

INMATEH -

**AGRICULTURAL
ENGINEERING**

SEPTEMBER - DECEMBER

No liability is assumed by the editorial staff for the content of scientific papers and opinions published in this volume. They represent the author's point of view

Managing Editorial Board - INMA Bucharest

Editor in Chief

Lucian-Ionel CIOCA, Professor, PhD.Eng., "Lucian Blaga" University of Sibiu

Executive Editor

Lucreția POPA
PhD.Eng, SR I

Assistant Editor

Nicolae-Valentin VLADUȚ
PhD.Eng, SR I
Mihai-Gabriel MATAȚHE
PhD.Eng, SR I

Logistic support, database

Virgil MURARU
PhD.Eng, SR I

Scientific Secretary

Cârdei Petre, math.

Official translator

RADU Daniela-Cristina, English

Editorial Board

- *QUENDLER Elisabeth – Austria, Vienna, Univ. of Natural Resources & Applied Life Sciences;*
- *Ir. HUYGHEBAERT Bruno – Belgia, Walloon Agricultural Research Center CRA-W;*
- *Van IMPE F.M. Jan – Belgia, KU Leuven University*
- *FABBRO Dal Inacio Maria - Brazil, Campinas State University;*
- *ATANASOV Atanas – Bulgaria, "Angel Kanchev" University of Rousse*
- *MOLINOS-SENANTE María – Chile, Pontificia Universidad Católica - Vicedecana, Escuela de Ingeniería UC*
- *BILANDZIJA Nikola – Croatia, Zagreb University, Faculty of Agriculture;*
- *KOSUTIC Silvio – Croatia, Zagreb University, Faculty of Agriculture;*
- *KOVACEV Igor - Croatia, Zagreb University, Faculty of Agriculture;*
- *GONZÁLEZ Omar – Republic of Cuba, Central University "Marta Abreu" de las Villas;*
- *KATHIJOTES Nicholas – Cyprus, University of Nicosia;*
- *HERAK David - Czech Republic, Czech University of Agriculture Prague;*
- *BORCHARD Nils – Finland, Natural Resources Institute Finland (Luke);*
- *SAUER Johannes – Germany, Technical University Munich;*
- *FENYVESI László – Hungary, Hungarian Institute of Agricultural Engineering Godollo;*
- *PEEYUSH Soni - India, Indian Institute of Technology, Kharagpur;*
- *MOHAMMADREZA Alizadeh – Iran, Department of Agricultural Engineering, Rice Research Institute of Iran (RRII);*
- *De WRACHIEN Daniele - Italy, State University of Milan;*
- *BIOCCA Marcello - Italy, Agricultural Research Council, Agricultural Engineering Research Unit;*
- *COLANTONI Andrea – Italy, University Viterbo;*
- *SARAUSSKIS Egidijus – Lithuania, Vytautas Magnus University, Faculty of Agricultural Engineering;*
- *KRIAUCIUNIENE Zita - Lithuania, Vytautas Magnus University;*
- *DUKE Mike – New Zealand, University of Waikato, Faculty of Science and Engineering;*
- *EWEMOJE Temitayo Abayomy – Nigeria, University of Ibadan, Faculty of Technology, Department of Agricultural and Environmental Engineering;*
- *SKIERUCHA Wojciech – Poland, Institute of Agro-physics Polish Academy of Sciences, Lublin;*
- *EKIELSKI Adam - Poland, Warsaw University of Life Sciences;*
- *KOT Sebastian - Poland, Czestochowa University of Technology*
- *SAVIN Lazar– Serbia, University of Novi Sad, Faculty of Agriculture, Department of Agricultural Engineering;*
- *SIMIKIC Mirko– Serbia, University of Novi Sad, Faculty of Agriculture, Department of Agricultural Engineering;*
- *MARTINOV Milan - Serbia, Faculty of Agriculture, Department of Agricultural Engineering,*
- *TURAN Jan – Slovakia, Technical University Kosice, Dept Elect & Multimedia Commun, Kosice;*
- *MADYIRA M. Daniel - South Africa, University of Johannesburg, Mechanical Engineering Science Department*
- *COZ FERNANDEZ Alberto – Spain, University of Cantabria, School of Nautical Studies, Department of Chemistry and Process & Resource Engineering;*
- *ERTEKIN Can - Turkey, Akdeniz University Antalia;*
- *KABAŞ Önder –Turkey, Antalia, Agricultural Scientific Research Institute of Batı Akdeniz;*
- *SELVI Kemal Çağatay - Turkey, Samsun, University of Ondokuz Mayıs, Faculty of Agriculture, Department of Machines for Agriculture;*
- *ÖTLEŞ Semih - Turkey, Ege University, Engineering Faculty, Food Engineering Department;*
- *MARUSCHAK Pavlo - Ukraine, Ternopil Ivan Pul'uj National Technical University, Department of Technical Mechanics and Agricultural Engineering;*
- *BULGAKOV Volodymyr – Ukraine, National University of Life and Environmental Sciences of Ukraine;*
- *PARASCHIV Gigel - Romania, Politehnica University of Bucharest;*
- *VOICU Gheorghe - Romania, Politehnica University of Bucharest;*
- *BIRIŞ Sorin - Romania, Politehnica University of Bucharest;*
- *MAICAN Edmond - Romania, Politehnica University of Bucharest;*
- *FILIP Nicolae - Romania, Technical University Cluj Napoca;*
- *COZAR Onuc-Romania, „Babes-Bolyai” University of Cluj-Napoca Romania, Faculty of Physics;*
- *VLASE Sorin - Romania, “Transilvania” University of Braşov;*
- *ȚENU Ioan - Romania, USAMV Iași;*
- *HERIŞANU Nicolae - Romania, Politehnica University of Timisoara;*
- *MARSAVINA Liviu - Romania, Politehnica University of Timisoara*
- *MARINCA Vasile - Romania, Politehnica University of Timisoara*
- *GERGEN Iosif - Romania, USAMVB Timișoara;*
- *BORDEAN Despina-Maria - Romania, USAMVB Timișoara;*
- *BUNGESCU Sorin - Romania, USAMVB Timișoara;*
- *RODINA Steliana – Romania, ICEADR, Bucharest;*
- *VOICEA Iulian - Romania, INMA Bucharest;*
- *DEAK Gyorgy - Romania, INCDFM Bucharest;;*
- *BELC Nastasia - Romania, IBA Bucharest;*
- *BUȚU Alina - Romania, INCDSB Bucharest;*
- *PAUN Mihaela - Romania, INCDSB, Bucharest*

CONTENT

		Page(s)
1.	DESIGN AND EXPERIMENTAL ANALYSIS OF ROTARY SPOON SOYBEAN PRECISION SEEDER / 转勺式大豆精密排种器设计与试验分析 Qichao LI ¹⁾ , Jinlong FENG ¹⁾ ¹⁾ College of Mechanical and Electrical, Lingnan Normal University, Zhanjiang 524048, China	13
2.	MACHINE FOR SPRING TECHNOLOGICAL HARVESTING OF INDUSTRIAL HEMP / МАШИНА ДЛЯ ТЕХНОЛОГІЧНОГО ВЕСНЯНОГО ЗБИРАННЯ ТЕХНІЧНИХ КОНОПЕЛЬ NALOBINA O.O. ¹⁾ , HOLOTIUK M.V. ²⁾ , BUNDZA O.Z. ¹⁾ , SHYMKO A.V. ¹⁾ , PUTS V.S. ²⁾ , MARTYNIUK V.L. ²⁾ ¹⁾ National University of Water and Environmental Engineering / Soborna str.11, Rivne, Ukraine; ²⁾ Lutsk National Technical University / Lvivska str., 75, Lutsk, Ukraine	25
3.	A HIGH-ACCURACY SHEEP FACE RECOGNITION MODEL BASED ON IMPROVED ResNet50 / 一种基于改进 ResNet50 的高精度羊脸识别模型 Xiwen ZHANG ^{1,2)} , Chuazhong XUAN ^{*2)} , Tao ZHANG ²⁾ , Quan SUN ^{1,3)} ¹⁾ Jiangsu Maritime Institute, College of Marine Electrical and Intelligent Engineering, Nanjing, China ²⁾ Inner Mongolia Agricultural University, College of Mechanical and Electrical Engineering, Inner Mongolia, China ³⁾ State grid Inner Mongolia Eastern Electric Power Co., , Hulunbuir, China	33
4.	NUMERICAL SIMULATION AND EXPERIMENTAL RESEARCH ON COMPACTION DEVICE OF SEEDBED LEVELING MACHINE / 苗床整平机镇压夯实装置数值模拟与试验研究 Bo-jun SHAN ^{1,2)} , Gang CHE ²⁾ , Lin WAN ^{1,2)} , Nai-chen ZHAO ¹⁾ , Qiang ZHANG ¹⁾ ¹⁾ College of Engineering, Heilongjiang Bayi Agricultural University, Daqing/P.R.China ²⁾ Key Laboratory of Intelligent Agricultural Machinery Equipment in Heilongjiang Province, Daqing / P.R.China	42
5.	RESEARCH AND DEVELOPMENT OF POWER DETECTION TECHNOLOGY AND DEVICE FOR KEY PARTS OF GREEN FODDER HARVESTER / 基于青饲收割机关键部件的动力检测技术与设备的研究与开发 Kang NIU ^{1,2)} , Xiaoyi CUI ^{1,2)} , Ruikang QIN ^{1,2)} , Yuqi WANG ^{1,2)} , Weijing WANG ^{1,2)} , Liming ZHOU ^{1,2)} , Yangchun LIU ^{1,2)} , Fengzhu WANG ^{1,2)} , Dongyang WANG ³⁾ , Weipeng ZHANG ^{1,2)} ¹⁾ Chinese Academy of Agriculture Mechanization Sciences Group Co., Ltd, Beijing ²⁾ State Key Laboratory of Agricultural Equipment Technology, Beijing ³⁾ Shenzhen Polytechnic University, Shenzhen, Guangdong, China	57
6.	EXPERIMENTAL STUDY ON TWO-SIDED LOOSENING SHOVEL OF DIGGING-PULLING CASSAVA HARVESTER / 挖拔式木薯收获机两侧式松土铲的试验研究 Wang YANG ¹⁾ , Xu WAN ¹⁾ , Junhui XI ¹⁾ , Debang ZHANG ¹⁾ , Yu HUANG ¹⁾ , Xian ZHENG ¹⁾ , Zhiheng LU ^{1*)} , Ganran DENG ²⁾ , Zhende CUI ²⁾ ¹⁾ College of Mechanical Engineering, Guangxi University, Nanning, China ²⁾ Institute of Agricultural Machinery, Chinese Academy of Tropical Agricultural Sciences, Zhanjiang, China	69
7.	RESEARCH ON CONTROL SYSTEM OF ELECTRIC-DRIVE WHEAT SHALLOW-BURIED DRIP IRRIGATION AND WIDE-WIDTH PRECISION SEEDER / 电驱式小麦浅埋滴灌-宽幅匀播机控制系统研究 Shenghe BAI ^{1,2)} , Yanwei YUAN ^{1,2)} , Liang WEI ²⁾ , Liming ZHOU ²⁾ , Kang NIU ²⁾ , Bo ZHAO ²⁾ , Jinhui ZHANG ³⁾ , Yuqi WANG ²⁾ , Wenyu TONG ²⁾ , Shuaiyang ZHANG ²⁾ , Lijing LIU ^{1,2)} , Zenglu SHI ⁴⁾ , Gang GUO ⁵⁾ ¹⁾ China Agricultural University, Beijing 100083, China; ²⁾ Chinese Academy of Agricultural Mechanization Sciences Group Co., Ltd, National Key Laboratory of Agricultural Equipment Technology, Beijing, China ³⁾ Dongliao county mechanical technology promotion station, Jilin, China ⁴⁾ College of Mechanical and Electrical Engineering, Xinjiang Agricultural University, Urumqi, China ⁵⁾ Heilongjiang Province's Gengzheng Agricultural Machinery Manufacturing Co., Ltd., Nanyang, China	81
8.	SIMULATION OF SOYBEAN SEED PHYSICAL PROPERTIES ON FILLING PERFORMANCE / 大豆种子物理特性对充种性能影响的仿真研究 Guoqiang DUN ^{*12)} , Na GUO ²⁾ , Xinxin JI ²⁾ , Jiaying DU ³⁾ , Yongzhen YANG ⁴⁾ ¹⁾ Harbin Cambridge University, Intelligent Agricultural Machinery Equipment Engineering Laboratory, Harbin / China; ²⁾ Northeast Forestry University, College of Mechanical and Electrical Engineering, Harbin / China; ³⁾ Jiamusi University, Jiamusi / China; ⁴⁾ Shantui Engineering Machinery Limited Company, Jining / China	95
9.	DESIGN OF AN UNMANNED TRANSFER VEHICLE LOOP DETECTION SYSTEM FOR GRAIN DEPOT SCENARIOS / 用于粮库场景的无人驾驶转运车回环检测系统设计 Boqiang ZHANG ¹⁾ , Dongding LI ¹⁾ , Tianzhi GAO ^{*1)} , Kunpeng ZHANG ²⁾ , Jinhao YAN ¹⁾ , Xuemeng XU ¹⁾ ¹⁾ School of Mechanical and Electrical Engineering, Henan University of Technology, Zhengzhou / China; ²⁾ College of Electrical Engineering, Henan University of Technology, Zhengzhou / China	105
10.	RESEARCH ON DEFECT IDENTIFICATION OF YU-LU-XIANG PEARS BASED ON IMPROVED LIGHTWEIGHT RESIDUAL NEURAL NETWORK MODEL / 基于改进轻量化卷积神经网络模型的玉露香梨缺陷识别研究 Chao ZHANG ^{1,2)} , Ning WANG ^{1,2)} , Chen LI ^{1,2)} , Jiexiong SUN ^{1,2)} , Qiuyue JIANG ^{1,2)} , Xiaoping HAN ^{*1,2)} , Juxia WANG ^{1,2)} ¹⁾ College of Agricultural Engineering, Shanxi Agricultural University, Taigu / China ²⁾ Key Technology and Equipment of Dry Farming Agricultural Machinery Shanxi Key Laboratory, Taigu / China	117

		Page(s)
11.	<p>IMPACT OF PARTIAL FREEZING WITH MODIFIED ATMOSPHERE PACKAGING ON PORK'S QUALITY / 气调微冻对猪肉品质的影响</p> <p>Huaming HOU^{1,3}, Dengming LI², Rui ZHANG¹, Wei NIU¹, Qingliang CUI^{1,3}, Yisheng CHEN^{*2}</p> <p>¹ College of Agricultural Engineering, Shanxi Agricultural University, Taigu / China; ² College of Food Science and Engineering, Shanxi Agricultural University, Taigu / China; ³ Dryland Farm Machinery Key Technology and Equipment Key Laboratory of Shanxi Province, Taigu / China</p>	127
12.	<p>CONSTRUCTION AND VALIDATION OF A PREDICTIVE MODEL FOR TOMATO ORGAN BIOMASS AT ORGAN SCALE BASED ON STACKING LEARNING / 基于堆叠学习的番茄器官尺度的生物量预测模型的构建与验证</p> <p>Qi LIU, Fengpei WANG, Gang LIU, Lian BAI, Wuping ZHANG¹</p> <p>Software College of Shanxi Agricultural University/China</p>	137
13.	<p>DESIGN AND TESTING OF PICKUP TOOTH CONVEYOR BELT TYPE BUCKWHEAT PICKUP DEVICE / 扒齿输送带式荞麦捡拾装置的设计与试验研究</p> <p>Chun WANG^{1,2}, Yongchao SHAO¹, Xiangyang LIU¹, Fuzeng YANG¹, Weiguo ZHANG^{*1}</p> <p>¹College of Mechanical and Electrical Engineering, Northwest Agriculture and Forestry University, Yangling 712100, China;²College of Biological and Agricultural Engineering, Jilin University, Changchun 130000, China</p>	152
14.	<p>DESIGN AND DEVELOPMENT OF SUNFLOWER INTELLIGENT INSERTION TRAY DRYER / 向日葵智能插盘晾晒机的设计与开发</p> <p>Qiang WANG¹, Xinyuan WEI¹, Keqi YAN¹, Qiyuan XUE¹, Yangcheng LV¹, Yaoyu Li^{1,2}, Wuping ZHANG¹, Fuzhong LI¹</p> <p>¹ College of Software, Shanxi Agricultural University, Taigu, Shanxi / China ² College of Agricultural Engineering, Shanxi Agricultural University, Taigu, Shanxi / China</p>	162
15.	<p>DESIGN AND EXPERIMENT OF HIGH MOISTURE CORN THRESHING DEVICE WITH LOW DAMAGE / 高水分玉米低损伤脱粒装置的设计与试验</p> <p>Qing Tang¹, Lan Jiang¹, Wenyi Yu², Jun Wu^{*1}, Gang Wang¹</p> <p>¹ Nanjing Institute of Agricultural Mechanization, Ministry of Agriculture and Rural Affairs of China, Nanjing, China; ² Jiangsu Province Grain and Oil Information Center, Nanjing, China</p>	172
16.	<p>RESISTANCE WIRE HEATING GROOVE-TYPE TEA DE-ENZYMING AND CARDING MACHINE: DESIGN AND TESTING / 电阻丝加热-槽式茶叶杀青理条机的设计与试验</p> <p>HaiJun BI^{1,2}, Chen XU^{1,2}, Kuan QIN^{3,4}, Lei YU⁵, Chengmao CAO^{3,4}, Dongsong XIA^{3,4}, Xinliang GUO^{1,2}, Yang LIU^{3,4}, Bin CHEN^{3,4}</p> <p>¹ State Key Laboratory of Tea Plant Biology and Utilization, Anhui Agricultural University, Hefei, China ² School of Tea Science, Anhui Agricultural University, Hefei, China ³ School of Engineering, Anhui Agricultural University, Hefei, China ⁴ Anhui Intelligent Agricultural Machinery Equipment Engineering Laboratory, Hefei, China ⁵ Anji Yuanfeng Tea Machinery Co. Ltd, Huzhou, China</p>	184
17.	<p>COUPLING UNMANNED AERIAL VEHICLE (UAV) MULTISPECTRAL IMAGERY AND INTEGRATED LEARNING TO CONSTRUCT A MONITORING AND PREDICTION MODEL FOR RELATIVE CHLOROPHYLL CONTENT (RCC) AND LEAF AREA INDEX (LAI) OF SORGHUM IN FIELDS / 基于无人多光谱图像和集成学习的田间高粱叶绿素相对含量与叶面积指数的监测预测模型</p> <p>Qi LIU, Huping LIU, Mengjiao XU, Lian BAI, Wuping ZHANG¹, Guofang WANG²</p> <p>¹ College of Software, Shanxi Agricultural University, Taigu, Shanxi / China ² College of Resources and Environment, Shanxi Agricultural University, Taigu, Shanxi / China</p>	199
18.	<p>A BIBLIOMETRIC-BASED ANALYSIS OF RESEARCH PROGRESS IN UNMANNED AERIAL REMOTE SENSING OF WHEAT / 基于文献计量的小麦无人机遥感研究进展分析</p> <p>Wenyu PENG, Junke ZHU*, Weiyi FENG, Hongjian ZHAO, Susu HUANG, Shenke LI, Aoqun HUANG, Zhicheng TANG</p> <p>School of Agricultural Engineering and Food Science, Shandong University of Technology, Zibo/ China</p>	209
19.	<p>DESIGN AND EXPERIMENTATION OF A MACHINE VISION-BASED QUALITY INSPECTION SYSTEM FOR GREEN ONION SEEDING / 基于机器视觉的大葱播种质量检测系统的设计与试验</p> <p>Fangyuan LU¹, Chong TAO², Zhiye MO¹, Mengqi ZHANG¹, Guohai ZHANG^{*1}, Xiangyu WU¹, Bolong WANG^{*1}</p> <p>¹ School of Agricultural Engineering and Food Science, Shandong University of Technology, Zibo/ China ² Binzhou Polytechnic, Binzhou/ China</p>	218
20.	<p>VEHICLE MASSIVE IMAGE DATA FILTERING AND USELESS IMAGE REUSE BASED ON FARMLAND BACKGROUND ANALYSIS / 基于农田背景分析的车载大数据图像过滤与无效图像再利用</p> <p>Hanlu JIANG, Fengzhu WANG, Gaoyong XING, Yangchun LIU, Weipeng ZHANG, Liming ZHOU</p> <p>State Key Laboratory of Agricultural Equipment Technology, Chinese Academy of Agricultural Mechanization Science Group Co., Ltd. Beijing, China</p>	230

		Page(s)
21.	<p>QUANTITATIVE ANALYSIS OF THE MIXING CHARACTERISTICS OF SIMULATED BROWN RICE PARTICLES BASED ON THE DISCRETE ELEMENT METHOD / 基于离散元模拟的糙米颗粒混合特性定量分析</p> <p>Yonghao ZHAI, Biao Xie, Yanxiang Yang, Quanbiao Hu, Wei You, Nian Liu, Qiang Zhang^{*)} College of Engineering, Huazhong Agricultural University, Wuhan / China; Key Laboratory of Agricultural Equipment in Mid-lower Yangtze River, Ministry of Agriculture, Wuhan / China</p>	242
22.	<p>DEVELOPING AN AUTOMATIC PRECISION SEEDING UNIT (APSU) FOR POT SEED PLANTING / تطوير وحدة زراعة آلية دقيقة لزراعة البنور في الأصص</p> <p>Mohamed ABO-HABAGA¹⁾, Zakaria ISMAIL¹⁾, Nariman MOUSTAFA¹⁾, Mahmoud OKASHA²⁾ ¹⁾Agricultural Engineering Department, Faculty of Agriculture, Mansoura University, Egypt ²⁾Agricultural Engineering Research Institute (AEnRI), Agricultural Research Center (ARC), Giza 12611, Egypt</p>	260
23.	<p>POD PEPPER TARGET DETECTION BASED ON IMPROVED YOLOv8 / 基于改进 YOLOv8 的朝天椒目标检测研究</p> <p>Jiayv SHEN, Qingzhong KONG, Yanghao LIU, Na MA^{*)} College of Information Science and Engineering, Shanxi Agricultural University, Taigu / China</p>	273
24.	<p>RESEARCH ON LOCUST TARGET DETECTION ALGORITHM BASED ON YOLO V7 -MOBILENETV3-CA / 基于 YOLOv7-MobileNetV3-CA 的蝗虫目标检测算法研究</p> <p>Dongfang QIU¹⁾ College of Information Science and Engineering, Shanxi Agricultural University, Jinzhong, Shanxi, China</p>	283
25.	<p>RESEARCH ON THE INFLUENCE OF VENTURI AERATOR CONFIGURATION ON OXYGEN ABSORPTION PERFORMANCE / 文丘里增氧器结构参数对吸氧性能的影响研究</p> <p>Longlong REN^{1,2,3)}, Qingfu GONG^{1,2)}, Zhenxiang JING¹⁾, Xiang HAN^{1,2)}, Ang GAO^{1,2)}, Yuepeng SONG^{1,2,3)} ¹⁾ Shandong Agricultural University, College of Mechanical and Electrical Engineering / China; ²⁾ Shandong Provincial Engineering Laboratory of Agricultural Equipment Intelligence / China; ³⁾ Shandong Provincial Key Laboratory of Horticultural Machinery and Equipment / China</p>	293
26.	<p>PARAMETER CALIBRATION AND EXPERIMENT OF DISCRETE ELEMENT SIMULATION OF SPHERICAL-LIKE SOYBEAN BASED ON DEM / 基于 DEM 的类球型大豆离散元仿真参数标定与试验</p> <p>Guangwei CHEN¹⁾, Fuxing LI¹⁾, FaYi QU^{*)}, Chong Jian ZHANG¹⁾ ¹⁾Northeast Forestry University, College of Mechanical and Electrical Engineering, Harbin / China; ²⁾Northeast Forestry University, Graduate School, Harbin / China</p>	303
27.	<p>DESIGN AND RESEARCH ON THE CRUSHING SYSTEM OF THE TANK CLEANING ROBOT / 贮罐清理机器人破碎系统的设计与研究</p> <p>Yong TIAN¹⁾, Jian SONG¹⁾, Fuxiang XIE^{*)} ¹⁾ School of Machinery and Automation, Weifang University, Shandong/ China</p>	316
28.	<p>LIGHTWEIGHT DESIGN OF THE SEEDING WHEEL STRUCTURE OF RICE DIRECT SEEDER BASED ON TOPOLOGY OPTIMIZATION / 于拓扑优化的水稻直播机排种轮结构轻量化设计</p> <p>Juan HUANG^{1,3)}, Jing HUANG²⁾, Jinhui CAI²⁾, Songlin SUN¹⁾, Caiwang PENG¹⁾ ¹⁾ College of Mechanical and Electrical Engineering, Hunan Agriculture University, Changsha, 410012, / China; ²⁾ College of Automotive and Mechanical Engineering, Changsha University of Science and Technology, Changsha / China; ³⁾ Hunan Provincial Key Laboratory of Intelligent Manufacturing Technology for High-performance Mechanical Equipment, Changsha / China</p>	325
29.	<p>OPTIMIZATION OF MELKASSA AGRICULTURAL RESEARCH CENTER (MARC) BEAN THRESHER PARAMETERS USING RESPONSE SURFACE METHOD (RSM) / የምላሽ ወለል ዘዴን (RSM) በመጠቀም የመልካሳ ግብርና ምርምር ማዕከል (MARC) የሶቶ-ቂ ማው-ቂያ ማሻን ማለኪያዎችን ማመቻቸት</p> <p>Biniam ZEWDIE¹⁾, Adesoji M. OLANIYAN²⁾, Amana WAKO¹⁾, Dereje ALEMU³⁾, Tamrat LEMA³⁾ ¹⁾ School of Mechanical, Chemical, and Materials Engineering, Departments of Agricultural Machinery Engineering, Adama Science and Technology University, P.O. Box 1888, Adama, Ethiopia. ²⁾ Department of Agricultural and Bioresources Engineering, Faculty of Engineering, Ikole-Ekiti, Nigeria. ³⁾ Ethiopian Institute of Agricultural Research; Agricultural Engineering Research, Adama, Ethiopia</p>	335
30.	<p>DESIGN AND EXPERIMENTAL RESEARCH OF A PORTABLE WALNUT HARVESTER BASED ON ELECTROMAGNETIC EXCITATION TECHNOLOGY / 基于电磁激励技术的便携式核桃采摘机设计与试验研究</p> <p>Na JIA¹⁾, Guangqiu LI¹⁾, Anguo HU²⁾, Qin CHEN¹⁾ ¹⁾ Northeast Forestry University, College of Mechanical and Electrical Engineering/ China; ²⁾ Yongkang Weili Technology Co, Ltd / China ^{*)} The Yunnan Provincial Academy of Forestry and Grassland Sciences YangBi Walnut Research Institute / China</p>	345
31.	<p>DESIGN AND EXPERIMENT OF ARRAY-BASED FINGERPLATE DIFFERENTIAL FLOW SENSOR FOR RICE GRAIN MONITORING / 阵列式指板差分水稻籽粒流量传感器的设计与试验</p> <p>Qibin LI¹⁾, Yang YU¹⁾, Gang GUO²⁾, Jinpeng HU¹⁾, Peng LIU¹⁾, Xiaoyu CHAI¹⁾, Yingfeng WANG¹⁾, Lizhang XU^{1*)} ¹⁾ College of Agricultural Engineering, Jiangsu University, Zhenjiang, China ²⁾ Zoomlion Heavy Industry Science & Technology Co., Ltd Changsh, China</p>	358

		Page(s)
32.	<p>ESTABLISHMENT AND CALIBRATION OF DISCRETE ELEMENT MODEL FOR COATED WHEAT SEED BASED ON STATIC AND DYNAMIC VERIFICATION TEST / 基于静态验证试验的包衣小麦种子离散元模型标定与优化</p> <p>Xuejun ZHANG^{1,2}, Ren GUO¹, Zenglu SHI^{1,2}, Jinshan YAN^{1,2}, Shenghe BAI³, Longfei YANG¹, Yongliang YU⁴, Duijin WANG⁴</p> <p>¹) College of Mechanical and Electrical Engineering, Xinjiang Agricultural University, Urumqi/ China; ²) Key Laboratory of Intelligent Agricultural Equipment of Xinjiang, Urumqi/ China ³) National Key Laboratory of Agricultural Equipment Technology, Chinese Academy of Agricultural Mechanization Sciences Group Co., Ltd., Beijing/ China ⁴) Xinjiang Tiancheng Agricultural Equipment Manufacturing Co, Tiemenguan/ China</p>	370
33.	<p>THEORETICAL STUDY OF TRACTION RESISTANCE OF HARROWS WITH HELICAL WORKING BODIES / ТЕОРЕТИЧНЕ ДОСЛІДЖЕННЯ ТЯГОВОГО ОПОРУ БОРОНИ З ГВИНТОВИМИ РОБОЧИМИ ОРГАНАМИ</p> <p>Volodymyr BULGAKOV¹, Adolfs RUCINS², Ivan HOLOVACH¹, Oleksandra TROKHANIAK¹, Mykola KLENDII³, Lucretia POPA⁴, Anastasiya KUTSENKO¹</p> <p>¹)National University of Life and Environmental Sciences of Ukraine, Ukraine; ²)Latvia University of Life Sciences and Technologies, Latvia; ³)Separated Subdivision of National University of Life and Environmental Sciences of Ukraine, Berezhan Agrotechnical Institute, Ukraine; ⁴) INMA, Bucharest / Romania</p>	380
34.	<p>DESIGN AND TESTING OF A GAP ADJUSTABLE ELASTIC LOW DAMAGE CORN PICKING HEADER BASED ON ADAMS / 基于 Adams 的间隙可调弹性低损玉米摘穗割台的设计与试验</p> <p>Xianghao LI¹, Yongli ZHAO¹, Hongda ZHAO¹, Shaochuan LI¹, Peisong DIAO^{1*}</p> <p>College of Agricultural Engineering and Food Science, Shandong University of Technology, Zibo, Shandong, China</p>	388
35.	<p>CAGE WHEEL TRACTIVE PERFORMANCE OF 4WD TRACTOR IN PADDY FIELD / PENGUJIAN TRAKSI RODA SANGKAR TRAKTOR RODA EMPAT DI LAHAN SAWAH</p> <p>Desrial^{1,2}, Hiroaki MURAOKA^{2,3}, Kunio DOI⁴, Ismi Makhmudah EDRIS²</p> <p>¹) Faculty of Agricultural Engineering and Technology, Bogor Agricultural University/ Indonesia; ²) Yanmar Agricultural Research Institute – IPB, Bogor Agricultural University, Indonesia / Indonesia; ³) Yanmar Holdings Co. Ltd./ Japan; ⁴) Yanmar Agribusiness Co., Ltd./ Japan</p>	401
36.	<p>INTEGRATED UAV TECHNOLOGIES USED IN THE ANALYSIS OF THE CONDITION OF CROPS IN VINEYARDS AND ORCHARDS / TEHNOLOGII INTEGRATE UAV UTILIZATE ÎN ANALIZA STĂRII CULTURILOR DIN VII ȘI LIVEZI</p> <p>George IPATE^{*1}, Iuliana GĂGEANU^{*2}, Andreea - Nicoleta BURCEA¹, Stefan DUMITRU¹, Mădălina- Elena ȘTEFAN¹, Dan CUJBESCU², Elena-Melania CISMARU²</p> <p>¹)University POLITEHNICA of Bucharest, Faculty of Biotechnical Systems Engineering / Romania ²) National Institute of Research–Development for Machines and Installations Designed for Agriculture and Food Industry INMA Bucharest, Romania</p>	409
37.	<p>COMPARATIVE EXPERIMENTAL STUDY ON OPERATION PERFORMANCE AND YIELD OF MAIZE SEEDERS OF DIFFERENT TYPES IN WHEAT STUBBLE FIELD / 麦茬地不同型式玉米播种机作业性能及产量对比试验研究</p> <p>Ting XU¹, Zehua HAO¹, Yinping ZHANG^{*1}, Kai XU², Ke LIU², Yunyou KANG², Hua ZHOU^{*1}, Dengyu LI²</p> <p>¹) School of Agricultural and Food Science, Shandong University of Technology, Zibo, China ²) Shandong Province agricultural machinery technology promotion station, Jinan, China</p>	421
38.	<p>RESEARCH ON POWER PARAMETERS OF A SCREW CONVEYOR WITH BLADED OPERATING BODY FOR TRANSPORTING AGRICULTURAL MATERIALS / LAUKSAIMNIECĪBAS BERAMKRAVU MATERIĀLU TRANSPORTĒŠANAS GLIEMEŽTRANSPORTIERA JAUDAS PARAMETRU PĒTĪJUMI</p> <p>Adolfs RUCINS¹, Volodymyr BULGAKOV², Ivan HOLOVACH², Oleksandra TROKHANIAK², Mykola KLENDII³, Lucretia POPA⁴, Vadym YAREMENKO²</p> <p>¹)Latvia University of Life Sciences and Technologies, Latvia; ²)National University of Life and Environmental Sciences of Ukraine, Ukraine; ³)Separated Subdivision of National University of Life and Environmental Sciences of Ukraine, Berezhan Agrotechnical Institute, Ukraine; ⁴) INMA Bucharest, Romania</p>	428
39.	<p>SWEET POTATO VINE CUTTING MACHINE: KEY COMPONENTS DESIGN AND EXPERIMENTAL RESEARCH / 甘薯切蔓机关键部件设计及试验研究</p> <p>Biao MA¹, Tianchan LI², Weiqiang LIN¹, Yongsheng CHEN³, Run ZHAO^{*1}, Yanyan SHI^{*1}</p> <p>¹)Nanjing Institute of Agricultural Mechanization, Ministry of Agriculture and Rural Affairs, Jiangsu / China; ²) Jiangsu Academy of Agricultural Sciences, Jiangsu / China; ³) Institute of Western Agriculture, CAAS, Xinjiang / China</p>	436
40.	<p>DESIGN AND EXPERIMENT OF SELF-PROPELLED MULTIFUNCTIONAL TRENCHING AND FERTILIZING MACHINE / 自走式多功能开沟施肥机的设计与实验</p> <p>Tengyun MA, Bin QI³, Xiaoming SUN^{*1}, Yuanqi LIU¹, Yuchao REN¹, Jiyuan SUN¹, Bohan ZHANG¹, Qiong WU²</p>	449

		Page(s)
	¹⁾ College of Agricultural Engineering and Food Science, Shandong University of Technology/ China; ²⁾ Zibo Normal College/ China	
41.	SIMULATION ANALYSIS AND OPTIMIZATION OF CONCAVE BAR POTATO-SOIL SEPARATION DEVICE / 凹杆式薯土分离装置仿真分析与优化 Qingmiao XIANG ¹⁾ , Bei WU ^{1,2)} , Fangping XIE ^{1,2)} , Zhichao FANG ^{1,2)} , Huanyuan QIAN ¹⁾ , Zhuo LI ¹⁾ ¹⁾ Hunan Agricultural University, College of Mechanical and Electrical Engineering, Changsha/China; ²⁾ Hunan Key Laboratory of Intelligent Agricultural Machinery and Equipment, Changsha/China	460
42.	IMPROVED YOLOv8N-BASED DETECTION OF GRAPES IN ORCHARDS / 基于改进 YOLOv8n 的果园葡萄检测方法 Shan TAO, Shiwei WEN, Guangrui HU, Yahao GE, Jingming WEN, Xiaoming CAO, Jun CHEN ^{*)} College of Mechanical and Electronic Engineering, Northwest A&F University, Yangling / China	473
43.	EGG QUALITY DETECTION BASED ON LIGHTWEIGHT HCES-YOLO / 基于轻量化的 HCES-YOLO 的鸡蛋品质检测算法 Zhimin TONG ^{*)} , Shengzhang LI, Chuanmiao SHI, Tianzhe XU, Yu ZHOU, Changhao LI ¹⁾ College of Electrical and Mechanical Engineering, Qingdao Agricultural University, Qingdao/ China	485
44.	MATHEMATICAL MODELING OF THE FORCE REQUIRED TO MOVE PLATFORMS INTENDED FOR SOIL SAMPLING / MODELAREA MATEMATICĂ A FORȚEI NECESARE DEPLASĂRII PLATFORMELOR DESTINATE PRELEVĂRII PROBELOR DE SOL Mario CRISTEA ¹⁾ , Mihai Gabriel MATACHE ¹⁾ , Robert-Dorin CRISTEA ^{*)} , Andreea-Iulia GRIGORE ¹⁾ , Laurențiu VLĂDUȚOIU ¹⁾ ¹⁾ National Institute of Research - Development for Machines and Installations Designed to Agriculture and Food Industry – INMA Bucharest / Romania	496
45.	DESIGN AND EXPERIMENT OF SWEET POTATO COMBINE HARVESTER BASED ON TWO-SEGMENT POTATO SOIL SEPARATION DEVICE / 基于两段式薯土分离装置甘薯联合收获机设计与试验 Ranbing YANG ^{1,2)} , Minsheng WU ^{1,2)} , Peng XU ³⁾ , Yongfei PAN ^{1,2)} , Danyang LV ^{1,2)} , Xiantao ZHA ^{*)1,2)} ¹⁾ School of Mechanical and Electrical Engineering, Hainan University, Hainan/ China; ²⁾ Key Laboratory of Tropical Intelligent Agricultural Equipment, Ministry of Agriculture and Rural Affairs, Hainan/ China; ³⁾ College of Engineering, Jiangxi Agricultural University, Jiangxi/ China	509
46.	SIMULATION AND EXPERIMENT OF POTATO EXCAVATOR / 马铃薯挖掘机仿真与试验 Boxuan CHEN ¹⁾ , Xuhong CHU ^{*)1)} , Bingshen HUANG ¹⁾ , Xiangdong LIU ¹⁾ , Yiyuan GE ¹⁾ ¹⁾ College of Mechanical Engineering, Jiamusi University, Jiamusi 154007, China	526
47.	EXPERIMENTAL STUDY ON THE PERFORMANCE OF CORN STALK CRUSHING DEVICE WITH STEPPED SAW DISK KNIFE / 阶梯式锯盘刀玉米秸秆粉碎装置性能试验研究 Yongtao YU, Yanjun LI, Fuxiang XIE ^{*)} , Jian SONG ^{*)} , Yong TIAN College of Machinery and Automation, Weifang University, Weifang, China	535
48.	BLOCKCHAIN TECHNOLOGY FOR ENHANCED TRACEABILITY AND SUSTAINABILITY OF PERSONAL PROTECTIVE EQUIPMENT IN ROMANIAN AGRICULTURE / TEHNOLOGIA BLOCKCHAIN PENTRU ÎMBUNĂȚIREA TRASABILITĂȚII ȘI SUSTENABILITĂȚII ECHIPAMENTELOR INDIVIDUALE DE PROTECȚIE ÎN AGRICULTURA DIN ROMÂNIA Daniel Onuț BADEA ^{*)1)} , Doru Costin DARABONT ¹⁾ , Lucian-Ionel CIOCA ²⁾ , Alina TRIFU ¹⁾ , Vlad-Andrei BARSAN ³⁾ ¹⁾ National Research and Development Institute on Occupational Safety - I.N.C.D.P.M. "Alexandru Darabont", 35A Ghencea Blvd., Sector 6, 061692, Bucharest, Romania ²⁾ Industrial Engineering and Management Department, Faculty of Engineering, Lucian Blaga University of Sibiu, 10 Victoriei Blvd., 550024, Sibiu, Romania; ³⁾ SC Continental SA Sibiu, Romania	543
49.	DISCRETE ELEMENT METHOD SIMULATION OF RICE GRAIN STACKING CHARACTERISTICS / 水稻籽粒堆积特性离散元法模拟研究 Liquan TIAN, Hong LI, Xian ZHANG ¹⁾ , Chunxiang LIU ²⁾ ¹⁾ Intelligent Manufacturing College, Jinhua University of Vocational Technology/Jinhua, China ²⁾ Heilongjiang Institute of Technology, Haerbin / China	554
50.	MOISTURE CONTENT DETECTION OF SOYBEAN GRAINS BASED ON HYPERSPECTRAL IMAGING / 基于高光谱成像的大豆籽粒含水率检测研究 Zhichang CHANG ¹⁾ , Man CHEN ^{1,2*)} , Gong CHENG ¹⁾ , Chengqian JIN ^{1*)} , Tengxiang YANG ¹⁾ ¹⁾ Nanjing Institute of Agricultural Mechanization, Ministry of Agriculture and Rural Affairs, Nanjing, Jiangsu / China; ²⁾ National Digital Agriculture Equipment (South China Intelligence Agricultural Machine) Innovation Sub-center, Nanjing, Jiangsu / China	562

		Page(s)
51.	<p>OBSTACLE AVOIDANCE PATH OF WHEELED AGRICULTURAL HANDLING ROBOTS IN WAREHOUSE BASED ON IMPROVED ACO-DWA ALGORITHM / 基于改进 ACO-DWA 算法的轮式农业机器人仓库搬运避障路径研究</p> <p>Kan ZHANG*¹⁾</p> <p>School of Computer Engineering, Shanxi Vocational University of Engineering Science and Technology, Jinzhong, Shanxi / China</p>	571
52.	<p>MULTI-UAV TASK ALLOCATION AND PATH PLANNING METHOD FOR AGRICULTURAL PATROL SCENE / 面向农业巡检场景的多无人机任务分配与路径规划方法</p> <p>Li SHENG *¹⁾</p> <p>School of Economics and Management, Wuhan Railway Vocational College of Technology, Wuhan, Hubei / China</p>	582
53.	<p>DESIGN AND EXPERIMENT OF LARGE STRAW CRUSHER WITH CYLINDER FEEDING HAMMER / 圆筒喂料锤片式大型秸秆粉碎机设计与试验</p> <p>Tao CHEN¹⁾, Shu-juan YI¹⁾, Song WANG¹⁾, Wen-sheng SUN¹⁾</p> <p>¹⁾College of Engineering, Heilongjiang Bayi Agricultural University, Daqing/P.R.China</p>	592
54.	<p>SIMULATION ANALYSIS AND EXPERIMENT OF CLEANING MECHANISM FOR TRACK-TYPE COMBINE HARVESTER BASED ON CFD-DEM / 基于 CFD-DEM 的履带式联合收获机清选装置仿真分析与试验</p> <p>Hongda ZHAO¹⁾, Xianghao LI¹⁾, Yongli ZHAO¹⁾, Shaochuan LI¹⁾, Peisong DIAO¹⁾</p> <p>¹⁾College of Agricultural Engineering and Food Science, Shandong University of Technology, Zibo, Shandong, China</p>	603
55.	<p>OPTIMIZING THE UNIT STRUCTURE OF THE DRAINAGE-TYPE CYCLONE SEPARATOR FOR SAND SAMPLE COLLECTION / 优化排水型旋风分离砂样采集器的单元结构</p> <p>Caoqi ZHANG¹⁾, Ariff Bin Banharudin MUHAMMAD^{1*)}, Taiming GUO²⁾, Jining ZHANG³⁾, Shipping WU⁴⁾</p> <p>¹⁾ Faculty of Electrical Engineering, Universiti Teknologi Malaysia, Johor Skudai/Malaysia ²⁾ Faculty of Computer Engineering, Universiti Teknologi Malaysia, Johor Skuda/Malaysia ³⁾ State Nuclear Electric Power Planning Design & Research Institute, Beijing/China ⁴⁾ Faculty of Humanities and Social Sciences, Datong No.12 Middle School Shanxi, 034400, P.R. China</p>	615
56.	<p>DESIGN AND EXPERIMENT OF DRAG REDUCTION CHARACTERISTICS OF CASSAVA BIONIC DIGGING SHOVEL BASED ON RED SOIL / 基于红土壤的木薯仿生挖掘铲减阻特性设计与试验</p> <p>Ranbing YANG^{1,3)}, Guiquan ZHOU^{1,3)}, Dongquan CHEN²⁾, Tao WANG^{1,3)}, Danyang LV²⁾, Xiantao ZHA^{*1,3)}</p> <p>¹⁾ School of Mechanical and Electrical Engineering, Hainan University, Hainan/ China; ²⁾ School of Information and Communication Engineering, Hainan University, Hainan/ China; ³⁾ Key Laboratory of Tropical Intelligent Agricultural Equipment, Ministry of Agriculture and Rural Affairs, Hainan / China</p>	625
57.	<p>THE IMPACT OF OHMIC HEATING ON RICE GRAIN HARDNESS AND HEATING UNIFORMITY COMPARED TO CONVENTIONAL COOKING METHODS / 欧姆加热与传统加热蒸煮米饭对米粒硬度与加热均匀性的影响</p> <p>Xinting DING, Xingshu LI</p> <p>College of Mechanical and Electronic Engineering, Northwest A&F University, Yangling, China</p>	642
58.	<p>RESEARCH ON THE CONTROL SYSTEM OF MOBILE STRAW COMPACTION MOLDING MACHINE BASED ON PSO-ELM-GPC MODEL / 基于 PSO-ELM-GPC 模型的移动式秸秆致密成型机控制系统研究</p> <p>Huiying CAI *¹⁾; Yunzhi LI¹⁾; Fangzhen LI¹⁾</p> <p>¹⁾ School of Computer Science and Technology, Shandong University of Finance and Economics, Jinan/ China</p>	652
59.	<p>OPTIMIZATION STUDY OF STRUCTURE AND OPERATING PARAMETERS OF DOUBLE-LAYER CENTRIFUGAL ATOMIZING NOZZLE BASED ON RESPONSE SURFACE METHODOLOGY / 基于响应面法的双层离心式雾化喷头结构与工作参数的优化研究</p> <p>Nan ZHOU, Yubin LAN^{*)}, Yu YAN, Lilian LIU</p> <p>¹⁾ College of Agricultural Engineering and Food Science, Shandong University of Technology, Zibo / China; ²⁾ Research of Institute of Ecological Unmanned Farm, Shandong University of Technology, Zibo / China</p>	662
60.	<p>STUDY ON THE EFFECT OF CURVED FUNNEL FOR SILO UNLOADING ON PARTICLE FLOW CHARACTERISTICS / 筒仓卸粮曲面漏斗对颗粒流动特性的影响研究</p> <p>Mingxu WANG^{1,2)}, Saiqiang LI¹⁾, Tao Gao¹⁾, Zhijie SONG⁴⁾, Kunlun LIU³⁾, Jianzhang WU³⁾, Jiangfeng OUYANG¹⁾</p> <p>¹⁾School of Mechanical & Electrical Engineering, Henan University of Technology, Zhengzhou, China ²⁾Henan Key Laboratory of Grain and Oil Storage Facility & Safety, Henan University of Technology, Zhengzhou, China ³⁾School of grain college, Henan University of Technology, Zhengzhou, China ⁴⁾Jiaozuo Creation Heavy Industry Co.,Ltd., Jiaozuo, China</p>	673

		Page(s)
61.	<p>REVIEW OF AGRICULTURAL PLASTIC FILM RECYCLING EQUIPMENT FROM CHINA / 农膜回收装备研究现状及展望</p> <p>Songmei YANG¹⁾, Benxu WANG¹⁾, Shaofeng RU^{*1)}, Xuegeng CHEN²⁾, Limin YAN²⁾, Jilong WU¹⁾</p> <p>¹⁾School of Mechanical and Electrical Engineering, Hainan University, Haikou / China ²⁾School of Mechanical and Electrical Engineering, Shihezi University, Shihezi / China</p>	683
62.	<p>RECOGNITION OF DROUGHT STRESS IN MILLET ON HYPERSPECTRAL IMAGING / 基于高光谱成像技术识别谷子干旱胁迫</p> <p>Rongxia WANG, Jiarui ZHANG, Jianyu CHEN, Yuyuan MIAO, Jiwan HAN, Lijun CHENG</p> <p>Shanxi Agricultural University, College of Software / China</p>	699
63.	<p>EVALUATION OF BRAKING DECELERATION DURING EMERGENCY BRAKING OF AGRICULTURAL TRACTORS / ОЦЕНКА НА СПИРАЧНОТО ЗАКЪСНЕНИЕ ПРИ АВАРИЙНО СПИРАНЕ НА ЗЕМЕДЕЛСКИ ТРАКТОРИ</p> <p>Daniel LYUBENOV¹⁾, Atanas Z. ATANASOV^{*1)}, Georgi KADIKYANOV¹⁾, Valentin VLADUT²⁾</p> <p>¹⁾University of Ruse "Angel Kanchev", 7017 Ruse / Bulgaria; ²⁾National Research - Development Institute for Machines and Installations Designed to Agriculture and Food Industry, 013813 Bucharest / Romania</p>	712
64.	<p>DESIGN AND EXPERIMENT OF AIR-SUCTION PRECISION SEED-METERING DEVICE FOR GARLIC / 大蒜气吸式精量排种器的设计与试验</p> <p>Fuhai FANG, Jingling SONG*, Zhuo WANG, Kunqiao LI, Yongzheng ZHANG, Long ZHOU, Chao LI</p> <p>Shandong University of Technology, College of Agricultural Engineering and Food Science, Zibo, China</p>	721
65.	<p>INVESTIGATION OF THE BULK MATERIAL MOVEMENT KINEMATICS IN CONICAL SCREW CONVEYOR / ДОСЛІДЖЕННЯ КІНЕМАТИКИ РУХУ СИПКОГО МАТЕРІАЛУ У ГВИНТОВОМУ КОНВЕЄРІ КОНІЧНОЇ ФОРМИ</p> <p>Oleg LYASHUK, Andrii DIACHUN, Ihor TKACHENKO, Mykola STASHKIV, Andrii BABII, Maria PANKIV, Zhanna BABIAK, Alexander MARUNYCH, Oleg LAKH, Artur STARIKH</p> <p>Ternopil Ivan Puluj National Technical University / Ukraine</p>	732
66.	<p>INTEGRATION OF EDEM BY ALTAIR SIMULATIONS FOR EFFICIENT DISTRIBUTION OF LARGE AND SMALL SEEDS IN AGRICULTURAL SYSTEMS OF VINEYARDS AND FRUIT TREES / INTEGRAREA SIMULĂRILOR EDEM DE LA ALTAIR PENTRU DISTRIBUȚIA EFICIENTĂ A SEMINȚELOR MARI ȘI MICI ÎN SISTEME AGRICOLE DE VIȚĂ DE VIE ȘI POMI FRUCTIFERI</p> <p>Dragoș-Nicolae DUMITRU¹⁾, Eugen MARIN¹⁾, Gabriel-Valentin GHEORGHE¹⁾, Dragoș MANEA¹⁾, Marinela MATEESCU¹⁾, Dragoș-Nicolae ANGHELACHE^{1,2)}, Elisabeta PRISACARIU¹⁾, Alin HARABAGIU¹⁾</p> <p>¹⁾INMA Bucharest/ Romania; ²⁾National University of Science and Technology POLITEHNICA Bucharest/Romania</p>	745
67.	<p>RESEARCH ON BILEVEL TASK PLANNING METHOD FOR MULTI-UAV LOGISTICS DISTRIBUTION / 面向多农业无人机物流配送的双层任务规划方法研究</p> <p>Zhibo LI*, Yuan LIU</p> <p>Business School, Chongqing Polytechnic University of Electronic Technology, Chongqing/China</p>	761
68.	<p>A LIGHTWEIGHT IMPROVED YOLOv5s MODEL-BASED RICE BLAST DETECTION METHOD AND MOBILE DEPLOYMENT / 基于轻量化改进 YOLOv5s 模型的稻瘟病检测方法及移动部署</p> <p>Fankai MENG¹⁾, Congkuan YAN¹⁾, Yuqing YANG¹⁾, Ruixing XING¹⁾, Dequan ZHU¹⁾, Aifang ZHANG²⁾, Qixing TANG^{1,3)}, Juan LIAO^{1,3)}</p> <p>¹⁾ College of Engineering, Anhui Agricultural University, Hefei / China; ²⁾ Institute of Plant Protection and Agricultural Product Quality and Safety, Anhui Academy of Agricultural Sciences, Hefei / China; ³⁾ East Anhui Comprehensive Experimental Station, Anhui Agricultural University, Mingguang /China</p>	771
69.	<p>SMART VENDING MACHINE, ENERGY INDEPENDENT, THERMALLY CONDITIONED, FOR PACKAGED AGRICULTURAL PRODUCTS / AUTOMAT DE VANZARE INTELIGENT, INDEPENDENT ENERGETIC, CONDITIONAT TERMIC, A PRODUSELOR AGRICOLE AMBALATE</p> <p>Ioan Mihail SAVANIU, Oana TONCIU³⁾, Bogdan BEBESELEA</p> <p>Technical University of Civil Engineering Bucharest / Romania</p>	787
70.	<p>OBSTACLE AVOIDANCE PLANNING OF GRAPE PICKING ROBOTS BASED ON DEEP REINFORCEMENT LEARNING / 基于深度强化学习的葡萄采摘机器人采摘路径避障规划</p> <p>Pei LIU*</p> <p>School of Economics and Management, Wuhan Railway Vocational College of Technology, Wuhan, Hubei/China</p>	797

		Page(s)
71.	<p>RESEARCH ON THE INFLUENCE OF THE MAIN VIBRATION-GENERATING COMPONENTS IN GRAIN HARVESTERS ON THE OPERATOR'S COMFORT / CERCETĂRI PRIVIND INFLUENȚA PRINCIPALELOR COMPONENTE GENERATOARE DE VIBRAȚII DIN CADRUL COMBINELOR DE RECOLTAT CEREALE ASUPRA CONFORTULUI CONDUCĂTORULUI</p> <p>Eugen MARIN¹⁾, Petru CÂRDEI¹⁾, Valentin VLĂDUȚ¹⁾, Sorin-Ștefan BIRIȘ²⁾, Nicoleta UNGUREANU²⁾, Sorin Tiberiu BUNGESCU³⁾, Iulian VOICEA¹⁾, Dan CUJBESCU¹⁾, Iuliana GĂGEANU¹⁾, Lorena-Diana POPA⁴⁾, Simona ISTICIOAIA⁴⁾, Gheorghe MATEI⁵⁾, Sorin BORUZ⁵⁾, Gabriel TELIBAN⁶⁾, Cristian RADU⁵⁾, Onder KABAS⁷⁾, Ioan CABA¹⁾, Joński MACIEJ⁷⁾</p> <p>¹⁾INMA Bucharest / Romania; ²⁾University POLITEHNICA Bucharest/ Romania; ³⁾USV "King Mihai I" Timișoara / Romania; ⁴⁾ARDS Secuieni / Romania; ⁵⁾University of Craiova / Romania; ⁶⁾University of Life Sciences Iași / Romania; ⁷⁾Akdeniz University / Turkey; ⁷⁾Warsaw University of Life Sciences / Poland</p>	808
72.	<p>RESEARCH ON DRIED DAYLILY GRADING BASED ON SSD DETAIL DETECTION WITH FEATURE FUSION / 基于特征融合细节检测 SSD 的干制黄花菜分级研究</p> <p>Xueli ZHANG^{1,2)}, Haiyan SONG^{*1,2)}, Decong ZHENG^{1,2)}, Renjie CHANG^{1,2)}, Chenfei LI^{1,2)}, Yile SUN^{1,2)}, Zonglin LIU^{1,2)}</p> <p>¹⁾ College of Agricultural Engineering, Shanxi Agricultural University, Taigu / China; ²⁾ Dryland Farm Machinery Key Technology and Equipment Key Laboratory of Shanxi Province, Taigu / China</p>	824
73.	<p>PATH PLANNING RESEARCH ON GRAPE PICKING ROBOTIC ARM BASED ON IMPROVED RRT ALGORITHM / 基于改进 RRT 算法的葡萄采摘机械臂路径规划研究</p> <p>Yifan HU^{1,2)}, Jianjun QIN^{1,2)}, Luyang WANG^{1,2)}, Xifu CHEN^{1,2)}, Yue ZHAO^{1,2)}</p> <p>¹⁾ Beijing University of Civil Engineering and Architecture, School of Mechanical-electronic and Vehicle Engineering, Beijing / China ²⁾ Beijing Engineering Research Center for Building Safety Monitoring, Beijing / China</p>	833
74.	<p>DEEP LEARNING PREDICTIVE MODEL FOR SOIL TEXTURAL ASSESSMENT / PAG TUKOY SA URI NG LUPA SA PAMAMAGITAN NG DEEP LEARNING MODEL</p> <p>Karla Jane G. QUINOL¹⁾, Carolyn Grace G. SOMERA^{*2)}, Marvin M. CINENSE²⁾, Nemesio A. MACABALE Jr.³⁾</p> <p>¹⁾Graduate Student, Department of Agricultural and Biosystems Engineering, College of Engineering, Central Luzon State University, Philippines; ²⁾Faculty, Department of Agricultural and Biosystems Engineering, College of Engineering, Central Luzon State University, Philippines; ³⁾Faculty, Department of Information and Technology, College of Engineering, Central Luzon State University, Philippines</p>	845
75.	<p>STRUCTURAL DESIGN AND POWER SIMULATION OF TRACKED ELECTRIC TRACTOR BASED ON ECONOMY / 基于经济性的履带式电动拖拉机结构设计与动力仿真</p> <p>Qikang LI^{1,2)}, Guodong NIU^{1,2*)}, Yuanyi LIU^{1,2)}, Xinyu SONG³⁾</p> <p>¹⁾Shandong University of Technology, Collage of Agricultural Engineering and Food Science, ZiBo, China ²⁾Shandong University of Technology, Institute of Modern Agricultural Equipment, ZiBo, China ³⁾Shandong University of Science and Technology, Collage of Mechanical and Electronic Engineering, QingDao, China</p>	854
76.	<p>POTATO APPEARANCE DETECTION ALGORITHM BASED ON IMPROVED YOLOV8 / 基于改进 YOLOV8 的马铃薯外观品相检测算法</p> <p>Huan ZHANG¹⁾, Zhen LIU¹⁾, Ranbing YANG^{1,2)}, Zhiguo PAN¹⁾, Zhaoming SU¹⁾, Xinlin LI¹⁾, Zeyang LIU¹⁾, Chuanmiao SHI¹⁾, Shuai WANG¹⁾, Hongzhu WU³⁾</p> <p>¹⁾ College of Electrical and Mechanical Engineering, Qingdao Agricultural University, Qingdao/ China ²⁾ College of Mechanical and Electrical Engineering, Hainan University, Haikou/ China ³⁾ Qingdao Hongzhu Agricultural Machinery Co., Ltd., Qingdao/ China</p>	864
77.	<p>REAL-TIME MECHANICAL FLOWER THINNING EQUIPMENT, CONTROLLED BY ARTIFICIAL INTELLIGENCE / ECHIPAMENT PENTRU RARIREA MECANICĂ A FLORILOR ÎN TIMP REAL, CONTROLAT FOLOSIND INTELIGENȚA ARTIFICIALĂ</p> <p>Mihai Gabriel MATAACHE¹⁾, Robert CRISTEA^{*1)}, Ana ZAICA¹⁾, Radu CIUPERCĂ¹⁾, Adrian IOSIF²⁾, Gheorghe VOICU²⁾</p> <p>¹⁾ INMA Bucharest/ Romania; ²⁾ University "POLITEHNICA" Bucharest/ Romania</p>	875
78.	<p>DEVELOPMENT OF FOGPONICS CULTIVATION SYSTEM FOR MICROGREENS WITH INTERNET OF THINGS MONITORING SYSTEM AND MACHINE LEARNING AUTOMATION/ PAGLINANG NG SISTEMA NG FOGPONICS PARA SA PAGTATANIM NG MGA MICROGREENS NA MAY SISTEMA NG PAGSUBAYBAY SA PAMAMAGITAN NG INTERNET OF THINGS AT AWTONASYON NG MACHINE LEARNING</p> <p>Jamal Omar S. SARANGANI¹⁾, Carolyn Grace G. SOMERA-ALMEROL^{*2)}, Marvin M. CINENSE²⁾, Khavee Agustus W. BOTANGEN³⁾</p> <p>¹⁾ College of Engineering, Central Luzon State University, Science City of Muñoz, Nueva Ecija, Philippines; ²⁾Faculty of Department of Agricultural and Biosystems Engineering, College of Engineering, Central Luzon State University, Science City of Muñoz, Nueva Ecija, Philippines; ³⁾Faculty of Department of Information Technology, College of Engineering, Central Luzon State University, Science City of Muñoz, Nueva Ecija, Philippines</p>	885

		Page(s)
79.	<p>OPTIMISATION AND TESTING OF STRUCTURAL PARAMETERS OF INTERNAL TANGENT CIRCLE EXTERNAL GROOVED WHEEL FERTILISER DISCHARGER / <i>内切圆外槽轮式排肥器结构参数优化与试验</i></p> <p>Shubin YAN¹⁾, Wendong ZHONG¹⁾, Guifang WU¹⁾, Xiangping BAI²⁾, Jianing DI¹⁾, Xiangpeng ZHAO¹⁾ ¹⁾Inner Mongolia Agricultural University, College of Mechanical and Electrical Engineering, Hohhot/China; ²⁾Inner Mongolia Autonomous Region Agricultural and Pastoral Technology Extension Center, Hohhot/ China</p>	895
80.	<p>DESIGN AND EXPERIMENT OF THE RECIPROCATING ADJUSTABLE STRIKING-VIBRATING COMBINED DEVICE for ROOT-SOIL SEPARATION of <i>GENTIANA</i> / <i>往复调节式龙胆根土分离敲-振组合装置设计与试验</i></p> <p>Hongguang CUI¹⁾, Guangshuo CHEN¹⁾, Zhanqiu XIE¹⁾, Wenzhong HUANG²⁾, Weiming BIAN²⁾, Liyan WU¹⁾, Cuihong LIU^{1*)} ¹⁾ Shenyang Agricultural University, College of Engineering, Shenyang / China; ²⁾ Fushun Agricultural and Rural Development Service Center, Fushun / China</p>	908
81.	<p>DESIGN AND TESTING OF SEEDING QUALITY MONITORING SYSTEM FOR COTTON HILL-DROP PLANTER / <i>棉花精量穴播器播种质量检测系统设计与试验</i></p> <p>Liming ZHOU^{1,2)}, Yuxi JI^{1,2)}, Shenghe BAI^{1,2)}, Gaoyong XING^{1,2)}, Liang WEI^{1,2)}, Yanwei YUAN^{1,2)}, Bo ZHAO^{1,2)}, Kang NIU^{1,2)}, Yangchun LIU^{1,2)} ¹⁾ Chinese Academy of Agricultural Mechanization Sciences Group Co., Ltd, State Key Laboratory of Agricultural Equipment Technology, Beijing, China; ²⁾ China Agricultural University, Beijing, China</p>	920
82.	<p>STRUCTURAL PARAMETERS OPTIMIZATION AND EXPERIMENT OF TRENCHING BLADES VIA DEM / <i>基于 DEM 的开沟刀结构参数优化与试验</i></p> <p>Haochao TAN, Congcong SHEN, Zhaoyang GUO, Deyu LI, Shuai MA, Liming XU¹⁾ College of Engineering, China Agricultural University, Beijing / China</p>	934
83.	<p>OPTIMIZING TRENCHING DEVICE OPERATIONAL PARAMETERS VIA MBD-DEM COUPLING FOR ENERGY SAVINGS / <i>基于 MBD-DEM 耦合法优化开沟装备作业参数以减少能源消耗</i></p> <p>Haochao TAN, Congcong SHEN, Junlong MA, Chunlin WU, Liming XU, Shuai MA¹⁾ College of Engineering, China Agricultural University, Beijing / China</p>	944
84.	<p>MECHANIZATION OF GRASSLAND FARMING BY TECHNOLOGICAL VARIANTS WITH MINIMAL INPUTS. A REVIEW / <i>MECANIZAREA LUCRĂRILOR AGRICOLE PE PAJÎȘTI PRIN VARIANTE TEHNOLOGICE CU INPUTURI MINIME. REVIEW</i></p> <p>Vasile MOCANU¹⁾, Tudor Adrian ENE¹⁾, Eugen MARIN²⁾, Neluș-Evelin GHEORGHÎĂ³⁾ ¹⁾ Research-Development Institute for Grasslands, Brasov / Romania; ²⁾INMA Bucharest / Romania ³⁾ University Polytechnic of Bucharest, Department of Biotechnical Systems, Faculty of Biotechnical Systems Engineering, Bucharest / Romania</p>	954
85.	<p>RESEARCH ON THE VISCO-ELASTIC BEHAVIOUR OF SOME VARIETIES OF CHEESE WITH MOLD, RIPENED UNDER SPECIFIC CONDITIONS / <i>CERCETĂRI PRIVIND COMPORTAREA VĂSCOELASTICĂ A UNOR SORTIMENTE DE BRÂNZĂ CU MUCEGAI, MATURATE ÎN CONDIȚII SPECIFICE</i></p> <p>Grațîela-Florinela PANĂ, Paula TUDOR, George IPATE, Mihaela BEGEA, Elena-Mădălina ȘTEFAN, Gheorghe VOICU[*] National University of Science and Technology POLITEHNICA Bucharest, Romania</p>	971
86.	<p>TRENDS IN THE DEVELOPMENT OF CONSERVATION / ECOLOGICAL AGRICULTURE IN THE CONTEXT OF CURRENT CLIMATE CHANGE – A REVIEW / <i>TENDINȚE ÎN DEZVOLTAREA AGRICULTURII CONSERVATIVE / ECOLOGICE ÎN CONTEXTUL SCHIMBĂRILOR CLIMATICE ACTUALE - O SINTEZĂ</i></p> <p>Nicolae-Valentin VLĂDUȚ¹⁾, Atanas ATANASOV^{*2)}, Nicoleta UNGUREANU^{*3)}, Larisa-Victoria IVAȘCU⁴⁾, Lucian-Ionel CIOCA^{5,6)}, Lorena-Diana POPA⁷⁾, Gheorghe MATEI⁸⁾, Sorin BORUZ⁸⁾, Valerian CEREMPEI⁹⁾, Victor ȚÎȚEI¹⁰⁾, Florin NENCIU¹⁾, Oana-Elena MILEA¹⁾, Ștefan DUMITRU¹⁾, Ioan CABA^{*1)} ¹⁾ INMA Bucharest / Romania; ²⁾ University of Ruse / Bulgaria; ³⁾ National University of Science and Technology Politehnica Bucharest / Romania; ⁴⁾ P.U. Timișoara / Romania; ⁵⁾ ULBS Sibiu / Romania; ⁶⁾ Academy of Romanian Scientists / Romania; ⁷⁾ ARDS Secuieni / Romania; ⁸⁾ University of Craiova / Romania; ⁹⁾ State Agrarian University of Moldova / Moldova; ¹⁰⁾ Alexandru Ciubotaru National Botanical Garden (Institute) of Moldova State University, Chișinău / Moldova</p>	980
87.	<p>RESEARCH AND OPTIMIZATION OF PARAMETERS CONCERNING THE INTERACTION MECHANISMS BETWEEN VERTICAL CUTTING BLADES AND STRAW IN CORN COMBINE HARVESTERS / <i>玉米联合收获机纵置切刀-秸秆互作机理研究与参数优化</i></p> <p>Zhao Zhu^{1,2)}, Liu Fengbo¹⁾, Shui Dongli¹⁾, Zhao Bintong³⁾, Wang Zhongnan^{*1)} ¹⁾Liaoning Agricultural Technical College, Yingkou / China ²⁾ College of Agricultural and Animal Science, Tacheng Vocational and Technical College, Tacheng / China; ³⁾ College of Engineering, Shenyang Agricultural University, Shenyang / China</p>	1033

		Page(s)
88.	<p>RATIONALE OF THE OPTIMAL SHAPE AND PLACEMENT ANGLE VARIATION PATTERN OF THE TILLAGE ROTARY BLADE / Հոդաւորուած Ֆորէշի Դաւադի Օրհտիւլ Զաի և Տեղադրուած Աւազան Փոփոխուած Օրհնաշարժութեան Հիստադրոհիս</p> <p>Arshaluys TARVERDYAN, Artur ALTUNYAN¹⁾, Albert GRIGORYAN Scientific Research Institute for Agricultural Mechanization and Automation, Armenian National Agrarian Univ., Yerevan, Armenia</p>	1047
89.	<p>ADVANCING PRECISION AGRICULTURE WITH UAV'S: INNOVATIONS IN FERTILIZATION / PROGRESUL AGRICULTURII DE PRECIZIE CU UAV-URI: INOVAȚII ÎN FERTILIZARE</p> <p>Gabriel-Valentin GHEORGHE, Dragoș-Nicolae DUMITRU, Radu CIUPERCĂ, Marinela MATEESCU, Stefano-Andrea MANTOVANI, Elisabeta PRISACARIU, Alin HARABAGIU INMA Bucharest/ Romania</p>	1057

DESIGN AND EXPERIMENTAL ANALYSIS OF ROTARY SPOON SOYBEAN PRECISION SEEDER

转勺式大豆精密排种器设计与试验分析

Qichao LI¹⁾, Jinlong FENG^{1*)}

¹⁾ College of Mechanical and Electrical, Lingnan Normal University, Zhanjiang 524048, China

*Corresponding authors, Email: qc_lee@126.com

DOI: <https://doi.org/10.35633/inmateh-74-01>

Keywords: soybean; precision sowing; rotary spoon style; seeder; fastest descent line

ABSTRACT

To optimize the structure of soybean precision seeder and improve the performance of sowing, a new rotary spoon precision seeder is designed, and the key component structure is designed using numerical calculation methods. Using a combination of bench experiments and field experiments for parameter optimization experiments, a multi factor quadratic orthogonal rotation combination design experiment is adopted. The experimental data is analyzed and processed using Design Expert 8.0.6 software to seek the optimal combination of parameters. The results show that when the working speed is 24.56 ~ 33.72 r/min and the forward speed is in the range of 1.31 ~ 2.21 m/s, the seeding qualification index is greater than 90% and the coefficient of variation is less than 10%, meeting the requirements of excellent seeding standards. This study uses a rotary spoon seeder to sow soybeans, providing a new idea and reference for the development of precision soybean seeders.

摘要

为优化设计大豆精密排种器结构, 提高播种作业性能, 设计一种新型转勺式精密排种器, 采用数值计算方法设计关键部件结构。通过台架试验与田间试验相结合的方法进行参数优选试验, 设计试验采用多因素二次正交旋转组合方法, 运用 Design Expert 8.0.6 软件分析处理试验数据, 寻求最优作业参数组合。结果表明: 工作转速 24.56~33.72 r/min, 前进速度 1.31~2.21 m/s 范围时, 播种合格指数>90%, 变异系数<10%, 达到播种优等标准要求。该研究利用转勺式排种器播种大豆, 为大豆精密排种器的研发提供了创新思路和借鉴参考。

INTRODUCTION

Soybean, as an important grain and oil crop, has been continuously expanded in planting scale, and the demand for precise sowing is increasing day by day. Precision sowing machinery is used to accurately and quantitatively sow seeds into predetermined positions in the soil, ensuring uniform three-dimensional spatial distribution between seeds. The core component of a soybean seeder is the seeder, whose structure and working principle determine the quality of sowing and directly affect soybean yield (Dayoub et al., 2021; Badua et al., 2021; Sharma et al., 2024; Noureldin et al., 2019; Wang et al., 2021; Šarauskiis et al., 2023). The main types of soybean seeders are mechanical and air suction. Air suction is applied due to its light damage to seeds and relaxed requirements for seed shapes, which is conducive to high-speed sowing by large machinery. However, its complex structure, high price, and high-power requirements are not conducive to the application of small machinery. Mechanical seeders have been widely used due to their simple structure, low cost, and strong applicability (Akhalaia et al., 2021; Baghoee et al., 2023; Chen et al., 2020; Akhalaya et al., 2021).

Many studies have been conducted on mechanical soybean seeders. Emrah et al (2021) designed a slotted wheel seeder device. Through optimizing the design of the slotted wheel, the damage to the seeder was reduced, and the lowest crushing rate was achieved at a forward speed of 2 m/s. Kumar et al (2017) designed a disc seeding device to overcome seed damage, seed loss, and uneven seed distribution. Laryushin et al (2021) designed a disc groove seeding device, in which the filling groove of the cross-section is designed as a ring shape to improve the uniformity of seeding. Kokuryu (2021) developed a slanted hole disc seeder that can supply seeds on both sides and is used for large-scale high-speed sowing. Hensh and Raheman (2022) designed an electromagnetic driven seeder that driven by a push-pull solenoid valve. The seeds are transported through a rectangular hole wheel disc and thrown out at the outlet to improve seeding accuracy.

Qichao LI, Associate professor, Ph.D.; Jinlong FENG, Lecturer, Ph.D.

Zhang *et al* (2022) optimized the height difference design of the hole edge at the filling end of the disc soybean seeder to reduce the overhead problem of soybean seeds during the filling process. Huang *et al* (2022) designed a side mounted guided soybean precision seeder with a hole structure that facilitates the shape of seed filling, solving the problem of poor seed filling effect of existing mechanical seeders during high-speed operations. Li *et al* (2024) designed a dual row seed disc-shaped hole staggered distributed seed planter. The independent dual cavity structure reduces the speed of the seeder and avoids the population accumulation and mutual interference affecting seed filling. The above studies mainly focus on improving the hole structure of the sowing, increasing sowing accuracy or reducing damage rate. However, these studies only focus on innovative optimization of the hole structure of the wheel sowing device, and there is relatively little researches and applications of the spoon soybean sowing device.

In response to the limitations of the above researches, to improve the operational quality of mechanical soybean precision seeders, a rotary spoon soybean precision seeder is designed. Its structure and working principle are analyzed, and the key component structural parameters are optimized. The multi factor quadratic orthogonal rotation combination experimental method is used to optimize the seeding and parameters of the seeder, providing theoretical support and innovative ideas for the development of precision soybean seeding.

MATERIALS AND METHODS

Structure and Working Principle of the Seeder

The overall structure of the seeder mainly consists of an upper cover, dual drive disc (cam groove limit track disc, drive turntable, seed spoon base), seed spoon, seed guide tube, seed container, seed storage box and other components, as shown in Fig. 1 (a). The seed spoon and dual drive disc are the core components, and their reasonable configuration can smoothly complete the tasks of seed filling, seed holding, and seed feeding. The structure of the seed spoon is a near spherical crown, which can reduce the probability of seed slipping and damage during seed picking, and improve seed adaptability. The other end is directly connected to the base installed on the drive turntable, and the tail end of the base is embedded in the grooves of the cam groove limit track disc. The design of the upper mouth of the seed guide tube is lengthened to increase the feeding stroke and improve the effective seeding. The side wall is provided with an open seed partition plate, which is in contact with the seed shell. The seed shell is divided into two parts: the seed filling area and the seed storage area. The seeds in the seed storage area can flow into the seed filling area through the opening, and the whole is closed by the upper cover. The final assembly drawing is shown in Fig. 1 (b).

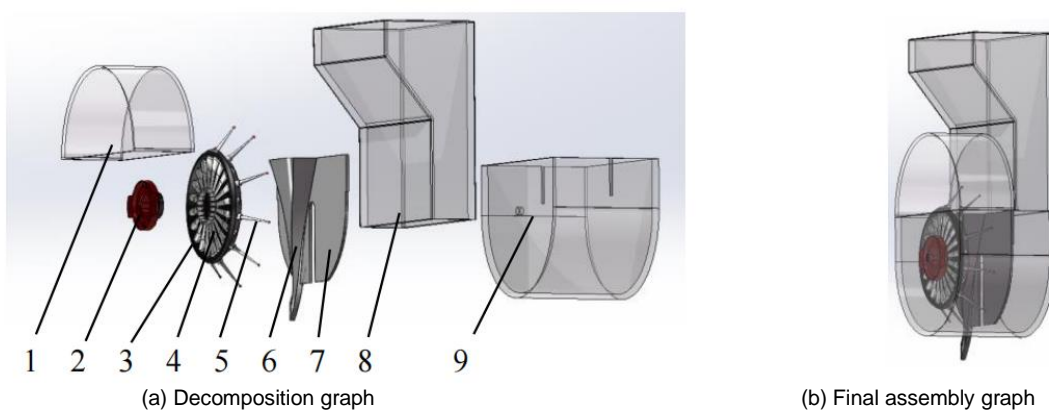


Fig. 1 - Structure of the seeder

1. Upper cover; 2. Cam groove limit track disc; 3. Drive turntable; 4. Base; 5. Seed spoon; 6. Seed guide tube; 7. Seed separator; 8. Seed storage box; 9. Seed container

The working process of the seeder is mainly divided into three stages: seed filling, seed holding, and seed feeding. During operation, the seeds in the seed storage box flow into the seed filling area under the action of gravity. The number of seeds flowing into the seed filling area is controlled by the seed container and the seed separator, ensuring that the number of seeds in the seed filling area is sufficient and in dynamic balance. The driving turntable drives the seed spoon and the base to rotate steadily in the circumferential direction. The tail end of the base is located in the grooves of the cam groove limit track disc. Under the joint action of the driving turntable and the cam groove limit track disc, the seed spoon and the base rotate regularly to ensure effective seed filling, stable seed holding, and precise seed feeding of the seed spoon.

When filling seeds, the seeds are divided under the rotation and agitation of the seed spoon, forming a population layer with different speeds. The seed filling process is completed under the combined action of its gravity, centrifugal force, collision friction between populations, and the force of the seed spoon. During the seed holding stage, the spoon slightly tilts upwards to ensure that a single seed does not fall off during rotation, achieving a smooth seed holding. When the seeds are transported to the sowing area, the spoon mouth flips downwards due to the rotation of the seed scoop. The seeds are precisely thrown into the seed guide tube under their gravity and centrifugal force, completing the sowing process.

Structural design of seed spoon

The seeding spoon is one of the key components of the spoon seeding device, and its structural shape, size parameters, and arrangement directly affect the seeding and feeding of the seeding device. Therefore, it is required that the seed scoop scoops the seeds and rotates them in all directions smoothly without falling off, and the seeds slide smoothly without obstacles when drop. 1000 soybean seeds (Zhonglong 3) are selected randomly for three-axis size measurement, and the average values are respectively $l = 5.3 \text{ mm}$, $w = 5.0 \text{ mm}$, $h = 4.9 \text{ mm}$ as approximately spherical.

The formula for calculating the projected cross-sectional area is as follows:

$$\begin{cases} S_h = \pi lw \\ S_w = \pi lh \\ S_l = \pi wh \end{cases} \quad (1)$$

where, S_h —The projected cross-sectional area when the seeds are in a supine state, mm^2

S_w —The projected cross-sectional area when the seeds are in a side-standing state, mm^2

S_l —The projected cross-sectional area when the seeds are in an upright state, mm^2

During the process of filling seeds with a seed spoon, the probability of the posture distribution of seeds scooped into the spoon under the action of gravity and friction is positively correlated with the projected cross-sectional area (Zhang, 1997), and it is an incompatible event.

The calculation formula is as follows:

$$P_h + P_w + P_l = 1 \quad (2)$$

$$\begin{cases} P_h = \frac{S_h}{S_h + S_w + S_l} \times 100\% \\ P_w = \frac{S_w}{S_h + S_w + S_l} \times 100\% \\ P_l = \frac{S_l}{S_h + S_w + S_l} \times 100\% \end{cases} \quad (3)$$

Where:

P_h —Probability of distribution in a supine position, %

P_w —Probability of distribution in a side-standing position, %

P_l —Probability of distribution in an upright position, %

According to Eqs. (2) and (3), the probabilities of seeds being placed in three positions of supine, side-standing, and upright in the seed spoon are calculated to be 34.4%, 33.8%, and 31.8%, respectively. Based on the geometric parameters of seeds and the probability of attitude distribution, combined with the principle of the steepest descent curve, the internal structure of the seed scoop is simplified. The solid of the seed scoop is optimized as a near spherical crown by rotating and scanning the curve, as shown in Fig. 2. The main structural parameters are the spoon mouth diameter D , the spoon depth H , and scanning curve parameters, and the design should follow principles $D > l > w > h > H > 0.7l$ (Gulati and Singi, 2003).

Based on the measurement of the three-axis size parameters of the seeds, a seed scoop is designed with an opening diameter of $D = 5.5 \text{ mm}$ and a depth of $H = 4.0 \text{ mm}$.

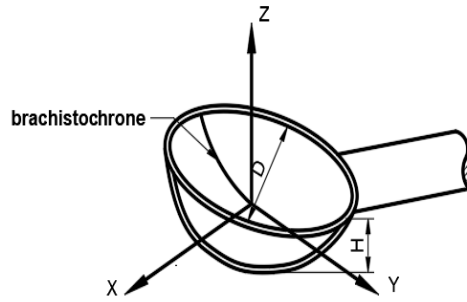


Fig. 2 - Seed spoon

When the seed rolls from the mouth to the bottom of the spoon, the shortest time path it experiences is the steepest descent curve. The particle M rolling from the starting point O to the non-directly below endpoint K is the curve with the shortest time, as shown in Fig. 3. The rolling circle with radius r rolls along the straight-line OB , and the trajectory swept by a point M on the edge of the circle is the steepest descent line between points O and K . θ is the angle of rotation, r is the radius of curvature, and the equation for the trajectory of the steepest descent line is (Akhshik et al., 2015) as follows:

$$\begin{cases} x = r(\theta - \sin \theta) \\ z = r(1 - \cos \theta) \end{cases} \quad \theta \in [0, \pi / 2] \quad (4)$$

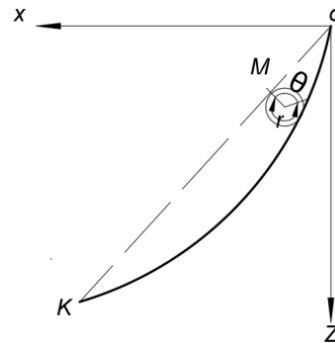


Fig. 3 - The principle of the steepest descent line

The abstract model schematic diagram based on the actual movement of the seed filling and scooping spoon is shown in Fig. 4. Using the center of the bottom of the seed spoon as the coordinate origin o , a spatial Cartesian coordinate system $o-vyz$ is established to study the motion state of seeds in the xoz plane, then

$$\begin{cases} mg \cos \beta = F_N \\ F_s = F_N \tan \varphi \end{cases} \quad (5)$$

- where m - the quality of a single seed, (g);
- g - gravitational acceleration, (m/s²);
- β - the tangent inclination angle of the truncated curve at the sliding point, (°);
- φ - the friction angle between seed and spoon, (°);
- F_N - the support of the spoon on seeds, (N);
- F_s - the friction force of spoon on seeds, (N).

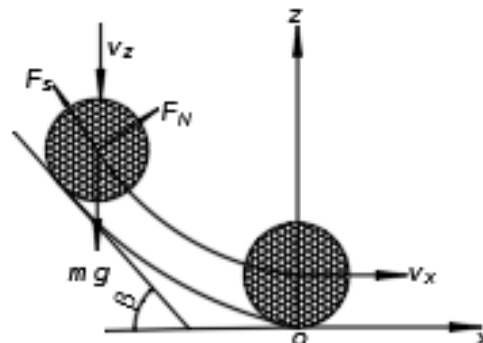


Fig. 4 - The cut-through curve of the fastest descent line

During the seed filling process, when the height of the seed rolling is h (the maximum value is the hole depth H), its lateral displacement is $\frac{\theta - \sin \theta}{1 - \cos \theta} h$. The work done by the frictional force F_s when the seed rolls down along the steepest descent line to the bottom of the spoon is as follows:

$$\int_0^{\frac{\theta - \sin \theta}{1 - \cos \theta} h} mg \cos \beta \tan \varphi dx = mgh \cos \beta \tan \varphi \frac{\theta - \sin \theta}{1 - \cos \theta} \quad (6)$$

According to the law of conservation of energy, that is:

$$\frac{1}{2} m(v_z^2 - v_x^2) + mgh = mgh \cos \beta \tan \varphi \frac{\theta - \sin \theta}{1 - \cos \theta} \quad (7)$$

where v_z - the initial descent speed of seeds, (m/s);

v_x - the seed termination horizontal speed, (m/s);

Combining and simplifying Eqs. (4) to (7), it can be obtained:

$$z = \frac{2gh \cos \beta \tan \varphi}{v_z^2 - v_x^2 + 2gh} x \quad (8)$$

From this, it can be concluded that the tangent inclination angle β is:

$$\beta = \arcsin \left[\sqrt{1 + \left(\frac{v_z^2 - v_x^2 + 2gh}{2gh \tan \varphi} \right)^2} - \frac{v_z^2 - v_x^2 + 2gh}{2gh \tan \varphi} \right] \quad (9)$$

The friction angle between the seed and the spoon is $\varphi = 33 \sim 43^\circ$. In an ideal state, the initial velocity of the seed is $v_z = 0$ m/s, and the velocity of rolling to the bottom of the spoon is $v_x = 0$ m/s. Substituting it into Eq. (9), the tangent angle β of the steepest descent curve can be obtained as $\beta = 30 \sim 37^\circ$.

Dual drive wheel design

The dual drive wheel disc consists of a drive turntable and a cam groove limit track disc, and a seed spoon base is installed on the drive turntable. The cam groove limit track disc is used to restrict the movement trajectory of the spoon base, and its model structure is shown in Fig. 5.

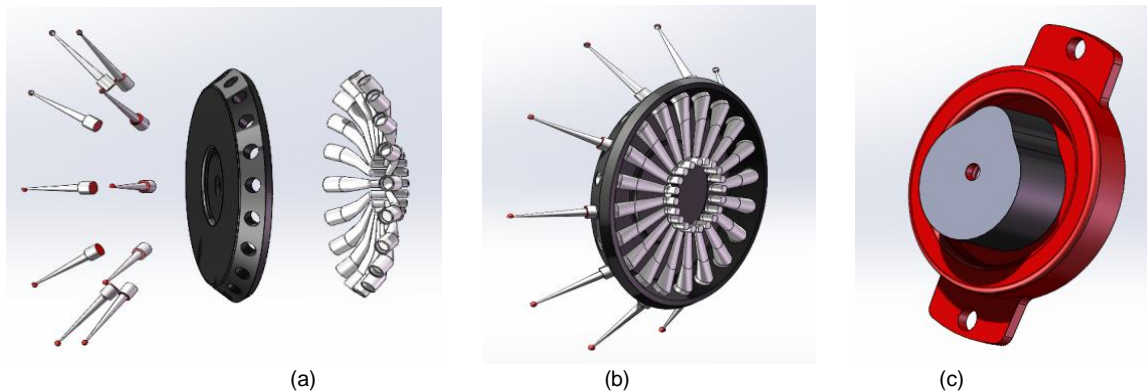


Fig. 5 - Dual drive disc structure

(a) Decomposition diagram of drive turntable and base; (b) Assembly diagram of seed spoon and drive turntable
(c) Cam groove limit track disc

The smooth coordination of the two plates can accurately and timely control the seed spoon to complete the tasks such as filling, holding, and feeding. The principle of dividing the working areas of the seeder should follow: the filling area should be designed as large as possible to ensure sufficient filling time, stable and reliable filling efficiency, and avoid too large filling area that causes seed wear; the seed holding area is the natural sliding of excessive seeds as soon as possible to ensure the smooth transportation of individual seeds to the planting area; the seeding area keeps the seeds thrown accurately and quickly, so as to prevent the spoon and seeds from crossing the seeding area and missing the seeding port. According to this principle, combined with the position of the population in the seeder, the angles of the filling area I, the holding area II, the sowing area III, the empty sowing area IV, are designed to be 130° , 90° , 50° and 90° , respectively, as shown in Fig. 6.

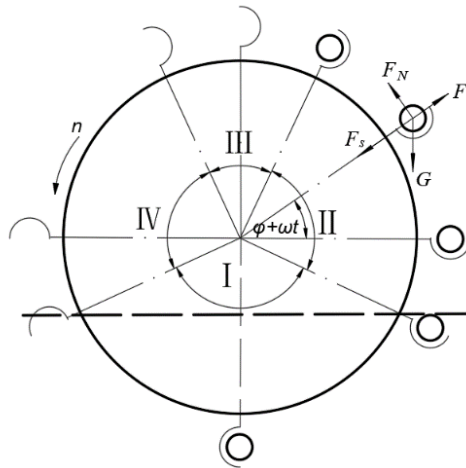


Fig. 6 - Regional division and seed stress analysis

To improve the seeding performance of the seeder, it is required that the force during seed transportation be stable. The critical condition for seeds to be relatively balanced in a spoon and not thrown away is analyzed. A mechanical model is established based on the D'Alembert principle:

$$\begin{cases} mg \sin(\varphi + \omega t) + F_s = F_e \\ F_N = mg \cos(\varphi + \omega t) \\ F_e = mR\omega^2 = 4\pi^2 mRn^2 \\ F_s = \mu F_N \end{cases} \quad (10)$$

where m —seed quality, (g);

μ —friction coefficient between seed and spoon wall (0.32~0.43)

F_e —centrifugal force of seeds, (N);

ω —angular velocity of motion, (rad/s);

$(\varphi + \omega t)$ —rotation angle, $(0, \pi/2)^\circ$

The second derivative of the radial decomposition in Eq. (8) is obtained as follows:

$$\frac{d^2 F_N}{d\omega^2} = -mgt^2 [\sin(\varphi + \omega t) + \mu \cos(\varphi + \omega t)] - 2mR \quad (11)$$

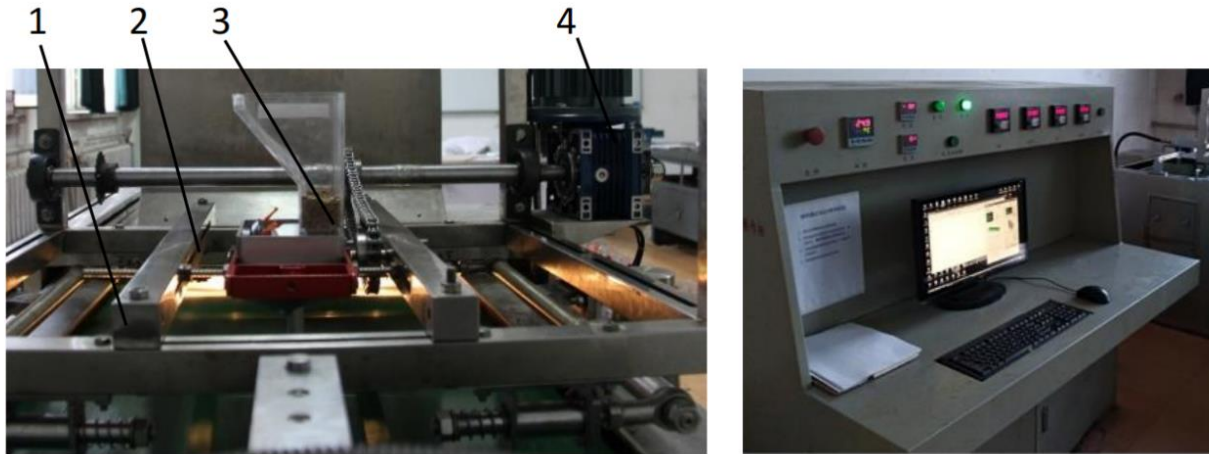
According to the rotation angle range $(0, \pi/2)$ of the seeding wheel, it can be determined that the second-order derivative of Eq. (11) is always less than zero, that is, the radial force function of the spoon holding seed is changing along the convex curve. Therefore, it can be inferred that as the working speed increases, the radial force on the seed first increases and then decreases. Therefore, the maximum centrifugal force on the seed should be at the inflection point.

To solve for the critical condition of the seed being thrown away, the working speed limit value n is obtained by organizing Eq. (10) as follows:

$$n \leq \sqrt{\frac{g[\sin(\varphi + \omega t) + \mu \cos(\varphi + \omega t)]}{4\pi^2 R}} \quad (12)$$

The larger the rotation radius of the seeding spoon of the seeder, the more spoons there are, and the lower the speed, the better the seeding. However, if the radius is too large and the spoon handle is too long, the seeding stability will be worse. The diameter of the drive turntable should not be too small, otherwise the number of seed spoons installed will be small, resulting in an increase in speed. Based on this, the radius of the drive turntable is set to 50 mm; the radius of the cam groove limit plate is 46 mm; the rotation radius R of the spoon is 56 mm; the number of spoons is 10, and the relative rotation angle is $25 \sim 90^\circ$. Substituting it into Eq. (12), it is calculated that if the working speed is below 40.37 r/min, the seeds will remain stable and not fly away, which sets the horizontal critical value of the working speed factor for the experiment.

Experimental materials and equipment



(a) Test bench for the seed planter performance (b) Data acquisition system

Fig. 7 - Seed performance test bench

1. Transmission bed belt; 2. Installation rack; 3. Seeder; 4. Motor

The experimental material is soybean (Zhonglong 3), and the experimental location is the Seed Performance Laboratory of Northeast Agricultural University. The experimental equipment includes the JPS-12 computer vision seeder performance testing platform and seeder, as shown in Fig. 7. During the experiment, the seeder is fixed on the test bench and maintained in a horizontal seeding state. The motor controls the speed of the seeder, and another motor controls the speed of the seedbed conveyor belt to simulate the forward state of the seeding machine. The data collection and statistical processing are carried out through the image acquisition and processing system of the test bench, so as to accurately measure different seeding performance indicators.

Test methods

According to the requirements of soybean growth and agronomic characteristics, combined with the actual sowing conditions in Heilongjiang Province, a single row sowing spacing of 8 cm is set to ensure uniform sowing during the operation. Referring to GB/T6973-2005 "Test methods for single seed drills (precision drills)" and JB/T1029-2001 "Specifications for single seed drills (precision drills)", the seeding qualification index and coefficient of variation are selected as the test indicators to evaluate the performance of the seeder. The calculation formula is as follows:

$$S = \frac{n_1}{N} \times 100\% \quad (13)$$

$$C = \sqrt{\frac{\sum(l - \bar{l})^2}{(N-1)\bar{l}^2}} \times 100\% \quad (14)$$

where S —qualification index, (%);

C —coefficient of variation, (%);

n_1 —number of qualified seeds per grain, (piece);

N —total theoretical seeds of hole spacing, (piece);

l —theoretical sowing distance, (cm);

\bar{l} —average sowing distance, (cm).

RESULTS AND ANALYSIS

Under the premise of determining the structural parameters of the seeder, the main factors affecting the performance of the seeder are the working speed and forward speed of the seeder. Therefore, two factors are selected as experimental factors, and a two factor five level quadratic regression rotation orthogonal combination design experiment is adopted to seek the optimal working parameter combination of the seeder. The working speed v_1 of the seeder is set in the range of 20 ~ 40 r/min, and the forward speed v_2 is set in the range of 1 ~ 3 m/s. The experimental design scheme and measurement results are shown in Table 1. Design Expert 8.0.6 software is used for analysis, as shown in Table 2.

Table 1

Experimental design and results

Number	Experimental factor		Performance index	
	Working speed v_1 / r·min ⁻¹	Forward speed v_2 / m·s ⁻¹	Qualified index S / %	variable coefficient C / %
1	-1	-1	88.01	11.97
2	+1	-1	81.59	7.67
3	-1	+1	76.08	13.95
4	+1	+1	74.46	11.56
5	-1.414	0	88.09	13.23
6	+1.414	0	79.23	10.65
7	0	-1.414	82.79	9.75
8	0	+1.414	70.16	11.78
9	0	0	90.88	9.22
10	0	0	93.62	8.93
11	0	0	90.67	7.93
12	0	0	89.49	7.34
13	0	0	94.91	6.91
14	0	0	93.67	6.32
15	0	0	92.55	7.67
16	0	0	90.39	8.99

Table 2

Measured test data from variance analysis

Indexes	Sources	Sum of squares	Degree of freedom	Mean square	F	P
Qualified indexes	Models	853.92	5	170.78	59.31	< 0.0001
	v_1	52.89	1	52.89	18.37	0.0016
	v_2	170.40	1	170.40	59.17	< 0.0001
	$v_1 v_2$	5.76	1	5.76	2.00	0.1876
	v_1^2	140.41	1	140.41	48.76	< 0.0001
	v_2^2	484.46	1	484.46	168.23	< 0.0001
	Residual	28.80	10	2.88		
	Fitting	2.70	3	0.90	0.24	0.8648
	Error	26.10	7	3.73		
	Sum	882.71	15			
Coefficient of variation	Models	74.73	5	14.95	16.80	0.0001
	v_1	13.36	1	13.36	15.02	0.0031
	v_2	9.55	1	9.55	10.74	0.0083
	$v_1 v_2$	0.91	1	0.912	1.03	0.3351
	v_1^2	33.72	1	33.72	37.91	0.0001
	v_2^2	17.18	1	17.18	19.32	0.0013
	Residual	8.89	10	0.89		
	Fitting	2.29	3	0.76	0.81	0.5281
	Error	6.61	7	0.94		
	Sum	83.62	15			

Note: ** means extremely significant (P < 0.01); * means significant (0.01 < P < 0.05), same as below.

According to the analysis in Table 2, the working speed and forward speed have an extremely significant impact on the sowing qualification index, coefficient of variation performance indicators, respectively. The regression equation is meaningful and the fitting degree is good.

The regression equations for fitting the seeding qualification index and coefficient of variation are as follows:

$$S = 92.02 - 2.57v_1 - 4.62v_2 + 1.2v_1v_2 - 4.19v_1^2 - 7.78v_2^2 \tag{15}$$

$$C = 7.80 - 1.29v_1 - 1.09v_2 - 0.48v_1v_2 + 2.05v_1^2 + 1.47v_2^2 \tag{16}$$

To analyze the relationship between sowing indicators and experimental factors more intuitively, Design Expert 8.0.6 software is used to establish corresponding surfaces between the indicators and the two factors, as shown in Fig. 8.

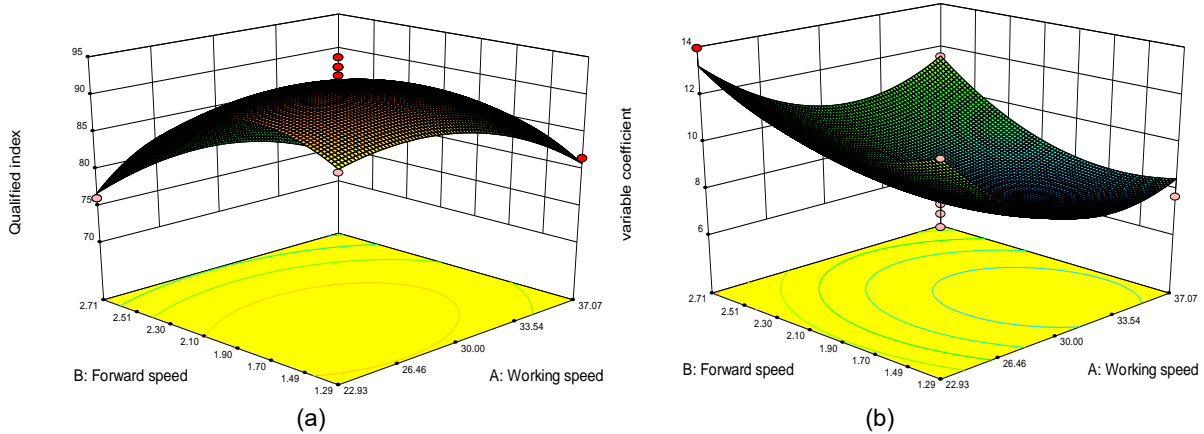


Fig. 8 - Effects of different working parameters on the indicators

(a) Effects of working speed and forward speed on the qualified index

(b) Effects of working speed and forward speed on the variable coefficient

According to Eq. (15) and Fig. 8 (a), it can be seen that the qualified index of seed spacing increases first and then decreases with the increase of working speed, and increases first and then decreases with the increase of forward speed. When the working speed is low, the change in the qualification index is gentle, and when it is high, the change increases significantly. When the working speed is around 28 r/min and the forward speed is around 1.8 m/s, the qualification index is the highest.

According to Eq. (16) and Fig. 8 (b), it can be seen that the coefficient of variation decreases first and then increases with the increase of working speed, and decreases first and then increases with the increase of forward speed. When the working speed is low, the coefficient of variation of uniformity changes rapidly, and when it is high, the change is gentle. When the forward speed is low, the coefficient of variation of uniformity changes smoothly, and when it is high, the change is faster. When the working speed is around 37 r/min and the forward speed is around 1.7 m/s, the coefficient of variation is the smallest.

Optimization of experimental results and parameter combinations

The optimal combination of working parameters is obtained by analyzing the experimental data, and different factors are optimized for design. According to the agronomic requirements of soybean sowing and combined with boundary conditions of various factors, a parameterized mathematical model is established. Following the requirements of precision sowing, a multi-objective variable optimization method is adopted to analyze the regression equations of sowing qualification index and coefficient of variation.

A nonlinear programming parameter model is established as follows:

$$\left\{ \begin{array}{l} \max S \\ \min C \\ s.t. \quad 20r \cdot \min^{-1} \leq v_1 \leq 40r \cdot \min^{-1} \\ \quad 1m / s \leq v_2 \leq 3m / s \\ \quad 90\% \leq S \leq 100\% \\ \quad 0 \leq C \leq 10\% \end{array} \right. \quad (17)$$

According to the optimization principle, Design Expert 8.0.6 is used for optimization analysis. It is found that when the working speed is 29.47 r/min and the forward speed of the machine is 1.78 m/s, the seeding of the seeder is optimal, with a qualified index of 92.90% for grain spacing and a coefficient of variation of 7.83%. According to the optimization analysis, the optimal parameter combination interval is shown in Fig. 9, that is, when the working speed is between 24.56 ~ 33.72 r/min and the forward speed is in the range of 1.31 ~ 2.21 m/s, the qualified index of sowing distance is greater than 90%, and the coefficient of variation of uniformity is less than 10%.

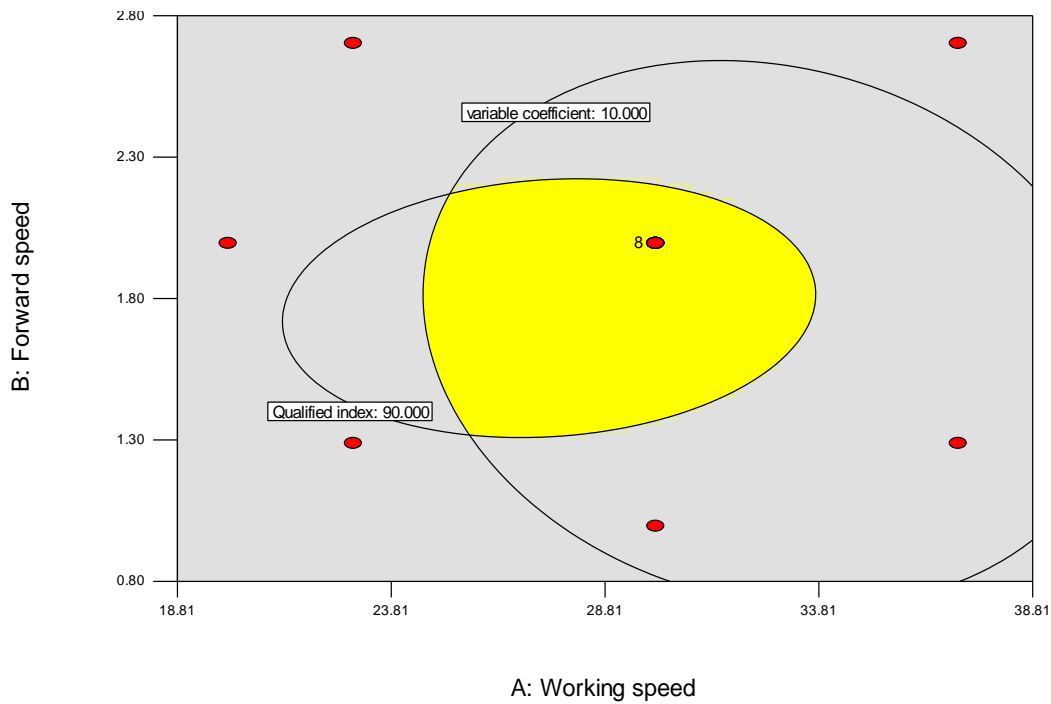


Fig. 9 - Parameters analysis

Field performance test

The field sowing performance test was conducted from June to July 2024 at the experimental base of Northeast Agricultural University. Before the experiment, soil was prepared and the soil moisture content was tested to be 17.8 %, with a solidity of 1.42×10^6 Pa, which meets the requirements of sowing agriculture. Based on the optimal parameter interval combination optimized by the bench performance test analysis, three sets of data were selected for the experiment. Each set of experimental data was tested three times and the average value was taken. The experimental process is shown in Fig. 10, and the results are shown in Table 3.



Fig. 10 - Field experiment

Table 3

Results of verification experiment				
Number	Working speed $v_1 / r \cdot \text{min}^{-1}$	Forward speed $v_2 / \text{m} \cdot \text{s}^{-1}$	Qualified index S / %	Variation coefficient C / %
1	26	1.5	91.81	9.12
2	29	1.8	92.92	8.16
3	32	2.1	90.69	9.46

According to Table 3, when the working speed of the seeder is 29 r/min and the forward speed is 1.8 m/s, the combination of the two factors is optimal. When the seeding qualification index is 92.92% and the coefficient of variation is 8.16%, the seeding is optimal. In addition, two sets of parameter combination experiments show that the sowing qualification index is greater than 90% and the coefficient of variation is less than 10%. The experimental results are basically consistent with the theoretical optimization results, meeting the requirements of optimal sowing standards.

CONCLUSIONS

(1) Based on the physical characteristics of soybean seeds, a seeder is designed. Its structure and working principle are analyzed, and the structural parameters of key components such as the seed spoon, drive turntable, and cam groove limit track are designed.

(2) The bench test investigates the optimal parameter combination of the working speed and forward speed of the seeder, so as to establish a mathematical model between the seeder indicators and experimental parameters. Design Expert software is used for analysis. When the working speed is 29.47 r/min and the forward speed is 1.78 m/s, it is an optimal condition, with a qualification index of 92.90% and a coefficient of variation of 7.83%. Optimizing the regression mathematical model, it is found that when the working speed is 24.5 ~ 33.72 r/min and the forward speed is in the range of 1.31 ~ 2.21 m/s, the qualified index of sowing distance is greater than 90%, and the coefficient of variation of uniformity is less than 10%. This meets the requirements of optimal sowing standards.

(3) Three sets of parameter combinations in the optimized parameter range are selected for field sowing test. When the working speed is 29 r/min and the forward speed is 1.8 m/s, the parameter combination is optimal, with a qualification index of 92.92% and a coefficient of variation of 8.16%, indicating the best seeding. The qualification index of the remaining two evaluation indicators is greater than 90%, and the coefficient of variation is less than 10%. The experimental results are consistent with the optimized model results.

ACKNOWLEDGEMENTS

Thanks to the Innovation team of intelligence and key technology research for agricultural machinery and equipment in Western of Guangdong province (Grant No. 2020KCXTD039), Horizontal project of intelligent seeder (Grant No. 23060351600030), University Special talent projects (Grant No. ZL22023).

REFERENCES

- [1] Akhalaia, B.K., Tsench, Y.S., Mironova, A.V. (2021). Development and Research of a Pneumatic Seed Drill Seed Metering unit. *Tekhnika i oborudovanie dlya sela (Техника и оборудование для села)*, Vol. 6, pp. 8-11. <http://dx.doi.org/10.33267/2072-9642-2021-6-8-11>
- [2] Akhalaya, B.K., Shogenov. Y.K., Starovoitov. S.I. (2021). Effect of Design Changes in Pneumatic Seeding Devices on Quality Indicators of Seeding. *Russian Agricultural Sciences*, Vol. 47, pp. 93-98. <https://doi.org/10.3103/S106836742101002X>
- [3] Akhshik, S., Behzad, M., Rajabi, M. (2015). CFD-DEM approach to investigate the effect of drill pipe rotation on cuttings transport behavior. *Journal of Petroleum Science and Engineering*, Vol. 127, pp. 229–244. <http://dx.doi.org/10.1016/j.petrol.2015.01.017>
- [4] Badua, S. A., Sharda, A., Strasser, R., Ciampitti. I. (2021). Ground speed and planter downforce influence on corn seed spacing and depth. *Precision Agriculture*, Vol. 22, pp. 1154-1170. <https://doi.org/10.1007/s11119-020-09775-7>
- [5] Baghooee, M., Karparvarfard, S.H., Azimi-Nejadian, H., Keramat-Jahromi, M., Balanian, H., Sardarpour, F. (2023). DEM Simulation for Seeding Performance of a Slotted Roller Seed-Metering Device for Planting Maize in Laboratory Condition. *Journal of Biosystems Engineering*, Vol. 48, pp. 428-436. <https://doi.org/10.1007/s42853-023-00202-z>
- [6] Chen, W., Zhang, B., Jiang, L., Qiu, T., Wang, L., Yang, S. (2020). Research status and development trend of seed-metering device in China. *American Journal of Agricultural Research*, Vol. 5(11), pp. 98-109. DOI: 10.28933/ajar-2020-06-3006
- [7] Dayoub, E., Lamichhane, J.R., Schoving, C., Debaeke, P., Maury, P. (2021). Early-Stage Phenotyping of Root Traits Provides Insights into the Drought Tolerance Level of Soybean Cultivars. *Agronomy*, Vol. 11(1): 188, <https://doi.org/10.3390/agronomy11010188>
- [8] Emrah, K., Yildiran, Y. (2021). Laboratory Scale of Seed Damage of Coarse-Grain Depending on Groove Diameter and Depth in Roller Devices. *Applied Engineering in Agriculture*, Vol. 37(3), pp. 411-416. <https://doi.org/10.13031/aea.14484>

- [9] Gulati, S., Singi, M. (2003). Design and development of a manually drawn cup type potato planter. *Indian Potato Assoc*, Vol. 30(1), pp. 61-62. India
- [10] Hensh, S., Raheman, H. (2022). Laboratory Evaluation of a Solenoid-Operated Hill Dropping Seed Metering Mechanism for Pre-germinated Paddy Seeds. *Journal of Biosystems Engineering*, Vol. 47, pp. 1-12, <https://doi.org/10.1007/s42853-021-00124-8>
- [11] Huang, Y., Li, P., Dong, J., Chen, X., Zhang, S., Liu, Y. (2022). Design and experiment of side-mounted guided high speed precision seed metering device for soybean (大豆高速播种机侧置导引式精量排种器设计与试验). *Transactions of the Chinese Society for Agricultural Machinery*, Vol. 53(10), pp. 44-53, 75. (in Chinese)
- [12] Kokuryu, T. (2011). High-Speed Seeding with an Inclined-plate Soybean Seeder: Development of the Inclined Cell Plate. *Japanese Journal of Farm Work Research*, Vol. 46(3), pp.107-114. Japan
- [13] Kumar, D., Tripathi, A., Kant, K., Devi, P., Prakash, V. (2017). Design and laboratory test of a seed metering device of sowing soybean seeds. *Asian Journal of Multidimensional research*. Vol. 6(2), pp. 57-66. India
- [14] Laryushin, N.P., Shukov, A.V., Abakumov, A.V. (2021). Laboratory studies of the sowing unit with the grooves of the coil made in the shape of a torus. *The Agrarian Scientific Journal (Аграрный научный журнал)*, Vol. 4, 82-84. <http://dx.doi.org/10.28983/asj.y2019i4pp82-84>
- [15] Li, Y., Zhao, S., Yang, L., Song, Q., Li, B., Yang, F. (2024). Design and Test of High-speed Precision Seeder of Independent Fractionated Soybean Double-row Brush. *Transactions of the Chinese Society for Agricultural Machinery*, Vol. 55(06), pp. 101-110. (in Chinese)
- [16] Noureldin, S., Artyom, D., Andrey, B., Aleksandr, L. (2019). A comparative analysis of precision seed planters. *E3S Web of Conferences*, Vol. 135, 1080. <https://doi.org/10.1051/e3sconf/201913501080>
- [17] Šarauskis, E., Kazlauskas, M., Bručienė, I., Naujokienė, V., Romaneckas, K., Buragienė, S., Steponavičius, D., Abdul Mounem, M. (2023). Impact of soil electrical conductivity-based site-specific seeding and uniform rate seeding methods on winter wheat yield parameters and economic benefits. *Precision Agriculture*, Vol. 24, pp. 2438-2455. <https://doi.org/10.1007/s11119-023-10047-3>
- [18] Sharma, A., Prakash, A., Bhambota, S., Kumar, S. (2024). Investigations of precision agriculture technologies with application to developing countries, *Environment, Development and Sustainability*, Vol. 2024, 18 February. <https://doi.org/10.1007/s10668-024-04572-y>
- [19] Wang, S., Sun, Y., Yang, C., Yu, Y. (2021). Advanced design and tests of a new electrical control seeding system with genetic algorithm fuzzy control strategy. *Journal of Computational Methods in Sciences and Engineering*, Vol. 21(3), pp. 703 -712. <http://dx.doi.org/10.3233/JCM-215126>
- [20] Zhang, B.P. (1997). *Xiandai Zhongzhi Jixie Gongcheng (现代种植机械工程)*. [M], China Machine Press, Beijing. (in Chinese)
- [21] Zhang, F., Qin, C., Wang, X. (2022). Study on leak in seeding prevention and seed protection of disc precision soybean metering device (圆盘精量大豆排种器型孔防空排设计与种子防护研究). *Journal of Agricultural Mechanization Research*, Vol. 44(8), pp. 65-70. DOI: 10.13427/j.cnki.njyi.2022.08.012 (in Chinese)

MACHINE FOR SPRING TECHNOLOGICAL HARVESTING OF INDUSTRIAL HEMP / МАШИНА ДЛЯ ТЕХНОЛОГІЧНОГО ВЕСНЯНОГО ЗБИРАННЯ ТЕХНІЧНИХ КОНОПЕЛЬ

NALOBINA O.O.¹⁾, HOLOTIUK M.V.²⁾, BUNDZA O.Z.¹⁾, SHYMKO A.V.¹⁾, PUTS V.S.²⁾, MARTYNIUK V.L.²⁾

¹⁾National University of Water and Environmental Engineering / Soborna str.11, Rivne, Ukraine;

²⁾Lutsk National Technical University / Lvivska str., 75, Lutsk, Ukraine;

Tel: +380960825360; E-mail: o.z.bundza@nuwm.edu.ua

DOI: <https://doi.org/10.35633/inmateh-74-02>

Keywords: hemp, machine, harvesting, technology, indicators.

ABSTRACT

The development of industrial hemp production necessitates the creation of new technical means and methods, and the refinement of technological approaches for cultivating and harvesting this crop. The harvesting process requires special attention, which is determined by the characteristics of this crop, the stems of which contain strong fibers making it difficult to cut them. The article discusses the efficiency of using the machine that was developed and manufactured for spring harvesting of hemp stalks. The parameters of the hemp stalks windrow were considered, taking into account the factors affecting its quality. In addition, there were selected the parameters to assess the quality of the resulting windrow. The research was carried out using probability theory and statistical methods. Through experimental studies, the functionality of the developed and manufactured machine was confirmed. It was established that the machine facilitates the formation of a uniform windrow from hemp stalks, with the skew cutting angle not exceeding 17°, which allows it to be collected with a baler, minimizing the risk of clogging.

РЕЗЮМЕ

Розвиток промислового коноплярства зумовлює необхідність створення нових технічних засобів і методів, а також удосконалення технологічних підходів до вирощування та збирання цієї культури. В Україні, де коноплярство переживає період активного зростання, існує особлива потреба в технічних рішеннях, здатних забезпечити якісний процес збирання врожаю і при цьому залишатися доступними для відносно невеликих господарств.

У статті розглядається ефективність розробленої та виготовленої машини для весняного збирання стебел конопель. Розглянуто параметри валка стебел конопель з урахуванням факторів, що впливають на його якість. Крім того, були обрані параметри для оцінки якості отриманого валка. Дослідження проводилися з використанням теорії ймовірностей та статистичних методів. За допомогою експериментальних досліджень підтверджено працездатність розробленої та виготовленої машини. Встановлено, що машина сприяє формуванню рівномірного валка зі стебел конопель, при цьому кут нахилу зрізу не перевищує 17°, що дозволяє збирати його прес-підбирачем, мінімізуючи ризик засмічення.

INTRODUCTION

Hemp is a crop that garners widespread interest among scientists, farmers and industrial producers due to its versatile applications. Currently, bast fibers are utilized for industrial applications in the textile, construction, automotive, and other industries both in Europe and China (Nalobina et al, 2017; Popa et al, 2022). Recently, bast fibers have also gained importance as a renewable raw material for the production of strong, lightweight composite (Pari et al., 2015).

Considering the potential of hemp cultivation and its diverse applications, Ukraine is experiencing a resurgence in this industry. This revival necessitates the adoption of innovative technologies for cultivation, harvesting and primary processing aimed at enhancing the product quality and reducing losses.

The increase in hemp cultivation in Ukraine underscores the need for widespread mechanization, particularly in hemp harvesting, which is the most labor-intensive phase of cultivation.

Hemp has become the focus of research for numerous scientists, covering a wide range of directions. These include investigations into the physical and mechanical properties of stalks and fibers (Moskalenko and Giliazetdinov, 2011; Xiaoping et al, 2013; Wu et al, 2010; Sankari, 2000).

Specifically, the research has revealed variations of hemp stem fiber across the different parts of the hemp stem. The mechanical properties (modulus of elasticity and hardness) of the fiber cell wall in the lower section were found to differ from the upper sections of the hemp stem (*Hrydiakin, 2015*). Hemp harvesting technologies are somewhat different from those used for harvesting other agricultural crops, and they require the use of specialized equipment capable of performing several technological operations in one pass. In addition, the process is complicated by the plant height at the time of harvesting, as well as the structure of the stems, which contain a strong fibrous layer and wood component. Therefore, an urgent issue in the hemp industry is the intensification of harvesting operations, the use of modern harvesting technologies and technical means to increase the level of mechanization in the industry.

The research by *Zaica et al., (2022)*; *Popa et al., (2022)*; *Assirelli et al., (2020)*; *Sadrmanesh and Chen (2019)*; *Huang et al., (2023)*; *Huang, Shen, Li, (2017)*; *Pari, Alfano, Scarfone., (2016)*; *Huang, Shen, Ji, Tian et al., (2020)*; *Zhu, Zhang, Yu.,(2018)*; *Li, Shu, (2010)*; *Burczyk., Kaniewski, (2003)*; *Bulgakov et al., (2015)*, and others are dedicated to solving this issue.

Burczyk and Kaniewski, (2008) proposed a method of harvesting hemp seeds and a device for its implementation, which provides mowing and cutting the stems into smaller parts, allowing effective use for the production of essential oils. This method is recommended for use during the hemp flowering phase. This device can be also used during the period of complete ripening of seeds in order to harvest them for further preparation of seed material.

The process of harvesting hemp seeds has also become the subject of scientific research by *Baraniecki et al, (2022)*, who investigated the operation of a B-800 mower, which was attached to a John Deere 6830 tractor with the power of 104.4 kW. The performance of this mower in hilly terrain was evaluated during hemp harvesting. The authors recommend to use this equipment in relatively small farms, which are usually unable to purchase expensive and bulky machinery for hemp harvesting.

The studies by *Păun A. et al, (2020)*; *Manea D. et al, (2023)*, who also investigated hemp harvesting equipment, contain the results obtained as part of the research project conducted by INMA Bucharest. The presented equipment was tested on the experimental site. The kinematic and power parameters were obtained, and their influence on the quality indicators of the harvesting process, in particular the cutting height of the stems, was investigated. The conducted research allowed the authors to provide certain recommendations on the harvesting process efficiency.

The research of *Bulgakov (2015)*; *Huang (2023)*; *Huang, Shen, Li (2017)*; *Huang, Shen, Ji, Tian et al. (2020)*; *Pari, Alfano, Scarfone (2016)* were devoted to the development and analysis of the hemp harvester performance. Combine harvesters are able to ensure harvesting in large and level fields. In addition, these are rather complex and bulky machines that are not suitable for use in small farm fields. A significant deterrent to the use of combines by small and medium-sized farmers is their high price. Therefore, some researchers (*Zhu et al., 2018*; *Li et al, 2010*) suggest using well-known headers. The authors found that the reapers were not effective due to frequent baler clogging, uneven stem cutting and breakage of cutting elements.

The analysis of the latest research helped conclude that the issue of efficiently organizing hemp harvesting operations is relevant, while the issues of harvesting technologies that would ensure obtaining high-quality products, both seeds and fiber, are not sufficiently studied. In addition, the machines produced by well-known machine-building companies are bulky and energy-consuming. Considering this, the research focused on developing the equipment and technologies for small farms, which will facilitate the development of the hemp industry, is highly relevant. Therefore, this study aims to develop a compact device for the spring harvesting of hemp stalks suitable for small farms and to evaluate its operational effectiveness.

MATERIALS AND METHODS

Hemp harvesting employs various technologies, including the one developed and introduced by the Institute of Bast Crops of the National Academy of Sciences of Ukraine which is known as spring hemp harvesting. According to this technology, crop harvesting is carried out in two stages. Initially, seeds are harvested using a combine harvester in autumn, followed by stalks harvesting in spring after rotting of the hard stalks at the root, requiring less effort for their removal. To break the stalks during the second stage, a rotary rake is offered to be utilized. However, this process results in uneven windrows of stalks with significant relative displacements. These uneven windrows can lead to clogging of balers during the pickup. Consequently, the baler must be stopped periodically to clear the clogs, thereby increasing the harvesting time (*Nalobina et al, 2017*).

In order to eliminate stoppages of the baler due to obtaining a uniform windrow from broken stalks in the field, a specialized machine for spring hemp harvesting was developed and manufactured (Fig. 1).

The newly manufactured machine operates as follows: the drive pulley 2 is powered by the power take-off shaft of the tractor, which in turn drives the belts equipped with firmly positioned fingers on them. During this period, following the winter season, the stalks are weakened at the root, making them prone to easy breakage. The fingers transport the stalks from left to right and place them in windrows. The machine offers two options for finger placement on the belts: sequential placement (Fig. 2) and a checkerboard pattern arrangement.

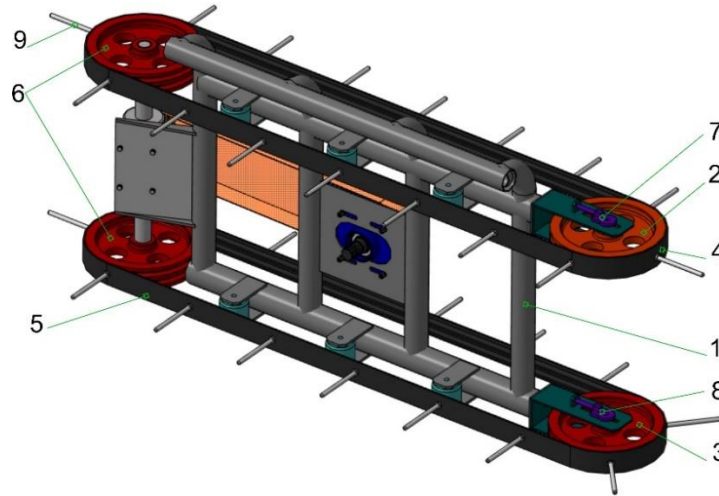


Fig. 1 - Machine for springtime hemp stalk breaking:
 1- frame, 2,3- upper and lower driving pulleys, 4,5- belts, 6-driven pulley, 7,8 – tightener, 9-finger



Fig. 2 – Machine for harvesting hemp stalks

To assess the functionality of the machine, the parameters of the process of forming a hemp stalks windrow will be examined, assuming the implementation of spring harvesting technology.

Figure 3 illustrates the parameters of the stalks windrow formation.

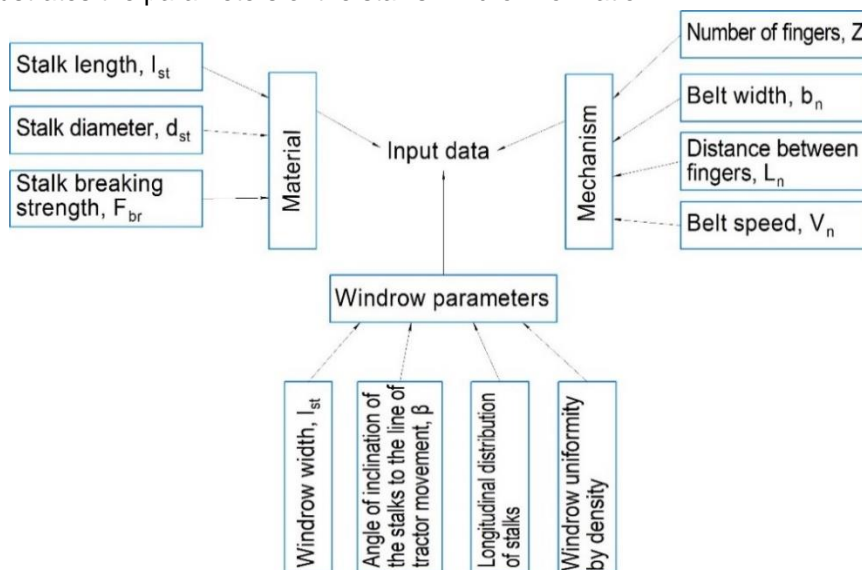


Fig. 3 - Factors influencing the windrow laying process and determining its quality

Consider the above factors.

1. Stalk length l_{st} . The given parameter depends on the variety of hemp, conditions for its cultivation. The average length of stalks (after removing the seed part) in the experimental field is 62.7 cm. The maximum length is 98.7 cm, the minimum is 57.9 cm. The diameter of stalks $d_{st} = 0.85...1.97$ mm. Breaking force is $F_{br} = 4.72...7.55$ N.

2. Machine parameters

The number of fingers on the upper and lower belts is 24 pieces. The width of the rubberized belt is 10 cm.

3. Windrow parameters

The width of the windrow l_w , laid out in the field depends on the uniformity of stalks composition conveyed from the fingers of the machine carrier, the difference in the stalks height after mowing the seed part, the uniformity of the field surface, and the speed of the machine movement.

The windrow width can be described by the following equation:

$$l_w = l_{avg} \cdot \delta \quad [m] \tag{1}$$

where:

l_{avg} – average stalk length, m;

δ – windrow extent in the field,

$$\delta = 1 + \frac{\Delta l}{l_{avg}} \quad [m] \tag{2}$$

where:

Δl is the value of displacement (relative to the distortion) of stalks in the windrow, which will depend on the displacement of the lower (upper) part of the stalks after they leave the fingers relative to some optional value.

In the field, the stalks are uneven in height. Taking into account the distribution of various heights, it can be observed that the tops of stalks are distributed according to the normal law (Fig.4).

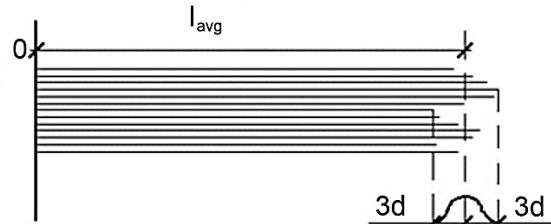


Fig. 4 - Distribution of the stalk tops

Taking into account the above, the assumption is adopted that after laying the windrow from broken hemp stalks and being moved by the machine in the field, the basal areas and tops are distributed according to the normal law. This implies that the density of the distribution of the tops $f(x_t)$ and the basal parts $f(x_b)$ will be determined as follows:

$$\begin{cases} f(x_t) = \frac{1}{\sigma_t \sqrt{2\pi}} \exp\left(-\frac{(x-\mu)^2}{2\sigma_t^2}\right) \\ f(x_b) = \frac{1}{\sigma_b \sqrt{2\pi}} \exp\left(-\frac{((x-l_{avg})-\mu)^2}{2\sigma_b^2}\right) \end{cases} \tag{3}$$

where:

μ – mathematical expectation;

σ^2 – variance of a random variable;

σ_t – mean square deviation of the basal parts and tops, respectively;

l_{avg} – the average length of stalks in the windrow.

Given that the probability of a random value (abscissa representing the position of the stalk top) falling within the expected interval is 99.7%, the system of equations (3) takes the form provided below:

$$\begin{cases} f(x_b) = \frac{1}{\sigma_t \sqrt{2\pi}} \exp\left(-\frac{(x_t-3\sigma_t)^2}{2\sigma_t^2}\right) \\ f(x_b) = \frac{1}{\sigma_b \sqrt{2\pi}} \exp\left(-\frac{(x_b-3\sigma_b)^2}{2\sigma_b^2}\right) \end{cases} \tag{4}$$

where: $x_t = x - l_{avg}$.

It should be noted that σ_t and σ_b are determined by the unevenness of the field, the stalk length, and the machine parameters.

An important indicator for evaluating the quality of the windrow spread in the field is the angle of inclination of stalks in the windrow. The ideal windrow configuration is achieved when the stalks in it are laid out parallel to each other and positioned at an angle of 90° to the direction of motion (Fig. 5).

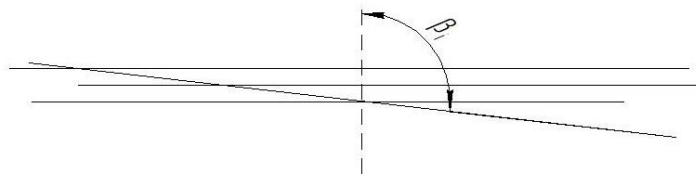


Fig. 5 - Pattern of displacement in the windrow (in relation to the direction of the machine motion)

The manifestation of the β_i value is probabilistic, thus it will be assessed using the part of the event occurrence (Chung, 2001).

Relative frequency of the event occurrence is:

$$p(\beta_i) = \frac{M}{N} \tag{5}$$

where:

M is the number of trials when event β_i occurred;

N is the number of all trials.

The uniformity of the windrow in terms of density is a significant indicator for evaluating the quality of the hemp harvester. The windrow spread in the field must exhibit uniform linear density to ensure unobstructed collection by the baler without any clogging and the formation of rolls with uniform density along their height. This is important for the preservation of rolls and their subsequent processing.

The number of stalks on one linear meter of the windrow laid out in the field is determined by the formula:

$$i = B_t \cdot i_0, \tag{6}$$

where:

B_t is the machine grip width, m;

i_0 is the stalk density (the number of stalks per square meter of the field), items/m².

The linear density, items/m² of stalks is determined as follows:

$$\rho = B_m \cdot i_0 \cdot \frac{V_M}{V_t}, \tag{7}$$

where:

B_m is the machine grip width, m;

i_0 is the stalk density (the number of stalks per square meter of the field), items/m².

V_m, V_b are the speeds of the machine and the belt with fingers, m/s.

RESULTS

The research was conducted in the fields of Rivne region, Ukraine. Stalks were harvested using spring technology. The newly developed and manufactured machine was used for harvesting.

The characteristics of the stalk density (average values over the two years of the research) are given in Table 1.

Table 1

Stem density parameters			
No.	Parameter name	Value	Measuring units
1	Stalk maximum height	98.7	cm
2	Stalk minimum height	57.9	cm
3	Average height value (100 stalks)	64	cm
4	Average stalk diameter	1.23	cm

The windrow width was determined by measuring one hundred one-meter-long windrow sections. The relative displacement of basal parts and tops was also measured. Statistical processing of the experimental data resulted in creation of a distribution graph confirming the earlier assumption regarding the normal distribution of these values (Fig.6).

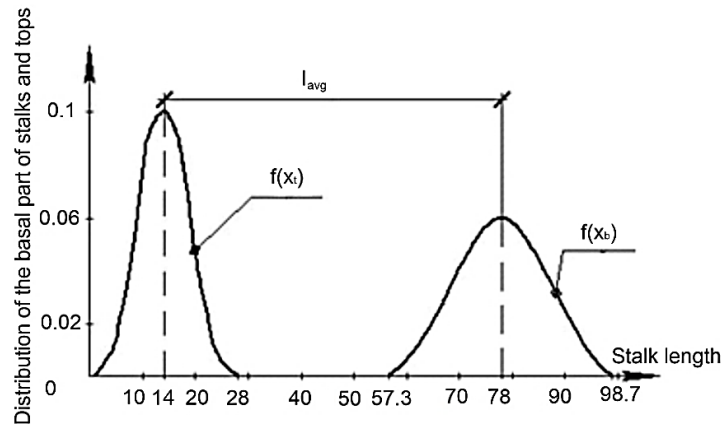


Fig. 6 - Distribution of the basal part of stalks and tops in the windrow (stalk length)

With the obtained distribution, given that $l_{avg}=64$ cm, the mean square deviation of the basal parts of stalks $\sigma_b = 4.6 \approx 5$ cm, the mean square deviation of the tops $\sigma_t = 6.6 \approx 7$ cm, no clogging is observed.

The results of the study of the skew cutting angle β_i are depicted in Fig.7.

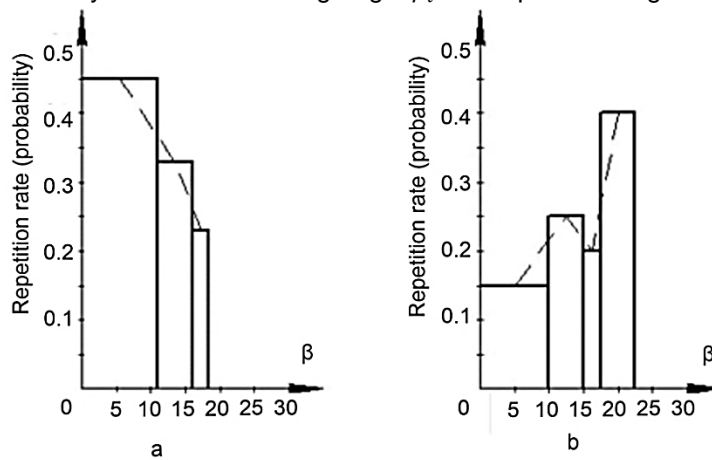


Fig. 7 - Distribution density of the probability of β_i indicator manifestation under the conditions of using the machine for harvesting hemp (mean values from one hundred one-meter-long plots):
 a- PTO shaft speed is 530 rpm; b - PTO shaft speed is 1123 rpm.

It is evident that reducing the rotation speed of the machine drive pulley and, accordingly the belt speed, has led to a decrease in the number of stalks deviating from the line perpendicular to the direction of the machine movement.

In addition to the speed of the machine belt movement, changes were made to the arrangement of the fingers on the belt. Experiments were also conducted with the machine where fingers were arranged in a checkerboard pattern. The results are shown in Fig.8.

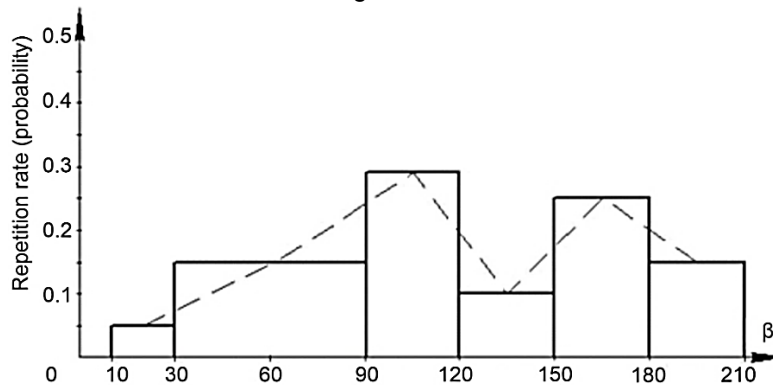


Fig.8 - Distribution density of the probability of β_i indicator manifestation under the conditions of arranging the fingers in a checkerboard pattern and the rotation speed of the PTO shaft set at 530 rpm

Due to significant stalks displacement along the windrow length, checkerboard arrangement of fingers is not efficient.

CONCLUSIONS

As a result of the field tests of the machine for hemp spring harvesting, it was determined that:

- the machine is to be manufactured with a sequential arrangement of fingers on 10 cm-wide belts with a distance between fingers of 41 cm;
- the diameter of the machine drive pulley is 250 mm with the pulley width of 100 mm;
- the tractor's PTO shaft is expected to have the rotation speed of 530 rpm.

Adherence to these conditions ensures the formation of a uniform windrow of hemp stalks in the field, enabling the baler to collect the windrow without clogging or stopping.

REFERENCES

- [1] Assirelli A., Dal Re, L., et al (2020). The Mechanical Harvesting of Hemp Using In-Field StandRetting: A Simpler Approach Converted to the Production of Fibers for Industrial Use. *Sustainability*, Vol.12, p.8795. DOI: <https://doi.org/10.3390/su12218795>. Monterotondo / Italy;
- [2] Baraniecki P., Latterini, F., et al (2022). Assessment of the Working Performance of an Innovative Prototype to Harvest Hemp Seed in Two Different Conditions of Terrain Slope. *Agronomy*, Vol. 12, p.185. DOI: <https://doi.org/10.3390/agronomy1201018>. Poznan / Poland;
- [3] Bulgakov V., Ivanovs S, Adamchuk V. (2015). Estimated mathematical model of plane-parallel motion of trailed hemp harvesting aggregate. *Engineering for rural development*, Jelgava, 20-22.05.2015. https://www.tf.lbtu.lv/conference/proceedings2015/Papers/005_Bulgakov.pdf. Kyiv / Ukraine;
- [4] Burczyk H., Kaniewski R. (2003). New Technology of Harvesting Hemp Grown for Seed. *Journal of Industrial Hemp*, Vol. 10(1), pp. 49-60. DOI: https://doi.org/10.1300/J237v10n01_05 Poznan / Poland;
- [5] Chen Y., Liu J., Gratton J.L. (2003). Engineering perspectives of the hemp plant, harvesting and processing: A review. *Journal of Industrial Hemp*, Vol.9 (2), pp. 23-39. DOI: https://doi.org/10.1300/J237v09n02_03 . Winnipeg / Canada;
- [6] Chung K. L. (2001). *A course in probability theory*. Academic press. 432 p., URL: <https://ru.scribd.com/document/44893783/Chung-K-L-a-Course-in-Probability-Theory-3ed-AP-2001>, San Diego / USA;
- [7] Manea D., Stroescu G., Popa L., Ionescu Al., Zaica Al. (2023). Management practices in industrial hemp harvesting and storage. *INMATEH Agricultural Engineering*, Vol. 69(1), pp.520-526. DOI: <https://doi.org/10.35633/inmateh-69-49> , Bucharest / Romania;
- [8] Hrydiakin O. (2015). *The study of physical and mechanical properties of hemp stalks (Дослідження фізико-механічних властивостей стебел конопель)*. NUBIP Bulletin. *Technology and energy of agricultural industry (Вісник НУБІП. Технології та енергетика АПК)*. Vol.215, pp.82-87, Kyiv/Ukraine;
- [9] Huang J.C., Shen C., Li X.W., et al.(2017). Design and tests of hemp harvester. *International Agricultural Engineering Journal*, Vol. 26(2), pp. 117–127, India
- [10] Huang J.C., Shen C., Ji A.M., Tian K.P., Zhang B., Ji A., Liu H., Shen C. (2020). Design and test of two-wheeled walking hemp harvester. *Int J Agric & Biol. Eng.*, Vol.13(1), pp.127–137. DOI: <http://dx.doi.org/10.25165/j.ijabe.20201301.5223> , Beijing/China;
- [11] Huang J., Tan L. , Tian K., Zhang B., Ji A., Liu H., Shen C. (2023). Formation mechanism for the laying angle of hemp harvester based on ANSYS-ADAMS. *Int J Agric & Biol. Eng.*, Vol. 16(4), pp.109-115. DOI: <https://doi.org/10.25165/j.ijabe.20231604.7978>, Beijing/China;
- [12] Li X, Shu C.X., Huang H.D., Tian B.P. (2010). Harvest cutting technology of thick-tall stem crops at home and abroad. *Journal of Agricultural Mechanization Research*, Vol. 8, pp. 1–6, Beijing / China;
- [13] Moskalenko B., Hiliazetdinov R. (2011). *Research on the resistance to breakage of hemp stalks bast fiber and technical crops (Дослідження стійкості до розриву стебел конопель луб'яного волокна та технічних культур)*. Institute of Bast Crops of the National Academy of Sciences of Ukraine (Інститут луб'яних культур НААН). Issue 1 (6), pp. 150-154, Kyiv/Ukraine;
- [14] Nalobina O., Kovalchuk R., Vasylychuk N. (2017). *The concept of development of the hemp industry of the agro-industrial complex of Ukraine (Концепція розвитку коноплярської галузі АПК України)*. *Machinery, energy, and transportation in the agro-industrial complex (Техніка, енергетика, транспорт АПК)*. Vol.1, pp.37-41, file:///C:/Users/Olena/Downloads/tetapk_2017_1_8.pdf Vinnytsia/Ukraine;
- [15] Pari L., Baraniecki P., Kaniewski R. et al. (2015). Harvesting strategies of bast fiber crops in Europe and in China, *Industrial Crops and Products*, Vol. 68, pp. 90-96, DOI:10.1016/j.still.2008.02.004, Poznan/Poland;

- [16] Paun A., Stroescu G., Zaica A, Ciuperca R., Bogdanof G. (2020). Analysis of the process of green hemp stalks sequential harvesting. *9th International Conference on Thermal Equipment, Renewable Energy and Rural Development*. DOI:10.1051/e3sconf/202018003026. INMA Bucharest/ Romania;
- [17] Popa L.D., Zaica A., Nedelcu A. (2022). Considerations on hemp stalk harvesting using specialized equipment. *INMATEH-Agricultural Engineering*, Vol. 68(3), p. 51. DOI:10.35633/inmateh-68-05 Bucharest / Romania;
- [18] Sadrmanesh V. & Chen Y. (2018). Bast fibres: structure, processing, properties, and applications. *International Materials Reviews*, Vol. 64 (7), pp. 381-406, DOI: <https://doi.org/10.1080/09506608.2018.1501171>, Winnipeg / Canada;
- [19] Sankari H. (2000). Comparison of bast fibre yield and mechanical fibre properties of hemp (*Cannabis sativa L.*) cultivars. *Industrial Crops and Products*, Vol. 11, Issue 1, pp. 344-348, DOI: [https://doi.org/10.1016/S0926-6690\(99\)00038-2](https://doi.org/10.1016/S0926-6690(99)00038-2), Jokioinen / Finland;
- [20] Xiaoping Li, Siqun Wang, Guanben Du, et al (2013). Variation in physical and mechanical properties of hemp stalk fibers along height of stem. *Industrial Crops and Products*, Vol. 42, pp. 344-348, DOI: <https://doi.org/10.1016/j.indcrop.2012.05.043>, Kunming / China;
- [21] Yan Wu, Siqun Wang, Dingguo Zhou, Cheng Xing, et al (2010). Evaluation of elastic modulus and hardness of crop stalks cell walls by nano-indentation. *Bioresource Technology*, Vol. 101, pp. 73-84. DOI: <https://doi.org/10.1016/j.biortech.2009.10.074>, Nanjing / China;
- [22] Zaica Al., Anghelache D., Zaica A., Diana Popa D., Teliban G. (2022). Technologies and technical equipment for farmers in the field of hemp cultivation. *International Symposium, ISB-INMATEH', Agricultural and Mechanical Engineering*, Bucharest, Romania, 6-8 October 2022. National Institute for Research-Development of Machines and Installations Designed for Agriculture and Food Industry - INMA Bucharest, pp. 554-559. Bucharest/ Romania;
- [23] Zhu H, Zhang Z. G., Yu G. (2018). Development and test of hemp swather. *Agricultural Engineering*, Vol. 8(2), pp. 95–98. DOI: 10.25165/j.ijabe.20201301.5223 (in Chinese).

A HIGH-ACCURACY SHEEP FACE RECOGNITION MODEL BASED ON IMPROVED ResNet50

一种基于改进 ResNet50 的高精度羊脸识别模型

Xiwen ZHANG^{1,2)}, Chuanzhong XUAN^{*2)}, Tao ZHANG²⁾, Quan SUN^{1,3)}

¹⁾Jiangsu Maritime Institute, College of Marine Electrical and Intelligent Engineering, Nanjing, China

²⁾Inner Mongolia Agricultural University, College of Mechanical and Electrical Engineering, Inner Mongolia, China

³⁾State grid Inner Mongolia Eastern Electric Power Co., Ltd. Ewenki autonomous banner power supply branch, Hulunbuir, China

Tel: 0471-4309215; ^{*}Corresponding author E-mail: xcz@imau.edu.cn

DOI: <https://doi.org/10.35633/inmateh-74-03>

Keywords: Sheep face recognition; Deep learning; High-accuracy model; ResNet50; Attention mechanism

ABSTRACT

Accurate identification of sheep is of significant importance for modern, intensive sheep farming. Traditionally, herders have used conventional methods to identify individual sheep, which are time-consuming, labour-intensive, and prone to considerable errors. In recent years, researchers have developed sheep face recognition models based on deep learning techniques to identify sheep using facial images. However, existing models suffer from insufficient theoretical research and limited recognition accuracy. To address these issues, this study develops a high-accuracy sheep face recognition model named ResNet-SFR. The core innovation of this model is the deepening of the feature extraction network of the original ResNet50, which enhances the model's ability to capture various facial features in sheep images, as well as improving its generalization and stability. Additionally, the Convolutional Block Attention Module (CBAM) attention mechanism is embedded into the original model to further enhance the identification of key features, significantly increasing the accuracy of sheep face recognition. Transfer learning is employed to pre-train the sheep face recognition model, further boosting the accuracy of ResNet-SFR. Experimental results show that on a self-constructed sheep face image dataset, ResNet-SFR achieves a recognition accuracy of 96.6%, demonstrating its superior performance in sheep face recognition tasks. The proposed ResNet-SFR not only offers high recognition accuracy but also exhibits strong applicability, meeting the practical needs of farm identification and showcasing promising application prospects.

摘要

羊只身份准确识别对现代化、集约化养羊业有着重要的应用意义。在过去，牧民们用传统的羊只身份识别方法对个体羊只进行身份识别，然而，传统方法既费时又费力，还存在较大的识别误差。近年来，学者们基于深度学习技术开发了羊脸识别模型，通过羊脸图像识别其对应的身份。然而，目前现有的羊脸识别模型存在理论研究不足和识别精度不足问题。针对上述问题，本研究开发了一组高精度羊脸识别模型，名为ResNet-SFR。该模型的核心创新在于将原ResNet50的特征提取网络进行加深，此举不仅增强了模型捕捉羊脸图像中不同脸部特征的能力，同时也提高了其泛化性与稳定性。此外，在原模型的基础上嵌入了CBAM注意力机制，进一步加强了模型对关键特征的识别，显著提高了羊脸识别的准确度。本研究采用了迁移学习对羊脸识别模型进行预训练，进一步提升了ResNet-SFR的识别精度。试验结果表明，在自制的羊脸图像数据集上，ResNet-SFR的识别精度达到了96.6%，证明了其在应对羊脸识别任务上的优越表现。本研究提出的ResNet-SFR在羊脸识别方面不仅识别精度高，且具有较强的应用性，符合养殖场识别的实际需求，展现了较好的应用前景。

INTRODUCTION

With the continuous development of intelligent animal husbandry, intelligent and intensive breeding methods have gained widespread attention. In modern sheep farms, it is necessary to collect various information about the sheep, such as birth dates, weight, vaccination records, and pregnancy status. With this information, herders can formulate scientific management strategies and improve feeding practices, thereby effectively managing the pasture and further reducing breeding costs (Billah et al., 2023). Accurate identification of sheep is a prerequisite for collecting individual information (Xue et al., 2024).

In the breeding process, the accuracy of sheep identification directly affects the effectiveness of individualized management. For instance, by identifying each sheep, it is possible to record and track its health status and production performance, ensuring that each sheep receives appropriate care and management

(Zhang *et al.*, 2023). Additionally, identifying sheep helps to promptly detect and isolate sick individuals, preventing the spread of diseases within the flock and thus reducing breeding risks and losses. Accurate identification also provides reliable data support for breeding programs, assisting farmers in selecting superior breeds and enhancing breeding efficiency. Ultimately, accurate sheep identification enables traceability of meat quality, meeting consumer demand for high-quality meat. Therefore, sheep identification has become an indispensable part of modern sheep farming (Salama *et al.*, 2019).

Traditional methods of sheep identification include paint markings, manual observation, and ear tags. However, these traditional methods have significant limitations. Manual observation is inefficient and inaccurate, making it unsuitable for large flocks (Hitelman *et al.*, 2022). Additionally, paint markings and ear tags require regular maintenance and cleaning by staff, further increasing breeding costs. Currently, some farms use RFID ear tags and readers for sheep identification. However, in complex environments, RFID ear tags often become damaged or lost, and the identification process is easily disrupted. In summary, relying solely on traditional sheep identification methods may be inconvenient for managing modern sheep farms (Sharma *et al.*, 2020).

With the development of information technology, biometric image recognition has gained increasing attention and has become a trend in the field of animal face recognition (Zhang *et al.*, 2022; Deng *et al.*, 2022). Biometric image recognition utilizes intelligent monitoring equipment and computer vision to capture stable biometric features of individuals, such as facial images, and then performs identification based on these individual features. In recent years, researchers have developed sheep face recognition models using deep learning techniques, training on sheep facial images to achieve identification. However, existing sheep face recognition models suffer from insufficient theoretical research and limited recognition accuracy. To address these limitations, this study developed a high-accuracy sheep face recognition model named ResNet-SFR. By integrating image recognition models and various improvement strategies, the aim is to overcome the limitations of traditional sheep identification methods. The feature extraction layers of the original ResNet50 network were deepened. Additionally, the CBAM attention mechanism was introduced to enhance feature extraction capabilities. Finally, transfer learning was employed to pre-train ResNet-SFR, further improving the model's recognition accuracy. Experimental results show that ResNet-SFR achieved the highest recognition accuracy, meeting the practical needs of modern sheep farms and providing technical support for sheep face recognition technology.

MATERIALS AND METHODS

Dataset

This study used a group of Small Tail Han sheep as test subjects. The Small Tail Han sheep is a widely bred sheep breed in China, known for its high reproductive rate and superior meat quality. The coat colour of the Small Tail Han sheep is predominantly white, with some individuals having black or brown spots on their faces. These spots are mostly concentrated around the eyes, ears, cheeks, or mouth. The sheep face images used in this study were collected in August 2020 at Tianjin Aoqin Animal Husbandry Co., Ltd. The collection details are as follows: A total of 50 test sheep were used, aged between 1 to 3 years. The test sheep were numbered from 1 to 50, with the numbers corresponding to their identity information. Before collecting the facial images, the test sheep were enclosed in a pen and allowed to move freely. A photographer used a Canon EOS 600D DSLR camera (Canon, Tokyo, Japan) to capture the sheep face images, which were saved in JPG format with a resolution of 2736×1824. The collection distance was over one meter. The collection times were from 9:00 AM to 11:00 AM and from 2:00 PM to 5:00 PM. To increase the complexity and practicality of the dataset, facial images of the test sheep were taken from different angles, including left profile, right profile, and frontal views. A schematic diagram of the sheep face image collection is shown in Fig.1.

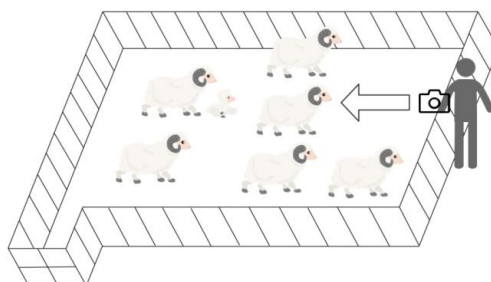


Fig. 1 - Schematic diagram of the sheep face image collection

Using the above methods, 50 facial images were collected for each test sheep. Sample images of the test sheep faces are shown in Fig.2.



Fig. 2 - Sample images of the test sheep faces

To enhance the applicability of the recognition model in practical scenarios, data augmentation was performed on the collected sheep face images. The specific data augmentation operations applied were: adjusting image brightness (-45% to 45%), adjusting image contrast (-45% to 45%), rotating the image 45 degrees to the left and right, and vertical flipping. Using these methods, 100 augmented images were generated for each test sheep to supplement the training of the recognition model. Ultimately, 150 facial images were retained for each test sheep, creating the sheep face image dataset. All images were randomly divided into training, validation, and test sets in a ratio of 8:1:1. The specific configuration of the sheep face image dataset is shown in Table 1.

Table 1

Dataset	The sheep face image dataset		
	Images	Size	Proportion
Training	6000	2736×1824	80%
Verification	750	2736×1824	10%
Testing	750	2736×1824	10%
Total	7500	2736×1824	100%

ResNet50

Convolutional Neural Networks (CNNs) achieve image recognition tasks by continuously extracting local features from images (Deng *et al.*, 2021). Ideally, a deeper feature extraction network can capture richer and more complex target features. However, with increased network depth, CNNs are prone to issues such as gradient vanishing and network degradation, which can further lead to reduced learning efficiency or ineffective improvement in accuracy. To address these issues, residual networks were proposed (He *et al.*, 2016). Residual networks successfully overcome these problems by introducing the concept of shortcut connections. The basic form of a residual network involves directly connecting the output of a layer to the input of a subsequent layer, which does not increase the model's parameter count or computational complexity. A schematic diagram of the residual network structure is shown in Fig.3. The input features x are processed through feature extraction to obtain output features $F(x)$. The residual network further adds the input features to the output features through a residual connection to obtain the final output features y . The specific calculation formula is as follows:

$$y = F(x) + x \quad (1)$$

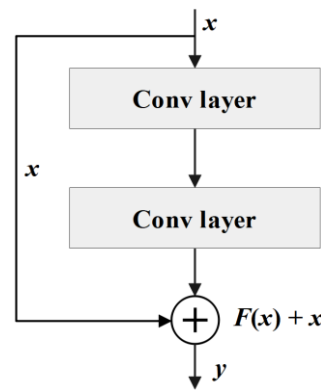


Fig. 3 - Schematic diagram of the residual network structure

ResNet50 is a residual network composed of forty-nine convolutional layers and one fully connected layer. It mainly consists of four basic modules: Block, Conv-Block, Identity-Block, and Block2 (Zhang et al., 2023). The Block module is composed of a convolutional layer and a max-pooling layer. The convolutional layer is responsible for the initial feature extraction from the input image and forms the initial feature representation. Next, the model uses the max-pooling layer to downsample the extracted features, reducing the spatial dimensions of the feature map. At the same time, the max-pooling layer helps to retain the main feature information, reduce computational complexity, and improve the model's adaptability to translation invariance.

The Conv-Block is used to change the dimensions of the input vector. The Conv-Block can be divided into two parts: the left side is the main branch, which includes two sets of convolutional layers with batch normalization and ReLU activation functions, as well as an additional set of convolutional layers that only have batch normalization. The right side consists of the residual branch, which includes a set of convolutional layers with batch normalization. The Conv-Block captures abstract features at different levels and achieves nonlinear mapping through convolutional operations. Therefore, the Conv-Block plays a role in extracting high-order features throughout the ResNet architecture.

The Identity-Block is also composed of two parts. The left side is the same as the main branch of the Conv-Block, while the right side is the residual branch, specifically connecting the input features with the output features of the main branch. In ResNet, the Identity-Block is used to handle cases where the input and output have the same dimensions. The Identity-Block effectively prevents the problem of gradient vanishing, retains the original input information of the module, and enables iterative learning of features layer by layer in subsequent layers.

In Block2, a global average pooling layer and a fully connected layer are used. The global average pooling layer's function is to obtain a feature vector with the average value of each channel. Then, the fully connected layer maps the final feature vector to specific classes, outputting the recognized target's class through the Softmax activation function, thus completing the entire image recognition task.

ResNet50, with its unique network structure, demonstrates superior recognition performance in numerous recognition tasks. The overall structure of ResNet50 is shown in Fig.4.

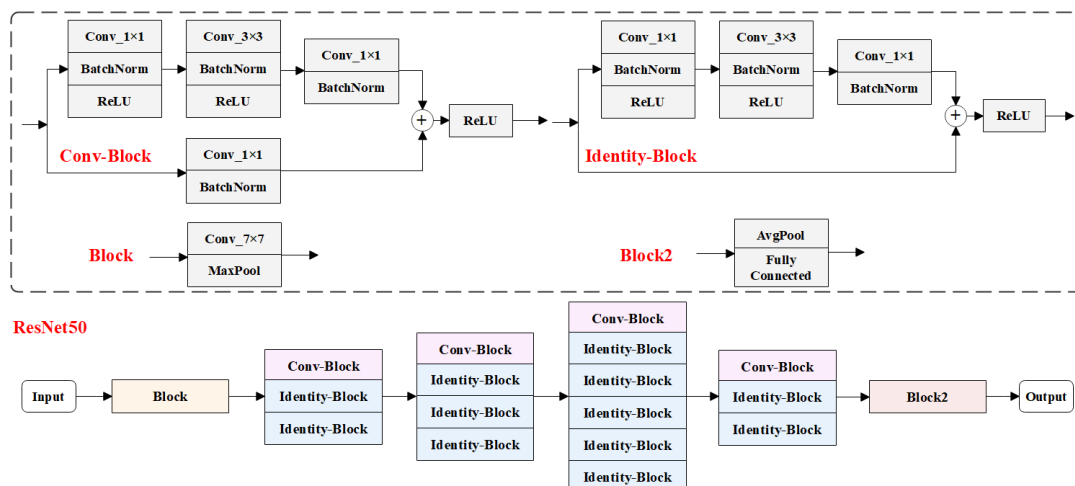


Fig. 4 - Overall structure of ResNet50

CBAM

The CBAM is an attention mechanism for CNNs that enhances feature representation by integrating both spatial and channel attention (Ni et al., 2024). The modular design of CBAM allows it to significantly improve model performance with relatively low computational cost (Zhang et al., 2023).

The CBAM module consists of two sub-modules: the channel attention module and the spatial attention module. The channel attention module first captures global information through global average pooling and global max pooling, and then generates channel attention weights using a shared multilayer perceptron (MLP). The input feature map is then multiplied by these channel attention weights to obtain the weighted feature map. The spatial attention module aggregates the input feature map along the channel dimension by performing global average pooling and max pooling, generating a two-dimensional feature map. This feature map then passes through a convolutional layer to generate spatial attention weights, which are multiplied by the channel-weighted feature map to obtain the final output (Fang et al., 2024).

The structure of CBAM is highly pluggable, making it easy to integrate into existing convolutional neural networks. Its workflow can be summarized as follows: first, channel dimension weighting is performed through the channel attention module, and then spatial dimension weighting is performed through the spatial attention module. This double weighting process enhances the representation ability of the input features. CBAM effectively increases the model's focus on important features, improving performance in the sheep face recognition task. The overall structure of the CBAM attention mechanism is shown in Fig.5.

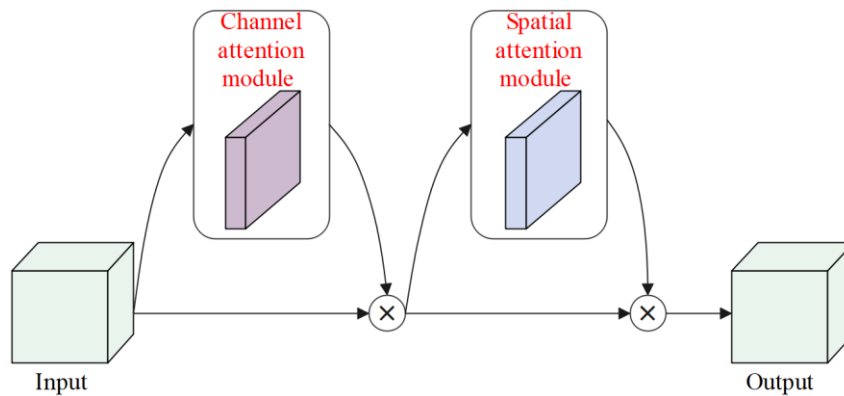


Fig. 5 - Overall structure of the CBAM attention mechanism

In the process of optimizing ResNet50, this study introduces the CBAM attention mechanism before the model's Block2 to further enhance performance. CBAM can adaptively adjust the responses at different positions in the feature map, making the model more focused on important regions in the image. Before Block2, ResNet50 completes the feature extraction of the final convolutional block and extracts the complete features of the target. Therefore, introducing the CBAM module before Block2 can effectively strengthen the sheep face-related features within the complete feature set and improve their representation. This design helps to enhance the model's focus on key features of the sheep face.

Deepening network

ResNet50 includes four sets of stacked convolutional block structures, each composed of Conv-Blocks and Identity-Blocks. Considering the high difficulty of the sheep face recognition task in this study, the network depth of ResNet50 was further increased to improve the model's feature extraction capability. The specific deepening method is as follows: an additional set of stacked convolutional blocks was added to the third and fourth sets of stacked convolutional blocks in ResNet50. The configuration of the added convolutional blocks is consistent with the second set of stacked convolutional blocks, including one Conv-Block and three Identity-Blocks. This design introduces deeper convolutional layers to extract more detailed sheep face features while maintaining the stability of the network structure. This approach aims to make the improved ResNet50 better suited for the sheep face recognition task, thereby enhancing the model's overall performance and generalization ability.

Transfer learning

Transfer learning is a model training method. Transfer learning is defined as using a model trained on task A as the initial model and retraining it for task B (Bo et al., 2024).

By leveraging the knowledge from the source domain data, transfer learning makes the model more robust and generalizable in the target domain. Additionally, transferring the knowledge of a complex model to a simplified model can achieve model lightweighting and accelerated inference (Liu *et al.*, 2024). The application of transfer learning not only improves model performance but also provides feasibility for the practical application of deep learning tasks in resource-constrained or data-limited situations.

In this study, the following method is used to apply transfer learning to multiple recognition models to achieve pre-training. First, the sheep face image dataset is divided into Dataset A and Dataset B. The training, validation, and test sets are all evenly split. In Method 1, the recognition model is first trained on Dataset A, and a pre-trained model is obtained once the training results are stable. This pre-trained model represents a model that has already learned the sheep face recognition task and achieved a "pre-learning" effect. The resulting pre-trained model is then further trained on Dataset B, and the final training results for Dataset B are obtained, which are considered as the final training results for Method 1. In Method 2, the recognition model is first trained on Dataset B to obtain a pre-trained model. Then, this pre-trained model is trained on Dataset A, resulting in the final training results for Method 2. The two sets of results are averaged to provide the final training results of the recognition model after transfer learning.

ResNet-SFR

To further enhance the recognition performance of the sheep face recognition model, this study employs the three improvement strategies mentioned above based on ResNet50, ultimately constructing the sheep face recognition model ResNet-SFR. The overall structure of ResNet-SFR is shown in Fig.6.

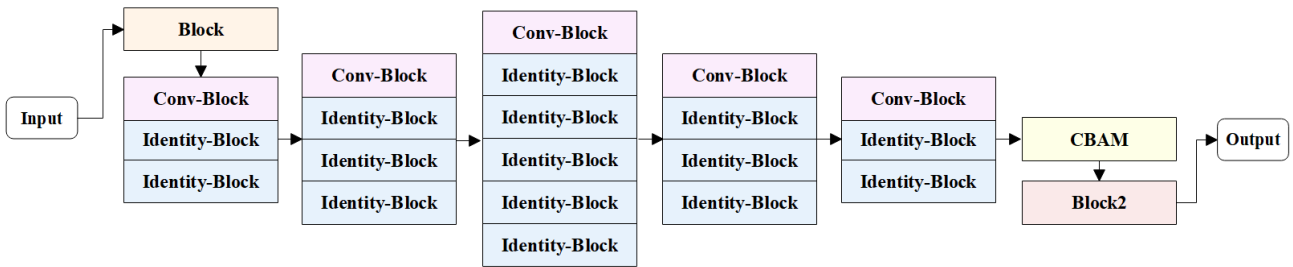


Fig. 6 - Overall structure of ResNet-SFR

Evaluation Metrics

The training platform used in this study is configured as follows: CPU is Intel Core i7-9700, GPU is NVidia GeForce RTX 2080Ti with 11 GB VRAM, memory is 16 GB, and the operating system is Windows 10. The software platform is PyCharm, with CUDA 11.3, PyTorch version 1.10.0, and Python version 3.8. During model training, the dynamic learning rate is set to 0.001, with 50 epochs and a batch size of 16.

In this study, the evaluation metrics for the sheep face recognition model include precision, recall, F1-score, and accuracy. Precision represents the percentage of correctly classified samples out of the total number of samples. Recall measures the ratio of correctly retrieved samples to the number of samples that should have been retrieved. Here, TP, FP, TN, and FN represent the counts of true positives, false positives, true negatives, and false negatives, respectively. The F1-score takes both precision and recall into account. Accuracy is one of the fundamental metrics for evaluating the performance of deep learning models, as it measures the proportion of correctly classified samples out of all samples. The ranges for F1-score, recall, precision, and accuracy are from 0% to 100%.

The formulas for these metrics are as follows:

$$\text{Precision} = \frac{TP}{TP + FP} \quad (2)$$

$$\text{Recall} = \frac{TP}{TP + FN} \quad (3)$$

$$\text{F1-score} = \frac{2 \times \text{Precision} \times \text{Recall}}{\text{Precision} + \text{Recall}} \quad (4)$$

$$\text{Accuracy} = \frac{TP + TN}{TP + TN + FP + FN} \quad (5)$$

RESULTS AND DISCUSSIONS

Training curve

To further investigate the training results of ResNet-SFR, an analysis was conducted on the training curves of ResNet50 and ResNet-SFR, specifically including accuracy curves and loss curves. The training curves for both models are shown in Fig.7. From the training curves, it can be observed that after the number of epochs exceeds 10, the recognition accuracy of ResNet-SFR is consistently higher than that of ResNet50. Additionally, the loss value for ResNet-SFR is consistently lower than that of ResNet50. Ultimately, the training accuracy of ResNet-SFR stabilizes at 96.6%. These results indicate that, compared to ResNet50, ResNet-SFR is more effective in learning the sheep face recognition task.

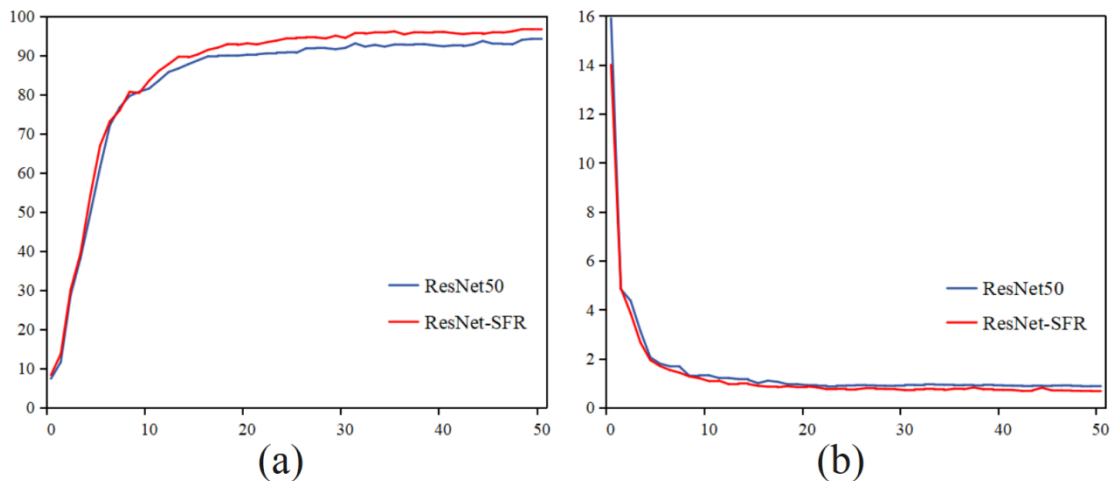


Fig. 7 - The training curves for both models
a. Accuracy curve; b. Loss curve

Comparison of Recognition Performance of Different Models

In this section, several classic deep learning models were selected for pre-training and their performance on the sheep face recognition task was evaluated. The chosen models include those previously used in sheep face recognition research, specifically: VGG16, ResNet18, MobileViT, AlexNet, RepVGG, YOLOv4, and ResNet50.

The pre-training results for each sheep face recognition model are shown in Table 2. From the results in Table 2, it can be seen that among the various recognition models, ResNet50 achieved the best performance on the sheep face image dataset, with an F1-score and accuracy of 93.9% and 94.3%, respectively. Based on these results, this study uses ResNet50 as the benchmark model for high-precision sheep face recognition and will proceed with targeted improvements to further enhance recognition accuracy.

Table 2

The training results of the sheep face recognition model		
Model	F1-score (%)	Accuracy (%)
VGG16	87.5	88.0
ResNet18	88.2	87.9
MobileViT	89.8	89.9
AlexNet	91.0	90.5
RepVGG	92.3	92.5
YOLOv4	93.0	93.6
ResNet50	93.9	94.3

Ablation Experiment

In this section, ablation experiments were conducted on ResNet-SFR to investigate the specific performance of several improvement strategies. The results of the ablation experiments on ResNet-SFR are shown in Table 3. Based on the three improvement strategies, eight combinations of improved models were tested. Here, TL represents models pre-trained using transfer learning.

From the results in Table 3, it can be observed that compared to ResNet50, deepening the network layers alone improved the F1-score and accuracy of the modified model by 0.8% and 0.7%, respectively.

Introducing the CBAM module alone improved the F1-score and accuracy by 1.0% and 0.4%, respectively. Using TL pre-training alone improved the F1-score and accuracy by 0.6% and 0.5%, respectively. These results indicate that each of the three improvement strategies positively enhanced the recognition performance of ResNet50.

When using two improvement strategies simultaneously, compared to the results from ResNet50, deepening the network layers and introducing the CBAM module improved the F1-score and accuracy of the modified model by 1.8% and 1.6%, respectively. Deepening the network layers and using TL pre-training improved the F1-score and accuracy by 1.5% and 0.9%, respectively. Introducing the CBAM module and using TL pre-training improved the F1-score and accuracy by 1.7% and 1.1%, respectively. Finally, when all three improvement strategies were applied together, ResNet-SFR achieved an F1-score and accuracy of 96.3% and 96.6%, respectively. Compared to ResNet50, the F1-score increased by 2.4% and the accuracy increased by 2.3%. The experimental results indicate that the proposed improvement strategies effectively enhance the recognition performance of ResNet50.

Table 3

ResNet50	Deepening network	CBAM	TL	F1-score (%)	Accuracy (%)
√				93.9	94.3
√	√			94.7	95.0
√		√		94.9	94.7
√			√	94.5	94.8
√	√	√		95.7	95.9
√	√		√	95.4	95.2
√		√	√	95.6	95.4
√	√	√	√	96.3	96.6

Comparison of Attention Mechanisms

In this section, different attention modules were introduced into ResNet50, and the training results were compared. The integration position of each attention module was consistent. The test results are shown in Table 4. In Table 4, the improved models with embedded attention modules all achieved performance enhancements. Specifically, when the CBAM module was added to ResNet50+Deepening network+TL, the improved model achieved higher recognition accuracy. In summary, the CBAM module was chosen as the attention mechanism improvement strategy for ResNet-SFR.

Table 4

ResNet50+Deepening network+TL	F1-score (%)	Accuracy (%)
/	95.4	95.2
+SE	95.6	95.5
+ECA	95.8	95.9
+CA	96.1	96.3
+CBAM(Ours)	96.3	96.6

CONCLUSIONS

This study presents a high-precision sheep face recognition model named ResNet-SFR, which builds upon the ResNet50 architecture and incorporates several advanced techniques to enhance performance. By deepening the network layers, integrating the CBAM attention mechanism, and employing transfer learning, ResNet-SFR significantly improves the accuracy and robustness of sheep face recognition.

The experimental results demonstrate that ResNet-SFR outperforms traditional methods and other deep learning models, achieving a recognition accuracy of 96.6% on the sheep face image dataset.

Compared to ResNet50, the proposed model shows a 2.4% improvement in F1-score and a 2.3% improvement in accuracy. These enhancements validate the effectiveness of the introduced modifications in capturing and utilizing complex features of sheep faces.

In addition, the comparative experiments with various attention mechanisms highlighted the superiority of the CBAM module, which further contributed to the model's performance boost. The comprehensive evaluation and ablation studies confirm that the combination of deepened network layers, CBAM, and transfer learning is instrumental in achieving high precision in sheep face recognition tasks.

Overall, this research not only provides a robust and accurate solution for sheep face recognition but also contributes valuable insights into improving recognition models through advanced techniques. The proposed ResNet-SFR model holds significant promise for practical applications in modern sheep farming and animal management.

ACKNOWLEDGEMENTS

We acknowledge that this work was supported by the Fundamental Research Funds of Inner Mongolia Agricultural University (BR221314 and BR221032), the Science and Technology Planning Project of Inner Mongolia Autonomous Region (2021GG0111), and the Research and Innovation Project for Doctoral Candidates in Inner Mongolia Autonomous Region (B20231075Z).

REFERENCES

- [1] Billah M., Wang X., Jiang Y., (2022), Real-time goat face recognition using convolutional neural network. *Computers and Electronics in Agriculture*, Vol 194, pp. 106730, China.
- [2] Bo C., Liu S., Liu Y., Guo Z., Wang J., Xu J., (2024). Research on Isomorphic Task Transfer Algorithm Based on Knowledge Distillation in Multi-Agent Collaborative Systems, *Sensors*, Vol. 24, Issue 14, pp. 4741, China.
- [3] Deng X., Zhang S., Shao Y., Yan X., (2022). A real-time sheep counting detection system based on machine learning. *INMATEH-Agricultural Engineering*, Vol 67, Issue 2, pp. 85-94, Romania.
- [4] Deng X., Yan X., Hou Y., et al. (2021). Detection of behaviour and posture of sheep based on YOLOv3. *INMATEH-Agricultural Engineering*, Vol. 64, Issue 2, pp. 457-466, Romania.
- [5] Fang S., Chen C., Li Z., Zhou M., Wei R., (2024). YOLO-ADual: A Lightweight Traffic Sign Detection Model for a Mobile Driving System, *World Electric Vehicle Journal*, Vol. 15, Issue 7, pp. 323, China.
- [6] He K., Zhang X., Ren S., Sun J., (2016). Deep residual learning for image recognition. In *IEEE Conference on Computer Vision and Pattern Recognition (CVPR)*, pp. 770-778, China.
- [7] Hitelman A., Edan Y., Godo A., Berenstein R., Lepar J., Halachmi I. (2022). Biometric identification of sheep via a machine-vision system. *Computers and Electronics in Agriculture*, Vol.194, pp. 106713, Israel.
- [8] Liu J., Liu H., He Y., Tong S., (2024). An Improved Detail-Enhancement CycleGAN Using AdaLIN for Facial Style Transfer. *Applied Sciences*, Vol. 14, Issue 14, pp. 6311, China.
- [9] Ni X., Wang F., Huang H., Wang L., Wen C., Chen D., (2024). A CNN- and Self-Attention-Based Maize Growth Stage Recognition Method and Platform from UAV Orthophoto Images, *Remote Sensing*, Vol.16, Issue 14, pp. 2672, China.
- [10] Salama A., Hassanien AE., Fahmy AA., (2019). Sheep identification using a hybrid deep learning and Bayesian optimization approach. *IEEE Access*, Vol.7, pp. 31681-31687, Egypt.
- [11] Sharma A., Jain A., Gupta P., (2020). Machine learning applications for precision agriculture: A comprehensive review. *IEEE Access*, Vol.9, pp. 4843-4873, India.
- [12] Xue J., Hou Z., Xuan C., Ma Y., Sun Q., Zhang X., Zhong L., (2024), A Sheep Identification Method Based on Three-Dimensional Sheep Face Reconstruction and Feature Point Matching. *Animals*, Vol.14, Issue 13, pp. 1923, China.
- [13] Zhang X., Hou Z., Xuan C., (2022). Design and experiment of recognition system for coated red clover seeds based on machine vision. *INMATEH-Agricultural Engineering*, Vol. 66 (1), pp. 62-72, Romania.
- [14] Zhang X., Xuan C., Ma Y., Su H., (2023). A high-precision facial recognition method for small-tailed Han sheep based on an optimised Vision Transformer, *Animal*, Vol.17, pp. 100886, China.
- [15] Zhang X., Xuan C., Xue J., Chen B., Ma Y., (2023), LSR-YOLO: A High-Precision, Lightweight Model for Sheep Face Recognition on the Mobile End. *Animals*, Vol 13, Issue 11, pp. 1824, China.
- [16] Zhang Y., Wang H., Liu J., (2023). A lightweight winter wheat planting area extraction model based on improved Deeplabv3+ and CBAM. *Remote Sensing*, Vol. 15, Issue 17, pp. 4156, China.

NUMERICAL SIMULATION AND EXPERIMENTAL RESEARCH ON COMPACTION DEVICE OF SEEDBED LEVELING MACHINE

苗床整平机镇压夯实装置数值模拟与试验研究

Bo-jun SHAN^{1,2)}, Gang CHE^{*1,2)}, Lin WAN^{*1,2)}, Nai-chen ZHAO¹⁾, Qiang ZHANG¹⁾

¹⁾College of Engineering, Heilongjiang Bayi Agricultural University, Daqing/P.R.China

²⁾Key Laboratory of Intelligent Agricultural Machinery Equipment in Heilongjiang Province, Daqing / P.R.China

Tel.: +86-459-13836961617; E-mail: chegangq180@126.com;

DOI: <https://doi.org/10.35633/inmateh-74-04>

Keywords: *impeller type, fertilizer discharger, EDEM, variable, experiment*

ABSTRACT

Currently, the compaction operations in rice seedling greenhouses are mostly performed manually or with simple machinery, resulting in significant discrepancies between the operational effects and requirements. Moreover, simple compaction machinery towed by small tractors cannot meet the dimensional requirements of rice seedling greenhouses. To address the issues of limited types of rice seedling compaction machinery and inability to meet the technical requirements for seedbed compaction quality, an eccentric compaction mechanism suitable for use in rice seedling greenhouses has been designed to reduce manual labor and improve soil firmness and evenness of seedbeds. Based on eccentric vibration theory, the motion equation of the leveling machine was established, and numerical simulations of the eccentric compaction mechanism were conducted using the RecurDyn-EDEM coupling method. Results indicate that the eccentric compaction mechanism effectively resolves the inability of traditional compaction devices to meet soil firmness requirements. Using a seedbed leveling machine independently developed by Heilongjiang Bayi Agricultural University, parameter optimization experiments were conducted using a second-order orthogonal rotational combination simulation method. The optimized parameter combination was: forward speed of 0.708 m/s, eccentric shaft rotation speed of 63.23 rad/s, and counterweight box mass of 50.99 kg, resulting in soil firmness of 3156.554 kPa and evenness of 0.02573 m. The experimental results were within 5% relative error of the simulation optimization results, indicating that the seedbed soil firmness and evenness meet agronomic requirements and have practical application value.

摘要

目前水稻育秧大棚中的镇压夯实作业多为人力或简易机械完成,其作业效果与要求相差较大,且简易镇压机械由小型拖拉机牵引作业,无法适应水稻育秧大棚中的尺寸要求。针对水稻育秧镇压机械种类少,压实质量无法满足育秧苗床的技术要求问题,设计一种适用于水稻育秧大棚内的偏心镇压夯实机构,用于减少人力提高苗床土壤坚实度以及平整度。基于偏心激振理论,建立整平机运动方程,通过运用 Recurdyn-EDEM 耦合的方法对偏心镇压夯实机构进行数值模拟。结果表明:采用偏心镇压夯实机构有效解决传统镇压装置无法满足土壤坚实度要求。采用黑龙江八一农垦大学自主研发苗床整平机,应用二次正交旋转组合仿真试验方法进行参数优化试验,优化参数组合:机车前进速度为 0.708 m/s,偏心轴转速为 63.23 rad/s,配重箱质量为 50.99 kg 时,土壤坚实度为 3156.554 kpa,平整度为 0.02573 m。试验结果与仿真优化结果相对误差在 5%之内,苗床土壤坚实度以及平整度达到农艺要求具有实际应用价值。

INTRODUCTION

In modern agricultural production, soil compaction is a crucial step in improving crop yield and quality. However, current agricultural compaction machinery is limited in variety and often too large to meet the dimensional requirements of greenhouse environments. Within greenhouses, compaction operations are mostly carried out manually by dragging heavy objects, resulting in significant discrepancies between operational effects and requirements, making large-scale application challenging.

¹Bo-jun Shan, master degree; Gang Che, Prof. Ph.D.; Lin Wan, Prof. Ph.D.; Nai-chen Zhao, Ph.D.; Qiang Zhang master degree;

Wang Jia L. et al. designed a variable pressure seedling belt compactor that can detect the compaction force during field operations of seeders through pressure sensors and digital displays, and adjust the force via a hydraulic system. They also analyzed the impact of compaction force on actual seed depth and plant spacing, thereby optimizing the appropriate range of compaction force (Jia L., Jiang Y., Sun J., et al., 2021). Luo Hongqi et al. researched a combination compactor capable of simultaneously compacting ridge sides and seeding bands (Luo H., Meng Y., Li X., 2019). The compaction wheel's soil contact area is circular, resulting in an arched ridge shape post-compaction, which is beneficial for maintaining ridge form. Ren Luquan et al., addressing soil adhesion issues during compaction roller operations, designed a bionic compaction roller (Zhang Y., Huang H., Ren L., 2013). This design incorporates a flexible rubber sleeve around the traditional roller body, with protruding ribs on the inner surface of the flexible outer sleeve creating a gap between the rubber sleeve and the roller body. This allows for deformation and vibration of the flexible outer sleeve during operation, thereby reducing soil adhesion to the roller. Foreign research on compaction implements is more extensive, with over 200 types of compactors in the United States alone. For example, contour-following compactors can perform compaction operations adapting to ground surface changes and can determine working width and number of units based on available power (Tolon-Becerra A., Tourn M., Botta G.F., Lastra-Bravo X., 2011; Botta G.F., Tolon-Becerra A., Tourn M., Lastra-Bravo X., Rivero D., 2012). Other types include tubular compactors, toothed disc compactors, anti-spray compactors, spiral compactors, double-sided tooth-meshing compactors, straight-faced fan compactors, and chrysanthemum-type compactors, all with varying degrees of application. Despite extensive research on soil compaction machinery by domestic and international scholars, studies on compaction machinery specifically for rice seedling greenhouses remain insufficient. Existing machinery struggles to achieve ideal compaction effects while meeting the dimensional requirements of rice seedling greenhouses.

Therefore, there is a need to design an efficient compaction mechanism suitable for use within greenhouses to reduce manual labor and improve seedbed soil firmness, thereby promoting crop growth. Through the Recurdyn-EDEM coupling method and eccentric vibration theory, an eccentric block-shaft motion model is established and numerically simulated to provide a theoretical basis for the design and optimization of soil compaction machinery for rice seedling greenhouses.

MATERIALS AND METHODS

Agronomic requirement

According to the "Technical Specifications for Intelligent Soil Preparation Equipment Testing in Standardized Rice Seedling Greenhouse Seedbeds" formulated by the National Grassroots Agricultural Technology Extension System Reform and Construction Project of the Beidahuang Group, the agronomic requirement for standardized rice seedbeds is "firm on top, loose below". Measurements of the 0-0.45 m soil layer should yield soil firmness values as shown in Table 1.

Table 1

Reference Range for Soil Firmness After Leveling			
Soil depth [m]	0~0.15	0.15~0.30	0.30~0.45
Soil solidity [kPa]	2600~2800	3000~3300	1800~2000

Referring to the provisions in "GB/T 5 668-2017", the post-tillage surface evenness is used as the performance evaluation indicator for seedbed leveling machines. The post-tillage surface evenness is measured perpendicular to the direction of machine advancement. A horizontal baseline is established above the highest point of the ground surface. At appropriate positions, a width equivalent to the working width of the prototype machine is divided into 10 equal parts. The distance from each division point to the ground surface is measured, and the average and standard deviation of these measurements are calculated. One point is measured for each pass, and the average of the standard deviations under working conditions represents the evenness. A post-tillage surface evenness of 0.05 m or less is considered satisfactory.

Based on these agronomic requirements, when designing a rice seedling greenhouse seedbed leveling machine, special attention must be paid to the design of the compaction device. On one hand, this device needs to effectively compact the surface soil to meet the required firmness standards. On the other hand, it must avoid over-compacting the lower soil layers to ensure the necessary looseness for root system growth, thereby meeting the evenness requirements specified in "GB/T 5 668-2017" (Gang C., Wei L., Lin W., 2023).

The whole machine structure and principle

The seedbed compaction device consists of a frame, gearbox, eccentric shaft mechanism, and counterweight box. The frame is composed of a body and a baseplate, with connection holes for the landing gear at the front end of the frame, and the frame bottom welded to the baseplate. The gearbox is a T6 spiral bevel gear reducer. The eccentric shaft mechanism comprises a main shaft, eccentric block, bearings, and bearing housings. The eccentric block is a solid iron block with a notch, allowing adjustment of its tightness against the main shaft by varying the depth of the adjusting screw. The counterweight box consists of compression springs and a weighted iron box. The power connection device is achieved through a fixed coupling, with power output connected to the tractor's output shaft via a universal joint. The speed is then increased through the gearbox and transmitted via V-belts to drive the eccentric shaft's rotation as shown in Figure 1.

The working process of the seedbed compaction device utilizes the rotation of the main shaft with its eccentric block to induce vibration in the entire machine, thereby causing continuous vibration of the counterweight box. As the tractor moves forward during operation, it pulls the machine, which to some extent contributes to leveling the ground.

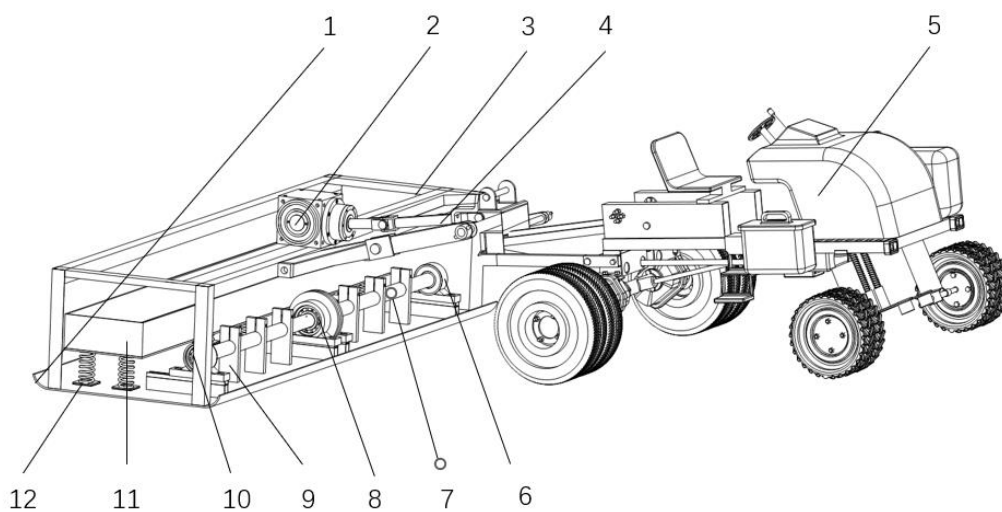


Fig. 1 –Overall Machine Structure

- 1. bottom plate; 2. transmission; 3. racks; 4. output shafts; 5. front; 6. bearing seats; 7. spindle; 8. belt wheels;
- 9. bearing; 10. bearings; 11. weight boxes; 12. main vocal spring

Motion equation

This paper employs an eccentric block structure. To facilitate manufacturing and reduce costs, a simpler block structure is used as shown in Figure 2. The excitation force generated by the eccentricity is:

$$F_{(t)} = m_1 e \omega^2 \tag{1}$$

where:

m_1 is the mass of the eccentric block, [kg]; e is the eccentricity, [m]; ω is the angular velocity of the eccentric block rotation, [rad/s].

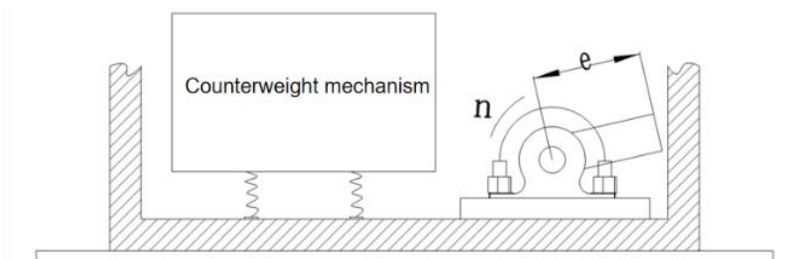


Fig. 2 –Simplified Motion Diagram of the Leveling Machine

The spring deformation is:

$$x = \frac{F(t) - F_0}{k} \quad (2)$$

where:

F_0 is the restoring force of the spring [N]; k is the spring stiffness coefficient, [N/mm].

According to Newton's second law, the springs system motion equation is:

$$m_2 \frac{d^2x}{dt^2} + kx = m_1 e \omega^2 \quad (3)$$

where:

m_2 is the weight of the counterweight mechanism [kg];

Based on trigonometric identities, the amplitude can be derived as:

$$A = \frac{m_1 e \omega^2}{k - m_2 \omega^2} \quad (4)$$

Based on agronomic requirements for a maximum soil firmness of 3300 kPa and design specifications allowing engine output speeds of 0 ~ 104.72 rad/s during operation, an excitation force of 4500 N is selected at 62.83 rad/s. This results in an eccentricity of 0.045 m, although typical eccentric mechanisms like vibrating screens generally use an eccentricity of 0.020 m (*Olumide O., Indresan G., Njema M.A., et al., 2021*).

To meet the agronomic requirement of a maximum seedbed soil firmness of 3300 kPa, the leveling machine must exert a significant downward force to ensure effectiveness. This necessitates a greater excitation force to achieve the required working amplitude. However, increasing the excitation force also increases the load, leading to reduced service life, increased energy consumption, and compromised machine reliability and cost-effectiveness. Therefore, drawing inspiration from large vibrating screen mechanisms, main vibration springs are installed beneath the tamping box. This increases the amplification factor of the vibration system, allowing the vibration system to resonate with the excitation system, thereby reducing power output burden and increasing amplitude. This effectively addresses the lifespan issues of key components, saves manual labor, and improves work efficiency.

Based on the agronomic requirement for maximum soil firmness of 3300 kPa and design specifications, the natural frequency of the compaction mechanism components is observed to ensure that internal structures do not resonate near the working frequency. The main vibration springs are then designed to bring the overall system's working frequency close to the natural frequency of 10 Hz for the vibration mode moving vertically up and down. When the overall system resonates, deformation primarily occurs in the elastic elements, allowing the internal structure of the compaction mechanism to be approximated as a rigid body (*Thiago B.L., Classon B.S.V., 2021*). This ensures internal structural stability and reliability while effectively reducing excitation force, extending the service life of shafts and bearings, and reducing the vibrating screen's energy consumption. Resonance occurs when the excitation frequency ω equals the system's natural frequency ω_0 , where:

$$\omega = \omega_0 = \sqrt{\frac{k}{m_2}} \quad (5)$$

The equation of motion at this point becomes:

$$m_1 \frac{d^2x}{dt^2} + c \frac{dx}{dt} + kx = m_1 e \omega^2 - m_2 \quad (6)$$

where: c is the damping coefficient, [N·s/m].

Calculations show that the springs can withstand a maximum load of 5000 N. With a stiffness coefficient of 1400 N/mm, the system's natural frequency is 10 Hz. The maximum load on the springs is a combination of the excitation force and the weight of the counterweight box, so the maximum weight of the counterweight box is 500 N, approximately 51.02 kg. In the subsequent simulation, the weight of the counterweight box is tentatively set at 50 kg.

The relationship between frequency and amplitude

According to previous calculations, after adding springs, the system's natural frequency is around 10 Hz, matching the excitation frequency. Resonance occurs when the excitation frequency is approximately 10 Hz, significantly increasing the amplitude to meet design requirements (Zhang C., 2020). Using RecurDyn software to solely consider the leveling machine's motion state, the spring stiffness coefficient is set to 1400 N/mm. Displacement conditions are captured within 1-1.5 seconds of movement on the Ground at shaft rotation speeds of 52.36 rad/s (8 Hz), 62.83 rad/s (10 Hz), and 75.40 rad/s (12 Hz) to observe the overall machine vibration and further verify if it meets design requirements in Figure 3.

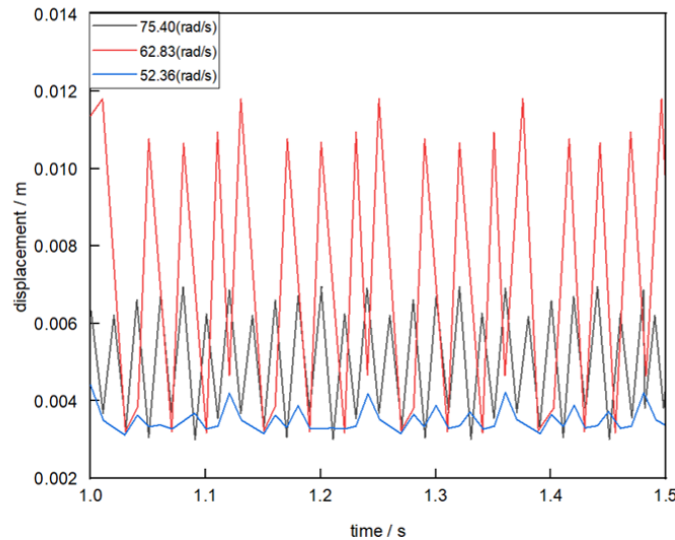


Fig. 3 –Relationship between excitation frequency and amplitude

The Z-axis displacement of the leveling machine at 52.36 rad/s (8 Hz), 62.83 rad/s (10 Hz), and 75.40 rad/s (12 Hz) is exported from RecurDyn. As the eccentric shaft speed (excitation frequency) increases, the overall machine amplitude shows a trend of first increasing and then decreasing (Lamandé et al, 2011). The maximum amplitude shown in the figure is 0.01082 m, with a vibration frequency of 9.86 Hz, which is close to both the excitation frequency and the previously calculated natural frequency, aligning with the expected design plan.

Model establishment

A simplified three-dimensional structural model of the seedbed leveling machine was created using SolidWorks 2020 and saved as an .x_b file. This file was then imported into the RecurDyn multibody dynamics simulation software. The soil compaction process of the leveling machine was simulated using the EDEM-RecurDyn coupling method (Ucgul M., Fielke J.M., Saunders C., 2014). The main parameters of the constructed seedbed soil compaction simulation model are shown in Table 3.

Table 3

Main Parameters of the Soil Particle Model	
Parameter name	Value
Soil particles density [kg/m ³]	2740
Soil particle shear modulus [Pa]	1.55e+08
Soil particle Poisson's ratio	0.29
Coefficient of restitution between soil particles	0.4
Static friction coefficient between soil particles	0.4
Dynamic friction coefficient between soil particles	0.11
Surface energy between soil particles [J/m ²]	0.159
Static friction coefficient between soil and leveling machine	0.5
Soil-Separate Rubbing coefficient between the leveling machines	0.48
Dynamic friction coefficient between soil and leveling machine	0.21

Comparison verification

To validate the significant effect of using an eccentric mechanism for soil compaction in the seedbed leveling machine, this study employed a comparative analysis method. The performance of traditional compaction devices (weight dragging), compaction mechanisms without springs, and compaction mechanisms with added springs were systematically evaluated.

First, a simplified model of the compaction mechanism was constructed in the multibody dynamics simulation software RecurDyn. For the traditional compaction device, the entire structure was set as a rigid body with an applied forward motion speed of 0.6 m/s to simulate actual operating conditions. Second, for the compaction mechanism without springs, the sand box and spring were set as a rigid body, with the eccentric block's shaft rotation speed set to 62.83 rad/s and a forward motion speed of 0.6 m/s, to study the effect of the eccentric mechanism on soil compaction performance. Finally, for the compaction mechanism with added springs, a spring system was introduced based on the above settings, with a stiffness coefficient set to 1400 N/mm. By setting the eccentric block's shaft rotation speed to 62.83 rad/s and maintaining a forward motion speed of 0.6 m/s, the contribution of the added spring system to soil compaction effectiveness could be comprehensively evaluated.

To obtain reliable experimental data, each mechanism underwent three repeated trials. By comparing and analyzing the changes in soil firmness under different operating conditions, the advantages of the seedbed leveling machine's eccentric mechanism in soil compaction could be objectively evaluated (Lamande M., Greve M.H., Schjonning P., 2018).

The results of this study indicate that compared to traditional compaction devices and compaction mechanisms without springs, the compaction mechanism with added springs can significantly improve soil compaction effectiveness. This provides important evidence for optimizing the design of seedbed leveling machines.

Based on actual soil conditions, through the selection and parameter settings of the soil trough model, and utilizing features such as the contact model in EDEM software, the actual operation of the implement can be replicated. The reliability of the simulated test results can be restored. Since EDEM software cannot calculate complex motions such as eccentric vibrations and spring elastic support, RecurDyn software is used to add motion and import it into EDEM to simulate and explore the distribution patterns of soil firmness (Elskamp F., Kruggel-Emden H., Hennig M., et al. 2015). Figure 4 shows the distribution of contact forces between soil particles at different depths during the compaction process of the leveling machine on seedbed soil. In the figure, a higher concentration of red particles indicates greater soil firmness in that area (Sun J., Chu H., Liu Q., 2022).

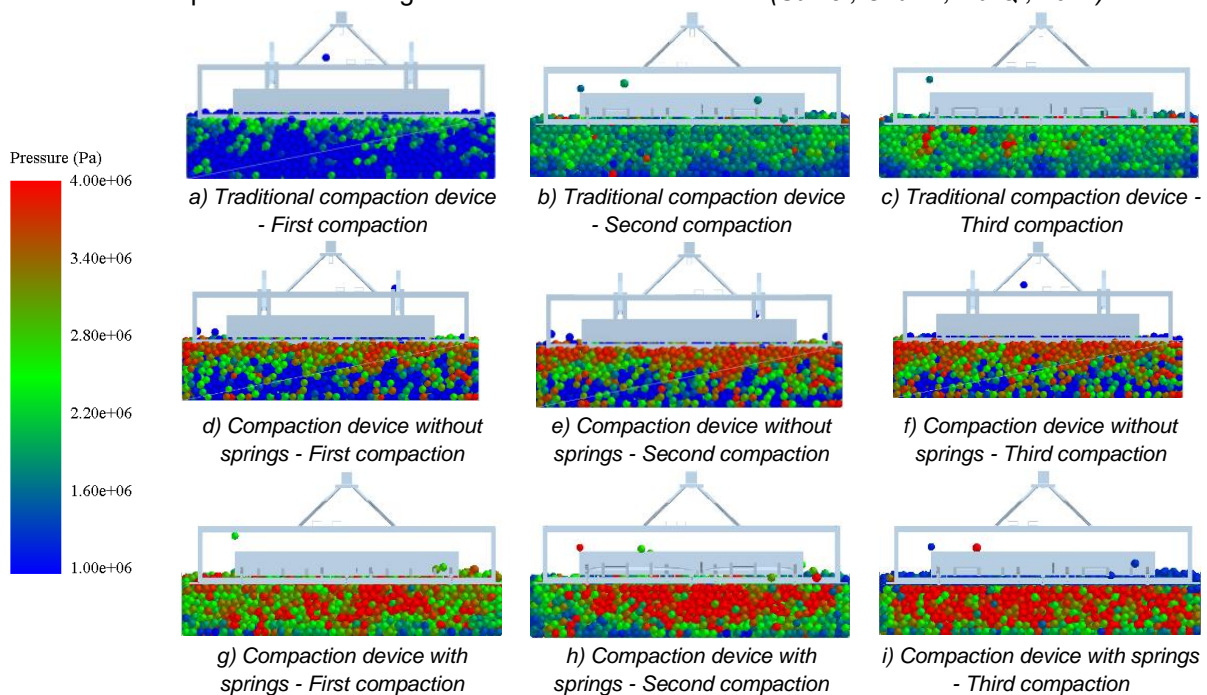


Fig. 4 – Comparative validation of different compaction devices

In summary, through the comparative analysis of the performance of different institutions in the soil consolidation of the soil, this study provides strong evidence, indicating that the application of eccentric institutions in the setting of the seedbed can significantly improve the effect of soil consolidation and meet the high standard requirements of modern agricultural production.

As shown in Figure 4c, the traditional compaction device cannot meet agronomic requirements. Data exported from the EDEM post-processing module after three compactions shows that the maximum firmness value in the 0-15 cm soil layer is 1820.2 kPa. In actual production, the mass of the compaction device is similar to that of the leveling machine, making the simulation results quite convincing.

Figure 4f indicates that the leveling machine without springs meets agronomic requirements in the 0 ~ 0.15 m soil layer after the third compaction. Although no springs are added, the eccentric mechanism can provide small-amplitude vibrations. The average firmness of five points in the 0.15 ~ 0.30 m soil layer is 2650.7 kPa, which does not meet the agronomic requirement range of 3000-3300 kPa. The smaller amplitude provides less downward force, and due to the internal friction characteristics of soil particles, energy cannot be transferred to deeper soil layers when the amplitude is small. Only by continuously increasing the shaft rotation speed can agronomic requirements be met.

As shown in Figure 4i, the firmness in the 0 ~ 0.15 m layer is 2770.4 kPa, 3124.1 kPa in the 0.15 ~ 0.30 m layer, and 1802.6 kPa in the 0.30 ~ 0.45 m layer. This meets the agronomic requirement of "firm on top, loose below" and aligns with practical needs, further validating the significant effect of the leveling machine compared to traditional compaction devices.

In conclusion, through systematic comparative analysis of different mechanisms' soil compaction performance, this study provides strong evidence that the application of eccentric mechanisms in seedbed leveling machines can significantly improve soil compaction effectiveness, meeting the high standards required in modern agricultural production.

Simulation test of seedling bed levelling machine

Single factor test

Single-factor experiments were conducted using machine forward speed, eccentric shaft rotation speed, and counterweight box mass as factors, with soil firmness and evenness as performance indicators. This was done to determine the influence patterns of each factor on the evaluation indicators of the leveling machine. When testing the motion parameters of the leveling machine's eccentric device, parameters were reset in Recurdyn and imported into EDEM for simulation, completing single-factor experiments of the leveling machine's motion parameters based on preliminary test results.

When the machine forward speed was in the range of 0.2 ~ 1.2 m/s, simulation revealed that the speed value should not be too high or too low. The front part of the compaction machine levels the surface soil of the seedbed, pushing the surface soil forward to "fill holes with pushed soil" as shown in Figure 5.

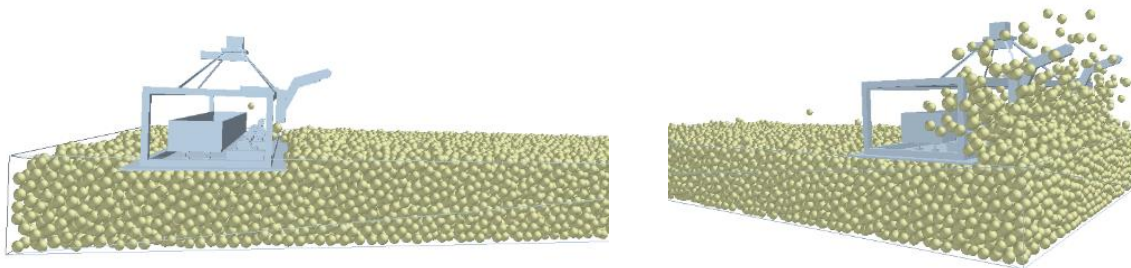


Fig. 5 – Effect of machine forward speed on seedbed

When the speed was in the range of 0.2 ~ 0.5, due to the low speed, too much soil accumulated at the front, causing the machine to stall in the field. When the speed was in the range of 0.9 ~ 1.2 m/s, the high speed caused severe scattering of soil particles during the pushing process.

When the machine forward speed was in the range of 0.5 ~ 0.9 m/s, soil firmness showed a gradual decreasing trend, while evenness did not change significantly. The test results are shown in Figure 6. This is because lower machine forward speeds result in higher compaction frequency per unit soil area, transferring more energy. As the machine forward speed increases, the compaction frequency per unit soil area decreases, leading to a gradual decrease in soil firmness in Figure 6. Therefore, a machine forward speed range of 0.5 ~ 0.9 m/s was selected for multi-factor experiments.

The eccentric shaft rotation speed is an important parameter of the leveling machine's motion, directly affecting the overall machine amplitude. The eccentric shaft drives the eccentric block, with faster rotation speeds resulting in higher excitation frequencies. Although the motion was simulated on a relatively ideal plane in previous sections, in reality, the interaction between the machine and soil also has some impact on the

motion. When the eccentric shaft rotation speed was in the range of 54.45 ~ 70.16 rad/s, soil firmness showed a trend of first increasing and then decreasing, while evenness showed a trend of first decreasing and then increasing, generally tending towards stability. When the eccentric shaft speed was below 54.45 rad/s, the amplitude clearly did not meet the design amplitude requirements and could not satisfy agronomic requirements after three compactions. Therefore, an eccentric shaft rotation speed range of 54.45 ~ 70.16 rad/s was selected in Figure 6.

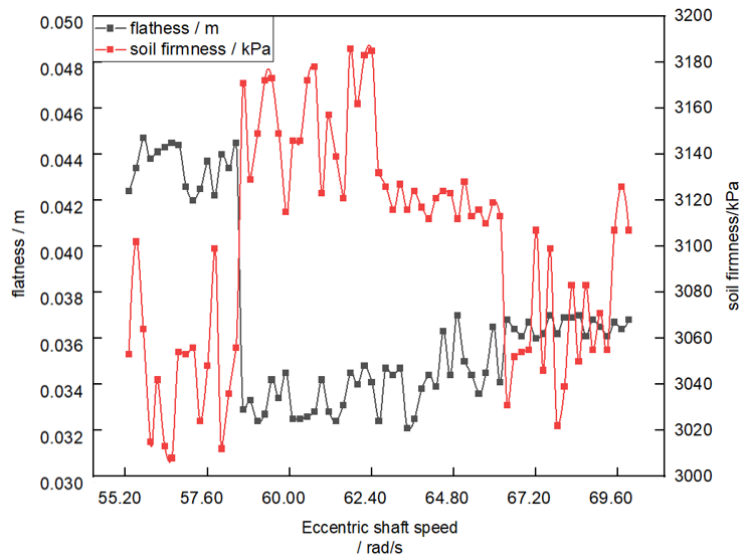


Fig. 6 – Effect of Eccentric Shaft Rotation Speed on Evaluation Indicators

The mass of the counterweight box provides static pressure for the compaction machinery, helping to maintain stable contact with the ground and transmitting pressure to the surface during compaction. The increased mass of the counterweight box adds inertia to the entire system, resulting in a more stable and controllable vibration response when the eccentric block generates excitation force. The mass of the counterweight box, together with the spring stiffness coefficient, determines the system's natural frequency. By changing the mass of the counterweight box, the system's natural frequency can be adjusted. During the compaction process, the counterweight box and spring system can store and release energy. When the eccentric block moves upward, the spring is compressed, increasing potential energy; when it moves downward, the spring releases energy, transferring it to the baseplate and ground, achieving the compaction function. When the counterweight box mass is less than 40 kg or greater than 50 kg, the main vibration spring compression does not meet design requirements and cannot achieve the designed amplitude. Therefore, the selected range for the counterweight box mass is 40 ~ 60 kg in Figure 7.

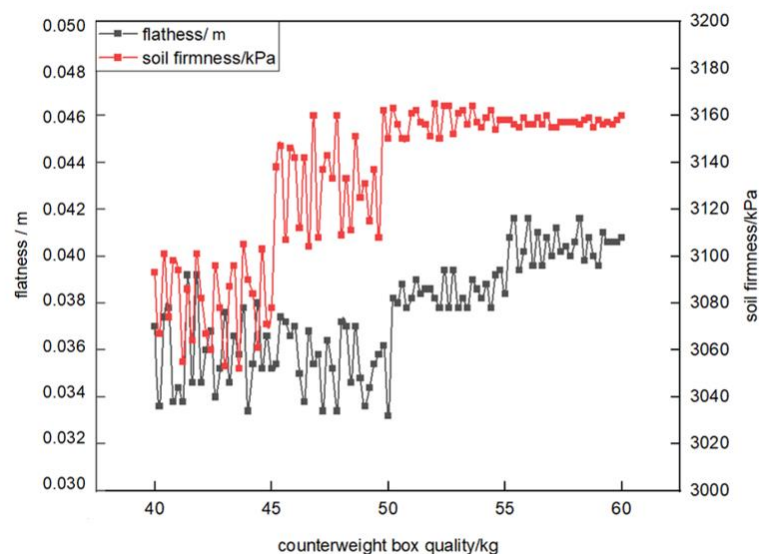


Fig. 7– Effect of Counterweight Box Mass on Evaluation Indicators

Parameter optimization experiment for compaction mechanism

Based on single-factor experiment results, the ranges for machine forward speed X_1 , eccentric shaft rotation speed X_2 , and counterweight box mass X_3 were determined. Referring to GB/T 5 668-2017, soil firmness at 15-30 cm depth Y_1 and evenness Y_2 were selected as performance evaluation indicators for the leveling machine. A three-factor, five-level quadratic orthogonal rotational central composite design was adopted. The experimental table was generated using Design-Expert software, with each group of experiments repeated 3 times. The coding of experimental factors is shown in Table 4.

Table 4

Level	Coding Value	Forward speed X_1 [m/s]	Eccentric shaft speed X_2 [rad/s]	Counterweight box mass X_3 [kg]
Upper star arm (+1.682)	+1.682	1	70.16	70
Upper level(+1)	+1	0.9	67.02	60
Zero level(0)	0	0.7	62.83	50
Lower level(-1)	-1	0.5	58.61	40
Lower star arm (1.682)	-1.682	0.4	55.50	30

Table 5

Serial number	Experimental factors			Test indicators	
	Forward speed X_1 [m/s]	Eccentric shaft speed X_2 [rad/s]	Counterweight box mass X_3 [kg]	Firmness [kPa]	Evenness [m]
1	-1	-1	1	3037.2	0.25
2	0	0	0	3165	0.37
3	0	0	0	3155.3	0.17
4	0	0	0	3131.7	0.02
5	0	0	0	3158.1	0.27
6	-1	1	1	3039.6	0.26
7	1	-1	-1	2963.5	0.02
8	0	0	0	3157	0.31
9	-1.68179	0	0	3025.6	0.22
10	1	1	-1	3022	0.05
11	0	-1.68179	0	2998.3	0.18
12	1.68179	0	0	3010.7	0.36
13	0	0	1.68179	3027.2	0.28
14	0	1.68179	0	3035.6	0.04
15	0	0	-1.68179	2988.2	0.01
16	0	0	0	3163.3	0.38
17	-1	-1	-1	3008.7	0.23
18	0	0	0	3163.6	0.02
19	-1	1	-1	3033.9	0.22
20	1	1	1	3036.1	0.04
21	0	0	0	3156.9	0.01
22	0	0	0	3160.2	0.32
23	1	-1	1	3027.3	0.35

After regression fitting using Design-Expert software, regression equations for the effects of various factors on soil firmness and evenness were obtained. Variance analysis and significance results analysis showed that all three regression variances were significant ($P < 0.01$), while the lack of fit P-value was not significant, indicating that the fitting of each regression equation was relatively optimal. Regression equations for the coded values of each factor were established.

$$\begin{aligned}
 Y_1 &= 3156.456 - 6.997X_1 + 11.54225X_2 + 13.011X_3 + 4.962X_1X_2 \\
 &\quad + 5.462X_1X_3 - 9.062X_2X_3 - 45.819X_1^2 - 46.243X_2^2 - 49.514X_3^2 \\
 Y_2 &= 2.778 - 0.193X_1 - 0.407X_2 - 0.223X_3 + 0.187X_1X_2 - 0.387X_1X_3 \\
 &\quad + 0.312X_2X_3
 \end{aligned}$$

(7)

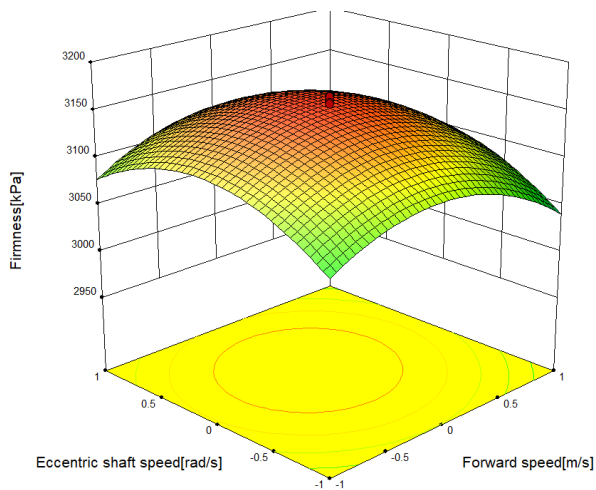
Analysis of test results

Figure 8a shows the effect of the interaction between eccentric shaft speed and forward speed on soil firmness when the counterweight box mass is 50 kg. The graph indicates that at a constant forward speed, as the eccentric shaft speed increases, soil firmness first increases and then decreases. When the eccentric shaft speed is constant, lower forward speeds result in higher firmness.

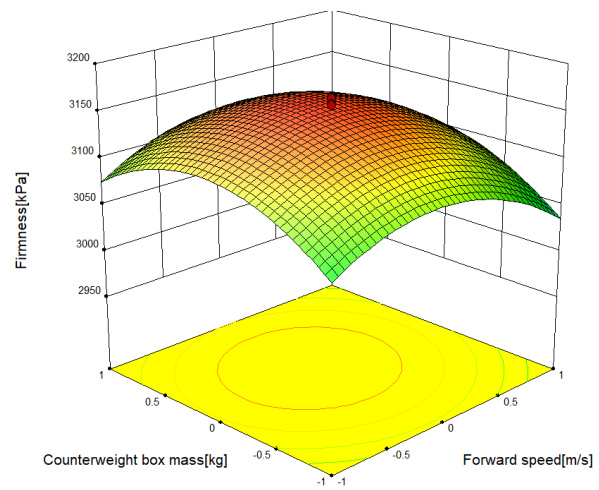
Figure 8b illustrates the effect of the interaction between counterweight box mass and forward speed on soil firmness when the eccentric shaft speed is 62.83 rad/s. The graph shows that at a constant forward speed, as the counterweight box mass increases, soil firmness first increases and then decreases. When the counterweight box mass is constant, lower forward speeds result in higher firmness.

Figure 8c depicts the effect of the interaction between counterweight box mass and eccentric shaft speed on soil firmness when the forward speed is 0.7 m/s. The graph reveals that as both counterweight box mass and eccentric shaft speed increase, soil firmness first increases and then decreases.

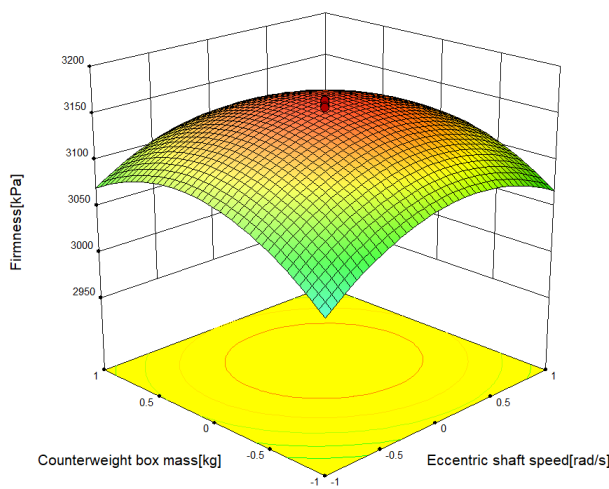
Figure 8d shows the effect of the interaction between eccentric shaft speed and forward speed on evenness when the counterweight box mass is 50 kg. The graph indicates that as both eccentric shaft speed and forward speed increase, evenness first rises and then falls. The eccentric shaft speed has a more significant impact on evenness.



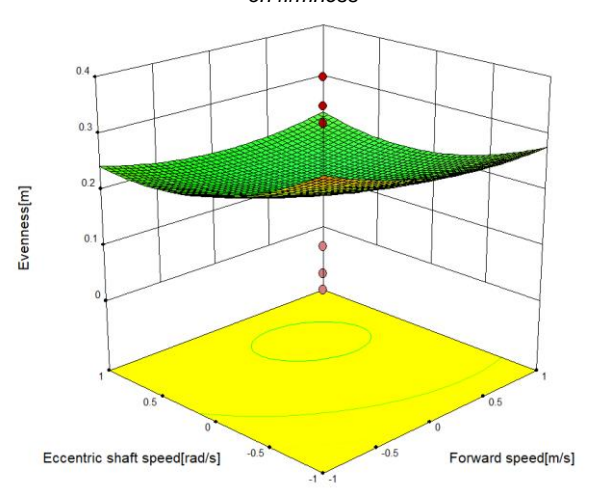
a) Effect of eccentric shaft speed and forward speed on firmness



b) Effect of eccentric shaft speed and counterweight box quality on firmness



c) Influence of forward speed and counterweight box mass on firmness



d) Influence of eccentric shaft rotation speed and advance speed on flatness

Fig. 8 – Response surface of each interaction factor to the evaluation indicators

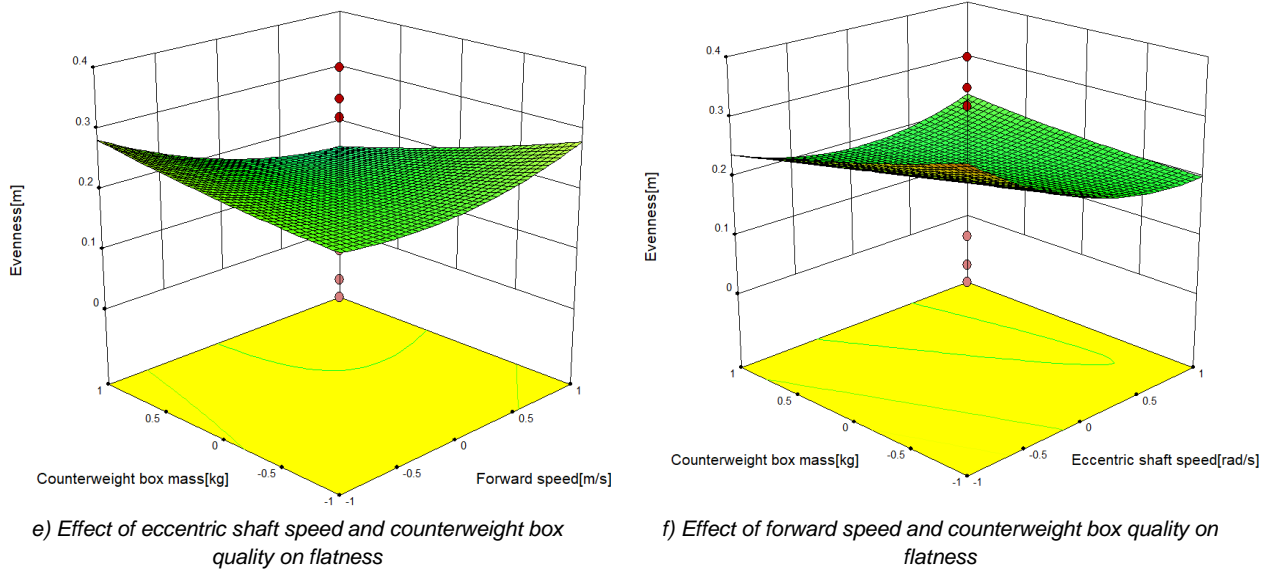


Fig. 8 – Response surface of each interaction factor to the evaluation indicators

Figure 8e illustrates the effect of the interaction between eccentric shaft speed and counterweight box mass on evenness when the forward speed is 0.7 m/s. The graph shows that as both eccentric shaft speed and counterweight box mass increase, evenness first increases and then decreases.

Figure 8f depicts the effect of the interaction between forward speed and counterweight box mass on evenness when the eccentric shaft speed is 62.83 rad/s. The graph reveals that as both forward speed and counterweight box mass increase, evenness first increases and then decreases. The eccentric shaft speed has a more significant impact on evenness.

Optimization and verification

Through simulation experiments with different parameter settings for the leveling machine's working device, the interactive effects of various experimental factors on soil firmness and evenness were obtained. Design-Expert software was used to optimize the data and establish a mathematical model expression as follows:

$$\begin{cases} \max Y_1 \\ \min Y_2 \\ s. t \begin{cases} 0.5 \text{ m/s} \leq X_1 \leq 0.9 \text{ m/s} \\ 58.61 \text{ rad/s} \leq X_2 \leq 67.02 \text{ rad/s} \\ 40 \text{ kg} \leq X_3 \leq 60 \text{ kg} \\ 3000 \text{ kPa} \leq Y_1(X_1, X_2, X_3) \leq 3300 \text{ kPa} \\ 0.01 \text{ m} \leq Y_2(X_1, X_2, X_3) \leq 0.04 \text{ m} \end{cases} \end{cases} \quad (8)$$

Using Design-Expert software for optimization, when the machine forward speed is 0.708 m/s, eccentric shaft rotation speed is 63.23 rad/s, and counterweight box mass is 50.99 kg, the soil firmness is 3156.554 kPa, and evenness is 0.025 m.

FIELD TEST

Test materials and equipment

The experiment was conducted in a greenhouse at Heilongjiang Bayi Agricultural University in Figure 9. Greenhouse No. 1 was selected as the experimental field, with dimensions of 60m × 12m and a moisture content of 15.1%. A Jinhe 2ZG-8KZ high-speed rice transplanter was used as the power source for the seedbed leveling machine. Operating parameters were controlled to be consistent with the simulation values for the rice seedling greenhouse experiment.

A DSA320 level and a TYY-2 soil hardness tester were used to measure soil elevation and firmness, respectively. Five points were sampled and averaged to meet the agronomic requirements of "GB/T 5 668-2017".



Fig. 9 – Field test

Test process and analysis

After the leveling experiment, multiple measurement points were evenly distributed in the test area for soil data collection. A level and soil hardness tester were used to measure seedbed soil elevation and firmness.

Following land leveling operations, the operational effect was evaluated by analyzing and comparing the relative errors of data obtained before and after the operation. Relevant indicators such as evenness and soil firmness were introduced to assess the operational effect.

The evaluation standard for leveling operations is the evenness after operation, which is assessed using the standard deviation of relative field surface elevations. Evenness is calculated according to equation (9):

$$S_i = \sqrt{\frac{\sum_{i=1}^n (h_i - \bar{h})^2}{n - 1}} \quad (9)$$

where: S_i is the evenness, [m]; h_i is the relative elevation of the i -th sampling point in the field; \bar{h} is the expected relative elevation for the field, [m]; generally refers to the average relative surface elevation of all measurement points within the field, i.e., the average design elevation, [m]; n is the number of all sampling points within the field.

A diagonal method was used to determine firmness sampling points in the selected area. Eleven points were evenly spaced along each diagonal, as shown in Figure 10. A TYY-2 soil hardness tester was used to measure seedbed soil firmness at 0.015 ~ 0.030 m depth. Firmness was measured and compared before and after the operation.



Fig. 10 – Diagonal point taking

After practical verification, the intelligent soil preparation machine for standardized rice seedling greenhouse seedbeds achieved the agronomic requirement of "firm on top, loose below". After the experiment, the evenness was 0.034 m, and the firmness at 0.015 ~ 0.030 m depth was 3102.5 kPa, meeting the agronomic requirements of "GB/T 5 668-2017".

RESULTS

Test results and analysis

The data recorded by the elevation meter was exported and processed using Origin 2021 software to obtain the seedbed evenness, as shown in Figure 11.

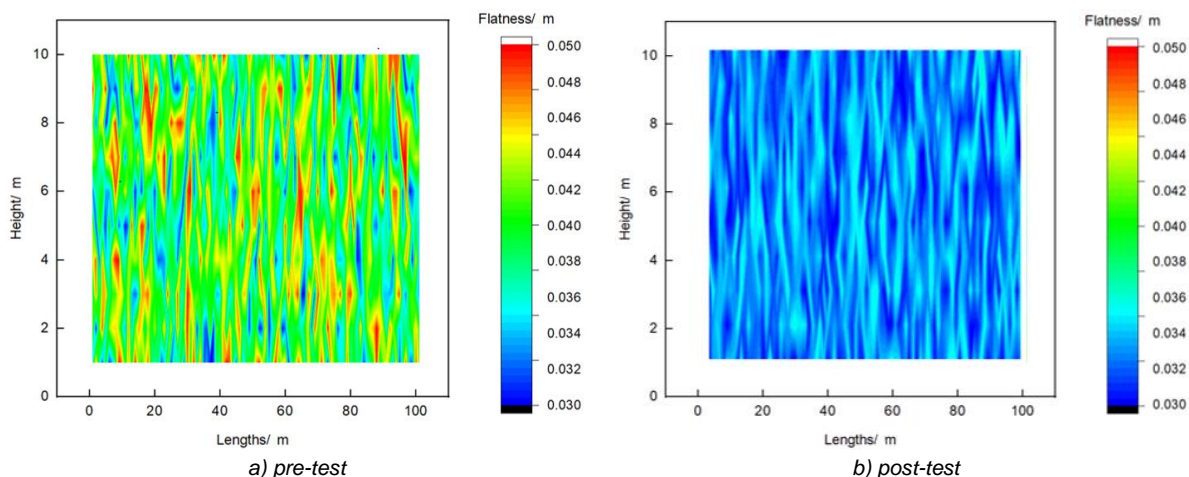


Fig. 11 – Ground evenness before and after experiment

Software calculations revealed that before the experiment, the red and yellow areas occupied 43.75% and 25.1% of the total area respectively, while the blue and green areas accounted for 31.15%. After three operations, the red and yellow highlighted areas decreased to 1.2% and 12.2%, while the blue and green areas increased to 86.6%. Therefore, the rice seedling greenhouse seedbed leveling machine had a significant effect on seedbed soil evenness.

During the rice soil preparation period in the experimental greenhouse at Heilongjiang Bayi Agricultural University, data on actual operational efficiency and seedbed firmness were collected for three seedbed leveling methods: traditional compaction device, compaction device without springs, and compaction device with springs. The results are shown in Figure 12.

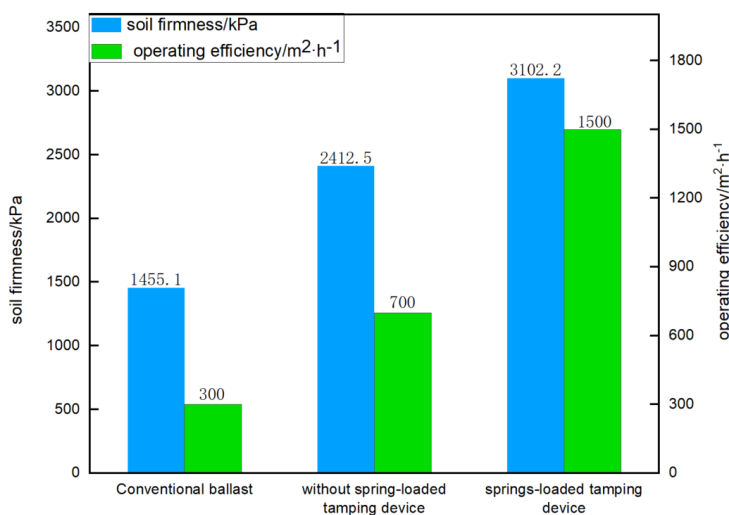


Fig. 12 – Comparison of leveling operation effects

Using the traditional compaction device for seedbed leveling operations could only level 300 m²/h of seedbed, with poor leveling effects that required repeated operations. The application of the compaction device with springs for seedbed leveling operations could level approximately 1500 m²/h of seedbed. The experimental results show that the leveling operation efficiency increased by about 400% compared to the traditional compaction device and by about 114.29% compared to the compaction device without springs.

The relative errors between the optimal simulation parameters and actual operation results are shown in Table 5 below:

Table 5

Optimization and test results		
Project	Soil firmness [kPa]	Flatness [m]
Optimization results	3156.554	0.0257
Actual results	3102.5	0.026
Relative error /%	1.75	2.3

The optimal parameter combination: machine forward speed of 0.708 m/s, eccentric shaft rotation speed of 63.23 rad/s, and counterweight box mass of 50.99 kg resulted in soil firmness of 3156.554 kPa and evenness of 0.02573 cm. The experimental results were within 5% relative error of the simulation optimization results, indicating that the seedbed soil firmness and evenness meet agronomic requirements and have practical application value.

CONCLUSIONS

To optimize the performance of the compaction device for rice seedling greenhouses and improve seedbed soil firmness and evenness, this paper analyzed and studied the main parameters affecting compaction effectiveness through theoretical analysis, simulation modeling and experimental validation. The factors influencing seedbed soil firmness were analyzed: a motion model of the compaction device was established, and the relationships between eccentric shaft rotation speed, eccentric block mass, spring stiffness coefficient, counterweight mechanism mass and amplitude were derived.

A soil compaction mechanism suitable for rice seedling greenhouse seedbeds was designed. RecurDyn software was used to simulate the compaction process. Results showed that when the vibration frequency was 9.86 Hz, the amplitude reached a maximum of 0.0108 m, which aligned with the expected design plan.

RecurDyn-EDEM coupling was used to simulate the compaction process, resulting in optimal combination parameters of 0.708 m/s for machine forward speed, 603.84 r/min for eccentric shaft rotation speed, and 50.99 kg for counterweight box mass. Field trials showed that the relative error between actual results and optimized results was less than 5%.

ACKNOWLEDGEMENT

This project is the special project of Central Government guiding local Science and Technology development (ZY20B05); National Grassroots Agricultural Technology Extension Project (NJ202105);

REFERENCES

- [1] Botta G.F., Tolon-Becerra A., Tourn M., Lastra-Bravo X., Rivero D. (2012). Motion resistance and soil compaction in relation to tractor design and different soil conditions. *Soil & Tillage Research*, Vol.120, pp.92-98. Argentina.
- [2] Elskamp F., Kruggel-Emden H., Hennig M., et al. (2015). Benchmarking of process models for continuous screening based on discrete element simulations. *Minerals Engineering*, Vol. 83, pp. 78-96. Germany.
- [3] Gang C., Wei L., Lin W. (2023). Design and test of automatic leveling system for rice seedling shed seedbed precision leveler (水稻秧棚苗床精平机自动调平系统设计与试验). *Journal of Agricultural Engineering*, Vol. 39, pp. 9-17, Heilongjiang /China.
- [4] Jia L., Jiang Y., Sun J., et al. (2021). Simulation and test of disc rotary roller of disc elastic tooth combined paddy field grader based on EDEM (基于 EDEM 的圆盘弹齿组合式水田平地机圆盘转辊仿真与试验). *Journal of Jiangxi Agricultural University*, Vol.06, pp.202-210, China.
- [5] Lamandé M., Greve M.H., Schjonning P. (2018). Risk assessment of soil compaction in Europe-Rubber tracks or wheels on machinery. *Catena*, Vol.167, pp.353-362. Denmark.
- [6] Lamandé M., Schjonning P., (2011). Effect of soil water content. *Soil and Tillage Research*, 114, 78-85.
- [7] Luo H., Meng Y., Li X. (2019). Three-dimensional model study of ridge no-tillage seeder (垄作免耕播种机三维模型研究). *Rural Economy and Science and Technology*, Vol.30, pp.68-70, China.
- [8] Olumide O., Indresan G., Njema M.A., et al. (2021). Development of a mechanistic model of granular flow on vibrating screens. *Minerals Engineering*, Vol.163, pp. 67-71. Cape Town /South Africa.

- [9] Sun J., Chu H., Liu Q. (2022). Research on soil compaction stress of hill track tractor contour operation on slopes (山地履带拖拉机坡地等高线作业土壤压实应力研究). *Journal of Agricultural Machinery*, Vol.53, pp.30-42, Shanxi /China.
- [10] Thiago B.L., Classon B.S.V. (2021). Analysis of the dynamic forces acting on a vibrating screen and its support structure using a scale mode. *Measurement*, Vol.176, pp. 109-116. Brazil.
- [11] Tolon-Becerra A., Tourn M., Botta G.F., Lastra-Bravo X. (2011). Effects of different tillage regimes on soil compaction, maize (*Zea mays L.*) seedling emergence and yields in the eastern Argentinean Pampas region. *Soil & Tillage Research*, Vol.117, pp.184-190. Spain.
- [12] Ucgul M., Fielke J.M., Saunders C. (2014). Three-dimensional discrete element modelling of tillage: determination of a suitable contact model and parameters for a cohesionless soil. *Biosystems Engineering*, Vol.121, pp. 105-117. Australia.
- [13] Zhang C. (2020). High stiffness elastic support design of inertia vibrating screen (惯性振动筛的高刚度弹性支撑设计). *Journal of Hubei University of Technology*, Vol. 35, pp. 22-27, Hubei /China.
- [14] Zhang Y., Huang H., Ren L., (2013). Research on soil cutting test and drag reduction mechanism of bionic bucket teeth of excavator (挖掘机仿生斗齿土壤切削试验与减阻机理研究). *Journal of Agricultural Machinery*, Vol.44, pp.264-267. China.

RESEARCH AND DEVELOPMENT OF POWER DETECTION TECHNOLOGY AND DEVICE FOR KEY PARTS OF GREEN FODDER HARVESTER

基于青饲收割机关键部件的动力检测技术与设备的研究与开发

Kang NIU^{1,2)}, Xiaoyi CUI^{1,2)}, Ruikang QIN^{1,2)}, Yuqi WANG^{1,2)}, Weijing WANG^{1,2)}, Liming ZHOU^{1,2)}, Yangchun LIU^{1,2)}, Fengzhu WANG^{1,2)}, Dongyang WANG³⁾, Weipeng ZHANG^{1,2*)}

¹⁾Chinese Academy of Agriculture Mechanization Sciences Group Co., Ltd, Beijing 100083

²⁾State Key Laboratory of Agricultural Equipment Technology, Beijing 100083

³⁾Shenzhen Polytechnic University, Shenzhen, Guangdong, China 518055

Corresponding author: Weipeng Zhang

DOI: <https://doi.org/10.35633/inmateh-74-05>

Keywords: corn forage harvester, sensor design, power detection, CAN-bus, test analysis

ABSTRACT

The study focuses on the self-propelled forage harvester and analyzes various parameters such as the working speed and torque of the cutting table, chopped roll, throwing fan, walking parts, and the output flow rate and pressure of the hydraulic pump of the feeding section. Field experiments show that the fan, walking, chopping roller, and grain crushing roller drive powers account for 7-8%, 7-10%, 24-28%, and 13-21% of the engine power, respectively. The driving power of the inner and outer sides of the cutting table, fan, and walking power account for a relatively stable proportion of the engine output power. The study collects and analyzes operation parameters simultaneously to provide a reference for evaluating the performance and optimizing the design of corn forage harvesters.

摘要

本研究针对自走式饲草收割机进行深入探讨, 系统分析了切割台、碎料辊、抛送风扇、行走机构等关键部件的工作速度与扭矩特性, 以及送料部分液压泵的输出流量与压力等重要参数。通过实地试验, 研究发现风扇、行走机构、切碎滚筒和谷物破碎滚筒的驱动功率分别占发动机总功率的 7-8%、7-10%、24-28% 和 13-21%, 且切割台内外侧、风扇及行走功率分配相对稳定。本研究同步收集并分析了运行参数, 旨在为玉米饲草收割机的性能评估及设计优化提供科学依据。

INTRODUCTION

China is a large agricultural country with about 1.8 billion mu of arable land. There are many kinds of crops, such as rice, wheat, corn, green fodder, and so on. The popular use of combine harvester mechanization level is increasing, automation, intelligence and standardization have become the trend in agricultural machinery development (Mao *et al.*, 2020). Currently, there are functions for monitoring, displaying, and alerting the rotational speeds of key rotating components in small and medium-sized combine harvesters, such as fans, threshing cylinder engines, and other essential parts. (Liang *et al.*, 2023). However, due to the relatively independent relationship between the parameters, it is impossible to control the association, and it is difficult to realize the automatic adjustment of the working parameters during the harvesting process to achieve the best harvesting quality of the operating state (Wang *et al.*, 2023).

Scholars at home and abroad have carried out a lot of research work on combine harvester operation power monitoring (Mohsenimanesh *et al.*, 2017, Siebald *et al.*, 2017), mainly using torque and speed to realize power online monitoring. Foreign green fodder harvesting machinery has been completely developed in the direction of automation, informatization, and intelligence. The representative results include, for example, the Case IN 8010 model developed by Case which is equipped with a power optimization system, power acquisition system, and operation quality monitoring system. During field harvesting, the collected loss rate and power are used as the control target of the power optimization system, which greatly improves the operation quality of the combine harvester (Pallottino *et al.*, 2019, Feuerstein *et al.*, 2014), which greatly improved the overall performance and automation level of the whole machine. Cho *et al.*, (2014), proposed a method to detect uncut crop edges during harvester operation using multiple sensors, which provided more valuable information for combine harvester operation monitoring.

Cho et al., (2021), proposed a method to accurately capture field spatial variability of corn forage and corn grain yield in the New York method that generated the most accurate grid maps of corn forage and grain yields at both the farm and field levels. It is useful to ensure accurate and precise spatial mapping of yield products to optimize corn growth management.

With modern agriculture showing intensive and large-scale development, high-end large-scale agricultural machinery and equipment play an increasing role in China's agricultural production, therefore, there is an urgent need for the corresponding field experiment validation methods and key parts and components of the operational parameters acquisition technology. The corresponding collection test devices and systems are developed (Wang, 2019). The field operation quality and operation load monitoring technology of the combine harvester were studied, and the acquisition system of threshing roller load characteristics was designed. The current research mainly detects single or several machine parameters, and the detection data are relatively independent of each other, lacking systematic basic data on operation quality and component working conditions, and the method of correlation analysis (Chen, et al., 2023, Zhou, et al., 2023). Liu et al., (2022), proposed a new semantic segmentation network RSHC U-Net for self-propelled forage harvesters to achieve better trailer hopper segmentation in forage harvesting images. Experts and scholars carried out corresponding control research on key parts of the combine harvester such as the fan, threshing roller, etc., and controlled them independently, collected the corresponding operating state parameters, and formulated the standards of precise control system (Zhang et al., 2022, Li et al., 2021, Wu et al., 2024), breaking through the combine harvester intelligent working condition monitoring technology and intelligent control technology (Martelli et al., 2015, Liu et al., 2022). Buryanov et al., (2019), developed a method for stripping plants from their roots, and this method has been proven to enhance the productivity and efficiency of combine harvesters by a factor of 1.4 to 2.0. Zhou et al., (2020), developed an effective step-less speed regulation mechanism for real-time control of the threshing drum and cleaning fan in combine harvesters.

This study is oriented to the field operation of corn forage harvester, to solve the key problems of insufficient field experiment data and lack of test validation means of China's agricultural machinery and equipment, focusing on research on field operation of the whole machine and the core working device power matching detection method, to provide testing technology support for the rapid acquisition of operational data of the test validation and performance evaluation system.

MATERIALS AND METHODS

Power monitoring methods

The cutting table, threshing roller, cleaning sieve, chopping roller and blowing fan are the core working parts of the forage harvester, and their working power is one of the key information for determining the working status and fault condition of the machinery in the field if the working load of the parts is too large, it is easy to lead to clogging of the rotating shaft, which will cause a serious impact on the driving parts; if the load is too small, the parts are in the unsaturated working state, and the feeding amount is insufficient, which affects the harvesting efficiency. In the harvesting process of corn forage harvester, the power of these core working mechanisms should be ensured to be in a better state as far as possible, so it is necessary to carry out on-line dynamic monitoring of the working power of the key working parts, to provide basic data support for the reasonable power distribution of the key working parts as well as the analysis of the influence of the working power of each part on the quality of the machine operation.

The most direct and effective way to monitor the power of the working parts is the online monitoring of the torque and speed of the rotating working shaft, as shown in Figure 1.

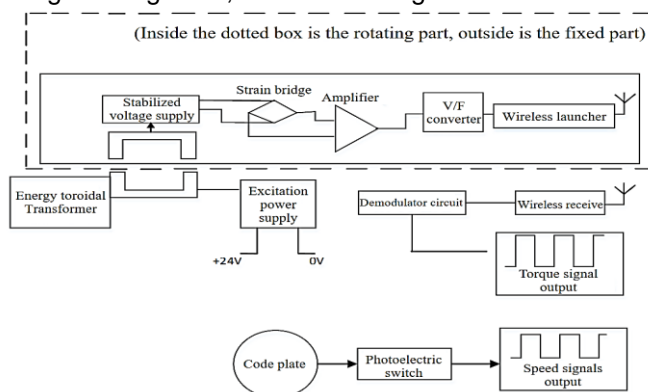


Fig. 1 - The principal diagram of the torque sensor

In this study, a specially designed and customized rotary strain-type torque sensor is used, applying the strain bridge electrical measurement technology, the special torsion-measuring strain gauges are pasted on the measured elastic shaft with strain adhesive to form a strain bridge, and a set of toroidal transformers located on the sensor provide power supply to the strain bridge non-contact, and amplify the weak elastic shaft subjected to torsion signals detected by the strain bridge, convert the voltage/frequency (V/F), so as to make the torque value be proportional to the measured frequency value, and finally a micro-power signal coupler is used to replace the toroidal transformer for non-contact transmission to output its frequency signal, which can effectively overcome the high-order harmonic generation brought about by the inductive coupling and the mutual interference between the energy toroidal transformer and the signal toroidal transformer, and its internal rotational speed measurement device based on the Hall element is also included.

The torque sensor uses a toroidal transformer non-contact transfer of energy, signal output using wireless telemetry, the torque signal wireless transmission is converted to wired transmission, thereby overcoming a series of problems such as torque angle phase difference, strain bridge collector ring issues, battery power supply concerns, and radio telemetry limitations.

Power monitoring principle

Conventional torque speed sensors require the use of a broken shaft to connect the sensor in series between the power source and the load, as shown in Figure 2. This kind of mounting form will cause great inconvenience to the sensor installation. For this reason, several new structures of torque speed sensors are designed in this study: strain gauges on the shaft method, extended shaft method, and replacement pulley method. Among them, the extended shaft method changes the transmission route of the original power, through the modification of the mechanical structure of the pulley, disconnecting the power transmission between the pulley and the pulley of the load shaft, the pulley first drives the inner rotary shaft of the torque-speed monitoring sensor, and then the outer rotary shaft of the torque-speed monitoring sensor transmits the power back to the load shaft, and the load condition of the working shaft can be obtained by the strain-bridge circuit affixed in the inner and outer shafts of the torque sensor. The load condition at the working shaft can be obtained through the strain bridge circuit attached between the inner and outer shafts of the torque sensor. The extended shaft method fixes the pulley disk of the torque sensor to the outer side of the rotating shaft through a number of bolts, and the head of the rotating shaft needs to be embedded in the rotating sleeve of the sensor, which in effect installs the sensor with a torque signal coupler between the power source and the load without disconnecting the drive shaft. The replacement pulley method is the application of the elastic modulus coefficient of better materials to make the power wheel, replace the original pulley, the use torsion strain gauges to detect the elasticity of the power wheel elastic deformation, so as to indirectly obtain the torque at the working shaft, and without the need to disconnect the shaft to complete the torque monitoring of the components.

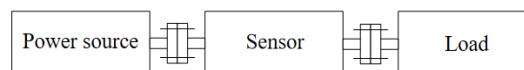


Fig. 2 - The connection diagram of the torque sensor

Corn forage harvester machine power detection technology

Torque Sensor Design

(1) Design of torque sensors for forage harvesters

The torque and speed monitoring sensor structure of each component of the forage harvester is designed by adopting various torque sensors such as the shaft-mounted type, the replacement pulley type, the hydraulic pressure and flow type, etc., as shown in Figure 3, including the walking parts, working hydraulic pump, cutting table large blade, cutting table small blade, chopping roller, clearing fan and grain crushing roller and other seven key working parts.



(a) Walking spline shaft

(b) Chopping roller

(c) Cutting table large and small size blade

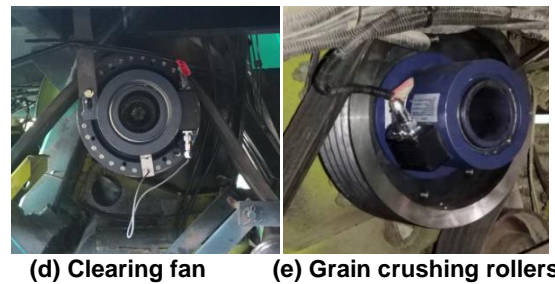


Fig. 3 - The torque and speed monitoring sensor of the forage harvester

Among them, some of the sensor prototypes of the two types of sensors for corn harvesting are shown in the physical drawings as in Figure 4. The designed torque monitoring sensor outputs a frequency pulse signal of 10 kHz at no load, 15 kHz at full load for forward rotation, and 5 kHz at full load for reverse rotation, with a full-scale measurement accuracy of 0.5%. In addition, a rotational speed sensor is integrated into the torque measuring device, and the working power of the rotating parts can be deduced according to:

$$P = T \times n / 9549 \text{ [kW]}$$

In the aforementioned equation, P denotes power, [kW], T signifies torque, [N m], and n represents the rotational speed of the motor, [r/min].

According to the driving power of the corn forage harvester, the working torque of the rotating parts at all levels is estimated, to determine the range of the torque sensor as 0 to 1500 Nm and 0 to 1000 Nm two kinds.



Fig. 4 - The prototype of the torque and speed monitoring sensor

Torque sensor calibration

The use of JZ200 torque sensor static calibration table on the selected torque sensor for static calibration, is shown in Figure 5.



Fig. 5 - The JZ200 static calibration device of the torque sensor

According to the formula $T = F' \cdot S$, where F' is the force perpendicular to the cross-section axis of the torque sensor, and S is the distance from force F' to the cross-section axis of the torque sensor. The torque sensor is calibrated to carry out the accuracy test of torque measurement, respectively, to the static calibration table loaded with different masses of standard weights, the system measurement value is recorded, then analyzing and processing is performed and the torque sensor's measurement error is obtained within 0.5%.

Among them, the torque sensor of the engine output intermediate shaft has a range of 1500 Nm and an operating voltage of 24 V. The static calibration was carried out in a room with a temperature of 22°C and a humidity of 60 % to obtain an accuracy of 0.5 % F.S. as shown in Table 1.

Table 1

The calibration results of the torque sensor in the engine output shaft

Load value [Nm]	Positive Signal		Reverse Signal	
	Frequency output (kHz)		Frequency output (kHz)	
	load	uninstallation	load	uninstallation
0	10.005	10.005	10.005	10.005
300	11.011	11.012	9.000	9.000
600	12.017	12.017	7.994	7.995
900	13.023	13.023	6.989	6.990
1200	14.029	14.029	5.983	5.985
1500	15.035	15.035	4.980	4.980

The range of the clearing fan shaft torque sensor is 1000 Nm, the operating voltage is 24 V, and the static calibration is carried out at a room temperature of 22°C and a humidity of 60% to obtain an accuracy of ±0.5 % F.S, as shown in Table 2.

Table 2

The calibration results of the torque sensor in clearing the fan shaft

Load value [Nm]	Positive Signal		Reverse Signal	
	Frequency output (kHz)		Frequency output (kHz)	
	load	uninstallation	load	uninstallation
0	10.005	10.005	10.005	10.005
200	11.010	11.009	9.002	9.003
400	12.015	12.015	8.000	8.000
600	13.020	13.020	6.997	6.998
800	14.025	14.025	5.995	5.995
1000	15.030	15.030	4.993	4.993

To test the dynamic performance of torque measurement, the procedure involves first controlling the speed of the test shaft to reach the preset desired value and maintaining stable operation for a certain period of time. After that, the test shaft is stopped and returned to its initial working state. Once the test shaft has completely stopped, the entire measuring system is shut down. The resulting dynamic step response curve of the torque sensor is illustrated in Figure 6.

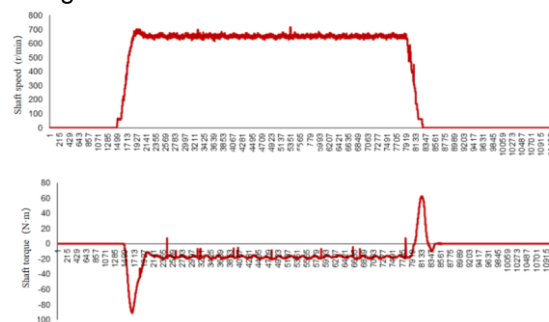


Fig. 6 - The dynamic loading curve of the torque sensor

As can be seen from the figure, the torque of the measured shaft is consistent with the trend of the rotational speed change. When the rotational speed of the measured shaft does not change, the torque measurement value basically remains stable, and when the rotational speed of the measured shaft suddenly increases or decreases, the torque measurement value enters a new steady state after a large transient pulse, which is in line with the torque change rule under the normal working condition of rotary shafts, indicating that the torque sensor designed in this research has good performance, and is able to monitor the torque information of the above key working shafts effectively. It shows that the torque sensor designed by this institute works well and can effectively monitor the torque information at the above key working shaft.

Vehicle-mounted data communication network

All the data from the vehicle-mounted sensors are sent to the host computer through the CAN-bus network for display and saving, as Figure 7 shows. The CAN network supports up to 110 nodes, simplifying circuit connections via a bus architecture for easy installation. Nodes communicate freely using differential signaling, often through shielded twisted-pair cables for robust anti-jamming. Additionally, it offers considerable communication distance.

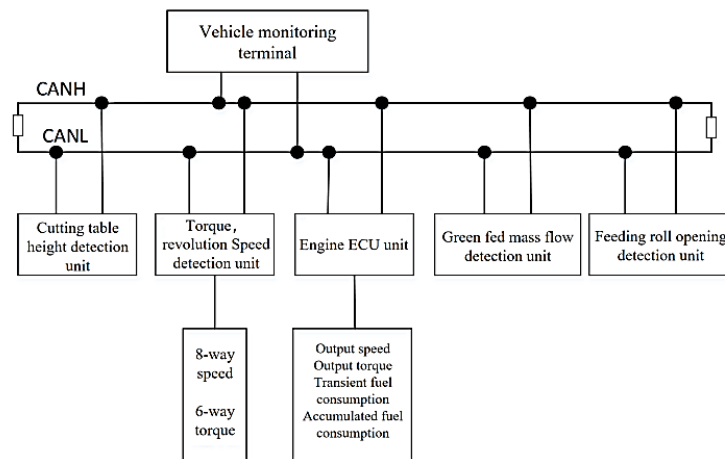


Fig. 7 - The network structure of CAN-bus communication in forage harvester

Each detection unit is a CAN node composed of a sensor, an acquisition controller and a CAN communication module. The acquisition controller collects data from on-site sensors in real time and saves the processing results in a memory unit, and it also has a network-wide unique identifier (ID) bound to a specific sensor. The vehicle monitoring terminal periodically sends out remote data query frames in accordance with the CAN2.0B protocol using the USB-CAN adapter. When the collection controller receives the remote frames, it compares its own ID with the ID of the remote frames, and if it matches, it returns a data frame containing the sensor data using its own ID as the identifier, and sends it to the bus network through the CAN communication module, and the monitoring computer, after receiving the data frames, updates the corresponding sensors according to their IDs. When the monitoring computer receives the data frame, it updates the data of the corresponding sensor according to the ID, thus realizing the real-time display and saving of the signals of each torque and speed sensor.

Power Acquisition Controller

The power monitoring system mainly involves the pulse signal acquisition of relevant torque sensors and speed sensors. Therefore, this study adopts PIC18F2580 as the processor for the design of the power acquisition controller and configures various peripheral hardware circuits with PIC18F2580 as the core to constitute a complete power monitoring controller hardware. The system structure is mainly composed of a microcontroller minimum system, pulse input signal acquisition and CAN data communication and other subsystems.

The CAN communication protocol in this study follows the SAE J1939 standard. It is a network protocol for high-speed communication between multiple ECUs that supports closed-loop control and has become a common standard for controller local area networks in trucks and buses. It uses CAN 2.0 as the core of the network, and each node in the network has a network-wide unique 29-bit J1939 identifier that identifies the type of parameter being transmitted on the CAN-bus network.

The pulse signals are counted by the 16-bit counters Timer0 and Timer1 within the microprocessor PIC18F2580, and the 16-bit timer Timer3 is used for timing, and the timing time selected in this study is 0.1 s. The timer block diagram is shown in Figure 8.

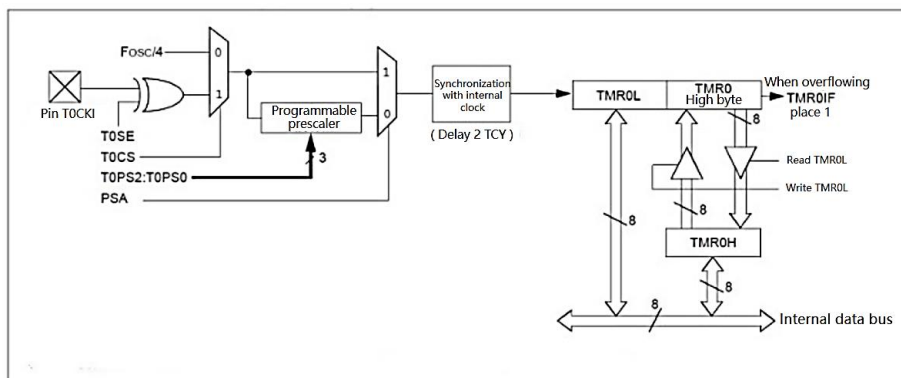


Fig. 8 - The timer block diagram

Its internal software acquisition process, is shown in Figure 9.

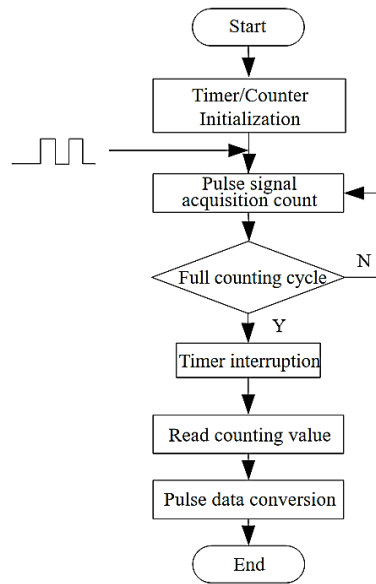


Fig. 9 - The program flow chart of pulse sampling

The PIC18F2580 microcontroller selected for this study incorporates the communication controller ECAN module, which follows the Bosch specified CAN2.0A or CAN2.0B protocol. The CAN-bus module consists of a protocol engine with a message buffer and a control module. The CAN protocol engine automatically handles all the functions of receiving and sending messages on the CAN-bus. Messages are sent by first loading the corresponding data registers. Status and errors can be detected by reading the corresponding registers. Any message detected on the CAN-bus is detected for errors and subsequently compared with a filter to determine whether it should be received and stored in one of the two receive registers. The internal software design consists of 3 main parts: initialization of the CAN node, data transmission and data reception.

Initialization is a crucial part of the CAN communication system's operation, serving as the prerequisite for the normal functioning of the CAN-bus. Initialization design includes the configuration of CAN module working mode, interrupt allow register setting, baud rate parameter setting, receive shield register setting, transmit priority setting and receive filter setting, etc., as shown in Figure 10.

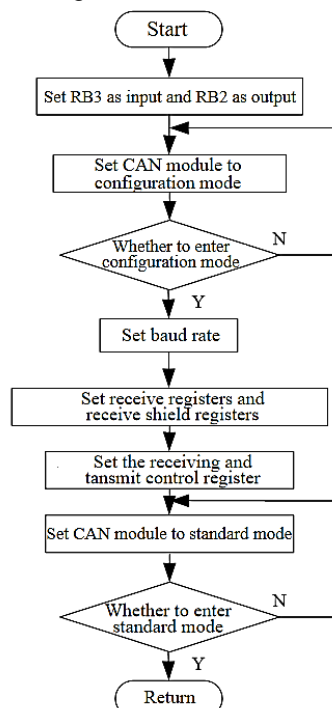


Fig. 10 - The flow chart of CAN initialization in the data acquisition controller

Selection of test factors

The travel speed of the self-propelled forage harvester is an important factor affecting the power consumption, and the change in travel speed will cause the change in feeding volume, with the increase in feeding volume, the rotational speed of each key part decreases slightly, and the torque rises, and the power consumption of the self-propelled forage harvester roughly shows an upward trend. At the same time, the height of the cutting table also affects the power consumption; at the same travel speed, the lower the height of the cutting table, the smaller the stubble height, and the feeding volume increases at the same time, in the process of the test. The local farmers in order to obtain a higher yield often require drivers to reduce the height of the cutting table to a minimum, generally 200 mm. In summary, the travel speed and height of the cutting table were selected as the two factors for the test arrangements. The machine's travel speed during normal operation is within the range of 3-10 km/h, and the height of the cutting table during normal operation is within the range of 150 mm to 250 mm, and the test arrangement is shown in Table 3.

Table 3

Test	Operational test schedule			
	1	2	3	4
Travel speed (km/h)	3	5	7	10
Cutting table height (mm)	200	200	200	200

Experimental Methodology Design

The field with good silage corn growth, length, and width meeting the test requirements was selected as the test area, and the corn at the starting point was harvested with the prototype before the test started to ensure the smooth start of the prototype. The operation of the self-propelled forage harvester and the acquisition of relevant data were carried out in accordance with the national standard GB80097-2008 "Test Methods for Harvesting Machinery Combine Harvester". Before entering the measurement area, the travel speed of the self-propelled forage harvester and the rotational speed of each key part reached a predetermined value and stabilized, and then entered the measurement area at a constant speed to start measurement. Each test was harvested in full width (cutting width 6 m), and the length of the harvesting interval and operating time were recorded during the test, and each group of tests was repeated twice to take the average value, and the condition of the machine was checked at the end of each group of tests, so as to be carried out in the next test. The condition of the prototype machine in the field test is shown in Figure 11.



Fig. 11 - Test prototype field operation

RESULTS

The system is capable of capturing real-time torque and rotational speed data for various critical components of the self-propelled forage harvester throughout its entire journey from entering the test area to exiting. Subsequently, it accurately calculates the power consumption of these critical components based on different test conditions. Figure 12 presents a clear illustration of the working power consumption curves for some experimental groups of the self-propelled forage harvester, with all these data derived from the aforementioned real-time data acquisition and calculation process. The power curves in the figure, from top to bottom, represent the chopping roller driving power, fan driving power, grain crushing roller driving power, walking driving power, outer cutting table driving power, and inner cutting table driving power.

To visualize the above contents more concretely and reflect the load fluctuation of the operating components, the average power and standard deviation under the four test conditions were calculated as shown in Table 4 and Table 5.

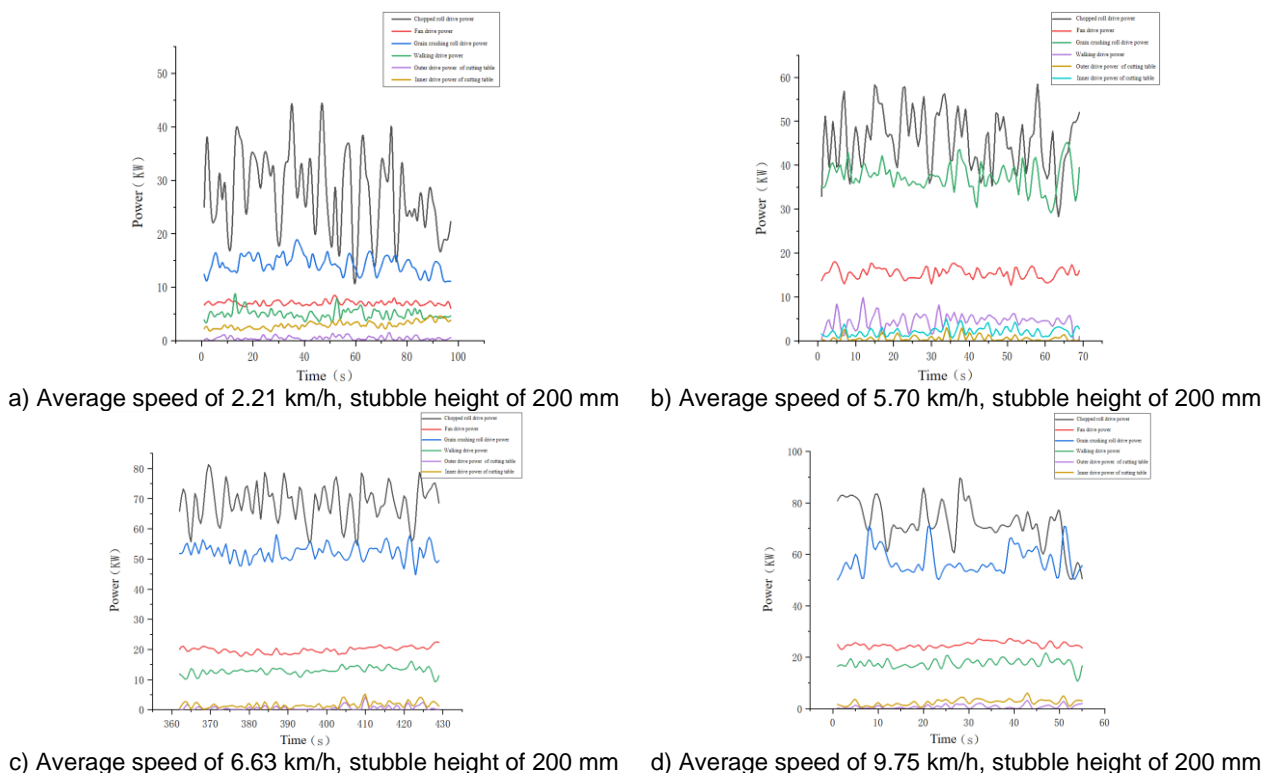


Fig. 12 - Power curve of each key part

Table 4

Power distribution table of key parts

Test number	Engine Output/kW	Chopping roller drive power/kW	Fan drive power/kW	Grain crushing drive power/kW	Walking drive power/kW	Inside cutter drive power/kW	Outside cutter drive power/kW
1	154.19	37.54	10.04	20.31	10.41	3.07	0.57
2	208.17	55.76	15.42	37.33	20.80	3.38	0.66
3	263.63	68.70	19.87	47.30	26.12	3.62	0.61
4	271.75	76.05	23.06	57.29	30.01	3.74	0.73

Table 5

Standard deviation of power value of each key part

Test number	Engine Output/kW	Chopping roller drive power/kW	Fan drive power/kW	Grain crushing drive power/kW	Walking drive power/kW	Inside cutter drive power/kW	Outside cutter drive power/kW
1	5.363	12.14	0.234	9.53	3.35	1.024	1.357
2	6.766	14.61	0.371	11.67	3.71	2.93	2.038
3	7.397	15.25	0.41	11.38	1.37	1.31	1.827
4	13.505	22.65	0.52	17.12	5.41	1.494	1.173

Analyzing and comparing the above power data, it is learned that, 1) the inner and outer drive power of the cutting platform is small, and the value changes are not very big with the increase of the average speed and the feeding amount; the drive power of the chopping roller, the drive power of the fan, the drive power of the grain crushing roller, and the drive power of the walking are large, and the value changes are more obvious with the increase of the average speed and the feeding amount. 2) the average speed of the test 4 reaches 9.75 km/h, and the standard deviation of the power values of the key parts of the test prototype is large. At this time, the feeding volume is close to the limit value, and the standard deviation of the power value of each key part of the test prototype is large, indicating that the machine under the average speed, the power of each key part is unstable, and the long-time operation in this situation affects the life of the machine.

Further, the proportion of each key part to the engine output power under different working conditions and the relationship between them is analyzed. Figure 13 shows the power proportion of each key part.

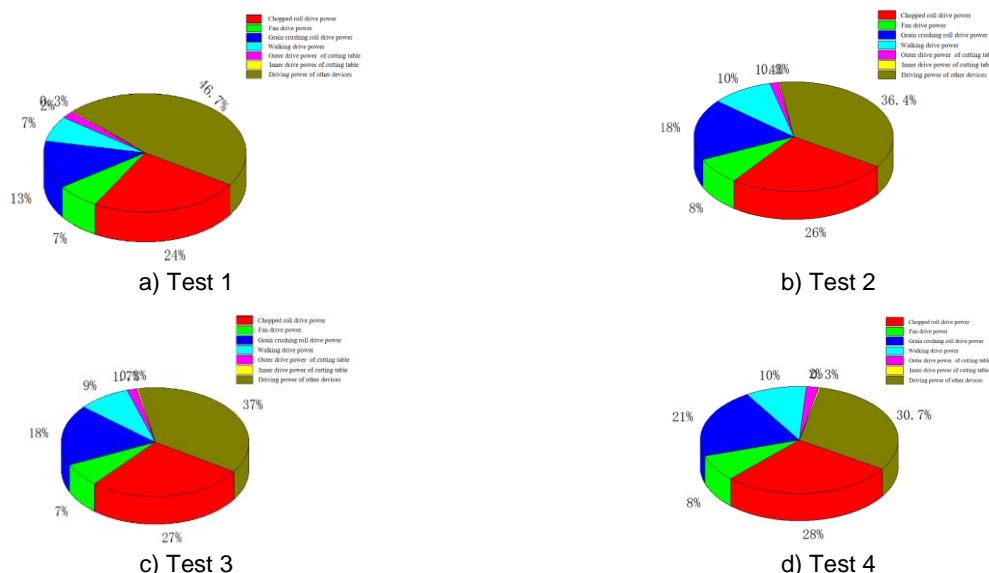


Fig. 13 - Power ratio chart of each key part

As can be seen in Figure 13: (1) the proportions of the inner and outer drive power of the cutting table, fan drive power and walking drive power to the engine output power are relatively stable, of which the proportion of fan drive power to the engine output power is 7% to 8%, and the proportion of walking drive power to the engine output power is 7% to 10%. Combined with Table 3-5 and Table 3-6, the standard deviation of the torque value of the fan drive shaft and walking drive shaft is small, and the load impact is relatively smooth. The inner and outer drive power of the cutting table accounts for 0.3% to 2% of the engine output power, which is small, but in the actual operation process, when the feeding volume is too large, it is easy to cause the cutting table blockage, in which case the load impact is larger. (2) The driving power of the chopping roller and the driving power of the grain crushing roller account for a large proportion of the engine output power, and the proportion of the range varies greatly. The proportion of chopping roller driving power is 24% to 28%, and the proportion of grain crushing roller driving power is 13% to 21%. When analyzing Table 4 and Table 5 together, Test 3 stands out as it ensures that the feed amount is close to the rated feed amount. Under this premise, the drive power for both the chopping roller and the grain crushing roller account for the smallest proportion of the engine's output power. Furthermore, the standard deviation of the torque value is smaller, indicating smoother fluctuations. Therefore, Test 3 represents the most ideal test conditions among the four groups of experiments.

CONCLUSIONS

This study realizes the torque and speed detection of the key components of the whole machine based on the strain bridge electrical measurement technology and CAN-bus communication technology, and the measurement parts cover most of the working parts of the test prototype. According to the structural characteristics of the working parts, wireless torque node, broken shaft method, strain gauges on the shaft method, extended shaft method, replacement pulley method and other methods are used to install torque sensors for the test prototype, and static calibration test and indoor bench loading test are carried out on the prototype of the torque sensors, which show that the torque sensors have a detection accuracy of 0.5%. This study can accumulate a large amount of field operation data of green fodder harvester under different working conditions, which can provide basic data support for the reasonable power allocation of each key working part of the whole machine and the analysis of the influence of the working power of each part on the operation quality of the machine. The results of the field test show that: the proportion of the inner and outer drive power of the cutting table, fan drive power and walking drive power of the green forage harvester to the engine output power are relatively stable, of which the proportion of the fan drive power to the engine output power is 7%-8%, the proportion of the walking drive power to the engine output power is 7%-10%, the proportion of the chopping roller drive power is 24%-28%, and the proportion of the driving power of grain crushing roller is 13%-28%, the proportion of the driving power of grain crushing roller is 13%-10%, and the proportion of the driving power of grain crushing roller is 13%-28%. When the speed is 6.63 km/h, under the premise of ensuring that the feeding amount is close to the rated feeding amount, the chopping roller driving power and the driving

power of grain crushing roller accounted for the smallest proportion of the engine output power, and the standard deviation of the torque value is small, and the fluctuation is relatively smooth, which is a more desirable test condition in the four groups of experiments.

ACKNOWLEDGEMENT

The work was sponsored by the Anhui Province science and technology major project (202203a06020027)

REFERENCES

- [1] Buryanov A., Chervyakov I. (2019). Using combines for cleaning grain crops by non-traditional technologies, *INMATEH - Agricultural Engineering*, Vol. 59(3), pp. 27-32, DOI: <http://doi.org/10.35633/INMATEH-59-03>.
- [2] Chen, M., Xu, G., Wei, M., Li, X., Wei, Y., Diao, P., Cui, P., Teng, S. (2023) Optimization design and experiment on feeding and chopping device of forage maize harvester. *International Journal of Agricultural and Biological Engineering*, Vol. 16(3), pp. 64-77, DOI: <https://doi.org/10.25165/j.ijabe.20231603.7922>.
- [3] Cho, W., Lida, M., Suguri, M., Masuda, R., Kurita, H. (2014) Using multiple sensors to detect uncut crop edges for autonomous guidance systems of head-feeding combine harvesters. *Engineering in Agriculture, Environment and Food*, Vol. 7(3), pp.115-121, DOI: <https://doi.org/10.1016/j.eaef.2014.02.004>.
- [4] Cho, J.B., Guinness, J., Kharel, T.P., et al. (2021) Spatial estimation methods for mapping corn forage and grain yield monitor data. *Precision Agriculture*, Vol. 22, pp. 1501-1520, DOI: <https://doi.org/10.1007/s11119-021-09793-z>.
- [5] Feuerstein, U., Swieter, A. (2014). Evaluation effectiveness of forage harvesters in forage preparation. *IOP Conf. Ser.: Earth Environ. Sci.* 699, 012050, DOI: https://doi.org/10.1007/978-94-017-9044-4_18.
- [6] Li, T., Li, N., Liu, C., Zhu, Z., Zhou, J., Zhang, H. (2021) Development of automatic depth control system employed in potato harvester (薯类收获机挖掘深度自动控制系统设计与试验). *Transactions of the Chinese Society of Agricultural Engineering*, Vol. 52(12), pp. 16-23, DOI: <https://doi.org/10.6041/j.issn.1000-1298.2021.12.002>.
- [7] Liang, Z., & Wada, M. E. (2023). Development of cleaning systems for combine harvesters: A review. *Biosystems Engineering*, Vol. 236, pp. 79-102, DOI: <https://doi.org/10.1016/j.biosystemseng.2023.10.018>.
- [8] Liu, L., Du, Y., Li, X., Liu, L., Mao, E., Guo, D., Zhang, Y. (2022) Trailer hopper automatic detection method for forage harvesting based improved U-Net. *Computers and Electronics in Agriculture*, Vol. 198, pp. 107046, DOI: <https://doi.org/10.1016/j.compag.2022.107046>.
- [9] Liu, Y., Sun, D., Ni, X., Wang, S., Wang, Xin. (2022) Optimization of a Low Loss Strategy for Combine Harvesters Based on Bayesian Network. *IFAC-PapersOnLine*, Vol. 55(32), pp. 259-264, DOI: <https://doi.org/10.1016/j.ifacol.2022.11.149>.
- [10] Mao, W., Han, S., Zhao, B. (2020). Study of remote monitoring system for forage harvester working condition based on Netty and Marshalling (基于 Netty 和 Marshalling 的青饲机工况远程监测系统研究). *Transactions of the Chinese Society of Agricultural Engineering*, Vol. 51, pp. 145-151, DOI: <https://doi.org/10.6041/j.issn.1000-1298.2020.08.016>.
- [11] Martelli, R., Bentini, Ma., Monti, A. (2015) Harvest storage and handling of round and square bales of gjan treed and switchgrass: an economic and technical evaluation. *Biomass Bioenergy*, Vol. 83, pp. 551-558, DOI: <https://doi.org/10.1016/j.biombioe.2015.11.008>.
- [12] Mohsenimanesh, A., Nieuwenhof, P., Neculescu, D. S., & Laguë, C. (2017). Monitoring a hydraulically-driven feed roll system with sensors on a prototype pull-type forage harvester. *Applied engineering in agriculture*, Vol. 33(1), pp. 23-30, DOI: <https://doi.org/10.13031/aea.11645>.
- [13] Pallottino, F., Antonucci, F., Costa, C., Bisaglia, C., Figorilli, S., & Menesatti, P. (2019). Optoelectronic proximal sensing vehicle-mounted technologies in precision agriculture: A review. *Computers and Electronics in Agriculture*, Vol. 162, pp. 859-873, DOI: <https://doi.org/10.1016/j.compag.2019.05.034>.
- [14] Siebald, H., Hensel, O., Beneke, F., Merbach, L., Walther, C., Kirchner, S. M., & Huster, J. (2017). Real-time acoustic monitoring of cutting blade sharpness in agricultural machinery. *IEEE/ASME Transactions on Mechatronics*, Vol. 22(6), pp. 2411-2419, DOI: <https://doi.org/10.1109/TMECH.2017.2735542>.

- [15] Wang, F., Zhao, B., Liu, Y., Wang, J., Jiang, H. (2023). Design and Experiment of Multi-parameter Detection System for Corn Forage Harvester (玉米青贮收获机多参数检测系统设计与试验). *Transactions of the Chinese Society of Agricultural Engineering*. Vol.54(1), pp.127-136, DOI: <https://doi.org/10.6041/j.issn.1000-1298.2023.01.013>.
- [16] Wang, J. (2019) *Development of metal foreign body detection system in harvesting machine*. Dissertation, Chinese Academy of Agricultural Mechanization Sciences, Beijing/China.
- [17] Zhou, X., Xu, X., Zhang, J., Wang, L., Wang, D., Zhang, P. (2023) Fault diagnosis of forage harvester based on a modified random forest. *Information Processing in Agriculture*, Vol. 10(3), pp. 301-311, DOI: <https://doi.org/10.1016/j.inpa.2022.02.005>.
- [18] Zhang, D., Yi, S., Zhang, J., Bao, Y. (2022) Establishment of millet threshing and separating model and optimization of harvester parameters. *Alexandria Engineering Journal*, Vol. 61(12), pp. 11251-11265, DOI: <https://doi.org/10.1016/j.aej.2022.04.048>.
- [19] Wu, Z., Chen, J., Ma, Z., Li, Y., Zhu, Y. (2024) Development of a lightweight online detection system for impurity content and broken rate in rice for combine harvesters. *Computers and Electronics in Agriculture*, Vol. 218, pp. 108689, DOI: <https://doi.org/10.1016/j.compag.2024.108689>.
- [20] Zhuohuai G., Zhou Z., Tao J., Ying L., Chongyou W., Senlin M. (2020). Development and test of speed control system for combine harvester threshing and cleaning device, *INMATEH – Agricultural Engineering*. Vol. 61 (2), pg. 305-314, DOI: <https://doi.org/10.35633/inmateh-61-33>

EXPERIMENTAL STUDY ON TWO-SIDED LOOSENING SHOVEL OF DIGGING-PULLING CASSAVA HARVESTER

挖拔式木薯收获机两侧式松土铲的试验研究

Wang YANG¹⁾, Xu WAN¹⁾, Junhui XI¹⁾, Debang ZHANG¹⁾, Yu HUANG¹⁾, Xian ZHENG¹⁾, Zhiheng LU^{1*)},
Ganran DENG²⁾, Zhende CUI²⁾

¹⁾College of Mechanical Engineering, Guangxi University, Nanning, 530004, China

²⁾Institute of Agricultural Machinery, Chinese Academy of Tropical Agricultural Sciences, Zhanjiang, 524091, China

Tel: +86 13552574667; E-mail: 8812316@163.com

DOI: <https://doi.org/10.35633/inmateh-74-06>

Keywords: *comprehensive optimization, digging-pulling cassava harvester, factor impact, loosening shovel, orthogonal test*

ABSTRACT

Cassava is one of the world's top three tuber crops, and its harvesting mechanization level is low. Digging-pulling cassava harvester is the main research direction of cassava harvesters. However, the soil-loosening components of the existing digging-pulling harvesters have poor loosening effect, high tuber damage rate, and large pulling force of cassava tubers after loosening. The two-sided loosening shovel that digs and loosens the soil on both sides of the tubers has low working resistance and is not easy to damage the tubers, but there are few reports on the impact of its operating performance. Therefore, this study focuses on three common types of two-sided soil-loosening shovels: the offset-wing shovel (OWS), L shovel (LS), and double-wing shovel (DWS). A two-factor, three-level orthogonal experiment is conducted, taking tillage depth (h) and shovel distance (b) as variables, then range analysis and factor impact analysis are carried out. Finally, through comprehensive comparison and optimization, a shovel type with best operational effects and its optimal working conditions are identified. The results show the LS demonstrated optimal performance when the breakage rate and pulling force were minimized. At the optimal combination of h of 0.25 m and b of 0.6 m, the LS has a breakage rate of 7.576% and a pulling force of 291.608 N. This study can provide basis for optimizing the design of loosening parts of digging-pulling cassava harvester.

摘要

木薯是世界三大薯类作物之一，其机械化收获水平低。挖拔式木薯收获机是木薯收获机的主要研究方向。但现有挖拔式木薯收获机的挖掘松土部件松土效果较差，伤薯率高，且松土后木薯块根拔起力大。而挖松块根两侧土壤的两侧式松土铲工作阻力小，不易伤薯，但目前其作业性能影响研究鲜有报道。因此，本文以偏翼铲、L铲、双翼铲三种常用的两侧式松土铲为对象，以耕深 h 和铲距 b 作为因素，分别进行两因素三水平正交试验，并对试验因素及结果进行极差分析和因素影响分析，最后通过综合比较和优化获得一种作业效果相对好的铲型及其较优的耕作条件。结果表明当断薯率和最大拔起力小时，L铲作业效果最优。该铲在耕深为 0.25m 和铲距为 0.6m 的较优组合时，断薯率为 7.576%，最大拔起力为 291.608N。本文可为挖拔式木薯收获机松土部件的优化设计提供依据。

INTRODUCTION

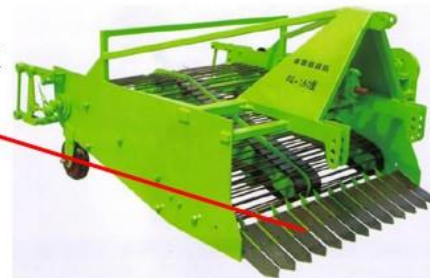
Harvesting is one of the most difficult and expensive operations worldwide (Awad, et al., 2022, Khater, et al., 2023). Cassava (*Manihot esculenta*) is widely cultivated in tropical and subtropical regions, and is one of the world's three major tuber crops along with potatoes and sweet potatoes. Its tuberous roots are rich in starch, known as the "king of starch" and "underground granary" (Wang, et al., 2019). Ranked sixth in terms of yield among food crops, cassava serves as a staple food for about six hundred million people worldwide (Jansson, et al., 2009, Vandegeer, et al., 2013). Moreover, it is a key component in industrial raw materials and a prominent source of biofuel energy (Li, et al., 2017, Parmar, et al., 2017, Sivamani, et al., 2018). However, primarily manual labor is still employed in cassava harvesting (Amponsah, et al., 2014, Chalachai, et al., 2013), which is labor-intensive and hampers the expansion of the cassava industry. Therefore, research of cassava harvesting machinery is important to the progress of the cassava industry.

Cassava harvesters are categorized into digging and loosening type, digging and shaking separation type, and digging-pulling type (Yang, et al., 2012). The digging and loosening type cassava harvester uses a digging shovel to separate cassava roots from the soil, then manually picks up the tubers after arching them out. This harvester has a simple structure, low manufacturing cost, and has been adaptable to various soil types. However, its working efficiency is low. The representative machines include the II type single-row cassava harvester developed by Cuba (Odigboh, 1991), the P-900 type double-row cassava tuber harvester (Fig. 1a) developed by Brazil (Chen, et al., 2022, Ospina, et al., 2002), the TEK mechanical harvester developed in Ghana (Amponsah, et al., 2018), and the 4UMS-390II cassava harvester designed by Xue et al. (Xue, et al., 2010). The digging and shaking separation type cassava harvester uses a digging shovel to lift the clods containing tubers and roots, which is then elevated and shaken along lifting chain to separate the soil from the cassava tubers. This cassava harvester is highly efficient but consumes a lot of power and is not adaptable to the various types of soil where cassava is planted. In sandy soils, the loss and damage rate of tuber is relatively low, while in clayey soil is higher. The representative machines include the API cassava tuber excavator from Malaysia (Akhir and Sukra, 2002), the vibrating cassava harvester developed by Gupta et al. in Thailand (Gupta, et al., 1999), the 4U-160 cassava harvester (Fig. 1b) produced by Henan Kunda Agricultural Machinery and Equipment Co. (Zhang, et al., 2012), and the 4UM-160 cassava harvester developed by Mo and Huang (Mo and Huang, 2012). The digging-pulling type cassava harvester first passes under the tubers to loosen the soil with its loosening shovels, then uses the clamping and uprooting device to pull out the tubers. Its representative machines include the cassava tuber digging and uprooting harvester developed by Cuba (Chalachai, et al., 2013), CHM-3407 digging and pulling cassava harvester developed by Estonian scientists (Thasontea and Chansiri, 2015), the Leipzig mechanical cassava harvester developed by the Leipzig University, Germany (Gupta, et al., 1999), the clamping strap pulling cassava harvester (Fig. 1c) developed by Hainan University (Liao, et al., 2012), and the clamping and pulling cassava (Fig. 1d) harvester developed by Guangxi University (Qi, et al., 2018). Compared with the previous two types of harvesters, the digging-pulling type cassava harvester can achieve fully mechanized harvesting of tuber roots. It has high operating efficiency, low power consumption, and strong adaptability to various cassava planting soils. This type of cassava harvester represents the primary focus of current study on cassava harvesting technology.



(a) Digging and loosening cassava harvester

Digging shovel



(b) Digging and shaking separation cassava harvester

Integral digging shovel



(c) Digging-clamping strap pulling cassava harvester

Two-sided loosening shovel



(d) Loosening-clamping pulling cassava harvester

Fig. 1 - Cassava Harvester

The loosening shovel is a crucial component of the digging-pulling cassava harvester. Its loosening performance significantly affects the harvest effect and traction resistance of the harvester. Currently, the loosening shovel exhibits poor loosening effectiveness, high traction resistance, and other issues. Therefore, it is essential to conduct a comprehensive study on the loosening components.

Agbetoye et al. (Agbetoye, et al., 1998) studied the effects on soil traction resistance and disturbance by varying the tillage depth using three types of bilateral loosening device: an L-tine, an A-blade, and a combination of a curved chisel tine. The results showed that the L-tine shovel had a better loosening effect, was simple to manufacture, and easy to adjust the working width. The effects of the L-tine shovel on the disturbance of the soil around the cassava tubers were later investigated through indoor soil trench tests and an orthogonal test in the field (Agbetoye and Ilevbare, 2012). Liao et al. developed an integral fence loosening shovel, a combined shovel and a bionic loosening shovel for digging-pulling cassava harvesters (Li, et al., 2022, Liao, et al., 2012, Liu, et al., 2014, Wang, et al., 2015). However, it has a high traction resistance and a high injury rate for cassava tuber. A two-sided offset-wing loosening shovel was designed by Liu (Liu, 2020). And a loosening shovel-stalk-tuber-root-soil system dynamics simulation model was established to conduct a quadratic regression generalized rotary combination design simulation test, so as to optimize operating conditions of the loosening shovel. The results indicated that the loosening effect was better at a tillage depth of 0.25 m and a shovel distance of 0.7 m. However, the maximum traction resistance of a single side shovel was high, reaching 4609 N. And the optimization results were not validated in the field yet. Moreover, in order to study the loosening mechanism of the shovel and the deformation process of tubers from a microscopic perspective, Yang et al. (Yang, et al., 2013a, Yang, et al., 2013b) established a biplane loosening shovel-stalk-tuber-root-soil system dynamics simulation model to numerically simulate and analyze the digging and loosening process of tubers.

The aforementioned studies indicate that the integral digging shovel, which excavates from the bottom of the tubers, experiences high traction resistance and a high cassava tuber injury rate. In contrast, the two-sided loosening shovel, which loosens the soil on both sides of the tubers, encounters low traction resistance and is less likely to cause tuber injuries. However, there is limited research on the impact of its operational performance. Therefore, this study focuses on three common types of double-sided soil-loosening shovels: the offset-wing shovel (OWS), the L shovel (LS), and the double-wing shovel (DWS). Using tillage depth and shovel distance as factors, a two-factor, three-level orthogonal test is conducted, range analysis and factor impact analysis are performed on the test factors and results. Finally, a relatively optimal shovel type and its improved operating conditions are identified through comprehensive comparison and optimization. This study provides a basis for optimizing the design of loosening components in digging-pulling cassava harvester.

MATERIALS AND METHODS

Two-sided loosening shovel

The double-wing shovel (DWS) used in the test was adapted from a two-sided deep loosening shovel with wings of equal size on both sides. The offset-wing shovel (OWS) had wings of different sizes on each side. These two shovels were designed with reference to the articles by Liu et al. (Liu, et al., 2017) and Liu (Liu, 2020) respectively. The L-shaped shovel was identified as the most effective loosening shovel in the Agbetoye's test (Agbetoye, et al., 1998). In this experiment, the L shovel (LS) was customized to match its dimensions, and a cutting edge was incorporated into the arm of the loosening shovel to enhance its breaking capability once it penetrates the soil. The three types of shovels are shown in Fig. 2.

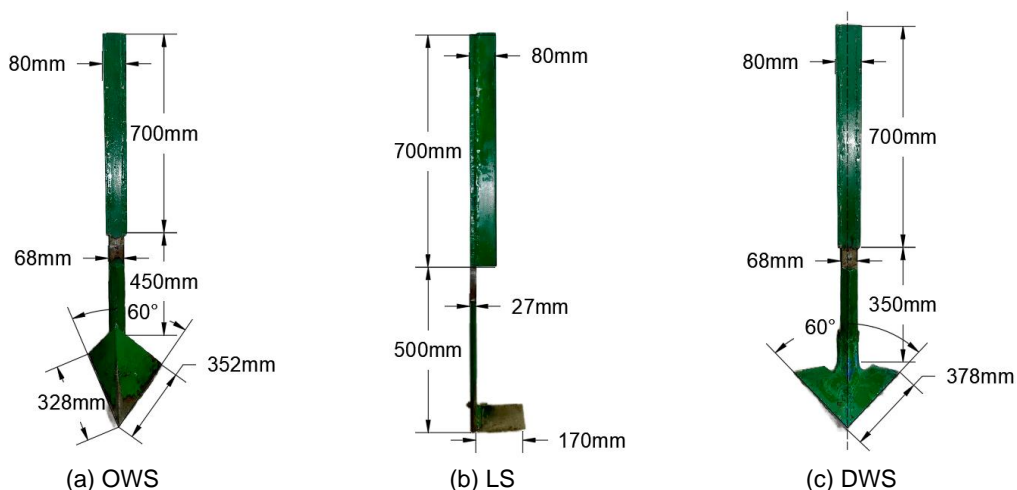


Fig. 2 - Three types of loosening shovels

Test site and equipment

The test site was Wei Zhou Village, Liangjiang Town, Wuming District, Nanning City, Guangxi, China (108°33'E, longitude; 23°51'N, latitude; and 171.6 m height). The cassava variety was Nanzhi 199, and it was planted in single rows with mulching film inserted obliquely, spaced 1 m between rows and 0.8 m apart. The soil's physical properties were measured using the five-point sampling method, as detailed in Table 1, with the values presented on a wet basis. In order to be consistent with a manual cassava harvesting scenario, only cassava stalks with a vertical distance of 30 cm from the ground were retained before the start of the test.

Table 1

Parameters of physical properties of soil				
Depth	Soil hardness on ridge	Soil hardness on furrow	Soil density	Soil moisture content
[cm]	[kg/cm ²]	[kg/cm ²]	[kg/m ³]	[%]
0-10	3.3	9.7	1547.2	22.83
10-20	12.9	12.6	1686.3	26.5
20-30	11.5	11.7	1653.3	29.19

Main instruments and equipment included the LOVOL-AUPAX 704 wheeled tractor (Weichai Lovol Intelligent Agricultural Technology Co., Ltd., China), three types of loosening shovels, the attachments for mounting the loosening shovels (Fig. 3), a custom-made device for testing the pulling force of cassava tuber roots (Fig. 4), and a custom-made instrument for measuring soil disturbance. Both the traction resistance of the loosening shovel and the force required to uproot cassava tubers were measured using a strain measurement method. Strain gauges were connected in a full bridge configuration, and DH5902 and DH5981 data acquisition systems (Jiangsu Donghua Testing Technology Co., Ltd., China) were utilized for the measurements.



Fig. 3 - Loosening shovel resistance test system

1 - Ground wheel; 2 - Resistance sensor; 3 - Loosening shovel; 4 - Three-point suspension hinge; 5 - Crossbeam

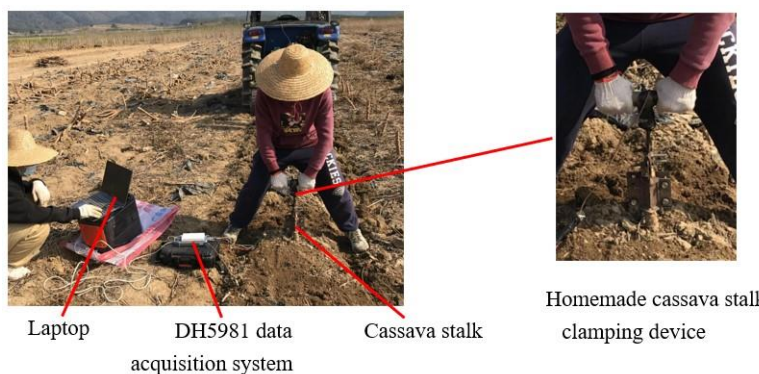


Fig. 4 - Cassava tuber pulling force test system

Test methods

Experimental design for loosening shovel operations

The position of the loosening shovel relative to the tuber has a significant impact on operational performance. Different types of loosening shovels have varying effects and different levels of soil disturbance on cassava tubers.

In this study, the tillage depth (h) and the installed shovel distance (b) – (the distance between the center of the two loosening shovel columns) – were considered as the experimental factors. The range of values for tillage depth and shovel distance were determined based on the depth of planting and the row distance of cassava. Each shovel type underwent a two-factor, three-level orthogonal test, and each trial of tests was repeated three times, with the results averaged.



Fig. 5 - Field test

Traction resistance and maximum pulling force test

Each trial started with adjusting the loosening shovel tillage depth and shovel distance. The tractor advanced at a speed of 0.9 km/h for 20 m at a constant speed, and the traction resistance (F_q) of the loosening shovel was determined using the traction resistance test system. The field test was shown in Fig. 5. After each trial loosening operation, three cassava plants were randomly selected in the operation area. The cassava stalks were clamped using a homemade cassava stalk clamping device, and the cassava was slowly pulled out vertically with both hands. The maximum cassava tuber pulling force (F_b) was determined using the pulling force test system (Fig. 4).

Soil fluffiness and soil disturbance coefficient test

Soil fluffiness (B) and soil disturbance coefficient (y) are indicators of the quality of loosened soil. According to Li's article (Li, et al., 2015), the pre-tillage soil surface curve was measured first between two cassava stalks, followed by the post-tillage soil surface curve and furrow bottom curve. The measurement process was illustrated in Fig. 6. Soil fluffiness and soil disturbance coefficient were calculated using Eq. (1) and (2), respectively.



White paper

Homemade soil disturbance tester



(a) Pre-tillage surface profile measurement

(b) Measurement of furrow bottom curve after tillage

Fig. 6 - Soil disturbance measurement

$$B = \frac{A_h - A_q}{A_q} \times 100\% \quad (1)$$

$$y = \frac{A_s}{A_q} \times 100\% \quad (2)$$

where:

A_h is area bounded by the ground surface after loosening operation and the theoretical furrow bottom (cm^2);

A_q is area bounded by the ground surface before loosening operation and the theoretical furrow bottom (cm^2),

A_s is area bounded by the ground surface before loosening operation and the actual furrow bottom (cm^2)

Breakage rate of cassava tuber test

Tuber breakage refers to the noticeable fracturing of cassava tubers caused by mechanical action during harvester operations, this study specifically examined the fracturing of cassava tubers that occurs during the loosening shovel operation. After the loosening shovel operation, the cassava tubers from each trial were manually dug out. Tubers with a length of less than 5 cm at the end were not counted as broken. The total number of tubers and the number of broken tubers were counted. According to Yang's article (Yang, et al., 2016), the breakage rate of cassava tuber (s) was derived from Eq. (3). In the formula, "n" represents the total number of tubers in one trial, and "a" represents the number of broken cassava tubers.

$$s = \frac{a}{n} \times 100\% \tag{3}$$

Factor impact analysis and optimization methods

(1) Range analysis: Based on the orthogonal test results of each loosening shovel, a range analysis was conducted to determine the effect size of the factors and the optimal combination of levels.

(2) Factor impact analysis: According to the test methods and results, the average values of the test indexes for the same tillage depth but different shovel distance was calculated, as well as for the same shovel distance but different tillage depth. Subsequently, a line graph illustrating the relationship between tillage depth, shovel distance, and the changes in the test indexes respectively was created. Finally, the impact pattern was analyzed by using the line graph.

(3) Comprehensive comparison and optimization: This study gave priority to small breakage rate of cassava tuber and optimal maximum pulling force. To achieve this, line graphs were used to compare the operational effectiveness of each shovel type based on the average maximum pulling force and average cassava tuber breakage rate data. Subsequently, the analysis identified the type of shovel that led to a relatively low breakage rate and pulling force. By analyzing the factors influencing these indicators, the study determined the most effective combinations. Finally, a comprehensive balancing method was used to identify the optimal combination with a relatively small breakage rate and maximum pulling force.

RESULTS

Test results of loosening shovel operation

A table of factor levels for loosening shovel operations is shown in Table 2, and the three loosening shovels test program and results are presented in Table 3.

Table 2

Table of factor levels

Levels	Factors	
	Tillage depth <i>h</i>	Shovel distance <i>b</i>
	[m]	[m]
1	0.2	0.6
2	0.25	0.7
3	0.3	0.8

Table 3

Orthogonal test program and results

Test number	Level of factors		Test indicators					
	Tillage depth <i>h</i>	Shovel distance <i>b</i>	Traction resistance <i>F_q</i>	Maximum pulling force <i>F_b</i>	Soil fluffiness <i>B</i>	Soil disturbance coefficient <i>y</i>	Breakage rate of cassava tuber <i>s</i>	
	[m]	[m]	[N]	[N]	[%]	[%]	[%]	
OWS	1	0.2	0.6	2523.160	375.463	25.995	21.198	13.402
	2	0.2	0.7	3638.887	531.259	18.494	18.529	4.587
	3	0.2	0.8	4250.371	629.584	11.201	12.707	9.790
	4	0.25	0.6	6094.149	251.879	15.747	23.462	4.587
	5	0.25	0.7	6332.209	468.624	14.360	26.046	11.034
	6	0.25	0.8	7167.747	434.775	10.027	18.243	10.000
	7	0.3	0.6	7727.880	436.194	16.170	26.300	17.105
	8	0.3	0.7	8199.327	333.535	14.222	32.075	19.403
	9	0.3	0.8	8642.769	346.363	7.586	11.896	33.793
LS	10	0.2	0.6	1465.699	435.754	16.092	15.905	7.237
	11	0.2	0.7	1800.573	385.229	22.229	16.590	7.914
	12	0.2	0.8	2116.673	567.920	17.490	9.728	6.202

	13	0.25	0.6	2626.817	291.608	16.036	17.669	7.576
	14	0.25	0.7	3102.530	315.218	10.331	16.998	9.286
	15	0.25	0.8	3863.050	338.540	10.173	16.337	4.348
	16	0.3	0.6	4936.538	278.263	12.151	17.516	15.108
	17	0.3	0.7	6031.200	402.959	7.752	19.618	19.841
	18	0.3	0.8	6504.520	351.904	6.250	17.561	20.313
DWS	19	0.2	0.6	1208.154	305.848	19.919	21.658	15.789
	20	0.2	0.7	1556.319	388.936	19.090	24.070	13.483
	21	0.2	0.8	2018.091	246.651	19.057	12.097	25.806
	22	0.25	0.6	3156.697	281.318	17.613	22.209	16.867
	23	0.25	0.7	3611.550	327.796	16.066	24.176	25.974
	24	0.25	0.8	4420.176	402.582	14.631	12.561	12.791
	25	0.3	0.6	5436.548	216.471	9.284	23.630	22.892
	26	0.3	0.7	6430.480	275.962	14.643	25.482	15.315
	27	0.3	0.8	6554.018	364.649	12.807	13.111	25.352

Range analysis

The results of the range analysis for each type of shovels are presented in Table 4. In the table, "k" represents the statistical mean, while subscripts 1, 2, and 3 denote the levels of the three factors, and "R" signifies the extreme variance of the statistical mean.

Table 4

Range analysis for three types of loosening shovels

Test indicators	Statistical averages	OWS		LS		DWS	
		Tillage depth <i>h</i>	Shovel distance <i>b</i>	Tillage depth <i>h</i>	Shovel distance <i>b</i>	Tillage depth <i>h</i>	Shovel distance <i>b</i>
		[m]	[m]	[m]	[m]	[m]	[m]
Traction resistance F_q	k_1	3470.806	5448.396	1794.315	3009.685	1594.188	3267.133
	k_2	6531.369	6056.808	3197.466	3644.768	3729.474	3866.116
	k_3	8189.992	6686.962	5824.086	4161.415	6140.348	4330.761
Maximum pulling force F_b	k_1	512.102	354.512	462.968	335.208	313.812	267.879
	k_2	385.093	444.473	315.122	367.802	337.232	330.898
	k_3	372.031	470.241	344.375	419.455	285.694	337.961
Soil fluffiness <i>B</i>	k_1	18.563	19.304	18.604	14.760	19.355	15.605
	k_2	13.378	15.692	12.180	13.437	16.103	16.600
	k_3	12.659	9.604	8.718	11.304	12.245	15.498
Soil disturbance coefficient <i>y</i>	k_1	17.478	23.653	14.075	17.030	19.275	22.499
	k_2	22.584	25.550	17.002	17.735	19.649	24.576
	k_3	23.424	14.282	18.232	14.542	20.741	12.590
Breakage rate of cassava tuber <i>s</i>	k_1	9.260	11.698	7.117	9.974	18.360	18.516
	k_2	8.541	11.675	7.070	12.347	18.544	18.257
	k_3	23.434	17.861	18.421	10.287	21.186	21.316
<i>R</i>	$R (F_q)$	4719.186	1238.566	4029.771	1151.730	4546.160	1063.629
	$R (F_b)$	140.071	115.729	147.846	84.246	51.538	70.082
	$R (B)$	5.904	9.699	9.886	3.455	7.111	1.101
	$R (y)$	5.945	11.268	4.157	3.193	1.466	11.986
	$R (s)$	14.893	6.186	11.351	2.373	2.827	3.059

As seen from the results of the range analysis of the OWS in Table 4, the extreme variance in the traction resistance of factor *h* is significantly larger than that of factor *b*. Therefore, the effect on the traction resistance is $h > b$. In terms of the effect of the maximum pulling force, $h > b$. Regarding the effect of soil fluffiness, $h < b$. With respect to the effect of the soil disturbance coefficient, $b > h$. In relation to the breakage rate of cassava tuber, $h > b$.

For the LS, the effect of the soil fluffiness is $h > b$. The magnitude of the extreme variance between *h* and *b* on the soil disturbance coefficient does not differ significantly. The main factors affecting the other test indicators of the LS, such as traction resistance, maximum pulling force, and breakage rate of cassava tubers, all have values where $h > b$.

The main relationship among the factors influencing the test indexes of the DWS, such as maximum pulling force, soil disturbance coefficient, and breakage rate of cassava tuber, is that $h < b$. Conversely, the factors of traction resistance and soil fluffiness exhibit the relationship $h > b$.

The optimal combinations of factors for each test index for the three types of shovels are determined from the results of the range analysis, as presented in Table 5.

Table 5

Optimal combinations of the three shovel factors

Test indicators	OWS	LS	DWS
Traction resistance F_q	$h_1 b_1$	$h_1 b_1$	$h_1 b_1$
Maximum pulling force F_b	$h_3 b_1$	$h_2 b_1$	$b_1 h_3$
Soil fluffiness B	$b_1 h_1$	$h_1 b_1$	$h_1 b_2$
Soil disturbance coefficient γ	$b_2 h_3$	$h_3 b_2$	$b_2 h_3$
Breakage rate of cassava tuber s	$h_2 b_2$	$h_2 b_1$	$b_2 h_1$

Factor impact analysis

The factor change impact diagrams are shown in Figs. 7-11. The three types of shovels are represented by different colors in the diagram. The black color represents the OWS, the red color represents the LS, and the blue color represents the DWS.

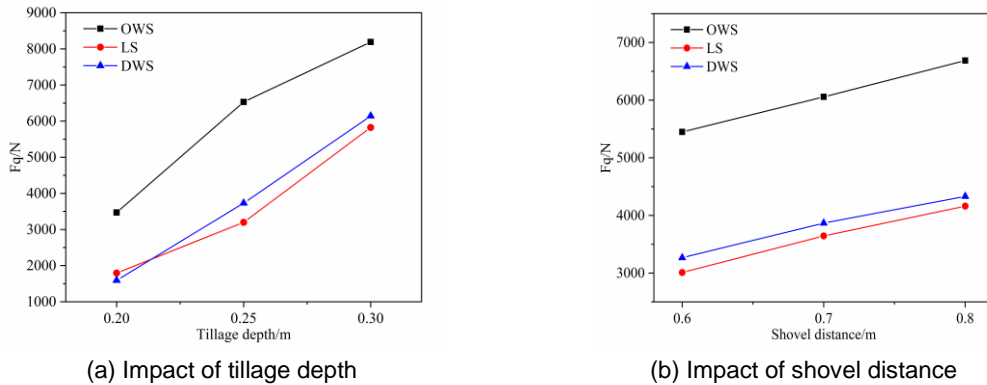


Fig. 7 - Effect of three shovels on traction resistance

According to Fig. 7(a), the traction resistances of the three types of shovels rise as the tillage depths increase. This is due to the loosening shovels plowed deeper, the positive pressure exerted by the soil above the shovel wings also increases, resulting in an increase in traction resistance.

Fig. 7(b) demonstrates that the traction resistances of the three shovels rise as the shovel distances increase. This is attributed to a large shovel distance, wide operating width, and the gradual contact of the loosening shovel's wings with the furrows. Additionally, the first layer of soil hardness in the furrows is greater than that of the ridges, thereby contributing to the increase in traction resistance.

Furthermore, Fig. 7 illustrates that the OWS exhibits significantly higher traction resistance compared to the other two shovels when the tillage depth and shovel distance are altered. On the other hand, the traction resistances of the LS and the DWS are closer.

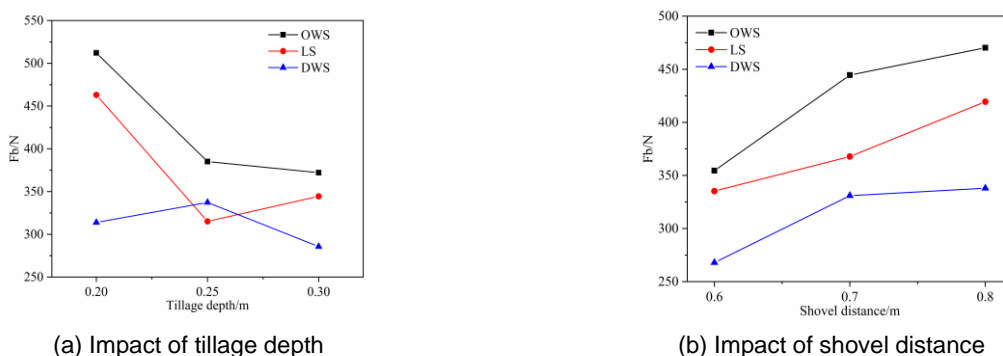


Fig. 8 - Effect of three shovels on maximum pulling force

As could be seen from Fig. 8(a), with the tillage depths increase, the maximum pulling force of the OWS decrease, while the maximum pulling force of the LS initially decreases and then increases. Both forces decrease by the same amount, and both of them have a relatively large decrease. The maximum pulling force of the DWS initially increases and then decreases with the increase in tillage depth, but the magnitudes of the increase and decrease are not significantly different.

From Fig. 8(b), it can be seen that with the increase in shovel distances, the maximum pulling forces of the three shovels increase. This is because the wider the shovel distance, the less the loosening shovel affects the cassava tubers in the middle. In addition, the trends of the OWS and DWS are essentially the same.

As shown in Fig. 8, when the tillage depth and shovel distance are varied, the maximum pulling force of the OWS is greater than that of the other two shovels.

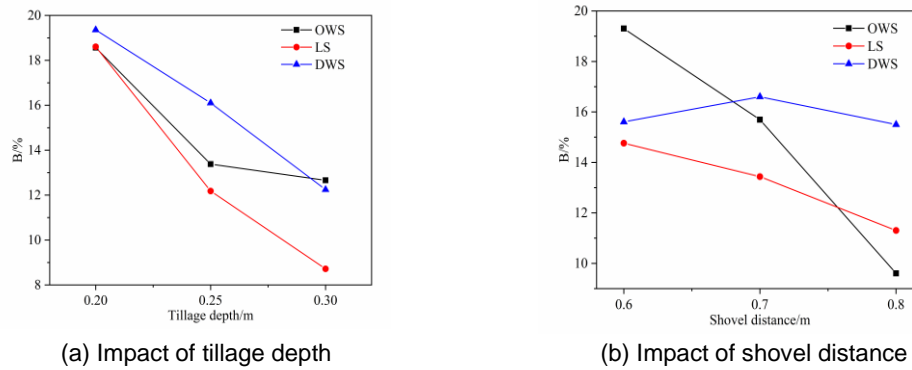


Fig. 9 - Effect of three shovels on soil fluffiness

As shown in Fig. 9(a), with the increase in tillage depths, the soil fluffiness of the three types of shovels decrease. This is due to the increase of tillage depth, the loosening shovel penetrates the soil to a greater depth, resulting in a decrease in soil surface elevation after tillage. This is consistent with the result that "soil fluffiness gradually decreases with the increase of deep loosening depth" obtained in the test by Li et al. (Li, et al., 2017). However, when the tillage depth of the DWS increases from 0.25 m to 0.3 m, the soil fluffiness does not change significantly, whereas the soil fluffiness of the LS decreases rapidly.

From Fig. 9(b), the soil fluffiness of the OWS and LS decrease with the increase of shovel distance, which is consistent with Shi's result (Shi, et al., 2021). However, the soil fluffiness of the OWS decreases rapidly. In addition, the soil fluffiness of the DWS is not significantly affected by the shovel distance.

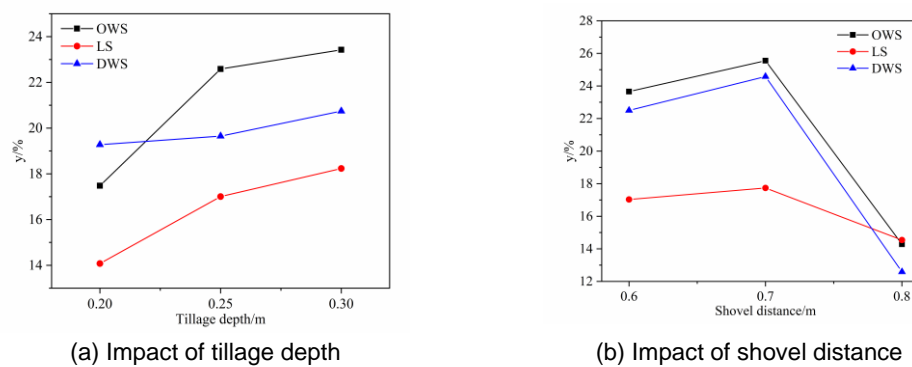


Fig. 10 - Effect of three shovels on soil disturbance coefficient

As shown in Fig. 10(a), the soil disturbance coefficients of the three types of shovels increase with the increase in tillage depth. This trend is associated with the rise of tillage depth and the subsequent decrease of soil surface elevation after tillage. Among them, the soil disturbance coefficients of the OWS and LS show more consistent trends. While the soil disturbance coefficient of the DWS does not vary significantly. And those of the LS are the smallest.

As depicted in Fig. 10(b), the soil disturbance coefficients of the OWS and DWS initially increase with the rise of shovel distance, followed by a sharp decrease. When the shovel distance is 0.8 m, the soil disturbance coefficient is significantly smaller compared to the other two shovel distance conditions. Furthermore, even though it also increases and then decreases with the increase of shovel distance, the soil disturbance coefficient of the LS does not change significantly.

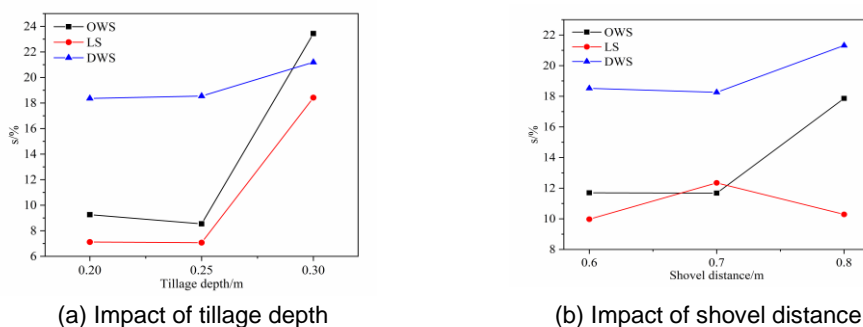


Fig. 11 - Effect of three shovels on breakage rate of cassava tuber

From Fig. 11(a), the cassava tuber breakage rates of the OWS and LS exhibit an initial slight decrease followed by a rapid increase as the tillage depths increase, displaying the same pattern. Conversely, the cassava tuber breakage rate linked to the DWS consistently maintains a relatively high level, demonstrating a gradual rise with the increase of tillage depth.

In Fig. 11(b), as the shovel distances increase, the cassava tuber breakage rates of the OWS and DWS show a gentle decrease followed by an increase. In contrast, the cassava tuber breakage rate of the LS increases initially and then decreases with the expansion of shovel distance.

Comprehensive comparison and optimization

The fluctuations in the average values of maximum pulling force and breakage rate of cassava tuber across various tillage depths and shovel distances for each type of shovel are illustrated in Figs. 8 and 11.

As shown in Fig. 8(a), the maximum pulling force exerted by the OWS diminishes as the tillage depth increases. The LS initially experiences a decrease followed by a slight increase, whereas the DWS demonstrates an initial increase followed by a decrease. The OWS exhibits the highest maximum pulling force, and the LS and DWS show similar maximum pulling forces at tillage depths of 0.25 m and 0.3 m. Analysis of Fig. 11(a) reveals that at tillage depths of 0.2 m and 0.25 m, the cassava tuber breakage rates are significantly lower for the LS and OWS compared to the DWS. Notably, the LS exhibits the lowest cassava tuber breakage rate among three shovels.

From Fig. 8(b), the maximum pulling forces exhibited by the three types of shovels increase with the extension of shovel distance. And the OWS demonstrates a higher maximum pulling force compared to the LS, which in turn surpasses the DWS. Analysis of Fig. 11(b) reveals a similar trend in cassava tuber breakage rate between the OWS and DWS, while the breakage rate of the LS initially increases and then decreases in relation to a rising shovel distance. Moreover, the DWS incurs a higher cassava tuber breakage rate compared to the other two shovel types. And the LS shows a relatively low breakage rate among the three.

Based on the aforementioned analysis, the OWS exhibits a low breakage rate but possesses the highest maximum pulling force. Conversely, the DWS demonstrates a small maximum pulling force but a high breakage rate. The LS shows the lowest breakage rate among the three shovel types and a maximum pulling force smaller than that of the OWS. In a comprehensive comparison, the LS emerges as the optimal shovel type due to its lowest breakage rate, relatively small pulling force, and low cost-effectiveness.

Finally, utilizing Table 5 and employing a comprehensive balance method, the optimal combination of the LS type is identified as (h_2, b_1) , indicating a tillage depth of 0.25 m and a shovel distance of 0.6 m.

CONCLUSIONS

(1) The order of factors affecting the traction resistance, maximum pulling force, and cassava tuber breakage rate of the OWS was $h > b$, and vice versa for other test indicators. The order of factors affecting the five test indexes of the LS was $h > b$. The order of factors affecting the maximum pulling force, soil disturbance coefficient, and cassava tuber breakage rate of the DWS was $b > h$, and the opposing order for other test indicators.

(2) The traction resistance and soil disturbance coefficient of the OWS, LS, and DWS increased with deeper tillage depths, while the soil fluffiness decreased. The maximum pulling force of the OWS decreased as tillage depth increased, while the LS initially decreased and then increased. The DWS's maximum pulling force initially mildly increased and then decreased. The cassava tuber breakage rate of the OWS and LS decreased slightly before rapidly increasing with deeper depth, while the DWS maintained a relatively high breakage rate that increased gradually. Additionally, the traction resistance and maximum pulling force of three

shovels increased with increasing shovel distance. The soil fluffiness of the OWS and LS decreased with increasing shovel distance, while the DWS initially increased and then decreased. The soil disturbance coefficient of three shovels gently increased and then decreased with increasing shovel distance. The breakage rate of the OWS and DWS increased after a slight decrease with increasing shovel distance, while the LS's breakage rate increased and then decreased. When it came to adjusting the tillage depth and shovel distance, the OWS exhibited higher traction resistance and maximum pulling force compared to the other two shovels.

(3) Between maintaining a low cassava tuber breakage rate and minimizing the maximum pull force, the LS was identified as the optimal shovel type. When operating at an optimal tillage depth of 0.25 m and shovel distance of 0.6 m, the breakage rate of cassava tuber was 7.576 %, and the maximum pulling force was 291.608 N.

ACKNOWLEDGEMENT

This study was supported by grants from the National Natural Science Foundation of China (Grant Nos. 32160422 and 51365005) and Guangxi Science and Technology Major Program (Grant No. Guike AA23073003).

REFERENCES

- [1] Agbetoye L.A.S, Ilevbare I., (2012), Evaluation of L-tines for soil disturbance during mechanised cassava harvesting, *2012 ASABE Annual International Meeting Sponsored by ASABE*, vol.12;
- [2] Agbetoye L.A.S., Kilgour J., Dyson J., (1998), Performance evaluation of three pre-lift soil loosening devices for cassava root harvesting, *Soil & Tillage Research*, vol.48, no.4, pp.297-302;
- [3] Akhir H.M., Sukra A.B., (2002), Mechanization possibilities for cassava production in Malaysia, *Cassava Research and Development in Asia: Exploring New Opportunities for an Ancient Crop*, International Center for Tropical Agriculture(CIAT), pp.271-276;
- [4] Amponsah S.K., Addo A., Gangadharan B., (2018), *Review of Various Harvesting Options for Cassava*, Chapter 16, pp.291-304;
- [5] Amponsah S.K., Sheriff J.T., Byju G., (2014), Comparative evaluation of manual cassava harvesting techniques in Kerala, India, *Agricultural Engineering International : The CIGR e-journal*, vol.16, no.2;
- [6] Awad M., Fouda O., Fathy W., El Balkemy W., Egela M., El-Fakhrany W., Okasha M., (2022), *A combined machine for collecting and chopping rice straw*, *Heliyon*, vol.8, no.8;
- [7] Chalachai S., Soni P., Chamsing A., Salokhe V.M., (2013), A critical review of mechanization in cassava harvesting in Thailand, *International Agricultural Engineering Journal*, vol.22, no.4, pp.81-93;
- [8] Chen L., Mou X., Xue J., Peng Z., Liu W., (2022), Research status and prospect of cassava mechanize planting and harvesting equipment at home and abroad (国内外木薯机械化种收装备研究现状与展望), *Agricultural Engineering*, vol.12, no.2, pp.10-16;
- [9] Gupta C.P., Paul S.C., Stevens W.F., (1999), Development of a vibrating cassava root harvester, *Agricultural Mechanization in Asia, Africa and Latin America*, vol.30, no.1, pp.1-55;
- [10] Jansson C., Westerbergh A., Zhang J., Hu X., Sun C., (2009), Cassava, a potential biofuel crop in (the) People's Republic of China, *Applied Energy*, vol.86, pp.S95-S99;
- [11] Khater A., Fouda O., El-Termezy G., Hamid S.A., El-Tantawy M., El-Beba A., Sabry H., Okasha M., (2023), Modification of the rice combine harvester for cutting and binding wheat crop, *Journal of Agriculture and Food Research*, vol.14;
- [12] Li D., Peng X., Liao Y., Guo D., Shi T., (2022), Design and experiment of bionic shovel for single row cassava root harvester (单行木薯块根收获机仿生铲的设计与试验), *Journal of Agricultural Mechanization Research*, vol.44, no.1, pp.174-182;
- [13] Li S., Cui Y., Zhou Y., Luo Z., Liu J., Zhao M., (2017), The industrial applications of cassava: current status, opportunities and prospects, *Journal of the Science of Food and Agriculture*, 97, 8, 2282-2290;
- [14] Li W., Zhang S., Huang Y., Zhu R., (2017), Distinct element method simulation and experimental research of subsoiling depth on soil disturbance (深松深度对土壤扰动影响的仿真与试验研究), *Journal of Agricultural Mechanization Research*, vol.39, no.11, pp.153-157;
- [15] Li X., Zhang D., Wang W., Cui T., (2015), Performance parameter optimization and experiment of forced-vibration subsoiler (受迫振动深松机性能参数优化与试验), *Transactions of the Chinese Society of Agricultural Engineering*, vol.31, no.21, pp.17-24;

- [16] Liao Y., Sun Y., Liu S., Cheng D., Wang G., (2012), Development and prototype trial of digging-pulling style cassava harvester, *Transactions of the Chinese Society of Agricultural Engineering*, 28, 2, 29-35;
- [17] Liu C., (2020), *Optimization study on operation parameters of cassava shovel (木薯松土铲作业参数优化研究)*, MSc Thesis, Guangxi University, Guangxi Zhuang Autonomous Region/China;
- [18] Liu J., Wang X., Li H., He J., (2017), Optimization of structural parameters of subsoiler based on soil disturbance and traction resistance (基于土壤扰动与牵引阻力的深松铲结构参数优化), *Transactions of the Chinese Society for Agricultural Machinery*, vol.48, no.2, pp.60-67;
- [19] Liu S., Weng S., Liao Y., Zhu D., (2014), Structural bionic design for digging shovel of cassava harvester considering soil mechanics, *Applied Bionics and Biomechanics*, vol.11, pp.1-11;
- [20] Mo Q., Huang M., (2012), Development and application of 4UM-160 cassava harvester (4UM-160 型木薯收获机的研发应用), *Guang Xi Agricultural Mechanization*, vol.3, pp.20-22+25;
- [21] Odigboh E.U., (1991), Single-row model II cassava harvester, *Agriculture Mechanization In Asia, Africa and Latin America*, vol.22, no.3, pp.63-66;
- [22] Ospina B., Cadavid L.F., Garcia M., (2002), Mechanization of cassava production in Colombia, *Cassava Research and Development in Asia. Centro International de Agricultura Tropical*, pp.277-287;
- [23] Parmar A., Sturm B., Hensel O., (2017), Crops that feed the world: Production and improvement of cassava for food, feed, and industrial uses, *Food Security*, vol.9, no.5, pp.907-927;
- [24] Qi P., Wang J., Yuan J., (2018), Design and experiment of digging and pulling harvester (挖拔式木薯收获机的设计与试验), *Guang Xi Agricultural Mechanization*, vol.14, pp.23-25;
- [25] Shi Z., Yu Z., Yang L., Yang M., (2021), On simulation and experiment of soil disturbance caused by airfoil subsoil shovel spacing (翼型深松铲铲间距对土壤扰动的仿真与试验), *Journal of Southwest China Normal University (Natural Science Edition)*, vol.41, no.4, pp.38-44;
- [26] Sivamani S., Chandrasekaran A.P., Balajii M., Shanmugaparakash M., Hosseini-Bandegharai A., Baskar R., (2018), Evaluation of the potential of cassava-based residues for biofuels production, *Reviews in Environmental Science and Bio-Technology*, vol.17, no.3, pp.553-570;
- [27] Thasontea M., Chansiri C., (2015), The potential on development of cassava combine harvester in Thailand, *Farm engineering and automation technology journal*, vol.1, no.2, pp.107-116;
- [28] Vandegeer R., Miller R.E., Bain M., Gleadow R.M., Cavnano T.R., (2013), Drought adversely affects tuber development and nutritional quality of the staple crop cassava (Crantz), *Functional Plant Biology*, vol.40, no.2, pp.195-200;
- [29] Wang T., Liao Y., Yang Y., Zheng M., Yuan C., (2015), The design and mechanical analysis of digging shovel of cassava harvest machine (木薯收获机多阶挖掘铲设计及其力学特性分析), *Journal of Agricultural Mechanization Research*, vol.37, no.10, pp.50-54;
- [30] Wang Z., Zhou J., Yang X., Liu Y., Liu F., (2019), Research progress of cassava tuber harvesting technology and machine (木薯块根收获技术与机具研究进展), *Agricultural Engineering*, 9, 1, pp.1-8;
- [31] Xue Z., Huang H., Li M., Qiu Z., Gao W., Cui Z., (2010), Study on 4UMS-390II cassava harvester (4UMS-390II 型木薯收获机的研制), *Journal of Agricultural Mechanization Research*, vol.32, no.8, pp.78-81+85;
- [32] Yang W., Jia F., Yang J., (2013a), Numerical simulation of digging processes of cassava root (木薯块根挖掘作业过程的数值模拟), *Engineering Mechanics*, vol.30, no.6, pp.301-307;
- [33] Yang W., Li X., Wang R., Yang J., Pan Q., Li J., (2016), Numerical simulation test of maximum stress of tuber in cassava lifting (木薯块根拔起的最大应力数值模拟及试验), *Transactions of the Chinese Society of Agricultural Engineering*, vol.32, no.6, pp.58-64;
- [34] Yang W., Yang J., Jia F., Wang Q., Huang Y., (2013b), Numerical simulation of digging operation of cassava root planted in red clay (种植于红粘土的木薯块根挖掘作业数值模拟), *Journal of Mechanical Engineering*, vol.49, no.09;
- [35] Yang W., Yang J., Zheng X., Jia F., (2012), Current research and development trends of cassava root harvest machinery and technology (木薯块根收获机械与技术研究现状及发展趋势), *Journal of Agricultural Mechanization Research*, vol.32, no.12, pp.230-235;
- [36] Zhang Y., Huang H., Cui Z., (2012), Harvesting principle and structure design of cassava harvester (国内木薯收获机采挖原理和结构设计), *Tropical Agricultural Engineering*, vol.36, no.5, pp.17-20;

RESEARCH ON CONTROL SYSTEM OF ELECTRIC-DRIVE WHEAT SHALLOW-BURIED DRIP IRRIGATION AND WIDE-WIDTH PRECISION SEEDER

电驱式小麦浅埋滴灌-宽幅匀播机控制系统研究

Shenghe BAI^{1,2)}, Yanwei YUAN^{1,2)}, Liang WEI²⁾, Liming ZHOU²⁾, Kang NIU²⁾, Bo ZHAO²⁾, Jinhui ZHANG³⁾, Yuqi WANG²⁾, Wenyu TONG²⁾, Shuaiyang ZHANG²⁾, Lijing LIU^{1,2)}, Zenglu SHI⁴⁾, Gang GUO⁵⁾

¹⁾ China Agricultural University, Beijing 100083, China

²⁾ Chinese Academy of Agricultural Mechanization Sciences Group Co., Ltd, National Key Laboratory of Agricultural Equipment Technology, Beijing 100083, China

³⁾ Dongliao county mechanical technology promotion station, Jilin 136200, China

⁴⁾ College of Mechanical and Electrical Engineering, Xinjiang Agricultural University, Urumqi 830052, China

⁵⁾ Heilongjiang Province's Gengzheng Agricultural Machinery Manufacturing Co., Ltd., Nanyang 473000, China

Tel: +86-13815375524; E-mail: 13815375524@163.com

DOI: <https://doi.org/10.35633/inmateh-74-07>

Keywords: Drip irrigation; Precision seeder; Electric-drive; Control system; Precision seeding and fertilization

ABSTRACT

To achieve precise seeding and fertilization operations for wheat and improve the intelligent level of wheat shallow buried drip irrigation and wide-width precision seeder, this article proposes a fusion speed measurement method by integrating ground encoder and satellite positioning module, and designs a control system of electric-drive wheat shallow-buried drip irrigation and wide-width precision seeder. The system includes STM32 main controller, DC servo motor, servo motor reducer, wheel encoder, vehicle navigation positioning module, vehicle control terminal, attitude sensor, voltage conversion module, etc. Based on the VisualTFT platform and equipped with a multi-functional touch screen, by designing the overall functions of terminal including obtaining speed from ground wheel encoder, obtaining speed from vehicle navigation positioning module, automatic switching of seeding mode speed source, motor speed control model, and remote transmission of positioning information, the system achieves the precise seeding and fertilization by adjusting the seeding/fertilization speed according to the forward speed of the tractor. The experimental study investigated the working performance of the control system of electric-drive wheat shallow-buried drip irrigation and wide-width precision seeder. Calibration test results showed that the speed accuracy of the ground wheel encoder was above 97.00%, The average seeding rate and fertilizer application rate were 22.4 g/r and 157.4 g/r, the standard deviations were 1.1 and 3.3, respectively. Field trial results showed that the seeding rate control error ranged from 3.0% to 5.3%, and the fertilization amount control error ranged from 3.0% to 6.0%. It meets the requirements for precise seeding and fertilization operations of shallow-buried drip irrigation and wide-width precision wheat seeder.

摘要

为实现小麦精量播种施肥作业过程,提高小麦浅埋滴灌-宽幅匀播机智能化水平,提出地轮编码器和卫星定位模块融合测速方法,设计了电驱式小麦浅埋滴灌-宽幅匀播机控制系统,包括STM32主控器、直流伺服电机、伺服电机减速器、地轮编码器、车载导航定位模块、车载控制终端、姿态传感器、变压模块等部分。基于VisualTFT平台,搭载多功能触摸屏,通过对地轮编码器速度获取、车载导航定位模块速度获取、播种模式速度源自动切换、电机调速控制模型、定位信息远程传输等终端功能整体设计,实现了随拖拉机前进速度调整排种/肥转速,达到精量播种施肥的目的。试验研究了电驱式小麦浅埋滴灌-宽幅匀播机控制系统工作性能,标定试验结果表明:地轮编码器测速精度都在97.00%以上,平均排种/肥量分别为22.4 g/r、和157.4 g/r,标准差分别为1.1和3.3;田间试验结果表明:播量控制误差范围为3.0%~5.3%,施肥量控制误差范围为3.0%~6.0%,符合实际小麦浅埋滴灌-宽幅匀播机精量播种施肥作业要求。

INTRODUCTION

Shenghe BAI, Ph.D. Stud. Eng.; Yanwei YUAN*, Prof. Ph.D. Eng.; Liang WEI, M.S. Stud. Eng.; Liming ZHOU, Prof. Ph.D. Eng.; Kang NIU, Prof. Ph.D. Eng.; Bo ZHAO, Prof. Ph.D. Eng.; Jinhui ZHANG, M.S. Stud. Eng.; Yuqi WANG, M.S. Stud. Eng.; Wenyu TONG, Ph.D. Stud. Eng.; Shuaiyang ZHANG, Ph.D. Stud. Eng.; Lijing LIU, Prof. Ph.D. Eng.; Zenglu SHI, Prof. Ph.D. Eng.; Gang GUO, Prof. Ph.D. Eng.

Xinjiang is a typical arid and semi-arid region and water-saving high-yield is the inevitable direction for the sustainable development of wheat production in Xinjiang (Wan, 2023). Subsurface drip irrigation with wide-row planting is an efficient water-saving, and yield-increasing cultivation technique for wheat, promoting cost. Reduction and income increase, which has received significant attention and promotion in recent years (Yu et al., 2023; Yao et al., 2021). Precision seeding is to provide uniform seed flow according to agronomic requirements, that is, adjusting seeding density can effectively coordinate the relationship between the number of spikes per unit area and the number of grains per spike of wheat. It further increases production and becomes the development trend of shallow buried drip irrigation and wide-row uniform planting of wheat in Xinjiang (Xue et al., 2023; Wang 2023). Currently, traditional wheat seeders mostly use ground wheel-driven seeders, combined with manual gearbox to adjust seeding amount and grain spacing. However, due to the complexity of field conditions and the large vibration of the machinery during operation, it is prone to issues such as wheel slippage, hanging, and chain jumping when operating at high speeds. In addition, the uneven speed of the tractor often results in poor seeding uniformity, seriously affecting the quality of seeding (Gui et al., 2024; Tang 2021). In addition, adjusting the seeding volume manually through the gearbox can only adjust the seeding volume in a fixed gear, which makes it difficult to meet the precise control requirements of seeding volume under different planting agronomic requirements and operating speeds (Liao et al., 2022; Sun et al., 2024). Electric drive seeding technology, as an important means to achieve precise adjustment of seed spacing and seeding volume, has the advantages of saving seeds, labor, and increasing efficiency, and has always been a research focus at home and abroad. Therefore, studying a control system for an electric-drive wheat shallow-buried drip irrigation-wide-width precision seeder is of great significance for achieving precise seeding of wheat in Xinjiang.

Research on precision seeding technology at home and abroad mainly focuses on the structural design and parameter optimization of seeders. There are various seeders with stable performance and high seeding accuracy currently being applied in production practice (Mударisov et al., 2020; Nielsen et al., 2018; Zhang et al., 2024; Jiang et al., 2019). To further achieve high-speed precision sowing and precise adjustment of sowing quantity, scholars have conducted extensive research on the driving and speed measurement methods of seeders (Gui et al., 2024; Feng et al., 2020; Wang et al., 2022; He et al., 2017). Karimi et al., (2019), developed a wheat seeder operation monitoring system, consisting of vehicle speed sensors, seed flow sensors, GPS, and electric drive modules. It achieves precise matching of seeding quantity and operation speed by controlling the electric drive module through the controller. Cay et al., (2018), designed a motor control system that integrates PWM and PID technologies, consisting of an encoder, a DC brushless motor, and its drive module. Inoti et al. (Ibrahim et al., 2018) developed a control system for pneumatic precision seeding, which features functions such as data collection, data processing, and seeding control. Domestically, Liao et al., (2022), Wu (2022), Liao et al., (2017), designed a speed-controlled seeding system based on two speed measurement methods: wheel encoder and BeiDou signal receiver. Zhang Zenghui, (2018), designed a model for intelligent operation and precise control system of wheat seeder, solving the problems of unstable seeding quality and traditional backward seeding technology caused by the use of ground wheel drive in domestic wheat seeders. Liu Wei, (2020), studied the monitoring and control technology of wheat sowing amount based on seeding flow information, providing feedback control on the actual sowing amount. Chen et al., (2022), designed a precision seeding control system based on BeiDou navigation, and the results showed that the system response time was ≤ 0.8 s. Jiang Zhenhan et al., (2024), designed a control system for an electrically-driven high-speed intelligent corn planting machine, which achieves real-time matching of planting spacing and machine forward speed. In summary, the current electronic control seeding technology is based on measuring speed using wheel speed sensors, Doppler radar, satellites, etc., and controlling the speed of electric motors or hydraulic motors to dispense seeds or fertilizers as needed. The wheel speed sensor has low speed measurement accuracy, the Doppler radar is expensive and not easy to promote, and there is a delay when the satellite is in non-uniform motion on the carrier. The above speed measurement method is single and cannot guarantee the accuracy of speed measurement under different working conditions and speeds, affecting the uniformity of sowing and making precision sowing difficult to achieve.

To address the above issue, this article proposes a speed measurement method that integrates ground wheel encoders and satellite positioning modules based on a single-axis rotary tillage wheat shallow buried drip irrigation-wide width uniform sowing machine.

It uses the STM32 microcontroller to build and develop the control system for the electric drive wheat shallow buried drip irrigation - wide-width uniform broadcasting machine, and conducts parameter calibration and field performance verification tests in order to improve the quality of wheat shallow buried drip irrigation - wide-width uniform broadcasting operations.

MATERIALS AND METHODS

Overall design of wheat shallow-buried drip irrigation and wide-width precision seeder

The wheat shallow-buried drip irrigation and wide-width precision seeder is mainly composed of two parts: mechanical structure and control system.

● **Mechanical structure**

The mechanical structure of the single-axis rotary tillage wheat shallow-buried drip irrigation and wide-width precision seeder includes components such as the frame, reducer, rotary tillage device, tail seeding assembly, shallow-buried drip irrigation belt device, pressing device, side fertilization device, and fertilization box. It can complete operations such as leveling of 9 rows of wheat seedbeds, laying drip irrigation belts, precise seeding, variable fertilization, and covering soil in one go.

During operation, the machine is suspended on the tractor at three points, connected to the gearbox through the power output shaft, driving the rotary tillage device to crush and level the soil and throw it up. The motor drives the seeding/fertilizing shaft, and the seeds and fertilizers are transported through the seeding/fertilizing tube. And under the action of the harrow, the seeds are evenly distributed on the crushed and leveled seedbed. The overturned soil is smoothly and orderly covered on the surface of the organic fertilizer under the action of the retaining plate. The drip tape rotates on the drip tape rack and is laid shallowly along the front of the machine under the action of the shallow-buried drip tape device. The compaction device completes the post-seeding soil compaction and leveling process.

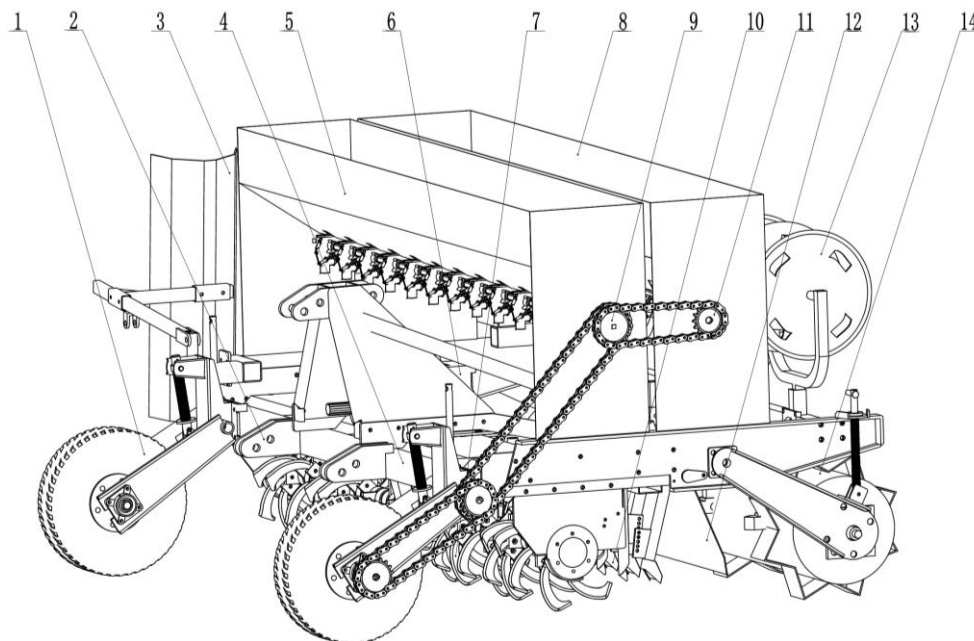


Fig. 1 - Mechanical structure diagram of Wheat Shallow-Buried Drip Irrigation and Wide-Width Precision Seeder

1. Ground wheel; 2. Three-point suspension; 3. Side fertilization device; 4. Frame; 5. Fertilizer box; 6. Reducer; 7. Rotary tillage device; 8. Seed box; 9. Fertilizer discharge shaft; 10. Swallowtail seeding assembly; 11. Seed discharge shaft; 12. Soil deflector; 13. Shallow buried drip irrigation tape device; 14. Pressing device.

● **Control system**

The overall structure of the control system of the electric-drive wheat shallow buried drip irrigation-wide width precision seeder is shown in Figure 2, mainly composed of STM32 main controller, DC servo motor, servo motor reducer, ground wheel encoder, vehicle navigation positioning module, vehicle control terminal, attitude sensor, voltage conversion module, etc.

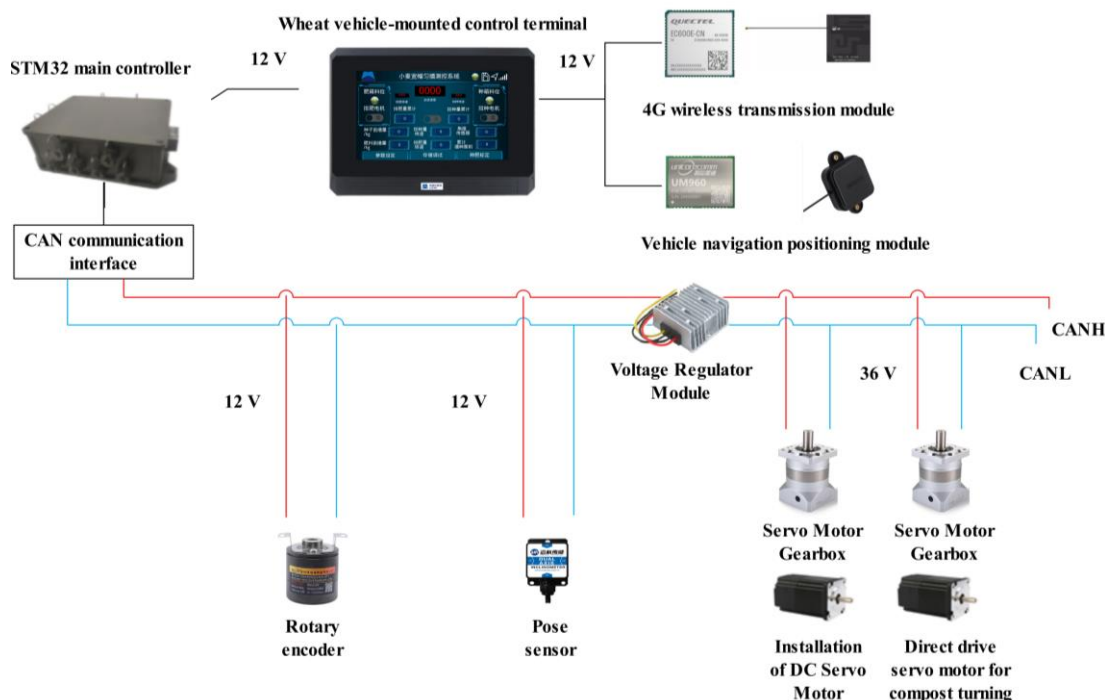


Fig. 2 - Overall control system composition diagram of electric-drive wheat shallow-buried drip irrigation and wide-width precision seeder

When the system starts working, it first installs the on-board control terminal in the tractor cab through operation. It sets parameters such as the number of planting/fertilizing units, working width, number of working rows, amount of planting/fertilizing per circle, amount of planting/fertilizing applied per mu (mu represents 666.7 square meters), angle threshold, etc., and sends them to the STM32 controller via the CAN bus. When the machine starts operating, the main controller first reads the angle value of the posture sensor to determine if the machine is on the ground. If it detects that the machine has landed, it will start the sowing and fertilizing operations, and turn on the motor enable switch. It reads the speed signals from the wheel encoder and the vehicle navigation positioning module, and generates motor control commands based on the speed signals and preset parameter information. It controls the servo motor to respond quickly, matching the planting/fertilizing rate with the forward speed of the tractor. The vehicle-mounted navigation positioning module obtains the seeding machine operation location information, uses a 4G wireless transmission module to remotely wirelessly transmit the positioning information to the cloud storage platform. When the tractor is working in variable speed mode, the main controller automatically selects the more accurate speed source between the wheel encoder and the vehicle navigation positioning module to drive the servo motor at the target speed for driving the planting/fertilizing shaft rotation. If the monitoring angle value is greater than the set threshold, the main controller stops sending motor drive pulses and stops reading speed signals. Continuously monitor and judge whether the tractor is landing, adjust the planting/fertilizer rotation speed according to the speed of the tractor to achieve precise seeding and fertilization.

System hardware design

● Main Controller

The main controller is the core of the control system, which needs to receive and process various sensor signals in real time, such as ground wheel encoders, vehicle navigation positioning modules, tilt sensors, and generates signals in real time to adjust the speed of the DC servo motor. This study used the STM32F407VET6 microcontroller produced by STMicroelectronics, which features a high-performance ARM Cortex-M4 core architecture. It has 32-bit arithmetic capability and interrupt masking function, with 100 external pins. The installation location is shown in Figure 3.

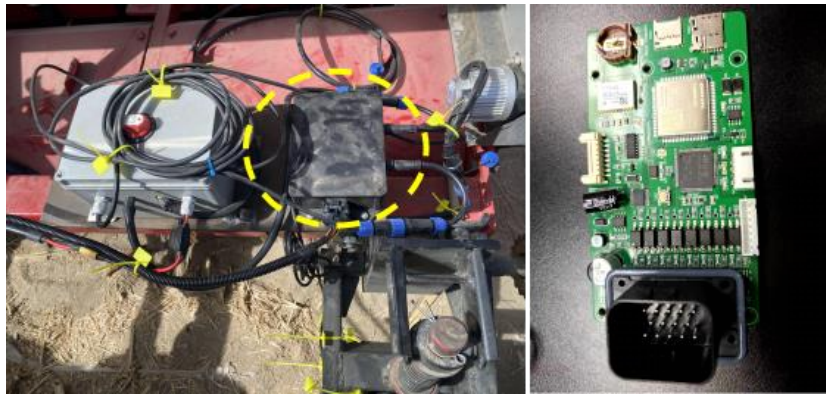


Fig. 3 - Installation diagram of main controller

- **Drive module**

The drive module consists of a DC servo motor, servo motor reducer, planting/fertilizing actuator, etc. The design of the single-axis rotary wheat shallow buried drip irrigation-wide width uniform sowing machine includes a seed sowing amount of 30 kg per mu, a fertilizer application amount of 10 kg per mu, a working width of 2850 cm, a sowing width of 30 cm, and a row spacing of 60 cm. To meet the requirements of machine operation speed and precise sowing, the transmission ratio for the planting reducer is selected as 20, and the transmission ratio for the fertilization reducer is 10. The driving torque of the servo motor is (Liao *et al.*, 2022):

$$N = \frac{KM}{\alpha\beta} \quad (1)$$

where:

N - motor drive torque, Nm;

K - the safety factor of the motor, which is set to 2;

M - the maximum load on the planting axis during operation, Nm;

α - the sprocket transmission ratio;

β - the gear ratio of the reducer.

The starting torque of the planting shaft measured by the digital torque wrench ATRITERBME-006 of Wuhu Aritter Mechanical and Electrical Equipment Co., Ltd. is 9.8 Nm, and the steady rotation torque is 7.4 Nm. The torque of the motor drive is calculated as 1.48 Nm according to formula (1). The 60AIM40 integrated torque servo motor produced by Hangzhou Yizhi Technology Co., Ltd. with a torque of 3 Nm is selected, which meets the operational requirements. It uses PF-60 servo motor with two-stage reducer to meet the transmission requirements. The installation location is shown in Figure 4.



Fig. 4 - Installation diagram of drive module

- **Rotary encoder**

Forward speed is an important measurement parameter for precision planting. This article features the IP68 single-turn waterproof and explosion-proof absolute value encoder produced by Brite Electronic, which has strong anti-interference capability and high-cost performance. The installation location is shown in Fig. 5.



Fig. 5 - Installation diagram of rotary encoder

- **Vehicle navigation positioning module**

The vehicle navigation positioning module uses the GPS/BeiDou dual-mode positioning module produced by Redcore IoT Technology to real-time obtain the positioning location of the seeder in the field operation (communicate with the control platform through the 4G CAT module to upload the machine operation position in real time). It sets the signal update frequency to calculate the forward speed and seeding area of the machine, with characteristics such as high gain, low standing wave ratio, and stable signal. The installation location is shown in Figure 6.



Fig. 6 - Installation diagram of vehicle navigation positioning module

- **Attitude sensor and pressure module**

The posture sensor uses the LVT425T-90 dual-axis tilt sensor produced by Microsensor, which real-time acquires the tilt angle value of the machine, and determines whether it exceeds the set angle threshold, that is, whether the machine is grounded. It features simplicity of use, reliable performance, and good scalability. The voltage booster module uses a non-isolated boost converter produced by Enpu Technology to convert the tractor voltage of 12 V to the operating voltage of the servo motor of 36 V, providing continuous and stable power for the drive module. The installation location is shown in Figure 1.

- **Vehicle control terminal**

The vehicle control terminal uses the DC80480KM070 model serial display night vision screen produced by Guangzhou Dacai. It is based on the VisualTFT platform to process, display, control, and store data. It has the advantages of good handling of workpiece movement and vibration, meeting the actual requirements of the electric drive wheat shallow buried drip irrigation-wide width seeder control system.

System Software Design

- **Overall design of terminal functions**

Based on the functional requirements of the precision seeding/fertilization control system, this article designs the system implementation process. The implementation process is shown in Figure 7. Initialize configuration before system startup, set system parameters, and obtain parameter values through corresponding protocol parsing. Start the system and cyclically check the working status of each sensor. After the control system is started, input the equipment parameters of the wheat shallow buried drip irrigation-wide width seeder through the touch screen (machine operation width, number of sowing and fertilizing rows, etc.), single circle sowing/fertilizer amount, target fertilizer application amount, target sowing amount of wheat, angle threshold, etc.

Establish the serial connection relationship between the main controller and the driver module, wheel encoder, onboard navigation positioning module, attitude sensor, etc. The embedded controller determines the target speed for planting/fertilizing by obtaining the operating posture and working speed of the machine, combined with the input parameters.

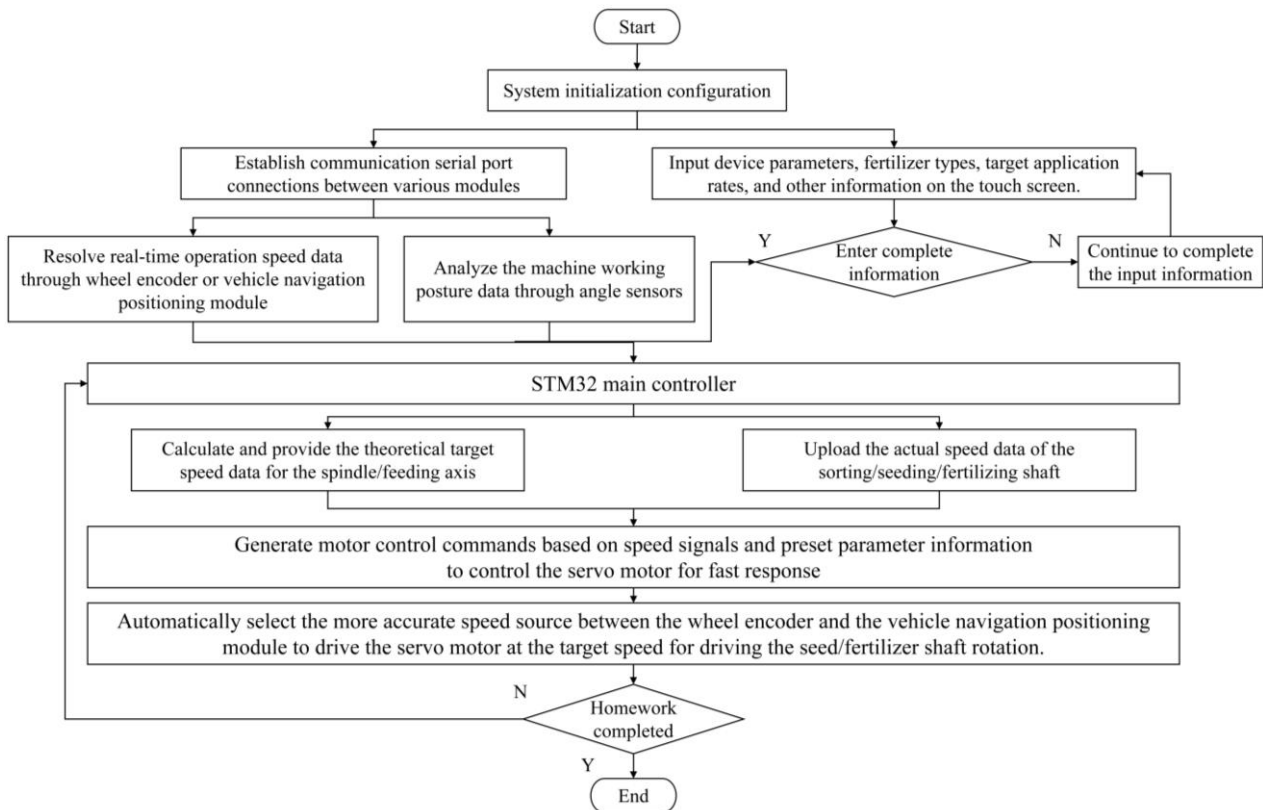


Fig. 7 - Control system implementation flowchart

(1) Rotary encoder speed acquisition

By using a precision rotary grating disk and optocoupler to generate count pulses that can be recognized for direction, the count pulses are transmitted to the STM32 controller to calculate the ground wheel rotation speed (i.e. implement forward speed), allowing real-time acquisition of implement movement data information. However, due to the phenomenon of wheel slippage, the wheel slippage coefficient must be considered. The formula for calculating the actual wheel speed (i.e. implement forward speed) is:

$$\begin{cases} v = \frac{\pi d(1 + \varepsilon)N}{tn} \\ v = \frac{33\pi(1 + \varepsilon)N}{25600t} \end{cases} \quad (2)$$

where:

- v - the speed of the machine, m/s;
- n - the number of speed pulse signals per revolution of the encoder, which is 1024;
- d — the diameter of the speed measuring wheel, which is 1.32 m;
- ε — the slip rate, generally taken as 0.05 to 0.12 (Zhang et al., 2021).

(2) Vehicle navigation positioning module speed acquisition

The UM220-IV outputs location information in the communication standard format of NMEA-0183 and accepts data input in ASCII format. It sets the output frequency of the module to 5 Hz through the MCU, and obtains valid information such as latitude, longitude, UTC time, and ground speed by parsing the mixed positioning data RMC frame of GPS and BeiDou. The basic format of RMC frame is as follows:

\$GNRMC, time, status, Lat, N, Lon, E, spd, cog, date, mv, mvE, mode*cs

Where spd is the ground speed, obtaining spd data can obtain the real-time speed v of the planter. The speed resolution process diagram is shown in Figure 8.

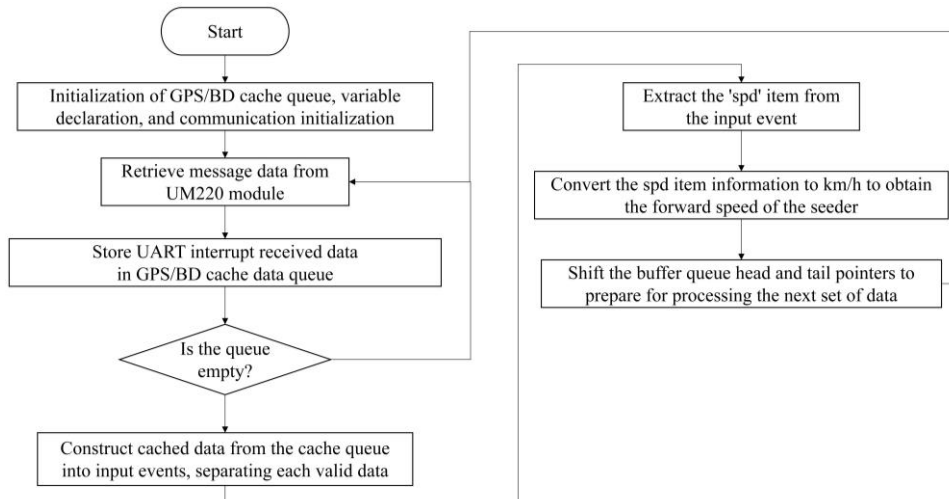


Fig. 8 - Flowchart of speed acquisition process for vehicle navigation positioning module

(3) The speed of sowing mode comes from automatic switching

When the tractor is working in variable speed mode, the main controller automatically selects the more accurate speed source between the wheel encoder and the vehicle navigation positioning module to drive the servo motor. The speed measured by the vehicle navigation positioning module is v_1 , the speed measured by the wheel encoder is v_2 , and the critical speed for switching speed measurement methods is v_3 . The speed source V selection mode is as shown in Table 1.

Table 1

Speed source switch logic		
Real-time speed	Measured speed	Speed Source
$> v$	$v_1 > v_2$	v_1
	$v_1 \leq v_2$	v_2
$\leq v$	/	v_1

(4) Motor Speed Control Model

To achieve precise planting control, the motor needs to dynamically match the forward speed of the tractor. The demand weight per unit time in the field is equal to the sowing quantity per unit time required by the sowing machine, and the calculation formula is:

$$\begin{cases} N_T = BS = XH \frac{1000v}{60} \cdot \frac{1.5}{1000} \\ N_B = \frac{V_s \rho n X}{1000} \end{cases} \quad (3)$$

Simplifying formula (3), the theoretical speed calculation formula of the seed meter (motor scheduling control model) can be obtained:

$$n = \frac{25BLv}{V_s \rho} \quad (4)$$

where: S - the planting area per unit time of the planter in the field, acres/min;

X - the number of rows planted by the seeder;

H - the row spacing of the planter, m;

v - the operating speed of the seeder, km/h;

N_T - the demand weight per unit time in the field, kg/min;

B - the seeding rate per acre, kg/acre;

N_B - the seeding amount per unit time of the seeder, kg/min;

V_s - the calculated volume of the seeding rotor, cm^3 ;

ρ - the bulk density of wheat seeds, g/cm^3 ;

n - the theoretical working speed of the planter, r/min.

(5) Remote transmission of location information

When transmitting positioning information of the seeder, the 4G wireless transmission module needs to be configured. The STM32F407 microcontroller configures the 4G wireless transmission module using AT commands, setting the data communication baud rate between the 4G wireless transmission module and the STM32F407 microcontroller USART1 (TXD_1) to 9600. 4G wireless transmission module connects to Alibaba Cloud server, port is 8090, connection type is long connection, and working mode is network transparent transmission mode. After the above configuration, the 4G module can transmit the positioning information of the planter through the network to the specified server port after receiving the positioning data packet sent by the STM32F407 microcontroller, realizing the remote transmission of the planter's positioning information.

● **Display Interface**

Based on the precision seeding/fertilization control algorithm and flow chart, the display interface of the electric-drive wheat shallow buried drip irrigation-wide width precision seeder control system is planned and designed on the VisualTFT platform. It is mainly divided into four major functional interfaces: main interface, parameter setting interface, storage debugging interface, and fertilizer calibration interface.

The main interface sets the switch for sowing, fertilizing, and motor control, displaying parameters such as amount of sowing applied per mu, amount of fertilizer applied per mu, sowing speed, fertilizing speed, machine forward speed, angle sensor, sowing area, etc., and provides alarm prompts for the material level in the seed and fertilizer boxes. The parameter setting interface mainly sets the number of seeders, the number of fertilizers, working width, angle threshold, number of working rows, wheel rotation radius, single circle seeding amount, single circle fertilization amount, amount of sowing applied per mu, amount of fertilizer applied per mu, etc., and can adjust the rotation direction of the motor. Debug the stored content of the prototype positioning status, operation information, etc. in the storage debugging interface. The fertilizer calibration interface is mainly used to calibrate the single circle seeding amount and single circle fertilization amount, as shown in Figure 9.



Fig. 9 - Display Interface

Performance test design of monitoring system

● **Parameter calibration**

(1) Wheel Encoder Speed Measurement

Accurate measurement of the forward speed of the machine is related to the control system for seeding/fertilizer rate calculation and control accuracy, and speed testing work is required. The wheat shallow buried drip irrigation-wide width precision seeder maintains a constant speed of 3-6 km/h and records the time it takes to pass through the calibration interval (100m*5m).

By transforming formula (2), the calculation formula for slip ratio is obtained:

$$\varepsilon = \frac{25600tv}{33\pi N} - 1 \tag{5}$$

The study selected 6% as the slip rate of the wheat shallow buried drip irrigation-wide width precision seeder. To verify the accuracy of the speed measurement, repeat the experiment 3 times and take the average value. Calculate the actual speed by dividing the distance traveled by the time taken.

(2) Seed planting/fertilizer measurement

To achieve precise seeding and fertilization, it is necessary to determine the seeding/fertilizer discharge rates of different planters/fertilizer applicators. The experimental materials selected were commonly used granular compound fertilizer and Xin Chun 6 wheat seeds. Before the experiment, the seeds/fertilizer are loaded into the seed/fertilizer box separately.



The servo motor is controlled by the controller to drive the slot wheel type seed/fertilizer dispenser to rotate at a certain speed. Place the feeding container at the discharge port, and the amount of seeds/fertilizer for sowing/fertilizing can be obtained by weighing the seeds/fertilizer in the feeding container. Then use a stopwatch to time the sowing/fertilizing, repeating the experiment three times at each speed.

● **Field performance test**

To verify the operation effect of the control system of the electric-drive wheat shallow-buried drip irrigation-wide-width precision seeder, a field test of precision seeding of wheat was conducted on March 30, 2024 in Yuli County, Bayingolin Mongol Autonomous Prefecture, Xinjiang Uygur Autonomous Region. The supporting power is John Deere 1204 tractor, the wheat variety is Xinchun 6, the compound fertilizer variety is Guizhuhua 27-17-7, and the seeding and fertilization experiment is conducted using the wheat shallow-buried drip irrigation-wide-width uniform sowing machine equipped with this system.

According to the national standards GB/T9478-2005 "Test methods for grain drill" (China Agricultural Machinery Standardization Technical Committee 2005) and GB/T35487-2017 "Variable rate fertilizer seeder control system" (China Agricultural Machinery Standardization Technical Committee 2017), the test process starts by powering on the system and resetting the data. Then start the machine moving forward by adjusting the throttle and shifting gears to control the forward speed of the machine. In this experiment, the machine was set to move at speeds of 1.0, 2.0, 3.0, 4.0, 5.0, and 6.0 km/h, with a seeding rate of 30.0 kg per mu and a fertilizer application rate of 10.0 kg per mu. At each speed, the machine operates on an area of 1 mu. The actual seeding and fertilization amounts are recorded in the experimental table.

RESULTS AND ANALYSIS

● **Parameter calibration**

(1) Wheel Encoder Speed Measurement

The test site is shown in Figure 10. The detection speed was calculated using formula (2), and the test results are shown in Table 2. The speed measurement accuracy during the test was above 97.00%, meeting the requirements for accurate speed measurement in seed/fertilizer testing work.



Fig. 10 - Wheel encoder speed test

Table 2

Test measurement results of wheel encoder speed calibration

Number	Actual Speed (km/h)	Detection speed (km/h)	Accuracy (%)
1	3.00	2.93	97.67
2	3.50	3.45	98.57
3	4.00	4.07	98.25
4	4.50	4.60	97.78
5	5.00	4.88	97.60
6	5.50	5.59	98.36
7	6.00	6.14	97.67

(2) Seed planting/fertilizer measurement

The test site is shown in Figure 11, and the test results are shown in Table 3. The average seeding/fertilizer application rates were 22.4 g/plant and 157.4 g/plant, with standard deviations of 1.1 and 3.3 respectively. It can be seen that the slot wheel type seed/fertilizer planter dispenses a larger amount of seeds/fertilizer per revolution at low speed and a smaller amount at high speed, which is mainly related to the weight of seeds/fertilizer carried out between the slot wheel outer side and the shell.



Fig. 11 - Seed planting/fertilizer application test

Table 3

Test measurement results of seeding/fertilizer dispenser capacity

Category	Number of trials	Manure spreader speed / (r/min)		
		10	30	50
Sowing quantity (g/r)	1	25.6	21.6	20.6
	2	24.8	21.6	19.6
	3	24.4	23.8	19.6
	Average	22.4		
	Standard Deviation	2.2		
Manure application (g/r)	1	163.4	148.6	148.8
	2	162.0	159.0	151.4
	3	165.6	164.8	153.0
	Average	157.4		
	Standard Deviation	6.6		

● **Field performance test**

The test site is shown in Figure 12, and the test results are shown in Table 4. Field trial results showed that the seeding rate control error ranged from 3.0% to 5.3%, and the fertilization amount control error ranged from 3.0% to 6.0%, meeting the requirements for practical operation of electrically driven wheat shallow buried drip irrigation-wide width precision seeder. However, there is still room for optimization in the accuracy of the prototype control. In the future, in-depth research on the working principle, key components, and control modules of the prototype is needed to improve its control accuracy.



Fig. 12 - Field test site

Table 4

System field monitoring test results

Forward speed (km/h)	Theoretical audience reach (kg)	Actual playback volume (kg)	Control Error (%)	Theoretical fertilization amount (kg)	Actual amount of fertilizer (kg)	Control Error (%)
1	30.0	31.5	5.0	10.0	10.5	5.0
2		31.3	4.3		10.3	3.0
3		28.9	3.7		9.4	6.0
4		29.1	3.0		9.5	5.0
5		28.4	5.3		9.4	6.0
6		28.6	4.7		9.6	4.0

CONCLUSIONS

In this paper an electrically driven control system for wheat shallow buried drip irrigation-wide width precision seeder was designed, parameter calibration tests were conducted, and field tests were carried out to verify the reliability of the system operation.

1) This article proposed a fusion speed measurement method integrating the ground wheel encoder and satellite positioning module. The control system was designed with a single-chip STM32 controller as the core, consisting of STM32 main controller, DC servo motor, servo motor reducer, ground wheel encoder, vehicle navigation positioning module, vehicle control terminal, attitude sensor, voltage conversion module, etc., to achieve precise wheat sowing and fertilization for an electric-drive shallow-buried drip irrigation and wide-width precision seeder.

2) Based on the VisualTFT platform, the software system developed for the electric drive control system can calibrate the single-circle seeding amount, single-circle fertilization amount, set the number of seed/fertilizer dispensers, working width, angle threshold, working rows, wheel rotation radius, seed amount of sowing applied per mu, amount of fertilizer applied per mu, etc. It can display real-time parameters such as seeding amount rotation speed, fertilization amount rotation speed, machine forward speed, machine posture status, seeding area, and has fault alarm and storage functions.

3) Calibration tests and field trials of the control system for an electric-drive wheat shallow-buried drip irrigation and wide-width uniform seeding machine showed that the system operated stably and reliably. In the parameter calibration test, the speed accuracy of the ground wheel encoder was above 97.00%, with average seeding/fertilizer amounts of 22.4g/r and 157.4g/r respectively, and standard deviations of 1.1 and 3.3. In field experiments, the seeding rate control error ranged from 3.0% to 5.3%, and the fertilization amount control error ranged from 3.0% to 6.0%, meeting the operational requirements of the actual electric-drive wheat shallow-buried drip irrigation and wide-width precision seeder.

Subsequent research will add fertilization prescription charts, flow monitoring sensors, and consider introducing other programming languages to take into account the development characteristics of other high-level programming languages, enhancing the monitoring performance of the system. Further research will collect more diverse data to enhance the robustness and adaptability of the model, ensuring greater stability, reducing control accuracy errors, improving the system's environmental adaptability and operational reliability, making the system functions more in line with actual production conditions, and adaptable to different operational scenarios.

ACKNOWLEDGEMENT

This work was supported by the Xinjiang Uygur Autonomous Region Major Science and Technology Special Projects (2022A02003-3).

REFERENCES

- [1] Cay A., Kocabiyik H., May S., (2018), Development of an electro-mechanic control system for seed-metering unit of single seed corn planters-Part I: design and laboratory simulation [J]. *Computers and Electronics in Agriculture*, 144: 71-79, London / UK.;
- [2] Cay A., Kocabiyik H., May S., (2018), Development of an electro-mechanic control system for seed-metering unit of single seed corn planters-Part II: field performance[J]. *Computers and Electronics in Agriculture*, 145:11-17, London / UK.;
- [3] Chen S.F., Yu C., Sun Q.X., Yang, J., Lu X.C., Li X.H., Liu, X., (2020), Research on Control System of Precision Seeder Based on Beidou Navigation [J]. *Journal of Agricultural Mechanization Research*, 44(08): 114-118, Heilongjiang / P.R.C.;
- [4] Feng Y.G., Jin C.Q., Yuan W.S., Chen M., Xu J.S., Liu Z., (2020), Research on precision electric seeding control system based on satellite velocity measurement for wheat [J]. *Journal of Chinese Agricultural Mechanization*, 41(12): 124-130, Jiangsu / P.R.C.;
- [5] Gui Z.L., Gu Y.Q., Xu L.X., He X., Zhu Y.H., Wang B.S., Wang W.Z., (2024), Design and experiment of electronic control system of wheat planter based on GNSS velocity measurement [J]. *Journal of Henan Agricultural University*, 58(03): 1-14, Zhengzhou / P.R.C.;
- [6] He X., Zhang D., Wei J., Wang M., Yu Y., Liu Q., Yan B., Zhao D., Yang L., (2017), Development of an electric-driven control system for a precision planter based on a closed-loop PID algorithm [J]. *Computers and Electronics in Agriculture*, 136(C): 184-192, London / UK.;

- [7] Ibrahim E.J., Liao Q., Wang L., (2018), Design and experiment of multirow pneumatic precision metering device for rapeseed [J]. *International Journal of Agricultural and Biological Engineering*, 11(05): 116-123, Beijing / P.R.C.
- [8] Jiang M., Liu C.L., Wei D., Du X., Cai P.Y., Song J.N., (2019), Design and Test of Wide Seedling Strip Wheat Precision Planter [J]. *Transactions of the Chinese Society for Agricultural Machinery (Transactions of the CSAM)*, 50(11): 53-62, Beijing / P.R.C.;
- [9] Jiang Z.H., Jiang Z.H., Wang Y.X., Wei Y.F., Yu Y., Sun Y.J., Sun Y.T., (2024), Design and experiment of control system of electric drive corn high speed operation seeder [J]. *Journal of Chinese Agricultural Mechanization*, 45(03): 24-30,57, Jiangsu / P.R.C.;
- [10] Karimi H., Navid H., Besharati B., Eskandari I., (2019), Assessing an infrared-based seed drill monitoring system under field operating conditions [J]. *Computers and Electronics in Agriculture*, 162: 543-551, London / UK.;
- [11] Liao Q.X., Lei X.L., Liao Y.T., Ding Y.C., Zhang Q.S., Wang L., (2017), Research progress of precision seeding for rapeseed [J]. *Transactions of the Chinese Society for Agricultural Machinery (Transactions of the CSAM)*, 48(09): 1-16, Beijing / P.R.C.;
- [12] Liao Q.X., Wu C., Zhang Q.S., Wang B.S., Du W.B., Wang L., (2022), Design and Experiment of Speed-dependent Seeding Control System of Rapeseed Precision Combined Seeding Machine [J]. *Transactions of the Chinese Society for Agricultural Machinery (Transactions of the CSAM)*, 53(12): 49-58+159, Beijing / P.R.C.;
- [13] Liu W., (2020), *Research on Seeding Rate Monitoring and Controlling Technology Based on Information of Seed Flow Rate for Wheat Drill* [D]. Jiangsu University, Zhenjiang / P.R.C.;
- [14] *National Agricultural Machinery Standardization Technical Committee.*, (2005), GB/T 9478-2005 Test method of grain strip machine [S]. China Agriculture Press, Beijing / P.R.C.;
- [15] *National Agricultural Machinery Standardization Technical Committee.*, (2017), GB/T 35487-2017 Variable fertilization planter control system [S]. China Agriculture Press, Beijing / P.R.C.
- [16] Nielsen S.K., Munkholm L.J., Lamandé M., Nørremark M., Edwards G.T.C., Green O., (2018), Seed drill depth control system for precision seeding [J]. *Computers and Electronics in Agriculture*, 144: 174-180, London / UK.;
- [17] Salavat M., Ildar B., Zinnur R., Ramil L., Elmas N., (2020), Numerical simulation of two-phase "air-seed" flow in the distribution system of the grain seeder [J], *Computers and Electronics in Agriculture*, 168: 105151, London / UK.;
- [18] Sun X.W., Xi X.B., Chen M., Huang S.J., Jin Y.F., Zhang R.H., (2024), Design and experiment of control system of wheat mechanized uniform sowing [J]. *Journal of Chinese Agricultural Mechanization*, 45(02): 27-32, Jiangsu / P.R.C.;
- [19] Tang W.B., (2021), *Design and research of vertical rotary tillage electric drive wide narrow row sowing compound machine* [D]. Henan Agricultural University, Zhengzhou / P.R.C.;
- [20] Wang W.L., (2023), *Effect of Optimizing Large Tube to Row Ratio Drip Irrigation Patterns on Yield and Water Use Efficiency of Spring Wheat and Its Physiological Mechanism* [D]. Shihezi University, Xinjiang / P.R.C.;
- [21] Wang W.W., Wu K.P., Zhang Y., Wang M.X., Zhang C.L., Chen L.Q., (2022), The development of an electric-driven control system for a high-speed precision planter based on the double closed-loop fuzzy PID algorithm [J]. *Agronomy*, 12(04): 945, Madison Wisconsin / USA.;
- [22] Wang Y.L., (2023), *Design and Research of Electric Control Wheat Precision Seeder* [D]. Henan Agricultural University, Zhengzhou / P.R.C.;
- [23] Wu C., (2022), *Design and Experiment of Speed-dependent Seeding Control System of Rapeseed Precision Combined Seeding Machine* [D]. Huazhong Agricultural University, Wuhan / P.R.C.;
- [24] Xue B., Zhou L.M., Niu K., Zheng Y.K., Bai S.H., Wei L.A., (2023), Sowing Depth Control System of Wheat Planter Based on Adaptive Fuzzy PID [J]. *Transactions of the Chinese Society for Agricultural Machinery (Transactions of the CSAM)*, 54(S1): 93-102, Beijing / P.R.C.;
- [25] Yao J.W., Qi Y.Q., Li H.H., Shen Y.J., (2021), Water saving potential and mechanisms of subsurface drip irrigation: a review [J]. *Chinese Journal of Eco-Agriculture*, 29(06): 1076-1084, Beijing / P.R.C.;
- [26] Yu H.L., Kan M.X., Xu Z.L., Ma R.Q., Liu A.K., Wang D.M., Wang Y.J., Yang Y.S., Zhao G.C., Chang X.H., (2023), Yield and dry matter accumulation of wheat in response to spring irrigation water in uniform sowing and strip sowing [J]. *Acta Agronomica Sinica*, 49(10): 2833-2844, Beijing / P.R.C.;

- [27] Zhang C.L., Liu T., Zheng Z.H., Fang J., Xie X.D., Chen L.Q., (2024), Design and test of the precision seeding dispenser with the staggered convex teeth for wheat sowing with wide seedling belt [J]. *Transactions of the Chinese Society of Agricultural Engineering (Transactions of the CSAE)*, 40(05): 47-59, Beijing / P.R.C.;
- [28] Zhang J.C., Yan S.C., Ji W.Y., Zhu B.G., Zheng P., (2021), Precision Fertilization Control System Research for Solid Fertilizers Based on Incremental PID Control Algorithm [J]. *Transactions of the Chinese Society for Agricultural Machinery (Transactions of the CSAM)*, 52(03): 99-106, Beijing / P.R.C.;
- [29] Zhang Z.H., (2018), *Research and Design of Control System for Wide Wheat Multifunction Precision Seeder* [D]. Shandong Agricultural University, Taian / P.R.C.

SIMULATION OF SOYBEAN SEED PHYSICAL PROPERTIES ON FILLING PERFORMANCE

大豆种子物理特性对充种性能影响的仿真研究

Guoqiang DUN ^{*12)}, Na GUO²⁾, Xinxin JI²⁾, Jiaying DU³⁾, Yongzhen YANG⁴⁾

¹⁾ Harbin Cambridge University, Intelligent Agricultural Machinery Equipment Engineering Laboratory, Harbin / China;

²⁾ Northeast Forestry University, College of Mechanical and Electrical Engineering, Harbin / China;

³⁾ Jiamusi University, Jiamusi / China;

⁴⁾ Shantui Engineering Machinery Limited Company, Jining / China;

Tel: 86 13836027042; E-mail: dunguoqiangpaper@163.com

DOI: <https://doi.org/10.35633/inmateh-74-08>

Keywords: Sphericity, EDEM, Filling performance, Response surface methodology, Variation coefficient.

ABSTRACT

Soybean seed physical properties is important on filling performance during planting. To evaluate the effect of sphericity and variation coefficient of mean diameter on seeding performance in seed metering device, seven soybean genotypes [The Ken Dou 40, Ken Feng 17, Qing Ren Black Soybean, Black Soybean, Hei He 44, Bei Jiang 91 and Dong Nong 52] were tested to measure the length, width, thickness, and calculate these sphericities, mean diameter and variation coefficient of mean diameter, respectively. The model of soybean seed with equal mean diameter was developed and the discrete element method was used to set the different sphericity and variation coefficient of mean diameter. A simulation study was performed in the model of the cell wheel feed followed by mathematical modeling of the experimental data, and the data with response to the surface methodology was analyzed. Results showed that while the sphericity had a significant effect on both single- and empty -seed rates, the variation coefficient of mean diameter had a significant effect on the multi -seed rate. With the increase of sphericity, the single-seed rate increases but empty-seed rate decreases. With the increase of variation coefficient of mean diameter, the multi-seed rate increases. Based on our results, the Ken Feng17, Ken Dou 40, Black Soybean and Qing Ren Black soybeans were only selected for bench test. The relative error between the experimental results and the theoretical values of the regression analysis was small; however, the respond trend of factor index was same. Our study suggested that the effect of sphericity and variation coefficient of mean diameter on seeding performance can be used by using simulation experiment.

摘要

大豆种子的物理特性对充种过程中的充填性能影响非常重要，为了探究球度与均径变异系数对种子在排种器中充填性能的影响，选取 7 种不同品种的大豆种子[垦豆 40, 垦丰 17, 青仁黑豆, 黑豆, 黑河 44, 北疆 91 和东农 52] 为试验对象，分别测量种子的长度、宽度、厚度，并计算种子的球度、均径变异系数，建立相同均径的大豆种子模型，并采用离散元法设置不同的球度和均径变异系数，并在窝眼轮式排种器模型中进行仿真试验。构造试验数据的数学模型，并进行响应曲面分析，结果表明：球度对单粒率和空粒率影响显著，均径变异系数对多粒率影响显著；随着球度的增加，单粒率升高，空粒率减小；随着均径变异系数的增加，多粒率升高。依据结果，选择垦丰 17、垦豆 40、黑豆和青仁黑豆进行台架试验，其试验值与回归方程输出理论值的相对误差较小，且具有相同的因素指标响应趋势，即利用仿真试验研究球度及均径变异系数对排种性能的影响具有可行性。

INTRODUCTION

Soybean is one of the most important legume grain crops associated with global food security. Soybeans as a crop is grown on an estimated 6% of the world's arable lands (Hartman et al., 2011). Global soybean production in the 2017-2018 market year was 346 million metric tons which represents 61% of the world's oilseeds production. Out of 12 major soybean producing countries, Brazil, Argentina and the U.S. produced over 82% of the world's soybeans. The U.S. was first in world soybean production with 119.5 million tons followed by Brazil at 112 million tons, and Argentina 54 million tons (USDA/NASS., 2017). China accounts for 4% of soybean production in the world, covering over 235 million hectares farmland. China accounts for 60% of worldwide soybean imports to meet the domestic demand. World growth of soybeans has been impressive as the growth has increased by about 350% since 1987 in response to the commercial growth of livestock and poultry industries.

While soybean is an important protein and oil source, the potential of greater benefits will achieve both economically and socially if soybeans can be sustainably and continuously grown with precision technology. Sustainable agricultural practices have the potential to maximize soybean production in response to increasing global demand; however, a systematic approach is needed to equilibrate soybean seeding techniques.

The effects of physical properties of soybean seeds on seeding performance is one of the key problems in current research on soybean breeding (Liu *et al.*, 2015; Horabik and Molenda, 2016; An *et al.*, 2017; Shi *et al.*, 2020). It's often problematic for the commercially available current metering devices to meet the seed filling requirements due to the differences of the geometric characteristics of the soybean seeds. The variable geometric characteristics of soybean seeds with internal friction among themselves resulted in irregular seeding of soybeans, therefore improving seeding performance has always been a research focus of the precision seed metering device. Use of planting equipment with adaptive seed metering devices can improve the efficiency of precision planting of seeds and reduce the cost of soybean production. While several studies have researched the relationship between soybean seeds filling and parameters of type hole, there are very limited research information available on filling performance of different sphericity and variation coefficient of mean diameter of soybean seeds in seed metering devices (Dun *et al.*, 2016; Coetzee, 2019; Zhao *et al.*, 2019).

With the development of computer technology, numerical simulation has been used in the design, analysis, and optimization of agricultural machinery. The discrete element method is a new numerical method for analyzing and solving the dynamics of discrete systems (Yang *et al.*, 2018; Zeng *et al.*, 2018; Han *et al.*, 2019). A recent study reported the influence factors of seed filling problem of corn seed distributor by using the discrete element method (Lu *et al.*, 2018). Similarly, another one proposed a method of seed discrete element modeling based on granular assembly by measuring and analyzing the parameter of soybean seeds (Wang *et al.*, 2018). Other studies have also dynamically simulated the working processes of seed metering device with discrete element method (Qian *et al.*, 2023). Based on the results of previous studies, the discrete element method has a great potential and space to optimize the performance of seed metering devices.

Based on the discrete element method, the soybean seeds with different sphericity and variation coefficient of mean diameter were simulated by using the model of Shuang Fu cell wheel feed. The effect of sphericity and variation coefficient of mean diameter on filling performance was evaluated to provide a theoretical basis on designing the seed meter device for soybean seeds. The simulation analysis on the seed metering device by discrete element numerical simulation will save costs, minimize test cycle, and provide references and calibration for the improvement of the precision planters.

MATERIALS AND METHODS

Measurement and calculation of physical characteristics of soybean seeds

The Ken Dou 40, Ken Feng 17, Qing Ren Black Soybean, Black Soybean, Hei He 44, Bei Jiang 91 and Dong Nong 52 were selected as test objects to study the effect of sphericity and variation coefficient of mean diameter on filling performance.

The parameters (length L , width W , and thickness T) of 100 seeds randomly selected from each variety were measured with SANTO 8014 digital caliper (measuring range 1~150 mm, accuracy 0.01 mm) as shown in Fig.1. The mean diameter, sphericity, and variation coefficient of soybean seeds were also calculated (Lu *et al.*, 2017; Xu *et al.*, 2017).

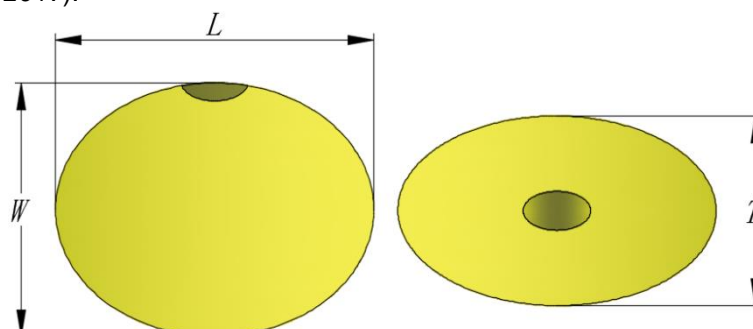


Fig. 1 - Schematic diagram of soybean seed size

Note: L seed length, mm, W seed width, mm, T seed thickness, mm.

The soybean seed was supposed to be a three-dimensional ellipsoid, according to the related researchers (Yuan *et al.*, 2022; Rorato *et al.*, 2019), the calculation formula of sphericity was as follows:

$$S_P = \frac{\sqrt[3]{LWT}}{L} \quad (1)$$

where: L is length of the seed, mm; W is width of the seed, mm; T is thickness of the seed, mm.

The variation coefficient can reflect the discrete degree of soybean mean diameter, and the calculation formula of variation coefficient was as follows:

$$C = \frac{S_d}{N} \times 100\% \quad (2)$$

where:

C is the variation coefficient of mean diameter, %; S_d is the standard deviation, mm; N is the average value, mm.

According to the measurement and calculation of the physical characteristics of the above seeds, mean diameter, range of sphericity, mean sphericity and variation coefficient of mean diameter were calculated as shown in Table 1.

Table 1

The data of soybean seed with descriptive statistics Table

Soybean variety	Mean diameter (mm)	The range of sphericity (%)	Mean sphericity (%)	Variation coefficient of mean diameter
Ken Dou 40	6.13	93.2 - 99.8	96	0.046
Ken Feng 17	6.66	88.7 - 99.8	96.4	0.041
Qing Ren Black Soybean	6.65	75.5 - 94.4	87.1	0.068
Black Soybean	7.52	81.3 - 95.2	89.9	0.057
Hei He 44	5.98	78.1 - 95.8	88.8	0.050
Bei Jiang 91	6.88	84.6 - 98.4	95.1	0.062
Dong Nong 52	6.69	90.8 - 98.4	95.5	0.043

Mean diameter of soybean seeds was supposed to be a constant value for studying the effect of sphericity and variation coefficient of mean diameter on seed filling performance. Because in the context of definite type hole, the smaller the mean diameter of soybean seeds is, the easier it is to fill the seeds. It was selected as the model of test that the smallest integer of mean diameter range is 6 mm and range of the sphericity is 70 - 100%, and range of variation coefficient of mean diameter is 0.041 - 0.068. Based on the information, our discrete element simulation test was developed.

The establishment of discrete element model

The contact parameters in EDEM

The material of the seed metering device was set as steel and the brush was nylon origin. Related research (Zhang *et al.*, 2018; Zhang *et al.*, 2017) have shown that the Poisson's ratio, shear modulus, and density of the soybean seed, steel surface and brush were supposed to be constant values. So, the coefficient of restitution, coefficient of static friction, and coefficient of rolling friction of the seed-seed, seed-brush, and seed-steel surface were calculated, as shown in Table 2.

Table 2

Basic parameters of soybean seed

Material	Parameters	Value
Soybean seed	Poisson's ratio	0.23
	Shear modulus (MPa)	63
	Density (kg/m ³)	1290
Brush	Poisson's ratio	0.40
	Shear modulus (MPa)	100
	Density (kg/m ³)	1150
Steel surface of seed metering device	Poisson's Ratio	0.30
	Shear modulus (MPa)	70000
	Density (kg/m ³)	7800
Seed-seed	Coefficient of restitution	0.30
	Coefficient of static friction	0.39
	Coefficient of rolling friction	0.17
Seed-brush	Coefficient of restitution	0.45
	Coefficient of static friction	0.50
	Coefficient of rolling friction	0.01
Seed-steel surface	Coefficient of restitution	0.52
	Coefficient of static friction	0.15
	Coefficient of rolling friction	0.09

Soybean seed model, establishment of seed metering device model and parameter setting

According to parameters in Table 1 and 2, the model of soybean seeds (mean diameter, 6 mm) was built with the granular assembly method. The relationship between seeds length, width and thickness and seeds sphericity was as follows:

$$\begin{cases} \frac{L+W+T}{3} = N \\ \frac{\sqrt[3]{L \times W \times T}}{L} \times 100\% = S_p \\ L = S + D \\ T = D \end{cases} \quad (3)$$

where: *L* is length, [mm]; *W* is width, [mm]; *T* is thickness, [mm]; *N* is mean diameter, [mm]; *S_p* is sphericity, [%]; *S* is the distance between the outside two balls, [mm]; *D* is the diameter of the ball, [mm].

In the following, a soybean seed with 85% sphericity will be used as an example to illustrate the process of constructing a soybean seed particle model. First, to simplify the calculation process, the thickness and width of the soybean seeds were supposed to be equivalent. According to Formula 3, the distance *S* between the outermost two balls is 1.52 mm and the diameter *D* of ball is 5.49mm. In the EDEM particle system, to begin with, three balls are generated. The three balls are on the same layer and have the same diameter, as well as the spherical centers of the three balls are (-0.76,0,0), (0,0,0) and (0.76,0,0) respectively. The three balls were used to simulate soybean seeds, and the final combination resulted in a soybean seed model with 85% sphericity. In this way, the spherical polymerization model of soybean seeds with the same diameter and other different sphericity was established. Soybean seed model is shown in Figure 2.

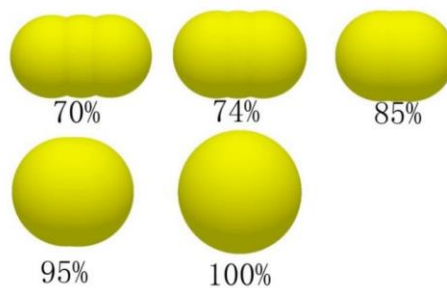


Fig. 2 - Soybean seed model

Quadratic orthogonal simulation experiment

Test parameters

The contact model (particle to particle and particle to geometry) was set as Hertz-Mindlin (no slip) build-in with discrete element simulation software EDEM 2.6. A 3D model removed the complex structure was built in the Solid works which could be imported into EDEM2.6, based on the Shuang Fu brush cell wheel feed (Figure. 3).

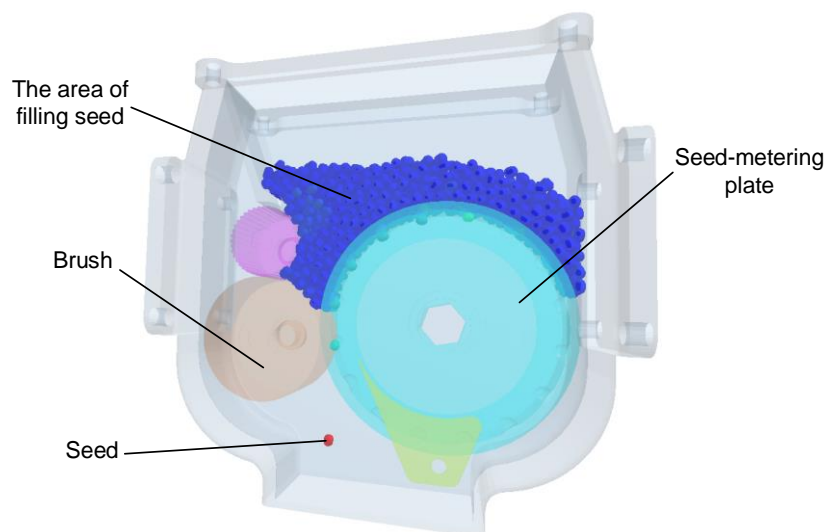


Fig. 3 - The EDEM model of seed metering device

Related previous studies (*Dun et al., 2016*) have shown that, there was the best effect on the cell wheel feed when the diameter of the holes on the cell wheel feed disk was 1.5 to 1.7 times as long as the seeds' mean diameter. Therefore, the diameter of holes was set to 9.6 mm, which was 1.6 times as long as the seeds' mean diameter, (*the mean diameter of seeds was 6 mm*). The diameter of the seeding disk was 130 mm, and 25 holes were arranged around it. The theoretical plant spacing was 5 cm, and the maximum working speed was 0.5 m/s. By calculation, the rotational speed of the seeding disk was 0.4 r/s, and the rotation speed of the brush was set to be 0.5 r/s.

The virtual particle factory was created at the upper seed box of the model. The central coordinate of the virtual plane was set as (0, 0, 110), the size of the long side was 80 mm, and the size of the short side was 30 mm. Particles were set in dynamic generation mode, and the number of particles was set as 300, and the generation speed was 5000 seeds per second. The particle diameter was subject to the normal distribution mode (*Ma et al., 2015; Wang et al., 2018; Wang et al., 2018*), and the soybean seeds' variation coefficient of mean diameter was matched with data presented in Table 2. The simulation started from 0 seconds and the particle's downward velocity was set to 2.5 m/s. The duration was 15 seconds, and the fixed time step was set to 5×10^{-6} s.

The sphericity and variation coefficient of mean diameter were selected as experimental factors, and the two-factor and five-level quadratic regression orthogonal test was designed to analyze the effect on filling performance. The experimental factors and horizontal code were shown in Table 3.

Table 3

Levels	Factors	
	Sphericity X1/%	Variation coefficient of mean diameter X2
+1.267	100	0.068
+1	96.8	0.065
0	85	0.055
-1	73.2	0.045
-1.267	70	0.041

Simulation data and analysis

Variance analysis

According to the two-factor five-level quadratic regression orthogonal experiment (*Li et al., 2023*) as designed above, the single-seed rate, empty-seed rate, and multi-seed rate were obtained by the simulation, as shown in Table 4. The data were analyzed by design-expert 8.0.6 software, as shown in Table 5.

Table 4

The result of simulation

Test serial number	Sphericity X ₁	Variation coefficient of mean diameter X ₂	The single seed rate Y ₁	The multi-seed rate Y ₂	The empty hole rates Y ₃
1	-1	-1	77.6	10.8	11.6
2	1	-1	87.9	8.4	5.3
3	-1	1	71.4	13.8	14.8
4	1	1	85.5	14.2	0.3
5	-1.267	0	62.9	11.6	20.5
6	1.267	0	89.1	10.6	0.2
7	0	-1.267	85.3	4.7	10
8	0	1.267	81.8	12.8	6.4
9	0	0	84.6	7.7	7.7
10	0	0	80.7	9.5	9.8
11	0	0	82.4	9.3	8.3
12	0	0	84.9	8.9	6.2
13	0	0	81.1	9.2	9.7

Table 5

Analysis of variance

Evaluation Index	Variation source	Sum of squares	Freedom	Mean square	F value	P value	Significance
The single seed rate	Model	561.93	5	112.39	15.17	0.0012	**
	X ₁	460.06	1	460.06	62.10	0.0001	**
	X ₂	23.56	1	23.56	3.18	0.1177	-

Evaluation Index	Variation source	Sum of squares	Freedom	Mean square	F value	P value	Significance
	X ₁ X ₂	3.61	1	3.61	0.49	0.5077	-
	X ₁ ²	69.11	1	69.11	9.33	0.0185	*
	X ₂ ²	5.59	1	5.59	0.75	0.4139	-
	Residual	51.86	7	7.41	-	-	-
	Lack of fit	36.77	3	12.26	3.25	0.1424	-
	Pure error	15.09	4	3.77	-	-	-
	Cor total	613.79	12	-	-	-	-
The multi-seed rate	Model	73.92	5	14.78	13.08	0.0019	**
	X ₁	1.48	1	1.48	1.31	0.2901	-
	X ₂	50.40	1	50.40	44.58	0.0003	**
	X ₁ X ₂	1.96	1	1.96	1.73	0.2294	-
	X ₁ ²	19.01	1	19.01	16.82	0.0046	**
	X ₂ ²	1.07	1	1.07	0.95	0.3620	-
	Residual	7.91	7	1.13	-	-	-
	Lack of fit	5.87	3	1.96	3.82	0.1142	-
	Pure error	2.05	4	0.51	-	-	-
Cor total	81.84	12	-	-	-	-	
The empty hole rate	Model	327.22	5	65.44	16.24	0.0010	**
	X ₁	300.14	1	300.14	74.50	< 0.0001	**
	X ₂	5.61	1	5.61	1.39	0.2764	-
	X ₁ X ₂	16.81	1	16.81	4.17	0.0804	-
	X ₁ ²	2.76	1	2.76	0.69	0.4349	-
	X ₂ ²	1.90	1	1.90	0.47	0.5144	-
	Residual	28.20	7	4.03	-	-	-
	Lack of fit	19.23	3	6.41	2.86	0.1683	-
	Pure error	8.97	4	2.24	-	-	-
Cor total	355.42	12	-	-	-	-	

Note: P<0.01 (Highly significant, **), 0.01<P<0.05 (Very Significant, *), P>0.05 (not significant)

The single-seed rate model indicated that the model has reached the highly significant level and the misfit was not significant to account for. By analyzing the reliability of the test model, the determination coefficient (R²=0.8621) was obtained, which indicated that the 86.21% of the response values came from the selected factors, so the test fits well. The significance test of the model showed that the P of X₁ was less than 0.01, and the P of X₁² was less than 0.05. indicating that the sphericity and sphericity square had a significant impact on the single-seed rate, while other interactions were less significant. The regression equation of the variation coefficient of mean diameter and sphericity was:

$$Y_1 = -92.10 + 4.71X_1 - 1809.70X_2 + 7.53X_1X_2 - 0.03X_1^2 + 9172.52X_2^2 \tag{4}$$

According to the P value, the less significant terms were removed one by one. The regression equation after removing was shown.

$$Y_1 = -162.91 + 5.12X_1 - 0.03X_1^2 \tag{5}$$

The multi-seed rate model P = 0.0019 shown that the model has reached the highly significant level and the misfit was not significant. By analyzing the reliability of the test model, the determination coefficient R²=0.9033 was obtained, which indicated the 90.33% of the response values came from the selected factors, so the test fits well. The significance test of the model showed that the P value of X₂, and X₁² was less than 0.01. It showed that the variation coefficient of mean diameter and sphericity square had significant effects, while other interactions were less significant. The regression equation of the variation coefficient of mean diameter and sphericity was:

$$Y_2 = +135.19 - 2.67X_1 - 662.08X_2 + 5.55X_1X_2 + 0.01X_1^2 + 4022.52X_2^2 \tag{6}$$

According to the P value, the less significant terms were removed one by one. The regression equation after removing was shown.

$$Y_2 = -2.12 + 248.13X_2 - 1.77E - 004X_1^2 \tag{7}$$

The empty-seed rate model P=0.0010 suggested that the model has reached the highly significant level and the misfit was not significant. By analyzing the reliability of the test model, the determination coefficient R²=0.9207 was obtained, which indicated that 92.07% of the response values came from the selected factors, so the test fitted well.

The significance test of the model showed that the P value of X_1 was less than 0.01. It showed that sphericity had significant effects, while other interactions were less significant. The regression equation of the variation coefficient of mean diameter and sphericity was:

$$Y_3 = +5.85 - 0.55X_1 + 1881.69X_2 - 16.25X_1X_2 + 5.22X_1^2 - 5347.94X_2^2 \quad (8)$$

According to the P value, the less significant terms were removed one by one. The regression equation after removing was shown.

$$Y_3 = +54.85 - 0.54X_1 \quad (9)$$

Response surface analysis

The response surface method was applied to analyze the effect and interaction of two factors on the test indicators (Figure 4).

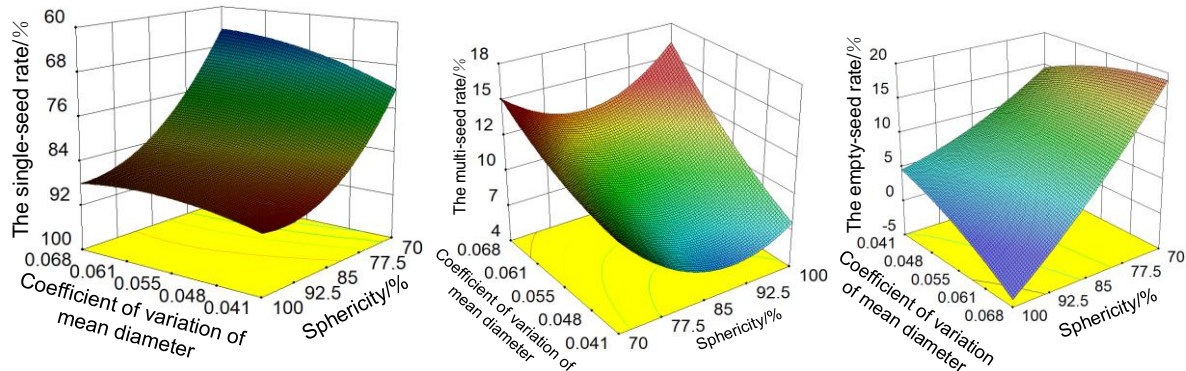


Fig. 4 - Response surface diagram of (a) single- seed, (b) multi-seed and (c) empty-seed rate

Fig. 4a was the response surface diagram of single-seed rate with the change of the experimental factors. When the sphericity was at a low level ($S_P=70\%$), the variation coefficient of mean diameter had little effect on the single-seed rate. However, when the sphericity had other levels, the single-seed rate decreased with the increase of variation coefficient of mean diameter. When the variation coefficient was at a high level ($C=0.068$), the sphericity had little effect on single-seed rate. However, in other levels, the single-seed rate increased with the increase of sphericity. In Fig. 4b is shown the response surface diagram of multi-seed rate with the change of the experimental factors. When the variation coefficient of mean diameter at a high level of ($C=0.068$), the multi-seed rate decreased and then increased with the increase of sphericity. However, in other levels, the sphericity had little effect on multi-seed rate and increased with the increase of the variation coefficient of mean diameter. The effect of the variation coefficient of mean diameter on multi-seed rate was more significant than the sphericity. In Fig. 4c is shown the response surface diagram of empty-seed rate with the change of experimental factors. With the increase of sphericity, the empty-seed rate decreased. When the sphericity was at a low level ($S_P=70\%$), the empty-seed rate increased with the increased of variation coefficient of mean diameter; however, when the sphericity had other levels, the empty-seed rate decreased with the increased of variation coefficient of mean diameter.

As the sphericity increased, the seed particle was closer to a positive sphere, and it was easier to enter the mold hole during seed filling, so single-seed rate increased, and empty-seed rate decreased. When the variation coefficient of mean diameter increased, the dispersion degree of seed particles became larger, and seeds became flatter and longer. As a result, the probability of filling more than two seeds in the mold hole would become bigger, and the multi-grain rate would increase accordingly.

Verification of bench test

Considering the feasibility of the test, the Shuang Fu brush cell wheel feed was used in bench test to verify the veracity of the simulation experience (Figure 5).



Fig. 5 - Verification of bench test

The working speed of the feeder was set as 0.5 m/s, the rotational speed of the seeding disk was 0.4 r/s, and the rotational speed of the brush was 0.5 m/s. In addition, Ken Feng 17 (sphericity 96.4%, variation coefficient of mean diameter 0.041), Ken Dou 40 (sphericity 96%, variation coefficient of mean diameter 0.046), Black soybean (sphericity 89.9%, variation coefficient of mean diameter 0.057) and Qing Ren black soybean (sphericity 87.1%, variation coefficient of mean diameter 0.068) were selected for testing on the performance test bench of JPS-12 seed feeder. The sphericity and variances coefficient of mean diameter were substituted into above regression equations (5), (7) and (9) to obtain the theoretical values of single, multiple and empty seed rates of the above seeds, as shown in Table 6.

Table 6

Data comparison						
Variety		Sphericity/%	Variation coefficient of mean diameter	Single-seed rate/%	Multi-seed rate/%	Empty-seed rate/%
Ken Feng17	Experimental value	96.4	0.041	85.5	9.2	5.3
	Theoretical value			87.49	6.41	2.79
	Relative error			2.27	43.53	89.96
Ken Dou40	Experimental value	96	0.046	83.5	10.7	5.8
	Theoretical value			87.46	7.66	3.01
	Relative error			4.53	39.69	92.69
Black soybean	Experimental value	89.9	0.057	79.3	12.8	7.9
	Theoretical value			85.88	10.59	6.30
	Relative error			7.66	20.87	25.40
Qing Ren Black Soybean	Experimental value	87.1	0.068	77.6	14.2	8.2
	Theoretical value			84.50	13.41	7.82
	Relative error			8.17	5.89	4.86

The experimental values of single-seed rate were little smaller than that of the theoretical values, in contrast, the experimental values of multi-seed rate and empty-seed rate were little larger than the theoretical values.

While the sphericity of Ken Feng 17, Ken Dou 40, Black soybean and Qing Ren Black Soybean decreased, the variation coefficient of mean diameter increased. It could be seen from Table 6 that the single-seed rate of Ken Feng 17, Ken Dou 40, Black Soybean and Qing Ren Black Soybean decreased, multi-seed rate and empty-seed rate increased. The relative error between the verified values and the theoretical values of the equation was small and had the same response trend to factor index. Therefore, it was feasible to study the effect of sphericity and variation coefficient of mean diameter on seeding performance by using simulation test.

CONCLUSIONS

(1) The physical parameters of Ken Dou 40, Ken Feng 17, Qing Ren Black Soybean, Black Soybean, Hei He 44, Bei Jiang 91 and Dong Nong 52 were measured. The sphericity range of seeds was 75.5 to 99.8% and the variation coefficient of mean diameter was 0.041 to 0.068.

(2) Based on the measured seed parameters, the simulation was carried out by using EDEM, and the simulation results were carried out by quadratic regression orthogonal experiment, and the mathematical models of single-, multi-, empty-seed rates, sphericity and variation coefficient of mean diameter were established, respectively.

(3) According to the analysis of response surface, with the increase of sphericity, the single-seed rate increased, and the empty-seed rate decreased, and with the increase of variation coefficient, the multi-seed rate increased.

(4) Ken Feng 17, Ken Dou 40, Black Soybean and Qing Ren Black Soybean were used in the bench test. While the sphericity of Ken Feng 17, Ken Dou 40, Black soybean and Qing Ren Black Soybean decreased, the variation coefficient of mean diameter increased, so the single-seed rate of Ken Feng 17, Ken Dou 40, Black Soybean and Qing Ren Black Soybean decreased in turn, but multi-seed rate and empty-seed rate increased. The relative error between the verified values and the theoretical values of the equation was small and had the same response trend to factor index. Therefore, it was feasible to study the effect of sphericity and variation coefficient of mean diameter on seeding performance by using simulation test.

ACKNOWLEDGEMENT

The authors were funded for this project by the National Key Research and Development Program Project (2018YFD0201001); Natural Science Foundation of Heilongjiang Province (LH2023E025); Northeast Forestry University Fundamental Research Funds for Central Universities (2572020BF03); Harbin Cambridge University Key Scientific Research Application Research Project (JQZKY2022021).

REFERENCES

- [1] An, X., Wang, S., Duan, H., Yang, C., Yu, Y., (2017). Test on Effect of the Operating Speed of Maize-soybean Interplanting Seeders on Performance of Seeder-metering Devices. *Procedia Engineering*, Vol.174, pp. 353-359, United States.
- [2] Chen, Z., Yu, J., Xue, D., Wang, Y., Zhang, Q., Ren, L., (2018). An approach to and validation of maize-seed-assembly modelling based on the discrete element method. *Powder Technology*, Vol.328, pp. 167-183, United States.
- [3] Coetzee, C., (2018). Particle upscaling: Calibration and validation of the discrete element method. *Powder Technology*, Vol.344, pp. 487-503, United States.
- [4] Dun, G., Chen, H., Zha, S., (2016). Parameter optimization and validation of soybean cell wheel seeding plate type-hole based on EDEM(基于 EDEM 的大豆窝眼轮式排种盘型孔参数优化与验证系统研究). *Soybean Sci*, Vol. 35(05), pp. 830-839, Heilongjiang / China.
- [5] Hartman, G. L., West, E. D., Herman, T. K., (2011). Crops that feed the World 2. Soybean-worldwide production, use, and constraints caused by pathogens and pests. *Food Security*, Vol. 3(1), pp. 5–17, United States.
- [6] Horabik, J., Molenda, M., (2016). Parameters and contact models for DEM simulations of agricultural granular materials: a review. *Biosystems Engineering*, Vol. 147, pp. 206-225, United States.
- [7] Han, D., Zhang, D., Jing, H., Yang, L., Cui, T., Ding, Y., Wang, Z., Wang, W., Zhang, T., (2018). DEM-CFD coupling simulation and optimization of an inside-filling air-blowing maize precision seed-metering device. *Computers and Electronics in Agriculture*, Vol. 150, pp. 426-438, United States.
- [8] Liu, D., Ning, X., Li, Z., Li, H., Yang, D., Gao, L., (2015). Discriminating and elimination of damaged soybean seeds based on image characteristics. *Journal of Stored Products Research*, Vol. 60, pp. 67-74, United States.
- [9] Lu, X., Xiong, Q., Cheng, T., Li, Q., Liu, X., Bi, Y., Li, W., Zhang, W., Ma, B., Lai, Y., Du, W., Man, W., Chen, S., Zhang, J., (2017). A PP2C-1 Allele Underlying a Quantitative Trait Locus Enhances Soybean 100-Seed Weight. *Molecular Plant*, Vol.10(5) , pp. 670-684, United States.
- [10] Lu, Y., Lv, Z., Zheng, W., Cai, Y., Liu, Z., (2018). Research and Experiment on Nest Hole Wheel Seed-metering Device of Maize-Based on EDEM(玉米窝眼轮排种器性能影响因素试验研究—基于 EDEM). *Journal of Agricultural Mechanization Research*, Vol. 40(06) , pp. 155-161, Heilongjiang / China.
- [11] Li, M., Liao, Q., Pei, L., Liao, Y., Wang, L., Zhang, Q., (2023). Design and Experiment of Rotary-cut Micro-ridge Seedbed Device for Rapeseed Direct Seeding Machine(油菜直播机旋切式微垄种床制备装置设计与试验). *Transactions of the Chinese Society of Agricultural Machinery*, Vol.54(05) , pp. 47-58+90, Beijing / China.
- [12] Ma, Z., Li, Y., Xu, L., (2015). Discrete-element method simulation of agricultural particles motion in variable-amplitude screen box. *Computers and Electronics in Agriculture*, Vol.118 , pp. 92-99, United States.
- [13] Qian, K., Liu, L., Liu, D., Sun, Q., Wang, D., Chen, K., Wang, J., Li, X., (2023). Simulation and Experiment of Seed Filling Characteristics of Different Peanut Varieties Based on EDEM(基于 EDEM 的不同品种花生种子填充特性仿真与试验). *Transactions of the Chinese Society of Agricultural Engineering*, Vol. 13(05), pp. 97-104, Beijing/ China.
- [14] Rorato, R., Arroyo, M., Andò, E., Gens, A., (2019). Sphericity measures of sand grains. *Engineering Geology*, Vol 254 , pp. 43-53, United States.
- [15] Shi, H., (2020). Research on Matching Cultivation Technique for Soybean Mechanized Harvest (适应大豆机械化收获配套栽培技术研究). *Modern Agricultural Sciences and Technology*, Vol. 24, pp. 9-10+13, Anhui / China.
- [16] United States Department of Agriculture (USDA)/National Agricultural Statistics Service (NASS). (2017). Available from: <http://www.nass.usda.gov/>

- [17] Wiącek, J., Molenda, M., Horabik, J., Ooi, JY., (2012). Influence of grain shape and intergranular friction on material behavior in uniaxial compression: Experimental and DEM modeling. *Powder Technology*, Vol. 217 , pp. 435-422, United States.
- [18] Wang, L., Li, R., Wu, B., Wu, Z., Ding, Z., (2018). Determination of the coefficient of rolling friction of an irregularly shaped maize particle group using physical experiment and simulations. *Particuology*, Vol. 38 , pp. 185-195, United States.
- [19] Wang, L., Wu, B., Wu, Z., Li, R., Feng, X., (2018). Experimental determination of the coefficient of restitution of particle-particle collision for frozen maize grains. *Powder Technology*, Vol. 338 , pp. 263-273, United States.
- [20] Wang, Y., Lyu, F., Xu, T., Yu, J., (2018). Shape and size analysis of soybean kernel and modeling (大豆籽粒形状和尺寸分析及其建模). *Journal of Jilin University(Engineering and Technology Edition)* , Vol. 48(02) , pp. 507-517, Jilin / China.
- [21] Xu, T., Yu, J., Yu, Y., Wang, Y., (2018). A modelling and verification approach for soybean seed particles using the discrete element method. *Advanced Powder Technology*, Vol. 29(12) , pp. 3274-3290, United States.
- [22] Yuan, X., Tao, G., Qu, J., Zhang, S., Chen, C., Yi, S., (2022). Compression Test and Crack Analysis of Sorghum Seeds (高粱种子的压缩试验与裂纹分析) . *Journal of Agricultural Mechanization Research*, Vol. 44(09) , pp. 217-223, Heilongjiang / China.
- [23] Yang, L., Chen, L., Zhang, J., Liu, H., Sun, Z., Sun, H., Zheng, L., (2018). Fertilizer sowing simulation of a variable-rate fertilizer applicator based on EDEM. *IFAC-PapersOnLine*, Vol. 51(17) , pp. 418-423, United States.
- [24] Zhang, T., Liu, F., Zhao, M., Liu, Y., Li, F., Ma, Q., Zhang, Y., Zhou, P., (2017). Measurement of physical parameters of contact between soybean seed and seed metering device and discrete element simulation calibration(大豆种子与排种器接触物理参数的测定与离散元仿真标定). *Journal of China Agricultural University*, Vol. 22(09) , pp. 86-92, Beijing / China.
- [25] Zhao, Y., Yang, S., Zhang, L., Chew, J., (2019). Understanding the varying discharge rates of lognormal particle size distributions from a hopper using the Discrete Element Method. *Powder Technology*, Vol. 342 , pp. 356-370, United States.
- [26] Zeng, Y., Jia, F., Xiao, Y., Han, Y., Meng, X., (2019). Discrete element method modelling of impact breakage of ellipsoidal agglomerate. *Powder Technology*, Vol. 346, pp. 57-69, United States.
- [27] Zhang, M., Wang, Z., Luo, X., Jiang, E., Dai, Y., Xing, H., Wang, B., (2018). Effect of double seed-filling chamber structure of combined type-hole metering device on filling properties(组合型孔排种器双充种室结构对充种性能的影响). *Transactions of the Chinese Society of Agricultural Engineering*, Vol. 34(12), pp. 88-15, Beijing/ China.

DESIGN OF AN UNMANNED TRANSFER VEHICLE LOOP DETECTION SYSTEM FOR GRAIN DEPOT SCENARIOS

用于粮库场景的无人驾驶转运车回环检测系统设计

Boqiang ZHANG¹, Dongding LI¹, Tianzhi GAO^{*1}, Kunpeng ZHANG², Jinhao YAN¹, Xuemeng XU¹

¹ School of Mechanical and Electrical Engineering, Henan University of Technology, Zhengzhou 450001 / China;

² College of Electrical Engineering, Henan University of Technology, Zhengzhou 450001 / China

Tel: 18003988576; E-mail: gtz1069312977@163.com

Corresponding author: Tianzhi GAO

DOI: <https://doi.org/10.35633/inmateh-74-09>

Keywords: Grain depot, Food logistics, LCD, SLAM, Deep learning, Feature extraction

ABSTRACT

The grain depot scenario is critical for grain logistics and transportation, and it is also a key setting for the efficient operation of intelligent grain logistics platform vehicles. A large number of repetitive and specific building structures, along with low-textured walls, characterize the grain depot scene. Loopback detection is an essential module in visual SLAM, and an efficient system can eliminate accumulated errors. While traditional systems rely on manually designed features, which struggle to adapt to the unique grain depot environment, this paper proposes a deep learning-based loopback detection system for grain transfer trucks. Leveraging a custom dataset capturing both grain depot environments and loopback scenarios, the system employs convolutional neural networks for identifying building equipment and door numbers, edge extraction for robust feature matching, and image template matching for efficient loopback verification. Extensive testing on the grain depot loopback dataset demonstrates that the system significantly improves loopback detection accuracy and efficiency, paving the way for reliable autonomous navigation in grain depots.

摘要

粮库场景是粮食物流转运的重要场景，同时也是智能粮食物流平台车高效运行的关键环节。粮库的大量重复和特殊建筑结构以及缺乏纹理的墙体颜色是粮库场景的特点。回环检测模块是视觉定位与建图的一个重要模块，有效的回环检测能够消除累积的误差，传统的回环检测使用的特征是人工设计的特征，在粮库的特殊场景下难以发挥出良好的效果。本文提出了一种基于深度学习的粮食转运车回环检测系统，利用录入了粮库环境和回环场景的定制化数据集，使用卷积神经网络识别建筑设备和门牌号码，通过边缘提取进行稳健的特征匹配，并采用图像模板匹配进行高效的回环验证。在粮库回环数据集上进行的广泛测试表明，该系统显著提高了回环检测的准确性和效率，为在粮库中实现可靠的自动导航铺平了道路。

INTRODUCTION

A nation's economy and quality of life are intrinsically linked to agricultural production, and food storage has been a cornerstone practice for farmers and traders throughout history. Grain storage is the main realization scenario of this paper, which is vital for the preservation of new grain, though significant breakthroughs in grain storage and transportation methods are still lacking. To tackle current problems in the grain storage and transfer process, an intelligent grain logistics platform vehicle has been developed to replace traditional grain transport trucks (Zhang et al., 2023). This vehicle efficiently handles the transfer of grain from the raw grain cleaning center to various storage facilities. Compared to traditional large-scale grain transport trucks, the intelligent logistics platform vehicle offers features such as autonomous route planning, dynamic obstacle avoidance, and simultaneous localization and mapping in unknown areas. These capabilities effectively reduce long waiting times for numerous trucks during the harvest season in grain depot parks, health hazards to workers caused by harsh working environments, and traffic accidents within the parks. Vehicle navigation in these scenarios relies heavily on Simultaneous Localization and Mapping (SLAM) technology. Achieving accurate localization and map-building results is crucial for efficient operation. To balance effectiveness with cost, this research focuses on vision sensor-based SLAM.

Boqiang ZHANG, Senior engineer Ph.D. Eng.; Dongding LI, M.S. Stud. Eng.; Tianzhi GAO, M.S. Stud. Eng.; Kunpeng ZHANG, A.P. Ph.D. Eng.; Jinhao YAN, M.S. Stud. Eng.; Xuemeng XU, Prof. Ph.D. Eng.

However, the unique features of grain depots pose challenges for traditional vision approaches. Their abundance of untextured granary buildings, floors, and specialized equipment can lead to unstable and inefficient feature detection and matching, particularly during loop detection.

Loop detection is a crucial part of the visual SLAM system, significantly reducing the cumulative error generated by the system by identifying and revisiting previously visited locations, thereby improving the accuracy of the constructed map. When the system detects a loop closure, it transmits this information to the backend for further optimization and error elimination, resulting in a more accurate map (Gao *et al.*, 2017).

Appearance-based loop detection methods are indeed prevalent in visual SLAM (Qu and Wang, 2011), where rich visual information readily provides sufficient appearance cues for the system to rely solely on camera data, bypassing the compounding errors inherent in trajectory data. Consequently, in visual SLAM, loop detection essentially boils down to comparing image similarities.

Classical loop detection algorithms, as highlighted by Wu *et al.* and Qiu *et al.* (Wu *et al.*, 2010; Qiu *et al.*, 2023), often rely on manually designed features like SIFT, SURF, ORB, and BRIEF (Rublee *et al.*, 2011) to represent images. However, this approach is not without its limitations. These traditional features, meticulously crafted by computer vision researchers, exhibit distinct characteristics: some are sensitive to environmental changes such as illumination variations, while others are hindered by computational complexity, limiting their broad applicability in diverse real-world scenarios.

With the rapid development of computer vision thanks to the continuous progress of deep learning techniques, CNNs have achieved great success in computer vision fields such as image classification, image segmentation, and target detection thanks to their powerful feature learning and representation capabilities (Hongtao *et al.*, 2016). Since 2015, there have been attempts to use deep learning to extract features from images and thus replace hand-crafted features.

Xia *et al.* used the AlexNet network for feature extraction (Xia *et al.*, 2017), followed by secondary training using Support Vector Machines (SVM) algorithm, and this loop detection model exhibited better robustness. Bai *et al.* proposed a CNN feature-based loop detection method that combines the pre-trained CNN intermediate layer output with the traditional sequence-based matching process output to reduce the computational complexity of the search strategy (Bai *et al.*, 2018).

Mukherjee *et al.* used a deep deconvolutional network to represent the scene as a low-dimensional vector and determine the loop by comparing this vector (Mukherjee *et al.*, 2019). Yang *et al.* proposed a parallel recurrent search and verification method that combines features from bag-of-words models and features from convolutional neural networks to act on loop detection (Yang *et al.*, 2021).

Wang *et al.* used a two-stage loop detection strategy to avoid blind matching (Wang *et al.*, 2021). Guo *et al.* used a VGG-19 network to extract the features of the images for the determination of loop detection by a locally sensitive hashing algorithm (Guo Jizhi *et al.*, 2021). Scene-specific loop detection is still relatively rare.

To enhance loop detection efficiency in grain depot scenarios, this paper proposes a Convolutional Neural Network (CNN)-based approach for visual SLAM. This approach aims to improve both the accuracy and recall rate of loop detection. Grain depot environments are characterized by unique structures, such as towering silos, shallow round bins, and spherical bins. These structures are omnipresent in grain depots and pose challenges for traditional geometric feature-based methods. CNNs, on the other hand, offer long-term stability and robustness to perspective and illumination changes, making them ideal for feature extraction in these scenarios. Therefore, this paper proposes a deep learning feature-assisted visual SLAM framework specifically tailored for grain depot environments.

MATERIALS AND METHODS

In the grain depot, the shape of each depot is consistent and regularly arranged. The SLAM system is prone to classify the depots in different locations as the same scene when performing loopback determination, thus delivering wrong fitting information to the back-end and causing confusion in the system. In this paper, the system was divided into two branches. One is a lightweight GhostNet network, which extracts the deeper features of the image after transfer learning training. The other branch is a network for number recognition, which uses the grain depot door number to distinguish different grain depots, as shown in Figure 1.

The loopback detection system as a whole is shown in Figure 2.



Fig. 1 - Grain warehouse door number

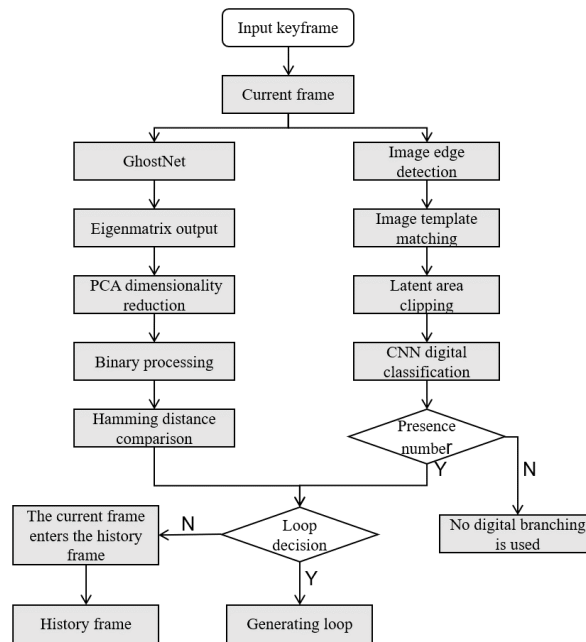


Fig. 2 - Algorithm flow chart

CNN Feature Extraction

CNNs have shown powerful performance within the field of computer vision for computer vision tasks such as target detection, image classification, and semantic segmentation. Traditional convolutional neural networks often contain a large number of parameters and complex computations, which are limited by the limited memory and computational resources of embedded devices, and it has become a new trend to study portable lightweight, and efficient convolutional neural networks (BI et al., 2024; Feng et al., 2024). For the above problems, the current common solution ideas are compact deep neural networks and efficient neural architecture design.

GhostNet network was proposed by Huawei Noah's Ark Lab in 2020, which is a lightweight CNN model with a smaller number of parameters and operations to ensure certain accuracy and can be deployed on removable embedded devices to meet the real-time requirements of visual SLAM systems. It divides the traditional convolution operation into two steps: the first step first generates feature maps with fewer channels using traditional convolution with less computation; the second step further generates more new feature maps using a small amount of computation on top of the generated feature maps using deep convolution; finally, the two feature maps are stitched together and the output is the final output. The idea of GhostNet is a phased convolutional computation module, which performs a linear convolution based on a few nonlinear convolutions to form a new feature map, and the large number of new feature maps obtained in this way is called Ghost of the previous feature maps. As shown in Figure 3, (a) figure shows the ordinary convolutional generation of feature maps, and (b) shows the Ghost module generation of feature maps.

The role of the GhostNet network itself is primarily to perform image classification and retrieval, rather than final output image features. From the network structure, the final fully connected layer serves as the output layer for image classification, and therefore is not considered as a feature extraction layer. The features extracted by the previous convolutional layer are too coarse to imply the global image. In this paper, the output of the FC8 layer of the GhostNet model is used as the features of the image, and the output of the FC8 layer is 1280 dimensional data.

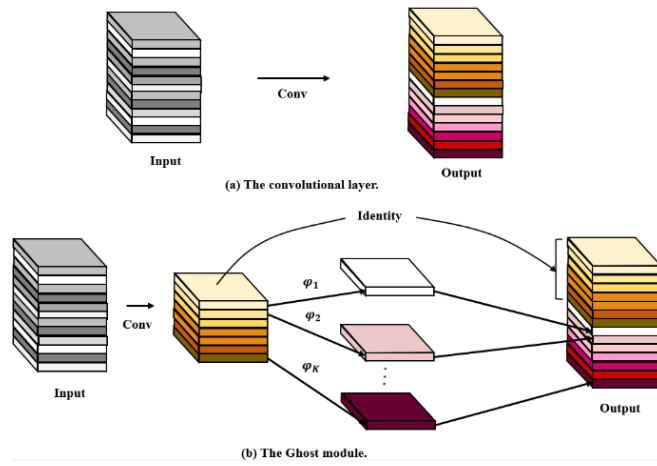


Fig. 3 - Comparison of normal convolution and Ghost module

Similarity Comparison

For the calculation of the distance between feature vectors, the more common and effective ones are the Euclidean distance and the cosine distance, if there are two feature vectors $a[a_1, a_2, a_3, \dots, a_n]^T$ and $b[b_1, b_2, b_3, \dots, b_n]^T$, then the cosine distance (Zou and Umugwaneza, 2008) between two vectors can then be expressed as:

$$d(a, b) = \frac{a^T \cdot b}{\sqrt{(a^T \cdot a) \times (b^T \cdot b)}} \tag{1}$$

When the feature vectors are of high dimension using the above two determination methods will be computationally intensive and affect the corresponding accuracy and precision, it is more important to use a more efficient computation method, which will help to improve the accuracy and real-time performance of the loop detection algorithm. Successful image retrieval methods have shown that data augmentation of the original feature vector can improve its ability to describe the image and increase computational efficiency. In this paper, Principal Component Analysis (PCA) (Salih Hasan and Abdulazeez, 2021) and binarization are used to augment the extracted features to improve the image feature representation.

The steps of data processing are as follows.

- 1) Calculate the covariance matrix Σ of the sample matrix, which is calculated as:

$$\Sigma = \frac{1}{m-1} X^T X \tag{2}$$

- 2) The SVD decomposition (Singular Value Decomposition) is performed on the covariance matrix Σ . The calculation is:

$$\Sigma = USV^T \tag{3}$$

The U and V unitary matrices in the formula are the left singular matrix and the right singular matrix.

- 3) The sample matrix is de-correlated using the left singular matrix U . The calculation is:

$$X_r = U^T X^T \tag{4}$$

- 4) Calculate the mean of each row of the sample matrix after dimensionality reduction.

$$mean = \frac{1}{m} \sum_{j=1}^m X_{ij}, i = 1, 2, \dots, n \tag{5}$$

- 5) The sample matrix is binarized. The calculation is done as follows:

$$Y_{ij} \begin{cases} 1, X_{ij} \geq mean \\ 0, X_{ij} < mean \end{cases} \tag{6}$$

After the above process, the feature vector of each image is represented as a low-dimensional binary vector. The distance between two images can be expressed as the corresponding Hamming distance. The Hamming distance, which is the number of different elements of two equal-dimensional feature vectors at corresponding positions, is often used to determine the similarity between two images in the field of image retrieval.

Improved Canny Edge Extraction

Although the Canny edge extraction algorithm is easier to use and the edges are extracted more accurately, the traditional Canny algorithm has some disadvantages. Only Gaussian filtering is used in the image filtering stage, which is better for removing continuous noise such as Gaussian noise. However, Gaussian filtering generally uses pre-set conditions and is not able to take a more targeted filtering of the image based on the actual information of the image, which may make the image blurred. The image is unable to effectively filter out other types of noise, such as salt and pepper noise. In the final stage of the Canny edge extraction algorithm a human input threshold is used to determine the pixels in the image, resulting in poor adaptation to the image. In this paper, the traditional Canny algorithm is improved in two ways: the original Gaussian filter was replaced with a hybrid filter consisting of a Gaussian filter and an adaptive median filter, and an adaptive thresholding scheme was chosen to replace the fixed threshold in the final stage of the original algorithm.

The Gaussian filter can smooth the image and remove some low-frequency noise, and the adaptive median filter can remove the salt and pepper noise in the image, etc. The combination of the two can better remove the noise in the image, improve the quality of the image, and retain the details of the image.

Adaptive median filtering (Yu *et al.*, 2016) is based on median filtering and addresses the window size problem, utilizing the advantages and disadvantages of filtering in both large and small windows, and adapting to change the size of the window according to the noise. After determining the filter window size, the adaptive median filter will set up judgment conditions to identify whether the median point is a noise point, which effectively avoids the problem of filter failure in median filtering. The adaptive median filter first constructs a rectangular window S with point (x,y) as the center point of the window. The following symbols are used to describe the principle: Z_{min} is the minimum gray value in the window S , Z_{max} is the maximum gray value in the window S , Z_{med} is the median gray value in the window S , Z_{xy} is the gray value of the coordinate (x,y) position, and S_{max} is the maximum window size allowed by S . The process of adaptive median filtering can be divided into two processes A and B.

$$A1 = Z_{med} - Z_{min} \quad (7)$$

$$A2 = Z_{med} - Z_{max}$$

$$B1 = Z_{xy} - Z_{min} \quad (8)$$

$$B2 = Z_{xy} - Z_{max}$$

If $A1 > 0$ and $A2 < 0$, go to process B. Conversely increase the size of the window. If after increasing the size of the window is not greater than S_{max} , repeat process A. Instead output Z_{med} . In process B if $B1 > 0$ and $B2 < 0$, then output Z_{xy} , and vice versa output Z_{med} .

It is inevitable that the edge information of the image will be lost when denoising with adaptive median filtering, in this paper, the determination of edge keeping was added in addition to the process of the determination of adaptive median filtering, and a new threshold was designed to protect the edge pixels. The calculation formula of the threshold value is (9).

$$T = \sqrt{\frac{1}{N-1} \sum_{i=1, j=1}^N (X_{ij} - \hat{X})^2} \quad (9)$$

In the formula, T is the threshold to be sought and \hat{X} is the average value of the pixels in the window.

The gray values of the elements surrounding the center element in the window are used as the basis for determination. When the difference between the gray value of the center element and the gray value of the surrounding elements is greater than the threshold value T , the number of pixels accounting for one-fourth to three-fourths of the total number of surrounding elements, the center pixel is judged to be an edge point, and vice versa is judged to be a non-edge point. The image produced by adaptive median filtering and the edge information image are superimposed to complete the output. The pseudo-code for this part of the program is as follows:

Algorithm 1 Adaptive median filtering for edge preservation

$A1 = Z_{med} - Z_{min}$, $A2 = Z_{med} - Z_{max}$

If $A1 > 0$ and $A2 < 0$ do

$B1 = Z_{xy} - Z_{min}$, $B2 = Z_{xy} - Z_{max}$

If $B1 > 0$ and $B2 < 0$ do

```

    Reserve  $Z_{xy}$ 
  Else do
    Reserve  $Z_{med}$ 
Else do
  Enlarge window
  If  $S \leq S_{max}$  do
    Return
  Else do
    Reserve  $Z_{xy}$ 
 $D = Z_{xy} - T$  (Take nine grids for example)
  If  $2 < D < 7$  do
    Reserve  $Z_{xy}$ 
  Else do
    Return
Merge image

```

Traditional Canny edge extraction algorithms use high and low thresholds to discriminate edge information, but the size of the high and low thresholds need to be set manually and have low adaptivity. In this paper, Otus adaptive thresholding algorithm (*Sha et al., 2016*) is used to give the high and low thresholds, the algorithm calculates the corresponding intra-class variance of the foreground and background through the different dividing values of the foreground and background parts of the detected target image, and the dividing value corresponding to the maximum value of the intra-class variance is the adaptive threshold calculated by Otus.

The coarse localization of the digital part uses the template matching technique in image processing technology. Template matching technique is a common image recognition technique, it first establishes a template library, the template library stores the content to be recognized, with the template library templates to traverse the input image, by searching for regions in the target image that match the given template to recognize a specific region in the image. In this paper, since only a coarse localization of the numbers on the granary is required, a template library consisting of numbers is constructed for template matching. In this paper, an image template library of 9 numbers from number 1 to number 9 is constructed with a size of 300pixel×300pixel, and an image can be selected from the template library to match with the input image when template matching is performed. The template library image is shown in Figure 4.



Fig. 4 - Digital template library

Construction of CNN for Number Classification

After coarse localization of the digital portion using image template matching, the portion where digits may be present is cropped from the image. The template matching technique achieves matching by finding the region in the target image that is most similar to the template image. However, this method may be affected by a number of factors that can lead to inaccurate matching. In contrast, convolutional neural network is a deep learning model that automatically extracts features from an image by learning a large amount of image data to achieve more accurate image recognition. Therefore, in this paper, a convolutional neural network is built to achieve accurate recognition of numbers.

The convolutional neural network built in this paper contains an input layer, a convolutional layer, a pooling layer, a fully connected layer and an output layer. The overall architecture of the network is shown in Table 1. The input to the network is a 28*28 image, a 5×5 convolution kernel is used in the first convolutional layer, followed by a 2×2 maximum pooling operation, and the above operation is repeated. At the end of the network is a fully connected layer and finally the network outputs the prediction through a fully connected layer of 10 neurons.

Table 1

Convolutional neural network structure			
Operator	Input	Out	Kernel
Input	$28 \times 28 \times 1$	$28 \times 28 \times 1$	
Conv	$28 \times 28 \times 1$	$24 \times 24 \times 32$	$5 \times 5 \times 1$
ReLU	$24 \times 24 \times 32$	$24 \times 24 \times 32$	
MaxPool	$24 \times 24 \times 32$	$12 \times 12 \times 32$	
Conv	$12 \times 12 \times 32$	$8 \times 8 \times 64$	$5 \times 5 \times 32$
ReLU	$8 \times 8 \times 64$	$8 \times 8 \times 64$	
MaxPool	$8 \times 8 \times 64$	$4 \times 4 \times 64$	
FC	$4 \times 4 \times 64$	1024	
FC	1024	10	

Loop generation

The key to loop detection is to effectively detect the matter that a camera or other sensor device has passed through the same place (Quan Meixiang *et al.*, 2016). If this thing can be successfully detected, more valid data can be provided to the back-end in a mature SLAM framework to get a globally consistent estimate (Di *et al.*, 2018). Image selection needs to be taken into account when detecting image similarity; if the selection is too close, it will result in too much similarity between two frames, which will make it difficult to detect the frames inside the history frames that produce a loop (Liu Guozhong and Hu Zhaozheng, 2017). For example, the detection results in the n th frame being the most similar to the $n-1$ and $n+1$ th frames, but obviously, such a loop judgment is meaningless. So, the order of the images should be processed in some way during the detection, assuming that the current frame is the n th frame and its neighbor has k frames of images, then the frame for loop similarity comparison should be outside the n th and k th frames.

RESULTS

Experimental environment

The equipment used in the test is an intelligent grain logistics platform vehicle, independently developed by Henan University of Technology. This self-driving vehicle is equipped with sensors such as LIDAR, a binocular camera, millimeter-wave radar, and RTK. It includes mounted devices like a storage unit, grain unloading system, wire control chassis, sensor module, and a core control unit computer. The vehicle can handle a 20-degree slope with a 3-ton load and features a large-capacity battery, ensuring it meets the operational requirements of a grain depot, as illustrated in Figure 5. The computer configuration used was an Inter(R) Xeon(R) CPU, an NVIDIA RTX3060 graphics card, 14 GB of RAM, and a software configuration of Python 3.8, CUDA 11.3, PyTorch 1.11.0, and an Ubuntu 20.04 operating system.

Grain Depot Environment Dataset and Model Training

For the grain depot scene in the actual environment, this paper uses monocular image acquisition equipment to produce a grain depot scene dataset, which has 1180 photos and divides the training set and test set according to 5:1. The dataset cover different environments with different lighting, shooting angles, shading, distance and size, which can easily reflect the existence of special buildings and special mechanical equipment in the grain depot environment.

The grain depot dataset produced in this paper contain three types of grain depots: cottage silos, shallow round silos, and vertical silos, which are widely used in most grain depots in China. In addition, the grain warehouse data set also includes common grain-related machinery and equipment for grain transportation, ventilation and drying, and bulk grain cleaning, such as steering conveyor, cleaning sieve, horizontal conveyor, mobile grain suction machine, bucket elevator, scraper conveyor, screw conveyor, grain picker, flat conveyor, tape conveyor, centrifugal ventilator, low-noise double-suction environmental protection centrifugal fan, grain warehouse insulation doors and windows, and weighing weighbridge. These devices play an important role in the harvest season, and these mechanical devices are generally used only in the grain depot environment and have a high degree of recognition. The grain depot data set is partially shown in Figure 6.



Fig. 5 - Henan University of Technology independently developed intelligent grain logistics platform vehicle



Fig. 6 - Grain depot dataset

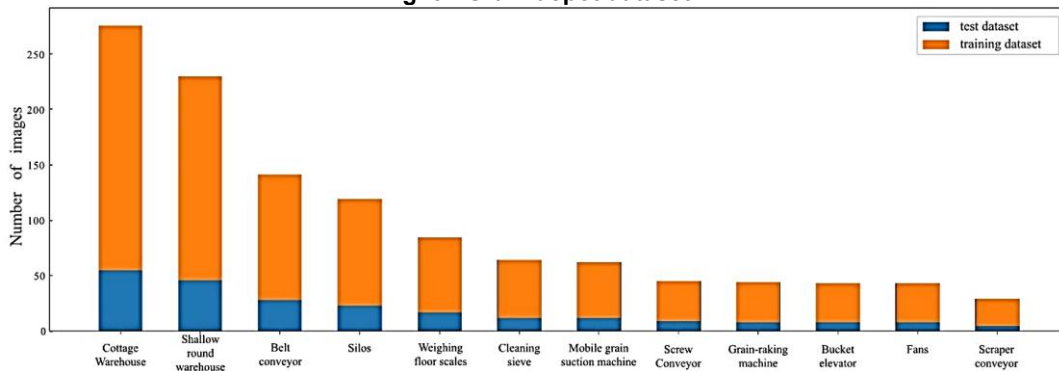


Fig. 7 - Number of images of each category in the grain depot dataset

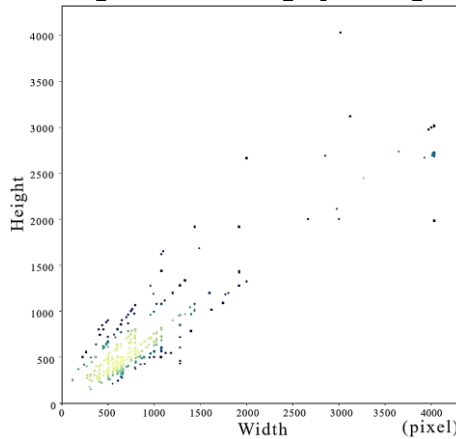


Fig. 8 - Distribution of grain depot dataset size

To address the limitation that the dataset produced in this paper cannot be as large as the world-renowned datasets, this paper employs data expansion strategies to augment the images within the grain depot dataset using various simple and effective methods, including flipping images left and right, random cropping, rotation, panning, noise perturbation, and luminance contrast transformation, thereby enhancing the model's robustness and adaptability to the grain depot scene. ImageNet dataset are computer vision dataset created by Fei-Fei Li, a professor at Stanford University, who led the creation of the ImageNet dataset. The dataset contains 14,197,122 images and uses pre-trained parameters to obtain good initial parameters for network training (Deng et al., 2009). This paper uses the GhostNet model trained on the ImageNet public dataset as the initialization weights for training the network, and this operation enables the network to show better performance in subsequent use.

SVHN (Street View House Number) Datasets is derived from Google Street View House Number and contains a large number of door numbers, as shown in Figure 9. The network is trained using the SVHN dataset as a way to adapt the classification of door numbers above the grain depot. In the grain depot environment, each depot has a consistent shape, and it is easy to classify depots in different locations as the same scene in the loopback detection system.



Fig. 9 - SVHN dataset

In this chapter training, Stochastic Gradient Descent (SGD) is used for training, the Famma of SGD is set to 0.1, the initial learning rate is 0.001, and 32 training images are selected for each iteration. Figure 10 and Figure 11 show the training of the pre-trained GhostNet network on the grain depot dataset. Figures 12 and 13 show the training of the SVHN dataset.

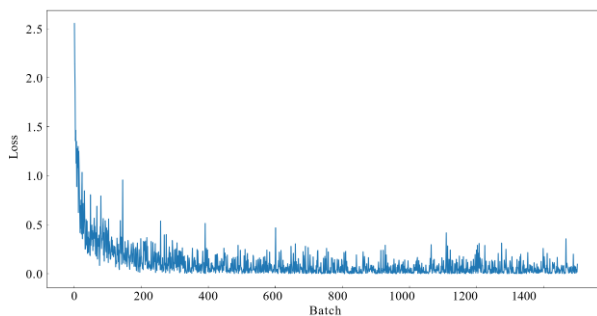


Fig. 10 - Loss function of training set

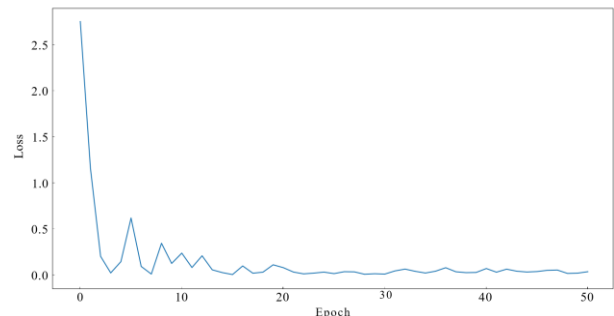


Fig. 11 - Test set loss function

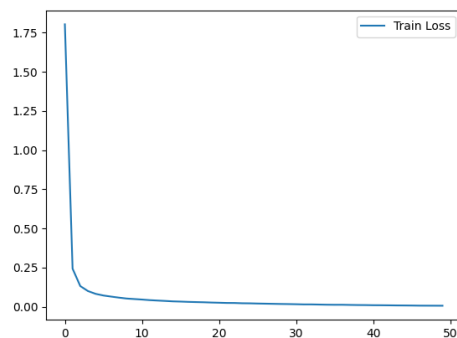


Fig. 12 - Loss function of training set

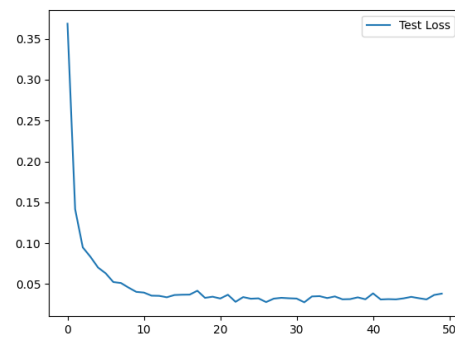


Fig. 13 - Loss function of training set

Edge extraction and template matching

The edge extraction algorithm is improved in the 'Improved Canny Edge Extraction' section of this paper, in which a hybrid filter combining Gaussian filter and adaptive median filter is used instead of the original Gaussian filter in the edge extraction algorithm, and adaptive high and low thresholds are used instead of manually setting the original high and low thresholds. This section makes a comparison between the hybrid filter and the improved edge extraction algorithm.

Gaussian noise and salt-and-pepper noise were added to the image, and Gaussian filter and the hybrid filter in this paper were used respectively for processing, and the effect was shown in Figure 14. From left to right, the original image, the image with Gaussian and Pepper noise added, the image processed using the Gaussian filter in the original algorithm, and the image processed using the hybrid filter in this paper, are shown.

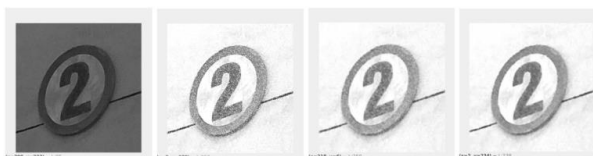


Fig. 14 - Comparison of the effect of filtering algorithms

The hybrid filtering algorithm proposed in this paper outperforms the Gaussian filtering algorithm used in the conventional Canny edge extraction method, both in terms of noise removal and edge information retention.

The traditional Canny edge extraction algorithm and the improved edge extraction algorithm are used to extract the edges of the grain depot image. The extraction results are shown in Figure 15.



Fig. 15 - Comparison of edge extraction effect

It can be seen that the original Canny edge extraction algorithm is prone to extract more noise during edge extraction and the edges are not well protected. After improvement, it can show better performance.

The system performs edge extraction on the images in the template library as well as on the input image, followed by coarse localization of the target on the input image using a template matching algorithm. In this, the input images are processed using image pyramid, which reduces the amount of computation and time spent by utilizing images of different resolutions for multi-scale processing. At the same time, by using images of different scales for matching, the accuracy and robustness of matching can be improved. As shown in Figure 16. After coarse localization of the part of the input image that may be a digit the part is cropped to ensure that the digit occupies most of the area in the cropped image, and the cropped image is fed into the previously constructed convolutional neural network for accurate digit recognition.

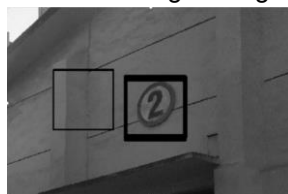


Fig. 16 - Results of image template matching

During the matching process, some parts that are not numbers can be matched, for example, the left box in Figure 16 is not a number, these parts can be well disposed of after entering into the convolutional neural network to ensure the accuracy of the system.

PR Curve Metrics

To verify the performance of the algorithm in this paper, comparisons are made in terms of Precision-Recall (PR) curve metrics, and extraction time of image features, respectively.

In the loop detection task, a classification can be made of the various phenomena that occur. The two images are judged by the algorithm to be the same scene as a loop. If the two images are not actually from the same scene, the phenomenon is called False Positive (FP); otherwise, it is True Positive (TP). If two images from the same scene are determined by the algorithm to be from different scenes, they are called False Negative (FN), otherwise, they become True Negative (TN). P and R in the PR curve are defined as shown in equation (10) (Shin and Ho, 2018).

$$Precision = \frac{TP}{TP + FP} \quad (10)$$

$$Recall = \frac{TP}{TP + FN} \quad (11)$$

Figure 17 shows the processing of the data after the features of the image have been extracted by the deep learning network. The performance when compared directly using cosine distance without data processing is different from the performance after performing principal component analysis to reduce the dimensionality and binarization. Therefore, in this paper, PCA and binarization were performed on the data.

The PR curve is an important metric for determining loop detection algorithms, and a good loop detection algorithm should have both high accuracy and recall. This paper uses the bag-of-words model DBoW3 and VGG16 (Simonyan K. and Zisserman A., 2014) for comparison, and VGG16 also uses PCA reduction and binarization for data processing.

Figure 18 shows the experimental results of the algorithm under the grain depot loop dataset, with the horizontal axis indicating the recall rate and the vertical axis indicating the correct rate. From the experimental results, it can be seen that the proposed loopback detection system in this paper has higher correctness and recall than the traditional bag-of-words model when performing loopback detection in a grain depot, and it is also more advantageous than a single convolutional neural network, which can be better applied to grain depot scenarios. When the classification of door numbers of grain depots is added, the accuracy and recall perform better than the single trained GhostNet network. Considering that there is not a door number in every location, the performance is only slightly better than a single network.

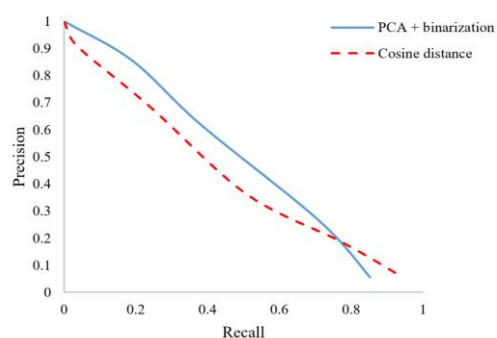


Fig. 17 - Data processing comparison chart

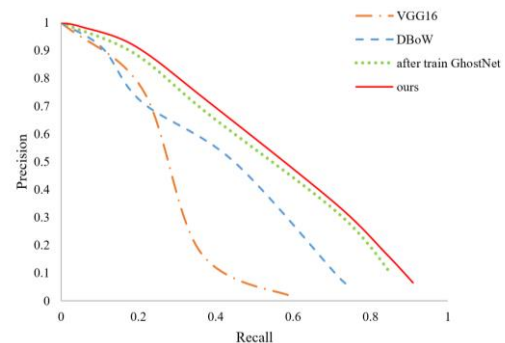


Fig. 18 - Grain depot scene loopback PR curve

CONCLUSIONS

Grain depots serve as critical lifelines for a nation's inhabitants. However, the influx of new grain each year poses numerous challenges that demand swift and decisive solutions. Employing modern equipment and technology in grain depots is a crucial path forward. This paper focused on addressing some of these challenges, specifically the repetitive building structures and low-textured environments that hinder the efficiency and accuracy of loop detection. Word bag models, commonly used in this context, suffer from limitations in both speed and accuracy.

This paper addressed the challenge of loopback detection in grain depots, where judging the similarity of unique buildings and consistent shapes can be difficult. A GhostNet architecture was leveraged to extract deep image features, which were then processed through PCA and binarization for enhanced representation. Additionally, a two-stage digit recognition branch was introduced. This branch utilized image template matching for coarse localization followed by CNNs for precise digit recognition. By combining these approaches, our loopback detection module for visual SLAM demonstrated robust performance in grain depots, paving the way for modernizing traditional grain storage facilities.

ACKNOWLEDGEMENT

The authors would like to thank the anonymous reviewers for their constructive suggestions. This work was partially supported by the National Key Research and Development Program of China [Grant Number 2022YFD2100201], the Henan Provincial Key R&D and Promotion Project [Grant Number 231111241100].

REFERENCES

- [1] Bai D., Wang C., Zhang B., Yi X., & Yang X. (2018). CNN Feature Boosted SeqSLAM for Real-Time Loop Closure Detection. *Chinese Journal of Electronics* 27(3): 488-499. <https://doi.org/https://doi.org/10.1049/cje.2018.03.010>
- [2] Bi Z., Li Y., Guan J., & Zhang X. (2024). Real-time Wheat Detection Based On Lightweight Deep Learning Network Repyolo Model. *INMATEH - Agricultural Engineering*. 72: 601-610. <https://doi.org/10.35633/inmateh-72-53>

- [3] Deng J., Dong W., Socher R., Li L. J., Li K., & Fei-Fei L. (2009). ImageNet: A large-scale hierarchical image database. *2009 IEEE Conference on Computer Vision and Pattern Recognition*. <https://doi.org/10.1109/CVPR.2009.5206848>
- [4] Kaichang D., Wenhui W., Hongying Z., Zhaoqin L., Runzhi W., & Feizhou Z. (2018). Progress and Applications of Visual SLAM. *Cehui Xuebao/Acta Geodaetica et Cartographica Sinica*, 47: 770-779. <https://doi.org/10.11947/j.AGCS.2018.20170652>
- [5] Gao X., Zhang T., Liu Y., & Yan Q. (2017). 14 lectures on visual SLAM: from theory to practice. 206-234.
- [6] Jizhi G., Fenglian L., Xinzhu Y., & Riwei W. (2021). The closed loop detection method of vision SLAM based on deep learning(基于深度学习的视觉 SLAM 闭环检测方法). *Journal of Optoelectronics Laser*. 32(06): 628-636. <https://doi.org/10.16136/j.joel.2021.06.0392>
- [7] Hongtao L., & Qinchuan Z. (2016). Applications of deep convolutional neural network in computer vision. *Journal of Data Acquisition and Processing*. 31(1): 1-17.
- [8] Guozhong L., & Zhaozheng H. (2017). Fast Loop Closure Detection Based on Holistic Feature from SURF and ORB (基于 SURF 和 ORB 全局特征的快速闭环检测). *Robot*. 39(01): 36-45. <https://doi.org/10.13973/j.cnki.robot.2017.0036>
- [9] Mukherjee A., Chakraborty S., & Saha S. K. (2019). Detection of loop closure in SLAM: A DeconvNet based approach. *Applied Soft Computing*. 80: 650-656. <https://doi.org/10.1016/j.asoc.2019.04.041>
- [10] Meixiang Q., Songhao P., & Guo L. (2016). An overview of visual SLAM (视觉 SLAM 综述). *CAAI Transactions on Intelligent Systems*. 11(06): 768-776.
- [11] Qu, L., & Wang H. (2011). An overview of Robot SLAM problem. *2011 International Conference on Consumer Electronics, Communications and Networks (CECNet)*. <https://doi.org/10.1109/CECNET.2011.5769022>
- [12] Rublee E., Rabaud V., Konolige K., & Bradski G. (2011). ORB: An efficient alternative to SIFT or SURF. *2011 International Conference on Computer Vision*. <https://doi.org/10.1109/ICCV.2011.6126544>
- [13] Hasan B. M. S., & Abdulazeez A. M. (2021). A Review of Principal Component Analysis Algorithm for Dimensionality Reduction. *Journal of Soft Computing and Data Mining* 2(1): 20-30.
- [14] Sha C., Hou J., & Cui H. (2016). A robust 2D Otsu's thresholding method in image segmentation. *Journal of Visual Communication and Image Representation* 41: 339-351.
- [15] Shin D. W., & Ho Y. S. (2018). Loop closure detection in simultaneous localization and mapping using learning based local patch descriptor. 30: 1-6.
- [16] Simonyan K., & Zisserman A. (2014). Very deep convolutional networks for large-scale image recognition. <https://doi.org/10.48550/arXiv.2006.12567>
- [17] Wang Z., Peng Z., Guan Y., & Wu L. (2021). Two-Stage vSLAM Loop Closure Detection Based on Sequence Node Matching and Semi-Semantic Autoencoder. *Journal of Intelligent & Robotic Systems* 101(2): 1-21. <https://doi.org/10.1007/s10846-020-01302-0>
- [18] Wu L., Hoi S. C., & Yu N. (2010). Semantics-Preserving Bag-of-Words Models and Applications. *IEEE Transactions on Image Processing* 19(7): 1908-1920. <https://doi.org/10.1109/TIP.2010.2045169>
- [19] Xia Y., Li J., Qi L., Yu H., & Dong J. (2017). An Evaluation of Deep Learning in Loop Closure Detection for Visual SLAM. *2017 IEEE International Conference on Internet of Things (iThings) and IEEE Green Computing and Communications (GreenCom) and IEEE Cyber, Physical and Social Computing (CPSCom) and IEEE Smart Data (SmartData)*. <https://doi.org/10.1109/iThings-GreenCom-CPSCom-SmartData.2017.18>
- [20] Yang Z., Pan Y., Deng L., Xie Y., & Huan R. (2021). PLSAV: Parallel loop searching and verifying for loop closure detection. *IET Intelligent Transport Systems* 15(5): 683-698. <https://doi.org/https://doi.org/10.1049/itr2.12054>
- [21] Yu W., Ma Y., Zheng L., & Liu K. (2016). Research of Improved Adaptive Median Filter Algorithm. *Proceedings of the 2015 International Conference on Electrical and Information Technologies for Rail Transportation*, Berlin, Heidelberg, Springer Berlin Heidelberg
- [22] Zhang B., Gao T., Chen Y., Jin X., Feng T., & Chen X. (2023). Research on unmanned transfer vehicle path planning for raw grain warehousing. *Journal of Intelligent & Fuzzy Systems* 45: 6513-6533. <https://doi.org/10.3233/JIFS-232780>
- [23] Zou B. J., & Umugwaneza M. P. (2008). Shape-Based Trademark Retrieval Using Cosine Distance Method. *2008 Eighth International Conference on Intelligent Systems Design and Applications*. <https://doi.org/10.1109/ISDA.2008.161>

RESEARCH ON DEFECT IDENTIFICATION OF YU-LU-XIANG PEARS BASED ON IMPROVED LIGHTWEIGHT RESIDUAL NEURAL NETWORK MODEL

基于改进轻量化卷积神经网络模型的玉露香梨缺陷识别研究

Chao ZHANG ^{1,2)}, Ning WANG ^{1,2)}, Chen LI ^{1,2)}, Jiaxiong SUN ^{1,2)}, Qiuyue JIANG ^{1,2)}, Xiaoping HAN ^{*1,2)}, Juxia WANG ^{1,2)} ¹

¹⁾ College of Agricultural Engineering, Shanxi Agricultural University, Taigu / China

²⁾ Key Technology and Equipment of Dry Farming Agricultural Machinery Shanxi Key Laboratory, Taigu / China

Tel: 15340798868; E-mail: hanxiaoping15@163.com

Corresponding author: Xiaoping HAN

DOI: <https://doi.org/10.35633/inmateh-74-10>

Keywords: Transfer learning, Attention mechanism, Lightweight network, Defect identification, Yu-Lu-Xiang pears

ABSTRACT

The skin of Yu-Lu-Xiang pears is brittle and easily damaged during picking and sorting. In order to reduce the secondary damage caused by mechanical automatic sorting of Yu-Lu-Xiang pear after harvest, optimize the sorting process and improve the sorting accuracy. Based on the MobileV2Net model, a lightweight convolutional neural network model EC-MobileV2Net-Fast, which integrated transfer learning and attention mechanism, was proposed to identify skin damage defects of Yu-Lu-Xiang pears. According to the defects of Yu-Lu-Xiang pears with different damage degrees, a dataset containing four characteristics was created. The model accuracy rate, single defect identification accuracy rate, recall, specificity, parameter and so on were taken as evaluation indexes, and the interpretation ability of the model decision was analyzed by Grad-CAM thermal map. Preliminary evaluation results showed that the model produced the highest level of accuracy, underscoring the potential of deep learning algorithms to significantly enhance defect recognition and classification. It can improve sorting efficiency, reduce labor costs and strictly control after-sales quality.

摘要

玉露香梨的果皮极其脆弱，在采摘和分拣过程中容易损坏。为了减少玉露香梨收获后机械自动分拣造成的二次损害，优化分拣工艺，提高分拣精度。本文以 MobileV2Net 模型为基础，提出了一种融合迁移学习和注意力机制的轻量化卷积神经网络模型 EC-MobileV2Net-Fast 用以识别玉露香梨表皮损伤缺陷。根据玉露香梨不同损伤程度所表现的缺陷创建了含有 4 种特征的数据集。以模型准确率、单一缺陷识别精确率、灵敏度、特异度、参数量等作为评价指标，采用 Grad-CAM 热力图分析模型决策的解释能力。初步评估结果表明，模型产生了最高水平的准确性，强调了深度学习算法在显著增强玉露香梨缺陷识别分类方面的潜力。可以提高分选效率、降低劳动力成本和严格把控售后质量。

INTRODUCTION

Yu-Lu-Xiang Pears is a high-quality new variety of medium-ripe pear. This variety was crossbred from Korla pear as mother and Snow pear as father in Shanxi Academy of Agricultural Sciences Fruit Tree Research Institute (Kai B., 2022). Yu-Lu-Xiang pears had the fragrant taste of Korla pears, were juicy, crispy and sugary, which was popular with consumers as soon as it came on the market (Haixia S. et al., 2023). Because the skin of Yu-Lu-Xiang pears was thin and brittle, they were easily damaged during the picking process. If the damaged part was exposed to the air, in a short period of time, the quality of Yu-Lu-Xiang pears would decline sharply or even deteriorate. This affected the storage, processing and sales of Yu-Lu-Xiang pears. Therefore, it was key to grade the pears quickly and accurately after harvest to ensure the quality and price of the fruits.

With the rapid development of computer vision and artificial intelligence, deep learning technology became increasingly important in many fields (Too E.C. et al., 2019). By simulating human brain neural network, deep learning algorithm realized automatic extraction and analysis of image feature data (Jiang P. et al., 2019).

¹ Chao ZHANG, As.M.S.Stud.; Ning WANG, As.M.S.Stud.; Chen LI, As.M.S.Stud.; Jiaxiong SUN, As.M.S.Stud.; Qiuyue JIANG, As.M.S.Stud.; Xiaoping HAN, Associate Professor, Doctor of Engineering; Juxia WANG, Associate Professor, Doctor of Engineering.

The main deep learning network models included Convolutional Neural Networks (CNNs), Recurrent Neural Networks (RNNs), and Generative Adversarial Networks (GANs). CNNs were the most important deep learning model in image recognition, which could achieve accurate classification through a large amount of data analysis and feature extraction. In the field of agriculture, this technology was mainly used in crop pest monitoring, field weed identification, and defect detection and classification of agricultural products (Weijian H. *et al.*, 2020), especially in fruit and vegetable defect detection.

A network model was constructed by integrating CBAM attention mechanism based on the ResNet34 model for healthy and defective kiwifruit, which achieved a recognition accuracy of 99.5% (Yunfei W., 2023). An optimized CNNs topology model was developed by Wei P *et al.* for apple surface defect detection (Wei P., 2023). Iosif A. *et al.*, (2023), used convolutional neural networks to evaluate apple quality, and the results showed that the deep learning model produced the highest accuracy and was able to accurately evaluate apple quality. Based on the ResNet model, by fine-tuning all layers of the model, a deep neural network model for external defect detection of tomatoes was proposed to achieve accurate extraction of external defect features of tomatoes (da Costa *et al.*, 2020). Yanhong proposed a lightweight convolutional model for tomato disease damage, which not only improved the recognition accuracy of the disease but also shortened the detection time. The model, after being improved, had high stability (Yanhong L. *et al.*, 2022). Zhang designed an identification and detection system for coated seeds, and the system achieved an identification accuracy of 96%, which thereby allowed for non-destructive testing of the coated seeds (Xiwen Z. *et al.*, 2022). Based on the previous research results (Bin W. *et al.*, 2023), the technical level of using machine learning methods to detect fruit defects needed to be improved.

Therefore, the theory of damage defect characteristics of other similar fruits was used for reference, and it was combined with the defect characteristics of Yu-Lu-Xiang pears (Shengqiao X. *et al.*, 2022). This paper developed a lightweight CNNs model, which fused the transfer learning (Zhongpei W. *et al.*, 2021) and channel attention mechanism (Jiapeng Q. *et al.*, 2023) based on the MobileV2Net model for identifying the defects of Yu-Lu-Xiang pears. The transfer learning enhanced the weight of the feature extraction layer and sped up the convergence of the model. Additionally, ECA channel attention mechanism enhanced the ability of the model to recognize and acquire subtle targets. The LeakyReLU activation function was employed to replace the ReLU6 activation function, addressing the issue where neuron parameters cannot be updated and resulted in death due to excessively small activation values. The results showed that the improved network model could effectively classify the skin damage of Yu-Lu-Xiang pears.

MATERIALS AND METHODS

Materials

The samples of Yu-Lu-Xiang pears were harvested from the Yu-Lu-Xiang pear base located in Beiguang Village, Taigu District, Jinzhong City, Shanxi Province in September 2023. The defects on the surface of samples include cracks, bumper injury and brown rot spots caused by diseases, etc. An image capturing obscura was made to ensure that the process of image acquiring was not interfered with by the external environment. The size of the obscura was 430mm × 430mm × 430mm, and the bottom plate used a white frosted board. The light source, an adjustable white ring LED tube with a color temperature of 5500K and a power of 8W, was installed at the top of inside the camera obscura, with a height of 40cm. The shooting equipment used a Panasonic G85 camera with 16 million pixels, which was placed on the top of outside of the camera obscura, and acquired the sample images through the reserved camera holes on the camera obscura. The image acquisition device is shown in Figure 1.

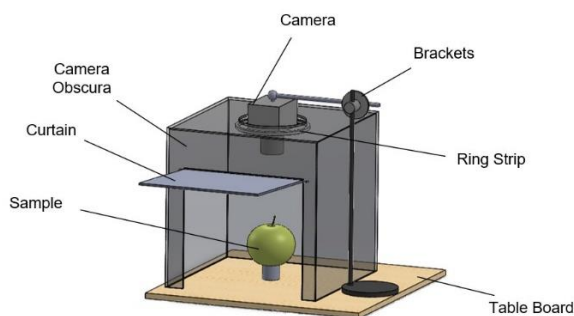


Fig. 1 - Image acquisition device

According to the grading standard of Korla pear (****Korla Pear, 2020*), Fresh pear (****Fresh Pear, 2008*) and the damage degree of samples, the Yu-Lu-Xiang pears were categorized into four types: Full, Crack, Damage, and Rot, as illustrated in Figure 2. The photos were taken according to the angles between shooting direction and the surfaces of the samples at 45° and 135°, respectively. A total of 520 original images with a resolution of 3424×3424 pixels were collected, of which 130 were Full, 128 were Crack, 128 were Damage, and 134 were Rot.



Fig. 2 - Examples of partial fruit samples

Image Preprocessing

Due to the large space occupied by the original images, the training speed of the model would have been slow if these data had been directly input into the training model. In this paper, the resolution of all original images was uniformly resized to 224×224×3 pixels through normalization processing to adapt to the input of model and improve the convergence speed of model. To improve the generalization ability of the CNNs and prevent overfitting in the training process, data enhancement techniques were used based on the original data including brightness adjustment, sharpness enhancement, noise addition, mirroring, rotation, and vertical flipping, this resulted in a total of 5200 sample images. Subsequently, the images were selected and divided into train and test sets in a 7:3 ratio by a self-designed random function for sample partitioning, with 3640 images in the train sets and 1560 images belonging to the test sets.

MobileV2Net Model Infrastructure

The MobileNet series network (*Jiaqi Q., 2022*) is a lightweight convolutional neural network that was proposed in 2017 (*Md Taimur Ahad et al, 2023*). The MobileV1Net was the primary network in this series, which adopts primarily the innovative convolutional mode of depthwise separable convolution in its structure to reduce the number of parameters and computational requirements of the model and significantly enhance its operational efficiency and real-time performance on mobile devices, and introduces the width factor α for flexible adjustment of the model size to reach a balance between accuracy and efficiency. Subsequently, the MobileV2Net occurred on the foundation of MobileV1Net, which had been continuously evolving. The MobileV2Net borrowed the inverse residual structure from the ResNet network, which avoided the gradient vanishing problem and improved the modeling effect (*Yang Z., 2021*).

As shown in Figure 3, the network architectures of MobileV1Net, MobileV2Net, and ResNet were illustrated. Compared to MobileV1Net, MobileV2Net introduced an additional step in its network structure, namely, the input features were beforehand subjected to a 1×1 convolution to increase the depth of feature maps through channel expansion. Compared with the ResNet, the MobileV2Net followed a data processing sequence with the opposite pattern of "expansion-convolution-compression". Furthermore, MobileV2Net employed depthwise separable (DW) convolutions for feature separation, whereas ResNet utilized standard convolutions for this purpose.

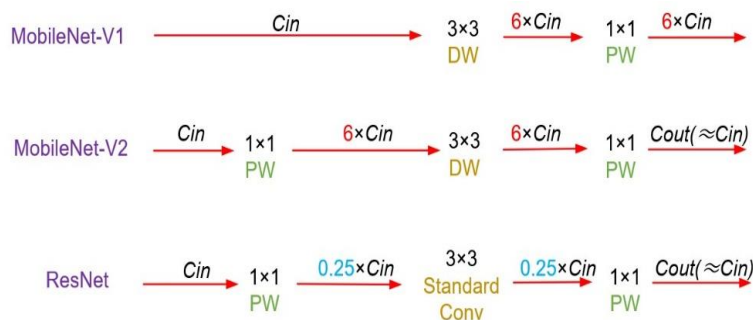


Fig. 3 - Network Comparison Structure

The inverse residual structure (Shortcut) controlled the residual connections through manipulating the stride size. When the stride was set to 1, the network adopted the inverted residual connection, as illustrated in Figure 3(a). Accordingly, when the stride was 2, the network utilized the direct connection between layers, as depicted in Figure 3(b). This structure not only enhanced the model's recognition accuracy but also maintained a relatively low computational complexity and parameter count. Therefore, the MobileV2Net was adopted widely in mobile devices and embedded systems.

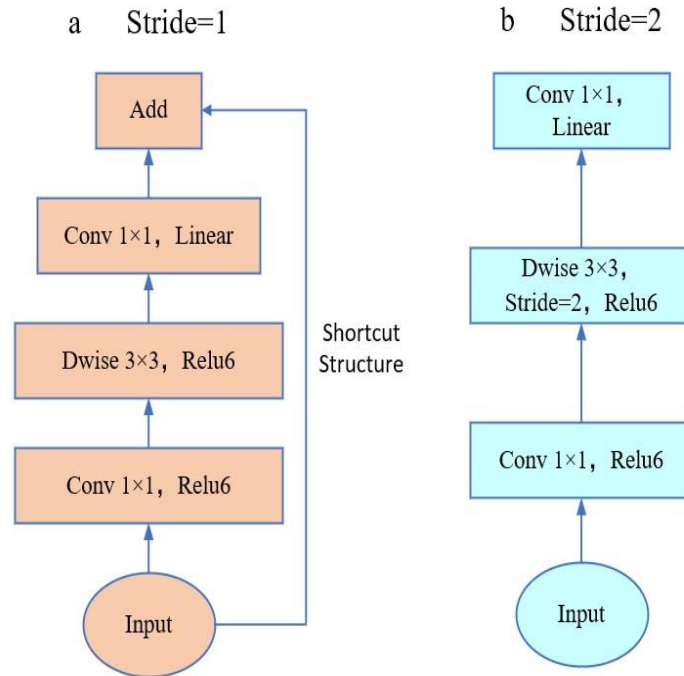


Fig. 4 - a: Stride =1 residual module; b: Stride=2 Directly connected modules

EC-MobileV2Net-Fast model

Figure 5 illustrated the constructed EC-MobileV2Net-Fast model. Initially, the pre-training network was gained by transfer learning on the ImageNet dataset, and established the target task as skin damage classification for Yu-Lu-Xiang pears.

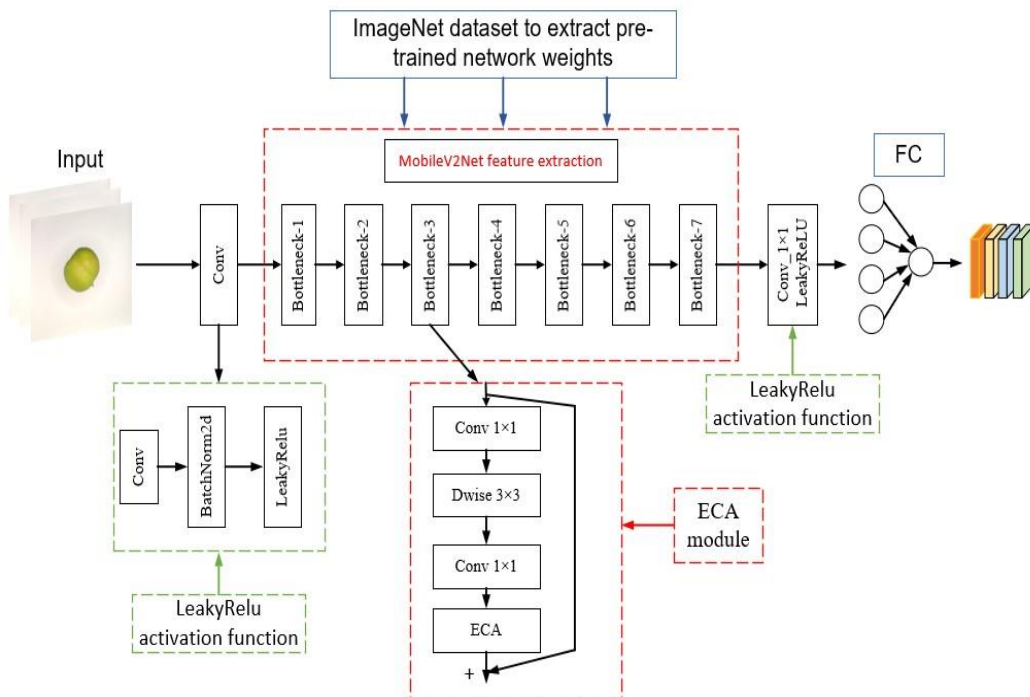


Fig. 5 - EC-MobileV2Net-Fast model

At the same time, the ECA channel attention mechanism was introduced to improve the model's capability of identifying and extracting subtle features. Furthermore, the Relu6 activation function was employed in the new network to substitute the LeakyRelu activation function, which took the problem of neuronal activity when the input was negative into account. Through these measures, the expression ability of the new model was enhanced, the negative input could generate non-zero output, avoided the neuronal death problem, and improved the classification efficiency.

RESULTS

Model Results

In this study, Windows10 was used as the operating system, with an Intel Core i5-13400H CPU, an NVIDIA GTX 4060 Ti GPU, 16GB of RAM, and a model running environment of Pytorch 1.7.1+cu110. To compare the effectiveness of the improved EC-MobileV2Net-Fast network model in this experiment and evaluate the classification performance for Yu-Lu-Xiang pears, eight classification network models were adopted: Vgg16, ResNet34, ResNet50, MobileV2Net, GoogleNet, DenseNet121, ShuffleNet and AlexNet. These networks were trained with 100 epochs, a learning rate (LR) of 0.0001, and a batch size of 16. To mitigate overfitting during training, the SGD optimizer and L2 regularization settings were employed. For specificity analysis, when all hyperparameters were kept constant, the Accuracy, the Recall, the Specificity, the Model size, the number of network parameters (Params), and the training time were selected as evaluation metrics, as summarized in Table 1.

Table 1

Comparison of test results

Model	Accuracy	Recall	Specificity	Params	Model size /MB	Training time/s
Vgg16	98.13%	0.981	0.994	134285380	512	6145
ResNet34	98.30%	0.982	0.994	21286724	81.3	2866
ResNet50	98.33%	0.983	0.994	23516228	90	3238
MobileV2Net	90.70%	0.907	0.968	2228996	8.74	2625
GoogleNet	98.00%	0.980	0.993	5977652	39.4	3730
DenseNet121	93.71%	0.937	0.979	6957956	27.1	3745
ShuffleNet	97.94%	0.979	0.993	1257704	4.96	2612
AlexNet	95.96%	0.959	0.986	14589636	55.6	1917
EC-MobileV2Net-Fast	99.67%	0.996	0.998	3504903	8.75	2630

As shown in Table 1, compared to other classification networks, the improved EC-MobileV2Net-Fast network exhibited advantages in terms of accuracy, model size, and training time. Overall, EC-MobileV2Net-Fast significantly reduced the computing and storage costs associated with network models, thereby further enhancing the practicality and efficiency of the network.

Table 2 showed the precision comparison of the model in identifying single defect samples of fruit. By comparing the precision of single samples, the performance of the model in terms of feature extraction and classification boundary demarcation for each type of fruit could be judged.

Table 2

The precision of identification of six types of models

Model	Single defect sample recognition precision			
	Full	Crack	Damage	Rot
Vgg16	0.990	0.966	0.981	0.987
ResNet34	0.975	0.989	0.997	0.971
ResNet50	0.977	0.981	0.995	0.980
MobileV2Net	0.960	0.830	0.955	0.888
GoogleNet	0.982	0.959	0.995	0.985
DenseNet121	0.965	0.896	0.962	0.926
ShuffleNet	0.982	0.966	0.981	0.987
AlexNet	0.977	0.932	0.997	0.935
EC-MobileV2Net-Fast	0.995	0.997	0.995	1.0

As was evident from Table 2, the improved EC-MobileV2Net-Fast model achieved an identification precision exceeding 0.995 for all four types of Yu-Lu-Xiang pear fruits. Notably, the most significant gains in precision were observed from the "crack" and "rot" defects, with values of 0.997 and 1.0 respectively. This outcome may have stemmed from the fact that the edge of the "crack" damage exhibited color characteristics similar to those of "rot" damage in the image information following air erosion.

The traditional network model struggled to capture the relevant fine details when processing such intricate information, thus failing to achieve accurate classification. In contrast, the improved model incorporated a channel attention mechanism, which enabled the network to focus on subtle features at the edges and enhanced its defect extraction capability.

During the model training process, real-time monitoring of the training dynamics was instrumental in gaining insights into the model's learning progress. Figure 6 presented a comprehensive dynamic evaluation of the model's performance by depicting the evolution of Loss and Accuracy for both the train and test sets across four distinct figures, namely (a), (b), (c), and (d). This visualization offered an intuitive understanding of how the model's performance evolved.

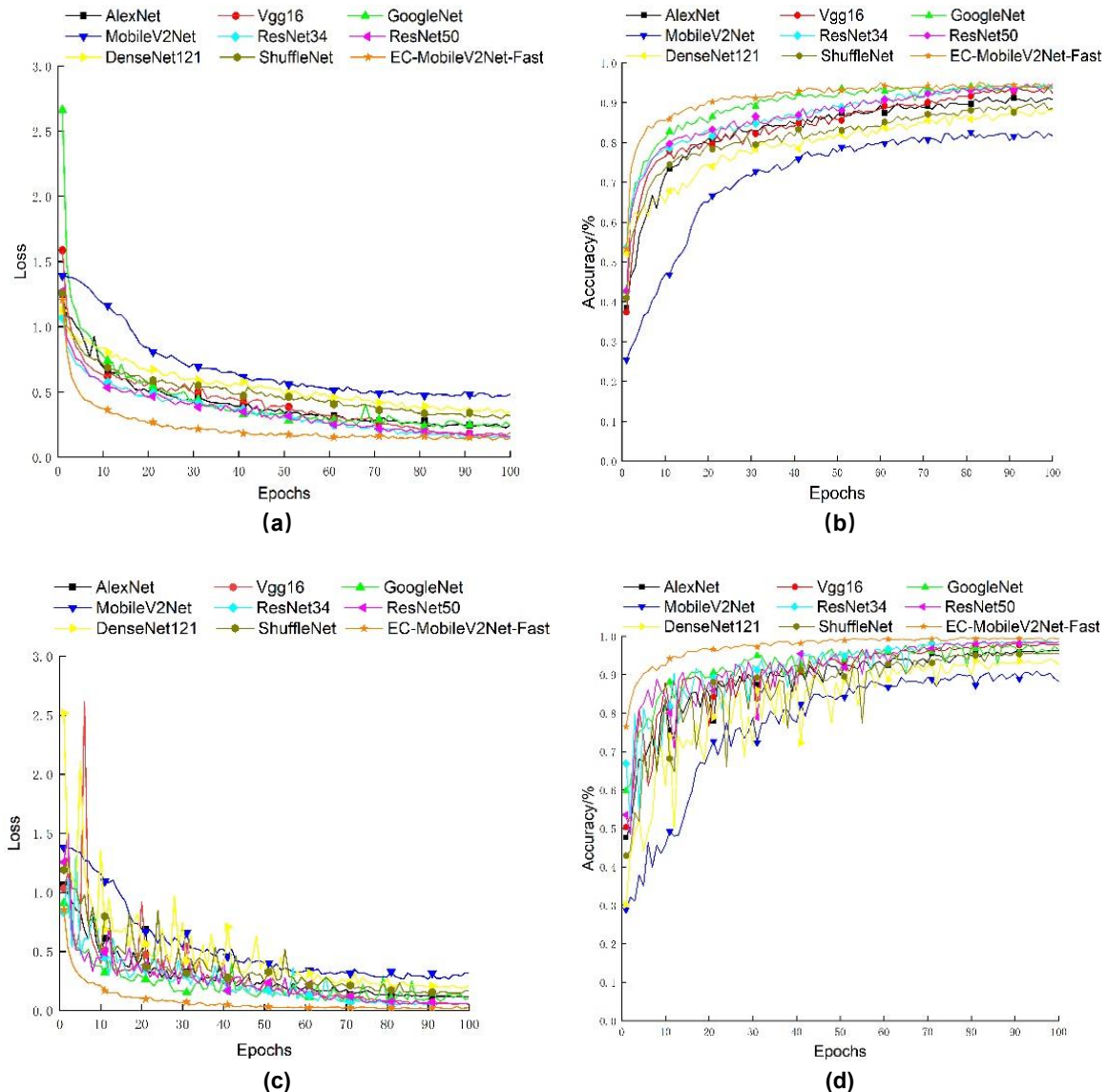


Fig. 6 (a) Train Loss Curve; (b) Train Accuracy Curve; (c) Test Loss Curve; (d) Test Accuracy Curve

Figures 6(a) and 6(b) illustrated the trend in the difference between the predicted and actual values of the model during the iterative process, while Figures 6(c) and 6(d) demonstrated the model's classification capabilities. The loss curve revealed that the improved network exhibited a lower loss rate and faster convergence compared to other networks. Typically, the loss rate curve and the accuracy curve exhibited a complementary trend; as the loss rate declined rapidly, the accuracy rate increased correspondingly, indicating that the network swiftly learned the characteristics of the input data and effectively mapped them to the correct output. After 50 iterations, the network had grasped the essential features of the input data and accurately mapped them to the desired output. In comparison with other models, the EC-MobileV2Net-Fast model demonstrated a marked improvement, with a substantially reduced loss rate and a peak accuracy rate achieved.

Ablation Comparison Test

To further explore the effectiveness of the network model, seven sets of ablation experiments were designed. The results of the ablation experiments were shown in Table 3, where "√" indicated that this item was adopted, and "x" indicated that this item was not adopted.

Table 3

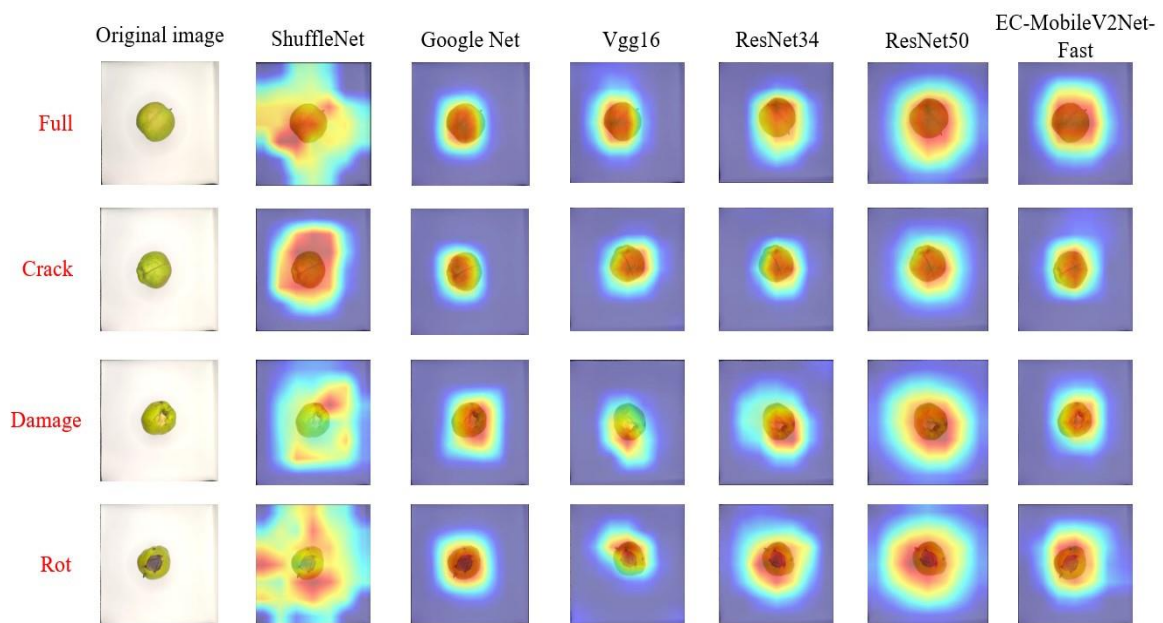
Comparison of ablation experiments

Model	Test 1	Test 2	Test 3	Test 4	Test 5	Test 6	Test 7
ECA module	√	x	x	√	√	x	√
Transfer learning	x	√	x	√	x	√	√
LeakyReLU	x	x	√	x	√	√	√
Accuracy	95.64%	91.85%	89.80%	99.40%	88.10%	90.83%	99.67%
Single picture inference time	15.5 ms	15.7 ms	14.8 ms	15.2 ms	15.3 ms	14.8 ms	14.4 ms

As evident from the table, the integration of the ECA module notably enhanced the model's feature extraction capability, thereby laid a robust foundation for high-precision recognition. The utilization of LeakyReLU, with its distinctive activation characteristics, expedited the model's inference process. Furthermore, the incorporation of transfer learning fortified the synergistic effects of the ECA and LeakyReLU modules, ultimately enabling the improved model to achieve optimal performance.

Feature Visualization Result

Among the aforementioned comparison models, the top five models with the highest accuracy were chosen for a thermal map comparison with the enhanced EC-MobileV2Net-Fast model. Randomly selected from the test set were four types of original images of Yu-Lu-Xiang pear fruits. The thermal maps of the final layer for all models were generated using Grad-CAM technology (Selvaraju R et al, 2019), as depicted in Figure 7(a). The layer-by-layer heat maps of the four damaged fruits based on the improved model EC-MobileV2Net-Fast are shown in Figure 7(b), the enhanced model demonstrated a superior capability in precisely pinpointing the defect locations and accurately highlighting the regions of interest (ROIs) for specific defect categories, This observation aligned with the manual sorting process, where similar regions of specific features were recognized for classification purposes.



(a)

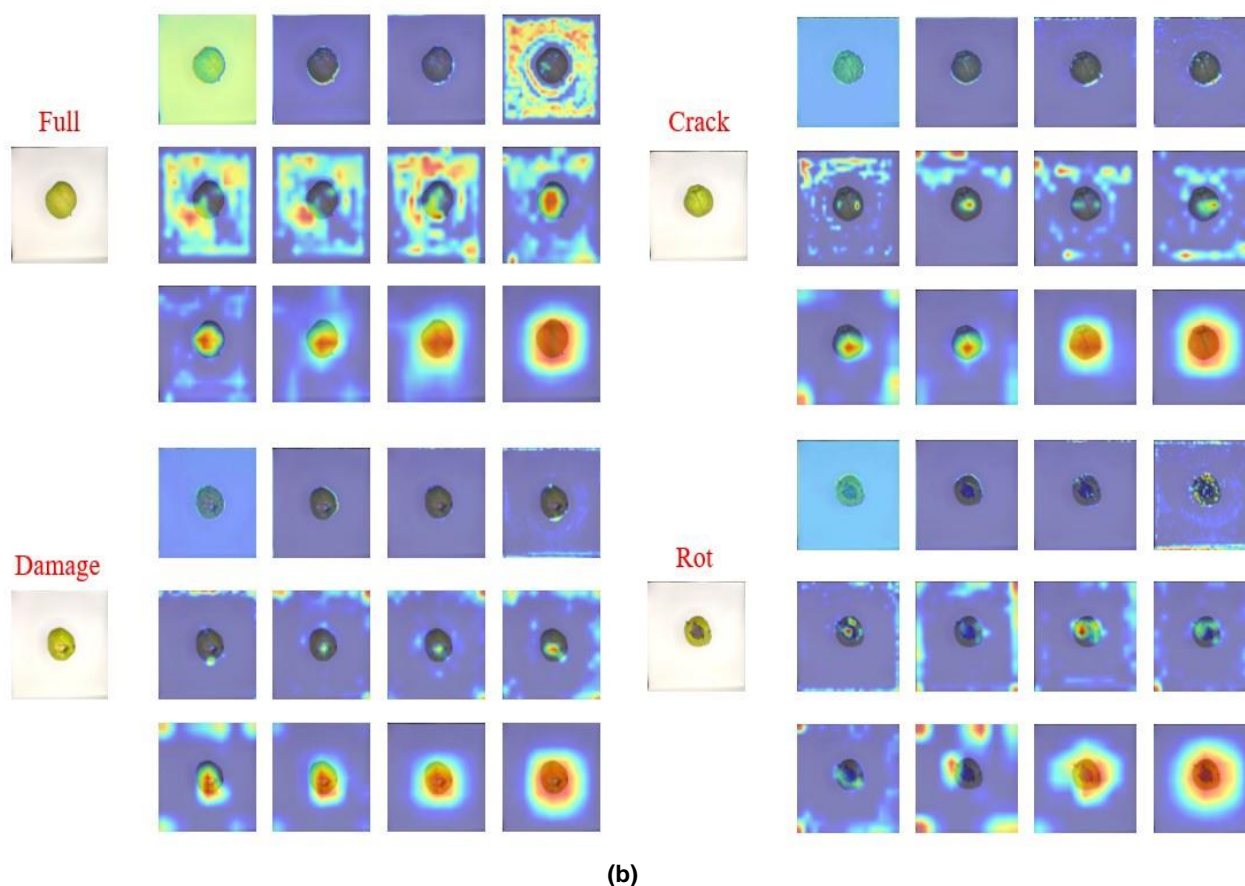


Fig. 7 – (a) Heat Map Comparison; (b) Improved model layer-by-layer heat map

CONCLUSIONS

In this study, an enhanced lightweight CNNs model, EC-MobileV2Net-Fast, was proposed specifically for recognizing various degrees of damage and defects on the surface of Yu-Lu-Xiang pears. By incorporating a channel attention mechanism, the focus on critical subtle feature areas was significantly augmented, which enabled the model to extract and identify these subtle yet vital features with greater precision. Consequently, the overall classification accuracy of the model was improved. Fused transfer learning into the model, using the feature extraction capability of the pre-trained model to make the model adapt to new tasks quickly with a small amount of data, accelerated the training process and improved the generalization ability of the model. By optimizing the activation function, the problem of neuron deactivation when the input was negative was effectively solved, and the stable performance of the model in complex environment was ensured.

Compared to the traditional classical models, including VGG16, ResNet34, ResNet50, MobileV2Net, GoogleNet, DenseNet121, ShuffleNet, and AlexNet, EC-MobileV2Net-Fast demonstrated remarkable enhancements on accuracy, the specific increases being of 1.54%, 1.37%, 1.34%, 8.97%, 1.67%, 5.96%, 1.73% and 3.71%, respectively. Moreover, the EC-MobileV2Net-Fast model also excelled in other key metrics of model, such as the recall and precision of single fruit recognition. Therefore, the model improvement strategies proposed in this study had substantially enhanced its classification capabilities, showcasing its superiority and robustness in recognizing surface damage defects of Yu-Lu-Xiang pears.

Therefore, this study provided a systematic classification method for the sorting of Yu-Lu-Xiang pears after harvesting, realized the non-destructive testing for Yu-Lu-Xiang pears defects, and provided theoretical and technical support for deepening the theoretical research of Yu-Lu-Xiang pears and automating the classification after transplantation to mobile devices.

ACKNOWLEDGEMENT

This research was supported by Shanxi Province's key research and development project [grant No: 202102020101012] and supported by the Shanxi Agricultural University Science and Technology Innovation and Promotion project [grant No: CXGC2023044]. The authors are grateful and honored to receive this support.

REFERENCES

- [1] Bin W., Lili L., (2023), Detection of defects of cerasus humilis fruits based on hyperspectral imaging and convolutional neural networks. *INMATEH Agricultural Engineering*, Taigu / China, Vol. 71, pp. 103-114.
- [2] da Costa Arthur., Figueroa H., Fracarolli J. (2020). Computer vision based detection of external defects on tomatoes using deep learning. *Biosystems Engineering*, Vol. 190, pp. 131-144.
- [3] Haixia S., Runrun W., Shujuan Z., Rui R., Liyang S., Xinyuan L., (2023), Determination of soluble solids content of Yu-Lu-Xiang pears based on visible/near-infrared spectroscopy (基于可见/近红外光谱技术的玉露香梨可溶性固形物含量检测). *Agricultural Products Processing*, Taigu / China, Vol. 14. pp. 46-48,54.
- [4] Iosif A., Maican E., Biris S., Popa L., (2023), Automated quality assessment of apples using convolutional neural networks. *INMATEH Agricultural Engineering*, Bucharest / Romania, Vol. 71, pp. 483-498.
- [5] Jiaqi Q., (2022), A MobileNet-based method for identification of crop leaf diseases (基于 Mobilenet 的农作物叶片病害识别方法). *Information and Computers (Theory Edition)*, Guilin / China, Vol. 33. pp. 181-184.
- [6] Jiang P., Chen Y., Liu B., He D., Liang C. (2019), Real-Time Detection of Apple Leaf Diseases Using Deep Learning Approach Based on Improved Convolutional Neural Networks, *IEEE Access*, Vol. 7, pp. 59069–59080.
- [7] Jiapeng Q., Dong X., Xiaohui H., Ruihong T., Guotian H., (2023), Detection method of tomato leaf diseases based on improved attention mechanism. *INMATEH Agricultural Engineering*, Yanglin / Shanxi, Vol. 70, pp. 615-625.
- [8] Kai B. (2022), *Research on non-destructive inspection of the quality of Yu-Lu-Xiang pears based on hyperspectral technology* (基于高光谱技术的玉露香梨品质无损检测研究). (Master's thesis). Shanxi Agricultural University, Shanxi / China.
- [9] Md Taimur Ahad., Yan Li., Bo Song., Touhid Bhuiyan, (2023), Comparison of CNN-based deep learning architectures for rice diseases classification. *Artificial Intelligence in Agriculture*, Vol. 9, pp. 22-35.
- [10] Selvaraju R., Cogswell M., Das A., Vedantam R., Parikh D., Batra D., (2019), Grad-CAM: Visual explanations from deep networks via gradient-based localization. *International Journal of Computer Vision*, Vol. 128, pp. 336-359.
- [11] Shengqiao X., Yang B., Qilin A., Jian S., Xiuying T., Fuxiang X., (2022), Identification system of tomato leaf diseases based on optimized mobilenet v2. *INMATEH Agricultural Engineering*, Weifang / China, Vol. 68, pp. 589-598.
- [12] Too E. C., Yujian L., Njuki S., Tingchun L. (2019), A comparative study of fine-tuning deep learning models for plant disease identification, *Computers and Electronics in Agricult*, Vol. 161, pp. 272–279.
- [13] Weijian H., Jie F., Tongxing D., Baoshan L., Naixue X., Bekkering E., (2020), “MDFC–ResNet: An Agricultural IoT System to Accurately Recognize Crop Diseases,” *IEEE Access*, Vol. 8, pp.115287–115298.
- [14] Wei P., Xilong Q., Shocheng W., Qingchun L. (2023), Apple surface defect detection based on improved CNN and data expansion (基于改进 CNN 和数据扩充的苹果表面缺陷检测). *Food and Machinery*, Hunan / China, Vol. 39, pp. 22-128,226.
- [15] Xiwen Z., Zhanfeng Hou., Chuazhong X., (2022), Design and experiment of recognition system for coated red clover seeds based on machine vision. *INMATEH Agricultural Engineering*, Neimenggu / China, Vol. 66, pp. 62-72.
- [16] Yanhong L., Hua Y., Xindong G., Yanwen L., Zhiwei H., Yiming H., Hongxia S., (2022), Fine-grained tomato disease recognition based on deep convolutional network. *INMATEH Agricultural Engineering*, Shanxi / China, Vol. 67, pp. 182-190.
- [17] Yunfei W., (2023), *Research on non-destructive testing method for external quality of kiwifruit* (猕猴桃外部品质无损检测方法研究). (Master's thesis). China Academy of Agricultural Mechanisation Science, Beijing / China.
- [18] Yang Z., Jun X., (2021), Face recognition system based on MobileNetV2 and Raspberry Pi (基于 MobileNetV2 与树莓派的人脸识别系统). *Computer system applications*, Shenyang / China, Vol.30, pp.67-72.
- [19] Zhongpei W., Meng Z., Wei D., Jingbo Zhu., Juanjuan Kong., Rong Q., (2021), Research on multi-model rice disease identification method based on transfer learning (基于迁移学习的多模型水稻病害识别方法研究). *Anhui Agricultural Sciences*, Anhui / China, Vol. 49. pp. 236-242.

- [20] ***Fresh pear: GB/T 10650-2008, (2008), *National standard for Fresh pears (鲜梨国家标准)*, Jinan Fruit Research Institute, All China Supply and Marketing Cooperative Society, Jinan / China.
- [21] ***Korla pear:DB65/T 4295-2020, (2020), *Xinjiang Korla pear fruit quality grading standard (新疆库尔勒香梨果品质量分级标准)*, Xinjiang Uygur Autonomous Region local standard, Xinjiang / China.

IMPACT OF PARTIAL FREEZING WITH MODIFIED ATMOSPHERE PACKAGING ON PORK'S QUALITY

气调微冻对猪肉品质的影响

Huaming HOU^{1,3)}, Dengming LI²⁾, Rui ZHANG¹⁾, Wei NIU¹⁾, Qingliang CUI^{1,3)}, Yisheng CHEN^{*2)}

¹⁾ College of Agricultural Engineering, Shanxi Agricultural University, Taigu 030801 / China;

²⁾ College of Food Science and Engineering, Shanxi Agricultural University, Taigu 030801 / China;

³⁾ Dryland Farm Machinery Key Technology and Equipment Key Laboratory of Shanxi Province, Taigu 030801 / China

Tel: +86-18404966321; E-mail: chenisheng@sxau.edu.cn

DOI: <https://doi.org/10.35633/inmateh-74-11>

Keywords: storage, pork, modified atmosphere packaging, partial freezing, quality

ABSTRACT

To preserve the original quality of fresh pork and prolong its shelf life, this study aimed to seek a no ionic residue efficient storage method. The partial freezing with modified atmosphere packaging (PF-MAP, -1°C, 75%O₂+20%CO₂+5%N₂) method was proposed and it was used to preserve fresh pork, and the storage effects with methods of refrigeration with MAP (R-MAP, 4°C), partial freezing with vacuum package (PF-VP, -1°C), refrigeration with vacuum package (R-VP, 4°C), partial freezing (PF, -1°C) and refrigeration (R, 4°C) were compared. The results indicated that after 8 days of storage, the total volatile basic nitrogen (TVB-N) content and total viable count (TVC) of pork under PF-MAP and R-MAP were much below the safety threshold limits, while the TVB-N content and TVC of the pork under PF-VP, R-VP, PF, R exceeded the safety limits. The drip and stewing losses of PF-MAP pork were lowest, which were 0.98% and 27.54%, respectively. The hardness and shear force of PF-MAP pork were 37.78 N and 38.38 N, respectively, which were significantly higher than other methods. The color of PF-MAP pork was bright, with a pH value of 6.08, an intense pork aroma, and perceived freshness. After 12 days of storage, the TNB-N content and TVC of PF-MAP pork remained significantly lower values, while the TVC of R-MAP pork approached the safety limit. After 20 days of storage, the TVB-N content and TVC of PF-MAP pork were 10.92 mg/100 g and 4.84 lg CFU/g, respectively, significantly lower than the threshold limits. Its drip loss, stewing loss, hardness, shear force, pH, and color (L*, a*, b* values) were all satisfactory, resembling fresh pork in color and aroma. In conclusion, PF-MAP can better maintain the quality of fresh pork.

摘要

为保持鲜猪肉品质, 延长其货架期, 该研究旨在寻求一种无离子残留的高效贮藏方法, 提出了一种气调包装微冻猪肉的贮藏方法, 测量其贮藏效果, 并与气调冷藏、真空微冻、真空冷藏、微冻、冷藏方法的贮藏效果相比较。结果表明, 贮藏 8 天时, 气调微冻和气调冷藏猪肉的挥发性盐基氮 (TVB-N) 含量和菌落总数 (TVC) 远低于安全限量, 而冷藏、微冻、真空冷藏和真空微冻猪肉的 TVB-N 含量和 TVC 已超过安全限量, 气调微冻猪肉的汁液流失率和蒸煮损失率最低, 分别为 0.98% 和 27.54%。气调微冻猪肉的硬度和剪切力均显著高于其他贮藏方法下的猪肉, 分别为 37.78 N 和 38.38 N。气调微冻猪肉的色泽鲜亮, pH 值为 6.08, 香气浓且感官上最为新鲜。贮藏 12 天时, 气调微冻猪肉的 TNB-N 含量和 TVC 仍显著低于安全限量, 而气调冷藏猪肉的 TVC 已达到安全限量。贮藏 20 天时, 气调微冻猪肉的 TVC-N 含量和 TVC 分别是 10.92 mg/100 g 和 4.84 lg CFU/g, 仍显著低于安全限量, 其汁液流失、蒸煮损失、硬度、剪切力、pH 和色度 L*、a*、b* 值皆较好, 色泽与新鲜猪肉相近, 仍保有猪肉香气。综上可知, 气调微冻方法能较好地保持鲜猪肉的品质。

INTRODUCTION

The Rongchang pig is a superior pig breed in China, hailed as the "treasure of China," with advantages such as easy feeding, good meat quality, and high reproductive performance (Leng et al., 2023). However, developments in the intensive processing industry have resulted in a demand to preserve Rongchang pork. In the past, pork in China was mainly distributed as fresh or frozen meat. Fresh meat is not suitable for storage, and freezing can cause severe damage to the quality of the meat. Chilled fresh meat has become increasingly popular in recent years. Although chilling improves the quality of meat for eating, it is limited by the growth of

¹ As A.P. Ph.D. Eng. Huaming HOU; Yisheng CHEN, Prof. Ph.D. Eng.; Dengming LI, M.S. Eng.

spoilage-related microbes during storage, which means it can only be stored for a maximum of 4-5 days (Zhao *et al.*, 2022). An efficient and safe method for preserving chilled fresh meat must be developed to extend the shelf life of chilled fresh pork, maintain its high quality, and ensure food safety.

Preservation by partial freezing refers to storing food slightly below its freezing point after rapid pre-cooling, resulting in a fresh appearance (Hoang *et al.*, 2016). After pre-cooling, the food can pass rapidly through the maximum ice crystal generation zone, thus avoiding damage to tissue and cell structure caused by ice crystals. Partial freezing technology allows some formation of ice crystals by water in the food, which effectively inhibits the activity of endogenous enzymes and the growth of spoilage-associated bacteria, thus maintaining the food quality (Cao *et al.*, 2023). Research has demonstrated that subjecting marine, meat, and meat products to partial freezing leads to a preserved state of freshness, significantly prolonging their shelf life by 1.5 to 4 times compared to conventional refrigeration methods (Tao *et al.*, 2023). The formation of uniform small ice crystals causes minimal damage to muscle fibers, thus making the procedure suitable for storing partially freezing fresh meat (Guo *et al.*, 2023). After partial freezing, there is no need to add protective ice blocks during short-term storage and transportation, thus reducing costs. Modified atmosphere packaging (MAP) involves the sealing of food in an artificially mixed gas environment using packaging materials to retard food spoilage, inhibit the growth of microorganisms and enzyme reactions in the food, and extend the shelf life of the product (Liu *et al.*, 2024). Common gasses used in MAP include O₂, CO₂, and N₂. O₂ can inhibit the reproduction of anaerobic bacteria, thus maintaining the fresh red color of the meat. In contrast, CO₂ can inhibit mold development and growth of aerobic bacteria, and N₂, besides its bacteriostatic effect, helps maintain the meat products' original texture, color, and taste (Abdullah *et al.*, 2024). Research has demonstrated that MAP has bacteriostatic capabilities and preserves meat products' tenderness, color, water retention, and other characteristics. It also slows down the oxidation process of proteins and lipids in meat while maintaining the integrity of cellular structures (Śmiecińska *et al.*, 2023).

Therefore, this study investigates the impact of combining MAP technology with partial freezing to preserve fresh Rongchang pork and maintain its storage quality. The present study measured and compared the alterations in the quality of fresh Rongchang pork during storage using various methods, including refrigeration, partial freezing, vacuum refrigeration, and vacuum partial freezing. These findings serve as a valuable reference for advancing preservation and processing techniques for fresh pork.

MATERIALS AND METHODS

Storage Experiment Design and Freezing-Point Determination

Six types of storage conditions were investigated. These were refrigeration (4°C, denoted as A), partial freezing (-1°C, denoted as B), vacuum refrigeration (4°C, denoted as C), vacuum partial freezing (-1°C, denoted as D), R-MAP (75%O₂+20%CO₂+5%N₂, 4°C, denoted as E), and PF-MAP (75%O₂+20%CO₂+5%N₂, -1°C, denoted as F). Fresh pork was used as the blank control (CK). The experimental indicators included the total volatile basic nitrogen (TVB-N), total viable count (TVC), drip-loss rate, cooking-loss rate, hardness, shear force, pH, and color and aroma components. Measurements were conducted at four-day intervals to assess variations in pork quality across various storage conditions until the conclusion of the storage period. Monitoring of pork under a specific storage condition was stopped when the safety indicators (TVB-N, TVC) surpassed the safety limits.

The freezing point of Rongchang fresh pork was determined in advance to determine the partial freezing temperature. After removing the fat and connective tissue, the pork was cut into small pieces measuring 5 × 5 × 5 cm. A calibrated thermometer probe (JM222, Tianjin Jiming Instrument Co., Ltd., China) was inserted into the geometric center of the piece of meat, followed by placing the meat in a -18°C freezer (BCD-607WKPZM(E), Midea Group Co., Ltd., China). The temperature was recorded every 20 s until the temperature at the center of the pork reached -18°C. A temperature-change curve was plotted, and when a platform period appeared in the temperature change, the temperature of this platform period was taken as the freezing point of the pork. This measurement was conducted three times and averaged (Li *et al.*, 2020).

The fresh Rongchang pork was sliced on a sanitized workstation, and the fresh pork quality markers were recorded. The pork was packaged in PE preservation boxes (Haoduohe Blister Packaging, China) for the refrigeration and partial freezing procedures. In contrast, for MAP treatment, the pork was packed using a MAP machine (BZJ-300, Wenzhou Dajiang Packaging Machinery Co., Ltd., China). The pork was packed using a vacuum-packaging machine (DZ520/2D, Yuanda Intelligent Packaging Machinery Co., Ltd., China) for vacuum treatment. The packaged pork was then stored in constant-temperature refrigerators (KB(E6), KAIGEN Biotechnology Co., Ltd., Germany) for refrigeration (4°C) and partial freezing (-1°C).

Safety Analysis of Stored Pork

Marketable pork is required to meet the safety standards of specific indicators. To meet these standards, the research team measured two common indicators used in pork inspection and quarantine: the TVB-N content and the TVC. The TVB-N content in Rongchang pork was determined using a fully automatic Kjeldahl apparatus (K9860, Hanon Group, China). The lean meat portion was minced using a food processor (DEM-JS200, Guangdong Deerma Technology Co., Ltd., China). A 10 g sample and 75 mL of distilled water were introduced to a distillation tube, shaken, and allowed to digest for 30 minutes. Next, 1 g of MgO was added, and the liquid was distilled using the Kjeldahl apparatus. In parallel, the distilled ammonia was absorbed in a 250 mL conical bottle containing 2 drops of methyl red-bromocresol green mixed indicator, 10 mL boric acid solution (20 g/L), and a standard hydrochloric acid solution (0.01 mol/L) was added after the mixture had reacted for 6 minutes until it turned pink. The amount of standard hydrochloric acid solution used was noted. Distilled water was used as a blank control. The TVC-N content was calculated using the following formula (Zhang *et al.*, 2024):

$$X = \frac{(V_1 - V_2) \times c \times 14}{m} \times 100 \quad (1)$$

where X is the content of TVB-N in the sample, in mg/100 g or mg/100 mL; V_1 is the volume of standard hydrochloric acid solution consumed by the sample, in mL; V_2 is the volume of standard hydrochloric acid solution consumed by the blank group, in mL; c is the concentration of standard hydrochloric acid solution, in mol/L; m is the mass or volume of the sample, in g or mL.

Before determining the TVC, all Petri dishes, physiological saline, and culture media were sterilized using a vertical pressure steam sterilizer (JC100D, Deqiang Purify, China). In a laminar flow cabinet (SWP-2, Kenton Instrument Co., Ltd., China), 25 g of pork and 225 mL of sterile physiological saline were placed in a sterile homogenization bag (Type 400, BKMAN LAB, China). A 1:10 sample homogenate was produced after homogenizing the material for one to two minutes using a homogenizer (SCIENTZ-11, Ningbo Scientz Biotechnology Co., Ltd., China). Three appropriate dilution gradients were selected for plate coating out of ten serial dilutions of the homogenate produced. Aliquots of 1 mL of the homogenate were placed in sterile Petri dishes containing 15-20 mL of plate-count agar and evenly spread. The petri dish was then placed in a sterile constant-temperature incubator (HWS-500H, Ningbo Yanghui Instrument Co., Ltd., China) for 48 ± 2 h, followed by plate counting.

Commodity Value of Stored Pork

Drip loss during pork storage has an impact on the commodity value. As a result, pork's drip and cooking loss rates were measured during storage. To determine the drip-loss rate, moisture on the surface of chilled fresh meat packaging was wiped off, and the meat and packaging were weighed using an analytical scale (JA2003, Sunny Hengping Instrument Co., Ltd., China) and recorded as m_1 . The package was then opened and the liquid inside the package was absorbed with absorbent paper for the second weighing, recorded as m_2 . Finally, the sample was removed from the packaging, and the mass of the packaging was weighed and recorded as m_3 . The drip loss rate was calculated by the following formula (Yao *et al.*, 2024):

$$\text{Drip loss (\%)} = \frac{m_1 - m_2}{m_1 - m_3} \times 100 \quad (2)$$

To determine the stewing loss rate, the refrigerated raw meat was taken out of its packing and weighed, noted as m_1 . Afterwards, it was immersed in a water bath (J-HH-2A, Shanghai LNB Instrument Co., Ltd, China) set at a temperature of 75°C for 20 minutes. It was then extracted, allowed to cool until the surface was devoid of moisture, and subsequently reweighed, documented as m_2 . The stewing loss rate was determined using the following formula (Gao *et al.*, 2023):

$$\text{stewing loss rate (\%)} = \frac{m_1 - m_2}{m_1} \times 100 \quad (3)$$

Organoleptic Properties of Stored Pork

The color, aroma, taste, and texture of pork represent intuitive indicators of its quality. Therefore, the color, aroma components, pH value, shear force, and hardness of the pork during storage were measured. The color of the chilled fresh meat was measured using a colorimeter (NR10QC, Hunan Lichen Instrument Technology Co., Ltd., China). Following the calibration process, the colorimeter's test port was positioned correctly in alignment with the sample, and results were documented once they reached a stable state. Three measurements were conducted for each sample, and the mean value was calculated (Che *et al.*, 2023).

The aroma components of the chilled fresh meat were measured using an electronic nose (C-Nose, Bosin Tech, China). One gram of chopped and evenly mixed sample was placed in a 15 mL headspace vial,

sealed with a polytetrafluoroethylene pad, and left at room temperature for 30 min. Electronic nose detection was examined using the headspace suction method, with each sample being measured three times (Zhang *et al.*, 2022).

The pH value of the chilled fresh meat was measured using a portable pH meter (PH828+, SIGMA TECHNOLOGY, China). Following the calibration process, the pH meter probe was put into the sample, and measurements were taken once the values became stable. Three measurements were taken for each sample, and the mean value was calculated.

The texture analyzer (TA-300W, CZMLD, China) was used to measure the shear force and hardness of the chilled fresh meat. When measuring the shear force, after measuring the cooking-loss rate, the meat sample was cut into strips of 1 × 1 × 3 cm and measured using a V-notch probe, using the parameters of deformation rate of 40%, trigger load of 3.8 N, test speed of 60 mm/min, and return speed of 100 mm/min (Feng *et al.*, 2023). When measuring the hardness, the cooked meat sample was cut into cubes of 1 × 1 × 1 cm and measured using a TA9 probe, with the parameters of deformation rate of 40%, trigger load of 3.8 N, test speed of 60 mm/min, return speed of 60 mm/min, and cycle number of 2 (McGuinness *et al.*, 2024).

Statistical Analysis

The raw data was organized and analyzed using Excel software. The measurement findings were presented as the average value plus or minus the standard deviation. The Origin2021 software was utilized for generating statistical graphs, while SPSS version 25.0 (IBM Corp., Armonk, NY, USA) was used for significance tests and correlation analysis.

RESULTS AND ANALYSIS

Freezing Point of Pork

Figure 1 shows a progressive reduction in the core temperature of the pork as the storage time increased. After 28 minutes, a platform phase was observed, with a temperature of -0.8°C , suggesting that the pork had reached its freezing point. As a result, the temperature for storing partially frozen items was adjusted to -1°C .

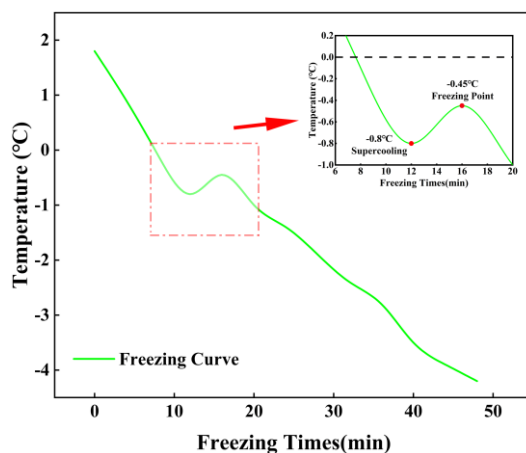


Fig. 1 - Freezing Curve of pork

Changes in TVB-N Content and TVC in Pork under Different Storage Conditions

TVB-N and TVC are essential indicators of meat freshness. A higher TVB-N content indicates greater amino acid degradation (Zhang and Zhao, 2023), while TVC reflects the degree of bacterial contamination in the meat. National meat safety standards stipulate that the TVB-N content of fresh pork should not exceed 15 mg/100 g (Cai *et al.*, 2024), and the TVC should not exceed 6 lg CFU/g (Xu *et al.*, 2018). As shown in Figure 2, as the storage time increased, both the TVB-N content and TVC of the pork in all groups tended to increase. On the eighth day, the level of TVB-N in the vacuum-packed and partially frozen pork surpassed the safe limit. Furthermore, the TVC of the pork in the vacuum-refrigerated and refrigerated groups exceeded the limit. On the twelfth day, the amount of TVB-N in the pork stored in a R-MAP environment was still below the acceptable limit, however its TVC value was above the limit. On the 20th day, the pork in the PF-MAP group had TVB-N levels of 10.92 mg/100 g and TVC levels of 4.84 lg CFU/g, which were still within the acceptable limits for freshness. This is possibly due to the effective protection of the protein structures in the meat by the MAP treatment (Hou *et al.*, 2023) and inhibition of bacterial growth in the partial-freezing environment.

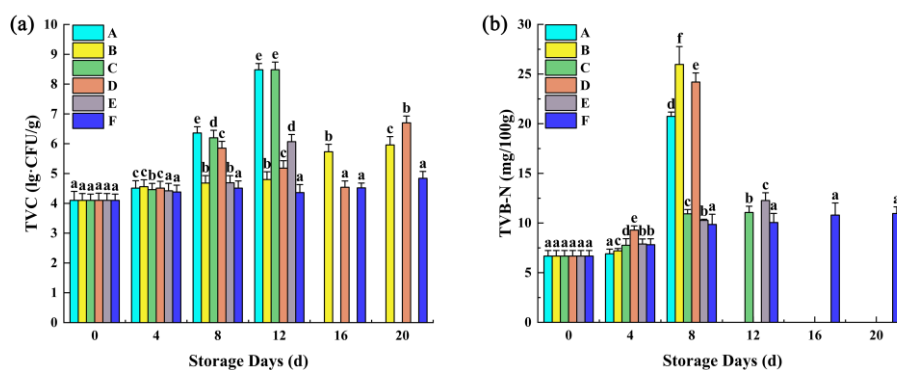


Fig. 2 - Changes of TVC and TVB-N content of pork during storage:

(a) Changes of TVC; (b) Changes of TVB-N content

Changes in Drip Loss Rate and Stewing Loss Rate of Pork under Different Storage Conditions

The drip loss and stewing loss rates are essential indicators of meat quality as they reflect the water-holding capacity of the meat. The annual economic losses caused by drip loss are immeasurable (Eom *et al.*, 2024). The higher the stewing loss rate, the smaller the water-holding capacity and the poorer the eating quality (Qin *et al.*, 2022). Figure 3a shows that as storage time extended, the drip-loss rate of pork in all groups increased gradually. During the first eight days of storage, drip loss rates in the refrigerated, vacuum-packed, PF-MAP, and R-MAP pork groups were low and gradually increased. After eight days, the drip loss was found to be lowest in the PF-MAP pork, with the slowest rate of rise, followed by the R-MAP pork. By day 20, the drip loss rate in the PF-MAP pork was 1.7%. As shown in Figure 3b, during the first four days of storage, the stewing-loss rate of the pork in all groups showed an upward trend, with a slower rate of increase in the vacuum-partial frozen, vacuum-refrigerated, and PF-MAP groups. From day 8, the stewing-loss rate of the PF-MAP pork was found to be the lowest, with the slowest increase rate. The R-MAP pork's stewing-loss rate tended to decline from days 8 to 12, and by day 12, it was nearly identical to that of the PF-MAP group. The partial freezing pork with MAP had a reasonably low stewing-loss rate of 29.76% till day 20. This is because some of the moisture in the pork created tiny ice crystals in the partially frozen environment, which caused the least damage to the pork's cells and tissue.

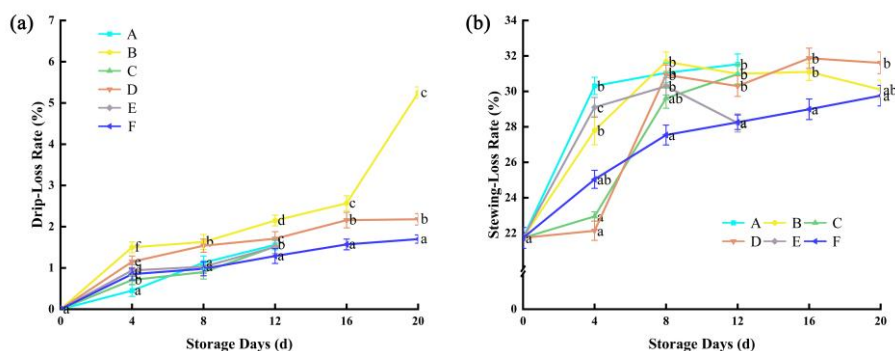


Fig. 3 - Changes in drip loss and stewing loss of pork during storage:

(a) changes of drip loss; (b) changes of stewing loss

Changes in Pork Color under Different Storage Conditions

Meat color is the most intuitive indicator of pork quality. Within a certain range, higher L^* values, larger a^* values, and smaller b^* values indicate fresher meat (Bohrer and Boler, 2017). Oxidation of proteins and lipids in pork increases the b^* value. As the storage time increased, the L^* , a^* , and b^* values in all the pork groups tended to increase. Figure 4a shows the color of the pork after 12 days of storage. The L^* , a^* , and b^* values of all the refrigerated pork groups are higher than the color values of the fresh pork. Among them, the R-MAP group's L^* , a^* , and b^* pork values were highest, showing a bright red-yellow color. This indicates that while MAP treatment enhanced the color of the pork, it did not significantly slow down the oxidation of proteins and lipids, as well as the growth of microbes. Figure 4b depicts the hue of the pork after a storage period of 20 days. The L^* , a^* , and b^* values of all the partially frozen pork groups were greater than the color values of the fresh pork. Among them, the L^* and a^* values of pork in the PF-MAP group were the highest, and its b^* value was closest to the b^* value of the fresh pork. This indicates that partial freezing effectively delayed the color

change caused by protein and lipid oxidation and microbial erosion in pork. Thus, PF-MAP treatment improves the color of stored pork.

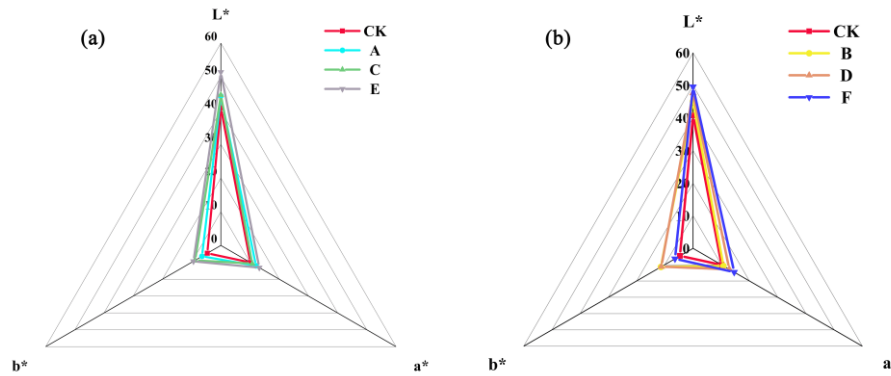


Fig. 4 - Colorimetric radar chart of pork under different storage conditions during storage:
 (a) Color comparison of pork under different refrigeration conditions after 12 days of storage;
 (b) Color comparison of pork under different frozen storage conditions after 20 days of storage

Changes in Aroma Components of Pork under Different Storage Conditions

From Figure 5a, it can be observed that the principal components 1 and 2 of the volatile compounds in fresh pork accounted for a combined percentage of 86.6%, and their distribution is relatively uniform with no significant differences. Figure 5b indicates that after eight days of storage, there was a substantial difference in the volatile components between the vacuum and fresh-pork groups, while other groups showed no significant differences compared to the fresh-pork group. In Figure 5c, after 12 days of storage, the volatile components of the MAP- partial freezing group showed no significant difference from those of fresh pork, while other groups showed some differences. Figure 5d indicates that after 20 days of storage, there were substantial differences in the volatile components of all the partial-freezing groups compared to fresh pork. However, the vacuum-partial and PF-MAP groups showed no significant differences in their volatile components. At this stage, both of these groups had lost their commodity value, suggesting that the freshness of the PF-MAP group fell somewhere between that of chilled fresh meat and spoiled meat. Furthermore, the pork in the PF-MAP group was in the transitional phase towards becoming spoiled meat. These findings indicate that using PF-MAP treatment can effectively slow down the degradation of volatile compounds in chilled fresh pork, hence maintaining the natural aroma of the pork.

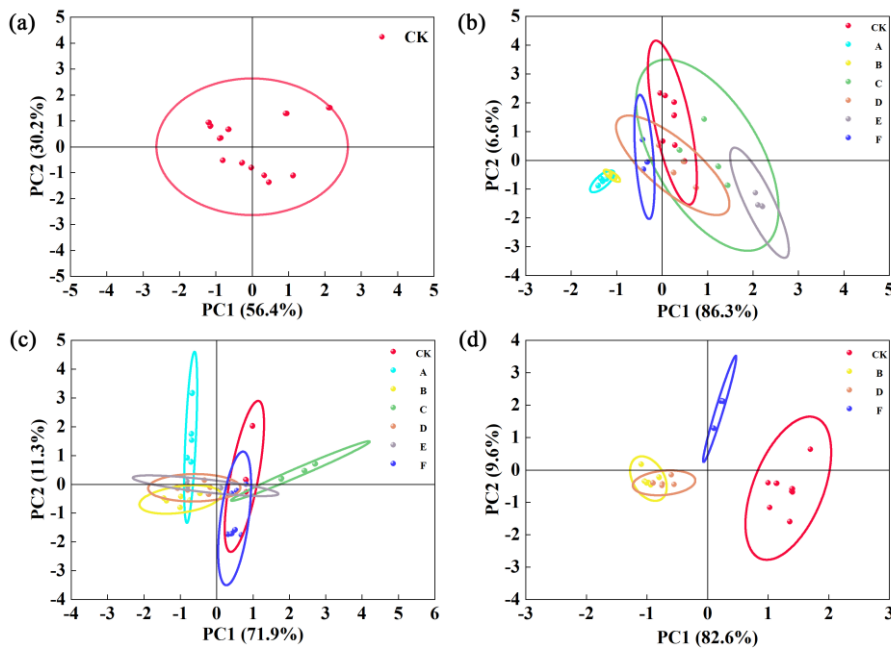


Fig. 5 - Principal component analysis (PCA) of the pork aroma during storage:
 (a) PCA of the fresh pork aroma; (b) PCA of the pork aroma after 8 days of storage;
 (c) PCA of the pork aroma after 12 days of storage; (d) PCA of the pork aroma after 20 days of storage

The main flavor-associated substances in pork are usually ribose and dicysteine. As shown in Figure 6, with the extension of storage time, the total amount of volatile components in chilled pork gradually decreased, indicating the continuous consumption of volatile flavor substances and thus reduced aroma. Figure 6a shows that the main volatile components in the fresh pork were nitrogen oxides, alkanes, sulfides, alcohols, aromatic compounds, and sulfur organic compounds. Figure 6b illustrates the volatile components in the various pork groups after four days of storage. The detected levels of W3S, W1C, W3C, and W5C in each group did not differ significantly from those of the fresh pork, while the remaining six components differed. The detected levels of W5S, W6S, W1S, W1W, and W2W in the pork in the PF-MAP and vacuum-partial-freezing groups were increased, with the vacuum treatment restricting the overall increase. The levels of volatile components in other groups displayed a declining pattern. Figures 6c and 6d display the levels of volatile components in all the groups that underwent partial freezing on days 16 and 20 of storage. The total concentration of volatile compounds in each partially frozen group was significantly lower than in the fresh pork.

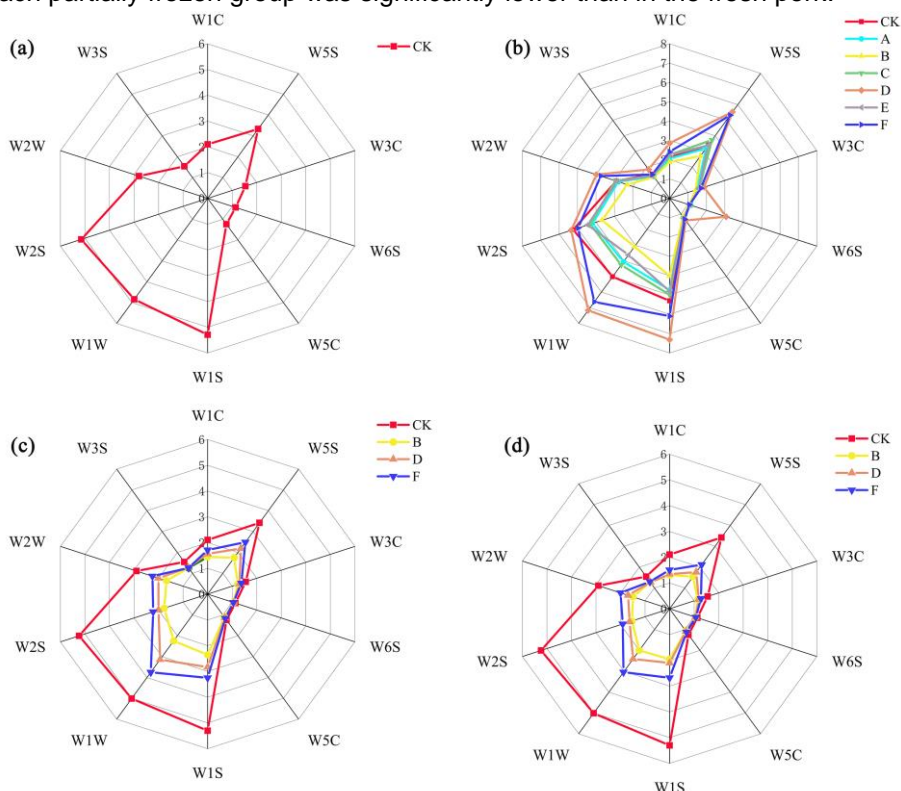


Fig. 6 - Radar plots of pork volatile components during storage

- (a) Radar plots of the fresh pork volatile components; (b) Radar plots of the pork volatile components after 4 days of storage; (c) Radar plots of the pork volatile components after 16 days of storage; (d) Radar plots of the pork volatile components after 20 days of storage

Furthermore, there were variations between the groups, particularly in the levels of W1S, W1W, W2S, and W2W. The total volatile component content in the PF-MAP group was significantly higher than in the vacuum-partial and partial-freezing groups. These findings suggest that fluctuations in the concentrations of W5S, W6S, W1S, W1W, and W2W during storage are linked to the freshness of chilled pork. Furthermore, using PF-MAP treatment is advantageous in preserving the volatile constituents of chilled fresh pork.

Changes in Pork pH under Different Storage Conditions

The pH value of pork is used as a reference index for measuring the freshness of the meat, as it affects the meat's color, tenderness, water retention, flavor, and shelf life. Generally, the pH value of primary fresh meat ranges from 5.18 to 6.12, while secondary fresh meat is between 6.13 and 6.16, with pH values above 6.17 indicating spoilage (Laack *et al.*, 2001). As shown in Figure 7, the pH values of the pork in each group generally showed an upward trend. In the first 12 days, the observed fluctuations in the pH values in all groups may be due to changes in the lactic acid content. After 12 days, the pH values began to increase, attributed to the breakdown of proteins and nitrogen-containing compounds in the meat by microorganisms and endogenous enzymes, leading to the formation of alkaline substances. During storage, the pH value of MAP-partially frozen pork remained relatively low with a slow increase.

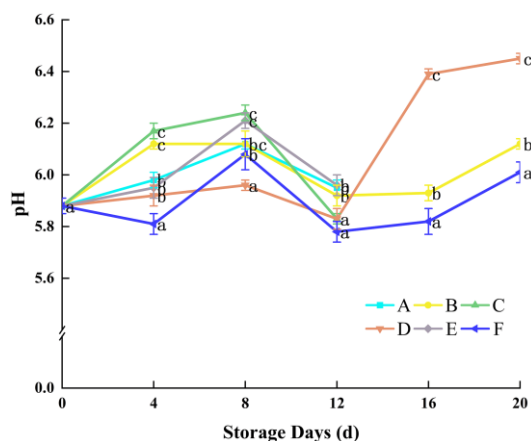


Fig. 7 - Changes in pH of pork during storage

In contrast, the vacuum-refrigerated and partially frozen groups had higher pH values. After 12 days, the pH values of the vacuum-partially frozen pork increased rapidly. After 20 days of storage, the pH value of the MAP-partially frozen pork was 6.01. Therefore, vacuum treatment is not conducive to maintaining the pH of pork, while the combination of MAP and partial freezing can better maintain the pH.

Changes in Pork Hardness and Shear Force under Different Storage Conditions

Hardness and shear force are important indicators reflecting the freshness and tenderness of pork. Within a certain range, greater hardness indicates freshness, and lower shear force indicates tenderness (LeMaster *et al.*, 2024). Figure 8a demonstrates that as the duration of storage extended, the meat's hardness in all groups tended to decline. During storage, the hydrolysis of myofibrillar proteins and the breakdown of peptide bonds between amino acids allow the collagen protein cross-linkages to break, which leads to a loss in hardness. Throughout the storage period, the pork in the PF-MAP group maintained a consistently high level of hardness, which was much greater than the hardness observed in the other groups.

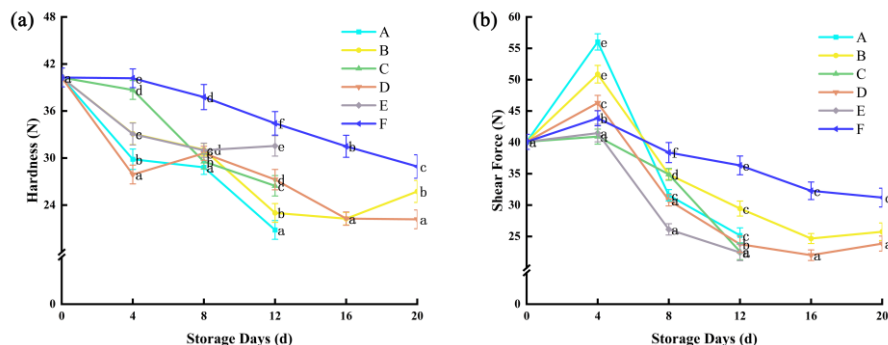


Fig. 8 - Changes in hardness and shear force of pork during storage: (a) Changes in hardness of the pork; (b) Changes in shear force of the pork

Furthermore, the hardness of the pork in this group reduced gradually over time. The hardness of the pork in the partial-freezing group ranked second, while the pork in the vacuum-partial-freezing group showed the fastest decrease in hardness. After 20 days of storage, the hardness of the pork in the PF-MAP group was 28.92 N. As shown in Figure 8b, the shear force of the pork in each group first tended to increase and then decrease, possibly due to the after-ripening of the chilled fresh meat leading to an increase in shear force, followed by the growth of ice crystals and microbial proliferation causing damage to muscle fibers, resulting in a decrease in the shear force. Over the initial four days of storage, the pork in the R-MAP, R-VP, and PF-MAP groups had low shear force values, suggesting excellent flesh tenderness. Over 4 days, the shear force of the pork in the PF-MAP group gradually declined but remained at a relatively high level, which was significantly higher than the other groups.

In contrast, the shear force in the other groups decreased quickly. After 20 days of storage, the shear force of the pork in the PF-MAP group was 31.2 N. Therefore, PF-MAP storage can reduce damage to the fiber structures of pork muscle, inhibit microbial proliferation, and help maintain the hardness and tenderness of the pork.

CONCLUSIONS

To prolong the shelf life of fresh pork, this study proposed and researched the effect of partial freezing with modified atmosphere packaging on the quality of fresh pork, and comparing with the methods of refrigeration with MAP, partial freezing with vacuum package, refrigeration with vacuum package, partial freezing, and refrigeration. The results showed that the effect of PF-MAP was the best, which could significantly inhibit the increase of TVB-N content and TVC in fresh pork, better retaining the juice, color, flavor, hardness and tenderness of fresh pork, and the storage period could reach more than 20 days. In conclusion, the storage method of PF-MAP can better maintain the quality of fresh pork, which can be used to solve the problem of short shelf life of fresh pork and provide a reference for the research and development of fresh pork storage technology.

ACKNOWLEDGEMENT

The authors are grateful for the financial support provided by Shanxi Basic Research Program youth fund project (NO. 20210302124606), 2022 Shanxi Province science and technology major special plan project 4 (NJ23-07-193), Central government guided local science and technology development fund projects (YDZJSX20231C008), Science and technology Innovation Fund project of Shanxi Agricultural University (NO. 2020BQ48), Scientific research project awarded by excellent Doctor of Shanxi Province for work in Shanxi (SXYBKY2019050), and Fundamental Research Program of Shanxi Province (NO. 202303021221106).

REFERENCES

- [1] Abdullah F.A.A., Dordevic D., & Kabourkova E., (2024), Oxidation Status and Antioxidant Activity of Analogue Meat Products in Modified Atmosphere Packaging. *Applied Sciences* 14(15), 6713-6713.
- [2] Bohrer B.M., & Boler D.D., (2017), Review: Subjective pork quality evaluation may not be indicative of instrumental pork quality measurements on a study-to-study basis. *The Professional Animal Scientist* 33(5), 530-540.
- [3] Cai M., Li X., Liang J., Liao M., & Han, Y., (2024), An effective deep learning fusion method for predicting the TVB-N and TVC contents of chicken breasts using dual hyperspectral imaging systems. *Food Chemistry* 456, 139847.
- [4] Cao R., Yan L., Xiao S., Hou B., Zhou X., Wang W., Bai T., Zhu K., Cheng J., & Zhang J., (2023), Effects of Different Low-Temperature Storage Methods on the Quality and Processing Characteristics of Fresh Beef. *Foods* 12(4), 782-782.
- [5] Che S., Susta L., & Barbut S., (2023), Effects of broiler chilling methods on the occurrence of pale, soft, exudative (PSE) meat and comparison of detection methods for PSE meat using traditional and Nix colorimeters. *Poultry science* 102(10), 102907-102907.
- [6] Eom J.U., Seo J.K., Y K.J., Song S., Kim G.D., & Yang H.S., (2024), Comparison of Chemical Composition, Quality, and Muscle Fiber Characteristics between Cull Sows and Commercial Pigs: The Relationship between Pork Quality Based on Muscle Fiber Characteristics. *Food science of animal resources* 44(1), 187-102.
- [7] Feng Y., Zhu X., Wang P., Xu X., Xiao Q., Liu X., Zeng X., & Zhao T., (2023), Analysis of the suitable thawing endpoint of the frozen chicken breast using video recording analysis, shear force, and bioelectrical impedance measurement. *Journal of texture studies* 55(1).
- [8] Gao H., Wang Z., Dai Y., Zeng J., & Li W., (2023), Effects of chia seed gum on the physicochemical properties of frozen dough and the quality of dumplings. *International journal of biological macromolecules* 253(P6), 127280-127280.
- [9] Guo Z., Wu S., Lin J., Zheng H., Lei H., Yu Q., & Jiang W., (2023), Active film preparation using pectin and polyphenols of watermelon peel and its applications for super-chilled storage of chilled mutton. *Food Chemistry* 417, 135838-135838.
- [10] Hoang H.M., Brown T., Indergard E., Leducq D., & Alvarez G., (2016), Life cycle assessment of salmon cold chains: comparison between chilling and superchilling technologies. *Journal of Cleaner Production* 126, 363-372.
- [11] Hou X., Zhao H., Yan L., Li S., Chen X., & Fan J., (2023), Effect of CO₂ on the preservation effectiveness of chilled fresh boneless beef knuckle in modified atmosphere packaging and microbial diversity analysis. *LWT* 187.
- [12] Laack R.L.v., Stevens S.G., & Stalder K.J., (2001), The influence of ultimate pH and intramuscular fat content on pork tenderness and tenderization. *Journal of animal science* 79(2), 392-397.

- [13] LeMaster M.N., Ha M., Dunshea F.R., Chauhan S., Darryl D.S., & Warner R.D., (2024), Impact of cooking temperature on pork longissimus, and muscle fibre type, on quality traits and protein denaturation of four pork muscles. *Meat Science* 209, 109395.
- [14] Leng D., Ge L., & Sun J., (2023), Characterization analysis of Rongchang pig population based on the Zhongxin-1 Porcine Breeding Array PLUS. *Animal bioscience* 36(10).
- [15] Li G.-y., Zhang J., Zhou Z.-w., Wang F., Chen D., Cao Y.-p., & Wu G., (2020), A novel freezing point determination method for oil-contaminated soils based on electrical resistance measurement and its influencing factors. *Science of the Total Environment* 721(pre-publish), 137821.
- [16] Liu K., Dong H., Peng J., Liao W., Yang X., & He Q., (2024), Design of equilibrium modified atmosphere packaging for postharvest cabbages preservation based on introducing available active sites into film materials as gas transport channels. *Food Research International* 177, 113900.
- [17] McGuinness L., Timlin M., Murphy J.P., Hennessy D., Fitzpatrick E., McCarthy K., O'Donovan M., O'Callaghan T.F., Kilcawley K.N., O'Riordan E.D., Brodkorb A., Sheehan J.J., & Feeney E.L., (2024), Impact of feeding regimes and lactation stage on sensory attributes of Cheddar cheese. *Food Research International* 180, 114046.
- [18] Qin O., Liu L., Muhammad Z., Wang L., & Chen Q., (2022), Application of portable visible and near-infrared spectroscopy for rapid detection of cooking loss rate in pork: Comparing spectra from frozen and thawed pork. *LWT* 160.
- [19] Śmiecińska K., Kubiak D., & Figger K., (2023), The Fatty Acid Profile, and the Content of Vitamin A, Vitamin E and Cholesterol in Beef (*M. longissimus lumborum*) Stored Under Different Modified Atmospheres. *Acta Universitatis Cibiniensis. Series E: Food Technology* 27(2), 173-184.
- [20] Tao Y., Guo Y., Li J., Ye K., Zhang Y., Zeng X., & Dou H., (2023), Effect of temperature fluctuation during superchilling storage on the microstructure and quality of raw pork. *Meat Science* 198, 109096-109096.
- [21] Xu F., Wang C., Wang H., Xiong Q., Wei Y., & Shao X., (2018), Antimicrobial action of flavonoids from *Sedum aizoon* L. against lactic acid bacteria in vitro and in refrigerated fresh pork meat. *Journal of Functional Foods* 40, 744-750.
- [22] Yao M., Chang L., Xu S., Zhang J., Li P., Tian B., Luo L., Yang D., Long Q., & Zou X., (2024), Comparison of production performance and meat quality characteristics between Guizhou Black goats and F4 generation hybrids of South African Kalahari Goats. *Scientific Reports*, 14(1), 18608-18608.
- [23] Zhang W., Han Y., Yang S., Wang S., Wu J., Jiao T., Wei J., Li D., Chen X., Chen Q., & Chen Q., (2024), Non-destructive prediction of total volatile basic nitrogen (TVB-N) content of *Litopenaeus vannamei* using A bi-channel data acquisition of Colorimetric sensing array. *Journal of Food Composition and Analysis* 128, 106026.
- [24] Zhang Y., Yun Z., Zhu M., Liu Z., & Huang Y., (2022), Oxidation and flavor changes in smoked bacon cured using bamboo extract concentrate combined with bamboo poles during storage. *Journal of Food Processing and Preservation* 46(5), e16556.
- [25] Zhang Z., & Zhao X., (2023), Effect of different packaging methods on the storage quality of beef sauce. *Chinese condiments* 48(08), 117-120.
- [26] Zhao F., Wei Z., Zhou G., Kristiansen K., & Wang C., (2022), Effects of Different Storage Temperatures on Bacterial Communities and Functional Potential in Pork Meat. *Foods*, 11(15), 2307-2307.

CONSTRUCTION AND VALIDATION OF A PREDICTIVE MODEL FOR TOMATO ORGAN BIOMASS AT ORGAN SCALE BASED ON STACKING LEARNING

基于堆叠学习的番茄器官尺度的生物量预测模型的构建与验证

Qi LIU, Fengpei WANG, Gang LIU, Lian BAI, Wuping ZHANG^{*)}

Software College of Shanxi Agricultural University/China

Tel: +86-15935664481; E-mail: zwping@126.com

DOI: <https://doi.org/10.35633/inmateh-74-12>

Keywords: Stacked Machine Learning; Tomato; Geometric Morphology Data; Linear Regression; Biomass Prediction Model; Organ-Scale

ABSTRACT

In this study, a stacked machine learning algorithm was constructed with tomato organ biomass as the research object, taking the geometric morphology data of tomato organs as the variables, utilizing eight classical machine learning algorithms as the base-model, and applying the linear regression algorithm as the stacked meta-model. This algorithm was then utilized to establish a prediction model for tomato biomass at the organ scale, and the biomass models of tomato plant leaves and fruits at the organ scale were constructed. The model has $R^2=0.86$, $MAE=0.49$, and $RMSE=0.81$ in predicting leaves, and $R^2=0.94$, $MAE=0.33$, and $RMSE=0.57$ in predicting fruits. The model has practical applications in predicting tomato yield and supply, providing market information, and supporting agricultural investment decisions. It also helps to optimize agricultural production and management, guide industrial development and planning, and improve the efficiency and competitiveness of the agricultural sector.

摘要

本研究以番茄器官生物量为研究对象，将番茄器官的几何形态数据作为变量，利用八种经典机器学习算法作为基础模型，并应用线性回归算法作为堆叠元模型，构建了一种堆叠式机器学习算法。然后利用此算法建立器官尺度上的番茄生物量预测模型，并构建了器官尺度上番茄植株叶片和果实的生物量模型。该模型在预测叶片方面的 $R^2=0.86$ ， $MAE=0.49$ ， $RMSE=0.81$ ；在预测果实方面的 $R^2=0.94$ ， $MAE=0.33$ ， $RMSE=0.57$ 。该模型在预测番茄产量和供应、提供市场信息、支持农业投资决策等方面具有实际应用价值，还有助于优化农业生产和管理，指导产业发展和规划，提高农业部门的效率和竞争力。

INTRODUCTION

Tomato (*Solanum lycopersicum* L.) is one of the most important vegetable crops in the world, and it has become one of the largest vegetable crops in the world's cultivation area (Li, 2013). Some studies have shown that the dramatic changes in global climate in the 21st century will have a significant impact on biodiversity, which, to some extent, also indicates that the cultivation of high-yielding and stable crop varieties will face greater uncertainty and higher difficulty (Damte, 2017). Therefore, it is necessary and important to obtain timely, rapid, and accurate information on crop growth and development and predict biomass.

Biomass is an important parameter for crop growth, which is directly related to the final yield, and the amount of biomass can effectively reflect the growth of crops (Colomina et al., 2014). Biomass modeling is the main method to estimate biomass, is an effective and relatively accurate investigation method (Wang et al., 2008), and has become a hot area of biomass research, rapid and accurate monitoring of biomass can be a timely understanding of crop growth and yield prediction, which is of great significance to the production and management of agriculture (Chen et al., 2016). However, the traditional methods for determining biomass are not only time-consuming, and slow, with large errors and low efficiency, but also cause damage to the crop during the measurement process, making it difficult to realize the measurement of biomass rapidly (Liu et al., 2021).

Domestic and international scholars have done a lot of research on biomass prediction modeling (Liu et al., 2023). Many scholars have used new science and technology, such as machine learning, in the production management of agriculture, to effectively realize the prediction and estimation of phenotypic indexes such as vegetation index, above-ground biomass, and chlorophyll content of crops with the help of new technology and new means, such as machine learning and artificial intelligence (Fu et al., 2021). Wang

et al., (2024) constructed a biomass prediction model for larch in Xiaoxinganling using diameter at breast height (D) and tree height (H) as variables and found that the machine learning algorithm could predict biomass better than the traditional algorithm. However, most of the current studies have focused on biomass prediction at the individual scale, and not many prediction models have been developed at the organ scale. Moreover, it has been shown that there is a significant correlation between the morphological data of tomato organs and the amount of material produced by them (*Dong et al.*, 2007). Therefore, in this study, a tomato organ biomass prediction model was developed at the organ scale based on machine learning techniques, taking tomato organ biomass as output parameters and tomato organ geometric morphology data as the input variables, to provide fast biomass prediction at the organ scale for tomato production, research, and breeding, to provide a theoretical basis and reference basis for tomato variety selection, cultivation management and production monitoring, and to provide experimental basis and scientific basis for tomato yield prediction and cost input.

MATERIALS AND METHODS

Test Material and Test Site

The test tomato variety is YOU CUI 8850, which is an infinite-growth large-fruited variety of tomato, a variety of medium-early maturity; the fruit is nearly round, turns red and bright in colour after maturity, has high hardness, a moderate size, and continuous fruit-setting ability; the weight of a single fruit is 190 g - 260 g; storage and transportation resistance, long shelf-life; resistance to the tomato yellowing curculio virus, blight, and tobacco mosaic virus, etc. The developmental stages of tomato fruit, specifically the green maturity and complete ripening phases, are shown in Fig. 1 and Fig. 2.



Fig. 1 - Green maturity of tomato fruits



Fig. 2 - Complete ripening of tomato fruits

The test site is located in Datong City, Shanxi Province, Yanggao County, West Lijia Soap Village, Tomato Industry Research Institute test base (longitude 113°40'42", latitude 40°09'50", elevation 1125 m) to carry out the test site for the meso-thermal temperate continental semiarid monsoon climate, the average annual temperature of 7.1°C, the temperature difference between day and night is obvious; the average annual number of hours of sunshine is 2,691.4 h; the average annual precipitation is 364.9mm; the annual frost-free period is 161 days; the soil is mainly loamy and of medium fertility. The test site is shown in Fig. 3.

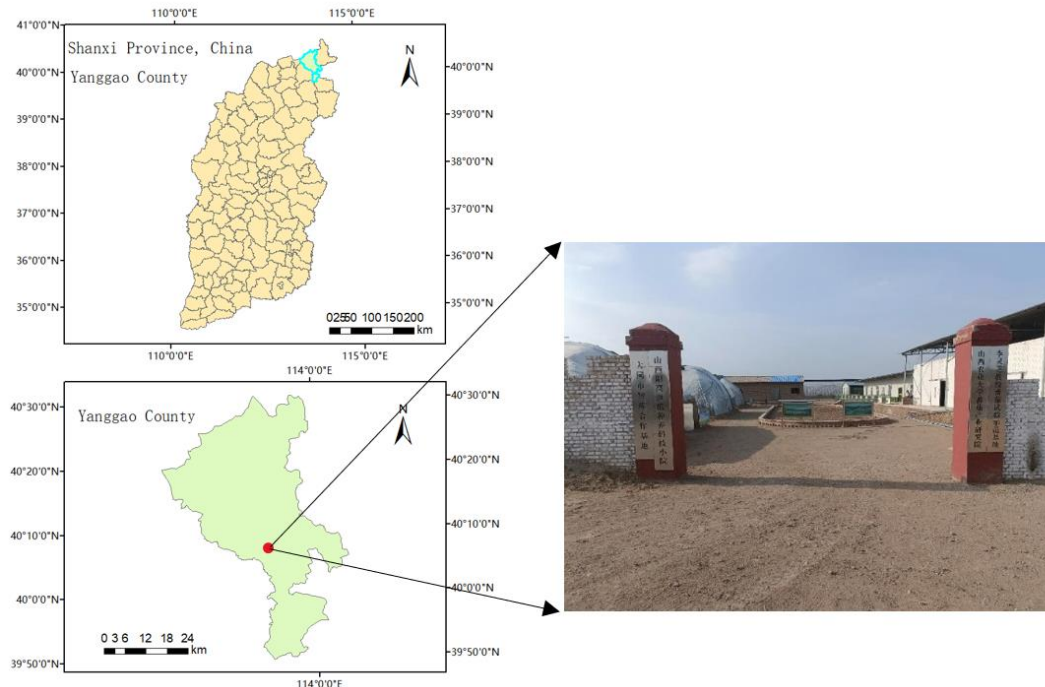


Fig. 3 - Visualization of test site locations

The experimental greenhouse was located in the north-south direction, with a length of 70 m, a span of 12 m, and a ridge height of 8.6 m. The planting ridge was in the shape of a trapezoid, with a length of 10 m, a width of 110 cm at the base of the ridge, a width of 60 cm at the surface of the ridge, a height of 40 cm, and a spacing of 50 cm between neighbouring ridges; the ridge was planted with two rows, two rows staggered, with a spacing of 50 cm between the rows and a spacing of 40 cm between the plants. The layout of tomato planting inside the greenhouse is shown in Fig. 4.



Fig. 4 - Inside the greenhouse tomato planting scene

The experiment started on May 15, 2023 when the tomato seedlings were planted and continued till August 13, 2023. The trial was managed routinely during the trial period.

The experimental environment used in this study: CPU: Intel(R) Core (TM) i7-13700K@3.40GHZ, 64GB of running memory, Operating System: Windows 11, GPU: NVIDIA GeForce RTX 4080 with 16GB video memory. The machine learning framework is scikit-learn 1.0.2, and the programming language is Python 3.7.0.

Data Acquisition and Processing

One week after planting, six YOUCUI8850 plants with consistent growth were selected for observation. Additionally, six plants with similar growth potential and morphology were selected for harvesting at intervals of 10-15 days, and a total of seven harvests were conducted. At each harvest, the selected plants were carefully removed from the soil and quickly brought back to the laboratory, where each of the aboveground organs of the tomato was individually sectioned from the base to the apical growth point. Then the length and width of each leaf, the transverse and longitudinal diameter of each fruit were quickly measured, after which each organ was placed in a kraft paper bag into the oven to kill the green at 105° for 30 minutes, and then dried at a constant temperature of 80°C, until the mass was constant. Then, the biomass (dry mass) of each organ was measured (Cheng et al., 2022).

Geometric morphometric data on tomato leaves and fruits from each harvest were recorded and they were numbered according to their position on the plant. Fig. 5 and Fig. 6 show the geometrical morphometric data of the leaves at different positions at each harvest. It can be seen that the length and width of the leaves at different positions showed an increasing trend with the growth time. Fig. 7 and Fig. 8 show the geometrical morphometric data of the fruits at different positions at each harvest, and it can be seen that the transverse and longitudinal diameters of the fruits at different positions show the same trend of growth with the change in growth time. Moreover, the average leaves and fruits biomass per plant at each harvest and the average plant height and stem thickness were recorded. As shown in Fig. 9, leaf biomass, fruit biomass, plant height, and stem thickness increased over time, indicating that the plants were maturing as they grew.

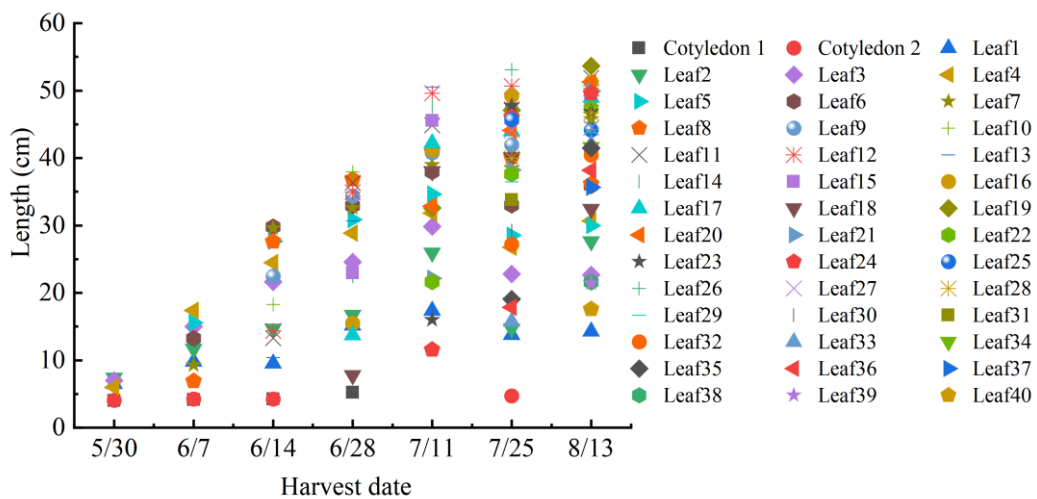


Fig. 5 - The data on leaf length per harvest

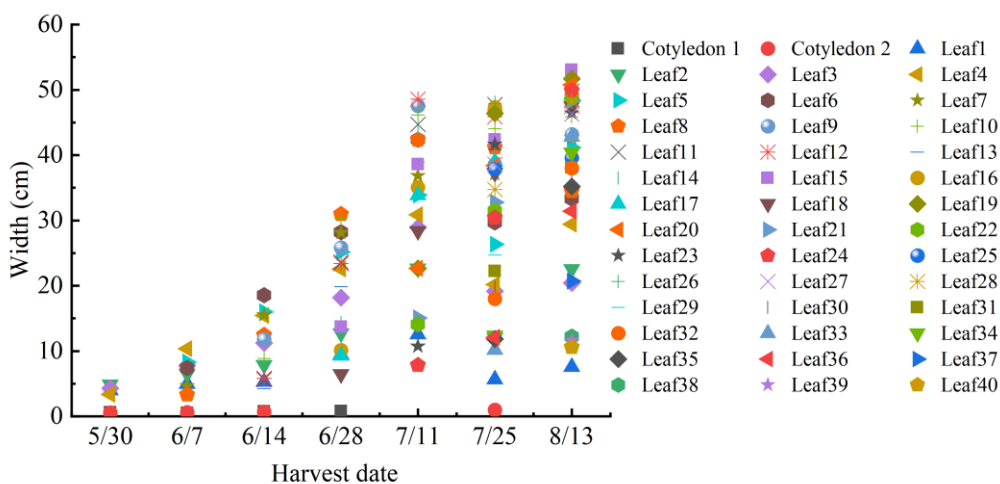


Fig. 6 - The data on leaf width per harvest

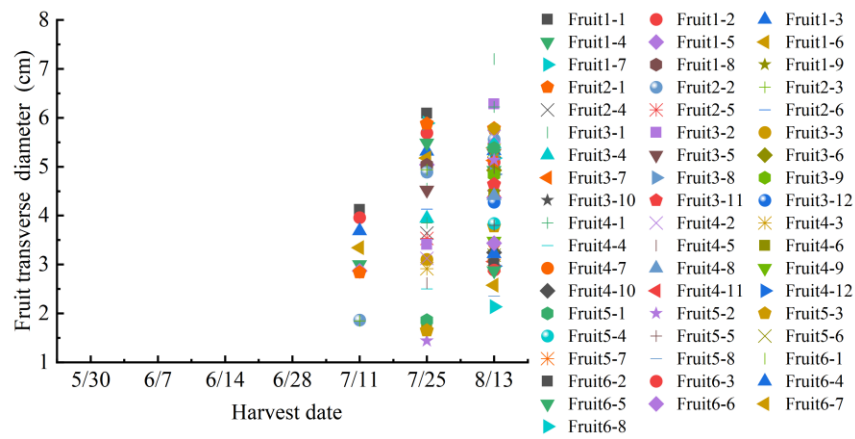


Fig. 7 - The data on fruit transverse diameter per harvest

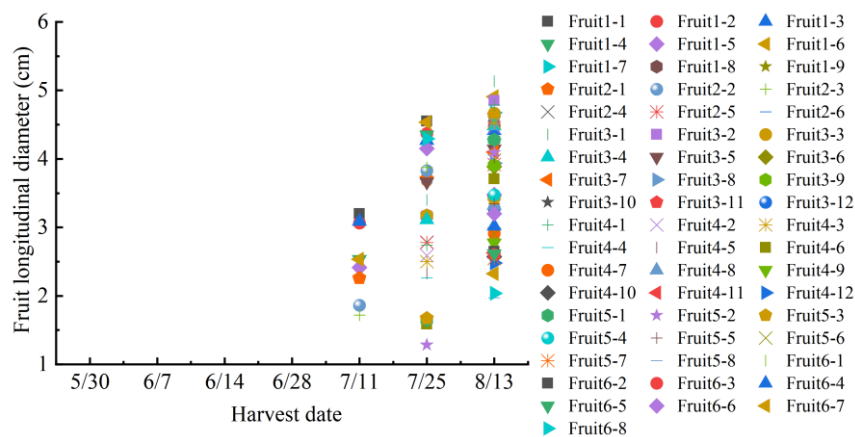


Fig. 8 - The data on fruit longitudinal diameter per harvest

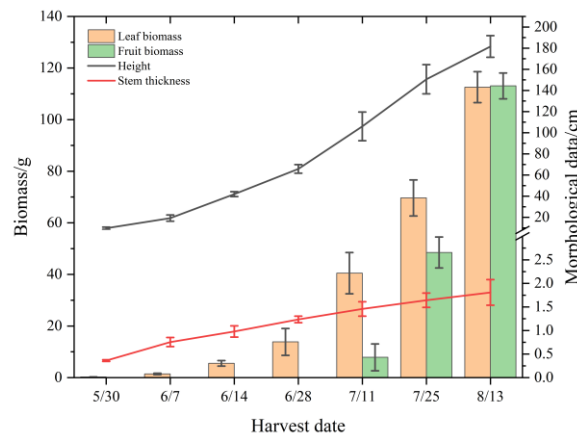


Fig. 9 - Average leaf and fruit biomass per plant and plant height and width per harvest

Model Selection

In this study, classical machine learning algorithms were used to predict the biomass of tomato organs. Among these algorithms, the generalized linear regression supported Ridge Regression (Ridge), Lasso regression algorithm (Least absolute shrinkage and selection operator, Lasso), and ElasticNet (EN) were used, Support Vector Machine algorithm (SVM), Multi-Layer perceptron (MLP), K-NearestNeighbor (KNN), Random Forest (RF) algorithm belonging to bagging in integrated learning, and Gradient Boosting Decision Tree (GBDT) algorithm which belongs to boosting in integrated learning. In addition, the above algorithmic models were also stacked based on the stacking mode of integrated learning to construct a model to realize the prediction of tomato biomass.

In the field of machine learning, the choice of algorithms and the tuning of parameters have always been headache-inducing challenges. Although there are many algorithms available, no algorithm is foolproof. As technology continues to evolve, new techniques have emerged that can provide some help in algorithm selection and parameter tuning, and one of the most popular techniques is Stacking.

Stacking is a technique used to enhance the performance of machine learning models (Maddaloni et al, 2022; Jahnavi et al., 2023). The technique generates final predictions by combining predictions from different algorithms. This approach can help to solve many machine learning problems, especially when a single algorithm is not sufficient to solve the problem. Stacking usually consists of two steps: the first step is to use multiple base models to generate predictions, and the second step is to use another model to integrate these predictions and generate the final prediction. The basic process of its implementation is generally divided into two steps. The first step is to generate the prediction results. In the first step, multiple base models were used to generate prediction results. For each base model, the training data are split into two parts: one part is used to train the model and the other part is used to generate the prediction results. Different models such as decision trees, random forests, support vector machines, multilayer perceptual machines, etc. can be used. Each model generates a prediction result; the second step integrates the prediction results. In the second step, another model is used to integrate these predictions and generate the final prediction results. Algorithms such as linear regression, logistic regression, random forests, support vector machines, neural networks, etc. can be used to accomplish this step. One thing that must be noted here is that the model in the second step must use the predictions from the first step as input. This will ensure the consistency of the entire Stacking process.

RESULTS

Result Evaluation

In this study, R^2 , Mean Absolute Error (MAE), and Root Mean Square Error (RMSE) were used to evaluate the model. The closer the value of R^2 is to 1, the better the interpretability and performance of the model. The smaller the MAE and RMSE values, the higher the consistency between the predicted values and the actual values, thus proving the more accurate prediction results of the model (Wang et al., 2022).

Construction and Evaluation of Tomato Leaf Biomass Prediction Model

The leaf is an important organ of the plant, which is the main tissue for photosynthesis, absorbing energy from sunlight through chlorophyll and other photosynthetic pigments and converting it into chemical energy to support plant growth and development. Leaves also absorb water from the plant body from the ground to the atmosphere through transpiration, facilitating water and nutrient uptake and transport, and regulating the temperature of the plant body.

By quickly realizing the prediction of leaf biomass, it is possible to understand the total amount and trends of leaves in different plant communities and ecosystems. This helps to assess the dynamic distribution and spatial pattern of plant biomass and reveals the structure and function of ecosystems, thus providing important information for ecological studies.

After all the data obtained from the seven experiments were divided into a training set and a test set according to the different organs in the ratio of 75% and 25%, then a model was constructed with the geometric morphology data of leaves (length and width of leaves) and its corresponding biomass data and the geometric morphology data were used as inputs to the model to predict its corresponding biomass. The eight classical machine learning models (Ridge, Lasso, EN, SVM, MLP, KNN, RF, and GBDT), with their corresponding hyperparameters are shown in Table 1.

Table 1

Hyperparameters of the 8 base models when the input feature of the model is the geometric shape of the leaves

Model	Para1	Value1	Para2	Value2	Para3	Value3
Ridge	alpha	10				
Lasso	alpha	0.01	max_iter	10		
EN	alpha	0.1	l1_ratio	0.9		
SVM	C	1	kernel	rbf		
MLP	activation	relu	hidden_layer_sizes	(25,25,25,25)	solver	adam
KNN	algorithm	ball_tree	leaf_size	3	n_neighbors	9
RF	min_samples_leaf	6	min_samples_split	0.1	n_estimators	6
GBDT	learning_rate	0.1	loss	lad	n_estimators	96

The above 8 base models are taken as base-model and linear regression algorithm is used as stacking meta-model. The above 8 classical machine learning models were integrated, using common input data, and 9 different sets of predicted data were obtained, after normalizing the predicted values with the actual values to construct a 1:1 comparison graph, the specific results are shown in Fig. 10 and Fig. 11.

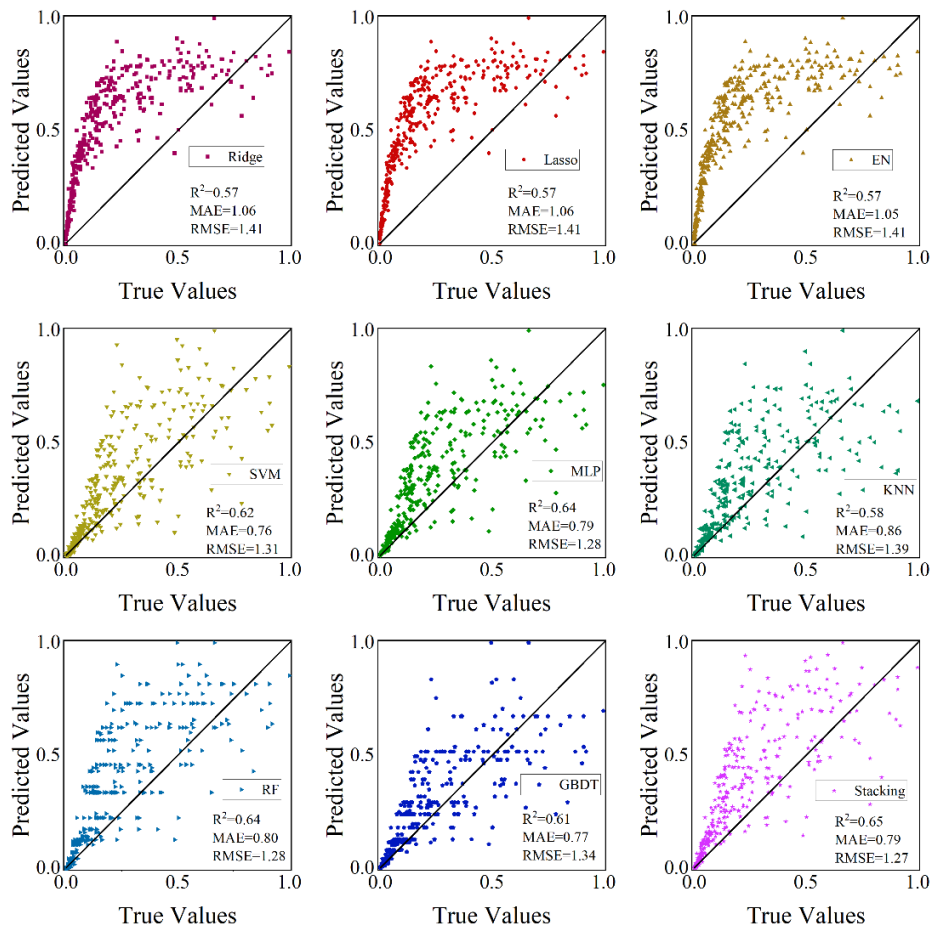


Fig. 10 - The 1:1 plot of predicted versus actual values for the nine models when the input feature of the model is the geometry of the blade

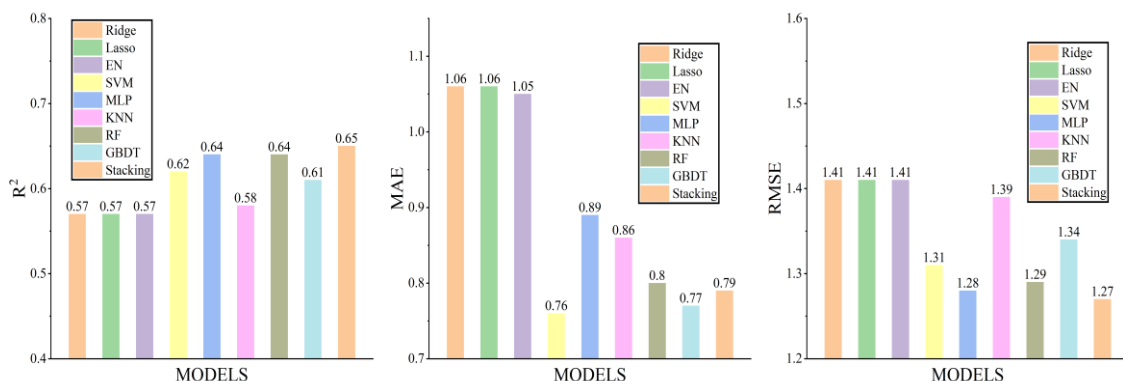


Fig. 11 - Comparison of the evaluation metrics of the nine models when the input feature of the model is the geometric form of the blade

The prediction results of MLP and RF in a single model are optimal. The model constructed based on the stacking approach is superior to the base learner whose prediction results are best. However, the prediction results of the nine models were not very good, so plant height and stem thickness of the current plant individuals of the leaf geometry data were added to the input features of the models. The results obtained were superior to the prediction results without adding the individuals' plant height and stem thickness.

The hyperparameters of the 8 machine-learning models with the addition of individual plant height and stem thickness are shown in Table 2.

Table 2
Hyperparameters of the 8 base models when the input features of the models are the geometric shape of the leaves and the height and stem thickness of the corresponding individual plants

Model	Para1	Value1	Para2	Value2	Para3	Value3
Ridge	alpha	1				
Lasso	alpha	0.001	max_iter	20		
EN	alpha	0.1	l1_ratio	0.1		
SVM	C	5	kernel	rbf		
MLP	activation	relu	hidden_layer_sizes	(25,25,25,25)	solver	adam
KNN	algorithm	kd_tree	leaf_size	1	n_neighbors	5
RF	min_samples_leaf	3	min_samples_split	0.1	n_estimators	51
GBDT	learning_rate	0.1	loss	ls	n_estimators	96

Similarly, the above 8 base models were used as the base-model and the linear regression algorithm was used as the meta-model for stacking. The obtained 9 sets of predicted data were normalized and a 1:1 comparison graph between them and the actual values was constructed, and the specific results are shown in Fig. 12 and Fig. 13.

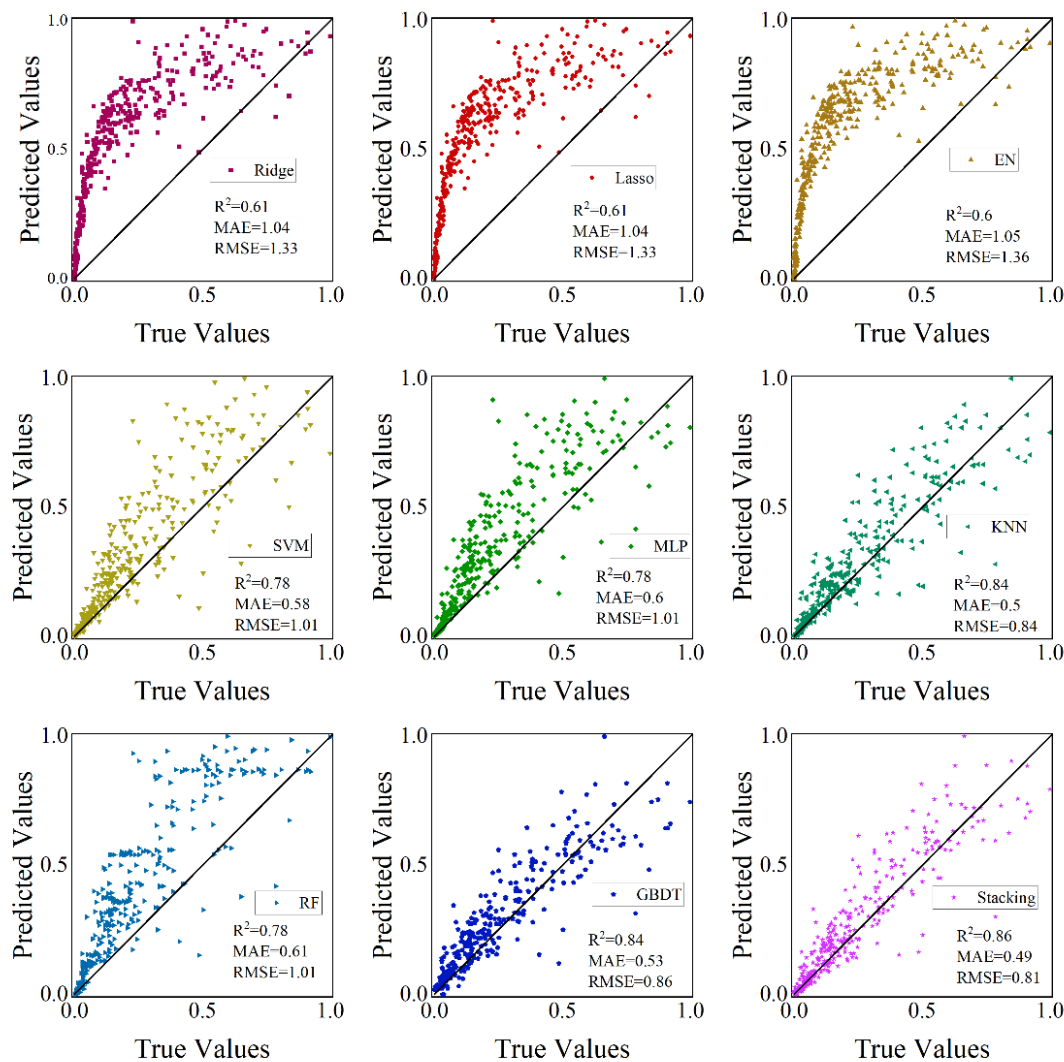


Fig. 12 - The 1:1 plot of predicted versus actual values for the nine models when the input features of the models are the geometric shape of the leaves versus the height and stem thickness of the corresponding individual plants

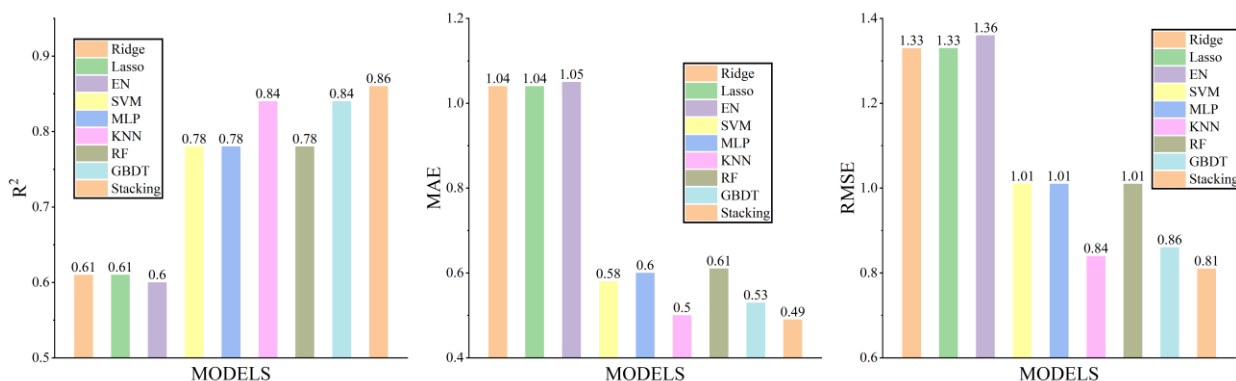


Fig. 13 - Comparison of the evaluation metrics of the nine models when the input features of the models are the geometric shape of the leaves with the height and stem thickness of the corresponding individual plants

The prediction accuracy of the model was significantly improved with the addition of plant height and stem thickness corresponding to individual plants, and it is desirable to have a prediction model with higher accuracy. In agriculture and horticulture, the prediction of plant leaf biomass enables the assessment of plant growth and yield potential. This helps to adjust fertilization and irrigation strategies, optimize the growing environment of crops, and improve agricultural productivity and resource efficiency. Leaf biomass prediction is important for ecological research and precision agriculture research, promoting sustainable development of agriculture and environmental protection.

Construction and Evaluation of Tomato Fruit Biomass Prediction Models

When a model is constructed with the geometric morphology data of the fruit (transverse and longitudinal diameters of the fruit) and its corresponding biomass data and the geometric morphology data are use as inputs to the model to predict its corresponding biomass, the 8 classical machine learning models (Ridge, Lasso, EN, SVM, MLP, KNN, RF, and GBDT), with their corresponding hyperparameters are shown in Table 3.

Table 3

Hyperparameters of the 8 base models when the input feature of the model is the geometric form of the fruit

Model	Para1	Value1	Para2	Value2	Para3	Value3
Ridge	alpha	50				
Lasso	alpha	0.1	max_iter	10		
EN	alpha	0.1	l1_ratio	0.1		
SVM	C	1	kernel	rbf		
MLP	activation	relu	hidden_layer_sizes	(30, 30, 30)	solver	adam
KNN	algorithm	ball_tree	leaf_size	3	n_neighbors	9
RF	min_samples_leaf	3	min_samples_split	0.1	n_estimators	21
GBDT	learning_rate	0.1	loss	huber	n_estimators	21

Similarly, the stacking model was constructed based on the above-mentioned base model. A 1:1 comparison plot was constructed with the actual values after normalizing the obtained 9 sets of predicted data, as shown in Fig. 14 and Fig. 15.

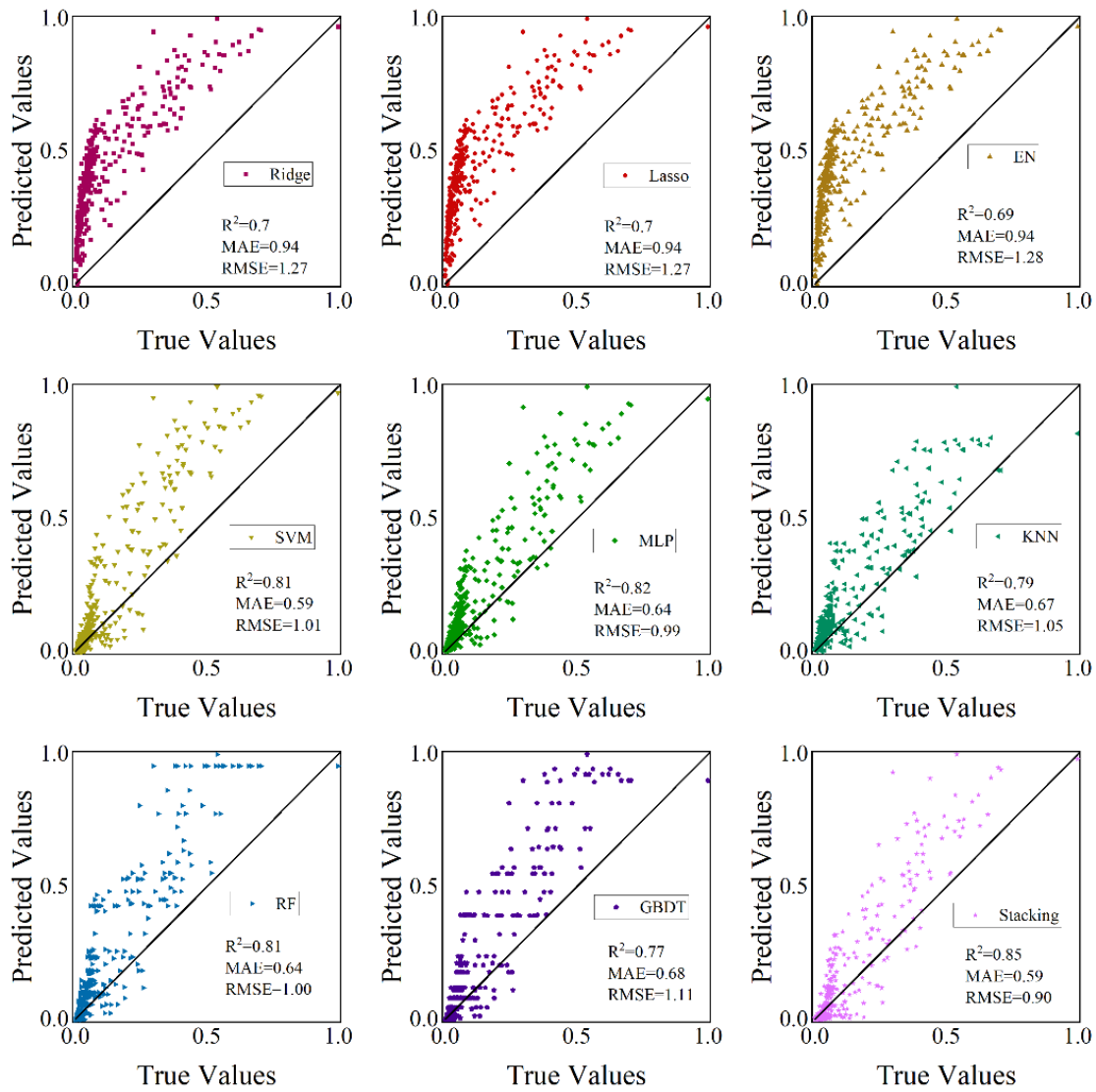


Fig. 14 - The 1:1 plot of predicted versus actual values for the nine models when the input features of the models are the geometric shape of the leaves versus the height and stem thickness of the corresponding individual plants

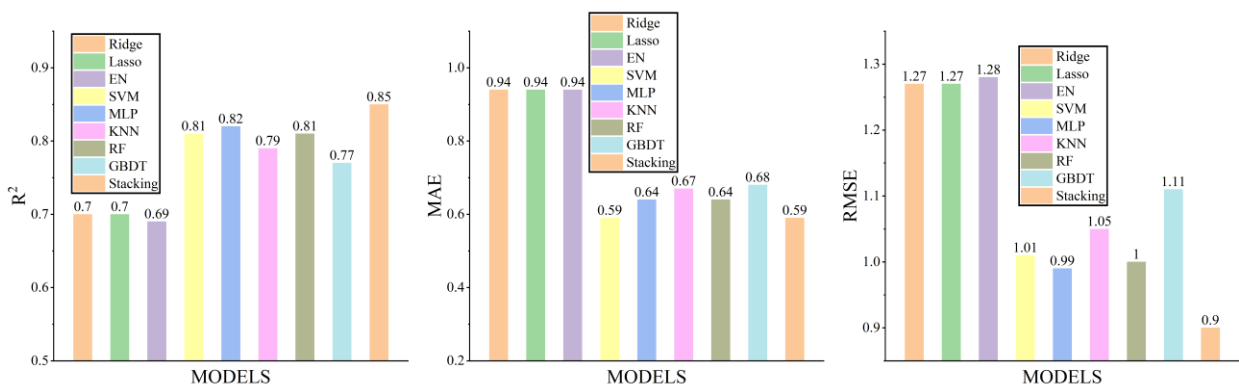


Fig. 15 - Comparison of the evaluation metrics of the nine models when the input feature of the model is the geometric form of the fruit

As in the case of the leaves, the plant height and stem thickness of the corresponding individual plant were added to the input features. The results obtained were again superior to the predictive models without the added plant height and stem thickness. The hyperparameters of the 8 machine learning models after adding individual plant height and stem thickness are shown in Table 4.

Table 4

Hyperparameters of the 8 base models when the input feature of the model is the geometric form of the fruit

Model	Para1	Value1	Para2	Value2	Para3	Value3
Ridge	alpha	10				
Lasso	alpha	0.1	max_iter	10		
EN	alpha	0.1	l1_ratio	0.9		
SVM	C	5	kernel	rbf		
MLP	activation	relu	hidden_layer_sizes	(25, 25, 25, 25)	solver	lbfgs
KNN	algorithm	ball_tree	leaf_size	3	n_neighbors	9
RF	min_samples_leaf	3	min_samples_split	0.1	n_estimators	21
GBDT	learning_rate	0.1	loss	huber	n_estimators	21

The above 8 base models were used as the base-model and the linear regression algorithm was used as the meta-model for stacking. The obtained 9 sets of predicted data were normalized and a 1:1 comparison graph between them and the actual values was constructed, as shown in Fig. 16 and Fig. 17.

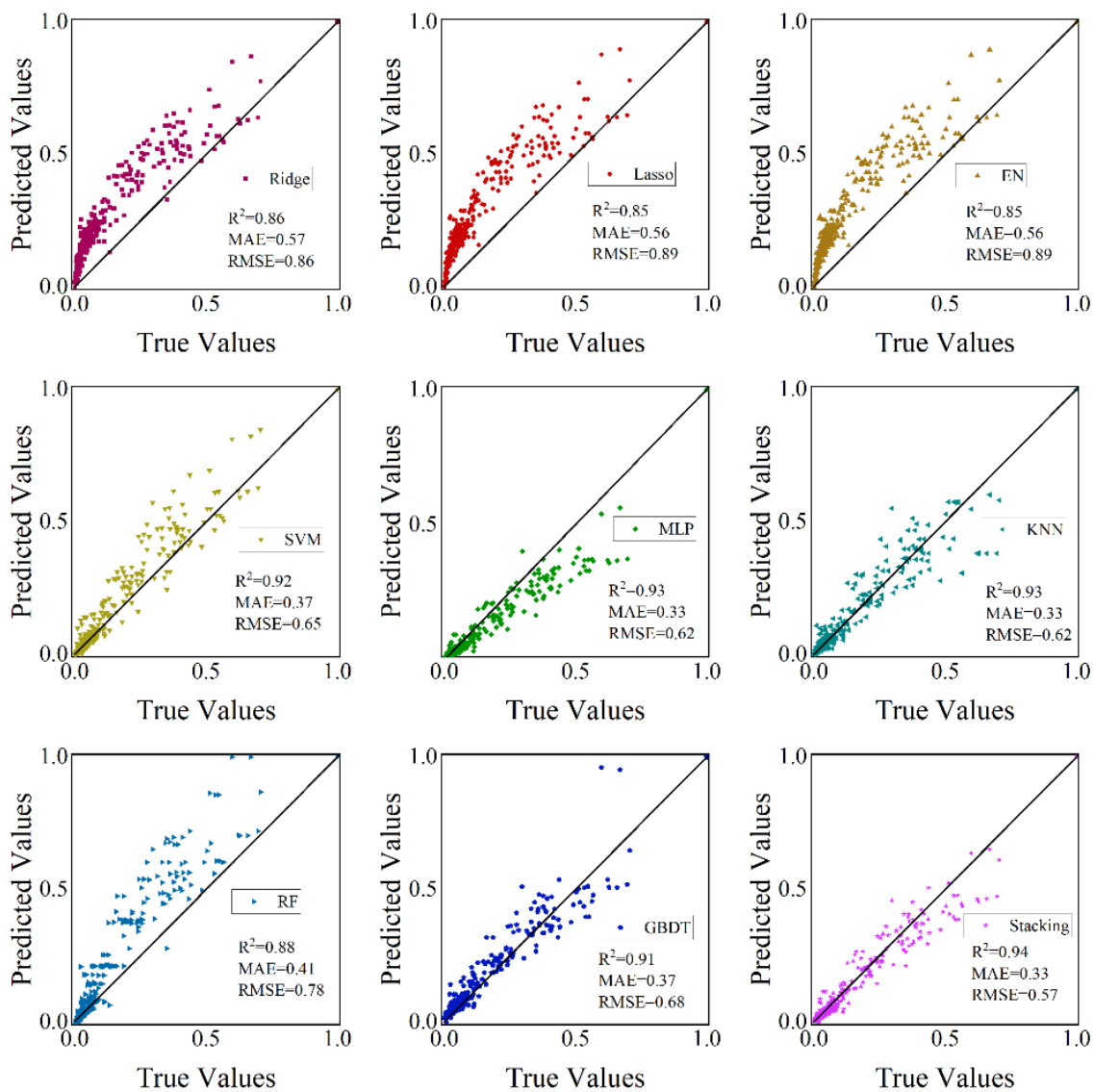


Fig. 16 - The 1:1 plot of predicted versus actual values for the nine models when the input features of the models are the geometric shape of the leaves versus the height and stem thickness of the corresponding individual plants

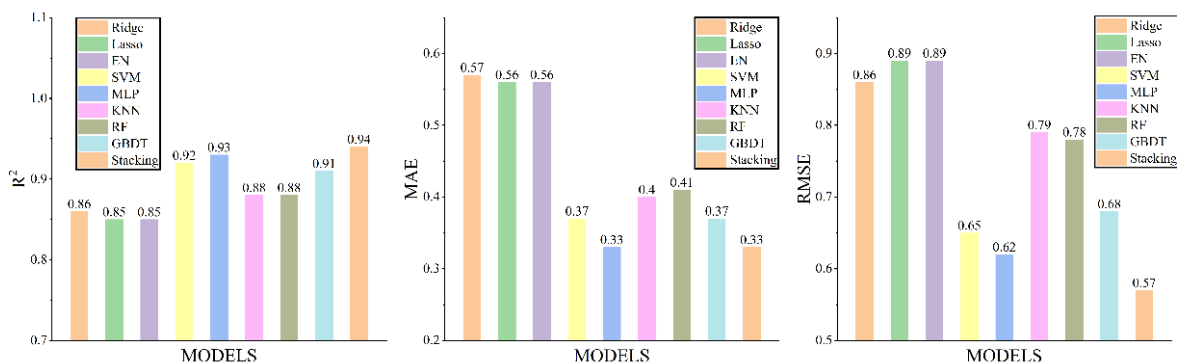


Fig. 17 - Comparison of the evaluation metrics of the nine models when the input features of the models are the geometric form of the fruit with the height and stem thickness of the corresponding individual plants

The leaf biomass prediction model constructed based on stacking had $R^2=0.65$, $MAE=0.79$ and $RMSE=1.27$, whereas the evaluation indexes of the leaf biomass prediction model constructed based on stacking improved to a certain extent after adding the height and stem thickness of the current individual tomato plants to the input features. Compared with the model without the addition of height and stem thickness, the R^2 increased by 0.21, MAE decreased by 0.3 and RMSE decreased by 0.46. The specific values were $R^2=0.86$, $MAE=0.49$, and $RMSE=0.81$. Similarly, the fruit biomass prediction model was constructed based on stacking, with $R^2=0.85$, $MAE=0.59$, and $RMSE=0.9$. After adding the plant height and stem thickness of the current tomato plant individuals to the input features, the evaluation indexes of the fruit biomass prediction model constructed based on stacking were improved to a certain extent, with an increase of 0.09 in the R^2 , a decrease of 0.26 in the MAE, and a decrease of 0.33 in the RMSE compared with that of the model with no addition of the plant height and stem thickness, with the specific values of $R^2=0.94$, $MAE=0.33$, and $RMSE=0.57$. It is evident that the model's prediction accuracy can be effectively improved after adding the corresponding plant height and stem thickness of individual plants.

Model validation

The predicted and measured values of different parts of tomato leaves and fruits at various periods were compared to assess the model's generalisation ability.

Fig. 18 shows the predicted values of leaves biomass at each growth cycle of the four positions compared with the measured values, and the results of section 9 were better, with $RMSE=0.1473$ g and $MAE=0.1072$ g between its predicted and actual values. The RMSE between the predicted and measured values of biomass of leaves during each growth cycle ranged from 0.1473 g to 0.5229 g; MAE ranged from 0.1072 g to 0.4190 g. By comparing the predicted and measured values of leaf biomass, it was found that the predicted values might be larger or smaller than the measured values. The predicted results of leaf biomass fluctuated wildly, and the reason for the significant fluctuation of leaf error might be the large error mixed in the data collection process of the experiment.

Fig. 19 shows the predicted values of fruits biomass at each growth cycle of the four positions compared with the measured values, and the results of section fruit 3-2 were better, with $RMSE=0.1206$ g and $MAE=0.0987$ g between its predicted and actual values. The RMSE between the predicted and measured values of biomass of fruits during each growth cycle ranged from 0.1206 g to 0.4113 g; MAE ranged from 0.0987 g to 0.2965 g. By comparing the predicted and measured values of fruit biomass, it was found that the predicted values might be larger or smaller than the actual values. However, the predicted results of fruit biomass fluctuated less compared with the results of leaf biomass, which might be due to the smaller samples of fruits.

Machine learning algorithms are highly flexible and computationally efficient and have been widely used for modeling and prediction of agricultural scenarios (Ribeiro et al., 2022; Saleem et al., 2021). The input factors selected in this study were all phenotypic indicators of individual tomato plants and did not include environmental factors. If the variables including environmental factors, location of planting area, and agronomic and management practices are coupled into the simulation of the biomass prediction model, the performance, accuracy, and generalization ability of the model will be greatly improved (Geng et al., 2021).

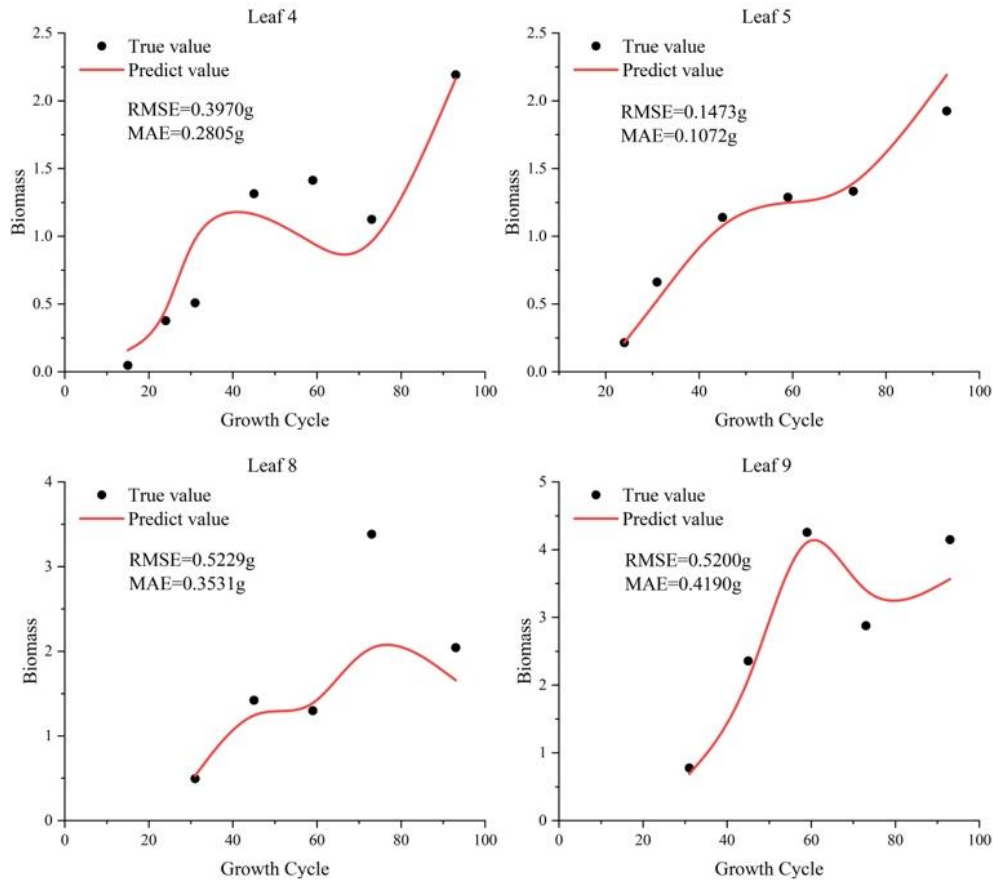


Fig. 18 - Comparison of predict and measured values of leaf biomass at different locations

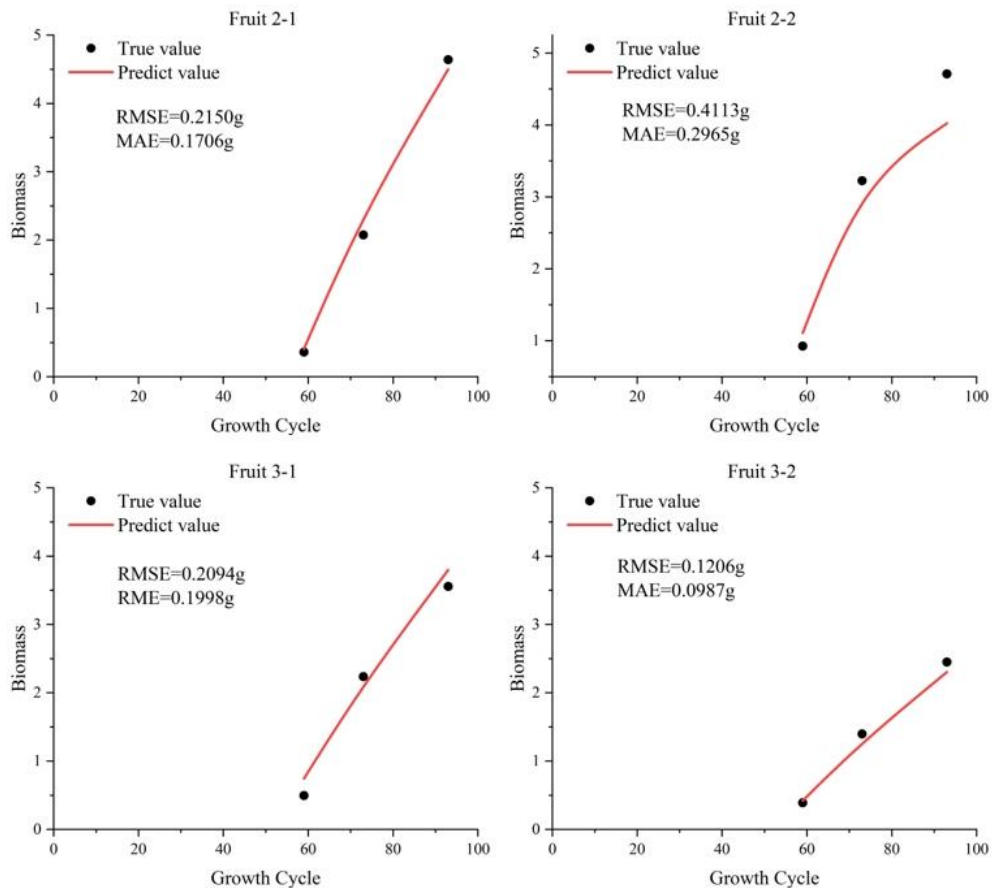


Fig. 19 - Comparison of predict and measured values of fruit biomass at different locations

CONCLUSIONS

In this study, tomato is taken as the research object, tomato organ morphology data were used as variables, morphological factors such as plant height and stem thickness were superimposed, and the biomass prediction model of tomato under organ scale is established based on machine learning and integrated learning, which specifies the optimal model construction method under organ scale and accurately realizes the biomass prediction of leaves and fruits of tomato.

The model is user-friendly and cost-effective. Farmers can anticipate fruit and leaf biomass by simply collecting geometrical-morphological data on tomato fruits and leaves using a measuring tool. The estimated cost of our test mainly includes measuring tools, ovens, computers, and other equipment, with a total of approximately 15,000 RMB. So that farmers can understand the growth status of the crop in real time, adjust cultivation and management measures and plant protection methods in a timely manner, and manage the tomato crop in a targeted manner to maximize yield and product quality.

Of course, this study still has the following shortcomings: first, the duration of the experiment needed to be shorter, and the subsequent tomato experiment needed to be conducted over a more extended period to improve the model's accuracy and generalization ability with more data. Second, the experiments were conducted only on tomatoes grown in solar greenhouses in the alpine region of the North China Plateau and did not consider other crops (e.g., cucumbers and eggplants, etc.), other growing regions (e.g., lamps in the North China Plateau), and other growing facilities (e.g., glass greenhouses), or field crops, and will be followed up with a more detailed experimental planning and experimental design to increase the abundance of the model's adaptability and the breadth of its use. Third, the acquisition of experimental data is manually obtained by hand, which has a certain degree of subjectivity and instability. This study did not consider the effects of pests and diseases, root systems, and soil on the whole process of tomato growth and development. In the following study, the effects of different environmental factors, agronomic measures and management conditions should be explored as well as the effects of pests and diseases on the biomass prediction model. Therefore, related research should be strengthened and it should be strived to construct more accurate and reliable biomass prediction models and to apply them to actual agricultural production to promote the progress of agricultural science and provide scientific basis and technical support for optimizing agricultural production.

ACKNOWLEDGEMENT

This research, titled 'Construction and validation of a predictive model for tomato organ biomass at organ scale based on stacking learning', was funded by the Shanxi Agricultural University Special Merit Program (XDHZFQY2022-02) and the Basic Research Program of Shanxi Provincial Science and Technology Department (202103021224123).

REFERENCES

- [1] Colomina I., Molina P. (2014). Unmanned aerial systems for photogrammetry and remote sensing: a review. *ISPRS Journal of Photogrammetry and Remote Sensing*. 92, 79-97.
- [2] Damtew A. (2017). Review on Genetics and Breeding of Tomato (*Lycopersicon esculentum Mill*). *Advances in Crop Science & Technology*, 05(05), 306.
- [3] Yuanyuan Fu, Guijun Yang, Xiaoyu Song, Zhenhong Li, Xingang Xu, Haikuan Feng, Chunjiang Zhao. (2021). Improved Estimation of Winter Wheat Aboveground Biomass Using Multiscale Textures Extracted from UAV-Based Digital Images and Hyperspectral Feature Analysis. *Remote Sensing*. 13(4), 581.
- [4] Liying Geng, Tao Che, MingGuo Ma., Junlei Tan, HaiBo Wang. (2021). Corn Biomass Estimation by Integrating Remote Sensing and Long-Term Observation Data Based on Machine Learning Techniques. *Remote Sensing*. 13(12), 2352.
- [5] Jahnvi Y., Elango P., Raja S.P., Nagendra Kumar P. (2023). A Novel Ensemble Stacking Classification of Genetic Variations Using Machine Learning Algorithms. *International Journal of Image and Graphics*. (02), 2350015.
- [6] Ji Wen Cheng, Shusen Wang, Yuyang Luo, Cen Zhang. (2022). Prediction model of above-ground biomass of Salix based on BP neural network (基于 BP 神经网络的沙柳地上生物量预测模型), *Forestry Science Research*. (003), 035.
- [7] Qi Liu, Yaxin Wang, Jie Yang, Wuping Zhang, Huanchen Wang, Fuzhong Li, Guofang Wang, Yuansen Huo, Jiwan Han. (2023). Smartagb: Aboveground Biomass Estimation of Sorghum Based on Spatial

- Resolution, Machine Learning, and Vegetation Index. *EAI Endorsed Transactions on Internet of Things*. 9(1), e1.
- [8] Lingzhi Li, (2013), Quantitative study of tomato growth with different nitrogen supply levels based on functional structure feedback mechanism (基于功能结构反馈机制下番茄生长对不同供氮水平定量化研究), [Doctoral dissertation, Shanxi Agricultural University]
- [9] Maddaloni P., Continanza D.N., Del Monaco A., Figoli D., Di Lucido M., Quarta F., Turturiello G. (2022). Stacking machine-learning models for anomaly detection: comparing AnaCredit to other banking datasets. *Bank of Italy Occasional Paper*. (689).
- [10] Qiaoxue Dong, Yiming Wang, Jialin Hou. (2007), Tomato structural-functional model: Organ-based functional model and validation (番茄的结构-功能模型Ⅱ:基于器官水平的功能模型与验证研究), *Chinese Journal of Ecological Agriculture*. (01),122-126.
- [11] Junior F.M.R., Bianchi R.A., Prati R.C., Kolehmainen K., Soininen J.P., Kamienski C.A. (2022). Data reduction based on machine learning algorithms for fog computing in IoT smart agriculture. *Biosystems Engineering*. 223, 142-158.
- [12] Saleem M.H., Potgieter J., Arif K.M. (2021). Automation in Agriculture by Machine and Deep Learning Techniques: A Review of Recent Developments. *Precision Agriculture*. 22(6), 2053-2091.
- [13] Weifeng Wang, Yuancai Lei, Xuefeng Wang, Haoyan Zhao. (2008). Review of forest biomass models (森林生物量模型综述), *Journal of Northwest Forestry College*. 23(2), 58-63.
- [14] Xu Wang, Yushuai Wang, Xuemeng Lian, Yuguang Wang, Lihua Yu, Gui Geng, (2022), Inversion of chlorophyll content in sugar beet canopy based on UAV multispectral technique (基于无人机多光谱技术的甜菜冠层叶绿素含量反演). *Sugar Crops of China*. 44(4), 36-42.
- [15] Zhong Xin Chen, Jianqiang Chen, Huajun Tang, Yun Shi, Peileng, Jia Liu, Limin Wang, Wenbin Wang, Yanmin Yao, (2016), Progress and perspectives on agricultural remote sensing research and applications in China (农业遥感研究应用进展与展望), *Journal of Remote Sensing*. 20(5), 748-767.
- [16] Yang Liu, Jue Huang, Qian Sun, Haikuan Feng, Guijun Yang, Fuqin Yang. (2021). Estimation of aboveground biomass of potato based on UAV digital image (利用无人机数码影像估算马铃薯地上生物量), *National Remote Sensing Bulletin*. 25(9), 2004-2014.
- [17] Zhaoying Mu, Zipeng Zhang, Hao Zhang, Lichun Jiang. (2024). Applying Machine Learning Algorithm Models to Predict Aboveground Biomass of *Larix gmelinii* in Xing'an (应用机器学习算法模型预测兴安落叶松地上生物量), *Journal of Northeast Forestry University*. 52(03), 41-47.

DESIGN AND TESTING OF PICKUP TOOTH CONVEYOR BELT TYPE BUCKWHEAT PICKUP DEVICE

扒齿输送带式荞麦捡拾装置的设计与试验研究

Chun WANG^{1,2)}, Yongchao SHAO¹⁾, Xiangyang LIU¹⁾, Fuzeng YANG¹⁾, Weiguo ZHANG¹⁾

¹⁾College of Mechanical and Electrical Engineering, Northwest Agriculture and Forestry University, Yangling 712100, China;

²⁾College of Biological and Agricultural Engineering, Jilin University, Changchun 130000, China

Tel: +86-18291918130; E-mail: wangchun11@nwfau.edu.cn

DOI : <https://doi.org/10.35633/inmateh-74-13>

Keywords: buckwheat harvest, pickup device, field experiment, response surface methodology

ABSTRACT

To address the high rate of grain loss in the two-stage harvest of buckwheat, a pickup tooth conveyor belt type buckwheat pickup device was developed to mitigate the grain loss in the buckwheat pickup process. The critical components of the pickup mechanism and conveyor mechanism were designed, and the essential parameters were determined. The operational efficiency of pickup tooth conveyor belt type buckwheat pickup device was verified through field orthogonal test. The field test results indicate that the loss rate is most significantly affected by the speed of the pickup tooth, followed by the tilt angle of the pickup tooth. the forward speed of the combine exerts minimal influence. After the multi-objective parameters of the regression equation model were optimized, the optimal parameters of the factors were obtained: the speed of the pickup tooth was 0.8 m/s, the forward speed of the combine was 1.1 m/s, and the tilt angle of the pickup tooth was 0°, Under this condition, the loss rate of buckwheat grain reached 6.92%.

摘要

针对荞麦两段式收获过程中籽粒损失率较高的问题, 设计了一种扒齿输送带式荞麦捡拾装置, 以减少荞麦捡拾过程中的籽粒损失。对关键零部件扒齿捡拾机构和输送机构进行了设计, 并确定了关键参数。通过田间正交试验验证扒齿输送带式荞麦捡拾装置的工作效果。田间试验结果表明, 扒齿线速度对损失率影响最大, 扒齿的倾角次之, 机器前进速度的影响最小。对建立的二次回归模型进行多目标参数优化后, 得到各因素最佳参数组合: 当捡拾速度为 0.8 m/s, 扒齿倾角为 0°, 机器前进速度为 1.1 m/s, 在上述条件下, 荞麦籽粒的损失率达到最小值为 6.92%。

INTRODUCTION

Buckwheat is extensively considered a multi-purpose grain crop due to its exceptional nutritional composition, high medicinal value, and notable health benefits (Wang et al., 2023). As living standards have improved, there has been increased awareness of nutrition and health, resulting in increased demand for buckwheat in both domestic and international markets (Qi et al., 2022). With the growth of buckwheat plants, the stems undergo bifurcation, flowers and branches intertwining each other. Buckwheat also exhibits a high stem-to-grain ratio, uneven grain maturity, and susceptibility of mature grains to detachment. Additionally, its stem has a high moisture content during harvest (Wang et al., 2020; Wang et al., 2022). Consequently, mechanized harvesting of buckwheat is challenging. Mechanized harvesting of buckwheat can be categorized into one-time combined harvesting and two-stage harvesting (Wang et al., 2018). The two-stage harvesting method allows grains to fully dried and ripen under sunlight and the moisture content of the stems was reduced. Consequently, it is considered the optimal mechanized harvesting method for buckwheat (Zhang et al., 2019). A two-stage pickup combine was utilized for pickup, threshing, and cleaning operations. The pickup device serves as a crucial component in the two-stage harvest, significantly affecting the overall quality of buckwheat harvesting (Wang et al., 2023).

Existing research has identified that the main types of two-stage harvesters consist of belt type, telescopic pickup type, and elastic drum type. Shi et al. (2011), from the Nanjing Agricultural Mechanization Research Institute, demonstrated that the application of a toothed belt pickup device for two-stage harvesting of oilseed rape achieved a minimum loss rate of 3.92%.

Li et al. (2016), from Hunan Agricultural University, demonstrated that an elastic-tooth drum pickup device achieved a theoretical minimum loss rate of 3.16% for two-stage pickup and harvesting of oilseed rape. Because of the unique characteristics of buckwheat harvesting, conventional pickup devices often impact buckwheat swath, resulting in grain loss during collection. Current research on pickup devices (e.g., grains, herbage, oilseed rape, and film residue recovery) can serve as a reference for this study (Ivan and Vlăduț, 2015; Ivan et al., 2015; Chen et al., 2020; Tian et al., 2020).

To address the above problems, a pickup tooth conveyor belt-type buckwheat pickup device was developed to shorten the pickup path and minimize impact on the buckwheat. Key components were designed, and field tests were conducted to verify the performance of the device. The optimal combination of working parameters was determined through orthogonal testing.

MATERIALS AND METHODS

Structural design and operational principle of the machine

The pickup tooth conveyor belt-type buckwheat pickup device primarily consists of a pickup mechanism, conveyor mechanism, pickup table, feed plate, and chain rake conveyor. The structure of the device is illustrated in Figure 1.



Fig. 1 - The structure diagram of the pickup tooth conveyor belt type buckwheat pickup device

1 – feed plate; 2 – chain rake conveyor; 3 – pickup table;
4 – pickup mechanism; 5 – conveyor mechanism

When the pickup tooth conveyor belt-type buckwheat pickup device is in operation, it is mounted in front of the combine and powered by the self-propelled mechanism. The pickup mechanism collects the buckwheat and transports it to the pickup table via a flexible scraper. The feed plate directs the collected buckwheat to the chain rake conveyor, which subsequently conveys it to the threshing and cleaning device.

Key component design and parameter determination

The design of pickup mechanism

The working principle of the pickup mechanism involves linear motion following the combine harvester's forward movement, while simultaneously rotational motion. As shown in Figure 2, its structure mainly includes driven shaft, driven sprocket, chain, mounting plate, driving shaft, driving sprocket, pickup tooth, rack, etc.

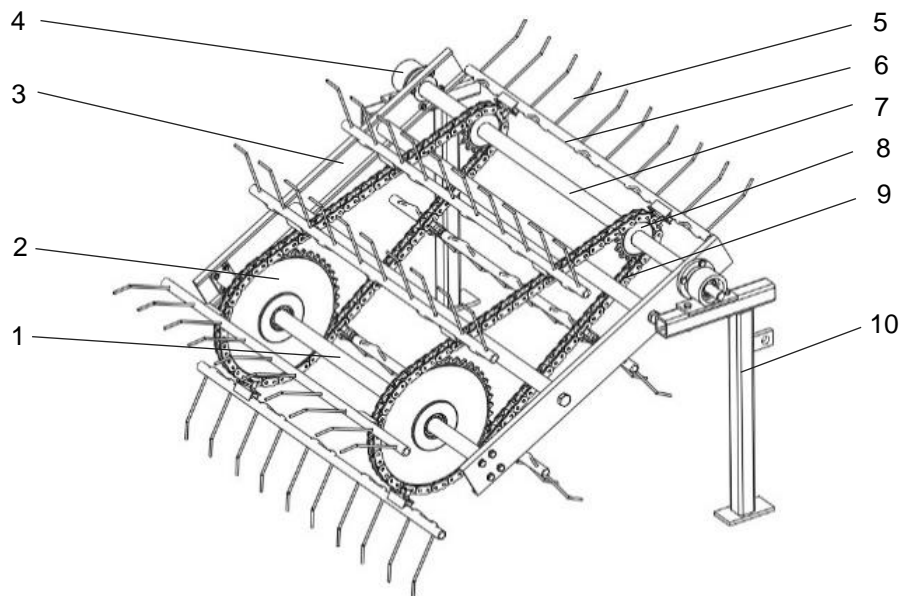


Fig. 2 - The structure diagram of the pickup mechanism

1 – driven shaft; 2 – driven sprocket; 3 – mounting plate; 4 – bearing with fix seat; 5 – pickup tooth; 6 – hollow shaft; 7 – driving shaft; 8 – driving sprocket; 9 – chain; 10 – rack.

(1) Width of the pickup mechanism

In practical operation, the width of the conveyor mechanism should be determined based on the width of the buckwheat swath after cutting. The working width of the pickup device must be greater than the maximum width of the buckwheat swath, which typically ranges from 500 to 1400 mm. Therefore, considering both the design requirements of agricultural machinery and practical working conditions, the width of the pickup mechanism is set to $W = 1600$ mm (China Academy of Agricultural Mechanization Sciences, 2007).

(2) Normal working conditions of the pickup mechanism

To effectively scrape the buckwheat swath onto the conveyor mechanism, the pickup tooth should avoid striking the buckwheat stems and grains at high speeds, as this can cause the grains to fall off. Therefore, the speed at the tip of the pickup tooth should be carefully determined. At a certain speed of the combine, if the speed of the pickup tooth is excessively small, buckwheat plants are difficult to pick up. At excessively high pickup tooth speeds, the buckwheat stalks and grains are struck with too much force, causing the grains to fall off. Therefore, controlling the speed of the pickup tooth is crucial for the effective handling of buckwheat plants. The motion path of pickup tooth is a combination of the forward motion of the pickup combine and the rotary motion of pickup tooth. To achieve effective pickup, the absolute speed of the pickup tooth (pickup tooth relative to the ground) when contacting the buckwheat swath should be opposite to the forward speed of the combine. This requires that the ratio of the speed of the pickup tooth (pickup tooth relative to the combine) to the forward speed of the combine be greater than 1. ($\lambda > 1$), that is

$$\omega R > V_m \quad (1)$$

where:

ω is the driven sprocket angular speed [rad/s]; R is the turning radius of the pickup tooth [mm]; V_m is the forward speed of the combine [m/s].

(3) The design of the pickup tooth

In this study, the pickup tooth was designed, and practical experience suggested that a specific bending angle of the pickup tooth can help increase the pickup rate.

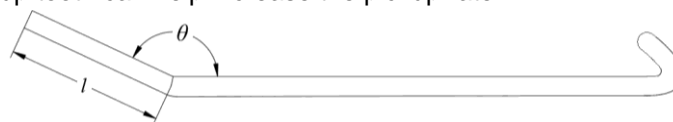


Fig. 3 – The design of the pickup tooth

Through the force analysis of the buckwheat plants picked up by the pickup mechanism, the suitable bending angle θ can be calculated, and the buckwheat plants were simplified into a particle. The force situation is presented in Figure 4, when the buckwheat plants were scraped to the conveyor mechanism by the pickup device.

To ensure the pickup tooth successfully picking up buckwheat, the friction between the buckwheat plants and the pickup tooth must exceed the gravity and centrifugal force acting on the plants at the pickup point. This ensures that the conditions required for scraping up the buckwheat plants are met.

$$F_f \geq G \cos \beta + F_r \cos \alpha \tag{2}$$

$$F_f = \mu F_N \tag{3}$$

$$F_r = m\omega R^2 \tag{4}$$

where:

F_f is the friction force on buckwheat plants when they are lifted [N]; G represents gravity of buckwheat plants [N]; β is the angle between the bending section of pickup tooth and the direction of gravity [°]; F_r is the centrifugal force received by buckwheat plants when they are picked up [N]; α is the angle between the bending section of the pickup tooth and the centrifugal direction [°]; μ is the friction coefficient between buckwheat plant and pickup tooth; F_N is the thrust exerted by the pickup pair when the buckwheat plant is scraped towards the conveyor mechanism [N].

According to the geometric relation, there are:

$$\alpha = 180^\circ - \theta \tag{5}$$

where: θ is the bending angle of pickup tooth

According to the principle of action and reaction

$$F_N = G \sin \beta + F_r \sin \alpha \tag{6}$$

Can be obtained from the Formula (2), (3), (4), (5), (6)

$$\mu g \sin \beta + \mu \omega R^2 \sin \alpha > g \cos \beta + \omega R^2 \cos \alpha \tag{7}$$

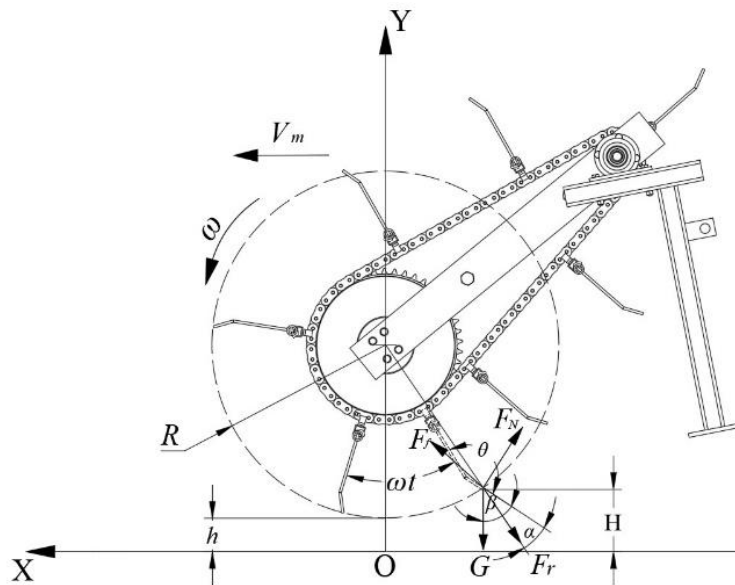


Fig. 4 – The stress situation of the pickup mechanism

The buckwheat plants were cut down by a swather and then aired for 7 days. Five areas were randomly selected to examine the thickness H of buckwheat at the natural laying state. The measurement times of the respective group were 3 time, and the average value was taken. Its laying thickness ranged from 44 to 61 mm. The smallest lay-up thickness was selected, which was 44 mm.

$$\beta - \alpha = \arccos[R/(R + H - h)] = 22.26^\circ \tag{8}$$

$$\beta = 22.26^\circ + \alpha = 202.26^\circ - \theta \tag{9}$$

where:

H is the thickness of buckwheat grass laying [mm]; h is the minimum distance between pickup tooth and ground [mm].

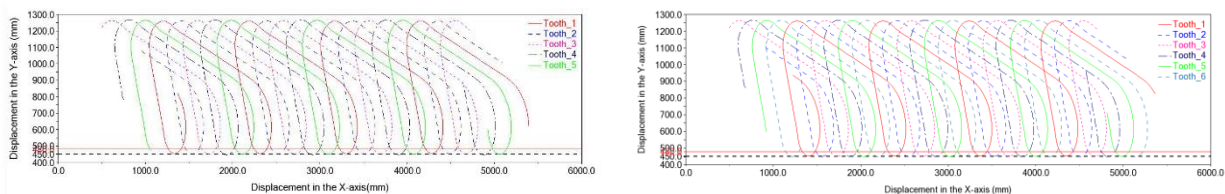
The coefficient of friction (μ) between buckwheat and the pickup tooth was 0.43. Substituting Eq. (9) into Eq. (7), the calculated bending angle of the pickup tooth is 129.01°, which is rounded to 130°. The length of the bent section of the pickup tooth (l) should exceed the thickness of the buckwheat layer, i.e., greater than 44 mm. Considering the stacking of some buckwheat swaths, the length of the bent section was set to 60 mm.

(4) Pickup tooth row spacing

The pickup tooth rotates relative to the combine as the joint harvester advances to collect the buckwheat, causing the tip of the pickup tooth to move in a staggered trajectory and creating a missing area. To improve pickup efficiency, the size of the missing area should remain within a reasonable range. The size of the missing area is primarily influenced by the forward speed of the combine, the speed of the pickup tooth, and the number of pickup tooth rows. The optimal spacing between pickup tooth rows is determined by analyzing the motion path of the pickup tooth tip.

Due to the complexity of pickup tooth trajectories, which are difficult to measure, this study uses ADAMS software to simulate the trajectories of pickup tooth tips across different rows. The model, created in SOLIDWORKS, was imported into ADAMS, where material properties, motion pairs, drives, chain systems, and tape systems were added.

The forward speed of the combine was set to $V_m=1.0$ m/s, the rotary speed of the pickup tooth was set to $\omega = 4$ rad/s, the simulation time was set to 5 s, and the number of simulation steps was set to 500. The motion tracks of pickup tooth tips for different rows are shown in Figure 6. The pickup tooth tips traverse the entire thickness of the buckwheat plant layer, allowing buckwheat plants to be moved to the conveyor mechanism, which confirms that the pickup tooth can pick up the buckwheat swath. As shown in Figure 5(a), with fewer than five rows of pickup tooth, not all buckwheat plants can be picked up; however, with six rows or more, all plants are effectively picked up. Therefore, the pickup tooth count should be more than six. The number of pickup tooth rows was determined based on the thickness of the buckwheat swath. In practical production, variations in the thickness of laid buckwheat plants were observed. Field experiments indicated that too many rows of pickup tooth can increase the contact with buckwheat stalks and grains, resulting in potential grain loss. Thus, the optimal design specifies seven rows of pickup tooth ($n = 7$)



(a) The motion trajectories of 5 rows of tooth

(b) The motion trajectories of 6 rows of tooth

Fig. 5 – The trajectories of pickup tooth

Parameter design and selection of conveyor mechanism

The conveyor mechanism works in tandem with the pickup mechanism to lift the buckwheat swath and convey it smoothly to the pickup table. Its structure is illustrated in Figure 6. Specifically, it mainly comprises a driving roller, driven roller, auxiliary roller, conveyor belt, flexible scraper, side plate, wheel, etc.

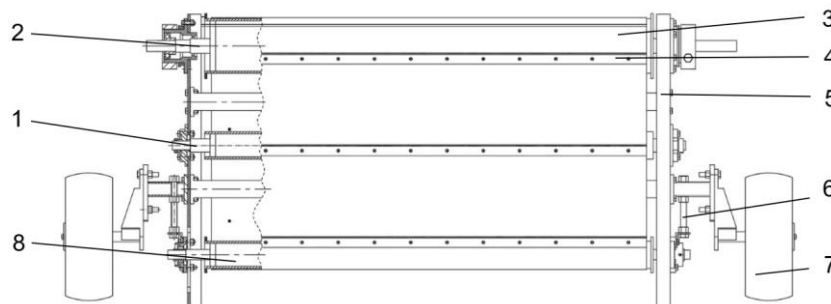


Fig. 6 – The structure diagram of conveyor mechanism

1 – auxiliary roller; 2 – driving roller; 3 – conveyor belt; 4 – flexible scraper; 5 – side plate; 6 – adjust screw; 7 – wheel; 8 – driven roller.

As depicted in Figure 6, the flexible scraper is attached to the conveyor belt through a bolted connection, and the conveyor belt is positioned around the driving roller, driven roller, and auxiliary roller. The driving and driven rollers are mounted on a side plate equipped with a sliding groove. The relative position of the driving and driven rollers is regulated by adjusting the screw for conveyor tensioning (Yu et al., 2017).

(1) Width of the conveyor mechanism

The role of the conveyor mechanism is to work in conjunction with the pickup mechanism to complete the pickup and transport of buckwheat plants. Consequently, the width of the conveyor mechanism should match that of the pickup mechanism, set at $w = 1600$ mm.

(2) Distance of flexible scraper

When the distance between the flexible scrapers is too large, it can cause an increase in the leakage and grain loss rates of the buckwheat swath. To reduce leakage, the line speed of the flexible scraper can be increased; however, increasing the speed also raises the impact force, which in turn increases the grain loss rate. Therefore, the distance l of the flexible scraper cannot be too large. If the distance l of the flexible scraper is too small, the number of scrapers will increase, leading to more frequent contact with the buckwheat swath and thus an increase in grain loss rate. Therefore, l should not be too small. According to agricultural machinery design standards, the tooth spacing for a typical spring-tooth conveyor mechanism ranges from 63 mm to 100 mm. The initial design proposes a flexible scraper interval of $l = 100$ mm.

Field experiment

The forward speed of the combine, the speed of the pickup tooth, and the tilt angle of the pickup tooth (the angle between the pickup tooth and the chain's normal direction) were selected as evaluation indices to explore optimal combinations of working parameters and to conduct field tests (Li *et al.*, 2024).

The field experiment was conducted on July 11, 2022, at the test field of Northwest Agriculture and Forestry University of Science and Technology, North Campus, located in Yangling District, Xianyang City, Shaanxi Province. The buckwheat variety planted was "Guqiao No.1," and the test plot covered an area of 4 acres. The test included measurements of buckwheat grain maturity and stalk and grain moisture content. The grain maturity rate was 73.4%, the stalk moisture content was 78.36%, and the grain moisture content was 27.58%. After nine days of drying post-harvest, the stalk moisture content was 57.63%, and the buckwheat grain moisture content was 15.81% (Zhang *et al.*, 2022). Subsequently, a combine equipped with a pickup tooth conveyor belt-type buckwheat pickup device was used to harvest the buckwheat, and the buckwheat grain loss rate was measured.



Fig. 7 – The site of the field trial

The field experiment was divided into multiple groups, with each group harvesting a buckwheat swath whose length being 20 m. The natural loss of fallen grains in the field was collected prior to the experiment. The natural fallen mass of buckwheat was recorded as m_1 . A colored strip of cloth was placed by the machine to collect debris, and the quality of the grains it captured was screened and recorded as m_2 . The mass of buckwheat grains on the ground after harvest by the pickup combine was recorded as m_3 , and the total grain loss mass was recorded as m . The grain loss mass m is calculated as follows:

$$m = m_3 - m_1 \quad (10)$$

The quality of the grains within the grain bin after the test was recorded as m_4 , and the grain loss rate Y is expressed as:

$$Y = \frac{m}{m_2 + m_3 + m_4} \quad (11)$$

RESULTS

Design-Expert software was used to conduct a secondary rotary combination design test on the test data, clarifying the optimal coordination of operational parameters for the pickup tooth conveyor belt-type buckwheat pickup device.

The test factors and levels are shown in Table 1, with each level selected to meet field operation requirements. The average value of the statistical results, obtained by repeating the test three times for each test group, is presented in Table 2.

Table 1

Table of factors and levels

Level	Factors		
	The forward speed of the combine, X_1	The speed of the pickup tooth, X_2	The tilt angle of the pickup tooth, X_3
	[m/s]	[m/s]	[°]
1	0.6	1.0	-10
2	0.8	1.2	0
3	1.0	1.4	10

Table 2

Experimental program and results

Number	Factors			Indicators	Number	Factors			Indicators
	X_1	X_2	X_3			Y	X_1	X_2	
1	0.8	1.2	0	7.36	10	1.0	1.0	0	10.23
2	0.8	1.2	0	6.89	11	0.8	1.2	0	8.04
3	1.0	1.2	10	8.37	12	0.6	1.2	-10	10.25
4	0.6	1.2	10	8.52	13	0.8	1.4	10	14.87
5	0.8	1.2	0	7.15	14	1.0	1.0	-10	9.06
6	0.8	1.0	10	8.80	15	0.6	1.2	0	16.63
7	1.0	1.4	0	13.62	16	0.8	1.0	-10	8.93
8	0.6	1.0	0	8.16	17	0.8	1.2	0	7.81
9	0.8	1.4	-10	15.41					

Regression model construction and testing

The experimental results were analyzed using Design-Expert software, and a quadratic regression equation model of grain loss rate Y was developed with X_1 , X_2 , and X_3 as independent variables. The significance of the regression equation model was verified through analysis of variance (ANOVA) and regression coefficient tests. The results are presented in Table 3.

Table 3

Regression equation variance analysis of pickup loss rate response surface

Indicators	Y				
Source	Sum of Squares	Degrees of Freedom	Mean Square	F value	P-value
Regression	154.55	9	17.17	56.19	<0.0001
X_1	1.34	1	1.34	4.40	0.0741
X_2	74.48	1	74.48	243.72	<0.0001
X_3	2.09	1	2.09	6.84	0.0346
X_1X_2	6.45	1	6.45	21.11	0.0025
X_1X_3	1.04	1	1.04	3.40	0.1075
X_2X_3	0.042	1	0.042	0.14	0.7217
X_1^2	4.24	1	4.24	13.88	0.0074
X_2^2	57.84	1	57.84	189.26	<0.0001
X_3^2	3.02	1	3.02	9.87	0.0164
Residual error	2.14	7	2.14		
Lack of fit	1.25	3	1.25	1.87	0.2749
Error	0.89	4	0.89		
Sum	156.69	16	156.69		

According to Table 3, the regression equation for the loss rate Y , expressed in coded values, was obtained by excluding the insignificant terms from the regression equation.

$$Y = 7.45 + 3.05X_2 - 0.51X_3 - 1.27X_1X_2 + 3.71X_2^2 + 0.85X_3^2 \tag{12}$$

The interaction between the other two factors and their effect on Y was analyzed by fitting the response surface, with any factor in Eq. 12 set to the zero level, as shown in Figure 8.

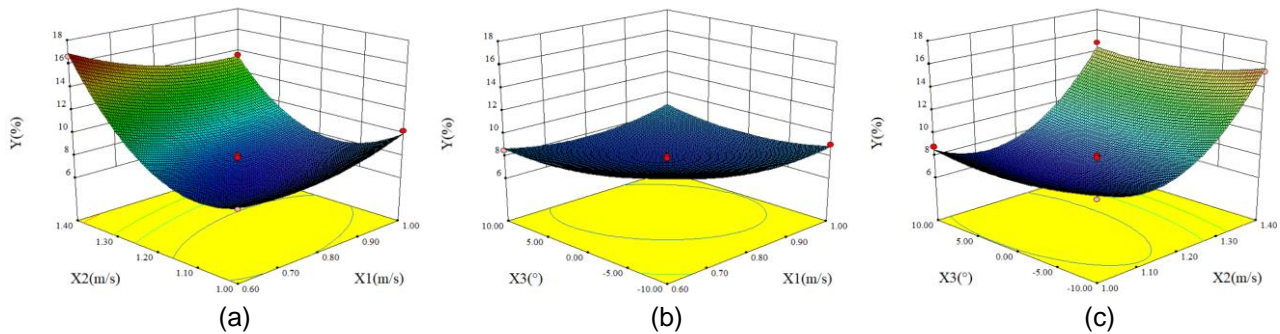


Fig. 8 – Response surfaces effect of factor interaction on test indicators

As shown in the response surface of Figure 8(a), when X_3 was set to 0° , X_1 and X_2 significantly affected Y . Y first decreased and then increased as X_1 and X_2 increased. When X_2 increased from 1.0 m/s to 1.4 m/s, the effect of X_1 on Y initially decreased and then increased; when X_1 increased from 0.6 m/s to 1.0 m/s, the effect of X_1 on Y tended to decrease. As shown in the response surface of Figure 8(b), Y first decreased and then increased with increasing X_1 and X_3 ; however, the effects of X_1 and X_3 on Y were not significant, consistent with the results of the regression equation variance analysis. As shown in the response surface of Figure 8(c), Y decreased and then increased with increasing X_2 and X_3 ; however, the effects of X_2 and X_3 on Y were also not significant, consistent with the regression equation variance analysis results.

Parameter optimization and experiment of Pickup tooth conveyor type buckwheat pickup device

The influence of the three test factors on grain loss rate was ranked as follows: the speed of the pickup tooth (X_2), the tilt angle of the pickup tooth (X_3), and the forward speed of the combine (X_1). To further determine the optimal parameter combination for the pickup tooth conveyor belt-type buckwheat pickup device, a regression equation model was used for multi-objective parameter optimization. Using the test influence factor range as boundary conditions and the minimum grain loss rate as the optimization objective, a mathematical model was established (Zhang et al., 2024):

$$\begin{cases} \min Y(X_1, X_2, X_3) \\ s. t. \begin{cases} 0.6 \text{ m/s} \leq X_1 \leq 1.0 \text{ m/s} \\ 1.0 \text{ m/s} \leq X_2 \leq 1.4 \text{ m/s} \\ -10^\circ \leq X_3 \leq 10^\circ \end{cases} \end{cases}$$

The Design-Expert software regression equation model was used to find the optimal parameters for the test impact factors: X_1 at 0.82 m/s, X_2 at 1.09 m/s, and X_3 at 1.43° . Under the optimal combination of parameters, the grain loss rate Y was 6.92%.

Based on the results of the multi-objective optimization and the practical operating requirements of the pickup tooth conveyor belt-type buckwheat pickup device, the test parameters were set as follows: the forward speed of the combine of 0.8 m/s, the speed of the pickup tooth of 1.1 m/s, and the tilt angle of the pickup tooth of 0° . Under these test conditions, three experiments were conducted, yielding a loss rate of 6.92%.

CONCLUSIONS

To address the problem of excessively high grain loss during the buckwheat pickup process in two-stage mechanized harvesting, a pickup tooth conveyor belt-type buckwheat pickup device was designed to reduce grain loss. The design of key components, including the pickup mechanism and conveyor mechanism, was conducted, and critical design parameters were determined. The operational parameters influencing grain loss rate were identified, and field tests were conducted.

Through the orthogonal, the quadratic regression equation model was established. The model analysis showed the speed of the pickup tooth had the most significant effect on the grain loss rate, followed by the tilt angle of the pickup tooth and the forward speed of the combine. The response surface method was used to analyze the orthogonal test results, and the regression equation model was solved by multi-objective optimization. The reasonable test parameters of pickup tooth conveyor belt type buckwheat pickup device were determined: the forward speed of the combine was 0.8 m/s, the speed of the pickup tooth was 1.1 m/s, and the tilt angle of the pickup tooth was 0° . Under these conditions, the grain loss rate was 6.92%.

ACKNOWLEDGEMENT

This research was funded by the Key Research and Development Project Plan of Shaanxi Province (Program No. 2023-YBNY-210), and Yulin City science and technology plan project (Program No.2023-CY-314).

REFERENCES

- [1] Chen, Y. Q., Hu, Z. C., Wang, S. Y., Cao, M. Z., Xu, H. B., Wang, G. P., Yan, J. C. (2020). Design and experiments of pickup device of peanut harvester after cutting peanut straws. *Transaction of Chinese Society of Agricultural Engineering*, Vol.36, Issue 16, pp.1-8, Beijing/P.R.C.;
- [2] Fan, R., Cui, Q. L., Lu, Q. (2022). Experimental study on non-planar screening device for buckwheat threshing material. *INMATEH-Agricultural Engineering*, Vol.66, Issue 1, pp.73-80, Bucharest/Romania;
- [3] Ivan Gh., Vlăduț V. (2015). The intensification of shaking process to the conventional cereal harvesting combines. *Proceedings of the 43 International Symposium on Agricultural Engineering "Actual Tasks on Agricultural Engineering"*. pp. 417-430, Opatija / Croatia;
- [4] Ivan Gh., Vlăduț V., Ganea I. (2015). Improving threshing system feeding of conventional cereal harvesting combine, *Proceedings of the 43 International Symposium on Agricultural Engineering "Actual Tasks on Agricultural Engineering"*. *Actual Tasks on Agricultural Engineering*. pp. 431-440, Croatia;
- [5] Li, H. Y., Wu, M. L., Luo, H. F. (2016) Experimental study on oilseed rape picking with a bullet-tooth drum picker. *Chinese agricultural science bulletin*, Vol.32, Issue 18, pp. 176-182, Beijing/P.R.C;
- [6] Li, Z. B., Ye, T., Nie, M. L., Lan, H. T., Zhang, X., Zhao, W. (2024). Design and testing of 4YZ-6 fresh core harvester grain splitting front end component. *INMATEH-Agricultural Engineering*, Vol.72, Issue 1, pp.820-829, Bucharest/Romania;
- [7] Liu, W. (2019) Research on key technologies and equipment for reducing losses in cutting and threshing of oil sunflower combing harvester. Doctor dissertation, Huazhong Agricultural University; Wuhan/P.R.C.;
- [8] Qi, L., Zheng, D. C., Li, L. H., Liu, F. J., Liu, Y. (2022). Research status of mechanized production technology and equipment of buckwheat in China. *INMATEH-Agricultural Engineering*, Vol.67, Issue 1, pp.487-496, Bucharest/Romania;
- [9] Shi, L., Wu, C. Y., Liang, S. N. (2011) Design and testing of a tooth belt picker for oilseed rape section harvesting. *Journal of Chinese agricultural mechanization*, Vol.32, Issue 4, pp. 75-78, Nanjing/P.R.C;
- [10] Tian D. L., Hou H. Y., Zhang J. (2020) Design and experimental study of chain-tooth residual film recycling machine, *Journal of Chinese Agricultural Mechanization*, Vol.41, Issue 09, pp.204-215, Nanjing/P.R.C.;
- [11] Wang, C., Zhang, W. G., Zhang, Y., Ding, H. B., Feng, S. K., Yang, F. Z. (2023). Design and experiment of scraper buckwheat pick-up device. *Journal of Southwest University (Natural Science Edition)*, Vol.45, Issue 12, pp.157-166, Chongqing/P.R.C.;
- [12] Wang, C., Shao, Y. C., Zhang, Y., Xin, Z., Chen, J., Zhang, W. G., Yang, F. Z. (2023). Design and experimental research of a comb-type buckwheat-harvesting device. *Agriculture*, Vol.13, pp. 1383-1403, Australia;
- [13] Wang, J. W., Yu, X. H., Zhang, J. L., Zheng, D. C., Li, Z. W., Song, H. Y. (2022). Design of inner and outer roller buckwheat thresher and field test. *INMATEH-Agricultural Engineering*, Vol.66, Issue 1, pp.111-120, Bucharest/Romania;
- [14] Wang, J. W., Li, Z. W., Hussain, S., Lu, Q., Song, H. Y., Zheng, D. C. (2020). Design and threshing outputs study of internal and external rotary roller buckwheat thresher. *INMATEH-Agricultural Engineering*, Vol.60, Issue 1, pp.173-182, Bucharest/Romania;
- [15] Wang, Q. (2018). Development and experimental research of tooth belt buckwheat pickup test platform. Master dissertation, Northwest A&F University; Yangling/P.R.C.;
- [16] Wu, J. (2023) Research on Key Technology of Threshing and Cleaning of Rape Combine Harvester on Sloping Land. Doctor dissertation, Agricultural Mechanization Engineering; Nanjing/P.R.C.;
- [17] Xu, B., Zheng, D. C., Cui, Q. L. (2022) Experimental research on three-level vibrating screening of buckwheat based on discrete element method. *INMATEH-Agricultural Engineering*, Vol.68, Issue 3, pp.191-200, Bucharest/Romania;
- [18] Yu, H. Z., Wang, W. M., Morigenbilige, Liu, W. F., Li, L., Cui, H. G. (2017) Experiment on performance of spring-finger cylinder pickup collector. *Transaction of the Chinese Society for Agricultural Machinery*, Vol.48, Issue 3, pp.106-112, Beijing/P.R.C.;

- [19] Zhang, Y. Q., Cui, Q. L., Wang, C., Li, H. B., Zhang, Z. Y. (2022). Test and analysis of mechanical properties of buckwheat stem during harvest. *INMATEH-Agricultural Engineering*, Vol.68, Issue 3, pp.275-282, Bucharest/Romania;
- [20] Zhang, K. K. (2019) Research on dynamics simulation and layout of the buckwheat picking harvest. Master dissertation, Northwest A&F University; Yangling/P.R.C.;
- [21] Zhang, Z. X., Jiang, H. L., He, X. N., Zhang, F. Y., Wang, J. S., Wang, D. W. (2024). Design and test of threshing and cleaning device for *Cyperus esculentus* combine harvester. *INMATEH-Agricultural Engineering*, Vol.72, Issue 1, pp.799-808, Bucharest/Romania;
- [22] ***China Academy of Agricultural Mechanization Sciences, (2007), *Agricultural Machinery Design Manual*. ISBN 97878022333352, China Agricultural Science and Technology Press, Beijing/ P.R.C..

DESIGN AND DEVELOPMENT OF SUNFLOWER INTELLIGENT INSERTION TRAY DRYER

向日葵智能插盘晾晒机的设计与开发

Qiang WANG ¹⁾, Xinyuan WEI ¹⁾, Keqi YAN ¹⁾, Qiyuan XUE ¹⁾, Yangcheng LV ¹⁾,
Yaoyu Li ^{1,2)}, Wuping ZHANG ^{1*)}, Fuzhong LI ¹⁾

¹⁾ College of Software, Shanxi Agricultural University, Taigu, Shanxi / China

²⁾ College of Agricultural Engineering, Shanxi Agricultural University, Taigu, Shanxi / China

Tel: +8603546287093; E-mail: zwping@126.com

Corresponding author: Zhang Wuping

DOI: <https://doi.org/10.35633/inmateh-74-14>

Keywords: sunflower; intelligent Plug-in Tray Dryer; Agricultural Engineering; You Only Look Once version 5 (YOLOv5); Lightweight and Ground Optimized Lidar Odometry and Mapping (LeGO-LOAM)

ABSTRACT

In order to meet the demand for mechanisation of sunflower segmented harvesting and tray insertion for drying, an intelligent tray insertion dryer was designed and developed. The machine integrates the functions of disc picking, disc flipping, bar clipping, lifting and inserting, and uses SolidWorks for accurate mechanism design and simulation, incorporating the YOLOv5 model for efficient recognition of flower discs and the LeGO-LOAM algorithm for accurate navigation and map building. In the experiment, 81 sunflower samples were collected to analyse data on disc diameter, plant height, rod diameter and stalk diameter, and to verify the recognition accuracy of the YOLOv5 model in different directions. The results showed that the precision of disc recognition was 95.54%, accuracy was 89.94%, recall was 95.54% and F1 value was 0.89. Using the LeGO-LOAM algorithm tested at different path lengths, the root-mean-square error of the navigational build trajectory was 0.15 m, with a standard deviation of 0.10 m. This technological integration improves the operational efficiency and supports the mechanisation of sunflower insertion tray drying.

摘要

为了满足向日葵分段收获和插盘晾晒的机械化需求,我们设计并开发了一款智能插盘晾晒机。该机集成了摘盘、翻盘、剪杆、升降和插盘等功能,采用 SolidWorks 进行精确的机构设计和模拟,融合了 YOLOv5 模型的高效识别花盘和 LeGO-LOAM 算法的精确导航建图。实验中,采集了 81 株向日葵样本,分析花盘直径、株高、杆径和梗径数据,并验证 YOLOv5 模型在不同方向上的识别精度。结果显示,花盘识别精度达 95.54%, 准确度为 89.94%, 召回率为 95.54%, F1 值为 0.89。利用 LeGO-LOAM 算法在不同路径长度下测试,导航建图轨迹的均方根误差为 0.15m, 标准差为 0.10m。这种技术整合提高了作业效率,为向日葵插盘晾晒机械化提供了支持。

INTRODUCTION

In the era of electronic information, intelligent agricultural machinery, as multifunctional equipment, is combined with automation technology to promote the development of modern agriculture (Jin *et al.*, 2021; Dhanaraju *et al.*, 2022). At present, the harvesting process of major food crops around the world has been commonly mechanised (Peng *et al.*, 2022). According to the Food and Agriculture Organization of the United Nations (FAO), the sunflower planting area in China has stabilised at around 1 million hectares in the last decade, with an annual output of between 2.4 million and 2.6 million tonnes (Moschen *et al.*, 2017). However, the mechanisation level of sunflower harvesting is still low, mainly relying on manual and limited mechanised means for sectioning and joint harvesting (Pan *et al.*, 2024).

The insertion of sunflower trays for drying can accelerate the dehydration process of flower trays and seeds, promote the full maturation of seeds, improve the appearance quality and overall cleanliness, and reduce the risk of mould caused by improper stacking. By inserting the disk directly on the stalks for drying, it not only effectively solves the shortage of drying sites, but also facilitates the efficient operation of walking threshing machines in the field, further improving the overall efficiency of field management.

Qiang WANG, M.S. Stud. Agr.; Xinyuan WEI, M.S. Stud. Eng.; Keqi YAN, M.S. Stud. Eng.; Qiyuan XUE, M.S. Stud. Agr.; Yangcheng LV, M.S. Stud. Agr.; Yaoyu Li, Ph.D.Eng.; Wuping ZHANG, Prof. Ph.D. Eng.; Fuzhong LI, Prof. Ph.D. Eng.

In this paper, an intelligent sunflower insertion tray drying machine is designed, which integrates the functions of picking, turning, cutting stems, lifting, inserting trays, etc., to meet the mechanization needs of sunflower harvesting and drying in the field environment. Traditional sunflower harvesting and drying methods usually rely heavily on manual operation or single-function harvesting equipment, which has problems such as low efficiency, high labour intensity, and unstable drying quality. At the same time, the traditional equipment usually can only complete the single task of cutting and handling, lack of insertion plate drying follow-up operation function, need to additionally configure other equipment or manual processing, thus increasing the operational complexity and cost.

To address these shortcomings, the intelligent sunflower insertion tray drying machine designed in this paper realizes the whole process automation from picking to drying through integrated design. The device combines deep learning and navigation technologies to accurately recognize the sunflower position and intelligently adjust the operation path and attitude to ensure the precise handling and consistency of each disk. Compared to traditional methods, the intelligent equipment has significant advantages in reducing labour costs and improving operational precision and efficiency, making it particularly suitable for small- and medium-scale sunflower planting sites. While controlling costs, the design can effectively improve field operation efficiency, providing a more efficient and intelligent solution for agricultural mechanization. (Dong *et al.*, 2017).

MATERIALS AND METHODS

Overall structure

In order to the integrity of the machine function and the intelligence of the insert tray drying work, this paper selects the idea of modular design (Li *et al.*, 2017). The functional structure of the machine body is designed first, and then the intelligent function is expanded to gradually transition from mechanisation to intelligence. It can make the structure of the machine complete and reliable, and also make the upgrading and transformation of the body more flexible, and finally complete the established function of insert tray drying.

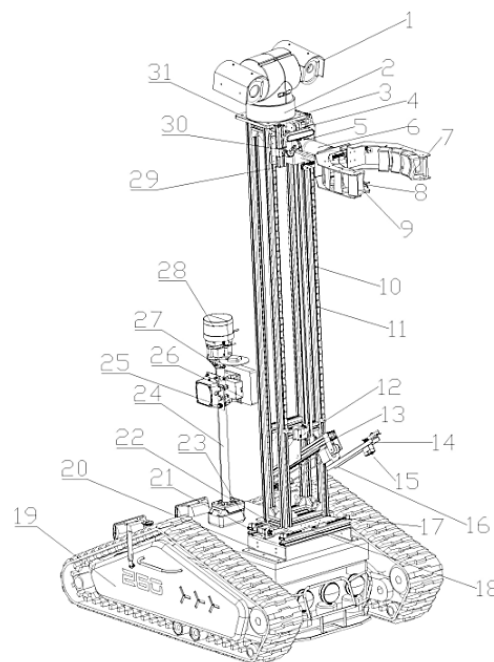


Fig. 1 - Schematic structure of Sunflower Intelligent Plug-in Tray Dryer

1. environmental information acquisition device; 2. environmental information acquisition device rotating servo; 3. environmental information acquisition device fixed frame; 4. flower disc gripping device moving frame; 5. flower disc gripping device servo motor; 6. flower disc gripping device tipping servo; 7. flower disc gripping device; 8. flower stalk cutting device servo motor; 9. flower stalk cutting device; 10. flower disc gripping device moving guide and main frame; 11. conveyor; 12. conveyor control motor; 13. stem cutting device fixed frame; 14. stem cutting device; 15. stem cutting device servo motor and distance sensor; 16. stem cutting device telescopic frame; 17. main body fixed frame; 18. frame left-right moving device; 19. crawler chassis; 20. frame left-right moving device fixed frame; 21. frame left-right moving device servo motor; 22. frame left-right moving device conveyor; 23. navigation receiver base; 24. support bar; 25. IMU attitude inertial sensor; 26. RTK receiver; 27. LiDAR fixture; 28. LiDAR; 29. binocular camera fixture; 30. binocular camera movable arm; 31. binocular camera



Fig. 2 - Sunflower Intelligent Insert Tray Dryer test prototype

According to the above design ideas, the sunflower intelligent plug tray drying machine overall structure design shown in Fig.1, is mainly divided into mechanical design part and intelligent equipment part (Young *et al.*, 2019). In the mechanical design part, by simulating the operation process of sunflower tray drying, six parts of grasping, shearing, turning, lifting, telescoping and moving are designed; the tracked chassis is selected and weighted, which fully takes into account the fact that the centre of gravity will be unstable after the completion of the design due to the discs being too high, and also makes it convenient for the agricultural machine to walk on the rugged field ground. In the intelligent equipment section, the integration of environmental information acquisition devices, binocular cameras, LiDAR, and RTK receivers enables the intelligent operation of sunflower planting and drying. The physical prototype is shown in Fig. 2.

Key Structure and Hardware Selection

Design of mechanical structures

This design of sunflower tea tray drying robot contains a flower tray grasping structure, a stem cutting device, a lifting device, a stem cutting device, and a rack moving device (shown in Fig.3). When the binocular camera moves upward, the camera and sensor integration technology recognizes and locates the flower plate (Fang *et al.*, 2018). After the localization is completed, the motor drives the gripper jaws to complete the gripping. In the case of failing to locate the flower disk, the device control system will speculate the position of the disk by recognizing the flower stem direction and some disk features. If the recognition fails, the device will slightly adjust the angle or height of the camera to help the camera better capture the front or side of the disk. After the capture is completed, the controller sends a signal and the motor drives the conveyor belt through gear transmission to realize the structure lifting and lowering. The stem shearing device consists of a fixed part and a moving part, and the motor drives the shearing device to telescope through gears and a conveyor belt. After grasping and turning over, the distance sensor measures the distance of the stem, and the motor controls the shears to complete the shearing. The frame moving device controls the conveyor belt to move on the guide rail through the motor and adjusts the horizontal position of the frame to ensure accurate completion of gripping and shearing. The power drive is driven by stepper motor with lead-acid battery power supply. The stepper motor has excellent positioning accuracy and speed control capability to ensure the accuracy and consistency of the shearing, lifting and inserting operations. Lead-acid batteries have low energy density, but are low cost and durable. A single charge can support continuous operation for about 2-3 hours, which meets the endurance requirements of small-scale field operations. Users can further extend the operating time by replacing the batteries.

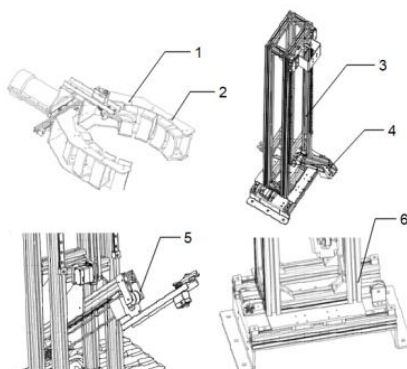


Fig. 3 - Schematic diagram of the mechanical structure of Sunflower Intelligent Insert Tray Dryer

1. stalk shearing device; 2. disc gripping structure; 3. lifting device; 4. stalk shearing device fixing component;
5. stalk shearing device moving component; 6. frame moving device

Intelligent structural design

The key structures of the intelligent design include the environmental information acquisition device, binocular camera and LIDAR (shown in Fig.4). The environmental information acquisition device is used to identify and locate sunflowers in the field, together with the LiDAR for distance judgement and equipment attitude adjustment (Shi et al., 2023; Peteinatos et al., 2014). A binocular camera enhances the recognition and localisation capabilities and assists the flower disc grasping structure for accurate grasping (Williams et al., 2019; Zhu et al., 2021). The LiDAR, on the other hand, is responsible for device localisation, helping to build graphics, plan routes, avoid obstacles and navigate (Bechar et al., 2016).

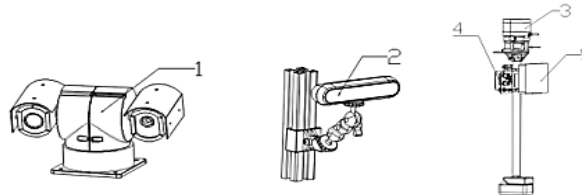


Fig. 4 - Schematic diagram of intelligent structure of Sunflower Intelligent Insertion Tray Dryer
1. Environmental Information Acquisition Unit (EIAU); 2. Binocular Camera; 3. LiDAR; 4. RTK Receiver; 5. IMU Attitude Sensor

Software design

Machine parameters are set through the configured host computer, as shown in Table 1. Set the baud rate in the "serial port settings" interface, open the serial port to receive real-time feedback data from the servo, and confirm that the computer is connected to the servo normally. Servo control module can independently or simultaneously control the servo ID1-7, the default speed of 1000, range 0-32766, angle range 0-32766, enter the servo position, select and click on the operation, the feedback position value will have a ± 5 error. The device supports initialisation and one-button neutrality function. At initialisation, all servos move left and right and return to the minimum angle/0 position; one-key neutral function sets the current servo position to 2048 neutral. In servo mode, the servos can perform different position movements. After writing the target position, click to complete the operation. The system currently only supports one write operation, and cannot be executed multiple times. When deleting the content, please delete all the written content at once and reset the servo to the minimum angle/0 position.

Table 1

Servo serial number and control parameters

Position	Helm number	Parameters and operating range
Top opening and closing grippers	ID 1	0-2600
Top rotating gripper	ID 2	0-1380
Upper and lower jointed robotic arms	ID 3	Upper unit to view servo position
Right and left articulated robotic arms	ID 4	Upper unit to view servo position
Upper scissor control joints	ID 5	5-2500
Lower scissor control joints	ID 6	5-2500
Forward control joints	ID 7	Upper unit to view servo position

Workflow

After the device enters the field, the environmental information acquisition device starts immediately, collects information about the surrounding environment, and identifies and localizes the sunflower plant through the deep learning algorithm. The LiDAR scans synchronously, plans an obstacle-free route and turns on the obstacle avoidance function, determines the position of the sunflower and the device, and feeds back the movement coordinates to the mobile control mechanism (see Fig.5). As the device approaches the target crop, it stops at a distance of about 10 cm from the sunflower. The gripper jaws begin to rise, and when the binocular camera recognizes the disk, the gripper jaws stop and feed back to the motor, which contracts and completes the fine-tuning to ensure that the disk is grabbed. After the jaws have contracted, the stalk cutter is activated and the motor controls the opening and closing of the scissors to cut the stalks from the disk. Subsequently, the stalk shearing device extends and is positioned by the distance sensor and the fine adjustment mechanism, stopping when the distance is 0. The scissors motor cuts the stalks. Subsequently, the clamping jaws flip to remove the flower disk and descend to the set distance, then the sunflower disk is firmly inserted into the stalks that have just been cut, completing the insertion of the flower disk for drying process. After the clamping jaws are reset, the mobile mechanism backs up, and the information acquisition device re-recognizes the next target and enters the next round of operation.

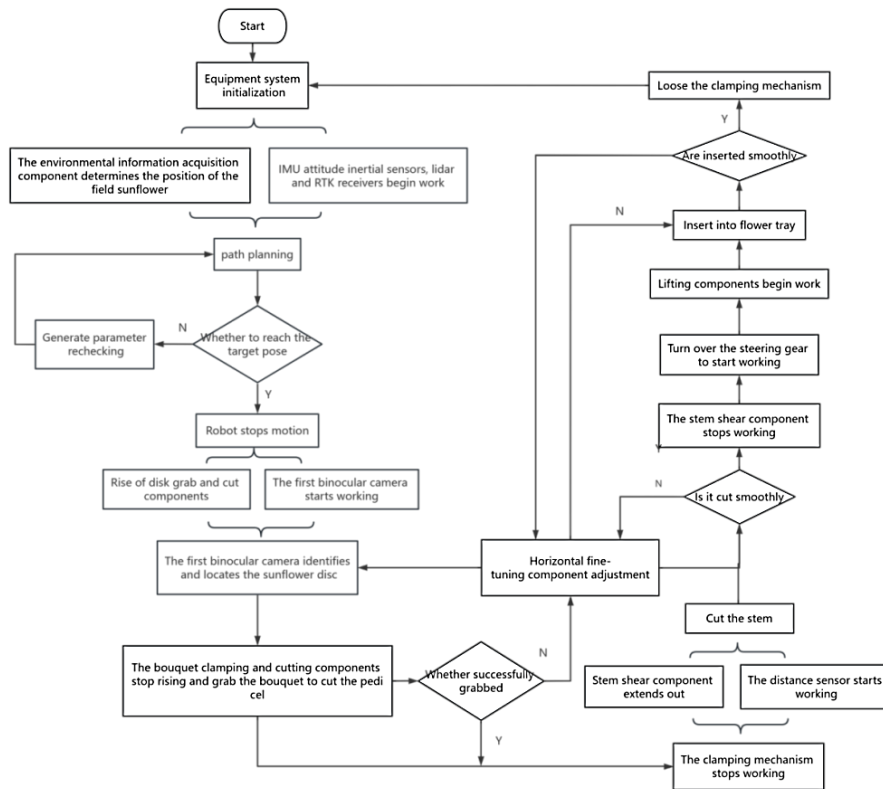


Fig. 5 - Planning of sunflower plug tray drying operation

Target identification design

In this study, the lightweight YOLOv5 target detection model was used to identify sunflower discs. The experimental data were obtained from the experimental base of Shanxi Agricultural University and the experimental base of its Economic Crops Research Institute in Wujiabao, Taigu District, Jinzhong City, Shanxi Province. To reduce the influence of light intensity and camera angle on the detection results, 2213 sunflower disc images in different weather, time and angle were taken. Meanwhile, 278 flower disc images were selected from the Kaggle floral public dataset, totalling 5697 images, including data expanded by contrast adjustment, flipping and mirroring. The dataset was annotated using LabelIMG tool and saved as an XML file in Pascal VOC format. The recognition process of sunflower discs is shown in Fig.6.

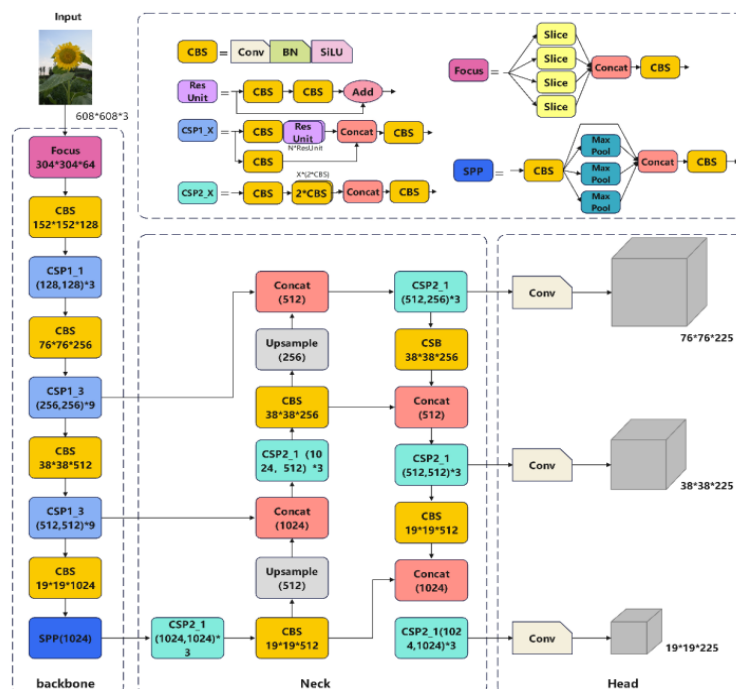


Fig. 6 - YOLOv5 detection model

Performance indicator

In order to represent the performance of the model, it was decided to use the Average Precision of the categories (Average Precision), the Mean of Average Precision of the categories (mAP), the F1-score, the number of parameters, and the model's occupied memory as model evaluation metrics. Precision P and Recall R can be defined by the following equations:

$$P = \frac{TP}{TP + FP} \times 100\% \tag{1}$$

$$R = \frac{TP}{TP + FN} \times 100\% \tag{2}$$

Therefore, the category accuracy AP can also be derived:

$$AP = \int_0^1 P(R) dR \tag{3}$$

mAP is the average of the AP values for multiple categories. If there are N categories, mAP can be expressed as:

$$mAP = \frac{1}{N} \cdot \sum_{i=1}^N AP_i \tag{4}$$

F1 is the reconciled average of precision and recall and is often used to evaluate the balance of the model. It is given by the formula:

$$F1 = 2 \times \frac{P \times R}{P + R} \tag{5}$$

Field path navigation design

In an agricultural environment, a machine vision-based navigation and positioning system performed well in good lighting conditions, with recognition accuracy of 97.8 percent (sunny) and 85.3 percent (cloudy), but decreased to 56.4 percent at night. Global navigation satellite systems (GNSS) provide real-time position information, but the error increases to ±5 metres in occluded environments. LiDAR becomes a reliable choice due to its high ranging accuracy and anti-interference, with the error controlled within ±0.1 m. Taking it into consideration, a navigation scheme is designed: machine vision is preferred when there is good light; when there are a lot of occlusions, switch to GNSS; rely on LiDAR for precise positioning in areas with low light or complex terrain. Fig.7 shows the path navigation design planning flow chart.

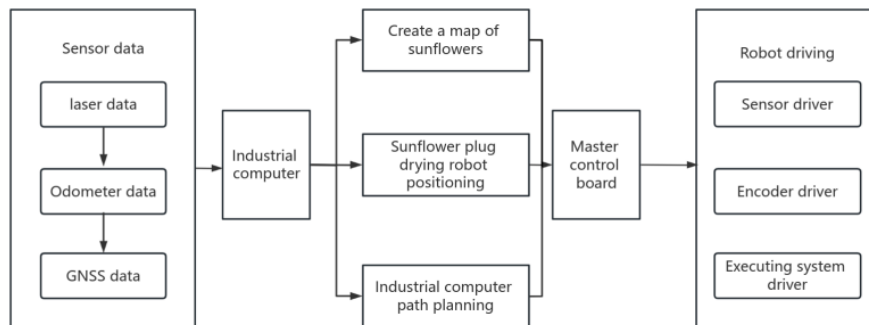


Fig. 7 - Flowchart of path navigation design

Assessment of indicator

In order to evaluate the performance of the algorithm, it was decided to use Root Mean Square Error (RMSE), Standard Deviation (STD) as the evaluation metrics for the LeGO-LOAM algorithm. The following are the formulas for these two metrics.

$$RMSE = \sqrt{\frac{1}{n} \sum_{i=1}^n (y_i - \hat{y}_i)^2} \tag{6}$$

$$STD = \sqrt{\frac{1}{n-1} \sum_{i=1}^n (x_i - \bar{x}_i)^2} \tag{7}$$

RESULTS

Tests and analyses of insert tray drying operations

To verify the feasibility of the plug tray drying experiment, 81 samples of drying sunflower plants were collected for destructive sampling and their disc diameter, plant height, stem diameter and stalk diameter were measured. Because the dryer design needs to take into account different plant heights, a wide range of plant heights was designed, ranging from 60 cm to 200 cm. Stable data on stem and peduncle diameters were concentrated in the range of 2 to 3 cm and less than 1 cm, respectively, which facilitated the design of mechanical clamping or shearing devices. Flower disc diameters were predominantly in the 20 cm range, influencing the design of mechanical devices to accommodate different disc sizes. Based on the data calculations, the final prototype design parameters included a base 106 cm long, 80 cm wide, and 204.5 cm high; a gripping jaw range of 18 to 36 cm and a lifting range of 98 to 196.5 cm; and a shear device with a maximum retractable distance of 31 cm and an opening and closing distance of 6 cm. These parameters ensure that the prototype is capable of efficiently and automatically executing sunflower plug tray drying operations. It has been experimentally verified that the processing time of a single disk is about 10 seconds, and about 330 disks can be processed in one hour. However, the specific area covered by the operation is subject to change according to the planting density.

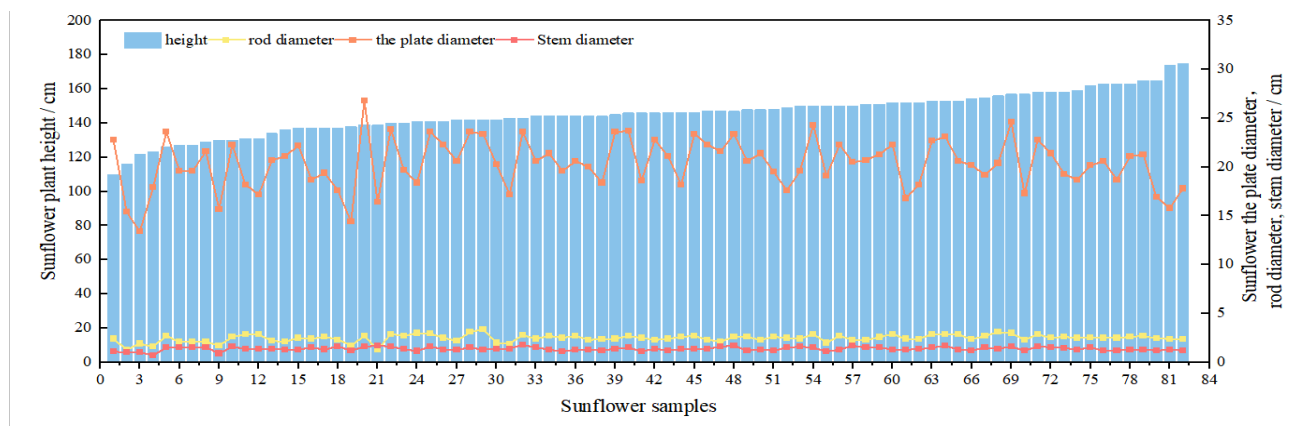


Fig. 8 - Sunflower sample data collection map

Plate drying test is the operator to operate the machine through the clamping claw assembly to grasp the flower plate and cut (a), flip the structure to control the clamping claw flip (b), the stem shear assembly to cut the flower stalk (c), left and right fine-tuning structure to move 5cm and with the lifting assembly to complete the lifting and moving the insertion of sunflower plate (d), and ultimately to achieve the drying of the flower plate. Due to precision limitations, each component's servo motor movement is subject to an error of ± 5 . After several adjustments to the position of each component, the basic motion parameter range of the servo was determined, greatly expanding the operational space for disc insertion and ensuring the successful completion of the task. The prototype test results are shown in Fig. 9.



Fig. 9 - Sunflower plug tray drying test plot

Analysis of sunflower identification detection results

Experimental validation shows that the YOLOv5 model performs well in the sunflower disc recognition task. The overall category accuracy reached 95.54%, precision was 89.94%, recall was 95.54%, and F1 value was 0.89 (Fig.10).

In the different orientation tests, the category precision of the model in the frontal, side, top, and back orientations were 96.00%, 95.00%, 95.50%, and 95.00%, respectively; the precision in all orientations exceeded 90.00%, and the recall rate exceeded 95.00%, as shown in Table 1. In the comprehensive evaluation, the highest F1 value was 0.92 for the frontal direction, and the rest of the directions remained at 0.91 (Fig.11). The results show that the YOLOv5 model not only has excellent overall recognition performance, but also has excellent robustness and efficiency in multi-direction tests.



Fig.10 - Sunflower recognition results

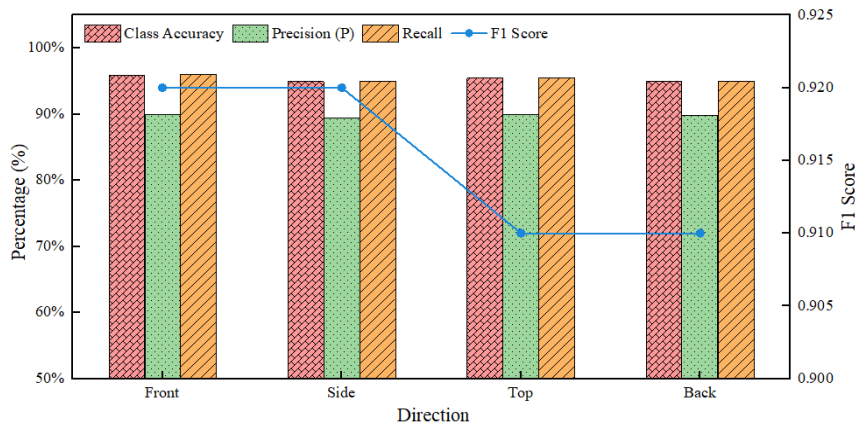


Fig. 11 - Multi-directional test results

Table 2

Multi-directional recognition test results				
Direction	Class Accuracy	Precision (P)	Recall	F1 Score
Front	96.00 %	90.00 %	96.00 %	0.92
Side	95.00 %	89.50 %	95.00 %	0.92
Top	95.50 %	89.90 %	95.50 %	0.91
Back	95.00 %	89.80 %	95.00 %	0.91

Navigational mapping test analysis

The methodology for constructing a map of the sunflower environment includes point cloud scanning and processing, SLAM loopback detection, point cloud alignment and graphical optimisation (Almazrouei et al., 2023). In this study, 16-line 3D LiDAR is used on a tracked mobile chassis for point cloud data acquisition at a speed of 0.5-1 m/s and a frequency of 10 Hz. The map is constructed using the LeGO-LOAM algorithm, and the experimental results show that the root-mean-square error (RMSE) of the trajectory is 0.15 m, with a standard deviation of 0.10 m. The purple line is the preset trajectory and the green line is the actual trajectory, and the purple line is the preset trajectory and the green line is the actual trajectory, which are highly consistent, but the green line in the turning area is slightly deviated, indicating that the error is mainly concentrated in the turning adjustment. The figure on the right represents the absolute position error of the trajectory in the spatial coordinate system, and the closer the colour is to red, the greater the error, which is consistent with the navigation trajectory diagram in the left figure.

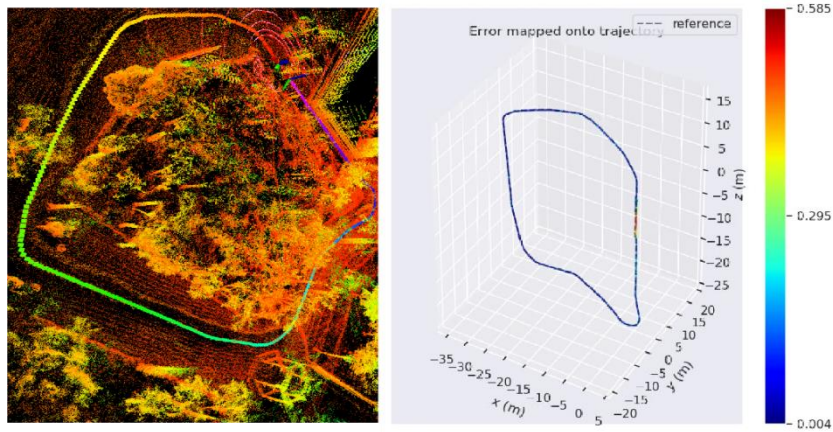


Fig. 12 - Graph of building test results

In this experiment, the path error of the robot was measured several times while navigating through a field of sunflowers. Table 2 lists the scheduled path length, actual path length, path deviation rate, error mean and error standard deviation data for the five sets of tests. Fig.12 demonstrates the trend of error with path length. The results show that when the predetermined path length is 100 metres, the error mean is 0.15 metres and the standard deviation is 0.10 metres; when the path length increases to 300 metres, the error mean is 0.17 metres and the standard deviation is 0.12 metres. Although the increase in path length resulted in a slight increase in error, the overall error remained low. The path deviation rates for all tests ranged from 0.20% to 0.26%, indicating that the actual path of the robot deviated very little from the intended trajectory. The algorithm performs stably in sunflower field navigation and meets the needs of sunflower insertion tray drying and autonomous navigation.

Table 3

Robot navigation test data

Test Number	1	2	3	4	5
Planned Path Length (m)	100	150	200	250	300
Actual Path Length (m)	100.2	150.3	300.4	250.6	300.8
Path Deviation Rate (%)	0.2	0.2	0.2	0.24	0.26
Mean Error (m)	0.15	0.14	0.16	0.15	0.17
Error Standard Deviation (m)	0.1	0.11	0.09	0.1	0.12

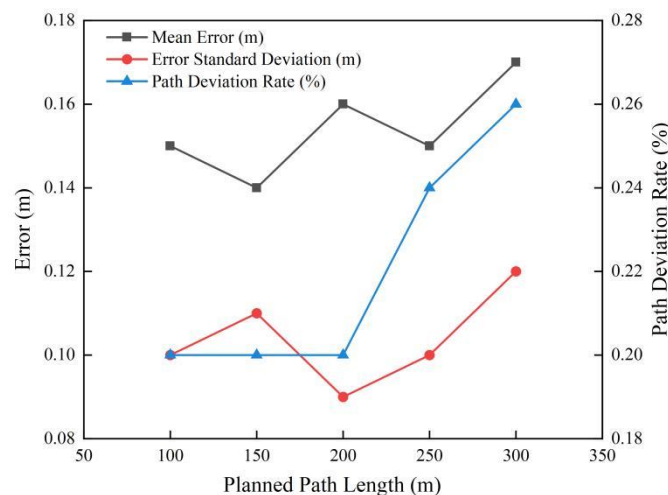


Fig. 13 - Path error analysis diagram

CONCLUSIONS

In this paper, an intelligent sunflower insertion tray drying machine is proposed, which has the functions of intelligent recognition of sunflower trays and navigation and map building, and significantly improves the work efficiency. Field experiments comprehensively verified the performance of the device.

The experimental results show that the category accuracy of the YOLOv5 model in the multi-direction test of the flower discs exceeds 95%, demonstrating good recognition stability and robustness.

The navigation building tests using the LeGO-LOAM algorithm show that the robot's path tracking error is small, with path deviation rates ranging from 0.20% to 0.26%. However, in the tests with different path lengths, the error in the turning area was large, reaching 0.3 m to 0.585 m. The turning mechanism needs to be optimised to reduce the error. The error of navigation building is mainly concentrated in the complex terrain area, and the point cloud processing algorithm should be optimised to improve the positioning accuracy.

In addition, it was found that the diameter of the flower discs was concentrated around 20 cm, which accounted for 85% of the total samples, and a more flexible jaw structure needs to be designed to increase the clamping range. In the future, the processing speed and range can be further optimized to adapt to the needs of larger-scale operations, which provides a proven solution for agricultural mechanization.

ACKNOWLEDGEMENT

This project was funded by the Construction Project of Modern Agricultural Industrial Technology System of Shanxi Province (2023CYJSTX05-17), the Key Research and Development Programme of Shanxi Province (202202140601021) and the Sub-theme of the National Key Research and Development Programme (2021YFD1600301-4).

REFERENCES

- [1] Jin, Y., Liu, J., Xu, Z., Yuan, S., Li, P. and Wang, J., 2021. Development status and trend of agricultural robot technology. *International Journal of Agricultural and Biological Engineering*, 14(4), pp.1-19.
- [2] Dhanaraju, M., Chenniappan, P., Ramalingam, K., Pazhanivelan, S. and Kaliaperumal, R., 2022. Smart farming: Internet of Things (IoT)-based sustainable agriculture. *Agriculture*, 12(10), p.1745.
- [3] Peng, J., Zhao, Z. and Liu, D., 2022. Impact of agricultural mechanization on agricultural production, income, and mechanism: evidence from Hubei province, China. *Frontiers in Environmental Science*, 10, p.838686.
- [4] Moschen, S., Gialdi, A.I.L., Paniego, N., Fernandez, P. and Heinz, R.A., 2017. Sunflower leaf senescence: a complex genetic process with economic impact on crop production. In *Senescence-Physiology or Pathology*. IntechOpen.
- [5] Pan, F., Chen, J., Zhang, H., Han, L., Dong, Y., Li, B. and Ji, C., 2024. Design and Experiment of Plate Taking Control System of Edible Sunflower (*Edulis Helianthus Catino L.*) Harvester. *Agriculture*, 14(4), p.592.
- [6] Dong, S., Yuan, Z., Gu, C., Yang, F., Fu, H., Wang, C., Jin, C. and Yu, J., 2017. Research on intelligent agricultural machinery control platform based on multi-discipline technology integration. *Transactions of the Chinese Society of Agricultural Engineering*, 33(8), pp.1-11.
- [7] Li, C.E., Tang, Y., Zou, X., Zhang, P., Lin, J., Lian, G. and Pan, Y., 2022. A novel agricultural machinery intelligent design system based on integrating image processing and knowledge reasoning. *Applied Sciences*, 12(15), p.7900.
- [8] Young, S.N., Kayacan, E. and Peschel, J.M., 2019. Design and field evaluation of a ground robot for high-throughput phenotyping of energy sorghum. *Precision Agriculture*, 20(4), pp.697-722.
- [9] Fang, B., Sun, F., Yang, C., Xue, H., Chen, W., Zhang, C., Guo, D. and Liu, H., 2018, May. A dual-modal vision-based tactile sensor for robotic hand grasping. In *2018 IEEE International Conference on Robotics and Automation (ICRA)* (pp. 4740-4745). IEEE.
- [10] Shi, J., Bai, Y., Diao, Z., Zhou, J., Yao, X. and Zhang, B., 2023. Row detection BASED navigation and guidance for agricultural robots and autonomous vehicles in row-crop fields: methods and applications. *Agronomy*, 13(7), p.1780.
- [11] Peteinatos, G.G., Weis, M., Andújar, D., Rueda Ayala, V. and Gerhards, R., 2014. Potential use of ground-based sensor technologies for weed detection. *Pest management science*, 70(2), pp.190-199.
- [12] Williams, H.A., Jones, M.H., Nejati, M., Seabright, M.J., Bell, J., Penhall, N.D., Barnett, J.J., Duke, M.D., Scarfe, A.J., Ahn, H.S. and Lim, J., 2019. Robotic kiwifruit harvesting using machine vision, convolutional neural networks, and robotic arms. *Biosystems Engineering*, 181, pp.140-156.
- [13] Zhu, K. and Zhang, T., 2021. Deep reinforcement learning based mobile robot navigation: A review. *Tsinghua Science and Technology*, 26(5), pp.674-691.
- [14] Bechar, A. and Vigneault, C., 2016. Agricultural robots for field operations: Concepts and components. *Biosystems Engineering*, 149, pp.94-111.
- [15] Almazrouei, K., Kamel, I. and Rabie, T., 2023. Dynamic obstacle avoidance and path planning through reinforcement learning. *Applied Sciences*, 13(14), p.8174.

DESIGN AND EXPERIMENT OF HIGH MOISTURE CORN THRESHING DEVICE WITH LOW DAMAGE

高水分玉米低损伤脱粒装置的设计与试验

Qing TANG¹⁾, Lan JIANG¹⁾, Wenyi YU²⁾, Jun WU^{*1)}, Gang WANG¹⁾

¹⁾ Nanjing Institute of Agricultural Mechanization, Ministry of Agriculture and Rural Affairs of China, Nanjing 210014, China;

²⁾ Jiangsu Province Grain and Oil Information Center, Nanjing 210014, China;

Tel: +86.15366092905; E-mail: 362268885@qq.com

DOI: <https://doi.org/10.35633/inmateh-74-15>

Keywords: corn, threshing damage, direct harvesting, optimize

ABSTRACT

To address the requirements of direct corn kernel harvesting in the Huang-Huai-Hai region of China, this study aimed to rectify issues related to kernel damage and low threshing rates observed in the operation of existing corn kernel direct harvesting machines. Initially, a novel threshing device was designed, incorporating staggered rotary motions for the threshing cylinder and concave grate. Subsequently, the experimental factors such as the speed of threshing drum, the speed of concave grate and the threshing gap were considered on the test bench, and the indexes such as corn grain crushing rate and threshing rate were evaluated. Moreover, orthogonal testing indicated that optimal threshing performance was achieved with a threshing cylinder speed of 287 rpm, a concave grate speed of 106 rpm, and a threshing clearance of 49 mm, resulting in a kernel crushing rate of 4.12% and a threshing rate of 94.18%. These experimental findings confirm the feasibility of the Rotating Concave Screen Threshing Device, underscoring its ability to significantly enhance corn threshing rates while minimizing kernel fragmentation and damage.

摘要

为了满足中国黄淮海地区玉米籽粒直接收获的要求, 本研究旨在解决现有玉米籽粒直收机操作中观察到的与籽粒损伤和脱粒率低相关的问题。设计了一种新型脱粒装置, 其中脱粒滚筒和凹板筛交错反向旋转运动。选取脱粒滚筒转速、凹板筛转速和脱粒间隙为试验因素, 玉米籽粒破碎率和脱净率等试验指标开展了台架试验。实验结果揭示了这些因素对玉米粒破碎率和脱净率的影响。正交试验表明, 当脱粒滚筒转速为 287 rpm、凹板筛转速为 106 rpm、脱粒间隙为 49 mm 时, 脱粒效果最佳, 籽粒破碎率为 4.12%, 脱净率为 94.18%。这些实验结果证实了旋转凹板筛脱粒装置的可行性, 强调了其在最大限度地减少谷粒破碎和损坏的同时显著提高玉米脱净率的能力。

INTRODUCTION

Corn stands as the preeminent cereal crop globally, playing a pivotal role in food production, chemical applications, and livestock feed due to its exceptional yield (Steponavičius *et al.*, 2023). In China, corn holds a prominent position as one of the three principal staple foods, boasting the largest planting area and the highest total output (Chen *et al.*, 2015). Notably, the Huang-Huai-Hai Wheat-Corn Rotation Region ranks as the second-largest corn-producing region in China. The harvested corn kernels from this region exhibit elevated water content, ranging between 30% and 35%. The corn harvesting process subjects the kernels to compression, impact, and abrasion by threshing components, precipitating issues such as kernel damage, skin breakage, and cracks. These challenges heighten the susceptibility to aflatoxin infection and mildew, posing a significant threat to food security. Addressing these concerns is crucial for ensuring the integrity of the corn supply chain and safeguarding food resources (Yang *et al.*, 2022).

Currently, mechanized corn harvesting predominantly takes two forms: ear harvesting and grain harvesting. Beyond a grain moisture content of 28%, the increased softness renders the grains susceptible to compression, leading to amplified losses (Wacker, 2005; Miu, 2015). A widely adopted approach involves peeling, threshing, and cleaning the corn cob in a single operation, yielding labor and time savings. This process entails the use of a stripper attached to the header for corn cob removal from the stem, followed by threshing using either a tangential or axial threshing device-essentially the central component of the combine harvester, crucially influencing the quality of the corn harvest (Yang *et al.*, 2016).

Notably, as the moisture content surpasses 14%, the grain breakage rate escalates with higher moisture levels. At a water content of 35%, the grain damage can reach up to 40% (Alonge A.F et al., 2000; Volkovas V. et al., 2006). The persistent challenge of elevated crushing rates in corn ears with high moisture content during grain harvesting remains a primary constraint on the advancement of corn mechanization (Li et al., 2014).

Initially, investigations into low-loss threshing technology were conducted abroad, revealing that the threshing process was contingent upon the corn variety and the design and adjustment of the threshing device (Wacker, 2005). A key strategy involved the redesign of the threshing device, encompassing the drum and concave plate, to mitigate grain damage, allowing the hulled grain to promptly exit the threshing drum after hulling (Chowdhury et al., 1978). Numerous scholars have delved into the impact of structural parameters of the threshing device on threshing damage and loss. Petkevichius et al. (2008a and 2008b), Spokas, et al. (2008) analyzed the influence of drum speed and concave gap on grain separation, revealing that a judicious increase in gap significantly reduced grain loss and crushing. Moreover, the movement of the ear in the threshing chamber was scrutinized, exposing varied movement speeds based on the ear's posture. Specifically, the ear parallel to the drum axis exhibited a faster movement speed than the ear perpendicular to the drum axis. Pužauskas et al., (2017), investigated the impact of the grid concave gap on grain damage, revealing that a concave gap of 62.5 mm could reduce the grain damage rate to less than 3%. Miodragovic et al., (2006), explored the influence of threshing gap on grain quality, establishing that an increased threshing gap was conducive to reducing grain crushing rates and improving grain threshing quality. In the domestic domain, scholars have probed the crushing mechanism of corn grain (Niu et al., 2011; Xu et al., 2009), exploring the influence of key working parameters such as moisture content and drum circumferential speed on the crushing rate of corn grain through the development of a small threshing test bench (Xiang et al., 2015; Yang et al., 2018). To comprehensively evaluate two distinct threshing drums, Yang et al., (2022), scrutinized the effects of various threshing parameters, including corn ear feed, drum circumferential speed, and threshing gap, on grain crushing rates under different moisture content conditions.

Currently, research on threshing technology predominantly focuses on traditional longitudinal or transverse axial threshing systems, examining the influence of threshing drum rotation speed, types of threshing elements, and threshing gap on threshing damage to identify optimal parameters. However, there remains a notable gap in the study of threshing damage for corn seeds with water content ranging between 20% and 30%, as well as those exceeding 30%. To address this gap, this paper introduces a low-damage threshing device designed to alleviate the issue of high moisture content corn grain threshing damage, thereby minimizing grain damage while ensuring an efficient corn grain threshing rate.

MATERIALS AND METHODS

High moisture corn

The focus of this study was Zhengdan 958, the predominant maize variety cultivated in the Huang-huai-hai region of China (see Figure 1).

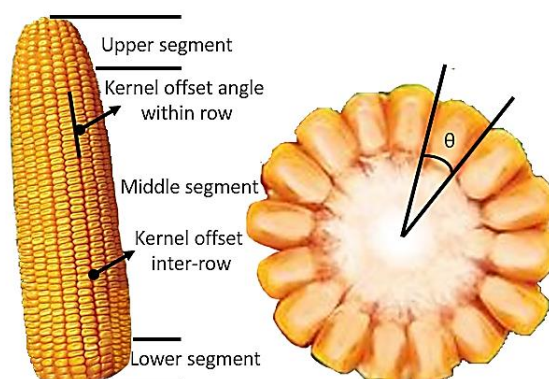


Fig. 1 - Zhengdan 958 corn

This variety exhibits a plant height ranging from 240 to 250 cm and an ear height of 100 to 110 cm. Characterized by a cylindrical ear, white axis, 18-20 cm ear length, approximately 5 cm ear thickness, 14-16 rows per ear, about 36 grains per row, yellow-colored grains, and a 1000-grain weight ranging from 300 to 350g.

To capture representative data, 50 ears were randomly selected for measurement using a vernier caliper, which included the diameter of the large end, the diameter of the small end, and the length of the ear. The resulting average values are presented in Table 1.

Table 1

Corn ear physical parameters				
parameter	Unit	Maximum value	Minimum	Average value
Big-endian diameter	mm	56.64	48.28	52.31
Little-endian diameter	mm	49.17	43.55	46.82
Ear length	mm	198.16	117.04	154.46

Preceding the experiment, ten ears were randomly chosen, and the moisture content of the grains was gauged using a grain moisture meter, with the average value determined through three measurements. The measuring tool employed was the Kate PM-8188 grain moisture measuring instrument, boasting a measurement range of 6-40% and an accuracy of 0.5%. The recorded grain moisture content registered at 30.12%, categorizing it as high-moisture corn grain.

Rotating concave screen threshing device

The research indicates that a high threshing drum speed is the primary factor contributing to grain damage (Paulsen et al., 2014; Miodragovic et al., 2006). Conversely, other parameters such as threshing gap and the type of threshing element exhibit minimal influence on grain damage (Brandini, 1969). For corn kernels with elevated water content, diminishing the rotating speed of the threshing drum proves effective in mitigating damage. However, corn kernels with low rotating speed face challenges in separating from the corn cob, resulting in an increased loss rate. To address this issue, this study proposes a threshing system featuring a 360-degree full-wrap concave screen and a counter-rotating separating drum. This design aims to minimize damage and extend the contact time between the corn cob and the threshing drum and concave screen, facilitating easier separation of the corn kernels. Figure 2 illustrates the structure of the proposed threshing device, highlighting key differences from traditional counterparts. Specifically, the concave screen wrap angle exceeds 270 degrees, reaching a full 360 degrees, and the rotary concave screen can rotate in the opposite direction relative to the threshing drum, differing from the fixed orientation of traditional concave screens.

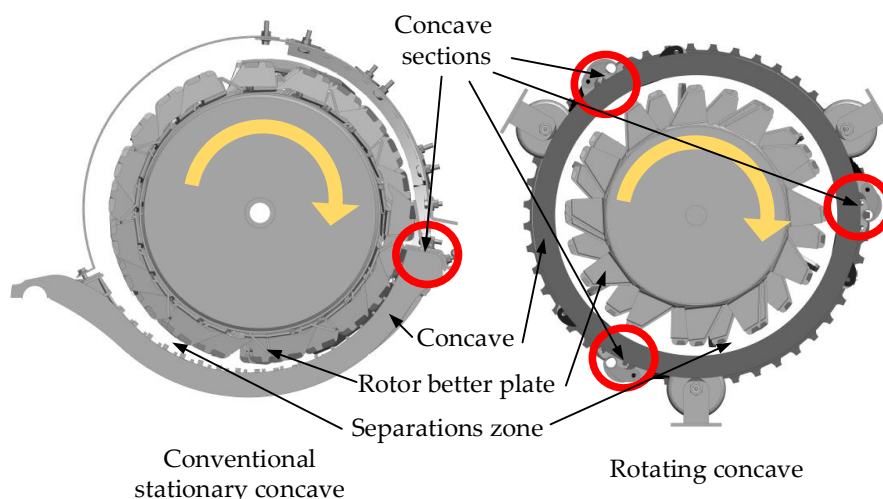


Fig. 2 - Working principles of the conventional stationary concave grate and rotary concave grate

Research findings indicate that the axial threshing device incurs lower grain damage compared to the tangential threshing device (Wacker, 2005; Poničan et al., 2009). Consequently, this study opts to enhance the longitudinal axial threshing device utilized in the CASE4099 combine. Figure 3 illustrates the structure of the modified threshing device.

This study aims to investigate the impact of a novel threshing system on reducing threshing damage. Given a fixed corn threshing power, both the method involving a small-diameter cylinder with high threshing speed and the one employing a large-diameter cylinder with low threshing speed can be utilized to achieve grain and ear shaft separation.

However, the adoption of a driven concave screen design in this paper imposes constraints on the layout of the concave screen and raises challenges for the drive system when using a large-diameter threshing cylinder. Additionally, as the cylinder diameter decreases, the inertia force increases, enhancing the cylinder's ability to overcome overload and ensuring a more stable working process. Hence, this paper employs the small-diameter with high threshing speed method. Following the guidelines in the agricultural machinery design manual, the recommended threshing speed for the axial flow cylinder is 10~12 m/s, with a cylinder rotation speed ranging from 300 rpm to 450 rpm. Accordingly, the selected cylinder diameter in this paper is 0.43 m, falling within the suggested range. The threshing area measures 1.30 m, and the separation area has a length of 1.03 m. The total length of the cylinder is 2.86 m, with the threshing area comprising 1.30 m and the separation area extending to 1.03 m. A threshing angle of 10° was chosen based on the reference book. Detailed parameters are presented in Table 2.

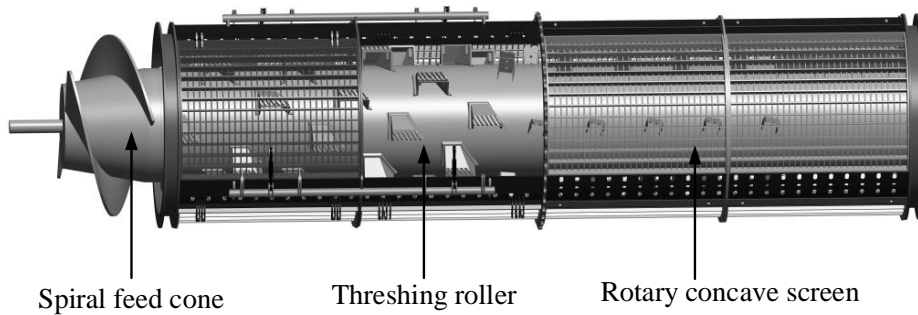


Fig. 3 - Schematic of modified threshing device

Table 2

Main parameters of threshing cylinder		
Parameter	Unit	Value
Cylinder diameter	mm	430
Cylinder length	mm	2860
Length of the threshing area	mm	1300
Length of the separation area	mm	1030
Threshing inclination	°	10°

Threshing cylinder

As depicted in Figure 4, the rotating concave screen threshing device comprises a spiral feeding cone, a closed threshing cylinder, and a rotary concave screen.

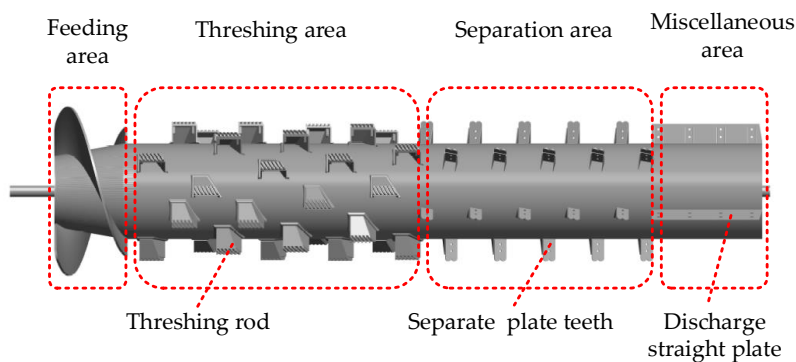


Fig. 4 - Schematic of the threshing cylinder

Notably, the rotary movement direction of the concave screen opposes that of the threshing cylinder. In the feeding process, corn ears undergo tangential and axial forces from the spiral cone, progressing along the cone toward the threshing cylinder. This journey is characterized by even stress on the ears due to the smooth surfaces of the feeding blade and cone, coupled with a uniform increase in the cylinder's diameter, preventing any damage. Upon entering the threshing cylinder, the corn kernel gradually dislodges through the kneading, squeezing, and impacting actions of the threshing element and concave screen, ultimately reaching the cleaning device via the concave screen.

The counter-directional movement of the concave screen compared to the threshing cylinder significantly amplifies the threshing wrapping angle, prolonging the threshing duration for corn ears in the device and enhancing the overall threshing rate. Furthermore, the reduction in the rotation speed of the threshing cylinder diminishes the impact of the corn threshing element on the corn ear, minimizing kernel shattering and associated damage.

Concave screen

The primary purpose of the concave screen is to facilitate the threshing and separation of corn ears in conjunction with the threshing cylinder. The proposed rotary concave screen comprises a frame, threshing concave screen section, and separation concave screen section. The frame encompasses the rotary track, transition plate, sprocket plate, threshing concave screen clearance adjustment plate, and separation concave screen fixed plate. Within the threshing concave screen section, six groups of concave grates are arranged, with three groups evenly distributed between the rotary track and transition plate, and the remaining three groups between the transition plate and the sprocket plate. Similarly, the separation concave screen section features six groups of concave grates, with three groups evenly distributed between the chain wheel plate and the transition plate, and the other three groups evenly distributed between the transition plate and the rotary track. A clearance adjustment device is incorporated into the threshing section concave screen to accommodate variations in corn varieties, ear diameter, feeding amount, and moisture content during harvest (refer to Figure 5).

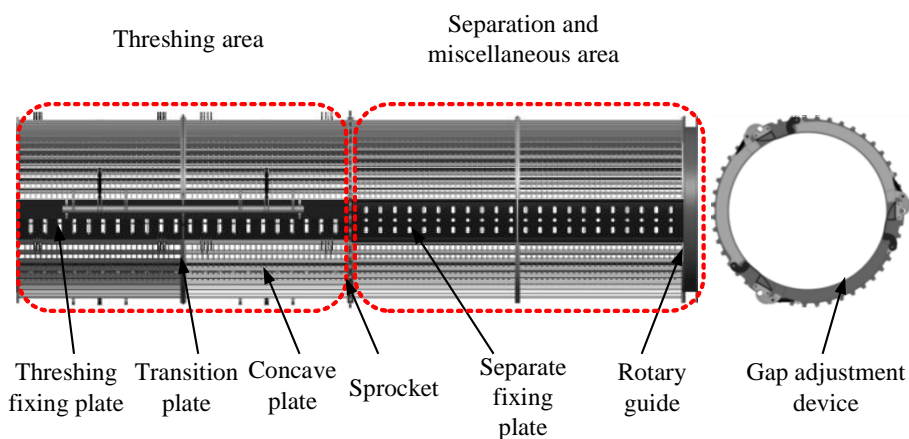


Fig. 5 - Schematic of rotary concave screen

The concave screen employs a grid format, consisting of both flat and round steel components, as illustrated in Figure 6. The structural parameters of the concave grate are established in accordance with guidelines outlined in the agricultural machinery design manual and pertinent literature, detailed in Table 3.

The grain passage rate through the concave screen is computed using Formula (1) (Miu et al., 2008).

$$P = \frac{(a_1 - a_2 - d)(b_1 - b_2 - d)}{a_1 b_1} \tag{1}$$

where: P = the grain passing rate of concave screen [%]; a_1 = center distance between round bars [mm]; a_2 = round steel diameter [mm]; b_1 = center distance between flat steels [mm]; b_2 = width of flat steel [mm]; d = average diameter of grain [mm].

Table 3

Structural parameters of concave screen			
parameter	Unit	Value	
Flat bar width	mm	5	
Diameter of round steel diameter	mm	5	
Flat bar spacing	mm	48	
Round bar spacing	mm	22	
Deflector helix angle	°	6	
Concave radian	°	90	
A minimum gap of concave grate and cylinder	mm	45	
Maximum gap of concave grate and cylinder	mm	55	

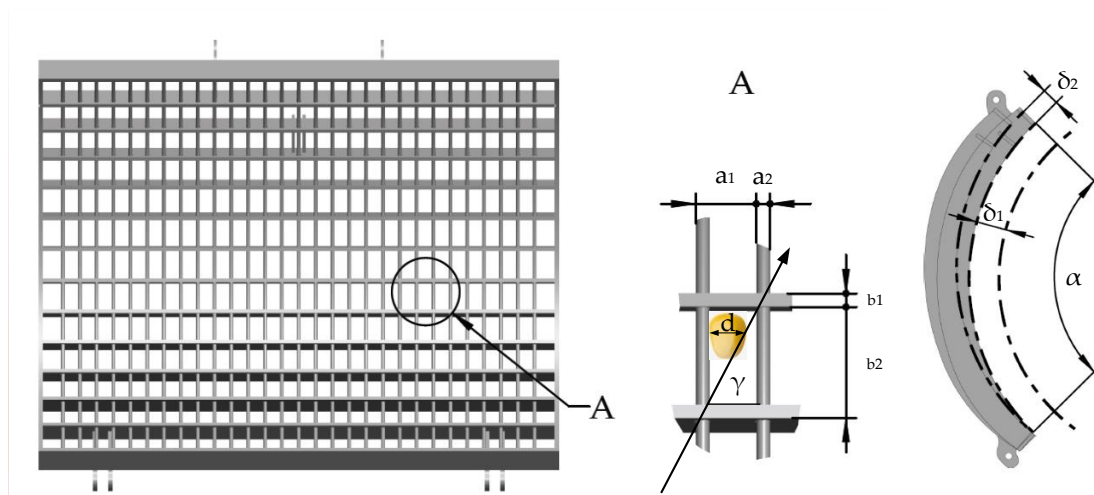


Fig. 6 - Structural parameters of concave grate

RESULTS AND DISCUSSION

Experimental scheme

Test indicators

During the corn ear harvesting process, essential qualitative evaluation indices for combine harvester performance encompass grain loss, grain breakage, work efficiency, and fuel consumption (Petkevichius et al., 2008; Kutzbach et al., 1999; Li et al., 2020). This study specifically focuses on the threshing quality of the threshing device in conditions of high grain water content, with no emphasis on work efficiency and fuel consumption. Grain loss is characterized by the proportion of grains threshed from the corncob to the total grain count, termed the grain threshing rate, and is computed using formula (2).

$$T = \frac{m_t}{m_t + m_w} \times 100\% \tag{2}$$

where *T*- seed cleaning rate, [%]; *m_t* - take off the grain weight, [g]; *m_w* - weight of non-threshed grain [g].

Grains damaged during harvesting can be classified into distinct categories based on the extent of damage, as illustrated in Figure 9 (Chowdhury et al., 1978; Ma et al., 2020).

The categories include: (1) Broken grains: comprising fragmented and crushed grains, none of which remain intact in this category, with at least one-third of the grains missing. (2) Defective seeds: exhibiting damage to the embryo, radicle, damage around the edge of the embryo, and pericarp loss in this section of the sample. (3) Cracked grains: featuring minute cracks but remaining intact in this portion of the sample.

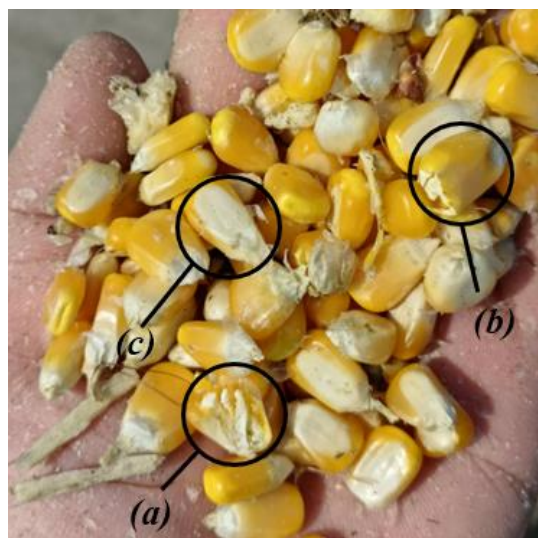


Fig. 9 - Categories of grain damage
(a)broken grains (b) defective grains (c) cracked grains

The proportion of impaired grain quality to the overall grain quality is termed the grain damage rate, and it is determined using formula (3).

$$P = \frac{m_s}{m_i} \times 100\% \quad (3)$$

where P - grain damage rate, [%]; m_s - damaged grain quality, [g]; m_i - total grain mass, [g].

Selection of test factors

Numerous researchers have indicated that the damage to corn kernels is influenced by the rotational speed of the threshing drum (*Petkevichius et al., 2008; Pastukhov et al., 2021; Pachanawan et al., 2021*). *Bumbar et al., (2018)*, discovered that optimizing threshing quality to minimize grain damage involves setting the peripheral speed within the range of 17–21 m/s. Given that the threshing mechanism in this study involves the opposite rotation of the threshing drum and the concave screen, the threshing drum's speed is lower than that of conventional designs, operating at 250–500 rpm, while the concave screen rotates at 50–150 rpm.

Another critical technological parameter affecting grain damage is the clearance between the threshing drum and the concave plate, which is contingent upon the size of the ear to be threshed (*Miu P.I. 2015; Steponavicius et al., 2018*). With corn ear diameter averaging around 5 cm in this investigation, the threshing gap is set at 45–55 mm.

Testing program

This study utilized the crushing rate and threshing rate as key indicators in the orthogonal test, with cylinder speed, concave grate speed, and threshing clearance serving as the test factors. The investigation aimed to elucidate the impact of optimized parameter combinations on the threshing system and assess the varying levels of these factors on threshing performance. To achieve this, an orthogonal test was meticulously designed based on the Box-Behnken Design using Design-Expert software. The specified ranges for the test factors were as follows: threshing cylinder speed ranging from 250 to 500 rpm, concave grate speed within the range of 50 to 150 rpm, and threshing clearance set between 45 and 55 mm. The respective levels of the different factors are detailed in Table 6.

Table 6

Level	Parameter levels		
	cylinder speed v_r , (rpm)	concave grate speed v_c , (rpm)	threshing clearance c , (mm)
-1	250	50	45
0	375	100	50
1	500	150	55

According to Design-Expert, there were 17 experiments, and the experimental results are shown in Table 7.

Table 7

Trial Protocol and Results					
Test number	Cylinder speed v_r , (rpm)	Concave speed v_c , (rpm)	Threshing clearance c , (mm)	Crushing rate X , (%)	Threshing rate Y , (%)
1	1	1	0	4.77	92.68
2	-1	-1	0	4.31	92.60
3	-1	0	-1	4.38	93.67
4	0	-1	1	4.39	89.54
5	0	0	0	4.35	94.24
6	1	0	-1	5.84	91.95
7	-1	0	1	4.19	90.84
8	1	-1	0	5.29	90.03
9	1	0	1	4.77	90.29
10	-1	1	0	3.95	91.83
11	0	0	0	4.35	94.04
12	0	1	1	4.25	90.55
13	0	0	0	4.31	94.22
14	0	0	0	4.47	93.85

Test number	Cylinder speed v_r , (rpm)	Concave speed v_c , (rpm)	Threshing clearance c , (mm)	Crushing rate X , (%)	Threshing rate Y , (%)
15	0	1	-1	4.73	92.53
16	0	-1	-1	5.39	91.76
17	0	0	0	4.31	94.22

Observing the results, the minimum recorded crushing rate stood at 3.95%. This occurred when the threshing cylinder operated at a speed of 250 rpm, the concave grate speed was set to 150 rpm, and the threshing clearance was fixed at 50 mm. Conversely, the maximum threshing rate reached 94.24% under different conditions, specifically with a threshing cylinder speed of 375 rpm, concave grate speed at 100 rpm, and a consistent threshing clearance of 50 mm.

RESULTS ANALYSIS AND DISCUSSION

Analysis of variance

In the analysis of experimental data, variance analysis was conducted using Design-Expert software. Coefficient items with a significance greater than 0.05 in the model were excluded. The outcomes of this analysis are detailed in Tables 8 and 9. The regression model expressing the relationship between the crushing rate, threshing rate, and the encoded values is provided below:

$$X = 4.36 + 0.48v_r - 0.21v_c - 0.34c - 0.22 v_r c + 0.13v_c c + 0.16 v_r^2 + 0.27c^2 \quad (R^2=0.992) \quad (4)$$

$$Y = 94.11 - 0.5v_r + 0.46v_c - 1.09c + 0.85 v_r v_c + 0.29v_r c - 0.87 v_r^2 - 1.46 v_c^2 - 1.56c^2 \quad (R^2=0.996) \quad (5)$$

All regression coefficients in the model exhibited a significance level below 0.05, and the lack of fit was deemed non-significant. These findings affirm a high degree of fitting for the regression model.

Table 8

source of variance	sum of variance	degree of freedom	mean square deviation	F value	P value
Model	3.88	9	0.43	96.31	< 0.0001
A	1.84	1	1.84	411.82	< 0.0001
B	0.35	1	0.35	78.83	< 0.0001
C	0.94	1	0.94	209.68	< 0.0001
AB	0.0064	1	0.0064	1.43	0.2707
AC	0.19	1	0.19	43.26	0.0003
BC	0.068	1	0.068	15.10	0.0060
A ²	0.11	1	0.11	25.15	0.0015
B ²	0.014	1	0.014	3.22	0.1158
C ²	0.31	1	0.31	70.37	< 0.0001
Residual	0.031	7	0.00448	1.08	
Lack of Fit	0.014	3	0.00468	96.31	0.4512
Pure Error	0.017	4	0.00432		
Cor Total	3.91	16			

Table 9

source of variance	sum of variance	degree of freedom	mean square deviation	F value	P value
Model	41.20	9	4.58	196.49	< 0.0001
A	1.99	1	1.99	85.41	< 0.0001
B	1.67	1	1.67	71.87	< 0.0001

source of variance	sum of variance	degree of freedom	mean square deviation	F value	P value
C	9.44	1	9.44	405.14	< 0.0001
AB	2.92	1	2.92	125.50	< 0.0001
AC	0.34	1	0.34	14.69	0.0064
BC	0.014	1	0.014	0.62	0.4576
A ²	3.17	1	3.17	136.23	< 0.0001
B ²	8.98	1	8.98	385.61	< 0.0001
C ²	10.22	1	10.22	438.80	< 0.0001
Residual	0.16	7	0.023		
Lack of Fit	0.050	3	0.017	0.58	0.6574
Pure Error	0.11	4	0.028		
Cor Total	41.37	16			

Analysis of Response Surface

An examination was carried out based on the regression equations for crushing rate and threshing rate. The results of the analysis revealed that the primary and secondary orders of the effects of various factors on the crushing rate were ACB, whereas the primary and secondary orders of the effects of various factors on the threshing rate were CAB.

Effects of Threshing Cylinder Speed and Concave Grate Speed on Threshing Performance

As depicted in Figure 10, both the cylinder speed and concave grate speed exhibited significant independent effects on the crushing rate, without any discernible interaction between them. The crushing rate demonstrated a noticeable upward trend with an increase in threshing cylinder speed, while it exhibited a gradual and less pronounced increase with higher concave grate speed. Concurrently, the cylinder speed, concave grate speed, and their interaction exerted extremely significant effects on the threshing rate. As both cylinder speed and concave grate speed increased, the threshing rate initially rose and then declined.

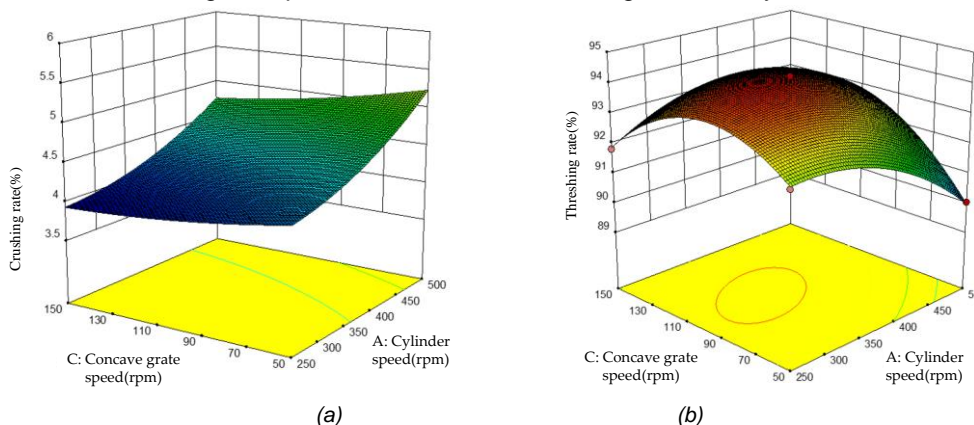


Fig. 10 - The effects of cylinder speed and concave grate speed on threshing performance
 (a) Cylinder speed and concave grate speed effect on crushing rate;
 (b) Cylinder speed and concave grate speed effect on threshing rate

Effects of Threshing Cylinder Speed and Threshing Clearance on Threshing Performance

As illustrated in Figure 11, both the cylinder speed and threshing clearance exhibited significant effects on both the crushing rate and threshing rate. Notably, the interaction between cylinder speed and threshing clearance had a substantial impact on the crushing rate, while a similar interaction exerted a significant effect on the threshing rate. Specifically, an increase in cylinder speed led to a marked escalation in the crushing rate. Conversely, an increase in threshing clearance resulted in a decline in the crushing rate, stabilizing thereafter. Furthermore, an increase in both cylinder speed and threshing clearance led to an initial rise and subsequent decline in the threshing rate.

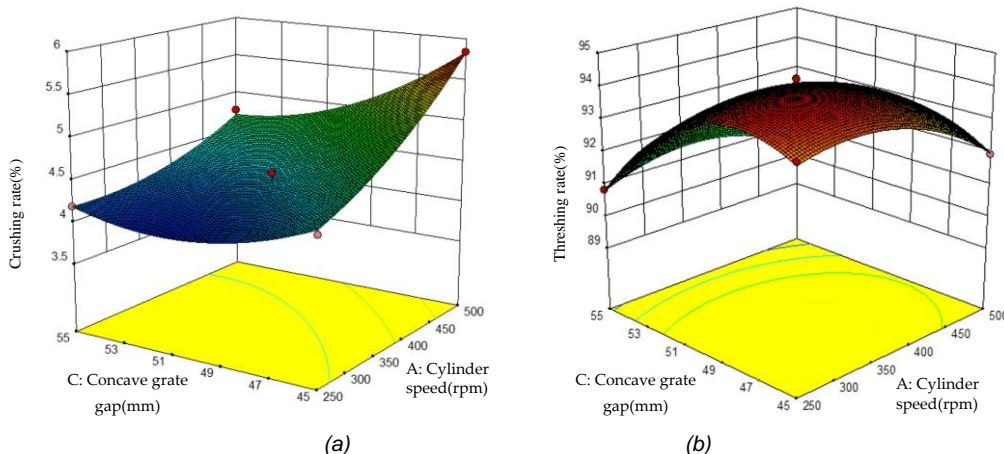


Fig. 11 - Effects of cylinder speed and concave grate gap on the threshing performance
 (a) Cylinder speed and concave grate gap effect on crushing rate; (b) Cylinder speed and concave grate gap effect on threshing rate

Effects of Concave Grate Speed and Threshing Clearance on Threshing Performance

According to Figure 12, the velocity of the concave grate and the clearance for threshing exhibited noteworthy impacts on the crushing rate, with their interaction significantly influencing the overall crushing rate. An escalation in threshing clearance resulted in a substantial decrease in the crushing rate, whereas an increase in the concave grate speed led to a modest reduction in the crushing rate. Simultaneously, both the concave grate speed and threshing clearance wielded substantial influence on the threshing rate, though their interaction demonstrated no discernible effect on the threshing rate. Consequently, elevations in both concave grate speed and threshing clearance yielded an initial increase followed by a subsequent decrease in the threshing rate.

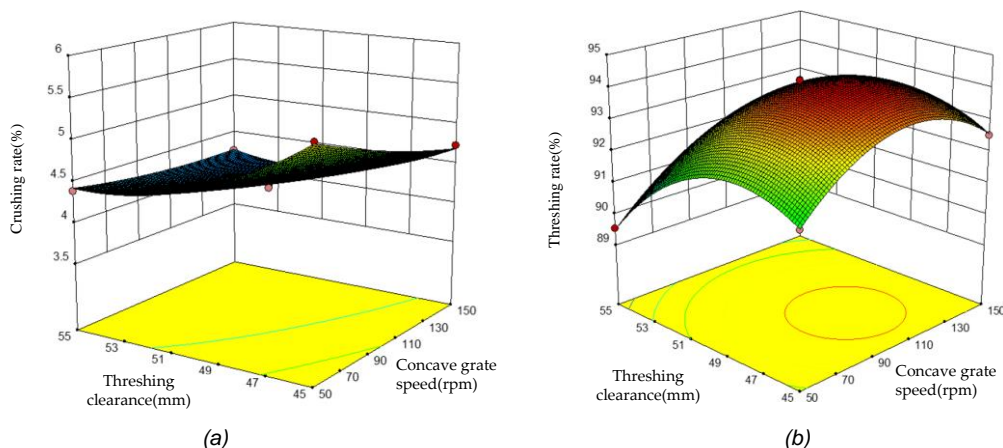


Fig. 12 - Effects of concave grate speed and threshing clearance on threshing performance
 (a) Concave grate speed and threshing clearance effect on crushing rate;
 (b) Concave grate speed and threshing clearance effect on threshing rate

Utilizing variance analysis and response surface analysis, the optimized combination of operational parameters was derived. The corn ear's kernel crushing rate achieved 4.12%, and the threshing rate reached 94.18% under the following conditions: a threshing cylinder speed of 287 revolutions per minute (rpm), concave grate speed of 106 rpm, and a threshing clearance of 49 millimeters.

CONCLUSIONS

This study introduces an innovative threshing device, wherein the threshing cylinder and concave grate can execute staggered rotational motions. The ensuing conclusions are as follows:

This device demonstrated a notable enhancement in the threshing rate while concurrently diminishing fragmentation and damage to corn kernels. The bench test showed that the optimal speed range for the threshing cylinder was 250–500 rpm, the concave grate should operate within the range of 50–100 rpm, and the threshing clearance should be set between 45–55 mm.

Utilizing the optimization function in Design-Expert 11.0, the optimal parameter combination was determined as follows: threshing cylinder speed = 287 rpm, concave grate speed = 106 rpm, and threshing clearance = 49 mm. Correspondingly, the corn kernel exhibited a crushing rate of 4.12% and a threshing rate of 94.18%. The most influential factor affecting the kernel crushing rate was the threshing cylinder speed, followed by threshing clearance and concave grate speed. Simultaneously, the most impactful factor influencing the threshing rate was the threshing clearance, followed by the threshing cylinder speed and concave grate speed.

ACKNOWLEDGEMENT

This research was supported by the low-loss threshing technology and device development for high-moisture corn, S202008-2, "The APC was funded by the basic scientific research business expenses".

REFERENCES

- [1] Alonge A.F, Adegbulugbe T.A. (2000). Performance evaluation of a locally developed grain thresher – II. *Agricultural Mechanization in Asia, Africa and Latin America*. 31(2):52–54.
- [2] Brandini A. (1969). Corn kernel forces during impact shelling. *Retrospective Theses and Dissertations*. 14482.
- [3] Bumbar I.V., Epifantsev V.V., Shchegorets O.V., Sinegovskaya V.T., Kuznetsov E.E., Kuvshinov A.A., Lontseva I.A., Kapustina N.A. (2018). Optimization of agrotechnical terms of harvesting of crops, design and operating parameters of crop-harvesting machines under conditions of the Amur region, Russian Federation. *Plant Archives*. 18(2): 2567–2572.
- [4] Chen Y, Xiao C, Wu D, Xia T, Chen Q, Chen F, Yuan L, Mi G. (2015). Effects of nitrogen application rate on grain yield and grain nitrogen concentration in two maize hybrids with contrasting nitrogen remobilization efficiency. *European Journal of Agronomy*. 62:79–89.
- [5] Chowdhury M.H., Buchele W.F. (1978). The nature of corn kernel damage inflicted in the shelling crescent of grain combines. *Transactions of the ASAE*. 21(4): 610-614.
- [6] Kutzbach H.D., Quick G.R. (1999). Harvesters and Threshers Grain. *CIGR Handbook of Agricultural Engineering*. 311-347.
- [7] Li S.F., Zhang C.X. Lu M., Liu W.G., Li X.H. (2014). Research development of kernel dehydration rate in maize. *Molecular Plant Breeding*. 12(4): 825–829.
- [8] Li X , Du Y , Guo J , Mao E. (2020).Design, Simulation, and Test of a New Threshing Cylinder for High Moisture Content Corn. *Applied Sciences*. 10(14):4925.
- [9] Miu P.I. (2015). *Cereal threshing and separating processes: threshing units*. Theory, Modelling, and Design. CRC Press: 189-260.
- [10] Miu P.I., Kutzbach H.D. (2008). Modeling and simulation of grain threshing and separation in threshing units—Part I. *Computers and Electronics in Agriculture*. 60(1): 96–104.
- [11] Ma Z., Han M., Li Y., Yu S., Chandio F.A. (2020). Comparing kernel damage of different threshing components using high-speed cameras. *International Journal of Agricultural and Biological Engineering*. 13(6): 215–219.
- [12] Miodragovic R., Djevic M. (2006). Contemporary combine harvesters in corn harvesting, *Annals of the Faculty of Engineering Hunedoara*. 4(3): 199-206.
- [13] Niu H.H., Zhao W.Y., Shi Z.L. (2011). Progress of research and application in mechanical properties of corn kernel. *Chinese Agricultural Mechanization*. 101–104.
- [14] Petkevichius S., Shpokas L., Kutzbach H.D. (2008). Investigation of the maize ear threshing process. *Biosystems engineering*. 99(4): 532–539.
- [15] Paulsen M.R., Pinto F.A.C., Sena D.G., Zandonadi R.S., Ruffato S., Costa A.G, Ragagnin V.A., Danao M.-G.C. (2014). Measurement of combine losses for corn and soybeans in Brazil. *Applied Engineering in Agriculture*. 30(6): 841-855.
- [16] Poničan J., Angelovič M., Jech J., Žitňák M., Findura P. (2009). The effect of the design concept of combine harvester threshing mechanism on the maize crop threshing quality. *Contemporary Agricultural Engineering*. 35(4): 268-274.

- [17] Pužauskas E, Steponavičius D, Jotautienė E, Petkevičius S. (2017). Substantiation of concave crossbar shape for corn ear threshing. *Mechanika*. 22(6):553-561.
- [18] Petkevičius S, Špokas L, Steponavičius D. (2008). Substantiation of technology parameter of wet maize ear threshing. *Agronomy Research*. 6:271-280.
- [19] Pastukhov A.G., Bakharev D.N., Parnikova T.V. (2021). Differentiated threshing of seed corn with minimal grain crushing. In IOP Conference Series: *Earth and Environmental Science*. 659:012095.
- [20] Pachanawan A., Chuan-Udom S., Doungpueng K. (2021). Development of drums for an axial flow maize shelling unit. *Engineering Journal*. 25(2):59–70.
- [21] Steponavičius D, Kemzūraitė A, Pužauskas E, Domeika R, Grigas A, Karalius D. (2023). Shape Optimization of Concave Crossbars to Increase Threshing Performance of Moist Corn Ears. *Agriculture*. 13(5):983.
- [22] Špokas L, Steponavičius D, Petkevičius S. (2008). Impact of technological parameters of threshing apparatus on grain damage. *Agronomy Research*. 6: 367–376.
- [23] Steponavičius D., Pužauskas E., Špokas L., Jotautienė E., Kemzūraitė A. (2018). Concave design for high-moisture corn ear threshing. *Mechanics*. 24(1):80–91.
- [24] Volkovas V, Petkevičius S, Špokas L. (2006). Establishment of maize grain elasticity on the basis of impact load. *Mechanika*. 62(6):64–67.
- [25] Wacker P. (2005). Maize grain damage during harvest. *Landtechnik*. 60(2): 84-85.
- [26] Xu L.Z., Li Y.M., Wang X.R. (2009). Research development of grain damage during threshing. *Trans. Transactions of the Chinese Society of Agricultural Engineering*. 25:303–307.
- [27] Xiang M.G., Zhang D.L., Li C.N., Bu L.X., Cui M. (2015). Analysis of influence factor on corn threshing performance. *Journal of Agricultural Mechanization Research*. 37: 188–191.
- [28] Yang L, Lü Q, Zhang H. (2022). Experimental study on direct harvesting of corn kernels. *Agriculture*. 12(7): 919.
- [29] Yang L., Cui T., Qu Z., Li K., Yin X., Han D., Yan B., Zhao D., Zhang D. (2016). Development and application of mechanized maize harvesters. *International Journal of Agricultural and Biological Engineering*. 9(3): 15-28.
- [30] Yang L.Q., Wang W.Z., Zhang H.M., Li L.H., Wang M., Hou M.T. (2018). Improved design and bench test based on tangential flow-transverse axial flow threshing system. *Transactions of the Chinese Society of Agricultural Engineering*. 34(1): 35–43.

RESISTANCE WIRE HEATING GROOVE-TYPE TEA DE-ENZYMING AND CARDING MACHINE: DESIGN AND TESTING

电阻丝加热-槽式茶叶杀青理条机的设计与试验

HaiJun BI^{1,2)}, Chen XU^{1,2)}, Kuan QIN^{3,4)}, Lei YU⁵⁾, Chengmao CAO^{3,4)}, Dongsong XIA^{3,4)},
Xinliang GUO^{1,2)}, Yang LIU^{3,4)}, Bin CHEN^{3,4)}

¹⁾ State Key Laboratory of Tea Plant Biology and Utilization, Anhui Agricultural University, Hefei, China

²⁾ School of Tea Science, Anhui Agricultural University, Hefei, China

³⁾ School of Engineering, Anhui Agricultural University, Hefei, China

⁴⁾ Anhui Intelligent Agricultural Machinery Equipment Engineering Laboratory, Hefei, China

⁵⁾ Anji Yuanfeng Tea Machinery Co. Ltd, Huzhou, China

Corresponding author, Tel: +8613965131157; E-mail address: bihaijun@ahau.edu.cn

First author, Tel: +8613965131157; E-mail address: bihaijun@ahau.edu.cn

DOI: <https://doi.org/10.35633/inmateh-74-16>

Keywords: Tea de-enzyming and Carding Machine, Thermal Analysis, Energy Savings, Energy Consumption, Design and Experimentation.

ABSTRACT

The force analysis of the tea leaves on the U-shaped tank of the resistance wire heating groove-type tea de-enzyming and carding machine is conducted, and then the track analysis on SolidWorks based on the force analysis. The coupled steady state thermal analysis is carried out on the heating tank of the two kinds of machinery. The comparative test and content analysis of the three prototypes and gas trough machines are conducted, and the average value of the three tests is considered. The results are presented. The output of the prototype is 3.80 kg h^{-1} , the strip rate is 88.38%, and the surface temperature of the pot groove reaches the requirement of finishing temperature.

摘要

对茶叶在电阻丝加热-槽式杀青理条机的 U 型锅槽的进行受力分析, 然后基于受力分析对茶叶在 Solidworks 上进行轨迹分析。对两种样机机械加热时的锅槽, 分别进行耦合稳态热分析。进行三组样机与燃气式槽式杀青机的对比试验以及内含物分析, 皆取 3 次试验结果的平均值; 结果表明; 样机台时产量为 3.80 kg h^{-1} , 成条率为 88.38%, 锅槽表面温度达到杀青温度要求。

INTRODUCTION

Green tea is the first type and currently the main tea in China, with most Chinese people consuming tea (You et al., 2023). Green tea differs from other tea types in that the first process of its manufacturing is tea chlorosis. In the process of tea chlorosis, the high-temperature passivation of enzyme activities stops the oxidation of polyphenols in fresh leaves, preventing the leaves of green tea from turning red. Tea chlorosis can also evaporate some of the water in the leaves, allowing them to become soft prior to kneading. Along with water evaporation, gas in fresh leaves has a low boiling point and evaporates, thus helping to improve the aroma of tea leaves. Therefore, the process of tea chlorosis plays a key role in the quality of green tea (Wang et al., 2022). Meanwhile, tea chlorosis and straightening play a vital role in tea processing, and knowing whether their effect is ideal is directly related to the appearance and quality of tea (Yang et al., 2022). Tea chlorosis is the application of external high temperature to tea leaves to transfer heat, which not only eliminates the oxidative enzyme activity of tea leaves but also contributes to evaporation by reducing the water content of tea leaves. Consequently, the tea leaves become fluffy, easy to knead and shape and can disperse easily, ensuring a fresh and fragrant green tea aroma (Yan et al., 2022). Straightening is the method of transforming tea leaves into strips after processing, which is conducive to the subsequent process and the formation of the quality of color, aroma, and taste of the tea leaves (Gan et al., 2018).

Japan has been a leading country in the research of green tea processing machinery. Since the 1970s, the development of tea processing machines in Japan has progressed rapidly, particularly for machinery involved in the steaming process of green tea and the management of tea plantations. The main equipment for processing steamed green tea is the steam fixing machine. This machine works on the principle that the condensation of steam generates a significant amount of latent heat, rapidly elevating the temperature of fresh leaves. This process effectively inactivates enzymes such as polyphenol oxidase in the tea leaves. Due to the strong penetrating power of the hot steam, the tea leaf surface temperature increases quickly, thus the fixing process is very fast. The entire steaming of fresh tea leaves can be completed in just a few seconds. After fixing, the leaves retain a good overall appearance and are less likely to develop a burnt taste. Despite the global renown of some of Japan's tea processing machinery, Japan does not produce the unique needle-shaped or flat-shaped teas that are exclusive to our country. In Japan, the focus is primarily on the production of matcha, and hence there has been extensive research conducted on matcha processing machinery, placing Japan at a leading level worldwide.

Domestic and foreign tea de-enzyming and carding machine mainly take the form of roller-type de-enzyming (gas, electricity, and coal), microwave tea de-enzyming and carding machines, electromagnetic tea de-enzyming and carding machines, heat radiation tea de-enzyming and carding machines, hot air tea de-enzyming and carding machines, and steam tea de-enzyming and carding machines (Xu *et al.*, 2014). The advantages of hot air tea de-enzyming and carding machines are its de-enzyming efficiency, quality, and stability, whereas its disadvantages include high energy consumption, easy scorching of leaf edges, appearance of fish-eye bubbles, long operation of cooling time, and low thermal efficiency (Ren *et al.*, 2022). Microwave tea de-enzyming and carding machines do not require preheating and result in a good appearance of green tea leaves, but the tea has a reduced aroma (i.e., no lasting phenomenon). The other disadvantages are high energy consumption, high replacement cost of the generator and other components, and low operating efficiency of the drum (Li *et al.*, 2019), which have led to a gradual decrease in the number of applications of microwave de-enzyming in recent years. Electromagnetic tea de-enzyming and carding machines use high-frequency electric field heating drums, which have the advantages of faster preheating speed, easier operation, and lower energy consumption compared with traditional electric heating drums, but the cost is higher. Heat radiation tea de-enzyming and carding machines applies the infrared "direct" action mode of internal molecules to generate heat, saving more than 30% of the energy produced by the traditional tunnel-type tea de-enzyming and carding machines with a quasistatic process, and the uniformity of the material has high requirements. Hot air tea de-enzyming and carding machines use heat convection to quickly remove the surface moisture of tea leaves, making them suitable for processing the large moisture contents of fresh leaves. As described above, most tea de-enzyming and carding machines are not equipped with heat-recovery devices, so their thermal efficiencies are low; generally, natural gas or electric heating is used, which raises the machine cost (Dai *et al.*, 2023). Steam green tea de-enzyming and carding machines have high-temperature steam penetration characteristics, so the rapid warming of fresh leaves does not easily scorch the leaves. This method also has high production efficiency, but the tea flavor is altered. Furthermore, the traditional processing methods differ greatly, indicating that applications can only be promoted in certain tea processing areas (He *et al.*, 2023). The main equipment for green de-enzyming is shown in Figure 1.

Currently, the tea de-enzyming and carding machine commonly used for tea chlorosis are groove-type tea de-enzyming and carding machine and roller-type tea de-enzyming and carding machine and so on. The gas heating-groove tea chlorosis and barbering machine, which use tea and hot air as raw materials, are composed of multicomponent and multiphase heat systems, but they are limited by the following problems: low thermal efficiency; pot grooves are easily deformed; and pot groove have inaccurate temperature measurements.

Recently, the degree of mechanization of tea processing has gradually increased, with the manual tea de-enzyming and carding mode shifting to the mechanical tea de-enzyming and carding mode to increase market penetration. While mechanical de-enzyming has brought process efficiency and extended market sales, attention should be given to tea quality and energy saving measures. At present, most of the tea de-enzyming and carding machines are not equipped with heat recovery devices, indicating low thermal efficiency; furthermore, using natural gas costs much higher (Jia *et al.*, 2023). In some applications, gas is considered inconvenient to use and requires replacement. Given the problems associated with mechanical tea de-enzyming and carding operations, the heating of groove-type tea de-enzyming and carding machines and the shift to electrical energy for heating must be studied.

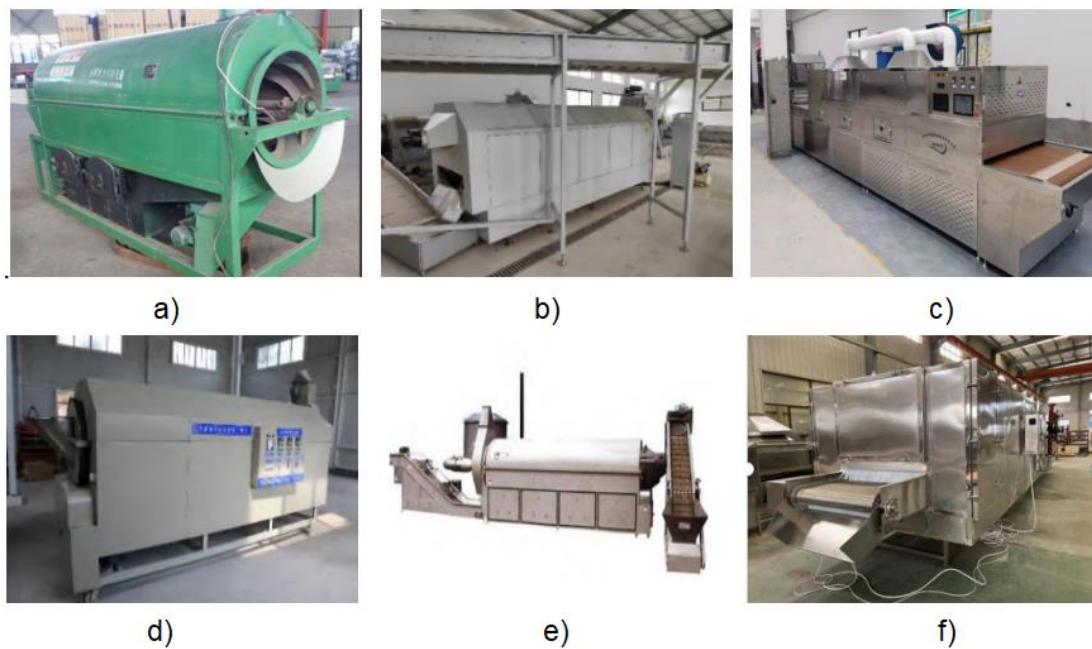


Fig. 1- Domestic and foreign tea de-enzyming and carding machine types

- a) Roller-type tea de-enzyming and carding machine; b) microwave tea de-enzyming and carding machine; c) electromagnetic tea de-enzyming and carding machine; d) heat radiation tea de-enzyming and carding machine; e) hot air tea de-enzyming and carding machine; f) steam tea de-enzyming and carding machine

With white tea production in Anji, Zhejiang Province, China taken as the background, this study comprehensively considered the production, tea chlorosis effect, and energy use with respect to the design of a resistance wire heating groove-type tea de-enzyming and carding machine. By optimizing the heating method of mechanical de-enzyming, in contrast to traditional mechanical tea de-enzyming and carding machines, resistance wire heating groove tea de-enzyming and carding machine can not only meet the greening standard requirements but also solve the problem of high energy consumption of tea finishing. The machine is also simple, easy to start, and practical to operate.

SolidWorks was used to create a simplified model, which was then combined with the simulation and thermodynamic analysis of the resistance wire heating groove-type tea de-enzyming and carding machine on Workbench 2022 R1, thus laying a solid foundation for the tea chlorosis operations of such machines.

MATERIALS AND METHODS

Key components

The depth size, width size, pot groove walls, and horizontal plane between the varying angle sizes of the *U*-shaped groove directly affect the efficiency of the tea *de-enzyming*. The crank slider mechanism in the connecting rod mechanism, which handles the transmission of the key components, is connected to the *U*-shaped groove, thus achieving a *U*-shaped groove reciprocating motion.

During movement, the connecting rod exerts a forward thrust and a downward pressure on the *U*-type multi-slot pot, the servo motor drives the active wheel to rotate, and the active wheel rotation drives the driven wheel, eccentric wheel, and connecting rod to perform a reciprocating linear motion. As the connecting rod undergoes a reciprocating linear motion, it drives the fixed push plate and the strip plate to swing back and forth to achieve a uniform stripping of tea leaves. The resistive wire heating device is installed below the *U*-shaped multi-slot pot. For the thermal efficiency of the resistance wire, the heating time and the stable heat supply to the pot slot are also key factors that directly affect tea chlorosis (Zhang *et al.*, 2022). A resistance wire heating device is installed at the bottom of the *U*-shaped multi-slot pot. For the thermal efficiency of the resistance wire, the heating time and the stable heat supply to the pot trough are also key factors directly affecting tea de-enzyming (Ju *et al.*, 2002).

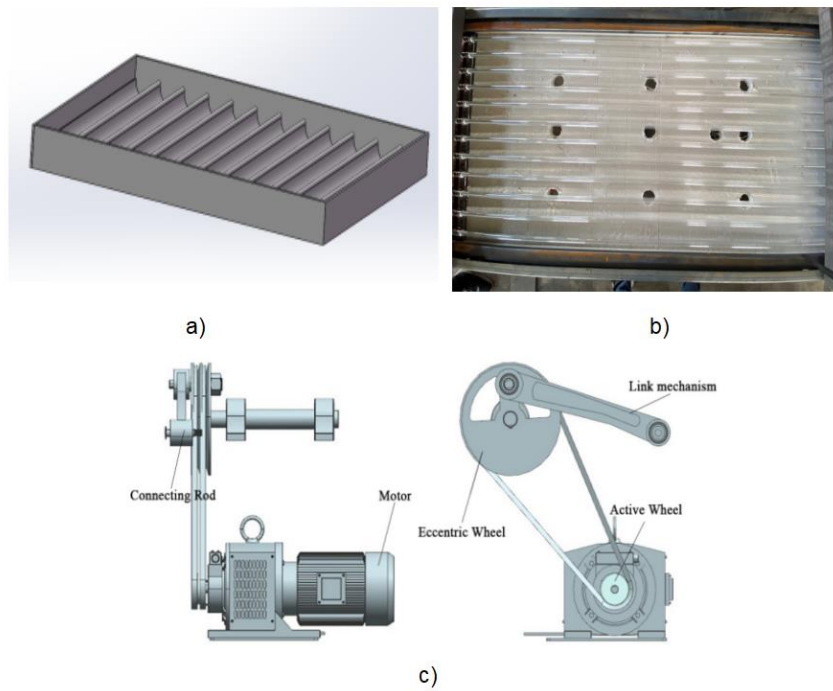


Fig. 2 - Schematic diagram of the structure of key components
 a) U-shaped multi-tank pot structure; b) resistance wire heating device structure; c) crank slider mechanism

Motion analysis and simulation of tea particles in the groove

The movement of tea particles in the potting machine is mainly divided into three stages. First, the tea leaves in the potting machine perform a throwing movement. Second, the tea leaves extrude through the inner wall of the potting machine in a state of throwing movement. Finally, the tea leaves fall back into the potting machine and collide after the throwing movement (Wu et al., 2019).

Acceleration analysis of tea particles before and after performing a lift-and-throw

Let us take a single tea leaf as a mass point while ignoring the effect of collision between tea particles and other elements in the U-shaped groove under the action of the power mechanism. The tea particles are thrown upward along the inner wall of the pot groove and toward the airspace above, subjecting the tea particles to acceleration and gravity.

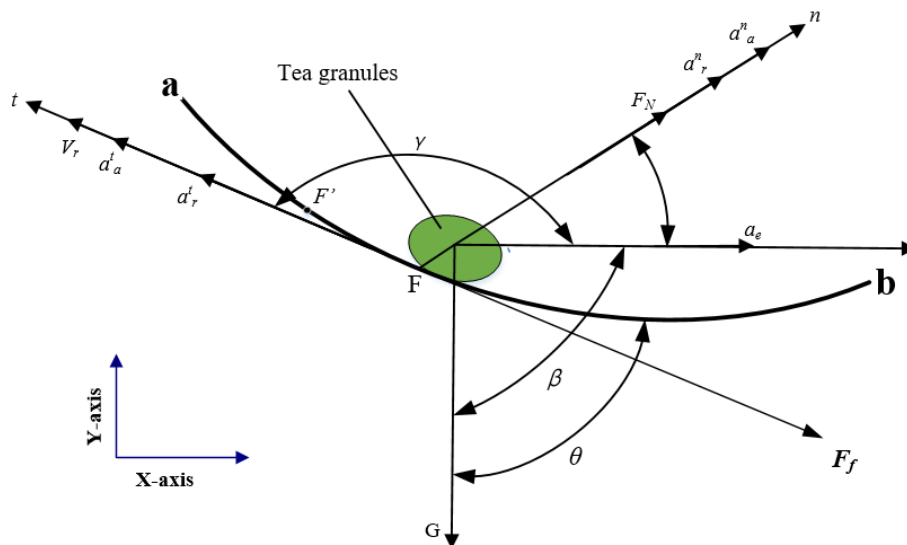


Fig. 3 - Tea-strip force subdiagram

A coordinate system is established with the XY axis. In the diagram, curve ab represents the U -shaped pot groove curve; G is the gravity force of tea particles ($G = mg$, where m is the mass of tea particles); F_N is the support force of the inner wall of the pot; F_f is the friction force between tea leaves and the inner wall of the pot; μ is the friction coefficient of the pot on the tea particles; V_r is the relative velocity of the tea particles along the surface of the pot; n and t are the normal vector of the surface of the pot and the tangential vector of the surface of the pot, respectively (the directions are in the same direction as that of V_r); a_a^n is the absolute acceleration of the tea particles during movement; (a_a) is the normal component of the absolute acceleration of the tea particles along the surface of the pot; $a_a^t - a_a$ represents the tangential component along the surface of the pot; a_r^n is the normal component of the acceleration of the tea leaves relative to the surface of the pot; a_r^t is the tangential component of the acceleration of the tea leaves relative to the surface of the pot; α is the angle between the acceleration of the pot's motion at a_e and the normal vector at n ; β is the angle between the gravitational force at G and the normal vector at n ; γ is the angle between the acceleration of the pot's motion at a_e and the tangential vector at t ; and θ is the angle between the tangential vector at t and the gravitational force at G . The variables can be expressed as:

$$V_{rx}n_x + V_{ry} + n_y = 0 \quad (1)$$

where V_{rx} and V_{ry} are the two components of V_r on the XY -axis, and n_x and n_y are the components of the normal vector n of the U -shaped pot groove curve ab on the XY -axis. On this basis, it is obtained:

$$n_x = \frac{-\frac{|V_{rx}|}{|V_{rx}|} V_{ry}}{\sqrt{V_{rx}^2 + V_{ry}^2}} \quad (V_{rx} \neq 0) \quad (2)$$

$$n_y = \frac{|V_{rx}|}{\sqrt{V_{rx}^2 + V_{ry}^2}} \quad (V_{rx} \neq 0) \quad (3)$$

The angle between two vectors can be obtained from the product of two vector quantities as follows:

$$\cos \alpha = \frac{a_e n_x}{|a_e| \sqrt{n_x^2 + n_y^2}} \quad (4)$$

$$\cos \beta = \frac{-G n_y}{|G| \sqrt{n_x^2 + n_y^2}} \quad (5)$$

$$\cos \gamma = \frac{a_e V_{rx}}{|a_e| \sqrt{V_{rx}^2 + V_{ry}^2}} \quad (6)$$

$$\cos \theta = \frac{-G V_{rx}}{|G| \sqrt{V_{rx}^2 + V_{ry}^2}} \quad (7)$$

The point acceleration summation formula is given by:

$$a_a^n = a_e^n + a_r^n \quad (8)$$

$$a_a^t = a_e^t + a_r^t \quad (9)$$

which further obtains $a_r^n = \frac{V_r \times V_r}{\rho}$, where ρ is the radius of curvature of the U -shaped pot groove. Eqs. (10) represents the situation when the tea particles are thrown upward along the pot groove under the action of the driving force $F_N < 0$. The friction force and relative average speed of the tea particles along the wall of the pot groove are in the opposite direction.

$$a_e^n = a_e \cos \alpha \quad (10)$$

The supporting reaction force on the tea particles on the inner wall of the U -shaped pot groove is given by:

$$F_N = -G \cos \alpha + ma_a^n \quad (11)$$

The friction applied to the tea particles on the inner wall of the U -shaped pot groove is expressed as:

$$\begin{cases} F_f = G \cos \theta - ma_a^t \\ F_f = \mu F_N \end{cases} \quad (12)$$

Eqs. (1) – (10) are combined to obtain the normal component of the absolute acceleration (a_a) of the tea particles along the surface of the pot during motion a_a^n .

Then, Eqs. (11) and (12) are combined to obtain:

$$a_a^t = g(m \cos b + \cos q) - ma_a^n \quad (13)$$

$$a_a^t = a_e \cos g \quad (14)$$

The tangential component of the accelerated motion of the tea leaves relative to the surface of the pot can be derived, i.e., a_a^n , by combining Eqs. (13) and (14) to further obtain a_r^t .

Analysis of the acceleration of the motion of the tea leaves after being thrown away from the inner wall of the pot trough

The summation of acceleration is given by the following known formulas:

$$a_{ay} = a_{rx} + a_{ex} \quad (15)$$

$$a_{ay} = a_{ry} + a_{ey} \quad (16)$$

The tea particles leave the inner wall of the pot trough and are in the air with only gravity acting on the tea. This action can be expressed as follows:

$$a_{ax} = 0 \quad (17)$$

$$a_{ay} = g \quad (19)$$

$$a_{ex} = a_e \quad (19)$$

$$a_{ey} = 0 \quad (20)$$

The components of vector a_a on the XY -axis are given by a_{ax} and a_{ay} , while those of vector a_e on the XY -axis are given by a_{ex} and a_{ey} .

Combining Eqs. (15) – (20) it is obtained:

$$a_{rx} = -a_e \quad (21)$$

$$a_{ry} = g \quad (22)$$

The velocity component of the tea particles in the U -shaped pot groove is taken as a moving coordinate system as follows:

$$\begin{cases} V_{rxF'} = V_{rxF} + a_{rx} \cdot \Delta t \\ V_{ryF'} = V_{ryF} + a_{ry} \cdot \Delta t \end{cases} \quad (23)$$

The tea particles moving in a U -shaped pot groove is taken as a moving coordinate system as follows:

$$\begin{cases} x_{F'} = x_F + V_{rxF'} \cdot \Delta t + a_e \cdot \Delta t^2 \\ y_{F'} = y_F + V_{ryF'} \cdot \Delta t - g \cdot \Delta t^2 \end{cases} \quad (24)$$

where V_{rxF} , V_{ryF} , $V_{rxF'}$, $V_{ryF'}$ is the relative velocity of motion V_r of the tea particles moving along the inner wall of the pot to points F and F' , which denote the velocity component of motion on the X and Y axes, respectively, and x_F , $x_{F'}$, y_F , $y_{F'}$ is the position of the tea particles at points F and B' .

SolidWorks-based simulation analysis of the trajectory of tea particles on the pot groove

The trajectory of tea particles in a pot groove represents a complex system. Tea particles are subject to sliding, rolling, and throwing movements during tumbling. Then, the tea particles fall into the pot groove by gravity and influence the pot groove to undergo sliding and rolling movements. In this study, for the simulation analysis, the problem is simplified, and two assumptions are made.

As the tea particles are light and soft, the normal vector velocity in the inner wall of the pot is almost equal to zero when they are thrown up and back to the pot.

When the tea particles roll along the surface of the pot, the rolling speed of the tea particles is zero.

During calculation, the initial motion of tea particles is located at the lowest part of the U -shaped pot groove. At this time, the initial velocity of the tea particles is zero.

On the basis of Eq. (26), motion simulation analysis is performed on SolidWorks, and the trajectory diagram of the de-enzyming process of tea particles in the U -shaped pot trough (Deng *et al.*, 1995) is derived (Fig. 4).

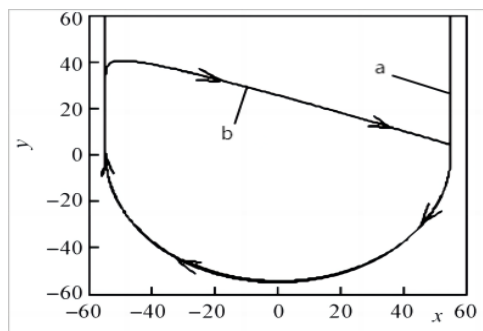


Fig. 4 - Simulation curves of tea leaf trajectory in the U -shaped pot groove

a) Pot trough curve and; b) simulation movement trajectory of tea leaves

From the trajectory diagram, the tea in the U -shaped pot trough undergoes periodic movement, and the change rule is essentially the same. With the heating of the tea chlorosis machine from the bottom of the pot trough, the tea particles in the U -shaped pot trough move in a cycle. Then, as a result of the heating effect, the tea particles at the bottom of the pot trough move with a relatively long trajectory because of rolling, friction, and heating. Thus, the heating of the tea pot trough mainly affects tea chlorosis. When the tea particles move at the bottom of the trough, the temperature at this part initially reaches the temperature of tea chlorosis. The temperature change at the bottom of the trough is small to allow the tea to be further heated and achieve the purpose of greening. The cloud motion trajectory analysis after the force analysis provides theoretical support for the subsequent simulation and experimental design.

Now the trough finishing machine is the gas type electric heating plate mechanical finishing way. In this study, the design of mechanical heating for the de-enzyming method involved replacing the gas type electric heating plate mechanical finishing with resistance wire heating. The other aspects were maintained, that is, the bottom of the U -shaped pot trough heating achieves the purpose of de-enzyming green.

Comparison of thermal analysis of Workbench-based simulation

SolidWorks coupled with ANSYS Fluent steady-state thermal simulation software was used to simulate the heating process of the pot trough of the resistance wire heating groove-type tea de-enzyming and carding machine and the gas heating-groove-type tea de-enzyming and carding machine. In the simulation thermal analysis, the basic parameters for setting the material of the de-enzyming and slitting machine were set according to the setting method proposed in the literature (Qin *et al.*, 2022). The results are shown in Table 1.

Table 1

Basic parameter setting		
Name (of a thing)	Parametric	Value
pot groove	Poisson's ratio	0.3
	Density (kg/m^{-3})	7800
	Shear modulus (Pa)	7×10^7

Simulation modeling of a U-shaped pot hole

This design was implemented in SolidWorks. The overall model of the groove-type tea de-enzying and carding machine and the overall mechanism were both established to perform simplification, particularly by ignoring the frame, motor, and other parts that are not in direct contact with the pot trough (Luo *et al.*, 2022). Then, the simulation models simulated by SolidWorks were saved in *.spt format and imported into Workbench 2022 R1.

Fluid Domain Geometry Model Extraction and Meshing

The pot groove model imported into Workbench 2022 R1 was extracted to determine the fluid domain of the simulation operation geometry model. The extracted fluid domain model was further inputted into Workbench 2022 R1, and the mesh was exported (Fig. 5).

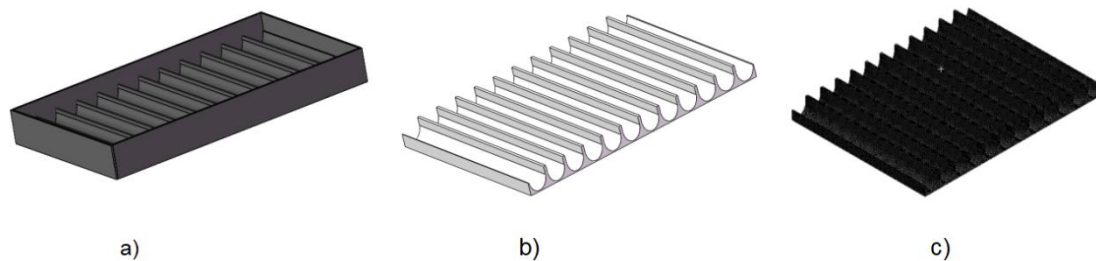


Fig. 5 - Simplified extracted fluid domain and meshing mode

a) Simplified pot model; b) extraction of the fluid domain model; c) meshing of the fluid domain

Thermodynamic simulation analyses of the operation process of the two machines were performed. The U-shaped pot groove can reach 300 °C and an ambient temperature of 22 °C, and other environmental impacts can be ignored. Other specific simulation parameters are shown in Table 2. The solution can be obtained after completing the various parameter settings.

Table 2

Main working parameters of the tea finishing machine	
parametric	Value
Specific heat (K)	1006.43
Thermal conductivity (K)	0.0242
Resistance wire resistivity	2.277×10^{-5}

Coupling simulation process

As shown in Figure 6, after processing the thermal analysis work in ANSYS Fluent, a static structure workgroup in the analysis system of the toolbox of Workbench 2022 R1 was created. The results of the model after the thermal analysis were combined with those of the static structure workgroup. The engineering data settings were selected, and the relevant parameters were confirmed for correctness.

The solutions in the steady-state thermal analysis module were linked with the settings in the static structure workgroup, resulting in the thermal deformation analysis of the pot groove under the heating condition of the resistance wire. After confirming that the parameters were correct, the solution in the steady-state thermal analysis module was associated with the settings in the static structure working group.

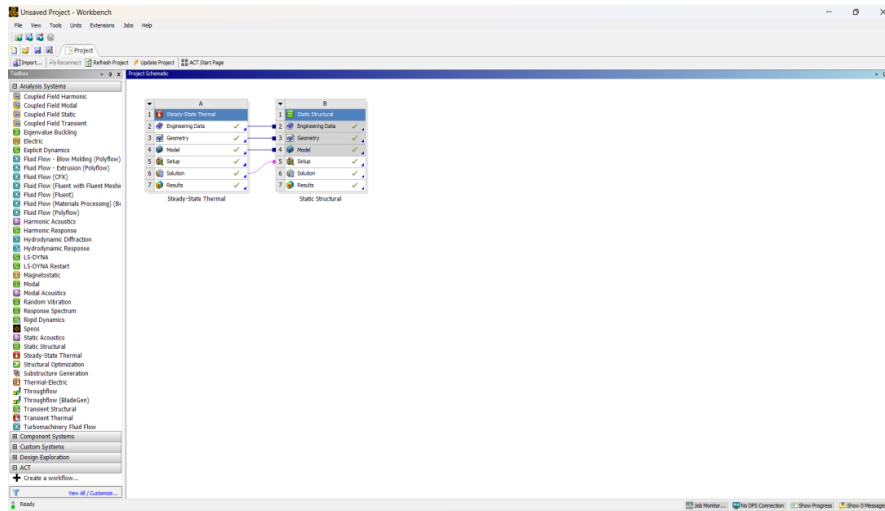


Fig. 6 - Coupled simulation with Workbench 2022 R1 static structure

The performance test

The reasonableness of the heating of the resistance wire heating–groove-type tea de-enzyming and carding machine to meet the quality standards of tea processing was verified by exploring the energy-saving effect and the quality of the tea after de-enzyming. A test was conducted in August 2023 at Yuanfeng Tea Machinery Co. Ltd. (Huzhou City, Zhejiang Province, Anji County, China). The control test was performed with a gas-type electric heating tea de-enzyming and carding machine, and the sample tea used in the test was Anji White Leaf No. 1. The test instruments were a stopwatch, infrared temperature gun, electronic scale, electronic balance, resistance wire-type tea chlorosis machine, and others. The test instruments and prototype machine are shown in Figure 7.



Fig. 7 - Test apparatus and de-enzyming equipment

a) Chronograph; b) electronic scale; c) infrared thermometer; d) electronic balance; e) resistance wire-type and groove-type tea de-enzyming and carding machine

Experimental design

The local white tea leaves in Anji were selected as the test material, and the motor speed was set to 240 r/min for both the resistance wire heating–groove-type tea de-enzyming and carding machine and the gas heating–groove-type tea de-enzyming and carding machine. The motor speed was approximately 180 r/min for both machines during the striping stage, and the time of tea chlorosis and striping was 10 min.

The tea leaves were divided into two portions, and each portion was further divided into three portions and put into two kinds of greening pots and troughs after withering in two batches. After withering, the tea leaves were put into the two kinds of greening pots. Finally, the mean value of the two kinds of de-enzyming results was taken as the experimental result. After the test tea samples were processed by greening by the two different machines, the finished tea was processed according to the same method of processing, and the inclusions were measured and analyzed. The test result was issued by the Science and Technology Building of Anhui Agricultural University.

After processing the finished three tea samples, a total of nine tea samples were taken and sent to the Anhui Agricultural University Science and Technology Building for testing, which issued a test report. The results of the inclusions are shown in Tables 5 and 6. The sensory review is shown in Fig. 5, in which the same kind of mechanically processed tea sample results take the average value.

Table time output: A stopwatch was used to record each de-enzyming time (bar end), and the total mass of tea leaves was weighed after the end of the de-enzyming according to the following formula:

$$P_0 = \frac{M_0}{t} \quad (25)$$

where: P_0 is the output in kg h^{-1} ; M_0 is the total mass of tea leaves after greening (kg); and t is the time needed for each greening (h).

Strip rate: The dried tea samples were collected after greening for picking. The broken tea, tea stems, and yellow leaves, and other excess impurities were selected, and the tea specimens, including their unstripped parts, were weighed and calculated according to the following formula:

$$Y_0 = \frac{Q_0}{T_0} \times 100\% \quad (26)$$

where: Y_0 is the rate of tea leaf formation; Q_0 is the mass of the formed portion after de-enzyming (kg); and T_0 is the sum of the formed and unformed portions of tea leaves (kg).

Surface temperature of the pot groove: Four corners of the pot groove position were checked, and an infrared thermometer was placed 15 cm from the tank surface. The temperature of the surface of the pot groove was measured. Each point was measured two to three times, and the average was taken as the pot groove's effective working temperature.

Energy consumption tests

The energy consumption of the resistance wire heating–groove-type tea de-enzyming and carding machine and the traditional electrically heated drum was also determined. A microwave de-enzyming and carding machine was used for the control experiment. The local white tea from Anji was used as the test material, and the total weight of the tea leaves was 50 kg. The drum de-enzyming and carding machine model was 6CS-100(D), whereas the microwave de-enzyming and carding machine model was CSW-30.

Key component design and analysis

The main parts of resistance wire heating–groove-type tea de-enzyming and carding machine are the *U*-shaped multi-trough pot, crank slider mechanism and resistance wire heating device, connecting rod, and motor (Haijun *et al.*, 2022). During operation, the machine delivers power to the *U*-shaped multi-slot pot through the belt drive and crank slider mechanism and achieves different rotational speeds with the changing frequency of the motor. This approach can meet the demands of tea processing technology. The heating parts of the resistance wire are distributed under the *U*-shaped multi-slot pot, which is driven by the crank slider mechanism to produce a reciprocating linear motion. The withered and adjusted tea leaf specimens are put into the *U*-shaped multi-slot pot of the machine, which is under a reciprocating driving force. Similarly, a reciprocating force drives the resistance wire heating device. With tea leaves processed in the reciprocating driving force, along with the effects of the pot groove walls and the friction between the tea particles and heat, both heating and water are uniformly lost via pot track friction extrusion, and the tea leaves are gradually sorted out for stripping (Sheng *et al.*, 1976).

RESULTS AND DISCUSSION

Static thermal analysis results

Coupled simulation was performed using SolidWorks and ANSYS Fluent. Simulation modeling and joint steady-state thermal analysis were conducted. The lowest temperature of the *U*-shaped pot groove heated by resistance wires is slightly higher than that of the gas-type mechanical heating. And the resistance wire groove heating steady state heat is more stable, conducive to uniform heating tea.

After completing the thermal analysis solution, ANSYS Fluent was used to postprocess it, and diagrams of thermal analysis for the two types of pot grooves (i.e., the resistance wire heating groove-type tea de-enzyming machine and the gas heating-groove-type tea de-enzyming and carding machine) were obtained (Fig. 8). When the maximum temperature is 300°C, the resistance wire heating pot and the gas-fired electric heating pot both generate heat at the bottom and achieve a temperature rise. Both pots reached the required temperature for tea de-enzyming at the bottom of the tank.

The solution in the static structure was selected for implementing the thermal analysis coupled with the static structure. Finally, the thermal deformation analysis of the pot groove heated by the resistance wire was obtained (Fig. 9).

The steady-state thermal and static structure of Workbench 2022 R1 was also used for joint simulation analysis. The thermal deformation of the U-shaped potting tank was analyzed under the heating of the resistance wire, with the temperature set to 300°C. The total deformation, equivalent stress, and equivalent elastic strain were also determined (Fig. 9). The total deformation of the potting tank itself is extremely small in the heating of the resistance wire. Furthermore, the total deformation value is small and can reach the standard requirement of tea de-enzyming machinery.

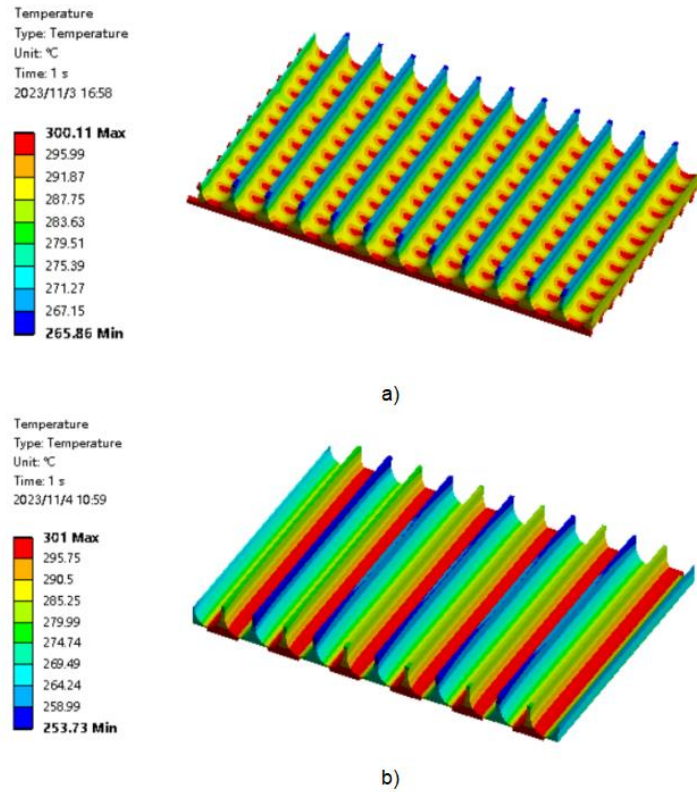


Fig. 8 - Thermal analysis of two mechanically heated pots and tanks
 a) Resistor wire heating; b) Gas heating

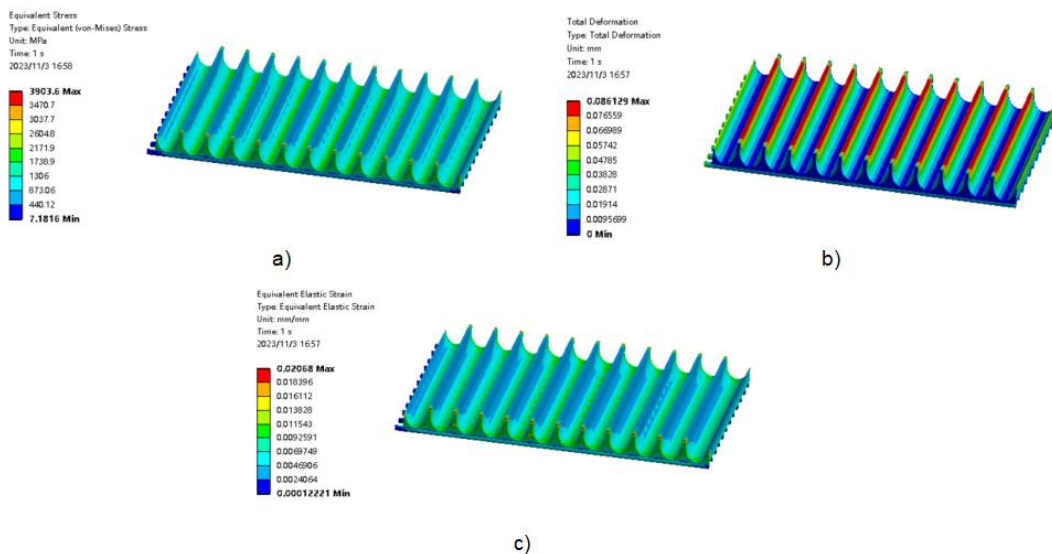


Fig. 9 - Analysis of thermal deformation of the pot groove under the condition of coupled resistance wire heating
 a) Equivalent effective stress; b) total deflection; c) equivalent elastic strain

Mechanical property test results

Tables 3 and 4 show the test data of the pot groove-type of gas-fired tea de-enzyming and carding machine and the resistance wire heating–the pot groove-type of gas-fired tea de-enzyming and carding machine, respectively. The average value of the three tests with output per hour was obtained, and the gas heating–groove tea de-enzyming was 3.88 kg h⁻¹, the rate of strips was 89.0%, and the surface temperature of the pot groove was 180 °C. The output per hour of the resistance wire heating–groove tea de-enzyming was 3.80 kg h⁻¹, the rate of strips was 88.38%, and the surface temperature of the pot groove was 142.6%. The comparative data of the two different mechanical heating methods indicate that the hourly output of the resistance wire heating–trough-type tea de-enzyming and slitting machine and strip rate did not decline, the efficiency of tea chlorosis did not decrease, and the surface temperature of the pot trough achieved the temperature requirements of tea de-enzyming.

Table 3

Test parameters	First test	Second test	Third test	average value
Output per hour (kg h ⁻¹)	3.79	3.98	3.88	3.88
Strip rate (%)	89.65	88.35	89.12	89.0
Potting surface temperature (°C)	184	177	180.5	180

Table 4

Test parameters	First test	Second test	Third test	average value
Output per hour (kg h ⁻¹)	3.68	3.85	3.86	3.80
Strip rate/per cent	87.45	88.7	89.10	88.38
Potting surface temperature (°C)	140	145	142.5	142.6

Table 5 shows the results of the inclusion test after the pot groove-type of gas-fired tea de-enzyming and carding. Table 6 shows the inclusion test results after the resistance wire heating groove-type tea de-enzyming. The inclusion test report indicates that the amino acid and polyphenol content of the tea samples in gas heating and resistance wire heating remains unchanged, but the water contents of the tea processed by the two mechanical heating methods are different. One of the resistance wire heating approach for tea de-enzyming has a water content of 5.9%, and the water content of gas heating after tea de-enzyming is 6.72%. The water content from the resistance wire heating is lower than that of the gas heating, with a reduction of 0.82%.

Table 5

Detection of compounds in tea leaves after the pot groove-type of gas-fired tea de-enzyming and carding machine

serial number	First test GB/8304-2002	Second test GB/T8313-2008	Third test GB/T8314-2002	Average value
Moisture (%)	7.11	6.60	6.46	6.72
Polyphenol (%)	16.6	16.8	16.3	16.57
Amino acid (%)	5	5	4	4.67

Table 6

Detection of compounds in tea leaves after the resistance wire heating groove-type tea de-enzyming machine

serial number	First test GB/8304-2002	Second test GB/T8313-2008	Third test GB/T8314-2002	Average value
Moisture (%)	5.66	5.40	6.65	5.90
Polyphenol (%)	16.5	16.3	16.1	16.30
Amino acid (%)	5	5	5	5

Table 7 presents the energy consumption test results. Mechanical energy test data for tea dehydration were carried out at the initial stage Under the condition of the same amount of tea. For the CSW-30 microwave tea de-enzyming and carding machine, the energy consumption was 45.4 kW, the preheating was 4.5 min, and the de-enzyming time was 94 min.

For the 6CS-100(D) drum tea de-enzyming and carding machine, the energy consumption was 196.1 kW, the preheating was 30 min, and the de-enzyming time was 70 min. The energy consumption of the resistance wire heating groove-type tea de-enzyming and carding machine was 34.6 kW, with a preheating time of 3 min and a de-enzyming time of 130 min. Compared with the 6CS-100(D) drum tea de-enzyming and carding machine, the energy consumption of the resistance wire heating groove-type tea de-enzyming and carding machine is saved by 10.8kW, and Compared with the energy consumption of the CSW-30 microwave tea de-enzyming and carding machine, the energy consumption of the resistance wire heating groove-type tea de-enzyming and carding machine is saved by 161.5kW. The energy consumption of the resistance wire heating groove-type tea de-enzyming and carding machine was lower than that of the 6CS-100(D) drum tea de-enzyming and carding machine and CSW-30 microwave tea de-enzyming and carding machine, it is proved that the resistance wire heating groove-type tea de-enzyming and carding machine has more energy-saving advantages. The energy consumption of the resistance wire heating groove-type tea de-enzyming and carding machine was 23.80% and 82.30% less than those of the 6CS-100(D) drum tea de-enzyming and carding machine and the CSW-30 microwave tea de-enzyming and carding machine, respectively.

Table 7

Energy consumption test record sheet

Processing	tea plant variety	Power (kW)	de-enzyming weight (kg)	Preheating / de-enzyming time (min)	Energy consumption (kg h ⁻¹)
Microwave	Anji white tea	30	50	4.5/94	45.4
Resistor Wire-type		16	50	3/130	34.6
Roller		130	50	30/70	196.1

Review results

After the test prototype processing of the resulting dry tea samples, under the appraisal of tea sensory evaluation experts, all the evaluation indexes could meet the requirements. The sensory review results of the three tests are shown in Table 8 and Figure 10.

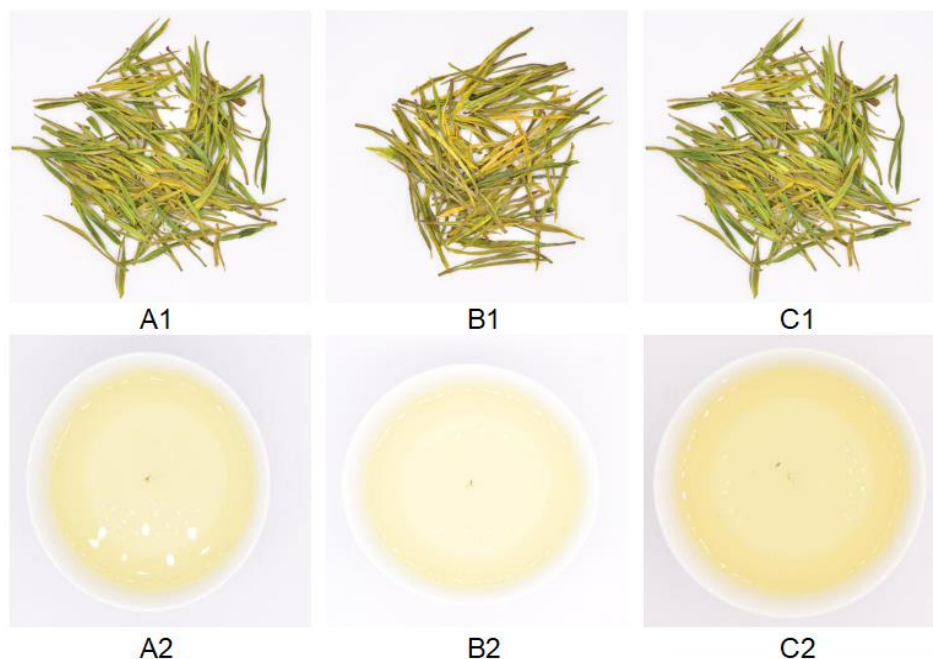


Fig. 10 - Results of tea review

A1) Experimental Sample Tea 1; A2) Soup color one; B1) Experimental Sample Tea 2; B2) Soup color two; C1) Experimental Sample Tea 3; C2) Soup color three

Table 8

Results of tea sensory evaluation

test group	color	a bar	color of soup	assessment result
1	fresh and moist (air)	lit. flat and vertical	yellowish	eligible (voter etc.)
2	emerald green	slightly curved	yellowish	eligible (voter etc.)
3	dark green	lit. flat and vertical	yellowish	eligible (voter etc.)

CONCLUSIONS

(1) The mechanical analysis of the force process of the tea specimens was processed by SolidWorks. In particular, a three-dimensional model of the resistance wire heating–groove-type tea de-enzyming and carding machine was built, and the *U*-shaped pot trough was simplified and analyzed. SolidWorks simulation was used to analyze the tea particles in the tea de-enzyming machinery via a movement trajectory process to obtain the trajectory of the tea. Coupled simulation was performed using SolidWorks and ANSYS Fluent. Simulation modeling and joint steady-state thermal analysis and thermal deformation analysis were conducted. The lowest temperature of the *U*-shaped pot groove heated by resistance wires is slightly higher than that of the gas-type mechanical heating.

(2) Under the same conditions, comparative results showed that the tea leaves heated by resistance wire tea de-enzyming had a lower water content than those heated by the gas heating–groove tea de-enzyming and carding machine.

(3) An energy consumption test was conducted on the resistance wire heating–trough-type tea de-enzyming and carding machine and the general tea de-enzyming and carding machine, followed by a comparative analysis. The energy consumption of the resistance wire–groove-type tea de-enzyming and carding machine was 82.36% and 23.80% less than those of the 6CS-100(D) drum greening machine and CSW-30 microwave tea de-enzyming and carding machine, respectively.

ACKNOWLEDGEMENT

This work was supported by the National Natural Science Foundation of China (52205509), Key Natural Science Research Project of Anhui Province Universities (2024AH050444), Anhui Provincial Natural Science Foundation Youth Fund Program (2208085QE155), Open Fund Program of State Key Laboratory of Tea Plant Biology and Utilization (SKLTOF20220118), and the Yuanfeng Tea Processing Technology Research and Quality Service Enhancement Enterprise Commissioning Project (KJ2022436).

REFERENCES

- [1] Bi, Haijun, Jia, Pengcheng, Kuan, Qin, Lei, Yu, Cao, Chengmao, Bai, Yuxuan. (2022). Optimization Design of Pot Slot Structure of Tea De-Enzyming and Carding Machine. *Agronomy-Basel*. 12, 2937.
- [2] Dai, Yunzhong., Chen, Xueqin., Zhao, Chunyan. (2023). Design of a new type of steam finishing device for tea processing. *Southern Agricultural Machinery*. 54 (08): 10-12.
- [3] Deng, Dexiang. (1995). Improvement of structured control flow chart (NS diagram) and modular programming diagram. *Computer Research and Development*. 32 (12): 21-26.
- [4] Jian, H., Qing, A., Ying, W., Jia, Y., Xiao, D. (2023). Research on the electromagnetic heating model of a small finishing machine based on COMSOL. *Electromechanical Engineering Technology*. 52 (08): 43-48.
- [5] Jia, Pengcheng. (2023). The influence of the structure of the pot trough on the quality of Anji white tea. *Anhui Agricultural University*.
- [6] Ju, Zhou, Zhengke, Hu, Xiang. (2002). The influence of vibration organization on the quality of needle-shaped famous tea. *Chinese Tea*. 24 (1): 32-33.
- [7] Li, Jie, Chen, Weizhu, Song, Pengxing. (2019). Electric heating tea finishing machine. *Chinese Patent*: CN209882955U, 01-08.
- [8] Luo, K., Wu, Z., Cao, C., Qin, K., Zhang, X., An, M. (2022). Biomechanical Characterization of Bionic Mechanical Harvesting of Tea Buds. *Agriculture*. 12(9): 1361.
- [9] Ning, G., Chang, S., Zheng, Z. (2018). Research progress of tea processing machinery in China. *Tea Processing in China*. (2): 31-37.
- [10] Qin, K., Zhao, Y., Zhang, Y., Cao, C., and Shen, Z. (2022). Lateral stress and its transmission law caused by operation of a double-wing subsoiler in sandy loam soil. *Frontiers in Environmental Science*. 2022: 1873.
- [11] Ren, Caihong., Li, Jie., Song, Zhiyu., Yang, Guang, Mei, Song., Jiang, Qinghai. (2022). Design and test of energy-saving far-infrared thermal radiation finishing machine. *Agricultural Development and Equipment*. (10): 33-37.
- [12] Sheng, Chang, (1976) 60 slot type finishing machine. *Tea Science and Technology Bulletin*. (08): 19.
- [13] Wu, Z., Cao, C., Wang, E., Luo, K., Zhang, J., and Sun, Y. (2019). A method for tea selection based on morphological feature parameters. *Transactions of the Chinese Society for Agricultural Machinery*. 35 (11): 315-321.

- [14] Wang, X., Wu, Z., Zhong, H., Huang, Y., Zhang, X., and Shi Z. (2022). Evaluation of the tea carding operation based on machine vision technology. *China Tea Processing*. (03): 40-45.
- [15] Xu, H., Tan, H., Li, G., Xie, Chi., Li, J. (2014). Study on the spiral motion model of leaf guide plate of roller type tea killing machine. *Journal of Tea Science*. 34 (4): 381-386.
- [16] You, Q., Shi, Y., Zhu, Y., Yang, G., Yan, H., Lin, Z., Lv, H. (2023). The influence of different processing techniques on the key aromatic ingredients of green tea. *Food Science*: 1-14 [2023-01-09].
- [17] Yang, Tianming, Ma, Yuqing, Liang, Mingzhi. (2022). The influence of different finishing methods on the content of fluorine and the main flavor substances in tea leaves. *Processing of agricultural products*. (22): 19-22.
- [18] Yan, Jianwei, Hu, Dongjun, Liu, Qihe (2022). Progress in tea organization technology and machinery. *China Agricultural Machinery Chemical News*. 43 (02): 75-83.
- [19] Zhang, Y., Tian, L., Cao, C., Zhu, C., Qin, K., and Ge, J. (2022). Optimization and validation of blade parameters for inter-row weeding wheel in paddy fields. *Frontiers in Plant Science*.

COUPLING UNMANNED AERIAL VEHICLE (UAV) MULTISPECTRAL IMAGERY AND INTEGRATED LEARNING TO CONSTRUCT A MONITORING AND PREDICTION MODEL FOR RELATIVE CHLOROPHYLL CONTENT (RCC) AND LEAF AREA INDEX (LAI) OF SORGHUM IN FIELDS

基于无人多光谱图像和集成学习的田间高粱叶绿素相对含量与叶面积指数的监测预测模型

Qi LIU, Huping LIU, Mengjiao XU, Lian BAI, Wuping ZHANG¹⁾, Guofang WANG²⁾

¹⁾ College of Software, Shanxi Agricultural University, Taigu, Shanxi / China

²⁾ College of Resources and Environment, Shanxi Agricultural University, Taigu, Shanxi / China

Corresponding authors: Zhang Wuping; Tel: +86-15935664481; E-mail: zwping@126.com

Guofang Wang, Tel: +86-15835470561; E-mail: guofang19800104@126.com

DOI: <https://doi.org/10.35633/inmateh-74-17>

Keywords: Sorghum, RCC, LAI, UAV, stack, spatial resolutions

ABSTRACT

This study mainly investigates the feasibility of monitoring and estimating the RCC (Relative Chlorophyll Content) and the LAI (Leaf Area Index) of sorghum by coupling integrated learning model with UAV multispectral image, clarifies the quantitative relationship between RCC and LAI of sorghum and the vegetation index based on different spatial resolutions, and constructs a Monitoring and prediction model for the RCC and the LAI of sorghum based on the UAV multispectral image and the vegetation index at different spatial resolutions. The model constructed based on integrated learning, and using the stacking approach had good prediction accuracies at three spatial resolutions, with the stacking model predicting $R^2=0.87$, $MAE=18.27$, and $RMSE=22.23$ for the RCC at spatial resolution of 0.017 m; $R^2=0.86$, $MAE=17.38$, and $RMSE=23.21$ for RCC at spatial resolution of 0.024 m; $R^2=0.80$, $MAE=18.62$, and $RMSE=24.12$ for RCC at spatial resolution of 0.030 m; $R^2=0.93$, $MAE=0.34$, and $RMSE=0.37$ for LAI at spatial resolution of 0.017 m; and $R^2=0.89$, $MAE=0.44$, and $RMSE=0.55$ for LAI at spatial resolution of 0.024 m. The model established by combining the vegetation index and integrated learning can quickly and accurately monitor and predict RCC and LAI of sorghum, which provides a scientific methodology and theoretical basis for scientific monitoring and predicting RCC and LAI of sorghum in the field.

摘要

本研究主要探讨了将集成学习模型与无人机多光谱影像耦合, 监测和估算高粱叶绿素相对含量和叶面积指数的可行性, 明确了基于不同空间分辨率的高粱叶绿素相对含量和叶面积指数与植被指数之间的定量关系, 构建了基于无人机多光谱影像和植被指数的不同空间分辨率高粱叶绿素相对含量和叶面积指数的预测模型。基于集成学习和堆叠方法构建的预测模型在三种空间分辨率下均具有良好的预测精度, 其中堆叠模型在空间分辨率为 0.017m 时预测叶绿素相对含量的 $R^2=0.87$, $MAE=18.27$, $RMSE=22.23$; 在空间分辨率为 0.024m 时预测叶绿素相对含量的 $R^2=0.86$, $MAE=17.38$, $RMSE=23.21$; 空间分辨率为 0.030 m 时叶绿素相对含量的 $R^2=0.80$, $MAE=18.62$, $RMSE=24.12$; 空间分辨率为 0.017m 时叶面积指数的 $R^2=0.93$, $MAE=0.34$, $RMSE=0.37$; 空间分辨率为 0.024m 时叶面积指数的 $R^2=0.89$, $MAE=0.44$, $RMSE=0.55$ 。植被指数与集成学习相结合而建立的模型能够快速且准确地监测和预测高粱的叶绿素相对含量和叶面积指数, 为科学监测、预测田间高粱的叶绿素相对含量和叶面积指数提供了科学的方法和理论依据。

INTRODUCTION

Sorghum [*Sorghum bicolor* (L.) Moench] is the fifth largest cereal crop in the world. It has a long history of cultivation in China, with high and stable yields and other characteristics, and has a unique drought-resistant, waterlogging-resistant, saline-resistant, barren, and other resistance to adversity, in the plains, hills, floodplains, saline and alkaline land. It can be planted with a variety of uses, such as food, brewing, feeding, energy, silage, etc., and the potential development of sorghum is huge.

The chlorophyll content is an important parameter to consider in crop growth. It has a direct relationship with the final yield, which can effectively reflect the growth status and nutritional status of crops (Pan et al., 2023). Therefore, rapid and accurate monitoring of the chlorophyll content of crops can provide a timely understanding of the crop growth status and can be used to make a scientific prediction of the final yield of

crops (Berjon *et al.*, 2022). LAI is an important physiological parameter reflecting the monitoring of crop phenotype (Liu *et al.*, 2012). The vegetation index obtained by remote sensing technology for the calculation of the band has a strong correlation with the LAI; the use of remote sensing technology can be used in small and medium-sized areas of the crop LAI prediction, to provide a strong support for agricultural management (Hunt *et al.*, 2008). The application of drones in crop monitoring is a hot spot in the current field of agricultural science and technology. With the rapid development of UAV technology, its application in precision agriculture is more and more extensive, especially in crop growth monitoring and management. UAV multispectral technology has a large number of applications in crop monitoring by applying the advantages of flexibility, simple operation, and ease of use (Tavakoli *et al.*, 2014).

Guo *et al.* found that the prediction effect of the prediction model established based on the support vector machine-based prediction model has the best prediction effect and also helps to retrieve SPAD values based on spectral and texture indices extracted from multispectral images using machine learning methods (Guo *et al.*, 2022). Sudu B *et al.* inverted summer maize SPAD values using UAV hyperspectral data based on multiple machine learning algorithms, and the results showed that UAV hyperspectral image data can be used to predict maize growth information and that machine learning-based prediction models can quickly and non-destructively predict maize SPAD values (Sudu *et al.*, 2022). Zhang *et al.* used an unmanned collection of hyperspectral images of winter wheat and multiple machine-learning models based on different algorithms to train an LAI inversion model (Zhang *et al.*, 2021). That shows UAV monitoring technology can accurately measure chlorophyll content and leaf area of field crops on a large scale and with high throughput, so effective monitoring of field sorghum can be realized by the means mentioned above.

However, most of the studies on growth monitoring and yield prediction of crops use vegetation indices, texture, and spectral information, but due to the differences in plant species, varieties, fertility periods, and research methods, the forms and parameters of the constructed models are different, which results in the conclusions obtained from a single experiment being often not universal (Tunca *et al.*, 2018). The research on monitoring and prediction of sorghum-based on RGB images of drones has also been rarely reported, and fewer studies have been carried out on the optimal spatial resolution for monitoring. Few studies have been reported on the monitoring and predicting sorghum based on RGB images from UAVs, and fewer studies have been conducted on the optimal spatial resolution for monitoring. Because of this, this study, based on previous studies, with the advantage of UAV in variable spatial resolution, attempts to obtain multispectral images by UAV and combine them with vegetation indices under different spatial resolutions by using machine learning to build a model and combine them with the experimental data related to RCC and LAI of sorghum obtained during the same period to realize the prediction of important indices of sorghum growth at the field scale. By comparing the differences in generalization ability and prediction accuracy among models, the best prediction model is identified to provide new theoretical support and technical means for data collection, production management, and yield estimation in sorghum growth monitoring.

MATERIALS AND METHODS

Test Material and Test Site

The test sorghum variety is JINZA No.22. The test site is located in Wujiabao Village, Taigu County, Jinzhong City, Shanxi Province, China. The region (elevation 800 m, longitude 112° 30' 51" E, latitude 37° 26' 41" N) has a temperate continental monsoon climate, with high temperature and rain in summer, cold and dry in winter, and four distinct seasons, with an altitude of about 795~805 m above sea level and an average annual frost-free period of 160-190 days. The average annual temperature is 10.6°C, the annual precipitation is 400 mm-600 mm, the main precipitation is concentrated in July-August, and the average annual sunshine is 1810 hours-2100 hours, which is suitable for the growth of sorghum, one season a year. The experiment was sown by manual spot sowing, with sowing row spacing of 0.3 m and plant spacing of 0.2 m. The sowing time was April 25, 2021, and the harvest was made on October 13, 2021, and the test was carried out by selecting the stage of pulling out, tasseling, and ripening of sorghum, and the conventional field management such as watering, fertilizer, and spraying of herbicides were carried out at appropriate time according to the experience, to prevent the interference of its cause.

Data Acquisition and Processing

In this study, a multispectral camera modeled as MicaSense RedEdge-MX is used, which has five spectral bands, namely, blue, green, red, red-edge, and near-infrared. The device is mounted on the 4-axis UAV platform of the DJI Phantom 4 Pro to collect multispectral images. The system includes a flight control system,

power supply system, stabilizing gimbal, remote control, display, etc. The image data are collected when the light intensity is moderate and the radiation is stable to ensure the accuracy of the collected image data. The multispectral sensors are calibrated before the start of the flight to ensure the accuracy of the multispectral image calibration. The RCC of the tested sorghums was determined using a hand-held portable chlorophyll meter (Instrument model: CM 1000, which has a range of values from 0-999) for chlorophyll determination. Four target sorghum plants were selected, and the RCC values of the top two fully expanded leaves were measured: a total of three parts of the leaf such as the leaf base, leaf middle, and leaf tip were measured, and a leaf was measured at least three times. Finally, all the measurements on the same leaf were averaged and taken as the RCC of the plant. The LAI of the tested sorghums was determined using a handheld portable leaf area meter (instrument model: LAI-2200C) using the modified LAI method.

The measurement of the relevant data was carried out simultaneously with the acquisition of multispectral photos by UAV to ensure the consistency of the collected data. Meanwhile, the UAV data measurements were carried out in a windless and cloudless period with suitable light to ensure the accuracy of the collected data. The valid data obtained during the experiment were divided into a training set and a validation set, in which the training set accounted for 70% and the validation set accounted for 30%. The processing and analysis of the data was done based on Python 3.6. The processing of the multispectral images acquired by the UAV was done through Agisoft PhotoScan and ArcGIS.

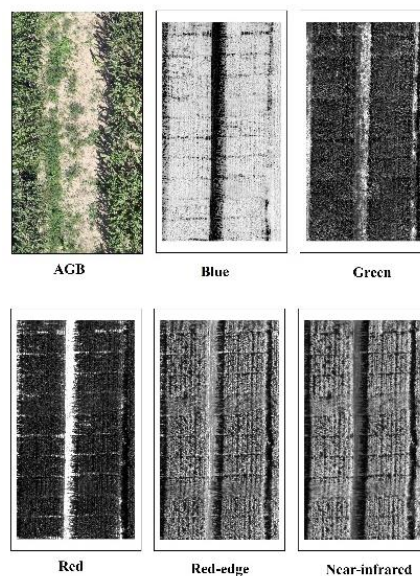


Fig. 1 - Multispectral images of unmanned aerial vehicles in different frequency bands of sorghum

Vegetation Indices Selection and Model Evaluation

Healthy green vegetation in the blue and red light band shows absorption, while in the green light and near-infrared band has a strong reflection. Hence, the vegetation index is the use of green vegetation in different bands of different characteristics, through the sensor obtained by the combination of different bands of information, to achieve the purpose of enhancing the vegetation information. It is essentially a comprehensive consideration of a variety of spectral information, and its certain mathematical transformations so that it enhances the vegetation information at the same time and minimizes the non-vegetation and other noise. There are hundreds of vegetation indices proposed in related research fields, and in this study, 11 vegetation indices that showed a high correlation with the RCC and LAI of the test species were selected.

Regarding the evaluation of the model prediction results, the coefficient of determination R^2 , Mean Absolute Error (MAE), and Root Mean Square Error (RMSE) are used in this study.

RESULTS

Analysis of Variations in RCC and LAI at Different Flight Altitudes

In this section, data on variations in RCC and LAI obtained through multispectral imaging technology using UAVs at different flight altitudes are presented. Measuring RCC and LAI provides essential insights into the growth status and health of plants. Changes in these indicators can help farmers promptly identify issues such as nutrient deficiencies, pest infestations, or diseases, enabling them to take appropriate measures to protect plant health and promote high-quality crop yields.

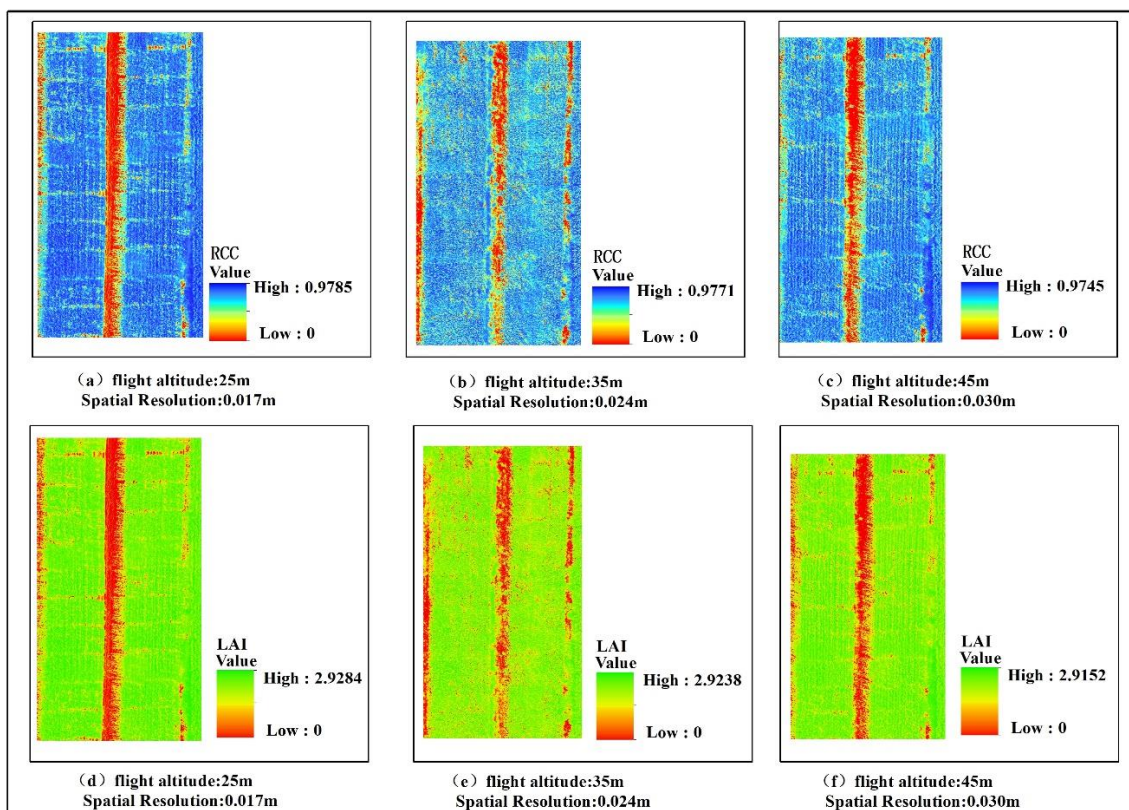


Fig. 2 - RCC and LAI spectra at different spatial resolutions

When the UAV flight altitude is 25 meters, the corresponding spatial resolution is 0.017 meters. At this spatial resolution, it was observed that the measured RCC and LAI values were 0.9785 and 2.9284, respectively, indicating that the health status of the plants is optimal at this height. As the flight altitude increases to 35 meters and 45 meters, the RCC and LAI values gradually decline, reaching 0.9771 and 2.9238 (at 35 meters), and 0.9745 and 2.9152 (at 45 meters), respectively. This trend suggests that higher flight altitudes may reduce the ability to capture vegetation characteristics, thereby affecting the accuracy of the monitoring data.

As shown in the figure 2, the variations in RCC and LAI measured at different flight altitudes are illustrated. The figure clearly indicates that RCC and LAI values are highest at a flight altitude of 25 meters, while both indicators show a declining trend as the flight altitude increases.

The reason for this variation may be attributed to increased light scattering and reflection at higher flight altitudes, which can affect the ability to capture vegetation characteristics. Additionally, higher altitudes may reduce the resolution of the sensors, making it more challenging to monitor subtle changes. Therefore, selecting an appropriate flight altitude and spatial resolution is crucial for optimizing vegetation monitoring effectiveness.

Construction and Evaluation of a Prediction Model for RCC

Measuring the RCC gives an idea of the growth status, nutritional status, and health of the plant. This is important for the timely detection of problems such as plant diseases, pests, or nutritional deficiencies, and by regularly monitoring chlorophyll content, farmers can take appropriate measures to protect plant health and improve crop yield and quality (Zhao *et al.*, 2023). Through the use of tools such as remote sensing technology or portable chlorophyll meters, chlorophyll content can be monitored in real-time over large areas of farmland, allowing early detection of poor plant growth or disease problems. At the same time, based on trends in chlorophyll content, crop yields can be predicted and measures can be taken to improve yields and stabilize agricultural production.

The corresponding spatial resolution at this flight altitude is 0.017 m with the flying altitude of 35 m. At this spatial resolution, the optimal parameter combinations are obtained for each model as shown in Table 1.

Table 1

The parameter information of independent machine learning models at spatial resolution of 0.017 m of RCC

Model	Para1	Value1	Para2	Value2	Para3	Value3
Ridge	Alpha	100				
Lasso	Alpha	10	Max_iter	20		
SVM	C	0.1	Kernel	Linear		
MLP	Activation	Tanh	Hidden_layer_sizes	(25, 25, 25, 25)	solver	lbfgs
KNN	Algorithm	Kd_tree	Leaf_size	1	n_neighbors	9
RF	Min_samples_leaf	8	Min_samples_split	0.1	n_estimators	46
GBDT	learning_rate	0.01	Loss	ls	n_estimators	51

The above 7 basic models are used as the base model and the linear regression algorithm is used as the stacking meta-model. After synthesizing the above independent machine learning models and using the same input data to get the prediction results obtained by the stacking model, a 1:1 comparison graph is constructed after normalizing the stacking model prediction results with a total of 8 sets of prediction results and actual values such as the prediction results of the aforementioned independent models, and the specific results are shown in Figure 3.

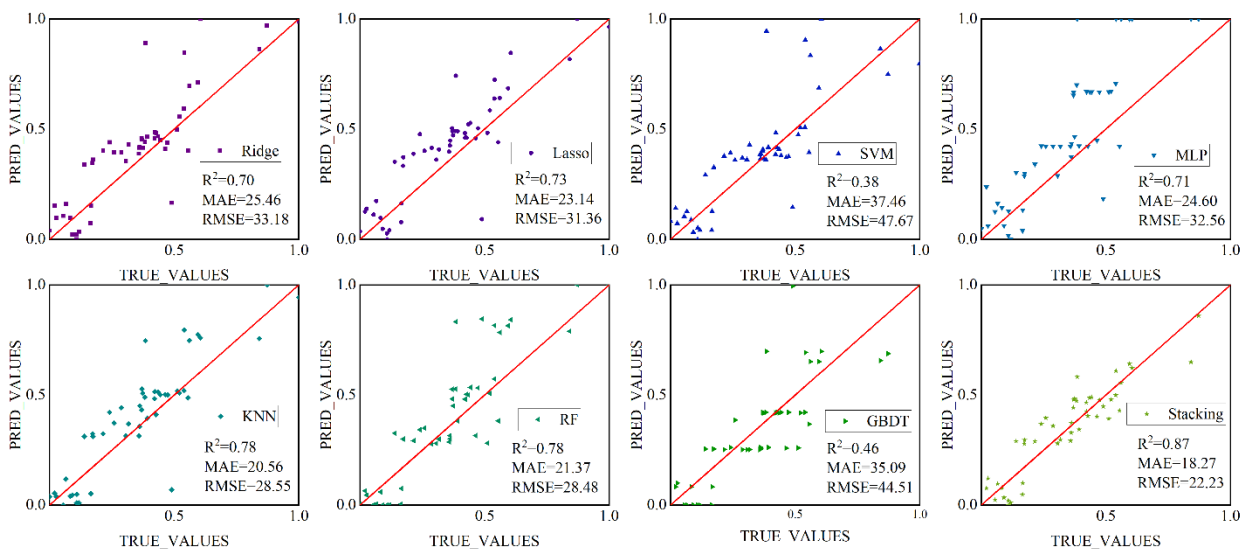


Fig. 3 - The plot of predicted versus measured values for eight models at spatial resolution of 0.017 m of RCC

At this spatial resolution, KNN and RF have the best prediction results among the seven independent machine learning models, with R²=0.78, MAE=20.56, and RMSE=28.55 for KNN, and R²=0.78, MAE=21.37, and RMSE=28.48 for RF. In contrast, the stacking model has R²=0.87, MAE=18.27, and RMSE=22.23, and its three evaluation indices are better than the KNN and RF models. Hence, the prediction results of the stacking model are better than the seven independent models.

The corresponding spatial resolution at this flight altitude is 0.024 m with the flying altitude of 35 m. At this spatial resolution, the optimal parameter combinations are obtained for each model as shown in Table 2.

Table 2

The parameter information of independent machine learning models at spatial resolution of 0.024 m of RCC

Model	Para1	Value1	Para2	Value2	Para3	Value3
Ridge	Alpha	0.1				
Lasso	Alpha	0.001	Max_iter	210		
SVM	C	100	Kernel	Rbf		
MLP	Activation	Logistic	Hidden_layer_sizes	(50, 50)	solver	lbfgs
KNN	Algorithm	Kd_tree	Leaf_size	1	n_neighbors	4
RF	Min_samples_leaf	89	Min_samples_split	0.1	n_estimators	6

Model	Para1	Value1	Para2	Value2	Para3	Value3
Ridge	Alpha	0.1				
GBDT	learning_rate	0.1	Loss	lad	n_estimators	51

The above 7 basic models are used as the base model and the linear regression algorithm is used as the stacking meta-model. After synthesizing the above independent machine learning models and using the same input data to get the prediction results obtained by the stacking model, a 1:1 comparison graph is constructed after normalizing the stacking model prediction results with a total of 8 sets of prediction results and actual values such as the prediction results of the aforementioned independent models, and the specific results are shown in Figure 4.

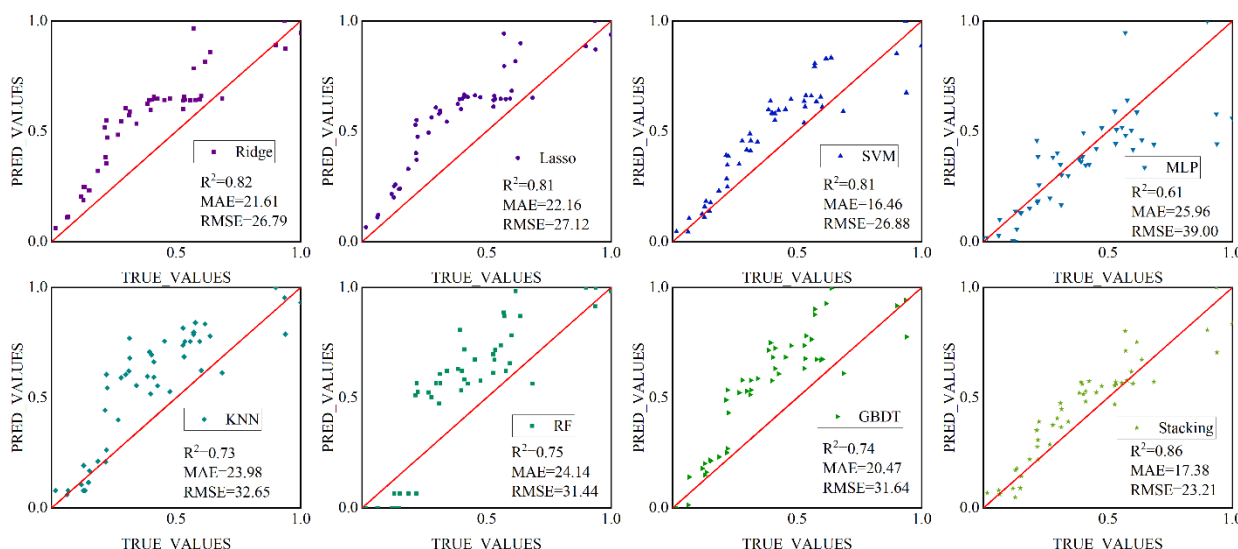


Fig. 4 - The plot of predicted versus measured values for eight models at spatial resolution of 0.024 m of RCC

At this spatial resolution, Ridge has the best prediction results among the seven independent machine learning models, with R²=0.82, MAE=21.61, and RMSE=26.79; the stacking model has R²=0.86, MAE=17.38, and RMSE=23.21, and all the evaluation metrics are better than Ridge model, so the stacking model's prediction results are better than seven independent models.

The corresponding spatial resolution at this flight altitude is 0.030 m with the flying altitude of 45 m. At this spatial resolution, the optimal parameter combinations is obtained for each model as shown in Table 3.

Table 3

The parameter information of independent machine learning models at spatial resolution of 0.030 m of RCC

Model	Para1	Value1	Para2	Value2	Para3	Value3
Ridge	Alpha	50				
Lasso	Alpha	10	Max_iter	10		
SVM	C	1	Kernel	Linear		
MLP	Activation	Tanh	Hidden_layer_sizes	(30, 30, 30)	solver	lbfgs
KNN	Algorithm	Kd_tree	Leaf_size	1	n_neighbors	9
RF	Min_samples_leaf	1	Min_samples_split	0.1	n_estimators	96
GBDT	learning_rate	0.1	Loss	lad	n_estimators	31

The above 7 basic models are used as the base model and the linear regression algorithm is used as the stacking meta-model. After synthesizing the above independent machine learning models and using the same input data to get the prediction results obtained by the stacking model, a 1:1 comparison graph is constructed after normalizing the stacking model prediction results with a total of 8 sets of prediction results and actual values such as the prediction results of the aforementioned independent models, and the results are shown in Figure 5.

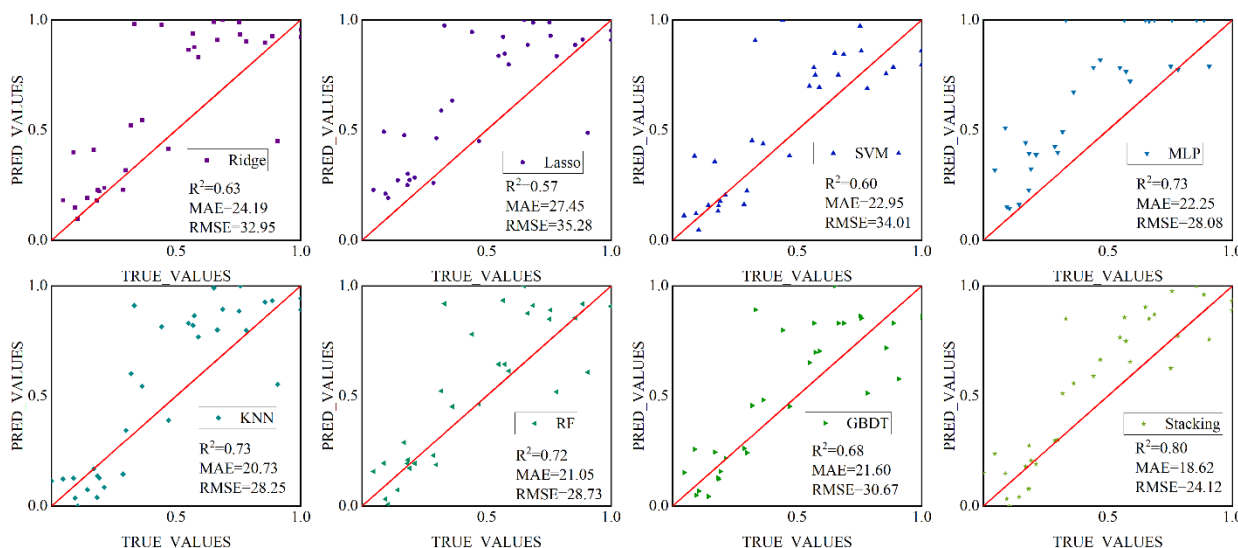


Fig. 5 - The plot of predicted versus measured values for eight models at spatial resolution of 0.030 m of RCC

At this spatial resolution, MLP and KNN have the best prediction results among the seven independent machine learning models, with R²=0.73, MAE=22.25, and RMSE=28.08 for MLP, and R²=0.73, MAE=21.05, and RMSE=28.73 for KNN. In contrast, the stacking model has R²=0.80, MAE=18.62, and RMSE=24.12, and its three evaluation indices are better than the MLP and KNN models. Hence, the prediction results of the stacking model are better than the seven independent models.

When the spatial resolution is 0.017 m, the KNN and RF models have the best prediction results, however, the stacking model's prediction results are better than the seven independent models with R²=0.87. When the spatial resolution is 0.024 m, the Ridge model has the best prediction results, and the stacking model's prediction results are better than the seven independent models with R²=0.86. When the spatial resolution is 0.030 m, the MLP, and the KNN model have the best prediction, but the stacking model's prediction is still better than that of the seven independent models, with R²=0.80.

Construction and Evaluation of a Prediction Model for LAI

The LAI is also an important indicator describing the vertical structure of vegetation, which reflects the amount of leaf area per unit surface area. By monitoring and analyzing changes in LAI, abnormal crop growth, malnutrition, or pest problems can be detected promptly and provide a scientific basis for agricultural management, such as fertilizer application, irrigation, and pest control, which can help to improve crop yield and quality, and LAI can be rapidly acquired and monitored by remote sensing technology, providing important information for land use, forestry resource management, water resource management, and so on (Yamaguchi et al., 2023). The monitoring of LAI by remote sensing can realize the rapid assessment of vegetation growth status in large-scale areas and provide scientific support for decision-making on resource management and environmental protection.

When the UAV flight altitude is 25 m, the spatial resolution of multispectral is 0.017 m. In this spatial resolution, 11 target vegetation indices are taken as inputs to 7 independent machine learning algorithm models, the models are trained on the training set, and the validation set data is used to validate and evaluate the obtained models, and the optimal parameter combinations of each model are shown in Table 4.

Table 4

The parameter information of independent machine learning models at spatial resolution of 0.017 m of LAI

Model	Para1	Value1	Para2	Value2	Para3	Value3
Ridge	Alpha	0.1				
Lasso	Alpha	0.001	Max_iter	20		
SVM	C	5	Kernel	Linear		
MLP	Activation	Identity	Hidden_layer_sizes	(30, 30, 30)	solver	adam
KNN	Algorithm	Kd_tree	Leaf_size	1	n_neighbors	4
RF	Min_samples_leaf	3	Min_samples_split	0.3	n_estimators	11
GBDT	learning_rate	0.1	Loss	ls	n_estimators	46

The above 7 basic models are used as base models and the linear regression algorithm is used as a stacking meta-model. After synthesizing the above independent machine learning models and using the same input data to get the prediction results obtained by the stacking model, a 1:1 comparison graph is constructed after normalizing a total of 8 sets of prediction results with the actual values such as the prediction results of the stacking model and the prediction results of the aforementioned independent models, the specific results are shown in Figure 6.

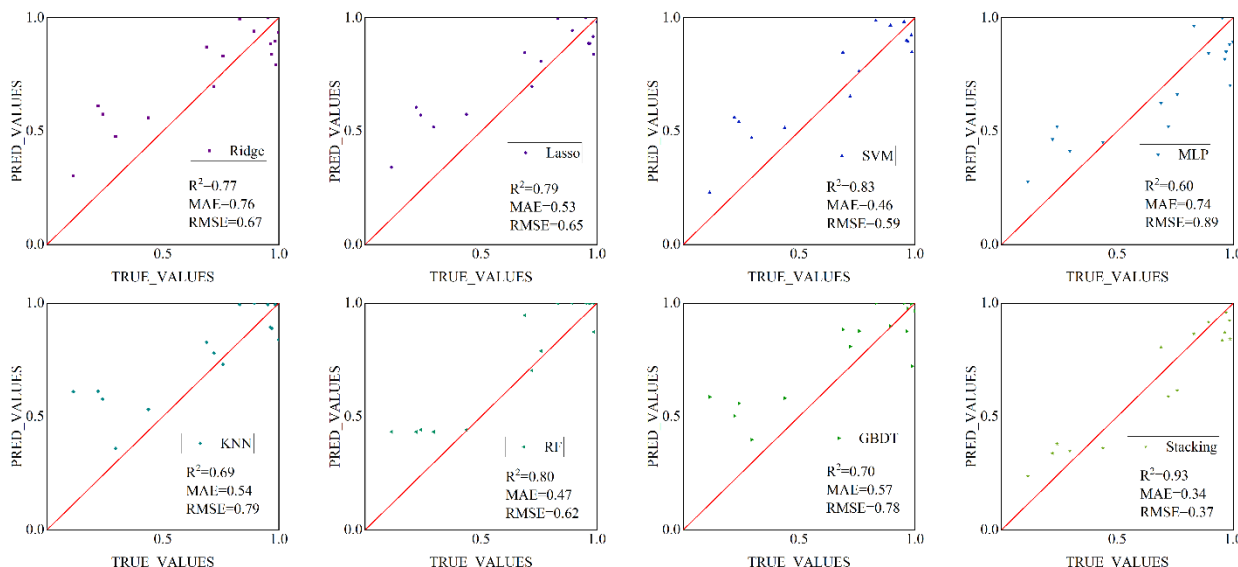


Fig. 6 - The predicted versus measured values for eight prediction models at spatial resolution of 0.017 m of LAI

At this spatial resolution, the best prediction among the seven independent machine learning models is the SVM model, which corresponds to R²=0.83, MAE=0.46, and RMSE=0.59. The stacking model has R²=0.93, MAE=0.34, and RMSE=0.37, and all the evaluation indices are better than those of the SVM model, so the stacking model's prediction results are better than seven independent models such as RF.

When the UAV flight altitude is 35 m, the spatial resolution of multispectral is 0.024 m. In this spatial resolution, The optimal parameter combinations for each model obtained at this spatial resolution are shown in Table 5.

Table 5

The parameter information of independent machine learning models at spatial resolution of 0.024 m of LAI

Model	Para1	Value1	Para2	Value2	Para3	Value3
Ridge	Alpha	50				
Lasso	Alpha	0.5	Max_iter	50		
SVM	C	10	Kernel	Rbf		
MLP	Activation	Relu	Hidden_layer_sizes	(25, 25, 25, 25)	solver	lbfgs
KNN	Algorithm	Kd_tree	Leaf_size	1	n_neighbors	1
RF	Min_samples_leaf	1	Min_samples_split	0.1	n_estimators	6
GBDT	learning_rate	1	Loss	lad	n_estimators	6

Then the above 7 basic models are used as the base model and the linear regression algorithm is used as the stacking meta-model. After synthesizing the above independent machine learning models and using the same input data to get the prediction results obtained by the stacking model, a 1:1 comparison graph is constructed after normalizing the stacking model prediction results with a total of 8 sets of prediction results and actual values such as the prediction results of the aforementioned independent models, and the results are shown in Figure 7.

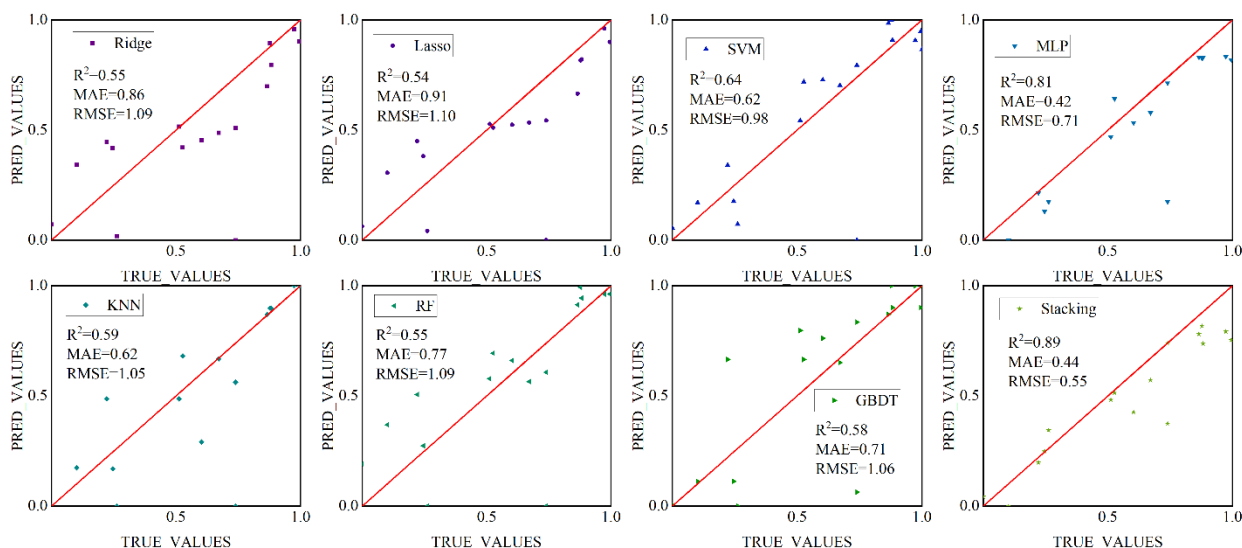


Fig. 7 - The predicted versus measured values for eight prediction models at spatial resolution of 0.024 m of LAI

At this spatial resolution, MLP has the best prediction results among the seven independent machine learning models, with $R^2=0.81$, $MAE=0.42$, and $RMSE=0.71$, the stacking model has $R^2=0.89$, $MAE=0.44$, and $RMSE=0.55$, and all the evaluation metrics are superior to those of the MLP model so that the stacking model's prediction results were better than seven independent models such as MLP.

When the spatial resolution is 0.017 m, the SVM model has the best prediction effect, but the stacking model has better prediction results than the seven independent models such as SVM, with $R^2=0.93$. When the spatial resolution is 0.024 m, the MLP model has the best prediction effect, and the stacking model still has better prediction results than the seven independent models such as MLP, with $R^2=0.89$. Unfortunately, not enough valid data were collected on the LAI of sorghum due to insufficient time at the spatial resolution of 0.030 m.

It was found that the models constructed at higher spatial resolution have higher R^2 values, lower MAE values, and lower RMSE values, indicating that increasing the resolution can improve the prediction accuracy of the models to some extent. Therefore, when conditions permit, lower flight altitude is considered to obtain higher spatial resolution and effectively improve the prediction model of RCC and LAI. Of course, the lower flight altitude, for a given monitoring area, represents the need to pay more monitoring time and slower monitoring speed, which needs to be measured according to the actual situation and trade-offs.

CONCLUSIONS

In previous studies, vegetation indices such as NDVI and EVI vegetation indices are mainly used to monitor crops in RCC and LAI prediction model (Tian & Min, 1998). Linear regression models or simple nonlinear regression models with simple spectral indices are usually used to monitor crop growth (Berger et al., 2020). However, because the spectral index varies greatly at different growth stages of crops, the monitoring accuracy and adaptability of the traditional methods need to be improved (Ramsanthosh et al., 2021). Instead, this study used the vegetation index of plants, coupled with a stacked learning model, to go about exploring the optimal sorghum RCC and LAI prediction model at different spatial resolutions. Compared with the traditional, single machine learning model-based prediction method, the prediction model constructed based on integrated learning and using the stacking approach has higher prediction accuracy and better prediction results, to realize the rapid monitoring and prediction of sorghum growth in field environments (Ashcraft & Karra, 2021; Yahata et al., 2017).

Although the prediction model constructed by combining the vegetation index with independent machine learning at different spatial resolutions can achieve high prediction accuracy, there are still some shortcomings in predicting and monitoring the values of RCC and LAI of sorghum. One of the challenges is that lower resolution results in a smaller amount of data obtained, as it requires less time to monitor the same area. This reduction in data volume affects both model construction and validation. Additionally, the parameter optimization method using grid search in this study is not sufficient, and a more dynamic update-based parameter optimization algorithm will be explored in future work. Furthermore, the unstable and unstructured environment of field crop survival, combined with the manual methods used to collect plant data, introduces a degree of subjectivity in data collection.

The study is also limited to a single species, with discontinuous observation times and a relatively small total sample size. These factors indicate that generalizing the conclusions of this study requires further exploration, testing, and research.

ACKNOWLEDGEMENT

This research, titled 'Coupling Unmanned Aerial Vehicle (UAV) Multispectral Imagery, Spatial Resolution, and Integrated Learning to Construct a Monitoring and Prediction Model for Leaf Area Index (LAI) and Relative Chlorophyll Content (RCC) of Sorghum in Fields', was funded by the Shanxi Agricultural University Special Merit Program (XDHZFY2022-02) and the Basic Research Program of Shanxi Provincial Science and Technology Department (202103021224123).

REFERENCES

- [1] Ashcraft, C., & Karra, K. (2021). *Machine Learning aided Crop Yield Optimization*. <https://doi.org/10.48550/arXiv.2111.00963>
- [2] Berger, T., Bernardi, A., Martini, D., Münzberg, A., & Troost, C. (2020). Combining Machine Learning and Simulation Modelling for Better Predictions of Crop Yield and Farmer Income. *10th International Congress on Environmental Modelling and Software*,
- [3] Berjon, A.J., Cachorro, V.E., Zarco-Tejada, P.J., & De Frutos P.J., Martin, P. (2023). Estimation of Leaf Area Index and chlorophyll content in barley by inversion of radiative transfer models at different growth stages. *IGARSS 2023: IEEE International Geoscience and Remote Sensing Symposium*, vols I - VII;
- [4] Guo, Y., Chen, S., Li, X., Cunha, M., Jayavelu, S., Cammarano, D., & Fu, Y. (2022). Machine Learning-Based Approaches for Predicting SPAD Values of Maize Using Multi-Spectral Images. *Remote Sensing*, 14(6), 1337. <https://www.mdpi.com/2072-4292/14/6/1337>
- [5] Hunt, E. R., Fujikawa, S. J., Yoel, D. W., & Cio. (2008). Remote sensing of crop leaf area index using unmanned airborne vehicles. *Pecora 17-The Future of Land Imaging...Going Operational.*, Colorado
- [6] Liu, Y., Liu, R., & Chen, J. M. (2012). Retrospective retrieval of long-term consistent global leaf area index (1981–2011) from combined AVHRR and MODIS data. *Journal of Geophysical Research*.
- [7] Pan, Y., Wu, W., Zhang, J., Zhao, Y., Zhang, J., Gu, Y., Yao, X., Cheng, T., Zhu, Y., & Cao, W. (2023). Estimating leaf nitrogen and chlorophyll content in wheat by correcting canopy structure effect through multi-angular remote sensing. *Computers and Electronics in Agriculture*, 208.
- [8] Ramsanthosh, V., Laxmi, A. S., Abhinay, C. S., Santosh, V., & Chopra, S. (2021). Review and Further Prospects of Plant Disease Detection Using Machine Learning. *International Journal of Scientific Research in Computer Science Engineering and Information Technology*, 105-115.
- [9] Sudu, B., Rong, G., Guga, S., Li, K., Zhi, F., Guo, Y., Zhang, J., & Bao, Y. (2022). Retrieving SPAD Values of Summer Maize Using UAV Hyperspectral Data Based on Multiple Machine Learning Algorithm. *Remote Sensing*, 14(21), 5407. <https://www.mdpi.com/2072-4292/14/21/5407>
- [10] Tavakoli, H., Mohtasebi, S., Alimardani, R., & Gebbers, R. (2014). Evaluation of different sensing approaches concerning to nondestructive estimation of leaf area index (LAI) for winter wheat. *International Journal on Smart Sensing and Intelligent Systems*. Vol.7, No.1, pp.357-359. DOI: 10.21307/ijssis-2017-659
- [11] Tian, Q., & Min, X. (1998). Advances in study on vegetation indices. *Advance in earth sciences*.
- [12] Tunca, E., Köksal, E. S., Çetin, S., Ekiz, N. M., & Balde, H. (2018). Yield and leaf area index estimations for sunflower plants using unmanned aerial vehicle images. *Environmental Monitoring and Assessment*. 190(11):682. doi: 10.1007/s10661-018-7064-x
- [13] Yahata, Onishi, Yamaguchi, Ozawa, Kitazono, Ohkawa, Yoshida, Murakami, & Tsuji. (2017). A Hybrid Machine Learning Approach to Automatic Plant Phenotyping for Smart Agriculture. *IEEE IJCNN*, 1787-1793.
- [14] Yamaguchi, H., Yasutake, D., Hirota, T., & Nomura, K. (2023). Nondestructive Measurement Method of Leaf Area Index Using Near-infrared Radiation and Photosynthetically Active Radiation Transmitted through a Leafy Vegetable Canopy. *HortScience*. Volume 58: Issue 1, pp.16-22
- [15] Zhang, J., Cheng, T., Guo, W., Xu, X., & Ma, X. (2021). Leaf area index estimation model for UAV image hyperspectral data based on wavelength variable selection and machine learning methods. *Plant Methods*, 17(1).
- [16] Zhao, R., An, L., Tang, W., Qiao, L., Wang, N., Li, M., Sun, H., & Liu, G. (2023). Improving chlorophyll content detection to suit maize dynamic growth effects by deep features of hyperspectral data. *Field Crops Research*, 297.

A BIBLIOMETRIC-BASED ANALYSIS OF RESEARCH PROGRESS IN UNMANNED AERIAL REMOTE SENSING OF WHEAT

基于文献计量的小麦无人机遥感研究进展分析

Wenyu PENG¹, Junke ZHU*¹, Mei HUANG^{1,2}, Yubin LAN^{1,3}, Hongjian ZHAO¹, Susu HUANG¹, Shenke LI¹, Aoqun HUANG¹, Zhicheng TANG¹

¹ School of Agricultural Engineering and Food Science, Shandong University of Technology, Zibo / China

² Qilu Normal University, Jinan/China

³ National Sub-Centre for International Collaboration Research Centre for Agricultural Aviation Intelligent Equipment, Zibo/China

Tel: +8618905338833; E-mail: zhujunke@126.com

Corresponding author: Junke ZHU

DOI: <https://doi.org/10.35633/inmateh-74-18>

Keywords: UAV; wheat; bibliometric; VOSviewer; CiteSpace

ABSTRACT

To gain a comprehensive understanding of the current status of unmanned aerial vehicle (UAV) technology in wheat crop growth monitoring and its development trajectory, this paper quantifies and visualizes the relevant literature published between 2015 and 2024 in the Web of Science database. By conducting a comprehensive analysis of high-frequency keywords, the article presents a summary of the prevailing research topics in this field. This can assist researchers in further familiarizing themselves with the relevant literature and providing a novel perspective on the utilization of UAV technology in wheat crop growth monitoring.

摘要

为深入探究无人机技术在小麦作物生长监测中的应用现状及其发展趋势，本文对 Web of Science 数据库中 2015 至 2024 年间发表的相关文献进行了量化与可视化分析。文章通过深入分析高频关键词等，归纳该领域的主流研究热点，可以帮助研究者进一步熟悉该领域相关文献，为理解无人机技术在小麦作物生长监测中的应用提供全新的视角。

INTRODUCTION

Wheat is the primary grain crop in China, comprising 25% of the total grain production area. China is the world's largest producer and exporter of wheat, and its production is closely linked to global food security. In 2023, wheat production decreased slightly by 0.9% to 134.53 million tons. The stable increase in production remains a significant challenge for China's agriculture sector. Standardized cultivation necessitates efficient monitoring and forecasting capabilities (Andrés *et al.*, 2023). The conventional approach to measuring crop loss, relying on sampling, is limited in precision and lacks the necessary accuracy for precision agriculture. Consequently, the advancement of rapid and precise monitoring technology is vital for the progress of intelligent agriculture. At present, Phang *et al.*, (2023), mainly discusses the differences between satellites and drones in data collection and introduces the advantages of drone remote sensing in data collection and analysis. Maes *et al.*, (2019), focused on analyzing the research progress of drone remote sensing technology in the areas of drought stress, weed and pathogen detection, nutritional status and growth vigor assessment, and yield prediction. Sishodia *et al.*, (2020), based on the analysis of remote sensing systems and remote sensing technology applications in agriculture, studied vegetation indices commonly used in remote sensing analysis to help scientists understand the spatial and temporal variations of crops. Most of these reviews focus on the progress of UAV applications in agriculture, with fewer articles providing a systematic summary of the field of remote sensing extraction of wheat crops.

Scientific literature databases are collections of disciplinary knowledge constructed by scholars in related fields, which carry the recording and dissemination of disciplinary knowledge (Bornmann *et al.*, 2020; Garg *et al.*, 2016). Statistical analysis of literature data can reveal current research hotspots, quickly capture the latest research trends, and effectively predict future research trends. In recent years, scholars have conducted analyses on remote sensing research on crop growth monitoring (Wang *et al.*, 2019), crop monitoring in smallholder farms using unmanned aerial vehicles (Gokool *et al.*, 2023), and the application of machine learning methods in agricultural management (Zhang *et al.*, 2021) based on bibliometric analysis. However, there are few reports on bibliometric analysis in the field of specific crop monitoring such as wheat.

In light of the aforementioned considerations, this paper utilizes a bibliometric methodology to categorize and examine the literature related to the monitoring wheat crops via unmanned aerial vehicles (UAVs). The number of countries of origin, authors, journals and keywords in this field over the past ten years are analyzed in order to offer a comprehensive overview of the development trajectory and evolution of research hotspots in the domain of remote sensing-based wheat crop extraction.

MATERIALS AND METHODS

Data source

This paper presents a specific search strategy constructed based on the Advanced search function in the WOS (Web of Science) core collection database, through which relevant literature can be filtered. Boolean logic operation rules were applied to construct the following search formula: The following search formula was constructed: "TS = (("UAV" OR "unmanned aerial vehicle" OR "remotely piloted aircraft") AND ("RGB*" OR "multispectral*" OR "hyperspectral*")) AND ("winter wheat" OR "wheat culture" OR "wheat cereal" OR "wheat*"))". The search was conducted between 1 January 2015 and May 2024, and only articles were included. After screening the search criteria, 548 literature records were initially obtained. The records were then subjected to further screening and cleaning in order to guarantee the accuracy and relevance of the data. By eliminating data that was unrelated to the topic and performing de-emphasis and merging processes, 347 valid documents were ultimately identified as the basis for subsequent analyses. These will provide a reference basis for future related studies.

Research tools and methods

In this paper, the research data were mapped and analyzed with the help of the VOSviewer and CiteSpace software. VOSviewer was utilized to map authorship and keyword co-occurrence due to its diversified visual functions in the areas of keywords, co-institutions, and co-authors, as well as its user-friendly mapping process and aesthetic image presentation. Meanwhile, the HistCite software was employed to categorize and extract data on a number of parameter indicators, including authors, countries, institutions, journals, and highly cited papers. Furthermore, an in-depth visualization and analysis of geographical collaboration networks among different countries were conducted in conjunction with VOSviewer and Scimago Graphica software.

Countries of citing papers analysis

The collaboration of national institutions in scientific research is increasingly recognized as a valuable avenue for accessing supplementary scientific resources, sharing, and the overall advancement of scientific research capabilities (Han et al., 2022). Using the VOSviewer software, a geographic network view of scientific research cooperation encompassing 42 countries was constructed (Figure 1).

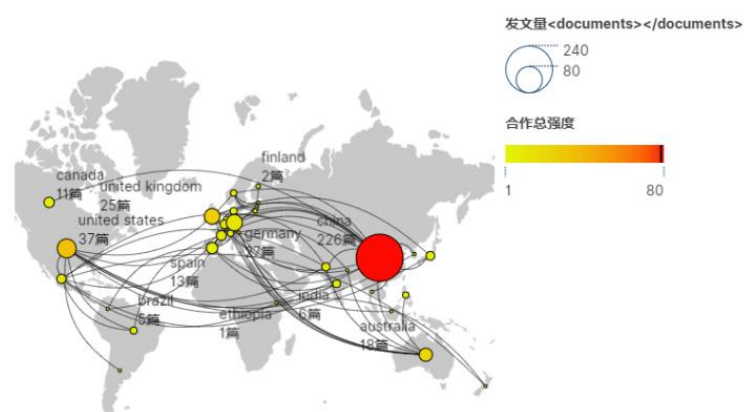


Fig. 1 - Network map of cooperation between the countries in the world in terms of publications

The size of the nodes is directly proportional to the quantity of articles sent by each country; thus, the larger the node, the greater the volume of articles. The thickness of the connecting line between nodes indicates the strength of the cooperation relationship between countries. A thicker line signifies a greater number of articles sent by the cooperating countries. Node color represents the level of intensity of the cooperation.

As illustrated in Figure 1, China and the United States demonstrate the most robust collaboration within the global scientific research network. The two countries have jointly published an impressive 30 papers, representing 13.27% and 81.08% of their respective total output. The two countries initially established a research partnership in 2017, subsequently reaching a peak in the number of co-authored papers in 2022.

Furthermore, China and the United Kingdom have also engaged in considerable scientific cooperation, with a total of 17 co-authored papers. Additionally, China and Germany have collaborated on nine scientific papers. These findings illustrate that China plays a pivotal role in international scientific research cooperation, maintaining active and frequent collaboration with numerous countries.

Authors of citing papers analysis

A comprehensive examination of the researcher community enables the identification of the most influential scholars and the primary research strengths in the field. In the domain of unmanned aerial vehicle wheat monitoring, there are 1,386 active authors. Of these, authors with only one paper account for 69.77% of the total, which is consistent with the Lotka-Price law (Irene *et al.*, 2013).

Table 1 presents the ten most prolific authors in the field of unmanned aerial vehicle (UAV) applications in wheat research. Yan Zhu, a prominent researcher in the field, leads the ranking with her exceptional research output. The next most prolific researchers are Cao Satellite and Yang Guijun, who have published 23 and 18 articles, respectively. It is noteworthy that all of the top ten authors are based in China, with six of them affiliated with Nanjing Agricultural University. This observation suggests that Chinese scholars are at the forefront of academic research in the field of UAV remote sensing applied to wheat crops, and that Nanjing Agricultural University, as a leading agricultural university in China, has achieved significant advancements in this area.

Table 1

Top 10 authors in the world in terms of number of publications				
Author	Institution	Papers	Local citation score / LCS	Global citation score / GCS
Zhu Yan	Nanjing Agricultural University	25	6	830
Cao Weixing	Nanjing Agricultural University	23	6	700
Tian Yongchao	Nanjing Agricultural University	18	1	710
Yang Guijun	Beijing Academy of Agricultural and Forestry Science	18	86	1258
Cheng Tao	Nanjing Agricultural University	17	5	563
Feng Haikuan	Nanjing Agricultural University	16	56	988
Yao Xia	Nanjing Agricultural University	15	1	594
Li Zhenhai	Technology Center for Information Agriculture	14	20	720
Liu Tao	Yangzhou University	10	1	64
Sun Chengming	Yangzhou University	10	1	49

Keywords of citing papers analysis

As the fundamental element of academic papers, the co-occurrence analysis of keywords can elucidate the research focal points and trends within particular scientific disciplines (Dong *et al.*, 2022). In this study, the VOSviewer software was employed to map the keyword density of 347 documents. It should be noted that some keywords may not be fully represented in the images due to the scale. In order to provide a more accurate representation of the research focus, the keywords with a frequency of at least 5 were selected for visualization.

As illustrated in Figure 2, the brightness of a keyword is directly proportional to its frequency of occurrence in the literature. In other words, the higher the brightness, the higher the frequency of occurrence of the keyword. Through the graphical analysis, it was found that, with the exception of unmanned aerial vehicle, high-frequency keywords such as vegetation indexes, leaf area index, biomass, and chlorophyll content constituted the representative terms in the field. Therefore, the in-depth analysis and discussion of these keywords are of great significance for understanding the current research status and future directions in this field.

This is mainly because machine learning algorithms have powerful pattern recognition and data mining capabilities when dealing with large-scale, high-dimensional unmanned aerial vehicle remote sensing data. It can automatically extract valuable information and features from complex data, thereby providing strong support for accurate wheat yield prediction and growth status assessment. Compared with traditional data analysis methods, machine learning methods show significant advantages in accuracy, generalization ability and adaptability, and can better cope with the diversity and complexity of unmanned aerial vehicle remote sensing data.

In order to gain a deeper understanding of the development process in this research area, this paper utilizes the CiteSpace software to analyze the evolution of keywords and to create a map of the keywords' time zones (Figure 3). Figure 3 illustrates the evolution of keywords over time. Each time period is represented by a vertical axis, and the keywords are displayed as annuli, with the size of the annulus indicates the frequency of keyword appearances and the color marking the time of keyword appearances. The connecting lines indicate the co-occurrence of keywords, thereby revealing the evolution of the research theme and the cross-disciplinary trend.

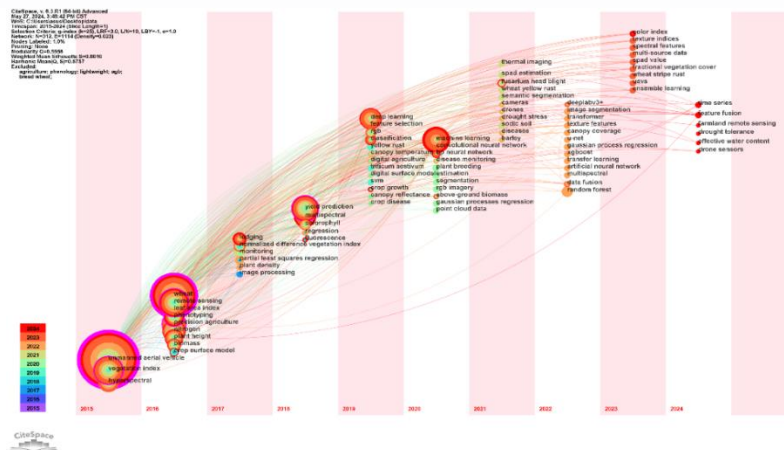


Fig. 3 - The mapping of keyword co-occurrence time zone

Figure 3 illustrates the uniform distribution of high-frequency keywords across time zones, which demonstrates the continuous development of this research field and the expansion of its scope. With regard to the acquisition of data, the initial focus was on hyperspectral, multispectral and RGB data (Yang *et al.*, 2022; Kang *et al.*, 2024; Ma *et al.*, 2023), which subsequently gave way to the utilization of integrated multi-source remote sensing data, encompassing hyperspectral and multispectral, visible and hyperspectral, RGB and multispectral, and other combinations. etc. which reflects the increasing depth of research on the use of unmanned aerial vehicles (UAVs) for remote sensing data acquisition over the past decade (Liu *et al.*, 2023; Yue *et al.*, 2021; Ding *et al.*, 2022). Ding *et al.*, (2020), employed a UAV to obtain multispectral, RGB, and thermal infrared images, subsequently constructing a multi-source fusion dataset to predict nitrogen content in wheat. Compare with traditional monitoring methods, unmanned aerial vehicle technology has higher precision in wheat growth monitoring and agricultural production management. Traditional manual monitoring methods are not only time-consuming and labor-intensive, but also prone to errors. While unmanned aerial vehicles can cover a wide area in a short time, and the obtained data is more accurate and comprehensive, which can provide a more reliable basis for agricultural production management.

The study of unmanned acquisition of information related to the growth process of wheat has emerged as a new and prominent area of research. The frequent appearance of keywords such as leaf area index, plant height, and nitrogen underscore the crucial role of wheat growth monitoring in attracting the attention of scholars (Song *et al.*, 2020; Yue *et al.*, 2017; Liu *et al.*, 2020) making it a major focus of research. Chen *et al.*, (2019), Chen *et al.*, (2020), Gao *et al.*, (2016) employed hyperspectral images to estimate the leaf area index. Li *et al.*, (2023); Wang *et al.*, (2024), employed multispectral images to estimate the leaf area index. Tao *et al.*, (2020), gathered hyperspectral images from an unmanned aerial vehicle (UAV) to ascertain the yield and plant height of wheat. Wang *et al.*, (2020), monitored the nitrogen content of wheat with the aid of hyperspectral data. The research on these parameters can help researchers understand the growth mechanism of wheat, grasp the dynamic changes of wheat growth in real time, adjust field management strategies in a timely manner, and improve yield and quality.

With respect to the research objectives, phenotyping constituted an early and consistent research focus in the field (Wan *et al.*, 2021). Since 2018, research has also gradually shifted towards prediction studies and inversion techniques (Han *et al.*, 2021). Zhu *et al.*, (2024), proposed a genetic algorithm-improved support vector machine algorithm for estimating wheat growth and yield in a trial of 12 wheat varieties and 3 levels of nitrogen fertilizer application, specifically Shannong 28. The yield model produced superior results ($R^2=0.70$). Sangjan *et al.*, (2024), extracted satellite images in conjunction with UAV images for the purpose of comparing the wheat yield prediction models of the two sampling methods. The findings indicated that the accuracy of the two prediction models is comparable. Through in-depth research, it is found that these two prediction models are comparable in terms of accuracy, but each has its own advantages in different application scenarios. For example, in large-scale farmland monitoring, the model combined with satellite images may have more advantages; while in small-scale precision agriculture, the model mainly based on drone images may perform better. Among them, the prediction of wheat yield and above-ground biological indicators and the drawing of inversion maps have become the most common and crucial practical forms in prediction research. With the continuous innovation of technology and the increasing abundance of data, this field is expected to achieve greater breakthroughs in aspects such as multi-source data fusion, intelligent analysis, and precision agriculture applications, providing more scientific and efficient decision support for agricultural production management.

With regard to technological innovation, the field has been developing at a particularly rapid pace. The concept of Partial Least Squares Regression (PLSR) has been widely introduced since 2017 (Zhang *et al.*, 2022), and subsequently, regression analysis has become a mainstream method for data analysis. Guo *et al.*, (2021), Fu *et al.*, (2021), proposed a multi-scale texture extraction method (GLCM). The extracted spectral features, multiscale texture features, and their combinations were analyzed using partial least squares regression (PLSR) and least squares support vector machine (LSSVM) regression models, which demonstrated high accuracy when based on multiscale texture. In recent years, the emergence of keywords such as support vector machine, random forest, and neural network reflects the extensive application of machine learning and deep learning techniques in this field (Ji *et al.*, 2024; Yang *et al.*, 2021; Lucks *et al.*, 2021). Arshad *et al.*, (2023), employed the vegetation index extracted from UAV images in conjunction with climate data, selected eight models in machine learning for combination, and found that the accuracy of the RF model was superior to that of the other models. Amorim *et al.*, (2022), utilized a drone to acquire multispectral images. The spectral images of wheat at three growth stages were extracted, and vegetation indices were then combined with three different machine learning models. It was found that the models were able to more accurately estimate the biomass of wheat at different periods. As technology advances and data collection becomes increasingly sophisticated, scholars are dedicating greater attention to data processing. Developing data analysis methods based on machine learning and deep learning can better mine and utilize monitoring data and provide more scientific decision support for agricultural production management.

RESULTS

The literature concentration in the field of unmanned aerial vehicles (UAVs) monitoring wheat crops is gradually increasing, forming two major global cooperation nodes with China and the United States as the cores. Chinese authors not only have a high output of papers but also pay attention to international exchanges and cooperation. They carry out cooperation with scholars from the United States, the United Kingdom and other countries. The number of co-authored papers accounts for 24.78% of China's total paper output. Chinese scholars are increasingly strengthening teamwork, promoting the optimal integration of research forces, and continuously broadening the breadth and depth of research.

The evolution of research hotspots in the field of UAV monitoring wheat is gradually becoming clear. Wheat, UAVs, yield, vegetation index, and machine learning are high-frequency keywords. However, as time goes by, keywords such as plant height, leaf area, nitrogen content, and deep learning continue to appear. The research hotspot has gradually shifted from the early single yield monitoring of wheat by UAVs to the direction of monitoring specific growth information of wheat. Through UAV monitoring means, researchers, on the one hand, pay attention to the nutritional components of wheat at different growth stages, and while maximizing the satisfaction of wheat growth needs, reduce fertilizer application; on the other hand, they pay attention to the relationship between indicators such as leaf area, plant height, nitrogen content and yield and quality, and more scientifically guide wheat production practice.

CONCLUSIONS

This paper takes the Web of Science database as the data source and selects relevant academic papers to conduct bibliometric analysis of the development trend of unmanned aerial vehicles for monitoring wheat crops. Due to the limited coverage of the database, a large number of high-quality journals are not retrieved. At the same time, due to the language limitations of the database, the vast majority of articles are mainly in English and cannot fully reflect the research situations in different language regions around the world. These limitations will have a certain impact when analyzing research hotspots.

In addition, this paper only screens for high-frequency words and does not consider a large number of low-frequency emergent words that appear at different time stages. These emerging fields that appear in the short term are not included in this analysis. When setting the co-occurrence intensity threshold for data visualization, some smaller research hotspots will be affected by the co-occurrence intensity and word frequency threshold selection of keywords.

Secondly, due to space limitations, this paper does not conduct citation analysis and journal analysis.

Finally, through bibliometric analysis, this paper analyzes and summarizes the time development trend of this discipline from three aspects: research field, research objective, and technological innovation, and does not conduct in-depth excavation and review from a disciplinary perspective. These limitations can be continuously studied and discussed in future work.

ACKNOWLEDGMENT

This work was supported by the Shandong Provincial Key R&D Program, Breeding and Industrialization of High-Yielding, High-Quality, High-Efficiency and Stress-Resistant Major New Wheat Varieties(2022LZGCQY002).

REFERENCES

- [1] Arshad, S., Kazmi, J. H., Javed, M. G., & Mohammed, S. (2023). Applicability of machine learning techniques in predicting wheat yield based on remote sensing and climate data in Pakistan, South Asia. *European Journal of Agronomy*, Vol: 147: 126837. Almeida-Ñauñay, A. F., Tarquis, A. M., López-Herrera, J., Pérez-Martín, E., Pancorbo, J. L., Raya-Sereno, M. D., & Quemada, M. (2023). Optimization of soil background removal to improve the prediction of wheat traits with UAV imagery. *Computers and Electronics in Agriculture*, Vol:205, Issue S0: 107559-107559.
- [2] Atkinson Amorim, J. G., Schreiber, L. V., de Souza, M. R. Q., Negreiros, M., Susin, A., Bredemeier, C., Trentin, C., Vian, A. L., de Oliveira Andrades-Filho, C., Doering, D., & Parraga, A. (2022). Biomass estimation of spring wheat with machine learning methods using UAV-based multispectral imaging. *International Journal of Remote Sensing*, Vol:43, Issue S13: 4758-4773.
- [3] Bornmann, L. (2020). Bibliometrics-based decision tree (BBDT) for deciding whether two universities in the Leiden ranking differ substantially in their performance. *Remote Sensing*, Vol:122, Iss.S2:1255-1258.
- [4] Chen, R.Q., Feng, H. K., Yang, F. Q., Li, C. C., Yang, G. J., Pei, H. J., Pan, L., & Chen, P. (2019). Estimation of leaf area index of winter wheat based on hyperspectral data of unmanned aerial vehicles. *IGARSS 2019-2019 IEEE International Geoscience and Remote Sensing Symposium*.
- [5] Chen, X. K., Li, F. L., Wang, Y. N., Shi, B. T., Hou, Y. H., & Chang, Q. (2020). Estimation of winter wheat leaf area index based on UAV hyperspectral remote sensing (无人机高光谱遥感估算冬小麦叶面积指数). *Transactions of the Chinese Society of Agricultural Engineering*, Vol: 36: 40-49.
- [6] Ding, F., Li, C. C., Zhai, W. G., Fei, S. P., Cheng, Q., & Chen, Z. (2022). Estimation of Nitrogen Content in Winter Wheat Based on Multi-Source Data Fusion and Machine Learning. *Agriculture-Basel*, Vol: 12, Issue S 11.
- [7] Dong, D., Sun, M., Xu, D., Han, S., Cui, L., Cao, S., Yang, Y., & Xu, S. (2022). Mapping the Hot Spots and Evolution Main Path of Whole-Body Vibration Training Since the 21st Century: A Bibliometric Analysis. *Front Bioeng Biotechnol*, Vol: 10: 920846.
- [8] Fu, Y. Y., Yang, G. J., Song, X. Y., Li, Z. H., Xu, X. G., Feng, H. K., & Zhao, C. J. (2021). Improved Estimation of Winter Wheat Aboveground Biomass Using Multiscale Textures Extracted from UAV-Based Digital Images and Hyperspectral Feature Analysis. *Remote Sensing*, Vol: 13, Issue S4: 581.
- [9] Gao, L., Yang, G. J., Yu, H. Y., Xu, B., Zhao, X. Q., Dong, J. H., & Ma, Y. B. (2016). Retrieving winter wheat leaf area index based on unmanned aerial vehicle hyperspectral remote sensing. *Transactions of the Chinese Society of Agricultural Engineering*, Vol: 32, Issue S22: 113-120.

- [10] Garg, K. C., & Kumar, S. (2016). Bibliometrics of global Ebola Virus Disease research as seen through Science Citation Index Expanded during 1987-2015. *Travel Medicine and Infectious Disease*, Vol:16, 64-65.
- [11] Gintaras Kabelka. (2013). Lietuvos filosofijos posovietinė transformacija: filosofijos kryptys, disciplinos, produktyvumas. *Problemos*, Vol: 83, Issue S0: 22-34.
- [12] Gokool, S., Mahomed, M., Kunz, R., Clulow, A., Sibanda, M., Naiken, V., Chetty, K., & Mabhaudhi, T. (2023). Crop monitoring in smallholder farms using unmanned aerial vehicles to facilitate precision agriculture practices: a scoping review and bibliometric analysis. *Sustainability*, Vol:15, Issue S4: 3557.
- [13] Guo, A. T., Huang, W. J., Dong, Y. Y., Ye, H. C., Ma, H. Q., Liu, B., Wu, W. B., Ren, Y., Ruan, C., & Geng, Y. (2021). Wheat Yellow Rust Detection Using UAV-Based Hyperspectral Technology. *Remote Sensing*, Vol: 13, Issue S1: 123.
- [14] Han, X., Wei, Z., Chen, H., Zhang, B. Z., Li, Y. N., & Du, T. S. (2021). Inversion of Winter Wheat Growth Parameters and Yield Under Different Water Treatments Based on UAV Multispectral Remote Sensing. *Frontiers in Plant Science*, Vol: 12: 609876.
- [15] Han, Y. S., Yang, Y. F., Chen, G., Yu, H. L., Zhang, Z. G., & Zhou, B. (2022). Emerging trends and focus of giant cell tumor of bone research from 2001-2021: A visualization research. *Front Oncol*, Vol:12, Issue S10: 25876.
- [16] Ji, J. T., Wang, X. F., Ma, H., Zheng, F. X., Shi, Y., Cui, H. W., & Zhao, S. S. (2024). Synchronous Retrieval of Wheat Cab and LAI from UAV Remote Sensing: Application of the Optimized Estimation Inversion Framework. *Agronomy-Basel*, Vol: 14, Issue S2: 359.
- [17] Kang, Y. L., Wang, Y., Fan, Y. M., Wu, H. Q., Zhang, Y., Yuan, B. B., Li, H. J., Wang, S. S., & Li, Z. (2024). Wheat Yield Estimation Based on Unmanned Aerial Vehicle Multispectral Images and Texture Feature Indices. *Agriculture-Basel*, Vol:14, Issue S2: 167.
- [18] Li, W. J., Weiss, M., Garric, B., Champolivier, L., Jiang, J. Y., Wu, W. B., & Baret, F. (2023). Mapping Crop Leaf Area Index and Canopy Chlorophyll Content Using UAV Multispectral Imagery: Impacts of Illuminations and Distribution of Input Variables. *Remote Sensing*, Vol: 15, Issue S6: 1539.
- [19] Liu, H. Y., Zhu, H. C., Li, Z. H., & Yang, G. J. (2020). Quantitative analysis and hyperspectral remote sensing of the nitrogen nutrition index in winter wheat. *International Journal of Remote Sensing*, Vol:41, Issue S3: 858-881.
- [20] Liu, Y., Sun, L., Liu, B. H., Wu, Y. F., Ma, J. C., Zhang, W. Y., Wang, B. Y., & Chen, Z. Y. (2023). Estimation of Winter Wheat Yield Using Multiple Temporal Vegetation Indices Derived from UAV-Based Multispectral and Hyperspectral Imagery. *Remote Sensing*, Vol: 15, Issue S19: 4800.
- [21] Lucks, L., Haraké, L., & Klingbeil, L. (2021). Wheat ear detection using neural networks and synthetically generated training data. *Tm-Technisches Messen*, Vol: 88, Issue S7-8: 433-442.
- [22] Ma, J. C., Wu, Y. F., Liu, B. H., Zhang, W. Y., Wang, B. Y., Chen, Z. Y., Wang, G. C., & Guo, A. (2023). Wheat Yield Prediction Using Unmanned Aerial Vehicle RGB-Imagery-Based Convolutional Neural Network and Limited Training Samples. *Remote Sensing*, Vol:15, Issue S23: 5444.
- [23] Maes, W. H., & Steppe, K. (2019). Perspectives for Remote Sensing with Unmanned Aerial Vehicles in Precision Agriculture. *Trends in Plant Science*, Vol:24, Issue S2: 152-164.
- [24] Phang, S. K., Chiang, T. H. A., Happonen, A., & Chang, M. M. L. (2023). From Satellite to UAV-Based Remote Sensing: A Review on Precision Agriculture. *IEEE Access*, Vol:11, 127057-127076.
- [25] Sangjan, W., Carter, A. H., Pumphrey, M. O., Hagemeyer, K., Jitkov, V., & Sankaran, S. (2024). Effect of high-resolution satellite and UAV imagery plot pixel resolution in wheat crop yield prediction. *International Journal of Remote Sensing*, Vol: 45, Issue S5: 1678-1698.
- [26] Song, Y., Wang, J. F., & Shang, J. L. (2020). Estimating effective leaf area index of winter wheat using simulated observation on unmanned aerial vehicle-based point cloud data. *IEEE Journal of Selected Topics in Applied Earth Observations and Remote Sensing*, Vol:13, 2874-2887.
- [27] Sishodia, R. P., Ray, R. L., & Singh, S. K. (2020). Applications of Remote Sensing in Precision Agriculture: A Review. *Remote Sensing*, Vol:12, Issue S19: 3136.
- [28] Tao, H. L., Feng, H. K., Xu, L. J., Miao, M. K., Yang, G. J., Yang, X. D., & Fan, L. L. (2020). Estimation of the yield and plant height of winter wheat using UAV-based hyperspectral images. *Sensors (Switzerland)*, Vol: 20, Issue S4: 1231.
- [29] Wan, L., Zhu, J. P., Du, X. Y., Zhang, J. F., Han, X. Z., Zhou, W. J., Li, X. P., Liu, J. L., Liang, F., He, Y., & Cen, H. Y. (2021). A model for phenotyping crop fractional vegetation cover using imagery from unmanned aerial vehicles. *Journal of Experimental Botany*, Vol: 72, Issue S13: 4691-4707.

- [30] Wang, L. J., Zhang, G. M., Wang, Z. Y., Liu, J. G., Shang, J. L., & Liang, L. (2019). Bibliometric analysis of remote sensing research trend in crop growth monitoring: A case study in China. *Remote Sensing*, Vol: 11, Issue S7: 809.
- [31] Wang, S. F., Tao, S., Li, Y., & Wang, W. (2023). Leaf area index inversion of winter wheat based on UAV multispectral imagery. *Fourth International Conference on Geology, Mapping, and Remote Sensing (ICGMRS 2023)*. Vol: 12978.
- [32] Wang, Y. N., Li, F. L., Wang, W. D., Chen, X. K., & Chang, Q. R. (2020). Monitoring of winter wheat nitrogen nutrition based on UAV hyperspectral images(基于无人机高光谱的冬小麦氮素营养监测). *Transactions of the Chinese Society of Agricultural Engineering*, Vol: 36, Issue S22: 31-39.
- [33] Yang, S. Q., Hu, L., Wu, H. B., Ren, H. Z., Qiao, H. B., Li, P. J., & Fan, W. J. (2021). Integration of Crop Growth Model and Random Forest for Winter Wheat Yield Estimation from UAV Hyperspectral Imagery. *IEEE Journal of Selected Topics in Applied Earth Observations and Remote Sensing*, Vol:14, 6253-6269.
- [34] Yang, X., Yuan, Z. R., Ye, Y., Wang, D. Z., Hua, K. K., & Guo, Z. B. (2022). Winter Wheat Total Nitrogen Content Estimation Based on UAV Hyperspectral Remote Sensing. *Spectroscopy and Spectral Analysis*, Vol: 42, Issue S10: 3269-3274.
- [35] Yue, J. B., Yang, G. J., Li, C. C., Li, Z. H., Wang, Y. J., Feng, H. K., & Xu, B. (2017). Estimation of Winter Wheat Above-Ground Biomass Using Unmanned Aerial Vehicle-Based Snapshot Hyperspectral Sensor and Crop Height Improved Models. *Remote Sensing*, Vol: 9, Issue S7: 708.
- [36] Yue, J. B., Zhou, C. Q., Guo, W., Feng, H. K., & Xu, K. J. (2021). Estimation of winter-wheat above-ground biomass using the wavelet analysis of unmanned aerial vehicle-based digital images and hyperspectral crop canopy images. *International Journal of Remote Sensing*, Vol:42, Issue S5: 1602-1622.
- [37] Zhang, J. Y., Liu, J. X., Chen, Y. Q., Feng, X. C., & Sun, Z. L. (2021) Knowledge mapping of machine learning approaches applied in agricultural management—a scient metric review with CiteSpace. *Sustainability*, Vol: 13, Issue S14: 7662.
- [38] Zhang, X. W., Zhang, K. F., Wu, S. Q., Shi, H. T., Sun, Y. Q., Zhao, Y. B., Fu, E. J., Chen, S., Bian, C. F., & Ban, W. (2022). An Investigation of Winter Wheat Leaf Area Index Fitting Model Using Spectral and Canopy Height Model Data from Unmanned Aerial Vehicle Imagery. *Remote Sensing*, Vol: 14, Issue S20: 5087.
- [39] Zhu, J. K., Li, Y. M., Wang, C. Y., Liu, P., & Lan, Y. B. (2024). Method for Monitoring Wheat Growth Status and Estimating Yield Based on UAV Multispectral Remote Sensing. *Agronomy-Basel*, Vol: 14, Issue S5: 991.
- [40] Zhu, Y. J., Liu, J. K., Tao, X. Y., Su, X. X., Li W. Y., Zha, H. N., Wu, W. G., & Li, X. W. (2023). A Three-Dimensional Conceptual Model for Estimating the Above-Ground Biomass of Winter Wheat Using Digital and Multispectral Unmanned Aerial Vehicle Images at Various Growth Stages. *Remote Sensing*, Vol: 15, Issue S13.

DESIGN AND EXPERIMENTATION OF A MACHINE VISION-BASED QUALITY INSPECTION SYSTEM FOR GREEN ONION SEEDING

基于机器视觉的大葱播种质量检测系统的设计与试验

Fangyuan LU¹⁾, Chong TAO²⁾, Zhiye MO¹⁾, Mengqi ZHANG¹⁾, Guohai ZHANG^{*1)}, Xiangyu WU¹⁾, Bolong WANG^{*1)}

¹⁾ School of Agricultural Engineering and Food Science, Shandong University of Technology, Zibo/ China

²⁾ Binzhou Polytechnic, Binzhou / China

Tel: +8615965534882; +8613581044910; E-mail: guohaizhang@sdu.edu.cn; 892460540@qq.com;

Corresponding author: Guohai ZHANG, Bolong WANG

DOI: <https://doi.org/10.35633/inmateh-74-19>

Keywords: Green onion seed, Machine vision, Primary concave defect segmentation algorithm, BP neural network, seeding quality detection

ABSTRACT

In response to the inefficiency and low accuracy issues of traditional detection algorithms in detecting the tray seeding process of green onions, this paper proposes a machine vision-based quality inspection system for green onion seeding. Considering the color characteristics of green onion seeds and the substrate soil, the original RGB images are converted into HSV images. The HSV color filtering algorithm is employed to separate green onion seeds from complex soil backgrounds. Image noise is removed using erosion-dilation operations and small-area methods. The projection method is utilized to determine the detection area of the tray and the position of the holes. Information about connected regions and their convex hulls is extracted, and eight feature parameters including perimeter, area, shape factor, perimeter ratio, area ratio, shape factor ratio, concave defect distance ratio, and error variance are used to establish a BP neural network for single and adherent seed classification. A concave point segmentation algorithm is used to separate adherent green onion seeds and count the number of green onion seeds in each hole to obtain seeding quality parameters of the seeder. Experimental results show that the average relative error of the system qualification rate is 2.24%, with maximum and minimum relative errors of 3.22% and 1.10%, respectively. The average absolute errors of the reseeding rate and void rate are 1.31% and 0.71%, respectively. The absolute error of the average number of particles is 0.025 particles, the overall accuracy rate of the integrated seeding quality detection is 98%, and the average processing time per image is 0.91 s. The research results provide reference data for precision seeding operations of green onion seeders.

摘要

针对传统的检测算法在检测大葱秧盘播种过程中，效率低下，检测精度低等问题，本文提出了一种基于机器视觉的大葱播种质量检测系统。针对大葱种子颜色和基质土壤的颜色特征，将原始 RGB 图像转换成 HSV 图像。通过 HSV 色彩过滤算法将大葱种子从复杂的土壤背景中分离。使用腐蚀膨胀操作以及小面积法去除图像噪声。使用投影法确定秧盘检测区域和穴孔位置。提取连通区域及其凸包的信息，使用了周长、面积、形状因子、周长比、面积比、形状因子比、凹缺陷距离比、误差方差 8 个特征参数，建立 BP 神经网络单粒种子与粘连种子分类模型。使用凹点分割算法将粘连的大葱种子分离，并统计每穴大葱种子数量，得到排种器的播种质量参数。试验结果表明，系统合格率的平均相对误差为 2.24%，最大和最小相对误差分别为 3.22% 和 1.10%；重播率和空穴率的平均绝对误差分别为 1.31% 和 0.71%；平均粒数的绝对误差为 0.025 粒、综合播种质量检测准确率为 98%、每幅图像平均处理时间为 0.91 s。研究结果为大葱排种器精密播种作业提供了参考数据。

Fangyuan LU, As. Ph.D. Eng; Chong TAO, M.S. Stud. Eng.; Zhiye MO, M.S. Stud. Eng.; Mengqi ZHANG, M.S. Stud. Eng.; Guohai ZHANG, As. Ph.D. Eng; Xiangyu WU, M.S. Stud. Eng.; Bolong WANG, As. Ph.D. Eng;

INTRODUCTION

As a biennial herb of allium in Liliaceae, green onion has high medical and economic value and has a long planting history in China. Additionally, it serves as a common vegetable and seasoning. With the increasing market demand, both the production and cultivation area of green onions have been steadily increasing year by year (Wang *et al.* 2019; Liu *et al.*, 2017). Currently, field seedling cultivation of green onions heavily relies on manual labor, resulting in low efficiency and high labor intensity. Hence, there is a need to promote mechanized planting of green onions. In the mechanized planting process of green onions, according to the agronomic planting requirements of green onion seedling trays, most adopt a seeding scheme of 1-3 seeds per hole (Peng *et al.*, 2017). However, existing mechanical seeders for green onions often encounter problems such as missed seeding and reseeded due to various factors, significantly impacting the seedling quality of green onion trays. Therefore, it is of great significance to inspect the seedling quality of green onion trays to promptly adjust seeding devices and enhance the production performance of green onion seedling production lines.

In the current research, methods such as manual counting, photoelectric counting and machine vision are usually adopted for the detection and evaluation of crop seeding quality (Zhang *et al.*, 2022). Most of the traditional seed detection methods for crop seeding quality are carried out manually. In this way, after a long period of work, human eyes are easily tired, which inevitably leads to counting errors and cannot ensure accuracy (Lv *et al.*, 2023). Therefore, the study of replacing artificial testing of seeding quality and performance of crops has attracted widespread attention from researchers at home and abroad (Li *et al.*, 2022). At present, the technology that replaces manual detection is photoelectric technology and machine vision technology for detection. Song *et al.*, (2011), designed and developed ZPXG-18 automatic photoelectric particle count meter and 1000-particle weight meter based on the newly discovered rotary disc inclined scraping principle, which allows for automatic particle sorting and separation. Let the disordered particles or seeds enter the groove tray with inclined grooves and arc grooves, driven by the bottom turntable to be diagonally scraped and shifted, automatically ordered and generated grain spacing, to obtain the reliable light transmission gap required by photoelectric counting, and to count the particles by presetting and rechecking the secondary counting. Dong *et al.*, (2019), developed a real-time online monitoring system for seeding performance of hybrid rice based on embedded machine vision and machine learning technologies. By scanning the outline of each image to check whether there are seeds in the nest, the number of holes is calculated, and then the deficiency rate of hybrid rice is calculated. Bai *et al.*, (2021), proposed a sweet corn seed detection method based on a voting mechanism to detect missing seeds in moving insert tray, replacing manual detection and improving the accuracy of corn seeding detection. Tan *et al.*, (2019), proposed the integral segmentation and counting method, which tested three hybrid rice varieties and realized the evaluation of seeding performance. At present, most of the researches are focused on the seeds of large grain crops such as rice and corn, but there are few researches on the sowing quality detection of small grain and irregular green onion seeds. Compared to traditional manual counting and photoelectric counting methods, the seeding detection technology based on machine vision demonstrates superior efficiency and accuracy when handling complex detection scenarios. Therefore, researching and developing a machine vision-based quality detection system for green onion sowing holds significant importance.

In this paper, a detection method based on machine vision and BP neural network is proposed to detect the seeding quality of scallion seedling tray. Firstly, a machine vision image acquisition platform is constructed to capture images. Then, the image processing algorithm is used to process the seed images of green onion in different soil environments. Finally, the seeding quality detection algorithm is designed based on BP neural network and main concave defect segmentation algorithm, and the experiment is verified.

MATERIAL AND METHODS

Testing system

The test system was installed on the precision scallion seedling feeder developed by the College of Agricultural Engineering and Food Science of Shandong University of Technology, and the scallion seeding quality detection system based on machine vision and BP neural network was set on the conveyor belt after the seedling tray was sown. The system is mainly composed of a computer, a light box, a high-definition industrial camera, and a network cable, as shown in Fig. 1.

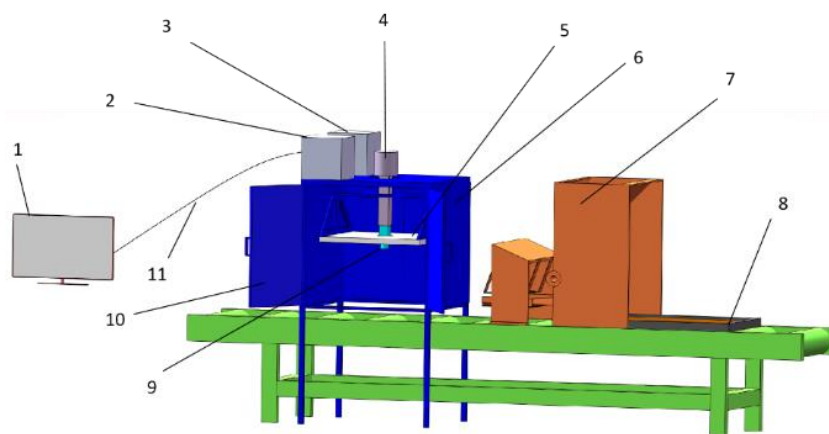


Fig. 1 - Schematic diagram of green onion sowing quality inspection system

1 – Light box; 2 - Light source; 3 - Network cable; 4 - Computer; 5 - Green onion seed; 6 - Rice seedling tray; 7 - High-definition industrial camera; 8 - Tray; 9 - Industrial camera; 10 - Light box door; 11 - Tata transmission line

The computer uses the DELL G15 5515, which is configured with a 3.30 GHz CPU and 16GB of baseband RAM. The light box uses stainless steel as the shell, and has a 600 mm×600 mm hole surface light source, and the camera passes through the hole. High-definition industrial cameras use the Keenes series CA-HF2100C, lens model CA-LHE12. When shooting, the computer uses a USB cable to control the high-definition industrial camera for shooting work. The size of the test seedling tray was 580 mm×280 mm, in which there were 12 holes in each row and 23 holes in each column. By adjusting the mounting height of the camera, the shooting range in the camera window is approximately 9×11 holes during each shooting.

Image preprocessing

The seedling plate images acquired by high-definition industrial cameras are RGB images, as shown in Fig. 1, in which the color of green onion seeds is black. In order to meet a wider application range, two kinds of soil were selected as the background soil of green onion seeds in this experiment, one is the matrix soil for cultivating vegetables, and the other is the planting soil from the planting area of green onion, as shown in Fig.2.

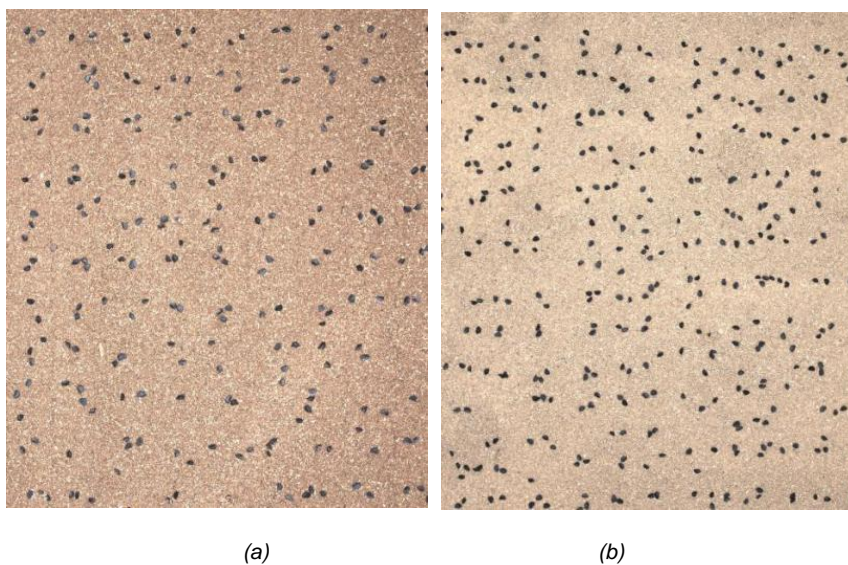


Fig. 2 - Captured RGB original image. (a) matrix soil; (b) Planting soil

In order to separate the green onion seeds from the complex soil background, the RGB image was first transferred into the HSV color space for processing. The resulting processed image was shown in Fig. 3.

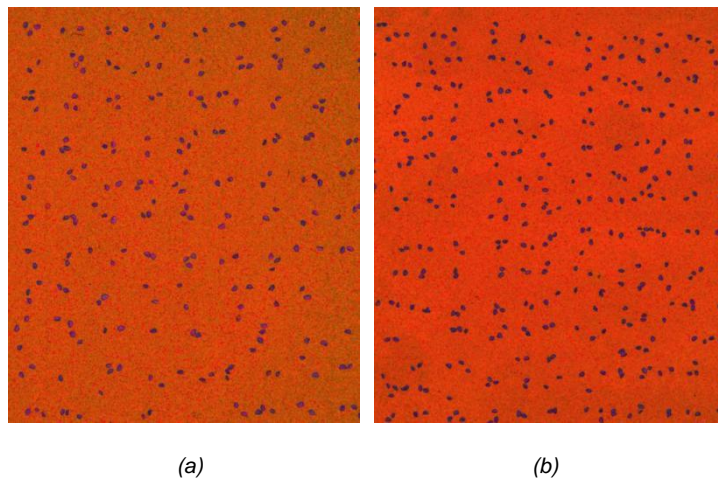


Fig. 3 - HSV color space image. (a) Matrix soil; (b) Planting soil

The experiment showed that after converting the acquired RGB image into an HSV image, the color of green onion seeds could be distinguished from the background soil, allowing for the effective extraction of the target objects. In the HSV color space, the color of green onion seeds differs significantly from the background soil color, enabling the initial extraction of green onion seeds by isolating specific color regions in the HSV space (Ren *et al.*, 2021). Additionally, due to the physical characteristics of the seeds or the presence of reflective phenomena, the color of scallion seeds in the HSV space image varies, as illustrated in Fig. 4.



Fig. 4 - Color of different green onion seeds. (a) RGB image ; (b) HSV image

Therefore, it was also necessary to obtain the best color interval through the experiment. In order to meet the goal of better extraction of green onion seed image under two soil backgrounds at the same time, it was necessary to determine the value range of H (hue), S (saturation) and V (value) of green onion seed in HSV image. EVENT_LBUTTONDOWN function and click callback function could be used to collect HSV parameters of the points of green onion seeds in the soil background from HSV images, as shown in Fig. 5. The coordinates of the collected pixels were indicated in parentheses, and the parameter values of H, S, and V are also provided in parentheses.

```

HSV value at position (1248, 254): [133 36 49]
HSV value at position (1435, 291): [140 13 61]
HSV value at position (1543, 298): [111 50 51]
HSV value at position (1230, 505): [156 14 94]
HSV value at position (1221, 512): [104 49 99]
HSV value at position (1207, 506): [108 56 78]
HSV value at position (1265, 478): [101 57 76]
HSV value at position (1541, 471): [111 52 64]
HSV value at position (1550, 481): [120 30 85]
HSV value at position (1261, 601): [120 13 40]
HSV value at position (1262, 607): [75 9 56]
    
```

Fig. 5 - Process diagram of collecting HSV information

Among H, S and V, H was the most important for color expression. The analysis of H value parameters of green onion seeds under the two soil backgrounds provided an important reference for extracting target images of green onion seeds. By collecting the color parameters of 2000 green onion seed pixels, the value range of H parameter could be obtained as shown in the following table.

Table 1

H value of green onion seeds under different soil background

Parameter	H minimum value	H maximum value	H mean value
Substrate soil as the background	42	140	115
The local loess is the background	47	149	122

Based on the H parameter of scallion seeds under the two soils, the optimal H value range for the target of extraction of scallion seeds was obtained through experiments as [42,169]. Moreover, there was no obvious difference between the S value and V value in the seed and soil background of green onion, so the value interval of S value and V value was set to the maximum range [0,255]. After defining the color value range of green onion seeds in the HSV space, the binary mask was created by the cv2.inRange function, as shown in Fig. 6.

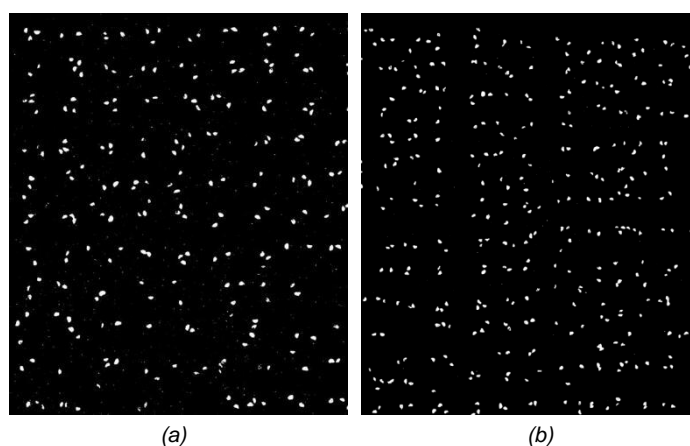


Fig. 6 - Binary mask image. (a) Matrix soil; (b) Planting soil

At this time, there were many small noise points in the image, so it was necessary to de-noise the image. Taking the matrix soil with more noise points as an example. Therefore, the binary mask was corroded and expanded, and large noise points in the image were removed by small area method. After processing by the above method, noise points in the image could be effectively filtered out, and finally the seedling was located by projection method, the processing results were shown in Fig. 7.

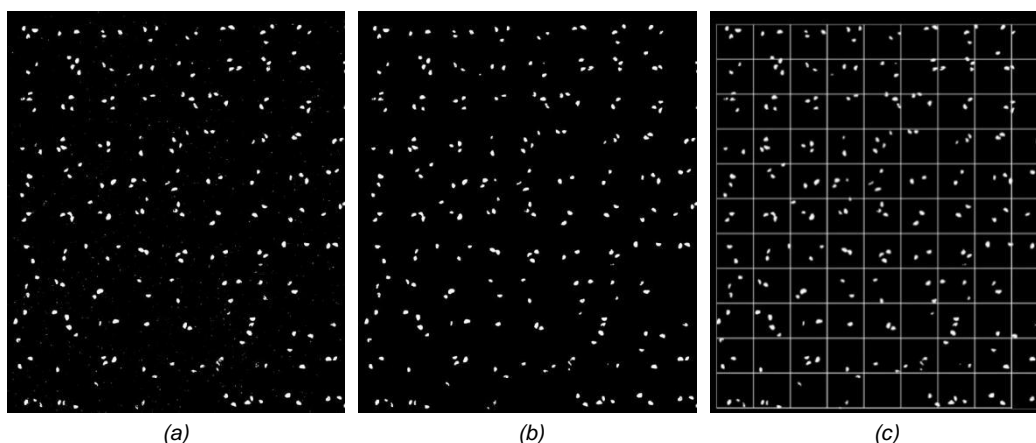


Fig. 7 - Images before and after noise reduction

(a) Original drawings; (b) Images after noise reduction; (c) Projection of legal post-image

The formula for corrosion expansion operation was as follows:

Corrosion operation:

$$(E(A, B))(x, y) = \min_{(i,j) \in B} A(x + i, y + j) \tag{1}$$

Expansive working:

$$(D(A, B))(x, y) = \max_{(i,j) \in B} A(x + i, y + j) \tag{2}$$

where:

$E(A, B)$ - Etch operation; $D(A, B)$ - Expansive working; A - Input image; B - Structural element; (x, y) - Pixel position in the image; (i, j) - Relative coordinates within structural elements; max - Take the maximum value of the corresponding pixel in all structure elements in B ; min - Take the minimum value of the corresponding pixel value in all structure elements in B .

Eigenvalue extraction

In the process of seeding, there would be a phenomenon of multi-grain adhesion of green onion seeds, which would make the image recognize multiple seeds into one grain during the contour recognition and counting process, thus affecting the accuracy of seeding detection.

Therefore, it was necessary to first classify the adhered multi-seed and single seed, and then segment the adhered seeds. In this study, BP neural network (Sun et al., 2022) was used to extract the adhered multi-seed, and the eigenvalue should be determined first.

In this study, three parameters, perimeter C_1 , area S_1 and form factor SF_1 , were selected as the shape features of green onion seeds, and five parameters, perimeter ratio P_r , area ratio A_r , error variance V_e , shape factor ratio S_r and concave defect distance ratio C_r , were selected as the external convex hull features as input values of BP neural network. For the single and multi-grain scallion seeds, the shape characteristics of the connected domain of scallion seeds in the simply connected domain were calculated, as shown in Table 2. The characteristic parameters of external convex hull of single and multi-grain adhesive green onion seeds were shown in Table 3.

Table 2

Simple connected region shape characteristics of different number of green onion seeds

Parameter	Shape characteristics of simple connected region of green onion seeds with different seed numbers		
	1	2	3
Number	1	2	3
Perimeter (pixels)	161	314	357
Area (pixels)	1505	3278	3757
Shape factor	0.72	0.41	0.37

Table 3

The characteristics of the outer convex envelope in the simply connected region of different number of green onion seeds

Parameter	Characteristic statistics of different number of green onion seeds with outer convex hull		
	1	2	3
Number	1	2	3
Perimeter ratio	1.03	1.34	1.481
Area ratio	0.93	0.72	0.65
Error variance	0.55	45.23	76.93
Form factor ratio	0.80	0.53	0.33
Concave defect distance ratio	0.13	5.74	8.34

Construction of BP neural network

BP neural network was a multi-layer feedforward neural network based on error calculation, and its weight was adjusted according to the error backward propagation algorithm in order to achieve continuous

error reduction. This process was similar to calculating the error through a forward neural network and then backpropagating to adjust the weight of the neuron until the error is minimized (Deng et al., 2022). In this study, the input layer of BP neural network was set with 8 neurons, representing 8 characteristic parameters. The output layer was set up with two neurons, one representing a single seed and one representing multiple seeds. This allows you to distinguish single seeds from multiple seeds. The performance of BP neural network was affected by the number of neurons in the hidden layer, and the number of neurons in the hidden layer was usually determined by a large number of tests and experiences. The empirical formula was expressed as formula 3.

$$NUM = \sqrt{p + q} + b \quad (3)$$

where:

NUM - Number of hidden layer neurons; p - Enter the number of layer vectors; q - Output the number of layer vectors; b - Adjustable empirical constant, the value range was [1,10].

In this paper, the traditional BP neural network was selected for training comparison with the optimized BP neural network. The optimized transfer function was Leaky ReLU, and the output layer transfer function was Purelin. The Adaptive Moment Estimation algorithm was used to train the deep neural network (Zhang et al., 2022).

Data set construction

Through image preprocessing, the binarized connected domain images of scallion seeds were extracted from the complex background. A total of 3602 images were obtained, including 2750 single scallion seeds and 852 multi-scallion seed images (Ding et al., 2019). In order to enhance the training effect and generalization performance of the model, methods such as amplification, rotation and noise increase were used to expand the data set. After expansion and processing, the data set has a total of 6033 images. The two kinds of pictures of single scallion seed and multi-scallion seed adhesion were used as the training set and the test set of BP neural network according to the ratio of 3:1:1. The dataset image was shown in the Fig. 8.

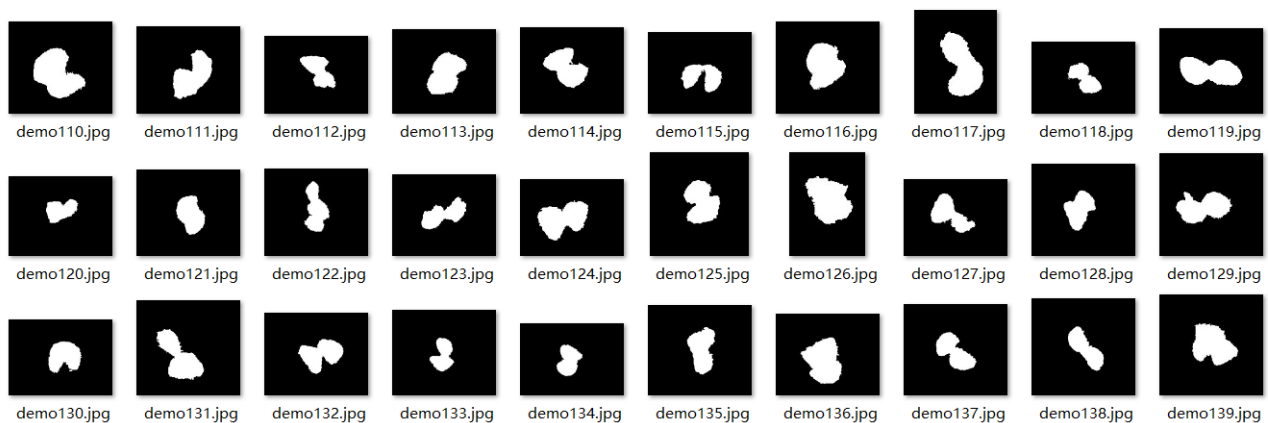


Fig. 8 - Dataset image

Main concave defect segmentation algorithm

On the edge or inside of a polygon, a line segment connecting two points can always be found. This polygon encompasses all points, and the smallest such polygon is termed a convex hull. For a geometry, the outer convex hull is a convex polygon whose boundary completely encloses all points within the given geometry. A concave defect represents a dip or void in the outline shape of an object. A concave point is a point that forms the boundary of a concave defect. The red dot in the figure identifies the concave spot on the image, the green line outline represents the outer convex envelope of the scallion seed, and the yellow area highlights the main concave defect area. Points D, E and F represent the starting point, the deepest point and the ending point of the largest concave defect area of the adhesive allium seeds, respectively. The other red pits in the image also represent the deepest point of the small concave defect, and each pit can be the deepest point of the concave defect, the starting point and the ending point, so the number of pits was equal (Zhu et al., 2023).

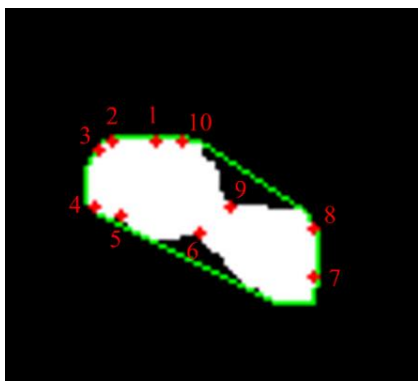


Fig. 9 - Concave detection sequence

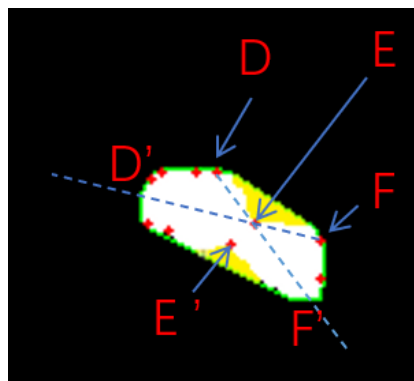


Fig. 10 - Principle diagram of main concave defect segmentation

There is no concave defect in the outer convex hull of single scallion seeds. However, for the multi-grain seeds, the outer convex hull has concave defects. It is necessary to use concave defect segmentation algorithm to divide these adhered onion seeds into single seeds. The determination of the concave defect depth threshold is critical. A lower threshold may lead to misidentification of minor concavities on the green onion seed surface as connection points between two seeds, resulting in erroneous segmentation. Conversely, an excessively high threshold may cause omission of key segmentation points, leading to missed segmentation. Therefore, it is imperative to select an appropriate concave defect depth threshold. Extensive preliminary experiments have determined that setting the concave defect depth threshold to 5.23 yields the highest accuracy in segmenting images of adhered green onion seeds (Nicolau *et al.*, 2023).

For the adhesive onion seeds, the workflow of image segmentation proposed in this study was as follows, illustrated by Fig. 10:

(1) Traversal and selection of main segmentation points: The system first traverses all concave points in the image to find the concave defect point with the greatest depth. By comparing the concave defect depth of this point with the size of the concave defect depth threshold 5.23, if the concave defect depth was greater than the threshold, this point (such as point E in Fig. 9) was identified as the main concave point of segmentation. If the depth of the concave defect was less than the threshold, the process stopped the current segmentation operation and moved to the next connected domain of the onion seed for detection.

(2) Determination of the secondary split point: Then, by extending the DF and EF line segments, an included angle $\angle D'EF'$ was formed, as shown in Fig. 9. In this specific region, the concave defect point with the largest depth was selected as the secondary segmentation point, and the deepest concave point in this region was the E' point. The image segmentation operation was completed by connecting EE'. If no concave point was found in the area of the included angle, the point closest to point E in the area of the included angle $\angle D'EF'$ was selected as the segmentation point. This point was usually the narrowest part of the seed outline, ensuring effective segmentation based on physical form in the absence of significant concave defects.

(3) Repeated adhesion detection and segmentation: The segmented image was tested for adhesion again. If there was still adhesion, Step 1 was performed again to continue the division of the adhesive seeds. If no adhesion was detected, the process proceeded to the detection of the connected domain of the next onion seed. The effect of the segmentation was shown in Fig. 11.



Fig. 11 - Adhesive seed segmentation effect

Field test

The image collection was carried out after the soil was covered and sown on the seedling tray, which was then moved to the image collection area by a conveyor belt. The speed of the conveyor belt was set to 600 plates per hour to ensure that when the plate enters the shooting area of the camera, the camera could cover 9×11 holes of the window, meaning each image contained 99 seedling holes. The camera shooting interval was set to 2.9 s, ensuring each seedling plate was shot twice, and each shooting area did not overlap. The average processing time of each image was 0.91 s, and the hole rate, pass rate, reseeding rate and average grain number were calculated. The error rate of test results was shown in Table 4. Finally, the number of green onion seeds in each hole in the seedling plate image was output. Among them, 0 seeds in each point were classified as empty point sowing, 1-3 seeds in each point were qualified, and 3 seeds in each point were repeated.

RESULTS

BP neural network training results

In this study, the traditional BP neural network architecture and the optimized BP neural network architecture were used for training. After 100 training cycles (epochs), the loss and accuracy trends of the two models were shown in Fig. 12.

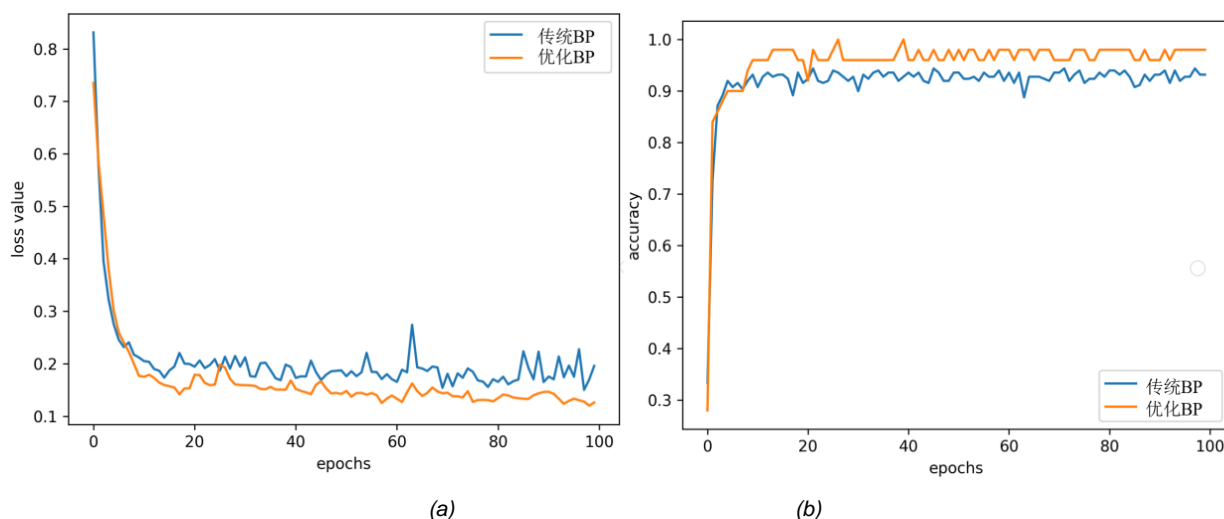


Fig. 12 - Loss rate versus accuracy rate. (a) Loss ratio; (b) Accuracy rate

It can be seen from Fig. 12(a) that after completing 20 iterations, the loss rate and accuracy of the two neural network models tend to converge basically. The loss rate of traditional BP neural network tends to be stable, in the range of about 0.19, but in the subsequent training process, the loss rate fluctuates significantly. In contrast, the optimized BP neural network showed a decreasing trend of loss rate after 20 iterations, and the final loss rate stabilized at about 0.14, and the corresponding fluctuation range was smaller, showing higher stability than the traditional BP neural network.

In terms of accuracy, as shown in Fig. 12(b), after iterative convergence, the classification accuracy of the traditional BP neural network was stable at about 93%, while the classification accuracy of the optimized BP neural network was stable at 98%. The performance of the optimized BP neural network continues to outperform the traditional BP neural network after convergence, especially in the later stage of training. The accuracy curve of the optimized model showed the advantage of higher stability and continuity.

The optimized BP neural network exhibits a lower loss rate, indicating that the gap between the model's predictions and the actual values has narrowed, thus improving prediction accuracy. Additionally, the increased accuracy reflects the model's enhanced ability to precisely distinguish between different categories in classification tasks. Overall, these improvements clearly demonstrate that the optimized BP neural network outperforms its pre-optimized version.

Field test verifies the results

In order to verify the accuracy of the system, a field test was carried out in the agricultural machinery greenhouse of Shandong University of Technology, as shown in Fig.13.



Fig. 13 - Field test

The error rates of qualified rate, replay rate, hole rate and average number of grains were obtained by comparing system detection with manual detection, as shown in the Table 4.

Table 4

The relative error rate of system and manual inspection

Number	Pass rate (%)	Replay rate (%)	Hole rate (%)	Average number of grains (grains)
	Relative error	Absolute error	Absolute error	Absolute error
1	2.15	2.02	0	0.02
2	2.17	1.01	1.01	0.02
3	2.10	2.02	0	0.03
4	1.10	0	1.01	0.02
5	2.08	1.01	0	0.04
6	3.19	2.02	1.01	0.03
7	1.12	1.01	0	0.03
8	2.06	1.01	1.01	0.01
9	3.22	1.01	2.02	0.02
10	3.16	2.02	1.01	0.03
Average error rate	2.24	1.31	0.707	0.025

Through the above experiments, the results of the seeding quality detection system and manual detection method were compared in this paper. In the measurement of pass rate, replay rate, hole rate and average number of grains, the system's detection errors were all within the acceptable error range. Specifically, the average relative error of the pass rate was 2.24%, the maximum relative error was 3.22%, and the minimum relative error was only 1.10%. The average absolute error value of the replay rate was 1.31%, and the average absolute error value of the hole rate was 0.71%. The absolute error of the average number of grains was 0.025 grains. According to the comprehensive index, the seeding quality detection system had high accuracy, and its detection speed was significantly better than the traditional manual detection method. Therefore, the system could effectively replace the manual inspection of green onion sowing quality, reduce the consumption of human resources, and improve the working efficiency.

CONCLUSIONS

(1) Design and hardware construction of the quality inspection system for scallion seedling and sowing on the scallion seedling tray: According to the size of the scallion precision seeder and the size of the scallion seed, a set of hardware image acquisition platform was built. These mainly include light boxes, light sources, cameras, lenses, and computers. Selecting the appropriate hardware could make the acquired image clearer, with higher contrast, which provided convenience for image processing.

(2) Image preprocessing and seed target extraction: A method was proposed to detect the seed quality of green onion in various soil environments. This method compared the two soil environment images in RGB and HSV color space, and found that the HSV space was more conducive to extraction of green onion seed targets. The fixed double threshold method was used to extract the green onion seed targets in HSV images, and the corrosion expansion method and small area method were used to enhance the images.

(3) Research on seeding quality detection algorithm: A method based on BP neural network was proposed to classify single seed and multiple adhered seeds. The classification model of single seed and adherent seed was successfully constructed by using 8 characteristic parameters, such as perimeter, area, shape factor, perimeter ratio, area ratio, error variance, shape factor ratio and concave defect distance ratio. In the training stage of BP neural network, the dataset was constructed, and data augmentation methods were applied to expand the dataset. The prediction performance of BP neural network was evaluated. The main concave defect segmentation algorithm was used to segment the adhered seeds, and the kernel method was used to judge the seed site belonging to the seeds on the seedling site line. Finally, the seeding quality of the whole image was assessed through a large number of seed quality testing experiments of green onions.

(4) Experimental verification: In the process of experimental verification, it was concluded that the average relative error between the qualified rate of system detection and manual detection was 2.24%. The maximum relative error was 3.22%, and the minimum relative error was 1.10%. Additionally, the average absolute error value of replay rate was 1.31%, and the average absolute error value of hole rate was 0.71%. The absolute error of average number of grains was 0.025 grains. The overall accuracy rate of the integrated seeding quality detection is 98% . The detection time of each image was 0.91 s.

ACKNOWLEDGEMENT

This research was supported by the Key Research and Development Project of Ningxia Hui Autonomous Region (2023BCF01052).

REFERENCES

- [1] Bai, J., Hao, F., Cheng, G., Li, C. (2021). Machine vision-based supplemental seeding device for plug seedling of sweet corn. *Computers and Electronics in Agriculture*, Vol. 188, pp. 106345.
- [2] Deng, X., Zhang, S., Shao, Y., Yan, X. (2022). A real-time sheep counting detection system based on machine learning. *INMATEH-Agricultural Engineering*, Vol. 67, Issue 2, pp. 85-94.
- [3] Ding, A., Zhang, X., Zou, X., Qian, Y., Yao, H., Zhang, S., Wei, Y. (2019). A novel method for the group characteristics analysis of yellow feather broilers under the heat stress based on object detection and transfer learning. *INMATEH-Agricultural Engineering*, Vol. 59, Issue 3, pp. 49-58.
- [4] Dong, W., Ma, X., Li, H., Tan, S., Guo, L. (2019). Detection of performance of hybrid rice pot-tray sowing utilizing machine vision and machine learning approach. *Sensors*, Vol. 19, Issue 23, pp. 5332.
- [5] Li, Y., Xiao, L., Li, W., Li, H., Liu, J. (2022). Research on recognition of occluded orange fruit on trees based on YOLOv4. *INMATEH-Agricultural Engineering*, Vol. 67, Issue 2, pp. 137.
- [6] Liu D., Gao H., Wang F., & Zhou J., (2017). Planting Agronomy and Mechanization Production Technology of Scallion in Zhangqiu (章丘大葱种植农艺及机械化生产技术), *Transactions of Agricultural Engineering*, Vol.7, Issue.1, pp.15-18+47.
- [7] Lv, Z., Zhang, W., Zeng, X., Han, Y., (2023). Design and experiment of potato seedling film-breaking device based on machine vision. *INMATEH-Agricultural Engineering*, Vol. 71, Issue 3, pp. 136.
- [8] Nicolau M.M., Alcover G.M., Hidalgo M.G., Jaume-i-Capo A. (2023). Improving concave point detection to better segment overlapped objects in images. *Multimedia Tools and Applications*, Vol.83, Issue 8, pp. 24339-24359. Peng S, Yang Y, Chen, L, Jiang Z., (2017). Analysis on planting and mechanized harvesting of Welsh onion (大葱种植与机械化收获分析), *Transactions of Journal of Chinese Agricultural Mechanization*, Vol.38, issue.9, pp.30-35.

- [9] Ren, X., Wang, H., Shi, X. (2021). Research on visual navigation path detection method for dense plum grove. *INMATEH-Agricultural Engineering*, Vol. 65, Issue 3, pp. 111.
- [10] Song R.S., Lan J.Z., Xia S.F., Hua J., (2011). Design of ZPXG-18 photoelectric instrument to automatically count and weigh up to 1 000 granules (ZPXG-18 型转盘斜刮式自动光电数粒仪和千粒重仪的设计), *Transactions of Acta Agriculturae Zhejiangensis*, vol.23, issue.5, pp.1023-1028
- [11] Sun, B., Mu, D., Dou, W., Sun, S., Jiang, M. (2022). Designing an intelligent irrigation system by using backpropagation neural network to predict water demand. *INMATEH-Agricultural Engineering*, Vol. 67, Issue 2, pp. 525-532.
- [12] Tan, S., Ma, X., Mai, Z., Qi, L., Wang, Y. (2019). Segmentation and counting algorithm for touching hybrid rice grains. *Computers and Electronics in Agriculture*, Vol. 162, pp. 493-504.
- [13] Wang H.X., Wu Y.Q., Li T.H., Zhang J.Q., & Hou J.L. (2019). Current situation and prospect of research on Welsh onion planting machinery (大葱种植机械研究现状与展望), *Transactions of Journal of Chinese Agricultural Mechanization*, Vol.40, Issue.2, pp.35-39.
- [14] Zhang, X., Hou, Z., Xuan, C., (2022). Design and experiment of recognition system for coated red clover seeds based on machine vision. *INMATEH-Agricultural Engineering*, Vol. 66, Issue.1, pp. 62-72.
- [15] Zhang, W., Han, Y., Huang, C., Chen, Z. (2022). Recognition method for seed potato buds based on improved YOLOv3-tiny. *INMATEH-Agricultural Engineering*, Vol. 67, Issue 2, pp. 364-373.
- [16] Zhu, Y., Wang, H., Li, Z., Zhen, T. (2023). Detection of corn unsound kernels based on GAN sample enhancement and improved lightweight network. *Journal of Food Process Engineering*, Vol. 47, Issue 1.

VEHICLE MASSIVE IMAGE DATA FILTERING AND USELESS IMAGE REUSE BASED ON FARMLAND BACKGROUND ANALYSIS

基于农田背景分析的车载大数据图像过滤与无效图像再利用

Hanlu JIANG, Fengzhu WANG, Gaoyong XING, Yangchun LIU, Weipeng ZHANG, Liming ZHOU

State Key Laboratory of Agricultural Equipment Technology, Chinese Academy of

Agricultural Mechanization Science Group Co., Ltd. Beijing 100083, China;

Tel: +86-(010)64882659; E-mail: liuyangchun@caams.org.cn

Correspondent author: Yangchun Liu

DOI: <https://doi.org/10.35633/inmateh-74-20>

Keywords: Image filtering; Background recognition; Effective farmland segmentation

ABSTRACT

The real-time images captured by agricultural machinery on-board monitoring equipment have complex backgrounds and different shooting angles. Especially for straw monitoring tasks, the utilization rate of images is relatively low. This paper presents a novel image classification and effective region segmentation method for straw returning in agriculture, leveraging semantic segmentation to enhance the efficiency of agricultural data analysis. The study addresses the challenges of manual straw cover analysis by proposing an automated approach to select images that meet monitoring standards. The methodology employs an encoder-decoder structure model, enriched with residual units, multi-scale convolution, and attention mechanisms. This model classifies images by calculating the pixel proportions of various scene categories and segments farmland areas to be inspected by incorporating distance information. The model's design is tailored to handle the complex and variable natural environments typical of vehicular monitoring scenarios, where semantic object boundaries can be fuzzy. The experimental results demonstrate that the proposed method achieves an overall sample classification accuracy of 93% for straw returning image classification and an 85.37% accuracy in dividing areas to be inspected. The method outperforms several mainstream semantic segmentation models, providing a more accurate and efficient means of processing agricultural monitoring images. The integration of distance information proves particularly beneficial in distinguishing the farmland areas under inspection, leading to clearer segmentation and more reliable data for agricultural decision-making. In conclusion, the study contributes to the field of agricultural intelligence by offering a robust method for image analysis that can be applied to optimize the use of straw return monitoring data.

摘要

农机车载监控设备拍摄的实时图像背景复杂，特别是对于秸秆定量检测任务，图像的利用率相对较低。本文提出了一种基于语义分割的图像高效分类和背景区域分割方法，通过计算各种场景类别的像素比例对图像进行分类，筛选出符合秸秆检测要求的图像，再并结合距离信息进一步分割秸秆检测区域，提高车载图像数据分析利用效率与秸秆检测准确度，以此来解决农田大数据杂乱，利用率低的问题。该方法采用编码器-解码器模型结构，融合了轻量型残差单元、多尺度卷积和注意力机制，在保证分割边界清晰的情况下降低模型参数。从不同模型的对比结果和可视化处理结果可以表明：该方法对秸秆图像分类的总体样本分类准确率为93%，对待检区域的划分准确率为85.37%，该模型对背景类别中农田的分割效果更好，空间位置更加准确。因此，本文的研究方法能提高秸秆信息化监测手段的应用效率，为农田监测图像的处理提供了一种更准确、更高效的方法。

INTRODUCTION

In recent years, with the aim of protecting the precious and rare black soil resources on Earth, there has been a particular emphasis on promoting conservation tillage techniques, such as straw mulch cover and no-tillage (Yu *et al.*, 2015), supported by information technology-enabled remote monitoring to enhance agricultural production. Currently, the monitoring terminals for conservation tillage have achieved the basic collection, transmission, and storage of agricultural big data, obtaining vast amounts of data on no-tillage machinery operation conditions and field straw vehicle monitoring images. However, for calculating the straw cover rate, data still require manual organization and human analysis, resulting in limited data application depth and low model technical content.

Therefore, it is imperative to strengthen the application research of data analysis technology in the context of conservation tillage, efficiently utilize straw cover images, and automatically select straw quantitative detection images that meet monitoring standards (Wu *et al.*, 2017).

Recent research findings indicate that in order to improve detection accuracy, image semantic segmentation methods are transitioning from probabilistic graphical models to deep learning models (Habas *et al.*, 2010; Chung *et al.*, 2010; Liu *et al.*, 2010; Long *et al.*, 2015; Chen *et al.*, 2018; Litjens *et al.*, 2017; Qi *et al.*, 2017; Jiang *et al.*, 2020). For instance, Zhou proposed a method that combines fully convolutional networks with conditional random fields for image semantic segmentation, merging probabilistic graphs with deep learning while maintaining computational sensitivity and global consistency (Zhou *et al.*, 2016). Ronneberger introduced a U-Net structure that effectively utilizes annotated samples through data augmentation, achieving end-to-end model training with fewer samples (Ronneberger *et al.*, 2015). Liu Kaidong employed U-Net as the backbone network and introduced a model based on R2U-Net and compact dilated convolution for segmenting and recognizing target muscle areas (Liu *et al.*, 2020). Badrinarayanan presented a fully convolutional neural network architecture called SegNet with an encoder-decoder structure (Badrinarayanan *et al.*, 2017). The encoder is used for object information parsing, while the decoder employs upsampling to restore the reduced feature maps to their original size. Lin introduced a universal multi-path optimization network, RefineNet, this model utilizes remote residual connections to capture all available information during the downsampling process, directly capturing high-level semantic features (Lin *et al.*, 2017). Zhao Shida applied generative adversarial networks and transfer learning to train ICNet, enabling fine segmentation of sheep skeletons' spine, ribs, and neck under different lighting conditions (Zhao *et al.*, 2021). Fang Peng integrated attention mechanisms, residual networks, and feature pyramids to extract image features, using a region generation network for broiler target classification, segmentation, and contour extraction (Fang *et al.*, 2021). Liu Wenya applied semantic segmentation to remote sensing images, proposing an automated extraction architecture based on DeepLabv3+ that can eliminate interference from field pixels and accurately extract urban green spaces (Liu *et al.*, 2021).

Although the above methods have solved the problem of detection accuracy in specific fields, there are still shortcomings in the domain of agricultural machinery onboard monitoring. Image quality is the key to straw detection, but it is often overlooked.

In view of the above problems, this paper addresses the impact of changes in the angle of in-vehicle cameras on the proportion of non-farmland backgrounds within the visual range and the visual distance on the division of areas to be inspected. It introduces a method for sample classification and the division of areas to be inspected based on semantic segmentation. Building upon the encoder-decoder structure, the paper incorporates key techniques such as residual units, multi-scale convolution, and attention mechanisms. It determines image categories by calculating the proportion of various background pixels in the image and simultaneously defines distance levels for the spatial distribution of farmland, establishing clear boundaries for the division of areas to be inspected in farmland.

MATERIALS AND METHODS

Problem analysis

The prerequisite for the application of straw return monitoring data is that the proportion of the fields to be inspected within the image range is large, and the distribution of straw is clear. It is common to retrofit agricultural machinery with rear-mounted cameras to make them intelligent. However, the stability and consistency of image quality are often compromised due to variations in the installation position and angle of the cameras.

Images captured by monocular cameras mostly follow a long-tail distribution, with areas closer to the camera having higher resolution, making it difficult to clearly observe the distribution of straw in distant pixels (Sreepada *et al.*, 2020). When the angle of view is too low, the machinery occupies the lower and middle parts of the image, obscuring the effective monitoring area of the field. When the angle of view is too high, the image may display a prominent skyline, the agricultural field area is reduced, and distant field objects appear blurred. Both of these image types fail to meet the requirements for straw monitoring.

As shown in Fig. 1, the left image illustrates the schematic of the manual method for measuring straw cover percentage using a rope. It uses a 50-meter rope divided into 250 collection points on average, it is placed along the diagonal of the plot to be tested, and the percentage of collection points where straw is present is calculated to determine the straw cover percentage of that plot. According to the area calculation formula, this method is most efficient when the plot is a square.

The 250 points can represent the collection area composed of 31,250 points. These collection points can be analogized to image resolution. Given that the YB-DB015A onboard camera has a spatial resolution of 320x240, it ensures that the agricultural background in the image is not less than 40%. As shown in the two images on the right, the intersection point of the camera's optical axis with the ground is always located at the center of the image. Therefore, as long as the center distance "c" exceeds 15 meters, it ensures that the pixel proportion of the areas to be inspected in the image is not less than 40%. Thus, based on the correspondence between the horizon vanishing point, the field of view angle " φ ," and the pitch angle " σ ," the maximum proportion of sky background at this point is 30%, and the machinery occupies no more than 10%.

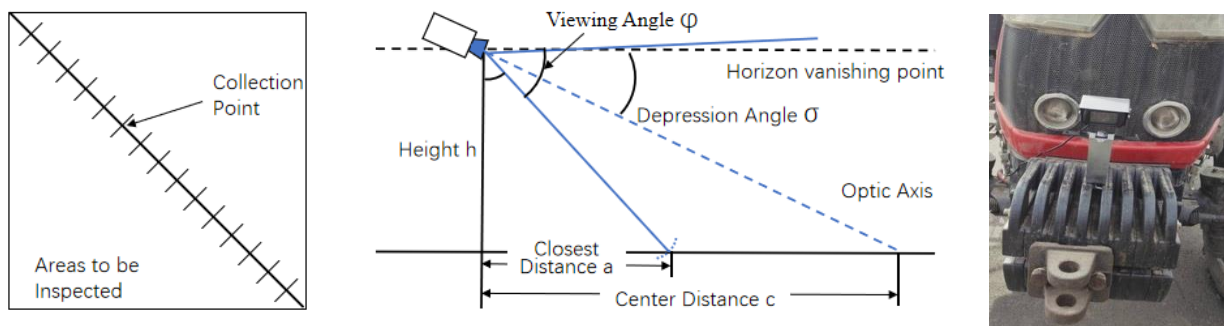


Fig. 1 - Pull rope method and camera imaging principle

Therefore, the image classification standards in this article are different from traditional images, it does not classify images based on scene categories but rather relies on combinations of pixel proportions in different scenes, images are divided into four categories (Xiao et al., 2015; Liang et al., 2020; Miao et al., 2015). Pixel-level semantic segmentation method perform both image classification and segmentation tasks simultaneously (Minaee et al., 2020; Jadhavo et al., 2018).

Experimental Data

To illustrate and verify the farmland background recognition and segmentation method proposed in this study, 1700 images were collected from straw application field monitored by image grabbing in Da'an City, Siping, Jilin province from April 15 through June 20, 2021. The conservation tillage types in Jilin province were Minimum-Tillage and No-Tillage of straw land covering. In order to meet the needs of straw monitoring, the monitoring terminals which are about more than 50 are installed on No-tillage planters, and the images were collected on sunny or daytime days at different times and environments. A YB-DB015A camera with a resolution of 320x240 was used and placed on front of the cab roof and initially tilted down 60 degrees toward the ground to get the straw image in front of the planter.

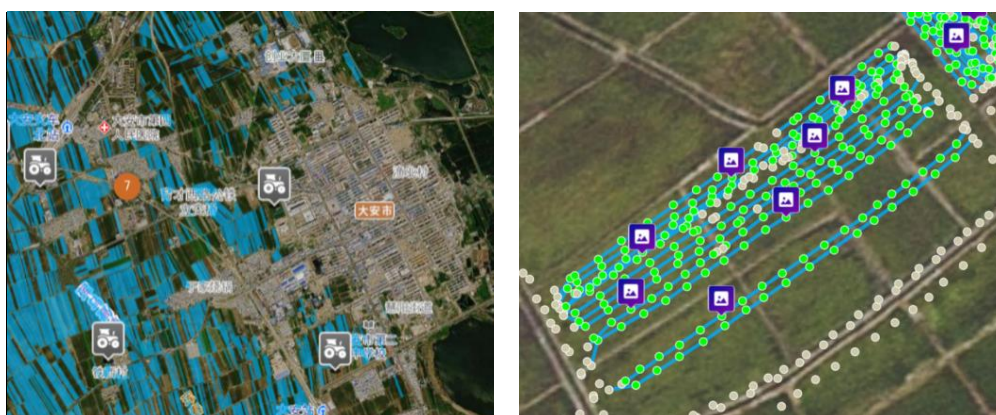


Fig. 2 - No-tillage layer in Da'an City

Based on the pixel proportions of different categories in the agricultural scene, sample images are divided into four classes (C1: high angle; C2: low angle; C3: standard image; C4: to-be-processed image). Each class has 365, 284, 325, and 726 images, respectively. As shown in Fig. 3, C1 images have a sky proportion greater than 30%, indicating a high angle that does not meet monitoring requirements.

C2 images have a machinery proportion exceeding 10%, indicating a low angle that does not meet monitoring requirements. C3 images have an agricultural field proportion of approximately 90%, representing standard images for straw cover monitoring. C4 images have a sky proportion less than 30% and a machinery proportion less than 10%, indicating to-be-processed images that can meet monitoring requirements through the division of areas to be inspected in the field.

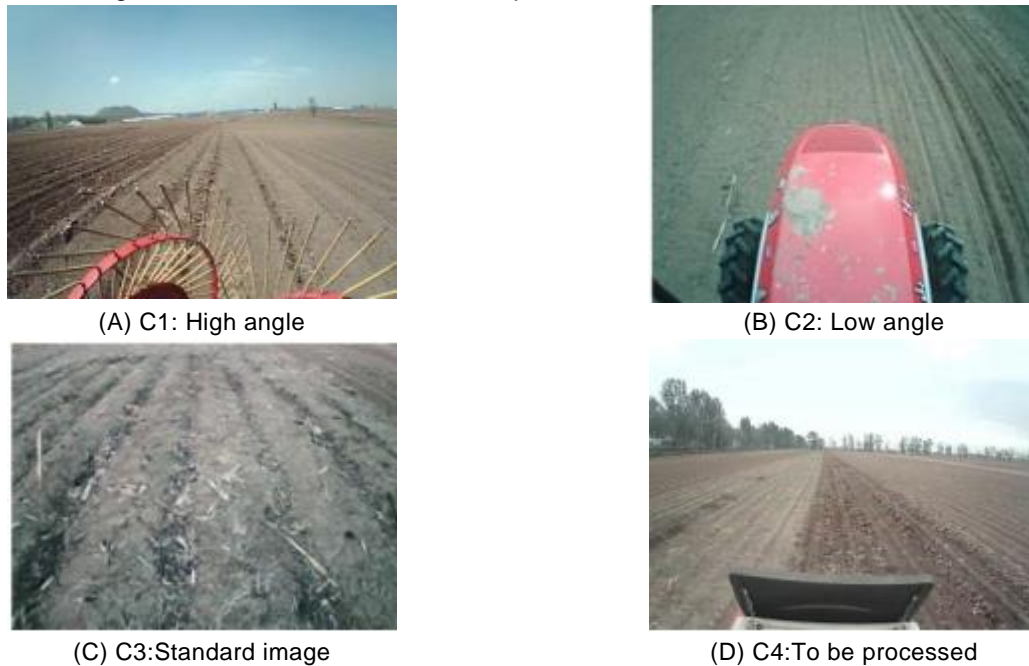


Fig. 3 - Typical images of four categories

All images were marked in LABELME and saved in red, green, and yellow in JSON format. In order to get label data, JSON was converted to single channel image. Moreover, for the fuzzy farmland in the distance (unable to distinguish straw distribution), distance information was used as supplementary information to segment effective farmland. The label picture and distance hierarchical map was showed in Fig. 4.

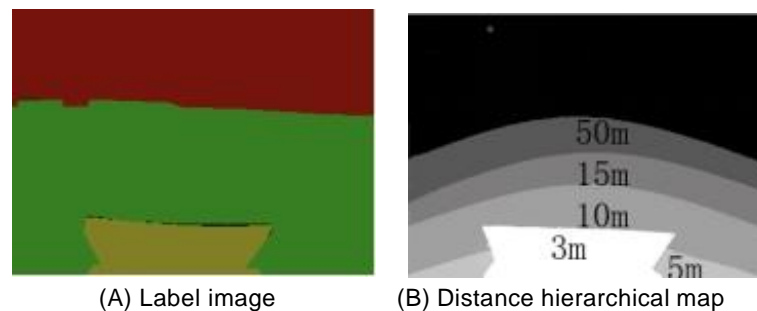


Fig. 4 - Annotated images of samples

Furthermore, the hardware setup used in this study consisted of a Precision T7920 tower workstation equipped with two Intel Xeon SP series processors and an Nvidia Quadro P2200 graphics card. The operating system utilized was Ubuntu Linux 18.04, and the development software included PyCharm and the PyTorch framework.

Model structure analysis

The design of model is an encoder-decoder structure, including a lightweight and efficient feature extraction module and a decoding module based on multi-scale convolution and ordinary convolution as shown in Fig. 5. In order to extract the background features in field, the encode module consists of three layers. Thus, the image was reduced to 80×60 pixels but increased to 128 features in the end by convolution and down sampling. The decode module includes multiple channels to analyze the semantic information between multi-scale features, wherefore the background label and distance level of the pixel are determined.

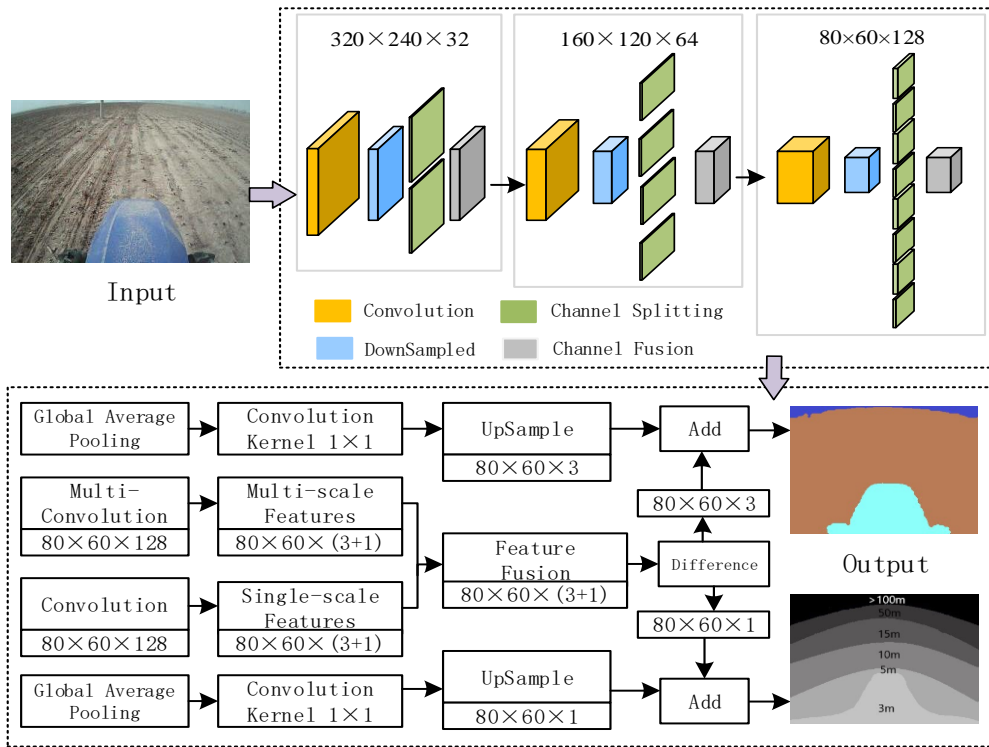


Fig. 5 - General structure diagram of the model

Small paraments encoder

In order to facilitate real time computation in filed, reducing the number of parameters and the calculation process are the key to model construction. In this study, with the increase of the number of encode layer, convolution kernel size and channel number play a major role. Assuming the optimization unit is not considered, the number of parameters is described as follows:

$$N_p \sim O(\sum_{l=1}^D K_{lx} \cdot K_{ly} \cdot C_{l-1} \cdot C_l) \tag{1}$$

where, C_{l-1} is the number of input channel; C_l is the number of output channel; K_{ly} and K_{lx} are the size of convolution kernel.

Then, the amount of calculation can be expressed as:

$$N_c \sim O(\sum_{l=1}^D K_{lx} \cdot K_{ly} \cdot M_{lx} \cdot M_{ly} \cdot C_{l-1} \cdot C_l) \tag{2}$$

where, M_{lx} and M_{ly} are the size of feature map in layer l.

Suppose the parameters of hybrid dilated convolution are not considered, the size of convolution kernel is 3x3, and the input channels are divided into two branches. Methods after improvement, the product of channels is reduced by 4 times, and convolution kernel is reduced by 1.5 times. Therefore, after the two channels are added, the parameters and the calculation are reduced to one third of the former one.

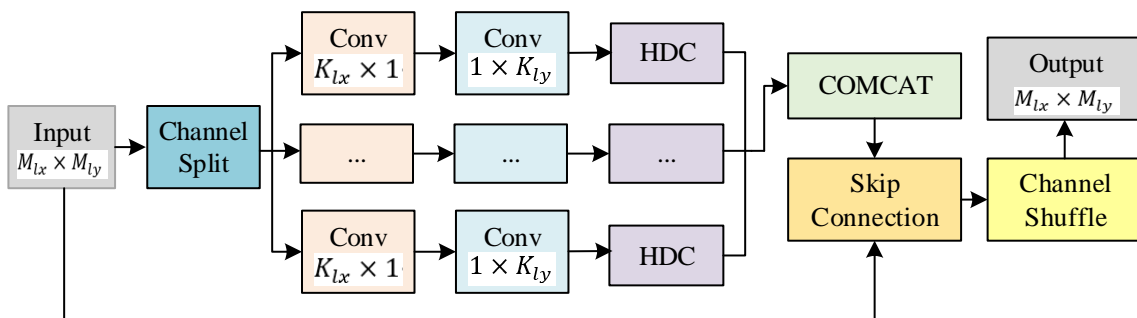


Fig. 6 - Residual network structure of block convolution

Additionally, in pixel-level semantic segmentation tasks, local information around the prediction points has a significant impact on predicting categories.

To expand the receptive field without sacrificing resolution, a Hybrid Dilated Convolution (HDC) is used to enhance local information, addressing the issue of information loss when restoring the image to its original size in the decoding module through upsampling and pixel addition, as shown in Fig. 7. Finally, after concatenating the channels of multiple branches, the original feature maps and the residuals extracted from each branch are fused in the form of skip connections to restore the original channel count. Due to the lack of correlation in feature dimensions caused by channel branches, it is necessary to shuffle the channel order of feature maps before entering a feature extraction module to enhance the global correlation of feature maps.

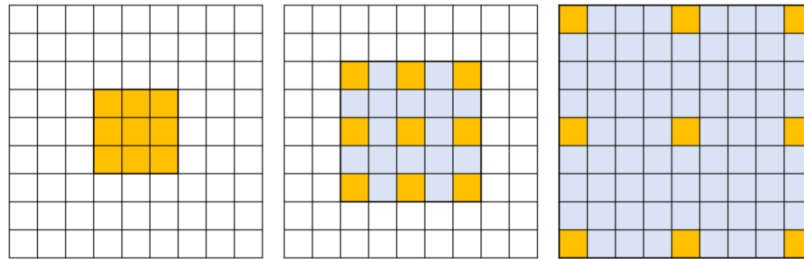


Fig. 7 - Dilation convolution with 3x3 kernel size

Multi-scale convolution decoder

Multi-scale convolution algorithm is a common method to extract different layers of semantic information. The output of the encoder is convolved in three different scales, for which 7x7, 5x5, and 3x3 convolution kernels were selected, respectively. The convolution kernel with large scale can capture the association between far away pixels, while the convolution kernel with small scale can extract the detail of near small targets. It is easier to analyze near machine and distant sky and farmland by combining convolution kernels of different sizes. Therefore, the size of the feature map is reduced in the initial process. As shown in Fig. 8, because the semantic segmentation task requires that the output size should be the same as the original image, it is necessary to design an upsample to recover the feature map. Subsequently, the same size features are fused by convolution with 1x1 convolution kernel. After 3 times of upsampling and 2 times of feature fusion, the output is the same size as the input feature map and semantic channel.

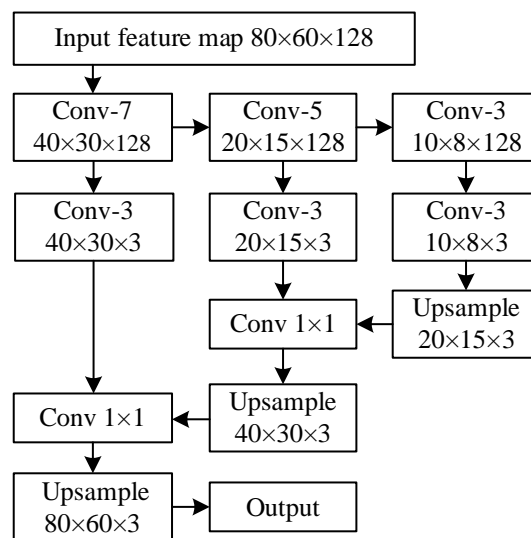


Fig. 8 - Structure of multi-scale convolution

Effective region segmentation based on distance information

Distance estimation and semantic segmentation are both of scene perception. Distance estimation describes the geometric relationship in space, while semantic information represents the entity meaning of different background of the scene. Therefore, the distance information is introduced into the decode module as the auxiliary information, both of which share context information to the purpose of segmenting effective farmland. The decoder consists of four branches, two of which are multiscale convolution module and normal convolution module. Except for the three semantic channels mentioned in the previous section, a distance channel is added.

After point multiplication, the output of the two modules is divided into semantic and distance parts. The other two branches complete global average pooling (GAP), convolution with 1×1 and up sampling in turn to retain the uniqueness of the two types of information. Finally, the semantic prediction results and distance classification results are obtained by adding the outputs of the two kinds of information.

RESULTS

Case Analysis Impact of Residual Networks on Training Accuracy

To address the increased difficulty in training deep networks, residual networks were introduced in this model to enhance the fitting capability of high-dimensional models, and improvements were made to the convolutional kernels and residual branches of the residual network, resulting in a three-fold reduction in the number of parameters. To verify the impact of introducing residual modules and improved residual modules on training accuracy, this section compares the training iteration accuracy curves for different models to highlight the advantages of residual modules. The experimental results are shown in Fig. 9. It can be observed from the curve variations that the model without residual modules exhibits lower training speed and iteration accuracy compared to the results with the introduction of residual modules. Additionally, the improved residual module, due to its significantly reduced number of parameters, has slightly lower iteration speed than the unimproved model. However, the final training accuracy of the model is essentially consistent with the unimproved version. Therefore, introducing residual networks in the model optimizes the training process and, after improvements, does not affect the model's training accuracy.

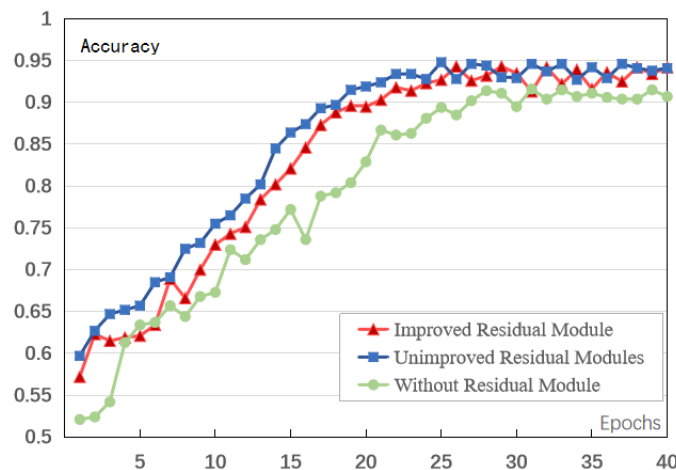


Fig. 9 - Iterative accuracy curve of sample training

Classification Results of Captured Image Samples

Among various semantic segmentation methods, this paper selected four representative networks for comparison: UNet with an encoder-decoder structure, RefineNet with residual optimization, PSPNet with pyramid pooling, and the prevailing DeepLabv3+. The model was trained using 1000 images, with 200 for validation and 500 for testing. From the classification results of the test images, it can be seen that the overall accuracy of all methods exceeds 90%, with this paper's method achieving the highest accuracy at 93%. The results clearly show that the three methods that utilize multi-scale convolution outperform UNet and RefineNet. This paper's method demonstrates greater accuracy in classifying C3 and C4, indicating that the model is more sensitive to pixels labeled as farmland. DeepLabv3+ performs well in all categories, particularly excelling in C2, suggesting that this model provides more accurate predictions for individual pixels.

Table 1

Results (%) of image classification

Number	Model	C1	C2	C3	C4	Accuracy
1	UNet	90.24	82.89	93.61	91.30	90.24
2	RefineNet	89.43	85.52	91.48	92.75	90.62
3	PSPNet	91.05	86.83	94.68	92.75	91.81
4	DeepLabv3+	93.49	92.10	92.55	92.27	92.63
5	Ours	92.68	89.47	94.68	93.71	93.00

The confusion matrix for this paper's method in Fig. 10 shows that C2 is easily misclassified as C3, indicating that some machinery pixels are incorrectly identified as farmland, resulting in the classification results of C3 exceeding the number of samples. However, there are no misclassifications between C3 and C4, primarily because most images that meet the requirements for C4 arise due to different seed machine models, causing the camera to capture both the sky and machinery within the normal monitoring angle. The proportions of both scenarios are less than the requirements for C1 and C2. Consequently, this paper's method not only achieves higher accuracy, while providing a more precise representation of the C4 category, which is the focus of this paper, effectively addressing the image classification issue.

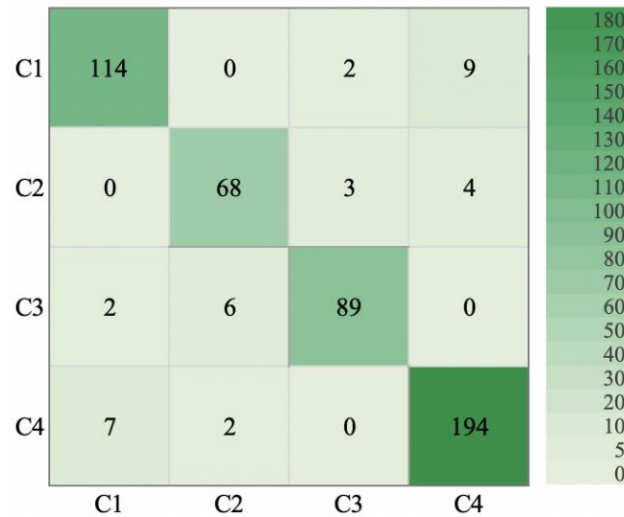


Fig. 10 - Confusion Matrix of our method

Background Segmentation and Areas to be Inspected Division Results

The background segmentation and areas to be inspected division results are presented in Table 2. Two sample images from classes C1 and C4, each containing three different types of plots, were selected for quantitative analysis of the model's performance. The C1 image was captured on a cloudy afternoon, while the C4 image was captured on a sunny morning. From the experimental results, it can be observed that the model proposed in this paper performed well in terms of total accuracy, intersection over union (IoU), and the number of parameters used. Particularly, compared to DeepLabv3+, one of the best-performing semantic segmentation models, although it did not have an advantage in single-pixel prediction accuracy, it achieved a roughly 20-fold reduction in model parameters, and achieved the best results in the segmentation of farmland areas to be inspected, with an accuracy of 85.37%. This is due to the residual modules maintaining high feature extraction capability even with reduced parameters, the entire encoder module exhibits higher encoding efficiency. Additionally, it indicates that the decoder, which combines multi-scale convolution and attention mechanisms, effectively highlights distance features. In the context of areas to be inspected division, it outperforms other semantic segmentation models significantly. Therefore, this method is the most suitable for the requirements of farmland areas to be inspected division.

Table 2

Results (%) of segmentation					
Background Categories and Evaluation Methods	UNet	RefineNet	PSPNet	DeepLabv3+	Ours
Sky	92.24	94.54	94.46	96.24	94.26
Machine	80.26	82.64	85.41	86.29	86.37
Fram	77.50	77.12	74.95	88.10	86.34
Areas to be Inspected	63.24	69.34	72.24	73.31	85.37
Total Accuracy	76.04	86.61	85.26	96.02	94.54
IoU	73.42	80.45	79.79	83.25	84.96
Model Parameters(M)	7.76	14.35	37.30	41.00	2.10

Visualization of Farmland Background Segmentation Results

The visualization of background segmentation results for C1 samples is shown in Figure 10. Comparing the ground truth and predicted results for various methods in Fig. 11, it can be observed that most algorithms accurately capture the boundary between the sky and farmland in the scene images. However, UNet exhibits confusion in boundary distinction, as machinery with darker colors tends to be confused with the surrounding farmland, resulting in poorer segmentation results. RefineNet produces segmentation regions that are similar to the center region of the ground truth, but with overly smooth boundaries. PSPNet's segmentation is influenced by the category with more pixels, causing the center region to shift downward. However, it has a clear boundary. DeepLabv3+ demonstrates good segmentation results and is visually similar to this paper's method, but the boundaries are more distinct. This paper's method achieves more accurate segmentation of the central farmland region, benefiting from the inclusion of distance information in the network, which enhances the spatial characteristics of the farmland category. This ensures that the farmland area is not misclassified as other categories in the entire image, aligning better with the task requirements of this paper.

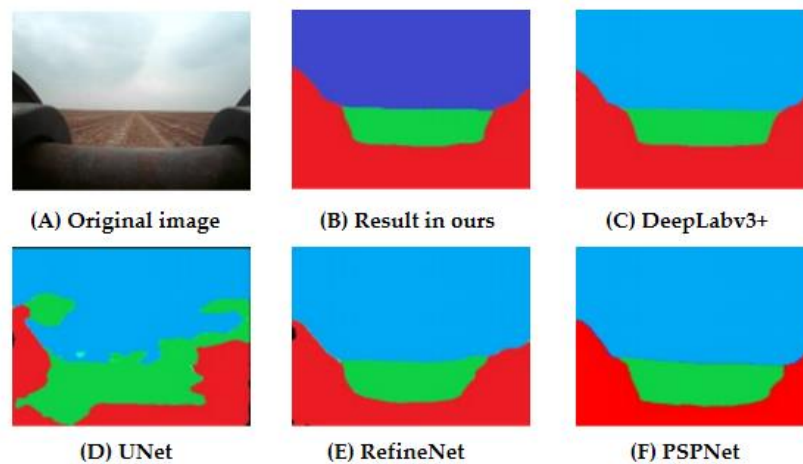


Fig. 11 - Farmland background segmentation image

Visualization of Areas to be Inspected Division Results

The visualization of areas to be inspected division results for C4 samples is shown in Fig. 12.

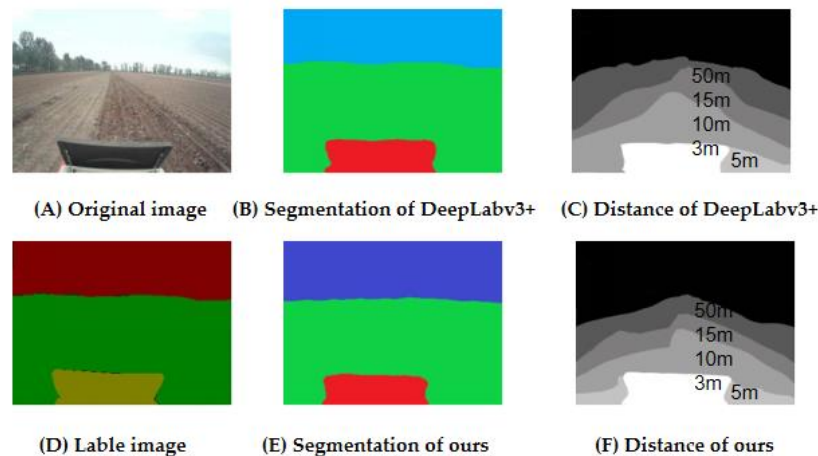


Fig. 12 - Effective region segmentation image

The results show that, in terms of background segmentation, both methods still exhibit no significant differences. This paper's method focuses more on the central location, while DeepLabv3+ shows more distinct boundaries. In the smoothed distance prediction map, DeepLabv3+ exhibits a more pronounced overflow phenomenon beyond the 10-meter level boundary. It also misclassifies a 5-meter area in the bottom left corner. The 50-meter boundary line aligns almost with the skyline, failing to separate farmland at a distance. This paper's method provides a clearer separation of areas for each level, without misclassification due to the lower proportion of samples. The position of the 50-meter level boundary is closer to the level map, allowing for better differentiation of distant information.

This paper uses the 15-meter level line as the boundary for areas to be inspected and obtains the division map of farmland areas to be inspected. From the map, it is evident that this paper's method produces a more accurate division of areas to be inspected. This is attributed to the decoding module, which includes both multi-scale convolution branches and a separate distance branch, allowing for better resolution of distance information during the division of areas to be inspected.

Experimental effect of straw cover detection

For the straw target detection task, the average deviation of various image regions after segmentation is generally more balanced and better than the results before segmentation. This is because after the division of the test area, there is no interference from the sky background and distant farmland in the sample image, making the test sample image closer to the standard image. However, in undivided image samples, the higher the camera angle, the greater the proportion of sky background in the image. In the white balance processing, the sky with a color closer to white replaces straw as the benchmark for color correction, rendering the color perception module for straw in the model ineffective. Therefore, without dividing the inspection area, when a large amount of straw is covered in the field, an angle that is too high will lead to a higher straw coverage rate, while when there is less straw covered, it will result in a lower straw coverage rate.

Table 3

Results of before and after effective region segmentation

Camera Angle	Before region segmentation		After region segmentation	
	Excessive straw	Fewer straw	Excessive straw	Fewer straw
Normal	0.974	1.062	0.974	1.062
Slightly high	1.095	0.892	0.965	1.054
Too high	1.134	0.851	0.963	1.087
Average Deviation	0.096		0.05	

CONCLUSIONS

(1) A novel approach for image classification and division of farmland areas to be inspected based on semantic segmentation is proposed. This method combines encoder-decoder structures, residual units, multi-scale convolution, and attention mechanisms. It classifies individual pixels in onboard captured images using semantic analysis, calculates the pixel proportions of various scene categories, and determines the image state. At the same time, it incorporates distance information into the segmentation of farmland areas to be inspected, making it possible to use a large number of images in the "to-be-processed" state as the calculation basis for quantitative analysis of straw returning.

(2) Experimental results indicate that, for onboard captured samples in various farmland scenes, the method proposed in this paper, based on semantic segmentation, achieves an overall sample classification accuracy of 93% for straw returning image classification and farmland areas to be inspected division, a background segmentation accuracy of 94.54%, and an areas to be inspected division accuracy of 85.37%. This method outperforms various mainstream semantic segmentation methods in straw monitoring applications, providing technical support for straw returning data processing and quantitative calculations.

(3) Compared with the results, it has been proven that the method proposed in this paper performs better in segmenting farmland in background categories and has more accurate spatial positions for vehicle captured samples in different agricultural scenes. This method integrates distance information to divide the image waiting area, which enables a large number of pending state images to serve as the calculation basis for quantitative analysis of straw returning to the field, effectively improving the application efficiency of straw monitoring images

ACKNOWLEDGEMENT

The work was sponsored by the National Key R&D Program Project of China (2022YFD2000300).

REFERENCES

- [1] Badrinarayanan V, Kendall A, Cipolla R. (2017). SegNet: A Deep Convolutional Encoder-Decoder Architecture for Image Segmentation. *IEEE Transactions on Pattern Analysis & Machine Intelligence*, USA.

- [2] Chen L C, Papandreou G, Kokkinos I. (2018). DeepLab: Semantic Image Segmentation with Deep Convolutional Nets, Atrous Convolution, and Fully Connected CRFs. *IEEE Transactions on Pattern Analysis and Machine Intelligence*, Vol. 40, pp. 834-848, United States.
- [3] Chung C, Chiu, MinY. (2010). A Robust Object Segmentation System Using a Probability-Based Background Extraction Algorithm. *IEEE Transactions on Circuits & Systems for Video Technology*, Vol. 20, pp. 518-528, United States.
- [4] Fang P, Hao H, Li T. (2021). Instance Segmentation of Broiler Image Based on Attention Mechanism and Deformable Convolution (基于注意力机制和可变形卷积的肉鸡图像实例分割). *Transactions of the Chinese Society for Agricultural Machinery*, Vol. 52, pp. 257-265, Beijing/China.
- [5] Habas P A, Kim K, Corbett-Detig J M. (2010). A spatiotemporal atlas of MR intensity, tissue probability and shape of the fetal brain with application to segmentation. *Neuroimage*, Vol. 53, pp. 460-470, United States.
- [6] Jadhav J K, Singh R P. (2018). Automatic semantic segmentation and classification of remote sensing data for agriculture. *Mathematical Models in Engineering*, Vol. 4, pp. 112-137, United States.
- [7] Jiang H, Zhang C, Zhang Z. (2020). Detection Method of Corn Weed Based on Mask R-CNN (基于 Mask R-CNN 的玉米田间杂草检测方法). *Transactions of the Chinese Society for Agricultural Machinery*, Vol. 51, pp. 227-235+254, Beijing/China.
- [8] Liang X, Li Y, Zhou Y. (2020). Study on the abandonment of sloping farmland in Fengjie County, *Three Gorges Reservoir Area, a mountainous area in China*. *Land Use Policy*, Vol. 97, pp. 104760, United Kingdom.
- [9] Lin G, Milan A, Shen C. (2017). RefineNet: Multi-path Refinement Networks for High-Resolution Semantic Segmentation. *2017 IEEE Conference on Computer Vision and Pattern Recognition (CVPR)*. *IEEE*, pp. 5168-5177, United States.
- [10] Litjens G, Kooi T, Bejnordi B E. (2017). A Survey on Deep Learning in Medical Image Analysis. *Medical Image Analysis*, Vol. 42, pp. 60-88, Netherlands.
- [11] Liu B, Cheng H D, Huang J. (2010). *Probability density difference-based active contour for ultrasound image segmentation*. *Pattern Recognition*, Vol. 43, pp. 2028-2042, United Kingdom.
- [12] Liu K, Xie B, Zhai Z. (2020). Target Muscle region Recognition in Ovine Hind Leg Segmentation Based on R2U-Net and Atrous Convolution Algorithm (基于 R2U-Net 和空洞卷积的羊后腿分割目标肌肉识别). *Transactions of the Chinese Society for Agricultural Machinery*, Vol. 51, pp. 507-514, Beijing/China.
- [13] Liu W, Yue A, Ji J. (2020). Urban green space extraction from GF-2 remote sensing image based on DeepLabv3 + semantic segmentation model (基于 DeepLabv3+语义分割模型的 GF-2 影像城市绿地提取). *Remote Sensing for Land and Resources*, Vol. 32, pp. 120-129, Beijing/China.
- [14] Long J, Shelhamer E, Darrell T. (2015). Fully Convolutional Networks for Semantic Segmentation. *IEEE Transactions on Pattern Analysis and Machine Intelligence*, Vol. 39, pp. 640-65, United States.
- [15] Miao R, Tang J, Chen. (2015). Classification of farmland images based on color features. *Journal of visual communication & image representation*, pp. 138-146, United States.
- [16] Minaee S, Boykov Y, Porikli F. (2020). Image Segmentation Using Deep Learning: A Survey. *IEEE Transactions on Software Engineering*, United States.
- [17] Qi C R, Su H, Mo K. (2017). PointNet: Deep Learning on Point Sets for 3D Classification and Segmentation. *2017 IEEE Conference on Computer Vision and Pattern Recognition (CVPR)*, Vol. 1, pp. 77-85, United States.
- [18] Ronneberger O, Fischer P, Brox T. (2015). U-Net: Convolutional Networks for Biomedical Image Segmentation. *International Conference on Medical Image Computing and Computer-Assisted Intervention*. Springer International Publishing, Vol. 9351, pp. 234-241, Germany.
- [19] Sreepada R, Patra B. (2020). Mitigating long tail effect in recommendations using few shot learning technique. *Expert Systems with Application*, Vol. 140, pp. 112887.1-112887.17, United States.
- [20] Wu J, Ye C, Sheng V S. (2017). Active learning with label correlation exploration for multi-label image classification. *IET Computer Vision*, Vol. 11, pp. 577-584, United Kingdom.

- [21] Xiao D, Jiang, Qi G. (2015). Extraction of farmland classification based on multi-temporal remote sensing data. *Transactions of the Chinese Society of Agricultural Engineering*, Vol. 31, pp. 145-150, Beijing/China.
- [22] Yu H, Liang X, Zhang Y. (2015). Effects of Different Straw Returning Modes on the Soil Microorganism and Enzyme Activity in Corn Field. *Journal of Agricultural Resources and Environment*, Vol. 32, pp. 305-311, Tianjin/China.
- [23] Zhao S, Wang S, Bai Y. (2021). Real-time Semantic Segmentation of Sheep Skeleton Image Based on Generative Adversarial Network and ICNet (基于生成对抗网络与 ICNet 的羊骨架图像实时语义分割). *Transactions of the Chinese Society for Agricultural Machinery*, Vol. 2, pp. 329-339+380, Beijing/China.
- [24] Zhou H, Zhang J, Lei J. (2016). Image semantic segmentation based on FCN-CRF model. *2016 International Conference on Image, Vision and Computing (ICIVC)*, Vol. 8, pp. 9-14, United Kingdom.

QUANTITATIVE ANALYSIS OF THE MIXING CHARACTERISTICS OF SIMULATED BROWN RICE PARTICLES BASED ON THE DISCRETE ELEMENT METHOD

基于离散元模拟的糙米颗粒混合特性定量分析

Yonghao ZHAI, Biao XIE, Yanxiang YANG, Quanbiao HU, Wei YOU, Nian LIU, Qiang ZHANG¹

College of Engineering, Huazhong Agricultural University, Wuhan / China;

Key Laboratory of Agricultural Equipment in Mid-lower Yangtze River, Ministry of Agriculture, Wuhan / China

Tel: +86 27 87282120; E-mail: zq604@mail.hzau.edu.cn

DOI: <https://doi.org/10.35633/inmateh-74-21>

Keywords: Sprouted brown rice machine tank, Grown rice, Discrete element method, Mixing characteristics, Quantitative analysis

ABSTRACT

The mixing characteristics and movement principles of brown rice particles in two different types of sprouted brown rice machine tanks were investigated based on the discrete element method. Through numerical simulation, the effects of different mixing process parameters on the mixing uniformity and energy consumption of brown rice particles were quantitatively analyzed. The optimal mixing parameters for blade-type sprouted brown rice machine were 40.16% filling degree and 20 r/min rotational speed and for drum-type sprouted brown rice machine were 37.9% filling degree and 20 r/min rotational speed. In addition, a drum-type sprouted brown rice machine mixing test platform was designed and constructed. Physical tests validated the accuracy of the discrete element simulation outcomes, confirming their consistency with physical test environments in terms of the change rule of the movement state and mixing uniformity of brown rice particles. This paper provides a significant theoretical basis and experimental support for the refinement of the design and the enhancement of the manufacturing process for the sprouted brown rice machine.

摘要

本文基于离散元法研究了糙米颗粒在两种不同类型的发芽糙米机罐体内的混合特性和运动规律。通过数值模拟,定量分析了不同混合工艺参数对糙米颗粒混合均匀度和能耗的影响,确定了最优混合工艺参数:叶片式发芽糙米机填充度 40.16%、转速 20r/min,滚筒式发芽糙米机填充度 37.9%、转速 20r/min。此外,还设计并搭建了一套滚筒式发芽糙米机混合试验平台,通过物理试验验证了离散元模拟仿真结果的准确性,表明仿真环境与物理试验环境下糙米颗粒的运动状态及混合均匀度的变化规律一致。这一研究为发芽糙米机的设计优化和生产工艺优化提供了重要的理论依据和实验支持。

INTRODUCTION

China is a large producer and consumer of rice. Brown rice obtained after coarse dehulling retains all the nutrients of rice, but its taste is poor and indigestible which is not easily accepted by the public. To address this issue, some scholars have developed sprouted brown rice, a whole grain variant. This product is derived from brown rice that has been cultivated to a specific bud length under optimal temperature and humidity conditions. Sprouted brown rice boasts an array of bioactive compounds, offering higher nutritional value and an enhanced flavor profile compared to traditional brown rice (Zhang *et al.*, 2021). Research on the production process of sprouted grains has been a hot and difficult issue in the deep processing of grains (Chen *et al.*, 2021).

Scholars at home and abroad have tried to improve the method of grain water absorption to improve the quality of sprouted grains. For example, Jia *et al.* (2012), introduced a new technique to produce sprouted brown rice by circulating humidification and conditioning treatment. The process used atomized humidification and supplemented with mixing to make the brown rice tumble and flow to achieve the required moisture content for germination (Yaraghi *et al.*, 2018). The uniformity of its mixing has a direct impact on the quality of sprouted brown rice. At present, the research and development of sprouted grains primarily remains confined to laboratory-based theoretical studies, centering on fundamental investigations into their nutritional makeup.

¹ Yonghao Zhai, B.S. Stud. Eng.; Biao Xie, M.S. Stud. Eng.; Yanxiang Yang, M.S. Stud. Eng.; Quanbiao Hu, M.S. Stud. Eng.; Wei You, M.S. Stud. Eng.; Nian Liu, Prof. Ph.D. Eng.; Qiang Zhang, Prof. Ph.D. Eng.

The humidification and conditioning processes involved in sprouted grain production face challenges, including a lack of clear methods for quantitatively describing the mixing mechanism of stratified particles. Difficulties in achieving uniform conditioning control significantly hinder widespread and high-quality application of this technology in the grain processing industry. Therefore, it is essential to examine the mixing and movement principles of brown rice within the sprouted brown rice machine.

Recently, discrete element numerical simulation has been widely used in the study of particle mixing laws in mixers (*Zuo et al., 2021*). This method can intuitively reflect the motion and mixing law of particle population and help to obtain the optimal mixing parameters and energy consumption data. The discrete element method is a numerical simulation method based on the assumption of discontinuity, which has become an important means to study particle mixing (*Bao et al., 2018; Zhang et al., 2020*). The discrete element method enables the acquisition of detailed information on individual particles, such as velocity and direction, which illuminates the underlying principles and characteristics of the particle population (*Chandratilleke et al., 2021*). By employing this method, the energy consumption of brown rice particles when they are mixed uniformly can be understood. Information such as the motion trajectory, position, velocity, direction and force of individual particles can be localized (*Tang et al., 2017*). The discrete element method can also be used to analyze the particle mixing behavior in a mixer (*Yu et al., 2022*). For example, *Zhao et al., (2019)*, used the discrete element method to analyze the motion trajectory of particles in the soil-fertilizer mixing process to obtain the mixing uniformity of fertilizer particles in the soil. *Chen et al., (2015)*, distinguished the radial mixing motion of particles in the drum into active zone, stable zone and mixing dead zone based on the discrete element method. *Wang et al., (2020)*, used the coefficient of variation and net power consumption as evaluation indexes to optimize the parameters such as rotational speed and filling degree through discrete element simulation. This optimization process aimed to identify the optimal combination of mixing parameters. *Yang et al (2021)* constructed a mathematical model of the correlation between the rotational speed of the screw mixer blades, the filling volume and the degree of particle mixing, and optimized the mixing process parameters based on this model.

Most scholars used discrete element numerical simulation to study the mixing kinematic properties of binary spherical particles in the drum. This revealed a link between drum rotational speed and particle states. As drum rotational speed rose, six kinematic states would appear successively: sliding, stepping, rolling, small waterfall, large waterfall and centrifugal (*Tsunazawa et al., 2022*). And there are three mixing mechanisms of convection, diffusion and shear in the mixing process (*Tanabe et al., 2019; Ebrahimi et al., 2021*). The degree of influence of each mixing stage on the mixing effect is different, and the mixing performance of particles with complex shapes is lower. Meanwhile, most scholars often apply similarity theory approach to obtain the relationship between the prototype mixer and model parameters. Similarity theory fused with discrete element numerical simulation studies favors the model scaling aspect.

In summary, the current research mostly uses spherical particles to validate the discrete element simulation, and there are fewer studies on real brown rice particles. Therefore, this paper primarily investigated the mixing characteristics of real brown rice grains in the tank. The two comparative test programs of reducing the tank and particle amplification were proposed based on the similarity theory. The two typical sprouted brown rice machine tanks of brown rice particles in the optimal mixing process parameters and the law of change of energy consumption were quantitatively analyzed. A physical test platform specifically designed for drum-type sprouted brown rice machine mixing was built. The accuracy and reliability of discrete element numerical simulation were validated by comparing the outcomes of the physical tests conducted on this platform with the simulation results.

MATERIALS AND METHODS

Discrete element numerical simulation system

Due to the large prototype of sprouted brown rice machine, computer hardware and EDEM software limitations, the simulation was based on similar theoretical principles to shrink the tank or enlarge the brown rice particles. In this paper, the mixing movement principles of brown rice particles under the two conditions of enlarged particles and reduced tank were compared and analyzed.

EDEM software was applied to simulate the particle mixing characteristics in the tank of a non-soaked sprouted brown rice machine with ellipsoidal particles with low water content and without considering the effect of adhesion. The Hertz-Mindlin (no slip) contact mechanics model was used. Table 1 lists the initial boundary and physico-mechanical parameters of the simulated tank and brown rice particles.

Table 1

Parameters required for simulation	
Parameters	value
Particle density/ ($\text{kg}\cdot\text{m}^{-3}$)	1538
Particle Poisson's ratio	0.4
Interparticle coefficient of recovery	0.6
Coefficient of static friction between particles	0.43
Coefficient of interparticle kinetic friction	0.01
Coefficient of static friction between particles and inner wall	0.3
Coefficient of kinetic friction between particles and inner wall	0.01
Coefficient of recovery of particles from the inner wall	0.6
Mixer tank density/ (steel, $\text{kg}\cdot\text{m}^{-3}$)	7800
Tank Poisson's ratio	0.3
Mixer tank shear modulus/ Pa	7×10^{10}
Particle shear modulus/ Pa	1.1×10^7

Numerical simulation conditions and test program for the tank of the blade-type sprouted brown rice machine

Blade type sprouted brown rice machine tank ensures uniform mixing and precise control during brown rice germination, improving germination quality, but can be costly due to the complexity of the technology and relatively complicated maintenance. Roller type sprouted brown rice machine has high production efficiency, simple operation and wide practicality, but with low loading factor, inconvenient drainage and high power consumption.

Blade type sprouted brown rice machine tank was mainly composed of three parts: tank shell, center shaft and drum bottom plate. The structure was simple and the processing cost was low. The three-dimensional model was shown in Fig. 1.

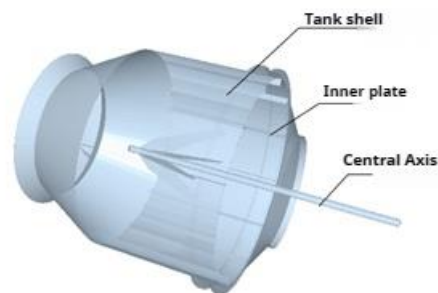


Fig. 1 - 3D model of the blade type sprouted brown rice machine tank

The diameter of the tank was 1600 mm, and the mixing area was 1000 mm long. There were 12 straight plates and 4 inclined plates in the drum, which were evenly distributed. There were four identical and evenly distributed mixing blades on the center shaft to match the mixing, with a blade angle of 42° , thickness of 2 mm, width of 210 mm and vertical distance of 220 mm. The brown rice grains simulated in the test were Dongnong 429, which were oval in shape. One hundred grains were randomly selected for measurement, with the long axis ranging from 5.5 mm to 6.8 mm, and the short axis ranging from 2.6 mm to 3.1 mm. Considering the effect of brown rice particle size, two particle models, long and short, were selected for the test.

Unchanged tank, enlarged grain, bladed sprouted brown rice machine tanks

In order to meet the simulation conditions, the size of the tank of the sprouted brown rice machine was kept unchanged and the brown rice particle model was enlarged. Five round balls with different radii were used to fill in, and the approximate short and long particle models were obtained, as shown in Fig. 2.

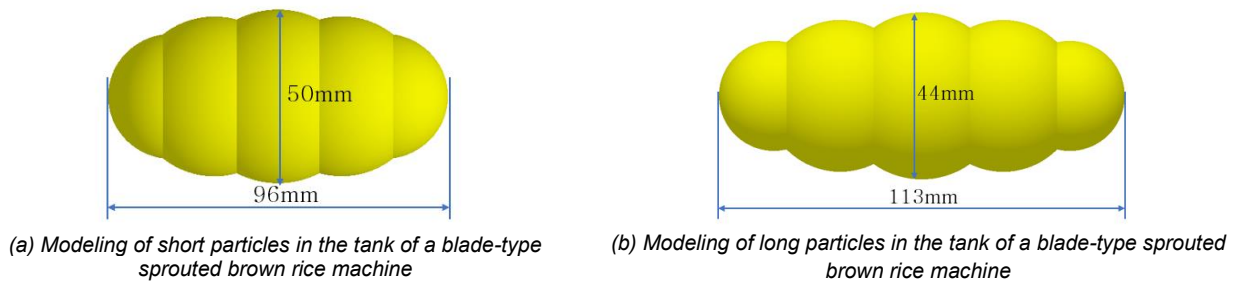


Fig. 2 - Two models of filled particles in the blade sprouted brown rice machine tank (particle amplification)

To ascertain the parameter range for rotational speed in the simulation test, different rotational speeds were employed in the simulation and the range of rotational speeds was determined based on the end-of-mix status. The method used to determine the range of the simulation test filling degree is consistent with the determination of the rotational speed. The particles were separated into upper and lower layers with different colors but the same number. The simulated mixing time was about 35 s, and the exact time was determined based on the final mixing status.

According to the relationship among rotational speed, number of particles and filling degree, the mixing parameters under particle amplification were determined, as shown in Table 2.

Table 2

The blade sprouted brown rice machine mixing parameters test program

Sprouted Brown Rice Machine Type	Particle type	Filling degree	Number of particles	Number of revolutions per minute
Blade Sprouted Brown Rice Machine	long grain	33.83%	4700	10r/min 20r/min 30r/min 40r/min
		44.59%	6400	
		55.23%	7600	
	short grain	40.16%	4800	
		50.5%	6000	
		60.83%	7600	

Reduced tank, no change in grain condition, blade type sprouted brown rice machine

According to the grain magnification, the tank was reduced by the same amount and the brown rice grain size was kept constant. The Blade Sprouted Brown Rice Machine tank was reduced by a factor of 16 and the diameter is reduced to 100 mm. The short and long grain models were shown in Fig. 3.

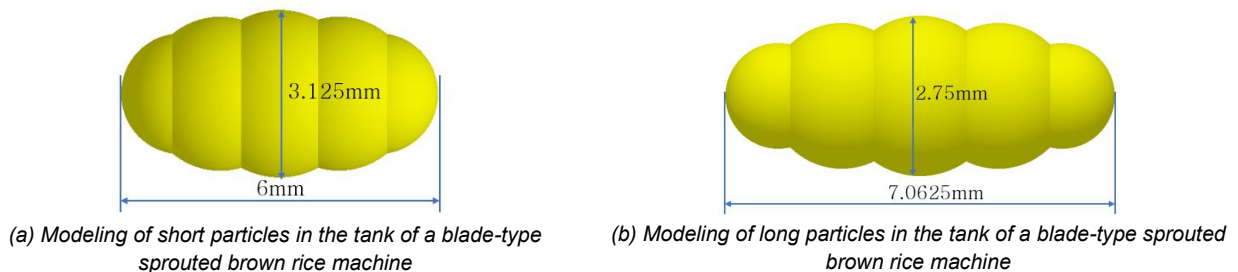


Fig. 3 - Two models of filled particles in the blade sprouted brown rice machine tank (tank reduction)

In order to comparatively analyze the particle mixing process under the two scaling modes of tank reduction and particle enlargement, the mixing parameters such as rotational speed and particle filling degree are consistent with Table 2.

Numerical simulation conditions and test program for drum type sprouted brown rice machine tanks

The whole tank of roller type sprouted brown rice machine consisted of two parts: tank shell and inner baffle, with relatively simple structure and no central axis. Its three-dimensional model is shown in Fig. 4.

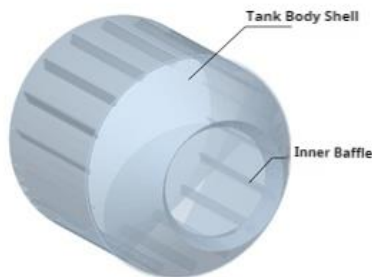


Fig. 4 - 3D model of the drum-type sprouted brown rice machine tank

Roller type sprouted brown rice machine had a diameter of 2000 mm and mixing area length of 1490 mm. Eighteen inner baffles were uniformly distributed, each 20 mm thick and 1400 mm long with 45° angle to tangent line. In this paper, long and short particle models were selected to investigate the effect of particle size on mixing characteristics.

Unchanged tanks, grain enlargement conditions, drum type sprouted brown rice machine tanks

In order to meet the simulation conditions, the size of the tank of the sprouted brown rice machine was kept constant and the brown rice particle model was enlarged. Five round balls with different radius were used to fill in, and the approximate short and long particle models were obtained as shown in Fig. 5.

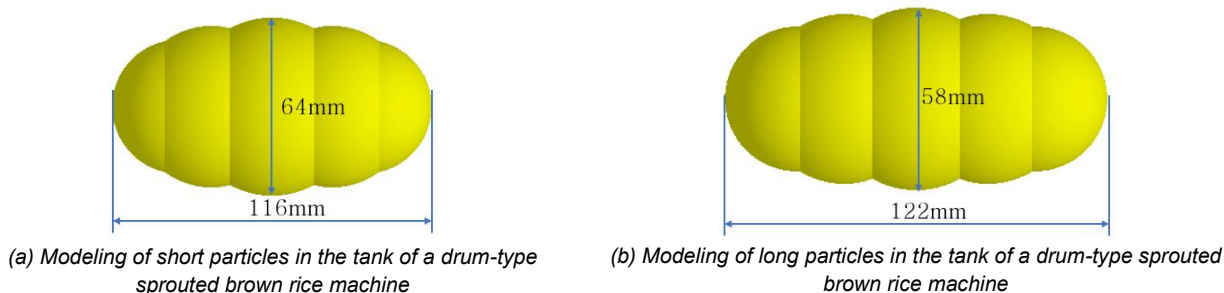


Fig. 5- Two models of filled particles in the drum-type sprouted brown rice machine tank (particle amplification)

The rotational speeds of the tank were 10 r/min, 20 r/min, 30 r/min and 35 r/min. The particles were divided into upper and lower layers in the initial state, with the upper layer being blue and the lower layer being red, and with the same number of particles in both colors. The mixing parameter settings under particle amplification conditions are shown in Table 3.

Table 3

Test program of the drum-type sprouted brown rice machine mixing parameters

Mixer Type	Particle type	Filling degree	Number of particles	Number of revolutions per minute
Cylindrical Sprouted Brown Rice Machine	long grain	37.9%	4800	10 r/min 20 r/min 30 r/min 35 r/min
		44.2%	6000	
		53.7%	7200	
	short grain	38.5%	4800	
		45.8%	6000	
		55.8%	7200	

Reduced tanks, unchanged grain conditions, drum-type sprouted brown rice machine tanks

Based on grain magnification above, reduce the tank by the same number of times and keep the brown rice grain size the same. Roller-type sprouted brown rice machine was reduced by a factor of 20 and the diameter was reduced to 100 mm. Its short and long grain models are shown in Fig. 6.

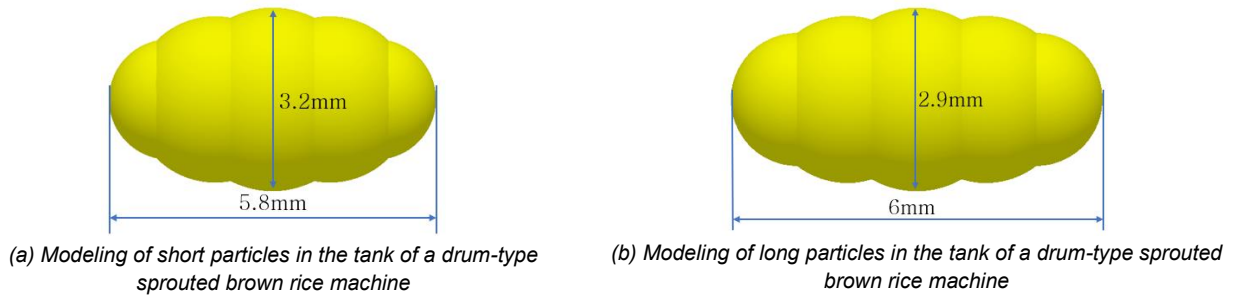


Fig. 6- Two models of filled particles in the drum-type sprouted brown rice machine tank (tank reduction)

To comparatively analyze the mixing process of particles under two scaling modes of tank reduction and particle enlargement, the mixing parameters such as rotational speed and particle filling degree of the drum-type sprouted brown rice machine were designed to be consistent with Table 2.

Simulation test parameter

Quantitative analysis of particle mixing systems

In this study, the separation index was used to characterize the degree of mixing homogeneity of brown rice particles in the mixing process (Cho *et al.*, 2017; Kamesh *et al.*, 2022). To obtain the separation index, the tank was divided into 6x6x8 operational domains. Since the difference or absence of the number of particles in the operational domains would affect the results, only the operational domains with the number of brown rice greater than 20 were calculated, and a weighting scheme was used to make the weights of the operational domains with a large number of particles larger (Zuo *et al.*, 2021). On this principle, the formula for the separation index of the two types of particles is as follows:

$$S = \sqrt{\frac{1}{k} \sum_{i=1}^{N_s} k_i (a_i - \bar{a})^2} \quad (1)$$

Where:

N_s - The total sample size;

a_i - The volume fraction of one type of brown rice grain within the sample;

\bar{a} - The volume fraction of a brown rice particle within the tank of the sprouted brown rice.

k can be expressed by the following equation:

$$k = \sum_{i=1}^{N_s} k_i \quad (2)$$

Here k_i is the sample weight which can be expressed as:

$$k_i = \frac{N_i}{N_t} \quad (3)$$

where:

N_i - the sample i is the total number of particles within the sample;

N_t - the total number of particles within all samples.

Effect of rotational speed on energy consumption

The EDEM software can only export the average output torque data when the mixer is rotating, so the following formula was usually used to calculate the energy consumption (Wang *et al.*, 2020):

$$W = 2\pi n T t \quad (5)$$

where:

n - the tank rotational speed (r/min);

T - the average output torque ($N \cdot m$);

t - the time for the granular system to reach homogeneous mixing.

Physical test equipment and program design

The physical test platform was mainly composed of switching power supply, stepping motor, motor driver, controller and hybrid roller, as shown in Fig. 14.

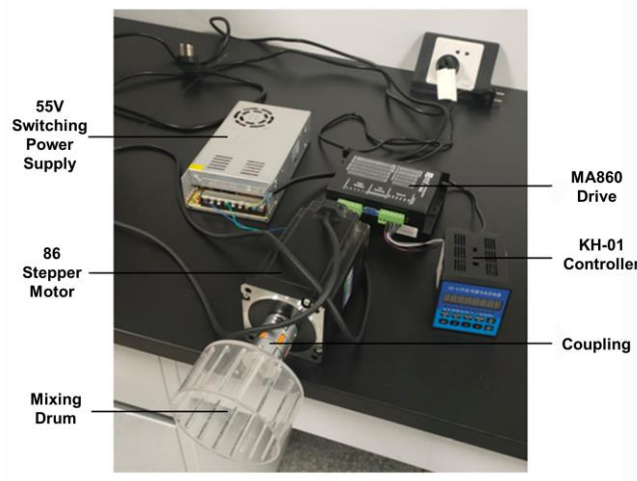


Fig. 14 – The mixing test platform of the drum-type sprouted brown rice machine

The drum-type sprouted brown rice machine tank rotated horizontally and its diameter, length, rotational speed and filling degree were the main parameters. The diameter of the drum was 100 mm, the angle of the inner bottom plate was 45° and there were 18 bottom plates. In order to investigate the effect of different transverse planes on the mixing of brown rice, three different lengths of tanks were used in the experiment: 75 mm, 50 mm and 25 mm, which were consistent with the simulation test conditions. The tank of its drum type sprouted brown rice machine was shown in Fig. 15.



Fig. 15 - Three different lengths of the drum-type sprouted brown rice machine tank
(left: 75 mm mid: 50 mm right: 25 mm)

The experimental research object was Japonica brown rice, dyed with vegetable dyes into red and blue, respectively, the lower layer was filled with blue, the upper layer was filled with red, and the number of brown rice particles of both colors was the same when they were filled. The dyed brown rice particles are shown in Fig. 16.



Fig. 16 - Brown rice particles after dyeing
(left: blue, right: red)

The mixing drum material was acrylic plate, which can clearly observe the mixing motion state of brown rice particles during the test. A high-speed video camera was used to photograph and videotape the mixing process of brown rice particles. Its physical test program design was shown in Table 3.

Table 3

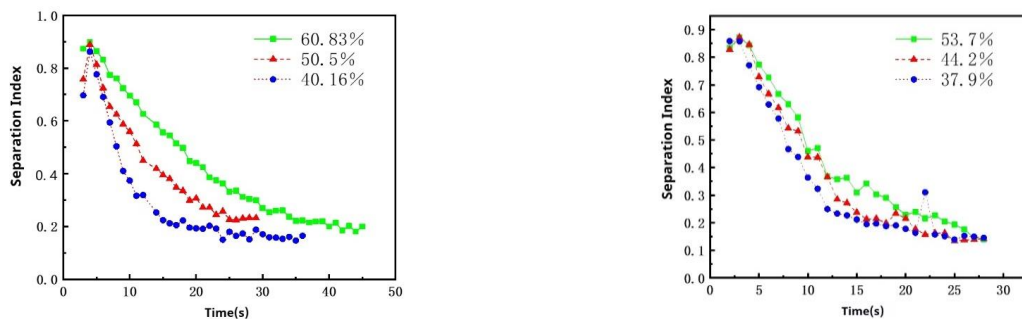
Validation test scheme design

Mixer Type	Number of revolutions per minute	Filling degree
Cylindrical Sprouted Brown Rice Machine	10 r/min	32% 45% 55%
	20 r/min	
	30 r/min	
	35 r/min	

RESULTS

Effect on separation index at the same rotational speed

According to the results of mixing uniformity calculations, the relationship curve between mixing time and separation index of particles in the tank of two typical sprouted brown rice machines under the conditions of particle amplification and rotation speed of 20 r/min was drawn, as shown in Fig. 7.



(a) Blade-type sprouted brown rice machine, 20 r/min, short grain

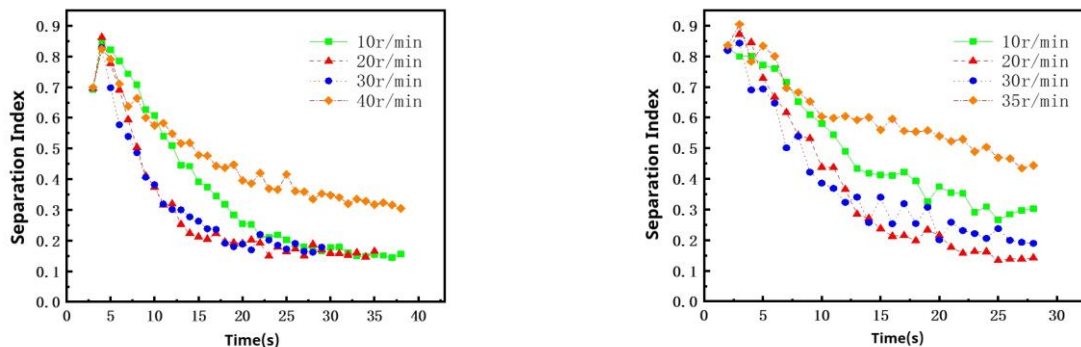
(b) Drum type sprouted brown rice machine, 20 r/min, long grain

Fig. 7- Variation curves of separation index with time at different filling degrees (particle amplification)

The separation index represents the uniformity of mixing, the lower the value, the better the mixing. Fig. 7. showed that the separation index first rises and then decreases rapidly at different filling degrees, and finally stabilizes, the lower the filling degree the faster the stabilization. The final mixing degree of the three filler degrees was similar at 20 r/min. The mixing speed was fast in the first 10 seconds of mixing, then the convection effect weakened, and the mixing effect was no longer obvious. Finally, the particles were uniformly distributed and tended to stabilize. The mixing speed was the fastest at the lowest filling degree, and the mixing degree was slightly better.

Effect on separation index at the same filling degree

At a fixed degree of filling (40.16% for the blade type and 44.2% for the drum type), Fig. 8 demonstrated the relationship between mixing time and separation index for different tank rotation speeds.



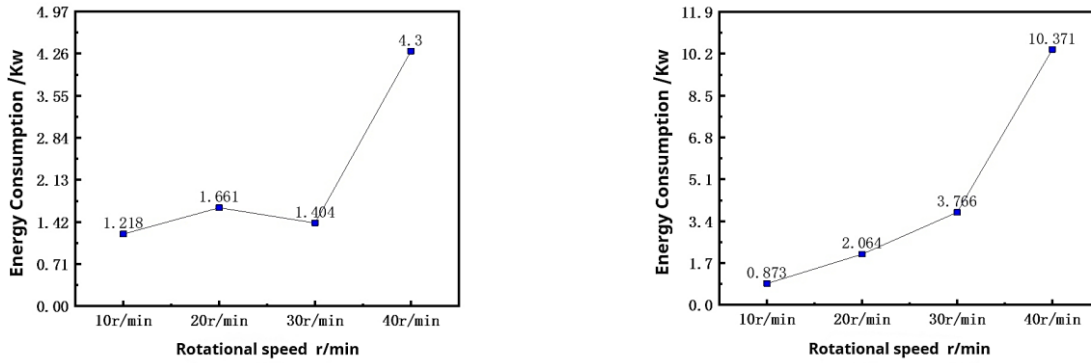
(a) Blade-type sprouted brown rice machine, 40.16%, short grain

(b) Drum-type sprouted brown rice machine, 44.2%, long grain

Fig. 8 - Variation curves of separation index with time at different rotational speeds (particle amplification)

Fig. 8 demonstrated the effect of different rotational speeds on the separation index. The separation index started with a small increase and then decreased rapidly and finally stabilized. Blade tanks showed a slower decrease in separation index at 10 r/min and 40 r/min, while 20 r/min and 30 r/min showed a faster decrease and better mixing. Roller tanks had the fastest initial decline at 30 r/min, but the 20 r/min group ended up with a higher degree of mixing. Excessive rotational speed can lead to particles being affected by centrifugal force and rotating with the tank without mixing, e.g. poor mixing in the 40 r/min and 35 r/min groups.

Effect of rotational speed on energy consumption

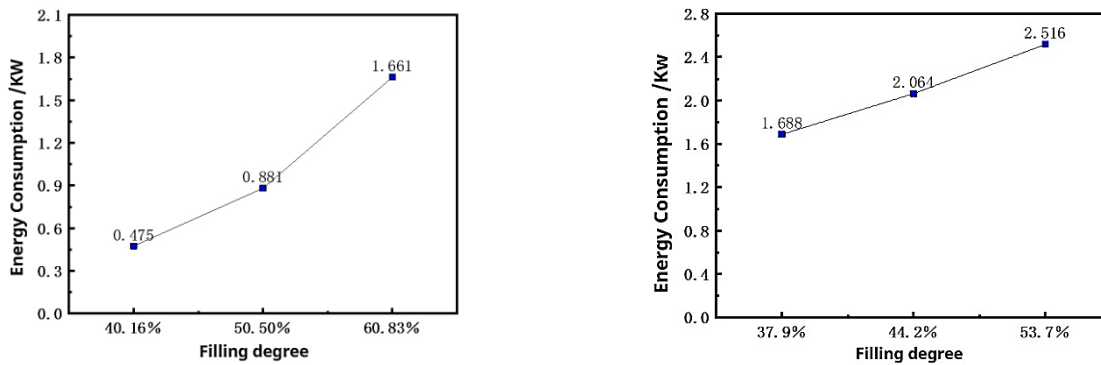


(a) Blade-type sprouted brown rice machine, 40.16%, short grain (b) Drum-type sprouted brown rice machine, 44.2%, long grain

Fig. 9 - The effect of rotational speed on energy consumption (particle amplification)

Fig. 9 demonstrated the variation of energy consumption with rotational speed when the particles were uniformly mixed. The energy consumption was calculated based only on the work done by the tank on the motion of the particles; other factors were not considered. And it also showed that energy consumption increased with increasing rotational speed. At 40.16% filling degree, the stabilized mixing time was similar, so faster rotational speed resulted in higher energy consumption, especially when the rotational speed exceeded 30 r/min, the energy consumption increased sharply.

Effect of filling degree on energy consumption



(a) Blade-type sprouted brown rice machine, 20 r/min, short grain (b) Drum-type sprouted brown rice machine, 20 r/min, long grain

Fig. 10 - Effect of filling degree on energy consumption (particle amplification)

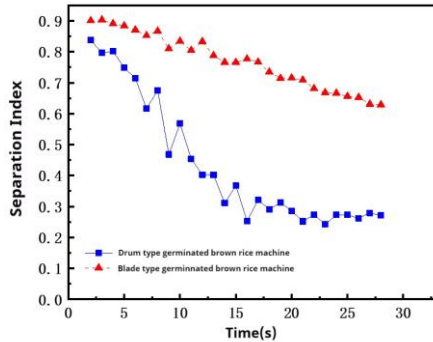
Fig. 10 showed that the energy consumption for particle movement increased gradually with increasing filling degree. Taking into account the filling degree, rotational speed and energy consumption, the optimum mixing parameters were: blade type sprouted brown rice machine was mixed at 40.16% filling degree and 20 r/min rotational speed, while the drum type was best at 37.9% filling degree and 20 r/min rotational speed.

Comparison of the mixing process of two types of sprouted brown rice machine tanks

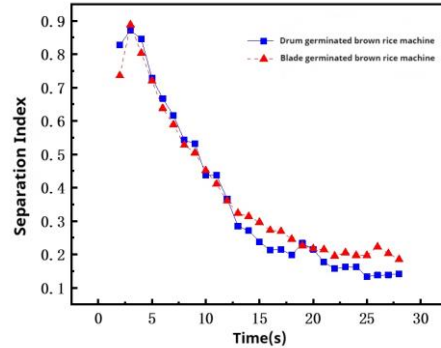
Both mixers went through three phases of rapid, slow mixing and mixing fluctuations in particle mixing involving convection, shear and diffusion mechanisms. The centrifugal motion appeared at 35 r/min in the

drum-type sprouted brown rice machine, while it appeared at 40 r/min in the blade-type sprouted brown rice machine, indicating that the rotational speed had a great influence on the particle mixing state in the drum-type tank. Both types of tank particle movement path were gradually narrowed elliptical helix and the degree of narrowing reflects the mixing effect, the superior the mixing effect, the more obvious changes in the movement path.

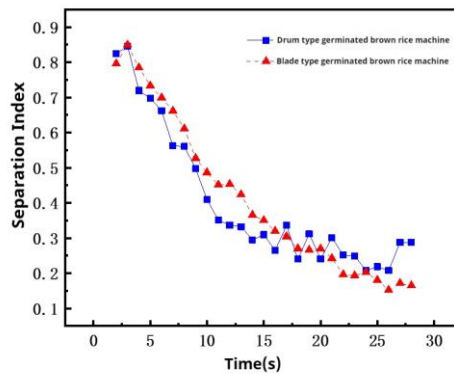
Comparison of two sprouted brown rice machine tank mixing ration analysis



(a) Long particles at 10 r/min, 55%



(b) Long particles at 20 r/min, 44%



(c) Long particles at 30 r/min, 55%

Fig. 11 - Changes of mixing degree of two kinds of machines with mixing time (particle amplification)

In this paper, the degree of particles mixing in the two kinds of germinated brown rice machines was compared and analyzed under the condition of particle amplification. As can be seen from Fig. 11, when the rotational speed was low, the mixing effect of the particles in the tank of the drum-type sprouted brown rice machine was generally better than the blade-type sprouted brown rice machine. When the rotational speed was higher than 30 r/min, the particles in the tank of drum-type sprouted brown rice machine were hindered from mixing due to centrifugal effect, so the mixing effect of blade-type sprouted brown rice machine was better.

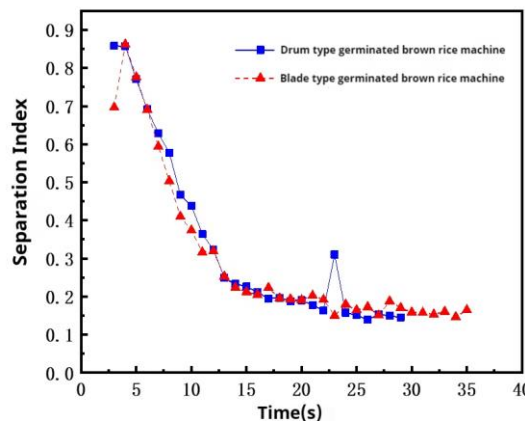


Fig. 12 - Changes of mixing degree with time under the optimal mixing parameters of two sprouted brown rice machines (particle amplification)

Fig. 12 showed the curves of the degree of mixing with time for the two sprouted brown rice machines under the conditions of optimal mixing parameters. The two curves had similar trends and reached the optimal mixing state after 25 s, indicating that the mixing effect of the two types of sprouted brown rice machine was consistent. Fig. 10 showed that the blade type sprouted brown rice machine had the filling degree of 40.16%, rotational speed of 20 r/min, energy consumption of 0.476 kw, while the drum type sprouted brown rice machine had the filling degree of 37.9%, rotational speed of 20 r/min, energy consumption of 1.687 kW. Considering the mixing effect and energy consumption, the blade type sprouted brown rice machine mixing performance was better.

Comparative analysis of mixing processes under particle enlargement and tank reduction conditions

In order to clarify the difference between the numerical results under the two conditions of particle enlargement and tank shrinkage, taking the blade type sprouted brown rice machine as an example, a comparison graph of the change of separation index with time under different rotational speeds was drawn, as shown in Fig. 13.

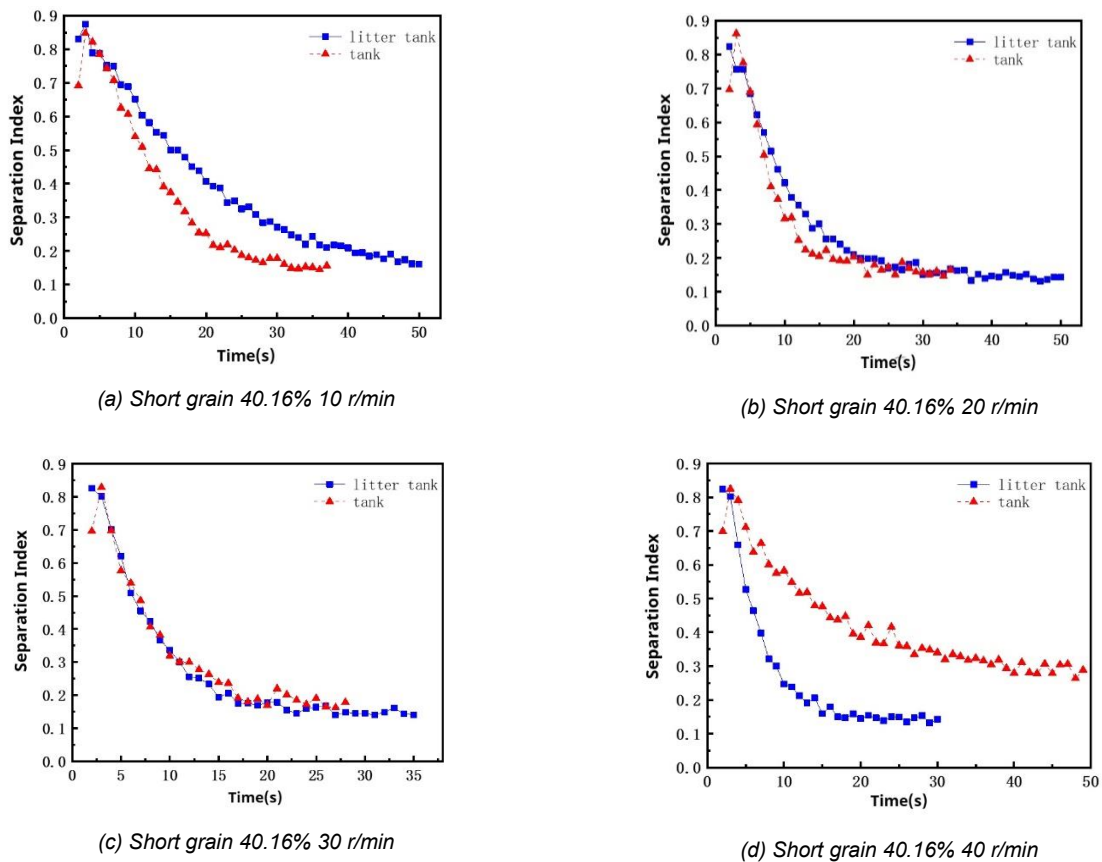


Fig. 13 - Comparison of mixing degrees at different rotational speeds under two scaling conditions

Fig. 13 illustrated the mixing of short particles at 40.16% filling at different rotational speeds for tank downsizing versus particle upsizing. Mixing uniformity was similar at 20 r/min versus 30 r/min, with little difference in the separation index values. At 10 r/min, tank downsizing was less efficient but the end of the mixing was similar. At 40 r/min, particle upsizing was reduced due to centrifugal force mixing efficiency. And the tank shrinkage test conditions were not affected.

Comparison of particle mixing patterns between physical and simulation tests of mixing drums

The physical test was conducted by using the full-factor test method to mix the brown rice particles in the drum with drum rotational speed and filling degree as variables, and a high-speed video camera was used to record the mixing process. Taking 75 mm tank, 45% filling degree, and rotational speeds of 10 r/min, 20 r/min, and 30 r/min as examples, the motion images of the physical test and the simulation test at different rotational speeds were compared, as shown in Fig. 17.

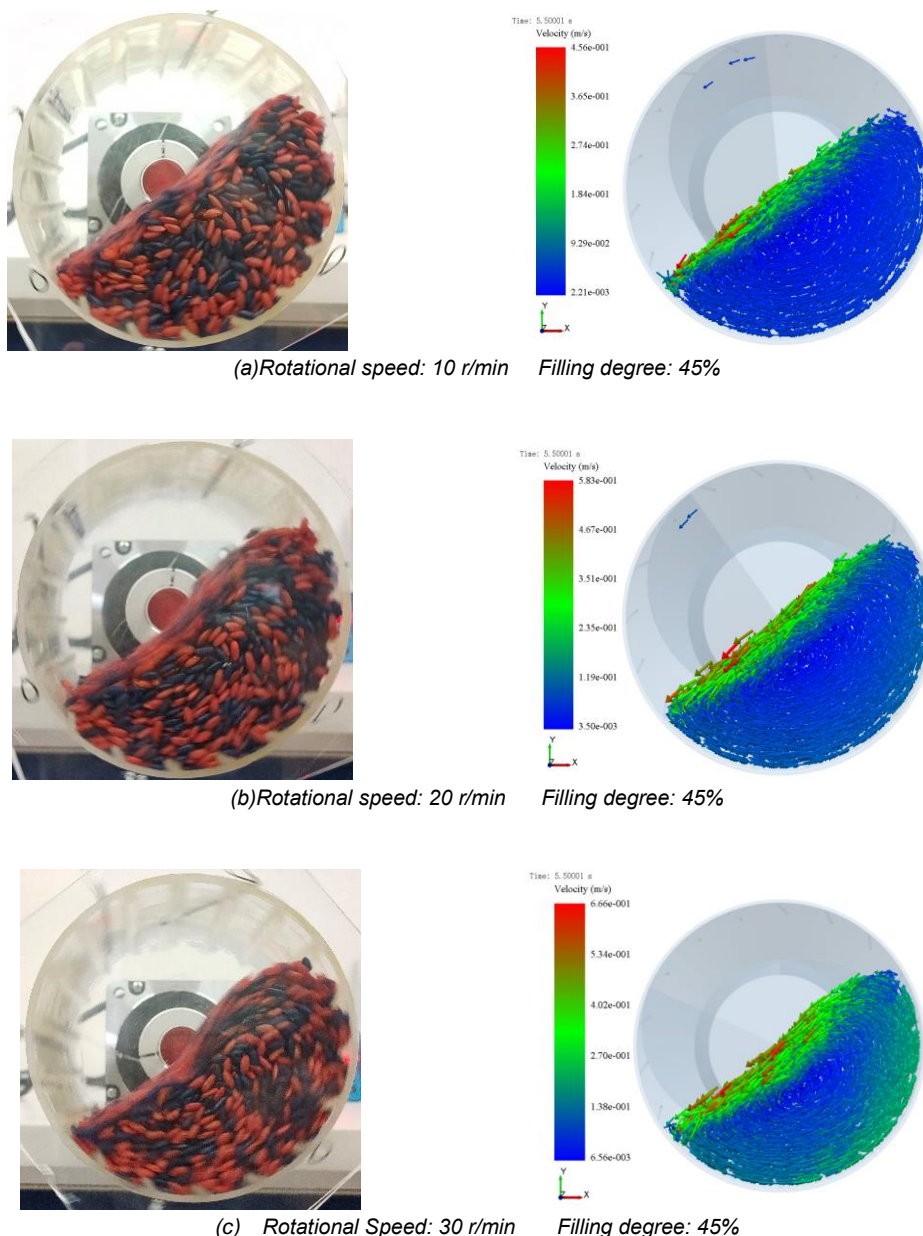


Fig. 17 - Comparison of particle mixing morphology between verification test and simulation test

From the physical test images, it can be seen that the brown rice particles move in a circular motion with the tank and the number of falling particles increases when the rotational speed increases, indicating faster mixing and higher efficiency. The comparative images in Fig. 17 showed that the brown rice particles were mainly in a rolling state with similar morphology during mixing. Under the same conditions, the falling height and flow range of the brown rice particles in the physical and simulation tests were the same, with no significant difference.

Quantitative analysis of particle mixing for physical tests

Comparison of 2D discrete element simulation and 3D discrete element simulation results

Transverse mixing has been the focus of particle mixing research due to its high efficiency and speed, compared to axial mixing of particles which is slower and occurs in smaller numbers. The 2D DEM simulation uses a small number of particles, as *WU et al., (2022)* to reduce the computational effort of the computer in the simulation process. The 2D model was considered as a cheap alternative model to the 3D model. Therefore, in this paper, the mixing uniformity is considered in a particular plane of the drum-type sprouted brown rice machine to represent the overall mixing uniformity.

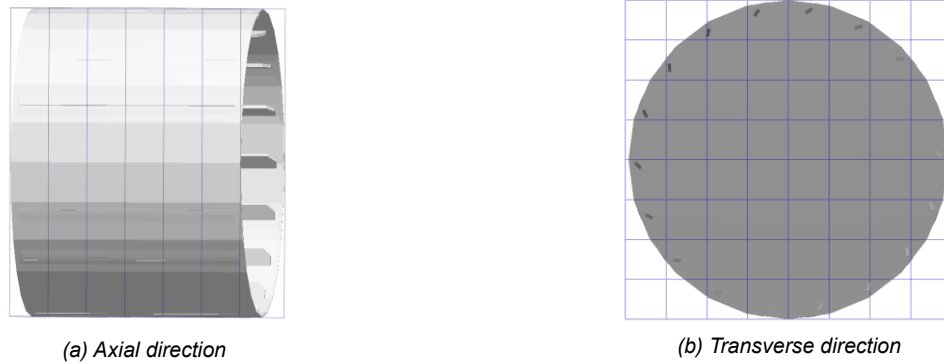
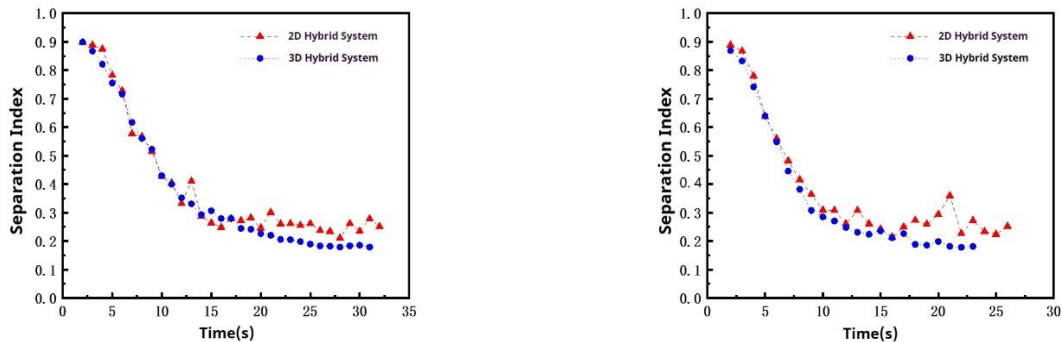


Fig. 18 - The grid division method of the drum-type sprouted brown rice machine

Fig. 18 divided the entire 3D mixing system of the drum-type sprouted brown rice machine into 384 subdomains, axially divided into 6 layers, each with a thickness of 8 mm (approximately equal to the length of the grain). The horizontal direction was divided into an 8 × 8 square grid. And the 64 subdomains of the first layer were used as the 2D mixing system.



(a) Short particles, rotational speed 30 r/min, 55%

(b) Short particles, rotational speed 35 r/min, 45%

Fig. 19 - Comparison of separation index between 2D hybrid system and 3D hybrid system (tank reduction)

Fig. 19 showed that the separation indices of the two mixing systems were similar in the steady state with the same decreasing trend. However, the 2D system had large fluctuations in the separation index due to the small number of particles. The 2D mixing system uniformity can characterize the overall mixing uniformity of the 3D system. Therefore, the overall mixing uniformity of the particles in the sprouted brown rice machine can be replaced by the lateral mixing on the 3D thin layer.

Brown Rice Grain Mixing Image Processing

The physical test of brown rice layered particle mixing was carried out at 45% filling degree and 30 r/min rotational speed conditions, and the lateral particle mixing motion was filmed with a high-definition video camera for 40 s. The mixing status was recorded every 5 s.



Fig. 20 - Image of particle blending at a mixing time of 5 s

Fig. 20(a) showed the original particle mixing image with a mixing time of 5 s. After cropping process, the middle circular mixing region was retained, as in Fig. 20(b), with a pixel interval of 630*630. To calculate the mixing uniformity, two colors of brown rice needed to be distinguished. The target image was segmented by comparing each pixel point in the image based on the gray level difference using the threshold editor in OpenCV. The distribution map of red and blue pixel points was finally obtained, as shown in Fig. 21.

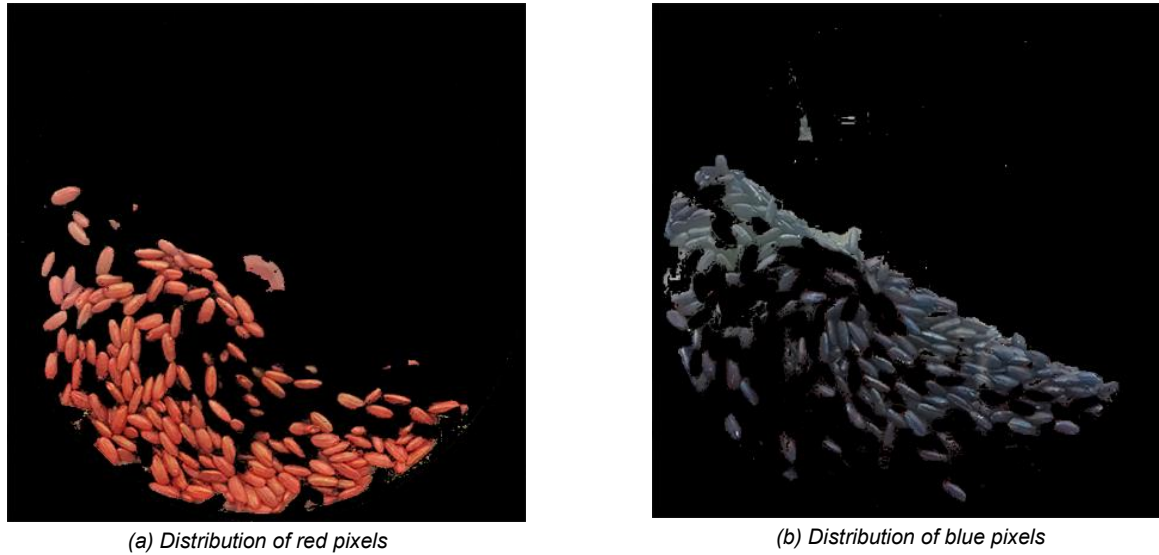


Fig. 21 - Pixel distribution map of two colors

Then the pixel distribution maps of two colors were divided into 5x5 grids using PS software. The regions of the pixel point distribution maps of the two colors corresponded to each other after segmentation. The grid division image was shown in Fig. 22.

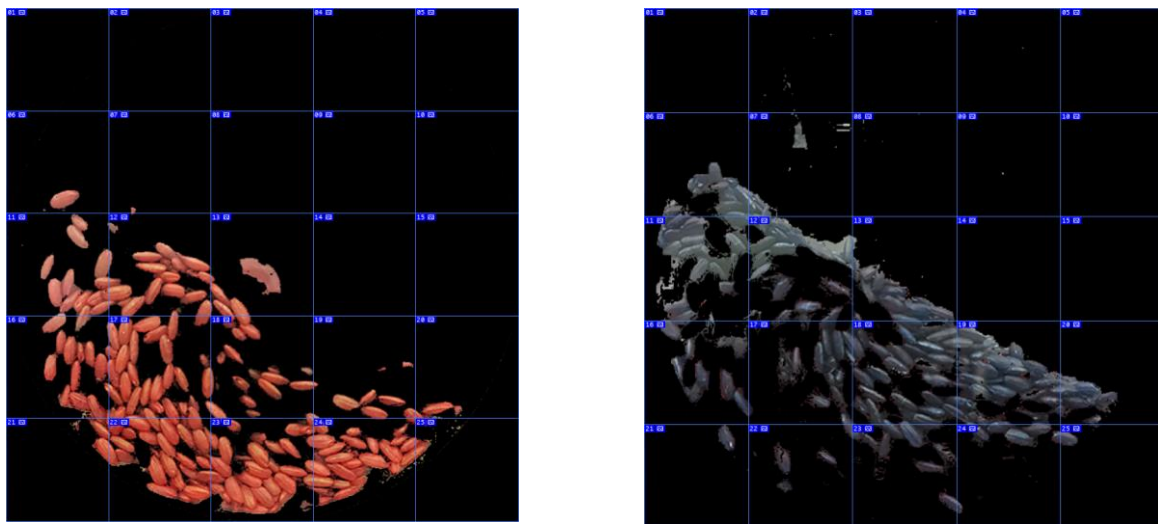


Fig. 22 - Meshing images
(left: red, right: blue)

OpenCV functions analyzed and processed image pixels. The processed image had only two colors, black and red (or blue). Using Python-OpenCV function to extract the number of red (or blue) pixel points in each image, after statistical analysis, it was known that the more pixel points, the greater the proportion of the corresponding color brown rice. After data processing, the separation index value of the mixing moment could be obtained. The whole image processing process was shown in Fig. 23.

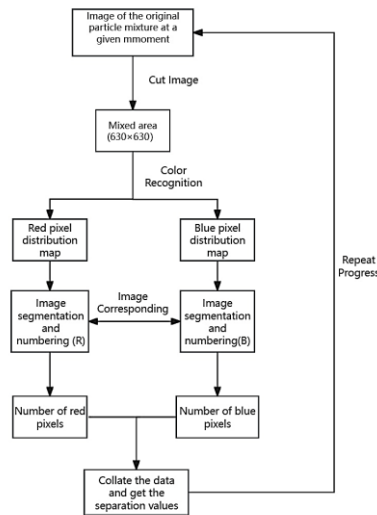
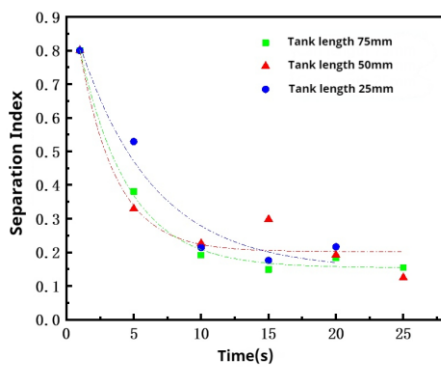


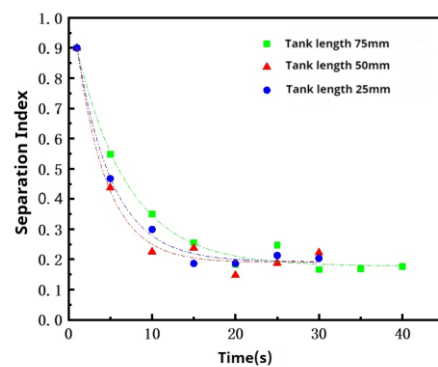
Fig. 23 - Image processing flowchart

Results of mixing uniformity of brown rice grains under physical test conditions

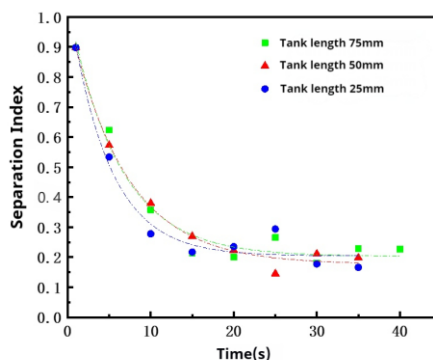
In order to clarify the effect of different transverse planes on the mixing process of brown rice particles, this study compares the change curves of separation index with mixing time for different tank lengths under different filling degree and drum rotational speed, as shown in Fig. 24.



(a) Filling degree: 32% Drum rotational speed: 20 r/min



(b) Filling degree: 45% Drum rotational speed: 30 r/min



(c) Filling degree: 55% Drum rotational speed: 30 r/min

Fig. 24 - Comparison of separation index of different tank lengths

Fig. 24 showed that the trend of particle mixing uniformity with time was the same for different tank mixing depths, and the values of separation index were similar from 0 to 15 s. It indicates that the mixing depth has a small effect on the mixing uniformity of brown rice. This study takes the 75 mm tank as an example to explore the variation rule of separation index with mixing time under physical test and simulation, as shown in Fig. 25.

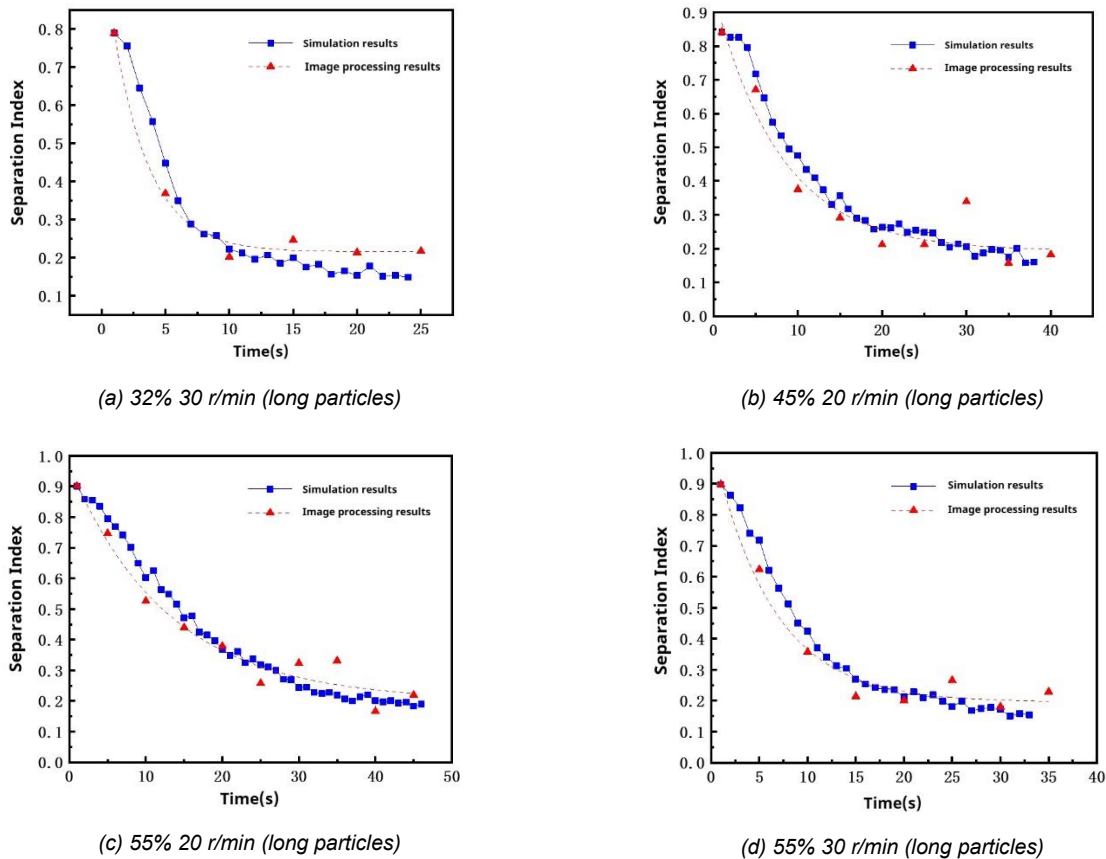


Fig. 25 - Comparison of separation indices of simulation environment and test environment

Fig. 25 showed that the separation index gradually decreased with increasing mixing time, i.e., the particles were mixed more uniformly. The trend of the separation index curves under the simulation and test environments is consistent, with a rapid decline at the initial stage, followed by a slower rate and eventual stabilization. Under the same mixing time, the two separation index values are similar, indicating that the change rule of mixing uniformity is consistent, which verifies the accuracy of the discrete element simulation.

CONCLUSIONS

In this paper, the discrete unit method was used to study the mixing process and movement law of brown rice particles in the tank of two kinds of sprouted brown rice machine. The mixing mechanism of brown rice particles under different mixing process parameters was quantitatively analyzed. And based on the results of the above research, a set of drum type sprouted brown rice machine mixing test platform was built. The accuracy of the discrete element simulation results was verified by physical test based on real brown rice particles. The main conclusions of the whole study are as follows:

(1) Appropriate mixing process parameters can significantly improve the working efficiency and mixing performance of sprouted brown rice machine. When the rotational speed is higher than 20 r/min, the mixing efficiency of the particle system decreases; the lower the filling degree, the higher the mixing efficiency of the particle system.

(2) There was comprehensive consideration of mixing uniformity and energy consumption to determine the optimal mixing process parameters of two kinds of sprouted brown rice machine. Blade type sprouted brown rice machine: filling degree was 40.16%, rotational speed was 20 r/min; Drum type sprouted brown rice machine: filling degree was 37.9%, rotational speed was 20 r/min. Under the optimal conditions for both sprouted brown rice machine tank mixing process parameters, the mixing performance of the blade type sprouted brown rice machine was better than that of drum type sprouted brown rice machine.

(3) A set of drum type sprouted brown rice machine mixing test platform was designed and built. The results showed that the simulation environment and physical test environment of brown rice particles motion state and mixing uniformity change rule is consistent. The accuracy of the discrete element simulation results is verified via the actual brown rice particle physical test.

ACKNOWLEDGMENTS

The authors express their acknowledgment to the National Natural Science Foundation of China (Grant No.32001423) and First Division Alar City Science and Technology Plan Project (Grant No. 2023ZB01) for financial support and all of the persons who assisted in this writing.

REFERENCE

- [1] Bao, Y., Lu, Y., Cai, Z., Gao, Z. (2018). Effects of rotational speed and fill level on particle mixing in a stirred tank with different impellers. *Chinese Journal of Chemical Engineering*, 26(6):1383-1391. <https://doi.org/10.1016/j.cjche.2017.11.010>
- [2] Chandratilleke, G., Jin, X., Shen, Y. (2021). DEM study of effects of particle size and density on mixing behavior in a ribbon mixer. *Powder Technology*, 392:93-107. <https://doi.org/10.1016/j.powtec.2021.06.058>
- [3] Chen, H., Zhao, X., Liu, Y., Xiao, Y., Liu, Y. (2015). Toward separation of D-type binary granular material tumbling mode in rotor(转筒内 D 型二元颗粒物料滚落模式的径向分离). *Journal of Agricultural Machinery*, 46(6):334-340. <https://doi.org/10.6041/j.issn.1000-1298.2015.06.048>
- [4] Chen, Y., Zhang M., Zhang, Y., Dang, Y., Wei, Z., Tang, X., Liu, G., Li, P. (2021). Effects of germination and extrusion on volatile flavor substances in brown rice(发芽及挤压膨化对糙米挥发性风味物质的影响). *Chinese Agricultural Science*, 54(1):190-202. <https://doi.org/10.3390/foods12071542>
- [5] Cho, M., Dutta, P., J, A. (2017). Non-sampling mixing index for multicomponent mixtures. *Powder Technology*,319:434-444. <https://doi.org/10.1016/j.powtec.2017.07.011>
- [6] Ebrahimi, M., Yaraghi, A., Jadidi, B., Ein-Mozaffari, F., Lohi, A. (2021). Assessment of bi-disperse solid particles mixing in a horizontal paddle mixer through experiments and DEM. *Powder Technology*, 381:129-140. <https://doi.org/10.1016/j.powtec.2020.11.041>
- [7] Jia, F., Wang, J., Lan, H., Han, S., Zhang, Q., Fu, Q. (2012). Effect of cyclic moisture conditioning treatment on γ -aminobutyric acid content of germinated brown rice(循环加湿工艺对发芽糙米中 γ -氨基丁酸含量的影响). *Transactions of the Chinese Society of Agricultural Engineering (Transactions of the CSAE)* 28(20): 288-292. <https://doi.org/10.3969/j.issn.1002-6819.2012.20.039>
- [8] Kamesh, R., Vaddagani, S., Sumana, C., Yamuna, R., Gopireddy, S., Urbanetz, N. (2022). Six-directional sampling method and mean mixing indices for solids blending performance analysis of DEM simulations. *Powder Technology*, 398:117051. <https://doi.org/10.1016/j.powtec.2021.117051>
- [9] Tanabe, S., Gopireddy, S., Minami, H., Ando, S., Urbanetz, N., Scherließ, R. (2019). Influence of particle size and blender size on blending performance of bi-component granular mixing: a DEM and experimental study. *European Journal of Pharmaceutical Sciences*,134:205-218. <https://doi.org/10.1016/j.ejps.2019.04.024>
- [10] Tsunazawa, Y., Soma, N., Sakai, M. (2022). DEM study on identification of mixing mechanisms in a pot blender. *Advanced Powder Technology*, 2022, 33(1):103337. <https://doi.org/10.1016/j.apt.2021.10.029>
- [11] Wang, D., Dang, C., Huang H., Liu, C. (2020). Mechanism analysis and parameter optimization of paddle-type diet mixer(桨叶式日粮混合机机理分析与参数优化). *Journal of Agricultural Machinery*, 51(6):122-131. <https://doi.org/10.6041/j.issn.1000-1298.2020.06.013>
- [12] Wu, W., Chen, K., Tsotsas, E. (2022). Prediction of particle mixing time in a rotary drum by 2D DEM simulations and cross-correlation. *Advanced Powder Technology*, 33(4):103512. <https://doi.org/10.1016/j.apt.2022.103512>
- [13] Yang, Y., Zhang, H., Wang, Z., Liu, Y., Lan, H., Zhang, Y. (2021). Optimization of spiral mixer parameters and construction of data model by discrete element method (离散元法的螺旋搅拌机参数优化及其数据模型构建). *Packaging and Food Machinery*, 39(1):56-61. <https://doi.org/10.3969/j.issn.1005-1295.2021.01.010>
- [14] Yaraghi, A., Ebrahimi, M., Ein-Mozaffari, F., Lohi, A. (2018). Mixing assessment of non-cohesive particles in a paddle mixer through experiments and discrete element method (DEM). *Advanced Powder Technology*, 2018, 29(11):2693-2706. <https://doi.org/10.1016/j.apt.2018.07.019>

- [15] Yu, M., Zhang, H., Guo, J., Zhang, J., Han, Y. (2022). Three-dimensional DEM simulation of polydisperse particle flow in rolling mode rotating drum. *Powder Technology*, 396:626-636. <https://doi.org/10.1016/j.powtec.2021.10.058>
- [16] Zhang, Q., Liu, N., Wang, S., Liu, Y., Lan H. (2019). Effects of cyclic cellulase conditioning and germination treatment on the γ -aminobutyric acid content and the cooking and taste qualities of germinated brown rice. *Food Chemistry*, 289:232-239. <https://doi.org/10.1016/j.foodchem.2022.102165>
- [17] Zhang, R., Jiao, W., Zhou, J., Qi, B., Liu, H., Xia, Q. (2020). Parameter calibration of discrete elemental model parameters for rice seeds with different filled particle radius(不同填充颗粒半径水稻种子离散元模型参数标定). *Journal of Agricultural Machinery*, 51(S1):227-235. <https://doi.org/10.6041/j.issn.1000-1298.2020.S1.026>
- [18] Zhao, C., Wu, X. (2019). Analysis of soil-fertilizer mixing process based on EDEM discrete element method(基于 EDEM 离散元法的土肥混合过程分析). *Chinese Journal of Agricultural Mechanical Chemistry*, 40(7):178-182. <https://doi.org/10.1016/j.still.2022.105591>
- [19] Zuo, Z., Gong, S., Xie, G., Zhang, J. (2021). DEM simulation of binary mixing particles with different density in an intensive mixer (基于 DEM 的强力混合机湿颗粒混匀过程中桨叶磨损分析). *Powder Technology*, 383:454-470. <https://doi.org/10.1016/j.powtec.2021.01.064>

DEVELOPING AN AUTOMATIC PRECISION SEEDING UNIT (APSU) FOR POT SEED PLANTING

تطوير وحدة زراعة آلية دقيقة لزراعة البذور في الأصص

Mohamed ABO-HABAGA¹⁾, Zakaria ISMAIL¹⁾, Nariman MOUSTAFA¹⁾, Mahmoud OKASHA²⁾

¹⁾Agricultural Engineering Department, Faculty of Agriculture, Mansoura University, Egypt

²⁾Agricultural Engineering Research Institute (AEnRI), Agricultural Research Center (ARC), Giza 12611, Egypt

Tel: +20-1003133841; E-mail: mahmoudokasha1988@yahoo.com

Corresponding author: Mahmoud Okasha

DOI: <https://doi.org/10.35633/inmateh-74-22>

Keywords: Automatic seeding; Greenhouse; Precision seeding

ABSTRACT

This research aims to develop an automatic precision seeding unit (APSU) for planting seeds in pots inside greenhouses. The study evaluated three seed suction nozzle diameters (0.5, 1.0, and 2.0 mm) and four types of seeds (Armenian cucumber, pepper, turnip, and okra). The key performance indicators involved the number of seeds captured per stroke, total time for seeding one pot, and deviation relative to the pots' centers. The results showed that a nozzle diameter of 1.0 mm was the most effective for okra and Armenian cucumber seeds, resulting in average yields of 1.0 and 1.46 seed(s) per pot, respectively. The 0.5 mm nozzle showed optimal performance for pepper and turnip seeds, achieving 1.33 and 1.46 seeds per pot, respectively. The average time for seeding one pot, including all three stages, is approximately 35 seconds. These findings endorse the improvement of productivity and accuracy in automated greenhouse seeding, furthering precision agriculture as a state-of-the-art technological strategy.

المخلص

تهدف هذه الدراسة إلى تطوير وحدة زراعة بذور آلية دقيقة قادرة على زراعة البذور في الأصص داخل البيوت المحمية. تم إجراء التجارب على ثلاثة أقطار مختلفة لفوهات الشفط وهي 0.5، 1.0، و 2.0 مم وأربعة أنواع مختلفة من البذور وهي: القثاء، الفلفل، اللفت، والبامية. وتم تقييم أداء وحدة الزراعة من حيث عدد البذور الملتقطة في المشوار الواحد، إجمالي الوقت المستغرق لزراعة أصيص واحد، والانحراف بالنسبة لمنتصف الاصيص. أظهرت النتائج أن قطر فوهة الشفط 1.0 مم كانت الأكثر فعالية لبذور البامية والقثاء، حيث كان متوسط عدد البذور الملتقطة 1 و 1.46 بذرة لكل أصيص على التوالي. بينما أظهرت فوهة الشفط ذات القطر 0.5 مم أداءً مثاليًا لبذور الفلفل واللفت، حيث كان متوسط عدد البذور الملتقطة 1.33 و 1.46 بذرة لكل أصيص على التوالي. وكان متوسط الزمن اللازم لزراعة أصيص واحد، بما في ذلك المراحل الثلاث، هو حوالي 35 ثانية. ومن ثم، تدعم هذه النتائج تحسين الإنتاجية والدقة في الزراعة الآلية داخل البيوت المحمية، مما يعزز الزراعة الدقيقة كاستراتيجية تكنولوجية متقدمة.

INTRODUCTION

The agriculture sector currently suffers from a labor shortage; thus, utilizing agricultural automation technologies presents an effective solution to mitigate reduced labor supply (Abo-Habaga et al., 2022; Amin et al., 2024a; Amin et al., 2024b). The primary goal of creating an agricultural automation robot is to minimize labor needs and improve food quality. This agricultural robot tackles significant obstacles farmers face, such as monitoring crop quality in real-time and performing tasks like plowing, seeding, spraying, harvesting, and fruit picking (Bu et al., 2020). The quality of sowing in mechanized processes is heavily reliant on the efficiency of sowing equipment, potentially impacting crop yield (Maleki et al., 2006; Urbaniak et al., 2008). For instance, the Agro-Bot is an autonomous robot with a combined seeding and watering system and a solar panel, making it a self-sufficient option for farming in remote areas. The Farmer Bot system offers information via internet connectivity, enhancing adaptability and remote accessibility; the Agro-Bot presents a workable substitute for conventional farming methods (Khandelwal et al., 2017). Various automation and technologies, ranging from basic integrated circuits to advanced microcontrollers, micro-computers, sensors, and Internet of Things (IoT) applications (Abdelmotalieb et al., 2015; Loukatos et al., 2021), have been utilized in agriculture through smart farming technologies (SFT) to facilitate data acquisition, analysis, evaluation, and precision application (Balafoutis et al., 2017a), resulting in notable economic, environmental, and labor benefits (Balafoutis et al., 2017b; Balafoutis et al., 2020). However, these applications are primarily found in large-scale farming, with limited efforts toward small-scale, automated urban agriculture.

Data acquisition tasks are supported by the advancement of computer vision techniques and the availability of various sensory data sources (Ardiansah *et al.*, 2021; Brisco *et al.*, 2014; Reyns *et al.*, 2002), while data analysis and evaluation are prevalent in agricultural research (Nash *et al.*, 2009; Iosif *et al.*, 2023). These strategies apply to seed planting, seed mapping, re-seeding, weed mapping, pesticide spraying, and irrigation. The operation of air-suction seed metering devices encompasses seed loading, conveyance, and discharge to guarantee precise seed distribution and optimal planting efficiency. For seeds with high sphericity, such as pea, soybean, rapeseed, and *Panax notoginseng*, the preferred method of planting involves air-suction seed-metering devices, known for their consistent and effective performance (Tang *et al.*, 2023). The suction force is a pivotal element in these devices, combining multiple forces, particularly the drag force, which is vital for determining seed attachment to the suction hole (Li *et al.*, 2021).

This study aims to develop an automatic precision seeding unit (APSU) for pot-location detection within a greenhouse to prevent pot omission and ensure accurate planting depth, using distance sensors to optimize depth while enabling three-directional movement with a seed suction nozzle for precise, single-seed placement per pot.

MATERIALS AND METHODS

The automatic precision seeding unit (APSU) manufacturing process and trial experiments were conducted in 2024 at the Department of Agricultural Engineering, Faculty of Agriculture, Mansoura University, Egypt. The APSU comprises hardware systems and software systems.

Hardware systems

The automatic precision seeding unit (APS) comprises the following components: (1) an information collection unit, including the camera, auxiliary equipment, and sensor group; (2) control unit, comprising the central control unit; (3) moving unit for movement in the X-Y directions; and (4) seeding unit, comprising the air source control device, a set of seed suction nozzles of different diameters, and an angularly adjustable seed box (Fig. 1).

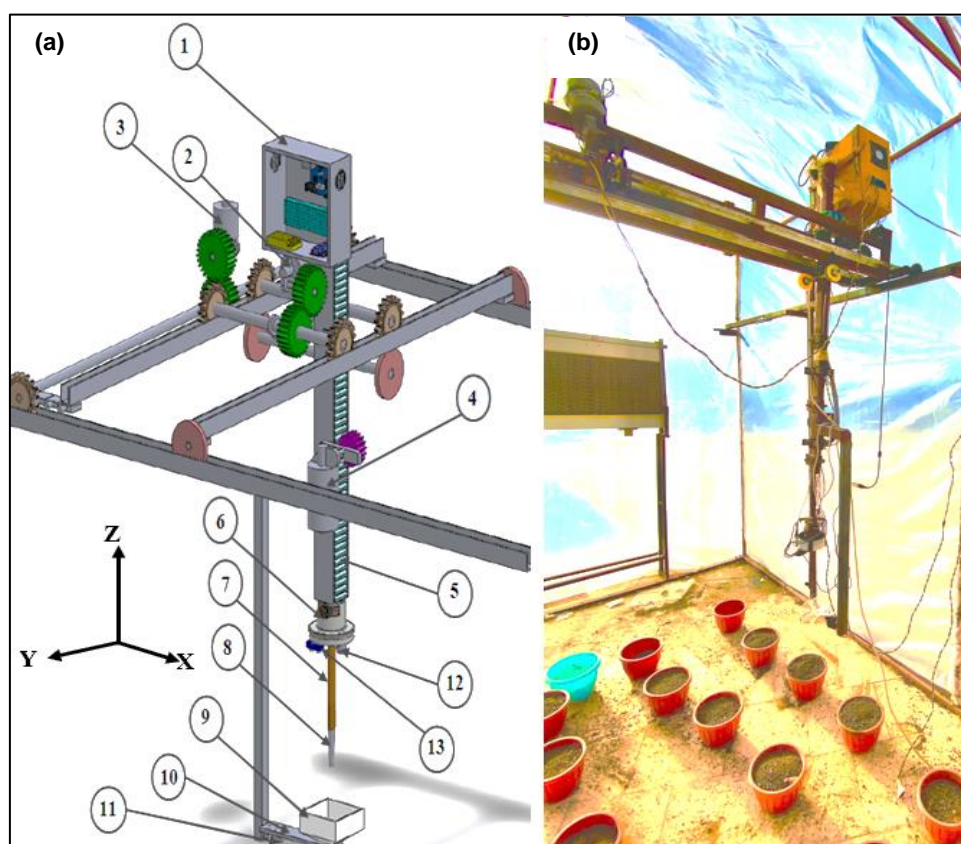


Fig. 1 – Layout and components of the automatic precision seeding unit (APSU): (a) 3D diagram, and (b) operation of the APSU inside the greenhouse

1 – Control box; 2 – Y-axis motor; 3 – X-axis motor; 4 – Z-axis motor with pinion gear; 5 – Rack; 6 – Seed suction motor; 7 – Seed suction pipe; 8 – Seed suction nozzle; 9 – Seed box; 10 – Seed box holder; 11 – Servo motor; 12 – Camera; 13 – Ultrasonic sensor

Information collection unit

The Logitech C270 Pro Stream camera was used in this study. It features a 720p HD resolution at 1280 × 720 pixels, with a maximum frame rate of 30 frames per second (fps) and a fixed-focus lens providing a 60-degree field of view. The camera supports high-definition (HD) 720p and captures images up to three megapixels. It was mounted vertically below the air suction motor, covering the image acquisition area of the planting pot, and was connected to the control unit to initiate operation. A distance sensor was used to adjust the gap between the planting nozzle and the seeds in the seed box, ensuring accurate planting depth and preventing interference between moving parts during the motion signaling process.

For accurate soil penetration depth, three HC-SR04 ultrasonic sensors were used to determine the planting arm position in the X, Y, and Z directions. Powered by a +5V DC supply, these sensors have a current below 2 mA, an operating current of 15 mA, an effective angle of less than 15°, and a measurement range of 2 to 400 cm with a resolution of 0.3 cm. They feature a measurement angle of 30°, a pulse trigger width of 10 μS, dimensions of 45 × 20 × 15 mm, and an approximate weight of 10 g. Built for robustness, they operate within a temperature range of -20°C to +70°C, making them suitable for various environmental conditions.

Control unit

The control unit consists of a PC, an Arduino Uno (AVR), a Raspberry Pi 4 Model B powered via a USB Type-C power supply delivering 5V at 3A, a 24V-10A power supply for appropriate voltage, a 2-channel and 1-channel relay module, and peripheral circuits. The primary function of this unit is to collect sensor signals to send to the PC, receive data processed by the PC, and transmit it to the Arduino. The Arduino distributes these signals across 14 channels to enable individual relay control.

Moving unit in the X-Y directions

A moving unit operates in the X-Y directions, with X-axis motion driven by a DC motor featuring a 55 mm diameter spur gear, 29 teeth, and a drive shaft with three spur gears. A 60 mm middle gear connects to the motor gear, flanked by two side gears with a 60 mm diameter and a 33 mm pitch. The Y-axis motion is also driven by a DC motor with specifications similar to the X-axis motor but with an 8 mm gear pitch and a length of 180 cm (Fig. 2).

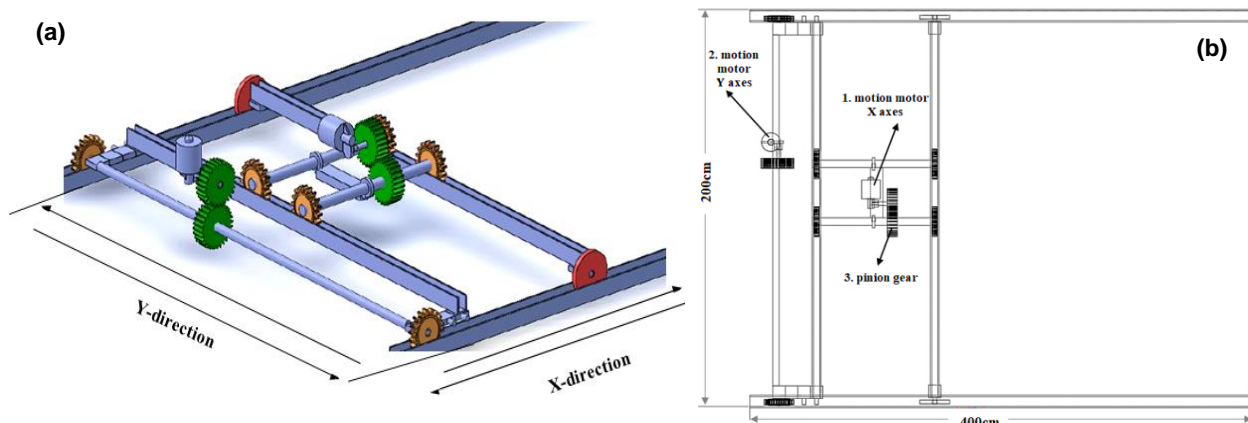


Fig. 2 – 3D view of the X- and Y-axis motion (a) and layout of the X- and Y-axis motion directions (b)

Seeding unit

The seeding unit includes Z-axis motion that is driven by a DC motor with a 23 mm diameter pinion gear, 14 teeth, and an 11 mm pitch aligned with a rack of 120 cm length and 2 cm width. The planting arm (PA) comprises three main components: the seed suction motor, suction pipe, and seed suction nozzle (Fig. 3).

The seed suction nozzle assembly consists of three cone-shaped air-suction nozzles with hole diameters of 0.5, 1.0, and 2.0 mm. The first nozzle, with a 0.5 mm hole diameter, is made of Teflon, while the other two are from steel. All nozzles have a standardized total length of 25 mm, including a 15 mm external thread length with a 10 mm diameter.

The suction pressure values were obtained through measurements conducted with three different nozzle sizes (2.0 mm, 1.0 mm, and 0.5 mm), resulting in recorded pressures of -0.20 bar, -0.16 bar, and -0.12 bar, respectively.

The suction pipe is fabricated from steel and has a length of 23 cm with an outer diameter of 2.25 cm. The lower part of the pipe features an internal thread for attaching diverse cone-shaped air-suction nozzles (Fig. 4).

The seed box, designed for sowing seeds in pots, is constructed from acrylic with dimensions of 133.92 × 125.92 × 80 mm (length × width × height), a thickness of 2.5 mm, and a slope angle of 30°. A carbon fiber seed box holder, measuring 20 cm in length and 4 mm in thickness, provides sturdy support. The MG946R metal gear servo motor was predominantly chosen for its high-angle precision. In contrast, the seed box was continuously rotated at a 90-degree angle by a standard electric motor when power was supplied, while the servo motor was halted after its instructed rotation was completed and awaited the following command.

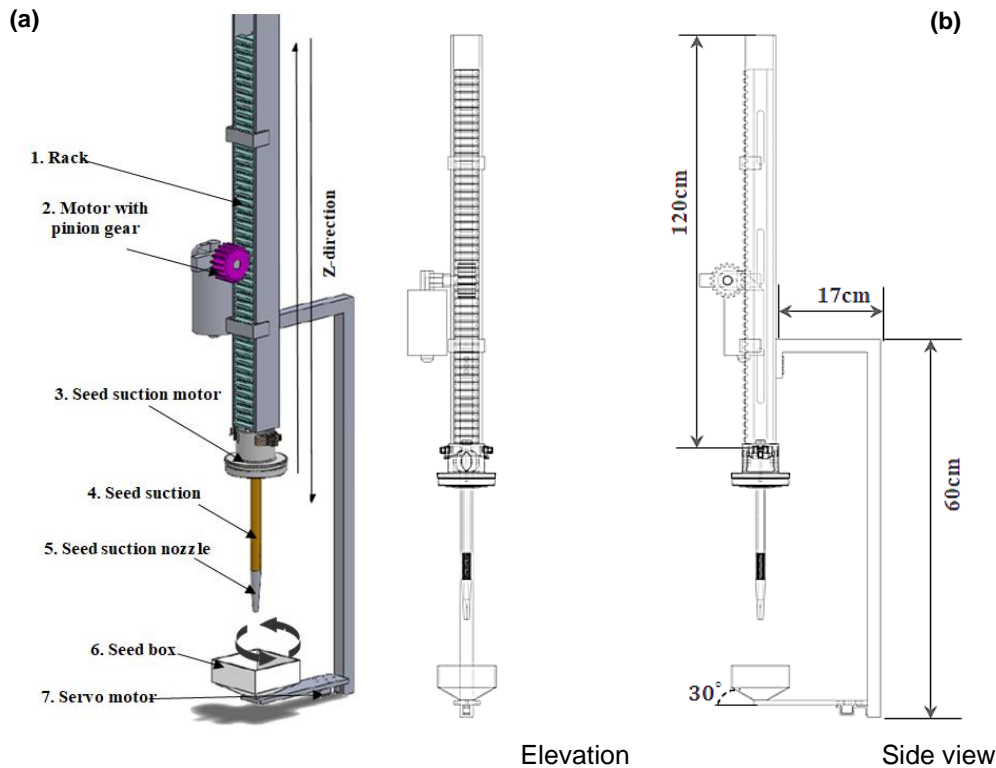


Fig. 3 – 3D view of the Z-axis motion of the PA motion (a) and elevation and side views of the PA (b)

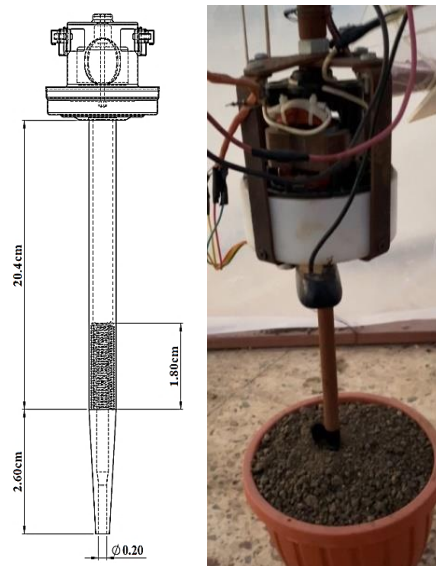


Fig. 4 – Suction-seeding pipe of PA

Software systems

This section outlines the methodologies for image acquisition, image processing, identification and positioning of plant pots, data management, and control of the precision seeding mechanism, encompassing tasks related to image analysis, data processing, and mechanical adjustments. An Arduino microcontroller was utilized for signal distribution and program execution. Figure 5 presents the software system flowchart after initialization.

Image acquisition

The Python script conducts real-time circle identification via a webcam feed, utilizing the OpenCV library for image processing and circle detection. The circle coordinates are transmitted to an Arduino using a serial link. Figure 6 presents a depiction of an image obtained using the industrial camera. If circles are identified, they are outlined in green with red centers on the frame. The center coordinates of each circle are converted to strings and transmitted to the Arduino via the serial connection.

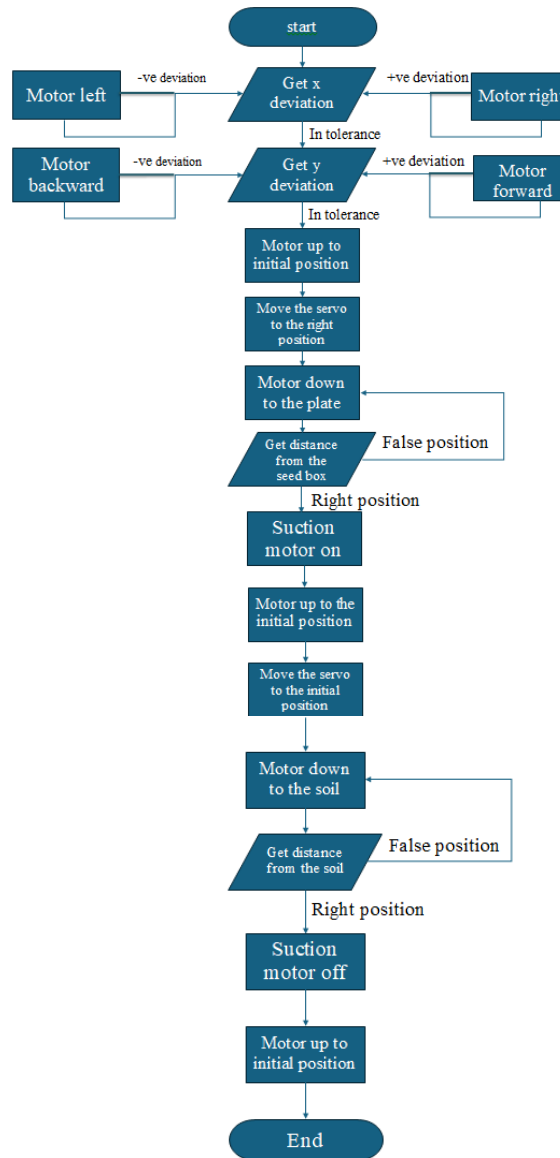


Fig. 5 – Flowchart of software system

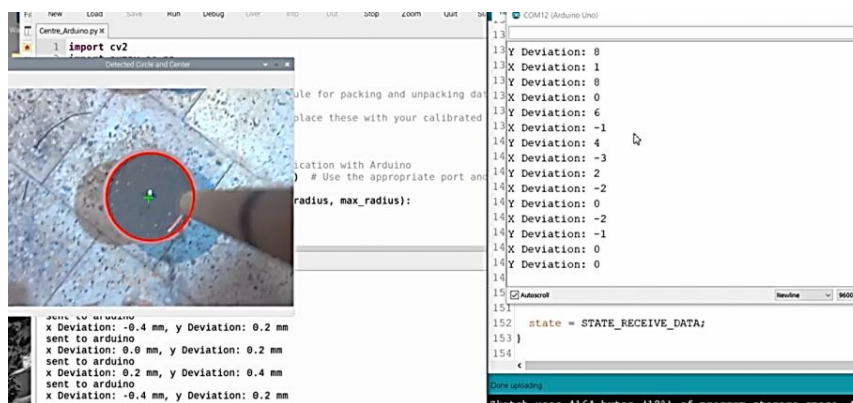


Fig. 6 – Drawing circles and sending coordinates

Image processing

The captured frame was converted from BGR color format to grayscale to simplify processing. A Gaussian blur was then applied to the grayscale image to reduce noise and enhance circle detection accuracy. Finally, the Hough Transform was used to identify circles in the blurred grayscale image (Fig. 7).

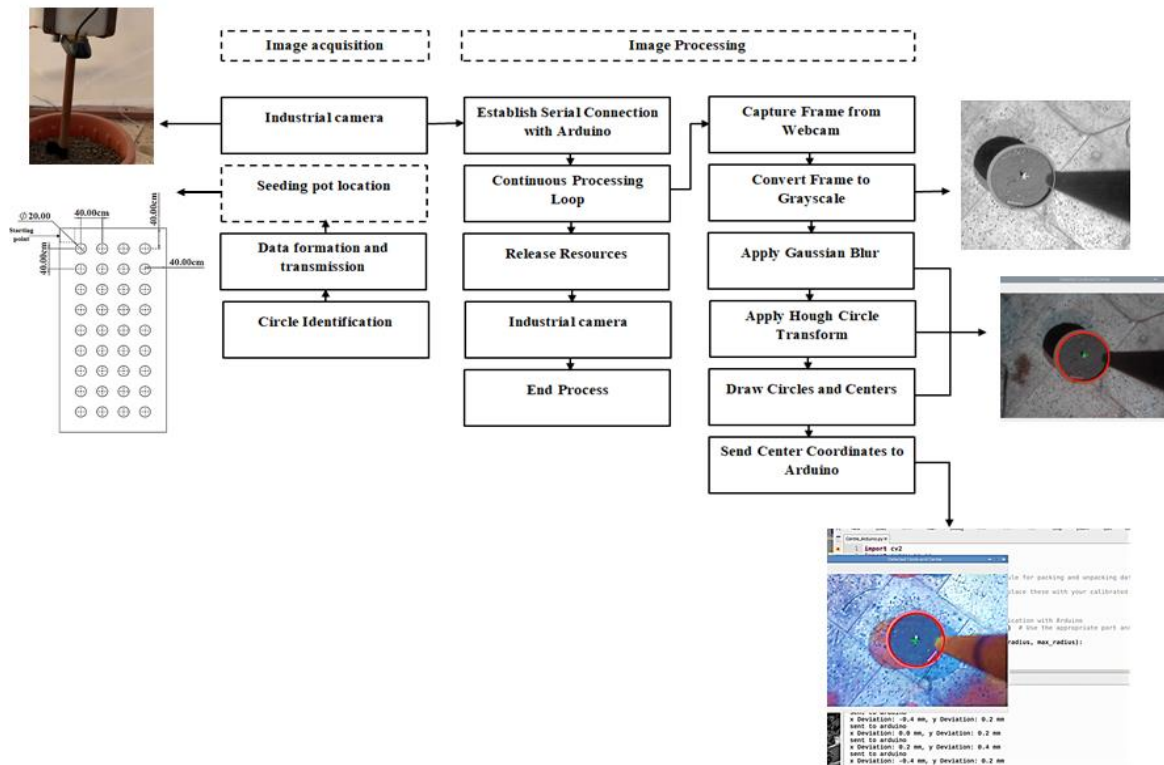


Fig. 7 – Image processing

Controlling the seed planting automation

The Arduino system governs various motors and a servo motor by following instructions through serial communication (mySerial). It controls motor movements, planting actions, and sensor data by utilizing different states and functions to automate the planting procedure—controls motors based on deviations ($x_deviation$ and $y_deviation$). Modify motor orientations and statuses according to discrepancies received from Raspberry Pi.

Controlling a suction motor

The Arduino sketch manages a suction motor connected to pin 8 of the Arduino board. The motor activates for half a second, followed by a two-second off period, continuously cycling through this pattern in the loop() function. Modifying the timing in the delay() functions will alter the motor's duration on and off. Upon reaching the intersection of the circle's radii (showing the planting point), the APSU starts the planting process. Initially, the seed box moves using a servo motor until it reaches a 90-degree angle, positioning it directly beneath the planting column. The suction motor responsible for seed collection is then activated. According to measurements from the ultrasonic sensor, the APSU moves downward in the Z direction until it reaches the seed box, which is positioned 31 cm below the maximum height. It picks up the seed and then moves upward in the Z direction to the maximum height until the seed box returns to its original position (Fig. 8).

Ultrasonic distance measurement

This Arduino sketch utilizes an ultrasonic sensor connected to pins A0 (trigger) and A1 (echo) to measure distances. It continuously reads distances, filters out invalid measurements, and displays the valid distance readings on the Serial Monitor (Fig. 9). The distance range and timing can be adjusted based on specific sensor characteristics and application requirements. Based on these readings, the arm plants seeds at the required depth.

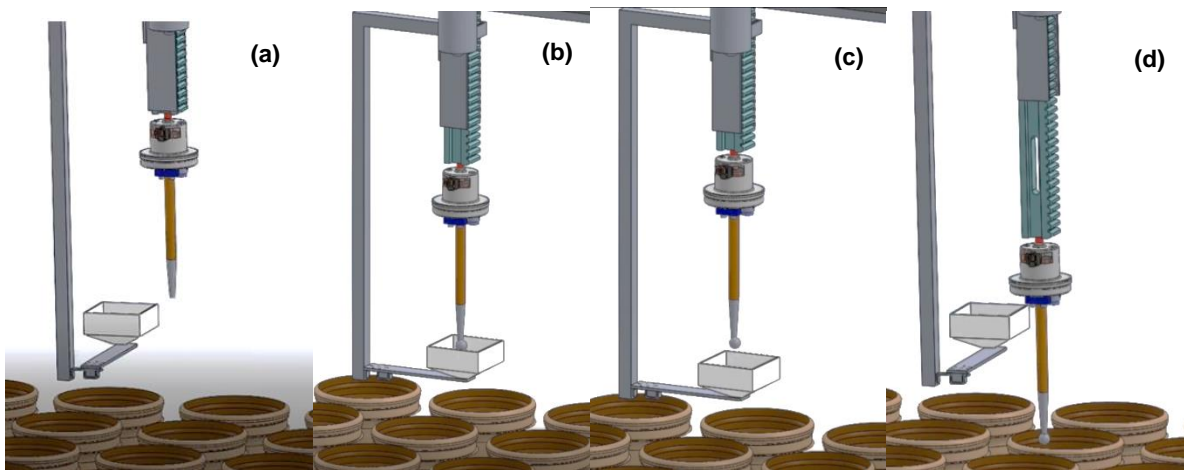


Fig. 8 – The process of picking up the seed from the rotating seed box, beginning at the starting position (a), followed by a downward vertical movement (b), then an upward vertical movement after suctioning the seed (c), and finally a downward vertical movement to place the seed in the pot after a 90° rotation by the servo motor (d)

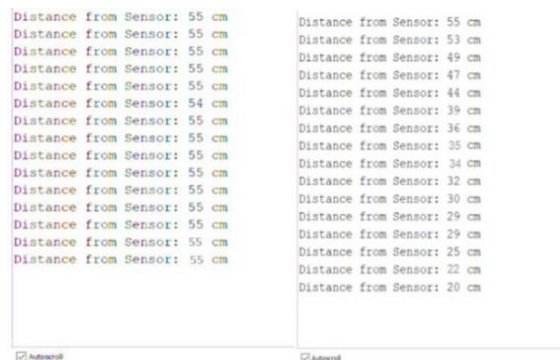


Fig. 9 – Ultrasonic readings and its height above the soil surface

Planting depth

The program was used for planting seeds in soil, relying on an ultrasonic distance sensor to measure depth. Variables like Servo_ANG and Servo_ANG_RE were assigned to set the servo motor's motion angles for seed placement. During the Put_Seeds() process, continuous checks were made on the distance (Dis_Z) to ensure accurate seed placement. The program can be adjusted to regulate planting depth by modifying conditions in functions like GetSeeds() and PutSeedsInSoil() to meet specific agricultural tasks.

The ultrasonic sensor is 20 cm from the suction pipe's end and varies in distance from the soil's surface (Fig. 10). Next, the planting depth is computed using Eq. (1).

$$Y = 20 - X \tag{1}$$

where Y represents the distance between the ultrasonic sensor and the soil surface [cm], 20 represents the suction pipe [constant height], and X denotes the planting depth [cm].

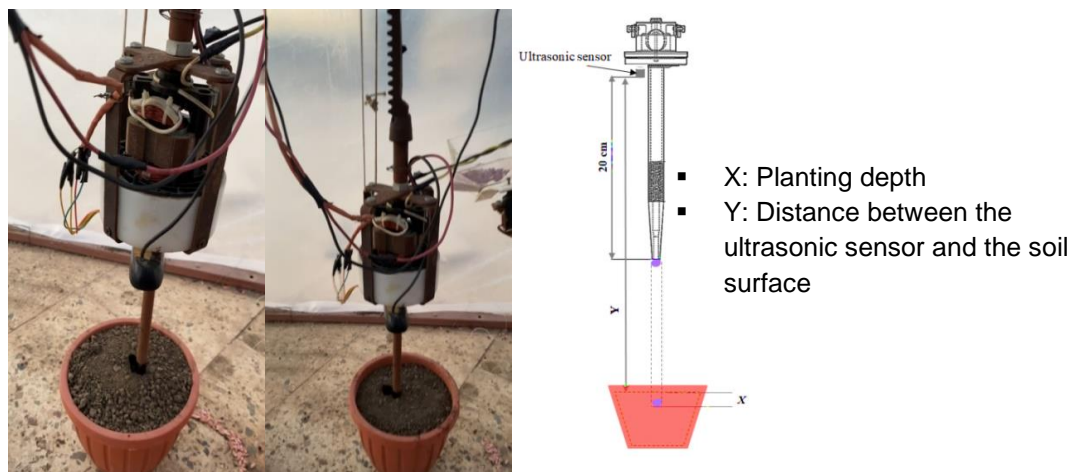


Fig. 10 – Determining planting depth

Time to complete the planting process

Each pot has a diameter and height of 20 cm. Thirty-six pots are arranged in an 8 m² area, with 9 pots placed longitudinally and 4 pots placed transversely, each spaced 20 cm apart. The distance between the pot edges and the greenhouse structure is 30 cm in all directions. The required planting time for this greenhouse was determined according to Eq. (2):

$$= (N \times (T_P + T_R)) + T_T + Turnaround\ time \tag{2}$$

$$= (36 \times 30) + (8 \times 4 \times 5) + (3 \times 5) = \frac{1255}{3600} = 0.35\ h$$

where *N* denotes the number of pots, *T_p* denotes the planting time [sec], *T_R* represents the resting time [sec], and *T_T* implies the transit time [sec].

RESULTS AND DISCUSSION

Camera deviation relative to the pots' centers

The code begins by including the SoftwareSerial library, which facilitates virtual serial communication on the Arduino. It then defines variables for storing deviations in the X and Y axes and processing incoming data. Figure 11 represents the precision and variability of the positioning system. Minimal deviations, ranging from -1.2 mm to 1.2 mm, were observed, demonstrating effective alignment control. Experiments 3 and 5 showed no deviation on the X-axis. Experiment 3 achieved accurate alignment in both X and Y directions, while Experiment 5 demonstrated a minor deviation in the Y direction (-0.6 mm). In the X direction, negative deviations of -0.2 mm and -0.4 mm were noted in Experiments 1 and 6, respectively, along with slight shifts in the Y direction. Experiment 2 showed the most substantial positive deviations in the X (1.2 mm) and Y (0.8 mm) axes, showing a significant shift from the central position. Experiment 4 showed a positive deviation of 1.2 mm in the X direction and a notable negative deviation of -1.2 mm in the Y direction, suggesting angular displacement. Despite the overall precision, adjustments may be needed to enhance accuracy because of the deviations observed in Experiments 2 and 4. These deviations might be because of mechanical discrepancies, limitations in the control system, or systematic inaccuracies. Enhanced calibration and more precise control algorithms have the potential to minimize these deviations and improve alignment with the pot centers.

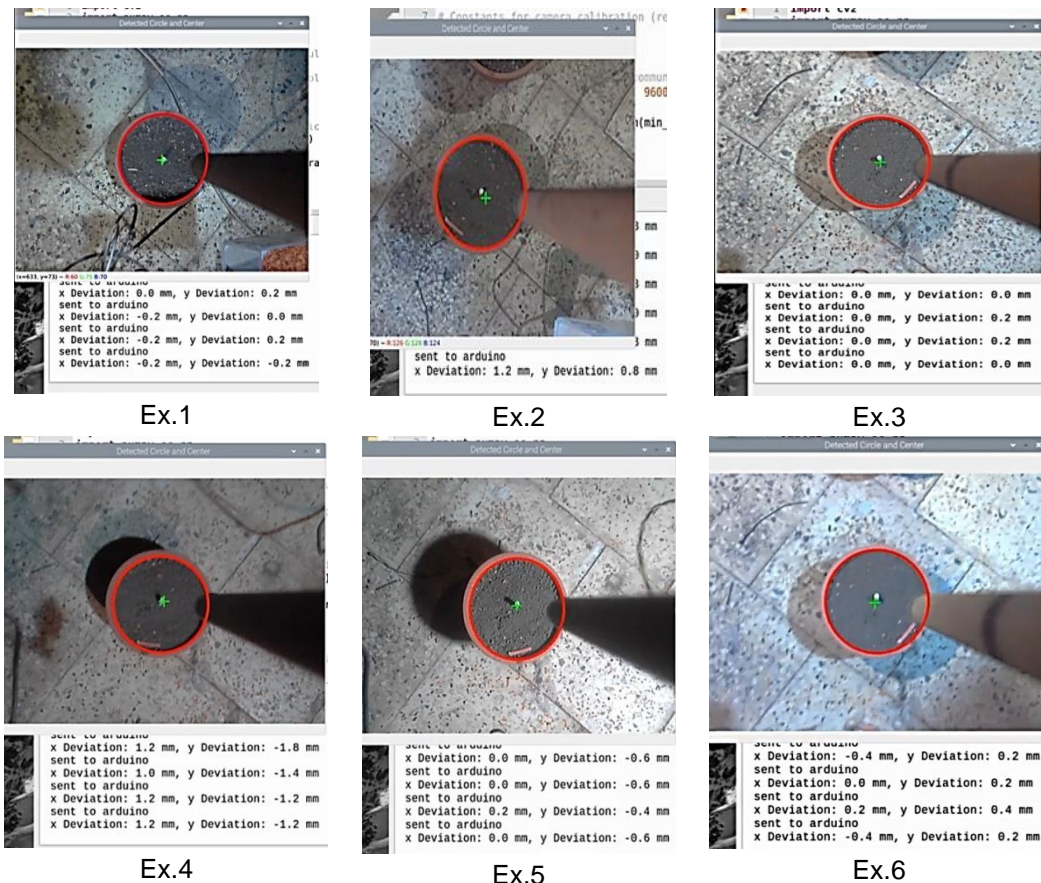


Fig. 11 – Deviations in the X and Y directions relative to the pots' centers

The number of seeds captured by air suction for different seed types and seed suction hole diameters

Figures 12-15 present the number of seeds collected through air suction, categorized by suction hole diameters (0.5 mm, 1 mm, and 2 mm) and seed varieties (okra, turnip, pepper, and Armenian cucumber) across fifteen experiments. Okra seeds show consistent behavior, achieving a nearly 100% success rate across diameters, indicating they can be efficiently used with various hole sizes. Some deviations were noted in specific experiments, possibly because of alignment issues. Turnip seeds displayed greater variability; smaller diameters (0.5 mm and 1 mm) had high success rates, while the 2 mm diameter resulted in multiple seeds being captured, reducing efficiency. Pepper seeds captured mostly 1 seed at 0.5 mm, with slightly higher averages at 1 mm (2.13 seeds) and a significant increase at 2 mm (average of 12.6 seeds), indicating challenges in capturing a single seed effectively. Armenian cucumber seeds also increased in capture with larger diameters, from 1 seed at 0.5 mm to an average of 3.93 seeds at 2 mm.

Recommendations based on these findings suggest using a 0.5 mm suction hole for turnip and pepper seeds and a 1 mm hole for okra and Armenian cucumber seeds to enhance planting efficiency and reduce waste.

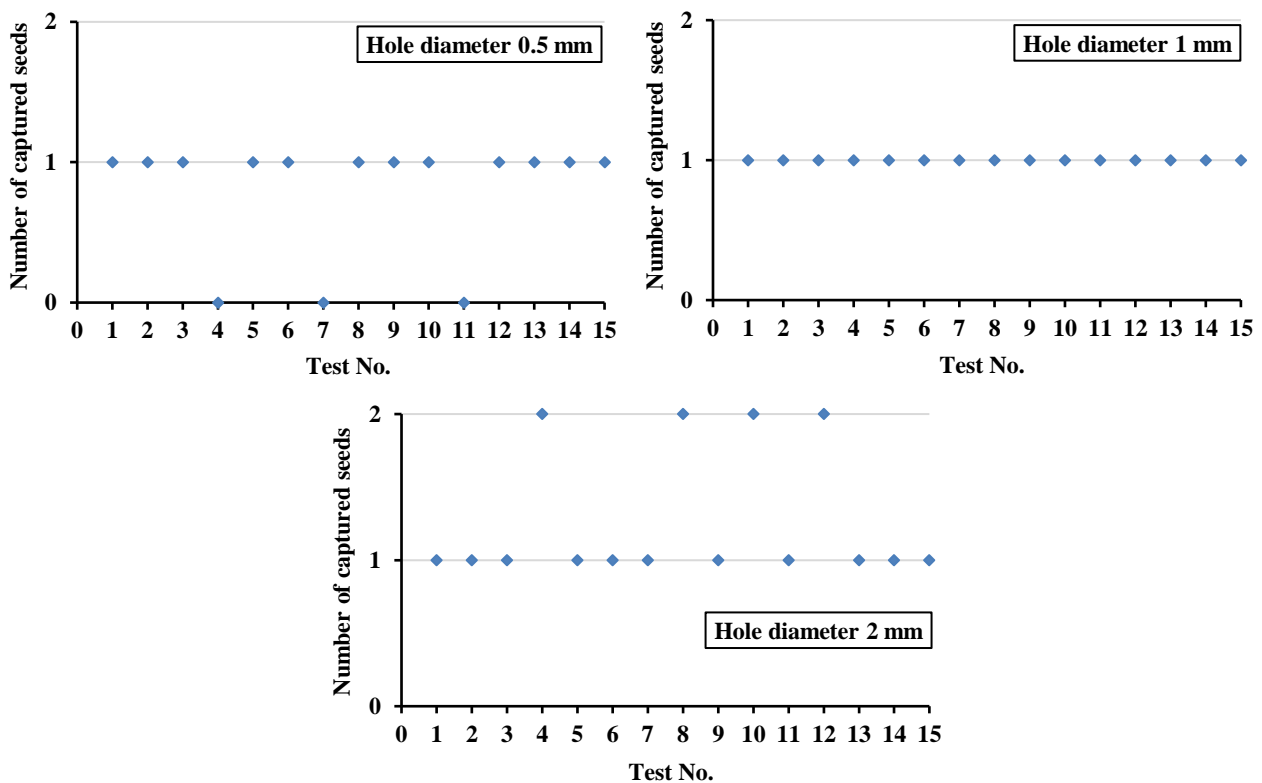


Fig. 12 – Number of captured okra seeds with suction hole diameters of 0.5, 1, and 2 mm

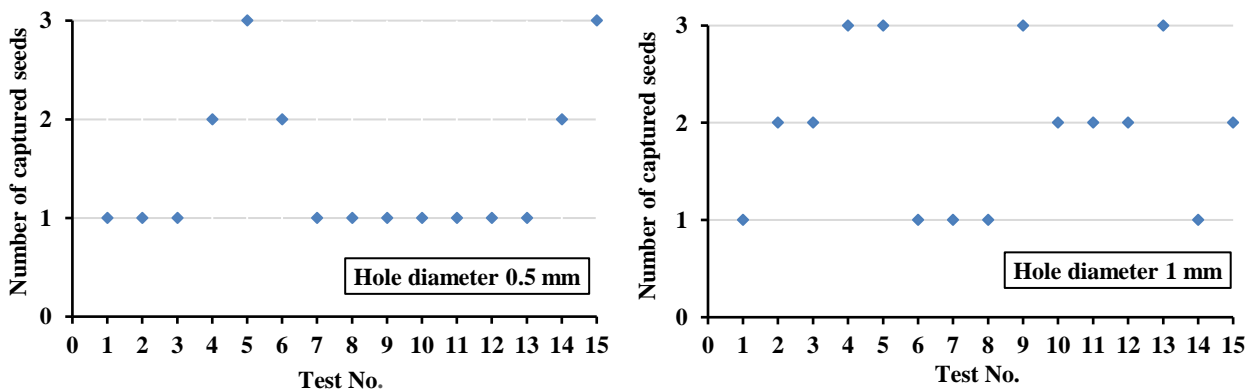


Fig. 13 – Number of captured turnip seeds with suction hole diameters of 0.5 and 1 mm

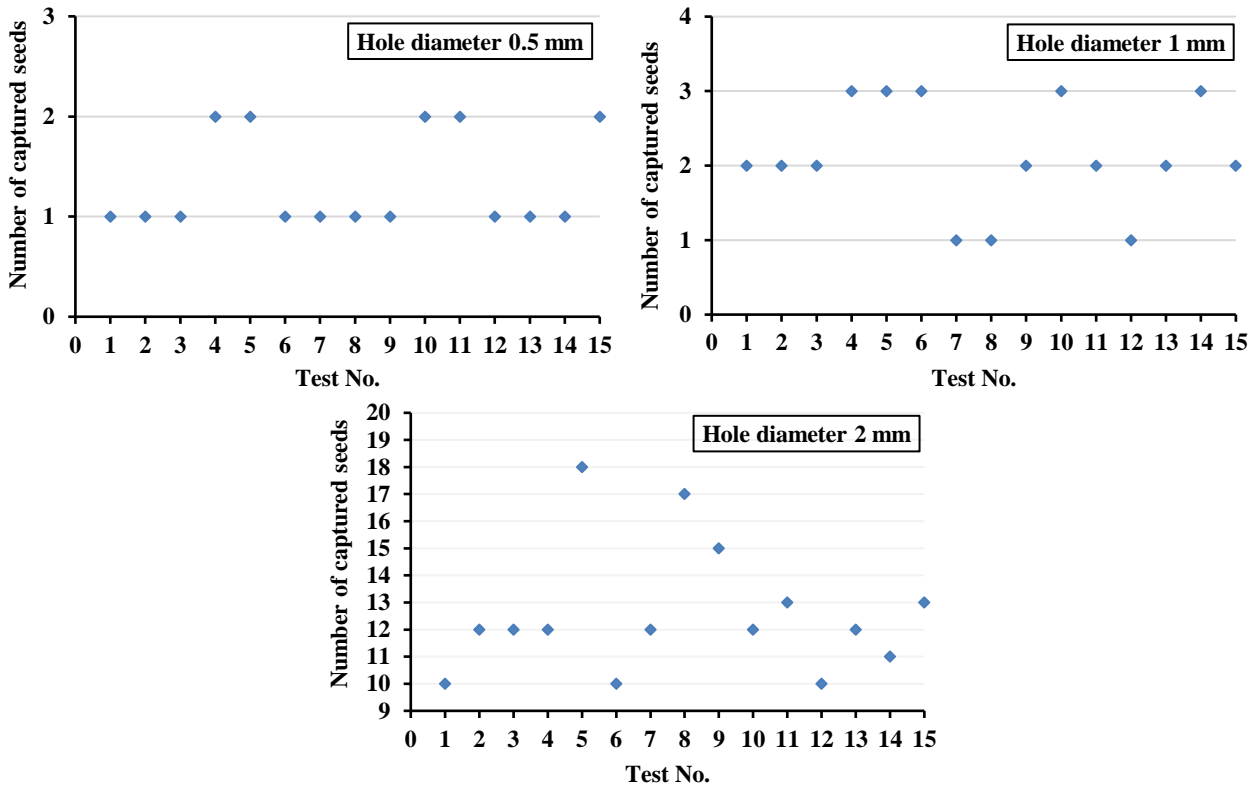


Fig. 14 – Number of captured pepper seeds with suction hole diameters of 0.5, 1, and 2 mm

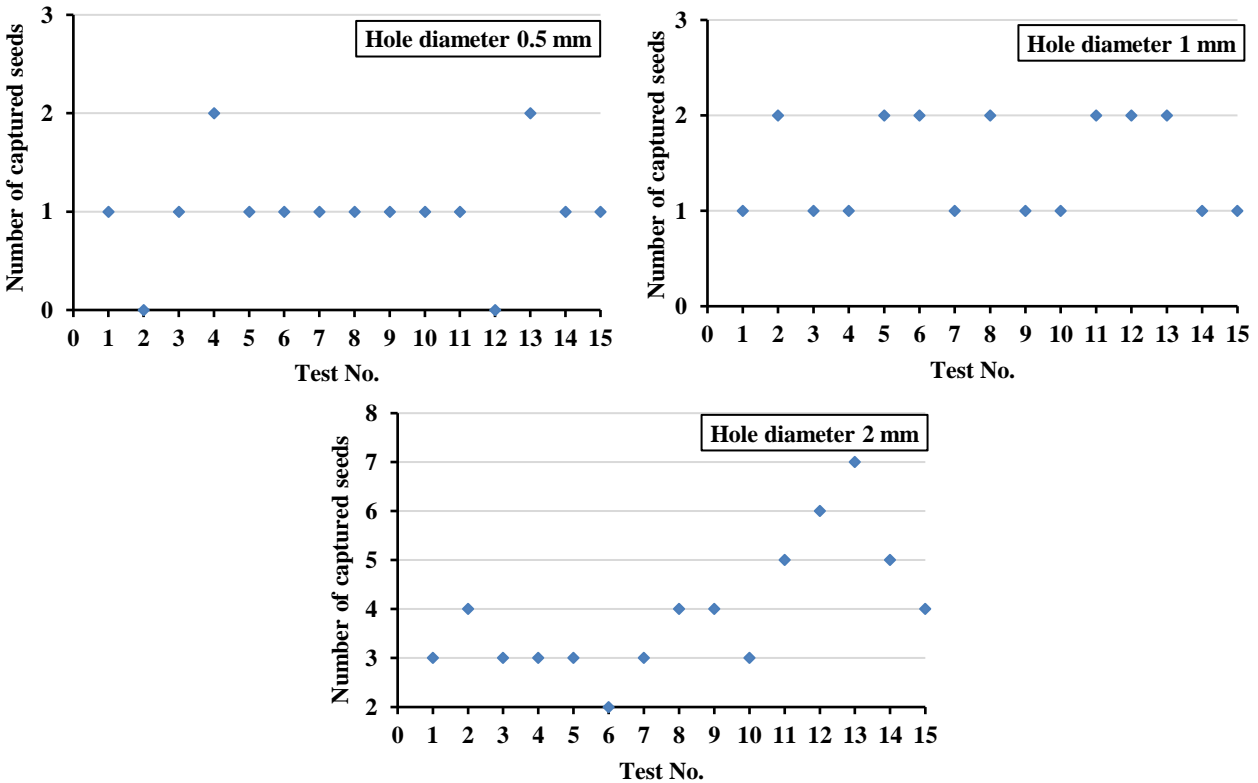


Fig. 15 – Number of captured Armenian cucumber seeds with suction hole diameters of 0.5, 1, and 2 mm

Planting depth and soil elevation

This program is intended for seed planting and employs an ultrasonic distance sensor to measure depth precisely. The planting arm adapts its elevation using reliable sensor readings to reach the predetermined planting depth of 3.0 cm. The depth was assessed at three distinct soil elevations, varying between 15 and 20 cm (Table 1). The results from nine trials exploring planting depths at varying soil elevations to maintain a target depth of 3.0 cm are presented in Table 1.

The data demonstrate how changes in soil elevation influence planting depth, which plays a crucial role in ensuring uniform seed placement and promoting optimal germination. Trials were conducted at three soil elevations: 20 cm, 18 cm, and 15 cm, showing that variations in soil elevation affect planting depth. At a soil elevation of 20 cm, the planting depth ranged from 2.5 cm to 3.2 cm, with an average of 2.9 cm. At 18 cm, planting depths varied between 2.7 cm and 3.3 cm, while at 15 cm, they ranged from 2.7 cm to 3.0 cm. The average planting depth across all trials was 2.9 cm, slightly below the target depth of 3.0 cm. The planting depth had a coefficient of variation (CV) of 8.28% and a standard deviation of approximately ± 0.24037 cm. Despite variations in soil elevation, the planting technique consistently maintained a depth close to 3 cm. The results indicate satisfactory performance, although minor adjustments and calibrations could further enhance accuracy and consistency.

Table 1

Different soil elevations with planting depth stability of 3.0 cm

Experiments	Soil elevation	Planting depth
Ex.1	20 cm	3.2 cm
Ex.2	20 cm	3.0 cm
Ex.3	20 cm	2.5 cm
Ex.4	18 cm	2.7 cm
Ex.5	18 cm	2.8 cm
Ex.6	18 cm	3.3 cm
Ex.7	15 cm	3.0 cm
Ex.8	15 cm	2.7 cm
Ex.9	15 cm	2.9 cm
Average (\bar{X})		2.9 cm
Standard deviation ($\pm SD$)		± 0.24037 cm
Coefficient of variation (CV)		8.28%

Total time for planting

Table 2 details the overall time needed for the planting procedure, comprising three separate time spans: planting time (T_P), resting time (T_R), and transit time (T_T). Planting time (T_P) is the overall period required for the mechanical planting process, which involves the planting arm's horizontal descent and subsequent vertical motions to achieve the desired planting depth and ensure precise seed placement in the soil. The duration of this phase is estimated to be approximately 20 seconds. Resting time (T_R) refers to the period following the suction motor's deactivation and the seed's subsequent release, enabling it to embed itself in the soil at a 3 cm depth. This period is critical to ensure the correct seed penetration before advancing to the subsequent seed, and it typically endures for approximately 10 seconds. This timing was determined through conducted experiments. Transit time (T_T) refers to the period needed for transferring between pots, commencing with the initiation of the planting arm's upward movement and ending when the subsequent downward movement commences. This phase lasts approximately 5 seconds. In conclusion, the overall time (T_{T0}) required for a complete planting cycle, encompassing all three elements, totals 35 seconds.

Table 2

Total time to complete the planting process

Required time	
Planting time (T_P)	20 s
Resting time (T_R)	10 s
Transit time (T_T)	5 s
Total time (T_{T0})	35 s

CONCLUSIONS

An automatic precision seeding unit was developed for planting pepper, turnip, Armenian cucumber, and okra seeds. The research introduced an approach to identifying planting pot positions and calculating pot radius to assist with planting at the prescribed depth. Investigating the precision seeding device's control system and mechanical structure yielded multiple discoveries. A practical approach for identifying circles and determining positions was introduced through image processing methods such as circle detection, morphological processing, and image reconstruction, showcasing exceptional precision.

Three seed suction nozzles were meticulously crafted to function through air suction, each with dimensions of 0.5 mm, 1 mm, and 2 mm, and set at precise pressure levels of -0.2 bar, -0.16 bar, and -0.12 bar, respectively, effectively fulfilling seed suction needs. A precision seeding unit automated planting procedures, including identifying pot locations, controlling the movement of the seeding unit, managing the seed box movement, and overseeing the seed uptake and release through the suction nozzle. The planting arm achieved a depth accuracy within a coefficient of variation of $\pm 8.28\%$, positioning at an average depth of 2.9 cm beneath the soil surface in contrast to the 3 cm target depth, despite fluctuations in soil height. The results illustrate the system's ability to offer a reliable solution for automated planting with consistent precision.

REFERENCES

- [1] Abdelmotaleb, I., Hegazy, R., Imara, Z., & Rezk, A. (2015). Development of an autonomous navigation agricultural robotic platform based on machine vision. *Misr Journal of Agricultural Engineering*, 32(4), 1421–1450. <https://doi.org/10.21608/mjae.2015.97589>
- [2] Abo-Habaga, M. M., Ismail, Z. E., & Okasha, M. H. (2022). Effect of tillage systems on a soil moisture content and crops productivity. *Journal of Soil Sciences and Agricultural Engineering, Mansoura University*, 13(7), 231–235. <http://doi.org/10.21608/JSSAE.2022.138432.1077>
- [3] Amin, A., Wang, X., Guoxiang, S., Shi, Y., Ndumiaassan, J. N., & Okasha, M. (2024a). Design and experimentation of a solar-powered robot for cleaning the greenhouse roofs. *Results in Engineering*, 23, 102602. <https://doi.org/10.1016/j.rineng.2024.102602>
- [4] Amin, A., Wang, X., Chen, Y., Guoxiang, S., Xuekai, H., Rottok, L. T., Sayed, H. A. A., & Okasha, M., Hassanien, R.H.E. (2024b). Enhancing Greenhouse Performance Through Robotic Roof Cleaning Solutions: A Review. *Journal of Field Robotics*. <https://doi.org/10.1002/rob.22459>
- [5] Ardiansah, I., Bafdal, N., Bono, A., Suryadi, E., & Husnuzhan, R. (2021). Impact of ventilations in electronic device shield on micro-climate data acquired in a tropical greenhouse. *INMATEH - Agricultural Engineering*, 63(1), 397–404. <https://doi.org/10.35633/inmateh-63-40>
- [6] Balafoutis, A. T., Beck, B., Fountas, S., Tsiropoulos, Z., Vangeyte, J., Van der Wal, T., Soto-Embodas, I., Gómez-Barbero, M., & Pedersen, S. M. (2017a). Smart Farming Technologies—Description, Taxonomy and Economic Impact. In *Progress in Precision Agriculture*; Springer: Cham, Switzerland, pp. 21–77.
- [7] Balafoutis, A., Beck, B., Fountas, S., Vangeyte, J., Van, D. W. T., Soto, I., Gómez, M., Barnes, A., & Eory, V. (2017b). Precision Agriculture Technologies Positively Contributing to GHG Emissions Mitigation, Farm Productivity and Economics. *Sustainability*, 9(8), 1339. <https://doi.org/10.3390/su9081339>
- [8] Balafoutis, A. T., Van Evert, F. K., & Fountas, S. (2020). Smart Farming Technology Trends: Economic and Environmental Effects, Labor Impact, and Adoption Readiness. *Agronomy*, 10(5), 743. <https://doi.org/10.3390/agronomy10050743>
- [9] Brisco, B., Brown, R. J., Hirose, T., Naim, H. M., & Staenz, K. (2014). Precision Agriculture and the Role of Remote Sensing: A Review. *Canadian Journal of Remote Sensing*, 24(3), 315–327. <https://doi.org/10.1080/07038992.1998.10855254>
- [10] Bu, L. X., Chen, C., Hu, G. R., Sugirbay, A., & Chen, J. (2020). Technological development of robotic apple harvesters: a review. *INMATEH - Agricultural Engineering*, 61(2), 151–164. <https://doi.org/10.35633/inmateh-61-17>
- [11] Iosif, A., Maican, E., Biriş, S., & Popa, L. (2023). Automated quality assessment of apples using convolutional neural networks. *INMATEH - Agricultural Engineering*, 71(3), 483–498. <https://doi.org/10.35633/inmateh-71-42>
- [12] Khandelwal, S., Kaushik, N., Sharma, S., Pandey, M. Kr., & Rawat, T. S. (2017). AgRo-Bot: Autonomous robot. *International Journal of Advanced Research in Computer Science*, 8(5), 2318–2320.
- [13] Li, J. H., Lai, Q. H., Zhang, H., Zhang, Z. G., Zhao, J. W., Wang, T. T. (2021). Suction force on high-sphericity seeds in an air-suction seed-metering device. *Biosystems Engineering*, 211, 125–140. <https://doi.org/10.1016/j.biosystemseng.2021.08.031>
- [14] Loukatos, D., Templalexis, C., Lentzou, D., Xanthopoulos, G., & Arvanitis, K. G. (2021). Enhancing a flexible robotic spraying platform for distant plant inspection via high-quality thermal imagery data. *Computers and Electronics in Agriculture*, 190(1), 106462. <http://dx.doi.org/10.1016/j.compag.2021.106462>

- [15] Maleki, M. R., Jafari, J. F., Raufat, M. H., Mouazen, A. M., & De Baerdemaeker, J. (2006). Evaluation of seed distribution uniformity of a multi-flight auger as a grain drill metering device. *Biosystem Engineering*, 94(4), 535–543. <https://doi.org/10.1016/j.biosystemseng.2006.04.003>
- [16] Nash, E., Korduan, P., & Bill, R. (2009). Applications of Open Geospatial web services in precision agriculture: A review. *Precision Agriculture*, 10(6), 546–560. <http://dx.doi.org/10.1007/s11119-009-9134-0>
- [17] Reyns, P., Missotten, B., Ramon, H., & De Baerdemaeker, J. (2002). A Review of Combine Sensors for Precision Farming. *Precision Agriculture*, 3, 169–182. <https://doi.org/10.1023/A:1013823603735>
- [18] Tang, H., Xu, C. S., Zhao, J. L., & Wang, J. W. (2023). Stripping mechanism and loss characteristics of a stripping-prior-to-cutting header for rice harvesting based on CFD-dem simulations and bench experiments. *Biosystems Engineering*, 229, 116–136. <https://doi.org/10.1016/j.biosystemseng.2023.03.023>
- [19] Urbaniak, S. D., Caldwell, C. D., Zheljzkov, V. D., Lada, R., & Luan, L. (2008). The effect of seeding rate, seeding date and seeder type on the performance of *Camelina sativa* L. in the Maritime Provinces of Canada. *Canadian Journal of Plant Science*, 88(3), 501–508. <https://doi.org/10.4141/CJPS07148>

POD PEPPER TARGET DETECTION BASED ON IMPROVED YOLOv8

/ 基于改进 YOLOv8 的朝天椒目标检测研究

Jiayv SHEN, Qingzhong KONG, Yanghao LIU, Na MA*)

College of Information Science and Engineering, Shanxi Agricultural University, Taigu / China

Tel: +86-13834188480; E-mail: manasxau@163.com

DOI: <https://doi.org/10.35633/inmateh-74-23>**Keywords:** pod pepper, machine vision, YOLOv8, attention mechanism**ABSTRACT**

Pod pepper (*Capsicum annuum* var. *conoides*), a common variety of chili pepper, poses a challenge for traditional object detection methods due to its complex morphological features and diverse types. This study focuses on the application of machine vision technology to address the issue of pod pepper object detection. Firstly, a large number of pod pepper sample images were collected, followed by data preprocessing and annotation. Subsequently, YOLOv3, YOLOv5, YOLOv6, and YOLOv8 pod pepper object detection models were established, with YOLOv8 yielding the best detection results with a mean Average Precision (mAP) value of 81.6%. Next, different attention mechanisms were incorporated into the YOLOv8 network structure, with experimental results indicating that the Triplet Attention mechanism performed the best in pod pepper object detection, achieving an mAP value of 82.5%, a 0.9% improvement over YOLOv8. To further optimize the effectiveness of the attention mechanisms, Triplet Attention was added at different positions within the YOLOv8 network. The experiment showed that the location of adding the attention mechanism significantly impacted the pod pepper detection results. When Triplet Attention was added at the 5th layer, the best detection performance was achieved, with an mAP value of 84.1%, a 2.5% improvement over the original YOLOv8. This research provides technical support for intelligent harvesting of pod pepper.

摘要

朝天椒是一种常见的辣椒品种，由于其形态特征复杂且种类较多，传统的目标检测方法在其识别方面存在一定的挑战。本研究基于机器视觉技术，针对朝天椒目标检测问题展开研究。首先，采集了大量朝天椒样本图像，并进行了数据预处理和标注整理。其次，建立了 YOLOv3、YOLOv5、YOLOv6、YOLOv8 朝天椒目标检测模型，对比不同检测模型效果，YOLOv8 检测结果最优，检测 mAP 值为 81.6%。然后在 YOLOv8 网络结构中添加不同注意力机制，实验结果表明 Triplet Attention 机制在朝天椒目标检测中表现最好，检测结果 mAP 值为 82.5%，比 YOLOv8 提升 0.9%。为了进一步验证注意力机制的效果最大优化性，将 Triplet Attention 添加到 YOLOv8 网络不同位置，试验结果表明添加注意力机制的位置对朝天椒检测结果有显著影响。当 Triplet Attention 添加到 5 层，检测效果最好，检测 mAP 值为 84.1%，相比原始 YOLOv8 提升 2.5%。该研究可为朝天椒智能采摘提供技术支持。

INTRODUCTION

In everyday cooking, chili peppers are a popular spice among consumers and have been used as an edible vegetable, flavouring, natural colouring agent and traditional medicine (Hernández-Pérez et al., 2020). Pepper is a good source of provitamin A; vitamins C and E; carotenoids; and phenolic compounds such as capsaicinoids, luteolin, and quercetin (Batiha et al., 2020). Pod pepper, a chili variety originating from tropical regions of South America, plays a crucial role in agriculture and food processing. Efficient monitoring and harvesting of Pod peppers are therefore essential in agricultural production. By selecting and cultivating high-yielding and disease-resistant varieties, both societal and economic benefits can be enhanced.

Traditional manual monitoring methods rely on visual observation by humans, which requires prolonged attention and repetitive labour. Extended monitoring periods can lead to fatigue, making the process time-consuming, labour-intensive, and subjectively inefficient. Moreover, employing manual labour is costly and lacks periodicity, while economic efficiency of crops remains a critical production factor. Additionally, the diverse and complex morphology of pod peppers grown in fields, compounded by weather conditions and foliage occlusion, objectively diminishes the depth and dimension parameters in colour image-based target detection tasks (Li et al., 2020), thereby reducing the accuracy of traditional detection models. Hence, there is a need for a cost-effective, field-appropriate detection method that promotes the integration of technology and agriculture.

Over the past few decades, precision agriculture techniques have been richly developed to refine agricultural management practices (Arakeri *et al.*, 2017). With the advancements in machine vision and deep learning technologies, automated analysis of target images using computers has rapidly progressed in fields such as crop monitoring and commercial recognition (Cai *et al.*, 2023). Initially, the integration of deep learning algorithms with agriculture focused on automated sorting of agricultural products and detection and diagnosis of plant diseases and pests. Sladojevic *et al.* first combined the Caffe deep learning framework with the detection of plant diseases and pests, achieving an average accuracy of 96.3% in pest detection across 13 different types of leaves (Sladojevic *et al.*, 2016). Kanda *et al.* utilized a Conditional Generative Adversarial Network, Convolutional Neural Network, and Logistic Regression to achieve an average accuracy of 96.1% in the recognition of eight plant leaf datasets. (Kanda *et al.*, 2021). Farooq *et al.* conducted structural optimization of YOLOv8 based on SSD, YOLOv5m, Scaled YOLOv4, CenterNet, and YOLOv8m results in an average accuracy of 93.8% for recognition of small foreign object fragments (Farooq *et al.*, 2024). Mahesh *et al.* used YOLOv3 to determine plant diseases based on symptoms on pepper leaves with a final average accuracy of 90% (Mahesh *et al.*, 2024). Sapkota *et al.* utilized the YOLOv8 object detection and instance segmentation algorithm in conjunction with geometric shape fitting of 3D point cloud data to accurately determine the size of unripe green apples in a commercial orchard environment, with a final result of RMSE values (2.35 mm for Azure Kinect and 9.65 mm for Realsense D435i) and MAE value (1.66 mm for Azure Kinect and 7.8 mm for Realsense D435i) (Sapkota *et al.*, 2024).

The aforementioned studies collectively demonstrate that object detection algorithms, particularly in the realm of agricultural modernization, show promising results in crop and fruit localization and recognition. Addressing the shortcomings of existing models in detecting pod peppers in field conditions, this study develops a pod pepper object detection model named YOLOv8-TripletAttention-5. Initially, a substantial dataset of pod pepper images was collected and annotated using labelImg. Subsequently, various YOLO series models were compared for their effectiveness in pod pepper detection, with YOLOv8 selected as the optimal base model. Different triplet attention mechanisms were then integrated at various positions on the YOLOv8 model, ultimately improving it by incorporating Triplet Attention at position 5. The results indicate a significant enhancement in efficiency and accuracy of pod pepper detection in challenging field environments where direct observation is less feasible. This research is poised to make a positive contribution to the modernization and sustainable development of agriculture.

MATERIALS AND METHODS

Data Acquisition and Pre-processing

The experimental pod pepper variety used in the study is Shengfeng Sanying No. 8. The dataset of images was collected from late July to early August 2023 at the Xiangfen County Clustered Pod Pepper Planting Base in Linfen City, Shanxi Province, China. With the purpose of this experiment is to improve the recognition accuracy of ripe pepper in the picking period, 689 images of ripe pepper were collected. The experiment captured various scenarios including obstructed and unobstructed views, as well as clear and rainy weather conditions, aiming to realistically depict the diverse situations encountered in agricultural fields during the harvest period. Figure 1 shows a selection of collected pod pepper images.



Fig. 1 - Partial Data Collection

Using Labellmg for pod pepper data annotation, the YOLO format was selected. Bounding boxes were carefully drawn around each pod pepper in the images using the mouse, aiming for accuracy and completeness to ensure that no pod peppers were missed. The class label "ctj" was assigned to each annotated pod pepper. The data was then randomly split into training, validation, and test sets in a ratio of 7:2:1 and saved accordingly. Ultimately, the training set comprised 482 images, the test set contained 138 images, and the validation set consisted of 69 images.

YOLO Series Algorithm

The YOLO (You Only Look Once) series is a convolutional neural network-based object detection algorithm widely used for its fast detection speed and high accuracy. The YOLO series addresses the detection problem by processing the entire image in a single pass. Unlike traditional sliding window methods, YOLO divides the image into a grid, with each grid cell responsible for detecting objects within its boundaries and predicting multiple bounding boxes, prioritizing those whose centres fall within the cell. This eliminates the need to examine sub-regions, significantly reducing computational complexity. YOLO simultaneously predicts bounding boxes and class probabilities for objects within each grid cell, allowing for efficient and accurate detection across different images without varying window or stride sizes. The YOLO series continually introduces improvements, such as more efficient feature extraction networks and mechanisms for handling varying sizes and aspect ratios, enhancing both detection accuracy and speed.

The rise of convolutional neural networks (CNNs) has propelled the advancement of deep learning, offering greater convenience in image feature extraction. YOLO is a real-time object detection algorithm that treats object detection as a single regression problem. Therefore, it can be trained end-to-end within a single network, enabling simultaneous prediction of the positions and classes of all objects. Unlike traditional algorithms, YOLO directly divides an initial image into non-overlapping small regions and generates feature maps through convolution. Each small region of the original image corresponds to each element of the feature map, with each element predicting the objects within its respective region. YOLO features higher detection speed and a simpler network structure compared to traditional methods. The YOLO algorithm implements end-to-end object detection through an independent CNN model, utilizing multiple layers of neural networks to perform convolutions and pooling directly on images to extract essential features. This approach offers significant advantages. The mesh-like structure of the YOLO algorithm, depicted in Figure 2, includes a pair of fully connected layers and twenty-four convolutional layers. When an image enters the YOLO network, features are first extracted via convolutional networks, followed by connection through fully connected layers to produce the final predictions.

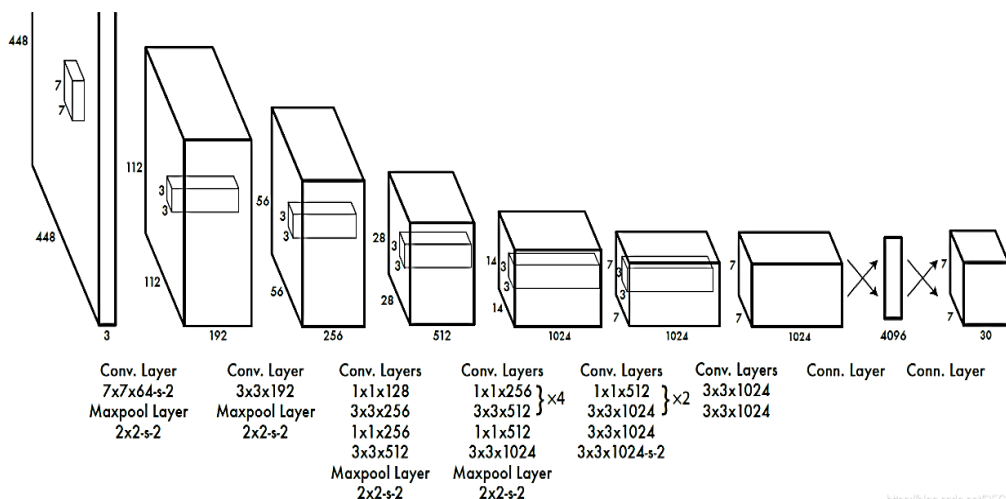


Fig. 2 - Partial network structure of the YOLO algorithm

The YOLO algorithm takes a complete image as input and outputs bounding boxes that determine the location of the target objects along with their corresponding class labels. The algorithm divides the entire image into grid cells, where each cell is responsible for predicting multiple bounding boxes and their associated class probabilities. It also predicts a confidence score for each bounding box, indicating the likelihood that the box contains an object and how confident this prediction is. The probability that an object belongs to each class within the predicted bounding box is represented by class probabilities. By setting a threshold, predictions with probabilities below the threshold can be filtered out to enhance detection accuracy.

YOLO excels in fast detection speed, ease of implementation and training, and performs well in detecting small objects. Additionally, it supports joint training with other tasks such as classification and segmentation, making it highly versatile for various applications.

YOLOv8 Model

YOLOv8 is an advanced object detection model built upon the foundation of YOLOv5, offering a new state-of-the-art (SOTA) model that further enhances performance and flexibility. The architecture of YOLOv8 is illustrated in Figure 3.

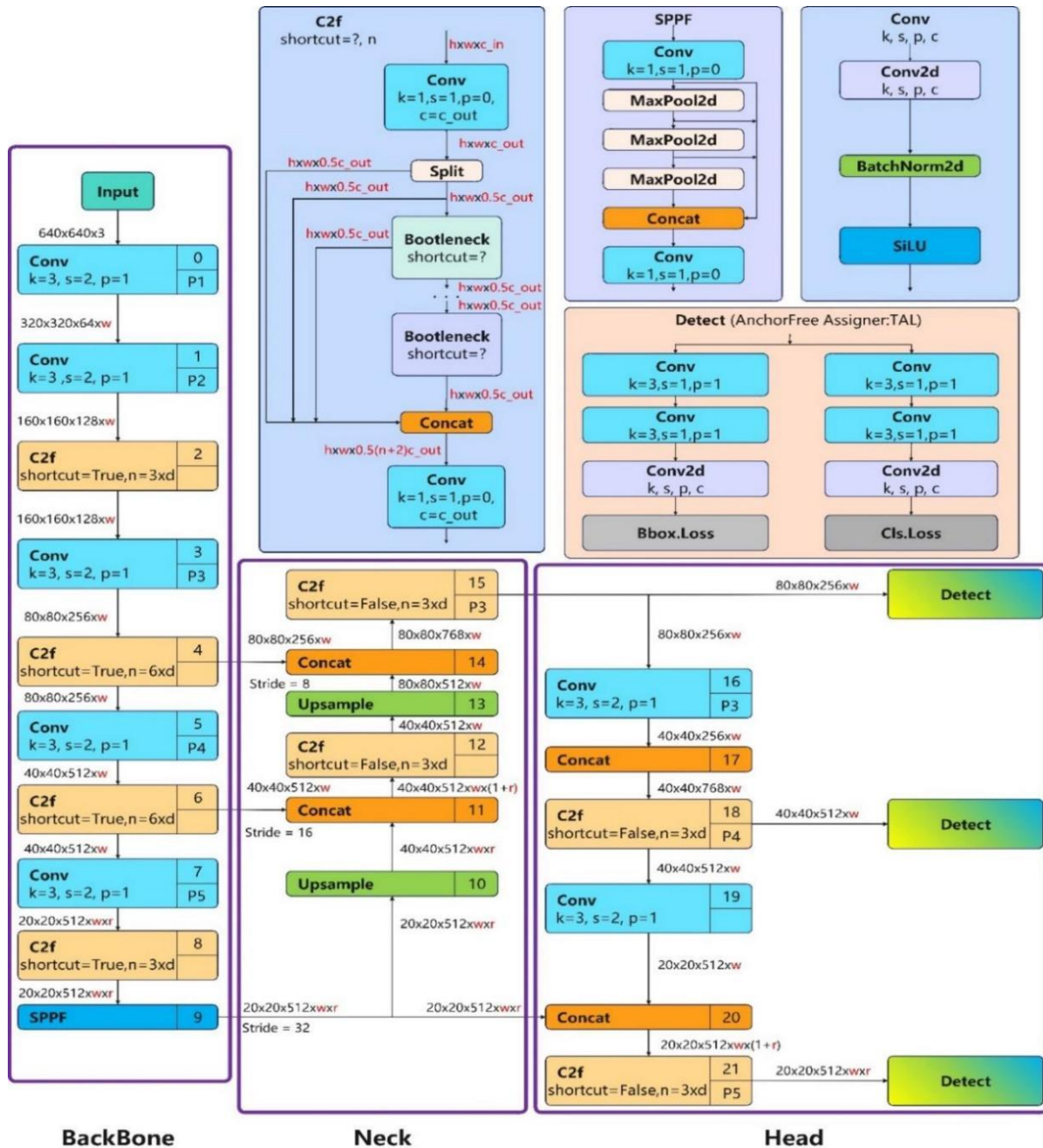


Fig. 3 –YOLOv8 Network Structure

Drawing from the design principles of YOLOv7 ELAN, YOLOv8 improves upon YOLOv5 by replacing the C3 structure with the more gradient-rich C2f structure in its backbone network and Neck section. It adjusts channel numbers for different scale models, significantly boosting model performance. YOLOv8 also introduces additional functionalities including image classification, object detection, and instance segmentation tasks. It supports command-line operation for model prediction, facilitating convenient testing and application. This study adopts YOLOv8 as the foundational algorithm for investigating target detection of Capsicum annum var. conoides.

Triplet Attention

The Triplet Attention mechanism is specifically designed for handling sequential data. It extends traditional bidirectional attention mechanisms by enabling models to consider information from the past, present, and future simultaneously when computing attention weights. The Triplet Attention mechanism consists of three independent attention weight vectors: one each for past, current, and future information importance. These three attention weights are then combined to form the final attention weights.

The Triplet Attention mechanism offers advantages such as comprehensive context understanding, reduced risks of information leakage and overfitting, and enhanced predictive performance. Therefore, this study will primarily focus on improving the YOLOv8 algorithm based on the Triplet Attention mechanism. Figure 4 illustrates the specific implementation process of Triplet Attention, which includes three branches: upper branch, middle branch, and lower branch.

The upper branch is utilized to compute attention weights for both the channel dimension (C) and the spatial dimension (W). This branch performs a Z-Pool operation on the input tensor, followed by a convolutional layer (Conv), and finally generates attention weights using the Sigmoid function.

The middle branch is employed to capture dependencies between the channel dimension (C) and the spatial dimensions (H) and (W). This branch first undergoes identical Z-Pool and convolutional operations, followed by the generation of attention weights using the Sigmoid function in a similar manner.

The lower branch is utilized to capture dependencies among the spatial dimensions. This branch performs Z-Pool and convolution operations without altering the input, followed by generating attention weights using the Sigmoid function.

The role of the Sigmoid function in each of the three branches is to perform logistic regression (scaling the results between 0 and 1 based on a multivariate linear regression foundation). By categorizing based on a midpoint of 0.5, the essence of the classifier is to identify boundaries. Therefore, when using 0.5 as the threshold, the solution of $\hat{y} = h_{\theta}(x) = \frac{1}{1 + e^{-\theta^T x}} = 0.5$ is sought, which is the solution at $z = \theta^T x = 0$.

After each branch generates attention weights, they are applied to the input, followed by aggregating the outputs of the three branches through averaging to obtain the triple attention outputs.

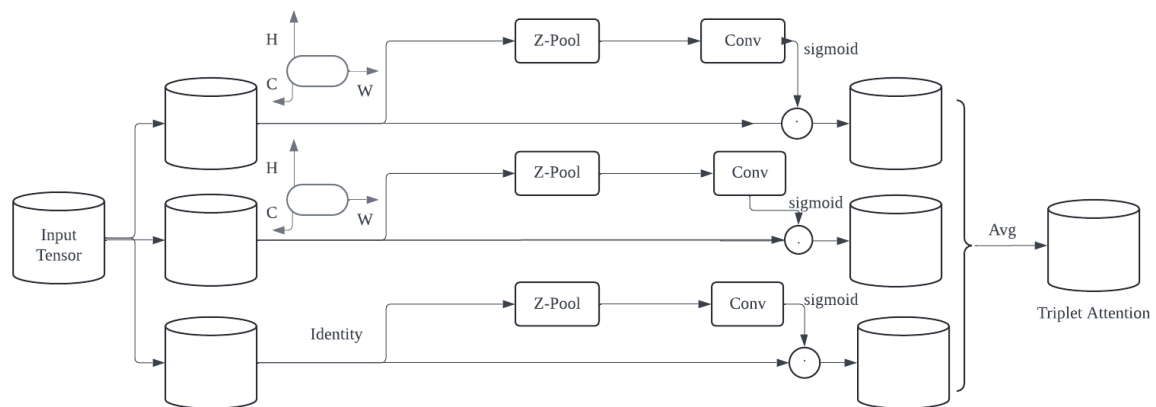


Fig. 4 –Triplet Attention Flowchart

Improved Methodology

In the context of field cultivation environments, the detection of pod pepper is influenced by stems, leaves, and weather conditions. In order to improve the accuracy of the model in the case of limited resources such as embedded devices and mobile applications, the YOLOv8n version of the YOLOv8 model is chosen, and improvements are made based on it. Attention mechanisms have been widely applied in various research fields and have shown potential to enhance traditional model detection performance (Yadav *et al.*, 2023). Therefore, five different attention mechanisms were integrated —SimAM (Yang *et al.*, 2021), DAttention (Xia *et al.*, 2022), CPCA (Huang *et al.*, 2023), SegNext_Attention (Guo *et al.*, 2022), and Triplet Attention (Misra *et al.*, 2021) into the 10th layer of the basic YOLOv8n model. Among these, Triplet Attention demonstrated the most promising results, prompting further testing by integrating it at different positions within the YOLOv8n model's backbone network to optimize detection performance. The experiments revealed that integrating Triplet Attention into the fifth layer of the backbone network yielded the best detection results. Figure 5 illustrates the modified architecture of the enhanced YOLOv8n model.

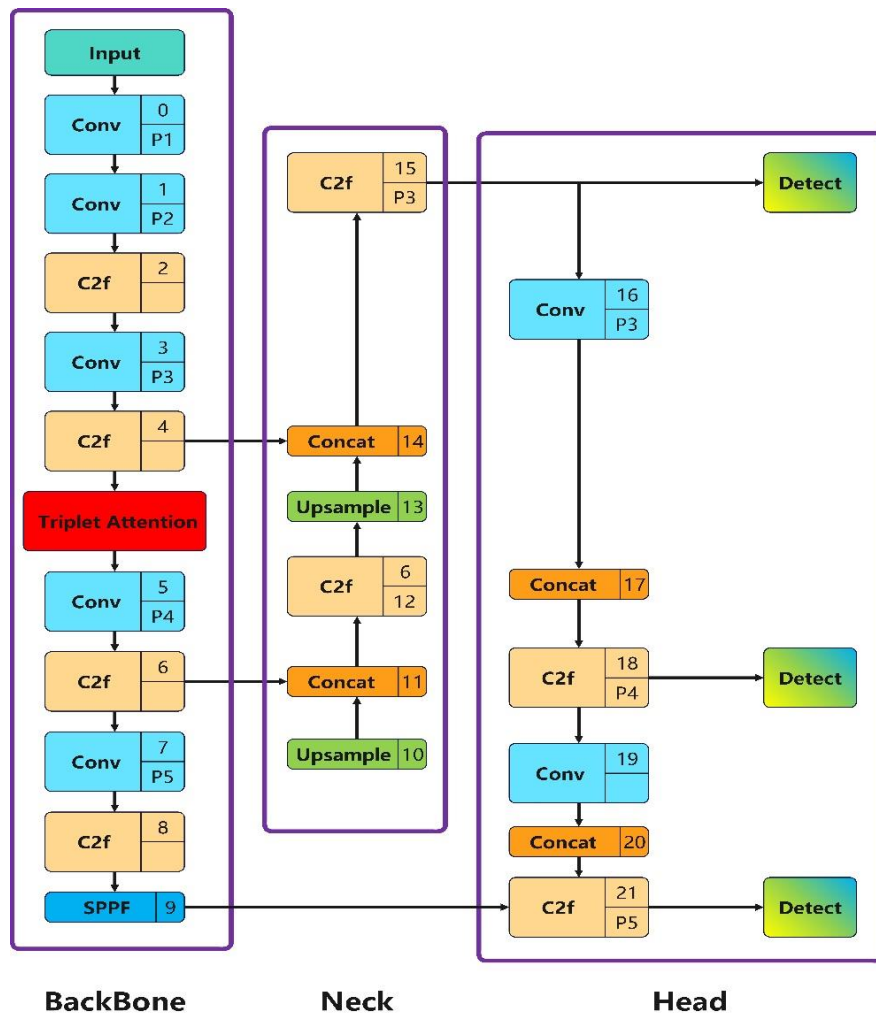


Fig. 5 –Improved YOLOv8 structure diagram

Model Evaluation Metrics

To quantitatively evaluate the performance of the proposed method against other comparative methods, this paper adopts three metrics as the evaluation standards for object detection: precision, recall, and mean average precision (mAP). These metrics can be computed using formulas 1 to 4.

precision calculation formula is:

$$\text{Precision} = \frac{TP}{TP + FP} \tag{1}$$

recall calculation formula is:

$$\text{Recall} = \frac{TP}{TP + FN} \tag{2}$$

mAP calculation formula is:

$$AP = \sum_n (R_n - R_{n-1})P_n \tag{3}$$

$$mAP = \frac{1}{|C|} \sum_{i=1}^{|C|} AP_i \tag{4}$$

In this context, TP and FP represent the numbers of correct and incorrect identifications, respectively. FN represents the number of actual cases that the network model failed to detect. n is the index of data points sorted in ascending order of recall rate. P_n is the precision of the data point indexed by n, R_n is the recall of the data point indexed by n, |C| represents the number of classes, AP_i represents the mean precision of class i.

RESULTS

The operating system used for the experiment was Windows 11. The GPU model was NVIDIA GeForce RTX 3050. The CPU model was 12th Gen Intel(R) Core(TM) i7-12700H 2.30 GHz. The system memory was 16GB, and the solid-state drive capacity 1TB.

The GPU acceleration libraries used were CUDA 12.3 and cuDNN 8.7. The Python version used was Python 3.11.7, and the deep learning framework PyTorch 2.3.1. The image size for deep learning training was 640x640 pixels, with 150 training epochs.

Comparison of detection results by model

As a category of rapid and efficient object detection algorithms, the YOLO series exhibits fast convergence during the detection process. Specifically, the loss functions of YOLOv3, YOLOv5, and YOLOv6 models stabilize around 100 epochs, while the YOLOv8 model stabilizes around 50 epochs. However, the Precision, Recall, and mAP values of YOLOv3, YOLOv5, and YOLOv6 models fluctuate significantly even when stabilized, resulting in relatively low accuracy, with only some achieving above 80%. In contrast, the Precision, Recall, and mAP values of the YOLOv8 model exhibit minimal fluctuations after stabilization and consistently achieve high accuracy, mostly exceeding 80%.

Table 1 summarizes the detection results for different YOLO models. Notably, YOLOv8 performed best with a precision of 77.9%, mAP of 81.6%, and mPA_{0.5:0.95} of 56.6%. These results indicate that YOLOv8 demonstrated superior detection performance for this experiment. Therefore, this study is based on YOLOv8 and further improves this model for the detection of *Capsicum annum* var. *conoides*.

Table 1

Order	Model	Precision (%)	Recall (%)	mAP (%)	mAP _{0.5:0.95} (%)
1	YOLOv3	78.6	72.8	79.2	55.3
2	YOLOv5	77.9	74.1	81.5	55.5
3	YOLOv6	76.5	72.8	81.3	56.5
4	YOLOv8	77.9	71	81.6	56.6

Improved Algorithm Performance

The study attempted to enhance YOLOv8 using various attention mechanisms, added to the 10th layer of the base YOLOv8 model, with improvements shown in Table 2. From Table 2, it can be observed that after adding five different attention mechanisms, the Triplet Attention mechanism resulted in an improvement of 6.3% in Recall, a 0.9% increase in mAP, and a 1.4% increase in mAP_{0.5:0.95}, demonstrating a superior overall enhancement compared to the other four mechanisms.

Table 2

Order	Model	Precision (%)	Recall (%)	mAP (%)	mAP _{0.5:0.95} (%)
1	YOLOv8	77.9	71	81.6	56.6
2	SimAM	75.3	79.8	81.8	56.8
3	DAttention	74.1	72.8	80.4	56.5
4	CPCA	79.2	70.5	80	56.4
5	SegNext_Attention	79.7	74.1	81.6	57.5
6	Triplet Attention	74.8	77.3	82.5	58

The application of Triplet Attention can enhance the performance of the YOLOv8 algorithm, but its specific effects depend on where it is applied and the specific requirements of the task. During experiments, it is essential to carefully evaluate its effects at different positions and select the most suitable configuration based on practical needs. Therefore, to further determine the advantages of integrating the Triplet Attention mechanism into YOLOv8 for pod pepper target detection, this study conducted experiments with Triplet Attention integrated at different positions within the YOLOv8 algorithm's backbone network. The detection results are presented in Table 3, where YOLOv8-TripletAttention-x denotes the specific position where Triplet Attention is added in the YOLOv8 network.

Table 3

Order	Model	Precision (%)	Recall (%)	mAP (%)	mAP _{0.5:0.95} (%)
1	YOLOv8-TripletAttention-2	76.7	76.6	83.7	58.3
2	YOLOv8-TripletAttention-3	75.9	79.1	82.8	57
3	YOLOv8-TripletAttention-4	85	68.8	82.8	58.5
4	YOLOv8-TripletAttention-5	79.7	76.6	84.1	58.9

Order	Model	Precision (%)	Recall (%)	mAP (%)	mAP _{0.5:0.95} (%)
5	YOLOv8-TripletAttention-6	78.5	74.8	82.1	56.7
6	YOLOv8-TripletAttention-7	81.6	75.1	83.9	58.4
7	YOLOv8-TripletAttention-8	76.5	77.1	82.1	56.2
8	YOLOv8-TripletAttention-9	79.1	74.4	81.7	56.9
9	YOLOv8-TripletAttention-10	74.8	77.3	82.5	58

Based on the experimental results comparison in Table 3, it is evident that the YOLOv8-TripletAttention-5 model achieved the highest overall accuracy, with an mAP of 84.1% and an mAP_{0.5:0.95} of 58.9%. It performed best in detecting pod peppers.

This study compared the precision, recall, mAP0.5 and mAP_{0.5:0.95} of the YOLOv8 model with that of the YOLOv8-TripletAttention-5 model during the process of gradual convergence as the number of training epochs increased, as shown in Fig. 6. It can be seen that when the overall results converged, the YOLOv8-TripletAttention-5 model outperformed the YOLOv8 model in the three metrics of precision, mAP0.5, and mAP0.5:0.95.

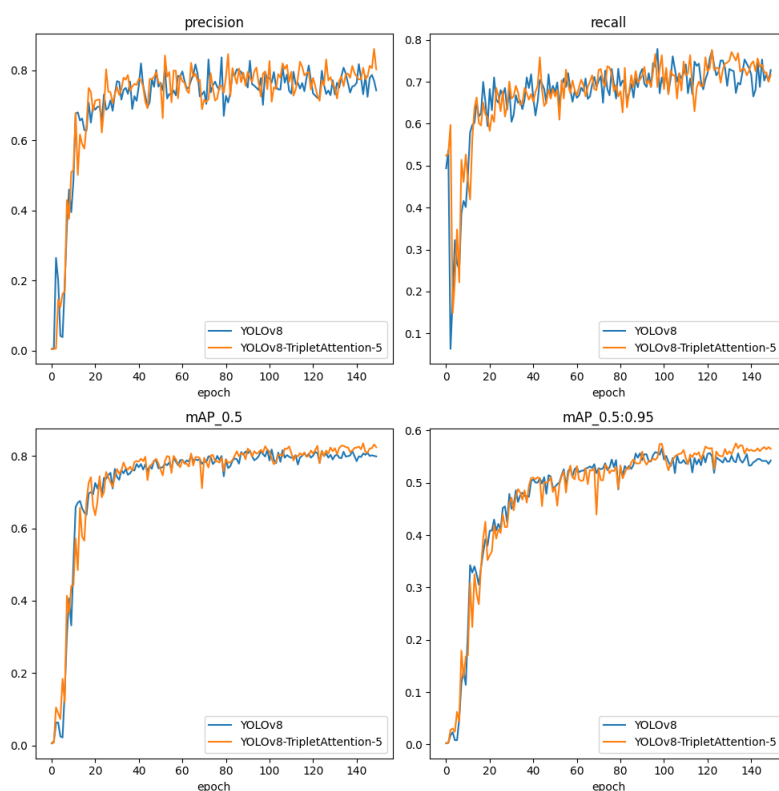


Fig. 6 – Performance curves of YOLOv8 model and YOLOv8-TripletAttention-5 model

Therefore, YOLOv8-TripletAttention-5 offers several advantages over the original YOLOv8 model: By incorporating the Triplet Attention mechanism, the model can better capture crucial information in images, thereby improving the accuracy and overall performance of object detection, specifically in detecting pod peppers. It also enhances the handling of both global and local information: the Triplet Attention mechanism balances attention between global and local information, making the model more effective in detecting targets of different scales. Moreover, it adapts better to complex backgrounds: the Triplet Attention mechanism assists the model in handling object detection tasks in complex backgrounds, thereby enhancing the model's robustness.

In summary, YOLOv8-TripletAttention-5 combines the distinct advantages of YOLOv8 and the triplet attention mechanism, complementing each other's strengths. This model shows superior performance in object detection tasks by enhancing accuracy and effectively handling complex backgrounds. Therefore, employing YOLOv8-TripletAttention-5 for the detection of *Capsicum annum* var. *conoides* is a scientifically sound approach.

Visualisation of Test Results

The trained YOLOv8-TripletAttention-5 model was validated using pod pepper dataset, and the detection results are shown in Figure 7. From Figure 7, it can be observed that our improved algorithm performs well in detecting unoccluded pod pepper, partially occluded pod pepper, small-sized pod pepper targets, as well as in both sunny and rainy conditions.

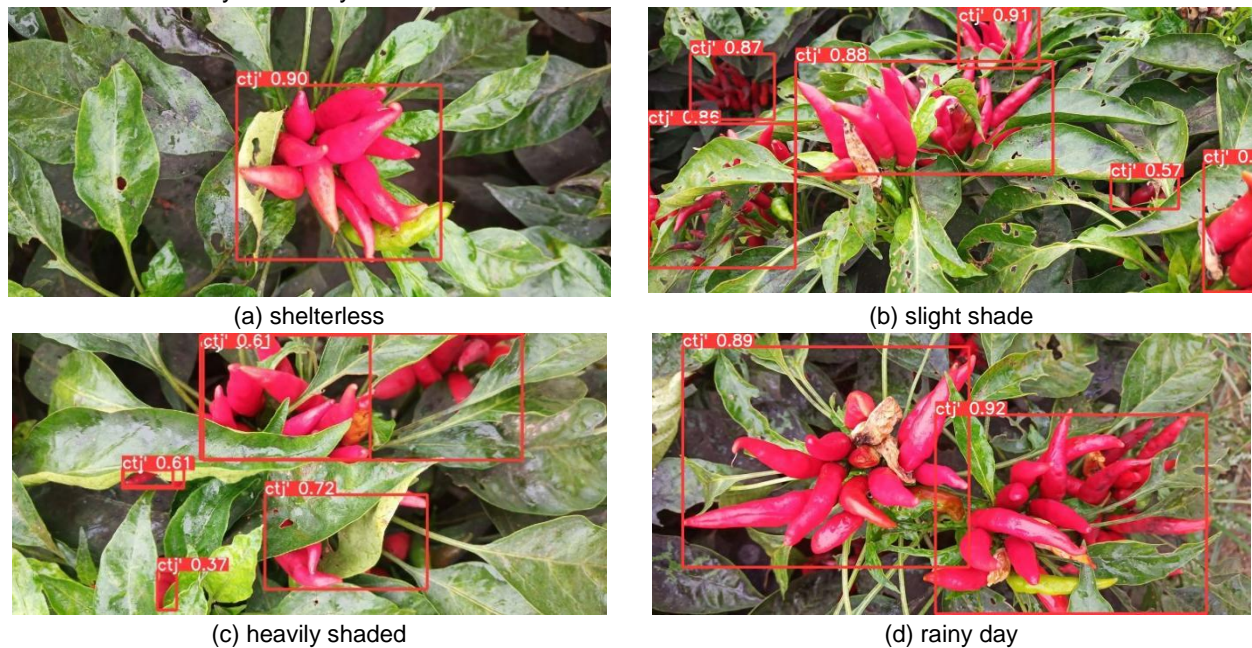


Fig. 7 - Partial detection

CONCLUSIONS

This study successfully developed an improved object detection research based on YOLOv8, named YOLOv8-TripletAttention-5, aimed at precise localization and recognition of pod pepper positions, applicable to related production contexts.

(1) The dataset for this study was constructed under various conditions including occlusion, no occlusion, sunny, and rainy weather.

(2) Using an incremental approach to enhance the YOLO model for pod pepper detection, different YOLO models were first compared and YOLOv8 was selected for its superior performance. Subsequently, various attention mechanisms were added, with Triplet Attention proving to be the most effective. Different positions for Triplet Attention were tested to further enhance the accuracy of the improved YOLOv8 model.

(3) This study introduced Triplet Attention into the YOLOv8 model at the 5th layer of the backbone network, establishing the YOLOv8-TripletAttention-5 model. Experimental results showed an mAP (mean Average Precision) of 84.1% for pod pepper detection, a 2.5% improvement over the original YOLOv8. The mAP 0.5:0.95 achieved 58.9%, indicating enhanced precision in object detection.

(4) By integrating Triplet Attention into the original YOLOv8 model, the study potentially improved the model's ability to extract critical information from data while balancing global and partial information, thereby enhancing its effectiveness in handling complex target scenarios.

Limitations of this experiment include achieving an mAP of 84.1% for pod pepper detection, necessitating further improvements in existing object detection algorithms to enhance accuracy and robustness. Additionally, the pod pepper dataset used in this research is limited in scene diversity, highlighting the need for a more comprehensive dataset to enrich sample diversity and improve model generalization. Lastly, because this experiment is in the stage of algorithm research, when it is really applied to the actual picking activities, it may also need to further study and design lightweight models or optimization algorithms for scenes with high real-time requirements, and finally apply it to mobile devices for real-time detection and harvest of Pod pepper.

ACKNOWLEDGEMENT

This research, titled "Pod pepper target detection based on improved YOLOv8", was funded by the Basic Research Program of Shanxi Province (202303021212115).

REFERENCES

- [1] Arakeri, M. P., Kumar, B. V., Barsaiya, S., et al. (2017). Computer vision based robotic weed control system for precision agriculture[C]. *International Conference on Advances in Computing, Communications and Informatics (ICACCI)*. IEEE, (pp. 1201-1205).
- [2] Batiha, G. E. S., Alqahtani, A., Ojo, O. A., et al. (2020). Biological properties, bioactive constituents, and pharmacokinetics of some Capsicum spp. and capsaicinoids[J]. *International journal of molecular sciences*, 21(15), 5179.
- [3] Cai W. T., Li Z. S., Han J. N., et al. (2023). Review on application of health monitoring in pigs based on computer vision[J]. *Heilongjiang Animal Science and Veterinary Medicine*, (24):22-30.
- [4] Farooq, J., Muaz, M., Khan Jadoon, K., et al. (2024). An improved YOLOv8 for foreign object debris detection with optimized architecture for small objects[J]. *Multimedia Tools and Applications*, 83(21), 60921-60947.
- [5] Guo M. H., Lu C. Z., Hou Q., et al. (2022). Segnext: Rethinking convolutional attention design for semantic segmentation[J]. *Advances in Neural Information Processing Systems*, 35:1140-1156.
- [6] Hernández - Pérez, T., Gómez - García, M. D. R., Valverde, M. E., et al. (2020). Capsicum annum (hot pepper): An ancient Latin - American crop with outstanding bioactive compounds and nutraceutical potential. A review[J]. *Comprehensive Reviews in Food Science and Food Safety*, 19(6), 2972-2993.
- [7] Huang H. J., Chen Z. G., Zou Y., et al. (2024). Channel prior convolutional attention for medical image segmentation[J]. *Computers in Biology and Medicine*, 178, 108784.
- [8] Kanda, P. S., Xia, K., & Sanusi, O. H. (2021). A deep learning-based recognition technique for plant leaf classification[J]. *IEEE Access*, 9, 162590-162613.
- [9] Li Y.J., Li X.P., Zhang W.G. (2020). Survey on vision-based 3D object detection methods[J]. *Computer Engineering and Applications*, 56(01):11-24.
- [10] Mahesh, T. Y., & Mathew, M. P. (2024). Detection of bacterial spot disease in bell pepper plant using YOLOv3[J]. *IETE Journal of research*, 70(3), 2583-2590.
- [11] Misra, D., Nalamada, T., Arasanipalai, A. U., et al. (2021). Rotate to attend: Convolutional triplet attention module[C]. *In Proceedings of the IEEE/CVF winter conference on applications of computer vision*, pp. 3139–3148.
- [12] Sapkota, R., Ahmed, D., Churuvija, M., et al. (2024). Immature green apple detection and sizing in commercial orchards using YOLOv8 and shape fitting techniques[J]. *IEEE Access*, 12, 43436-43452.
- [13] Sladojevic, S., Arsenovic, M., Anderla, A. et al. (2016). Deep neural networks based recognition of plant diseases by leaf image classification[J]. *Computational Intelligence and Neuroscience*, 2016(1), 3289801.
- [14] Xia Z., Pan X., Song S., et al. (2022). Vision transformer with deformable attention[C]. *In Proceedings of the IEEE/CVF Conference on Computer Vision and Pattern Recognition*, 4794-4803.
- [15] Yadav, A., & Vishwakarma, D. K. (2023). MRT-Net: Auto-adaptive weighting of manipulation residuals and texture clues for face manipulation detection[J]. *Expert Systems with Applications*, 232.120898.
- [16] Yang L., Zhang R. Y., Li L., et al. (2021). Simam: A simple, parameter-free attention module for convolutional neural networks[A]. *In International Conference on Machine Learning*, 139:11863-11874.

RESEARCH ON LOCUST TARGET DETECTION ALGORITHM BASED ON YOLO V7 -MOBILENETV3-CA

基于 YOLOv7-MobileNetV3-CA 的蝗虫目标检测算法研究

Dongfang QIU ¹⁾

College of Information Science and Engineering, Shanxi Agricultural University, Jinzhong, Shanxi, China

Tel: +86 177034433; E-mail: qdf_0106@126.com

DOI: <https://doi.org/10.35633/inmateh-74-24>

Keywords: locust detection, YOLO v7, MobileNetV3, CA attention mechanism

ABSTRACT

To accurately detect various kinds of locusts in real-time and make locust detection more universal, a locust data set that contained different species of locusts was created through the Internet crawler and public dataset IP102, and a locust target detection algorithm YOLOv7-MobileNetV3-CA was proposed in this paper. Firstly, to reduce the size of model parameters, the backbone of YOLOv7 was replaced by MobileNetV3, secondly, a CA (Coordinate Attention) attention mechanism was added to further improve the detection accuracy of locusts after feature enhancement. The experiment showed that the precision of locusts identification was 95.96%, the recall rate was 92%, the AP was 95.74%, and the F1 was 0.92. Compared with YOLOv7, the model size was reduced by 27%, and the AP was improved by 4.48%. Compared with YOLOv4, YOLOv4 MobileNetV3, YOLOv5, and SSD algorithms, AP has improved by 51.16%, 26.81%, 11.9%, and 11.75%, respectively. Experiments have shown that this algorithm performs well in detecting locusts of different scales, scenes, and types, and can provide reference for real-time locust detection.

摘要

为了能实时准确地检测各类蝗虫目标,使得蝗虫检测更具有普适性,本文通过互联网爬虫及公有数据集IP102形成蝗虫数据集,提出了YOLOv7-MobileNetV3-CA的蝗虫目标检测算法。首先,为了降低模型参数量,使用MobileNetV3替换YOLOv7骨干网。其次,在特征加强后加入了CA (Coordinate Attention) 注意力机制,以进一步提高蝗虫的检测精度。实验表明,蝗虫的检测精确率为95.96%,召回率92%,mAP为95.74%,F1为0.92,与YOLOv7相比,模型大小降低27%,mAP提高了4.48%。与YOLOv4、YOLOv4-MobileNetV3、YOLOv5、SSD算法相比,mAP分别提高了51.16%、26.81%、11.9%、11.75%。试验表明本算法对不同尺度、不同场景及不同种类的蝗虫检测效果较好,可以为蝗虫实时检测提供参考。

INTRODUCTION

There are various types of locusts in the world, such as desert locusts, rice locusts, grass locusts, flying locusts, and so on. Locust plague caused by large-scale locusts can cause destructive damage to agricultural, forestry. Locust plague can even cause animal husbandry production, further cause serious economic losses and famine due to food shortages (Kang et al, 2019). Locust plague has been the focus of agricultural pest control all over the world. Therefore, there is an urgent need to establish a locust detection system with higher accuracy and that can detect more types of locusts (Yu et al, 2021).

At present, the detection methods for locusts include artificial ground investigation, climate prediction, phenological prediction, radar detection technology, GPS/GIS detection, etc. However, due to the small size of locusts, methods that rely on manual detection methods cost highly and perform weakly in real time. Detection relying on remote sensing satellites can only be achieved by making models from historical data, resulting in low real-time accuracy. With the development of information technology, establishing locust disaster detection by image processing and pattern recognition provides a new method that can improve the efficiency of locust control.

Early locust recognition was mainly based on image processing methods. Someone used the frame difference method to determine the motion area in the image, and then counted locusts attempting to further extract locust information using chromaticity and morphological features (Mao et al, 2008). Some researchers used fuzzy patterns to identify locusts (Zheng et al, 2010).

¹ Qiu Dongfang, As. Lect. M.S. Msc

However, the traditional image processing greatly relies on the manually designed features, the accuracy of locust detection based on traditional image process is low due to the small size, variety and complex growth environment of the locust. The development of deep learning and computer vision provides a new way for automatic detection, and convolutional neural networks can better express image features compared with traditional *image processing*. With high detection accuracy, the computer vision based on the deep learning is widely used in agriculture, including intelligent harvesting (*Chen et al, 2024; Yu et al, 2024; Zhi et al, 2023; Huang et al, 2024; Wang et al, 2023; Wang et al, 2023; Matache et al, 2022*), crop yield estimation (*Ma et al, 2024; Wang et al, 2024; Xu et al, 2022; He et al 2021*), weed recognition (*Zhao et al, 2021; Cao et al., 2023; Fan et al, 2021*), animal facial recognition (*Ning et al, 2023; Wang et al, 2023*), pest and disease detection (*Zhang et al, 2023; Liu et al, 2023; Zhou et al, 2022; Mu et al, 2022; Ma et al, 2023*) and other agricultural fields. In recent years, locust detection has been successfully addressed using various deep learning-based object detection models; for example,

Ma et al., (2022), implemented locust detection in grasslands utilizing the YOLOv5 algorithm, while *Li et al., (2021)*, achieved video detection of flying locusts using the SSD object detection algorithm. *Bai et al., (2022)*, applied a combination of MCG2 and YOLOv4 for the detection and recognition of flying locusts. Additionally,

Kumar et al., (2021), employed deep learning techniques for the early detection of locust populations. However, these methods could all detect a single species or a certain growth stage of locusts.

Due to the limitations in diagnosing various locust species, the current locust detection systems cannot be widely promoted and applied. The wide variety, small size, complex and various growth environments, and the scale of locust images, make it difficult to collect them. To improve the locust detection accuracy, a locust data set that contained various kinds of locusts was created by internet crawler and public dataset IP102 in this paper. Furthermore, the data set was expanded by mosaic method. A YOLOv7-MobileNetV3-CA algorithm was proposed to identify locusts in the dataset images. To reduce the size of the detection model, it was replaced the backbone of YOLOv7 with MobileNetV3. Then, to further improve the detection accuracy, a coordination attention (CA) attention mechanism was added after feature enhancement. The proposed algorithm can further provide a new way to detect locusts.

MATERIALS AND METHODS

Locust Data Set and Its Pre-processing

The image data set created in this paper is part from the public data set IP102 (*Wu et al, 2019*) (crop pest data set) and part from the Internet. After filtering and choosing, 544 valid images were finally included in the data set, including 96 images from IP102 and 448 from the Internet. Afterwards, 84 images were expanded in the data set with the Mosaic method. The data set included grass locusts, rice locusts, desert locusts, and other locust species. Fig.1 shows partial images in the dataset.



Fig. 1 - The examples of the locust data

Images from the data set were manually labelled. The label format was XML. When creating the image label in the dataset, the following principles were followed: (1) Annotating the entire locust target; (2) Giving annotation with occlusion but clear visible locust (3) Not labelling locust targets with unclear targets. One example regarding label annotation is presented in Fig.2.



Fig. 2 - Example of the labelled image

YOLOv7-MobileNetV3-CA model

The existing convolutional neural networks based on deep learning have high detection accuracy and high model complexity, but they cannot meet the needs of real-time detection. To further improve detection efficiency while ensuring detection accuracy, a YOLOv7-MobileNetV3-CA model was proposed. Firstly, the backbone of YOLOv7 was replaced with a lightweight MobileNetV3 network, and the coordination attention was added after feature enhancement. The improved YOLOv7 MobileNetV3-CA model structure is shown in Fig.3. The improved model not only behaves better; but also has smaller model size than the original model YOLOv7.

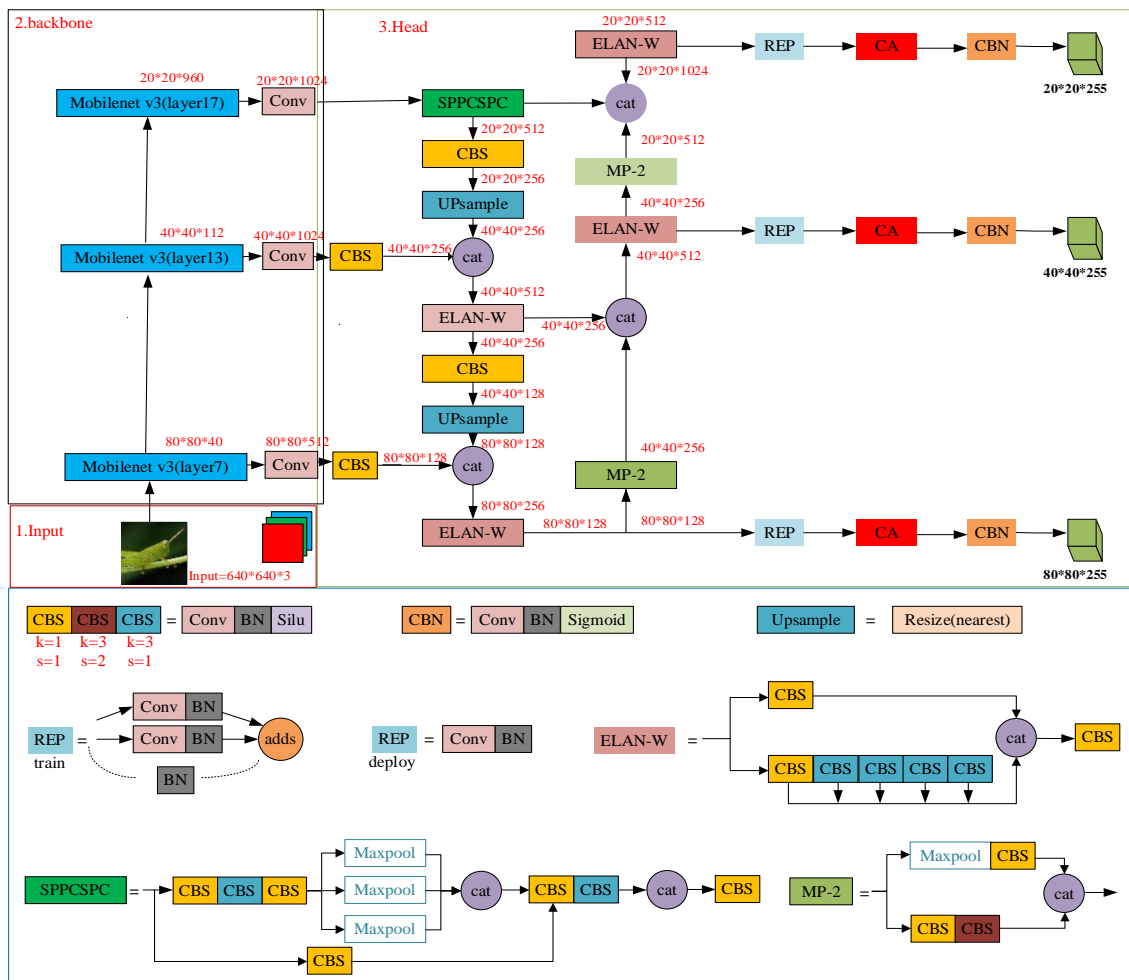


Fig. 3 - YOLOv7-MobileNetV3-CA model structure

MobileNetV3 Model

MobileNet is a kind of lightweight network model that includes MobileNetV1 (Howard et al, 2017), MobileNetV2, and MobileNetV3. MobileNetV3 is widely used in image recognition (Mao et al, 2023; Li et al, 2023), and its overall architecture follows the design of MobileNetV2, adopting lightweight structures such as depth wise separable convolution and residual blocks, and optimizing and upgrading modules, including bottleneck structure, SE module, and NL module. It has performed well in tasks such as image classification, object detection, and semantic segmentation on mobile devices. The network structure is shown in Table 1.

Table1

The structure of the MobileNetV3						
Input	Operator	exp size	#out	SE	NL	s
2242x3	Conv2d	-	16	-	HS	2
1122x16	bneck,3*3	16	16	-	RE	1
1122x16	bneck,3*3	64	24	-	RE	2
562x24	bneck,3*3	72	24	-	RE	1
562x24	bneck,5*5	72	40	√	RE	2
282x40	bneck,5*5	120	40	√	RE	1
282x40	bneck,5*5	120	40	√	RE	1
282x40	bneck,3*3	240	80	-	HS	2
142x80	bneck,3*3	200	80	-	HS	1
142x80	bneck,3*3	184	80	-	HS	1
142x80	bneck,3*3	184	80	-	HS	1
142x80	bneck,3*3	480	112	√	HS	1
142x112	bneck,3*3	672	112	√	HS	1
142x112	bneck,5*5	672	160	√	HS	2
72x160	bneck,5*5	960	160	√	HS	1
72x160	bneck,5*5	960	160	√	HS	1
72x160	conv2d,1*1	-	960	-	HS	1
72x960	pool,7*7	-	-	-	-	1
12x960	conv2d,1*1,NBN	-	1280	-	HS	1
12x1280	conv2d,1*1,NBN	-	k	-	-	1

Note: Operator represents the block structure that the feature layer will operate on, and exp size represents the number of channels after the inverse residual structure rises within the bneck; # Out represents the number of channels in the feature layer when inputting bneck, and SE represents whether to use SE attention mechanism; NL represents which activation function to use, Hs represents h-swish, and RE represents Rule.

Coordination Attention

The Coordination Attention (CA) is a lightweight network attention method (Hou, et al) that can capture channel and location information, helping to more accurately locate and identify the target of detection. It mainly consists of two steps: coordinate information embedding and coordinate attention generation. To obtain attention to image width and height and encode precise positional information, CA first divides the input feature map into two directions: width and height, and performs global average pooling to obtain feature maps in both directions, as shown in formulas (1) and (2):

$$z_c^h = \frac{1}{W} \sum_{0 \leq i \leq W} x_c(h, i) \quad (1)$$

$$z_c^w = \frac{1}{H} \sum_{0 \leq i \leq H} x_c(j, w) \quad (2)$$

z_c^w , z_c^h represent the width and height of the feature maps, respectively, W and H represent the width and height of the image, and $x_c(i, j)$ represent the pixel of (i, j) . Next, the feature maps in both the width and height of the global are concatenated together. Then, they are fed into a shared convolution module with a kernel, reducing their dimensionality to the original C/r . Then, the batch normalized feature map F_1 is used to obtain a feature map f with a size of $1 \times (W+H) \times C/r$ by the sigmoid activation function, as shown in formula (3).

$$f = \delta \left(F_1 \left(\left[z_c^h, z_c^w \right] \right) \right) \quad (3)$$

Subsequently, to obtain feature maps F_h and F_w with the same number of channels as before, the feature map f is convolved with a 1×1 kernel according to its original height and width. Then, the attention weights g_h and g_w in the width direction of the feature map are obtained by the sigmoid function, which is shown in formulas (4) and (5).

$$g^h = \sigma \left(F_h(f^h) \right) \quad (4)$$

$$g^w = \sigma \left(F_w(f^w) \right) \quad (5)$$

After the above calculation, the attention weights of the input feature map in the height and width direction will be obtained. Finally, the final feature map with attention weights in the width and height will be obtained by multiplying and weighting the original feature map, which is shown in the formula (6). The total structure is shown in Fig.4.

$$y_c(i, j) = x_c(i, j) \times g_c^h(i) \times g_c^w(j) \tag{6}$$

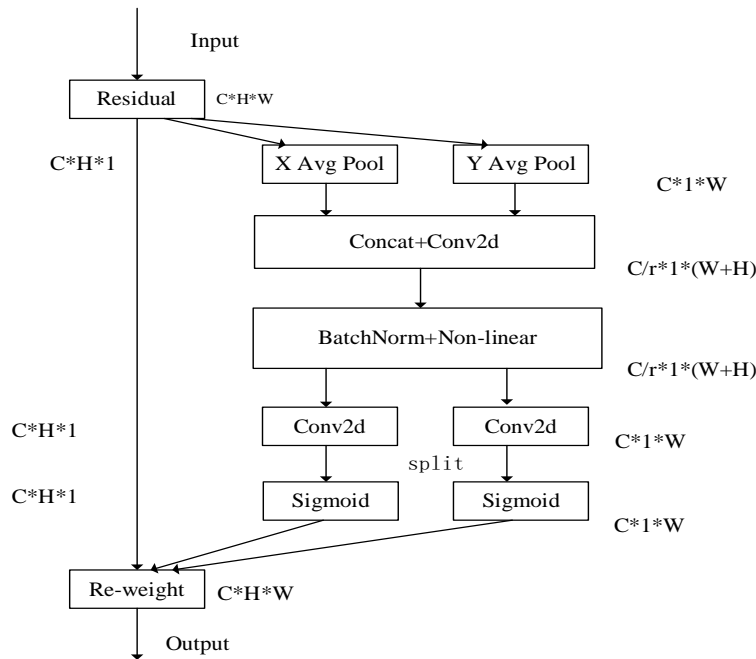


Fig. 4 - The structure of the CA

Model Evaluation Metrics

The locusts' identification required consideration of detection accuracy and the real-time detection ability of the model. Precision, Recall, F1 score, and Average Precision (AP) were chosen as evaluation metrics to evaluate the detection accuracy. The calculations are as follows.

$$Precision = \frac{TP}{TP + FP} \tag{7}$$

$$Recall = \frac{TP}{TP + FN} \tag{8}$$

$$F1 = \frac{2TP}{2TP + FP + FN} \tag{9}$$

where:

- TP (True Positive): represents the number of correct predictions as positive samples.
- FP (False Positive): represents the number of incorrect predictions as positive samples.
- TF (False Positive): represents the number of correct predictions as negative samples.
- FN (False Negative): represents the number of incorrect predictions as negative samples.

AP (Average Precision): It is calculated by computing the precision-recall curve and the area under the curve (AUC). AP represents the average precision across all levels. Besides, model Size represents the model complexity.

RESULTS

The model was trained on a server with a GPU model of NVIDIA GeForce RTX-3090, 4 cores CPU, 35GB memory, Python 3.6.9 software, and a deep learning framework using Python 1.12.

The Result of the YOLOv7- MobileNetV3-CA

To verify the performance of YOLOv7-MobileNetV3-CA, 54 locust images in the test set were tested and evaluated. The model achieved Precision of 95.96%, Recall of 92%, AP of 95.74%, and F1 of 0.92, model size being 27.37 MB.

Some detection examples are shown in Fig.5, showing that YOLOv7-MobileNetV3-CA performs well in locust detection and recognition under complex conditions such as various of types, scenes, number of targets, and scales.

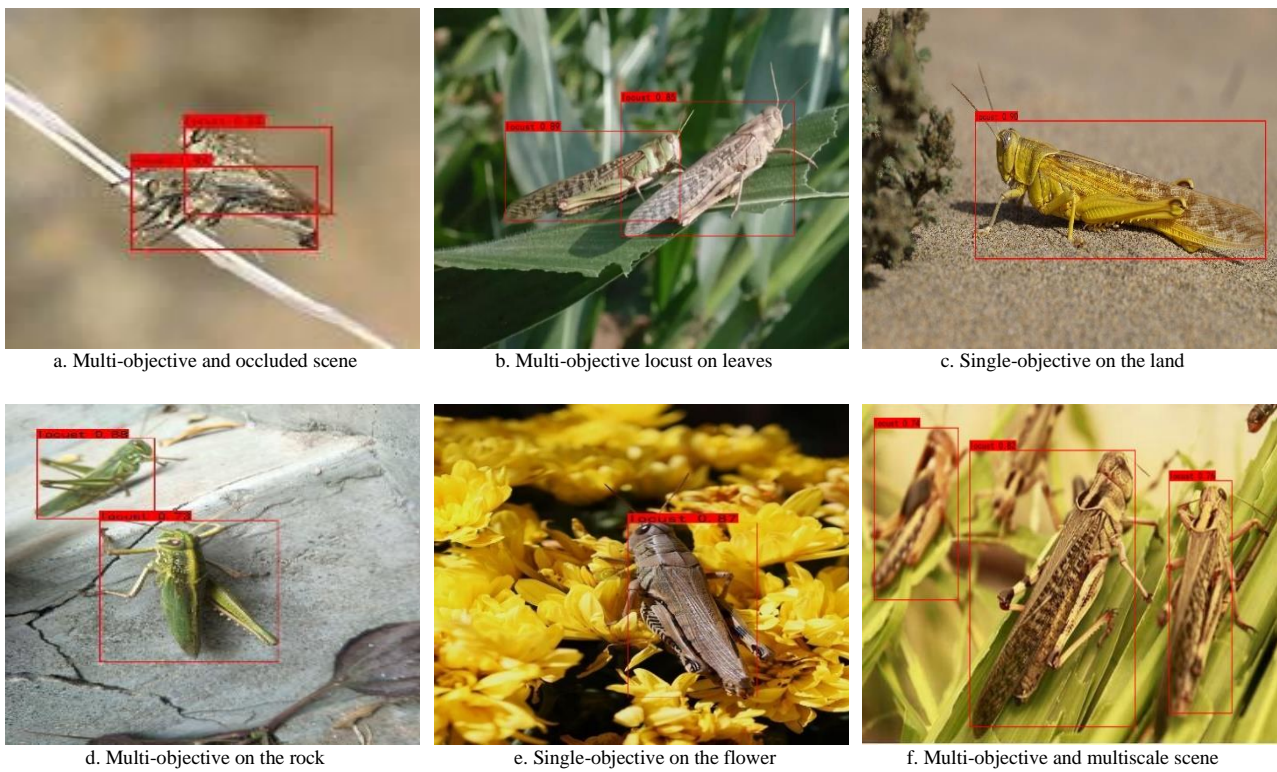


Fig. 5 - The detection result of the YOLOv7-MobileNetV3-CA

Ablation Experiment Results

To further verify the effectiveness of the model, ablation experiments were conducted to demonstrate the effectiveness of the model, comparing detection results and evaluation indicators were used to demonstrate the effectiveness. The detection results of YOLOv7, YOLOv7-CA, and YOLOv7-MobileNetV3 are shown in Fig.6, and it was found that the final model YOLOv7- MobileNetV3-CA performed best on occlusion images with various dimension scales of the locusts.

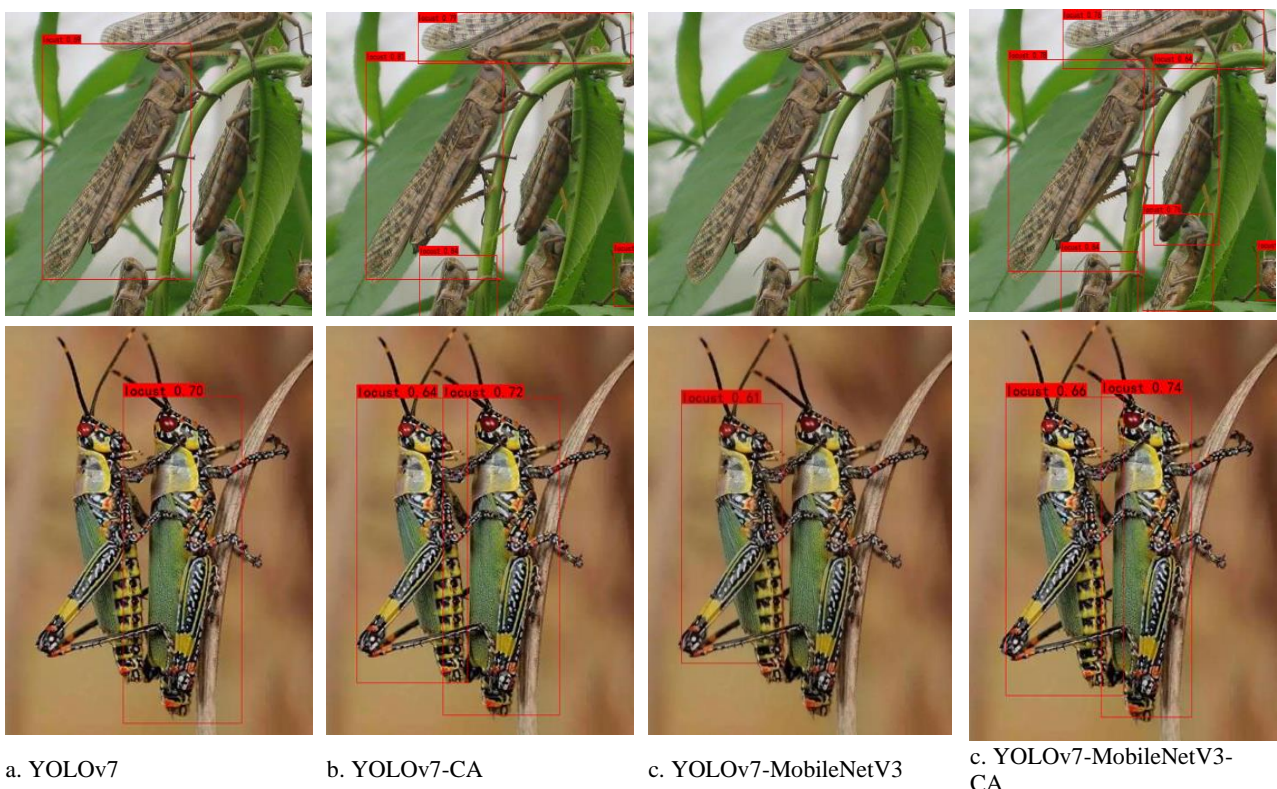


Fig. 6 - The detection results of the ablation experiment

The evaluation indicators of the model YOLOv7, YOLOv7-CA, YOLOv7-MobileNetV3, and YOLOv7-MobileNetV3-CA are shown in Table 2. It was found that adding the CA attention mechanism to YOLOv7, made the recall rate, precision and F1 to achieve the following values: 0.99%, 0.91%, 0.01, respectively, AP decreased by 5.98%, because the addition of the attention mechanism resulted in overfitting of the model. After replacing the backbone network of YOLOv7 with MobileNetV3, the detection performance of the model significantly decreased. The reason for this is that the model underwent depth wise separable convolution, which not only greatly reduced the number of parameters but also significantly reduced the detection accuracy of the model. Finally, by adding the CA attention mechanism, the detection accuracy of the model was greatly improved. YOLOv7-MobileNetV3-CA has increased AP by 4.4%, recall by 18.61%, detection accuracy by 1.48%, F1 by 0.12, while the model size decreased by 27% compared to YOLOv7.

Table 2

The evaluation of ablation experiment					
model	AP	Recall	Precision	F1	Model size/MB
YOLOv7	91.26%	69.35%	93.48%	0.80	37.62
YOLOv7-CA	86.24%	70.34%	94.39%	0.81	37.88
YOLOv7-MobileNetV3	65.37%	48.65%	83.08%	0.61	27.31
YOLOv7-MobileNetV3-CA	95.74	87.96%	95.96%	0.92	27.36

Comparative Experimental Results

To further validate the performance of the model YOLOv7-MobileNetV3-CA, it was compared with YOLOv4, YOLOv4-MobileNetV3, YOLOv5, and SSD models. The detection results are shown in Fig.7. By comparison, it was found that when multiple targets and occlusion exist in the image, YOLO v4 can detect the full target area, not the single target, while YOLOv5 and YOLOv4-MobileNetV3 did not perform well. SSD could detect some locusts, and YOLOv7-MobileNetV3-CA presented in this paper had the best detection performance, detecting more locusts compared with other models.

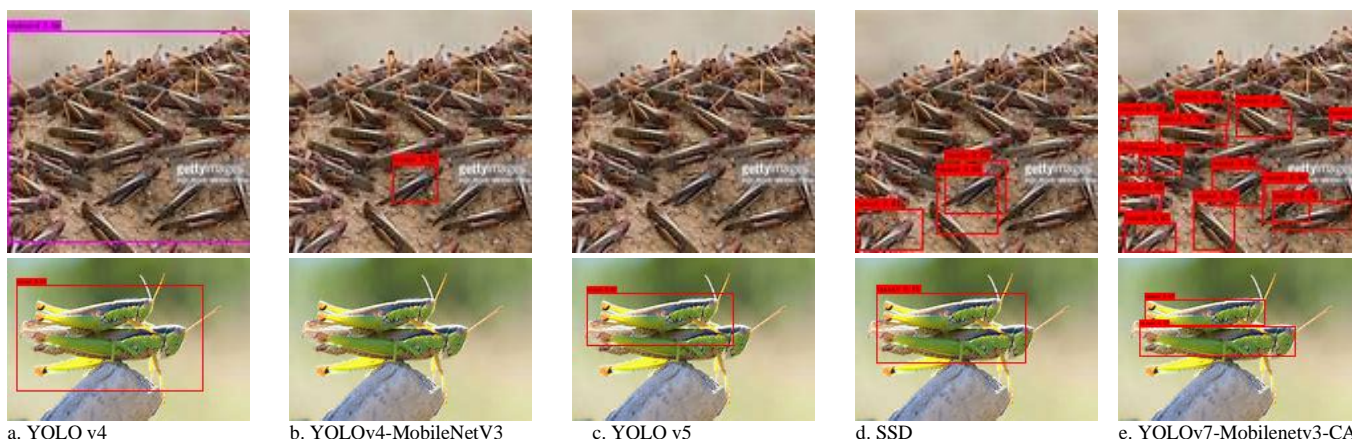


Fig.7- The comparing detection result

To objectively evaluate the performance of the model, YOLOv7-MobileNetV3-CA was compared with YOLOv4, YOLOv4 MobileNetV3, YOLOv5, SSD, and YOLOv7, using evaluation indicators including precision, F1, Recall, Average Precision (AP), and the model size. The results are shown in Table 3. Overall, the YOLOv7-MobileNetV3-CA behaved best on the detection ability compared with other models. Its model size was smaller compared with YOLOv4, YOLOv5, SSD, and YOLOv7.

Table 3

The evaluation of the models					
Model	Precision	F1	Recall	AP	Model size/MB
YOLO v4	90.48%	0.68	55.07%	73.00%	64.36
YOLO v4-MobileNetV3	80.00%	0.36	23.53%	70.01%	12.69
YOLO v5	88.57%	0.67	53.45%	83.83%	47.05
SSD	88.68%	0.82	75.81%	83.99%	26.28
YOLO v7	93.48%	0.80	69.35%	91.26%	37.62
YOLOv7-MobileNetv3-CA	95.96%	0.92	87.96%	95.74%	27.36

CONCLUSIONS

In this paper, a locust images data set was created from the public dataset IP102 and Internet crawlers and then images were manually labelled using LabelImage software. Besides, an improved locust detection algorithm YOLOv7-MobileNetV3-CA was proposed, which replaces the backbone of YOLOv7 with MobileNetV3 to catch model features and to reduce the parameters of the model. After the features were enhanced, a CA attention mechanism was added to improve the detection accuracy of the model. Finally, by comparing with other target detection algorithms, the following conclusions were drawn: (1) Compared with YOLOv7 model, the AP of the proposed model is increased by 4.48%; (2) Compared with YOLOv7, the model size has been reduced by 27%, achieving a lightweight model. (3) Compared with the classic object detection algorithms YOLO v4, YOLO v4 MobilenetV3, YOLO v5, and SSD, the average detection accuracy has been improved by 22.74%, 25.73%, 11.9%, and 11.75%, respectively, and the detection behaves best compared with other models. (4) This model shows good detection ability for different kinds of locusts in various scenes. Therefore, the proposed algorithm can provide a new way for locust detection.

ACKNOWLEDGEMENT

This paper was supported by the Science and Technology Innovation Fund of Shanxi Agricultural University (Grant number: 2019022)

REFERENCES

- [1] Bai, Z., Tang, Z., Diao, L., Lu, S., Guo, X., Zhou, H., Liu, C., Li, L. (2022). Video target detection of East Asian migratory locust based on the MCG2-YOLOv4 network. *International Journal of Tropical Insect Science*. Vol.42, pp.793–806. USA.
- [2] Cao, Y., Zhao, Y., Yang, L. (2023). Weed Identification Method in Rice Field Based on Improved DeepLabv3 (基于改进 DeepLabv3+的水稻田间杂草识别方法). *Transactions of the Chinese Society for Agricultural Machinery*. Vol.54, pp.242-252, Beijing/China.
- [3] Cheng, F., Cheng, C., Zhu, X., Shen, D.&Zhang, X. (2024) Detection of camellia oleifera fruit maturity based on improved YOLOv7 (基于改进 YOLOv7 的油茶果实成熟度检测). *Transactions of the Chinese Society of Agricultural Engineering (Transactions of the CSAE)*, Vol.40, pp.177-186, Beijing/China.
- [4] Fan, X.; Zhou, J., Xu, Y., Li, K., Wen, D. (2021). Identification and Localization of Weeds Based on Optimized Faster R—CNN in Cotton Seedling Stage (基于优化 Faster R-CNN 的棉花苗期杂草识别与定位). *Transactions of the Chinese Society for Agricultural Machinery*, Vol.52, pp.26-34, Beijing/China.
- [5] He, X., Luo, H., Qiao, M., Tian, Z., Zhou, G. (2021). Yield estimation of winter wheat in China based on CNN-RNN network (基于 CNN-RNN 网络的中国冬小麦估产). *Transactions of the Chinese Society of Agricultural Engineering*, Vol.37, pp. 124-132, Beijing/China.
- [6] Hou, Q., Zhou, D., Feng, J. (2021), Coordinate Attention for Efficient Mobile Network Design. *2021 IEEE/CVF Conference on Computer Vision and Pattern Recognition (CVPR)*, pp.13708-13717, Nashville/USA.
- [7] Howard A.G., Zhu M., Chen B. et al. (2017). MobileNets: Efficient Convolutional Neural Networks for Mobile Vision Applications, *Computer Science*. USA. <https://doi.org/10.48550/arXiv.1704.04861>.
- [8] Huang, H., Zhang, H., Hu, Xiao. &Nie, X. (2024) Recognition and Localization Method for Pepper Clusters in Complex Environments Based on Improved YOLO v5 (基于改进 YOLO v5 的复杂环境下花椒簇识别与定位方法). *Transactions of the Chinese Society for Agricultural Machinery*. Vol.55, pp.243-251. Beijing/China.
- [9] Kang, L., Wei, L. (2022). Progress of acridology in China over the last 60 years (中国蝗虫学研究 60 年). *Journal of Plant Protection*, Vol.49, pp.4-16, Beijing/China.
- [10] Kumar, K.S., Abdul Rahman, A. (2021). Early Detection of Locust Swarms Using Deep Learning. *Advances in Machine Learning and Computational Intelligence. Algorithms for Intelligent Systems*. pp.303–310. Springer, Singapore. DOI: 10.1007/978-981-15-5243-4_27
- [11] Li, L., Bai, Z., Diao, L., Tang, Z., Guo, X. (2021). Video Detection and Counting Method of East Asian Migratory Locusts Based on K SSD F (基于 K-SSD-F 的东亚飞蝗视频检测与计数方法). *Transactions of the Chinese Society for Agricultural Machinery*, Vol.52, pp.262-266, Beijing/China.
- [12] Li, R., Mamat, S, Sheng, Y., He, X. (2023). Identification and application flaut based on CA-MobileNet-V2 (基于 CA-MobileNet-V2 的核桃病害识别与应用). *Acta Agriculturae Zhejiangensis*, Vol.35, pp.2977-2987, Zhejiang/China.

- [13] Liu, F., Wang, S., Pang, S., Han, Z. (2024), Detection and recognition of tea buds by integrating deep learning and image-processing algorithm. *Journal of Food Measurement and Characterization*, Vol.18, pp.2744–2761, America.
- [14] Liu, S., Hu, B., Zhao, C. (2023). Detection and identification of cucumber leaf diseases based improved YOLOv7 (基于改进 YOLOv7 的黄瓜叶片病虫害检测与识别). *Transactions of the Chinese Society of Agricultural Engineering (Transactions of the CSAE)*, Vol.39, pp.163-171, Beijing/China.
- [15] Ma, C., Zhang, H., Ma, X., Wang, J., Zhang, Y., Zhang, X. (2024). Method for the lightweight detection of wheat disease using improved YOLOv8(基于改进 YOLOv8 的轻量化小麦病害检测方法). *Transactions of the Chinese Society of Agricultural Engineering*, Vol.40, pp.187-195, Beijing/China
- [16] Ma, N., Li, Y., Xu, M., Yan, H. (2023). Improved YOLOv8-based automated detection of wheat leaf diseases, *INMATEH - Agricultural Engineering*, Vol. 71, no.3, pp.499-510, Bucharest / Romania.
- [17] Ma, H., Zhang, M., Dong, K., Wei, S., Zhang, R., Wang, S. (2022). Research of Locust Recognition in Ningxia Grassland Based on Improved YOLO v5 (基于改进 YOLOv5 的宁夏草原蝗虫识别模型研究) *Transactions of the Chinese Society for Agricultural Machinery*, Vol.53, Beijing/China.
- [18] Mu J., Wang J, Liu S, Wang Z, Jiang H, Ma B, Zhang Z, Hu X (2022), A pest accurate segmentation method based on critical point nonlinear enhancement, *INMATEH - Agricultural Engineering*, vol. 68, pp.21-31. Bucharest / Romania. <https://doi.org/10.35633/inmateh-68-02>
- [19] Mao, T, Yu, I, Zhou, X, Yao, T., Wan, W., Xiong, B., Ou, Q. (2023),. Human behavior recognition method in infrared image based on improved MobileNet V1 (基于改进 MobileNetV1 的红外图像人体行为识别方法). *Journal of Liaoning Technical University (Natural Science)*, Vol.42, pp.362-369, Liaoning/China.
- [20] Mao, W., Zheng, Y., Zhang, Y., Yuan, Y., Zhang, X. (2008). Grasshopper detection method based on machine vision (基于机器视觉的草地蝗虫识别方法) *Transactions of the Chinese Society of Agricultural Engineering*. Vol.24, pp.155-158, Beijing/China.
- [21] Matache, M.G., Marin, F.B., Gurauc., Gurau, G., Marin M. (2022), Găgeanu I., Ionescu A., Neural network testing for spot-application of phytosanitary substances in vegetable crops using a self-propelled electrical sprayer, *INMATEH - Agricultural Engineering*, Vol. 68, pp.471-480, Bucharest / Romania. DOI : <https://doi.org/10.35633/inmateh-68-46>
- [22] Ning, J., Lin, J., Yang, S., Wang, Y., Lan, X. (2023), Face Recognition Method of Dairy Goat Based on Improved YoLo V5s(基于改进 YOLO v5s 的奶山羊面部识别方法). *Transactions of the Chinese Society for Agricultural Machinery*, Vol. 4, pp.331-337. Beijing/China.
- [23] Wang, L., Liu, Q, Cao, Y., Hao, X. (2023). Posture recognition of group-housed pigs using improved Cascade Mask R-CNN and cooperative attention mechanism (基于改进 Cascade Mask R-CNN 与协同注意力机制的群猪姿态识别). *Transactions of the Chinese Society of Agricultural Engineering (Transactions of the CSAE)*, Vol.39. Beijing/China.
- [24] Wang, J., Zhou, J., Zhang, Y., Hu, H. (2023). Multi-pose dragon fruit detection system for picking robots based on the optimal YOLOv7 model (基于优选 YOLOv7 模型的采摘机器人多姿态火龙果检测系统) *Transactions of the Chinese Society of Agricultural Engineering*, Vol.39, pp.276-283. Beijing/China.
- [25] Wang, X., Xu, Y., Zhou, J., Chen, J. (2023). Safflower picking recognition in complex environments based on an improved YOLOv7(基于改进 YOLOv7 的复杂环境下红花采摘识别) *Transactions of the Chinese Society of Agricultural Engineering (Transactions of the CSAE)*, Vol.39, pp.169-176. China.
- [26] Wang, P., Du, J., Zhang, Y., Liu, J., Li, H., Wang, C. (2024). (基于遥感多参数和 CNN-Transformer 的冬小麦单产估测). *Transactions of the Chinese Society for Agricultural Machinery*, Vol.55, pp.173-182, Beijing/China.
- [27] Wu, X., Zhan, C., Lai, K., et al (2019). "IP102: A Large-Scale Benchmark Dataset for Insect Pest Recognition. *2019 IEEE/CVF Conference on Computer Vision and Pattern Recognition*, DOI: 10.1109/CVPR.2019.00899.
- [28] Xu, D., Ma, W., Tan, Y., Liu, X., Zheng, Y., Tian, Z. (2022) Yield estimation method for tea buds based on YOLOv5 deep learning (基于 YOLO v5 深度学习的茶叶嫩芽估产方法). *Journal of China Agricultural University*, Vol.27, pp.213-220. Beijing/China.
- [29] Yu, H., Shi, W. (2021) Outbreak monitoring and control technology of desert locust *Schistocerca gregaria* (沙漠蝗灾发生、监测及防控技术进展). *Journal of Plant Protection*, Vol.48, pp.28-36. Beijing/China.

- [30] Yu, J., Chen, W., Guo, Y., Mu, Y., Fan, C. (2024). Improved Oriented R-CNN-based model for oriented wheat ears detection and counting (基于改进 Oriented R-CNN 的旋转框麦穗检测与计数模型). *Transactions of the Chinese Society of Agricultural Engineering (Transactions of the CSAE)*, Vol.40, pp.248-257, Beijing/China.
- [31] Zhang, G., Lyu, Z., Liu, H., Liu, W., Long, C., Huang, C. (2023). Model for identifying lotus leaf pests and diseases using improved DenseNet and transfer learning (基于改进 DenseNet 和迁移学习的荷叶病虫害识别模型). *Transactions of the Chinese Society of Agricultural Engineering*. Vol.39, pp.188-196. Beijing/China
- [32] Zhao, H., Cao, Y., Yue, Y., & Wang, H. (2021). Field weed recognition based on improved DenseNet (基于改进 DenseNet 的田间杂草识别). *Transactions of the Chinese Society of Agricultural Engineering*, Vol.37, pp.136-142, Beijing/China.
- [33] Zheng, Y., Wu, G., Wang, Y. & Mao, W. (2010) Locust images detection based on fuzzy pattern recognition (基于模糊模式的蝗虫图像识别方法). *Transactions of the Chinese Society of Agricultural Engineering* Vol.26, pp. 21-25, Beijing/China.
- [34] Zhou, W., Niu, Y., Wang, Y, Li, D. (2022). Rice pests and diseases identification method based on improved YOLOv4-GhostNet *Jiangsu J. of Agr.* Vol.38, pp.685-695. Jiangsu/China.

RESEARCH ON THE INFLUENCE OF VENTURI AERATOR CONFIGURATION ON OXYGEN ABSORPTION PERFORMANCE

文丘里增氧器结构参数对吸氧性能的影响研究

Longlong REN^{1,2,3*)}, Qingfu GONG^{1,2)}, Zhenxiang JING¹⁾, Xiang HAN^{1,2)}, Ang GAO^{1,2)}, Yuepeng SONG^{1,2,3*)}

¹⁾ Shandong Agricultural University, College of Mechanical and Electrical Engineering / China;

²⁾ Shandong Provincial Engineering Laboratory of Agricultural Equipment Intelligence / China;

³⁾ Shandong Provincial Key Laboratory of Horticultural Machinery and Equipment/ China

Tel:15550851588; E-mail: renlonglong123@126.com; uptonsong@163.com

DOI: <https://doi.org/10.35633/inmateh-74-25>

Keywords: Venturi oxygen; Oxygen absorption performance; Numerical simulation; Experimental verification

ABSTRACT

In order to address the issue of low oxygen stress caused by crops in traditional facility agriculture, this paper designed and optimized a venturi aeration device to enhance the oxygen content in the rhizosphere of crops in facility orchards. With the assistance of Comsol software, visual analysis of the flow field was conducted using Computational Fluid Dynamics (CFD) technology, exploring the impact of throat deviation and air inlet positioning on the suction efficiency of the aerator. The results indicated that the eccentric venturi configuration significantly improved suction efficiency. Moreover, positioning the air inlet on the contracted side of the eccentric venturi throat increased suction efficiency by 12.7%. Analysis of flow field characteristics of various venturi aerator configurations identified key factors influencing suction capacity, including throat flow velocity, vortex morphology in the diffuser section, and distribution of turbulent energy within the aerator. To validate the accuracy of the numerical simulations, an oxygen absorption performance testing apparatus was constructed and simulation results were compared with experimental data. The analysis revealed an error range between the two results of 1.67% to 7.74%, confirming the reliability of the simulations. This study has provided a theoretical foundation and technical methodology for the structural design and optimization of venturi aerators.

摘要

为了解决传统设施农业中对作物造成的低氧胁迫问题，本文设计并优化了一种文丘里增氧装置，旨在提高设施果园作物根际的氧含量。借助 Comsol 软件，基于流体动力学（CFD）技术进行流场的可视化分析，并探究喉管的偏移程度及进气口的位置对增氧器的吸气效率的影响。研究结果表明，偏心文丘里配置能显著提升吸气效率。此外，将进气口设置在偏心文丘里管喉管的收缩端一侧，能够使吸气效率提高 12.7%。通过分析文丘里增氧器不同构型的流场特性，得到影响吸气流量的关键因素主要包括喉管处的流速、扩散段的漩涡形态及增氧器内部的湍流能量分布情况。为了验证数值模拟仿真的准确性，构建了一套吸氧性能测试装置，并将仿真结果与试验结果进行了对比，结果比较分析表明二者之间的误差范围介于 1.67%至 7.74%，验证了仿真结果的可靠性。该研究为文丘里增氧装置的结构设计与优化提供了理论依据和技术方法。

INTRODUCTION

In recent years, with the growth of global population and the acceleration of urbanization, facility agriculture, as an efficient agricultural production mode, has attracted more and more attention and promotion (Ding et al., 2023; Li et al., 2021). However, due to the long time required for drip irrigation, hypoxia stress often occurs in the rhizosphere of crops, which greatly limits the improvement of crop yield and quality (Zahra et al., 2021; Zhu et al., 2020). Root hypoxia not only limits the absorption of water and nutrients by plants (Salvatierra et al., 2020), but also hinders the metabolic process of crops, thereby inhibiting their growth and development (León et al., 2021; Kapoor et al., 2022).

Venturi aerator is widely used in facility agriculture as an aerator. Through the design of specific structural parameters, it can effectively increase the oxygen concentration in the root area and promote the healthy growth of crops. The oxygenation effect of the oxygenation device directly affects the oxygen content of the water body during irrigation and the effect on soil aeration. Therefore, it is particularly important to optimize the design of the oxygenation device.

In the early 21st century, the United States developed an innovative irrigation method called AUDI technology, which improves the gas environment of roots by directly transporting oxygen to plant roots, thereby increasing crop yield (Xie *et al.*, 2019). The large-scale farmland irrigation system based on computer control developed by Eldar-Shany Automatic Control Technology is considered to be one of the cutting-edge control systems in the field of intelligent agriculture (He *et al.*, 2021). Li Yunkai *et al.* from China Agricultural University added ultra-micron bubble generators to the water and fertilizer integration device to increase the oxygen content of the water body (Li *et al.*, 2015). Liu Jun *et al.* from Jiangsu Academy of Agricultural Sciences optimized and designed a new type of U-shaped structure substrate tank to increase the oxygen content of irrigation water (Liu *et al.*, 2014). Fan Xingke *et al.* developed an eccentric venturi aerator, and found that its performance exceeded the traditional coaxial design (Fan *et al.*, 2014). In addition, Wang Haitao *et al.* compared the flow field distribution of the same axis and the eccentric venturi through the finite element analysis method, and revealed that the eccentric venturi has less head loss due to the smaller conflict of multi-directional velocity in the throat, which makes it more efficient (Wang *et al.*, 2018).

At present, a variety of venturi aerator irrigation devices have been developed at home and abroad, but there are significant differences in the effect and application of these devices. In addition, the research on the specific influence mechanism of different structural parameters on the aeration performance of venturi aerator is relatively insufficient. Based on this, according to the agronomic requirements of aerated irrigation in facility agriculture, this paper deeply discusses the specific influence of the key structural parameters of venturi aerator on its oxygen absorption performance in the integrated water and fertilizer system of facility agriculture, and optimizes the design of venturi aerator, which is of great significance for improving agricultural production efficiency and promoting crop growth.

MATERIALS AND METHODS

Structural model

Venturi aerator is a common aeration device used to inject air into water to provide oxygen (Yagci *et al.*, 2020). Its theoretical basis is Bernoulli equation. The general form of Bernoulli equation is as follows:

$$P + \frac{1}{2}\rho v^2 + \rho gh = c \quad (1)$$

In the above formula, P is the hydrostatic pressure; ρ is the fluid density; v is the fluid velocity; g is the acceleration of gravity; h is the height of the fluid at this point; c is a constant.

Based on the venturi effect in hydrodynamics, a venturi aerator is designed to increase oxygen content in water (Yao *et al.*, 2022). This device guides the water flow through a narrow channel inside, thereby generating a low-pressure environment in the local area. In the narrow part of the venturi aerator, this low-pressure environment causes the surrounding air to be inhaled and mixed with the water flow, thereby increasing the oxygen content in the water body. The conventional coaxial venturi structure is shown in Fig. 1.

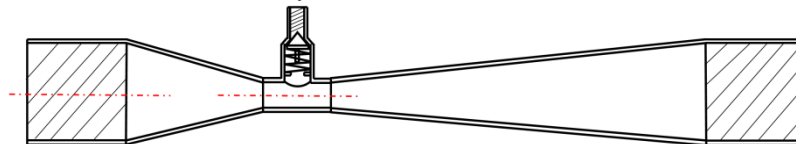


Fig.1 - The conventional coaxial venturi structure diagram

By optimizing the design of the venturi aerator, especially adjusting its internal structure, the flow field characteristics during operation can be significantly improved, thereby improving the suction efficiency and overall performance of the aerator. According to the agronomic requirements and existing problems of aerated irrigation in facility agriculture (Wen *et al.*, 2023), the structure of venturi aerator was optimized, and the concentric structure was optimized as an eccentric structure, as shown in figure 2.

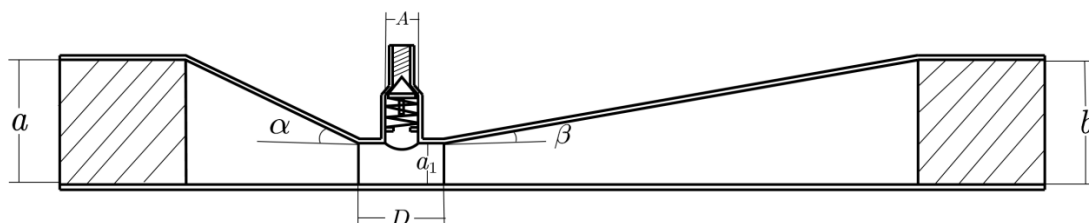


Fig. 2 - Structure diagram of eccentric venturi aerator

a. The diameter of inlet straight pipe section; b. The diameter of outlet straight pipe section; α. The angle of contraction section; β. The angle of diffusion section L; a₁. Throat diameter; D. Throat length; A. Inlet diameter

The basic structure of eccentric venturi aerator includes six main parts: inlet straight pipe section, contraction section, throat pipe, diffusion section, outlet straight pipe section and suction pipe. The key parameters include contraction section angle α , diffusion section angle β , throat diameter a_1 , throat diameter-length ratio λ ($\lambda = D/a_1$), throat contraction ratio γ ($\gamma = a_1/a$), throat length D and inlet diameter A . The difference of these parameters will significantly affect the working performance and efficiency of venturi aerator. Aiming at the offset distance S of the throat relative to the central axis of the overall structure and the distance L from the inlet to the contraction end of the throat, a series of models with different parameters were constructed to carry out experimental and numerical simulation analysis. After dividing the distance parameters, five different S values were set, which were S_1 (0 mm), S_2 (2.5 mm), S_3 (5 mm), S_4 (7.5 mm) and S_5 (10 mm). And five different L values, L_1 (5 mm), L_2 (7.5 mm), L_3 (10 mm), L_4 (12.5 mm) and L_5 (15 mm). The specific structural parameters of the venturi aerator are shown in Table 1.

Table 1

Structure parameters of the eccentric venturi aerator	
Structure name	Numerical value
Diameter of inlet straight pipe section (mm)	30
Outlet straight pipe diameter (mm)	30
Angle of contraction segment ($^\circ$)	25
Diffusion section angle ($^\circ$)	8
Throat diameter (mm)	10
Throat pipe length (mm)	20

Numerical simulation

When using Computational Fluid Dynamics (CFD) technology to visualize the flow field, a three-dimensional model is first created by SolidWorks, as shown in Figure 3, and Comsol 6.1 is used for meshing for subsequent analysis. The model meshing is shown in Figure 4. In order to ensure the calculation accuracy while reducing the consumption of computing resources, it is necessary to perform mesh independence verification to determine the optimal mesh size.

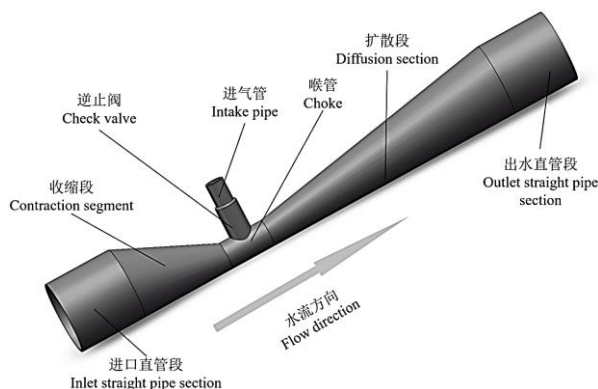


Fig. 3 - 3D model of eccentric venturi aerator

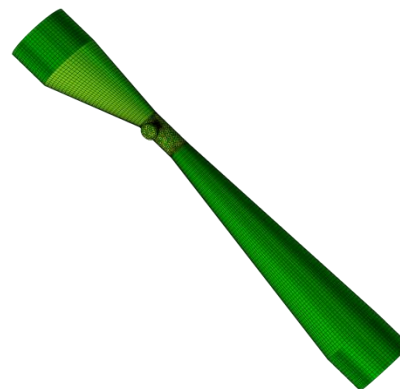


Fig. 4 - Model grid division diagram

According to the research of Zhang et al. (Zhang et al., 2021), the simulation accuracy is mainly affected by the mesh size, and the correlation with the calculation condition is low. Based on this, grid independence verification was carried out under specific working conditions (inlet flow rate was 1 m/s, outlet and inlet pressure were both 0 MPa), and the change rate of fertilizer suction flow was used as the test index to explore the relationship between the number of grids and the change rate of fertilizer suction flow. The results show that when the difference between the calculation results is less than 0.5 %, the grid density has little effect on the accuracy of the calculation results. Therefore, the grid configuration can be regarded as a suitable computational grid (Xing et al., 2021).

In order to further optimize the calculation accuracy of the model and reduce the calculation cost, a combination of hexahedral and tetrahedral grids is used for meshing. Tetrahedral meshes are used in the throat area to accurately capture the complex flow phenomena of gas-liquid mixing, while hexahedral meshes are used in other areas of the model to improve the computational efficiency and the accuracy of flow field analysis. The curve of the relationship between the maximum grid size and the change of air flow velocity obtained by simulation calculation is shown in figure 5. After comprehensive consideration, it is finally determined that the model shows the best analysis effect under the condition that the maximum grid size is 0.0016 m.

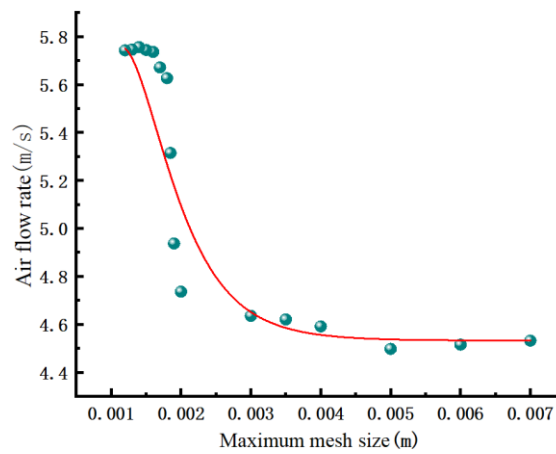


Fig. 5 - Curve of the relationship between the maximum grid size and the variation of air flow velocity

RESULTS

Analysis of the influence of different configurations of venturi aerator

In the study of structural optimization of venturi aerator, two key structural parameters *S* (the offset distance of the throat relative to the central axis of the overall structure) and *L* (the distance from the inlet to the contraction end of the throat) need to be considered comprehensively. The *S5* venturi aerator designed in this paper is a prototype design proposed by Kong Lingyang et al. (Kong et al., 2013). The design is characterized by a downward bias of the throat and a smooth wall away from the suction side. Based on this prototype, the *L* parameters are optimized by adjusting the values to obtain the best structural configuration. Accordingly, the venturi aerator design can be summarized into nine different combinations, namely *S1L1*, *S2L1*, *S3L1*, *S4L1*, *S5L1*, *S5L2*, *S5L3*, *S5L4* and *S5L5*. The design explores whether different combination configurations will affect the suction efficiency of the venturi tube, and further explores its influence principle. This paper will discuss the specific effects of these combined configurations on the performance of venturi aerators through in-depth analysis.

The fluid dynamics simulation analysis of nine different configurations of venturi aerators was carried out to observe their air suction performance under uniform flow rate conditions (1 m/s). CFD is used to simulate the flow characteristics of each configuration, and the corresponding air suction flow rate is combined. The results are presented in figure 6 in the form of point-line diagram. It can be seen from the figure that the simulated maximum air suction flow rate reaches 5.73 m/s, and the structure with this value is *S5L1*.

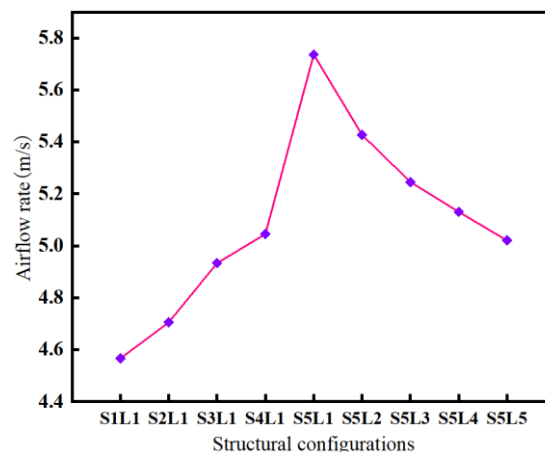


Fig. 6 - The influence of throat position on air flow velocity

It can be seen from Fig. 6 that under the condition of fixed inlet relative position (*L*), with the increase of throat deflection (*S*), the air velocity increases obviously and reaches the peak at *S5*. In the case of selected *S5* skewness, it is observed that the air flow rate gradually decreases with the increase of the relative position (*L*) of the inlet, and the rate of flow rate decrease gradually slows down. After examining nine different combinations of relative position and skewness of inlets, it is found that the structure of *S5L1* combination produces the highest air flow velocity, which is 20.2 % higher than that of *S1L1* combination. This result shows that the configuration of the venturi aerator has a significant effect on the air velocity.

In describing the performance parameters of venturi aerator, the gas-liquid ratio (the ratio of the liquid volume flow rate of the venturi aerator to the volume flow rate of the inhaled air) is usually used to measure the aerator 's suction capacity. The formula is:

$$\varepsilon = \frac{Q_V}{Q_W} \tag{2}$$

In the above formula, ε is the gas-liquid ratio; Q_V is the volume flow rate of air; Q_W is the liquid volume flow rate.

As shown in Figure 7, the relationship between the gas-liquid ratio and the venturi configuration follows the same trend as the previous analysis data. With the increase of the skewness S , the gas-liquid ratio gradually increases, and reaches the maximum value of 0.408 at $S5$. On the contrary, with the increase of the relative position L of the inlet, the gas-liquid ratio shows a gradual downward trend, and the gas-liquid ratio is the highest at $L1$. When comparing 9 different configurations of venturi aerators, it was found that the venturi aerator with $S5L1$ structure had the highest gas-liquid ratio, which was 12.7 % higher than that of $S5L5$.

Through the detailed analysis of the changes of structural parameters S and L , it can be concluded that the increase of skewness S has a significant positive effect on the air intake efficiency of the venturi aerator, while the increase of the relative position L of the inlet has a negative effect on the air intake efficiency. Therefore, under the structural configuration of $S5L1$, the overall suction efficiency of the venturi aerator is optimal.

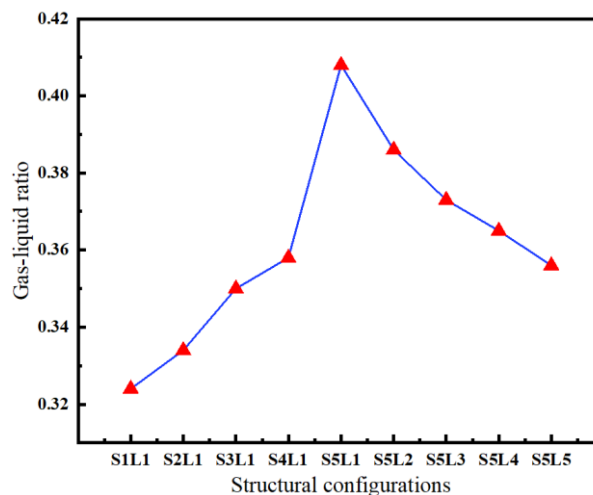


Fig. 7 - Effect of throat position on gas-liquid ratio

Analysis of the influence of inlet velocity of S5L1 venturi aerator on suction volume

Fig.8 shows the relationship between the water flow velocity and the suction gas flow velocity in the S5L1 venturi aerator and its corresponding fitting curve. It can be seen from the diagram that with the increase of water flow velocity, the gas flow velocity also increases accordingly. This phenomenon is consistent with the prediction of Bernoulli 's principle, that is, the increase of fluid velocity will reduce its own pressure, and then increase the pressure difference at the inlet, and finally increase the gas velocity at the inlet.

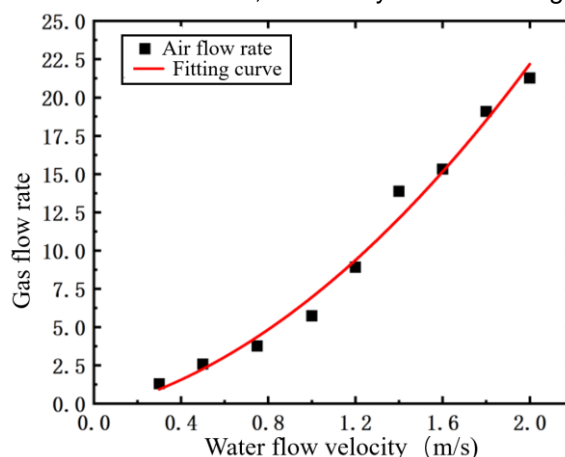


Fig. 8 - Influence of water velocity on air velocity

With the increase of water flow velocity, the gas suction volume at the inlet shows an increasing trend. However, an increase in the velocity of the water flow can also lead to an increase in the flow rate of the water. These two factors work together on the suction efficiency of the aerator. According to the data analysis shown in Fig.9, it can be seen that the gas-liquid ratio gradually increases with the increase of water flow velocity. In the area where the water flow velocity is lower than 0.8 m/s, the growth rate of gas-liquid ratio is low and fluctuates to some extent. When the water flow velocity is in the range of 0.8 m/s to 1 m/s, the growth of the gas-liquid ratio is significantly accelerated, and after exceeding 1.4 m/s, the growth rate slows down and gradually stabilizes. Within the specified range of flow rates in the simulation calculations, it is evident that increasing the inlet flow rate results in a corresponding increase in the inlet suction flow rate. Moreover, a notable linear correlation exists between the water flow rate and the gas flow rate at the inlet.

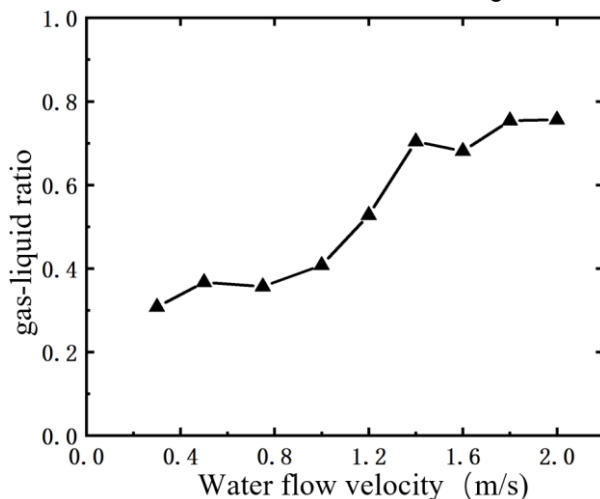


Fig. 9 - Influence of water velocity on gas-liquid ratio

Experimental verification

The test sample was printed by a 3D printer with an accuracy of 0.5 mm, and the printing material was high toughness resin. Figure 10 is the solid model of S5L1 venturi aerator. The fluid is injected into the aerator through the left inlet. When it passes through the contraction area, the flow rate increases and the pressure decreases. When it flows through the throat section, a negative pressure is generated, and the external gas can be sucked into the aerator through the inlet. Subsequently, the gas-liquid two-phase mixture is discharged from the outlet to achieve the purpose of gas-liquid mixing.



Fig. 10 - Physical drawing of S5L1 venturi aerator

To ensure precise measurement of the flow characteristics of the S5L1 venturi aerator, a turbine flowmeter was employed for data collection in this study, offering a measurement range of 9 to 100 L/min. When assessing air flow velocity, the gas flow parameters were acquired using a glass rotor flowmeter. Based on simulation outcomes, a glass rotor flowmeter with a range of 6 to 45 L/min was selected to encompass the required measurement scope for the experiment.

In order to verify the accuracy of the numerical simulation results, a suction performance test system was designed and built, as shown in Figure 11. The test platform uses a submersible pump to provide a pressure water source. The submersible pump is equipped with a flow regulation function. In the test, the water flow through the venturi aerator is controlled by adjusting the operating state of the submersible pump. The turbine flowmeter is connected in series behind the submersible pump to read the water flow through the aerator in real time. The inlet end of the venturi tube is externally connected with the glass rotor flowmeter. The inlet end of the flowmeter leads to the external environment, and the outlet end is connected with the inlet port of the aerator.

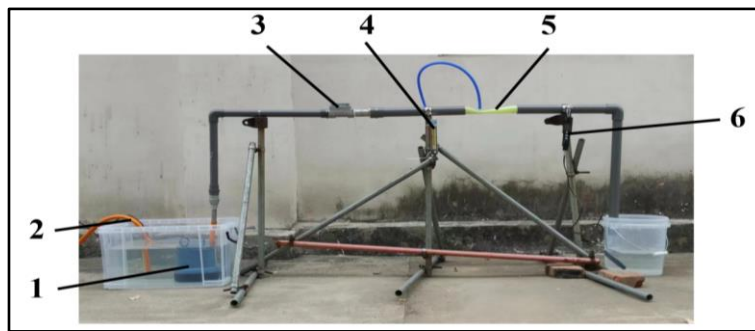


Fig. 11 - Inspiratory performance test device

1. Submersible pump; 2. Permanent water; 3. Turbine flowmeter; 4. Glass rotor flow meter;
5. Venturi aerator type S5L1; 6. Dissolved oxygen measuring instrument

During the experimental operation, the flow rate is gradually increased from low to high, and after each adjustment of the flow rate, the readings of the turbine flowmeter and the glass rotor flowmeter in the stable state are recorded respectively to obtain accurate flow data. According to the test device, the simulation reliability verification test was carried out. The test explored the relationship between the inlet flow rate and the air flow rate by adjusting the inlet flow rate of the venturi aerator. Figure 12 shows the trend and change curve of the simulated value and the experimental value. The experimental results show that the trend of the simulation data is basically the same as that of the experimental data, and the error range between the two is between 1.67 % and 7.74 %, which is within the acceptable error range. In addition, the data comparison verifies the accuracy and applicability of the computational simulation model, which proves that it can be effectively used to explain the optimization results.

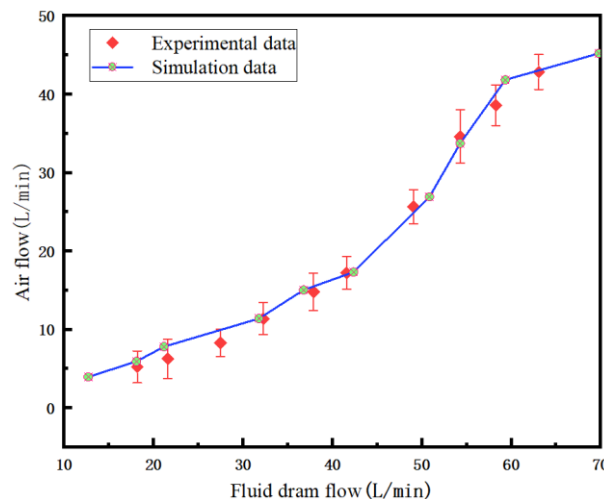


Fig. 12 - Comparison of simulation data with experimental data

Analysis of velocity characteristics of throat pipe

Figure 13 is the distribution of flow velocity characteristics of venturi aerators with different configurations. On the premise of the same working environment, according to the Bernoulli principle, it can be observed that in the throat area, the increase of the flow rate leads to the decrease of the negative pressure near the inlet area, which improves the suction efficiency and reduces the energy loss. With the gradual downward movement of the throat position from *S1* to *S5*, the flow rate of the throat shows an increasing trend, which reaches the maximum at the *S5* position. When the position of the throat is kept unchanged at *S5*, when the position of the air inlet gradually moves from *L1* to *L5*, the flow velocity of the throat shows a decreasing change, which is consistent with the previous experimental results of the inspiratory capacity. Through the velocity distribution map, it can be further observed that when the liquid flows through the inlet, the velocity increases obliquely downward. This phenomenon is caused by the external air introduced by the inlet above the throat. The mixing of the air and the water flow leads to the increase of the volume of the mixed fluid, which causes the increase of the flow rate. At the same time, because the air enters the throat along the normal direction of the air inlet, the flow velocity at the throat shows an oblique downward trend due to the influence of the water flow to the right side.

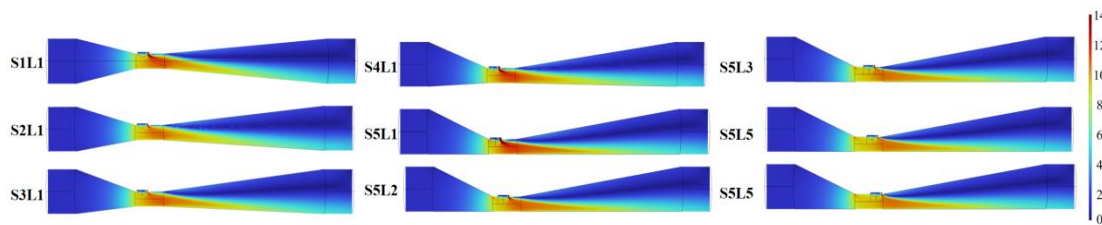


Fig. 13 - Distribution of velocity characteristics of venturi aerator

Vortex characteristics analysis

In order to accurately describe the position of the vortex center, this paper processes each vortex simulation result image. A plane rectangular coordinate system is established on the non-diffusion side of the outlet pipe, and this side is used as the coordinate origin (O). The X axis of the coordinate system extends along the inverse direction of the water flow, while the Y axis is vertical upward. In this way, the geometric characteristics of the vortex can be analyzed more clearly, as shown in Fig.14.

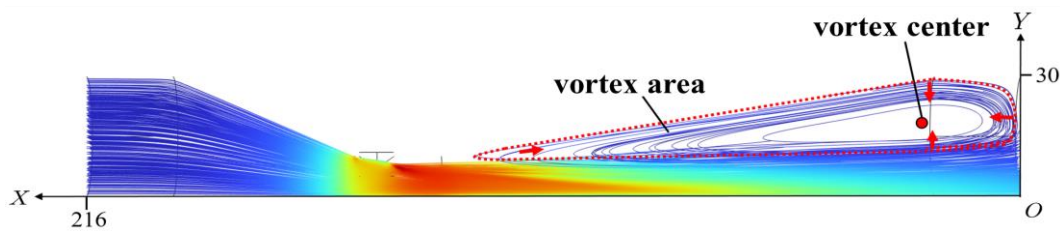


Fig. 14 - Location of vortex region and vortex center

The vortex boundary and the vortex center are processed to express the position of the vortex center on the coordinate system based on the plane right-angled coordinate system established above and measure its data loci marked on the X and Y axes of the coordinate system, and the processed vortex annotation map is shown in Figure 15.

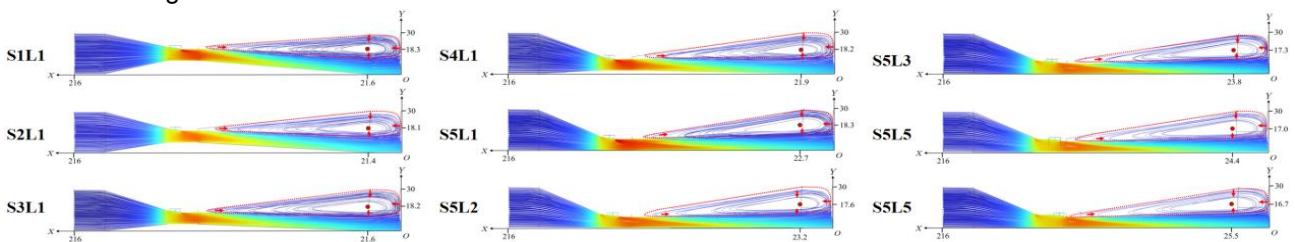


Fig. 15 - Vortexes of venturi aerators with different configurations

During the increment of the throat position from *S1* to *S5*, the change of the position of the vortex center is not significant and mainly moves irregularly in a small range. At the same time, the area of the vortex region shows a gradual reduction trend, in which the area of the vortex decreases by 256.5 mm² at the *S5* position compared with the *S1* position, which is a decrease of 20.9%. For the change of inlet position from *L1* to *L5*, the vortex center of the eccentric venturi oxygenator shifted in both X and Y axes. In this case, the vortex center was shifted to the left by 2.8 mm in the X-axis direction and downward by 1.6 mm in the Y-axis direction, with a combined shift distance of 3.2 mm downward from the left. In addition, there was a significant increase in the vortex area of 318.0 mm², which is an increase of 32.9%, as shown in Table 2.

Table 2

Vortex characteristics of the aerator at different intake positions

Venturi aerator configuration	Vortex center position		Vortex area (mm ²)
	X-axis (mm)	Y-axis (mm)	
S1L1	21.6	18.3	1223.75
S2L1	21.4	18.1	1172.61
S3L1	21.6	18.2	1095.47
S4L1	21.9	18.2	1030.33
S5L1	22.7	18.3	967.2
S5L2	23.2	17.6	1013.8
S5L4	24.4	17.0	1171.4
S5L5	25.5	16.7	1285.2

Under the same working conditions, the vortex area of the venturi aerator under the *S5L1* configuration is the smallest, which leads to the relative increase of the effective area of the mainstream water flow. In addition, the vortex center of the *S5L1* venturi aerator is closest to the throat and the air inlet, resulting in the vortex area beginning to affect the working environment near the air inlet and hindering the inflow of gas. In contrast, the vortex area in the *S5L5* configuration is small and the vortex center is far away, so the interference to the working environment near the inlet is small, and the inflow of external air is hardly affected by the vortex. Compared with the *S5L1* configuration, the venturi aerator with the *S1L1* configuration has a more significant skewed flow due to the expansion of its diffusion section along the upper and lower directions. Therefore, it can be concluded that the mainstream area is mainly concentrated on the far side of the suction pipe, resulting in a large vortex in the diffusion section, which may affect the working efficiency of the aerator.

Analysis of turbulent kinetic energy distribution characteristics

Figure 16 is the turbulent kinetic energy distribution cloud map of the throat with different skewness *S1-S5* and the inlet pipe at different positions of the throat *L1-L5*. Turbulent kinetic energy is an intuitive indicator to measure the degree of turbulence in the flow field. The higher turbulent kinetic energy reflects that the flow field is more complex, and the interaction, collision and mixing between the layers are more intense, resulting in an increase in local head loss (Li et al., 2020). In the configuration of *S1-S4*, the venturi aerator shows obvious turbulent kinetic energy concentration in the throat area. With the increase of skewness *S*, the concentration of turbulent kinetic energy gradually decreases until the concentration of turbulent kinetic energy basically disappears in the *S5* state. This trend is due to the fact that different *S* values change the contraction structure at both ends of the venturi aerator, which affects the flow characteristics of the water flow into the throat and causes a significant concentration of turbulent kinetic energy in the throat area. For the case of *L1-L5*, the maximum turbulent kinetic energy appears in the middle region of the diffusion section. The reason is that with the increase of *L* value, the vortex area inside the venturi aerator expands accordingly, and the range and offset of the vortex area also increase. This causes the backflow in the vortex region to collide with the water flow in the mainstream region, making the flow pattern more chaotic and the turbulence intensity increased accordingly. In addition, when the air is sucked into the throat through the air inlet, it mixes with the water flow and collides violently in multiple directions, resulting in the disorder of the water flow in the throat, thereby increasing the turbulence intensity.

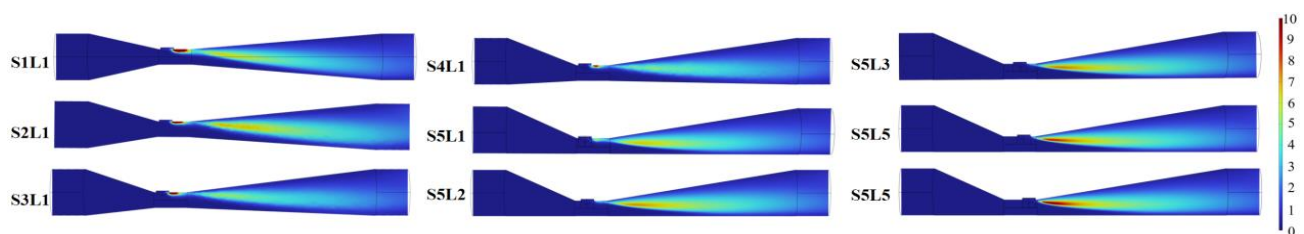


Fig. 16 - Distribution of turbulent kinetic energy of venturi aerators with different configurations

CONCLUSIONS

In this paper, the effects of the offset distance of the throat center and the relative position of different inlets at the throat on the suction performance and flow characteristics of the venturi aerator are compared and analyzed. The specific conclusions are as follows:

(1) Under normal working conditions, there is a good linear relationship between the deviation degree of the throat of the venturi aerator and the inspiratory efficiency. In addition, the relative position of the air inlet and the throat of the venturi aerator also shows a linear correlation with the inspiratory efficiency. When the venturi aerator is configured as *S5L1* configuration, its inspiratory efficiency reaches the maximum.

(2) The simulation results of 9 configurations under the same working conditions show that the performance of *S5L1* type is the best. Specifically, this configuration has the highest flow velocity at the throat, the smallest vortex area in the diffusion section, and the lowest turbulent kinetic energy. These three flow characteristics work together to make the *S5L1* venturi aerator have the highest suction efficiency.

(3) Through the experimental study of the suction performance test bench and the calculation and analysis of the corresponding simulation model, this study reveals that there is a significant positive linear correlation between the liquid flow rate and the air flow rate in the venturi aerator. The variation trend of the simulation value is generally consistent with the actual value of the test, and the error range between the two is 1.67 % to 7.74 %.

ACKNOWLEDGEMENT

This work was sponsored by “Key R&D Program of Shandong Province, China” (2024TZXD045, 2024TZXD038); Shandong modern agricultural industrial technology system - special fund for fruit innovation team (SDAIT- 06 -12) - special fund for fruit facilities, machinery and equipment post.

REFERENCES

- [1] Ding, Y.H., Zhang, Y.H., Sun, N., Fu, G.H., Lin, S., Chen, C. (2023). International experience and enlightenment of facility agriculture development in China (我国设施农业发展的国际经验与启示). *Jiangsu Agricultural Sciences*, Vol.51(16), pp.1-8.
- [2] Fan, X.K., Kong, L.Y. (2014). The Selection of Venturi Injector in the Drip Irrigation System (滴灌系统中文丘里施肥器的选配方法). *Journal of Irrigation and Drainage*, Vol.33 (1), pp. 26-29.
- [3] He, Q.H., Zheng, L., Chu, Y. H., Dou, Q.Q., Ci, W.L., Sun, Y.T. (2021). Research status and prospect of the head of fertigation system (水肥一体化系统首部研究现状与展望). *Chinese Journal of Agricultural Chemistry*, Vol.42 (1), pp. 122-129.
- [4] Kapoor, R., Kumar, A., Sandal, S.K., Sharma, A., Raina, R., Thakur, K.S. (2022). Water and nutrient economy in vegetable crops through drip fertigation and mulching techniques: a review. *Journal of Plant Nutrition*, Vol.45(15), pp.2389-2403.
- [5] Kong, L.Y., Fan, X.K. (2013). Experimental Study on Fertilizer Suction Performance of Venturi Injector (文丘里施肥器吸肥性能试验研究). *Water Saving Irrigation*, Vol.7, pp. 4-6.
- [6] León, J., Castillo, M.C., Gayubas, B. (2021). The hypoxia-reoxygenation stress in plants. *Journal of experimental botany*, Vol.72(16), pp. 5841-5856.
- [7] Li, H., Li, H., Huang, X.Q., Han, Q.B., Yuan, Y., Qi, B. (2020). Numerical and experimental study on the internal flow of the venturi injector. *Processes*, Vol.8(1), pp.64.
- [8] Liu, J., Tao, J.P., Yan, J.M., Luo, K.Y., Han, J.M., Zheng, H.Q., Lv, X.L. (2014). A method of water, fertilizer and gas fertilization (一种水肥气施肥方法). CN103918393A.
- [9] Li, W.F., Lin, F.L., Xiang, J.L., Xu, Q.Y., Li, H.P. (2021). Development Status and Countermeasures of Facility Agriculture (浅析设施农业发展现状及对策). *Guangdong Sericulture*, Vol.55(03), pp.12-15.
- [10] Li, Y.K., Liu, X.J., Xu, F.P., Wang, X.R., Zhang, Q.L., Jia, R.Q. (2015). A water-fertilizer-gas integrated drip irrigation system and drip irrigation method (一种水肥气一体化滴灌系统及滴灌方法). CN103141206B.
- [11] Salvatierra, A., Toro, G., Mateluna, P., Opazo, I., Ortiz, M., Pimentel, P. (2020). Keep calm and survive: Adaptation strategies to energy crisis in fruit trees under root hypoxia. *Plants*, Vol.9(9), pp.1108.
- [12] Wang, H.T., Wang, J.D., Yang, B., Mo, Y. (2018). Numerical simulation of Venturi injector with non-axis-symmetric structure (非对称结构文丘里施肥器数值模拟). *Journal of Drainage and Irrigation Machinery Engineering*, Vol.36(11), pp. 1098-1103.
- [13] Wen, H.Y., Yu, Z.Z., Wang, C., Zhang, D.M., Wang, H.X., Zou, H. F. (2023). Analysis on the Research Status and Development Trend of Aerobic Irrigation Technology (增氧灌溉技术研究现状与智能化发展趋势分析). *Journal of Agricultural Mechanization Research*, Vol.45(3), pp.1-7.
- [14] Xie, P.J., Zhang, Y.B. (2019). Development and application of green and efficient water-fertilizer-gas irrigation system (绿色高效水肥气灌溉系统研发与应用). *Southern Agriculture*, Vol.13(31), pp.77-80.
- [15] Xing, S.B., Wang, Z.H., Zhang, J.Z., Liu, N.N., Zhou, B. (2021). Simulation and verification of hydraulic performance and energy dissipation mechanism of perforated drip irrigation emitters [J]. *Water*, Vol.13(2), 171.
- [16] Yagci, A.E., Unsal, M., Ercan, B. (2020). Investigation the aeration performance of a new aerator: Venturi conduit. *Fresenius Environmental Bulletin*, Vol.29(2), pp.917-930.
- [17] Yao, N.Z., Wang, H., Wang, B., Wang, X.S. (2022). Venturi-effect rotating concentrators and nonreciprocity characteristics based on transformation hydrodynamics (基于变换流体力学的文丘里效应旋聚器的设计与非互易特性研究). *Acta Phys Sin*, Vol.71(10), pp.104701.
- [18] Zahra, N., Hafeez, M.B., Shaukat, K., Wahid, A., Hussain, S., Naseer, R., Raza, A., Iqbal, S., Farooq, M. (2021). Hypoxia and Anoxia Stress: Plant responses and tolerance mechanisms. *Journal of Agronomy and Crop Science*, Vol.207(2), pp.249-284.
- [19] Zhang, H.G., Tang, S.Y., Yue, H.R., Wu, K.J., Zhu, Y.M., Liu, C., Liang, B., Li, C. (2021). Comparison of computational fluid dynamic simulation of a stirred tank with polyhedral and tetrahedral meshes. *Iranian Journal of Chemistry & Chemical Engineering-International English Edition*, Vol.39(4), pp.311-319.
- [20] Zhu, Y., Cai, H., Song, L.B., Wang, X.W., Shang, Z.H., Sun, Y.N. (2020). Aerated irrigation of different irrigation levels and subsurface dripper depths affects fruit yield, quality and water use efficiency of greenhouse tomato. *Sustainability*, Vol.12(7), pp. 2703.

PARAMETER CALIBRATION AND EXPERIMENT OF DISCRETE ELEMENT SIMULATION OF SPHERICAL-LIKE SOYBEAN BASED ON DEM

基于DEM的类球形大豆离散元仿真参数标定与试验

Guangwei CHEN¹⁾, Fuxing LI¹⁾, FaYi QU^{*2)}, Chong Jian ZHANG¹⁾

¹⁾Northeast Forestry University, College of Mechanical and Electrical Engineering, Harbin / China;

²⁾Northeast Forestry University, Graduate School, Harbin / China

Tel: +86 15663693373; E-mail: qufae@163.com

DOI: <https://doi.org/10.35633/inmateh-74-26>

Keywords: Spherical-like soya bean, Material properties, discrete element simulation, Stacking angle

ABSTRACT

This paper focuses on the lack of spherical-like soybean simulation parameters when guiding the optimization and design of agricultural machinery and equipment through discrete element simulation. The spheroidal soybean variety SN29 was used as a study subject; the intrinsic properties and physico-mechanical properties of the spherical soybean were determined through actual measurements and the simulation of spherical-like soybean particles with Hertz-Mindlin (no-slip) as the contact model was established. The collision recovery, static, and rolling friction coefficients of the spherical-like soybean and acrylic sheet material were measured by the natural drop and inclined plane methods, combined with discrete element simulation and bench experiments. They were 0.474, 0.496, and 0.0361, respectively. The relative errors between the measured stacking angles and the simulated stacking angles were used as indicators, and the contact parameters between the particles were used as variables for the design of the steepest climb experiment. The collision recovery coefficient, static friction coefficient, and rolling friction coefficient between spherical-like soybean particles were determined to be 0.35, 0.30, and 0.074, respectively, by orthogonal rotational combination experiment and multi-objective optimization. The relative error between the simulated and measured stacking angles was only 1.09%, as verified by the experiment. This proves that the discrete element simulation parameters of the studied spherical-like soybean can reflect its real characteristics and be used as the parameter basis for discrete element simulation.

摘要

针对类球形大豆在应用离散元仿真指导相关农机设备优化设计时缺乏仿真参数的问题。以类球形大豆品种SN29为研究对象，通过实际测量和万能试验机，确定了类球形大豆的本征特性与物理力学特性，并建立了以Hertz-Mindlin (no-slip)为接触模型的类球形大豆仿真颗粒模型。通过跌落法和斜面法，结合离散元仿真及台架试验，测得类球形大豆与亚克力板材料的碰撞恢复系数、静摩擦系数和滚动摩擦系数，分别为0.474、0.496和0.0361。以实测与仿真堆积角的相对误差为指标，颗粒间接触参数为变量，设计了最陡爬坡试验，并通过正交旋转组合试验及多目标优化，确定了类球形大豆颗粒间的碰撞恢复系数、静摩擦系数和滚动摩擦系数，分别为0.35、0.30和0.074。经试验验证，仿真堆积角与实测堆积角的平均相对误差仅为1.09%。这证明了研究所得的类球形大豆离散元仿真参数能够反映其真实特性，可作为离散元仿真时的参数依据。

INTRODUCTION

As an essential source of protein, edible oil, and livestock feed, soybean is widely cultivated worldwide and an indispensable crop in agricultural production (Guo *et al.*, 2023). As the demand for soybeans continues to grow, it has become crucial to improve the mechanization of the soybean chain (Shi *et al.*, 2021; Chang *et al.*, 2024). In the design and optimization of agricultural machinery and equipment, discrete element (DEM) simulation software is often used to simulate the motion state of crops during sowing, harvesting, and clearing; the advantages of this method are that seasonal and experimental conditions do not restrict it, and it has a lower trial-and-error cost compared with actual experiments, which has led to its wide application in the design and optimization of agricultural machinery and equipment (Zhao *et al.*, 2021; Zhang *et al.*, 2022).

¹GuangWei CHEN Assoc.Prof.; Fuxing LI, Postgraduates.; FaYi QU, Assistant Research Fellow; ChongJian ZHANG, Postgraduates.

In the process of using discrete element simulation (DEM) to guide the design and optimization of agricultural machinery and equipment, due to the differences in the intrinsic characteristics and physical parameters of different crops, to simulate the actual movement patterns of crops in farm machinery and equipment, exact measurements and other means are usually used to obtain their accurate physical parameters (Hao *et al.*, 2021). The relevant parameters' authenticity determines the simulation results' accuracy and reliability (Xie *et al.*, 2024). At present, domestic and foreign scholars' studies on the calibration of crop parameters have mainly used actual measurements, cylinder lifting method, inclined surface method and falling method to calibrate the intrinsic characteristics and physical parameters of grain and oil crops and straws, such as white kidney beans, chili peppers, sunflower seeds and alfalfa stems and stalks (Yang *et al.*, 2024; Chen *et al.*, 2024; Wang *et al.*, 2022; Chen *et al.*, 2023). However, the calibration of discrete element parameters for spherical-like soybeans grown in Northeast China is still insufficient, resulting in the lack of accurate and effective simulation parameters for spherical-like soybeans when using discrete element simulation to guide the optimization and design of agricultural machinery and equipment, which to a certain extent restricts the optimization and development of the design of farm machinery and equipment for spherical soybean varieties.

In order to determine the physical parameters of the spherical-like soybean, this study obtained the basic material properties of the soya bean and its contact parameters with the acrylic material by combining bench experiments and discrete element simulation experiments. The steepest climb experiment was designed using the interparticle contact parameter as a variable and the minimum error between the measured and simulated stacking angles as an indicator; by designing orthogonal rotational combination experiments with the help of Design Expert 13 software, the optimum contact parameters between the soybean seeds were finally determined through target optimization and validation experiments. The study results can provide accurate, reliable, and reasonable simulation models and parameter support when discrete element simulation guides the design and optimization of agricultural machinery and equipment for spherical soybean varieties.

MATERIALS AND METHODS

Determination of intrinsic properties and discrete element models for spherical-like soybeans

Experiment Material Selection

The representative spherical-like soybean variety SN29 from Suihua, Northeast China, was selected as the experiment material. It was harvested in October 2023, collected from farmers' homes in February 2024, and sealed using ziplock bags after collection to prevent moisture loss.

Hundred-grain weight and triaxial dimensions

Using an electronic balance with an accuracy of $500\text{g} \pm 0.01\text{g}$, three groups of materials were randomly selected, and each group was repeated three times, resulting in a consolidated 100-grain weight of 20.84 g. Five hundred soybeans were randomly selected, and using a vernier caliper with an accuracy of 0.01 mm, the geometrical dimensions of their length (L), thickness (T), and width (W) were measured and recorded, and the mean values were obtained to be 7.49 mm, respectively, 7.33 mm and 6.58 mm. The specific measurement positions and tools are shown in Fig. 1.



Fig. 1 - Soybean seed geometry measurement positions and tools

In order to provide a basis for establishing the discrete element simulation model, the equivalent diameter and sphericity of soybeans were calculated using Eq. (1) and (2). The combined sphericity was 95.1%, and the combined average diameter was 7.1 mm, resulting in a high overall sphericity. Combining the various data, the histogram of the normal distribution of the equivalent diameters of spherical-like soya-like beans versus the three-axis sizes was plotted using Origin2022, and it can be seen that the various size intervals conformed to the normal distribution, as shown in Fig. 2. In order to avoid repetition or ambiguity, all the descriptions of 'spherical-like soya beans' in the following were replaced by 'soybean' instead.

$$D_{es} = (L \times T \times W)^{\frac{1}{3}} \quad (1)$$

$$\varepsilon = \frac{D_{es}}{d_s} \times 100 \tag{2}$$

where:

D_{es} is the equivalent diameter, [mm]; L , T , W are the length, width, and thickness, [mm]; ε is the sphericity, [%]; d_s is the diameter of the external ball of the soybean (long axis dimension), [mm].

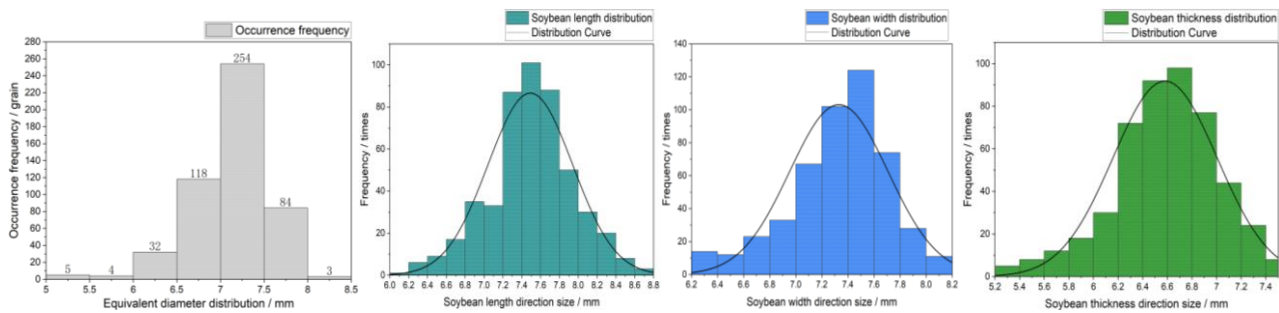


Fig. 2 - Histogram of equivalent diameter and triaxial size distribution of soybean

Moisture content and density

The density of soya beans was measured using the drainage method. The measuring cylinder was filled with a certain volume of pure water, say 40ml (40 cm³), noted as V1. A random portion of soya bean was taken and weighed, noted as M. After putting the soybeans into the measuring cylinder, the combined volume of the two is noted as V2. The density of the soybeans is $[M/(V2- V1)] \times 1000$. After three experimental measurements, the average density of the spherical-like soybeans was 1,252 kg/m³.

The moisture content of the soya beans was determined using the pyrolytic weight principle, using the high-temperature rapid drying unit of the MS100 Halogen Moisture Meter. The masses of the soybeans before and after drying were noted as M1 and M2, respectively, and the moisture content was $[(M1-M2)/M1] \times 100\%$. After three measurements, the average value was taken to obtain an average moisture content of 10.93% for the soybeans. The above density and moisture content measurement equipment is shown in Fig. 3.

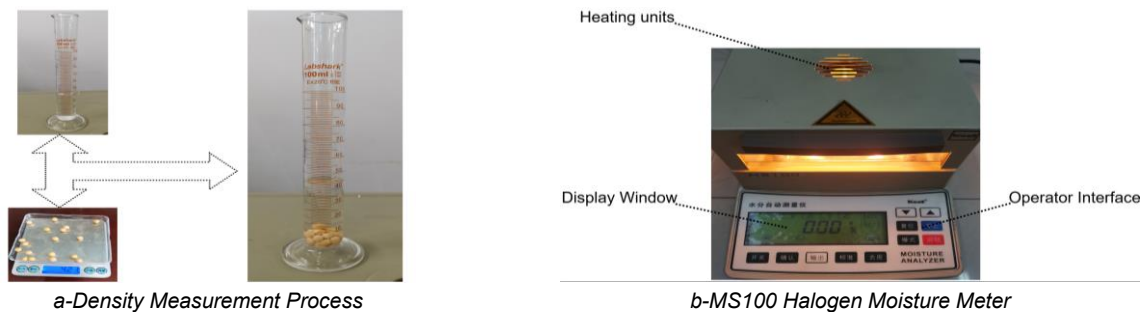


Fig. 3 - Density and moisture content measuring equipment

Poisson's ratio and modulus of elasticity

Poisson's ratio is a physical quantity that describes the ratio of positive radial strain to positive axial strain of a material in unidirectional tension or compression. It is also known as the transverse deformation coefficient (Zhang et al., 2024). Ten soybeans were randomly selected and subjected to Poisson's ratio uniaxial compression experiments using a CTM2500 universal materials experimenting machine. The handle controlled the moving beam to apply the load along the soybean thickness direction at a 5 mm/min descending speed. When the particles made cracking sounds, the pressure was stopped immediately, the moving beam was lifted quickly, and the changes in the soybeans' length and thickness direction dimensions before and after compression were recorded. Substituting the measured data into Eq. (3), the Poisson's ratio of soybeans ranged from 0.17 to 0.35, with an average value of 0.23.

$$\mu = \frac{L_1 - L_2}{W_1 - W_2} = \left| \frac{V_L}{V_W} \right| \tag{3}$$

where: μ is the Poisson's ratio of soybean; L_1 is the length of soybean before compression, [mm]; L_2 is the length of soybean after compression, [mm]; W_1 is the thickness of soybean before compression, [mm]; W_2 is the thickness of soybean seed after compression, [mm]; V_L is the deformation of compression in the direction of the length, [mm]; V_W is the deformation of the direction of the thickness of soybean, [mm].

The modulus of elasticity and shear modulus of soybean refer to the ability of a material to resist deformation when subjected to a force and are essential components of the simulation parameters. Ten soybeans were randomly selected and measured using a universal experimenting machine concerning the ASAE S368.4 DEC2000 (R2008) standard published by the American Society of Agricultural and Biological Engineers (Shirvani M et al., 2014). When the experimenting machine detects that the compression curve exceeds the elastic deformation interval of the soybean, the moving beam will automatically stop the downward pressure and lift upward, outputting the relevant data of the compression experiment and completing the whole measurement process of the modulus of elasticity.

Substituting the obtained values into Eq. (4) and (5), the modulus of elasticity of soybean was calculated as 43.54-109.79 MPa, and the average value was 79.71 MPa. Substituting the values of modulus of elasticity and Poisson's ratio into Eq. (6) gives the range of shear modulus of the soybean as 17.7 to 44.63 MPa with an average value of 32.4 MPa. The described CTM2500 universal materials experimenting machine and its measurement principle are shown in Fig. 4.

$$E = \frac{0.38F(1 - \mu^2)}{D^{\frac{3}{2}}} \left[2K \left(\frac{1}{R_1} + \frac{1}{R'_1} \right)^{\frac{1}{3}} \right]^{\frac{3}{2}} \tag{4}$$

where:

$$\begin{cases} R_1 = \left[(L/2)^2 + (W/2)^2 \right] / W \\ R'_1 = \left[(T/2)^2 + (W/2)^2 \right] / W \\ \cos \theta = \frac{(1/R'_1 - 1/R_1)}{(1/R'_1 + 1/R_1)} \end{cases} \tag{5}$$

where:

E is the modulus of elasticity of soybean particles, [MPa]; F is the compression load on soybeans, [N]; μ is the Poisson's ratio of soybeans, according to the above calculations it can be known as 0.23; D is the deformation of soybeans, [mm]; R_1 is the radius of curvature of the upper contact surface between soybeans and the circular compression table, [mm]; R'_1 is the radius of curvature of the lower contact surface of the fixed platform of the soybeans and particles, [mm]; K value is an intermediate constant value (calculated using the $\cos\theta$ formula in Eq.(6) and obtained after searching in the ASAE S368.4 DEC2000 (R2008) standard).

$$G = E/2(1 + \mu) \tag{6}$$

where:

G is the shear modulus of soybean particles, [MPa]; E is the modulus of elasticity of soybean, [MPa]; μ is the Poisson's ratio of soybean.

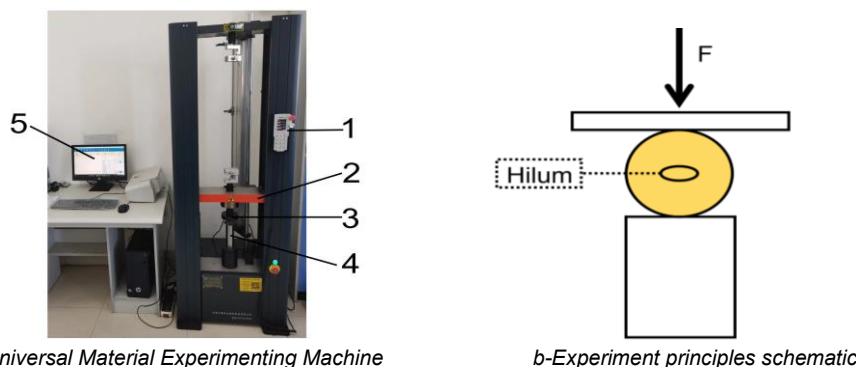


Fig. 4 - Soybean compression experiment equipment and schematic diagram

1. Control Handle; 2. Movable Crossbar; 3. Mobile Pressurized Circular Table; 4. Fixed Material Platform; 5. Computer Control Terminal.

Discrete element modeling of soybean

When the sphericity of the particles is greater than 90%, the single spherical particles that come with the system can be used to build a discrete element simulation model, and this means it can effectively improve the simulation efficiency under the premise of ensuring the reliability of the simulation (Zhang et al., 2024). The integrated sphericity of the calibrated soybean was 95.1%, which met the above modeling conditions.

A discrete element simulation model was developed based on a determined equivalent average diameter of 7.1 mm for soybeans. The soybean particle and discrete element simulation model are shown in Fig. 5.

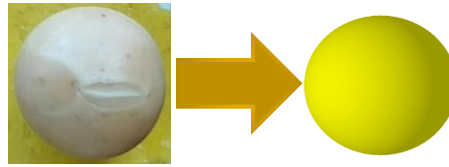


Fig. 5 - Soybean particle and discrete element simulation modeling

Contact Model and Contact Material

Since soybean is a bulk material, particles have no adhesion, and the forces are relatively simple. Therefore, Hertz-Mindlin (no sliding) was chosen as the contact model for the discrete element simulation (Dun et al., 2022). When simulating the production process of soybean cleaning or sowing, frequent contact and collisions between particles occur, which is not limited to between soybean particles but also between soybeans and the surrounding wall material. In this paper, acrylic sheets were chosen as the wall material for the study. It has a Poisson's ratio of 0.5, a shear modulus of 1.77×10^8 Pa, and a density of 1180 kg/m^3 .

Calibration of contact parameters between spherical soybeans and acrylic sheets

Collision recovery coefficients

The collision recovery coefficient between soybeans and acrylic sheets was determined using the natural drop method. The experimental equipment required for this method included a high-definition digital camera, grid paper, a vacuum pump, and an acrylic plate. The vacuum pump was switched on to hold the soybean pellets at a height of 250 mm. After the pellets were stabilized, the vacuum pump was switched off and the soybean pellets were subjected to a free-fall motion, with a high-definition digital camera used to record the fall and rebound of the pellets. The recorded video was processed by slow playback and combined with grid paper to measure and record the maximum height of the bouncing of the soybean particles.

Ten soybeans were randomly selected to repeat the above experiment, and the mean value was taken to obtain an average bounce height of 59.93 mm for the soybeans. The measured values were substituted into Eq. (7) to calculate the collision recovery coefficient between the soybeans and the acrylics, which ranged from 0.41 to 0.57.

$$e = \frac{v_1}{v_0} = \frac{\sqrt{2gh_{max}}}{\sqrt{2gH}} = \sqrt{\frac{h_{max}}{H}} \quad (7)$$

where: e is the collision recovery coefficient; V_1 is the pre-collision normal velocity, [m/s]; V_0 is the post-collision normal velocity, [m/s]; h_{max} is the maximum height of bouncing of the soybean after the collision, [mm]; H is the height of the soybean when it is released, [mm].

The static friction coefficient A_2 and rolling friction coefficient A_3 between soybean and acrylic plate, as well as the collision recovery coefficient B_1 , static friction coefficient B_2 , and rolling friction coefficient B_3 between soybean particles, do not have a significant effect on the bouncing height of soybeans on the acrylic plate; in order to avoid interference, the simulation experiment can be set to these parameters to 0. Based on the bench experiment, the collision recovery coefficient parameters range between soybeans and the acrylic plate is 0.4 to 0.6, and the setting interval is 0.05. A total of 5 groups of experiments were conducted, each repeated three times, and the average value was taken. The experiment program and results are shown in Table 1. The above bench experiment, principles, and simulations are shown in Fig. 6.

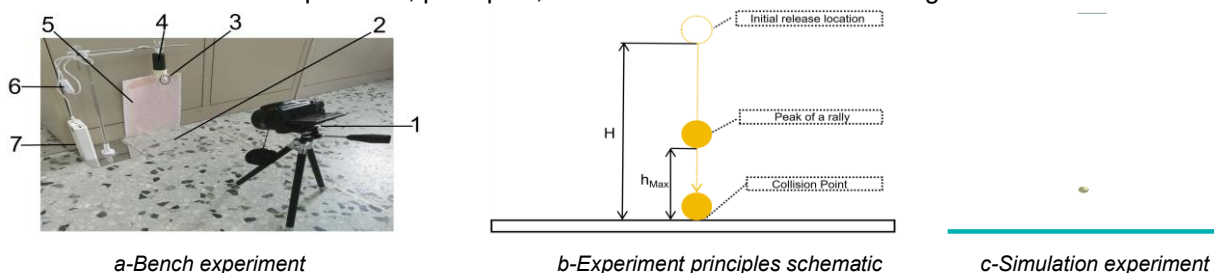


Fig. 6 - Calibration of the collision recovery coefficient between soya beans and acrylic sheets

1. High-Definition Digital Camera; 2. Acrylic Sheet; 3. Soybean Pellet; 4. Vacuum Pump; 5. Grid Paper; 6. Switch; 7 Power Supply.

Table 1

Collision recovery coefficient simulation design of experiments scheme and results

Experiment (group)	e	h_{max} (mm)
1	0.40	46.04
2	0.45	55.63
3	0.50	66.76
4	0.55	79.56
3	0.60	95.04

To demonstrate the relationship between the soybeans' static friction coefficients in Table 2 and the angle of static friction, a quadratic polynomial fit was used to obtain the fitted curves for both, which are shown in Fig. 9. The equation of the fitted curve is given in Eq. (8).

$$h_{max} = 384.28571e^2 - 140.42571e + 40.826 \quad (R^2=0.99981) \quad (8)$$

The average value of the maximum bounce coefficient between the soybean and the acrylic plate measured in the bench experiment was 59.93 mm, which was substituted into Eq. (8) to obtain e as 0.474. The value was substituted into the simulation software for validation. The experiment was repeated three times, and the maximum rebound height of the simulation experiment was measured to be 60.83 mm, which had a percentage error of only 1.479 with that of the estimated value of the bench experiment. From this, the collision recovery coefficient e between the soybean and the acrylic plate is 0.474.

Static friction coefficient

In this experiment, the friction coefficient between soybean particles and acrylic sheets was determined by the inclined plane method with the help of a homemade coefficient of friction experimenting device and high-definition video recording technology. To prevent the rolling of the soybeans, 16 uniformly sized soybeans, four in each group, were selected and glued together following a quadrilateral shape. The equipment was adjusted to a horizontal position for the experiment, and the angle gauge was zeroed. The pellet plate was placed on the device's left plane, the handle was slowly rotated, and a video recording device was used to capture the entire process of the soybean plate from rest to sliding. The video was played slowly to record the angle-measuring device reading as the soybean plate slid. Three trials were repeated for each group of soybean plates, and the average of the angles was taken to give a static friction angle of 26.397° for the soybeans. Substituting the measured angle into Eq. (9), the static friction coefficient between the soybeans and the acrylic plates was found to be 0.38 to 0.56.

$$\mu_s = \frac{F_{smax}}{P} = \frac{mg \sin(\alpha_s)}{mg \cos(\alpha_s)} = \tan \alpha_s \quad (9)$$

where: μ_s is the collision recovery coefficient; F_{smax} is the maximum static frictional resistance between the soybean and the acrylic plate, [N]; P is the positive pressure, the vertically downward force exerted by the soybean particles on the acrylic plate under the action of gravity, [N]; m is the mass of the soybean to have been experimented, [Kg]; and α_s is the static friction angle between the soybean and the acrylic material, [°].

Rolling friction coefficient A_3 between soybean and acrylic plate, as well as the collision recovery coefficient B_1 , static friction coefficient B_2 , and rolling friction coefficient B_3 between soybean particles, do not have a substantial effect on the angle of static friction α_s between the soybean and the acrylic plate; to avoid interference, the simulation experiment can be set to these parameters to 0. Based on the bench experiment, the static friction parameters range between soybeans and the acrylic plate is 0.35 to 0.6, and the setting interval is 0.05. A total of 6 groups of experiments were conducted, each repeated three times, and the average value was taken. The experiment program and results are shown in Table 2. The above bench experiment, principles, and simulations are shown in Fig. 7.

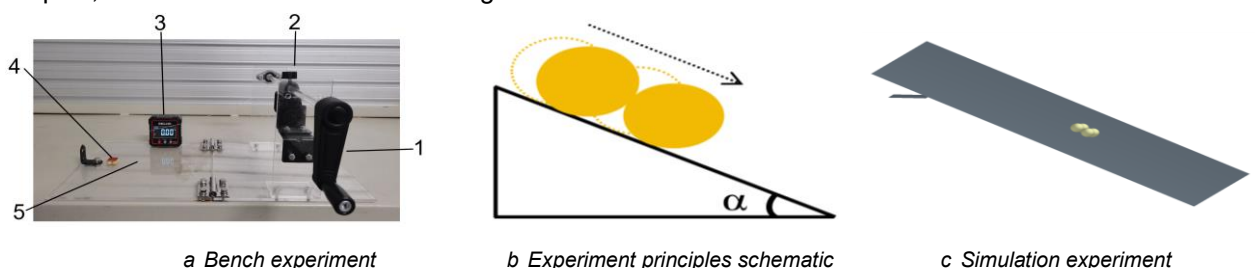


Fig. 7 - Calibration of the static friction coefficient between soya beans and acrylic sheets
 1. Handle; 2. Limit Switch; 3. Angle Gauge; 4. Soybean Plate; 5. Acrylic Sheet.

Table 2

Scheme and results of simulation design of experiments for static friction coefficient

Experiment (group)	A_2	α_s [°]
1	0.35	20.22
2	0.40	22.80
3	0.45	24.90
4	0.50	26.16
5	0.55	29.28
6	0.60	31.40

To demonstrate the relationship between the static friction coefficients of the soybeans in Table 2 and the angle of static friction, a quadratic polynomial fit was used to obtain the fitted curves for both, which are shown in Fig.9. The equation of the fitted curve is given in Eq. (10).

$$\alpha_s = 12.71429A_2^2 + 31.69286A_2 + 7.77786 \quad (R^2=0.98647) \quad (10)$$

The average static friction angle between the soybean and the acrylic plate measured in the bench experiment was 26.397°, which was substituted into Eq. (10) to obtain that α_s was 0.474. The value was substituted into the simulation software for validation. The experiment was repeated three times, and the static friction angle α_s of the simulation experiment was measured to be 26.7°, which had a percentage error of only 1.14 compared with that of the estimated value of the bench experiment. From this, the static friction coefficient A_2 between the soybean and the acrylic plate was 0.493.

Rolling friction coefficient

The rolling friction coefficient between the soya bean and the acrylic sheet was still determined using the inclined plane method. Ten uniformly sized soybeans with high sphericity were selected and placed horizontally on the top of the left plane of the friction coefficient experimenting equipment. The handle was slowly rotated, and a high-definition video camera was used to capture the soybean particles from static to rolling. The video was played slowly to record the angle-measuring device reading as the soybean particles rolled. Three trials were repeated for each group of soybean particles, and the average of the angles was taken to give a static friction angle of 2.375° for the soybeans. Substituting the measured angle into $\mu_r = \tan\alpha_r$, the rolling friction coefficient between the soybeans and the acrylic plates was found to be in the range of 0.022-0.063.

Collision recovery coefficient B_1 , static friction coefficient B_2 , and rolling friction coefficient B_3 between soybean particles have no effect on the rolling friction angle between the soybean and the acrylic plate. To avoid interference, the simulation experiment can be set to these parameters to 0. Based on the bench experiment, the rolling friction coefficient parameters range between soybeans and the acrylic plate is 0.02 to 0.07, and the setting interval is 0.01. A total of 6 groups of experiments were conducted, each repeated three times, and the average value was taken. The experiment program and results are shown in Table 3. The above bench experiment, principles, and simulations are shown in Fig. 8.

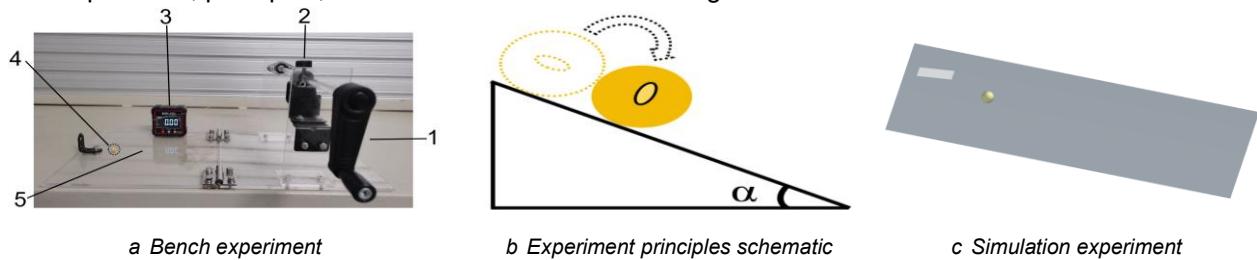


Fig. 8 - Calibration of the rolling friction coefficient between soya beans and acrylic sheets
 1. Handle; 2. Limit Switch; 3. Angle Gauge; 4. Soybean Pellet; 5. Acrylic Sheet.

Table 3

Scheme and results of dynamic friction coefficient simulation design of experiments

Experiment (group)	A_3	α [°]
1	0.02	1.38
2	0.03	2.28
3	0.04	2.46
4	0.05	3.12
5	0.06	3.66
6	0.07	4.26

To demonstrate the relationship between the rolling friction coefficients of the soybeans in Table 3 and the rolling friction angle, a quadratic polynomial fit was used to obtain the fitted curves for both, which are shown in Fig. 9. The equation of the fitted curve is given in Eq. (11).

$$\alpha_r = -10.71429A_3^2 + 55.82143A_3 + 0.37286 \quad (R^2=0.97259) \quad (11)$$

The average value of the rolling friction angle between the soybean and the acrylic plate measured in the bench experiment was 2.375, which was substituted into Eq. (11) to obtain that α_r was 0.0361. The value was substituted into the simulation software for validation.

The experiment was repeated three times, and the friction angle α of the simulation experiment was measured to be 2.34°, which had a percentage error of only 1.47 with that of the estimated value of the bench experiment. From this, the rolling friction coefficient A_3 between the soybean and the acrylic plate was 0.0361.

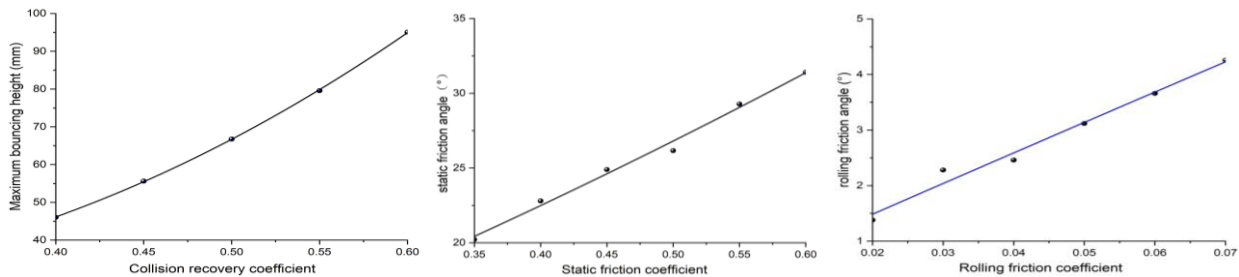


Fig. 9 - Fitted calibration curves for parametric relationships between spheroidal-like soybeans and acrylic plates

RESULTS

Calibration of inter-seed contact parameters in spherical-like soybeans

Selection of calibration method

Although the main body of the soybean particles has spherical characteristics, the shape and thickness are not the same; in the determination of the contact parameters between the particles, there may be obstruction, collision, bouncing, and other interferences, resulting in significant differences in the determination of the parameters, which, to a certain extent, will affect the accuracy of the measurement results (Zhang *et al.*, 2022). It was found that the collision recovery coefficient, the static friction coefficient, and the rolling friction coefficient all affect the stacking angle during the falling and molding process. Therefore, this study used a combination of stacking angle simulation experiments and bench experiments to determine the optimal parameter interval for soybean interparticle contact parameters by performing the steepest climb experiment with the contact parameters between particles as variables and the relative errors between measured and simulated stacking angles as indicators. With the help of Design Expert 13 software, a regression orthogonal combination experiment was designed to determine the optimal contact parameters between spherical soybean particles through analysis of variance (ANOVA) and objective optimization.

Measured and simulated calibration of stacking angle

Material stacking angle is an essential parameter for measuring powder or granular materials' flow and friction characteristics. The angle of accumulation of soya beans was determined experimentally using the cylinder lifting method. The experiment device consists of a bottomless cylinder and a support plate. According to the regulations, the inner diameter of the acrylic cylinder should be at least 4 to 5 times the diameter of the soybean, and the height should be three times the inner diameter. (Xu *et al.*, 2023). Therefore, the cylinder size used for the experiment was 40[mm]×120[mm], and the support plate was 200[mm]×200[mm]×5[mm], both made of acrylic.

A bottomless cylinder filled with soybeans is slowly and uniformly lifted so the soybeans will slowly fall due to gravity, into the acrylic plate to form a pile; at this time the acrylic plate and the soybean pile are formed by the angle of inclination that is the stacking angle. When the cylinder is fully lifted and the stack is shaped to be stationary, the front and side images of the stacked corner are taken in a horizontal position using a high-definition camera. The stacking angle picture is binarized using Matlab software and combined with the least squares method through edge detection to extract the contour curve for fitting. The tangent value of the slope of the fitted curve is the stacking angle. Repeating three experiments to take the average value, the soybean stacking angle was 22.50 degrees. The determination process is shown in Fig.10.

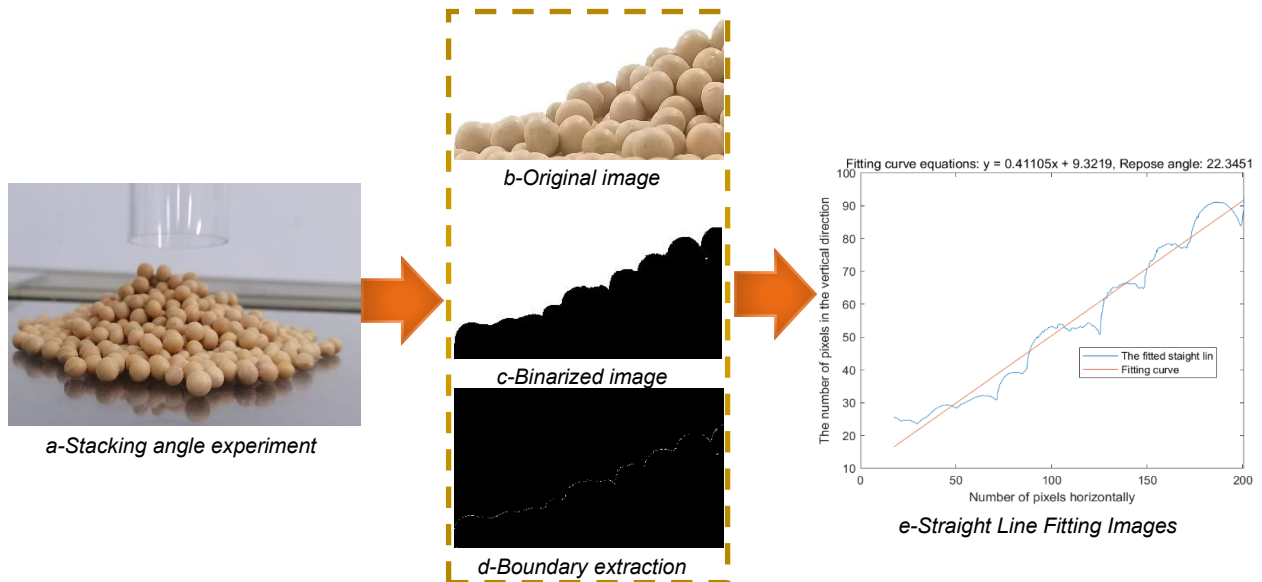


Fig. 10 - Bench experiment stacking angle measurement procedure

For the stack angle simulation experiment, the experiment setup was modeled at a 1:1 scale and imported into the Discrete Element Simulation software. The soybean interparticle contact parameters, B_1 , B_2 , and B_3 , used in the simulation were determined as ranges of values based on the General Elemental Materials Database (GEMM) module under the Bulk Materials tab of the Discrete Element Simulation Software, as well as on recently published literature (Sun et al., 2021; Qu et al., 2024; Dun et al., 2024). Specifically, B_1 : 0.15 to 0.75, B_2 : 0.2 to 0.50, and B_3 : 0.02 to 0.20. Poisson's ratio, shear modulus, and the contact parameters e , A_2 , and A_3 between the soybean and the acrylic sheet material were taken from the above measurements. To facilitate observation and measurement, the appearance of the soybean pile was processed, and then the angle tool that comes with the software was used to measure from the x, y, -x, and -y directions and take the average value; the measurement process is shown in Fig. 11.

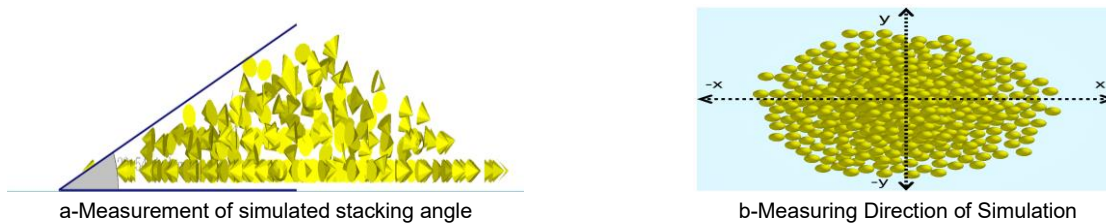


Fig. 11 - Measurement of simulated stacking angle

Steepest ascent experiment

To determine the optimal parameter interval for soybean interparticle contact parameters, the steepest climb experiment was designed using the soybean inter-grain contact parameters B_1 , B_2 and B_3 as the experiment factors, and the relative error of stacking angle between the bench experiment and the simulation experiment as the experiment indexes, in conjunction with the range of values of the soybean inter-grain contact parameters obtained as mentioned above. The experiment program and results are shown in Table 4, and the relative error calculation formula is shown in Eq. (12). The experiment results show a tendency for the error to decrease and then increase. According to the magnitude of the error value, The third set of data has the smallest error value, so it can be used as a level 0 test factor for the quadratic orthogonal rotational combination test, while the second and fourth sets of data are used as factor-1 and level 1 test factors, respectively.

$$\delta = \frac{|\theta' - \theta|}{\theta} \tag{12}$$

where:

- δ is the relative error of stacking angle;
- θ' is the simulated stacking angle, [°];
- θ is the measured stacking angle, [°].

Table 4

Steepest ascent experiment and results

Code	Experiment factors			Experiment results	
	Collision recovery coefficient B ₁	Static friction coefficient B ₂	Rolling friction coefficient B ₃	Repose angle θ' [°]	Relative error δ [%]
1	0.15	0.20	0.02	9.25	58.89
2	0.25	0.25	0.05	19.03	15.42
3	0.35	0.30	0.08	23.10	2.67
4	0.45	0.35	0.11	25.59	13.73
5	0.55	0.40	0.14	31.74	41.06
6	0.65	0.45	0.17	35.40	57.33
7	0.75	0.50	0.20	36.66	62.93

Central-Composite experimental design and results analysis

To clarify the optimal combination of the inter-particle contact parameters B₁, B₂, and B₃, a quadratic orthogonal rotational combination experiment was designed using Design Expert 13 software, with the range of values of the parameters determined by the steepest ascent experiment as the factors and the simulated stacking angle as the experiment index. The simulation factor level table is shown in Table 5, and the Experiment plan and results are shown in Table 6.

Table 5

Factor level table

Level	Experiment factors		
	Collision recovery coefficient B ₁	Static friction coefficient B ₂	Rolling friction coefficient B ₃
-1.682	0.18	0.22	0.03
-1	0.25	0.25	0.05
0	0.35	0.30	0.08
1	0.45	0.35	0.11
1.682	0.52	0.38	0.13

Table 6

Experiment plan and results table

Code	Experiment factors			Repose angle θ' [°]	Code	Experiment factors			Repose angle θ' [°]
	B ₁	B ₂	B ₃			B ₁	B ₂	B ₃	
1	0.25	0.25	0.05	19.03	11	0.35	0.22	0.08	24.13
2	0.45	0.25	0.05	18.54	12	0.35	0.38	0.08	25.15
3	0.25	0.35	0.05	21.52	13	0.35	0.3	0.03	17.95
4	0.45	0.35	0.05	21.09	14	0.35	0.3	0.13	26.75
5	0.25	0.25	0.11	25.78	15	0.35	0.3	0.08	22.45
6	0.45	0.25	0.11	24.77	16	0.35	0.3	0.08	23.18
7	0.25	0.35	0.11	26.98	17	0.35	0.3	0.08	22.97
8	0.45	0.35	0.11	25.05	18	0.35	0.3	0.08	22.40
9	0.18	0.3	0.08	22.68	19	0.35	0.3	0.08	23.64
10	0.52	0.3	0.08	21.32	20	0.35	0.3	0.08	23.34

The results of the data in Table 6 were analyzed by ANOVA and multiple regression fitting, and the results of the ANOVA are shown in Table 7. The regression equation for the angle of accumulation of soybeans is Eq. (13). From the ANOVA results in Table 7, it can be seen that the model has an extremely significant effect on the stacking angle (p<0.01), and the out-of-fit term (p>0.05) is not significant, which means that the model has a better fit in this data range. The effect of B₁, B₂, B₃, B₂² on stacking angle was highly significant (p<0.01), B₂B₃, B₁² on stacking angle was significant (0.01<p<0.05), and the effect of B₁B₂, B₁B₃, B₃² was not significant (p>0.05).

The coefficient of determination R²=0.9807 and the corrected coefficient of determination R²adj=0.9632, which is close to 1, and the standard deviation is 2.12%, which is a small difference, meaning that the model can be used to accurately respond to the real situation of the stacking angle and its prediction.

$$\theta' = 23.01 - 0.4479B_1 + 0.6213B_2 + 2.73B_3 - 0.1075B_1B_2 - 0.2525B_1B_3 - 0.4450B_2B_3 - 0.3880B_1^2 + 0.5875B_2^2 - 0.2973B_3^2 \tag{13}$$

Table 7

Variance analysis of regression equation

Source of variation	Sum of Squares	Degree of Freedom	Mean Square	F Value	P Value
Model	119.56	9	13.28	56.32	< 0.0001**
B ₁	2.76	1	2.76	11.72	0.0065**
B ₂	5.07	1	5.07	21.47	0.0009**
B ₃	101.36	1	101.36	429.67	< 0.0001**
B ₁ B ₂	0.0924	1	0.0924	0.3919	0.5453
B ₁ B ₃	0.5100	1	0.5100	2.16	0.1722
B ₂ B ₃	1.58	1	1.58	6.72	0.0269*
B ₁ ²	2.26	1	2.26	9.56	0.0114*
B ₂ ²	4.27	1	4.27	18.08	0.0017**
B ₃ ²	1.10	1	1.10	4.65	0.0565
Residual	2.36	10	0.2359		
Lack of fit	1.14	5	0.2276	0.9321	0.5298
Pure error	1.22	5	0.2442		
Sum	121.92	19			

Note: 0.01<p<0.05 (significant effect, *); p<0.01 (highly significant effect, **)

Combination of Optimal Parameters and Verification of Stacking Angle

The objective optimization module of Design-Expert 13 software was applied to optimally solve the regression model Eq. (14) with the inter-soybean contact parameter interval as the optimization variable and the objective of minimizing the relative error value of the measured stacking angle and the simulated stacking angle. The objective and constraint equation conditions are shown below.

$$\begin{cases} \min \theta'(B_1, B_2, B_3) \\ s. t. \begin{cases} 0.18 \leq B_1 \leq 0.52 \\ 0.22 \leq B_2 \leq 0.38 \\ 0.03 \leq B_3 \leq 0.13 \end{cases} \end{cases} \quad (14)$$

Based on the above constraints and objectives, the collision recovery coefficient B₁ of the spherical-like soya bean is obtained as 0.35, the static friction factor B₂ is 0.3, and the rolling friction factor B₃ is 0.074.

To check whether the obtained soybean contact parameters B₁, B₂, and B₃ are accurate and reliable, the optimized optimal parameter combinations are verified for the stacking angle. The experiment was repeated five times, and the average value of the simulated stacking angle was 22.26°, with an average relative error of only 1.09% from the bench experiment stacking angle of 22.5°, which is in high agreement and proves that the simulation parameters and results obtained are authentic and valid. Stacking angle test simulations, as shown in Figure 12, and a summary of the results of the above simulations are shown in Table 8.

Table 8

Analysis of the simulation experiment

Code	Repose angle θ' [°]	Relative error δ [%]
1	22.16	1.64
2	22.38	0.53
3	22.45	0.22
4	22.23	1.20
5	22.08	1.86

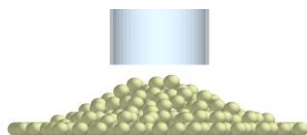


Fig. 12 - Experimental simulation of stacking angle

CONCLUSIONS

(1) Aiming at the lack of simulation parameters for spherical soybeans in the application of discrete element simulation to guide the optimization and design of agricultural machinery and equipment, this paper calibrates the parameters of spherical soybean variety SN29. The intrinsic properties of the material were determined by means of actual measurements, and a simulated particle model with a particle size of 7.1 mm was established based on the measured parameters.

(2) The collision recovery coefficients, Static friction coefficient, and rolling friction coefficient between the spherical soybean and the acrylic sheet were measured using the natural fall method and the inclined plane method through a combination of bench experiments and simulation experiments and were 0.474, 0.496 and 0.0361, respectively.

(3) The frontal and lateral stacking angles between the spheroidal soybeans and the acrylic panels were measured by the cylinder lift method in combination with a high-definition video camera and Matlab software, and the combined stacking angle was calculated to be 22.5°. The steepest climb experiment was designed to determine the optimum range of contact parameters between spherical-like soybean particles. With the help of Design-Expert 13 software, the parameter ranges obtained from the steepest climb experiment were used as variables. The simulated stacking angle was used as an index to design a three-factor, five-level quadratic orthogonal rotary combination experiment, and the results were optimized and analyzed and the ANOVA table and regression equation of the influencing factors and stacking angle were obtained. Through further optimization of the solution, the spherical-like optimal collision recovery coefficient between soybean particles was 0.35, the static friction coefficient was 0.3, and the rolling friction coefficient was 0.074.

(4) For the optimal parameter combinations obtained, the stacking angle verification experiments were carried out, and the relative error between the simulated stacking angle and the measured stacking angle was only 1.09 %. It shows that the calibration parameters have high credibility, which can provide a parameter basis for the design optimization and discrete element simulation of spherical soybean agricultural equipment.

REFERENCES

- [1] Chang J., Bai X., Lu Z. (2024). Research on the development of agricultural mechanization based on the perspective of agricultural products import and export trade (基于农产品进出口贸易视角的农业机械化发展研究) [J]. *Journal of Chinese Agricultural Mechanization*, Vol. 45(1), pp. 315-321.
- [2] Chen T., Yi S., Li Y., Tao G., Qu S. (2023). Establishment of Discrete Element Model and Parameter Calibration of Alfalfa Stem in Budding Stage (苜蓿现蕾期茎秆离散元模型建立与参数标定) [J]. *Transactions of the Chinese Society for Agricultural Machinery*, Vol. 54(5), pp. 91-100.
- [3] Chen X., Wang X., Bai J., Fang W., Hong T., Zang N., Wang G. (2024). Virtual parameter calibration of pod pepper seeds based on discrete element simulation [J]. *Heliyon*, Vol. 10(11).
- [4] Dun G., Mao N., Liu W., Wu X., Zhou C., Ji W. (2022). Design and Experiment of Four-bar Translational Seed Metering Device for Soybean Plot Breeding (四杆平移式大豆小区育种排种器设计与试验) [J]. *Transactions of the Chinese Society for Agricultural Machinery*, Vol. 53(4), pp. 70-78.
- [5] Dun G., Wu X., Ji X., Zhang F., Ji W. (2024). Simulation and Optimization of Soybean Plot Metering Device with Double Swing Plate (双摆盘式大豆小区排种器的仿真优化) [J]. *Journal of Agricultural Science and Technology*, Vol. 26(6), pp. 82-90.
- [6] Guo S., Xu J. (2021). Development status and existing problems of the soybean food industry in China (中国大豆食品产业发展现状及存在的问题) [J]. *Journal of Food Science and Technology*, Vol. 41(3), pp. 1-8.
- [7] Hao J., Wei W., Huang P., Qin J., Zhao J. (2021). Calibration and experimental verification of discrete element parameters of oil sunflower seeds (油葵籽粒离散元参数标定与试验验证) [J]. *Transactions of the Chinese Society of Agricultural Engineering (Transactions of the CSAE)*, Vol. 37(12), pp. 36-44.
- [8] Qu J., Dai F., Shi R., Zhao W., Ma H. (2024). Design and experiment of a combined planter for soybean and corn compound planting in a Northwest arid area (西北旱区大豆玉米复合种植联合播种机的设计与试验) [J]. *Journal of China Agricultural University*, Vol. 29(05), pp. 103-114.
- [9] Shi H. (2021). On the Process of Soybean Developing to the Worldwide Crop (大豆成为世界性作物的历程探析) [J]. *Agricultural Archaeology*, Vol. (06), pp. 71-78.
- [10] Shirvani M., Ghanbarian D., Ghasemi-Varnamkhasti M. (2014). Measurement and evaluation of the apparent modulus of elasticity of apple based on Hooke's, Hertz's, and Boussinesq's theories [J]. *Measurement*, Vol. 54, pp. 133-139.
- [11] Sun J., Yang H., Liu Y. (2021). Calibration and model optimization of simulation contact parameters of potassium fertilizer particles based on discrete element method [J]. *AMA*, Vol. 32(3), pp. 4651-4668.
- [12] Wang S., Yu Z., Zhang W. (2022). Study on the modeling method of sunflower seed particles based on the discrete element method [J]. *Computers and Electronics in Agriculture*, Vol. 198, pp. 107012.
- [13] Xu Z., Wang S., Yi Z., Pan J., Lv X. (2023). Parameter calibration of chili seed discrete element based on JKR model (基于JKR模型的辣椒籽离散元参数标定) [J]. *Journal of Chinese Agricultural Mechanization*, Vol. 44(9), pp. 85-95.

- [14] Xie W., Ou Y., Jiang P., Meng D., Luo H. (2024). Calibrating and optimizing the discrete element parameters for clamping section stems during rape shoot harvesting (面向夹持采收的油菜薹夹段茎秆离散元参数标定与优化) [J]. *Transactions of the Chinese Society of Agricultural Engineering (Transactions of the CSAE)*, Vol. 40(7), pp. 104-116.
- [15] Yang H., He J., Lu J., Wang T., Wang Y., Guo Y. (2024). Parameters Calibration for Discrete Element Model Simulation of White Kidney Bean Seeds [J]. *INMATEH-Agricultural Engineering*, Vol. 72(1), pp.77-86. <https://doi.org/10.35633/inmateh-72-07>
- [16] Zhao H., Huang Y., Liu Z., Liu W., Zheng Z. (2021). Applications of discrete element method in the research of agricultural machinery: A review[J]. *Agriculture*, Vol. 11(5), pp. 425.
- [17] Zhang G., Chen L., Liu H., Dong Z., Zhang Q. (2022). Calibration and experiments of the discrete element simulation parameters for water chestnut (荸荠离散元仿真参数标定与试验) [J]. *Transactions of the Chinese Society of Agricultural Engineering (Transactions of the CSAE)*, Vol. 38(11), pp. 41-50.
- [18] Zhang H., Han X., Yang H., Chen X., Zhao G. (2024). Calibrating and simulating contact parameters of the discrete element for apple particles (苹果颗粒离散元接触参数标定与仿真试验) [J]. *Transactions of the Chinese Society of Agricultural Engineering (Transactions of the CSAE)*, Vol. 40(12), pp. 66-76.
- [19] Zhang H., Ceng X., Li H., Tian Y., Fan G. (2024). Simulated Contact Parameters Calibration and Experiment of Controlled-release Fertilizer Particles (控释肥颗粒群仿真接触参数标定与试验) [J]. *Transactions of the Chinese Society for Agricultural Machinery*, Vol. 55(6), pp. 80-90.
- [20] Zhang S., Zhang R., Chen T., Fu J., Yuan H. (2022). Calibration of Simulation Parameters of Mung Bean Seeds Using Discrete Element Method and Verification of Seed-metering Experiment [J]. *Transactions of the Chinese Society of Agricultural Machinery*, Vol. 53(3), pp. 71-79.

DESIGN AND RESEARCH ON THE CRUSHING SYSTEM OF THE TANK CLEANING ROBOT

贮罐清理机器人破碎系统的设计与研究

Yong TIAN¹⁾, Jian SONG¹⁾, Fuxiang XIE^{*1)}

¹⁾ School of Machinery and Automation, Weifang University, Shandong/ China;

Tel: +86-18863637275 ; E-mail: 20210007@wfu.edu.cn

DOI: <https://doi.org/10.35633/inmateh-74-27>

Keywords: Large tanks, robot, crushing system, EDEM, optimal operating parameters, crushing rate

ABSTRACT

The existing equipment for cleaning large tanks has the problems of simple structure and single function. In order to solve this problem, a robot is designed to clean solid residues in tank, which integrates shoveling, crushing, sweeping and suction. And the crushing system of the robot is structurally designed and analyzed. Firstly, the crushing system is simulated and analyzed by using EDEM software. Then, the optimal operating parameters of the crushing device are determined by studying the effects of rotary knife pitch, rotary knife speed and rotary depth on the crushing rate. Finally, the crushing test is carried out on the cleaning robot, and the crushing rate is obtained as 83.6%, and the results show that the robot control system meets the design requirements. The study provides a certain reference for the research and development of the cleaning robot.

摘要

现有清理大型贮罐的装置结构简单、功能单一，为解决这一问题，以贮罐作为研究清理对象，提出了一种清理贮罐中固体残留物的机器人设计方案，研制了一种集铲装、破碎、清扫、吸尘为一体的清理装置，并对破碎装置进行了优化设计分析。使用EDEM软件对机器人进行仿真分析，研究旋耕刀间距、旋耕刀转速和旋耕深度对破碎率的影响，分析确定了破碎装置的最优工作参数；通过对清理机器人进行性能试验，破碎试验得到破碎率为83.6%，该研究从结构设计到试验验证，为清理机器人的研究与发展提供了一定的参考。

INTRODUCTION

At present, there are two main cleaning methods for large storage tanks, one is to utilize a mechanical arm carrying a water spray device. The residue is flushed with the water spray device, and then the residue is stirred and mixed with the mechanical arm, and finally the mixture is extracted with the pump. Another way is to use the cleaning robot to clean up, the robot carries a crushing tool and high-pressure water spray device. The method is the use of high-pressure crushing device for residue crushing, and then the use of water jetting device for flushing, and finally the use of pumps to extract the mixture (Li, 2021; Naser, 2015; Tan, 2021).

In the 1980s, some developed countries began to research and design the storage tank cleaning device. Fig.1(a) shows the C-104NESL tracked folding vehicle (Michal, 2012), which has a folded width of 685 mm and an unfolded width of 1016 mm, with a front-mounted push shovel that can be used alone to concentrate the dried sludge in the tanks, and with nozzles and absorbers to work in conjunction with the push shovel in a remotely-controlled manner. Fig.1(b) shows the Industrobot cleaning robot developed by Offshore Cleaning systems in the United States, and Fig.1(c) shows the hydrotanker developed by Petroleum Ferment Company, which utilizes water jets to rinse the bottom of the tank (Chen, 2019). These two cleaning devices have a push shovel at the front and work in conjunction with the water jets above them, and are mainly used for cleaning large tanks.

Fig.1(d) shows the oil tank cleaning robot, which is an automated robot specialized in cleaning the residue at the bottom of the tank, with the functions of moving, adsorption and cleaning, and the cleaning methods mainly include water jet cleaning, mechanical force cleaning and ultrasonic cleaning (Song, 2020). Fig.1(e) shows a silt cleaning robot (Nagatani et al., 2013), which utilizes a forward device to feed the silt to the pump inlet, where it undergoes a rotating device to break up the debris, and then enters the silt transfer system. This device is mainly used for the cleaning of pools and urban pipelines. Fig.1(f) shows a multifunctional sweeper, which is a cleaning device integrating sweeping, vacuuming, sprinkling, mopping, recycling and transportation (Naser, 2015). The device is manually remote-controlled, the bottom of the car is equipped with a sweeping disk with a water spraying device and a sponge device used to absorb water, which is mainly used for roadway sweeping operations.

Fig.1(g) shows that the Chinese Academy of Sciences developed for nuclear power plant underwater operations, "underwater foreign body salvage robot" (Lee et al., 2013). The robot length is 420 mm, the width - 198 mm, the height - 236 mm and it can realize the underwater cleaning and salvage operations.

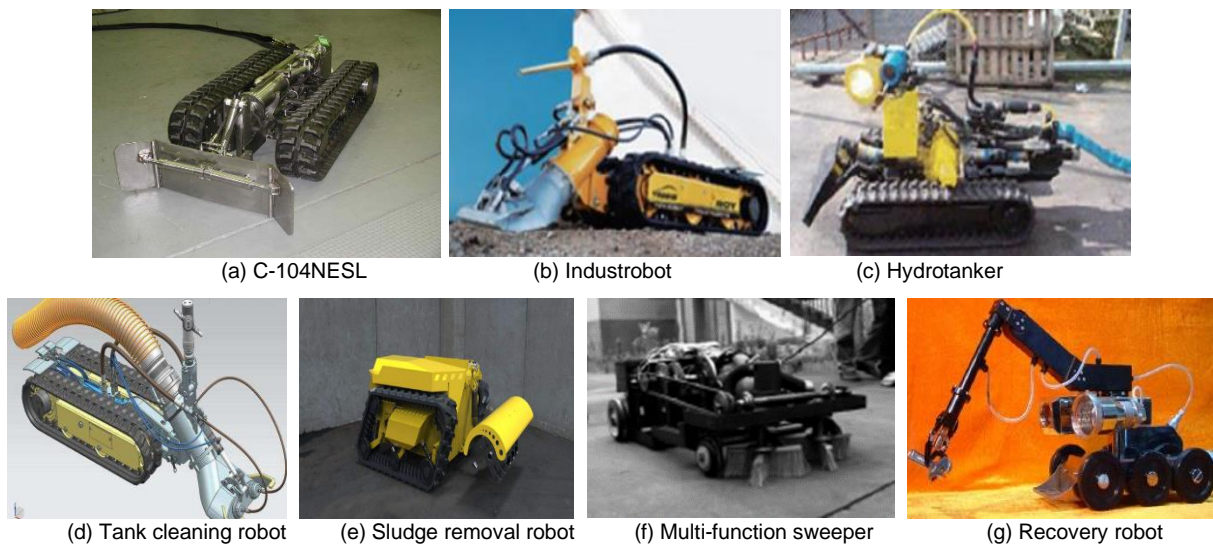


Fig. 1 - Robotic arm cleaning device

Regarding the long-term residue in the storage tank, the cleaning effect is also greatly affected due to the complexity of the environment (Grape, 2014; Mochizuki, 2014; Sawade, 2012; Zhong et al., 2015). Therefore, designing a relevant cleaning device to solve these problems has important research significance and application value. This paper mainly focuses on the research and design of a cleaning device for solid residues in large storage tanks, and uses the software EDEM to simulate and analyze the crushing device, to study the effects of changes in the rotational speed, tilling depth and tillage knife spacing of the rotary blade on the crushing effect, and obtain the optimal combination of parameters.

MATERIALS AND METHODS

Design of Tank Cleaning Robot

The residual substances at the bottom of the tank mainly include slurries, salt cakes, or sediments, and have a certain hardness after prolonged storage (Du et al., 2020; Liu et al., 2024). Due to the small opening of the storage tank, there is consequent difficulty in removing the residuals at the bottom of the tank. In this paper, the overall structural design of the cleaning robot is carried out in consideration of the internal composition of the tank.

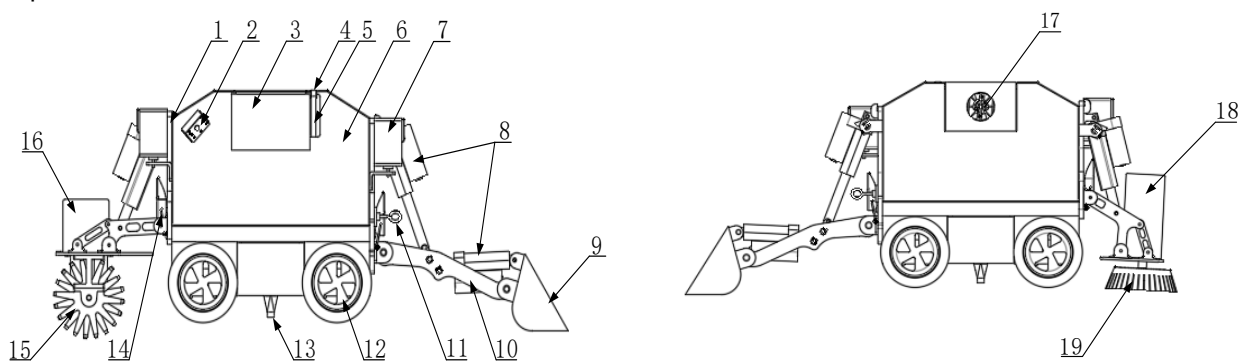


Fig. 2 - Structure of the cleaning robot

1-fixing plate, 2-camera, 3-dust collection box, 4-synchronous wheel, 5-synchronous belt, 6-main box, 7-searchlight, 8-electric actuator, 9-bucket, 10-linkage, 11-hooks, 12-rubber tires, 13-suction nozzle, 14-locking buckle, 15-rotary cutter, 16-protection shell of rotary motor, 17-fan, 18-protection illumination of sweeping motor, 19-brush plate

In view of the structural characteristics of nuclear storage tanks and the functions to be realized and requirements to be met, on the basis of ensuring the functionality, it is preferred to achieve the simplest structure and high stability, which is convenient for disassembly and replacement.

The overall structure is shown in Fig.2. The cleaning robot takes the vehicle body as the main body, and the front and rear suspensions are operated. The connection between the device modules and the vehicle body is fixed by latches to facilitate disassembly and replacement. Depending on the operation requirements, different device modules are hung. During the cleaning operation, the camera feeds back the situation in the storage tank to the ground display screen, and the robot is operated by the control box. Firstly, the residue or hard sediment is crushed by the crushing device, and then the disturbed residue is sent to the collection container by the shovel loading device. The fine particles are absorbed by the vacuum cleaning device, sucked into the dust collection box through the suction nozzles at the bottom of the vehicle, and finally the absorbed residue is poured into the collection container to complete the entire residue cleaning and collection work.

As an important part of the cleaning operation, the main function of the crushing is to use the designed mechanism to break the hard residue, so that the crushing device is more convenient and quicker to crush the residue into the collection container. The quality of its structural design has a significant impact on the crushing effect and working efficiency of the cleaning robot. The crushing scheme of rotary tillage blades has been adopted, using multiple disc rotary tillage blades as crushing tools. This scheme has the advantages of good disturbance resistance and high work efficiency for residues with low scab hardness. The specific rotary plowing crushing three-dimensional model is shown in Fig. 3.

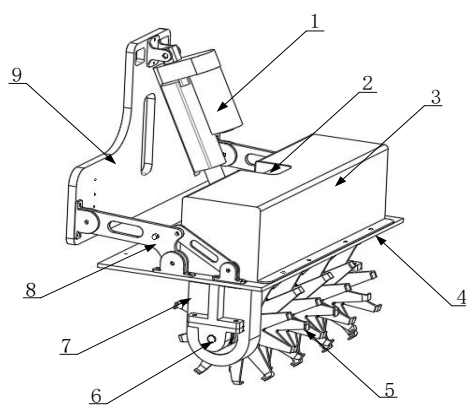


Fig. 3 - Three-dimensional diagram of rotary plowing and crushing device

1-lifting push rod, 2-motor, 3-motor shroud, 4-baffle plate, 5- rotary cutter, 6-bearing, 7-sprocket cover, 8-linkage, 9-fixing plate

RESULTS

Simulation Analysis of Crushing System

Crushing is an important part of the cleaning operation, and its main function is to break the hard residue using the designed mechanism. The setting of relevant parameters of the rotary blade has different effects on the crushing effect, and the influencing factors mainly include the tool spacing, rotary tillage depth, tool rotation speed and forward speed. In this paper, EDEM is used to simulate the crushing process of the rotary blade. During the simulation process, the simulation of residues and rotary tillage tools is achieved by calculating the forces on particles. Reasonable parameter settings and contact models to some extent determine the effectiveness of the simulation. The variation range of the forward speed is small, so it is not considered. A tool spacing of 10 mm to 20 mm is determined in the simulation, and the rotational speed of the rotary blade is set at 200 rpm to 350 rpm. In simulation, the radius of the particle model is usually set to 2 mm, 5 mm, and 10 mm (*Li et al., 2023; Zhu, 2016*). Based on the characteristics of the residue in the cleaned tank, the particle model radius is set to 2 mm, the bonding radius is set to 3 mm, and the rotary tiller simulation is shown in Fig.4.

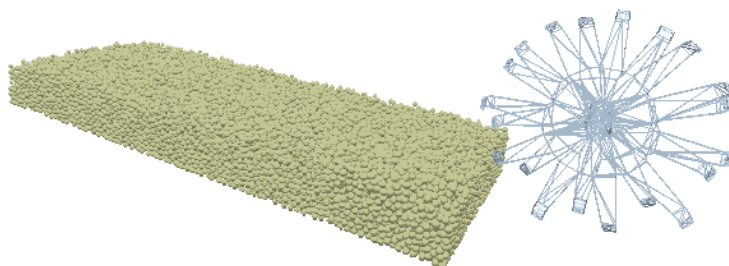


Fig. 4 - Analog simulation of rotary cutter

Breakage rate is an important manifestation of crushing effect. This article calculates the breakage rate by the number of bond breaks between particles. (Yu, 2018). The number of bond breaks between particles is statistically calculated by using post-processing Analyst in EDEM software, and then calculate the breakage rate by the given formula, which is expressed as follows:

$$I = \frac{N_b}{N_b + N_i} \times 100\% \quad (1)$$

where: I is the fragmentation rate, N_b is the number of broken particle bonds in the spinning zone, and N_i is the number of intact particle bonds in the spinning zone.

- Analysis of Orthogonal Tests

Taking the tool spacing, rotary tillage depth and tool speed as the influencing factors, and they are respectively marked as A, B, and C, and the breakage rate and forward resistance are taken as the response values, -1, 0, and 1 are respectively the low, medium, and high levels, and a three-factor three-level Box-Behnken test is established.

Applying the Box-Behnken response surface design principle, a total of 17 test points are designed in the experiment to evaluate and calculate the experimental error (Sun *et al.*, 2023), and the Box-Behnken response surface test results and analysis are obtained, as shown Table 2.

Table 1

Box-Behnken test factor level table				
Factor code		Experimental factors		
		Low-level -1	Mid-level 0	High-level 1
A	Tool spacing (mm)	10	15	20
B	Rotary depth (mm)	20	30	40
C	Tool speed (rpm)	150	200	250

Table 2

Box-Behnken Response Surface Test					
Serial No.	Tool spacing (mm)	Rotary depth (mm)	Tool speed (rpm)	Horizontal resistance (N)	Crushing rate (%)
1	10.00	30.00	150.00	5.80	83.48
2	20.00	20.00	200.00	5.82	82.59
3	15.00	30.00	200.00	5.89	86.24
4	15.00	30.00	200.00	5.71	86.45
5	20.00	40.00	200.00	7.91	88.05
6	15.00	30.00	200.00	5.82	86.40
7	10.00	30.00	250.00	5.90	88.03
8	20.00	30.00	150.00	5.89	82.16
9	15.00	30.00	200.00	5.75	86.35
10	10.00	40.00	250.00	7.54	90.68
11	15.00	30.00	200.00	5.91	86.32
12	15.00	40.00	150.00	7.86	85.93
13	15.00	20.00	250.00	6.25	84.36
14	10.00	20.00	200.00	5.60	81.53
15	20.00	30.00	250.00	6.30	88.84
16	10.00	40.00	200.00	6.84	89.44
17	15.00	20.00	150.00	5.24	78.33

● Analysis of the Effect of Factors on Horizontal Resistance

The variance of horizontal resistance was analyzed using Design-Expert V8.0.6 software and the results are shown in Table 3. From the results of the analysis in Table 3, it can be seen that the *P* value of the horizontal resistance regression model is less than 0.001, indicating that the regression model is significant. The value of *P* of the misfit term is 0.0708, which is greater than 0.05, so the misfit term is not significant, indicating that the model is more reliable. The *P*-value shows that rotary tillage depth *B* has a more significant effect on horizontal resistance, tool spacing *A* has the second most significant effect on horizontal resistance, and tool speed *C* has a non-significant effect on horizontal resistance. After analyzing, it can be seen that the order of influence of the three factors on horizontal resistance is *B*>*A*>*C*, i.e., tool depth>tool spacing>tool speed. Among them, the interaction term *BC* has a very significant effect (*P*<0.001) and *AB* has a significant effect (*P*<0.01). The secondary term *B*² had a highly significant (*P*<0.001) effect on the results.

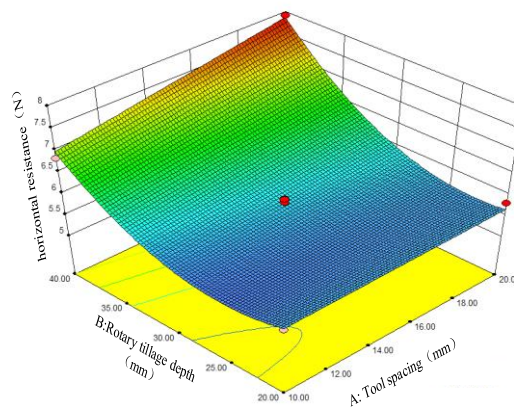
Table 3

Analysis of Variance for Horizontal Resistance						
Source	square sum	DOF	mean square	F	P	significance
model	9.95	9	1.11	52.10	<0.0001	***
A	0.40	1	0.40	18.67	0.0035	**
B	6.37	1	6.37	300.34	<0.0001	***
C	0.21	1	0.21	9.96	0.0160	*
AB	0.18	1	0.18	8.51	0.0224	*
AC	0.024	1	0.024	1.13	0.3226	
BC	0.38	1	0.38	17.83	0.0039	**
A ²	2.368e-06	1	2.368e-06	1.116e-04	0.9919	
B ²	2.22	1	2.22	104.53	<0.0001	***
C ²	0.10	1	0.10	4.81	0.0643	
residual	0.15	7	0.021			
lost proposal	0.12	3	0.040	5.29	0.0708	
pure error	0.030	4	7.48e-03			
sum	10.10	16				

Note: * indicates *p*<0.05 (significant); ** indicates *p*<0.01 (highly significant); *** indicates *p*<0.001 (highly significant).

In order to better analyze the effect of the test factors on the horizontal resistance, choose one of the three test factors to be fixed as the zero level, choose the other two factors to observe the effect on the crushing rate, and use the response surface generated in the software to observe the size of the effect of each factor on the horizontal resistance.

As shown in Fig. 5, it can be seen that the depth of rotary tillage has a significant impact on the horizontal resistance of the cutting tool, and the effect of rotary tillage depth on the horizontal resistance of the cutting tool is more significant than the effect of tool spacing.



(a) tool spacing

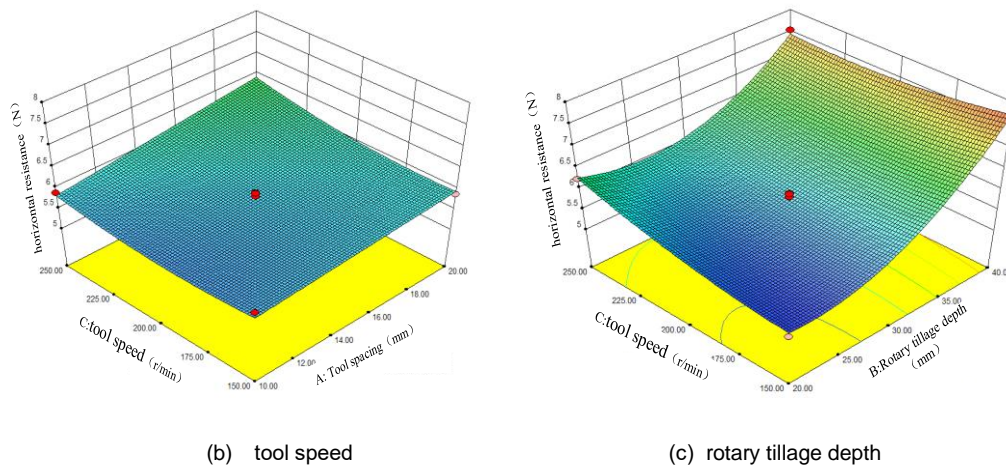


Fig. 5 - Response surface on tool horizontal resistance

For rotary tillage depths between 20 mm and 30 mm, the increase in horizontal resistance is small, while for rotary tillage depths greater than 30 mm, the increase is significant. The tool speed and tool spacing have no significant effect on the horizontal resistance of the tool, and the horizontal resistance experienced by the tool does not change significantly with changes in tool speed and tool spacing.

● Analysis of the effect of factors on crushing rate

Table 4

Analysis of Variance for Crushing Rate						
Source	square sum	DOF	mean square	F	P	significance
model	162.17	9	18.02	1361.31	<0.0001	***
A	0.088	1	0.088	6.66	0.0364	*
B	93.09	1	93.09	7033.09	<0.0001	***
C	60.56	1	60.56	4574.88	<0.0001	***
AB	1.50	1	1.50	113.37	<0.0001	***
AC	1.13	1	1.13	85.69	<0.0001	***
BC	0.41	1	0.41	30.94	<0.0008	***
A ²	0.023	1	0.023	1.72	0.2313	
B ²	3.23	1	3.23	244.10	<0.0001	***
C ²	1.78	1	1.78	134.81	<0.0001	***
residual	0.093	7	0.013			
lost proposal	0.067	3	0.022	3.52	0.1280	
pure error	0.025	4	6.370E-003			
sum	162.26	16				

Note: * indicates $p < 0.05$ (significant); ** indicates $p < 0.01$ (highly significant); *** indicates $p < 0.001$ (highly significant).

As can be seen from the results of the analysis in Table 4, the regression model is significant, and the lost proposal is not significant, indicating that the model is relatively reliable. From the P-value, it can be seen that B and C have a significant impact on horizontal resistance. After analysis, it can be seen that the three factors on horizontal resistance are in the order of $C > B > A$, that is, tool speed > rotary plowing depth > tool spacing. Among them, the interaction terms AB, AC and BC had highly significant effects ($P < 0.001$). The secondary terms B² and C² had highly significant ($P < 0.001$) effect on the results. A² had no significant effect on the results. Use software to generate corresponding response surfaces and intuitively study the impact of various factors on the fragmentation rate, as shown in Fig.6.

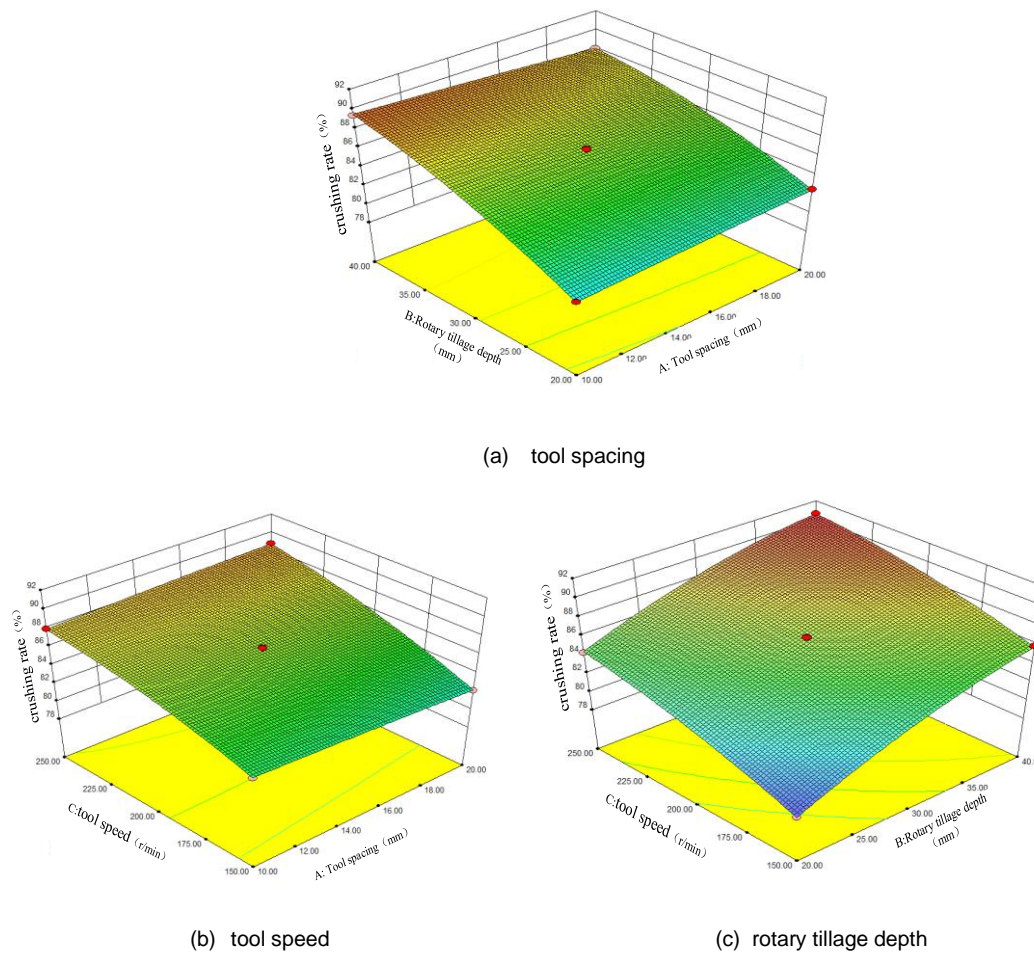


Fig. 6 - Response surface on fragmentation rate

● Parameter Optimization

The purpose of parameter optimization is to ensure that the crushing device can obtain better crushing effect and smaller horizontal resistance within the scope of meeting the operational indexes. Taking the horizontal resistance y_1 and the crushing rate y_2 as the function of the test indexes, the optimal combination of the tool spacing A , the tool rotational speed B and the rotary tillage depth C is selected, analyzed and solved by using Design-Expert with the objective function and constraints as follows:
Objective function:

$$\begin{cases} y_1(A, B, C) \rightarrow \max \\ y_2(A, B, C) \rightarrow \min \end{cases} \quad (2)$$

Constraints:

$$s.t. \begin{cases} 10 \leq A \leq 20 \\ 20 \leq B \leq 40 \\ 150 \leq C \leq 250 \end{cases} \quad (3)$$

It can be seen through simulation that the optimal combination of parameters for the designed crushing device is determined in the case of satisfying the constraints and the objective function tool spacing of 10 mm, rotary depth of 30 mm, tool speed of 230 rpm, horizontal resistance of 5.8 N, and a crushing rate of 88.30%, according to the optimal combination of the measured parameters applied to the actual crushing operation.

Prototype Development and Testing

To verify the feasibility of the tank cleaning robot, a site that meets the requirements of the project party was selected for testing, and the crushing rate was used as the main verification indicator for the experiment:

$$E = \frac{G_s - G_a}{G_s} \times 100\% \tag{4}$$

where: E for the crushing rate; G_a for the mass of the pieces less than 4 cm in the crushing zone; G_s for the total mass of the material in the crushing zone. And five 0.2 m*0.2 m boxes were homemade, and the mass of all the soil in the tillage layer in the boxes and the clods of soil with the longest side less than 4 cm were weighed (Yu, 2021). The experimental results are shown in Fig.7.



Fig. 7 - Sample machine test

The traveling speed was set to 0.1 m/s, 0.2 m/s, 0.3 m/s, 0.4 m/s, the tool spacing was 10 mm, the tool speed was set to 230 rpm, and the depth of rotary tillage was 30 mm. Through the experimental comparisons under different advancing speeds, the crushing rate under the optimal parameters obtained from the simulation was tested. The results were analyzed and the data were obtained.

As can be seen from Table 5, when the traveling speed is 0.1m/s, the highest crushing rate is 83.6%, and when the traveling speed is 0.4 m/s, the lowest crushing rate is 74.2%. Through the value of speed and crushing rate analysis, in the value range of the higher speed crushing rate gradually decreased, when the traveling speed of 0.1 m/s crushing device in the low-speed operation is closer to the simulation results, the device is more suitable for low-speed operation under the use of simulation parameters.

Table 5

Comparison of Crushing Rate Tests						
Travel speed (m/s)	Crushing rate E (%)					average value
	test1	test 2	test 3	test 4	test 5	
0.1	86	83	80	85	81	83.6
0.2	81	82	80	83	79	81
0.3	83	73	81	75	73	77
0.4	72	76	78	70	75	74.2

CONCLUSIONS

In this article, EDEM software is used to simulate the fragmentation of rotary tillage equipment. By selecting a reasonable particle contact model, the rotary tillage blade is simulated. The blade spacing, blade speed, and rotary tillage depth are used as experimental factors, and horizontal resistance and fragmentation rate are used as experimental indicators to study the effects of the three experimental factors on the experimental indicators. By analyzing the regression equation and response surface, the significance of each experimental factor on the experimental indicators was determined. And through parameter optimization, the optimal parameter combination was obtained. Finally, based on the optimized simulation parameters, an experiment was conducted and a crushing rate of 83.6% was obtained at a speed of 0.1 m/s. The error between the experimental data and the simulation data was relatively small.

ACKNOWLEDGEMENT

This research has received support from the Weifang Science and technology development plan project (2022GX005).

REFERENCES

- [1] Chen L., (2019). *Design of explosion-proof cleaning robot system for residual oil at the bottom of horizontal tanker (卧式油罐车罐底残油防爆型清理机器人系统设计)*. Master dissertation, Anhui University of Technology, Anhui/China.
- [2] Du, J., Zhang, W., Zhu, Y., (2020). Characterization of power distribution of rotary buried knife roller based on discrete element method (基于离散元法的旋埋刀辊功率分配特性研究). *Journal of Anhui Agricultural University*, Vol. 47, pp. 1031-1037, Anhui/China.
- [3] Grape, S., Svaerd, S., Hellesen, C., Jansson, P., & Lindell, M., (2014). New perspectives on nuclear power—generation iv nuclear energy systems to strengthen nuclear non-proliferation and support nuclear disarmament. *Energy Policy*, Vol. 73, pp. 815-819, England.
- [4] Lee, W., Hirai, M., & Hirose, S., (2013). Gunryu iii: reconfigurable magnetic wall-climbing robot for decommissioning of nuclear reactor. *Advanced Robotics*, Vol. 27, pp. 1099-1111, Japan.
- [5] Li, X., (2021). *Intermediate level liquid radwaste tank decommissioning technological plan design (中放废液贮罐退役工艺方案设计)*. Master dissertation, University of South China, Guangdong/China.
- [6] Li, S., Diao, P., Zhao, Y., Miao, H., Li, X., & Zhao, H., (2023). Calibration of discrete element parameters for soil in high-speed tillage (高速耕作条件下土壤离散元参数标定). *INMATEH - Agricultural Engineering*, Vol. 71, pp. 248-258, Romania.
- [7] Liu, Z., Shang, S., Ma, S., Hou, Y., Dong, T., & He, X., (2024). Optimization by coupled RecurDyn-EDEM simulation: Optimization tests of a three-stage low-loss separation device for potato soil (RecurDyn-EDEM 耦合仿真优化: 三段式薯土低损分离装置优化试验). *INMATEH - Agricultural Engineering*, Vol. 72, pp. 138-147, Romania.
- [8] Michal, V., (2012). Remote operation and robotics technologies in nuclear decommissioning projects – ScienceDirect. *Nuclear Decommissioning*, pp. 346-374.
- [9] Mochizuki, M., Singh, R., Nguyen, T., & Nguyen, T., (2014). Heat pipe based passive emergency core cooling system for safe shutdown of nuclear power reactor. *Applied Thermal Engineering*, Vol. 73, pp. 699-706, England.
- [10] Nagatani, K., Kiribayashi, S., Okada, Y., Otake, K., Yoshida, K., & Tadokoro, S., (2013). Emergency response to the nuclear accident at the Fukushima Daiichi Nuclear Power Plants using mobile rescue robots. *Journal of Field Robotics*, Vol. 30, pp. 44-63, USA.
- [11] Naser, H., (2015). Analysing the long-run relationship among oil market, nuclear energy consumption, and economic growth: an evidence from emerging economies. *Energy*, Vol. 89, pp. 421-434, England.
- [12] Sawade, C., Turnock, S., Forrester, A., & Toward, M., (2012). Improved rehabilitation and training techniques through the use of motion simulation – core strength conditioning for elite rowers – ScienceDirect. *Procedia Engineering*, Vol. 34, pp. 646-651, Netherland.
- [13] Song Z., Zhou C., Zhang S., (2020). Application of dredging robot in culvert dredging project (清淤机器人在暗涵疏浚工程中的应用). *Northwest Hydropower*, Vol. 1, pp. 70-73, Shanxi/China.
- [14] Sun, J., Yang, L., Xu, B., & Guo, Y., (2023). Design and experiment of a single-row small grain precision seeder (单行小籽粒精少量播种机设计与试验). *INMATEH - Agricultural Engineering*, Vol. 70, pp. 127-136, Romania.
- [15] Tan, X., (2021). Analyzing Chinese nuclear energy development situation and outlook (浅析中国核能发展状况及展望). *China Plant Engineering*, Vol. 19, pp. 235-236, Beijing/China.
- [16] Yu, C., (2018). Development and test of straw pulling mechanism of mobile tobacco straw pulling and crushing machine (移动式烟秆拔秆破碎机拔秆机构的研制及试验). Master dissertation, Guizhou University, Guizhou/China.
- [17] Yu, C., (2021). Construction and validation of a multi-phase coupled simulation model of knife roller-straw-soil (刀辊-麦秆-土壤多相耦合仿真模型构建及验证). Master dissertation, Anhui Agricultural University, Anhui/China.
- [18] Zhong, Y., Z., Fu, Y., Gao, P., (2015). Retrieval methods and techniques for tank stored HLLW (槽贮高放废物回取方法和技术). *Guangdong Chemical Industry*, Vol.1, pp. 13-14, Guangdong/China.
- [19] Zhu, H., (2016). Simulation and experimental research on furrowing working parts of no-tillage fertilizer planter (免耕施肥播种机开沟工作部件仿真与试验研究). Master dissertation, South China Agricultural University, Guangdong/China.

LIGHTWEIGHT DESIGN OF THE SEEDING WHEEL STRUCTURE OF RICE DIRECT SEEDER BASED ON TOPOLOGY OPTIMIZATION

基于拓扑优化的水稻直播机排种轮结构轻量化设计

Juan HUANG^{1,3)}, Jing HUANG²⁾, Jinhu CAI²⁾, Songlin SUN¹⁾, Caiwang PENG¹⁾

¹⁾ College of Mechanical and Electrical Engineering, Hunan Agriculture University, Changsha, 410012, / China;

²⁾ College of Automotive and Mechanical Engineering, Changsha University of Science and Technology, Changsha, 410114, / China;

³⁾ Hunan Provincial Key Laboratory of Intelligent Manufacturing Technology for High-performance Mechanical Equipment, Changsha 410114 / China;

Tel: 18810537386; E-mail: caijinhu@csust.edu.cn and hnnndssl@163.com

DOI: <https://doi.org/10.35633/inmateh-74-28>

Keywords: seeding wheel, Abaqus, topology optimization, lightweight design

ABSTRACT

Abaqus software is used to analyze the seeding wheel's stress distribution and displacement deformation during the working process, and the seeding wheel's stress distribution and displacement cloud maps are obtained. Topology optimization analysis was conducted on the seeding wheel to obtain the optimized finite element model. Based on the finite element model, the original 3D model was modified to obtain the topologically optimized 3D model of the seeding wheel. The results show that the optimized seeding wheel reduces its mass by 48.4%, achieving a lightweight design of the seeding wheel structure.

摘要

运用 Abaqus 软件分析排种轮在工作过程中的应力分布和位移变形, 得到排种轮的应力分布云图和位移云图。对排种轮进行拓扑优化设计, 得到了优化后的有限元模型, 根据有限元模型对原始三维模型进行修正, 得到拓扑优化后的排种轮三维模型。结果表明, 优化后的排种轮其质量减少 48.4%, 实现了排种轮结构轻量化设计。

INTRODUCTION

The seeder is the core component of the rice direct seeder, and the performance of the seeder directly affects the quality and efficiency of rice sowing. The seeding wheel is the key component of the seeder. Therefore, the design, analysis, and optimization of the seeding wheel are important links in the design process of rice direct seeders. The lightweight design of the seeding wheel can reduce the use of materials and improve the performance of the seeding wheel. Structural optimization design, as one of the effective means of lightweight design, is mainly divided into structural topology optimization, structural size optimization, and structural shape optimization (Bendsoe et al., 2003; Karadere et al., 2020). Topology optimization aims to obtain the optimal distribution of materials within a given design domain. When designers lack direct experience guidance and cannot determine the initial configuration of the structure, topology optimization design reveals innovative structural configurations under established loads through certain constraints such as stress and displacement, maximizing material potential and significantly improving the quality and efficiency of engineering design (Sui et al., 2017). In recent years, topology optimization has made significant progress in both theoretical research and practical applications. With the continuous development of numerical analysis technology, structural topology optimization methods have been widely applied in fields such as architecture, shipbuilding (Jang et al., 2014), aerospace (Berrocal et al., 2019; Zhu et al., 2015), and automotive (Karadere et al., 2020; Wu et al., 2016).

Since Bendsoe and Kikuchi proposed topology optimization in their groundbreaking paper in 1988, topology optimization has undergone tremendous development. Currently, research algorithms for topology optimization mainly include homogenization methods (Ganghoffer et al., 2023; March et al., 2023), variable density methods (Wang et al., 2024), level set methods (Gao et al., 2021; Wang et al., 2015; Zhang et al., 2017), and evolutionary structural optimization methods (He et al., 2016; Huang et al., 2011; Huang et al., 2010). Among them, the variable density method is more mature and most widely used. The interpolation models of the variable density method include SIMP (Solid Isotropic Microstructures with Penalization) and RAMP (Rational Approximation of Material Properties), and the SIMP method is mainly adopted. In recent years, Hassani et al. (Hassani et al., 2012) proposed for the first time the isogeometric topology optimization method based on the SIMP method and combined it with the isogeometric analysis method.

This method improves the solving efficiency and suppresses the checkerboard phenomenon. Subsequently, Liu et al. (Liu et al., 2018) studied the topology optimization problem involving stress constraints in continuum structures based on the SIMP method and isometric analysis theory. Lieu and Lee (Lieu et al., 2017) proposed a multi-resolution isometric topology optimization method using the SIMP method and isometric geometric framework, which can achieve high-resolution topology optimization design with less computational complexity. Subsequently, Xuan et al. (Liang et al., 2019) proposed a universal multi-scale material interpolation model based on the SIMP method, and used this model to complete the multi-scale, multi-material parallel topology optimization design of vibration acoustic structures. After more than 30 years of development, the SIMP method has matured and is almost the most well-known and representative topology optimization method. In addition to the classic flexible optimization problem of elastic structures, it also has effectiveness in nonlinear structural optimization, stress optimization, and other aspects. In addition, this method has also demonstrated good performance in many physical problems and has been successfully applied to thermoelastic structures, fluid problems, acoustic problems, and optical problems.

In this paper, the variable density method is used for the topology optimization of the rice direct seeder's seeding wheel. Finite element simulation technology is used to simulate and analyze the stiffness and strength of the structure of the rice direct seeder's seeding wheel and obtain its displacement and stress distribution. In response to practical application needs, the optimization module of Abaqus software was used for structural topology optimization design, and the optimized topology model was obtained, providing a basis for the optimization design of the seeding wheel structure of the rice direct seeder.

MATERIALS AND METHODS

1. Finite element simulation analysis of the seeding wheel

1.1. Implementation of Topology Optimization in Abaqus

As one of the large general-purpose nonlinear finite element analysis software, Abaqus covers a variety of unit models, and material models and supports a variety of analysis processes with its excellent computational power and simulation performance. For basic linear elastic problems, or problems involving multiple substances, complex mechanical processes, and nonlinear combinations, Abaqus can give satisfactory results whether implicit or explicit solutions are chosen. In this paper, Abaqus is adopted to achieve the topology optimization design of the seeding wheel. The optimization design in Abaqus relies on the powerful analysis and calculation power of computers and carries out structural optimization based on optimization theory. According to the objective function and constraints set by users, the optimal solution of structural design is obtained through accurate calculation. Abaqus/CAE topology Optimization Module is abbreviated as ATOM. Abaqus provides two algorithms for topology optimization: general-purpose algorithm and conditional algorithm. The general topology optimization algorithm takes the pseudo-density and stiffness of the structure as the objective function and constraint and can deal with most topology optimization problems. In the design structure, the conditional algorithm will optimize the stress and strain energy of the unit nodes, which is the basis of the design, and the calculation efficiency is higher, the design effect is better, mainly solving more specific problems.

1.2 Modeling

Abaqus has a common interface with SolidWorks software. Models established through SolidWorks can be imported into Abaqus for subsequent mesh partitioning and finite element simulation. The results obtained through Abaqus topology optimization can be imported into SolidWorks for measurement, and the common units and coordinates between software can be kept consistent.

The initial 3D model of the seeding wheel was created using SolidWorks software, as shown in Fig. 1. The material of the seeding wheel is stainless steel, with an initial volume of 338752 mm³ and an initial mass of 2663 g. To facilitate grid partitioning and computational analysis, the seeding wheel model is simplified. Because the spur gear pair can be equivalent to two elastic circular contacts during the meshing process, the gear teeth are simplified to a cylindrical surface, resulting in a simplified seeding wheel model as shown in Fig.2.

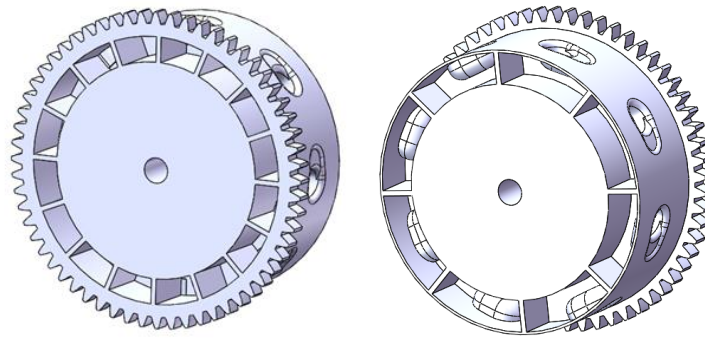


Fig. 1 - 3D model of the seeding wheel

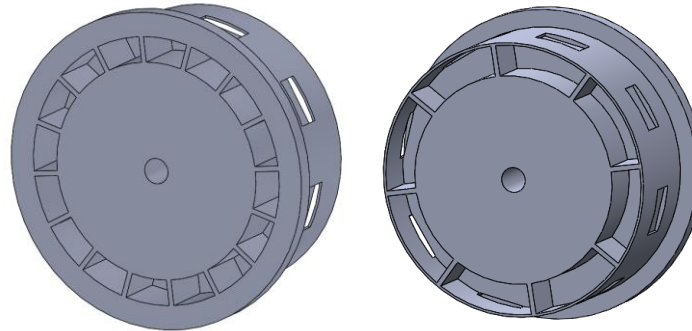


Fig. 2 - Simplified model of the seeding wheel

The protruding surface on one side of the model in Fig. 2 is the simplified gear teeth. The material of the seeding wheel is stainless steel, which has good plasticity and toughness and is suitable for processing and manufacturing. Its mechanical properties are shown in Table 1.

Table 1

Mechanical property				
Density (kg/m ³)	Poisson's ratio	Elastic modulus / (GPa)	Yield strength (MPa)	Tensile strength (MPa)
7860	0.27	207	272	685

1.3 Finite element model settings

Import the simplified seeding wheel model into the finite element analysis software Abaqus, and use tetrahedral elements to mesh it. The total number of mesh elements is 94209, and the meshed model is shown in Fig. 3. Set material properties: elastic modulus $E = 2.07 \times 10^{11}$ Pa, Poisson's ratio $\mu = 0.27$, and density $\rho = 7860$ kg/m³.

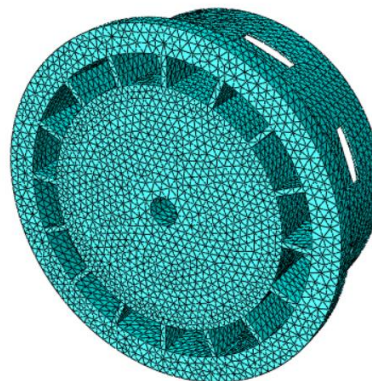


Fig. 3 - Grid division of the seeding wheel

Set boundary conditions in Abaqus software, and the seeding wheel rotates around the central axis while working, with the central axis fixed. Fix the inner surface of the center hole of the seeding wheel completely, and the constraint method is shown in Fig. 4. Adding load points on the model surface and applying loads, the actual loads on the seeding wheel during operation are simplified to the loads shown in Fig. 5.

The size of these loads is all 200 N, and the direction is shown in Fig. 5. At the same time, to obtain a structure that can withstand the corresponding loads, loads as shown in Fig. 6 are added to the front side of the seeding wheel, and loads as shown in Fig. 7 are added to the rear side of the seeding wheel, all of which are 100 N in size.

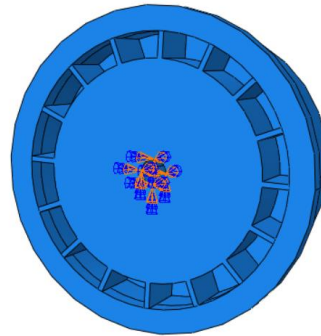


Fig. 4 - Boundary condition settings

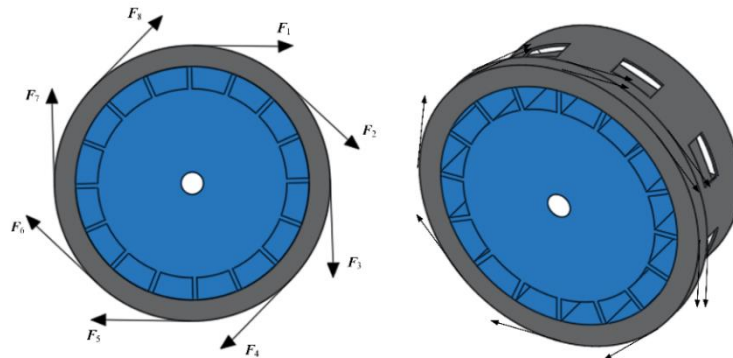


Fig. 5 - Direction of surface load on gear teeth

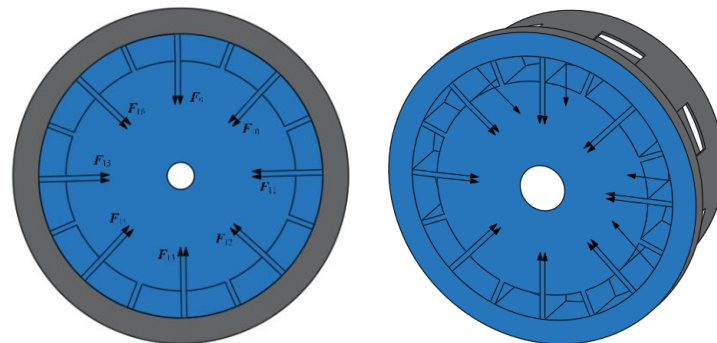


Fig. 6 - Loads applied on the front side of the seeding wheel

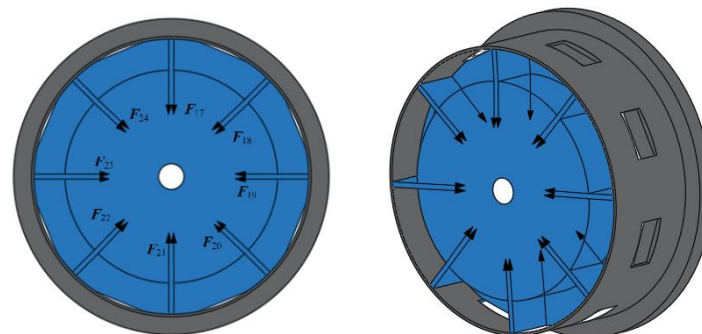


Fig. 7 - Loads applied to the rear side of the seeding wheel

2. Topological optimization mathematical model

2.1 Basic Theory of Variable Density Method

The variable density method characterizes the mapping relationship between unit density and material elastic modulus in the form of a continuous function, thereby transforming discrete optimization problems into continuous optimization problems. The basic idea is to use artificially assumed density variable units and set

the density values of the units as continuous variables between [0,1]. In structural topology optimization, when density variable units are introduced, many intermediate density units will appear in the results. However, in the actual manufacturing process, there are only two filling states for a unit: with material and without material, and the presence of intermediate density greatly reduces the manufacturability of the structure. So, effective measures should be taken to suppress the generation of intermediate density units. To reduce intermediate density, a material interpolation model with an intermediate density penalty function is proposed, which promotes the optimization of materials towards extreme values of all 0 or all 1, which is beneficial for material production and processing.

2.2 SIMP method topology optimization model

In structural topology optimization, the interpolation models of the variable density method include the Solid Isotropic Microstructures with Penalization (SIMP) and the Rational Approximation of Material Properties (RAMP). At present, the SIMP model is mature and mainly used, and the material interpolation model based on SIMP is:

$$E(x_i) = E_{\min} + (x_i)^p (E_0 - E_{\min}), x_i \in [0,1] \tag{1}$$

where: $E(x_i)$ is the elastic modulus, E_0 is the elastic modulus of the solid element, and E_{\min} is the minimum positive stiffness to prevent singularity in the stiffness matrix. p is the penalty factor, x_i represents the relative density of each unit. When x_i is set to 1, it indicates that there is material filling here, and when x_i is set to 0, it indicates that there is no material filling here.

Due to $E_{\min} \ll E_0$, Eq. (1) can be transformed into:

$$E(x_i) = E_{\min} + (x_i)^p (E_0 - E_{\min}) = x_i^p E_0, x_i \in [0,1] \tag{2}$$

By using the density interpolation function of continuous variables to represent the correspondence between the relative density and elastic modulus of structural units, a smooth material interpolation model can be obtained. The size of the penalty factor p varies, and its inhibitory effect on intermediate density units also varies. Usually, the inhibitory effect increases with the increase of the p value, but when the p value is too large, it often leads to the occurrence of the checkerboard phenomenon. Bendsoe and Sigmund (*Bendsoe et al., 2003*) pointed out theoretically that the material corresponding to the SIMP interpolation model can be simulated through microstructure by satisfying condition $p \geq 3$, and it can be ensured that the obtained material exists physically. In general, when the penalty factor p satisfies the following equation, the SIMP model can be considered as a material model.

$$p \geq \max \left\{ \frac{2}{1-\nu^0}, \frac{4}{1+\nu^0} \right\} \quad 2D \tag{3}$$

$$p \geq \max \left\{ 15 \frac{1-\nu^0}{7-5\nu^0}, \frac{3(1-\nu^0)}{2(1-2\nu^0)} \right\} \quad 3D$$

where: ν^0 is the Poisson's ratio of the material.

Under the constraint of a given structural volume, with the objective function of minimizing the compliance of a continuum structure, the topology optimization mathematical model based on the SIMP method is:

$$\begin{aligned} & \text{find } X=(x_1, x_2, x_3, \dots, x_i)^T \in R \\ & \quad i=1, 2, \dots, m \\ & \min c = \mathbf{F}\mathbf{U} = \mathbf{U}^T \mathbf{K}\mathbf{U} = \sum_{i=1}^m (x_i)^p u_i^T k_0 u_i \\ & \text{s.t. } \mathbf{K}\mathbf{U} = \mathbf{F} \\ & \quad V = fV_0 = \sum_{i=1}^m x_i v_i \\ & \quad 0 < x_{\min} \leq x_i \leq x_{\max} \leq 1 \end{aligned} \tag{4}$$

This model is used to solve the minimum compliance of the optimized structure under volume or mass constraints so that the optimization results can reach the maximum stiffness under the constraint conditions. Where, X is the unit design variable and c is the structural compliance. \mathbf{F} and \mathbf{U} are the load vector and

displacement vector, respectively, and \mathbf{K} represents the unit stiffness matrix. k_0 is the initial unit stiffness matrix, f is the retained volume fraction, V_0 is the initial volume, v_i is the unit volume, x_{\min} and x_{\max} are the minimum and maximum values of the design variables, and m is the number of units.

To obtain higher computational efficiency, the optimization method based on derivative information is generally adopted in the process of solving optimization problems. To implement such a method, the corresponding sensitivity analysis must be carried out.

The structural objective function is as follows.

$$c = FU = U^T KU = \sum_{i=1}^m (x_i)^p u_i^T k_0 u_i \tag{5}$$

Taking the partial derivative of the objective function over the design variable x_i yields

$$\frac{\partial c}{\partial x_i} = \sum_{i=1}^m p(x_i)^{p-1} u_i^T k_0 u_i \tag{6}$$

RESULTS

3. Topology optimization of the seeding wheel

3.1 Static analysis

The static analysis of the seeding wheel was carried out. The stress and displacement cloud maps of the seeding wheel were obtained, as shown in Fig. 8 and Fig. 9. It can be seen from Fig. 8 that, compared with other positions inside the seeding wheel, the stress at the point where loads acts are slightly larger, but are still far less than the yield strength of the material. As can be seen from Fig. 9, the maximum displacement of the seeding wheel is 1.336×10^{-8} mm, and its deformation is very small. According to the data obtained from the analysis, there is room for structural optimization and lightweight design of the seeding wheel.

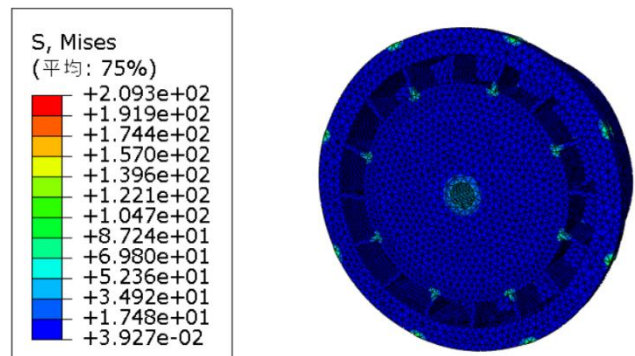


Fig. 8 - Stress program of the seeding wheel

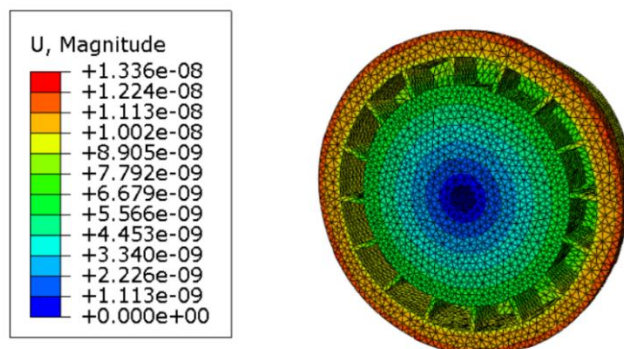


Fig. 9 - Displacement program of the seeding wheel

3.2. Topology Optimization Analysis

The seeding wheel operates under a single load case. The topology optimization of the seeding wheel aims to minimize the structural strain energy and the allowable volume of the material is set to 50% of the design domain. Due to the transmission function of the seeding wheel gear, this part cannot be used as a design domain for optimization design. The size and position of the seeding hole cannot be changed arbitrarily. therefore, this part should also be set as a non-design domain.

As shown in Fig. 10, during the topology optimization process, the blue area represents the designable domain and the gray area represents the non-design domain.

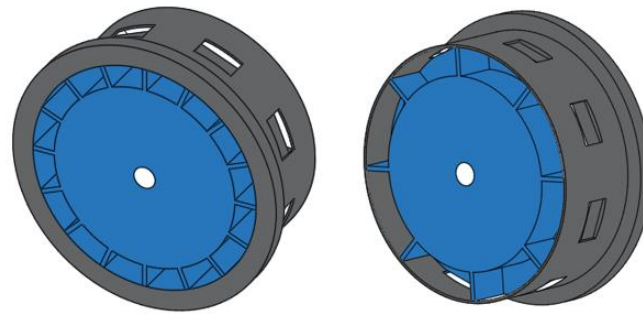


Fig. 10 - Design domain of the seeding wheel

After topology optimization calculation, the seeding wheel reached the optimal result after 30 iterations of analysis, as shown in Fig. 11. Then, the optimized seeding wheel model was exported and the original 3D model was modified using SolidWorks to obtain the optimized 3D model as shown in Fig. 12.

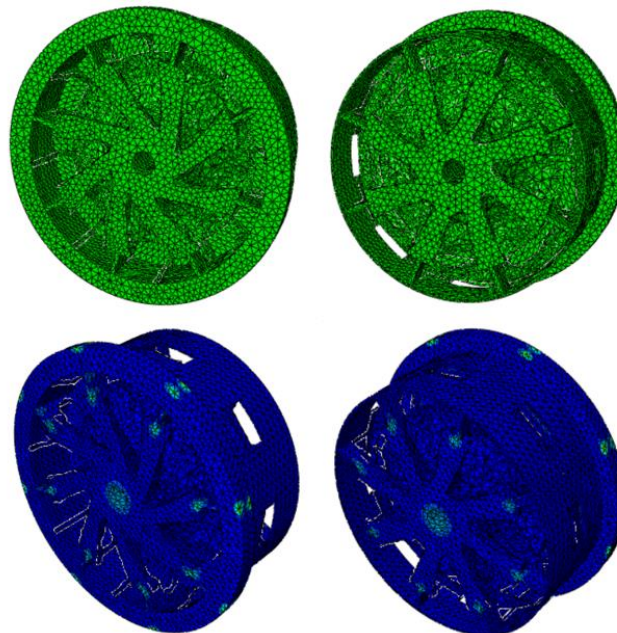


Fig. 11 - Topology optimization results of the seeding wheel

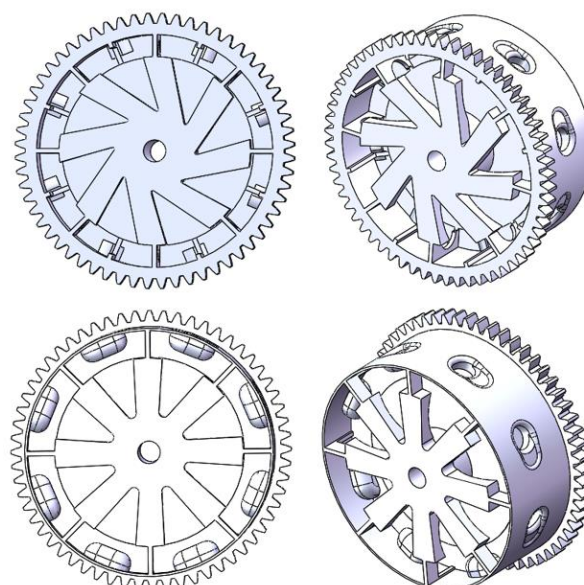
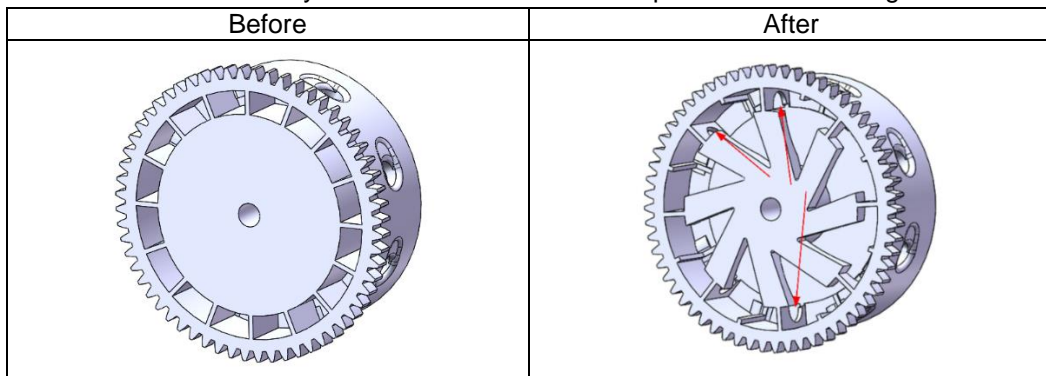


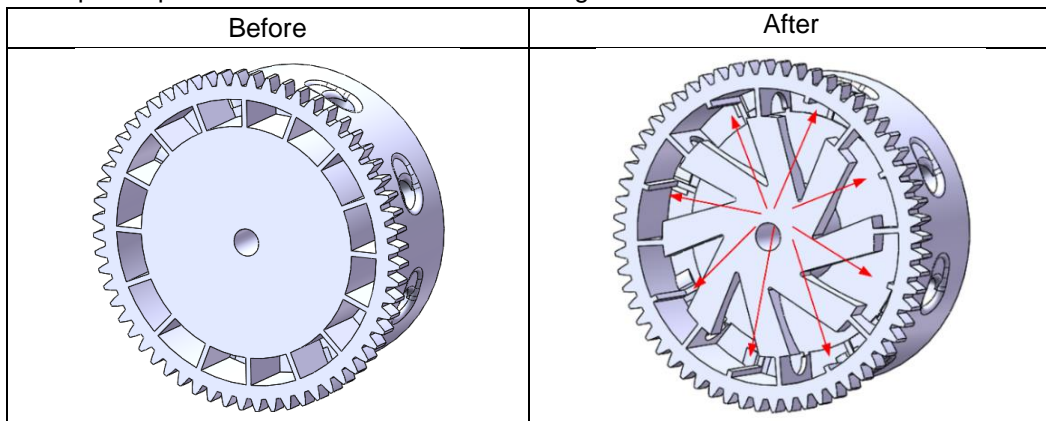
Fig. 12 - Revised 3D model

Comparing the optimized seeding wheel model with the original 3D model, it can be seen that:

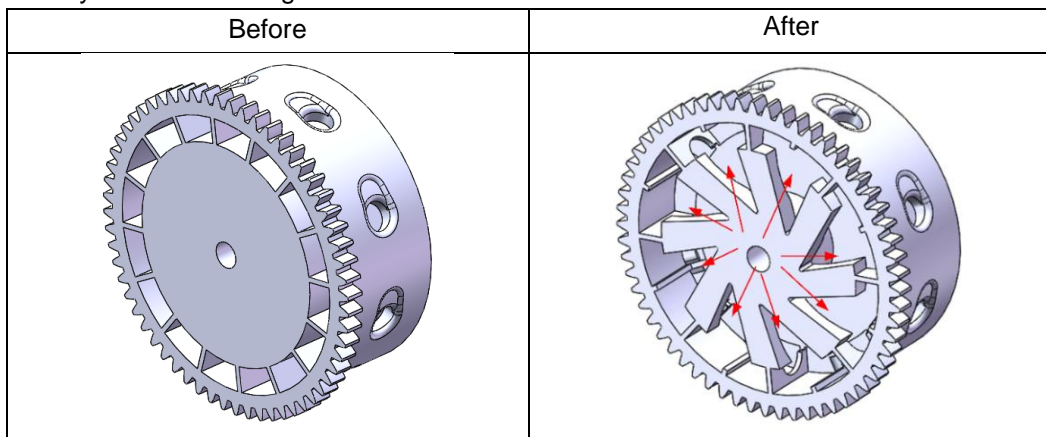
(1) There are curved holes uniformly distributed on the front side plates of the seeding wheel.



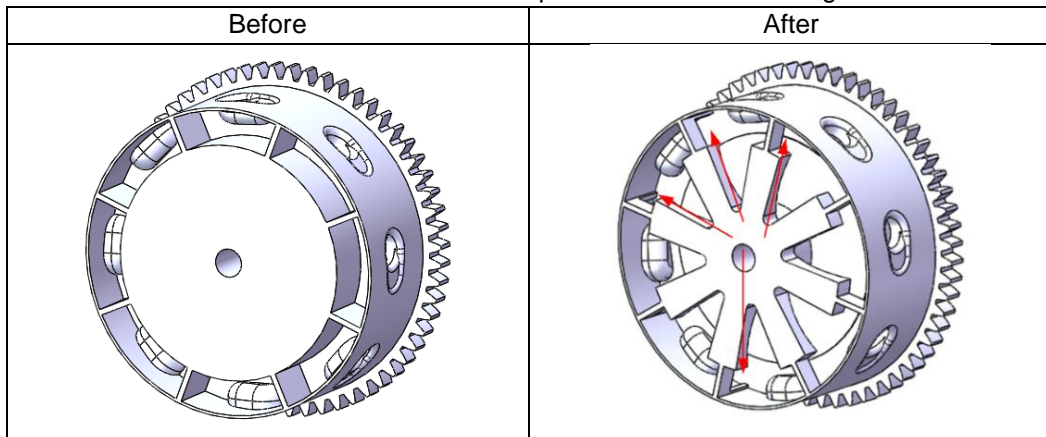
(2) Remove the partial plate on the front side of the seeding wheel



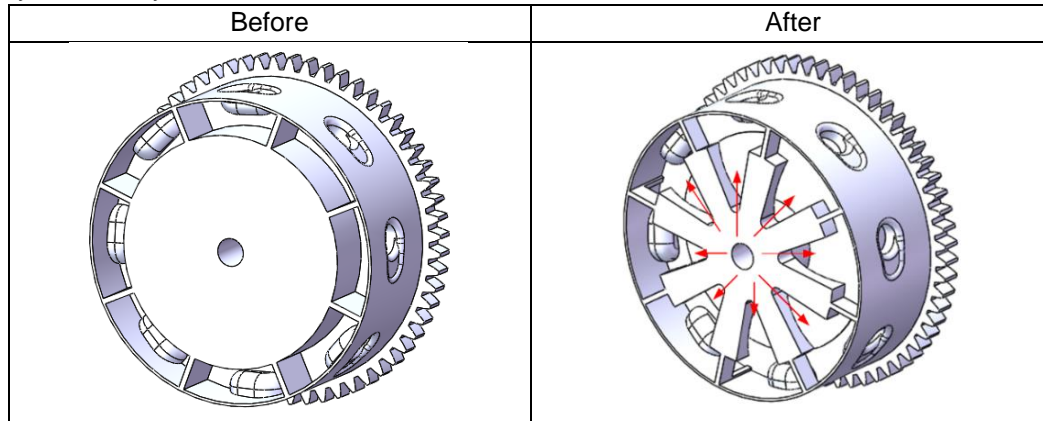
(3) Part of the material is removed from the front side of the seeding wheel, and the remaining material is evenly distributed along the arc direction.



(4) Remove the material from the inner side of the side panel behind the seeding wheel.



(5) Remove some materials from the rear side of the seeding wheel and distribute the remaining materials symmetrically.



The optimized seeding wheel model has a volume of 174729 mm³ and a mass of 1373 g. Compared to the original model, the volume and mass have decreased by 48.4%, greatly reducing the distribution of structural materials and achieving a lightweight design of the seeding wheel structure.

CONCLUSIONS

In this paper, the finite element analysis was carried out on the seeding wheel of the rice direct seeder, and the static simulation analysis was carried out by Abaqus software. The stress and displacement program of the seeding wheel were obtained. The mathematical model of topology optimization based on the SIMP method is given, the topology optimization module of Abaqus software is used to optimize the seeding wheel, and the optimized structure of the seeding wheel is obtained. The optimized model was imported into SolidWorks software for 3D model correction, and the 3D model of the seeding wheel after topology optimization was obtained. Compared with the original 3D model, the volume and mass of the optimized seeding wheel were reduced by 48.4%, which greatly reduced the material use and realized the lightweight design of the seeding wheel without affecting the performance of the seeding wheel.

REFERENCES

- [1] Bendsoe, M. P., & Sigmund, O. (2003). *Topology optimization: theory, methods, and applications*: Springer Science & Business Media.
- [2] Berrocal, L., Fernández, R., González, S., Periñán, A., Tudela, S., Vilanova, J., Lasagni, F. (2019). Topology optimization and additive manufacturing for aerospace components. *Progress in Additive Manufacturing*, 4, 83-95.
- [3] Ganghoffer, J.-F., Wazne, A., & Reda, H. (2023). Frontiers in homogenization methods towards generalized continua for architected materials. *Mechanics Research Communications*, 130, 104114.
- [4] Gao, H., Liang, J., Li, B., Zheng, C., & Matsumoto, T. (2021). A level set based topology optimization for finite unidirectional acoustic phononic structures using boundary element method. *Computer Methods in Applied Mechanics and Engineering*, 381. doi:10.1016/j.cma.2021.113776
- [5] Hassani, B., Khanzadi, M., & Tavakkoli, S. M. (2012). An isogeometrical approach to structural topology optimization by optimality criteria. *Structural and Multidisciplinary Optimization*, 45(2), 223-233. doi:10.1007/s00158-011-0680-5
- [6] He, G., Huang, X., Wang, H., & Li, G. (2016). Topology optimization of periodic structures using BESO based on unstructured design points. *Structural and Multidisciplinary Optimization*, 53, 271-275.
- [7] Huang, R., & Huang, X. (2011). *Matlab implementation of 3D topology optimization using BESO*.
- [8] Huang, X., & Xie, M. (2010). *Evolutionary topology optimization of continuum structures: methods and applications*: John Wiley & Sons.
- [9] Jang, I. G., Kim, K.-S., & Kwak, B. M. (2014). Conceptual and basic designs of the Mobile Harbor crane based on topology and shape optimization. *Structural and Multidisciplinary Optimization*, 50, 505-515.
- [10] Karadere, G., Düzcan, Y., & Rıza Yıldız, A. (2020). Light-weight design of automobile suspension components using topology and shape optimization techniques. *Materials Testing*, 62(5), 454-458.

- [11] Liang, X., & Du, J. (2019). Concurrent multi-scale and multi-material topological optimization of vibro-acoustic structures. *Computer Methods in Applied Mechanics and Engineering*, 349, 117-148. doi:<https://doi.org/10.1016/j.cma.2019.02.010>
- [12] Lieu, Q. X., & Lee, J. (2017). Multiresolution topology optimization using isogeometric analysis. *International Journal for Numerical Methods in Engineering*, 112(13), 2025-2047. doi:<https://doi.org/10.1002/nme.5593>
- [13] Liu, H., Yang, D., Hao, P., & Zhu, X. (2018). Isogeometric analysis based topology optimization design with global stress constraint. *Computer Methods in Applied Mechanics and Engineering*, 342, 625-652. doi:<https://doi.org/10.1016/j.cma.2018.08.013>
- [14] March, N. G., Gunasegaram, D. R., & Murphy, A. B. (2023). Evaluation of computational homogenization methods for the prediction of mechanical properties of additively manufactured metal parts. *Additive Manufacturing*, 64, 103415.
- [15] Sui, Y., & Peng, X. (2017). *Modeling, solving and application for topology optimization of continuum structures: ICM method based on step function*: Butterworth-Heinemann.
- [16] Wang, Y., Luo, Z., Kang, Z., & Zhang, N. (2015). A multi-material level set-based topology and shape optimization method. *Computer Methods in Applied Mechanics and Engineering*, 283, 1570-1586.
- [17] Wang, Z., Wang, D., & Jia, H. (2024). A Novel Fully Decoupled Scheme for the MHD System with Variable Density. *Computational Methods in Applied Mathematics*(0).
- [18] Wu, P., Ma, Q., Luo, Y., & Tao, C. (2016). Topology optimization design of automotive engine bracket. *Energy and Power Engineering*, 8(04), 230.
- [19] Zhang, W., & Kang, Z. (2017). Robust shape and topology optimization considering geometric uncertainties with stochastic level set perturbation. *International Journal for Numerical Methods in Engineering*, 110(1), 31-56.
- [20] Zhou, M., & Rozvany, G. (1991). The COC algorithm, Part II: Topological, geometrical and generalized shape optimization. *Computer Methods in Applied Mechanics and Engineering*, 89(1-3), 309-336.
- [21] Zhu, J., Zhang, W., & Xia, L. (2015). Topology Optimization in Aircraft and Aerospace Structures Design. *Archives of Computational Methods in Engineering*, 23(4), 595-622. doi:10.1007/s11831-015-9151-2

OPTIMIZATION OF MELKASSA AGRICULTURAL RESEARCH CENTER (MARC) BEAN THRESHER PARAMETERS USING RESPONSE SURFACE METHOD (RSM)

/

የምላሽ ወለል ዘዴን (RSM) በመጠቀም የመልካሳ ግብርና ምርምር ማዕከል (MARC) የቦሎቄ መውቂያ ማሽን መለኪያዎችን ማመቻቸት

Biniam ZEWDIE^{1*}, Adesoji M. OLANIYAN², Amana WAKO¹, Dereje ALEMU³, Tamrat LEMA³

¹School of Mechanical, Chemical, and Materials Engineering, Departments of Agricultural Machinery Engineering, Adama Science and Technology University, P.O. Box 1888, Adama, Ethiopia.

²Department of Agricultural and Bioresources Engineering, Faculty of Engineering, Federal University Oye-Ekiti, Ikole-Ekiti Campus, Post Code 370001, Ikole-Ekiti, Nigeria.

³Ethiopian Institute of Agricultural Research; Agricultural Engineering Research, Melkassa Agricultural Research Center, P.O.Box 436, Adama, Ethiopia

Tel: +2519-1040-8218/+2519-1582-8327; email: nzq2001nzq@gmail.com

Corresponding author: Biniam Zewdie Ghebrekidan

DOI: <https://doi.org/10.35633/inmateh-74-29>

Keywords: Optimization, Bean Thresher, Response Surface Method (RSM), Parameters, and Experimental Design

ABSTRACT

In this study, the Agricultural Research Center of Melkassa examined the performance of a laboratory loop type bean thresher. As a function of different drum speeds (450, 550, and 650 rpm), concave apertures (25, 35, and 45 mm), feed rates (550, 650, and 750 kg/h), and moisture levels (5, 10, and 15%), the extent of grain deterioration, threshing efficiency, and rate of implantation were examined. Utilizing response surface techniques, the experimental design for optimization was developed. The response variables were significantly impacted by each independent variable. With a cylinder speed increase of 7.5 to 10.83 ms⁻¹, the percentages of grain damaged, threshed, and germination decreased from 45.98 to 47.97%, 96.81 to 99.69%, and 85.75 to 55.98%, respectively. Despite an increase in seed germination, damaged grain and threshing efficiency decreased as the moisture content increased. Grain deterioration and threshing efficiency decreased, however seed sprouting improved in tandem with an increase in feed rate and convex aperture. The cylinder speed of 8.25 ms⁻¹, the concave clearance of 37.4 mm, the feed rate of 672 kg/h, and the moisture content of 11.6% (db) were found to be the ideal parameters. In this case, the ideal ranges for seed sprouting, threshing efficiency, and grain impairment were found to be 3, 98.3, and 84.29%, respectively.

አገልግሎት-ጥናት

በዚህ ጥናት የመልካሳ ግብርና ምርምር ማዕከል የላብራቶሪ ሉፕ ዓይነት የቦሎቄ መውቂያ ማሽን አፈጻጸምን መርምሯል። እንደየተለያዩ የሲሊንደር ጥገና ፍጥነት (450, 550 እና 650 rpm), ሽግግር ቀዳዳዎች (25, 35 እና 45 ሜ)፣ የምግብ መጠን (550, 650 እና 750 ኪ.ግ. በሰዓት) እና የእርጥበት ደረጃዎች (5, 10, እና 15%) ፣ የእህል መበላሸት መጠን, የመውቂያ ቅልጥፍና እና የመትከል መጠን ተፈትሸዋል. የምላሽ ወለል ቴክኒኮችን በመጠቀም፣ ለማመቻቸት የሙከራ ንድፍ ተዘጋጅቷል። የምላሽ ተለዋዋጮች በእያንዳንዱ ገለልተኛ ተለዋዋጭ ጉልህ ተጽዕኖ አሳድረዋል. የሲሊንደር ፍጥነት ከ 7.5 ወደ 10.83 ms⁻¹ በመጨመር የተነሳ፣ የተወቃ እና የበቀለው እህል በመቶኛ ከ45.98 ወደ 47.97%፣ ከ96.81 ወደ 99.69% እና ከ85.75 ወደ 55.98% ቀንሷል። የዘር ማብቀል ቢጨምርም የእርጥበት መጠኑ እየጨመረ ሲሄድ የተበላሸ እህል እና የመውቂያው ውጤታማነት ቀንሷል። የእህል መበላሸት እና የመውቂያ ቅልጥፍና ቀንሷል፣ ነገር ግን የዘር ማብቀል ከአመጋገብ ፍጥነት እና ከኮንቬክሽን ክፍት ቦታ ጋር ተያይዞ ተሸሽሏል። የሲሊንደር ፍጥነት 8.25 ms⁻¹፣ የሽላ 37.4 ሜ ማዳጃ፣ የምግብ ፍጥነት 672 ኪ.ግ በሰዓት እና 11.6% (db) የእርጥበት መጠን በጣም ጥሩ መለኪያዎች ሆነው ተገኝተዋል። በዚህ ሁኔታ ለዘር ማብቀል፣ የመውቂያ ቅልጥፍና እና የእህል እክል ተስማሚ ክልሎች 3፣ 98.3 እና 84.29% በቅደም ተከተል ተገኝተዋል።

INTRODUCTION

According to Joshi et al. (2022), the common bean (*Phaseolus vulgaris* L.) is the third most consumed legume globally and one of the primary sources of nutrition for both people and animals in Africa. The seed and pod are used to make animal feed, and the seed has a high protein and carbohydrate content (Uebersax et al., 2023).

Ethiopia is the world's largest producer of edible legumes, with 560,191 hectares of farmed land and 208,913 tons of beans produced in 2019 (Delelegn T., 2022). Common beans are among the most important legumes (Bento et al., 2022). The common bean crop is threshed by a machine after being harvested by hand. Grain is separated from the pod and stalk by the thresher using pressure and impact force (Que et al., 2024). Grains sustain significant damage from the crop migrating between the thresher unit's stirring components and from inadequate clearance among static as well as moving portions (Lee et al., 2023). Grain that has been damaged has the lowest shelf life and is less resilient to pests and diseases (Adewoyin, 2023). Grain grading is the primary factor that determines its marketability; fragmented seeds result in a lower grain grade (Parker et al., 2022). In addition, damaged grains prevent seeds from germinating (Chandra et al., 2024).

Grain damage, threshing loss, and mingled chaff with the grain are the most qualitative indicators of a thresher operation's effectiveness. In their examination of the design features of a thresher apparatus, Ghebrekidan et al. (2024) found those technological parameters such as drum speed and concave-to-drum clearance, as well as the rate at which materials were fed into the device, had a substantial impact on the threshing performance. Furthermore, the crop cultivar, moisture content, and biometrical indices all had an impact on the threshing process, according to Juraev et al. (2023). In order to assess a thresher's performance, the most prestigious particles are combined with grain damage and threshing loss (Strecker et al., 2022). The velocity of material feeding into the device, along with technological aspects like drum acceleration and convex-to-drum aperture, had a substantial impact on the shredding performance, as per Ghebrekidan et al. (2024) analysis of the design elements of a thresher apparatus. The biometrical parameters, moisture level, and crop genotype were also found to have an impact on the threshing process by Jan et al. (2021).

Ejara et al. (2018) conducted an interesting inquiry in which they distinguished several criteria into conventional bean threshing quality indices: loss of grains, grain impairment, level of separation, and size of the pod decrease. The aperture, the wire loop type drum, the convex, and the drum peripheral velocity were shown to be two crucial elements in the threshing of common beans. Ghebrekidan et al. (2024) looked at the parameters of the common bean separation mechanism. It was demonstrated that the primary factors influencing crop quality were peripheral speed and the distance between the cylinder and the concaves. The findings of their experiment using the tangential threshing mechanism indicated that the rate of grain breakage improved from 3.8 to 6.01% when the cylinder perimeter speed was enhanced from 9.4 to 21.4 m/s. Numerous threshing units were used by Umbataliyev et al. (2023) for common bean seeds. Using a multitude of sorts of drums, rates, as well as rate of feed, they assessed the thresher's performance in terms of throughput capacity, threshing effectiveness, damage to the grain, losses of the grain, differentiation, as well as specific utilization of energy. They discovered that the apparent damage to the grain increased along acceleration as well as flow rate. Kidney bean threshers were examined by Wang and Cichy (2024) using variables such as seed moisture level, clearance rates, and cylinder rpm. The outcomes demonstrated that moisture level, cylinder speed, and convex level all had a major impact on the germination of threshed seeds.

The success rate of threshing, output capacity, and grain damage and losses of a longitudinal flow barrier utilized in common beans were all significantly impacted by the feed rate, moisture content, and threshing drum beat, according to Huertas et al. (2023). The percentage of damaged grains and threshed pods in a loop-type bean thresher was investigated in relation to the impact of the drum's speed, moisture level, and pod size (Lisciani et al., 2024). The findings showed that the pod size had the biggest impact on damage intensity, while the drum speed had the least. It was further suggested that the optimal circumstances for common bean threshing would be a water content ranging from 12 to 15% and a drum speed of 9.5 ms^{-1} . The potential of the response surface methodology for optimizing the threshing of common beans in respect to machine-crop factors has not been investigated, despite the fact that several studies have been carried out on the threshing of various agricultural crops. The main objective of this study was to increase threshing efficiency, reduce grain damage, and maximize seed germination when threshing common beans. To achieve this, the response surface approach is used to improve technological parameters such as cylinder acceleration, convex clearance levels, feed rate, and moisture level.

MATERIALS AND METHODS

Selected improved varieties of common beans from the Oromia regional State in Ethiopia were provided by the Awash Melkassa Research Center. A digital vernier caliper (TA, M5 0–300 mm, China) was used to measure the three primary axial dimensions of the beans: with an accuracy of 0.01 mm, the measurements are dimensions (L, mm), (W, mm), and (T, mm).

The experimental findings indicated that the average mean values for thickness (4.962 ± 0.50 mm), width (6.316 ± 0.502 mm), and length (9.848 ± 0.802 mm) were, accordingly. After common beans were harvested by hand, the threshing procedure was carried out using a laboratory wire loop/rasp type drum thresher. The assembled thresher and a collaborative assessment of it are depicted in Fig.1. With 33 teeth spaced 100 mm apart along each of the device's four axes, the drum measured 730 mm in length. The concave was made from 720 mm long steel sheets that had been rolled and perforated.



Fig. 1 – MARC Bean thresher schematic diagram and participatory evaluation assessment

Experimental design

Based on the multifactorial experiment principle with three independent replications, the experiment utilized a split-split plot design. The main plot was assigned to the two varieties of crops levels, the sub plot was assigned to the three threshing drum speed levels, and the sub-sub plot was assigned to the three feeding levels, each with three replications (Table 1). The Response Surface Method was utilized to maximize the threshing performance, and statistical R-studio software was utilized to analyze all the data gathered during the laboratory and field performance evaluations.

Table 1

Randomization Layout								
R1			R2			R3		
S ₁ F ₁ M ₁	S ₂ F ₂ M ₂	S ₃ F ₃ M ₃	S ₁ F ₁ M ₃	S ₂ F ₂ M ₁	S ₃ F ₃ M ₂	S ₁ F ₁ M ₂	S ₂ F ₃ M ₃	S ₁ F ₁ M ₁
S ₃ F ₂ M ₁	S ₁ F ₂ M ₂	S ₂ F ₁ M ₃	S ₃ F ₂ M ₃	S ₁ F ₂ M ₁	S ₂ F ₁ M ₂	S ₂ F ₂ M ₂	S ₁ F ₂ M ₃	S ₂ F ₂ M ₁
S ₂ F ₃ M ₁	S ₃ F ₁ M ₂	S ₁ F ₃ M ₃	S ₃ F ₁ M ₃	S ₂ F ₁ M ₁	S ₂ F ₂ M ₂	S ₃ F ₃ M ₂	S ₃ F ₁ M ₃	S ₃ F ₃ M ₁
S ₃ F ₃ M ₁	S ₂ F ₃ M ₂	S ₁ F ₁ M ₃	S ₃ F ₃ M ₃	S ₂ F ₃ M ₁	S ₁ F ₁ M ₂	S ₃ F ₁ M ₂	S ₂ F ₁ M ₃	S ₃ F ₁ M ₁
S ₂ F ₁ M ₁	S ₁ F ₃ M ₂	S ₂ F ₃ M ₃	S ₂ F ₁ M ₃	S ₃ F ₁ M ₁	S ₂ F ₃ M ₂	S ₃ F ₂ M ₂	S ₃ F ₃ M ₃	S ₂ F ₃ M ₁
S ₁ F ₂ M ₁	S ₃ F ₂ M ₂	S ₃ F ₂ M ₃	S ₁ F ₂ M ₃	S ₁ F ₃ M ₁	S ₃ F ₂ M ₂	S ₁ F ₂ M ₂	S ₁ F ₃ M ₃	S ₁ F ₂ M ₁
S ₁ F ₃ M ₁	S ₂ F ₁ M ₂	S ₃ F ₁ M ₃	S ₁ F ₃ M ₃	S ₃ F ₂ M ₁	S ₃ F ₁ M ₂	S ₁ F ₃ M ₂	S ₂ F ₂ M ₃	S ₁ F ₃ M ₁
S ₂ F ₂ M ₁	S ₃ F ₃ M ₂	S ₁ F ₂ M ₃	S ₂ F ₃ M ₃	S ₃ F ₃ M ₁	S ₁ F ₂ M ₂	S ₂ F ₁ M ₂	S ₃ F ₂ M ₃	S ₃ F ₂ M ₁
S ₃ F ₁ M ₁	S ₁ F ₁ M ₂	S ₂ F ₂ M ₃	S ₂ F ₂ M ₃	S ₁ F ₁ M ₁	S ₁ F ₃ M ₂	S ₂ F ₃ M ₂	S ₁ F ₁ M ₃	S ₂ F ₁ M ₁

S = drum speed, F = feed rate, M = moisture content, & R = replications

Response surface method (RSM)

Four independent parameters were considered for optimization: moisture content (5, 10, and 15% wb), convex aperture (25, 35, 45 mm), speed of cylinder (7.5, 9.17, 10.83 ms^{-1}), and rate of feeding (550, 650, 750 kg^{-1}). Germination of seeds percentage, threshing efficiency, and damage to grain were the three dependent variables in the experimental method of optimization. To fit the experimental results, a polynomial equation of second order was thus developed using the method of response surfaces and central composite experiment design.

According to the findings of earlier research and the limitations of the manufactured thresher (*Que et al., 2024*) the levels of convex aperture, moisture level, and chamber rate were chosen (*Savic et al. 2019*). In the end, 54 experiments were conducted utilizing triplets of implementation for the independent variables in a CCD-type experimental design, as shown in Table 1. In a random order, the trials were carried out. In the latter half of the parameters with encode, three replications were conducted to determine the relationship model describing the two main parameters' sum of square errors and lack of fitness (*Güvercin and Yıldız, 2018*). Design-Expert 12 was used to optimize the several responses simultaneously.

Evaluation procedure

The chamber rate, flow rate, Level of moisture, and convex aperture width of the thresher were evaluated at three different levels on a firm surface after installation and adjustments. With regards to the trial, the consequence of their separate parameters on sprouting, threshing efficiency and grain damage was taken into account. Samples were randomly prepared and put into the thresher once it was turned on in order to obtain the thresher performance indices. According to *Wang and Cichy (2024)*, the effectiveness of threshing (TE), the aptitude for threshing (TC), effective cleaning (CE), and proportional of losses were determined using the following relationships in order to assess the threshing machine's effectiveness.

RESULTS

i) Threshing Efficiency

The figures 2a–c were prepared using optimal feeding amounts of 672 kg/h , 37.4 cm concave clearance, and 8.25 ms^{-1} drum speed.

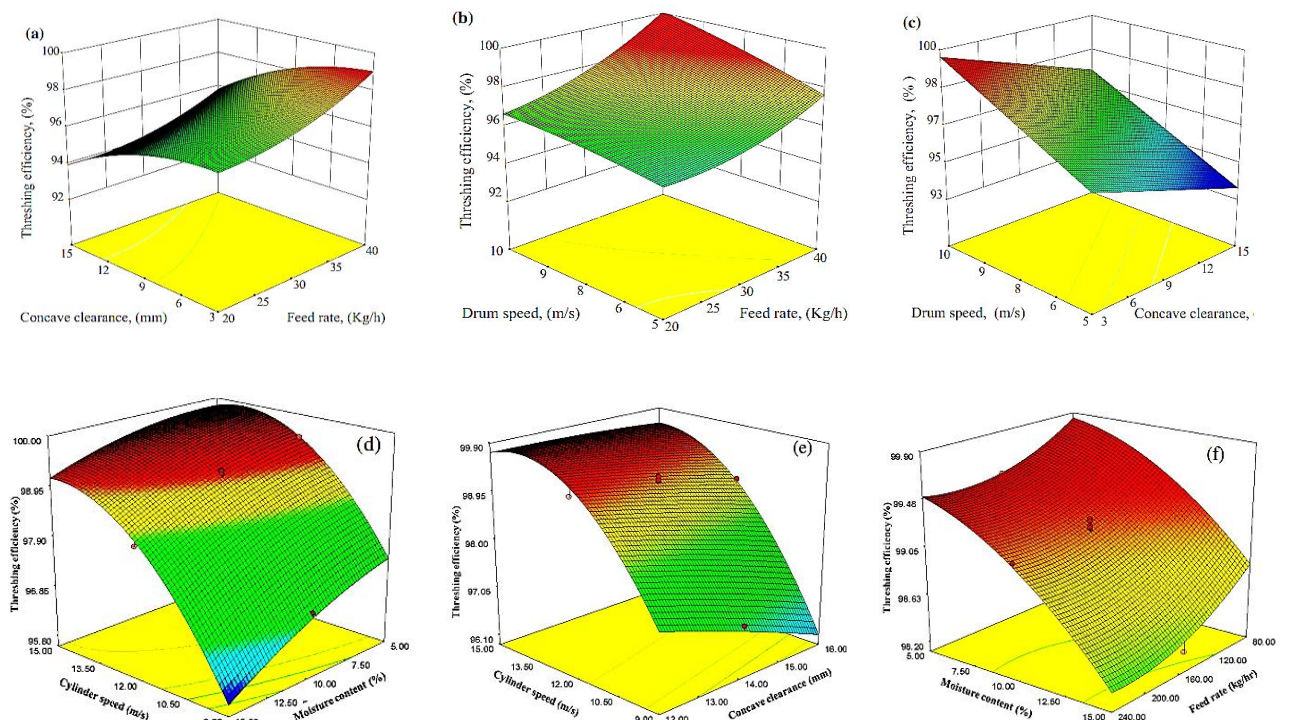


Fig. 2 - The implications of those parameters on the threshing efficiency

(a) feed rate and concave clearance; (b) drum speed and feed rate; (c) drum speed and concave clearance; (d) cylinder speed and moisture content; (e) cylinder speed and concave clearance; and (f) moisture content and feed rate.

Threshing efficiency improved together with Concave geometry clearance and rate of feed, as Figure 2a presented. Threshing efficiency attained a highest of 98.7% at an average feed rate of 672 kg/h and a convex clearance of 37.4 cm. Figure 2b illustrates how increasing the rate of feed and speed of the drum led to an enhancement to the effectiveness of threshing. The most significant threshing efficiency (99.7%) was ascertained with an intake rate of 672 kg/h and a drum with a speed of 8.25 ms⁻¹. In contrast, the efficiency of threshing climbed in tandem with the drum speed improved and convex clearance dropped. The drum speed at which the highest efficiency (99%) was achieved was 8.25 ms⁻¹ and a concave clearance of 37.4 mm (Fig. 2c). Threshing efficiency improved when the rubbing force between the bean and the canvas concave increased, corresponding with a decrease in convex clearance between the concave strip and the concave bar. As perimeter rate climbed, so did momentum and thrust of impact on the trembling, which in turn boosted threshing efficiency as drum speed climbed. When it came to bean threshers, *Umbataliyev et al. (2023)* discovered similar patterns.

The experimental findings are illustrated in Fig. 2-d to -f. throughout the range of input components examined, the threshing efficiency varied between 95.1 and 99%. At the 1% confidence level, Table 2 illustrates that threshing efficiency was significantly impacted through the rate of feed, cylinder speed, level of moisture, and convex clearance. The impact of the cylinder speed on common bean effectiveness of threshing is illustrated in Fig. 2-d. When cylinder speed was increased from 7.5 to 9.17 ms⁻¹, threshing efficiency climbed from 96.81 to 99.21% with a moisture level of 11.6%. Furthermore, as anticipated, the highest cylinder speed (10.83 ms⁻¹) produced the highest threshing efficiency rating (99.69%).

As concave aperture increased, threshing efficiency decreased, as Figure 2-e illustrates. In light of improvements in convex aperture from 35 to 45 mm, the threshing efficacy reduced from 97.45 to 96.16% at 7.5 ms⁻¹ with the chamber's frequency. Convex space did not significantly influence performances at speed of drum exceeding 9.17 ms⁻¹. The higher cylinder speed resulted in refined threshing efficiency because of an increased impact force. The rationale for lowest threshing efficiency at the highest concave clearance was the insufficient force exerted on the pods, which caused them to fall out without separating the seeds. At the 1% confidence level, the concave clearance and cylinder speed influences on the threshing efficiency interacted significantly. There was a negative correlation between the feed rate and threshing efficiency. As the feed consumption rate went up from 550 to 750 kgh⁻¹, the average threshing efficiency reduced from 99.52 to 99.09% in (Figure 2f).

Outcomes of the investigation indicated that the detrimental impact of cylinder speed on crop threshing was mitigated as the rate of feed escalated due to an increase in the width of the trim slice between the cylinder and concave. For every drum speed level, *Huertas et al. (2023)* found that as feed rate climbed the effectiveness of threshing decreased.

The efficiency of threshing dramatically dropped as the input material's level of moisture escalated, as shown in Fig. 2-f. There was a correlation between the highest (99.52%) and minimum (98.31%) effectiveness of threshing and the amounts of water of 5% and 15%, within that sequence. At increasing levels of water content, there was a greater impact of moisture content on threshing efficiency. *Que et al. (2024)* also reported a similar outcome. Pods and seeds are more easily split because there is less tension holding the pod together and the pods are more brittle due to reduced seed moisture concentrations. Threshing efficiency dropped as a result of increased pod cohesion brought on by the plant materials' increased flexibility at higher moisture contents.

The ANOVA illustrated in Table 2 ($p < 0.001$) implies that the predicted value of F (19.81) is high, indicating that a model with quadratic parameters could be a good fit for the outcomes of the experiment. Table 2 illustrates the F-values that demonstrate the significant impact of the feed rate, convex clearance, and drum speed in terms of linear regression on the effectiveness of shredding at the 1% significance level. In this case, the ratio changed to 16.577, indicating a strong pulse. *Savic and Savic-Gajic (2021)* assert that this framework can be used for maneuvering within the realm of design. This model's predicted R² (0.81) and adjusted R² (0.89). Using polynomial form fitting, the regression model illustrating the threshing efficiency change with regard to the independent parameters (*feed rate, F_r*), (*drum speed, v_s*) and (*concave clearance, C_c*) was produced. The simplified polynomial model was obtained by removing terms from the quadrilateral model that are not significant (*Savic et al. 2019*)

Table 2

Response surface quadratic model-based analysis of variance for common bean threshing

Source of variation	df ^a	Response	
		Grain damage	Threshing efficiency
Model	54	164.62**	99.73**
Cys	1	1437.46**	930.83**
Fr	1	78.75**	21.01**
Cc	1	70.63**	60.35**
Mc	1	232.06**	144.55**
Cys x Fr	1	15.69**	13.34**
Cc x Fr	1	0.83ns ^b	0.082ns
Fr x Mc	1	15.46*	0.92ns
Cc x Cys	1	124.03**	35.36**
Cc x Mc	1	3.59ns	0.78ns
Cys x Mc	1	94.68**	21.16**
(Mc) ²	1	5.38*	2.51ns
(Cys) ²	1	93.47**	52.46**
(Fr) ²	1	0.46ns	1.60ns
(Cc) ²	1	1.45ns	0.090ns
Res.	15		
Pe	5		
Corr. total	69		

*Significant at the 5% level; **highly significant at the 1% level; ^a Degrees of freedom, ^b Non-significant, Fr = Feed rate, Cs = Drum speed, Cc = Convex aperture, Mc = Level of moisture, Res. = Residual, Pe = pure error, Corr. = Total Correlation

ii) Grain Damage

The variation among the investigation's outcomes illustrated that the convex aperture, chamber rate, rate of feeding, and levels of water content all exhibited a significant impact on the amount of grain damage (Table 2). The most significant factors were determined to be the cylinder speed, which was followed by rate of feeding, moisture level, and convex aperture. First-order interactions were prioritized according to relevance: cylinder speed x level of moisture, feed rate x level of moisture, and cylinder speed x convex aperture. The implications of convex clearance and speed of cylinder on the percentage of grain damage are shown in Fig. 3a. This figure illustrates how the rotational frequency at which the drum is threshed enhances the amount of grain impairment. Damage of grains escalated from 4.98 to 47.97% at the convex of 35 mm when the drum speed increased from 7.5 to 10.83 ms⁻¹. When cylinder speed was raised from 7.5 to 10.83 ms⁻¹, grain breakage escalated from 1.71 to 33.29% at a convex aperture of 35 mm. During threshing, the common bean was subjected to higher impact levels, which increased damage. However, as concave clearance improved, grain damage drastically decreased.

Grain damage and rate of feeding interacted inversely with each other across independent variables. Since the crop was subjected to more intense contact at the lower feed rate, the reduction in grain damage was approximately 50% (Fig. 3b) when the concave clearance of 37.4 mm was attained while upgrading the intake rate from 550 to 750 kg/h. Additionally, according to *Ghebrekidan et al. (2024)*, grain damage increased as feed rate diminished. When the amount of moisture escalated, the proportion of grain damage dropped dramatically, as shown in Fig. 3c. On the other hand, grain loss went from 33.42 to 57.79% when the amount of moisture decreased at a speed of 10.83 m/s, from 15% to 5%. At lower cylinder speeds, the impact of moisture content on grain damage was minimal. When moisture content was reduced from 15% to 5%, grain damage increased from 5.52 to 10.51% at a cylinder speed of 7.5m/s. Grain elastic behavior increased with increasing moisture content; hence, more energy was needed to crack the grain. Moisture content has also been identified by several researchers as a significant factor influencing grain impairment (*Huertas et al., 2023; Chandra et al., 2024*).

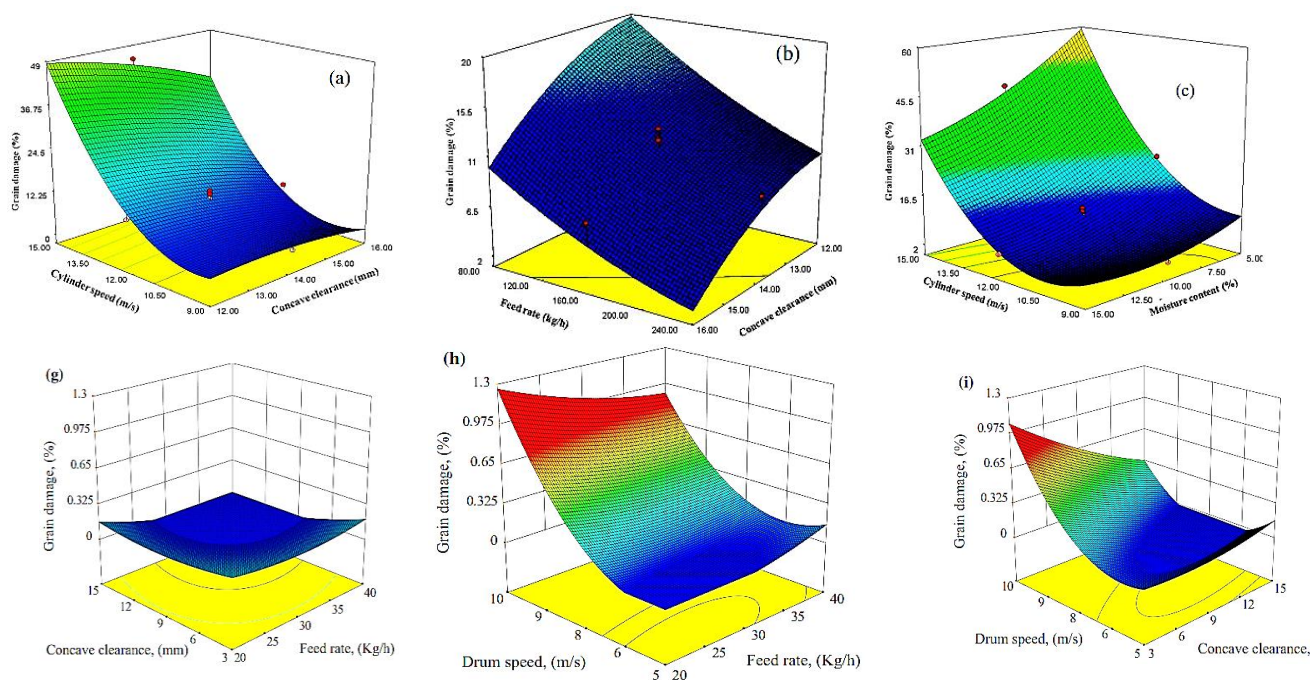


Fig. 3 - The implications on grain damage percentage of (a) cylinder speed and concave clearance, (b) feed rate and concave clearance, (c) cylinder speed and moisture content, (g) concave clearance and feed rate, (h) drum speed and feed rate, and (i) drum speed and concave clearance

A 672 kg/h rate for feeding, a concave clearance of 35 cm, and a drum speed of 8.25 m/s were the optimal parameters for preparing the Fig. 3g-i. As illustrated in Fig. 3g, the greatest damage to the grain appeared at 35-45 mm convex clearance at rates of feed varied from 650-750 kg/h. There was no evidence of damage to grains within the 35-38 mm convex clearance range at 650-675 kg/h amount of intake. The greatest amount of grain impairment has been observed to be 3.5% at 25 cm convex spacing and 750 kg/h amount of intake. Figure 3h showed the proportion of damaged grains emerged in tandem with raised rate of feed and drum rpm. With an amount of intake 750 kg/h and a drum rate of 10.83 m/s, the ultimate breakdown of grain was achieved, at 3.3%.

Likewise, there was an increase in damage to grains when the drum speed climbed and the convex clearance diminished. At a chamber inclination of 10.83 m/s and a convex space of 25 mm, the highest possible 3.8% loss of grain was seen (Fig 3i). The reduction in convex clearance led to an increase in the contacting action between the grains and the covering stripe, degrading the grains. Moreover, it happened because there was more intimate interaction among the beans and the canvas strip and the segments of the chamber that are convex. Significant forces from impacts were detected when the drum was moving faster. The maximum grain damage was caused by those maximal impact forces. At lower drum speeds, the maximum grain damage is caused by these maximum impact forces, and vice versa. Grain damage was found to be decreased at higher feed rates because maximum feed rates share the power of collision and contacting force produced by drums in rotation, whereas minimum feed rates handle the greatest the power of collision and contacting force, which results in highest degree of scratches. Similar findings with respect to the multi-threshing machine were published in *Huertas et al., (2023)*, *Chandra et al., (2024)*. The greater feed that was shared by the impact and rubbing power of the revolving drum resulted in less degradation of grain when the degree of feeding escalated.

The influence of the rate of feeding (kg/h), speed of the drum (m/s), and convex clearance (mm) on common bean damage was investigated using the implementation of the ANOVA described in Table 2. The linear parameters of rate of feeding, drum speed, convex space, interaction coefficient curvature space x speed of drum, and nonlinear term convex clearance all had a significant impact on grains damage at the 1% level of significance, based on the F-values in Table 2. At the 5% significance level, the rate feed x drum speed interaction term also significantly influenced the degree of grain impairment. The damage to the beans was not significantly impacted by the relationship between the terms flow rate x concave aperture or the quadrilateral in relation to convex geometry and intake rate variables, irrespective of the significance threshold of 10% ($p < 0.1$).

Sufficient accuracy is used to measure the signal to noise proportion. Therefore, the ratio should be higher than four. In this instance, the ratio changed to 22.74, indicating a strong signal. To navigate the design space, one can apply this model (Savic *et al.*, 2019; Savic and Savic-Gajic, 2021). This model's predicted R^2 (0.89) and adjusted R^2 (0.95). Polynomial form fitting was used to generate the regression equation that shows a variation of the percentage of grain damage (GD, %) with respect to the independent parameters (*feed rate, F_r*), (*drum speed, v_s*) and (*concave clearance, C_c*). The exponential model's insignificant terms had been eliminated to create the simplified multiplication framework (Savic *et al.*, 2019).

iii) Optimization of MARC bean thresher

The graphical optimization and optimal outcomes are shown in Figure 4. The machine's independent design parameters, which are connected to these outcomes, establish the optimal ranges of cleaning efficiency, threshing efficiency, and grain damage. The predicted percentages for cleaning efficiency, grain damage, and threshing efficiency were 85%, 0.086%, and 97.94%, respectively. By using graphical optimization, the optimal values of several variables were found, including concave clearances of 25-45 mm with 87.94% efficiency of threshing, 85% cleaning effectiveness, and 0.086% fractures.

The marked region of Fig 4a-c displays the collective outcomes of this optimization. The same values were obtained by the numerical and graphical optimization techniques (Benaseer *et al.*, 2018; Umbataliyev *et al.*, 2023). These optimal features guided the development of the drum, which was then finished and its performance assessed to validate the chosen parameters. The findings indicated that the percentage of cleaning, detrimental to the grain and spinning was 86% compared to 85%, 99%, and 0.1%, respectively, compared to predictions of 97.94% and 0.086%. As a result, a cylinder speed of 8.25 ms^{-1} , convex aperture of 37.4mm, rate of feed 672 kg h^{-1} , and level of moisture 11.6% were recommended for threshing common beans.

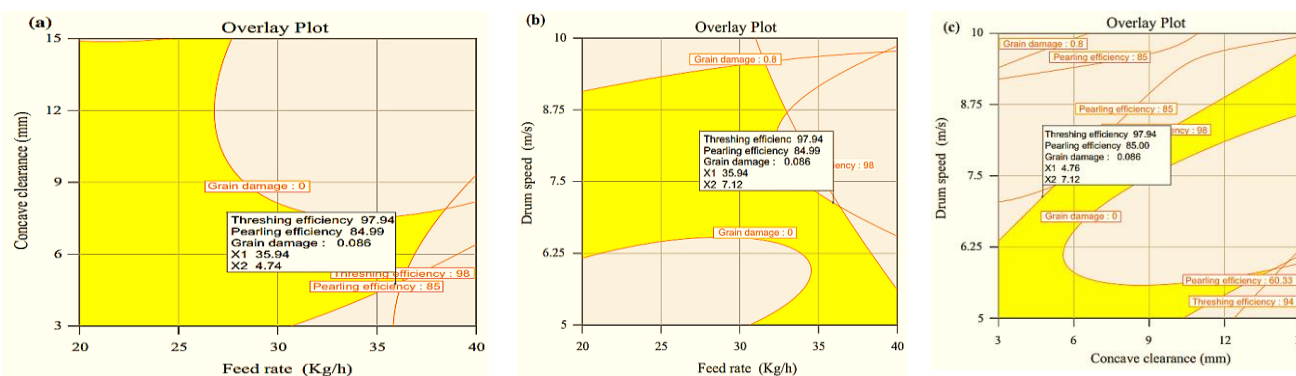


Fig. 4 - Graphical optimization of the operating parameters of the threshing drum

- (a) Superimposed contours for threshing efficiency, pearling efficiency, and damage to bean at varying feed rates and concave clearance; (b) Superimposed contours for threshing efficiency, pearling efficiency, and speed of the drum at varying feed rates; and (c) Superimposed contours for threshing efficiency, drum speeds, and concave clearance at varying feed rates.

CONCLUSIONS

The threshing drum of the MARC bean thresher is one of its essential parts and its performance is depending on its operational parameters. Important variables influencing grain damage, threshing efficiency and cleaning efficiency in common bean threshed seed quality are the feed rate, moisture level, convex aperture, and drum speed. The most significant crop and machine measurement was cylinder speed, which was subsequently the moisture level. The percentage of damaged grain improved from 45.98 to 47.97% and the overall threshing efficiency elevated from 96.81 to 98.69% when the speed of drum was varied from 7.5 to 10.83 ms^{-1} . Increased moisture content was associated with increased grain damage, efficiency of threshing and rates of seed germination. The proportion of grain impairment, and threshing efficiency were all significantly ($P < 0.01$) impacted by concave clearance. Within the 550 - 750 kg h^{-1} rate of feed range, there was variation in the average value of damage to grain (16.65-7.67%) and threshing efficiency (96.52-28.09%). As a result, a cylinder speed of 8.25 ms^{-1} , convex aperture of 37.4 mm, rate of feed 672 kg h^{-1} , and moisture level of 11.6% were recommended for threshing common beans.

ACKNOWLEDGMENTS

The author Biniam Zewdie Ghebrekidan would like to thank department of Agricultural Engineering & Food Process Engineering from Awash Melkassa Agricultural Research Center; Haramaya University (HrU), and Adama science & Technology University (ASTU) for the provision of the improved common bean seed varieties and laboratory facilities, respectively.

REFERENCES

- [1] Adewoyin, O.B. (2023). Pre-Harvest and Postharvest Factors Affecting Quality and Shelf Life of Harvested Produce. In *New Advances in Postharvest Technology*. IntechOpen. 42, 28-420
- [2] Benaseer, S., Masilamani, P., Albert, V. A., Govindaraj, M., Selvaraju, P., & Bhaskaran, M. (2018). Impact of harvesting and threshing methods on seed quality: A review. *Agricultural Reviews*, 39(3), 183–192.
- [3] Bento, J.A.C., Gomes, M.J.C., Bassinello, P.Z., Martino, H.S.D., de Souza Neto, M.A., & Oomah, B.D. (2022). Benefits of Carioca Beans (*Phaseolus vulgaris*) Molecular Mechanisms to Human Health and Nutrition. *Molecular Mechanisms of Functional Food*, 112-141.
- [4] Chandra, R.J., Masilamani, P., Suthakar, B., Rajkumar, P., Sivakumar, S. D., & Manonmani, V. (2024). Effect of Moisture Content on Combine Harvested Seed Crop and its Quality. *Journal of Experimental Agriculture International*, 46(3), 114-138.
- [5] Delelegn, T. (2022). *Design Development and Performance Evaluation of a Common Bean (Phaseolus Vulgaris) Thresher* (Doctoral dissertation, Haramaya University).
- [6] Ejara, E., Mohammed, W., & Amsalu, B. (2018). Genetic variability, heritability and expected genetic advance of yield and yield related traits in common bean genotypes (*Phaseolus vulgaris* L.) at Abaya and Yabello, Southern Ethiopia. *African Journal of Biotechnology*, 17(31), 973-980.
- [7] Ghebrekidan, B.Z., Olaniyan, A.M., Wako, A., Tadesse, A.G., Alemu, D., & Lema, T. (2024). Gravimetric characteristics and friction parameters of common bean (*Phaseolus vulgaris* L.). *Turkish Journal of Agricultural Engineering Research*, 5(1), 76-93.
- [8] Güvercin, S., & Yıldız, A. (2018). Optimization of cutting parameters using the response surface method. *Sigma Journal of Engineering and Natural Sciences*, 36(1), 113-121.
- [9] Huertas, R., Karpinska, B., Ngala, S., Mkandawire, B., Maling'a, J., Wajenjeche, E., & Foyer, C.H. (2023). Biofortification of common bean (*Phaseolus vulgaris* L.) with iron and zinc: Achievements and challenges. *Food and Energy Security*, 12(2), e406.
- [10] Jan, S., Rather, I. A., Sofi, P.A., Wani, M.A., Sheikh, F.A., Bhat, M.A., & Mir, R.R. (2021). Characterization of common bean (*Phaseolus vulgaris* L.) germplasm for morphological and seed nutrient traits from Western Himalayas. *Legume Science*, 3(2), e86.
- [11] Joshi-Saha, A., Sethy, S.K., Misra, G., Dixit, G.P., Srivastava, A.K., & Sarker, A. (2022). Biofortified legumes: Present scenario, possibilities and challenges. *Field Crops Research*, 279, 108467
- [12] Juraev, D.T., Dilmurodov, S.D., Kayumov, N.S., Xujakulova, S.R., & Karshiyeva, U.S. (2023). Evaluating Genetic Variability and Biometric Indicators in Bread Wheat Varieties: Implications for Modern Selection Methods. *Asian Journal of Agricultural and Horticultural Research*, 10(4), 335-351.
- [13] Lee, G.H., Moon, B.E., Basak, J.K., Kim, N.E., Paudel, B., Jeon, S.W., Kook J., Kang M.Y., Ko H.J., Kim, H.T. (2023). Assessment of Load on Threshing Bar During Soybean Pod Threshing. *Journal of Biosystems Engineering*, 48(4), 478-486. DOI: 10.1007/s42853-023-00206-9
- [14] Lisciani, S., Marconi, S., Le Donne, C., Camilli, E., Aguzzi, A., Gabrielli, P., & Ferrari, M. (2024). Legumes and common beans in sustainable diets: nutritional quality, environmental benefits, spread and use in food preparations. *Frontiers in Nutrition*, 11, 1385232.
- [15] Parker, T.A., Gallegos, J.A., Beaver, J., Brick, M., Brown, J.K., Cichy, K., & Gepts, P. (2022). Genetic resources and breeding priorities in *Phaseolus* beans: Vulnerability, resilience, and future challenges. *Plant breeding reviews*, 46, 289-420.
- [16] Que, K., Tang, Z., Wang, T., Su, Z., & Ding, Z. (2024). Effects of Unbalanced Incentives on Threshing Drum Stability during Rice Threshing. *Agriculture*, 14(5), 777.
- [17] Savic, I.M., & Savic Gajic, I.M. (2021). Optimization study on extraction of antioxidants from plum seeds (*Prunus domestica* L.). *Optimization and Engineering*, 22, 141-158.
- [18] Savic, I.M., Nikolic, I.L., Savic-Gajic, I.M., & Kundakovic, T.D. (2019). Modeling and optimization of bioactive compounds from chickpea seeds (*Cicer arietinum* L). *Separation Science and Technology*, 54(5), 837-846.

- [19] Strecker, K., Bitzer, V., & Kruijssen, F. (2022). Critical stages for post-harvest losses and nutrition outcomes in the value chains of bush beans and nightshade in Uganda. *Food Security*, 14(2), 411-426.
- [20] Uebersax, M.A., Cichy, K.A., Gomez, F.E., Porch, T.G., Heitholt, J., Osorno, J.M., Kamfwa K, Bales, S. (2023). Dry beans (*Phaseolus vulgaris* L.) as a vital component of sustainable agriculture and food security-A review. *Legume science*, 5(1), DOI: 10.1002/leg3.155.
- [21] Umbataliyev, N., Smailova, G., Toilybayev, M., Sansyzbayev, K., Koshanova, S., Snapp S., Bekmukhanbetova, S. (2023). Optimization of the Technological Process of Threshing Combine Harvester. *Eastern-European Journal of Enterprise Technologies*, 124(1).
- [22] Wang, W., & Cichy, K. A. (2024). Genetic variability for susceptibility to seed coat mechanical damage and relationship to end-use quality in kidney beans. *Crop Science*, 64(1), 200-210.

DESIGN AND EXPERIMENTAL RESEARCH OF A PORTABLE WALNUT HARVESTER BASED ON ELECTROMAGNETIC EXCITATION TECHNOLOGY

基于电磁激励技术的便携式核桃采摘机设计与试验研究

Na JIA¹⁾ Guangqiu LI¹⁾ Anguo HU²⁾ Qin CHEN^{*3)}

¹⁾ Northeast Forestry University, College of Mechanical and Electrical Engineering/ China;

²⁾ Yongkang Weili Technology Co, Ltd / China

^{*3)} The Yunnan Provincial Academy of Forestry and Grassland Sciences YangBi Walnut Research Institute/ China;

Tel: +86 18686870636; E-mail: 876765338@qq.com

Corresponding author: Qin Chen

DOI: <https://doi.org/10.35633/inmateh-74-30>

Keywords: Electromagnetic excitation technology, Walnut harvesting machine, Portable machinery, Agricultural mechanization, Parameter optimization

ABSTRACT

With the development of agricultural mechanization and the expansion of fruit tree cultivation, effective harvesting techniques have become crucial for boosting yield and reducing labor costs. This is particularly true in hilly areas with complex terrains where traditional, large-scale harvesting machinery struggles to be effective. This study designed and experimentally validated a portable walnut harvester based on electromagnetic excitation technology, aiming to enhance harvesting efficiency and reduce labor intensity in these areas. The harvester integrates electromagnetic excitation technology with the design of a lightweight, handheld electric cart, optimizing the machine's adaptability and operational flexibility across various terrains. Through field testing, the vibration effects of the machine under different branch diameters and impact locations were evaluated, and the impact parameters were optimized using Design-Expert software. Experimental results indicate that the machine can operate effectively at maximum pitch angles while delivering powerful impact forces to harvest walnuts efficiently. Furthermore, by optimizing the vibration frequency and impact location for branches of different diameters, recommended parameters for using the equipment were provided. This study not only demonstrates the potential application of electromagnetic excitation technology in agricultural machinery but also offers a viable mechanized solution for orchards in similarly complex terrains.

摘要

随着农业机械化的发展和果树种植业的扩展，有效的采摘技术成为提升产量和降低劳动成本的关键。尤其在地形复杂的丘陵地区，传统的大型采摘机械难以发挥效用。本研究设计并实验验证了一种基于电磁激励技术的便携式核桃采摘机，旨在提高这些地区的采摘效率并减轻劳动强度。该采摘机结合了电磁激励技术和轻便的手扶式电动推车设计，优化了机械在不同地形下的适应能力和操作灵活性。通过实地测试，我们评估了机器在不同枝杆直径和撞击位置下的激振效果，并采用 Design-Expert 软件进行了撞击参数的优化。实验结果表明，该机械能在最大俯仰角度下有效操作，同时提供强大的撞击力，有效地采摘核桃。此外，通过对不同直径枝杆的激振频率和撞击位置的优化，提供了设备使用的推荐参数。该研究不仅展示了电磁激励技术在农业机械中的应用潜力，也为类似地形复杂的果园提供了一种可行的机械化解方案。

INTRODUCTION

As global populations continue to rise and advancements in agricultural mechanization progress, efficient crop harvesting technologies are becoming increasingly vital. Walnuts, a fruit of significant economic value, are extensively cultivated in various provinces in China such as Yunnan, Xinjiang, and Sichuan (Wei Li, 2023; Jia Meng et al., 2023). Particularly in Yunnan Province, walnut cultivation leads the nation with an area of 286.87 thousand hectares and a production of 1.48 million tons (Honghong Yu et al., 2019). Due to the distinct seasonality of walnut harvesting, delays in harvesting can directly impact the quality of the walnuts and result in substantial economic losses. Consequently, enhancing the efficiency of walnut harvesting has been a focal point in forestry and fruit industry research.

In recent years, as the level of agricultural mechanization has improved, the development and application of large-scale vibratory harvesting machines have achieved notable success. For instance, in 2017, *Hoshyarmanesh et al.* designed a vibratory olive harvester, identifying the optimal excitation frequency for olive trees at 20Hz (*Hoshyarmanesh et al., 2017*). Castro-Garcia S developed a vibratory harvester for citrus fruits, determining through simulations and experiments that the resonance range for different maturities of citrus lies between 4.5 to 5Hz (*Castro-Garcia S et al., 2017*). In 2019, Zicheng Gao developed a suspended vibratory camellia fruit harvester, using dual eccentric blocks as the source of vibration and a tracked chassis for mobility. Their trials indicated that the acceleration of camellia fruit tree branches varied cyclically with vibration, with the vibratory frequency and clamping height significantly affecting trunk amplitude, and fruit drop rate correlating positively with harvesting frequency and inversely with clamping height. At a frequency of 15Hz and a clamping height of 1300mm, the fruit drop rate and flower drop rate reached 95.1% and 4.8%, respectively (*Zicheng Gao et al., 2019*). In 2022, Xiaoqiang Du designed a tracked tea oil fruit vibratory harvester, employing a crank rocker to drive multiple rows of tapping rods, achieving a fruit harvesting rate of 87.56% and a bud drop rate of 25.86% at 360r/min hydraulic motor operation (*Xiaoqiang Du et al., 2022*). In 2023, Shuqi Shang designed an apple vibratory harvester using eccentric blocks as the source of vibration, towed by a tractor. At a vibration frequency of 10Hz, an amplitude of 1.6cm, and a clamping height of 58.7cm, the fruit detachment rate reached 95.9% with a fruit damage rate of only 1.3% (*Shuqi Shang et al., 2023*).

Although large-scale vibratory harvesting machines have shown significant effectiveness in improving the efficiency of orchard fruit harvesting, their application in mountainous and hilly areas still poses major challenges. These machines typically rely on eccentric blocks to generate the necessary vibratory force, leading to an increase in overall weight, which restricts mobility and operability. In areas with complex terrain and steep slopes, the operational safety and flexibility of these devices are substantially reduced, and the high cost of the equipment further limits their widespread use in these regions (*Wenting Jin et al., 2023*).

Given the challenges posed by complex terrains, the development of portable walnut harvesting equipment becomes crucial. In 2018, Chengmao Cao designed a portable walnut harvester that mimics human-like high-altitude beating actions using an eccentric wheel and a driven pendulum piece. Although experimental data indicated that this device exhibited a higher picking cleanliness, the small impact area per beat resulted in lower harvesting efficiency, and prolonged manual operation increased the labor intensity for workers (*Chengmao Cao et al., 2018*). Subsequently, in 2021, Zensong Li developed an integrated manual and automatic walnut harvester. Experiments demonstrated that at excitation frequencies of 16-18 Hz, the machine achieved average picking rates of 83.9%-88.0%. However, increased excitation amplitude and duration led to greater damage to branches and shoots (*Zensong Li et al., 2021*). In 2023, Huibin Zhu and Zhang Wenkai designed a gasoline-powered walnut harvesting machine, which exhibited an optimal picking cleanliness of 86.5% in simulation tests. Nevertheless, due to limitations in the design of the clamping points, its cleanliness could not be further improved, highlighting the necessity to consider more adjustable clamping points in the design to optimize performance (*Huibin Zhu et al., 2023*).

These studies indicate that despite some progress in addressing walnut harvesting challenges in mountainous and hilly regions through portable harvesting equipment, the design reliance on eccentric masses as excitation sources continues to restrict the portability and ease of operation of these devices. Electromagnetic excitation technology, as an innovative solution, demonstrates significant advantages due to its simple structure, light weight, strong and controllable excitation force. This technology not only effectively reduces the equipment weight but also allows for the adjustment of excitation frequency to flexibly meet the harvesting needs of different tree species and fruits, greatly enhancing the practicality and application range of portable walnut harvesting devices.

MATERIALS AND METHODS

System Overview and Operating Principle

System Components

The overall structure of the portable walnut harvester based on electromagnetic excitation technology includes the following main components: an impact clamping device (comprising an impact device and a clamping device), a control rod, an adjustable support column, Hanging Connector, an electric dual-wheel handcart, and associated motor and electromagnetic control devices. The schematic of this structure is detailed in Fig. 1.

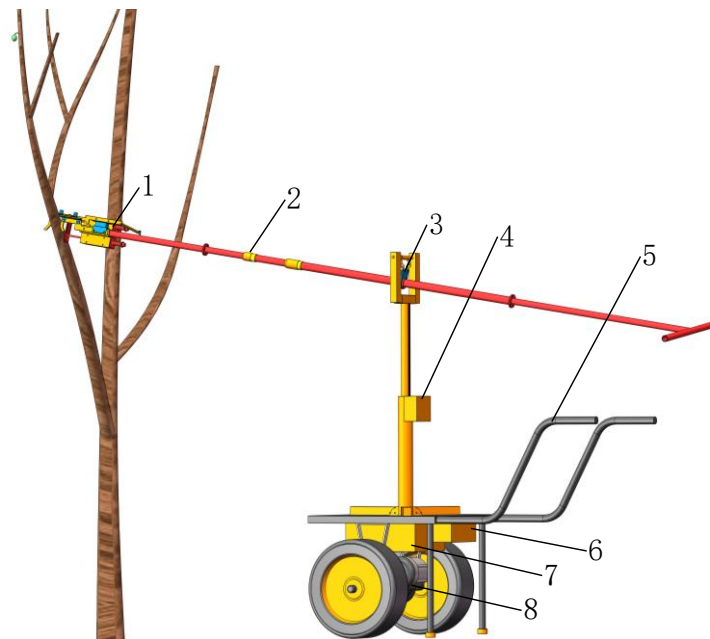


Fig. 1 - Schematic Diagram of Walnut Harvester Structure

1. Impact Clamping Device; 2. Control Rod; 3. Hanging Connector; 4. Adjustable Support Column; 5. Electric dual-wheel handcart; 6. Control Box; 7. Power Storage Compartment; 8. 0.8kW Motor

The impact clamping device consists of a clamping device and an impact device, both fixed to the control rod via a convex connecting plate. The clamping device utilizes a pre-tensioned spring to achieve a clamping gap corresponding to the varying thicknesses of branches, which is then locked by the magnetic force of a rectangular solenoid.

This design allows the clamping device to adaptively grip branches of different thicknesses using the self-weight of the impact clamping device. The exciting electromagnet provides an effective impact force, enabling efficient excitation of the branches. The control rod is suspended from the head of the adjustable support column via a chain, significantly reducing the transfer of vibrational forces to the operator during excitation, thereby enhancing operational comfort.

The adjustable support column is connected to the Electric dual-wheel handcart through bolts, allowing operators to quickly switch between targets during the harvesting process. The Electric dual-wheel handcart is equipped with a differential to drive both wheels, with a motor power of 0.8 kW and a maximum climbing angle of 40° , sufficient to meet the mobility and on-the-spot turning requirements of the harvester in hilly areas. The motor control device of the Electric dual-wheel handcart and the control device for the exciting electromagnet are both housed within a control box, sharing a power source to simplify system configuration and operation.

Before initiating the harvesting operation, operators must first adjust the Electric dual-wheel handcart to ensure it maintains an appropriate distance from the main trunk of the walnut tree. This process involves adjusting the position of the Electric dual-wheel handcart and its telescopic section, as well as the height of the adjustable support column based on the distribution height of the branches, thus optimizing the ergonomics of the operation and enhancing harvesting efficiency.

The operator controls the control rod to position the clamping device above the target branch. Subsequently, the operator reduces the force applied at the handle of the operation section, allowing the impact clamping device to naturally fall and engage the branch into the working interval of the clamping device. Under the tension provided by the pre-tensioned spring, the clamping device automatically adapts to branches of different thicknesses, ensuring the stability of subsequent clamping operations. Once positioned, the air switch is activated, energizing the rectangular solenoid, which then locks the clamping gap formed to match the diameter of the clamped branch, completing the clamping process.

Following this, the switch of the exciting electromagnet controller is triggered. According to the preset operating frequency of the control system chip, the exciting electromagnet drives the push plate to impact the clamped branch. The impact of the push plate accelerates the fruit at the end of the branch; when the inertial force exerted on the fruit exceeds the binding force of the fruit stem, the fruit detaches from the branch, completing the harvesting process.

Design of Key Components

Design of the Control Rod Structure

The control rod is a critical component of the portable walnut harvester, directly impacting the equipment's operational flexibility and efficiency. In this design, the control rod consists of several functional parts, including the connection segment, control segment, telescopic segment, Rotating Clamp Head, and Hanging Connector, with the detailed structure presented in Fig. 2. The design of the control rod focuses on enhancing the ergonomic adaptability of operations and reducing physical labor intensity.

The Hanging Connector on the control rod are linked to the adjustable support column via a chain, allowing the control rod to be suspended in mid-air, effectively reducing the reactive forces transmitted to the operator's hands during the excitation process. In terms of connections, the control segment, connection segment, and telescopic segment utilize flange connections, which allow for rapid disassembly and assembly through hand-tightened nuts, greatly increasing the efficiency of equipment maintenance and adjustment.

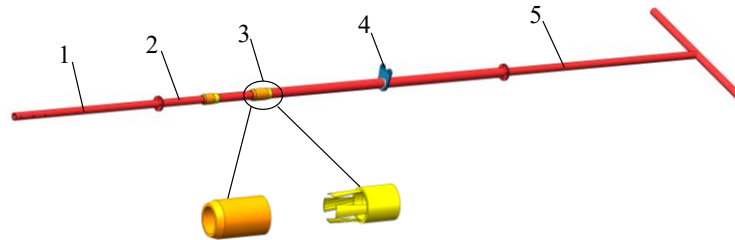


Fig. 2 - Schematic Diagram of the Control Rod Structure

1. Connection Segment; 2. Telescoping segment; 3. Rotating Clamp Head; 4. Hanging Connector; 5. Control Segment

The control rod is made from stainless steel hollow tubes, designed to reduce overall weight and enhance structural corrosion resistance, adapting to various field environments. The telescopic segment is designed as a combination of three stainless steel tubes of different thicknesses and lengths, connected by a Rotating Clamp Head, allowing for rapid adjustment of the control rod length to accommodate different operator habits and work environments. The adjustable range of the control rod length is from 1.3 to 2.6 meters, meeting the needs from low to high work requirements, and the longest rod segment does not exceed 1.3 meters when disassembled, facilitating transportation and storage.

The flexible suspension of the telescopic segment allows the control rod to rotate or swing circumferentially on the adjustable support column via Hanging Connector, accommodating branches growing at various angles. Based on ergonomic design, the operator's hand-holding position is maintained at a height of 0.8 to 1.2 meters to optimize the operating experience and efficiency. The support panel height of the Electric dual-wheel handcart is 0.6 meters, which, in conjunction with the adjustment of the control rod, can meet different harvesting height requirements.

Taking practical harvesting heights of 3.2 meters and 0.9 meters as examples, the angle between the control rod and the horizontal plane as well as the lifting range of the adjustable support column were precisely calculated using formulas (Formulas 1-4), ensuring the accuracy and safety of the operation.

$$\sin \theta = \frac{l}{H - h_1} \quad [^\circ] \quad (1)$$

where: l - length of the control rod, [m]; H - actual harvesting height, [m]; h_1 - height of the control rod grip, [m]; θ - Pitch angle of the control rod, [°].

Using equation (2) to calculate the pitch angle of the control rod, the height of the fixed position of the Hanging Connector is determined:

$$\theta = \arcsin \frac{l}{H - h_1} \quad [^\circ] \quad (2)$$

$$h = \tan \theta (l_1 - h_2) \quad [\text{m}] \quad (3)$$

$$h = \tan \left(\arcsin \frac{l}{H - h} (l_1 - h_2) \right) \quad [\text{m}] \quad (4)$$

where: l_1 - horizontal distance between the control rod grip and the adjustable support column, [m]; h_2 - height of the Electric dual-wheel handcart panel, [m]; h - height of the adjustable support column's head, [m].

The calculations indicate that the optimal fixed position for the Hanging Connector on the control rod should be at 1.3 m, while the lifting range of the adjustable support column should be set between 0.6 and 1.2 m to accommodate different working conditions. Under these settings, the pitch angles of the control rod will be 12.68° and 31.26°, respectively, ensuring optimal ergonomics and operator comfort during operation.

Design and Development of the Impact Clamping Device

The impact clamping device is a core component, consisting of parts such as the push plate, exciting electromagnet, convex connecting plate, and clamping mechanism (including the clamping head, pre-tensioned spring, slide rail, and rectangular solenoid), with the specific structure shown in Fig 3. Both the exciting electromagnet and the rectangular solenoid, along with the clamping head, are bolted onto the control rod. By clamping the branches, the weight of the impact clamping device and most of the reactive force during excitation are transferred to the branch, significantly reducing the labor intensity for workers engaged in prolonged operations. The two exciting electromagnets have the same model and are installed at the corresponding position on the convex connecting plate to ensure that the kinetic energy output of the exciting electromagnet to the pushing plate can be balanced during the excitation process. The dynamic clamping head is connected to the fixed clamping head via a slide rail and connected at the end to the pre-tensioned spring, facilitating adaptive clamping.

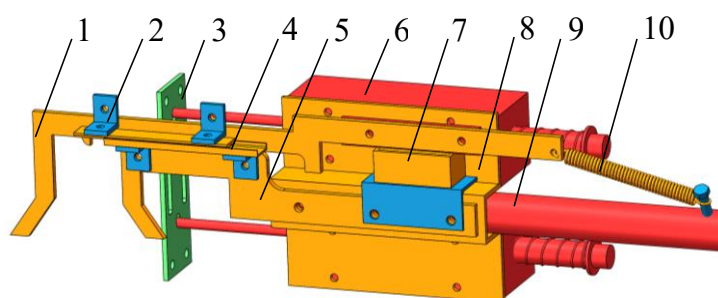


Fig. 3 - Schematic Diagram of the Impact Clamping Device Structure

1. Dynamic Clamp Head; 2. Angle Bracket; 3. Push Plate; 4. Slide Rail; 5. Fixed clamp head; 6. Exciting electromagnet; 7. Rectangular solenoid; 8. Convex Connection Plate; 9. Connection Segment; 10. Pre-tension Spring

Design and Development of the Impact Device

The key to the design of the impact device lies in ensuring the optimal ratio of kinetic energy to weight of the push plate, to maximize impact efficiency without compromising the stability and durability of the equipment. The impact clamping device operates in an upward-looking posture; thus, the exciting electromagnet needs to overcome the gravitational work of the push plate during excitation. Excessive weight of the push plate could significantly affect the excitation frequency and impact kinetic energy of the electromagnet, while too light a weight may lead to deformation of the push plate or insufficient impact energy. Therefore, to ensure that the impact device's kinetic energy meets the harvesting requirements, the weight and material properties of the push plate are especially crucial. Using NM450 material for the push plate, which has a yield strength exceeding 1100 MPa and impact resistance and wear resistance three times that of the commonly used Q235 material, enhances the impact performance and long-term durability of the entire device (Yi Cao *et al.*, 2023).

Upon impact, walnut branches facilitate the accelerated motion of the fruit. According to tests on the separation force between walnut fruit and branches, the average separation force along the stem direction is 8N. As the direction of force application increasingly deviates from the fruit's growth direction, the required separation force decreases. Based on the average weight of mature walnuts, 60-80g, using formula (5), the necessary acceleration for walnut detachment is calculated to ensure that excitation at any angle can effectively harvest the fruit (Tuqiang Chen *et al.*, 2023; Chunshou Ye *et al.*, 2022).

$$F_f = m_h a_f \quad [\text{N}] \quad (5)$$

where: F_f - force required for fruit detachment, [N] ; m_h - weight of a single walnut, [g]; a_f - acceleration needed for fruit to detach from the branch, [m/s²].

During the harvesting process, when the walnut's acceleration reaches 100 m/s², effective harvesting can be achieved. As per equation (6), the magnitude of the electromagnetic force is influenced by factors including the length of the striking pin and the coil's excitation current. Therefore, based on this data, when selecting the model of the exciting electromagnet, it is advisable to choose a model with a long striking pin and high current to ensure optimal mechanical performance (Mengkun Lu *et al.*, 2023; Tong Huang *et al.*, 2018).

$$F_D = \frac{dW}{dx} = \frac{1}{2} i^2(t) \frac{\partial L(x)}{\partial x} \text{ [N]} \tag{6}$$

where: F_D - Electromagnetic force, [N]; W - Magnetic energy, [J]; $L(x)$ - Inductance value related to the position of the striking pin, [H]; $i(t)$ - Excitation current of the coil, [A].

Models with longer movable striking pin and greater current capabilities to enhance the impact strength and reliability of the equipment were preferred. The selected model of the exciting electromagnet is DC24 - 100mm, characterized by its compact size, lightweight, operating voltage of 24V, current of 8A, stroke of 100mm, and operating frequency set between 1 - 3.5 Hz. It provides a maximum impact force of over 50N, making it highly suitable for the needs of this project.

Optimization Experiments of the Impact Device

In this study, the performance evaluation of the excitation electromagnet was conducted by overcoming the gravity of the push plate. In order to further explore the impact force of the impact device under different postures, a series of impact tests was designed considering the influence of the design parameters of the picking machine. Acceleration sensors were pasted on the surface of the push plate to collect experimental data (Hou, Junming, et al., 2024). Two different weights (100g and 600g) of push plates were used, and four experiments were conducted at elevation angles of 0°, 10°, 20° and 30°, with four groups in each experiment. Each group lasted for 4s, and the duration of each group was divided into five equal parts, taking the average value as the numerical value of that stage. The specific experimental setup is shown in Figure 4, and the experimental results are shown in Figure 5.

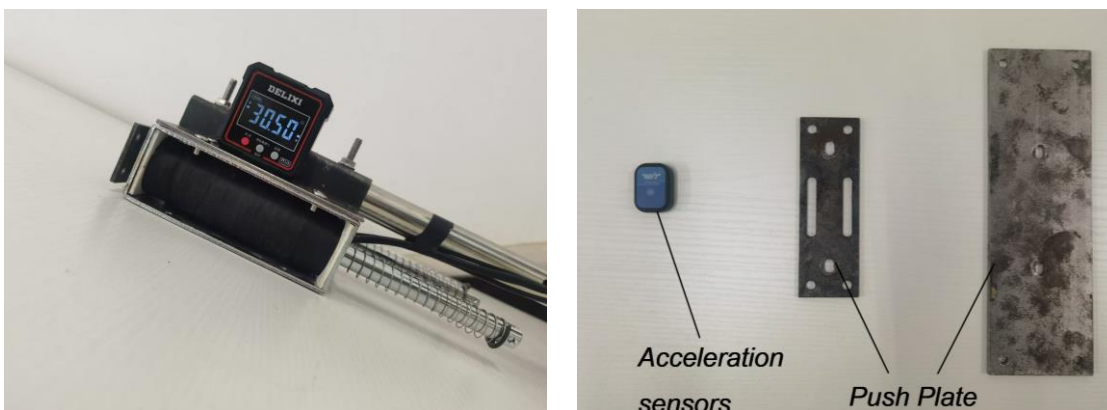


Fig. 4 - Device for Impact Testing

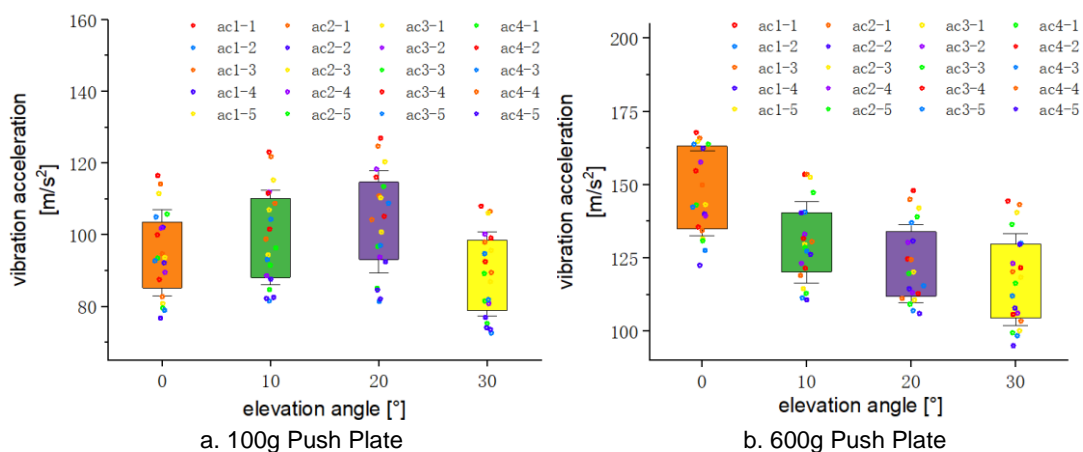


Fig. 5 - Performance Testing of the Impact Device

As shown in Fig 6a, the 100g push plate recorded a maximum acceleration of 118 m/s² at a 0° tilt angle, while a peak acceleration of 128 m/s² was observed at a 20° tilt angle, indicating an initial increase and subsequent decrease in acceleration with increasing tilt angle. Furthermore, the operating frequency of the push plate had a minimal impact on the test results.

The iron core was measured to weigh 437g, and based on formula (16), the maximum instantaneous impact force of the 100g push plate under peak acceleration was calculated to be 68.75N. This calculation provides a direct quantification of the impact performance of the impact device.

$$F_s = (m_2 + m_3) a \quad [N] \tag{16}$$

where: F_s - the impact force measured by the impact device, [N]; m_2 - mass of the striking pin, [m]; m_3 - mass of the push plate, [m]; a - acceleration recorded, [m/s²].

For the 600g push plate, Fig. 6b shows that the highest acceleration recorded was 170 m/s² at a 0° tilt angle, with a decreasing trend in acceleration as the tilt angle increased, reaching 151 m/s² at 30°. Unlike the 100g push plate, the 600g push plate significantly impacts the operating frequency of the impact device.

Accordingly, the instantaneous impact force for the 600g push plate at maximum acceleration was calculated to be 176N. This result highlights the significant increase in impact force due to increased weight and also points to the influence of weight on the overall operating frequency of the device.

In this study, a detailed analysis of the effects of tilt angle and push plate mass on the performance of the impact device was conducted. Experimental results indicate that the mass of the push plate and the tilt angle are important factors affecting the impact force. Specifically, when the mass of the push plate is low, the impact force initially increases and then decreases with increasing tilt angle. This phenomenon can be explained by changes in the efficiency of kinetic energy transfer at different angles: an initial increase in tilt may facilitate more effective energy transfer, while at higher tilt angles, impact efficiency begins to decrease due to mechanical structural limitations.

Conversely, for heavier push plates, increasing the tilt angle leads to a gradual decrease in impact force. This is mainly because the increased weight leads to greater kinetic energy loss during transfer, especially at larger tilt angles. Additionally, the mass of the push plate significantly affects the operating frequency of the exciting electromagnet, requiring the electromagnet to operate at lower frequencies to maintain sufficient impact force for heavier push plates.

Therefore, when selecting a push plate, it is essential to consider the combined effects of tilt angle and operating frequency of the electromagnet. This comprehensive consideration aims to optimize the overall performance of the impact device, ensuring optimal impact force under various working conditions. Table 1 lists detailed data on the impact forces under different configurations.

Table 1

Impact Force of the Impact Device				
Elevation angle [°]	0	10	20	30
Impact force [N]	155-130	150-125	142-110	135-105

Design and Analysis of the Clamping Device

The clamping device achieves precise positioning of the branches to be clamped through the self-weight of the impact clamping device and the guide angle, and confirms the clamping gap relative to the diameter of the clamped branch using a pre-tensioned spring, ultimately utilizing the magnetic attraction principle of the Rectangular solenoid to lock the clamping gap formed around branches of varying thicknesses. Whether the clamping device can form and lock a corresponding clamping gap for branches of different thicknesses depends on the tension provided by the pre-tensioned spring and the magnetic force of the Rectangular solenoid. Therefore, an analysis and calculation of the forces during the clamping process are necessary, as shown in Fig. 6.

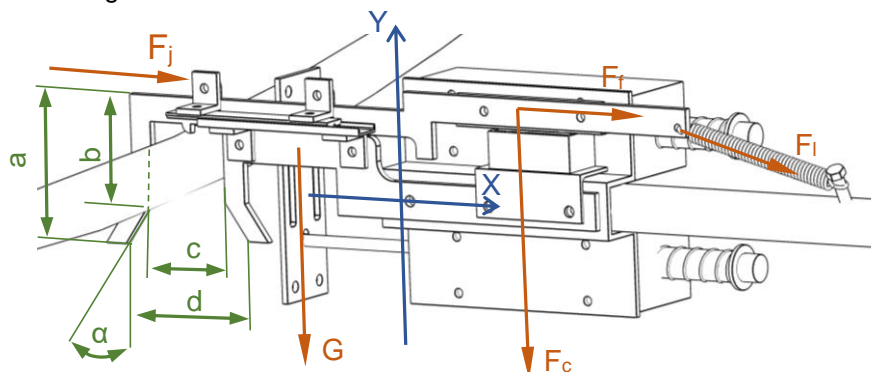


Fig. 6 - Force Analysis Diagram of the Clamping Device

Analyzing the forces in the coordinate system yields:

$$\begin{cases} F_y = F_l \sin \alpha + \mu F_N - nG \cos \alpha \\ F_x = F_l \cos \alpha + nG \sin \alpha \end{cases} \quad (7)$$

where: F_l - tension provided by the pre-tensioned spring, [N]; μ - coefficient of friction between the clamping device and the bark; n - ratio of the support force to gravity acting on the impact clamping device; G - gravity of the impact clamping device, [N]; α - deflection angle of the guide angle, [°];

If the clamping device is to adapt to branches of various thicknesses, it is required:

$$\begin{cases} F_y < 0 \\ F_x = -F_N \end{cases} \quad (8)$$

Combining and simplifying the above expressions, it is obtained:

$$F_l < \frac{\sin \alpha + \mu \cos \alpha}{nG(\cos \alpha - \mu \sin \alpha)} \text{ [N]} \quad (9)$$

For a cylindrical helical spring:

$$F_l = k \cdot \Delta x \text{ [N]} \quad (10)$$

where: k - spring stiffness coefficient, [N/m]; Δx - spring extension, [mm].

The clamping mechanism is self-adapting to a wide range of branch thicknesses, provided that the distance between the ends of the guide angles, d , is greater than the diameter of the largest clamped branch. The cross-sectional diameters of walnut tree branches mostly range from 30 to 90 mm, tapering from the main trunk to the end of the branch. Hence, the working range of the clamping $d > 50$ mm.

From this, the guide angle can be deduced:

$$\alpha = \arctan \frac{a-b}{d-c} \text{ [°]} \quad (11)$$

Using equations (3), (4), and (5), the spring stiffness coefficient can be determined:

$$k = \frac{\sin(\arctan \frac{a-b}{d-c}) + \mu \cos(\arctan \frac{a-b}{d-c})}{\Delta x n G \left[\cos(\arctan \frac{a-b}{d-c}) - \mu \sin(\arctan \frac{a-b}{d-c}) \right]} \text{ [N/m]} \quad (12)$$

Analysis of the clamping force:

$$\begin{cases} F_g = G \sin \theta \\ F_z + F_g = F_j \\ F_j = F_f + F_l \\ F_f = \mu_2 F_c \end{cases} \quad (13)$$

where:

F_g - support force from the branch on the impact clamping device, [N]; F_z - impact force, [N]; F_i - Resultant force of the pre-tension and the pull provided by the Rectangular solenoid, [N]; F_f - Friction force between the Rectangular solenoid and the dynamic clamping head, [N]; μ_2 - static friction coefficient between the Rectangular solenoid and the dynamic clamping head; F_c - magnetic force of the electromagnet, [N].

From equation (9), the required magnetic force of the Rectangular solenoid can be calculated:

$$F_c = \frac{G \sin \theta + F_z - F_l}{\mu_2} \text{ [N]} \quad (14)$$

The higher the harvesting height of the harvester, the stronger the magnetic suction force required to clamp the branches during impact by the exciting electromagnet. Taking the maximum clamping gap and the highest working height as examples, let $a = 70$ mm, $b = 40$ mm, $c = 65$ mm, $d = 110$ mm, $\theta = 30^\circ$, $n = 0.5$. The spring extension deformation corresponds to the clamping diameter of the clamping device, $0 \leq \Delta x \leq 40$ mm.

At this point, $\Delta x = 40\text{mm}$, the spring provides the maximum tensile force, thus meeting the requirements across the entire range. From this, the guide angle is determined to be $\alpha = 35^\circ$, the spring progression coefficient $k < 376.4\text{N/m}$, $F_c = 473\text{N}$.

Based on the formula for the spring stiffness coefficient:

$$k = \frac{Gd^4}{8D^3n} \text{ [N/m]} \quad (15)$$

From this analysis, the guide angle is determined to be 35° , with the spring progression coefficient being less than 376.4 N/m , and the tensile force provided is 473 N . According to the formula for the spring stiffness coefficient:

RESULTS

Walnut Harvester Picking Trials

During the harvesting process, it is essential to consider how the impact device adapts to walnut branches of varying thicknesses and changes in excitation points. The excitation effect differs significantly depending on the branch diameter: thinner branches show a more pronounced response under excitation, with a wider range and greater efficiency; by contrast, optimizing the harvesting efficiency of thicker branches should be a focal point. Therefore, in order to provide a practical reference for harvesting, this study was planned to conduct multi-point excitation tests on walnut branches of different diameters using different excitation frequencies.

Branches with diameters ranging from 30mm to 56mm and lengths exceeding 2.5m were selected, with data collection facilitated by an in-house developed IM948 sensor module fitted in an electronic walnut. This device utilizes Bluetooth technology to transmit acceleration data to a computer terminal within a frequency range of $0.5\text{-}250\text{Hz}$. The sensor's acceleration component has a range of $\pm 16\text{g}$, with a minimum change unit accurate to 0.01g . The use of the electronic walnut simulates the acceleration response of the fruit at the end of the branch post-excitation, thus verifying the excitation effects of the harvester and providing a scientific basis for orchard harvesting (see Fig.7).



Fig. 7 - Schematic diagram of the harvesting trials

Trial Strategy and Outcomes

Based on device performance and user experience, branches with diameters of 30mm , 43mm , and 56mm and lengths exceeding 2.5m were selected as test subjects. At positions 800mm , 1200mm , and 1600mm from the main branch, excitation frequencies of 1.67Hz , 2.50Hz , and 3.33Hz were set for testing. During the tests, the electronic walnut mounted on the branches was used to collect dynamic acceleration data of the fruit at the branch ends.

A three-factor, three-level response surface analysis using Design-Expert software was conducted to thoroughly assess the impact of branch diameter, excitation point, and excitation frequency on the excitation effect. The experimental factors and levels are detailed in Table 2, which provides an overview of the comprehensive experimental parameter settings.

Table 2

Table of Trial Factor Levels

Level	Excitation frequency / A	Branch diameter / B	Vibration excitation point / C
	[Hz]	[mm]	[mm]
-1	1.66	30.00	800
0	2.50	43.00	1200
+1	3.33	56.00	1600

The average values of the experimental data for each group were calculated and entered into the experimental design and results table, as shown in Table 3.

Table 3

Trial design and results

Treatment group	excitation frequency / A	branch diameter / B	vibration excitation point / C	vibration acceleration / Y
	[Hz]	[mm]	[mm]	[m/s ²]
1	3.33	56	1200	72
2	2.50	43	1200	93
3	2.50	43	1200	93
4	1.66	56	1200	63
5	1.66	43	800	61
6	1.66	30	1200	110
7	3.33	30	1200	142
8	1.66	43	1600	118
9	2.50	30	800	100
10	2.50	43	1200	93
11	3.33	43	1600	132
12	2.50	56	1600	85
13	2.50	43	1200	93
14	2.50	30	1600	150
15	2.50	56	800	47
16	3.33	43	800	85
17	2.50	43	1200	93

A second-order multivariate regression fit of the data in Table 2 was performed using Design-Expert software, yielding the results of the analysis of variance (ANOVA) for walnut fruit acceleration, as displayed in Table 4.

Table 4

Trial ANOVA table

	Sum of Squares	Df	F-value	P-value
Model	12568.51	9	294.00	<0.001**
A	780.13	1	164.24	<0.001**
B	6903.13	1	1453.29	<0.001**
C	4608.00	1	970.11	<0.001**
AB	132.25	1	27.84	0.012*
AC	25.00	1	5.26	0.055
BC	36.00	1	7.58	0.028*
A²	55.33	1	11.65	0.011*
B²	0.066	1	0.014	0.909
C²	23.75	1	5.00	0.060
Residual	33.25	7		
Lack of Fit	33.25	3	0.629	
Pure Error	0	4		
Cor Total	12601.76	16		

Note: "***" indicates highly significant, and "*" indicates significant.

This study conducted a detailed analysis of the acceleration of walnut fruit post-excitation and determined the order of importance of influencing factors based on experimental data. The results indicate that branch diameter, excitation point, and excitation frequency significantly impact acceleration, with the order of influence being: branch diameter > excitation point > excitation frequency. The regression model derived from the analysis is as follows:

$$Y = 92.80 + 9.87A - 29.38B + 24.00C - 75AB - 2.50AC - 3.00BC + 3.72A^2 + 0.22B^2 + 2.48C^2 \quad (17)$$

The model's goodness-of-fit test indicated that the lack-of-fit value was greater than 0.1, confirming the model's high adaptability. The model's high significance was validated with a P-value of 0.0001, and a coefficient of determination (R²) of 0.9574, indicating that over 95% of the response values can be explained by this model, thus confirming the accuracy of the regression equation in predicting the post-excitation acceleration of walnut fruit.

To further understand the impact of each factor on acceleration, response surface analysis plots for significant interaction factors were generated based on the regression equation, as shown in Fig.8. The analysis revealed:

Optimization of Harvesting Parameters

In the operation of walnut harvesting machines, the excitation effects significantly vary for branches of different diameters, even under the same excitation point and frequency. For thin branches, excessively strong excitation forces may cause branch breakage, while thick branches may require multiple excitations to achieve the desired harvesting effect. To enhance harvesting efficiency and optimize energy utilization, optimization calculations of harvesting parameters were conducted using Design-Expert software, aiming to provide more effective harvesting guidance.

The optimization objective function considered the interactions between excitation force, frequency, and position, with detailed solution analysis conducted through mathematical modeling and constraints (Eq.18).

$$\begin{cases} 100 \leq Y \\ 1.6 \leq A \leq 3.3 \\ 30 \geq B; 30 \leq B \leq 43; 43 \leq B \leq 56 \\ 800 \leq C \leq 2500 \end{cases} \quad (18)$$

The results of the harvesting parameter optimization, as shown in Fig. 9, are as follows:

(a) As the excitation frequency increases, the excitation point required to achieve the necessary acceleration significantly decreases. Therefore, increasing the excitation frequency while ensuring harvesting effectiveness can effectively expand the excitation range. The recommended harvesting parameters are an excitation frequency of 3.33Hz and an excitation point 450mm from the main branch junction.

(b) For branches with diameters ranging from 30mm to 43mm, increasing the excitation point can significantly enhance the excitation effect, while reducing the excitation frequency helps to decrease energy consumption. Therefore, the suggested harvesting parameters are an excitation frequency of 1.66Hz and an excitation point 1400mm from the main branch junction.

(c) For branches with diameters ranging from 43mm to 56mm, the impact of excitation frequency on the excitation effect is minimal, so the frequency can be reduced as much as possible to lower energy consumption. The recommended harvesting parameters are an excitation frequency of 1.66Hz and an excitation point 1800mm from the main branch junction.

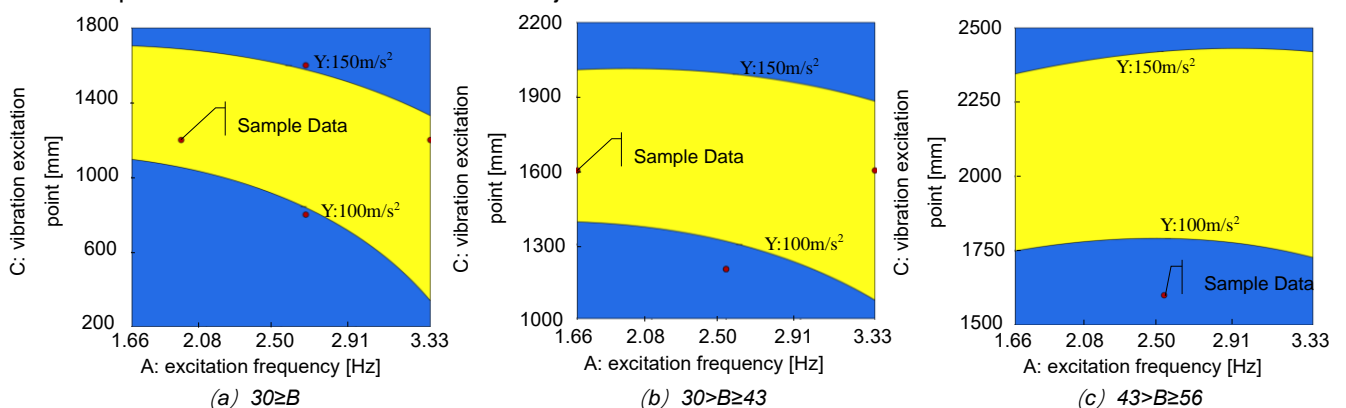


Fig. 9 - Optimization Plot for Harvesting Parameters

CONCLUSIONS

This study successfully designed and experimentally validated a portable walnut harvesting machine tailored for the unique planting patterns of China's hilly regions. The main conclusions and contributions are as follows:

1. The walnut harvester, integrated with an Electric dual-wheel handcart, demonstrated exceptional climbing and obstacle-crossing capabilities, suitable for the complex terrain of hilly areas. Through an adjustable support column and a suspension design, the impact device located at the end of the control rod effectively reduces the transmission of excitation force to the operator while providing flexible control to accommodate various branch growth angles. This significantly improves harvesting efficiency and reduces the labor intensity for farmers.

2. Impact tests indicate that lightweight push plates are less affected by pitch angle and excitation frequency, whereas heavier push plates exhibit greater impact kinetic energy. However, as the pitch angle increases, the impact decreases and the kinetic energy shows a trend of initially increasing then decreasing. Using a push plate made of NM450 material (weight 300g), an impact force of up to 130N was produced at the maximum pitch angle, optimizing the excitation effect.

3. Electronic fruits prepared using the IM948 sensor module were used to collect data, verifying the machine's impact effects under various excitation frequencies, positions, and branch diameters. Experimental results indicated that both the excitation point and branch diameter significantly influence fruit acceleration, with notable effects from excitation frequency as well. Using the Design-Expert software for parameter optimization, the picking parameters for branches of different diameters were optimized. Consequently, for branches with diameters less than 30mm, a recommended excitation frequency of 3.33Hz and an excitation point 450mm from the main branch junction; for branches with diameters of 30 to 43mm, an excitation frequency of 1.66Hz and an excitation point 1400mm from the main branch junction; and for branches with diameters of 43 to 56mm, an excitation frequency of 1.66Hz and an excitation point 1800mm from the main branch junction.

ACKNOWLEDGEMENT

This project is supported by two funding sources. The first one is the National Key Research and Development Program of China, with the project titled "Research and Development of Harvesting Equipment for Walnuts and Goji Berries" (2022YFD2202105).

The second one is the Yunnan Province Rural Revitalization Science and Technology Special Project, titled "Yunnan Province Yangbi County Walnut Industry Science and Technology Special Group" (202204BI090011).

REFERENCES

- [1] Castro-Garcia S., Blanco-Roldan G.L., Louise F., Gonzalez-Sanchez E.J., Gil-Ribes J.A., (2017), Frequency response of late-season 'Valencia' orange to selective harvesting by vibration for juice industry. *Biosystems Engineering*, vol.155, pp.77-83, DOI:[10.1016/J.BIOSYSTEMSENG.2016.11.012](https://doi.org/10.1016/j.biosystemseng.2016.11.012);
- [2] Chengmao Cao, Chao Zhan, Yan Sun, Zeze Li, Wentian Wu, Ran Ding., (2018), Design and Experiment of Portable Walnut High-altitude Pat-picking Machine (便携式山核桃高空拍打采摘机设计与试验). *Transactions of the Chinese Society for Agricultural Machinery*, vol.49, no.3, pp.130-137, Beijing/China, DOI: [10.6041/j.issn.1000-1298.2018.03.015](https://doi.org/10.6041/j.issn.1000-1298.2018.03.015);
- [3] Chunshou Ye, Kangnni Su, Yuhe Ma, Chenyu Liao, Baoqing Wang, Haifang Hu., (2022), Effect of Walnut-Corn Intercropping on Fruit Quality and Yield of Walnut (核桃-玉米间作对核桃果实品质及产量的影响), *Acta Agriculturae Boreali-occidentalis Sinica*, vol.31, no.10, pp.1365-1373, Shanxi/China, DOI: [10.7606/j.issn.1004-1389.2022.10.013](https://doi.org/10.7606/j.issn.1004-1389.2022.10.013);
- [4] Honghong Yu, Ya Li, Lingzhi Liao., (2019), Research on the Development Strategy of Walnut Industry in Yunnan Province (云南省核桃产业发展策略研究), *Problems of Forestry Economy*, vol.39, no.4, pp.427-434, Fujian/China, <https://doi.org/10.16832/j.cnki.1005-9709.2019.04.013>;
- [5] Hoshyarmanesh, H., Dastgerdi, H. R., Ghodsi, M., Khandan, R., Zareinia, K., (2017), Numerical and experimental vibration analysis of olive tree for optimal mechanized harvesting efficiency and productivity, *Computers and Electronics in Agriculture*, vol.132, pp.34-48, <https://doi.org/10.1016/j.compag.2016.11.014>;

- [6] Huibin Zhu, Wenkai Zhang, Gaocao Ke, Zhenbai Li, Hui Li, Leimu Dan., (2023), Design and Experimental Research on Vibratory Walnut Harvester for Mountainous Areas in Yunnan (云南山地核桃振动采摘机的设计与试验研究), *Journal of Agricultural Mechanization Research*, vol.45, no.2, pp.130-139, Heilongjiang/China, DOI:[10.13427/j.cnki.njyi.2023.02.009](https://doi.org/10.13427/j.cnki.njyi.2023.02.009);
- [7] Jia Meng, Xiaopu Fang, Xuanming Shi, Yu Zhang, Jian Liu., (2023), The Current Situation, Problems, and Suggestions for the Development of Walnut Industry in China (我国核桃产业发展现状、问题与建议), *China Lipid*, vol.48, no.1, pp.84-86+103, Shanxi/China, <https://doi.org/10.19902/j.cnki.zgyz.1003-7969.220637>;
- [8] Junming Hou, Yachen Yu, Ziyuan Tang, Liang Zhang, Jiuyu Jin, Wei Wang., (2024), Optimization and experiment on mechanical vibration harvesting process parameters of mulberry, *Journal of INMATEH - Agricultural Engineering* Vol. 72, No. 1 / 2024, DOI: <https://doi.org/10.35633/inmateh-72-49>;
- [9] Mengkun Lu, Junhong Zhang, Xielie Yi, Zhifang Yuan., (2023), Numerical Algorithm of Electromagnetic Force of Cylindrical Push-Pull Electromagnet (圆柱形推拉式电磁铁的电磁力数值算法), *Science Technology and Engineering*, vol.23, no.30, pp.12958-12965, Beijing/China, DOI: [10.3969/j.issn.1671-1815.2023.30.023](https://doi.org/10.3969/j.issn.1671-1815.2023.30.023);
- [10] Qiqi Shang, Chengpeng Li, Xiaoning He, Dongwei Wang, Haiqing Wang Shuai Yang., (2023), Design and Experiment of High-acid Apple Vibrating Picker (高酸苹果振动式采摘机设计与试验). *Transactions of the Chinese Society for Agricultural Machinery*, vol.54, no.3, pp.115-125, Beijing/China, DOI:[10.6041/j.issn.1000-1298.2023.03.012](https://doi.org/10.6041/j.issn.1000-1298.2023.03.012);
- [11] Tong Huang, Baoquan Guo, Tong Zhang, Huping Mao, Ning Ding., (2018). Dynamic characteristics of electromagnetic damper under impact loading (冲击载荷作用下电磁阻尼器动力学特性). *Science Technology and Engineering*, vol.18, no.32, pp.174-178, Beijing/China, DOI: [10.3969/j.issn.1671-1815.2018.32.026](https://doi.org/10.3969/j.issn.1671-1815.2018.32.026);
- [12] Tuqiang Chen, Guiqing Xu, Jiazhen Chen, Shensi Liu, Jinyao Li, Haifang Hu., (2023), Effects of different water supply amounts on physiology, growth, and fruit quality of walnut trees. (不同灌水量对核桃树生理、生长和果实品质的影响), *Chinese Journal of Ecology*, vol.42, no.11, pp.2578-2587, Beijing/China, Doi: [10.13292/j.1000-4890.202311.016](https://doi.org/10.13292/j.1000-4890.202311.016) Zicheng Gao, Kaijie Zhao, Lijun Li, Guoyou Pang., (2019), Design and experiment of suspended vibratory actuator for picking *Camellia Olerfera* fruits (悬挂振动式油茶果采摘执行机构设计与试验). *Transactions of the Chinese Society of Agricultural Engineering (Transactions of the CSAE)*, vol.35, no.21, pp. 9-17, Beijing/China, DOI: [10.11975/j.issn.1002-6819.2019.21.002](https://doi.org/10.11975/j.issn.1002-6819.2019.21.002);
- [13] Wei Li., (2023), Analysis and Reflection on the Development Issues of Walnut Industry in China (我国核桃产业发展问题的几点分析与思考), *Northwest Horticulture*, vol.308, no.1, pp.5-7, Shanxi/China , DOI:[10.3969/j.issn.1004-4183.2023.02.002](https://doi.org/10.3969/j.issn.1004-4183.2023.02.002);
- [14] Wenting Jin, Jinhui Zhao., (2023), Tengfei Zhuang, Zhongjun Liu, Xuejun Yang, Lijing Liu., Review on Theory and Equipment of Mechanical Vibration Picking of Forest Fruits (林果机械振动采摘理论与装备研究进展). *Transactions of the Chinese Society for Agricultural Machinery*, vol.54, no.s1, pp.144-160, Beijing/China, DOI:[10.6041/j.issn.1000-1298.2023.S1.016](https://doi.org/10.6041/j.issn.1000-1298.2023.S1.016);
- [15] Xiaoqiang Du, Chen Ning, Lei Yin He, Yin Qian, Guofeng Zhang, Xiaohua Yao., (2022), Design and Test of Crawler-type High Clearance *Camellia oleifera* Fruit Vibratory Harvester (履带式高地隙油茶果振动采收机设计与试验). *Transactions of the Chinese Society for Agricultural Machinery*, vol.53, no.7, pp.113-121, Beijing/China, DOI:[10.6041/j.issn.1000-1298.2022.07.011](https://doi.org/10.6041/j.issn.1000-1298.2022.07.011);
- [16] Yi Cao, Zhaodong Wang, Di Wu, Ti Zhang., (2011), Microstructure and mechanical properties of HSLA wear-resistant steel NM400 (NM400 高强度低合金耐磨钢的组织与性能), *Journal of Northeastern University (Natural Science)*, Shenyang/China, vol.32, no.2, pp.241-244;
- Zensong Li, Chengmao Cao, Delin Wu, Jianyu Zhang., (2021), Design and experiment of hand-operated self-integrated picking machine for *Carya cathayensis* (手自一体式山核桃采摘机的设计与试验), *Acta Agriculturae Zhejiangensis*, vol.33, no.7, pp.1309-1319, Zhejiang/China, DOI: [10.3969/j.issn.1004-1524.2021.07.17](https://doi.org/10.3969/j.issn.1004-1524.2021.07.17).

DESIGN AND EXPERIMENT OF ARRAY-BASED FINGERPLATE DIFFERENTIAL FLOW SENSOR FOR RICE GRAIN MONITORING

阵列式指板差分水稻籽粒流量传感器的设计与试验

Qibin LI¹⁾, Yang YU¹⁾, Gang GUO²⁾, Jinpeng HU¹⁾, Peng LIU¹⁾, Xiaoyu CHAI¹⁾, Yingfeng WANG¹⁾, Lizhang XU^{1*)}

¹⁾ College of Agricultural Engineering, Jiangsu University, Zhenjiang 212013, China

²⁾ Zoomlion Heavy Industry Science & Technology Co., Ltd Changsha 410013, China

Correspondence email: justxlz@ujs.edu.cn

DOI: <https://doi.org/10.35633/inmateh-74-31>

Keywords: Grain Flow Sensor; Auger elevators; Array Structure; Dual-Plate Differential; Random Forest

ABSTRACT

Most existing grain flow sensors are designed for paddle-type elevators, with limited focus on applications in auger elevators. This paper addresses the yield monitoring needs during rice harvesting operations, specifically targeting auger-based outlets through experimental research. An array-type differential grain flow sensor was developed and an indoor test bench was constructed to evaluate its performance. The study compares the effectiveness of time-domain and frequency-domain differential processing, alongside various filtering methods, for pre-processing the sensor's raw signals. Additionally, a grain flow regression model was built using the Random Forest algorithm. Experimental results demonstrated that the monitoring errors during field tests ranged from -6.42% to 8.23%, indicating that the sensor met the requirements for rice yield monitoring. This sensor provides valuable data for feed rate detection, speed regulation, and adjustments to the threshing and cleaning systems in combine harvesters, offering significant practical implications for the promotion and development of precision agriculture.

摘要

现有的籽粒流量传感器大多面向于刮板式升运器，鲜有针对搅龙式升运器工作场景的籽粒流量传感器。本文面向搅龙式出粮口，针对水稻收获作业的产量监测需求进行试验研究，开发了阵列式指板差分结构的籽粒流量传感器，研制了籽粒流量传感器室内试验台，对比了时域、频域差分处理以及不同滤波方法对所采集的传感器原始信号的预处理效果，并基于随机森林算法构建了籽粒流量回归模型。试验结果表明田间试验监测误差为-6.42%~8.23%，能够满足水稻收获的产量监测需求，可以为联合收获机喂入量检测、前进速度调控或者脱粒清选装置的作业参数调节提供数据参考，对精准农业的推广和发展也具有重要的实际意义。

INTRODUCTION

The mapping of grain yield during harvesting operations is a crucial component of precision agriculture, and an accurate and reliable grain flow monitoring sensor is fundamental for generating yield distribution maps (Vinod Chandra et al., 2024; Kasera et al., 2024). With advancements in sensor and GPS technologies, yield monitoring systems have been widely adopted in Europe and the United States (Yin et al., 2024). In these regions, large wheeled harvesters are commonly used, which often incorporate scraper elevators that allow for high grain flow rates and concentrated impact areas, making signal acquisition relatively straightforward (Cheng et al., 2023). However, in the Huang-Huai-Hai region of China, a rotation system of rice and oilseed or rice and wheat is typically implemented. In this context, compact and highly adaptable tracked harvesters have become the mainstream model for rice harvesting in southern paddy fields (He et al., 2023). These machines generally employ auger-type elevators for grain transport, as illustrated in Fig. 1.

According to the measurement principle, yield detection methods can be categorized into types such as mass measurement and volume measurement. Among these, the impulse-based grain flow sensor, which falls under mass measurement, has become one of the most widely used measurement methods due to its simple structure, ease of installation, and low cost (Bantchina et al., 2024). In the research on impulse-based grain flow sensors, Hu et al (2009) designed a dual-plate differential impulse grain flow sensor to address vibration interference, effectively mitigating the impact of vehicle vibrations on measurement accuracy.

Qibin Li (M.Eng. student), Yang Yu (Research Associate), Gang Gu (Engineer), Jinpeng Hu (Doctor), Peng Liu (Doctor), Xiaoyu Chai (Research Associate), Yingfeng Wang (M.Eng. student), Lizhang Xu (Professor)

Liu *et al* (2018) developed a dual-plate differential impulse grain flow sensor with a curved impact plate based on the scattering patterns of grain from scraper elevators. They conducted a spatiotemporal analysis of yield distribution data collected over two consecutive years in the same field. Li *et al* (2015) analyzed the impact patterns of grains, determined the optimal sampling frequency based on the sampling theorem, and compared two different signal processing methods: double-threshold filtering and arithmetic mean. Wei *et al* (2014) addressed the issue of vibration noise interference in impulse grain flow sensors by employing signal dual-plate differential techniques and wavelet transformation for filtering the raw signals. Shoji *et al* (2009) established a nonlinear grain flow model suitable for local combine harvesters in Japan, which, after validation through yield tests, demonstrated a relative root mean square error of 4.4% when the elevator speed was stable.

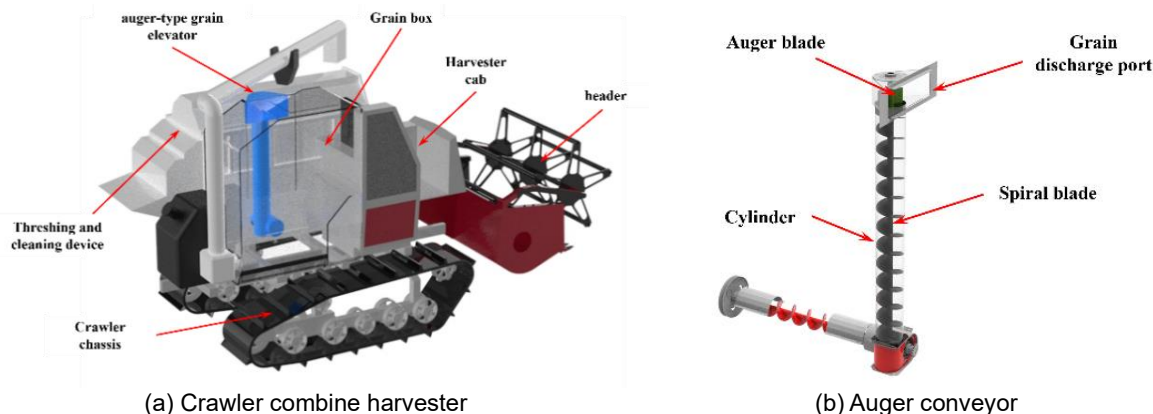


Fig.1 - Grain conveying system of the crawler combine harvester

In summary, existing impulse flow sensors rarely address applications in auger elevators. Therefore, this study focuses on the auger elevator of tracked combine harvesters, designing an array-type paddle impact grain flow sensor. The signal processing method was optimized to enhance vibration interference resistance through frequency-domain differential processing and filtering. A grain flow regression model was constructed based on the Random Forest algorithm. Finally, field tests were conducted during rice harvesting using the self-developed grain flow sensor, achieving online monitoring of yield information throughout the harvesting process.

MATERIALS AND METHODS

Design of the Grain Flow Sensor Structure

Compared to scraper elevators, auger elevators convey a smaller grain flow and exhibit a less concentrated scattering of grains at the discharge outlet. To identify the optimal installation position for the sensor, the scattering distribution characteristics of grains at the discharge outlet was analyzed and EDM simulations of the grain transport process in auger elevators were conducted. The simplified auger model was imported into EDEM software (2021, Altair Engineering Inc., Troy, MI, USA), with the auger speed set at 860 rpm. A particle factory was established at the base of the auger, and data was saved at a time step of 0.01 seconds over a total simulation time of 5 seconds. The mechanical property parameters of the rice grains and the contact coefficients of the working components were set based on the literature (Zhao *et al.*, 2023; Ma *et al.*, 2023; Xing *et al.*, 2024). The scattering distribution of rice grains under different flow rates is illustrated in Fig. 2. The simulation results indicate that the rice grains scatter in a fan-shaped distribution, flowing along the side walls of the auger and falling into the grain tank, while the middle area experiences wave-like scattering of grains influenced by the auger blades. It is clear that monitoring all grain impact signals at the outlet would require a sensor monitoring plate with a large surface area, which could interfere with the normal flow of grains into the tank and even block the auger outlet.

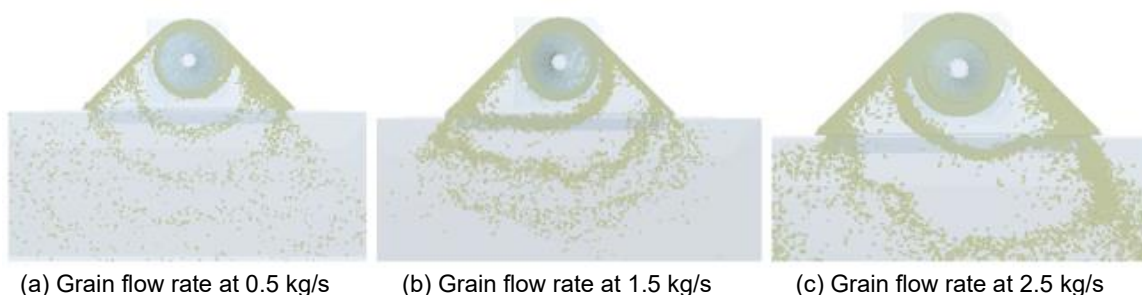


Fig. 2 - Rice Grain Discharge Characteristics at Different Flow Rates

To address this challenge, a multi-point monitoring method using dual-plate differential sensors, leading to the development of a custom grain flow monitoring sensor, as illustrated in Fig. 3, is proposed. The sensor is organized into three monitoring units: left, center, and right. Each unit consists of an impact paddle sensor and a reference paddle sensor. These paddle sensors are designed with point pressure sensors and paddles, secured by a gantry installation bracket and universal vibration-damping steel wires. All paddles are constructed from stainless steel. The impact paddle sensor captures the force from the grain flow, while the reference paddle sensor monitors vibrations and zero-point drift in that location. The front and rear paddles are parallel and do not make contact, with their sides bent at a 90° angle to enhance their strength. The universal vibration-damping steel wires help mitigate interference from vibrations during harvesting operations.

To ensure that the monitoring units on both sides receive normal impacts from the grain flow, the left and right sensors are installed perpendicular to the auger discharge outlet, while the center sensor is positioned parallel to it. The monitoring surfaces of the left and right units form an angle of 35.5° with the surface of the center unit, creating a symmetrical arrangement. Each paddle has an area of 135 × 40 mm, and the pressure sensors are single-point types (AT8501, AUTODA, China) with a maximum capacity of 300 grams, based on the design parameters derived from our earlier simulation analysis

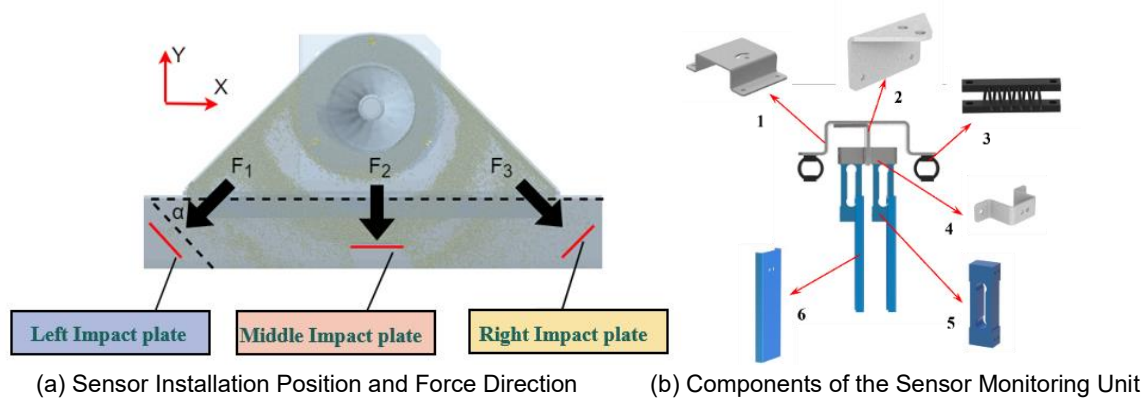


Fig. 3 - Differential Grain Flow Sensor with Array Structure

- 1 - Gantry mounting bracket. 2 - Mounting plate. 3 - Universal damping steel wire. 4 - Small gantry bracket.
- 5 - Pressure sensor. 6 - Plate.

Sensor signal conditioning circuit design

The hardware circuit of the array-type paddle differential flow sensor primarily consists of a power supply circuit, measurement circuit, differential amplification circuit, and bandpass filtering circuit, as illustrated in Fig.4.

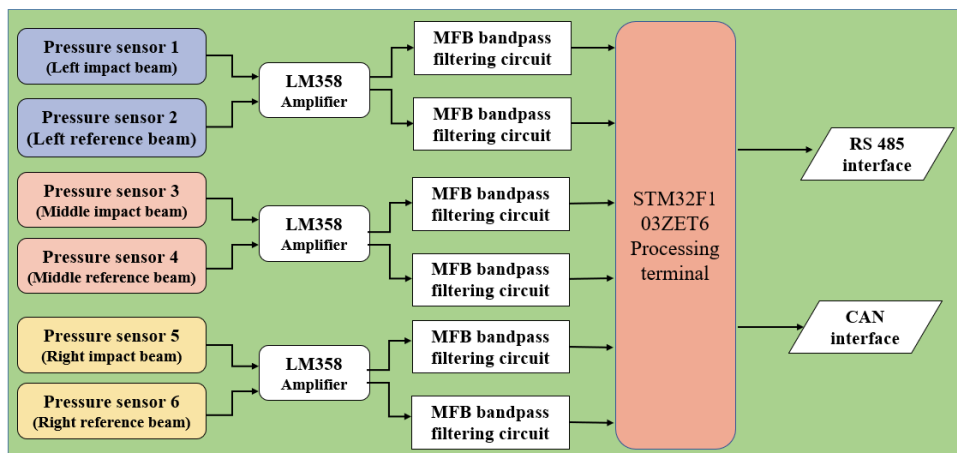


Fig. 4 - Hardware Circuit Diagram

The AT8501 pressure sensor generates only 10 mV of voltage under a 5 V excitation voltage with a 300 g load, necessitating the use of an LM358 amplification chip to enhance the weak signal. Given that the amplified strain signals require bandpass filtering, the choice of cut-off frequencies significantly affects the measurement accuracy of the sensor. Therefore, an adjustable center frequency second-order multiple feedback bandpass filter is utilized to meet the dynamic flow monitoring requirements. To facilitate the recording and analysis of experimental data, the sensor can directly output real-time flow signals via RS-485 or CAN communication after processing the signals within the microcontroller.

Development of the Grain Flow Indoor Test Bench

To further shorten the development cycle, this study developed an indoor grain flow test bench to simulate the grain conveying conditions of a tracked combine harvester in the field. The dimensions of the auger blades and the inner diameter of the auger cylinder match those of the 4LZ-6.0 combine harvester and are capable of achieving the machine's rated auger speed. The test bench enables calibration of the relationship between grain flow rate and sensor electrical signals and allows for the acquisition of background vibration noise to explore optimal noise reduction methods.

The physical setup of the grain flow test bench, shown in Fig. 5, consists primarily of the following components: an array-type differential flow sensor, a material receiving frame, a vertical auger, a measuring device, a grain hopper, a three-phase AC asynchronous motor, a frequency converter, and an opening adjustment flap. During the test, grains in the hopper are pushed by a horizontal auger to the bottom of the vertical auger, lifted to the auger outlet, and then discharged into a glass receiving frame. A funnel below the receiving frame, equipped with a load cell-based measuring device, records the cumulative change in grain mass, allowing for the calculation of key information such as the average flow rate. The grain flow rate is adjusted using a flap at the bottom of the hopper.

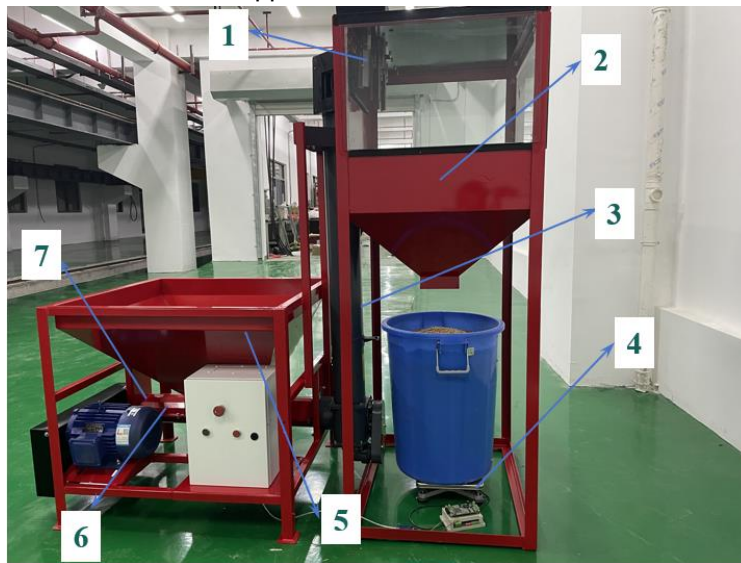


Fig. 5 - Test bench for the flow sensor experiment

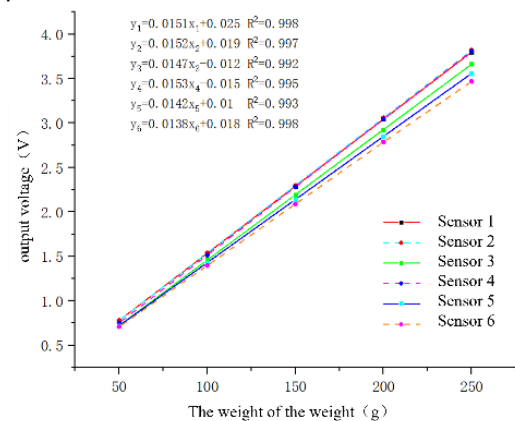
- 1 - Flow sensor. 2 - Material receiving frame. 3 - Auger grain elevator. 4 - Measuring device. 5 - Grain hopper.
- 6 - Three-phase AC asynchronous motor and frequency converter. 7 - Opening adjustment baffle.

Sensor Signal Differentiation and Denoising

To ensure that the vibration and impact amplitudes of all sensors are on the same scale, static calibration of each sensor was conducted using standard weights. As shown in Fig. 6(a), standard weights were applied at random positions on the monitoring paddles to obtain the static force characteristic curves for each sensor, illustrated in Fig. 6(b). The output signals from the six parallel beam pressure sensors demonstrated excellent linearity within their measurement range, meeting the required specifications for use.



(a) Static calibration test



(b) Static force characteristics

Fig. 6 - Static calibration of the pressure sensors

Damping alone cannot completely eliminate the influence of vibrations; therefore, the raw vibration signals from the sensors mounted on the machine were collected and the vibration signals from each differential unit in both the time domain and frequency domain were processed to compare the denoising effects. The signals detected by the impact paddle sensor and the vibrations measured by the reference paddle sensor represent a pair of common-mode signals. To ensure the effectiveness of the signal differentiation, the original signal acquisition frequency for the pressure sensors was set to 500 Hz, in accordance with the Nyquist sampling theorem, during the collection of vibration signals under no-load conditions. The collected raw signals are depicted in Fig. 7, with time-domain and frequency-domain differential analyses performed on the original output signals from the three paddle groups, as shown in Figs. 8 and 9.

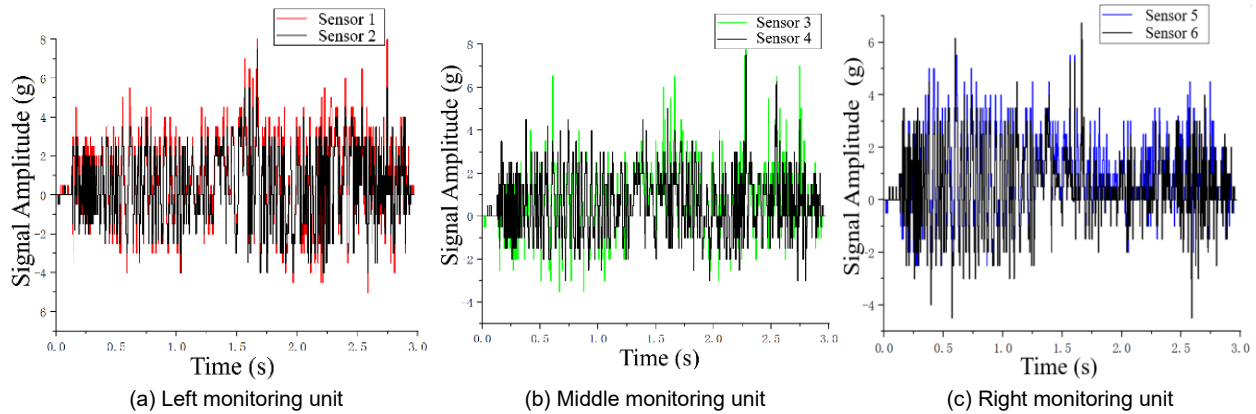


Fig. 7 - The original vibration signal of each monitoring unit

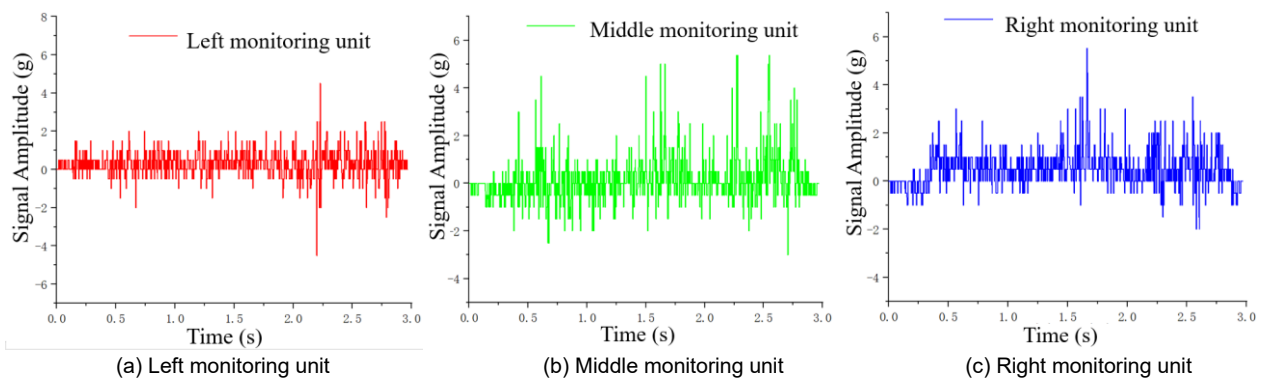


Fig. 8 - Time domain difference signal of each monitoring unit

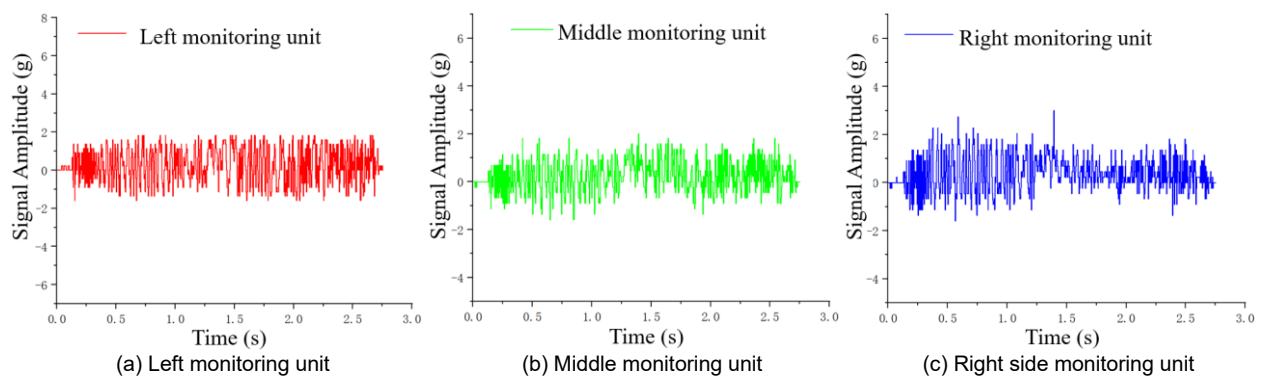


Fig. 9 - The frequency domain differential signal of each monitoring unit

As shown in Fig. 7, it is evident that the vibration amplitudes of each paddle in the raw signal under no-load conditions are similar, yet the signal concentration varies and exhibits significant oscillations. After performing time-domain differentiation, the amplitudes, means, and standard deviations of the signals from each monitoring unit decreased, resulting in improved signal concentration and demonstrating effective differentiation. However, the phase subtraction in the time domain does not completely eliminate sudden changes in acceleration, as some peaks still remain. In contrast, conducting signal differentiation in the frequency domain effectively reduces the frequency of peak occurrences, preventing peaks exceeding 6 g.

A further comparison of the mean and standard deviation between frequency-domain and time-domain differencing, as shown in Table 1, indicates that the mean and standard deviation of the signals from the left, middle, and right monitoring units all decreased. This suggests that frequency-domain differencing significantly improves the signal concentration during the impact phase, and the effect of background vibration noise reduction for each monitoring unit's sensor is relatively stable.

Table 1

Mean and variance of each sensor						
Monitoring unit	Left monitoring unit		Middle monitoring unit		Right monitoring unit	
Sensor number	Time Domain	Frequency Domain	Time Domain	Frequency Domain	Time Domain	Frequency Domain
Signal average /g	0.29	0.26	0.25	0.15	0.48	0.38
Signal standard deviation /g	0.72	0.71	1.02	0.66	0.79	0.74

Sensor Signal Filtering and Noise Reduction

The grain flow consists of discrete particle flows, which, when combined with background noise generated by machine vibrations, results in signals obtained through frequency-domain differentiation that are not entirely stable. To further enhance monitoring accuracy, additional filtering of the signals is required. Therefore, this study employs various filtering algorithms for secondary filtering based on the frequency-domain differentiated signals, aiming to identify the optimal secondary filtering method.

The data acquisition process during the bench tests is as follows: the motor speed is controlled, and each trial involves pre-weighing 40 kg of rice grains to be fed into the hopper. The opening of the adjustment baffle is fixed to regulate the flow rate to approximately 1.5 kg/s, with three repetitions of each trial. This study evaluates nine different filtering methods for secondary filtering, with their effects illustrated in Fig. 10.

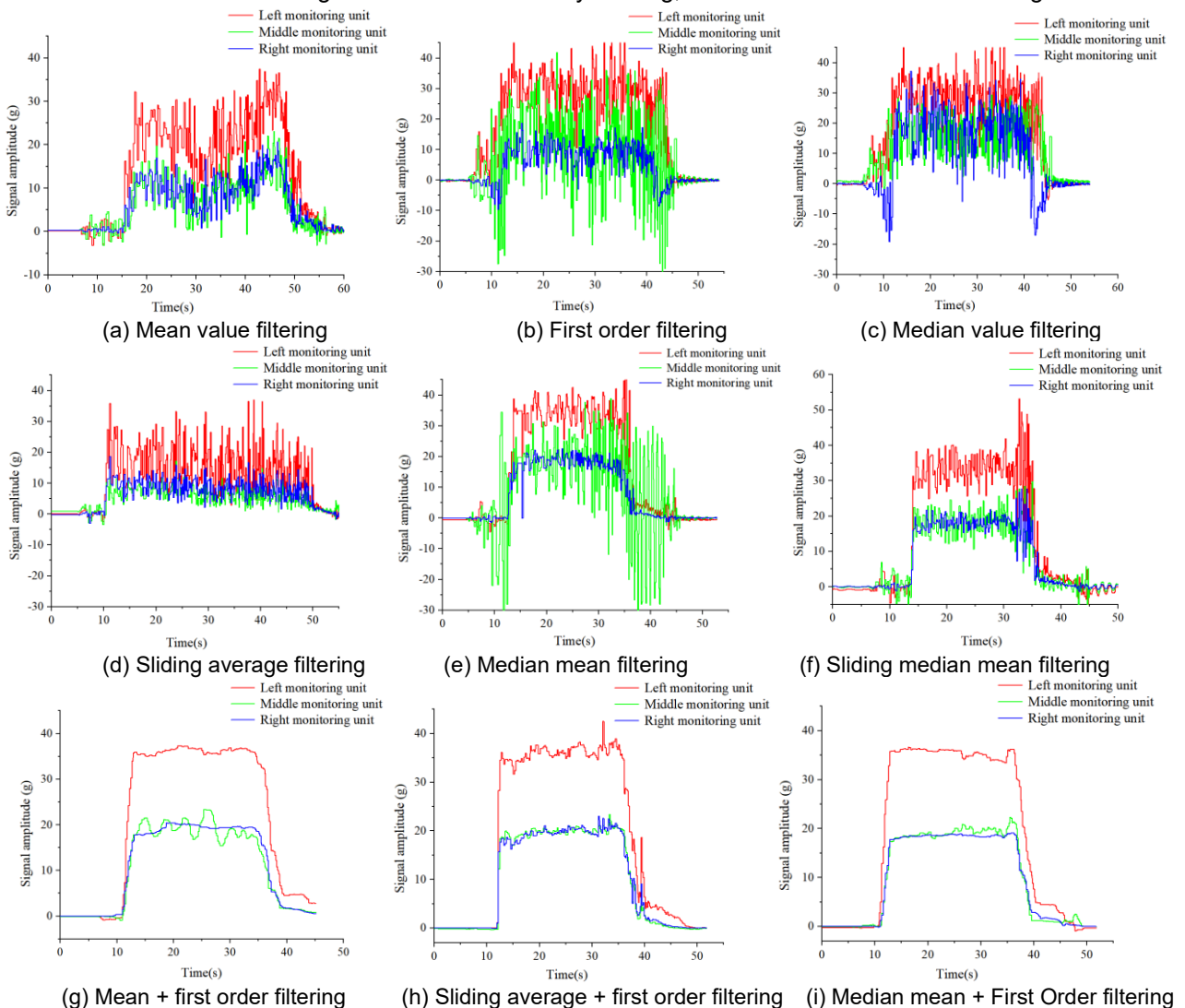


Fig. 10 - Effects of different secondary filtering methods

The initial assessment of the above data indicates that the performance of first-order filtering, average filtering combined with first-order filtering, sliding average filtering combined with first-order filtering, and median average filtering combined with first-order filtering is relatively satisfactory.

To further compare the filtering effects, the ratio of the sum of the monitoring values (Sum) from the secondary filtering to the mass of the input grains (m), referred to as the conversion coefficient (k) under flow conditions is evaluated. By comparing the standard deviation of the conversion coefficient (k), the effectiveness of the various filtering methods can be determined.

As shown in Table 2, the standard deviation of the ratio Sum/m is smallest for median average filtering combined with first-order filtering among the various filtering methods. The grain flow impacts the impact plates in a non-simultaneous and discrete manner over time, which, when combined with machine vibrations, leads to high-frequency fluctuations in the original signal. Median average filtering dynamically removes extreme values from the collected data, mitigating sampling deviations caused by occasional impact disturbances, and effectively reduces measurement errors of the flow sensor. The subsequent application of first-order filtering after median average filtering leverages its advantage in high-frequency data acquisition and provides good suppression of periodic vibration interference from the combine harvester's working components.

Table 2

Comparison of the different secondary filtering effects of three crops

Secondary filtering method	Standard deviation of k		
	Left group	Middle group	Right group
First order filtering	46.75	110.65	132.91
Mean + First order filtering	79.936	41.19	56.52
Sliding average filtering + First order filtering	68.35	148.87	62.74
Median mean filtering + First order filtering	58.63	41.25	52.76

In summary, the signal processing flow for the sensor is as shown in Fig. 11: the signals from each monitoring unit are differentiated in the frequency domain, transformed into three independent time-domain signals through inverse discrete Fourier transform, and then subjected to secondary filtering (median average filtering combined with first-order filtering) to achieve stable monitoring signals.

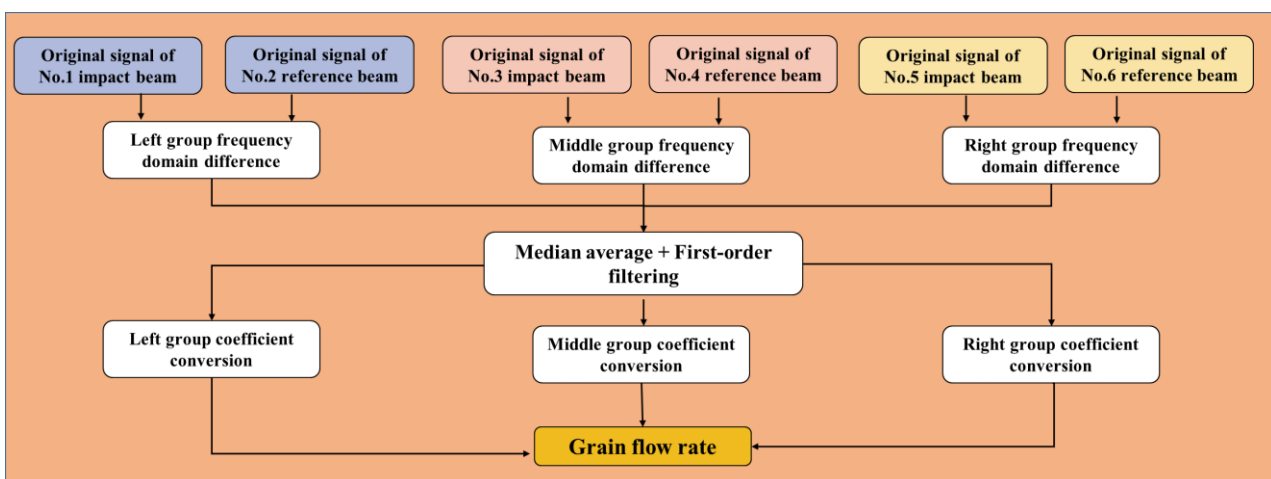


Fig. 11 - The signal processing flow of the flow sensor

RESULTS AND ANALYSIS

Establishment of the grain flow measurement model

To establish a mathematical metering model for grain flow, this study collected sensor signals from the grain flow test bench, capturing the output signals from three monitoring unit sensors along with the changes in accumulated mass of rice grains at various flow rates, as illustrated in Fig. 12.

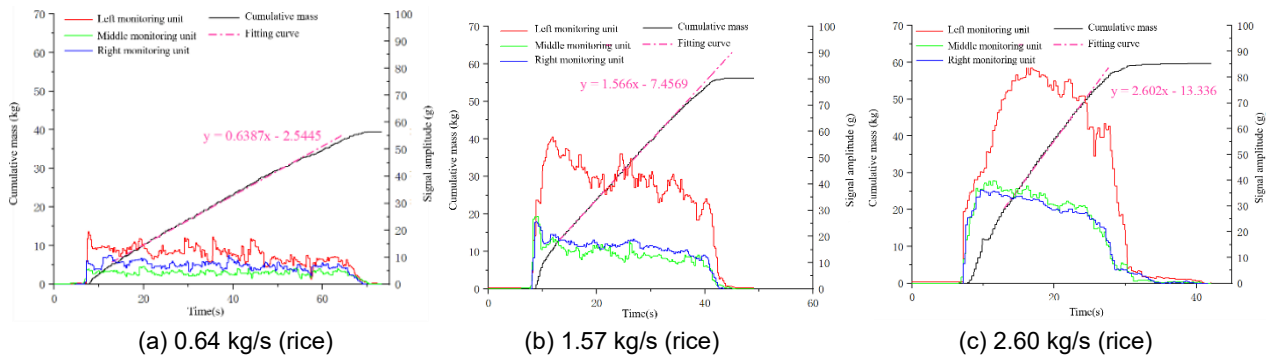


Fig. 12 - Changes in the rice accumulative quality and signal amplitude of each monitoring unit under different flow rates

It can be observed that the signal amplitude of the monitoring units is correlated with the slope of the cumulative mass curve. The significant differences in signal amplitude among the left, middle, and right units are attributed to the orientation of the vertical grain auger. The auger blades are tilted leftward, with a counter clockwise rotation (viewed from above), causing the right fan blades to throw grains towards the left side, as shown in Fig. 13(a). As the flow rate increases, the fill level within the auger blades rises, resulting in more grains being dispersed towards the left and middle monitoring units, specifically in the $\angle AOD$ region shown in Fig. 13(b). This indicates that the flow rate variations at the three monitoring positions are not synchronized, making it unreasonable to represent the overall grain flow rate based on a single monitoring location.

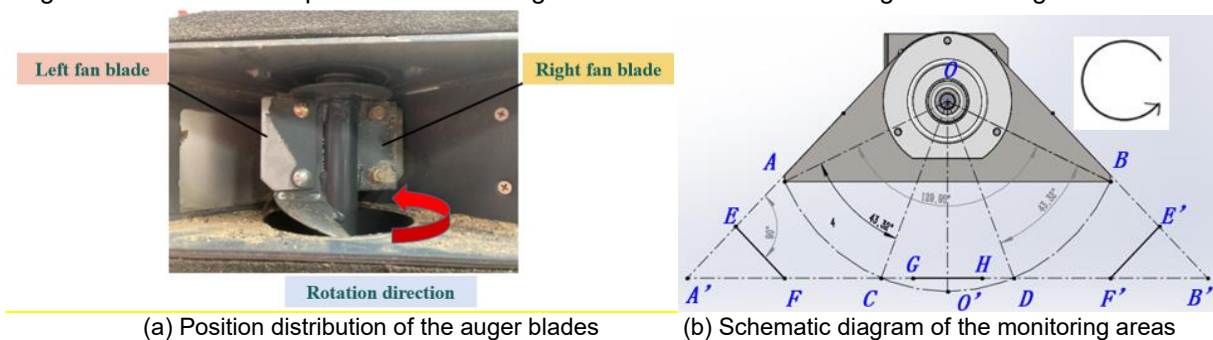


Fig. 13 - Position distribution of the auger blades

For the designed array-type paddle differential flow sensor, the differing amplitudes of signals from the left, center, and right monitoring units indicate that the gain varies under the same flow conditions. This suggests that the three monitoring units correspond to three distinct fan-shaped regions where the distribution of grain dispersion is uneven. Traditional linear or multivariate nonlinear regression methods do not yield satisfactory results for flow regression modelling. In contrast, the Random Forest algorithm offers advantages such as parallel processing, low computational overhead, fewer parameters to adjust, and ease of implementation compared to other common machine learning methods (Zhou et al., 2023; Ravishankar et al, 2023).

Therefore, this study employs the Random Forest algorithm to establish a regression model for grain flow.

It is important to note that due to the poor fluidity of the grains, the descent speed of the rice grains in the feed hopper decreases with pressure, resulting in an overall declining trend in the amplitudes of the three monitoring units under the same opening. Consequently, using the long-time interval change in cumulative mass Δm to represent the true flow is not reasonable. During the stable flow phase from t_1 to t_2 , the sum of the signal amplitudes S from each monitoring unit over a unit time interval Δt is positively correlated with the average flow rate Q over that time interval. The model is constructed as follows:

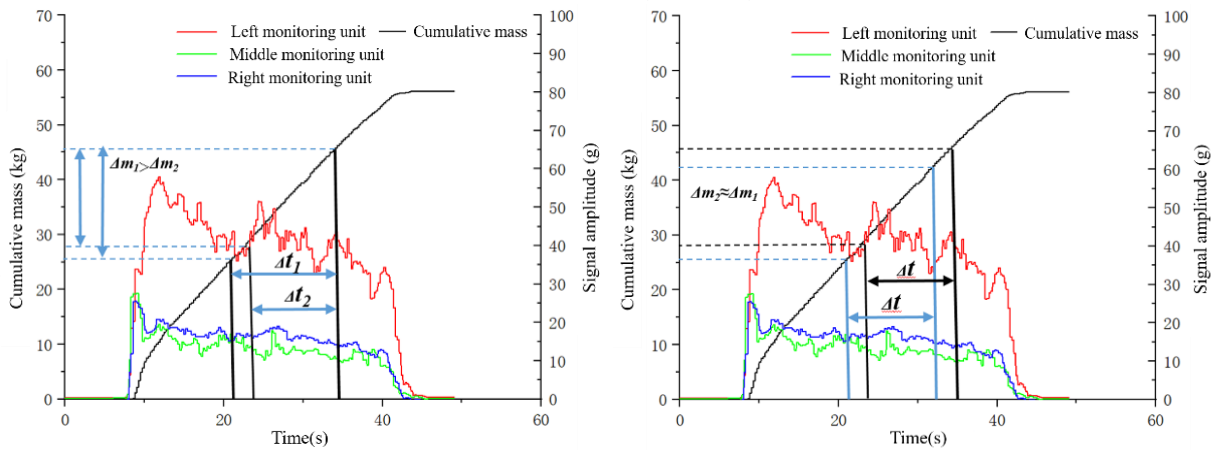
$$y = f(x_1, x_2, x_3) \tag{1}$$

In the equation, y represents the grain flow rate per unit time Δt , and x_1, x_2 and x_3 are the values of $S/\Delta t$ for the left, middle, and right monitoring units, respectively. The model for the average grain flow rate Q within Δt is given by:

$$\frac{\Delta m}{\Delta t} = f\left(\frac{S_1}{\Delta t}, \frac{S_2}{\Delta t}, \frac{S_3}{\Delta t}\right) \quad (2)$$

Due to the continuous variation in signals from the three monitoring units, the sum of the signal amplitudes S per unit time also changes accordingly. This implies that time displacement in the time domain will result in changes to the "rectangular" area S of each monitoring unit's signal, which, in turn, causes slight variations in Δm due to deviations in the cumulative mass data. By selecting different unit time steps Δt , a more diverse set of samples can be created, as shown in Fig. 14. Additionally, there is a small amount of zero drift at the beginning and end of the experiment, with the drift amount within 0.5 g. Data from this time period can be used to construct zero drift samples, which are represented as follows:

$$\frac{\Delta m}{\Delta t} = 0 = f\left(\frac{S_1}{\Delta t}, \frac{S_2}{\Delta t}, \frac{S_3}{\Delta t}\right) \quad (3)$$



(a) Method for changing Δt (b) Method for maintaining a fixed Δt
Fig. 14 - Construction of the original dataset

In field harvesting operations, the complexity of zero-drift caused by machine start-stop, turns, and other conditions makes it more challenging to filter zero-drift data from linear models compared to bench tests. However, this issue can be easily addressed in a random forest regression model.

Therefore, the sample construction for the random forest regression model only needs to focus on the following time points: the point where the cumulative mass curve begins to change slope, indicating that grains have started to be discharged from the outlet but remain unstable. This point is denoted as t_R , any sensor signals before this point are considered as zero-drift data. The moment when the testing platform reaches its rated speed, at which point the grain discharge becomes relatively stable. This moment is noted as t_1 .

The time when the screw conveyor begins to show a significant decrease in grain flow, with clear reductions in sensor data and the cumulative mass curve's slope gradually approaching zero. This moment is recorded as the end of stable flow, noted as t_2 . After t_2 , the slope of the cumulative mass curve remains at zero. The initial time when this occurs is denoted as t_S , continuing until the end of data collection at t_N . The period from t_S to t_N represents the zero-drift phase. The divisions of these time periods are illustrated in Fig. 15.

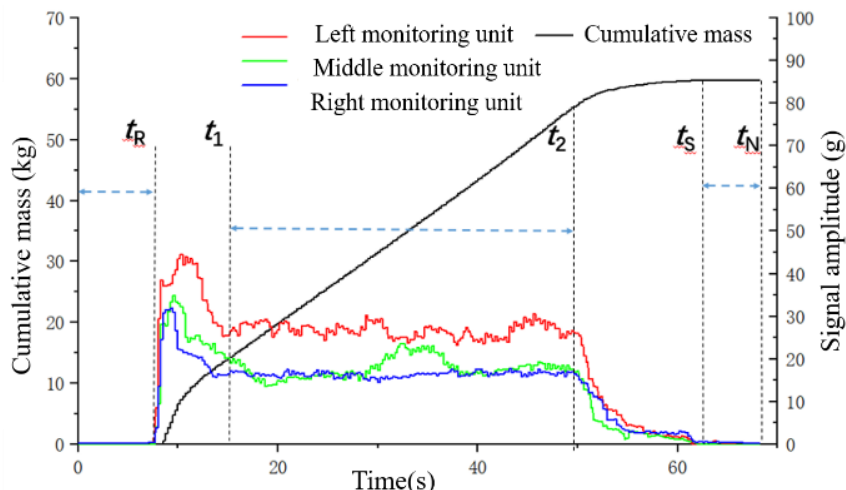


Fig. 15 - The division of the time periods of a single group of experimental data

After selecting specific time periods, an array $[x_1, x_2, x_3, y]$ is constructed using Formula 2, where y represents the grain flow within the time interval Δt , and x_1, x_2 and x_3 correspond to the values of $S/\Delta t$ from the left, middle, and right monitoring units, respectively.

Choosing a very small flow calculation period Δt can increase computational load and lead to sample bias, especially under high flow conditions. Conversely, a very large Δt may fail to capture flow variations adequately. To determine the optimal size of Δt , this study selected 0.4 s, 0.8 s, and 1.2 s as candidate parameters. After obtaining the samples, the rice regression model is established. 80% of the dataset is used for training, while 20% is used for testing. The depth of the decision trees is set to 4. The test results for different time steps Δt are shown in Table 3.

Table 3

Sample test of the traffic regression model based on the random forest algorithm

Δt	Sample size	Training score	Test score
0.4	1103	0.56	0.68
0.8	370	0.96	0.87
1.2	213	0.99	0.36

Note: The training score and test score are fitting evaluations between 0 and 1, where 0 is the worst and 1 is the best.

From the above table and Fig. 16, a time step of $\Delta t = 0.8$ seconds is selected as the average time interval for predicting flow, leading to the final grain flow model constructed as $[t_0, t_0 + 0.8]$.

$$Q = f(1.25S_1, 1.25S_2, 1.25S_3, y) \tag{4}$$

In the equation, the dynamic output method for flow is as follows: first, the discrete integral area $[S_1, S_2, S_3]$ for each monitoring unit over each second is calculated. Each discrete integral area is divided by the time step Δt to obtain the input array $[x_1, x_2, x_3]$. Subsequently, based on the trained Random Forest flow regression model, the flow values after internal evaluation are output.

Sensor performance test verification

To further validate the monitoring accuracy of the grain flow sensor, a field harvesting verification experiment was conducted in November 2023 at Jiangsu University's experimental field. The selected plot was relatively flat, with the rice variety being Changnong Jing 10, a bulk density of 639 g/L, and a grain moisture content of 21%. The test machine used was a 4LZ-6.0 multifunctional intelligent combine harvester, operating at a feed rate of 6 kg/s and a cutting width of 2.2 m. The experimental site is shown in Fig. 16(a), with the GPS positioning device mounted on the top of the cab, and the grain flow sensor installed as depicted in Fig. 16(b).

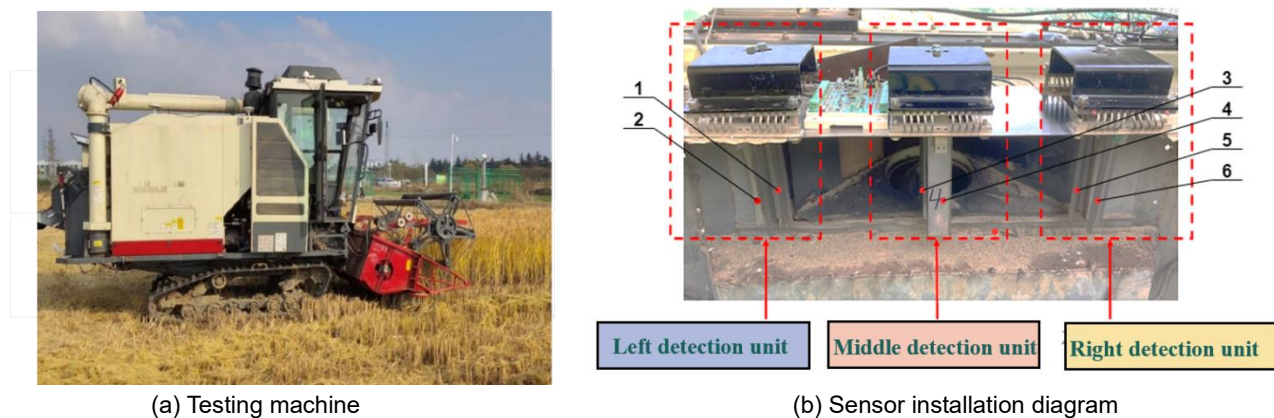


Fig .16 - Physical map of the sensor installation

1. Left impact unit. 2. Left reference unit. 3. Middle impact unit. 4. Middle reference unit.
5. Right impact unit. 6. Right reference unit.

The rice yield measurement validation experiment consisted of five groups, with a uniform harvesting speed over a full cutting width of 30 meters. Cumulative yield data from the grain flow sensor were recorded alongside manual weighing data to compare and verify the sensor's field accuracy. The results are summarized in Table 4. The field trial indicated that the designed grain flow sensor achieved satisfactory monitoring performance, with monitoring errors ranging from -6.42% to 8.23% during stable harvesting conditions.

Table 4

Validation test results			
Crop	Actual Quality (kg)	Random Forest Regression Model	
		Predicted Quality (kg)	Error (%)
Rice	122.49	132.57	8.23%
	105.13	99.43	-5.42%
	94.23	97.49	3.46%
	97.28	91.04	-6.42%
	119.39	125.19	4.85%

Discussion

This study addresses the uneven dispersal characteristics of grain ejection from auger outlets by designing an array-type grain flow sensor that utilizes a multi-point distribution and dual-board differential arrangement for monitoring grain flow. However, this study did not consider the impacts of machine tilt and varying grain moisture content. Future work will incorporate tilt sensors to capture the machine's inclination and moisture monitoring sensors to assess grain moisture variations. Additionally, the grain dispersal patterns under different operating conditions will be analyzed and the yield measurement model will be optimized to enhance the versatility of the grain flow sensor developed in this study.

While this research primarily focused on rice crops, the monitoring principles indicate that the developed grain flow sensor is applicable to a variety of crops. Future experimental studies will be conducted on rice, wheat, rapeseed, and other crops to develop a universal grain flow sensor. Furthermore, by integrating positional information from the harvesting machine, it is aimed to generate visualized yield distribution maps to guide precision farming and management for the next crop season.

CONCLUSIONS

To monitor the flow variation of rice grains in real-time, a multi-point monitoring and dual-board differential scheme was proposed based on the dispersal characteristics of grains ejected from the auger outlet of a crawler-type combine harvester, leading to the design of an array-type differential grain flow sensor.

The differential effects of the original signals from the flow sensor were compared in both the frequency and time domains, alongside various filtering and noise reduction methods. The optimal signal processing approach was identified as frequency-domain differentiation combined with "median filtering + first-order filtering," resulting in stable sensor signals.

A grain flow measurement model for rice was constructed using the Random Forest algorithm, and field harvest experiments were conducted for validation. The results indicated that the measurement error during stable field operations ranged from -6.42% to 8.23%.

ACKNOWLEDGEMENT

Shandong Province Key Research and Development Plan (Science and Technology Demonstration Project) Project (2022SFGC0201), Jiangsu Agricultural Science and Technology Independent Innovation Fund Category I project (CX (22) 1005), The Natural Science Foundation of Jiangsu Province (BK20230544), Postgraduate Research & Practice Innovation Program of Jiangsu Province (KYCX22_3678) and Postgraduate Research & Practice Innovation Program of Jiangsu Province (KYCX24_3989).

REFERENCES

- Bantchina, B.B., Qaswar, M., Arslan, S., Ulusoy, Y., Gündoğdu, K. S., Tekin, Y., Mouazen, A. M. (2024). Corn yield prediction in site-specific management zones using proximal soil sensing, remote sensing, and machine learning approach. *Computers and Electronics in Agriculture*, 225, 109329. <https://doi.org/10.1016/j.compag.2024.109329>
- Cheng, S., Han, H., Qi, J., Ma, Q., Liu, J. An, D., Yang, Y. (2023). Design and Experiment of Real-Time Grain Yield Monitoring System for Corn Kernel Harvester. *Agriculture*, 13, 294. <https://doi.org/10.3390/agriculture13020294>
- He, Y., Zhou, J., Sun, J., Jia, H., Liang, Z., Awuah, E. (2023). An adaptive control system for path tracking of crawler combine harvester based on paddy ground conditions identification. *Computers and Electronics in Agriculture*, 210, 107948. <https://doi.org/10.1016/j.compag.2023.107948>

4. Hu, J.W., Luo, X.W., Ruan, H., Chen, S.R., Li, Y.M. (2009). Design of a dual-plate differential impact-based yield sensor (双板差分冲量式谷物流量传感器设计). *Transactions of the Chinese Society for Agricultural Machinery*, 40(4), 69-72. [http://dx.doi.org/10.3969/j.issn.1000-1298.\[year\].4.\[sequence\]](http://dx.doi.org/10.3969/j.issn.1000-1298.[year].4.[sequence]) (China)
5. Li, X.C., Li, M.Z., Zheng, L.H., Zhang, M., Wang, X.J., Sun, M.Z. (2015). Test and optimization of sampling frequency for yield monitor system of grain combine harvester (谷物联合收获机测产系统采样频率优化与试验). *Nongye Jixie Xuebao/Trans. Transactions of the Chinese Society for Agricultural Machinery*, 46(S1), 74-78. <http://dx.doi.org/10.6041/j.issn.1000-1298.2015.S0.013> (China)
6. Vinod Chandra, S.S., Anand Hareendran, S., Ghassan, F. A. (2024). Precision farming for sustainability: An agricultural intelligence model. *Computers and Electronics in Agriculture*, 226, 109386. <https://doi.org/10.1016/j.compag.2024.109386>
7. Liu, R., Zhang, Z., Zhang, M., Yang, W., Li, M. (2018). Performance analysis and modelling of impact-based sensor in yield monitor system. *IFAC-PapersOnLine* 51(17), 613–618. <https://doi.org/10.1016/j.ifacol.2018.08.129>
8. Kasera, R.K.; Gour, S.; Acharjee, T. (2024). A comprehensive survey on IoT and AI based applications in different pre-harvest, during-harvest and post-harvest activities of smart agriculture. *Computers and Electronics in Agriculture*, 216, 108522. <https://doi.org/10.1016/j.compag.2023.108522>
9. Ma, Z., Traore, S.N., Zhu, Y., Li, Y., Xu, L., Li, Y. (2022). DEM simulations and experiments investigating grain tank discharge of a rice combine harvester. *Computers and Electronics in Agriculture*, 198, 107060. <https://doi.org/10.1016/j.compag.2022.107060>
10. Ravishankar, M., Siddharth, S., Yadav, A. A., Kassa, S.R. (2023). Integrating IoT and Sensor Technologies for Smart Agriculture: Optimizing Crop Yield and Resource Management. *2023 IEEE Technology & Engineering Management Conference-Asia Pacific (TEMSCON-ASPAC)*. IEEE, 1-5. <https://doi.org/10.1109/TEMSCON-ASPAC59527.2023.10531339>
11. Shoji, K., Itoh, H., Kawamura, T. (2009). In-situ non-linear calibration of grain-yield sensor: Optimization of parameters for flow rate of grain vs. force on the sensor. *Engineering in Agriculture, Environment and Food*, 2(3), 78-82, [https://doi.org/10.1016/S1881-8366\(09\)80008-6](https://doi.org/10.1016/S1881-8366(09)80008-6)
12. Yin, C., Zhang, Q., Mao, X., Chen, D., Huang, S., Li, Y. (2024). Research of real-time corn yield monitoring system with DNN-based prediction model. *Frontiers in Plant Science*, 15, 1453823. <https://doi.org/10.3389/fpls.2024.1453823>
13. Wei, X.H., Zhang, J.M., Dan, Z.M., Liu, C.L. (2014). Signal processing method of impact-based grain flow sensor for predicted yield (冲量式谷物流量传感器测产信号处理方法). *Transactions of the Chinese Society of Agricultural Engineering*, 30(15), 222-228. (China) <http://www.tcsae.org/article/doi/10.3969/j.issn.1002-6819.2014.15.029>
14. Xing, S., Yu, Y., Cao, G., Hu, J., Zhu, L., Liu, J., Wu, Q., Li Q., Xu L. (2024). Design and Parametric Optimization Study of an Eccentric Parallelogram-Type Uprighting Device for Ratoon Rice Stubbles. *Agriculture*, 14(4), 534. <https://doi.org/10.3390/agriculture14040534>
15. Zhao, J., Zhao, H., Tang, H., Wang, X., Yu, Y. (2023). Bionic threshing component optimized based on MBD-DEM coupling simulation significantly improves corn kernel harvesting rate. *Computers and Electronics in Agriculture*, 212, 108075. <https://doi.org/10.1016/j.compag.2023.108075>
16. Zhou, X., Xu, X., Zhang, J., Wang, L., Wang, D., Zhang, P. (2023). Fault diagnosis of silage harvester based on a modified random forest. *Information Processing in Agriculture*, 10(3), 301-311. <https://doi.org/10.1016/j.inpa.2022.02.005>

ESTABLISHMENT AND CALIBRATION OF DISCRETE ELEMENT MODEL FOR COATED WHEAT SEED BASED ON STATIC AND DYNAMIC VERIFICATION TEST

基于静动态验证试验的包衣小麦种子离散元模型标定与优化

Xuejun ZHANG^{1,2}, Ren GUO¹, Zenglu SHI^{1,2}, Jinshan YAN^{1,2}, Shenghe BAI³, Longfei YANG¹, Yongliang YU⁴, Duijin WANG⁴

¹) College of Mechanical and Electrical Engineering, Xinjiang Agricultural University, Urumqi/ China;

²) Key Laboratory of Intelligent Agricultural Equipment of Xinjiang, Urumqi/ China

³) National Key Laboratory of Agricultural Equipment Technology, Chinese Academy of Agricultural Mechanization Sciences Group Co., Ltd., Beijing/ China

⁴) Xinjiang Tiancheng Agricultural Equipment Manufacturing Co, Tiemenguan/ China

Correspondent author: Xuejun ZHANG; Tel: +8615199093163; E-mail: tuec@163.com;

DOI: <https://doi.org/10.35633/inmateh-74-32>

Keywords: coated wheat seed, repose angle, simulation, parameter calibration, seed metering

ABSTRACT

This study calibrated discrete element parameters for coated wheat seeds through static and dynamic validation tests. Using physical experiments, key parameters were measured, and a discrete element model was created. Optimal parameters were identified via the Plackett-Burman test, steepest ascent experiment, and Box-Behnken design. Validation tests showed that the relative error between the simulated and actual angle of repose was 1.31%, and the relative error in seeding uniformity and seed displacement uniformity was less than 5%. These findings provide theoretical support for optimizing seed dispenser structures in precision wheat sowing.

摘要

本研究基于静动态试验对包衣麦种参数进行离散元标定, 采用物理试验测得其物性参数和接触参数, 建立离散元模型; 采用 PLACKETT-BURMAN 试验, 最陡爬坡实验、BOX-BEHNKEN 试验获得显著影响因素的最佳参数组合, 通过静态圆筒提升实验与动态排种器台架试验进行验证。结果表明, 仿真休止角与实际休止角相对误差为 1.31%, 播量一致性和排种均匀性的变异系数相对误差平均值均低于 5%, 可为麦种精量化播种中排种器结构优化提供理论参考。

INTRODUCTION

Wheat is the second-largest grain crop globally and one of the primary staple crops in China. As an important wheat-producing area, Xinjiang's stable yield is of great significance to guarantee national food security (Chen *et al.*, 2019; Lang *et al.*, 2016; Zhang *et al.*, 2018). According to statistics, the sown area of wheat in China reached 23518.5 thousand hectares in 2022 (Nbo S, 2023). The widespread adoption of mechanized wheat production technology and equipment has significantly reduced labour costs and increased production efficiency (Li *et al.*, 2024).

Sowing is a crucial step in the mechanized production of wheat. As the core component of mechanized sowing, the performance of the seed metering device directly impacts the seeding quality of the wheat planter. The structure of the seed metering device is intricate and compact, and the interactions between wheat seeds, as well as between the seeds and the metering components, are complex. Traditional analysis methods cannot directly study the movement patterns of seeds and the seeding mechanism during this process, making it necessary to rely on computer simulations. The Discrete Element Method (DEM) is particularly well-suited for analysing the movement of granular materials (Han *et al.*, 2018; Zhang *et al.*, 2022). Applying DEM to the seed metering process of wheat seeds is an effective approach; however, the accuracy of the DEM model is highly dependent on the precision of the physical parameters calibrated between the seeds and the metering components. Therefore, calibrating the discrete element parameters for coated wheat seeds is of utmost importance. International scholars have undertaken significant work in calibrating particle parameters.

Liu *et al.* optimized and calibrated the discrete element simulation parameters of wheat using repose angles obtained from experiments and simulations, finding no significant difference between the simulated and experimental values (Liu *et al.*, 2016).

Lu *et al.* conducted discrete element simulations of the friction angles (including two repose angles and a sliding friction angle) of rice seeds. They used the experimental results of the three friction angles of the seeds as correction indicators to obtain calibrated parameters, with a relative error of less than 2.75% compared to the physical test results (Lu *et al.*, 2018). The reliability and accuracy of the discrete element simulation method have been corroborated through extensive bench and field experiments in recent years (Zhi *et al.*, 2021). Since the seed metering device directly interacts with coated wheat seeds, and the coating process alters some contact parameters (Hu *et al.*, 2018), the parameters used in existing DEMs are not sufficiently accurate for coated wheat seeds. Few scholars have employed coated wheat seed parameters for discrete element analysis in their seed metering device designs, leading to insufficient precision in the data for coated wheat seeds. This lack of precision hampers research on the seed metering mechanism and structural optimization for devices using coated wheat seeds, making it necessary to calibrate the parameters for these seeds.

To further enhance the accuracy of discrete element parameters for coated wheat seeds, physical experiments were conducted to determine their geometric characteristics, physical properties, and contact parameters. These data were used to establish a DEM that reflects the intrinsic parameters of the coated wheat seeds. The parameters were optimized using *Plackett-Burman* (PB) test, *steepest ascent* (SA) test, and *Box-Behnken design* (BBD) test. The accuracy of the model was validated by comparing simulation results with bench tests of the seed metering device. This provides reliable DEM parameters for studying the seeding mechanism and optimizing the structure of wheat seed metering devices.

MATERIALS AND METHODS

Measurement of basic physical parameters

For the widely cultivated "Xindong 20" variety in southern Xinjiang, 10,000 plump, undamaged seeds were selected to determine the basic physical parameters of coated wheat seeds. These seeds were randomly divided into 10 groups, each containing 1,000 seeds. Each group was weighed using an electronic balance with an accuracy of 0.01 g to calculate the average weight and determine the thousand-seed weight (38.32 g). Additionally, 100 seeds were randomly selected from each group and measured with a calliper to obtain their characteristic dimensions (length L 6.17 mm \times width W 3.31 mm \times thickness T 2.86 mm), as illustrated in Fig. 1.

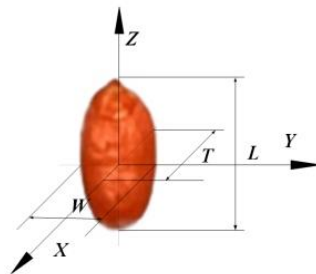


Fig. 1 - Schematic diagram of three-dimensional sizes

The volume of the coated wheat seeds was measured by the drainage method, and the density of the coated wheat seeds was calculated to be $1260 \text{ kg}\cdot\text{m}^{-3}$.

Poisson's ratio and shear modulus

The Poisson's ratio is one of the important mechanical characteristics of coated wheat seeds. It was determined using a combination of theoretical definitions and experimental measurements (Shi *et al.*, 2018).

The coated wheat seeds, being small and irregularly shaped, were subjected to a compression deformation test using an RCM-4002 universal testing machine (range: 0-2 kN) in the thickness direction, as shown in Figure 2. The seeds were placed on the lower pressing plate, and the upper pressing plate applied a load at a speed of 0.5 mm/s for 3 seconds. The test was repeated six times. The Poisson's ratio of the coated wheat seeds was calculated to be 0.3 by measuring their length and thickness before and after the test.

To determine the elastic modulus, a compression test was performed using the same universal testing machine. The seeds were placed horizontally on the test bench, and a circular pressing plate applied a load along the thickness direction at a speed of 2 mm/min for 10 seconds, after which the machine was stopped. The compression force-displacement curve, as shown in Figure 3, was generated using the computer software's post-processing module. The test was repeated six times, and the average value was recorded.

The contact area was determined as the projected area in the thickness direction. Due to the irregular shape of the seed, its contact area was calculated using SolidWorks by creating a 3D model based on the measured dimensions of the seed, resulting in a contact area of $3.02 \times 10^{-6} \text{ m}^2$.

$$G = \frac{F/s}{2(1+\delta)(\Delta l/l)} \tag{1}$$

where:

G - the shear modulus of the coated wheat seed, Pa; F is the applied force, N, s is the contact area, m^2 , δ - Poisson's ratio of coated wheat seed, dimensionless. Δl is the deformation, mm, and l is the sample height, mm.

Finally, using equation (1), the shear modulus of the coated wheat seed was calculated to be $4.93 \times 10^8 \text{ Pa}$.

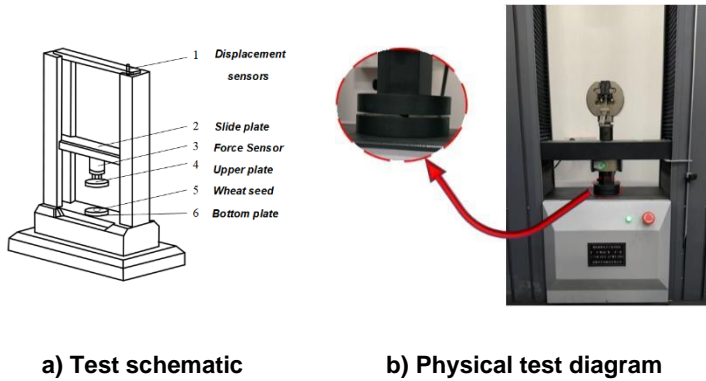


Fig. 2 - Compression test of coated wheat seed

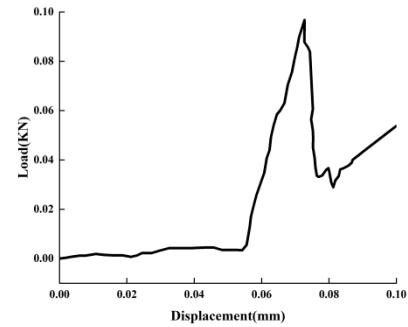


Fig. 3 - Compression-displacement curve

Angle of repose determination test

The repose angle was used as the standard parameter in this study, as its measurement accuracy directly influences the reliability of simulation parameter calibration. An acrylic cylinder with an inner diameter of 39 mm and a height of 120 mm was selected based on the material characteristics of the wheat seeds (Wu et al., 2002). The lower end of the cylinder was initially blocked with a baffle. Once the cylinder was completely filled with coated wheat seeds, the baffle was quickly removed, allowing the seeds to fall freely and form a conical pile. After the seeds settled, the slope of the pile was recorded as the repose angle.

A high-definition camera captured a frontal image of the seed pile. This image was processed using MATLAB software for grayscale conversion, binarization, and extraction of boundary pixels (Ma et al., 2024), as illustrated in Figure 4. The extracted boundary pixels were then fitted using the image digitization tool in Origin software to determine the single-sided repose angle of the coated wheat seeds, as shown in Figure 5. Here, H represents the horizontal pixel points, and R represents the vertical pixel points. After 10 repeated experiments, the average repose angle of the coated wheat seeds was found to be 31.14° in the physical tests.

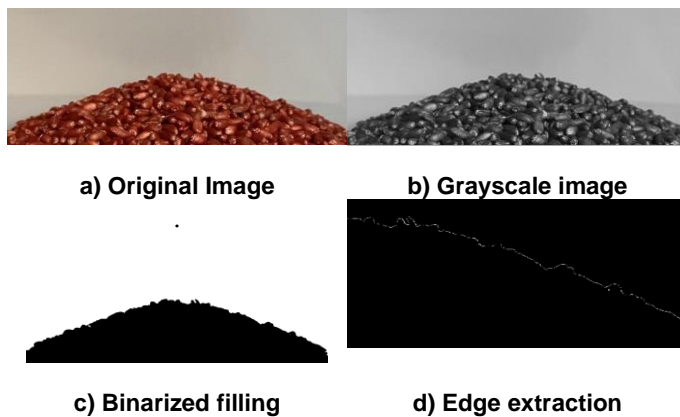


Fig. 4 - Repose Angle Profile Extraction Process

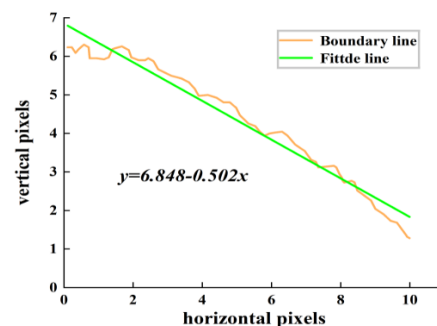


Fig. 5 - Seed single-sided angle of repose fitting image

Coefficient of static and rolling friction

In this experiment, a custom-built device was used to measure the friction coefficients between coated wheat seeds, as well as between the seeds and acrylic plates. The experimental setup is shown in the fig. 6. Coated wheat seeds were placed on an acrylic plate mounted on an iron base, and the static friction coefficient (SFC) was determined by measuring the angle at which the seeds began to slide as the inclined plane was raised (Hao *et al.*, 2021). Double-sided tape was used to attach the coated wheat seeds to the acrylic plate, ensuring that the seed surfaces were aligned as accurately as possible. During the test, the coated wheat seeds were placed on the seed plate, and the testing procedure followed the same steps as previously described. After 30 repeated trials, the seed-seed SFC was found to range from 0.2 to 0.8, with an average of 0.60. The seed-acrylic SFC was found to range from 0.3 to 0.7, averaging 0.51. The rolling friction coefficient (RFC) was measured using the same approach. The seed-seed RFC was in the range of 0 to 0.1, with an average of 0.05, the seed-acrylic RFC was found to range from 0 to 0.1, with an average of 0.01.

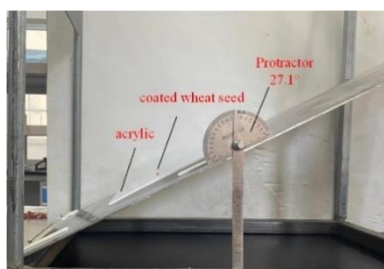


Fig. 6 - Friction coefficients test

Collision recovery coefficient (CRC)

Newton's law of collision was used to calculate the CRC. A 200 mm graduated ruler was placed vertically on the acrylic board, with the graduated side facing the camera. To minimize experimental error due to air resistance, the coated wheat seeds were released from a height H of 120 mm above the material board (Teng *et al.*, 2007; Zhou *et al.*, 2021). The seeds bounced off the acrylic board, and the entire collision and motion process was recorded using the slow-motion video feature on a Huawei Mate50, set to 240 frames per second. Each frame of the video was analysed to record the height h corresponding to the highest rebound point. The experiment was repeated six times. The acrylic board was then replaced with a seed-coated board, and the experiment was repeated six times using the same procedure. The coefficient of restitution was calculated using the following formula:

$$e = \frac{v_1}{v_0} = \frac{\sqrt{2gh}}{\sqrt{2gH}} = \sqrt{\frac{h}{H}} \quad (2)$$

where: e - the collision response factor, dimensionless; v_1 - the instantaneous velocity normal to the collision, mm s^{-1} ; v_0 - the instantaneous velocity before the collision, mm s^{-1} ; h - the maximum bounce height, mm ; H - the seed release height, mm .

According to equation (2), the seed-seed and seed-acrylic CRC were calculated to be 0.48 and 0.54.

Establishment of discrete element model

Based on the measured physical dimensions of the coated wheat seeds, a 3D model was created using SolidWorks. The completed seed model was then converted to STL format and imported into EDEM. Research by scholars has shown that minor differences in the shape outline do not significantly impact simulation results (Horabik *et al.*, 2016; Shi *et al.*, 2022). Therefore, this model uses single-sphere particles for the Generate Particle function. The physical appearance, physical model, and DEM of the coated wheat seeds are shown in Figure 7. The material in contact with the coated wheat seeds is an acrylic board, the parameters of which have been determined by reference to the literature (Boac *et al.*, 2014). The Poisson's ratio of Acrylic is 0.40, the shear modulus is 1.6×10^9 Pa, and the density is 1385 kg m^{-3} .

In the simulation of the repose angle of coated wheat seeds, a simulation tool model was established based on the actual dimensions of the experimental tools. A virtual particle factory was created above the acrylic cylinder, where particles were allowed to fall freely to the bottom of the cylinder, generating a total of 3,000 coated wheat seeds. Once the particles stabilized, the baffle was quickly removed, and the particles formed a stable pile on the base, as shown in Figure 8. The Hertz-Mindlin (no slip) contact model embedded in EDEM software was used, in line with the physical characteristics of the coated wheat seeds as granular materials.

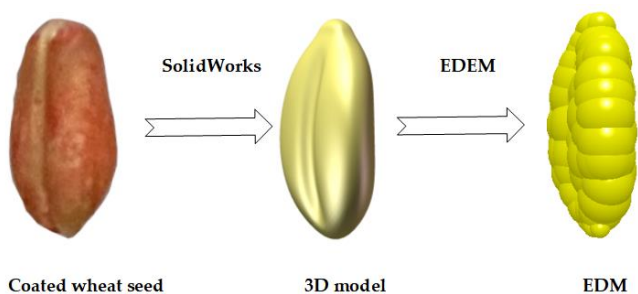


Fig. 7 - Discrete element modeling process

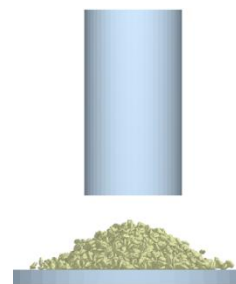


Fig. 8 - Repose angle simulation test

RESULTS

Plackett–Burman (PB) Test

Using the repose angle of the coated wheat seeds as the response value, the PB module in Design-Expert 13.0 software was employed for experimental design to identify the significant factors affecting the repose angle (Jia et al., 2014). Given that the minimum number of factors for the experiment was 11, and with 8 real parameters considered, the remaining 3 factors were filled with virtual parameters. Each parameter was set at two levels, high and low, coded as +1 and -1, as shown in Table 1.

A total of 12 experiments were conducted. After the simulation of the repose angle of the seeds was completed, the simulated repose angle was measured using the same method as in the physical experiments, with the results shown in Table 2.

Table 1

PB test measure range table

Symbol	Parameters	Unit	Low level (-1)	High level (+1)
X ₁	Poisson's ratio of seed		0.14	0.46
X ₂	Shear modulus of seed	MPa	1.5	10
X ₃	Seed-seed CRC		0.2	0.6
X ₄	Seed- acrylic CRC		0.4	0.7
X ₅	Seed-seed SFC		0.2	0.8
X ₆	Seed- acrylic SFC		0.3	0.7
X ₇	Seed-seed RFC		0	0.1
X ₈	Seed- acrylic RFC		0	0.1
X ₉ , X ₁₀ , X ₁₁	Virtual parameters		-	-

Table 2

PB test protocol and results

No.	X ₁	X ₂	X ₃	X ₄	X ₅	X ₆	X ₇	X ₈	X ₉	X ₁₀	X ₁₁	Repose angle θ/°
1	1	1	-1	1	1	1	-1	-1	-1	1	1	24.96
2	-1	1	1	-1	1	1	1	-1	-1	-1	1	29.04
3	-1	1	1	1	-1	-1	-1	1	-1	1	1	16.23
4	1	-1	1	1	1	-1	-1	-1	1	-1	1	23.87
5	1	-1	-1	-1	1	-1	1	1	-1	1	1	28.11
6	-1	-1	-1	1	-1	1	1	-1	1	1	1	26.12
7	1	1	-1	-1	-1	1	-1	1	1	-1	1	17.35
8	-1	1	-1	1	1	-1	1	1	1	-1	-1	25.31
9	1	-1	1	1	-1	1	1	1	-1	-1	-1	33.04
10	-1	-1	1	-1	1	1	-1	1	1	1	-1	25.66
11	1	1	1	-1	-1	-1	1	-1	1	1	-1	22.54
12	-1	-1	-1	-1	-1	-1	-1	-1	-1	-1	-1	17.15

The test results were analysed by ANOVA using Design-Expert 13.0 software to obtain the significant results of each simulation parameter as shown in Table 3. As can be seen from Table 3, the P<0.01 for seed-seed RFC (X₇) is extremely significant on the particle simulation rest angle; the P<0.05 for seed-seed SFC (X₅) and seed-acrylic SFC (X₆) is significant on the particle simulation rest angle; and the remaining experimental parameters with P>0.05 are not significant on the particle simulation rest angle.

Steepest ascent (SA) Test

Based on the results in Table 3, X₅, X₆, and X₇ were selected as the significant factors for the steepest ascent experiment (Ma et al., 2020), while the other non-significant parameters were assigned the average values from the physical experiments. Specifically, the Poisson's ratio of coated wheat seeds was 0.3, shear modulus was taken as 4.93 × 10⁸ Pa, seed-seed CRC was 0.48, seed-acrylic CRC was 0.54, and seed-acrylic RFC was 0.01.

Table 3

Analysis of the significance of parameters according to the PB test

Parameters	Effect	Sum of Squares	Contribution / %	p-Value	Significance
X ₁	1.7267	8.9441	3.076	0.209	
X ₂	-3.0867	28.5825	9.83	0.0651	
X ₃	1.8967	10.792	3.7116	0.1781	
X ₄	1.6133	7.8085	2.6855	0.233	
X ₅	4.0867	50.1025	17.2311	0.0326	*
X ₆	3.8267	43.9301	15.1083	0.0385	*
X ₇	6.49	126.36	43.4575	0.0093	**
X ₈	0.3367	0.34	0.1169	0.7762	

Note: * indicates a significant impact (0.01 < P < 0.05) ; ** indicates that the effect is extremely significant (P < 0.01).

Table 4

Design and results of the SA test

No.	X ₅	X ₆	X ₇	Repose angle θ / °	Relative error / %
1	0.20	0.30	0	0	100
2	0.35	0.40	0.03	19.53	37.28
3	0.50	0.50	0.06	26.23	15.77
4	0.65	0.60	0.09	29.67	4.72
5	0.80	0.70	0.12	33.15	6.45

From the results in Table 4, it is evident that the relative error was minimized at experiment 4, determining that the optimal range lies around this point. Therefore, No. 4 was selected as the centre point, with No. 3 and No. 5 serving as the low and high levels, respectively, for the subsequent BBD.

Box-Behnken (BBD) test

Based on the BBD principle and the results of the PB and SA tests, the significant parameters seed-seed SFC (X₅), seed-acrylic SFC (X₆), and seed-seed RFC (X₇) were selected as high (+1), medium (0), and low (-1), the three levels of No. 5, No. 4, and No. 3 for the design of the experiment, respectively, as shown in Table 5 (Hou et al., 2020). The values of the non-significant parameters were kept the same as in the SA test.

Table 5

Test factor codes for the BBD test

No.	X ₅	X ₆	X ₇	Repose angle θ / °	Relative error / %
1	0.20	0.30	0	0	100
2	0.35	0.40	0.03	19.53	37.28
3	0.50	0.50	0.06	26.23	15.77
4	0.65	0.60	0.09	29.67	4.72
5	0.80	0.70	0.12	33.15	6.45

Table 6

Design and results of BBD test

No.	Factor			Relative error / %
	X ₅	X ₆	X ₇	
1	-1	-1	0	15.45
2	1	-1	0	3.82
3	-1	1	0	5.20
4	1	1	0	0.9
5	-1	0	-1	16.21
6	1	0	-1	11.43
7	-1	0	1	3.28
8	1	0	1	4.78
9	0	-1	-1	14.10
10	0	1	-1	9.22
11	0	-1	1	1.64
12	0	1	1	4.14
13	0	0	0	2.76
14	0	0	0	4.27
15	0	0	0	5.39

Following the design and results of BBD test (Table 6), a second-order regression equation for the simulated repose angle was derived through multivariate regression fitting using Design-Expert 13.0.

$$\theta = 29.85 + 1.12X_5 + 0.93X_6 + 2.14X_7 - 0.57X_5X_6 + 0.26X_5X_7 + 0.07X_6X_7 - 0.55X_5^2 - 0.14X_6^2 - 0.19X_7^2 \quad (3)$$

According to the variance analysis of the model (Table 7), X_5 , X_6 , and X_7 had extremely significant effects on the repose angle of the particles, while the $X_5 X_6$, X_5^2 showed significant effects. The P-value of the repose angle regression model is 0.003 ($P < 0.01$), indicating that the model is highly significant. The lack-of-fit term has a P-value of 0.6564 ($P > 0.05$), suggesting a good fit between the model and the actual data. The coefficient of determination (R^2) is 0.9884, with an adjusted R^2 of 0.9675, a coefficient of variation (CV) of 1.25%, and an accuracy of 22.2219, all of which demonstrate that the test results are highly reliable and precise.

Table 7

Variance analysis of the results of the BBD test						
Parameters	Sum of Squares	df	Mean Square	F-value	p-Value	Significance
Modal	56.17	9	6.24	46.94	0.003	**
X_5	9.97	1	9.97	74.98	0.003	**
X_6	6.88	1	6.88	51.77	0.008	**
X_7	36.51	1	36.51	274.63	<0.001	**
$X_5 X_6$	1.30	1	1.30	9.78	0.0261	*
$X_5 X_7$	0.2756	1	0.2756	2.07	0.2094	
$X_6 X_7$	0.0196	1	0.0196	0.1474	0.7168	
X_5^2	1.10	1	1.10	8.29	0.0346	*
X_6^2	0.0711	1	0.0711	0.5347	0.4974	
X_7^2	0.1351	1	0.1351	1.02	0.3597	
Residual	0.6647	5	0.1329			
Lack of Fit	0.3261	3	0.1087	0.6420	0.6564	
Pure Error	0.3386	2	0.1693			
Cor Total	56.83	14				

Note: * indicates a significant impact ($0.01 < P < 0.05$); ** indicates that the effect is extremely significant ($P \leq 0.01$).

Based on the results of the ANOVA, the interaction between seed-seed SFC and seed- acrylic SFC ($X_5 X_6$) has a significant effect on the repose angle of the particles ($P < 0.05$). The response surface plot for $X_5 X_6$, generated using Design-Expert 13, visually illustrates the interaction effects between these parameters, as shown in Figure 9. As the values of these two parameters increase, the repose angle of the particles also shows an upward trend.

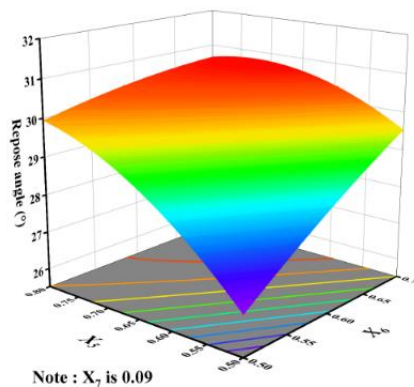


Fig. 9 - Response surface of the interaction between factors on the repose angle

Determine the optimal parameter combination

To identify the optimal simulation parameters and achieve the best possible fit to the actual repose angle, the relative error η was used as the optimization criterion. In Design-Expert 13.0, the response values were optimized, with the objective function and constraints set accordingly.

$$\begin{cases} \min \eta(A, B, C) \\ s.t. \begin{cases} 0.5 \leq A \leq 0.8 \\ 0.5 \leq B \leq 0.7 \\ 0.06 \leq C \leq 0.12 \end{cases} \end{cases} \quad (4)$$

The optimal simulation parameters for seed-seed SFC, seed-acrylic SFC, and seed-seed RFC were solved to be 0.62, 0.69, and 0.1, respectively.

Static verification test

To verify the reliability and accuracy of the calibrated discrete element simulation parameters for coated wheat seeds, these optimal parameters were input into EDEM for three simulation trials. As shown in Figure 10, the repose angles of the coated wheat seeds were found to be 30.27°, 29.78°, and 32.15°, respectively. The relative error between the average repose angle from physical tests (31.14°) and the average repose angle from simulation tests (30.73°) was 1.31%. This indicates that the calibrated parameters can serve as a valuable reference for future simulation studies of coated wheat seeds.



a) Real test schematic
b) Comparison chart
Fig. 10 - Comparison of simulated angle of repose and actual angle of repose fitting plots

Dynamic verification test

To validate the consistency between the DEM and the actual physical model, a precision seed-metering test bench for wheat was established, as shown in Figure 11.

The coated wheat seeds of the "Xindong 20" variety were selected for the bench test. The seed-metering wheel had a diameter of 52 mm, with 12 teeth per row, arranged in a staggered pattern across two rows.



Fig. 11 - Coated wheat seed metering test device



Fig. 12 - Simulation test of coated wheat seed rowing

The seeder model was simplified, and the DEM of the coated wheat seeds, along with the optimal contact parameters obtained from calibration, was imported into EDEM for simulation, as shown in Figure 12.

In accordance with the GB/T 9478-2005 "Test Methods for Grain Drills," the variation coefficients for seeding consistency (determined by counting the number of seeds discharged by the seed-metering wheel after three revolutions, with three groups of 10 measurements each, and then calculating the coefficient of variation) and seeding uniformity (by dividing the conveyor belt into ten 100×50 mm grids, counting the number of seeds in each grid, repeating three times, averaging the results, and calculating the coefficient of variation) were used as key parameters.

The formulas are shown in 5, 6. The relative error between the variation coefficients from the simulation and the bench tests at different speeds was used as a reference indicator.

$$S = \sqrt{\frac{1}{n-1} \sum (X - \bar{x})^2} \tag{5}$$

$$a = \frac{100S}{\bar{x}} \tag{6}$$

where: *S* - the standard deviation, dimensionless; *n* - the number of zones, dimensionless; *X* - the number of seeds per zone, pcs; \bar{x} - the mean number of seeds per zone, pcs; *a* - the coefficient of variation, dimensionless.

The experimental results (Table 8) show that the average relative error in the variation coefficients for seeding consistency and uniformity was less than 5%, indicating that the optimal parameter combination obtained from calibration can provide theoretical support for precision wheat seeding and the structural optimization of the seed-metering device.

Table 8

Coefficient of variation of discharge consistency and seeding uniformity at different speeds

Velocity km/h-1	Coefficient of variation of displacement consistency C ₁ / %			Coefficient of variation of seeding uniformity C ₂ / %		
	Simulation text	Bench text	Relative error	Simulation text	Bench text	Relative error
	5	2.42	2.38	1.68	8.77	8.47
6	1.97	2.02	2.48	5.14	4.93	4.26
7	2.19	2.14	2.34	7.33	7.55	2.91

CONCLUSIONS

Through physical experiments, the "Xindong 20" wheat seeds were found to have a Poisson's ratio of 0.3, a shear modulus of 4.93×10^8 Pa, and a natural angle of repose of 31.14° . The SFC between seed-seed and seed-acrylic were determined to be 0.60 and 0.51, respectively; the RFC were 0.05 and 0.01, respectively; and the CRC were 0.48 and 0.54.

The PB test identified seed-seed and seed-acrylic SFC, along with seed-seed RFC, as the significant influencing parameters. Subsequent SA test further refined these parameter ranges to 0.5-0.8, 0.5-0.7, and 0.06-0.12.

Using a BBD response surface test, a quadratic regression model was established to describe the relationship between the significant influencing parameters and the angle of repose. Analysis of the interaction between seed-seed SFC and seed-acrylic SFC showed that the angle of repose increased as the values of these two parameters rose. By optimizing the relative error of the angle of repose, the optimal simulation parameters were determined to be 0.62 for seed-seed SFC, 0.69 for seed-acrylic SFC, and 0.1 for seed-seed RFC. Validation experiments using these optimal parameters showed a relative error of 1.31% in the simulated angle of repose, indicating no significant difference.

Under different speed conditions, the average relative error between the variation coefficients of seeding consistency and uniformity in both bench and simulation tests was less than 5%. These results demonstrate that the DEM and the simulation parameters can effectively support the optimization of seed-metering device structures in precision wheat seeding.

ACKNOWLEDGEMENT

This work was supported by Major Science and Technology Special Projects in Xinjiang Uygur Autonomous Region, China (Project No. 2022A02003-3).

REFERENCES

- [1] Boac J.M., Casada M.E., Maghirang R.G., Harner J.P. (2010). Material and interaction properties of selected grains and oilseeds for modeling discrete particles. *Transactions of the ASABE* 53(54):1201-1216.
- [2] Chen Y.Y., Lu C.H. (2019). Future Grain Consumption Trends and Implications on Grain Security in China. *Sustainability* 11(19): 5165.
- [3] Han D., Zhang D., Jing H., Yang L., Cui T., Ding Y., Wang Z., Wang Y., Zhang T. (2018). DEM-CFD coupling simulation and optimization of an inside-filling air-blowing maize precision seed-metering device. *Computers and Electronics in Agriculture* 150(7):426-438.
- [4] Hao J., Wei W., Huang P., Qin J., Zhao J. (2021). Calibration and experimental verification of discrete element parameters of oil sunflower seeds. *Transactions of the CSAE* 37(12): 36-44.
- [5] Horabik J., Molenda M. (2016). Parameters and contact models for DEM simulations of agricultural granular materials: A review. *Biosystems engineering* 147(7): 206-225.
- [6] Hu M.J., Zhou Y., Tang Z.C., Xu Z.Y., Wang H.L., Wang P.T. (2018). Mechanical properties of the delinted and coated cottonseed. *Journal of Anhui Agricultural University* 45(01):175-180.
- [7] Jia F., Han Y., Liu Y., Cao Y., Shi Y., Yao L., Wang H. (2014). Simulation prediction method of repose angle for rice particle materials. *Transactions of the Chinese Society of Agricultural Engineering* 30(11): 254-260.
- [8] Lang X.T., Ma H.L. (2016). Wheat production efficiency and region differences in Xinjiang (新疆小麦生产效率及地区差异研究). *Chinese Journal of Agricultural Resources and Regional Planning* 37(10): 127-133.

- [9] Li H.W., Cheng Y.G., Chen X.H., Zhang Y.F., Weng C.J., Bo K., Gao Q.H., Ban H.G., Su G.Y. (2024). Development status and trend of mechanization of the whole process of wheat production (小麦生产全程机械化发展现状及趋势). *China Agricultural Machinery Quality and Supervision* 1(05): 3-6+13.
- [10] Liu F., Zhang J., Li B., Chen J. (2016). Calibration of parameters of wheat required in discrete element method simulation based on repose angle of particle heap. *Transactions of the Chinese Society of Agricultural Engineering* 32(12): 247-253.
- [11] Lu F.Y., Xu M., Tan S.Y., Chen L.T., Zeng L.C., A P. (2018). Simulative calibration and experiment on main contact parameters of discrete elements for rice bud seeds. *Transactions of the Chinese Society of Agricultural Machinery* 49(2): 93-99.
- [12] Ma D., Shi S., Hou J., Zhou J., Li H., Li J. (2024). Calibration and Experimentation of Discrete Elemental Model Parameters for Wheat Seeds with Different Filled Particle Radii. *Applied Sciences* 14(5): 2075.
- [13] Ma Y., Song C., Xuan C., Wang H., Yang S., Wu P. (2020). Parameters calibration of discrete element model for alfalfa straw compression simulation. *Transactions of the CSAE* 36(11): 22-30.
- [14] NBo S. (2023). Statistical bulletin of the People's Republic of China on National Economic and social development 2022 (中华人民共和国 2022 年国民经济和社会发展统计公报)
- [15] Shi L.R., Sun W., Zhao W.Y., Yang X.P., Feng B. (2018). Parameter determination and validation of discrete element model of seed potato mechanical seeding. *Transactions of the Chinese Society of Agricultural Engineering* 34(06): 35-42.
- [16] Shi L.R., Zhao W.Y., Yang X.P. (2022). Effects of typical corn kernel shapes on the forming of repose angle by DEM simulation. *Int J Agric & Biol Eng* 15(2): 248–255.
- [17] Teng G., Jia Z.H., Zhou K.D. (2007). A theoretical model for the coefficient of restitution calculation of point impact (计算点接触碰撞恢复系数的一种理论模型). *Ji Xie She Ji Yu Yan Jiu* (2023). *Machine Design and Research*. 3: 14-15.
- [18] Wu A.X.S., Y Z., Liu X.P. (2002). *Theory of Granular Dynamics and Its Application*, Metallurgical Press: Beijing, China, p.18.
- [19] Zhang W.X., Wang F.Y. (2022). Parameter calibration of American ginseng seeds for discrete element. *Int J Agric & Biol Eng* 15(6): 16–22.
- [20] Zhang Z.G., Fan L.F., Ma X.H., Lin J.Y., Zhu H.R., Qiu S.J. (2018). Spatial-temporal patterns of Xinjiang's grain output increase and the contribution factors during 2007–2015. *Arid Land Resour. Environ* 32(09):71-75.
- [21] Zhi W.Z., Xu M., Xiu L.C., Ze H.L., Xi C.W. (2021). Critical review of applications of discrete element method in agricultural engineering. *Transactions of the Chinese Society of Agricultural Machinery* 52(4): 1-20.
- [22] Zhou L. (2021). DEM-based modelling of maize seeds and the simulation analysis and experimental study of the seed-sowing. *Jilin Agricultural University*: Jilin, China.

THEORETICAL STUDY OF TRACTION RESISTANCE OF HARROWS WITH HELICAL WORKING BODIES

ТЕОРЕТИЧНЕ ДОСЛІДЖЕННЯ ТЯГОВОГО ОПОРУ БОРОНИ З ГВИНТОВИМИ РОБОЧИМИ ОРГАНАМИ

Volodymyr BULGAKOV¹, Adolfs RUCINS²), Ivan HOLOVACH¹), Oleksandra TROKHANIAK¹),
Mykola KLENDII³), Lucretia POPA⁴), Anastasiya KUTSENKO¹)

¹National University of Life and Environmental Sciences of Ukraine, Ukraine;

²Latvia University of Life Sciences and Technologies, Latvia;

³Separated Subdivision of National University of Life and Environmental Sciences of Ukraine, Berezhany Agrotechnical Institute, Ukraine;

⁴National Institute of Research–Development for Machines and Installations Designed for Agriculture and Food Industry–INMA, Bucharest / Romania

*Corresponding author's E-mail: adolfs.rucins@lbtu.lv; vbulgakov@meta.ua

DOI: <https://doi.org/10.35633/inmateh-74-33>

Keywords: tillage machines, traction resistance, angle of attack, model

ABSTRACT

The paper presents a general view of the new working surface of the harrow with helical working bodies. With the help of SOLIDWORKS software package, a computer model of this soil tillage equipment with helical working bodies for surface tillage has been created. The obtained new analytical dependence made it possible to determine the traction resistance of the harrow, equipped with a spiral working element which, in turn, served as the basis for constructing graphs, showing a change in the traction resistance depending on various values angle of attack of the harrow and the soil resistance. On the basis of a computer model of a helical tillage body created in the SOLIDWORKS program, it was found that when the angle of attack of the body increases, the traction resistance P increases, as well, and its greatest increase is observed for the maximum diameter D . It was found that the thickness of the screw λ has a much smaller effect on the traction resistance P compared to the diameter D .

АНОТАЦІЯ

У статті представлено загальний вигляд нової робочої поверхні борони з спіральними робочими органами. За допомогою програмного забезпечення SOLIDWORKS створено комп'ютерну модель цього ґрунтообробного знаряддя з гвинтовими робочими органами для поверхневого обробітку ґрунту. Отримана нова аналітична залежність дала можливість визначити тяговий опір борони, оснащеної спіральним робочим органом, що у свою чергу послужило основою для побудови графіків, що показують зміну тягового опору в залежності від різних величин кута атаки борони та опору ґрунту. На основі комп'ютерної моделі гвинтового ґрунтообробного знаряддя, створеного в програмі SOLIDWORKS, встановлено, що при збільшенні кута атаки спіральної борони зростає також тяговий опір P , причому найбільше його збільшення спостерігається для максимального діаметру D . Встановлено, що товщина спіралі λ значно менше впливає на тяговий опір P порівняно з діаметром D .

INTRODUCTION

To perform technological operations of tillage it is necessary to choose a rational set of units that will have high productivity, low cost and operating costs, to ensure optimal conditions for plant growth. Technologies, units and complexes for tillage are being improved to ensure tillage quality and reduce energy costs.

The issues under consideration are the subject of works, published by many authors. In addition, considerable attention is paid to the study of the energy parameters of machine and tractor units, in particular soil-cultivating ones, the working bodies of which will not only perform these technological processes efficiently, but will also have minimal energy costs. If the energy costs of the tillage machines are assessed only by the main indicator – traction resistance, then it is necessary to take into account many factors, the consideration of which is mandatory. First of all, the traction resistance of such aggregates directly depends on the design parameters of the tillage machines, and this is the type, size, shape of the working parts and their number in the unit.

Besides this, the material used in their manufacture and its physical and mechanical properties, the manufacturing technology and quality, the properties of the working surfaces, etc. are important. When studying the traction resistance, the physical and mechanical properties of the soil and the climatic conditions in which the soil is cultivated are essential. And finally, technical and operational conditions are also important, such as precise adjustment of the working parts to a preset processing depth, the state of sharpness and wear of the cutting edges of the tillage machines, etc. There are works (Lech, 2001; Bulgakov et al., 2022a; Olt et al., 2022) devoted to taking these factors into account when studying the soil-cultivating machine-tractor aggregates to reduce the traction resistance. In addition, it should be remarked that there are well-known works in this area, which most deeply present the analytical and experimental results on reducing the traction resistance of the tillage machines (Pylypaka et al., 2019; Bulgakov et al., 2017, 2022b; Pylypaka et al., 2018). The use of spiral working bodies as a working element in soil cultivation, as well as the study of the quality of their work and the selection of optimal design, kinematic and energy parameters are the subject of the works (Bulgakov et al., 2019; Pylypaka et al., 2021; Pastushenko et al., 2020; Hevko et al., 2020; Klendiy and Dragan, 2021; Hristov et al., 2016; Lyashuk et al., 2016).

Several previous studies have focused on the physical and mechanical properties of the treated soil to determine the parameters that have the greatest impact upon the crop germination and emergence (Tagar, et al., 2020).

In the work by Serrano et al., (2007), a study of the dynamics of the system: "Tractor-tiller attachment" is presented, for soil cultivation. The configuration of the combination tractor-harrow, based on the measurement of the traction required under the operating conditions, provides important information on the recommended power, required for each harrow model produced. Due to this type, it is possible to make decisions on the selection of an appropriate combination of the specified system. This is what will make it possible to increase the productivity of the tractor harrow and improve the efficiency of the field surface processing.

Conventional free-rotating disc implements require multiple harrow passes after moldboard ploughing to achieve the desired soil treatment (Kumari and Raheman, 2024), resulting in harmful soil compaction, excessive consumption of fuel and delay in sowing.

In addition, poor penetration of passively driven discs (Nalavade et al., 2010) creates the need to add extra weight to the disc harrows, resulting in increased traction, excessive slippage, increased fuel consumption and excessive soil compaction.

Therefore, at the present time, the main task in the creation and substantiation of the parameters of new constructions of transport-technological agricultural machines and their working bodies, providing the expansion of technological possibilities, is the development of such constructions that would ensure a reduction of energy and material resources with improved conditions for their operation, wide multi-functionality, mechanization and automation of production processes. The aim of this study is to reduce the traction resistance of a harrow, equipped with spiral working bodies, based on the theoretical determination of its optimal design parameters.

MATERIALS AND METHODS

Traction resistance of disk and screw working bodies are determined by soil resistance forces acting on the blade and working surface of disks or spirals. Application of this or that type of construction of these working bodies leads to the prevalence of a certain type of deformation of the soil layer. Therefore, the traction resistance of one working body in the direction of movement of the machine-tractor unit will be determined using such an analytical expression:

$$P = k \cdot A_n + \mu \cdot Q + \varepsilon \cdot A_S \cdot V^2 \quad (1)$$

where: k – specific traction resistance of the working body, ($k = 20000 \dots 70000 \text{ N} \cdot \text{m}^{-2}$); A_n - the total area of the screw surface immersed in the soil, [m^2];

A_S – cross-sectional area of the soil layer subject to tillage, [m^2];

μ – the coefficient of rolling resistance;

Q – weight of harrow with helical working bodies, [N];

ε – coefficient depending on the shape of the working body and soil properties, [$\text{N} \cdot \text{s}^2 \cdot \text{m}^{-4}$];

V – unit movement speed, [$\text{m} \cdot \text{s}^{-1}$].

In the relation 1, $k \cdot A_n$ - resistance, which takes into account the resistance of working bodies; $\mu \cdot Q$ - harrow weight; $\varepsilon \cdot A_s \cdot V^2$ - placement and form of working bodies.

Value A_s can be expressed by the product of the angle of attack α by the area A [m²] the contact of one coil with the soil. Taking this into account, the dependence (1) will have the form (2):

$$P = n A \sin \alpha \cdot [1 + \tan(\gamma + \varphi)] \cdot (k + \varepsilon \cdot V^2) + \mu \cdot Q \quad (2)$$

where:

n – the number of coils of the helical surface, simultaneously buried in the soil;

φ – angle of elevation of the helical surface of the tillage body, $\varphi = \arctan(h \cdot R^{-1})$ [deg];

β – the angle of the harrow section to the direction of travel of the machine [deg];

γ – angle between the front working surface of the soil tillage body coil and the harrow surface [deg];

h – screw pitch [m];

R – screw implement radius [m].

Using the SOLIDWORKS software package, a computer model of an implement with helical working bodies for surface tillage was created (Fig. 1).

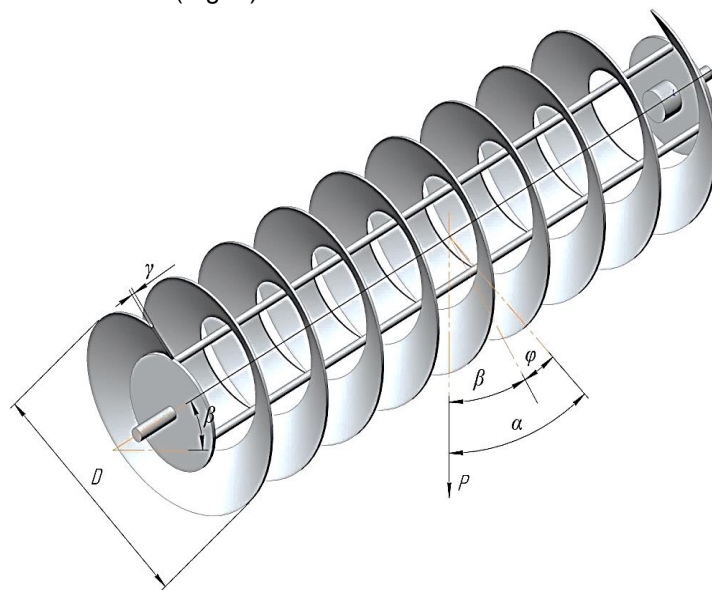


Fig. 1 – Calculation scheme of the screw working body

A general view of the working surface of the screw harrow is shown in Fig. 2.



Fig. 2 – General view of the working surface of the screw harrow

The area A of contact of one coil of the helical surface of the implement with the soil can be determined by the relationship (3).

$$A = \int_0^{\arccos(1-a/R)} \left(R \cdot \sqrt{R^2 + b^2} - \frac{R-a}{\cos \theta} \cdot \sqrt{\frac{(R-a)^2}{\cos^2 \theta} + b^2} \right) d\theta \quad (3)$$

where: θ – angle of spiral segment [deg];

R – outside radius of the helical surface, [m];

a – tillage depth, [m]; b – screw pitch, [m].

After integrating the expression (3) and the corresponding transformations, relation (4) is obtained:

$$P = n \left[R^2 \cdot \arccos \left(1 - \frac{a}{R} \right) - (R - a) \cdot \sqrt{2Ra - a^2} \right] \sin \alpha \cdot [1 + \tan(\gamma + \varphi)] (k + \varepsilon V^2) + \mu Q \quad (4)$$

Thus after carrying out the next transformation, the analytical expression that allows determining the traction resistance P of a harrow equipped with a spiral working body can be presented in the following final form (5):

$$P = kn \left[R^2 \cdot \arccos \left(1 - \frac{a}{R} \right) - (R - a) \cdot \sqrt{2Ra - a^2} \right] \sin \alpha \cdot [1 + \tan(\gamma + \varphi)] + \mu Q \quad (5)$$

Using the obtained analytical expression (5) in its final form makes it possible to perform calculations of the traction resistance P of a harrow, equipped with a spiral working element, using a personal computer. However, at first it is necessary to specify the numerical values of the constants included in expression (5).

In this case it is assumed that: the harrow weight $Q = 1720$ N – (this mass value will provide the required depth of the soil cultivation, equal to $a = 0.08$ m; for a tillage depth equal to $a = 0.10$ m the harrow is loaded up to the weight of $Q = 1950$ N; outside radius of the helical surface $R = 0.28$ m; number of coils of the helical surface, simultaneously buried in the soil $n = 10$ (2 working bodies of 5 turns each); attack angle $\alpha = 20^\circ \dots 40^\circ$; the reduced conditional coefficient of rolling friction can be set in such limits $\mu = 0.07 \dots 0.012$. It depends on the properties of the soil and the material of the screw surface.

RESULTS

The analysis of the calculated data shows that with increasing the angle α from 20 to 40° the traction resistance of the harrow with helical bodies increases linearly (Fig. 3).

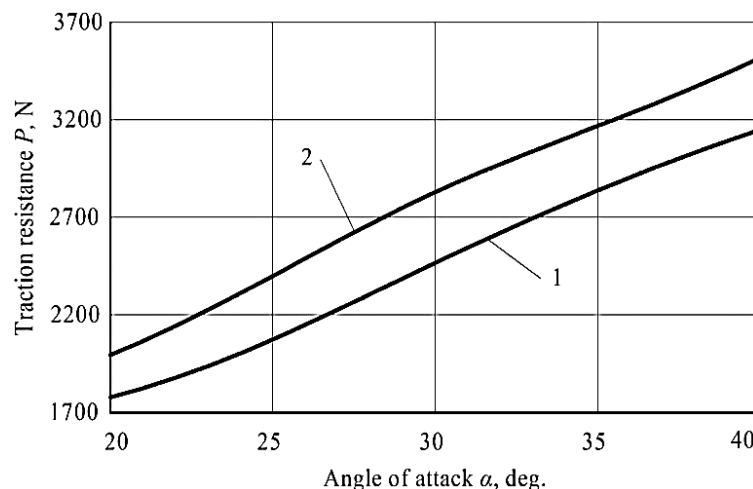


Fig. 3 – Dependencies of the traction resistance of the harrow with helical working bodies on changes in the angle of attack α with $k = 20000$ N·m⁻²
1 – for a tillage depth of 0.08 m, 2 – for a tillage depth of 0.10 m

Within one value of tillage depth (lines 1, 2 and 3) this gain is 42...44%. At the same time, within the limits of one value of parameter α , the value of P when changing the depth of tillage from 0.08 to 0.10 m increases by 11...13%.

Consequently, within the accepted limits of variation, the angle of attack parameter α has a greater influence on the increase in traction resistance P for a harrow with a working element in the form of a spiral body than the depth of tillage.

Hence, it is quite obvious that to reduce it, preference should be given to smaller values of the parameter α . The depth of tillage in this case will be determined by the agricultural requirements for the technological operation performed by the harrow.

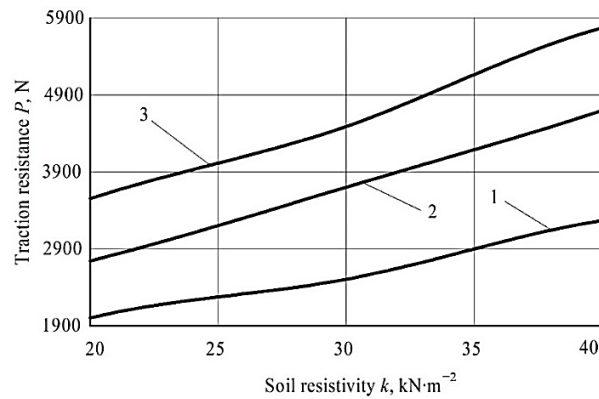


Fig. 4 – Dependencies of the traction resistance of the harrow with helical working bodies on changes in the value of the resistivity of the soil k , width = 0.1 m

1 – for angle of attack $\alpha = 20^\circ$; 2 – for angle of attack $\alpha = 30^\circ$; 3 – for angle of attack $\alpha = 40^\circ$

The analysis of the obtained dependencies (Fig. 4) shows that the traction resistance of a harrow equipped with a spiral working body at $a = 0.1$ m within the limits of the change in soil resistivity $k = 20 \dots 40$ $\text{kN}\cdot\text{m}^{-2}$ increases linearly. In this case, the resistance for the angle of attack $\alpha = 20^\circ$ changes within the range of $P = 1980 \dots 3210$ N, which is 1.62 times, for tillage depth, $\alpha = 30^\circ$ varies within the range of $P = 2820 \dots 4630$ N, which is 1.64 times and for tillage depth, $\alpha = 40^\circ$ changes in the range of $P = 3555 \dots 5871$ N, which is 1.65 times.

In order to study the angle of attack of the helical working body and obtain the corresponding graphical relationships to the traction resistance, simulation of the corresponding conditions of the experience was carried out. The working body was clamped on both sides and a force perpendicular to the plane rotated by an angle β . During the modelling of the helical working body, the variables were the following parameters: the value of the angle β ; the thickness of the helical spiral of the working body λ ; the diameter of the helical working body D . Further on the PC a graphic image of the displacement (Fig. 5), the components of the working body under the action of traction resistance and torque were obtained.

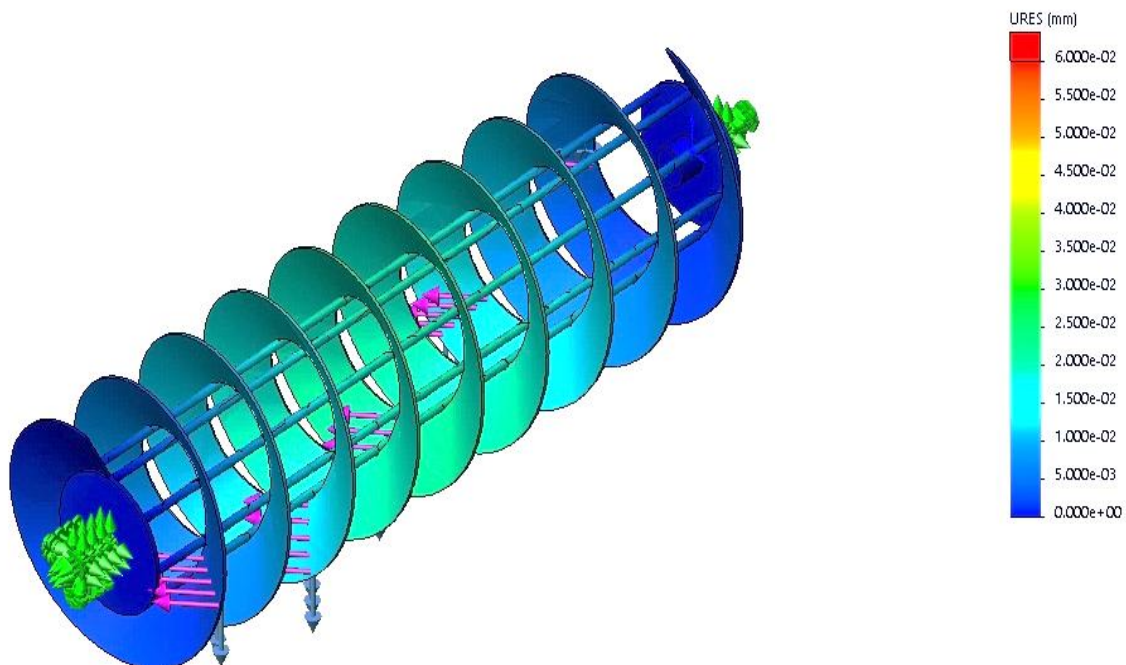


Fig. 5 – Movement of the helical body's components under the influence of traction resistance and torque

According to the results of the simulation, the angle of attack of the helical working body was obtained, while changing the value of the angle β , the thickness of the helical spiral of the working body λ , the diameter of the helical working body D and traction P .

The corresponding graphical relationships are shown in Figs.6-8.

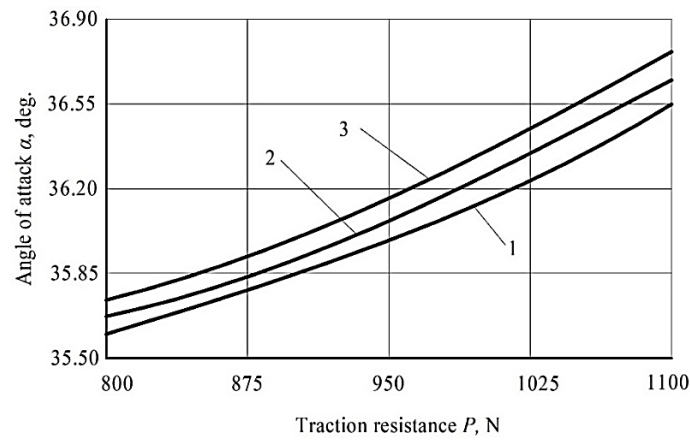


Fig. 6 – Dependencies of changes in the value of traction resistance on the angle of attack of the helical working body at different thicknesses of the helical body
 1 – $\lambda = 0.006$ m; 2 – $\lambda = 0.008$ m; 3 – $\lambda = 0.01$ m

As can be seen from the graphical relationships, the tractive force P increases as the angle of attack of the body increases. The greatest increase is observed for the diameter of the body $D = 0.6$ m, and the smallest – for $D = 0.4$ m (Fig. 8).

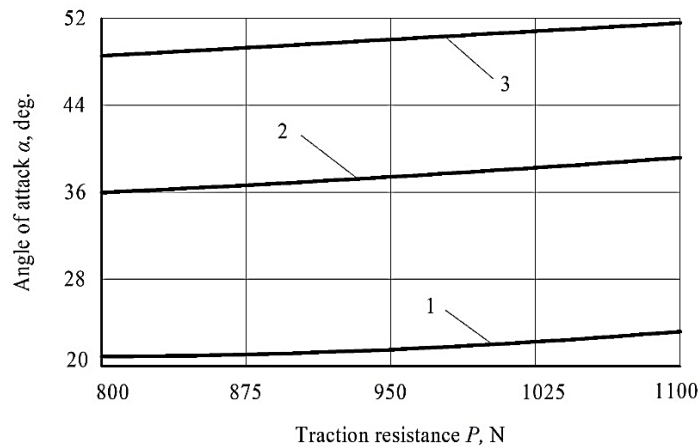


Fig. 7 – Dependencies of the change in the value of traction resistance on the angle of attack of the screw working body at different angles of the working body
 1 – $\beta = 10^\circ$; 2 – $\beta = 25^\circ$; 3 – $\beta = 40^\circ$

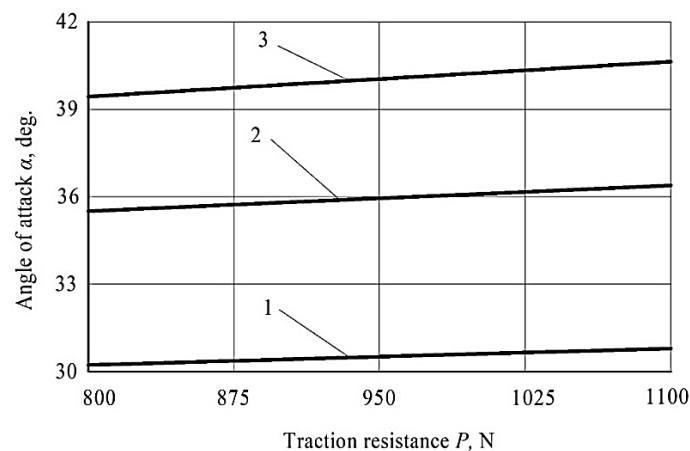


Fig. 8 – Dependencies of changes in the value of traction resistance on the angle of attack of the helical working body at different diameters of the helical body
 1 – $D = 0.4$ m; 2 – $D = 0.5$ m; 3 – $D = 0.6$ m

As can be seen from the graphical relationship shown in Fig. 6, the thickness of the helical spiral λ has much less influence on the angle of attack α , compared to diameter D . The graphical dependencies themselves are close to linear.

The comparison of the obtained results allows us to conclude about the similarity of the values obtained and the corresponding graphical dependencies constructed on their basis.

CONCLUSIONS

Based on the analysis of literature sources and patent search, the design of the harrow with helical working body was developed and manufactured. With the help of SOLIDWORKS software package, a computer model of the equipment with helical working body for surface tillage was created. On the basis of the derived relations for determining the traction resistance of the harrow with helical working body, graphical dependence of its value on the angle of attack α and the soil resistivity k has been plotted. It was found that within one value of tillage depth (lines 1, 2 and Fig. 3) this increase is 42...44%. At the same time, within the limits of one value of parameter α the value P at a change of tillage depth from 0.08 to 0.10 m grows by 11...13%. Consequently, the parameter of the angle of attack α , within the accepted limits of its variation, has a practically greater influence on the growth of the traction resistance P of a harrow with a helical working body than the depth of tillage. At the same time, within one value of parameter α the value of P at a change of tillage depth from 0.08 to 0.10 m grows by 11...13%. Consequently, the angle of attack parameter α , within the accepted limits of its variation, has a practically greater influence on the growth of the traction resistance P of helical harrows than the working depth.

It was also found that within the limits of the change in soil resistivity $k = 20...40 \text{ kN}\cdot\text{m}^{-2}$, it increases linearly. In this case, the resistance for the angle of attack $\alpha = 20^\circ$ changes within the range of $P = 1980...3210 \text{ N}$, which is 1.62 times, for tillage depth, $\alpha = 30^\circ$ changes within the range of $P = 2820...4630 \text{ N}$, which is 1.64 times for tillage depth, $\alpha = 40^\circ$ changes within the range of $P = 3555...5871 \text{ N}$, which is 1.65 times.

It was found that with increasing the angle of attack of the working body traction force P increases, and its greatest increase is observed for the maximum diameter of the working body D , while the thickness of the screw has a much smaller influence on the angle of attack α , compared with the diameter D .

Comparison of the obtained results allows us to conclude about the similarity of the values obtained and the corresponding graphical dependencies constructed on their basis.

REFERENCES

- [1] Bulgakov, V., Trokhaniak, O., Klendii, M., Ivanovs, S., & Dukulis, I. (2022a). Reserch on the Impact of the Operating Modes and Main Design Parameters on the Efficiency of the Machine for Preparing and Packing Slaked Lime. *INMATEH – Agricultural Engineering*, 67(2), 323-330. DOI: <https://doi.org/10.35633/inmateh-67-33>
- [2] Bulgakov, V., Olt, J., Ivanovs, S., Trokhaniak, O., Gadzalo, Ja., Adamchuk, V., Chernovol, M., Pascuzzi, S., Santoro, F., Arak, M. (2022b). Research of a contact stresses in swivel elements of flexible shaft in screw conveyor for transportation of agricultural materials. *Estonian Academic Agricultural Society. Agraarteadus*, 33(1), 67-73. doi:10.15159/jas.22.12
- [3] Bulgakov, V., Pascuzzi, S., Nikolaenko, S., Santoro, F., Sotirios Anifantis, A., Olt, J. (2019). Theoretical study on sieving of potato heap elements in spiral separator. *Agronomy Research*. Volume 17, No 1, 33-38.
- [4] Bulgakov, V., Adamchuk, V., Nozdrovický, L., Ihnatiev, Ye. (2017). Theory of Vibrations of Sugar Beet Leaf Harvester Front-Mounted on Universal Tractor. *Acta Technologica Agriculturae*, 20(4), 96-103.
- [5] Hevko, R., Rohatynskyi, R., Hevko, M., Lyashuk, O., Trokhaniak, O. (2020). Investigation of sectional operating elements for conveying agricultural materials. *Research in Agricultural Engineering*, 66 (1), 18-26, DOI: 10.17221/25/2019-RAE
- [6] Hristov, G., Zahariev, P., Beloiev, I. (2016). A review of the characteristics of modern unmanned aerial vehicles. *Acta Technologica Agriculturae*, 19(2), 33-38.
- [7] Klendiy, M.B., Dragan, A.P. (2021). Justification of the design of the working body of the screw section of the combined tillage tool. *Perspective technologies and devices*, 18, 66-72. (in Ukrainian).
- [8] Kumari, A., Raheman, H. (2024). Development of a Novel Draft Sensing Device with Lower Hitch Attachments for Tractor-Drawn Implements. *Journal of Biosystems Engineering*, 49, 20-28.

- [9] Lech, M. (2001). Mass flow rate measurement in vertical pneumatic conveying of solid. *Powder Technology*, 114(1–3), 55-58.
- [10] Lyashuk, O., Vovk, Y., Sokil, B., Klendii, V., Ivasechko, R., Dovbush, T. (2019). Mathematical model of a dynamic process of transporting a bulk material by means of a tube scraping. *Agricultural Engineering International: CIGR Journal*, 21(1), 74-81.
- [11] Nalavade, P. P., Salokhe, V. M., Niyamapa, T., Soni, P. (2010). Performance of Free Rolling and Powered Tillage Discs. *Soil and Tillage Research*, 109(2), 87-93.
- [12] Olt, J., Bulgakov, V., Trokhaniak, O., Klendii, M., Gadzalo, I. A., Ptashnik, M., Tkachenko, M. (2022). Harrow with screw-type operating tools: Optimisation of design and process parameters. *Agronomy Research*, 20(4), 751-763.
- [13] Pastushenko, S.I., Klendy, N.B., Klendy, M.I. (2020). Investigation of the traction resistance of the experimental version of the harrow with screw working bodies. *Scientific Bulletin of the Taurida State Agrotechnological University*, 2(10), 1-14. (in Ukrainian).
- [14] Pylypaka, S., Klendii, M., Klendii, O. (2018). Particle motion on the surface of a concave soil-tilling disk. *Acta Polytechnica. Journal of Advanced Engineering*, 58(2), 201-208.
- [15] Pylypaka, S.F., Klendii, M.B., Nesvidomin, V.M., Trokhaniak, V.I. (2019) Particle motion over the edge of an inclined plane that performs axial movement in a vertical limiting cylinder. *Acta Polytechnica. Journal of Advanced Engineering*, 59 (3), 67-76.
- [16] Pylypaka, S.F., Klendii, M.B., Trokhaniak, V.I., Kresan, T.A., Hryshchenko, I.Y., Pastushenko, A.S. 2021. External rolling of a polygon on closed curvilinear profile. *Acta Polytechnica. Journal of Advanced Engineering*, 61(1), 270-278.
- [17] Serrano, J. M., Peça, J.O., da Silva, J.M., Pinheiro, A., Carvalho, M. (2007). Tractor energy requirements in disc harrow systems. *Biosystems Engineering*, 98 (3), 286-296.
- [18] Tagar, A. A., Adamowski, J., Memon, M. S., Do, M. C., Mashori, A. S., Soomro, A., S. (2020). Soil fragmentation and aggregate stability as affected by conventional tillage implements and relations with fractal dimensions. *Soil and Tillage Research*, 197, 104494, 10.1016/j.still.2019.104494

DESIGN AND TESTING OF A GAP ADJUSTABLE ELASTIC LOW DAMAGE CORN PICKING HEADER BASED ON ADAMS

基于 Adams 的间隙可调弹性低损玉米摘穗割台的设计与试验

Xianghao LI¹⁾, Yongli ZHAO¹⁾, Hongda ZHAO¹⁾, Shaochuan LI¹⁾, Peisong DIAO^{1*)}

College of Agricultural Engineering and Food Science, Shandong University of Technology, Zibo, Shandong, 255000, China

Tel: +86-15036943900; E-mail: dps2003@163.com

Corresponding author: Peisong Diao

DOI: <https://doi.org/10.35633/inmateh-74-34>

Keywords: corn picking header; elastic low-damage; compression spring; gap adjustment; adaptive

ABSTRACT

To address the high damage rate and impurity content in corn ear picking, this study proposes the design of a gap-adjustable elastic low damage corn picking header. Theoretical analysis of the adaptive gap adjustment mechanism for the picking plate and the flexible picking mechanism will be conducted. Simulation experiments will be performed considering three factors: the stiffness coefficient of the compression spring, the rotational speed of the stalk-pulling roller, and the thickness of the flexible body. The test results indicate that the minimum collision force on the fruit cluster occurs when the stiffness coefficient of the compression spring is 36 N/mm, the rotational speed of the stalk-pulling roller is 700 r/min, and the thickness of the flexible body is 6 mm. When the header tilt angle was 25 degrees and the working speed was 3 km/h, using the stalk roller speed as the experimental variable, the collision force of the gap-adjustable elastic low-damage corn picking header was compared to that of the ordinary plate-type corn picking header. The results indicated that the collision force of the gap-adjustable elastic low-damage corn picking header was reduced by more than 25 % compared to the ordinary plate-type corn picking header.

摘要

为解决玉米割台摘穗损伤率高以及含杂率高的问题，本研究提出设计一台间隙可调弹性低损玉米摘穗割台。对摘穗板间隙自适应调节结构和柔性摘穗机构进行理论分析，在压缩弹簧的刚度系数、拉茎辊转速、柔性体厚度三因素下，进行仿真试验。试验表明，在压缩弹簧刚度系数为 36 N/mm、拉茎辊转速 700 r/min、柔性体厚度为 6 mm 时，果穗碰撞力最小。在割台倾角为 25°，作业速度为 3 km/h 时，以拉茎辊转速为试验变量，将间隙可调弹性低损玉米摘穗割台和普通板式玉米摘穗割台进行果穗碰撞力对比，试验结果表明，弹性低损玉米摘穗割台比普通板式玉米摘穗割台碰撞力减少 25% 以上。

INTRODUCTION

Corn is an important grain and economic crop in China. High ear damage rates and high stalk loss rates have always been significant issues during the operation of corn harvesters' headers (Bu et al., 2016; Cui et al., 2019; Zhang et al., 2021). In recent years, with the widespread use of corn harvesters, the issue of ear picking loss caused by the header has become increasingly severe (Chen, 2014; Guo et al., 2018). Therefore, there is an urgent need to address the ear picking losses caused during the corn header picking process.

The main reason for corn ear damage is that the external force on the kernels exceeds the connecting strength between the kernels and the cob. When corn experiences a forward pulling picking force, it is prone to damage at the bottom of the ear and kernel breakage (Chen et al., 2021; Yi et al., 2016; Shin et al., 2020). The primary causes of stalk loss and blockage are the inability of the picking plate to adaptively adjust to the corn plant. Researchers at home and abroad have conducted extensive studies on the mechanisms of kernel damage during corn picking. Chen analyzed the physiological characteristics of corn kernels and found that kernel moisture content is a key factor affecting kernel breakage (Chen et al., 2009).

Xianghao LI, M.S. Stud.; Yongli ZHAO, M.S. Stud.; Hongda ZHAO, M.S. Stud. Shaochuan LI, Ph.D Stud.; Peisong DIAO professor Dr.

Tai performed simulation tests on the kinematic and dynamic performance of the corn stalk separation device, corn plant, and ear-picking rollers using ADAMS virtual simulation technology, and developed a method for evaluating both the corn stalk separation and ear-picking performance (Tai et al., 2020). Li measured the number of kernels shed under the impact of three different shapes of punch heads and concluded that the wedge-shaped punch head was most conducive to kernel shedding (Li et al., 2014). Zhang Hongmei analyzed the collision process of corn ears and found that picking losses were mainly related to the picking mechanism and materials (Zhang et al., 2024). Chen Meizhou through high-speed photography, discovered that ear retention on the picking roller and bouncing were the main causes of secondary damage during picking (Chen et al., 2017). He Junlin studied the mechanism and characteristics of ear damage caused by roller-type picking devices and found that roller type and roller gap were important factors affecting ear damage (He et al., 2006). Srivastava studied the shear properties of corn under impact loads and found that the shear strength of corn is inversely proportional to moisture content and directly proportional to impact velocity (Srivastava et al., 1976).

In terms of measures to reduce corn picking damage, scholars have also conducted extensive research. Fu Qiankun designed a wheel-type rigid-flexible coupling low-damage corn picking header and found that its kernel loss rate was significantly lower than that of the plate-type picking mechanism through comparative experiments (Fu et al., 2019). Li Tianyu addressing the issue of high ear damage rates in corn harvesting devices, conducted an in-depth analysis of the shearing mechanism for ear picking and designed a shearing-type ear picking mechanism (Li et al., 2023). Luo Huizhong designed a narrow-width low-damage picking header using the principle of elastic buffering to achieve flexible low-damage picking (Luo et al., 2021). Geng Duanyang studied the picking mechanism of upright roller-type headers and found that the main causes of picking damage were the picking gap not meeting plant passage requirements, large impact forces during the picking process, and suboptimal ear positions during picking. They optimized the structure and motion parameters of the upright roller (Geng et al., 2017; Xin, 2020; Zhang et al., 2005; Geng et al., 2017). Zhang Zhilong designed a comb-type picking unit that reduced ear damage by upward combing picking (Zhang et al., 2014). Cheng Xiupei designed an upward pulling ear-picking corn harvesting device based on the principle of top-down ear picking (Cheng et al., 2016). Zhu Guangqiang designed a bionic picking device for fresh corn by mimicking the manual ear-picking posture (Zhu et al., 2023). The JOHN DEERE company in the United States reduced corn kernel loss by adjusting the hydraulic picking plate parameters in the 708C header. Zhang Zhen identified the factors influencing corn harvesting losses through experimental research and theoretical analysis, and determined the optimal parameter combination for efficient corn ear picking (Zhang et al., 2021).

MATERIALS AND METHODS

Structural Design

Through the analysis of the corn ear-picking process, it is found that the impact force on the corn ear is mainly related to the stiffness coefficient and damping coefficient of the ear-picking system. To reduce the stiffness coefficient and increase the damping coefficient of the ear-picking plate, a flexible surface and buffer spring ear-picking mechanism were designed. To reduce the impurity rate of corn stalks, a self-adaptive adjustment device for the gap between the ear-picking plates was designed. As shown in Figure 1, the structural diagram of the gap-adjustable low-damage elastic corn ear-picking header consists of the main frame, gearbox, stalk-pulling roller, gathering chain, transmission device, flexible cantilever ear-picking plate, and ear-picking plate gap-adjusting device.

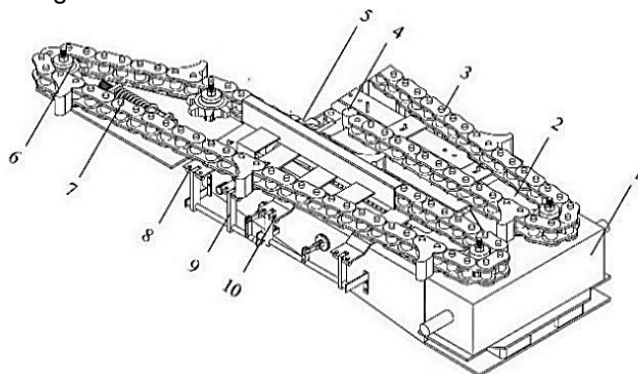


Fig.1 - Structural diagram of the low-damage elastic corn ear-picking header

1. Gearbox; 2. Frame; 3. Gathering chain; 4. Elastic ear-picking device; 5. Stalk-pulling roller; 6. Driven gear; 7. Gathering chain tensioning device; 8. Front ear-picking plate; 9. Ear-picking plate gap-adjusting mechanism; 10. Rear ear-picking plate

Working Principle

Under the combined action of the conical guide section at the front end of the stalk-pulling roller and the gathering chain, the corn stalk enters the gap between the ear-picking plates. Since the initial gap between the designed ear-picking plates is smaller than the diameter of the corn stalk, when the corn stalk enters the gap, the ear-picking plates move to both sides under the squeezing force of the corn stalk, thereby increasing the gap. Under the action of the spring adjustment device, the gap between the ear-picking plates can be adaptively adjusted according to the diameter of the corn stalk. After the corn stalk enters the ear-picking position, the stalk-pulling roller clamps and pulls downwards. The corn ear collides with the ear-picking plate, and under the action of the flexible surface and buffer spring, the kinetic energy of the collision is converted into potential energy of the spring and flexible body and dissipated, reducing the grain loss caused by the collision. When the flexible cantilever ear-picking plate is subjected to the pressure of the corn ear, the ear-picking plate moves downward under the compression of the buffer spring, reducing the gap between the ear-picking plates, increasing the clamping force on the ear stem, making it easier to pick the ear and reducing the collision force on the ear.

Design of the Self-Adaptive Gap Adjustment Device for the Picking board

The designed self-adaptive gap adjustment device for the ear-picking plate can adjust the gap according to the diameter of the corn plant. The self-adaptive gap adjustment system for the ear-picking plate, as shown in Figure 2, mainly consists of the ear-picking plate, spring adjustment device, rotating shaft, rotating plate, and connecting plate.

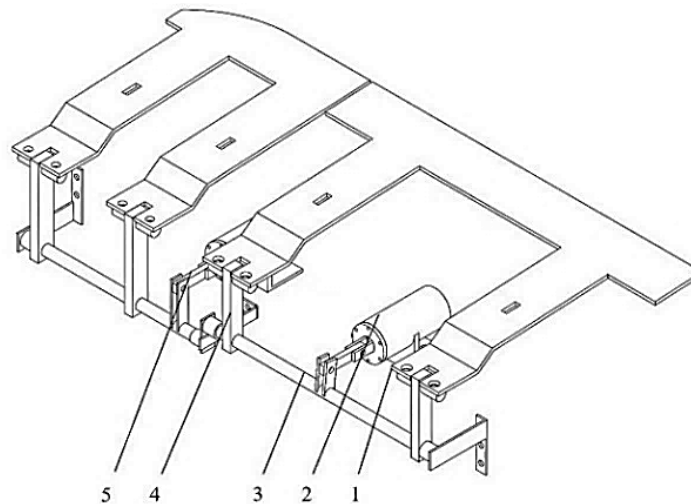


Fig. 2 - Adaptive adjustment system for the gap between heading plates

1. Ear picking plate; 2. Spring adjustment device; 3. Rotating shaft; 4. Rotating plate; 5. Connecting plate

When adjusting the gap of the ear-picking plate, the gap reaches its minimum value under the pre-tightening force of the spring adjustment device and the action of the limit slot. To ensure the consistency of the movement of the ear-picking plate during gap adjustment and to avoid the mechanism from getting stuck during the adjustment process, the self-adaptive adjustment device is designed as a rotating shaft type. To ensure quick and accurate adjustment, the spring is placed vertically with respect to the frame. Therefore, the circular motion of the rotating plate needs to be converted into the linear motion of the spring. A connecting plate is designed between the rotating shaft and the adjustment spring to ensure the uniformity and continuity of spring adjustment. To ensure the adjustment range of the ear-picking plate, a limit slot is set on the ear-picking plate to limit the maximum and minimum adjustment range of the ear-picking plate. Figure 3 shows the movement analysis of the heading plate during the gap adjustment process.

As shown in Figure 3, the adjustment range of the ear-picking plate gap is related to the length L of the rotating plate and the rotation angle α of the rotating shaft.

$$d = L \sin \alpha \quad (1)$$

where: d - Horizontal adjustment range of the ear-picking plate, mm; L - Length between the two mounting holes of the rotating shaft, $L = 70\text{mm}$; α - Rotation angle of the rotating shaft, $^\circ$.

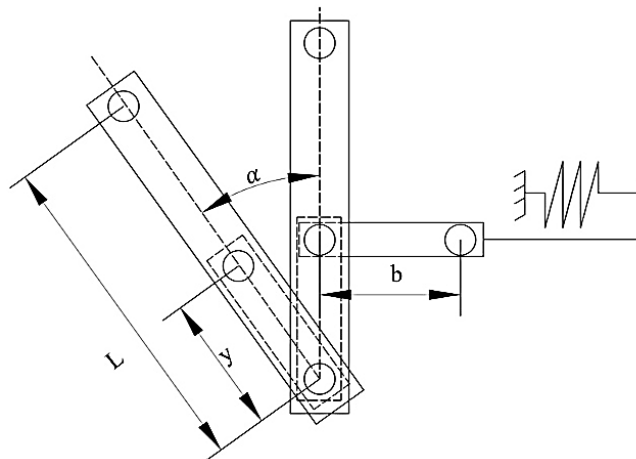


Fig. 3 - Movement analysis diagram of the gap adjustment device for ear picking plates

The adjustment range of the ear-picking plate gap depends on the physical characteristics of the corn ear and the corn plant. By measuring the physical characteristics of the corn ear and the corn plant, the minimum diameter of the larger end of the corn ear is 42.4 mm, and the minimum diameter of the corn plant at the ear-picking position is 19.3 mm. To ensure better working performance, the self-adaptive adjustment range of the ear-picking plate gap is designed to be 18-40 mm. That is, $d_{max} = 11$ mm, substituting into formula (1), the value of α is 9° .

The stiffness coefficient and length of the spring are key parameters of the design. By analyzing the movement of the ear-picking plate, the compression length of the spring is:

$$x = (y \sin \alpha + b) - \sqrt{b^2 - (y - y \cos \alpha)^2} \tag{2}$$

where: x - Compression amount of the spring, mm; y - Distance from the center of the rotating shaft to the connecting plate hole, mm; b - Length of the connecting plate, mm

Due to the limitation of the installation position, the length of the connection between the rotating shaft and the connecting plate is designed to be 35 mm, and the length of the connecting plate $b = 40$ mm, resulting in the maximum compression length of the spring being 6.8 mm.

Design of Spring Adjustment Device

The stiffness coefficient of the spring is a crucial parameter affecting the self-adaptive gap adjustment of the picking plates. If the spring stiffness coefficient is too high, it can cause the stalks to break, whereas if it is too low, the picking plates may oscillate and fail to quickly adjust the gap according to the diameter of the corn stalks, resulting in poor gap adjustment performance. Figure 4 shows the structure of the spring adjustment device, which mainly consists of an outer cylinder, a compression spring, and a pull rod. An adjustment slot is provided on the outer cylinder to adjust the pre-tightening force of the spring.

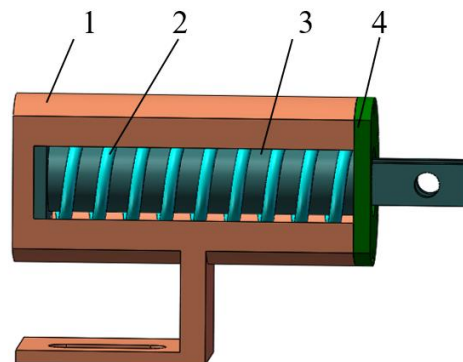


Fig. 4 - Spring adjustment device
 1. Outer cylinder; 2. Spring; 3. Tie rod; 4. Outer cylinder cover

During the gap adjustment process, the clamping force of the picking plates on the stalks is shown in Figure 5.

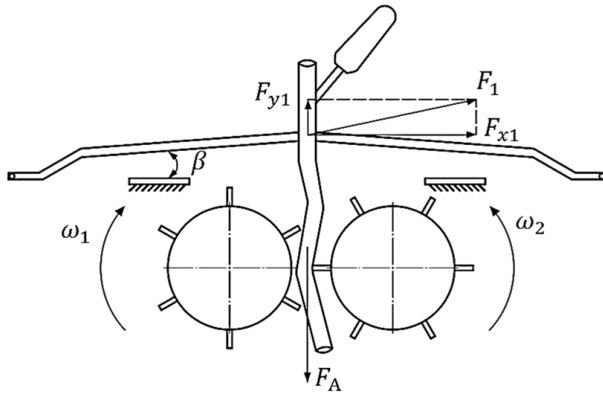


Fig. 5 - Force Diagram of Corn Stalks During Gap Adjustment

β -represents the angle between the picking plate and the bracket;
 F_1 - The clamping force of a single picking plate on the stalks, N;
 F_A - The stem roller has the maximum force on the corn stalk, N

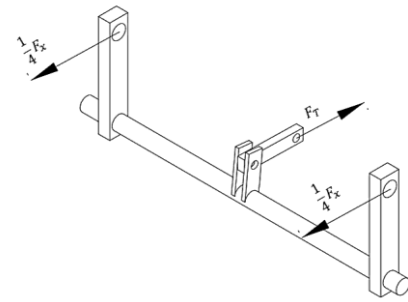


Fig. 6 - Force analysis of lever structure

The forces acting on the corn stalks in the horizontal and vertical directions are:

$$\begin{cases} F_x = 2F_1 \cos \beta \\ F_y = 2F_1 \sin \beta \end{cases} \quad (3)$$

F_x - Sum of forces on corn stalks in the horizontal direction; F_y - Sum of forces on corn stalks in the vertical direction.

To prevent the clamping force of the picking plates from being too high and causing the stalks to break, the following condition must be met:

$$F_x f + F_y < F_L \quad (4)$$

where:

f - the friction coefficient between the picking plate and the corn stalks; F_L -the pulling force required to break the corn stalks, N.

Figure 6 illustrates that the picking plate and the spring adjustment device can be regarded as a lever mechanism, where the two rotating plates on the pivot axis can be seen as lever arms:

$$\frac{1}{2} F_x L = F_T y \quad (5)$$

$$\frac{L}{y} = 2 \quad (6)$$

Sorted out:

$$F_T = F_x < \frac{F_L}{0.22 + \tan \beta} \quad (7)$$

where: F_T - The elastic force of the spring

The corn ear attachment is the weakest part of the corn stalk. Tensile tests on corn plants using an electronic universal testing machine show that when the moisture content of the corn kernels is 30%, the force required to break the stalk at the ear attachment is no less than 300 N. The pulling force for the corn ear stalk ranges from 264 N to 673 N, with an average value of 468.5 N. To ensure that the stalk does not break during ear picking, F_L is taken as 200 N. Substituting this into equation (8):

$$F_T < \frac{200}{0.22 + \tan \beta} \quad (8)$$

Due to installation position constraints, $\beta < 10^\circ$, solving for $F_T < 500$ N. During operation, excessive horizontal clamping force of the picking plates will also affect the pulling speed of the corn plants. Therefore, the spring stiffness coefficient should be as small as possible while ensuring operational effectiveness. The best ear-picking effect is achieved when the corn ear is picked at 1/3 to 1/2 of the pulling section. Hence, the spring stiffness coefficient should be chosen to be moderate.

Design of Flexible Picker Device

When picking ears of corn, the corn ears fall off under the obstruction of the picking plates, which results in significant impact between the ears and the picking plates. Therefore, the picking plates are treated with a flexible material to reduce the direct impact. The picking plates are made of 3 mm thin steel plates covered with a layer of flexible rubber material. During the self-adaptive gap adjustment process of the picking plates, to avoid interference between two corn plants, the picking plates are designed in two segments. Each segment interacts with only one corn plant during ear picking. The relationship between the length of the first segment of the picking plate and the corn plant spacing B is:

$$S \leq \frac{B}{\cos\theta} \tag{9}$$

where: θ - header inclination angle.

When the header inclination angle is between 20-30°, the ear-picking loss is minimized. This study selects a header inclination angle of 25°. The corn plant spacing B generally ranges from 250 to 330 mm. To minimize interference between two corn plants, the plant spacing B is set to 200 mm, and the picking plate length $S \leq 220$ mm. The length of the pulling section of the pulling roller used in this study is 610 mm, and the total length of the pulling roller is 730 mm. Therefore, the total length of the picking plates is designed to be 730 mm, with the length of the second segment being 510 mm.

During ear picking, the picking plates are compressed downward by the impact force of the ears, thereby increasing the collision time between the ears and the picking plates and reducing ear damage. The movement of the picking plates during ear picking is shown in Figure 7.

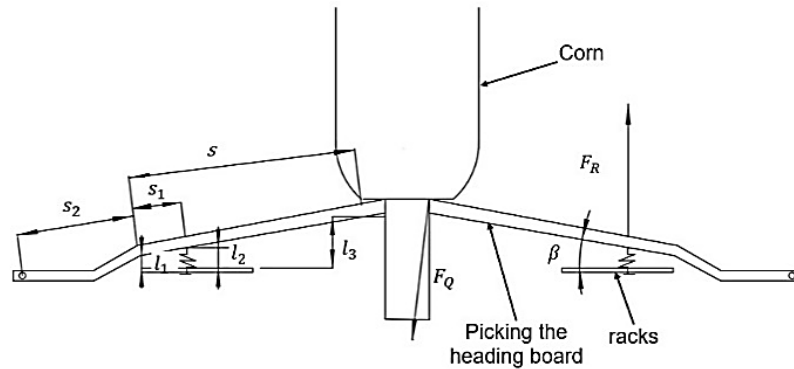


Fig. 7 - Movement of picking plates during ear picking

F_Q -represents the collision force of the ears on the picking plates, N ; F_R -represents the supporting force of the compression spring on the picking plates, N ; l_1 -represents the minimum gap between the picking plates and the bracket, mm ; l_2 -represents the compression length of the compression spring, mm ; l_3 -represents the maximum gap between the picking plates and the bracket, mm ; s_1 -represents the length from the bending point of the picking plates to the spring, mm ; s_2 -represents the length from the installation hole of the picking plates to the bending point, mm ; s -represents the length of the bending point of the picking plates, mm

Due to installation size constraints, the maximum height between the picking plates and the bracket should not exceed 30 mm, and the maximum height is:

$$l_3 = l_1 + s \sin \beta \tag{10}$$

The maximum compression height of the buffer spring

$$l_2 = s_1 \sin \beta + l_1 \tag{11}$$

This design requires that during ear picking, the picking plates can compress the spring to the maximum value, the impact force between the ears and the picking plates is greater than the supporting force of the buffer spring on the picking plates. The maximum working load of the buffer spring occurs when the picking plates are compressed to the lowest point, so it must be ensured that the torque exerted by the corn ears driving the picking plates to rotate is greater than the torque resisting the rotation of the picking plates by the buffer spring, i.e.:

$$F_Q \cdot s + s_2 > F_R \cdot (s_1 + s_2) \cos \beta \tag{12}$$

The row spacing for corn planting is 600-700 mm. This study designs the row spacing of the corn header to be 630 mm, and the length of the picking plates is designed to be 270 mm, with $s = 200$ mm, $s_1 = 50$ mm, and $s_2 = 70$ mm.

Therefore:

$$\frac{s + s_2}{s_1 + s_2} = \frac{27}{12} \tag{13}$$

As previously mentioned, the pulling force of the corn ear stalk ranges from 264 N to 673 N. To pick the ears without causing blockage:

$$F_Q \cos \beta < \frac{1}{2} F_{Amin} \tag{14}$$

where: F_{Amin} - the minimum pulling force of the ear stalk, $F_{Amin}=264$ N.

From equations 24, 25, and 26, the maximum elastic force of the compression spring is:

$$F_R \leq \frac{F_{Amin} (s + s_2)}{2(s_1 + s_2)} \tag{15}$$

This study designs the minimum height between the picking plates and the bracket $l_1=10$ mm. Calculations show that β does not exceed 5° ; taking $\beta=5^\circ$, the maximum compression height of the compression spring $l_2=15.23$ mm. Calculations show that: $F_R \leq 297$ N. To minimize the impurity rate of the stalks, the maximum elastic force of the spring is taken as 250 N, resulting in a spring stiffness coefficient not exceeding 20.2 N/mm. To reduce the vibration of the picking plates when unloaded, a certain pre-tightening force must be applied to the spring. Based on the weight of the picking plates, the pre-tightening force of the buffer spring is designed to be no less than 50 N. The buffer spring should withstand more than 10^6 cycles of cyclic impact during ear picking, classified as Class I load. Table 1 shows the main parameters of the spring.

Table 1

Main parameters of compression springs

Project	Spring parameters	Project	Spring parameters
Diameter of the material	3.5 mm	Spring center diameter	22 mm
Ultimate load	484.52 N	The amount of deflection in a single turn	3.481 mm
Number of valid laps	7	Total number of laps	9
Stiffness factor	19.86 N/mm	Single-turn stiffness	139 N/mm
Helix angle	5.78°	Free height	54.25 mm
Outside diameter	25.5 mm	Inner diameter	18.5 mm
Pitch	7 mm	Unfolded length	622.04 mm
The amount of deformation under the ultimate load	24.367 mm		

RESULTS

Harvesting header Model building

During the optimal corn harvest season, the physical properties of corn are measured to establish models of corn ears and stalks. Based on the reference materials, the physical properties of the corn and picking plate were determined, and the corresponding parameters were configured in ADAMS as shown in Table 2 (Gao et al., 2003; Zhang, 2003).

Table 2

Physical properties of steel and rubber

Type of material	Elastic modulus (N/m ²)	Density (N/m ³)	Poisson's ratio
steel	2.06x10 ¹¹	7800	0.3
rubber	7.84x10 ⁶	1500	0.47
Ears of corn	1.37x10 ⁸	1197	0.4
Corn stalks	1.1x10 ¹⁰	450	0.3

To make the simulation results of the self-adaptive gap adjustment of the picking plates more realistic, simulations are conducted on different nodes of the same stalk during the simulation process. Additionally, a modal analysis of the corn stalks is performed in ANSYS software. This allows for a clear visualization of the operation of the self-adaptive gap adjustment structure of the picking plates as the diameter of the stalks changes. Based on actual measurements of corn stalks, the simulation targets the five nodes below the ear, with diameters of 41 mm, 37 mm, 34 mm, 30 mm, and 24 mm, and a length of 150 mm. The simulation model after setting is shown in Figure 8.

During the simulation of the corn ear-picking process, flexible Bushing connections are established between the stalk and the ground, and between the stalk and the ear. Collision force sensors are added between the corn ear and the picking plates. When the sensor value exceeds 500 N, the bushing force fails, causing the ear to separate from the ear stalk.

The simulation model after setting is shown in Figure 9.

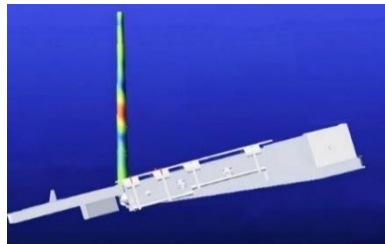


Fig. 8 - Single-factor simulation process

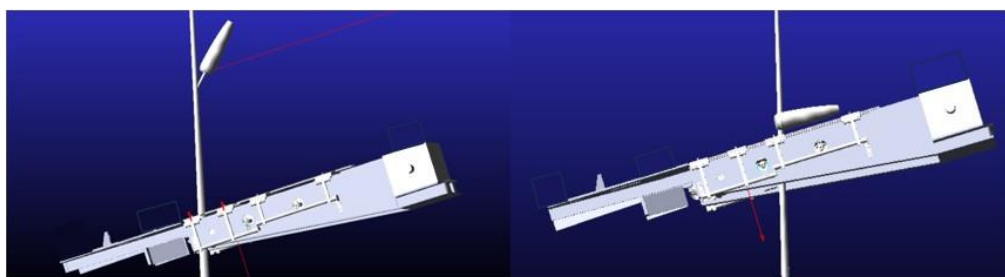


Fig. 9 - Simulation process of heading

Simulation results of the adaptive adjustment mechanism for ear-picking plate clearance

To analyze the impact of the spring stiffness coefficient on the self-adaptive gap adjustment of the picking plates, a single-factor experiment on the stiffness coefficient of the compression spring was conducted. Figure 10 shows the displacement curve of the picking plates in the y-axis direction under different spring stiffness coefficients.

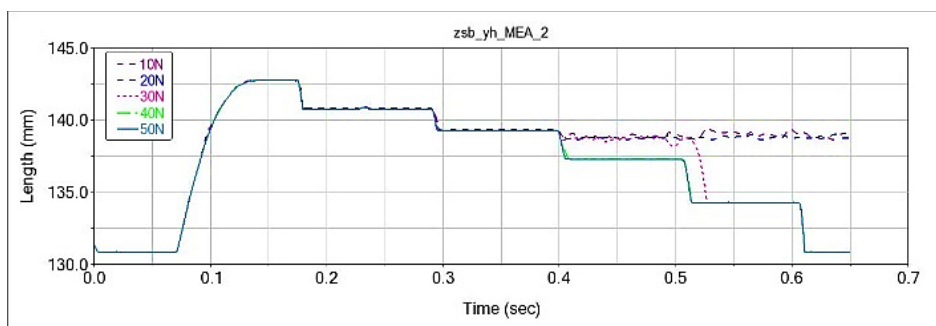


Fig.10 - Dynamic analysis of heading plates under different spring stiffnesses

From Figure 10, it can be seen that the corn plant contacts the picking plates at 0.07 seconds, causing the picking plates to move outward until reaching the maximum value. When the spring stiffness coefficient is 10 N/mm, the picking plates cannot move when the corn stalk diameter reaches 30 mm. This is mainly due to the internal friction within the picking plate adjustment device, preventing the picking plates from moving and causing oscillation. When the spring stiffness coefficient is 20 N/mm, the picking plates cannot quickly adjust to the changes in the corn stalk diameter when it decreases to 30 mm, though the vibration amplitude of the picking plates is reduced. When the spring stiffness coefficient is 30 N/mm, the picking plates can adjust according to the corn stalk diameter, but the adjustment process is delayed when the stalk diameter is 30 mm, preventing quick adjustments. When the spring stiffness coefficient is 40 N/mm, the picking plates stabilize when the corn plant diameter is 24 mm, with minimal displacement fluctuation. The fluctuation at a stiffness coefficient of 50 N/mm is similar to that at 40 N/mm, indicating that the optimal spring stiffness is between 30 N/mm and 40 N/mm.

Experimental Factors and Indicators

A three-factor, three-level quadratic regression rotational orthogonal experiment was conducted to analyze the collision force on the corn ears during the ear-picking process. The factors included the stiffness coefficient of the compression spring for the self-adaptive gap adjustment of the picking plates, the rotational speed of the pulling roller, and the thickness of the flexible material. Table 3 shows the factors and levels of the virtual orthogonal experiment.

Table 3

Virtual orthogonal test factors and levels			
Experimental level	The stiffness coefficient of the compression spring /(N/mm)	Stem pulling roller speed / ^o	The thickness of the flexible material / mm
1	30	700	2
2	35	850	4
3	40	1000	6

Using Design-Expert 13 software, the experimental design and analysis were conducted. Each combination was tested three times, and the virtual orthogonal experiment scheme and results are shown in Table 4. The stiffness coefficient of the compression spring, the rotational speed of the pulling roller, the thickness of the flexible material, and the ear contact force are represented by x_1 , x_2 , x_3 , and Y , respectively.

Table 4

Test protocol design and test results				
Serial number	x_1 / (N/mm)	x_2 / ^o	x_3 / mm	Y / N
1	30	700	4	563
2	40	700	4	536
3	30	1000	4	954
4	40	1000	4	902
5	30	850	2	728
6	40	850	2	716
7	30	850	6	672
8	40	850	6	628
9	35	700	2	561
10	35	1000	2	969
11	35	700	6	510
12	35	1000	6	870
13	35	850	4	638
14	35	850	4	640
15	35	850	4	632
16	35	850	4	645
17	35	850	4	642

Variance analysis of the experimental results was conducted using Design-Expert 13 software, yielding the response function for the ear contact force Y .

$$Y = 639.4 - 16.87x_1 + 190.63x_2 - 36.75x_3 - 6.25x_1x_2 - 8x_1x_3 - 12x_2x_3 + 28.92x_1^2 + 70.42x_2^2 + 17.68x_3^2 \quad (16)$$

Variance analysis of the experimental results, as shown in Table 5, indicates that the regression model for the ear contact force is highly significant with a $P \leq 0.0001$, and the lack of fit test value $P > 0.05$ (0.4163), indicating a high degree of fit for the regression equation. The determination coefficient R_2 is 0.9995, indicating that the model can explain more than 99 % of the evaluation indices. Therefore, the working parameters of the elastic low-damage corn picker header can be optimized using this model.

Table 5

ANOVA of quadratic response surface regression model					
Variance source	Sun of squares	Degree of freedom	Mean square	F	P
Model	332400	9	36936.81	1428.89	<0.0001
x_1	2278.12	1	2278.12	88.13	<0.0001
x_2	290700	1	290700	11245.77	<0.0001

Variance source	Sun of squares	Degree of freedom	Mean square	F	P
x_3	10804.50	1	10804.50	417.97	<0.0001
x_1x_2	156.25	1	156.25	6.04	0.0436
x_1x_3	256.00	1	256.00	9.90	0.0162
x_2x_3	576.00	1	576.00	22.28	0.0022
x_1^2	3522.76	1	3522.76	136.28	<0.0001
x_2^2	20882.87	1	20882.87	807.85	<0.0001
x_3^2	1315.39	1	1315.39	50.89	0.0002
Residual	180.95	7	25.85		
Lack of Fit	85.75	3	28.58	1.20	0.4163
Pure Error	95.20	4	23.80		
Cor Total	332600	16			

Note: P<0.01 (highly significant**); P<0.05(significant*).

The impact of each parameter on the regression equation can be reflected by the P<0.01 indicates a highly significant impact, and P<0.05 indicates a significant impact.

In the ear contact force Y model, x_1 , x_2 , x_3 , x_2x_3 , x_1^2 , x_2^2 and x_3^2 are all highly significant, while x_1 , x_2 and x_1 , x_3 , are significant.

Response Surface Analysis of Each Factor

The experimental results show significant differences in ear collision forces under different structural parameters. Response surface analysis of the experimental results was conducted to determine the optimal parameters for the elastic low-damage corn picker header. Figure 11 shows the response surfaces of each factor in the regression model.

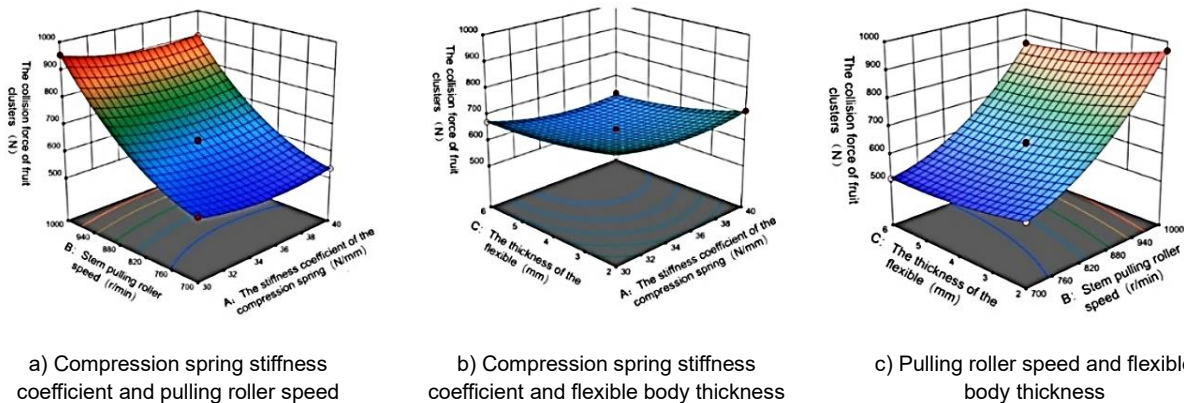


Fig. 11 - The influence of different factors on the collision force of fruit ears

From Figure 11a, it can be seen that when the rotational speed of the pulling roller is constant, the ear collision force initially decreases and then stabilizes and slightly increases with the increase in the spring stiffness coefficient. This is because the increase in the spring stiffness coefficient allows the picking plates to clamp the ear stalk during ear-picking, reducing the force exerted by the pulling roller on the stalk. When the spring stiffness coefficient exceeds 36 N/mm, the clamping force on the ear stalk by the picking plates becomes too large, preventing the corn ears from being quickly picked upon contact with the picking plates, leading to an increase in the ear collision force. When the spring stiffness coefficient is constant, the ear collision force is positively correlated with the rotational speed of the pulling roller, as an increase in the pulling roller speed increases the downward speed of the corn plant, leading to a higher ear collision force according to the kinetic energy theorem. The influence of the rotational speed of the pulling roller on the ear collision force is greater than that of the spring stiffness coefficient.

From Figure 11b, it can be seen that when the spring stiffness coefficient is constant, the ear collision force decreases with the increase in the thickness of the flexible material. When the thickness of the flexible material exceeds 4 mm, the ear collision force stabilizes as the flexible material's elastic performance dissipates most of the collision kinetic energy of the ear. Thus, when the thickness of the flexible material exceeds 4 mm, the ear collision force remains stable.

From Figures 11a, 11b, and 11c, it can be seen that the factors affecting the ear collision force, in order of significance, are the rotational speed of the pulling roller, the thickness of the flexible material, and the stiffness coefficient of the compression spring. Using Design-Expert 13 software to solve the regression equation with the constraint of minimizing the ear collision force, the optimal solution is obtained: a spring stiffness coefficient of 36 N/mm, a pulling roller speed of 700 r/min, and a flexible material thickness of 6 mm.

Comparative Validation Experiment

Comparative experiments were conducted between the designed elastic low-damage corn picker header and a conventional plate-type corn header under different working conditions. The experiments were conducted with the designed spring stiffness coefficient of 36 N/mm and a flexible picking plate thickness of 6 mm. The gap between the picking plates of the conventional plate-type header was set to 35 mm. Figure 15 shows the comparison of ear force and collision acceleration at a pulling roller speed of 700 r/min, a header inclination angle of 25°, and a travel speed of 3 km/h.

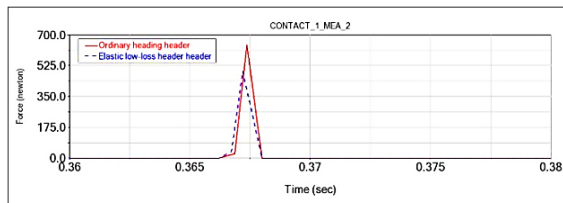


Fig.12a-Comparison of ear collision forces during ear

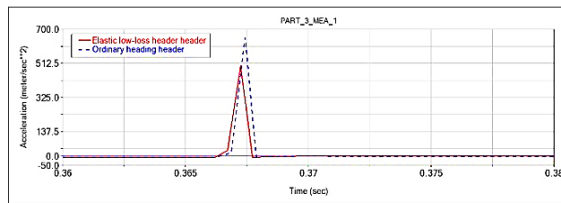


Fig.12b-Comparison of acceleration at ear collision

Fig.12 - Comparative analysis of ear collision force and acceleration

From Figure 12, it can be seen that the collision force of the elastic low-damage corn picker header is 505 N, compared to 648 N for the conventional plate-type header. The collision acceleration of the elastic low-damage corn picker header is 500 m/s², compared to 655 m/s² for the conventional plate-type header. This indicates that the designed elastic low-damage corn picker header can effectively reduce collisions.

Table 6 shows the factors and results of the comparative experiments. At a pulling roller speed of 700 r/min, the collision force on the ears is reduced by 25.66 % compared to the conventional plate-type header. At a pulling roller speed of 850 r/min, the collision force is reduced by 30.81 %, and at a pulling roller speed of 1000 r/min, the collision force is reduced by 31.71 %. This demonstrates that the designed elastic low-damage corn picker header can effectively reduce the collision force on the ears.

Table 6

Comparative analysis of elastic and low-damage corn ear picking header and ordinary plate header

Serial number	Stem pulling roller speed (r/min)	Header inclination / °	Travel speed (km/h)	Elastic and low-damage header ear contact force / N	Ear contact force of ordinary plate header / N
1	700	25	3	505	648
2	850	25	3	613	886
3	1000	25	3	840	1230

CONCLUSIONS

An elastic low-damage corn picker header was designed to address the high rate of ear damage and the issue of ear loss and clogging present in current corn picking devices. The design achieves high efficiency and low damage in corn harvesting. Structural design and parameter calculations were conducted for the picking plate gap adjustment device, picking plates, and compression spring adjustment structure.

Virtual simulation experiments of the corn ear-picking process were conducted using ADAMS software. The range of the stiffness coefficient of the compression spring for the picking plate gap adjustment mechanism was determined to be 30-40 N/mm through simulation. The contact force during the corn ear-picking process was analyzed using sensors and script control methods. Virtual orthogonal experiments analyzed the collision force on the corn ears under different spring stiffness coefficients, pulling roller speeds, and flexible material thicknesses. Response surface analysis determined the optimal parameter combination for harvesting: a spring stiffness coefficient of 36 N/mm, a pulling roller speed of 700 r/min, and a flexible material thickness of 6 mm.

Comparative experiments under different pulling roller speeds, with a header inclination angle of 25° and a forward speed of 3 km/h, showed that the designed elastic low-damage corn picker header reduced the collision force on the ears by more than 25 % compared to the conventional plate-type header, meeting operational requirements.

ACKNOWLEDGEMENT

This project is funded by the integration of agricultural machinery research and development, manufacturing, promotion, and application in Shandong Province (NJYTHSD-202318).

REFERENCES

- [1] Bu, L., Zhang, D., Li T., Jia C., Cui, M., (2016). Analysis and simulation of ear holding device for non-aligned corn header (不对行玉米收获机割台扶禾装置的分析与仿真). *Journal of Agricultural Mechanization Research*, Vol. 38, pp. 57-60+242, Shandong/China.
- [2] Chen, M., Sun, X., Cheng, X., Jia, X., Li, Q., (2017). Effect of height difference between ears snapping rollers on corn kernel loss in horizontal roller-type ears snapping mechanism (卧辊式摘穗机构摘穗辊高度差对玉米籽粒损失的影响). *Transactions of the Chinese Society of Agricultural Engineering*, Vol. 33, pp. 63-68, Shandong/China.
- [3] Chen, Z., (2015). Key Technologies and Equipment for Full-Value Harvesting of Corn (玉米全价值收获关键技术与装备). *Science Press*, Vol. 1, Beijing/China.
- [4] Chen, Z., Wassgren, C., Ambrose, R., (2021). Measured damage resistance of corn and wheat kernels to compression, friction, and repeated impacts. *Powder Technology*, Vol. 380, pp. 638-648, Indiana/USA.
- [5] Cheng, X., Jia, X., Chen, M., Li, Q. (2016). Bench test and analysis of corn harvester with upward stalk pulling and ear snapping mechanism (上拉茎掰穗式玉米收获台架试验与分析). *Transactions of the Chinese Society of Agricultural Engineering*, Vol. 32, No. 22, pp. 50-55, Shandong/China.
- [6] Cui, T., Fan, C., Zhang, D., Yang, L., Li, Y., Zhao, H., (2019). Research progress analysis of corn mechanized harvesting technology (玉米机械化收获技术研究进展分析). *Transactions of the Chinese Society of Agricultural Machinery*, Vol. 50, pp. 1-13, Beijing/China.
- [7] Fu, Q., Fu, J., Wang, F., Chen, Z., Ren, L., (2019). Design and parameter optimization of wheel-type rigid-flexible coupling corn ear snapping header for reducing loss (轮式刚柔耦合减损玉米摘穗割台的设计与参数优化). *Transactions of the Chinese Society of Agricultural Engineering*, Vol. 35, pp. 21-30, Jilin/China.
- [8] Gao, M., Guo, K., Yang, Z., Li, X., (2003). Mechanical properties testing of corn stalks (玉米秸秆的力学特性测试研究). *Transactions of the Chinese Society of Agricultural Machinery*, Vol. 4, pp. 47-49+52, Shanxi/China.
- [9] Geng, D., Li, Y., He, K., Jin, C., Ni, G., Zhang, M. (2017). Design and test of a clearance clamping and conveying device for vertical roller corn harvester header (立辊式玉米收获机割台间隙夹持输送装置设计与试验). *Transactions of the Chinese Society of Agricultural Machinery*, Vol. 48, pp. 130-136, Shandong/China.
- [10] Geng, D., Li, Y., Meng, F., Meng, P., Ni, G., Zhang, M, (2017). Design and test of multi-edge vertical roller ear snapping device for corn harvester (玉米收获机多棱立辊式摘穗装置设计与试验). *Transactions of the Chinese Society of Agricultural Machinery*, Vol. 48, pp. 84-91, Shandong/China.
- [11] Guo, Y., Zhan, P., Li, X., Zhu, J., (2018). Research on corn harvest loss in China: Based on a survey of five counties in five provinces (中国玉米收获损失研究: 基于5省5县的调查). *Journal of Maize Sciences*, Vol. 26, pp. 130-136, Beijing/China.
- [12] He, J., Tong, J., Hu, W., Guo, Y., (2006). Effects of roller shape and operating speed on corn ear snapping performance of corn harvesters (辊型和作业速度对玉米收获机摘穗性能的影响). *Transactions of the Chinese Society of Agricultural Machinery*, Vol. 37, pp. 46-50, Jilin/China.
- [13] Li, T., Guan, X., Zhou, F., (2023). Mechanistic analysis and experimental study of a shear-type low-loss fresh corn ear-picking mechanism. *Computers and Electronics in Agriculture*, Vol. 213, pp. 108191, Guangxi/China.
- [14] Li, X., Du, Z., Ma, D., Gao, C., Ma, F., (2014). Discrete analysis of maize ear at different impact head. *Applied Mechanics and Materials*, Vol. 651-653, pp. 323-327, Henan/China.
- [15] Luo, H., Jiang, X., Qin, D., Zuo, P., Zhang, F., Zhang, L., (2021). Design and experiment of narrow-width and low-damage corn ear snapping header (窄幅低损伤摘穗割台设计与试验). *Journal of Northeast Agricultural University*, Vol. 52, pp. 66-76, Sichuan/China.
- [16] Shin, C., YUN, T., Choi, H., Kim, T., (2020). Experimental study on the structural safety of the corn harvester attached to a tractor. *Journal of the Korean Society of Manufacturing Process Engineers*, Vol. 19, pp. 24-29, Chungcheongbuk-do/ Korea.

- [17] Srivastava, A., Herum, F., Stevens, K (1976). Impact parameters related to physical damage to corn kernels. *Agricultural and Food Sciences*, Vol. 19, pp. 1147-1151.
- [18] Tai, J., Li, H., Du, Y., Guan, Y., Mao, E., Long, X., (2020). Simulation analysis on the performance of splitting and picking devices of corn harvester. *INMATEH - Agricultural Engineering*, Vol. 62, pp. 69-78, Bucharest/Romania.
- [19] Used John Deere 708C Corn and Row Crop headers For Sale -John Deere MachineFinder [EB/OL]. [2021/3/3]. <https://www.machinefinder.com/ww/en-US/categories/used-combine-headers/makes/john-deere/models/708c>.
- [20] Xin, S., (2020). *Research on the mechanism and key technologies of vertical roller corn ear snapping (立辊式玉米摘穗机理与关键技术研究)*. PhD dissertation, Gansu Agricultural University, Ganshu/China.
- [21] Yi, K., Zhu, D., Zhang, X., Yao, Z., Liu, Z., (2016). Influence of moisture content on direct mechanized harvesting of corn kernels (含水率对玉米籽粒机械化直接收获的影响). *Journal of Chinese Agricultural Mechanization*, Vol. 37, pp. 78-80, Anhui/China.
- [22] Zhang, D., Sun, Y., Zhao, H., Wang, X., (2005). Design of vertical roller corn ear snapping and stalk chopping device (立辊式玉米摘穗与茎秆切碎装置的设计). *Transactions of the Chinese Society of Agricultural Machinery*, Vol. 36, pp. 50-52, Shandong/China.
- [23] Zhang, H., Chen, B., Hu, J., Li, Z., He, X., Wang, W., (2024). Comparative experiment of ear snapping devices for fresh corn based on collision characteristics (基于碰撞特性的鲜食玉米摘穗装置对比试验). *Journal of Henan Agricultural University*, Vol. 58, pp. 87-95, Henan/China.
- [24] Zhang, K., Chen, H., Wang, Y., Zhang, J., Xu, F., Zhao, X., (2021). Design and simulation of ear snapping device for corn header (玉米割台摘穗装置的设计与仿真). *Journal of Shandong Agricultural University (Natural Science Edition)*, Vol. 52, pp. 1042-1048, Shandong/China.
- [25] Zhang, Y., (2003). Study on crushing mechanical properties of corn straw (玉米秸破碎力学特性的研究). *Journal of Heilongjiang Bayi Agricultural University*, Vol. 4, pp. 43-45, Heilongjiang/China.
- [26] Zhang, Z., Chi, R., Du, Y., Pan, X., Dong, N., Xie, B., (2021). Experiments and modeling of mechanism analysis of maize picking loss. *International journal of agricultural and biological engineering*, Vol. 14, pp. 11-19, Beijing/China.
- [27] Zhang, Z., Zhang, D., Cui, T., Yang, Li., Li, K., (2014). Design and test of corn ear snapping unit with comb teeth (玉米梳齿摘穗单体机构设计与试验). *Transactions of the Chinese Society of Agricultural Engineering*, Vol. 30, pp. 1-9, Beijing/China.
- [28] Zhu, G., Li, T., Zhou, F., Wang, W., (2023). Design and experiment of bionic ear snapping device for fresh corn (鲜食玉米仿生摘穗装置设计与试验). *Journal of Jilin University (Engineering and Technology Edition)*, Vol. 53, pp. 1231-1244, Jilin/China.

CAGE WHEEL TRACTIVE PERFORMANCE OF 4WD TRACTOR IN PADDY FIELD

/

PENGUJIAN TRAKSI RODA SANGKAR TRAKTOR RODA EMPAT DI LAHAN SAWAH

Desrial^{*1,2)}, Hiroaki MURAOKA^{2,3)}, Kunio DOI⁴⁾; Ismi Makhmudah EDRIS²⁾

¹⁾ Faculty of Agricultural Engineering and Technology, Bogor Agricultural University/ Indonesia;

²⁾ Yanmar Agricultural Research Institute – IPB, Bogor Agricultural University, Indonesia / Indonesia;

³⁾ Yanmar Holdings Co. Ltd./ Japan;

⁴⁾ Yanmar Agribusiness Co., Ltd./ Japan

Tel: +62-81310286750 E-mail: desrial@apps.ipb.ac.id

DOI: <https://doi.org/10.35633/inmateh-74-35>

Keywords: *tractive, cage wheel, rubber wheel, 4WD tractor*

ABSTRACT

In Indonesia, the use of four-wheel drive (4WD) tractors in paddy fields has been introduced, replacing two-wheel tractors. However, the condition of Indonesian paddy fields is commonly deep due to the absence of hard pan layer that make lower tractive performance of 4WD tractors. This research designed a special cage wheel for a 4WD tractor and compared it to a commonly used rubber wheel. The result showed that the cage wheel could increase the drawbar pull by 39.5% and drawbar power by 66.2%. It could also reduce wheel slippage by 21.9% and decrease sinkage by 15.9%.

ABSTRAK

Di Indonesia, traktor roda empat tengah diintroduksikan untuk menggantikan traktor roda dua. Namun, kondisi lahan sawah yang dalam membuat kinerja traksi traktor roda empat menjadi rendah. Penelitian ini bertujuan untuk mendesain roda sangkar dan membandingkan kinerjanya dengan roda karet yang umum digunakan di traktor roda empat. Hasil menunjukkan bahwa roda sangkar meningkatkan drawbar pull 39.5% dan drawbar power 66.2%. Roda sangkar ini juga mampu menurunkan slip roda sebesar 21.9% dan ketenggelaman sebesar 15.9%.

INTRODUCTION

Lately, in Indonesia, there has been a noticeable shift towards the adoption of 4WD within paddy fields, replacing the previously dominant two-wheel tractors. Yet, this transition to 4WD tractors has brought forth a significant challenge - the notably deep condition of the paddy fields, attributed to the absence of hardpan layers (Jusran *et al.*, 2019). In narrow muddy paddy fields, general agricultural machinery is difficult to show good performance (Chen *et al.*, 2020). Moreover, the depth of mud tends to increase year by year due to the deposition of soil brought by high mud content in irrigation water.

The absence of a soil hardpan makes difficult trafficability for any machines for crop maintenance (Setiawan *et al.*, 2013). Wheel sinkage is a common problem occurred in tractors or other machinery in a wet deep paddy field in Indonesia. The sinkage of agricultural machinery has been the topic of intensive research in the past and will continue to be in the future (Pradhan *et al.*, 2015). Insufficient shear resistance in paddy soil often leads to sinking, slipping, or even the inability to travel (Chen *et al.*, 2024).

One of the efforts to provide better traction and trafficability for an agricultural tractor is by using a cage wheel. Implementing a cage wheel on a two-wheel tractor holds the potential to significantly enhance the traction performance of the tractor when operating in a wet paddy field (Eswari *et al.*, 2018) as well as in wetland cultivation (Pradhan *et al.*, 2016). In Indonesia, cage wheels have been commonly used for two-wheel tractors and commercially available in the market. However, cage wheel for 4WD tractors has just been introduced, so there is no academic paper yet on how cage wheels can improve the tractive performance of 4WD tractors compared to standard rubber wheels. Therefore, this research intended to compare the performance of the cage wheels which were specifically designed for 4WD tractors with rubber wheels.

The cage wheels are made using heavy-duty angle and iron & steel material (Kumar *et al.*, 2018). Tractive performance depends greatly on the dimensions, shapes, and materials of the wheels used and the soil conditions (Nizamani and Cebro, 2018). The cage wheel provides a floating effect to power tiller in wet paddy fields, in addition to puddling the soil (Pradhan and Verma, 2017).

The aim of this research was to design a special cage wheel for a 4WD tractor, assess its tractive and trafficability performance, and subsequently compare it with the performance of a standard rubber wheel of the 4WD tractor.

MATERIALS AND METHODS

• Cage wheel design and prototype

The cage wheel tested in this research was specially designed by Yanmar Agribusiness Co. Ltd. Japan for Yanmar Tractor EF453T series. The main design criteria of cage wheel were that the cage wheel could provide a good traction force as well as lifting force to support the vehicle against sinkage, and the lugs arrangement could prevent soil blocking between lugs in wet paddy field. Based on these criteria, "V" shape lugs were selected to provide a good traction for forward as well as reverse travel direction. Moreover, "V" shape lugs had lower effect of destroying the hard pan of paddy field. The optimum number of lugs of the designed cage wheel was 12 lugs, with 150 mm width of forward lug face and 80 mm width of reverse lug face. Lug angle of forward lug face was 35° , while for reverse lug face was 45° . The weight of one cage wheel was 164 kg and overall dimension of the designed cage wheel is shown in Figure 1.

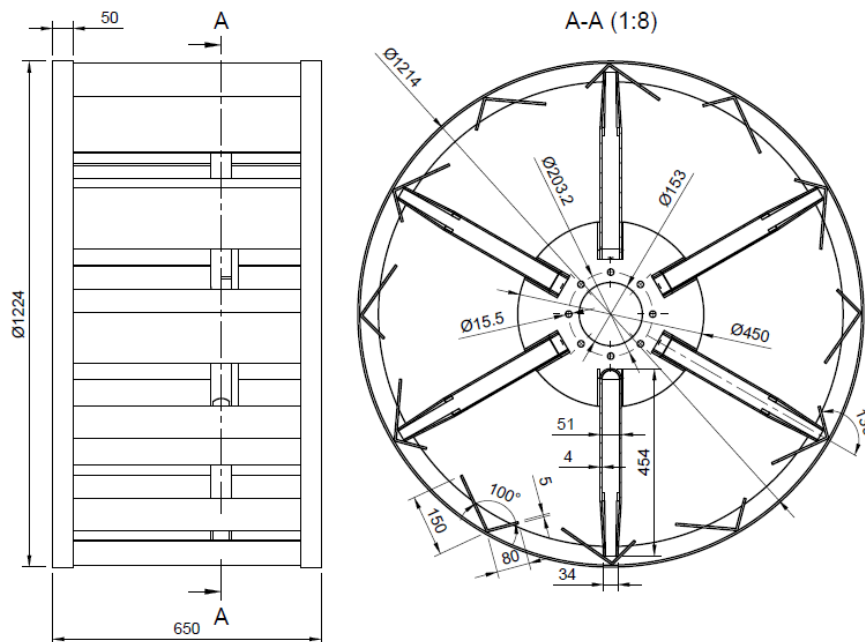


Fig. 1 – Cage wheel design

The prototype of cage wheel was manufactured by Yanmar Agricultural Research Institute - IPB University Indonesia. Given the prevalent absence of farm roads connecting paddy fields in Indonesia, a pragmatic approach was taken. In this regard, 12 pairs of supplementary small lugs were strategically affixed to the outer rim of the cage wheel, as visually depicted in Figure 2. Those additional lugs were designed to improve the cage wheel traction especially when the tractor is traveling between paddy field borders.



Fig. 2 - Cage wheel prototype installed on the tested tractor

• Location and equipment

The performance test was taken place in the Department of Mechanical and Biosystem Engineering, IPB University, Indonesia. The performance tests for cage wheels and rubber wheels were carried out on the

same paddy fields. The size of the paddy fields was 30x30 m and divided into two, half was used for measuring the performance of the cage wheels and the other half was used for measuring the performance of the rubber wheels. Land preparation of the test field was done using two passes of rotary tiller. Soil cone index was measured before the test and the location for measuring the soil cone index was on the 10x10 m grid as shown in Figure 3. The soil sample of paddy field was also taken before the test for analysing the soil texture classification.

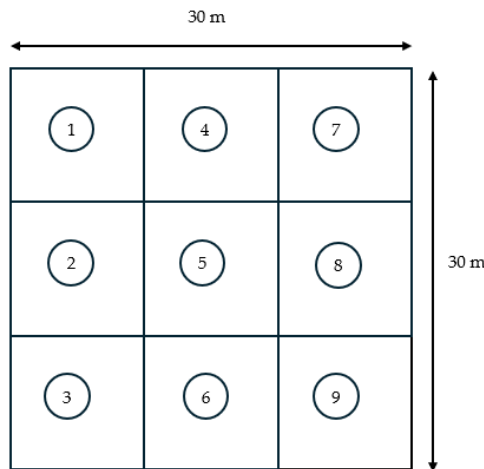


Fig. 3 - Location of soil cone index and soil sampling

The tractor subjected to testing in this research was the YANMAR EF453T, a 4WD tractor with an engine power output of 33.8 kW. Standard rubber wheels of this tractor having size 13.6-26 with 121 cm diameter, 4 ply rating with R-2 lug type and total weight of tractor with rubber wheel was 1450 kg. To determine the drawbar pull of the tested tractor, a KUBOTA L3608, another 4WD tractor with an engine power output of 26.5 kW, was employed as the load tractor. The drawbar pull was measured using a drawbar-type load cell, namely Kyowa LTR-S-SA1, which had a capacity of 5 tons. An ultrasound sensor (Ultrasonic Range Sensor Module HC-SR04) was utilized to measure the tractor's sinkage. Signal data from load cell and ultrasound sensor were recorded in a digital data logger. For the measurement of soil cone index, a digital soil compaction meter named Field Scout SC900 was employed. The tractor's actual forward speed was measured using a measuring tape and stopwatch.

• **Experimental details**

The parameters included in the tractive performance test were actual forward speed, drawbar pull, drawbar power, and coefficient of traction. While the trafficability performance is expressed by wheel slippage, sinkage, and turning radius. The tractive performance test was measured by following the Indonesian Standard for Tractor Performance Test (SNI 7416:2019) with the setup being shown in Figure 4. Tractor was operated at gear position: main gear 1, secondary gear 2, and engine speed 2000 rpm. This engine speed was selected because it was recommended rated engine speed for long run application by the tractor manufacture.

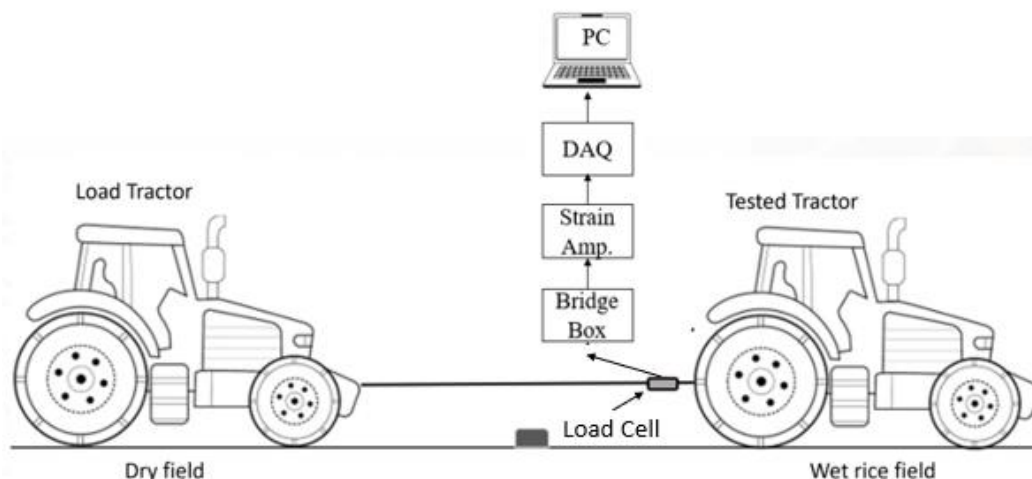


Fig. 4 - Setup of tractive performance test

To calculate tractive performance, Equation 1 and 2 were used (Macmillan, 2002; Pradhan et al., 2017; Hensh et al., 2022).

$$P = F \times v \quad (1)$$

where:

P is drawbar power, kW; F is drawbar pull, kN; and v is tractor forward speed, m/s.

$$CoT = F/W \quad (2)$$

where:

CoT is the coefficient of traction and W is the total tractor's weight, kN (Jusran et al., 2019). The total tractor's weight with cage wheels was 1536 kg and the total tractor's weight with rubber wheels was 1450 kg. Wheel slippage was calculated by Equation 3.

$$S = (S_o - S_i)/S_o \times 100 \quad (3)$$

where:

S is wheels slippage, %; S_o is traveling distance of five-wheel revolutions on hard surface terrain, m; and S_i is traveling distance of five-wheel revolutions on test field, m.

Trafficability parameter was shown by wheel sinkage as a measure of a wheel's depth below the terrain surface (Creager et al., 2017) which was measured by using an ultrasound sensor for distance measurement as expressed in Equation 4.

$$z = d_o - d_i \quad (4)$$

where:

z is sinkage, m, d_o is the distance from bottom of tractor body to the terrain surface in hard soil, m; and d_i is the distance from the bottom of tractor body to the terrain surface during test, m.

The turning radius was defined as the distance from the centre of the outer wheel tread to the point where the tractor completed a U-turn. This measurement was taken using a measuring tape, as illustrated in Figure 5. The duration of performing U-turn was measured by a stopwatch.

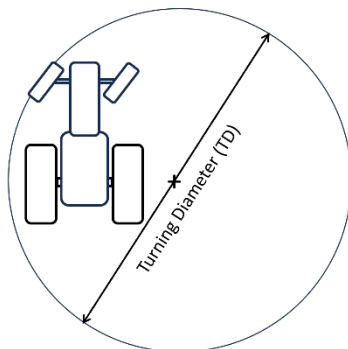


Fig. 5 – Setup and field measurement of turning diameter (TD)

RESULTS

• Test field condition

Based on soil texture analysis, the test soil was categorized as silty clay according to USDA Soil Texture Classification, that consisted of sand 6.7%, silt 52.2% and clay 41.1%. The high content of silt and clay >40% found in this research was in accordance with the findings of Fakhroh et al., (2019) who stated that soil texture of Indonesian paddy field in the study area was dominated by clay and silt with the clay fraction more than 55%.

The soil cone index result is plotted in Figure 6. Based on this graph, it can be understood that the soil cone index started increasing at the soil depth of 20 cm. Then it began to be stable at the soil depth of 30 cm. This indicates that it already touches the hardpan. This soil depth is commonly found in a wet paddy fields in Indonesia. Seemingly, the depth hardpan layer more than 30 cm was also found by Guturu et al., (2016) in the wet paddy field in India.

• Tractive performance of the cage wheel

The tractive performance for cage wheel showing relation between wheel slip, drawbar pull and drawbar power is shown in Figure 7. It can be seen from the figure, that the maximum drawbar pull was 11.5 kN at a slippage of 48.2%. The trend shows that after this point the drawbar pull kept constant while slippage tends to increase. The maximum drawbar power 3.2 kW was reached at a wheel's slippage 27.3%.

Soekarno and Salokhe (2003) studied that the drawbar power of a power tiller with cage wheel reached a maximum value at 15% wheel slip and then decreased further with the increase of wheel slip. When the slippage increases over the above slip values, the drawbar power decreases to zero at 100% of wheels slip (Triratanasirichai et al., 1990). After the maximum drawbar power was achieved, drawbar power tends to decrease because the increment of drawbar pull was lower than the decreasing of forward speed. Thus, since the drawbar power is the product of drawbar pull and forward speed, then the drawbar power was reduced after it reached the maximum point.

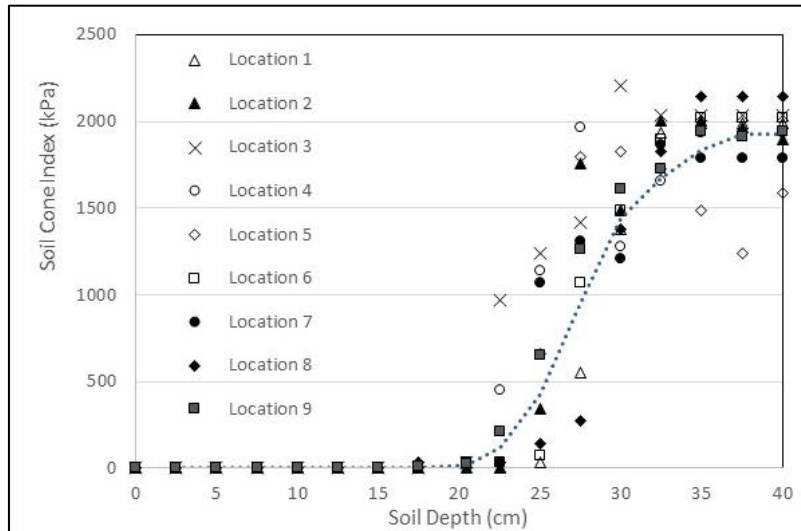


Fig. 6 – Soil cone index graph

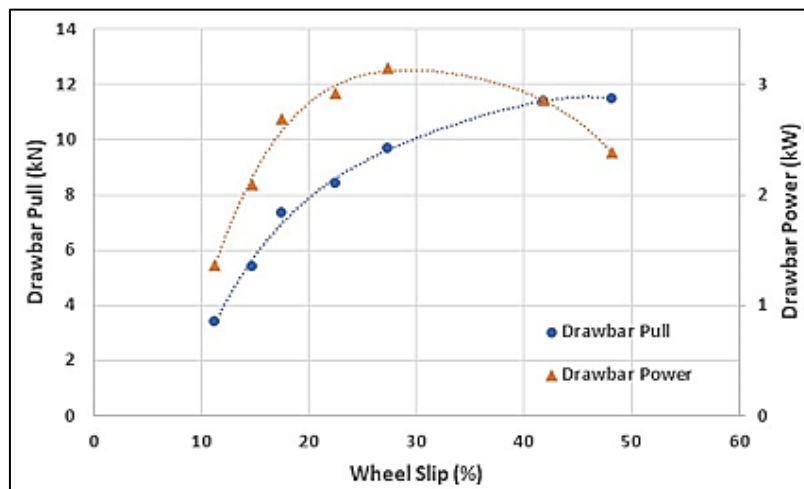


Fig. 7 – The drawbar pull and drawbar power at different wheel slip for cage wheel

The correlation between forward speed and sinkage based on certain slippage is shown in Figure 8. Based on the figure, the forward speed was decreasing with the increase of wheel slip. At the lowest drawbar pull, the wheels slip was 11.2% resulting in the forward speed 0.4 m/s and then the wheel slip continually increased with the increase of drawbar pull thus the forward speed was decreased. For each level of load applied to the test tractor, the sinkage varied slightly, but there was no trend of either increase or decrease with the increase of wheel slip.

This indicates that the cage wheels can provide sufficient lifting force to keep the tractor from sinking. The maximum sinkage was 32.8 cm which occurred at 14.7% and 22.5% wheels slip. Pradhan et al., (2015) who studied the effect of sinkage and sticking on a cage wheel attached to a power tiller found that more sinkage and sticking will cause more fuel consumption, more slippage, and reduce speed.

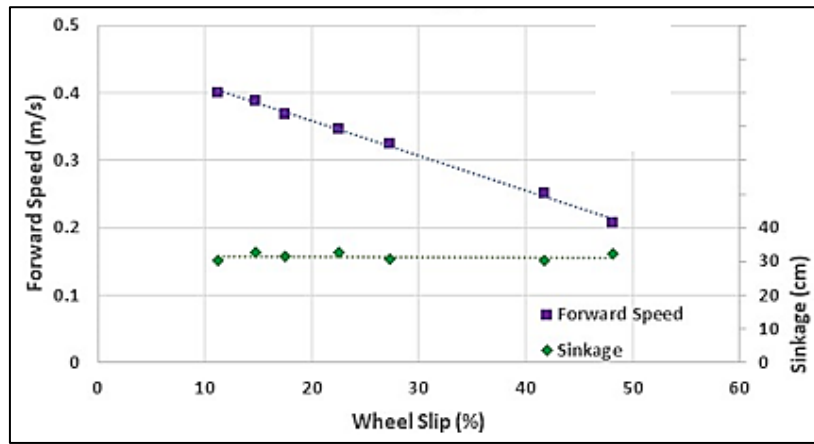


Fig. 8 – The forward speed and sinkage graph at different wheel slip for cage wheel

• **Tractive performance of the rubber wheel**

The result of the drawbar pull, drawbar power, wheels slippage, forward speed, and sinkage of rubber wheel are presented in Figure 9 and Figure 10. Based on the drawbar pull graph of rubber wheel (Figure 9), it shows similar trend to the cage wheel's result in Figure 7. The maximum drawbar pull was 7.7 kN at wheels slip 52.6%. The trend shows that after this slip no more drawbar power can be increased. The maximum drawbar power of 1.9 kW was reached at the wheel slip 35%.

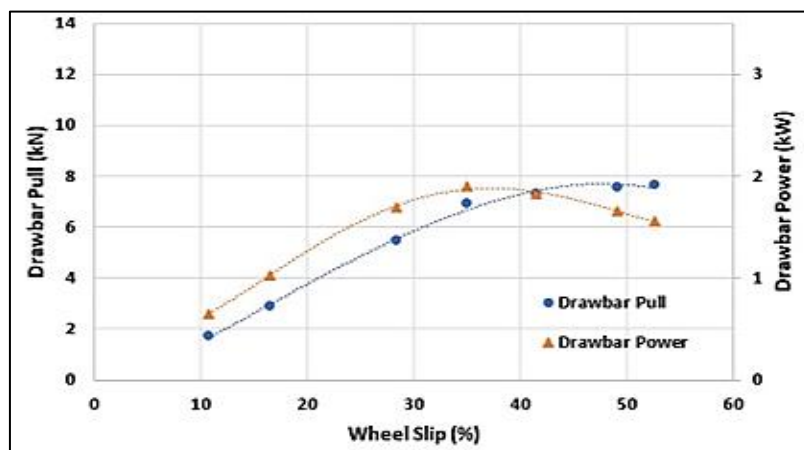


Fig. 9 – The drawbar pull and drawbar power at different wheel slip for rubber wheel

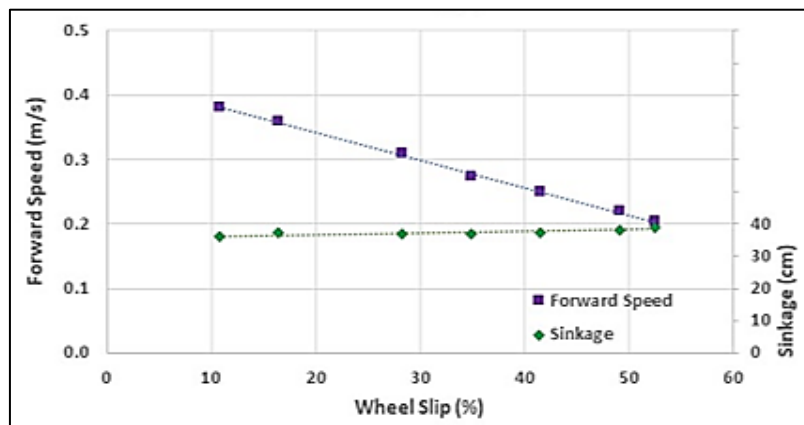


Fig. 10 – The forward speed and sinkage graph at different wheel slip for rubber wheel

The correlation between forward, wheel slip, and sinkage of a tractor with a rubber wheel is shown in Figure 10. The initial wheels slip was 10.8% resulting in the forward speed 0.38 m/s then the wheel slip continually increased with the increasing of drawbar pull thus the forward speed was decreasing. The maximum sinkage was 39.1 cm which occurred at the maximum wheel slip of 52.6%.

- **Comparison of tractive and trafficability between the cage wheel and rubber wheel**

The drawbar pull and drawbar power which resulted from cage wheels (Figure 7) were higher compared with rubber wheel (Figure 9). A higher drawbar pull resulted from the cage wheels was due to the higher traction and shallower sinkage. The condition of shallower sinkage of the cage wheels (Figure 8) was due to higher lifting force of the cage wheel. Consequently, this shallower sinkage will reduce the rolling resistance of the cage wheel. Drawbar pull is a result of traction deducted by rolling resistance.

This shows that the cage wheel gave better tractive performance compared with the rubber wheel. The drawbar performance depends on several factors such as the type of tractor, constructive and operating parameters, and type of the ground (Nastasoiu and Ispas, 2017).

According to Figure 8 and Figure 10, the sinkage resulting from cage wheels shows shallower than from rubber wheels. The forward speed of the tractor using cage wheels also resulted to be higher. This was found to be higher because of the presence of the spike on the cage wheels. Those spikes make the diameter of the cage wheels wider thus it increases the forward speed. The sinkage that occurred in the tractor with cage wheels was less because it follows the theory that the usage of cage wheels will give floating action when the lug touches the soil itself. So, it is proven that cage wheels have better sinkage compared to rubber wheels.

At maximum drawbar power as shown in Table 1, the tractive performance of the cage wheels resulted in decreasing wheel slip by -21.9%, higher drawbar power by 66.2%, higher drawbar pull by 39.5%, higher forward speed by 19.1%, and shallower sinkage by 15.9%. The CoT at the tractor using cage wheels is higher by 31.7% compared with the tractor using rubber wheels.

Table 1

Wheel type	Wheel slip	Drawbar power	Drawbar pull	Forward speed	Sinkage	CoT
	[%]	[kW]	[kN]	[m/s]	cm	
Tractor with cage wheel (CW)	27.3	3.2	9.7	0.33	30.9	0.64
Tractor with rubber wheel (RW)	35.0	1.9	6.9	0.27	36.8	0.49
Comparison: CW vs RW	-21.9 %	66.2 %	39.5 %	19.1 %	-15.9 %	31.7 %

The trafficability performance of cage wheels and rubber wheels are shown in Table 2. From the table, the cage wheels had a wider turning radius and longer U-turn time compared with rubber wheels. Commonly, cage wheels are more difficult in trafficability aspect. The turning radius and U-turn performance were tested without a brake to make U-turn.

Table 2

Wheel type	Turning radius	U-turn time	Sinkage
	[m]	[s]	[cm]
Tractor with cage wheel (CW)	9.3	29.2	32.3
Tractor with rubber wheel (RW)	7.1	25.5	38.7
Comparison: CW vs RW	31.6 %	14.5 %	-16.4 %

The width of the cage wheel was 65 cm while the width of the rubber wheel was 34 cm. For that reason, the total width of the tractor with cage wheel was 237 cm and the total width of the rubber wheel was 161 cm. As the turning radius was affected by the total width of the tractor, the turning radius of tractor with cage wheel become higher.

CONCLUSIONS

Based on the result, it can be concluded that 4WD tractor with cage wheels could provide better tractive performance compared with 4WD tractors using rubber wheels. This was indicated by the increase in drawbar pull, drawbar power, wheel slippage, and coefficient of traction. However, the trafficability result of the cage wheels caused a wider turning radius and longer U-turn time compared with rubber wheels. Sinkage which resulted from cage wheels was shallower compared with sinkage which resulted from rubber wheels.

ACKNOWLEDGEMENT

The author would like to deliver gratitude to Yanmar Agribusiness Co. Ltd. Japan for financial support and to the Department of Mechanical Engineering and Biosystem, Faculty of Agricultural Engineering and Technology of Bogor Agricultural University Indonesia for facility support.

REFERENCES

- [1] Chen, Z., Gu, J., & Yang, X. (2020). A novel rigid wheel for agricultural machinery applicable to paddy field with muddy soil. *Journal of Terramechanics*, 87, 21-27. <https://doi.org/10.1016/j.jterra.2019.11.001>
- [2] Chen, D.; Xu, Y.; Song, Y.; Xom, M.; Wu, L.; Kong, A.; Wang, H.; Dai, P.; Yu, H. (2024). A bionic walking wheel for enhanced trafficability in paddy fields with muddy soil, *Biomimetics*, 9(2), 1-19. <https://doi.org/10.3390/biomimetics9020068>
- [3] Creager, C., Asnani, V., Oravec H., & Woodward A. (2017). Drawbar Performance (DP) Procedures for Off-Road Vehicle Testing. *National Aeronautics and Space Administration*. https://core.ac.uk/download/pdf/1415194_87.pdf.
- [4] Eswari, S.; Kumar, K.K.; & Mamilla, V. R. (2018). Design and analysis of kinematic cage wheel. *International Journal for Research in Engineering Application & Management*, 4, 1-5.
- [5] Fakhroh, Z., Mulya, S.P., Suryaningtyas, D.T., & Mulyanto, B. (2019). Soil and regional characteristics of paddy field in Ngoro Sub-district, Mojokerto, Indonesia: understanding land use change. *IOP Conf. Series: Earth and Environmental Science*, Indonesia, 399, 012067.
- [6] Guturu K., Jesudas, D. M., & Kumar, A. S. (2016). Variation in surface and hardpan levels of wet rice fields. *Indian Journal of Ecology* 2016, 43(Special Issue), 000-000.
- [7] Hensh, S., Chattopadhyay, P. S., & Das, K. (2022). Drawbar performance of a power tiller on a sandy loam soil of the Nadia district of West Bengal. *Research in Agricultural Engineering*, 68, 41 – 46.
- [8] Jusran, Setiawan, R.P.A., & Subrata, I.D.M. (2019). Prototyping and performance test of single wheel tractor for rice plants maintenance. *Jurnal Keteknik Pertanian*, 7, 147-154.
- [9] Kumar, K.K., Sindhuri, K., & Ramprasad, G. (2018). Modify the design of kinematic cage wheel to improve the factor of safety (reduce the stresses). *International Journal of Management, Technology and Engineering*, 8, 607-621.
- [10] Macmillan, R.H. (2002). The Mechanics of Tractor – Implement Performance. *Australia: University of Melbourne*. <https://iagre.org/kcfinder/upload/files/documents/Ross%20Macmillan%20Intro%20-%20Chapter%201.pdf>
- [11] Nastasoiu, M., & Ispas, N. (2017). Determining the theoretical drawbar performance characteristics of tractors, considering the variation of the wheels radii during tractor operation. *Scientific Bulletin*, 27, 89 – 96. <https://doi.org/10.26825/bup.ar.2017.012>
- [12] Nizamani Z. F., & Cebro, I. S. (2018). Measurement of wetland penetration resistance at various points of pressure. *International Journal of Engineering and Applied Technology (IJEAT)*, 1, 23-36. <https://doi.org/10.5281/zenodo.1541344>
- [13] Pradhan, P., Verma, A., Kiran, K., & Ragesh, K.T. (2015). Performance of power tiller with different cage wheels in wet land. *International Journal of Agricultural Science and Research*, 5, 23-32.
- [14] Pradhan, P., Verma, A., Naik, R., & Guru, P. (2016). Traction and drawbar performance characteristic of power tiller attached cage wheel. *BIBECHANA*, 13, 38-49. <http://dx.doi.org/10.3126/bibechana.v13i0.13351>
- [15] Pradhan P., & Verma A. (2017). Cage wheel for traction improvement in power tiller. *Journal of Plant Development Sciences*, 9, 631-636.
- [16] Pradhan, P., Verma, A.K., Naik, R.K., & Guru, P.K. (2017). Draftability of power tiller with different lug angle of cage wheels in puddle soils for paddy. *International Journal of Bio-resource and stress management*, 8, 079-084. <http://dx.doi.org/10.23910/IJBSSM/2017.8.1.1766>
- [17] Setiawan R.P.A., Astika, W., Subrata, D.M. & Azis, A. (2018). Design of iron wheel of a light tractor for crop maintenance in unconsolidated paddy field. *Proceedings of the International Symposium on Agricultural and Biosystem Engineering*, Indonesia.
- [18] Soekarno, S., & Salokhe, V. (2003). Soil reactions on the cage wheels with staggered echelons of half-width lugs and perfect chevron lugs in wet clay soil. *Agricultural Engineering International: the CIGR Journal of Scientific Research and Development*, 1-25.
- [19] Susanto, H., Supardi, J., Darsan, H., & Fitriadi, N. (2023). Testing Cage Wheels Driven on Peaty Paddy Fields. *Transactions of the Chinese Society of Agricultural Machinery*, 54(7), 30-40.
- [20] Triratanasirichai, K., Oida, A., & Honda, M. (1990). The performance of cage wheels for small power tillers in agricultural soil. *Journal of Terramechanics*, 27, 193-205. [https://doi.org/10.1016/0022-4898\(90\)90011-A](https://doi.org/10.1016/0022-4898(90)90011-A)

INTEGRATED UAV TECHNOLOGIES USED IN THE ANALYSIS OF THE CONDITION OF CROPS IN VINEYARDS AND ORCHARDS

TEHNOLOGII INTEGRATE UAV UTILIZATE ÎN ANALIZA STĂRII CULTURILOR DIN VII ȘI LIVEZI

George IPATE*¹⁾, Iuliana GĂGEANU*²⁾, Andreea - Nicoleta BURCEA¹⁾, Stefan DUMITRU¹⁾,
Mădălina- Elena ȘTEFAN¹⁾, Dan CUJBESCU²⁾, Elena-Melania CISMARU²⁾

¹⁾University POLITEHNICA of Bucharest, Faculty of Biotechnical Systems Engineering / Romania

²⁾ National Institute of Agricultural Machinery, Bucharest, Romania

E-mail: george.ipate@upb.ro, iulia.gageanu@gmail.com

DOI: <https://doi.org/10.35633/inmateh-74-36>

Keywords: DJI drone, GIS, sensors, surveillance, UAV, vegetation indices

ABSTRACT

The use of UAV (Unmanned Aerial Vehicle) technology or drones in the monitoring of vineyards and orchards offers multiple benefits, improving the monitoring, management, and productivity of crops. The main goal of this study was to implement a cost-effective integrated UAV technology that includes the necessary hardware and software elements for analyzing the health and growth of agricultural crops in general, with a particular focus on vineyards and orchards. Based on the analysis, agronomists, experts in the field, or ordinary farmers can implement appropriate management measures, such as adjusting the irrigation process, applying fertilizers or phytosanitary treatments, and potentially using shading for the crops. Continuous crop monitoring allows for the evaluation of the effectiveness of the implemented measures and the adjustment of the crop management strategy. Another important objective was the use of high-precision sensors that can be easily attached to a commercial civil drone. The developed system should have a compact size and low energy consumption and even allow for IoT connectivity. To collect and record data from these sensors, a program written in Python is used, containing specific blocks for data acquisition from each sensor to facilitate the monitoring of environmental factors or energy consumption. Experimental tests conducted in the orchard space at the Faculty of Biotechnical Systems Engineering of the National University of Science and Technology Politehnica in Bucharest, Romania, led to the creation of maps showing the health status of the crops based on vegetation indices. The tests demonstrated that UAVs could rapidly cover large areas and collect detailed data without requiring extensive human resources or costly equipment. The results of the analysis of the drone's flight performance underscore the considerable potential of UAV technologies in revolutionizing precision agriculture, particularly in orchards, providing farmers with powerful tools to improve the sustainability and productivity of their crops.

REZUMAT

Utilizarea tehnologiei UAV (Vehicul aerian fără pilot) sau dronelor în supravegherea viilor și livezilor oferă multiple beneficii, îmbunătățind monitorizarea, gestionarea și productivitatea culturilor. Scopul principal al acestui studiu a constat în implementarea unei tehnologii UAV integrate cu cost redus care să conțină elementele hardware și software necesare analizei stării de sănătate și creștere a culturilor agricole în general, cu particularizare în zona de vii și livezi. Pe baza analizei, agronomii, experții în domeniu sau fermierii obișnuiți implementează măsuri de management adecvate, cum ar fi ajustarea procesului de irigare, aplicarea fertilizatorilor sau tratamente fitosanitare, eventual acoperirea cu umbrare a culturilor. Monitorizarea continuă a culturilor permite evaluarea eficiența măsurilor implementate și ajustarea strategiei de gestionare a culturilor. Un alt obiectiv important a fost utilizarea de senzori cu precizie ridicată ce pot fi atașați cu ușurința unei drone civile comerciale. Sistemul realizat se impune să aibă un gabarit și un consum de energie redus, și chiar să permită o conectivitate IoT. Pentru a colecta și înregistra datele de la acești senzori, se folosește un program scris în limbajul Python conținând blocuri specifice pentru achiziția datelor fiecărui senzor, pentru a facilita procesul de monitorizare a factorilor de mediu sau consumul energetic. Testele experimentale realizate în spațiul livezii din Facultatea de Ingineria Sistemelor Biotehnice a Universității Naționale de Știință și Tehnologie Politehnica București, România, au condus la crearea hărților care arată starea sănătății culturii pe baza indicilor de vegetație. Testele au arătat că UAV-urile pot acoperi rapid suprafețe mari și pot colecta date detaliate fără a necesita resurse umane extinse sau echipamente costisitoare. Rezultatele analizei comparative a performanțelor de zbor ale dronei în cele două misiuni executate (zbor liber și cu încărcare)

subliniază potențialul considerabil al tehnologiilor UAV în revoluționarea agriculturii de precizie, în special în podgorii și livezi, oferind fermierilor instrumente puternice pentru a îmbunătăți sustenabilitatea și productivitatea culturilor lor.

INTRODUCTION

Enforcing intelligent applications in agricultural activities is an imperative and pressing concern worldwide (Abo-Habaga et al., 2024).

Photogrammetric analysis of crop conditions in vineyards and orchards is a modern and advanced method for monitoring and evaluating the health and development of agricultural crops using aerial images captured by drones or other aerial platforms. This technique provides a precise and efficient way to obtain detailed information about crop conditions over large areas without the need for on-site inspections. Drones equipped with high-resolution cameras capture images of vineyards and orchards from various angles and at different altitudes to detect plant health issues. The captured images are processed and geometrically corrected to create accurate orthophotos—geographically accurate two-dimensional maps that provide an exact representation of the terrain. The orthorectification process is necessary to eliminate distortions caused by terrain topography and camera angles. Using photogrammetry techniques, three-dimensional (3D) models of the terrain, vines, or trees can be created, allowing for detailed assessment of plant height, vegetation density, and structure. These 3D models are useful for volumetric analysis and for monitoring changes over time (Ipate et al., 2015; Remondino et al., 2011; Sassu et al., 2021; Xue & Su, 2017).

Based on the captured multispectral images, vegetation indices, such as the Normalized Difference Vegetation Index (NDVI), are calculated, providing information about plant health and vigor. The values of these indices allow for the identification of areas experiencing plant stress, such as those affected by drought, diseases, or nutritional deficiencies. The generated maps and obtained data are analyzed to detect specific crop issues, such as areas affected by pests, diseases, water shortages, or other stress factors. This information can be used to make informed decisions regarding irrigation, fertilizer application, or phytosanitary treatments. Photogrammetric analysis enables periodic real-time monitoring of crops, providing up-to-date data and allowing for quick interventions when problems are detected (Toscano et al., 2024; Fascista A., 2022; Cavalari C., 2023; Vidican et al., 2023; Velez et al., 2023).

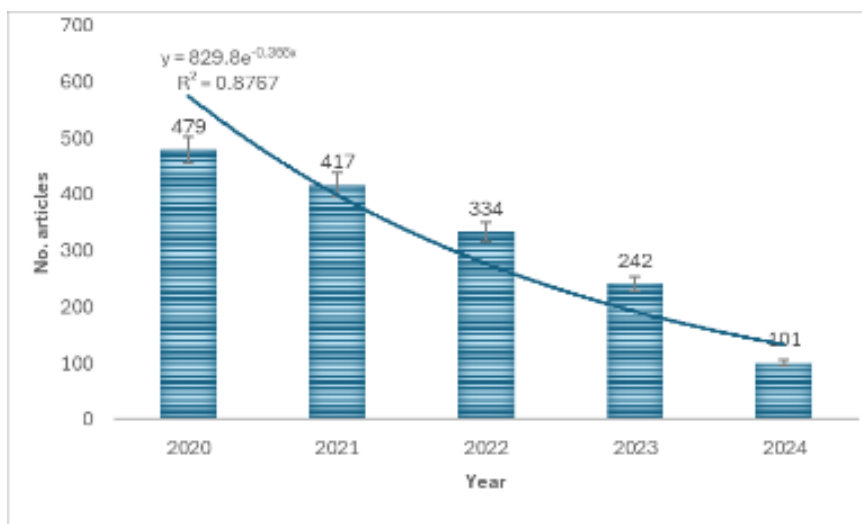


Fig. 1 – The evolution of the number of scientific articles in the last 5 years on the topic of using drones for monitoring vineyards and orchards

The present study began with an in-depth search on the most comprehensive scientific database platform, Google Scholar, using a combination of the defined key terms “UAV drone monitoring orchard and vineyards” (Singh et al., 2022). In just 0.11 seconds, 4,140 papers were detected, of which 563 are review articles. The graph in Figure 1 shows the number of articles published over the years 2020-2024. A clear downward trend in the number of published articles is observed, from 479 in 2020 to 101 in 2024. This decrease is described by an exponential curve, indicating a rapid decline in the early years, followed by a slower decrease in the subsequent years.

This trend may suggest a decrease in interest or resources allocated to this specific field, or a shift in focus to another area of research. However, without additional information, definitive conclusions about the reasons for this decline cannot be drawn.

The works cited in references *Zhang et al., (2021)*; *Lopez-Granados et al., (2020)* provide a comprehensive review of the existing literature concerning crop management in vineyards and orchards using aerial drones, highlighting the significant potential of UAV technology; these reviews emphasize various applications of UAVs in managerial decision-making processes, focusing particularly on the diversity of data processing techniques and the accuracy of monitoring capabilities. In the studies referenced as *Zhou et al., (2021)*; *Bilotta & Bernardo, (2021)*; *Kasimati et al., (2023)*, there is a detailed discussion on the critical importance of utilizing drones for crop forecasting and selective harvesting, as well as for pest control and the efficiency of irrigation systems; these studies underscore the transformative impact of drone technology on agricultural practices. Moreover, in the paper referenced as *Modica et al., (2020)*, it is anticipated that an increasingly substantial source of information will be provided by unmanned aerial vehicle (UAV) platforms, which are predominantly equipped with multispectral optical cameras, to map, monitor, and analyze the temporal and spatial variations in crops through specialized maps of spectral vegetation indices. The discussion further mentions the necessity for solid knowledge in geographic information systems (GIS) and computer image processing, which are essential for field data collection and the creation of vegetation health maps; the capture of aerial images and video files for plant health analysis, along with their integration into GIS programs, facilitates the early detection of fruit tree health issues, thereby enabling the rapid implementation of measures to optimize crop yields.

Currently, the development of drones and their equipment with the most advanced sensors is clearly essential for monitoring and data collection. In the case of applying treatments through spraying in orchards, such as those for fruit trees, olive trees, or citrus, the role of aerial drones remains one of the most controversial aspects, deeply connected to economic, technical, and environmental fields. In the study done by *Campos et al., (2019)*, a major objective was to determine possible correlations between experimental data from remote sensing and the actual characteristics of the upper parts of trees or plants, including branches and leaves. This correlation is necessary for the development of a variable-rate application technology for treatments, based on the health status maps previously developed (*Ioja et al., 2024*; *Ghazal et al., 2024*).

Special attention is given in some works to the use of artificial intelligence in the processing and understanding of images captured by UAVs during the monitoring and evaluation of production in fruit orchards or vineyards (*Lopez-Garcia et al., 2022*; *Popescu et al., 2023*). The complex characteristics of UAV trajectories and flights in these areas are easily managed through the implementation of neural network systems. The structure of the applications, databases, software, and the performances obtained are systematically analyzed to recommend the most effective solutions to end-users. The complex applications analyzed, such as crop and tree identification and classification, disease and pest detection, production evaluation, and growth condition assessment, lead to significant improvements in efficiency and accuracy in orchard management, providing essential information for optimizing interventions and maximizing agricultural yield (*Poblete et al. 2017*; *Zhou et al., 2021*).

Convolutional neural networks (CNNs) are used in the monitoring of orchards and vineyards to analyze aerial or ground images captured by drones, satellites, or fixed cameras (*Zhang et al., 2021*; *Popescu et al., 2023*; *Osco t al., 2020*; *Chen et al., 2019*). These networks are capable of identifying and classifying various critical aspects of crops, such as plant health, the presence of pests, development stages, and even water stress.

- **Monitoring Plant Health:** CNNs can detect early signs of diseases or nutritional deficiencies by analyzing variations in the color and texture of leaves and fruits (*Khattak et al., 2021*). This enables rapid intervention to prevent the spread of problems.
- **Pest Identification:** By analyzing images in detail, convolutional networks can recognize the presence of pests and affected areas, aiding in the application of precise and effective treatments (*Liu & Wang, 2020*).
- **Yield Estimation:** CNNs can be used to count fruits or assess their size and distribution in real-time (*Vasconez et al., 2020*; *Miranda et al., 2023*), providing more accurate estimates of the expected harvest.
- **Development Stage Detection:** Convolutional networks can analyze images to determine the growth stages of plants, allowing for better planning of harvesting and other agricultural activities.

The main goal of this paper is to develop an innovative agricultural crop monitoring system based on an aerial drone, which can have various applications and contribute to more efficient resource use. By implementing better-informed and more tailored agricultural practices to the specific conditions of each plantation, the system also aims to significantly reduce the negative environmental impact. From this proposed goal, several key research objectives emerge, as follows: the **Aerial Photogrammetry** section briefly describes the approaches to image processing for providing detailed and useful information. By formalizing the task as a sequential labeling problem, the **Image Processing** section designs an image classifier for identifying plant diseases using the K-means algorithm. The **Convolutional Neural Networks** section reports significant improvements in understanding the use of the method primarily for image recognition and classification. Considerations regarding real-time object detection are presented in this paper in the **Fruit Recognition in an Orchard with YOLOv4** section. An analysis of the drone battery's energy efficiency in various scenarios is addressed in the **Flight Performance Analysis** section. These objectives aim to develop efficient and scalable systems capable of integrating artificial intelligence technologies to provide precise information for optimizing agricultural processes.

MATERIAL AND METHODS

I. Aerial Photogrammetry

Photogrammetry is a well-developed technology that combines photography and precise measurements to provide detailed and useful information about the surrounding world. The final products of photogrammetry include digital 3D models of the terrain, topographic maps, orthophotos (geometrically corrected aerial images), and various precise measurements of dimensions, volumes, and distances (Srinivas *et al.*, 2012; Zhang *et al.*, 2023). The photogrammetry process includes:

- Capturing images from different angles to ensure complete coverage of the object or terrain being studied;
- Orientation and calibration using Ground Control Points (GCPs) and algorithms to align and calibrate the images, correcting any distortions;
- 3D reconstruction of the object or terrain using photogrammetry software by analyzing the perspective differences in the captured images.

When creating an orthophoto mosaic (Figure 2) from multiple aerial or satellite images, each image must be geometrically corrected and then stitched together with other images to cover the entire area of interest (Gharibi & Habib A., 2018; Rosell & Sanz, 2012; Altunbasak *et al.*, 2003). Seamlines define the locations where these images are joined.

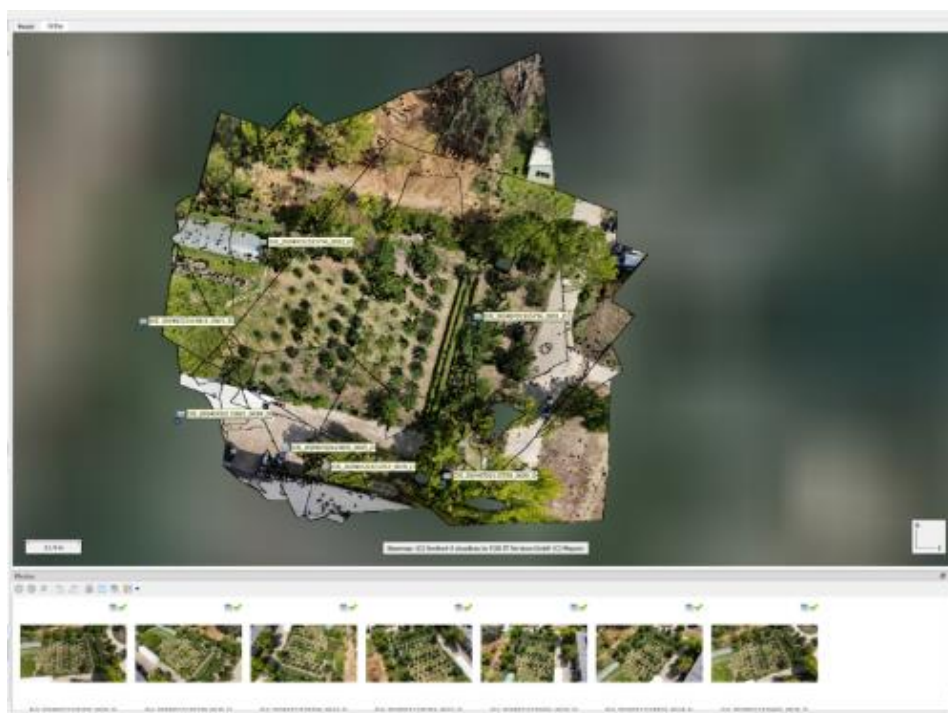


Fig. 2 – Orthomosaic with Image Identification and Seamlines (Screenshot from Agisoft Program)

Radial correction is an important process in photogrammetry and image processing, aimed at eliminating radial distortions introduced by the camera's optical system. These distortions often occur at the edges of the image, where straight lines may appear curved. The radial correction process involves modeling and compensating for these distortions to restore the correct geometry of the image.

Classification of Radial Distortions:

- Barrel Distortion: Straight lines at the edges of the image appear to curve outward, giving the image a "barrel" shape. This type of distortion is common in wide-angle lenses.
- Pincushion Distortion: Straight lines at the edges of the image appear to curve inward, toward the center, creating a "pincushion" effect.

The *mathematical model* for radial correction is based on modeling radial distortions using polynomials or various mathematical functions. The most common model for correcting radial distortion is based on a higher-order polynomial that describes how a pixel shifts depending on its distance from the optical center (Altunbasak et al., 2003).

a) Coordinates before correction: Let's assume we have the coordinates of a point in the image, (x,y) , which are the pixel coordinates before correction. Radial distortion affects these pixels based on their radial distance from the optical center of the image.

b) Radial distance (1): The radial distance r is the distance from the center of the image (assuming the distortion is symmetric relative to the optical center) to the point (x,y) :

$$r = \sqrt{x^2 + y^2} \quad (1)$$

c) Radial distortion model. Radial distortion can be modeled with a polynomial of the 2nd (2) or 3rd (3) order. The basic formula to calculate the new position of the corrected point is:

$$x_{cor} = x \cdot (1 + k_1 \cdot r^2 + k_2 \cdot r^4 + k_3 \cdot r^6 + \dots) \quad (2)$$

$$y_{cor} = y \cdot (1 + k_1 \cdot r^2 + k_2 \cdot r^4 + k_3 \cdot r^6 + \dots) \quad (3)$$

where the coefficients k_1, k_2, k_3 , etc., are the radial distortion coefficients, which are determined practically through camera calibration.

d) Camera calibration. The camera calibration process involves photographing a known pattern (such as a grid of points or a checkerboard) and adjusting the coefficients so that the model in the image matches the real model. Camera calibration can be performed using specific algorithms, such as Zhang's method, which is commonly used in computer vision (Zhang Y.J., 2023).

e) Applying the correction. After the coefficients are determined, the above formula is used to recalculate the positions of each pixel in the corrected image. Essentially, the formula is applied to every pixel in the image to obtain a new position that corrects the effect of radial distortion.

f) Interpolation. In the correction process, since points may be shifted to positions that do not exactly coincide with a pixel, interpolation of color values is necessary. Common interpolation methods include bilinear interpolation or cubic interpolation to ensure a smooth transition and a corrected image without visible artifacts.

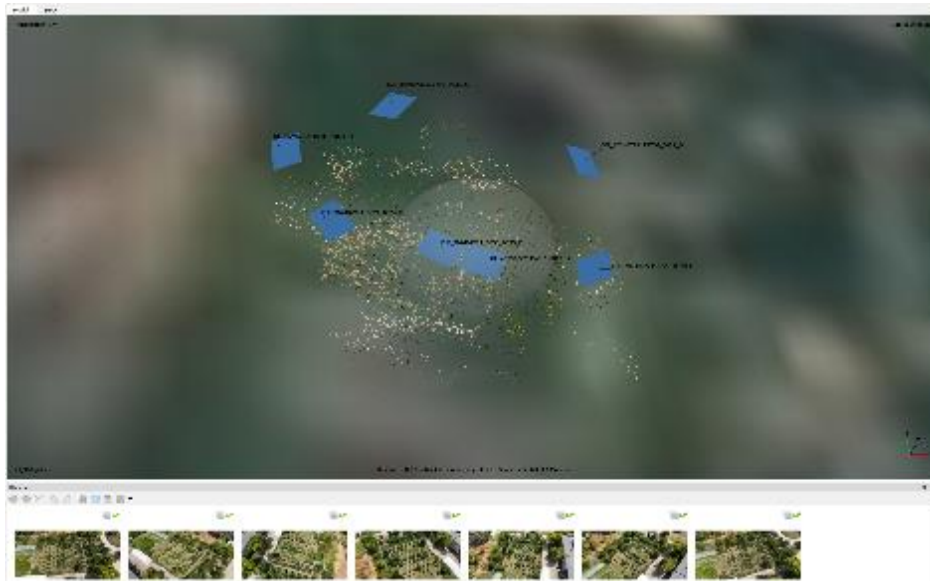


Fig. 3 – Point cloud construction with identification of used images (screenshot from Agisoft program)

For practical implementation examples, in programming languages like MATLAB or Python, there are functions and libraries (such as OpenCV) that can automatically apply these corrections once the distortion coefficients are known.

The Digital Surface Model (DSM) represents the actual surface of the Earth, including all objects that cover it. It is constructed based on the point cloud through interpolation or triangulation to create a continuous surface. A point cloud from the Digital Surface Model (DSM) represents a collection of points in three-dimensional coordinates (X, Y, Z) that describe the terrain surface and all objects on it, such as buildings, vegetation, and other structures (Figure 3). The DSM is different from a Digital Terrain Model (DTM), which represents only the terrain surface without any objects above it. In addition to spatial coordinates, each point can also have other attributes, such as the intensity of reflected light (in the case of LIDAR), color (in the case of RGB photogrammetry), or other spectral data (Beumier & Idrissa, 2016).

II. Hardware components

The DJI Mini 4 Pro is a commercial drone from the DJI series, and it is one of the smallest and lightest, weighing just 249 grams (Figure 4 a). It is easy to transport and can be used in many countries without requiring registration or a license. Equipped with a high-performance 1-inch sensor camera, it is capable of capturing high-resolution images and superior quality 4K HDR video. An advanced 3-axis gimbal technology (Figure 4 b) ensures electronic stabilization of the video camera, allowing for continuous and stable image capture. With a flight time of up to 34 minutes, due to the intelligent battery that includes safety features such as overcharge and overheating protection, the drone also has advanced obstacle avoidance systems for safe navigation, significantly reducing the risk of accidents. For precise positioning and accurate tracking of planned trajectories, the drone uses GPS (Global Positioning System) and GLONASS technology. Various automated and intelligent flight modes, such as QuickShots, ActiveTrack, and Point of Interest, make it easy to capture impressive images and videos. Intelligent features allow the drone to automatically return to the takeoff point in case of a weak signal, low battery, or at the user's command. The drone benefits from the OcuSync system, which provides stable and clear video transmission over long distances, up to 10 km, allowing for more precise control and a safer flying experience. Data encryption for the DJI Mini 4 Pro against interception involves the use of technologies and protocols that protect data transmitted between the drone and the controller (pilot) or between the drone and data storage servers. This includes encryption of video streams, telemetry, control data, and other sensitive information that might be transmitted or stored. The encryption protocol used by DJI is based on AES (Advanced Encryption Standard), a strong and widely used cryptographic standard.



Fig. 4 – DJI Mini 4 Pro with payload (a) and gimbal (b)

RESULTS

The experimental location was an arable area situated within the campus of the Faculty of Biotechnical Systems Engineering at the University Politehnica of Bucharest (at the coordinates of the takeoff/landing point 44.440218° N and 26.045350° E) at an altitude of 78 m, as shown in Figure 5 a and b. The topography of the site is relatively homogeneous and flat. The orchard, containing various fruit tree species, generally apples, pears, plums, nectarines, peaches, apricots, and rows of grapevines, was monitored through the execution of two flight missions. The experiments conducted in this study were carried out with maximum safety concerning other aircraft, infrastructure, and individuals, in accordance with the regulations of the Romanian Civil Aeronautical Authority (AACR). The flight missions were conducted within the pilot's visual range at a maximum altitude of 80 meters above ground level to avoid collisions. The flight missions were planned in compliance with all current regulations (as per flight request No. 10139 - 202473091447 approved by the Ministry of National Defense).

The processing of the captured aerial images (focused on a point of interest (POI) configured at the center of the monitored area) from the selected points along the route (Figure 5c) and the analysis of vegetation indices were carried out using the Agisoft Metashape Professional software. To analyze the drone's performance in terms of energy consumption, maneuverability, and flight autonomy, two missions were conducted: one free flight and one flight with a payload, both following the same planned route. Along the route, 7 waypoints were configured/designed at an altitude of 78 meters above the ground, from which images of the monitored area, including the fruit orchard and rows of grapevines, were captured. Additionally, a point of interest was configured at a distance of 1 meter above the ground, located in the center of the monitored area.

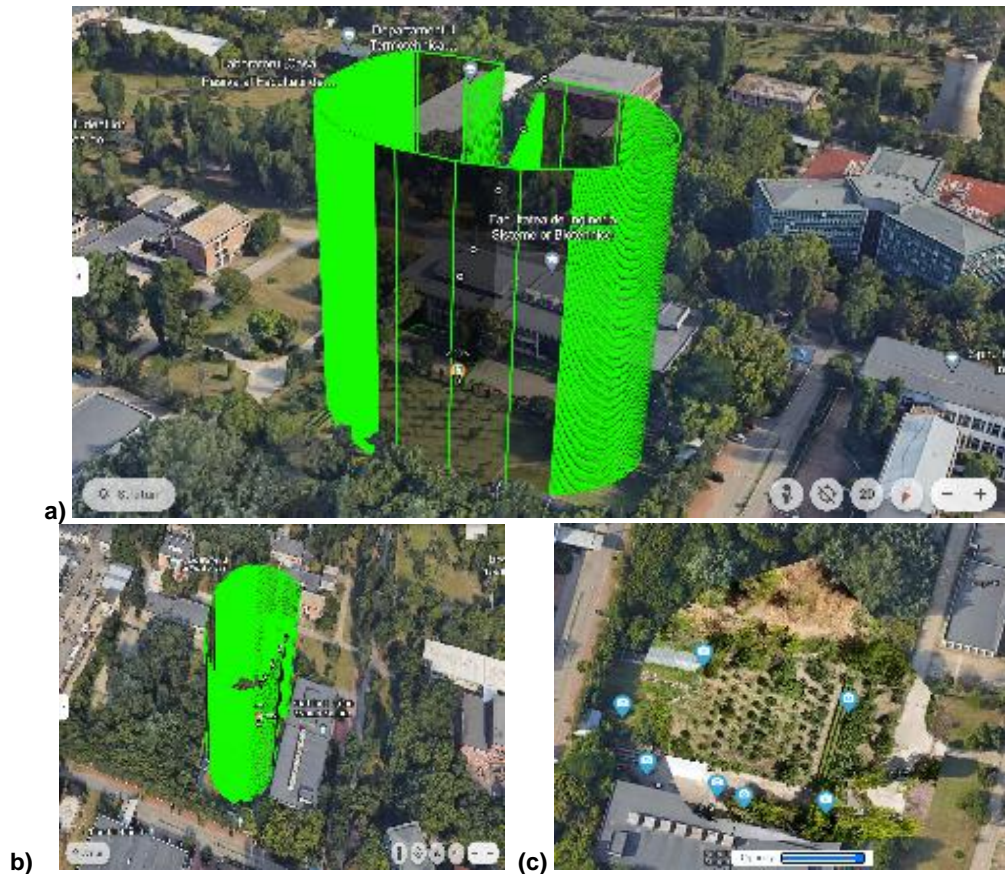


Fig. 5 – Experiment location - University Politehnica of Bucharest campus: (a) Flight mission 1, Google Earth screenshot; (b) Flight mission 2; (c) Image capture locations in the monitored area

Photogrammetric Analysis

In the method proposed by the study (Alganci *et al.*, 2018), the processing of the digital surface model (DSM) involves several steps, starting with image capture and ending with model analysis. Figure 6 shows one of the aerial photographs taken by the drone with a high-definition camera at point 5 of the route, located at coordinates Lon 26.065390 and Lat 44.440345, to create a digital surface model.



Fig. 6 – The image captured at point 5 of the planned route

The camera is equipped with a 1/1.3-inch CMOS sensor and supports up to 4x digital zoom, allowing for the capture of distant details without significantly compromising image quality. It can capture photos at a resolution of up to 48 megapixels, ensuring extremely detailed images; real-time video transmission is supported at 1080p over distances of up to 10 km. The geographic coordinates of the points along the flight path where the camera was programmed to capture images are provided in Table 1.

Table 1

Geographic coordinates of the waypoints along the flight path

Waypoints	Longitude (E)	Latitude (N)
Waypoint1	26.045899	44.440040
Waypoint2	26.046240	44.440021
Waypoint3	26.046326	44.440355
Waypoint4	26.045724	44.440513
Waypoint5	26.045390	44.440345
Waypoint6	26.045493	44.440151
Waypoint7	26.045788	44.440079

The Red-Blue Normalized Difference Vegetation Index (NDVI-RB), sometimes also referred to as the Visible Color Difference Index in the context of the red and blue bands, is determined using the following relationship (Qiao *et al.*, 2022):

$$VNDVI_{RB} = \left(\frac{R-B}{R+B} \right) \tag{4}$$

This value represents a ratio that captures the characteristics of vegetation, contrasting the reflectance of the red (R) and blue (B) bands to highlight areas where red light is absorbed (indicating photosynthetic activity) and blue light is reflected. The image in Figure 7 was processed using the unstandardized formula of the vegetation index, displayed in an NDVI (Normalized Difference Vegetation Index) palette.

Applying a specific NDVI color palette to this index means that the image is colored in a way that highlights areas with high vegetation health (green) and areas with low vegetation health or non-vegetative areas (in brown, yellow, or light tones). The NDVI color palette ranges from -1 to 1, with higher values (closer to 1) indicating dense and healthy vegetation, and lower values (closer to -1) indicating bare soil, water, or deteriorated vegetation. Green areas indicate regions where the absorption of the red band is high relative to the blue band, signifying healthy plant material. Brown and lighter colors represent vegetation health ranging from moderate to low or areas with sparse vegetation. In the context of the applied formula, this suggests areas where the difference between red and blue reflectance is less pronounced, indicating potentially stressed vegetation or bare soil.



Fig. 7 - Normalized Difference Red-Blue Vegetation Index (NDVI-RB).

The Normalized Difference Index of Visible Colors (VNDVIBR - Visible Normalized Difference Vegetation Index - Blue Red) presented in Figure 8 is less common compared to the classic NDVI, but it can be used to evaluate vegetation based on reflectance in the blue (B) and red (R) bands, especially in situations where near-infrared (NIR) band data is not available.

It is calculated using the following formula (Qiao *et al.*, 2022):

$$\text{VNDVI}_{BR} = \left(\frac{B-R}{B+R} \right) \quad (5)$$

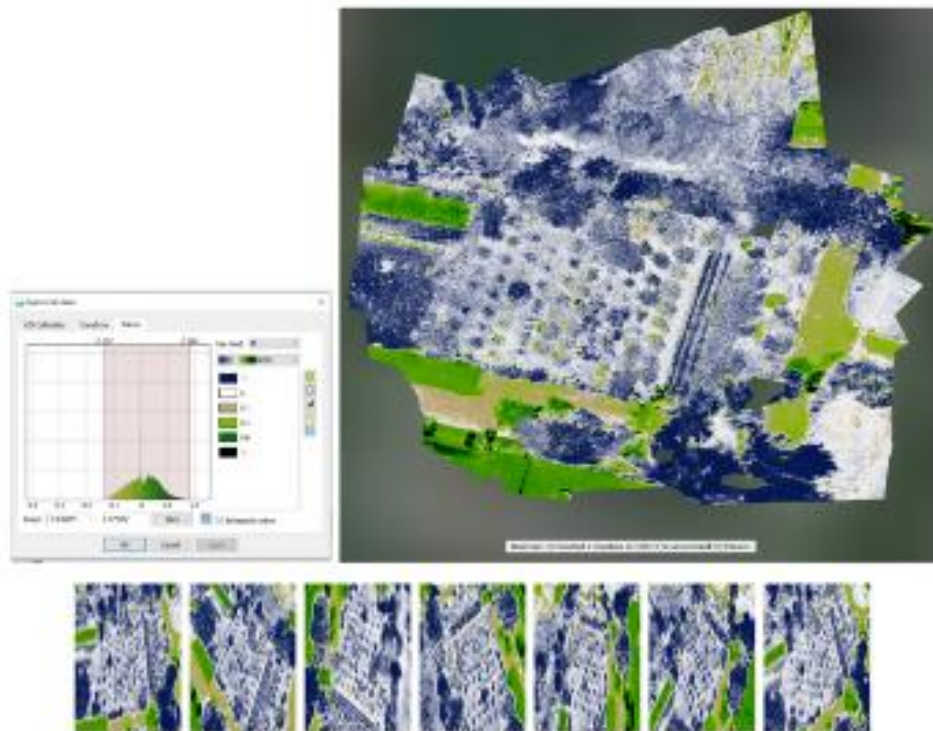


Fig. 8 - Normalized Difference Blue-Red Vegetation Index (NDVI-BR)

Because healthy vegetation usually absorbs red light (used in photosynthesis) and reflects more light in the blue band, this index is somewhat unusual, but it can still provide useful information about the relative health and type of vegetation. In this context, lower values (towards -1) represent healthier and more vigorous vegetation, while values closer to 0 and towards 1 represent areas with less vegetation, stressed or less vigorous vegetation, or even the absence of vegetation.



Fig. 9 - Vineyard monitoring: (left) color image showing the rows of vines; (right) low contrast image where the details exhibit strong negative activation (dark) as well as positive activation (bright)

In Figure 9, a comparison is presented between the color and black-and-white images used to highlight certain characteristics or anomalies in the vegetation, which might be important for monitoring the vineyard's condition. The left frame shows a color image depicting a vineyard with 3 rows of vines. The vegetation is dense and well-defined, with the leaves and stems of the plants clearly visible. In the background, a building and a few trees can be seen, indicating that the vineyard is located in a natural environment, in the garden of the Faculty of Biotechnical Systems Engineering. The right frame shows the same image, but in a black-and-white format with reduced contrast. The image is more difficult to interpret visually, but it seems to depict the same area or a similar area, though the details are much more blurred. The contrast between dark and light areas may indicate the presence of differences in temperature, humidity, or vegetation health that are not evident in the color image.



Fig. 10 – Implementation of artificial intelligence algorithms in image processing for orchard monitoring

Figure 10 shows the implementation of artificial intelligence algorithms to extract specific information from a natural scene. These three images, taken together, suggest a process of vegetation analysis and monitoring, where different image processing techniques are used. In the first frame (left), the image is an ordinary color one, showing the vegetation in natural conditions, with clear details of the trees and surrounding vegetation. The sky is blue, the vegetation is green and healthy, and the background includes trees and possibly other elements of the natural environment. The second frame (middle) presents a slight adjustment in saturation, although the differences from the first image are subtle. This frame is used to highlight certain details of the vegetation or to prepare the image for further analysis. The third frame (right) shows an image with strong contrast, with accentuated dark areas. The vegetation appears much more defined, and fine details of leaves and branches are highlighted. This processing can be used to isolate certain characteristics of the vegetation, such as density or the health status of the plants, and this image might be intended for spectral analysis or to detect anomalies or variations in vegetation composition.

CONCLUSIONS

The application of unmanned aerial vehicle (UAV) technology and artificial intelligence in precision agriculture provides a significant advantage in managing current issues. This combination of technologies facilitates efficient operations and rapid interventions, optimizing resources and thus contributing substantially to increased production and minimized expenses.

The use of applications that implement artificial intelligence algorithms for assessing the health of crops is essential for precise and automated monitoring in agriculture, offering the ability to quickly and efficiently analyze complex images to detect problems or quantify yields. In conclusion, this information is extremely important for optimizing resources in various work scenarios, as well as for planning future operations within the agricultural farm.

The presented study has fully demonstrated its usefulness, contributing to the expansion of knowledge in the field of vineyard and orchard monitoring through a significantly more cost-effective solution compared to those currently available on the open market.

REFERENCES

- [1] Alganci, U., Besol, B., & Sertel, E. (2018). Accuracy assessment of different digital surface models. *ISPRS International Journal of Geo-Information*, 7(3), 114.
- [2] Altunbasak, Y., Mersereau, R. M., Patti, A. J. (2003). A fast parametric motion estimation algorithm with illumination and lens distortion correction. *IEEE Transactions on Image Processing*, 12(4), 395-408.
- [3] Beumier, C., Idrissa, M. (2016). Digital terrain models derived from digital surface model uniform regions in urban areas. *International Journal of Remote Sensing*, 37(15), 3477-3493.
- [4] Bilotta, G., Bernardo, E. (2021). UAV for precision agriculture in vineyards: a case study in Calabria. *Italian Conference on Geomatics and Geospatial Technologies*, pp. 28-42. Cham: Springer International Publishing.
- [5] Campos, J., Llop, J., Gallart, M., García-Ruiz, F., Gras, A., Salcedo, R., Gil, E. (2019). Development of canopy vigour maps using UAV for site-specific management during vineyard spraying process. *Precision Agriculture*, 20(6), 1136-1156.
- [6] Cavalaris, C. (2023). Challenges and opportunities for cost-effective use of unmanned aerial system in agriculture. *Unmanned Aerial Systems in Agriculture*, 197-229.
- [7] Chen, Y., Lee, W. S., Gan, H., Peres, N., Fraisse, C., Zhang, Y., & He, Y. (2019). Strawberry yield prediction based on a deep neural network using high-resolution aerial orthoimages. *Remote Sensing*, 11(13), 1584.

- [8] Fascista, A. (2022). Toward integrated large-scale environmental monitoring using WSN/UAV/Crowdsensing: A review of applications, signal processing, and future perspectives. *Sensors*, 22(5), 1824.
- [9] Gharibi, H., & Habib, A. (2018). True orthophoto generation from aerial frame images and LiDAR data: An update. *Remote Sensing*, 10(4), 581.
- [10] Ghazal, S., Munir, A., & Qureshi, W. S. (2024). Computer vision in smart agriculture and precision farming: Techniques and applications. *Artificial Intelligence in Agriculture*, 13, pp. 64-83, <https://doi.org/10.1016/j.aiia.2024.06.004>.
- [11] Ioja, I., Nedeff, V., Agop, M., Nedeff, F. M., Tomozei, C. (2024). Software uses in precision agriculture based on drone image processing – A review. *9th International Conference on Energy Efficiency and Agricultural Engineering (EE&AE)*, pp. 1-6.
- [12] Ipate, G., Voicu, G., Dinu, I. (2015). Research on the use of drones in precision agriculture. *University Politehnica of Bucharest Bulletin Series*, 77(4), 1-12.
- [13] Kasimati, A., Lomis, A., Psiroukis, V., Darra, N., Koutsiaras, M. G., Papadopoulos, G., & Fountas, S. (2023). Unmanned aerial systems applications in orchards and vineyards. *Unmanned Aerial Systems in Agriculture*, pp. 93-109. Academic Press.
- [14] Khattak, A., Asghar, M. U., Batool, U., Asghar, M. Z., Ullah, H., Al-Rakhami, M., Gumaei, A. (2021). Automatic detection of citrus fruit and leaves diseases using deep neural network model. *IEEE access*, 9, 112942-112954.
- [15] Liu, J., Wang, X. (2020). Tomato diseases and pests detection based on improved Yolo V3 convolutional neural network. *Frontiers in plant science*, 11, 898.
- [16] López-García, P., Intrigliolo, D., Moreno, M. A., Martínez-Moreno, A., Ortega, J. F., Pérez-Álvarez, E. P., Ballesteros, R. (2022). Machine learning-based processing of multispectral and RGB UAV imagery for the multitemporal monitoring of vineyard water status. *Agronomy*, 12(9), 2122.
- [17] López-Granados, F., Torres-Sánchez, J., Jiménez-Brenes, F. M., Oneka, O., Marín, D., Loidi, M., Santesteban, L. G. (2020). Monitoring vineyard canopy management operations using UAV-acquired photogrammetric point clouds. *Remote Sensing*, 12(14), 2331.
- [18] Miranda, J. C., Gené-Mola, J., Zude-Sasse, M., Tsoulas, N., Escolà, A., Arnó, J., Gregorio, E. (2023). Fruit sizing using AI: a review of methods and challenges. *Postharvest Biology and Technology*, 206, 112587.
- [19] Modica, G., Messina, G., De Luca, G., Fiozzo, V., & Praticò, S. (2020). Monitoring the vegetation vigor in heterogeneous citrus and olive orchards. A multiscale object-based approach to extract trees' crowns from UAV multispectral imagery. *Computers and Electronics in Agriculture*, 175, 105500.
- [20] Osco, L. P., De Arruda, M. D. S., Junior, J. M., Da Silva, N. B., Ramos, A. P. M., Moryia, É. A. S., Gonçalves, W. N. (2020). A convolutional neural network approach for counting and geolocating citrus-trees in UAV multispectral imagery. *ISPRS Journal of Photogrammetry and Remote Sensing*, 160, 97-106.
- [21] Poblete, T., Ortega-Farías, S., Moreno, M. A., & Bardeen, M. (2017). Artificial neural network to predict vine water status spatial variability using multispectral information obtained from an unmanned aerial vehicle (UAV). *Sensors*, 17(11), 2488.
- [22] Popescu, D., Ichim, L., Stoican, F. (2023). Orchard monitoring based on unmanned aerial vehicles and image processing by artificial neural networks: a systematic review. *Frontiers in Plant Science*, 14, 1237695.
- [23] Qiao, L., Tang, W., Gao, D., Zhao, R., An, L., Li, M., Song, D. (2022). UAV-based chlorophyll content estimation by evaluating vegetation index responses under different crop coverages. *Computers and electronics in agriculture*, 196, 106775.
- [24] Remondino, F., Barazzetti, L., Nex, F. C., Scaioni, M., & Sarazzi, D. (2011). UAV photogrammetry for mapping and 3D modeling: Current status and future perspectives. In *Proceedings of the International Conference on Unmanned Aerial Vehicle in Geomatics (UAV-g): Zurich, Switzerland*, pp. 25-31. International Society for Photogrammetry and Remote Sensing (ISPRS).
- [25] Rosell, J. R., & Sanz, R. (2012). A review of methods and applications of the geometric characterization of tree crops in agricultural activities. *Computers and electronics in agriculture*, 81, 124-141.
- [26] Sassu, A., Gambella, F., Ghiani, L., Mercenaro, L., Caria, M., Pazzona, A. L. (2021). Advances in unmanned aerial system remote sensing for precision viticulture. *Sensors*, 21(3), 956.
- [27] Singh, A. P., Yerudkar, A., Mariani, V., Iannelli, L., Glielmo, L. (2022). A bibliometric review of the use of unmanned aerial vehicles in precision agriculture and precision viticulture for sensing applications. *Remote Sensing*, 14(7), 1604.

- [28] Srinivas, P., Venkataraman, V. R., & Jayalakshmi, I. (2012). Digital aerial orthobase for cadastral mapping. *Journal of the Indian Society of Remote Sensing*, 40(3), 497-506.
- [29] Toscano, F., Fiorentino, C., Capece, N., Erra, U., Travascia, D., Scopa, A., D'Antonio, P. (2024). Unmanned Aerial Vehicle for Precision Agriculture: A Review. *IEEE Access*, vol. 12, pp. 69188-69205, doi: 10.1109/ACCESS.2024.3401018.
- [30] Vasconez, J. P., Delpiano, J., Vougioukas, S., & Cheein, F. A. (2020). Comparison of convolutional neural networks in fruit detection and counting: A comprehensive evaluation. *Computers and Electronics in Agriculture*, 173, 105348.
- [31] Vélez, S., Martínez-Peña, R., & Castrillo, D. (2023). Beyond vegetation: A review unveiling additional insights into agriculture and forestry through the application of vegetation indices. *J*, 6(3), 421-436.
- [32] Vidican, R., Mălinaş, A., Ranta, O., Moldovan, C., Marian, O., Gheţe, A., Cătunescu, G. M. (2023). Using remote sensing vegetation indices for the discrimination and monitoring of agricultural crops: a critical review. *Agronomy*, 13(12), 3040.
- [33] Xue, J., Su, B. (2017). Significant remote sensing vegetation indices: A review of developments and applications. *Journal of sensors*, 1, 1353691.
- [34] Zhang, C., Valente, J., Kooistra, L., Guo, L., Wang, W. (2021). Orchard management with small unmanned aerial vehicles: A survey of sensing and analysis approaches. *Precision agriculture*, 22(6), 2007-2052.
- [35] Zhang, J., Xu, S., Zhao, Y., Sun, J., Xu, S., & Zhang, X. (2023). Aerial orthoimage generation for UAV remote sensing. *Information Fusion*, 89, 91-120.
- [36] Zhang, Y. J. (2023). Camera calibration. In *3-D Computer Vision: Principles, Algorithms and Applications*. Springer Nature Singapore, pp. 37-65.
- [37] Zhou, X., Yang, L., Wang, W., & Chen, B. (2021). UAV data as an alternative to field sampling to monitor vineyards using machine learning based on UAV/sentinel-2 data fusion. *Remote Sensing*, 13(3), 457.

COMPARATIVE EXPERIMENTAL STUDY ON OPERATION PERFORMANCE AND YIELD OF MAIZE SEEDERS OF DIFFERENT TYPES IN WHEAT STUBBLE FIELD

麦茬地不同型式玉米播种机作业性能及产量对比试验研究

Ting XU¹⁾, Zehua HAO¹⁾, Yinping ZHANG^{*1)}, Kai XU²⁾, Ke LIU²⁾, Yunyou KANG²⁾, Hua ZHOU^{*1)}, Dengyu LI²⁾

¹⁾ School of Agricultural and Food Science, Shandong University of Technology, Zibo (255000), China

²⁾ Shandong Province agricultural machinery technology promotion station, Jinan (250013), China

Correspondent author: Yinping ZHANG; Hua ZHOU

Tel: +86 15165333108; E-mail: zhangyinping929@163.com; sdy2000@163.com

DOI: <https://doi.org/10.35633/inmateh-74-37>

Keywords: mechanical seeding quality; plant spacing qualified rate; plants height consistency; yield of maize; seeder type; operation efficiency

ABSTRACT

Mechanical seeding quality is a key factor affecting the yield of maize in stubble fields. To choose for high-performance seeders and determine the appropriate operating speed, comparative sowing tests were conducted using spoon-wheel seeders, lightweight and heavyweight finger-clip seeders, and air-suction seeders in six districts of Shandong Province. Three working speeds, low speed, medium speed and high speed, were set up to determine the qualified rate of plant spacing, the consistency of plants height and the yields under different working speeds. The results showed that the qualified plant spacing rate, plants height consistency, and yield of the spoon-wheel and lightweight finger-clip seeders were significantly affected by the operating speed, decreasing as the speed increased. At high speeds, the qualified plant spacing rates were less than 80%, and plants height consistency were less than 85%. Heavyweight finger-clip and air-suction seeders' qualified plant spacing rates, plants height consistency, and yields were not significantly affected by the operating speed, remaining stable across different speeds and significantly higher than those of the spoon-wheel and lightweight finger-clip seeders. The differences in qualified plant spacing rates and plants height consistency were more significant at higher speeds, along with obvious yields increase advantage. The yields increase ranged from 3.50% to 7.84% at low speeds, 4.32% to 9.31% at medium speeds, and 7.64% to 11.65% at high speeds. This study provides a reference for the selection of high-performance seeders for maize in stubble fields and the determination of suitable operating speeds.

摘要

机械播种质量是影响麦茬地玉米产量的关键因素,为筛选高性能播种机,并确定适宜的作业速度,使用勺轮式、指夹式(轻型、重型)和气吸式播种机在山东省6个区县进行播种对比试验,试验设置低速、中速和高速3种作业速度,测定不同作业速度下的株距合格率、苗高一致性和产量,结果表明:勺轮式和轻型指夹式播种机的株距合格率、苗高一致性以及产量均受作业速度影响显著,随作业速度增大而降低,高速作业时株距合格率小于80%,苗高一致性小于85%;重型指夹式和气吸式播种机株距合格率、苗高一致性以及产量受作业速度的影响不显著,各速度下株距合格率、苗高一致性以及产量均较稳定,显著高于勺轮式和轻型指夹式播种机,并且作业速度越高,株距合格率和苗高一致性差异越显著,增产优势也越明显,低速增产幅度为3.50%~7.84%,中速增产幅度为4.32%~9.31%,高速增产幅度为7.64%~11.65%。本研究为麦茬地玉米高性能播种机的筛选和适宜作业速度的确定提供参考。

INTRODUCTION

Maize is an important grain crop, high-quality feed, and industrial raw material. China imports an average of 20 million tons of maize annually (Zhong *et al.*, 2024). With limited arable land resources, it is important to increase maize production to get rid of the dependence on imports (Bao *et al.*, 2023; Wang *et al.*, 2023).

The quality of mechanized sowing significantly impacts maize yield, and uniform seed spacing and consistent planting depth are the main embodiment of good sowing quality (Du *et al.*, 2023; Yang *et al.*, 2016; Suan *et al.*, 2021; Sanavi *et al.*, 2006; Badua *et al.*, 2021). Gan *et al.* (1995), found that the depth of sowing directly affects the seedling emergence rate of seeds, which results in a reduction of yield due to the increase

of sterile plants. Griepentrog *et al.*, (1998), pointed out that the spacing of sowing affects the crop's use of light, water and soil nutrients, which influences the level of yield. Li Yueming found that different seed viability at different sowing depths and various seed traits had different effects on yield (Li *et al.*, 2019). Fu Weiqiang found that the inconsistency of seeding depth seriously affected the uniformity of seedling stage and the yield in later stage (Fu *et al.*, 2019). Han Dandan and Zhang Shaohua pointed out that poor plant spacing uniformity fails to meet agronomic requirements and would cause a lot of waste of seeds (Han *et al.*, 2023; Zhang *et al.*, 1981). Under the same conditions of the previous crop's surface, the performance of the seeder is the main factor affecting the quality of sowing. Currently, there are various types of maize seeders on the market, with differing performances and varying sowing quality (Cheng *et al.*, 2023). The seed metering device and furrow opener are the key components that significantly influence the quality of sowing (Gao *et al.*, 2021; K. *et al.*, 2022). Seed metering devices mainly include spoon wheel type, the finger-clip type and the gas suction type, and the openers mainly include the hoe shovel type, the double disc type and the hoe shovel double disc combined type (Zhao *et al.*, 2022; Singh *et al.*, 2005; Yazgi *et al.*, 2007; Vamerali *et al.*, 2006; Aliakbar *et al.*, 2013). In order to choose high performance seeder and improve the quality of maize seeding, comparative tests of maize seeding were carried out in different districts of Shandong Province.

MATERIALS AND METHODS

Test locations and materials

The locations of the tests were relatively concentrated plots in six areas, Wenshang County, Hanting District, Huantai County, Shanghe County, Qihe County, and Zoucheng City, of Shandong Province. Based on local climatic conditions and production practices, commonly used spoon-wheel type, finger-clip type and air-suction type maize seeders from the market were selected. The row spacing, plant spacing, theoretical sowing amount, and other parameters were determined, as shown in Table 1. The test plots had relatively consistent conditions in terms of light, moisture, and soil nutrients, with flat terrain and no slopes. The length of the plot was no less than 70 meters, and the wheat straw from the previous crop was returned to the field in full cover, without ploughing or straw treatment in any way.

Table 1

The basic situation of sowing in each experimental site

Test site	Maize variety	Seeder type	Trencher type	Seeder weight (kg)	Theoretical spacing (cm)	Theoretical seeding amount (grain/hm ²)
Wenshang county	Huamei No.1	Spoon-wheel type	Hoe shovel	685	17	98 040
		Heavyweight finger-clip type	Double-disc	1 260	17	98 040
		Air-suction type	Double-disc	1 600	17	98 040
Hanting district	Denghai 605	Spoon-wheel type	Hoe shovel	1 000	23	72 465
		Lightweight finger-clip type	Hoe shovel	890	23.5	70 920
		Air-suction type	Double-disc	1 970	22.3	74 745
Huantai county	Denghai 1966	Spoon-wheel type	Hoe shovel	310	25	66 660
		Lightweight finger-clip type	Hoe shovel	295	25	66 660
		Air-suction type	Double-disc	2 300	25	66 660
Shanghe county	Denghai 605	Spoon-wheel type	Hoe shovel	300	24	69 450
		Lightweight finger-clip type	Hoe shovel	360	24	69 450
		Air-suction type	Double-disc	1 520	24	69 450
Qihe county	Denghai 605	Spoon-wheel type	Hoe shovel	350	20	83 340
		Heavyweight finger-clip type	Hoe shovel + Double-disc	1 280	20	83 340
		Air-suction type	Hoe shovel + Double-disc	1 500	20	83 340
Zoucheng city	Denghai 1717	Spoon-wheel type	Hoe shovel	690	23	72 465
		Lightweight finger-clip type	Hoe shovel	570	23	72 465
		Air-suction type	Double-disc	1 410	23	72 465

Test methods

The test was set up with three working speeds: low speed (5 ± 1 km/h), medium speed (7 ± 1 km/h), and high speed (9 ± 1 km/h), across nine test plots. Unify seed bed conditions, operator, seeding time and field management after sowing. After 10 days of emergence, the plant spacing and plant height were measured, then the plant spacing qualified rate and plant height consistency were calculated. The theoretical yield of maize was measured before harvest.

Test metrics

(1) Plant spacing qualified rate

Two seeding rows were randomly selected on the round trip of the seeding plot (a total of four rows). In the stable seeding area, the plant spacing of 20 plants was measured consecutively in each row. The plant spacing qualified rate Z was calculated according to equation (1). Take an average of four lines of measurement results.

$$Z = \frac{Z_H}{20} \times 100\% \quad (1)$$

where: Z_H is the numbers of qualified plant spacing, which was greater than 0.5 times the theoretical plant spacing and less than or equal to 1.5 times the theoretical plant spacing, pcs.

(2) Plant height consistency

Two seeding rows on the round trip of the seeding plot (a total of four rows) were randomly select. In the stable seeding area, the height of 20 plants was measured consecutively. The plant height consistency H was calculated according to equation (2) - (5). Take an average of four lines of measurement results.

$$h = \frac{\sum_{i=1}^{20} h_i}{20} \quad (2)$$

$$H_0 = \sqrt{\frac{\sum_{i=1}^{20} (h_i - h)^2}{20 - 1}} \quad (3)$$

$$p = \frac{H_0}{h} \times 100\% \quad (4)$$

$$H = 1 - p \quad (5)$$

where: h is the average plant height, cm; h_i is the height of plants, cm; H_0 is the standard deviation of plants height, cm; p is the coefficient of variation of plants height; H is the coefficient of plant height consistency.

(3) Yield of maize

During the harvest period, the method of artificial actual production measurement was adopted. For each experimental treatment, three measurement points were selected using the diagonal sampling method, and 2 rows of maize, 10 meters long, were selected from each point. The actual area S of the harvesting sample point was calculated according to equation (6).

$$S = 10 \times 2 \times b \quad (6)$$

where: S the actual sampling area, m²; b is the maize planting row spacing, m.

The cobs in the sample points were harvested and weighed manually, and 20 cobs selected randomly were threshed and weighed manually. The seed rate α was calculated according to equation (7).

$$\alpha = \frac{g}{G} \times 100\% \quad (7)$$

where: α is the value of seed yield rate of the sampled cobs, %; g is the value of grain weight of 20 cobs, kg; G is the value of total weight of 20 cobs, kg.

Maize moisture content was measured with a moisture tester, and the average value β was measured at three measuring points. The yield Q per hectare of each test point was calculated according to equation (8), and the average of three measurements was taken.

$$Q = \frac{W \times \alpha \times (1 - \beta) \times 10000}{S \times (1 - 14\%)} \quad (8)$$

where: Q is the value of yield per hectare, kg/hectare; W is the total weight of harvested cobs, kg.

Data Processing

Microsoft Excel 2016 was used for data analysis and processing.

RESULTS AND ANALYSIS

(1) Plant spacing qualified rate analysis

The uniformity of plant spacing affects the effective use of light, water and soil nutrients, and the uniformity of plant spacing is conducive to the high yield of crops. Figure 1 shows the qualified rates of plant spacing for different types of seeders at low, medium, and high operating speeds. As can be seen from the figure, at the same speed, except for low-speed treatment in Hanting District, the qualified rate of plant spacing of air-suction seeder is significantly higher than that of spoon-wheel and lightweight finger-clip seeder, being around 90%, with the highest reaching 96.25%. This indicates that the air-suction seeder has better seeding performance, especially in medium-high speed operation, where the plant spacing is more stable. The analysis shows that the reason for the lower qualified rate of plant spacing for the air-suction seeder in the low-speed treatment in Hanting District is that, under low-speed operation, the tractor's power take-off shaft speed is low, resulting in insufficient fan wind pressure. This leads to missed seeding occurrences, which causes the qualified rate of plant spacing to be lower. In Wenshang County and Qihe County, the qualified rates of plant spacing for the heavyweight finger-clip seeders are not significantly different from those of the air-suction seeder, and both are higher than those of the spoon wheel seeders. In other areas, the qualified rates of plant spacing for the lightweight finger-clip seeders are not significantly different from those of the spoon wheel seeders, and both are significantly lower than those of the air-suction seeder.

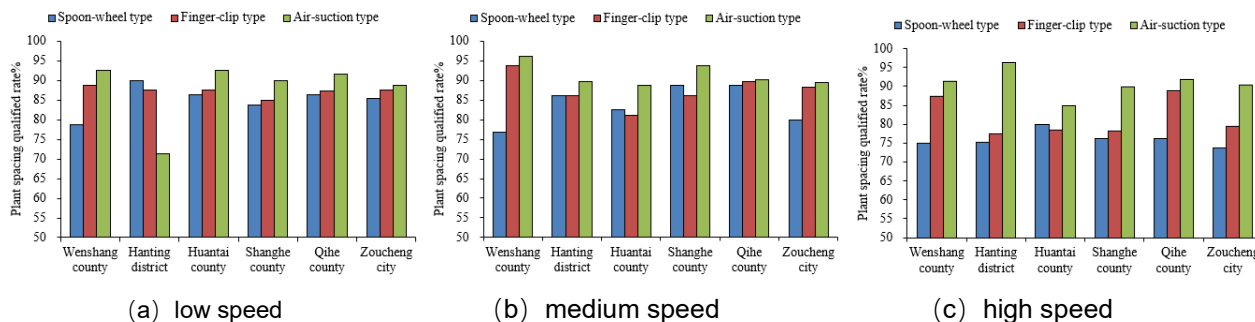


Fig. 1 - Plant spacing qualified rate at different working speeds

Through the analysis of plant spacing qualified rate, it can be seen that under the same operation speed, the seeding uniformity of air-suction seeder and heavyweight finger-clip seeder is higher than that of spoon wheel and lightweight finger-clip seeder. This difference is particularly significant at high operating speeds. Comparing the qualified rates of plant spacing for the same seeder at different operating speeds reveals that the spoon wheel and lightweight finger-clip seeders are significantly affected by speed. The qualified rate of plant spacing decreases as the speed increases, dropping below 80% at high speeds. In contrast, the heavyweight finger-clip and air-suction seeders are not significantly affected by speed, with their qualified rates of plant spacing generally remaining above 90% even at high speeds.

(2) Plant height consistency analysis

Overall, the plant height consistency of the spoon wheel and lightweight finger-clip seeders is significantly affected by operating speed. As the operating speed increases, plant height consistency decreases, dropping below 85% at high speeds. In contrast, the plant height consistency of the air-suction and heavyweight finger-clip seeders is not significantly affected by speed, maintaining a uniformity of around 90% \pm 2% across different speeds. Comparing the plant height consistency at the same speed, the air-suction type and heavyweight finger-clip seeders have higher uniformity than the spoon wheel and lightweight finger-clip seeders. This difference is especially significant at medium and high speeds. The reason is that the air-suction type and heavyweight finger-clip seeders have a heavier overall weight (greater than 1200 kg), providing sufficient individual downforce. Additionally, the four-bar linkage contour-following mechanism performs well in contouring, and the use of double-disc openers with depth limiters ensures stable furrow depth. However, due to the light weight of the whole machine (less than 1000 kg), the opener of the spoon-wheel and lightweight finger-clip seeder have serious bumps during high-speed operation in the stubble field. Although there is a four-link imitation, the pressure of the single unit is limited, especially in the case of stubble, large soil and large amount of straw, maize seeding monomer jumps significantly and the depth of the furrow is unstable.

At the same time, hoe-shovel openers have poor soil backfill performance at high-speed operation, resulting in uneven soil thickness covering the seeds and poor plant height consistency. Nevertheless, in Figure 2, the consistency of plant height of the air-suction seeder in Huantai County is lower than that of the spoon wheel type and the traditional finger-clip type at the same speed. The investigation revealed that the stubble height of Huantai test site was greater than 25 cm and the straw cutting length was greater than 20 cm due to the rush to harvest wheat before rain. Moreover, on the test day, the air humidity was high, which increased the toughness of the straw, making it difficult to cut off. During the seeder's operation, slight clogging occurred, with root stubble being dragged by the straw clearing discs and accumulating on the seedbed (as shown in Figure 3). This accumulation affected soil coverage and led to inconsistent sowing depth. Furthermore, the uncut long straw was pressed into the seed furrow by the double discs, so that the seeds could not be in close contact with the soil. This affected the emergence time and resulted in poor consistency of plant height, as shown in Figure 4.

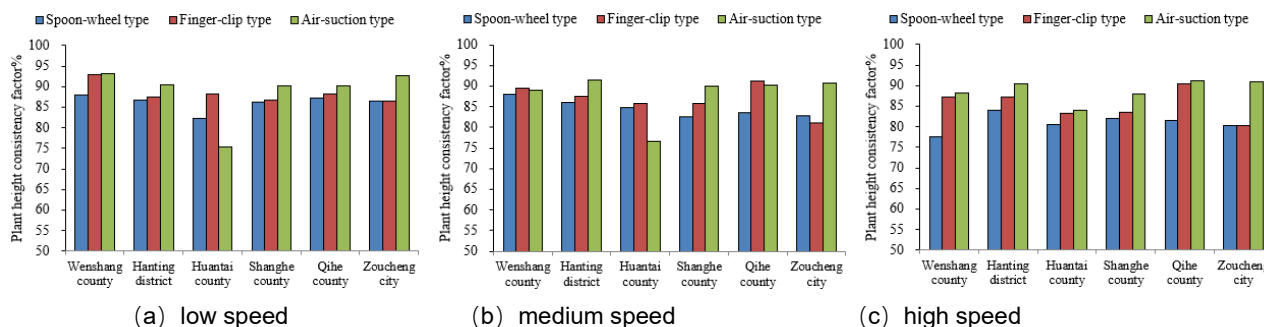


Fig. 2 – Plants height consistency at different operating speeds



Fig. 3 – Passive clearing of seed bed unevenness due to straw tray congestion



Fig. 4 – Seedling emergence of maize sown on straw and not sown on straw

Through the analysis of plant height consistency, it is evident that compared to hoe-shovel openers, double-disc openers are better at ensuring consistent seeding depth. However, the crop residue and root stubble from the previous crop must meet operational requirements for this advantage to be realized. Finger-clip and air-suction seeder used in Qihe County installed hoe-shovel opener in front of the double-disc opener, broke the stubble first and then used the double-disc opener. The consistency of plant height was more than 90%, indicating that hoe-shovel and double-disc opener were more suitable for maize seeding in the stubble field.

(3) Maize yield analysis

Figure 5 shows maize yields at different operating speeds. Comparing the yields of the same seeder at different operating speeds reveals that, overall, the yields of spoon wheel and lightweight finger-clip seeders decrease as the operating speed increases. In contrast, the yields of heavyweight finger-clip and air-suction seeders are less affected by speed, with no significant differences in yield across different speeds. Comparing the output of different types of seeders at the same speed, it can be seen that there is little difference in the output of spoon wheel type and lightweight finger-clip type on the whole. Except for the air-suction seeder in Hanting District, which experienced missed seeding at low speeds, and the lower yield of the air-suction seeder in Huantai County due to previous crop stubble, the yields of the spoon wheel and lightweight finger clip seeders in other areas were significantly lower than those of the heavyweight finger-clip and air-suction seeders.

This indicates that heavyweight finger-clip and air-suction seeders are conducive to achieving higher maize yields. At low speeds, the yield increase ranges from 3.50% to 7.84%; at medium speeds, the yield increase ranges from 4.32% to 9.31%; at high speeds, the yield increase ranges from 7.64% to 11.65%. This demonstrates that the yield advantage of heavyweight finger-clip and air-suction seeders becomes more significant under higher operating speeds.

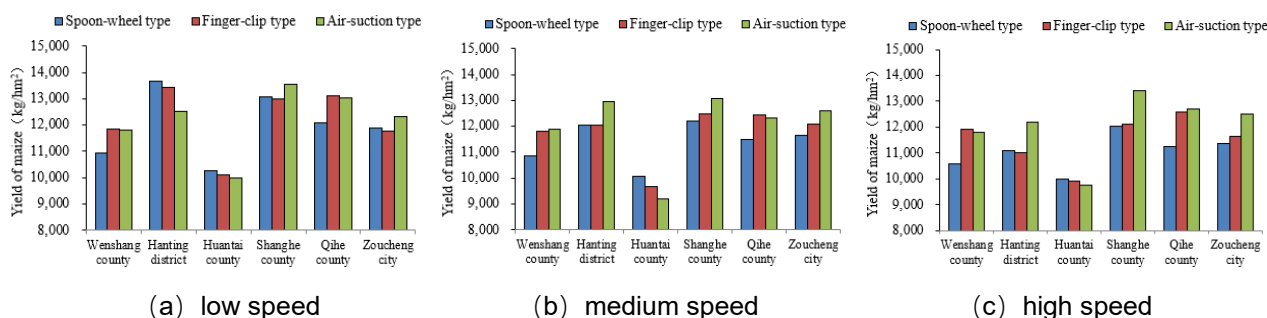


Fig. 5 – Maize yield at different operating speeds

CONCLUSIONS

This study conducted sowing comparison tests in six counties in Shandong Province to analyse the plant spacing, plant height consistency, and yields of four types of seeders—spoon wheel, lightweight finger-clip, heavyweight finger-clip, and air-suction—at different operating speeds. The following conclusions are drawn:

(1) The plant spacing, plant height consistency and yield of spoon-wheel and lightweight finger-clip seeder were significantly affected by speed, and decreased with the increase of speed, so these seeders are not suitable for high-speed operations. The plant spacing, plant height consistency, and yield of heavyweight finger-clip and air-suction seeders are not significantly affected by operating speed. These metrics remain stable across different speeds and are significantly higher than those of spoon wheel and lightweight finger-clip seeders. Moreover, the higher the operating speed, the more pronounced the differences become.

(2) Spoon-wheel and lightweight finger-clip seeders are suitable for medium and low speed operations, and the operating speed is generally not more than (7 ± 1) km/h. The air-suction and heavyweight finger-clip seeders are suitable for high, medium, and low-speed operations. However, when operating at low speeds with air-suction seeders, it is important to increase the fan speed to prevent missed seeding.

(3) Compared with the hoe-shovel opener, the double-disc opener can better ensure the consistency of sowing depth. However, the stubble and root residue from the previous crop must meet operational requirements. To ensure consistent seeding depth, a hoe-shovel opener can be installed in front of the double-disc opener to first clear the stubble, followed by the use of the double-disc opener for furrowing. For plots with more straw, it is also possible to install an active stubble-breaking and straw-clearing device in front of the double disc opener to prevent seeder clogging.

ACKNOWLEDGEMENTS

This work was supported by the Shandong Province Science and Technology Smets Innovation Ability Improvement Project (NO.2023TSGC0339 and 2024TSGC0271) and Shandong Province Major Agricultural Technology Collaborative Extension Project (No. SDNYXTTG-2024-03 and SDNYXTTG2023-01).

REFERENCE

- [1] Aliakbar Solhjou, Jacky M.A. Desbiolles, John M.Fielke. (2013). Soil translocation by narrow openers with various blade face geometries[J]. *Biosystems Engineering*, Vol. 114, pp. 259-266. Netherlands.
- [2] Badua, S.A., Sharda, A., Strasser, R. Strasser,R., Ciampitti,I. (2021). Ground speed and planter downforce influence on corn seed spacing and depth. *Precision Agric*, Vol. 22, pp. 1154-1170. Netherlands.
- [3] Bao Yongjun, Yuan Zhiming, Yao Lei, Tao Zhenshui. (2023). Popularization and Application of Increasing Yield Technology of Maize Mechanized Cultivation [J] (玉米机械化增产栽培技术的推广应用). *Agricultural Technology & Equipment*, Vol. (01), pp. 45-47. Shanxi/China.
- [4] Cheng Yan. (2023). Research on the development status and optimal design of maize sowing machinery [J] (玉米播种机械发展现状与优化设计研究). *China Southern Agricultural Machinery*, Vol. 54(15), pp. 94-96. Jiangxi/China.

- [5] Du Zhaohui, He Xiantao, Yang Li, Zhang Dongxing, Cui Tao, Zhong Xiangjun. (2023). Research progress on precision variable-rate seeding technology and equipment for maize [J] (玉米精准变量播种技术与装备研究进展). *Transactions of the Chinese Society of Agricultural Engineering*, Vol. 39(9), pp.1-16. Beijing/China.
- [6] Fu Weiqiang. (2019). *Study on key technology of quality control for maize no-tillage precision seeding (玉米免耕精密播种质量控制关键技术研究)* [D]. China Agricultural University. Beijing/China.
- [7] Gao Jiansheng, Cui Huini, Tian Dianbin, Dong Guohao, Guo Jianjun, Guo Zhihun, Li Yongjun, Guo Lianghai. (2021). Effects of Sowing Machine on the Seedling Quality and Yield of Summer Maize [J] (播种机具对夏玉米播种质量及产量的影响). *Journal of Anhui Agricultural Sciences*, Vol. 49(04), pp. 207-208. Anhui/China.
- [8] GAN Y, STOBBE E H. (1995). Effect of variations in seed size and planting depth on emergence, infertile plants, and grain-yield of spring wheat[J]. *Canadian Journal of Plant Science*, Vol. 75(3), pp. 565-570.
- [9] Griepentrog H W. (1998). Seed Distribution Over the Area [J]. *Rivista Di Ingegneria Agraria*, pp. 1-4. Italy.
- [10] Han Dandan, He Bin, Yang Wenyu, et al. (2023). Design and experiment of an integrated air-suction soybean-corn strip intercropping planter [J](气吸式大豆-玉米带状间作播种机的设计与试验). *Journal of Gansu Agricultural University*, Vol.58(4), pp. 260-268. Gansu/China.
- [11] K. Shah, M. S. Alam, F. E. Nasir, M. U. et al. (2022). "Design and Performance Evaluation of a Novel Variable Rate Multi-Crop Seed Metering Unit for Precision Agriculture," in *IEEE Access*, Vol. 10, pp. 133152-133163. USA.
- [12] Li Yueming, Wang Cheng. (2019). Effects of Different Sowing Depth on Seed Vigor of Maize Varieties [J](不同播种深度对不同玉米品种种子活力的影响). *Seed*, Vol.38(02), pp. 30-36. Guizhou/China.
- [13] SANAVI S N, Raoufat M H. (2006). Comparative performance of four planter furrow opener and row cleaner arrangements in a conservation tillage corn production system[J]. *Iran Agricultural Research*, Vol. 24. Iran.
- [14] Singh R.C., Singh G, Saraswat D.C. (2005). Optimisation of Design and Operational Parameters of a Pneumatic Seed Metering Device for Planting Cottonseeds[J]. *Biosystems Engineering*, Vol. 92(4), pp. 429-438. Netherlands.
- [15] Suan Y, Cui T, Xia G, Gao X., Li Y., Qiao M., Xu Y. (2021). Effects of different moisture content and varieties on physico-mechanical properties of maize kernel and pedicel[J]. *Journal of Food Process Engineering*, Vol. 44(9), pp. 1-11. USA.
- [16] Vamerali T., Bertocco M., Sartori L. (2006). Effects of a new wide-sweep opener for no-till planter on seed zone properties and root establishment in maize (*Zea mays*, L.): A comparison with double-disk opener[J]. *Soil and Tillage Research*, Vol. 89, pp. 196-209. Netherlands.
- [17] Wang Keshan. (2023). Achievements and Experiences of China's Food Security in the New Era [J](新时代我国粮食安全保障的成就与经验). *Reform*, Vol. (09), pp. 99-109. ChongQing/China.
- [18] Yang Li, Yan Bingxin, Zhang Dongxin, Zhang Tianliang, Wang Yunxia, Cui Tao. (2016) Research Progress on Precision Planting Technology of Maize [J](玉米精密播种技术研究进展). *Transactions of the Chinese Society for Agricultural Machinery*, Vol. 47(11), pp. 38-48. Beijing/China.
- [19] Yazgi A, Degirimvencoglu A. (2007). Optimisation of the seed spacing uniformity performance of a vacuum-type precision seeder using response surface methodology[J]. *Biosystems Engineering*, Vol. 97(3), pp. 347-356. Netherlands.
- [20] Zhang Shaohua. (1981). Talking about the sowing trial work of the maize precision spot planter [J](谈谈玉米精量点播机的播量试验工作). *Modernizing Agriculture*, Vol. (02), pp. 6-9. Hei Longjiang/China.
- [21] Zhao H, Zhang D, Yang L, Cui T, Song W, He X, Wu H, Dong J. (2022). Optimal Design and Experiment of Critical Components of Hand-Pushing Corn Plot Precision Planter. *Agriculture*, Vol. 12(12), pp. 2103. Switzerland.
- [22] Zhong Yanming. (2024). Corn imports remain high [J](玉米进口持续保持高位). *China Customs*, Vol. (04), pp. 66-67. Beijing/China.

RESEARCH ON POWER PARAMETERS OF A SCREW CONVEYOR WITH BLADED OPERATING BODY FOR TRANSPORTING AGRICULTURAL MATERIALS

LAUKSAIMNIECĪBAS BERAMKRAVU MATERIĀLU TRANSPORTĒŠANAS GLIEMEŽTRANSPORTIERA JAUDAS PARAMETRU PĒTĪJUMI

Adolfs RUCINS¹⁾, Volodymyr BULGAKOV²⁾, Ivan HOLOVACH²⁾, Oleksandra TROKHANIAK²⁾, Mykola KLENDII³⁾, Lucretia POPA⁴⁾, Vadym YAREMENKO²⁾

¹⁾Latvia University of Life Sciences and Technologies, Latvia;

²⁾National University of Life and Environmental Sciences of Ukraine, Ukraine;

³⁾Separated Subdivision of National University of Life and Environmental Sciences of Ukraine, Berezhaný Agrotechnical Institute, Ukraine;

⁴⁾National Institute of Research–Development for Machines and Installations Designed for Agriculture and Food Industry–INMA, Bucharest / Romania

*Corresponding author's E-mail: adolfs.rucins@lbtu.lv; vbulgakov@meta.ua

DOI: <https://doi.org/10.35633/inmateh-74-38>

Keywords: conveying, grain material, screw conveyor, blade, rotation frequency, conveyor fill factor, torque

ABSTRACT

The article presents the results of theoretical and experimental laboratory investigations of an improved screw conveyor for bulk agricultural materials that has been created, which, instead of a solid spiral winding, fixed to the drive shaft, uses a spiral winding, formed by separate curvilinear planes (blades), which are also separately fixed to the shaft, yet as a whole form a single spiral. An analytical dependence was obtained for determination of the magnitude of the torque on the drive shaft of this transport working element. The numerical values, obtained as a result of the laboratory experiments, made it possible, when conducting a regression analysis, to derive a new analytical expression in the form of a regression equation. The analysis of the regression equation shows that these factors, which have a significant impact upon the increase in the torque, are the factors: x_1 (D) – the diameter of the fixed casing in which the screw is installed and x_2 (ψ) – the filling factor of the conveyor with the transported bulk material. Increasing the value of the factor x_3 (n), i.e., the rotation speed of the vane working body leads to a decrease in the torque value.

ANOTĀCIJA

Šajā rakstā ir sniegti teorētisko un eksperimentālo pētījumu rezultāti par pilnveidotu gliemežtransportieri lauksaimniecības materiālu beramkravu transportēšanai, kurā pie piedziņas vārpstas piestiprināta nepārtraukta spirāles tinuma vietā tiek izmantots spirāles tinums, ko veido atsevišķas izliektas plāksnes (lāpstiņas), kas arī ir piestiprinātas pie vārpstas, bet kopumā veido vienu spirāli. Veikti teorētiski un eksperimentāli pētījumi, lai noteiktu šī uzlabotā gliemežtransportiera jaudas parametrus, jo īpaši tā piedziņas vārpstas griezes momentu dažādu beramo lauksaimniecības materiālu transportēšanas laikā. Tika iegūta analītiska sakarība, lai noteiktu šīs piedziņas vārpstas griezes momenta vērtību. Eksperimentālo pārbaužu rezultātā iegūtās skaitliskās vērtības ļāva regresijas analīzes laikā iegūt jaunu analītisku izteiksmi regresijas vienādojuma formā. Šis vienādojums atspoguļo citu parametru, kas šajā gadījumā izmantoti kā kontrolējamie faktori, ietekmes pakāpi uz griezes momenta vērtību. Regresijas vienādojuma analīze liecina, ka faktori, kas būtiski ietekmē griezes momenta pieaugumu, ir: x_1 (D) - fiksētā korpusa, kurā uzstādīta spirāle, diametrs un x_2 (ψ) - transportiera piepildījuma koeficients ar transportēto beramo materiālu. Tika konstatēts, ka, palielinoties faktora x_3 (n) - spirāle, kurā spirālveida vijums veidots no izliektu plāksņu (lāpstiņu) komplektiem, kas piestiprināti pie piedziņas vārpstas, rotācijas kustības ātruma - vērtībai, turpretī griezes momenta vērtība samazinās.

INTRODUCTION

Screw conveyors in the agricultural industry are widely used in the transportation of bulk materials, in particular grain, seed materials, granulated fertilizers, feed, etc. However, existing screw conveyor designs do not fully meet all operational requirements.

Their main disadvantages are higher energy costs, damage to the bulk material and the complexity of manufacturing screw conveyor operating bodies, especially with their large overall dimensions.

From the analysis of studies of screw conveyors, it can be concluded that the vast majority of the authors paid attention to the conclusion of analytical relationships to determine the design and kinematic parameters of the screw operating bodies and, to a lesser extent, their energy-power parameters (*Klendij, 2016; Olt et al., 2022; Lyashuk et al., 2018*).

Known experimental studies are mainly aimed at determining the parameters of the operating bodies, which would ensure their high functional and operational performance with the minimum permissible mass of the operating body, thus reducing energy consumption for the transportation process (*Mondal, 2018; Hevko et al., 2016a; Hristov et al., 2016*).

In addition, the previously published works, devoted to the study of transportation of bulk agricultural materials deserve attention.

Thus, in the work by *Fan et al., (2023)* the mechanism of transportation of mixed corn stalks in a screw conveyor was investigated and the parameters, influencing the transportation performance of the screw conveyor were determined. Besides, using the discrete element method, the author had created a simulation model of the process of transporting the corn stalks by a screw conveyor. Multifactorial modeling was also performed.

Zhang et al., (2020), have shown an analysis of the bulk material conveying process by a horizontal screw feeder using the EDEM software. The work determines the influence of the feed upon the productivity, filling rate and the conveying speed of the feeder.

Zhou et al., (2019), presented a simulation test analysis of three factors (the screw inclination angle, the screw pitch, the screw rotation speed) that affect the ability of the screw to convey the grain materials. The author obtained the significance ratio of the transportation parameters and the best combination of the three specified design and kinematic factors.

There are also investigations of the screw conveyors to determine their productivity depending on the angle of inclination of the conveying line, the rotation speed of the screw itself, its length when transporting conventional granular materials, such as rice, corn, sorghum and gari, with a moisture content of 13% (*Li et al., 2022; Pezo et al., 2015*).

The previously published works point to significant intentions of the foreign authors to optimize the transport capabilities of the screw conveyors, used specifically for transportation of bulk agricultural materials by changing various parameters of these working bodies.

Known experimental studies are mainly aimed at determining the parameters of the operating bodies, which would ensure their high functional and operational performance with the minimum permissible mass of the working body, thus reducing energy consumption for the transportation process. In some publications, as an alternative to the helical body of conventional design, a bladed body in the form of flat blades forming a helical surface is considered (*Hevko et al., 2016b; Bulgakov et al., 2022a; Hevko et al., 2021*).

The purpose of this study is to determine the torque on the drive shaft of a screw conveyor with a bladed operating body when transporting bulk materials agro-industrial production to eliminate the occurrence of drive breakage during operation.

MATERIALS AND METHODS

The screw working element that was improved is a conventional screw conveyor which, instead of a solid spiral winding, welded to the drive shaft, uses a similar winding, which is formed by separate curvilinear planes (blades), that are also separately fixed to the shaft, yet, as a whole, this makes up a single spiral. As it is known, the use of a solid spiral winding, fixed on the drive shaft, has a number of essential disadvantages. Thus, it significantly complicates the technology of obtaining (rolling from sheet steel) the spiral itself. Further, there are significant costs for its fixation (welding) on the drive shaft. As it turned out, the working element of the screw conveyor of an improved design, proposed by us, is mounted from separate stamped curvilinear blades. In this case the spiral winding retains all its properties, its manufacture is possible for any length of the screw conveyor, the reparability of the structure will be significantly increased since the replacement of a damaged or deformed blade will be much easier than repairing a solid spiral. It is much easier to weld these small blades onto the drive shaft. Thus, in this case the production of an improved design is significantly simplified and the material consumption of these transport working bodies is reduced.

Figure 1 shows the bladed operating body, which is used for conveying bulk materials.



Fig. 1 – General view of the bladed operating body

This operating body is made in the form of a drive shaft, on the surface of which inclined flat blades, bounded by semi-ellipses, alternate with each other, and their angles of inclination also alternate in sign, which allowed to reduce the material intensity and simplify the design of these screw conveyors. It is expedient to manufacture such blades by a simpler method, by stamping sheet material with subsequent welding of the blades to a cylindrical shaft.

To carry out experimental studies, an experimental setup for the study of the conveyor with a bladed operating body, the general view of which is shown in Fig. 2., was built.



Fig. 2 – General view of a conveyor in which a bladed operating body is used to transport loose materials:
1 – frame; 2 – fixed cylindrical cover; 3 – shaft of the bladed operating body; 4 – electric motor; 5 – hopper

The experimental study to determine the value of torque transmitted by the shaft of the bladed operating body of the screw conveyor was as follows. First, the software in the personal computer was started to control the process and signal to the appropriate speed of the electric motor 4. Frequency converter (Altivar 71) with Power Suite v.2.5.0 software was used for starting the electric motor and regulating the speed of rotation, thus allowing to perform smooth starting and regulation of the necessary speed of the electric motor 4. The electronic system the Altivar 71 was used as a modern system that, due to the ability to be connected to a computer network has a virtual oscilloscope that allows you to track the change in the parameters you are looking for over time with specific numerical values.

At setting the required rotation speed with the help of computer via Altivar 71 system, the command to electric motor 4 was transmitted and it started rotating the shaft of the bladed operating body 3, with the set parameters. Bulk material from the hopper 5 was fed through the open slide gate to the experimental setup under the stationary cylindrical cover 2. Further the loose material was transported, and the data on the magnitude of the load transmitted to the bladed operating body was recorded on a personal computer.

For theoretical determination of the energy-power parameters of the screw conveyor, in particular, to determine the torque on the shaft with a bladed operating body, the known dependencies are used. First of all, let's consider the analytical dependence for determining the conveying power of the screw conveyor, which will be equal to (Gevko and Rogatynsky, 1989):

$$N = \rho \cdot g \cdot Q \cdot W \cdot L \quad (1)$$

where:

ρ – bulk density of the transported material; g – acceleration of gravity; Q – volume flow; W – coefficient of specific friction losses along the length of transportation; L – conveying length.

Since the mass flow rate of the load given by the operating body can be determined as $Q_m = \rho \cdot g \cdot Q$ then the load portion Δm , coming down from one blade per its revolution is determined according to the following dependence:

$$\Delta m = 2\pi \cdot \rho \cdot g \cdot Q \cdot \omega^{-1} \quad (2)$$

Power parameters of the new screw conveyor, in particular the torque T , on its shaft can be determined through the impact force acting on the working surfaces of its blades. Thus, such an impact force F , applied to the second blade can be determined through the impact momentum of the angular momentum theorem (Gevko and Rogatynsky, 1989):

$$\bar{F} = \Delta m \cdot (\bar{V}_+ - \bar{V}_-) \cdot (\Delta t)^{-1} \quad (3)$$

where:

\bar{V}_- and \bar{V}_+ – averaged velocity vectors of the array before and after contact with the operational surface;
 Δt – material contact time with the operational surface.

From the analysis (3) it follows that it is the value of the force F , and therefore, the energy loss for contact and friction of the load will be minimal at $\bar{V}_+ - \bar{V}_- \rightarrow \min$. In addition, the minimum energy loss on the acceleration of the material by the operating body, is determined by the dependence:

$$W_k = \Delta m \cdot (V_+^2 - V_-^2) \cdot 2^{-1} \quad (4)$$

In this case, the power spent on overloading the cargo can be determined by a relationship similar to (1):

$$N = \rho \cdot g \cdot Q \cdot W_f \cdot L \quad (5)$$

where:

L – the length of the overload zone given; W_f – overload loss coefficient, exceeding the specific loss coefficient of the conveyor W .

Depending on the design $W_f = (1.2 \dots 1.5)$.

The value of torque on the drive shaft of the conveyor with a bladed operating body can be determined by the following dependence:

$$T = N \cdot \omega^{-1} = 9554 \cdot \rho \cdot g \cdot Q \cdot W_f \cdot L \cdot n^{-1} \quad (6)$$

where: n and ω – rotational speed and angular velocity of the screw conveyor drive shaft.

To determine the effect of transportation parameters of bulk material and design parameters of the conveyor on the value of the torque T , a full-factor experiment was conducted $FFE - 3^3$, i.e. determination of the torque dependence on the change of three main factors: the inner diameter of the fixed casing D , conveyor fill factor ψ and the rotation speed of the operating body n .

Since during the experiments the variable independent factors are heterogeneous and have different units, and the numbers expressing the value of these factors are of different orders, they were reduced to a single system of calculations by switching from actual values to coded values presented in Table 1.

Table 1

Setting the coefficients that determine the efficiency of the improved screw conveyor in the form of codes in a multifactorial experiment, as well as the levels of their variation when determining the torque on the drive shaft

Factors	Identification		Variation interval	Levels of variation, natural/coded		
	Coded	Natural				
Inner diameter of the fixed conveyor hood D , m	X_1	X_1	0.02	0.06/-1	0.08/0	0.1/+1
Conveyor fill factor, ψ	X_2	X_2	0.2	0.3/-1	0.5/0	0.7/+1
Rotation frequency of the bladed body, n , rpm	X_3	X_3	200	200/-1	400/0	600/+1

The experimental investigations, conducted in the laboratory conditions, made it possible to determine the specific values of torque T from the main design and kinematic parameters that characterize the process of screw transportation of the bulk materials.

These parameters are:

- internal diameter of the fixed housing D , coded by the index x_1 ;
- filling factor of the screw conveyor ψ , coded by the index x_2 ;
- the speed of rotation of the screw conveyor, designated as its rotation frequency, n and can be designated by code x_3 .

Experimental studies to determine the value of torque T of a conveyor with a bladed operating body were carried out during the transportation of wheat with a bulk weight of $760 \text{ kg}\cdot\text{m}^{-3}$ and humidity W , 12 to 15%, which made it possible to construct analytical regression equations.

The obtained results of the laboratory experimental study were processed by means of modern statistical methods, using a PC. Besides, mainly the regression and correlation analysis methods were used. The purpose of such processing of the results was to obtain regression equations reflecting the dependencies between all the parameters studied.

For these purposes a plan was drawn up of a full-factorial experiment, allowing for the regression model to be created and the optimization parameter to be selected. The plan was carried out in the following sequence.

The response functions (the optimization parameter), i.e. the torque $T=f(D, \psi, n)$, which was determined as a result of the experiment, can be represented as a complete square polynomial, for there is every reason to consider a mathematical model of the process under study. It should be pointed out that its structure may be similar to the structures of other three-factor experiments:

$$T = b_0 + b_1x_1 + b_2x_2 + b_3x_3 + b_{12}x_1x_2 + b_{13}x_1x_3 + b_{23}x_2x_3 + b_{11}x_1^2 + b_{22}x_2^2 + b_{33}x_3^2 \quad (7)$$

where: $b_0, b_1, b_2, b_3, b_{12}, b_{13}, b_{23}, b_{11}, b_{22}, b_{33}$ – coefficients of corresponding values x_i ; $x_1; x_2; x_3$ – relevant coding factors.

The regression equation for determining the value of the maximum torque during transportation of wheat on the experimental unit is as follows:

$$T = 2.35 + 129.5 \cdot D + 21.7 \cdot \psi + 0.00924 \cdot n - 0.0675 \cdot D \cdot n - 0.000008 \cdot n^2 - 12 \cdot \psi^2. \quad (8)$$

The resulting regression equation (8) can be used to determine the value of torque T during transportation by a conveyor with a bladed operating body, depending on the diameter of the fixed housing D , coefficient ψ of conveyor filling and frequency n of the rotation of the bladed implement during the transport of wheat within the following limits of input factors: $0.06 \leq D \leq 0.1$ (m); $0.3 \leq \psi \leq 0.7$; $200 \leq n \leq 600$ (rpm).

RESULTS

To determine the torque value theoretically T of the conveyor take the following initial data: the conveyor filling factor ψ - 0.5, bulk weight of wheat ρ - $760 \text{ kg}\cdot\text{m}^{-3}$, bulk weight of peas ρ - $700 \text{ kg}\cdot\text{m}^{-3}$, bulk weight of corn ρ - $800 \text{ kg}\cdot\text{m}^{-3}$, bulk weight of fodder ρ - $250 \text{ kg}\cdot\text{m}^{-3}$, outer radius of the bladed operating body R - 0.05 m, radius of the shaft on which the blades are fixed r - 0.023 m, rotational speed of the bladed operating body, n - 200-600 rpm, the length of the overload zone is given L - 1.4 m, overload loss factor W_f - 1.44.

Results of analytical torque determination T on the drive shaft of a screw conveyor with a bladed operating body are shown in Fig. 3.

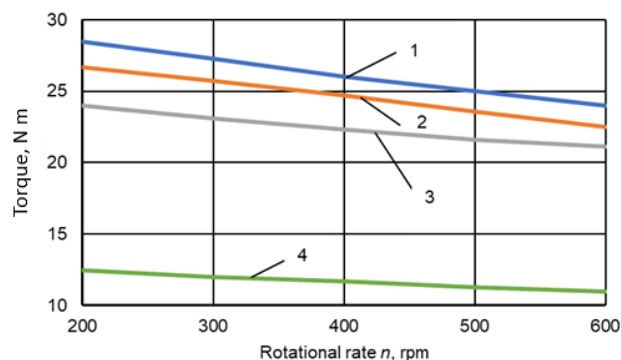


Fig. 3 – Torque dependencies T on the drive shaft of a screw conveyor with a bladed operating body from its speed n for the conveyor fill factor $\psi = 0.5$ during transportation:

1 – corn; 2 – peas; 3 – wheat; 4 – fodder

The analysis of the graphical dependencies shown in Fig. 3 shows that the torque T on the drive shaft of a screw conveyor with a bladed operating body, when transporting grain material with a conveyor filling factor $\psi = 0.5$, at a speed limit n of the impeller, varying between 200-600 rpm tends to decrease. And this reduction occurs linearly. At the same time, the torque T during transportation of corn varies within 28.73 to 23.92 N·m. In the investigated range of torque values received, the specified reduction is 16.8%. When transporting peas, the torque T decreases within 26.84 to 22.63 N·m, which corresponds to a reduction equal to 15.7%. When transporting wheat, the torque T varies between 24.32 to 20.54 N·m. This torque reduction is 15.5%. And when transporting mixed fodder, the torque T varies within the range of 12.42 to 10.87 N·m. Thus, in this case its reduction is 12.5%.

According to the results of laboratory experimental studies to determine the torque T on the drive shaft of a screw conveyor with a bladed operating body using the application program "STATISTICA 10" graphically reproduced the intermediate general regression models in the form of quadratic responses and their two-dimensional sections of the torque value as a function of two variable factors $x_{i(1,2)}$ a constant level of the corresponding third factor $x_{i(3)} = \text{const}$ (Fig. 4).

Analysis of the above regression equation shows that the main factors influencing the increase in the value of torque T are: the diameter of the fixed housing $x_1(D)$ the conveyor fill factor $x_2(\psi)$, the factor value increase $x_3(n)$. The rotation speed of the bladed operating body leads to a decrease in torque.

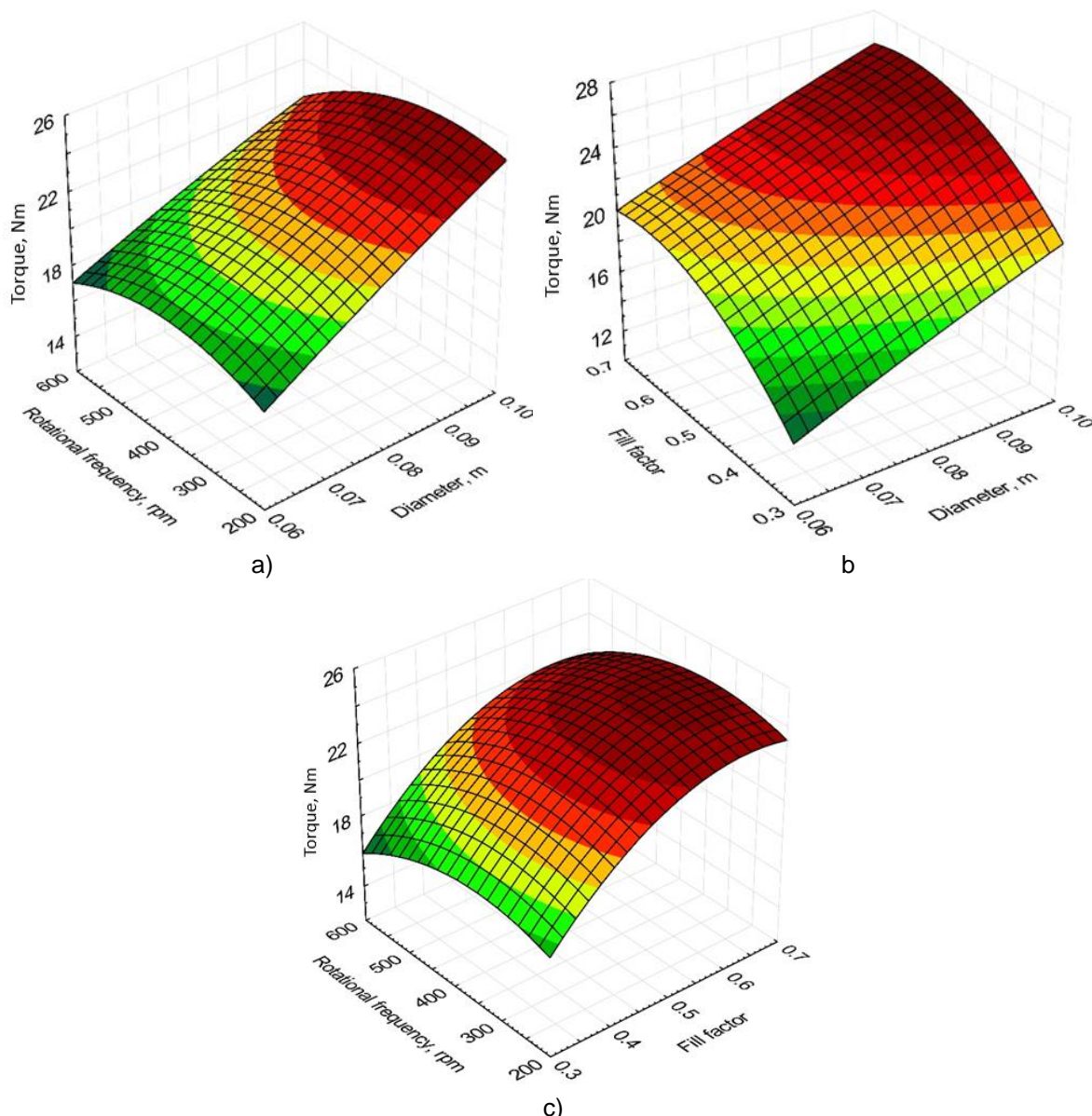


Fig. 4 – Response surfaces of the torque value T on the drive shaft of a screw conveyor with a bladed operating body during the transportation of wheat

If the diameter D varies within the range 0.06-0.1 m, the torque T increases by 17.9%, if the conveyor fill factor ψ increases from 0.3 to 0.7 m, the torque T increases by 17.4%, and when changing the rotational speed n of the bladed operating body within the range of 200-600 rpm, the torque T decreases by 4.9%.

A comparison of the results of theoretical and experimental studies has shown that with $n = 400$ rpm, $\psi = 0.5$ and different values of D in the range of 0.06-0.1 m the discrepancy of the obtained values of the torque T is 4.8...15.7%.

As shown by the studies done by *Lyashuk et al., 2018; Pylypaka, et al., 2019; Bulgakov, et al., 2022b; Pastushenko et al., 2021; Bulgakov, et al., 2024*, the values of the torque T of the conveyor with a bladed operating body are almost equal to the values of the torque of the conveyor with a screw operating body when transporting similar bulk solids (error not more than 5%).

Thus, the improved screw working element is a perspective transporting working element, used in agriculture, precisely due to the simplicity of its manufacture. In addition, it has been established that the use of curved blades, attached to the drive shaft instead of a solid spiral, does not lead to a reduction in the transportation capabilities of this working element.

In figure 4 are shown the response surfaces of the magnitude of torque T on the drive shaft of a screw conveyor, using flat curved blades instead of a solid spiral winding during the transportation of wheat depending on: a) $T = f(D; n)$; b) $T = f(D; \psi)$; c) $T = f(\psi; n)$.

Thus, the results of the conducted laboratory experimental studies give every reason to believe that the improved screw conveying working element has undoubted advantages in terms of the power parameters, in comparison with similar working elements. However, if it is taken into account that the production of an improved working element, formed by flat curved blades, obtained by stamping, will be significantly cheaper than the production of similar elements with continuous spiral winding, then its use will be more than efficient.

CONCLUSIONS

Based on the analysis of literary sources and patent search of preliminary exploratory studies, an improved design of a screw working element was developed and manufactured, in which, instead of a solid spiral winding, flat curved blades of small sizes are welded to the drive shaft, which, as a whole, make up a spiral winding. To study the power parameters of the improved screw working element, an experimental setup was created, which made it possible to determine the torque on the drive shaft during the transportation of the bulk agricultural materials.

The analytical dependence for determining the value of the torque on the drive shaft of the conveyor with a bladed operating body was obtained. The analysis of the obtained dependence shows that the torque on the drive shaft of the conveyor with a bladed operating body when transporting grain material tends to decrease with increasing speed. Thus, for the conveyor fill factor $\psi = 0.5$, within the rotational speed n of the bladed operating body, varying between 200-600 rpm tends to decrease. And this reduction occurs linearly. At the same time, the torque T during transportation of corn varies within 28.73-23.92 N·m. In the investigated range of torque values received, the specified reduction is 16.8%. When transporting peas, the torque T decreases within 26.84 to 22.63 N·m, which corresponds to a reduction equal to 15.7%. When transporting wheat, the torque T varies between 24.32 to 20.54 N·m. This reduction equals 15.5%. And when transporting mixed fodder, the torque T varies within the range of 12.42 to 10.87 N·m in such a way that its decrease is 12.5%.

According to the results of experimental studies, the corresponding regression equation for the response surface to establish the effect on the value of torque of controllable factors was built. Analysis of the above regression equation shows that the main factors influencing the increase in torque value T are the following factors: the diameter of the fixed housing $x_1(D)$ and the conveyor fill factor $x_2(\psi)$. However, an increase in the value of the factor $x_3(n)$, i.e., the rotation speed of the vane working body leads to a decrease in the torque value.

When changing the diameter D of the cylindrical shell within 0.06 to 0.1 m the torque T increases by 17.9%, the change in the ψ -loading ratio of the conveyor from 0.3 to 0.7 m the change of torque T increases by 17.4%, a when changing the rotational speed n of the bladed operating body within the range of 200-600 rpm, the torque decreases only by 4.9%.

REFERENCES

- [1] Bulgakov, V., Trokhaniak, O., Klendii, M., Ivanovs, S., & Dukulis, I. (2022a). Reserch on the impact of the operating modes and main design parameters on the efficieny of the machine for preparing and packing slaked lime. *INMATEH – Agricultural Engineering*, 67(2), 323-330. DOI: 10.35633/inmateh-67-33
- [2] Bulgakov, V., Trokhaniak, O., Holovach, I., Adamchuk, V. Klendii, M., Ivanovs, S. (2022b). Investigation of the performance of a screw conveyor with a working body, made in the form a shaft with inclined flat blades. *INMATEH – Agricultural Engineering*, 67(2), 406-411. DOI: 10.35633/inmateh-67-41.
- [3] Bulgakov, V., Rucins, A., Holovach, I., Trokhaniak, O., Polishchuk, D. (2024). Design development and results of experimental research on grain damage by a new screw conveyor. *INMATEH – Agricultural Engineering*, vol. 73(2). doi : <https://doi.org/10.35633/inmateh-73-32>
- [4] Fan, Z.P., Ma, Z., Wang, H.B., Yu, Z.H. (2023). Optimization of Screw Conveying of Kneaded Corn Stalks Based on Discrete Element Method. *INMATEH – Agricultural Engineering*, 69(1), 626-634. DOI: 10.35633/inmateh-69-60
- [5] Gevko, B.M., Rogatynsky, R.M. (1989). *Screw feeders of agricultural machines*. Lviv. Graduate School, 176. (in Ukrainian).
- [6] Hevko, R.B.; Lyashuk, O.L.; Dzyura, V.O.; Dovbush, T.A.; Trokhaniak, O.M.; Liashko, A.P. (2021). Experimental studies of the process of loose material transportation by a pneumatic-screw conveyor. *INMATEH – Agricultural Engineering*, vol. 63(1), 63-49.
- [7] Hevko, R.B., Rozum, R.I., Klendiy, O.M. (2016a). Development of design and investigation of operation processes of loading pipes of screw conveyors, *INMATEH – Agricultural engineering*, vol. 50(3), pp. 89-96.
- [8] Hevko, R.B., Klendiy, M.B., Klendii, O.M., 2016b: Investigation of a transfer branch of a flexible screw conveyer, *INMATEH – Agricultural Engineering*, vol. 48(1), pp. 29-34.
- [9] Hristov, G., Zahariev, P., Beloev, I. (2016). A review of the characteristics of modern unmanned aerial vehicles. *Acta Technologica Agriculturae*, 19(2), 33-38.
- [10] Hevko, R.B.; Lyashuk, O.L.; Dzyura, V.O.; Dovbush, T.A.; Trokhaniak, O.M.; Liashko, A.P. (2021). Experimental studies of the process of loose material transportation by a pneumatic-screw conveyor. *INMATEH – Agricultural Engineering*, vol. 63(1), 63-49.
- [11] Klendii, M.B., Klendii, O.M. (2016). Interrelation between incidence angle and roll angle of concave disks of soil tillage implements. *INMATEH – Agricultural Engineering*, 49 (2), 13-20.
- [12] Li, A., Jia, F., Han, Ya., Chen, P., Zhang, J., Wang, Y., Fei, J., Shen, Sh., Hao, X., Feng, W. (2022). Effect of the rotational speeds of the screw conveyor and milling roller on the behaviour of grain flows in the connected chamber of a vertical “conveying-milling” rice mill. *Biosystems Engineering*, 224, 161-182
- [13] Lyashuk, O.L., Sokil, M.B., Klendiy, V.M., Skyba, O.P., Tretiakov, O.L., Slobodian, L.M., Slobodian, N.O. (2018). Mathematical model of bending vibrations of a horizontal feeder-mixer along the flow of grain mixture. *INMATEH – Agricultural Engineering*, 55(2), 35-44.
- [14] Mondal, D. (2018). Study on filling factor of short length screw conveyor with flood-feeding condition. *Mater. Today Proc.*, 5, 1286-1291.
- [15] Olt, J., Bulgakov, V., Trokhaniak, O., Klendii, M., Gadzalo, I. A., Ptashnik, M., Tkachenko, M. (2022). Harrow with screw-type operating tools: Optimisation of design and process parameters. *Agronomy Research*, 20(4), 751-763.
- [16] Pastushenko, S.I., Klendiy, N.B., Trokhanyak, A.N. (2021). Investigation of the torque of a screw conveyor with a bladed working body. *Scientific Bulletin of the Taurida State Agrotechnological University*, 2(11), 1-11.
- [17] Pezo, L., Jovanović, A., Pezo, M., Čolović, R., Lončar, B. (2015). Modified screw conveyor-mixers – Discrete element modeling approach. *Advanced Powder Technology*, 26(5), 1391-1399.
- [18] Pylypaka, S., Klendii, M., Trokhaniak, V., 2019: Particle motion over a plane, which rotates about a horizontal axis and makes a certain angle with it. *Bulletin of the Karaganda University. «Mathematics» series*, 1(93), 129-140.
- [19] Zhang Y. W., Wang W., Liu H. Y., Zhang W. G., Lu J. C. (2020). Simulation analysis of multi-point feed horizontal screw feeder based on EDEM, *Port Loading and Unloading*, 6, 10-13.
- [20] Zhao F. C., Wang C. G., Wulan T. Y. (2019). Research on parameter optimization of spiral conveying device. *China Agricultural Science and Technology Review*, 21(6), 70-78.

SWEET POTATO VINE CUTTING MACHINE: KEY COMPONENTS DESIGN AND EXPERIMENTAL RESEARCH

甘薯切蔓机关键部件设计及试验研究

Biao MA¹⁾, Tianchan LI²⁾, Weiqiang LIN¹⁾, Yongsheng CHEN³⁾, Run ZHAO^{*1)}, Yanyan SHI^{*1)}

¹⁾Nanjing Institute of Agricultural Mechanization, Ministry of Agriculture and Rural Affairs, Jiangsu/China;

²⁾ Jiangsu Academy of Agricultural Sciences, Jiangsu /China; ³⁾ Institute of Western Agriculture, CAAS, Xinjiang/China

Tel:+8615366092802,E-mail: 949704383@qq.com ; Tel:+8615366092810,E-mail: nriamyan@163.com

Correspondent authors: Run Zhao, Yanyan Shi

DOI: <https://doi.org/10.35633/inmateh-74-39>

Keywords: Sweet potato, Vine, Straw crushing, Flail knife

ABSTRACT

In response to technical challenges such as the difficulty in cutting long sweet potato vines in ridge furrows, low stem crushing rate, long stubble residues, and sweet high potato damage rate with the direct shredding and returning machine for sweet potato vines, this study conducted research on ridge furrow long vine removal and crushing technology, as well as optimization experiments on operating parameters. A ridge furrow boot-type vine picking knife structure, a "dynamic embedding static" shaft end anti-entanglement mechanism, and a ridge-like crushing chamber structure were designed. A high-efficiency sweet potato vine shredding and returning machine was developed, with ridge surface vine length qualification rate and ridge top stubble height as the main control indicators. The study conducted a 3-factor, 3-level orthogonal experiment in typical regions to analyze the factors of machine forward speed, knife roller speed, and ground clearance height, which significantly influence the performance. The results indicate that the optimal working parameters for the sweet potato vine cutting machine are a knife roller speed of 2000 r/min, a forward speed of 0.6 m s⁻¹, and a ground clearance height of 10 mm. The vine crushing length qualification rate reached 94%, and the stubble height of 5.3 cm exceeded the various indicators, meeting the agricultural requirements for sweet potato harvesting.

摘要

针对甘薯秧蔓直接粉碎还田机械垄沟秧难切断、茎秆粉碎率低、留茬长、伤薯率高等技术难题，本文开展了垄沟长蔓清除粉碎技术研究、作业参数最优化试验研究，设计了垄沟靴型挑秧刀结构，“动嵌静”轴端防缠绕机构和仿垄形粉碎仓机构，研制了一款高清除性甘薯秧蔓粉碎还田机，以垄面薯蔓长度合格率和垄顶留茬高度为主控指标，将机具前进速度、刀辊转速和离地高度这三个显著影响指标的因素在典型地区进行3因素3水平正交试验。结果表明甘薯切蔓机的最优工作参数：刀辊转速为2000r/min，前进速度为0.6m s⁻¹，离地高度为10mm。薯蔓粉碎长度合格率94%，留茬高度5.3cm高于各项指标，满足了甘薯收获农艺要求。

INTRODUCTION

Sweet potatoes have been cultivated in China for over 400 years. In 2022, China's total sweet potato planting area was 2.25 million hectares, accounting for 30% of the world's planting area, with a total production of 49.196 million tons, representing 55% of the world's production (Mu et al., 2019).

The crushing of sweet potato vines is a crucial step in sweet potato harvesting, directly affecting the efficiency and effectiveness of the harvest. Developed countries have conducted early and relatively mature research on vine shredders (Amer et al., 2014). Countries like the UK and the US mainly use large-scale equipment, including large multi-row vine shredding and returning machines, as well as large combined harvesters that can complete digging, conveying, forced separation of vines, cleaning, sweet potato collection, and vine throwing operations in one go. These machines require significant power, close coordination between agricultural machinery and practices, and are designed for shorter varieties of sweet potato vines. For example, the TSP1900 large tractor-mounted sweet potato harvester produced by the Stanton company in the UK is currently not applicable in China due to its vine removal and harvesting mode. Countries like Japan and South Korea, where the field sizes are relatively small, mostly adopt the direct vine shredding and returning mode before sweet potato harvesting, using small single-row machines. The technology of small-scale vine shredding has certain reference value for China.

In recent years, with the emergence of large-scale sweet potato plantations and severe shortage of rural labor, the market demand for sweet potato machinery has been increasing. The development of sweet potato cutting and vine removal devices in China has entered a new stage, with the successive development of some sweet potato vine cutting machines (Mu *et al.*, 2018). Currently, most domestically developed sweet potato vine cutting machines are improved and designed based on rice, wheat, corn, and potato shredding and returning machines. Sweet potato vines mostly grow horizontally, and aside from vine removal, it is essential to prevent long vines from entangling or blocking during subsequent digging and harvesting. The different physical and growth characteristics, as well as agricultural practices of sweet potatoes, lead to poor adaptability of other machinery used for vine cutting. Therefore, existing sweet potato vine cutting machines still have significant limitations, including high resistance, high energy consumption, low crushing qualification rates, long stubble residue lengths, low ridge furrow vine removal rates, and high sweet potato damage rates (Ma *et al.*, 2014; Zheng *et al.*, 2019). After operations, manual or mechanical secondary cleaning in the ridges is often required, restricting their widespread promotion and application. Aiming at the above problems, this paper, through structural design and experimental research, overcame the difficulty in cutting long sweet potato vines in ridge furrows, low stem crushing rate, long stubble residues, and sweet high potato damage rate with the direct shredding and returning machine for sweet potato vines, and developed an efficient and high-clearance vine crushing and returning machine to provide a good working environment for sweet potato harvesting.

MATERIALS AND METHODS

Sweet Potato Vine Cutting Machine Structure and Working Principle

The sweet potato vine cutting machine is mainly composed of the hood assembly, camshaft roller assembly, suspension mechanism, gearbox assembly, transmission mechanism, tensioning components, and ridge-like depth wheel components. Its basic structure is shown in Figure 1. The power transmission path during operation is as follows: the power output shaft at the rear of the tractor transmits power to the gearbox assembly through the universal joint drive shaft (Ma *et al.*, 2015; Lv *et al.*, 2016; Zhou *et al.*, 2022). The gearbox assembly increases the speed and changes direction, then transfers the power to the camshaft roller assembly through pulleys and V-belts.

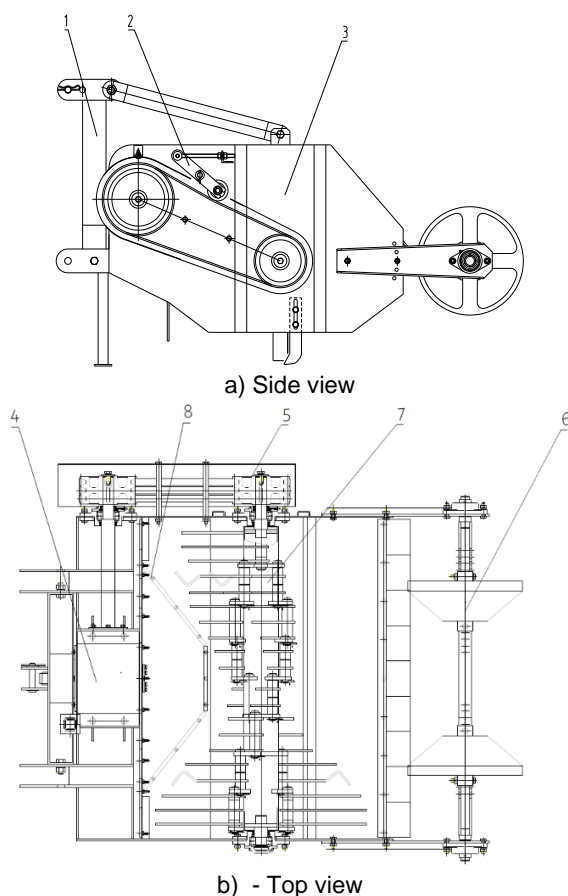


Fig. 1 - The structure diagram of sweet potato vine-cutting machine

1. Traction frame; 2. Tensioning gear; 3. Casing assembly; 4. Gearbox assembly; 5. Transmission mechanism; 6. Ridge-like deep limit wheel assembly; 7. Profile cutter roll assembly; 8. Ridge-like hood

Sweet Potato Vine Cutting Machine Working Principle

During operation, the vine cutting machine is suspended behind the tractor through the suspension mechanism. It connects the power output shaft at the rear of the tractor and the input shaft of the cutting machine gearbox through universal joints. After opening, the power output controls the speed at the rated speed. Then, the ridge-like depth wheel is mounted on the ridge, and the tractor moves forward at a constant speed (Mu et al., 2021). The knife roller is driven to rotate at high speed through the transmission system to cut and directly crush the vine. The high-speed rotation of the knife roller creates negative pressure in the semi-enclosed crushing chamber. The vine is sucked into the crushing chamber under the negative pressure at the feed inlet, and after multiple impacts, cutting, tearing, and kneading actions, it forms crushed segments that are scattered and returned to the field. When completing a turn at the end of each ridge operation, the power output is closed, the rear suspension is lifted, and then the machine is turned around.

Key Component Parameter Determination

Length of the Vine-cutting knife

If the clearance between the vine-cutting knife and the ground is too large, it may miss cutting the vines that grow close to the ground. If the vine-cutting knife enters the soil, it will impact the tool, knife holder, and knife roller, causing strong vibration of the machine, which will greatly affect the service life, stability, and reliability of the machine. Additionally, it may cause damage to the sweet potatoes, so it should be avoided as much as possible to prevent the vine-cutting knife from entering the soil. The determination of the vine-cutting knife length should vary according to the changes in the ridge shape, gradually increasing from the ridge top to the ridge furrow, with the vine-cutting knife tip about 4 cm away from the ridge surface. Furthermore, to ensure the proper coordination of the vine-cutting knife with the ridge-like hood for vine cutting, the distance between the vine-cutting knife and the upper hood should be controlled at 23 mm.

The number of blades is 40 pieces, using double helix staggered symmetrical arrangement, each pair of blades in the rotation process of the centrifugal force generated in the same plane, opposite direction, the same size, good balance, small vibration.

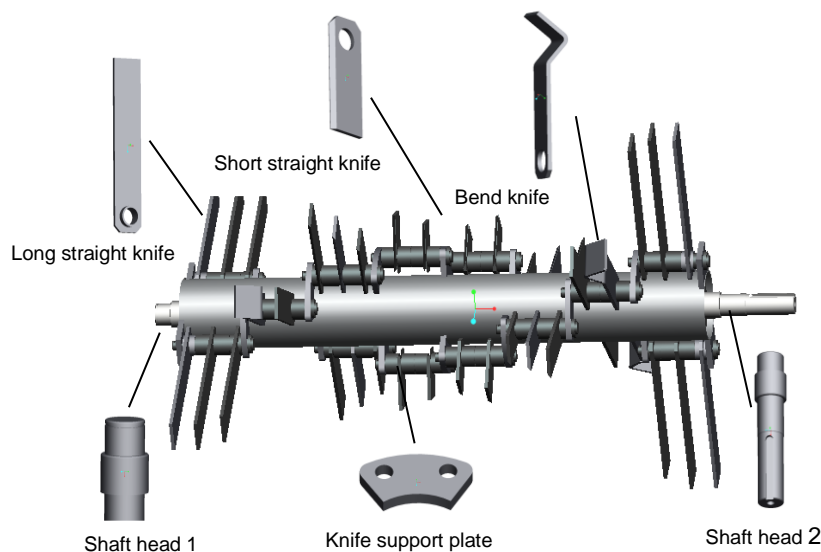


Fig. 2 - The structure diagram of cutter roller combination mechanism

Design of boot-shaped knife for raising vine

In order to solve the phenomenon of insufficient cleaning of ridge and vine, a pair of picking knife is added to the bottom of both sides of the vine cutting machine. By using the combination of boot-type ridge lifting knife with self-sliding angle and the long cutter outside the cutter roll, the broken vine will automatically slide down along the boot angle to realize automatic cleaning, and effectively solve the entanglement and blocking problem of ridge and long vine on subsequent harvesting machinery, improving the operation smoothness. The inclination Angle β of the blade tip of the seedling picking knife should be satisfied, and the friction angle of the soil on the blade is $23^\circ - 26^\circ$, so 60° is taken here. In order to facilitate the upward slippage of the vine being picked, the knife tip is designed at a 55° angle. The 65Mn material is used, the blade is double-sided, and the tip needs heat treatment.

Determination of Knife Roller Speed

If the knife roller speed is too low, the vine may not be crushed sufficiently. On the other hand, if the speed is too high, it will increase power consumption and exacerbate the wear and tear of the machine. Therefore, the speed should be determined within a reasonable range, ideally lower to ensure the vines are fully crushed. During machine operation, the absolute speed of the vine-cutting knife is the composite of the forward speed of the whole machine and the rotation speed of the knife roller. To avoid vine pushing during operation, the vine-cutting knife's motion trajectory needs to be a cycloidal curve, as shown in Figure 3.

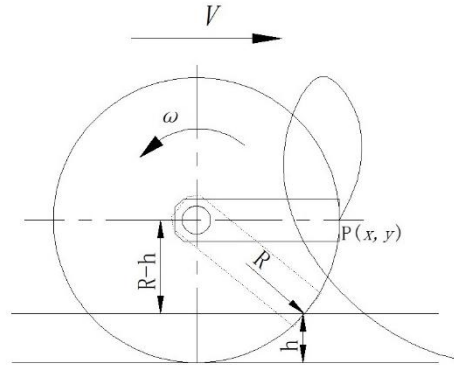


Fig. 3 - The trajectory of the vine-cutting knife

Let $P(x, y)$ be a point on the tip of the vine-cutting knife for vine cutting, assuming the coordinates of the origin are at position $O(0,0)$ at the initial time of 0.

It can be seen that:

$$\begin{cases} x = Vt - R \cos \omega t \\ y = R \sin \omega t \end{cases} \quad (1)$$

where: V is the forward speed of the vine cutting machine, (m s⁻¹);

t is the duration of the knife roller movement, (s);

R is the maximum radius of rotation for the vine-cutting knife in vine cutting, (m);

ω is the angular speed of the knife roller for vine cutting, (rad/s);

h is the distance from the ground on the tip of the knife, (m);

Differentiating equation (1) with respect to t as the independent variable:

$$\begin{cases} V_x = V + R \sin \omega t \\ V_y = R \cos \omega t \end{cases} \quad (2)$$

In equation (1):

V_x is the horizontal component velocity (m s⁻¹)

V_y is the vertical component velocity (m s⁻¹)

In a stable operating state of the sweet potato vine cutting machine, with $V_p=0.48\text{m s}^{-1}$, effective cutting height $h=0.15\text{m}$, maximum vine-cutting knife rotation radius $R=0.326\text{m}$, and based on "Agricultural machinery design manual", $V_c=30\text{m s}^{-1}$. As shown in Figure 3, in order to ensure that the sweet potato vines are fully crushed, the absolute value of the horizontal component velocity of the vine-cutting knife must not be lower than the linear speed V_c required for vine cutting. From the given condition, $\sin\omega t=(R-h)/R$, combining the above formulas, the speed of the knife roller can be determined.

$$n \geq 30 (V_c - V) / [\pi (R - h)] \quad (3)$$

Substituting the above data into formula (3), the rotational speed n of the sweet potato vine cutting knife roller should not be less than 1602 r/min.

Ridge-like Depth Wheel Assembly

When the vine cutting machine is too low, the vine-cutting knife may enter the soil, causing damage to the sweet potatoes, generating strong vibrations in the machine, leading to damage and increased energy consumption. On the other hand, if the vine cutting machine is too high, it may result in insufficient crushing of the vine. The main components of the depth wheel assembly include: width adjustment tube, height adjustment support arm, dumbbell-shaped ground wheel, support shaft, and bearing seat. Due to different ridge specifications in different regions, the depth wheel can adjust the machine's operating state according to different specifications.

The adjustable width range is 190 mm to 430 mm, and the adjustable height range is 290 mm. Additionally, the depth wheel is designed with a conical surface to clamp the side of the ridge, preventing the machine from swaying from side to side, facilitating smooth operation, and improving work quality (Wu et al., 2021). The structural diagram of the depth wheel assembly is shown in Figure 4.

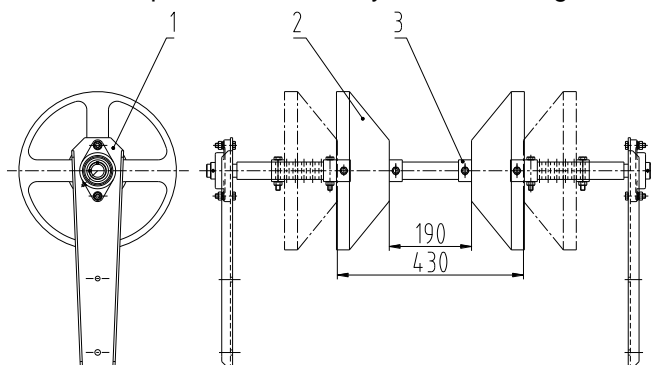


Fig. 4 - The basic structure of depth-control wheel combination
1. Height adjustment arm; 2. Land wheel; 3. Width regulating tube

Solutions for anti-winding device

The root cause of the winding is found that the gap between the end of the knife roll and the bearing seat is too large. Therefore, reducing or even eliminating the gap is the design idea of the anti-winding technology of the shaft end. It is found that the diameter of the bearing seat is less than the diameter of the cutter roller barrel, and the idea of extending the bearing seat into the shaft barrel is put forward. Translate the side plate of the cutter roll inward to leave space, and then extend the bearing seat into the shaft barrel, as shown in Figure 5. The experiment proved that the anti-entanglement had a good effect, and almost no entanglement problem occurred.

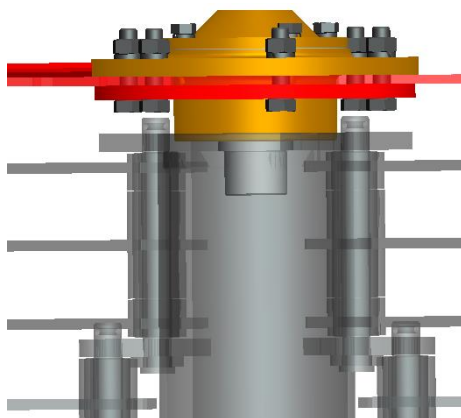


Fig. 5 - The technology of winging preventing at the shaft end

Sweet Potato Vine Cutting Machine Field Test

Test Conditions

The test site selected is the Sweet Potato Base of the Commercial Crop Research Institute in Shangqiu City. The terrain of the site is flat, free of obstacles, with sandy loam soil, measuring 60 meters long and 22 meters wide. The average soil moisture content is 7.3%. The average soil compaction is 120.3 kPa. The average plant spacing is 22.2 cm, ridge height is 20.4 cm, ridge top width is 30.8 cm, ridge base width is 64.6 cm, and ridge spacing is 89.5 cm.

Physical Characteristics of Sweet Potatoes in the Test Site

(1) Variety Selection

The selected variety for the experiment is Shangshu 19, which has a large planting area in China and is highly representative. The vine length ranges from 1 to 3.5 meters, with around 8 branches at the base and no trichomes at the top of the stem.

(2) Vine Length, Diameter, and Moisture Content

At ten random locations in the test site, measurements were taken for the vine length, vine diameter, and stem moisture content. The average values obtained through measurements are 259.4 cm for length, 0.57 cm for diameter, and 89.4% for moisture content.

(3) The tensile and shear tests of sweet potato stem were carried out by universal testing machine. The average tensile force was 110 N and the average cutting force was 106 N.

Field Test and Analysis

In order to determine the optimal combination of machine operating parameters, field tests were conducted at the Sweet Potato Experimental Base of the Commercial Crop Research Institute in Liangyuan District, Shangqiu City. The weather conditions were sunny, with an environmental temperature of 23.5°C and humidity of 43.6%. The sweet potato variety used was Shangshu 19.

Factors Affecting Experimental Indicators

Field tests and equipment inspections refer to the "Draft Regulations for Sweet Potato Vine Crushing and Returning Machine Tests and Inspections" and the "Technical Regulations for Mechanized Ridge Harvesting Operations of Sweet Potatoes."

There are many factors that influence the indicators of sweet potato vine crushing and returning machines (such as the qualification rate of vine crushing length on ridge surface and the average height of stubble left at the top of the ridge), including design factors, processing and manufacturing factors, planting mode factors, crop growth conditions, field conditions, and machine operating parameter factors. The following experiments will focus on the impact of machine operating parameters on the indicators. Among the operating parameters, the factors that have a significant impact on the operational indicators are the forward speed of the machine (v), the rotational speed of the knife roller (ω), and the height of the knife roller above the ground (h).

Single-factor Experiments Affecting the Quality of Sweet Potato Vine Crushing and Returning Machine Operation

Through single-factor experiments, analyze the impact of each influencing factor on the quality of sweet potato vine crushing and returning machine operation, observe the trend of each factor's impact on the qualification rate of vine crushing length (The qualified length of potato vine crushing is not more than 150 mm) and a significant effect on the height of stubble left at the top of the ridge, determine the range of values for each factor, conduct orthogonal experimental research on each factor and its levels, determine the primary and secondary factors affecting vine crushing, and identify the optimal parameter combination for each factor.

(I) Impact of Forward Speed on Operational Quality

(1) Experimental Plan

To study the effect of machine forward speed on the sweet potato vine crushing effect, with the knife roller speed set at 1800 rpm and the lifting height of the vine-cutting knife set at 20 mm, the tractor drives the vine cutting machine to advance at five different speeds of 0.7 m s⁻¹, 0.65 m s⁻¹, 0.6 m s⁻¹, 0.55 m s⁻¹, and 0.5 m s⁻¹. The qualified rate of sweet potato vine length and stubble height at ridge top were used as the main control index. During the experiment, the machine worked for 20 meters per row, excluding the first and last 5 meters. Measurements of various indicators of sweet potato vine crushing will be taken at three points within a stable 10-meter working area in the middle, to study the relationship between machine forward speed and crushing effect.

(2) Experimental Results and Analysis

Field experiments were conducted according to the experimental plan, and the qualification rate of vine crushing length on the ridge surface and the average height of stubble left at the top of the ridge were obtained under different forward speeds of the machine. Single-factor analysis of variance on the impact of different forward speeds on operational quality was conducted using SPSS and Excel software, with results shown in Figure 6.

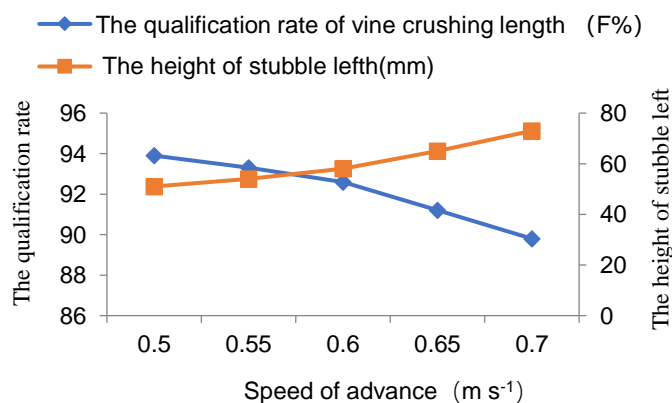


Fig. 6 - The influence of forward speed on indexes

The analysis results indicate that the machine's forward speed has a significant impact on the qualification rate of vine crushing length on the ridge surface and a significant effect on the height of stubble left at the top of the ridge. From a comprehensive analysis of the experimental results, it can be concluded that the qualification rate of sweet potato vine crushing decreases with increasing machine forward speed, while the height of stubble left at the top of the ridge increases with the machine's forward speed.

(II) Impact of Knife Roller Speed on Operational Quality

(1) Experimental Plan

To study the effect of the cutting knife roller speed on the quality of sweet potato vine crushing and returning machine operation, the forward speed of the machine was set at 0.6 m s^{-1} , the lifting height was set at 20 mm, and the knife roller speed was set at 1600 rpm, 1700 rpm, 1800 rpm, 1900 rpm, and 2000 rpm. Since the parameter values when the speed is set to 1800 rpm were repeated in the third group of the experiment on the impact of knife roller speed on operational quality, this group was omitted in this round of experiments. The qualified rate of sweet potato vine length and stubble height at ridge top were used as the main control index. During the experiment, the machine worked for 20 meters per row, excluding the first and last 5 meters. Measurements of various indicators of sweet potato vine crushing were taken at three points within a stable 10-meter working area in the middle to study the relationship between the cutting machine's knife roller speed and crushing effect.

(2) Experimental Results and Analysis

Field experiments were conducted according to the experimental plan, obtaining the qualification rate of vine crushing length on the ridge surface and the average height of stubble left at the top of the ridge under different roller speeds. Single-factor analysis of variance on the impact of knife roller speed on operational quality was conducted using SPSS and Excel software, with results shown in Figure 7. The analysis results indicate that the roller speed has a highly significant impact on the qualification rate of vine crushing length on the ridge surface and a significant effect on the height of stubble left at the top of the ridge.

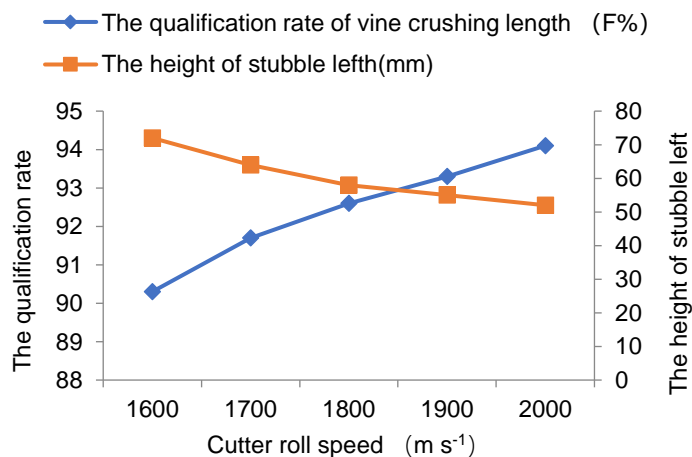


Fig. 7 - The influence of cutter roller speed

From a comprehensive analysis of the experimental results, it can be concluded that the qualification rate of sweet potato vine crushing increases with the increase in roller speed, while the height of stubble left at the top of the ridge decreases with the increase in roller speed.

(III) Impact of Knife Roller Lifting Height on Operational Quality

(1) Experimental Plan

To study the effect of the knife roller lifting height on the quality of sweet potato vine crushing and returning machine operation, the forward speed of the machine was set at 0.6 m s^{-1} , the knife roller speed was set at 1800 m s^{-1} , and the knife roller lifting height was set at 10 mm, 15 mm, 20 mm, 25 mm, and 30 mm. The qualified rate of sweet potato vine length and stubble height at ridge top were used as the main control index. During the experiment, the machine worked for 20 meters per row, excluding the first and last 5 meters. Measurements of various indicators of sweet potato vine crushing were taken at three points within a stable 10-meter working area in the middle to study the relationship between the knife roller lifting height and the crushing effect.

(2) Experimental Results and Analysis

Field experiments were conducted according to the experimental plan, obtaining the qualification rate of vine crushing length on the ridge surface and the average height of stubble left at the top of the ridge under different lifting heights of the knife roller. Single-factor analysis of variance on the impact of the knife roller at different lifting heights on operational quality was conducted using SPSS and Excel software, with results shown in Figure 8. The analysis results indicate that the knife roller lifting height has a highly significant impact on the qualification rate of vine crushing length on the ridge surface and the height of stubble left at the top of the ridge.

From a comprehensive analysis of the experimental results, it can be concluded that the qualification rate of sweet potato vine crushing increases with decreasing lifting height, while the height of stubble left at the top of the ridge decreases with decreasing lifting height.

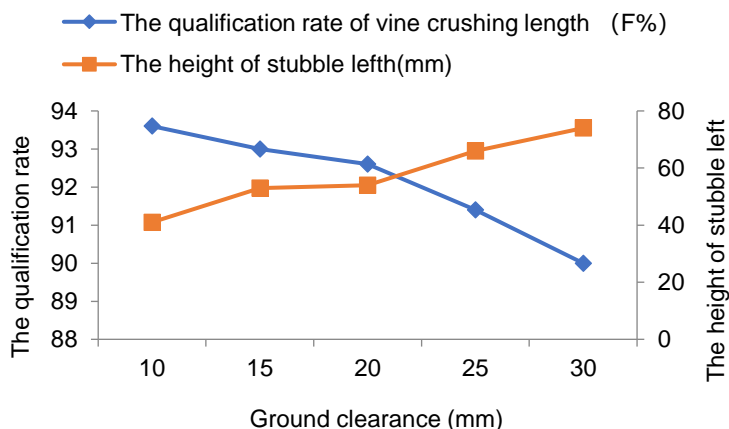


Fig. 8 - The influence of the height from the ground

Orthogonal Experiment Affecting Operational Quality

Through single-factor experiments, it is known that the machine's forward speed, knife roller speed, and knife roller lifting height in the working parameters of the sweet potato vine crushing and returning machine all play significant roles in the operational quality of the machine. The following orthogonal experiment will be conducted to determine the primary and secondary factors affecting the qualification rate of vine crushing length on the ridge surface and the average height of stubble left at the top of the ridge, as well as the optimal combination of working parameters.



Fig. 9 - Working conditions of vine-cutting machine

(1) Experimental Plan and Results

In this round of experiments, based on the single-factor experiments, with the qualification rate of vine length on the ridge surface (The qualified length of potato vine crushing is not more than 150 mm) and the height of stubble left at the top of the ridge as the main control indicators, a 3-factor 3-level orthogonal experiment was conducted on the three significant influencing factors of machine forward speed, knife roller speed, and lifting height. The levels of each factor are shown in Table 1, taking into account the primary interactions between the factors. The experimental design was based on the L27 orthogonal table. The plan and results are shown in Table 2.

Table 1

Factor	Level		
	-1	0	1
A Speed of advance (m s ⁻¹)	0.7	0.6	0.5
B Cutter roll speed (rpm)	1600	1800	2000
C Ground clearance (mm)	10	20	30

Table 2

Test number	Factor													The qualification rate of vine crushing length F (%)	The height of stubble left H (mm)
	A	B	AxB		C	AxC		BxC		Empty list					
1	1	1	1	1	1	1	1	1	1	1	1	1	1	89.5	66
2	1	1	1	1	2	2	2	2	2	2	2	2	2	88.9	72
3	1	1	1	1	3	3	3	3	3	3	3	3	3	87.4	74
4	1	2	2	2	1	1	1	2	3	2	2	3	3	91.1	63
5	1	2	2	2	2	2	2	3	1	3	3	1	1	89.8	73
6	1	2	2	2	3	3	3	1	2	1	1	2	2	89.6	74
7	1	3	3	3	1	1	1	3	2	3	3	2	2	92.9	52
8	1	3	3	3	2	2	2	1	3	1	1	3	3	92.5	59
9	1	3	3	3	3	3	3	2	1	2	2	1	1	91.2	67
10	2	1	2	3	1	2	3	1	1	2	3	2	3	90.8	68
11	2	1	2	3	2	3	1	2	2	3	1	3	1	90.3	72
12	2	1	2	3	3	1	2	3	3	1	2	1	2	89.2	75
13	2	2	3	1	1	2	3	2	3	3	1	1	2	91.6	41
14	2	2	3	1	2	3	1	3	1	1	2	2	3	92.6	58
15	2	2	3	1	3	1	2	1	2	2	3	3	1	88.0	74
16	2	3	1	2	1	2	3	3	2	1	2	3	1	94.4	49
17	2	3	1	2	2	3	1	1	3	2	3	1	2	94.1	52
18	2	3	1	2	3	1	2	2	1	3	1	2	3	92.9	59
19	3	1	3	2	1	3	2	1	1	3	2	3	2	93.2	49
20	3	1	3	2	2	1	3	2	2	1	3	1	3	93.0	57
21	3	1	3	2	3	2	1	3	3	2	1	2	1	91.7	68
22	3	2	1	3	1	3	2	2	3	1	3	2	1	94.8	47
23	3	2	1	3	2	1	3	3	1	2	1	3	2	93.9	51
24	3	2	1	3	3	2	1	1	2	3	2	1	3	90.2	63
25	3	3	2	1	1	3	2	3	2	2	1	1	3	95.8	48
26	3	3	2	1	2	1	3	1	3	3	2	2	1	94.1	50
27	3	3	2	1	3	2	1	2	1	1	3	3	2	93.3	59

(2) Analysis of Variance of Experimental Results

The results obtained from the orthogonal experiment were subjected to variance analysis using SPSS software to determine the primary and secondary factors affecting the qualification rate of vine length on the ridge surface and the height of stubble left at the top of the ridge, as well as the significance of these factors. With a given significance level of 0.05, the results are shown in Table 3.

Table 3

The result of analysis variance

Source	Dependent Variable	Type III Sum of Squares	df	Mean Square	F	Sig.
Calibration Model	F	132.171a	18	7.343	4.002	.026
	H	2748.667c	18	152.704	6.048	.007
Intercept	F	227553.840	1	227553.840	124020.058	.000
	H	101200.333	1	101200.333	4007.934	.000
A	F	37.254	2	18.627	10.152	.006
	H	679.556	2	348.778	13.813	.003
B	F	44.827	2	22.414	12.216	.004
	H	709.556	2	354.778	14.051	.002
C	F	41.956	2	20.978	11.433	.005
	H	1028.222	2	514.111	20.361	.001
AxB	F	4.095	4	1.024	.558	.700
	H	151.556	4	37.889	1.501	.289
AxC	F	.559	4	.140	.076	.987
	H	80.889	4	20.222	.801	.557
BxC	F	3.479	4	.870	.474	.754
	H	80.889	4	20.222	.801	.557
Error Total	F	14.679	8	1.835	/	/
	H	202.000	8	25.250	/	/
Total	F	227700.690	27	/	/	/
	H	104151.000	27	/	/	/
Corrected Total	F	146.850	26	/	/	/
	H	2950.667	26	/	/	/

a. R -squared = 0.900 (Adjusted R -squared = 0.675); b. The calculation result using $\alpha = 0.05$

c. R -squared = 0.932 (Adjusted R -squared = 0.778)

From the analysis in Table 7, the primary and secondary factors affecting the qualification rate of vine length on the ridge surface and the height of stubble left at the top of the ridge are as follows:

(1) Significance Analysis

Factors A, B, and C have a very significant impact on the qualification rate of vine length on the ridge surface and the height of stubble left at the top of the ridge. Other interactions do not significantly affect the qualification rate of vine length on the ridge surface and the height of stubble left at the top of the ridge.

(2) Primary and Secondary Factors Analysis

The ranking of primary and secondary factors affecting the qualification rate of vine length on the ridge surface is as follows: $B > C > A$, meaning that knife roller speed > lifting height > forward speed. The ranking of primary and secondary factors affecting the height of stubble left at the top of the ridge is as follows: $C > B > A$, meaning that lifting height > knife roller speed > forward speed.

(3) Weighted Comprehensive Scoring Method to Determine the Optimal Parameter Combination

From the results of the analysis of variance, it is evident that the significance and primary-secondary relationships of each factor on each indicator are different. In order to comprehensively assess various indicators and determine the optimal parameter combination to achieve the best crushing effect, a weighted comprehensive scoring method is used to analyze the experimental results. The cleaning of sweet potato vines is to facilitate the work of the sweet potato harvester in the following steps. Leaving too many long vines will cause the sweet potato harvester to become entangled or even blocked, affecting the efficiency of the sweet potato harvester and potentially causing damage to the harvester. In addition, work efficiency needs to be taken into account as well. Work efficiency increases with the increase in the machine's forward speed. The time required for the machine to travel 10 m in a stable working state, denoted as T , is added as an evaluation indicator to the comprehensive index. Considering the importance of each indicator, with a total weight of 100 points, the qualification rate of vine length on the ridge surface (F) is assigned 40 points, the height of stubble left at the top of the ridge (H) is assigned 30 points, and the time to pass 10 m (T) is assigned 30 points. Additionally, to calculate the weighted comprehensive index, the qualification rate of vine length is converted to the non-qualification rate to ensure that all indicators have the same trend. The weighted comprehensive index Z can be calculated using the following formula:

$$Z_i = \sum_{j=1}^r W_j \frac{y_{ij}}{y_{j\max}} \quad (4)$$

Z_i represents the calculated weighted evaluation index of the i -th experiment group, where $i = 1, 2, 3, \dots, 27$; W_j represents the "weight" value of the j -th indicator, where $j = 1, 2, 3$, with $W1 = 40, W2 = 30, W3 = 30$; y_{ij} represents the j -th indicator in the first experiment group, where y_{1j} is the non-qualification rate of vine length on the ridge surface, y_{2j} is the height of stubble left at the top of the ridge, and y_{3j} is the time to pass 10 m; y_{jmax} represents the maximum value of the j -th indicator among all 27 experiment groups.

The results of calculating the weighted comprehensive index Z by inputting the data of each parameter into the formula are shown in Table 4.

Table 4

Test results of the comprehensive index

Test number	Factor												Composite indicator Z	
	A	B	AxB		C	AxC		BxC		Empty list				
1	1	1	1	1	1	1	1	1	1	1	1	1	1	80.2
2	1	1	1	1	2	2	2	2	2	2	2	2	2	85.9
3	1	1	1	1	3	3	3	3	3	3	3	3	3	91.5
4	1	2	2	2	1	1	1	2	3	2	2	3	3	73.9
5	1	2	2	2	2	2	2	3	1	3	3	1	1	81.9
6	1	2	2	2	3	3	3	1	2	1	1	2	2	82.9
7	1	3	3	3	1	1	1	3	2	3	3	2	2	64.0
8	1	3	3	3	2	2	2	1	3	1	1	3	3	68.0
9	1	3	3	3	3	3	3	2	1	2	2	1	1	75.2
10	2	1	2	3	1	2	3	1	1	2	3	2	3	80.4
11	2	1	2	3	2	3	1	2	2	3	1	3	1	83.5
12	2	1	2	3	3	1	2	3	3	1	2	1	2	87.4
13	2	2	3	1	1	2	3	2	3	3	1	1	2	67.5
14	2	2	3	1	2	3	1	3	1	1	2	2	3	70.8
15	2	2	3	1	3	1	2	1	2	2	3	3	1	91.6
16	2	3	1	2	1	2	3	3	2	1	2	3	1	61.7
17	2	3	1	2	2	3	1	1	3	2	3	1	2	63.8
18	2	3	1	2	3	1	2	2	1	3	1	2	3	70.3
19	3	1	3	2	1	3	2	1	1	3	2	3	2	70.4
20	3	1	3	2	2	1	3	2	2	1	3	1	3	74.1
21	3	1	3	2	3	2	1	3	3	2	1	2	1	82.5
22	3	2	1	3	1	3	2	2	3	1	3	2	1	64.6
23	3	2	1	3	2	1	3	3	1	2	1	3	2	69.0
24	3	2	1	3	3	2	1	1	2	3	2	1	3	85.3
25	3	3	2	1	1	3	2	3	2	2	1	1	3	61.8
26	3	3	2	1	2	1	3	1	3	3	2	2	1	68.0
27	3	3	2	1	3	2	1	2	1	1	3	3	2	74.0

Performing variance analysis on the comprehensive scoring results, the results are shown in Table 5.

Table 5

The result of comprehensive score analysis variance

Source	Dependent Variable	Type III Sum of Squares	df	Mean Square	F	Sig.
Calibration Model	Z	2084.287 ^a	18	115.794	9.666	.001
Intercept	Z	152656.001	1	152656.001	12743.655	.000
A	Z	160.814	2	80.407	6.712	.019
B	Z	945.254	2	472.627	39.455	.000
C	Z	773.081	2	386.540	32.268	.000
AxB	Z	101.690	4	25.423	2.122	.170
AxC	Z	36.890	4	9.223	.770	.574
BxC	Z	66.557	4	16.639	1.389	.320
Error	Z	95.832	8	11.979	/	/
Total	Z	154836.120	27	/	/	/
Corrected Total	Z	2180.119	26	/	//	

a. R-squared = 0.956 (Adjusted R-squared = 0.857); b. The calculation result using alpha = 0.05

From the table, it is evident that factors A, B, and C have a very significant impact on the comprehensive index. The primary and secondary factors affecting the comprehensive index of the operation of the vine shredder and returning machine are $B = C > A$, meaning that the knife roller speed = lifting height > forward speed. Through visual analysis of the comprehensive index, it is determined that the optimal parameter combination is the 16th group A2B3C1, with a forward speed of 0.6 m s^{-1} , knife roller speed of 2000 r/min , and lifting height of 10 mm .

Operational Index Testing

The machine parameters are set as follows: forward speed of 0.6 m s^{-1} , knife roller speed of 2000 r/min , lifting height of 10 mm . The vine shredder is tested by the Mechanical Industry Agricultural Machinery Product Quality Testing Center. The test results show a vine length qualification rate of 94% and a stubble height of 5.3 cm , which are much higher than the standards in "JB/T6678-2001 Straw Shredder for Returning to the Field," the "Sweet Potato Vine Shredder Test and Inspection Method (Draft)," and the "Technical Regulations for Sweet Potato Mechanized Ridge Harvesting Operations." The machine has achieved high efficiency in vine removal.

CONCLUSIONS

This article introduces the structure and working principle of the vine cutting machine, determines the operating parameters of key components, measures the soil conditions, ridge conditions, and physical characteristics of sweet potato vines at the experimental site. By conducting field performance tests on the sweet potato vine shredder, the technical performance, vine shredding quality, and operational efficiency of the machine are determined. The study verifies whether the developed sweet potato high-efficiency vine cutting machine meets the design requirements and inspection standards, assesses its operational reliability and performance stability, and evaluates its operational quality. Through orthogonal experiments, it is revealed that the primary and secondary factors affecting the qualification rate of vine shredding length on the ridge surface are ranked as $B > C > A$, indicating that the knife roller speed > ground clearance height > forward speed. The primary and secondary factors affecting the height of the ridge top stubble are ranked as $C > B > A$, meaning that the ground clearance height > knife roller speed > forward speed. Using a weighted comprehensive analysis and scoring method, the optimal working parameter combination for the sweet potato vine cutting machine is determined to be a forward speed of 0.6 m s^{-1} , a knife roller speed of 2000 r/min , and a ground clearance height of 10 mm .

ACKNOWLEDGEMENT

This research was supported by Chinese Academy of Sciences foresight strategic science and technology pilot project (XDA0440404), National key research and development plan project(2022YF200210203), Major scientific and technological tasks of the Chinese Academy of Agricultural Sciences(CAAS-ZDRW202407).

The authors wish to thank the useful comments of the anonymous reviewers of this paper.

REFERENCES

- [1] Mu Guizhi, Xin Qingqing, Xuan Guantao, Lv Zhaoqin, Wang Haining, Xin Qingsong. (2019). Design and experiment of Ridge Cutting crushing and Throwing Device for sweet potato vine Recovery Machine (甘薯秧蔓回收机仿垄切割粉碎抛送装置设计与试验). *Transactions of the Chinese Society for Agricultural Machinery*, 50 (12), pp.53-62, Shandong/China.
- [2] Amer N.N. Kakahy, Ahmad D., Akhir M.D., Sulaiman S., Ishak A. (2014). Effects of rotary mower blade cutting angles on the pulverization of sweet potato vine[J]. *Agriculture and Agricultural Science Procedia*, 30(2), pp. 95 – 101, Iraq.
- [3] Mu Guizhi, Zhang Xianguang, Lv Zhaoqin, Guo Zimeng. (2018). Design and simulation analysis of the knife roller of the profiling sweet potato seedling killing machine (仿形甘薯杀秧机刀辊的设计与仿真分析). *Journal of Chinese Agricultural Mechanization*, 39(5), pp. 21-26, Shandong /China.
- [4] Ma Biao. (2014). *The research and optimized design on the high performance of cutting vine technology and mechanism of sweet potato* (甘薯高清除性切蔓技术及其装置研究与优化设计). Hefei: Anhui Agricultural University, Jiangsu/China.

- [5] Zheng Wenxiu, Lv Zhaoqin, Zhang Wanzhi, Liu Zhengyi, Lu Yao, Li Yudao. (2019). Design and test of single row sweet potato vine recycling machine (单行甘薯秧蔓回收机设计与试验). *Transactions of the CSAE*, 35(6), pp. 1 – 9, Shandong/China.
- [6] Ma Biao, Hu Lianglong, Xu Liangyuan, Tian Lijia, Ji Fulai, Wang Bing. (2015). Design and Dynamic balance analysis of cutter roll of sweet potato vine crushing machine (甘薯秧蔓粉碎还田机刀辊设计与动平衡分析). *Journal of Chinese Agricultural Mechanization*, 36 (4), pp. 18 ~ 21, Jiangsu/China.
- [7] Lv Jinqing, Shang Qinqin, Yang Ying, Li Zihui, Li Jicheng, Liu Zhongyuan. (2016). Design and experimental on potato haulm cutter (马铃薯杀秧机设计优化与试验). *Transactions of the Chinese Society for Agricultural Machinery*, 47(5), pp. 106 – 114, Heilongjiang/China.
- [8] Zhou Zihan, Shang Shuqi, Wang Dongwei, He Xiaoning, Tan Ying, Dong Cheng. (2022). Sweet potato seedling special cut harvest machines, design and test (甘薯秧蔓收获机专用割台设计与试验). *Journal of Chinese agricultural mechanization, lancet*, (12), pp. 26-32, Shandong /China.
- [9] Mu Guizhi, Qi Xieteng, Zhang Wanzhi, Lv Zhaoqing, Zhang Tingting, Wang Shuwen, Wang Gongpu. (2021). Chopped sweet potato seedling discrete element simulation parameters measurement and calibration (碎甘薯秧离散元仿真参数测量与标定). *Journal of Chinese agricultural mechanization*, vol.(11), pp. 72-79, Shandong/China.
- [10] Wu Teng, Hu Lianglong, Wang Gongpu, Hu Zhichao, Yan Wei, Wang Bing. (2017). Design and experiment of Walking Machine for returning shredded sweet potato to field (步行式甘薯碎蔓还田机的设计与试验). *Transactions of the Chinese Society of Agricultural Engineering*, 33(16), pp. 8-17, Jiangsu/China.

DESIGN AND EXPERIMENT OF SELF-PROPELLED MULTIFUNCTIONAL TRENCHING AND FERTILIZING MACHINE

自走式多功能开沟施肥机的设计与实验

Tengyun MA¹⁾, Bin QI^{1*)}, Xiaoming SUN^{*)}, Yuanqi LIU¹⁾, Yuchao REN¹⁾, Jiyuan SUN¹⁾,
Bohan ZHANG¹⁾, Qiong WU²⁾

¹⁾ College of Agricultural Engineering and Food Science, Shandong University of Technology/ China;

²⁾ Zibo Normal College/ China

Tel: +86-15966964198; E-mail: sdutid@163.com

DOI: <https://doi.org/10.35633/inmateh-74-40>

Keywords: Orchard mechanization, Trenching and fertilizing machine, Rotary tiller

ABSTRACT

In orchard management, trenching operations are labor-intensive and have low efficiency, and mechanization is of crucial importance for the development of the fruit industry in China. In view of the many deficiencies of the existing chain-type and disc-type trenching machinery, this paper designs a self-propelled multifunctional orchard trenching machine. Its core component, the double-disc trenching disc, is an innovative design. Compared with the traditional single-disc trenching disc, it effectively reduces the trenching power consumption while ensuring the trenching depth and width, and significantly improves the operation efficiency. The trenching machine is composed of a frame, a gearbox, a double-disc trenching disc, a trenching knife, a soil retaining plate, etc. Field tests show that the operation speed reaches 1.2 kilometers per hour, the trenching depth is 31.2 cm, the width is 30.5 cm, and the stability coefficient of the trenching depth is 97.2%. Its power consumption is in a relatively good parameter group. When the cutter roller speed is 400 r/min, the forward speed is 0.8 km/s, and the trenching depth is 0.3 m, the average power consumption value of the trenching component is measured to be approximately 7.63 kW, with an 11.18% reduction in power consumption compared with the current trenching machines. And it meets the requirements of orchard agronomy and industry standards. In terms of improving productivity, its high-efficiency operation performance can greatly shorten the trenching operation time in the orchard, enabling fruit growers to arrange production more reasonably and increase fruit output. In reducing labor costs, mechanization replaces manpower, reduces manpower input, reduces labor cost expenditures, and at the same time avoids the instability of manpower operations. For the sustainability of orchard operations, the precise and stable trenching operation helps to optimize the utilization of land resources, ensure the quality of orchard agronomy, maintain the long-term production capacity of the orchard, promote the sustainable development of the orchard, and inject new impetus into the mechanization process of the fruit industry.

摘要

果园管理中开沟作业劳动密集且效率低，机械化对中国果业发展至关重要。鉴于现有链式、盘式开沟机械存在诸多不足，本文设计了一种自走式多功能果园开沟机。其核心部件双盘开沟盘为创新设计，相比传统单盘式开沟盘，在保证开沟深度和宽度的同时，有效降低了开沟功耗，显著提升了作业效率。该开沟机由机架、变速箱、双盘开沟盘、开沟刀和挡土板等组成，田间试验表明，作业速度达 1.2 公里/小时，开沟深度为 31.2 cm，宽度为 30.5 cm，深度稳定性系数为 97.2%，其功耗较优参数组，刀辊转速为 400 r/min，前进速度为 0.8 km/s，开沟深度为 0.3 m，测得此时开沟部件平均功耗值约为 7.63 kW，较目前开沟机相比功耗降低 11.18%。且符合果园园艺和行业标准要求。在提高生产力方面，其高效作业性能可大幅缩短果园开沟作业时间，使果农能更合理安排生产，提升水果产量。降低劳动力成本上，机械化替代人力，减少了人力投入，降低人力成本支出，同时避免人力作业的不稳定性。对于果园运营可持续性，精准稳定的开沟作业有助于优化土地资源利用，保证果园园艺质量，维持果园长期生产能力，推动果园可持续发展，为水果行业机械化进程注入新动力。

INTRODUCTION

China is the world's largest fruit producer, with the planting area and output of fruit varieties ranking first in the world. It has become the third largest agricultural planting industry after food and vegetables (Yinghong, 2019).

The fruit industry is a labor-intensive industry. With the increase in fruit orchard planting area and labor costs in recent years, labor shortages have become one of the important reasons hindering the development of China's fruit industry (Jianhui, 2012). The operation of trenching and fertilizing is the most important part of orchard management. Reasonable trenching and fertilizing operations are important ways to increase fruit yield and improve fruit quality. The current trenching and fertilizing operation in domestic orchards mainly relies on manual completion, with high intensity, low efficiency, low standardization, and easy to delay farming time, severely affecting the development process of China's fruit industry. Therefore, mechanized trenching operation has become an inevitable trend in large-scale orchard trenching and fertilizing operations.

Currently, domestic research scholars have conducted a series of research on orchard trenching machines. Yichuan *et al.*, (2015), designed the 2FK-40 orchard trenching and fertilizing machine, with a disc-type trenching blade design, maximum trenching depth of 40 cm, adjustable depth, and trenching distance of 50-80 cm from the crop roots. The machine can complete trenching, fertilizing, and covering soil operations at one time without damaging the crop roots. Ruihua *et al.*, (2018), developed a grape trenching and fertilizing machine, which can complete trenching, fertilizing, and covering soil at one time, and the trenching depth can meet the agronomic requirements of the grape orchard. Zhou *et al.*, (2023), designed and developed a deep organic fertilizer trenching device suitable for fruit planting modes such as grapes and jujubes in Xinjiang, which achieves mechanized trenching operation and meets the requirements of deep organic fertilizer application, with the characteristics of simple structure and stable performance.

The above research has to some extent alleviated the problem of high labor intensity in orchards, but there are still some shortcomings in meeting the agronomic requirements of orchards, as well as the reliability and energy consumption of the machinery.

Based on this, this paper comprehensively considers the requirements of orchard planting modes, agronomy, and energy conservation, that is, the trenching depth and width should be greater than 30 cm, and the structural design should minimize power consumption while ensuring compliance with agronomic requirements. A self-propelled multifunctional orchard trenching machine is developed to realize mechanized trenching operation.

Overall structure and working principles

A rotary tillage blade assembly is installed at each end of the trenching power output shaft. The rotary tillage blade assembly is welded with a rotary tillage blade seat and equipped with a rotary tillage blade. During trenching and fertilization, the trenching and fertilization guide cover guides and throws the soil thrown out during trenching, fills the trench, and simultaneously applies fertilizer. The machine is composed of a track chassis, matching power, gearbox, additional reducer, working chain, tool, spiral soil discharger, hydraulic cylinder, etc., and has the characteristics of compact structure, flexible rotation, and excellent trenching quality, as shown in figure 1.

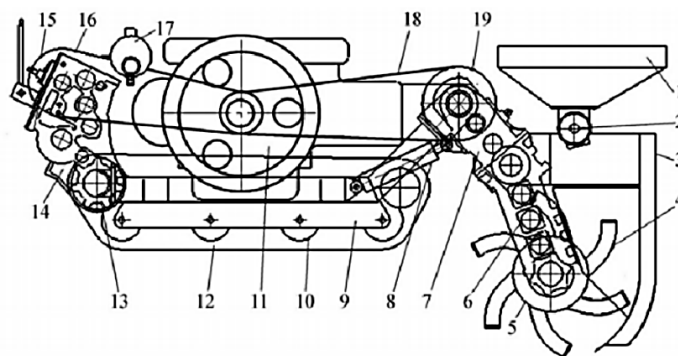


Fig. 1– Transmission box clutch

1. Fertilizer box; 2. Manure spreader; 3. Cultivator hood; 4. Rotary tiller blade; 5. Rotary tiller blade mounting bracket; 6. Trenching transmission box; 7. Transmission box; 8. Hydraulic cylinder; 9. Frame; 10. Track support wheel; 11. Diesel engine; 12. Track; 13. Track drive wheel; 14. Gearbox; 15. Gearbox clutch; 16. V-belt; 17. Hydraulic oil tank; 18. Transmission box V-belt

The self-propelled multi-functional trenching and fertilizing machine developed in this study uses 65Mn steel for the tool material. It has the characteristic of good rigidity, which enables the trenching cutter to maintain good shape stability during the operation process and is not easy to deform, thus ensuring the accuracy and continuity of the trenching operation and ensuring that the trenching depth, width, etc. meet the requirements. Moreover, due to its high tensile strength and wear resistance, during the trenching operation, the trenching cutter can withstand large tensile forces.

Especially when cutting hard soil or encountering obstacles in the soil, the high tensile strength of 65Mn steel can ensure that the trenching cutter is not easy to break, extend its service life, reduce the downtime for maintenance caused by cutter damage, and improve the operation efficiency (Qi, 2023). The wear resistance of 65Mn steel can effectively reduce the wear rate of the cutter, enabling it to maintain good cutting performance after long-term use, reducing the frequency of cutter replacement, saving costs, and also helping to ensure the stability of the trenching quality. In addition, the double-disc trenching cutter can make the soil receive more reasonable forces during the trenching process. When the cutter discs rotate, the two discs work together to optimize the cutting and ejecting angles of the soil. For example, compared with a single disc, the double discs can eject the soil from different angles, making the soil more evenly distributed on both sides of the trench, effectively preventing the soil from piling up in the trench and affecting the trenching quality. This good soil ejecting effect provides convenient conditions for subsequent operations such as fertilizing and back filling. If the soil cannot be well ejected from the trench, the efficiency of subsequent fertilizing and back filling will be affected, and the double-disc cutter discs can better solve this problem. During the rotation of the double-disc cutter discs, due to their symmetrical structure, the stability of the entire trenching machine during work is enhanced. The two cutter discs share the resistance during the trenching process, reducing unstable situations such as machine shaking caused by excessive unilateral force. In terms of power consumption, the double-disc cutter discs can more evenly distribute power while ensuring the trenching effect. Compared with the single-disc cutter discs, the double-disc cutter discs can make more efficient use of power, reducing the overall power consumption of the trenching operation to a certain extent, which is beneficial to energy conservation and reducing operation costs (Miao et al., 2022).

During the working process, start the crawler multifunctional working machine, and control the power output, rotation speed and steering of the orchard crawler multifunctional working machine by operating the handle. The power of the multifunctional working machine is output through the rear power output shaft, transmitted to the gearbox at the right rear end of the frame via the universal shaft, and the gearbox transmits the power to the trenching cutter disc. The rotation of the trenching cutter disc drives the trenching cutter to rotate for trenching operation. When the rotation speed of the trenching cutter disc reaches the requirement, the driver controls the hydraulic system to lower the frame according to the trenching depth requirement until the required trenching depth is achieved. When the trenching machine is working, the soil cut by the trenching cutter disc is thrown to the right side of the trench under the action of the soil deflector, and the trenching machine completes the trenching operation. The performance parameters of the machine are shown in Table 1.

Table 1

Main technical parameter of the orchard trencher	
Parameter	Numeric value
Supporting power / kW	≥18
The size of the whole machine (Length*width*height) / (m*m*m)	1.1*0.9*1.02
Maximum speed of output shaft / (r·min ⁻¹)	540
Trench width / (m)	0.3
Trenching depth / (m)	0.35
Speed of work/ (km·h ⁻¹)	0.8~1.5

Key component design

The trenching disc is an important component of the trenching assembly, and the structural design parameters of the trenching disc determine the trenching depth and width, while also significantly affecting the power consumption and stability of the trenching process. Currently, in the design of trenching discs that can meet the requirements for trenching depth, single discs are mostly used, which makes it difficult to ensure the trenching width. Therefore, based on the single-disc trenching disc, a dual-disc trenching disc has been

designed, which can better meet the requirements for trenching width and effectively achieve soil ejection (Pingyuan *et al.*, 2017). The main design parameter is the diameter D of the trenching disc.

The disc diameter D is the main parameter of the trenching machine's trenching disc, which has a significant impact on the soil ejection distance, power consumption, transmission form, and overall machine size of the trenching machine. Currently, in China, the general empirical formula for the design of the size of the rotating trenching machine disc is based on literature (Xue *et al.*, 2018).

The diameter of the trenching machine disc is:

$$D = (1.2 \sim 1.4)H \quad (1)$$

where:

D —Cutterhead diameter, [mm];

H —Trenching depth, [mm].

Based on the working requirements for deep fertilization trenching in orchards and the design requirements of the project, the minimum trenching depth is about 30 cm, and the maximum is about 40 cm. According to formula (1), the range of the disc diameter is 360 mm to 560 mm.

The diameter of the trenching disc has a significant impact on the power consumption of trenching. Under the premise of meeting the minimum trenching depth of 30 cm, the smaller the diameter D of the trenching disc, the less power is consumed for trenching. Therefore, to ensure that the trenching disc cuts the soil evenly and can throw the cut soil blocks onto the trench surface with less power consumption, the trenching disc is designed as a double-disc type. The diameter of the designed trenching disc is selected to be 430 mm. To reduce the mass of the trenching disc and lower the overall power consumption, the trenching disc is processed into a circular ring shape, as shown in Figure 2.

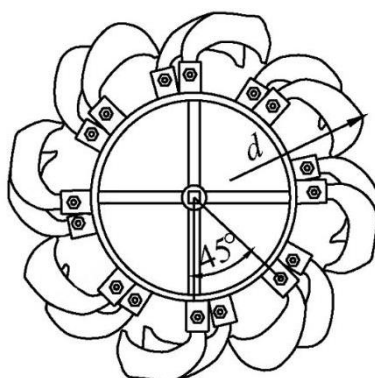


Fig. 2 –Structure diagram of stepped trenching cutter

The structure and arrangement of the trenching blades have a significant impact on the performance of the trenching machine. Currently, the main structural forms of trenching blades used for trenching are chisel blades, right-angle blades, and curved blades. The selected trenching curved blades have a wider cutting face width than the standard rotary tilling curved blades of the national standard, which can effectively carry soil and have good soil ejection performance. To ensure the stability of the trenching machine and the continuity of soil cutting, each layer of the double-disc trenching blade disc is evenly equipped with 8 trenching blades. The installation positions of the trenching blades on adjacent discs are staggered by 45°. This stepped trenching blade disc is equipped with a total of 16 trenching blades, which are fixed to the blade seats on the edge of the trenching blade disc by bolts. After the installation of the trenching blades, the rotating radius R of the blade disc with the trenching blades installed is determined to be 385 mm.

The JC-28 self-propelled small orchard trenching machine of Jingchi brand consumes a power of 6.98 KW when the trenching rotational speed is 500 $\text{r} \cdot \text{min}^{-1}$, the forward speed is 1.0 km/h, and the trench depth is 0.15 m. In contrast, under the same working requirements, the designed self-propelled multi-functional trenching and fertilizing machine consumes a power of 5.96 KW, saving 14.6% of the power consumption. However, considering the differences in the experimental environment, the specific values may deviate.

Three-position design and strength analysis of the tool

First, a 3D scanner is used to scan the rotary tilling blade to establish an accurate model of the rotary tilling blade, as shown in Figure 4. The camera resolution of the 3D scanner is 1280×1024 pixels, with a scanning accuracy of 20 micrometers and a scanning speed of 1.3 seconds per frame. The front and back sides of the rotary tilling blade are scanned to obtain the models of both sides, as shown in Figure 5. The scanned models of both sides are imported into the software Geomagic Studio 12 for model stitching and merged into the final complete model, as shown in Figure 6.



Fig. 4 – Scanning Process with COM1M-12 Type Grating 3D Scanner

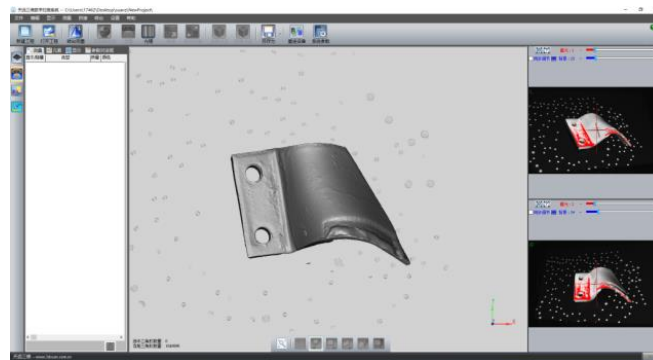


Fig. 5 – Scanned Single-Sided Model

The 3D model of the rotary tilling blade merged by Geomagic Studio 12 is preprocessed using SolidWorks 3D software. In the Start menu, execute the "ANSYS21.0—Workbench" command. The working load of the rotary tilling blade can be determined according to literature (*Mariam, 2018*), with the load magnitude being 500 N. Based on the above force analysis, the load is uniformly applied to the rotary tilling blade. A new material is added in the engineering data properties, and the new material name "65Mn" is entered. The specific material parameters are shown in Table 2. Then, meshing is carried out. The mapping meshing method is adopted to mesh the irregular rotary tilling blade model. The meshing situation of the rotary tilling blade is shown in Figure 6. Since the blade edge of the rotary tilling blade is the first to be subjected to force, it is necessary to check whether the deformation and stress of the rotary tilling blade meet the design requirements, providing a reference for subsequent optimization and improvement.

Table 2

Simulation Experiment Parameters of 65Mn Steel	
Material Properties	Numeric value
Elastic Modulus / (kPa)	2*10 ⁸
Poisson's ratio / %	0.3

Soil moisture content / %	16
Yield strength / (kPa)	7.85×10^5
Tensile strength / (kPa)	9.8×10^5
Mass density / ($\text{kg} \cdot \text{m}^3$)	7.81×10^3

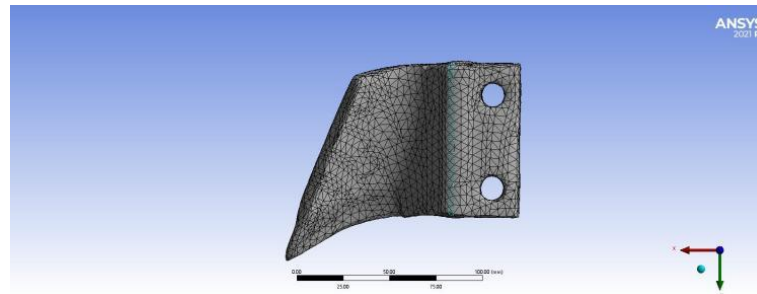


Fig. 6 – Mesh Division of Rotary Tilling Blade

As shown in Figure 7, it is the strength cloud map of the rotary tilling blade.

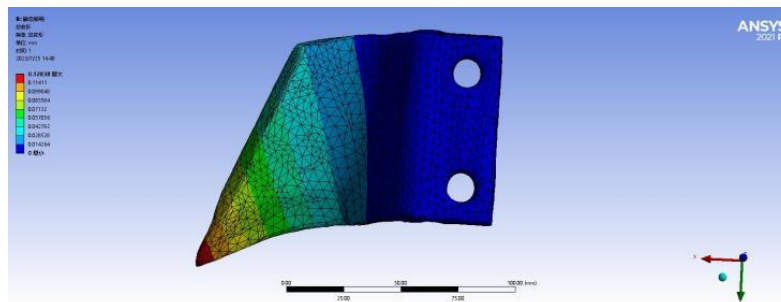


Fig. 7 – Stress Cloud Map of the Rotary Tilling Blade

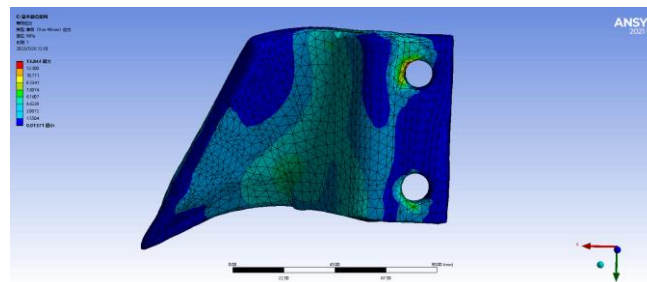


Fig. 8 – Displacement Variation of the Rotary Tilling Blade

From Figure 7, it can be seen that the maximum stress of the rotary tilling blade is 55.48 MPa, which is located at the lower edge of the blade. The reason for this is that the lower edge of the rotary tilling blade is the first to come into contact with the soil. In addition, significant stress also occurs at the mounting hole and the position of the secondary cutting edge, with an average stress of 30 MPa, which is less than the allowable stress of 300 MPa for 65Mn steel. The displacement variation at the mounting hole and the handle of the rotary tilling blade also leads to relatively large deformation, and the average deformation meets the requirements. The maximum displacement of the rotary tilling blade occurs at the blade edge and the upper half, with the maximum displacement being 0.4 mm. There is also obvious deformation at the mounting hole and the handle position, which is due to the stress concentration at the mounting hole, and the average deformation is 0.38 mm. Based on the above analysis, the rotary tilling blade meets the design requirements.

The primary function of the soil deflector plate is to arrange the soil thrown up by the trenching blades in an orderly manner on the right side of the trench, preventing the soil from re-entering the trench and affecting the quality of the trenching. The soil deflector plate mainly consists of an arc plate, side straight plate, flexible plate, and fixed installation square tube, as shown in Figure 3. When the trenching blade disc cuts the soil, the soil is thrown up at a certain speed along with the rotation of the disc. At this moment, the soil strikes the arc plate, and further breaks and falls under the impact of the arc plate. To ensure that the soil is arranged in an orderly manner on the right side of the trench and to reduce the overall weight of the machine, a flexible plate is installed on the right side of the arc plate.

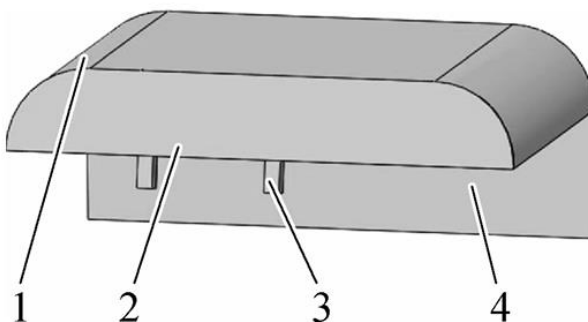


Fig. 3 – Structure diagram of diversion cover

1. Arc Plate; 2. Side Straight Plate; 3. Fixed Installation Square Tube; 4. Flexible Plate

Field experiments and analysis of results

Based on the relevant agronomic requirements for trenching in orchards, this paper designed a double-disc trenching device and carried out relevant simulation experiments. To verify whether the prototype can meet the agronomic requirements for trenching in orchards, trenching tests were conducted at Shandong University of Technology in 2023. On the day of the test, the weather was sunny with a light breeze, and the temperature was 16°C. A relatively flat area was selected at the test site for the trenching test. During the test process, the blade thickness was 6 mm, the depth of cut was 30 mm, and the cutting speed of the blade was 7.7 m/s. The test mainly involved equipment such as tape measures, speedometers, computer data acquisition systems, TJSD 750 firmness meters, and cutting rings. The test conditions are shown in Table 3.

Table 3

Test conditions	
parameter	numeric value
Test site (Length * Width) / (m*m)	50*40
Test the terrain of the site in terms of slope	flat
Soil moisture content/%	16
Ambient temperature/°C	17
Soil density / (kg*m³)	2190
Soil compactness / (kPa)	1342

During the trial process, the self-propelled multi-functional orchard trencher is suspended on the orchard crawler multi-functional machine. The operation is stable and the work is safe and reliable during the trenching project, which allows for better trenching and soil-throwing operations. At the same time, the trencher can be raised and lowered by manipulating the orchard crawler multi-functional machine to meet the depth requirements for trenching. As shown in Figure 8.



Fig. 9 – Field Experiment

To inspect the stability of the trenching depth of the trencher, measurements were taken at five points along the direction of travel during two cycles of the machine's operation, as shown in Figure 10. The test data for the trenching depth are presented in Table 4.

Table 4

Measurement results of trenching depth						
Depth/m	Test point 1	Test point 2	Test point 3	Test point 4	Test point 5	Average depth
Itinerary 1	0.304	0.325	0.318	0.329	0.316	0.317
Itinerary 2	0.321	0.318	0.305	0.309	0.327	



Fig. 10 – Trenching depth measurement

Both the trenching width and the trenching depth were measured at the same measuring point. The distance between the two sides of the trench was measured with a ruler, and this distance was the trench width, as shown in Figure 11. The measurement results of the trenching width are presented in Table 5.



Fig. 11 – Trenching width measurement

Table 5

Measurement results of trenching width

Width/m	Test point 1	Test point 2	Test point 3	Test point 4	Test point 5	Average width
Itinerary 1	0.305	0.304	0.304	0.308	0.306	0.307
Itinerary 2	0.307	0.308	0.306	0.308	0.310	

The formula for the trench - depth stability coefficient is:

$$S = \sqrt{\frac{\sum_{i=1}^n (h_i - h)^2}{N - 1}} \tag{2}$$

$$V = \frac{s}{h} \times 100\% \tag{3}$$

$$U = 1 - V \tag{4}$$

In the formula:

- h_i —represents the trenching depth at the i th measuring point, in mm;
- N —represents the total number of measuring points within the travel distance, and $N = 10$;
- h —represents the average value of the trenching depth, in mm;
- s —represents the standard deviation of the trenching depth, in mm;
- V —represents the coefficient of variation of the trenching depth, in %;
- U —represents the stability coefficient of the trenching depth, in %;

The calculated stability coefficient of the trenching depth $U = 97.2\%$.

To further verify the working performance of the trencher, the main performance indicators of the trencher, including trench width, depth, and operating speed, were measured according to the Chinese agricultural industry standard "NY/T740—2003 Field Trenching Machinery Operation Quality" (Liufang and Peng, 2007). The results are shown in Table 6. The calculated stability coefficient for the trenching depth is 97.2%, which complies with the Chinese agricultural industry standard that the stability coefficient for trenching depth should not be less than 80%, indicating good trenching quality.

Table 6

Experimental performance result		
parameter	Design values	Test results
Trenching depth/m	≥ 0.3	0.317
Trench width/m	≥ 0.3	0.307
Speed of work/ (km·h ⁻¹)	0.8~1.5	1.2

Based on Table 5 and the experiment, the trencher, operating at a forward speed of 1.2 km/h, achieved a trench depth of 31.27 cm and a width of 30.5 cm. Both the depth and width of the trench, as well as the operating speed, meet the design requirements. Additionally, the depth of the trench can be controlled by the hydraulic lifting device of the orchard multi-functional machine, which can be adjusted according to actual needs. This can effectively satisfy both the design requirements and the horticultural demands of the orchard (Jiqiang et al., 2021).

Control experiment design

Experimental analysis was carried out by comparing with the existing trenching machines (Kang, 2017). After field tests, the comparison results of the power consumption of the double-disc trenching knives and the trench depth stability are shown in Table 7. Compared with the existing trenching machines, the specific productivity and the trenching stability coefficient of the existing trenching machines are 0.45 kJ/kg and 84% - 85% respectively. The specific productivity is the energy consumed for excavating a unit mass of soil within a unit time. For the trenching machine described in this paper, the specific productivity is 0.35 kJ/kg and the trenching stability coefficient is 95.69%. They are respectively reduced by 22.22% and increased by 11.2% - 12.5% compared with those of the existing trenching machines.

Table 7

Comparative test data

Trenching speed / (r·min ⁻¹)	Forward speed / (km·h ⁻¹)	Ditch depth/m	Power consumption / kW		Reduced value / %	Stability coefficient / %		Added value / %
			Existing trenching machines	The designed trenching machine		Existing trenching machines	The designed trenching machine	
400	0.8	0.15	4.95	4.24	14.34	87.73	94.26	6.53
		0.20	6.24	5.51	11.69	88.82	95.34	6.62
		0.25	7.04	6.34	9.94	89.21	96.01	6.80
		0.30	8.59	7.63	11.18	92.10	97.11	5.01
		0.35	10.99	9.98	9.19	92.45	95.75	3.30
Average value			7.562	6.738	11.268	90.062	95.694	5.652

Limiting factors in the field experiment

1) The experimental site was selected in a relatively flat area of Shandong University of Technology. However, the actual orchard terrain is complex and diverse, with different degrees of slopes, differences in soil compaction, and the presence of obstacles. This experimental site cannot fully represent the actual terrain conditions of all orchards, which may lead to certain deviations in the performance of the machine when it is actually applied in different orchards compared to the experimental results. For example, in orchards with larger slopes, the stability of the machine and the control of trenching depth may face greater challenges, and this factor was not fully considered in the experiment.

2) Although the operating speed of the machine reached 1.2 kilometers per hour, the trenching depth was 31.2 cm, the width was 30.5 cm, and the trench depth stability coefficient was 97.2% in the experiment, these performance indicators were measured under specific conditions such as the cutter roller speed (e.g., 400 r/min), forward speed (0.8 km/s), and trenching depth (0.3 m). When these working conditions change, the performance of the machine may be affected. The experiment did not conduct in-depth research on the performance changes of the machine under long-term continuous operation.

In the field experiment of the self-propelled multifunctional trenching and fertilizing machine, although certain achievements have been made, due to the limitations of the experimental site, soil conditions, and other factors, as well as the fact that the changes in machine performance under different working conditions have not been fully clarified, further testing and optimization in a wider range of actual application scenarios are needed to comprehensively evaluate the performance and applicability of the machine.

CONCLUSIONS

1) In response to the development needs of orchard mechanization and the deficiencies of existing trenching machinery, a self-propelled multifunctional orchard trenching machine has been successfully developed. The innovative design of its double-disc trenching disc effectively reduces power consumption while ensuring the trenching depth (reaching 31.2 cm) and width (reaching 30.5 cm), significantly improving the operation efficiency. The operation speed reaches 1.2 kilometers per hour, meeting the requirements of orchard agronomy and industry standards, and strongly promoting the process of orchard mechanization, fulfilling the demand for efficient trenching machinery mentioned in the introduction.

2) The finite element analysis of the rotary tillage knife shows that the maximum stress is 13.84 MPa and the average deformation is 0.01 mm. The location and causes of the maximum deformation are identified, which provides a reference for the selection of tool materials and the improvement of the structure. It ensures the accuracy and continuity of trenching, improves the trenching quality, and guarantees the sustainable operation of the orchard.

3) Field tests show that the performance indicators of the trencher are good. The trench depth stability coefficient reaches 97.2%, meeting the standard requirements. And it performs excellently under specific working conditions, fully verifying the rationality of the design. The high-efficiency operation performance can shorten the trenching time in the orchard, help fruit growers arrange production reasonably, increase fruit output, achieve the research goals of improving orchard productivity and promoting the sustainable development of the orchard, and provide strong support for the development of orchard mechanization.

4) The control experiment comparing with the existing trenching machines shows that the specific productivity of the designed trenching machine is reduced by 22.22%, and the trenching stability coefficient is increased by 11.2% - 12.5%. This further proves its advantages in energy conservation and operation stability,

provides a better choice for orchard mechanized operations, and helps to improve the overall management level and economic benefits of the orchard.

ACKNOWLEDGEMENT

This work was supported by the Shandong Province Science and Technology Minor Enterprises Innovation Ability Promotion Project (Project number: 2023TSGC1014) and the Key Project of Undergraduate Teaching Reform Research in Shandong Province (Z2022263).

REFERENCES

- [1] Jiangtao Q., Hewei M., Chengsong L., (2017). Design of ditching devices suitable for deep application of organic fertilizer in orchards (适于果园深施有机肥开沟装置设计). *Agricultural Mechanization Research*. Vol. 39, ISSN1003-188X, pp.34-37, China.
- [2] Jianhui J., (2012). *Design of deep fertilizer applicator in vineyard (葡萄园化肥深施机的设计)*. Master's thesis. Shandong Agricultural University, Tai'an, China.
- [3] Jianming K., (2017). Design and Experiment of Ditching Blades for Ditching and Fertilizing Machines in High-Density Orchards (密植果园开沟施肥机开沟刀片设计与试验). *Transactions of the Chinese Society for Agricultural Machinery*. Vol. 48, ISSN1000-1298, pp.68-74, China.
- [4] Jiqiang Z., Ziru N., Yuhua L., (2021). Design and experiment of horizontal rotary cultivator based on scallion transplanter (基于大葱移栽机的卧式旋耕机的设计与试验). *Agricultural Mechanization Research*. Vol. 8, ISSN1003-188X, pp.41-45, China.
- [5] Liufang S., Peng S., (2007). Power Consumption analysis of the blades of forward and reverse rotary tillage stubble removal machines (正反转旋耕灭茬机刀片的功耗分析). *Agricultural Mechanization Research*. ISSN1003-188X, pp.87-89, China.
- [6] Mariem A., (2018). Parameterizing wheat leaf and tiller dynamics for faithful reconstruction of wheat plants by structural plant models. *Field crops research*. Vol. 218, ISSN0378-4290, pp. 213-230, French.
- [7] Miao W., Zhigang L., Mingze D., (2022). Simulation Study on the Wear of 65Mn Circular Saw Blades Based on the Orchard Model (基于 Orchard 模型的 65Mn 圆锯片磨损仿真研究). *Tool Engineering*. Vol. 56, ISSN1000-7008, pp.54-58, China.
- [8] Pingyuan X., Zhou Y., Zhiqian S., (2017). Triaxial working resistance test and operation parameter optimization of rotary tillage knives (旋耕刀三向工作阻力试验及作业参数优化). *Transactions of the Chinese Society of Agricultural Engineering*. Vol. 33, ISSN1002-6819, pp. 51-58, China.
- [9] Qi Z., (2023). *Simulation analysis of the distribution of residual stress in the tensioning of 65mn circular saw blade matrix by roll pressing and process optimization (65Mn 材质圆锯片基体辊压适张残余应力分布仿真分析及工艺优化)*. Master's thesis. Qingdao University. China.
- [10] Ruihua X., Dongjun W., Hewei M., (2018). Design and experiment of 2FPG - 40 grape ditching and fertilizing machine (2FPG-40 型葡萄开沟施肥机的设计与试验). *Journal of Chinese Agricultural Mechanization*. Vol. 39, ISSN2095-5553, pp.36-40, China
- [11] Xue C., Zhou Z., Huagang H., (2018). Optimization of working parameters of rotary tilling knife based on ADAMS and ANSYS simulation analysis (基于 ADAMS 旋耕刀工作参数优化及 ANSYS 仿真分析). *Modern Agricultural Science and Technology*. ISSN1007-5739, pp.167-170, China.
- [12] Yichuan H., Zhihui T., Xiangjin M., (2015). Design and experiment of 2FK-40 type orchard opening and fertilizing machine(2FK-40 型果园开沟施肥机的设计与试验). *Agricultural Mechanization Research*. ISSN1673-9205, pp.173-174, China.
- [13] Yinghong L., (2019). Analysis on management measures and key points of planting technology of fruit trees in the new period (新时期果树栽培管理措施及种植技术要点分析). *Agricultural Development & Equipment*, Vol.33, ISSN1002-6819, pp. 51-58, China.

SIMULATION ANALYSIS AND OPTIMIZATION OF CONCAVE BAR POTATO-SOIL SEPARATION DEVICE

凹杆式薯土分离装置仿真分析与优化

Qingmiao XIANG¹⁾, Bei WU^{1,2)}, Fangping XIE^{1,2)}, Zhichao FANG^{1,2)}, Huaiyuan QIAN¹⁾, Zhuo LI¹⁾

¹⁾ Hunan Agricultural University, College of Mechanical and Electrical Engineering, Changsha/China;

²⁾ Hunan Key Laboratory of Intelligent Agricultural Machinery and Equipment, Changsha/China

Tel: +86 15802521582; E-mail: wubei@hunau.edu.cn

Corresponding author: Bei Wu

DOI: <https://doi.org/10.35633/inmateh-74-41>

Keywords: potato harvester, separation device, EDEM, sticky soil

ABSTRACT

The limited separation efficiency of potato-soil separation equipment in the southern potato planting areas is attributed to the high viscosity of the soil. To enhance the performance of the lifting chain separation device, a concave bar was designed. Structural parameters influencing the efficiency of potato-soil separation by bars were determined through kinetic analysis during the separation and transportation of potato-soil mixtures. Both a potato simulation model and a sticky soil simulation model were developed. Simulation tests indicated that the concave bar outperforms the straight bar in separation efficiency. Key factors investigated include the angle of the concave side, the width of the concave bar, the depth of the concave bar, and the installation angle. Orthogonal simulations were conducted using separation efficiency and the maximum force on potatoes as evaluation metrics. The results demonstrated that with a concave side angle of 15°, a concave bar width of 450 mm, a concave bar depth of 60 mm, and an installation angle of 30°, the separation efficiency of the potato-soil mixture reached 79.7%, with a maximum force on potatoes of 35.218 N, achieving the highest separation efficiency. Based on these results, test devices were constructed, and field tests were performed. The field test results showed a damage rate of 1.58%, a potato epidermal injury rate of 1.03%, and a loss rate of 2.87%. These results comply with national standards and validate the reliability of the simulation findings.

摘要

南方马铃薯种植地区因土壤黏性大导致薯土分离装置分离效果差。为了提高升运链式分离装置的分离效率，设计一种凹形杆。在薯土分离和运输过程中的力学分析的基础上，确定了影响筛分杆对薯土分离效果的结构参数。构建了马铃薯模型和粘性土壤模型。通过仿真试验，明确了凹杆的分离效果优于直杆。选取凹杆边角、凹杆宽度、凹杆深度和安装倾角为试验因素，以薯土混合体分离效率与薯块最大受力为评价指标开展了仿真正交试验。结果表明，当凹杆边角为15°，凹杆宽度为450mm，凹杆深度为60mm，安装倾角为30°，此时薯土混合体分离效率为79.7%，薯块最大受力为35.218N，薯土分离效果最好。根据试验结果搭建试验样机，进行田间试验。田间试验结果统计得到伤薯率为1.58%，破皮率为1.03%，损失率为2.87%，符合国家标准，验证了仿真结果可靠性。

INTRODUCTION

China is a major potato-producing country, with an annual cultivation area exceeding 6 million hectares, demonstrating significant potential for industrial development. The potato has emerged not only as a key crop for enhancing farmers' income but also as a crucial component in the "all-encompassing approach" strategy, which aims to strengthen national food security (Xin et al., 2023). Soil properties vary significantly across different potato-growing regions in China. The Northeast is characterized by cohesive soils, the Northwest by sandy soils, and the South by sticky soils. The development of potato harvesting machinery is uneven across these regions, with higher levels of mechanization in the northern areas where production processes are more advanced. In contrast, the southern regions face challenges such as small and fragmented farmland plots and high soil moisture content during the rainy season, which result in lower levels of mechanized production (Li et al., 2016). The potato harvesters developed in China are primarily designed for agronomic practices such as mound or flat planting typical of the northern regions.

Qingmiao Xiang, M.S. Stud.; Bei Wu, Lect. Ph.D.; Fangping Xie, Prof. Ph.D.; Zhichao FANG, Lect. Ph.D.; Huaiyuan Qian M.S. Stud.; Zhuo Li M.S. Stud.

Only a limited number of harvesting machines are suitable for winter potato harvesting in the South. Research on potato harvesting machinery in Europe and the United States began early, focusing mainly on self-propelled and traction types. Currently, the primary development trend in these regions is towards high-power combined harvesting machinery. Foreign potato harvesters have advanced significantly in areas such as automation control and the intelligentization of hydraulic systems. Some models are equipped with GPS navigation systems, enabling the monitoring of technical parameters through geographic information systems (Wei et al., 2020; Zhao et al., 2021; Wei et al., 2019). In Asia, small potato harvesting machines are produced in a few countries and regions, such as Japan and Korea. However, these machines face several challenges when used in China. They often have poor adaptability to the diverse arable land conditions and agronomic requirements across different regions of China. Additionally, they tend to be expensive, with high operating costs, limited after-sales service, and inadequate spare parts supply channels, which complicates their widespread adoption (Qing, 2020; Li et al., 2016; Dou et al., 2019).

Domestic potato harvesters are primarily classified into combined and segmented types, with small and medium-sized models being more advanced. The main types of potato-soil separation devices include bar type, vibration type, and cylinder type. In the southern regions, where the soil is often moist and sticky, the bar type separation device is preferred. This design is particularly effective for separating potatoes from sticky soil (Zhou et al., 2021). The problem of improving the quality of potato tuber separation by improving the digging working parts from the construction of potato harvesters is investigated (Hrushetsky et al., 2019). To reduce damage and improve the retrieval rate of whole potatoes, changes in the materials used for separation bars can be beneficial. For instance, incorporating rubber into metal bars and auxiliary devices has been explored (Zi et al., 2016; Li et al., 2022). On the basis of the analysis of the state of motion of potatoes and soil on the separating device, the mechanism of the separation process was understood and the separation devices were improved (Xin et al., 2023; Nalobina et al., 2021). Additionally, modifying the movement pattern of the bars by implementing a dual separation approach combining vibration and waveform has been shown to enhance potato-soil separation and minimize losses (Zhong et al., 2020; Wei et al., 2019). A curved bar design and a curved-straight bar exchange configuration have been developed to enhance potato-soil separation, improving effectiveness and reducing clogging. However, there has been limited research on how changing the shape of the bar affects separation efficiency, and there is currently no detailed theory regarding the optimal shape and mounting configuration of the curved bar (Lv et al., 2015; Xing et al., 2024; Zhong et al., 2023; Ji et al., 2022). Due to the scarcity of harvesters suited for sticky soils in southern regions (Ji et al., 2022; Lv et al., 2017; Bei et al., 2021), this paper focuses on optimizing the structural parameters and assembly methods of concave bars. Simulation models of potato-soil mixtures were developed to theoretically analyze the separation process. Key factors such as the angle of the concave side, width of the concave, and installation angle were studied. Orthogonal tests were conducted to evaluate separation efficiency and maximize potato recovery. The results confirmed the rationality and feasibility of the concave-bar potato-soil separation device.

Structure and theoretical analysis

Structure of the whole machine

In this paper, a potato-soil separation device is designed specifically for the sticky soils prevalent in southern regions. Due to the high soil adhesion characteristics, a lift chain separator was selected as the model for this study. The lifting chain potato-soil separation device is a critical component of a potato harvester, consisting of a frame, digging shovel, gearbox, transmission system, separation device, and vibration unit. It is known for its stable conveying performance, effective separation when paired with a vibration unit, straightforward structure, and strong adaptability. According to agricultural machinery design manuals, the length of the initial separation device typically ranges from 1.2 to 1.5 meters, with the inclination angle of the plane formed by the chain bar between 22° and 34°. In this study, a 30° angle was chosen to address the significant adhesion issues associated with southern sticky soil (Wei et al., 2018). To enhance the crushing and splitting of the potato-soil mixture, increasing the amplitude of vibration by adjusting the vibration unit could be considered. However, this approach might lead to increased damage to the potatoes (Jin et al., 2020; Xie et al., 2020). To address this issue, this paper proposes the use of concave bars. These bars are designed to induce fractures in the potato-soil mixture through an unbalanced force within a groove-like space, facilitating the crushing and separation of the mixture during the transfer process of the separation device. The structure of the entire machine is illustrated in Fig. 1.

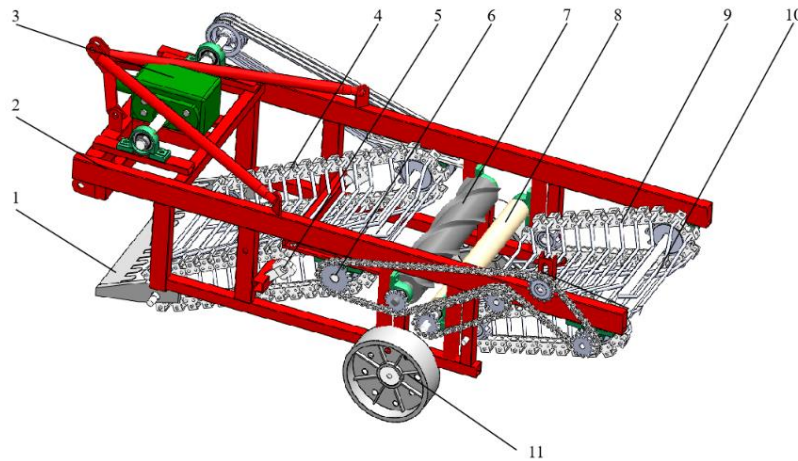


Fig. 1 - Structure of potato harvester in the form of concave bar

1- Digging shovel; 2 - Frame; 3 - Gearbox; 4- First separation device; 5 - Vibration unit; 6- Transmission system; 7- Cleaning roller; 8- Smooth roller; 9- Second separation device; 10- Concave bar 11- Walking wheel

The process of potato-soil separation can be summarized as follows: The tractor tows the potato harvester, which excavates the soil-potato mixture using the digging shovel. This mixture then enters the separation device. Within the device, the mixture is subjected to unbalanced forces in the grooves of the bars, causing it to break apart. The vibration unit generates impact collisions that help to overcome the adhesive forces between soil particles. This causes the internal structure of the soil to break down into smaller masses and particles. The separation device's design ensures that the broken soil and potatoes are separated, with the soil and potatoes falling to the ground through the gaps in the bars. Essentially, the process of crushing the soil transforms it from a continuous medium model into a discrete medium model, allowing for more efficient separation of soil and potatoes.

Theoretical analysis of potato transport process

Potatoes are cultivated in sticky soil environments, resulting in a lumpy potato-soil mixture when harvested by digging shovels. Separating this mixture efficiently using a straight-bar lifting chain proves challenging. To address this, the paper presents an optimized design featuring downward concave chain bars. As illustrated in Figure 2, the bars and their cross-sections were subjected to mechanical analysis to enhance the separation process.

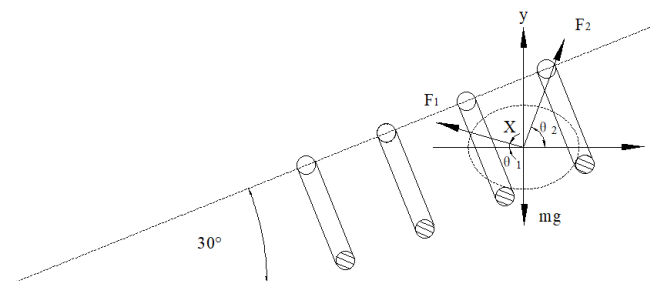


Fig. 2 - Mechanical analysis of potato

A coordinate system is established where the positive x-axis is directed opposite to the machine's forward direction, and the positive y-axis is oriented opposite to the direction of gravity. The equilibrium equation can then be derived based on this coordinate system, as follows:

$$F_1 \sin \theta_1 + F_2 \sin \theta_2 - mg = 0 \tag{1}$$

$$F_2 \cos \theta_2 - F_1 \cos \theta_1 = 0 \tag{2}$$

The simplification is as follows:

$$F_1 = \frac{mg \cos \theta_2}{\sin(\theta_1 + \theta_2)} \tag{3}$$

$$F_2 = \frac{mg \cos \theta_1}{\sin(\theta_1 + \theta_2)} \tag{4}$$

where:

F_1 is force of support of the front one bar on the potato, [N]; F_2 is force of support of the back one bar on the potato, [N]; θ_1 is angle between F_1 and the horizontal plane, [°]; θ_2 is angle between F_2 and the horizontal plane, [°]; mg is gravity of potato.

When the horizontal combined force on the potato is aligned with the positive x-axis, the potato will remain stable and not flow back during transportation. This stability is calculated as follows:

$$\sum F_x = F_2 \cos \theta_2 - F_1 \cos \theta_1 \geq 0 \tag{5}$$

Theoretical analysis of soil transport process

Large chunks of the potato-soil mixture are picked up by the digging shovels and conveyed to the concave bar. Due to varying coefficients of kinetic friction between the soil and potatoes against the bar, as well as the uneven forces exerted by the large soil lumps in the bar's grooves, the separation device can break and fragment. This results in the soil breaking into several particles and smaller lumps. When the mixture falls and collides with the bars, it generates significant and variable inertial forces. These forces can cause soil particles to fall through gaps in the bar and small soil pieces to break further. The sticky soil lump is idealized as a rectangular body for theoretical analysis. When a bar strikes this soil block, the instantaneous inertial force is much greater than the inertial force due to bar vibrations. Assuming the acceleration a perpendicular to the plane of the bar is the acceleration of the soil block, Figure 3 illustrates that to effectively crush the soil block, the crushing moment must exceed the moment of the internal forces' adsorption. The moment equation at point Q is given as follows:

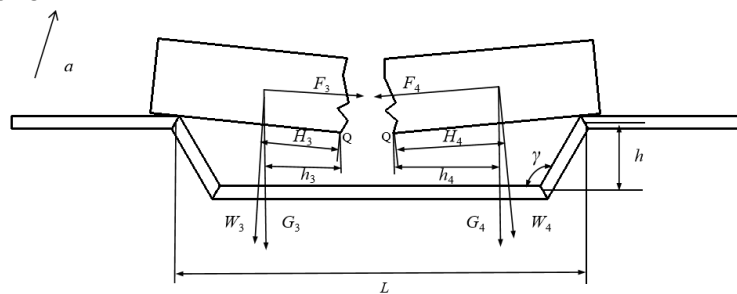


Fig. 3 - Mechanical analysis of soil

$$\begin{cases} G_3 h_3 + W_3 H_3 > F_3 H \\ G_4 h_4 + W_4 H_4 > F_4 H \end{cases} \tag{6}$$

where: G_3 and G_4 is gravity of the soil block, [N]; W_3 and W_4 is inertial force of the soil block, [N]; h_3 and h_4 is vertical distance of the gravitational force on the soil block to point Q, [mm]; H_3 and H_4 is vertical distance from the inertial force on the soil block to point Q, [mm]; L is width for concave bar, [mm]; h is depth for concave bars, [mm]; γ is angle of the concave side, [mm]; F_3 and F_4 is cohesion of the soil block, [N].

The magnitude of the inertial forces W_3 and W_4 of the soil block are specified as follows:

$$\begin{cases} W_3 = -m_3 a \\ W_4 = -m_4 a \end{cases} \tag{7}$$

Bringing equations (6) and (13) into equation (12), as follows:

$$\begin{cases} 2A\pi^2 m_3 f^2 \cos(2\pi ft + a) h_3 + m_3 g H_3 > F_3 H \\ 2A\pi^2 m_4 f^2 \cos(2\pi ft + a) h_4 + m_4 g H_4 > F_4 H \end{cases} \tag{8}$$

It is the moment equation for crushing, as follows:

$$M_0 = 2A\pi^2 m_i f^2 \cos(2\pi ft + a) h_i + m_i g H_i \tag{9}$$

From the equation, the crushing capacity of the separation device is proportional to the square of the amplitude and frequency generated by the vibration unit.

Assuming that the height of the soil block is $2H$ and its length is L , it follows from the geometric relationship that:

$$\begin{cases} H = \frac{h}{2} \\ H_3 = H_4 = \frac{L}{4} \\ h_3 = h_4 = \cos(\gamma - \frac{\pi}{2}) h \end{cases} \tag{10}$$

Soil brokenness is directly proportional to soil strength, and adhesion is the main factor. The cohesion of the soil is as follows

$$F = c \cdot S \tag{11}$$

where:

c is soil bonding strength, [kPa]; S is area of soil breaks, [cm²].

The quality of the soil is as follows:

$$m = \mu \cdot V \tag{12}$$

where:

μ is soil capacity, [g/cm³]; V is volume of the soil block, [cm³].

Bringing Eqs. (19), (20) and (21) into Eqs. (16) and (17). When the function of acceleration goes to the maximum, the maximum crushing moment generated by the separation device is as follows:

$$2A\pi^2\mu\frac{hL^2}{4}f^2\cos(2\pi ft+a)\cos(\gamma-\frac{\pi}{2})h+\mu\frac{hL^3}{16}g > c\cdot\frac{Lh^2}{8} \tag{13}$$

The inertia force distance indeed plays a crucial role in breaking the soil block, as it generates the dominant moment needed to overcome the block's resistance. When the block breaks, its displacement aligns with both the inertial force direction and the internal bonding force direction. The relationship between the concave's width, depth, and angle, and the crushing moment is positively correlated. This correlation implies that as these dimensions increase, the moment required for soil crushing also increases. Additionally, the energy required to break the soil block depends on its cohesive forces, which are significantly influenced by the soil's moisture content. More moisture typically reduces soil cohesion, making the soil block easier to break.

MATERIALS AND METHODS

Simulation model of potato

The study of potato, soil, and bar interactions, especially using Discrete Element Method (DEM), provides valuable insights. Potatoes and soil lumps have distinct mechanical properties: soil lumps exhibit excitation and depolymerization, while bars, particularly chain bars, show rigidity (Zhong et al., 2020). Analyzing how these properties affect collisions and fragmentation on concave bars helps understanding how different bar parameters influence the behavior of potato-soil mixtures. This can be critical for optimizing processes in agricultural and industrial applications.

Given the extensive variety of potato shapes, the study simplified the model by representing potatoes as multisphere aggregates. This approach facilitated the analysis by approximating the complex geometry of potatoes with a more manageable and computationally efficient model, as shown in figure 4.

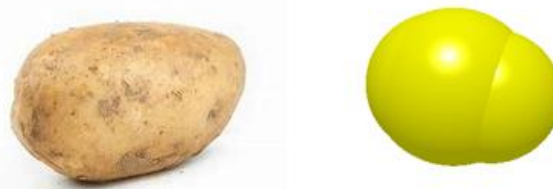


Fig. 4 - EDEM models of potato

For the study of potato triaxial minimum thickness dimensions, the potato model was configured with triaxial dimensions of 62 mm x 52 mm x 52 mm. The model generation time in the 'Particle Factory' software was set to 0.5 seconds, with a total of 20 models created. Potatoes and soils were distributed based on data from actual potato harvests. A monolayer distribution method was employed, wherein potatoes were randomly dropped onto a subsoil layer. Simulation parameters are detailed in Table 1 (Zhong et al., 2020; Wen et al., 2018).

Table 1

Simulation parameter of potato	
Parameter	Numerical value
Poisson's ratio of potato	0.5
Shear modulus of potato/ MPa	1.3
Density of potato	1100

Parameter	Numerical value
Potato-potato restitution coefficient	0.97
Potato-potato static friction coefficient	0.5
Potato-potato rolling friction coefficient	0.02

Simulation model of soil

Considering the characteristics of southern sticky soils, this paper employs the cohesive particle model, specifically the 'Hertz-Mindlin with Bonding V2' contact model, which incorporates bonding between soil particles. Soil particles in southern regions are noted for their high cohesion. When the particle radius is defined, the bonding radius of wet particles can be determined from the material density and moisture content using the formula for the contact radius of soil particles, as follows:

$$w_c = \frac{m_2}{m_1 + m_2} = \frac{\rho_2 v_2}{\rho_1 v_1 + \rho_2 v_2} \quad (14)$$

where:

w_c is soil moisture content, [%]; m_1 is quality of soil particles, [kg]; m_2 is quality of water, [kg]; ρ_1 is density of soil, [kg/m³]; ρ_2 is density of water, [kg/m³]; v_1 is volume of soil particles, [m³]; v_2 is volume of water, [m³].

For reference, the radius of soil particles is usually set to 3 mm. Based on actual tests, the moisture content of southern sticky soils is 26%. The contact radius of soil particles could be calculated as 3.75 mm. The simulation parameters are shown in Table 2 (Zhong *et al.*, 2020; Xie *et al.*, 2020).

Table 2

Simulation parameter of soil	
Parameter	Numerical value
Poisson's ratio of potato	0.5
Shear modulus of potato / MPa	1.3
Density of potato / kg/m ³	1100
Potato-potato restitution coefficient	0.97
Potato-potato static friction coefficient	0.5
Potato-potato rolling friction coefficient	0.02

Simulation model of separation device

To streamline the simulation process, this study disregards the effects of seedlings and vines on soil fragmentation and the movement characteristics of potato pieces. Additionally, air resistance during the falling process after material ejection is omitted. Components such as bars and other parts of the machine were constructed from 65Mn steel. Figure 5 illustrates the simulation model of the potato harvester, which features concave bars.

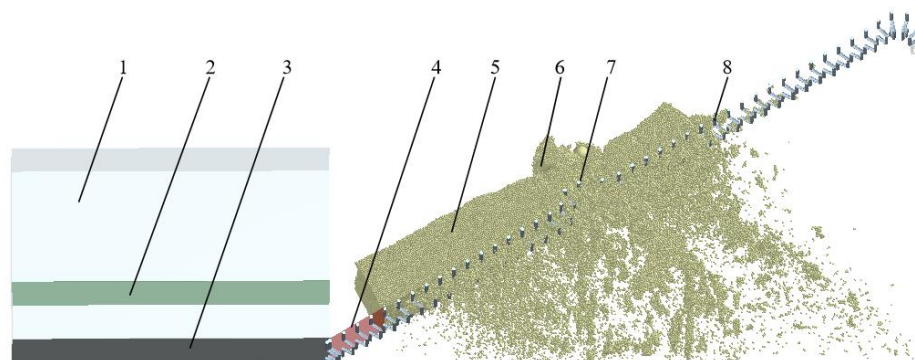


Fig. 5 - Simulation model

- 1- Factory; 2 - Plates for compacted soil; 3 - Conveyor belt model; 4- . Digging shovel; 5 - Soil; 6- Potato; 7- Vibration device; 8- Concave bar

Table 3 shows the soil and bar simulation parameters. The main parameters of the simulation are shown in Table 4 (Zhong *et al.*, 2020; Xie *et al.*, 2020; Li *et al.*, 2022).

Table 3

Simulation parameters of separation device

Parameter	Numerical value
Potato-soil restitution coefficient	0.06
Potato-soil static friction coefficient	0.5
Potato-soil rolling friction coefficient	0.01
Potato-bar restitution coefficient	0.5
Potato-bar static friction coefficient	0.4
Potato-bar rolling friction coefficient	0.1
Soil-soil of normal stiffness per unit area / (N·m ⁻¹)	1.4 × 10
Soil-soil the maximum normal strength / MPa	0.235
Soil-soil of shear stiffness per unit area / (N·m ⁻¹)	1 × 10 ⁶
Soil-soil the maximum shear strength/ (MPa)	0.186
Poisson's ratio of bar	0.3
Shear modulus of bar/ (MPa)	3.1 × 10 ⁵
Density of bar / (kg·m ⁻³)	7800
Soil-bar restitution coefficient	0.16
Soil-bar static friction coefficient	0.6
Soil-bar rolling friction coefficient	0.35

Table 4

Main parameters

Parameter	Numerical value
Diameter of the bar / (mm)	11
Length of the bar / (mm)	630
Velocity of the bar / (m/s)	1.7
Distance between the centers of adjacent bars / (mm)	50
Time interval between movements of adjacent bars / (s)	0.02941
Angular velocity of the bar / (rad/s)	20.98765
Vibration frequency / (Hz)	5

A 630 mm × 1000 mm × 600 mm 'Factory' was constructed to characterize the potato-soil mixture. Within this 'Factory,' the potato factory and two soil particle factories were established. To accurately simulate the harvesting environment, the subsoil generation began at 0 seconds, with a total of 600,000 generations. The subsoil was fully generated before the creation of the potatoes. Following the completion of the topsoil layer, which involved generating 130,000 particles, the soil was compacted at 0.8 seconds, resulting in a 180 mm 'soil-potato-soil' mixture. To simulate the forward movement of the harvester, a 'moving plane' model was integrated into the floor and front settings of the 'Factory.' During the potato-soil separation process, soil clumps adhered to each other and collided with the concave chain bar, causing them to crush and disperse the potato-soil mixture throughout transportation.

Factors of orthogonal experiment

Based on research and practical production experience (Jun, 2010), Figure 6 illustrates the factors coded A, B, C, and D, which correspond to the angle of the concave side, the width of the concave, the depth of the concave, and the angle of installation, respectively. Table 5 presents the orthogonal experiment design, with separation efficiency and maximum force on potatoes used as evaluation indices.

Table 5

Coding with factors and levels

Level	Factor			
	A	B	C	D
	Angle of the concave side /°	Width of concave /mm	Depth of concave /mm	Angle of installation/°
1	90	250	12	-30
2	120	350	36	0
3	150	450	60	30

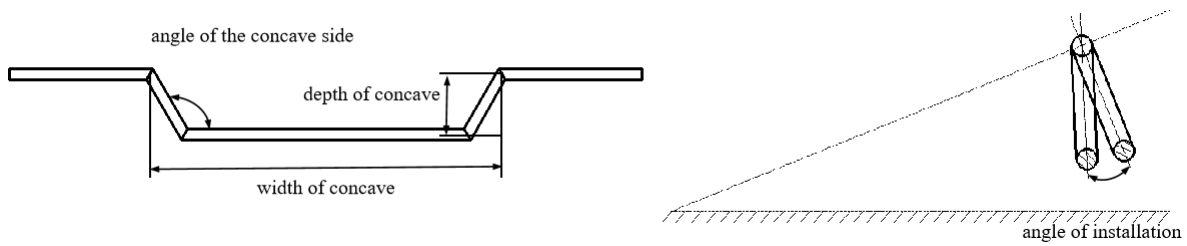


Fig. 5 - Schematic diagram of factors

Methodology for testing evaluation indicators

Separation efficiency is evaluated by collecting data from the 'particle factory' and from the position where the bar reaches its end. A mass sensor is set up at the end of the separation device to measure the soil mass. The separation efficiency is then calculated using the following formula:

$$E = 1 - \frac{M_r}{M_t} \tag{15}$$

where:

E is separation efficiency, [%]; M_r is remaining mass of soil at the end of the separation device, [kg]; M_t is total mass of soil after completion of soil generation in the "Factory", [kg].

The method for determining the maximum force on the potato involves using a 'Grid Bin Group' to measure the force exerted on potatoes within the separation plane. Subsequently, 'Manual Selection' is employed to calibrate and measure the force on 20 individual potatoes, with data exported for analysis. The recorded 'Compressive Force' represents the maximum force applied to each potato. Observations of the potato-soil mixture on the sieving device revealed that potato movement was most active between 2.5 and 4 seconds, with the highest collision frequency during this interval. Assuming that collisions occur in the same area on the potato block within this period, the forces on the 20 potatoes are summed separately for this time frame, and the maximum value is selected. This maximum value is used to assess the force applied to the potato under these conditions and determine potential damage. According to potato damage experiments, a force greater than 200 N on the potato surface is likely to cause damage (Wei et al., 2023; Li and Ji, 2022). Thus, a threshold of 200 N is used to evaluate whether the potato has been damaged.

RESULTS

Concave vs. straight bars

Simulation experiments used EDEM's "Hertz Mindlin with bonding" contact model as a model for soil particle bonding. The "Grid Bin Group" was set to count the number of bond keys, and the data was exported as Figure 7.

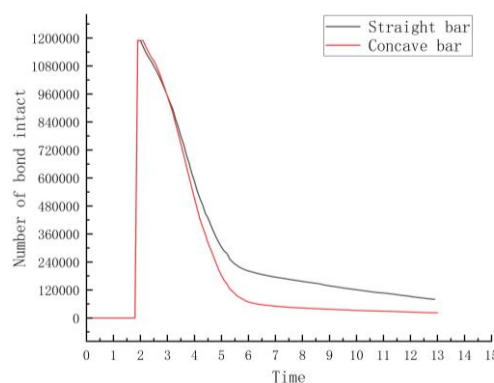


Fig. 7 - Bond Number of bond connections

From the figure, it is evident that after soil formation was completed at 1.8 seconds, bond connections between soil particles began to form. During transportation on the separation device, these soil clumps were broken apart, reducing the bond connections between particles. Over time, the rate at which these bonds decreased was more pronounced on separation devices with concave bars compared to those with straight bars. This observation indicates that the crushing capacity of concave bars is superior to that of straight bars.

Experimental results and analysis

Table 6 presents an analysis of variance (ANOVA) performed on the results of the orthogonal experiments to examine the impact of four factors—angle of the concave side bar, width of the concave, depth of the concave, and angle of installation—on separation efficiency and maximum force on the potato. Since factor A had the least effect on both indicators, it was used as the control group in the ANOVA.

Table 6

Results of orthogonal experiment and range analysis							
Indicator	Serial number	Factor				Results	
		A	B	C	D	Separation efficiency (%)	Maximum force on potatoes (N)
	1	1	1	1	1	61.2	34.991
	2	1	2	2	2	72.0	41.694
	3	1	3	3	3	77.5	33.134
	4	2	1	2	3	74.9	42.125
	5	2	2	3	1	68.7	33.546
	6	2	3	1	2	73.3	33.681
	7	3	1	3	2	73.6	35.420
	8	3	2	1	3	77.0	45.674
	9	3	3	2	1	67.8	30.927
Separation efficiency (%)	K_1	210.7	209.7	211.5	197.7		
	K_2	217.0	217.6	214.7	218.9		
	K_3	218.3	218.6	219.8	229.4		
	k_1	70.2	69.9	70.5	65.9		
	k_2	72.3	72.5	71.6	73.0		
	k_3	72.8	72.9	73.3	76.5		
	R	2.5	3.0	2.8	10.6		
	Sequence	4	2	3	1		
Maximum force on potatoes (N)	K_1	109.819	112.536	114.346	99.464		
	K_2	109.351	120.914	114.745	110.794		
	K_3	112.021	97.742	102.100	120.933		
	k_1	36.606	37.512	38.115	33.155		
	k_2	36.450	40.305	38.248	36.931		
	k_3	37.340	32.581	34.033	40.311		
	R	0.890	7.724	4.215	7.156		
	Sequence	4	1	3	2		

Table 7

Results of variance analysis					
Indicator	Origin	Sum of squared deviations	Mean square	F-value	P-value
Separation efficiency (%)	width of concave	0.002	< 0.001	1.444	0.409
	depth of concave	0.001	< 0.001	1.080	0.481
	angle of installation	0.017	0.009	15.903	0.059
Maximum force on potatoes (N)	width of concave	91.777	45.889	67.713	0.015
	depth of concave	34.445	17.223	25.414	0.038
	angle of installation	76.895	38.447	56.733	0.017

Table 7 indicates that the factors had weakly significant effects on separation efficiency. Due to the orthogonal design, there was no correlation between factors, resulting in a large p-value for the non-significant factor C. Table 8 presents the revised ANOVA obtained by excluding factor C. This is because the sum of squared deviations for the remaining factors remains constant when one factor is removed. The results revealed that the angle of installation was significant ($p < 0.05$), indicating that it has a substantial effect on the

screening efficiency of potato-soil mixtures. Polar analysis showed that the factors affecting separation efficiency are ranked as follows: $D > B > C > A$. The installation angle has the most significant impact on efficiency, while the angle of the concave side bar has the least. The optimal parameters for achieving the best separation efficiency are a 150° angle for the concave side bar, a concave width of 450 mm, a concave depth of 60 mm, and an installation angle of 30° .

Table 8 revealed that the width of the concave, the depth of the concave, and the angle of installation all had significant effects ($p < 0.05$) on the maximum force exerted on potatoes. The data from polar analysis showed that the factors influencing the maximum force are ranked as follows: $B > D > C > A$. The width of the concave bar had the greatest impact, while the angle of the concave side bar had the least influence. Thus, the optimal parameters for minimizing the maximum force on potatoes are a 120° angle for the concave side bar, a concave width of 450 mm, a concave depth of 60 mm, and an installation angle of -30° .

Table 8

Consolidated results of variance analysis

Indicator	Origin	Sum of squared deviations	Mean square	F-value	P-value
Separation efficiency (%)	width of concave	0.002	< 0.001	1.389	0.348
	angle of installation	0.017	0.009	15.290	0.013*
Maximum force on potatoes (N)	width of concave	91.777	45.889	67.713	0.015*
	depth of concave	34.445	17.223	25.414	0.038*
	angle of installation	76.895	38.447	56.733	0.017*

Table 9 indicated that two sets of parameter schemes were simulated to determine the optimal combination. The results showed that with an angle of 150° for the concave side bar, a concave width of 450 mm, a concave depth of 60 mm, and an installation angle of 30° , the separation efficiency reached 79.7%. Additionally, the maximum force on the potatoes did not exceed 200 N in both combinations, ensuring that the potatoes remained undamaged.

Table 9

Simulation results with optimal parameters

Composition	Separation efficiency [%]	Maximum force on potatoes [N]
A ₃ B ₃ C ₃ D ₃	79.7	35.218
A ₂ B ₃ C ₃ D ₁	77.9	32.787

Field experiment

The field experiment utilized a towed harvester with bars set to a 150° angle for the concave side bar, a concave width of 450 mm, a depth of 60 mm, and an installation angle of 30° . Conducted at Yingchang Agricultural Machinery Cooperative in Liuyang City, China, the potatoes (Jiaying 2 variety) were grown in row crops with a soil moisture content of 22.4%. The loss rate, damage rate and potato epidermal injury rate were measured in the field experiment are. The detailed measure methods are as follows:

Lost potatoes are buried potatoes and non-dug potatoes. The loss rate was calculated as follows:

$$T_1 = \frac{W_1 + W_2}{W} \times 100\% \quad (16)$$

where: T_1 is lost rate, [%]; W_1 is mass of buried potatoes, [kg]; W_2 is mass of non-dug potatoes, [kg]; W is total mass of potatoes, [kg].

Damaged potatoes are the damaged part of all potatoes. The damage rate was calculated as follows:

$$T_2 = \frac{W_3}{W} \times 100\% \quad (17)$$

where: T_2 is damage rate, [%]; W_3 is mass of damaged potatoes, [kg].

Potatoes of epidermal injury are the part of all potatoes with broken skin. The potato epidermal injury rate is calculated as follows:

$$T_3 = \frac{W_4}{W} \times 100\% \quad (18)$$

where:

T_3 is potato epidermal injury rate, [%]; W_4 is mass of potatoes of epidermal injury, [kg].

Figure 8 illustrates the results of the field harvesting experiment, and Table 10 presents the data. The results showed that the damage rate was 1.58% and the potato epidermal injury rate was 1.03%, and the loss rate was 2.87%, which met the standard requirements (NY/T 648-2015).



Fig. 8 - Field harvest experiment and results

Table 10

Results of field tests							
Groups	Mass of damage potato [kg]	Mass of potato epidermal injury [kg]	Mass of loss potato [kg]	Total mass [kg]	Damage rate [%]	Potato epidermal injury rate [%]	Loss rate [%]
1	0.12	0.09	0.27	8.75	1.37	1.03	3.09
2	0.19	0.1	0.25	9.18	2.07	1.09	2.72
3	0.15	0.08	0.32	9.07	1.65	0.88	3.53
4	0.11	0.1	0.19	8.85	1.24	1.13	2.15
Average					1.58	1.03	2.87
Standard requirements					≤2	≤3	≤4

CONCLUSIONS

Due to the high soil moisture content prevalent in southern potato cultivation environments, separating potatoes from the soil during harvesting presents significant challenges. To address this issue, a concave lifting chain device was employed, and the structural parameters of the concave chain bars were optimized. The results of this approach are summarized as follows:

- (1) A potato-soil mixture model was developed using EDEM software. A simulation model of a concave bar-type potato-soil separation device was constructed to investigate the effects of various structural parameters on the separation process. The influence of these parameters on the potato-soil separation was elucidated through theoretical analysis.
- (2) A comparative simulation experiment was conducted using both the concave bar-type and straight bar models for potato-soil separation. The number of bonds in the soil model was quantified for each model. The analysis of the results indicated that the soil-breaking capacity of the concave bar-type separation device was superior to that of the straight bar model.
- (3) Orthogonal simulation experiments were conducted to identify the optimal parameter combinations for the concave bar potato-soil separation device through comprehensive analysis. The field experiment, conducted under the conditions of a 150° angle for the concave side bar, a concave width of 450 mm, a concave depth of 60 mm, and an installation inclination angle of 30°, demonstrated that the relevant test indices met national standards.

ACKNOWLEDGEMENT

The study was supported by Project supported by Natural Science Foundation of Hunan Province(2024JJ5194), Changsha Municipal Natural Science Foundation (kq2208071) and A Project Supported by Scientific Research Fund of Hunan Provincial Education Department (23A0181).

REFERENCES

- [1] Dou, Q., Sun, Y., Sun, Y., Shen, J., & Li, Q. (2019). Current situation and development of potato harvesting machinery at home and abroad (国内外马铃薯收获机械现状与发展). *Journal of Chinese Agricultural Mechanization*, Vol. 40, pp. 206-210, Nanjing/China.
- [2] Hrushetsky, S.M., Yaropud, V. M., Duganets, V. I., Pryshliak, V. M., Kurylo, V. L., & Agrarian, S. (2019). Research of constructive and regulatory parameters of the assembly working parts for potato harvesting machines. *INMATEH-Agricultural Engineering*, Vol. 59, pp. 101-110, Romania.
- [3] Ji, L., Yi, N., Yu, S. (2022). Design and experiment of separating and lifting device of potato harvester-based one equivalent radius method (马铃薯收获机分离升运装置设计与试验——基于当量半径法). *Journal of Agricultural Mechanization Research*, Vol.44, pp. 199-206+256, Heilongjiang/China.
- [4] Jin, L., Xiao, Y., Yi, L., Zi, L., Ji, L., & Chang, D. (2020). Analysis and Experiment of Potato Damage in Process of Lifting and Separating Potato Excavator (马铃薯挖掘机升运分离过程块茎损伤机理分析与试验). *Transactions of the Chinese Society for Agricultural Machinery*, Vol. 51, pp. 103-113, Beijing/China.
- [5] Jun, G., Xu, L., & Cai, W. (2010). Parameters optimization in regression of linear equation based on experiments designed by orthogonal L₉ (34) (正交设计 L₉ (3~4) 的渐进优化线性回归方法). *Computers and Applied Chemistry*, Vol. 27, pp. 1503-1508, Beijing/China.
- [6] Li, J., Xu, M., Tao, W., Xue, C., & Guo, S. (2016). Application status and research prospect of southern winter planting potato harvesting machine (南方冬种马铃薯收获机的应用现状与研究展望). *Journal of Agricultural Mechanization Research*, Vol.38, pp. 263-268, Heilongjiang/China.
- [7] Li, X., Ji, L. (2022). Design of a new potato combine harvester. *Acta Mechanica Malaysia*, Vol.15, pp. 44-46, Acta Mechanica Malaysia, Malaysia.
- [8] Li, Y.B., Zhang, Z.G., Wang, Y.M., Wang, H.Y., Fang, Y.I., & Zhang, Z.D. (2022). Design and experiment of multistage conveying and separating device for potato harvester (马铃薯收获机多级输送分离装置设计与试验). *Journal of Shenyang Agricultural University*, Vol.52, pp. 758-768, Shenyang/China.
- [9] Lv, J., Sun, H., Dui, H., Peng, M., & Yu, J. (2017). Design and experiment on conveyor separation device of potato digger under heavy soil condition. *Transactions of the CSAM*, Vol.48, pp. 146-155, Beijing/China.
- [10] Lv, J., Tian, Z., Yang, Y., Shang, Q., & Wu, J. (2015). Design and experimental analysis of 4U2A type double-row potato digger (4U2A 型双行马铃薯挖掘机的设计与试验). *Transactions of the Chinese Society of Agricultural Engineering*, Vol.31, pp. 17-24, Beijing/China.
- [11] Nalobina, O., Shymko, A., Bundza, O., Holotiuk, M., Herasymchuk, O., & Puts, V. (2021). Theoretical analysis of strength resistance to displacement of improved digging working body of potato harvesting combine. *INMATEH-Agricultural Engineering*, Vol. 65, pp. 312-320, Romania.
- [12] Qing, Z. (2020). Research status and development prospect of potato harvesting machinery at home and abroad. *Agricultural Engineering*. Vol.10, pp. 7-10, USA.
- [13] Wei Z, W., Li, H., Chuan, S., Xue, L., Wen, L., Guo, S., & Fa, W. (2018). Improvement of potato harvester with two segments of vibration and wave separation (振动与波浪二级分离马铃薯收获机改进). *Transactions of the CSAE*, Vol. 34, pp. 42-52, Beijing/China.
- [14] Wei, D., Chun, W., & Sheng, X. (2020). Test research on the impact peak force and damage depth of potato. *INMATEH-Agricultural Engineering*, Vol. 61, pp. 105-114, Romania.
- [15] Wei, W., Ran, Y., Zhi, P., Yi, Q., Jian, Z., Dong, C., Xin, G., & Shi, Lyu. (2023). Design and Experimental Study of Single Plant Harvester for Potato Breeding Experiments. *Agriculture*, Vol. 14, pp. 71, Switzerland.
- [16] Wei, Z., Li, H., Sun, C., Su, G., Liu, W., & Li, X. (2019). Experiments and analysis of a conveying device for soil separation and clod-crushing for a potato harvester. *Applied engineering in agriculture*, Vol. 35, pp.987-996, USA.
- [17] Wen, L., Jin, H., Hong, L., Xue, L., Kan, Z., & Zhong, W. (2018). Calibration of simulation parameters for potato minituber based on EDEM (基于离散元的微型马铃薯仿真参数标定). *Nongye Jixie Xuebao/Transactions of the Chinese Society of Agricultural Machinery*, Vol.49, pp. 125-135+142, Beijing/China.
- [18] Wu, B., Huang, T., Qiu, X., Zuo, T., Wang, X., & Fang, X. (2021). Design and experimental study of potato-soil separation device for sticky soils condition. *Applied Sciences*, Vol.11, pp.10959, Switzerland.
- [19] Xie, F., Wu, Z., Wang, X., Liu, D., Wu, B., & Zhang, Z. (2020). Calibration of discrete element parameters of soils based on unconfined compressive strength test (基于无侧限抗压强度试验的土壤离散元参数标定). *Transactions of the Chinese Society of Agricultural Engineering*, Vol. 36, pp. 39-47, Beijing/China.

- [20] Xie, S., Wang, C., & Deng, W. (2020). Collision damage test and acceleration characteristic analysis of potato (马铃薯碰撞损伤试验与碰撞加速度特性分析). *Journal of China Agricultural University*, Vol. 25, pp. 163-169, Beijing/ China.
- [21] Xin, H., Long, L., Xing, L., Yu, X., Tao, J., Wei, L. (2023). Design and test of potato conveying and grading device with variable space, *INMATEH-Agricultural Engineering*, Vol. 69, pp. 681-692, Romania.
- [22] Xing, W., Zhong, W., Guo, S., Peng, M., Fa, W., Xiang, Z., & Xian, W. (2024). Design and Experiment of Simple Harmonic Disturbance Separation Device for Potato Harvester (马铃薯收获机扰动分离装置设计与试验). *Nongye Jixie Xuebao/Transactions of the Chinese Society of Agricultural Machinery*, Vol. 55, pp. 101-112, Beijing/China.
- [23] Zhao, Z., Hai, W., Yan, L., Xi, Y., Issa, Ibrahim., & Zhen, Z. (2021). Design and Experiment of Multi-stage Separation Buffer Potato Harvester (多级分离缓冲马铃薯收获机设计与试验). *Nongye Jixie Xuebao/Transactions of the Chinese Society of Agricultural Machinery*, Vol.52, pp. 96-109, Beijing/China.
- [24] Zheng, Z., Zhao, H., Liu, Z., He, J., & Liu, W. (2021). Research progress and development of mechanized potato planters: A review. *Agriculture*, Vol. 11, pp. 521, Switzerland.
- [25] Zhong, W., Guo, S., Xue, L., Fa, W., Chuan, S., & Peng, M. (2020). Parameter optimization and test of potato harvester wavy sieve based on EDEM (基于离散元的马铃薯收获机波浪形筛面参数优化与试验). *Nongye Jixie Xuebao/Transactions of the Chinese Society of Agricultural Machinery*, Vol. 51, pp. 109-122, Beijing/China.
- [26] Zhong, W., Xing, W., Xue, L., Fa, W., Zhi, L., & Cheng, J. (2023). Design and Experiment of Crawler Self-propelled Sorting Type Potato Harvester (履带自走式分拣型马铃薯收获机设计与试验). *Nongye Jixie Xuebao/Transactions of the Chinese Society of Agricultural Machinery*, Vol. 54. pp, 95-106, Beijing/China.
- [27] Zhou, J., Yang, S., Li, M., Chen, Z., Zhou, J., Gao, Z., & Chen, J. (2021). Design and experiment of a self-propelled crawler-potato harvester for hilly and mountainous areas. *INMATEH-Agricultural Engineering*, Vol. 64, pp. 151-158, Romania.
- [28] Zi, L., Jiang, J., Chang, Z., Qun, Y., & Xiu, S. (2016). Design and Experimental Study on The Conveying Chain Soil Cleaning Device of Potato Harvester (薯类收获机输送链条清土装置的设计和试验研究). *Journal of Agricultural Mechanization Research*, Vol.38, pp. 123-127, Heilongjiang/China.

IMPROVED YOLOv8N-BASED DETECTION OF GRAPES IN ORCHARDS

基于改进 YOLOv8n 的果园葡萄检测方法

Shan TAO, Shiwei WEN, Guangrui HU, Yahao GE, Jingming WEN, Xiaoming CAO, Jun CHEN^{*)}
College of Mechanical and Electronic Engineering, Northwest A&F University, Yangling 712100, China
Tel: +86-13572191773; E-mail: chenjun_jdxy@nwsuaf.edu.cn
DOI: <https://doi.org/10.35633/inmateh-74-42>

Keywords: Fresh table grapes, Automatic detection, Algorithm lightweight design, YOLOv8n

ABSTRACT

To address the issues of low detection accuracy, slow speed, and large parameter size in detecting fresh table grapes in natural orchard environments, this study proposes an improved grape detection model based on YOLOv8n, termed YOLOGPnet. The model replaces the C2f module with a Squeeze-and-Excitation Network V2 (SENetV2) to enhance gradient flow through more branched cross-layer connections, thereby improving detection accuracy. Additionally, the Spatial Pyramid Pooling with Enhanced Local Attention Network (SPPELAN) substitutes the SPPF module, enhancing its ability to capture multi-scale information of the target fruits. The introduction of the Focaler-IoU loss function, along with different weight adjustment mechanisms, further improves the precision of bounding box regression in object detection. After comparing with multiple algorithms, the experimental results show that YOLOGPnet achieves an accuracy of 93.6% and mAP@0.5 of 96.8%, which represents an improvement of 3.5 and 1.6 percentage points over the baseline model YOLOv8n, respectively. The model's computational load, parameter count, and weight file size are 6.8 Gflops, 2.1 M, and 4.36 MB, respectively. The detection time per image is 12.5 ms, showing reductions of 21.84%, 33.13%, 30.79%, and 25.60% compared to YOLOv8n. Additionally, comparisons with YOLOv5n and YOLOv7-tiny in the same parameters reveal accuracy improvements of 0.7% and 1.9%, respectively, with other parameters also showing varying degrees of enhancement. This study offers a solution for accurate and rapid detection of table grapes in natural orchard environments for intelligent grape harvesting equipment.

摘要

针对自然果园环境下鲜食葡萄的检测精度低、速度慢、参数量较大等问题，本研究提出了一种基于改进 YOLOv8n 的葡萄检测模型（YOLOGPnet）。该模型使用压缩与激励网络（Squeeze-and-Excitation Network V2, SENetV2）替换了 C2f 模块，通过更多的分支跨层连接使梯度流更加丰富，提高模型的检测精度；并将 SPPF 模块替换为增强局部注意力的空间金字塔池化网络（Spatial Pyramid Pooling with Enhanced Local Attention Network, SPPELAN），提升了网络捕捉目标果实的多尺度信息的能力；通过使用 Focaler-IoU 损失函数，和引入不同的权重调整机制提高了目标检测中的边界框回归精度问题。试验结果表明，YOLOGPnet 的精确度和 mAP@0.5 分别为 93.6%、96.8%，相较于 YOLOv8n，分别提高了 3.5 和 1.6 个百分点。该模型的计算量、参数量和权重文件大小分别为 6.8 Gflops、2.1 M 和 4.36 MB，单幅图像检测耗时为 12.5 ms，相较于 YOLOv8n，分别降低了 21.84%、33.13%、30.79% 和 25.60%。该研究为智能化葡萄采摘装备在自然果园环境下准确且快速地检测鲜食葡萄提供了一种解决方案。

INTRODUCTION

According to the Food and Agriculture Organisation of the United Nations (in full English, FAO), the global production of grapes reached about 80.1×10^8 kg in 2022 (Khan N et al., 2021). Grape harvesting, as a labour-intensive operation, is challenged by global labour resource constraints, and harvesting robotics is becoming increasingly important in grape growing (Zhao et al., 2023). Traditional target detection in dense berry class mainly relies on colour, shape and texture features, and with the development of deep learning technology, a large number of deep learning-based target detection methods with high accuracy and robustness have emerged (Ying et al., 2023).

Over the years, researchers worldwide have extensively studied machine vision technology for fruit and vegetable target recognition and picking point localization (Song et al., 2023). Lu et al. (2021) proposed the Swin-T-YOLOv5 model to detect grape clusters at different growth stages. Zhao et al. (2022) introduced an improved YOLOv4 method for predicting grape cluster picking points.

Wu et al. (2023) developed the Ghost-HRNet model, integrating object detection and key point localization to focus on grape peduncle positioning. *Ning et al. (2021)* innovatively used an improved Mask R-CNN to select optimal picking points at the horizontal central positions near the critical centroid of the peduncle area. *Zhang et al. (2023)* employed YOLOv5 GAP to detect green grape clusters effectively in densely grown and shaded environments. *Su et al. (2022)* proposed a lightweight grape detection method by integrating feature maps of different resolutions. *Wang et al. (2020)* introduced the SwinGD model for visual recognition of grape clusters. *Cha et al. (2021)* replaced Faster R-CNN's backbone with VGG16 to achieve accurate detection of Red Globe grapes in natural environments. *Zhu et al. (2021)* improved the YOLOX-Tiny model to detect red and green grape clusters. *Sun et al. (2023)* proposed the MRWYOLOv5s model, achieving a mAP of 97.74%, an improvement of 2.32% over the original model. *Li et al. (2021)* developed the YOLO grape model for detecting grape clusters of various colors, achieving an F1-score of 90.93% for green grapes and an average F1-score of 91.42%. *Zhao et al. (2022)* designed a lightweight end-to-end YOLO-GP model with integrated picking point prediction. *Cha et al. (2023)* employed transfer learning for Red Globe grape detection in natural settings. *Zhang et al. (2023)* utilized YOLOv5 GAP for accurate detection of densely grown grape clusters. *Liu et al. (2024)* proposed the YOLOX-RA model for fast and precise detection of densely grown and occluded grape clusters. *Lu et al. (2022)* developed the Swin-Transformer-YOLOv5 model, achieving 97% detection accuracy under cloudy conditions. *Guo et al. (2023)* introduced the YOLO y4+ model, which enhanced robustness in unstructured environments using a parameter-free attention mechanism. *Zhang et al. (2022)* developed the Grape-Internet dataset, improving detection efficiency through lightweight processing. *Qiu et al. (2022)* enhanced detection speed with an improved SM-YOLOv4 algorithm, achieving a detection time of 10.82 ms. *Yang et al. (2024)* proposed the YOLOv8s-grape detection method, significantly improving mAP and detection efficiency. *Jiang et al. (2024)* introduced the YOLOv8n-GP model, effectively enhancing feature extraction for grape stems.

In addition to its extensive application in grape harvesting, the YOLO series of algorithms has been widely used for target recognition and pest detection in other fruits and vegetables, providing valuable insights for improving recognition algorithms in this study. *Wen et al. (2024)* proposed a lightweight detection model based on an improved YOLOv8 network, incorporating partial convolution (Pconv) blocks to enhance apple detection under occlusion and varying lighting conditions. *Chen et al. (2024)* modified the YOLOv5 backbone by adding Transformer modules with attention mechanisms, replacing the original PAFPN Neck with a bidirectional weighted fusion BiFPN structure, and integrating a P2 shallow downsampling module in the Head structure. These modifications improved the accuracy of apple detection in natural environments by 3.7%. *Zhao et al. (2022)* conducted detection experiments on melon fruits using YOLOv3, YOLOv4, YOLOv5s, and an improved ResNet_YOLO model, finding YOLOv5 to perform best and demonstrating the feasibility of mixed detection for images of four Cucurbitaceae fruits. *Ren et al. (2024)* introduced MSC1-YOLOv8s, which enhanced the model's ability to capture multi-scale disease features in grape leaf images and achieved a real-time detection efficiency of 37.2 ms.

These studies have made significant progress in grape cluster target detection and picking point localisation, providing strong technical support to further improve fruit and vegetable recognition accuracy, but in the actual grape picking work it is necessary to ensure the recognition accuracy of fruit targets as well as to achieve the lightweight of the visual model, so this study improves and compares the existing models from these two aspects.

MATERIALS AND METHODS

Construction of grape image data set in orchard environment

Image acquisition

The grape fruit images in this dataset were captured between August 20th and 23rd, 2023, at the Caixin Research Base in Yangling District, Xianyang City, Shaanxi Province. Due to the challenge of distinguishing green grapes (such as Shine Muscat, Bijou, and Zuijinxiang) from the similarly colored leaves, green grape varieties were selected as the experimental subjects. Based on varying shooting distances, the images were categorized into close-range (0.5m), mid-range (1.2m), and long-range (2m) shots, and were captured using a HUAWEI P60 smartphone. A total of 1,536 images were collected under different lighting conditions and in complex environments, of which 1,100 images were used for training, 200 for validation, and 236 for testing. The training set was used for model training and parameter tuning, the validation set for optimizing the network structure, and the test set for evaluating the model's generalization capability.

The images were uniformly cropped to a resolution of 1240×1240, and resized to 640×640 pixels during training to ensure efficient inference and accuracy. The dataset includes grape clusters of various forms, with up to 20 clusters appearing in long-range images, and close-range images presenting cases of overlapping and occlusion.

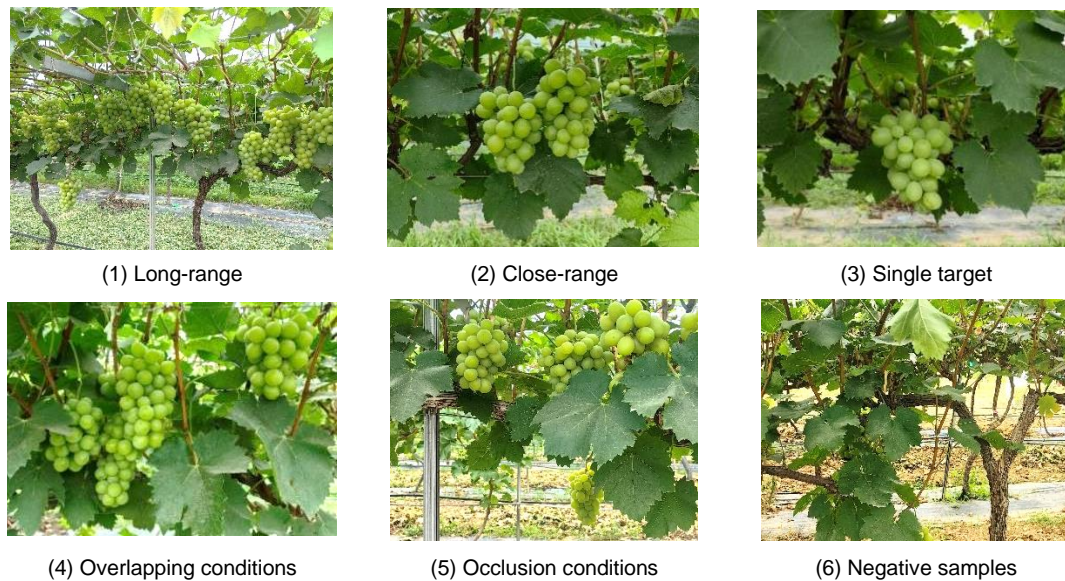


Fig. 1 - Grape fruit collection image example

The sample images were manually annotated using the Labelling software, where the grape cluster regions were labeled with minimum enclosing bounding boxes. This process generated XML files in VOC format, extracting information such as the coordinates of the center point, bounding box width, and height, which were then saved as TXT label files. The entire image dataset was divided into training, validation, and test sets. A diverse dataset enhances the model's generalization ability and robustness, while also improving the model's adaptability to different scales. On the self-constructed dataset, YOLOv8 employed various data augmentation techniques, including mosaic augmentation, mixup augmentation, random perturbation, and color distortion, effectively expanding the dataset size.

Detection model based on improved YOLOv8 YOLOGpnet

YOLOv8 is categorized into five models—n, s, m, l, and x—designed for different application scenarios. As the model depth increases, detection accuracy improves. YOLOv8n, with the smallest number of parameters, offers the fastest detection speed. To ensure real-time performance, this study focuses on enhancing the YOLOv8n model. The architecture consists of four components: the Input, Backbone, Neck, and Head.

As shown in Figure 2, YOLOGpnet replaces the C2f structure of the baseline model with SENetV2 in the Backbone. C2f is an improved version of the C3 structure in YOLOv5, whereas SENetV2 enriches the gradient flow through more branched cross-layer connections, enhancing feature representation capabilities. It aims to improve recognition accuracy by optimizing spatial feature extraction and channel-level representation. Additionally, the SPPF module is replaced by the SPPELAN module, allowing the network to better adapt to input images of varying sizes, capture multi-scale information, and improve feature map expression and object detection performance. In the Neck network, a Path Aggregation Network (PAN) is employed to enhance feature fusion for objects at different scales. The Head network decouples the classification and detection processes and is mainly responsible for loss calculation and bounding box selection. Loss computation includes positive and negative sample assignment strategies and the calculation of the loss function, with the regression branch incorporating Distribution Focal Loss (DFLoss) and Complete Intersection over Union Loss (CIOULoss). YOLOGpnet replaces CIOULoss with the Focaler-IoU loss function, improving the accuracy of bounding box prediction by optimizing class imbalance and bounding box regression through a weight adjustment mechanism.

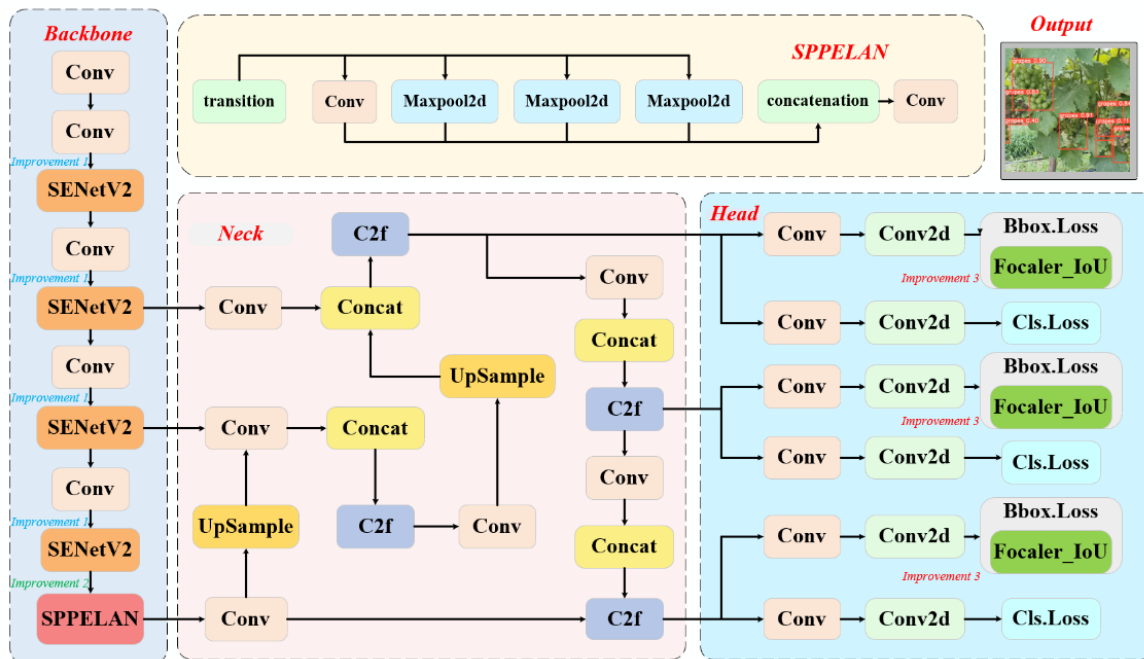
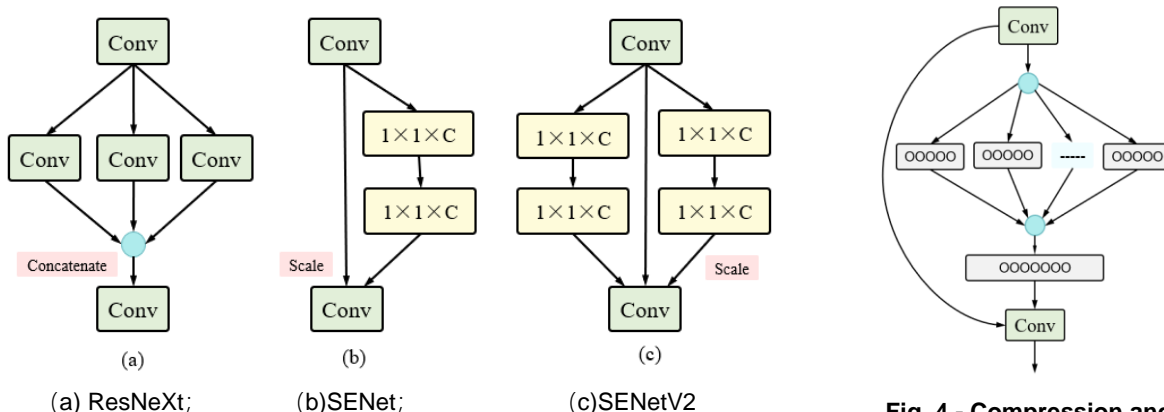


Fig. 2 - YOLOGpnet model structure

SENetV2 module

The multi-layer structure of deep neural networks makes it difficult to effectively propagate learned features, which can lead to performance degradation. This issue can be mitigated by enhancing feature propagation through shortcut connections in residual modules. The Squeeze-and-Excitation Network V2 (SENetV2) is an image classification model based on convolutional neural networks (CNNs), which improves recognition accuracy by extracting spatial features and optimizing channel representations. Figure 3 compares three network modules: ResNeXt merges features through a multi-branch CNN structure; SENet applies global average pooling, fully connected layers, and Sigmoid activation after standard convolution to obtain channel weights and scale the features; SENetV2 combines the characteristics of both, employing a multi-branch fully connected layer to squeeze and excite the features before scaling them.



Note: Concatenate refers to the merging operation, Scale refers to the scaling operation, and $1 \times 1 \times C$ denotes a fully connected layer with a size of 1×1 and C channels.

Fig. 3 - Comparison of neural network modules

Fig. 4 - Compression and excitation module structure diagram

The design of SENetV2 enhances feature representation granularity and the ability to integrate global information through a multi-branch structure. The proposed SaE module (as shown in Figure 4) dynamically adjusts channel weights through the squeeze-and-excitation process, either enhancing or suppressing specific channel features. The output of the squeeze operation is passed through a multi-branch fully connected layer for excitation and then restored to its original shape. By incorporating multi-branch dense layer design, SENetV2 significantly improves prediction accuracy while maintaining nearly the same number of parameters. It enhances the network's ability to capture both intra-channel and inter-channel patterns, effectively accounting for dependencies between channels.

The training process is illustrated in Fig.5. Extensive experiments demonstrate that SENetV2 surpasses existing architectures in terms of accuracy.

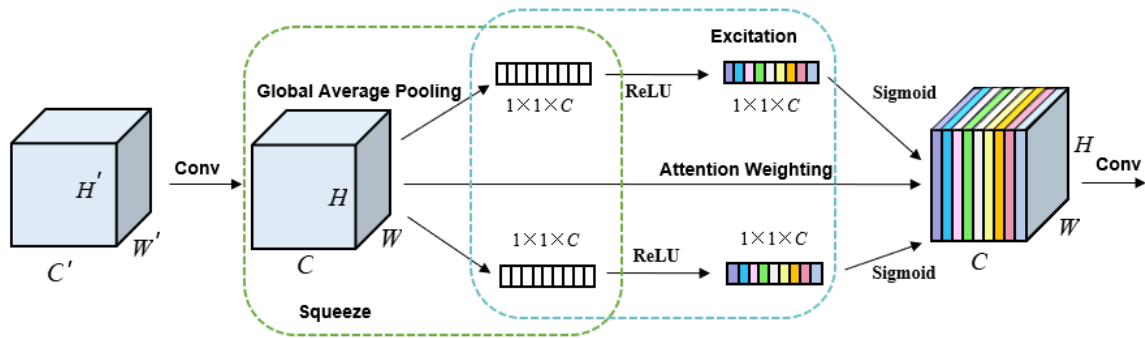
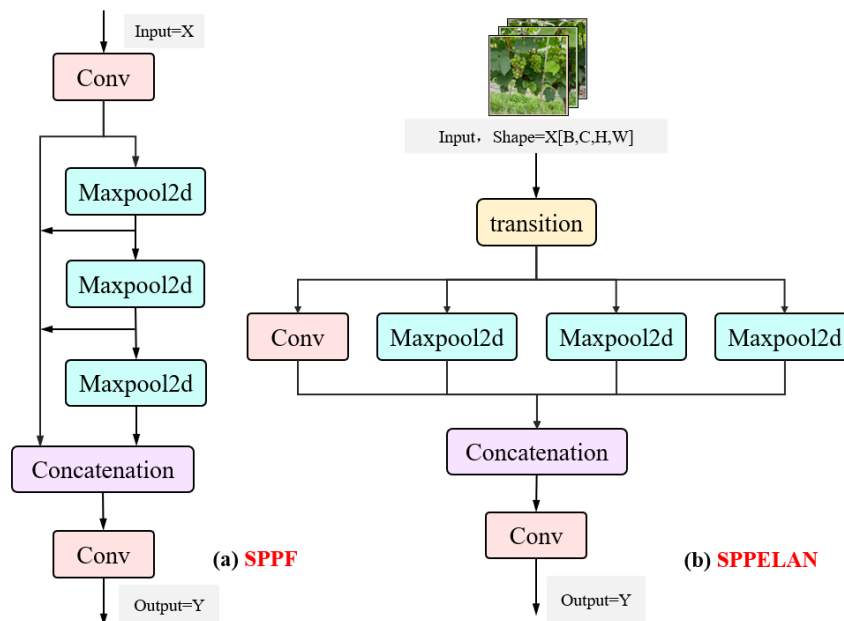


Fig. 5 - Compression and excitation module

SPPELAN module

The Spatial Pyramid Pooling with Enhanced Local Attention Network (SPPELAN) module is designed to improve model performance. It consists of two key components: Spatial Pyramid Pooling (SPP) and the Enhanced Local Attention Network (ELAN). Figure 6 compares the processing flows of SPPF and SPPELAN. SPP generates fixed-size features through multi-scale pooling, enhancing the network's ability to capture multi-scale information and improving its adaptability to input images of varying sizes and object detection performance. ELAN, utilizing a local attention mechanism, dynamically adjusts feature weights, allowing the network to focus more on critical regions. This makes it particularly effective in complex backgrounds and for detecting small objects, which is especially useful in fruit recognition tasks within orchard environments. The feature maps processed by SPP and ELAN are then fused, further enhancing the model's representational capacity.



Maxpool2d refers to the application of 2D max pooling on an input signal composed of multiple input planes.

Fig. 6 - (a)SPPF Module (b)SPPELAN Module

Focaler-IoU loss function

The loss function is a critical tool for measuring the difference between model predictions and actual results. In the regression branch of YOLOv8's head network, Distribution Focal Loss (DFLoss) and Complete Intersection over Union Loss (CIoULoss) are combined. YOLOGPnet replaces CIoULoss with Focaler-IoU. The CIoU loss function (Formula 1) primarily considers the overlap degree and size differences between bounding boxes, making it susceptible to scale variations and reducing detection accuracy. IoU represents the intersection over union between the predicted and ground truth boxes, α is a weighting coefficient, ν reflects the aspect ratio difference between the predicted and ground truth boxes, $\rho^2(b^{gt}, b)$ denotes the Euclidean

distance between their center points, and c is the diagonal length of the smallest enclosing box of the two. To improve the accuracy of grape picking point recognition, optimizing the choice of loss functions is crucial.

To improve the accuracy of grape picking point identification, optimizing the choice of the loss function is especially important.

$$CIoU_Loss = 1 - IoU + \alpha v + \frac{\rho^2(b^{gt}, b)}{c^2} \quad (1)$$

The Focaler-IoU loss function combines Focal Loss and IoU Loss to address issues of class imbalance and bounding box regression accuracy in object detection. Focal Loss, as defined in Equation (2), balances the weights of positive and negative samples through the parameter α and adjusts the importance of hard and easy samples using the parameter γ ; \hat{p} represents the predicted probability of the model. IoU evaluates the overlap between the predicted and ground truth bounding boxes, with Equation (3) representing the ratio of the intersection area to the union area of the predicted and true boxes. IoU Loss, as defined in Equation (4), optimizes the position of the predicted box by maximizing its IoU with the ground truth box, thereby improving regression accuracy, where B_p is the predicted bounding box and B_t is the ground truth bounding box.

Focaler-IoU focuses on different regression samples and reconstructs the IoU loss using linear mapping, emphasizing the impact of hard and easy samples in bounding box regression. Equation (5) defines the mechanism by which the loss is adjusted according to the IoU value: when IoU is below the lower threshold d , the loss is set to 0; when IoU exceeds the upper threshold u , the loss is set to 1; and when IoU falls between d and u , the loss increases linearly with the IoU value. This design focuses on samples with moderate overlap, enhancing the model's feature extraction capability.

$$Focal\ Loss = -\alpha(1-\hat{p})^\gamma \log(\hat{p}) \quad (2)$$

$$IoU = \frac{Area\ of\ Overlap}{Area\ of\ Union} = \frac{|B_p \cap B_t|}{|B_p \cup B_t|} \quad (3)$$

$$IoU\ Loss = 1 - IoU(B_p, B_t) \quad (4)$$

$$IoU^{focaler_Loss} = \begin{cases} 0, & IoU < d \\ \frac{IoU-d}{u-d}, & d \leq IoU \leq u \\ 1, & IoU > u \end{cases} \quad (5)$$

RESULTS

EXPERIMENTAL DESIGN AND ANALYSIS

Evaluation indicators

To validate the detection capability of the YOLOGPnet algorithm, the specific calculation formulas for accuracy and mean Average Precision (mAP) used in this study are provided in Equations (6) and (7) as evaluation metrics for detection performance, TP refers to the number of samples correctly predicted as positive by the model, while FP represents the number of samples incorrectly predicted as positive. N denotes the total number of target categories to be detected or classified by the model, and AP_i is the average precision of the i category. The model's performance is assessed using mAP@0.5%, parameter count, and GFLOPs. Additionally, for evaluating the real-time performance of the grape orchard detection and harvesting task, the model's inference speed is measured using the frames per second (FPS) for single-image inference.

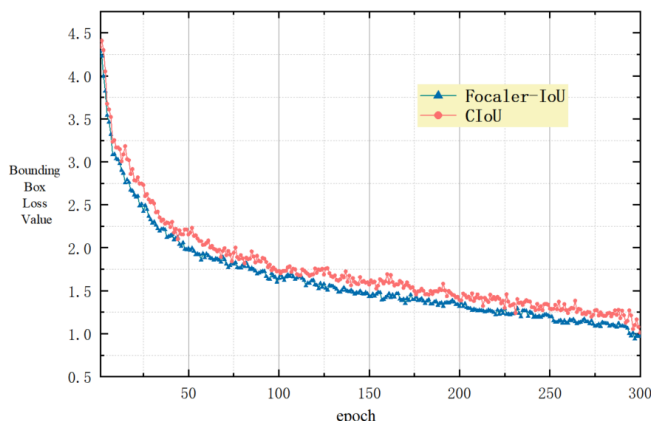
$$P = \frac{TP}{TP + FP} \quad (6)$$

$$mAP = \frac{1}{N} \sum_{i=1}^n AP_i \quad (7)$$

Performance Validation of the Loss Function

The optimization of the loss function allows the predicted results to better approximate the true values. Figure 7 compares the CIoU loss function used in the original YOLOv8n model with the Focaler-IoU loss function introduced in this study. Their convergence speed and loss values are similar; however, when using the CIoU loss function for the bounding box, the regression is slower, and the final loss value after convergence is higher. The Focaler-IoU loss function introduced in this study demonstrates a faster and more stable convergence, gradually converging after 280 epochs with the lowest final loss value. This not only accelerates the convergence speed of the model but also improves its accuracy.

As shown in Figure 8, the blue bounding boxes represent the detection results using Focaler-IoU Loss, while the green bounding boxes correspond to the results using CloU Loss. Focaler-IoU Loss enables the bounding boxes to more closely approximate the minimum enclosing rectangles of the target grapes, resulting in superior detection performance.



CloU indicates that the model uses CloU Loss as the bounding box loss function; Focaler-IoU indicates that the model uses Focaler-IoU Loss as the bounding box loss function.

Fig. 7 - Comparison of Bounding Box Loss Convergence with Improved Methods

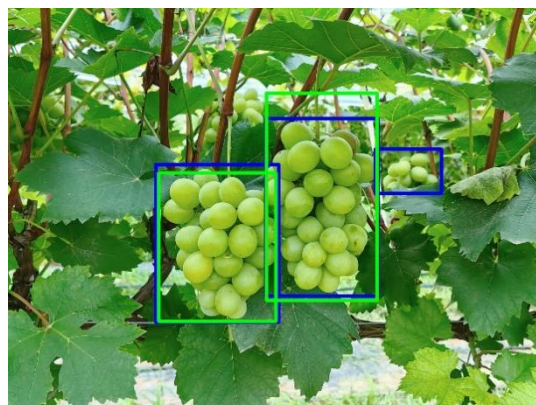


Fig. 8 - Comparison of Detection Performance between CloU Loss and Focaler-IoU Loss

Comparison of Detection Results from Different Models

To evaluate the detection performance of different models on the grape cluster dataset, this study selected YOLOv5s, YOLOv7-tiny, YOLOv8n, and the improved model YOLOGPnet for experiments on the same test set. The detection results of each model were compared and analyzed using metrics such as accuracy. Two-stage object detection algorithms were excluded from the comparison due to their large computational load and weight file size, which do not meet the requirements for lightweight real-time detection and are unsuitable for use in orchard environments. The YOLO series is more appropriate for the lightweight real-time detection demands of this dataset. The experimental results of different models are presented in Table 2.

Comparative Experimental Results of Different Models on the Test Set

Table 2

Model	Precision (%)	mAP @0.5 (%)	Gflops	Parameter (M)	Weight File (MB)	Inference Time per Image (ms)
YOLOv5s	92.9	95.7	10.3	3.8	7.4	15.9
YOLOv7-tiny	91.7	94.6	7.8	2.8	4.5	12.1
YOLOv8n	90.1	95.2	8.7	3.2	6.3	16.8
Improved Model YOLOGpnet	93.6	96.8	6.8	2.14	4.36	12.5

The comparative results show that the proposed YOLOGPnet model outperforms YOLOv5n, and YOLOv7-tiny across all evaluation metrics. Compared to YOLOv5s, the proposed model improves accuracy and mAP@0.5 by 0.7 and 1.1 percentage points, respectively, while reducing computational load, parameter count, and weight file size by 33.98%, 43.68%, and 41.08%, respectively, with an increase in detection speed of 3.4 ms. The model significantly reduces computational resource consumption while maintaining high accuracy, making it suitable for deployment on mobile devices due to its smaller memory footprint and weight file size.

As shown in Table 3, the improved model achieves an accuracy of 93.6% and an mAP@0.5 of 96.8%, representing increases of 3.5 and 1.6 percentage points, respectively, compared to the original YOLOv8n model. Additionally, all other metrics show improvements across different models. The model's weight file size is reduced by 30.79%, while parameter count and detection time are reduced by 33.13% and 4.3 ms, respectively. Overall, the model demonstrates outstanding performance in grape cluster detection, with significantly enhanced recognition accuracy.

Ablation Study

To verify the effectiveness of the proposed improvements, ablation experiments were conducted under the same experimental conditions using the original YOLOv8n as the baseline. By testing different combinations of the SENetV2, SPPELAN module, and Focaler-loU loss function, the accuracy, mAP@0.5, computational load, weight file size, and single-image detection time were evaluated on the same grape dataset. The results are shown in Table 3. In these experiments, A represents replacing the C2f module in YOLOv8n's backbone network with SENetV2, B represents replacing the SPPF module with SPPELAN, and C represents replacing the Ciou loss function with Focaler-loU. The symbol "x" indicates that the improvement strategy was not applied, while "√" indicates that the improvement strategy was applied.

Table 3

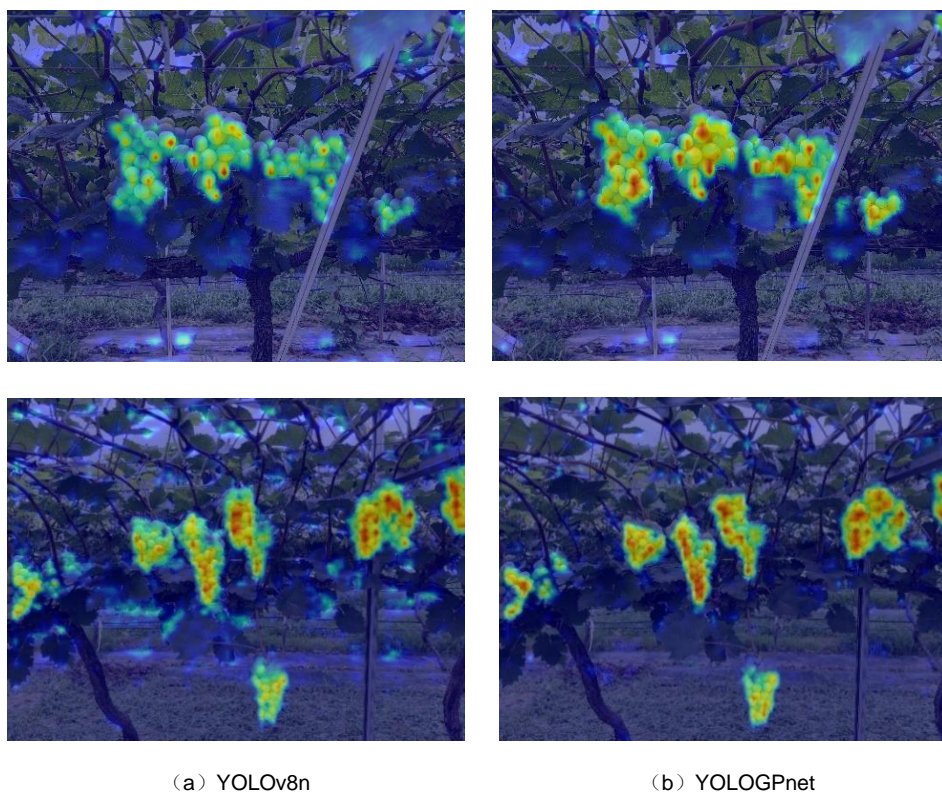
Ablation Study of Different Improvement Methods								
A	B	C	Precision (%)	mAP @0.5 (%)	Gflops	Parameter (M)	Weight File (MB)	Inference Time per Image (ms)
—	—	—	90.1	95.2	8.7	3.2	6.3	16.8
√	—	—	93.2	96.4	7.3	2.7	4.3	12.0
—	√	—	91.9	95.3	7.6	2.6	4.7	14.1
—	—	√	90.9	95.1	8.2	3.1	6.1	12.6
√	√	—	93.4	96.6	6.7	2.1	4.2	11.8
√	—	√	92.7	96.1	7.2	2.3	4.9	12.9
√	√	√	93.6	96.8	6.8	2.14	4.36	12.5

Compared to the baseline YOLOv8n model, the YOLOv8n+A model improved detection accuracy and mAP@0.5 by 3.1 and 1.2 percentage points, respectively, while reducing the computational load, parameter count, weight file size, and single-image detection time by 16.09%, 37.5%, 31.75%, and 28.57%, respectively. This improvement is attributed to the introduction of SENetV2, which enhances feature extraction capabilities through the squeeze-and-excitation operations while reducing model parameters, thus validating its effectiveness in both lightweight design and performance enhancement. The YOLOv8n+B model improved detection accuracy and mAP@0.5 by 1.8 and 0.1 percentage points, respectively, while reducing the computational load, parameter count, weight file size, and detection time by 12.64%, 18.75%, 25.4%, and 16.07%, respectively. The SPPELAN module reduced feature redundancy and enhanced the extraction of detailed features, further improving model performance. The YOLOv8n+C model increased detection accuracy by 0.8 percentage points, although mAP@0.5 decreased slightly by 0.1 percentage points. However, single-image detection time decreased by 4.2 ms, with parameter count and weight file size remaining almost unchanged.

Compared to YOLOv8n, the YOLOv8n+A+B+C model improved accuracy and mAP@0.5 by 3.5 and 1.6 percentage points, respectively, while reducing computational load, parameter count, weight file size, and detection time by 21.84%, 34.38%, 30.79%, and 25.60%, respectively. When compared to the YOLOv8n+A+B model, accuracy and mAP@0.5 improved by 0.2 percentage points, with computational load remaining nearly the same. Compared to the YOLOv8n+A+C model, the YOLOv8n+A+B+C model reduced detection time by 0.4 ms, while increasing accuracy and mAP@0.5 by 0.9 and 0.7 percentage points, respectively. Additionally, the computational load, parameter count, and model size decreased by 5.56%, 8.70%, and 11.02%, respectively, demonstrating significantly superior overall performance compared to the YOLOv8n+A+C model.

Heatmap Visualization

To intuitively evaluate the detection performance of the YOLOGPnet model, this study utilizes Grad-CAM to generate heatmaps for visualizing the target detection process. In the heatmaps, red and yellow regions represent areas that have a greater influence on the model's decision-making. Figure 9 displays the detection results for several grape images, indicating a high level of consistency between the YOLOGPnet model and the original images. Compared to the original model, YOLOGPnet more accurately identifies overlapping fruits and shows improved feature capture along the edges of the fruits. This demonstrates its enhanced ability to extract and focus on features in complex backgrounds and for weak semantic targets.



(a) YOLOv8n (b) YOLOGPnet
Fig. 9 - Heatmap of Grape Image Detection

Comparison of Detection Performance Across Models Under Different Conditions

To validate the performance and generalization ability of the improved model in real grape orchard environments, this study randomly selected 30 images under different shooting conditions, including close-range, long-range, cloudy, and sunny scenes. The images contain complex situations such as fruit overlap and leaf occlusion, without applying image augmentation, to simulate a realistic orchard environment. Comparative experiments were conducted using the YOLOv5s, YOLOv7-tiny, YOLOv8n, and YOLOGPnet models. Figures 10 and 11 display the prediction results of each model, with purple, green, red, and blue bounding boxes representing the predictions of YOLOv5s, YOLOv7-tiny, YOLOv8n, and YOLOGPnet, respectively. Missed and misdetections are marked with light blue and yellow circles.

Close-range grape images help analyze model detection performance in complex situations such as overlap and occlusion. Figure 10 shows that detecting green grapes is challenging due to their similar color to the orchard background. Under sufficient lighting, the distinction between grapes and the background is clearer, and all four models perform relatively well. However, YOLOv8n performs poorly in cases of severe occlusion, while YOLOv7-tiny tends to identify overlapping grapes as a single target. Additionally, both models mistakenly detect branches as grapes. In contrast, YOLOGPnet demonstrates excellent detection accuracy in complex scenes, with its predicted bounding boxes more closely approximating the minimum enclosing rectangles of the targets, reducing gaps and over-wrapping, and improving the accuracy of picking point prediction. YOLOGPnet only exhibited one instance of an inaccurate bounding box, whereas the other models showed more misdetections, and YOLOv8n even missed the target entirely.

Long-range grape images better reflect the performance of each model in multi-object detection, particularly under poor lighting conditions, which further test the models' generalization capabilities. On cloudy days, the brightness of the grapes and leaves decreases, making the boundaries less distinct and the detection of overlapping and occluded grapes more difficult. Figure 11 shows that YOLOv5s and YOLOv8n performed poorly in long-range detection under all weather conditions, with many missed and misdetections. YOLOv7-tiny performed better on sunny days compared to cloudy conditions. Meanwhile, YOLOGPnet had only two misdetections under all conditions, and the bounding box convergence remained excellent in long-range images, indicating good adaptability to lighting variations.

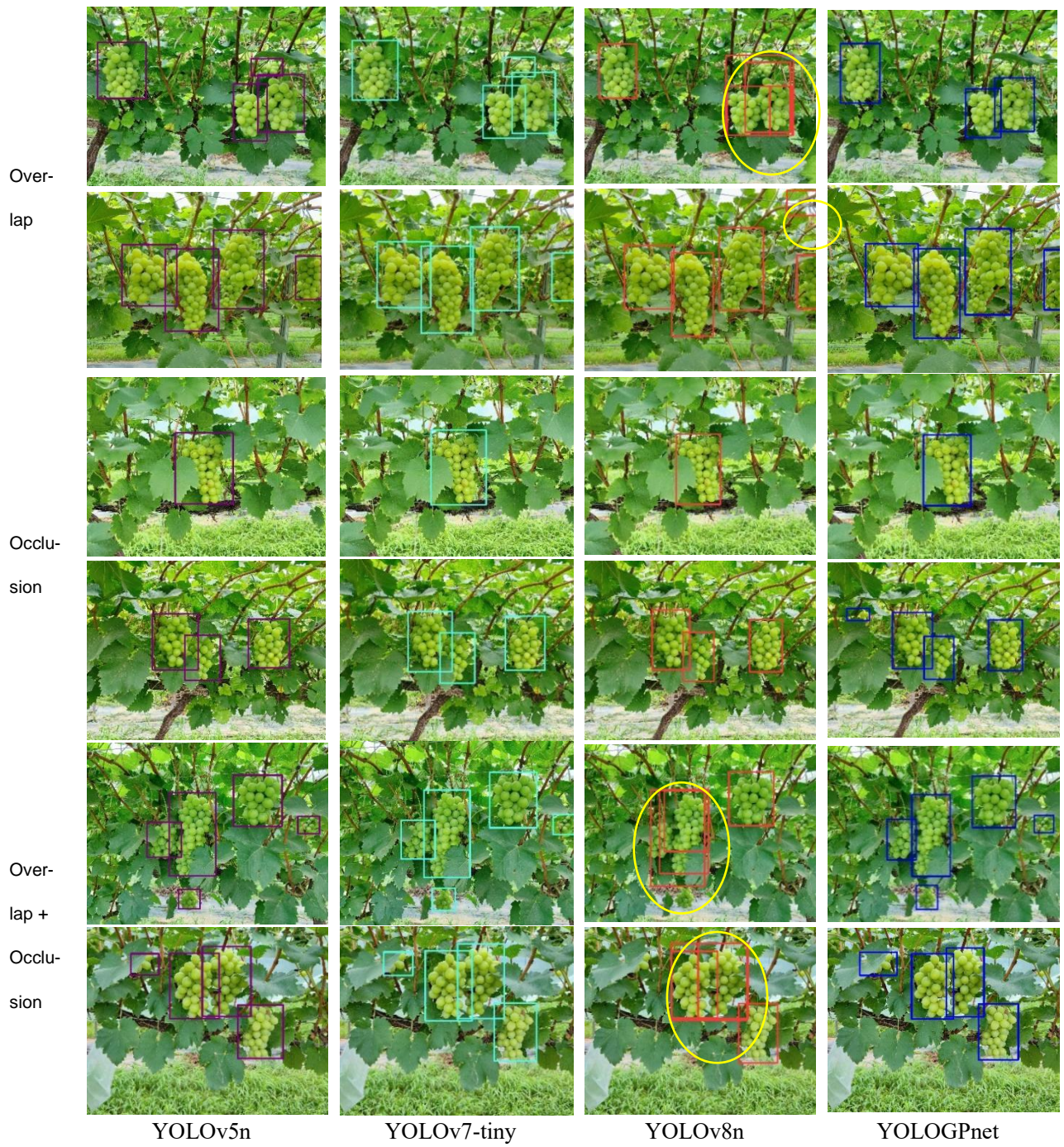
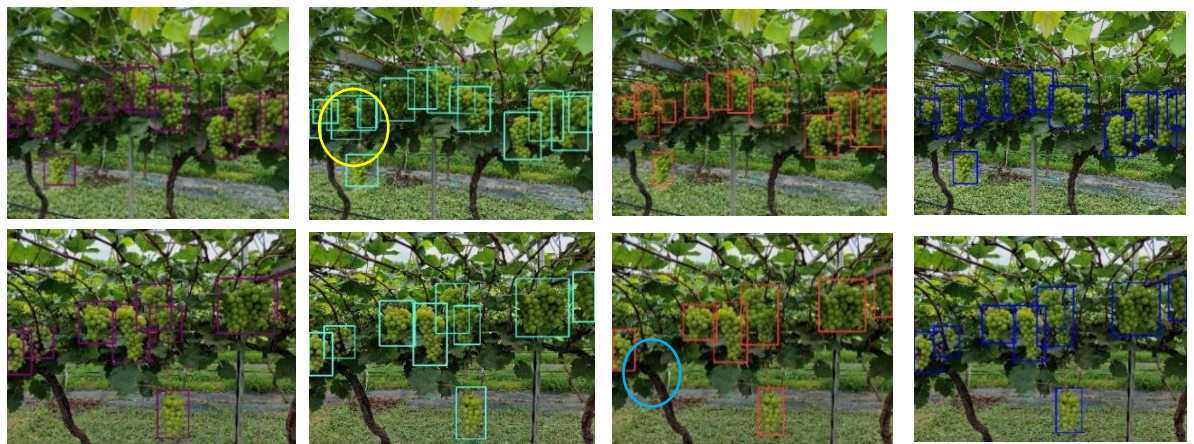


Fig.10 - Comparative Detection Results of Multiple Models under Different Conditions (Close-range)



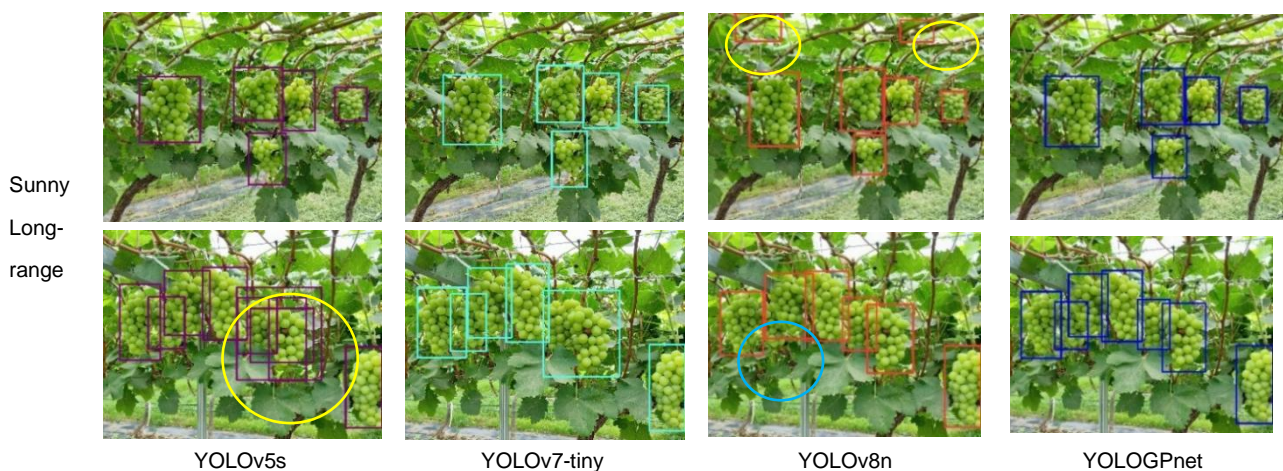


Fig.11 - Comparative Detection Results of Multiple Models under Different Weather Conditions (Long-range)

CONCLUSIONS

This study proposes the YOLOGPnet model, which demonstrates significant performance improvements. By incorporating SENetV2 and SPPELAN modules, the model effectively addresses the limitations in multi-scale feature extraction, while the Focaler-IoU loss function further enhances regression accuracy and predictive performance. Comparative experiments under varying lighting conditions validate the practicality and robustness of YOLOGPnet, showing fewer false positives and missed detections compared to other models, with predicted bounding boxes more closely aligning with target fruits. The improvements in evaluation metrics and detection performance indicate that YOLOGPnet maintains high accuracy and stability in complex environments, making it particularly suitable for resource-constrained applications.

ACKNOWLEDGEMENT

This research was supported by the National Natural Science Foundation of China (No.32272001) and Qinchuangyuan “Scientist + Engineer” Team Development Program of the Shaanxi Provincial Department of Science and Technology (No.2023KXJ-016) .

REFERENCES

- [1] Cha, Z., Zhou, W., Wu, J., (2021). Field-based recognition of Red Globe grape bunches using transfer learning and the Faster R-CNN model(基于迁移学习 Faster R-CNN 模型田间红提葡萄果穗的识别). *Journal of Shihezi University (Natural Science Edition)*, Vol. 1, pp.26-31, Xinjiang/China.
- [2] Chen, Y., Niu, Y., Cheng, W., Zheng, L., Sun, D., (2024). Apple detection method in the natural environment based on improved YOLOv5. *Inmateh- Agricultural Engineering*, Vol. 72, pp.183-192, Romania.
- [3] Guo, C., Zheng, S., Cheng, G., Zhang, Y., Ding, J., (2023). An improved YOLOv4 used for grape detection in unstructured environments. *Frontiers in Plant Science*, Vol.14, 1209910, Switzerland.
- [4] Jiang, T., Li, Y., Feng, H., Wu, J., Sun, W., Ruan, Y., (2024). Research on a trellis grape stem recognition method based on YOLOv8n-GP. *Agriculture*, Vol.9, 1449, Switzerland.
- [5] Khan, N., Fahad, S., Naushad, M., (2020). Grape production critical review in the world . <https://ssrn.com/abstract=3595842>.
- [6] Li, H., Li, C., Li, G., Chen, L., (2021). A real-time table grape detection method based on an improved YOLOv4-tiny network in complex backgrounds. *Biosystems Engineering*, Vol.212, pp.347-359, , England.
- [7] Liu, B., Zhang, Y., Wang, J., Luo, L., Lu, Q., Wei, H., Zhu W., (2023). An improved lightweight network based on deep learning for grape recognition in unstructured environments. *Information Processing in Agriculture*, Vol.2, pp.202-216, Beijing/China
- [8] Liu, P., Zhu, Y., Zhang, T., Hou, J., (2020). Recognition and image segmentation algorithm for closely packed grape bunches under natural conditions (自然环境下贴叠葡萄串的认可与图像分割算法). *Transactions of the Chinese Society of Agricultural Engineering*, 2020, Vol. 6, pp.161-169, Beijing/China.

- [9] Lu, J., Lei, W., (2021). Over lapping grape segmentation algorithm based on full convolutional network and concave point search(基于全卷积网络与凹点搜索的重叠葡萄分割算法). *Journal of Optoelectronics-Laser*, Vol. 03, pp. 231-240, Tianjin/China.
- [10] Lu, S., Liu, X., He, Z., Zhang, X., Liu, W., Karkee, M., (2022). Swin-Transformer-YOLOv5 for real-time wine grape bunch detection. *Remote Sensing*, Vol.14, pp.53-58, Switzerland.
- [11] Ning, Z., Luo, L., Liao, J., Wen, H., Wei, H., Lu, Q., (2021). Grape stem recognition and optimal picking point positioning based on deep learning (基于深度学习的葡萄果梗识别与最优采摘定位). *Transactions of the Chinese Society of Agricultural Engineering*, Vol. 9, pp. 222-229, Beijing/China.
- [12] Qiu, C., Tian, G., Zhao, J., Liu, Q., Xie, S., Zheng, K., (2022). Grape maturity detection and visual pre-positioning based on improved YOLOv4. *Electronics*, Vol.14, 2677, Switzerland.
- [13] Ren, J., Zhang, H., Wang, G., Dai, C., Teng, F., Li, M., (2024). Real-time grape disease detection model based on improved YOLOv8s. *INMATEH-Agricultural Engineering*, 72(1). *INMATEH - Agricultural Engineering*, Vol. 72, pp.96-105, Romania.
- [14] Song, Y., Yang, S., Zheng, Z., Ning, J., (2023). Tea-picking point semantic segmentation algorithm based on multi-head self-attention mechanism (基于多头自注意力机制的茶叶采摘点语义分割算法). *Transactions of the Chinese Society for Agricultural Machinery*, Vol. 09, pp. 297-305, Beijing/China.
- [15] Su, S., Chen, R., Fang, X., Zhu, Y., Zhang, T., Xu, Z., (2022). A novel lightweight grape detection method. *Agriculture*, Vol. 9, 1364, Switzerland.
- [16] Sun, J., Wu, Z., Jia, Y., Gong, D., Wu, X., Shen, J., (2023). Grape detection in orchard environments based on improved YOLOv5s (基于改进 YOLOv5s 的果园环境葡萄检测). *Transactions of the Chinese Society of Agricultural Engineering*, 2023, Vol.18, pp.192-200, Beijing/China.
- [17] Wang, J., Zhang, Z., Luo, L., Zhu, W., Chen, J., Wang, W., (2021). SwinGD: A robust grape bunch detection model based on Swin transformer in complex vineyard environments. *Horticulturae*, Vol. 7, 492, Switzerland.
- [18] Wen, S., Zhou, J., Hu, G., Zhang, H., Tao, S., Wang, Z., & Chen, J., (2024). PcMNet: an efficient lightweight apple detection algorithm in natural orchards. *Smart Agricultural Technology*, Vol.9, 100623, Netherlands.
- [19] Wu, Z., Xia, F., Zhou, S., Xu, D., (2023). A method for identifying grape stems using keypoints. *Computers and Electronics in Agriculture*, Vol. 209, 107825, England.
- [20] Yang, W., Qiu, X., (2024). A lightweight and efficient model for grape bunch detection and biophysical anomaly assessment in complex environments based on YOLOv8s. *Frontiers in Plant Science*, 2024, Vol.15, 1395796, Switzerland.
- [21] Yang, Y., Han, Y., Li, S., Yang, Y., Zhang, M., Li, H., (2023). Vision-based fruit recognition and positioning technology for harvesting robots. *Computers and Electronics in Agriculture*, Vol. 213, England.
- [22] Zhang, C., Ding, H., Shi, Q., Wang, Y., (2022). Grape cluster real-Time detection in complex natural scenesbased on YOLOv5s deep learning network. *Agriculture*, Vol.14,1242, Switzerland.
- [23] Zhang, T., Wu, F., Wang, M., Chen, Z., Li, L., Zou, X., (2023). Grape-bunch identification and picking point location on occluded fruit axes based on YOLOv5-GAP. *Horticulturae*, Vol. 4, 498, Switzerland
- [24] Zhao, C., Fan, B., Li, J., Feng, Q., (2023). Advances, challenges, and trends in agricultural robotics technology (农业机器人技术进展、挑战与趋势). *Smart Agriculture (Bilingual)*, Vol. 04, pp. 1-15, Beijing/China.
- [25] Zhao, R., Zhu, Y., Li, Y., (2022). An end-to-end lightweight model for grape and picking point simultaneous detection. *Biosystems Engineering*, Vol. 223, pp. 174-188 , England.
- [26] Zhao, F., Zhang, J. W., Zhang, N., Zhang, N., Tan, Z., Xie, Y., Zhang, S., Han, Z., Li, M., (2022). Detection of cucurbits' fruits based on deep learning. *INMATEH- Agricultural Engineering*, Vol. 72, pp.321-330, Romania.

EGG QUALITY DETECTION BASED ON LIGHTWEIGHT HCES-YOLO

/ 基于轻量化的 HCES-YOLO 的鸡蛋品质检测算法

Zhimin TONG¹⁾, Shengzhang LI, Chuanmiao SHI, Tianzhe XU, Yu ZHOU, Changhao LI¹⁾ College of Electrical and Mechanical Engineering, Qingdao Agricultural University, Qingdao/ ChinaTel: +8615845982569; E-mail: leicahit@qau.edu.cn

Corresponding author: Zhimin Tong

DOI: <https://doi.org/10.35633/inmateh-74-43>**Keywords:** YOLOv8n, Egg quality detection, HGNetV2, ContextGuideFusionModule, EfficientHead**ABSTRACT**

The quality detection of eggs based on deep learning faced many problems, such as similar feature colors and low computational efficiency, which resulted in an increased probability of false detection or missed detection. To effectively solve these problems, this paper proposed an egg quality detection method based on YOLOv8n, which integrated the ContextGuideFusionModule, EfficientHead, and SIOU loss functions by improving the backbone network. The recognition rate from the field test was 88.4%, indicating that the algorithm could meet the real-time monitoring requirements, effectively identify the quality status of eggs, and provide support for intelligent poultry house management.

摘要

基于深度学习的鸡蛋的品质检测面临特征颜色相近, 计算效率低等诸多问题, 导致误检或漏检的概率增加。为有效解决这些问题, 本文提出了一种基于 YOLOv8n, 通过改进骨干网络, 集成 ContextGuideFusionModule、EfficientHead 和 SIOU 损失函数的鸡蛋品质检测方法。现场试验识别率为 88.4%, 表明该算法能满足实时监测, 有效的识别鸡蛋的品质状态, 为智能化禽舍管理提供支持。

INTRODUCTION

Eggs, as one of the main foods for humans, are rich in protein, fat, and other important nutrients. With the improvement of food safety awareness, the quality of eggs is getting more and more attention. The appearance of eggs is one of the important indexes to evaluate their quality, which is usually negatively correlated with egg age (Eddin et al., 2019; Hisasaga et al., 2020; Malfatti et al., 2021). Traditional methods for assessing egg appearance utilized the Haugh unit (HU) to evaluate quality by measuring the weight and protein height of the eggs. However, this approach was often destructive and applicable only to sampling, failing to meet the demands of modern agriculture for large-scale production. Such losses were unacceptable to hatcheries, the food processing industry, and consumers (Guanjun et al., 2019). Currently, non-destructive testing of egg defects primarily relied on transmission techniques, which typically required observing the eggs under a light source. For instance, Omid et al. extracted features of crack regions through spatial transformations of the HSV color space of images, constructing a corresponding discriminant system with an accuracy rate of 94.5% (Omid et al., 2013). Cruz-Tirado et al. combined near-infrared spectroscopy with a PLS-DA model to identify fresh and unfresh eggs, achieving an accuracy of 87% (Cruz-Tirado et al., 2021). Dong et al. developed a method based on VIS-NIR spectroscopy that established a quantitative model for the freshness of different egg varieties through global updates, direct standardization, and slope/deviation correction (Dong et al., 2020). However, this method proved inefficient in practical applications, with poor sanitation conditions and a propensity for errors. Therefore, there was an urgent need for a rapid and non-invasive technique to evaluate egg quality.

Research indicated that abnormal eggs exhibited noticeable color differences compared to normal eggs, which can be identified by taking multiple sets of egg surface images to extract abnormal features. For example, Yao et al. employed hyperspectral imaging (HSI) technology to assess both the internal and external quality of eggs, achieving an overall accuracy rate of 93.33% (Yao et al., 2022). Luo et al. constructed an egg collection system to obtain images of severely damaged eggs and applied an improved YOLOv5 algorithm for their identification, ultimately achieving an accuracy of 92.4% (Luo et al., 2023).

Narushin *et al.*, (2023), and Sehirli *et al.*, (2022), conducted a comparative analysis of various non-destructive detection methods based on existing studies. In recent years, with the continuous improvement of computing power, many researchers have begun to use deep learning technology to quickly and accurately judge the quality and grade of agricultural products, thereby improving their added value and market competitiveness (Okinda *et al.*, 2020; Turkoglu *et al.*, 2021; Zhao *et al.*, 2023). Du *et al.*, (2024), realized the effective identification of young apples by improving the YoLOV5 algorithm, with an average accuracy of 82.2%. Liang *et al.* (2024), realized the effective identification of maize pests and diseases by improving the YoLOV8 n algorithm, and the average accuracy reached 94.8 %. Compared to other YOLO models, YOLOv8 demonstrated higher detection precision and efficiency in object detection tasks, showcasing remarkable overall performance (Gevorgyan *et al.*, 2022; Xu *et al.*, 2024; Yang *et al.*, 2023). Consequently, some scholars applied the YOLOv8 algorithm to target detection in the livestock industry to enhance production efficiency and product quality (Wang *et al.*, 2024; Yang *et al.*, 2023). However, previous studies mainly focused on the assessment of single quality parameters, while research on the multi-quality detection of eggs remained relatively scarce. Therefore, this paper designs a lightweight model method to accurately identify the quality of eggs. This project optimizes the YoLOv8n algorithm, uses the HGNetv2 (Zhao *et al.*, 2024) network to replace the original backbone network, and introduces the pyramid network ContextGuideFusionModule (Hu *et al.*, 2018). The lightweight grouping convolution detection head EfficientHead (Zhang *et al.*, 2019) is used and the CIOU loss function is replaced with the SloU (Gevorgyan *et al.*, 2022) loss function, named HCES-YOLOv8 algorithm. The algorithm aims to replace the traditional detection methods to achieve effective detection of objects in many fields such as animal husbandry production lines, thereby improving the detection effect.

The purpose of this study is to use the improved YoLOv8 network to perform multiple quality assessments of egg quality, focusing on:

- (1) The morphological characteristics of egg appearance were extracted to identify different quality problems, such as color, breakage and contaminants, etc.;
- (2) Create a multiple egg quality assessment data set to fill the existing non-destructive quality test data and facilitate a more comprehensive assessment of egg quality;
- (3) The original network of YoLOv8n was improved to establish a model suitable for egg quality detection.

MATERIALS AND METHODS

Image acquisition system

An egg image acquisition platform is built in the laboratory, as shown in Fig. 1. The main hardware of the system consists of four parts: camera, 15w LED light source, computer and conveyor belt. The industrial camera used in this study is a CMOS type, which can capture a 1920×1080 pixel RGB image using a 90° distortionless fixed-focus lens. In this study, the LED light source was placed directly above the egg slope to illuminate the characteristics of the egg surface and facilitate the observation of the upper surface of the egg. This method is easy to install and can meet the image acquisition requirements of light source installation.

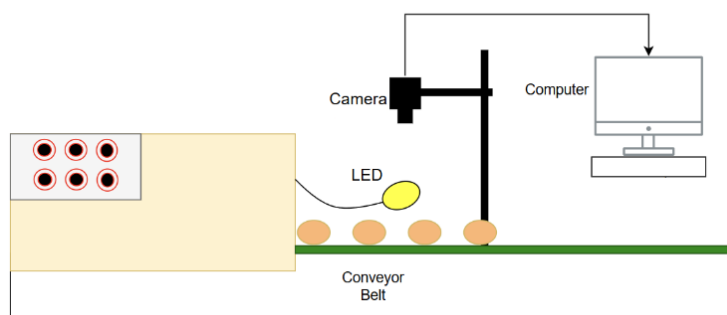


Fig. 1 – Egg image acquisition system

Image acquisition

In this study, eggs were used as experimental subjects, and the selected egg samples were obtained from Kaimeng Farm in Wudi County. In order to improve the experimental results, the obtained images will be manually classified. According to the eggshell characteristics, the eggs were divided into white spotted eggs, brown spotted eggs, pink skin eggs, white skin eggs, blood-stained eggs, broken shell eggs, dirty eggs and normal eggs. A total of 1100 images were taken, and Fig. 2 is the egg category map. The bounding boxes and categories of all objects in each image are labelled, and the corresponding annotation files are generated.

In order to simulate different conditions and enhance the robustness of the model, data enhancement methods such as mirroring, rotation, cropping, and brightness transformation are randomly used, and brightness transformation coefficients are randomly generated in the interval to double the number of images. After selection, 3300 enhanced egg images constitute an egg quality detection data set, numbered in order. Finally, the data set was divided into training set, validation set and test set according to the ratio of 7: 2: 1, including 2310, 660 and 330 egg images, respectively.

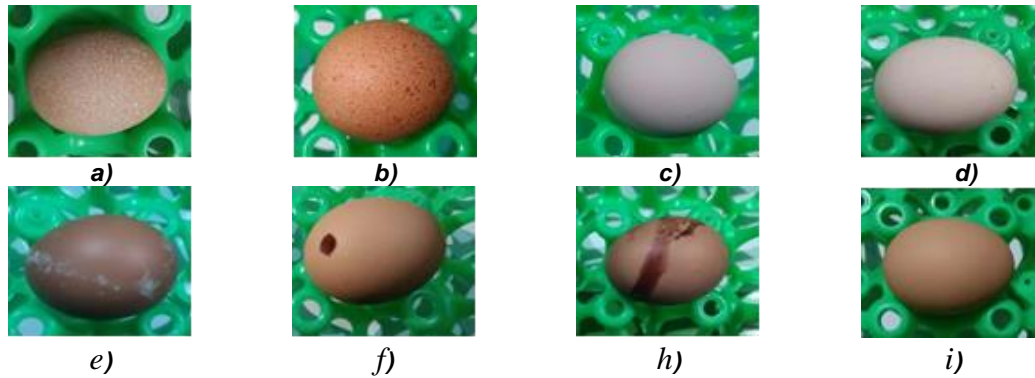


Fig. 2 – Egg category distinction diagram

a) White spotted egg; b). Brown spotted egg; c) Pink skin egg; d) White skin eggs; e) Bloody eggs; f) Broken egg; h) Dirty egg; i) Normal egg

YOLOv8n model

YOLO model is a single-stage target detection algorithm. Its core idea is to divide the image into regions and predict them, which has the characteristics of fast and efficient training. The backbone feature extraction network of YOLOv8 consists of CBS module, C2f module and SPPF module. The C2f module combines the design of the C3 module and the efficient lightweight attention network, which enhances the feature fusion ability and speeds up the inference speed. Based on the concept of spatial pyramid pooling, the SPPF module has lower parameters and calculation amount, which effectively expands the receptive field of the model and improves the recognition accuracy. Compared with YOLOv5, the head part of YOLOv8 has been greatly changed. The decoupling head structure is used to separate the classification and detection head, and it is changed from Anchor-Based to Anchor-Free, which significantly improves the target detection accuracy and alleviates the problem of inaccurate positioning and classification errors in complex scenes.

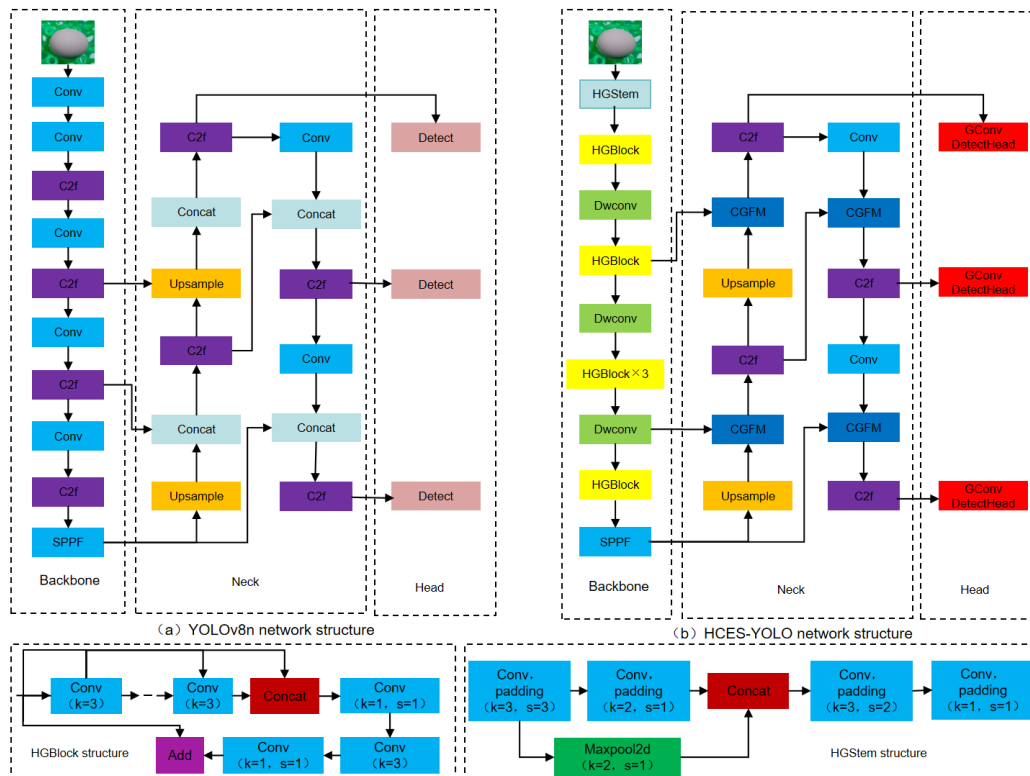


Fig. 3 –YOLOv8n and HCES-YOLO network structure

HCES-YOLO model

In this study, the Backbone and Neck parts of YOLOv8 were improved. The lightweight backbone network HGNetv2 is used to replace the original YOLOv8 backbone to reduce the computational load and model size, and the calculation speed is improved by the optimized Transformer structure. On this basis, the ContextGuideFusionModule is introduced, and the channel attention mechanism is used to weight the feature map, so as to improve the feature expression ability. The detection head of the original YOLOv8 is also optimized and the standard convolution is replaced with grouping convolution to reduce the amount of parameters and calculation, and the calculation efficiency is improved. In this study, the SIOU loss function is used in the model to comprehensively consider the shape similarity and spatial relationship of the target, so as to improve the accuracy of target location. The YOLOv8n model and the improved lightweight HCES-YOLO model are shown in Fig. 3.

Lightweight backbone network HGNetv2

The latest version of YOLOv8n has improved in accuracy and speed, but its backbone network still has limitations, especially in terms of computational complexity. This limits the application of YOLOv8n on resource-constrained devices. At the same time, as the depth and width of the network increase, the size of the model also increases, resulting in increased storage and transmission costs, which is a significant problem for applications that need to be deployed on edge devices. In addition, although YOLOv8n has improved in multi-scale feature fusion, it still has room for improvement in dealing with fine-grained features and global information.

Therefore, HGNetv2 is used to significantly optimize the original DETR network structure, which has many advantages. First, it uses a lightweight basic network, which significantly reduces the computational load and model size, and is suitable for running on resource-constrained devices. Secondly, through the optimized Transformer structure, HGNetv2 improves the calculation speed while maintaining high precision, which is especially suitable for real-time target detection tasks. In addition, HGNetv2 abandons the traditional NMS processing, so that the network can be optimized together during the training process, thereby improving the generalization ability and performance of the model.

The network structure of HGNetv2 includes pretreatment Stem layer, HG block, learnable LDS layer and GAP layer. The Stem layer is responsible for the initial processing of the input data for subsequent feature extraction. The HG block enhances the detection ability of targets of different scales by hierarchically processing data. The LDS layer performs downsampling to reduce the computational load and increase the receptive field. The GAP layer converts the feature map into a vector, which can improve the robustness to spatial transformation. The final classification layer includes a convolutional layer and a fully connected layer to complete the classification task. The HGNetv2 structure is shown in Fig.4.

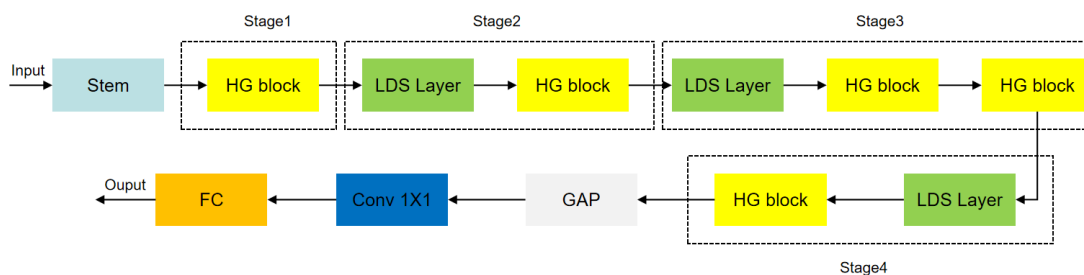


Fig. 4 – HGNetv2 structure

Pyramid Network ContextGuideFusionModule

The Concat module of YOLOv8 is widely used in computer vision tasks, which fuses different levels of features by stitching feature maps on channel dimensions. Although this method is efficient and has low computational cost, its simple splicing fails to consider the correlation between levels, resulting in insufficient information fusion. In addition, simple stitching cannot distinguish the importance of each feature map, and all features are treated equally. This may lead to the loss of egg image details, resulting in false detection and missed detection, and may also be detrimental to the final performance of the egg quality detection model. In contrast, ContextGuideFusionModule provides a more advanced and detailed feature fusion method to overcome the limitations of simple stitching. Through careful design, CGFM not only simply stitches feature maps, but also achieves more effective feature integration through weight adjustment and attention mechanism.

The core of ContextGuideFusionModule is Squeeze-and-Excitation Attention (SEAttention). This mechanism emphasizes important features and suppresses unimportant channels by weighting the importance of each channel. Specifically, SEAttention first uses the global average pooling to compress the spatial dimension of each channel into a scalar, representing the global feature of the channel. Then, these scalars are nonlinearly transformed through the fully connected layer to generate the weight of each channel. Finally, the weighted feature map is obtained by multiplying the original feature map by elements. After completing the feature adjustment, ContextGuideFusionModule realizes feature fusion by weighted addition, and the structure is shown in Fig. 5. The specific step is to multiply the two input feature maps by their corresponding weights, and then add them to form a fused feature map. This method not only retains the important information in the input feature map, but also enhances the information complementarity between different feature maps through weight adjustment, thereby improving the feature expression ability and model performance.

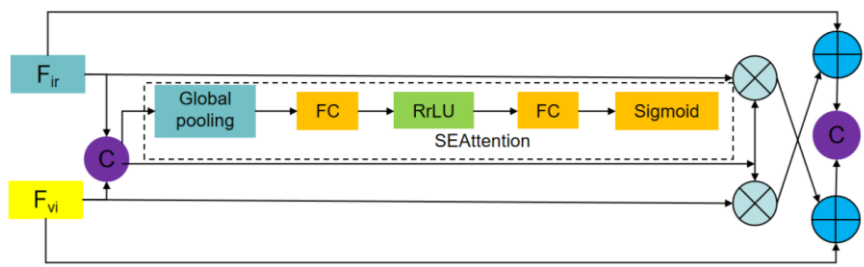


Fig. 5 – ContextGuideFusionModule structure

Lightweight detection head EfficientHead based on grouping convolution

Head of YOLOv8n uses independent classification and localization branches. Since the sample allocation strategy is task-independent, there is a lack of information interaction between classification and localization tasks. This will lead to inaccurate prediction positions with high scores and inaccurate prediction scores with accurate positions. At the same time, the classification and positioning are separated, and the model calculations are independent of each other, which will cause the Head part to be complicated and the calculation amount to be huge. Based on the above shortcomings, this paper designs a new detection head EfficientHead with reference to the idea of grouping convolution.

As a lightweight convolution operation, group convolution divides the input data and convolution kernel into multiple groups, and each group performs convolution operation independently, which greatly reduces the amount of parameters and calculations, as shown in Fig. 6. Grouping convolution effectively reduces the amount of parameters and calculations by grouping the input feature maps, and improves the computational efficiency of the model, which is especially suitable for the training of deep networks and large-scale data sets. In order to further reduce the model complexity and computational complexity without affecting the detection accuracy, this paper improves the detection head part of YOLOv8.

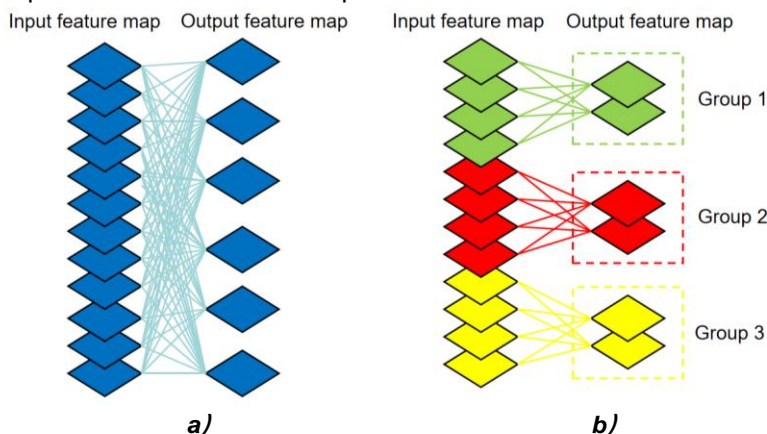


Fig. 6 –Comparison of the implementation process of conventional convolution and group convolution
 a) conventional convolution; b) group convolution

YOLOv8 adopts a decoupling head structure, and two parallel branches extract location features and category features respectively. Each layer uses a 1×1 convolution to complete the classification and positioning tasks. Based on the original YOLOv8 head structure, this paper replaces the standard convolution with group convolution, as shown in Fig. 7.

This improved method combines the advantages of group convolution, which can effectively reduce the complexity and computational complexity of the model. At the same time, the detection accuracy is maintained, so that the model can also perform well in a limited computing resource environment.

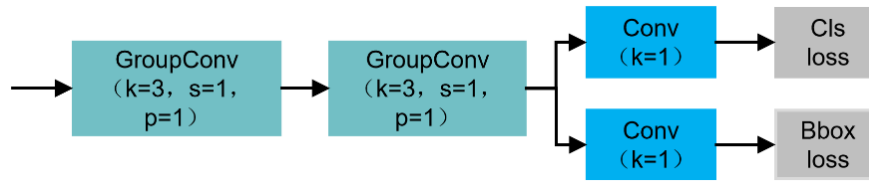


Fig. 7 – Lightweight detection head EfficientHead structure diagram

SloU loss function

The loss function is the key to evaluate the performance of the model, especially in deep learning target detection. The CloU loss function adopted by the YOLOv8n network focuses on the position and size of the bounding box, but does not consider the directional mismatch between the label box and the prediction box. In contrast, the SloU loss function introduces four parts: angle, distance, shape, and IoU to comprehensively evaluate the position, size, and direction of the object. By redefining the distance loss and combining the angle loss, SloU considers the distance and angle between the center of the object and the center of the predicted bounding box, enhances the robustness to shape changes, and helps to cope with deformation in the image. In addition, SloU is suitable for multi-class target detection, without additional complexity, ensuring the convergence speed of the algorithm, and is insensitive to target size changes to avoid excessive errors. Its differentiability enables the model to optimize parameters through back propagation, thereby improving the accuracy of small target detection in egg images.

RESULTS

Experimental environment

The computer configuration used for training and testing in this article is CPU model: Intel (R) Core97-12900H, GPU model: Nvidia GeForce RTX3060. The program compilation environment is: Window11 system, Pytorch1.1.0, python3.8, CUDA11.0, OpenCV library, and other parameters use YOLOv8 default parameters.

Performance evaluation index

In order to effectively evaluate the performance of the HCES-YOLOv8n model, five indicators—accuracy, recall rate, mAP, GFLOPs, and parameter quantity—were used to assess the performance of the model, as shown in Equations (1) - (4).

$$P = \frac{T_p}{T_p + F_p} \quad (1)$$

$$P = \frac{T_p}{T_p + F_n} \quad (2)$$

$$AP = \int_1^0 P(R) dR \quad (3)$$

$$mAP = \frac{\sum_1^n AP}{n} \quad (4)$$

In the formula, T_p was the number of correctly predicted targets, F_p was the number of incorrectly predicted targets, and F_n was the number of omitted targets to be predicted. P was the accuracy rate, defined as the proportion of samples correctly predicted as the target to the samples predicted as the target. R was the recall rate, defined as the proportion of samples correctly predicted as the target to all target samples. AP was the average accuracy, and n was the number of detected categories.

Ablation experiment

The purpose of this study was to improve the YOLOv8n network and develop a lightweight egg quality detection algorithm. To evaluate the impact of various improvements, ablation experiments were conducted under the same training environment and hyperparameters, testing a total of 8 schemes. Models 2, 3, and 4 added the HGNetv2 module and ContextGuideFusionModule to the original model, respectively, and replaced the original structure with EfficientHead, all of which were single module changes. Models 5, 6, and 7 added ContextGuideFusionModule and EfficientHead one by one based on HGNetv2, and replaced the original loss function of YOLOv8 with SloU. All models detected the same image, and the effect was shown in Fig. 8.

From the perspective of detection effect, the improved model reduced missed detections and false detections, successfully identifying eggs with small features. The evaluation indexes of the seven models were sorted out, as shown in Table 1.

Table 1 showed that under the same experimental conditions, after replacing the original backbone with HGNetv2, the accuracy, recall, and average accuracy of the model increased by 1.8%, 3%, and 3%, respectively, while the floating-point operations and parameter scale were reduced by 1.2G and 0.66M, respectively. Using the ContextGuideFusionModule structure, the accuracy, recall, and average accuracy increased by 1.8%, 3.1%, and 2.7%, respectively. Using the DetectEfficient structure, the model's performance improved while the floating-point operations and parameter scale were reduced by 3.3G and 1.41M, respectively. Combined with HGNetv2 and ContextGuideFusionModule, the accuracy, recall, and average accuracy increased by 2.9%, 3.7%, and 3.4%, respectively, and the floating-point operations and parameter scale decreased by 1.1G and 0.5M, respectively. After improving DetectEfficient based on Model 5, the floating-point operations and parameter scale were reduced by 2.4G and 0.58M, respectively, while the accuracy and recall rate remained almost unchanged. Finally, after replacing CIOU with SIOU in model 6, the accuracy and recall rate increased by 0.3% and 1.0%, respectively. In summary, these four improved strategies effectively enhanced the performance of the model while maintaining high detection accuracy.

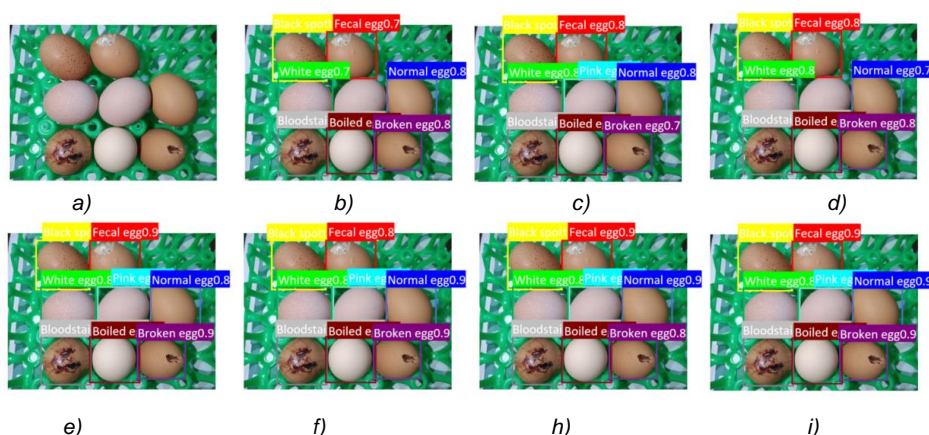


Fig. 8 – Ablation experiment detection effect diagram

Table 1

Performance comparison of ablation experiments

Network model	HGNetv2	ContextGuide FusionModule	Efficient Head	SIOU	P/%	R/%	mAP@0.5%	FLOPs/G	Parameter size / MB
Model 1	—	—	—	—	80.2	78.6	85.4	8.1	3.01
Model 2	√	—	—	—	82.0	81.6	88.4	6.9	2.35
Model 3	—	√	—	—	82.0	81.7	88.1	8.3	3.16
Model 4	—	—	√	—	80.5	80.8	86.9	4.8	1.60
Model 5	√	√	—	—	83.1	82.3	88.8	7.0	2.51
Model 6	√	√	√	—	83.7	82.5	88.7	4.6	1.93
Model 7	√	√	√	√	84.0	83.5	88.6	4.6	1.93

A is the original image, b is the detection result of the YOLOv8n model, and c ~ j is the detection result of models 3 ~ 7.

Comparative experiments of different lightweight backbone networks

In the previous section, several improvements were implemented to YOLOv8n and verified their effectiveness. To further prove the effectiveness of the introduced lightweight HGNetv2 backbone network, comparative experiments were conducted with other lightweight backbone networks.

The GhostHGNetv2, RepHGNetV2, and EfficientViT networks were used in this experiment. These networks served as replacements for the backbone network of the benchmark model and were compared with the HGNetv2 proposed in this paper. Table 2 listed the comparative experimental results of different lightweight backbone networks. It could be seen from the experimental results in Table 2 that both GhostHGNetv2 and RepHGNetv2 showed improvements in accuracy, but the recall rate and average accuracy hardly changed. In contrast, StarNet's recall rate and average accuracy improved, but its accuracy declined.

The HGNetv2 proposed in this paper not only successfully reduced the floating-point operations by 14.8% and the number of parameters by 21.9%, but also achieved significant improvements in accuracy, recall, and average accuracy. This result demonstrated that HGNetv2 could effectively improve the overall performance of the model while maintaining high efficiency.

Table 2

Comparative experiments of different lightweight trunks

Network model	P/%	R/%	mAP@0.5%	FLOPs/G	Parameter size / MB
YOLOv8n (Baseline)	80.2	78.6	85.4	8.1	3.01
GhostHGNetv2	83.8	78.5	85.8	6.8	2.31
RepHGNetV2	82.3	78.8	85.9	6.9	2.37
StarNet	79.5	81.1	86.2	7.1	2.40
HGNetv2	82.0	81.6	88.4	6.9	2.35
YOLOv8n (Baseline)	80.2	78.6	85.4	8.1	3.01
GhostHGNetv2	83.8	78.5	85.8	6.8	2.31

Model performance

To verify the performance of HCES-YOLO in the training process, the training effect was evaluated by observing the change trend of the SIOU loss function value compared to the original loss function. The model comparison curve was shown in Fig. 9. In Fig. 9 (a), as training deepened, the loss value of the bounding box gradually decreased, indicating that the model continued to improve the positioning accuracy of the bounding box. In Fig. 9 (b), the decreasing trend of classification loss showed that the model was gradually enhanced in its ability for category discrimination. Fig. 9 (c) illustrated that the model also had high recognition ability for a few categories of samples. The stationary state curve in Fig. 9 indicated that there was no overfitting or underfitting phenomenon during the model training process. Throughout the training process, the model learned effective feature representation, demonstrating that it had good stability and generalization ability when completing the recognition task. From the above, it could be concluded that the loss value of the improved HCES-YOLO model converged faster compared to the original YOLOv8n loss function, and the loss value was smaller than that of YOLOv8n. This indicated that the improved method in this paper effectively enhanced the convergence ability of the model.

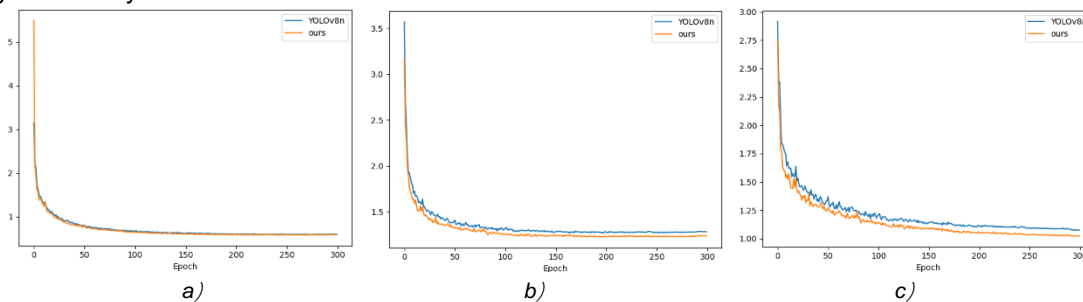


Fig. 9 - Loss function comparison curve

a) Box Loss; b) CLS Loss; c) DFL Loss

Comparative experiment of different models

In this paper, a series of improvements were made to the YOLOv8n model to enhance the accuracy and efficiency of target detection, and the performance was compared with other mainstream models through experiments. Following the principle of control variables, the data training and evaluation in Table 3 were carried out in a unified hardware and software environment. The experimental results showed that Faster R-CNN, as a two-stage object detection algorithm, generated a large number of redundant boxes due to the need to produce candidate boxes, which increased the computational burden, and the recall rate was not satisfactory. The recall rate and average accuracy of the SSD algorithm on the egg quality dataset were 70.4% and 71.4%, respectively. Although multi-scale feature fusion was used, the response was insufficient when dealing with small targets, which affected accuracy, leaving a gap compared to other algorithms.

Single-stage object detection algorithms such as Tood and YOLOv7 had similar accuracy, recall, and average accuracy to YOLOv8n, but their floating-point operations and parameter scale were much larger than those of YOLOv8n. Although the floating-point operations and parameter scale of YOLOv5n were lower than

those of YOLOv8n, its performance index was not as good as that of YOLOv8n. In summary, YOLOv8n significantly reduced computing resources and memory usage while achieving better detection results, thereby improving the interpretability of the model. Therefore, this paper chose YOLOv8n as the original model. Compared with YOLOv8n, HCES-YOLOv8 improved accuracy by 3.8%, recall rate by 4.9%, and average accuracy by 3.2% on key indicators, respectively. At the same time, the floating-point operations and parameter scale were greatly reduced, making the model lighter and especially suitable for resource-constrained devices. The comparative experimental results clearly showed that the HCES-YOLOv8 algorithm exhibited superior performance in the field of egg quality target detection.

Table 3

Performance comparison of different models

Network model	P/%	R/%	mAP@0.5%	FLOPs/G	Parameter size / MB
Faster R-CNN	—	76.6	79.2	182.3	41.37
SSD	—	70.4	71.4	33.6	25.6
Tood	—	80.1	86.6	172	32.03
YOLOv5n	75.4	84.4	83.3	7.2	2.51
YOLOv7	77.7	80.1	86.6	103.2	34.79
YOLOv8n	80.2	78.6	85.4	8.1	3.01
PSCW-YOLOv8n	84.0	83.5	88.6	4.6	1.93

Test result

To verify the practicality of the improved model, real-time detection of egg quality in the egg image acquisition system was carried out. According to the research, the egg-feeding capacity of a single processing line was 10,000 to 20,000 eggs per hour, and the required egg-feeding speed was 3 to 5 meters per minute. Therefore, it was planned to conduct experiments on the laboratory test platform to evaluate the performance of the improved YOLOv8n model in practical applications. 300 eggs were obtained from the farm and all categories of samples were uniformly mixed. Before the start of the experiment, all the sample eggs were manually placed on the tray on the conveyor belt, with the surface eggs in the area with obvious features facing upward, and there was no obstruction between the eggs.

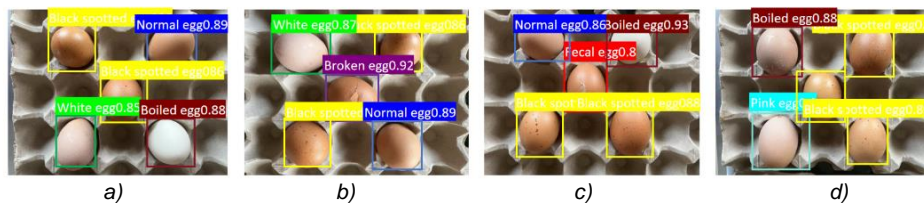


Fig. 10 - Model real-time detection effect diagram

After starting the drive motor, all the eggs were transported at a set speed. The egg image was collected by the camera, and the trained improved YOLOv8n model was introduced to detect the egg quality, with the detection result being output at the end. The eggs detected each time were counted and their accuracy was assessed. The accuracy of egg quality was 88.4%. Fig. 10 showed a random screenshot from the detection process. It could be seen from Fig. 10 that the detection model proposed accurately detected the quality of the eggs appearing in the visual window and met the real-time detection requirements of the egg assembly line collection work on the farm.

CONCLUSIONS

In this study, an egg quality detection model was established based on an improved YOLOv8n network, which can effectively recognize small targets. The test results on the same dataset show that the improved model achieves an accuracy of 84.0%, a recall of 83.5%, and an average accuracy of 88.6% in egg quality detection, outperforming the original YOLOv8n network and other detection models. Its computational cost was also reduced and its accuracy in identifying minor damages and pollution was improved. On-site experiments were conducted on the testing platform built in the laboratory, and the improved YOLOv8n model can effectively detect leaking eggs during movement at a conveying speed range of 3 to 5 m/min. The comprehensive detection performance reached 88.4%, providing a new solution for rapid non-destructive testing of eggs.

ACKNOWLEDGEMENT

The author has been supported by the “Aquaculture solid waste treatment and resource utilization equipment development” (Project number: 2023TSGC0741).

REFERENCES

- [1] Cruz-Tirado, J.P., Da Silva Medeiros, M.L., Barbin, D.F. (2021). On-line monitoring of egg freshness using a portable NIR spectrometer in tandem with machine learning. *Journal of Food Engineering*, 306, 110643
- [2] Dong, X., Zhang, B., Dong, J., Lu, B., Hu, C., Tang, X. (2020). Egg freshness prediction using a comprehensive analysis based on visible near infrared spectroscopy. *Spectroscopy Letters*, 53(7), 512-522
- [3] Eddin, A.S., Ibrahim, S.A., Tahergorabi, R. (2019). Egg quality and safety with an overview of edible coating application for egg preservation. *Food chemistry*, 296, 29-39
- [4] Gevorgyan, Z. (2022). SloU loss: More powerful learning for bounding box regression. arXiv. *arXiv preprint arXiv:2205.12740*, 10
- [5] Guanjun, B., Mimi, J., Yi, X., Shibo, C., Qinghua, Y. (2019). Cracked egg recognition based on machine vision. *Computers and electronics in agriculture*, 158, 159-166
- [6] Hisasaga, C., Griffin, S.E., Tarrant, K.J. (2020). Survey of egg quality in commercially available table eggs. *Poultry Science*, 99(12), 7202-7206
- [7] Hu, J., Shen, L., Sun, G. (2018) *Squeeze-and-excitation networks*. Paper presented at the Proceedings of the IEEE conference on computer vision and pattern recognition.
- [8] Liang, Q., Zihan, Z., Jingye, S., Jiang, T., Ningning, G., Haiyang, Y.U., Yiyuan, G.E. (2024). Multi-target detection method for maize pests based on improved YOLOv8. *INMATEH-Agricultural Engineering*, 73(2), pp.227-238
- [9] Luo, Y., Huang, Y., Wang, Q., Yuan, K., Zhao, Z., Li, Y. (2023). An improved YOLOv5 model: Application to leaky eggs detection. *LWT*, 187, 115313
- [10] Malfatti, L.H., Zampar, A., Galvão, A.C., Da Silva Robazza, W., Boiago, M.M. (2021). Evaluating and predicting egg quality indicators through principal component analysis and artificial neural networks. *Lwt*, 148, 111720
- [11] Narushin, V.G., Kent, J.P., Salamon, A., Romanov, M.N., Griffin, D.K. (2023). Density of egg interior: Looking inside an egg while keeping it intact. *Innovative Food Science & Emerging Technologies*, 87, 103387
- [12] Okinda, C., Sun, Y., Nyalala, I., Korohou, T., Opiyo, S., Wang, J., Shen, M. (2020). Egg volume estimation based on image processing and computer vision. *Journal of Food Engineering*, 283, 110041
- [13] Omid, M., Soltani, M., Dehrouyeh, M.H., Mohtasebi, S.S., Ahmadi, H. (2013). An expert egg grading system based on machine vision and artificial intelligence techniques. *Journal of food engineering*, 118(1), 70-77
- [14] Sehirli, E., Arslan, K. (2022). An application for the classification of egg quality and Haugh unit based on characteristic egg features using machine learning models. *Expert Systems with Applications*, 205, 117692
- [15] Turkoglu, M. (2021). Defective egg detection based on deep features and Bidirectional Long-Short-Term-Memory. *Computers and Electronics in Agriculture*, 185, 106152
- [16] Wang, Z., Hua, Z., Wen, Y., Zhang, S., Xu, X., Song, H. (2024). E-YOLO: Recognition of estrus cow based on improved YOLOv8n model. *Expert Systems with Applications*, 238, 122212
- [17] Xu, W., Liu, C., Wang, G., Zhao, Y., Yu, J., Muhammad, A., Li, D. (2024). Behavioral response of fish under ammonia nitrogen stress based on machine vision. *Engineering applications of artificial intelligence*, 128, 107442
- [18] Yang, S., Wang, W., Gao, S., Deng, Z. (2023). Strawberry ripeness detection based on YOLOv8 algorithm fused with LW-Swin Transformer. *Computers and Electronics in Agriculture*, 215, 108360
- [19] Yang, W., Wu, J., Zhang, J., Gao, K., Du, R., Wu, Z., Firkat, E., Li, D. (2023). Deformable convolution and coordinate attention for fast cattle detection. *Computers and Electronics in Agriculture*, 211, 108006
- [20] Yao, K., Sun, J., Chen, C., Xu, M., Zhou, X., Cao, Y., Tian, Y. (2022). Non-destructive detection of egg qualities based on hyperspectral imaging. *Journal of Food Engineering*, 325, 111024
- [21] Yonghui, D.U., Ang, G., Yuepeng, S., Jing, G., Wei, M.A., Longlong, R. (2024). Young apple fruits detection method based on improved YOLOv5. *INMATEH-Agricultural Engineering*, 73(2), pp.84-93

- [22] Zhang, Q., Li, J., Yao, M., Song, L., Zhou, H., Li, Z., Meng, W., Zhang, X., Wang, G. (2019). Vargnet: Variable group convolutional neural network for efficient embedded computing. *arXiv preprint arXiv:1907.05653*
- [23] Zhao, M., Cang, H., Chen, H., Zhang, C., Yan, T., Zhang, Y., Gao, P., Xu, W. (2023). Determination of quality and maturity of processing tomatoes using near-infrared hyperspectral imaging with interpretable machine learning methods. *LWT*, 183, 114861
- [24] Zhao, Y., Lv, W., Xu, S., Wei, J., Wang, G., Dang, Q., Liu, Y., Chen, J. (2024) *DETRs beat YOLOs on real-time object detection*. Paper presented at the Proceedings of the IEEE/CVF Conference on Computer Vision and Pattern Recognition.

MATHEMATICAL MODELING OF THE FORCE REQUIRED TO MOVE PLATFORMS INTENDED FOR SOIL SAMPLING

MODELAREA MATEMATICĂ A FORȚEI NECESARE DEPLASĂRII PLATFORMELOR DESTINATE PRELEVĂRII PROBELOR DE SOL

Mario CRISTEA ¹⁾, Mihai Gabriel MATAACHE ¹⁾, Robert-Dorin CRISTEA ^{*1)}, Andreea-Iulia GRIGORE ¹⁾,
Laurențiu VLĂDUȚOIU ¹⁾

¹⁾ National Institute of Research - Development for Machines and Installations Designed to Agriculture and Food Industry –
INMA Bucharest / Romania;

^{*)} E-mail: robertcri@yahoo.com

DOI: <https://doi.org/10.35633/inmateh-74-44>

Keywords: self-propelled platform, soil sampling, traction force, mathematical model.

ABSTRACT

Self-propelled platforms designed for soil sampling represent a remarkable technological advancement in the field of soil research, providing efficient and precise collection of essential data regarding soil composition. These platforms are equipped with advanced technologies and sophisticated sampling systems, offering researchers the opportunity to obtain detailed data in an automated and replicable manner. In this article, the technical features of self-propelled platforms for soil sampling and their significance in advancing soil sciences research will be investigated.

In this paper, a mathematical model is described to aid in the design of the propulsion system of self-propelled platforms intended for soil sample collection under conditions of movement on horizontal or sloping terrain. With this mathematical model, the forces required for the platform to move can be calculated, considering the constraints specific to each project. When the project is completed, and key parameters such as the total weight of the platform, dimensions, payload weight, and transmission gear ratios are known, the minimum power required for the engine to move the platform can be calculated.

REZUMAT

Platformele autopropulsate destinate prelevării probelor de sol reprezintă un avans tehnologic remarcabil în domeniul cercetării solului, furnizând o colectare eficientă și precisă a datelor esențiale privind compoziția solului. Aceste platforme sunt dotate cu tehnologii avansate și sisteme de eșantionare sofisticate, oferind cercetătorilor oportunitatea de a obține date detaliate într-un mod automatizat și reproductibil. În acest articol, vom explora în profunzime caracteristicile tehnice ale platformelor autopropulsate destinate prelevării probelor de sol, precum și importanța lor în avansarea cercetărilor în domeniul științelor solului. În această lucrare este descris un model matematic care ajută la proiectarea sistemului de propulsie a platformelor autopropulsate destinate prelevării probelor de sol în condițiile de deplasare pe un teren orizontal sau un teren aflat în pantă. Cu ajutorul acestui model matematic se pot calcula forțele de care este nevoie ca platforma să execute o deplasare ținând cont de constrângerile care se impun la fiecare proiect în parte. Atunci când este realizat proiectul și sunt cunoscute, de exemplu, greutatea totală a platformei, dimensiunile dar și greutatea utilă și rapoartele de transmitere ale transmisiei, se poate calcula puterea minimă necesară pentru motor ca platforma să se poată deplasa.

INTRODUCTION

Self-propelled platforms designed for soil sampling are an innovative paradigm in soil research, providing an advanced and precise method for collecting essential data on soil composition and properties. These technologically advanced vehicles have become the focal point for researchers in the soil sciences, enabling detailed and accurate data collection, with a significant impact on understanding pedological processes and the practical application of research results (Oprescu R.M. et al, 2023).

Self-propelled platforms benefit from rapid advancements in autonomous system technologies, robots, sensors, and navigation algorithms. For the navigation of self-propelled platforms in open or enclosed spaces, the development of computational models is necessary to enable movement under conditions of maximum safety and the utilization of optimized routes (Ibrahim A. et al., 2023). These not only facilitate data collection but also make significant contributions to optimizing research processes in the field of soil studies (Zawilski, B.M. et al, 2023).

Using mathematical models of precise movement of self-propelled platforms on agricultural land, simulation models can be created to increase efficiency, but also to reduce soil damage (*Bulgakov V. et al, 2018*). It can also simulate the pressure exerted by self-propelled platforms equipped with various agricultural machinery, such as sprayers (*Li W. et al, 2022*).

The evolution of self-propelled platforms has been substantial in recent years, transitioning from simple devices to sophisticated and intelligent vehicles. The use of autonomous robots in soil research has marked a significant leap in data collection, facilitating access to challenging areas and ensuring increased accuracy in sample collection. This technological evolution has been fueled by advanced research in the fields of artificial intelligence and navigation algorithms (*Vaeljaots F. et al, 2018*).

An essential aspect of self-propelled platforms is represented by their advanced sampling systems. These systems are designed to collect representative samples, taking into account the specific characteristics of the soil, such as texture, water content, and chemical composition. Specialized sensors and integrated tools enable researchers to obtain detailed information about the physical and chemical properties of the soil in real-time (*Huuskonen J., Oksanen T., 2018; Tan K.H., 2005*).

The use of self-propelled platforms in soil research has a significant impact on agricultural resource management. The collected data provides essential information for optimizing agricultural practices, including irrigation needs, fertilizer application, and chemical substance management. This personalized approach contributes to resource efficiency and reduces environmental impact (*Viăduț V. et al, 2020*).

While the agricultural sector has made significant progress in implementing robotic automation in various processes, there are still notable challenges associated with mechanization in specific environments and techniques, such as vineyard cultivation and orchard management in mountainous or steep terrain. These challenges stem from difficult topographic conditions, extreme fragmentation of vineyards, variability in weather conditions, rich biodiversity, and other concomitant factors. Real-time tracking of soil robots in environments like forests, pastures, and vineyards has seen the development of environmental detection methods using YOLO (You Only Look Once) and a multi-target tracking algorithm designed for monitoring ground robot activities through real-time digital video transmissions (*Cao X. et al., 2023*). In the context of this complexity, farmers show an increased interest in implementing precision spraying/mowing robots characterized by financial efficiency, operational safety, and autonomy, with the ability to operate effectively in vineyards situated on steep slopes. The purpose of these efforts is to reduce costs, optimize agricultural process efficiency, and minimize the negative impact on the environment associated with agricultural activities (*Vanghele N.A. et al, 2021*).

Air Technical Industries (ATI), based in Mentor, Ohio, has designed and developed a self-propelled platform with remarkable capabilities (figure 1) (<https://www.mhnetwork.com/self-propelled-platform-truck-tug/>).



Fig. 1 - Air Technical Industries platform

The propulsion of this platform is provided by an electric motor powered by a 24-volt nominal voltage battery.

The fruit harvesting device ARGILÉS AF-5 (figure 2) is equipped with a Kubota 3-cylinder, 25-horsepower engine. Its operation can be managed through a radio remote control, providing the user with flexible control over the machine.



Fig. 2 - ARGILÉS AF-5, Machine for fruit picking, cutting, thinning, hail netting, etc.
(<https://argiles.es/informacion-producto/af5/?lang=en>)

Additionally, this machine exhibits a maximum speed of 14 km/h, contributing to the efficiency and speed of the fruit harvesting process (<https://argiles.es/informacion-producto/af5/?lang=en>).



Fig. 3 - UGV Robotics Plus
(<https://www.powermotiontech.com/sensors-software/automation/media-gallery/21254335/robotics-plus-unveils-unmanned-ground-vehicle-for-agricultural-operations?id=21254335&slide=2>)

Through this Unmanned Ground Vehicle (UGV), also known as an autonomous ground vehicle, Robotics Plus aims to contribute to addressing the labor shortage issue faced by the contemporary agricultural industry. The vehicle in question has been designed in a compact format, facilitating maneuverability within tightly spaced row crops, characteristic of orchards, vineyards, and other similar agricultural applications. The use of an electric steering system and independent motors gives the UGV the ability to make turns on its rear axle (figure 3).

The implementation of a hybrid propulsion system, with diesel-electric power, is an advantage in reducing fuel consumption and emissions while maintaining sufficient power for the efficient execution of agricultural activities throughout the working day (<https://www.powermotiontech.com/sensors-software/automation/media-gallery/21254335/robotics-plus-unveils-unmanned-ground-vehicle-for-agricultural-operations?id=21254335&slide=2>).



Fig. 4 - OMNiDRIVE self-propelled platform

(<https://www.agriculture.com/news/technology/raven-announces-new-product-brand-and-autonomous-growth-platform>)

The self-propelled electric platform developed by OMNi, Raven – OMNiDRIVE (figure 4), shows the capability to efficiently replace certain agricultural machinery, thereby enabling farmers to perform various tasks throughout the growing season. Mission launches can be carried out both autonomously and through direct control from a tablet. A notable feature of this platform is the absence of dedicated personnel for its operation (<https://www.agriculture.com/news/technology/raven-announces-new-product-brand-and-autonomous-growth-platform>).



Fig. 5 - The smart mower R 150

(<https://hse-uav.com/products/r150-2023-autonomous-tractor-mower>)

Drawing on expertise in autonomous driving and artificial intelligence (AI) training, XAG has implemented new enhancements to its UGV R150 system (figure 5). The XAG R150 can be characterized as an "open and scalable utility-loading platform," capable of integrating various modules for activities such as precision spraying, fertilizing, and mowing of crops. The RevoMower 2.0 system, designed to facilitate grass cutting in complex terrestrial environments like farmlands, marshes, and orchards, is part of this platform. Equipped with a 6 kW power motor, the XAG R150 demonstrates the ability to efficiently control weeds and small shrubs (<https://hse-uav.com/products/r150-2023-autonomous-tractor-mower>).



Fig. 6 - UGV Husky

(<https://clearpathrobotics.com/blog/2021/01/husky-ugv-drives-smart-precision-agriculture-for-steep-slope-vineyards/>)

The AgRobIT project, based on the UGV Husky platform (figure 6), proposes a simplified architecture built on a ROS (Robot Operating System) stack solution, consisting of three main ROS packages: localization and mapping, path planning and control, and mission supervisor. AgRobIT has successfully used the achievements of INESC TEC over the past four years, including VineSLAM (a cost-effective, modular, and reliable localization system capable of working with or without available GNSS and integrating semantic information) and AgRobPP (path planning and control systems aware of soil compaction and the robot's center of gravity) (<https://clearpathrobotics.com/blog/2021/01/husky-ugv-drives-smart-precision-agriculture-for-steep-slope-vineyards>.)

MATERIALS AND METHODS

The mathematical model was developed using relationships describing vehicle dynamics since the platforms are subject to the same forces, moments, and efforts. The resulting mathematical model aims to determine the force required by a motor for the platform to move. A series of steps were followed to study the forces involved in all the mechanisms that make up the propulsion system. In general, the propulsion system consists of an engine, gearbox, final drive, and wheel or track. Most of the forces influencing movement occur at the wheel or track level. For this reason, the study method began with wheel kinematics.

Wheel kinematics is a branch of mechanics that deals with the study of the motion and behavior of wheel systems, including the analysis of relationships between wheel motion and associated parameters such as speed, acceleration, and position in space. This discipline is crucial in engineering, especially in fields involving the design of vehicles or other systems that utilize wheels, such as mobile robots, autonomous vehicles, or any other application involving the motion and orientation of wheels.

In the context of constant speed motion, figure 7, the wheels experience the torque M_R and the gravitational force or the load on the wheel G_R (acting perpendicular to the direction of motion and applied at the center of the wheel). As a result of the interaction of these two loads, the rolling resistance reaction Z_R , the traction force F_t , and the friction force X occur (Băisan, 2020).

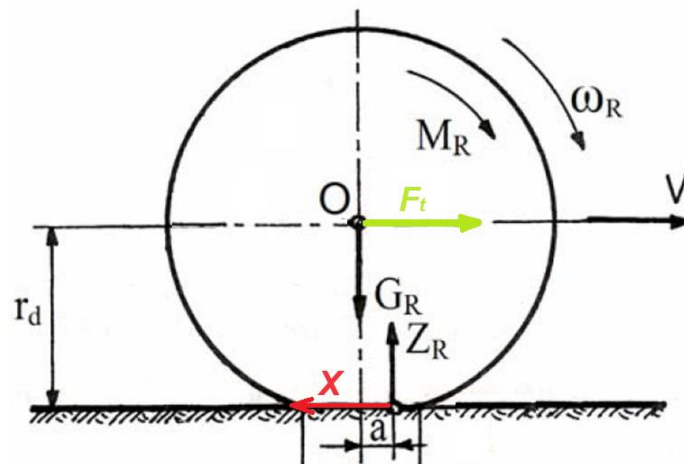


Fig. 7 - Equilibrium of the drive wheel on a non-deformable roadway (Băisan, 2020)

As, upon contact with the rolling surface, the wheel undergoes deformation along the length L , and the pressure forces are not symmetrical, the Z_R reaction will experience a displacement at a distance from the wheel's vertical axis.

The equilibrium equations (Băisan, 2020) in the case of constant speed rolling can be expressed by:

$$X - F_t = 0 \quad (1)$$

$$Z_R - G_R = 0 \quad (2)$$

$$X r_d + Z_R a - M_R = 0 \quad (3)$$

From equations (1), (2), and (3) follows the relationship:

$$X = \frac{M_R}{r_d} - Z_R \frac{a}{r_d} \text{ [N]} \quad (4)$$

where:

X – friction force [N]; F_t – tractive force [N]; Z_R – reaction force [N]; G_R – load on the wheel [N]; M_R – wheel torque [Nm]; r_d – dynamic wheel radius [m]; a – distance by which the reaction force Z_R is shifted forward [m].

In the scenario of a wheel rolling on a deformable track, figure 8, while maintaining a constant speed, it is assumed that the deformation involves the existence of a cylindrical surface in front of the wheel and a flat surface behind it. Distinct forces and reactions act on the wheel in this configuration, namely R_1 on the cylindrical surface and R_2 on the flat surface. By combining these, the resultant R is obtained, which is decomposed into two main components: the tangential force X and the vertical reaction Z_R . This allows the formulation of equilibrium equations for the wheel, capturing the complex interactions between the wheel and the deformable track while maintaining a constant speed during the rolling process.

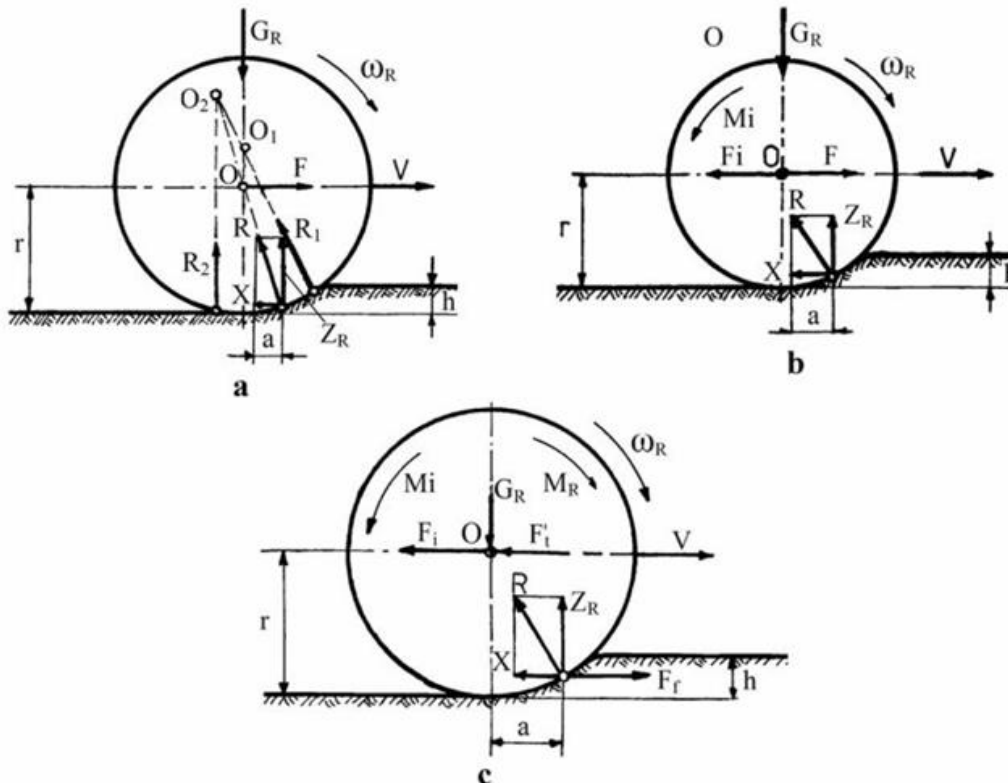


Fig. 8 - Wheel balance when traveling on a deformable roadway (Bäisan, 2020)

In this case the tangential reaction is:

$$X = F = Z_R \frac{a}{r} = G_r f = R_r \text{ [N]} \tag{5}$$

If the inertial force is also considered:

$$X = F - F_i = F - m_R \frac{dv}{dt} \text{ [N]} \tag{6}$$

To obtain the power balance, the inertia force (F_i), the translational speed of the wheel (V), are entered into relation (6):

$$V = \omega_R r \text{ [m/s]} \tag{7}$$

$$FV = M_r \omega_R + M_i \omega_R + F_i V \tag{8}$$

For the case where the wheel runs on deformable terrain at variable speed, the equilibrium equations are:

$$F_t - X - F'_t - F_i = 0 \tag{9}$$

$$Z_R - G_R = 0 \quad (10)$$

$$M_R - F_t r - M_i = 0 \quad (11)$$

where: F_t – traction force [N]; M_R – torque at the wheel [Nm]; M_i – moment of inertia [Nm]; F'_t – traction force reaction [N].

In the case of movement with constant speed $F_i = 0$ and $M_i = 0$, and the torque required for movement (M_R) is:

$$M_R = F_t r + M_i \text{ [Nm]} \quad (12)$$

$$r = \frac{V}{\omega_r} \text{ [m]} \quad (13)$$

In relation (12) add slip and theoretical speed (V_t), substitute r from relation (13) and F_t , and get:

$$M_R \omega_R = F_t (V_t - V) + XV + F'_t + FiV + M_i \omega_R \text{ [Nm]} \quad (14)$$

The deceleration is introduced into the calculations and it is obtained:

$$M_R \omega_R = F_t (V_t - V) + XV + F'_t \pm FiV \pm M_i \omega_R \text{ [Nm]} \quad (15)$$

It can be seen that the motor power required at the driving wheel ($M_R \omega_R$), in the context of variable speed travel on a deformable raceway, consists of the sum of the powers lost by the slippage of the driving wheel for running (XV), to imprint an accelerated motion ($F_i V$), and for an accelerated rotational movement ($M_i \omega_R$), respectively the power transmitted to the vehicle body ($F_t V$).

Depending on the characteristics of the raceway, at the point of contact with the tire, it is possible to manifest a maximum adhesion force. The ratio of this force to the normal reaction at the wheel is defined by the adhesion coefficient (φ) (Băisan, 2020):

$$\varphi = \frac{X_{max}}{Z_R} \Leftrightarrow X_{max} = \varphi Z_R \quad (16)$$

For the maximum grip force, a maximum moment at the driving wheels ($M_{R max}$) results, corresponding to a maximum force at the grip limit ($F_{R max}$).

$$M_{R max} = r_d (\varphi + f) Z_R \text{ [Nm]} \quad (17)$$

$$F_{R max} = \frac{M_{R max}}{r_d} = (\varphi + f) Z_R \text{ [N]} \quad (18)$$

In the situation where the vehicle has more than one driven wheel, the evaluation of the maximum adhesion force involves the use of the adhesion weight (G_{ad}), representing the sum of the normal reactions of the roadway on the driven wheels:

$$X_{max} = \varphi G_{ad} \text{ [N]} \quad (19)$$

When the movement takes place on an inclined terrain the maximum motor torque and the maximum force at the motor wheels is:

$$M_{R max} = r_d (\varphi + f) G_{ad} \cos \alpha \text{ [Nm]} \quad (20)$$

$$F_{R max} = (\varphi + f) G_{ad} \cos \alpha \text{ [N]} \quad (21)$$

There is the situation when the moment at the wheel is minimal, namely when the adhesion force is zero:

$$M_{R min} = r_d f Z_R \text{ [Nm]} \quad (22)$$

The torque at the wheel must satisfy the following inequality:

$$M_{R \min} < M_R \leq M_{R \max} \quad (23)$$

Slippage of the drive wheel occurs when the drive torque is maximum, thus a relative frictional speed appears in the contact area of the tire with the ground. In the case of wheels subjected to brake action (the braking moment, M_f , may also occur), the relationship can be formulated as:

$$M_f = Xr_d - Z_R a \text{ [Nm]} \quad (24)$$

For maximum braking torque there is:

$$M_{f \max} = \varphi r_d Z_R - Z_R a = Z_R r_d (\varphi - f) \text{ [Nm]} \quad (25)$$

The determination of rolling resistance involves the use of the coefficient of rolling resistance, denoted f and defined as the ratio of the adhesion coefficient (a) to the wheel radius (r_d). The rolling resistance coefficient exhibits an approximately linear increase with platform speed.

Due to the ability of a platform to move on various types of tracks, the coefficient of rolling resistance is influenced by a multitude of factors. For this reason, for mathematical purposes, average values were adopted, adjusted according to the specific condition of the running surface.

Traction force is dependent on the coefficient of friction (μ) between the tire and the running surface, along with the radial load exerted on the wheel (G_R). Its expression can be formulated as follows (Băisan, 2020).

$$F_t = \mu G_R + \sigma \sum_{i=1}^n A_{vi} \text{ [N]} \quad (26)$$

where: A_v – the projection area of each tire protrusion located on a vertical plane in the running surface; n – the number of protrusions of the tire that come into contact with the ground.

The traction force of the vehicle influences the adhesion weight utilization coefficient φ_{ad} .

$$\varphi_{ad} = \frac{F_t}{G_{ad}} \quad (27)$$

For wheeled platforms the slip coefficient of the driving wheels is calculated with the relation (Băisan, 2020):

$$\delta = a \frac{F_t}{G_{ad}} + b \left(\frac{F_t}{G_{ad}} \right)^c \quad (28)$$

The coefficients a , b and c depend on the type of tire, the air pressure in the tire and the type of soil on which the platform moves, the usual values being presented in the specialized literature (Băisan, 2020).

In the context of the vehicle traveling on a deformable roadway, the evaluation of the adhesion coefficient requires consideration of the fact that the maximum traction force ($F_{t \max}$), at which slippage of the driving wheels is considered acceptable (δ_{ad}), is defined as equal to X_{\max} :

$$\varphi = \frac{X_{\max}}{G_{ad}} = \frac{F_{t \max}}{G_{ad}} \quad (29)$$

For a platform moving on a track inclined at an angle α at a speed V , the forces and moments acting on it can be observed in figure 9.

This figure shows the rolling resistance moments on each axle (M_{r1} and M_{r2}), the tangential reaction forces (X_1 and X_2), and the reaction forces from the track surface (Z_1 and Z_2) (Băisan, 2020).

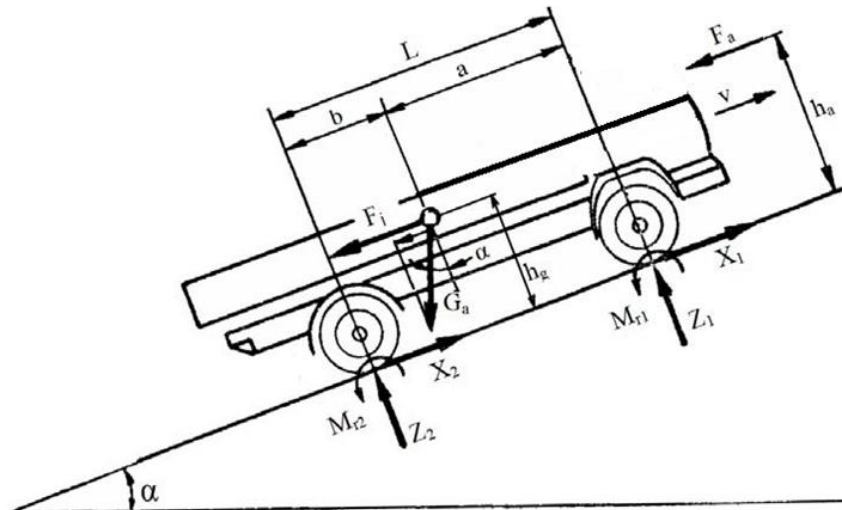


Fig. 9 - Diagram of forces and moments acting on the platform (Băisan, 2020)

The traction force at the wheel is determined using the following relationship (Băisan, 2020):

$$F_t = F_r + F_p + F_a + F_i = fG_a \cos \alpha + G_a \sin \alpha + C_x \frac{1}{2} A \rho v^2 + \frac{G_a}{g} \delta_{rot} \frac{dv}{dt} \quad [\text{N}] \quad (30)$$

The effective motor torque is calculated according to the following relationship:

$$M_e = \frac{P_m}{\omega} \quad [\text{Nm}] \quad (31)$$

In general cases, the balance of powers is determined with the help of the relationship (Băisan, 2020):

$$P_e = P_{tr} + P_r + P_p + P_i + P_a + P_\delta = F_t v \delta + \frac{v f G_a \cos \alpha}{10^3} + \frac{v G_a \sin \alpha}{10^3} + v \frac{G_a \delta_{rot} dv}{g 10^3 dt} + \frac{C_x A \rho v^3}{2 \cdot 10^3} + \frac{\delta F_m v}{10^3 (1 - \delta)} \quad [\text{W}] \quad (32)$$

where: A – surface area exposed to air resistance [m^2]; F_t – traction force [N]; M_e – effective motor moment [Nm]; i_{tr} – total transmission ratio; η_{tr} – transmission efficiency [%]; r – wheel radius [m]; F_a – air resistance force [N]; F_p – the force required to climb the slope [N]; F_i – inertial force; F_r – rolling resistance force; C_x – aerodynamic coefficient; ρ – air density; G_a – total weight; v – speed [m/s]; α – the angle of inclination of the slope [degrees]; f – rolling resistance coefficient; δ – slip coefficient, δ_{rot} – coefficient of influence of the masses in the rotation movement; P_e – effective power [W]; P_{tr} – power lost during transmission; P_r – the power required to overcome the rolling resistance; P_p – the power required to climb the slope [W]; P_i – the power required to overcome the inertial force [W]; P_a – the power required to overcome the air resistance force [W]; P_δ – power lost during skating [W]; P_m – engine power [W]; ω – angular speed of the motor shaft [rad/s].

RESULTS

Calculating traction force in vehicle dynamics is essential for several key aspects of vehicle design, efficiency, and performance.

When calculating traction force for vehicles such as self-propelled platforms, some resistance forces are often neglected, for instance, air resistance, friction force in bearings or rollers, and in certain situations, even inertia force. These forces are not considered due to the reduced travel speed in such cases and the high gear ratios used, which greatly amplify the braking force when the engine is no longer accelerating (engine brake).

A crucial factor in calculating moments or forces at the wheel axis is the transmission. The transmission gear ratios must be known for each speed stage, as well as the final drive transmission, which can be a simple differential.

Currently, it is recommended that the engine force applied to the platform's propulsion system has a power reserve of at least 20%.

Case Study

In this simulation, the above relationships were used to calculate the minimum force needed for the movement of a self-propelled platform on a rigid surface with non-deformable wheels, intended for transporting loads up to a maximum of 2000 kg (load weight – 19613.3 N). The platform dimensions are (length x width x height, mm) – 4396 x 1848 x 1501, the mass of the platform – 1150 kg (weight – 11277,64 N), wheel radius - 0.295 m, total transmission ratio – 14.02, angle α ranging from 0 to 11.5 degrees, air density $\rho = 1.225 \text{ kg/m}^3$, transmission efficiency $\eta_{tr} = 0.93$, mass influence coefficient in rotational motion $\delta_{rot} = 1.144$, considering $dv/dt = 0.2 \text{ m/s}^2$, maximum travel speed – 2.2 m/s, aerodynamic coefficient $C_x = 0.65$, rolling resistance coefficient $f = 0.0132$, normal gravitational acceleration $g = 9.806 \text{ m/s}^2$, $A = 2.48 \text{ m}^2$ and sliding coefficient $\delta = 0.8-0.9$ are known.

At the time of the experiment, the self-propelled platform is in the design stage, a car was used to validate the mathematical model. During the experiments, the maximum angle of the slope was 11.5 degrees and the measurement of the traction force was measured with the help of a dynamometer placed between the car and the tractor with which it was towed. The force at which the car starts moving was measured. Model optimization will be performed when the platform is ready for experimentation.

To calculate the traction force, relationship (30) was used, where all known data was substituted. The forces needed for movement were studied under two different operating conditions: when the platform is unloaded, and the propulsion system is used for movement on a horizontal surface, as well as on a surface with an incline ranging from 5 to 25 degrees. In the second case, the platform was loaded with the maximum proposed load under simulation conditions.

Table 1 presents the force values resulting from calculations when the platform is unloaded, and Table 2 shows the force values when the platform is loaded with the maximum load. The inertia force and the air resistance force have exceedingly small values and are typically neglected.

Table 1

Forces required for the movement of the self-propelled platform calculated for unloaded travel

F_t (N)	F_r (N)	F_p (N)	F_a (N)	F_i (N)	Angle α	Measured data F_t (N)
414.07	148.92	0.00	1.93	263.23	0.00	412.02
906.02	148.77	492.09	1.93	263.23	2.50	1098.72
1396.75	148.35	983.25	1.93	263.23	5.00	1294.92
1885.33	147.64	1472.53	1.93	263.23	7.50	1383.21
2660.25	145.93	2249.17	1.93	263.23	11.50	2266.11

Table 2

Forces required for the movement of the self-propelled platform calculated for travel with the maximum load

F'_t (N)	F'_r (N)	F'_p (N)	F'_a (N)	F'_i (N)	Angle α	Measured data F'_t (N)
561.64	202.40	0.00	1.48	357.76	0.00	558.86
1230.26	202.20	668.82	1.48	357.76	2.50	1491.93
1897.23	201.63	1336.36	1.48	357.76	5.00	1758.91
2561.27	200.66	2001.36	1.48	357.76	7.50	1879.13
3614.49	198.33	3056.91	1.48	357.76	11.50	3078.97

where:

F'_t - traction force (with maximum load) [N]; F'_r - rolling resistance force (with maximum load) [N]; F'_p - force required for uphill movement (with maximum load) [N]; F'_a - air resistance force [N]; F'_i - inertia force [N].

Figure 10 shows the graph with the variation of the forces required to move on horizontal ground or on a slope.

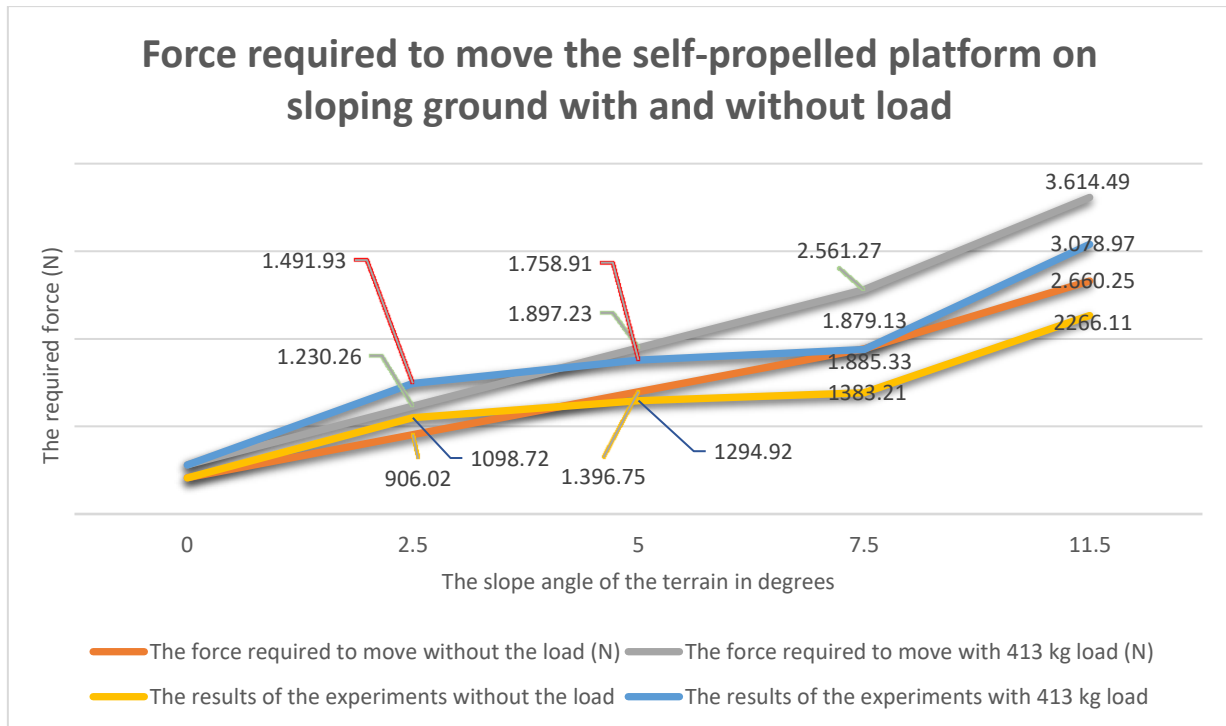


Fig. 10 – The graph with the variation of the forces as a function of the load and the slope angle

To calculate the power needed for displacement, relation (32) was used, all known data were replaced. In tables 3 and 4, the values resulting from the calculations were entered, the same displacement conditions were used as in the case of determining the forces.

Table 3

Power required to move the self-propelled platform calculated for moving without load

P_e (W)	P_r (W)	P_p (W)	P_{tr} (W)	P_i (W)	P_a (W)	P_δ (W)	Angle α	Measured power P_e (W)
820.80	0.33	0.00	819.86	0.58	0.02	0.02	0.00	815.80
1795.99	0.33	1.08	1793.92	0.58	0.02	0.06	2.50	2175.47
2768.76	0.33	2.16	2765.57	0.58	0.02	0.10	5.00	2563.94
3737.26	0.33	3.24	3732.95	0.58	0.02	0.14	7.50	2738.76
5273.35	0.32	4.95	5267.29	0.58	0.02	0.18	11.50	4486.90

Table 4

Power required to move the self-propelled platform calculated for moving with full load

P'_e (W)	P'_r (W)	P'_p (W)	P'_{tr} (W)	P'_i (W)	P'_a (W)	P'_δ (W)	Angle α	Measured power P'_e (W)
1112.52	0.13	0.00	1112.04	0.23	0.01	0.11	0.00	1106.54
2436.95	0.13	0.42	2435.92	0.23	0.01	0.24	2.50	2954.01
3758.10	0.13	0.85	3756.52	0.23	0.01	0.38	5.00	3482.64
5073.45	0.13	1.27	5071.31	0.23	0.01	0.51	7.50	3720.68
7159.71	0.13	1.94	7156.69	0.23	0.01	0.72	11.50	6096.36

where:

P'_e - effective power (with maximum load) [W]; P'_r - power required to overcome rolling resistance (with maximum load) [W]; P'_p - power required for uphill movement (with maximum load) [W]; P'_{tr} - power lost in transmission (with maximum load) [W]; P'_i - power required to overcome inertia force (with maximum load) [W]; P'_δ - power lost in slipping (with maximum load) [W].

Figure 11 shows the variation graph of the power required to move the self-propelled platform when moving on a horizontal or sloping ground with zero load or maximum load.

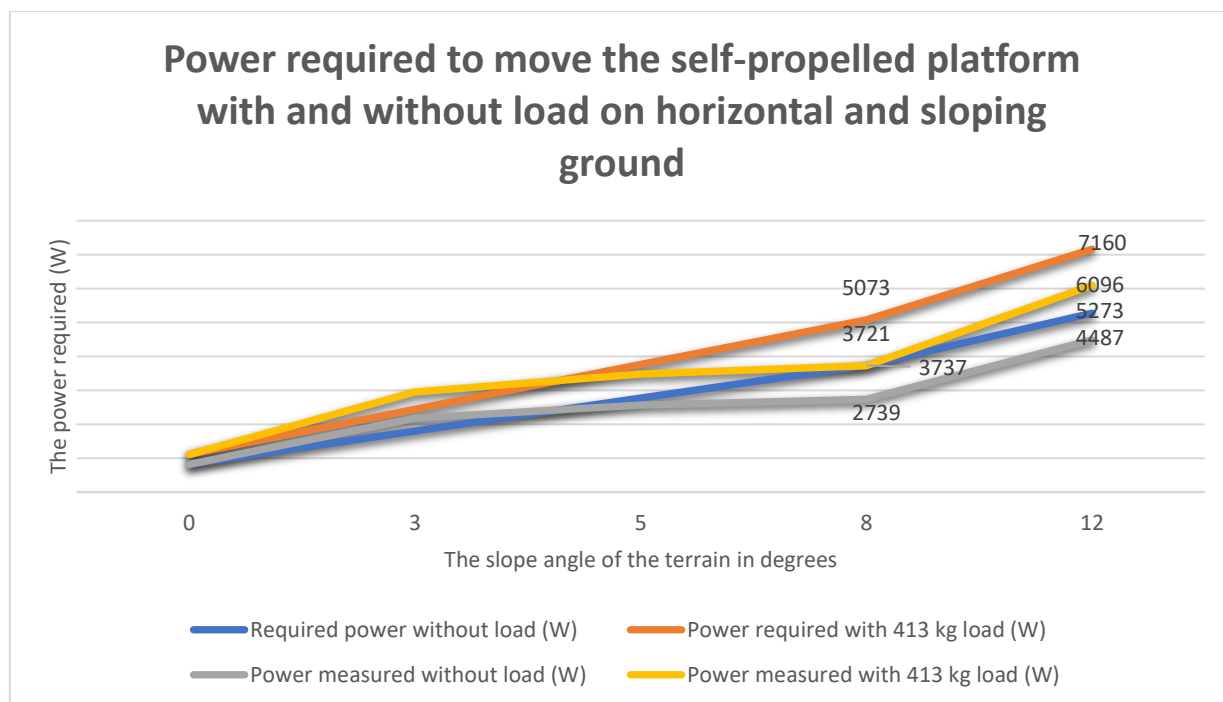


Fig. 11 – The graph with the variation of the power required to move the self-propelled platform in conditions of movement on a horizontal ground but also on a slope, without load but also with the maximum load

CONCLUSIONS

Self-propelled platforms represent a significant advancement in soil research, bringing forth numerous benefits. Technological advancements have transformed them into essential tools for the research community, facilitating the collection of precise data, optimizing research processes, and contributing to a deeper understanding of biogeochemical processes in the soil. The ongoing use of these platforms and the improvement of associated technologies will continue to support progress in soil research and the development of sustainable agricultural practices.

When calculating the power or force required for a motor to propel a platform, it is imperative to possess specific information about the vehicle's component subassemblies or those imposed by the project. The calculation method presented in this work is applicable to wheeled platforms with a 4x2 transmission, with travel speeds up to a maximum of 15 km/h, and a maximum mass not exceeding 2500 kg. In the case of these platform types, some of the resistance forces to movement are characterized by low values and can be neglected. Factors influencing the power of the propulsion system include the transmission, tire type, dimensions, and the platform's intended use. Following the necessary calculations, the power requirement interval for the motor, corresponding to the project's requirements, can be selected from the power requirement graphs.

The mathematical model presented in this paper proves to be a valuable tool in the design process of self-propelled platforms equipped with wheels. Its integration into the calculation algorithms of design software results in a significant reduction of the time required for simulation and the implementation of experimental models for these self-propelled platforms.

ACKNOWLEDGEMENT

This work was supported by the Romanian Research and Innovation Ministry, through the Project entitled: "An intelligent automated system designed for georeferenced soil sampling." -- PN 23 04 01 02. Contract no./date 9N/ 01.01.2023.

REFERENCES

- [1] Băisan I. (2020). Tractors, automobiles, and propulsion systems for agricultural machinery – Part I (Tractoare, automobile și sisteme de propulsie a mașinilor agricole – partea I), *documentary material for third-year students, specialization MIAIA*, "Gheorghe Asachi" Technical University, Faculty of Mechanics, Iași.

- [2] Bulgakov V., Pascuzzi S., Santoro F., Anifantis A.S., (2018). Mathematical Model of the Plane-Parallel Movement of the Self-Propelled Root-Harvesting Machine. *Sustainability*, 2018, 10:3614.
- [3] Cao X., Wang Z., Zheng B., Tan Y. (2023). Improved UAV-to-Ground Multi-Target Tracking Algorithm Based on StrongSORT, *Sensors (Basel, Switzerland)*, vol. 23, no. 22: 9239.
- [4] Huuskonen J., Oksanen T. (2018). Soil sampling with drones and augmented reality in precision agriculture, *Computers and Electronics in Agriculture*, vol. 154, pp 25–35.
- [5] Ibrahim A., Torres-Calderon W., Golparvar-Fard M. (2023). Reinforcement learning for high-quality reality mapping of indoor construction using unmanned ground vehicles, *Automation in Construction*, vol. 156.
- [6] Li W., Yang F., Mao E., Shao M., Sui H., Du Y. (2022). Design and Verification of Crab Steering System for High Clearance Self-Propelled Sprayer. *Agriculture* 2022, 12, 1893.
- [7] Oprescu R.M., Nenciu F., Vocea I., Cujbescu D., Persu C. (2023). Considerations for machinery used for mechanical weed control in organic farming, *ISB INMA TEH International Symposium*, pp. 600-611.
- [8] Tan K.H., (2005) -Soil sampling, preparation and analysis, 2nd edition, *New York: CRC Press*, pp. 672, eBook ISBN 9780429178993.
- [9] Vaeljaots E., Lehiste H., Kiik M., Leemet T. (2018). Soil sampling automation case-study using unmanned ground vehicle, *17th International Scientific Conference Engineering for Rural Development*, Jelgava, pp. 982-987.
- [10] Vanghele N.A., Petre A. A., Matache A., Stanciu M.M, (2021) - Agriculture 5.0 - Review, *Annals of the University of Craiova*, vol. 51/2/2021, pp. 576-583.
- [11] Vlăduț V., Petre A., Vocea I., Matei Gh., Boruz S., Popa D, Isticioaia S., Biriș S. St, Ungureanu N., Epure M., Dumitru C., Atanasov At. (2020), Agriculture 4.0 - The Use of Smart Technologies for High-Performance Agriculture, *Annals of the University of Craiova - Agriculture, Montanology*, pp. 594-692.
- [12] Zawilski B. M., Granouillac F., Claverie N., Lemaire B., Brut A., Tallec T., (2023). Calculation of soil water content using dielectric-permittivity-based sensors -- benefits of soil-specific calibration, *Geoscientific Instrumentation, Methods and Data Systems*, Vol. 12, pp. 45-56.
- [13] *** <https://www.mhnetwork.com/self-propelled-platform-truck-tug/>
- [14] *** <https://argiles.es/informacion-producto/af5/?lang=en>
- [15] *** <https://www.powermotiontech.com/sensors-software/automation/media-gallery/21254335/robotics-plus-unveils-unmanned-ground-vehicle-for-agricultural-operations?id=21254335&slide=2>
- [16] *** <https://www.agriculture.com/news/technology/raven-announces-new-product-brand-and-autonomous-growth-platform>
- [17] *** <https://hse-uav.com/products/r150-2023-autonomous-tractor-mower>
- [18] *** <https://clearpathrobotics.com/blog/2021/01/husky-ugv-drives-smart-precision-agriculture-for-steep-slope-vineyards>

DESIGN AND EXPERIMENT OF SWEET POTATO COMBINE HARVESTER BASED ON TWO-SEGMENT POTATO SOIL SEPARATION DEVICE

基于两段式薯土分离装置甘薯联合收获机设计与试验

Ranbing YANG^{1,2)}, Minsheng WU^{1,2)}, Peng XU³⁾, Yongfei PAN^{1,2)}, Danyang LV^{1,2)}, Xiantao ZHA^{*1,2)}

¹⁾ School of Mechanical and Electrical Engineering, Hainan University, Hainan/ China;

²⁾ Key Laboratory of Tropical Intelligent Agricultural Equipment, Ministry of Agriculture and Rural Affairs, Hainan/ China;

³⁾ College of Engineering, Jiangxi Agricultural University, Jiangxi/ China

Corresponding author: Xiantao Zha

Tel: +8618627838628; E-mail: zhaxt@hainanu.edu.cn

DOI: <https://doi.org/10.35633/inmateh-74-45>

Keywords: agricultural machinery, sweet potato, two-segment potato-soil separation, low damage harvesting, field experiment

ABSTRACT

Aiming at the problems of high skin-breaking rate and high impurity rate of sweet potato during harvesting operations, a low-damage fresh-eating sweet potato combine harvester based on a two-segment potato-soil separation device was designed by using a "d"-type elevator chain combined with a double-buffer clearing platform technology. The results show that the best working parameters of the harvester are a vibrating shaft frequency of 5.2 Hz, elevator chain speed of 0.37 m/s, and cleaning platform speed of 0.58 m/s, in which the sweet potato skin-breaking rate is 1.09% and the impurity rate is 1.90%, which is in line with the standard.

摘要

针对甘薯收获作业过程中存在甘薯破皮率高、含杂率高的问题,采用“d型升运链式薯土分离装置+双重缓冲清选平台”技术,设计了一种基于两段式薯土分离装置的低损鲜食甘薯联合收获机。结果表明,收获机最佳工作参数为振动轴频率 5.2Hz、升运链速度 0.37m/s、清选平台速度为 0.58m/s,此时甘薯破皮率为 1.09%、含杂率为 1.90%,符合标准。

INTRODUCTION

The sweet potato is characterized by a high and stable yield, drought resistance and barrenness tolerance, extensive adaptability, rich nutrition, etc. It occupies an important position in global agricultural production, and its market demand is increasing (Bovell-Benjamin, 2007; dos Santos et al., 2019; Xie et al., 2022; Cláudio et al., 2020; Mohanraj et al., 2014). The current sweet potato harvesting method adopts a semi-mechanized operation mode, which causes the sweet potatoes to break during the potato soil separation process and mix with excessive soil, weeds and other impurities, seriously affecting the quality and market competitiveness of sweet potatoes (Hu et al., 2014; Chen, 2020). In order to improve the performance of sweet potato harvesters, researchers conducted research from different angles. Hrushetsky and Fu developed an excavation device for potato harvesters, which significantly improved the excavation efficiency and reduced resistance, but had little impact on the peeling rate and potato soil separation rate (Hrushetsky et al., 2019; Fu et al., 2023). The peeling rate and potato soil separation rate are the most important indicators for evaluating the performance of fresh sweet potato harvesters. Therefore, it is of great significance to develop high efficiency and low damage fresh sweet potato combine harvester, explore and optimize potato soil separation device, improve sweet potato harvest efficiency and reduce the rate of peeling and impurity.

In recent years, researchers have continuously innovated and optimized the structure of the potato-soil separator to improve its harvesting efficiency and sweet potato quality. For example, to reduce the skin-breaking rate of sweet potatoes, Marciniak, Cui, Ismail and Bulgakov developed a small-scale traction-type sweet potato harvester, and the developed machinery shortened the length of the potato-soil separating device, which resulted in less collision between sweet potatoes and rods and therefore a lower skin-breaking rate of

^{1,2)} Ranbing Yang, Prof. Ph.D. Eng; Minsheng Wu, M.S. Stud. Eng; Yongfei Pan, Ph.D. Eng; Danyang Lv, Ph.D. Eng; Xiantao Zha, Ph.D. Eng.

³⁾ Peng Xu, Ph.D. Eng.

sweet potatoes. However, the conveyor device has a compact structure and a short conveyor stroke, resulting in a poor soil-clearing effect and high subsequent labor intensity (Marciniak et al., 2022; Cui et al., 2020; Ismail et al., 2014; Bulgakov et al., 2021; Feng et al., 2024). To improve the efficiency of potato-soil separation, researchers have increased the length and number of stages of the potato-soil separation device to reduce the impurity rate of sweet potatoes. For instance, Beznosyuk designed a multi-segment potato harvesting machine with transportation and clearing roles and mounted the multi-segment potato-soil separation device longitudinally to reduce the longitudinal clearance of sweet potatoes and the fall height during potato collection (Beznosyuk et al., 2022). Li designed a ring-shaped damage-reducing potato collection and transportation device that uses a multi-stage transportation and cleaning method to clean the potato soil mixture of stones and vines, and the harvested potato crop is transported to the collection box (Li et al., 2023). The above type of potato-soil separation device saves labor costs and has a high harvesting efficiency. The disadvantage is that, due to the excessively long potato-soil separation device, the number of collisions between sweet potatoes and the conveying device increases, resulting in an increased rate of skin breakage. In addition, due to the lack of manual cleaning, some stones and soil pieces are simple to transport into the collection box following the conveyor chain, which requires secondary cleaning (Wei et al., 2023).

Combining the advantages and disadvantages of integrated and multi-segment potato-soil separation devices, some researchers have developed and designed a two-segment potato-soil separation device with a manual cleaning assistance platform. Yang created a new traction-type potato crop picking and bagging machine equipped with a two-segment flexible conveyor and a hydraulic control system, and they designed a rubberized bionic finger in the first segment of the elevator chain, which reduces the collision of the potato crop falling in the harvesting process (Yang X. et al., 2024). Wang designed a self-propelled potato crop harvester for hilly and mountainous areas with a two-segment potato-soil separation device; the first segment of the potato-soil separation device is installed with a fingers-type crushing mechanism, and the second segment of the elevator chain is installed with a scraper to protect the sweet potatoes, which improves the harvesting efficiency and reduces the skin-breaking rate (Wang et al., 2023). The two-segment potato-soil separation device improves the efficiency of potato-soil separation at the same time, supplemented by manual cleaning to minimize the impurity rate of sweet potatoes. However, there is still the problem of a high rate of broken skin in sweet potatoes, which still needs to be optimized by research and development personnel.

For the above problems, this paper develops and designs a two-segment potato-soil separation device that can complete the integration of the operations of sweet potato conveying, soil removal, cleaning, and collecting at one time, aiming at reducing the skin-breaking rate and impurity rate of sweet potato. The first segment of the "d" elevator chain potato-soil separation device realizes elevator chain straight bar sweet potato fall prevention, and the second segment of the double buffer cleaning platform realizes the optimization design of sweet potato fall damage. Field experiments were conducted using orthogonal testing to analyze and discuss the influence of each parameter on the skin-breaking rate and impurity rate, then to determine the optimal parameter combinations to improve the efficiency of sweet potato harvesting and to reduce the skin-breaking rate and impurity rate of sweet potatoes.

MATERIALS AND METHODS

Harvester structure and working principle

Combined with the agronomy of fresh-eating sweet potato cultivation in Hainan, China, a low-damage sweet potato combine harvester was designed based on a two-segment potato-soil separating device. The harvester consists of a profiling device, a digging device, a potato-soil separating device, a transmission system, a control console, and a traveling device, and its structure and object are shown in Figure 1.

In the sweet potato harvesting process, the harvester moves forward, and the profiling device carries out heaving motion according to the height of the ridge, realizing adaptive adjustment of digging depth. The digging shovel transports the potato-soil mixture to the first segment "d" type elevator chain potato-soil separation device, and a vibrating device is installed at the front end of the elevator chain to sieve off the redundant soil by vibrating it. The potato-soil mixture rotates with the elevator chain, passing through the drop buffer device to the second segment of the double buffer cleaning platform. The sweet potatoes are then cleaned by staff and placed on the inside of the potato collection board. The conveyor belt of the secondary double buffer cleaning platform carries the sweet potatoes to the rear conveying buffer device, and with the rotation of the rear conveying roller, it further cleans the soil adhering to the surface of the sweet potatoes. Finally, the sweet potatoes are decelerated by the rear rubber buffer curtain and fall into the potato collection basket to complete the harvesting process.

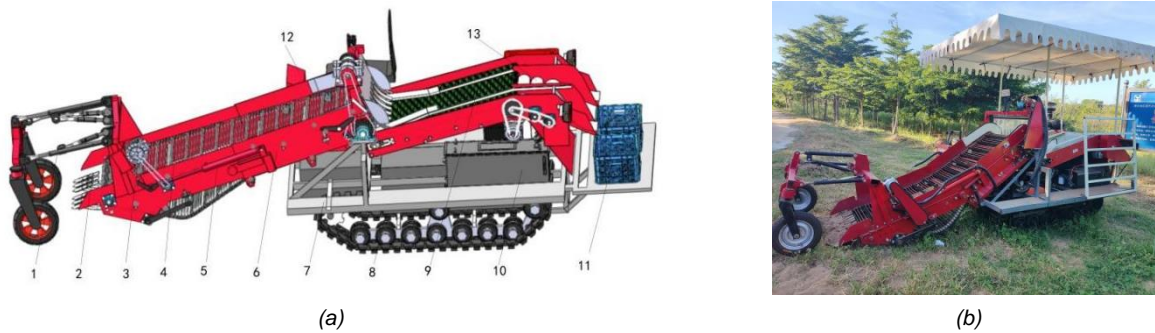


Fig. 1 - Low-damage fresh sweet potato combine harvester

(a) Structure: 1 - profiling device; 2 - digging device; 3 - "d"-type elevator chain potato-soil separating device; 4 - hydraulic control device; 5 - frame; 6 - picking platform; 7 - crawler walking device; 8 - double buffer cleaning platform; 9 - fuel tank and power device; 10 - potato collection basket; 11 - control console; 12 - front falling buffer device; 13 - rear conveying buffer device. (b) Physical object

Transmission system and technical parameters

The transmission system of the low-loss fresh sweet potato combine harvester consists of hydraulic transmission and mechanical transmission, as shown in Figure 2. The engine transmits the power to the gearbox through the output shaft, which then transmits the power to the crawler-traveling device through the output shaft. The engine provides power for the hydraulic pump, and the change of the inclination angle of the elevator chain is controlled by the hydraulic pump's inlet and outlet oil volumes. The engine transmits the power to the vibrating shaft through the gearbox and the crank-rocker mechanism, which is used to separate the potato from the soil. The engine provides power for the "d" type elevator chain potato-soil separation device, double buffer cleaning platform, and conveying buffer device through the chain drive.

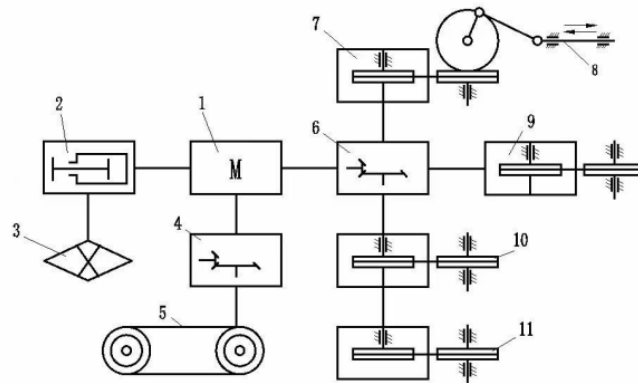


Fig. 2 - Schematic diagram of the transmission system of a low-damage fresh-eating sweet potato combine harvester

1 - engine; 2 - hydraulic pump; 3 - elevator chain inclination control; 4 - gearbox; 5 - crawler walking device; 6 - reducer; 7 - motor; 8 - vibrating shaft; 9 - elevator chain; 10 - conveyor belt; 11 - conveyor roller

Based on the harvesting demand of China's "Gaoxi 14" fresh sweet potato, the technical parameters of the low-damage fresh-eating sweet potato combine harvester are shown in Table 1.

Table 1

Technical parameters of low-damage fresh-eating sweet potato combine harvester	
Parameters	Values
Structure form	Self-propelled
Power matching (HP)	70
Size (LxWxH)/(mm*mm*mm)	5500x2200x2000
Working width (mm)	1000
Digging depth (mm)	100-150 (below the bottom of the mound)
Operating speed (m/s)	0.2-0.7
Operating efficiency (m ² /h)	1400-2100
Potato collection method	Basket/Bagging
The whole machine's weight (kg)	2180

Design of one-segment "d" elevator chain potato-soil separation device

The compact structure of the traditional elevator chain and the use of tensioning devices limit the undulation and vibration of the elevator chain, which only ensures the vibration of the elevator chain on the vibrating shaft, with no extra space to support the vibration of the elevator chain in other positions. In addition, the clay loam and weeds carried by the traditional elevator chain are not cleaned in time, which makes it easy to increase its load and cause clogging of the chain plate and drive shaft (Wang et al., 2014). For the above problems, this paper develops a first-segment "d" elevator chain potato-soil separation device, as shown in Figure 3. Near the digging shovel, the longer elevator chain is retained so that it falls under the action of the gravity of the rollers and the elevator chain itself, forming a structure similar to the letter "d". As shown in Figure 3 partial enlargement, the "d"-type elevator chain connecting belt is made of soft rubber material, conveying surface roller spacing between 30 and 50 cm between the rollers. Due to the elevator chain's self-gravity and potato-soil mixture quality, it is easy to cause the elevator chain to produce concave changes. Rollers can re-lift the elevator chain to achieve the conveying effect of gentle vibration and improve the efficiency of potato-soil separation. In the process of chain lifting, the excess elevator chain provides a force buffer for the conveying process. The falling part of the elevator chain can sieve the soil in time through the chain movement and the inertial swing of vehicle walking to reduce the redundancy of weeds and soil congestion at the front end of the elevator chain.

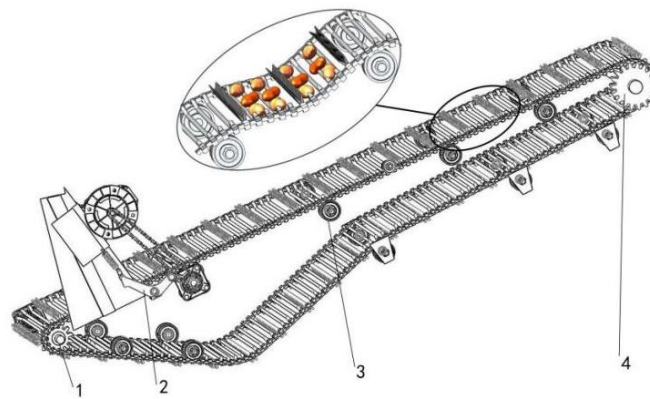


Fig. 3 - Structure of first-segment "d" elevator chain potato-soil separation device
 1 - follower shaft; 2 - vibration device; 3 - rollers; 4 - active shaft

The elevator chain uses four continuous curved bars and one straight rubber bar. Nitrile rubber (NBR), a material that is small in hardness and has better adhesion to metal, forms both the rubber connecting belt and the rubber sleeve of the straight bar (Shen, 2021). The straight bar's rubber sleeve shape is similar to the letter "V," which effectively protects the sweet potato when it rolls over in the elevator chain. Figure 4 illustrates the structural analysis of sweet potatoes in the elevator chain's curved bar zone.

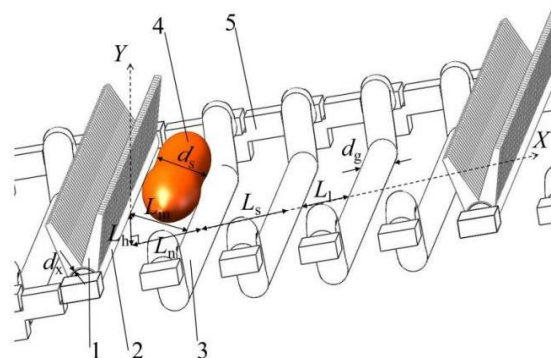


Fig. 4 - Sweet potatoes in the interval of the elevator chain curved bars
 1 - rubber sleeve for the straight bar; 2 - straight bar; 3 - curved bar; 4 - sweet potato model; 5 - rubber connecting band.

It can be obtained from the analysis of Figure 4:

$$\begin{cases} L_s = L_l + d_g \\ L_h = \sqrt{(L_m + d_g + d_x)^2 - L_n^2} \end{cases} \quad (1)$$

where:

L_s is the centroid-distance between the curved rod and the curved bar on the X-axis, [mm]; L_n is the centroid-distance between the straight rod and the curved bar on the X-axis, [mm]; L_l is the gap between the curved rod and the curved bar, [mm]; d_g is the diameter of the bar, [mm]; L_h is the centroid-distance between the straight rod and the curved bar on the Y-axis, [mm]; L_m is the gap between the straight rod and the curved bar, [mm], and d_x is the thickness of the rubber sleeve wrapped around the straight rod bar, [mm].

In the current sweet potato harvester elevator chain structure, the bar diameter typically ranges from 9-11 mm (Li *et al.*, 2022). Combined with the actual operating conditions, a bar diameter d_g of 10 mm was selected. To reduce production costs and improve the elevator chain's stability, the distance between the links should be the same, i.e., $L_n=L_s$. To ensure optimal conveying performance, a large bar gap can enhance the efficiency of potato-soil separation. However, to decrease the loss of sweet potatoes, the bar gap should be smaller than the minimum short axis size. In the "agricultural machinery promotion appraisal outline" of potato harvester operation standard, the DG/T078-2022 establishes a minimum size of 25 mm for the sweet potato harvest loss rate (Ministry of Agriculture and Rural Affairs, 2022). As a result, the gap between the straight bar and the curved bar, L_m , was set at 24 mm. The rubber sleeve thickness d_x , wrapped in the straight bar, d_x is 2 mm (Wu, 2022), meeting the design requirements. By substituting the above parameters into Equation (1), the centroid-distance between the straight rod and the curved bar on the Y-axis (L_h) can be calculated from the gap between the curved rod and the curved bar (L_l) as Equation (2).

$$L_h = \sqrt{1296 - (L_l + 10)^2} \quad (2)$$

Equation (2) reveals a gradual decrease in L_h as L_l increases. The center of mass spacing (L_h) between the straight bar and the curved bar on the Y-axis is one of the crucial parameters to stop the sweet potato from rolling downward after popping up. A too-small L_h parameter increases the risk that the sweet potato will cross the straight bar. This study chose a gap of 20 mm between the curved bars (L_l) to increase both L_h and L_l to larger values. The calculation of Equation (2) approximates L_h to 20 mm, resulting in a center-of-mass spacing of 30 mm between the curved bars and the X-axis (L_s), which meets the design requirements.

Two-segment double buffer cleaning platform front drop buffer device design

During the sweet potato harvesting, the sweet potato falls from the elevator chain to the secondary double buffer cleaning platform. It then falls from the potato drop channel to the collection basket. These two stages are likely to cause sweet potato skin breakage. The double buffer cleaning platform incorporates a front falling buffer device and a rear conveying buffer device to decrease the rate of broken skin resulting from the falling and collision of sweet potatoes. The double buffer design effectively slows down the impact force of sweet potatoes during the falling process, thereby greatly reducing their damage. Figure 5 illustrates the structural design of the secondary double buffer cleaning platform device.

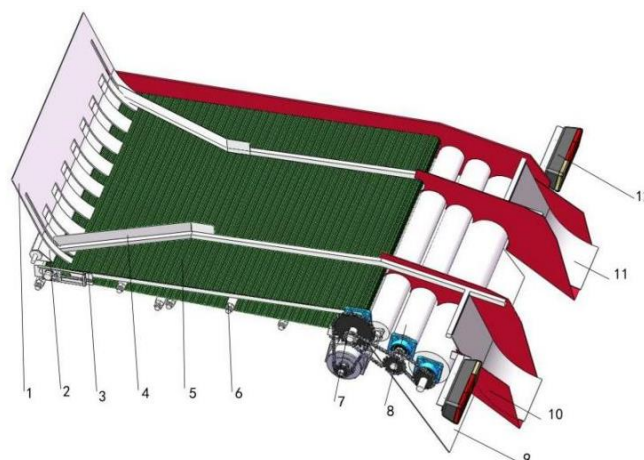


Fig. 5 - Structure of a Secondary Double Buffer Cleaning Platform Device

1 - front rubber buffer curtain; 2 - front buffer protection plate; 3 - conveyor belt tensioning device; 4 - potato collection plate;
5 - clearing platform conveyor belt; 6 - rack support shaft; 7 - gear set; 8 - rear conveyor roller; 9 - sand leakage board;
10 - falling potato channel; 11 - rear rubber buffer curtain; 12 - tail light

The elevator chain's instantaneous throwing speed causes the sweet potato to continue moving in a vertical direction. This situation leads to a significant increase in the sweet potato's fall speed as well as a significant increase in the rate of broken skin. Therefore, the elevator chain ends with the installation of the front fall buffer device, which consists of a front rubber buffer curtain and a front buffer protection plate at the bottom of the conveyor belt. It can reduce the speed of sweet potato throwing and, at the same time, block the gravel and sand brought by the elevator chain to protect the pickers. Figure 6 shows that the sweet potato from the elevator chain falls to the secondary double buffer cleaning platform movement process, this time ignoring the potato-soil collision impact.

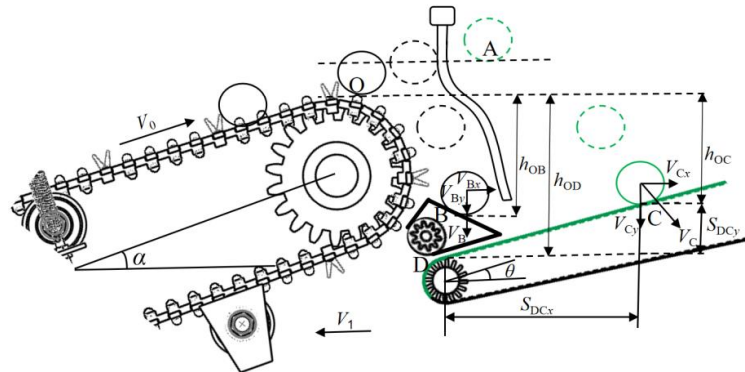


Fig. 6 - The movement of sweet potato falling from the elevator chain to the secondary double buffer cleaning platform

The conveyor belt on the cleaning platform is the reference surface for the sweet potato's displacement. Since the sweet potato and the conveyor belt are subject to the action of the vehicle speed V_1 simultaneously, the influence of the vehicle speed V_1 on the displacement of the sweet potato at this stage is negligible. This study viewed the OC section's motion without a front drop buffer device as the parabolic motion of a sweet potato, and by analyzing the kinematics of the sweet potato, the following formula was derived:

$$\begin{cases} V_C^2 - V_0^2 = 2gh_{OC} \\ h_{OC} = h_{OD} - S_{DCx} \tan \theta \\ S_{DCx} = V_{Cx} t_{OC} - V_{Bx} t_{OB} \\ V_{Cx} = V_0 \cos \alpha \\ V_C = -V_0 + gt_{OC} \end{cases} \quad (3)$$

where:

V_C is the combined speed of sweet potatoes falling in the OC section, [m/s]; V_0 is the speed of the "d" type elevator chain, [m/s]; g is the acceleration of gravity, [m/s²], and g is valued at 9.8. h_{OC} is the vertical distance from point O to point C , [m]; h_{OD} is the vertical distance from point O to point D , [m]; S_{DCx} is the horizontal distance from point D to point C , [m]; θ is the inclination angle of the conveyor belt, [°]; V_{Cx} is the horizontal component velocity at the moment of falling of the sweet potato in the OC section, [m/s]; t_{OC} is the time of the sweet potato's movement from point O to point C , [s]; V_{Bx} is the horizontal component velocity at the moment of falling of the sweet potato in the OB section, [m/s]; t_{OB} is the time of the sweet potato's movement from point O to point B , [s]; α is the angle of the elevator chain and the ground, [°].

When the sweet potato is thrown up, due to the role of the front rubber buffer curtain, the speed of the sweet potato in the x -direction is gradually reduced to 0, so there is no speed effect on the sweet potato in the y -direction. Therefore, the velocity analysis in the y direction for the OB section of the front drop buffer device can be considered a free-fall motion, yielding the following formula:

$$\begin{cases} V_{Bx} = 0 \\ V_B^2 = V_{By}^2 = 2gh_{OB} \end{cases} \quad (4)$$

In the OB and OC sections, the sweet potato movement process follows the law of energy conservation. Therefore, this study analyzes the scenario with and without the shelter curtain and discovers that the sweet potato generates energy change before coming into contact with the conveyor belt.

$$\Delta E = \Delta E_{OB} - \Delta E_{OC} = \frac{1}{2} mV_B^2 - \frac{1}{2} mV_C^2 \tag{5}$$

Substituting Equation (3) and Equation (4) into Equation (5), the simplification leads to the following:

$$\Delta E = \frac{m}{2} \left[2gh_{OB} - V_0^2 - 2gh_{OD} + 2(V_C + V_0)V_0 \cos \alpha \tan \theta \right] \tag{6}$$

Among them, the static friction coefficient between sweet potato and nitrile rubber (NBR) is $\mu=0.61$, and the friction coefficient between sand and rubber takes a value ranging from 0.605 to 0.621 (Shen, 2021; Yang *et al.*, 2021). To ensure that the sweet potato and sandy soil are steadily elevated on the conveying rubber belt, the inclination angle θ of the sweet potato on the rubber belt should satisfy $\theta \leq \arctan 0.605$, that is, $\theta \leq 31.17^\circ$. In conjunction with the pickup personnel at work on the pickup height, the conveyor belt inclination angle was set to 18° . Figure 5 illustrates that after designing the transmission ratio for each gear diameter, the h_{OD} approximation takes the value of 35 cm, and the h_{OB} approximation takes the value of 30 cm. It can be seen from Equation (6) that the speed of the elevator chain and the inclination angle of the elevator chain are within the range of meeting agronomic demand, and the energy change is maintained at $\Delta E < 0$. It indicates that the installation of buffer curtains and buffer protection boards can effectively reduce the initial energy of the instant sweet potato falling, thereby reducing the rate of broken skin on the sweet potato. In summary, this study determined that the buffer protection plate's sloping surface had an inclination angle of 45° and a width of 7 cm, meeting the design requirements.

Two-segment double buffer cleaning platform rear conveyor buffer device design

The cleaning platform's conveyor belt transports the clean sweet potatoes to the rear conveying roller. At this time, the sweet potatoes have a faster final velocity and a higher falling height, which makes it easy to cause them to break their skin. Therefore, this study installs a rear conveyor buffer device at the end of the cleaning platform's conveyor belt, which directs the sweet potatoes into the potato collection channel through the rear conveyor roller. It also installs a rear rubber buffer curtain on the potato collection channel's surface to ensure stable transportation. To ensure stable transportation of the sweet potatoes on the rear conveying roller, the force analysis in Figure 7 illustrates the relationship between the sweet potatoes and the roller.

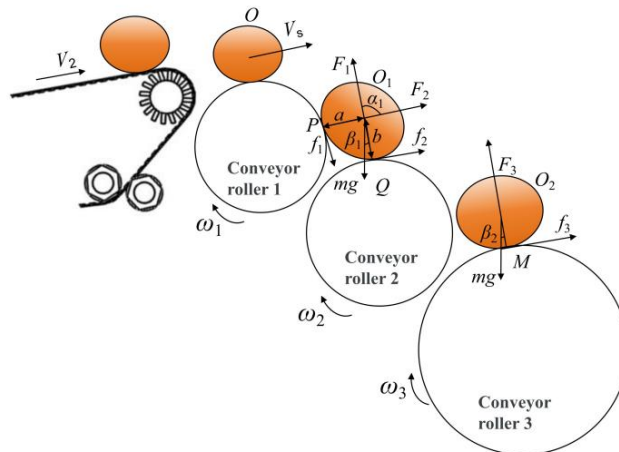


Fig. 7 - Force analysis of sweet potato between rear conveyor rollers of a secondary cleaning platform

O denotes that the sweet potato is transported in the conveying roller 1, and O_1 denotes the force analysis of the sweet potato under the simultaneous action of the two conveying rollers. When the sweet potato generates motion under the action of conveying rollers, it should satisfy that the resultant moment and resultant force at point Q are more than zero. O_2 denotes the force analysis performed by a single conveying roller.

$$\begin{cases} \sum_Q M = \mu F_2 \left[a + b \sin \left(\alpha_1 - \frac{\pi}{2} \right) \right] + mgb \sin \beta_1 - F_2 b \sin (\pi - \alpha_1) \geq 0 \\ \sum_Q F = \mu F_2 \cos \alpha_1 - mgb \sin \beta_1 + \mu F_1 + F_2 \cos (\pi - \alpha_1) \geq 0 \\ \sum_M F = mg \sin \beta_2 - \mu F_3 \end{cases} \tag{7}$$

where:

μ is the friction coefficient of sweet potato on the conveying roller; a is the distance between the center of mass of O_1 and the point P, [mm]; b is the distance between the center of mass of O_1 and the point Q, [mm]; α_1 is the angle between the support force F_1 and F_2 , [°]; mg is the gravity of O_1 , [N]; β_1 is the angle between the gravity of the sweet potato and the distance b , [°]; F_2 is the support force of sweet potato at the point P, [N]; β_2 is the angle between the gravity of the sweet potato and the O_2M , [°], and the O_2M is the line connecting the center of mass of O_2 to the contact point M .

The analysis of sweet potato force revealed that the sweet potato's gravity, which is impossible to regulate artificially, primarily affects the support force and friction force in Equation (7). However, it can affect the values of α_1 , β_1 , and β_2 by changing the dimensions and position of the rear conveying roller and making the sweet potato transport stable. Figure 6 and Equation (7) show that increasing the diameter of conveying roller 2 leads to an increase in α_1 . It increases the resultant moment and resultant external force at the Q point, thereby enhancing the power of the sweet potato's tumble. Increasing the diameter of conveying roller 3 increases β_2 , that is, increasing the resistance of the sweet potato at point M diagonally downward. Meanwhile, this causes an increase in the transportation distance on the conveying roller's surface, which can effectively reduce the sweet potato's transportation speed. As a result, it is necessary to reduce the transportation speed of the sweet potatoes to ensure that they have enough power to turn over each conveying roller. The size of the rear conveying roller can be set to gradually increase, which is conducive to the stable transportation of sweet potatoes. Combining the structural design of the secondary cleaning platform, which determines that the diameter of conveying roller 1 is 8 cm and the diameter of conveying roller 2 is 10 cm, ensures the stable transportation of sweet potatoes. Determine that the diameter of conveying roller 3 is 18 cm, aiming to guarantee the transportation of sweet potatoes while at the same time reducing its transportation speed. Wrapping NBR on the conveying roller's surface results in a static friction coefficient of $\mu=0.61$, which improves conveying performance.

Key experimental parameters - Vibration frequency

In the sweet potato harvesting process, in order to prevent the sweet potato from crossing the straight bar strip from appearing to be repeatedly falling and thus causing damage, the amplitude and frequency of the vibration axis need to be limited. As shown in Figure 8, sweet potatoes with different short-axis radii have a high probability of being in the curved bar interval when stabilized (Yang R.B. et al., 2024). The minimum force required for the sweet potato to cross the straight bar is the critical velocity V_t required for the movement of B to C.

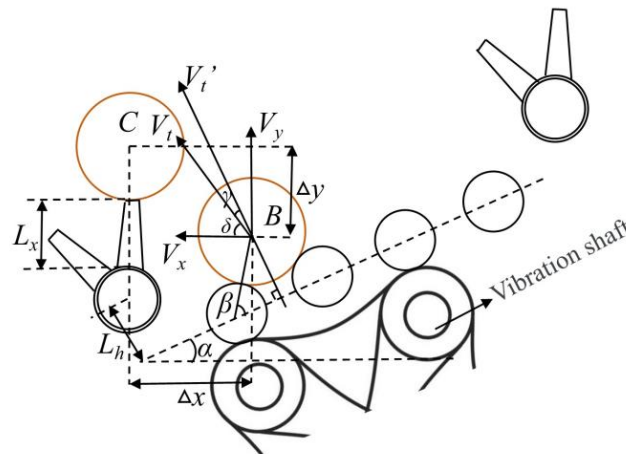


Fig. 8 - Motion analysis of sweet potato as it passes through the vibrating device during the lift-off process

The horizontal displacement Δx and vertical displacement Δy required for the sweet potato to move from B to C in the critical state are as follows:

$$\begin{cases} \Delta x = (L_h \tan \alpha + L_s) \cos \alpha + \frac{1}{2}(d_g + d_s) \cos(\beta + \alpha) \\ \Delta y = L_h \cos \alpha - L_s \sin \alpha + d_x + L_x + \frac{1}{2}(d_g + d_s) [1 - \sin(\beta + \alpha)] \end{cases} \quad (8)$$

where:

Δx is the horizontal displacement of the sweet potato, [mm]; Δy is the vertical displacement of the sweet potato, [mm]; and L_s is the height of the rubber sleeve of the straight bar, which is approximated as the distance between the sweet potato and the rubber sleeve of the outer ring of the straight bar in the critical state in the collision analysis, [mm]. β is the angle of the sweet potato B when it is stationary at the interval of the bent bar [°]. Analyzed from Figure 8, $\cos\beta = L_s / (d_s + d_g)$.

According to the equations for uniformly decelerated linear motion in the vertical state and uniformly accelerated linear motion in the horizontal state, the critical velocity V_t required for the sweet potato to move from B to C is:

$$V_t = \sqrt{V_x^2 + V_y^2} = \sqrt{\frac{g\Delta x^2}{2\Delta y} + 2g\Delta y} \quad (9)$$

where:

V_y is the component velocity of sweet potato in the vertical direction, [mm/s]; V_x is the component velocity of sweet potato in the horizontal direction, [mm/s]; g is the acceleration of gravity, [m/s²], and g takes the value of 9.8.

The critical velocity, V_t , is at an angle δ in the horizontal direction:

$$\delta = \arctan \frac{V_y}{V_x} = \arctan \frac{2\Delta y}{\Delta x} \quad (10)$$

The elevator chain, with the vibration axis rotating to periodic up-and-down reciprocating motion, can be regarded as "simple harmonic motion", as shown in Figure 8 (Lv et al., 2017). Set the vibration device to start at $t=0$, and the elevator chain's displacement in the vertical chain surface is 0. In one cycle, the vibration axis can provide four times the maximum amplitude. The elevator chain and the vibrating shaft share the same resonance frequency, allowing us to derive the following relationship between the vibration displacement Y and time t :

$$Y = \frac{A}{2} \cos(4\pi f \cdot t + \pi) + \frac{A}{2} \quad (11)$$

where:

Y represents the elevator chain's displacement on the vertical chain surface, [mm]; f signifies the vibration shaft's frequency, [Hz]; and A signifies the vibration shaft's maximum amplitude, [mm].

This study solves the derivative of Y with respect to t to derive the velocity V_t' , which the vibrating device provides to the elevator chain perpendicular to the chain surface:

$$V_t' = -2A\pi f \sin(4\pi f \cdot t + \pi) \quad (12)$$

To prevent the sweet potato from crossing the straight bar and causing repeated damage, the vibration device's maximum collision velocity, V_t' , must ensure that the component velocity on the trajectory of the sweet potato from B to C is always smaller than the critical velocity, V_t . Figure 8 shows that V_t' takes the maximum value of $2A\pi f$, and there exists an angle γ between the maximum collision velocity V_t' and the critical velocity V_t , which yields the following equation.

$$2A\pi f \cos\left(\frac{\pi}{2} - \alpha - \arctan \frac{2\Delta y}{\Delta x}\right) < \sqrt{\frac{g\Delta x^2}{2\Delta y} + 2g\Delta y} \quad (13)$$

Combined with the above elevator chain structure design and actual operational requirements, the optimal amplitude A of the vibration shaft of the sweet potato combine harvester is 18.2 mm (Liu, 2021). Equation (13) indicates that a sweet potato crossing the straight bar can cause repeated damage when f is less than 8.4. Simultaneously, if the vibration frequency is too low, it will result in a poor separation effect between the potato and soil, so the vibration shaft frequency f takes the value of 3-8 Hz.

Key experimental parameters - Elevator chain speed

Too slow a speed on the elevator chain is likely to cause congestion of the potato-soil mixture, and too fast a speed is likely to damage the sweet potato. To ensure stable transportation of the potato-soil mixture, the elevator chain's speed, and the harvester's forward speed should meet the following formula:

$$V_1 = \lambda V_0 \quad (14)$$

where:

V_1 is the forward speed of the harvester, [m/s]; λ is the speed coefficient, which generally takes the value of 0.8-2.5 (Lv *et al.*, 2015); and V_0 is the speed of the elevator chain, [m/s].

The faster the harvester advances, the greater the sweet potato harvest area per unit of time. However, too fast forward speed may lead to more impacts and friction on the sweet potato during digging and conveying, thus increasing its rate of broken skin. The sweet potato planting method involves planting two rows on one ridge, meaning that the agronomic characteristics of sweet potato planting and the picker's working speed influence the forward speed of the harvester.

$$V_1 = \frac{X\eta d}{2n} \quad (15)$$

where:

X is the number of pickers; η is the number of sweet potatoes picked up per second by a single picker; d is the distance between sweet potato plants, [m]; n is the number of sweet potatoes contained per plant.

During the sweet potato harvesting period, agronomic investigations and operational efficiency analyses were carried out. The harvester has four pickers and can pick 2-3 sweet potatoes per second. The sweet potato plant spacing is 0.3 m, and each plant bears 3-6 potatoes. Calculated by Equation (15), the forward speed of the harvester is in the range of 0.2-0.6 m/s. Usually, the ratio of the speed of the elevator chain to the speed of the vehicle during harvesting is slightly more than 1 (Chen *et al.*, 2019). So, in this paper, λ is taken to be 0.85. Equation (14) calculates the selected range of elevator chain speed V_0 , which is 0.235-0.706 m/s. The elevator chain speed V_0 is 0.25-0.75 m/s for convenience of calculation.

Key experimental parameters - Clearing platform speed

Figure 7 demonstrates how the throwing velocity V_s of sweet potato O influences the sweet potato's falling position at the conveying roller. This indicates that it affects α_1 , β_1 , and β_2 in Equation (7), which affects the stability of sweet potato transportation. The V_s is affected by both the velocity V_2 of the clearing platform and the angular velocity ω_1 of the rearward conveyor roller 1. This study employs gears and chain connections to maintain consistency between the speed of the cleaning platform and the linear speed of the conveyor roller 1, thereby minimizing the risk of skin breakage of sweet potatoes that fall onto the conveyor roller 1 due to their significant speed differences. Therefore, cleaning platform speed V_2 is one of the key factors affecting sweet potato harvesting. Yang determined that the clearing platform of the secondary conveying and separating device has a speed range of 0.4-0.8 m/s (Yang R.B. *et al.*, 2024).

Key performance parameters - The rate of broken skin of sweet potatoes

In this field trial, the sweet potato skin-breaking rate (B_R) and impurity rate (I_R) were used as evaluation indices, referencing the DG/T078-2022 potato harvester operation standard in the "Agricultural Machinery Extension Appraisal Syllabus" (Ministry of Agriculture and Rural Affairs, 2022). Equation (16) describes how to calculate the skin-breaking rate as follows:

$$B_R = \frac{m_3}{m_1 + m_2} \times 100\% \quad (16)$$

where:

B_R is the sweet potato skin-breaking rate, [%]; m_1 is the total mass of harvested sweet potato in two trips, [kg]; m_2 is the total mass of missed pickup sweet potato in two trips, [kg]; m_3 is the total mass of skin-breaking sweet potato, [kg].

Key performance parameters - Impurity rate of sweet potatoes

Determination of impurity content refers to the ratio of impurities in the potato box after harvest to the total mass of the box, which includes small potatoes, vines, and soil mass. The impurity rate was calculated according to Equation (17), which is described below:

$$I_R = \frac{m_4}{m_1 + m_4} \times 100\% \tag{17}$$

where: I_R is the impurity content of sweet potato, [%]; m_4 is the mass of impurities, [kg].

Method of field experiment

The field experiment site of this study was the sweet potato planting base of the Intelligent Agricultural Machinery (Nada Town, Danzhou City, Hainan Province, China). The sweet potato variety was “GaoXi 14”, the width of the sweet potato ridge was 650 mm, the width of the bottom of the ridge was 1000 mm, the height of the ridge was 200 mm, the soil compactness of the bottom of the ridge was 1305 kPa, the density of the soil was 1.82 g/cm³, and the water content was 12.87 %. Instruments and equipment required for the test included a low-damage fresh-eating sweet potato combine harvester, a non-contact tachometer (DLY-2301), an electronic protractor (precision of 0.01), a potato collection basket, and an electronic scale.

To investigate the variation rule of vibrating shaft frequency, elevator chain speed, and clearing platform speed on the effect of skin-breaking rate and impurity rate, as well as to obtain the optimal parameter combination, this study combines the previous analysis to determine that the vibrating shaft frequency f is 3-8 Hz, the elevator chain speed V_0 is 0.25-0.75 m/s, and the cleaning platform speed V_2 is 0.25-0.75 m/s. The skin-breaking rate of sweet potatoes and the impurity rate were taken as the evaluation indexes. Table 2 displays the test factor level codes.

Table 2

Factor level coding table			
Level	Experimental factor		
	A: Vibrating shaft frequency (Hz)	B: Elevator chain speed (m/s)	C: Cleaning platform speed (m/s)
-1	3	0.25	0.4
0	5.5	0.5	0.5
1	8	0.75	0.8

This study used Design-Expert 13.0 to conduct a three-factor, three-level Box-Behnken test, repeating each set of tests three times to get the average (Ferreira et al., 2007; Chen et al., 2024). Table 3 displays the experimental results.

Table 3

Response surface results					
Trial No.	Experimental Factors			Evaluation Indicator	
	A (Hz)	B (m/s)	C (m/s)	B_R (%)	I_R (%)
1	3	0.25	0.6	0.95	2.47
2	8	0.25	0.6	1.18	1.77
3	3	0.75	0.6	1.42	3
4	8	0.75	0.6	1.51	2.5
5	3	0.5	0.4	1.38	1.75
6	8	0.5	0.4	1.47	1.53
7	3	0.5	0.8	1.04	2.81
8	8	0.5	0.8	1.37	1.86
9	5.5	0.25	0.4	1.29	1.74
10	5.5	0.75	0.4	1.86	2.12
11	5.5	0.25	0.8	1.25	2.56
12	5.5	0.75	0.8	1.58	2.95
13	5.5	0.5	0.6	1.1	1.82
14	5.5	0.5	0.6	1.11	1.92
15	5.5	0.5	0.6	1.19	1.84
16	5.5	0.5	0.6	1.18	1.82
17	5.5	0.5	0.6	1.18	1.89

The field experiment and the effect are shown in Figure 9.



Fig. 9 - Field experiment

RESULTS

Regression equation analysis of field experiment results

As shown in Table 4, the Design Expert 13 software fitted the data to determine the significance of each influential factor, and it performed an ANOVA for B_R and I_R to establish the regression equation.

Table 4

ANOVA for regression equations										
Source	Broken skin B_R [%]					Impurity content I_R [%]				
	Sum of Squares	D/F	Mean Square	F-value	P-value	Sum of Squares	D/F	Mean Square	F-value	P-value
Model	0.8029	9	0.0892	53.01	< 0.0001**	3.52	9	0.3909	58.65	< 0.0001**
A-Vibration shaft frequency	0.0685	1	0.0685	40.67	0.0004**	0.7021	1	0.7021	105.34	< 0.0001**
B-Lift chain speed	0.3613	1	0.3613	214.66	< 0.0001**	0.5151	1	0.5151	77.29	< 0.0001**
C-Cleaning platform speed	0.0722	1	0.0722	42.90	0.0003**	1.16	1	1.16	173.32	< 0.0001**
AB	0.0049	1	0.0049	2.91	0.1317	0.0100	1	0.0100	1.50	0.2602
AC	0.0144	1	0.0144	8.56	0.0222*	0.1332	1	0.1332	19.99	0.0029**
BC	0.0144	1	0.0144	8.56	0.0222*	0.0000	1	0.0000	0.0038	0.9529
A ²	0.0047	1	0.0047	2.81	0.1377	0.0519	1	0.0519	7.78	0.0269*
B ²	0.0904	1	0.0904	53.70	0.0002**	0.9143	1	0.9143	137.19	< 0.0001**
C ²	0.1626	1	0.1626	96.61	< 0.0001**	0.0014	1	0.0014	0.2162	0.6561
Residual	0.0118	7	0.0017			0.0467	7	0.0067		
Lack of Fit	0.0043	3	0.0014	0.7665	0.5694	0.0386	3	0.0129	6.37	0.0529
Pure Error	0.0075	4	0.0019			0.0081	4	0.0020		
Cor Total	0.8147	16				3.57	16			
R ²	0.9855					0.9869				

Note: $P < 0.01$ indicates highly significant, **, $0.01 < P < 0.05$ indicates significant, *.

Table 4 reveals that the rates of broken skin and impurity rate regression models are highly significant, whereas the lack of fit relationship is not. It indicates that the regression model analysis can better reflect the relationship between the skin-breaking rate or impurity rate, the vibration shaft frequency, the elevator chain speed, and the cleaning platform speed. The factors A , B , C , AC , B^2 , and C^2 have highly significant effects on B_R , whereas the factors AC and BC have significant effects on B_R . According to the F values of A , B , and C , the three factors have a significant impact on the skin-breaking rate in the order of elevator chain speed, cleaning platform speed, and vibrating shaft frequency. The factors A , B , C , AC , and B^2 have a highly significant impact on I_R , while A^2 significantly influences I_R in the order of clearing platform speed, vibrating shaft frequency, and elevator chain speed.

The non-significant terms are not involved in the data analysis, so the regression model of B_R and I_R is optimized as follows:

$$\begin{cases} B_R = 3.162 - 0.035A - 0.746B - 6.377C + 0.12AC - 1.2BC + 2.316B^2 + 4.868C^2 \\ I_R = 2.075 - 0.097A - 6.457B + 3.908C - 0.365AC + 0.018A^2 + 7.472B^2 \end{cases} \quad (18)$$

After optimizing the regression model, the coefficient of determination R^2 for B_R is 0.9737, meaning it can explain approximately 97.37% of the variation in the response variable. The coefficient of determination R^2 of I_R is 0.9837, which indicates that the regression model about I_R can explain about 98.37% of the variation in the response variable. The closeness of the R^2 to 1 signifies that a better fit of the model results in a smaller difference between the predicted and actual values. To show more intuitively the fitting degree of the optimized regression model, the predicted and actual values are plotted as line graphs for analysis. Figure 10(a) shows the comparison results between the actual and predicted values of B_R , and Figure 10(b) demonstrates the comparison results between the actual and predicted values of I_R . In this case, green line segments represent the actual values, while red lines represent the predicted values. The figure clearly shows a satisfactory fit between the predicted and actual values.

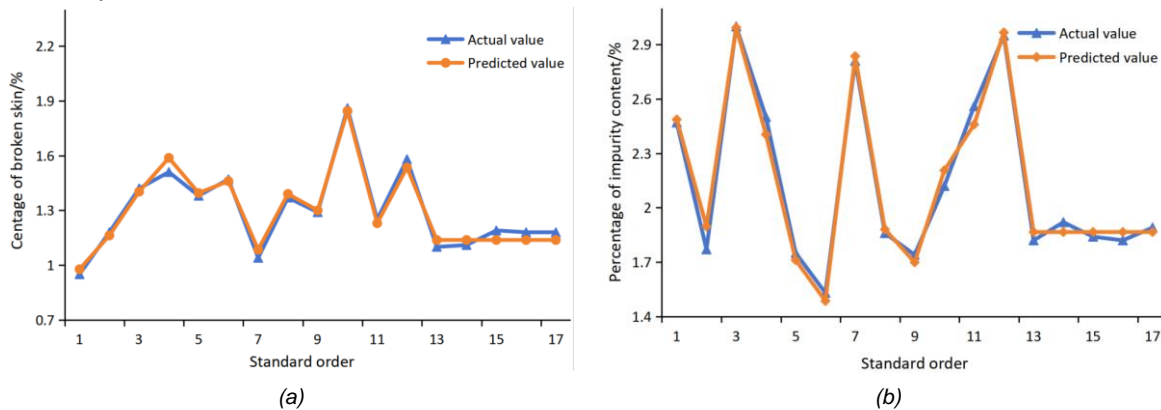


Fig. 10 - Comparison of data predicted by regression models

(a) Comparison of data predicted by B_R regression models; (b) Comparison of data predicted by I_R regression models

Parameter Optimization

The quality and integrity of sweet potatoes are key factors affecting their marketing. The sweet potato's B_R significantly influences its quality, with a set weight of 70%. In contrast, I_R primarily influences the efficiency of sweet potato harvesting and has a relatively small impact on sweet potato quality, with a set weight of 30%. To further investigate the optimal parameters of the harvesting process, it is necessary to perform parameter optimization on the above experimental results and construct a mathematical model. The optimized objective function and determined constraints are as follows:

$$\begin{cases} \min B_R(A, B, C) \\ \min I_R(A, B, C) \\ s.t. \begin{cases} 3 \leq A \leq 8 \\ 0.25 \leq B \leq 0.75 \\ 0.4 \leq C \leq 0.8 \end{cases} \end{cases} \quad (19)$$

Parameter optimization determines the optimal combination of parameters. Among them, the vibrating shaft frequency was 5.153 Hz, the elevator chain speed was 0.368 m/s, and the clearing platform speed was 0.578 m/s. At this point, the B_R of sweet potatoes was 1.06%, and the I_R was 1.86%.

Field experiment validation

The field experiment was conducted using the best parameter combination to verify the accuracy of the above regression equation and the best parameter combination, and the results are shown in Figure 11. The B_R and I_R of sweet potatoes were analyzed under this parameter condition. This test was conducted at the Intelligent Agricultural Machinery and Equipment Research Institute's sweet potato planting base (Nada Town, Danzhou City, Hainan Province, China). After taking the approximate values, the experimental parameters yielded a vibrating shaft frequency of 5.2 Hz, an elevator chain speed of 0.37 m/s, and a clearing platform speed of 0.58 m/s. Table 4 displays the experimental results, revealing a B_R of 1.09 % and an I_R of 1.90 % for sweet potatoes. Despite the slight increase in B_R and I_R , the relative errors were less than 5 %, indicating the reliability of the regression model.



Fig. 11 - Field experiment to verify harvesting effectiveness

Table 5

Experimental validation results		
Items	B_R	I_R
Predicted Value	1.06%	1.86%
Validation Value	1.09%	1.90%
Relative Error	2.83%	2.15%

Discussion

This research processed the data from Table 4 and combined it with the response surface results to analyze and explain the test factors that significantly affected B_R and I_R .

Table 4 reveals that the vibration shaft frequency and the cleaning platform speed significantly influence B_R , with Figure 12(a) displaying the response surface. Meanwhile, the elevator chain speed is 0.5 m/s, and the B_R increases gradually as the vibrating shaft frequency. This indicates that the higher frequency of the vibration axis makes the number of collisions between sweet potatoes and bars increase. This situation makes it easy for the sweet potatoes to cross the straight bars, resulting in repeated falls and collisions that increase B_R .

Figure 12(a) shows that B_R tends to decrease and then increase as the cleaning platform's speed increases. It indicates that when the speed of the clearing platform is small, the number of sweet potatoes piled up on the clearing platform per unit time is larger. Meanwhile, the slow speed of the rear conveyor roller may lead to the accumulation and jamming of sweet potatoes, and the friction between sweet potatoes increases the B_R . If the clearing platform's speed is excessively high, it could potentially damage the sweet potatoes during the conveying process due to the high impact force, thereby increasing the B_R .

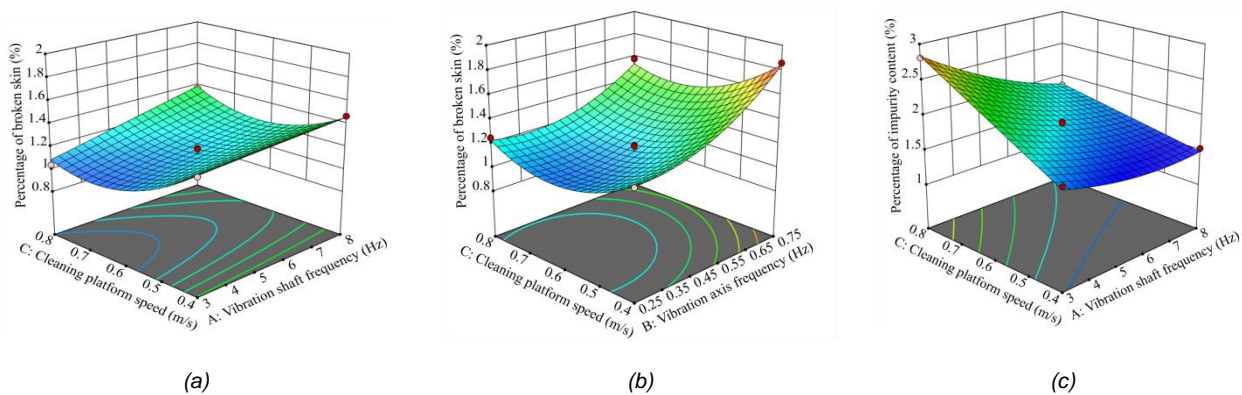


Fig. 12 - Significant and highly significant interaction response surfaces

(a) AC interaction response surface of B_R ; (b) BC interaction response surface of B_R ; (c) AC interaction response surface of I_R

Table 4 shows that elevator chain speed and clearing platform speed have a significant influence on B_R . Figure 12(b) displays the response surface, where the vibration axis frequency is 5.5 Hz. Figure 12(b) shows that the B_R increases gradually as the elevator chain speed increases.

When the elevator chain speed is low, the number of collisions between the sweet potato and the elevator chain bars is smaller, and the collision amplitude is small. As a result, the B_R remains at a low level with no obvious changes. As the elevator chain speed increases, the sweet potato generates more friction as it passes through the vibrating shaft and the rollers, leading to a significant increase in B_R and more noticeable changes.

Table 4 demonstrates that the vibration shaft frequency and the clearing platform's speed significantly influence the I_R , as depicted in Figure 12 (c), where the elevator chain's speed is 0.5 m/s. Figure 12 (c) shows that the I_R decreases gradually as the vibration shaft frequency increases. It shows that increasing the vibration shaft frequency will make the number of collisions between the impurities increase, which leads to the impurities gradually falling into the ground from the bar gap, reducing the I_R .

Figure 12(c) shows that I_R increases gradually as the clearing platform speeds up. It indicates that when the speed of the cleaning platform is less, the soil attached to the sweet potato can be cleaned out by the rear conveyor roller, and the broken soil removed is discharged to the surface through the sand leakage plate, which reduces the I_R of the sweet potato. The cleaning platform's increased speed prevents the timely completion of manual and conveyor roller cleaning operations, resulting in a gradual increase in I_R .

CONCLUSIONS

(1) This study designed a low-damage fresh-eating sweet potato combine harvester based on a two-segment potato-soil separating device and described its whole machine structure and working principle. The one-segment potato-soil separator device is designed with a "d" type elevator chain structure and a vibrating device. The two-segment double buffer cleaning device incorporates a front-falling buffer device and a rear-conveying buffer device. This harvester can effectively solve the problem of high B_R and I_R in the sweet potato harvesting process.

(2) The paper presents a design that uses a straight bar on the elevator chain and a kinematic analysis of sweet potatoes to prevent falls. The study shows that using a vibration axis frequency (f) of 3-8 Hz can reduce collisions and mitigate repeated damage caused by sweet potatoes hitting the straight bar. This research determined the speed of the elevator chain V_0 as 0.25-0.75 m/s through the agronomic survey of sweet potato planting and the analysis of pickers' operating efficiency. The analysis of the sweet potato force in the rear conveyor roller of the secondary cleaning platform determines the speed of the cleaning platform V_2 to be 0.4-0.8 m/s.

(3) This research conducted the quadratic regression orthogonal combination test, using the vibrating shaft frequency, elevator chain speed, and cleaning platform speed as test factors and the B_R and I_R as evaluation indexes. The results indicate that reducing the vibration shaft frequency and elevator chain speed and increasing the cleaning platform speed appropriately can reduce the B_R of the sweet potato harvesting process. Conversely, increasing the vibration shaft frequency and elevator chain speed appropriately and decreasing the cleaning platform speed can reduce the I_R of the sweet potato harvesting process. The field validation results showed that the optimal parameter combinations were a vibrating shaft frequency of 5.2 Hz, an elevator chain speed of 0.37 m/s, and a cleaning platform speed of 0.58 m/s.

At this time, the B_R of sweet potatoes was only 1.09 %, and the I_R was only 1.90 %, which meets the design standard of potato harvesting machinery. Overall, this harvester can significantly improve harvesting efficiency, and there is an obvious improvement in sweet potato B_R and I_R .

ACKNOWLEDGEMENT

Research on the device and mechanism of low damage cassava coupled excavation based on dynamic rupture characteristics of cassava-soil complex. (Project No. 52265029).

REFERENCES

- [1] Beznosyuk R.V., Evtekhov D.V., Borychev S.N., Kostenko M.Y., Rembalovich G.K., (2022), Justification of parameters of a finger hump of potato harvesters when vibrating canvas, *IOP Conference Series: Earth and Environmental Science*, vol. 981, no. 4, ISSN 1755-1315, p. 042051, United Kingdom.
- [2] Bovell-Benjamin A.C., (2007), Sweet Potato: A Review of its Past, Present, and Future Role in Human Nutrition, *Advances in Food and Nutrition Research*, vol. 52, ISSN 1043-4526, pp. 1–59, Valencia/Spain.

- [3] Bulgakov V., Bonchik V., Holovach I., Fedosiy I., Volskiy V., Melnik V., Ihnatiev Ye., Olt J., (2021), Justification of parameters for novel rotary potato harvesting machine, *Agronomy Research*, vol. 19, no.2, ISSN 1406-894X, pp. 1–11, Estonia.
- [4] Chen M., Liu X., Hu P., Zhai X., Han Z., Shi Y., Zhu W., Wang D., He X., Shang S., (2024), Study on rotor vibration potato-soil separation device for potato harvester using DEM-MBD coupling simulation, *Computers and Electronics in Agriculture*, vol. 218, ISSN 0168-1699, p. 108638, United Kingdom.
- [5] Chen X.D., Hu Z.C., Wang B., You Z.Y., Peng B.L., Hu L.L., (2019), Design and parameter optimization of sweet-potato-stalk separator for single row sweet potato combine harvester (单垄单行甘薯联合收获机薯秧分离机构设计与参数优化), *Transactions of the Chinese Society of Agricultural Engineering (Transactions of the CSAE)*, vol. 35, no. 14, ISSN 1002-6819, pp. 12-21, Beijing/China.
- [6] Chen X.D., (2020), *Study Sweet-potato-stalk Separation Characteristics and Structure Optimization of in Self-propelled Sweet Potato Combine Harvester (自走式甘薯联合收获机薯茎分离特性研究与机构优化)*, Master's Thesis, Anhui Agriculture University, Anhui/China.
- [7] Cláudio E. Cartabiano-Leite, Ornella M. Porcu, Alicia F. de Casas, (2020), Sweet potato (*Ipomoea batatas* L. Lam) nutritional potential and social relevance: a review, *International Journal of Engineering Research and Applications*, vol. 10, no. 6, ISSN 2248-9622, pp. 23–40, India.
- [8] Cui Z.K., Zhang H., Zhou J., Li T., (2020), Design and test of 4U-750 trailing type sweet potato harvester (4U-750 牵引式甘薯收获机设计与试验), *Journal of Chinese Agricultural Mechanization*, vol. 41, no. 5, ISSN 2095-5553, pp. 01-05, Jinan/China.
- [9] dos Santos T.P.R., Franco C.M.L., Mischan M.M., Leonel M., (2019), Behavior of Sweet Potato Starch After Spray - Drying Under Different Pretreatment Conditions, *Starch - Stärke*, vol. 71, no. 9–10, ISSN 0038-9056, 1521-379X, p. 1800245, Germany.
- [10] Feng B., Wang H.C., Wang G.P., Sun W., Shi L.R., Tian B., (2024), Optimization and Experiment of Operating Parameters of Separating Screen of Small Potato Harvester (小型马铃薯收获机分离筛作业参数优化与试验), *Journal of Agricultural Mechanization Research*, vol.46, no.10, pp.138-144+152, Harbin/China.
- [11] Ferreira S.L.C., Bruns R.E., Ferreira H.S., Matos G.D., David J.M., Brandão G.C., da Silva E.G., Portugal L.A., dos Reis P.S., Souza A.S., dos Santos W.N., (2007), Box-Behnken design: An alternative for the optimization of analytical methods, *Analytica Chimica Acta*, vol. 597, no.2, pp. 179–186, Netherlands.
- [12] Hu L.L., Tian L.J., Ji F.L., Wang B., (2014), Research on the working mode of sweet potato production mechanization (甘薯生产机械化作业模式研究), *Journal of Chinese Agricultural Mechanization*, vol. 35, no. 5, ISSN 2095-5553, pp. 165-168, Nanjing/China.
- [13] Fu Y., Ren S.Y., Tang P., Leng Y.C., Chen X.H., Tu X.Y., Lv X.R., (2023), Design and simulation test of digging device for small potato harvester, *INMATEH – Agricultural Engineering*, vol. 69, no. 1, ISSN 2068–4215, pp. 145-158, Romania.
- [14] Hrushetsky S.M., Yaropud V.M., Duganets V.I., Duganets V.I., Pryshliak V.M., Kurylo V.L., (2019), Research of constructive and regulatory parameters of the assembly working parts for potato harvesting machines, *INMATEH – Agricultural Engineering*, vol. 59, no. 3, ISSN 2068–4215, pp. 101-110, Romania.
- [15] Ismail Z.E., Amine E.E., El-Shabrawy T.H., Faleih H.S., (2014), Investigate a simple design for sweet potato harvesting, *Misr Journal of Agricultural Engineering*, vol. 31, no. 4, pp.1331–1346, Egypt.
- [16] Liu C.L., (2021), *Study on Design and Damage Law of Sweet Potato Combine Harvester (甘薯联合收获输送分离装置设计及损伤规律研究)*, Master's Thesis, Shandong Agricultural University, Tai'an/China.
- [17] Li J.C., Lv Y.N., Sun Y.K., Lin Y.L., (2022), Design and Experiment of Separating and Lifting Device of Potato Harvester-Based on Equivalent Radius Method (马铃薯收获机分离升运装置设计与试验——基于当量半径法), *Journal of Agricultural Mechanization Research*, vol. 44, no. 12, ISSN 1003-188X, pp. 199-206+256, Harbin/China.
- [18] Li X.Q., Wang X.H., Liu Y., Wang F., Meng P.X., Wang J.M., (2023), Design and Experiment of Circular Reducing and Collecting Potato Lifting Device for Potato Combine Harvester (马铃薯联合收获机环形减损集薯升运装置设计与试验), *Transactions of the Chinese Society for Agricultural Machinery*, vol. 54, no. 12, ISSN 1000-1298, pp. 109-120, Beijing/China.
- [19] Lv J.Q., Sun H., Dui H., Peng M.M., Yu J.Y., (2017), Design and Experiment on Conveyor Separation Device of Potato Digger under Heavy Soil Condition (粘重土壤下马铃薯挖掘机分离输送装置改进设计与试验), *Transactions of the Chinese Society for Agricultural Machinery*, vol. 48, no. 11, ISSN 1000-1298, pp. 146-155, Beijing/China.

- [20] Lv J.Q., Tian Z.G., Yang Y., Shang Q.Q., Wu J.E., (2015), Design and experimental analysis of 4U2A type double-row potato digger (4U2A 型双行马铃薯挖掘机的设计与试验), *Transactions of the Chinese Society of Agricultural Engineering (Transactions of the CSAE)*, vol. 31, no. 6, ISSN 1002-6819, pp. 17-24, Beijing/China.
- [21] Marciniak A., Przybyl K., Koszela K., Duda A., Szychta M., (2022), Analysis of the strength of an innovative design of an organic farming potato harvester, *In Journal of Physics: Conference Series*, vol. 2212, no. 1, ISSN 1742-6596, p. 012028, United Kingdom.
- [22] Ministry of Agriculture and Rural Affairs, PRC, (2022), *Agricultural machinery promotion appraisal outline: potato harvester (农业机械推广鉴定大纲: 薯类收获机)*, DG/T 078-2022, 22.2.2022, Beijing/China.
- [23] Mohanraj R., Sivasankar S., (2014), Sweet potato (*Ipomoea batatas* [L.] Lam)-A valuable medicinal food: A review. *Journal of medicinal food*, vol. 17, no. 7, ISSN 1096-620X, pp. 733-741, United States.
- [24] Shen H.Y., (2021), *Sweet potato combined harvesting arc grid handover Research and Optimization of Scraper Chain Conveying Mechanism (甘薯联合收获弧栅交接刮板链输送机构研究与优化)*, Master's Thesis, Chinese Academy of Agricultural Sciences Thesis, Nanjing/China.
- [25] Wang B., Hu L.L., Hu Z.H., Tian L.J., Ji F.L., Ma B., (2014), Damage mechanism study of chain-lever elevator sweet potato harvester (链杆式升运器薯土分离损伤机理研究), *Journal of China Agricultural University*, vol. 19, no. 02, ISSN 1007-4333, pp. 174-180, Beijing/China.
- [26] Wang F.A., Cao Q.Z., Li Y.B., Pang Y.L., Xie K.T., Zhang Z.G., (2023), Design and Trafficability Experiment of Self-propelled Potato Harvester in Hilly and Mountainous Areas (丘陵山区自走式马铃薯联合收获机设计与通过性试验), *Transactions of the Chinese Society for Agricultural Machinery*, vol. 54, no. s2, ISSN 1000-1298, pp. 10-19, Beijing/China.
- [27] Wei Z.C, Han M., Su G.L., Zhang H., Li X.Q., Jin C.Q., (2023), Design and Experiment of a Bagging and Unloading Potato Combine Harvester (装包卸包型马铃薯联合收获机设计与试验), *Transactions of the Chinese Society for Agricultural Machinery*, vol. 54, no. 10, ISSN 1000-1298, pp. 92-104, Beijing/China.
- [28] Wu D.Y., (2022), *Experimental Study on Collision Damage of Rod Lifting Chain to Potato and Parameter Design (马铃薯与杆条升运链碰撞损伤试验研究与参数设计)*, Master's Thesis, Northwest A&F University, Xianyang/China.
- [29] Xie Y.Z., Bian X.F., Jia Z.D., Ma P.Y., Yu Y., Zhang Q., Liu S., (2022), Development status and prospect of fresh sweet potato industry in China (中国鲜食甘薯产业发展现状及其发展前景). *Jiangsu Journal of Agricultural Sciences*, vol. 38, no. 06, ISSN 1000-4440, pp. 1694-1701, Nanjing/China.
- [30] Yang R.B., Zhang J., Shang S.Q., Tian G.B., Zhai Y.M., Pan Z.G., (2024), Design and Test of Secondary Conveyor Separator Device for Sweet Potato Combine Harvester (甘薯联合收获机二级输送分离装置的设计与试验), *Journal of Jilin University (Engineering and Technology Edition)*, ISSN 1671-5497, pp.1-14, Changchun/China.
- [31] Yang S., Zheng M.J., Wu W.J., Zhao C.L., (2021), Calibration of Physical Characteristics of Wind Sand Particles Based on Discrete Element Method (基于离散元的风沙沙粒物理特性参数标定), *Journal of Shijiazhuang Tiedao University (Natural Science Edition)*, vol. 34, no. 01, ISSN 2095-0373, pp. 49-57. Shijiazhuang/China.
- [32] Yang X., Wu Y., Wang L., Liu F., Zhao X., Bai H., Dong W., Kong X., Hu H., Zhong W., Xuan D., Yang A., Ma Y., (2024), Design and Performance Test of 4UJ-180A Potato Picking and Bagging Machine, *Agriculture*, vol. 14, no. 3, ISSN 2077-0472, p. 454, Basel/Switzerland.

SIMULATION AND EXPERIMENT OF POTATO EXCAVATOR

马铃薯挖掘机仿真与试验

Boxuan CHEN¹⁾, Xuhong CHU^{*1)}, Bingshen HUANG¹⁾, Xiangdong LIU¹⁾, Yiyuan GE¹⁾¹⁾ College of Mechanical Engineering, Jiamusi University, Jiamusi 154007, China

Tel: +86-15046495399; E-mail: chuxuhongemail@163.com

DOI: <https://doi.org/10.35633/inmateh-74-46>**Keywords:** agricultural machinery, potato, excavation shovel, loosening shovel**ABSTRACT**

In this study, the potato excavator with loosening shovel was designed in order to solve the problems of serious soil obstruction and high excavation resistance during the potato harvest. Using EDEM discrete element simulation software, potato excavation simulation experiments were carried out on soil broken effects and excavation resistance. Through the comparative analysis with loosening shovel and without, the results showed that the increase of soil broken effects was close to 52%, and the excavation resistance decreased by 16.57%. Through the two-factor and three-level field orthogonal experiment with excavation depth and loosening depth as influencing factors, the optimal operating parameters was determined for potato excavators: the excavation depth was 23 cm and the loosening depth was 20 cm. At this time, the excavation potato rate was 98.21%, and the rate of damaged potato was 1.31%. The traction resistance was 1826 N, which met the requirements of relevant industry standards. Through comparative analysis of simulation experiments and field experiment, it was found that when the excavation depth was 23 cm and the loosening depth was 20 cm, the error value of traction resistance was 11.3% between simulation experiments and field experiments. The discrete element simulation analysis can provide a preliminary reference for potato excavation design.

摘要

设计带松土铲的马铃薯挖掘机以解决小规模种植马铃薯收获时挖掘铲壅土严重、挖掘阻力大等问题。利用 EDEM 离散元仿真软件, 进行马铃薯挖掘仿真试验, 发现增加松土铲对土壤的破碎效果增幅接近 52%, 挖掘阻力降低 16.57%。进行以挖掘深度、松土深度为影响因素的两因素三水平的田间正交试验, 确定马铃薯挖掘机的最优作业参数: 挖掘深度 23cm, 松土深度 20cm。此时明薯率为 98.21%, 伤薯率为 1.31%, 挖掘效果最好, 牵引阻力 1826N, 符合相关行业标准的要求。通过仿真试验与田间试验对比分析, 当挖掘深度增加至 23cm 时, 仿真试验与田间试验牵引阻力的误差值低至 11.3%。离散元仿真分析为马铃薯挖掘机设计提供了前期参考。

INTRODUCTION

Potatoes are an important food crop that can be used as raw materials in various fields such as food processing, petrochemicals, and healthcare, in addition to being consumed directly (Luo et al., 2020; An et al., 2022; Devaux et al., 2021).

Extensive research has been conducted in the field of designing or simulating potato excavator. Aiming at the potato cropping pattern in the hilly area of southwest China, a small digging device for potato harvester was designed by Fu et al. (2023). The simulation experiment was carried out by the discrete element (DEM) software. The simulation results showed that the excavation potato rate was 87.3%. A small vibrating shovel excavator was designed by Joel et al. (2023), which was superior to the ordinary excavator in terms of soil crushing and drag reduction. A potato digging shovel with a non-smooth surface structure was designed based on bionics theory by Zhao et al. (2023). Through the simulation comparison test results showed that the soil adhered to the mechanical surface can be effectively reduced by 93.3%. A self-propelled crawler and potato harvester was designed by Zhou et al. (2021). The harvester could complete the tasks of digging potatoes, separating potatoes from the soil, transporting potatoes, and collecting potatoes in a single operation. Aiming at the problems of traditional potato excavation shovel, such as high resistance, easy to wear, high fuel consumption, high cost and so on, Bao Jianlun (2021) of Jilin University designed a bionic self-sharpening excavation shovel, which mimics the incisors of rabbits.

Boxuan CHEN, Master Degree; Xuhong CHU*, Tutor; Bingshen HUANG, Professor; Xiangdong LIU, Professor; Yiyuan GE, Professor.

Through experimental research and analysis, it was found that it was better than ordinary excavation shovel in self-sharpening and drag reduction. Li's bionic excavation shovel designed according to pangolin scales and Fan Yu's bionic excavation shovel designed by observing the arch mouth of wild boar were both effective in drag reduction (Li et al., 2020; Fan et al., 2022). An experimental sample of digging working parts for potato harvesting machines was developed and manufactured by Hrushetsky et al. (2019), whose verification in operation confirmed their work ability and efficiency. Wei Mengyang (2018) designed a drum potato harvester and simulated the key components. The excavator shovel was in the shape of an arrow, but it had high power consumption and serious damage to the potato. Lv Jinqing et al. (2018) designed a lifting chain potato excavator, its two excavation shovels correspond to a ridge, and the oblique angle of the blade on both sides of each excavation shovel was different, and the shovel pieces adjacent to the two excavation shovels bend downward to a certain angle, reducing the oblique angle of the shovel edge adjacent to the excavation shovel, but the groove shape of the whole excavation shovel was still approximately flat, which not only increases the slip cutting but also ensures the smooth shape of the ditch. The 4U2A double-row potato harvester was also designed, which was characterized by the design of an anti-blocking system, which solved the problems of high resistance and anti-entanglement of weeds (Lv et al., 2015).

At present, there are many studies on reducing resistance for potato excavation. In this study, a kind of potato excavator with loosening shovel was designed by our group, aiming at the problems such as lack of small potato digging machinery, poor digging effect and serious soil choking phenomenon.

The tractor was connected to the whole machine through three-point suspension. The soil loosening shovel first loosened the soil, the excavation shovel excavated the potato and the soil and transported it to the vibrating screen, which separated the potato soil and laid the potato on the ground. The tractor transmission shaft was connected with the gearbox through the universal joint, and the gearbox adjusted the transmission ratio, input the power into the chain drive through the transmission shaft, drove the vibrating screen to work, and shook up and down the vibrating screen to achieve the purpose of separating the potato soil, as shown in Fig.1 (Chen et al., 2023).

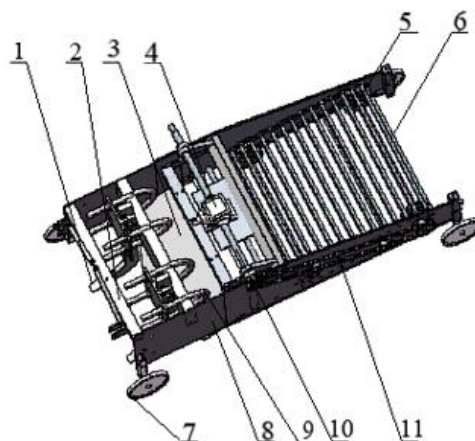


Fig. 1 - General assembly diagram of potato excavator

1. loosening shovel; 2. three-point suspension; 3. excavation shovel; 4. gearbox; 5. driving wheel; 6. vibration sieve;
7. ground wheel; 8. frame; 9. U bolts; 10. transmission shaft; 11. chain drive

MATERIALS AND METHODS

Discrete element simulation analysis of potato excavating process

The soil trough and potato models for excavation simulation experiments were generated by using the discrete element software EDEM. The soil trough and potato were both composed of particles in EDEM simulation.

Generation of soil trough model

The actual shape and size vary between different soil particles, so it is not possible to replace all soil with a spherical particle simply. In this study, the soil particle models were generated after simplification, including single sphere particles, double sphere particles, and three sphere particles, all with a particle radius of 4 mm as shown in Fig. 2. The contact radius between soil particles was 4 mm, and the soil particles were connected by Bond key. Through the particle factory, the soil trough model was generated with a length of 2000 mm, a width of 700 mm, and a height of 260 mm, as shown in Fig. 3.

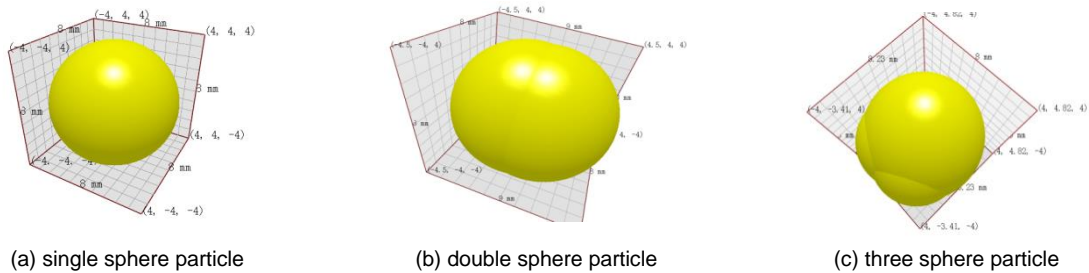


Fig. 2 - Model of Soil particle

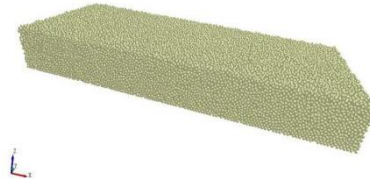


Fig. 3 - Soil trough model

Generation of potato model

In order to improve the calculation speed and facilitate analysis, this article used potatoes with the same size for simulation. The potato model was created by using SolidWorks, and imported into EDEM software. The potato model was filled with spherical particles in EDEM, as shown in Fig. 4. Three boxes were added to the soil trough, all of which were set as virtual structures. The spacing between the three boxes was set to 60 mm, and all with dimensions of 500 mm in length, 300 mm in width, and 200 mm in height. Three particle factories were set directly above the three boxes, as shown in Fig. 5. When generating particles, first the bottom soil particles were generated with a depth of 60 mm, and then potatoes and soil particles were simultaneously generated above them. The number of potatoes generated in each box was 22.

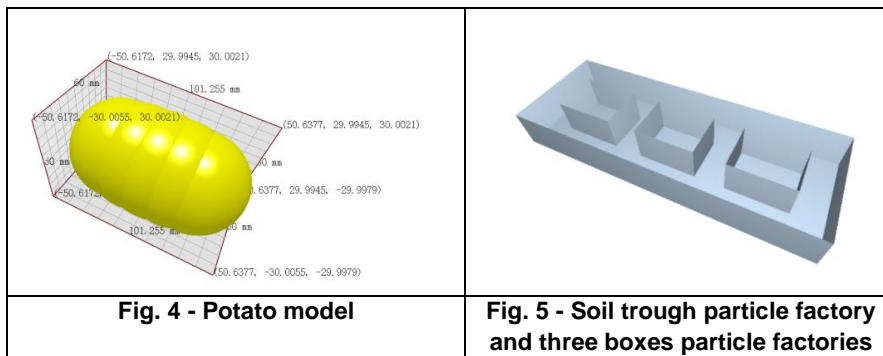


Fig. 4 - Potato model

Fig. 5 - Soil trough particle factory and three boxes particle factories

The Hertz-Mindlin (no slip) contact model was set up between potatoes and soil particles. In order to prevent the potato bouncing, the descent speed of potato particles was reduced during the potato model formation.

By consulting the relevant materials (Xin et al., 2020; Fan et al., 2022) and EDEM material library, the parameter values were shown in Table 1 and Table 2, which were used in discrete element analysis.

Table 1

Basic parameters of discrete element method simulation	
Material parameters	Value
Soil moisture content, %	13.33
Soil particle density, g/cm ³	1.57
Poisson's ratio of soil	0.3
Soil shear modulus, Pa	1.01×10 ⁶
Potato density, g/cm ³	1.05
Potato moisture content, %	80.3
Potato shear modulus, Pa	25.01×10 ⁶
Poisson's ratio of potato	0.45
Excavation shovel shear modulus, Pa	7.01×10 ⁷
Excavation shovel density, g/cm ³	7.85
Poisson's ratio of excavation shovel	0.5

Table 2

Contact parameters between particles			
	Restitution coefficient	Static friction coefficient	Dynamic friction coefficient
Potato - Excavation shovel	0.72	0.56	0.16
Potato-Potato	0.31	0.39	0.04

To avoid excessively long computation time, the simulation experiment time step was set to 20%, and the grid size was set to 8 mm. The save time was set to 0.5 s.

Using the EDEM software to simulate the potato excavating process. The excavation shovel model (which was generated by SolidWorks software) was imported into EDEM software, then the position of the excavation shovel was set, the simulation process was started.

Field experiment

The orthogonal experiment was selected, and the two-factor three-level orthogonal experiment with excavation depth A and loosening depth B as influencing factors were selected. The level of experiment factors was shown in Table 3.

Table 3

The levels of experiment factors		
Level	Experiment factors	
	Excavation depth $x_1 / (cm)$	Loosening depth $x_2 / (cm)$
1	13	10
2	18	15
3	23	20

Because the interaction between the two factors should be considered, the orthogonal table L9 (3⁴) was selected to arrange the experiment. According to the requirements of the Agricultural Industry Standard of the People's Republic of China NY/T1130-2006, the assessment indicators were selected including the traction resistance, the rate of excavation potato and the rate of damaged potato.

RESULTS

Discrete element simulation analysis results

Simulation analysis of excavation without loosening shovel

In order to study the disturbance of soil particles when digging and shoveling into the soil and the movement state of soil particles, the schematic diagram of the velocity of soil particles at different times during excavation was intercepted, as shown in Fig. 6.

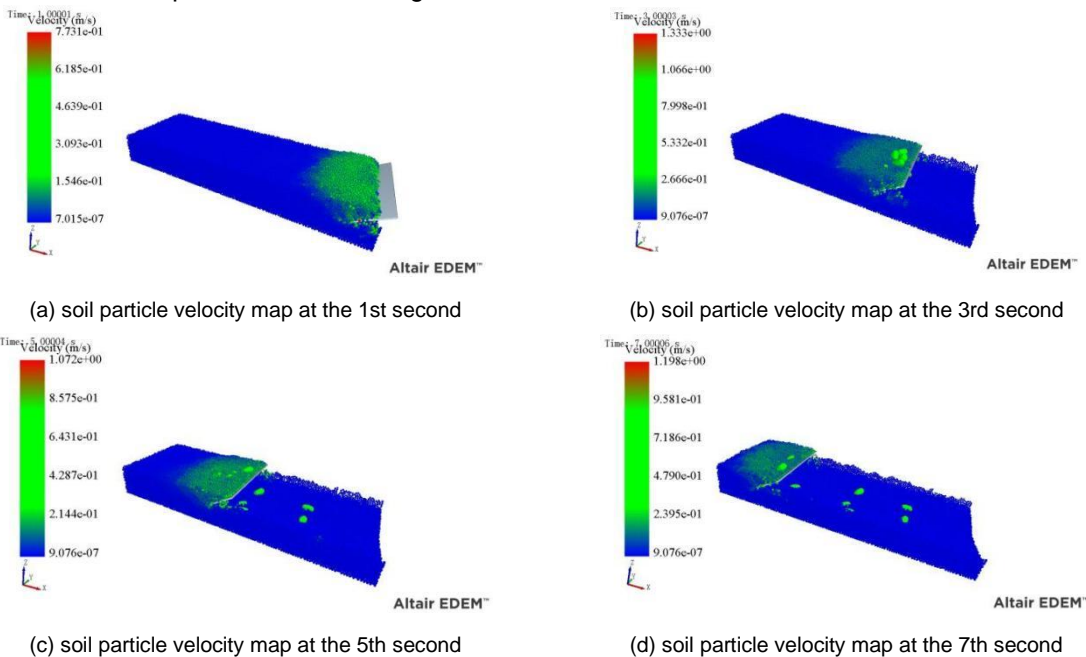


Fig. 6 - Motion velocity map of soil particles at different times

In Fig. 6, it indicated an increasing speed from blue to red, with large bright green tubers representing potato tubers. As can be seen from Fig. 6, after the potato excavation shovel digging at 1st second, the soil particles in the front and middle end of the shovel blade increased obviously, showing a light green color. With the increase of time, from 3rd second to 5th second, the speed of soil particles further increased, showing a bright green. When the time reached 7th second, when the soil particles slip from the excavation shovel, several red particles appeared, indicating that when the soil particles moved backward on the excavation shovel, they did parabola movement without the support of the excavation shovel. The speed of soil particles were further accelerated under the action of excavation shovel and gravity. From Fig. 6 (b), it can be found that most of the soil particles in the middle part of the excavation shovel had a higher speed, while the soil particles in the two sides of the excavation shovel were slower than those in the middle part, and the soil disturbance was more concentrated in the middle part.

Simulation analysis of excavation with loosening shovel

As shown in Fig. 7, after adding the loosening shovel, it was found that the soil showed a large area of red particles, the velocity of soil particles increased, and the disturbance of soil particles were greater. The loosening shovel could increase the disturbance to the soil and increased the disturbance range, and there was an obvious change in the soil particle velocity on both sides of the excavation shovel. The soil movement area increased obviously, and the soil height above the excavation shovel also increased obviously.

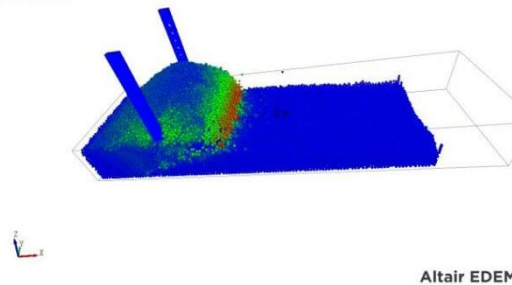


Fig. 7 - Excavation process of potato with loosening shovel

Comparative analysis with loosening shovel and without loosening shovel

When digging potatoes, soil blocks can easily cause soil blockage at the entrance of the excavator. Therefore, the crushing effect on soil was also an indicator for testing the performance of excavation devices. In EDEM, the soil crushing effect was replaced by the breaking of the connection bond. As shown in Fig. 8, the solid line represented the soil particle breaking effect of the excavation shovel with loosening shovel, and the dotted line represents the soil particle crushing effect of the excavation shovel without loosening shovel. It can be found from Fig. 8 that the crushing effect of soil was improved close to 52% by adding loosening shovel. Both the tip and handle of loosening shovel had a certain influence on the crushing effect.

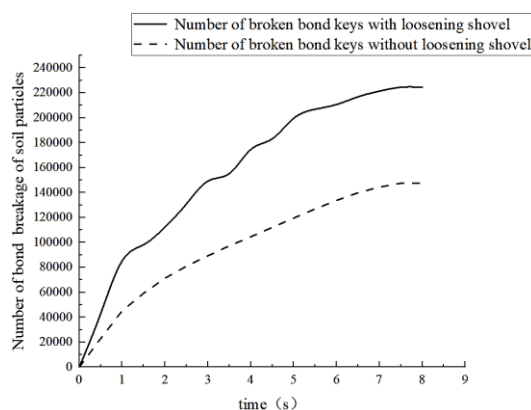


Fig. 8 - Comparison of broken number of soil particle bonds with and without loosening shovel

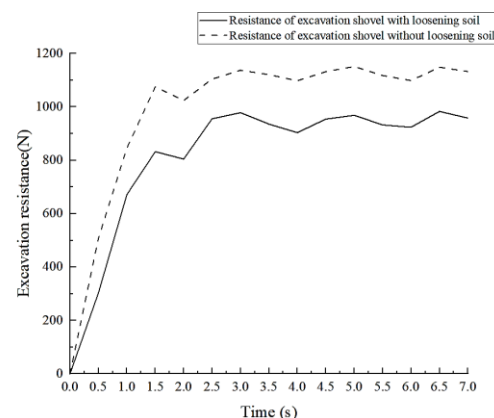


Fig. 9 - Comparison of excavation resistance with and without loosening shovel

It can be seen from Fig. 9 that the resistance of the excavation shovel with loosening shovel was obviously lower than without loosening shovel. The average excavation resistance was calculated in a stable area after 1.4 seconds.

The excavation resistance of the excavation shovel without loosening shovel was 1111.60 N, while that of the excavation shovel with loosening shovel was 927.39 N. The resistance of the excavation shovel with loosening shovel was 16.57% lower than that of the excavating shovel without loosening shovel.

Effect of excavation depth on traction resistance with loosening shovel

Excavation depth was one of the important influencing factors of traction resistance. When the excavation depth was too shallow, although the traction resistance was low, it may increase the rate of damaged potatoes and reduce the rate of excavation potatoes; when the excavation depth was too deep, it increased the traction resistance and excavated too much soil which may lead to the occurrence of soil blockage and increase the energy consumption and wear of working equipment. The discrete element simulation was used to analyze the influence of different excavation depth on the traction resistance when the machine speed was 1.1 m/s and the loosening depth was 20 cm, as shown in Table 4.

Table 4

Excavation depth / cm	Traction resistance / N
13	1205.58
18	1403.92
23	1619.43

Field experiment results

The experiment results were shown in Table 5.

Table 5

Experiment number	Experiment factors				Assessment indicators		
	Excavation depth A / (Level)	Loosening depth B / (Level)	AxB	Empty column	Traction resistance / (N)	Excavation potato rate / (%)	Damaged potato rate / (%)
1	1	1	1	1	1372	87.31	4.51
2	1	2	2	2	1445	88.5	3.22
3	1	3	3	3	1562	89.77	2.92
4	2	1	2	3	1507	96.42	3.11
5	2	2	3	1	1610	96.55	2.73
6	2	3	1	2	1724	96.79	1.42
7	3	1	3	2	1672	98.15	2.87
8	3	2	1	3	1730	98.17	2.49
9	3	3	2	1	1826	98.21	1.31
Traction resistance	K ₁	4379	4551	4826	Optimal solution: A ₁ B ₁		
	K ₂	4841	4785	4778			
	K ₃	5228	5112	4844			
	R	849	561	66			
Excavation potato rate	K ₁	262.58	281.88	282.27	Optimal solution: A ₃ B ₃		
	K ₂	289.76	282.22	282.13			
	K ₃	294.53	282.77	282.47			
	R	31.95	0.89	0.2			
Damaged potato rate	K ₁	10.65	10.49	8.42	Optimal solution: A ₃ B ₃		
	K ₂	7.26	8.44	7.64			
	K ₃	6.67	5.65	8.52			
	R	3.98	4.84	0.88			

Because there were relatively many experiment indexes, the comprehensive balance method was used to determine the optimal solution in this experimental analysis. For factor A (excavation depth), the range of traction resistance and excavation potato rate were the largest, A1 and A3 were selected respectively. The range of damaged potato rate was relatively small, so the A3 was selected. The A3 was the best factor after comprehensive analysis. For factor B (loosening depth), the range of damaged potato rate was the largest, so the B3 was selected. The traction resistance and excavation potato rate had less influence on B1 and B3 respectively, so the B3 was the best after comprehensive analysis.

The depth of loosening soil should be deeper than the actual growth depth of potato. According to the field experiment, it was found that although the loosening shovel was set on the side of the ridge, it still caused some damage to potato. With the increase of the loosening depth, the damaged potato rate decreased gradually.

As shown in Fig. 10, the solid line represents the excavation potato rate, and the dotted line represents the damaged potato rate. When the excavation depth was smaller than the actual growth depth of potato, the loosening shovel had a certain influence on the excavation rate. With the depth of loosening increased, the excavation potato rate gradually increased. The reason was that during the operation of the loosening shovel, the soil and potatoes moved upwards. Therefore, it can reduce the actual excavation depth to a certain extent with the loosening shovel.

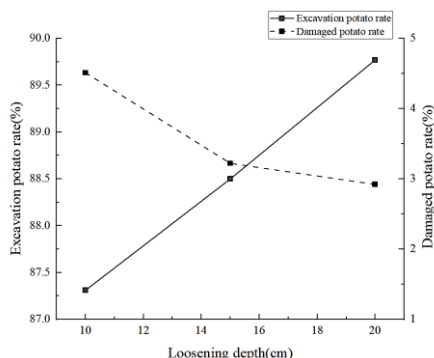


Fig. 10 - The effect of loosening depth on excavation potato rate and damaged potato rate

The significant factor affecting the excavation potato rate was the excavation depth of the shovel. When the excavation depth was 23 cm, the excavation potato rate was the highest. Loosening shovel also had a certain effect on the excavation potato rate, and the excavation potato rate was the highest when the depth of loosening was 20 cm. From the perspective of considering the excavation potato rate, the excavation potato rate was the highest when the depth of loosening was 20 cm and the depth of excavation was 23 cm.

The significant factor affecting the damaged potato rate was the excavation depth. When the excavation depth was 13 cm, the damaged potato rate was the highest. When the excavation depth was 23 cm, the damaged potato rate was the lowest. Therefore, under the condition of only considering reducing the rate of damaged potato, the excavation depth was 23 cm and the depth of loosening was 20 cm.

Through the above analysis, the optimal operating parameters of the potato excavation were determined: the excavation depth was 23 cm, the loosening depth 20 cm. At this time, the excavation effect was the best, including the traction resistance was 1826 N, the rate of excavation potato was 98.21%, the rate of damaged potato was 1.31%.

Comparative analysis with loosening shovel and without loosening shovel

The field experiment measured the traction resistance, excavation potato rate and damaged potato rate without loosening shovel when the excavation depth was 13 cm, 18 cm, 23 cm, as shown in Table 6. The comparative analysis was shown in Fig. 11. The dotted line represented the traction resistance of the excavation device without loosening shovel at different excavation depth, and the solid line represented the traction resistance of the excavation device with loosening shovel at different excavation depth. It can be found that with the increase of excavation depth, the traction resistance with loosening shovel was similar to that without loosening shovel. It showed that with the increase of excavation depth, the effect of loosening shovel to reduce excavation resistance was more obvious. The comparison of excavation potato rate and damaged potato rate with loosening shovel and without loosening shovel was shown in Fig. 12. It can be found from the picture that when the excavation depth was insufficient, the loosening shovel can improve the excavation potato rate to a certain extent, but when the loosening depth was insufficient, the damaged potato rate was higher, and the excavation potato rate decreased with the increase of the loosening depth. When the depth of loosening soil was 18 cm, the damaged potato rate with loosening shovel was similar to that without loosening shovel, indicating that when the depth of loosening was greater than 18 cm, increasing loosening shovel had little effect on the damaged potato rate.

Table 6

The experiment results without loosening shovel

Experiment number	Experiment factors		Inspection indexes		
	Excavation depth A / (cm)	Loosening depth B / (cm)	Traction resistance / (N)	Excavation potato rate / (%)	Damaged potato rate / (%)
1	13	0	1027	87.42	2.03
2	18	0	1189	96.53	1.41
3	23	0	1332	98.15	1.25

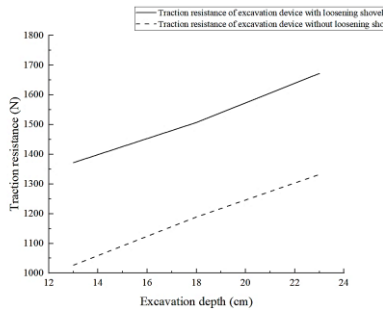


Fig. 11 - Comparative analysis of traction resistance with and without loosening shovel

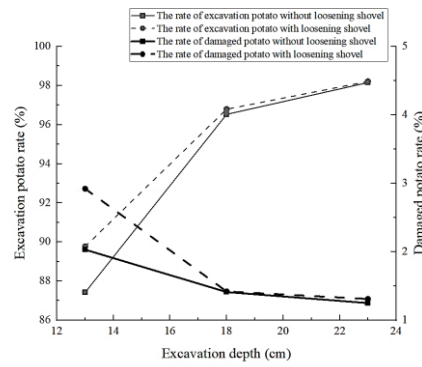


Fig. 12 - Comparative analysis of excavation potato rate and damaged potato rate with and without loosening shovel

Comparative analysis of discrete element simulation and field experiment

When loosening depth was 20 cm, the comparison of traction resistance between field experiment and simulation experiment with different excavation depth was shown in Fig. 13. It can be found that the maximum difference of traction resistance between field experiment and simulation experiment appeared when the excavation depth was small. With the increase of excavation depth, the difference of traction resistance between field experiment and simulation experiment decreased gradually. When the excavation depth was 23 cm, the error value of traction resistance was 11.3% between simulation experiments and field experiments.

It can be seen from Fig. 13 that the traction resistance of discrete element simulation was relatively small compared with field experiments. The main reason was that the working environment was relatively bad in the field experiment, and the simulation experiment only considered the force of soil and potato on the excavation shovel in the ideal state, but the influence of other factors was not considered. In addition, there were some differences in physical and mechanical properties between the soil particle model in the discrete element analysis and the actual soil particles in the field, which was also one of the reasons why the traction resistance of the discrete element simulation was relatively small compared with the field experiment.

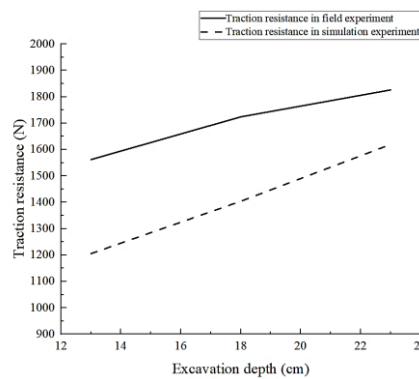


Fig. 13 - Comparative analysis of discrete element simulation and field experiment

CONCLUSIONS

(1) Based on the discrete element simulation analysis of the potato excavation process, it was found that including the loosening shovel increased the disturbance to the soil, and the crushing effect of the loosening shovel on the soil was improved close to 52%. The excavation resistance with loosening shovel was 16.57% lower than that of the excavating shovel without loosening shovel. Under the same working conditions, the service life of the excavation shovel with loosening shovel was longer.

(2) Based on the field experiment with excavation depth and loosening depth as influencing factors, the two-factor and three-level orthogonal experiment was carried out to obtain the optimal operation parameters of the excavation device. When the excavation depth was 23 cm and the loosening depth was 20 cm, the operation effect was the best at this time, while the traction resistance was 1826 N. The excavation potato rate was 98.21%, and the damaged potato rate was 1.31%, which met the requirements of relevant industry standards.

(3) Through comparative analysis of discrete element simulation and field experiments, it was found that the traction resistance value obtained from discrete element simulation was lower than that obtained from field experiments. The main reason was that the simulation experiment only considered the forces exerted by soil and potatoes on the excavation shovel under ideal conditions, without taking into account the influence of other factors. When the excavation depth was 23 cm and the loosening depth was 20 cm, the error value of traction resistance was 11.3% between simulation experiments and field experiments. The discrete element simulation analysis can provide a preliminary reference for potato excavation design.

ACKNOWLEDGEMENT

The authors acknowledge the support received from the scientific research project of Heilongjiang Province Universities Basic Scientific Research Business Cost (2018-KYYWF-0927).

REFERENCES

- [1] An M., Sun W., Han Y., Yang R.Y., Yan S., Kong F.T., Cao S.S. (2022). A dataset of the statistics on potato transaction price in the wholesale market in China from 2012 to 2018 (2012 - 2018 年中国马铃薯批发市场交易价格调查统计数据集). *Chinese Scientific Data: Chinese and English Online Version*, 7(3):213-222.
- [2] Bao J.L. (2021). Design and experiment of bionic self-sharpening for potato digging shovel. (仿生自磨锐马铃薯挖掘铲的设计与试验). *Jilin University*, China.
- [3] Chen B.X., Chu X.H., Liu X.D., Huang B.S., Cao C.Y., Sun P.Q., Ma L.X., Ge Y.Y., Yu Y.H., Ma L.L. (2023). A machine for cutting potato vine and potato harvester. (一种马铃薯切秧挖掘一体机). [P]. China.
- [4] Devaux A., Goffart J.P., Kromann P., Andrade P.J., Polar V., Hareau G. (2021) The potato of the future: opportunities and challenges in sustainable agri-food systems. *Potato Research*. 64, 681–720.
- [5] Fan Y. (2020). Research on potato digging mechanism based on discrete element method and design of bionic shovel (基于离散元法的马铃薯挖掘机理研究及仿生铲设计). *Shenyang Agricultural University*, China.
- [6] Fu Y., Ren S.Y., Tang P., Leng Y.C., Chen X.H., Tu X.Y., Lv X.R. (2023). Design and simulation test of digging device for small potato harvester. *INMATEH Agricultural Engineering*. 69(1).
- [7] Hrushetsky S.M., Yaropud V.M., Duganets V.I., et al. (2019). Research of constructive and regulatory parameters of the assembly working parts for potato harvesting machines. *INMATEH Agricultural Engineering*. 59(3).
- [8] Li J.W., Jiang X.H., Ma Y.H., Tong J., Hu B. (2020). Bionic design of a potato digging shovel with drag reduction based on the discrete element method (DEM) in clay soil [J]. *Applied Sciences*, 10(20).
- [9] Luo Q.Y., Gao W.J., Lv J.F., Gao M.J. (2022). Analysis of the development situation of China's potato industry from 2021 to 2022 (2021—2022 年中国马铃薯产业发展形势分析). *Innovation of Potato Industry and Seed Industry. Institute of Agricultural Resources and Agricultural Regionalization, Chinese Academy of Agricultural Sciences*, 4.
- [10] Lv J.Q., Tian Z.E., Yang Y., Shang Q.Q., Wu J.E. (2015). Design and experimental analysis of 4U2A type double-row potato digger (4U2A 型双行马铃薯挖掘机的设计与试验). *Journal of Agricultural Engineering*, China, 31(06):17-24.
- [11] Lv J.Q., Wang P.R., Li Z.H., Li J.C., Liu Z.Y. (2018). Design of key components for potato excavator (马铃薯挖掘机关键部件的设计). *The Potato Industry and Poverty Alleviation*, China, 304-311.
- [12] Joel T.P.A., Wang J.X., Zhao H., Jia B.X., Sun W., Tian B. (2023). Design and drag reduction performance of small vibrating shovel potato excavator (小型振铲式马铃薯挖掘机的设计与减阻性能研究). *Agricultural Equipment & Vehicle Engineering*, China, 61(05):1-4.
- [13] Wei M.Y. (2018). The design and simulation analysis of key components of the roller potato harvester. (滚筒式马铃薯收获机关键部件的设计及仿真分析). *Hubei University of Technology*, China.
- [14] Xin Q.Q. (2020). Simulation and test of potato seedling crushing and throwing device based on fluent-EDEM. (基于 Fluent-EDEM 的马铃薯秧粉碎抛送装置仿真与试验). *Shandong Agricultural University*, China.
- [15] Zhao P., Yu T.K., Xu G.F., Guo R.J., Li H., Xu H.F., Jin T.C., Ji D. (2023). Design and drag reduction performance analysis of a potato harvest shovel based on the surface texture characteristics of pangolin scale. *INMATEH Agricultural Engineering*. 70(2).
- [16] Zhou J.G., Yang S.M., Li M.Q., Chen Z., Zhou J.D., Gao Z.N., Chen J. (2021). Design and experiment of a self-propelled crawler-potato harvester for hilly and mountainous areas. *INMATEH Agricultural Engineering*. 64(2).

EXPERIMENTAL STUDY ON THE PERFORMANCE OF CORN STALK CRUSHING DEVICE WITH STEPPED SAW DISK KNIFE

阶梯式锯盘刀玉米秸秆粉碎装置性能试验研究

Yongtao YU, Yanjun LI, Fuxiang XIE*, Jian SONG, Yong TIAN
 College of Machinery and Automation, Weifang University, Weifang 261000, China
 Tel: +86-182-6566-9383; E-mail: yyt2015110104@163.com
 Corresponding author: Fuxiang Xie
 DOI: <https://doi.org/10.35633/inmateh-74-47>

Keywords: stalk returning, stepped saw disc knife, sawing and crushing, single-factor experiment, high-speed camera

ABSTRACT

Responding to the problem of over-returning of corn stalk to the field, this article proposes a comprehensive utilization model that returns 30% of corn stalk to the field from above the surface and recycles the remaining 70% as fodder is proposed. For the problems of poor quality of stalk crushing and fast knife wear, the experimental platform for corn stalk crushing with vertical shaft stepped saw disc knife was designed. The effects of different factors on the qualified rate of stalk cutting length and cutting power were investigated. The qualified rate of cutting length was the best 96.57% when the plant spacing was 20 cm. The cutting power was the smallest 322.94 W when the rotational speed of knife roller was 600 r/min. The stalk crushing process was analysed by high-speed camera, and the stalk crushing mechanism was clarified.

摘要

针对玉米秸秆还田量过大的问题, 本文提出了将玉米秸秆自地表以上 30% 还田, 其余 70% 回收作饲料的综合利用模式。针对秸秆粉碎质量差、刀片磨损快等问题, 设计了立轴阶梯式锯盘刀玉米秸秆粉碎试验台, 实现秸秆离地粉碎。通过单因素试验, 探究了刀辊转速、喂入速度、钳住角、拨禾星轮转速、株距对秸秆切断长度合格率和切割功率的影响规律。当株距为 20 cm, 切断长度合格率达到最高为 96.57%。当刀辊转速为 600 r/min 时, 切割功率达到最小为 322.94 W。通过高速摄像对秸秆粉碎过程进行了分析, 明晰了秸秆粉碎机理。

INTRODUCTION

Stalk crushing and returning to the field has many advantages, which is the main way of stalk utilization at present (Ramm et al., 2024; Li et al., 2024; Miranda et al., 2021; Liu et al., 2019; Yeboah et al., 2017). However, the amount of stalk returned to the field is too large and cannot be effectively decomposed and utilized. In addition, the traditional devices for returning corn stalk to the field are mainly the hammer claw type and the dumping knife type. It is near-ground operation, and the knife inevitably contact with soil, stones and so on, resulting in rapid wear and bluntness of the knife blunt. Therefore, it cannot cut of the stalk fibre effectively, and the operation power consumption is large (Zhang et al., 2019; Yu et al., 2019).

To improve the cutting effect and reduce the cutting power, scholars have studied the cutting theory, mechanism design and parameter optimization of corn stalk returning devices. Gupta et al., (1996), studied the effect of operating parameters of single disc cutter on the cutting performance of sugarcane. Mello et al., (2000), compared the differences between angled and serrated blades in reducing cutting loss and cutting force through experiment, and analysed them by high-speed cameras. Igathinathane et al., (2010), tested the effect of cutting angle on cutting force and cutting power of corn stalk. Geng et al., (2021), designed a corn stalk kneading and conveying device to achieve stalk conveying while cutting stalk. Zhao et al., (2022), designed a cutting knife for corn stalk by bionic the mandibular teeth of ants. Sun et al., (2019), designed a differential speed stalk returning machine with circular saw knives and crushing knives working in the same direction. Wang et al., (2020), designed a chopping device to improve the decomposition rate of stalk returning to the field. Zhao et al., (2021), designed a bionic stalk returning knife based on primnoa mouthparts to reduce the cutting power. Liu et al., (2021), designed a dynamic supported corn stalk chopping device with different rotational speed of disc knife.

Yongtao Yu, Lecturer Ph.D.; Yanjun Li, A.P. Ph.D.; Fuxiang Xie, Prof. Ph.D.; Jian Song, Prof. Ph.D.; Yong Tian, Lecturer Ph.D.

Song *et al.*, (2024), experimented the parameters of stalk returning machine and obtained the optimal parameter combination. However, there are fewer studies on the appropriate amount of stalk returned to the field and the related mechanical devices based on it.

Aiming at the problems of poor quality of stalk crushing and fast knife wear, an experimental platform for corn stalk crushing with stepped saw disc knife composed of multiple circular saw knives of different diameters was designed to achieve off-ground crushing of stalk. The factors affecting the qualified rate of cutting length and cutting power of corn stalk were experimented through the experimental platform, and the stalk crushing process was analysed by high-speed camera. The research provides theoretical basis and design basis for the design of stalk crushing device of corn harvester.

MATERIALS AND METHODS

The crushing experimental platform with stepped saw disc knife

The comprehensive utilization mode of corn stalk

If the entire corn stalk is returned to the field, the amount of returned stalk is too large, which not only affects the subsequent sowing and emergence of wheat, but also the stalk cannot be effectively decomposed and utilized (Li *et al.*, 2022; Zhu, 2019; Qiao, 2019). Recycling all of them cannot fully utilize the effect of stalk returning to the field on improving soil organic matter and promoting wheat yield. So, a comprehensive utilization model that returns 30% of corn stalk to the field from above the surface and recycles the remaining 70% as fodder is proposed (Dong *et al.*, 2010; Wang *et al.*, 2013), as shown in Fig. 1.

Fig. 1 - The comprehensive utilization mode of corn stalk

The machine structure and operating principle of the experimental platform

It is difficult to accurately adjust the operating parameters and inconvenient to collect data when the field experiment is conducted directly by the corn stalk returning machine. Therefore, based on the principle of comprehensive utilization of corn stalk, an experimental platform of stepped saw disc is designed, which mainly consists of three parts: stepped saw disc crushing device, clamping feeding device, control and data acquisition system, as shown in Fig. 2. The clamping feeding, crushing, and data collection of corn stalks are completed at one time.

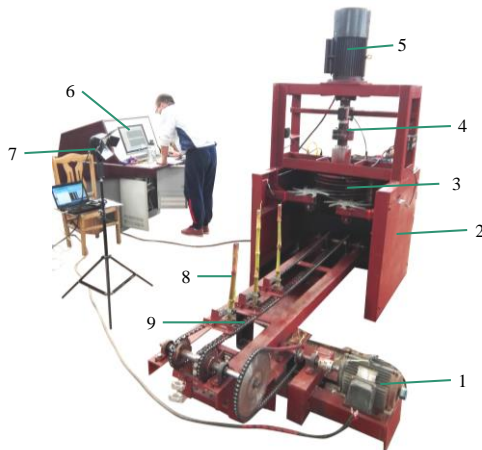


Fig. 2 - The crushing experimental platform with stepped saw disc knife

1 - Motor of clamping feeding device; 2 - Crushing device of stepped saw disc knife; 3 - Stepped saw disc knife; 4 - Torque sensor; 5 - Motor of the crushing device; 6 - Devices of control and data collection; 7 - High-speed camera; 8 - Corn stalk; 9 - Clamping feeding device

The core component of the stepped saw disc knife consists of multiple circular saw knives of different diameters, as shown in Fig. 3. The saw disc knives are arranged in a stepped manner, and their diameter gradually decreases from top to bottom. There is a relative velocity between neighbouring saw disc knives. Not only cutting the stalk, but also tearing it, which is more conducive to the crushing and subsequent decay of the stalk. In addition, the corn stalks are crushed in an upright state, the saw disc knife does not touch the soil, so the saw teeth can remain sharp for a long time to ensure better crushing effect (Zhang et al., 2021).

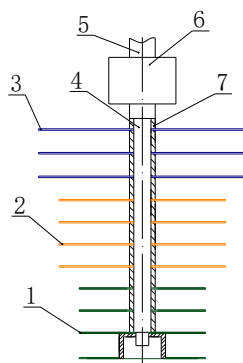


Fig. 3 - The stepped saw disc knife

1 - Circular saw knife with a diameter of 200 mm; 2 - Circular saw knife with a diameter of 280 mm;
3 - Circular saw knife with a diameter of 360 mm; 4 - Shaft of the knife; 5 - Shaft of the motor; 6 - Coupling; 7 - Bushing

Sawing and crushing experiment of corn stalk

Experimental materials

The corn variety used for the experiment is Zhengdan 958, and the average value of stalk diameter is 20.78 mm, and the average value of moisture content is 78.30%. Corn stalks with equivalent outer diameter and without epidermal damage are selected for the experiment.

Experimental indexes

Referring to the relevant standards (GB/T 5262 - 2008; NY/T 500 - 2015), the experiment is conducted with the qualified rate of stalk cutting length and cutting power as the experiment indexes.

The qualified rate of cutting length F_n :

$$F_n = \frac{m_z - m_b}{m_z} \times 100\% \tag{1}$$

m_b - the mass of stalk with unqualified lengths [kg]; m_z - the total mass of stalk [kg].

The cutting power P_q :

$$P_q = \frac{n(T_z - T_k)}{9550} \tag{2}$$

T_k - the torque during idling [N·m]; T_z - the total torque during operation [N·m].

Single-factor experiment

The rotational speed of the knife roller, stalk feeding speed (i.e. machine forward speed), clamping angle, rotational speed of the dial wheel and stalk plant spacing are taken as the experimental factors, and the experiment is repeated five times to take the average value. The level coding table of experimental factor is shown in Table 1. The rotational speed of the knife roller of 800 r/min, feeding speed of 1.45 m/s, rotational speed of the dial wheel of 110 r/min, clamping angle of 15° and plant spacing of 30 cm are taken as the zero level.

Table 1

Level coding table of experimental factors

Level	Factors				
	Rotational speed of the knife roller [r/min]	Feeding speed of the stalk [m/s]	Clamping angle [°]	Rotational speed of the dial wheel [r/min]	Plant spacing of the stalk [cm]
1	600	0.75	-15	50	20
2	700	1.10	0	80	25
3	800	1.45	15	110	30
4	900	1.80	30	140	35

RESULTS

Rotational speed of the knife roller

The stalk that has been cut and crushed is shown in Fig. 4, in which most of them are cut into small sections of 30 mm, the length of which meets the requirements, and the stalk fibre can be effectively cut. The length meets the requirements, and the stalk fibres can be effectively cut. The tearing of stalk by the teeth of the saw disc knife is shown in Fig. 4(a). However, the length of individual stalks after cutting is unqualified, as shown in Fig. 4(b), the stalks are half cut and half torn. There are also stalks that are not completely cut, as shown in Fig. 4(c).



Fig. 4 - Crushed stalk

The effects of the rotational speed of the knife roller on the qualification rate of cutting length and cutting power are shown in Fig. 5. The qualified rate of cutting length of corn stalk shows a trend of increasing and then decreasing with the increase of the knife roller rotational speed, and the qualified rate of cutting length is non-linearly correlated with the rotational speed of the knife roller. When the rotational speed of the knife roller is 800 r/min, the qualified rate of cutting length reaches best 85.59%. The reason is that, with the increase of rotational speed of the knife roller, the impact of knife roller on corn stalk increases, and the stalk is difficult to feed into the knife roller, which leads to the decrease of qualified rate of cutting length. The cutting power increases with the increase of rotational speed of the knife roll. The cutting power is the smallest 322.94 W when the rotational speed of the knife roll is 600 r/min. The growth rate of cutting power is basically the same, and they are linearly correlated. The rotational speed of the knife roller is the main factor affecting the cutting power.

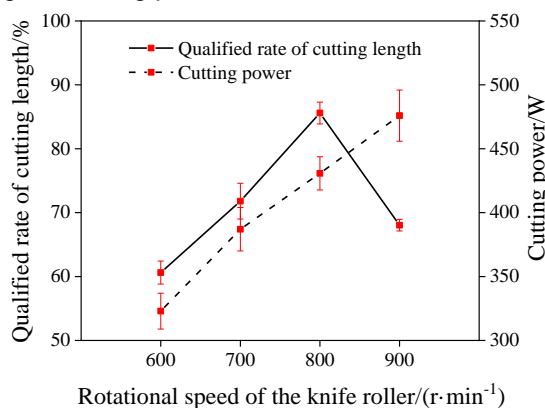


Fig. 5 - Effect of the rotational speed of the knife roller on the experimental indexes

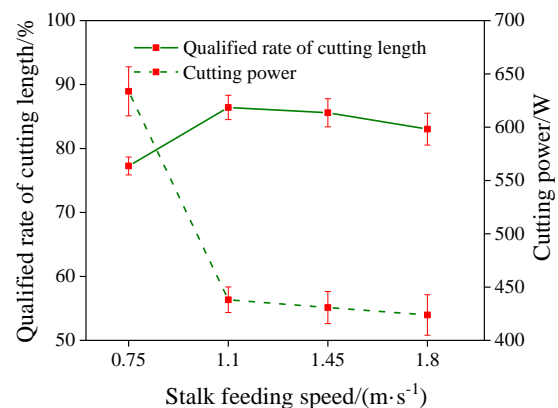


Fig. 6 - Effect of the feeding speed on the experimental indexes

Stalk feeding speed

The effects of stalk feeding speed on the qualification rate of cutting length and cutting power are shown in Fig. 6. The qualified rate of cutting length shows a trend of increasing and then decreasing with the increase of stalk feeding speed.

When the feeding speed is 1.10 m/s, the qualified rate of cutting length reaches the best level 86.42%. The reason is that, with the increases of feeding speed, the number of corn stalks cut by the knife rollers per unit time increases, and the effective cutting time of a single corn stalk decreases, resulting in inadequate cutting of the stalks. Secondly, with the increase of feeding speed, the collision and impact between corn stalks and knife rollers increase, and the stalks cannot be fed efficiently, resulting in a decrease in the qualified rate of cutting length.

The cutting power decreases with the increase of feeding speed, and they are negatively correlated. The cutting power reaches a minimum of 423.81 W when the feeding speed is 1.80 m/s. The reason is that with the increase of feeding speed, the effective cutting time of single corn stalk is reduced, and the stalk is not sufficiently cut, and even missing cutting due to stalk cannot be fed. When the feeding speed increases from 0.75 m/s to 1.10 m/s, the cutting power is reduced by 30.88%, which is a significant reduction. The reduction is significantly reduced when the feeding speed exceeds 1.10 m/s. It shows that as the feeding speed continues to increase, its effect on cutting power becomes less and less.

Clamping angle

The effects of clamping angle on the qualification rate of cutting length and cutting power are shown in Fig. 7. The qualified rate of cutting length shows a trend of first increase and then decrease with the increase of clamping angle. When the clamping angle is 15°, the qualified rate of cutting length reaches the best 88.58%. When the clamping angle is -15°, the qualified rate of cutting length is the lowest 65.40%. The reason is that at this time, the rotation direction of the dial wheel is opposite to the direction of stalk feeding, which is not conducive to the feeding of stalk. This indicates that when corn stalk is fed into the knife rollers from an area with negative clamping angle, the cutting effect is not ideal. The cutting power increase and then decrease with the increase of clamping angle. When the clamping angle is 15°, the cutting power reaches a maximum of 440.75 W. When the clamping angle is -15°, the cutting power reaches a minimum of 372.11 W.

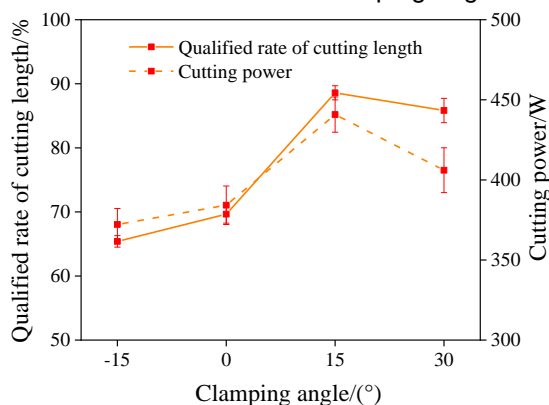


Fig. 7 - Effect of the clamping angle on the experimental indexes

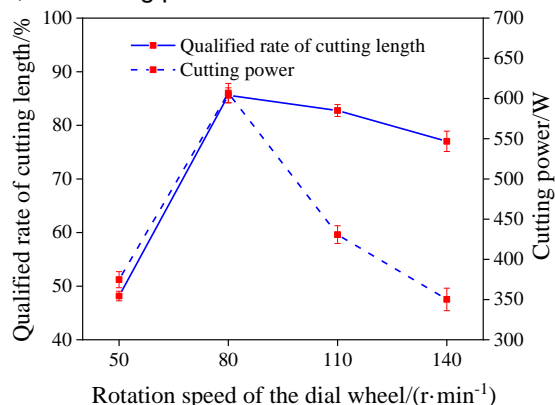


Fig. 8 - Effect of the rotational speed of the dial wheel on the experimental indexes

Rotational speed of the dial wheel

The effects of the rotational speed of the dial wheel on the qualification rate of cutting length and cutting power are shown in Fig. 8. The qualified rate of cutting length increase and then decrease with the increase of the rotational speed of the dial wheel. When the rotational speed of the dial wheel is 80 r/min, the qualified rate of cutting length reaches the best level 85.59%. The reason is that, with the increase of the rotational speed of the dial wheel, the speed of the stalk in the instant of cutting suddenly increases, the impact between the stalk and the knife roller increases, which reduces the qualified rate of cutting length. The cutting power increases and then decreases with the increase of the rotational speed of the dial wheel. The cutting power is the smallest 350.16 W when the rotational speed of the dial wheel is 140 r/min. At this time, the rotational speed of the dial wheel is too fast and cannot match with the knife roller speed and stalk feeding speed, and the stalk is not sufficiently cut or missed, which leads to a smaller cutting power.

Plant spacing of the stalk

The effects of plant spacing on the qualification rate of cutting length and cutting power are shown in Fig. 9. The qualified rate of cutting length decreases with the increase of plant spacing, and they are negatively correlated. When the plant spacing is 20 cm, the qualified rate of cutting length is the best 96.57%. With the increases plant spacing, the qualified rate of cutting length gradually decreases, but the decrease of each section does not exceed 10%.

It indicates that its effect on the qualified rate of cutting length becomes smaller and smaller with the increases of plant spacing. The cutting power decreases with the increase of plant spacing and the decrease of cutting power is essentially the same. When the plant spacing is 35 cm, the cutting power is the smallest 358.33 W. With the increase of plant spacing, the feeding gap between neighbouring corn stalks increases, and the probability of stalk congestion decreases, so the cutting power gradually decreases.

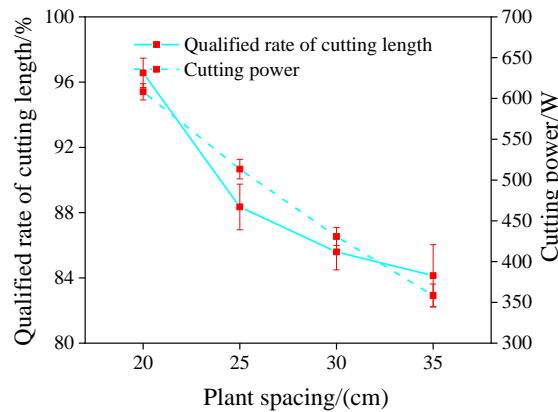


Fig. 9 - Effect of the stalk plant spacing on the experimental indexes

The analysis of high-speed camera

The process of crushing corn stalks with the stepped saw disc knife is analysed by high-speed camera, and the results are shown in Fig. 10. Corn stalk fixed on the clamping feeding device is transported to the knife rollers. Since the diameter of the saw disc knife in the upper region of the knife roll is the largest, the upper part of the stalk is cut first, as shown in Fig. 10 (a) and (b). The saw teeth squeeze the stalk for sliding cut, cutting the stalk while tearing and crushing it. After the upper part of the stalk is crushed, the middle part of the stalk starts to be cut and crushed by the saw disc knives in the middle area of the knife rollers, as shown in Fig. 10 (c) and (d). To the lower part of the stalk, as shown in Fig. 10 (e) and (f), at this point, a corn stalk is completely crushed. Through the high-speed camera analysis of the stalk crushing process, the corn stalks are cut sequentially from top to bottom, which meets the design requirements of the stepped saw disc knife.

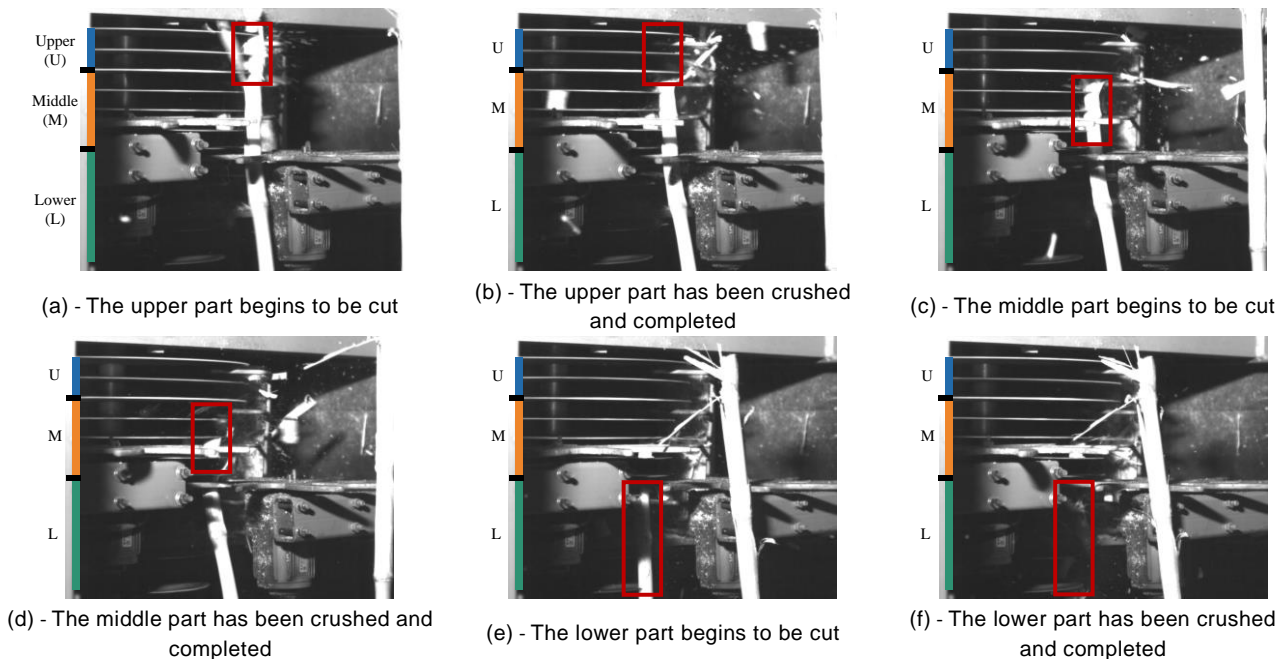


Fig. 10 - The crushing process of corn stalk

The failure of stalk during crushing is analysed by high-speed camera, and the failure of stalk is shown in Fig. 11. Fig. 11(a) shows that the stalk is broken due to collision and impact by the knife rollers. Fig. 11(b) shows that the stalk is congested in the cutting process because the feeding speed of the stalk is too fast. In Fig. 11(c), the stalk is difficult to be cut without being clamped by the saw disc knife when the clamping angle is negative.

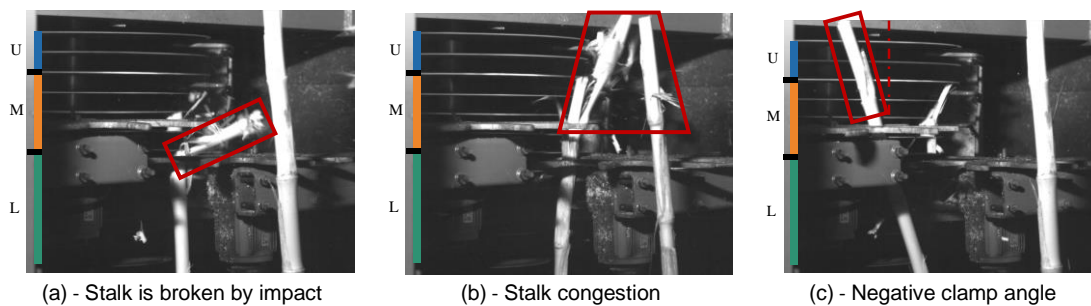


Fig. 11 - The cutting failure of corn stalk

CONCLUSIONS

(1) A comprehensive utilization model that returns 30% of corn stalk to the field from above the surface and recycles the remaining 70% as fodder was proposed. Based on this, the experimental platform for corn stalk crushing with stepped saw disc knife was designed to achieve off-ground crushing of stalk.

(2) The results of the single-factor experiment showed that the qualified rate of cutting length increased and then decreased with the increase of knife roller rotational speed, feeding speed, clamping angle and dial wheel rotational speed, and decreased with the increase of plant spacing. When the plant spacing was 20 cm, the qualified rate of cutting length is the best namely 96.57%.

(3) The results of the single-factor experiment showed that the cutting power increased with the increase of knife roller rotational speed, decreased with the increase of feeding speed and plant spacing, and increased and then decreased with the increase of clamping angle and the dial wheel rotational speed. When the rotational speed of the knife roll was 600 r/min, the cutting power was the smallest 322.94 W.

(4) The high-speed camera analysis of the corn stalk crushing process showed that the stepped saw disc knife could completely cut off the stalk fibres and improved the quality of corn stalk crushing.

ACKNOWLEDGEMENT

This work was supported financially by the Start-up Foundation for Doctoral Research of Weifang University (N0.2022BS30), Shandong Province Key R&D Program (2022CXGC010612), and the Shandong Province Higher Education Institutions Young Innovation Team Talent Introduction Program.

REFERENCES

- [1] Dong, Y., Fan, H., Wang, J., Wang, J., (2010). Preliminary report of returning corn straw into soil on soil fertility (玉米秸秆还田培肥效果研究). *Guangdong Agricultural Sciences*, Vol. 2, ISSN 1004-874X, pp. 77-78+85, China.
- [2] GB/T 5262-2008, Measuring methods for agricultural machinery testing conditions-general rules (农业机械试验条件 测定方法的一般规定). China.
- [3] Geng, A., Gao, A., Zhang, Y., Zhang, J., Zhang, Z., & Hu, X., (2021). Development and test of corn straw kneading and conveying device. *INMATEH - Agricultural Engineering*, Vol. 65, No. 3, ISSN 2068-4215, pp. 29-38, Romania.
- [4] Gupta, C., Lwin, L., Kiatiwat, T., (1996). Development of a self-propelled single-axle sugarcane harvester. *Applied Engineering in Agriculture*, Vol. 12, No. 4, ISSN 0883-8542, pp. 427-434, United States.
- [5] Ighathinathane, C., Womac, A., Sokhansanj, S., (2010). Corn stalk orientation effect on mechanical cutting. *Biosystems Engineering*, Vol. 107, No. 2, ISSN 1537-5110, pp. 97-106, England.
- [6] Li, S., Li, B., Wang, C., Sun, P., (2024). Effects of maize straw returning on soil fertility index and carbon sequestration ability. *Heilongjiang Agricultural Sciences*, No. 5, pp. 32-38, China.
- [7] Li, W., Yang, J., Jin, W., Ma, L., Ge, Y., Zhang, J., Zhuansun, Y., (2022). Investigation of the decomposition pattern of corn straw in cold land under different field return methods. *INMATEH - Agricultural Engineering*, Vol. 68, No. 3, ISSN 2068-4215, pp. 693-701, Romania.
- [8] Liu, P., He, J., Lou, S., Wang, Y., Zhang, Z., & Lin, H., (2021). Design and experiment for dynamic supporting type maize straw chopping retention device with different rotational speeds of disc blade (异速圆盘动态支撑式玉米秸秆粉碎装置设计与试验). *Transactions of the Chinese Society for Agricultural Machinery*, Vol. 52, No. 10, ISSN 1000-1298, pp. 41-50, China.

- [9] Liu, P., Zhang, Z., He, J., Li, H., & Wang, Q., (2019). Kinematic analysis and experiment of corn straw spreading process. *INMATEH - Agricultural Engineering*, Vol. 58, No. 2, ISSN 2068-4215, pp. 83-92, Romania.
- [10] Mello, R., Harris, H., (2000). Cane damage and mass losses for conventional and serrated bale cutter blades. *Conference of the Australian Society of Sugar Cane Technologists*, No. 22, pp. 84-91, Australian.
- [11] Miranda, M., García-Mateos, R., Arranz, J., Sepúlveda, F., Romero, P., & Botet-Jiménez, A., (2021). Selective use of corn crop residues: energy viability. *Applied Sciences*, Vol. 11, No. 7, ISSN 1454-5101, pp. 3284, Romania.
- [12] NY/T 500-2015, Operating quality for straw-smashing machines (秸秆粉碎还田机 作业质量). China.
- [13] Qiao, H., (2019). Problems and countermeasures of returning corn straw to the field (玉米秸秆还田存在的问题及对策). *Xiandai Nongye Keji*, No. 14, ISSN 1007-5739, pp. 174+183, China.
- [14] Ramm, S., Voßhenrich, HH., Hasler, M., Reckleben, Y., & Hartung, E., (2024). Comparative analysis of mechanical in-field corn residue shredding methods: evaluating particle size distribution and rating of structural integrity of corn stalk segments. *Agriculture - Basel*, Vol. 14, No. 2, ISSN 2077-0472, pp. 263, Switzerland.
- [15] Song, J., Li, H., Zhang, H., Liu, X., Sun, W., Chen, Y., Wang, S., & Yuan, Y., (2024). Simulation optimization and experiment of parameters for maize straw chopping and returning machine (玉米秸秆切碎还田机参数仿真优化与试验). *Forestry Machinery & Woodworking Equipment*, Vol. 52, No. 2, ISSN 2095-2953, pp. 37-42, China.
- [16] Sun, N., Wang, X., Li, H., He, J., Wang, Q., Wang, J., Liu, Z., & Wang, Y., (2019). Design and experiment of differential sawing rice straw chopper for turning to field (差速锯切式水稻秸秆粉碎还田机设计与试验田). *Transactions of the Chinese Society for Agricultural Machinery*, Vol. 35, No. 22, ISSN 1000-1298, pp. 267-276, China.
- [17] Wang, B., Chi, S., Tian, S., Ning, Y., Chen, G., Zhao, H., & Li, Z., (2013). CH₄ uptake and its affecting factors in winter wheat field under different stubble height of straw returning (不同留茬高度秸秆还田冬小麦田甲烷吸收及影响因素). *Transactions of the Chinese Society of Agricultural Engineering*, Vol. 29, No. 5, ISSN 1002-6819, pp. 170-178, China.
- [18] Wang, L., Zhang, Z., Liu, T., Wang, Y., Jia, F., & Jiang, J., (2020). Design and experiment of device for chopping stalk of header of maize harvester (玉米收获机割台砍劈式茎秆粉碎装置设计与试验). *Transactions of the Chinese Society for Agricultural Machinery*, Vol. 51, No. 7, pp. 109-117, China.
- [19] Yeboah, S., Lamptey, S., Zhang, R., Li, L., (2017). Conservation tillage practices optimizes root distribution and straw yield of spring wheat and field pea in dry areas. *Journal of Agricultural Science*, Vol. 9, No. 6, ISSN 0021-8596, pp. 37-48, England.
- [20] Yu, Y., Zhang, J., Geng, A., Zhang, Z., Yang, Q., & Zhang, J., (2019). Design and test of roller strip chopping device (对辊式秸秆切碎装置的设计与试验). *Journal of Agricultural Mechanization Research*, Vol. 41, No. 3, ISSN 1003-188X, pp. 93-98, China.
- [21] Zhang, J., Yu, Y., Yang, Q., Zhang, J., Zhang, Z., & Geng, A., (2018). Design and experiment of smashed straw unit for high stubble maize double header (高留茬玉米秸秆复式割台粉碎还田装置设计与试验). *Transactions of the Chinese Society for Agricultural Machinery*, Vol. 49, No. S1, ISSN 1000-1298, pp. 42-49, China.
- [22] Zhang, Z., Yu, Y., Yang, Q., Geng, A., & Zhang, J., (2021). Development and evaluation of finger wheel and cutting disc combined device for stalk returning. *INMATEH - Agricultural Engineering*, Vol. 64, No. 2, ISSN 2068-4215, pp. 54-64, Romania.
- [23] Zhao, Z., Wang, Z., Zhao, B., Song, Y., & Xin, M., (2022). Design and research of a cutting blade for corn stalks based on a bionic principle. *INMATEH - Agricultural Engineering*, Vol. 68, No. 3, ISSN 2068-4215, pp. 711-721, Romania.
- [24] Zhao, J., Wang, X., Zhang, J., Liu, H., Wang, Y., & Yu, Y., (2021). Coupled bionic design based on primnoa mouthpart to improve the performance of a straw returning machine. *Agriculture - Basel*, Vol. 11, No. 8, ISSN 2077-0472, pp. 775, Switzerland.
- [25] Zhu, J., (2019). Analysis of the advantages and disadvantages of corn straw returning technology (浅析玉米秸秆还田技术的利弊). *Problem Discussion*, Vol. 37, No. 15, ISSN 1005-2690, pp. 145+147, China.

BLOCKCHAIN TECHNOLOGY FOR ENHANCED TRACEABILITY AND SUSTAINABILITY OF PERSONAL PROTECTIVE EQUIPMENT IN ROMANIAN AGRICULTURE

TEHNOLOGIA BLOCKCHAIN PENTRU ÎMBUNĂȚIREA TRASABILITĂȚII ȘI SUSTENABILITĂȚII ECHIPAMENTELOR INDIVIDUALE DE PROTECȚIE ÎN AGRICULTURA DIN ROMÂNIA

Daniel Onuț BADEA^{*1)}, Doru Costin DARABONT¹⁾, Lucian-Ionel CIOCA²⁾, Alina TRIFU¹⁾, Vlad-Andrei BARSAN³⁾

¹⁾ National Research and Development Institute on Occupational Safety - I.N.C.D.P.M. "Alexandru Darabont",
35A Ghencea Blvd., Sector 6, 061692, Bucharest, Romania

²⁾ Industrial Engineering and Management Department, Faculty of Engineering, Lucian Blaga University of Sibiu,
10 Victoriei Blvd., 550024, Sibiu, Romania

³⁾ SC Continental SA Sibiu, Romania

Corresponding author: Daniel Onuț Badea

Tel: +403131726; E-mail: dbadea@protectiamuncii.ro

DOI: <https://doi.org/10.35633/inmateh-74-48>

Keywords: agriculture, blockchain technology, personal protective equipment, traceability

ABSTRACT

Blockchain technology provides a secure and transparent method to improve the traceability and sustainability of personal protective equipment (PPE) in Romanian agriculture. By enabling comprehensive monitoring of PPE across its lifecycle, blockchain addresses gaps in safety and compliance. It ensures adherence to safety standards while reducing risks of counterfeit or defective products. However, several challenges hinder adoption. High costs, limited digital infrastructure, and low digital literacy among farmers create significant barriers. Overcoming these requires targeted investments in rural digital infrastructure and training programs designed to enhance stakeholders' skills. Public-private partnerships and pilot projects are essential to demonstrate the technology's benefits and build trust among users. Gradual implementation, supported by collaboration between public and private sectors, can transform Romanian agriculture. Blockchain's integration can lead to better productivity, improved safety, and greater sustainability. This study examines blockchain's potential in PPE management, offering insights into its applications, benefits, and necessary steps for successful adoption in the agricultural sector. Through strategic action, Romanian agriculture can leverage blockchain to achieve safer practices and long-term sustainability.

REZUMAT

Tehnologia blockchain oferă o metodă sigură și transparentă pentru a îmbunătăți trasabilitatea și sustenabilitatea echipamentelor individuale de protecție (EIP) în agricultura din România. Prin monitorizarea cuprinzătoare a EIP pe parcursul ciclului său de viață, blockchain abordează lacunele privind siguranța și conformitatea. Aceasta asigură respectarea standardelor de siguranță, reducând în același timp riscurile de produse contrafăcute sau defecte. Cu toate acestea, mai multe provocări împiedică adoptarea tehnologiei. Costurile ridicate, infrastructura digitală limitată și alfabetizarea digitală scăzută în rândul fermierilor creează bariere semnificative. Depășirea acestora necesită investiții direcționate în infrastructura digitală rurală și programe de formare concepute pentru a îmbunătăți competențele părților interesate. Parteneriatele public-privat și proiectele pilot sunt esențiale pentru a demonstra beneficiile tehnologiei și pentru a construi încrederea utilizatorilor. Implementarea treptată, susținută de colaborarea între sectorul public și cel privat, poate transforma agricultura din România. Integrarea blockchain poate duce la o productivitate mai bună, siguranță îmbunătățită și sustenabilitate sporită. Acest studiu analizează potențialul blockchain în managementul EIP, oferind perspective asupra aplicațiilor, beneficiilor și pașilor necesari pentru o adoptare reușită în sectorul agricol. Prin acțiuni strategice, agricultura românească poate valorifica blockchain pentru a obține practici mai sigure și sustenabilitate pe termen lung.

INTRODUCTION

This research explores blockchain's potential to improve traceability and sustainability for personal protective equipment in Romania's agricultural sector. Blockchain, a secure, decentralized ledger for recording and verifying transactions, offers transparency and environmental benefits. In the context of PPE, it can help ensure compliance with safety standards and improve inventory tracking. Yet, adoption faces challenges: high costs, limited infrastructure, and a lack of expertise (*Sendros et al. 2022, Cuellar and Johnson, 2022*).

The study reviews relevant literature to outline the background and trends in blockchain applications within agriculture. Expert consultations provide additional insights from professionals in blockchain and agriculture, while hypothetical scenarios suggest possible uses of blockchain for tracking personal protective equipment (PPE). The findings emphasize a balanced approach involving both public and private sector support. Key recommendations include targeted investments in infrastructure, education, and pilot projects to address barriers and promote broader adoption. Overall, blockchain has the potential to drive a more efficient and sustainable agricultural sector in Romania.

Moreover, consumer perceptions significantly impact purchasing behavior, especially in food safety. Research indicates that when consumers better understand product diagnostics, a key cognitive factor, they make more informed choices (*Buaprommee and Polyorat, 2016*). This perception of safety is influenced by product details and by emotional and cognitive elements. Improving transparency and delivering accurate information helps reduce information asymmetry, fostering consumer confidence and promoting sustainable purchasing.

One of the key advantages of blockchain technology is its ability to create transparency which is made possible through a secure immutable ledger that tracks and validates every single transaction so that there is complete traceability in the supply chain itself. It allows agricultural products to demonstrate adherence to international standards in food safety and environmental protection thereby enabling them to establish consumer trust (*Guna et al., 2023*). Furthermore, apart from being the basis to apply this technology, resource management and information systems also fall under the category of agriculture since blockchain can provide "data transparency" and "transaction traceability" alongside accurate tracking of the products in the entire supply chain leading to unprecedented improvements on product quality and safety (*Westerlund et al., 2021*).

Blockchain technology offers more than just food traceability. It also improves the management of PPE for farmers and agricultural workers. Items such as gloves, masks, eyewear, and protective suits are essential for protecting these workers from exposure to chemicals, dust, noise, and other agricultural risks for safety and health. Through blockchain, PPE can be tracked effectively, ensuring that only quality-assured equipment is available and accessible (*Borah et al., 2020*). This streamlined monitoring supports better inventory control, cuts down on waste, and encourages sustainable farming practices (*Lin et al., 2020*).

Blockchain technology use in Romanian agriculture for PPE traceability is in its early stages. High startup costs and inadequate infrastructure in rural areas create adoption challenges. Many farmers lack the skills and resources to work with blockchain, pointing to a need for targeted training. An unclear legal framework also adds uncertainty, discouraging investment and slowing innovation. For success, collaboration among farmers, distributors, regulators, and other stakeholders is essential, with well-planned efforts to address these barriers.

This study examines blockchain's role in enhancing PPE traceability and sustainability in Romanian agriculture. It reviews key literature, gathers insights from local experts, and outlines example pathways for potential implementation. The research addresses critical questions: How can blockchain strengthen PPE traceability and transparency? What advantages might it offer to farmers, equipment manufacturers, and distributors? What challenges could arise in adopting blockchain for PPE management within Romanian agriculture? Through this approach, the study sheds light on the possibilities and obstacles that blockchain technology presents for advancing PPE management.

MATERIALS AND METHODS

In this study, a mixed-methods approach, including a literature review, expert discussions, and the development of hypothetical scenarios, is employed to examine the potential of blockchain technology for enhancing PPE traceability and sustainability in Romania's agricultural sector. This multi-faceted approach aims to uncover blockchain's potential for managing PPE in agriculture, along with the benefits it may offer and the unique challenges associated with its adoption in Romania.

The methodology begins with a comprehensive literature review, drawing from diverse scientific studies, guidance documents, and technical reports published by international organizations and respected

global research institutions, such as the Food and Agriculture Organization (FAO, 2024) and the European Agency for Safety and Health at Work (EU-OSHA, 2024). This review explores the use of blockchain in agriculture and related sectors for PPE and other essential safety commodities, presenting examples from countries such as the USA, Australia, and the Netherlands. These cases illustrate blockchain's applications in tracing PPE throughout supply chains, thereby helping to ensure compliance with quality standards and reduce counterfeiting risks.

The literature review analyzes best practices and challenges in applying blockchain to improve the traceability and sustainability of PPE in agriculture across different international contexts. For example, in the United States, blockchain technology is used to monitor PPE for agricultural workers, ensuring compliance to federal regulations and supporting worker health (Wang et al., 2022). In Australia, it manages the lifecycle of equipment, from production to disposal, promoting recycling and reducing waste (Zhang and Fröhling, 2024). Meanwhile, the Netherlands uses blockchain to foster collaboration between manufacturers, distributors, and regulatory bodies, providing full traceability and building trust among stakeholders (Louis Dreyfus Company, 2018). Together, these examples offer practical insights for implementing blockchain in Romanian agriculture, emphasizing the importance of traceability and sustainability in PPE management.

Blockchain technology offers specific benefits for Romanian agriculture, especially in the areas of PPE traceability and sustainability. To support this theoretical analysis, the methodology also involved informal discussions with local experts in agriculture and blockchain. In a relaxed setting, these discussions gathered qualitative insights on participants' perceptions, knowledge, and experiences with blockchain in agriculture. Participants, including farmers, cooperative representatives, sustainability consultants, and researchers, focused on blockchain's advantages in PPE management, the challenges in implementation, and the technological readiness of stakeholders. Conversations with local experts in agriculture and blockchain confirmed much of the literature findings and also helped clear up the ambiguity surrounding the Romanian context for applying blockchain in agriculture. Farmers (n=10), agricultural cooperative representatives (n=2), sustainability consultants (n=13), and researchers (n=5) were further consulted in 30 discussions to establish the challenges and practices described here. There is agreement that the application of blockchain to enhance the traceability and control of PPE in Romanian agriculture is valid, but the possibility for large-scale implementation in practice is debated. These discussions revealed practical insights into local needs, identifying both benefits and obstacles in adopting blockchain.

Further exploring blockchain's role, the methodology examines its implementation in PPE management for Romanian agriculture through three hypothetical scenarios: optimistic, moderate, and pessimistic. Based on the literature review and expert discussions, these scenarios capture different levels of public and private sector involvement. Each scenario presents unique implications for blockchain adoption, offering insights into the necessary conditions, as well as potential risks and opportunities.

To support the decision-making process, a flowchart (see Figure 4) was developed. This flowchart maps out key steps and decision points for each scenario, serving as a tool to structure expert discussions and clarify available options and challenges at each stage. By examining different implementation scenarios, the flowchart highlights critical factors for the successful adoption of blockchain in agriculture.

This approach combines theoretical analysis with practical insights and hypothetical scenarios, providing a comprehensive view of innovation in PPE management. The findings lead to recommendations for how blockchain can help create a safer, more efficient, and sustainable agricultural environment in Romania.

RESULTS

The literature highlights blockchain's potential to transform agriculture, particularly in PPE management, by enabling product tracking across the entire lifecycle, from production and distribution to use and recycling. Blockchain's decentralized, secure, and immutable characteristics provide a transparent and reliable means to monitor supply chains, ensuring adherence to safety and quality standards, which is crucial for PPE that protects agricultural workers' health.

By enhancing traceability and transparency, blockchain supports better compliance with PPE standards in agriculture (Panwar, 2023). Blockchain allows farms to effectively monitor PPE supply and usage, thereby improving worker safety and adherence to protection standards. For instance, smart contracts can trigger notifications if essential equipment is not used correctly, increasing safety without the need for physical inspections. However, high implementation costs and data privacy issues present major challenges, especially for smaller farms with limited access to digital skills and infrastructure.

While the benefits are clear, adopting blockchain in Romania faces significant hurdles. The high costs of implementation make it challenging, especially for small and medium-sized farms with limited budgets. Moreover, rural digital infrastructure is often inadequate for blockchain's requirements, such as high-speed internet and advanced data storage. There is also substantial resistance to change; many farmers rely on traditional practices and may be hesitant to adopt new technologies without clear evidence of benefits. Additionally, low digital literacy and limited access to training restrict farmers' ability to understand and use blockchain effectively. These issues underscore the need for financial, infrastructural, and educational support to facilitate blockchain's integration into Romanian agriculture. Romania also lacks the legislation needed to support or regulate blockchain use in agriculture, leaving many potential adopters uncertain and hesitant to invest. While there have been a few local efforts, such as a project in Timiș County exploring blockchain for tracking agricultural products, these initiatives remain isolated and experimental. In southern counties where agriculture is widespread, there's no sign of major projects using blockchain for PPE management. Despite growing interest, the lack of regulatory backing and funding is a key obstacle to broader adoption (EBSI4RO, 2022).

Internationally, groups such as the UN's Food and Agriculture Organization (FAO) highlight blockchain's promise for increasing transparency, traceability, and efficiency in agricultural supply chains. However, FAO also points out that significant challenges, such as technology gaps, weak digital infrastructure, and limited political and financial support, continue to restrict its use (Sylvester, 2019). These issues closely mirror those in Romania, where high costs, limited digital infrastructure, and hesitation from farmers make it tough to apply blockchain widely in agriculture.

Despite its potential to enhance traceability and sustainability in agriculture, particularly in managing PPE, several key issues must be addressed to assess blockchain's feasibility and impact. These include significant financial investment, enhancements to digital infrastructure, raising digital literacy among farmers, and developing a supportive legal framework. Without tackling these challenges, blockchain adoption in Romanian agriculture may remain limited, restricting the sector's ability to leverage the full benefits of this technology. This analysis highlights a mix of benefits, challenges, and potential associated with blockchain's role in Romanian agriculture. Supported by literature, the research shows blockchain's potential to increase transparency, efficiency, and safety in agricultural practices, especially in PPE management. Nonetheless, significant obstacles remain, which could limit the technology's broader adoption across Romania.

However, the literature point to significant obstacles. One primary issue is the high cost of implementation. Blockchain systems require substantial investments in hardware, software, and ongoing maintenance, costs that are often prohibitive for small and medium-sized farms with limited budgets. Furthermore, in many rural areas of Romania, the technological infrastructure is lacking. Limited access to high-speed internet and advanced data storage capabilities increases the complexity and cost of blockchain implementation, posing a substantial challenge to its effective deployment across the agricultural sector.

Another significant barrier to blockchain adoption is the lack of education and training. Many farmers in Romania rely on traditional methods and may hesitate to adopt new digital tools without a clear understanding of their benefits. This reluctance is reinforced by limited digital literacy and inadequate access to training resources, which could otherwise help farmers understand and apply blockchain technology. Additionally, the absence of a clear legislative framework creates further complications, adding uncertainty and discouraging investment. The literature underscores the need for regulatory guidelines to support blockchain, while local experts point out that current policies fall short in addressing these challenges.

Public-private partnerships also represent a key opportunity to promote blockchain technology. Such collaborations could leverage the resources and expertise of both sectors to tackle the financial and technical challenges of blockchain adoption. Experts suggest that these partnerships could create a supportive ecosystem by offering funding, infrastructure, and training programs designed for Romanian farmers. Additionally, legislative support at both national and local levels could play a crucial role in fostering blockchain investment. Clear regulatory frameworks and political backing are highlighted in the literature as essential steps for overcoming initial barriers and achieving sustainable integration of blockchain into agricultural practices.

Despite these challenges, the literature reveals opportunities to encourage blockchain adoption in Romanian agriculture. One promising approach is to launch pilot projects that showcase the technology's benefits. Pilot projects could build trust among stakeholders by demonstrating blockchain's effectiveness in a controlled setting. These projects would allow stakeholders to observe blockchain's impact on agricultural practices, identify potential barriers, and refine the implementation process before considering broader adoption. Figure 1 highlights both significant advantages and notable obstacles in implementing blockchain technology for agriculture, particularly in enhancing PPE traceability, data security, and supply chain integrity.

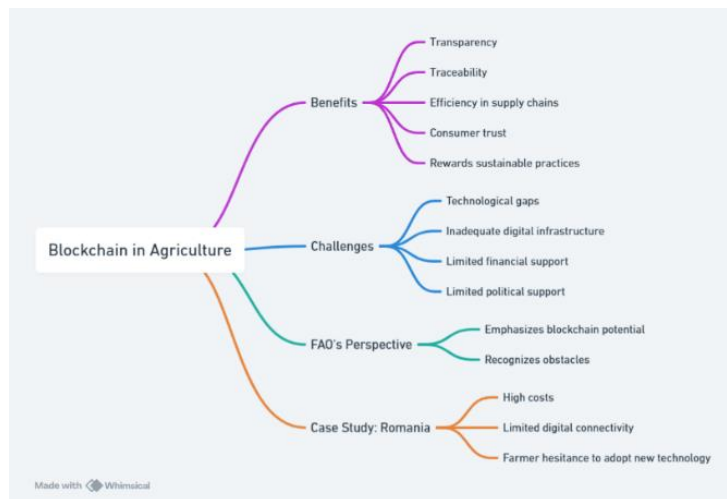


Fig. 1 - Insights from literature on blockchain benefits and challenges in agricultural PPE implementation

This visualization shows a balance of consensus on advantages and obstacles in blockchain implementation for agriculture. There is strong agreement on blockchain's benefits for trust and traceability, while there's equally high consensus on cost and infrastructure as significant challenges.

Approximately 70% of experts surveyed by this research team agree that there is very high potential for blockchain to improve the traceability and transparency of PPE in agriculture. As one expert stated, the transparency, accuracy, and trust levels with blockchain are much higher than traditional agriculture data systems. This demonstrates a perception that blockchain could help keep a supply chain honest, ensure compliance with safety standards, and address issues with defective or counterfeit PPE. Experts noted that blockchain provides a means to create secure, tamper-proof transaction logs across the supply chain to ensure quality and safety standards are maintained, playing a critical role in PPE management. Additionally, 65% of respondents think that trust in agricultural machinery will rise through the use of blockchain, which indicates that, in summary, the general view of blockchain is favorable when it comes to providing truthful and secure information. This confidence in trust factors could allow the agricultural industry, at a larger scale, to accept and adopt new technologies.

Additionally, 65% think the technology would boost trust in agricultural equipment due to its data security and authenticity. Another 60% emphasize that blockchain could facilitate real-time monitoring of PPE, which is important to prevent defective or counterfeit products and make agricultural operations safer. They claim that the ability to receive immediate access to reliable status updates on PPE information, as well as real-time data about equipment quality, could transform how PPE is managed, ensuring that only compliant and safe equipment is used. This is particularly relevant for Romanian agriculture, where the integrity and quality of PPE are directly related to safety within the work environment and the efficiency of processes.

However, expert discussions also revealed important barriers to the implementation of blockchain technology in Romanian agriculture (Figure 2). More than half (55%) of respondents cited high implementation costs and the lack of technological infrastructure in rural areas as the top barriers to blockchain usage. This highlights an obvious area for improvement, as many rural regions in Romania do not have the high-speed internet and cutting-edge digital infrastructure required to develop blockchain applications, which demands significant investment. Additionally, 50% of the respondents identified a lack of education and training to be a major obstacle. This indicates that farmers and other stakeholders may remain on the sidelines when it comes to utilizing and deploying a new technology such as blockchain without more clarity on what it does and how it can be applied. Moreover, since most farmers rely on traditional practices, it is difficult to implement blockchain in Romanian agriculture because they might be reluctant to adopt the new skills needed or to invest in the digital tools required for blockchain. Furthermore, due to the limited number of technical personnel available to train them, exploring blockchain remains challenging. The data suggests a need for targeted education programs so that stakeholders can acquire essential knowledge about blockchain technology, reducing hesitancy and fostering an environment that supports the adoption of new technologies.

On an optimistic perspective, there is an opportunity to advocate for blockchain adoption. Three-quarters of experts (75%) endorsed the launch of pilot projects to showcase the advantages of blockchain technology in practice. This strong endorsement reflects a readiness among experts to innovate with new technologies, try them out in controlled environments, and assess blockchain's benefits while addressing any

practical challenges. Pilot projects are considered essential for scaling up: they are seen as demonstrations of blockchain's benefits, such as enhanced traceability and transparency, turning hypothetical obstacles into real-world experiences. Such projects would foster confidence among farmers and other stakeholders by proving blockchain's practicality, potentially leading to quicker acceptance and wider adoption.

The answers related to opinions on blockchain technology in Romanian agriculture are quite balanced (see Figure 2). Interest in leveraging blockchain is significant, but some key impediments continue to challenge executives. The advantages, such as enhanced traceability, increased transparency, and greater trust in the agricultural supply chain, are evident, yet financial and educational barriers associated with the technology remain substantial, experts say. There are no easy answers to whether or not to adopt blockchain in Romanian agriculture, judging by the mixed responses of those polled. People are excited about innovation; there is so much innovation that can help to address some of our world's biggest challenges, but we are still missing practical strategies to implement it and make it current and relevant to people's everyday life.

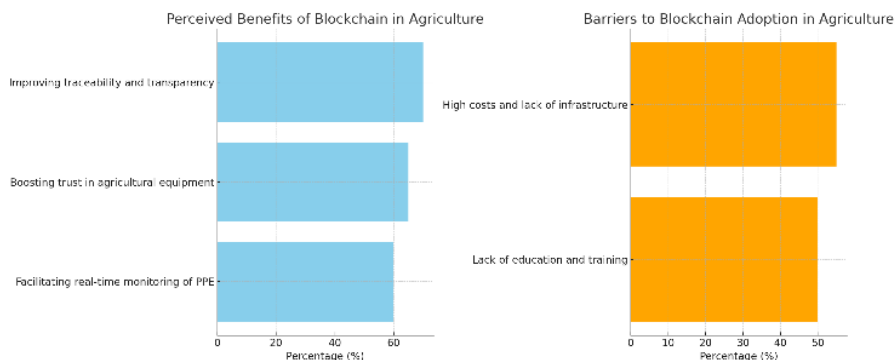


Fig. 2 - Expert perceptions on the benefits of blockchain in agriculture and the barriers to its adoption

Blockchain holds significant promise for strengthening PPE management in agriculture, offering improvements in both efficiency and sustainability. However, several considerations must be addressed to assess its practicality. Implementing this technology requires substantial investment, as well as enhancements in digital infrastructure. Additionally, increasing digital literacy among farmers and establishing a clear legislative framework should be prioritized. Without tackling these challenges, blockchain adoption in Romanian agriculture will likely remain limited, preventing the sector from fully realizing the technology's potential.

The analysis of blockchain's role in Romanian agriculture highlights benefits, challenges, and opportunities. Findings and expert insights suggest that blockchain can improve transparency, efficiency, and safety in agricultural practices, especially in PPE management. However, significant barriers could limit widespread adoption. Literature and expert input both emphasize blockchain's practical advantages, particularly for PPE traceability. Its secure, unchangeable nature enables tracking PPE across its lifecycle, from production to recycling, reducing risks of counterfeit or faulty equipment and helping to maintain safety standards. International examples from the Netherlands, the USA, and Australia show blockchain's effectiveness in PPE monitoring, enhancing transparency, consumer trust, and quality compliance, such as in PPE management on Dutch organic farms.

Achieving a balance is essential to fully unlock blockchain's potential in agriculture. This requires focused investment in infrastructure, education, and pilot projects. As shown in Figure 2, an integrated approach, guided by expert recommendations, could foster blockchain adoption in Romania. Addressing both the benefits and barriers allows Romania to leverage blockchain's capabilities in agriculture effectively. Figure 3 offers a comparison of the benefits and challenges, synthesizing scientific research and expert insights to identify factors that could either drive or hinder adoption. While the literature emphasizes the need for legislative support and political commitment, experts advocate for pilot projects and public-private partnerships as practical ways to demonstrate blockchain's value. By tackling issues such as high costs, limited infrastructure, and inadequate incentives, they propose solutions tailored to the unique needs of Romania's agricultural sector.

This research explores three possible paths for blockchain in Romanian agriculture. In an optimistic scenario, strong public-private collaboration drives adoption. In a moderate scenario, the private sector leads with limited government support. In a pessimistic scenario, blockchain adoption relies entirely on private investment, without public involvement. These scenarios create a clear framework for understanding potential directions and challenges for using blockchain, especially in PPE management.

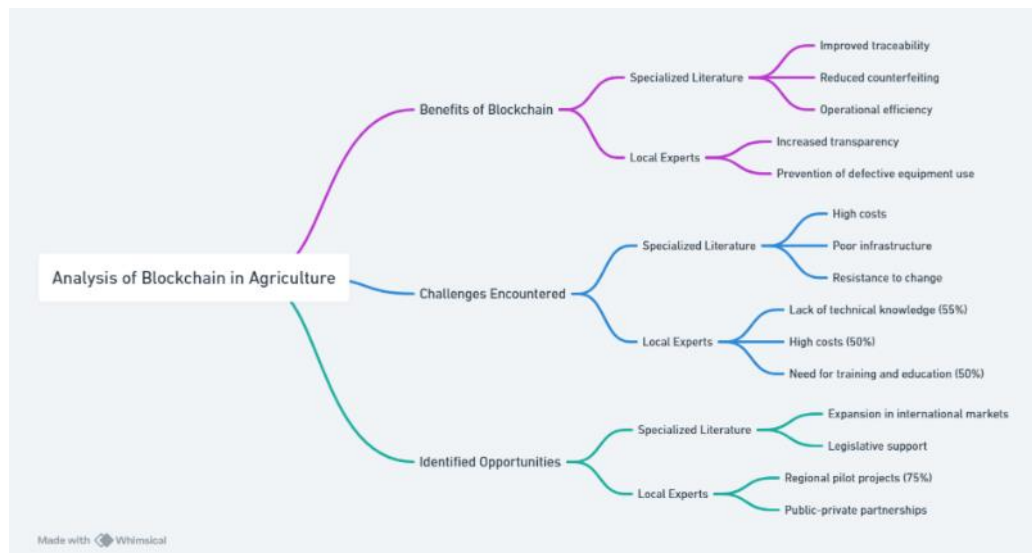


Fig. 3 - Comparison of the benefits and challenges of blockchain in Romanian agriculture

In the optimistic scenario, blockchain adoption moves advances through a strong partnership between the public and private sectors, making implementation faster and efficient. The government actively supports this process with financial support, grants, subsidies, and tax breaks, helping to reduce costs for farmers and PPE producers and promoting early adoption. This collaboration also establishes a national blockchain platform, co-managed with tech companies contributing expertise and innovation. The platform is designed to enable efficient, real-time monitoring of PPE across the supply chain by using blockchain's secure, decentralized ledger. The initial rollout includes pilot projects in regions with solid agricultural infrastructure, such as areas with established digital networks and cooperative farms. These projects serve as testing grounds to showcase the platform's ability to improve traceability and enhance operational efficiency. Within approximately two years, the blockchain platform could become operational at the national level, offering clear advantages such as enhanced transparency and traceability in PPE, which would ultimately improve safety standards and foster greater trust among farmers and consumers. This forms a self-reinforcing cycle, where initial success attracts further investment and broader adoption across the sector. Alignment between the private sector and favorable public policies, such as streamlining policies, reduced bureaucracy, and establishing lasting incentives, supports sustained growth and blockchain adoption. This creates a positive feedback loop, with the public and private sectors progressing from initial effort to steady collaboration, proving resilient and scalable in response to evolving market demands.

In the moderate scenario, blockchain implementation is led by private sector initiatives, with limited but strategic public sector support. Technology companies specializing in blockchain, PPE manufacturers, and large agricultural cooperatives collaborate to develop an independent blockchain platform suited to the unique needs and challenges of Romanian agriculture. While the public sector provides less financial backing, it plays a key supporting role by promoting partnerships, encouraging collaboration among major stakeholders, and reducing administrative and regulatory obstacles that could hinder adoption. This scenario allows for a phased and controlled approach to implementation. Initial efforts focus on high-value crops or regions with strong private sector interest, giving stakeholders a chance to test blockchain technology across different agricultural settings. These trials help identify practical challenges, such as technical issues, user acceptance, and integration with existing systems, while strategies are gradually adjusted based on real-world feedback. Although this approach moves slower than the optimistic scenario, it still delivers moderate gains in PPE traceability, transparency, and operational efficiency over time. The private sector gains from flexibility to innovate and adapt, while the public sector's limited but focused involvement provides a necessary regulatory framework and support for scaling successful models. There are risks associated with the moderate scenario. In the absence of public funding or a proper policy framework, widespread adoption might not be feasible, particularly in developing areas, or for smaller farmers who might lack the means to invest in innovative technologies. Implementation may take longer or be less rewarding since private actors will tend to pursue only those projects based on their economic and strategic profitability. In this scenario, there is a need for trust between and collaboration among private stakeholders, with the public sector focusing on creating an enabling environment for innovation and adoption of technology.

In the pessimistic scenario, blockchain adoption depends only on private investment, without any support from the public sector. This means start-ups, tech companies, and agricultural cooperatives bear on all the financial risk. They face tough challenges such as high costs, limited digital infrastructure, and the absence of legislation that might encourage new technology in agriculture. Without public grants, subsidies, or tax breaks to help with initial expenses, small and mid-sized businesses or individual farmers may find it hard to join in. Many farmers, accustomed to traditional practices, could be hesitant to adopt a complex technology like blockchain. This hesitation is made worse by the lack of training or educational programs that might help them understand blockchain's practical uses and benefits. As a result, blockchain use stays limited, seen only in a few pilot projects or small-scale initiatives. Overall, its impact on PPE management, traceability, and efficiency in agriculture remains minor, and the broader potential of blockchain technology goes mostly untapped. In this scenario, without support from the public sector, it's unlikely that blockchain adoption will expand widely. The agricultural sector risks missing out on digital advances that could improve efficiency and results. Without a clear regulatory framework, private companies also face legal uncertainties, which may discourage investment and limit the testing of blockchain.

A comparison of these three scenarios shows that a balanced approach, where public and private sectors share risks and responsibilities, offers the best path for adopting blockchain in agriculture. Public investments play a key role in building digital infrastructure, establishing clear regulations, and making technology accessible to farmers. Private investments add innovation, agility, and quick responses to market needs, supporting adaptation and scalability.

Successful implementation of blockchain requires collaboration among the public sector, private companies, technology providers, and the farming community. This collaborative model could improve operational efficiency, boost traceability, and enhance the safety of protective equipment in agriculture. It would also address barriers like high costs, limited infrastructure, and resistance to new technology by pooling resources and coordinating efforts.

These scenarios show different pathways for implementing blockchain in Romanian agriculture and underscore the need for a supportive environment with public investment in education, training, and infrastructure. The findings indicate that while blockchain has strong potential to improve PPE management in agriculture, its success will depend on coordinated efforts from both the public and private sectors. This collaborative effort may include additional investments in training programs to boost digital literacy among farmers, reduce resistance to new technologies, and establish a legislative framework that encourages innovation and supports blockchain adoption. The future of blockchain in Romanian agriculture depends on the commitment partnership of both public and private stakeholders willing to invest and collaborate to overcome existing challenges. A combined approach, drawing on the strengths of each sector, is essential for realizing blockchain's potential and building a more efficient, transparent, and sustainable agricultural system.

Figure 4 maps out the decision-making process, highlighting on the key steps and points essential for implementation across the different scenarios. The success of blockchain adoption depends on several factors: the readiness of digital infrastructure, available financial resources, stakeholder commitment, and a supportive regulatory framework. A balanced strategy, combining public support with private innovation, can create a sustainable model for blockchain adoption, improving traceability, efficiency, and safety in PPE management in agriculture.

The flowchart for implementing blockchain in Romania's agricultural sector begins by identifying needs for better traceability and sustainability in PPE management. Initially, it reviews specific areas where blockchain could improve processes, from production to recycling. Following this, an evaluation of costs and infrastructure is conducted, considering available funding, existing technology, and the readiness of farmers and stakeholders to adopt this approach. If resources are determined to be adequate, the plan advances to execution with support from public institutions and private companies. In the absence of sufficient resources, the diagram suggests seeking supplementary funding sources, such as grants or subsidies.

A key decision point assesses whether costs and infrastructure meet project needs. If these conditions are met, the process advances to a pilot phase to test blockchain in a controlled setting. This stage allows for adjustments to technology and strategy, based on outcomes across different regions. Positive results from the pilot phase lead to a recommendation for nationwide implementation, potentially positioning Romania as a leader in agricultural technology. If results don't meet expectations, the strategy may require adjustments, which could include technology improvements, new partnerships, or additional funding, with two final options: broader adoption if successful, or a revised approach if necessary.

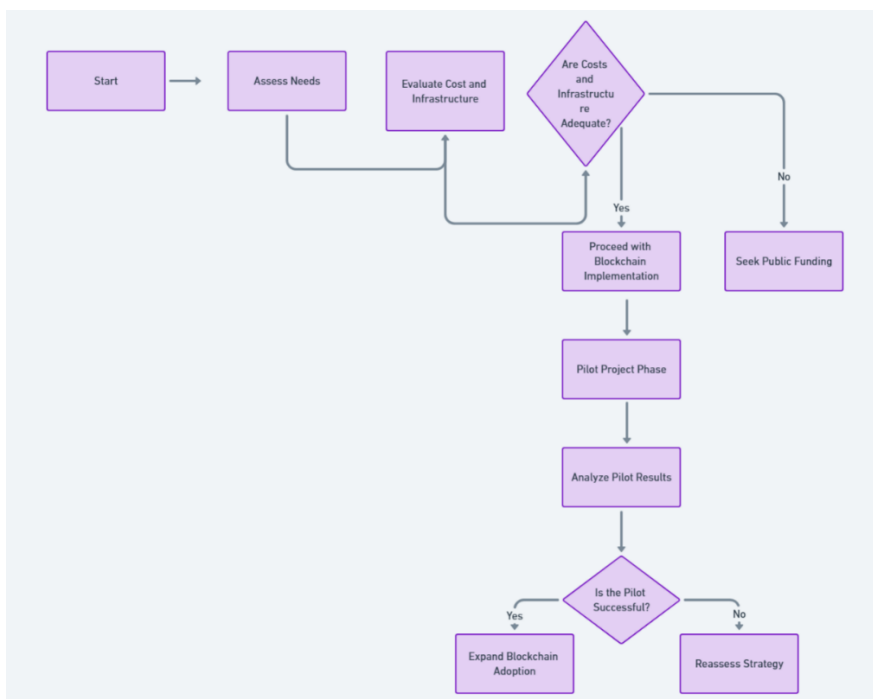


Fig. 4 - Flowchart for decision-making in implementing blockchain for agriculture PPE management

The flowchart presents a systematic method for integrating blockchain technology into the agricultural sector, emphasizing the necessity of collaboration between public and private entities to overcome challenges and amplify benefits. It provides guidance for decision-makers and stakeholders to identify essential actions and decisions necessary for effective and sustainable blockchain adoption. Both the expert opinion chart (Figure 2) and the flowchart (Figure 4) indicate that successful blockchain implementation relies on a combination of resources, government support, and local stakeholder engagement. The proposed scenarios offer a foundation for creating strategies tailored to the specific needs of Romanian agriculture.

Recent research underscore blockchain's transformative potential in agricultural supply chains, while also pointing out the challenges of its implementation. A report from the *Food and Agriculture Organization (FAO)* suggests that blockchain could significantly boost transparency, traceability, and operational efficiency, improve market access for smallholder farmers, reduce intermediary involvement, and promote fair pricing. However, the report also notes several barriers, including unclear regulations, the absence of universal standards, and insufficient infrastructure in rural areas (FAO, 2024). Additionally, another research suggests that integrating blockchain with Internet of Things (IoT) devices could improve the agricultural data management, but it also raises concerns about the high costs of implementation, legal uncertainties related to smart contracts, and connectivity limitations (AGDAILY, 2024). A systematic review of blockchain in the agri-food supply chain indicates that, whereas the technology can improve food safety, its adoption is limited by the need for significant investments, technical skills, and supportive policies (Management Review Quarterly, 2024). This aligns with the observations of Walaszczyk et al. (2022), who note that evolving consumer expectations are likely to boost demand for better food traceability and secure, tamper-proof systems. A robust traceability process provides consumers with comprehensive "farm to fork" information, enhancing food safety oversight and underscoring the importance of such innovations within the agri-food sector.

This study encounters several limitations. Information derived from discussions with regional experts and literature reviews may introduce bias, as expert opinions are often shaped by personal experiences, which could limit the broader applicability of the results. Since the research is focused on agriculture in Romania, findings may not apply to regions with different technological, economic, or regulatory contexts. Additionally, the proposed implementation scenarios rely on projections and assumptions regarding costs, infrastructure, and political support, which may not fully capture actual conditions or account for variables such as economic changes, policy shifts, or rapid technological advances that could impact blockchain adoption. Additionally, the proposed implementation scenarios are based on projections and assumptions about costs, infrastructure, and political backing, which might not accurately represent actual conditions or take into account factors such as economic fluctuations, policy changes, or rapid technological advancements that could influence the adoption of blockchain technology.

Future research should involve empirical studies that collect quantitative and qualitative data from a diverse range of stakeholders, farmers, distributors, and regulatory bodies, to better understand blockchain's potential in agriculture. Comparative case studies across different regions could highlight effective practices and successful strategies. Additionally, research should assess the economic impact of blockchain on farmers' incomes, market transparency, and operational efficiency. Developing regulatory frameworks and supportive policies for blockchain implementation, along with exploring international collaboration for a favorable legislative environment, are essential areas for further investigation.

CONCLUSIONS

Blockchain technology can enhance the traceability and sustainability of PPE in Romanian agriculture. By enabling secure and transparent monitoring throughout the PPE lifecycle, it ensures compliance with safety standards and reduces counterfeit risks. These features contribute to safer working conditions and support sustainable agricultural practices.

The adoption of blockchain faces significant barriers, including high costs, inadequate digital infrastructure in rural areas, and low digital literacy among farmers. Strategic investments in infrastructure and customized training programs are necessary to address these challenges and enable wider adoption.

Collaborations between public institutions and private stakeholders are critical for providing funding, developing infrastructure, and offering training. Such partnerships can demonstrate blockchain's benefits, build trust among users, and create a solid foundation for large-scale implementation. Pilot projects serve as valuable testing grounds, allowing stakeholders to identify challenges, refine strategies, and showcase blockchain's value before scaling up. Clear and supportive legislation is essential to encourage investment and reduce regulatory uncertainty. A well-defined legal framework will enable seamless integration of blockchain into agricultural practices, fostering trust and confidence among stakeholders. A balanced approach, combining public and private efforts, is key to overcoming existing barriers.

By addressing these issues and leveraging partnerships, blockchain can transform Romanian agriculture into a safer, more efficient, and sustainable sector.

REFERENCES

- [1] Agdaily. (2024). *Blockchain technology in agriculture: Opportunities and barriers*. AGDAILY. <https://www.agdaily.com/smartnews/blockchain-technology-transforming-agricultural-industry/>
- [2] Borah, M.D., Naik, V.B., Patgiri, R., Bhargav, A., Phukan, B., & Basani, S.G.M. (2020). Supply chain management in agriculture using blockchain and IoT. In Kim, S., & Deka, G. (Eds.), *Advanced applications of blockchain technology* (pp. 185-198). Studies in Big Data, vol. 60. Springer, Singapore. https://doi.org/10.1007/978-981-13-8775-3_11
- [3] Buaprommee, N., & Polyorat, K. (2016). The antecedents of purchase intention of meat with traceability in Thai consumers. *Asia Pacific Management Review*, 21(3), 161–169. <https://doi.org/10.1016/j.apmr.2016.03.001>
- [4] Cuellar, D., & Johnson, Z. (2022). Barriers to implementation of blockchain technology in agricultural supply chain. Cornell University. <https://doi.org/10.48550/arxiv.2212.03302>
- [5] European Agency for Safety & Health at Work. (n.d.). Information, statistics, legislation, and risk assessment tools. <https://osha.europa.eu/en>
- [6] Food and Agriculture Organization (FAO). (2024). *Blockchain for agriculture: Opportunities and challenges*. FAO. <https://www.fao.org/3/cb9047en/cb9047en.pdf>
- [7] Guna Sekhar Sajja, K. P., Rane, K., Phasinam, T., Kassaruk, E., Okoronkwo, & Prabhu, P. (2023). Towards applicability of blockchain in agriculture sector. *Materials Today: Proceedings*, 80(3), 3705–3708. <https://doi.org/10.1016/j.matpr.2021.07.366>
- [8] Lin, W., Huang, X., Fang, H., Wang, V., Hua, Y., Wang, J., Yin, H., Yi, D., Yau, L., & Lin, W. (2020). Blockchain technology in current agricultural systems: From techniques to applications. *IEEE Access*, 8, 143920-143937. <https://doi.org/10.1109/ACCESS.2020.3014522>
- [9] Louis Dreyfus Company. (2018). Blockchain for traceability. <https://www ldc.com>
- [10] Management Review Quarterly. (2024). Systematic review of blockchain in the agri-food supply chain. <https://link.springer.com/article/10.1007/s11301-024-00205-1>
- [11] Panwar, A., Khari, M., Misra, S., & Sugandh, U. (2023). Blockchain in agriculture to ensure trust, effectiveness, and traceability from farm fields to groceries. *Future Internet*, 15, 404. <https://doi.org/10.3390/fi15120404>

- [12] EBSI4RO. (2022). *Romanian Blockchain Ecosystem*. <https://ebsi4ro.ro/ro/romanian-blockchain-ecosystem/>
- [13] Sendros, A., Drosatos, G., Efraimidis, P.S., & Tsirliganis, N.C. (2022). Blockchain applications in agriculture: A scoping review. *Applied Sciences*, 12(16), 8061. <https://doi.org/10.3390/app12168061>
- [14] Sylvester, G. (2019). *E-agriculture in action: Blockchain for agriculture, opportunities and challenges*. FAO. ISBN 978-92-5-131227-8. <https://openknowledge.fao.org/handle/20.500.14283/ca2906en>
- [15] Walaszczyk, A., Koszewska, M., & Staniec, I. (2022). Food traceability as an element of sustainable consumption: Pandemic-driven changes in consumer attitudes. *International Journal of Environmental Research and Public Health*, 19(9), 5259. <https://doi.org/10.3390/ijerph19095259>
- [16] Wang, B., Lin, Z., Wang, M., Wang, F., Xiangli, P., & Li, Z. (2022). Applying blockchain technology to ensure compliance with sustainability standards in the PPE multi-tier supply chain. *International Journal of Production Research*, 61(1), 1-17. <https://doi.org/10.1080/00207543.2022.2025944>
- [17] Westerlund, M., Nene, S., Leminen, S., & Rajahonka, M. (2021). An exploration of blockchain-based traceability in food supply chains: On the benefits of distributed digital records from farm to fork. *Technology Innovation Management Review*, 11(6), 6-18. <http://doi.org/10.22215/timreview/1446>
- [18] Zhang, L., & Fröhling, M. (2024). Integration of blockchain and life cycle assessment: A systematic literature review. *International Journal of Life Cycle Assessment*. <https://doi.org/10.1007/s11367-024-02371-1>

DISCRETE ELEMENT METHOD SIMULATION OF RICE GRAIN STACKING CHARACTERISTICS

水稻籽粒堆积特性离散元法模拟研究

Liquan TIAN, Hong LI, Xian ZHANG¹⁾, Chunxiang LIU²⁾

¹⁾ Intelligent Manufacturing College, Jinhua University of Vocational Technology/Jinhua, China

²⁾ Heilongjiang Institute of Technology, Haerbin/ China

Corresponding author: Liquan Tian; E-mail: tlqbuct@foxmail.com

DOI: <https://doi.org/10.35633/inmateh-74-49>

Keywords: rice grains, image processing, model of discrete element, angle of repose

ABSTRACT

Accurately determining the angle of repose for irregular and dispersed agricultural grain materials requires a simulation model that effectively represents the actual grain shapes and utilizes numerical methods to analyze their stacking behavior. This study focuses on "Yongyou 15" rice grains, employing 3D raster scanning technology to obtain precise contour data. Through a reverse modeling process, a detailed 3D geometric model of the grains was developed, resulting in a discrete element model comprising 618 grains of varying diameters, created using granular polymer theory. Discrete element analysis software (EDEM) was integrated with MATLAB image processing to simulate the falling and stacking process of the rice grains within a stainless steel bottomless cylindrical tube. The contour of the grain heap was analyzed using linear fitting, followed by a micro-mechanical investigation of the grain heap structure. The analysis indicated that the pressure depression within the heap is caused by the oblique transmission of contact forces. The simulated angle of repose under experimental conditions was $31.29^\circ \pm 0.41^\circ$, differing by only 0.81% from the actual measured angle of $31.04^\circ \pm 0.21^\circ$ obtained through physical stacking experiments. These results demonstrate that combining numerical simulations with image feature extraction is a reliable and efficient method for assessing the stacking properties of agricultural materials.

摘要

为了准确确定不规则、分散的农业物料籽粒的休止角，需要建立与真实物料形状高度相似的籽粒仿真模型，并采用数值方法对物料的堆积特性进行仿真研究。本研究以“甬尤 15 号”水稻籽粒材料为例，利用三维光栅扫描技术获取籽粒的轮廓数据，采用逆向建模过程生成籽粒的三维几何模型，基于颗粒-聚合物理论建立由 618 个不等径颗粒组成的水稻籽粒离散元模型。利用离散元分析软件 EDEM 和 MATLAB 图形图像处理技术，模拟了水稻籽粒在不锈钢无底圆柱形管中落料和堆积过程，并对堆积图像轮廓采取线性拟合，同时对籽粒堆微观力学结构进行研究，得到籽粒堆压力凹陷的原因，来自籽粒堆内部接触力的斜向传递特征。模拟试验条件得到休止角为 $31.29^\circ \pm 0.41^\circ$ ，与实际堆积试验休止角 $31.04^\circ \pm 0.21^\circ$ 对比，偏差为 0.81%。结果表明，数值模拟结合图像特征提取的方法对测量农业物料堆积特性有效可行。

INTRODUCTION

In agricultural engineering, grain materials play a critical role as the primary operational medium for agricultural machinery, influencing its efficiency and performance through their dynamic response behaviors and contact interactions. During the stacking process, grains exhibit complex motion states that reflect key properties such as flow, scattering, and friction. Analyzing the stacking behavior of these materials holds substantial scientific and engineering importance, providing essential insights and practical guidance for enhancing agricultural machinery operations.

With the continuous development of computer technology, the discrete element method (DEM) has become a widely used tool for simulating grain materials (Zeng *et al.*, 2021; Wen *et al.*, 2020; Zhang *et al.*, 2022; Wang *et al.*, 2020; Hu *et al.*, 2023). Shu *et al.* (2023) focused on agricultural particle characteristics and calibrated DEM parameters for rapeseed discharge during combined harvesting, validating these parameters through cleaning platform experiments and CFD-DEM gas-solid coupling tests.

¹ Liquan Tian, M.S. Stud. Eng.; Hong Li, Prof. Ph.D. Eng.; Xian Zhang, M.S. Stud. Eng.; Chunxiang, Liu M.S. Eng.

Similarly, *Ma et al., (2020)*, *Hao et al., (2021)*, *Shi et al., (2020)*, and *Zhang et al., (2020)*, calibrated DEM parameters for various grains, including alfalfa seeds, sunflower seeds, flax seeds, and corn grains, providing essential reference data for agricultural material simulations. Accurate simulations of agricultural materials require calibration of both the intrinsic material properties and contact parameters (*Wu et al., 2020*; *Shi et al., 2019*; *Zhang et al., 2022*). Numerical methods not only serve as an efficient alternative to direct measurements but also allow predictions of grain behavior under specified stacking conditions. For instance, *Jia et al., (2014)*, employed a discrete element stacking approach using nine filled spheres to model rice grains. However, the significant disparity between the model and actual grain shapes led to reduced simulation stability. *Zhang et al., (2020)*, explored the influence of varying the radii of filled spheres on grain dynamics, discovering that smaller radii yielded results closer to experimental observations. Recently, advancements in 3D scanning technology have facilitated reverse modeling of grain shapes and solid particle morphology with higher precision, offering a powerful tool for improving the accuracy of grain material simulations (*Lumay, Boschini & Traina, 2012*).

The discrete element method (DEM) analyzes the macroscopic behavior of granular flows by iteratively calculating the motion dynamics of individual particles within the medium (*Ajayi & Sheehan, 2012*). In this research, DEM is utilized to simulate the formation process of a rice grain heap as it flows through a bottomless stainless steel cylinder. MATLAB is employed to process grain heap images, enabling the analysis of stacking properties such as the angle of repose and internal contact forces. This study introduces a numerical simulation and prediction approach for the stacking behavior of agricultural grains, offering key DEM model parameters for the development and optimization of rice sowing and harvesting machinery.

MATERIALS AND METHODS

Main structure and working principle

This research focuses on simulating the small-scale static stacking behavior of rice grains. Due to the low moisture content of the grains during the harvest season, adhesive forces are negligible. The displacement, force, and velocity of the grains during stacking are primarily influenced by the extent of overlap between the grains and the contact surfaces. The accuracy of the simulation outcomes largely depends on the selected contact model in the DEM. In this study, the Hertz-Mindlin mechanical model is adopted to simulate contact interactions during the stacking process, as depicted in Fig 1. This model simplifies the collision forces at contact points by decomposing them into normal and tangential components, which are represented using a parallel system of springs and dampers.

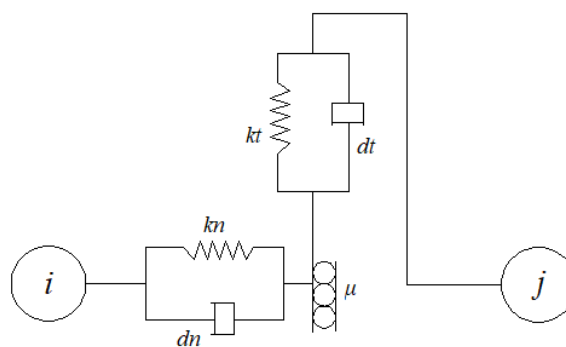


Fig. 1 – Hertz-Mindlin contact model

The model was applied to calculate the forces acting on a given granule *i* during the rice grain stacking process. These forces include the granule weight $m_i g$, the normal collision contact force F_n between granules, the normal damping force, the tangential collision force F_t , and the tangential damping force. Based on Newton's second law, the translational motion equation for each granule can be expressed as follows.

$$m_i \frac{dv_i}{dt} = m_i g + \sum_{j=1}^{n_i} (F_n + F_n^d + F_t + F_t^d) \tag{1}$$

Moreover, rice grains are also subject to the actions of tangential torque T_t and rolling friction torque T_r :

$$I_i \frac{d\omega_i}{dt} = \sum_{j=1}^{n_i} (T_t + T_r) \tag{2}$$

where m and I are the mass and rotational inertia of the granule, respectively; n_i represents the total number of granules in contact with the granule i ; v represents the movement speed of the granule; ω_i is angular velocity; and t denotes time.

During the stacking process of rice grains, contact collisions occur either between grains or between grains and other objects. These collisions result in small elastic deformations at the contact points, generating a degree of overlap to counteract the forces involved. The tangential collision force F_t is constrained by Coulomb's friction force $\mu_s F_n$ where μ_s represents the static friction coefficient. If the tangential collision force exceeds the Coulomb friction force, the grains will slide along the contact surface, and in such cases, F_t is primarily determined by $\mu_s F_n$. Based on the equations provided in Table 1, rolling motion occurs during the stacking process due to the interplay between tangential torque and rolling friction torque. Rolling friction torque, which depends on the rolling friction coefficient μ_r , was incorporated into the model to account for its influence on the degree of resistance to grain rolling.

Table 1

The forces and moments experienced by the grain in motion		
Force and moment	Unit	Formula derivation
Normal force	Contact force	$F_n = \frac{4}{3} E^* (R^*)^{1/2} \delta_n^{3/2}$
	Damp force	$F_n^d = -2 \sqrt{\frac{5}{6}} \cdot \frac{\ln e}{\sqrt{\ln^2 e + \pi^2}} \cdot \sqrt{S_n m^* v_n^{rel}}$
Tangential force	Contact force	$F_t = -S_n \delta_t$
	Damp force	$F_t^d = -2 \sqrt{\frac{5}{6}} \cdot \frac{\ln e}{\sqrt{\ln^2 e + \pi^2}} \cdot \sqrt{S_t m^* v_t^{rel}}$
Frictional force	Torque	$T_t = R_i \times (F_t + F_t^d)$
	rolling friction torque	$T_r = -\mu_r F_n R_i \hat{\omega}$

where E^* is equivalent elastic modulus; R^* is equivalent granule radius; δ_n and δ_t denote normal and tangential overlaps, respectively; S_n and S_t represent normal and tangential stiffness, respectively; e is recovery coefficient; v_n^{rel} and v_t^{rel} are normal and tangential relative velocity, respectively; m^* is equivalent mass; $\hat{\omega}$ is the unit angular velocity of the object at contact point; μ_r is rolling friction factor.

Modeling of Rice Grains

Rice grains possess a complex geometry with significant variations in curvature, making it challenging for traditional modeling techniques to accurately capture their physical characteristics. Advanced digital imaging and CT scanning technologies have been utilized in discrete element modeling to achieve more precise material representations (Du et al., 2012). This study focused on the "Yongyou 15" rice variety, employing 3,500 unthreshed and unsorted grains to construct a detailed 3D model (Yu et al., 2014). A 3D laser scanner was used to obtain point cloud data of the grains, as illustrated in Figure 2a. This data was processed to reconstruct a 3D solid model of the grains, as shown in Figure 2b. The finalized 3D model was imported into EDEM software, where the particle properties were configured with a smoothing value of 8 and a minimum grain radius of 0.2. Using the software's automatic packing module, a discrete element model consisting of 618 grains with varying diameters was successfully developed, depicted in Figure 2c.

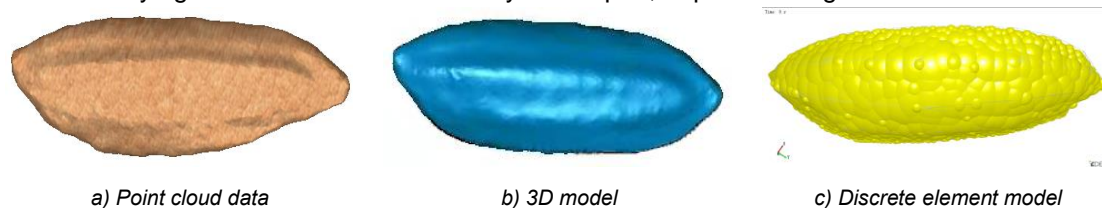


Fig. 2 - Three-dimensional model of rice grain

Modeling of contact geometry parameters and model stacking

This research examines rice grains and utilizes the discrete element method (DEM) to simulate their stacking behavior. A bottomless stainless-steel cylindrical tube is employed to guide the material flow, with simulation parameters determined based on relevant studies, as summarized in Table 2.

Table 2

Material parameters used in simulation	
Parameters	Value
Poisson's ratio of rice grain	0.25
Shear modulus of rice grain / MPa	86.5
Density of rice grain / (kg·m ⁻³)	1086
Poisson's ratio of stainless steel	0.29
Shear modulus of stainless steel / MPa	75000
Density of stainless steel / (kg·m ⁻³)	7800
Coefficient of restitution between rice grains	0.81
Coefficient of static friction between rice grains	0.35
Coefficient of restitution between rice grain and stainless steel	0.40
Coefficient of rolling friction between rice grains	0.01
Coefficient of static friction between rice grain and stainless steel	0.56
Coefficient of rolling friction between rice grain and stainless steel	0.02

The dimensions of the stainless-steel cylindrical tube were determined based on the size of the rice grains. Specifically, the tube diameter was set to be 4–5 times the maximum grain diameter, with a height-to-diameter ratio of 3:1. Given the average rice grain length of 7.6 mm, a tube with a diameter of 40 mm and a height of 120 mm was selected. Using the Geometry module in the EDEM software, a discrete element model of the cylindrical tube was created with these specifications and appropriate material properties. This model was used to simulate the dropping and stacking of rice grains both within the cylindrical tube and on a stainless-steel plate. The Particle Factory module in EDEM, positioned above the tube, dynamically generated three-dimensional models of rice grains that fell into the tube. Once the tube was filled with these grain models, it was slowly lifted vertically away from the plate, enabling the grains to form a heap on the plate.

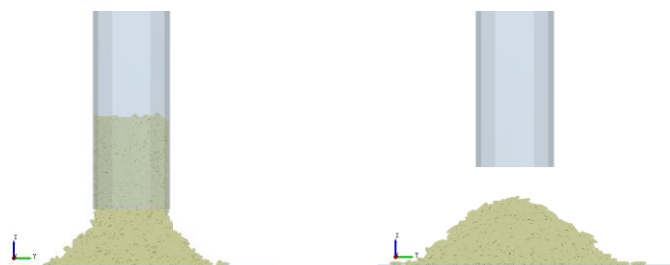


Fig. 3 – Stacking simulation of rice grain

When simulating the stacking process of a 3D rice grain model using a bottomless stainless-steel cylindrical tube, several key factors must be taken into account. These include the shape and properties of the grain model, such as static friction, rolling friction, and the restitution coefficient, as well as the specifications of the cylindrical tube. Additionally, the lifting speed of the tube plays a crucial role in determining the formation of the grain heap. To prevent the heap from spreading excessively, which could affect the accuracy of the repose angle measurements, a slower lifting speed is employed to maintain the heap's stability. A lifting speed of 1 mm/s was chosen to minimize edge diffusion and preserve the structural integrity of the heap.

Measurement of the Repose Angle

After generating the 3D model of the rice grain heap, the angle of repose is calculated using image processing techniques. In this process, the x and y coordinates correspond to pixel values, which do not have physical units. The rice heap image is symmetrically divided into left and right halves, as shown in Figure 4a.

MATLAB image processing tools are then employed to extract and binarize the boundary contours of the heap on one side. These contours, detected in grayscale as illustrated in Figure 4b, are analyzed to identify the slope boundary of the grain heap. The boundary is subsequently fitted linearly, and the resulting equation is used to calculate the slope, denoted as k . The final angle of repose is then determined using Equation (3).

$$\theta = \frac{\arctan |k| \times 180^\circ}{\pi} \tag{3}$$

In this study, the stacking angle of rice grains, denoted as θ , is numerically measured using the slope (k). Given that the stacking process of rice grains exhibits a degree of randomness, accurate measurement of the repose angle requires careful analysis. The angle of repose was measured using image processing along both the x and y axes, with measurements taken five times in each direction, as illustrated in Figure 4. This approach ensures a reliable and precise determination of the stacking angle.

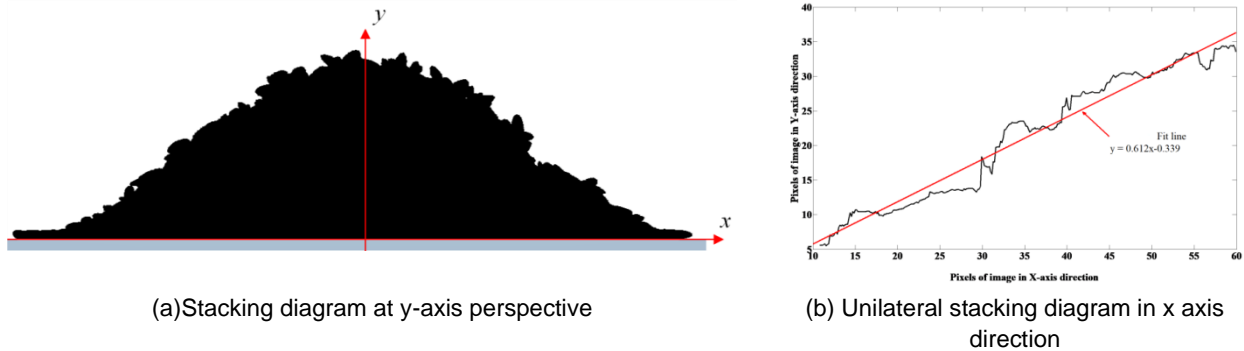


Fig. 4 –Stacking results of rice grains in different directions

Using the same method, the repose angles of the rice heap from five repeated simulations were measured as 30.71°, 31.47°, 31.05°, 31.93°, and 31.27°. The average angle of repose was calculated to be 31.29°, with a standard deviation of 0.41°. Thus, the angle of repose obtained from the discrete element method simulation for the rice grains is 31.29° ± 0.41°.

Verification test of stacking

To validate the accuracy of the angle of repose prediction method, natural stacking tests were conducted using real rice grains, a stainless-steel cylinder, and the necessary equipment. Since grain moisture content significantly affects its physical properties, the rice grains were conditioned to a moisture content range of 16%-20% to closely align with the simulation conditions, based on physical and mechanical parameters from literature on the collision mechanics of harvested grains. The specifications of the stainless-steel cylinder were set to match those used in the simulation. To ensure consistency between the simulated and experimental conditions, post-processing tools in EDEM software were used to count the number of grains in the cylinder, which amounted to 3,500 grains with a total mass of 101.15 grams.

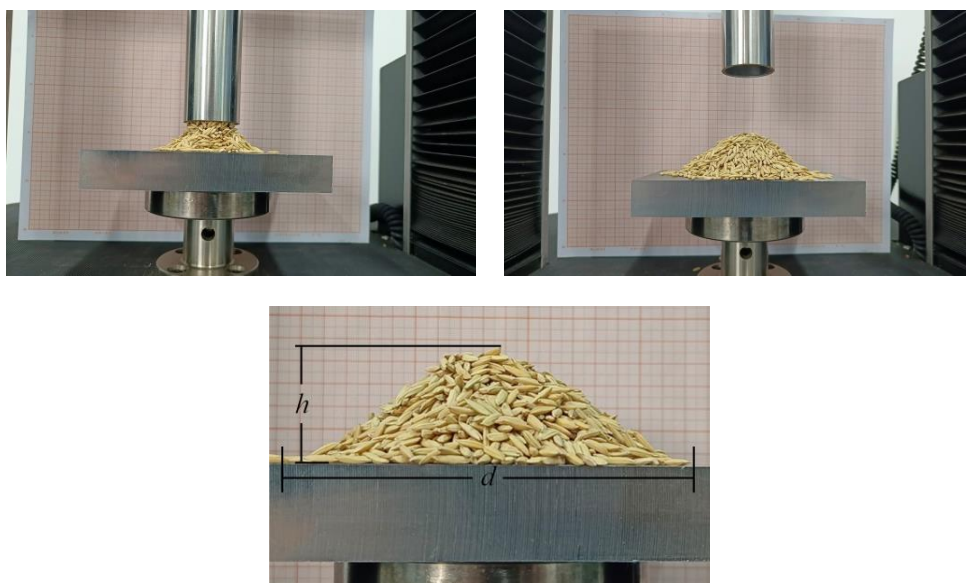


Fig. 5 – Physical stacking test

Angle of repose of rice grains was measured with the conventional method several times in different directions in the test, so as to obtain the bottom diameter d and height h of grain stack and take their averages. The actual test angle of repose θ' was calculated by Equation (4).

$$\theta' = \arctan\left(\frac{2h}{d}\right) \quad (4)$$

where θ' is the measured angle of repose of rice grains; h and d are the stacking height and diameter of rice grains, respectively.

The experimental procedure to measure the natural angle of repose involved filling the cylinder with rice grains, which were then lifted using a microcomputer-controlled electronic universal testing machine at a constant speed of 1 mm/s, in alignment with the simulation conditions. After the rice grains had settled and the heap's slope surface stabilized, the angle of repose and related measurements were recorded. This process was repeated five times, resulting in the following natural repose angles: 30.82°, 31.21°, 31.16°, 31.25°, and 30.74°. The average natural angle of repose was calculated as 31.04°, with a standard deviation of 0.21°, yielding a final repose angle of 31.04° ± 0.21°.

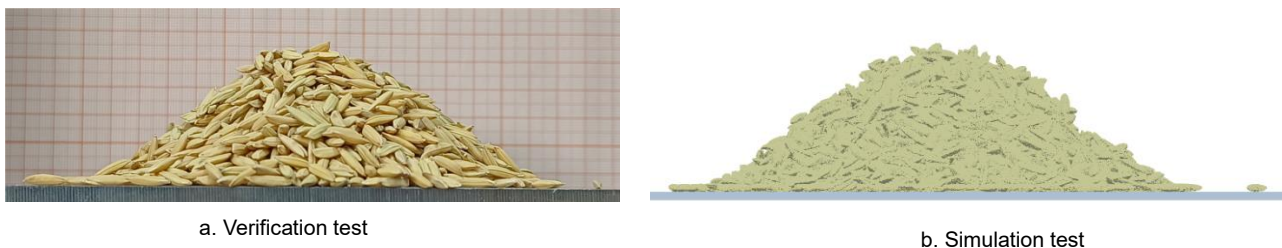


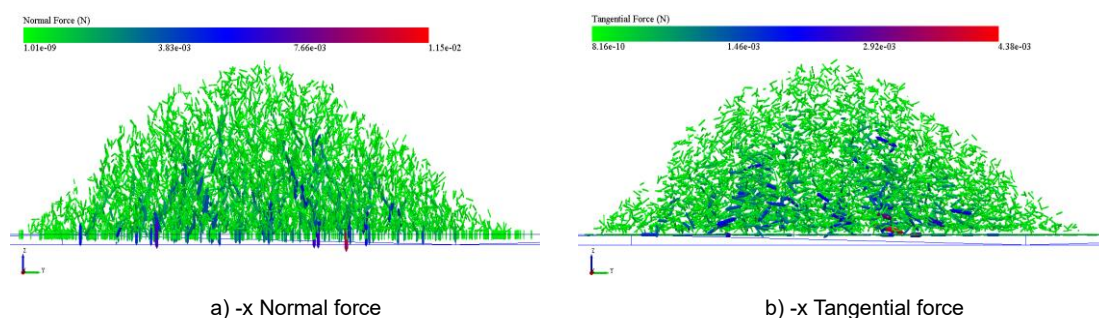
Fig. 6 – Simulation and experimental comparison of natural stacking angle of repose of rice grains

Fig. 6 compares the natural and simulated rice grain heaps, showing that while the overall stacking forms are similar, there is a slight difference in the smoothness of the slope surface. This variation can be attributed to the simulation's use of uniform geometric dimensions for the rice grains, while in reality, even after screening, individual grains exhibit minor irregularities. Additionally, the simulated angle of repose is slightly higher than the natural one. This discrepancy arises because the simulation model employs multi-sphere aggregates, which increase the contact area between adjacent grains, thus enhancing friction and reducing the flowability of the grains. The error between the simulated and natural angles of repose is 0.80%, indicating that the material parameters used in the discrete element method, along with the image processing techniques, provide a reasonably accurate simulation of the stacking behavior of rice grains.

Analysis of Contact Forces in Grain Heap

To gain a deeper understanding of the stacking characteristics of rice grains, the contact force chains within the grain heap were visualized by hiding the geometric body and particle models.

This approach allowed for a clearer examination of the micro-mechanical structure of the heap. Figure 7 illustrates the distribution of contact forces within the grain heap, where the magnitude of the forces is represented by different colors. Stronger forces are depicted as strong force chains, while weaker ones are identified as weak force chains. Given the nearly symmetrical structure of the grain heap, statistical analysis was performed on the contact forces in just one-half of the heap.



- [6] Jia F.G., Han Y.L., Liu Y., Can Y.P., Shi Y.F., Tao L.N., Wang H. (2014). Simulation prediction method of repose angle for rice particle materials (稻谷颗粒物料堆积角模拟预测方法). *Transactions of the CSAE*, 30(11): 254-260.
- [7] Lumay G, Boschini F, Traina K. (2012). Measuring the flowing properties of powders and grains (粉末和颗粒的流动特性测量). *Powder Technology*, 224: 19-27.
- [8] Ma W.P., You Y., Wang D.CH., Yin Sh.J., Xun X.L. (2020). Parameter calibration of alfalfa seed discrete element model based on RSM and NSGA-II (基于 RSM 和 NSGA-II 的首蓿种子离散元模型参数标定). *Transactions of the Chinese Society for Agricultural Machinery*, 51(8): 136-144.
- [9] Ma Y.H., Song CH.D., Xuan CH. ZH., Wang H.Y., Yang SH., Wu P. (2020). Parameters calibration of discrete element model for alfalfa straw compression simulation (首蓿秸秆压缩仿真离散元模型参数标定). *Transactions of the Chinese Society of Agricultural Engineering*, 36(11): 22-30.
- [10] Shi L.R., Ma Zh. T., Zhao W.Y., Yang X.P., Sun B.G., Zhang J.P. (2019). Calibration of simulation parameters of flax seeds using discrete element method and verification of seed-metering test (胡麻籽粒离散元仿真参数标定与排种试验验证). *Transactions of the Chinese Society of Agricultural Engineering*, 35(20): 25-33.
- [11] Shu C.X., Yang J., Wan X.Y., Yan J.CH., Liao Y.T., Liao Q.X. (2022) Calibration and experiment of discrete element simulation parameters for combined harvesting of rapeseed extracts (联合收获油菜脱出物离散元仿真参数标定与试验). *Transactions of the Chinese Society of Agricultural Engineering (Transactions of the CSAE)*, 38(9): 34-43.
- [12] Wang Y., ZHANG Y., Yang Y. (2020). Discrete element modelling of citrus fruit stalks and its verification (柑桔果柄离散元建模及其验证). *Biosystems Engineering*, 200:400-414.
- [13] Wen X.Y., Jia H.L., Zhang SH.W., Yuan H.F., Wang G., Chen T.Y. (2020). Calibration method of friction coefficient of granular fertilizer by discrete element simulation (基于 EDEM-Fluent 耦合的颗粒肥料悬浮速度测定试验). *Transactions of the Chinese Society for Agricultural Machinery*, 51(2): 115-122, 142.
- [14] Wu M.CH., Cong J.L., Yan Q., Zhu T., Peng X.Q., Wang Y.SH. (2020). Calibration and experiments for discrete element simulation parameters of peanut seed particles (花生种子颗粒离散元仿真参数标定与试验). *Transactions of the Chinese Society of Agricultural Engineering*, 36(23): 30-38.
- [15] Yu J.Q., Shen Y.F., Niu X.T., Fu H., Ni T.H. (2014). Simulation test for metering process of horizontal disc precision metering device based on discrete element method (组合内窝孔精密排种器清种过程的离散元法仿真分析). *Transactions of the Chinese Society of Agricultural Engineering*, 24(5): 105-109.
- [16] Zhang R.F., Zhou J.L., Liu H., Shi S., Wei G.J., He T.F. (2022). Determination of Interspecific Contact Parameters of Corn and Simulation Calibration of Discrete Element (玉米颗粒粘结模型离散元仿真参数标定方法研究). *Transactions of the Chinese Society for Agricultural Machinery*. 53:69-77.
- [17] Zhang R.F., Jiao W., Zhou J.L., Qi B., Liu H., Xia Q.Q. (2020). Parameter Calibration and Experiment of Rice Seeds Discrete Element Model with Different Filling Particle Radius (不同填充颗粒半径水稻种子离散元模型参数标定). *Transactions of the Chinese Society for Agricultural Machinery*. (51):227-235. Doi: 10. 6041 /J. ISSN. 1000-1298. 2020. S1. 026.
- [18] Zhang SH.W., Zhang R.Y., Chen T.Y., Fu J., Yuan H.F. (2022). Calibration of simulation parameters of mung bean seeds using discrete element method and verification of seed-metering test (绿豆种子离散元仿真参数标定与排种试验). *Transactions of the Chinese Society for Agricultural Machinery*, 53(3): 71-79.
- [19] Zeng Zh.W., Ma X., Cao X.L., Li Z.H., Wang X.CH. (2021). Critical Review of Applications of Discrete Element Method in Agricultural Engineering (离散元法在农业工程研究中的应用现状和展望). *Transactions of the Chinese Society for Agricultural Machinery*. (52):1-20. Doi: 10.6041 /J. ISSN. 1000-1298. 2021. 04. 001.

MOISTURE CONTENT DETECTION OF SOYBEAN GRAINS BASED ON HYPERSPETRAL IMAGING

基于高光谱成像的大豆籽粒含水率检测研究

Zhichang CHANG¹⁾, Man CHEN^{1,2*)}, Gong CHENG¹⁾, Chengqian JIN^{1*)}, Tengxiang YANG¹⁾

¹⁾ Nanjing Institute of Agricultural Mechanization, Ministry of Agriculture and Rural Affairs, Nanjing, Jiangsu / China;

²⁾ National Digital Agriculture Equipment (South China Intelligence Agricultural Machine) Innovation Sub-center, Nanjing, Jiangsu / China;

Tel: +8602584346113; E-mail: chm_world@163.com; jinchengqian@126.com

DOI: <https://doi.org/10.35633/inmateh-74-50>

Keywords: Soybean; Moisture content; Hyperspectral imaging; Detection

ABSTRACT

Using hyperspectral imaging technology for rapid, non-destructive detection of soybean grain moisture content provides technical support for high-quality soybean harvesting. A total of 90 samples of soybean grains from different varieties were collected, with hyperspectral images acquired in the wavelength range of 900–1700 nm. The moisture content of each soybean grain sample was determined using the direct drying method as specified in GB 5009.3-2016. The samples were divided into a calibration set and a prediction set based on a 4:1 ratio using the sample partitioning method of Joint X-Y Distance. Eight preprocessing methods were applied to the raw spectral data, including baseline correction, moving average, Savitzky-Golay filtering, normalization, standard normal variate transformation, multiple scatter correction, first derivative, and deconvolution. Feature wavelengths were then extracted using the successive projections algorithm and the competitive adaptive reweighted sampling algorithm. Finally, a partial least squares regression model for predicting the moisture content of soybean grains was developed based on these feature wavelengths. The results show that the correlation coefficient and the root mean square error of the optimal model for the prediction set were 0.92 and 0.2371, respectively. The moisture spectrum inversion model can precisely and rapidly predict the moisture content of soybean grains non-destructively, thereby determining the timing of mechanical soybean harvesting and enhancing the quality of soybean harvesting, storage, and processing.

摘要

采用高光谱成像技术实现大豆籽粒含水率的快速无损检测，为大豆高质量收获提供技术支撑。采集了 90 个不同品种大豆籽粒样本在 900 ~ 1700 nm 的高光谱图像，采用 GB 5009.3-2016 中的直接干燥法测定每种大豆籽粒样本的水分含量。基于联合 X-Y 距离的样本划分法按照 4:1 的比例划分样品，建立校正集和预测集。采用基线校正、移动平均、Savitzky-Golay 滤波、归一化、标准正态变量变换、多元散射校正法、一阶导数、去卷积 8 种算法方法对原始光谱数据进行预处理，基于连续投影算法和竞争性自适应重加权算法提取特征波长，最后建立基于特征波长的偏最小二乘回归的大豆籽粒含水率预测模型。结果表明，最优模型预测集相关系数和均方根误差分别为 0.92 和 0.2371。水分光谱反演模型可以准确快速无损预测大豆籽粒含水率，从而制定大豆机收时间，提升大豆收获、存储、加工品质。

INTRODUCTION

China is one of the world's major producers and consumers of soybeans (Li et al., 2023). The country's soybean planting area is approximately 9 to 10 million hectares, with an annual production of around 18 to 20 million tons (Liu et al., 2022). Soybean cultivation in China is mainly concentrated in the Northeast region and the Huang-Huai-Hai Plain. In recent years, there has been a shift in China's soybean production model, moving from traditional, small-scale farming to a more large-scale, mechanized, and intelligent approach (Li et al., 2023).

Moisture detection in soybeans is of great significance in mechanized production, as moisture content directly affects the efficiency and quality of various stages such as harvesting, transportation, storage, and processing. Moisture content is a key factor in determining the optimal harvest time for soybeans (Mo et al., 2020).

Zhichang Chang, Stud. Eng.; Man Chen, Associate Prof. Ph.D. Eng.; Gong Cheng, Stud. Eng.; Chengqian Jin, Prof. Ph.D. Eng.; Tengxiang Yang, Research Associate. Ph.D. Eng.

When the moisture content is too high, harvesting machinery may face operational difficulties, which can cause machine blockages, reduced harvesting efficiency, and increased risks of grain breakage or damage. On the other hand, if the moisture content is too low, soybean pods are more likely to crack, leading to increased field losses. By monitoring the moisture content of soybeans in real time, farmers and machine operators can select the best harvest time, minimize losses, and improve harvesting efficiency.

Traditional methods for detecting soybean moisture content include the drying method and the Karl Fischer titration method. These methods are recognized as standard due to their high detection accuracy and reliable results. However, they are time-consuming, involve complex procedures, and require specialized equipment and laboratory conditions, making them unsuitable for on-site, real-time detection. In recent years, with the rapid advancement of sensing technology, online detection techniques for soybean moisture content have developed quickly (Zhang *et al.*, 2023). These techniques include methods such as capacitance (Zhang *et al.*, 2021), resistance (Zhao *et al.*, 2018), near-infrared spectroscopy (Chen *et al.*, 2023), microwave measurement (Song *et al.*, 2023), infrared thermal radiation (Shi *et al.*, 2024), and machine vision and imaging technology (Wu *et al.*, 2022). These methods offer advantages like fast detection speed, high accuracy, and the ability to perform non-destructive, real-time measurements, making them widely used in modern agriculture. A rapid detection method for tomato water stress based on terahertz spectroscopy was proposed, integrating three-dimensional terahertz features and using support vector machines for the rapid detection of tomato water stress (Zhang *et al.*, 2021). A spectral classification model was developed to distinguish the moisture levels of different alfalfa seeds (Yang *et al.*, 2024). A method based on near-infrared spectroscopy and random forest variable selection was applied to identify soybean seed cracks, achieving an accuracy rate of 84% (Wang *et al.*, 2023). A microwave radar measurement system was employed for fast, non-destructive, and high-precision detection of grain moisture content, with standard errors of 0.564% and 0.983% for predicting moisture content in soybeans and wheat, respectively (Li *et al.*, 2022). A portable near-infrared and visible light spectrometer, combined with multivariate analysis, was used for non-destructive detection of rice moisture content, and the root mean square error of the optimal model was 0.388 (Zhang *et al.*, 2023). Additionally, a method based on terahertz imaging technology was applied to measure the moisture content of soybean leaves, with a root mean square error of 0.0465 (Bu *et al.*, 2018). Most existing technologies focused on a single variety, and the model's generalization was weak, making it unable to accurately detect parameters of multiple varieties. Given the wide variety of soybean cultivars in China, constructing a robust moisture detection model suitable for multiple cultivars is the focus of this study.

Therefore, this study focuses on 90 different soybean cultivars and utilizes hyperspectral imaging technology combined with chemometric methods to establish and identify the optimal prediction model for detecting soybean moisture content in the range of 900–1700 nm. This approach provides a new method for monitoring moisture content during soybean harvesting, storage, and processing.

MATERIALS AND METHODS

Sample Collection for the Experiment

In order to improve the generalization of the model, the samples used in the experiment were collected from major soybean-producing regions in China, including the Northeast Plain, Huang-Huai Plain, and Yangtze River Basin. These samples included 90 different varieties such as Heihe 43, Suinong 28, Zhonghuang 301, Wanhuang 506, Zhonghuang 37, Zhongdou 43, Zhongdou 41, Nandou 5, and Xiangchun Bean 26. During the soybean harvest season, the samples were mechanically harvested, cleaned to remove impurities, and then sealed in bags. They were labeled and brought back to the laboratory for further analysis.

Determination of Moisture Content in Experimental Samples

The moisture content of each soybean sample was measured using the direct drying method as outlined in GB 5009.3-2016 "National Food Safety Standard for the Determination of Moisture in Foods.", as shown in Fig.1.

The calculation formula for moisture content is as follows:

$$X = \frac{m_1 - m_2}{m_1 - m_3} \times 100 \quad (1)$$

where: X is moisture content in the sample, expressed as g/100 g;

m_1 is mass of the weighing bottle (with sea sand and glass rod) and the sample, in grams (g);

m_2 is mass of the weighing bottle (with sea sand and glass rod) and the sample after drying, in grams (g);

m_3 is mass of the weighing bottle (with sea sand and glass rod), in grams (g);

100 is conversion factor to express moisture content as a percentage.

When the moisture content is ≥ 1 g/100 g, the result is reported with three significant figures. When the moisture content is <1 g/100 g, the result is reported with two significant figures (Zhang *et al.*, 2023). Each soybean variety was measured three times, and the average value was used as the moisture content for that variety.



Fig. 1 – Measurement of moisture content in soybean samples

Spectral Measurement of Experimental Samples

The hyperspectral data acquisition system for soybean samples consists of three main components: a near-infrared hyperspectral imaging system, a halogen lamp light source, and a motion control system, as illustrated in Figure 2. This system uses the Pika NIR-320 Hyperspectral Imaging Camera from Resonon Inc., USA. It features a spectral range of 900–1700 nm, a spectral resolution of 8.8 nm, a spectral bandwidth of 4.8 nm, and 168 spectral channels. The system employs a halogen lamp to provide the necessary illumination for hyperspectral imaging across the full wavelength range. It includes a finned heat dissipation structure, complemented by a high-performance cooling fan, and is equipped with a voltage and current stabilizer to enhance the stability and reliability of the light source. This system integrates the light source and sensor into a single unit, allowing for high-precision synchronization between the sensor and the linear light source. It also facilitates easy adjustment of the camera's relative position to the target sample, accommodating the needs of capturing diverse and complex samples. This setup ensures comprehensive and accurate hyperspectral imaging by providing stable illumination, precise spectral measurements, and flexible positioning for various sample types.

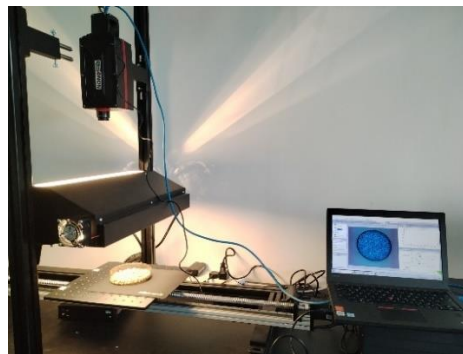


Fig. 2 – Hyperspectral data acquisition system

To minimize the impact of dark current and uneven light source intensity on hyperspectral images, black and white calibration of the hyperspectral images is required (Jin *et al.*, 2022; Guo *et al.*, 2023). Place a white reference board with a reflectance of 0.99 in the sample acquisition area (Chen *et al.*, 2019). Capture an image of this white board to obtain the white calibration image (Chen *et al.*, 2019), denoted as I_w . Cover the hyperspectral camera lens and capture an image to obtain the black calibration image, denoted as I_d .

The calibration formula for correcting hyperspectral images can be expressed as follows:

$$I_t = \frac{I - I_d}{I_w - I_d} \quad (2)$$

where, I_t is calibrated hyperspectral image, I is raw hyperspectral image of the sample.

During the sample scanning process, the exposure time was set to 7.3 ms, and the movement speed of the displacement platform was 3.512 cm/s. The hyperspectral data were analyzed using the SpectronPro software that comes with the Pika NIR-320 hyperspectral imaging system.

For each hyperspectral image, a region of interest (ROI) with a side length of 200 pixels was selected. The average spectrum of this ROI was extracted and used as the spectral information for the soybean sample. This approach ensures that the spectral data accurately represent the sample within the defined area of interest.

Spectral Data Preprocessing

During the spectral data acquisition with the Pika NIR-320 hyperspectral imaging system, due to differences in particle size and absorbance of the sample, variations occur during the diffuse reflection process, resulting in decreased spectral repeatability. Derivative is the most commonly used method to eliminate additive effects. Standard normal variate transformation (SNV) and multiple scatter correction (MSC) are commonly used methods to eliminate multiplication effects, which can to some extent reduce the impact of solid particle size or scattering effects on spectral data. Orthogonal signal correction (OSC) and net analyte signal (NAS) are non-independent methods of response variables, mainly used to remove spectral variations that are unrelated to the response variable, with the aim of simplifying the analysis model and improving its predictive ability. Therefore, baseline correction (BC), moving average, Savitzky-Golay filtering, normalization, SNV, MSC, first derivative, and deconvolution methods were used to preprocess the raw spectral data and remove irrelevant information.

Moisture Content Estimation Based on Spectral Information

Using the sample set partitioning based on joint X-Y distance (SPXY) method, the soybean samples were divided into a calibration set and a prediction set in a 4:1 ratio.

The raw spectral data contain a large amount of redundant and useless spectral information as well as various noises, which can reduce computation speed and affect the accuracy and precision of the model predictions. Therefore, the continuous projection algorithm (SPA) and competitive adaptive reweighted sampling (CARS) were used for dimensionality reduction and to select feature wavelengths.

Partial least squares regression (PLSR) was employed to establish the mathematical relationship between spectral information and soybean moisture content. PLSR constructs a linear regression model that indirectly describes the relationship between independent and dependent variables, effectively addressing the issue of high linear correlation among spectral variables.

The performance of the soybean moisture content PLSR model was evaluated using the coefficient of determination (R_c^2 , R_{cv}^2 and R_p^2) and the root mean square error (R_{mse} , R_{msecv} and R_{msep}) for the calibration set, cross-validation set, and prediction set. Generally, a well-performing model should have a high coefficient of determination and a low root mean square error.

Data analysis

The results were processed by Microsoft Office Excel (version 2021, Microsoft Corp., USA) and Matlab (version 2021a, MathWorks Corp., USA). Single factor analysis of variance (ANOVA) was carried out with IBM SPSS Statistics (version 24, IBM Corp., USA).

RESULTS

Spectral Feature Analysis of Soybean Samples with Different Moisture Contents

Figure 3 shows the spectral reflectance curves of soybean samples. The distinct reflectance dip near 1210 nm is attributed to the second overtone vibration band of C-H bonds in organic compounds.

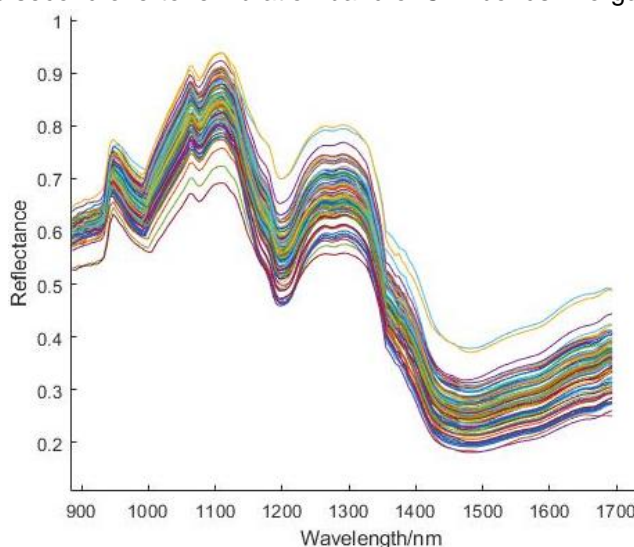


Fig. 3 – Original spectral curves of near infrared of 90 soybean samples

The reflectance dip at 1450 nm is related to the overtone vibration of O-H bonds, both of which are characteristic spectral bands for moisture content. The raw spectrum contains background information and noise, and the spectral data before 950 nm and after 1650 nm do not provide useful sample information. Therefore, spectral bands from 950 to 1650 nm, totaling 145 bands, are retained for modeling.

Sample Set Partitioning

The SPXY method divided the 90 samples into calibration and prediction sets in a 4:1 ratio, resulting in 72 samples for calibration and 18 samples for prediction. The moisture content range in the soybean samples is shown in Table 1. The calibration set covers the full range of moisture content present in the prediction set, indicating that the sample set partitioning is scientific and reasonable.

Table 1

Statistical data of soybean water content in sample set divided by SPXY method					
Sample Set	Number of Samples	Moisture Content			
		Maximum Value	Minimum Value	Average Value	Standard Deviation
Calibration Set	72	12.114	6.124	8.451	1.619
Prediction Set	18	10.952	6.344	8.237	1.652

Spectral Data Preprocessing

In this experiment, quantitative analysis of soybean moisture content was performed by establishing PLSR models based on both the raw spectra and spectra preprocessed using eight different methods. The results are shown in Table 2.

From Table 2, it can be observed that the PLSR model based on the raw near-infrared spectra has the R_p^2 of 0.7995 and the R_{msep} of 0.4205, indicating good stability of the model. After preprocessing with baseline correction, standard normal variate transformation, multiple scatter correction, and first derivative, the models exhibited the R_p^2 values higher than those of the raw spectrum-based model and the R_{msep} values lower than 0.4205. The performance of the models improved with these four preprocessing methods, and the stability of the cross-validation set was better.

The three preprocessing methods with the best performance (BC, SNV and MSC) were selected for further model processing.

Table 2

PLSR model based on different pretreatment methods							
Preprocessing Methods	PCs	Calibration Set		Cross-Validation Set		Prediction Set	
		R_c^2	R_{mse}	R_{cv}^2	R_{msecv}	R_p^2	R_{msep}
Raw spectral	9	0.8181	0.5072	0.6916	0.8598	0.7995	0.4205
Baseline Correction	14	0.8780	0.3267	0.5906	1.0961	0.8535	0.3612
Moving Average	9	0.8080	0.5353	0.6922	0.8581	0.7876	0.4454
Savitzky-Golay filtering	9	0.8095	0.5311	0.6889	0.8675	0.7799	0.4617
Normalization	10	0.8215	0.4640	0.7093	0.7557	0.8515	0.4230
Standard Normal Variate	9	0.8347	0.4329	0.6734	0.8555	0.8929	0.2838
Multiplicative Scatter Correction	9	0.8312	0.4393	0.6754	0.8447	0.9052	0.2646
Derivative Spectroscopy	6	0.8369	0.4525	0.7186	0.7809	0.8100	0.4051
Deconvolution	9	0.8157	0.5139	0.6919	0.8590	0.7935	0.4331

Selection of Feature Wavelengths

Among the 145 retained spectral bands, there is still a significant amount of redundant information. To improve modeling speed and model robustness, feature wavelengths need to be extracted from the spectral data. This study applied the continuous projection algorithm and competitive adaptive reweighted sampling algorithm to extract feature wavelengths from spectral data preprocessed by baseline correction, standard normal variate transformation, and multiple scatter correction.

Figure 4 illustrates the process of extracting feature wavelengths from the spectral data preprocessed with multiple scatter correction using the continuous projection algorithm. The selection process is determined by the size of the root mean square error, with smaller values indicating better model performance. The R_{msep} varies with the number of relevant wavelengths.

As shown in Figure 3(a), when the minimum R_{msep} is 0.4786, the number of extracted feature wavelengths is 7. The corresponding wavelengths in the original data are shown in Figure 3(b), with the 7 feature wavelengths being 966.15, 1301.8, 1142.68, 1085.21, 1418.51, 1214.81, and 951.93 nm, accounting for 4.83% of the total wavelengths.

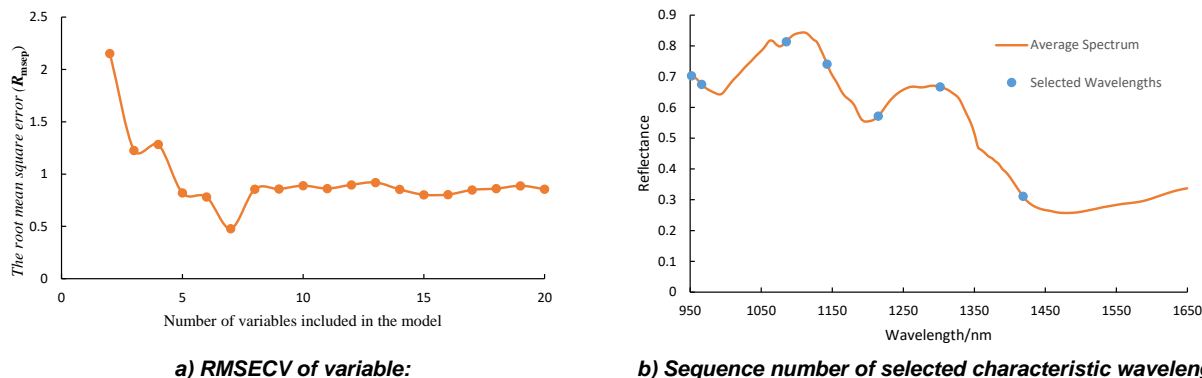


Fig.4 Process of SPA algorithm in screening characteristic wavelength of soybean water content

Similarly, for the spectral data preprocessed by standard normal variate transformation, 2 feature wavelengths were extracted when the minimum R_{msep} is 0.5601. These 2 feature wavelengths are 1496.77 and 951.93 nm, accounting for 1.38% of the total wavelengths.

For the spectral data preprocessed by baseline correction, 5 feature wavelengths were extracted when the minimum R_{msep} is 0.9474. These 5 feature wavelengths are 1330.9, 1457.59, 1219.63, 1142.68, and 1418.51 nm, accounting for 3.45% of the total wavelengths.

Figure 5 shows the results of extracting feature wavelengths from spectral data preprocessed using the competitive adaptive reweighted sampling algorithm after baseline correction, standard normal variate transformation, and multiple scatter correction.

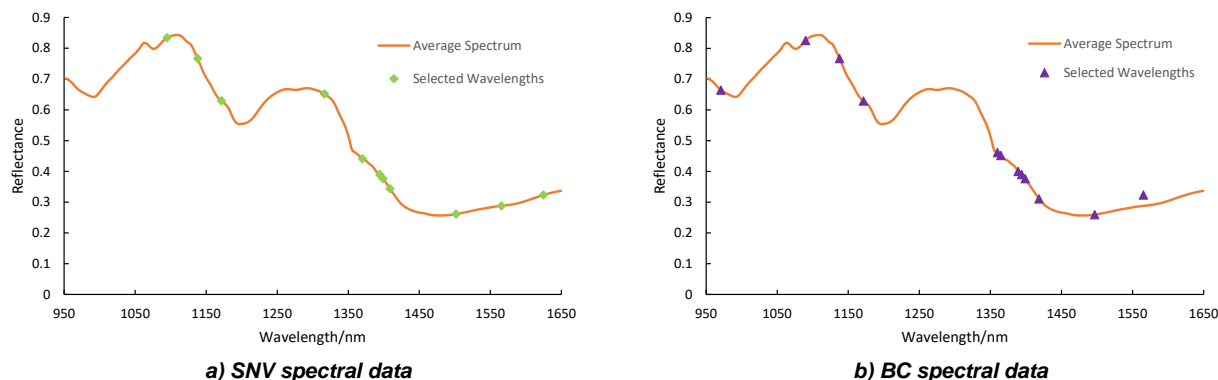


Fig. 5 - Result of CARS algorithm in screening characteristic wavelength of soybean water content

For the spectral data preprocessed by multiple scatter correction, 19 feature wavelengths were extracted. These wavelengths are 1085.21, 1089.99, 1133.09, 1137.89, 1176.3, 1306.64, 1311.49, 1316.34, 1369.78, 1374.64, 1389.25, 1394.12, 1399.00, 1413.63, 1496.77, 1501.68, 1570.49, 1580.34, and 1624.75 nm, accounting for 13.10% of the total wavelengths.

For the spectral data preprocessed by standard normal variate transformation, 11 feature wavelengths were extracted. These wavelengths are 1094.78, 1137.89, 1171.5, 1316.34, 1369.78, 1394.12, 1399.00, 1408.75, 1501.68, 1565.56, and 1624.75 nm, accounting for 7.59% of the total wavelengths.

For the spectral data preprocessed by baseline correction, 12 feature wavelengths were extracted. These wavelengths are 970.9, 1089.99, 1137.89, 1171.5, 1360.05, 1364.91, 1389.25, 1394.12, 1399.00, 1418.51, 1496.77, and 1565.56 nm, accounting for 8.28% of the total wavelengths.

Model Optimization

PLSR models for predicting soybean moisture content were established using the original spectral data from the 950–1650 nm wavelength range, as well as spectral data preprocessed by baseline correction, standard normal variate transformation, and multiple scatter correction.

The root mean square error of prediction for the prediction set was used as the metric to evaluate model performance, with lower R_{msep} values indicating better prediction accuracy. As shown in Table 3, the MSC-PLSR model has the lowest R_{msep} value of 0.2646, indicating that the PLSR model based on the 950–1650 nm wavelength spectra with MSC preprocessing has good prediction performance and stability.

To improve modeling speed and model robustness, SPA and CARS algorithms were used to select feature wavelengths for building soybean moisture content prediction models. These include SPA-BC-PLSR, SPA-MSC-PLSR, SPA-SNV-PLSR, CARS-BC-PLSR, CARS-MSC-PLSR, and CARS-SNV-PLSR. As shown in Table 3, compared to the SPA and full-band models, the PLSR models using feature wavelengths selected by the CARS algorithm had lower R_{msep} values. Among the models based on feature wavelengths, CARS-MSC-PLSR and CARS-SNV-PLSR had the lowest R_{msep} values of 0.2401 and 0.2371, respectively. This suggests that the models using feature wavelengths selected by the CARS algorithm performed better, likely due to CARS's effectiveness in reducing spectral collinearity.

Table 3

PLSR model based on different pretreatment methods								
NO	Models	Number of Wavelengths	Calibration Set		Cross-Validation Set		Prediction Set	
			R_c^2	R_{msec}	R_{cv}^2	R_{msecv}	R_p^2	R_{msep}
1	PLSR	145	0.8181	0.5072	0.6916	0.8598	0.7995	0.4205
2	BC- PLSR	145	0.8780	0.3267	0.5906	1.0961	0.8535	0.3612
3	MSC- PLSR	145	0.8312	0.4393	0.6754	0.8447	0.9052	0.2646
4	SNV- PLSR	145	0.8347	0.4329	0.6734	0.8555	0.8929	0.2838
5	SPA-BC- PLSR	5	0.6673	0.9014	0.6222	1.0236	0.837	0.3683
6	SPA-MSC- PLSR	7	0.6797	0.8543	0.6231	1.0053	0.8191	0.4497
7	SPA-SNV- PLSR	2	0.5804	1.1109	0.5454	1.2034	0.7098	0.5601
8	CARS -BC- PLSR	12	0.811	0.503	0.7289	0.7214	0.8771	0.3053
9	CARS -MSC- PLSR	19	0.8547	0.3826	0.786	0.5638	0.9105	0.2401
10	CARS -SNV- PLSR	11	0.845	0.3984	0.7877	0.5459	0.92	0.2371

DISCUSSION

Moisture content is a critical factor influencing the quality of soybean grains. However, determining the moisture content of soybean seeds is both time-consuming and expensive. Therefore, a rapid and non-destructive method for determining the moisture content in soybean seeds is essential. Guo Zhen applied visible near-infrared hyperspectral imaging technology (400–1000 nm) in conjunction with a wavelength selection algorithm to determine the moisture content of soybean seeds. They found that the combination of the interval variable iterative space shrinkage approach and the successive projections algorithm, based on the original spectra, was the most suitable model for determining the moisture content of soybean seeds (Guo *et al.*, 2023). Jin Chengqian employed near-infrared hyperspectral imaging technology for rapid and non-destructive detection of soybean moisture content. They found that the SPA algorithm provided better predictive performance for feature wavelength modeling, and selected the Normalize-SPA-PCR model, which demonstrated good stability and predictability, allowing for accurate prediction of soybean moisture content (Jin *et al.*, 2022). These findings suggest that the moisture inversion model constructed using spectral imaging technology can enable rapid detection of soybean moisture. This method provides a new approach for soybean moisture detection.

Furthermore, the CARS algorithm utilizes adaptive reweighted sampling technology to quickly identify variables that are most sensitive to moisture changes, thereby obtaining the optimal variable combination and reducing the consumption of computational resources. SNV enhances the stability of spectral data by performing a standard normal variate transformation, making the data more closely align with a normal distribution. Therefore, the combination of SNV and CARS algorithms for processing soybean spectral data can yield reliable prediction results.

CONCLUSIONS

(1) Eight preprocessing methods were used to develop a PLSR model for the spectral data in the 900–1700 nm range. The model with the highest R_c^2 value and lowest R_{msep} value was achieved after applying MSC, indicating that MSC performed best in full-band modeling and prediction.

(2) Two methods, SPA and CARS, were used to extract characteristic wavelengths, effectively reducing the spectral dimensionality. The characteristic wavelengths extracted by SPA accounted for 4.83%, 1.38%, and 3.45% of the spectral data, while those extracted by CARS accounted for 13.10%, 7.59%, and 8.28%.

(3) By combining preprocessing methods, feature wavelength extraction methods, and modeling methods, the effectiveness of 10 models was compared, and the CARS-SNV-PLSR model was selected as the optimal one. The CARS-SNV-PLSR model showed a high R_c^2 value of 0.92 and a low R_{msep} value of only 0.2371, indicating good stability and prediction performance. This model enables rapid, accurate, and non-destructive detection of soybean moisture content.

ACKNOWLEDGEMENT

We greatly appreciate the careful and precise reviews by the anonymous reviewers and editors. This research was financially supported by the National Natural Science Foundation of China, grant number 32272004, 32171911; the National Key Research and Development Program of China, grant number 2021YFD2000503; the Natural Science Foundation of Jiangsu, grant number BK20221188.

REFERENCES

- [1] Bu, Z.Y., Li, Z.F., Song, F.H., Li, B. & Li, J. (2018). Determination of moisture content in soybean leaves based on terahertz imaging (基于太赫兹成像技术的大豆叶片水分含量测定). *Acta Agriculturae Zhejiangensis*, Vol.30, pp.1420-1426. DOI: 10.6041/j.issn.1004-524.2018.08.21
- [2] Chen, J.W., Zhou, D.Q., Cui, C.C., Ren, Z.J. & Zuo, W.J. (2023). Prediction Model of Farinograph Characteristics of Wheat Flour Based on Near Infrared Spectroscopy (近红外光谱的小麦粉粉质特性预测模型研究). *Spectroscopy and Spectral Analysis*, Vol.43, pp.3089-3097. DOI: 10.3964/j.issn.1000-0593(2023)10-3089-09
- [3] Chen, M., Ni, Y.L., Jin, C.Q., Xu, J.S., Yuan, W.S. (2019). High spectral inversion of wheat impurities rate for grain combine harvester (谷物联合收割机收获小麦含杂率高光谱反演研究). *Transactions of the Chinese Society of Agricultural Engineering (Transactions of the CSAE)*, Vol.35, pp.22-29. DOI: 10.11975/j.issn.1002-6819.2019.14.003
- [4] Chen, M., Xu, J.S., Jin, C.Q., Zhang, G.Y., Ni, Y.L. (2019). Inversion model of soybean impurity rate based on hyperspectral (基于高光谱的大豆含杂率反演模型). *Journal of China Agricultural University*, Vol.24, pp.160-167. DOI: 10.11841/j.issn.1007-4333.2019.09.17
- [5] Guo, Z., Zhang, J., Ma, C.Y., Yin, X., Guo, Y.M., Sun, X. & Jin, C.Q. (2023). Application of visible-near-infrared hyperspectral imaging technology coupled with wavelength selection algorithm for rapid determination of moisture content of soybean seeds. *Journal of Food Composition and Analysis*, Vol.116, pp.105048. DOI: 10.1016/j.jfca.2022.105048
- [6] Jin, C.Q., Guo, Z., Zhang, J., Ma, C.Y., Tang, X.H., Zhao, N. & Yin, X. (2022). Non-destructive detection and visualization of soybean moisture content using hyperspectral technique (大豆水分含量的高光谱无损检测及可视化研究). *Spectroscopy and Spectral Analysis*, Vol.42, pp.3052-3057. DOI: 10.6041/j.issn.1000-0593(2022)10-3052-06
- [7] Li, C.X., Zhao, C.Y., Ren, Y., He, X., Yu, X.T. & Song, Q. (2022). Microwave traveling-standing wave method for density-independent detection of grain moisture content. *Measurement*, Vol.198, pp.111373. DOI: 10.1016/j.measurement.2022.111373
- [8] Li, Y., Wang, M.M., Lü, B., & Yu, H.S. (2023). Comparative analysis of soybean production efficiency in the main production areas in the context of rural revitalization (乡村振兴背景下主产区大豆生产效率比较分析). *Soybean Science*, Vol.43, pp.120–128.
- [9] Liu, L.L., Li, J.F., Shu, Y., Chen, X.Y., & Tang, G.X. (2022). Current situation of soybean production and consumption in China and strategies to improve self-sufficiency rate (我国大豆生产消费现状及提升自给率策略). *Chinese Journal of Oil Crop Sciences*, Vol.44, pp.242-248. DOI: 10.1016/j.issn.1007-9084.2022015

- [10] Li, Y., Xie, Q.Z., Liu, B.Q., He, S.Q., Wu, X.Z., Yang, Q., Liu, Z., Shi, X.L., Zhang, M.C., Yang, C.Y., Yan, L., Zhang, R.F., & Tao, P.J. (2023). Life cycle analysis of soybean production in typical district of the North China Plain (华北平原典型区大豆生产全生命周期分析). *Chinese Journal of Eco-Agriculture*, Vol.31, pp.1416–1427.
- [11] Mo, F., Wang, G.X., & Hu, M.Z. (2020). Analysis of soybean production status in northeast China based on cost (基于成本视角的东北地区大豆生产现状分析). *Soybean Science*, Vol.39, pp.947–953. DOI: 10.11861/i.issn.10009841.2020.06.0947
- [12] Shi, W.Q., Li, Y.H., Wei, Z., Yu, J.K., Zhao, C. & Qiu, J.K. (2024). Monitoring and zoning soybean maturity using UAV remote sensing. *Industrial Crops & Products*, Vol.222, pp.119470. DOI: 10.1016/j.indcrop.2024.119470
- [13] Song, Y.H., Gao, S.S., Chu, X.X., Zhou, Y.M., Xu, Y.Q., Sun, T., Zhou, G.X. & Liu, X.Q. (2023). Non-destructive detection of moisture and fatty acid content in rice using hyperspectral imaging and chemometrics. *Journal of Food Composition and Analysis*, Vol.121, pp.105397. DOI: 10.1016/j.jfca.2023.105397
- [14] Wang, L.S., Huang, Z.L. & Wang, R.J. (2023). Discrimination of cracked soybean seeds by near-infrared spectroscopy and random forest variable selection. *Infrared Physics and Technology*, Vol.115, pp.103731. DOI: 10.1016/j.infrared.2021.103731
- [15] Wu, J.Z., Zhang, L., Li, J.B., Liu, C.L., Sun, X.R. & Yu, L. (2022). Detection model of moisture content of single maize seed based on hyperspectral image and ensemble learning (基于高光谱与集成学习的单粒玉米种子水分检测模型). *Transactions of the Chinese Society for Agricultural Machinery*, Vol.53, pp.302-308. DOI: 10.6041/i.issn.1000-298.2022.05.031
- [16] Yang, S.F., Jia, Z.C., Yi, K., Zhang, S.H., Zeng, H.G., Qiao, Y., Mao, P.S. & Manli Li (2024). Rapid prediction and visualization of safe moisture content in alfalfa seeds based on multispectral imaging technology. *Industrial Crops & Products*, Vol.222, pp.119448. DOI: 10.1016/j.indcrop.2024.119448
- [17] Zhang, J., Guo, J., Wang, S.H., Yue, M.H., Zhang, S.S., Peng, H.H., Yin, X., Du, J., Zhao, N. & Ma, C.Y. (2023). Comparison of methods for water content in rice by portable near-infrared and visible light spectrometers (便携式近红外和可见光光谱仪检测水稻水分含量方法比较研究). *Spectroscopy and Spectral Analysis*, Vol.43, pp.2059-2066. DOI: 10.6041/j.issn.1000-0593(2023)07-2059-08
- [18] Zhang, T., Guan, H.O., Ma, X.D. & Shen, P.P. (2023). Drought recognition based on feature extraction of multispectral images for the soybean canopy. *Ecological Informatics*, Vol.77, pp.102248. DOI: 10.1016/j.ecoinf.2023.102248
- [19] Zhang, X.D., Duan, Z.H., Mao, H.P., Gao, H.Y., Shi, Q., Wang, Y.F., Shen, B.G. & Zhang, Q. (2021). Tomato water stress state detection model by using terahertz spectroscopy technology (利用太赫兹光谱技术构建番茄水分胁迫状态检测模型). *Transactions of the Chinese Society of Agricultural Engineering (Transactions of the CSAE)*, Vol.43, pp.121-128. DOI: 10.11975/j.issn.1002-6819.2021.15.015
- [20] Zhao, X.T., Zhang, S.J., Li, B. & Li, Y.K. (2018). Study on Moisture Content of Soybean Canopy Leaves under Drought Stress Using Terahertz Technology (太赫兹光谱技术用于干旱胁迫下大豆冠层含水量检测研究). *Spectroscopy and Spectral Analysis*, Vol.43, pp.3089-3097. DOI: 10.3964/j.issn.1000-0593(2018)08-2350-05

OBSTACLE AVOIDANCE PATH OF WHEELED AGRICULTURAL HANDLING ROBOTS IN WAREHOUSE BASED ON IMPROVED ACO-DWA ALGORITHM

基于改进 ACO-DWA 算法的轮式农业机器人仓库搬运避障路径研究

Kan ZHANG^{*})

School of Computer Engineering, Shanxi Vocational University of Engineering Science and Technology, Jinzhong, Shanxi / China

Tel: +8613834246680; E-mail: zk321672024@126.com

Corresponding author: Kan Zhang

DOI: <https://doi.org/10.35633/inmateh-74-51>

Keywords: Artificial potential field; Ant colony algorithm; Agricultural robot; Path optimization; Obstacle avoidance

ABSTRACT

The existing obstacle avoidance control algorithms for wheeled agricultural warehouse handling robots are prone to the local optimal solution in the process of path optimization and collision can easily occur during multi-robot simultaneous operation. Given this, the obstacle avoidance of wheeled agricultural warehouse handling robots was explored in this study, and an obstacle avoidance path planning algorithm for wheeled agricultural handling robots in warehouse based on improved ACO-DWA algorithm was proposed. Then, the moving trajectory of agricultural warehouse handling robots during handling process was studied, and their spatial kinematics equation was given. Next, the real-time pose of agricultural warehouse handling robots was detected, and their motion path was planned considering the real-time position of obstacles and the target locations of handling. In addition, the obstacle avoidance controlling quantity of agricultural warehouse handling robots was calculated according to the deviation between the pose of robots and the planned path. Supported by a controller, the obstacle avoidance control work of agricultural warehouse handling robots was realized. It was concluded through the effect experiment that compared with the traditional method, the improved ACO-DWA algorithm designed in this study significantly reduced the number of collisions between agricultural robots, and through practical application, the proposed algorithm can meet the needs of improving warehouse logistics management efficiency.

摘要

针对现有轮式农业机器人仓储搬运避障控制算法存在的路径寻优易陷入局部最优解, 及多机器人同时作业易发生碰撞等问题, 对轮式农业机器人的仓库避障控制进行了研究, 并提出提出了一种基于改进 ACO-DWA 算法的轮式农业机器人仓库搬运避障路径规划算法; 对农业机器人仓储机器人搬运过程中的移动轨迹进行了研究, 给出了机器人空间运动学方程。检测农业农业机器人仓储搬运实时位姿, 考虑障碍物实时位置和搬运目标地点, 规划机器人移动路径。根据农业机器人位姿与规划路径之间的偏差, 计算农业机器人仓储搬运避障控制量, 在控制器的支持下, 实现农业机器人仓储搬运避障控制工作。通过效果测试实验得出结论: 与传统方法相比, 本文所设计的改进 ACO-DWA 算法, 农业机器人之间发生碰撞的次数也显著少于传统避障控制算法, 经实际应用能够满足提升仓储物流管理效率的需求。

INTRODUCTION

Agricultural warehouse handling robots capable of automatic navigation, intelligent identification and efficient cargo handling have been increasingly widely applied to the fields of agricultural products warehousing and agricultural logistics, helping enterprises to realize automatic, intelligent and efficient agricultural warehouse management (Hao *et al.*, 2022). In dynamic and complicated warehouse environments, the autonomous navigation and obstacle avoidance of agricultural warehouse handling robots are the key to ensuring efficient and safe operations. When it comes to the obstacle avoidance of agricultural warehouse handling robots, they perceive the surrounding environment and identify obstacles in a real-time manner through sensors and plan a collision-free path according to a certain algorithm, so as to successfully evade obstacles and reach the destination (Guo *et al.*, 2022).

Obstacle avoidance control methods for agricultural warehouse handling robots have been proposed in order to ensure the obstacle avoidance effect and enhance the safety of robots during movement to the greatest extent on the premise of ensuring the handling work quality. Agricultural handling robots, which integrate various key technologies, such as deep visual sensor positioning, obstacle detection & path planning, energy consumption and thermal management and system integration & optimization, have experienced rapid development and application in the military and civilian field (Dang, 2021). Especially with the modernization, informatization and intelligent development of agricultural production, plant protection robots that can operate autonomously in fields and on edges of fields possess broad development prospects, which, on the one hand, reduce the labor intensity of agricultural production, and on the other hand, improve working performance and quality (Zheng et al., 2021).

Agricultural handling robots have gradually replaced manual labor to conduct such logistics operations as handling and sorting in real production, promoting the intelligent upgrading of agricultural warehouses and driving them to develop towards intelligent and unmanned directions. The research on the obstacle avoidance path of agricultural warehouse handling robots has been successively carried out, but the order of task allocation, the path planning of robots, and multi-robot collaborative handling remain to be deeply explored to ensure the practical application and popularization of handling robots (Li et al., 2021). Meanwhile, the current research difficulty lies in how to coordinate handling robots with other automation equipment in the warehouse and how to conduct path planning for handling robots under the interference of other movable automation equipment to ensure the most efficient operation of the warehouse.

Path planning, a key issue in the technical field of agricultural warehouse handling robots, determines how robots travel to the designated target, involving the perception and calculation of environmental information. At present, the algorithms used in path node search mainly include intelligent algorithms (ant colony optimization (ACO) algorithm (Rosemann et al., 2012), genetic algorithm (Sarkar et al., 2012), algorithms based on graph search (A^* (Ornek et al., 2022), Hybrid A^* (Zhai et al., 2022)). A^* algorithm has been widely used, but when searching in complex unstructured scenes, it is characterized by a large calculated quantity, serious memory consumption and narrow channels, which will easily generate oscillation. Aiming at the slow operation speed of A^* algorithm, Qian et al. (2019) designed a tracking controller with global convergence by following the idea of backstepping, which can avoid the local stability problem caused by the linearization method when handling nonlinearity problems. Ji et al. (2021) reduced the number of inflection points using the differential method, which, however, increased the calculated quantity. Ding et al. (2022) proposed the jump point search method, but this method failed to guarantee the global optimal path in complex irregular maps. Hossain et al. (2022) used the fourth-order Bezier curve to express the trajectory shape, whose plasticity, however, was restricted by the limitations of the Bezier curve, making it inapplicable to the complex road surface. During the actual operation process in orchard environments, the kinematical constraints of robots should be ensured in addition to obstacle avoidance constraints and distance cost. Therefore, the methods combining path planning and trajectory optimization have been proposed by some scholars, and the planned paths have been subjected to trajectory optimization.

Kobayashi and Motoi (2022) applied the differential flatness technique to the controller design, and expressed the state variables and input variables with the output and its derivatives of the system. By selecting reasonable output variables, the system can be effectively reduced in dimension, which is convenient for the design and solution of the controller. Wang et al. (2022) successfully designed a trajectory tracking controller for nonholonomic systems with the help of the input-output feedback local linearization method together with the dynamic expansion method, and achieved a good trajectory tracking effect by means of simulation.

The existing control algorithms of warehouse logistics robots correct travel paths and evade obstacles on the paths based on high-definition cameras, radar sensors, and distance sensors. For example, Zohaib et al. (2014) proposed an Automated Guided Vehicle (AGV), which can realize autonomous navigation and obstacle avoidance on the basis of manually setting the control program. However, AGV robots have some problems in global path optimization, and they are prone to local optimum so as to select noneconomical paths (Zohaib et al., 2014). Hichri et al. (2022) put forward a path optimization algorithm based on Q-learning on the basis of neural network model and machine learning algorithm. According to the instructions, the existing economical control algorithms for warehouse logistics robots have been selected, and the correction of travel paths and the obstacle avoidance along the paths have been realized mostly based on high-definition cameras, radar sensors and distance sensing. For example, Tan et al. (2022) used the backstepping method to construct two kinds of motion controllers from two situations: local minor error and global arbitrary error, which

successfully solved the trajectory tracking problem of mobile robots and extended them to nonholonomic systems with simple dynamic models.

Wang *et al.* (2022) proposed an Automated Guided Vehicle (AGV), which can realize autonomous navigation and obstacle avoidance on the basis of manually setting the control program. However, AGV robots have some problems in global path optimization, and they are prone to local optimum so as to select noneconomical paths (Wang *et al.*, 2022). Zhou *et al.* (2022) proposed a path optimization algorithm based on Q-learning on the basis of neural network model and machine learning algorithm, which can select a more economical path according to instructions and avoid obstacles along the path. Zhang *et al.* (2021) divided different priority sequences for handling robots according to different handling tasks, and low-priority robots should proactively give way to high-priority robots under this sequence condition.

Based on the above analysis, an obstacle avoidance path planning algorithm for wheeled agricultural warehouse handling robots based on improved ACO-DWA algorithm was put forward in this study. Under dynamic environments, image acquisition and preprocessing were performed, dynamic obstacles in the video were positioned according to feature recognition, and the obstacle avoidance path of agricultural warehouse handling robots was planned based on obstacle positioning results. Then, the travel cost of agricultural robots was fused into the objective function of search nodes using the improved ACO-DWA algorithm, path planning was conducted online according to the environmental map, and the acquired path planning effect was evidently better than that obtained by the traditional DWA algorithm in path length, obstacle avoidance ability and calculation time.

MATERIALS AND METHODS

The basic principle for optimally designing the obstacle avoidance control method of agricultural warehouse handling robots is described as follows: the dynamic obstacles in the agricultural warehouse were identified and positioned through image acquisition, image preprocessing, feature extraction and feature recognition. Then, the obstacle avoidance path of agricultural warehouse handling robots was planned according to obstacle positioning results. Next, the controlled quantity of obstacle avoidance was calculated considering the current handling position of agricultural robots, and the agricultural robot's task of obstacle avoidance control was completed under the support of a controller.

Determination of obstacle position in the environment via visual positioning technology

(1) Generation of dynamic environmental images during handling in warehouse

In the optimally designed obstacle avoidance control method for agricultural warehouse handling robots, the dynamic environment of agricultural warehouse handling robots was acquired through a single visual sensor, and the generation result of obstacle images at any moment is displayed as follows:

$$I(x_i(t), y_i(t)) \begin{cases} k_c x_i \cdot f \cdot \cos \alpha \\ k_c y_i \cdot f \cdot \sin \alpha \end{cases} \quad (1)$$

Where k_c is the imaging coefficient of the single visual sensor; f represents the focal length; α stands for the imaging angle of an obstacle, i.e., the included angle between the obstacle and the built-in sensor in the agricultural warehouse handling robot (Dang, 2021). To follow the rule of "everything looks small in the distance and big on the contrary" in the obstacle image, the distance between the imaging sensor and the obstacle should be measured as follows:

$$d = \frac{H(k_1 f - h \tan \alpha)}{k_1 f \tan \alpha + h} \quad (2)$$

In Formula (2), H and h represent the height of the imaging equipment and the height of the imaging plane, respectively; k_1 is the constant coefficient whose value depends on the work parameters of the single visual sensor. Using the above method, the generation result of dynamic obstacle images can be obtained. Since the optimally designed obstacle avoidance control method operates under dynamic environments, the acquisition frequency of dynamic obstacle images should be set. Controlled by the drive program, obstacle images are continuously acquired, completing the task of image acquisition.

(2) Environmental image preprocessing

In order to provide effective reference for the obstacle avoidance work of agricultural warehouse handling robots, the initial obstacle image was taken as the processing object, and the preprocessing work of the initial obstacle image was completed through image filtering, image enhancement, image correction,

obstacle target extraction, etc. Image filtering aimed to filter out the noise information in the obstacle image. Median filtering and mean filtering were combined to ensure the denoising effect on the image. The principle of median filtering is to replace the value of each pixel in the image with the median value of the pixel in the neighborhood. Mean filtering can facilitate the image pixel to change more smoothly, belonging to a linear filtering method. The filtering results of the initially acquired obstacle image in the warehouse environment of agricultural handling robots are exhibited as follows:

$$\begin{cases} g_1(x,y) = \text{med}\{I(x-k, y-1), (k, l \in U)\} \\ g_2(x,y) = \frac{1}{m} \sum I(x,y) \end{cases} \quad (3)$$

Where U is the 2D template of the image; m represents the number of pixel points contained in the initial image; $g_1(x,y)$ and $g_2(x,y)$ correspond to the median and mean filtering results, respectively. Under the irradiation of natural light, an object will generate a shade at the bottom or on the surface of another object. The shades of two objects may be overlapped if they are close to each other, leading to the failure to independently extract the image of the obstacle with shade crossing and making it necessary to eliminate the shaded area of the image and complete the image enhancement. The processing results are depicted as below:

$$g_z(x,y) = R(i,j) \times G(i,j) \quad (4)$$

Where $R(i,j)$ and $G(i,j)$ are the pixel value in the initial image and the grey level histogram, respectively. $G(i,j)$ is calculated as per the following formula:

$$G(i,j) = f_{sum} \left(\frac{I(x,y)}{m} \right) \quad (5)$$

Where $f_{sum}()$ is the sum function. Image calibration mainly aims at the deviation of light to improve the light distribution of the image so that the image can be more uniform and natural. This technology is applicable to such scenarios as images with rich details in the shaded part, backlighting scenarios and images with color deviations. The light calibration process of images can be quantitatively expressed as below:

$$g_j = k_c \cdot I^{\gamma_{gamma}}(x,y) \quad (6)$$

Where k_c is the constant coefficient and k_{gamma} denotes the Gamma coefficient. On this basis, the obstacle objects in the initially acquired image were extracted by means of background subtraction. Background subtraction is a preprocessing method that performs the differential operation on the image to be processed and the background reference image by taking the background of one frame in the image sequence as the reference and obtains the binarized image of the object through threshold division. This method can effectively extract objects from the background. The extraction results of obstacle objects are as follows:

$$Z(x,y) = \begin{cases} 1, & |I(x,y) - B(x,y)| < \delta \\ 0, & \text{otherwise} \end{cases} \quad (7)$$

where $B(x,y)$ is the visual image generation background of agricultural warehouse handling robots; δ represents the background difference threshold. Repeating the above operation, the preprocessing results for the obstacle images of agricultural warehouse handling robots can be obtained.

(3) Identification of obstacles in dynamic environment

Whether any obstacle exists in the dynamic environment corresponding to the current visual field of the agricultural warehouse handling robot is judged by means of feature matching. In the process of obstacle identification, the corresponding matching standard, marked as τ_B , should be set first according to the features of possible obstacles in the warehouse environment. Then, the matching result between the extracted environmental image feature and the feature standard is:

$$\zeta(i) = \frac{\tau_T \cdot \tau_B(i)}{\|\tau_T\| \cdot \|\tau_B(i)\|} \quad (8)$$

where $\tau_B(i)$ is the edge feature standard of the i -th type of obstacles. The relevant data are substituted into Formula 10. If the calculated feature matching degree is higher than the threshold ζ_0 , i -th type of obstacles exist in the current dynamic environment, or otherwise, such obstacles do not exist (Ornek et al., 2022). The specific value of variable i is adjusted according to the above method and the operation is repeated until completing the obstacle identification in the dynamic environment.

Obstacle avoidance path planning of agricultural warehouse handling robots

When the real-time position of dynamic obstacles in the dynamic warehouse handling environment, the motion path of robots is planned, ensuring that the planned path will not be overlapped with the obstacle at the same moment. The real-time pose detection result of the agricultural warehouse handling robot is taken as the initial position. Considering the target location of the warehouse handling task, the initial motion path is generated, expressed as follows:

$$L_0 = \frac{x_r(y_m - y_r)}{x_m - x_r} + y_r \quad (9)$$

In Formula 9, (x_m, y_m) stands for the coordinates of the final target position for the agricultural warehouse handling robot to execute the handling task, and the initially generated motion path is a straight path. According to the movement speed of the robot, its actual node position at any moment can be acquired and compared with the visual positioning information of the dynamic obstacle at the corresponding moment, and then the relationship between their distance and the threshold is judged. If the calculated distance is higher than the threshold, there is no collision risk between the robot and the obstacle, making it unnecessary to adjust the position of this path node, or otherwise, this path node should be adjusted through the following method:

$$\begin{cases} x_r(t) = x_r(t) + \Delta x \\ y_r(t) = y_r(t) + \Delta y \end{cases}, (x_r(t), y_r(t)) \in L_0 \quad (10)$$

where Δx and Δy are the adjustment quantities of the agricultural warehouse handling robot in horizontal and vertical directions, respectively. Each node on the initially generated motion path of the robot is adjusted according to the above method and connected with two continuous front and rear nodes, the adjusted path is subjected to smoothing, and thus the path planning of the robot is completed. Since both the robot and obstacle are under dynamic changes, it is necessary to dynamically update the planned path according to the pose detection result of the robot and the visual positioning result of the obstacle.

ALGORITHM DESIGN

ACO algorithm

(1) State transfer rate. At time t , the state transfer state of the ant from the state node i to the adjacent state node j can be defined as below:

$$P_{ij}^m(t) = \begin{cases} \frac{\tau_{ij}^\alpha(t) \cdot \eta_{ij}^\beta(t)}{\sum_{S \in U^m} \tau_{is}^\alpha(t) \cdot \eta_{is}^\beta(t)}, & \text{if } j \in U^m \\ 0, & \text{else} \end{cases} \quad (11)$$

where $P_{ij}^m(t)$ is the state transfer probability of the m -th ant from the state node i to the state node j at time t ; $\tau_{ij}^\alpha(t)$ is the pheromone concentration the path (i, j) , in which α is the information heuristic factor, reflecting the influence of pheromone on the path selection of ants; $\eta_{ij}^\beta(t)$ represents the heuristic function for the m -th ant to choose the adjacent state node j at the state node i , in which β is the expected heuristic factor, indicating the importance of heuristic information in guiding the search process of the ant colony; U^m denotes the set of next nodes not accessed by the ant; s is the set of selectable nodes adjacent to the current position; $\tau_{is}^\alpha(t)$ is the pheromone concentration of the m -th ant between the current state node i and each adjacent state node; $\eta_{is}^\beta(t)$ is the heuristic function of the m -th ant between the current node i and each adjacent state node.

The heuristic function $\eta_{ij}(t)$ can be expressed as below:

$$\eta_{ij}(t) = 1 / D_{ij} \quad (12)$$

where D_{ij} is the distance between the state nodes i and j .

(2) Pheromone concentration updating model

The currently common pheromone concentration updating models include ant-density system (ADS), ant-quantity system (AQS) and ant-cycle system (ACS). ADS and AQS models adopt the local updating strategy while ACS model applies the global updating strategy. Considering the algorithm solving speed and

obstacle avoidance ability, AQS model was taken as the prototype in this study. Assuming that the set of state nodes on the path (i, j) passed by the m -th ant in the current cycle is $X\{(i, j) | i = 1, 2, \dots, n; j = 1, 2, \dots, n\}$, then:

$$\Delta\tau_{ij}^m(t) = \begin{cases} \frac{Q}{D_{ij}}, & \text{if } (i, j) \in X \\ 0, & \text{else} \end{cases} \quad (13)$$

where $\Delta\tau_{ij}^m(t)$ is the pheromone concentration increment on the path of the m -th ant moving from the state node i to the adjacent state node j at time t , Q is the pheromone intensity, which is a constant greater than 0.

Improved DWA algorithm design

The classical DWA algorithm converts the position control of robots into speed control and describes the obstacle avoidance problem into the optimization problem of robot speed space with constraints, including speed, heading direction and surrounding environmental obstacles' position constraints. The speed set that depends on the physical constraints of obstacles around the robot's moving trajectory nodes and is composed of the robot's longitudinal speed and yaw rate limitations must meet the following formula:

$$U_s = \{(u_a, \omega_r) | 0 \leq u_a \leq u_{amax}, -\omega_{rmax} \leq \omega_r \leq \omega_{rmax}\} \quad (14)$$

It can be considered that the robot's traveling trajectory is composed of n broken line segments with n time frames, and it is believed that the connection point between broken line segments is close to the obstacle position to the greatest extent on the premise of meeting the expansion size limitation of the obstacle. To protect the robot from colliding with any obstacle during the movement, it can be obtained the speed set after time dt must meet the following formula according to the limitation of kinematic conditions:

$$U_a = \{(u_a, \omega_r) | u_a \leq \sqrt{2 \cdot \text{dist}(u_a, \omega_r) \cdot \dot{u}_a}, \omega_r \leq \sqrt{2 \cdot \text{dist}(u_a, \omega_r) \cdot \dot{\omega}_r}\} \quad (15)$$

where $\text{dist}(u_a, \omega_r)$ is the straight-line distance between the robot and the obstacle at the next moment.

Assuming that the speed set of the robot at the present moment is $u_{acurr} + \omega_{amax}$, then the speed set U_d at the next moment must satisfy the following condition:

$$U_d = (u_{ad}, \omega_{rd}) = \begin{cases} u_{acurr} - u_{amax} dt \leq u_a \leq u_{acurr} + u_{amax} dt \\ \omega_{rcurr} - \omega_{rmax} dt \leq \omega_r \leq \omega_{rcurr} + \omega_{rmax} dt \end{cases} \quad (16)$$

The final speed set U can be expressed as below:

$$U = U_s \cap U_a \cap U_d \quad (17)$$

The speed set at the next moment is predicted through the objective function. The objective function defined in this study comprehensively considers the movement speed, driving direction and collision safety, as follows:

$$G(u_{ad}, \omega_{rd}) = l \cdot \theta + m \cdot \text{dist}(u_a, \omega_r) + n \cdot u_{amax} \quad (18)$$

where θ represents the included angle between the robot's driving direction and the target line; $\text{dist}(u_a, \omega_r)$ indicates the shortest distance between the robot position and the obstacle; l , m , and n are the angle, distance and vehicle speed weight coefficients, respectively.

A greater value of the objective function indicates the greater excellence of the speed set. During the path planning process, the robot needs to acquire position and speed information from multiple sensors, while these signals are usually not always continuous, and the evaluation result may have a specific error. To reduce the error, the above 3 weight coefficients are generally normalized into a number within $[0, 1]$.

Out of the above considerations, an improved ACO-DWA algorithm was proposed in this study based on the advantages of the ACO algorithm in global optimization and continuous convergence of search process. The weight coefficient of the objective function was made self-adaptive by the ACO algorithm. This algorithm significantly reduces the bypassing distance and path planning time of the robot and improves the through capacity and safety in scenarios with dense obstacles. Hereby the specific dynamic updating process of the above weight coefficients according to the ACO algorithm will be detailed.

DAW algorithm improvement fusing ACO algorithm

It is assumed that at time t , there are obstacles of a certain density in the area of the robot's driving direction. If the number of obstacles in this area is K , the shortest distance between the robot and the i -th obstacle is D_i and the azimuth angle is θ_i . When M is greater than the threshold, this area is distributed with dense obstacles. The shortest distance D_{ij} between the i -th obstacle and the j -th obstacle is defined as follows:

$$D_{ij} = \sqrt{D_i^2 + D_j^2 - D_i D_j \cos(\theta_i - \theta_j)}, \theta_i \gg \theta_j \quad (19)$$

Considering the safety and maneuverability of the robot when passing through obstacles and in order to measure the through capacity of the robot between two obstacles, the number of its pass-through functions D_s is defined as below:

$$D_s = a \cdot \frac{\theta_{\max}}{\omega_{r\max}} + b \cdot \frac{u_{\max}}{\dot{u}_a} \quad (20)$$

where $\omega_{r\max}$ is the maximum value in ω_r ; θ_{\max} is the maximum value in θ ; coefficient a reflects the influence of the robot's deviation in direction on the through capacity and it is taken as 0.6 according to the modeling experience of grid maps. Coefficient b indicates the influence of the robot's speed on the through capacity, and it is taken as 0.4 according to the modeling experience of grid maps, too.

Introducing the expansion radius σ of obstacles, the condition for the robot to pass through two obstacles safely is:

$$D_s > \frac{D_{ij}}{\sigma} \quad (21)$$

where σ is set to 0.3 according to the modeling experience of grid maps. The updating model for dynamic pheromone is as follows:

$$\Delta \tau_{ij}^m = \begin{cases} \frac{\sigma \cdot D_{s\max} - D_{ij}}{D_{ij} - \sigma \cdot D_{s\min}}, \delta > \varepsilon \\ \frac{D_{ij} - \sigma \cdot D_{s\max}}{D_{ij} - \sigma \cdot D_{s\min}}, \delta \leq \varepsilon \end{cases} \quad (22)$$

where $\delta = D_{\max} - D_{\min}$, in which ε is the acceptable error in the n -th iteration, being a constant; D_{\max} refers to the maximum number of pass-through functions of the robot when moving between any two obstacles after traveling to the local obstacle avoidance area; D_{\min} is the minimum number of pass-through functions of the robot when moving between any two obstacles after traveling to the local obstacle avoidance area.

Algorithm flow

Step 1: The starting point and target point of the robot's movement are positioned after acquiring the environmental map information through a laser radar; the information of all state nodes in space are acquired and the adjacency matrix and heuristic information matrix are calculated;

Step 2: Parameter initialization. The number of iterations is initialized as N , the ant colony scale as M , the information heuristic factor as α , the expected heuristic factor as β , pheromone evaporation coefficient as ρ , and the pheromone concentration as τ ;

Step 3: The density of obstacles, the actual distance between the robot and each obstacle and their orientations are calculated in a real-time manner;

Step 4: Path selection and updating. The adjacency matrix is inquired, the feasible node set for the robot to move from the current node i to the next node is acquired, and the probability for the m -th ant to select adjacent nodes is solved. Whether the ant enters an area with dense obstacles is judged with such information as the density of obstacles, the actual distance between the robot and each obstacle and their orientations according to the captured map information during node updating; if yes, turn to Steps 5-7; if not, all weight coefficients in Step 5 are made constant;

Step 5: The node set greater than the threshold $dist(u_a, \omega_r)$ is eliminated from the planned global path nodes, the ant number is updated, the distance between obstacles and the number of the robot's pass-through functions D_s are calculated via the vehicle-mounted processor, the values of D_{\max} and D_{\min} are acquired, the pheromone is calculated and updated, and the dynamically updated weight coefficients l , m and n are obtained;

Step 6: The alternative speed space $U(u_a, \omega_r)$ is solved, and the 3 weight coefficients are respectively normalized to obtain the optimal speed set of the robot at time $t+1$;

Step 7: This speed is executed, and whether the target point is reached is judged; if yes, end the iteration process; if not, return to Step 1.

RESULTS

Experimental environment and parameter settings

A square area (side length: 30m×30m) was chosen as the experiment site for the agricultural warehouse handling robot, which was subjected to grid partitioning. The layout of shelves and the scene picture are displayed in Fig. 1.

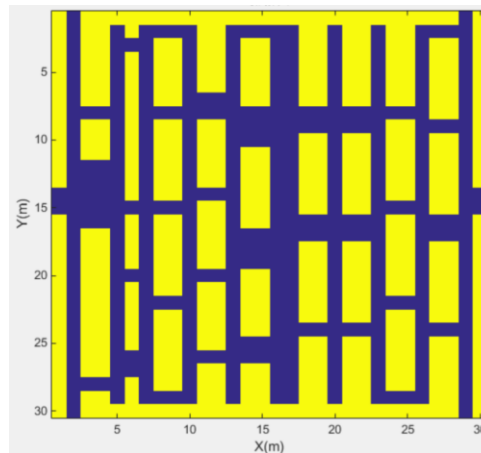


Fig. 1 - Warehouse site diagram based on grid method arrangement

In Fig. 2, the yellow cube indicates the immovable shelf, and the blue area is the passage. The length, width and height of the agricultural handling robot used in the experiment are 0.7, 0.5 and 0.4 m respectively, and the warehouse logistics handling robot itself has the telescopic lifting function, with the maximum bearing capacity of 100 kg.

At the same time, the robot is also equipped with a set of sensor suites, including a wireless communication module and a visual radar system, which are used to receive the background instruction information, deal with emergencies and avoid collisions. And the best travel path was chosen using the improved ACO-DWA algorithm from the global perspective. The speed and angular velocity of the agricultural handling robot are 2 m/s and 2.5 rad/s, respectively, the maximum number of iterations of the improved ACO-DWA algorithm is 800, and the value range for the core parameter of the policy gradient algorithm is 0.7-2.2. The obstacle avoidance path for the wheeled agricultural warehouse handling robot acquired through the improved ACO-DWA algorithm is exhibited in Fig. 2.

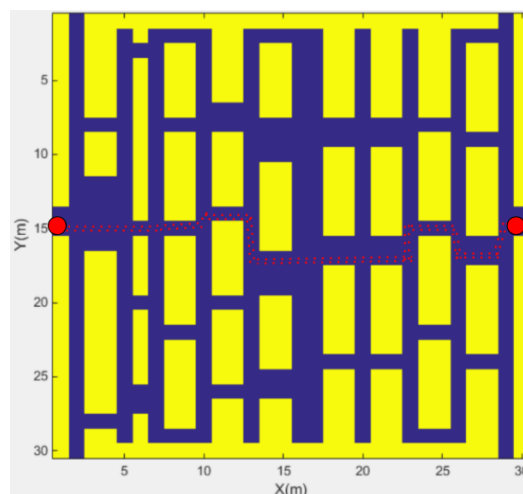


Fig. 2 - The travel path selected improved by ACO-DWA algorithm

In Fig. 3, the improved ACO-DWA algorithm proposed in this study planned the travel path from the perspectives of global planning and collision avoidance of moving obstacles, and chose a more economical path; the number of iterations of the improved ACO-DWA algorithm in global optimization was analyzed, and the algorithm iteration efficiency was higher under general circumstances, proving that the algorithm possesses stronger data training ability. If the number of algorithm iterations was too great and even exceeded the maximum number of iterations, the algorithm would be easily stuck in local optimum, failing to realize the

optimization within a global scope. In the process of path optimization, the maximum number of iterations of each algorithm was set to 800, the improved ACO-DWA algorithm gained the optimal result, and the agricultural handling robot turned for 10 times in the warehouse, with a driving distance of 42 m.

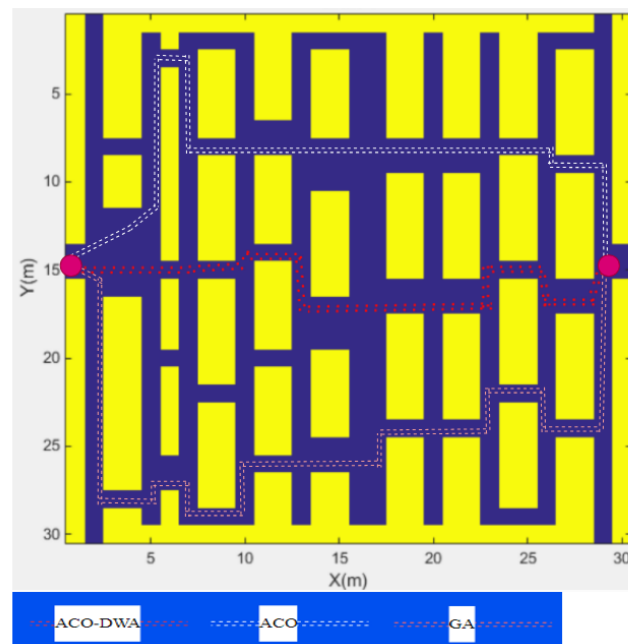


Fig. 3 - The travel path selected by each algorithm

Comparison of experimental data

To verify the improved ACO-DWA algorithm proposed in this study, path planning was performed from two angles: global planning and collision avoidance of moving obstacles, and a relatively economical path was chosen; as for the traditional ACO algorithm and genetic algorithm, turning occurred for 9 and 16 times, respectively, for the sake of avoiding other warehouse handling robots, which affected the overall travel speed. The paths obtained by the 3 algorithms for completing this handling task are exhibited in Figure 3.

Since the improved ACO-DWA algorithm selected a near path and can perceive and judge other moving obstacles around based on policy gradient and plan a new local path in advance, it spent the shortest time; for the other two traditional path planning algorithms, retracing occurred for avoiding obstacles, which influenced the final time consumption.

From the convergence speed of the algorithm, the convergence time of the improved ACO-DWA algorithm returned to zero after the 413th iteration, while the ACO algorithm and genetic algorithm completed the convergence only after approaching the maximum number of iterations, being 726 and 755, respectively. The iterative performance of the algorithm determines the efficiency of the algorithm and also has an important impact on the obstacle avoidance ability of the algorithm for selecting the optimal travel path. The experimental data showed that when a relatively complicated agricultural warehouse handling scenario, turning took place for 9 and 16 times, respectively, under obstacle avoidance planning based on the traditional ACO algorithm and genetic algorithm; under the control of the improved ACO-DWA algorithm, the policy gradient-based algorithm effectively avoided collisions during the simultaneous operation of multiple warehouse handling robots, and turning only occurred for 10 times. Besides, the policy gradient-based algorithm would adjust the direction of motion and speed of the robot timely according to the local obstacle distribution on site, which not only ensured traveling according to the path planned by the improved ACO-DWA algorithm as a whole but also effectively realized the avoidance of local moving obstacles.

CONCLUSIONS

In the dynamic warehouse environment, the obstacle avoidance control method of agricultural warehouse handling robots based on visual positioning and dynamic rectification is an efficient, accurate and highly adaptable method, which is of great practical significance for strengthening warehousing operation efficiency and safety. Visual positioning technology enables the robot to acquire and process environmental information in real time, and avoid obstacles through the real-time rectification of the robot's trajectory. With the increasing complexity of the working environment for warehouse handling robots, robots should not only

avoid static obstacles but also evade other robots on the path, that is, multiple robots working simultaneously are dynamic obstacles. In the path planning of logistics robots, the overall path of robots should be planned first, and the dynamic obstacles in local areas should be avoided by dynamic real-time rectification, which proposes higher requirements for the real-time communication of robots and the real-time selection of local paths. Therefore, the dynamic real-time rectification and obstacle avoidance based on the spatial coordinate transformation of robots will become one of the main development trends of warehouse logistics robots in the future.

In this study, a path planning method for wheeled agricultural warehouse handling robots was proposed. The improved DWA algorithm integrating the ACO algorithm can effectively improve the operation efficiency of the algorithm, reduce the bypassing distance around obstacles, shorten the path planning time and enhance the driving safety. The effectiveness and universality of the improved ACO-DWA algorithm were verified through simulation tests. This method evidently accelerates the optimization and convergence rate of the global path for agricultural warehouse handling robots. The applicability of the algorithm under scenarios with dynamic obstacles will be further explored on this basis.

REFERENCES

- [1] Dang, X. (2021). Automatic obstacle avoidance control method of packaging robot based on gravitational potential field (基于引力势场的包装机器人自动避障控制方法). *Packaging Engineering*, Vol.42, pp. 254-259, Chongqing/China.
- [2] Ding, H. W., Cao, X. G., Wang, Z. S., Dhiman, G., Hou, P., Wang, J., Li, A.S., & Hu, X. (2022). Velocity clamping-assisted adaptive Salp swarm algorithm: balance analysis and case studies. *Mathematical Biosciences and Engineering*, Vol. 19, pp. 7756-7804, United States.
- [3] Guo, H. Q., Fu, L. X., Zhang, Y., & Mao, J. L. (2022). Robot obstacle avoidance path planning method based on dynamic obstacles (基于动态障碍物的机器人避障路径规划方法). *Video Engineering*, Vol. 46, pp. 73-77, Beijing/China.
- [4] Hao, K., Zhang, H. J., Li, Z. S., & Liu, Y. L. (2022). Path planning of mobile robot based on improved obstacle avoidance strategy and double optimization ant colony algorithm (基于改进避障策略和双优化蚁群算法的机器人路径规划). *Transactions of the Chinese Society for Agricultural Machinery*, Vol. 58, pp. 303-312, Beijing/China.
- [5] Hichri, B., Gallala, A., Giovannini, F., & Kedziora, S. (2022). Mobile robots path planning and mobile multirobots control: a review. *Robotica*, Vol. 40, pp. 4257-4270, United Kingdom.
- [6] Hossain, T., Habibullah, H., Islam, R., & Padilla, R. V. (2022). Local path planning for autonomous mobile robots by integrating modified dynamic-window approach and improved follow the gap method. *Journal of Field Robotics*, Vol. 39, pp. 371-386, United States.
- [7] Ji, X. Y., Feng, S., Han, Q. D., Yin, H. F., & Yu, S. W. (2021). Improvement and fusion of A* algorithm and dynamic window approach considering complex environmental information. *Arabian Journal for Science and Engineering*, Vol. 46, pp. 7445-7459, Saudi Arabia.
- [8] Kobayashi, M., & Motoi, N. (2022). Local path planning: dynamic window approach with virtual manipulators considering dynamic obstacles. *IEEE Access*, Vol. 10, pp. 17018-17029, United States.
- [9] Li, J., & Qin, W. (2021). Design of mobile robot obstacle-avoidance control system based on vision system (基于视觉的移动机器人避障控制系统设计). *Machine Tool & Hydraulics*, Vol. 49, pp. 24-28, Guangdong/China.
- [10] Ornek, B. N., Aydemir, S. B., Duzenli, T., & Ozak, B. (2022). A novel version of slime mould algorithm for global optimization and real world engineering problems. *Mathematics and Computers in Simulation*, Vol. 198, pp. 253-288, Netherlands.
- [11] Qian, Q. W., Wu, J. F., & Wang, Z. (2019). Optimal path planning for two-wheeled self-balancing vehicle pendulum robot based on quantum-behaved particle swarm optimization algorithm. *Personal and Ubiquitous Computing*, Vol. 23, pp. 393-403, Germany.
- [12] Sarkar, R., Barman, D., & Chowdhury, N. (2022). Domain knowledge based genetic algorithms for mobile robot path planning having single and multiple targets. *Journal of King Saud University-Computer and Information Sciences*, Vol. 34, pp. 4269-4283, Saudi Arabia.

- [13] Tan, Z., Liang, H. G., Zhang, D., & Wang, Q. G. (2022). Path planning of surgical needle: a new adaptive intelligent particle swarm optimization method. *Transactions of the Institute of Measurement and Control*, Vol. 44, pp. 766-774, United Kingdom.
- [14] Wang, Z., Ding, H., Wang, J., Hou, P., Li, A., Yang, Z., & Hu, X. (2022). Adaptive guided Salp swarm algorithm with velocity clamping mechanism for solving optimization problems. *Journal of Computational Design and Engineering*, Vol. 9, pp. 2196-2234, Netherlands.
- [15] Wang, Z., Ding, H., Yang, Z., Li, B., Guan, Z., & Bao, L. (2022). Rank-driven Salp swarm algorithm with orthogonal opposition-based learning for global optimization. *Applied Intelligence*, Vol. 52, pp. 7922-7964, Netherlands.
- [16] Zhai, L. Z., & Feng, S. H. (2022). A novel evacuation path planning method based on improved genetic algorithm. *Journal of Intelligent and Fuzzy Systems*, Vol. 42, pp. 1813-1823, Netherlands.
- [17] Zhang, L., Zhang, Y. J., & Li, Y. F. (2021). Mobile robot path planning based on improved localized particle swarm optimization. *IEEE Sensors Journal*, Vol. 21, pp. 6962-6972, United States.
- [18] Zheng, J., Gao, Y., Lei, Z., Yang, C. J., Wang, C., & Oderman, G. (2021). Real time search of agricultural machinery based on matrix sequence sensor. *INMATEH-Agricultural Engineering*, Vol. 4, pp. 425-433, Romania.
- [19] Zohaib, M., Pasha, S. M., Javaid, N., Salaam, A., & Iqbal, J. (2014). An improved algorithm for collision avoidance in environments having U and H shaped obstacles. *Studies in Informatics and Control*, Vol.23, pp. 97-106, Romania.

MULTI-UAV TASK ALLOCATION AND PATH PLANNING METHOD FOR AGRICULTURAL PATROL SCENE

面向农业巡检场景的多无人机任务分配与路径规划方法

Li SHENG *)

School of Economics and Management, Wuhan Railway Vocational College of Technology, Wuhan, Hubei/ China

Tel: +8613307177200; E-mail: shirley1204_2016@foxmail.com

Corresponding author: Li Sheng

DOI: <https://doi.org/10.35633/inmateh-74-52>

Keywords: Agricultural patrol, multi-UAV, task allocation, path planning; maximum endurance constraint

ABSTRACT

A multi-unmanned aerial vehicle (UAV) task allocation and path planning model with the maximum endurance constraint was constructed specific to the agricultural patrol scene. Moreover, an optimized ant colony optimization (ACO) algorithm applicable to grid map environment was proposed given such problems of the traditional ACO algorithm as limited path search direction and field of view, failure to find the shortest path and proneness to deadlock. This method preprocessed the grid map environment, extracted the feature points of obstacles, and selected such feature points as the way-finding access nodes; then, the construction efficiency of the solution was enhanced via the nonuniform pheromone distribution based on ACO algorithm, the guiding function of path search was strengthened using Tent chaotic mapping, and the pheromone evaporation coefficient was dynamically adjusted to prevent the algorithm from too early convergence. The experimental results show that the proposed method more conforms to the operational requirements of rotary-wing UAVs with limited cruising ability in comparison with the existing methods. Besides, the convergence efficiency of the improved ACO algorithm embedded with the niche genetic algorithm is 30.55% higher than that of the traditional ACO algorithm. The experimental results verify the practicability and effectiveness of the proposed method.

摘要

针对农业巡检场景的多无人机任务分配与路径规划问题, 构建一种最大航程约束的多无人机任务分配与路径规划模型。针对传统蚁群算法存在的路径搜索方向和视野受限、无法找到最短路径、容易发生死锁等问题, 提出了一种适用于网格地图环境下的优化蚁群算法。该方法对网格地图环境进行预处理, 提取障碍物的特征点, 并选择这些特征点作为寻路访问节点; 然后, 基于蚁群算法, 采用信息素不均匀分布来提高解的构造效率, 采用 Tent 混沌映射增强路径搜索的引导作用, 动态调整信息素挥发系数以避免算法过早收敛。实验结果表明, 提出的方法相比于现有方法更符合续航能力有限的旋翼无人机作业需求, 且相比于传统蚁群算法, 提出的嵌入小生境遗传算法的改进蚁群算法与传统蚁群算法相比, 算法收敛效率提升 30.55%。实验结果证明了所提方法的实用性和有效性。

INTRODUCTION

In the development process of modern agriculture, agricultural intelligent patrolling unmanned aerial vehicles (UAVs) are becoming an important force to promote agricultural production efficiency, environmental protection and intelligence. These UAVs are equipped with advanced sensing technology and artificial intelligence system, which can quickly and accurately patrol farmland and collect and analyze key data (Ning and Zhao., 2019). As the level of agricultural mechanization is continuously elevated, UAVs have been widely applied to various agricultural fields, and good path planning serves as the technical support for autonomous flight (Duan and Wang, 2004). With the constant scientific and technological development, UAVs have been extended to a lot of industries, while their movement cannot be separated from path planning. So-called path planning refers to finding the path along which UAVs can safely reach the destination from the starting point according to the requirements of the fastest speed and the lowest energy consumption under known or unknown environmental information (Dong et al., 2023). This kind of planning can be divided into global path planning and local path planning. In this study, the global path planning problem under static environment is mainly considered.

Multi-UAV patrol for agricultural patrol scene is one of the important means of ensuring the stable operation of agricultural systems. Facing the agricultural patrol scene, rotary-wing UAV patrol instead of manual patrol integrates the merits of high safety, low cost, strong operability and high accuracy (Kong *et al.*, 2023). However, single UAVs are of limited cruising ability, failing to efficiently complete the electricity patrol task on a large scale, which, however, can be generally achieved by multi-UAV collaborative operation. Therein, multi-UAV task allocation and path planning are crucial technical challenges (Yu *et al.*, 2023). First, UAV groups need to perform reasonable patrol task allocation, contributing to the shortest time spent in completing the patrol task or the shortest flight distance. Second, UAVs must evade obstacles in the environment, ensuring that UAVs can safely execute the patrol task.

In most of the existing studies, multi-UAV task allocation is considered separately from path planning. A classical task allocation method, ant colony optimization (ACO) algorithm, can provide the optimal allocation scheme under most circumstances (Corregidor-Castro *et al.*, 2021). In addition, biological intelligence methods have also been extensively used to solve the task allocation problem (Palomaki *et al.*, 2017). However, all the above methods belong to centralized settings. Despite the simple logic, they are inapplicable to large-scale task allocation. Different from centralized allocation methods, distributed task allocation methods can usually achieve high calculation efficiency and acceptable distribution schemes (Baik and Valenzuela, 2021). Market auction-based methods have been highly concerned since it can balance the computational complexity and solving quality very well (Sun *et al.*, 2019). Such methods complete task allocation by driving UAVs to receive the prices offered by all neighbors. In a recent study, Doull *et al.* (2021) put forward a distributed task allocation algorithm by introducing the alternating direction method of multipliers (ADMM), and experimentally proved that the proposed method can harvest the best convergence under most circumstances. Although the above market auction-based methods can rapidly provide acceptable task allocation schemes, they have not considered the path planning problem, making it necessary to solve the obstacle avoidance path of UAVs via path planning algorithms after obtaining the task allocation scheme (Avendaño-Valencia *et al.*, 2021). In addition, multi-UAV task allocation and path planning have been simultaneously considered by some methods. Aiming at logistics distribution scene, Xu *et al.* (2020) added the collision constraint of UAVs into the objective function to solve the problems of multi-UAV task allocation and path planning. Dulava *et al.* (2015) considered the problems of multi-UAV task allocation and motion planning under dense obstacle scene. Zhu and Wang (2020) introduced three-dimensional Dubins curve to disperse the heading angle of UAVs, and solved it by integrating task allocation and path planning. Hayes *et al.* (2020) put forward a joint optimization method of task allocation and path planning for balancing resources. However, the above methods either do not consider the coupling problem between task allocation and path planning, or do not consider obstacle avoidance in the environment. In fact, multi-UAV task allocation and path planning constitute a mutually coupling problem, so they must be considered as a whole. Zhao *et al.* (2021) introduced Dubins curve, considered the heading angle of UAVs, and solved the problems of task allocation and path planning by combining ACO and self-organizing map (SOM) algorithm. Coombes *et al.* (2020) estimated the length of UAVs' obstacle avoidance path using the improved A* algorithm and solved the coupling problem of task allocation and path planning. Hodgson *et al.* (2018) introduced vector direction to modify UAV's direction of motion and realize their automatic obstacle avoidance, and completed task allocation in combination with SOM method. Ullah *et al.* (2022) solved the problems of air-land collaborated task allocation and path planning through improving mixed integer linear programming (MILP) method and genetic algorithm (GA). Nevertheless, the above methods are faced with the bottleneck of slow solving speed and it is difficult to ensure the real-timeliness of the system in large-scale multi-UAV patrol scene. In addition, large-scale open environment usually needs to be considered to solve the problems of task allocation and path planning in electricity patrol scene. Due to the cruising ability limitation of rotary-wing UAVs, the maximum endurance constraint of UAVs must be taken into account in task allocation. However, the problems of task allocation and path planning under electricity patrol have been rarely directly considered by the existing methods. Although some methods have considered the maximum endurance constraint of UAVs, they give solutions slowly or fail to consider environmental obstacles.

The battery capacity of UAVs is limited, which leads to their weak cruising ability and failure to execute long-time large-scale patrol tasks. Hence, how to realize efficient patrol by taking full use of limited capacity has become an important challenge faced in electric transmission line patrol. In the patrol process of UAVs, the patrol time and energy consumption are mainly related to the trajectory design of UAVs. In reality, UAVs will start from the nest/service center, fly to the patrol region for data collection and finally return to the nest/service center. To improve the patrol efficiency of UAVs, the distance or energy consumption for UAVs to execute tasks has been reduced in relevant work by optimizing the trajectory of UAVs (Zeng *et al.*, 2019).

Chabot and Francis (2016) considered the convex polygonal coverage path planning and designed a path planning algorithm with low energy consumption on the premise of meeting the resolution of patrol images. Huang et al. (2023) put forward an accurate honeycomb decomposition method to seek for the least number of turning times in UAV coverage path planning. Jones et al. (2021) put forward a path planning algorithm of energy aware coverage, which reduced energy consumption by optimizing the trajectory of UAVs and their patrol speed. Linchant et al. (2015) minimized the energy consumption in the patrol process by optimizing the trajectory, flight speed and resource allocation of UAVs. Chung et al. (2021) proposed a reinforcement learning-based UAV trajectory design method, which dynamically adjusted the trajectory through multiple UAV-environment interactions and solved the non-convexity of the problem, but it failed to obtain the optimal trajectory or radically solve the trajectory optimization problem of UAVs. In relevant literature regarding patrol scene, the system energy efficiency (Cao et al., 2019) and sensing performance have been improved by optimizing the trajectory and resource allocation of UAVs. Bowley et al. (2019) proposed a continuous trajectory design scheme of networked UAVs based on TD3 to minimize the patrol time of UAVs with communication constraints satisfied. Facing the challenge of energy limitation of UAVs, Qayyum et al. (2020) minimized the energy consumption of UAV patrol by jointly optimizing the trajectory of UAVs, sensor data unloading and sensor wireless energy transmission. Augustine and Burchfield (2022) proposed a routine inspection system for UAVs driven by mobile edge computing to solve the challenge of providing effective data perception and automatic transmission for wind turbine inspection. While ensuring the accuracy of data, it minimized the energy consumption of UAVs by jointly optimizing the trajectory and calculating operation. Aiming at the central requirements for efficient danger detection and disaster management in the future network physical system of intelligent patrol nodes, Wang and Zhang (2017) put forward a new path planning algorithm for autonomous inspection of large-scale geographic regions and considered all aspects of energy consumption for UAV groups during inspection, including the energy required by flight, hovering and data transmission. The results show that the path planning problem can be effectively solved within polynomial time. When designing the patrol trajectory of UAVs, the returning of UAVs to the nest for charging in actual patrolling process has not been taken into account, but instead, it is generally assumed that UAVs have enough energy in the process of patrolling. In fact, however, the single endurance of UAVs will fail to support the completion of all patrol tasks when the number of patrol points exceeds a certain value.

Based on the above discussion, such problems of the traditional ACO algorithm as limited path search direction and field of view, failure to find the shortest path and proneness to deadlock and unsmooth path were mainly considered in this study. Given these problems, a task application and path planning method facing the agricultural patrol scene was proposed, which solved the coupling problem of path planning and task allocation while considering the maximum endurance constraint of UAVs. Moreover, the following improves were made: (1) The grid map environment was preprocessed, i.e., extracting feature points; (2) in the process of path search, these feature points were used as path nodes; (3) on the basis of such feature points, path planning was performed through the improved nonuniform pheromone distribution, two-way parallel path search, Tent chaotic mapping and the dynamic adjustment of the pheromone evaporation coefficient.

MATERIALS AND METHODS

Problem description

In the agricultural patrol scene, it is assumed that a nest (a vehicle parked on the UAV parking platform, which can accommodate multiple rotary-wing UAVs) is responsible for one patrol region. After completing patrol task allocation in the nest, UAVs start flying to the maintenance region, access patrol tasks allocated one by one, and autonomously fly back to the nest after completing such tasks. During the flight process, UAVs need to bypass no-fly zones like buildings, trees and electromagnetic field interference and ensure that the flight distance should be as short as possible. It is noteworthy that since all patrol tasks are implemented on ground, UAVs were assumed to fly according to a constant height during the flight process, and thus task allocation and path planning were carried out in 2D space.

Mathematical model

$U = \{1, 2, \dots, i, L, m\}$ is set as the index set of UAVs in the nest, where m represents the number of UAVs. $T = \{1, 2, \dots, j, \dots, n\}$ is set as the index set of n patrol tasks in the patrol region. Without loss of generality, v_j is defined as the importance factor of task j . Since each patrol task has the same priority in this study, $v_j = 1$. λ_j denotes the distance discount factor.

To guarantee the monotonic decrease of the optimized objective function, $\lambda_i < 1$ should be met, and better solving quality could be achieved if $\lambda_i = 0.9$ was empirically taken in this study. According to the literature *Yang et al. (2020)* the total reward value $f_i(T_i)$ for all tasks in the patrol task set T_i accessed by UAV can be expressed by Equation (1).

$$f_i(T_i) = \sum_{j=1}^{|T_i|} v_j \lambda_i^{d(Path_i^j)} \tag{1}$$

where $|\cdot|$ is the number of elements in the set; $T_i(T_i \subseteq T)$ stands for the patrol task set allocated to UAV i according to the access sequence; $Path_i$ is the shortest obstacle avoidance path for the task set T_i accessed by the UAV; $Path_i^j$ is the sub-path of $Path_i$, indicating the path for UAV i to access the task $j(\forall j \in T_i)$; $d(Path_i^j)$ is the length of the sub-path $Path_i^j$.

During the process of task allocation, the undistributed task k is added into the set T_i to obtain the marginal reward value $\omega_i(k)$ of the UAV i , as seen in Equation (2):

$$\omega_i(k) = f_i(T_i \cup \{k\}) - f_i(T_i), \forall k \in T, k \notin T_i \tag{2}$$

Therefore, the expression of $\omega_i(k)$ can be acquired by combining Equations (1) and (2), as seen in Equation (3).

$$\omega_i(k) = \sum_{j=1}^{|T_i \cup \{k\}|} v_j \lambda_i^{d(Path_i^j)} - \sum_{j=1}^{|T_i|} v_j \lambda_i^{d(Path_i^j)}, \forall k \in T, k \notin T_i \tag{3}$$

where $\omega_i(k)$ ensures that the objective function is a submodular function, which has a significant attribute of progressive decrease in marginal gain, i.e., the more the tasks allocated to the UAV i , the smaller the marginal gain $\omega_i(k)$ obtained by the UAV through selecting the patrol task k . The convergence of the algorithm is ensured by the progressive decrease attribute of the marginal gain (*Baik et al., 2021*).

To sum up, the total reward function for all UAVs to complete task allocation can be described by Equation (4).

$$\begin{cases} \max \sum_{i=1}^{|U|} \left(\sum_{j=1}^{|T_i|} x_{ij} \cdot v_j \cdot \lambda_i^{d(Path_i^j)} \right) \\ \text{s.t. } |T_i| \leq L_i, \forall i \in U \\ \sum_{i=1}^{|U|} (x_{ij}) = 1, \forall j \in T \\ d(Path_i) \leq D_{max}^i, \forall i \in U \end{cases} \tag{4}$$

where x_{ij} means that if the task j is allocated to the UAV i , $x_{ij} = 1$, or otherwise, $x_{ij} = 0$. The constraint condition is described as follows: the number of tasks allocated to each UAV does not exceed the maximum number of tasks L_i accessed by the UAV; each task is only allocated to one UAV, while one UAV can be allocated with multiple tasks; the length of the obstacle avoidance path for UAVs to execute patrol tasks should not exceed their maximum endurance D_{max}^i .

Principle of ACO algorithm

As a swarm intelligence algorithm, ACO refers to the intelligent behavior exhibited by a group of non-intelligent or slightly intelligent individuals through collaboration, providing a new possibility for solving complex problems (*Kong et al., 2023*). ACO was first proposed by Italian scholars *Colormi A., Dorigo M. et al.* in 1991. Through two decades of development, ACO algorithm has achieved enormous progress in theoretical and applied research (*Doull et al., 2021*). ACO algorithm, a bionics algorithm, is enlightened by ant foraging behavior in nature (*Ullah et al., 2022*). During foraging in nature, ant colonies can always find one optimal path from the ant nest to the food source. The optimization mechanism of ACO algorithm, which is a new intelligent optimization algorithm, is divided into adaption stage and collaboration stage. When efforts are made to obtain the optimal solution, ACO dynamically optimizes the objective function from an unordered state to an ordered state.

The actual behavior of ants was simulated through a multi-UAV task allocation and path planning model specific to the agricultural patrol scene, and the definitions were presented as follows: m stands for the number of ants; d_{ij} is the distance from the patrol point i to j , and $d_{ij} = \{i, j = 1, 2, \dots, n\}$; τ_{ij} is the pheromone concentration between patrol points; ρ is the pheromone attenuation factor, which is an adjustable parameter within $[0, 1]$; η_{ij} represents the heuristic factor of the edge, also referred to as visibility, and $\eta_{ij} = 1/d_{ij}$;

P_{ij}^k indicates the probability for ant k to move from patrol point i to j ; $tabu_k$ is the patrol point currently passed by ant k ; $allowed_k$ denotes the patrol point where ant k can choose to move, and $allowed_k = \{0,1,2,3,\dots,m\} - tabu_k$. β is the influence coefficient of expected heuristic factor on the selected path during the movement of ants; α is the influence coefficient of pheromone on the selected path.

At initial moment, the pheromone on each path is equal, i.e., $\tau_{ij} = C$ (C is a constant). The direction of ant motion $k(k = 1,2,3,\dots,m)$ depends on the pheromone on the selectable path under the current state. In this case, the random proportion rule serves as the transfer rule of the ant system, and the probability for ants to transfer to the selectable path is displayed in Equation (5).

$$P_{ij}^k = \begin{cases} \frac{\tau_{ij}^\alpha(t) \cdot \eta_{ij}^\beta(t)}{\sum_{s \in allowed_k} \tau_{is}^\alpha(t) \cdot \eta_{is}^\beta(t)}, & j \in allowed_k \\ 0, & \text{else} \end{cases} \tag{5}$$

Ants select the next patrol node at patrol node i , as seen in Equation (6).

$$j = \begin{cases} \operatorname{argmax} \{ \tau_{ij}^\alpha(t) \cdot \eta_{ij}^\beta(t) \}, & j \in allowed_k \\ J, & \text{else} \end{cases} \tag{6}$$

q is assumed to a random variable and $q \in [0,1]$; q_0 is an adjustable parameter and $q_0 \in [0,1]$. After ants complete one complete path selection cycle through n moments, the pheromone on each path will change accordingly, as seen in Equations (7) and (8).

$$\tau_{ij}(t = n) = \rho \cdot \tau_{ij}(t) + \Delta\tau_{ij} \tag{7}$$

$$\Delta\tau_{ij}(t) = \sum_{k=1}^m \Delta\tau_{ij}^k \tag{8}$$

where $\Delta\tau_{ij}^k$ is the pheromone of ant k on patrol nodes i and j in the current cycle; $\Delta\tau_{ij}(t)$ means the increment of pheromones of ant k on patrol nodes i and j in the current cycle. The selection model for the pheromone increment is exhibited in Equation (9).

$$\Delta\tau_{ij}^k = \begin{cases} \frac{Q}{d_{ij}}, & \text{if the } k\text{th ant passes through the path } (i, j) \\ 0, & \text{miscellaneous} \end{cases} \tag{9}$$

where Q is a constant.

Patrol path constraint of ACO algorithm

The patrol points on the multi-UAV task allocation and patrol path on the agricultural patrol scene are namely the paths passed during the whole patrol process and each hover photographing point, and all UAVs need to keep an enough safe distance with patrol points. Since patrol begins until ending, the hover photographing points passed by UAVs are denoted by spatial sequence points $\{O, G_1, G_2, \dots, G_n, D\}$. O is the starting point, D is the endpoint, and G_1, G_2, \dots, G_n are the hover photographing patrol points within 3D grids during the patrol process. The connection diagram of patrol points on each path are displayed in Fig. 1.

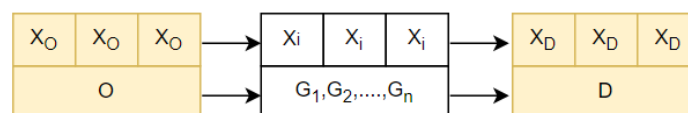


Fig. 1 - Connection diagram of patrol points on each path

In order to transform the safety requirements of patrol paths into constraints that can be used to improve ACO algorithm, UAV patrol path planning was simplified from a 3D problem into a path optimization problem within the 2D plane (Zhu et al., 2022). In the process of multi-UAV task allocation and patrol path planning specific to the agricultural patrol scene, numerous constraints, such as UAVs' cruising ability and endurance and the safe distance of patrol paths and topographical conditions, should be considered. First, the minimum patrol energy consumption and the maximum patrol distance were determined as the comprehensive indexes in multi-UAV task allocation and patrol path planning facing the agricultural patrol scene, and the integral operation was performed for the comprehensive indexes on the patrol path to obtain the comprehensive index function as seen in Equation (10).

$$\begin{cases} F = \int_0^L [\lambda \omega_f + \gamma \omega_t] dt \\ \lambda + \gamma = 1 \end{cases} \quad (10)$$

where F is the comprehensive index function; L represents the patrol distance during the patrol process of UAVs; ω_f and ω_t are the minimum energy consumption constraint and the maximum patrol distance constraint, respectively; λ and γ represent the weight coefficients corresponding to the minimum energy consumption constraint and the maximum patrol distance constraint, respectively.

During the whole path optimization process, the edge combination of patrol paths can be obtained after determining the position of each spatial sequence point. Therefore, the comprehensive index function F_i of the i -th path can be obtained as per F .

$$\begin{cases} F_i = \lambda \omega_{fi} + \gamma \omega_{ti} \\ \lambda + \gamma = 1 \end{cases} \quad (11)$$

where ω_{fi} is the minimum energy consumption constraint of the i -th path; ω_{ti} is the maximum patrol distance constraint.

(1) Calculation method for energy consumption. The energy consumption of UAVs during patrol is directly proportional to the flight distance of patrol work, as seen in Equation (12).

$$\begin{cases} \omega_f = \varepsilon \times L \\ \omega_{fi} = \varepsilon \times L_i \end{cases} \quad (12)$$

(2) Maximum patrol distance. When the maximum cruising ability of UAVs is V_{max} , the maximum patrol distance is displayed in Equation (13).

$$V \leq V_{max}, V = \sum_{i=1}^{n-1} v_i \quad (13)$$

where V is the flight distance of spatial sequence points passed during multi-UAV task allocation and patrol process on the agricultural patrol scene; v_i is the flight distance on the i -th cruising path.

RESULTS

Simulation experiment

In this study, a total of 105 patrol points during agricultural UAV patrol process were assumed and their positions are expressed by their coordinate values X and Y , as shown in Fig. 2. The patrol speed of agricultural UAVs and the coordinates of 105 detection points are already known.

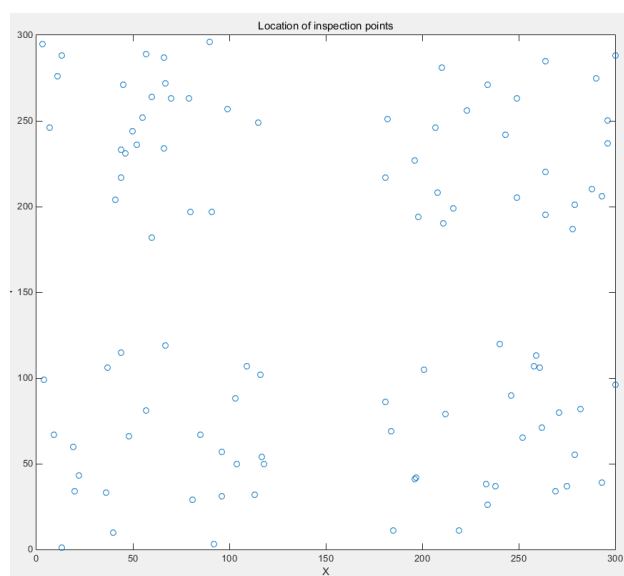


Fig. 2 - Layout plan for patrol points of agricultural UAVs

In this study, the experiment was implemented via Matlab2018a of Intel i7 processor. The multi-UAV task allocation and path planning model facing the agricultural patrol scene was solved through the improved ACO algorithm. During the simulation experiment, 100 patrol points were arranged, and the maximum patrol distance and endurance of UAVs were 120 km and 60 min, respectively. Other parameters were set to $\alpha=1.5$, $\beta=2$, $\rho=0.1$ and $Q=106$. When the maximum number of iterations was $N_{cmax}=2500$ and the number of ants was $m=30$, agricultural UAVs must park at all monitoring points during patrol. A simulation test was performed respectively using the improved ACO algorithm and the traditional ACO algorithm, and the corresponding calculation results were compared.

Result analysis

In order to eliminate the influence of various random factors and verify the advantages and disadvantages of the improved ACO algorithm designed in this study, the improved ACO algorithm was used to solve the problem of multi-UAV task allocation and patrol path optimization specific to the agricultural patrol scene for 2500 times. The convergence curve of the improved ACO algorithm is shown in Fig. 3, and the optimal travel path of multi-UAV patrol under this scene is shown in Fig. 4.

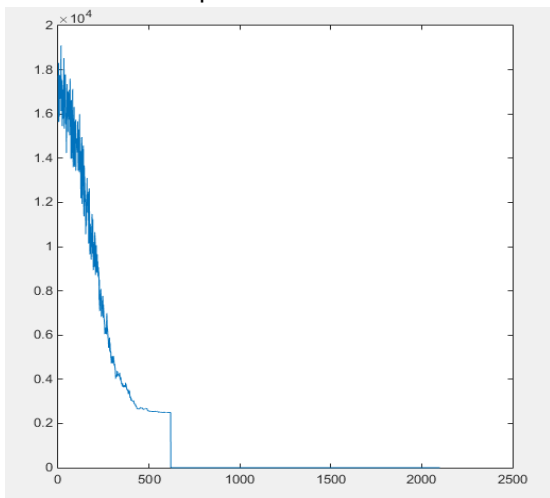


Fig. 3 - Convergence curve of improved ACO algorithm

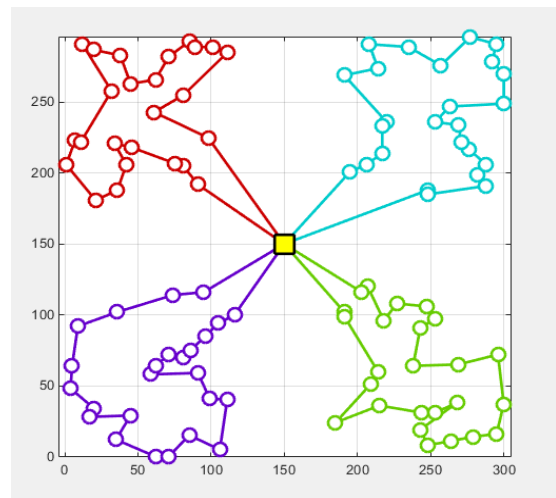


Fig. 4 - Optimal driving path of agricultural patrol UAVs

In order to verify the effectiveness of the model and algorithm, the optimization model established in this study was solved using the traditional ACO algorithm with the same parameters on the same platform. To achieve more scientific and effective experimental results, the maximum number of iterations of the traditional ACO algorithm was also set to 2500. The convergence curve of the traditional ACO algorithm is displayed in Figure 5, and the optimal multi-UAV patrol path on the agricultural patrol scene is exhibited in Fig. 6.

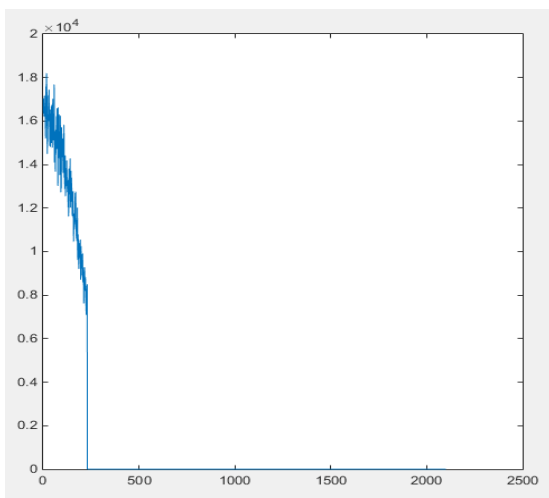


Fig. 5 - Convergence curve of traditional ACO algorithm

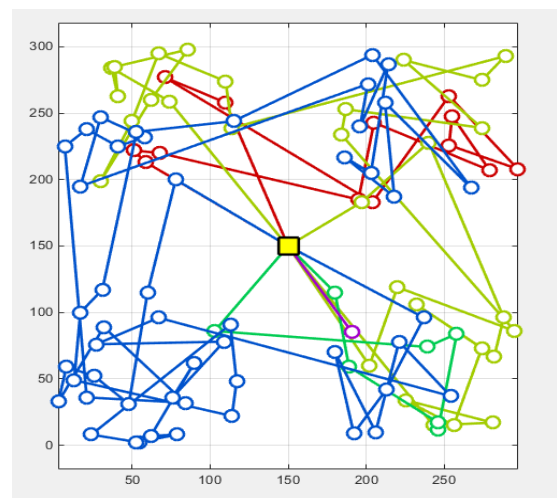


Fig. 6 - Optimal driving path of agricultural patrol UAVs

The improved ACO algorithm was compared with the traditional ACO algorithm in the patrol path and total driving distance of agricultural patrol UAVs as well as the algorithm convergence time. In comparison with the traditional ACO algorithm, the improved ACO algorithm embedded with the niche genetic algorithm showed strong exploratory and convergent properties, accompanied by the better value of the objective function. The comparison between the two algorithms is as seen in Table 1.

Table 1

Comparison between two algorithms				
Algorithm	Number of UAVs	Driving distance (m)	Total cost (yuan)	Algorithm time consumption (s)
Improved ACO algorithm	4	19327.291	452.031	440.81
Traditional ACO algorithm	5	24732.394	500.799	575.48

The servo motor power of agricultural patrol UAVs was about 2200 W, and the total power of other equipment was about 80 W. Agricultural patrol UAVs needed to stop at each parking point and rotate the cloud platform for detection. The average residence time at each detection point was about 4 s, and the average drive speed of patrol UAVs was about 1 m/s. Each patrol UAV was equipped with a 50 Ah lithium battery pack, for which a 200 W AC charger was adopted. After completing inspection each time, the agricultural patrol UAV needed to return to the charging room for charging, followed by the next inspection. Therefore, the total time spent in each inspection included two parts: task time and charging time. It could be known from Table 1 that the improved ACO algorithm embedded with the niche genetic algorithm performed better than the traditional ACO algorithm in the number of UAVs, driving distance, total cost and algorithm time consumption. The traditional ACO algorithm needed 5 UAVs to put agricultural product orders in and manage warehouse output, while only 4 ones were needed by the improved ACO algorithm embedded with the niche genetic algorithm to complete the same task, improving the efficiency by 20%; in the aspect of driving distance of UAVs, the total driving distance of the traditional ACO algorithm for agricultural UAVs was 24732.394 m, while the total driving distance of the improved ACO algorithm embedded with the niche genetic algorithm for completing the same task was 19327.291 m, and the path was shortened by 27.96%; the total cost spent by the traditional ACO algorithm in agricultural UAVs was 500.799 yuan, while that for the improved ACO algorithm embedded with the niche genetic algorithm to complete the same task was 452.031 yuan, saving the cost by about 10.79%; in terms of algorithm time consumption, it took 575.48 s for the traditional ACO algorithm to converge, while the convergence time for the improved ACO algorithm embedded with the niche genetic algorithm was 440.81 s, with the algorithm efficiency improved by 30.55%. It could be seen from Table 1 that the improved ACO algorithm showed stronger optimization ability and convergence than the traditional ACO algorithm. As intuitively observed from the algorithm convergence curves, the optimal path length acquired by the improved ACO algorithm was better than that of the traditional ACO algorithm when it comes to the total patrol distance of agricultural UAVs.

CONCLUSIONS

In this study, the multi-UAV task allocation problem facing the agricultural patrol scene was summarized, and the existing relevant work was reviewed. Specifically, a distributed task allocation and path planning algorithm was put forward aiming at the task allocation and path planning algorithm on the agricultural patrol scene. This method fully considered the coupling of task allocation with path planning in the process of task allocation, thus ensuring that the patrol task allocated to UAVs conformed to reality more. Besides, the maximum endurance constraint of UAVs was considered. The experiment manifested that when UAVs executed the patrol task, the improved ACO algorithm embedded with the niche genetic algorithm in this study had a total cruising range nearly 5405.103 m shorter than that obtained by the current advanced algorithms. In comparison with the traditional ACO algorithm, the proposed algorithm improved the convergence efficiency by 30.55%. In a word, the effectiveness and practicability of embedding the niche genetic algorithm were experimentally verified. Relevant research not only proves that Tent optimization ant colony algorithm has a good application in UAV inspection path optimization, enriching the practical application value of the algorithm, but also provides a reference for the theoretical research of related algorithms. However, a faster global path planning algorithm is not considered in this study for the time being, and the proposed algorithm will be further verified in real application scenarios deployed in the future.

REFERENCES

- [1] Augustine, J. K., & Burchfield, D. (2022). Evaluation of Unmanned Aerial Vehicles for Surveys of Lek – Mating Grouse. *Wildlife Society Bulletin*, Vol. 46, pp. 1–13, United States.
- [2] Avendaño-Valencia, L. D., Abdallah, I., & Chatzi, E. (2021). Virtual fatigue diagnostics of wake-affected wind turbine via Gaussian process regression. *Renewable Energy*, Vol. 170, pp. 539–561, United Kingdom.
- [3] Baik, H., & Valenzuela, J. (2021). An optimization drone routing model for inspecting wind farms. *Soft Computing*, Vol. 25, no. 3, pp. 2483–2498, United States.
- [4] Bowley, C., Mattingly, M., Barnas, A., Ellis-Felege, S., & Desell., T. (2019). An Analysis of Altitude, Citizen Science and a Convolutional Neural Network Feedback Loop on Object Detection in Unmanned Aerial Systems. *Journal of Computational Science*, Vol. 34, pp. 102–116, Netherlands
- [5] Cao, P., Liu, Y., Yang, C., Xie, S., & Xie, K. (2019). MEC-driven UAV-enabled routine inspection scheme in wind farm under wind influence. *IEEE Access*, Vol. 7, pp. 179252–179265, United States.
- [6] Chabot, D., & Francis, C. M. (2016). Computer-Automated Bird Detection and Counts in High-Resolution Aerial Images: A Review. *Journal of Field Ornithology*, Vol. 87, pp. 343–359, United States.
- [7] Chung, H. M., Maharjan, S., Zhang, Y., & Strunz, K. (2021). Placement and routing optimization for automated inspection with unmanned aerial vehicles: a study in offshore wind farm. *IEEE Transactions on Industrial Informatics*, Vol. 17, no. 5, pp. 3032–3043, United States.
- [8] Coombes, M., Fletcher, T., Chen, W. H., & Liu, C. (2020). Decomposition-based mission planning for fixed-wing UAVs surveying in wind. *Journal of Field Robotics*, Vol. 37, no. 3, pp. 440–465, United Kingdom.
- [9] Corregidor-Castro, A., Holm, T. E., & Bregnballe, T. (2021). Counting Breeding Gulls with Unmanned Aerial Vehicles: Camera Quality and Flying Height Affects Precision of a Semi-Automatic Counting Method. *Ornis Fennica*, Vol. 98, pp. 33–45, Finland.
- [10] Dong, Z., Li, H., Ge, J., & Cheng, J. (2023). Path planning of UAV 3D environment based on improved ant colony algorithm (改进蚁群算法的无人机三维环境路径规划). *Bulletin of Surveying and Mapping*, pp. 153-157, Beijing/China.
- [11] Doull, K. E., Chalmers, C., Fergus, P., Longmore, S., Piel., A.K., & Wich, S.A. (2021). An Evaluation of the Factors Affecting ‘Poacher’ Detection with Drones and the Efficacy of Machine-Learning for Detection. *Sensors*, Vol. 21, pp. 1–24. Switzerland.
- [12] Duan, H., & Wang, D. (2004). A Novel Improved Ant Colony Algorithm with Fast Global Optimization and its Simulation (一种快速全局优化的改进蚁群算法及仿真). *Information and Control*, pp. 241-244, Liaoning/China.
- [13] Dulava, S., Bean, W. T., & Richmond, O. M. W. (2015). Environmental Reviews and Case Studies: Applications of Unmanned Aircraft Systems (UAS) for Waterbird Surveys. *Environmental Practice*, Vol. 17, pp. 201–210, United States.
- [14] Hayes, M. C., Gray, P. C., Harris, G., Sedgwick, W. C., Crawford, V. D., Chazal, N., Crofts, S., & Johnston, D. W. (2021). Drones and Deep Learning Produce Accurate and Efficient Monitoring of Large-Scale Seabird Colonies. *Ornithological Applications*, Vol. 123, pp. 1–16, United States.
- [15] Hodgson, J. C., Mott, R., Baylis, S. M., Pham, T. T., Wotherspoon, S., Kilpatrick, A. D., Segaran, R. R., Reid, I., Terauds, A., & Koh, L. P. (2018). Drones Count Wildlife More Accurately and Precisely than Humans. *Methods in Ecology and Evolution*, Vol. 9, pp. 1160–1167, United Kingdom.
- [16] Huang, X., Wang, G., Lu, Y., & Jia, Z. (2023). Study on a boat-assisted drone inspection scheme for the modern large-scale offshore wind farm. *IEEE Systems Journal*, Vol. 17, no. 3, pp. 4509–4520, United States.
- [17] Jones, L. R., Godollei, E., Sosa, A., Hucks, K., Walter, S. T., Leberg, P. L., & Spring, J. (2021). Validating an Unmanned Aerial Vehicle (UAV) Approach to Survey Colonial Waterbirds. *Waterbirds*, Vol. 43, pp. 263–270, United States.

- [18] Kong, W. L., Wang, F., Zhou, P. H., & Wang, H. F. (2023). Three-Dimensional Path Planning of UAVs Based on Improved Ant Colony Algorithm (改进蚁群算法的无人机三维路径规划). *Electronics Optics & Control*, Vol. 30, no. 3, pp. 63-69. Henan/China.
- [19] Linchant, J., Lisein, J., Semeki, J., Lejeune, P., & Vermeulen, C. (2015). Are Unmanned Aircraft Systems (UASs) the Future of Wildlife Monitoring? A Review of Accomplishments and Challenges. *Mammal Review*, Vol. 45, pp. 239–252, United kingdom.
- [20] Ning, Y., & Zhao, R. (2019). Logistics UAV path planning based on improved ant colony algorithm (基于改进蚁群算法的物流无人机路径规划). *Electronic Technology and Software Engineering*, pp. 142-146, Beijing/China.
- [21] Palomaki, R. T., Rose, N. T., Bossche, V. D. M., Sherman, T. J., & De Wekker, S. F. J. (2017). Wind estimation in the lower atmosphere using multirotor aircraft. *Journal of Atmospheric and Oceanic Technology*, Vol. 34, no. 5, pp. 1183–1191, United States.
- [22] Qayyum, A., Ahmad, I., Iftikhar, M., & Mazher, M. (2020). Object detection and fuzzy based classification using UAV data. *Intelligent Automation & Soft Computing*, Vol. 26, no. 4, pp. 693–702, United States.
- [23] Sun, H., Zhou, F., & Hu, R. Q. (2019). Joint offloading and computation energy efficiency maximization in a mobile edge computing system. *IEEE Transactions on Vehicular Technology*, Vol. 68, no. 3, pp. 3052–3056, United States.
- [24] Ullah, M. A., Mikhaylov, K., & Alves, H. (2022). Enabling mMTC in remote areas: LoRaWAN and LEO satellite integration for offshore wind farm monitoring. *IEEE Transactions on Industrial Informatics*, Vol. 18, no. 6, pp. 3744–3753, United States.
- [25] Wang, L., & Zhang, Z. (2017). Automatic detection of wind turbine blade surface cracks based on UAV-taken images. *IEEE Transactions on Industrial Electronics*, Vol. 64, no. 9, pp. 7293–7303, United States.
- [26] Xu, D., Sun, Y., Ng, D. W. K., & Schober, R. (2020). Multiuser MISO UAV communications in uncertain environments with no-fly zones: robust trajectory and resource allocation design. *IEEE Transactions on Communications*, Vol. 68, no. 5, pp. 3153–3172, United States.
- [27] Yang Lei, Fan Junfeng, Liu Yanhong, Li En, Peng Jinzhu, Liang Zize (2020) A review on state-of-the-art power line inspection techniques [J]. *IEEE Transactions on Instrumentation and Measurement*, vol. 69, no.12, pp.9350–9365.
- [28] Yu, J., Guo, J., Zhang, X., Xie, T., Zhou, C., & Liu, N. (2023). UAV Path Planning Based on Improved Cellular Ant Colony Algorithm (基于改进元胞蚁群算法的无人机路径规划). *Electronics Optics and Control*, Vol. 30, no. 3, pp. 46-50, Henan/China.
- [29] Zeng, Y., Xu, J., & Zhang, R. (2019). Energy minimization for wireless communication with rotary-wing UAV. *IEEE Transactions on Wireless Communications*, Vol. 18, no. 4, pp. 2329–2345, United States.
- [30] Zhao, H., Chen, G., Hong, H., & Zhu, X. (2021). Remote structural health monitoring for industrial wind turbines using short-range Doppler radar. *IEEE Transactions on Instrumentation and Measurement*, Vol. 70, pp. 1–9, United States.
- [31] Zhu, Y. C., & Wang, S. W. (2022). Efficient aerial data collection with cooperative trajectory planning for large-scale wireless sensor networks. *IEEE Transactions on Communications*, Vol. 70, no. 1, pp. 433–444, United States.

DESIGN AND EXPERIMENT OF LARGE STRAW CRUSHER WITH CYLINDER FEEDING HAMMER

圆筒喂料锤片式大型秸秆粉碎机设计与试验

Tao CHEN¹⁾, Shu-juan YI^{*1)}, Song WANG¹⁾, Wen-sheng SUN¹⁾

¹⁾College of Engineering, Heilongjiang Bayi Agricultural University, Daqing/P.R.China

Tel: +86-459-13836961877; E-mail: yishujuan_2005@126.com

Corresponding author: Shu-juan Yi

DOI: <https://doi.org/10.35633/inmateh-74-53>

Keywords: Animal husbandry; Straw; Cylinder feeding; Crushing machinery; Test

ABSTRACT

In order to solve the problems of small feeding amount, high manual labor intensity and low work efficiency of the existing straw crusher, a large straw crusher with cylinder feeding hammer is designed. The key parts of the machine are designed and calculated, and the mechanism of corn straw crushing in the crusher is analyzed, and the theoretical factors affecting the working effect of the crusher are obtained. With the rotational speed of crushing shaft, diameter of sieve and clearance of sieve-hammer as test factors, and the productivity, qualification rate of crushing length as performance evaluation indicators, a quadratic regression orthogonal rotation combination test with three factors and five levels was carried out. The regression mathematical model of test factors and performance evaluation indicators was established by using Design-Expert 13.0 software. With the goal of simultaneously maximizing the qualified rate of productivity and crushing length, multi-objective optimization solutions were carried out for the rotational speed of crushing shaft, diameter of sieve and clearance of sieve-hammer, and the optimal parameter combination was determined as follows: the rotational speed of crushing shaft is 1709.24 r/min, the diameter of sieve is 22.83mm, the clearance of sieve-hammer is 15.38 mm, the verification test shows that the productivity is 9187.98 kg/h, and the qualification rate of crushing length is 93.87%. The machine improves the efficiency of crushing operation and can meet the design requirements.

摘要

为解决现有的饲草粉碎机喂入量小,人工劳动强度大,工作效率低等问题,设计了一种圆筒喂料锤片式大型秸秆粉碎机。对该机的关键部件进行了设计计算,并对玉米秸秆在粉碎机内的粉碎机理进行了分析,得到了影响粉碎机工作效果的理论因素。以粉碎轴转速、筛孔直径、筛锤间隙为试验因素,以生产率、粉碎长度合格率为性能评价指标,进行三因素五水平二次回归正交旋转组合试验,利用 Design-Expert 13.0 软件对试验结果进行方差分析,建立了试验因素与性能评价指标的回归数学模型。以生产率和粉碎长度合格率同时最大化为目标,对粉碎轴转速、筛孔直径、筛锤间隙进行多目标寻优求解,确定了最优参数组合为:粉碎轴转速 1709.24r/min、筛孔直径 22.83mm、筛锤间隙 15.38mm,验证试验表明,生产率 9187.98kg/h、粉碎长度合格率 93.87%。该机提高了粉碎作业效率,能够满足设计要求。

INTRODUCTION

Crop straw is an important biomass energy in the world, the global annual output being of up to 2.4 billion tons. China's straw production ranks first in the world. Corn, rice and wheat straw resources account for a large proportion. In recent years, the proportion of straw resources have increased, of which the proportion of corn straw resources increased the fastest, accounting for 32.34%. China's corn stalk output reached 267.4651 million tons. Corn straw is rich in cellulose, hemicellulose and lignin, and has high nutritional value. China has always adhered to agricultural priority in the utilization of crop straw, vigorously advocated the promotion of straw fertilizer, feed, energy, base and raw material utilization, and constantly promoted the comprehensive utilization of straw industry to improve quality and efficiency. In the process of feed utilization, the corn straw is used to feed livestock by cutting, crushing or kneading processing methods, which can improve the grazing rate and digestibility of straw, increase the utilization rate of straw, and effectively solve the problem of feed shortage in animal husbandry (Xu et al., 2020; Zhao et al., 2019; Zhang et al., 2021).

¹⁾Tao Chen, Ph.D.; Shu-juan Yi, Prof. Ph.D.; Song Wang, Ph.D.; Wen-sheng Sun, Ph.D.;

As one of the important links of straw processing, crushing is to cut off the straw to expose the internal nutrients, improve palatability, and improve the contact area with the digestive liquid of livestock, promote the absorption of nutrients, reduce the rumination and chewing time, and reduce the energy consumed by the chewing of livestock. As a common processing equipment of straw, the operation effect of the mill directly affects the processing cost and quality of straw (Wu *et al.*, 2022; Li *et al.*, 2023). The length of forage fodder required by ruminants is between 30 and 50 mm, and cutting too long or too short is not conducive to absorption. Before mixing, the length of the fodder obtained by crushing needs to be 50-80 mm to prevent it being too short after mixing and cutting.

At present, the straw shredders on the market are small machinery, the process of crushing straw requires manual feeding, labor intensity is large, increasing labor costs, and in the process of artificial feeding, the crushing rotor is idling most of the time, resulting in low work efficiency. With the increase of breeding scale, the existing straw crushing machinery cannot meet the needs of China's large-scale pasture construction (Liu *et al.*, 2019; Zhang *et al.*, 2024; Chen *et al.*, 2024).

Taking corn stalk as the research object, this paper designs a large straw crusher with cylinder feeding hammer, which can realize continuous grinding operation by rotating cylinder, greatly reducing labor cost and improving operation efficiency. The key mechanisms such as feeding and crushing were designed and calculated, the structural parameters were determined, and the performance test was carried out. It provides reference for the research and development of forage processing machinery for the construction of large pastures in China.

MATERIALS AND METHODS

Overall composition and working principle

The whole machine is mainly composed of frame, walking wheel, feeding device, crushing device, screw discharge device, conveyor belt, hydraulic system and transmission system. The overall structure is shown in Fig. 1.

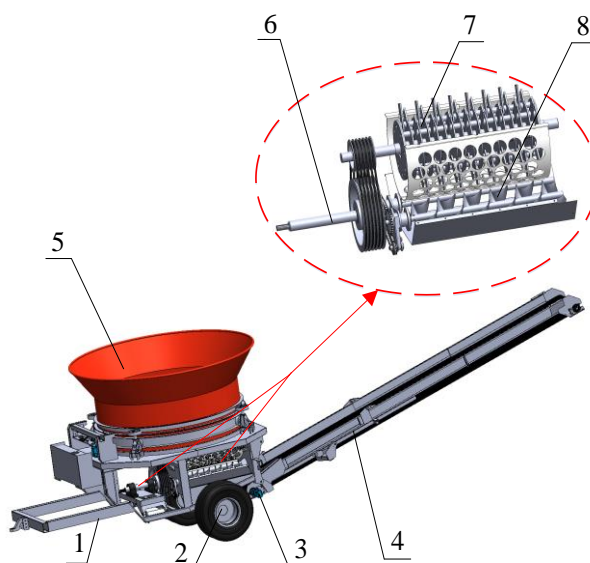


Fig. 1 - Structure diagram of cylinder feeding hammer type large straw crusher

1. Machine frame; 2. Walking wheels; 3. Hydraulic system; 4. Conveyor belt; 5. Feed cylinder; 6. Transmission system; 7. Crushing and sifting device; 8. Discharge device

The crusher is pulled by the tractor, and the rear power output shaft of the tractor drives the transmission system and the hydraulic system to provide power for the crusher to crush. During operation, the grasping machine grabs the straw into the cylinder, the straw enters the crushing bin under the action of gravity and rotating driving force, the rotor assembly in the crushing bin rotates at a high speed under the drive of the belt drive to crush the straw, the crushing straw enters the discharge bin through the sieve, and the double screw conveyor in the discharge bin transmits the broken straw to the discharge port by the chain drive and falls on the conveyor belt. The conveyor belt is driven by the hydraulic motor to transport the broken straw back for collection and complete the crushing operation.

In order to prevent overloading of crushing rotor due to excessive feeding amount, a feed cylinder speed control system was established, as shown in Fig. 2.

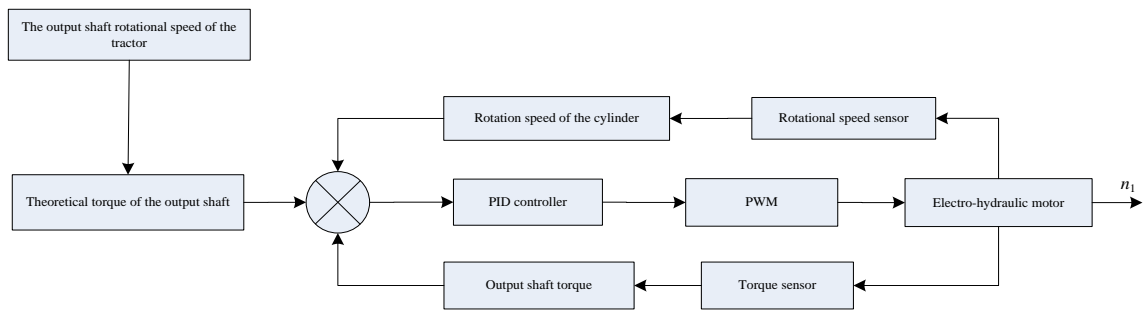


Fig. 2 - Feed cylinder speed control schematic diagram

Key component design

Cylinder design

As shown in Fig. 3, v_1 is the feed speed of the straw at the middle point of the circumference radius of the bottom surface of the cylinder, A_1 is the cross-sectional area of the volume of each cut of the hammer, and H is the feed distance of the straw during each cut interval of the hammer.

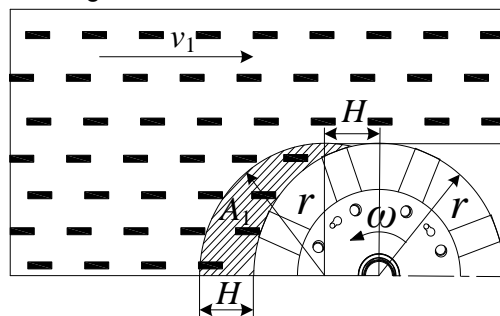


Fig. 3 - Feeding diagram

According to the target production efficiency of the machine, the feeding efficiency V should not be less than $50\text{m}^3/\text{h}$, and the feeding efficiency is:

$$V = 60znlA_1 \tag{1}$$

where: z is the number of cuts for one rotation of the grinding shaft, 8; n is the crushing rotor rotational speed; l is the length of hammer mounting disc, 750 mm.

As shown in Fig.2, the area of A_1 is:

$$A_1 = Hr \tag{2}$$

$$H = \frac{60v_1}{nz} \tag{3}$$

The feed velocity v_1 of the straw at the midpoint of the circumference radius of the bottom of the cylinder is:

$$v_1 = \frac{2\pi n_1 r_1}{60} \tag{4}$$

Where: n_1 is rotational speed of cylinder; r_1 is the radius at the midpoint of the circumference of the bottom of the cylinder, 1150 mm.

According to formula (1)~(4), n_1 should be greater than or equal to 2.15 r/min. In the actual working process, there will be relative sliding between the straw and the cylinder, and the straw is not tightly filled, so the rotational speed of n_1 of the cylinder is 15~20 r/min.

Hammer design

At present, the blade of straw crusher can be divided into hammer claw type, straight knife type, curved knife type and T-type according to the shape (Liu et al., 2011). Hammer claw blade has large volume and mass, large moment of inertia, good crushing effect, but large power consumption. The straight blade has the advantages of simple structure, small mass, small efficiency consumption, suitable for soft straw, usually used with fixed knife, and good crushing quality. The machete is suitable for hard straw, but the blade strength is low. T-type has complex structure, many cutting edges, large moment of inertia and large power consumption, which is suitable for straw crushing.

In this paper, the hammer is designed as a rectangular zigzag shape, which can increase the friction between the hammer and the material while striking and breaking the straw, and also produce better sliding and stabbing effects. The structure is shown in Fig.4.

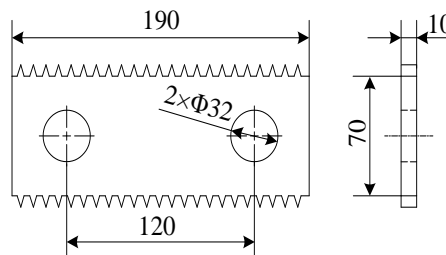


Fig. 4 - Hammer structure diagram

Determination of rotary radius and crushing speed of hammer

The size of the rotary radius of the hammer has a direct influence on the crushing effect, balance and overall size of the crusher. Increasing the rotary radius of the hammer can increase the cutting line speed of the hammer without changing the crushing speed, but increasing the rotary radius of the hammer will increase the overall size of the machine, increase the dynamic unbalance factor of the machine, and increase the energy consumption. Combined with the design size and production efficiency of the machine, the rotary radius r of the hammer is determined to be 330 mm. Then the grinding speed is:

$$n = \frac{60v}{2r\pi} \tag{5}$$

where: n is crushing speed, r/min; v is Hammer cutting line speed, m/s

According to the agricultural machinery design manual (*Agricultural Machinery Design Manual: The First Volume.*, 2007), the linear cutting speed of the hammer ≥ 34 m/s is appropriate. According to formula (5), when the grinding shaft speed is ≥ 996 r/min, the hammer cutting line speed is ≥ 34 m/s, so the minimum grinding speed is determined to be 996 r/min.

Design of sieve

The sieve is a part that screens and separates the crushed straw, so that the crushing straw with a geometric size less than the diameter of the sieve hole is separated from the crushing bin, and can also collide with the material that is not completely crushed to promote the further crushing of the material (Cao et al., 2016; Tian et al., 2016). Because of its simple structure and convenient manufacture, the round hole screen is widely used in the crusher (Cao et al., 2016; Tian et al., 2011). The diameter of sieve is an important parameter that affects the grinding quality and productivity of the mill. The diameter of the sieve hole is large, which can make the crushed material pass through the sieve plate more easily. Although the productivity of the machine is increased and the power consumption is reduced, the length of the crushed corn stalk is larger. The diameter of sieve is too small, so that the crushed material cannot easily pass through the sieve, resulting in excessive crushing, and increased power consumption. The relationship between the diameter of the screen and the length of the broken straw should be as follows:

$$l = (0.25 \sim 0.33)d \tag{6}$$

where: l is length of broken straw, mm; d is diameter of sieve, mm

According to the calculation of equation (6), combined with the actual requirements of crushing operation, the diameter of sieve should range from 15 to 25 mm. The structure is shown in Fig. 5. Two circular screen sieves with the same parameters should be used together.

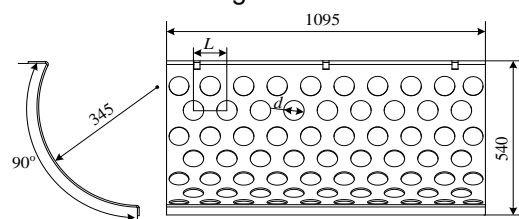


Fig. 5 - The structure of sieve

In order to further clarify the influence of sieve diameter on the crushing efficiency and quality of the machine, this paper optimizes it through experiments.

Design of discharge mechanism

The discharge device of the crusher designed in this paper adopts the double screw conveyor mechanism to change the passive discharge into the active discharge, which can improve the discharge efficiency (Chen et al., 2015; Xu et al., 2019; Xu et al., 2020). According to the production efficiency and discharge requirements of the designed crusher, the design structure of the double screw conveyor is shown in Fig.6.

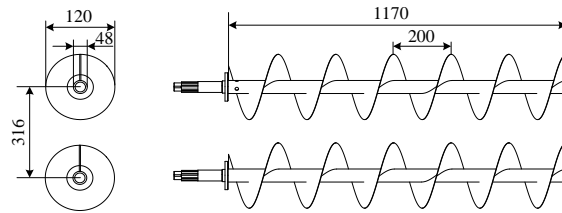


Fig. 6 - Structure diagram of double screw conveyor

In addition to the characteristics of the material itself, the factors that affect the change of the movement trajectory of the broken straw also include the stress and speed distribution, etc. In order to study the discharge stability of the device, the speed distribution of any broken straw is analyzed, as shown in Fig. 7.

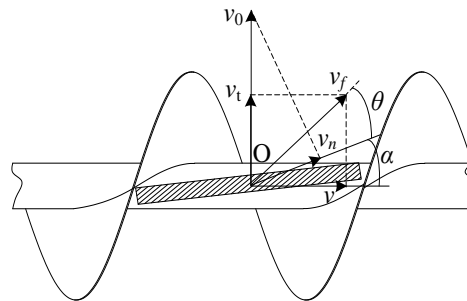


Fig. 7 - Velocity distribution broken straw

where: O is the position of the broken straw; v_0 is the implicated velocity, v_n is the absolute velocity when friction is ignored, v_f is the absolute velocity when friction is considered, v is the axial velocity after v_f decomposition, v_t is the tangential velocity after v_f decomposition, m/s. α is the angle between v_n and v , ($^\circ$); θ is the angle between v_f and v_n , ($^\circ$).

If a broken straw is selected at any radius r , there are two main motion modes, that is, relative sliding with the spiral surface and horizontal motion along the direction of the spiral axis. The circumferential velocity (implicated velocity) of the broken straw is $v_0=r\omega$, and the direction is the tangent direction of the broken straw. Absolute velocity $v_n=v_0\sin\alpha$ without friction; Considering the absolute velocity $v_f=v_n/\cos\theta$ in the case of friction, v_f is decomposed to obtain axial velocity v and tangential velocity v_t .

The axial speed makes the straw move along the direction of the spiral axis, and the tangential speed makes the broken straw flip in the screw conveyor. According to the velocity analysis, the axial velocity of the broken straw is:

$$v = v_f \cos(\alpha + \theta) = \frac{r\omega \sin \alpha}{\cos \theta} \cos(\alpha + \theta) \tag{7}$$

From the above analysis, it can be seen that when the movement speed of the broken straw in the conveying direction is $v>0$, the broken straw can move along the conveying direction, and vice versa. According to the requirements of smooth and efficient discharge, the rotational speed of the screw conveyor is set to 1000-2000 r/min, and the corresponding speed range of the conveying direction can be calculated to be 0.72-1.08 m/s, and the speed values are greater than 0, reaching the condition of the movement of the broken straw.

Analysis of corn straw crushing mechanism

The main crushing forms of corn stalk include smash, impact crushing and rubbing crushing (Ma et al., 2016; Wang et al., 2017). Smash crushing refers to the crushing form caused by the high-speed rotating hammer hitting the corn stalk, impact crushing refers to the crushing form caused by the corn stalk hitting the screen after being hit by the hammer, and rubbing crushing refers to the crushing form caused by the rubbing between the corn stalk, the sieve and the hammer.

Smashing process

The corn stalk enters the crushing bin through the feed port and is hit by the high-speed rotating hammer and broken, as shown in Fig.8.

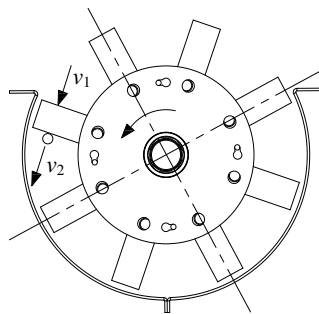


Fig. 8 - Schematic diagram of smashing process of corn stalk

Under the condition that the weight of the hammer plate and the airflow resistance are ignored, it can be known by the impulse-momentum theorem:

$$P\Delta t = m(v_1 - v_2) \tag{8}$$

Namely:

$$P = \frac{m(v_1 - v_2)}{\Delta t} \tag{9}$$

where: P is the impact force of the hammer on the corn stalk, N; Δt is strike action time, s; m is corn stalk mass, kg; v_1 is linear velocity at the end of the hammer, m/s; v_2 is the velocity of the corn stalk before the strike force, m/s.

According to equation (9), when the mass m of the corn stalk is constant, the greater the relative velocity of the hammer to the corn stalk, the greater the strike force on the corn stalk. The strike time Δt depends on the hardness of corn stalk, and the higher the hardness, the shorter the strike time; low hardness means long strike time. When the strike force exceeds the cohesion of the corn stalk, the corn stalk is broken.

Impact crushing

After being hit by the hammer, the corn stalk quickly hits the sieve, as shown in Fig. 9. When the impact force is greater than its cohesive force, the corn stalk is further broken.

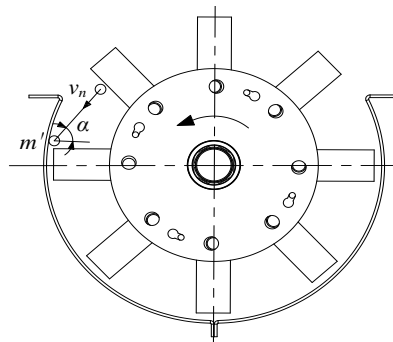


Fig. 9 - Schematic diagram of corn stalk impact crushing process

According to the impulse-momentum theorem, the impact force between the corn stalk and the sieve is:

$$N_1 = \frac{m'}{\Delta t_1} (1 + \lambda) v_n \cos \alpha \tag{10}$$

where: N_1 is Impact force between the corn stalk and the sieve, N; v_n is Initial impact velocity of corn stalk, m/s; m' is the mass of corn stalk before impact, kg; Δt_1 is Impact time, s; λ is elastic recovery coefficient of corn stalk; α is incidence angle of corn stalk to sieve, ($^\circ$).

According to formula (10), under the condition that the structure of the crushing chamber is fixed, the impact force between the corn stalk and the sieve is mainly affected by the initial impact velocity v_n and the elastic recovery coefficient λ of the corn stalk. The elastic recovery coefficient λ of corn stalk is related to its water content. Corn straw is a fibrous material, elastoplastic deformation is large, and most of its impact with the sieve will bounce back, only a small amount of corn straw will be broken, therefore, impact crushing is not the main crushing form of this crusher.

Rubbing crushing

Because there is relative movement between the corn stalk and the hammer and sieve, the corn stalk is further broken by rubbing, as shown in Fig.10.

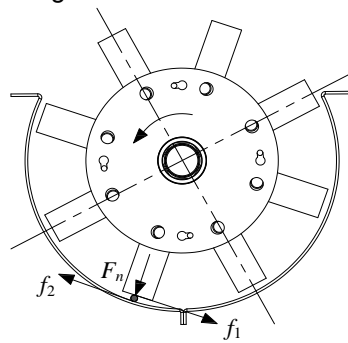


Fig. 10 - Schematic diagram of corn straw rubbing crushing process

The end of the hammer piece and the surface of the screen piece have extrusion and kneading effect on the corn stalk respectively, and the kneading force is respectively:

$$f_1 = \mu_1 F_n \quad (11)$$

$$f_2 = \mu_2 \left(m \frac{v^2}{D + \delta} + F_n \right) \quad (12)$$

where: f_1 is the kneading force of corn stalk and hammer, N; f_2 is the kneading force of corn stalk and sieve, N; F_n is extrusion pressure of the hammer on the corn stalk unit, N; μ_1 is friction coefficient between the corn stalk element and the hammer; μ_2 is friction coefficient between corn stalk and sieve; v is the speed of the corn stalk, m/s; D is rotor assembly diameter, m; δ is clearance of sieve hammer, m.

When the kneading force is greater than the cohesion of the corn stalk, the corn stalk will be broken.

RESULTS AND DISCUSSIONS

Performance test

Test condition

The test was carried out at the test site of Inner Mongolia Ruifeng Agricultural and Animal Husbandry Machinery Co., LTD. The corn straw used in the experiment was provided by corn growers in Datong District, Daqing City, Heilongjiang Province, with a moisture content of 35%. The test site is shown in Fig. 11.



Fig. 11 - Test site

Experimental design

With the rotational speed of crushing shaft, diameter of sieve and clearance of sieve-hammer as test factors, and the productivity, qualification rate of crushing length as performance evaluation indicators (calculation method is shown in the formula 13-14), the orthogonal rotation combination test of three factors and five levels of quadratic regression was carried out. The rotational speed of crushing shaft 1000-2000 r/min, diameter of sieve 15-25 mm, clearance of sieve-hammer 10-20 mm are selected, test factor coding as shown in the table 1, each group of tests were repeated three times, the average value of which was taken as the final test result, data processing and statistical analysis were carried out by Design-Expert 13.0 software. The test results are shown in the table 2.

Productivity y_1

The weighed straw was fed, the time required to crush all the straw was recorded, and the productivity y_1 was calculated as:

$$y_1 = \frac{m}{t} \times 3600 \tag{13}$$

where: m is quality of straw for test, kg; t is test time, s.

Qualification rate of crushing length y_2

At the same time interval, the sample of the crushing straw was picked up at the discharge port for 3 times, each time 300 g, and the mass was weighed after mixing and screening, and the qualified rate of crushing length y_2 was calculated:

$$y_2 = \frac{m_0}{m_1} \times 100\% \tag{14}$$

where: m_0 is the mass of the broken straw with a length of 50~80 mm in the sample, kg; m_1 is sample mass of broken straw, g.

Table 1

Factor level coding table

Coding	Factor		
	Rotational speed of crushing shaft $x_1 / \text{r}\cdot\text{min}^{-1}$	Diameter of sieve x_2 / mm	Clearance of sieve-hammer x_3 / mm
1.682	2000	25	20
1	1797.27 (1800)	22.97 (23)	17.97 (18)
0	1500	20	15
-1	1202.73 (1200)	17.03 (17)	12.03 (12)
-1.682	1000	15	10

Table 2

Test scheme and results

Number	x_1	x_2	x_3	$Y_1 / \text{kg}\cdot\text{h}^{-1}$	$Y_2 / \%$
1	1	1	1	9090.21	94.61
2	1	1	-1	8865.40	94.64
3	1	-1	1	9452.07	93.21
4	1	-1	-1	9257.15	93.08
5	-1	1	1	8895.94	93.32
6	-1	1	-1	9013.76	93.41
7	-1	-1	1	9082.55	92.12
8	-1	-1	-1	9088.32	92.79
9	1.682	0	0	8970.74	94.29
10	-1.682	0	0	8700.32	92.60
11	0	1.682	0	8890.60	94.59
12	0	-1.682	0	9649.43	92.52
13	0	0	1.682	9508.91	92.31
14	0	0	-1.682	9266.34	93.43
15	0	0	0	9637.16	92.38
16	0	0	0	9617.43	92.51
17	0	0	0	9474.76	92.37
18	0	0	0	9594.31	92.73
19	0	0	0	9570.22	92.69
20	0	0	0	9668.64	92.52
21	0	0	0	9671.60	92.39
22	0	0	0	9706.13	92.34
23	0	0	0	9595.08	92.82

Analysis of variance and significance test were performed on the experimental results. The results are shown in the table 3.

Table 3

Analysis of variance							
Evaluation index	Source of variance	Sum of square	Degree of freedom	Mean square	F	P	Significance
Y ₁	Model	2.06E+06	9	2.29E+05	27.82	< 0.0001	**
	x ₁	1.17E+05	1	1.17E+05	14.21	0.0023	**
	x ₂	3.13E+05	1	3.13E+05	37.97	< 0.0001	**
	x ₃	16820.25	1	16820.25	2.04	0.1765	-
	x ₁ ²	8953.23	1	8953.23	1.09	0.316	-
	x ₂ ²	12681.08	1	12681.08	1.54	0.2365	-
	x ₃ ²	11778.82	1	11778.82	1.43	0.253	-
	x ₁ x ₂	1.24E+06	1	1.24E+06	150.1	< 0.0001	**
	x ₁ x ₃	2.49E+05	1	2.49E+05	30.28	0.0001	**
	x ₂ x ₃	1.11E+05	1	1.11E+05	13.51	0.0028	**
	Residual error	1.07E+05	13	8232.29	-	-	
	Lack of fit	69639.88	5	13927.98	2.98	0.0823	
	Error	37379.83	8	4672.48	-	-	
	Sum total	2.17E+06	22	-	-	-	
Y ₂	Model	1.33E+01	9	1.47E+00	35.2	< 0.0001	**
	x ₁	3.30E+00	1	3.30E+00	78.78	< 0.0001	**
	x ₂	4.96E+00	1	4.96E+00	118.47	< 0.0001	**
	x ₃	0.46	1	0.46	11.05	0.0055	**
	x ₁ ²	0.15	1	0.15	3.68	0.0774	-
	x ₂ ²	0.099	1	0.099	2.36	0.1481	-
	x ₃ ²	0.025	1	0.025	0.6	0.4508	-
	x ₁ x ₂	1.80E+00	1	1.80E+00	42.89	< 0.0001	**
	x ₁ x ₃	2.24E+00	1	2.24E+00	53.38	< 0.0001	**
	x ₂ x ₃	2.80E-01	1	2.80E-01	6.7	0.0225	*
	Residual error	5.40E-01	13	0.042	-	-	
	Lack of fit	0.29	5	0.058	1.83	0.2132	
	Error	0.25	8	0.032	-	-	
	Sum total	1.38E+01	22	-	-	-	

Analysis of variance

As can be seen from the table, the rotational speed of crushing shaft x_1 and the diameter of sieve x_2 have extremely significant effects on the productivity, while the clearance of sieve-hammer x_3 has no significant effect on the productivity y_1 . The rotational speed of crushing shaft x_1 , the diameter of sieve x_2 , and the clearance of sieve-hammer x_3 all have extremely significant effects on the qualification rate of the crushing length y_2 . The main and second order of influencing factors on productivity are respectively the diameter of sieve, the rotational speed of crushing shaft and the clearance of sieve-hammer, and the main and second order of influencing the qualification rate of the crushing length are respectively the rotational speed of crushing shaft, the diameter of sieve and clearance of sieve-hammer. The interaction between the rotational speed of crushing shaft and the diameter of sieve (x_1x_2), the interaction between the rotational speed of crushing shaft and clearance of sieve-hammer (x_1x_3) has a very significant effect on productivity and the qualification rate of the crushing length. The interaction between the diameter of sieve and clearance of sieve-hammer (x_2x_3) has a significant effect on the productivity and the qualification rate of the crushing length. The significance level and the mismatch test of the regression equation are greater than 0.05, and the difference is not significant, indicating that the predicted value of the regression equation has a significant relationship with the actual value obtained through the analysis of the test results. The regression equation of each factor and evaluation index obtained after removing the non-significant item is shown as follows:

$$\begin{aligned}
 y_1 = & 9615.38 + 92.54x_1 - 151.29x_2 + 35.09x_3 - 33.45x_1x_2 + 39.81x_1x_3 \\
 & - 38.37x_2x_3 - 278.87x_1^2 - 125.26x_2^2 - 83.67x_3^2
 \end{aligned}
 \tag{15}$$

$$y_2 = 92.53 + 0.49x_1 + 0.60x_2 - 0.18x_3 + 0.14x_1x_2 + 0.11x_1x_3 + 0.056x_2x_3 + 0.34x_1^2 + 0.38x_2^2 + 0.13x_3^2 \quad (16)$$

Parameter optimization and verification test

In order to obtain the best parameter combination of crushing machinery operation performance, the multi-objective optimization algorithm in Design-Expert 13.0 software was used to maximize the productivity and the maximum qualification rate of the crushing length. The optimization mathematical model is established through analysis.

$$\begin{cases} \max y_1(x_1, x_2, x_3) \\ \max y_2(x_1, x_2, x_3) \\ s.t. \begin{cases} 1000r/min \leq x_1 \leq 2000r/min \\ 15mm \leq x_2 \leq 25mm \\ 10mm \leq x_3 \leq 20mm \end{cases} \end{cases} \quad (17)$$

The optimal parameters of the crusher are as follows: the rotational speed of crushing shaft is 1709.24 r/min, the diameter of sieve is 22.83 mm, the clearance of sieve-hammer is 15.38 mm, predicted productivity is 9264.69 kg/h, and the qualification rate of the crushing length is 94.04%.

In order to verify the reliability of the optimization results, the optimization results were verified under the same test conditions. Each group of tests was repeated three times, and the average value of the three test results was calculated as the actual value of the evaluation index under the same conditions. The relative error between the actual results and the optimization results is less than 2%, which proves that the mathematical model and the optimization results are accurate and reliable, and the crusher has a good working performance. The crushed straw is shown in Fig.12.



Fig.12 - Straw after grinding

CONCLUSIONS

(1) Aiming at the low crushing efficiency of the existing straw shredder, a large straw shredder with cylinder feeding hammer was designed, which improved the crushing efficiency through continuous cylinder feeding and could meet the needs of China's large pasture construction.

(2) Through the variance analysis of the test results, it is found that the main and secondary factors affecting the productivity are the rotational speed of crushing shaft, the diameter of sieve and the clearance of sieve-hammer. The main and secondary factors affecting the qualification rate of the crushing length are the rotational speed of crushing shaft, the diameter of sieve and the clearance of sieve-hammer.

(3) Optimized by Design-Expert 13.0 software to obtain the best combination of parameters for crushing operation: the rotational speed of crushing shaft is 1709.24 r/min, the diameter of sieve is 22.83 mm, the clearance of sieve-hammer is 15.38 mm, the verification test shows that the productivity is 9187.98 kg/h, and the qualification rate of the crushing length is 93.87%.

ACKNOWLEDGEMENT

This work was supported by National Natural Science Foundation of China (52275246) and Heilongjiang Bayi Agricultural University Graduate Innovative Research Project (YJSCX2023-Z02).

REFERENCES

- [1] Bao, L., Li, Z., & Dongxing, Z. (2011). Force and motion states of hammer mill at unloaded running (锤片式粉碎机空载运行中锤片的受力及运动状态) [J]. *Transactions of the Chinese Society of Agricultural Engineering*, Vol.27, pp. 123-128. Henan/China.

- [2] Defu, W., Mo, W., & Liqiao, L. (2017). Mechanism Analysis and Parameter Optimization of Hammer Mill for Corn Stalk (锤片式粉碎机粉碎玉米秸秆机理分析与参数优化) [J]. *Transactions of the Chinese Society for Agricultural Machinery*, Vol.48, pp. 165-171. Heilongjiang / China.
- [3] Fudi, Z., Siming, W., & Wenming, H. (2019). Analysis of mechanization utilization and development path of corn straw (玉米秸秆机械化利用情况与发展途径分析) [J]. *Agricultural Machinery Use and Maintenance*, Vol.51, pp. 48. Heilongjiang/China.
- [4] Haijun, Z., Yi, Q., & Haiqing, T. (2024). Design and Experimental Optimization of V-shaped Hammer for Hammer Mill. *INMATEH-Agricultural Engineering*, Vol. 73, pp.191-200. Zhejiang/China.
- [5] Haiqing, T., Fengfu, Q., Weifeng, L., Baosheng, H., Chunguang, W. (2011). Design and Experiment of Piecewise Arc-shaped Screen on Hammer Mill to Grinding Performance (锤片式粉碎机分段圆弧筛片设计与粉碎性能试验) [J]. *Transactions of the Chinese Society for Agricultural Machinery*, Vol.42, pp.92-95. Inner Mongolia/China.
- [6] Haiqing, T., Haiqing, W., Tao, H., Di, W., Fei, L., & Baosheng, (2018). Design of combination sieve for hammer feed mill to improve crushing performance (锤片饲料粉碎机组合形筛片设计改善粉碎性能) [J]. *Transactions of the Chinese Society of Agricultural Engineering*, Vol.34, pp. 45-52. Inner Mongolia
- [7] Hongcheng, L. (2023). Study on Influence Mechanism and Optimization of the Hammer Mill Grinding Performance (锤片式粉碎机工作性能影响机理与优化研究). Hubei/China.
- [8] Hongyang, X. (2020). Mechanization treatment of corn stalk and its development characteristics (玉米秸秆的机械化处理方式与发展特点) [J]. *Agricultural Machinery Use and Maintenance*, pp.101. Heilongjiang/China.
- [9] Kun, W., & Yuepeng, S. (2022). Research Progress Analysis of Crop Stalk Cutting Theory and Method (农作物茎秆切割理论与方法研究进展分析) [J]. *Transactions of the Chinese Society for Agricultural Machinery*, (in Chinese). Vol.53, pp. 1-20. Shandong / China.
- [10] Liying, C., Yuepeng, Z., Yubao, Z., & Yanyan, L. (2016). Influence of screen parameters optimization on screening efficiency of feed hammer mill (筛片参数优化对饲料粉碎机筛分效率的影响) [J]. *Transactions of the Chinese Society of Agricultural Engineering*, Vol. 32, pp. 284-288. Inner Mongolia
- [11] Liying, C., Xinghua, S., Jianxin, W., & Yu, B. (2016). Design and Experiment of Separation Device of Hammer Feed Mill (锤片式饲料粉碎机分离装置设计与试验)[J]. *Transactions of the Chinese Society for Agricultural Machinery*, Vol. 47, pp. 128-133. Inner Mongolia/China.
- [12] Qian, M., Fei, L., & Manquan, Z. (2016). Working mechanism and structure optimization of hammer of rubbing machine (揉碎机揉碎机理分析及锤片结构优化)[J]. *Transactions of the Chinese Society of Agricultural Engineering*, Vol.32, pp. 7-15. Inner Mongolia/China.
- [13] Tao, C., Shujuan, Y., Yifei, L., Guixiang, T., Xin, M., & Shanmin, Q. (2024). Design and Test of Cutting and Crushing Cooperative Silk Kneading Machine (铡切揉碎协同式牧草揉丝机设计与试验). *Transactions of the Chinese Society for Agricultural Machinery*, Vol. 55, pp. 149-159. Heilongjiang
- [14] Tiejun, W., Tieliang, W., Hongguang, C., Yuanjuan, G., Subo, T., & Ruili, W. (2021). Design and Experiment of Adjustable Feeding Straw Bale-breaking and Rubbing Filament Machine (喂入调节式秸秆破包揉丝机设计与试验)[J]. *Transactions of the Chinese Society for Agricultural Machinery*, Vol.52, pp. 148-158. Liaoning / China.
- [15] Xiaoqing, Z., Zifan, W., & MUYOU, C. et al. (2021). Analysis of current situation of crop straw yield and comprehensive utilization in China (中国农作物秸秆产量及综合利用现状分析). *Journal of China Agricultural University*, Vol.26, pp. 30-41. Inner Mongolia/China.
- [16] Xiongfei, C., Xiwen, L., Zaiman, W., Minghua, Z., Lian, H., Wenwu, Y., Shan, Z., Ying, Z., Houding, W., & Le, Z. (2015). Design and experiment of fertilizer distribution apparatus with double-level screws (两级螺旋排肥装置的设计与试验) [J]. *Transactions of the Chinese Society of Agricultural Engineering*, Vol.31, pp. 10-16. Guangdong / China.
- [17] Xuemeng, X., Feixiang, L., Yongxiang, L., Changpu, S., Kunpeng, M., & Jing, C. (2019). Design and Experiment of Quantitative Variable Pitch Screw (定量变距螺旋结构设计及试验)[J]. *Transactions of the Chinese Society for Agricultural Machinery*, Vol.50, pp. 89-97. Henan/China.
- [18] Xuemeng, X., Feixiang, L., Changpu, S., Yongxiang, L., & Dongtao, C. (2020). Optimization Design and Experiment of Wheat Flour Equal Pitch Screw Feeding Device (小麦粉等距螺旋喂料装置优化设计与试验)[J]. *Transactions of the Chinese Society for Agricultural Machinery*, Vol.51, pp.150-157. Henan/China.

SIMULATION ANALYSIS AND EXPERIMENT OF CLEANING MECHANISM FOR TRACK-TYPE COMBINE HARVESTER BASED ON CFD-DEM

基于 CFD-DEM 的履带式联合收获机清选装置仿真分析与试验

Hongda ZHAO¹⁾, Xianghao LI¹⁾, Yongli ZHAO¹⁾, Shaochuan LI¹⁾, Peisong DIAO^{1*)}

¹⁾College of Agricultural Engineering and Food Science, Shandong University of Technology, Zibo, Shandong, 255000, China

E-mail: dps2003@163.com

Corresponding author: Peisong Diao

DOI: <https://doi.org/10.35633/inmateh-74-54>

Keywords: Pre-screening device; Cleaning system; CFD-DEM; Material accumulation

ABSTRACT

This research aims to solve the problem of material accumulation on the screen surface of the cleaning device of tracked combine harvester and proposes an innovative solution of designing a pre-screening device based on the traditional cleaning device. The problem of material accumulation on the screen surface is improved, which in turn enhances the cleaning efficiency. In this study, CFD-DEM coupled simulation technology is used to simulate and analyse the cleaning device, and the effects of airflow velocity, vibration frequency and amplitude on the cleaning effect are explored, and the impurity content and loss rate are used as evaluation indexes. Through orthogonal experimental analysis, the optimal parameter combination of the cleaning device was determined as airflow velocity 11 m/s, vibration frequency 9 Hz, amplitude 30 mm, impurity content rate 2.10% and loss rate 1.62%. The experimental results show that increasing the pre-screening device can significantly improve the material separation effect, reduce the loss and improve the cleaning efficiency.

摘要

本研究旨在解决履带式联合收获机清选装置的筛面物料堆积问题，提出了在传统清选装置基础上设计预筛装置的创新方案。改善了物料在筛面上的堆积问题，进而提升清选效率。本研究采用 CFD-DEM 耦合仿真技术，对清选装置进行模拟分析，探讨了风速、振频、振幅对清选效果的影响，并以含杂率和损失率作为评价指标。通过正交实验分析，确定了清选装置的最优参数组合为风速 11 m/s，振频 9Hz，振幅 30mm。含杂率为 2.10%，损失率为 1.62%。实验结果表明，增加预筛装置能够显著改善物料分离效果，减少损失，提高清选效率。

INTRODUCTION

Combine harvesters are a vital component of contemporary agricultural practices, facilitating the integration of numerous processes, including cutting, conveying, threshing, separating, cleaning, and grain collection, into a single operation. Among the various essential components of the combine harvester, the cleaning system is undoubtedly one of the most crucial. The performance of the combine harvester is significantly influenced by key structural parameters, which in turn impact the operational quality and harvesting efficiency of the machine.

The stability of the combine harvester's operation allows the vibration sieve in the cleaning unit to be designed with a wider range of amplitude and frequency adjustments, rendering it suitable for high humidity and high-viscosity soil conditions. This ensures that high cleaning efficiency is maintained even in complex environments. However, these challenging conditions also give rise to issues such as material accumulation on the sieve surface and an increased risk of sieve clogging, which ultimately affects cleaning efficiency.

To address the issues of material accumulation and decreased cleaning efficiency, Zhang H. et al., (2022), combination of numerical simulation and experimental validation was employed to optimise the design of the cleaning device, resulting in a notable enhancement in the separation of grains. Li Hongchang et al., (2012), conducted computational fluid dynamics (CFD) and discrete element method (DEM) numerical simulations on the movement of materials over the vibrating screen of an air-screen cleaning unit. Furthermore, Guo Shuangjiang et al., (2021), coupled EDEM and Fluent to find the optimum operating parameters of the flushing unit. In response to these challenges, this study proposes an improved solution in the form of the addition of a pre-screening device to the traditional cleaning unit.

By optimising the structural design of the pre-screening device and the operational parameters of the cleaning unit, the airflow distribution on the sieve surface is improved, which in turn reduces material accumulation and decreases the workload of the vibrating screen, thereby further enhancing cleaning efficiency. It is anticipated that the introduction of the pre-screening device will facilitate preliminary separation of materials prior to their entry into the vibrating screen. This is expected to result in a reduction in the load on the vibrating screen, thereby enhancing the efficiency of the cleaning process.

In order to conduct a comprehensive analysis and validation of the performance of the enhanced cleaning system, this paper employs a simulation approach that integrates Computational Fluid Dynamics (CFD) and the Discrete Element Method (DEM). In recent years, a considerable number of researchers have conducted a variety of studies, resulting in notable advancements. For example, *Christian Korn et al., (2017)*, present a verification of the feasibility of the simulation model and an identification of potential avenues for improvement through a combination of numerical simulation and experimental comparison. *Xu Lizhang et al., (2014)*, from Jiangsu University, employed a two-phase solid-liquid flow method to simulate and analyse the cleaning system of a rice harvester. *Liang Zhenwei et al., (2018)*, and colleagues from Jiangsu University employed a two-phase gas-solid flow model in conjunction with practical test bench methods to enhance several pivotal factors of the fan in a multi-duct cleaning system. This resulted in a reduction of the impurity and loss rates by 0.5%. These studies primarily concentrate on the optimisation of parameters pertaining to the cleaning unit, yet they fail to adequately address the issue of material accumulation at the rear of the sieve surface.

In conclusion, this paper employs a coupled simulation approach combining CFD and DEM with practical experiments to simulate and validate the cleaning unit of a crawler-type combine harvester. The objective of this study is to enhance the efficiency of the cleaning process, reduce the impurity rate, and minimise the loss rate. This will be achieved through the design of the pre-screening device and the optimisation of the cleaning system parameters. Ultimately, this will determine the optimal working parameters for the cleaning unit of the crawler-type combine harvester and identify the optimal structure for the pre-screening device.

MATERIALS AND METHODS

Principle design of simulation structure

The cleaning device represents a fundamental component of the combine harvester, comprising a fan, vibrating screen, grain auger, residual auger, and pre-screening device. Upon initiation of operation, the cleaning screen and oscillating plates engage in a reciprocating motion, enabling the sequential conveyance of material from the upper oscillating plate through the middle one to the lower oscillating plate. During this process, the fan generates an airflow that expels the majority of lightweight impurities from the machine. The combination of the fish-scale and woven screens on the vibrating screen facilitates a more efficient and dispersed separation process. During the cleaning process, the wheat grains are conveyed to the grain bin by the grain auger, while any non-grain impurities are directed to the secondary cleaning stage via the residual auger. This mechanism serves to guarantee the quality of the grains, while also markedly enhancing the efficiency of the harvesting process, as illustrated in Figure 1.

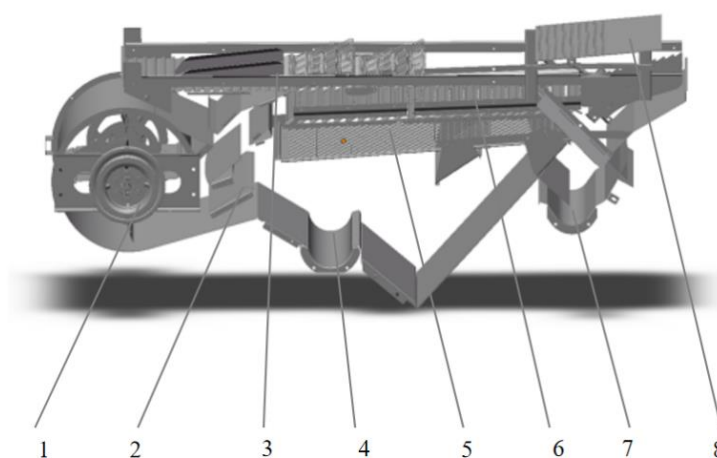


Fig.1 Structure of the cleaning device

1. Blower; 2. Dividing plate; 3. Upper shaking plate; 4. Seed conveying device; 5. Lower sieve woven sieve;
6. Fish scale sieve; 7. Debris conveying device; 8. Pre-screening device

The pre-screening device comprises a crank mechanism, comprising a drive motor, slide rails, a support

frame and a crank arm. The implementation of a pre-screening process at the rear of the cleaning system has the potential to significantly reduce material accumulation on the screen surface, thereby decreasing the overall working load of the vibrating screen and subsequently enhancing the efficiency of the cleaning process. The installation of the pre-screening device at the rear end of the concave sieve of the combine harvester allows for the effective pre-cleaning of the rear-end mixture of wheat. The pre-cleaning operation has the effect of significantly alleviating the workload of the vibrating screen. Consequently, the majority of the wheat mixture can be transferred to the central area of the vibrating screen, where cleaning efficiency is higher. Furthermore, the pre-screening device guarantees the uniform distribution of impurities across the screen surface, thus preventing the accumulation of materials caused by impurities directly falling onto the screen. This not only optimises the handling of impurities but also effectively prevents grains that have not been adequately processed from being discharged at the rear of the machine, thereby reducing losses during the cleaning process, as illustrated in Figure 2.

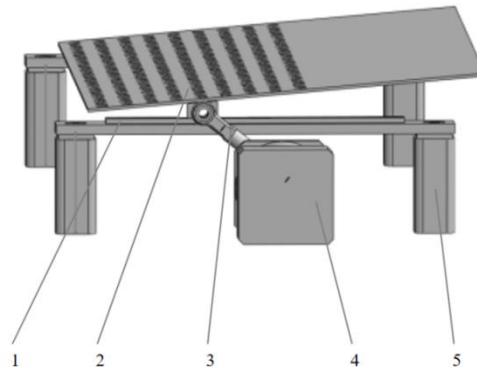


Fig. 2 - Pre-screening device

1. Pre-screen plate slide; 2. Pre-screen plate; 3. Curved arm; 4. Drive motor; 5. Support structure

Establishment of the Simulation Model Structure

In order to reduce the amount of computational energy consumed and to enhance the speed of the simulation, the model was simplified during its construction. The three-dimensional modelling software SolidWorks was employed to create a simplified representation of the cleaning section, retaining only those components that significantly impact the cleaning process, such as the oscillating plate, upper screen, and lower screen. With regard to dimensions, apart from a reduction in the width of the cleaning chamber, all other measurements were based on the actual dimensions of the harvester in real-world settings, with the exception of the aforementioned simplification.

In particular, the length of the cleaning chamber is 2000 mm, with a width of 720 mm and a height of 800 mm. The oscillating plate has a length of 540 mm and is situated 200 mm from the top of the cleaning chamber. The upper vibrating screen is composed of 20 fish-scale screens, whereas the lower screen employs a woven mesh design, measuring 860 mm in length and 735 mm in width. The apertures in the screen are square in shape, measuring 1.8 mm by 1.8 mm, with a distance of 2 mm between units. The distance between the upper screen and the lowest point of the oscillating plate is 160 mm, while the gap between the upper and lower screens is 200 mm. The upper and lower screens are of identical thickness, measuring 1 mm.

Simulation of the mathematical model and the parameters settings

Establishment of the Wheat Threshing Material Discrete Element Model

A discrete element model (DEM) for wheat threshing material was developed with the objective of simulating the behaviour of particles during the cleaning process. The objective of the model was to accurately represent the physical properties of wheat grains, chaff, and other impurities, which are crucial for understanding the separation mechanism in the cleaning system.

The construction of the DEM model for wheat threshing material necessitated the determination of the physical properties of the material's various components. The triaxial dimensions of wheat grains, when placed horizontally, were found to be 6.20-6.76 mm in length, 2.50-2.98 mm in width, and 2.30-2.98 mm in thickness, as indicated by the measurements. The mean values for length, width, and thickness were found to be 6.76 mm, 2.98 mm, and 2.88 mm, respectively.

The length of the short stalks ranged from 12.65 mm to 83.22 mm, with an outer diameter of 1.27 mm

to 3.23 mm and a wall thickness of 0.32 mm to 0.55 mm. The mean values for short stalk length, outer diameter, and wall thickness were found to be 22.95 mm, 2.21 mm, and 0.41 mm, respectively.

The discrete element modelling method was employed to model the various components of the threshed wheat material, which mainly consisted of grains and short stalks, using the triaxial dimensions of wheat grains as a basis. To guarantee the veracity and precision of the simulation experiments, models were constructed for all components, and the multi-sphere particle filling method in EDEM software was employed to streamline, overlap, and populate the particle models of each component. This approach yielded discrete element models of the various components of the wheat threshing material, as illustrated in Figure 3.

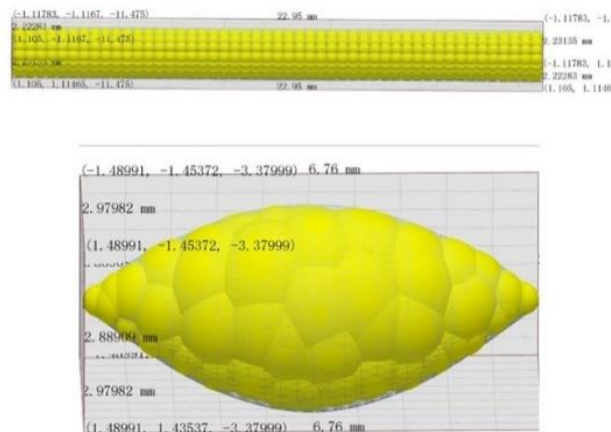


Fig. 3 - Discrete meta-model of wheat exudates

Physical Properties and Contact Parameters of Wheat Threshing Material

In accordance with the findings of prior research and the outcomes of pertinent experiments, the attribute parameters of the discrete element model for the diverse components of the wheat threshing material throughout the simulation process are presented in Table 1. The interaction parameters of each material are shown in Table 2.

Table 1

Material properties			
Material	Poisson's ratio	Shear modulus (MPa)	Density (kg/m ³)
grain	0.3	2.6	1350
Short stems	0.4	1	104
Cleaning room	0.3	7800	7800

Table2

The interaction parameters of each material			
Contact form	Material coefficient	Coefficient of static friction	Rolling friction coefficient
Grains - Grains	0.2	1.00	0.01
Grains - short stems	0.3	0.5	0.01
Grain-cleaning chamber	0.45	0.35	0.01
Short stalk - short stalk	0.22	0.5	0.01
Short stalk - cleaning	0.3	0.36	0.01

The wheat grain mass constitutes 90.32% of the total mass of the threshed material, while short stalks account for 4.18%, and light impurities account for 5.5%. The impurities present in wheat grains are primarily composed of short stalks, while light impurities (such as dust, wheat husks, and fragmented leaves) are frequently dislodged from the grain and rarely accumulate in the grain tank beneath the cleaning apparatus.

Accordingly, subsequent research will not consider these light impurities as subjects for investigation,

and will instead focus on the impact of short stalks. This is due to the fact that the primary impurities present in the grain tank during the cleaning process are short stalks.

Simulation of the mathematical model

Particle collision model

In order to accurately simulate the collisions between particles, as well as between particles and the screen surface, the Hertz-Mindlin (no-slip) contact model was employed within the EDEM software. The motion of the particles was determined in accordance with the mechanical equilibrium equations.

$$m_p \frac{dv_p}{dt} = F_D + F_{GB} + F_{SA} + F_{Ma} \quad (1)$$

$$I_p \frac{d\omega_i}{dt} = T \quad (2)$$

In the formula:

m_p represents the particle mass (kg); V_p represents the particle velocity; t —the total simulation time (s); F_D —the drag force (N); F_{GB} —the gravitational force (N); F_{SA} —the Saffman lift force (N); F_{Ma} —the Magnus lift force (N); I_p —the moment of inertia of the particle; w_n —the angular velocity of the particle (rad/s); T —the torque acting on the particle (N·m)

Fluid-phase control mode

Simulation of parameter settings

In the single-factor simulation experiments, the simplified device model was imported into the EDEM software, and the material properties of the sieve box and sieve plate were specified. Additionally, the motion parameters of the sieve box were set. In the course of the simulation, the Hertz-Mindlin no-slip contact model was utilised. A particle factory was positioned above the oscillating plate and configured to generate wheat grain and short stalk models as previously defined. The particle factories were configured to generate these components in a dynamic manner, with a total of 2,000 wheat grains and 400 short stalks. In the single-factor airflow velocity experiment, the CFD-DEM coupling method was employed to investigate the impact of airflow velocity on the experimental outcomes.

In this simulation, EDEM was coupled with Fluent, with the Hertz-Mindlin (no-slip) contact model selected in EDEM. The simplified cleaning device model was imported into EDEM, where the particle models were created. A particle factory was positioned directly above the oscillating plate. In Fluent, the ANSYS Workbench Design Modeler was employed to streamline the model and obtain the internal flow channel computational domain. Furthermore, in the Meshing module, an unstructured tetrahedral mesh was utilised to discretise the cleaning system model. Once all the requisite parameters had been set, the simulation experiments were initiated.

RESULTS

The findings of existing research indicate that the fan speed of the airflow-sieve cleaning device, in conjunction with the structural and dynamic parameters of the vibrating screen, exert a considerable influence on the efficacy of the device in terms of cleaning performance. Accordingly, this study has selected three experimental factors for analysis in the context of the cleaning device of the tracked rice-wheat combine harvester: fan speed, vibrating screen frequency, and vibrating screen amplitude. The evaluation indices for the single-factor experiments were the grain impurity content and cleaning loss rate. These indices were subjected to analysis with the objective of evaluating the operational performance of the cleaning device under different working parameters, with a view to determining the optimal combination of working parameters.

A review of the relevant literature and prior experimental data informed the decision-making process regarding the scope of the single-factor experiments. The fan speed was set between 8 m/s and 12 m/s, the reciprocating vibrating screen frequency ranged from 6 to 10 Hz, and the vibration amplitude was set between 20 mm and 40 mm. In the course of the simulation trials, two factors were maintained at a constant level in each experiment in order to investigate the impact of these parameters on the operational performance of the airflow-sieve cleaning device of the tracked combine harvester.

The influence of fan speed on the cleaning result

A simulation analysis was conducted to investigate the impact of fan speed on cleaning efficiency under

conditions where the vibrating screen frequency was set at 9 Hz and the screen amplitude at 35 mm. The fan speed was adjusted to 8 m/s, 9 m/s, 10 m/s, 11 m/s, and 12 m/s to observe the behaviour of the wheat threshing mixture within the cleaning device, with the objective of determining the optimal fan speed range. Following the simulation, the data pertaining to the impurity content and cleaning loss rate were duly recorded.

As the fan speed increased during the simulation, the force exerted on the threshed material in the airflow field also increased. This resulted in a prolonged suspension time and a backward shift in the position where the material landed on the screen. This resulted in an increase in wheat grain losses. At relatively low fan speeds, the threshed material fell rapidly onto the screen surface, resulting in a reduction in the quantity of blown-off impurities and an increase in the impurity content of the grains. However, the grains remained at a greater distance from the discharge port, thus reducing the probability of their loss and maintaining a low cleaning loss rate.

As illustrated in the accompanying figure 4, the gradual increase in fan speed was accompanied by a decrease in the impurity content of the wheat, while the cleaning loss rate exhibited a gradual increase. In the fan speed range of 8 m/s to 9 m/s, the impurity content decreased from 4.31% to 3.01%, indicating effective removal of light impurities within this range. Meanwhile, the cleaning loss rate remained at a relatively low level of approximately 1.7%. Upon further increasing the fan speed to 10 m/s, the impurity content decreased to 1.89%, while the cleaning loss rate rose to 2.51%. This resulted in an intersection point between the two trends.

Further increases in fan speed to 11 m/s and 12 m/s resulted in a reduction in impurity content to 1.16% and 0.95%, respectively. However, this was accompanied by an increase in cleaning loss rate, which reached 3.99% and 5.21%, respectively. This trend suggests that, within a certain range, an increase in fan speed effectively separates impurities, resulting in a gradual reduction in impurity content. However, when the fan speed exceeded 10 m/s, the excessive airflow intensity resulted in a greater likelihood of the wheat grains being blown off the screen, leading to a notable increase in the loss rate. In light of the observed variations in impurity content and cleaning loss rate, it can be inferred that the optimal fan speed range is likely to be between 9 m/s and 10 m/s, where the impurity content is relatively low and the loss rate is kept at a minimum level.

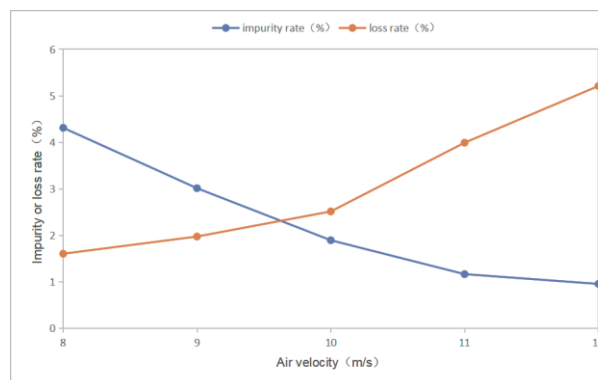


Fig. 4 - Schematic diagram of cleaning results

The influence of the vibrating frequency of the shaker on the sorting result

A simulation analysis was conducted to investigate the effect of vibrating screen frequency on cleaning performance for wheat. The vibrating screen amplitude was set at 30 mm and the fan speed at 10 m/s, with frequencies ranging from 6 to 10 Hz. The simulation results indicated that as the vibration frequency increased, the velocity of the threshed material also increased, while the residence time of the material on the screen surface decreased accordingly. This consequently reduced the probability of the material passing through the screen mesh. Upon contact with the screen, the high vibration frequency caused the material to scatter with ease and gain significant initial velocity, rendering it more susceptible to ejection from the cleaning chamber by the fish-scale screen. Consequently, the grain loss rate increased, while the proportion of grains in the screened material decreased, resulting in an elevated impurity content.

Further analysis demonstrated that, as illustrated in the figure 5, an increase in the vibrating screen frequency resulted in a gradual upward trend in the cleaning loss rate, while the grain impurity content initially exhibited a decrease and then an increase. As the vibration frequency increased from 6 Hz to 10 Hz, the cleaning loss rate exhibited a notable rise from 2.41% to 3.02%. Concurrently, the impurity content demonstrated a decline from 3.21% to 2.15%.

However, this trend reversed, with the cleaning loss rate rising once more to reach 2.34%. This can be attributed to the increased jumping frequency of wheat grains under higher vibration frequency, as well as their

accelerated horizontal velocity, which increased the likelihood of them jumping directly towards the discharge port, resulting in increased losses. Furthermore, as the loss rate increased, the proportion of wheat grains in the screened material decreased, resulting in an elevated impurity content. In conclusion, the optimal cleaning effect was achieved when the vibration frequency was between 8 Hz and 9 Hz, as this resulted in the lowest impurity content and cleaning loss rate.

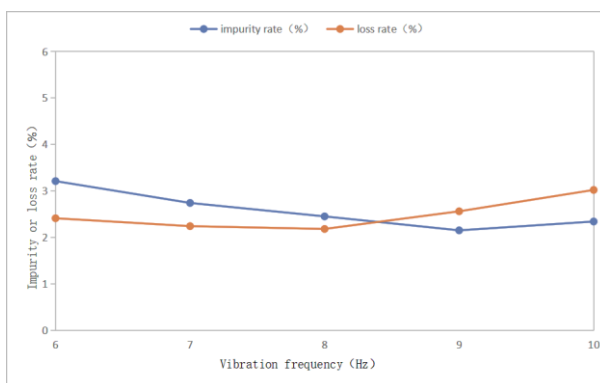


Fig. 5 - Schematic diagram of cleaning results

The Influence of Vibrator Amplitude on Sorting Results

The objective of this investigation was to ascertain the impact of vibrating screen amplitude on cleaning performance for wheat. To this end, different amplitude settings were applied to a simulation model under conditions of a fan speed of 10 m/s and a vibration frequency of 9 Hz. The amplitudes simulated included 20 mm, 25 mm, 30 mm, 35 mm, and 40 mm, with the objective of observing the behaviour of threshed wheat material on each screen surface and determining the optimal amplitude range. As illustrated in Figure 6, the numerical simulation results demonstrated that an amplitude of 30 mm resulted in an even distribution of the threshed wheat material on the screen, thereby achieving optimal sieving performance. Furthermore, this amplitude setting minimised both the grain loss rate and impurity content.

Conversely, at an amplitude of 30 mm, the sieving effect of the threshed wheat material on both the upper and lower screen surfaces was optimal, with minimal grain loss and the highest cleaning efficiency, resulting in stable operational performance. In conclusion, the results demonstrated that an amplitude of 30 mm was able to maintain a low loss rate while effectively reducing impurity content, achieving the best cleaning performance under the given fan speed and vibration frequency conditions.

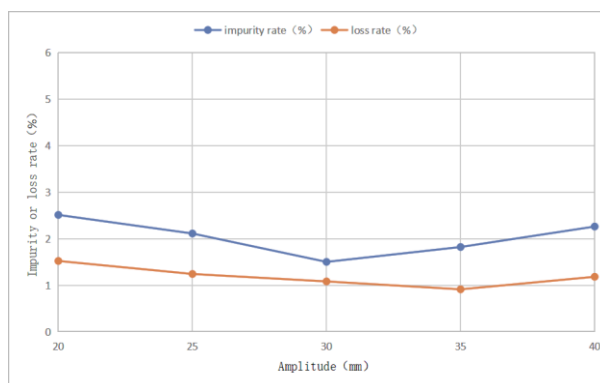


Fig. 6 - Schematic diagram of cleaning results

Pre-screening device structure optimisation

The CFD simulation analysis yielded two main conclusions regarding the airflow field distribution within the cleaning chamber. Firstly, the airflow velocity was observed to be relatively low in the area above the twentieth fish-scale screen. Secondly, a similarly low airflow velocity was observed in the area above the tenth fish-scale screen from the end as illustrated in Figure 7. In light of these findings, the structure and dimensions of the pre-screening plate were subsequently optimised.

In order to prevent the accumulation of wheat threshed material in a single area of the screen, which could result in an increased load, the pre-screening device's screen plate was designed to consist of a return plate and a perforated screen.

The wheat threshed material that falls from the end of the concave screen is propelled forward by the return plate. A proportion of the threshed material is able to pass through the perforated screen and fall onto

the surface of the vibrating screen in advance, thereby performing a pre-cleaning function. The material that does not pass through continues to move forward and ultimately falls onto the vibrating screen surface from the end of the perforated screen.

The dimensions of the screen plate were determined based on the width of the cleaning chamber, which was set at 810 mm, while the length was established as 4000 mm, according to the distance from the twentieth fish-scale screen to the machine outlet. The width of the perforated screen within the screen plate is identical to that of the screen plate itself, with a total length of 215 mm. This distance is determined by the distance from the tenth fish-scale screen from the end to the vibrating screen outlet, with the return plate measures 185 mm in length. The diameter of the perforations in the screen was determined based on the average length of the short stalks present in the threshed material, with a final measurement of 12 mm established.

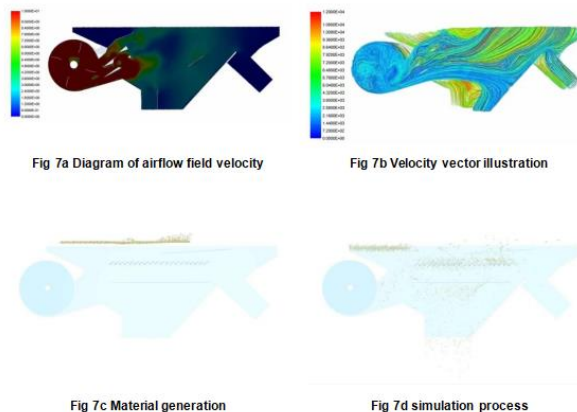


Fig. 7 - Selection simulation process

Orthogonal test numerical simulation and result analysis

Orthogonal experimental results

An orthogonal coupled simulation experiment was conducted, in which fan speed, vibration frequency and amplitude were identified as factors, with impurity content and grain loss rate of wheat kernels identified as evaluation indices. In accordance with the findings of the single-factor experiment detailed, the optimal intervals for these three parameters were identified and selected for further orthogonal simulation, as shown in Table 3.

Table 3

Virtual Orthogonal Experiment Factors and Level Table			
Level	Test Factors		
	A airflow velocity (m/s)	B oscillation (Hz)	C amplitude (mm)
1	9	7	25
2	10	8	30
3	11	9	35

Analysis of the contamination rate results

Table 4

Experimental plan and results					
Number	A airflow velocity (m/s)	B oscillation (Hz)	C amplitude (mm)	Trash content (%)	Loss rate (%)
1	9	7	25	3.51	2.60
2	9	8	30	3.12	2.00
3	9	9	35	2.61	1.94
4	10	7	30	3.19	2.51
5	10	8	35	2.80	2.12
6	10	9	25	3.72	2.20
7	11	7	35	2.30	1.73
8	11	8	25	3.03	1.91
9	11	9	30	2.10	1.62

Table 5

Analysis of Impurity Rate Range			
Serial number	A airflow velocity (m/s)	B oscillation (Hz)	C amplitude (mm)

K1	12.0	10.5	10.7
K2	9.5	9.2	8.1
K3	7.8	8.6	9.5
K1	4.0	3.5	3.57
K2	3.17	3.07	2.7
K3	2.6	2.87	3.17
range	1.4	0.63	0.87
Primary and secondary factors	airflow velocity (A) > oscillation (B) > amplitude (C)		
Optimization plan	airflow velocity (A):=9m/s oscillation (B)= 25mm amplitude (C)= 7Hz		

As demonstrated in table 4 and table 5, a reduction in impurity content is associated with enhanced cleaning efficiency. A range analysis of the various factors revealed that airflow velocity (A) had the most significant impact on impurity content, with the lowest impurity content observed at an airflow velocity of 9 m/s. The second most influential factor was amplitude (B), with an amplitude of 25 mm demonstrating the optimal cleaning effect. Vibration frequency (C) was found to exert the least influence on impurity content, with a frequency of 7 Hz yielding favourable results. It can therefore be concluded that the order of influence on impurity content is as follows: airflow velocity > amplitude > vibration frequency. In light of the aforementioned findings, the optimal parameter combination for minimising impurity content and maximising cleaning efficiency in the cleaning process is an airflow velocity of 9 m/s, an amplitude of 25 mm, and a vibration frequency of 7 Hz.

Table 6

Analysis of Variance with Impurity Rate						
	Type III sum of squares	df	mean square	F	Sig	
Correction model	8.960	6	1.493	296.670	0.003	
Intercept	46.444	1	46.444	9124.312	0.000	
Airflow velocity	8.361	2	4.180	418.119	0.001	
Vibration frequency	0.541	2	0.270	27.356	0.024	
Amplitude	0.299	2	0.150	15.534	0.046	
Error	0.021	2	0.010			
Total	56.414	9				
Total of corrections	8.970	8				

Table 6 presents the analysis of variance (ANOVA) for impurity content following the completion of the orthogonal experiments. In accordance with the F distribution table, the critical value is $F_{0.05(2,2)} = 19$. As illustrated in the table, the F-values for airflow velocity, vibration frequency, and amplitude are all greater than $F_{0.05(2,2)} = 1$. This suggests that there is a significant impact of airflow velocity, vibration frequency, and amplitude on impurity content. The F values indicate that airflow velocity has the greatest influence on impurity content, followed by vibration frequency and then amplitude. This finding is in accordance with the conclusions previously drawn from the range analysis.

Analysis of loss rate results

Table 7

Loss Rate Range Analysis			
Serial number	A airflow velocity (m/s)	B oscillation (Hz)	C amplitude (mm)
K1	7.6	7.3	6.8
K2	6.9	6.3	6.5
K3	5.5	6.4	6.7
K1	2.53	2.43	2.27
K2	2.3	2.1	2.17
K3	1.83	2.13	2.23
range	0.7	0.33	0.1
Primary and secondary factors	airflow velocity (A) > oscillation (B) > amplitude (C)		
Optimization plan	airflow velocity (A):=11m/s oscillation (B)= 30mm amplitude (C)= 9Hz		

A review of the data in the table reveals a clear correlation between the loss rate and the cleaning effect: the lower the loss rate, the more effective the cleaning. The range analysis of the various factors indicates that airflow velocity (A) exerts the most significant influence on the loss rate, with the lowest loss rate occurring at an airflow velocity of 11 m/s.

The subsequent most influential factor is amplitude (B), whereby a 30 mm amplitude is observed to yield the optimal cleaning effect. Vibration frequency (C) exerts the least influence on the loss rate, with the optimal

performance observed at 9 Hz. Therefore, the order of influence on loss rate among airflow velocity, amplitude, and vibration frequency is as follows: airflow velocity > amplitude > vibration frequency. It can therefore be concluded that the optimal parameter combination for minimising the loss rate during the cleaning process is an airflow velocity of 11 m/s, an amplitude of 30 mm, and a vibration frequency of 9 Hz, which yields the lowest loss rate and the best cleaning effect.

Table 8

	Type III sum of squares	df	mean square	F	Sig
Correction model	0.926	6	0.154	297.513	0.003
Intercept	48.780	1	48.780	11745.231	0.000
Airflow velocity	0.683	2	0.342	243.154	0.001
Vibration frequency	0.273	2	0.136	136.385	0.005
Amplitude	0.089	2	0.045	91.000	0.011
Error	0.021	2	0.010		
Total	50.866	9			
Total of corrections	0.926	8			

The conclusions shown in Table 8 are consistent with the conclusions drawn in Table 6.

Comprehensive analysis of loss rate and impurity rate

In the cleaning system, the effects of airflow velocity, feed rate, and vibration frequency on impurity content and cleaning rate are significant, resulting in an inverse relationship between impurity content and cleaning rate. Accordingly, in order to achieve equilibrium between these two pivotal indicators and to enhance the efficacy of the cleaning process, the comprehensive weighted average methodology is employed to evaluate the simulation outcomes pertaining to impurity content and cleaning rate. The calculation method is as follows:

$$Z_i = W_1 \times \frac{y_{i1}}{y_{1max}} + W_2 \times \frac{y_{i2}}{y_{2max}} \tag{3}$$

In the formula:

Z_i —Weighted score for the i -th experiment; W_1 —Weight of impurity content, $W_1=30\%$;

W_2 —Weight of loss rate, $W_2=70\%$, y_{i1} —Impurity rate of the i -th experiment;

y_{1max} —Maximum impurity content in the experiment; y_{i2} —Loss rate of the i -th experiment;

y_{2max} —The maximum loss rate in all experiments

Table 9

Number	A airflow velocity (m/s)	B oscillation (Hz)	C amplitude (mm)	Trash content (%)	Loss rate (%)	Weighted score
1	9	7	25	3.51	2.60	98.306
2	9	8	30	3.12	2.00	79.007
3	9	9	35	2.61	1.94	73.279
4	10	7	30	3.19	2.51	93.303
5	10	8	35	2.80	2.12	79.658
6	10	9	25	3.72	2.20	91.923
7	11	7	35	2.30	1.73	65.125
8	11	8	25	3.03	1.91	80.973
9	11	9	30	2.10	1.62	60.550

A lower weighted score is indicative of a lower impurity content and loss rate, thereby indicating an enhanced cleaning performance. As illustrated in the aforementioned table, Experiment 9 has the lowest weighted score of 60.550, thereby identifying it as the optimal parameter combination. The optimal parameter combination is as follows: airflow velocity A = 11 m/s, vibration frequency B = 9 Hz, and amplitude C = 30 mm.

CONCLUSION

The objective of this study was to develop a novel pre-screening device to address the limitations of traditional cleaning systems during grain harvesting, specifically the issues of cleaning efficiency and grain loss. The device effectively alleviates the accumulation of material on the sieve surface, thereby significantly enhancing the separation of material.

The pre-screening device has the effect of reducing the workload of the cleaning mechanism, thereby improving the efficiency of the cleaning process and the overall performance of the harvesting operation. This

design optimisation not only enhances the operational stability of the cleaning mechanism but also provides a novel reference point for the future development of combine harvesters.

The optimal parameter combination for the cleaning mechanism is as follows: A CFD-DEM simulation analysis was conducted to determine the optimal operating parameters for the cleaning system. A comprehensive analysis of airflow velocity, vibration frequency, and amplitude led to the conclusion that the optimal combination for cleaning performance is an airflow velocity of 11 m/s, a vibration frequency of 9 Hz, and an amplitude of 30 mm. This combination ensures an optimal balance between a low impurity rate and a low grain loss, thereby significantly enhancing the overall cleaning performance of the combine harvester during field operations.

REFERENCES

- [1] Badretdinov, I., Mudarisov, S., Lukmanov, R., Ibragimov, R., Permyakov, V., Tuktarov, M, (2020). Mathematical modeling and study of the grain cleaning machine sieve frame operation, *INMATEH – Agricultural Engineering*, vol.60(1), 19-28.
- [2] Chen, S., (2021). Simulation and key parameters optimisation of wheat harvester clearing based on CFD-DEM (基于 CFD-DEM 小麦收获机清选仿真与关键参数优化). *Jinan University*.
- [3] Christian, K., Thomas, H., (2017). Coupled CFD-DEM Simulation of Separation Process in Combine Harvester Cleaning Devices. *Landtechnik*, Vol. 72, No. 5.
- [4] Dai, F., Song, X. F., Zhao, W. Y., (2019). Motion simulation and test on threshed grains in tapered threshing and transmission device for plot wheat breeding based on CFD-DEM. (基于 CFD-DEM 的小麦育种锥形脱粒和传输装置中的运动模拟和脱粒测试). *International Journal of Agricultural and Biological Engineering*, 12(1): 66-73.
- [5] Li D.J., Hou, J.L., Wang, D.W., Chang, Z.J., (2024). Design and testing of peanut sieving prototype machine. *INMATEH –Agricultural Engineering*, 73(2), 760-770.
- [6] Guo, S.J., Ma, X.D., Liu, Z.H., Chen, G.H., Wang, S., (2021). Simulation study and parameter discussion of wind sieve type grain cleaning. (风筛式谷物清选模拟研究及参数讨论). *Agricultural Mechanisation Research*, 43(02): 10-15.
- [7] Han, D.D., Zhang, D.X., (2018). DEM-CFD coupling simulation and optimization of an inside-filling air-blowing maize precision seed-metering device. (DEM-CFD 耦合模拟与优化玉米精准播种装置). *Computers and Electronics in Agriculture*, 150: 426-438.
- [8] Han, D.D., Zhang, D.X., Jing, H.R., Cui, T., Yang, L., (2018). DEM-CFD coupling simulation and optimization of an inside-filling air-blowing maize precision seed-metering device (DEM-CFD 耦合模拟和优化内部填充式吹气玉米精密种子计量装置). *Computers and Electronics in Agriculture*, 150: 426-438.
- [9] li, Y.M., Zhao, Z., Chen, J., Xu, L. Z. (2007). Nonlinear motion law of material on air-and-screen cleaning mechanism (风筛式清选装置上物料的非线性运动规律). *Transactions of the Chinese Society of Agricultural Engineering*, 23(11): 142-147.
- [10] Li, H.Z., Li, Y.M., Tang, Z., (2011). Numerical simulation and analysis of shaker simulation based on EDEM (基于 EDEM 的振动筛仿真数值模拟与分析). *Transactions of the Chinese Society of Agricultural Engineering*, 27(5): 117-121.
- [11] Li, H.C., Li, Y.M., Tang, Z., Xu, L.Z., (2012). CFD-DEM numerical simulation of material movement on the vibrating screen of the air sieve cleaning device (风筛式清选装置振动筛上物料运动 CFD-DEM 数值模拟). *Transactions of the Chinese Society of Agricultural Engineering*, 43(2): 79-84.
- [12] Liang, Z.W., LI, Y.M., Ma, P.P., Wei, C.C., Wang, J.P., (2018). Structural optimisation and test of the cleaning device of longitudinal flow combine harvester. (纵轴流联合收获机清选装置结构优化与试验). *Research on Agricultural Mechanisation*. 40(05): 170-174.
- [13] Mircea, C., Nenciu, F., Vlăduț, V., Voicu, Gh., Gageanu, I., Cujbescu, D. (2020), Increasing the performance of cylindrical separators for cereal cleaning, by using an inner helical coil. *INMATEH – Agricultural Engineering*, vol.62(3), 249-258.
- [14] Ning, X.B., Xu, I., Sun, C.H., Yang, H.S., (2019). Fan's parameters optimization and internal flow field distribution in multi-duct cleaning device of combine harvester (联合收获机多风道清选装置气流场分布与风机参数优化) *Journal of Agricultural Mechanization Research*, 41(6):32-37.
- [15] Tang, X.H., Zhao, N., Guo, B., Jin, C.Q., Yu, M. Q., Li, J.Q., Qing, B., (2022). Design and test of multi-parameter adjustable cleaning loss distribution inspection test bench (多参数可调式清选损失分布检测

- 试验台设计与试验). *Research of Agricultural Mechanisation*, 44(12): 148-155.
- [16] Wang, J., Li, Z., Hussain, S., Lu, Q., Song, H., Zheng, D, (2020). Design and threshing outputs study of internal and external rotary roller buckwheat thresher, *INMATEH –Agricultural Engineering*, vol.60(1), 173-182.
- [17] Liu, L. W., Liu, F., Wei, C. Y., Peng, F., Wang, J.Q., (2024). Design and simulation analysis of the tuber harvest screening machine. *INMATEH –Agricultural Engineering*, vol.73(2), 534-545.
- [18] Xiao, X.X., Li, B., Wu, C.Y., Qi, X.D., Hu, T., (2018). Motion analysis of the cylindrical sieve cleaning process of two early rice varieties based on DEM-CFD. (基于 DEM-CFD 两种早稻品种圆筒筛清选过程的运动分析). *Mechanical Design*, 35(10): 32-37.
- [19] Xu, L.Z., Yu, L.J., LI, Y.M., Ma, Z., Wang, C.H., (2014). Numerical simulation of the internal flow field of a double outlet multiduct centrifugal fa. (双出风口多风道离心风机内部流场数值模拟). *Journal of Agricultural Machinery*, 45(10): 78-86.
- [20] Yuan, Z.X., DAI, F., ZHAO, W.Y., Shi, R.J., Zhao, Y.M., (2023). Simulation analysis and test of CFD-DEM based air-screen cleaning device for huisache (基于 CFD-DEM 的胡麻风筛式清选装置仿真分析与试验). *Agricultural Research in Arid Regions*, 41(06):281-290.
- [21] Zhao, Z., Yang, X., Zhang, G., (2022). Analysis and optimization test of operation process of cleaning device of corn seed harvester, *INMATEH –Agricultural Engineering*, vol.68(3), 211-220;
- [22] Zhu, P. F., (2019). Simulation research on grain air-and-screen cleaning process and optimization of key parameters. (谷物风筛清选仿真研究及关键参数优化设计). *Hangzhou: Zhejiang University*.
- [23] Zhang, H., Wang, Z., & Zhao, J, (2022). Simulation of grain cleaning process in combine harvester using CFD-DEM coupling method. *Biosystems Engineering*, 204, 53-65.

OPTIMIZING THE UNIT STRUCTURE OF THE DRAINAGE-TYPE CYCLONE SEPARATOR FOR SAND SAMPLE COLLECTION

优化排水型旋风分离砂样采集器的单元结构

Caoqi ZHANG¹⁾, Muhammad Ariff Bin BAHARUDIN^{1*)}, Taiming GUO²⁾, Jining ZHANG³⁾, Shiping WU⁴⁾

¹⁾ Faculty of Electrical Engineering, Universiti Teknologi Malaysia, Johor Skudai/Malaysia

²⁾ Faculty of Computer Engineering, Universiti Teknologi Malaysia, Johor Skuda/Malaysia

³⁾ State Nuclear Electric Power Planning Design & Research Institute, Beijing/China

⁴⁾ Faculty of Humanities and Social Sciences, Datong No.12 Middle School Shanxi, 034400, P.R. China

Tel: +60172178749; E-mail: mariff@utm.my

Corresponding author: Muhammad Ariff Bin Banharudin

DOI: <https://doi.org/10.35633/inmateh-74-55>

Keywords: Sand sampler, sampling efficiency, orthogonal experiment, regression model, wind erosion

ABSTRACT

This paper introduces a cyclone separation sand sampler with diversion flow to enhance soil wind erosion monitoring accuracy. Using CFD simulations and orthogonal testing, the optimal structural parameters for improved sampling efficiency were determined. A response model showed strong predictive capability with a *P*-value less than 0.0001 and *R*² of 0.9482. Wind tunnel tests demonstrated that the new sampler achieved a 91.44% efficiency, surpassing the 90.81% of the traditional design. The research provides valuable data for more accurate wind-sand flow monitoring, aiding in desertification prevention and improving wind erosion assessments in grasslands.

摘要

本文介绍了一种带有导流装置的旋风分离式沙尘采样器，以提高土壤风蚀监测的精度。通过 CFD 仿真和正交试验，确定了优化后的结构参数以提高采样效率。响应模型显示其预测能力较强，*P* 值小于 0.0001，*R*² 为 0.9482。风洞试验结果表明，新型采样器的采样效率达到 91.44%，高于传统设计的 90.81%。该研究为更准确的风沙流监测提供了有价值的参考数据，有助于防治荒漠化并改善草原风蚀评估。

INTRODUCTION

In recent years, nearly 180 million hectares of grasslands have undergone severe degradation. The degradation phenomenon has led to a continuous decline in grassland quality (Song, 2016). Soil wind erosion is the main factor causing grassland degradation, which is jointly restricted by climate, soil, vegetation, and human factors (Jhang *et al.*, 2019). The sand sampler is a type of wind erosion testing device, which is employed to measure the quantity of sand transported in the wind-sand flow and the wind-sand flow and the structure of the wind-sand flow (Liu *et al.*, 2019; Li *et al.*, 2022). It is an indispensable instrument for studying soil wind erosion and grassland degradation and observing the structural characteristics of wind sand flow in indoor and outdoor wind tunnels (Khan *et al.*, 2021).

Recently, domestic scholars have conducted extensive research on the sampling efficiency of the internal flow field of sand sampler units using aerodynamic (CFD) principles for different sand sampler devices (Petrichenko, 2020). The CFD method was used to study the internal velocity flow field and the principle of velocity reduction of the diversion counter flow sand sampler (Song *et al.*, 2018). The coupling method of CFD and the discrete element method were used to study and analyze the motion of gas-solid two-phase flow in a sand sampler (Yang, 2021). The CFD method was used to study the relationship between the internal velocity flow field and size parameters of a cyclone separation sand sampler unit (Huang *et al.*, 2015). In the case of the existing cyclone separation sand sampler, the sampler method of particles has not been researched. The use of sandbags and sandboxes to collect particles has also resulted in a significant reduction in the velocity of airflow backflow inside the sampler box, becoming the main reason for affecting the sampling efficiency. Based on this, a drainage method has been proposed in this article to make particles in the drainage tube only affected by gravity, reducing the reflux speed of the airflow, and thereby, the sampling efficiency of the sand sampler will be improved (Chen *et al.*, 2018).

A cyclone separation sand sampler of drainage type was designed, and the mathematical model between the sampling efficiency, structural parameters, and airflow velocity of its sand sampler unit was studied in this paper (Yan *et al.*, 2024). Firstly, the velocity and flow field of the sand sampler unit was simulated, and Design Expert software was used to design the sampling efficiency experiment (Xu *et al.*, 2023; Dumitru *et al.*, 2024). Secondly, the experimental data was classified and statistically analyzed, and a sampling efficiency response model using orthogonal experimental methods was established. Finally, the effects of the structural parameters of the sand sampler unit, airflow velocity, and their interaction on sampling efficiency were studied, providing corresponding theoretical references for the design and structural optimization of the drainage-type cyclone separation sand sampler (Zhang *et al.*, 2023; He *et al.*, 2024).

To summarize, in recent years, approximately 180 million hectares of grasslands have suffered severe degradation, primarily caused by soil wind erosion, which is influenced by climate, soil, vegetation, and human factors. The sand sampler, as a key device for measuring sand transport volume and wind-sand flow structure, is widely used in the study of soil wind erosion and grassland degradation. Existing research mainly focuses on improving the sampling efficiency of the internal flow field of sand samplers using CFD methods. This paper proposes a drainage-based cyclone separation sand sampler to reduce airflow reflux speed and improve sampling efficiency, providing theoretical references for the design and structural optimization of drainage-type sand samplers.

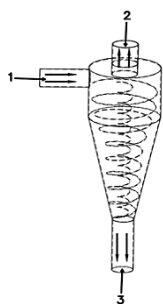
MATERIALS AND METHODS

Drainage type sand sampler unit

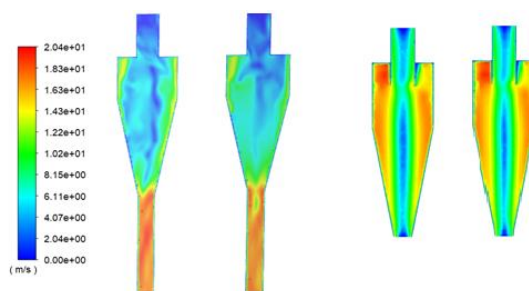
The system is divided into two plate assemblies, a field terminal, and a remote client. The system's overall framework is shown in Fig. 1, and its appearance is shown in Fig. 2.

At present, drainage and sampler treatment on the particles after gas-solid sampling has not been conducted in the cyclone separation type sand sampler research. In order to improve the sampling efficiency, this study focuses on optimizing the drainage tube, which is connected to the sand sampler unit using PVC rigid pipes, as shown in Figure 1. The left side of the sand flow enters from the air inlet. In the sand sampler unit, the purified gas is discharged from the upper exhaust funnel, and particles are collected from the lower sand discharge port. The direction of movement of the airflow and particles is the same. Through drainage, the reflux speed of the airflow is reduced, thereby improving the sampling efficiency of the sand sampler unit.

The research process was conducted through CFD simulation to analyze the velocity flow field of the drainage and traditional sand sampler units, as shown in Figure 2. The flow velocity field reflects the changes in particle motion velocity within the sand sampler unit. The smaller the velocity near the exhaust pipe, the fewer particles escaped, thus verifying the higher sampling efficiency (Patil *et al.*, 2022; Li, 2022).



1. Air inlet 2. Exhaust outlet 3. Sand discharge outlet
Fig. 1 - Particle motion trajectory diagram



(a) Drainage type (b) Traditional type
Fig. 2 - Numerical simulation distribution diagram of velocity flow field

In the simulation experiment, the variable factor is wind speed, and the amount of particle injection at the inlet is set. When the residual calculation is completed, the corresponding velocity flow field and the capture and escape amount of particles are obtained. The sampling efficiency of the capture amount of particles, the injection amount, and the final particle capture amount are the standards for measuring the sampling efficiency. Simulation experiments have found that particles are significantly affected by gravitational acceleration in the drainage tube, reducing the impact of reflux on particles. The sampling efficiency of the drainage and traditional sand sampler units increases with the increase in wind speed, and the sampling efficiency of both types of sand sampler units shows an upward trend within 10-13 m/s. In an ideal state, the sampling efficiency of the drainage sand sampler unit can reach 100% at a wind speed of 13 m/s.

The sampling efficiency of traditional sand sampler units is 99.7%. As a result, the sampling efficiency of the cyclone separation sand sampler unit with an increased drainage tube is significantly higher than that of the cyclone sampling sand sampler unit without a drainage tube. The line chart in Figure 3 intuitively shows that the sampling efficiency of the drainage-type sand sampler unit is better than that of the traditional-type sand sampler unit. The calculation formula for sampling efficiency:

$$X = S_1 / S_2 \tag{1}$$

Formula (1) where S_1 is the sand sampler capacity, S_2 represents the sand transport capacity, X is the dispersion efficiency.

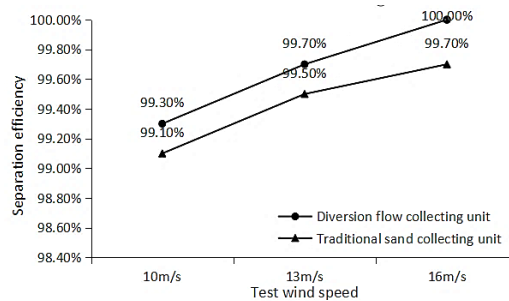


Fig. 3 - Comparison diagram of flow diversion and conventional sampling efficiency

Design optimization and result analysis of 2 drainage sand sampler units Overall Plan Design

Through simulation, adding a drainage tube to the sand sampler unit can improve the sand sampler rate of the cyclone separation sand sampler instrument. Regarding the factors that may affect the sampling efficiency of the sand sampler unit, the CFD simulation method was used to calculate the flow field of the drainage cyclone separation sand sampler unit. The effects of inlet wind speed (A), outlet diameter (B), exhaust pipe diameter (C), exhaust pipe insertion depth (D), cylinder section height (E), and cone section height (F) on the sampling efficiency of the sand sampler unit were studied. The interaction between different influencing factors was analyzed through orthogonal experiments.

A response model was established using the six-factor, three-level Box-Behnken response surface analysis method. The natural wind speed of sand lifting under natural conditions was 13.8 m/s, and the inlet wind speed in the orthogonal experiment, with values of 10 m/s, 13 m/s, and 16 m/s, was used as the reference wind speed for simulation. The level of experimental factors is shown in Table 1.

Table 1

Test factors and level of sampling efficiency

Test factors	Factor code	Factor level code		
		-1	0	1
Air inlet wind speed / (m/s)	A	10	13	16
Sand outlet diameter / mm	B	10	12.5	15
Exhaust funnel diameter / mm	C	20	25	30
Insertion depth of exhaust funnel / mm	D	0	10	20
Height of cylinder section / mm	E	40	50	60
Cone segment height / mm	F	80	90	100

Establishment and Regression Analysis

Design Expert software was used to establish a regression model for the influencing factors. Regression model variance analysis, R2 comprehensive analysis, and response surface analysis of the interaction between the influencing factors were conducted. The best parameter combination was obtained through the fitting degree of the model.

Multiple models were applied to model simulation data, and the model analysis results are shown in Table 2. The lower the P-value in the table (rejecting the original assumed value), the higher the fitting degree of the model. The F-value is a test of the fit of the regression equation, and the larger the value, the higher the fit of the model; R2 represents the fit test of the model on the data, and the closer its value is to 1, the higher the fit of the model. According to the data comparison and analysis results of multiple model variances in Table 2, the P values of the linear model, 2FI model, quadratic equation model, and cubic equation model are all less than 0.05, indicating that the model fitting is relatively significant. The f-values indicate that the fitting degree of the linear and quadratic models is better than that of the 2FI and cubic models.

The comprehensive analysis of R2 fitted by the four models in Table 3 shows that the R2 value of the quadratic equation model is 0.9980, the R2 value of the cubic equation model is 0.9482, both greater than 0.9, the R2 value of the linear model is 0.6428, and the R2 value of the 2FI model is 0.8004, both less than 0.9, indicating that the quadratic equation model and the cubic equation model have a high correlation with the test, and the model is more accurate. Based on the analysis results in Tables 2 and 3, a quadratic equation model was selected for the sampling efficiency response model.

Table 2

Analysis of variance of multiple regression models for sampling efficiency

Model type	Sum of squares	Free degree	Mean square value	F-value	P-value
Average value	48.82	1	48.82		
Linear	0.020	6	3.381E-003	19.69	< 0.0001
2FI	0.0241	15	1.607E-004	0.91	<0.0001
Quadratic equation	0.04192	6	6.986E-004	12.36	< 0.0001
Cubic equation	0.01411	18	7.842E-005	10.91	0.0009
residual	0.00575	8	7.187E-006		

Table 3

Square analysis of regression model R of sampling efficiency

Model type	Standard deviation	R2	R2 predicted value	Sum of squares of predicted residuals
Linear	0.013	0.7153	0.6428	0.010
2FI	0.013	0.8004	0.5477	0.013
Quadratic equation	7.517E-003	0.9980	0.7293	0.076
Cubic equation	2.681E-003	0.9482	0.4809	0.015

Table 4 shows the confidence analysis of the quadratic equation model and the influencing factors in the model. The estimated parameters of the factors in the table are the average values of the upper and lower values of the 95% confidence interval of the parameters, where VIF is the variable expansion factor, and the value between 0 and 10 is reasonable data for testing multicollinearity. Estimating the absolute value of parameters can infer the magnitude of the impact of each influencing factor on the response value. The results are: E>C>A>D>B>F (primary term), CD>DF>BC>AE>CE>AC>EF>AF>BD>BE>BF>CF>AB>AD>DE (interaction term of different factors), D2>E2>F2>B2>C2>A2 (secondary term), and the positive and negative values of the estimated parameters of each influencing factor can also indicate the direction of the response value, AC, AD, AE, AF, BD, BE, DE, DF, EF, A2, B2, C2, D2 E2 and F2 are adverse effects. In contrast, the other terms are positive effects. The positive effect is that the sampling efficiency increases with the increase of the independent variable, while the adverse effect is the opposite.

Table 4

Estimation of parameters of regression model of sampling efficiency

Factors	Estimating parameters	Free degree	Standard deviation	95% confidence interval		VIF
				Lower value	Upper value	
Domain	0.97	1	0.03069	0.97	0.98	
A	0.02667	1	0.01534	-0.00487	0.05821	1.00
B	0.02208	1	0.01534	-0.00945	0.05362	1.00
C	0.07042	1	0.01534	0.03888	0.010	1.00
D	0.026	1	0.01534	0.023	0.029	1.00
E	0.09292	1	0.01534	0.06138	0.012	1.00
F	0.01958	1	0.01534	-0.01196	0.05112	1.00
AB	0.01875	1	0.02658	-0.03588	0.07338	1.00
AC	-0.0475	1	0.02658	-0.010	0.07126	1.00
AD	-0.015	1	0.01879	-0.05363	0.02.363	1.00
AE	-0.0625	1	0.02658	-0.06088	0.04.838	1.00
AF	-0.04	1	0.02658	-0.0963	0.01463	1.00
BC	0.06625	1	0.02658	0.01162	0.012	1.00
BD	-0.00375	1	0.02658	-0.05838	0.05088	1.00

Factors	Estimating parameters	Free degree	Standard deviation	95% confidence interval		VIF
				Lower value	Upper value	
BE	-0.03125	1	0.01879	-0.06988	0.00738	1.00
BF	0.02875	1	0.02658	-0.02588	0.08338	1.00
CD	0.011	1	0.02658	0.05287	0.016	1.00
CE	0.05625	1	0.02658	0.00162	0.011	1.00
CF	0.02625	1	0.01879	-0.01238	0.06488	1.00
DE	-0.01375	1	0.02658	-0.06838	0.04088	1.00
DF	-0.0075	1	0.02658	-0.06213	0.04713	1.00
EF	-0.04375	1	0.02658	-0.09838	0.01088	1.00
A2	-0.03028	1	0.02344	-0.07845	0.01790	1.30
B2	-0.05819	1	0.02344	-0.011	-0.01002	1.30
C2	-0.04486	1	0.02344	-0.09304	0.00332	1.30
D2	-0.015	1	0.02344	-0.019	-0.09710	1.30
E2	-0.013	1	0.02344	-0.018	-0.08252	1.30
F2	-0.06736	1	0.02344	-0.012	-0.01919	1.30

RESULTS

Model validation

Before selecting the response model, each model's p-value and F-value R2 values were compared, and the quadratic equation model was validated through the residual standard probability plot of the model. As shown in Figure 4, the distribution of points on the residual average probability graph is approximately a straight line, with minor errors, indicating that the model is relatively reliable.

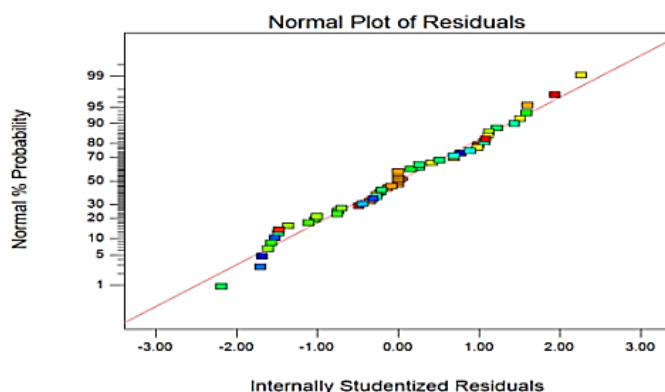


Fig. 4 - The student residual positive probability diagram of the sampling efficiency model

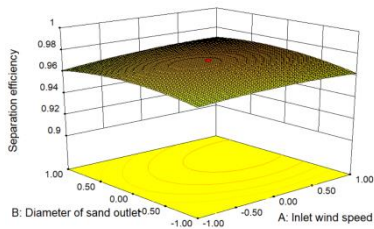
Analysis of Factors Influencing sampling Efficiency

The sand sampler's sampling efficiency is an important parameter for measuring the equipment's accuracy. A three-dimensional surface graph analyzed the interaction of six influencing factors on efficiency.

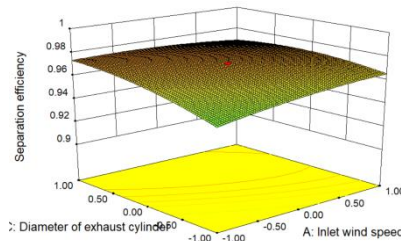
Figure 5 (a) shows the response surface of the interaction between the diameter of the sand outlet (B) and the inlet wind speed (A). When the diameter of the sand outlet is constant, the sampling efficiency increases with the increase of the inlet wind speed, with the maximum values being 0.72 and 0.962, respectively. The minimum wind speed for sand lifting is 13.8 m/s. When the diameter of the sand outlet increases from 10 mm to 12.5 mm, there is an insignificant upward trend in sampling efficiency. When the diameter of the sand outlet increases from 12.5 mm to 15 mm, there is an insignificant downward trend in sampling efficiency, and both have a small impact on sampling efficiency.

Figure 5 (b) shows the response surface of the interaction between the diameter of the exhaust funnel (C) and the inlet wind speed (A). When the diameter of the exhaust pipe is fixed, the sampling efficiency shows a significant increase and then a slow decrease with the increase in wind speed, with a maximum value of 0.97 and a minimum value of 0.955. When the inlet wind speed is constant, the sampling efficiency shows an insignificant trend of increasing and then decreasing with the increase of the exhaust pipe diameter, indicating that the exhaust pipe diameter has a particular impact on the sampling efficiency.

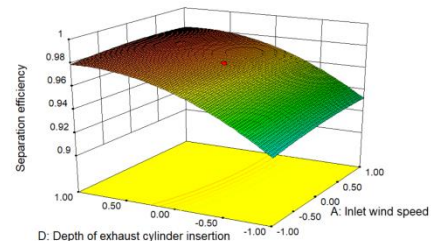
Figure 5 (c) shows the response surface of the interaction between the interpolation depth (D) of the exhaust funnel and the inlet wind speed (A). When the interpolation depth of the exhaust funnel is constant, the sampling efficiency shows a trend of slowly increasing and then slowly decreasing with the increase of the inlet wind speed, but its effect is insignificant. The highest sampling efficiency is 0.98, and the lowest is 0.976. When the inlet wind speed is constant, improving the sampling efficiency is achieved by changing the interpolation depth of the exhaust funnel. The sampling efficiency significantly increases when the interpolation depth of the exhaust funnel is between 0 mm and 15 mm but does not significantly decrease when the interpolation depth of the exhaust funnel is between 15 mm and 20 mm.



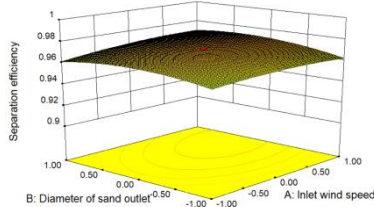
(a) Response surface of interaction between sand outlet diameter and inlet wind speed



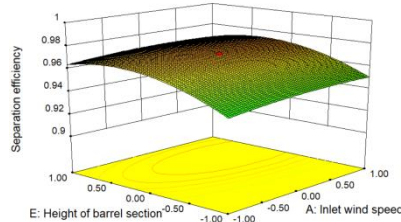
(b) Response surface of interaction between exhaust pipe diameter and inlet wind speed



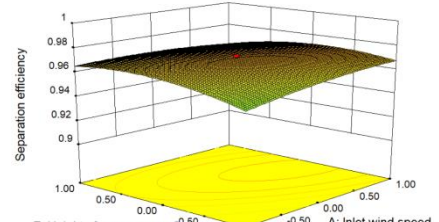
(c) Response surface of interaction between interpolation depth and inlet wind speed



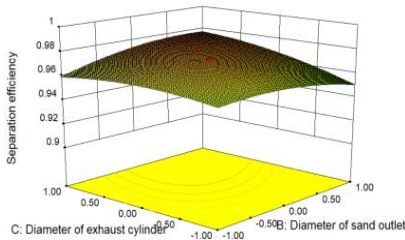
(d) Response surface for the interaction between the height of the cylinder section and the wind speed at the inlet



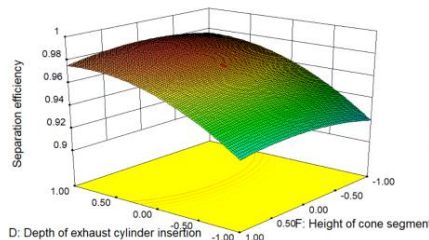
(e) Response surface for the interaction between the height of the cone section and the wind speed at the inlet



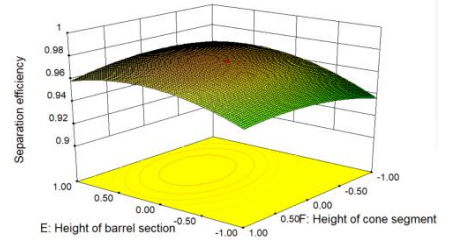
(f) Response surface for the interaction between the diameter of the sand outlet and the diameter of the exhaust funnel



(g) Response surface for the interaction between the insertion depth of the exhaust funnel and the height of the cylinder section



(h) Response surface for the interaction between the height of the cone section and the insertion depth of the exhaust funnel



(i) Response surface for the interaction between the height of the cone section and the height of the cylinder section

Fig. 5 - Response surface of second order interaction

Figure 5 (d) shows the response surface of the interaction between the height of the cylinder section (E) and the inlet wind speed (A). When the air inlet wind speed is constant, with the increase of the height of the cylinder section, the sampling efficiency shows a clear upward trend, while the downward trend is not apparent. The sampling efficiency reaches 0.974 when the cylinder section parameters reach 55 mm, and the sampling rate reaches 0.96 when the cylinder section parameters reach 60 mm. When the height of the cylinder section is constant, the increase in sampling efficiency is relatively small with the increase in wind speed, indicating that the influence of wind speed on sampling efficiency is significant.

Figure 5 (e) shows the response surface of the interaction between the height of the cone section (F) and the inlet wind speed (A). When the inlet wind speed is constant, the sampling efficiency slowly increases and then decreases with the increase of the height of the cone section. The height of the cone segment shows a significant upward trend within the range of 80 mm to 90 mm. When the inlet wind speed is constant, the sampling efficiency reaches its maximum value. When the height of the cone segment is 90 mm, the sampling efficiency can reach 0.965. The decrease in sampling efficiency is not significant within the range of 90 mm to 100 mm in the height of the cone section. When the height of the cone section is 100 mm, the sampling efficiency can reach 0.961. When the height of the cone section is constant, the sampling efficiency shows a trend of increasing and then decreasing with the increase of the inlet wind speed.

Figure 5 (f) shows the interaction response surface between the diameter of the sand outlet (B) and the diameter of the exhaust funnel (C). The diameter of the exhaust funnel and the diameter of the sand outlet have a significant impact on the sampling efficiency. When the diameter of the sand outlet is constant, the sampling efficiency increases with the increase of the diameter of the exhaust pipe. When the diameter of the exhaust pipe is large, the sampling efficiency increases with the increase of the diameter of the sand outlet. When the diameter of the exhaust pipe is small, the sampling efficiency shows a trend of increasing and then decreasing with the increase in the diameter of the sand outlet. When the diameter of the exhaust funnel is 30 mm, and the diameter of the sand outlet is 10 mm, the sampling efficiency is 0.96. When the diameter of the sand outlet is 15 mm, the sampling efficiency can reach 0.978.

Figure 5 (g) shows the response surface of the interaction between the insertion depth (D) of the exhaust funnel and the height of the cylinder section (E). When the height of the cylinder section is constant, the sampling efficiency shows an upward trend as the insertion depth of the exhaust funnel increases. When the insertion depth of the exhaust funnel is 0 mm and 20 mm, the sampling efficiency is 0.925 and 0.978, respectively. When the insertion depth of the exhaust funnel is constant, the sampling efficiency shows a trend of rapidly increasing and then slowly decreasing as the height of the cylinder section increases.

Figure 5 (h) shows the response surface of the interaction between the height of the cone section (F) and the insertion depth of the exhaust funnel (D). When the insertion depth of the exhaust pipe is constant, the efficiency shows an upward trend with the increase in the height of the cone section. When the insertion depth of the exhaust funnel is 0 mm and 20 mm, the efficiency can reach 0.923 to 0.978. As the height of the cone section increases, the sampling efficiency shows a slow increase and then a slow decrease trend. As mentioned above, the insertion depth of the exhaust funnel is constant, and the sampling efficiency can reach 0.975 and 0.982 with heights of 80 mm and 90 mm, respectively.

Figure 5 (i) shows the response surface of the interaction between the height of the cone section (E) and the height of the cylinder section (F). When the height of the cylinder section is 40 mm and 50 mm, the sampling efficiency can reach 0.95 and 0.966, and at 60 mm, the sampling efficiency can reach 0.952. As the height of the cone section increases, the sampling efficiency shows an upward trend. When the height of the cylinder section is significant, the sampling efficiency shows a downward trend as the height of the cone section increases.

Parameter optimization

Using the Design Expert response surface optimization method to process data on the dimensions of 54 sets of models, the system automatically seeks the optimal result through regression equations and response surface analysis. The optimization results are shown in Table 5, with the first line being the default optimal result sought by the system.

Table 5

The results after the sand collecting unit have undergone systematic optimization

	A	B	C	D	E	F	Expected value
1	0	1	1	0	1	0	1
2	0	0	1	1	0	1	1
3	0	0	0	0	0	0	1
4	1	0	0	1	-1	0	1
5	1	0	1	0	0	-1	1
6	-1	0	0	1	-1	0	1

Micro Wind Tunnel Testing

The optimal structure of the drainage-type cyclone separation sand sampler unit was determined through simulation experiments, and various components were mechanically processed. Subsequent validation tests were conducted. The test equipment adopts the movable wind erosion wind tunnel and micro wind tunnel of Inner Mongolia Agricultural University to test the sand sampler unit and sand sampler instrument separately. The thermal sensitive velocimeter is used to control the test wind speed accurately, and high-precision electronic scales are used to weigh the sand samples before and after the test accurately. For artificial screening of sand particles with a particle size less than 0.5 millimeters, considering the simulation of actual natural phenomena, the selected sand particles do not require drying treatment.

Prepare 12 sand samples, each weighing 60 g. The sand sampler consists of six sand sampler units. Because the six sand sampler units on the sand sampler have the same structure except for different heights above the ground, one sand sampler unit on the sand sampler is selected for sampling and weighing the sand volume. Four wind speeds of 7 m/s, 9 m/s, 11 m/s, and 13 m/s were used for the test. Three tests were

conducted at each wind speed, and the average of the three tests was taken to ensure the accuracy of the test. After the experiment, the sand samples collected in the sand sampler bag will be weighed using a high-precision electronic scale, and the average value of three experiments will be taken. The experimental device is shown in Figure 5. The gas-solid sampling efficiency values of the drainage type sand sampler unit calculated at four wind speeds of 7 m/s, 9 m/s, 11 m/s, and 13 m/s are 97.43%, 97.55%, 97.71%, and 98.92%, with an average sampling efficiency of 97.95%. The gas-solid sampling efficiency values of traditional-type sand sampler units are 96.54%, 96.82%, 97.24%, and 98.51%, with an average sampling efficiency of 97.32%. The effect of the drainage-type sand sampler unit is better than that of the traditional type sand sampler unit (Fig.6).



Fig. 6 - Miniature wind tunnel test drawing

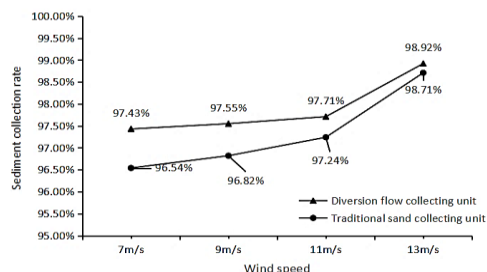


Fig. 7 - Comparison of sampling efficiency between diversion flow and traditional type

The gas-solid sampling efficiency values of the drainage type sand sampler unit calculated at four wind speeds of 7 m/s, 9 m/s, 11 m/s, and 13 m/s are 99.11%, 97.71%, 97.55%, and 97.43%, respectively. The average sampling efficiency is 97.95%, better than the traditional formula with 96.54%, 96.82%, 97.24%, and 98.71%, and the average sampling efficiency is 97.32% (Figure 7). The sampling efficiency of the drainage type and traditional sand sampler units shows a significant upward trend with the increase in wind speed. When the wind speed is low, the difference in sampling efficiency between the drainage type and traditional sand sampler units is more significant and needs to be improved. At the same wind speed, the sampling efficiency of the drainage type is better than that of the traditional type, and the experimental results meet the design expectations.

Wind Erosion Wind Tunnel Test

Conduct wind erosion wind tunnel tests to measure the sand sampler effect. Place the drainage type sand sampler used in micro wind tunnel tests in the groove of the wind erosion wind tunnel (Figure 8). The minimum height of the air inlet of the sand sampler unit from the ground is 20 mm, and the maximum height is 520 mm. Each sand sampler unit is spaced 100 mm apart, making collecting sand at different heights easy. The sand transportation adopts a floor-laying method, and the test sand is divided into 4 parts, with each part of 10000 g laid flat in the wind tunnel channel. Tie plastic bags under the drainage pipe to collect sand samples. Conduct experiments at four wind speeds of 7 m/s, 9 m/s, 11 m/s, and 13 m/s. After the experiment, weigh the sand's weight collected by the sand sampler unit at each height.

Calculate the fitting values of the sand sampler volume for the drainage-type cyclone separation sand sampler at different wind speeds and heights. The larger the determination coefficient R2 and the better its fit, the lower and upper bounds of the integration are taken as the height above the ground. Integrate the sand sampler volume at different heights to obtain the actual sand transport volume. The test research shows that the sand sampler volume of the sand sampler is a power function with the increase of the sampler height, which satisfies the equation 1:

$$q = ax^b \tag{2}$$

where q is the sand concentration at the height of sand sampler, a and b is the coefficient of the equation, x is the height of sand sampler (mm). Actual sand sampler capacity:

$$Q = \int_1^{52} q dx \tag{3}$$

At wind speeds of 7 m/s, 9 m/s, 11 m/s, and 13 m/s, the sand sampler efficiency is 67.19%, 88.36%, 93.46%, and 92.52%, respectively. During the experiment, the wind tunnel wind speed ranged from 9 m/s to 13 m/s, and the sand sampler efficiency varied steadily, with an average value of 91.44%, meeting the design requirements. Moreover, calculate the sampling efficiency of the traditional cyclone separation and sand sampler at wind speeds of 7 m/s, 9 m/s, 11 m/s, and 13 m/s, which are 66.88%, 87.82%, 92.24%, and 91.48%, respectively. During the experiment, the sampling efficiency of the wind tunnel wind speed in the range of 9 m/s to 13 m/s changed smoothly, with an average value of 90.81%. The comparison of sand sampler efficiency of two sand sampler singletons is shown in Figure 9.



Fig. 8 - Wind erosion wind tunnel test drawing

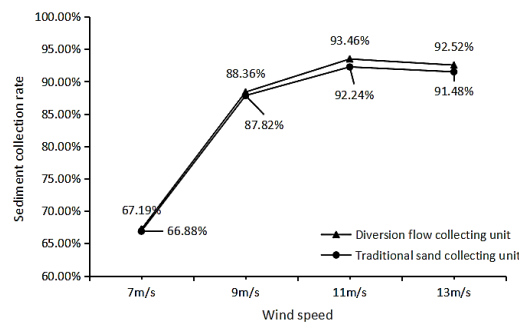


Fig. 9 - Line chart of sampling efficiency

CONCLUSIONS

Grasslands are crucial ecosystems in China, vital for maintaining ecological balance, preventing soil erosion, and conserving water resources. However, due to climate change and human activities, they have suffered significant degradation, with soil wind erosion being a major factor. Accurate monitoring of wind erosion is essential for the protection and restoration of these ecosystems. Dust samplers are key tools for detecting wind erosion, measuring sand transport and flow structure. However, current cyclone-type samplers have limitations in sampling efficiency.

This paper introduced a drainage-type cyclone dust sampler, which added a drainage pipe beneath the cyclone separator to reduce air backflow and improve efficiency. To optimize its design and enhance monitoring accuracy, this study presented the following research efforts:

(1) An Experimental design was conducted on the sampling efficiency of the sand sampler unit of the drainage-type cyclone separation sand sampler using the Box-Behnken response surface analysis method. The sampling efficiency was used as the experimental indicator to establish a mathematical model between the sampling efficiency and experimental factors (inlet wind speed, outlet diameter, exhaust pipe diameter, exhaust pipe insertion depth, cylinder section height, cone section height).

(2) The significance of each factor on the experimental indicators was estimated through model parameters: $E > C > A > D > B > F$ (primary term), $CD > DF > BC > AE > CE > AC > EF > AF > BD > BE > BF > CF > AB > AD > DE$ (interaction term of different factors), $D_2 > E_2 > F_2 > B_2 > C_2 > A_2$ (secondary term).

(3) Taking sampling efficiency as the optimization index, the optimal sampling efficiency of the sand sampler unit model was obtained in the experiment when the parameter values were as follows. The cylinder diameter was 60 mm, the cylinder section height was 60 mm, the cone section height was 90 mm, the exhaust pipe diameter was 30 mm, the exhaust pipe interpolation depth was 10 mm, and the sand outlet diameter was 15 mm.

(4) The cyclone separation sand sampler of drainage type performance was tested using wind tunnel tests. The experimental study showed that the average sampling efficiency of the sand sampler was 91.44% at wind speeds of 7 m/s to 13 m/s, indicating good performance. The drainage cyclone separation sand sampler unit obtained in this study provides a good measurement standard for monitoring the degree of land desertification. The sampling efficiency of the sand sampler unit reflects the actual sand concentration in the natural state of wind sand flow, providing a reference for obtaining more accurate and reliable wind sand flow data and improving the current situation of grassland wind erosion. Monitoring grassland degradation and soil erosion by wind with a sand sampler can reflect the real speed change, which provides a reliable theoretical reference for protecting nature and preventing land desertification in China.

ACKNOWLEDGEMENT

The authors were funded for this project by the National Natural Science Foundation of China (NSFC) (No.51869030) and science and technology project of Xinjiang Production and Construction Corps (No.2021CB021).

REFERENCES

- [1] Chen, Y. (2018). *Research on Automatic Variable Spraying Technology and Related Parameter Optimization of Spraying Machine Based on Multisource Information (基于多源信息的自动变量喷涂技术及喷涂机相关参数优化研究)*. PhD thesis. Univ. Inner Mongolia agricultural, Hohhot/China.

- [2] Cao, A-N; Wu, C-D; Zhang, B; Chen, Z; Jia, W-D; Li, W. (2023). Simulation and Analysis of Spray Barrel Motion for Unmanned spray Vehicles Replacing Pesticides (替代农药的无人喷雾车喷雾筒运动仿真与分析). *Research on Agricultural Mechanization*, Vol. 45(08), pp. 10-17, Heilongjiang/China.
- [3] Dumitru, D.; Bălăţatu, C.; Marin, E.; Gheorghe, G-V.; Manea, D.; Mateescu, M.; Cismaru, M-E. (2024). Technologies and constructive solutions regarding the inter-row management of vineyard and fruit trees, *INMATEH - Agricultural Engineering* 72(1), pp. 848-860.
- [4] Huang, Y; Zhao, M-Q. (2015). Optimization design of cyclone separation sand collector based on numerical simulation and wind tunnel test (基于数值模拟和风洞试验的旋风分离集砂器优化设计). *Transactions of the Chinese Society of Agricultural Engineering*, 31(16): 50-56, Hohhot/China.
- [5] He, X-Y; Ma, S-K; Liu, Z-X; Wang, W-D; Shang, S-Q; Li, G-H; Li, H-X. (2024)., Calibration and testing of saline soil parameters based on EDEM discrete element methodology, *INMATEH - Agricultural Engineering* 73(2), pp. 822-833.
- [6] Jhang, S-S., Lo, Y-L., Le, T-N. (2019). Systematic modeling approach for analyzing the powder flow and powder energy absorptivity in direct energy deposition system. *Int J Adv Manuf Technol* 105(1-4), 1765–1776.
- [7] Khan Sher Afghan, Ibrahim Omar Mohamed, Aabid Abdul. (2021). CFD analysis of compressible flows in a convergent-divergent nozzle. *Materials Today: Proceedings*,46(P7): 2835-2842.
- [8] Liu, H-Y; Chen, Z; Hou, Z-F; Tong, X; Zong, Z-Y. (2019). Development and test of soil wind erosion real-time monitoring system based on GPRS (基于 GPRS 的土壤风蚀实时监测系统开发与试验). *Transactions of the Chinese Society of Agricultural Engineering*, 35(05): 163-172, Hohhot/China.
- [9] Li, H-S. (2022). Design of cyclone classification control system based on Fluent. *Computer measurement and control*, 30(04): 128-133+154.
- [10] Li, B-P; Chen, X-C; Ying, Z; Li, J-R; Zhang C-X. (2022). Wind tunnel simulation of different soil moisture conditions on surface wind erosion in desert steppe of Inner Mongolia (内蒙古荒漠草原不同土壤湿度条件对地表风蚀的风洞模拟). *Arid area resources and environment*, 36 (09):126-132, Hohhot/China.
- [11] Petrichenko M.R., Sergeev V.S., Nemova D, Kotov E.V., Tarasova D.S. (2020). CFD simulation of the convective flows in the vertical caverns. *Magazine of Civil Engineering*, 8 (92): 172.
- [12] Patil Vaibhav D. Pise Gargee, Nandgaonkar Milankumar R. (2022). Analysis of Phase Change Material used as Thermal Energy Storage Unit in Catalytic Converter. *IOP Conference Series: Materials Science and Engineering*,1248(1).
- [13] Song, T. (2016). *Study on the internal flow field characteristics of the combined automatic sand collector with shunt hedge and multistage expansion (分流绿篱多级膨胀组合式自动集砂器内部流场特性研究)*. Master's thesis. Inner Mongolia Agricultural University, Hohhot /China
- [14] Song, T; Meng, X-J; Bian, B-C. (2018). Design parameter analysis of diverging hedge and multi-stage expansion automatic sand collection box (分流绿篱与多级膨胀式自动集沙箱设计参数分析). *Chinese Journal of Agricultural Mechanization*2018, 39 (12): 83-87, Hohhot/China.
- [15] Xu, B; Cui, Q-L; Zheng, D-C. (2023). Improvement design and simulation analysis on centrifugal disc organic fertilizer spreader, *INMATEH - Agricultural Engineering* 70(2), pp. 329-336.
- [16] Yang, Q. (2021). *Numerical simulation and optimization of gas-solid flow characteristics in a sand collector (集砂器内气固流动特性数值模拟与优化)*, Master's thesis. Wuhan University of Technology, Wuhan/China.
- [17] Yan, M; Jin, A-F; Gao, W-X. (2024). Optimization of joint sand barrier spacing and characterization of wind-sand flow study based on CFD numerical simulation, *INMATEH - Agricultural Engineering* 73(2), pp. 855-869.
- [18] Zhang, F; Shao, W; Zhao, S; Zhu, J; Li, P. (2023). Simulation test and verification of material conveying for small and medium-sized air suction jujube picking machine based on CFD DEM coupling, *INMATEH - Agricultural Engineering* 71(3), pp. 535-547.

DESIGN AND EXPERIMENT OF DRAG REDUCTION CHARACTERISTICS OF CASSAVA BIONIC DIGGING SHOVEL BASED ON RED SOIL

基于红土壤的木薯仿生挖掘铲减阻特性设计与试验

Ranbing YANG^{1,3}, Guiquan ZHOU^{1,3}, Dongquan CHEN², Tao WANG^{1,3}, Danyang LV², Xiantao ZHA^{*1,3}

¹⁾ School of Mechanical and Electrical Engineering, Hainan University, Hainan/ China;

²⁾ School of Information and Communication Engineering, Hainan University, Hainan/ China;

³⁾ Key Laboratory of Tropical Intelligent Agricultural Equipment, Ministry of Agriculture and Rural Affairs, Hainan/ China;

Corresponding author: Xiantao Zha

Tel: +8618627838628; E-mail: zhaxt@hainanu.edu.cn

DOI: <https://doi.org/10.35633/inmateh-74-56>

Keywords: Agricultural machinery, Cassava harvester, Digging shovel, Bionic, Drag reduction, Discrete element

ABSTRACT

Aiming at the digging shovel of the red soil harvester in the cassava planting area, problems such as high digging resistance and difficulty in breaking the soil when harvesting cassava tubers will lead to blockage at the connection between the digging device and the transmission device. Using the rabbit's front paws as a bionic prototype, three-dimensional scanning and reverse engineering technologies were employed to extract their unique geometric features. These quantified geometric structural characteristics were then applied to the design of an excavation shovel, aiming to reduce resistance during excavation operations. Based on the discrete element (EDEM) coupled RECURDYN, using the resistance of the excavation shovel and the Bonding key breakage rate as evaluation indicators, the discrete element orthogonal analysis of three factors including the shovel tooth length, shovel tooth width, and shovel edge inclination angle was carried out based on the simulation test results. Test was performed to determine the best parameter combination for drag reduction and crushing rate of the bionic shovel; the working resistance of the shovel was used as an evaluation index to verify the excavation performance of the bionic shovel through field tests. The optimal parameter combination of the bionic shovel based on the discrete element simulation test is the tooth length of 220 mm, the tooth width of 65.1 mm, and the blade inclination 60°. The excavation resistance of this combination is 1733.66 N and the maximum soil fragmentation rate is 92.9%. Through field tests, it can be found that when the excavation depth is 310 mm and the forward speed is 300 mm/s. The Type 1 bionic digging shovel exhibits a reduction in resistance of 6.84%, while the Type 2 bionic digging shovel demonstrates a more significant reduction of 9.21%, compared to the traditional digging shovel. Tests have shown that the bionic shovel type 2 has excellent soil excavation characteristics and can complete cassava excavation operations in tropical red soil areas. It can provide a design reference for reducing drag and saving energy for cassava harvesters.

摘要

针对木薯种植区域的红土壤收获机挖掘铲在进行收获木薯块茎时挖掘阻力大、土壤破碎困难等问题会导致挖掘装置与传输装置连接处出现堵塞情况，以兔子的前爪为仿生原型，采用三维扫描和逆向工程技术提取其独特的几何特征。然后将这些量化的几何结构特征应用于挖掘铲的设计，旨在减少挖掘作业期间的阻力。基于离散元（EDEM）耦合 RECURDYN，以挖掘铲所受阻力、Bonding 键破碎率为评价指标，基于仿真试验结果进行了铲齿长度、铲齿宽度、铲刃倾角等 3 个因素的离散元正交试验，确定仿生铲的减阻的和破碎率最佳的参数组合；通过田间试验以挖掘铲所受工作阻力为评价指标验证仿生挖掘铲的挖掘性能。基于离散元仿真试验可得的仿生铲最佳参数组合为铲齿长度 220mm、铲齿宽度 65.1mm、铲刃倾角 60°，该组合的挖掘阻力为 1733.66N 和较大的土壤破碎率为 92.9%。通过田间试验可得挖掘深度为 310mm、前进速为 300mm/s 时，试验表明仿生铲 2 型有优秀的土壤挖掘特性，能在热带红土壤地区完成木薯挖掘作业，能为木薯收获机减阻节能做出设计参考。

^{1,3} Ranbing Yang, Prof. Ph.D. Eng; Guiquan Zhou, M.S. Stud. Eng; Tao Wang, Assoc. Prof. M. Eng; Xiantao Zha, Ph.D. Eng.

² Dongquan Chen, Ph.D. Eng; Danyang Lv, Ph.D. Eng.

INTRODUCTION

Hainan Province is located in a tropical rain forest climate area (Li *et al.*, 2014). Under the conditions of high temperature, high humidity and high concentration of biological organic matter, it is easy to form red soil with heavy clay soil. However, cassava, which is highly adaptable to the environment and can grow in relatively harsh environments, is one of the excellent tropical economic crops. Observation in the practice of cassava planting fields shows that heavy soil is the main cause of resistance when the shovel is working. Therefore, when operating cassava harvesters under red soil conditions in tropical areas of Hainan Province, excavation drag reduction is the key technology to achieve high-efficiency and low-energy consumption harvesting of cassava.

Biomimetic design is a methodology that leverages biological structures, functions, and mechanisms found in nature to address engineering challenges and enhance performance by emulating the remarkable characteristics of natural systems. The extensive application of biomimetic and reverse engineering technologies within the engineering domain has demonstrated that simulation technology can effectively mitigate the challenges associated with limited experience in the design of mechanical components. The rise of bionics has led to practical applications demonstrating that bionic soil contact components can significantly save energy and reduce drag (Cui *et al.*, 2019; Zhang *et al.*, 2022). The potato digging shovel is a critical soil-contacting component of agricultural machinery. Energy efficiency, drag reduction, and wear performance are essential indicators for these parts. Numerous scholars and research teams, both domestically and internationally, have conducted studies and provided substantial data supporting the development of bionic digging shovels (Zhao *et al.*, 2021).

For instance, Fan Yu *et al.* explored the excavation mechanism and aimed to reduce excavation resistance by employing discrete element analysis to examine the soil fragmentation principles from a microscopic perspective during the excavation process. They applied bionic design principles to the structure of the potato soil contact device, drawing inspiration from the arch mouth of wild boars. Subsequently, they coupled these external characteristics with the potato digging shovel and conducted a mechanical analysis of the tool. The test results indicate that the application of bionic theory can effectively reduce digging resistance during potato harvesting (Fan *et al.*, 2020).

Duanmu Lingjian *et al.* (2020) addressed the issues of high digging resistance and limited adaptability of cassava digging shovels by selecting the forepaw toes of the yellow-haired rat as a bionic prototype to design a shovel-toothed bionic digging shovel. This design effectively reduces drag and allows for adjustments in the number of teeth according to the specific needs of the digging shovel. Zou Xiangxiang and colleagues developed a bionic digging shovel inspired by the shape of the front toe claws of the Oriental mole cricket to tackle the challenges of inserting the digging shovel into the soil and achieving a low soil breaking rate during cassava harvesting (Zou *et al.*, 2013). Their analysis concentrated on the static strength of the cassava digging shovel structure using finite element analysis. Sun *et al.* designed a bionic trencher to address high resistance and viscosity issues encountered with trenchers, drawing from the hydrophobic drag-reducing characteristics of shell texture. This design effectively reduces drag, minimizes adhesion, and facilitates detachment (Sun *et al.*, 2020).

Yu *et al.* (2022) focused on the large digging resistance and complex root systems associated with potato digging shovels, creating a bionic shovel based on the outer contour of mole toes. They conducted a static strength analysis and a discrete element structural analysis of the digging shovel, employing both finite element and discrete element methods, which effectively reduced the traction power required by the harvester and enhanced the fatigue strength of the digging shovel.

In summary, the structural design of agricultural machinery that incorporates bionics can effectively reduce digging resistance during operation and enhance the soil crushing performance of such machinery. The focus of bionic structural design lies in the combination of appropriate bionic objects. This paper addresses the technical challenges posed by high clay resistance and the presence of heavy soil clods that are difficult to break in the red soil of Hainan's cassava cultivation. Using an ordinary cassava digging shovel as a prototype, the structure is enhanced by integrating the drag reduction curve of a rabbit claw's outer contour, along with the addition of an arched structure to optimize soil-breaking performance. The Bionic Rabbit Paw Cassava Digging Shovel is designed with reference to conventional digging shovels, aiming to achieve energy savings and reduced drag during operations.

MATERIALS AND METHODS

Analysis on the mechanism of excavating shovel resistance

When the excavating shovel is in operation, it can be divided into two distinct phases: penetrating the soil and excavating it. Bekker's semi-empirical formula is employed to develop a mathematical model that describes the volume of soil excavated, as well as the shear and normal stresses experienced during the penetration phase (Zhang et al., 2015). Additionally, Rankine's earth pressure theory is applied to establish a mathematical model that elucidates the relationship between elastic soil properties and excavation depth during the soil excavation process (Zhao et al., 2017; Li et al., 2023).

Excavating shovel force analysis

When the cassava digging shovel is working, the cassava digging shovel encounters four primary types of resistance, as illustrated in Figure 1. These include the positive pressure F_p exerted by the soil on the digging shovel, the frictional resistance F_{f1} between the soil and the digging shovel, the penetration resistance F_{f2} that occurs as the front end of the digging shovel penetrates the soil, and the inertial force F_a exerted by the soil on the digging shovel.

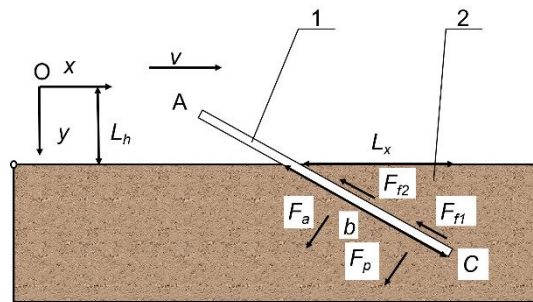


Fig. 1 - Force analysis of digging shovel during operation
1 – Digging shovel; 2 – Soil

Calculation of depth of penetration

As shown in Figure 1, O is the origin. The coordinates of points A and C and the distance L_h from the coordinate origin to the ground are known. It can be obtained that the horizontal projected length L_x of the digging shovel before it enters the soil and the length b of the digging shovel submerged in the soil are:

$$L_x = \frac{(y_c - L_h)(x_c - x_a)}{y_c - y_a} \tag{1}$$

$$b = \sqrt{L_x^2 + (y_c - L_h)^2} \tag{2}$$

where L_x is the horizontal length of the shovel into the soil; L_h is the distance from the coordinate origin to the ground; x_a is x coordinate of point A; y_a is y coordinate of point A; x_c is x coordinate of point C; y_c is y coordinate of point C; b is the length of the shovel into the soil.

Penetration resistance analysis and calculation

As shown in Figure 2, the angle of the shovel tip is θ , the excavating shovel width is d , and the shovel tip length is e . When the excavating shovel enters the soil, it is subject to the positive pressure F_σ of the soil on the excavating shovel and the shear stress F_τ of the soil on the excavating shovel. The penetration resistance when the front end of the digging shovel penetrates into the soil is F_{f2} .

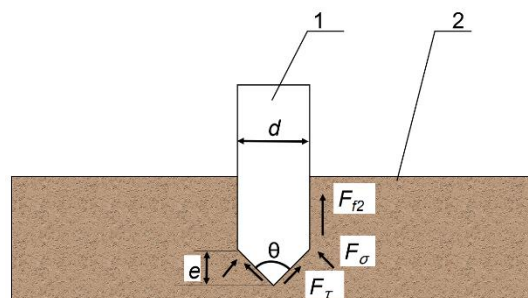


Fig. 2 - Stress analysis of shovel surface
1– Digging shovel; 2– Soil

It can be seen from Figure 2 that the geometric relationship between the blade tip length e , the angle θ between the excavation blade tip and the excavation blade width d is:

$$e = \frac{d}{2 \tan(\theta / 2)} \tag{3}$$

According to the relationship between digging shovel penetration and load in Bekker's semi-empirical formula, it can be obtained:

$$\sigma_y = \frac{k_1}{d} + k_2 y^n \tag{4}$$

$$\tau_{\max} = c_0 + \sigma_y \tan \alpha \tag{5}$$

$$\tau = \tau_{\max} \left(1 - e^{-\frac{b}{k_0}}\right) \tag{6}$$

where:

σ_y - the positive pressure at depth y , [MPa]; n - the soil subsidence coefficient; k_1 - the soil cohesive deformation modulus coefficient; k_2 - the friction deformation

14 ption modulus coefficient; τ_{\max} - the maximum shear stress at depth y , [MPa]; c_0 - soil cohesion N/mm²; α - Soil internal friction angle; τ - the Simplified shear stress at depth y , [MPa]; k_0 - Shear deformation modulus coefficient.

When the digging shovel enters the soil, the positive pressure F_σ exerted by the soil on the digging shovel is:

$$F_\sigma = \frac{b}{\cos(\theta / 2)} \int_0^b \sigma_y d_y \tag{7}$$

When the digging shovel enters the soil, the shear stress F_τ exerted by the soil on the digging shovel is:

$$F_\tau = \frac{b}{\cos(\theta / 2)} \int_0^b \tau d_y \tag{8}$$

The penetration resistance F_{f2} is:

$$F_{f2} = 2F_\sigma \sin \frac{\alpha}{2} + 2F_\tau \cos \frac{\alpha}{2} \tag{9}$$

Positive pressure analysis and calculation

According to Rankine's earth pressure theory, a mechanical model of the digging shovel and the surrounding soil is established, as illustrated in Figure 3. In this model, the normal stress σ_z on the digging shovel at a depth of z is denoted, while q represents the normal pressure exerted by the soil on the digging shovel. Additionally, β indicates the angle of slip between the slip line and the plane of the shovel.

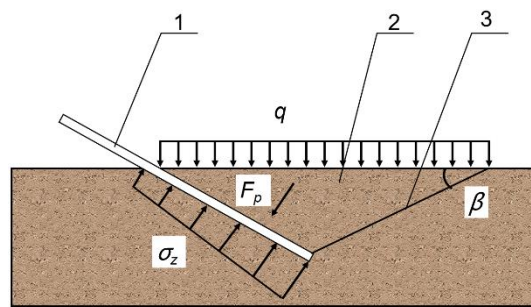


Fig. 3 - Stress analysis of shovel surface
1- Digging shovel; 2- Soil; 3- Slip line

σ_z is the normal stress and slip angle on the digging shovel at depth z :

$$\sigma_z = \gamma z \tan^2 \left(\frac{\pi}{4} + \frac{\alpha}{2}\right) + q \tan^2 \left(\frac{\pi}{4} + \frac{\alpha}{2}\right) + 2c_0 \tan^2 \left(\frac{\pi}{4} + \frac{\alpha}{2}\right) \tag{10}$$

$$\beta = \frac{\pi}{4} - \frac{\alpha}{2} \tag{11}$$

According to Rankine earth pressure theory, the positive pressure of the soil on the digging shovel is:

$$F_p = b \int_0^b \sigma_z d_z \tag{12}$$

$$F_p = \frac{1}{2} \gamma b^3 \tan^2 \left(\frac{\pi}{4} + \frac{\alpha}{2}\right) + qb^2 \tan^2 \left(\frac{\pi}{4} + \frac{\alpha}{2}\right) + 2c_0 b^2 \tan^2 \left(\frac{\pi}{4} + \frac{\alpha}{2}\right) \tag{13}$$

where: γ - the soil bulk density [N/mm³].

Digging shovel resistance calculation

According to Figure 3, the soil slip volume V is:

$$V = \frac{b^2}{2 \tan \beta} d \tag{14}$$

The inertial force of the soil on the digging shovel is:

$$F_a = \rho Va \tag{15}$$

where: ρ - the soil density [kg/mm³]; a - the slip acceleration of soil relative to digging shovel [m/s²].

The friction force of the soil on the digging shovel is:

$$F_{f1} = \mu F_p \tag{16}$$

where: μ - the kinetic friction factor between soil and digging shovel.

To sum up, the total resistance F of the sliding soil to the digging shovel is:

$$F = \sqrt{(F_{f1} + F_{f2})^2 + (F_p + F_a)^2} \tag{17}$$

According to the formula presented above, the width of the digging shovel, the depth to which it penetrates the soil, and the angle of the shovel tip all influence the digging resistance encountered during operation. In practical cassava harvesting, the conditions are complex and variable. The digging resistance is also affected by factors such as the size and shape of soil particles, soil moisture content, crop growth conditions, and other related variables.

Bionic cassava digging shovel design

Bionic prototype

The excavation device, as the primary component of the potato harvester, significantly influences both the operational efficiency of the machine and the quality of the harvested potato products. Within this excavation device, the excavation shovel teeth serve as the core elements that impact soil crushing and operational resistance. This article selects the adult Giron rabbit, a breed derived from California cave rabbits in the United States, as the bionic model. To maintain the stability of their burrows, Giron rabbits typically excavate in soil characterized by higher viscosity and hardness (Liu et al., 2010). The bionic sample rabbit measures 44 cm in length, 20 cm in height, and has a front foot width of 3 cm, with its front toe claws illustrated in Figure 4.



Fig. 4 - Bionic prototype rabbit paw

Digging shovel design

To obtain a comprehensive three-dimensional point cloud map of the toe claws, a high-precision 3D object scanner (supplied by Beijing Tianyuan 3D Technology Co., Ltd., with a scanning accuracy of up to 0.023 mm and a resolution of up to 0.02 mm) was utilized to perform a 360-degree scan of the toe claws, thereby establishing a three-dimensional point cloud model. Subsequently, the three-dimensional point clouds were processed and denoised using FreeScan Trak software, resulting in a three-dimensional image in STL format, as illustrated in Figure 5.

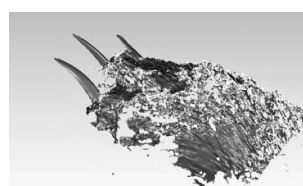


Fig. 5 - 3D cloud point diagram of bionic prototype rabbit paw toe

The front toe of the rabbit paw serves as the primary tool for digging holes. The unique biological curvature of its outer contour is the key factor that ensures effective soil cutting performance (Yu et al., 2019; Jia et al., 2019). The outline curve of the front toe is illustrated in Figure 6. To obtain a true and reliable representation of the outer contour curve of the toe claw, coordinate data from the cloud point diagram were extracted, and polynomial fitting was performed on this data using MATLAB. The resulting four distinct outer contour curves are presented in Figure 7. The fitting degree (R^2) of the contour curve equations exceeds 0.99, confirming that the accuracy of the extracted outer contour curve aligns with the actual biometric curve, thus meeting the necessary fitting requirements.

The equation is:

$$y_1 = 9.606 \times 10^{-11} x^4 - 1.767 \times 10^{-7} x^3 - 1.449 \times 10^{-4} x^2 + 0.3919x + 82.65 \tag{18}$$

$$y_2 = -2.329 \times 10^{-10} x^4 + 4.934 \times 10^{-7} x^3 - 6.256 \times 10^{-3} x^2 + 0.3979x + 328.1 \tag{19}$$

$$y_3 = 1.97 \times 10^{-15} x^6 - 6.836 \times 10^{-12} x^5 + 9.182 \times 10^{-9} x^4 - 5.881 \times 10^{-6} x^3 + 1.81 \times 10^{-3} x^2 - 0.138 \tag{20}$$

$$y_4 = -2.02 \times 10^{-15} x^6 + 6.373 \times 10^{-12} x^5 - 7.336 \times 10^{-9} x^4 + 3.6 \times 10^{-6} x^3 - 5.621 \times 10^{-4} x^2 + 0.04x + 345.7 \tag{21}$$

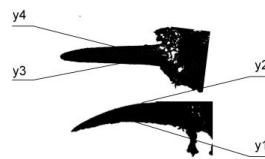


Fig. 6 - Bionic model rabbit paw outer contour

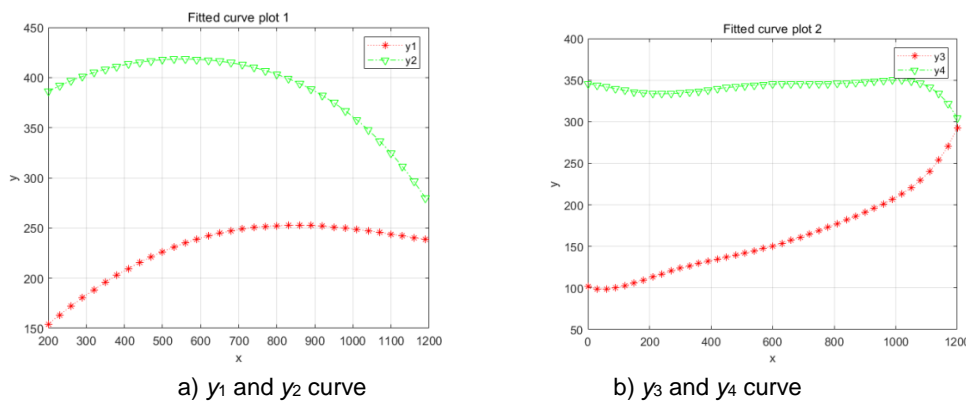


Fig. 7 - Outer contour function curve graph

Using the aforementioned contour curve equation as a reference, the outer contour surface of the bionic shovel is reconstructed utilizing SolidWorks software (Yu et al., 2022; Shi et al., 2014). The bionic shovel teeth are designed as fitting surfaces, with the side view projection curve serving as the horizontal reconstruction curve. Curve y_1 is designated as the upper ridge line, while curve y_2 represents the lower ridge line. The outer contour curves of the shovel blade are identified as curves y_3 and y_4 . Consequently, a three-dimensional model of bionic shovel type 1 is established, as illustrated in Figure 8b. To this model, a bionic claw arch structure is incorporated, resulting in the creation of three-dimensional bionic shovel type 2, as depicted in Figure 8c. Additionally, a control group consisting of ordinary shovel teeth is included to establish a three-dimensional model of a conventional shovel, as shown in Figure 8a. For the bionic shovel, θ is the angle between the tangents of curves y_3 and y_4 , and the intersection of the tangents is the same as that of the conventional shovel of the same specification.

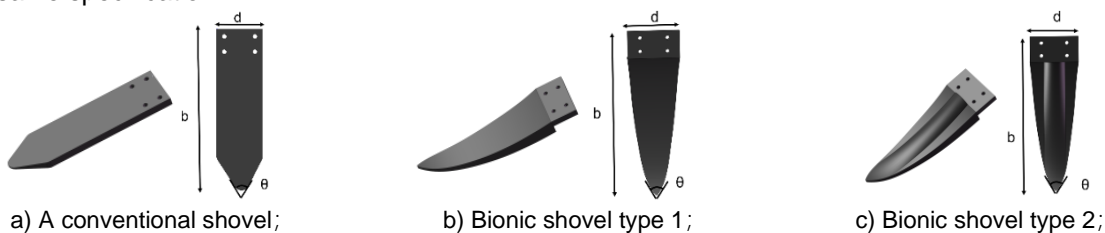


Fig. 8 - Excavating shovel 3D model

b – Digging shovel length; c – Digging shovel width; θ – Digging blade angle

Discrete element simulation experiment

Discrete element model of soil and its cassava

Research indicates that an increase in the number of Discrete Element Method (DEM) particles can significantly enhance simulation efficiency while maintaining calculation accuracy, albeit with an increase in computation time (Yang *et al.*, 2018; Zhou *et al.*, 2023). Consequently, this article categorizes soil particles into four distinct types. Additionally, a five-point sampling method was employed to collect soil samples from the experimental field. Following the screening of these samples through a soil sieve, it was noted that soil particles larger than 5 mm, as well as those ranging from 2 mm to 5 mm in diameter, exhibited irregular shapes. Specifically, particles exceeding 5 mm were confirmed to be irregularly shaped. For modelling purposes, particles larger than 5 mm were represented using a four-sphere model, while those measuring between 2 mm and 5 mm were represented with a three-sphere model. Particles smaller than 2 mm were found to be approximately spherical, leading to the selection of a single-sphere model for this category. The classification of particle types and sizes is illustrated in Figure 9.

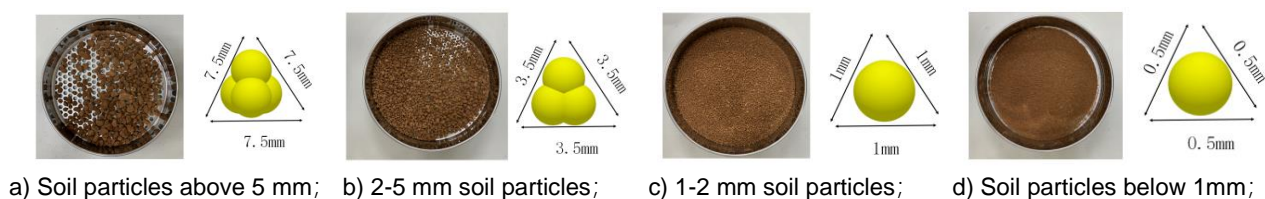


Fig. 9 - Soil particle discrete element model

During the cassava harvesting process, cassava stems are a primary focus of research regarding the fragmentation of the cassava-soil complex. This paper presents findings from a field investigation conducted at the Experimental Base of the Tropical High Efficiency Crops Agricultural Machinery Research Institute in Danzhou City, Hainan Province. The study revealed that cassava exhibits a growth pattern characterized by numerous tubers and straight, elongated stems. Most cassava stem models are approximately evenly distributed across the eight spatial quadrants (Yang *et al.*, 2022). Additionally, in the cassava planting area, physical parameters of the cassava were collected through direct measurements and averaged. The stem length can reach up to 60 cm, with a radius of about 4 m and an average depth of approximately 30 cm after maturity. The cassava stem itself measures around 30 cm. This article employs SolidWorks software to create a three-dimensional model, which is then saved and imported into EDEM for rapid particle filling. The discrete element model of cassava tubers is illustrated in Figure 10.

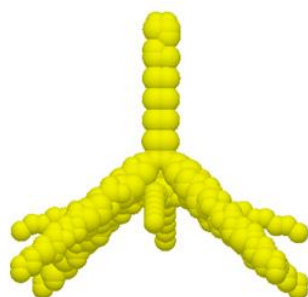


Fig. 10 - Cassava discrete element model

EDEM discrete element simulation model and its parameter settings

Hainan Province is situated in a tropical environment characterized by high temperatures and humidity. The accumulation of organic matter in this region facilitates the formation of red soil, which exhibits high viscosity resistance and significant thickness. Notably, the rainy soil in Hainan tends to adhere to cassava digging shovels. To simplify the calculation model, this article treats the soil as a viscous body. The "Hertz-Mindlin and JKR" contact model employs viscous particles as the theoretical foundation for analyzing the aggregation and separation motions between these particles (Ding *et al.*, 2017; Yang *et al.*, 2015; Abo *et al.*, 2004). Given the physical properties of Hainan's red soil, this paper adopts the "Hertz Mindlin with JKR Cohesion" contact model as the collision contact model for soil particles (Sridhar *et al.*, 2010; Mouazen *et al.*, 2002). The physical parameters utilized in the simulation materials (Wu *et al.*, 2020) are presented in Table 1.

Table 1

Material parameters and contact parameters	
Parameter	Value
Density of soil particles / (kg·m ⁻³)	1656
Density of shovel / (kg·m ⁻³)	7850
Poisson's ratio of soil	0.45
Poisson's ratio of shovel	0.3
Shear modulus of soil / Pa	1.5×10 ⁶
Shear modulus of shovel / Pa	7.1×10 ¹⁰
Coefficient of static friction for soil-soil	0.41
Coefficient of rolling friction for soil-soil	0.35
Coefficient of restitution for soil-soil	0.43
Coefficient of static friction for soil–shovel	0.56
Coefficient of rolling friction for soil-shovel	0.18
Coefficient of restitution for soil-shovel	0.56
Cohesion interaction of soil-soil / (J·m ⁻²)	7.90
Cohesion interaction of soil-shovel / (J·m ⁻²)	6.10

Discrete element complex of cassava-soil

Based on an on-site agronomic investigation conducted at the Tropical High Efficiency Crop Agricultural Machinery Institute in Danzhou City, Hainan Province, the distribution patterns of soil particles were analyzed, the field shape was measured, and the cassava planting conditions were documented. The cassava-soil complex vector model is illustrated in Figure 11. The field ridges are designed to be trapezoidal, with specified lower and upper bottom widths. The plant spacing and ridge spacing are also defined. Measurements of soil compactness using instruments indicate that greater soil depth correlates with increased pressure. This article categorizes the terraced field ridges into three layers based on depth: deep soil, middle soil, and shallow soil. Following the stabilization of particles in EDEM, they are introduced into the excavation device of the cassava harvester. In Recurdyn, the motion pair of the excavation device is added, with the start mode set from 0 s to 1 s, allowing for a gradual acceleration to 300 mm/s via a linear function, after which it maintains a constant speed. In the post-processing interface, the resistance of the shovel teeth and the disturbance of soil particles during the operation of each type of shovel are analyzed.

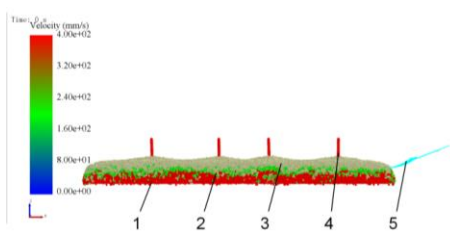


Fig. 11 - EDEM simulation diagram

1- Deep soil; 2- Middle soil; 3- Shallow soil; 4- Cassava; 5- Digging shovel

Simulation results and analysis

Comparative analysis of soil particle breaking ability

The impact of the excavating shovel on soil bonding is illustrated in Figure 12. Figure 12a demonstrates that after the soil bonding is disrupted by the blade of the ordinary excavating shovel, the bonding does not change once the soil reaches the shovel surface. Conversely, Figure 12b indicates that after the soil enters the shovel surface of bionic excavating shovel type 1, the bonding key increases along the curvature radius of the shovel surface, leading to an increase in force. As shown in Figure 12c, when the soil interacts with the shovel surface of bionic excavating shovel type 2, the arch structure significantly damages the bonding between soil particles. A portion of the soil slides upward along the shovel surface and enters the transition plate process, while some soil particles overcome the bonding force and slide laterally back to the ground.

Consequently, the primary working resistance of the excavating shovel arises from the reaction force of the soil against the transition plate. Therefore, reducing the amount of soil entering the transition plate can effectively decrease the working resistance.

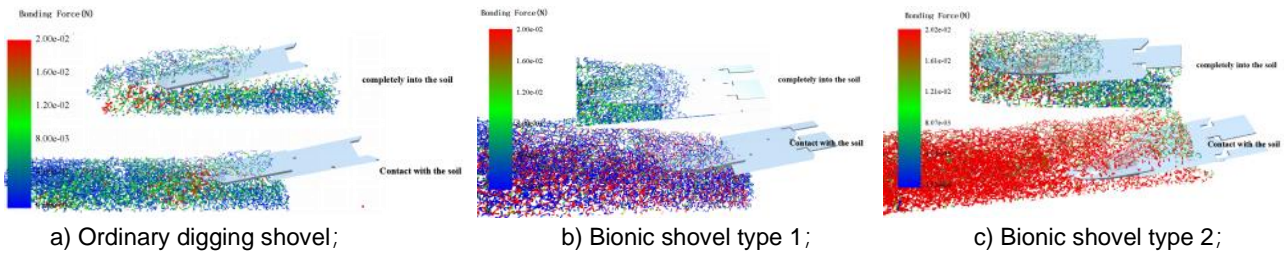


Fig. 12- Distribution diagram of soil particle cohesion force of digging shovel

Comparative analysis of excavation resistance

In the simulation, the forward speed of the frame is set to 300 mm/s, the soil penetration angle is set to 15°, the excavation depth is set to 40 mm, and the total simulation test time is set to 4 s. The simulation results are illustrated in the accompanying figure 13. Notably, the resistance experienced by the bionic digging shovel type 2 is significantly lower than that of the ordinary digging shovel and bionic digging shovel type 1. As depicted in Figure 13, the resistance of the excavating shovel increases sharply upon initial contact with the soil, reaching a stable value after 3 s. Consequently, this study considers the average value of the data from 3 s to 4 s as the resistance of the excavating shovel. The excavation depth achieved is 310 mm. At depths of 290 mm and 270 mm, the excavation resistance of the bionic excavating shovel type 1 is reduced by 6.84%, 4.58%, and 4.84% compared to the ordinary shovel, yielding an average reduction of 5.42%. In contrast, the excavation resistance of the bionic excavating shovel type 2 is reduced by 9.21%, 9.89%, and 10.12% relative to the ordinary shovel, with an average reduction of 9.74%. These results indicate a significant decrease in soil penetration resistance. The results show that bionic shovel type 2 is more effective.

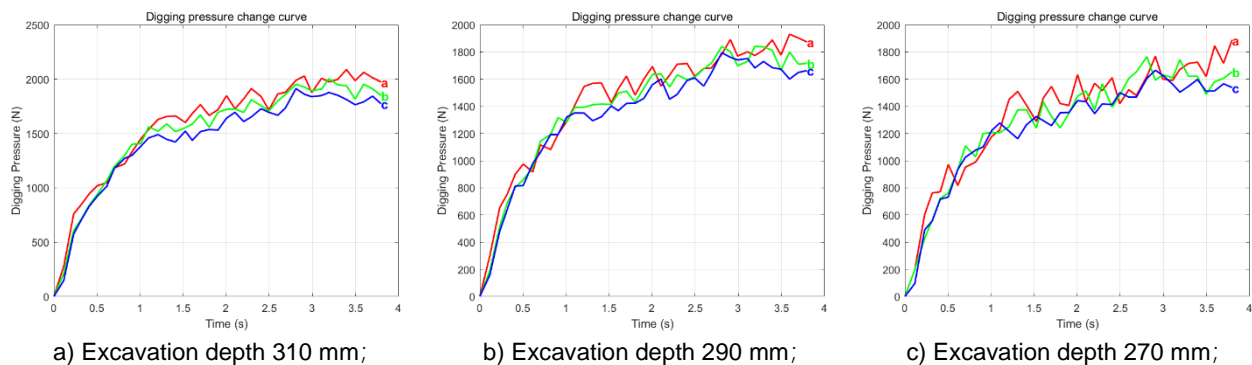


Fig. 13- Resistance curves for 3 excavation depths

a- A conventional shovel; b- Bionic shovel type 1; c- Bionic shovel type 2

Optimization test of structural parameters of bionic shovel

Experimental factors

According to the resistance analysis, the width of the digging shovel, the depth of its penetration into the soil, and the angle of the shovel tip are the primary factors influencing the resistance generated during its operation (Tagar et al., 2015; Barr et al., 2018). To identify the optimal combination of structural parameters for the bionic shovel type 2, simulations of excavations with various parameter combinations are conducted within a consistent simulation environment. These combinations are evaluated based on excavation resistance and soil breakage rate, where the soil breakage rate λ is defined as follows:

$$\lambda = \frac{N_0 - N_1}{N_0} \tag{22}$$

where:

- λ - Soil damage rate;
- N_1 - Bonding Number at the ending of simulation;
- N_0 - Bonding Number at the start of simulation.

According to the agronomic inspection of the planting site, the spacing between cassava planting rows is set at 1 m to 1.2 m. To maintain an appropriate gap between the digging shovels while completely excavating the cassava stems, this article specifies the digging shovel width to be between 65 mm and 85 mm. Additionally, to analyze the depth of the cassava stems buried in the soil, the excavation blade width is established at 220 mm to 260 mm (Xiong *et al.*, 2022). To achieve a better drag reduction effect during excavation without compromising the excavation efficiency, the inclination angle of the excavation blade is recommended to be between 55° and 60° (Fan *et al.*, 2020). To simplify the number of experiments and minimize simulation errors, the Box-Behnken Design (BBD) experimental design was employed, resulting in 17 groups of orthogonal experiments encompassing 3 factors and 3 levels. The experimental factors of bionic shovel type 2 are coded as presented in table 2.

Table 2

Coded value	Factor		
	Digging shovel length <i>b</i> A(mm)	Digging shovel width (<i>d</i>) B(mm)	Digging blade angle (θ) C(°)
-1	220	65	50
0	240	75	55
1	260	85	60

Test result analysis

After adjusting the physical dimensions of the excavating shovel in accordance with the 17 sets of test parameters, import the modified shovel design into the EDEM software. Conduct simulated excavation on the same soil model and record both the resistance encountered by the excavating shovel and the soil fragmentation rate during the excavation process. The results are presented in table 3.

Table 3

Serial number	Digging shovel length A (mm)	Digging shovel width B (mm)	Digging blade angle C (°)	Digging Resistance (N)	Soil breakage rate λ
1	-1	-1	0	1733.66	91.4
2	1	-1	0	1939.54	92
3	-1	1	0	1972.14	92.7
4	1	1	0	2078.01	93.4
5	-1	0	-1	1851.07	92.4
6	1	0	-1	2034.9	92.7
7	-1	0	1	1928.46	93.6
8	1	0	1	2051.42	94
9	0	-1	-1	1823.09	91.7
10	0	1	-1	2055.59	92.6
11	0	-1	1	1830.46	93
12	0	1	1	2067.5	93.4
13	0	0	0	2007.4	92.3
14	0	0	0	2012.5	92.7
15	0	0	0	2013.72	92.4
16	0	0	0	2030.36	91.8
17	0	0	0	2033.2	92.6

Regression model establishment and significance testing

To conduct a comprehensive analysis of the effects of excavation blade length, width, and inclination angle on working resistance, variance analysis was performed on the test results, as presented in the tables 4 and 5.

According to the variance analysis results presented in the table 4, it can be concluded that the empirical significance value of the regression model is $F = 55.15$, $P < 0.0001$. The simulated linear terms, including shovel tooth length (A) and shovel tooth width (B), as well as the quadratic terms (A^2 and B^2), significantly impact excavation resistance, with extreme significance ($P < 0.01$). Furthermore, the quadratic term AB also has a significant effect on excavation resistance ($P < 0.05$). Consequently, the order of influence of each individual factor on excavation resistance is as follows: tooth width (B) > tooth length (A) > blade inclination angle (C). Other factors do not have a significant impact. After eliminating the insignificant terms, the coded regression equation for soil resistance is obtained:

$$Y_1 = 2019.436 + 77.3175A + 105.81125B - 25.0025AB - 33.148A^2 - 55.4505B^2 \quad (23)$$

According to the variance analysis results for the soil fragmentation rate presented in Table 5, the empirical significance value of the regression model is $F = 6.82$ and $P = 0.0096$. The simulated first-order factors, specifically the shovel tooth width (B) and blade inclination angle (C), have a highly significant impact on the soil fragmentation rate ($P < 0.01$). Additionally, the quadratic term C^2 demonstrates a significant effect on the soil fragmentation rate ($P < 0.05$). The table indicates that the order of influence of each individual factor on the soil fragmentation rate is as follows: blade inclination angle (C) > blade tooth width (B) > blade tooth length (A), while other factors do not exhibit a significant influence.

After removing the insignificant terms, the coded regression equation for the soil fragmentation rate is obtained:

$$Y_2 = 165.419375 + 0.52125B - 2.2105C + 0.0223C^2 \quad (24)$$

Table 4

Work resistance variance analysis					
Source	Sum of Squares	df	Mean Square	F	p
Model	1.64×10 ⁵	9	18162	55.15	< 0.0001
A(**)	47823.97	1	47823.97	145.22	< 0.0001
B(**)	89568.17	1	89568.17	271.97	< 0.0001
C	1601.5	1	1601.5	4.86	0.0632
AB(*)	2500.5	1	2500.5	7.59	0.0283
AC	926.29	1	926.29	2.81	0.1374
BC	5.15	1	5.15	0.0156	0.904
A ² (**)	4626.48	1	4626.48	14.05	0.0072
B ² (**)	12946.35	1	12946.35	39.31	0.0004
C ²	1654.95	1	1654.95	5.03	0.0599
Residual	2305.32	7	329.33		
Lack of Fit	1770.89	3	590.3	4.42	0.0926
Pure Error	534.43	4	133.61		
Cor Total	1.66×10 ⁵	16			

Note: (**) indicates that the item is extremely significant ($P < 0.01$), (*) indicates that the item is significant ($P < 0.05$).

Table 5

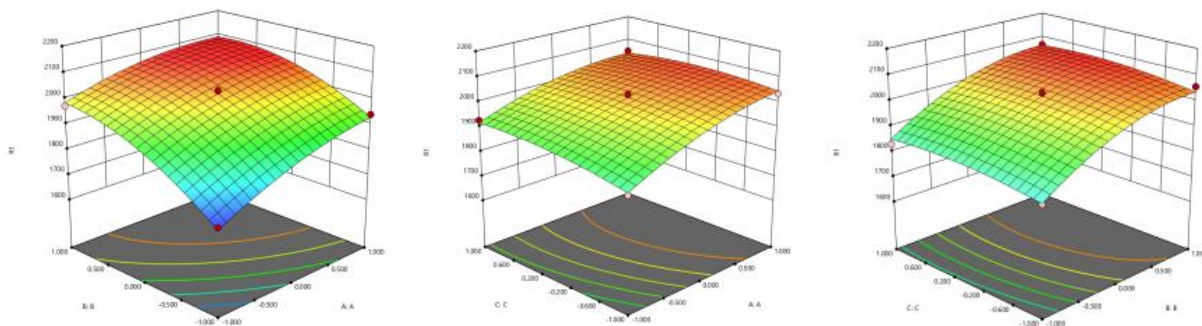
Variance analysis of soil breakage rate					
Source	Sum of Squares	df	Mean Square	F	p
Model	7.03	9	0.7815	6.82	0.0096
A	0.5	1	0.5	4.36	0.0751
B(**)	2	1	2	17.46	0.0041
C(**)	2.64	1	2.64	23.09	0.002
AB	0.0025	1	0.0025	0.0218	0.8867
AC	0.0025	1	0.0025	0.0218	0.8867

Source	Sum of Squares	df	Mean Square	F	p
BC	0.0625	1	0.0625	0.5455	0.4842
A ²	0.2792	1	0.2792	2.44	0.1625
B ²	0.2476	1	0.2476	2.16	0.185
C ² (*)	1.31	1	1.31	11.42	0.0118
Residual	0.802	7	0.1146		
Lack of Fit	0.31	3	0.1033	0.8401	0.5385
Pure Error	0.492	4	0.123		
Cor Total	7.84	16			

Note: (**) indicates that the item is extremely significant ($P < 0.01$), (*) indicates that the item is significant ($P < 0.05$).

Response surface analysis and target optimization

The response surface is illustrated in Figure 14. The interactive effect of blade length A and blade width B on excavation resistance is depicted in Figure 14a. With the blade inclination angle C fixed at 0 coded value and blade length A held constant, an increase in shovel width B leads to a rise in excavation resistance. This increase is pronounced in the range of 65-75 mm and more gradual in the range of 75-85 mm. Conversely, when shovel tooth width B is kept constant, excavation resistance increases with an increase in shovel tooth length A. The change is significant in the range of 220-240 mm, becomes more gradual in the range of 240-260 mm, and exhibits a slight downward trend after reaching a plateau. The interactive effect of blade length A and blade inclination angle C on excavation resistance is shown in Figure 14b. When blade tooth width B is fixed at 0 coded value and blade tooth length A remains unchanged, excavation resistance does not exhibit significant changes as blade inclination angle C increases, although there is a slight upward trend at higher excavation resistances. The interactive effect of shovel tooth width B and blade inclination angle C on excavation resistance is presented in Figure 14c. When shovel tooth length A is fixed at 0 coded value and shovel tooth width B remains constant, excavation resistance does not show significant changes with an increase in blade inclination angle C. However, when blade inclination angle C is held constant, excavation resistance tends to increase as shovel tooth width B increases.

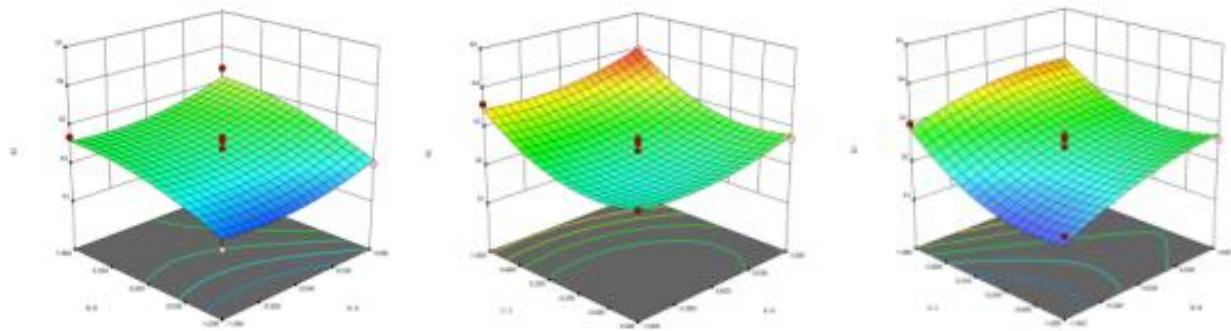


a) Response surface plots of A and B; b) Response surface plots of A and C; c) Response surface plots of B and C;

Fig. 14 - Excavation resistance response surface plot

The response surface is illustrated in Figure 15. The interactive effect of shovel tooth length A and shovel tooth width B on the soil breakage rate is depicted in Figure 15a. When the blade inclination angle C is fixed at 0 coded value and the shovel tooth length A remains constant, there is a slight upward trend in the soil crushing rate as the shovel width B increases, although this trend is not pronounced. Conversely, when the shovel tooth width B is held constant, the soil breakage rate does not exhibit significant changes with increasing shovel tooth length A. The interactive effect of shovel tooth length A and blade inclination angle C on the soil fragmentation rate is shown in Figure 15b.

When the shovel tooth width B is fixed at 0 coded value and the shovel tooth length A remains unchanged, the soil fragmentation initially decreases as the blade inclination angle C increases, then subsequently increases. Similarly, when the blade inclination angle C is held constant, soil fragmentation first decreases and then increases with an increase in blade length A. The interactive effect of blade width B and blade inclination angle C on the soil fragmentation rate is illustrated in Figure 15c. For a fixed shovel tooth length A at 0 coded value and constant shovel tooth width B, an increase in the blade inclination angle C results in a decrease in soil crushing, followed by an increase. When the blade inclination angle C remains constant, an increase in shovel tooth width B leads to a gradual increase in digging resistance.



a) Response surface plots of A and B; b) Response surface plots of A and C; c) Response surface plots of B and C

Fig. 15 - Soil breakage rate response surface plot

In order to obtain the optimal bionic shovel parameters with smaller excavation resistance and larger soil breakage rate, this paper performs an optimal horizontal combination of test factors and establishes a mathematical model based on the boundaries of the test factors as follows:

$$\begin{cases} \min Y_1 \\ \max Y_2 \\ s.t. \begin{cases} 220mm \leq x_1 \leq 260mm \\ 65mm \leq x_2 \leq 85mm \\ 50^\circ \leq x_3 \leq 60^\circ \end{cases} \end{cases} \quad (25)$$

In the multi-objective optimization module of the Design Expert 13 software, the optimal parameter combination for the bionic shovel, which achieves both minimal excavation resistance and a higher soil breakage rate, consists of a shovel tooth length of 220 mm, a shovel tooth width of 65.1 mm, and a shovel edge inclination angle of 60°. This combination results in an excavation resistance of 1733.66 N and a maximum soil fragmentation rate of 92.9%. A simulation test was conducted using this optimal parameter combination in EDEM, yielding an excavation resistance of 1671.51 N and a soil fragmentation rate of 93.1%. The error between the predicted response value and the experimental value was within 5%, thereby verifying both the accuracy and reliability of the model.

RESULTS

Field test machines and materials

The test machine utilized in this study, as illustrated in the accompanying figure 16, primarily comprises a depth shape prevention device, an excavation device, a vibration separation device, a secondary transmission and sorting table, and a central control unit. The depth shape prevention device is designed to control and stabilize the working excavation depth. The shovel teeth of the excavation device crush the soil, which is subsequently directed into the vibration separation device via a connecting plate to facilitate the separation of potato soil. Finally, the material is conveyed to the secondary transmission and sorting platform for manual sorting. This secondary transmission effectively integrates mechanical separation of the potato soil, while manual sorting significantly mitigates damage to the cassava caused by collisions.



Fig. 16 - Soil breakage rate response surface plot

- 1- Power unit; 2- Control device; 3- Track; 4- Vibrating wheel; 5- Hydraulic device; 6- Excavation device; 7- Alignment device;
- 8- Frame; 9- Support wheel; 10- Separating screen; 11- Power supply unit; 12- Sorting table drive shaft; 13- Anti-collision device;
- 14- Secondary transmission sorting table

The excavation device of the cassava harvester is illustrated in the figure 17. It primarily consists of shovel teeth, connecting plates, and transition plates. The shovel teeth measure 220 mm in length and 65 mm in width, while the transition plate measures 980 mm in length and 300 mm in width. To facilitate testing, the connecting plate features openings. The fixed holes allow for the installation of two types of bionic shovel teeth, one type of ordinary shovel teeth, and transition plates onto the cassava harvester's excavation device. Additionally, a pressure sensor is installed at the bottom of the shovel to measure the excavation resistance encountered during operation.

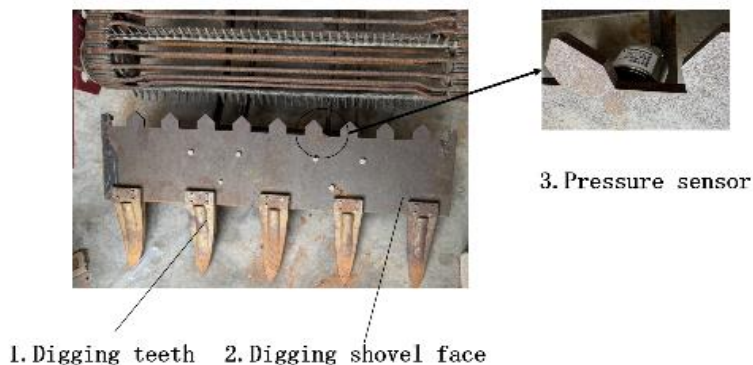


Fig. 17- Excavation device
 1- Digging teeth; 2- Digging shovel face; 3- Pressure sensor

To verify the soil-breaking effect of bionic excavation, three types of digging shovels were installed on a cassava harvester for field tests conducted in the cassava planting base. The digging depth was set to 310 mm, and the forward speed was maintained at 300 mm/s. The results of the excavation effects on the ridge field are illustrated in Figure 18. The image indicates that both the ordinary shovel and bionic shovel type 1 produced larger soil clumps. In contrast, bionic shovel type 2 resulted in a more uniform soil breakage, demonstrating superior performance, which aligns with the simulation results.



Fig. 18- Comparison chart of field excavation effects
 1- Ordinary digging shovel; 2- Bionic shovel type 1; 3- Bionic shovel type 2

The spacing between the conveyor chains of the cassava harvester is 40 mm. Consequently, this paper employs a soil sieve with a diameter of 20 mm to conduct five sets of sampling screenings across three ridge fields. As shown in Table 6, the proportion of soil particles with a diameter of 20 mm or greater for ordinary shovels is 18.94%. In contrast, the bionic shovel type 1 has a soil particle diameter of 20 mm or greater accounting for 16.98%, while the bionic shovel type 2 shows that soil particles of 20 mm or greater comprise 11.92%. Thus, it can be concluded that the bionic shovel type 2 exhibits superior soil breaking ability compared to both the ordinary shovel and bionic shovel type 1.

Table 6

The proportion of surface soil diameter above 20			
Sampling serial number	Bionic shovel type 1 (%)	Bionic shovel type 2 (%)	Ordinary digging shovel (%)
1	16.5	12.3	18.3
2	17.6	11.2	19.5
3	17.3	11.6	20.3
4	15.9	12.8	17.8
5	17.6	11.7	18.8
average value	16.98	11.92	18.94

Excavation resistance comparison test

The pressure sensor and information transmission module installed at the base of the digging shovel collect and transmit the excavation resistance values in real time. To simplify the testing process, the digging depth was set to 310 mm, and the forward speed was maintained at 300 mm/s. The resistance change curve over time is illustrated in Figure 19. Notably, the resistance value rapidly increases to a stable level upon entering the soil. It is evident that the resistance encountered by the bionic shovel type 2 is significantly lower than that experienced by the ordinary shovel and the bionic shovel type 1.

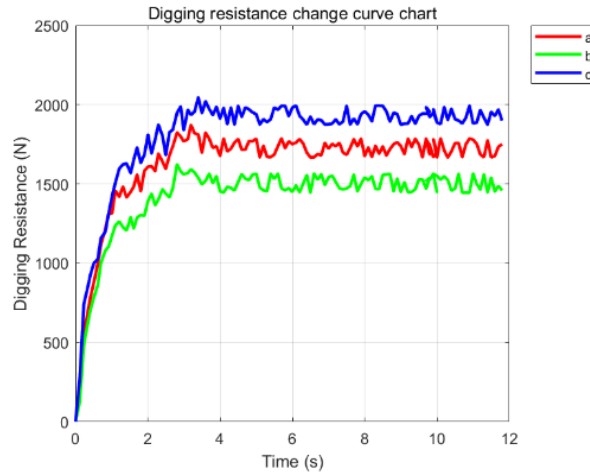


Fig. 19- Digging resistance change curve chart
a- Bionic shovel type 1; b- Bionic shovel type 2; c- Ordinary digging shovel

To ensure the accuracy of the data, each model of excavator shovel was tested 10 times, and the average data from 4 s to 12 s is shown in Figure 19. The results of the excavation resistance tests are presented in the table 7. The average resistance experienced by the Ordinary digging shovel during operation is 1886.842 N. The average resistance for Bionic shovel type 1 is 1729.390 N, and the average resistance for Bionic shovel type 2 is 1600.316 N. Calculations show that the resistance of the Type 1 Bionic Shovel is reduced by 8.34% compared to the conventional shovel. In addition, the Type 2 Bionic Shovel has a 15.19% reduction in resistance compared to a conventional digging shovel. In the simulation results in Figure 3, the digging depth is 310 mm, and the resistance of the Type 1 Bionic Shovel is reduced by 6.84% compared to the conventional shovel. Compared with the conventional shovel, the resistance of the Type 2 bionic shovel is reduced by 9.21%. The margin of error between simulation and experiment is within 10%, which verifies the reliability of the simulation. In terms of digging performance, the Type 2 Bionic Shovel outperforms the Normal Shovel and the Type 1 Bionic Shovel.

Table 7

The proportion of surface soil diameter above 20

Sampling serial number	Bionic shovel type 1 / (N)	Bionic shovel type 2 / (N)	Conventional digging shovel / (N)
1	1712.397	1627.799	1854.514
2	1721.62	1573.192	1872.327
3	1712.786	1617.638	1876.475
4	1710.114	1573.576	1871.152
5	1751.522	1569.991	1907.87
6	1714.208	1629.65	1903.715
7	1730.245	1570.074	1894.575
8	1753.198	1601.268	1906.316
9	1761.941	1629.691	1900.092
10	1725.87	1610.28	1881.385
average value	1729.39	1600.316	1886.842

CONCLUSIONS

This article presents the design of a cassava digging shovel specifically tailored for the extensive and dense red soils found in tropical regions. Utilizing a bionic rabbit claw toe biological curve structure, the shovel effectively reduces digging resistance and enhances the soil breakage rate during excavation tasks. The following conclusions are drawn:

1) Simulation test results for cassava digging indicate that at excavation depths of 310 mm, 290 mm, and 270 mm, the digging resistance of bionic digging shovel type 1 is reduced by 6.84%, 4.58%, and 4.84%, respectively, yielding an average reduction of 5.42% compared to the ordinary shovel. In contrast, the digging resistance of bionic digging shovel type 2 is decreased by 9.21%, 9.89%, and 10.12%, with an average reduction of 9.74%. The digging performance of bionic digging shovel type 2 significantly surpasses that of both bionic digging shovel type 1 and the ordinary shovel.

2) An analysis of the simulation test results reveals that the optimal parameter combination for bionic excavating shovel type 2 includes a tooth length of 220 mm, a tooth width of 65.1 mm, and a specific blade inclination, resulting in an excavation resistance of 1733.66 N and a substantial soil fragmentation rate of 92.9%.

3) Field test results demonstrate that bionic digging shovel type 2 possesses a superior ability to break soil, the Type 1 bionic digging shovel exhibits a reduction in resistance of 6.84%, while the Type 2 bionic digging shovel demonstrates a more significant reduction of 9.21%, in comparison to the traditional digging shovel achieving, thereby meeting the requirements for cassava harvesting.

ACKNOWLEDGEMENT

This work was funded by the National Natural Science Foundation of China, Research on the device and mechanism of low damage cassava coupled excavation based on dynamic rupture characteristics of cassava-soil complex, grant number 5226050106.

REFERENCES

- [1] Abo E., Hamilton R., Boyle J. H., (2004), Simulation of soil blade interaction for sandy soil using advanced 3D finite element analysis, *Soil and Tillage Research*, vol. 75, pp. 61-73, Netherlands.
- [2] Barr J. B., Ucgul D. J. M., Fielke J. M., (2018), Simulating the effect of rake angle on narrow opener performance with the discrete element method, *Biosystems Engineering*, vol. 171, ISSN 1537-5110, pp. 1-15, Netherlands.
- [3] Cui G., Ma Y., Yang D., Jia J. X., Li Y., (2019), Research situation of bionic resistance reducing technology about potato digging shovel (马铃薯挖掘铲仿生减阻技术研究概况), *Agricultural Engineering*, vol. 9, ISSN 2095-1795, pp. 19-22, Beijing/China.
- [4] Ding Q., Ren J., Belal E. A., Zhao J., Ge S., Li Y., (2017), Discrete element analysis of subsoiling process in wet sticky paddy soil (湿粘水稻土深松过程离散元分析), *Transactions of the Chinese Society for Agricultural Machinery*, vol. 48, ISSN 1000-1298, pp. 38-48, Beijing/China.
- [5] Duanmu L., (2020), Design and research on bionic excavating shovel for cassava harvester (木薯收获机仿生挖掘铲减阻设计与研究), *Jilin University*, Jilin/China.
- [6] Fan Y., (2020), Research on potato digging mechanism and bionic shovel design based on discrete element method (基于离散元法的马铃薯挖掘机理研究及仿生铲设计), *Shenyang Agricultural University*, Shenyang /China.
- [7] Jia H., Guo M., Zhao J., Huang D., Zhuang J., (2019), Design and test of bionic wide-ridge soybean tilling-sowing machine, *International Journal of Agricultural and Biological Engineering*, vol. 12, ISSN 1934-6344, pp. 42-51, China.
- [8] Li J., Li X., Hu B., Gu T., Wang Z., Wang H., (2023), Analysis of the resistance reduction mechanism of potato bionic digging shovels in clay and heavy soil conditions, *Computers and Electronics in Agriculture*, vol. 214, ISSN 1872-7107, pp. 1761-1761, Netherlands.
- [9] Li X., Liu X., Mao Y., Chen X., (2014), Desalination effect of flue gas desulfurization gypsum on tidal flat soil in the Weishi area (烟气脱硫石膏对围垦滩涂土壤的脱盐作用), *Journal of Environmental Engineering Technology*, vol. 6, ISSN 1674-991X, pp. 503-527, Beijing/China.
- [10] Liu H., (2010), Understanding the living habits of rabbits (认识兔子的生活习性), *Jilin Animal Husbandry and Veterinary Medicine*, vol. 31, ISSN 1672-2078, pp. 40-40, Jilin/China.
- [11] Mouazen A. M., Ramon H., (2002), A numerical–statistical hybrid modelling scheme for evaluation of draught requirements of a subsoiler cutting a sandy loam soil, as affected by moisture content, bulk

- density and depth, *Soil and Tillage Research*, vol. 63, ISSN 0167-1987, pp. 155-165, Netherlands.
- [12] Shi L., (2014), Design and simulation research on the potato bionic digging shovel, *Agricultural Research in the Arid Areas*, vol. 0, ISSN 1000-7601, pp. 0-0, China.
- [13] Sridhar H., Richard W., Marklin, Paula E. P., Cariapa V., (2010), A Shovel With a Perforated Blade Reduces Energy Expenditure Required for Digging Wet Clay, *Human Factors*, vol. 52, ISSN 0018-7208, pp. 492-502, America.
- [14] Sun J., Wang Y., Zhang S., Yun H., Jin T., Zhang Z., (2020), The mechanism of resistance-reducing / anti-adhesion and its application on biomimetic disc furrow opener, *Mathematical Biosciences and Engineering*, vol. 17, ISSN 1547-1063, pp. 4657-4677, Arizona State/America.
- [15] Susila E., Hryciw R. D., (2003), Large displacement FEM modelling of the cone penetration test (CPT) in normally consolidated sand, *International Journal for Numerical and Analytical Methods in Geomechanics*, vol. 27, ISSN 0363-9061, pp. 585-602, United Kingdom.
- [16] Tagar A. A., Ji C., Adamowski J., Malard J., Chen S., Ding Q., Abbasi N. A., (2015), Finite element simulation of soil failure patterns under soil bin and field testing conditions, *Soil and Tillage Research*, vol. 145, ISSN 0167-1987, pp. 157-170, Netherlands.
- [17] Wu P., Zhang X., Li Y., Li M., Dong X., Liang D., (2020), Study on the accumulation characteristics of lateritic soil model based on discrete element method (基于离散元的砖红土壤模型堆积特性研究), *Journal of Agricultural Mechanization Research*, vol. 42, ISSN 1003-188X, pp. 145-150, Heilongjiang /China.
- [18] Xiong C., Zhou D., Deng G., Li G., Cui Z., He F., Li L., (2022), Design and testing of an automatic control system for digging depth of a vibrating chain cassava harvester (振动链式木薯收获机挖掘深度自动控制系统设计与测试), *Journal of Huazhong Agricultural University (Natural Science Edition)*, vol. 41, ISSN 1000-2421, pp. 217-226, Hubei /China.
- [19] Yang J., Yang W., Yang J., (2022), Measurement of cassava stem parameters and EDEM simulation parameter calibration (木薯种茎参数测量及 EDEM 仿真参数标定), *Journal of Agricultural Mechanization Research*, vol. 44, ISSN 1003-188X, pp. 197-202, Heilongjiang /China.
- [20] Yang W., Li J., Yang J., Wei L., (2015), Numerical Simulation of An Experienced Farmer Lifting Tubers of Cassava for Designing A Bionic Harvester , *CMES-Computer Modeling in Engineering & Science*, vol. 104, ISSN 1526-1492, pp. 471-491, America.
- [21] Yang Y., Tong J., Ma Y., Li M., Jiang X., Li J., (2018), Design and experiment of bionic soil-cutting blade based on the multi-toe structure characteristics of mole rats (基于鼯鼠多趾结构特征的仿生切土刀片设计与试验), *Transactions of the Chinese Society for Agricultural Machinery*, vol. 49, ISSN 1000-1298, pp. 122-128, Beijing/China.
- [22] Yu J., Ma Y., Wang S., Xu Z., Liu X., Wang H., Qi H., Han L., Zhuang J., (2022), 3D Finite Element Simulation and Experimental Validation of a Mole Rat's Digit Inspired Biomimetic Potato Digging Shovel, *Applied sciences*, vol. 12, ISSN 2076-3417, pp. 108315-108315, Switzerland.
- [23] Yu J., Wang R., Tong X., Zou W., (2019), Surface reconstruction of rabbit claws and extraction of characteristic curves (兔子爪趾曲面重构及特征曲线的提取), *Journal of Chinese Agricultural Mechanization*, vol. 40, ISSN 2095-5553, pp. 43-47, Jiangsu/China.
- [24] Zhang C., Zhao Z., (2015), Advanced Kinematics (高等机构学), *China Machine Press*, Beijing/China.
- [25] Zhang Z., Xue H., Wang Y., Xie K., Deng Y., (2022), Design and experiment of Panax notoginseng bionic excavating shovel based on EDEM (基于离散元法的三七仿生挖掘铲设计与试验), *Transactions of the Chinese Society for Agricultural Machinery*, vol. 53, ISSN 1000-1298, pp. 100-111, Beijing/China.
- [26] Zhao C., Bai B., (2017), Principles of Soil Mechanics (土力学原理), *Tsinghua University Press*, Beijing/China.
- [27] Zhao J., Lu Y., Guo M., Fu J., Wang Y., (2021), Design and experiment of bionic stubble breaking-deep loosening combined tillage machine, *International Journal of Agricultural and Biological Engineering*, vol. 14, ISSN 1934-6344, pp. 123-134, China.
- [28] Zhou W., Xue N., Song K., Nuan W., Wang J., Fu Q., Na M., Tang H., Wang Q., (2023), Bionic Optimization Design and Discrete Element Experimental Design of Carrot Combine Harvester Ripping Shovel. *Processes*, vol. 11, ISSN 2227-9717, pp. 1526-1526, Switzerland.
- [29] Zou X., Liao Y., Ma Q., Liu S., Zhu D., (2013), Bionic design and finite element analysis of excavating shovel for cassava harvester (木薯收获机挖掘铲仿生设计及其有限元分析), *Science Technology and Engineering*, vol. 13, ISSN 1671-1815, pp. 10122-10128, Beijing/China.

THE IMPACT OF OHMIC HEATING ON RICE GRAIN HARDNESS AND HEATING UNIFORMITY COMPARED TO CONVENTIONAL COOKING METHODS

欧姆加热与传统加热蒸煮米饭对米粒硬度与加热均匀性的影响

Xinting DING, Xingshu LI¹⁾

College of Mechanical and Electronic Engineering, Northwest A&F University, Yangling 712100, China

Tel: +86-15596823831; E-mail: xingshu-li@nwsuaf.edu.cn

DOI: <https://doi.org/10.35633/inmateh-74-57>

Keywords: Ohmic heating, Heating uniformity, Rice grain hardness, Cooking method of rice

ABSTRACT

This study investigated the effects of ohmic heating on rice grain hardness and heating uniformity compared to conventional cooking methods. A self-developed ohmic heating system was utilized to cook rice, and the performance was evaluated against that of a traditional heating. The uniformity of rice temperature and the hardness of rice grains under different water-to-rice ratios were measured using a 5-channel temperature acquisition system and a texture analyzer, and the performance of the two heating methods was comprehensively evaluated. The results indicated that the ohmic heating equipment effectively controlled the temperature variations at each stage, with the maximum heating rate error being 1.24% and the R^2 value of the heating curve fitting exceeding 0.9997. Compared to traditional cooking methods, although the temperature difference during the ohmic heating of rice reached 18.32~31.85°C, which is greater than the 21.42~29.94°C observed in traditional heating, the hardness variation of rice at different locations was significantly lower than that achieved with conventional methods. This was primarily attributed to the fact that as the insulation time was extended, the hardness differences between different layers of rice gradually decreased, ultimately resulting in the hardness of the upper, middle, and lower layers of rice being within the range of 18~21 N, thus achieving a more uniform texture of the rice. The results show that ohmic heating technology has great potential to reduce the rice hardness, and provides theoretical basis and technical support for designing more efficient rice cooking equipment.

摘要

本文研究了欧姆加热对米饭粒硬度和加热均匀性的影响，并与传统烹饪方法进行了比较。使用了自行开发的欧姆加热系统对米饭进行烹饪，同时以传统电饭煲作为对照。采用5通道温度采集系统和质构仪测量了不同水米比例下的米饭温度均匀性和米粒硬度，全面评估了两种加热方式的性能。研究结果显示，欧姆加热设备有效控制了各阶段的温度变化，加热速率误差最大为1.24%，加热曲线线性拟合 R^2 大于0.9997。与传统烹饪方法相比，虽然欧姆加热米饭过程中温差达到18.32~31.85°C，大于传统加热的21.42~29.94°C，但是欧姆加热各个位置的米饭硬度差异远小于传统加热方法。这主要得益于随着保温时间的延长，不同层米饭之间的硬度差异逐渐减小，最终上中下层米饭硬度均在18~21N之间，实现了更均匀的米饭质地。研究结论表明，欧姆加热技术具有改善米饭烹饪品质的巨大潜力，为设计更高效的米饭烹饪设备提供了理论基础和技术支持。

INTRODUCTION

The primary method of rice consumption involves cooking the rice-water mixture to form rice, predominantly through traditional heating methods. However, traditional heating methods transfer heat via the container, leading to uneven heating and inconsistent rice quality. Therefore, scholars have recently adopted volumetric heating methods such as microwave and radio frequency to cook rice (Thuengtung and Ogawa, 2020; Verma et al., 2024; Rostamabadi et al., 2024). Although these methods enhance electrical energy utilization, they are hindered by high energy consumption, costs, safety issues, and failure rates, limiting their broader adoption.

Researchers have recently employed ohmic heating technology for rice cooking in order to enhance its overall quality. Jittanit et al., (2017), conducted ohmic heating and conventional heating tests on four types of rice samples. The study found that ohmic heating resulted in softer rice compared to conventional methods. Additionally, the energy consumption and energy cost of the ohmic method were approximately 73% to 90% of that of the conventional cooking method. Furthermore, ohmic cooking was demonstrated to be energy-efficient, reducing the come-up time of the conventional cooking method by 48%.

Specifically, the constant rate values indicated that ohmic cooking could soften rice grains at a greater rate compared to other cooking methods (*Gavahian et al., 2019*). Therefore, ohmic heating technology has great potential in rice cooking. However, existing studies have only selected samples from a specific location in the rice to compare and analyze the temperature and food properties under different heating methods (*Ding et al., 2020*), and have not analyzed the temperature and food property differences from a three-dimensional perspective. That is to say, the uniformity of heating and the hardness differences between ohmic heating and conventional heating have not been investigated.

A rice cooking device based on ohmic heating was developed in this study, which is capable of achieving precise temperature control, including temperature rise phase and insulation phase. The ohmic heating rate was then adjusted to make the heating process similar to that of traditional resistance wire heating. At different water-to-rice ratios, the differences and similarities between ohmic heating and traditional heating in terms of temperature uniformity and rice hardness were compared, and the reasons for these differences were explored. This study provides a theoretical basis for the design of a more comprehensive ohmic heating steamed rice cooking device.

MATERIALS AND METHODS

Materials

The rice used for the experiment was selected for uniform grain quality and it was japonica rice of high-quality. The initial moisture content was $11.86 \pm 0.19\%$ on a wet basis. The rice was packaged and filled with carbon dioxide, and stored in a cool, ventilated and dry place. As home cooking of rice typically uses tap water, this experiment also used tap water. Prior to each set of experiments, the water was stored in a large container to ensure the consistency of the tap water quality (*Kanjanapongkul, 2017*).

Rice cooking method

(1) Ohmic heating

Ohmic heating, also known as resistive heating or Joule heating, is fundamentally based on the electrical conductivity of food materials to directly convert electrical energy into thermal energy. When an electric field is applied across the two ends of the material, the current passes through the material, causing heat generation within it, thereby achieving heating. The ohmic heating system (Fig. 1) consisted of a sinusoidal alternating current power supply (OYHS-9805, Ouyang Huas Power Co., Ltd., Shenzhen, China), a self-made control system, an ohmic heating vessel, and a personal computer (ZX6-CP5S1, Hasee Computer Co., Ltd., Shenzhen, China) (*Ding et al., 2021*). The sinusoidal alternating current power supply was set to output an AC voltage of 220 V. Temperature measurements were taken at the center of the rice-water interface. The temperature data collected by the control system were transmitted to the personal computer via serial communication for storage and analysis. The ohmic heating vessel used for cooking rice was fabricated from five 5 mm thick acrylic plates welded together. The lid was a foam board equipped with a sealing rubber gasket. The electrodes were made of a pair of 1 mm 316L stainless steel plates (*Jun et al., 2007*).

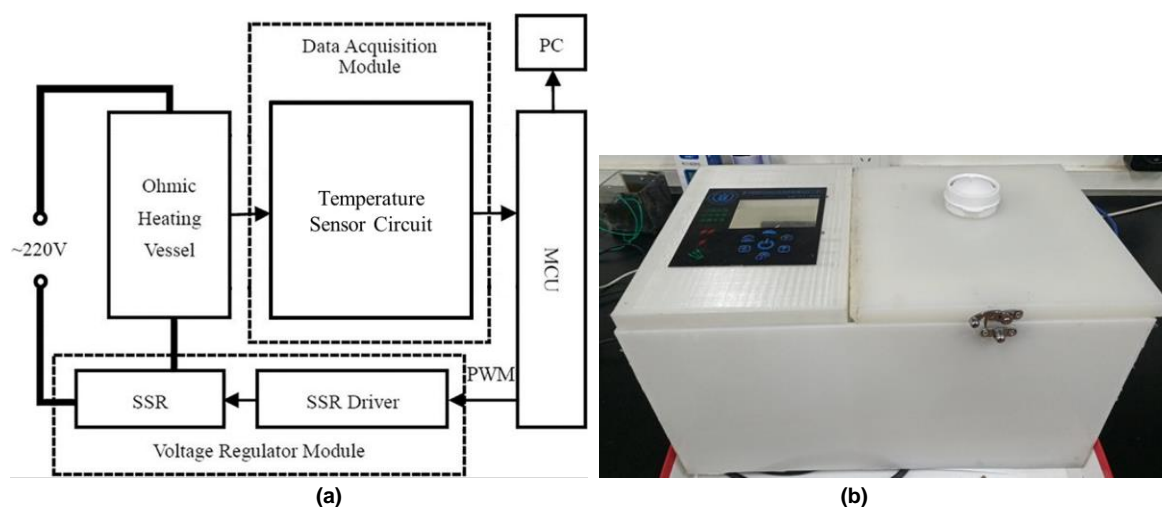


Fig. 1 - Schematic diagram and appliance of ohmic heating system for rice cooking

(2) Traditional heating

A traditional rice heating appliance, the resistance wire type non-high-pressure electric rice cooker (FD10E, Guangdong Tianji Electric Co., Ltd., China), was utilized. The data acquisition module of the ohmic heating rice cooking system was employed to monitor the temperature at the center of the rice-water mixture within the electric rice cooker.

Test method

During the experiments with the two heating methods, 100 g of rice was weighed using an electronic balance, and tap water at 25°C was mixed with the rice according to the water-to-rice ratios (v/w) of 1.25:1, 1.50:1, 1.75:1, and 2.00:1, and then soaked in a water bath maintained at a constant temperature of 25°C for 30 minutes (Ding *et al.*, 2020).

To standardize the heating process of both traditional and ohmic heating for rice cooking, a thermocouple was used to record the central temperature of the rice-water mixture in the traditional heating method. Based on the traditional heating process, the temperature control program of the ohmic heating control system was modified to ensure that the central temperature changes in ohmic heating were the same as those in traditional heating.

To compare the hardness uniformity and temperature uniformity of rice cooked by the two heating methods, temperature measurements and hardness sampling were taken at five different positions in both heating containers, as shown in Fig. 2. The cross-section of the electric rice cooker is circular, so the bottom center of the heating pot was taken as the origin, and temperature measurements and sampling were taken at points 1 (110, 10), 2 (55, 10), 3 (0, 10), 4 (55, 0), and 5 (0, 0). The cross-section of the ohmic heating tank is square, so the bottom corner was taken as the origin, and temperature measurements and sampling were taken at points 1 (0, 0, 0), 2 (20, 18.7, 15), 3 (40, 35.5, 30), 4 (40, 35.5, 15), and 5 (40, 35.5, 0).

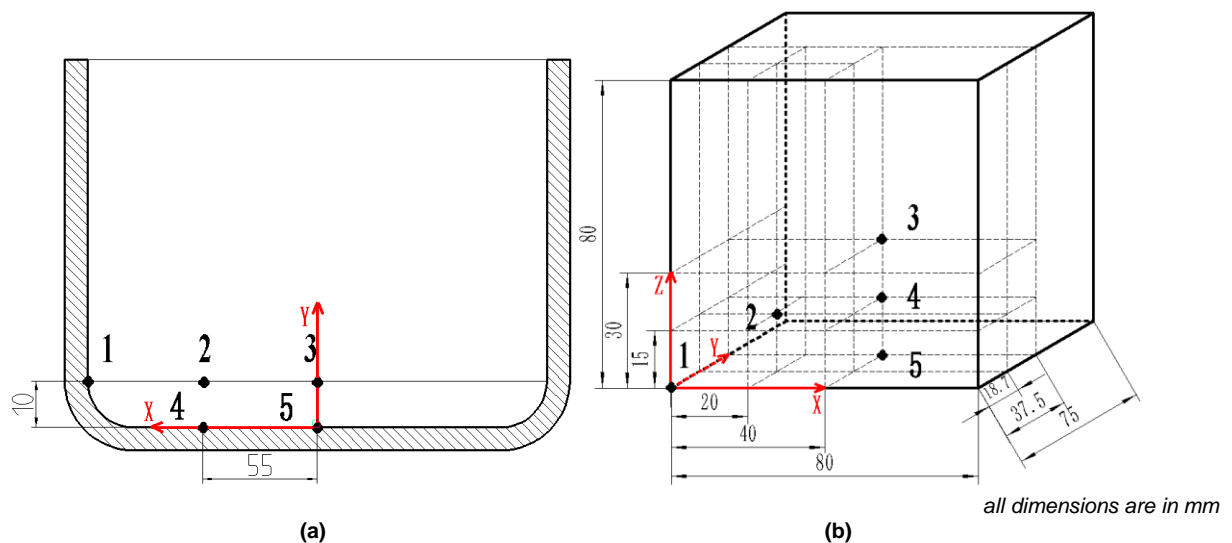


Fig. 2 - Schematic diagram of temperature collection and sample collection point in electric rice cooker (a) and ohmic heating device (b)

After cooking the rice, approximately 50 rice grains from each location were collected and placed in a sealed bag (80 mm × 120 mm), with air expelled and the bags sealed. The rice was then cooled to approximately 23°C, which is room temperature.

Temperature control comparison

After soaking, the rice-water mixture was poured into the electric rice cooker for rice cooking. The temperature change at the central point was measured, and the cooking process in the traditional heating was divided into two stages: heating and insulation. The heating process was further divided into a heating lag phase and a uniform heating phase. During the uniform heating phase, as the water-to-rice ratio increased from 1.25:1 to 2.00:1, the heating rate decreased from 5.034°C/min to 4.344°C/min. Therefore, the heating rate of the ohmic heating device was set to 5°C/min. During the insulation phase, the temperature of the rice in the electric rice cooker was maintained at $97.95 \pm 0.5^\circ\text{C}$. It took approximately 20 minutes from the moment the insulation indicator light was turned on until the buzzer sounded. Thus, the insulation temperature of the ohmic heating device was set to 98°C, with an insulation time of 20 minutes.

Table 1

Traditional heating and ohmic heating temperature parameters

Heating Method	Traditional heating				Ohmic heating			
	1.25:1	1.50:1	1.75:1	2.00:1	1.25:1	1.50:1	1.75:1	2.00:1
Water-rice ratio(v/w)								
Heating fitting equation (T, °C; t, s)	T=0.0839 t+5.3403	T=0.0823 t+3.7058	T=0.0807 t+4.8436	T=0.0724 t+6.4575	T=0.0826 t+22.214	T=0.0825 t+21.424	T=0.0823 t+22.877	T=0.0825 t+22.222
R^2	0.9848	0.9887	0.9882	0.9869	0.9997	1.0000	0.9999	1.0000
Heating rate (°C/min)	5.034	4.938	4.842	4.344	4.956	4.95	4.938	4.95
Relative error (%)	-	-	-	-	0.88%	1%	1.24%	1%
Minimum temperature(°C)	97.06	95.48	97.36	98.03	97.5	97.87	97.93	97.75
Maximum temperature(°C)	98.38	98.28	98.39	98.22	98.93	98.62	98.5	98.81
Maximum temperature difference(°C)	1.32	2.80	1.03	0.19	1.43	0.75	0.57	1.06
Mean insulation temperature (°C)	98.05	97.80	97.87	98.10	98.15	98.12	98.06	98.44
Standard deviation of insulation temperature	0.23	0.69	0.16	0.05	0.27	0.16	0.10	0.27

(1) Heating Lag Phase

During the initial 4 minutes of the heating cycle of traditional heating, despite continuous power supply and output, the temperature remains constant. This is attributed to the gradual heating of the heating plate, which subsequently transfers heat to the inner pot. Only after the inner pot reaches a certain temperature does the rice-water mixture begin to heat up. This heating method exhibits a certain degree of heating lag. In contrast, Ohmic heating is a volumetric heating method. Once the rice-water mixture is electrified, it immediately heats up, with no heating lag.

(2) Heating Temperature Rise Phase

After the rice begins to heat up with both heating methods, the actual heating rate of ohmic heating is between 4.938°C/min and 4.956°C/min, with an error less than 1.24% from the preset heating rate. The linear fitting correlation coefficient R^2 for the traditional heating's temperature rise curve ranges from 0.9848 to 0.9887, which is lower than that of the ohmic heating device, ranging from 0.9997 to 1.0000. This indicates that the temperature of the ohmic heating has a better linear relationship with time, with a stable and constant rate of temperature rise. Considering both the heating rate error and the linear fitting, the control system has a good control effect on the heating rate of ohmic heating.

(3) Insulation Phase

In the insulation phase, initially, the heating plate of the traditional heating continues to be electrified and generates heat, causing the rice temperature to gradually reach its maximum. After heating ceases, while heat is lost with the steam, the high-temperature ceramic inner pot continues to provide a small amount of heat to the rice until the 20-minute insulation period ends. The insulation temperature difference under different water-to-rice ratios ranges from 0.19°C to 2.80°C, and the standard deviation of the insulation temperature is between 0.05 and 0.69. In contrast, the ohmic heating device, under the influence of the PID algorithm, is always in a dynamically input state according to the temperature change, meaning the internal temperature of the rice-water mixture fluctuates around 98°C. The insulation temperature difference under different water-to-rice ratios is between 0.57°C and 1.43°C, with a standard deviation of the insulation temperature ranging from 0.10 to 0.27. Both the temperature difference and standard deviation are slightly better than those of the traditional heating. The results show that the PID algorithm can effectively control the insulation temperature, and the insulation effect of the ohmic heating device is slightly better than that of the traditional heating.

Temperature uniformity measurement method

Temperature during the heating process is a critical factor affecting the hardness of food. To better understand the temperature variations at different locations during the rice cooking process, T-type armored thermocouples from a 5-channel temperature acquisition system (model WRCK-191, Shanghai Wolan Instrument Co., Ltd., Shanghai, China) were vertically inserted through the foam board and secured at the five points shown in Fig. 2. The tips of the thermocouples were used to monitor the temperature changes at five locations in the heating container in real time. To avoid the influence of the current on the thermocouples during ohmic heating, the T-type armored thermocouples were insulated with Teflon tubes (Zhou *et al.*, 2005). After the temperature data were collected by the microcontroller, they were sent to the PC in real time via serial communication and stored. Prior to temperature measurement, the thermocouples were calibrated using the water bath method at temperatures of 15, 25, 40, 50, 60, 75, and 95°C. The experiments showed that the temperature differences between different thermocouples were less than 0.25°C, making them suitable as temperature sensors for assessing uniformity.

Methods for measuring hardness of rice grains

Experiments were designed with a water-to-rice ratio of 1.50:1. One hundred grams of rice was evenly divided into three portions, and the rice was layered into three strata using cheesecloth for the ohmic heating experiment, with the ohmic heating conditions remaining constant. The power supply was halted at insulation times of 0, 5, 10, 15, and 20 minutes, respectively, to measure the changes in the hardness of the rice at different strata as a function of insulation time.

Four intact rice grains from the rice samples cooked under different conditions were taken and placed in a cross shape at the center of the texture analyzer's (TA-XTC, Shanghai Baosheng Industrial Development Co., Ltd., China) stage to test their hardness, as shown in Fig. 3. The test employed a TA/36 cylindrical probe, with a pre-test speed of 3 mm/s, test speed and post-test speed of 1 mm/s, a trigger force of 5 g, 70% deformation compression, and a 5-second compression interval (Miao *et al.*, 2016; Zhu *et al.*, 2010; Zhou *et al.*, 2017). The experiment was repeated six times with 24 rice grains.

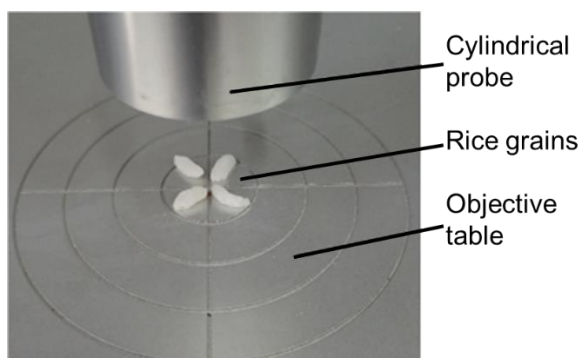


Fig. 3 - Rice grain placement diagram during rice hardness test

RESULTS AND ANALYSIS

Effect of heating method on hardness of rice grains

The hardness of rice at different sampling points in the traditional heating and ohmic heating equipment under different water-to-rice ratios is shown in Fig. 4. The results indicate that regardless of the heating method, the hardness at the same location decreases with an increase in the amount of water added. As can be seen from Fig. 4a, under the same water-to-rice ratio in traditional heating, there is a significant difference in hardness. The rice grains near the heating pot wall are harder, especially at point 4, which is harder than point 5, followed by point 1, while points 2 and 3 show little difference and have the lowest hardness. As shown in Fig. 4b, under the same water-to-rice ratio, the differences in hardness at various locations in ohmic heating are smaller. Table 5-5 indicates that under the same water-to-rice ratio, the standard deviation of the hardness of rice cooked in the traditional heating is much greater than that of ohmic heating, thus the hardness of rice cooked by ohmic heating is more uniform. The poor uniformity in hardness and the occurrence of scorching in rice cooked by the traditional heating (Fig. 5) are mainly due to the uneven heating of the rice during the cooking process in the traditional heating. Overheating leads to the loss of moisture in the rice, increasing its hardness and resulting in scorching. Therefore, it is necessary to study the temperature differences at different locations in the rice-water mixture during the rice cooking process.

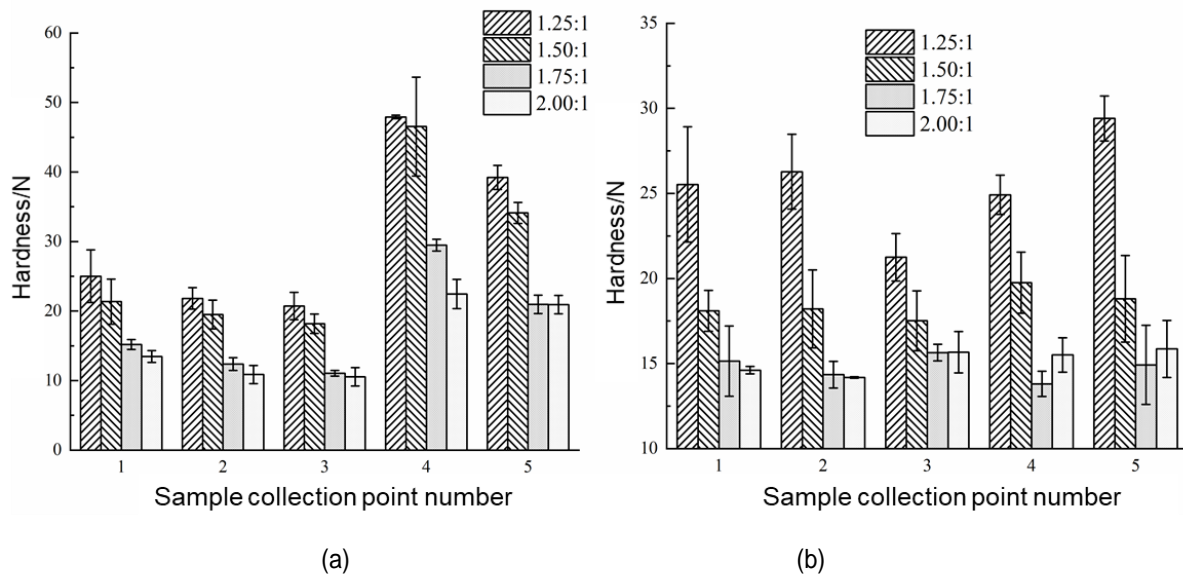


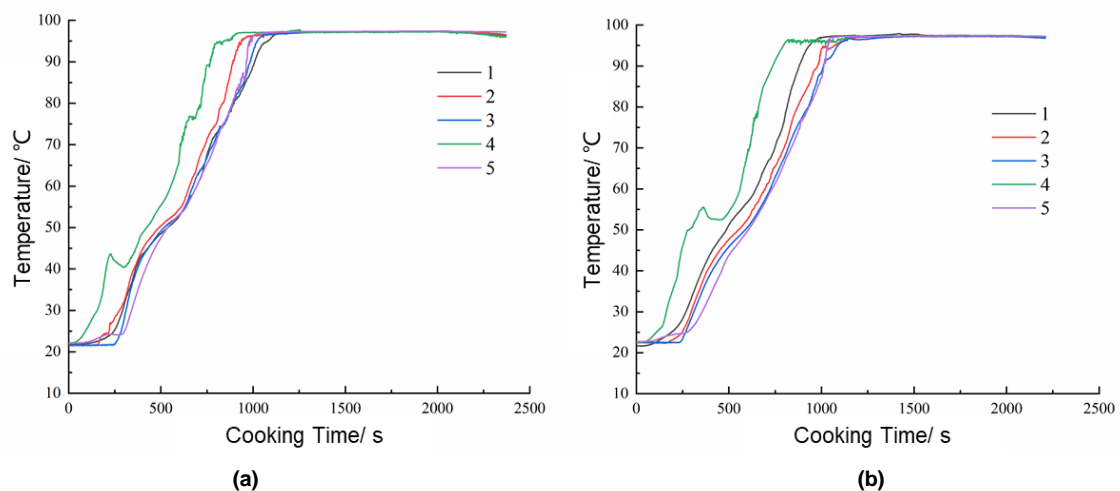
Fig. 4 - Rice hardness of rice at different sampling points in traditional heating (a) and Ohmic heating equipment (b) under different water-rice ratio



Fig. 5 - Rice shape at the bottom of rice cooked by traditional heating (a) and ohmic heating (b) with a water-to-rice ratio of 1.50:1

Effect of heating method on temperature uniformity

During the cooking of rice with the two heating methods, a 5-channel temperature acquisition system was used to measure the temperature changes at different locations of the rice-water mixture. The specific temperature curves and analysis are as shown in Fig. 6 and Fig. 7.



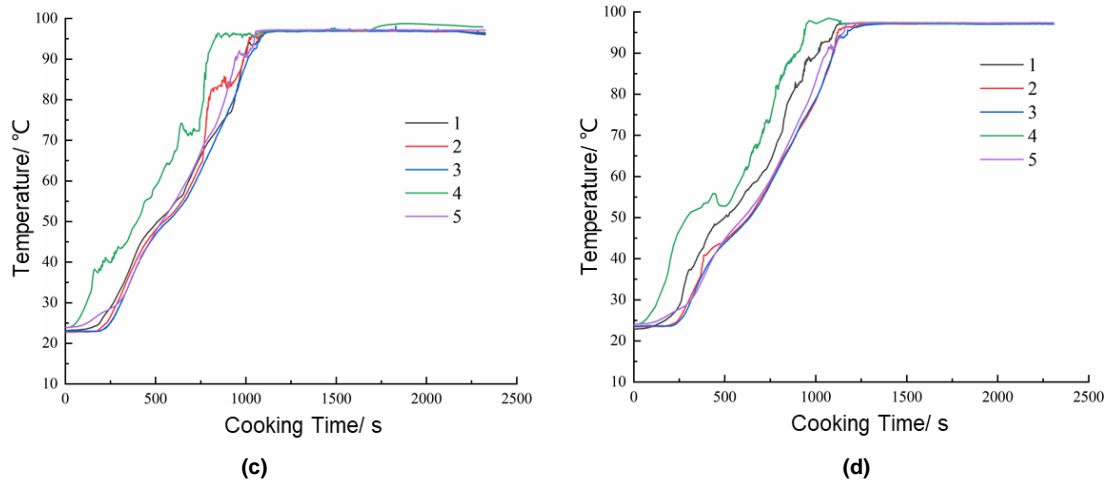


Fig. 6 - Traditional heating temperature curve of rice water mixture at the water-rice ratio of 1.25:1(a), 1.50:1(b), 1.75:1(c), 2.00:1(d)

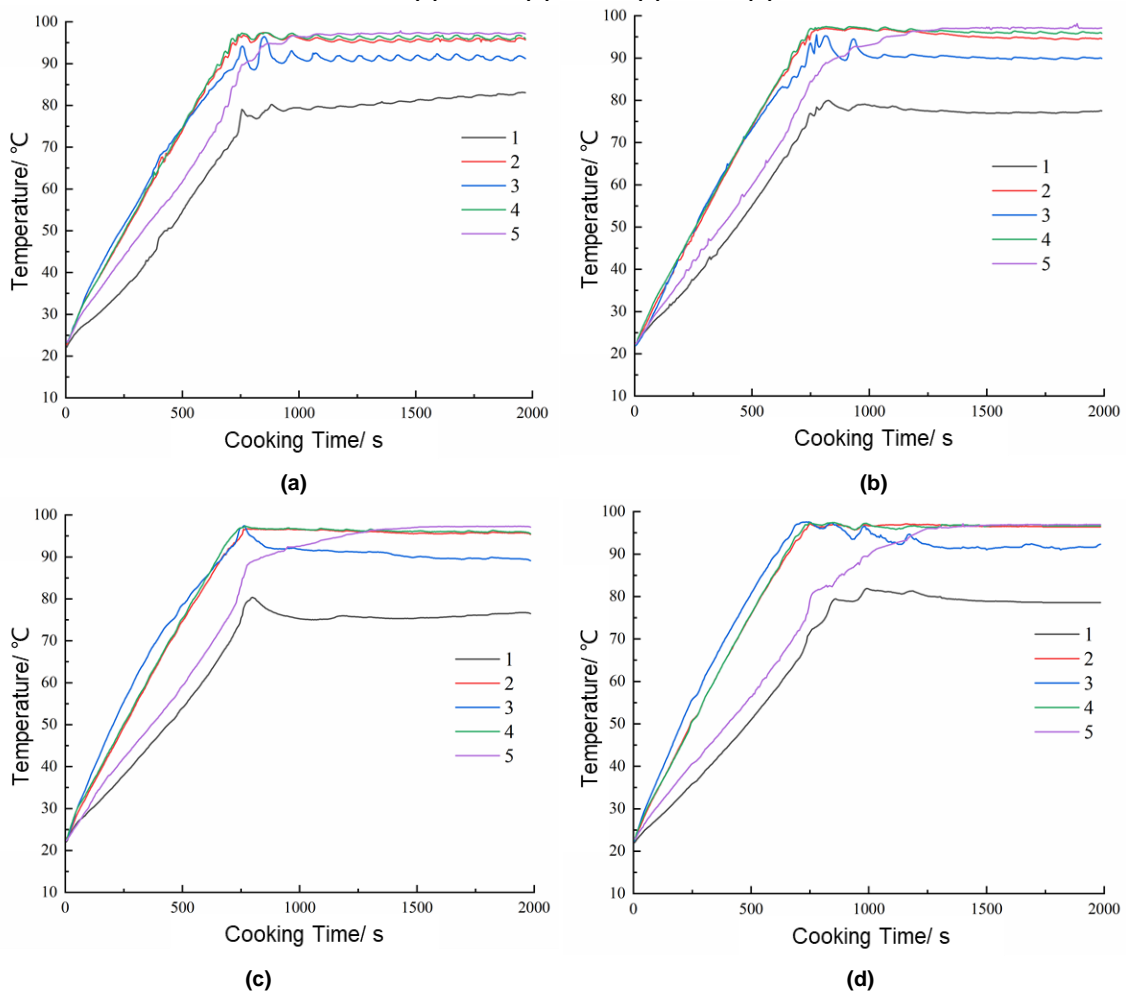


Fig. 7 - Ohmic heating temperature curve of rice water mixture at the water-rice ratio of 1.25:1(a), 1.50:1(b), 1.75:1(c), 2.00:1(d)

Fig. 6 indicates that the temperature at point 4 (the heating plate area) in the electric rice cooker is significantly higher than at other locations, and the temperature at point 1 (near the inner wall) is also slightly higher than at points 2, 3, and 5. Table 2 shows that the maximum temperature difference across the four water-to-rice ratios ranges from 21.42°C to 29.94°C. Comparing the hardness of rice cooked at different locations in the electric rice cooker reveals that the temperature near the heating inner wall is higher and the hardness of the rice is also higher. In particular, the hardness at point 4 is greater than at point 5, followed by point 1, while points 2 and 3 show little difference and have the lowest hardness. This suggests that hardness is related to temperature, meaning that the hardness of the finished rice is also higher where the temperature is higher, and scorching phenomena occur at locations with higher temperatures.

Table 2

The internal maximum temperature difference of the two heating methods at different water-rice ratios

Water-Rice Ratio (v/w)	Traditional heating (°C)	Ohmic heating (°C)
1.25:1	24.50	20.45
1.50:1	29.94	18.32
1.75:1	21.67	24.60
2.00:1	21.42	31.85

The temperature curves for ohmic heating, as shown in Fig. 7, clearly demonstrate that at the same height, the temperature at point 1 is significantly lower than at point 5, and the temperature at point 2 is slightly lower than at point 4. This indicates that the temperature closer to the container wall is lower. This can be attributed to the fact that point 1 is situated at the bottom corner, where heat dissipates in three directions, while point 5 is near the center of the container bottom where heat primarily dissipates in one direction towards the bottom. Point 2 is closer to the container wall than point 4. This is primarily because the heating method involves the food generating its own heat. The side of the rice near the wall loses more heat to the surroundings, hence the lower temperature. That is, the internal temperature of the rice-water mixture in ohmic heating is higher than the external temperature, which is quite different from the temperature distribution in traditional heating.

At different heights on the same cross-section (points 3, 4, and 5), during the heating phase, the temperature at point 3 is slightly higher than at point 4, while point 5 is significantly lower. This is due to point 3 initially being in the water layer, with rice settling at the bottom due to gravity. On the same cross-section, the material is the same, with the vertical section from top to bottom consisting of a water layer, a loose rice layer, and a compact rice layer. The conductive substances in the rice are released into the water, making the electrical conductivity of the water layer greater than that of the rice-water mixture layer. The bottom rice (point 5) is more compact, leading to a decrease in electrical conductivity from top to bottom, resulting in the water layer generating more heat and warming up more quickly. Point 5, however, has the lowest temperature due to its low electrical conductivity and heat dissipation.

During the insulation phase, the temperature at the top layer (point 3) gradually decreases after reaching the set insulation temperature and then remains stable. There are two main reasons: firstly, the gradual reduction of water in the upper layer, leading to increased porosity and a decrease in electrical conductivity, resulting in less heat generation. Secondly, the upper rice is in contact with air, leading to relatively more heat loss. The temperature at point 5 continues to increase during the early stages of the insulation phase, eventually surpassing points 3 and 4. The main reasons are that the bottom rice-water mixture always has more water, with a relatively higher electrical conductivity than points 3 and 4, continuously generating heat. Additionally, the contact surface temperature with the container gradually increases, meaning that point 5 has no heat loss, resulting in the highest temperature. With the increase in the water-to-rice ratio in ohmic heating, the maximum temperature difference increases from 18.32°C to 31.85°C.

From the temperature changes of the rice-water mixture at various locations during ohmic heating for rice cooking, it can be seen that although the temperature uniformity in ohmic heating is generally acceptable, even with certain temperature differences during the ohmic heating process, there is no occurrence of excessively high temperatures. As shown in Fig. 4b, the differences in hardness at various locations under the same water-to-rice ratio in ohmic heating are smaller, indicating that the internal hardness of the rice cooked by ohmic heating is more uniform. However, the temperature curve shows that during the heating phase, the upper water layer temperature is higher than the middle, and the bottom temperature is the lowest. Observations reveal that the upper rice absorbs water and expands more quickly, thus the uniformity of the hardness of rice cooked by ohmic heating is influenced not only by temperature but it may also be related to the ohmic heating process.

Influence of holding stage on hardness of different rice layers during ohmic heating

Experiments were designed with a water-to-rice ratio of 1.50:1. Rice was divided into three layers using cheesecloth for the experiment, and the hardness of the rice at different layers was measured as a function of the insulation time. As shown in Figure 8, the following results were obtained: after heating was completed without insulation, the hardness of the upper layer of rice was approximately 35.89±3.29 N, the middle layer was 49.15±2.84 N, and the lower layer was 63.48±10.22 N. There was a significant difference in hardness, with the upper layer of rice being softer.

As the insulation time increased, after 5 minutes of insulation, the moisture in the upper layer was gradually absorbed, and the hardness of the rice decreased to 17.18 ± 3.10 N. Subsequently, the hardness change was not significant, while the hardness of the middle and lower layers of rice decreased more, with the lower layer still having the highest hardness of 27.39 ± 2.32 N. At 10 minutes of insulation, the hardness of the middle layer of rice reached an equilibrium value (15.64 N to 18.76 N). The hardness of the bottom layer of rice continued to decrease but remained higher than that of the middle and upper layers. After 15 minutes of insulation, the hardness of the rice across all layers tended to stabilize, with no significant differences in hardness observed.

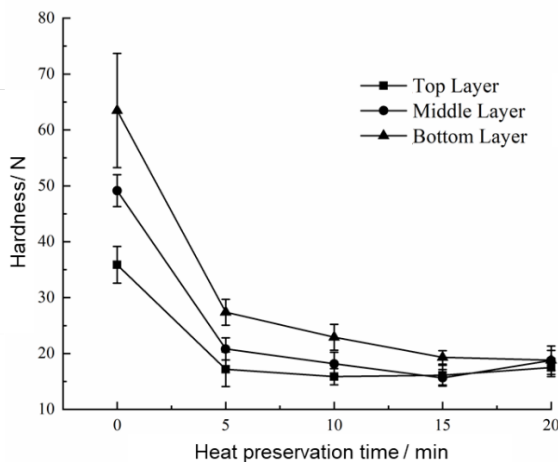


Fig. 8 - The hardness of different layers of rice varies with the holding time

This indicates that during the heating phase, the upper part of the rice, due to its higher temperature, absorbs water and expands, softening earlier. As the rice gradually absorbs water, the free liquid in the upper layer decreases, leading to the formation of gaps, which in turn causes a decrease in electrical conductivity and a reduction in heat generation. Meanwhile, the lower layer still contains liquid, and the rice continues to be heated and absorbs water, gradually softening until the rice cooking is completed.

Thus, it is demonstrated that although the upper layer of the rice-water mixture is at a higher temperature than the lower layer during the ohmic heating process, leading to a faster softening of the upper rice, the softening rate of the upper rice gradually decreases in the later stages of insulation due to the reduction of moisture. In contrast, the lower rice continues to soften, ultimately resulting in a more uniform hardness of the rice cooked by ohmic heating.

CONCLUSIONS

In this study, a self-made ohmic heating device was utilized to cook rice and compared with traditional heating devices in terms of the hardness of rice grains and temperature changes at various positions within the container. The results indicated that the ohmic heating device effectively controlled the temperature changes at each stage, with a maximum heating rate error of 1.24% and a linear fitting R^2 greater than 0.9997, thereby ensuring that the ohmic heating process was similar to traditional heating. As the water-to-rice ratio increased, the rice grains absorbed more water, leading to a decrease in the hardness of the cooked rice. Additionally, the heating method significantly affected the hardness and temperature uniformity of the rice. Specifically, compared to traditional cooking methods, although the temperature difference at different positions during the ohmic heating process reached $18.32\text{--}31.85^\circ\text{C}$, which was greater than the $21.42\text{--}29.94^\circ\text{C}$ observed in traditional heating, the hardness difference of rice at various positions was much smaller with ohmic heating. This was primarily attributed to the fact that as the insulation time was extended, the hardness difference between different layers of rice gradually decreased, ultimately resulting in a hardness range of 18–21 N for the upper, middle, and lower layers of rice, achieving a more uniform hardness. In contrast, the traditional heating method led to uneven hardness in the rice and the presence of burnt spots, indicating that ohmic heating could more effectively maintain the consistency of rice hardness.

However, ohmic heating requires the placement of electrodes on both sides of the food, through which an electric current passes to heat the food. Consequently, the food species to be heated must possess a sufficient amount of free ions, that is, a higher electrical conductivity. Additionally, the corrosion of electrode plates and the safety of equipment usage are urgent issues that need to be addressed before the large-scale application of ohmic heating.

REFERENCES

- [1] Dias-Martins, A. M., Cappato, L. P., Mattos, M. D., Rodrigues, F. N., Pacheco, S., & Caryalho, C. W. P. (2019). Impacts of ohmic heating on decorticated and whole pearl millet grains compared to open-pan cooking. *Journal of Cereal Science*, 85: 120-129. <https://doi.org/10.1016/j.jcs.2018.11.007>
- [2] Ding, X., Xiong, X., Li, S., Wang, S., & Li, X. (2020). Effects of ohmic heating on the cooking process energy consumption and quality of cooked rice (欧姆加热对米饭蒸煮过程能耗及其品质的影响). *Transactions of the Chinese Society of Agricultural Engineering*, 36(24): 310-318. <https://doi.org/10.11975/j.issn.1002-6819.2020.24.036>
- [3] Ding, X.T., Liu, J.K., Xiong, X.F., Wang, S.J., & Li, X.S. (2021). Influence of ohmic heating on the electrical conductivity, volume, and rice quality of each component of the water-rice mixture. *Innovative Food Science & Emerging Technologies*, 72: 102757. <https://doi.org/10.1016/j.ifset.2021.102757>
- [4] D'cruz, V., Chandran, M., Athmaselvi, K.A., Rawson, A., & Natarajan, V. (2023). Ohmic heating using electrolytes for paddy parboiling: A study on thermal profile, electrical conductivity, milling quality, and nutritional attributes. *Journal of Food Process Engineering*, 46(3): e14276. <https://doi.org/10.1111/jfpe.14276>
- [5] Gavahian, M., Chu, Y. H., & Farahnaky, A. (2019). Effects of ohmic and microwave cooking on textural softening and physical properties of rice. *Journal of Food Engineering*, 243: 114-124. <https://doi.org/10.1016/j.jfoodeng.2018.09.010>
- [6] Jittanit, W., Khuenpet, K., Kaewsri, P., Dumrongpongpaiboon, N., Hayamin, P., & Jantarangsri, K. (2017). Ohmic heating for cooking rice: Electrical conductivity measurements, textural quality determination and energy analysis. *Innovative Food Science & Emerging Technologies*, 42: 16-24. <https://doi.org/10.1016/j.ifset.2017.05.008>
- [7] Jun, S., Sastry, S., & Samaranayake, C. (2007). Migration of electrode components during ohmic heating of foods in retort pouches. *Innovative Food Science & Emerging Technologies*, 8(2): 237-243. <https://doi.org/10.1016/j.ifset.2007.01.001>
- [8] Kanjanapongkul, K. (2017). Rice cooking using ohmic heating: Determination of electrical conductivity, water diffusion and cooking energy. *Journal of Food Engineering*, 192: 1-10. <https://doi.org/10.1016/j.jfoodeng.2016.07.014>
- [9] Miao, W., Wang, L., Xu, X., & Pan, S. (2016). Evaluation of cooked rice texture using a novel sampling technique. *Measurement*, 89:21-27. <https://doi.org/10.1016/j.measurement.2016.03.072>
- [10] Rostamabadi, H., Yildirim-Yalcin, M., Demirkesen, I., Toker, O.S., Colussi, R., do Nascimento, L.A., Sahin, S., & Falsafi, S.R. (2024). Improving physicochemical and nutritional attributes of rice starch through green modification techniques. *Food Chemistry*, 458: 140212. <https://doi.org/10.1016/j.foodchem.2024.140212>
- [11] Thuengtung, S., & Ogawa, Y. (2020). Comparative study of conventional steam cooking and microwave cooking on cooked pigmented rice texture and their phenolic antioxidant. *Food Science & Nutrition*, 8(2): 965-972. <https://doi.org/10.1002/fsn3.1377>
- [12] Tumpunuvatr, T., & Jittanit, W. (2024). Application of ohmic heating in cooking mixtures of brown rice and whole grains: total phenolic content, antioxidant activities, vitamin B1, some minerals, and energy consumption. *International Journal of Food Properties*, 27(1): 431-447. <https://doi.org/10.1080/10942912.2024.2327334>
- [13] Verma, D.K., Tripathy, S., & Srivastav, P.P. (2024). Microwave heating in rice and its influence on quality and techno-functional parameters of rice compositional components. *Journal of Food Composition and Analysis*, 128: 106030. <https://doi.org/10.1016/j.jfca.2024.106030>
- [14] Zhu, B., Li, B., Zheng, X. D., Xu, B. L., Liang, S., Kuang, X., & Ma, M. H. (2010). Study on predictive models relating physicochemical properties to texture of cooked rice and the application in rice blends. *Journal of Texture Studies*, 41(2): 101-124. <https://doi.org/10.1111/j.1745-4603.2010.00216.x>
- [15] Zhou, Y., Yan, L., Yin, Y., & W, Y. (2005). Ohmic heating temperature field of liquid food materials with fruit granule (含水果颗粒液态食品物料通电加热温度场研究). *Transactions of the Chinese Society of Agricultural Engineering*, 21(05): 159-162.
- [16] Zhou, X., Wang, H., Zhou, Y., Zhang H., & Hu, Y. (2017). Influence of different cooking methods on eating quality of rice (不同烹煮方式对米饭食味品质的影响). *Food Science*, 38(11): 75-80. <https://doi.org/10.7506/spkx1002-6630-201711013>

RESEARCH ON THE CONTROL SYSTEM OF MOBILE STRAW COMPACTION MOLDING MACHINE BASED ON PSO-ELM-GPC MODEL

基于 PSO-ELM-GPC 模型的移动式秸秆致密成型机控制系统研究

Huiying CAI ^{*1)}; Yunzhi LI ¹⁾; Fangzhen LI ¹⁾

¹⁾ School of Computer Science and Technology, Shandong University of Finance and Economics, Jinan/ China

Tel: +86-18640598736; E-mail: caihuiying323@163.com

DOI: <https://doi.org/10.35633/inmateh-74-58>

Keywords: mobile straw compaction molding machine, biomass pellets, extreme learning machine, decoupling control

ABSTRACT

To address the issue of mutual influence and coupling between the main shaft speed and feeding amount of the mobile straw compaction molding machine, which is beneficial for the intelligent operation of the compaction molding, this paper designs a PSO-ELM-GPC control model. This model integrates Particle Swarm Optimization (PSO) algorithm, Extreme Learning Machine (ELM), and Generalized Predictive Control (GPC). It uses the ELM optimized by PSO to predict the output of the main shaft speed and feeding amount, and adjusts the input of the GPC controller based on the deviation weight adjustment unit. Field simulation experiments show that the maximum dynamic deviation of the speed is 1.72%, and the deviation from the target value is 1.52%. The maximum dynamic deviation of the feeding amount is 1.22%, and the deviation from the target value is 1.42%. The PSO-ELM-GPC model designed in this paper can promptly correct the uncertainties in speed and feeding amount control caused by disturbances.

摘要

为解决移动式秸秆致密成型机主轴转速与喂入量相互影响相互耦合的问题，以利于致密成型机智能化作业，本文设计了 PSO-ELM-GPC 控制模型，集粒子群优化、极限状态机、广义预测控制于一体，采用粒子群优化后的极限状态机对主轴转速与喂入量做出预测输出，依据偏差权重调整单元对 GPC 控制器输入量做出调节。场地模拟试验表明，转速最大动态偏差为 1.72%，与目标值的偏差为 1.52%；喂入量最大动态偏差为 1.22%，与目标值的偏差为 1.42%。本文设计的 PSO-ELM-GPC 模型可及时校正干扰引起的转速与喂入量控制引起的不确定问题。

INTRODUCTION

China has abundant straw resources, with a total straw volume reaching 8.56×10^8 tons in 2023. Biomass pellets made from corn straw extrusion are a low-carbon and clean energy source, which is of great significance for building an environmentally friendly society and promoting rural revitalization (Gheorghe et al., 2024). Mobile compaction molding machines integrate straw collection, crushing, dust removal, and pellet production in the field, which can greatly reduce production and labor costs, and have become an important way to promote the comprehensive utilization of straw. However, there is a coupling issue between the straw feeding amount and the main shaft speed during the operation of mobile straw compaction molding machines. The mismatch and lack of coordination between the feeding amount and main shaft speed affect the efficiency of the compaction molding machine in field operations.

To improve the work efficiency of mobile compaction molding machines, scholars at home and abroad have conducted extensive research. By analyzing the straw compacting process, the main factors affecting work efficiency are identified as straw feeding amount, main shaft speed, and straw moisture content. Rostami et al., (2022), studied the mutual influence of combine forward speed, reel index, field capacity, and pre harvest loss of a new designed combine harvester. Abbas, (2019), investigated the combine harvester speed, threshing cylinder speed and concave clearance on threshing losses and some related parameters during harvesting and suggested a strong correlation relationship between these parameters.

¹ Huiying Cai, Associate Prof.; Yunzhi Li, Associate Prof.

Choi *et al.*, (2018), fabricated and evaluated the performance of the grain flow sensor suitable to the mid-sized full-feed type combine for rice, soybean, and barley, indirectly indicated the relationship between grain flow rate and production efficiency. Chansrakoo *et al.*, (2018), investigated the influence of grain moisture content, rotor speed, and feed rate to the performance of a short axial-flow soybean unit. Birania *et al.* (2021) studied the relationship between feed rate and output of the small-scale pellet-making machine and specified that a satisfactory output could be obtained at a certain feed rate. Wang Wei *et al.*, (2024) established a work speed control model for the compaction molding machine based on a stable feeding amount on mobile compaction molding machines. Although the above research has made some progress, the coupling problem between feed rate and pressure roller spindle speed has not been considered. The coupling issue between the feeding amount and speed requires further in-depth research to further improve the work efficiency of the compaction molding machine.

Reasonable feeding amount and main shaft speed determine the work efficiency of the compaction molding machine. If the feeding amount is too large and the main shaft speed of the roller is low, the granulating device of the compaction molding machine is prone to clogging. If the feeding amount is too small and the main shaft speed is too high, the energy consumption is high, which affects the work efficiency of the compaction molding machine. To solve the coupling characteristics between feed rate and spindle speed and improve the efficiency of the molding machine, this paper takes the 560XC straw collection compaction molding machine designed by Liaoning Ningyue Agricultural Machinery Equipment Co., Ltd. as the research object. In view of the coupling problem between feeding amount and main shaft speed, a new decoupling control method is established based on POS and ELM, using GPC technology. The effectiveness and correctness of this algorithm are verified through field harvest tests and field trials.

MATERIALS AND METHODS

Structure and working principle of the control system

Overall structure

The control system of the mobile straw compaction molding machine consists of a hydraulic control device, a speed sensor, and a pellet molding device, as shown in Fig. 1. During operation, the mobile straw compaction molding machine is crushed by the front picking device, then thrown into the spiral conveyor, crushed for the second time, and conveyed through the feeding tube, and finally, the straw strands are squeezed and formed inside the forming device. The working process is shown in Fig. 2. The main shaft speed of the molding device is controlled by the hydraulic device, with the STM32F407 as the main microcontroller. The speed sensor gives a feedback to the main shaft speed. The driving speed determines the straw feeding amount.



Fig. 1 - Diagram of the straw compaction molding machine

1 – Hydraulic control device; 2 – Speed Sensor; 3 – Pellet forming device; 4 – Biomass pellet

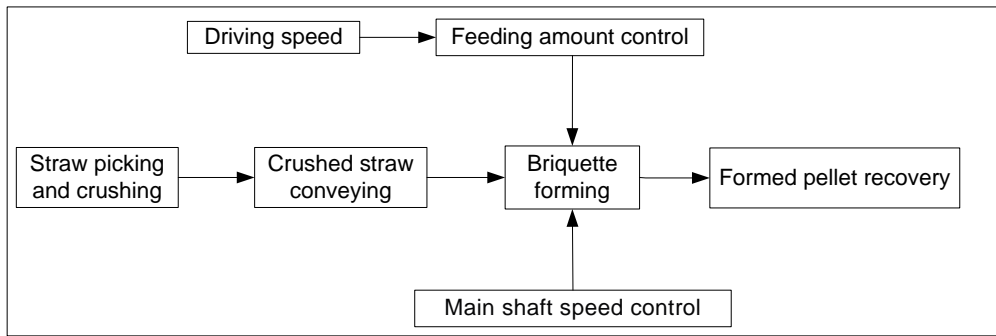


Fig. 2 - Flow diagram for straw pelletizing process of the molding machine

Composition and Working Principle of the Control System

The control system of the mobile straw compaction molding machine consists of an industrial computer, microcontroller control, driving hydraulic transmission, granulation main shaft hydraulic transmission, granulation main shaft speed sensor, and driving speed sensor. The principle of the control system is shown in Fig. 3. The microcontroller’s D/A output terminal 1 controls the driving hydraulic transmission mechanism, with the driving speed feedback by the driving speed sensor. D/A output terminal 2 controls the granulation main shaft hydraulic transmission mechanism, with the main shaft speed feedback by the granulation main shaft speed sensor. The industrial computer displays all control and monitoring information.

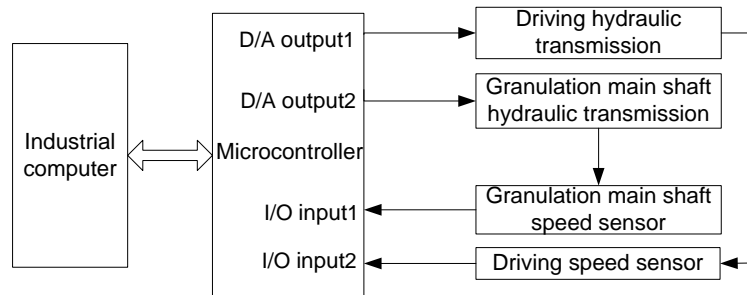


Fig. 3 - Structure of the molding machine control system

PSO-ELM Forecasting Method

ELM (Extreme Learning Machine)

ELM is intelligent algorithm that used widely in agriculture (John, 2021). It is a feedforward neural network with a single hidden layer, as shown in Fig. 4. During training, the input layer weight matrix and the hidden layer matrix of the ELM are randomly selected. By simply providing the number of neurons in the hidden layer, the global optimal target value can be obtained. It has the advantages of fast training speed and strong generalization ability.

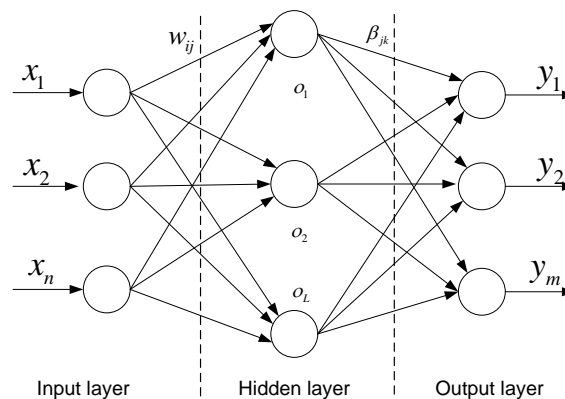


Fig. 4 - Structure of the molding machine control system

The input matrix of n neurons in the input layer is denoted as $X = [x_{i1}, x_{i2}, \dots, x_{in}]^T$. The output matrix is denoted as $Y = [y_{i1}, y_{i2}, \dots, y_{im}]^T$. The M model of the hidden layer activation function $g(x)$ is denoted as:

$$\sum_{i=1}^L \beta_{jk} g(\omega_{ij} \cdot x_{ij} + b_i) = y_i, j = 1, 2, \dots, N \tag{1}$$

where:

β_{jk} is the connection weight between the hidden layer and the output layer neurons; ω_{ij} is the connection weight between the input layer and the hidden layer neurons; b_i is the threshold of the i -th neuron in the hidden layer; y_i is the actual output value.

The hidden layer output matrix H can be expressed as:

$$H = \begin{pmatrix} g(w_1 \cdot x_1 + b_1) & \dots & g(w_L \cdot x_1 + b_L) \\ \vdots & \ddots & \vdots \\ g(w_1 \cdot x_N + b_1) & \dots & g(w_L \cdot x_N + b_L) \end{pmatrix} \quad (2)$$

where:

$w_i = [\omega_{i1}, \omega_{i2}, \dots, \omega_{iN}]^T$, represent the weight vector.

The network output is denoted as:

$$H\beta = Y' \quad (3)$$

The weight matrix denoted as $w = [\omega_1, \omega_2, \dots, \omega_N]^T$, threshold vector $b = [b_1, b_2, \dots, b_L]^T$. When $L = N$, the prediction result is independent of the size of w and b . The network output can approximate the training samples. That is:

$$\sum_{j=1}^N \|y_j - t_j\| = 0 \quad (4)$$

$$\min \|H\beta - T\| < \varepsilon \quad (5)$$

where:

T is the desired network output; ε is the network output error, when N is sufficiently large, $\varepsilon < 0$.

The connection weight value calculated by the minimum norm least squares criterion is:

$$\beta = H^+T \quad (6)$$

where:

H^+ is the pseudo-inverse of H .

Optimization for ELM by PSO

Due to the strong nonlinear characteristics between the main shaft speed and feeding amount of the compaction molding machine, the ELM is used for its simple structure, fast training speed, and strong nonlinear characterization ability to predict the main shaft speed and feeding amount. However, the random initialization of w and b in ELM can lead to the generation of useless neurons during operation, which affects the prediction accuracy. To reduce the error, this paper adopts the PSO (Particle Swarm Optimization) algorithm (Naveed, 2024; Chen, 2023) to optimize w and b , establishing a PSO-ELM (Swarm Optimization Algorithm-Extreme Learning Machine) forecasting model.

A population consisting of n particles is represented as $X = [x_1, x_2, \dots, x_n]$, which searches for the optimal value within this space. The parameters of particle i consists: velocity $V_i = [v_{i1}, v_{i2}, \dots, v_{iD}]^T$, position $X_i = [x_{i1}, x_{i2}, \dots, x_{iD}]^T$, individual extreme value $P_i = [P_{i1}, P_{i2}, \dots, P_{iD}]^T$; global extreme value $P_g = [P_{g1}, P_{g2}, \dots, P_{gD}]^T$.

During the iteration process, the particles continuously search for the optimal velocity and position based on P_i and P_g , updating as:

$$V_{id}^{k+1} = \omega V_{id}^k + c_1 r_1 (P_{id}^k - X_{id}^k) + c_2 r_2 (P_{gd}^k - X_{id}^k) \quad (7)$$

$$X_{id}^{k+1} = X_{id}^k + V_{id}^{k+1} \quad (8)$$

where:

w is the inertia weight; $i = 1, 2, \dots, n$; $d = 1, 2, \dots, D$; k is the current iteration number; c_1, c_2 are acceleration factors to be negative constants; r_1, r_2 are random numbers distributed between $[0, 1]$. The velocity and position are continuously updated according to the particle fitness value to obtain the optimal solution.

Using the PSO-ELM method to predict the main shaft speed and feeding amount of the compaction molding machine, the model's w and b are optimized as particles in PSO to improve their accuracy, as shown in the Fig. 5.

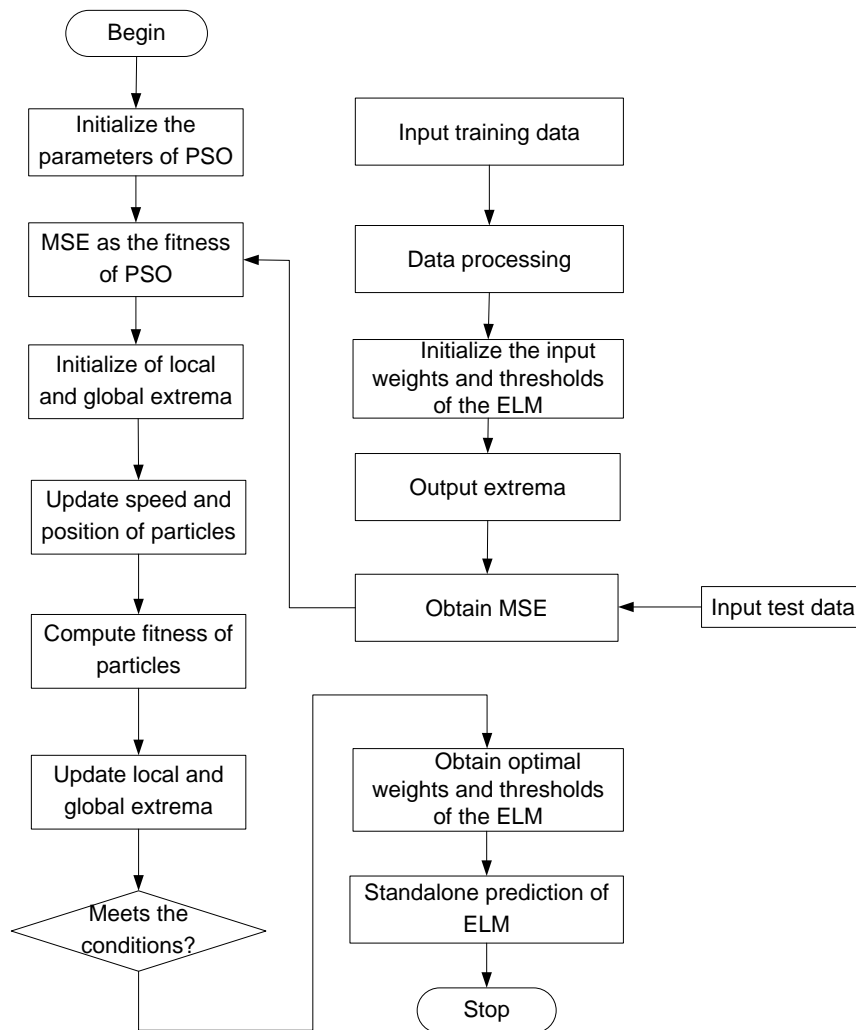


Fig. 5 - Flowchart of PSO-ELM model

RESULTS

Generalized Predictive Decoupling Control Based on PSO-ELM Model

Generalized Predictive Controller Design

The CARIMA (Controlled Autoregressive Integrated Moving Average) model (Ma, 2022) expression is denoted as:

$$A(z^{-1})y(k) = B(z^{-1})u(k-1) + \frac{C(z^{-1})\varepsilon(k)}{\Delta} \tag{9}$$

where:

$$A(z^{-1}) = 1 + a_1z^{-1} + a^2z^{-2} + \dots + a_nz^{-n}$$

$$B(z^{-1}) = b_0 + b_1z^{-1} + b^2z^{-2} + \dots + b_mz^{-m}$$

During field operations of the compaction molding machine, the environment is complex, which can lead to model mismatch and affect control accuracy. By introducing a performance function that minimizes multi-step prediction and control increments, a control sequence for future moments can be obtained, enhancing the system's stability. The performance index function is expressed as:

$$J_1(k) = E[\sum_{j=1}^P (y_M(k+j) - y_r(k+j))^2 + \sum_{j=0}^{L-1} \lambda (\Delta u(k+j))^2] \tag{10}$$

where: $E[\cdot]$ is the variance function; L is the control horizon; λ is the control increment weighting coefficient; $y_M(k+j)$ is the predicted value at time $k+j$; P is the control time domain; $\Delta u(k+j)$ is the control change between adjacent sampling times.

After introducing and solving the Diophantine equation (Fernandez B., 2018), the predicted model's output value at time $k + j$ is obtained as:

$$Y = G\Delta U + H\Delta\tilde{u} + F\tilde{y}(k) \tag{11}$$

where:

$$Y = [y(k+1) \cdots y(k+N)]^T$$

$$\Delta U = [\Delta u(k) \cdots \Delta u(k+M-1)]^T$$

$$\Delta u = [\Delta u(k-1) \cdots \Delta u(k-n_b)]^T$$

$$\tilde{y}(k) = [y(k) \cdots y(k-n_a)]^T$$

$$G = \begin{bmatrix} g_1 & & 0 \\ \vdots & \ddots & \\ g_M & \cdots & g_1 \\ \vdots & \ddots & \vdots \\ g_N & \cdots & g_{N-M+1} \end{bmatrix}$$

$$H = \begin{bmatrix} g_{1,1} & g_{1,2} & \cdots & g_{1,n_b} \\ g_{2,2} & g_{2,3} & \cdots & g_{2,n_b+1} \\ \vdots & & \ddots & \vdots \\ g_{N,N} & \cdots & \cdots & g_{N,N+n_b-1} \end{bmatrix}$$

$$F = \begin{bmatrix} f_{1,0} & f_{1,2} & \cdots & f_{1,n_a} \\ f_{2,0} & \ddots & & \vdots \\ \vdots & & \ddots & \vdots \\ f_{N,0} & \cdots & \cdots & f_{N,n_a} \end{bmatrix}$$

To ensure a smooth transition of the compaction molding machine's main shaft speed to the set value w , the reference trajectory is in the form of a first-order smoothing model, which is expressed as:

$$\begin{cases} y_r(t) = y(t) \\ y_r(t+j) = ay_r(t+j-1) + (1-a)w \end{cases} \tag{12}$$

where:

a is the softening coefficient, $a \in [0, 1]$; $y_r(t)$ is the desired output value of the speed; $y(t)$ is the actual output value of the speed; w is the set value of the speed.

Substituting Equation (11) into Equation (10), and taking the derivative of the performance index function J with respect to t , the optimal solution expression for $J_1(k)$ can be obtained as:

$$u(t) = u(t-1) + (G^T G + \lambda I)^{-1} G^T (W - H\Delta u - F y(k)) \tag{13}$$

where: I and W are the identity matrix with different size.

Generalized Predictive Control of the Molding Machine Based on the PSO-ELM Model

The process control structure diagram of predictive decoupling control method based on the PSO-ELM model for the main shaft speed and feeding amount of the molding machine is shown in Fig. 6.

Monitoring the output values of the main shaft speed and the feeding amount entering the compaction molding machine, denoted as $y = \{y_1, y_2\}$, calculate the deviation $e = \{e_1, e_2\}$ of the output values from the reference values $\omega = \{\omega_1, \omega_2\}$, and use this deviation as the input of the decoupling controller. The decoupling controller adaptively adjusts its strategy based on the deviation to improve decoupling performance. After optimization by the controller, the control amount $u = \{u_1, u_2\}$ adjusts the main shaft speed and feeding amount, thereby improving the production efficiency of the biomass pellets produced by the compaction molding machine.

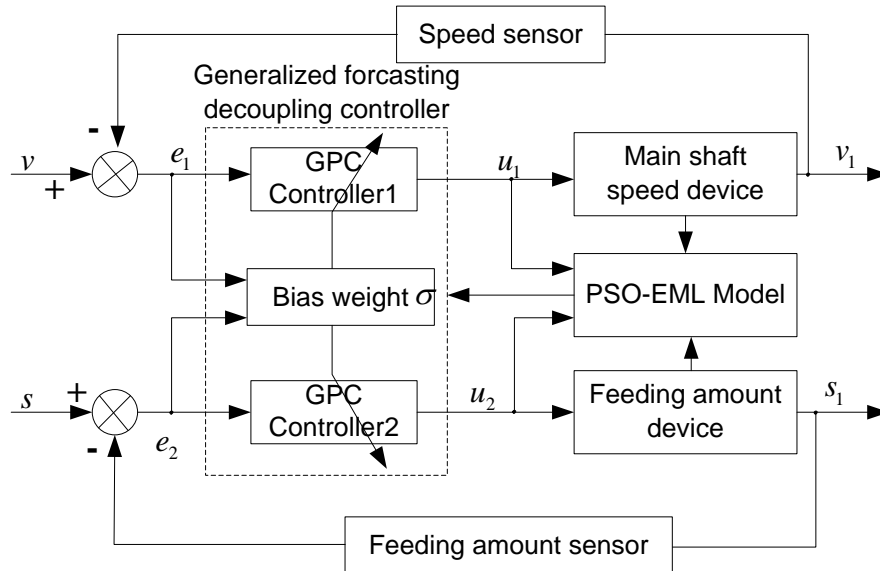


Fig. 6 - Process control structure of the molding machine based on the PSO-ELM model

In the decoupling controller, the deviation weight is decoupled based on the deviation between the predicted output value and the reference trajectory. When a certain deviation occurs between the predicted output value y of the main shaft speed loop and the reference value ω , the deviation weight $\alpha_i(k+t)$ of the feeding amount loop is adjusted to increase the output error weight of the feed rate loop, thereby increasing the control increment at the next moment and reducing the impact of the output change of the main shaft speed loop on the feeding amount loop, achieving the purpose of suppressing loop coupling. Similarly, the coupling effect of feed rate on speed can be eliminated according to this principle. The calculation formula for $\alpha_i(k+t)$ is expressed as:

$$\alpha_i(k+t) = \alpha_i(0) + \sum_{p=1}^2 \theta_{ip} \left[\hat{y}_p(k+p) - \omega_p(k+t) \right]^2 \tag{14}$$

where: $\alpha_i(0)$ is the initial value of $\alpha_i(k+t)$; θ_{ip} is the amplification coefficient.

Transfer function models for speed control and feed rate control are established through experiments. They are expressed as equation (15) and equation (16) respectively.

$$G_1(s) = \frac{8.34 \times 10^{-3}}{\left(\frac{s^2}{495.7^2} + \frac{3.6}{495.7} s + 1 \right)} \tag{15}$$

$$G_2(s) = \frac{21932.4}{s(0.0034s+1) \left(\frac{s^2}{5.4^2} + \frac{4}{27} s + 1 \right)} \tag{16}$$

Experiments and analysis

To verify the effectiveness of the generalized predictive decoupling control system proposed in this paper, a simulation harvest test was conducted on March 20, 2024, at Liaoning Ningyue Agricultural Machinery Equipment Co., Ltd. in Heishan County, Liaoning Province.

A 560XC straw compaction molding machine was selected for the experiments. A rectangular straw bed measuring 60 meters in length and 2 meters in width was laid out in the experiment site, as shown in Fig.7.

The main test equipment included an industrial computer (ZPC150-T112 model), a feed rate sensor (NY-DF01), and a speed sensor (SC12-20K). The industrial computer processor was Intel(R) Core(TM) i5-3337U CPU@1.8Hz, with a 64-bit Windows 10 operating system and 16GB of memory.



Fig. 7 - Granulation experiment

The performance comparison of the field granulation experiment controllers is shown in Table 1. In the PSO-ELM-GPC controller, the adjustment time of the speed of the main shaft is shortened by 8.1% and 32.7% compared to the GPC and PID controllers (Savaniu *et al.*, 2023; Hajjahmadi *et al.*, 2024), with the smallest speed overshoot of 8.42%. The adjustment time of the feed rate is shortened by 19.9% and 34.7% compared to the GPC and PID controllers, with the smallest feed rate overshoot of 8.97%.

The speed error curve and the feed rate error change curve are shown in Fig. 8 and Fig. 9, respectively. Under the control of the PSO-ELM-GPC model, the maximum dynamic deviation of the speed is 1.72%, with a deviation of 1.52% from the target value; the maximum dynamic deviation of the feed rate is 1.22%, with a deviation of 1.42% from the target value.

Table 1

Controller performance parameters				
Control algorithm	main shaft speed		feeding amount	
	Regulation	Overshoot	Regulation	Overshoot
	[s]	[%]	[s]	[%]
PID	11.62	10.35	14.34	12.46
GPC	8.51	9.32	11.69	10.82
PSO-ELM-GPC	7.82	8.42	9.36	8.97

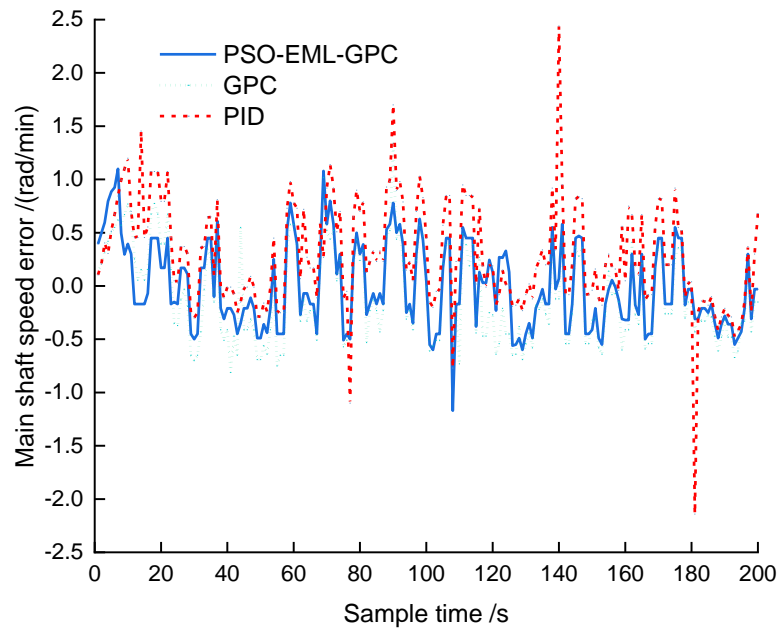


Fig. 8 - Error curve of main shaft speed

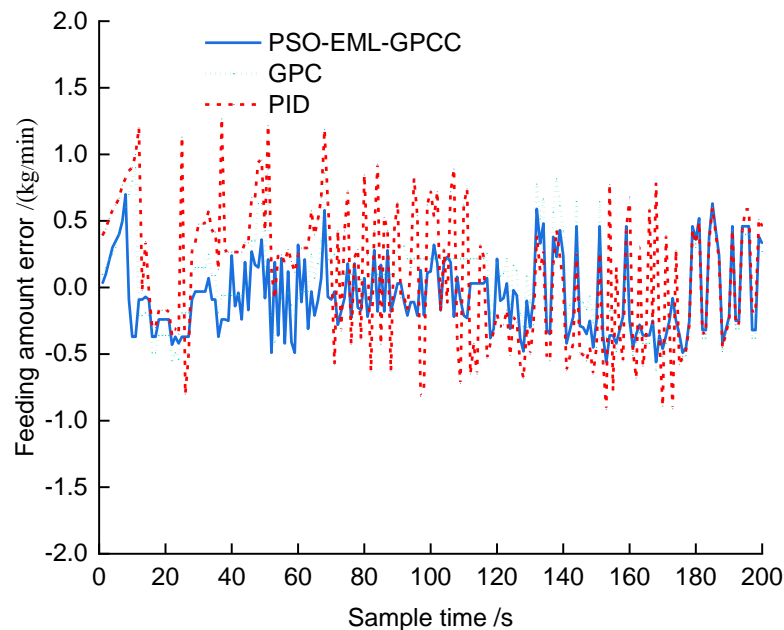


Fig. 9 - Error curve of feeding amount

CONCLUSIONS

(1) A PSO-ELM-GPC decoupling controller model was designed to eliminate the mutual influence between the main shaft speed and feeding amount of the mobile densification molding machine.

(2) In the PSO-ELM-GPC decoupling controller model, PSO was used to optimize the parameters in ELM, which predicts the main shaft speed and feeding amount. The input deviation weight adjustment unit adjusts the input of the GPC controller.

(3) Field simulation experiments showed that the maximum dynamic deviation of the speed was 1.72%, with a deviation of 1.52% from the target value; the maximum dynamic deviation of the feed rate was 1.22%, with a deviation of 1.42% from the target value. The PSO-ELM-GPC model designed in this paper can meet the on-site operation requirements of the mobile straw compaction molding machine.

ACKNOWLEDGEMENT

The results of the work are obtained using the straw granulator provided by Liaoning Ningyue Agricultural Machinery Equipment Co., Ltd.

REFERENCES

- [1] Abbas, A. A. (2019). The effect of combine harvester speed, threshing cylinder speed and concave clearance on threshing losses of rice crop. *Journal of Engineering and Applied Sciences*. <http://10.36478/jeasci.2019.9959.9965>
- [2] Abdeen, M. A., Xie, G., Salem, A. E., Fu, J., & Zhang, G. (2022). Longitudinal axial flow rice thresher feeding rate monitoring based on force sensing resistors. *Scientific Reports*, 12(1), 1369. <https://www.nature.com/articles/s41598-021-04675-w>
- [3] Birania, S., Yadvika, Garg, M. K., Gupta, R., Kumar, R., & Kumar, N. (2021). Development and performance evaluation of biomass pellet machine for on-farm sustainable management and valorization of paddy straw. *Environmental Engineering and Management Journal*, 20(12), 2013-2023. <http://10.30638/eemj.2021.187>
- [4] Chansrakoo, W., Chuan-Udom, S. (2018). Factors of operation affecting performance of a short axial-flow soybean threshing unit. *Engineering Journal*, 22(4), 109-120. <http://10.4186/ej.2018.22.4.109>
- [5] Chen, L. I. (2023). Path planning of fruit and vegetable picking robots based on improved A* algorithm and particle swarm optimization algorithm. *INMATEH-Agricultural Engineering*, 71(3). <https://doi-org-s.libyc.nudt.edu.cn:443/10.35633/inmateh-71-41>
- [6] Choi, M. C., Lee, K. H., Jang, B. E., Kim, Y. J., & Kim, S. K. (2018). Grain flow rate sensing for a 55 kW full-feed type multi-purpose combine. *International Journal of Agricultural and Biological Engineering*, 11(5), 206-210. <http://10.25165/ijabe.20181105.2686>
- [7] Fernandez, B., Herrera, P. J., & Cerrada, J. A. (2018). Self-tuning regulator for a tractor with varying speed and hitch forces. *Computers and Electronics in agriculture*, 145, 282-288. <https://doi.org/10.1016/j.compag.2017.12.027>
- [8] Gheorghe, D., & Neacsu, A. (2024). The influence of additives upon the energetic parameters and physicochemical properties of environmentally friendly biomass pellets. *Journal of the Mexican Chemical Society*, 438-454. <https://doi.org/10.29356/jmcs.v68i3.2032>
- [9] Hajiahmadi, F., Jafari, M., & Reyhanoglu, M. (2024). Machine learning-based control of autonomous vehicles for solar panel cleaning systems in agricultural Solar Farms. *AgriEngineering*, 6(2), 1417-1435. <https://doi.org/10.3390/agriengineering6020081>
- [10] John, S., & Rose, A. L. (2021). Machine learning techniques in plant disease detection and classification-a state of the art. *INMATEH-Agricultural Engineering*, 65(3), 362-372. <https://doi.org/10.35633/inmateh-65-38>
- [11] Ma, C., Li, X., Xiang, G., & Dian, S. (2022). A TS Fuzzy quaternion-value neural network-based data-driven generalized predictive control scheme for mecanum mobile robot. *Processes*, 10(10), 1964. <https://doi.org/10.3390/pr10101964>
- [12] Naveed, M. H., Gul, J., Khan, M. N. A., Naqvi, S. R., Štěpanec, L., & Ali, I. (2024). Torrefied biomass quality prediction and optimization using machine learning algorithms. *Chemical Engineering Journal Advances*, 19, 100620. <https://doi.org/10.1016/j.cej.2024.100620>
- [13] Rostami, M. A., Shaker, M., Bakhtiari, M. R. (2022). Economic and technical feasibility of replacing conventional combines with a new straw crusher combine. *Agricultural Engineering International: CIGR Journal*, 24(3), 93-102.
- [14] Savaniu, I.M., Chiriță, A.P., Popovici, I.A., Tonciu, O., Culcea, M., Neagu, A., & Stefan, V. (2023). Optimizing and integrating electromechanical actuators in agricultural excavator booms for enhanced efficiency and battery longevity. *INMATEH - Agricultural Engineering*, 71(3), 335-344. <http://10.35633/inmateh-71-29>
- [15] Wang, W., Ji, D., Gong, Y. J., Bai, X. W., Li, N., & Li H. Y. (2024). Spindle speed control method of straw picking compactor (基于 GPC-ILC 的秸秆捡拾致密成型机主轴转速控制方法研究). *Transactions of the Chinese Society of Agricultural Machinery*, 55(4), 83-90. <http://10.6041/j.issn.1000-1298.2024.04.008>

OPTIMIZATION STUDY OF STRUCTURE AND OPERATING PARAMETERS OF DOUBLE-LAYER CENTRIFUGAL ATOMIZING NOZZLE BASED ON RESPONSE SURFACE METHODOLOGY

基于响应面法的双层离心式雾化喷头结构与工作参数的优化研究

Nan ZHOU, Yubin LAN^{*)}, Yu YAN, Lilian LIU

¹⁾ College of Agricultural Engineering and Food Science, Shandong University of Technology, Zibo / China;

²⁾ Research of Institute of Ecological Unmanned Farm, Shandong University of Technology, Zibo / China

Tel: +86 13922707507; E-mail: ylan@sdu.edu.cn

Corresponding author: Yubin LAN

DOI: <https://doi.org/10.35633/inmateh-74-59>

Keywords: Plant protection drone, Centrifugal atomizing nozzle, Response surface method, Structural optimization, Atomization performance

ABSTRACT

In view of the problems such as the lack of comprehensive analysis of working parameters and structural parameters and the imperfection of the atomization model in existing studies, a dual-layer centrifugal atomizing nozzle was designed to optimize the droplet volume median diameter and droplet spectrum width. The key influencing factors, including atomizing disc speed, flow rate, and the number of atomizing teeth, were selected for optimization. Both single-factor and three-factor, three-level response surface optimization experiments were conducted to determine the optimal number of atomizing teeth for different combinations of disc speed and flow rate. Furthermore, with the spray width as the objective function, a Box-Behnken experimental design was employed to investigate the effects of atomizing disc speed, flow rate, and spray height on the atomization performance of the centrifugal nozzle. A multiple quadratic response surface regression model for spray width was also developed. The results indicated that both individual factors and their interactions had a significant impact on the droplet volume median diameter, droplet spectrum width, and spray width. The optimized number of atomizing teeth was found to be 50, and the adjusted R-squared values for the above three regression equations were 0.9977, 0.9893, and 0.9485, respectively. This study provides a theoretical basis for optimizing the nozzle structure and improving the quality of plant protection operations.

摘要

针对现有研究中喷头工作参数和结构参数综合分析不足、雾化模型不完善的问题，本文设计了一种基于响应面法的双层离心式雾化喷头，旨在优化雾滴体积中径和雾滴谱宽度。研究选取雾化盘转速、流量和雾化齿个数作为关键影响因素，通过单因素和三因素三水平响应面优化试验，得到了不同转速和流量组合下雾化齿的最佳数量。进一步，以优化后的喷幅为目标函数，采用 Box-Behnken 试验分析了雾化盘转速、流量和喷雾高度对离心喷头雾化性能的影响，并构建了喷幅的多元二次响应面回归模型。结果表明，单因素及各因素间交互作用对雾滴体积中径、雾滴谱宽度和喷幅均具有显著影响。优化后的雾化齿数量为 50，雾滴体积中径、雾滴谱宽度、喷幅的校正决定系数分别为 0.9977、0.9893、0.9485，表明模型拟合效果良好。本研究为喷头结构优化和提升航空植保作业质量提供了理论依据和指导。

INTRODUCTION

Throughout the growth cycle of crops, chemical control has become the primary choice for controlling diseases, pests and weeds in China due to its high efficiency and rapidity (Zhang et al., 2014). As a large agricultural country, China has problems such as excessive pesticide application and low pesticide utilization, leading to environmental pollution and agricultural product quality and safety problems (Li et al., 2012). With the development of agricultural science and technology, plant protection UAVs (Unmanned Aerial Vehicle) are more and more widely used in crop application by virtue of their advantages such as high efficiency, high speed and excellent application effect (Lan et al., 2018; Lan et al., 2019). As the core component of the drone spraying system, the plant protection spraying nozzle plays a crucial role in determining the quality of spraying (Deng et al., 2020). Among them, the rotary disk centrifugal atomizing nozzle belongs to the ultra-low-volume atomizing nozzle, such nozzle atomization uniformity is better, can be adjusted through the rotational speed

and flow rate to control the liquid particle size. In recent years, the application in the field of plant protection has become widespread (Chen *et al.*, 2018).

In recent years, in order to enhance the uniformity of liquid spraying and improve the atomization performance of droplets, many scholars at home and abroad have carried out a large number of experimental studies on centrifugal atomizing spray nozzles. Liu *et al.*, (2012), used a high-speed camera to observe the specific forms of three atomization modes, namely droplet atomization, ribbon atomization, and film atomization, and found that they can transform into each other under different flow rates and atomizing disk speed. Ru *et al.*, (2012), designed a remotely controllable centrifugal atomized spraying system with the help of a German multi-purpose unmanned helicopter, and investigated the effects of the atomizing disk speed and flow rate on the spray nozzle atomization performance. Yang *et al.*, (2023), in order to analyze the impact of flow rate changes in the application system on the spraying effect, designed a three-layer intelligent centrifugal variable spray nozzle that can satisfy four levels of flow rate adjustments, realizing the variable and controllable spraying of the medicinal liquid. Zhou *et al.*, (2016), studied the influence of the diameter, number of teeth and groove shape of the rotary cup on the atomization performance of the nozzle and optimized the structural parameters of the rotary cup through the analysis of the atomization mechanism of the rotary cup centrifugal nozzle. Most of these studies are aimed at optimizing the operating parameters of existing centrifugal atomizing spray nozzles, or improving the structure of centrifugal atomizing spray nozzles under fixed operating parameters. However, the structural optimization of centrifugal atomizing spray nozzles and atomization performance under different operating parameters have not been systematically studied.

In order to realize the comprehensive matching of nozzle structure and working parameters and improve the atomization performance, this research designs a double-layer centrifugal atomizing nozzle, which completes the secondary atomization of the liquid to obtain finer droplets. Design and construction of variable spray test system, combined with one-factor test and Box-Behnken response surface method, systematically studied the impact of different atomizing disc structure and working parameters on the atomization effect of the spray nozzle, and analyzed and came up with the best combination of parameters for atomization effect, aiming at realizing the “optimal bioparticle size”, and providing theoretical support for the application of plant protection drone spraying technology. The aim is to realize the “optimal biological particle size” and provide theoretical support for the application of plant protection UAV drug application technology.

MATERIALS AND METHODS

Double-layer centrifugal atomizing nozzle structure design and working principle

In this study, a centrifugal atomizing nozzle with a double-layer atomizing disc was designed. Compared with the traditional rotary disc centrifugal atomizing nozzle, a lower atomizing disc with atomizing teeth was coaxially added below the original atomizing disc, and both of them realized the secondary atomization of the liquid through the coaxial reversal movement of the transmission part.

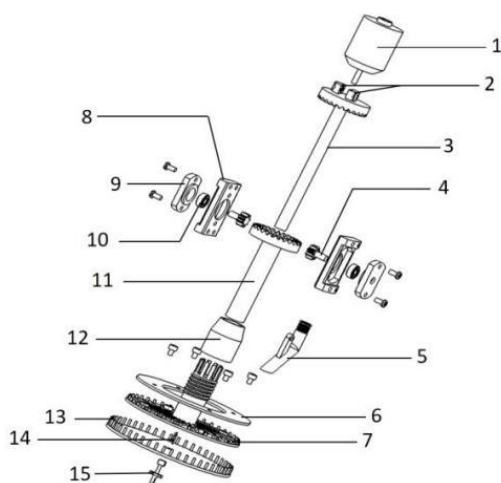


Fig. 1 – Structure diagram of double-layer centrifugal atomizing nozzle



Fig. 2 – Physical picture of double-layer centrifugal atomizing nozzle

1 - Motor; 2 - Motor connector; 3 - Input end gear; 4 - Cylindrical gear; 5 - Liquid inlet pipe; 6 - Upper atomization plate cover; 7 - Upper atomization plate; 8 - Support frame; 9 - Bearing end cover; 10 - Bearing; 11 - Output end gear; 12 - Locking ring; 13 - Lower atomizing disc; 14 - Spring; 15 - Remove parts

As shown in Fig. 1, the nozzle is mainly composed of DC motor, transmission part (end face gear and cylindrical gear), liquid inlet pipe, upper atomizing disk, lower atomizing disk, quick release parts and other structures. The motor is connected to the power supply, high-speed rotation, driven by the transmission structure consisting of end face gear and cylindrical gear. When the motor rotates clockwise, through the connection of the quick-release components, the input face gear drives the upper atomizing disk to rotate clockwise, while the output face gear drives the lower atomizing disk to rotate counterclockwise, thus realizing the coaxial reverse rotation of the upper and lower atomizing disks. The liquid enters the cavity of the upper atomizing disk through the inlet pipe. The surface of the upper disk is equipped with diversion grooves, which guide the liquid flow. As the upper atomizing disk rotates at high speed, the centrifugal force propels the liquid along the grooves. At the edge of the disk, the liquid comes into contact with the lower atomizing disk and collides with the atomizing teeth. This collision generates intense shearing forces, breaking the liquid into smaller droplets (Gong *et al.*, 2019). The picture of the double-layer centrifugal atomizing nozzle is shown in Fig. 2.

Test Methods

Control program and materials

Variable pressure-regulated, flow-regulated and liquid concentration-regulated are the three most widely used variable application methods in agricultural production (Feng *et al.*, 2021), in which the flow-regulated type outperforms the other two in terms of transient response. For the purpose of effectively controlling the impact of specific factors on the atomization performance of spray nozzles, a variable spraying system with adjustable flow rate and speed is built in this research, see Fig. 3.

Among them, the speed control system is mainly composed of PWM signal generator, DC power supply, motor drive module and brushless motor. The PWM signal generator generates different output control signals by constantly adjusting the width of each pulse signal, thus realizing the precise control of the voltage of the nozzle motor and the adjustable control of the rotational speed. Liquid part mainly includes sprayer tank, pump, one-way throttle valve, flowmeter and hose, etc. By adjusting the valve handle of the one-way throttle valve, the circulation area of the liquid circuit is controlled, so as to control the flow of the whole liquid circuit. The real-time flow rate of the liquid circuit is presented via the digital display of the flowmeter.

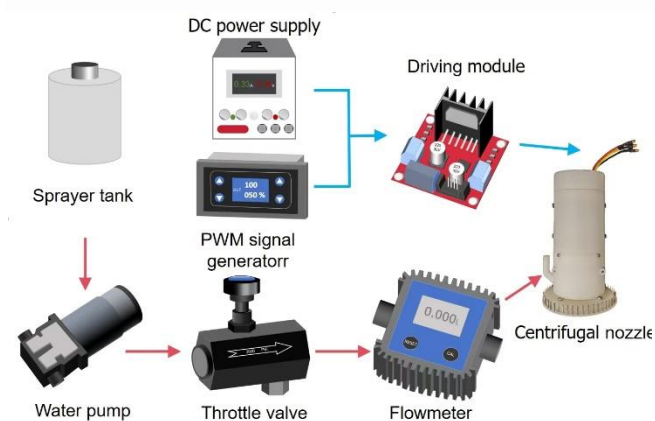


Fig. 3 – Diagram of variable spray system

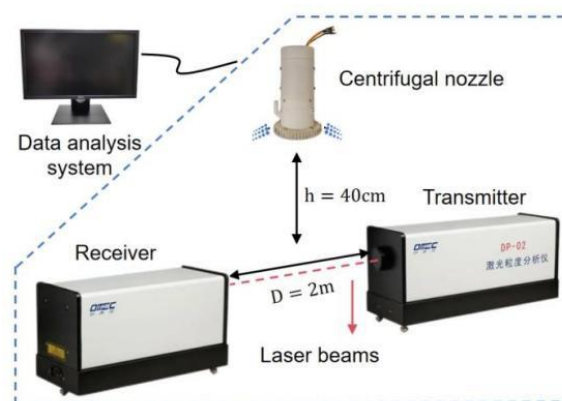


Fig. 4 – Droplet size test system

Droplet size test system

The droplet size testing system mainly consists of variable spray system, aluminum alloy support frame, laser particle size analyzer and data analysis system, in which the sending port of the laser particle size analyzer maintains a horizontal distance of 2m from the receiving port. As shown in Fig. 4, the centrifugal nozzle was installed vertically downward on the support frame, and the vertical distance from the laser beam was maintained at 40 cm. Its central axis was kept perpendicular to the laser beam of the laser particle sizer and the ground to ensure that the laser beam passed through the spray at the maximum cross-section of the spray, and the centrifugal nozzle spray was stabilized, which in turn was used to measure the particle size of the medicinal liquid.

Spray width test system

The spray nozzle comprehensive performance precision test device includes three parts: spraying system, droplet collection tank and control system.

As shown in Fig. 5, the spray nozzle is installed vertically downward, and after starting the power supply, the spraying system is first opened to wet the droplet collection tank. When it is completely wet, the deflector plate is put down to keep the centrifugal spray nozzle spraying steadily. In the test bench, if one of the collected liquids reaches 90% of the capacity of the cylinder, the spraying system is immediately closed, and the deflector plate is put away. The spray volume collected in each cylinder is measured and the spray width of the double-layer centrifugal atomizing nozzle is obtained through the output of the control system.

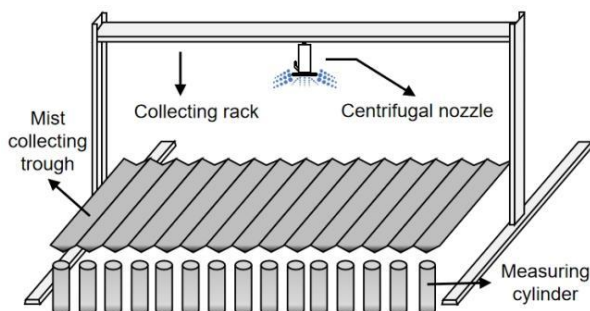


Fig. 5 – Sprinkler comprehensive performance precision test device

Atomization performance evaluation index

In the actual farmland operation, by selecting the appropriate range of liquid particle size, the desired pest control effect is then obtained, in which the median particle size of the volume of droplets can reflect the range of most of the droplet size, and the droplet size distribution width (RS) can better show the uniformity of the distribution of droplets. The smaller the droplet size distribution width, the better the uniformity of the droplet particle size distribution (Lan et al., 2016). This is typically calculated using Equation (1),

$$RS = \frac{D_{v90} - D_{v10}}{D_{v50}} \tag{1}$$

where D_{v10} , D_{v50} and D_{v90} denote 10%, 50%, and 90%, respectively, of the total volume of the entire system for droplets smaller than this particle size value.

In addition, the spray width can provide certain technical references for path planning in plant protection operations, which plays a vital role in improving spraying efficiency and operation quality. In summary, the above three features were selected as the evaluation indexes of centrifugal spray nozzle atomization performance in this experiment.

Response surface method optimization of nozzle structural parameters

Response surface methodology as an optimization tool, through a series of steps of screening tests, determining key factors, modeling and model testing, the key factors are tested at different levels of combinations, and through regression analysis of the whole process, the response values under the corresponding levels of factors are simulated, and the optimal way of combining factors is predicted, and this method has been widely used in many fields in practice (Wang et al., 2005; Hanrahan et al., 2006).

Single factor test

Taking the volume median diameter of droplets and the droplet size distribution width as evaluation indicators, the effect of various factors on the atomization capability of spray nozzle was studied and analyzed.

Table 1

Single-factor experimental design	
Factors	Values
Atomizing disk speed	3000, 4000, 5000, 6000, 7000, 8000, 9000
Flow rate	600, 700, 800, 900, 1000
Number of teeth	0, 5, 25, 50, 75, 100

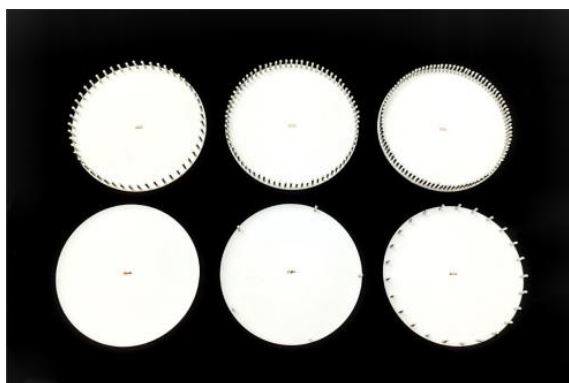


Fig. 6 – Lower atomizing disk with different number of teeth

A constant flow rate of 800 ml/min was set, and the atomization disk speed was maintained at 6000 r/min. The atomization disk had 50 teeth, and the spray medium used was water. The physical structure of different teeth under the atomization disk is illustrated in Fig. 6. The test factors and their corresponding values are summarized in Table 1. Each group of tests was repeated three times to ensure accuracy.

Box-Behnken test

Based on the analysis of the results of single-factor experiments, using Design-expert 13.0 software, the atomizing disk speed (A), the flow rate (B), and the number of atomization teeth (C) were identified as key factor, and the volume median diameter of droplets and the droplet size distribution width were set as dependent variables. Then, the Box-Behnken experiment analysis and design with three factors and three levels were carried out. Tables 2 and 3 respectively show the levels of the response surface experiment factors and the experiment design and results.

Table 2

Box-Behnken test factors and horizontal coding for structural optimization

Factors	Values		
	Atomizing disk speed (r/min)	Flow rate (ml/min)	Number of teeth
-1	3000	600	25
0	6000	800	50
1	9000	1000	75

Table 3

Design and results of Box-Behnken test for structural optimization

Group	Values			D _{v50}	RS
	Atomizing disk speed	Flow rate	Number of teeth		
1	9000	1000	50	81.46	0.98
2	6000	600	25	76.36	1.26
3	6000	600	75	79.94	1.42
4	6000	800	50	79.17	0.94
5	6000	800	50	80.64	0.96
6	3000	600	50	124.49	1.31
7	3000	1000	50	146.72	1.14
8	6000	1000	75	101.14	1.23
9	6000	800	50	79.23	0.93
10	9000	800	75	75.21	0.94
11	3000	800	25	134.96	1.14
12	6000	800	50	80.84	0.93
13	9000	800	25	73.37	0.82
14	3000	800	75	136.32	1.17
15	6000	1000	25	96.33	1.23
16	6000	800	50	80.94	0.97
17	9000	600	50	67.94	0.99

According to Table 3, it can be seen that the maximum value of the volume median diameter of droplets is 146.72 μm, the minimum value is 67.94 μm, and the droplet size distribution width ranges from 1.42 to 0.82. This result indicates that all the three variables selected in the test have a significant effect on the atomization performance of the double-layer centrifugal atomizing nozzle.

Model fitting analysis

Multivariate regression fitting and analysis were carried out on the experimental data obtained in Table 3. Using Design-expert 13.0 software, the multivariate quadratic response surface regression equations of the target functions, namely the volume median diameter of droplets (Y1) and the droplet size distribution width (Y2), with factors A, B, and C were established. The expressions are shown in Equation (2) and Equation (3), and the analysis of variance results of Y1 and Y2 were obtained, as shown in Table 4.

$$Y1=80.16-30.56A+9.62B+1.45C-2.18AB+0.12AC+0.3075BC+20.76A^2+4.23B^2+4.05C^2 \tag{2}$$

$$Y2=0.946-0.1287A-0.05B+0.0388C+0.04AB+0.0225AC-0.04BC-0.0543A^2+0.2132B^2+0.1257C^2 \tag{3}$$

Table 4

Regression model analysis of variance

Source	Sum of squares		Mean of squares		F-value		P-value	
	Y1	Y2	Y1	Y2	Y1	Y2	Y1	Y2
A	7473.14	0.1326	7473.14	0.1326	5086.64	432.77	< 0.0001	< 0.0001
B	739.59	0.0200	739.59	0.0200	503.40	65.27	< 0.0001	< 0.0001
C	16.79	0.0120	16.79	0.0120	11.43	39.20	0.0117	0.0004
AB	18.97	0.0064	18.97	0.0064	12.91	20.89	0.0088	0.0026
AC	0.0576	0.0020	0.0576	0.0020	0.0392	6.61	0.8487	0.0370
BC	0.3782	0.0064	0.3782	0.0064	0.2574	20.89	0.6275	0.0026
A ²	1813.86	0.0124	1813.86	0.0124	1234.61	40.44	< 0.0001	0.0004
B ²	75.45	0.1915	75.45	0.1915	51.35	624.86	0.0002	< 0.0001
C ²	68.91	0.0666	68.91	0.0666	46.90	217.28	0.0002	< 0.0001
Model	10307.57	0.4555	1145.29	0.0506	779.55	165.15	< 0.0001	< 0.0001
Lack of fit	7.14	0.0008	2.38	0.0003	3.03	0.8333	0.3614	0.5413
Residual	10.28	0.0021	1.47	0.0003				
Pure Error	3.15	0.0013	0.7865	0.0003				
Cor Total	10317.85	0.4576						

Y1: R²_{Adj}=0.9977; R²=0.9990 Y2: R²_{Adj}=0.9893; R²=0.9953

Note: P<0.01 (indicates highly significant), P<0.05 (indicates significant), same below.

The P-values in both of the above regression models are less than 0.0001, which means that the models have an extremely significant impact on both the volume median diameter of droplets and the droplet size distribution width. The misfit terms > 0.05 are all non-significant, which means that the experimental errors are small. Where, R² is the coefficient of determination and R²_{Adj} is the corrected coefficient of determination, equal to 0.9977 and 0.9893, indicating that 99.77% and 98.93% of the test data, respectively, are applicable to the above fitted equations. Therefore, all the above regression models showed good reliability and fitting accuracy.

RESULT ANALYSIS

The impacts of a single factor on D_{v50} and RS.

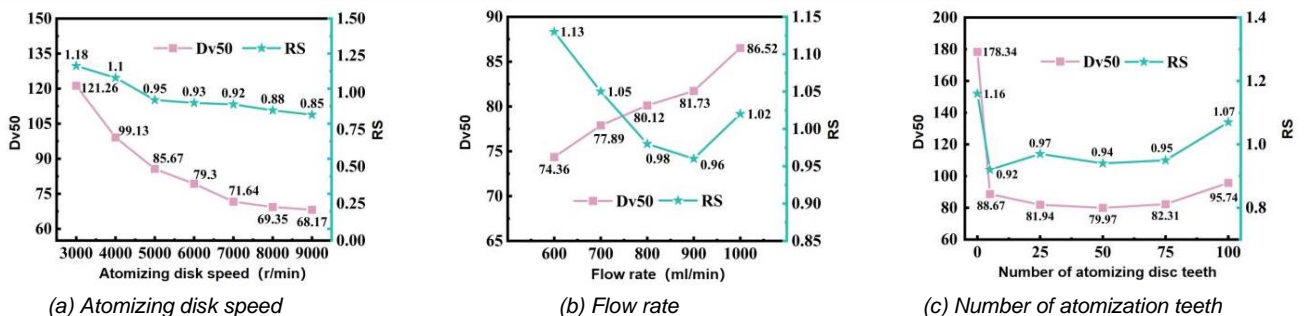


Fig. 7 – Influence of a single factor on the objective function

(1) The atomizing disk speed

As can be seen in Fig.7(a), both the volume median diameter of droplets and the droplet size distribution width are negatively correlated with the atomizing disk speed. This means that as the rotation speed of the atomization disk increases, the obtained droplet size becomes smaller and the droplet distribution becomes more uniform. This is mainly due to the fact that the centrifugal force on the liquid is gradually rose along with the growth of the atomizing disk speed, which further stretches the liquid into finer filaments, increases the friction with the surrounding air in the process, and achieves a second atomization when contacting the nebulizing teeth at the edge of the lower nebulizing disk, and thus it is rapidly broken into finer droplets.

(2) Flow rate

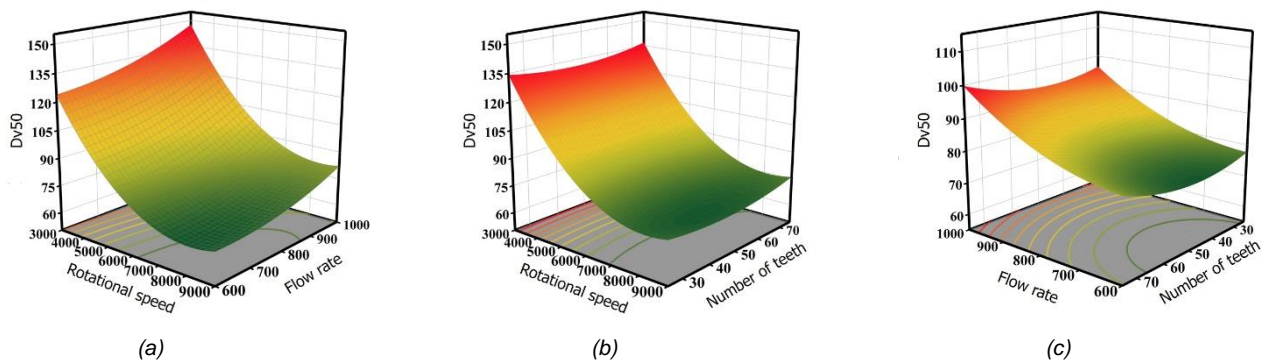
As can be seen in Fig.7(b), with the increase of flow rate, the volume median diameter of droplets increases gradually, and the experimental value increases gradually from 74.36 μm to 86.52 μm , while the droplet size distribution width decreases and then increases, and reaches a minimum value of 0.96 when the flow rate is 900 ml/min. When the flow rate is increased to 1,000 ml/min, the nozzle is unable to break the excess liquid completely, which leads to the non-uniformity of droplet size, and the droplet size distribution width increases to 1.02, but still meets the conditions of low-volume spraying for UAV plant protection operations. The width of droplet spectrum increased to 1.02, but it still meets the condition of low volume spraying for UAV plant protection operation.

(3) The number of atomization teeth

From Fig.7(c), it can be seen that the volume median diameter of droplets and the droplet size distribution width show a tendency of decreasing and then increasing with the increase of the number of atomizing teeth. When the number of teeth increases from 0 to 5, the decreasing rates of the volume median diameter of droplets and the droplet size distribution width are relatively large, which indicates that the atomization teeth have an obvious impact on the fragmentation of the liquid medicine. When the number of teeth is 50, the volume median diameter of droplets and the droplet size distribution width reach their minimum values of 79.97 μm and 0.94 respectively, and as the number of teeth continued to increase to 100, the narrow spacing of the teeth prevented the liquid from being thrown out smoothly, which in turn prevented it from being broken completely, resulting in an increasing trend in the volume median diameter of droplets and the droplet size distribution width.

The impacts of the interactions of various factors on D_{v50} and RS.

According to the analysis of variance in Table 4, the influences of the interactions of various factors on the volume median diameter of droplets and the droplet size distribution width are shown as $AB > BC > AC$ and $AB = BC > AC$, respectively, which is consistent with the results of the response surface plots in Fig. 8. As shown in Figs. 8(a) - 8(c), the volume median diameter of droplets was negatively correlated with the atomizing disk speed, while positively correlated with the flow rate, and the volume median diameter of droplets decreased and then increased with the increase in the number of atomization teeth, which was consistent with the results of the one-factor analysis. From Fig. 8(d), it can be seen that when the flow rate is at a low value, the size of the rotational speed has a greater effect on the droplet size distribution width. From Fig. 8(f), it can be observed that the droplet size distribution width first decreases and then increases with the increase in the flow rate and the number of teeth. At this time, the lowest point of the response surface curve falls within the test area, which can be seen that the response surface test can achieve the best structural parameters of the acquisition of the spray nozzle atomization performance to achieve the optimization.



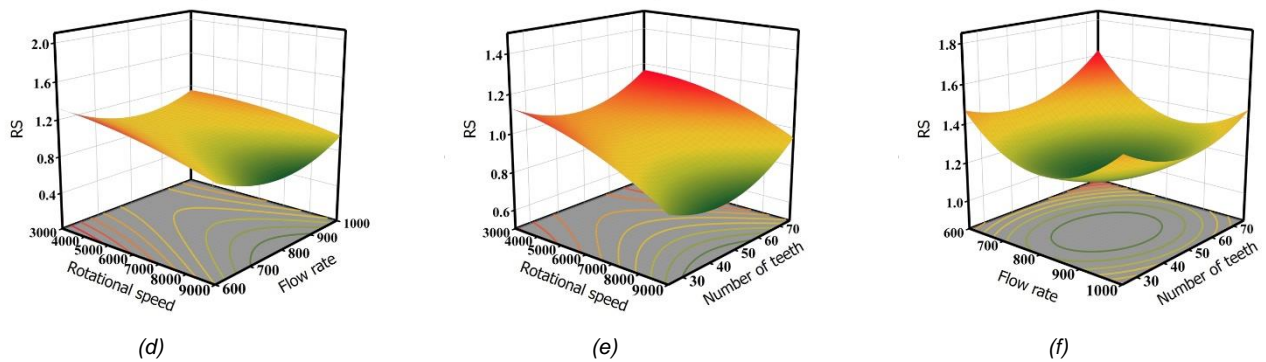


Fig. 8 – Response surface diagram of the influence of interaction of various factors on the middle diameter of droplet volume and the droplet spectral width

Based on the response surface curves and the actual test conditions, when atomizing disk speed is 8500 r/min, the flow rate is 750 ml/min, and the number of atomization teeth is 50, the structural parameters of the centrifugal spray nozzle are optimal. At this time, the volume median diameter of droplets is 67.4 μm, and the droplet size distribution width is 0.82, both of which can meet the requirements of low-volume spraying for unmanned aerial vehicle pesticide application.

Spray width response surface method optimization test

Table 5

Spray width Box-Behnken test factor and level coding

Factors	Values		
	Atomizing disk speed(r/min)	Flow rate(ml/min)	Height(m)
-1	3000	600	1
0	6000	800	1.5
1	9000	1000	2

Table 6

Spray width Box-Behnken test design and results

Group	Factors			Spray width(cm)
	Atomizing disk speed	Flow rate	Height	
1	6000	600	2	144.66
2	6000	1000	2	154.87
3	3000	600	1.5	111.34
4	6000	800	1.5	149.36
5	6000	1000	1	164.97
6	9000	800	1	163.35
7	3000	1000	1.5	122.29
8	9000	1000	1.5	146.93
9	6000	800	1.5	146.79
10	6000	800	1.5	140.31
11	9000	600	1.5	142.39
12	3000	800	1	107.64
13	9000	800	2	139.36
14	6000	800	1.5	147.06
15	6000	600	1	153.14
16	3000	800	2	125.37
17	6000	800	1.5	144.98

Spray height refers to the vertical distance between the nozzle and the crop canopy, the flight height of the UAV in actual operation has a significant impact on the application effect, according to the actual operational specifications and indoor conditions to determine the spray height of the value range of 1-2m (Hu et al., 2005). Using Design-expert 13.0 software, spray width was set as the response variable, and the atomizing disk speed (A), the flow rate (B), and the spray height (D) were selected as the independent variables, and three-factor, three-level response surface tests and analyses were designed and conducted. Table 5 and Table 6 show the response surface test factor levels and experimental design and results, respectively.

Model fitting analysis

The experimental data obtained in Table 6 were imported into Design-expert 13.0 software to carry out the fitting and analysis, and the multivariate quadratic response surface regression equations of the objective function spray width (Y3) with the factors A, B, and D, respectively, with the expressions as shown in Eq. (4) were established, and the analysis of variance (ANOVA) results of Y3 were obtained, as shown in Table 7.

$$Y3=145.7+15.67A+4.69B-3.1D-1.6AB-10.43AD-0.405BD-17.72A^2+2.76B^2+5.95D^2 \quad (4)$$

Table 7

Analysis of variance of spray width regression model				
Source	Sum of squares	Mean of squares	F-value	P-value
A	1965.33	1965.33	145.01	< 0.0001
B	176.06	176.06	12.99	0.0087
D	77.13	77.13	5.69	0.0485
AB	10.27	10.27	0.7579	0.4128
AD	435.14	435.14	32.11	0.0008
BD	0.6561	0.6561	0.0484	0.8321
A ²	1322.29	1322.29	97.56	< 0.0001
B ²	32.05	32.05	2.36	0.1680
D ²	149.13	149.13	11.00	0.0128
Model	4111.98	456.89	33.71	< 0.0001
Lack of fit	48.87	16.29	1.42	0.3614
Residual	94.87	13.55		
Pure Error	46.00	11.50		
Cor Total	4206.85			

$R^2_{Adj}=0.9485; R^2=0.9774$

The P-values in the above regression models are well below the significance level of 0.0001, indicating a highly significant difference between the models. The misfit term > 0.05 is not significant, indicating that the error generated in the test is at a low level. Where, $R^2 = 0.9774$, $R^2_{Adj} = 0.9485$, indicating that the above regression model has good reliability and accuracy. Thus, it is feasible to predict and analyze the change in spray width by this regression model.

Response surface analysis

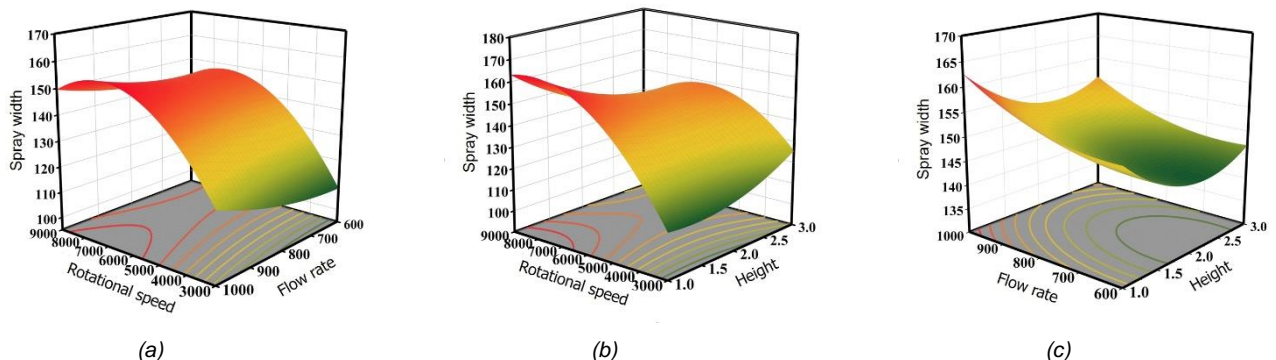


Fig. 9 – Response surface diagram of the influence of interaction of various factors on the spray width

From Fig. 9(a) and (b), it can be seen that when other factors remain constant, the spray width shows a tendency to increase and then decrease with the increase in rotational speed. This is because with the increase of the atomizing disk speed, the fog droplets obtain a greater initial velocity, the spray width increases; however, as the rotational speed continues to increase, the particle size of the droplets decreases, which leads to the liquid being more susceptible to the influence of the external environment and drift, the impossibility of being deposited on the surface of the test bench, resulting in a decrease in the spray width. As shown in Fig. 9 (a) and (c), when the rotational speed and height are certain, the spray width and the size of the flow rate are positively correlated, and the number of droplets will continuously increase with the increase of the flow rate in the liquid circuit, and the larger the droplet particle size, the larger the spray width. From Fig. 9(b), it can be seen that at low rotational speeds, the spray width increases with the increase in height, whereas at high rotational speeds the trend of the spray width is the opposite. This may be due to the fact that the increase in rotational speed decreases the droplet size, and the liquid is more prone to drift and loss, resulting in a decrease in spray width. In summary, it can be seen that this regression model can provide some reference value for the selection of working parameters of UAV in aerial plant protection operation.

CONCLUSIONS

This research proposes a double-layer centrifugal atomizing nozzle that can realize the secondary atomization of liquid medicine, combining single-factor experiments and the response surface method, and systematically exploring the effect of the structural parameters and working parameters of the double-layer centrifugal atomizing nozzle on its atomization performance.

(1) According to the single-factor experiments, within the test range, the volume median diameter of droplets and the droplet size distribution width of the centrifugal nozzle show the same trend with the increase in the number of atomization teeth, that is, they first decrease and then increase. Meanwhile, both of them are negatively correlated with the atomizing disk speed. On the other hand, the volume median diameter of droplets increases linearly with the increase in the flow rate, while the droplet size distribution width first decreases and then increases.

(2) In the response surface optimization experiment, three key factors that have significant effects on the volume median diameter of droplets and the droplet size distribution width are selected: the atomizing disk speed, the flow rate, and the number of atomization teeth, and a Box-Behnken analysis experiment with three factors and three levels is carried out. Through the analysis of variance of the obtained regression models, the R_{Adj}^2 values of the two are 0.9977 and 0.9893 respectively, indicating that the models have good fitting performance. Finally, the optimized number of atomization teeth is 50.

(3) The response surface method is used to establish a quadratic polynomial regression model of the atomizing disk speed, the flow rate, and the spray height with the spray width. The results show that $R_{Adj}^2=0.9485$ and $R^2=0.9774$, and the regression model has high accuracy and fitting degree, indicating that the response surface method has certain feasibility and theoretical guiding significance for the prediction and control of the spraying width in aerial plant protection operations.

ACKNOWLEDGEMENT

This work was supported by the National Key Research and Development Program of large-load intelligent UAV for plant Protection (2023YFD2000200) and the Key Research and Development Project of Ningxia Hui Autonomous Region (2023BCF01051).

REFERENCES

- [1] Chen, J., Liu, W., Yuan, Y., (2018). Application and development trend of nozzles on UAV (无人机雾化喷头的使用现状与发展趋势). *China Plant Protection Guide*, Vol. 38, no 3, pp. 66-70.
- [2] Deng, W., Chen, L., Zhang, R., Tang, Q., Xu, G., Xu, M., (2020). Research Status and Suggestions on Plant-protection Nozzles in China (植保施药喷头研发现状分析). *Modern Agricultural Equipment*, Vol. 41, no 6, pp. 58-63.
- [3] Feng, Y., Pei, L., Chen, Xiao., (2021). Summary of the key technology of variable rate application (变量施药关键技术综述). *Journal of Chinese agricultural mechanization*, Vol.42, no 12, pp.65-71.
- [4] Gong, J., Fan, W., Peng, J., (2019). Application analysis of hydraulic nozzle and rotary atomization sprayer on plant protection UAV. *International Journal of Precision Agricultural Aviation*, Vol.2, no 1.

- [5] Hanrahan, G., & Lu, K., (2006). Application of factorial and response surface methodology in modern experimental design and optimization. *Critical Reviews in Analytical Chemistry*, Vol.36, pp.141-151.
- [6] Hu, H., Ren, X., Ma, X., (2021). Control effect on cotton aphids of insecticides sprayed with unmanned aerial vehicles under different flight heights and spray volumes. *International Journal of Precision Agricultural Aviation*, Vol.4, no 1.
- [7] Li, L., Li, H., He, X., Andreas H., (2012). Development and experiment of automatic detection device for infrared target (红外靶标自动探测器的研制及试验). *Transactions of the Chinese Society of Agricultural Engineering*, Vol. 28, no 12, pp. 159-163.
- [8] Lan, Y., & Chen, S., (2018). Current status and trends of plant protection UAV and its spraying technology in China. *International Journal of Precision Agricultural Aviation*, Vol. 1, no 1.
- [9] Lan, Y., Chen, S., Deng, J., Zhou, Z., Ou, Y., (2019). Development situation and problem analysis of plant protection unmanned aerial vehicle in China (中国植保无人机发展形势及问题分析). *Journal of South China Agricultural University*, Vol. 40, no 5, pp. 217-225.
- [10] Liu, J., Yu, Q., Guo, Q., (2012). Experimental investigation of liquid disintegration by rotary cups. *Chemical Engineering Science*, Vol. 73, pp. 44-50.
- [11] Lan, Y., Peng, J., Jin, Ji., (2016). Research status and development of pesticide spraying droplet size (农药喷雾粒径的研究现状与发展). *Journal of South China Agricultural University*, Vol.37, no 6, pp.1-9.
- [12] Ru, Y., Jia, Z., Fan, Q., Che, J., (2012). Remote Control Spraying System Based on Unmanned Helicopter (无人直升机远程控制喷雾系统). *Transactions of the Chinese Society for Agricultural Machinery*, Vol. 43, no 6, pp.47-52.
- [13] Wang, Y., & Wang, C., (2005). The Application of Response Surface Methodology (响应面法的理论与应用). *Journal of Minzu University of China (Natural Science Edition)*, no 3, pp.236-240.
- [14] Yang, G., Lan, Y., Geng, L., Zhang, B., Yi, L., Han, X., (2023). Experimental Research on Three-layer Intelligent Centrifugal Variable Sprinkler (三层智能离心式变量喷头试验研究). *Journal of agricultural mechanization research*, Vol.45, no 8, pp.155-160.
- [15] Zhang, D., Lan, Y., Chen, L., Wang, X., Liang, D., (2014). Current Status and Future Trends of Agricultural Aerial Spraying Technology in China (中国农业航空施药技术研究进展与展望). *Transactions of the Chinese Society for Agricultural Machinery*, Vol. 45, no 9, pp. 53-59.
- [16] Zhou, Q., (2016). Research of Narrow Droplets Spectral Atomization Property of Centrifugal Nozzle in Low Volume Aviation Spray (航空低量窄雾滴谱旋转离心喷嘴雾化性能研究). *Chinese Academy of Agricultural Sciences*.

STUDY ON THE EFFECT OF CURVED FUNNEL FOR SILO UNLOADING ON PARTICLE FLOW CHARACTERISTICS

筒仓卸粮曲面漏斗对颗粒流动特性的影响研究

Mingxu WANG^{1,2*}, Saiqiang LI¹, Tao Gao¹, Zhijie SONG⁴, Kunlun LIU³, Jianzhang WU³, Jiangfeng OUYANG¹

¹School of Mechanical & Electrical Engineering, Henan University of Technology, Zhengzhou 450001, China

²Henan Key Laboratory of Grain and Oil Storage Facility & Safety, Henan University of Technology, Zhengzhou 450001, China

³School of grain college, Henan University of Technology, Zhengzhou 450001, China

⁴Jiaozuo Creation Heavy Industry Co.,Ltd., Jiaozuo 454000, China

Tel: 18623717728; E-mail: wmx20032002@163.com

DOI: <https://doi.org/10.35633/inmateh-74-60>

Keywords: Curved funnel, DEM, Shrinkage rate, Flow characteristics

ABSTRACT

In order to adapt to the needs of modern intelligent warehousing and reduce the unloading side pressure of grain silo, the influence of curved funnel on the unloading process is designed and analyzed, and this paper uses EDEM simulation software and Hertz Mindlin model for analysis. The results found that compared with the unloading characteristics of the conical funnel, the unloading side pressure is effectively improved; in the unloading process, with the increase of the shrinkage rate, the critical position of the flow transformation increases and the flow velocity of the particle group accelerates. However, the flow velocity of the particle group decreases when it reaches the critical position of 250 mm. Combined with the corresponding analysis, this paper uses the Froude number to quantitatively express the mobility of particles. As the shrinkage rate of the curved funnel and the unloading height increase, the Froude number also increases. This paper analyzes and calibrates the curved funnel for soybean unloading in silos, which will provide useful reference for avoiding arching and clogging during the unloading process of grain particles.

摘要

为适应现代化智能仓储的需求，减少粮食筒仓卸料侧面压力，设计并分析了曲面漏斗对卸料过程的影响，本文利用 EDEM 仿真软件，使用 Hertz-Mindlin 模型进行分析。结果发现，相比于锥形漏斗的卸料特性，有效改善卸料侧压力；卸载过程中，随着收缩率的增大，流形变换的临界位置增大，颗粒群的流动速度加快。然而，当达到临界位置 250mm 时，颗粒群的流速减慢。结合相应分析本文采用弗劳德数对颗粒的流动性进行了定量表述，随着曲面漏斗收缩率和卸料高度的增加，弗劳德数也在增大。本文对筒仓大豆卸料曲面漏斗的分析标定，将为解决粮食颗粒的卸料过程避免结拱和堵塞提供有益的参考。

INTRODUCTION

Silo as the main facility for grain storage, has many advantages, such as: it occupies a small area, it is easy to build, can be added to a variety of monitoring equipment, it is easy to use, it is conducive to the transfer of grain, and so on, therefore, worldwide it is more used for the storage of grain, sand and other bulk particles. In addition to bearing permanent load and variable load, the silo also bears the effect of grain storage on the silo during use (Ayuga F. et al., 2001). The effect of grain storage on silo is large, the action time is long, and it changes with time, which is the main factor affecting the safety of silo structure. The dynamic pressure of the silo will increase during the unloading process (Zhao et al, 2013), and overpressure phenomenon often occurs in the lower part of the silo.

Through a large number of studies by scholars, it is known that the conventional conical hopper silo will be clogged during unloading due to a number of factors such as the complexity of the bulk material, and even the silo wall is thus impacted, leading to the destruction of the silo. Pressure reducing tubes (Wang et al, 2001; Yuan et al, 2020; Wang et al, 2023) or fluid modifiers (Qu et al, 2012) are installed inside the silo to change the particle flow pattern, but in practice, the pressure reducing tubes are not easy to install and fix, and fluid modifiers can be damaged (Qu et al, 2012). One or both side chutes (Yuan et al, 2019) are installed on the side of the silo to change the particle flow pattern to reduce the side pressure, but the eccentric discharge is not well adapted. In this paper, the analysis of the law of influence of such a combined funnel on the unloading of a silo, when only one section of the unloading funnel is a curved funnel portion and the rest is still a conical funnel portion, is investigated.

Simulation of unloading from curved funnels with different degrees of curvature

Curved funnel model analysis

In order to study the influence of the bending degree of the curved funnel on the simulation of silo unloading, the height of 200 mm curved funnel is selected, and then the angle of the arc is used to represent the curvature of the surface, the arc angle of 20°~60° is selected for a total of five levels. After calculation, if the arc angle is greater than 60°, it will lead to the minimum discharge diameter change. Figure 1 shows the two-dimensional image of the curved funnel.

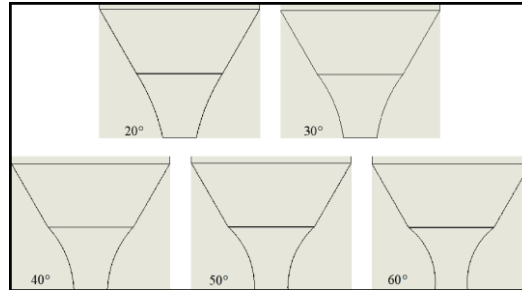


Fig. 1 - Curved funnels with different degrees of curvature

Shrinkage can be used to express the degree of curvature of the surface, which is expressed as the ratio of the difference between the area of the upper and lower two cross-sections and the ratio of the larger area of the two cross-sections in a unit distance of the longitudinal distribution of the discharge funnel; it is calculated by the formula shown below:

$$C = \frac{dS}{Sdy} = \frac{2\pi x dx}{\pi x^2 dy} = \frac{2}{y} \ln\left(\frac{2}{D_r} x\right) \tag{1}$$

where *C* is the shrinkage rate; *S* is the cross-sectional area; *dS* is the difference between the upper and lower cross-sectional areas; *dy* is the unit distance of the longitudinal distribution; and *D_r* is the outlet diameter of the funnel.

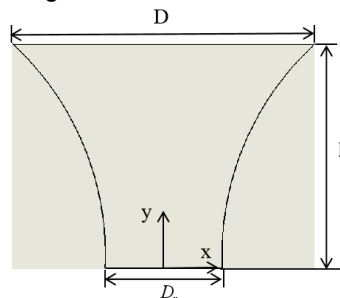


Fig. 2 - Schematic diagram of funnel cross-section

Figure 2 is the schematic diagram of the vertical section of the curved funnel. The shrinkage rate of the curved funnel with different arc angles can be calculated, as shown in Table 1:

Table 1

The shrinkage rate of five different funnels	
Angle of a circle arc	Shrinkage rate/C
20°	0.089
30°	0.106
40°	0.125
50°	0.146
60°	0.171

The silo model was imported into EDEM software and unloading simulation was carried out, as shown in Figure 3 for the 3D model of the silo.

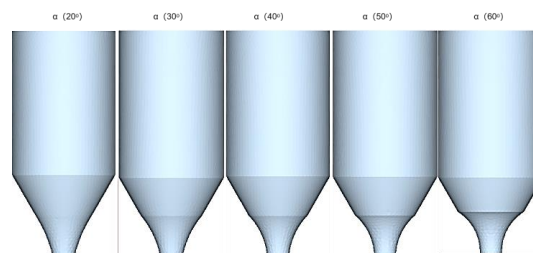


Fig. 3 - 3D model of the simulation test

The software uses the Hertz Mindlin model to calculate the indirect contact force of particles. The indirect contact force of particles includes normal force and tangential force, among which the calculation of normal force is based on Hertz theory. The calculation of tangential force is based on Mindlin's theory, which satisfies Coulomb's law of friction and accurately describes the interactions between particles. The particle model selected in this article is the four sphere particle model of soybean particles, and the corresponding three-dimensional model is shown in Figure 4.

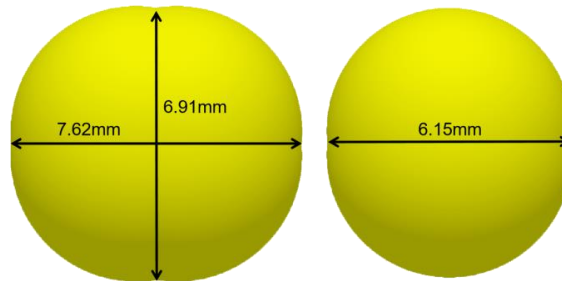


Fig. 4 - Three dimensional dimensions of soybean particles

The relevant physical attribute parameters and simulated attribute parameters are shown in the table:

Table 2

Physical parameters		
Material	Parameter	Numerical value
Soybean	Poisson's ratio	0.23
	Young's modulus (MPa)	63
	Particle density (kg/m ³)	1211
Silo	Poisson's ratio	0.5
	Young's modulus (MPa)	35
	Particle density (kg/m ³)	1180

Table 3

Contact parameters		
Material	Parameter	Numerical value
Particle - Particle	Coefficient of static friction	0.39
	Collision recovery coefficient	0.3
	Coefficient of dynamic friction	0.17
Particle - Silo	Coefficient of static friction	0.474
	Collision recovery coefficient	0.47
	Coefficient of dynamic friction	0.1

As can be seen in Figure 5 the average unloading rate of the conical hopper silo is 2.68 kg/s, while the unloading rate of the curved hopper silo accelerates with the increase of hopper shrinkage, and the growth slows down after the curved hopper arc angle of 40°.

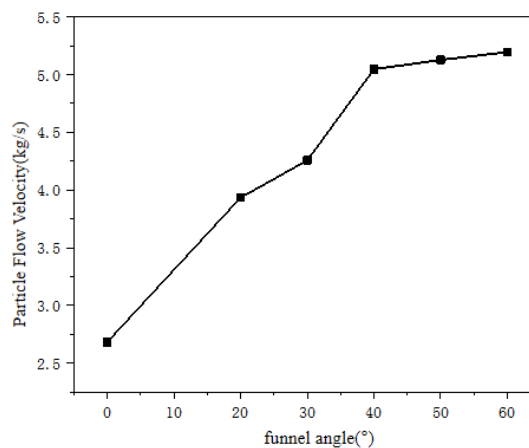


Fig. 5 - Comparison of discharge rate

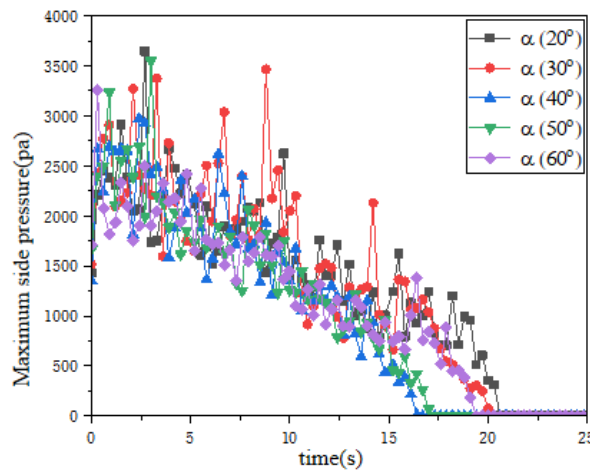


Fig. 6 - Maximum pressure of curved funnels with different shrinkage rates

From the analysis, it can be seen that the lateral pressure of the silo wall during unloading reaches the maximum value at the initial stage of unloading, and then shows an oscillating pattern of gradual decrease. It can be seen that the curved funnel plays the role of pressure reduction in the unloading process of the silo, and there is a difference in the degree of influence of different shrinkage of the curved funnel on the unloading of the silo. Among them, the unloading pressure of the simulation group with curved funnel shrinkage of 0.125 has the largest reduction, which reaches 27.1%.

Analysis of particle flow in curved funnel silos

In order to facilitate the observation of the changes in the particle flow form during the unloading process, the particle groups were stained hierarchically in the EDEM and divided into yellow and blue color, which was used to identify the particle flow form in the unloading. Figure 7 shows the comparison of the unloading particle flow patterns of the six simulation groups.

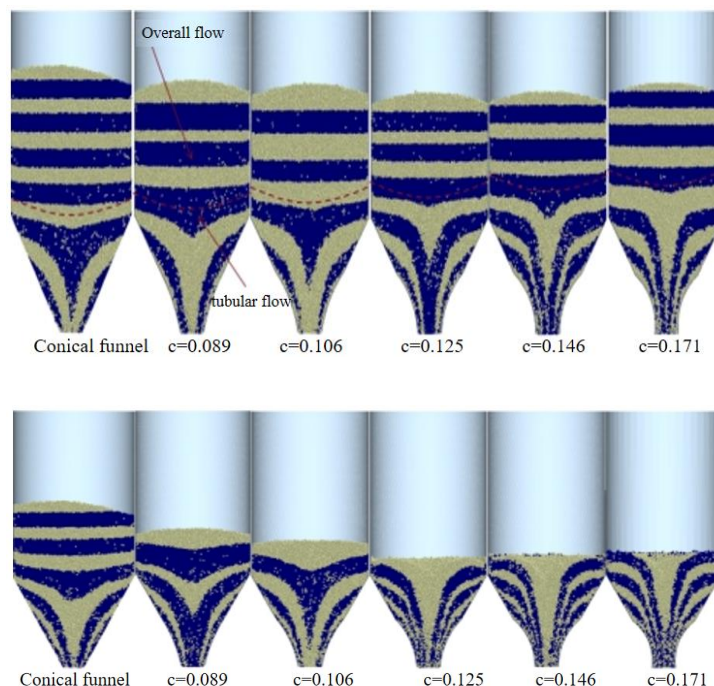


Fig. 7 - Flow pattern of particles from t=6s to t=15s

From the figure, it can be seen that when the shrinkage rate of the curved funnel is small, the critical position of the two forms of flow is low; as the shrinkage rate of the curved funnel increases, the critical position of the overall flow and the tubular flow increases, but the enhancement of the mobility of the particles slows down after the shrinkage rate increases to a certain extent.

Unloading flow rate analysis of curved funnel silos

A silo particle velocity cloud was created to analyze the change in velocity of the particles during unloading, as shown in Figure 8.

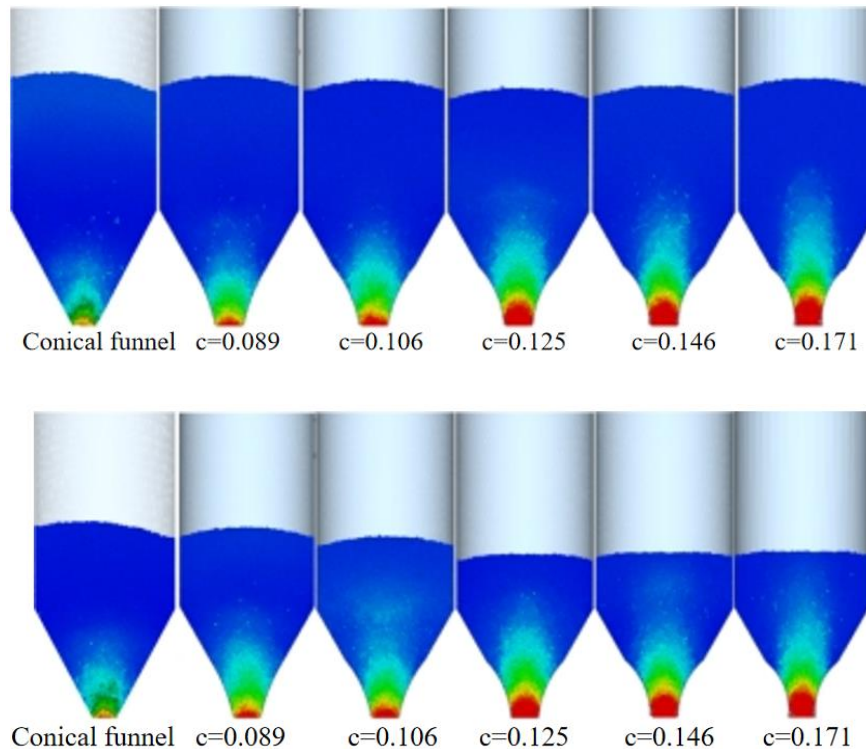


Fig. 8 Particle flow velocity cloud from t=6s to t=12s

The overall unloading process of the silo was investigated by laterally dividing the grid set into 11 regions, and the velocity of particles with different height in silo was collected along silo wall-center-silo wall, and the velocity of particles at each height was analyzed. It was ensured that each layer of the observation window was to contain multiple falling soybean particles, and each of the small grids created was a 20mm40mm rectangular observation window, as shown in Figure 9.

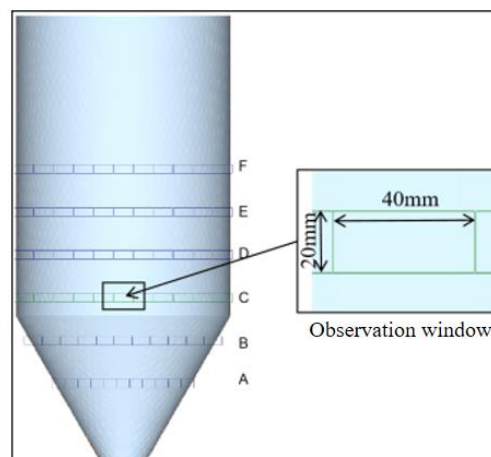


Fig. 9 - Particle flow rate observation window

The results in Figure 10 show that there are two stages in the variation of particle flow velocity with shrinkage: one in which the flow velocity of the particles is large and the difference in the flow velocity of the laterally distributed particles is obvious; and the other in which the flow velocity of the particles is small and the difference in the flow velocity of the laterally distributed particles is very small.

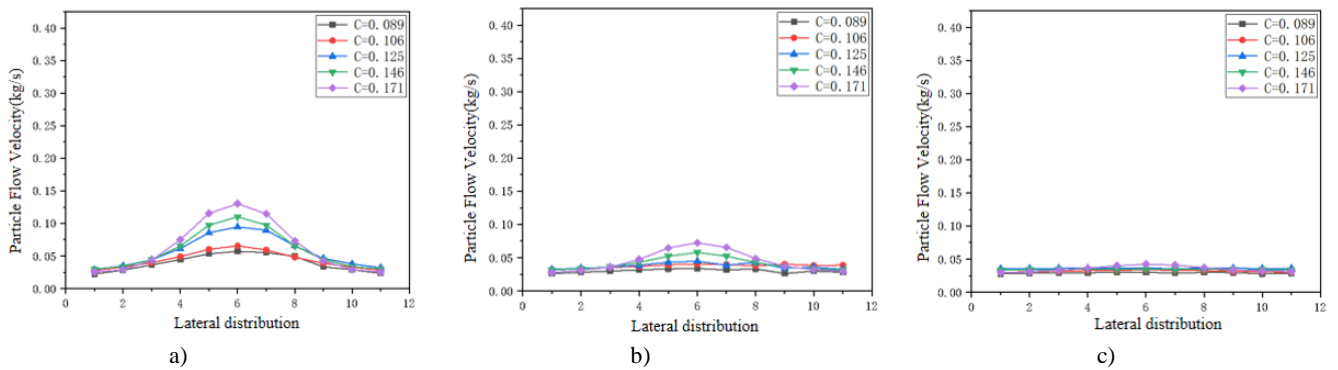


Fig. 10 - Mean particle flow velocity within regions a to c

The particle flow velocity in the observation window at the center of the lateral distribution was analyzed. As Figure 11 shows the comparison of the flow velocity of the center particles unloaded from silos with different shrinkage rates, it can be seen that the flow velocity of the center particles becomes faster with increasing shrinkage rate, while the flow velocity of the center particles gradually slows down with decreasing depth of the silo.

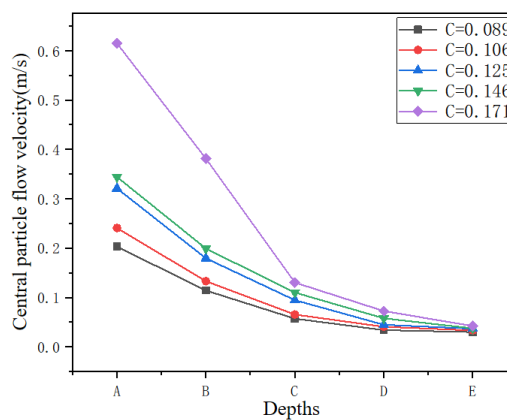


Fig. 11 - Comparison of central particle flow rates for different shrinkage rates

Simulation of unloading from curved funnel with different heights

When only a part of the hopper is curved, the dynamic lateral pressure of the silo wall, particle flow pattern and velocity change law are simulated by changing the shrinkage rate of the curved funnel, and the velocity of particles in the hopper is faster. Further study is made to change the height of the curved funnel in the discharge funnel to study the change rule of simulated silo discharge. The test model is divided into six variables, namely H (100mm), H (150), H (200mm), H (250mm), H (300mm), H (350mm), as shown in Fig.12.

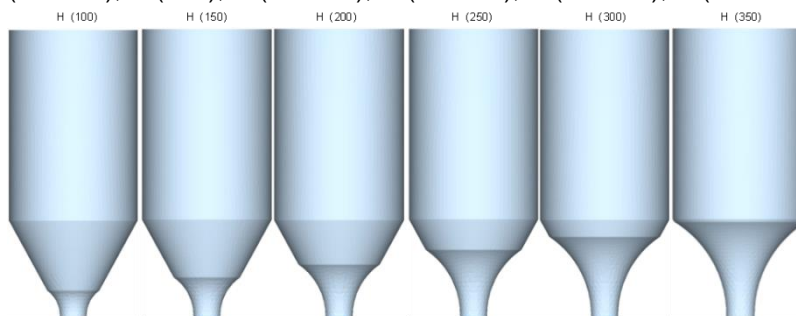


Fig. 12 - Unloading simulation test model

Effect of height of curved funnel on discharge pressure

The simulated maximum pressure values for six groups of curved funnel discharge with different heights are shown in Figure 13. When the height of the curved funnel is 100 mm, the maximum discharge pressure P of the silo is 3.56 kPa, which is a decrease of 11% compared to the maximum pressure value of the conical funnel group; when H=150 mm, the P is 3.33 kPa, which is a decrease of 16.7%; when H=200 mm, the decrease is 18.7%; when H=250 mm, the decrease is 21%; when H=300 mm, the decrease is 29.7% and 22.4% for H=350 mm.

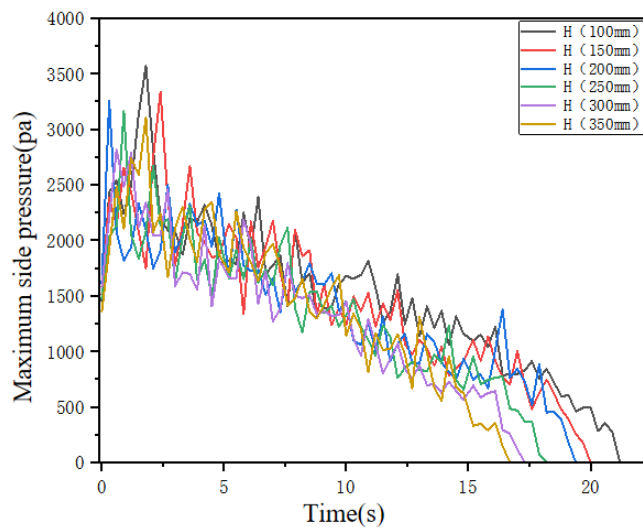


Fig. 13 - Maximum pressure values for different heights of curved funnel discharge simulation

From the above simulation test, it can be seen that the pressure variation law during unloading is similar to the discussed law. The influence of curved funnel with different height on the dynamic side pressure of silo discharging is also different. Among them, the simulation group with the height of 100 mm of curved funnel has the smallest unloading pressure drop, and the simulation group with the height of 300 mm has the largest unloading pressure drop.

Unloading flow analysis of curved funnel silos

The unloading flow pattern was analyzed, as shown in Figure 14, which compares the unloading particle flow pattern of the seven simulation groups.

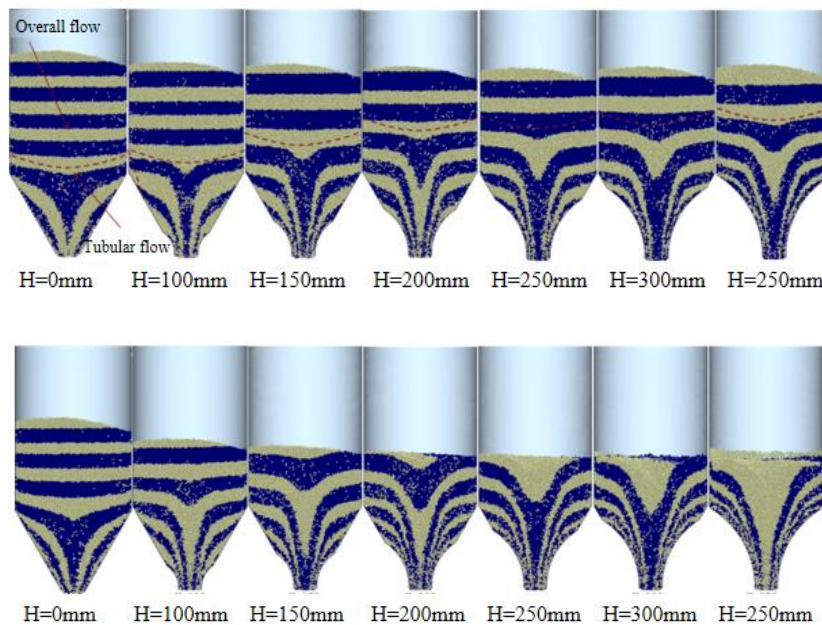


Fig. 14 - Comparison of particle flow regimes in the simulation group from t=6s to t=12s

The above analysis shows that when the height of the curved funnel is small, the critical positions of the two flow forms are low; with the increase of the height of the curved funnel, the critical positions also rise. From the conical funnel H=0 mm simulation group to the H=250 mm simulation group, the critical position of the flow situation in the subsequent simulation group also increased with the increase of the curved funnel height, but the amplitude was not obvious. With the increase of the height of the curved funnel, the flowability of the particles in the silo also increases.

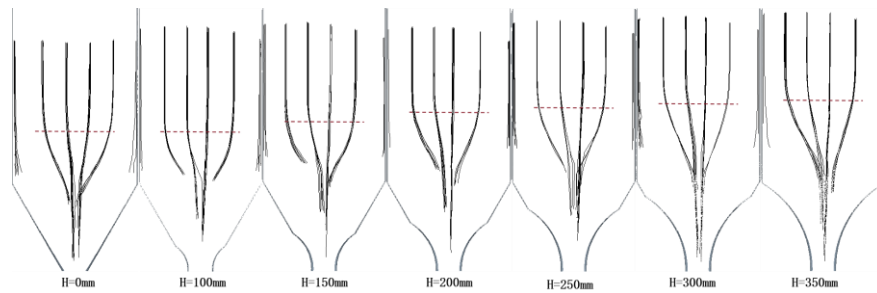


Fig. 15 - Critical positions of the two flow patterns

Unloading flow rate analysis of curved funnel silos

As can be seen from Figure 16, the particle flow rate in the curved funnel silo is larger than that in the conical funnel silo, and distributed along the wall-center-wall of the silo, the particle flow rate follows the law of slow-fast-slow change. The particle flow rate of the simulation group with a curved funnel height of 200 mm is significantly higher than that of the other simulation groups, and the other simulation groups follow the law that the particle flow rate increases with the increase of the curved funnel height.

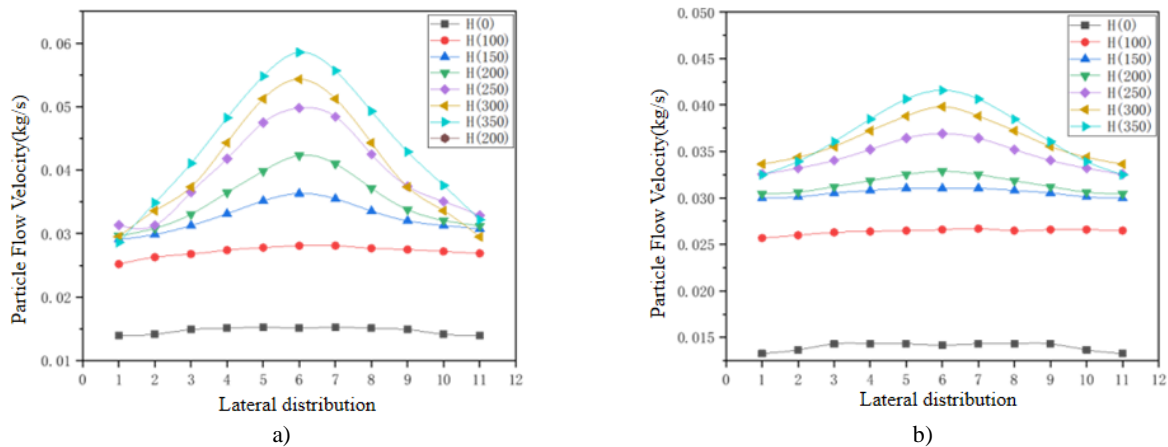


Fig. 16 - Mean particle flow velocity within regions a to b

From the above analysis, as the height of the curved funnel increases, the particle mobility becomes better and the particle flow rate is accelerated, which speeds up the outflow of particles from the top of the silo and reduces the time that the mixed flow situation exists.

Quantitative analysis of particle fluidity

In this paper, a dimensionless parameter, the Froude number, has been chosen as a means of quantitatively analyzing the mobility of particles.

The Froude number is the ratio of the inertial force to the gravitational force of the particles and is specified as follows:

$$F_r = \frac{v}{\sqrt{g \cdot L}} \tag{2}$$

where:

v is the velocity of the particle; g is the gravitational acceleration; L is the characteristic length of the object.

By analyzing the above formulas, Lehmann derived the non-square Froude number for axisymmetric containers as shown below:

$$F_r = \frac{M}{\rho_s \cdot \sqrt{g} \cdot D_r^{2.5}} \tag{3}$$

where:

M is the average discharge rate; ρ_s is the bulk density of the particles; g is the gravitational acceleration; D_r is the diameter of the outlet.

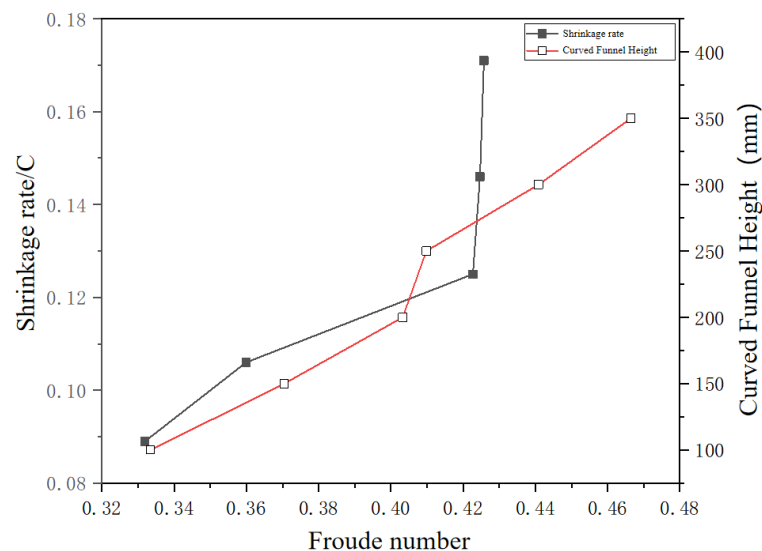


Fig. 17 - Relationship between variables and Froude number

Figure 17 shows the trend of Froude number for shrinkage $C=0.089$ to 0.171 and the trend of Froude number for height $H=100$ mm to 350 mm. The results show that the Froude number increases as the shrinkage rate increases and slows down after $C=0.125$; the Froude number increases as the height of the curved funnel increases and the rise rate increases after $H=250$ mm.

CONCLUSIONS

In this paper, the unloading of curved funnel silo is simulated. The effects of shrinkage rate and the height of curved funnel on discharge flow pattern and velocity were analyzed, the influence trend of curved funnel on particle flow was quantitatively analyzed, and the influence of the decrease of maximum lateral pressure at $C=0.146$ compared with that of curved funnel on discharge flow pattern and flow rate was analyzed, and the influence of curved funnel on particle flow capacity was quantitatively analyzed. It was found that different shrinkage rates and heights of curved funnel silos had different reduction of maximum lateral pressure compared with conical funnel silos. However, because the dynamic discharge pressure is affected by the complex flow characteristics of the internal particles, and does not change in a fixed law, the maximum side pressure drop is optimized at $H=350$ mm. During the simulated unloading process, the flow characteristics of the particles change with the change of shrinkage of the curved funnel. As the shrinkage increases, the critical position of the flow transition of the particle flow rises, the "V" shape of the central particle becomes more obvious, the flow velocity of the particles is accelerated, and the difference of the flow velocity of the particles in the lateral distribution is larger, but the trend of the particle flow velocity rise slows down when the shrinkage increases to a certain level. The flowability of particles changes significantly with the height of the curved funnel.

From the macroscopic level of analysis, with the increase of height, the critical position of the flow shape transformation rises, but with the increase of height to 250 mm later, the trend of the critical position rising slows down, and the end of the mixed flow is advanced; from the microscopic level of analysis, with the increase of height, the flow rate of particles accelerates, and the flow rate of the central particles is significantly larger than that of the surrounding particles. The flowability of the particles was quantitatively analyzed using a dimensionless parameter, the Froude number. The results showed that the Froude number increased with the increase of shrinkage, but slowed down after $C=0.125$; the Froude number increased with the increase of height, and the rise rate increased after $H=250$ mm. The flowability of the particles becomes better with the increase of the Froude number, which quantitatively expresses that the curved funnel improves the flowability of the particles.

ACKNOWLEDGEMENT

This research was supported by Training plan of young backbone teachers in colleges and universities in Henan Province (2020GGJS088), Opening subject of Henan key laboratory of grain and oil storage construction and safety (2021KF-B02), Science and Technology Research Project of Henan (No. 232103810084) and Science and Technology Key Research Program of Henan Provincial Department of Education(24A460004),"National Key Research and Development Programs under the 14th Five-Year Plan (2021YFD2100600)

REFERENCES

- [1] Ayuga F., Guaita M., Aguado P.J., (2001). Discharge and the eccentricity of the hopper influence on the silo wall pressures [J]. *Journal of Engineering Mechanics*, Vol. 127, pp. 1067-1074.
- [2] Cundall P.A, Strack O.D.L., (1979). A discrete numerical model for granular assemblies [J]. *Geotechnique*, Vol. 29, pp. 47-65.
- [3] Du Mingfang, Zhang Zhao, Zhou Jian., (2004). Numerical simulation of granular flow with silo pressure and its flow pattern (筒仓压力及其流态的颗粒流数值模拟) [J]. *Special Structures*, Vol. 04, pp. 39-41.
- [4] GB 50322-2011 *Design specification for steel plate silos for grain* [J].
- [5] Jenike A.W., (1987). A theory of flow of particulate solids in converging and diverging channels based on a conical yield function [J]. *Powder technology*, 1987, Vol. 50, pp. 229-236.
- [6] Johnston T., (2001). Silo Technology-Pressure Measurements During Flow in a 23.4 m Diameter x 66.7 m High Raw Meal Blending Silo at a Cement Plant [J]. *Bulk Solids Handling*, Vol. 21, pp. 149-152.
- [7] Matchett A.J., (2007). The shape of the cohesive arch in hoppers and silos-Some theoretical considerations [J]. *Powder Technology*, Vol. 171, pp. 133-145.
- [8] Mathews J C, Wu W., (2016). Model tests of silo discharge in a geotechnical centrifuge[J]. *Powder Technology*, Vol. 293, pp. 3-14. [J]. *Science, Technology and Engineering*, Vol. 20, pp. 2384-2389.
- [9] Mellmann J, Hoffmann T, Füll C., (2014). Mass flow during unloading of agricultural bulk materials from silos depending on particle form, flow properties and geometry of the discharge opening[J]. *Powder Technology*, Vol. 253, pp. 46-52.
- [10] Qu Hengxu, (2012). Analysis of pressure change in the range of decompression cone of cement silo (水泥筒仓减压锥范围内压力变化分析) [J]. *Journal of Jiamusi College of Education*, Vol. 05, pp. 417-418.
- [11] Wang Peiyan, (2023). Mechanism study on the influence of typical conical fluid change on silo unloading (典型锥形流对筒仓卸料的影响机理研究) [D]. *Henan University of Technology*, Vol. 34, pp.712-719.
- [12] Wan J., Wang F., Yang G., (2018). The influence of orifice shape on the flow rate: A DEM and experimental research in 3D hopper granular flows [J]. *Powder Technology*, Vol. 335, pp. 147-155.
- [13] Wang Ruiquan, Liu Hongru, Xu Xiaojuan, (2001). Experimental study on grain inlet and outlet of vertical silo with decompression tube (立筒仓减压管进出粮试验研究) [J]. *Grain Circulation Technology*, Vol. 03, pp. 16-17.
- [14] Wieckowski Z., (2000). Numerical modeling of silo discharge [M]. *Computing in Civil and Building Engineering*. Vol. 84, pp. 764-771.
- [15] Xu, Z.J., Liang, P.F., (2022). Modified lateral pressure formula of shallow and circular silo considering the elasticities of silo wall and storage materials [J] *Scientific Reports*, Vol. 55, pp.772-781 .
- [16] Yuan Fang, Du Qian, Xu Zhijun., (2020). Dynamic lateral pressure of silo sidewall unloading with built-in pressure-reducing tube (内置减压管的筒仓侧壁卸料动态侧压力) [J]. *Science, Technology and Engineering*, Vol. 20, pp. 2384-2389.
- [17] Yuan Fang, Jiang Xuejia, Zhang Jian, (2019). Comparative study on discharge pressure of double sidewall unloading silos with different height-to-diameter ratios (高径比不同的双侧壁卸料筒仓卸料压力对比研究) [J]. *Journal of Henan University of Technology (Natural Science Edition)*, 2019, Vol. 40, pp. 108-113.
- [18] Zhao Song, (2013). Silo storage pressure analysis and its application (筒仓贮料压力分析及其应用) [D]. *Wuhan University of Technology*, Vol.44, pp.833-841.

REVIEW OF AGRICULTURAL PLASTIC FILM RECYCLING EQUIPMENT FROM CHINA

/ 农膜回收装备研究现状及展望

Songmei YANG¹, Benxu WANG¹, Shaofeng RU^{*1}, Xuegeng CHEN², Limin YAN², Jilong WU¹¹School of Mechanical and Electrical Engineering, Hainan University, Haikou / China²School of Mechanical and Electrical Engineering, Shihezi University, Shihezi / China

Corresponding author: Shaofeng RU

Tel: +86089866295121; E-mail: rshaofeng@hainanu.edu.cn

DOI: <https://doi.org/10.35633/inmateh-74-61>**Keywords:** agricultural plastic film, pollution, recycling, machinery, mulch, polyethylene**ABSTRACT**

The treatment of polyethylene film in farmland mainly relies on residual film recycling machinery. However, there is a lack of detailed reports on the characteristics of agricultural residual film recycling machinery and guidance direction for further optimization. This article conducted a detailed literature review, first introducing the hazards of pollution. Then, the operational principles of residual film mechanized recycling equipment were explained from three aspects. Finally, the research direction of residual film pollution control equipment is clarified: it is urgent to reduce the impurity content in residual film and facilitate the resource utilization.

摘要

规模化地膜覆盖栽培技术在高寒干旱地区应用广泛。农田残留膜污染问题因其严重影响农田耕作质量、生态环境和农业可持续发展而备受关注。目前，可生物降解塑料薄膜尚未得到广泛应用，因此聚乙烯薄膜仍然是主流的塑料薄膜材料。农田聚乙烯薄膜的处理主要依靠残膜回收机械设备。然而，目前还没有关于农业残膜回收机械特性的详细报道，也缺乏对残膜回收机器进一步优化的相关指导方向。本文对农残膜回收机进行了详细的文献综述，首先介绍了农残膜污染的危害；然后，从三个方面阐述了操作原理：苗期地膜、耕作层残膜、表层全膜机械化回收设备；聚乙烯农用薄膜需要与农用薄膜、机械和农艺要求相结合，才能实现完全回收；最后，明确了残膜污染控制设备的研究方向：迫切需要降低残膜的杂质含量，促进残膜的资源化利用。

INTRODUCTION

Due to its versatility and lightness, plastic films are increasingly being used in various fields (Horodytska et al., 2018). For instance, plastic films are being used in express delivery, take-out tableware, and agricultural mulch films. Polyethylene film has become the fourth important agricultural production material after seeds, fertilizers, and pesticides (Deutsche Gesellschaft für Internationale Zusammenarbeit (GIZ) GmbH, 2022). Cultivation techniques of plastic film covering offers several advantages, including increased temperature and moisture, weed suppression, and increased crop yields, and is being used worldwide (Gao et al., 2019; Jiang et al., 2017). The use of agricultural film has been shown to increase the yield of cotton, corn, and other crops by approximately 30% (Jiang et al., 2023c). The application of agricultural plastic film planting technology in China has a history of about 40 years. Data from the past 5 years shows that the use of agricultural plastic film in China accounts for approximately 70% of the global total (Jin et al., 2020). In China, the plastic film planting rate of cotton in Xinjiang is 96.6%, while the peanuts and tobacco plastic film planting rates in Shandong Province and Hubei Province have reached 100% (Cui et al., 2024). Fig.1 illustrates the usage and coverage area of agricultural plastic film in China over the years (Liang et al., 2019), showing that China ranks first in the world in terms of coverage area and usage (Jiang et al., 2020).

However, with the widespread use of plastic films, while increasing crop yield, the issue of plastic film residues has also emerged. The accumulation of residual film from continuous mulching of farmland, coupled with the long-term use of ultra-thin farmland mulching films and inadequate awareness of the hazards of residual film pollution among farmers, has resulted in serious residue of farmland mulching films (Zhang et al., 2019a).

Songmei Yang, Lecturer; Benxu Wang, Postgraduate student; Shaofeng Ru, Associate Professor; Xuegeng Chen, Academician of Chinese Academy of Engineering; Limin Yan, Professor; Jilong Wu, Postgraduate student.

This residue hinders root growth and inhibits soil capillary action (Koskei *et al.*, 2021), affecting soil water holding capacity and the functional relationship between the microbial activity and water stable aggregates (de Souza Machado *et al.*, 2018), greatly impacting the quality of farmland cultivation and the ecological environment (Cao *et al.*, 2023a), and can even lead to a reduction in crop yield (Ding *et al.*, 2022b; Hu *et al.*, 2020). These large pieces of plastic film can further break down into micro/nano plastics with a particle size of less than 5 mm, and there is an annual trend of migration into deeper soil layers (Yan *et al.*, 2008). The content of microplastics pollutants in soil has exceeded that of marine ecosystems (Iqbal *et al.*, 2020). The presence of microplastics not only poses a threat to soil organisms and crop growth but also has the potential to contaminate groundwater and enter the food chain, thus endangering human health (Ding *et al.*, 2022a).

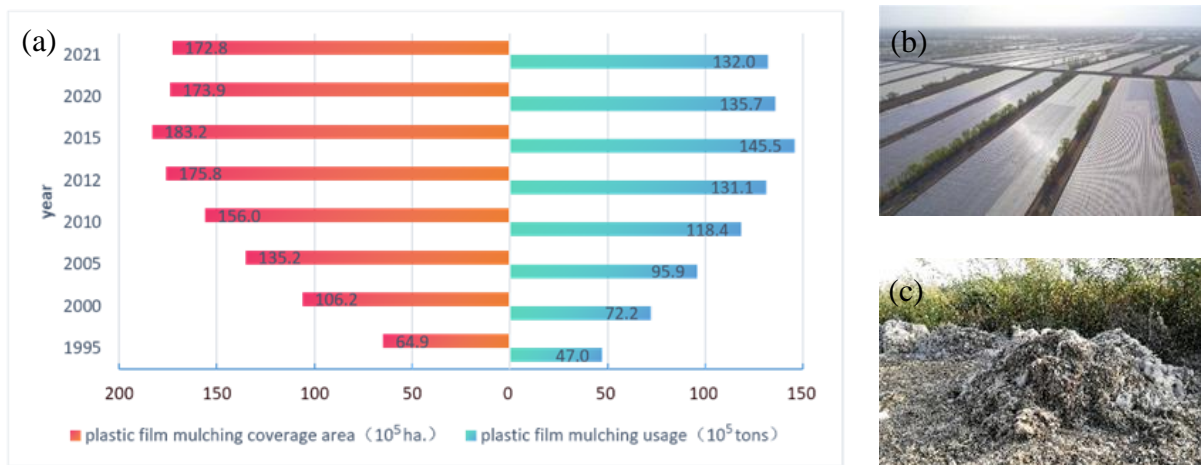


Fig. 1 -The use of agricultural film in China

(a) Annual usage and coverage area of agricultural plastic film in China; (b) Scenes after mulching and sowing in farmland; (c) Accumulation of residual film on the ground.

Polyethylene plastic film is known for its stability and can take decades or even hundreds of years to completely degrade (Niu *et al.*, 2023). Statistics show that the average plastic film residue intensity in China is $67.5 \text{ kg}\cdot\text{hm}^{-2}$ (Liang *et al.*, 2019). The Xinjiang Uygur Autonomous Region, which has the largest cotton planting area in China, experiences nearly 100% cotton mulching. Consequently, it is the region with the most severe agricultural plastic film pollution, with an average residue amount of $255.0 \text{ kg}\cdot\text{hm}^{-2}$ (Liu *et al.*, 2022). The arid climate and water resource shortages in regions like Inner Mongolia and Gansu have led to a significant use of mulch film, resulting in severe pollution from residual film. The average amount of residual mulch film in the crop layer is $127.1 \text{ kg}\cdot\text{hm}^{-2}$ (Yin *et al.*, 2022). Over time, the amount of residual plastic film in the tillage layer has been increasing (Yang *et al.*, 2023). According to estimates by scholars, the farmland in northwest China alone contains approximately 1.0×10^6 tons of residual macroplastics and 2.7×10^5 tons of residual microplastics as of 2020 (Cao *et al.*, 2023b).

The main methods of disposing polyethylene mulching film residues in farmland include landfilling and recycling. However, the agricultural film recycling rate in China is currently less than $2/3$ (Zhang *et al.*, 2021). Discarding and burying agricultural film waste resources are considered single-line economy methods (Dong *et al.*, 2022a; Lu *et al.*, 2023). On the other hand, recycling mulch film resources promotes a circular economy. Fig. 2 illustrates three main ways of reusing resources after recycling residual film. The recycled plastic film can be used for power generation, processed into plastic particles or wood plastic granules for subsequent production. From this, it can be seen that the recycling of agricultural residue film is a win-win measure, which is not only beneficial for environmental protection, but also for waste utilization.

In recent years, there has been significant attention given to biodegradable plastics due to their degradable properties. Biodegradable mulch films are considered as potential substitutes for polyethylene mulch films. However, the comprehensive performance of degradable mulch films is currently inferior to traditional polyethylene agricultural films in all aspects, and they also have a higher cost. Moreover, there are concerns about the potential risks and impact on the food chain (Ding *et al.*, 2022b; Shen *et al.*, 2020; Sintim *et al.*, 2021), which has limited their widespread promotion and application (Jiang *et al.*, 2023a). Therefore, until degradable mulch films can be widely adopted, polyethylene mulch films continue to be the primary choice for farmland.

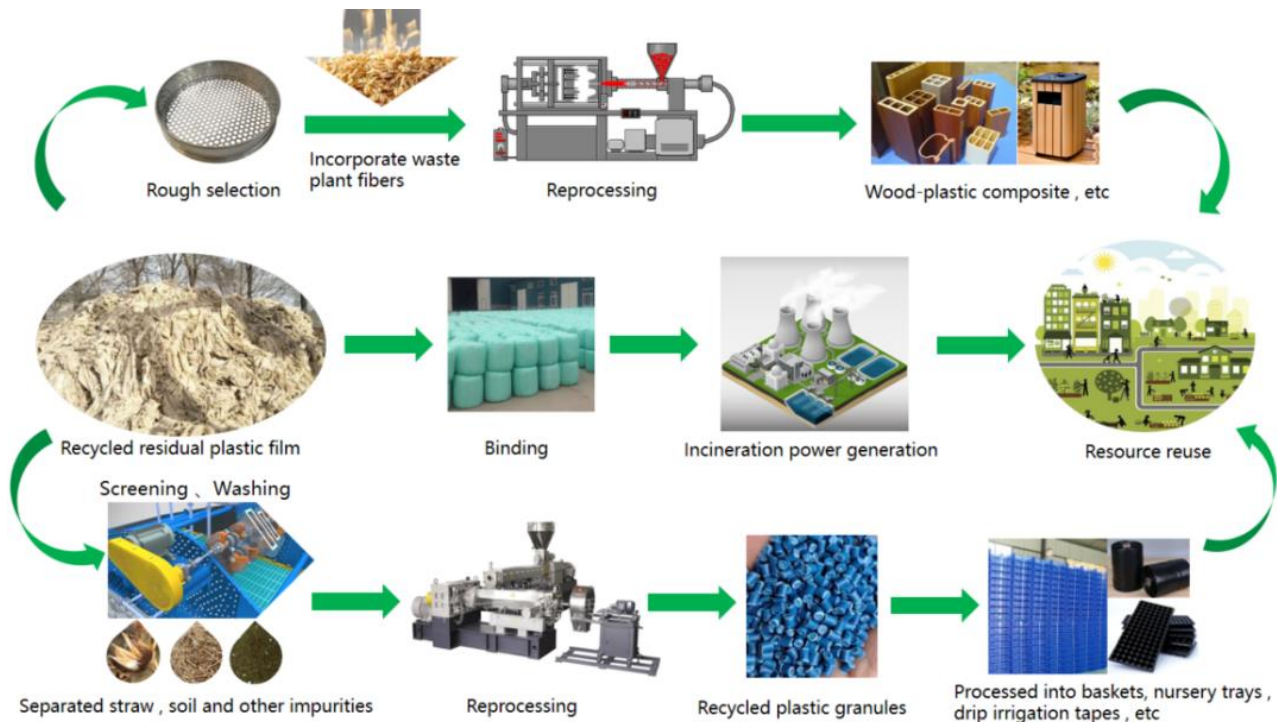


Fig. 2 - Three methods for reusing residual plastic film recycling resources

In summary, the primary task in treating residual film pollution in farmland is to recycle it. However, manual recycling has low efficiency, so mechanized recycling is an effective means to solve the problem of residual film pollution. This article summarizes the structural characteristics and applicable conditions of typical residual film recycling and post-treatment machinery, looks forward to the key technologies for residual film pollution control, provides reference for further optimization of residual film recycling machines, and puts forward suggestions for farmland residual film pollution control.

CURRENT RESEARCH STATUS OF PLASTIC FILM RECYCLING MACHINES

The issue of plastic film recycling is a global concern, and mechanical recycling is currently the most commonly used method to address this problem (Sica et al., 2015). In countries and regions such as Japan and Europe, agricultural mulch films with a minimum thickness of 0.02 mm are predominantly used (Jin et al., 2020), as depicted in fig. 3. Due to the thickness, strength, and durability of these films, a simple film rolling machine can effectively achieve the purpose of residual plastic film recycling, with simple machinery and high picking efficiency.

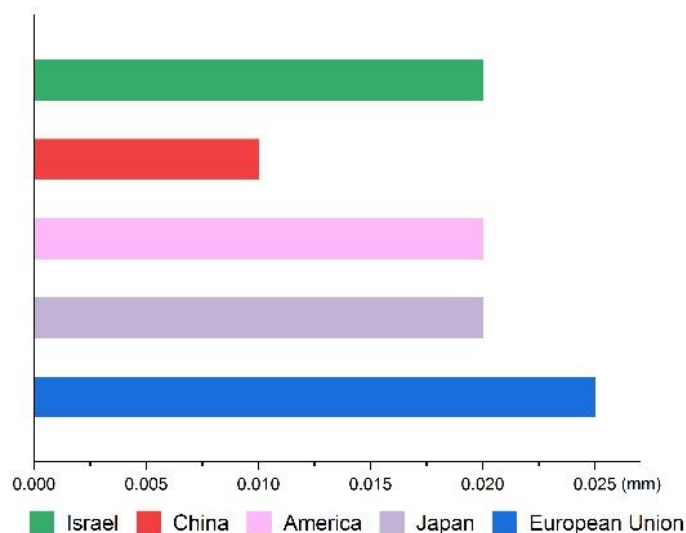


Fig. 3 - The thickness of applied plastic film in several representative countries

Before 2018, China's agricultural plastic film followed the national mandatory standard GB 13735-1992 'Polyethylene Blown Agricultural Mulch Covering Film' (Jin *et al.*, 2020). The standard stipulated that the thickness of the plastic film should be 0.008–0.02 mm. When the limit deviation of the plastic film with a thickness of 0.008 mm was ± 0.003 mm, it was considered a qualified product. As a result, plastic films with a thickness of 0.006–0.008 mm (Yan *et al.*, 2014) were commonly used due to their low cost, despite being easily damaged. Over the course of more than 20 years, the thinness of these films made them prone to aging, breaking, and tearing, thereby increasing the difficulty of recycling. Each year, the broken plastic film fragments mix into the soil, leading to the accumulation of microplastics. Moreover, the plastic film rolling machine cannot be used in this scenario. In May 2018, the revised national mandatory standard GB 13735-2017 'Polyethylene Blown Agricultural Mulch Covering Film' (Yang, 2020) was implemented. This new standard requires a minimum mulch film thickness of 0.01 mm and includes revisions to the tensile properties and weather resistance, resulting in better integrity of the recovered mulch film and facilitating mechanized recycling.

Based on the traditional agricultural film collecting operation time and process requirements, residual plastic film recycling machines can be categorized into three types: seedling stage plastic film recycling machines, post-autumn residual film recycling machines, and pre-sowing residual film recycling machines (Li *et al.*, 2020). With the advancement of mulch film standards, the integrity and strength of the residual film during recycling have improved. Therefore, considering the integrity of the residual plastic film and the operating principle of the residual plastic film recycling machine, the machine can be further classified into seedling stage residual film recycling machines, tillage layer residual film recycling machines, and surface whole film recycling machines. Both the seedling stage mulch recycling machine and the surface whole film recycling machine can recover the entire film. The difference is that the seedling stage mulch recycling machine needs to avoid the field seedlings during operation, whereas the tillage layer residual film recycling machine can be used to recycle broken residual film at any time after land preparation.

Seedling stage plastic film recycling machine

Recycling plastic film during the seedling stage refers to the collection of residual film covering the surface of crops before irrigation. During this stage, the mulch film is laid for a short period of time, resulting in minimal aging, good integrity, and little accumulation of soil and impurities. This makes it easier to mechanically remove the film. As a result, in areas with favorable irrigation conditions, some researchers have suggested recycling mulch films during the seedling stage.

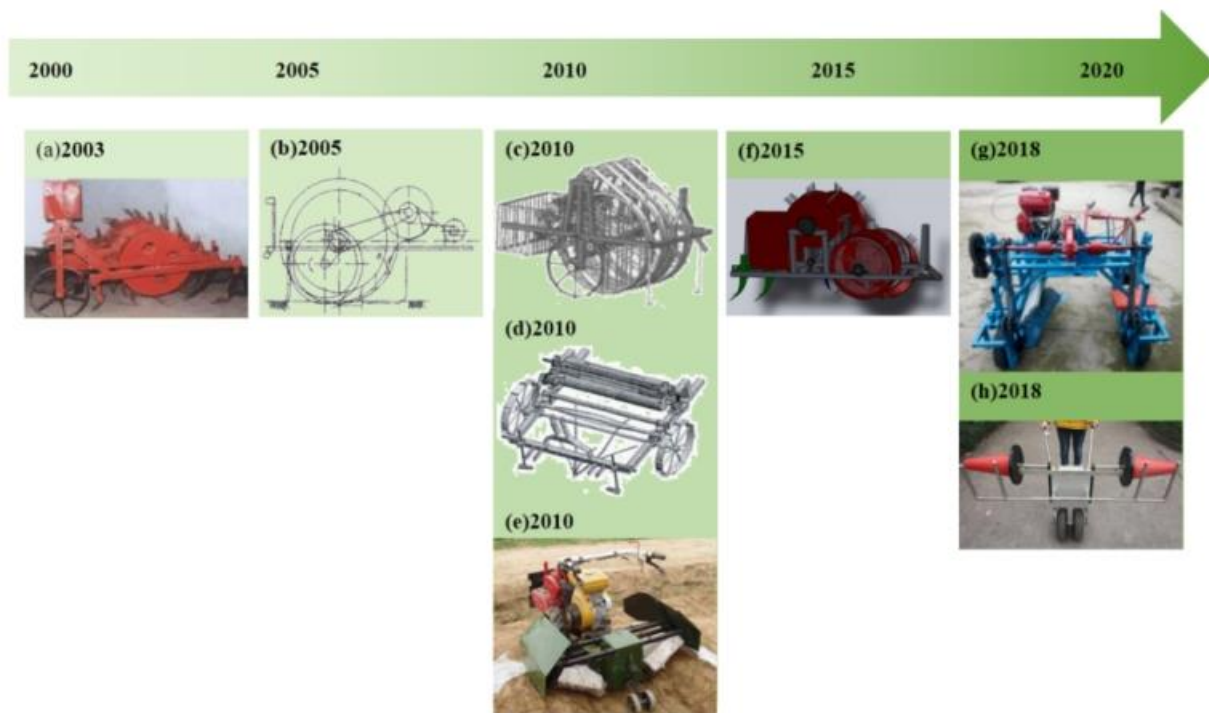


Fig. 4 - Representative seedling stage plastic film recycling machine

(a) MS-2 corn seedling stage film harvesting and tillage combined operation machine (Dong *et al.*, 2003) (b) Roll type cotton seedling residual film recycling machine (Xue *et al.*, 2005) (c) Plastic film collector for corn fields (Yang *et al.*, 2010b) (d) Plastic film collector for cotton fields during seedling period (Yang *et al.*, 2010a) (e) Plastic film collector in tobacco seedling stage (Cui, 2011) (f) Corn seedling film harvester (Wu, 2015) (g) Plastic film recycling machine for tobacco seedlings in mountainous areas (Liu, 2019) (h) Light and simple film stripper in tobacco seedling stage (Wang, 2019)

The cotton seedling stage residual film recycling machine (Xue et al., 2005) and the corn seedling stage film recycling and intertillage combined machine (Dong et al., 2003; Wu, 2015) as shown in the fig. 4 both utilize film rolling methods. In these machines, the film ends need to be manually wound on the film rolling wheel. When the remaining film roll reaches a certain level, the machine will stop, and then the film will be removed manually. This type of seedling residual film recycling machine may cause film tearing during the rolling process, while the floating synchronous film-rolling type seedling film recycling machine uses a floating synchronous film-rolling mechanism to effectively prevent film tearing, breakage, or retention (Yang et al., 2010a; Yang et al., 2010b).

Based on the analysis above, it is evident that the plastic film recycling machine used in the seedling stage often employs mulch film winding technology or a combination of film lifting mechanism to assist the winding machine. This approach is primarily utilized for mulch recycling in crops that do not require a significant increase in ground temperature during later stages of growth, such as corn. The mulch film recycling machine at the seedling stage takes on different forms depending on the crop variety, agronomic technology, and other requirements. However, it is important to note that recycling mulch films in the seedling stage can result in increased crop irrigation and soil compaction, particularly in dry agricultural areas that rely on drip irrigation technology under the film. Presently, there are limited methods available for recycling mulch films in the seedling stage.

Cultivated layer residual film recycling machine

The objective of recycling residual film in the tillage layer is to recover the blocky residual film present in the soil after plowing and levelling the land in spring, as well as the severely damaged plastic film after harvesting autumn crops. To address the issue of residual film pollution in the soil plow layer, various scientific research institutes have conducted studies on machines and tools for recycling residual film in farmland plow layer (Chen et al., 2020; Guo et al., 2020; Jin et al., 2018; Shi et al., 2019; Shi et al., 2023b; Wang et al., 2008; Zhang et al., 2019b). Currently, there are two main methods for recycling residual film in the tillage layer. The first method involves using an elastic toothed residual film recovery machine with a rake-like structure to gather the residual film together. The second method is the roller-type residual film recycling method, where a roller with multiple teeth is used. As the roller rotates, the residual film in the tillage layer adheres to the teeth and is then mechanically or pneumatically removed.

1. Elastic tooth type residual film recovery machine

The key components of the elastic tooth typed residual film recovery machine are typically made of manganese alloy materials such as No. 60 or 65 manganese steel and have an arc shape. During operation, the elastic tooth punctures the film and immediately collect it on the teeth for retrieval. The residual film is unloaded after reaching the end of the field. The elastic tooth type residual film recovery machine (Shi et al., 2017b) shown in fig. 5(a) only penetrates the film and requires manual removal. Some researchers have suggested adding a film unloading mechanism to the elastic toothed residual film recovery machine (Shi et al., 2017a; Tian, 2020; Tian et al., 2018; Wang, 2018), which allows for the completion of film collecting, stripping, and unloading processes in a single operation, thereby enhancing the efficiency of residual film recovery.



Fig. 5 - Representative tooth type residual film recovery machine

(a) tooth type residue plastic film collector of ridged peanut (Shi et al., 2017b). (b) Cotton stalk chopping and residual plastic film collecting combined operation Machine (Tian, 2020; Tian et al., 2018) (c) Standing cotton stalks raking-film machine with wide folding and monomer profiling (Wang, 2018; Wang et al., 2017)

Compared with other forms of residual film recycling machines, the elastic tooth type residual film recovery machine has a lower recovery rate of residual film, typically around 50%, and a high impurity content rate. However, it has gained wide usage in Xinjiang, Gansu, and Inner Mongolia in China due to its simple structure, low cost, and high operating efficiency.

2. Roller type residual film recycling machine

Fig. 6 illustrates various types of roller-type residual film recovery machines. These machines take advantage of the roller's rotation during operation. When it reaches the lowest point, the teeth of the roller penetrates the residual film, and a stripping device is positioned to remove the film, thus completing the residual film recycling operation. The roller-type residual film recovery device, as shown in Fig. 6(b) (Zhang, 2023; Zhang et al., 2023), features pick-up teeth installed on the outer edge of the roller. The pick-up roller collects the residual plastic film, and the stripping device removes it from the roller, depositing it in the film collection box to complete the residual film recovery operation. The corn full-film double-furrow residual film recovery machine as illustrated in fig. 6(e) (Dai et al., 2016), which differs from the previous devices in that it uses an eccentric pickup roller to collect the residual film. After the film is stripped off by the stripping device, it is rolled up and recycled by the film rolling roller, which is driven by ground wheels to maintain synchronicity. The strip-shaped residual film baling machine, as shown in fig. 6(f) (Niu et al., 2017), is specifically designed for picking and packaging strip-shaped residual film. This machine effectively removes most impurities through two operations involving the impurity cleaning roller and the eccentric pickup roller.

Each roller-type residual film recycling machine operates based on different working principles, with the main distinction being the working principle of its core component — the pickup roller. The pickup device in the roller-type residual film recovery machine can be categorized into two types: concentric roller-type pickup device and eccentric roller-type pickup device. This classification is based on the relative motion relationship between the pickup teeth and the roller, as well as the positional relationship between the center line of the pickup teeth assembly and the center line of the roller.

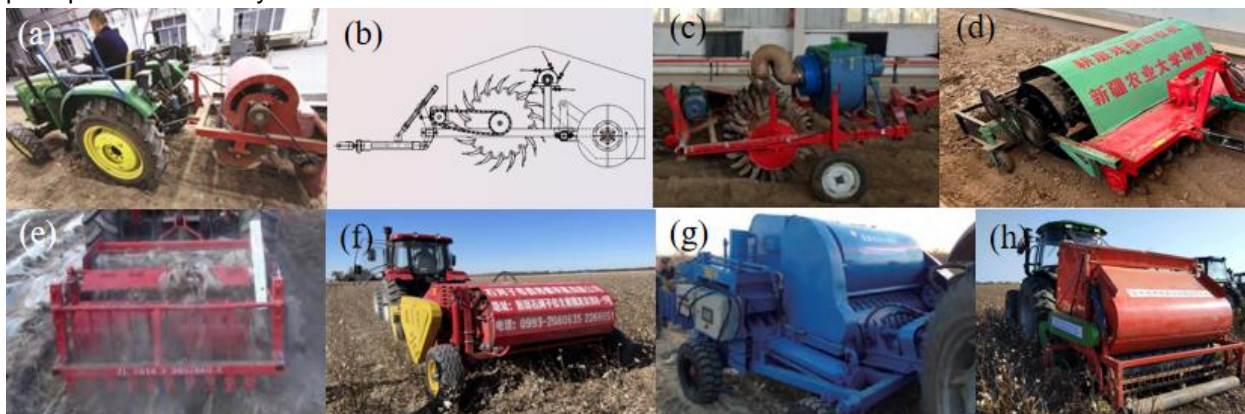


Fig. 6 - Representative roller-type residual film recovery machines

(a) Nail-teeth roller-type residual film recovery device (Chen et al., 2020);

(b) 1SMB-3600A residual film recycling machine (Zhang, 2023; Zhang et al., 2023); (c) Comb toothed pneumatic film removal type plow layer residual film recovery machine (Guo et al., 2020); (d) Roller type residual film recovery machine (Shi et al., 2023b); (e) Collector for corn whole plastic film mulching on double ridges (Dai et al., 2016); (f) Collecting and Separating Device for Strip Plastic Film Baler (Niu et al., 2017); (g) Roller-type elastic tooth residual film recovery machine (Liu, 2023); (h) 4JSM-2000 type combined operation machine for cotton stalk chopping and plastic film recovery (You, 2021; You et al., 2017b)

2.1. Concentric roller-type pickup device

The pick-up elastic teeth and the roller in the concentric roller-type pick-up device are typically combined into a single unit without any relative movement between them. The rotation center lines of the two components coincide with each other. 1SMB-3600A type fragmented film collector (Zhang, 2023; Zhang et al., 2023) which features a residual film pickup roller with arc-shaped teeth, as depicted in fig. 7. The residual film pickup roller and the film stripping roller rotate in opposite directions during operation. The film-picking teeth on the roller pick up the residual film from the tillage layer and transport it to the stripping area. Subsequently, the residual film attached to the teeth is peeled off by the stripping roller and collected in the residual film collection device.

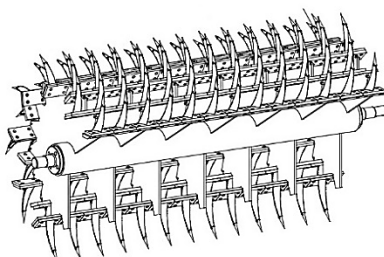


Fig. 7 - Roller of 1SMB-3600A type fragmented film collector

2.2. Eccentric roller-type pickup device

The pickup teeth and the roller of the eccentric roller-type pickup device can move relative to each other. There are two forms of the eccentric roller based on its principle: the eccentric shaft type and the crankshaft type. In the eccentric shaft type, the residual film pickup teeth assembly rotates synchronously with the roller, but their center lines do not coincide. The elastic teeth expand and contract through the strip holes on the roller (Niu et al., 2017; You et al., 2017a), as shown in fig. 8(a). On the other hand, in the crankshaft type, the residual film pickup elastic teeth are installed on the connecting rod of the crankshaft at the shaft diameter position. The elastic teeth can rotate relative to the connecting rod shaft diameter, while the pickup roller remains fixed and collinear with the center of the crankshaft. As the crankshaft rotates, the elastic teeth expand and contract through the holes on the roller (Dai et al., 2016; Jin et al., 2018; Niu et al., 2017), as shown in fig. 8(b). Regardless of the form of the eccentric roller used, the pickup teeth and the roller undergo relative radial movement to pick up the residual film. When the elastic teeth are fully extended, they pick up the residual film. As the elastic teeth shrink, the residual film is picked up by them and returned to the roller for film removal. This marks the beginning of the impurity cleaning and residual film collection stage.

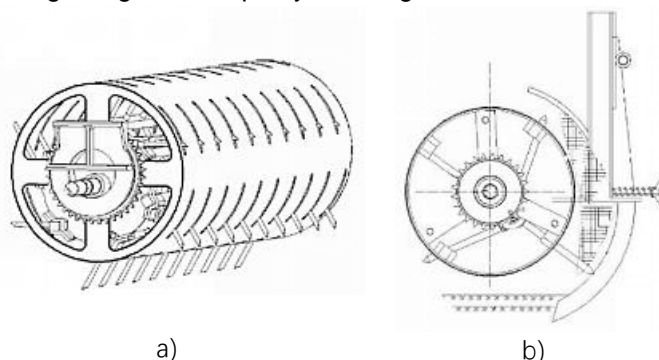


Fig. 8 - Schematic diagram of eccentric roller structure.
(a) Eccentric shaft roller (b) crankshaft eccentric roller

The advantage of the roller-type residual film recycling machine is its high work efficiency. The concentric roller-type residual film recycling machine is suitable for recycling small pieces of broken plastic film, while the eccentric roller type residual film recycling machine is more suitable for recycling large pieces of plastic film. This is due to the relative movement between the pickup teeth and the roller of the eccentric roller-type residual film recycling machine. It is easy to accumulate in the opening of the roller if the broken small pieces of film are not removed promptly from the elastic teeth, resulting in issues such as poor movement of the elastic teeth or even blockage.

In addition to the two methods mentioned above for recovering residual film from the tillage layer, there is also a screening method available (Luo et al., 2018; Xu et al., 2017; Yan et al., 2017; You et al., 2017c), as shown in fig. 9.



Fig. 9 - Screening type residual film recovery machine.
(a) Shovel screen residual film recycling machine (Yan et al., 2017; You et al., 2017c); (b) Chain screen cultivator residue film recycling machine (Luo et al., 2018); (c) Net chain peanut residue film recycling machine (Xu et al., 2017)

During the operation of the screening-type residual film recovery machine, the soil lifting mechanism is responsible for transporting the soil from the tillage layer to the screening device. The soil is then filtered under the action of vibration, allowing the collection of the residual film. Typically, these machines are equipped with an excavation shovel at the front of the unit. This method is particularly effective for collecting smaller residual film fragments. The film-soil mixture is excavated by the shovel and directed to the vibration separation mechanism, where the soil is separated from the remaining film. It is important to note that this type of machine has a large and complex structure, as well as high power consumption.

Surface film recycling machine

In arid areas or areas where under-film drip irrigation is used, residual film is typically recycled after the crops are harvested. This recycling process does not have any negative impact on the quality of the crops, and is currently the mainstream method of residual film recovery. The implementation of the national standard GB 13735-2017 'Polyethylene Blown Agricultural Mulching Film' has significantly improved the performance of mulching film after crop harvest, ensuring its integrity and strength. As a result, Chinese scientific researchers have developed various tooth chain-type residual film recycling machines for surface film recycling (Cao *et al.*, 2023c; Jiang *et al.*, 2019; Jiang *et al.*, 2023b; Jin *et al.*, 2022; Wen *et al.*, 2021; Yang *et al.*, 2020; Yang *et al.*, 2021; Yang *et al.*, 2018).

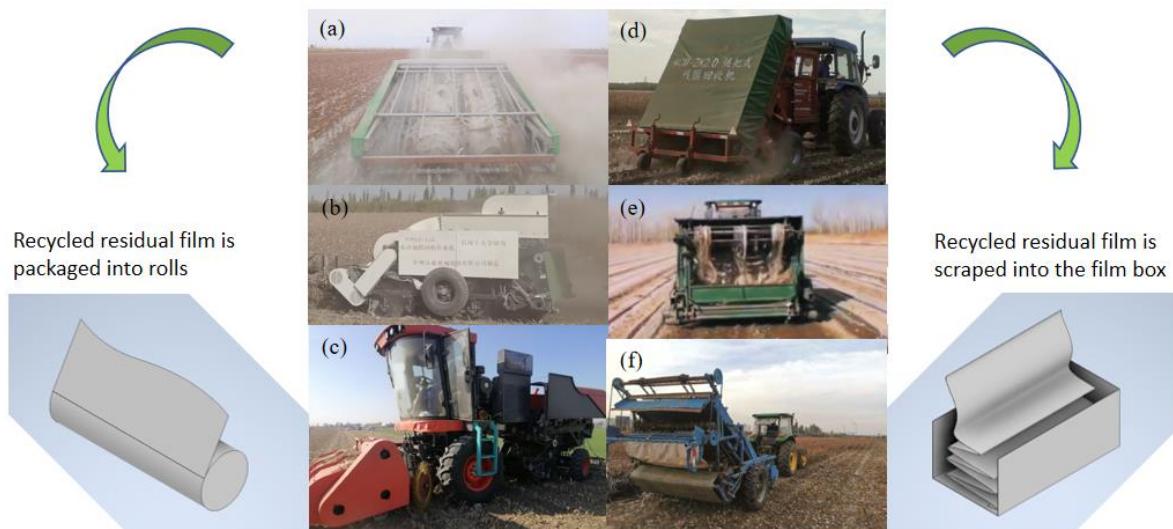


Fig. 10 - Representative model of tooth-chain-type residual film recycling machine.

(a) Passive cotton field residual plastic film recycling machine (Yang, 2020; Yang *et al.*, 2018). (b) Second stage chain plate straw crushing and plastic film recycling combined operation machine (Wen *et al.*, 2021). (c) Self-propelled straw crushing and residual film recycling combined operation machine (Jiang *et al.*, 2023a). (d) Side row cotton straw returning and residual plastic film recycling combined operation machine (Cao *et al.*, 2023c; Xie *et al.*, 2020). (e) Vertical double-row chain residual film recycling machine (Shi *et al.*, 2023a). (f) Clamping finger-chain type residual film collector (Duan, 2017; Tang *et al.*, 2020)

The tooth-chain-type residual film recovery machine is commonly used in conjunction with the straw return machine to perform joint operations. This machine can simultaneously crush cotton stalks and recover residual film, thereby improving operational efficiency and reducing land compaction. The tooth-chain-type residual film recycling machine is capable of performing multiple functions such as soil entry, film lifting, impurity cleaning, film stripping, and film collection. Its main operating component is a ring-shaped device composed of a tooth-chain that can pick up and transport plastic film. The straw returning machine breaks down straw into pieces and transports them to the ground on both sides or behind the unit where the residual film has been collected. During the process of straw breaking, the straw return machine creates negative pressure which helps remove light impurities from the membrane surface, thus creating favorable conditions for the operation of the residual film recovery machine. The tooth-chain-type residual film recovery machine, as shown in fig. 10 (a)-(c), allows for easy packaging of the residual film into film rolls for transportation and processing. Similarly, the tooth-chain-type residual film recovery machine shown in fig. 10(d)-(f) collects the residual film and places it into a film collecting box.

The device shown in fig. 11 (a) is the key core component of the recycling machine in fig. 10(a). The pickup, impurity cleaning, and film removal device in fig. 11(a) cleverly flips the film surface with the movement of the chain, allowing impurities to fall into the screw conveyor for removal. The device shown in fig. 11 (b) is the key core component of the recycling machine in fig. 10 (d), which transports the mulch film upwards using elastic teeth and a supporting plate, with the angle of the elastic teeth adjusted for effective stripping. Additionally, the tooth-chain-type residual film recovery machine also has vertical double-row chain-type (Shi *et al.*, 2023a), which utilizes the angle of the chain row arrangement for convenient impurity removal and film stripping under the force of gravity. In addition to mechanical cleaning devices, residual film removal devices can also use methods such as air flow assisted impurity removal (Peng *et al.*, 2023).

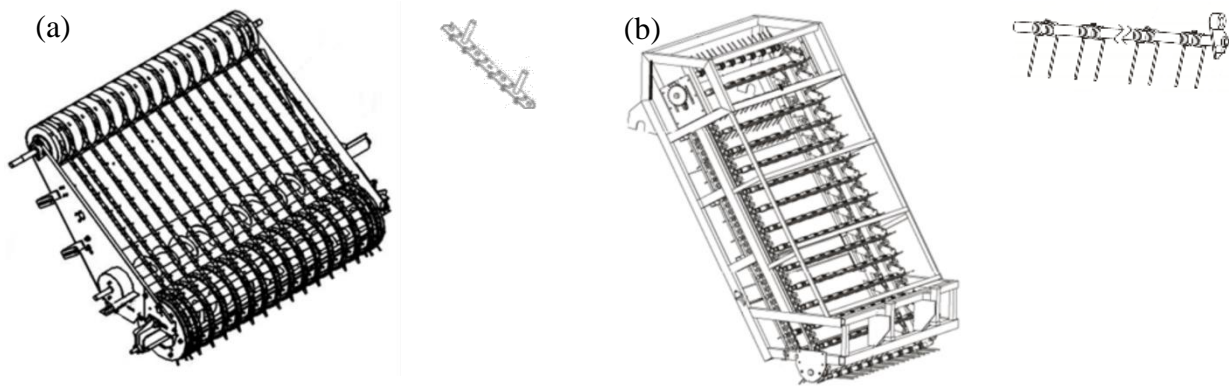


Fig. 11 - Key core components of the tooth-chain-type residual film recycling machine

(a) Key core components of the passive residual film recycling machine;

(b) The key core components of the side row cotton straw returning and residual plastic film recycling combined operation machine

There is no significant correlation between the amount of mulch film in farmland soil, the planting pattern, and the age of the mulch film. However, it is related to the recovery rate of residual film in the current season (Wang *et al.*, 2020). Therefore, the solution to the problem of residual film pollution in farmland is to completely recycle the mulch film laid in the current season, gradually recycle the film fragments in the soil (Zhao *et al.*, 2017). The tooth chain type residual film recovery machine can effectively recycle the entire film and has the advantage of a high recovery rate of residual film. In recent years, research has focused on improving the impurity removal rate and film unloading efficiency. This area shows good prospects for industrial development. Currently, there are agricultural machinery enterprises conducting small-scale trial production and demonstration and promotion.

RESIDUAL FILM POST-TREATMENT EQUIPMENT

The research on equipment for recovering agricultural residue film has achieved preliminary results (Dong *et al.*, 2022b; Lv *et al.*, 2015; Yang, 2005; Zhang, 2015). However, the mechanically recycled residual film is often contaminated with impurities like soil and straw, making it challenging to directly process it into plastic particles for reuse. To address this issue, residual film post-processing equipment plays a crucial role in effectively separating the residual film from impurities. This separation process is beneficial for subsequent processing and reuse of the residual film, contributing to its resource utilization.

According to different separation principles, residual film and impurity separation technology can be divided into three categories: air separation, electrostatic separation, and water washing separation. Various equipment has been developed based on the different physical properties of the residual film and impurities as depicted in fig. 12, which exhibit different behaviors in wind, electrostatic fields, and water.



Fig. 12 - Representative residual film post-treatment equipment

(a) Trommel sieve type film miscellaneous wind separator (Kang *et al.*, 2022). (b) Washing and separation device of residual film mixture collected by machine (Li, 2018). (c) Film-stubble separation device under high-voltage electrostatic adsorption (Li, 2023)

A roller screen type film and impurity air separator, which utilizes the combined action of roller screen rotation and air blowing to disperse the film and impurity mixture (Kang et al., 2022; Peng et al., 2020). The residual film with a smaller density is blown towards the circular film collecting box at the end of the cylindrical screen, while impurities such as cotton stalks with high density and high suspension speed are thrown out from the sieve holes of the cylindrical screen through inertia. The mechanism of film-stubble separation under high-voltage electrostatic adsorption was studied (Li, 2023; Li et al., 2022). After bench testing, it was found that the residual film adsorption rate was 90%, while the separation rate of residual film and impurities was 78%. However, further improvements are still needed. A water washing and separation device for mechanical collection of residual film mixture was developed (Hu et al., 2024; Li, 2018; Li et al., 2019). This device can separate the residual film and impurities based on the different positions of the floating layer of the material in the vortex flow field of the water tank.

URGENT RESEARCH WORK TO BE CARRIED OUT

Residual film recovery rate and impurity content rate are two important evaluation indicators for residual film recovery, but they are mutually exclusive. When recycling the residual film, film picking teeth are inserted into the soil to lift the plastic film from the ground. However, if the entire film is recycled, impurities such as soil and straw on the surface of the plastic film cannot be removed immediately and will be wrapped in the film roll or collected in the film collecting box. A higher recovery rate of residual film requires the device to penetrate the soil deeply during the pick-up stage, resulting in a higher impurity content rate, and vice versa. Although current residual film recycling machinery achieves a high recovery rate, it still faces the challenge of high impurity content. The recycled residual film becomes mixed with straw and soil, making it difficult to separate. In particular, the high soil content hinders resource utilization. Therefore, in the forthcoming research, our focus will be on upgrading or improving the technology to reduce the impurity content of the residual film while maintaining a high recovery rate.

SUMMARY AND OUTLOOK

The ultimate trend is to replace polyethylene mulch films with degradable films, and national standards have been established for fully biodegradable agricultural ground covering films (Lin et al., 2024). However, since the environmental impact of fully biodegradable mulch films is currently unknown (Min et al., 2022), polyethylene mulch films will continue to be the dominant choice for the next 10 years or so, resulting in a long coexistence period between the two. The use and recycling/degradation conditions of PE film and biodegradable film are different, as shown in fig. 13. Research units in China have conducted studies on recycling equipment for polyethylene residual films, designing different machines based on different crops and production models. Through extensive practice, it has been determined that only the combination of agronomy, agricultural machinery, and agricultural film can create basic conditions for the mechanized film recycling effectively. By gradually removing the old residual plastic film in the soil without generating new film residue, the content of residual film in the soil will decrease over time. Mechanized recycling of residual film is an essential step towards achieving this. After mechanized recycling, the residual film can be transformed into a valuable resource, contributing to a circular economy and providing raw materials for processing enterprises. This approach is beneficial for environmental protection and sustainable development. Therefore, developing an efficient and practical residual film recycling machine holds great practical significance.

This article provides a review of the recent advancements of residual film recycling machinery and post-processing technology and equipment in China. The aim is to enhance recycling efficiency and reduce environmental pollution. However, the utilization of polyethylene mulch films requires more than just the availability of corresponding technology and equipment. It necessitates government guidance on the use of compliant mulch films, departmental supervision and implementation, national participation in governance, centralized recycling at outlets, initial deep processing by enterprises, and comprehensive resource utilization. These measures are essential for effectively promoting the recycling and reuse of waste agricultural films, mitigating 'white pollution' in the fields, and achieving a 'win-win' situation for ecological and social benefits. Therefore, in future agricultural production, in addition to technical aspects, it is crucial to steadily promote agricultural film pollution control from the following perspectives:

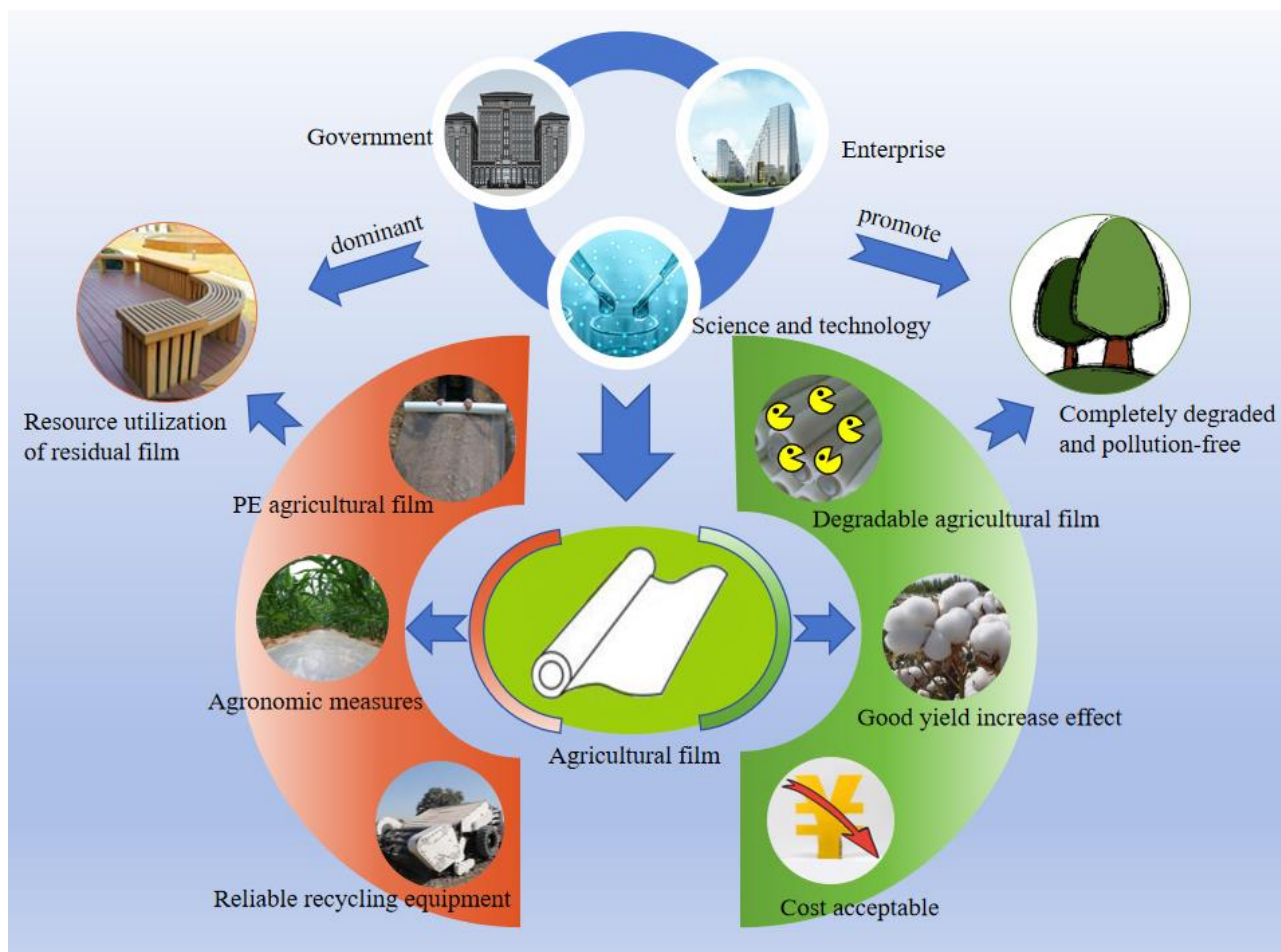


Fig. 13 - Usage conditions of PE agricultural film and degradable film

To control the thickness of agricultural film and minimize plastic pollution, it is crucial to use a high-strength weather-resistant film of a certain thickness. This will prevent the film from breaking into small pieces during harvest and enable mechanized recycling without damage. By completely recycling the film that very year and gradually reducing the stock of residual film in farmland, the goal of reducing volume and increasing efficiency can be achieved. To accomplish this, it is essential to strengthen market supervision, enforce standardized quality for agricultural mulch films, set higher requirements for suppliers, prohibit the use of recycled materials in agricultural mulch films, establish a quality tracking mechanism, and ensure compliance with national standards for agricultural film thickness.

To ensure the recovery rate of mulch film, it is important to clarify the goals and responsible persons for leaving residual film from the fields. Currently, plastic film recycling and processing in China is extensive. However, it is necessary to establish clear responsibilities and obligations for government departments at all levels, producers, sellers, and users. This will help improve the waste plastic film recycling system. Specifically, the responsibilities and obligations of film users for leaving residual film from the fields should be defined, and strict measures should be implemented to control the recycling rate of residual plastic film that very year.

To improve the number and coverage areas of residual film recycling outlets and reuse companies, it is crucial to address the current challenges. Our investigation reveals that many farmers either loosely recycle the residual film during land preparation in autumn or directly incorporate it into the soil without any recycling methods. A major contributing factor is the lack of recycling outlets for residual film. Even if farmers are willing to recycle the residual film, the absence of recycling outlets forces them to either accumulate it in the fields or resort to burning. Therefore, it is essential to establish recycling outlets in areas where agricultural film is extensively used. One approach is to support relevant cooperatives in a planned manner, enabling them to undertake the comprehensive management of residual film on farmland. Additionally, it is important to provide support to waste film reuse enterprises. These measures will enhance farmers' willingness to recycle residual film and improve the overall recovery rate.

ACKNOWLEDGEMENT

The authors were funded for this project by Hainan Provincial Natural Science Foundation of China (521QN0869) and Hainan Provincial Academician Innovation Platform Research Project (SQ2021YSPTJXRWS0011).

REFERENCES

- [1] Cao, J., Gao, X., Cheng, Z., Song, X., Cai Y., Siddique, K.H., Zhao X., Li, C. (2023a). The harm of residual plastic film and its accumulation driving factors in northwest China. *Environmental Pollution*. 318:120910.
- [2] Cao, J., Gao, X., Hu, Q., Li, C., Song, X., Cai Y., Siddique, K.H., Zhao, X. (2023b). Distribution characteristics and correlation of macro- and microplastics under long-term plastic mulching in northwest China. *Soil and Tillage Research*, 231:105738.
- [3] Cao, S., Xie, J., Yang, Y., Liu, Y., Lu, Y., Sun, B. (2023c). Design and experiment of side row cotton straw returning and residual film recovery combined machine. *Journal of Jilin University (Engineering and Technology Edition)*, 53(05):1514-1528.
- [4] Chen, X., Chen, X., Li, J., Li, C., Yang Y. (2020). Design and test of nail-teeth roller-type residual film recovery device before sowing. *Transactions of the Chinese Society of Agricultural Engineering*, 36(02):30-39.
- [5] Cui, F. (2011). *Study on Used Plastic Film Collector in Tobacco Seedling Stage*. [Master's thesis, Shandong Agricultural University].
- [6] Cui, J. X., Xu, J. Z., Bai, R. H., Liu, Q., He, W. Q., Yan, C. R. (2024). Analysis of the behavior and driving forces of the application, recovery, and management of plastic mulch film by farmers in typical areas of China. *Journal of Agricultural Resources and Environment*. 41 (01):175-186.
- [7] Dai, F., Zhao, W., Zhang, F., Wu, Z., Song, X., Wu, Y. (2016). Optimization and experiment of operating performance of collector for corn whole plastic film mulching on double ridges. *Transactions of the Chinese Society of Agricultural Engineering*, 32(18):50-60.
- [8] de Souza Machado A.A., Lau C.W., Till J., Kloas W., Lehmann A., Becker R., Rillig M.C. (2018). Impacts of microplastics on the soil biophysical environment. *Environmental Science Technology*, 52, 9656-9665.
- [9] Deutsche Gesellschaft für Internationale Zusammenarbeit (GIZ) GmbH (2022). Analysis Report on Current Status of PE Mulch Film Application in China & 2022 Series Report of Sino-European Sustainable Transition Towards Circular Economy. *Sino-German Project for Upgrading Plastics Management in Agriculture*.
- [10] Ding, F., Jones, D. L., Chadwick, D. R., Kim, P. J., Jiang, R. and Flury, M. (2022a). Environmental impacts of agricultural plastic film mulch: Fate, consequences, and solutions. *Science of The Total Environment*. 836:155668.
- [11] Ding, F., Yan, C. and Wang, J. (2022b). An Overlooked Issue in Black Soil Protection: Plastic Film Accumulation and Pollution. *Chinese Journal of Soil Science*. 53(01):234-240.
- [12] Dong, H., Yang, G., Zhang, Y., Yang, Y., Wang, D., Zhou, C. (2022a). Recycling, disposal, or biodegradable-alternative of polyethylene plastic film for agricultural mulching? A life cycle analysis of their environmental impacts. *Journal of Cleaner Production*. 380:134950.
- [13] Dong, J., Li, S., Bi, X., Wang, G., Wang, J., Wang, W., Tong, N. (2022b). Design and Experimental Research of a New Film-Picking Mulch Film Recovery Machine with Impurity Separation Function. *Process*. 10(3):455.
- [14] Dong, X., Na, M., Li, Y., Zhang, H., Yang, X., Hou, S. (2003). Research on MS-2-type corn seedling stage film harvesting and tillage combined operation machine. *Journal of Agricultural Mechanization Research*. 2003(02):175-176.
- [15] Duan, W. (2017). Design of clamping finger-chain type device for recycling agricultural plastic film. [Master's thesis, Shihezi University].
- [16] Gao, H., Yan, C., Liu, Q., Ding, W., Chen, B., Li, Z. (2019). Effects of plastic mulching and plastic residue on agricultural production: A meta-analysis. *Science of The Total Environment*. 651:484-492.
- [17] Guo, W., He X., Wang L., Zhao P., Hu C., Hou S., Wang X. (2020). Development of a comb tooth loosening and pneumatic stripping plough layer residual film recovery machine. *Transactions of the Chinese Society of Agricultural Engineering*, 36(18):1-10.
- [18] Horodytska, O., Valdés F. J., Fullana A. (2018). Plastic flexible films waste management – A state of art review. *Waste Management*. 77:413-425.

- [19] Hu, B., Yuan C., Xie Y., Guo, M., Luo, X., Pan, F., Li J. (2024). Design and test of cutting film and removal impurities device based on negative pressure conveying of water pump. *Journal of Jilin University (Engineering and Technology Edition)*, 2024, (1): 268-280. DOI: 10.13229/j.cnki.jdxbgxb.20221045.
- [20] Hu, C., Wang X. F., Wang S. G., Lu B., Guo W. S., Liu C. J., Tang X. Y. (2020). Impact of agricultural residual plastic film on the growth and yield of drip-irrigated cotton in arid region of Xinjiang, China. *International Journal of Agricultural and Biological Engineering*. 13(1):160-169.
- [21] Iqbal S., Xu J., Allen S.D., Khan S., Nadir S., Arif M.S., Yasmeen T. (2020). Unraveling consequences of soil micro- and nano-plastic pollution on soil-plant system: implications for nitrogen (N) cycling and soil microbial activity. *Chemosphere*, 260, 127578.
- [22] Jiang, D., Chen X., Yan L., Mo Y., Yang S., Wang Z. (2019). Optimization of working parameters of cleaning system for master-slave residual plastic film recovery machine. *Transactions of the Chinese Society of Agricultural Engineering, China*, 35(19):1-10.
- [23] Jiang, D., Chen X., Yan L., Yang J., Li Y. (2023a). Mechanical and friction properties of agricultural plastic film during autumn harvest period of cotton in Xinjiang, China. *Environmental Science and Pollution Research*. 30(38):89238-89252.
- [24] Jiang, D., Chen X., Yan L., Zhang R., Wang Z., Wang M.E. (2020). Research on technology and equipment for utilization of residual film in farmland). *Journal of Chinese Agricultural Mechanization*. 41(01):179-190.
- [25] Jiang, D., Yan L., Chen X., Mo Y., Yang J. (2023b). Design and experiment of nail tooth picking up device for strip type residual film recycling and baling machine. *International Journal of Agricultural and Biological Engineering*. 16(6):85-96.
- [26] Jiang, H., Lei Q., Zhang B., Wu S. (2023c). Effects of Mulching and Application of Organic and Chemical Fertilizer on Greenhouse Gas Emission and Water and Nitrogen Use in Summer Maize Farmland. *Environmental Science*. 44(06):3426-3438.
- [27] Jiang, X. J., Liu W. J., Wang E. H., Zhou T. Z., Xin P. (2017). Residual plastic mulch fragments effects on soil physical properties and water flow behavior in the Minqin Oasis, northwestern China. *Soil and Tillage Research*. 166:100-107.
- [28] Jin, T., Xue Y. H., Zhang M. M., Zhou T., Liu H. J., Zhang K., Xi B. (2020). Research Advances in Regulations, Standards and Recovery of Mulch Film. *Ecology and Environmental Sciences*. 29(02):411-420.
- [29] Jin, W., Liu J., Xu C., Zhang X., Bai S. (2022). Design, Simulation and Experimentation of a Polythene Film Debris Recovery Machine in Soil. *Applied Sciences*, 12: 1366.
- [30] Jin, W., Zhang, X., Yan, J., Yuan, P., Bai, S., Fang, X. (2018). Characteristic analysis and working parameter optimization of crankshaft type cotton field surface residual film collecting machine. *Transactions of the Chinese Society of Agricultural Engineering, China*, 34(16):10-18.
- [31] Kang, J., Xie C., Wang X., Chen Y., Wang C., Peng Q. (2022). Design and test of screen hole clearing device for trommel sieve type membrane miscellaneous wind separator. *Transactions of the Chinese Society for Agricultural Machinery*. 53(09):91-98.
- [32] Koskei, K., Munyasya A. N., Wang Y. B., Zhao Z. Y., Zhou R., Indoshi S. N., Xiong Y. C. (2021). Effects of increased plastic film residues on soil properties and crop productivity in agro-ecosystem. *Journal of hazardous materials*. 414: 125521.
- [33] Li, D., Zhao W., Xin S., Liu X., Qu H., Xu Y. (2020). Current situation and prospect of recycling technology of farmland residual film. *Journal of Chinese Agricultural Mechanization*. 41(05):204-209.
- [34] Li, J. (2018). Study on the water- separating device of residual film mixture collected by machine. [Master's thesis, Shihezi University].
- [35] Li, J., Luo X., Hu B., Wang M., Yao Q. (2019). Research and Experiment of the Water-separating Device for Residual Film Mixture. *Journal of Agricultural Mechanization Research*. 41(05):152-156.
- [36] Li, X. (2023). Design and experiment of membrane - stubble separation device under high voltage electrostatic adsorption. [Master's thesis, Tarim University].
- [37] Li, X., Xing J., Hu C., Wang L., Guo W., He X., Wang X. (2022). Application and Development Prospect of Electrostatic Technology in Agriculture. *Xinjiang Agricultural Mechanization*. (01):18-21+46.
- [38] Liang, R., Chen X., Zhang B., Meng H., Jiang P., Peng X., Li W. (2019). Problems and countermeasures of recycling methods and resource reuse of residual film in cotton fields of Xinjiang. *Transactions of the Chinese Society of Agricultural Engineering, China*, 35(16):1-13.

- [39] Lin, J., Li, X., Chai, X., He, C. (2024) Comparison of aging properties of starch/ PBAT degradable mulching film in different environments. *Acta Materiae Compositae Sinica*. 2024:1-8.
- [40] Liu, C. (2023). Design and research of drum elastic tooth residual film recovery machine. [Master's thesis, Shihezi University].
- [41] Liu, Y., Zhou, M., Zhai, X. (2022). Will participating in the agricultural film recycling affect the income of farmers? Case study in Xinjiang. *Journal of Arid Land Resources and Environment*. 36(03):59-66.
- [42] Liu, Z. (2019). Development and experiment of a plastic film recycling machine for tobacco seedlings in mountainous areas. [Master's thesis, Guizhou University].
- [43] Lu, L., Li, W., Cheng, Y., Liu, M. (2023). Chemical recycling technologies for PVC waste and PVC-containing plastic waste: A review. *Waste Management*. 166:245-258.
- [44] Luo, K., Yuan P., Jin W., Yan J., Bai S., Zhang C., Zhang X. (2018). Design of chain-sieve type residual film recovery machine in plough layer and optimization of its working parameters. *Transactions of the Chinese Society of Agricultural Engineering, China*, 34(19):19-27.
- [45] Lv, Z., Zhang L., Zhang G., Liu S. (2015). Design and test of chain guide rail-type plastic film collector. *Transactions of the Chinese Society of Agricultural Engineering, China*, 31(18):48-54.
- [46] Min, W., Wang C., Wang L., Yi T., Bian J., Zhi M., Zhao X. (2022). Effects of Biodegradable Film Raw Material Particles on Soil Properties, Wheat Growth, and Nutrient Absorption and Transportation. *Environmental Science* 43(01):560-568.
- [47] Niu, A., Wu J., Zhao X. (2023). Infrared Spectrum Analysis of Degradation Characteristics of PPC Plastic Film Under Different Covering Methods. *Spectroscopy and Spectral Analysis*. 43(02):533-540.
- [48] Niu, Q., Ji C., Zhao Y., Chen X., Zheng X., Li H. (2017). Design and Experiment on Collecting and Separating Device for Strip Plastic Film Baler. *Transactions of the Chinese Society for Agricultural Machinery*. 48(05):101-107.
- [49] Peng, Q., Li C., Kang J., Shi G., Zhang H. (2020). Improved Design and Test on Pneumatic Cylinder Sieve Film Hybrid Separator. *Transactions of the Chinese Society for Agricultural Machinery*. 51(08):126-135.
- [50] Peng, Q., Li K., Wang X., Zhang G., Kang J. (2023). Design and Test of Stripping and Impurity Removal Device for Spring-Tooth Residual Plastic Film Collector. *Agriculture*. 13(1):42.
- [51] Shen, M., Song B., Zeng G., Zhang Y., Huang W., Wen X., Tang W. (2020). Are biodegradable plastics a promising solution to solve the global plastic pollution? *Environmental Pollution*. 263:114469.
- [52] Shi, L., Hu Z., Gu F., Wu F., Chen Y. (2017a). Design on automatic unloading mechanism for teeth type residue plastic film collector. *Transactions of the Chinese Society of Agricultural Engineering*, 33(18):11-18.
- [53] Shi, L., Z. Hu, F. Gu, Wu F., Wu P. (2017b). Design and parameter optimization on teeth residue plastic film collector of ridged peanut. *Transactions of the Chinese Society of Agricultural Engineering*, 33(02):8-15.
- [54] Shi, Z., Tang X., Zhen J., Yan J., Zhang X., Jin W. (2019). Performance test and motion simulation analysis of nail tooth type mechanism for collecting plastic residue. *Transactions of the Chinese Society of Agricultural Engineering*, 35(04):64-71.
- [55] Shi, Z., Zhang X., Cheng J., Zhou X., Zhang C. (2023a). Design and test of film transfer and unloading device of vertical double-row chain residual film recycling machine. *Agricultural Research in the Arid Areas*. 41(03):257-265.
- [56] Shi, Z., Zhang X., Liu X., Kang M., Yao J., Guo L. (2023b). Analysis and Test of the Tillage Layer Roll-Type Residual Film Recovery Mechanism. *Applied Sciences*. 13(13):7598.
- [57] Sica, C., Dimitrijevic A., Scarascia-Mugnozza G., Picuno P. (2015). Technical Properties of Regenerated Plastic Material Bars Produced from Recycled Agricultural Plastic Film. *Polymer-Plastics Technology and Engineering*. 54(12):1207-1214.
- [58] Sintim, H. Y., Bandopadhyay S., English M. E., Bary A., Liquet y González J. E., DeBruyn J. M., Flury M. (2021). Four years of continuous use of soil-biodegradable plastic mulch: impact on soil and groundwater quality. *Geoderma*. 381:114665.
- [59] Tang, Y., Yongman Z., Wang J., Wang Z. (2020). Design and experiment of film removing device for clamping finger-chain type residual film collector. *Transactions of the Chinese Society of Agricultural Engineering*, 36(13):11-19.
- [60] Tian, X. (2020). *Design and Research of Cotton stalk crushing and Film casting combined working Machine*. [Master's thesis, Shihezi University].

- [61] Tian, X., Zhao Y., Chen X., Yan L., Wen H., Gou H., Ji C. (2018). Development of 4JSM-2000A type combined operation machine for cotton stalk chopping and residual plastic film collecting. *Transactions of the Chinese Society of Agricultural Engineering*, 34(10):25-35.
- [62] Wang, K. (2018). *Design and study on standing cotton stalks raking-film machine with wide folding and monomer profiling*. [Master's thesis, Shihezi University].
- [63] Wang, K., Hu B., Luo X., Chen X., Zheng X., Yan L., Gou H. (2017). Design and experiment of monomer profiling raking-film mechanism of residue plastic film collector. *Transactions of the Chinese Society of Agricultural Engineering*, 33(08):12-20.
- [64] Wang, X., Shi J., Guo J., Chen F. (2008). Experimental study and design on film raking mechanism of hanging film raker with cotton-stalk crushing and returning to field. *Transactions of the Chinese Society of Agricultural Engineering*, (01):135-140.
- [65] Wang, X. R., Wang K. R., Li Y. C., Wang B., Liu J., Wang F. L., Song N. N. (2020). Analysis on pollution situation of mulch film residual in farmland soils in QINGDAO city, *Fresenius Environmental Bulletin*. 29(7A):5822-5829.
- [66] Wang, Y. (2019). Design and Study on Simplified Film Stripper for Tobacco Seedling. [Master's thesis, Southwest University].
- [67] Wen, H., Gou H., Chen X. (2021). Development of a second-order chain plate straw crushing and plastic film recycling combined operation machine. *Agricultural Development & Equipments*, 235(07):40-41.
- [68] Wu, S. (2015). *Design and Experiment of Picking Up Film Removing Mechanism of Film Machine on Corn Seedling*. [Master's thesis, Northeast Agricultural University].
- [69] Xie, J., Yang Y., Cao S., Zhang Y., Zhou Y., Ma W. (2020). Design and experiments of rake type surface residual film recycling machine with guide chain. *Transactions of the Chinese Society of Agricultural Engineering*, 36(22):76-86.
- [70] Xu, H., Hu Z., Wu F., Gu F., Wei H., Yan J. (2017). Design and experiment of network chain type residual plastic film collector for peanut field. *Transactions of the Chinese Society of Agricultural Engineering*, 33(17):1-9.
- [71] Xue, W., Wang C., Zhu Z., Wang X. (2005). Design of a Roll Film Cotton Seedling Residual Film Recycling Machine. *Transactions of the Chinese Society for Agricultural Machinery*, (03):148-149+147.
- [72] Yan, C., Liu E., Shu F., Liu Q., Liu S., He W. (2014). Review of Agricultural Plastic Mulching and Its Residual Pollution and Prevention Measures in China. *Journal of Agricultural Resources and Environment*, 31(02):95-102.
- [73] Yan, C., Wang X., He W., Ma H., Cao S., Zhu G. (2008). The residue of plastic film in cotton fields in Shihezi, Xinjiang. *Acta Ecologica Sinica*, 28(07):3470-3474.
- [74] Yan, W., Hu Z., Wu N., Xu H., You Z., Zhou X. (2017). Parameter optimization and experiment for plastic film transport mechanism of shovel screen type plastic film residue collector. *Transactions of the Chinese Society of Agricultural Engineering*, 33(01):17-24.
- [75] Yang, D. (2005). Research on loosening shovel and curl-up film roller of the Machine for Retrieving the used plastic film after harvesting. Master's degree. [Master's thesis, China Agricultural University].
- [76] Yang, L., Heng T., He X., Yang G., Zhao L., Li Y., Xu Y. (2023). Spatial-temporal distribution and accumulation characteristics of residual plastic film in cotton fields in arid oasis area and the effects on soil salt transport and crop growth. *Soil and Tillage Research*. 231:105737.
- [77] Yang, L., Liu J., Zhang D., Hou S., Xu F. (2010a). Design and Experiment of plastic Film Collector for Cotton Fields during Seedling Period. *Transactions of the Chinese Society for Agricultural Machinery*. 41(S1):73-77.
- [78] Yang, L., Zhang D., Hou S., Xu F. (2010b). Analysis of Structural Parameters and Experiment of Plastic Film Collector for Corn Fields During Seedling Period. *Transactions of the Chinese Society for Agricultural Machinery*. 41(12):29-34.
- [79] Yang, S. (2020). Design and Key Technology Research of Passive Cotton Field Residual Plastic Film Recycling Machine. [Doctoral dissertation, Jilin University].
- [80] Yang, S., Chen X., Yan L., Jiang D. (2020). Performance of three different spades for residual plastic film recycling machine. *Applied Engineering in Agriculture*, 36(2):187-195.
- [81] Yang, S., Chen X., Yan L., Mo Y., Jiang D., Zhang H. (2021). Design and experiment on belt-type curl-up film device for residual plastic film recycling machine. *Transactions of the Chinese Society for Agricultural Machinery*, 52(02):135-144.

- [82] Yang, S., Yan L., Mo Y., Chen X., Zhang H., Jiang D. (2018). Design and Experiment on Collecting Device for Profile Modeling Residual Plastic Film Collector. *Transactions of the Chinese Society for Agricultural Machinery*, 49(12):109-115+164.
- [83] Yin, S., Zhao B., Mi J., Liu H., Guo X., Wu Y., Liu J. (2022). Current scenario and future trends of plastic film residue in farmland topsoil in Inner Mongolia, China. *Journal of Agro-Environment Science*, 41(09):1985-1992.
- [84] You, J. (2021). *Design and test of 4JSM-2000 type combined operation machine for cotton stalk chopping and plastic film recovery*. [Doctoral dissertation, Shenyang Agricultural University].
- [85] You, J., Chen X., Zhang B., Wu J. (2017a). Design and experiment of 4JSM-2000 type combined operation machine for cotton stalk chopping and residual plastic film collecting. *Transactions of the Chinese Society of Agricultural Engineering, China*, 33(10):10-16.
- [86] You, J., Zhang B., Wen H., Kang J., Song Y., Chen X. (2017b). Design and Test Optimization on Spade and Tine Combined residual Plastic Film Device. *Transactions of the Chinese Society for Agricultural Machinery*. 48(11):97-104.
- [87] You, Z., Hu Z., Wu H., Zhang Y., Yan J., Yan W., Zhou X. (2017c). Design and experiment of 1MCDS-100A typed shovel-sieve residual film recovery machine. *Transactions of the Chinese Society of Agricultural Engineering, China*, 33(09):10-18.
- [88] Zhang, B. (2015). *Design and Study of Film Recycling Film Recycling Machine in Autumn*. [Master's thesis, Xinjiang Agricultural University].
- [89] Zhang, B., Wang Z., Jin S. (2019a). Current situation and prospect of agricultural film pollution treatment in China. *World Environment*, (06):22-25.
- [90] Zhang, Q.Q., Ma Z.R., Cai Y.Y., Li H.R., Ying G.G. (2021). Agricultural Plastic Pollution in China: Generation of Plastic Debris and Emission of Phthalic Acid Esters from Agricultural Films. *Environmental Science Technology*, 55(18):12459-12470.
- [91] Zhang, X., Liu J., Shi Z., Jin W., Yan J., Yu M. (2019b). Design and parameter optimization of reverse membrane and soil separation device for residual film recovery machine. *Transactions of the Chinese Society of Agricultural Engineering*, 35(04):46-55.
- [92] Zhang, Z. (2023). *Study on the mechanism of picking up and recovering the residual film of sowing layer based on arc-shaped nail-tooth roller*. [Doctoral dissertation, Shihezi University].
- [93] Zhang, Z., Li J., Wang X., Zhao Y., Xue S., Su Z., Liang J. (2023). Design and test of 1SMB-3600A type fragmented mulch film collector for sowing layer soil. *Soil and Tillage Research*, 225:105555.
- [94] Zhao, Y., Chen X., Wen H., Zheng X., Niu Q., Kang J. (2017). Research Status and Prospect of Control Technology for Residual Plastic Film Pollution in Farmland. *Transactions of the Chinese Society for Agricultural Machinery*, 48(06):1-14.

RECOGNITION OF DROUGHT STRESS IN MILLET ON HYPERSPECTRAL IMAGING

/ 基于高光谱成像技术识别谷子干旱胁迫

Rongxia WANG¹⁾, Jiarui ZHANG¹⁾, Jianyu CHEN¹⁾, Yuyuan MIAO¹⁾, Jiwan HAN¹⁾, Lijun CHENG¹⁾¹⁾ Shanxi Agricultural University, College of Software / China

Tel: +86 16634257091; E-mail: wangrongxia@stu.sxau.edu.cn

Correspondent author: Jiwan HAN, Lijun CHENG

DOI: <https://doi.org/10.35633/inmateh-74-62>**Keywords:** hyperspectral imaging, drought stress, characteristic wavelengths, image features**ABSTRACT**

Millet is one of China's primary traditional food crops, and drought can adversely impact their yield and quality. To quickly detect the degree of drought stress in cereal grains, this study establishes a nondestructive classification model based on hyperspectral imaging technology. The raw spectral data underwent preprocessing using six pretreatment methods and various combinations of these methods. Subsequently, three distinct algorithms were employed for feature wavelength selection. To assess the severity of drought stress on millet, classification models were developed by integrating texture and color features, utilizing Support Vector Machine (SVM), Partial Least Squares Discriminant Analysis (PLS-DA), and Multilayer Perceptron (MLP) algorithms. The results indicate that the D1st-SVM model, based on CARS wavelength selection, exhibits the highest modeling performance when feature wavelengths are fused with significant texture and color variables, achieving an accuracy rate of 93%. These findings suggest that drought identification in millet can be performed quickly and nondestructively by integrating image features through hyperspectral imaging technology.

摘要

谷子是我国传统主要粮作之一，干旱对其的产量和品质都会产生不利影响。为了快速检测谷子受干旱胁迫程度，本研究基于高光谱成像技术建立一种无损的分类模型。本研究对原始光谱数据进行六种预处理方法，以及这些方法的不同组合，对光谱数据中的噪声进行处理。采用3种不同算法进行特征波长的选取。融合纹理特征和颜色特征，基于支持向量机（support vector machine, SVM）、最小二乘判别分析（partial least-squares discriminant analysis, PLS-DA）和多层感知机算法（Multilayer Perceptron, MLP）建立分类模型，来识别谷子受干旱胁迫程度。结果表明特征波段融合重要纹理特征、重要颜色特征变量时，基于CARS波长选择的D1st-SVM模型的建模性能最高，预测集的分类准确率为93%。研究结果表明，利用高光谱成像技术融合图像特征可以快速、无损地识别谷子是否受到干旱胁迫。

INTRODUCTION

In northern China, precipitation levels are low, with uneven seasonal distribution and significant inter-annual variability, leading to the predominance of semi-arid and arid areas. Millet is one of the primary cereal crops in these dry and semi-arid regions, characterized by its drought tolerance, high water and fertilizer utilization rates, broad adaptability, and strong resistance to adverse conditions (Wang *et al.*, 2022). Despite these attributes, drought stress often threatens millet's growth and development, which significantly impacts yield (Yang *et al.*, 2022). Drought is one of the most common and severe abiotic stress factors, adversely affecting the growth and productivity of many plants in dry and semi-arid regions (Hussain *et al.*, 2018). As one of the crops with the highest water utilization rates (Zou *et al.*, 2019), millet's photosynthesis mechanism can suffer irreversible damage due to drought stress (Gerhards *et al.*, 2019), inhibiting root system growth and reducing the efficiency of nutrient absorption and utilization, ultimately leading to slower growth and decreased yield. Therefore, accurately identifying the degree of drought stress in millet, supplying water effectively, and rationally managing water resources are crucial. In recent years, remote sensing technology (Chen *et al.*, 2022) and near-infrared spectroscopy (Wan *et al.*, 2020), among other advanced technologies, have played significant roles in detecting drought stress by assessing efficient water utilization by crops and enabling rational irrigation. However, natural conditions and spectral resolution limitations make it challenging to capture the comprehensive changes in crops under drought stress. Consequently, high spectral imaging technology, which combines imaging and spectroscopy (Mansoor *et al.*, 2024), has become a current research hotspot.

In high-throughput plant phenotyping platforms, hyperspectral imaging technology is extensively employed for the non-destructive and close-range assessment of plant physiological traits (Mohd Asaari *et al.*, 2022). Hyperspectral imaging technology can detect subtle changes in plant responses to abiotic stressors, such as reduced crop growth and stomatal closure resulting from drought stress (Mansoor *et al.*, 2024; Barradas *et al.*, 2021). This technology also minimizes plant damage and reduces chemical pollution (Gerhards *et al.*, 2019). It enables rapid prediction of metabolite profiles in crop leaves and accurate classification of drought-affected crops using spectral data (C A B *et al.*, 2021). Hyperspectral imaging technology has been extensively utilized to analyze crop drought stress. For example, using hyperspectral characteristics, Zhou *et al.* (2021) applied hyperspectral imaging as a high-throughput phenotyping method to detect drought stress in citrus trees early. Ioannis *et al.* (2024) utilized hyperspectral imaging technology to detect drought stress in broccoli within agricultural environments. However, these methods primarily rely on single spectral data analysis, limiting models' adaptability and decision-making capabilities in practical applications (Xu *et al.*, 2022). Therefore, integrating multiple types of information can enhance model performance and robustness. Fusing image features with hyperspectral data offers distinct classification, recognition, and model optimization advantages. Dong *et al.* (2015) improved the accuracy of wheat variety classification by combining hyperspectral imaging with image feature extraction techniques. Hyperspectral imaging can obtain color features that are correlated with specific characteristics (Alessandro *et al.*, 2024). Abdullah *et al.* (2024) established a rice classification model through the integration of spectral and color features, thereby attaining accurate discrimination between viable and non-viable rice seeds. Qiao *et al.* (2024) optimized feature variables in the corn kernel moisture content prediction model by fusing color features and texture information using hyperspectral imaging technology, thus improving prediction accuracy. These studies indicate that hyperspectral imaging technology, combined with image feature fusion, holds great potential for identifying plant drought stress, providing insights into plant responses to water scarcity (Mansoor *et al.*, 2024).

This study uses millet as the research object and uses a high-throughput plant phenotyping platform to collect spectral data. The spectral data is preprocessed, and feature wavelengths are selected. By combining high-spectral imaging technology with machine learning methods, the image, and spectral features are fused to classify and identify millet drought stress, and an optimal classification model is constructed to realize real-time identification of drought stress degree in millet fields, aiming to provide a fast and non-destructive detection method for millet drought stress identification.

MATERIALS AND METHODS

Materials

The experiment was conducted in the phenotyping platform greenhouse at Shanxi Agricultural University, with an average temperature of 32.5 to 34.6°C and an average humidity of 51.3 to 53.8% RH. The materials were provided by Shanxi Agricultural University and included drought-resistant varieties of millet, specifically "Dao Ba Qi" (B15), "Xiao Miao Jin" (B19), and "Yin Tian Han" (B74), along with sensitive varieties "Liao Gu No. 1" (B294) and "Ji Gu 28" (B354). These varieties were planted in pots in the same batch and under identical conditions, using a uniformly mixed substrate of nutrient soil and vermiculite in a 3:1 ratio. Each variety was assigned three gradients and three replicate groups, resulting in 45 pots of millet plants cultivated.

Drought-stress experiments were initiated one week after the plants reached the four-leaf and one-heart stages. Soil moisture content was monitored using soil moisture sensors, and the drought stress state of the millet was further controlled using the weighing method. Three different drought treatment levels were established:

- no drought stress (soil moisture content at 65% ± 2%)
- moderate drought stress (soil moisture content at 40% ± 2%)
- severe drought stress (soil moisture content at 30% ± 2%)

The remaining fertilization schedules, methods, and management measures were maintained consistently. Prior to the manifestation of noticeable traits in the moderately drought-stressed plants, hyperspectral data were collected weekly, resulting in 315 data samples.

Hyperspectral acquisition system

Spectral data were acquired using a high-throughput crop phenotyping automatic extraction system, with the hyperspectral component of this system illustrated in Fig.1. This component comprises a hyperspectral camera, six halogen lamps (with a power of 500 W), a whiteboard, belts, a conveyor belt, a computer, and a three-phase asynchronous motor connected by circular wiring, among other components.

The spectrometer operates within a spectral range of 400 to 1,000 nm (ImSpector V10E, SPECIM, Finland), encompassing 224 distinct wavelength bands. It features a spectral resolution of 5.5 nm and a spatial pixel dimension of 1024 pixels. The system operates within an enclosed darkroom environment to minimize external light interference and enhance the quality of the collected data. The acquired data are stored in binary data stream format.

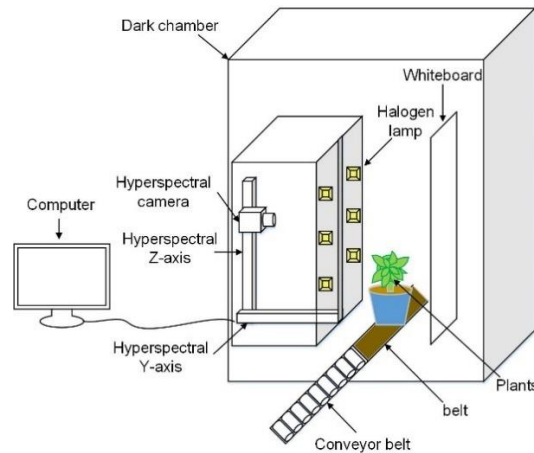


Fig. 1 - Hyperspectral part of the high-throughput automatic crop phenotype extraction system

Before collecting hyperspectral images, the system needs to be preheated for 30 minutes to eliminate the influence of uneven light and dark current on image quality (Jia *et al.*, 2020). Moreover, the relevant parameters of the system are set: the camera's exposure time is set to 11.6 ms, the platform's moving speed is set to 15 mm/s-1, and the object distance is set to 120 cm. During the data collection procedure, the whiteboard has to be calibrated to lower the complexity of calculations and the noise produced during the spectral data collection (Pouria *et al.*, 2021). In terms of a specific operation, first cover the lens cap, collect a dark current spectral data I_d , then open the lens cap and collect a whiteboard spectral data I_r and get the reflectance I of the corrected rice image according to formula 1:

$$I = \frac{I_r - I_d}{I_w - I_d} * 100 \quad (1)$$

where: I denotes the reflectance of the corrected rice image; I_r denotes the reflectance of the original image; I_d indicates the dark current-corrected image; and I_w signifies the whiteboard-corrected image.

The system was calibrated at one-hour intervals throughout the experiment.

Image Feature Extraction

The texture features of grains are extracted using the gray-level co-occurrence matrix (GLCM). In GLCM, the frequency of specific gray-level appearance between each pair of pixels is statistically calculated based on the given displacement direction and distance in an image, and this statistical information is integrated into a matrix (Prasad *et al.*, 2022). In this study, the distance is set to 1, and the energy, entropy, contrast (Contrast), correlation, and homogeneity are calculated at four different directions of 0° , 45° , 90° , and 135° .

Color features are extracted by creating a high-quality actual color (RGB) synthesis image using the red (625.67 nm), green (547.99 nm), and blue (470.31 nm) channels. The HSV color space provides an intuitive representation of color properties (Yang *et al.*, 2022). The RGB color information is mapped to the HSV color space, where the H, S, and V channels' first-order, second-order, and third-order moments are calculated. Color moments serve as a method for expressing color features; since color information is primarily concentrated in the lower-order moments (Yang *et al.*, 2022), the use of first-order, second-order, and third-order moments is sufficient to represent color distribution in digital images (Jiang *et al.*, 2022). The first-order moment indicates the average color, the second-order moment represents the dispersion of color, and the third-order moment reflects the skewness of color.

Hyperspectral image acquisition and preprocessing

From each sample dataset, a total of 224 images can be extracted, with segmentation performed to identify the region of interest (ROI) within the images, and the average spectral reflectance for this region calculated. Specifically, the grayscale image at 676.56 nm, which delineates the plant contours, is first extracted from the binary data.

This is due to the observation that in the spectral images of millet, the grayscale intensity initially deepens before lightening. At the 676.56 nm wavelength, the grayscale image reaches its darkest state, resulting in the most pronounced contrast between the plant and the background at this wavelength. Subsequently, a threshold segmentation method separates the millet plants from the background, producing a binary image. Image masking techniques are then applied to isolate the plant region in the image, designating it as the region of interest (ROI). Finally, the average reflectance of all pixels within the ROI is calculated to obtain the spectral reflectance, as illustrated in Fig. 2.

A range of preprocessing algorithms was utilized to mitigate the impacts of light scattering, baseline drift, and other confounding factors on the samples (Zhang *et al.*, 2021). These algorithms include first derivative (D1st), second derivative (D2nd), standard normalized variate (SNV), multiplicative scatter correction (MSC), Savitzky-Golay filtering (SG), and detrending. Furthermore, by the specific characteristics of each algorithm, SNV was integrated with detrending, while SG was paired with both D1st and D2nd to facilitate more effective preprocessing of the original spectrum.

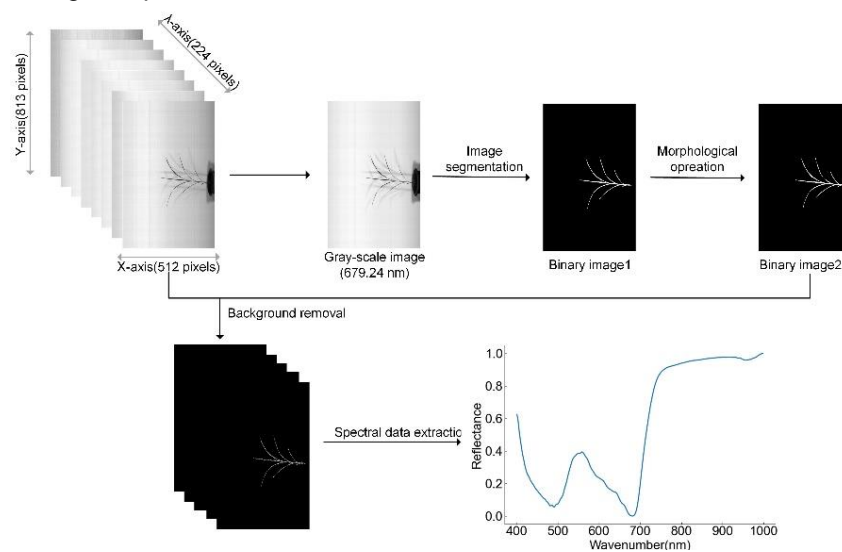


Fig. 2 - Spectral reflectance extraction process

Feature wavelength selection

Hyperspectral images encompass a substantial volume of spectral data, characterized by significant collinearity and redundant information; thus, selecting relevant feature wavelengths is imperative. The methodologies employed for the selection of feature wavelengths include Competitive Adaptive Reweighted Sampling (CARS), Successive Projections Algorithm (SPA), and Variable Iterative Space Shrinkage Approach (VISSA). CARS is a feature selection technique that integrates Monte Carlo sampling with partial least squares regression coefficients (Li *et al.*, 2009), facilitating the identification of the most pertinent spectral features while streamlining the data processing workflow. SPA sequentially selects projection directions that best preserve the key characteristics of the original data, mapping high-dimensional data into a lower-dimensional subspace to achieve dimensionality reduction (Milanez *et al.*, 2017). This process preserves critical and distinct data features while effectively capturing differences among various categories. VISSA assesses feature importance by evaluating the contributions of individual features to the spectral data, thereby selecting optimal wavelength combinations (Zhang *et al.*, 2020). This approach aids in identifying features that are rich in information and significance, while also accounting for inter-feature correlations.

Classification model

This study conducts a comparative analysis of three classification algorithms: Support Vector Machine (SVM), Partial Least Squares Discriminant Analysis (PLS-DA), and Multilayer Perceptron (MLP) to identify the optimal model for classifying millet based on varying levels of drought severity. SVM is a machine learning approach that can be employed in classification, regression, and outlier detection (Kuswidiyanto *et al.*, 2023). This research uses a polynomial kernel function to map the input data into a higher-dimensional feature space, where an optimal hyperplane is established to segregate data from distinct categories effectively. Additionally, five-fold cross-validation is implemented, with optimization performed on both the penalty factor and kernel parameters; specifically, the penalty factor is varied within a range of 0 to 100.

PLS-DA conducts rotation and projection of the data through Partial Least Squares, effectively handling the problem of multicollinearity among features and enhancing classification accuracy (Allen et al., 2017). During the modeling process, the number of principal components is selected within the range of 5 to 30; too few may result in insufficient information that affects classification accuracy, while too many can lead to overfitting. Therefore, selecting an optimal number of principal components that retain critical information is essential for achieving effective classification (Feng et al., 2024). MLP can achieve good prediction and classification performance on unseen data. It adapts to tasks of varying scales and complexities by adjusting both the number of layers and the number of neurons in each layer (Saeideh et al., 2017). It enhances model performance and generalization capabilities by employing various activation functions, regularization parameters, and other techniques. MLP demonstrates notable proficiency in nonlinear modeling for classification tasks.

The quality of classification models is evaluated by accuracy. The calculation formula is shown in Equation (2), which represents the proportion of correctly classified samples out of the total sample number.

$$Accuracy = \frac{TP+TN}{TP+FN+TN+FP} * 100 \quad (2)$$

where: TP represents the number of samples predicted to be positive and they are also positive; TN represents the number of samples predicted to be negative and they are also negative; FP stands for the number of samples predicted to be positive, but they are negative; while FN represents the number of samples predicted to be negative, but they are positive.

RESULTS

Spectrum characteristics analyses

The spectral reflectance of millet plant samples shows similar trends in the wavelength range of 400 to 1,000 nm (Fig. 3-a). The reflectance trends of all samples within this range are generally similar. Specifically, within the 540 to 590 nm range, a prominent absorption peak forms due to chlorophyll's relatively weak light absorption in the green light region (520 to 600 nm). This spectral band corresponds to lower photosynthesis efficiency in plants, resulting in higher spectral reflectance in this range (Zhao et al., 2016). Conversely, within the 660 to 710 nm range, an absorption trough appears due to chlorophyll's strong light absorption efficiency in the red edge region (630 to 690 nm). This area represents a spectral band with higher photosynthesis efficiency, enabling plants to exhibit vigorous photosynthetic activity (Zhao et al., 2016). Starting from the 690 nm range, the reflectance sharply increases with wavelength until reaching a maximum near 760 nm, forming the plant-specific red edge position.

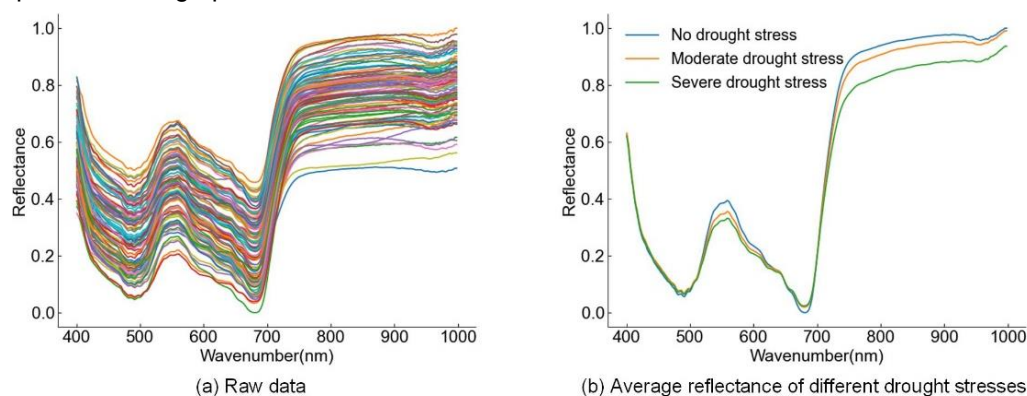


Fig. 3 - Characterization curves of spectrum of millet samples

To analyze the impact of drought severity on millet spectra, the average spectral curves of millet under no drought stress, moderate drought stress, and severe drought stress conditions are considered representatives of different drought severities. The overall trends of the spectral curves for millet under various drought severities are similar, as shown in Fig. 3 (b). However, significant differences in spectral curves are observed at the peak wavelength range of 540-590 nm, the trough wavelength range of 660-710 nm, and the high reflectance region of 730-1000 nm. Spectral reflectance decreases with increasing drought severity within the wavelength ranges of 540-590 nm and 730-1000 nm. This is attributed to the reduced water content in the millet, which affects the transmission and scattering of light, subsequently leading to a decline in spectral reflectance. Conversely, the reflectance increases with drought severity in the wavelength range of 660-

710nm, which falls within the red edge region where chlorophyll absorption in millet is strongest. This is due to decreased chlorophyll content under drought conditions, increasing reflectance. These spectral differences demonstrate the feasibility of utilizing hyperspectral imaging technology to identify the drought severity in millet.

Spectral data preprocessing results

After applying various preprocessing techniques and their combinations, significant variations were observed in the spectral curves, as illustrated in Fig. 4. Specifically, following the application of MSC and SNV preprocessing (Fig. 4-a, b), the spectral data exhibited increased concentration, with both methods yielding similar trends in the spectral curves. This similarity can be attributed to the shared objective of both preprocessing methods: standardizing the spectral morphology across all samples to a unified baseline and amplitude, thereby mitigating non-chemical variations within the spectral data. After applying SG filtering (Fig. 4-c), the curve appeared smoother compared to its original counterpart, with a notable reduction in fluctuations and noise within the dataset, facilitating subsequent analytical procedures. The spectral curve resulting from D1st processing (Fig. 4-d) revealed pronounced peaks in the 510-540 nm and 700-780 nm wavelength bands compared to the original spectrum, aiding in feature extraction and analysis within the spectral dataset. Following D2nd preprocessing (Fig. 4-e), significant fluctuations were observed in the spectral curve, highlighting the high sensitivity of this method to changes within the spectrum and its ability to accentuate subtle variations present. Upon Detrend from the original spectral data (Fig. 4-f), the initially observed concave feature within the 660-710 nm range became more pronounced, and a distinct downward trend was evident in the 750-1000 nm range. This preprocessing technique effectively eliminated trends or background components from the spectrum, thereby redirecting analytical focus towards the intrinsic fluctuation characteristics of each spectrum and enhancing both analytical accuracy and reliability.

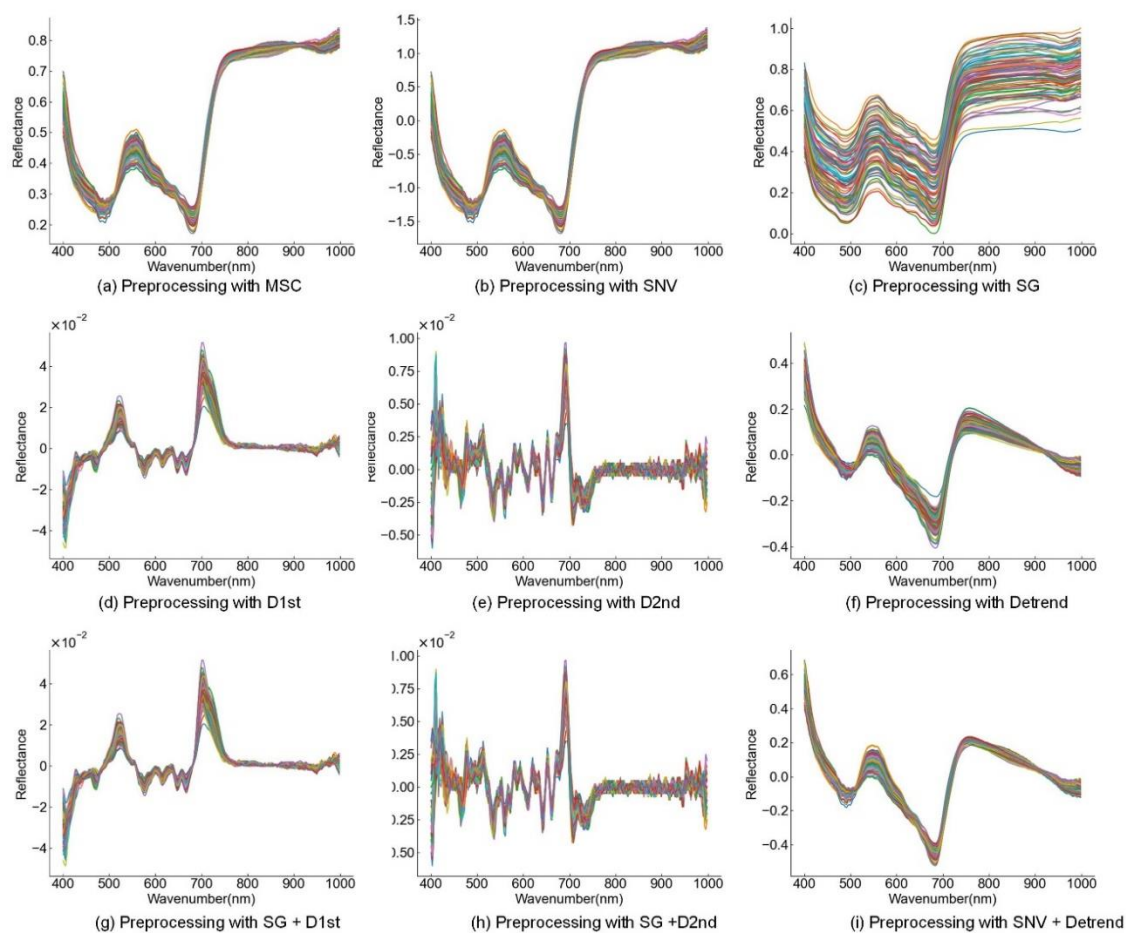


Fig. 4 - Spectral curves of different preprocessing methods

Two distinct combinations are employed to process the spectral data by integrating the characteristics of various preprocessing methods. The spectral data subjected to SG filtering is utilized for D1st calculation (Fig. 4-g), resulting in both smoothing and enhancement of local features within the spectral dataset. When SG filtering is combined with D2nd processing (Fig. 4-h), it not only smooths the data but also accentuates

details within the spectral curve, thereby improving the accuracy of subsequent classification efforts. Additionally, when SNV is integrated with detrending (Fig. 4-i), the results indicate that the spectral curve retains consistency with trends observed post-detrending while exhibiting a more concentrated distribution. This combination effectively corrects systematic errors in the spectral data while mitigating effects introduced by detrending.

Modeling analysis based on full wavelengths

Utilizing data that has undergone preprocessing with varying techniques as input can have a notable impact on the outcomes of modeling exercises. Table 1 compares the performance of different preprocessing methods within diverse modeling contexts. When employing raw, unprocessed data (RAW) for modeling, the MLP model exhibited optimal performance, achieving an accuracy rate of 81.3% in the predictive set classification task. A comparative analysis of model classification performance across various preprocessing methods reveals that spectral data processed using D1st, SNV, Detrend, and the combined SNV-Detrend techniques demonstrate superior modeling outcomes. In the context of the SVM models, applying D1st processing led to the highest performance, with a predictive set accuracy of 86.0%.

Furthermore, implementing the D1st processing technique in both the PLS-DA and the MLP models resulted in accuracy rates surpassing those of other preprocessing methods, precisely 79.0% and 84.8%, respectively. This underscores the advantage of the D1st processing method across diverse modeling paradigms. By emphasizing pivotal features within the original data, the D1st processing technique substantially enhances classification accuracy. Consequently, the decision was made to advance with spectral data processing and analysis based on the 1Dst processing methodology.

Table 1

	Classification results of millet drought degree based on Full spectrum					
	Training set accuracy(%)			Test set accuracy(%)		
	SVM	PS-DA	MLP	SVM	PLS-DA	MLP
Raw	91.9	80.4	87.9	81.3	77.9	82.5
D1st	89.9	91.4	91.4	86.0	79.0	84.8
D2nd	81.4	79.3	81.4	80.2	74.4	79
SNV	84.9	79.8	90.4	84.8	79.0	83.7
MSC	89.4	84.2	84.9	82.5	76.7	77.9
Detrend	86.4	85.9	89.4	82.5	79.0	82.5
SG	87.4	80.4	83.4	76.7	70.9	73.2
SG-D1st	89.9	93.9	86.4	80.2	75.5	75.5
SG-D2nd	75.3	79.8	74.8	70.9	66.2	70.9
SNV-Detrend	89.4	83.4	87.9	84.8	77.9	83.7

Feature wavelength selection results

This study employed three distinct algorithms, CARS, SPA, and VISSA, to extract characteristic wavelengths from the preprocessed spectral data. The precise distribution of the selected wavelengths is graphically depicted in Fig. 5.

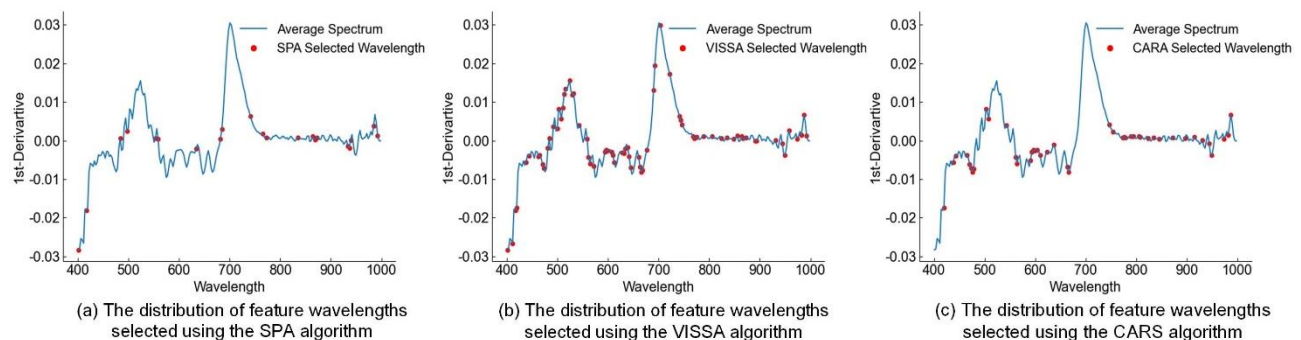


Fig. 5 - Distribution of characteristic wavelengths selected by different algorithms

The SPA algorithm selects 21 bands, the VISSA algorithm selects 74 bands, and the CARS algorithm selects 70 bands. The SPA algorithm selects fewer characteristic wavelengths from the spectral data, and the distribution is more dispersed. In contrast, the VISSA and CARS algorithms concentrate their selected characteristic wavelengths in 590–680 nm and 760–1000 nm, respectively, while exhibiting a more scattered distribution in other bands.

The CARS algorithm utilizes Monte Carlo sampling iterations and an exponential decay function to adjust the selection probability of each wavelength band adaptively, ultimately selecting the optimal combination of bands that contribute most significantly to modeling. Simultaneously, the number of Monte Carlo sampling iterations is determined through cross-validation assessment to achieve optimal algorithm performance and efficiency. In the CARS analysis, the Monte Carlo runs are set to 50, with a ratio of 3:1 for the training set to the test set in each run, and a 5-fold cross-validation is employed for Root Mean Square Error of Cross-Validation (RMSECV). The process of selecting characteristic variables by CARS is illustrated in Figure 6. Specifically, Fig. 6 (a) shows the exponential decrease in characteristic wavelengths as the number of Monte Carlo sampling iterations increases. Fig. 6 (b) depicts the changes in RMSECV during the Monte Carlo sampling iterations, with the RMSECV reaching a minimum value of 0.386 at the 18th iteration. Fig. 6(c) displays the trend of changes in the regression coefficient paths during each Monte Carlo sampling process. The vertical blue line in the figure indicates that the RMSECV value is minimum at the 18th iteration, with 70 characteristic wavelengths extracted.

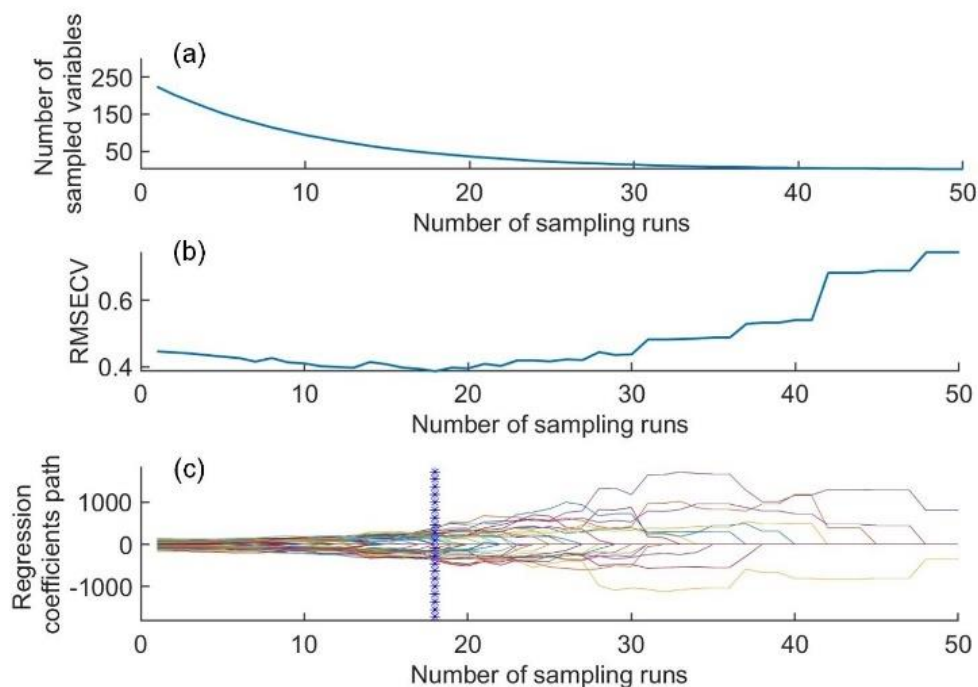


Fig. 6 - Changes of related parameters during the sampling operations of CARS

Modeling analysis based on feature wavelength

The results of modeling the important bands for different feature selection algorithms are shown in Table 2. When analyzing the data based on the entire wavelength spectrum, the SVM classification model achieved notably better results, exhibiting training set and prediction set classification accuracies of 89.9% and 86%, respectively. In comparison, the MLP classification model performed slightly worse, achieving accuracies of 88.9% on the training set and 84.8% on the prediction set. On the other hand, the PLS-DA classification model showed a high accuracy of 91.4% on the training set but struggled on the prediction set, achieving only 79% accuracy. Three feature wavelength selection algorithms were employed to extract critical wavelengths from the spectrum for modeling to enhance classification accuracy further and simplify the model. The classification model performance improved significantly after applying the CARS algorithm for feature selection, surpassing the performance of the other two algorithms. The VISSA algorithm yielded classification results similar to the CARS algorithm, but its prediction set accuracy was 2% lower. In contrast, the performance of the models declined after applying the SPA for feature selection, indicating that the SPA might not have captured the most relevant information for classification during feature extraction.

Table 2

	Classification results of millet drought degree based on important spectral bands					
	Training set accuracy (%)			Test set accuracy (%)		
	SVM	PS-DA	MLP	SVM	PLS-DA	MLP
Full spectrum	89.9	91.4	88.9	86	79	84.8
SPA	80.4	74.8	79.4	77.9	75.5	76.8
VISSA	86.4	83.4	88.9	87.2	77.9	83.7
CARS	91.9	88.9	87.9	87.2	79	83.7

Overall, the classification performance of the CARS-SVM and VISSA-SVM models improved compared to the original spectral modeling. Notably, the CARS-SVM model demonstrated an accuracy of 91.9% on the training set and 87.2% on the prediction set, exhibiting superior performance among all models. However, the classification accuracy of the other models, despite using selected feature wavelengths, did not match the level achieved with the original spectral data. This suggests that, while the selected feature wavelengths are representative, they do not fully encapsulate the spectral information required for precise classification of drought severity in millet.

Results of texture and color feature selection

Following the application of principal component analysis to the hyperspectral image, three principal component images were extracted, with contribution rates of 99.7%, 0.13%, and 0.11% (Fig. 7). Consequently, the optimal principal component image exhibiting a contribution rate of 99.7% was utilized for subsequent texture feature extraction. A total of 20 texture features were identified using the GLCM method. To mitigate information redundancy, correlation analyses were conducted between the extracted feature values at various angles and different drought severities in millet, ultimately resulting in the selection of seven significant texture feature variables.

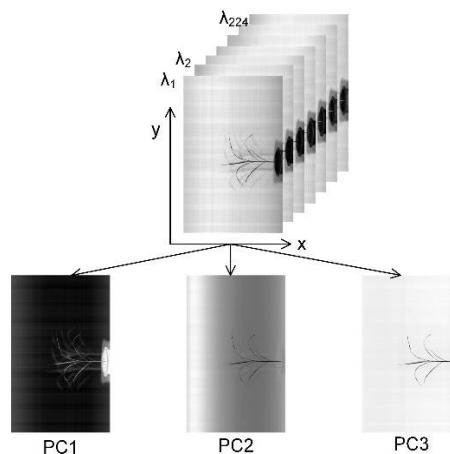


Fig. 7 - The first three principal component images of the millet samples

Color features were derived by calculating the first-order, second-order, and third-order moments of the H, S, and V channels from the RGB image, yielding a total of 9 feature values. A correlation analysis was performed to optimize further the feature combination between the color features and millet drought severity, ultimately resulting in the selection of 6 significant color feature variables. The extracted image texture information, color information, and spectral data were subsequently fused for modeling analysis.

Modeling analysis based on the fusion of spectral information and image information

Incorporating texture and color features into the spectral data significantly enhanced the classification accuracy of drought severity in millet (Table 3). Following the integration of spectral data with texture and color features, the performance of the three classification models remains broadly consistent with that achieved using only spectral feature wavelength extraction. The spectral data were fused with texture and color features, respectively, and the performance of the three classification models was consistent with that of the spectral data feature wavelength alone. However, when the spectral data was independently fused with important texture features (Texture*) and important color features (Color*), the performance of all models was slightly improved.

Specifically, adding important texture features improved the test set accuracy of the SVM model by 4.6%, the PLS-DA model by 3.5%, and the MLP model by 4.6%. The fusion of important color features improved the test set accuracy of the PLS-DA and MLP models by 2.3% and 4.6%, respectively, but had no significant impact on the performance of the SVM model.

Furthermore, integrating spectral data with important texture and color features significantly enhances the performance of classification models. Among these, the SVM model demonstrates superior classification accuracy, achieving an accuracy rate of 98.9% for the training set and 93% for the test set; closely following is the MLP model, which attains accuracy rates of 92.4% for the training set and 89.5% for the test set; in contrast, the PLS-DA model exhibits relatively lower classification accuracy, with rates of 90.9% for the training set and 83.7% for the test set. These findings indicate that integrating selected important texture and color features can effectively improve drought classification accuracy in millet.

Table 3**Classification results of millet drought degree by integrating spectrum, texture features and color features**

	Training set accuracy (%)			Test set accuracy (%)		
	SVM	PS-DA	MLP	SVM	PLS-DA	MLP
Raw	91.9	80.4	87.9	81.3	77.9	82.5
D1st	89.9	91.4	91.4	86.0	79.0	84.8
CARS-D1st	91.9	88.4	87.9	87.2	79.0	83.7
Spectrum + Texture	92.9	85.4	94.4	87.2	80.2	87.2
Spectrum + Texture*	99.4	84.9	90.4	91.5	82.5	88.3
Spectrum + Color	92.9	85.4	93.4	86.0	80.2	87.2
Spectrum + Color*	91.4	87.9	88.4	87.2	81.3	88.3
Spectrum + Texture* + Color*	98.9	90.9	92.4	93.0	83.7	89.5

In conclusion, hyperspectral imaging technology effectively facilitates the acquisition of millet data across varying drought levels, thereby enabling precise classification of drought severity. Integrating spectral data with texture and color features has significantly enhanced classification accuracy, offering a rapid, non-destructive, and efficient approach for monitoring drought conditions in millet.

CONCLUSIONS

This paper employed various preprocessing algorithms and their combinations alongside different feature band selection techniques to process hyperspectral data. Concurrently, image feature information was integrated to construct a classification model to categorize millet based on varying degrees of drought stress accurately. The research findings indicate that the model integrating pre-processing, feature wavelength extraction, and machine learning algorithms is feasible for predicting the maturity of rapeseed. Among them, the 1st-CARS-SVM model, which incorporates significant texture and color features, has the optimal classification performance, with a classification accuracy of 93%, attaining an enhancement in model classification accuracy. The study validates the potential of hyperspectral imaging technology in the detection of plant drought stress.

This model offers a rapid and non-destructive approach for identifying the degree of drought stress in millet, which holds the potential to provide significant scientific support for enhancing millet yield and irrigation management. However, the model still requires improvement, such as the influence of geographical environment, different years, and growing conditions on the growth process of millet, which may result in variations in the spectral characteristics of millet. In the subsequent working process, these issues will be further taken into account to enhance the model's universality.

ACKNOWLEDGEMENT

We would like to express our sincere gratitude to all authors for their support and contributions to this manuscript. This research is supported by the Shanxi Province Basic Research Program for Young Scientists (NO. 202303021222039).

REFERENCES

- [1] Alessandro, M., Joby, M. P. C., Sathishkumar, S., & Robert M. (2024). Are unmanned aerial vehicle-based hyperspectral imaging and machine learning advancing crop science?[J], *Trends in plant science*, 29(2): 196-209. <https://doi.org/10.1016/j.tplants.2023.09.001>
- [2] Allen, A., Williams, M. R., & Sigman, M. E. (2019). Application of likelihood ratios and optimal decision thresholds in fire debris analysis based on a partial least squares discriminant analysis (PLS-DA) model[J]. *Forensic Chem*, 16: 100188. <https://doi.org/10.1016/j.forc.2019.100188>
- [3] Barradas, A., Correia, P. M. P., Silva, S., Mariano, P., Pires, M. C., Matos, A. R., da Silva, A. B., & da Silva, J. M. (2021). Comparing Machine Learning Methods for Classifying Plant Drought Stress from Leaf Reflectance Spectra in Arabidopsis thaliana[J]. *Applied Sciences*, 11(14): 6392-6392. <https://doi.org/10.3390/app11146392>
- [4] Burnett, A. C., Serbin, S. P., Davidson, K. J., Ely, K. S., & Rogers, A. (2021). Detection of the Metabolic Response to Drought Stress Using Hyperspectral Reflectance[J]. *Journal of experimental botany*, 72(18): 6474-6489. <https://doi.org/10.1093/jxb/erab255>
- [5] Chen, Y., Wang, P., Zhang, Y., & Yang, J. (2022). Comparison of Drought Recognition of Spring Maize in Northeast China Based on 3 Remote Sensing Indices[J](基于 3 种遥感指数的东北春玉米干旱识别对比). *Journal of Applied Meteorological Science*, 33(04): 466-476. <https://doi.org/10.11898/1001-7313.20220407>
- [6] Dong, G., Guo, J., Wang, C., Chen, Z., Zheng, L., & Zhu, D. (2015). The Classification of Wheat Varieties Based on Near Infrared Hyperspectral Imaging and Information Fusion[J](基于近红外高光谱成像及信息融合的小麦品种分类研究). *Spectroscopy and Spectral Analysis*, 35(12): 3369-3374. [https://doi.org/10.3964/j.issn.1000-0593\(2015\)12-3369-06](https://doi.org/10.3964/j.issn.1000-0593(2015)12-3369-06)
- [7] Feng, H., Chen, Y., Song, J., Lu, B., Shu, C., Qiao, J., Liao, Y., & Yang, W. (2024). Maturity Classification of Rapeseed Using Hyperspectral Image Combined with Machine Learning[J]. *Plant phenomics (Washington, D.C.)*, 6:0139. <https://doi.org/10.34133/plantphenomics.0139>
- [8] Gao, C., Ji, X., He, Q., Gong, Z., Sun, H., Wen, T., & Guo, W. (2023). Monitoring of Wheat Fusarium Head Blight on Spectral and Textural Analysis of UAV Multispectral Imagery[J]. *Agriculture*, 13(2):293-293. <https://doi.org/10.3390/agriculture13020293>
- [9] Gao, S., & Xu, J.H(2022). Hyperspectral image information fusion-based detection of soluble solids content in red globe grapes[J]. *Computers and Electronics in Agriculture*, 196. <https://doi.org/10.1016/j.compag.2022.106822>
- [10] Gerhards, M., Schlerf, M., Mallick, K., & Udelhoven, T. (2019). Challenges and Future Perspectives of Multi-/Hyperspectral Thermal Infrared Remote Sensing for Crop Water-Stress Detection: A Review [J]. *Remote Sensing*, 11(10): 1240. <https://doi.org/10.3390/rs11101240>
- [11] Hussain, H. A., Hussain, S., Khaliq, A., Ashraf, U., Anjum, S. A., Men, S., & Wang, L. (2018). Chilling and Drought Stresses in Crop Plants: Implications, Cross Talk, and Potential Management Opportunities [J]. *Frontiers in Plant Science*, 9393. <https://doi.org/10.3389/fpls.2018.00393>
- [12] Jia, B., Wang, W., Ni, X., Lawrence, K. C., Zhuang, H., Yoon, S.-C., & Gao, Z. (2020). Essential processing methods of hyperspectral images of agricultural and food products[J]. *Chemometrics and Intelligent Laboratory Systems*, 198. <https://doi.org/10.1016/j.chemolab.2020.103936>
- [13] Jiang, X., Tian, J., Huang, H., Hu, X., Han, L., Huang, D., & Luo, H. (2022). Nondestructive visualization and quantification of total acid and reducing sugar contents in fermented grains by combining spectral and color data through hyperspectral imaging [J]. *Food Chemistry*, 386: 132779-132779. <https://doi.org/10.1016/j.foodchem.2022.132779>
- [14] Kuswidiyanto, L. W., Kim, D. E., Fu T., Kim, K. S., & Han X. (2023). Detection of Black Spot Disease on Kimchi Cabbage Using Hyperspectral Imaging and Machine Learning Techniques [J]. *Agriculture*, 13 (12). <https://doi.org/10.3390/agriculture13122215>
- [15] Li, H., Liang, Y., Xu, Q., & Cao, D. (2009). Key wavelengths screening using competitive adaptive reweighted sampling method for multivariate calibration[J]. *Analytica Chimica Acta*, 648(1): 77-84. <https://doi.org/10.1016/j.aca.2009.06.046>
- [16] Malounas, I., Paliouras, G., Nikolopoulos, D., Liakopoulos, G., Bresta, P., Londra, P., Katsileros, A., & Fountas S. (2024). Early Detection of Broccoli Drought Acclimation/stress in Agricultural Environments Utilizing Proximal Hyperspectral Imaging and AutoML [J], *Smart agricultural technology*, 8: 100463 <https://doi.org/10.1016/j.atech.2024.100463>

- [17] Mansoor, S., & Chung, Y. S. (2024). Functional phenotyping: Understanding the dynamic response of plants to drought stress[J]. *Current Plant Biology*, 38: 100331. <https://doi.org/10.1016/j.cpb.2024.100331>
- [18] Milanez, K., Nóbrega, T. C. A., Nascimento, D. S., Galvao, R. K. H., & Pontes, M. J. C. (2017). Selection of robust variables for transfer of classification models employing the successive projections algorithm. *Anal. Chim. Acta* 984: 76–85. <https://doi.org/10.1016/j.aca.2017.07.037>
- [19] Mohd Asaari, M. S., Mertens S., Verbraeken, L., Dhondt, S., Inze, D., Koirala, B., & Scheunders, P. (2022). Non-destructive analysis of plant physiological traits using hyperspectral imaging: A case study on drought stress [J]. *Computers and Electronics in Agriculture*, 195. <https://doi.org/10.1016/j.compag.2022.106806>
- [20] Pouria, S., Nicolas, V., & Malcolm, J. H. (2021). A Neural Network Method for Classification of Sunlit and Shaded Components of Wheat Canopies in the Field Using High-Resolution Hyperspectral Imagery [J], *Remote sensing*, 13(5): 898-898. <https://doi.org/10.3390/rs13050898>
- [21] Prasad, G., Vijay, G. S., & Kamath, C. (2022). Comparative study on classification of machined surfaces using ML techniques applied to GLCM based image features [J]. *Materials Today: Proceedings*, 62(P3): 1440-1445. <https://doi.org/10.1016/j.matpr.2022.01.285>
- [22] Qiao, M., Xia, G., Yang, X., Cui, T., Fan, C., Li, Y., Han, S., & Jun, Q. (2024). Prediction of moisture content for single maize kernel based on viscoelastic properties: constitutive model and force-time graph [J]. *Journal of the science of food and agriculture*, 140, 104(11): 6594-6604. <https://doi.org/10.1002/jsfa.13483>
- [23] Saeideh, F., Hossein, A. M., Abbas, R., S. Amirhassan M., & Hassan S. (2017). Identification and Classification of Three Iranian Rice Varieties in Mixed Bulks Using Image Processing and MLP Neural Network [J]. *International Journal of Food Engineering*. 13(5): 20160121-20160121. <https://doi.org/10.1515/ijfe-2016-0121>
- [24] Siam, A. A., Salehin, M. M., Alam, M. S., Ahamed, S., Islam, M. H., & Rahman, R. (2024). Paddy Seed Viability Prediction Based on Feature Fusion of Color and Hyperspectral Image with Multivariate Analysis [J], *Heliyon*, 10(17). <https://doi.org/10.1016/j.heliyon.2024.e36999>
- [25] Sun, J., Zhou, X., Wu, X., Zhang, X., & Li, Q. (2016). Identification of moisture content in tobacco plant leaves using outlier sample eliminating algorithms and hyperspectral data[J]. *Biochemical and Biophysical Research Communications*, 471(1): 226-232. <https://doi.org/10.1016/j.bbrc.2016.01.125>
- [26] Wan, Y., Ouyang, J., Yuan, H., Wu, Q., Xiang, D., & Zhao, G. (2020). Effect of Drought Stress on Physiological Characteristics and Infrared Spectrum Characterization of Tartary Buckwheat [J] (干旱胁迫对苦荞生理特征和红外光谱表征特性的影响). *Journal of Chengdu University (Natural Science Edition)*, 39(03): 230-233+240. <https://doi.org/10.3969/j.issn.1004-5422.2020.03.002>
- [27] Wang, Z., Liu, X., Yu, A., Cheng, K., Li, H., Tian, G., Wang, Y., Chen, X., Zhang, P., & Liu, H. (2022). Changes of Physiological Response to Drought Stress and Selection of Drought Resistance Indexes in Different [J] (不同谷子品种萌发期对于干旱胁迫生理响应的变化及抗旱指标筛选). *Journal of Agricultural Science and Technology*, 22(12): 39-49. <https://doi.org/10.13304/j.nykjdb.2019.0749>
- [28] Xu, P., Zhang, Y., Tan, Q., Xu, K., Sun, W., Xing, J., & Yang, R. (2022). Vigor identification of maize seeds by using hyperspectral imaging combined with multivariate data analysis[J]. *Infrared physics and technology*, 126. <https://doi.org/10.1016/j.infrared.2022.104361>
- [29] Yang, L., & Qin, H. (2022). Study on Peanut Appearance Quality Detection Based on Color and Texture Features [J] (基于颜色和纹理特征的花生仁外观品质检测研究). *Chinese Agricultural Science Bulletin*, 38(27): 151-156. <https://doi.org/10.11924/j.issn.1000-6850.casb2021-0918>
- [30] Yang, Y., Li, K., Wei, S., Guga, S., Zhang, J., & Wang, C. (2022). Spatial-temporal distribution characteristics and hazard assessment of millet drought disaster in Northern China under climate change [J]. *Agricultural Water Management*, 272. <https://doi.org/10.1016/j.agwat.2022.107849>
- [31] Zhang, L., Sun, J., Zhou, X., Nirere, A., Wu, X., & Dai, R. (2020). Classification detection of saccharin jujube based on hyperspectral imaging technology [J]. *Journal of Food Processing and Preservation*, 44(8). <https://doi.org/10.1111/jfpp.14591>
- [32] Zhang, X., Sun, J., Li, P., Zeng, F., & Wang, H. (2021). Hyperspectral detection of salted sea cucumber adulteration using different spectral preprocessing techniques and SVM method [J]. *LW T*, 152. <https://doi.org/10.1016/j.lwt.2021.112295>

- [33] Zhao, Z.J., Shan, G.L., Duan, X.H., Jiang, H., Ren, J., Chen, G., & Chu, X.H. (2016). Study on spectral reflectance and physiological characteristics of three cool-season turfgrass under drought stress [J]. *Grassland and Turf*, 36(06): 23-29. <https://doi.org/10.3969/j.issn.1009-5500.2016.06.004>
- [34] Zhou, J. J., Zhang, Y. H., Han, Z. M., Liu, X. Y., Jian, Y. F., Hu, C. G., & Dian, Y. Y. (2021). Evaluating the Performance of Hyperspectral Leaf Reflectance to Detect Water Stress and Estimation of Photosynthetic Capacities[J]. *Remote Sensing*, 13(11): 2160-2160. <https://doi.org/10.3390/rs13112160>
- [35] Zou, C., Li, L., Miki, D., Li, D., Tang, Q., Xiao, L., Rajput, S., Deng, P., Peng, L., Jia, W., Huang, R., Zhang, M., Sun, Y., Hu, J., Fu, X., Schnable, P. S., Chang, Y., Li, F., Zhang, H., Feng, B., Zhu, X., Liu, R., & Schnable, J. C. (2019). The genome of broomcorn millet[J]. *Nature communications*, 10(1): 436. <https://doi.org/10.1038/s41467-019-08409-5>

EVALUATION OF BRAKING DECELERATION DURING EMERGENCY BRAKING OF AGRICULTURAL TRACTORS

ОЦЕНКА НА СПИРАЧНОТО ЗАКЪСНЕНИЕ ПРИ АВАРИЙНО СПИРАНЕ НА ЗЕМЕДЕЛСКИ ТРАКТОРИ

Daniel LYUBENOV¹), Atanas Z. ATANASOV*¹), Georgi KADIKYANOV ¹), Valentin VLADUT ²)

¹) University of Ruse "Angel Kanchev", 7017 Ruse / BULGARIA;

²) National Research - Development Institute for Machines and Installations Designed to Agriculture and Food Industry, 013813 Bucharest, / ROMANIA

Tel: +359 885 497 406; E-mail: aatanasov@uni-ruse.bg

DOI: <https://doi.org/10.35633/inmateh-74-63>

Keywords: Tractor, Braking Deceleration, Road Safety, Crash Investigation

ABSTRACT

The use of tractors for transporting agricultural produce is a widespread practice in Bulgaria and imposes high requirements for traffic safety. Assessing the braking performance of these vehicles is essential for effective risk management and accident prevention. This study provides a database of experimentally obtained data on the braking deceleration of Zetor Crystal HD 170 and Belarus 952.3 tractors under various braking conditions, gathered using modern equipment under real road conditions. The results offer valuable insights for expert analyses in accident investigations involving these vehicles and contribute to developing strategies for enhancing road safety.

РЕЗЮМЕ

Използването на трактори за транспортиране на селскостопанска продукция е широко разпространена практика в България и налага високи изисквания за безопасност на движението. Оценката на спирачните свойства на тези превозни средства е от ключово значение за управлението на риска и предотвратяването на пътнотранспортни произшествия. В настоящата работа е представена база от експериментално получени данни за спирачното закъснение на трактори Zetor Crystal HD 170 и Belarus 952.3 при различни условия на спиране, получени чрез съвременна апаратура в реални пътни условия. Получените резултати предоставят ценна информация за бъдещи експертни анализи при разследване на инциденти с тези транспортни средства и допринасят за предприемането на мерки за подобряване на пътната безопасност.

INTRODUCTION

Effective emergency braking of agricultural tractors is essential for ensuring safety both for the tractor driver and surrounding road users. Braking deceleration, as a primary indicator of braking system performance, is crucial for enabling rapid stopping in critical situations. A comparative analysis of tractor deceleration across different wheel drives and driving speeds is presented by Gurevicius *et al.* (2017). Additionally, Aykan *et al.* (2023) conducted notable studies on the braking performance of tractor-trailer combinations under various operating conditions.

In Bulgaria, road safety is at a very low level compared to other European Union countries (*European Commission, 2024*), despite the „Vision Zero“ road safety framework adopted in our country, as well as in other countries (*Lopoo et al., 2024*). Improving road safety is a particularly relevant issue for our country. Many responsible institutions view road safety primarily as a set of legal regulations governing traffic, vehicle standards, and driver requirements. However, to effectively enhance road safety, this approach must evolve to encompass a broader perspective considering road safety as a complex interplay of scientific, social, and economic factors that support safe, efficient traffic flow and protect human life. One essential component of this multifaceted approach is the expert investigation of road accidents, which includes analysing causes, understanding the mechanisms of incidents, and exploring preventive measures.

A fundamental aspect of expert assessment in any traffic accident is determining the vehicle stopping distance. Accurate identification of this distance is essential for evaluating whether the accident was preventable. Calculating the stopping distance requires several input factors, among which braking deceleration during emergency braking is one of the most critical.

In Bulgaria, tractors are commonly used to transport agricultural produce and fertilizers across municipal and republican road networks. A substantial portion of agricultural transport involves moving plant and livestock products or securing inputs for production. Due to the seasonal nature of agricultural work, this transport requires a significant number of vehicles. Cargo specificity often dictates the selection of specialized trailers, and to accommodate cargo varying bulk densities, additional superstructures may be installed on trailers, which alters the trailer mass depending on the type of cargo. Factors such as cargo type, trailer configuration, and road conditions impact the braking deceleration of tractors.

While technical literature provides information on emergency braking deceleration for passenger vehicles, data specific to agricultural tractors is limited and often pertains to different conditions and applications (Pradhan *et al.*, 2024; Ahokas *et al.*, 2003; Canli *et al.*, 2023). Some studies, such as those by Janulevičius *et al.* (2002), offer theoretical insights into braking efficiency for tractor-transport aggregates. However, under real road conditions, the complex interaction of factors can limit the applicability of these findings for forensic accident analyses.

The absence of data on agricultural tractors' braking deceleration under Bulgarian road conditions is a notable research gap. This lack of information complicates the preparation of auto-technical reports for accidents involving tractors. Therefore, this study aims to fill this gap by investigating the braking deceleration of tractors during emergency braking under real road conditions in Bulgaria, providing essential data to enhance traffic safety analysis and accident investigation accuracy.

MATERIALS AND METHODS

Braking is the movement of vehicles at a speed that decreases to a certain value or to a complete stop. If the braking is performed with the maximum possible braking deceleration, it is generally called emergency braking.

To study the dynamic properties of vehicles, various equipment can be used: sensors installed in tires (Higuchi *et al.*, 2023; Ise *et al.*, 2017); measuring the effective braking distance or using an accelerometer (Uzunov *et al.*, 2022); fifth wheel (Ivanov *et al.*, 2022), etc. These methods have various limitations. Today, to study the dynamic properties, GPS equipment is widely used, which has a number of advantages related to versatility, precision and ease of operation (Phan *et al.*, 2023; Pandey *et al.*, 2023; Famiglietti *et al.*, 2020).

To study the braking deceleration of tractors during emergency braking, specialized global positioning systems (GPS) equipment for precise measurements VB20SL from the company RaceLogic Ltd – England (<https://www.racelogic.co.uk/index.php/en/>) was used. The main module of the equipment is a satellite receiver that uses data from GPS (Fig. 1).



Fig. 1 - Satellite receiver VB20SL

According to the technical specification, some of the main parameters that can be registered by the system are: speed - from 0.1 to 1609 km/h, dispersion 0.1 km/h; distance - accuracy 0.05%, dispersion 0.001m; acceleration - up to 20 g, accuracy 0.5%, dispersion 0.01 g. The VBOX Tools software is used to visualize and process the recorded data. The data is presented in different windows: main window, showing the acceleration as a function of the distance travelled or time; window presenting a table with the recorded data; window showing the vehicle's trajectory.

The experiment was conducted in 2023 at the Dimera Neykov EOOD agricultural farm in the city of Glodjevo, Bulgaria. The weather conditions were: temperature 13.5 °C, wind speed 2 km/h and humidity 83%. The study was conducted with Zetor Crystal HD 170 tractors and Belarus 952.3 tractor (Fig. 2 and 3).

The Belarus 952.3 tractor is equipped with Rosava 13.6R20 (380/70R20) front tires. The rear ones are Seha 16.9-38 (420/85R38). For the purpose of the experiment, an RSD-4 trailer equipped with Barum 245/70R17.5 tires was attached to the Belarus 952.3 tractor. The Zetor Crystal HD 170 tractor was equipped with Mitas 480/65R28 front tires and Mitas 600/65R38 rear tires. A Remel-RS-14 trailer equipped with Alliance 400/60-15.5 tires was attached to the Zetor Crystal HD 170 tractor.



Fig. 2 – Object of study: a) Tractor Zetor Crystal HD 170; 6) road surface and tire skid marks



Fig. 3 – Object of study: a) Tractor Belarus 952.3; 6) road surface and tire skid marks

The main technical data of the tractor Zetor Crystal HD 170 are shown in Table 1.

Table 1

Technical data of the tractor Zetor Crystal HD 170 and Belarus 952.3

Technical data	Zetor Crystal HD 170	Belarus 952.3
Rated engine power, kW	120	70
Rated engine speed, rpm	2100	1800
Weight of the tractor, kg	5760	4800
Wheelbase, mm	2840	2450
Front tires	480/65R28	380/70R20
Rear tires	600/65R38	420/85R38
Permitted maximum load of front axle (kg)	4200-6000	2360-2500
Permitted maximum load of rear axle (kg)	6500-7000	3104-4500
Recommendations front tires pressure, kPa	150-190	120-150
Recommendations rear tires pressure, kPa	140-160	110-120

In the process of emergency braking, 4 main phases of change in braking deceleration are distinguished: phase 1 – decelerated movement of the vehicle without activated braking system. It begins when the accelerator pedal is released. Braking deceleration occurs due to various resistances (from movement, air, etc.); phase 2: braking deceleration increases when the brake pedal is pressed to a maximum value for the specific conditions; phase 3: during this phase the brake pedal is pressed. Braking deceleration is relatively constant; phase 4: during this phase the brake pedal is still pressed. The braking deceleration of the vehicle decreases almost linearly, and immediately before reaching the zero value a peak with positive acceleration is observed, which is due to the longitudinal oscillations of the vehicle. In this study, the results obtained are for phase 2, which is characterized by a relatively constant deceleration for the specific real road conditions.

The methodology of the experimental study of the braking deceleration includes conducting a series of emergency stops on a horizontal dry road with asphalt pavement, such as the pavement on municipal and republican roads in Bulgaria. The speed at the beginning of the stops is within 20 - 30 km/h. The series of tests for both tractors were conducted in four different scenarios: stopping the tractor without a trailer attached; stopping with an empty trailer with the braking system on; stopping with an empty trailer with the braking system off; stopping with a full trailer with the braking system on; stopping with a full trailer with the braking system off. The mass of the load for the Belarus tractor is 3000 kg, and for the Zetor - 3600 kg.

The results of the study were processed with SPSS Statistics 19 (Statistical Package for the Social Sciences) - a software package used for interactive statistical analysis. This tool is implemented through descriptive menus, so as to satisfy the practical needs for statistical analysis of data collected with the presented equipment and used in science, police and court in expert analysis of road traffic accidents.

RESULTS

An actual record of the acceleration change in a Belarus 952.3 tractor during braking without an attached trailer is illustrated in Figure 4. The red ellipse highlights the region corresponding to the measurement of the average braking deceleration for each test.

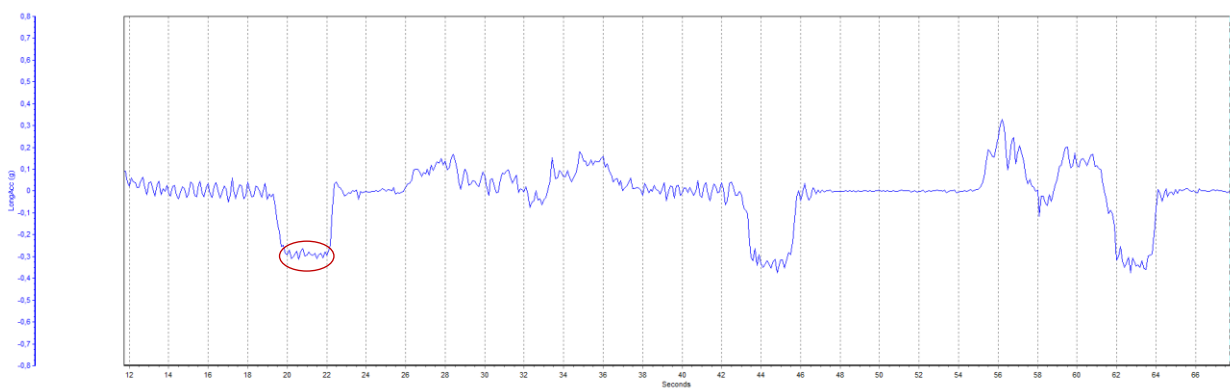


Fig. 4 – The variation in acceleration during a Belarus 952.3 emergency braking

From the part of the experiments presented in the figure, it can be seen that the negative accelerations reach values of 0.38 g or 3.73 m/s².

Fig. 5 presents a real recording of the change in acceleration of a Zetor Crystal HD 170 tractor when braking without a trailer attached.

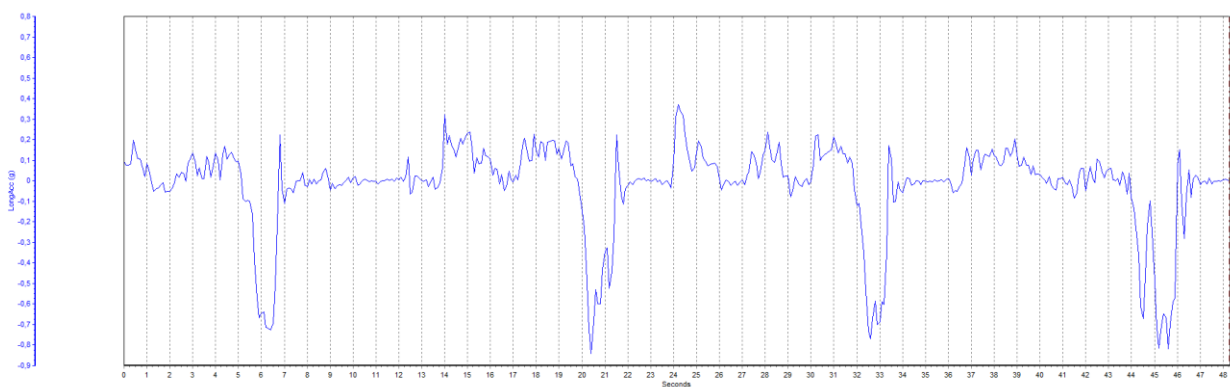


Fig. 5 – The variation in acceleration during a Zetor Crystal HD 170 emergency braking

From Fig. 5 it can be seen that in some of the tests for the tractor Zetor Crystal HD 170 the negative acceleration reaches a value of 0.85 g or 8.34 m/s² which are more than twice as large as those of the Belarus 952.3 tractor.

The results for the main statistical characteristics of the braking deceleration for the Belarus 952.3 tractor for different braking conditions are summarized in Table 2.

The mean values of the braking deceleration of the Belarus 952.3 tractor for different braking scenarios vary from 3.10 to 1.84 m/s². The smallest value obtained is 1.62 m/s², respectively, when braking with a full trailer with the brake system turned off.

Table 2

Statistical characteristics of the experimental results for Belarus 952.3 tractor

Belarus Statistics	No trailer	Empty trailer with brakes	Empty trailer without brakes	Full trailer with brakes	Full trailer without brakes
Number Valid	10	10	10	10	10
Mean	3.1009	2.7115	2.2229	2.1180	1.8413
Standard Error of Mean	0.03698	0.04837	0.02190	0.05173	0.04110
Median	3.0951	2.7027	2.2318	2.0846	1.8541
Mode	2.84	2.48	2.12	1.95	1.89
Standard Deviation	0.11694	0.15297	0.06924	0.16359	0.12998
Variance	0.014	0.023	0.005	0.027	0.017
Skewness	-1.060	-0.091	-0.113	0.367	-0.397
Standard Error of Skewness	0.687	0.687	0.687	0.687	0.687
Minimum	2.84	2.48	2.12	1.92	1.62
Maximum	3.23	2.91	2.32	2.34	2.00

The largest value obtained is 3.23 m/s², respectively, when braking the tractor without a trailer attached. The Table 3 summarizes the results of the study conducted on the interval estimates of the braking decelerations of the Belarus 952.3 tractor for the various braking scenarios.

Table 3

Interval estimates of the mean braking deceleration of the Belarus 952.3 tractor

Descriptives		Statistic	Std. Error
No trailer	Mean	3.1009	0.03698
	95% Confidence Interval for Mean	Lower Bound	3.0173
		Upper Bound	3.1846
Empty trailer with brakes	Mean	2.7115	0.04837
	95% Confidence Interval for Mean	Lower Bound	2.6021
		Upper Bound	2.8209
Empty trailer without brakes	Mean	2.2229	0.02190
	95% Confidence Interval for Mean	Lower Bound	2.1734
		Upper Bound	2.2725
Full trailer with brakes	Mean	2.1180	0.05173
	95% Confidence Interval for Mean	Lower Bound	2.0010
		Upper Bound	2.2350
Full trailer without brakes	Mean	1.8413	0.04110
	95% Confidence Interval for Mean	Lower Bound	1.7484
		Upper Bound	1.9343

From interval estimates of the mean braking decelerations for the different braking conditions it can be assumed that in 95% of cases their values would fall between the specified limits. The results for the main statistical characteristics of the braking deceleration for the Zetor Crystal HD 170 tractor for the different braking scenarios are summarized in Table 4.

Table 4

Statistical characteristics of the experimental results for Zetor Crystal HD 170 tractor

Zetor Crystal HD 170 Statistics	No trailer	Empty trailer with brakes	Empty trailer without brakes	Full trailer with brakes	Full trailer without brakes
Number Valid	10	10	10	10	10
Mean	6.7100	5.9664	5.0070	4.3527	3.6523
Standard Error of Mean	0.04029	0.05467	0.04103	0.02425	0.02516
Median	6.7248	6.0086	5.0276	4.3605	3.6738
Mode	6.46	5.66	4.83	4.26	3.54
Standard Deviation	0.12740	0.17290	0.12975	0.07670	0.07957
Variance	0.016	0.030	0.017	0.006	0.006
Skewness	-0.534	-0.589	-0.075	-0.026	-0.024
Standard Error of Skewness	0.687	0.687	0.687	0.687	0.687
Minimum	6.46	5.66	4.83	4.26	3.54
Maximum	6.88	6.17	5.20	4.45	3.79

For this tractor, the mean values of the braking deceleration for the different braking scenarios vary from 6.71 to 3.65 m/s². The smallest value obtained is 3.54 m/s², respectively, when braking with a full trailer with the brake system turned off. The largest value obtained is 6.88 m/s², respectively, when braking the tractor without a trailer attached.

The conducted research and the obtained results also establish the influence of the load mass on the braking properties. When braking a Zetor Crystal HD 170 tractor with a trailer with a 3600 kg load, the mean value of the braking deceleration is 27% less than when braking with an empty trailer.

Table 5 presents the results of the study on interval estimates of braking deceleration of the Zetor Crystal HD 170 tractor for different braking scenarios.

Table 5

Interval estimates of average braking decelerations of the Zetor Crystal HD 170 tractor

Descriptives			Statistic	Std. Error
No trailer	Mean		6.7100	0.04029
	95% Confidence Interval for Mean	Lower Bound	6.6189	
		Upper Bound	6.8012	
Empty trailer with brakes	Mean		5.9664	0.05467
	95% Confidence Interval for Mean	Lower Bound	5.8428	
		Upper Bound	6.0901	
Empty trailer without brakes	Mean		5.0070	0.04103
	95% Confidence Interval for Mean	Lower Bound	4.9142	
		Upper Bound	5.0998	
Full trailer with brakes	Mean		4.3527	0.02425
	95% Confidence Interval for Mean	Lower Bound	4.2978	
		Upper Bound	4.4076	
Full trailer without brakes	Mean		3.6523	0.02516
	95% Confidence Interval for Mean	Lower Bound	3.5953	
		Upper Bound	3.7092	

From the results in Table 5, the limits within which 95% of the cases of mean braking decelerations fall for the different scenarios can be determined.

When road accidents occur, the police, the prosecutor's office or the court appoint technical expertise to clarify the circumstances. The main task of the expertise is to provide an answer to the possibility of preventing the accident by the participants. In this regard, one of the most important issues is to determine the vehicles stopping distance. This is the minimum distance that the vehicle travels when stopping, from the moment of perceiving danger to a complete stop. It can be calculated according to the following relationship:

$$VSD = t_d V + t_v V + \frac{V^2}{2b_{dec}} \quad [\text{m}] \quad (1)$$

where: VSD – is the vehicle stopping distance, m; t_d - the driver reaction time, s; t_v – the vehicle reaction time, s; V – the vehicle velocity, m/s; b_{dec} – the braking deceleration, m/s².

The driver's reaction time depends on the traffic situation and the probability of an accident. In Bulgarian judicial practice, basic values for this time are used from 0.6 to 1.4 seconds. In special situations (driving at night, alcohol consumption, etc.) the driver's reaction time should be increased.

The reaction time of the vehicle includes the time for activating the braking system and for increasing the braking deceleration. The time for activating the braking system depends on the type of braking system. In Bulgarian case law, it is usually accepted from 0.2 to 0.4 seconds. The time for increasing the braking deceleration depends on the coefficient of friction between the tires and the road and the category of the vehicle. In Bulgarian case law, it is usually accepted from 0.2 to 0.6 seconds.

Using the experimentally obtained mean braking deceleration data under real road conditions, the vehicles stopping distance for both tractors at different speeds was calculated. A value of 0.8 seconds was used for the driver's reaction time, and 0.6 seconds for the vehicle's reaction time.

The results for the vehicles stopping distance during emergency braking of the Belarus 952.3 tractor for the different conditions are presented in Table 5. The results for the Belarus 952.3 tractor show an increase in the stopping distance when braking at a speed of 10 km/h with a full trailer without brakes by 16.5% compared to braking a tractor without a trailer – the boundary conditions of the study.

Table 5

Belarus 952.3 Stopping Distance

Braking conditions	No trailer	Empty trailer with brakes	Empty trailer without brakes	Full trailer with brakes	Full trailer without brakes
Braking Deceleration					
Mean values, m/s ²	3.10	2.71	2.22	2.12	1.84
Stopping Distance, m					
10.00 km/h (2.78 m/s)	5.14	5.32	5.63	5.71	5.99
20.00 km/h (5.56 m/s)	12.77	13.49	14.75	15.07	16.18
30.00 km/h (8.33 m/s)	22.85	24.46	27.29	28.03	30.52
40.00 km/h (11.11 m/s)	35.46	38.33	43.35	44.67	49.10
50.00 km/h (13.89 m/s)	50.56	55.04	62.90	64.95	71.87

For a speed of 50 km/h the increase is 42.2%. It is found that the braking deceleration has a more sensitive effect on the length of the vehicles stopping distance at higher speeds. At low speeds, the reaction time has a more sensitive effect on the length of the stopping distance.

Evaluating the influence of the mass of the transported load, it was found that when braking at a speed of 10 km/h and the braking system is on, the vehicles stopping distance increases by 7.3% (with a load of 3000 kg). For a speed of 50 km/h, this increase is 18%.

The results for the vehicles stopping distance during emergency braking of the Zetor Crystal HD 170 tractor for different conditions are presented in Table 6.

Table 6

Zetor Crystal HD 170 Stopping Distance

Braking conditions	No trailer	Empty trailer with brakes	Empty trailer without brakes	Full trailer with brakes	Full trailer without brakes
Braking Deceleration					
Mean values, m/s ²	6.71	5.97	5.01	4.35	3.65
Stopping Distance, m					
10.00 km/h (2.78 m/s)	4.47	4.54	4.66	4.78	4.95
20.00 km/h (5.56 m/s)	10.09	10.37	10.87	11.34	12.02
30.00 km/h (8.33 m/s)	16.83	17.47	18.59	19.64	21.17
40.00 km/h (11.11 m/s)	24.75	25.89	27.87	29.74	32.46
50.00 km/h (13.89 m/s)	33.82	35.60	38.70	41.62	45.88

For this tractor (Table 6), for the limit scenarios of the study, the results show an increase in the vehicles stopping distance when braking at a speed of 10 km/h with a full trailer without brakes by 10.7% compared to braking a tractor without a trailer – the limit conditions of the study. For a speed of 50 km/h, the increase is 35.7%. A significant difference in the length of the braking distance is established for the different scenarios of conducting the study for high speeds. This proves the need to accurately describe the circumstances (mass of the transported load, condition of the braking system, etc.) when each specific accident occurs in order to make the correct choice of braking deceleration and to calculate with high accuracy the stopping distance.

Evaluating the influence of the mass of the transported load for the Zetor Crystal HD 170 tractor, it was found that when braking at a speed of 10 km/h and the braking system is on, the vehicles' stopping distance increases by 5.3% (with a load of 3600 kg). For a speed of 50 km/h this increase is 16.9%.

CONCLUSIONS

As a result of this work, experimental data on the braking deceleration of Zetor Crystal HD 170 and Belarus 952.3 tractors under different braking scenarios in real road conditions were obtained.

The confidence intervals and statistical characteristics of the obtained results for all braking scenarios for both tractors are determined.

The mean values of the braking deceleration of the Belarus 952.3 tractor for the different braking scenarios vary within the limits from 3.10 to 1.84 m/s². The largest value obtained is 3.23 m/s² when stopping the tractor without an attached trailer.

For the Zetor Crystal HD 170 tractor, the mean values of the braking deceleration for the different braking scenarios vary within the limits from 6.71 to 3.65 m/s². The largest value obtained is 6.88 m/s² when stopping the tractor without an attached trailer.

The influence of the load mass on the braking properties was assessed. When stopping a Zetor Crystal HD 170 tractor with a trailer carrying 3600 kg of load, the main braking deceleration was 27% less than when stopping with an empty trailer. The vehicles stopping distance for both tractors at different speeds for all braking scenarios was calculated.

The results obtained provide important information for expert analysis in the investigation of tractor accidents and contribute to the implementation of measures to improve road safety.

ACKNOWLEDGEMENT

This study is financed by the European Union-NextGenerationEU, through the National Recovery and Resilience Plan of the Republic of Bulgaria, project № BG-RRP-2.013-0001-C01.

REFERENCES

- [1] Ahokas, J., & Kosonen, S. (2003). Dynamic behaviour of a tractor-trailer combination during braking. *Biosystems Engineering*, 85 (1), pp. 29-39. DOI 10.1016/S1537-5110(03)00035-7
- [2] Aykan, H., Çarman, K., Canlı, E., Ekinci, Ş. (2023). Evaluation of Tractor-Trailer Combination Braking Performance in Different Operating Conditions. *Süleyman Demirel Üniversitesi Fen Bilimleri Enstitüsü Dergisi*, 27(2), 219-225. <https://doi.org/10.19113/sdufenbed.1191413>
- [3] Canlı, E., Carman, K., Soylu, S., & Cıtil, E. (2023). Experimental assessment of a PID control solution for braking safety of transportation by agricultural tractor trailer combinations. *International Journal of Heavy Vehicle Systems*, 30 (2), pp. 211-231. DOI 10.1504/IJHVS.2023.132318
- [4] European Commission. Statistical pocketbook 2024. Road fatalities - country rankings. https://transport.ec.europa.eu/facts-funding/studies-data/eu-transport-figures-statistical-pocketbook/statistical-pocketbook-2024_en
- [5] Famiglietti, N., Nguyen, B., Fatzinger, E., & Landerville, J. (2020). Bicycle Braking Performance Testing and Analysis. *SAE Technical Papers*, Code 159263. DOI 10.4271/2020-01-0876
- [6] GPS equipment for precision measurements VB20SL. <https://www.racelogic.co.uk/index.php/en/>
- [7] Gurevicius, P., Janulevicius, A. (2017). Tractor MFWD braking deceleration research between different wheel drive, *16th International Scientific Conference Engineering for rural development*, Jelgava, 24-26.05.2017, DOI: [10.22616/ERDev2017.16.N173](https://doi.org/10.22616/ERDev2017.16.N173)
- [8] Higuchi, M., Suzuki, Y., Sasano, T., & Tachiya, H. (2023). Measurement of road friction coefficient using strain on tire sidewall. *Precision Engineering*. Volume 84, Pages 28-36. <https://doi.org/10.1016/j.precisioneng.2023.07.001>
- [9] Ise, T., Higuchi, M., Suzuki, Y., & Tachiya, H. (2017). Measurement on friction coefficients of tire grounding surface in arbitrary directions under high-load. *Experimental Mechanics*. Volume 57, November 2017, Issue 9, Pages 1383 – 13931. <https://doi.org/10.1007/s11340-017-0309-8>
- [10] Ivanov, Z., Sitnik, L., Dimitrov, R., Wrobel, R., Mihaylov, V., Skobiej, K., Ivanov, D., & Andrych-Zalewska, M. (2022). Investigation Of Braking Deceleration In Vehicle. *8th International Conference on Energy Efficiency and Agricultural Engineering, EE and AE 2022 – Proceedings*. Code 181234. DOI 10.1109/EEAE53789.2022.9831283
- [11] Janulevičius, A., Giedra, K. (2002) The evaluation of braking efficiency of tractor transport aggregate, *Transport*, 17:4, 152-158, DOI: [10.1080/16483840.2002.10414033](https://doi.org/10.1080/16483840.2002.10414033)
- [12] Lopoo, L.M., Cardon, E., Souders, S., Kroner Dale, M., & Ngo, U. (2024). An evaluation of a Vision Zero traffic-calming intervention, an urban transportation safety policy. *Journal of Urban Affairs*. <https://doi.org/10.1080/07352166.2024.2314040>
- [13] Pandey, P.K., Arora, H., & Kumar, B.A. (2023). Development of Driving Cycles for Electric Buses in Patna, India. *8th International Conference on Models and Technologies for Intelligent Transportation Systems, MT-ITS 2023*, Code 192575. DOI 10.1109/MT-ITS56129.2023.10241532
- [14] Phan, C., Meza Buendia, S.A., Nguyen, B.M., Fatzinger, E., & Landerville, J. (2023). Electric Motorcycle Acceleration, Braking, and Regenerative Coast-Down Deceleration Testing and Analysis. *SAE Technical Papers*, Code 187990. DOI 10.4271/2023-01-0631
- [15] Pradhan, N.C., Sahoo, P.K., Kushwaha, D.K., Bhalekar, D.G., Mani, I., Kumar, K., Singh, A.K., Kumar, M., Makwana, Y., & Aruna, T.N. (2024). ANN-PID based automatic braking control system for small agricultural tractors. *Journal of Field Robotics*, 41 (8), pp. 2805-2831. DOI 10.1002/rob.22393

- [16] Uzunov, H., Dimitrov, K., & Dechkova., S. (2022). Experimental Determination of the Tire-Road Friction Coefficient for a Vehicle with Anti-Lock Braking System. *AIP Conference Proceedings* 2557. Article number 030001-1. <https://doi.org/10.1063/5.0103769>

DESIGN AND EXPERIMENT OF AIR-SUCTION PRECISION SEED-METERING DEVICE FOR GARLIC

大蒜气吸式精量排种器的设计与试验

Fuhai FANG, Jingling SONG*, Zhuo WANG, Kunqiao LI, Yongzheng ZHANG, Long ZHOU, Chao LI¹

Shandong University of Technology, College of Agricultural Engineering and Food Science, Zibo (255000), China

Tel: +86-13675338192; E-mail: songjingling@sdut.edu.cn

DOI: <https://doi.org/10.35633/inmateh-74-64>

Keywords: Garlic; Air-suction seed metering device; Single seed extraction; Garlic seed orientation; Image recognition

ABSTRACT

To address the challenges associated with garlic single-seed extraction, including seed damage, blockages, and the inefficiency of directional placement for irregularly shaped garlic seeds, an air-suction seed metering device, integrated with image recognition and orientation technology, was developed. The working principle of the product is expounded, and comprehensive analysis and design of key components—such as the seed dispenser, directional needle, and combined suction block—are presented. A test bench was constructed using Jinxiang hybrid garlic as the experimental material, with the negative pressure in the air chamber, the rotation speed of the seed dispenser, and seed quantity in the seed chamber as the primary experimental factors. The performance indicators included the single seed rate, cavitation rate, and double grain rate. A three-factor, five-level orthogonal design was employed to assess the effects of each factor and their interactions on the single seed rate. The optimal operating parameters for garlic species A, B, and C were identified as follows: the negative pressure in the air chamber was 11.85 kPa, 12.03 kPa, and 13.21 kPa, respectively; the rotation speed of the seed dispenser was 7.13 r/min, 6.85 r/min, and 7.25 r/min, respectively; and the seed quantity in the seed chamber was 138.97 mm, 140.90 mm, and 141.24 mm, respectively. The corresponding single seed rates were 95.98%, 96.50%, and 96.23%, respectively. Under these optimal operating conditions, the study further explored the effects of the positional parameters of garlic seeds of different grades, as well as the positional parameters of the directional needle, on the preliminary directional performance. The optimal positional parameters were subsequently determined. The results of this study offer critical insights and establish conditions for the intelligent orientation of garlic planting machines.

摘要

针对目前大蒜单粒取种技术易损伤且易堵塞，及定向技术对形状不规则蒜种效果不佳问题，设计了一种结合图像识别定向技术的气吸式精量定向排种器。阐述了其工作原理并分析设计了排种盘、定向针和组合吸块等部件。通过搭建试验台，选用金乡杂交蒜为试验材料，以气室负压、排种转速、种室内种子量为试验因素，以单粒率、空穴率、双粒率为试验指标，进行三因素五水平旋转正交试验，分析了各因素及其交互作用对单粒率的影响，得出 A、B、C 三级蒜种的最佳工作参数：气室负压分别为：11.85 kpa、12.03kpa、13.21 kpa，排种盘转速分别为 7.13r/min、6.85r/min、7.25r/min，种室内种子量分别为 138.97 mm、140.90mm、141.24mm，对应单粒率分别为 95.98%、96.50%、96.23%。在最佳工作参数下，探究不同等级蒜种，定向针的位置参数对初步定向性能的影响，确定了最佳位置参数。研究结果可为大蒜种植机的智能化定向提供条件。

INTRODUCTION

As the world's largest producer and exporter of garlic (Binbin et al., 2019), China is facing an increasing demand for mechanized planting solutions (Xiaoxin et al., 2023). In garlic cultivation, positioning the bud tip upwards during planting has been shown to significantly improve seedling emergence and enhance plant quality (Tao et al., 2021).

Extensive research, both domestically and internationally, has focused on mechanized single-seed extraction and bud tip orientation technologies for garlic. Common single-seed extraction methods include

¹ Fuhai Fang, M.S. Stud.; Jingling Song, Prof.; Zhuo Wang, M.S. Stud.; Kunqiao LI, M.S. Stud.; Yongzheng Zhang, M.S. Stud.; Long Zhou, Lecturer; Chao LI, M.S. Stud.

chain spoon (Ruichuan et al., 2013), rotary spoon (Maheswarr et al., 2007), clamping (Hiroki et al., 2008), rotary cylinder (Yuzhen et al., 2017), and rotary mechanisms (Shichun et al., 2009), among others. However, these methods are often plagued by issues such as seed skin damage, clogging, and seed leakage, which significantly reduce planting efficiency. Garlic seed bud tip orientation technologies typically include techniques such as the three-stage directional bucket (Aijun et al., 2018) and double duckbill (Jialin et al., 2018), among others. Despite their widespread use, these methods show limited effectiveness in orienting hybrid garlic seeds, which account for nearly two-thirds of the garlic planted in China. Machine vision technology has emerged as a promising solution for improving the mechanized orientation of hybrid garlic seeds (Zhen et al., 2023). In recent years, researchers such as Fang Chun (Chun et al., 2019), Gao Chi (Chi et al., 2010), Yang Qingming (Qingming et al., 2010), Robles (Robles et al., 2016), and Paul (Paul, 2015) have conducted significant studies on image recognition methods for garlic seed bud tip identification and orientation.

This study aims to leverage machine vision technology for the mechanized orientation of garlic seeds by designing an air-suction seed metering device. This device will incorporate image recognition technology to enable the precise placement of single garlic seeds. The ultimate goal is to establish a mechanical foundation for integrating image recognition orientation technology into garlic planting machinery, thereby improving seeding accuracy and efficiency.

MATERIALS AND METHODS

The structure and working principle

As illustrated in Figure 1, the air-suction seed metering device for garlic primarily consists of several key components, including a seed dispenser, directional needles, an image acquisition and recognition device, a directional adjusting device, combined suction blocks, and other associated elements (Jingling et al., 2021). Multiple evenly spaced circular holes are arranged along the circumference of the seed dispenser, with corresponding combined suction blocks installed at these locations. Each suction block features a central suction hole. The combined suction block interacts with the directional adjusting device to achieve precise orientation of the seeds.

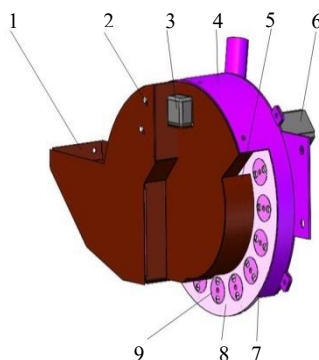


Fig. 1 - Structure diagram of garlic air suction precision directional seed dispenser

1. Seed chamber shell; 2. Directional needles; 3. Image acquisition and recognition device; 4. Air chamber shell; 5. Seed stirrer;
6. Directional adjusting device; 7. Sealing rubber strip; 8. Seed dispenser; 9. Combined suction block

As illustrated in Figure 2, the seed dispenser is divided into four distinct zones. When the seed-metering device is working, the initial air pressure in the air chamber is low, and a small amount of garlic seeds are taken out under the action of negative pressure. The suction holes are gradually filled with garlic seeds, and the final negative pressure of the air chamber reaches a basically stable state. As the seed dispenser rotates, the excess garlic seeds are removed under the action of the directional needles, leaving only one seed. Its length direction is adjusted to be tangential to the distribution circle at the center of the suction hole. The image acquisition and recognition device works at workstation 1 to determine the direction of the bud tip (forward or backward). The recognition result is sent to the directional adjusting device using the control method of the delayed queue. Considering the recognition time of the image acquisition and recognition device, the orientation adjusting device is arranged at workstation 2 to function. If the bud tip is facing backward, the directional adjusting device remains stationary. If the bud tip is facing forward, the directional adjusting device rotates the working surface of the combined suction block 180° to complete the orientation of the garlic seeds. When the garlic seeds leave the air chamber, they lose the adsorption effect of the negative pressure and fall

into the lower device by the gravity of the seeds themselves.

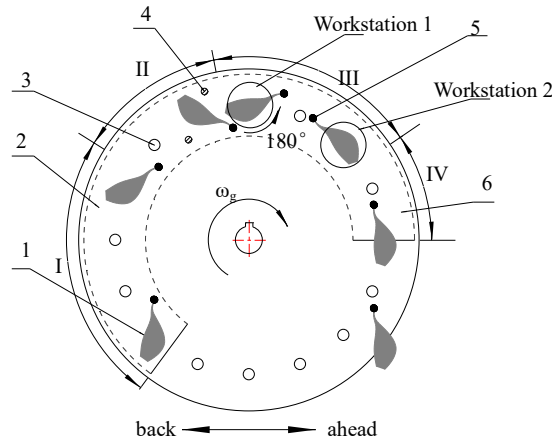


Fig. 2 - Diagram of the division of seed dispenser and the movement of garlic seeds

I. Seed suction zone; II. Preliminary orientation zone; III. Secondary orientation zone; IV. Seeding zone
 1. Garlic seed; 2. Seed dispenser; 3. Suction hole; 4. Directional needle; 5. The bud tip of garlic seeds; 6. Air chamber

Design and analysis of key components

Design of seed dispenser

The number of suction holes

The number of suction holes plays a crucial role in determining the seeding effectiveness within the seed suction zone (Ziheng et al.,2024). Therefore, it is essential to select an appropriate number of suction holes. The total number of suction holes on the seed dispenser should comply with the following formula (1).

$$Z = \frac{60v_m}{sn_p(1-p_0)} \tag{1}$$

Where:

- v_m is the operating speed of the planter, (m/s) ;
- s is the plant spacing, (m) ;
- n_p is the speed of the seed dispenser, (r/min) ;
- p_0 is the slip coefficient of the ground wheel, which is 8.5% in this paper.

Considering that the operating speed of the seeder exceeds 0.22 m/s and the plant spacing ranges from 0.08 to 0.12 m, the speed of the seed dispenser was set at 7 r/min. Based on these parameters, the number of suction holes was determined to be 16. Consequently, the central angle between adjacent suction holes was calculated to be 22.5°.

The diameter of the suction hole

Due to the irregular shape and significant size variation of garlic seeds, the selection of the suction hole diameter is critical. This diameter must be determined based on the size of the garlic seeds (Principles of Design of Seeding Machinery, 1982).

$$\begin{cases} d_c = (0.64 \sim 0.66) b_1 \\ (k_{min} + h_{min}) / 2 \leq b_1 \leq (k_{max} + h_{max}) / 2 \end{cases} \tag{2}$$

where:

- d_c is the diameter of the suction hole, (mm) ;
- b_1 is the average value of garlic seed width and thickness, (mm) ;
- k_{min} is the minimum value of garlic seed width, (mm) ;
- h_{min} is the minimum value of garlic seed thickness, (mm) ;
- k_{max} is the maximum value of garlic seed width, (mm) ;
- h_{max} is the maximum value of garlic seed thickness, (mm) ;

The size of Jinxiang hybrid garlic (Tao et al.2018) can be inserted into the formula (2) and the value range of the diameter of the suction hole should be 8.1~14.2 mm.

The radius of the distribution circle at the center of the suction hole

As illustrated in Figure 3, to prevent interference between two adjacent garlic seeds, the distance between the centers, O_1 and O_2 , of the two adjacent suction holes must satisfy the following condition:

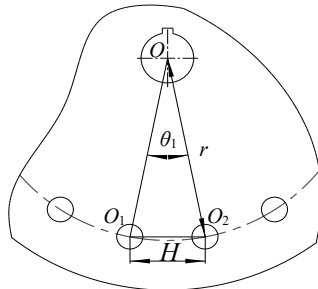
$$H \geq 2L_{max} - d_{cmin} \tag{3}$$

where: L_{max} is the maximum length of the garlic seeds, (mm);

d_{cmin} is the minimum value of suction holes, (mm);

Jinxiang hybrid garlic: L_{max} is 31.90 mm (Tao et al., 2018), then H is larger than 55.70 mm. In the isosceles triangle $O O_1 O_2$, the radius of the distribution circle of the center of the suction hole is larger than 142.31 mm, so 145 mm are taken in this paper.

Fig. 3 - Local schematic diagram of seed dispenser



O is the center of the seed dispenser; O_1 is the center of the suction hole circle; O_2 is the center of the adjacent suction hole circle.

Determination of directional needle positional parameters

The diversity of garlic adsorption states

Due to the irregular shape and size of garlic seeds, and the large gaps between adjacent garlic seeds, garlic seeds will randomly appear in a variety of adsorption states, as shown in Figure 4. In order to adapt to the diversity of garlic seed adsorption states, the number of directional needles is designed to be two, distributed on both sides of the center circle of the suction hole.

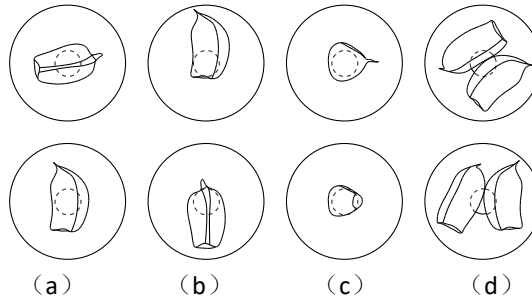


Fig. 4 - Different adsorption states of garlic species

Normal position parameters

The normal positional distance between the internal and external directional needles significantly influences the effectiveness of the preliminary orientation and seed-clearing process. As shown in Figure 5, garlic seeds pass through the internal and external directional needles in the direction of their thickness or width. Since the maximum width is greater than the maximum thickness, only the width dimension needs to be considered. The normal distance (E) between the internal and external directional needles, the radius (p) of the internal directional needle distribution circle, and the radius (q) of the external directional needle distribution circle must satisfy the following formula (4).

$$\begin{cases} \frac{k_{max}}{2} + \frac{d_d}{2} \leq r - p \leq L_{min} - \frac{d_{cmax}}{2} + \frac{d_d}{2} \\ \frac{k_{max}}{2} + \frac{d_d}{2} \leq q - r \leq L_{min} - \frac{d_{cmax}}{2} + \frac{d_d}{2} \\ E = q - p \end{cases} \tag{4}$$

where: k_{max} is the maximum value of the width of the garlic seed, mm;

L_{min} is the minimum length of the garlic seed, mm;

d_{cmax} is the maximum value of the suction holes, mm;

d_d is the diameter of the inner and outer directional needles, and it is taken 3 mm in this paper;

The size of Jinxiang hybrid garlic (*Tao et al.2018*) and the radius of the distribution circle of the center of the suction hole (r) can be inserted into the formula (4) and the value range of the normal distance E should be 25.14~38.32 mm.

Tangential position parameters

To prevent the garlic seeds from simultaneously contacting both the internal and external directional needles and being displaced, it is necessary to maintain a specific relative position between the internal and external directional needles in the tangential direction, which should be satisfied with F being larger than L_{max} , taking $F=50$ mm.

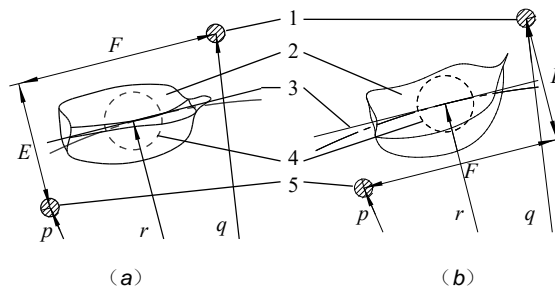


Fig. 5 - Garlic seeds passed through the directional needle smoothly

1. External directional needle; 2.Garlic seed; 3.The tangential direction of the suction hole; 4. Suction hole; 5.Internal directional needle

Combined suction block

Analysis of the motion process

In the secondary orientation process, the two levers of the directional adjusting device are mounted on the air chamber side of the seed dispenser. The initial positions of the levers and the two working edges of the combined suction block are aligned along the tangent direction of the suction hole distribution circle. These components must satisfy two key conditions: 1) The levers must be able to rotate 180°, and during this rotation, the garlic seeds should also rotate approximately 180° to ensure effective directional adjustment; 2) Upon completion of the lever rotation, the combined suction block must return to its initial position relative to the seed dispenser (namely, reset), and ensure that no interference occurs between the combined suction block and the levers when the system reaches the direction-adjusting station in the subsequent cycle, thereby maintaining the continuity of the directional adjustment process.

The seed dispenser rotates clockwise with an angular velocity ω_g , while the lever rotates counterclockwise around point O' with an angular velocity ω_z when the garlic seed requires adjustment. Each action involves a 180° rotation, which drives the combined suction block to rotate synchronously, as depicted in Figure 6.

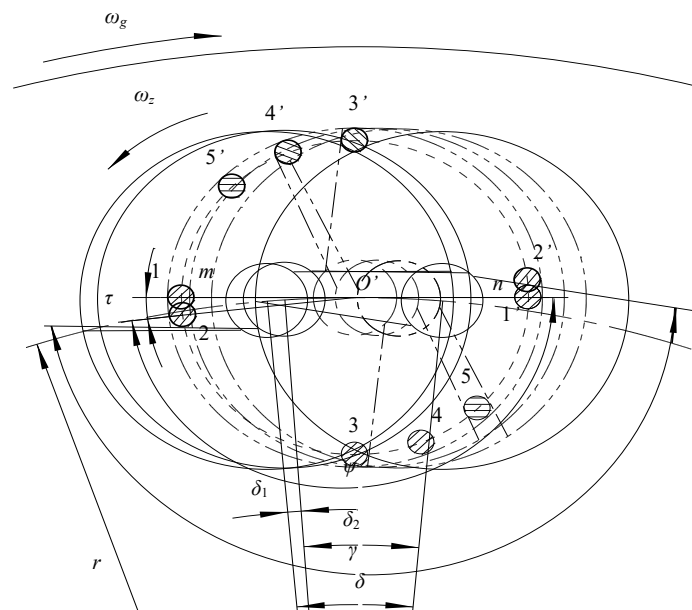


Fig. 6 - Movement process of the combined suction block

Position of the working edge of the combined suction block

Initially, the positions of lever *m* and lever *n* are at positions 1 and 1', respectively. As the lever begins to rotate counterclockwise, lever *m* first contacts the working edge of the corresponding combined suction block at position 2, initiating its rotation. When lever *m* reaches position 3, it disengages from the working side, and lever *n* continues to rotate the combined suction block. Upon lever *n* rotation to position 4', both levers are in the idle state. When lever *m* reaches position 5, it again engages the working edge before lever *n*, continuing to drive the combined suction block's rotation. At the end of the rotation cycle, lever *m* returns to position 1', and lever *n* returns to position 1. At this point, both levers have completed a full working cycle.

The 180° rotation of the lever is divided into two phases: idling time τ and effective rotation time ψ , with the corresponding rotation angles of the seed dispenser being δ_1 and δ_2 , respectively. The combined suction block undergoes a 180° rotation in synchrony with the rotation of δ_2 in the seed dispenser, during which the garlic seed is adjusted accordingly. For the garlic seed to be properly oriented, the idling time of the lever and the corresponding revolution time of the seed dispenser must be carefully coordinated.

As illustrated in Figure 7, a right-angle coordinate system is established with the center of the combined suction block, O_c as the origin, the x-axis tangential, and the y-axis normal to the system. The end of the lever's rotation is tangent to the working edge of the combined suction block during detachment. Therefore, the initial position of the working edge of the combined suction block must be tangent to the lever. The coordinates of the tangent point (G) are given by:

$$\begin{cases} x = r_2 \tan \beta_2 \cos \beta_2 \\ y = r_2 \cos \beta_2 - r \end{cases} \quad (5)$$

included among these:

$$\begin{cases} r_1 = \sqrt{r^2 + (d_a/2)^2} \\ r_2 = r_1 + d_b/2 \\ \beta_1 = \arctan \frac{d_a/2}{r} \\ \beta_2 = \beta_1 - \frac{\delta}{2} \end{cases} \quad (6)$$

where:

r_1 is the radius of the distribution circle at the center of the lever, (mm) ;

r_2 - the radius of the distribution circle at the tangent point G (mm) ;

d_a - the lever installation diameter (mm) ;

d_b - the diameter of the lever (mm) ;

β_1 - the angle between the center O' of the lever mounting and the center of the lever circle on the seed dispenser (°);

β_2 - the angle between the center O_c of the combined suction block and the center of the lever circle on the seed dispenser (°) .

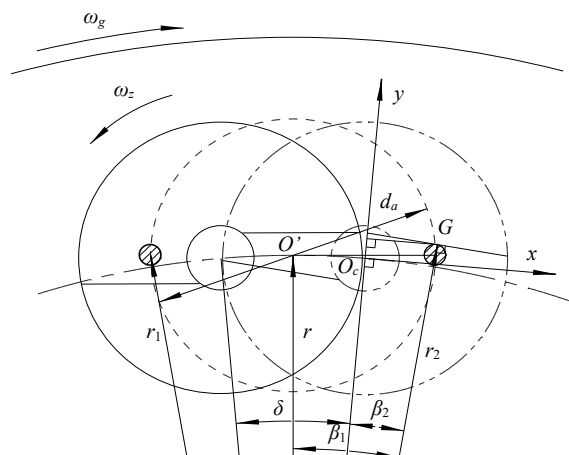


Fig. 7 - Analysis of the working state at the end of the lever rotation

Requirements for lever rotation

Due to the rotation of the seed dispenser, the lever may interfere with the subsequent arrival of the combined suction block's working edge as the lever nears the end of its rotation. The critical state of interference occurs when the outer circumference of the combined suction block becomes tangent to the motion trajectory of the outermost point of the lever, as illustrated in Figure 8. In this scenario, the combined suction block being adjusted begins to move toward the end of the lever's rotation, with the rotation angle of the combined suction block denoted as ε . Therefore, it is necessary for the time T required for the lever to complete one full working cycle to be less than the time t required for the seed dispenser to rotate by the angle ε . The calculation formula for t is given by:

$$\begin{cases} t = \varepsilon / \omega_g \\ \theta = \arccos \frac{2r^2 - (d_z/2 + d_a/2 + d_b/2)^2}{2r^2} \\ \varepsilon = 22.5^\circ - (\theta - \delta/2) \end{cases} \quad (7)$$

where:

θ is the central angle corresponding to the center of the combined suction block and the center of the lever installation on the seed dispenser under the interference critical state ($^\circ$);

d_z is the diameter of the combined suction block (mm);

According to equation (7):

$$T < \frac{1}{\omega_g} \left[22.5^\circ - \arccos \frac{2r^2 - (d_z/2 + d_a/2 + d_b/2)^2}{2r^2} + \frac{\delta}{2} \right] \quad (8)$$

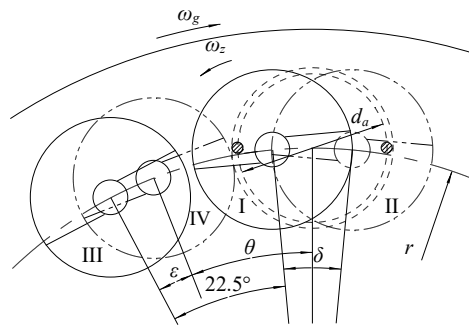


Fig. 8 - Analysis of the interference state of the lever

I is the initial position of the combined suction block; II is the end position of the rotation of the combined suction block; III is the initial position of the next combined suction block; IV is the interference position that the next combined suction block and the lever rotation

RESULTS AND ANALYSIS

The experimental apparatus and materials

The test was conducted using the JPS-12 seed dispenser performance test bench. The pneumatic system of the original test bench was upgraded to accommodate the specific air pressure requirements of the seed dispenser, as illustrated in Figure 9.

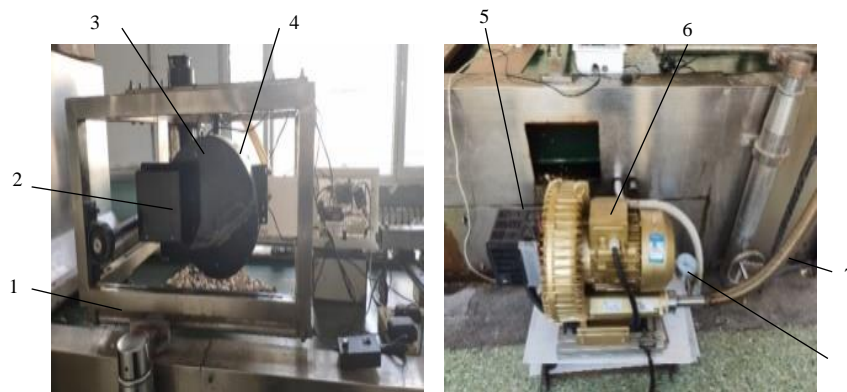


Fig. 9 - Physical diagram of the test bench

- 1. test benches; 2. seed dispenser; 3. image acquisition and recognition device; 4. directional adjusting device;
- 5. 7.5 kW Panasonic-MK30 inverter; 6. 3 kW GHBH-7D5-36-1R8 fan; 7. air pipe; 8. pressure gauge

Jinxiang hybrid garlic was selected as the test material, with seed thickness used as the basis for grading (Tao et al., 2018). The garlic seeds were categorized into three size classes: A (12–15 mm), B (15–18 mm), and C (18–21 mm). This grading process is designed to enhance the operational performance and efficiency of the garlic planting machine.

Single seed performance test

The experimental design

The diameters of the suction holes for garlic seeds in size classes A, B, and C were determined to be 10 mm, 11 mm, and 12 mm, respectively, based on preliminary pre-tests. To optimize the operating parameters of the seed dispenser, a three-factor, five-level rotary orthogonal experimental design was conducted using Design Expert software, in accordance with the GB/T 6973-2005 standard for Single-Grain (Precision) Seed Sowers (GB/T 6973-2005, 2005). The test factors selected were the negative pressure of the air chamber, the rotational speed of the seed dispenser, and the quantity of seeds in the seed chamber, while the test indices included the single grain rate, cavitation rate, and double grain rate. Upon analyzing the effects of these three factors on garlic seeds of different grades, it was found that the results were consistent across grades. As an example, the analysis focuses on B-size garlic seeds, which correspond to a suction hole diameter of 11 mm. The test factors and their corresponding codes are summarized in Table 1.

Table 1

Test factor coding table			
Code	Factors		
	X_1 / kPa	X_2 / (r/min)	X_3 /mm
-1.682	10.3	5.3	90
-1	11.0	6.0	110
0	12.0	7.0	140
1	13.0	8.0	170
1.682	13.7	8.7	190

Note: X_1 , X_2 , and X_3 are the negative pressure of the air chamber, the rotation speed of the seed dispenser, and the quantity of seeds in the seed chamber, respectively. The quantity of seeds in the seed chamber is measured by the height from the bottom of the air chamber to the surface of the seeds. And the scale is marked inside the seed chamber for easy reading of the experiment.

The experimental results and analysis

A total of 23 experimental runs were conducted. The study included 14 sets of analysis points and 9 sets of zero points. Each set of experiments was repeated 3 times, and the average value was taken as the experimental result.

The experimental data were then input into the Design-Expert software for statistical analysis and regression fitting (Chao, 2022). Through analysis of variance (ANOVA) for the single grain rate, cavitation rate, and double grain rate, non-significant factors were identified and eliminated. The resulting regression equations for each index and factor are as follows:

$$\begin{cases} Y_1 = 96.31 + 1.91X_1 - 1.19X_2 + 0.59X_3 + 1.76X_1X_2 + 0.78X_2X_3 - 4.50X_1^2 - 1.86X_2^2 - 2.24X_3^2 \\ Y_2 = 2.41 - 5.28X_1 + 2.48X_2 - 1.40X_3 - 0.79X_1X_2 + 2.90X_1^2 + 1.28X_2^2 + 2.18X_3^2 \\ Y_3 = 1.32 + 3.37X_1 - 1.29X_2 + 0.81X_3 - 0.97X_1X_2 + 0.68X_1X_3 - 0.53X_2X_3 + 1.60X_1^2 + 0.59X_2^2 \end{cases} \quad (9)$$

In the equation, Y_1 , Y_2 , and Y_3 are the single-grain rate, cavitation rate, and double-grain rate, respectively.

By using the dimensionality reduction method, one of the parameters of the negative pressure in the air chamber, the rotational speed of the seed dispenser, and the seed quantity in the seed chamber were adjusted to zero. A response surface graph was drawn to show the interaction between the other two factors on each indicator. Through response surface analysis, it was found that within the range of the air chamber pressure of 11~13 kPa, the seed dispenser speed of 6~8 r/min, and the seed quantity in the chamber of 110~170 mm, optimization solution is carried out under the condition of maximizing single seed rate and minimizing cavitation rate and double grain rate. The optimal parameter combination of the seed-metering device is obtained as follows: the negative pressure in the air chamber is 12.03 kPa, the rotational speed of the seed dispenser is 6.85 r/min, and the seed quantity in the seed chamber is 140.90 mm. At this time, the single seed rate is 96.50%, the cavitation rate is 1.87%, and the double grain rate is 1.63%.

Using the same method as above. For Grade A garlic, it was found that the negative pressure in the air chamber is 11.85 kPa, the rotational speed of the seed dispenser is 7.13 r/min, and the seed quantity in the seed chamber is 138.97 mm. At this time, the single seed rate is 95.98%, the cavitation rate is 2.13%, and the double grain rate is 1.89%. For Grade C garlic, it was found that the negative pressure in the air chamber is 13.21 kPa, the rotational speed of the seed dispenser is 7.25 r/min, and the seed quantity in the seed chamber is 141.24 mm. At this time, the single seed rate is 96.23%, the cavitation rate is 2.59%, and the double grain rate is 1.18%.

Preliminary orientation performance tests

Preliminary directional seed discharge performance indicators

In garlic planting, after individual grain orientation, the garlic seeds are first dropped into the receiving hopper, from which a vertical planting device then inserts them into the soil. To assess the orientation performance, garlic seeds were dropped into the hopper at various angles. The results showed that when the angle between the longitudinal axis of the garlic seeds and the normal line of the center distribution circle of the suction holes ranged from 40° to 90°, the upward rate of the bud tip exceeded 95%. Consequently, this range was established as the preliminary directional qualification standard. The preliminary orientation rate is calculated as follows:

$$M = \frac{N}{Q} \times 100\% \tag{10}$$

where: *M* is the preliminary orientation rate;

N is the number of garlic seeds qualified for preliminary orientation;

Q is the number of test garlic seeds.

Table 2

Percentage of bud tips facing up under different erection degrees of garlic species

Uprightness / °	Bud tip upward rate / %
0~20	85.66
20~40	91.16
40~60	95.61
60~80	96.33
80~90	98.75

Effects of directional needle position parameters on preliminary directional performance

Under the optimal working parameters, experimental studies were conducted on different grades of garlic. After the garlic varieties were classified according to thickness, it was observed that both the width and length of each grade increased with thickness. Consequently, the actual value of the distance *E* should be adjusted accordingly, compared to the theoretical analysis value. The experimental process is shown in Figure 10.

Fig. 10 - Diagram of the operation of the seed metering device



The positional parameters and test results for the directional needle are presented in Table 3.

Table 3

Statistical table of orientation effect of different grades of garlic seeds

Garlic seed level	<i>E</i> / mm	<i>r-p, q-r</i> / mm	Initial orientation rate / %
A	30	20.10	90.45
		17.13	95.33
		14.17	88.64
		11.19	53.20

Garlic seed level	E / mm	$r-p, q-r$ / mm	Initial orientation rate / %
B	35	22.13	75.64
		19.16	88.75
		16.19	96.04
		13.22	68.41
C	40	24.16	86.15
		21.19	92.62
		18.22	95.31
		15.25	57.21

The experimental results indicated that when the distances $r-p$ and $q-r$ are too small, the garlic seeds are prone to either falling prematurely or experiencing excessive angular deviation, leading to orientation failure. Additionally, since most garlic seeds are adsorbed below the center of the suction hole, the internal directional needle is more likely to cause the garlic seeds to be dislodged compared to the external directional needle.

CONCLUSIONS

(1) This study designed an air-suction seed metering device, incorporating a seed dispenser, directional needles, and combined suction blocks. This dispenser is equipped with the capabilities for single-seed extraction and preliminary orientation. Combined with image recognition and orientation technology, it can achieve continuous single-grain discharge of garlic seeds with the bud tip facing upward.

(2) A three-factor, five-level experimental design was employed, with the negative pressure in the air chamber, the rotational speed of the seed dispenser, and the number of seeds in the seed chamber as the test variables. The results indicated that, under the optimal operating parameters, the single-seed rate for garlic species A, B, and C were 95.98%, 96.50%, and 96.23%, respectively. The corresponding cavitation rates were 2.13%, 1.87%, and 2.59%, while the double-seed rates were 1.89%, 1.63%, and 1.18%, respectively. These results demonstrate that the performance of the system meets the requirements for the mechanization of garlic sowing.

(3) Through preliminary directional performance testing, the positional parameters of the directional needles for different grades of garlic seeds were determined. The radii of the distribution circles for the internal and external directional needles for garlic species A, B, and C were found to be 128 mm and 158 mm, 129 mm and 164 mm, and 124 mm and 164 mm, respectively.

ACKNOWLEDGEMENT

This research was supported by the Natural Science Foundation of Shandong Province (ZR2022ME103) and the 2022 Agricultural Application Technology Innovation Project of Jinan City (CX202216).

REFERENCES

- [1] Aijun G., Xiaoyu L., Jialin H., Zhilong Z., Ji Z., Jun C. (2018). Design and experiment of automatic directing garlic planter (自动定向大蒜播种机的设计与试验). *Transactions of the Chinese Society of Agricultural Engineering*, vol.34, no.11, pp. 17-25; Shandong/China.
- [2] Binbin Y., Yixiang Z., Banghong Z., (2019). Garlic Production Layout and Its Trade Patterns in China (中国大蒜生产布局及贸易格局分析), *Agricultural Outlook*, vol.15, no.11, pp. 6;
- [3] Chun F., Fuzhen S., Chongguang R. (2019). Identifying bulbil direction of garlic based on deep learning (基于深度学习的大蒜鳞芽朝向识别研究). *Application Research of Computers*, vol.36, no.02, pp. 598-600+610; Shandong/China.
- [4] Chao L. (2022). *Experimental study on garlic air-suction seed metering device for image recognition and orientation technology application*. MSc Thesis, Shandong University of Technology, Shandong/China.
- [5] Chi G., Shaoping X., Shenshu L., Qinlao Y. (2010). The Experimental Study of Recognition for Garlic Bud Scales Direction [J] (大蒜鳞芽方向识别的实验研究). *Journal of Agricultural Mechanization Research*, vol.32, no.10, pp. 136 -139; Shanxi/China.

- [6] GB/T 6973-2005, (2005) . Test method for single grain (precision) seeder (单粒(精密)播种机试验方法) . (in Chinese)
- [7] Hiroki M., Takeo H., Norio M. (2008) . *Bulb Planting Machine for Garlic or The Like*. JP2008131877 Japan.
- [8] Hongceng X, Chao L, Rui F, Junke Z, Chengqian J. (2021) . Effect of garlic planting position on garlic growth and yield (蒜种植方位对大蒜生长发育及产量的影响) , *Journal of Chinese Agricultural Mechanization*, vol.42, no.02, pp. 74-78; Shandong/China.
- [9] Jingling S., Pengfei X., Hongcen X., Shanru C., (2021), *Air suction type garlic directional seeding device*. CN201910346857.1, China.
- [10] Jialin H., Shenghai H., Ziru N., Yanqiang W., Tianhua L. (2018) Mechanism Analysis and Test of Adjusting Garlics Upwards Using Two Duckbill Devices (双鸭嘴式大蒜正头装置调头机理分析与试验) , *Transactions of the Chinese Society for Agricultural Machinery*, vol.49, no.11, pp. 87-96; Shandong/China.
- [11] Maheswarr T.K., Varma M.R. (2007) . Modification and performance evaluation of garlic planter, *Agricultural Engineering Today*, vol.31, no.02, pp. 11-14;
- [12] Paul F., (2015) A Garlic Clove Direction Detection based on Pixel Counting [C]. *Proceedings of the 2014 1st Student Computer Science Research Conference*.
- [13] Qingming Y., Juanling L., Ruiyin H. (2010) . Direction identification of garlic seeds based on image processing (基于图像处理的大蒜蒜瓣朝向识别) . *Acta Agriculturae Zhejiangensis*, vol.22, no.01, pp. 119 - 123; Jiangsu/China.
- [14] Robles S.N., Hlawinska S.J.R., Hernández A.R. (2016) Garlic apex localization by digital image analysis techniques (Localización del ápice del ajo mediante técnicas de análisis digital de imagen) . *Agrociencia*.
- [15] Ruichuan L, Xue S., Dianwei Q., Zhenjiao Z., Chuantao S., Zhaomiao Z., Qingsong H. (2013) . Research on the Garlic Planter Device Metering Single Seed (某大蒜播种机单粒排种装置的研究) , *Agricultural Equipment & Vehicle Engineering*, vol.51, no.06, pp. 5-8; Shandong/China.
- [16] Shichun J., Feng Z., Qing L., Fuxin L. (2009) . Research and Design on Rotary Garlic Single-Clove Directional Seed Metering Device (旋转式蒜瓣单粒定向取种器的研究设计) , *Agricultural Equipment & Vehicle Engineering*, pp. 18-20; Shandong/China.
- [17] Tao X., Jingling S., Zhichao C. (2018) . Physical properties of garlic seeds related to grading and planting[J]. *International Agricultural Engineering Journal*, vol.27, no.03, pp. 309-315; Shandong/China.
- [18] Xiaoxin C., Mengwei W., Li B., Xiaodong L. (2023) . Research on driving factors of Chinese garlic export growth (中国大蒜出口增长的驱动因素研究) , *China Cucurbits and Vegetables*, vol.36, no.10, pp. 153-160; Hebei/China.
- [19] Yuzhen W., Donglin Z., Yonglan L., Guannan X. (2017) Method Inquisition of Garlic Bud Screening and Upright Planting (大蒜芽端筛选及直立种植方案探究) , *Journal of Agricultural Mechanization Research*, vol.39, no.10, pp. 113-118; Jiangsu/China.
- [20] Ziheng F., Jing Z., Jincheng C., Feng P., Baiwei W., Chao J. (2024). Design and Experimental Analysis of an Air-Suction Wheat Precision Hill-Seed Metering Device. *Agriculture*. vol.14, no.11; Xinjiang/China.
- [21] Zhen C., Jingling S., Hongceng X., Mingliang Z. (2023) . A Review of Intelligent Orientation Techniques for Garlic Seeds Based on Machine Vision (基于机器视觉的蒜种智能定向技术综述). *Journal of Intelligent Agricultural Mechanization*, vol.04, no.02.
- [22] ****Principles of design of seeding machinery* (播种机械设计原理) , 1982. Beijing: China Machine Press. (in Chinese)

INVESTIGATION OF THE BULK MATERIAL MOVEMENT KINEMATICS IN CONICAL SCREW CONVEYOR

ДОСЛІДЖЕННЯ КІНЕМАТИКИ РУХУ СИПКОГО МАТЕРІАЛУ У ГВИНТОВОМУ КОНВЕЄРІ КОНІЧНОЇ ФОРМИ

Oleg LYASHUK, Andrii DIACHUN, Ihor TKACHENKO, Mykola STASHKIV, Andrii BABII, Maria PANKIV, Zhanna BABIAK, Alexander MARUNYCH, Oleg LAKH, Artur STARIKH

Ternopil Ivan Puluj National Technical University / Ukraine

Tel: +380967517889; E-mail: oleglashuk@ukr.net

DOI: <https://doi.org/10.35633/inmateh-74-65>

Keywords: conveyor, screw, conic shape, transporting, mixing.

ABSTRACT

New design of the conic shape screw conveyor is presented in the paper and the results of theoretical investigations of the bulk material kinematic movement in this conveyor were shown. Dependencies for finding kinematic and operating parameters, which provide long-term stability of such mixers were found. Stand equipment for investigation of the transporting efficiency and mixing of the bulk materials have been developed and manufactured. Mechanic screw conveyors' properties at high frequency range of rotation, under smooth and sharp starting, rotation frequency change and reversing in the automatic regime have been studied taking advantage of the ALTIVAR 71 and multipurpose measuring system with accelerometers for finding dynamic loadings by PC. The results of experimental investigations of the efficiency depending on the screw pitch and every next turn, the screw conic surface inclination and the screw rotation frequency are presented. It will make possible to clear the process of the bulk materials transporting and mixing for every possible combination of the initial parameters. Specifically, increasing the increment of the cargo displacement radius per turn from 1 mm to 5 mm results in a velocity increase ranging from 1.28 times to 2.44 times. Moreover, increasing the inclination angle of the forming cone surface from 1 degree to 2 degrees provides a 1.18-fold increase in productivity, and varying the increment of the screw pitch from 0.004 m to 0.01 m per turn results in a 1.07-fold decrease in productivity. Increasing the rotation frequency of the conical screw α from 200 r/min to 500 r/min leads to a doubling of productivity.

РЕЗЮМЕ

У статті представлено нову конструкцію гвинтового конвеєра конічної форми, подано результати теоретичних досліджень кінематику руху сипкого матеріалу у вищезгаданому конвеєрі. Виведені залежності для визначення кінематичних та експлуатаційних параметрів, що забезпечують стабільну роботу таких змішувачів. Розроблено і виготовлено стендове обладнання для дослідження продуктивності транспортування та змішування сипких матеріалів, а також характеристик механічних гвинтових конвеєрів в широкому діапазоні частоти обертання, при плавному та різкому пуску, зміні частоти обертання і реверсуванні в процесі досліджень в автоматизованому режимі за допомогою перетворювача частоти серії ALTIVAR 71 та універсальної вимірювальної системи з акселерометрами для визначення динамічних навантажень з отриманням відповідних даних у ПК. Представлено результати експериментальних досліджень продуктивності залежно від кроку шнека на кожному послідовному витку, кута нахилу твірної конічної поверхні шнека, частоти обертання шнека, які дозволять краще зрозуміти процес транспортування та змішування сипких матеріалів для кожної відповідної комбінації вхідних параметрів. Зокрема при збільшенні приросту радіуса переміщення вантажу на одному витку від 1 мм до 5 мм призводить до зростання швидкості вантажу від 1,28 рази до 2,44 рази. При цьому збільшення кута нахилу твірної конусної поверхні шнека від 1 град до 2 град забезпечує зростання продуктивності в 1,18 рази, а зміна величини приросту кроку шнека на кожному послідовному витку від 0,004 м до 0,01 м призводить до спадання продуктивності в 1,07 рази. Збільшення частоти обертання конусного шнека від 200 об/хв. до 500 об/хв. призводить до зростання продуктивності в 2 рази.

INTRODUCTION

The development of production and improvement of the transportation machines' efficiency can be achieved due to the creation of new and improvement of available screw conveyors with advanced technological capabilities. The application of such screw conveyors makes it possible to increase the accuracy of bulk material feeding and provide wide range of transportation efficiency.

Screw conveyors with variable geometry of the screw operating body and casing in the direction of material movement are designed to transport, mix and dose bulk materials and are usually installed at the beginning of the screw conveyor transport system (Pysarenko et al., 1988; Zareiforoush et al., 2010; Loveikin and Rogatynska, 2011; Aulin et al., 2019; Zalutskyi et al., 2018; Trokhaniak et al., 2020). Due to the application of such conveyors, the accuracy of the minute feeding of bulk material increases (Tian et al., 2018; Zaica et al., 2016; Zaica et al., 2020).

The use of variable speed drive increases the accuracy of bulk material dosing and ensures the achievement of wide range of transportation productivity. Screw conveyors with variable geometry of screw operating bodies are available in a wide range of cross-sectional dimensions, lengths, configurations and construction materials (Hevko et al., 2021; Bulgakov et al., 2022; Bulgakov et al., 2023; Hud et al., 2023). The SC loading area is usually completely filled with material under gravitation and connected to square, rectangular or cylindrical hopper by means of conical or straight neck (Lyashuk et al., 2019).

In the papers of Haaker et al., (1993), Zaica et al., (2020), it was determined that the maximum amount of material supply Q_0 per revolution of the screw operating body is the value equal to or less than $0.75Q_{max}$, where Q_{max} is the material supply being equal to the maximum value of the ratio of the turn pitch to the turn diameter. Beyond this value, the increase of turn pitch does not provide the increase of material movement productivity. Also, based on theoretical analysis, it was found that the minimum ratio of the turn pitch to the turn diameter should be at least 0.25.

In the paper of Yongqin (1997), Lyashuk et al., (2018), Lyashuk et al., (2022), three main methods of increasing material capture in the feed direction are proposed: the use of screw operating body with variable turn pitch, with conical shaft of the screw operating body, and conical screw operating body.

In the paper of Fernandez et al., (2009), Moorthi et al., (2022), six different designs of screw operating bodies are investigated for the determination of their effect on the efficiency of bulk material transportation, uniformity of material capture from the hopper, and power consumption during transportation.

In the paper of Roberts (1991), Ross and Isaacs (1961) the interaction of bulk material particles with each other were investigated in two different ways. Roberts, 1991, and Aulin et al., 2018, studied the vortex motion of grains in the screw conveyor theoretically and experimentally. The measured free vortex motion was correlated quite accurately with the obtained vortex motion of the grains based on theoretical equations. However, during force vortex motion, the grain mass demonstrated behavior similar to that of the solid body, while significant hysteresis effect was obtained in the resulting material vortex profile.

In the paper of Nilsson (1971), the theoretical analysis was based on the pressures generated around the screw operating body in the axial plane. For screw conveyors, it is difficult to maintain high efficiency at significant rotation speeds of the screw operating because centrifugal forces prevent bulk material from entering the screw operating body. Such investigations and innovations will make it possible to increase the efficiency of bulk materials transportation by designing and substantiating the screw conveyor parameters.

On the basis of structural synthesis and experimental investigations (Mondal, 2021; Lyashuk et al., 2023), it was found that conical screw conveyors, compared to cylindrical ones, make it possible to improve the quality of mixing bulk material during its transportation. Therefore, it is necessary to investigate the kinematics of bulk material movement in conical screw conveyor.

MATERIALS AND METHODS

During the operation of conical screw conveyor, the coordinates of bulk material placement and its movement nature are determined by angular parameters θ_1 and θ (Hevko et al., 2015; Lyashuk et al., 2019). In order to determine the nature of load movement, let us consider the movement of the selected material volume in xyz coordinates (Fig. 1).

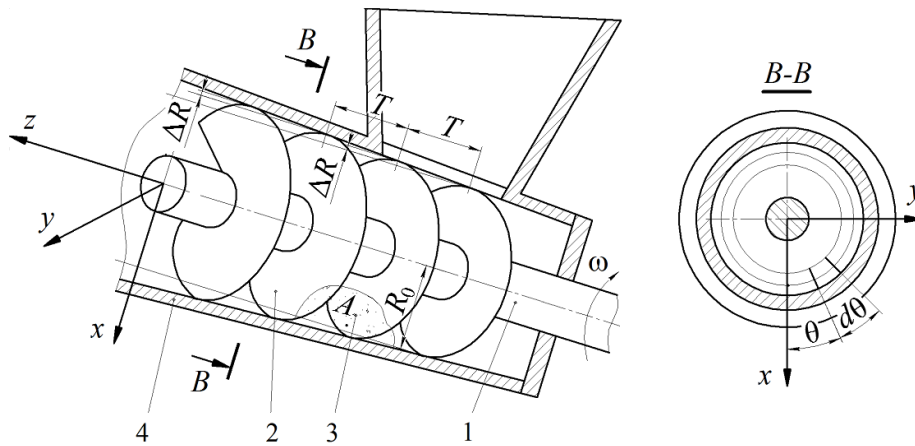


Fig. 1 – Calculation diagram of the movement of a selected load volume in the conical screw conveyor
 1 – drive shaft; 2 – conical screw; 3 – selected load volume; 4 – conical casing

The high-speed mode of conveyor operation, where simultaneous transportation and mixing of load take place, is investigated. Under simultaneous contact of the selected material volume *A* with the surface of the conical screw and the conical surface of the fixed casing, its placement is determined by radial parameter R_0 and angular parameters θ_1 and θ (Hevko et al., 2015; Rohatynskiy et al., 2015; Yu et al., 2022).

Let us represent the change of the outer screw radius R and the inner casing radius by linear dependence, where the initial radius of the screw R_0 increases by ΔR for each subsequent turn.

One screw turn corresponds to the angular parameter $\theta_1=2\pi$, then the function of changing the screw radius and load movement radius can be written as follows:

$$R(\theta_1) = R_0 + \frac{\Delta R \theta_1}{2\pi} \tag{1}$$

The increase in the screw radius and the load movement radius on one turn is:

$$\Delta R = \frac{R_{\max} - R_0}{i}, \tag{2}$$

where R_{\max} - maximum screw radius in the bulk material unloading area, m; i - is the number of turns involved in the movement of bulk cargo along helical trajectory.

The number of turns involved in the movement of bulk cargo along helical trajectory is determined by the following dependence:

$$i = \frac{\omega_v t}{2\pi}, \tag{3}$$

where ω_v - angular velocity of bulk material movement, rad/s; t - time of cargo movement from the loading area to the unloading area, s.

The time of cargo movement from the loading area to the unloading area is determined by the following formula:

$$t = \frac{2L\pi}{(\omega - \omega_v)T}, \tag{4}$$

where L - the length of the screw operating part, m; ω - the angular speed of the screw rotation, rad/s; T - the screw turn pitch, m.

Having substituted Eq. 4 into Eq. 3, is obtained:

$$i = \frac{\omega_v L}{(\omega - \omega_v)T}. \tag{5}$$

Then the increase in the screw radius and the load movement radius on one turn is:

$$\Delta R = \frac{T(R_{\max} - R_0)(\omega - \omega_v)}{\omega_v L}. \tag{6}$$

In the parametric form, with sufficient approximation, the coordinates of the selected material volume *A* are determined by the following dependencies:

$$\begin{cases} x_A = \left(R_0 + \frac{\Delta R \theta_1}{2\pi} \right) \cos \theta; \\ y_A = \left(R_0 + \frac{\Delta R \theta_1}{2\pi} \right) \sin \theta; \\ z_A = \frac{T(\omega_1 t - \theta)}{2\pi}, \end{cases} \quad (7)$$

where: x_A, y_A, z_A – are material coordinates, m.

The equations of conical screw with constant pitch $T=2\pi C$ rotating with angular velocity ω in parametric form are as follows:

$$\begin{cases} x_s = \left(R_0 + \frac{\Delta R \theta_1}{2\pi} \right) \cos(\theta_1 + \omega t); \\ y_s = \left(R_0 + \frac{\Delta R \theta_1}{2\pi} \right) \sin(\theta_1 + \omega t); \\ z_s = c\theta_1 = (T/2\pi)\theta_1. \end{cases} \quad (8)$$

The equation of the conical operating surface of the stationary screw conveyor casing looks like:

$$\begin{cases} x_k = \left(R_0 + \frac{\Delta R \theta_2}{2\pi} \right) \cos \theta_2 \\ y_k = \left(R_0 + \frac{\Delta R \theta_2}{2\pi} \right) \sin \theta_2; \\ z_k = u_2, \end{cases} \quad (9)$$

where θ_2 – angular parameter of the point of the screw casing surface, rad; u_2 – radial parameter of the point of the screw casing surface, m.

The projections of material movement velocity are found by differentiating the equations in Eq. 7:

$$\begin{cases} \dot{x}_A = \frac{\Delta R}{2\pi} \frac{d\theta_1}{dt} \cos \theta - \left(R_0 + \frac{\Delta R \theta_1}{2\pi} \right) \sin \theta \frac{d\theta}{dt}; \\ \dot{y}_A = \frac{\Delta R}{2\pi} \frac{d\theta_1}{dt} \sin \theta + \left(R_0 + \frac{\Delta R \theta_1}{2\pi} \right) \cos \theta \frac{d\theta}{dt}; \\ \dot{z}_A = \frac{T}{2\pi} \left(\omega - \frac{d\theta}{dt} \right). \end{cases} \quad (10)$$

The screw velocity is determined by the following dependencies:

$$\begin{cases} \dot{x}_{1s} = - \left(R_0 + \frac{\Delta R \theta_1}{2\pi} \right) \omega \sin \theta; \\ \dot{y}_{1s} = \left(R_0 + \frac{\Delta R \theta_1}{2\pi} \right) \omega \cos \theta; \\ \dot{z}_{1s} = 0. \end{cases} \quad (11)$$

Taking into account dependencies in Eq. 10 and Eq. 11, velocities of material movement relatively to the screw in the direction of axes x, y, z are found:

$$\begin{cases} \dot{x}_1 = \frac{\Delta R}{2\pi} \frac{d\theta_1}{dt} \cos \theta + \left(R_0 + \frac{\Delta R \theta_1}{2\pi} \right) \sin \theta \left(\omega - \frac{d\theta}{dt} \right); \\ \dot{y}_1 = \frac{\Delta R}{2\pi} \frac{d\theta_1}{dt} \sin \theta - \left(R_0 + \frac{\Delta R \theta_1}{2\pi} \right) \cos \theta \left(\omega - \frac{d\theta}{dt} \right); \\ \dot{z}_1 = \frac{T}{2\pi} \left(\omega - \frac{d\theta}{dt} \right). \end{cases} \quad (12)$$

The modulus of material velocity relatively to the screw and conical casing is determined by the corresponding formulas (Rohatynskiy et al., 2015):

$$|\dot{s}_1| = \sqrt{\dot{x}_1^2 + \dot{y}_1^2 + \dot{z}_1^2}; \tag{13}$$

$$|\dot{s}_2| = \sqrt{\dot{x}_2^2 + \dot{y}_2^2 + \dot{z}_2^2}. \tag{14}$$

Having substituted Eq. 12 into Eq. 13 and Eq. 10 into Eq. 14, taking into account that the material is in constant contact with the casing, after reductions, is obtained:

$$|\dot{s}_1| = \sqrt{\left(\left(R_0 + \frac{\Delta R \theta_1}{2\pi} \right)^2 + \frac{T^2}{4 \cdot \pi^2} \right) \cdot \left(\omega - \frac{d\theta}{dt} \right)^2 + \frac{1}{4\pi^2} \Delta R^2 \left(\frac{d\theta_1}{dt} \right)^2}; \tag{15}$$

$$|\dot{s}_2| = \sqrt{\left(R_0 + \frac{\Delta R \theta_1}{2\pi} \right)^2 \left(\frac{d\theta}{dt} \right)^2 + \frac{T^2}{4 \cdot \pi^2} \left(\omega - \frac{d\theta}{dt} \right)^2 + \frac{1}{4\pi^2} \Delta R^2 \left(\frac{d\theta_1}{dt} \right)^2}. \tag{16}$$

The acceleration of the material is found by differentiating equations in Eq. 10:

$$\begin{cases} \ddot{x}_A = \frac{\Delta R}{2\pi} \frac{d^2\theta_1}{dt^2} \cos \theta - \frac{\Delta R}{\pi} \frac{d\theta_1}{dt} \sin \theta \frac{d\theta}{dt} - \left(R_0 + \frac{\Delta R \theta_1}{2\pi} \right) \cos \theta \left(\frac{d\theta}{dt} \right)^2 - \left(R_0 + \frac{\Delta R \theta_1}{2\pi} \right) \sin \theta \frac{d^2\theta}{dt^2}; \\ \ddot{y}_A = \frac{\Delta R}{2\pi} \frac{d^2\theta_1}{dt^2} \sin \theta + \frac{\Delta R}{\pi} \frac{d\theta_1}{dt} \cos \theta \frac{d\theta}{dt} - \left(R_0 + \frac{\Delta R \theta_1}{2\pi} \right) \sin \theta \left(\frac{d\theta}{dt} \right)^2 + \left(R_0 + \frac{\Delta R \theta_1}{2\pi} \right) \cos \theta \frac{d^2\theta}{dt^2}; \\ \ddot{z}_A = -\frac{T}{2\pi} \frac{d^2\theta}{dt^2}. \end{cases} \tag{17}$$

Let us consider the stable mode of cargo movement in high-speed conical screw conveyor-mixer, where the material moves along helical trajectory (Fig. 2) and for which the following conditions are provided at the steady-state mode:

$$\frac{d\theta}{dt} = \text{const} = \omega_v; \quad \frac{d^2\theta}{dt^2} = 0; \quad \frac{d\theta_1}{dt} = \text{const} = \omega_v; \quad \frac{d^2\theta_1}{dt^2} = 0.$$

For the provided conditions from Eq. 12, the projections of the material movement velocity relative to the conical screw on the axis of coordinate system *xyz* are found:

$$\begin{cases} \dot{x}_1 = \frac{\Delta R \omega_v}{2\pi} \cos(\omega_v t) + \left(R_0 + \frac{\Delta R \omega_v t}{2\pi} \right) \sin(\omega_v t) (\omega - \omega_v); \\ \dot{y}_1 = \frac{\Delta R \omega_v}{2\pi} \sin(\omega_v t) - \left(R_0 + \frac{\Delta R \omega_v t}{2\pi} \right) \cos(\omega_v t) (\omega - \omega_v); \\ \dot{z}_1 = \frac{T}{2\pi} (\omega - \omega_v). \end{cases} \tag{18}$$

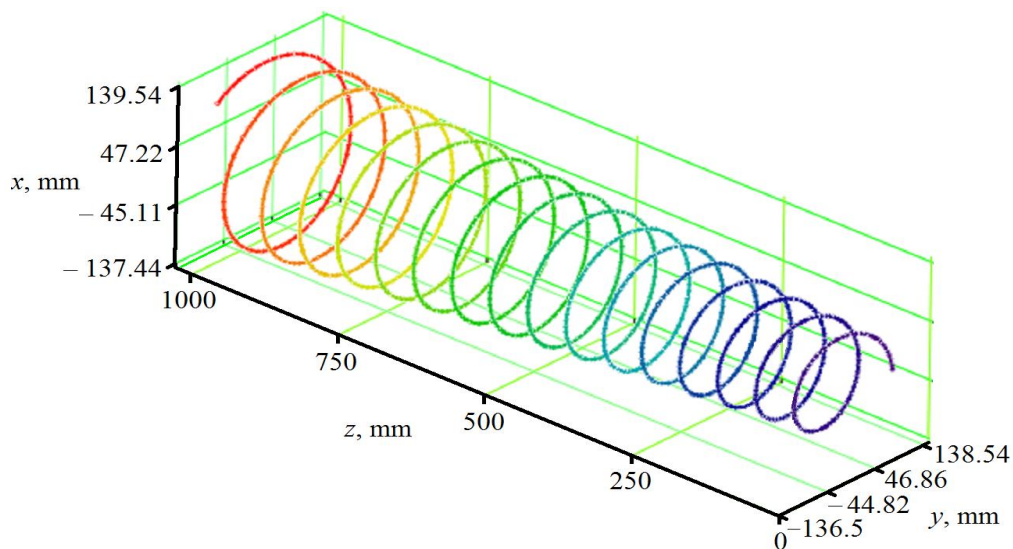


Fig. 2 – Chart of the bulk cargo trajectory in high-speed conveyor with the screw and conical casing:

$$R_0 = 75 \text{ mm}; R_{\text{max}} = 140 \text{ mm}, L = 1000 \text{ mm}, \Delta R = 3.97 \text{ mm}, i = 16$$

Projections of the material velocity relatively to the conical casing on the axes of coordinate system xyz :

$$\begin{cases} \dot{x}_2 = \frac{\Delta R \omega_v}{2\pi} \cos(\omega_v t) - \left(R_0 + \frac{\Delta R \omega_v t}{2\pi} \right) \sin(\omega_v t) \omega_v; \\ \dot{y}_2 = \frac{\Delta R \omega_v}{2\pi} \sin(\omega_v t) + \left(R_0 + \frac{\Delta R \omega_v t}{2\pi} \right) \cos(\omega_v t) \omega_v; \\ \dot{z}_2 = \frac{T}{2\pi} (\omega - \omega_v). \end{cases} \quad (19)$$

The modules of the material velocity from Eq.15 and Eq.16 are determined by the following formulas:

$$|\dot{s}_1| = \sqrt{\left(\left(R_0 + \frac{\Delta R \omega_v t}{2\pi} \right)^2 + \frac{T^2}{4 \cdot \pi^2} \right) \cdot (\omega - \omega_v)^2 + \frac{1}{4\pi^2} \Delta R^2 \omega_v^2}; \quad (20)$$

$$|\dot{s}_2| = \sqrt{\left(\left(R_0 + \frac{\Delta R \omega_v t}{2\pi} \right)^2 + \frac{1}{4\pi^2} \Delta R^2 \right) \omega_v^2 + \frac{T^2}{4 \cdot \pi^2} (\omega - \omega_v)^2}. \quad (21)$$

The material acceleration is determined by Eq.17:

$$\begin{cases} \ddot{x}_A = -\frac{\Delta R \omega_v^2}{\pi} \sin(\omega_v t) - \left(R_0 + \frac{\Delta R \omega_v t}{2\pi} \right) \omega_v^2 \cos(\omega_v t); \\ \ddot{y}_A = \frac{\Delta R \omega_v^2}{\pi} \cos(\omega_v t) - \left(R_0 + \frac{\Delta R \omega_v t}{2\pi} \right) \omega_v^2 \sin(\omega_v t); \\ \ddot{z}_A = 0. \end{cases} \quad (22)$$

Based on Eq. 20, the graphs of changes in the velocity of the movement of material selected volume relatively to the screw in conical screw conveyor were constructed (Fig. 3, Fig. 4).

Based on the graphs in Fig. 3 and Fig. 4, it was found that the increase in ΔR of the cargo movement radius on one turn of the conical screw conveyor significantly affects the increase in the cargo speed, which contributes to the intensification of the mixing process. That is, the increase in the growth ΔR of the cargo movement radius on one turn from 1 mm to 5 mm results in the increase in the cargo speed from 1.28 times to 2.44 times.

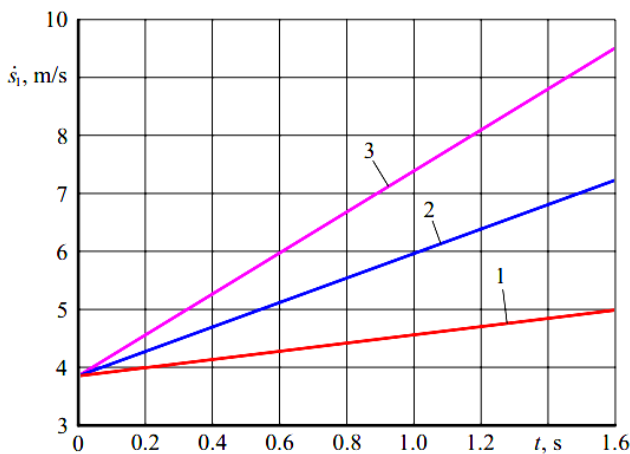


Fig. 3 – Chart of changes in the velocity of the movement of material selected volume relatively to the screw in conical screw conveyor over time $R_0=75$ mm:
1 – $\Delta R = 1$ mm; 2 – $\Delta R = 3$ mm; 3 – $\Delta R = 5$ mm

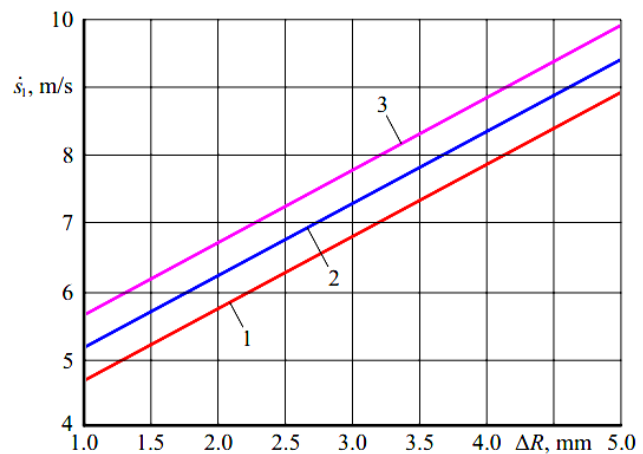


Fig. 4 – Chart of changes in the velocity of the movement of material selected volume relatively to the screw in conical screw conveyor from the increase in the cargo movement radius on one turn:
1 – $R_0=70$ mm; 2 – $R_0=80$ mm; 3 – $R_0=90$ mm

RESULTS

In order to carry out experimental investigations, a special laboratory installation was designed and manufactured. It includes: multifunctional screw conveyor, replaceable conical-shaped casings, screws with variable turn pitch, screws with corrugated surface and variable pitch for mixing materials during transportation. The installation is shown in Fig. 5.

The installation structure features include the use of conical screw conveyor-mixer equipped with the casing with adjustable hole sizes designed to spill the material during transportation. It makes possible to increase the transportation efficiency by mixing bulk materials with simultaneous stirring.

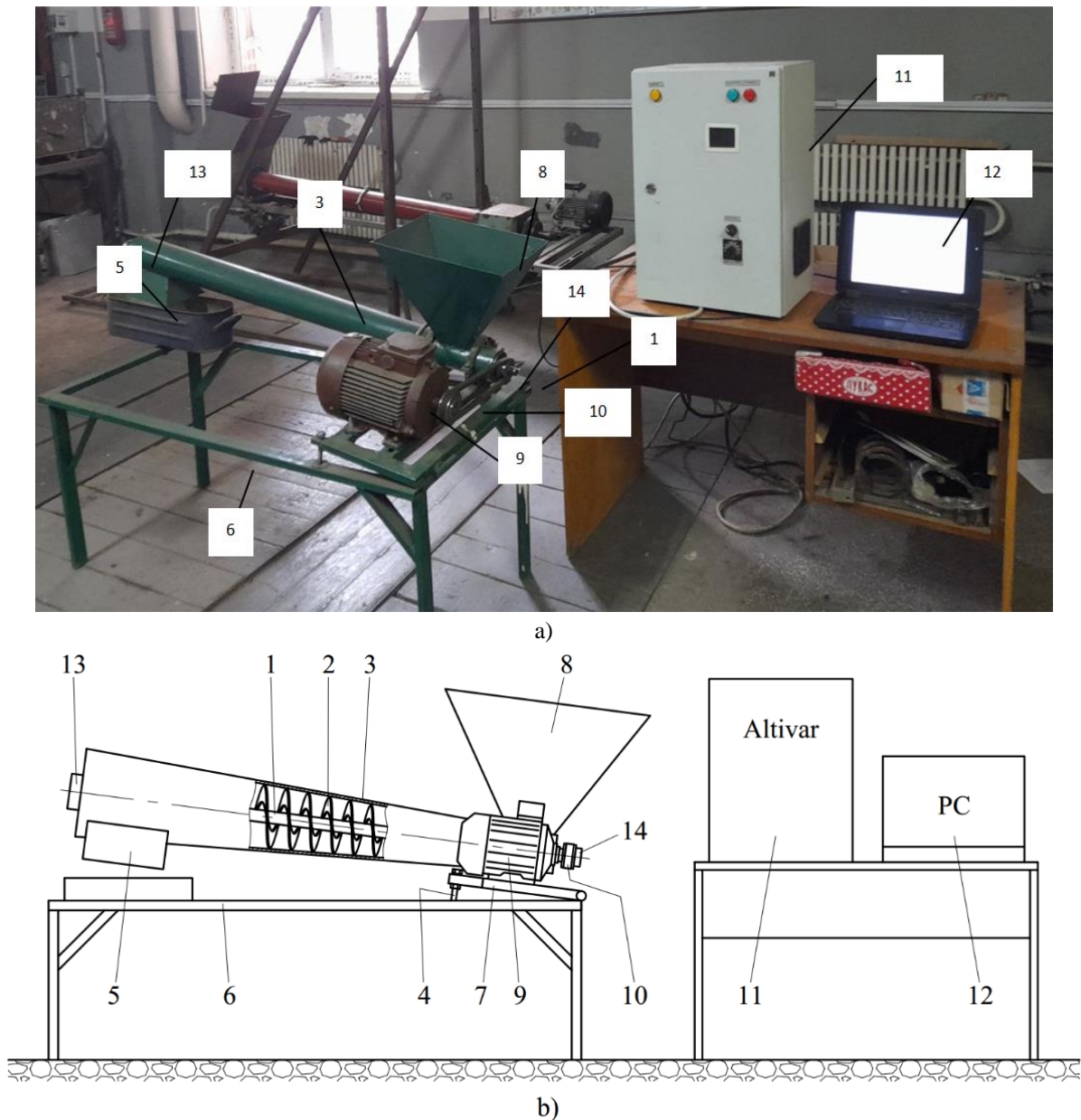


Fig. 5 – Experimental installation for the investigation of conical screw conveyor-mixer characteristics:

a – general view of the installation; b – schematic diagram of the installation; 1 – screw shaft; 2 – screw surface with the increasing gap between the shaft and the screw; 3 – conical casing; 4 – mechanism for adjusting the overload height; 5 – unloading nozzle; 6 – frame; 7 – movable table; 8 – hopper; 9 – electric drive; 10 – belt drive; 11 – drive rotation frequency converter; 12 – personal computer; 13 – accelerometer DN-3-M1; 14 – accelerometer DN-4-M1

After calculations, design and manufacture of the screw conveyors, the following limits of variation of input factors were determined:

- the amount of the screw pitch increase on each subsequent $\Delta T = 0.004-0.01$ m;
- the inclination angle of the screw conical surface $\alpha = 1-2$ deg;
- the speed of conical screw rotation $n = 200-500$ r/min;
- height of the protrusions (corrugations) on the outer diameter of the screw surface $A = 0.004-0.012$ m;
- rotational speed of the corrugated screw $n_1 = 70-270$ r/min.

The main design parameters of the conical screw are determined:

- for the lower level of variation of the experimental factors: maximum pitch of the conical screw on the last turn $T_{max} = 0.129$ m, maximum diameter of the conical screw $D_{max} = 0.151$ m, the number of turns $i = 13$;
- for zero level of variation of the experimental factors: maximum pitch of the conical screw on the last turn $T_{max} = 0.156$ m, maximum diameter of the conical screw $D_{max} = 0.175$ m, number of turns $i = 11.86$;
- for the upper level of variation of the experimental factors: maximum pitch of the conical screw on the last turn $T_{max} = 0.178$ m, maximum diameter of the conical screw $D_{max} = 0.2$ m, number of turns $i = 10.84$.

For the research, 18 different types of conical screws were manufactured. Experimental investigations of the designed and manufactured laboratory model of the multifunctional screw conveyor with replaceable casings and conical screws with variable pitch and with special corrugated conical screws with variable pitch for materials mixing during transportation were carried out. During these investigations the regularities of changes in the productivity of screw conveyors with ordinary conical screws from changes in three main factors were established: the value of the increase in the screw pitch ΔT at each step, the angle of inclination of the conical screw surface α , the screw rotation frequency n during the transportation of wheat and pea grains, and the efficiency of screw conveyors with common conical screw depending on changes in three main factors: the increase in the pitch of corrugated screw on each subsequent turn ΔT , the height of the corrugations on the outer diameter of the screw surface A , and the corrugated screw rotation frequency n_1 .

The general view of the regression equations for the efficiency of screw conveyors with common conical screws from changes in three main factors: the value of the increase in the screw pitch on each subsequent turn ΔT , the angle of inclination of the conical screw surface α , the screw rotation frequency n , i.e., $Q_1 = f(\Delta T, \alpha, n)$ based on the results of full factorial experiments 3^3 and the regression equation for determining the efficiency is derived:

- for wheat transportation:

$$Q_{1w(\Delta T, \alpha, n)} = 0.499 - 49.66\Delta T + 0.393\alpha + 0.0164n - 10\Delta T\alpha - 0.0889\Delta Tn + 0.00233\alpha n + 2555.55\Delta T^2 - 0.0268\alpha^2 - 7.42 \cdot 10^{-6}n^2; \tag{23}$$

- for peas transportation:

$$Q_{1p(\Delta T, \alpha, n)} = 0.605 - 67.722\Delta T + 0.345\alpha + 0.01387n - 8.66\Delta T\alpha - 0.0777\Delta Tn + 0.00204\alpha n + 2222.22\Delta T^2 - 0.0235\alpha^2 - 6.49 \cdot 10^{-6}n^2. \tag{24}$$

Based on the obtained results of experimental investigations and the derived regression Eq. 23 and Eq. 24, the response surfaces of the dependence of the efficiency of moving bulk material by screw conveyor with common conical screw with variable pitch of turns were constructed using software, as shown in Fig. 6.

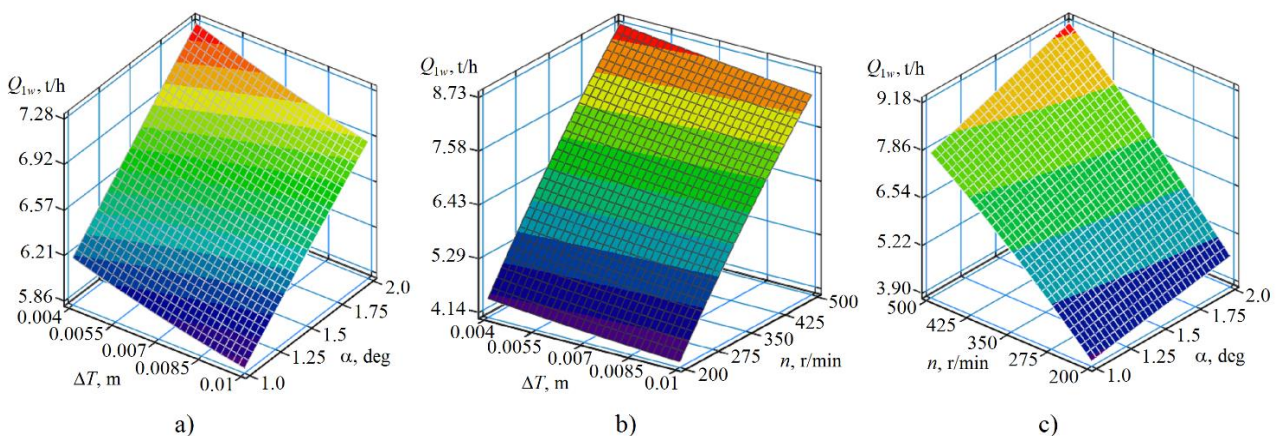


Fig. 6 – Response surfaces of the dependence of efficiency Q on the conveyor drive:
 a – $Q = f(\Delta T, \alpha)$ at $n = 350$ r/min; b – $Q = f(\Delta T, n)$ at $\alpha = 1.5$ deg.; c – $Q = f(n, \alpha)$ at $\Delta T = 0.004$ m

From Figures 6 and regression equations Eq. 23 and Eq. 24, it can be concluded that with the increase in the angle of inclination of the generative conical surface of the corrugated screw, the screw rotation frequency, and the decrease in the value of the incremental screw pitch at each subsequent turn, the efficiency of transporting bulk material increases. Maximum efficiency during wheat transportation was 9.44 t/h, and the minimum was 3.8 t/h. Maximum efficiency during the transportation of peas was 8.26 t/h, and the minimum was 3.32 t/h.

The increasing in the speed of conical screw n from 200 r/min to 500 r/min resulted in 2-fold increase in transportation efficiency. At the same time, the increase in the angle of inclination of the screw conical surface α from 1 degree to 2 degrees resulted in the increase of efficiency by 1.18 times, and change in the value of the increase in the screw pitch on each subsequent turn ΔT from 0.004 m to 0.01 m resulted in the decrease of efficiency by 1.07 times.

In order to implement the procedure for processing experimental data according to the method described in (<https://www.hbmprensia.com>, <https://www.ncode.com>), the operation project containing the following structural elements (glyphs): Excel Input, Multi Column to Time Series, Butterworth Filter, Meta Data Display, Time Series to Multi Column Output, Frequency Spectrum and XY Display was constructed. The general view of the interface of the operation project for processing experimental data in nCode GlyphWorks environment is shown in Fig. 7.

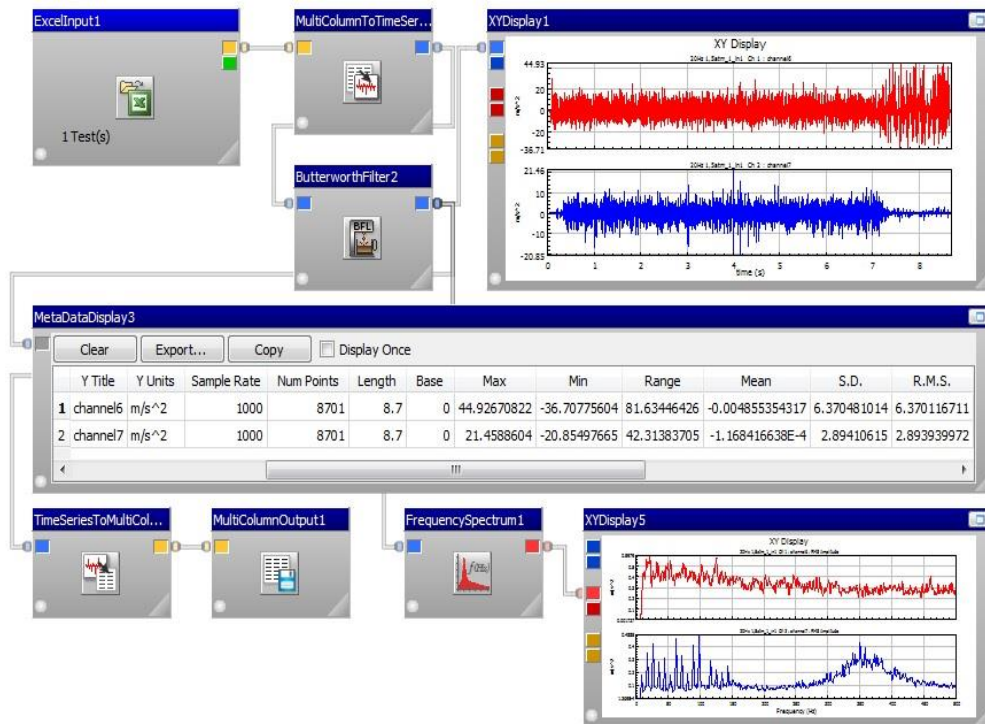


Fig. 7 – General view of the operation project in nCode GlyphWorks environment

The results of experimental data processing by nCode GlyphWorks for individual combinations of the investigated parameters are shown in Figs. 8 - 11.

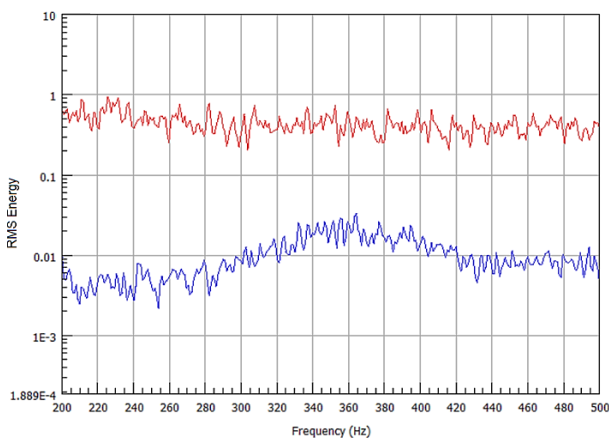


Fig. 8 – Frequency spectrum of the mean square deviation of the oscillations' energy density (10 Hz, 200 r/min)

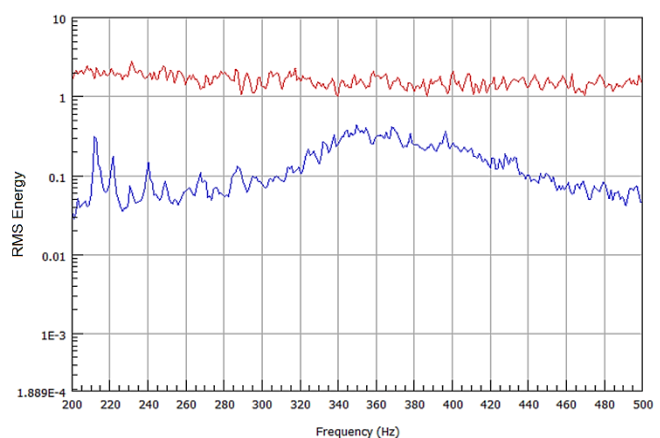


Fig. 9 – Frequency spectrum of the mean square deviation of the oscillations' energy density (20 Hz, 300 r/min)

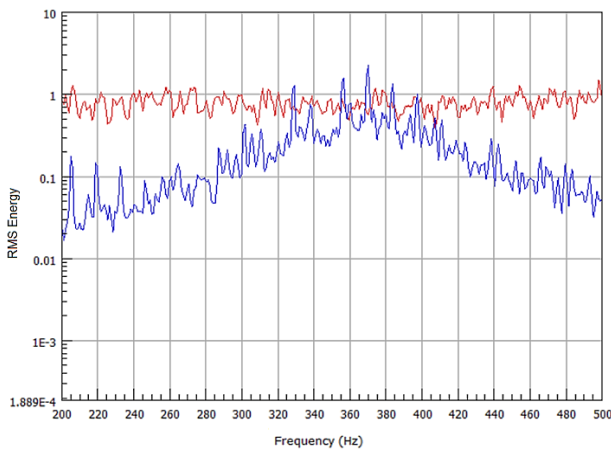


Fig. 10 – Frequency spectrum of mean square deviation of the oscillations' energy density (30 Hz, 400 r/min)

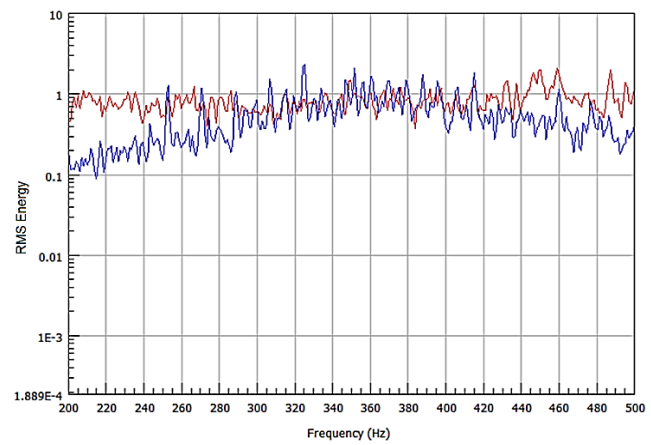


Fig. 11 – Frequency spectrum of mean square deviation of the oscillations' energy density (40 Hz, 500 r/min)

Using the SOLIDWORKS software package, a computer simulation of a screw conveyor for transporting bulk materials was created. To model the per-second throughput of the screw conveyor, the discrete element method (Rocky DEM) - a numerical method designed for calculating the movement of a large number of particles such as molecules, sand grains, gravel, and other granular media—was employed (Fig. 12).

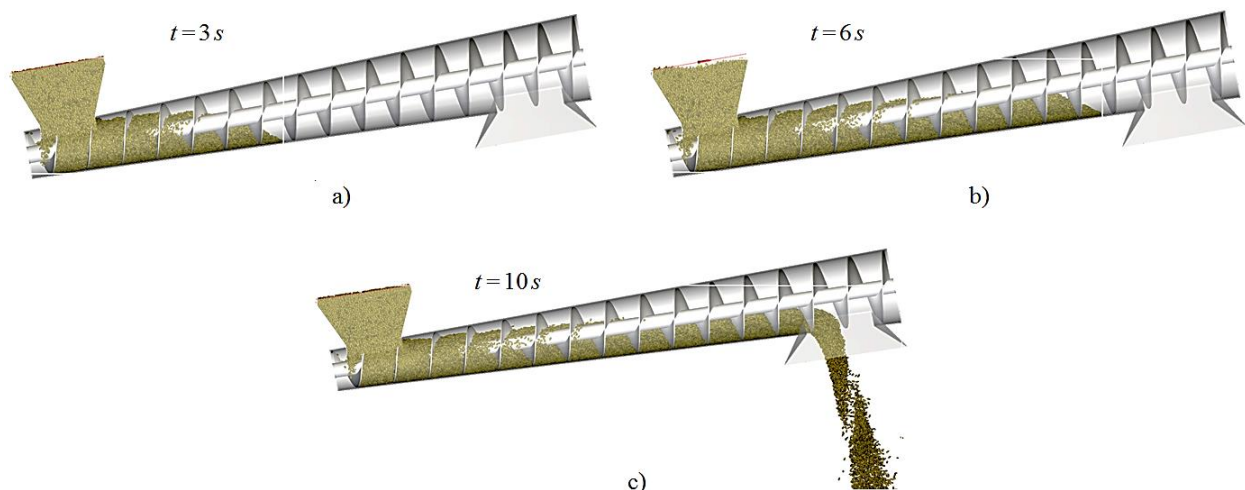


Fig. 12 – Graphical dependences of the second efficiency Q of the screw conveyor on the rotational speed of the operating body $n = 300$ r/min at $\alpha = 10$ deg

During the simulation of the screw conveyor for transporting bulk material, it was established that for an inclination angle of $\alpha = 10^\circ$ and a rotational speed of $n = 300$ rpm, the maximum throughput of the screw conveyor is observed between 7 and 10 seconds after startup when the hopper is filled with material. It was precisely within this time interval that samples were taken and the grain material was weighed to determine the per-second throughput of the screw conveyor.

Based on the analysis of computer simulation results of the grain material transportation process, it has been established that the per-second throughput Q of the screw conveyor increases linearly with the rotational speed n of the working element in the range from 200 to 500 r/min. However, a further increase in n does not contribute to the conveyor's throughput growth and even slightly decreases its value. This is explained by the fact that significant centrifugal forces hinder the normal loading of the conveyor. When determining the per-second throughput of the screw conveyor for other values of α and n , corresponding time intervals were identified during which the conveyor's throughput was maximal. Specifically, by increasing the internal diameter of the casing from 150 to 200 mm and within the inclination angle range of the working element to the horizon $\alpha = 0 \dots 10$, the throughput of the transportation process increases by 1.18–1.23 times.

CONCLUSIONS

The technological process of bulk materials transportation by conical screw conveyor is theoretically substantiated in order to determine the kinematic and operational parameters that ensure its stable operation. The analytical dependences for determining the change in the outer radius of the screw R and the inner casing radius at which the initial radius of the screw R_0 increases by value ΔR at each subsequent turn, are obtained. It is found that the increase in ΔR of the cargo movement radius on one (each subsequent) turn of the conical screw conveyor significantly affects the increase in cargo velocity, which contributes to the intensification of the mixing process. In particular, with the increase in radius ΔR of the cargo movement on one (each subsequent) turn from 1 mm to 5 mm, the load movement velocity increases from 1.28 times to 2.44 times.

Bench equipment for the investigation of the bulk materials transportation efficiency was developed and manufactured. In the course of experimental studies, it was testified that with the increase in the inclination angle of the screw conical surface, the screw rotation frequency and the decrease in the screw pitch growth at each subsequent turn, the maximum efficiency during wheat transportation was 9.44 t/h, and the minimum was 3.8 t/h. With the increase of the conical screw velocity n from 200 r/min to 500 r/min, the efficiency increases by 2 times. At the same time, the increase in the inclination angle α of the forming surface of the conical screw from 1 degree to 2 degrees provides 1.18-fold increase in efficiency, and the change in the value of the screw pitch growth on each subsequent turn ΔT from 0.004 m to 0.01 m results in 1.07-fold decrease in efficiency.

REFERENCES

- [1] Aulin V., Lyashuk O., Tykhyi A., Karpushyn S., Denysiuk N., (2018), Influence of rheological properties of a soil layer adjacent to the working body cutting element on the mechanism of soil cultivation, *Acta Technologica Agriculturae*, Vol. 21, no.4, pp.153–159, Nitra/Slovakia;
- [2] Aulin V., Lysenko S., Lyashuk O., Holub D., Chernai A., (2019), Wear resistance increase of samples tribomating in oil composite with geo modifier KgMf-1, *Tribology in Industry*, Vol. 41, no.2, pp.156–165, Kragujevac/ Serbia;
- [3] Bulgakov V., Trokhaniak O., Adamchuck V., Chernovol M., Korenko M., Dukulis I., Ivanovs S.A., (2022), Study of dynamic loads of a flexible sectional screw conveyor, *Acta Technologica Agriculturae*, Vol.25, no3, pp.131–136, Nitra/Slovakia;
- [4] Bulgakov V., Pascuzzi S., Adamchuck V., Olt J., Ruzhylo Z., Trokhaniak O., Santoro F., Arak M., Nowak J., Beloev H., (2023), Research into power and load parameters of flexible screw conveyors for transportation of agricultural materials, *Farm Machinery and Processes Management in Sustainable Agriculture*, Vol. 289, pp. 61–75;
- [5] Haaker G., Poppelen M.P., Jongejan M.P., Bekhuis J.H., (1993), Improvement of Screw Feeder Geometry for Better Draw-Down Performance. *International Symposium of Reliable Flow of Particulate solids*, pp. 551-561. Oslo/ Norway;
- [6] Hevko R.B., Zalutskyi S.Z., Tkachenko I.G., Lyashuk O.L., & Trokhaniak O. (2021), Design development and study of an elastic sectional screw operating tool. *Acta Polytechnica*, Vol. 61, no. 5, pp. 624–632, Prague/ Czech Republic;
- [7] Hewko B.M., Popovich P.V., Diachun A.Y., Lyashuk O.L., Liubachivskyi R.O., (2015), The study of bulk material kinematics in a screw conveyor-mixer, *INMATEH: Agricultural Engineering*, Vol.47, no.3, pp.156-163, Bucharest/Romania;
- [8] Hud V., Lyashuk O., Hevko, I., Ungureanu N., Vlăduț N-V., Stashkiv M., Hevko O., Pik A., (2023), Enhancement of Agricultural Materials Separation Efficiency Using a Multi-Purpose Screw Conveyor-Separator. *Agriculture*, Vol.13, p. 870;
- [9] Fernandez J.W., Cleary P.W., McBride W., (2011), Effect of Screw Design on Hopper Draw Down by a Horizontal Screw Feeder. *Seventh International Conference on CFD in the Minerals and Process Industries CSIRO*, 9-11 December, pp. 1-6; Melbourne /Australia;
- [10] Loveikin V., Rogatynska L., (2011), A Model of Loose Material Transportation by Means of High-Speed Conveyers with Elastic Operating Devices (Модель транспортування сипкого вантажу швидкохідними гвинтовими конвеєрами з еластичними робочими органами), *Bulletin of Ternopil Ivan Puluj National Technical University (Вісник ТНТУ ім. І. Пулюя)*, Vol.16, pp.66-70, Ternopil/Ukraine;

- [11] Lyashuk O., Vovk Y., Sokil B., Klendii V., Ivasechko R., Dovbush T. (2019), Mathematical model of a dynamic process of transporting a bulk material by means of a tube scraping, *Agricultural Engineering International: CIGR Journal*, Vol. 21, no 1, pp. 74-81, Japan;
- [12] Lyashuk O., Sokil M., Vovk Y., Levkovych M., Tson O., Kondratyuk D., Dmytrenko V., (2019), Analysis of resonance oscillations of extruder elastic screw conveyor, *International Journal of Engineering Research in Africa*, Vol.43, pp. 49–58, Switzerland;
- [13] Lyashuk O.L., Hevko, I.B., Hud, V.Z., Tkachenko, I.G., Hevko, O.V., Sokol, M.O., Tson, O.P.; Kobelnyk, V.R., Shmatko, D.Z. & Stanko, A.I. (2022), Research of non-resonant oscillations of the “telescopic screw – fluid medium system”. *INMATEH-Agricultural Engineering*, Vol.68, no. 3, pp. 499-510, Bucharest/Romania;
- [14] Lyashuk, O.L., Sokil, M.B., Klendiy, V.M., Slobodian, L.M., Slobodian, N.O. (2018). Mathematical model of bending vibrations of a horizontal feeder-mixer along the flow of grain mixture, *INMATEH-Agricultural Engineering*, vol.55, no. 2, pp. 35-45, Bucharest/Romania;
- [15] Lyashuk O., Rohatynskiy R., Hevko I., Dmytriv O., Tson O., Tkachenko I., Sokol M., Leshchuk R., Kobelnyk V. (2023) Investigation of bulk material transportation by screw conveyor with hinge-pan operating device, *Key Engineering Materials, Engineering Materials*, Vol. 948, pp. 169-182, Switzerland;
- [16] Mondal D., (2021), Design consideration of a laboratory size screw conveyor with variable speed for experimentation purpose-a methodological approach, *Techno Societal*, Vol. 68, no. 2, pp. 705–714;
- [17] Moorthi S., Megaraj, M., Nagarajan L., Karthick A., Bharani M., Patil P.P., (2022), Dynamic analysis and fabrication of single screw conveyor machine, *Advances in Materials Science and Engineering*, Vol. 10, pp.1–10, United States;
- [18] Pysarenko H.S., Yakovlev A.P., Matveev V.V., (1988), Reference on strength of materials (Справочник по сопротивлению материалов), *published by Naukova Dumka (видавництво Наукова думка)*, p.736, Kyiv/Ukraine;
- [19] Nilsson I. G., (1971), On the vertical screw conveyor for non-cohesive bulk materials, *Acta Polytechnica Scandinavica, Mechanical Engineering Series*, no. 64, Stockholm;
- [20] Roberts A. W., (1991), Determining Screw Geometry for Specified Hopper Draw-Down Performance. Proc. of Bulk 2000 Conference. *Institution of Mechanical Engineers*, pp. 111-116, London/United Kingdom;
- [21] Rohatynskiy R. M., Hevko Iv. B., Diachun A. Ye., (2015), The research of the torsional vibrations of the screw in terms of impulsive force impacts, *Naukovyi Visnyk Natsionalnoho Hirnychoho Universytetu (Науковий вісник Національного гірничого університету)*, Vol.149, no.5, pp. 64-68, Dnipropetrovsk/ Ukraine;
- [22] Ross I. J., Isaacs G. W., (1961), Capacity of Enclosed Screw Conveyors Handling Granular Material, *Transactions of the ASAE*, Vol. 4, no. 1, pp. 97-104;
- [23] Tian Y., Yuan P., Yang F., Gu J., Chen M., Tang J., Su Y., Ding T., Zhang K., Cheng Q., (2018), Research on the Principle of a New Flexible Screw Conveyor and Its Power Consumption, *Applied Sciences*, Vol.8, no.7, pp.1038;
- [24] Trokhaniak O. M., Hevko R. B., Lyashuk O. L., Dovbush T. A., Pohrishchuk B. V., Dobizha N. V., (2020), Research of the of bulk material movement process in the inactive zone between screw sections, *INMATEH: Agricultural Engineering*, Vol. 60, no. 1, pp. 261–268, Bucharest/Romania;
- [25] Yongqin Yu. (1997), Theoretical modelling and experimental investigation of performance of screw feeders, Doctor of Philosophy thesis, p. 226;
- [26] Yu W., Zhang K., Li D., Zou D., Zhang S., (2022), Numerical modeling of concrete conveying capacity of screw conveyor based on DEM, *Powder Technology*, Vol. 29, no.6, pp.361–374, Netherlands;
- [27] Zaica A., Olan M., Bunduchi G., Zaica A., Gageanu P., Paun A., (2020), Factors that influence coverage degree in seed treatment equipment having brush screw conveyor, *Engineering for rural development*, 20.-22.05.2020, pp.1325-1330, Jelgava/Latvia;
- [28] Zaica A., Visan A., Paun A., Gageanu P., Bunduchi G., Zaica A., Stefan V., Manea D., (2016), The coating process of corn grains using a treatment machine with brush screw conveyor, *Proceedings of the 44th International Symposium on Agricultural Engineering: Actual Tasks on Agricultural Engineering*, 23-26 February 2016, pp.333-345, Opatija/Croatia;

- [29] Zaica A., Visan A., Zaica A., Olan M., Bunduchi G., (2019), Coating process of corn grains using treatment machine with brush screw conveyor, *Engineering for rural development*, 22.-24.05.2019, pp.233-238, Jelgava/Latvia;
- [30] Zalutskyi S.Z., Hevko R.B., Hladko Y.B., Tkachenko I.H., Klendii O.M., (2018), Loose material flow motion on surface of screw with overlapping elastic sections (*Рух потоку сипкого матеріалу по поверхні шнека з еластичними секціями, що перекриваються між собою*), *Kharkiv P. Vasylenko National Technical University of Agriculture (Харківський національний технічний університет сільського господарства імені Петра Василенка)*, Vol.11, pp.81-90, Kharkiv/Ukraine;
- [31] Zareiforoush H., Komarizadeh M.H., Alizadeh M.R., (2010), Review on screw conveyors performance evaluation during handling process, *Journal of Scientific Review*, Vol. 2, no. 1, pp.55–63;
- [32] ***<https://www.hbmprensia.com>;
- [33] ***<https://www.ncode.com>.

INTEGRATION OF EDEM BY ALTAIR SIMULATIONS FOR EFFICIENT DISTRIBUTION OF LARGE AND SMALL SEEDS IN AGRICULTURAL SYSTEMS OF VINEYARDS AND FRUIT TREES

INTEGRAREA SIMULĂRILOR EDEM DE LA ALTAIR PENTRU DISTRIBUȚIA EFICIENTĂ A SEMINȚELOR MARI ȘI MICI ÎN SISTEME AGRICOLE DE VIȚĂ DE VIE ȘI POMI FRUCTIFERI

Dragoș-Nicolae DUMITRU¹⁾, Eugen MARIN¹⁾, Gabriel-Valentin GHEORGHE¹⁾, Dragoș MANEA¹⁾,
Marinela MATEESCU¹⁾, Dragoș-Nicolae ANGHELACHE^{1,2)}, Elisabeta PRISACARIU¹⁾, Alin HARABAGIU¹⁾

¹⁾INMA Bucharest/ Romania

²⁾National University of Science and Technology POLITEHNICA Bucharest/Romania

E-mail: dumitrudragos.nicolae@gmail.com; dragos1989anghelache@gmail.com

DOI: <https://doi.org/10.35633/inmateh-74-66>

Keywords: simulation, EDEM, agriculture, vineyards, fruit trees, distribution, seeds

ABSTRACT

Efficient seed distribution is crucial for maximizing crop yields in agricultural systems, particularly in vineyards and orchards where both large and small seeds are used. This research investigates the integration of EDEM by Altair simulations to enhance the distribution process of these seeds. Utilizing discrete element modeling (DEM), the study provides a comprehensive analysis of seed behavior during dispersal, including interactions with varying terrain and environmental conditions. Through detailed simulations, the research identifies critical parameters that influence seed placement accuracy, such as seed size, distribution patterns, and environmental factors. The results reveal that EDEM simulations can optimize the distribution of seeds, leading to reduced seed wastage and improved crop density uniformity. This integration not only facilitates a more precise sowing process but also offers valuable insights into the dynamics of seed distribution in complex agricultural systems. The findings suggest that adopting this simulation technology can significantly advance precision agriculture practices, offering tangible benefits for the efficiency and productivity of vine and fruit tree cultivation.

REZUMAT

Distribuția eficientă a semințelor este crucială pentru maximizarea randamentelor culturilor în sistemele agricole, în special în podgorii și livezi unde sunt folosite atât semințe mari, cât și mici. Această cercetare investighează integrarea EDEM prin simulările Altair pentru a îmbunătăți procesul de distribuție a acestor semințe. Folosind modelarea cu elemente discrete (DEM), studiul oferă o analiză cuprinzătoare a comportamentului semințelor în timpul împrăștierii, inclusiv interacțiunile cu terenul și condițiile de mediu variate. Prin simulări detaliate, cercetarea identifică parametrii critici care influențează acuratețea plasării semințelor, cum ar fi dimensiunea semințelor, modelele de distribuție și factorii de mediu. Rezultatele arată că simulările EDEM pot optimiza distribuția semințelor, ceea ce duce la reducerea pierderii de semințe și la o uniformitate îmbunătățită a densității culturii. Această integrare nu numai că facilitează un proces de însămânțare mai precis, dar oferă și perspective valoroase asupra dinamicii distribuției semințelor în sistemele agricole complexe. Descoperirile sugerează că adoptarea acestei tehnologii de simulare poate avansa în mod semnificativ practicile agricole de precizie, oferind beneficii tangibile pentru eficiența și productivitatea cultivării viței de vie și a pomilor fructiferi.

INTRODUCTION

In modern agriculture, precision in seed distribution plays a pivotal role in optimizing crop yields, particularly in specialized systems such as those used for vines and fruit trees. Accurate placement of seeds is essential not only for maximizing productivity but also for ensuring uniform plant growth and efficient resource utilization. However, the task of distributing seeds evenly becomes increasingly complex when dealing with a variety of seed sizes, ranging from large fruit tree seeds to smaller vine seeds. Traditional seeding methods often encounter challenges in achieving uniform distribution, leading to issues such as uneven growth, reduced yield, and increased wastage.

Recent advancements in simulation technology have introduced innovative solutions to these challenges. One such advancement is the integration of the Discrete Element Method (DEM) by Altair, a powerful tool for modeling and analyzing granular flow and seed behavior.

EDEM by Altair offers advanced capabilities for simulating the dynamics of seed movement within seeding systems, providing critical insights into how seeds interact with different seeding mechanisms. This simulation technology enables researchers to refine and optimize seeding devices, enhancing their performance and accuracy in handling both large and small seeds.

The optimization of the sowing period is crucial for enhancing the speed, seed quality, and overall yield of crops. As highlighted by *An X. et al., (2023)*, current agricultural practices face significant challenges, including uneven seed distribution, crowded seedling growth, and high leakage rates during planting. While mechanical seeders offer stability, they often struggle with consistency in seed placement, and pneumatic seeders, although more precise, are energy-intensive and unstable. To address these issues, the development of a centrifugal wheat strip seeding device has emerged as a promising solution for improving high-speed seeding efficiency.

Recent advancements in simulation technology, particularly Computational Fluid Dynamics (CFD) and Discrete Element Method (DEM), have significantly contributed to the optimization of agricultural equipment. In this context, *Cârlescu P. et al., (2022)*, emphasized that drying is the most common method for preserving corn seeds, albeit requiring substantial energy and time. The integration of CFD and DEM enables the design and simulation of more efficient dryer models, allowing for enhanced understanding of gas-solid interactions. In their study, the RNG k- ϵ turbulence model was utilized to effectively simulate fluid flow while analyzing the behavior of maize seeds as assemblies of spheres. The results indicated that a truncated cone-shaped dryer, optimized for airflow velocities, significantly improved both pneumatic transport and seed drying efficiency.

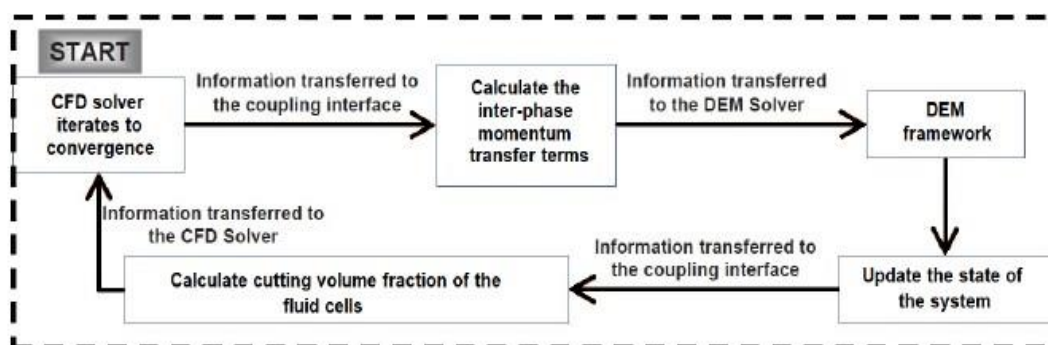


Fig. 1 - Coupled simulation of CFD-DEM

(Cârlescu P. et al., 2022)

Figure 1 illustrates a computational process that integrates CFD (Computational Fluid Dynamics) and DEM (Discrete Element Method) solvers. The process begins with the CFD Solver Iteration, where the CFD solver iterates until it achieves convergence. Next, the information is sent to the Coupling Interface, which calculates the inter-phase momentum transfer terms. The data is then transmitted to the DEM Solver, which updates the system's state. The Feedback Loops indicate that information is exchanged between the DEM framework and the CFD solver, as well as within the CFD solver itself, involving the calculation of fluid cell cutting volume fractions. This iterative approach ensures accurate simulations by continuously updating and sharing information between the solvers.

Moreover, the application of EDEM for modeling the behavior of wheat grains further enhances our understanding of the filling process during sowing. *Song C. et al., (2021)*, investigated the size and behavior of wheat grains through precise measurements, which were then used to create a three-dimensional map for simulation. Their findings revealed that the API automatic filling model demonstrated higher accuracy in replicating real wheat grains compared to manual filling models, with an error margin of only 3.08%. This underscores the importance of accurate modeling in improving the effectiveness of seed metering devices.

This article presents a comprehensive study on the integration of EDEM simulations by Altair to address the complexities associated with distributing various seed sizes in agricultural systems tailored for vines and fruit trees.

By employing sophisticated modeling techniques, this research aims to improve the precision of seed distribution processes, thereby advancing planting strategies and contributing to more efficient crop management. The study examines the impact of these simulations on optimizing seed flow dynamics, reducing distribution errors, and enhancing the overall effectiveness of seeding equipment. Through detailed analysis and validation, the research seeks to offer practical solutions for achieving uniform seed distribution and improving the operational efficiency of agricultural systems.

MATERIALS AND METHODS

Equipment and System Design

Cheng B. et al., (2022), study highlights the importance of precision in fertilizer application to improve efficiency. Traditional mechanical systems often suffer from blockages and uneven distribution, especially in multi-row setups. While pneumatic systems offer better efficiency, research on fertilizer particle movement is limited. This study designs and evaluates a pneumatic fertilizer discharge system, incorporating a distributor, corrugated pipe, elbow, fertilizer box, quantifier, jet feeder, and fan. High-speed airflow is used for mixing and transport. Simulations with EDEM-FLUENT confirmed smooth particle movement and minimal backflow. Bench tests at 35–40 m/s wind speed showed fertilization efficiencies of 0.29–0.41 kg/s and consistent row discharge, achieving stable, multi-row application.

The article by Han D. et al., (2018), highlights the global significance of maize as an essential crop for animal feed, medicine, and chemical production. In China, where annual maize production surpasses 200 million tons, precision planting is vital for maximizing seed utilization and yield. Han D. and his team developed and simulated a pneumatic maize seed-metering device, illustrated in Figure 2, using EDEM software. This device, modeled with six components and analyzed through EDEM-CFD simulations, demonstrated strong alignment with experimental data. The study identified optimal design parameters, including a lower lateral hole position, a hole width of 2.0 mm, and an arc length of 10 mm, enhancing performance while minimizing pressure loss. These insights form a basis for advancing pneumatic seed-metering device designs.

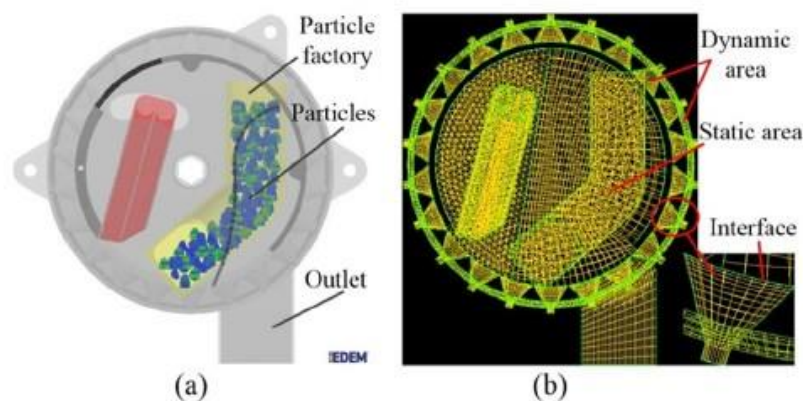


Fig. 2 - 3D simulation models, including a simplified EDEM model of the seed metering device.

(Han D. et al., 2018)

The study by Sun J. et al., (2020), investigates the grooved-wheel drilling device, which is widely used for seeding and fertilizing in developing countries due to its cost-effectiveness and versatility. Despite its popularity, the device encounters challenges such as particle breakage and wheel jamming, which impact precision. To enhance its performance, Sun J. and his team used EDEM simulation software to analyze particle velocity and force during operation. To validate these simulations, a new grooved wheel was created using 3D printing. The team employed a custom-built experiment bench to measure fertilizer distribution and optimize the device. For accurate simulations, spherical particles and the Hertz-Mindlin contact model were utilized.

The grape industry's significance in regions with harsh winters, such as Central Asia, is emphasized due to the labor-intensive vine-burying practices commonly used. Yang Q. et al., (2021), address the limitations of traditional vine-digging machines, which often lack precision and risk vine damage. To enhance efficiency and minimize damage, the study proposes a non-contact blower designed to remove soil from grapevines using air flow. The design and performance of the blower were evaluated using EDEM and CFD software, with a 22kW centrifugal fan serving as the prototype. Field tests conducted in Ningxia, China, demonstrated that the blower successfully cleared over 70% of soil in low moisture conditions and 80% under typical field conditions, achieving an average efficiency of 77.10% without damaging the vines.

System Configuration and Parameter Optimization

Ding H. et al., (2019), developed a fertilizer guide device aimed at ensuring uniform application aligned with seed lines. Using EDEM software, they optimized key design elements such as the shunt part angle (33°), vertical distance (76 mm), and horizontal position (25 mm), which significantly improved fertilizer distribution, with minimal

impact from the groove angle. These findings, validated through simulations and experiments, offer valuable insights for enhancing agricultural practices. Similarly, *Ding S. et al., (2018)*, optimized a dual-band fertilizer applicator shown in Figure 3, which applies starter and base fertilizers separately to improve nutrient utilization and cost-effectiveness. Their design, featuring a two-compartment hopper, fluted roller, and adjustable tubes, demonstrated through DEM simulations and tests that precision, uniformity, and efficiency were improved, reducing costs.

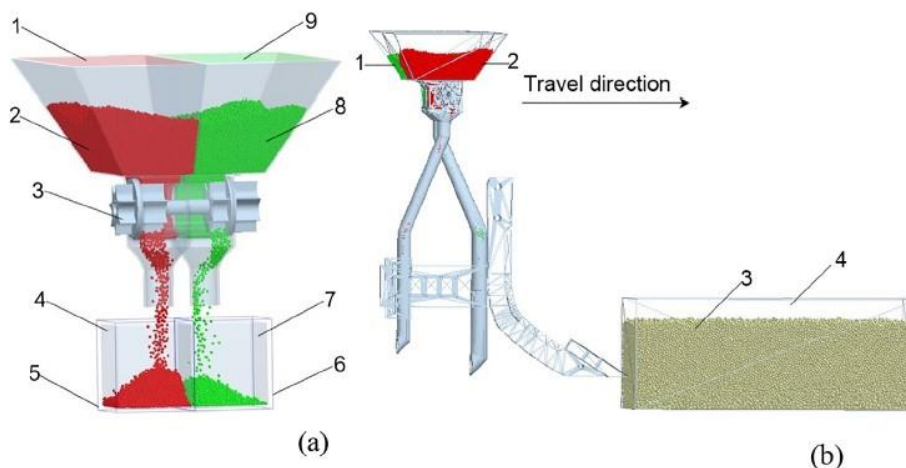


Fig. 3 - EDEM working model
(*Ding S. et al. 2018*)

The system presented in Figure 3 includes (a) working model of the metering assembly with components such as 1 - the starter fertilizer compartment, 2 - starter fertilizer, 3 - fluted roller, 4 - starter fertilizer collection boxes, 5 - monitoring zones for starter fertilizer, 6 - monitoring zone for base fertilizer, 7: base fertilizer collection box, 8: base fertilizer, 9: base fertilizer compartment along with (b) integrated model for fertilizer metering and banding that 1 - features base fertilizer, 2 - starter fertilizer, 3 - soil particles, and 4 - soil bin.

The study by *Zou H. et al., (2023)*, highlights the need for improved sowing accuracy in agriculture, noting that domestic equipment typically achieves 90-95% accuracy compared to up to 98% with foreign technology. To address this, a new seed reseeding device is introduced shown in Figure 3, featuring a needle seeder and electromagnetic vibration mechanism to enhance suction and reduce missed seeds. Optimal settings include an inlet speed of 8 m/s, a 1.8 mm aperture, an 18 mm lead, and a V-shaped nozzle. Simulations with EDEM and ANSYS/Fluent confirmed these settings, resulting in improved suction efficiency and precision. The device effectively handles about 4 seeds, significantly boosting sowing accuracy and efficiency.

Mechanical and air-suction seed metering devices for soybean cultivation in Northeast China were compared in a study by *Dun G. et al., (2022)*. While mechanical devices are more affordable, they tend to be less precise, whereas air-suction devices provide higher accuracy but come with increased power consumption. Dun G. and the team conducted simulations to determine the optimal parameters for the seed-metering wheel, achieving over 90% single-seed accuracy, which was validated through bench tests. Similarly, *Jia H.L. et al., (2018)*, focused on high-speed precision seeding, developing an agitated seed metering device that outperformed traditional units. Optimized parameters improved speed and accuracy, reaching a qualified seeding index of 93.9%. Lastly, *Wang J. et al., (2017)*, introduced a ripple surface pickup finger design for maize seed metering, resolving issues related to seed size and shape variations. The optimized design improved performance by 12.34%, confirmed by both simulations and tests.

In their study, *Lei X. et al., (2016)*, emphasized the importance of precision planters for rapeseed and wheat in China's Yangtze region, particularly focusing on centralized pneumatic planters. By employing DEM-CFD simulations, Lei X. and the team optimized the air-assisted seed metering system, determining the ideal airflow velocity and throat length for efficient seed movement. Similarly, *Li K. et al., (2023)*, introduced a fan-driven airflow system for high-speed sowing in Xinjiang's arid climate, optimizing the seed delivery pipeline for better precision. Their CFD-DEM simulations identified a 15° pipe angle and round table diversion, achieving high seeding accuracy and minimal missed seeds. *Liu R. et al., (2022)*, addressed challenges in high-speed maize planting, using DEM-CFD simulations to optimize seed ejection parameters like intake position, angles, and airflow velocity. Their innovations improved seed spacing and ejection speed, essential for precision planting.

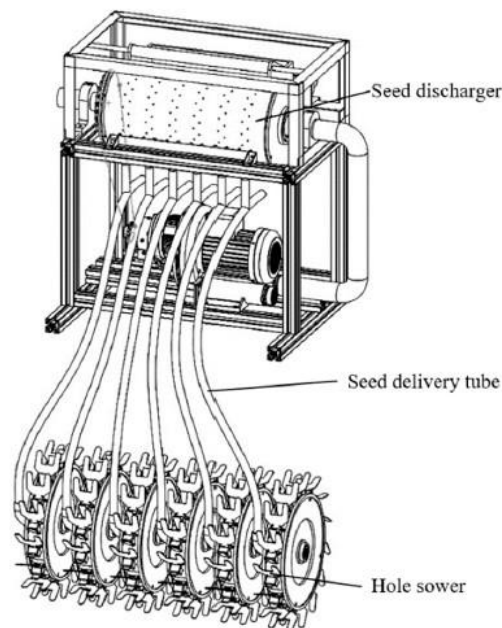


Fig. 4 - Split seeding system
(Lu B. et al. 2022)

Centralized seed metering systems for maize were the focus of a study by Lu B. et al., (2019), presented in Figure 4, which highlighted their relevance for modern precision farming. They employed EDEM and CFD simulations to analyze seed flow dynamics and improve the metering system's performance. The research pinpointed the optimal combination of airflow rate and seed inlet angle, leading to smoother seed movement and increased planting accuracy. Bench tests validated the simulation results, confirming improved uniformity in seed distribution. Similarly, Ma C. et al., (2023), improved corn planting efficiency with a belt-type seed guide device that reduces collisions and ensures uniform discharge. Optimized with simulations, the device's key parameters, like a 560 r/min wheel speed, enhanced high-speed sowing. Ma W. et al., (2023), focused on mechanized seeding for sesbania, using DEM simulations to optimize seed dynamics. Their study identified key factors affecting seed movement, with a model validation error of only 2.74%, ensuring accuracy.

Ren D. et al., (2022), optimized a hazelnut harvester cleaning device for mountainous regions, achieving a 95.12% net fruit rate through CFD and DEM simulations. Shi L. et al., (2023), used DEM to improve quinoa seeding machinery by analyzing seed properties and friction, boosting efficiency. Sun S. et al., (2024), introduced a vibrational seed supply system for irregular seeds like peppers, reaching 90.75% single-grain accuracy. Tang H. et al., (2022), enhanced maize seeding by optimizing the seed drop tube in a precision device, improving uniform seed delivery and performance. Wang H. et al., (2022), developed a precise garlic seed-metering device, achieving a 91.86% single-seed rate using EDEM simulations. Wang S. et al., (2022), improved sunflower seed harvesting by comparing DEM models, finding cuboid models most accurate for seed dynamics. Wang Y. et al., (2023), optimized soybean planting with a friction-based seed-filling method, showing that friction and particle size improve seeding efficiency. Zhao J. et al., (2024), optimized pneumatic seed delivery systems using DEM and CFD simulations, reducing pressure loss and enhancing seed distribution uniformity.

Mechanization and Performance Evaluation

Guo H. et al., (2021), emphasized the economic importance of garlic in China and the need for mechanization to improve sowing efficiency. They introduced a garlic seed metering mechanism optimized for single-seed accuracy, achieving over 80% accuracy in field tests. To enhance the efficiency of rice planting with seedling transplanting machines, Wang J. et al., (2020), examined prevalent issues such as seedling damage and low planting accuracy. They designed an innovative gripper mechanism aimed at ensuring gentle handling and precise placement of seedlings. Both simulations and field tests revealed that this new mechanism significantly reduced damage rates and improved planting accuracy over traditional models. These findings indicate the mechanism's strong potential to improve overall transplanting performance. Guo J. et al., (2002), developed a high-speed mechanical corn planter with an inclined seed-metering device. DEM simulations and field tests showed a 92.83% qualified seeding rate and low error rates, confirming the planter's efficiency and meeting industry standards.

The benefits of mixed sowing oats and vetch was explored by *Liao Y. et al. (2023)* for improved yield and soil fertility, focusing on optimizing air-blowing seed-metering devices for small forage seeds. Using DEM-CFD simulations, they identified optimal parameters, such as a 60° seeding angle and air velocity of 35-40 m/s, to enhance seed movement and distribution. Bench tests validated the results. Another study by *Liao Y. et al., (2023)*, talks about optimized pneumatic seeders for oats and vetch, achieving the best consistency at 25 m/s airflow velocity through DEM-CFD simulations, ensuring uniform distribution. *Li Y. et al., (2020)*, reviewed advancements in cotton seeders, highlighting that, mechanical devices optimized with cushioning and retracting spoons, can achieve over 93% precision. Simulations and tests confirmed optimal performance at 50 r/min and a 15° tilt, making the spoon-wheel device highly effective for cotton sowing.

Liu J.S. et al., (2020), optimized fertilizing machinery for alfalfa, which is underutilized in China despite its high protein content. Using EDEM simulations and orthogonal experiments, the study improved fertilization uniformity by 18.9%, with optimal parameters of 16 mm knob-width, 45° slanting angle, and 27.5 mm horizon-distance. *Ma D. et al., (2024)*, improved DEM simulations of wheat seed dynamics by using the multi-sphere method, finding that a 0.32 mm filling ball radius achieved the best accuracy with a 6.54% error rate. *Ma W. et al., 2022*, designed an alfalfa seed airflow collection system, optimizing the Venturi ejector to improve seed mobility and feeding efficiency, validated by experimental tests. *Miao Z. et al., (2019)*, focused on precision seeding for afforestation using air-suction seeders. EDEM simulations identified the best vibration settings (20 Hz, 5 mm amplitude), improving seed suction and distribution accuracy.

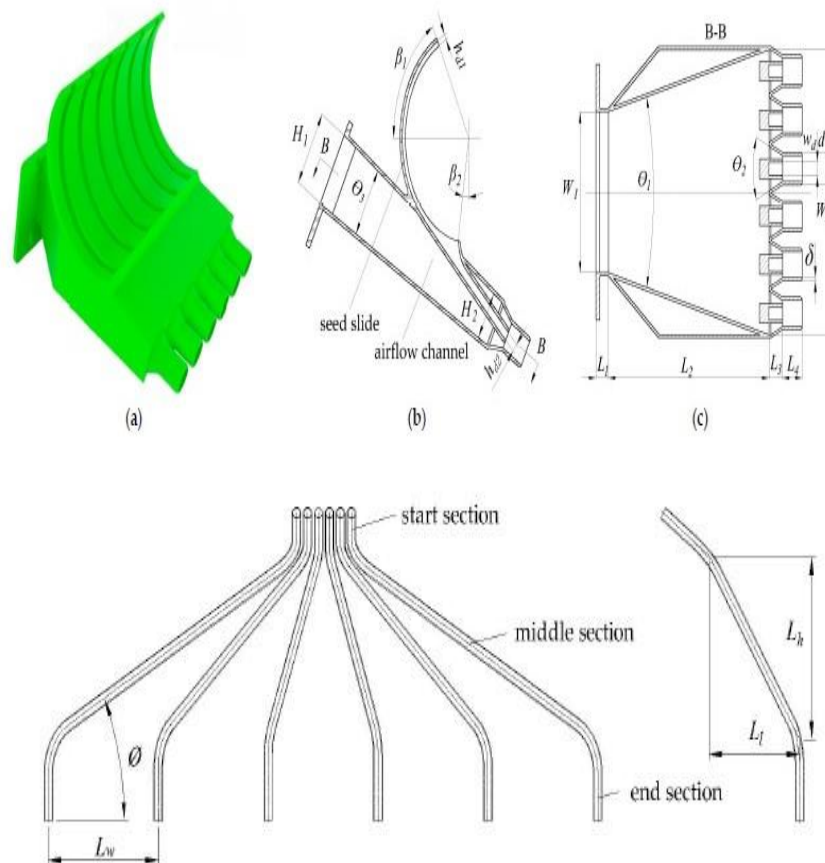


Fig. 5 - Structural design of the distribution manifold

(Wang B. et al. 2023)

Wang B. et al., (2023), study highlights sesame's significance as an oil crop and the limitations of traditional seeding methods, which often lead to uneven distribution. Single-seed seeding requires additional coating, while hill-seeding provides better distribution without it. The research develops an air-assisted seed-guiding device to enhance seeding quality and uniformity, addressing issues like poor seed mobility and tube blockages. The device shown in Figure 5, featuring a blower, manifold, and seed tubes, was optimized through CFD-DEM simulations and bench tests, achieving an 86.80% qualified rate and 6.00% miss-seeding rate. Field tests confirmed its effectiveness, with an average of 1.32 seedlings per hill and an 83.45% qualified rate, meeting precision hill-seeding requirements for sesame.

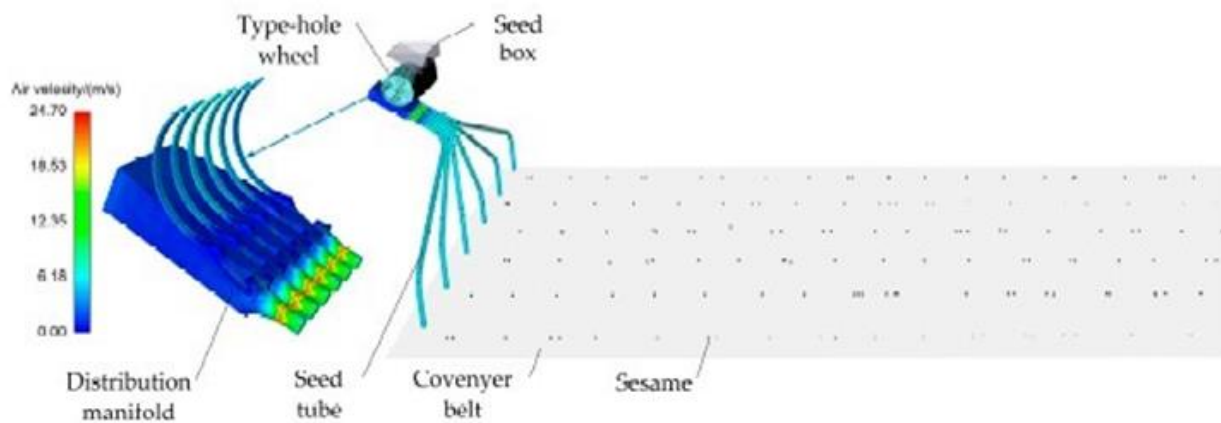


Fig. 6 - CFD-DEM simulations and bench tests

(Wang B. et al., 2023)

Wang J. et al., (2024), optimized a side-filled rice precision seeder to minimize seed damage and improve hole formation. Using DEM and MBD simulations, along with high-speed camera analysis, they determined that a rotation speed of 47 r/min, a 19° seeding angle, and a 180 mm seeding height provide optimal performance. Wang M. et al., (2022), focused on improving sugarcane billet planters, using DEM simulations to optimize the seed-filling process. They found that a 117° rake bar angle and increased billet presence near the rake bar improved seed-filling uniformity. Wang L. et al., (2024), enhanced mechanized wheat planting by optimizing air-assisted seeding technology. DEM simulations showed that heptagon and pentagon wheels increased seed fluidity and stability, with higher feeding speeds further improving seed distribution. These advancements are vital for improving the efficiency of wheat and rice planting machinery.

Xiao Y. et al., (2022), emphasized the importance of uniform seeding in rapeseed planting, noting that an air-feeding seed metering system can improve efficiency. They used DEM-CFD simulations to compare different seed tube structures—corrugated, hole-type, and round tubes—finding that corrugated and hole-type tubes enhanced seed distribution, although hole-type tubes resulted in more collisions. Yan D. et al., (2021), proposed a new Discrete Element Method (DEM) approach for better soybean particle modeling, identifying that multi-ball models (five, nine, and thirteen balls) improve simulation accuracy, especially for less spherical particles. In a subsequent study, Yan D. et al., (2022), focused on calibrating rolling friction coefficients for soybean seeds, using 5-, 9-, and 13-sphere models. Their findings indicated that precise measurement of rolling friction is crucial for accurate simulations, with high accuracy confirmed through multiple tests.

Zha X. et al., (2020), propose a six-row pneumatic deep precision fertilization device for rice transplanters to address issues like fertilizer waste and uneven growth in traditional methods. Featuring a spiral distribution system and precise control through sensors and PID, the device showed a high accuracy rate, with only a 3.53% error in tests. Zhang B. et al., (2024), introduced a new sugarcane seed metering device to solve problems like blockages and seed damage. With compliant walls and vibration relief, the device improved seed flow, boosting discharge rate by 43.7% and reducing blockages, leading to better accuracy and efficiency.

Zhang X. et al., (2022), developed a pneumatic seeder for single-seed precision planting. They identified optimal parameters using Ansys Fluent: a 15 mm air pipe diameter, a 105° angle, and a 34 mm negative pressure aperture. Their tests achieved an average airflow velocity of 102.59 m/s, reducing pressure loss and improving efficiency by optimizing airway structures. Zhao X. et al., (2022), addressed challenges in strip sowing for wheat, proposing a new seed metering device that uses positive and negative pressures to enhance seed uniformity and minimize damage. Their device features a roller with five rows of 2.0 mm holes and achieved an 80.62% qualified seeding rate with low reseeded (9.22%) and miss-seeding (10.16%) rates, meeting industry standards.

Both the integration of electromechanical actuators in agricultural excavator booms and the utilization of EDEM simulations for seed distribution aim to improve the efficiency of agricultural machinery. The primary focus of integrating electromechanical actuators is to optimize movement and power use, which directly impacts the machine's operational performance and battery life. The optimization of actuators ensures that agricultural machinery, such as excavator booms, operates smoothly and requires less power Savaniu et al., (2023). This is crucial for electric and hybrid agricultural machines, which benefit from extended operational periods due to improved energy management.

Vending Machine Mechatronics employ microcontrollers and sensors to ensure that dose delivery is accurately monitored and adjusted based on real-time data *Savaniu et. al., (2024)*. The integration of feedback loops enables the machine to adapt to different conditions, maintaining consistent energy use and reducing waste. Similarly, EDEM simulations can be integrated with planting equipment's control systems to optimize the seeding process. Real-time data from sensors about soil conditions, terrain, and seed type can inform the equipment's operation, ensuring that the seed distribution is energy efficient and precise.

Mechatronic Delivery system in vending machines is designed to use minimal energy while maintaining effective product delivery. The spiral mechanism ensures precise control over the portioning and release of products, allowing for energy-efficient operation. The study of energy consumption within this context highlights how different components interact to optimize power use *Savaniu et. al., (2024)*.

Also, *Zhu H. et al., (2023)*, tackled issues with no-till planters affected by vibrations from straw and root stubble. They proposed a shaftless spiral seed discharge device that improves seed delivery on uneven terrain. Field trials showed this device outperformed traditional methods, meeting no-till standards and enhancing performance under high-vibration conditions.

For this study, a complex design and simulation process were developed, starting with making a seed distributor using SolidWorks modeling software. The spreader design has been created with the goal of achieving even and efficient distribution, taking into account factors such as seed size, distribution speed and soil type. SolidWorks was chosen because of its ability to generate accurate and detailed models, facilitating both distributor structure analysis and component performance evaluation. To validate the efficiency of the spreader and to simulate the seed distribution process on the soil, the software EDEM by Altair was used, a simulation program based on the discrete element method (DEM). This technology is particularly useful in simulating the movement and interaction of small particles such as seeds in a complex environment such as soil. The simulation in EDEM allowed us to analyze with great accuracy the behavior of the seeds as they are transported through the hose and reach the soil. This approach provided us with relevant data on the trajectory of the seeds, their fall speed, as well as the distribution on the soil surface. Based on the results obtained from the simulations, iterative adjustments to the model were performed in SolidWorks, testing the improvements through additional simulations in EDEM. This iterative design and testing process enabled the distributor design to be gradually optimized, ensuring the efficiency and reliability required for use in real-world agricultural application conditions.

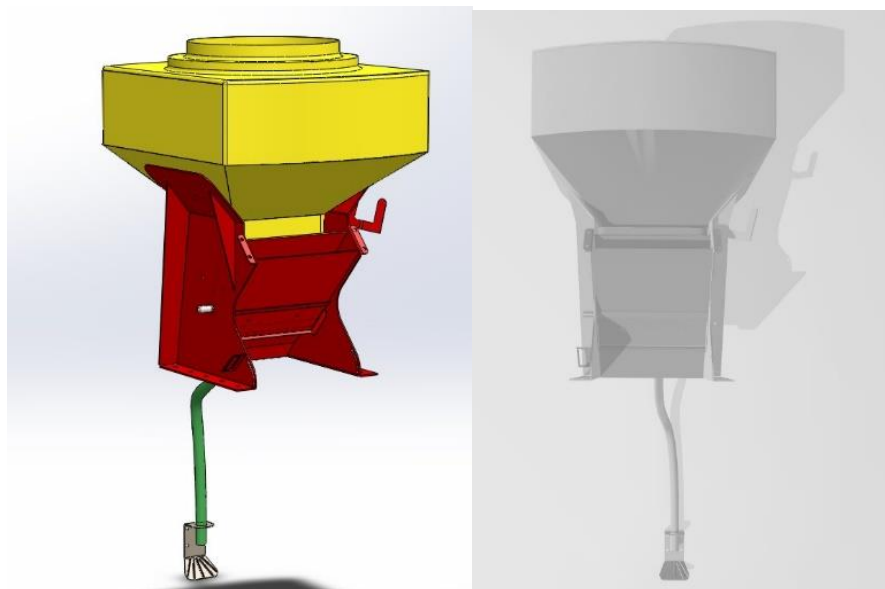


Fig. 7 - Seed distributor with SolidWorks Software

Figure 7 shows the model of the seed distributor made in SolidWorks, together with its version in STL format, ready to be imported into the EDEM by Altair simulation software. For the simulation, three distinct types of seeds were selected:

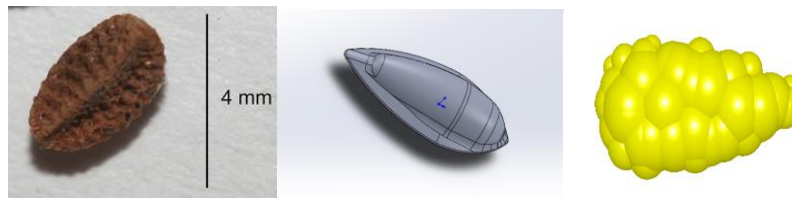


Fig. 8 - Phacelia tanacetifolia seed

(<https://gobotany.nativeplanttrust.org/species/phacelia/tanacetifolia/>)

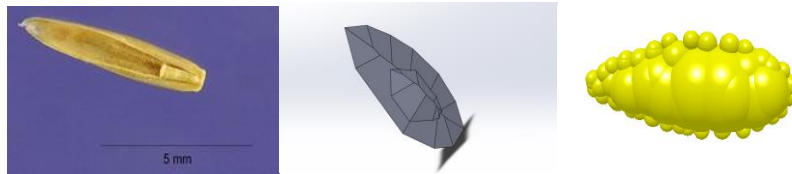


Fig. 9 - Lolium perenne seed

(https://keyserver.lucidcentral.org/weeds/data/media/Html/lolium_perenne.htm)

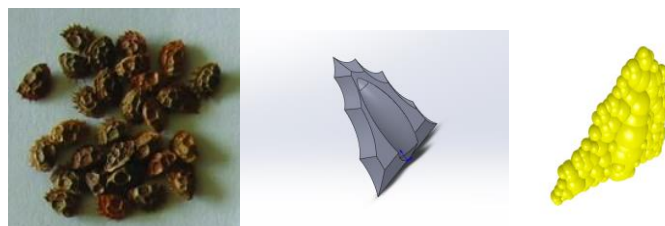


Fig. 10 - Onobrychis viciifolia seed

(https://www.researchgate.net/figure/Onobrychis-viciifolia-seed-variability-1208-1292-1257-and-1126-correspond-to-different_fig2_231803498)

In figures 8, 9 and 10 types of seeds are presented: Phacelia tanacetifolia, Onobrychis viciifolia and Lolium perenne. To ensure the most accurate simulation, detailed CAD models of each seed type were created, which were imported into EDEM by Altair. This approach allowed us to generate particles with characteristics specific to each type of seed, thus optimizing the accuracy of their distribution simulation.

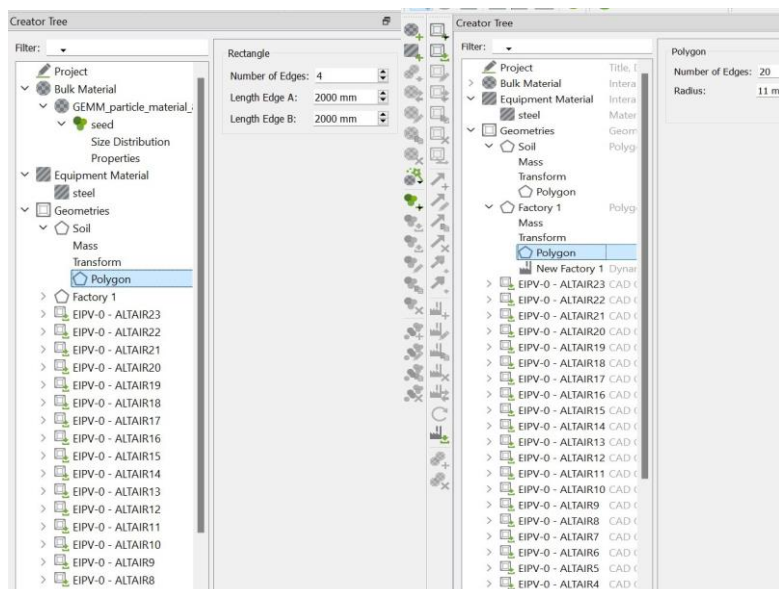


Fig. 11 - Soil and factory in creator tree

In the creator tree presented in Figure 11, polygons are utilized to model both the soil and the factory for the simulation of seed distribution. First, a polygon is created to represent the soil, which serves as the primary environment where the seeds will be dispersed. This polygon outlines the boundaries of the soil area, providing a clear visual representation of the terrain in which the simulation occurs.

Next, a second polygon is designed for the factory, which acts as the origin or source of the seeds. The factory is positioned near the soil, symbolizing where the seeds are coming from before they are scattered onto the field. These polygons are crucial because they not only define the spatial elements of the simulation but also set the stage for modeling seed movement and distribution across the defined landscape. Once the soil and factory polygons are in place, the simulation is initiated by distributing seeds within the soil polygon. The seeds are randomly placed within the soil boundaries, imitating the natural process of sowing. This simulation allows visualizing how the seeds are spread over the terrain, offering insights into patterns of distribution and helping to assess potential coverage of the area.

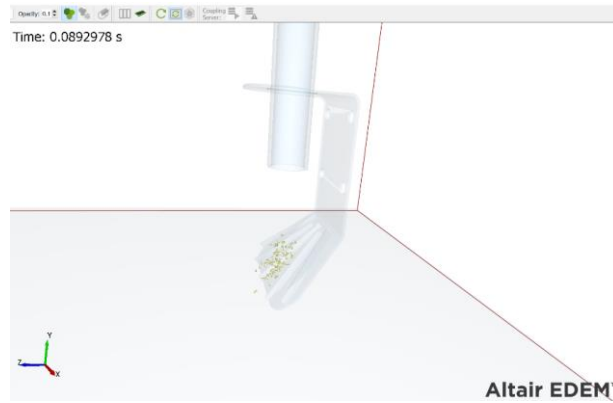
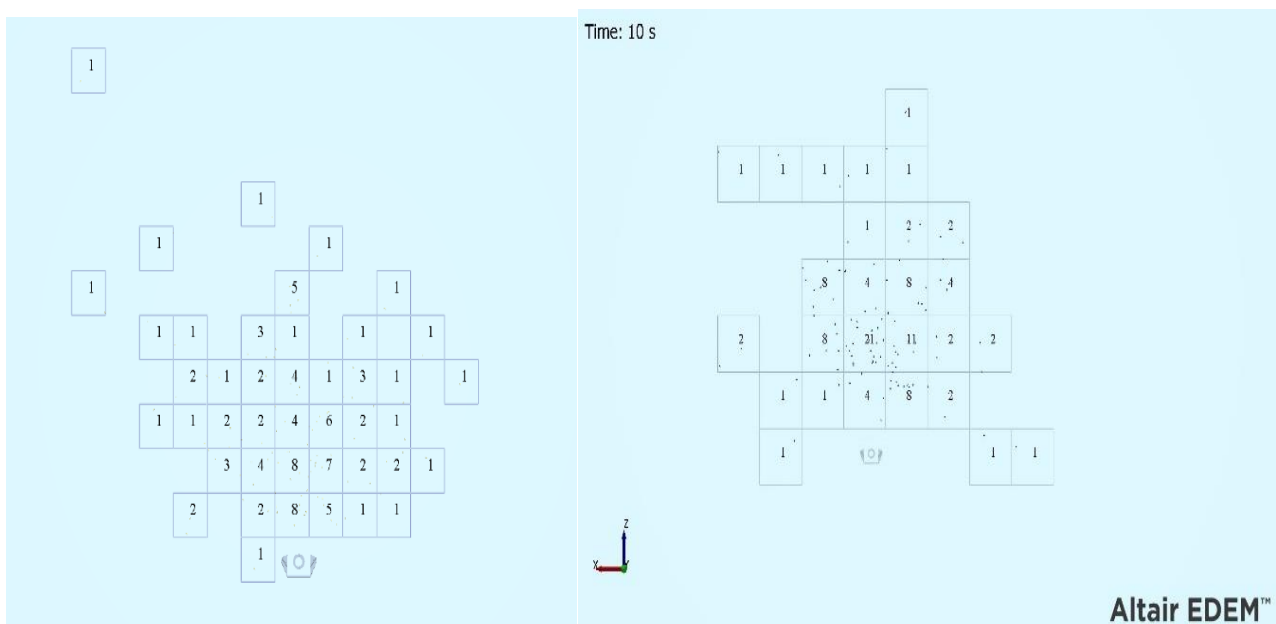


Fig. 12 - Interaction between seed-distribution board

In Figure 12 the interaction between the seeds and the distribution board is presented, during the seeding process. The distribution board is positioned at a 45° angle, which plays a critical role in directing the seeds as they make contact with the board. This angle helps ensure that the seeds are efficiently distributed across the soil surface by optimizing their trajectory after collision, promoting a more uniform spread. The 45° inclination is specifically chosen to balance the forces acting on the seeds during impact, minimizing bounce or clumping and enhancing overall seeding efficiency.

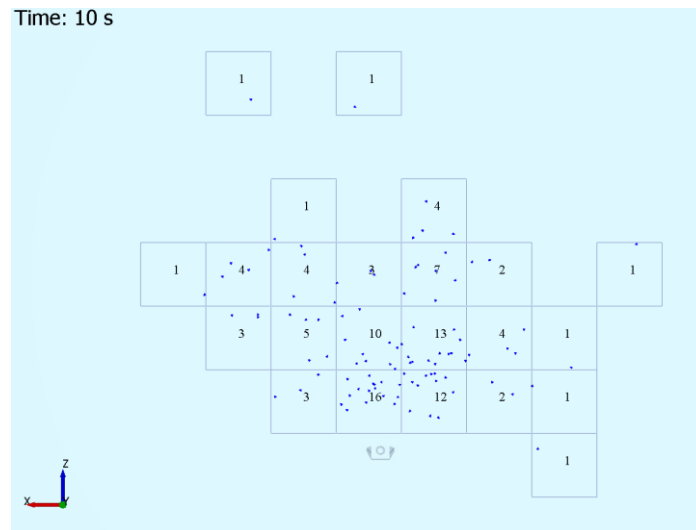
RESULTS

In this section, the results of a 3D scatter plot representing the spatial distribution of seeds within the defined area are presented. A detailed quantitative analysis has been conducted, focusing on several key aspects: density analysis, variance in seed distribution, hotspot identification, and standard deviation.



a) 3D Scatter plot *Phacelia tanacetifolia*

b) 3D Scatter plot *Lolium perenne*



c) 3D Scatter plot *Onobrychis viciifolia*
Fig. 13 - 3D Scatter plot for the seeds

In figure 13 a) and b), the highest seed concentration is marked by the number 10, positioned in the bottom left quadrant of the image. Figure 13 c) displays a grid composed of multiple squares, each containing a varying number of dots to represent seeds. The arrangement suggests a symmetrical distribution, with the middle row showing the densest seed concentration.

A quantitative analysis was conducted based on a 3D scatter plot for *Onobrychis viciifolia* seeds generated using EDEM software by Altair. The analysis involved converting the 3D seed data into a simplified 2D grid format presented in Table 1, where each cell in the grid represented the number of seeds within a corresponding square area of the plot.

Table 1

2D grid for 3D scatter plot *Onobrychis viciifolia*

Square Number	1	2	3	4	5	10	13	16
Seed	1	2	3	4	5	10	13	16
Seed	1	2	3	4	0	0	0	0
Seed	1	2	0	4	0	0	0	0
Seed	1	0	0	0	0	0	0	0
Seed	1	0	0	0	0	0	0	0
Seed	1	0	0	0	0	0	0	0
Seed	1	0	0	0	0	0	0	0
Seed	1	0	0	0	0	0	0	0

To obtain the total seed count, the sum of all values in the grid was used to get the total number of seeds. The output is the total sum. Total number of seeds equals 76.

For the average density, the total number of seeds is divided by the total number of squares to get the average seed density per square. The average density equals 1.1875.

For the variance and standard deviation, it is calculated how much the number of seeds in each square deviates from the average density. The variance and standard deviation will show how evenly seeds are distributed cross the grid.

The formula to calculate variance is as follows:

$$\sigma^2 = \frac{1}{N} \sum_{i=1}^N (x_i - \mu)^2 \tag{1}$$

where σ^2 is the variance, N the total number of regions or cells, μ is the average density (mean), x_i is the number of seeds in i -th region (the values in the table), $(x_i - \mu)^2$ is the squared difference between each seed count and the mean.

The variance of the seed density is approximately 8.53 seeds² per region.

The standard deviation is the square root of the variance.

$$\sigma = \sqrt{\sigma^2} \tag{2}$$

The standard deviation of the seed density is approximately 2.92 seeds per region. This gives a sense of how much the seed counts vary from the mean, on average.

To identify seed hotspots, a hotspot can be defined as a region where the number of seeds is significantly higher than the average density, where the seed count exceeds a certain threshold.

The hotspot threshold can be calculated and it can be noted as follows:

$$T_{hotspot} = \mu + \sigma \tag{3}$$

where $T_{hotspot}$ is the seed hotspot, μ is the average seed density and σ is the standard deviation.

In this case, the hotspot threshold will be 4.1075 which indicates that any region where the seed count exceeds would be classified as a hotspot.

For the *Phacelia tanacetifolia* seeds, the total seed count was calculated to be 99 seeds, representing the cumulative number of seeds distributed across all cells in the grid. The average seed density was found to be 0.538 seeds per cell, reflecting the mean seed distribution across the entire grid.

To assess the variability in seed distribution, the variance was calculated, yielding a value of 1.846, indicating a moderate spread of seed counts across the grid. The standard deviation, which measures the average deviation from the mean, was determined to be 1.359. This value provided insights into the clustering of seeds in specific regions of the grid.

Also, for the *Lolium perenne* seeds the total seed count was calculated to be 100, representing the cumulative number of seeds distributed across all cells in the grid. The average seed density was found to be 1.389 seeds per cell, reflecting the mean seed distribution across the entire grid.

To assess the variability in seed distribution, the variance was calculated, yielding a value of 10.599, indicating a moderate spread of seed counts across the grid. The standard deviation, which measures the average deviation from the mean, was determined to be 3.256. This value provided insights into the clustering of seeds in specific regions of the grid.

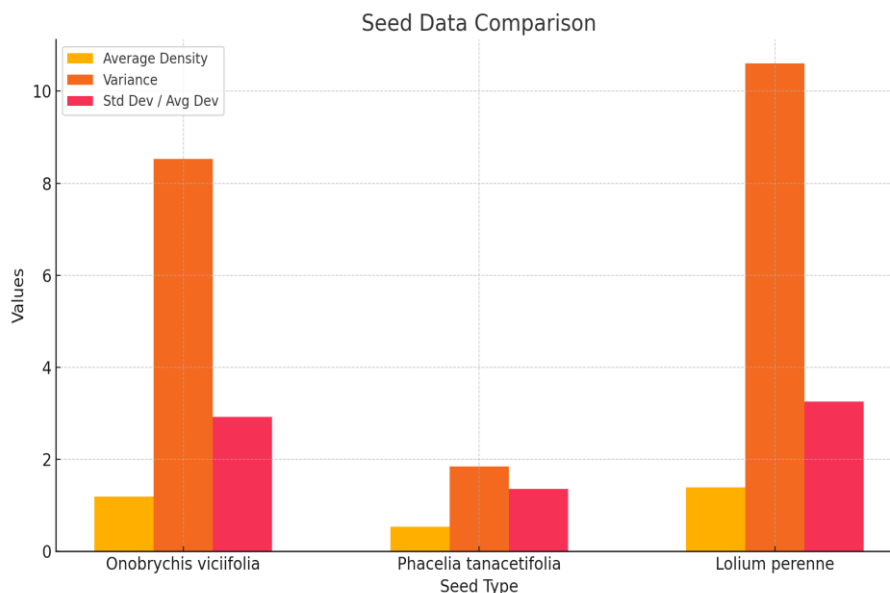


Fig. 14 – Seed Data Comparison

In Figure 14, the seed data comparison is presented. This comparison highlights the differences in statistical properties among the three seed types. The comparison of the three seed types—*Onobrychis viciifolia*, *Phacelia tanacetifolia*, and *Lolium perenne* reveals significant differences in their statistical properties. *Onobrychis viciifolia* and *Lolium perenne* exhibit similar average densities and standard deviations, but *Lolium perenne* has a slightly higher variance. *Phacelia tanacetifolia*, on the other hand, shows lower values across all metrics, indicating more consistent and less variable properties.

CONCLUSIONS

In conclusion, the adoption of EDEM by Altair Software is a transformative step toward enhancing the accuracy and efficiency of equipment design and material flow analysis. This advanced discrete element modeling tool allows for in-depth simulations of particle interactions and system behavior under a wide range of conditions, which is essential for predicting wear, optimizing processes, and reducing operational risks. By leveraging the powerful computational capabilities of EDEM, engineers can make informed decisions that improve performance and productivity before even conducting physical experiments.

However, while simulations offer a valuable preliminary understanding, their true value lies in their correlation with real-world outcomes. In the future, physical experiments will be conducted on the actual equipment, enabling a direct comparison between the simulation data and experimental results. This validation process is essential for assessing the software's reliability in predicting real-world scenarios and detecting any potential discrepancies. This hands-on approach aims to further refine the simulation models, ensuring they closely reflect real-world performance and strengthening confidence in EDEM's application for future projects. This integration of simulation and experimentation will be a key to advancing the accuracy and effectiveness of both equipment design and operational efficiency.

ACKNOWLEDGEMENT

The results were obtained with the support of MCID through the NUCLEU Program, contract no. 9N/01.01.2023 project PN 23 04 02 03 "Innovative technology for covering the interval between the rows of vines and fruit trees to avoid degradation of the soil structure".

REFERENCES

- [1] An, X., Cheng, X., Wang, X., Han, Y., Li, H., Liu, L., Liu, M., Liu, M., Zhang, X., (2023). Design and experimental testing of a centrifugal wheat strip seeding device. *Agriculture*, 13(10): 1883, <https://www.mdpi.com/2077-0472/13/10/1883>
- [2] Cârlescu, P., Țenu, I., Băetu, M., Arsenoia, V., Roșca, R., (2022). Simulation of grain seed motion in a hybrid dryer with CFD-DEM coupling approach. *a X-a International Conference on Agriculture, Food and Environment, HAICTA 2022, CEUR Workshop Proceedings*, 3293, pg.116
- [3] Cheng, B., He, R., Xu, Y., Zhang, X., (2022), Simulation analysis and test of pneumatic distribution fertilizer Discharge System, *Agronomy* 2022, 12(10), 2282, <https://doi.org/10.3390/agronomy12102282>
- [4] Ding, H., An, X., Wu, G., Li, L., Zhu, Q., (2019). Optimization and Simulation of Fertilizer Guide Device Parameters Based on EDEM Software. *11th International Conference on Computer and Computing Technologies in Agriculture (CCTA)*, pp.377-388, 10.1007/978-3-030-06179-1_38ff. fffhal-02111539
- [5] Ding, S., Bai, L., Yao, Y., Yue, B., Fu, Z., Zheng, Z., Huang, Y., (2018). Discrete element modelling (DEM) of fertilizer dual-banding with adjustable rates, *Computers and Electronics in Agriculture*, <https://doi.org/10.1016/j.compag.2018.06.044>
- [6] Dun, G., Mao, N., Gao, Z., Wu, X., Liu, W., Zhou, C., (2022). Model construction of soybean average diameter and hole parameters of seed-metering wheel based on DEM, *International Journal of Agricultural and Biological Engineering*, 15(1): 101–110, DOI: 10.25165/j.ijabe.20221501.5914
- [7] Guo, H., Cao, Y., Song, W., Zhang, J., Wang, C., Wang, C., Yang, F., Zhu, L., (2021). Design and simulation of a garlic seed metering mechanism, *Agriculture* 2021, 11(12), 1239, <https://doi.org/10.3390/agriculture11121239>
- [8] Guo, J., Yang, Y., Muhammad, M.S., Tan, C., Wang, L., Tang, P., (2002). Design and simulation for seeding performance of high-speed inclined corn metering device based on discrete element method (DEM), *National Center for Biotechnology Information*, 12(1):19415, doi: 10.1038/s41598-022-23993-1
- [9] Han, D., Zhang, D., Jing, H., Yang, L., Cui, T., Ding, Y., Wang, Z., Wang, Y., Zhang, T., (2018). DEM-CFD coupling simulation and optimization of an inside-filling air-blowing maize precision seed-metering device. *Computers and Electronics in Agriculture*, 150:426-438, DOI: 10.1016/j.compag.2018.05.006
- [10] Jia, H.L., Chen, Y.L., Zhao, J.L., Guo, M.Z., Huang, D.Y., Zhuang, J., (2018). Design and key parameter optimization of an agitated soybean seed metering device with horizontal seed filling. *International Journal of Agricultural and Biological Engineering*, 11(2): 76–87, DOI: 10.25165/j.ijabe.20181102.3464
- [11] Lei, X., Liao, Y., Liao, Q., (2016). Simulation of seed motion in seed feeding device with DEM-CFD coupling approach for rapeseed and wheat, *Computers and Electronics in Agriculture*, 131:29-39, <https://doi.org/10.1016/j.compag.2016.11.006>

- [12] Liao, Y., You, Y., Hui, Y., Zhang, X., Wang, D., (2023). Mixed Seeds of Oat and Vetch Based on DEM-Fluent Coupling Motion Simulation in a Venturi Tube, *Processes* 2023, 11(4):1095, <https://doi.org/10.3390/pr11041095>
- [13] Li, K., Li, S., Ni, X., Lu, B., Zhao, B., (2023). Analysis and Experimental of Seeding Process of Pneumatic Split Seeder for Cotton, *Agriculture* 2023, 13(5), 1050, <https://doi.org/10.3390/agriculture13051050>
- [14] Li, Y., Xing, S., Li, S., Liu, L., Zhang, X., Song, Z., Li, F., (2020). Seeding Performance Simulations and Experiments for a Spoon-Wheel Type Precision Cottonseed-Metering Device Based on EDEM, *Mechanical Engineering Science*, 2(1), <https://journals.viserdata.com/index.php/mes/article/view/2615>
- [15] Liao, Y., You, Y., Wang, D., Hui, Y., Xing, K., Sun, W., (2023). Motion simulation of oat and vetch seeds in dispensers based on DEM-CFD, https://papers.ssrn.com/sol3/papers.cfm?abstract_id=4639581, https://papers.ssrn.com/sol3/papers.cfm?abstract_id=4639581
- [16] Liu, J.S., Gao, C.Q., Nie, Y.J., Yang, B., Ge, R.Y., Xu, Z.H., (2020). Numerical simulation of Fertilizer Shunt-Plate with uniformity based on EDEM software, *Computers and Electronics in Agriculture*, 178(10):105737, <https://doi.org/10.1016/j.compag.2020.105737>
- [17] Liu, R., Liu, L., Li, Y., Liu, Z., Zhao, J., Liu, Y., Zhang, X., (2022). Numerical Simulation of Seed-Movement Characteristics in New Maize Delivery Device. *Agriculture* 2022, 12(11), 1944, <https://doi.org/10.3390/agriculture12111944>
- [18] Lu, B., Ni, X., Li, S., Li, K., Qi, Q., (2022). Simulation and Experimental Study of a Split High-Speed Precision Seeding System. *Agriculture* 2022, 12(7):1037, <https://doi.org/10.3390/agriculture12071037>
- [19] Ma, C., Yi, S., Tao, G., Li, Y., Wang, S., Wang, G., Gao, F., (2023). Research on Receiving Seeds Performance of Belt-Type High-Speed Corn Seed Guiding Device Based on Discrete Element Method. *Agriculture* 2023, 13(5), 1085
- [20] Ma, D., Shi, S., Hou, J., Zhou, J., Li, H., Li, J. (2024). Calibration and Experimentation of Discrete Elemental Model Parameters for Wheat Seeds with Different Filled Particle Radii. *Applied Sciences* 2024, 14(5):2075, DOI: 10.3390/app14052075
- [21] Ma, W., Zhang, S., Jin, C., Yin, X., Zhang, G., Zhu, L., (2022). Optimization Design of an Alfalfa Seed Airflow Collection and Drainage System Based on Numerical Simulation. *Processes*, 10(11):2281, DOI: 10.3390/pr10112281
- [22] Ma, W., Zhang, S., Yin, X., Chen, K., Zhu, L.A., (2023). Calibration of the Contact Parameters of a Sesbania Seed Discrete Element Model Based on RSM. *Processes*, 11(12):3381, DOI: 10.3390/pr11123381
- [23] Miao, Z., Li, Z., Xu, K., Wu, L., Ning, S., Song, G., Liu, Y., (2019). Numerical Simulation Analysis of Pinus sylvestris var. Mongolica seeds Vibration Situation Based on EDEM. *2018 4th International Conference on Environmental Science and Material Application*, 252 052111, DOI 10.1088/1755-1315/252/5/052111
- [24] Ren, D., Yu, H., Zhang, R., Li, J., Zhao, Y., Liu, F., Zhang, J., Wang, W., (2022). Research and Experiments of Hazelnut Harvesting Machine Based on CFD-DEM Analysis. *Agriculture* 2022, 12(12), 2115; <https://doi.org/10.3390/agriculture12122115>
- [25] Savaniu, I.M., Tonciu, O., Culcea, M., Bizgan, A., Badea, F., Apostolescu, T.C., Văleanu, D.M. "A Study on the Energy Consumption of a Mechatronic Delivery System with a Spiral used in an Innovative Energy-Efficient Vending Machine for Urban Use, *International Journal* 16 (2024): 100
- [26] Savaniu, I.M., Tonciu, O., Culcea, M., Bizgan, A., Badea, F., Radu, C. Energetically Efficient Mechatronic Systems for Dose Delivery in Energetically Independent Vending Machine for Cold Products." *International Journal of Mechatronics and Applied Mechanics* 15 (2024): 35-44.
- [27] Savaniu, I.M., Chiriță, A.P., Popovici, I.A., Tonciu, O., Culcea, M., Neagu, A., Blejan, R. and Ștefan, V., 2023. Optimizing and Integrating Electromechanical Actuators in Agricultural Excavator Booms for Enhanced efficiency and Battery Longevity, *INMATEH-Agricultural Engineering*, 71(3).
- [28] Shi, L., Zhao, W., Sun, B., Sun, W., Zhou, G., (2023). Determination and analysis of basic physical and contact mechanics parameters of quinoa seeds by DEM. *International Journal of Agricultural and Biological Engineering*, 16(5):35-43, DOI: 10.25165/j.ijabe.20231605.7837
- [29] Song, C., Cao, Shukun C., KuiZeng, G., WenLong, C., Cui, S., Ma, J., (2021). Research on wheat modeling method based on EDEM. *Journal of Physics Conference Series*, 1798(1):012048, <https://iopscience.iop.org/article/10.1088/1742-6596/1798/1/012048>

- [30] Sun, J., Chen, H., Duan, J., Liu, Z., Zhu, Q., (2020). Mechanical properties of the grooved-wheel drilling particles under multivariate interaction influenced based on 3D printing and EDEM simulation. *Computer and Electronics in Agriculture*, 172(8):105329, DOI: 10.1016/j.compag.2020.105329
- [31] Sun, S., Hu, B., Wu, X., Luo, X., Wang, J., (2024). Research on a Vibrationally Tuned Directional Seed Supply Method Based on ADAMS-EDEM Coupling and the Optimization of System Parameters. *Agriculture*, 14(3):433, DOI: 10.3390/agriculture14030433
- [32] Tang, H., Xu, F., Xu, C., Zhao, J., Wang, Y., (2022). The influence of a seed-drop tube of the inside-filling air-blowing precision seed-metering device on seeding quality. *Computers and Electronics in Agriculture*, vol. 204, 107555, <https://doi.org/10.1016/j.compag.2022.107555>
- [33] Wang, B., Liao, Q., Wang, L., Shu, C., Cao, M., Du, W., (2023). Design and Test of Air-Assisted Seed-Guiding Device of Precision Hill-Seeding Centralized Seed-Metering Device for Sesame. *Agriculture*, 13(2):393, DOI: 10.3390/agriculture13020393
- [34] Wang, H., Sun, X., Li, H., Fu, J., Zeng, X., Xu, Y., Wang, Y., Liu, H., Lü, Z., (2022). Design and Parameter Optimization of a Finger Clip Plate Garlic Seed-Metering Device Based on EDEM. *Agronomy*, 12(7):1543, DOI: 10.3390/agronomy12071543
- [35] Wang, J., Tang, H., Wang, J., Li, X., Huang, H., (2017). Optimization design and experiment on ripple surface type pickup finger of precision maize seed metering device. *International Journal of Agricultural and Biological Engineering*, 10(1): 61–71., DOI: 10.3965/j.ijabe.20171001.2050
- [36] Wang, J., Yao, Z., Xu, Y., Guo, F., Guan, R., Li, H., Tang, H., Wang, Q., (2024). Mechanism Analysis and Experimental Verification of Side-Filled Rice Precision Hole Direct Seed-Metering Device Based on MBD-DEM Simulations. *Agriculture*, 14(2):184, DOI: 10.3390/agriculture14020184
- [37] Wang, L., Liao, Q., Xi, R., Li, X., Liao, Y., (2024). Influence of an equal width polygon groove-tooth wheel on feeding performance of the seed feeding device for wheat. *Computers and Electronics in Agriculture*, 217(8):108565, DOI: 10.1016/j.compag.2023.108565
- [38] Wang, M., Liu, Q., Ou, Y., Zou, X., (2022). Numerical Simulation and Verification of Seed-Filling Performance of Single-Bud Billet Sugarcane Seed-Metering Device Based on EDEM. *Agriculture*, 12(7):983, DOI: 10.3390/agriculture12070983
- [39] Wang, S., Yu, Z., Aorigele, Zhang W., (2022). Study on the modeling method of sunflower seed particles based on the discrete element method. *Computers and Electronics in Agriculture*, vol. 198, 107012, <https://doi.org/10.1016/j.compag.2022.107012>
- [40] Wang, J., Wenqi, Z., Liquan, T., Shuwei, L., Zhao Z., (2017). Virtual simulation analysis and verification of seed-filling mechanism for dipper hill-drop precision direct rice seeder. *International Journal of Agricultural and Biological Engineering*, 10(6): 77–85., DOI: 10.25165/j.ijabe.20171006.2981
- [41] Wang, Y., Kang, X., Wang, G., Ji, W., (2023). Numerical Analysis of Friction-Filling Performance of Friction-Type Vertical Disc Precision Seed-Metering Device Based on EDEM. *Agriculture*, 13(12):2183, DOI: 10.3390/agriculture13122183
- [42] Xiao, Y., Ma, Z., Wu, M., Luo, H., (2022). Numerical Study of Pneumatic Conveying of Rapeseed through a Pipe Bend by DEM-CFD. *Agriculture*, 12(11):1845, DOI: 10.3390/agriculture12111845
- [43] Yan, D., Yu, J., Liang, L., Wang, Y., Yu, Y., Zhou, L., Sun, K., Liang, P., (2021). A Comparative Study on the Modelling of Soybean Particles Based on the Discrete Element Method. *Processes*, 9(2):286, DOI: 10.3390/pr9020286
- [44] Yan, D., Yu, J., Wang, Y., Sun, K., Zhou, L., Tian, Y., Zhang, N., (2022). Measurement and Calibration of DEM Parameters of Soybean Seed Particles. *Agriculture*, 12(11):1825, DOI: 10.3390/agriculture12111825
- [45] Yang, Q., He, M., Du, G., Shi, L., Zhao, X., Shi, A., Addy, M., (2021) Design and Experimental Study of a Wine Grape Covering Soil-Cleaning Machine with Wind Blowing. *AgriEngineering*, 3(1):50-72, DOI: 10.3390/agriengineering3010004
- [46] Zha, X., Zhang, G., Zhang, S., Hou, Q., Wang, Y., Zhou, Y., (2020). Design and experiment of centralized pneumatic deep precision fertilization device for rice transplanter. *International Journal of Agricultural and Biological Engineering*, 13(6):109-117, DOI: 10.25165/j.ijabe.20201306.5479
- [47] Zhang, B., Wang, J., Yang, X., Chen, B., (2024). A DEM-MBD based method for regulating transfer flux in the supply and discharge of cane seed particles. *Computers and Electronics in Agriculture*, 218(2):108732, DOI: 10.1016/j.compag.2024.108732

- [48] Zhang, X., Wen, Z., Wang, Q., Li, H., Zhang, Z., Liu, J., (2022) Research on Characteristics of Airway Pressure Loss in Seeding-Wheel-Type Pneumatic Seeder. *Agriculture*, 12(12):2021, DOI: 10.3390/agriculture12122021
- [49] Zhao, J., Li, Y., Liu, L., Liu, Z., (2024). Structural Design of Pressurized Tube Based on the Discrete Element Method–Computational Fluid Dynamics Coupled Simulation. *Applied Sciences*, 14(9):3836, DOI: 10.3390/app14093836
- [50] Zhao, X., Bai, W., Li, J., Yu, H., Zhao, D., Yin, B., (2022). Study on positive-negative pressure seed metering device for wide-seedling-strip-seeding. *International Journal of Agriculture and Biological Engineering*, 15(6):124-133, DOI: 10.25165/j.ijabe.20221506.7261
- [51] Zhu, H., Wu, X., Bai, L., Li, R., Guo, G., Qin, J., Zhang, Y., Li, H., (2023). Design and experiment of a soybean shaftless spiral seed discharge and seed delivery device. *Scientific Reports*, 13, 2075, DOI: 10.21203/rs.3.rs-3103875/v1
- [52] Zou, H., Wu, M., Shen, Y., Xu, R., Zhang, C., Wang, M., (2023). Simulation Study on Reseeding Link of an Air-Suction Precision Tray Seeder. *Preprints 2023*, 2023062264, <https://doi.org/10.20944/preprints202306.2264.v1>

RESEARCH ON BILEVEL TASK PLANNING METHOD FOR MULTI-UAV LOGISTICS DISTRIBUTION

面向多农业无人机物流配送的双层任务规划方法研究

Zhibo LI*, Yuan LIU

Business School, Chongqing Polytechnic University of Electronic Technology, Chongqing/China

Tel: +8617815380036; E-mail: Lizhibo68513@126.com

Corresponding author: Zhibo LI

DOI: <https://doi.org/10.35633/inmateh-74-67>

Keywords: Agricultural UAV, Bilevel planning model, Improved PSO algorithm, Path planning, Task allocation

ABSTRACT

Multi-unmanned aerial vehicle (UAV) collaborative task planning and distribution path planning are the core content of agricultural UAV logistics distribution. In this study, the multi-UAV collaborative task planning and the distribution path planning were discussed, and such constraint conditions as UAV load capacity, battery capacity and flight time were comprehensively considered, aiming to reduce the number of UAVs and their power consumption. To ensure the safe and efficient completion of multi-UAV logistics distribution tasks, 3D agricultural ultralow space was subjected to environment modeling, and a bilevel planning model for collaborative planning of UAV distribution route and flight path was constructed. Then, an improved particle swarm optimization (PSO) algorithm with the improved learning factor and inertia coefficient was designed on the basis of PSO framework, and the global optimal solution in the current iteration was improved using variable neighborhood descent search. The feasibility of the proposed algorithm was verified by analyzing a practical case. With the central city area of XX City as the study area, 1 logistics & freight transportation center was taken as the central warehouse (coordinates: 50, 50, unit: km) and 50 intelligent express cabinets as the express cabinets of UAVs. The obtained results were comparatively analyzed with those acquired through the basic PSO algorithm. The results manifest that the proposed algorithm performs better than the compared algorithms. The improved PSO algorithm is superior to the basic PSO algorithm in aspects of total UAV flight distance, number of UAVs used and algorithm convergence time, indicating that the model and algorithm established in this study are feasible and effective.

摘要

多无人机任务协同规划与配送路径规划是农业无人机物流配送的核心内容，探讨多无人机任务协同规划与配送路径规划的农业无人机群配送路径的规划问题，综合考虑无人机载重量、无人机电池容量、无人机飞行时间等约束条件，目标为降低无人机数量及耗电量。为保障安全、高效完成多农业无人机物流配送任务，首先对三维农业超低空间进行环境建模，构建了一种无人机配送线路以及航迹协同规划的双层规划模型。基于粒子群算法框架设计了一种改进学习因子与惯性系数的改进粒子群算法，利用变邻域下降搜索对当前迭代中的全局最优解进行改进。通过实际案例分析，验证了该算法的可行性，以XX市中心城区为研究区域。选取1个物流货运中心作为中心仓库位置坐标(50,50)，单位(km)、50个智能快递柜作为无人机快递柜位置。将所得结果与基础粒子群算法进行对比分析，结果表明，本算法性能优于对比算法，改进 PSO 得到的无人机飞行总距离，启用无人机数量和算法收敛时间等方面均优于基础粒子群算法，说明本文构建的模型与算法是可行的和有效的。

INTRODUCTION

Comprehensively driven by unmanned technological progress, policy assistance and market demand, unmanned aerial vehicles (UAVs) have been widely used in agricultural plant protection, traffic monitoring, logistics and transportation, bringing new opportunities to urban logistics (Liu et al., 2024). UAV logistics enterprises are actively promoting the pilot of UAV in medical treatment and food delivery, but due to the limitation of endurance, the current research and practice focus on the terminal distribution of UAVs and the vehicle-aircraft joint distribution mode, which still faces cohesion and technical problems in practical application (Li et al., 2024). Although the existing pure UAV distribution can meet certain needs, it is difficult to cope with the challenges in large-scale commercialization and complex scenarios in the future.

Therefore, it is more critical and necessary to explore the logistics UAV distribution mode in complex environments (Wei et al., 2024).

The rapid development of urban residents' consumption power has contributed to the rapid development of e-commerce and the explosive growth of the logistics industry, yet also accompanied by urban traffic congestion, express delivery delay, etc. (Fan et al., 2024). UAVs have the advantages of strong mobility, high flexibility and low cost, providing a new path to solve the "one kilometer at the terminal" of urban logistics, and exploratory practice has been carried out in lots of cities in China and abroad (Zhang et al., 2023). The core task of multi-UAV logistics distribution is manifested in two aspects: allocation of distribution tasks, i.e., giving the order of goods delivery according to customer needs; distribution path planning, also called trajectory planning or route planning, namely, giving the flight path of UAVs to each task point (Xu et al., 2024).

The current research on UAV logistics distribution mostly focuses on small-scale terminal delivery scenarios, and UAV charging factors have been fully considered in some studies. In terms of safety flight and UAV distribution task allocation, Zhao et al. (2019) comprehensively considered such constraint conditions as the operational reliability and flight performance of UAVs and established a multi-UAV collaborative task allocation model in logistics transportation with the minimum safety risk and logistics cost as the objective functions. Li et al. (2015) built a UAV task allocation model fully considering flight range, task revenue and task completion time window. Zhang et al. (2018) applied the particle swarm optimization (PSO) algorithm to solve the multi-UAV task allocation problem after realizing the discretization of UAVs through binary matrix encoding. With the minimum number of UAVs distributed and the shortest total range as the objectives, Shao et al. (2020) constructed a multi-objective function to solve the path collaboration problem in the cruising process of UAVs and solved it through the multi-objective evolutionary algorithm.

As for multi-UAV distribution path planning, specific research results have been achieved regarding multi-UAV collaborative path planning based on single-UAV path planning research. Ma et al. (2021) combined PSO with Hook-Jeeves search algorithm, first solved the path information of single UAVs, and then coordinated the arrival time through the centralized path planning layer, thus realizing the cooperative path planning of multiple UAVs; when coping with the needs of multiple UAVs to execute multi-target reconnaissance tasks in the military field, Liu et al. (2022) improved the traditional A* algorithm, K-means algorithm and depth traversal method and dynamically adjusted the task allocation according to real-time changes. Liu et al. (2023) proposed a hybrid differential crow search algorithm based on Levy flight strategy, which added pruning and Logistic chaotic mapping mechanism to the fast traversal random tree algorithm, and initialized the path through the improved rapidly exploring random tree (RRT), so as to improve the efficiency of heterogeneous UAV path planning.

When it comes to the research on the integration of task allocation and path planning, Yuan et al. (2020), designed a two-layer mutual coupling task planning solution strategy, and used a nested two-layer model to solve the task allocation, attack sequence and path planning problems of multiple military UAVs in a two-dimensional environment. Wu et al. (2021) designed a two-stage hybrid algorithm based on Deep Reinforcement Learning (DRL). In the first stage, DRL algorithm was used to generate the distribution routes of multiple UAVs visiting customers in sequence, and in the second stage, A* algorithm was applied to search the shortest path of each UAV. The current research on multi-UAV collaborative path planning focuses on 2D space, while urban 3D spatial environments have been rarely involved. Hwang et al. (2015) put forward the concept of "the last mile of UAV delivery" earlier. Tassone et al. (2016) raised the FSTSP problem, distinguished the distribution nodes of UAVs and trucks, carried out distribution with a truck carrying a UAV, and constructed a hybrid integer planning model and heuristic algorithm for solving. Chen et al. (2021) proposed the TSP-D problem, which made the UAV and the truck exist in the same distribution network, and the UAV could start from the same location and return to the truck. Zhou et al. (2018) further studied the TSP-D problem, improved the hybrid integer planning model and solved it by designing the simulated annealing algorithm. Yang et al. (2020) designed a dynamic planning algorithm for TS-D problem, which could solve larger-scale problems. Zhang et al. (2022) put forward the VRP-D problem with the objective of minimizing the completion time of distribution, which included multiple trucks and multiple UAVs. Agha et al. (2023) added effective inequations to the proposed model, allowed UAVs to implement closed-loop flight, and designed a heuristic algorithm to solve large-scale examples. Another application scenario widely concerned in the academic circles is the distribution of emergency medical materials using UAVs.

Ma et al. (2021) studied the distribution of drugs for chronic diseases and the recovery of test samples in rural areas using UAVs, and used decomposition method and Lagrange relaxation algorithm to accurately solve the problem. Hao et al. (2017) proposed a UAV path model based on the minimization of time and cost.

Hu et al. (2020) studied the scheduling optimization of UAVs, considered the battery energy consumption rate related to the load capacity of UAVs, established a hybrid integer planning model and used the boundary generation algorithm of the original problem and the dual problem to speed up the solving process. Han et al. (2021) explored the drug distribution problem of UAVs in the last mile of the disaster-stricken area, and established a mixed integer planning model considering the energy consumption of UAVs related to load capacity and flight distance.

In this study, environment modeling was performed using the grid method in an urban ultralow (<120 m) 3D environment. Considering the constraints of obstacles, a bilevel planning model for UAV task allocation and collaborative path planning was proposed. The problems at the upper and lower levels were mutually nested and influenced each other. Given that both levels of the model belonged to NP-hard problem, the upper-level model was solved by introducing the genetic algorithm, and an improved PSO algorithm was designed to solve the bottom-level model problem. Finally, the effectiveness of the algorithm and model was analyzed by means of simulation.

MATERIALS AND METHODS

Problem description

The path planning problem of logistics UAVs can be defined as an undirected complete graph $G = (V, A)$, where V represents the set of vertexes, including customer point information set, warehouse point 0 and obstacle information set; A denotes the set of arcs. All customer points are distributed on the transportation network. UAV k fully loaded with cargoes starts from warehouse point 0, arrive at the customer point i to be served, each customer point i has a receipt demand B_i , the service time of the UAV at customer point i is τ_i , within which the UAV can complete unloading work by default, and after serving customer point i , the UAV continues to fly to the next customer point until the residual load capacity C_{ik} or residual battery capacity of UAV k is not enough to arrive at the next customer point (in this case, the residual battery capacity of the UAV can support the UAV to return to warehouse point 0 from the current location), and then returns to warehouse point 0.

During the flight process, UAVs will be affected by weather, environment and other external factors. This study mainly focuses on path planning. Assuming that UAVs fly under ideal environment, greater attention is then paid to the constraints of UAVs themselves. The flight time and mileage of UAVs are directly influenced by their power consumption, which, in turn, is closely related to their load capacity. To be more practical, the influence of cargo load capacity on the residual battery capacity of UAVs is taken into account. Song et al. (2018) put forward a flight time weight function based on the present load capacity and proved that the battery power consumption is linearly correlated with the load capacity.

Then, the power consumption based on the current residual load capacity of UAVs can be calculated as follows (1) and (2):

$$f(C_{ik}) = 1 + \left(\frac{U-1}{Q}\right) C_{ik}, \forall i \in \Omega_j, k \in \Omega_K \quad (1)$$

$$E(i, j, C_{ik}) = f(C_{ik})e(d_{ij}/S_p), \forall i \in \Omega_j, j \in \Omega_j, k \in \Omega_K \quad (2)$$

where k is UAV number; i and j are customer point numbers, $i, j \in \{1, 2, 3, \dots, N\}$; N denotes the total number of customer points. $i, j = 0$ indicates the warehouse point; represents the residual load capacity of UAV k when starting from customer point i ; Q is the maximum load capacity of UAVs; U is a proportionality factor; $f(C_{ik})$ means the power consumption factor under load capacity of C_{ik} ; e is the power consumption of UAVs within unit time; S_p is the flight speed of UAVs; d_{ij} is the distance from customer point i to j ; $E(i, j, C_{ik})$ is the battery power consumption when UAVs fly from customer point i to j under load capacity of C_{ik} ; E represents the total battery capacity of UAVs; Ω_j is the set of customer points; Ω_K is the UAV number set. When calculating the power consumption of a UAV when unloading cargoes at one customer point, the residual load capacity is calculated according to the load capacity before unloading at the current customer point.

Model hypotheses

The model hypotheses are described as follows:

- (1) Each customer point is served and only once;
- (2) The flight loop of each UAV is completed within the limited duration of the battery;
- (3) It is assumed that only one distribution center exists in this area;
- (4) All UAVs are of the same model but different speeds, load capacities and ranges;
- (5) UAVs unload cargoes at each customer point within the same time;
- (6) The weights of cargoes to be distributed by UAVs to each customer are different, and the unloading time is also different.

Modeling

The objective functions and constraint conditions of the bilevel task planning problem facing multi-UAV logistics distribution are as below:

$$F_U = \alpha \sum_{k \in \Omega_K} \sum_{j \in \Omega_J} X_{0jk} + \beta \sum_{k \in \Omega_K} \sum_{i \in \Omega_F} \sum_{j \in \Omega_F} f(C_{ik})(d_{ij}/S_p + \tau_j) \tag{3}$$

$$\sum_{j \in \Omega_F} \sum_{k \in \Omega_K} X_{ijk} = 1, \forall j \in \Omega_J \tag{4}$$

$$\sum_{i \in \Omega_F} \sum_{k \in \Omega_K} X_{ijk} = 1, \forall j \in \Omega_J \tag{5}$$

$$\sum_{j \in \Omega_J} X_{0jk} = \sum_{i \in \Omega_J} X_{i0k}, \forall k \in \Omega_K \tag{6}$$

$$\sum_{i \in \Omega_J} \sum_{j \in \Omega_F} B_i X_{ijk} \leq Q, \forall k \in \Omega_K \tag{7}$$

$$\sum_{i \in \Omega_F} X_{ijk} = \sum_{i \in \Omega_F} X_{jik}, \forall j \in \Omega_J, \forall k \in \Omega_K \tag{8}$$

$$T_{jk} \geq T_{ik} + d_{ij}/S_p + \tau_j - M(1 - X_{ijk}), \forall i \in \Omega_F, \forall j \in \Omega_F, \forall k \in \Omega_K \tag{9}$$

$$C_{ik} \geq C_{jk} + B_j - M(1 - X_{ijk}), \forall i \in \Omega_F, \forall j \in \Omega_F, \forall k \in \Omega_K \tag{10}$$

$$O_{ik} \geq O_{jk} + f(C_{ik})(d_{ij}/S_p + \tau_j) - M(1 - X_{ijk}), \forall k \in \Omega_K \tag{11}$$

$$\sum_{i \in \Omega_F} \sum_{j \in \Omega_F} X_{ijk} (f(C_{ik})(d_{ij}/S_p + \tau_j)) \leq E, \forall k \in \Omega_K \tag{12}$$

$$T_{ck} \geq 0 \tag{13}$$

$$C_{ik} \geq 0 \tag{14}$$

$$O_{ik} \geq 0 \tag{15}$$

$$X_{ijk} \in \{0,1\} \tag{16}$$

Formula (3) is the optimized objective function, including reducing the number of UAVs and their total power consumption. α represents the weight coefficient for the number of UAVs; β denotes the weight coefficient for power consumption. When $\alpha=1$ and $\beta=0$, the only optimization objective is to reduce the number of UAVs; when $\alpha=0$ and $\beta=1$, the only optimization objective is to reduce the power consumption of UAVs. Another weight method is adopted, a very great positive integer M is taken, and when α is close to 1, β is the reciprocal of M . To ensure that value range of the part after the plus sign on the right side of Formula (3) is 0-1, $M > 2E$ should be satisfied; As the change in the number of UAVs before the plus sign on the right side of Formula (3) is an integer variable, Formula (3) indicates that the main optimization objective is to reduce the number of UAVs while the secondary objective is to reduce the power consumption of UAVs. Formula (4) means that for any customer point, the corresponding backward node can only be a point, i.e., ensuring that each customer point will be served only once. Formula (5) indicates that for any customer point, the corresponding forward node can only be a point, i.e., ensuring that each customer point will be served only once. Formula (6) ensures that each UAV starts from the warehouse point and finally returns to this point. Formula (7) manifests that the load capacity of UAVs during one flight should not exceed the maximum load capacity of UAVs. Formula (8) means that if UAV k works at customer point i , it must be UAV k that leaves after completing the work, i.e., ensuring that each customer point can only be served by one UAV simultaneously. Formula (9) indicates the flight time change when a UAV flies from customer point i to customer point j . Formula (10) denotes the change of the residual load capacity when UAV k flies from customer point i to customer point j . Formula (11) constrains that when UAV k flies from customer point i to customer point j , the residual battery capacity when leaving customer point i should be greater than the residual battery capacity when leaving customer point j . Formula (12) ensures that the total power consumption for a UAV to complete

one loop should be greater than or equal to the total battery capacity of this UAV. Formula (13) ensures that the residual time of UAVs is a positive value.

Formula (14) ensures that the residual load capacity of UAVs is positive. Formula (15) ensures that the residual battery capacity of UAVs is positive. Formula (15) is a decision variable, when UAV k flies from customer point i to customer point j , $X_{ijk} = 1$, otherwise, it is equal to 0.

How to solve the path optimization problem accurately and efficiently has always been a major problem. In the existing research, heuristic algorithm is generally used to solve similar problems. As a heuristic algorithm, whale optimization algorithm has been widely developed and applied because of its simple mechanism, few parameters and strong optimization ability. By improving the standard PSO algorithm, models can be solved faster and more effectively.

PSO algorithm

The PSO algorithm assumes that every member of the population is a particle with no mass and the same volume, and each particle has a memory and moves at a specific speed. Each particle is extended to form an n -dimensional structure, and all particles are given the fitness value of the function. When the PSO algorithm is started, the particles will be distributed at any position in space, that is, initializing the random solution set. In the subsequent iterative evolution, the particles will not only remember their own "best experience" but also learn from other particles' "best experience", and then constantly adjust the direction and speed of movement to move to the destination with "best experience". The particle moves in the space limited by the optimization condition, and its movement direction is influenced by three factors: the movement speed of the particle, the best position of itself and the best position of the whole population.

The PSO algorithm model is described as follows: Assuming an E -dimensional search space, the particle swarm P consists of m particles, and all particles therein move at a specific speed. The position of the m particles is expressed as $X = \{x_1, x_2, x_3, \dots, x_n\}$, their speed as $V = \{v_1, v_2, v_3, \dots, v_n\}$, and their position in the space as E -dimensional vector X . $X = (x_{i1}, x_{i2}, x_{i3}, \dots, x_{iE}), (i = 1, 2, 3, \dots, n)$. For instance, the L -dimensional position of the i -th particle is X_{iL} . During algorithm operation, the particles will share information with other particles according to their own path memory, the position of each particle is continuously adjusted as per its movement speed, and the speed of the i -th particle is $V = (v_{i1}, v_{i2}, v_{i3}, \dots, v_{iE}), (i = 1, 2, 3, \dots, n)$. Assuming that the best historical position reached by one particle is expressed as $p_i = (p_{i1}, p_{i2}, p_{i3}, \dots, p_{iE}), (i = 1, 2, 3, \dots, n)$, the best position obtained by all particles in the particle swarm is $g_i = (g_{i1}, g_{i2}, g_{i3}, \dots, g_{iE}), (i = 1, 2, 3, \dots, n)$. Each particle is slightly correlated with the objective function and fitness value, and the particle position X is substituted into the objective function to obtain the corresponding function fitness value. By comparing fitness values, their matching degree with the objective function can be judged, and finally particles will continuously adjust their speed and position to find out the optimal solution of the objective function.

During algorithm operation, particles share information with other particles based on their own path memory. The position of each particle is continuously adjusted according to their movement speed, and the speed of the i -th particle is expressed as $V = (v_{i1}, v_{i2}, v_{i3}, \dots, v_{iE}), (i = 1, 2, 3, \dots, n)$. Assuming that the best historical position reached by one particle is denoted as $p_i = (p_{i1}, p_{i2}, p_{i3}, \dots, p_{iE}), (i = 1, 2, 3, \dots, n)$, the best position obtained by all particles in the particle swarm is $g_i = (g_{i1}, g_{i2}, g_{i3}, \dots, g_{iE}), (i = 1, 2, 3, \dots, n)$. Each particle is slightly correlated with the objective function and fitness value, and the particle position X is substituted into the objective function to obtain the corresponding function fitness value. By comparing fitness values, their matching degree with the objective function can be judged, and finally particles will continuously adjust their speed and position to find out the optimal solution of the objective function.

Taking seeking for the minimum value in the structure for example, the individual iterative formula is shown in Formula (17):

$$p_i^{\bar{n}+1} = \begin{cases} f(X_i^{-n+1}), & \text{if } f(X_i^{-n+1}) < p_i^{-n} \\ p_i^{-n}, & \text{else} \end{cases} \quad (17)$$

Particles operate with the algorithm, and their speed and position changes are expressed by Formulas (18) and (19):

$$v_{ie}^{K+1} = v_{ie}^K + c_1 r_1 (p_{ie}^K - x_{ie}^K) + c_2 r_2 (p_{ge}^K - x_{ie}^K) \quad (18)$$

$$x_{ie}^{K+1} = x_{ie}^K + v_{ie}^{K+1} \quad (19)$$

In the above formula, $i = 1, 2, 3 \dots, K; e = 1, 2, 3, \dots, K; c_1$ and c_2 generally fluctuate within 0-4, usually taken as 2; r_1 and r_2 are random numbers within $[0, 1]$. x_{ie}^k indicates the present e-dimensional position of particle i in the K -th iteration.

Improved PSO algorithm

Given the abovementioned advantages and disadvantages of PSO algorithm and in order to overcome the proneness of PSO algorithm to local optimum and realize the stronger optimization ability and the higher convergence rate, algorithm parameters were first improved, and learning factors c_1 and c_2 and inertia weight ω were subjected to algorithm optimization. The learning factors c_1 and c_2 were improved as follows: Self-learning factor c_1 and social learning factor c_2 tended to change synchronously in the running process of the improved PSO algorithm, and the two continuously changed within $[c_{min}, c_{max}]$ with time during the whole optimization process. This optimization measure improved the learning ability of particles before algorithm operation, and particles were searched globally; after algorithm improvement, the social learning ability of particles was relatively weak but their self-learning ability was strong, which could accelerate convergence to obtain the optimal solution faster. The value of the learning factor upon the t -th iteration is solved as per Formula (20):

$$c_1 = c_2 = c_{max} - \frac{c_{max} - c_{min}}{t_{max}} \times t \tag{20}$$

The inertia weight ω was improved as below: The linear decrease in ω could easily lead to the local optimum of the PSO algorithm. To avoid this circumstance, in the improved PSO algorithm, ω was set to a variable number randomly distributed with movement during operation. First, at the initial evolution stage with the gradual closeness to the optimal point, relatively efficient values might be randomly generated to accelerate the algorithm convergence rate; then, if the algorithm failed to search the optimal value in the initial stage, values would be randomly generated according to the specific circumstance to overcome the local optimum induced by linear decrease. The calculation formula for ω is as shown in Formula (21).

$$\begin{cases} \omega = \mu + \sigma * N(0,1) \\ \mu = \mu_{min} + (\mu_{max} - \mu_{min}) * rand(0,1) \end{cases} \tag{21}$$

Where $N(0,1)$ represents the variable number following a quasi-normal distribution; $rand(0,1)$ denotes a variable number within 0-1. In addition to the improvement of learning factors c_1 and c_2 and inertia weight ω , the model results could reach the optimum if relevant parameters were adjusted according to the established model in this study.

RESULTS

Hardware environment and parameter settings

To verify the effectiveness of the model and algorithm under different scales, the central city area of XX City was taken as the study area. Taking the location distribution as the standard, several nodes whose distribution relatively conform to the problem description were screened out, including 1 logistics & freight transportation center as the central warehouse (position coordinate: 50,50, unit: km) and 50 intelligent express delivery cabinets as the UAV express delivery cabinets plus the quantity demanded, as shown in Table 1.

Table 1

Position coordinates of UAV express delivery cabinets and quantity demanded

No.	X (km)	Y (km)	Quantity demanded (kg)	No.	X (km)	Y (km)	Quantity demanded (kg)
1	37	30	1	26	46	46	2
2	57	79	3	27	78	72	2
3	78	21	1	28	37	11	1
4	18	62	1	29	98	23	1
5	67	50	1	30	83	37	1
6	55	76	2	31	10	49	2
7	32	58	2	32	28	100	3
8	54	76	2	33	58	30	1

No.	X (km)	Y (km)	Quantity demanded (kg)	No.	X (km)	Y (km)	Quantity demanded (kg)
9	10	53	1	34	66	18	4
10	33	61	1	35	4	78	4
11	78	45	1	36	4	68	2
12	59	12	2	37	37	42	2
13	16	11	3	38	64	74	1
14	76	55	1	39	79	30	1
15	80	2	4	40	79	68	1
16	13	43	4	41	28	8	2
17	37	54	2	42	38	30	3
18	55	18	2	43	44	100	1
19	32	29	1	44	25	1	4
20	68	40	1	45	78	26	4
21	75	94	2	46	33	74	2
22	60	89	2	47	27	79	2
23	65	33	1	48	76	79	1
24	58	7	1	49	35	61	1
25	77	69	1	50	67	95	1

The battery capacity of UAVs was, $6.48 \times 10^6 C$, the power consumption within unit time was $70.4 C/s$, the maximum load capacity was 15 kg, the no-load duration of flight was 120 min, the full-load duration of flight was 30 min, the flight speed was 20 m/s, the hovering time was 30 s, and the proportionality coefficient was $U=1.5$. This example was solved using the improved PSO algorithm. The population size of the algorithm was designed as 100, the number of VND iterations as 100, and the cycle index as 100. The duration of flight was taken as the mean value (120 min) of full-load duration and no-load duration, i.e., $\alpha = 1, M = 50000, \beta = 1/M$.

Simulation results

Based on the above designed model, the example was solved using the improved PSO algorithm. The results show that a total of 6 UAVs are needed to serve all customer points as required, the algorithm convergence curve is displayed in Fig 1, and the customer points served by each UAV are exhibited in Fig 2.

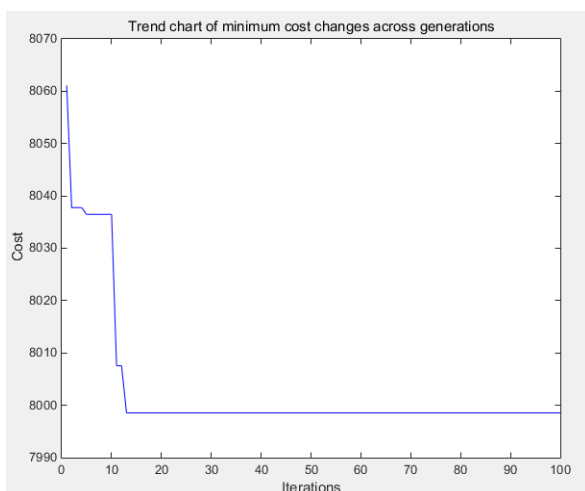


Fig. 1 – Convergence curve of improved PSO algorithm

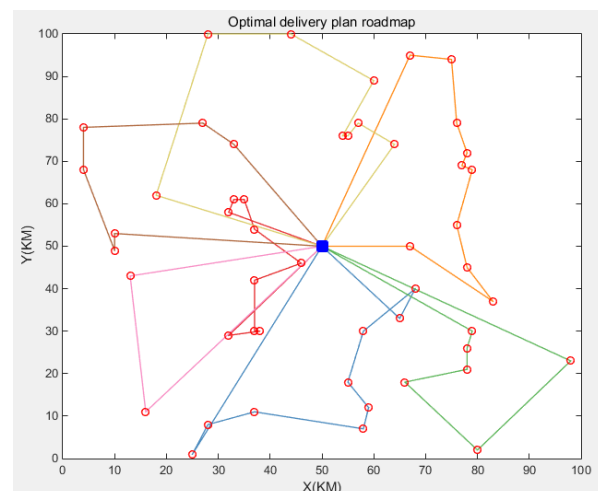


Fig. 2 – Optimal distribution path of improved PSO algorithm

The calculation example was solved using the improved PSO algorithm, and the UAV path results obtained by the improved PSO algorithm are displayed in Table 2.

In Table 4. No.1 represents UAV distribution station, and No.2-51 denote 50 demand points; a total of 7 UAVs return to the distribution station after completing the distribution task. The total flight distance is 998.56 km and the algorithm convergence time is 854.72 s.

Table 2

UAV path of improved PSO algorithm	
S/N	UAV path
UAV1	0→7→10→49→17→26→37→1→42→19→0
UAV2	0→44→41→28→24→12→18→33→20→23→0
UAV3	0→39→45→3→34→15→29→0
UAV4	0→50→21→48→27→25→40→14→11→30→5→0
UAV5	0→38→2→6→8→22→43→32→4→0
UAV6	0→9→31→36→35→47→46→0
UAV7	0→16→13→0

Algorithm verification

To further verify the effectiveness of the algorithm, the basic PSO algorithm was adopted to test an example under the same simulation conditions. The difference between the basic PSO algorithm and the improved PSO algorithm is that the former lacks the optimization of learning factors and inertia weights. The experimental results obtained by the basic PSO algorithm based on repeated tests are shown in Table 3, the convergence curve of the algorithm is shown in Fig 3, and the path of the UAVs is shown in Fig 4. A total of 8 UAVs return to the distribution station after completing the distribution task. The total flight distance is 1074.12 km, and the convergence time of the algorithm is 992.56 s.

According to the experimental results in Table 2 and Table 3, the improved PSO is superior to the basic PSO algorithm in solving the bilevel task planning problem for multi-agricultural UAV logistics distribution. Besides, the improved PSO performs better than the basic PSO in terms of the total flight distance, the number of UAVs enabled and the convergence time of the algorithm. This shows that the optimization of learning factors and inertia weights by improved PSO ensures the diversity of particle swarm, enhances the local search ability of the algorithm, and improves the accuracy and quality of the solution. This manifests that PSO can better arrange the customer distribution order, meet the time window of customers to the greatest extent, and improve their consumption experience. Therefore, for the bilevel task planning problem of multi- UAV logistics distribution, the improved PSO algorithm has more advantages than the basic PSO algorithm, because particles have the characteristics of dynamically tracking extreme values and storing historical memories, and it is easier to detect changes in the external environment, so as to jump out of the previous environment to adapt to the new environmental conditions, making it easier to search for the global optimal solution to the problem.

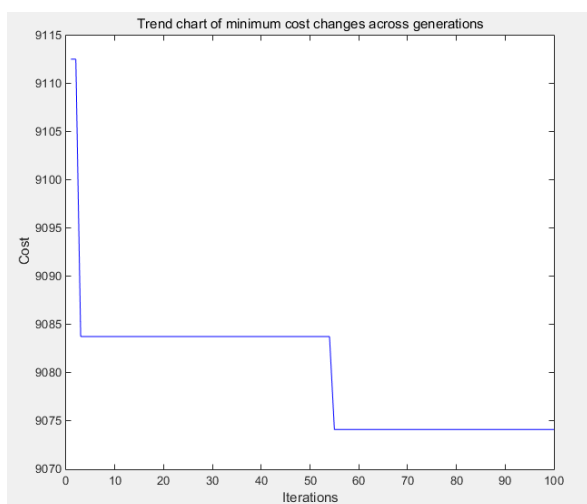


Fig. 3 – Convergence curve of basic PSO algorithm

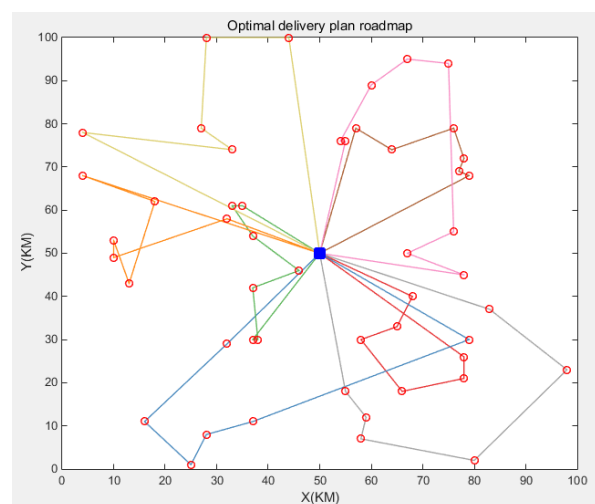


Fig. 4 – Optimal distribution path of basic PSO algorithm

Table 3

UAV path of basic PSO algorithm

S/N	UAV path
UAV1	0→20→23→33→34→3→45→0
UAV2	0→39→28→41→44→13→19→0
UAV3	0→1→42→37→26→17→10→49→0
UAV4	0→7→31→9→16→4→36→0
UAV5	0→35→46→47→32→43→0
UAV6	0→40→25→27→48→38→2→0
UAV7	0→6→8→22→50→21→14→5→11→0
UAV8	0→30→29→15→24→12→18→0

CONCLUSIONS

The bilevel task planning for multi-UAV logistics distribution is one of the hot topics in the academic circles in China and abroad at this stage. Multi-UAV task allocation and path planning do not exist independently, so their coupling relationship must be considered to carry out integrated research. Considering the factors of energy consumption and time window, UAV path problem modeling and solving algorithm were investigated in this study, which can not only provide decision-making reference for the R & D, application and promotion of logistics UAVs in relevant enterprises but also enrich and extend the theoretical research on vehicle paths in the academic circles. Specifically, the model was solved by designing the improved PSO algorithm, which could gain an effective task allocation and path planning scheme and provide theoretical guidance for practicing the bilevel task planning problem of multi-UAV logistics distribution. The established bilevel task planning model for multi-UAV logistics distribution and the adopted example can be referenced by other research work. In the follow-up research, accurate algorithms with better solving efficiency or heuristic algorithms with better solving effects can be searched for, and the modeling and solving algorithm for the extended problem of bilevel task planning for multi-UAV logistics distribution can also be explored. In addition, this article focuses on the flight path at the planning level and does not address the issue of flight conflicts at the operational level. In the future, the focus will be on solving this problem.

REFERENCES

- [1] Agha, K., & Vojdani, A. (2023). Adaptive Path Planning for UAVs in GPS-Denied Environments. *Aerospace Science and Technology*, Vol. 118, pp. 107892, France.
- [2] Chen, W., & Wu, X. (2021). Autonomous UAV path planning in dynamic environments using an algorithm and fast marching method. *Robotics and Autonomous Systems*, Vol. 139, pp. 103747, Netherlands.
- [3] Fan, H.M., Gan, L., Zhang, Y.G., & Bai, X. (2024). Optimization of collaborative distribution path between time-dependent vehicles and UAVs with no-fly zone (有禁飞区的时间依赖型车辆与无人机协同配送路径优化). *Control Theory & Application*, Vol. 41, pp. 321-330, Guangdong/China.
- [4] Han, P., & Zhao, Y. F. (2021). An air route planning model of unmanned aerial vehicles under constraints of ground safety. *Transactions of Nanjing University of Aeronautics and Astronautics*, Vol. 38, pp. 298-305, Nanjing/China.
- [5] Hao, L., Tang, J., Wang, Q., Tao, H., Ma, X., Ma, D., & Ji, H. (2017). Fractal characteristics of tight sandstone reservoirs: A case from the Upper Triassic Yanchang Formation, Ordos Basin, China. *Journal of Petroleum Science and Engineering*, Vol. 158, pp. 243-252, Beijing/China.
- [6] Hwang, Y. H., & Agha, K. (2015). Path Planning and Navigation for Autonomous UAVs in Unknown Environments. *Journal of Intelligent & Robotic Systems*, Vol. 78, pp. 227-239, Netherlands.
- [7] Hu, Y., Guo, Y., Shangguan, J., Zhang, J., & Song, Y. (2020). Fractal characteristics and model applicability for pores in tight gas sandstone reservoirs: A case study of the Upper Paleozoic in Ordos Basin. *Energy & Fuels*, Vol. 34, pp. 16059-16072, United States.
- [8] Li, N., & Xin, C. Y. (2024). "Vehicle + UAV" urban logistics distribution path optimization based on clustering-Floyd-genetic algorithm (基于聚类-Floyd-遗传算法的“车辆+无人机”城市物流配送路径优化). *Science Technology and Engineering*, Vol. 24, pp. 141-150, Beijing/China.

- [9] Li, X., Liu, L., & Ding, Z. (2015). A Hybrid Particle Swarm Optimization for Multi-UAV Path Planning. *Computers. Environment and Urban Systems*, Vol. 53, pp. 62-75, United Kingdom.
- [10] Liu, S., & Zhang, L. (2023). Dynamic and Adaptive Path Optimization for Autonomous Drone Delivery Systems. *IEEE Transactions on Systems, Man, and Cybernetics: Systems*, Vol. 53, pp. 3592-3605, United States.
- [11] Liu, X. X., Xu, Z. F., Li X. L., & Xu, J. H. (2024). Research on the Path of Vehicle+UAV Delivery Model Based on a Two-stage Approach (基于两阶段法的车+无人机配送模式路径研究). *Journal of Taiyuan University of Science and Technology*, Vol. 45, pp. 409-414+420, Shanxi/China.
- [12] Liu, Z., & He, Z. (2022). Energy-Efficient Path Planning for UAV-Based Delivery Systems. *International Journal of Environmental Research and Public Health*, Vol. 16, pp. 7907, Switzerland.
- [13] Ma, J., & Hu, S. (2021). Multi-UAV Path Planning in Urban Environments for Package Delivery: A Review. *International Journal of Robotics and Automation*, Vol. 36, pp. 14-25, United States.
- [14] Shao, S., Peng, Y., He, C., & Du, Y. (2020). Efficient path planning for UAV formation via comprehensively improved particle swarm optimization. *ISA transactions*, Vol. 97, pp. 415-430, United States.
- [15] Song, B. D., Park, K., & Kim, J. (2018). Persistent UAV Delivery Logistics: MILP Formulation and Efficient Heuristic. *Computers & Industrial Engineering*, Vol. 120, pp. 418-428, United States.
- [16] Tassone, D., & Amato, N. (2016). A Review on UAV Path Planning Algorithms and Applications. *In Proceedings of the 2016 IEEE International Conference on Robotics and Automation (ICRA)*, pp. 3999-4004, United States.
- [17] Wei, M., Wu, L., & Sun, B. (2024). An optimization model of emergency distribution path for UAVs with multiple material types (一类多物资类型无人机应急配送路径优化模型). *Mathematics in Practice and Theory*, Vol. 54, pp. 215-218, Beijing/China.
- [18] Wu, X., Yin, Y., Xu, L., Wu, X., Meng, F., & Zhen, R. (2021). Multi-UAV task allocation based on improved genetic algorithm. *IEEE Access*, Vol. 9, pp. 100369-100379, United States.
- [19] Xu, L., Yang, L. C., Zhu, W. X., & Zhong, S. J. (2024). Research on optimization of collaborative distribution path between UAVs and vehicles under rural E-commerce logistics (农村电商物流下无人机与车辆协同配送路径优化研究). *Computer Engineering and Applications*, Vol. 60, pp. 310-318, Beijing/China.
- [20] Yang, J., & Wang, Y. (2020). Task Scheduling and Path Planning for Autonomous UAVs in Large-Scale Networks. *International Journal of Robotics and Automation*, Vol. 35, pp. 104-113, United States.
- [21] Yuan, J., & Zhang, D. (2020). A Review on Path Planning for UAVs: Key Issues and Solutions. *Aerospace Science and Technology*, 99, 105721. China
- [22] Zhang, X., & Zhang, X. (2018). Drone Delivery System: Optimal Path Planning with Multiple Depots and Uncertain Demand. *Computers and Industrial Engineering*, Vol. 116, pp. 383-398, United Kingdom.
- [23] Zhang, Y., & Li, W. (2022). Deep Reinforcement Learning for UAV Path Planning in Complex Environments. *IEEE Transactions on Systems, Man, and Cybernetics: Systems*, Vol. 52, pp. 5730-5741, United States.
- [24] Zhang, Y., & Wei, D. C. (2023). Automatic optimization method of UAV logistics distribution path based on improved genetic algorithm (基于改进遗传算法的无人机物流配送路径自动优化方法). *Modern Computers*, Vol. 29, pp. 72-74, Shandong/China.
- [25] Zhao, J., Liu, W., & Wang, H. (2019). Optimization of Drone Delivery Path Using Genetic Algorithm and Ant Colony Optimization. *Journal of Intelligent & Robotic Systems*, Vol. 95, pp. 479-491.
- [26] Zhou, H., & Shi, P. (2018). Path Planning for UAVs in Urban Environments with Mission Constraints. *Journal of Intelligent & Robotic Systems*, Vol. 92, pp. 297-310, Netherlands.

A LIGHTWEIGHT IMPROVED YOLOv5s MODEL-BASED RICE BLAST DETECTION METHOD AND MOBILE DEPLOYMENT

基于轻量化改进 YOLOv5s 模型的稻瘟病检测方法及移动部署

Fankai MENG¹⁾, Congkuan YAN¹⁾, Yuqing YANG¹⁾, Ruixing XING¹⁾, Dequan ZHU¹⁾,
Aifang ZHANG²⁾, Qixing TANG^{1,3)}, Juan LIAO^{1,3)}

¹⁾ College of Engineering, Anhui Agricultural University, Hefei 230036 / China;

²⁾ Institute of Plant Protection and Agricultural Product Quality and Safety, Anhui Academy of Agricultural Sciences, Hefei 230031/ China;

³⁾ East Anhui Comprehensive Experimental Station, Anhui Agricultural University, Mingguang, 239400 / China

E-mail: liaojuan@ahau.edu.cn

DOI: <https://doi.org/10.35633/inmateh-74-68>

Keywords: Rice blast detection; YOLOv5s; Lightweight; GhostConv; BiFPN; SE; Android Studio

ABSTRACT

For achieving more efficient recognition results and deployment on mobile devices, a rice blast recognition model was constructed by making lightweight improvements to YOLOv5s. First, using YOLOv5s as the base, GhostConv was introduced to replace standard convolution in its backbone and neck, and LightC3 module was built to improve the C3 module in the neck. This significantly reduced the computational burden and model size. Furthermore, Concat operator was replaced with BiFPN and SE attention mechanism was integrated to maintain accuracy when reducing model complexity. These modifications enhanced the model's ability to capture fine-grained features and multi-scale information. The experimental results showed that the designed model had a 49% decrease in the number of model parameters and a 50% decrease in FLOPs without a decrease in precision on self-built rice blast dataset, compared with the YOLOv5s, achieving the good balance between detection performance and model lightweight. Then, an APP named RiceBlastDetector was built based on the model, achieving accurate detection in the scenario with the different characterization scale disease spots from experiments in the field, which can provide a reference for detecting other crop diseases.

摘要

为了在移动设备上实现更高效的识别结果与部署,我们通过对 YOLOv5s 进行轻量化改进构建了一个稻瘟病识别模型。首先,以 YOLOv5s 为基础,引入 GhostConv 替换其骨干和颈部的标准卷积,并构建 LightC3 模块,这显著减轻了计算负担和模型大小。接着,用 BiFPN 替换 Concat 算子,并集成 SE 注意力机制,从而在保持精度的同时降低复杂度,这些改进增强了模型捕捉细粒度特征和处理多尺度信息的能力。通过自建数据集验证,该模型在不损失精度的情况下,参数减少了 49%,浮点运算次数降低了 50%,这证明了我们在实现模型轻量化的同时保持高检测性能这一方法的有效性。我们还构建应用程序,用于田间的精准检测,为其他农作物病害的检测提供了参考,而且该应用程序有提升农业生产力和促进可持续农业实践的潜力。

INTRODUCTION

In terms of food production, rice ranks as one of the key crops in China, playing a crucial role in ensuring food security for the population. However, rice production is often hindered by diseases such as brown spot, rice stalk, and rice blast, which often occur and can cause considerable yield losses (Malvade et al., 2022). Among them, rice blast disease affects rice globally because of its rapid occurrence and easy infection. Rice blast varies significantly throughout the rice plant's development stages and can be divided into seedling blast, leaf blast and ear blast according to the time and location of rice infection, among which leaf blast and ear blast are the most harmful, which can reduce rice yield by 10%~30%, or even more than 50% (Asibi et al., 2019; Yang et al., 2020). Hence, it is necessary to identify and control rice blast in the early stage, which is very important to ensure a stable and efficient rice production.

The conventional process of disease recognition in agriculture relies heavily on the expertise of agronomists or plant pathologists who visually examine and manually identify lesions based on their shape, color, and other characteristics. However, this conventional method is often inefficient and subjective. As computer vision technology advances, numerous studies have concentrated on automating the detection of rice diseases using pattern recognition and machine learning techniques (Daniya et al., 2019; Sanghavi et al., 2021; Manavalan et al., 2020), where the essential challenge is to first extract characteristic feature information

of rice diseases from the images by using image processing and then using the classifier to judge whether the crop is infected or not according to a single image feature such as color, shape and texture or a combination of multiple features. The effectiveness of these machine learning-based methods is affected by challenges such as location of rice disease infection, variations between different diseases, manual feature extraction, and various factors present in the natural environment, leading to potentially insufficient accuracy. Therefore, there is a need for research focused on developing effective feature extraction and detection algorithms for rice blast disease.

Recently, deep learning technology has shown great prospects for application in agricultural target detection due to its ability to extract effective features, which have been extensively utilized for detecting diseases in plant leaves (*Bedi et al., 2021*), citrus fruit and leaves (*Khattak et al., 2021*), teas (*Sun et al., 2023*), maize (*Khan et al., 2023*), and other crops (*Nandhini et al., 2022*). To detect rice disease, *Zhou et al. (2019)* presented an algorithm that integrates the improved k-means clustering with Faster R-CNN, achieving a detection accuracy of 97.53%. *Rahman et al. (2020)* developed a small two-stage rice disease detection model based on CNN with 93.30% recognition accuracy. *Dogra et al. (2023)* designed a brown spot disease detection model based on CNN-VGG19 and transfer learning and achieving a detection accuracy of 93% on the developed rice leaf disease dataset. *Jia et al. (2023)* presented a rice disease detection model, where MobileNetV3 was used to design YOLOv7's backbone and the CA attention module was introduced in feature fusion to improve the model to integrate more key feature information, achieving an average precision of 98%.

The aforementioned studies have strongly demonstrated the feasibility of applying deep learning to recognize crop diseases (*Yan et al., 2022*). However, deep learning-based models often require significant computational resources such as high-performance workstations or servers equipped with powerful GPUs during both training and inference phases. Furthermore, most of existing deep learning-based methods prioritize higher accuracy while leading to more complex neural network models with a large number of parameters and longer prediction times. This complexity makes them difficult to deploy on embedded devices or mobile platforms, hindering their practical applications in agriculture. In this regard, some scholars have also started to focus on the lightweight CNN models for target identification. *Cheng et al. (2022)* present a lightweight method for crop pest recognition utilizing YOLOv3Lite, which integrated the lightweight sandglass module and the CA attention module into its residual structure. The method achieved a computational cost of 9.8 GFLOPs, which is only 8.1% of that of YOLOv3. *Li et al. (2024)* introduced a lightweight YOLOv8s algorithm that integrated the lightweight GhostNet to build the YOLOv8s' backbone. The approach reduced the size of model by 50.2% and FLOPs by 43.1% compared to the original YOLOv8s. In the field environment, the most portable method is to deploy neural networks in smartphones with limited computing power and use them for object detection such as crop disease detection and fruit detection (*Yu et al., 2024*). Although these approaches lay a foundation for lightweight studies in crop disease detection models, it is important to note that they are mainly designed for use on desktop computers. This focus makes it challenging to develop applications suitable for low-computation platforms. Additionally, the above studies on the model structure of general lightweight crop diseases most are based on the crops with little difference in crop disease symptoms, but similar or different symptoms of rice blast disease can develop at different stages, or on different plant parts, resulting in low accuracy of the above methods directly applied to rice blast recognition.

Aiming to better address the practical challenges of agricultural production, this study designs an improved YOLOv5 algorithm by effectively integrating various lightweight modules for rice blast detection, and develops a local Android-based application for identifying and detecting rice blast, enabling deployment on mobile devices. The algorithm replaces the standard convolution in the YOLOv5s' backbone and neck with the GhostConv module. And it substitutes the C3 modules of the YOLOv5s' backbone with GhostC3 and in the neck with LightC3 modules, thereby reducing the computational load. Furthermore, to enhance model perception of disease-related features, the lightweight channel attention mechanism squeeze-and-excitation (SE) is placed before the SPFF module and incorporated into the Bottleneck module of the YOLOv5s' neck, respectively. Additionally, the BiFPN network is introduced in the YOLOv5s' neck network to integrate more multi-scale features, and the convergence speed during model training is improved using EIoU loss. Finally, the optimized and lightweight model is implemented on mobile devices for practical monitoring of rice blast disease.

MATERIALS AND METHODS

In this study, rice blast images are captured from the experimental bases of the Rice Research Institute and the Institute of Plant Protection and Agricultural Product Quality and Safety, Anhui Academy of Agricultural

Sciences, Hefei, China. The Plant Protection Institute primarily focuses on researching the mechanisms and technologies for managing diseases and insect pests that affect crops such as rice, wheat, rapeseed, and vegetables in Anhui Province, and the Rice Research Institute is mainly engaged in basic and applied research on rice genetics and breeding, biotechnology, and development of new cultivation technologies. The images were captured from June to September 2023 using a Canon EOS 100D camera and a Huawei mobile phone. The collected image resolutions have 5184×3456 pixels and 4032×3024 pixels, respectively. To ensure the quality of the image labels, the acquired images showing rice blast disease were reviewed and validated by experts in plant protection, and then a total of 2620 images were obtained, including 1200 of ear blast and 1420 of leaf blast.

Taking into account that the high resolution of images can complicate model training and cause potential GPU memory overloads and failures, the original images were cropped to the lower resolution of images at a size of 640×640 pixels to build the dataset for this study. To label the rice blast lesions in the images, the Labelling software was utilized to manually annotate each infected area, thereby producing the ground truth (GT) labels necessary for the model. The dataset comprises both GT and RGB images, with the specific counts for ear blast and leaf blast illustrated in Table 1. Fig. 1 gives samples of the RGB images and the corresponding GT images. To train the model and evaluate its performance, the built rice blast dataset consisted of training, validation, and test sets according to the ratio of 7:2:1.

Table 1

Rice blast disease dataset composition				
	Train	Validation	Test	Total
Ear blast	840	240	120	1200
Leaf blast	994	284	142	1420



Fig. 1 - RGB and ground truth (GT) images

Lightweight rice blast detection model

YOLOv5 is a widely used one-stage object detection model (Wang *et al.*, 2022). Based on the model's width and depth, YOLOv5 comes in four variations: x, l, m, and s. Among these, YOLOv5s has the least depth and width in terms of network features, while the other three versions have enhancements that increase both depth and width based on this model (Lin *et al.*, 2022). In this study, YOLOv5s was used as the framework for the rice blast detection model, which was composed of three networks: backbone for disease characteristics acquisition, neck for characteristics fusion and a target category prediction network (Yonghui *et al.*, 2024). In order to decrease computational and memory costs and lightweight model which can be more easily deployed on mobile phone, the YOLOv5s model has been refined through various improvements in this study, specifically:

1) using GhostConv instead of the standard convolution of YOLOv5s' backbone and neck to reduce the number of model's parameters;

2) utilizing GhostC3 module instead of C3 modules of backbone network and adding the SE attention module before SPPF module to lower computational costs and enhance the model's capability to extract features;

3) building a LightC3 module to serve as a replacement for the C3 modules of YOLOv5s' neck and introducing the BiFPN module to reduce computational burden and enhance the fusion of multi-scale features. Based on the above improvements, the architecture of the lightweight model is shown in Fig. 2.

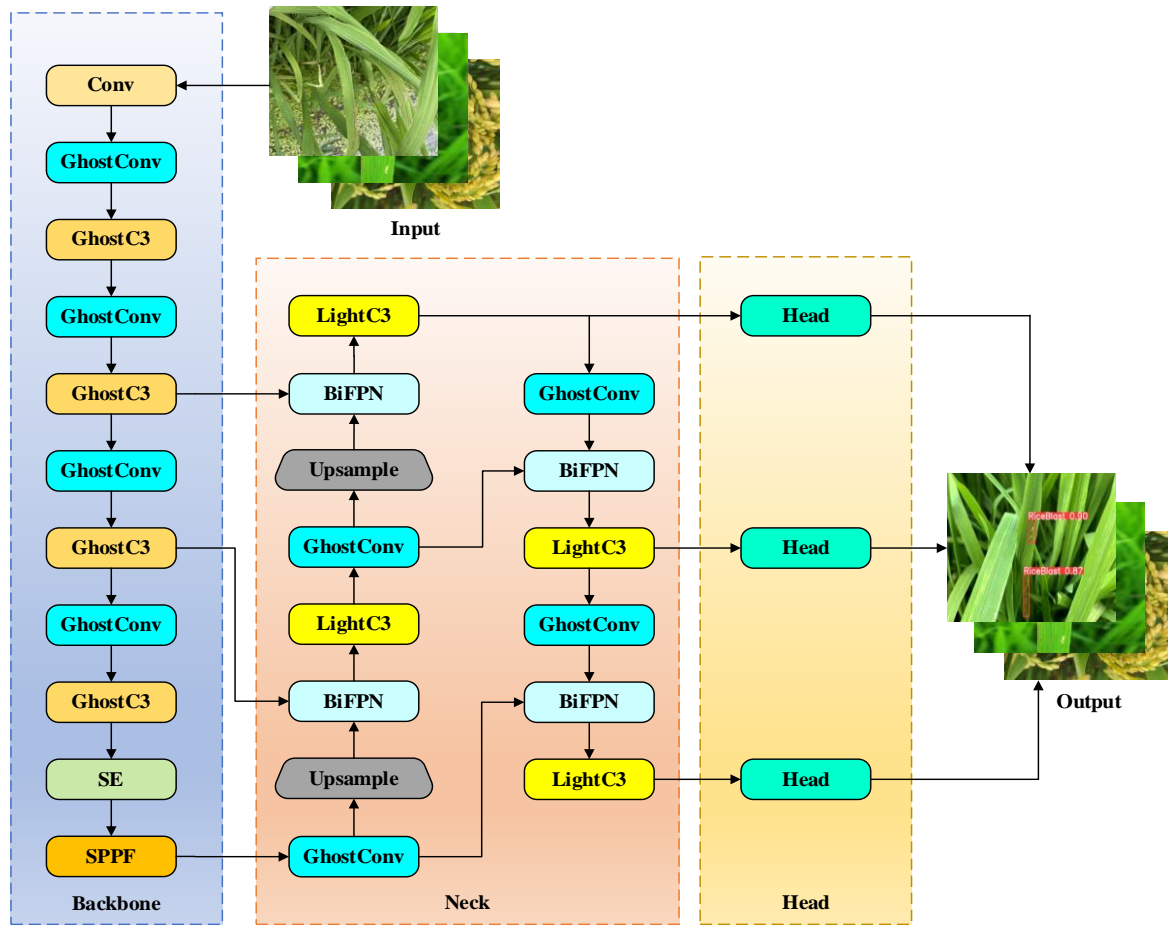


Fig. 2 - The structure of improved YOLOv5s model

Lightweight backbone network

The backbone network of YOLOv5s, with its combination of several Convs, C3, and SPP modules, is well-suited for extracting features from rice disease images, but it also presents challenges related to the number of parameters and information redundancy. To optimize the model for more efficient detection of rice diseases, the lightweight convolution GhostConv (Han et al., 2022) is introduced in the backbone network instead of Convs, as shown in Fig. 3. In the GhostConv, a 1x1 standard convolution is utilized to decrease the channel count of input feature maps. Lightweight linear transform operations are then used to generate additional feature maps, which are then added to the previously limited number of feature maps to output a feature map with the required number of channels.

Let $X \in R^{n \times h \times w}$ be the input of the channel, height and width of n, h and w, respectively, in Fig. 3. The output with m channels is denoted as $Y \in R^{m \times h' \times w'}$. Using Ghost convolution operation, s, additional feature maps are generated, where an identity mapping operation and m(s-1) linear operations are performed. Hence, the theoretical acceleration factor of ghost convolution in relation to standard convolution with the kernel size $n \times d \times d \times m$ is:

$$\begin{aligned}
 r &= \frac{h \times w \times n \times k \times k \times m}{\frac{m}{s} \times h \times w \times n \times d \times d + (s-1) \times \frac{m}{s} \times h' \times w' \times d' \times d'} \\
 &= \frac{s \times n \times k \times k}{n \times d \times d + (s-1) \times d' \times d'} \\
 &\approx \frac{s \times n}{n + (s-1)} \approx s
 \end{aligned}
 \tag{1}$$

where $d \times d$ and $d' \times d'$ represent the convolution kernel size for the identity mapping operation and the linear operation, respectively.

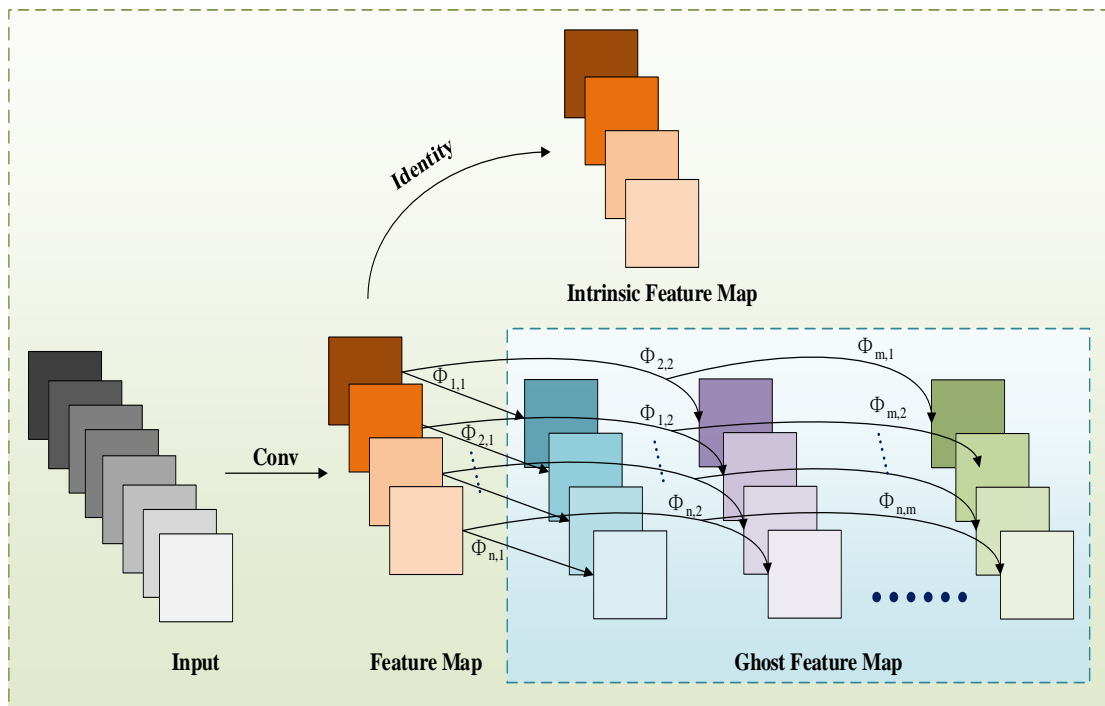


Fig. 3 - The structure of GhostConv module

From Equation (1), it can be seen that GhostConv presents a compelling alternative to standard convolutional layers, achieving significant reductions in both memory usage and FLOPs. Based on this, the improved backbone therefore uses the GhostC3 module (Han et al., 2022) instead of the original C3 module.

As shown in Fig. 4, the GhostConv and GhostBottleneck structures have been used to replace the traditional standard convolution and bottleneck structures, creating a lightweight C3 module in the backbone. The GhostBottleneck module, which refers to the residual structure in ResNet, replaces standard convolution with GhostConv to reduce the computational burden and memory usage (Yang et al., 2022).

The GhostBottleneck module's structure is given in Fig. 4, which is suitable for stride = 1 and stride = 2. In Fig. 4, the GhostBottleneck module contains two GhostConv modules and one shortcut when stride = 1. The first GhostConv module expands the input feature map, while the second GhostConv module has the same number of channels as the input by mapping the output of the first module. Subsequently, the output of the second GhostConv module is added to the input of the first GhostConv module to achieve a shortcut connection. Additionally, batch normalization (BN) is applied after the two GhostConv modules to prevent gradient vanishing and to speed up training and convergence. Besides, a depth-separable convolution (DWConv) (Wen et al., 2023) is inserted between the two GhostConv modules when stride = 2, as shown in Fig. 4. The depth convolution of DWConv is used to down-sample the output from the first GhostConv, while the point-wise convolution of DWConv is utilized to generate the intrinsic features for efficiency.

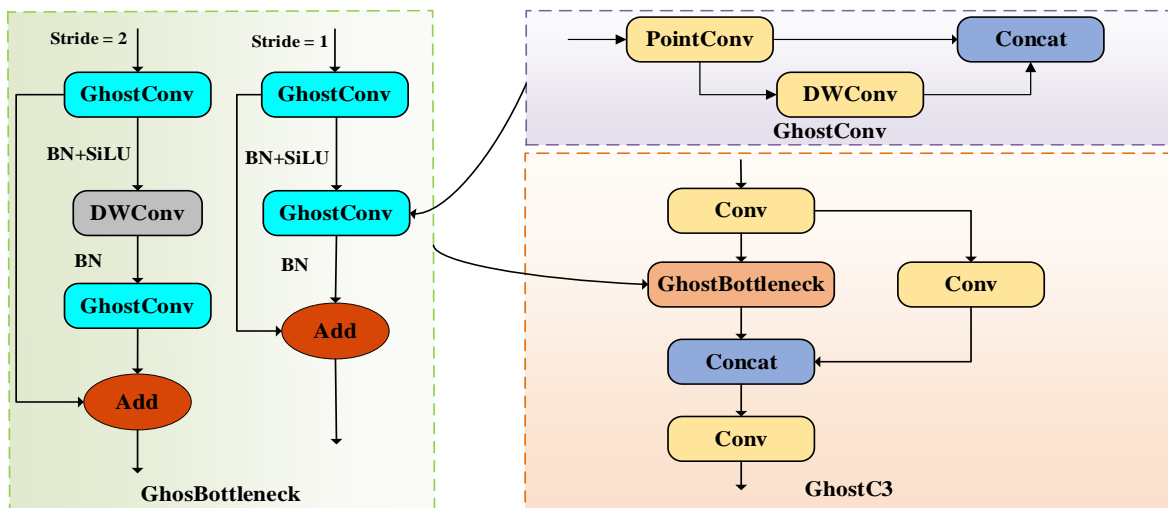


Fig. 4 - The structures of GhostC3 and GhostBottleneck modules

Added attention module

As mentioned above, using GhostConv and GhostBottleneck modules can effectively lightweight the YOLOv5s' backbone. However, in the field natural environment, the background is complex and variable, such as multiple rice plants, changing light conditions, large healthy rice leaves and other complex background information, while the disease characteristics of early leaf blast and ear blast are relatively small. During the model training process, these complex background elements will also be transmitted. As the model deepens, the weight of these background elements in the feature map may grow, potentially overwhelming the target information and negatively impacting the model's performance (Ye et al., 2023). Additionally, in the YOLOv5s backbone network, the convolutional layer primarily extracts feature information from adjacent positions within each feature map. However, it does not consider the correlation among channel information, even though each channel contains distinct feature data. Therefore, the squeeze-and-excitation (SE) attention mechanism (Xin et al., 2020) is positioned before the SPFF module to consider the relationships between channels and dynamically adjust their weights, so as to enhance the model's perception of diseases while suppressing the influence of irrelevant information, thereby enhancing the model's perception of disease feature and improving overall accuracy.

Figure 5 illustrates the structure of SE module, which consists of squeeze, excitation and scale steps. The squeeze operation uses global average pooling to compress each 2D feature channel into a single real number with a global acceptance field. Let $\mathbf{X} = [\mathbf{x}_1, \mathbf{x}_2, \dots, \mathbf{x}_C] \in \mathbf{R}^{C \times H \times W}$ be the input. The output $\mathbf{S} \in \mathbf{R}^C$ from the squeeze operation is given in Equation (2). Following this, an excitation process is performed to assess the relationships of the different channels and output weights that represent the importance of the different channels. The excitation operation consists of a sequence of layers with 1×1 convolution, ReLU and sigmoid activation, which is defined by Equation (3). Following the excitation operation, the scale operation employs multiplication to weight the previously selected features for each channel, effectively rescaling the original features along the channel dimension. The output $\hat{\mathbf{X}} \in \mathbf{R}^{C \times H \times W}$ of the scale operation is expressed in Equation (4). According to Equation (4), the output generated by the SE module is obtained by rescaling the input with the activation of each channel. Therefore, the SE module assigns weight values to each channel of the feature map, enhancing the contribution of important features while reducing the impact of less relevant ones. This process enhances the network's capacity to learn important features related to rice diseases.

$$s_c = F_{se}(\mathbf{x}_c) = \frac{1}{W \times H} \sum_{i=1}^W \sum_{j=1}^H \mathbf{x}_c(i, j) \tag{2}$$

$$\mathbf{z} = \text{Sigmoid}(\mathbf{W}_2 \times \text{ReLU}(\mathbf{W}_1 \mathbf{S})) \tag{3}$$

$$\hat{\mathbf{x}}_c = z_c \times \mathbf{x}_c \tag{4}$$

where s_c is the c -th element of \mathbf{S} , and $\mathbf{x}_c \in \mathbf{R}^{H \times W}$ is a feature map at the c -th channel. $\mathbf{W}_2 \in \mathbf{R}^{r \times C}$ and $\mathbf{W}_1 \in \mathbf{R}^{C \times \frac{C}{r}}$ are weights generated for each feature channel, and r is reduction ratio. $\text{Sigmoid}(\bullet)$ refers to the sigmoid function. $\hat{\mathbf{x}}_c$ is the c -th element of $\hat{\mathbf{X}} = [\hat{\mathbf{x}}_1, \hat{\mathbf{x}}_2, \dots, \hat{\mathbf{x}}_C]$.

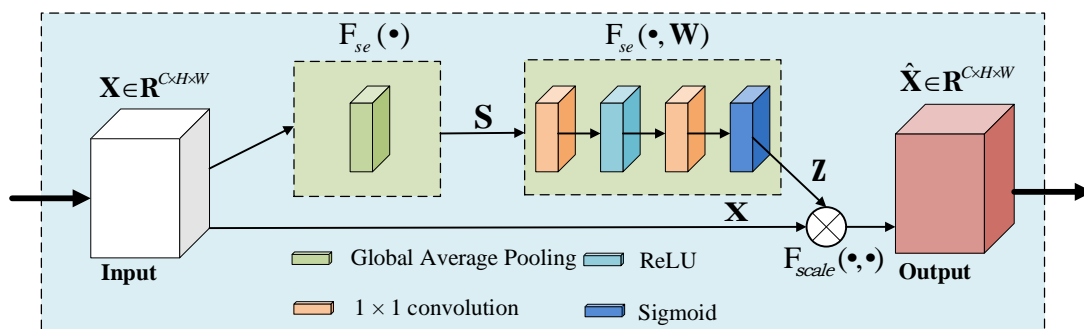


Fig. 5 - The structure of SE module

Enhanced feature fusion

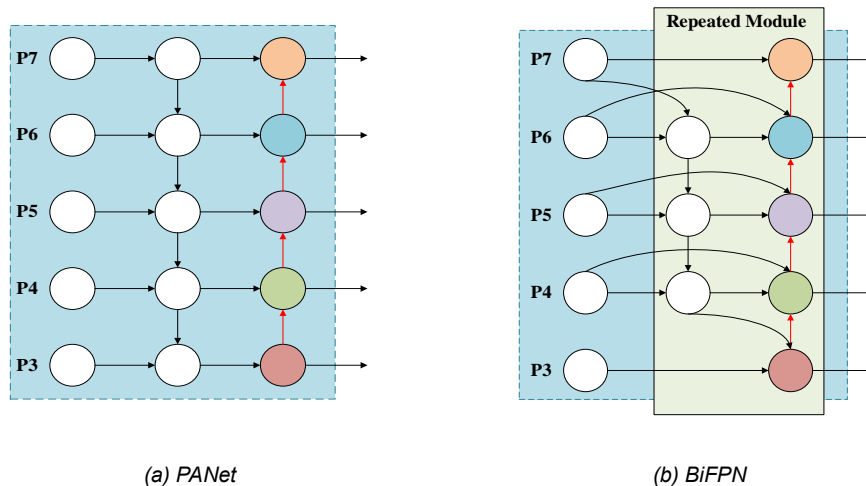


Fig. 6 - Structures of PANet and BiFPN modules

In the original YOLOv5s, the neck network performs convolution, up-sampling, and concatenation operations on features output from the YOLOv5s' backbone before being sent to the detection layer. In this process, the PANet structure in the feature pyramid is utilized to establish connections between different level feature information, as seen in Fig. 6(a). In PANet, the feature fusion process is achieved with a direct summation operation, which can potentially cause some loss of critical feature information originally extracted from the YOLOv5 backbone, particularly important features of small objects in shallow layers. However, early disease spots on rice leaves and panicles often manifest as small targets, and the characterization scale for diseases like leaf blast can vary significantly. Moreover, these small target lesions frequently coexist with larger targets such as healthy leaves. During the training process, the model may prioritize learning from the larger targets, hereby diminishing attention to or neglecting the small target lesions. This can adversely affect the accuracy in distinguishing between similar representations of diseases and small target lesions in images. Therefore, it becomes crucial to improve the ability to fuse features at different scales of the model through weighted designs.

To effectively fuse multi-scale features, a bidirectional feature pyramid network (BiFPN) (Li et al., 2022) is introduced and integrated in the YOLOv5 neck. As illustrated in Fig. 6(b), BiFPN does not utilize a single top-down and bottom-up path like PANet. Instead, BiFPN employs a pair of paths as a feature layer, fusing different level features from top to bottom and bottom to top. It assigns additional weights to each input, enabling the model to gradually learn the importance of each feature during the training process of feature aggregation. In this study, BiFPN is integrated to replace the Concat operation in the neck network according to the fact that different input features possess varying resolutions and contribute differently to feature fusion. This improvement based on BiFPN module can enhance the transmission of feature information crossed different network layers, and allow the model to better understand and learn the importance of features by integrating features from multiple levels both top-down and bottom-up. Hence, it can make all levels of the feature pyramid better balanced to provide a more global and semantic feature representation, which is helpful to accurately detect rice blast disease in complex environments, and improve the detection performance of different scale targets.

Lightweight neck network

Despite the lightweight in the YOLOv5s' backbone due to the aforementioned improvements, the feature fusion process still makes a significant contribution to the total number of parameters, affecting the speed of fusion. To achieve a lightweight neck network, standard convolution is replaced with the efficient GhostConv. Additionally, LightBottleneck module is designed based on the DWConv module, since DWConv extracts local detail features while utilizing fewer parameters compared to traditional convolution, thereby reducing the model's computational burden (Liu et al., 2023). The structure of LightBottleneck is given in Fig. 7. The LightBottleneck replaces the Bottleneck design in the original C3, resulting in the creation of a new module called LightC3. This reduces the parameter count associated with standard convolution, leading to a smaller model size. Furthermore, to reduce the redundant feature information introduced by the LightBottleneck and

to enhance feature discrimination and representation between channels during the fusion of multiple scale features without significantly increasing the computational load, the SE module is incorporated into the LightBottleneck module. As shown in Fig. 7, the SE module calculates the weights for each channel by leveraging global average pooling in conjunction with fully connected layers, allowing for adaptive adjustment of each channel's weight in the feature maps. It enables the network to better leverage multi-scale inputs by emphasizing significant features while diminishing irrelevant ones. Thus, it enhances the network's capacity to percept the key information about the disease characteristics, especially crucial features of small objects. In summary, the LightBottleneck module is designed based on DWConv and SE modules, which can enhance efficiency and accuracy in obtaining information related to disease features, thus lightweight model while maintaining accuracy in detecting rice blast disease.

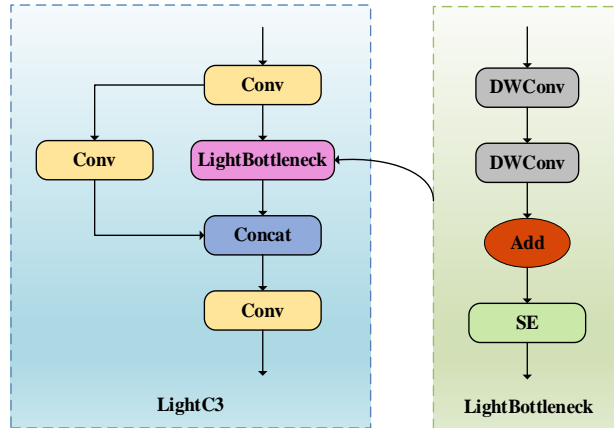


Fig. 7 - The structure of LightC3 module

Loss function

The loss function used in YOLOv5 is $CIoU$, which is expressed as follows:

$$L_{CIoU} = 1 - IoU + \frac{\rho^2(b^p, b^{gt})}{c^2} + \alpha v \tag{5}$$

where IoU is the intersection ratio of a predicted box b^p and a ground-truth box b^{gt} ; c denotes the length of the shortest diagonal of the smallest bounding box that encompasses both b^p and b^{gt} ; $\rho^2(b^p, b^{gt})$ is the Euclidean distance between the center points of b^p and b^{gt} ; α and v are used to calculate the discrepancy of the width-to-height ratio of b^p and b^{gt} , which are calculated as follows:

$$v = \frac{4}{\pi^2} \left(\arctan \frac{w^{gt}}{h^{gt}} - \arctan \frac{w}{h} \right)^2 \tag{6}$$

$$\alpha = \frac{v}{(1 - IoU) + v} \tag{7}$$

where w and h , h^{gt} and w^{gt} are the height and width of b^p , and height and width of b^{gt} , respectively.

From Equation (5), it is important to note that $CIoU$ involves the overlap area, aspect ratio, and the distance between the central points when calculating the loss between b^p and b^{gt} . However, it does not account for the differences in width and height between b^p and b^{gt} , resulting in a slower convergence speed. Thus, the $EIoU$ Loss (Zhang et al., 2022) is used in this study, which is calculated as follows:

$$\begin{aligned} L_{EIoU} &= L_{IoU} + L_{dis} + L_{asp} \\ &= 1 - IoU + \frac{\rho^2(b^p, b^{gt})}{(w^c)^2 + (h^c)^2} + \frac{\rho^2(w, w^{gt})}{(w^c)^2} + \frac{\rho^2(h, h^{gt})}{(h^c)^2} \end{aligned} \tag{8}$$

where w^c and h^c represent the width and height of the smallest box that encompasses b^p and b^{gt} . In Equation (8), the loss function is composed of L_{IoU} , L_{dis} and loss L_{asp} . These components effectively quantify the differences in overlap area, central point position, and the variations in width and height between b^p and b^{gt} , leading to faster convergence and accurate localization.

RESULTS AND ANALYSIS

Experimental setup and evaluation metrics

The experimental setup used a GeForce RTX 4080 16G GPU, an Intel I7-11700K CPU running at 2.5 GHz, and operating on Windows 11. The software involved Python 3.9, CUDA 12.1, and the PyTorch 1.13.0 framework. The initial learning rate was 0.01. The batch size was 64. The training epochs were 300. The stochastic gradient descent (SGD) optimizer was employed, weight decay at 0.0005. The momentum was 0.937. To assess model complexity and detection performance, precision (P), recall (R), the number of parameters, FLOPs, and mean average precision (mAP) were considered, which were calculated as follows:

$$P = \frac{TP}{TP + FP} \quad (9)$$

$$R = \frac{TP}{TP + FN} \quad (10)$$

$$mAP = \frac{1}{N} \sum_{i=1}^N \int_0^1 P dR \quad (11)$$

where TP denote positive samples that were correctly detected, while FP refer to negative samples incorrectly classified as positive, and FN represent positive samples that were not detected. N indicates the total number of categories. Higher mAP values indicate better detection performance.

Ablation experiment results

The YOLOv5s model is the basic framework for this study. The use of GhostConv and LightC3 modules contributed to lightweight model. Additionally, BiFPN was introduced for feature fusion, while SE attention mechanism was added to strengthen the focus on the disease features. To assess the effect of each introduced module on the performance of the rice blast disease detection, ablation experiments were conducted on eight models using the same training parameters. Table 2 displays comparisons of evaluation metrics for various enhancement methods, with “√” marking the inclusion of each improvement strategy in the network. The detection results for each model are show in Fig. 8.

From Table 2 and Fig. 8, it is observed that the integration of the LightC3 module reduced model parameters as well as FLOPs, the recall and mAP by 14.39%, 13.29%, respectively, and achieved rice blast detection results that were on par with YOLOv5s. The addition of GhostConv alone led to a reduction of 33.9% in FLOPs and a 0.6% decrease in mAP and increased the precision of leaf blast and ear blast by 0.9% and 0.2%, respectively. These show that adding the LightC3 or GhostConv module notably decreased model parameters and FLOPs, with only a minor reduction of mAP, indicating that integrating the LightC3 and GhostConv modules into the YOLOv5s model is a practical solution for deployment on resource-constrained mobile devices. Precision, recall and mAP metrics are improved with the introduction of BiFPN only compared to YOLOv5s. As depicted in Fig. 8, compared with YOLOv5s, the YOLOv5-B obtained better detection results for ear blast and leaf blast, indicating that BiFPN can improve detection of targets at different scales. Furthermore, compared with the baseline model, the model that incorporated the BiFPN module along with LightC3 or GhostConv achieved reductions in model parameters by 15.67% and 35.19%, respectively, and increased the precision. With the simultaneous introduction of LightC3, GhostConv and BiFPN modules, model parameters and FLOPs were reduced by 49.93% and 50.63% respectively. However, it causes a decrease in recall and mAP by 2.5% and 1.4%, respectively, since the detection results of YOLOv5-BGL on small-scale targets were worse than those of other models, as shown in Fig. 8. This proposed model incorporates the SE module within the YOLOv5s' backbone with incorporation of the LightC3, GhostConv and BiFPN modules achieved 3.58M parameters and 7.9 G FLOPs, which reduced by 49% and 50% compared with YOLOv5s. In terms of accuracy, the detection performance was comparable to YOLOv5s, with only 0.6% and 1.0% decrease in recall and mAP, respectively. Additionally, the proposed model integrated the SE module in the neck network, which can enhance feature discrimination and representation between channels in the multi-scale feature fusion process without adding too much calculation amount, thus yielding superior performance over YOLOv5-BGL with respect to detecting different scale disease targets. Thus, this demonstrates that the proposed model obtains an optimal balance between disease identification performance and lightweight.

Table 2

Results of ablation experiments

Light C3	Ghost Conv	BIFPN	SE	Model	P (leaf blast)	P (ear blast)	R	mAP	Params (M)	FLOPs (G)
				YOLOv5s	0.977	0.963	0.936	0.976	7.02	15.8
✓				YOLOv5-L	0.977	0.958	0.931	0.967	6.01	13.7
	✓			YOLOv5-G	0.986	0.965	0.938	0.970	4.64	10.0
		✓		YOLOv5-B	0.992	0.985	0.938	0.978	6.90	15.7
✓		✓		YOLOv5-BL	0.982	0.969	0.934	0.967	5.92	13.6
	✓	✓		YOLOv5-BG	0.987	0.972	0.938	0.976	4.55	9.90
✓	✓	✓		YOLOv5-BGL	0.966	0.932	0.911	0.962	3.55	7.80
✓	✓	✓	✓	Ours	0.986	0.963	0.930	0.966	3.58	7.90

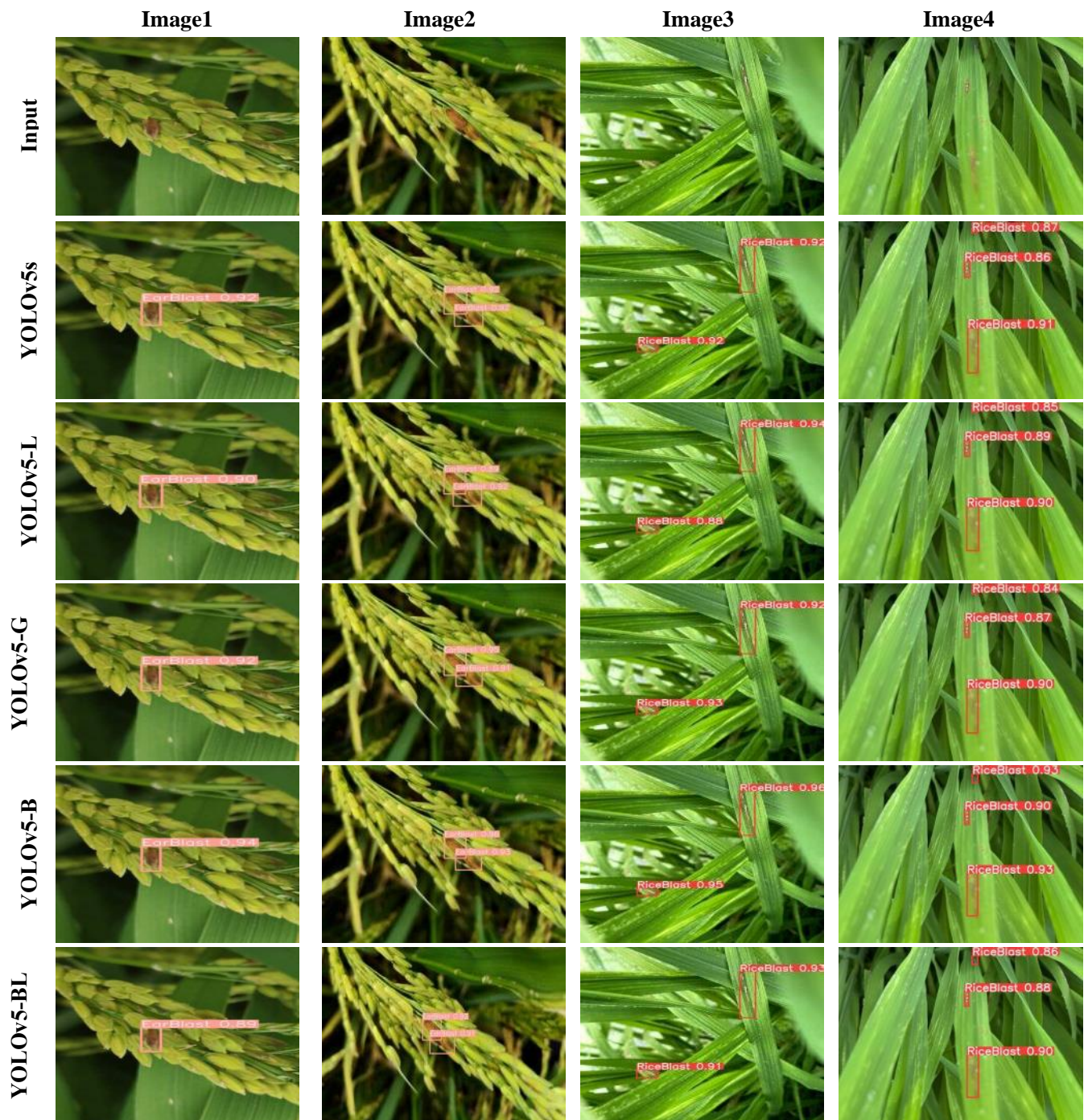




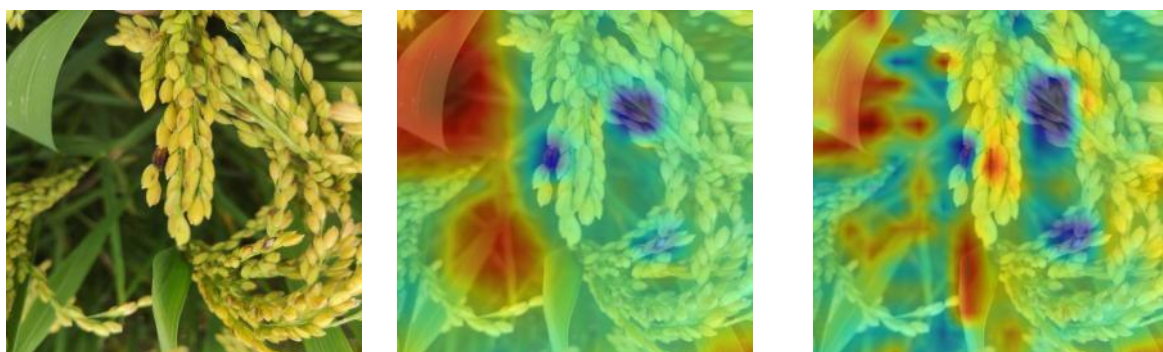
Fig. 8 - Rice blast detection results of each model based on YOLOv5s

Performance comparison using different attention mechanisms

To assess the effectiveness of the incorporated SE module, the additional attention mechanisms such as SimAM (Yang et al., 2021), CA (Hou et al., 2021) and CBAM (Woo et al., 2018) were compared. Table 3 shows comparison results with the use of various attention mechanisms on our dataset. Our improved model demonstrated optimal performance including precision, recall, mAP, and the number of parameters, as well as FLOPs, compared to the other two attention modules. Moreover, Fig. 9 shows the heat map of the YOLOv5-BGL without SE and after adding SE, which can intuitively display the degree of regional attention and the higher the feature is, the higher the heat map value at the corresponding position. It can be noted that the heat map shown in Fig. 9(c) shows that the extracted features of small rice blast are more focused and accurate compared with Fig. 9(b). As a result, incorporating the SE module led to improved accuracy in perception of disease features, especially for smaller target objects.

Table 3

Results of the comparison of different attention mechanisms						
Model	P	R	mAP	Params(M)	FLOPs(G)	
YOLOv5-BGL	0.949	0.911	0.962	3.55	7.80	
YOLOv5-BGL +SimAM	0.960	0.900	0.949	3.55	7.80	
YOLOv5-BGL +CA	0.957	0.913	0.955	3.57	7.90	
YOLOv5-BGL +CBAM	0.949	0.905	0.955	4.01	8.70	
YOLOv5-BGL +SE(Ours)	0.975	0.930	0.966	3.58	7.90	



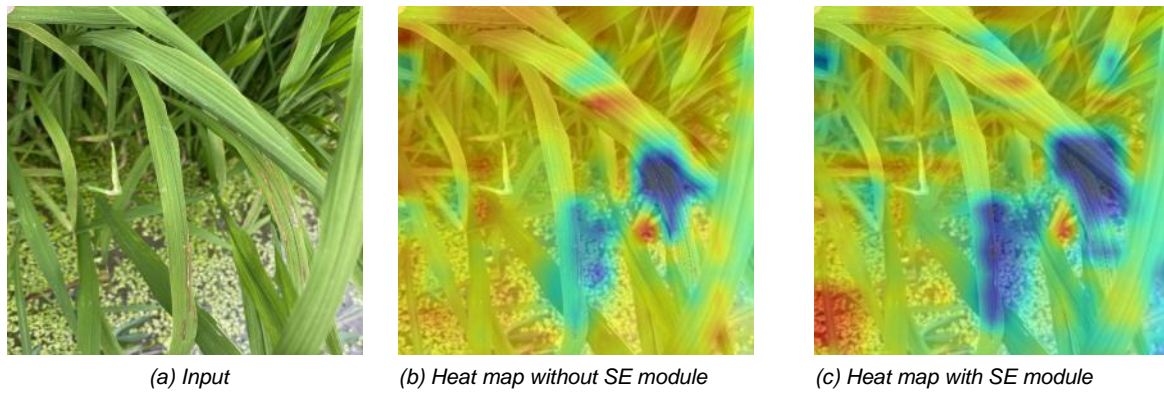


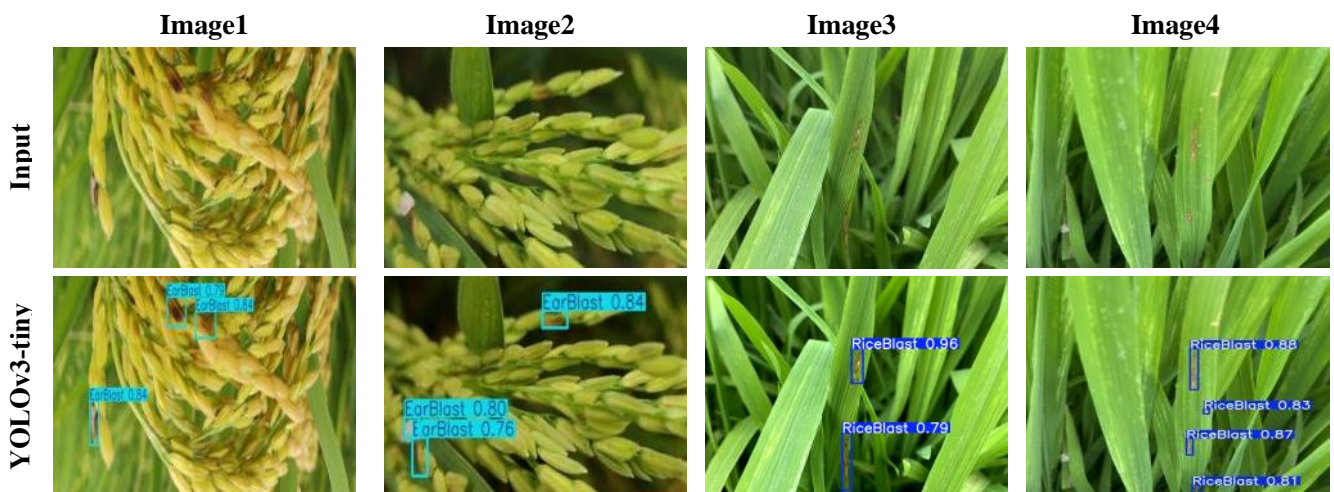
Fig. 9 - The heat map of the final output result of the model

Performance comparison using different detection model

To evaluate the efficiency and lightweight of the model for rice blast disease recognition, our model was compared to the YOLOv3-tiny, YOLOv4-tiny, YOLOv5s, YOLOv7-tiny, and YOLOv8s. The performance comparisons are given in Table 4. As shown in Table 4, while the YOLOv8s achieves high scores in detection accuracy of rice blast disease, it does not compare favorably to the proposed model in terms of parameters, FLOPs as well as model size. Comparison with the other lightweight models including YOLOv3-tiny, YOLOv4-tiny, and YOLOv7-tiny, the proposed model outperforms them across all metrics. Compared with the YOLOv5s model, the reductions in precision, recall, and mAP do not exceed 2%. However, there is a 49% decrease in model parameters, a 50% decrease in FLOPs, and a 74.61% decrease in model size, respectively. Additionally, as shown in Fig. 10, the detection performance of the YOLOv5s, YOLOv8s and the proposed model does not differ much in the case of rice blast detection. However, the target confidence of the YOLOv7-tiny and YOLOv4-tiny models were lower than that of the other three models, while in early disease spots on rice leaves and panicles, the YOLOv7-tiny and YOLOv4-tiny models, on the other hand, demonstrated some missing detections. Hence, it can be concluded that the proposed lightweight model outperforms comparable algorithms for rice blast detection, featuring fewer FLOPs and a more lightweight architecture that is suitable for mobile deployment.

Table 4

Results of the comparison of different detection model						
model	P	R	mAP	Params(M)	FLOPs(G)	Size(M)
YOLOv3-tiny	0.891	0.805	0.871	8.67	12.9	17.5
YOLOv4-tiny	0.759	0.387	0.337	6.01	16.2	23.57
YOLOv5s	0.977	0.936	0.976	7.01	15.8	14.1
YOLOv7-tiny	0.761	0.714	0.774	6.01	13.2	12.28
YOLOv8s	0.986	0.942	0.977	11.1	28.4	22.54
Ours	0.975	0.930	0.966	3.58	7.90	7.61



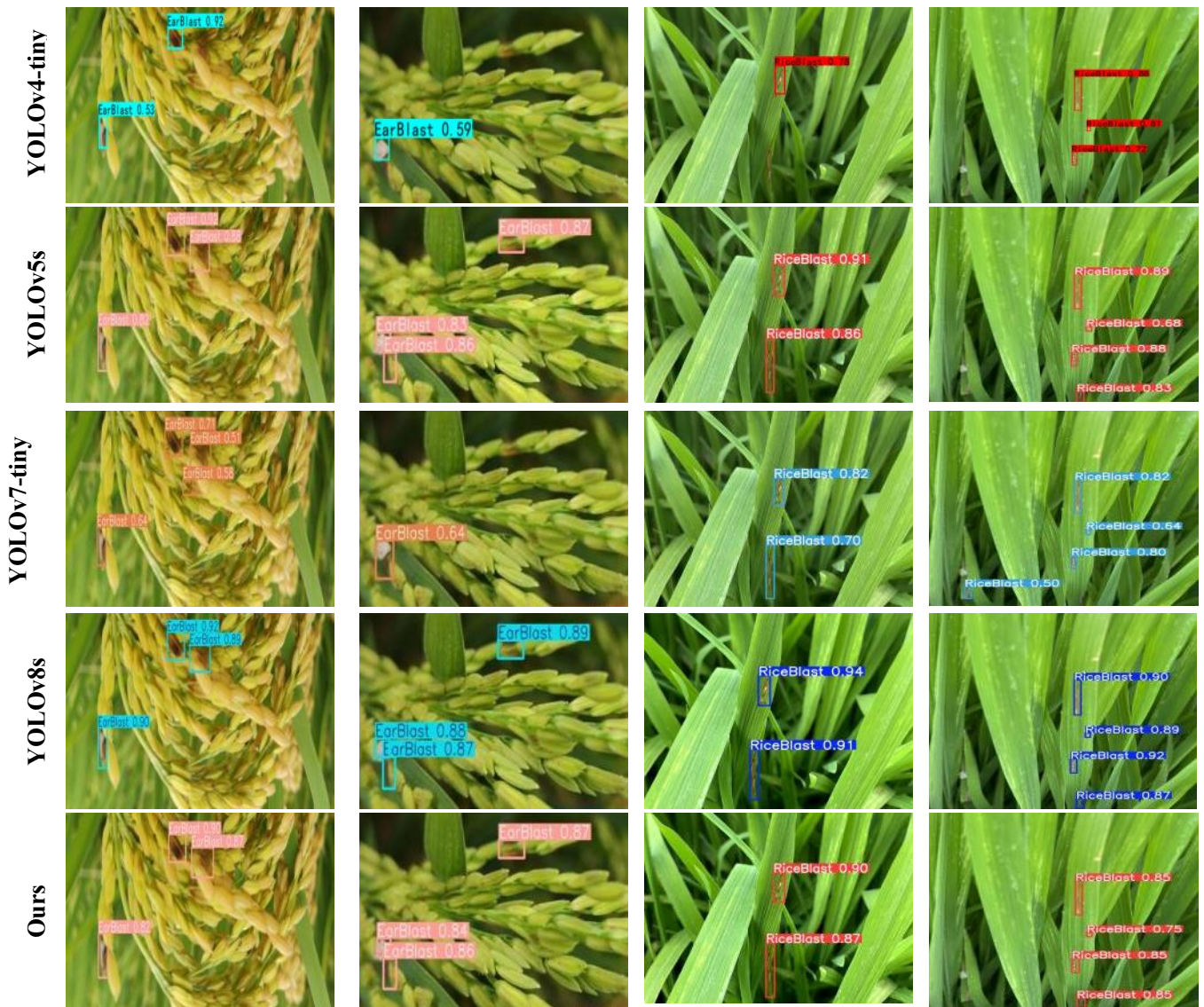


Fig. 10 - Comparison of rice blast detection results

Android deployment experimentation

The NCNN framework was used to quantify the trained rice blast model and then created an application RiceBlastDetector based on the model, as illustrated in Fig.10. The app was packaged as an APK file, generated using Android Studio, and installed on a Redmi K30 Pro smartphone running Android 12. As shown in Fig.11, the app's main interface features a unit for displaying image framing, photo button and video button. The user can use images saved on the phone or call the smartphone camera through “photo” or “video” button. The image framing display unit is capable of showing labels for disease categories, confidence scores, and predicted boxes. The effect of rice blast detection using the APP in the field is shown in Fig. 12. It can be seen from Fig.12 that the APP can achieve accurate detection in the scenario with the different characterization scale disease spots.

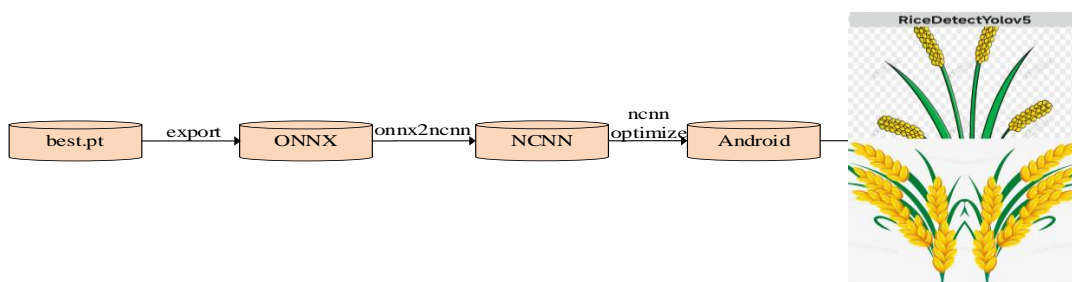


Fig. 11 - Model quantification and APP interface

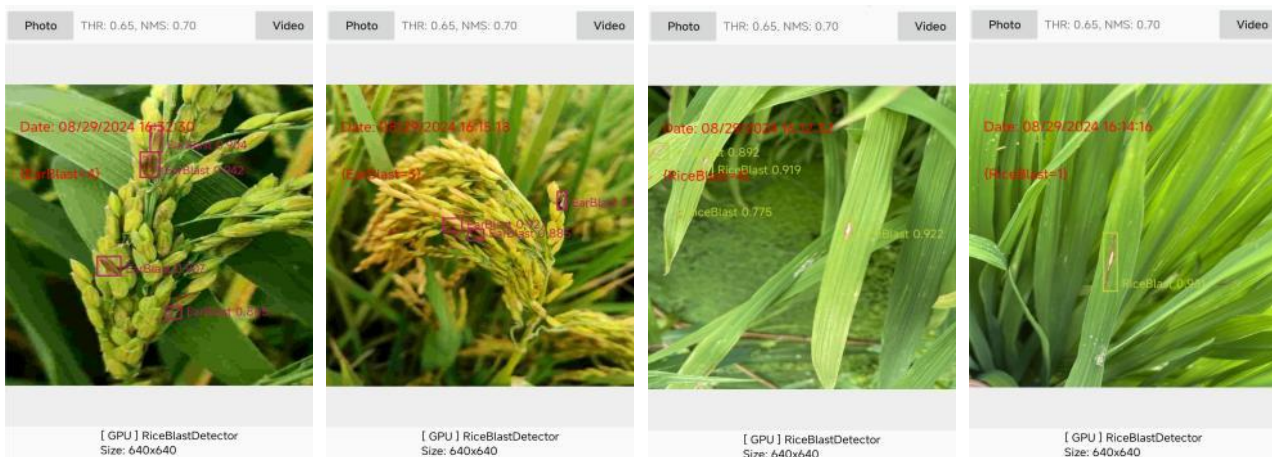


Fig. 12 - Detection rice blast based on APP

CONCLUSIONS

To effectively lightweight the rice blast detection model under the premise of ensuring the recognition performance, a lightweight YOLOv5s model was designed, verified and deployed on Android devices, facilitating detection of rice blast. The model replaced the standard convolution in its backbone and neck with GhostConv and implemented the LightC3 module, reducing complexity. The BiFPN module was used for multi-scale feature fusion, and the SE module was integrated into the backbone to enhance detection precision. The RiceDiseaseDetector app was developed and used for field detection. The results indicate that the designed model has a 49% decrease in model parameters, a 50% decrease in FLOPs, and a 74.61% decrease in model size, respectively, compared with the YOLOv5s model, which provides technical support for future intelligent plant protection initiatives. Furthermore, this approach can serve as a reference for detecting other minor rice disease-related issues.

ACKNOWLEDGEMENT

Thank you to all the participating authors. The research was funded by the National Key Research and Development Program (2022YFD2001801-3) and the National Natural Science Foundation of China (No.32201665).

REFERENCES

- [1] Asibi, A. E., Chai, Q., & Coulter, J. A. (2019). Rice blast: A disease with implications for global food security [J]. *Agronomy*, 9(8), 451.
- [2] Bedi, P., & Gole, P. (2021). Plant disease detection using hybrid model based on convolutional autoencoder and convolutional neural network [J]. *Artificial Intelligence in Agriculture*, 5, 90-101.
- [3] Cheng, Z., Huang, R., Qian, R., Dong, W., Zhu, J., & Liu, M. (2022). A lightweight crop pest detection method based on convolutional neural networks. *Applied Sciences*, 12(15), 7378.
- [4] Daniya, T., & Vigneshwari, S. (2019). A review on machine learning techniques for rice plant disease detection in agricultural research [J]. *System*, 28(13), 49-62.
- [5] Dogra, R., Rani, S., Singh, A., Albahar, M. A., Barrera, A. E., & Alkhayat, A. (2023). Deep learning model for detection of brown spot rice leaf disease with smart agriculture. *Computers and Electrical Engineering*, 109, 108659.
- [6] Han, K., Wang, Y., Xu, C., Guo, J., Xu, C., Wu, E., & Tian, Q. (2022). GhostNets on heterogeneous devices via cheap operations. *International Journal of Computer Vision*, 130(4), 1050-1069.
- [7] Hou, Q., Zhou, D., & Feng, J. (2021). Coordinate attention for efficient mobile network design. In *Proceedings of the IEEE/CVF conference on computer vision and pattern recognition* (pp. 13713-13722).
- [8] Jia, L., Wang, T., Chen, Y., Zang, Y., Li, X., Shi, H., & Gao, L. (2023). MobileNet-CA-YOLO: An improved YOLOv7 based on the MobileNetV3 and attention mechanism for Rice pests and diseases detection. *Agriculture*, 13(7), 1285.

- [9] Khan, F., Zafar, N., Tahir, M. N., Aqib, M., Waheed, H., & Haroon, Z. (2023). A mobile-based system for maize plant leaf disease detection and classification using deep learning [J]. *Frontiers in Plant Science*, 14, 1079366.
- [10] Khattak, A., Asghar, M. U., Batool, U., Asghar, M. Z., Ullah, H., Al-Rakhami, M., & Gumaei, A. (2021). Automatic detection of citrus fruit and leaves diseases using deep neural network model [J]. *IEEE access*, 9, 112942-112954.
- [11] Li, R., Li, Y., Qin, W., Abbas, A., Li, S., Ji, R., Wu Y., & Yang, J. (2024). Lightweight Network for Corn Leaf Disease Identification Based on Improved YOLO v8s. *Agriculture*, 14(2), 220.
- [12] Li, T., Zhang, Y., Li, Q., & Zhang, T. (2022). AB-DLM: an improved deep learning model based on attention mechanism and BiFPN for driver distraction behavior detection. *IEEE Access*, 10, 83138-83151.
- [13] Lin, Y., Chen, T., Liu, S., Cai, Y., Shi, H., Zheng, D., Lan, Y., & Zhang, L. (2022). Quick and accurate monitoring peanut seedlings emergence rate through UAV video and deep learning. *Computers and Electronics in Agriculture*, 197, 106938.
- [14] Liu, K., Wang, J., Zhang, K., Chen, M., Zhao, H., & Liao, J. (2023). A lightweight recognition method for rice growth period based on improved YOLOv5s. *Sensors*, 23(15), 6738.
- [15] Malvade, N. N., Yakkundimath, R., Saunshi, G., Elemmi, M. C., & Baraki, P. (2022). A comparative analysis of paddy crop biotic stress classification using pre-trained deep neural networks [J]. *Artificial Intelligence in Agriculture*, 6, 167-175.
- [16] Manavalan, R. (2020). Automatic identification of diseases in grains crops through computational approaches: A review [J]. *Computers and Electronics in Agriculture*, 178, 105802.
- [17] Nandhini, M., Kala, K. U., Thangadarshini, M., & Verma, S. M. (2022). Deep learning model of sequential image classifier for crop disease detection in plantain tree cultivation. *Computers and Electronics in Agriculture*, 197, 106915.
- [18] Rahman, C. R., Arko, P. S., Ali, M. E., Khan, M. A. I., Apon, S. H., Nowrin, F., & Wasif, A. (2020). Identification and recognition of rice diseases and pests using convolutional neural networks. *Biosystems Engineering*, 194, 112-120.
- [19] Sanghavi, K., Sanghavi, M., & Rajurkar, A. M. (2021). Early stage detection of Downey and Powdery Mildew grape disease using atmospheric parameters through sensor nodes [J]. *Artificial Intelligence in Agriculture*, 5, 223-232.
- [20] Sun, Y., Wu, F., Guo, H., Li, R., Yao, J., & Shen, J. (2023). TeaDiseaseNet: multi-scale self-attentive tea disease detection [J]. *Frontiers in Plant Science*, 14, 1257212.
- [21] Wang, H., Xu, Y., He, Y., Cai, Y., Chen, L., Li, Y., Sotelo, M. A., & Li, Z. (2022). YOLOv5-Fog: A multiobjective visual detection algorithm for fog driving scenes based on improved YOLOv5. *IEEE Transactions on Instrumentation and Measurement*, 71, 1-12.
- [22] Wen, Y., Xue, J., Sun, H., Song, Y., Lv, P., Liu, S., Chu, Y., & Zhang, T. (2023). High-precision target ranging in complex orchard scenes by utilizing semantic segmentation results and binocular vision. *Computers and Electronics in Agriculture*, 215, 108440.
- [23] Woo, S., Park, J., Lee, J. Y., & Kweon, I. S. (2018). Cbam: Convolutional block attention module. In *Proceedings of the European conference on computer vision (ECCV)* (pp. 3-19).
- [24] Xin, D., Chen, Y. W., & Li, J. (2020). Fine-grained butterfly classification in ecological images using squeeze-and-excitation and spatial attention modules. *Applied Sciences*, 10(5), 1681.
- [25] Li, Y., Xiao, L., Li, W., Li, H., Liu, J. (2022). Research on recognition of occluded orange fruit on trees based on YOLOv4. *INMATEH-Agricultural Engineering*, 67(2), 137-146.
DOI: <https://doi.org/10.35633/inmateh-67-13>
- [26] Yang, N., Yu, J., Wang, A., Tang, J., Zhang, R., Xie, L., Shu F., & Kwabena, O. P., (2020). A rapid rice blast detection and identification method based on crop disease spores' diffraction fingerprint texture [J]. *Journal of the Science of Food and Agriculture*, 100(9), 3608-3621.
- [27] Yang, L., Zhang, R. Y., Li, L., & Xie, X. (2021, July). Simam: A simple, parameter-free attention module for convolutional neural networks [C]. In *International conference on machine learning* (pp. 11863-11874). PMLR.
- [28] Yang, Y., Wang, L., Huang, M., Zhu, Q., & Wang, R. (2022). Polarization imaging based bruise detection of nectarine by using ResNet-18 and ghost bottleneck. *Postharvest Biology and Technology*, 189, 111916.

- [29] Xia, Y., Lei, X., Herbst, A., & Lyu, X. (2023). Research on pear inflorescence recognition based on fusion attention mechanism with YOLOv5. *INMATEH-Agricultural Engineering*, 69(1), 11-20. DOI: <https://doi.org/10.35633/inmateh-69-01>
- [30] Du, Y., Gao, A., Song, Y., Guo, J., Ma, W., Ren, L. (2024). Young apple fruits detection method based on improved YOLOv5. *INMATEH-Agricultural Engineering*, 73(2), 84-93.
- [31] Yu, C., Feng, J., Zheng, Z., Guo, J., & Hu, Y. (2024). A lightweight SOD-YOLOv5n model-based winter jujube detection and counting method deployed on Android. *Computers and Electronics in Agriculture*, 218, 108701.
- [32] Zhang, Y. F., Ren, W., Zhang, Z., Jia, Z., Wang, L., & Tan, T. (2022). Focal and efficient IOU loss for accurate bounding box regression. *Neurocomputing*, 506, 146-157.
- [33] Zhou, G., Zhang, W., Chen, A., He, M., & Ma, X. (2019). Rapid detection of rice disease based on FCM-KM and faster R-CNN fusion. *IEEE access*, 7, 143190-143206.

SMART VENDING MACHINE, ENERGY INDEPENDENT, THERMALLY CONDITIONED, FOR PACKAGED AGRICULTURAL PRODUCTS

AUTOMAT DE VANZARE INTELIGENT, INDEPENDENT ENERGETIC, CONDITIONAT TERMIC, A PRODUSELOR AGRICOLE AMBALATE

Ioan Mihail SAVANIU, Oana TONCIU¹, Bogdan BEBESELEA¹,

Technical University of Civil Engineering Bucharest / Romania;

* E-mail: oana.tonciu@utcb.ro.ro

DOI: <https://doi.org/10.35633/inmateh-74-69>

Keywords: vending machine, energy independent, packaged agricultural products, mechatronics, energy-efficient farming.

ABSTRACT

In the context of the development of intelligent systems in the agricultural field, systems that help farmers in agricultural production, the realization of intelligent systems to help them in the commercialization of agricultural products is both actual and necessary. The commercialization of agricultural products directly by the farmer, at the farm gate, requires specially authorized spaces, personnel, connection to utilities, etc., which limits the possibilities for sale of products by farmers, thus losing both the final customer and the farmer, as the product enters the distribution chain, which implies an additional cost and uncertainties regarding the product origin. The article presents the SVIEE-R equipment, an automatic and autonomous system for selling agricultural products at the farm gate, which does not require the presence of a salesperson or connection to electricity and which can store agricultural products that require refrigeration, such as: vegetables, fruits, dairy products, etc. The intelligent SVIEE-R vending machine is a smart system that continuously informs both the farmer and the customer about the stock level of stored products, the storage temperature, and can be placed anywhere due to the energy independence provided by an array of photovoltaic panels and accumulators.

REZUMAT

In contextul dezvoltării sistemelor inteligente in domeniul agricol, sisteme care ii ajuta pe fermierii in partea de productie agricola, realizarea de sisteme inteligente, care sa ii ajute in partea de comercializare a produselor agricole, este actuala si necesara. Comercializarea produselor agricole direct de fermier, la poarta fermei, necesita spatii special amenajate autorizate, personal, racordare la utilităţii, etc, aspecte care limitează posibilităţile de comercializarea directa a produselor de către aceştia, astfel pierde atât clientul final cat si fermierul întrucât produsul intra in lanţul de distribuţie, ceea ce presupune un cost suplimentar si nesiguranţa in ceea ce priveşte originea produsului. Articolul prezinta echipamentul SVIEE-R care este un sistem automat si autonom de vânzare a produselor agricole, la poarta fermei, care nu necesita prezenta unui vânzător, racordare la energie electrica si care poate stoca produse agricole care necesita refrigerare cum ar fi: legume, fructe, produsele lactate, etc. Automatul inteligent SVIEE-R este un sistem inteligent care informează in permanenta atât fermierul si clientul in ceea ce priveşte stocul de produse depozitate, temperatura de păstrare si care poate fi amplasat oriunde datorita independentei energetice asigurata de o matrice de panouri fotovoltaice si acumulatori.

INTRODUCTION

In the context of the development of intelligent systems in the agricultural field, systems that help farmers in the agricultural production part, the realization of intelligent systems that help them in the marketing of agricultural products is current and necessary. Vendomats in agriculture are an innovative solution for selling agricultural products directly to consumers, eliminating middlemen and giving farmers more control over pricing and distribution. These vending machines can be used to sell a wide range of agricultural products such as: fresh or pasteurized milk, yoghurts, cheeses, butter; fresh eggs from chicken, duck or quail; fruits and vegetables, packaged in small quantities; fresh or processed meat in the case of vendomats equipped with freezing systems; fruit juices, some vendomats can prepare the juice on the spot from fresh fruit; honey, pollen,

¹ Ioan Mihail Savaniu, PhD. Eng., Associate professor; Oana Tonciu, PhD. Eng., Lecturer;
Bogdan Bebeselea, PhD. Student Eng.

propolis, phages; etc. Vendomates can help farmers by selling seeds (wheat, maize, vegetables) or fertilizers (granulated, liquid) in the vicinity of their plantations, depending on the season. Smart vending machines for farms or agricultural stores can commercialize animal fodder (grains, flours, granules) packaged in small or medium quantities. The advantages of using vendomats in agriculture are: availability 24 hours / 7 days, speed in purchasing products; farmers can sell products at the farm gate or place products at specialized fairs, intermediaries are eliminated and product prices decrease; personnel costs are reduced; the customer has the guarantee of the origin of the purchased product (**ZETOMAT, 2024). The use of vending machines equipped with refrigeration systems, similar to the SVIEE-R vending machine, is important for fresh agricultural products, these are perishable and require special storage conditions (controlled temperature, humidity, etc.). Smart vending machines, such as the one presented in the article, constantly communicate to the farmer the demand from customers, so he can either estimate the demand while reducing losses due to product expiration, or constantly provide products in order not to disappoint customers.

In the article “*Vending machines proving popular with producers*”, (2021), are presented solutions for farmers to market their products using vending machines with specialized boxes that are accessed through a software application. These vending machines are connected to the electricity grid and the internet and according to reports from farmers in the UK are used to market products such as eggs, chilled or frozen various agricultural products, dairy products, etc. The vending machines can provide information to the customer via an application about the stock of products and can reserve products.

The dispenser manufacturer Zuply in the article “*On-farm sales solutions*” (2024), offers vending machine solutions for agricultural products in the form of lockers or pusher machines. Vendomats the form of lockers or pusher machines have the possibility to refrigerate the products and are equipped with a touch screen through which the buyer can find various information about the products to be sold. For farmers in Romania, ZETOMAT (**ZETOMAT, 2024), offers various solutions for vending machines for agricultural products, solutions that significantly influence the profitability for farmers and bring multiple benefits for both producers and farmers.

The use of food vending machines in urban areas is increasing, as the authors of *Rombach et al, (2022)*, conclude. As the inhabitants of big cities appreciate fresh food directly from the producer, the vending machine market is growing. Farmers need to develop networks for selling agricultural products directly at the farm gate as well as vending machines for packaged products (*Sabău et al, 2023*).

In Germany, a system has been developed for farmers to sell different agricultural products by vending machines, called REGIOMAT (**Das Prinzip Regiomat, 2024). Thus, products such as fresh country milk, eggs, cheese, bread, honey, frozen products can be marketed in this system. Thus, regional products are marketed directly by the producer without intermediaries. The solutions presented above are vending machines that are connected to the public electricity grid and in some cases have to be installed in enclosed spaces to be protected from the outside environment.



Fig. 1 - Example of SVIEE-R vendomat placement in rural areas

The agricultural products vending machine SVIEE - R, presented in the article, is energy independent and realized in such a way that it can be placed in an open environment in any rural area, at the small farmer's door, as shown in Fig. 1, near a stable, near an orchard, near greenhouses, etc.

The SVIEE-R is equipped with a refrigeration system that allows the storage of agricultural products, products that require preservation at low temperatures. The automat allows the commercialization of the products through an application that transmits to the customer information about the products inside, photos of the products to be commercialized, their stock, their shelf life, their payment. The computerized system transmits information to the farmer about product stocks, indoor temperature, the amount of energy produced and stored in the accumulators, system errors, vandalism. The SVIEE-R system is designed as a closed box without glazed surfaces or screens to limit vandalism, as it can be placed in unpopulated areas. The closed enclosure construction ensures the storage of agricultural products in dark areas without exposure to solar radiation.

The validation of the use of the SVIEE-R vending system by farmers, a vending machine that can be placed anywhere in the rural environment without the need to be connected to the electricity grid, involved verifying the stability of the vending machine to wind action, ensuring the optimal temperature for storing agricultural products in the thermally conditioned enclosure, and the energy autonomy of the vending machine. The article presents the studies undertaken in order to establish the possibility of using the SVIEE-R vending system in rural areas by farmers in order to commercialize agricultural products at the farm gate.

MATERIALS AND METHODS

The SVIEE-R energy-independent agricultural product vending system developed within the POC 121420 project, shown in Fig. 2, is composed of the following systems: the power supply system using an array of three photovoltaic panels, the command-and-control system, the product cooling system, the thermally insulated enclosure for product storage, the product storage system, the product delivery system.

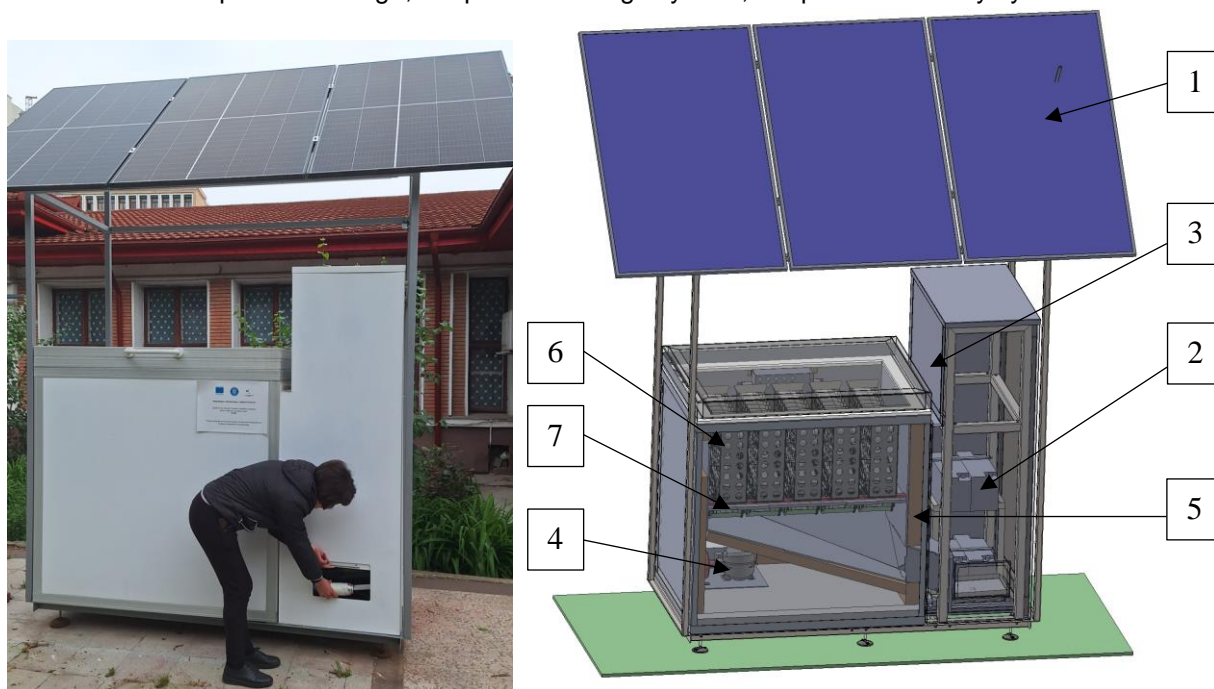


Fig. 2 – SVIEE-R system for selling agricultural products

The components illustrated in Fig. 2 of the SVIEE-R power supply system are: 1 - solar panels, type TSM, 405 DE09. 08, maximum power 405 W; 2 - batteries, type Victron GEL 12 v 130 AH; 3 - MPPT, type Victron 150/70 Tr. In Fig. 2 are shown: 4 - cooling system, 5 - thermally insulated enclosure, 6 - storage system, 7 - delivery system. The flow of electricity produced by the three photovoltaic panels is sent to the battery array and is managed by the MPPT type charge regulator. The MPPT regulator is known for their efficiency in converting the voltage from the photovoltaic panels to the battery charging voltage. The DC/DC conversion efficiency of these systems is 98% (****MPPT solar charger manual, 2024*).

The storage and delivery system for packaged agricultural products is shown in Fig. 3. The storage system consists of a sheet-metal casing with openings for ventilation and uniform cooling. The storage unit allows the storage of 32 containers with dimensions of 62 mm and height of 160 mm, the casing is designed in such a way that the containers move gravitationally which the product delivery system.

The operation analysis and evaluation of the electrical energy consumption of the delivery system was presented in the article “*Energetically efficient mechatronic systems for dose delivery in energetically independent vending machine for cold products*” (Savaniu et al, 2024), thus the average energy consumption for the delivery of one container is 1.115 W.

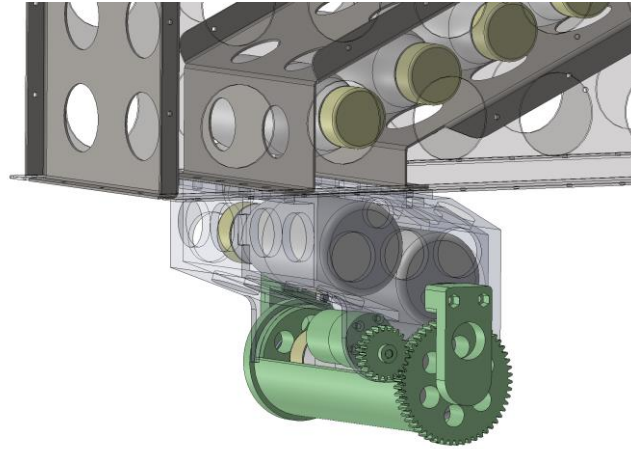


Fig. 3 – Delivery system for agricultural products packed in PET containers

The operation of the SVIEE-R implies in the first stage its supply with agricultural products packaged in Polyethylene terephthalate (PET) bottles which are stacked in the 5 storage units of the system located in the thermally insulated enclosure. From the thermally insulated enclosure the containers are unloaded by the delivery system, see Fig. 3, into the lower tank of the enclosure, from where they gravitationally reach the product pick-up area, see Fig. 2. The customer picks up the containers through the front delivery door, as shown in the picture in Fig. 2 where a person picks up the ordered product.

The SVIEE-R is equipped with a complex system of sensors whose measured values are continuously sent via the Internet to a server. The collected data is stored on the server to be later analyzed either in real time through an internet browser or downloaded as a database. The data stored on the server can be: temperature in the thermally insulated enclosure, ambient temperature, consumption for the refrigeration system [W], consumption for the product delivery system [W], data provided by the photovoltaic system via the MPPT solar charge controller (Battery [mV], Battery injected current [mA], Solar voltage [mV], Solar power [W], etc.).

The location of the SVIEE-R vending machine in rural areas requires a wind stability study. If a stability calculation is not carried out, it may happen that the vending machine may tip over, as shown in Fig. 4, when a similar vending system has been affected by wind action with very high intensity.

The stability of the vending machine is mainly determined by its mass, which in the case of the SVIEE-R vending machine, according to the data in Table 1 and applying formula (1) is 796.99 kg.

$$GV = TSSP + TSTLP + TSF \quad (1)$$



Fig. 4 – SVIEE vending machine overturned because of wind action

Table 1

No.	Name	Quantity	Density (kg/cm ³)	Total mass (Kg)
1	Thermal insulation Komacel 10 mm thick - cold room	101542.45 cm ³	5 x10 ⁻³	50.77
2	Thermal insulation Termoconfort 100 mm thick - cold room	955166.4 cm ³	0.034 x10 ⁻³	32.47
3	Thermal insulation BOND 3 mm thick - cold room	14444.44 cm ³	1.55 x10 ⁻³	22.39
4	Product storage system	5 trays	-	77.15
5	Metal structure made of aluminum profiles - cold room	1	-	20.62
6	Refrigeration installation (compressor. vaporizer. condenser. fan. support)	1	-	16.85
Total storage space for TSSP products				220.25
1	Outer casing - 3 mm thick steel sheet	1	-	80.44
2	External casing - 40 mm thick polystyrene thermal insulation	1	-	14.46
3	Product delivery system	1	-	8.65
4	Command and control system	1	-	2.43
5	Vendomat metal chassis	1	-	167.45
6	Metal structure supporting photovoltaic panels	1	-	85.01
Total technical and product delivery space TSTLP				358.44
1	GEL 12-130 batteries	4	-	152.00
2	Photovoltaic panels TSM 405-DE09.08	3	-	63.30
3	MPPT 150-70TR	1	-	3.00
Total photovoltaic system TSF				218.30

The stability study takes into account the forces acting on the machine as shown in Fig. 5. Thus, there is balance, in relation to the tipping edge, of the moments given by the force of weight given by the mass of the machine without being loaded with products and the force of weight of the counterweight made of concrete in relation to the moment generated by the force of wind action on the photovoltaic panels, as shown in Fig. 5. In order to ensure stability, which allows the safe use of the automat in open areas specific to the rural environment areas exposed to wind action, it is necessary to determine the size and then mount a counterweight at the base of the automat. The mass of the counterweight must be determined following a stability calculation.

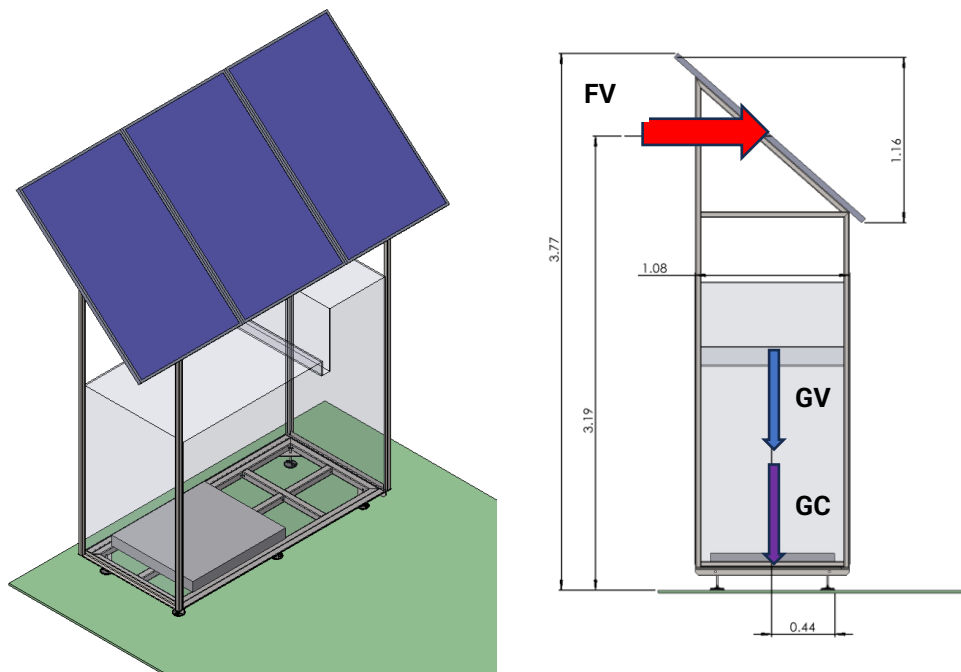


Fig. 5 – SVIEE-R vending stability calculation scheme

The tests on the validation of the commercialization of agricultural products by the SVIEE-R automat concerned dairy products packaged in plastic containers of the kefir and sana categories. Fermented dairy products, such as yoghurt, kefir, sana, buttermilk or fermented cream, must be kept at low temperatures to prevent the growth of micro-organisms that can spoil the product.

The optimal storage temperature is 2°C - 6°C, this temperature is provided by the product cooling system of the vending machine and the thermally insulated enclosure for product storage maintains this temperature, ensuring optimal storage of fermented dairy products. It is necessary to maintain this temperature range because below 2°C there is a risk of freezing, which can affect the texture and taste of the product, and above 6°C the risk of spoilage increases and the product may lose its properties, becoming unsafe for consumption. Storing at the correct temperature not only prevents spoilage but also helps to maintain the probiotic benefits of fermented products.



Fig. 6 – Loading the SVIEE-R with fermented dairy products. Temperature check with thermal camera.

The legislation in force in Romania, *The Sanitary Veterinary Regulation on additional conditions for the transportation, storage, marketing and veterinary sanitary control of milk and milk products* (***) *Sanitary Veterinary Regulation, 2004*) provides for the following for the marketing of agricultural dairy products: the optimal microclimate (temperature, humidity, ventilation) must be ensured for the product in question; for the purpose of its permanent control, the products must be arranged in an orderly manner, by assortment, lot or batch, and they must be visibly marked by means on which the assortment, quantity, date of entry of the product and the date of expiry of the shelf life must be obligatorily inscribed. Verification of the optimal temperature preservation of fermented dairy products consisted in feeding the vending machine with 25 containers loaded with sana, labeled S in Fig. 6 and 25 containers loaded with kefir, labeled K in Fig. 6. The containers had an average mass of about 350 g.

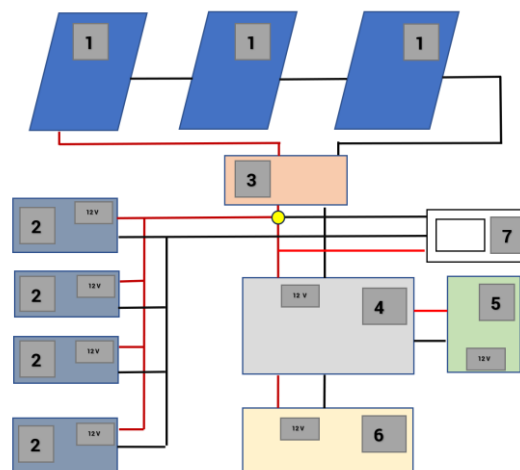


Fig. 7 – Block diagram of the SVIEE-R controller and current analyzer connection

The evaluation of the energy consumption of the SVIEE-R was carried out using a current analyzer type HIOKI PW3198 mounted according to the diagram in Fig. 8. The components of the electrical system of the energy independent vending machine are: 1 - solar panels, type TSM, 405 DE09. 08, maximum power 405 W; 2 - accumulators, type Victron GEL 12 v 130 AH; 3 - MPPT, type Victron 150/70 Tr; 4 - command and control system, of our own manufacture; 5 - cooling system powered at 12 V DC consisting of compressor, vaporizer, condenser; 6 - product delivery system, of our own manufacture; 7 - current analyzer type HIOKI PW3198.

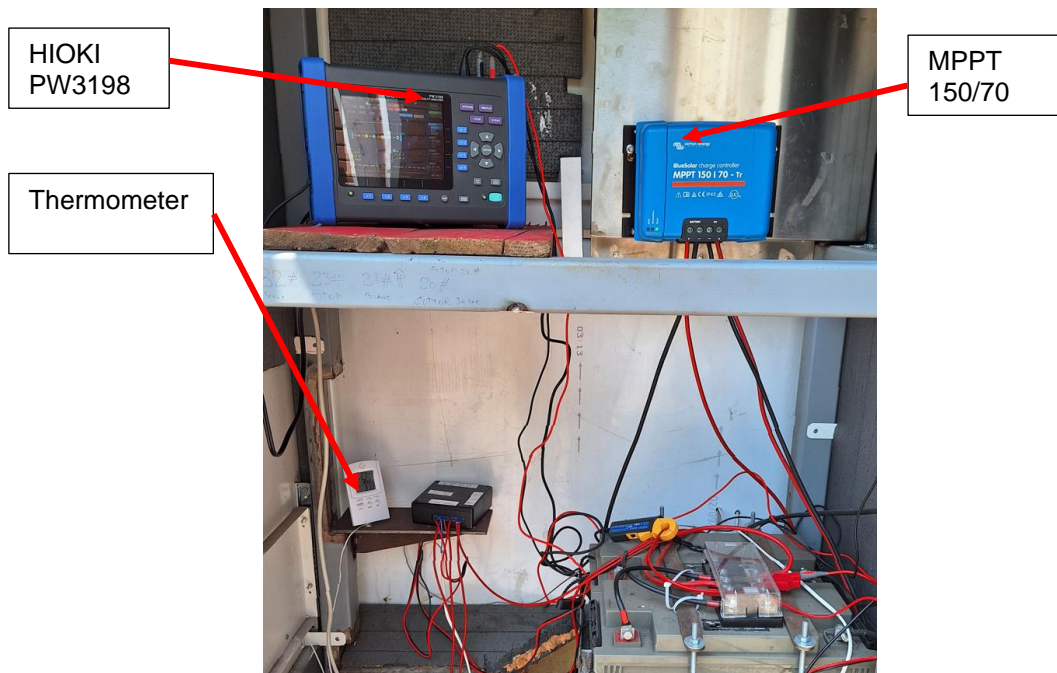


Fig. 8 – SVIEE-R command and control system

The HIOKI PW3198 power quality analyzer has the measurement accuracy Voltage: $\pm 0.1\%$ of nominal voltage; Current: $\pm 0.2\%$ rdg. $\pm 0.1\%$ f.s. + current sensor accuracy; Active power: $\pm 0.2\%$ rdg. $\pm 0.1\%$ f.s. + current sensor accuracy (** Hioki E.E. Corporation PQ ONE, 2024). The equipment, throughout the duration of the tests, collected data on supply voltage, current and electrical energy absorbed by the electromechanical actuator. The data stored in the storage medium of the equipment were analyzed with the PQ ONE software which allows the presentation of the values of the electrical energy absorbed by the electromechanical actuator in graphical or tabular form (** Hioki E.E. Corporation, 2024).

RESULTS

In order to verify the stability of the SVIEE-R vending machine to the variable action due to the wind, its action will be considered on the three photovoltaic panels placed at a height of about 3.19 m. Thus, according to the Design Code - Evaluation of Wind Action on Buildings - CR 1-1-4/2012 (** Indicative CR 1-1-4/2012) the average value of the dynamic wind pressure $q_m(z)$, acting on the solar panels, is determined by the formula:

$$q_m(z) = c_r^2(z) * q_b \quad (2)$$

where: $q_m(z)$ is the mean value of the dynamic wind pressure at a height z above the terrain (without taking into account the orography of the site); q_b is the reference value of the dynamic wind pressure (in the case of our tests, on the territory of Romania according to the map of CR 1-1-4/2012, the maximum reference value of the dynamic pressure can be 0.7 kPa); $c_r^2(z)$ is the roughness factor for the dynamic wind pressure (in case of location in terrain category II Open field - grassy terrain and/or with isolated obstacles (trees, buildings) at distances of at least 20 times the height of the obstacle) the case considered in the stability check for the location of the vending machine in rural areas. The value of the roughness factor, adopted according to the methodology of CR 1-1-4/2012, is 0.816.

In evaluating the stability of the SVIEE-R vending machine, a dynamic wind pressure value of 0.466 kPa at the solar panels was considered. Considering the area of a photovoltaic panel of 1.92 m² (length 1.754 m, width 1.096 m) and the area in the wind direction of 3.81 m² the total wind force is 1775.46 N.

Solving the equilibrium equation of moments (3), a counterweight value of 515.14 kg is obtained for the analyzed case of the SVIEE - R vending machine.

$$GC = \frac{3.19}{0.44} * FV - GV = 7.25 * 1775.46 N - 796.99 kg * 9.81 m/s^2 = 5053.61 N \quad (3)$$

The evaluation of the stability of the machine can also be done with the help of a simulation realized in SolidWorks. In this sense, the vending machine SVIEE-R was designed in the 3D virtual environment of SolidWorks, in order to simulate with the help of the Motion Analysis subroutine of SolidWorks the stability under the action of wind (** SolidWorks - Motion Analysis, 2022).

In this sense, the vending machine was placed in the virtual environment on a rigid flat surface, fixed in space, contact with a friction coefficient of 0.20 between the vending machine and the flat surface and the gravitational acceleration of 9.81 m/s^2 were considered. Using the Motion Analysis subroutine in SolidWorks the delivery system of cold products from the thermally insulated enclosure to the recipient was tested in a 3D virtual environment in which it was possible to run several working scenarios.

After running the simulations and using the tools provided by Motion Analysis, the stability of the automat was tested considering several working scenarios in terms of wind direction and counterweight size. The result obtained after running the simulator, for a scenario in which the automat loses its stability is shown in Fig. 9.



Fig. 9 – SolidWorks simulation of the loss of stability of SVIEE-R

The temperature maintenance and energy consumption tests were performed between 24/06/2023 and 25/06/2023. During the test period the average ambient temperature was 25.5 degrees Celsius. During this period, containers loaded with fermented dairy products were stored in the storage units in the thermally insulated enclosure of SVIEE-R. After loading, the SVIEE-R automat was started and the temperature inside the enclosure was checked at 15 min time interval with the thermometer mounted as shown in Fig. 8 and qualitatively with a PCE-TC24 thermal chamber, as illustrated in Fig. 6. The thermometer used had the temperature measuring range: $-5 \dots 50^\circ\text{C}$, measurement accuracy: $\pm 0.1^\circ\text{C}$. The thermal chamber had the temperature measuring range: $-20 \dots +380^\circ\text{C}$, measurement accuracy: $\pm 2^\circ\text{C}$. The average temperature recorded was 5.78 degrees Celsius.

The electrical energy consumption of the vending machine was recorded by the HIOKI PW3198 and the results regarding the voltage and current absorbed by the vending machine are presented in Fig. 10. After analyzing the collected data, an average consumption of 0.47 KW/h was recorded. Considering the 6.24 KW storage capacity of the automat there is an autonomy of about 13 hours in case there is no electricity production from photovoltaic panels.

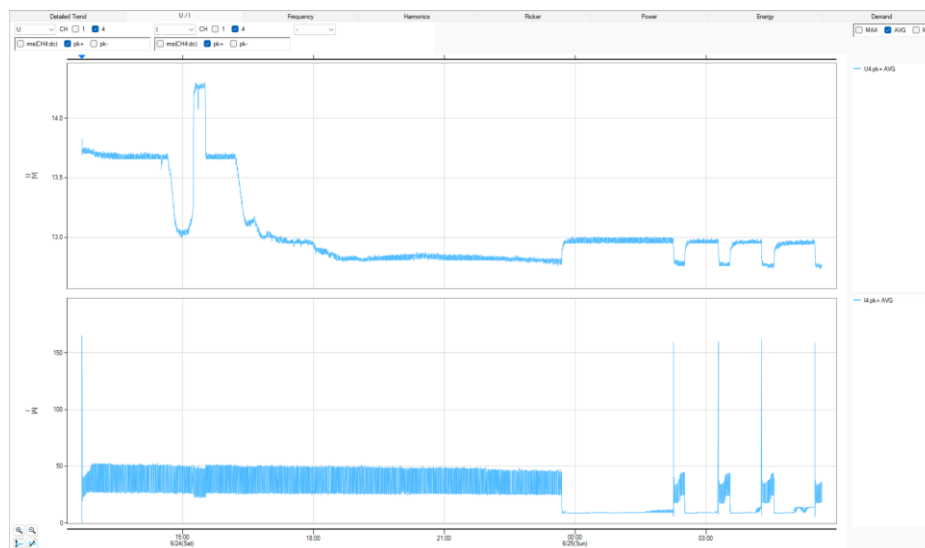


Fig. 10 – Current and voltage absorbed by SVIEE-R during the test period

CONCLUSIONS

Agricultural vending machines are more than a technological novelty; they represent a shift towards modernizing farming practices while maintaining inclusivity and sustainability. With proper implementation and support, they can revolutionize the way farmers access essential resources, boosting productivity and efficiency in the agricultural sector.

The research presented in the article recommends the use of the SVIEE-R energy independent vending machine in rural areas in order to co-market fermented dairy products at the farm gate. The use of the SVIEE-R energy independent vending machine ensures the safe commercialization of dairy food products by ensuring and maintaining a recommended refrigeration temperature for dairy products.

Providing the automat with an appropriate counterweight allows it to be placed anywhere, without the need for an additional foundation to anchor it. The automat is designed to be able to operate in the outdoor environment and in any environmental conditions.

The use of an energy-independent SVIEE-R has a significant impact on the environment and is intended for future sustainable agriculture - *Sustainable agriculture in the EU* (**Sustainable agriculture in the EU, 2024). SVIEE-R sales systems are intended for use on farms seeking to reduce greenhouse gas emissions. The supply of quantities of products tailored to the customer's requirements makes it possible to ensure that the food is always fresh and healthy and tailored to the customer's needs. Sales systems can determine the eating habits of specific communities and provide agricultural products 24 hours/7 days. The innovative energy efficient vending system SVIEE-R presented in the article is adapted to the European Green Deal adopted by the European Union, which assumes that by 2030 greenhouse gas emissions will be reduced by 55% (to 1990 levels), and a new binding EU-wide target has been set to improve energy efficiency by 11.7% by 2030. Member States will have to achieve annual savings of 1.49% on average between 2024-2030 (**The European Green Deal, 2024).

ACKNOWLEDGEMENT

This research was financially supported in part by the Competitiveness Operational Program—project name: Innovative Energy Efficient Sales Systems for Urban Areas (acronym, SVIEE, MySMIS code 121420), a co-financed project from the European Regional Development Fund by Operational Program Competitiveness.

FUNDING

This article was funded by UTCB - Technical University of Civil Engineering Bucharest, from Doctoral School funding (FCS).

REFERENCES

- [1] Rombach, M., Dean, D.L., Baird, T., Rice, J. (2022). Fruit Vending Machines as a Means of Contactless Purchase: Exploring Factors Determining US Consumers' Willingness to Try, Buy and Pay a Price Premium for Fruit from a Vending Machine during the Coronavirus Pandemic. *Covid*, 2(12), 1650-1665. <https://doi.org/10.3390/covid2120119>
- [2] Sabău, M. M., Mititean, P., Pocol, C. B., & Dabija, D.C. (2023). Factors Generating the Willingness of Romanian Consumers to Buy Raw Milk from Vending Machines. *Foods*, 12(11), 2193. <https://doi.org/10.3390/foods12112193>
- [3] Savaniu, M., Tonciu, O., Culcea M., Bizgan, A., Badea, F., Badea, C.R. (2024). Energetically efficient mechatronic systems for dose delivery in energetically independent vending machine for cold products. *International Journal of Mechatronics and Applied Mechanics*, Issue 15. DOI: 10.17683/ijomam/issue15.5
- [4] ***ZETOMAT Vending machines for fresh produce (Automate pentru vânzarea produselor proaspete), (2024), <https://zetomat.ro/>
- [5] ***Vending machines proving popular with producers, (2021). https://www.farminguk.com/news/vending-machines-proving-popular-with-producers_57970.html
- [6] ***On-farm sales solutions, (2024). <https://www.zuply.eu/branch/agriculture/>
- [7] ***Das Prinzip Regiomat, (2024). <https://www.regiomat.de/das-prinzip>
- [8] ***MPPT solar charger manual SmartSolar MPPT 150/70 up to 250/100 VE.Can, (2024). https://www.victronenergy.com/upload/documents/Manual_SmartSolar_MPPT_150-70_up_to_250-100_VE.Can/29694-MPPT_solar_charger_manual-pdf-en.pdf
- [9] *** Sanitary Veterinary Regulation on additional conditions for the transportation, storage, marketing and veterinary control of milk and milk products (Norma Sanitar Veterinară privind condițiile suplimentare pentru transportul, depozitarea, comercializarea și controlul sanitar veterinar al laptelui și produselor lactate), (2004), <https://legislatie.just.ro/public/DetaliiDocument/58860>
- [10] *** Hioki E.E. Corporation PQ ONE, (2024).
- [11] https://www.hioki.com/global/support/download/software/versionup/detail/id_562

- [12] *** Hioki E.E. Corporation, *Power Quality Analyzer PW3198*, (2024).
- [13] https://www.hioki.com/global/products/pqa/power-quality/id_5824
- [14] ***Design code assessment of wind action on buildings (*Cod de proiectare evaluarea actiunii vântului asupra constructiilor*), *Indicativ CR 1-1-4/2012*, 2012.
- [15] https://www.mdipa.ro/userfiles/reglementari/Domeniul_I/I_20_1_CR_1_1_4_2012.pdf
- [16] *** *SolidWorks – Motion Analysis*, (2022). <https://www.solidworks.com/>
- [17] *** *Sustainable agriculture in the EU*, (2024). https://agriculture.ec.europa.eu/sustainability_en
- [18] *** *The European Green Deal*, (2024). https://commission.europa.eu/strategy-and-policy/priorities-2019-2024/european-green-deal_en

OBSTACLE AVOIDANCE PLANNING OF GRAPE PICKING ROBOTS BASED ON DEEP REINFORCEMENT LEARNING

基于深度强化学习的葡萄采摘机器人采摘路径避障规划

Pei LIU*

School of Economics and Management, Wuhan Railway Vocational College of Technology, Wuhan, Hubei/China

Tel: +8613871280920; E-mail: wh20090803@126.com

Corresponding author: Pei LIU

DOI: <https://doi.org/10.35633/inmateh-74-70>

Keywords: deep reinforcement learning; grape; obstacle avoidance; path planning; picking robot

ABSTRACT

Given that picking robots are faced with many picking tasks in the field operation environment and the target and obstacles are located at random and uncertain positions, an obstacle avoidance planning method for the picking path of virtual robots based on deep reinforcement learning was proposed to achieve rapid route planning of robots under a lot of uncertain tasks. Next, the random motion strategy of virtual robots was set according to the physical structure of robot bodies. By comparatively analyzing the advantages and disadvantages of the observed values input by different networks, an environmental observation set was established in combination with actual picking behaviors as the network input; then, a reward function was established by introducing the idea of target attraction and obstacle repulsion contained in the artificial potential field method, aiming to evaluate the behavior of virtual robots and increase the success rate of obstacle avoidance. The results of the simulation experiment showed that the success rate obtained by virtual robots in completing the picking task reached 95.5% under obstacles set at different positions. The coverage path length of the deep reinforcement learning algorithm was reduced by 272.79 in compared with that of genetic algorithm, with a reduction rate of 5.09%. The total time consumed by navigation was 1549.24 s, which was 83.15 s shorter than that of the traditional algorithm. The study results manifest that the system can efficiently guide virtual robots to rapidly reach the random picking points on the premise of avoiding obstacles, meet picking task requirements and provide theoretical and technical support for the picking path planning of real robots.

摘要

针对采摘机器人在野外作业环境中, 面临采摘任务数量多, 目标与障碍物位置具有随机性和不确定性等问题, 提出一种基于深度强化学习的虚拟机器人采摘路径避障规划方法, 实现机器人在大量且不确定任务情况下的快速轨迹规划。根据机器人本体物理结构设定虚拟机器人随机运动策略, 通过对比分析不同网络输入观测值的优劣, 结合实际采摘行为设置环境观测集合, 作为网络的输入; 引入人工势场法目标吸引和障碍排斥的思想建立奖惩函数, 对虚拟机器人行为进行评价, 提高避障成功率。仿真实验结果显示, 不同位置障碍物设置情况下虚拟机器人完成采摘任务成功率达 95.5%, 深度强化学习算法覆盖路径长度相比于遗传算法减少了 272.79in, 缩短了 5.09%, 整体导航用时 1549.24s, 相比于传统算法缩短了 83.15s。研究结果表明, 本系统能够高效引导虚拟机器人在避开障碍物的前提下快速到达随机采摘点, 满足采摘任务要求, 为真实机器人采摘路径规划提供理论与技术支撑。

INTRODUCTION

With the growth of global population and the acceleration of urbanization, there is an increasing shortage of agricultural labor force and agricultural production is faced with severe challenges. Meanwhile, consumers have increasingly higher quality and safety requirements for agricultural products, facilitating agricultural production to develop towards intelligent and automatic directions. Emerging rightly under this background, picking robots are the product of combining modern agricultural technologies and robot technologies, aiming to solve such problems as the shortage of agricultural labor force, the improvement of production efficiency and the quality guarantee of agricultural products (Ma et al., 2024). Picking robots are capable of picking operations continuously and stably and immune to the influence of human fatigue and emotions, thus significantly improving production efficiency.

Compared with manual picking, picking robots can complete the picking task faster, reduce the picking cycle and improve the output of agricultural products (Cong *et al.*, 2024). With the shortage of agricultural labor force, labor costs are rising. If applied, picking robots can effectively reduce the dependence on manual labor and reduce labor costs. At the same time, picking robots can also avoid problems such as production delay and output decline caused by labor shortage (Cao *et al.*, 2023).

China is one of the important fruit producers in the world, with its main fruit varieties ranking first in the world since 2012. The labor required for fruit picking accounts for about 40% of the labor required for the whole production process, and the efficiency and quality of fruit picking greatly affect the economic benefits of fruit (Zhao *et al.*, 2023). As population aging is accelerated, the labor cost is getting higher and higher, and the economic and efficient market requirements cannot be satisfied just by relying upon manual picking. Agricultural automatic picking robots can effectively replace manual picking, and solve labor shortage to a great extent (Xu and Zhou., 2023). In the unstructured working environment, how to make the picking robot reach the picking point accurately and quickly and complete the picking task on the premise of ensuring safe operation is a difficulty in the field of manipulator control and also the key to determining whether robots can pick fruit successfully and efficiently. Therefore, the path planning of picking robots is very important.

Literature review on the field of picking robots (especially agricultural robots) mainly includes vision system, path planning, robot control, task scheduling, crop identification, force control and mechanical design. The following are the references and reviews in some key fields, covering the technologies, challenges and latest progress related to picking robots.

In terms of robot path planning methods, such algorithms as A-Star (A*) algorithm (Lehmann and Fendt, 2020), ant colony optimization algorithm (Wang and Zhang, 2021), genetic algorithm (San *et al.*, 2018) and artificial potential field method (Liu and He, 2022) had been widely used in vehicle navigation and path planning research of mobile robots. In the aspect of manipulators, the above algorithms had been mostly used to study the planning problem of low-degree-of-freedom (DOF) manipulators, with some defects such as slow convergence and low efficiency (Zhou and Yu, 2023). In order to solve the path planning problem of multi-DOF manipulators in high-dimensional space, Sun *et al.* (2020) put forward the rapidly-exploring random trees (RRT) algorithm, which avoids space modeling of the traditional method through the collision detection of sampling points in the state space. This algorithm, which could effectively solve the path planning problem in high-dimensional space under complex constraints, had been extensively applied to mobile robot path planning and multi-DOF manipulator path planning (Sun *et al.*, 2020). Considering the disadvantages of the RRT algorithm, Gupta and Shankar (2022) made lots of improvements of this algorithm in optimizing the algorithm path and accelerating the search speed (Gupta *et al.*, 2022). As for the optimization of the algorithm path, the progressively optimal RRT* algorithm and its improved algorithm are the representatives, but the quality of the planned path is improved at the sacrifice of greatly increasing time consumption. In the aspect of accelerating the search speed, Li and Chen (2022) proposed the bidirectional random search tree (BI-RRT) algorithm. On the basis of RRT algorithm, a double-tree extension link was introduced, and two random trees were generated at the same time from the starting point and the end point to search, which greatly reduced the search time. However, this algorithm adopted the idea of random node extension of RRT algorithm, thus having the disadvantage of no goal-oriented configuration. Nof and Sgobbi (2022) put forward the RRT-connect algorithm, which connected two random search trees of BI-RRT algorithm through greedy search strategy, reduced the number of sampling nodes and accelerated the convergence speed of the algorithm. Wei *et al.* improved the RRT-connect algorithm, which further accelerated the search speed. Chen and Zhang (2021) introduced the concept of target gravity and the adaptive parameter adjustment method, and proposed the AtBi-RRT algorithm based on double RRT algorithms, which realized the fast collision-free motion planning of litchi picking.

In the research on agricultural robots, Luo and Wei (2015) introduced the background of agricultural robot technology, covering various applications from crop monitoring to automatic picking, and discussed how unmanned aerial vehicles, mobile robots and other technologies can improve efficiency in agricultural production. Li *et al.* (2011) summarized the progress of fruit picking robot technology, focusing on crop identification, manipulator design and picking strategy, especially their application in automatic picking. Nguyen and Liu (2020) proposed the vision-based crop identification method, which covered the application of deep learning, image processing, stereo vision and other technologies, and analyzed the advantages and disadvantages of different fruit identification methods. Mohanan and Salgoankar (2018) reviewed the application of machine vision in precision agriculture, especially the key technologies in crop monitoring and picking, including visual sensors, image processing technology and deep learning model.

Jiang and Zhao (2020) discussed the path planning of agricultural robots in complex farmland environment, especially the challenges in unstructured environments, such as obstacle avoidance and optimal path search. *Hu et al. (2014)* introduced the route planning method of agricultural robots in a dynamic environment, considering obstacles and the spatial limitation between different crops as well as the optimal picking path design. *Devours et al. (2016)* systematically reviewed the design and control strategy of the manipulator of the picking robot, covering the aspects of force control, grasping and releasing mechanism, adaptive picking of crops and so on.

Ali and Silva (2019) discussed a variety of robot mechanical designs suitable for picking tasks, especially the selection of end effectors, force control strategies and design methods suitable for different crops. *Cui et al. (2016)* discussed the potential of multi-robot cooperation in precision agriculture, especially their application in automatic picking tasks, and analyzed the challenges and opportunities faced by multi-robot cooperation.

Xie and Liu (2019) analyzed the latest research on multi-robot cooperative picking in greenhouse environment, focusing on distributed task scheduling, cooperative path planning and coordination mechanism among robots. *Bac et al. (2014)* discussed the application of deep learning in agricultural robots, with the emphasis laid on the latest research results in the fields of crop detection, automatic picking and image processing based on deep neural networks. *Luo et al. (2016)* discussed the application of artificial intelligence in agricultural picking robots, especially in crop identification, path planning and decision-making systems. Future trends include multimodal learning and adaptive control.

Hernandez and Calderon (2018) discussed the special challenges faced by picking robots for soft fruits (such as strawberries and blueberries), especially the research progress in visual recognition, tactile perception and force control. *Brogli and Rucker (2017)* explored the future development direction of agricultural robot technology, including automatic picking, cooperative robot system, intelligent crop identification and the combination of robots and the Internet of Things. These documents cover a number of key technologies in the field of picking robots, from basic visual perception to complex path planning and cooperation tasks, to the application and challenges of deep learning, and each document is helpful to understand the technological breakthroughs and development trends of agricultural robots in different application scenarios. Agricultural picking robots can not only improve production efficiency but also play an important role in coping with labor shortage and improving crop yield and quality.

Aiming at the above problems, an obstacle avoidance planning system for the picking path of virtual robots based on reinforcement learning was designed with four-DOF picking robots as the study objects. First, the random motion strategy of virtual robots was set according to the physical structure of robots, and environmental observed quantity was reasonably set as the network input by analyzing the actual picking behavior. Then, a reward function was established by introducing the idea of target attraction and obstacle repulsion of the artificial potential field method. Given that the path planning is affected by the range repulsion of the artificial potential field method, a directional penalty obstacle avoidance function was proposed through the motion collision analysis of virtual robots, and the behavior of virtual robots was evaluated, guiding virtual robots to reach the target picking point as soon as possible on the premise of evading obstacles. Finally, the interactive communication between simulation environment and reinforcement learning was established using machine learning agents (ML-Agents) module, and the virtual robots were subjected to picking training via the distributed proximal policy optimization (DPPO) algorithm, expecting to realize the intelligent obstacle avoidance path planning of picking robots.

MATERIALS AND METHODS

In the design of the grape picking robot, the operation was completed in cooperation with the mobile platform under the single-arm picking mode. The configuration design of the 4-DOF manipulator was completed based on picking operation scenes. The picking environment and overall structure of robots are exhibited in Fig. 1.

In order to meet the collection operation needs of grape picking robots, a detachable grape grid collection box was designed. The detachable structure design was convenient for the robot to replace the collection box at the collection point after full loading; the grid structure design could not only avoid the contact damage of fruit stacking in ordinary collection boxes but also provide the location information of collection points for the path planning of collection operations, so as to realize the pre-planning of collection operation paths and save the collection path planning time.



Fig. 1- Schematic diagram of robot picking environment and overall structure

Kinematic model of the manipulator

In the structural design of the picking manipulator, the coordinates of the full-rotation chain-like robot were configured, and the manipulator was completely positioned in the working space via the 4 DOF. Next, the connecting rod coordinate system of the manipulator was established through the D-H parameter method, and its D-H parameters are listed in Table 1.

Table 1

Manipulator D-H parameters

#	$\theta/(\text{°})$	d/mm	a/cm	α/cm
0-1	θ_1	0	0	90
1-2	θ_2	0	270	0
2-3	θ_3	0	180	0
3-4	θ_4	0	180	90

In the forward kinematics solving of the manipulator, the homogeneous transformation matrix of the terminal of the picking manipulator relative to the base coordinate system is 0T_H , the formula is shown in (1).

$${}^0T_H = {}^0T_1 {}^1T_2 {}^2T_3 {}^3T_4 \tag{1}$$

Each row of the D-H parameter table is substituted into Equation (1) to obtain the rotational transformation matrix ${}^nT_{n+1}$ from the previous joint coordinate system $\{n\}$ to the next joint coordinate system $\{n+1\}$, the formula is shown in (2).

$${}^nT_{n+1} = Rot(z, \theta_{n+1}) \times Trans(z, d_{n+1}) \times Trans(x, a_{n+1}) \times Por(x, \alpha_{n+1}) = \begin{bmatrix} C\theta_{n+1} & -S\theta_{n+1}C\alpha_{n+1} & S\theta_{n+1}S\alpha_{n+1} & a_{n+1}C\theta_{n+1} \\ S\theta_{n+1} & C\theta_{n+1}C\alpha_{n+1} & -C\theta_{n+1}S\alpha_{n+1} & a_{n+1}S\theta_{n+1} \\ 0 & S\alpha_{n+1} & C\alpha_{n+1} & d_{n+1} \\ 0 & 0 & 0 & 1 \end{bmatrix} \tag{2}$$

The 4-DOF manipulator was designed based on the Pieper criterion, closed-form solutions exist in inverse kinematics, so the inverse kinematic solution of the manipulator was solved through the analytical method. The obstacle avoidance path planning algorithm of grape picking robots needs to detect the collision information between the manipulator and obstacles. The spatial position and pose of such obstacles as grape vines and leaves coming down in the orchard environment will change easily due to the disturbance of the external environment. To better encircle obstacles, the OBB bounding box with strong tightness, good real-timeliness and random direction was adopted.

Terminal operation path planning

The research on the terminal operation path planning of grape picking robots is mainly divided into the following two parts: The first is the picking operation path planning. According to the known position information, the obstacle-avoidance picking configuration of the manipulator from the initial position to the target position is calculated, and if a group of configurations can realize obstacle-avoidance picking, the obstacle-avoidance path is planned by the deep reinforcement learning algorithm to complete the picking operation. In case that there is no group of configurations that can realize obstacle avoidance picking or the

obstacle avoidance path planning fails, the flexible obstacle avoidance path is planned by the flexible obstacle avoidance strategy to complete the picking operation; if the flexible obstacle avoidance path planning fails, the position of the mobile platform is adjusted and the above operations are repeated at the new position. After picking, robots will return to the original position along the planned path. The second collection operation path planning. The coordinate information of the grape collection point position and the initial position of the manipulator are known. The path of the manipulator from the initial position to the placement position of each collection point is planned in advance by the deep reinforcement learning algorithm, and the collection paths such as b1, b2 and b3 are obtained. After the collection is completed, robots will return to the original position along the planned path. Among them, obstacle avoidance path planning refers to the collision detection of the whole connecting rod of the manipulator, so as to obtain the obstacle avoidance path along which the manipulator will not collide with obstacles during the whole operation. Flexible obstacle avoidance path planning refers to the flexible obstacle avoidance path through which the connecting rod of the manipulator can push aside the flexible obstacles such as vines and leaves laterally and complete the picking operation. In the collection operation, if the traditional collection box is used, it is necessary to identify and locate the grape placement point and conduct path planning once again in each collection operation; if the grid collection box with known location information of collection points is used, time can be greatly saved by directly calling the collection path planned in advance during operation.

Guided reward mechanism design

After initializing actions and states, agents can randomly draw different action strategies according to states, but they fail to evaluate the quality of actions according to states. Designing the guided reward function can evaluate agents' behavior, increase the probability of high-scoring behavior and reduce the probability of low-scoring behavior, and then guide the agents to make correct actions in various environmental states. The reward mechanism determines the effect of training results. A reasonably designed reward function can improve the training speed, reduce the consumption of computer resources and make the training results converge faster. In most cases, continuous reward and penalty information can continuously let the agent get feedback on the action strategy adopted, which is more effective than sparse reward and penalty signals. In this study, a continuous reward function was constructed based on the deep reinforcement learning algorithm, and the agents were guided to reach the target correctly by designing the guidance function and obstacle avoidance function. At the same time, a time function is set to guide the agents to complete the task faster.

When the gravity is set using the traditional artificial potential field method, its value is determined by the current position of the object; when setting the reward function, gravity is represented by the reward signal, which should be determined by the action of the agent. When the terminal actuator cutting point is close to the target point due to the change in the agent's action, a reward will be given and is directly proportional to the approaching distance, otherwise, a penalty will be posed. Under a state s_t , a certain distance exists between the terminal actuator cutting point $pend=(x_{st}, y_{st}, z_{st})$ of the virtual robot and the target picking point $p_{goal}=(x_0, y_0, z_0)$, which is expressed by the target distance D_{s_i} . If this distance is continuously reduced during the training process, the action strategy of the robot is correct and this behavior should be rewarded. The formula for setting the guidance function is shown in (3)-(6):

$$D_{s_i} = \sqrt{(x_{s_i} - x_0)^2 + (y_{s_i} - y_0)^2 + (z_{s_i} - z_0)^2} \quad (3)$$

$$D_{min} = \begin{cases} D_{s_0} & (i = 0) \\ \min(D_{s_i}, D_{min}) & (i \neq 0) \end{cases} \quad (4)$$

$$R_{goal} = \begin{cases} (D_{min} - D_{s_i})k_1 & (D_{s_i} \neq 0) \\ k_2 & (D_{s_i} = 0) \end{cases} \quad (5)$$

where D_{min} is the minimum value of the target distance in one picking round; D_{s_0} represents the initial value of D_{min} under initial state of the picking round; R_{goal} is the reward & penalty value of the target distance; k_1 and k_2 are constants.

As the agent does random actions, D_{s_i} changes, and the minimum value between the two is taken for D_{min} according to Equation (4). When the target distance is shortened, a low reward will be given according to the distance shortened, otherwise, a low penalty will be posed; when the target distance is 0, the robot correctly reaches the target picking point, a high reward will be given, and this round will be ended.

Setting of obstacle avoidance function

When the repulsive force is set by the deep reinforcement learning algorithm, as long as the object enters the potential field of the obstacle, it will be affected by the repulsive force, and the influence is sometimes unnecessary and will affect the planning of the shortest path. As shown in Figure 5, when the obstacle avoidance function is set based on the idea of the artificial potential field method, the repulsive force is represented by a penalty signal. In this case, the shortest path for the virtual robot to reach the target point is a straight line, but its path is deviated due to the influence of the potential field of the obstacle. In order to solve this problem, the spatial motion of the virtual robot was divided into 3 parts: leftward and rightward motion along x axis, back and forth motion along y axis and upward and downward motion along z axis. The range penalty of the obstacle was divided into the penalty of the above three directions of motion, and whether the movement of each rotating shaft of the virtual robot along the x, y and z axes in the current posture might collide with obstacles was judged. If it was possible, the penalty in this direction would be given, otherwise, the penalty in this direction would not be posed, so as to avoid unnecessary penalty on the virtual robot in the correct collision-free movement.

According to the physical structure of the picking robot, each rotating joint shaft of the virtual robot is regarded as a cylinder for the analysis. The random motion strategy of the virtual robot is divided into the motion along axes x, y and z. Given the similarity of motion collision analysis in the directions of the 3 axes, only the upward and downward motion of the rotating joint shaft 4 along axis z was subjected to the collision analysis, and other motion conditions could be obtained in a similar way. Assuming that the current coordinates of the virtual robot's rotating joint shaft 4 are (x_q, y_q, z_q) and those of the obstacle are (x_o, y_o, z_o) , it is necessary to judge whether the rotating shaft 4 will collide with the obstacle during upward and downward motion so as to determine whether to give the penalty. First, the z axis of this rotating shaft experiences translation to a position consistent with the z axis of the obstacle, i.e., the coordinates of this rotating shaft are set to (x_q, y_q, z_o) . In this case, the two are located on x-y plane, as shown in Fig. 2.

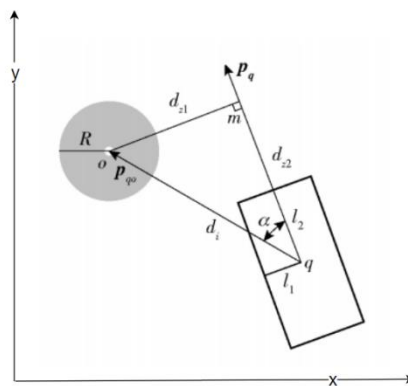


Fig. 2 - Collision analysis of upward and downward motion direction of the virtual robot's rotating shaft

In Figure 2, o represents the obstacle midpoint; R stands for the radius of the obstacle; q is the critical point of the virtual robot's rotating shaft; l_1 is the distance from q to the horizontal cylindrical surface, i.e., the radius of the cylinder; l_2 is 1/2 of the cylinder length; vector p_{qo} denotes the direction vector pointing to the obstacle midpoint o with q as the starting point; vector pq is the current forward direction vector of the virtual picking robot's rotating shaft; α is the included angle between vectors p_{qo} and pq; d_i is the distance between points o and q, which can be calculated through coordinates; d_{z1} represents the horizontal distance between points o and q; d_{z2} is the longitudinal distance between points o and q. It can be known from Figure 6 that d_{z1} and d_{z2} can be solved based on d_i , as follows (6):

$$\begin{cases} d_{z1} = d_i \sin \alpha \\ d_{z2} = d_i \cos \alpha \quad (\alpha > \pi / 2) \\ \alpha = \pi - \alpha \end{cases} \quad (6)$$

When the horizontal distance between points o and satisfies $d_{z1} \leq R + l_1$ and their longitudinal distance meets $d_{z2} \leq R + l_2$, the rotating shaft will probably collide with the obstacle only during upward and downward motion. Hence, the obstacle avoidance coefficient k_z in z direction is set.

When the above collision conditions are met, k_z is 1, otherwise, it is 0. The obstacle avoidance function in the upward and downward motion direction of this rotating shaft is expressed as below (7):

$$R_{obs-z} = k_z \frac{1}{d_z} \tag{7}$$

Similarly, the obstacle avoidance coefficient and function in left-right and back-forth motion directions are set. The obstacle avoidance coefficient and the overall obstacle avoidance function can be expressed as follows (8)-(9):

$$\begin{cases} k_{xi} = \begin{cases} 1, (d_{xi} \leq R + l_{i1} \ \&\& \ d_{xi} \leq R + l_{i2}) \\ 0, \text{else} \end{cases} \\ k_{yi} = \begin{cases} 1, (d_{yi} \leq R + l_{i1}) \\ 0, (d_{yi} > R + l_{i1}) \end{cases} \\ k_{zi} = \begin{cases} 1, (d_{zi} \leq R + l_{i1} \ \&\& \ d_{zi} \leq R + l_{i2}) \\ 0, \text{else} \end{cases} \end{cases} \tag{8}$$

$$\begin{cases} \sum_{i=1}^4 k_{xi} \frac{1}{d_{xi}} + k_{yi} \frac{1}{d_{yi}} + k_{zi} \frac{1}{d_{zi}} & (H \cap O_{obs} = \emptyset) \\ k_{obs} & (H \cap O_{obs} \neq \emptyset) \end{cases} \tag{9}$$

where d_{xi} is the distance between the x-coordinate of the critical point on the virtual robot's rotating shaft i and the x-coordinate of the obstacle, i.e., the left-right distance; d_{yi} represents the longitudinal distance; l_{i1} and l_{i2} stand for the cylinder radius of manipulator i and 1/2 of the cylinder length, respectively; k_{obs} is a collision penalty constant; HO_{obs} is the space set of the virtual robot and obstacle.

Equation (9) takes effect only when the virtual robot enters the range of obstacle repulsion, and its penalty increases as the distance between the critical point on each rotating shaft of the virtual robot and the characteristic direction of the obstacle decreases; in case of robot-obstacle collision, a high penalty will be posed and this round will be ended.

Setting of time function

The time penalty function R_p is set according to the distance traveled under the initial state, calculated as follows (10):

$$R_p = \frac{k_t}{D_{s_0}} \tag{10}$$

where k_t is the time penalty constant.

The designed total reward function is the cumulative sum of the above 3 functions, which can be expressed as bellows (11):

$$R = R_{goal} + R_{obs} + R_p \tag{11}$$

RESULTS

In order to verify the effectiveness of the algorithm, a simulation experiment was performed on the MATLAB platform. After establishing the forward and inverse kinematics models of the manipulator, the position of the manipulator joint 1 was set to (0,0,0), and the initial position configuration of the manipulator was set to (0°, -60°, 120°, 0°), which ensured the flexibility of bidirectional movement to the target position of the fruit stalk picking point and the collection position of the collection box. A deep reinforcement learning algorithm was compiled, and the step size was set to 2°, and the path planning simulation experiment was carried out in different environments.

Picking path planning of deep reinforcement learning algorithm

The simulation experiment scene was set as a 700in×700in operation area of the grape picking robot. See Fig. 3 for the specific distribution of picking points in the operation area. The path planning problem of multiple picking points in obstacle-free space was solved using the deep reinforcement learning algorithm, the grape picking task was completed based on this algorithm, and the convergence curve of the algorithm is displayed in Fig. 4. The grape picking robot's path planning based on the deep reinforcement learning algorithm is exhibited in Fig. 5. From the convergence of the fitness curve of 49 task points in Figure 2, the optimal traversal path was found through the 132nd epoch of the deep reinforcement learning algorithm. The deep reinforcement learning algorithm achieved a relatively good convergence effect, indicating its strong model solving ability.

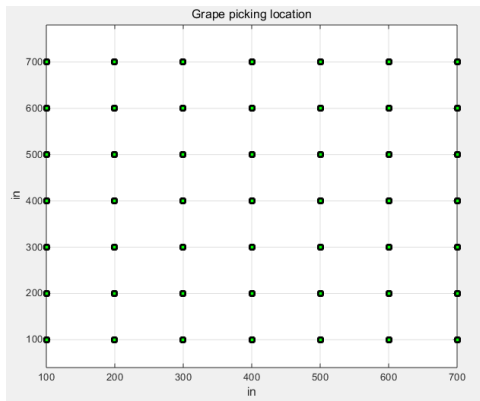


Fig. 3 - Length of operation area and position coordinates of picking points (m)

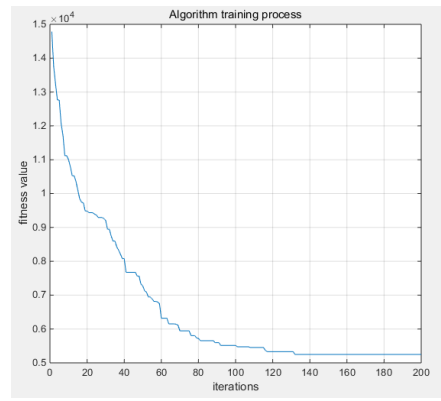


Fig. 4 - Convergence curve of deep reinforcement learning algorithm

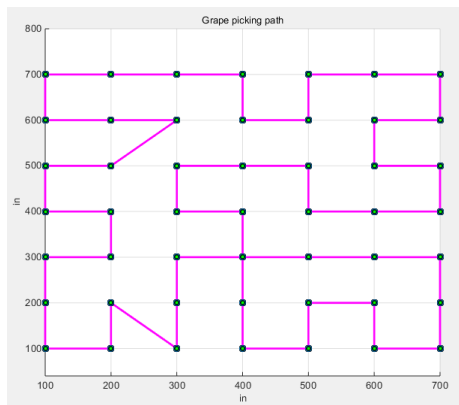


Fig. 5 - Path planned by deep reinforcement learning algorithm

Algorithm verification

To explore the stability of the algorithm and verify the effectiveness of the deep reinforcement learning algorithm, the traditional genetic algorithm solving model was also designed in this study. The number of grape picking points was 49, the minimum value of two-dimensional coordinates was 100in, the maximum value of two-dimensional coordinates was 700in, the maximum number of epochs in genetic algorithm parameters was popsize (population size) =100, the tournament size was tournament_size=5, the crossover probability was pc=0.95, and mutation probability was pm=0.1. Model solving was performed to obtain the path diagram of the traditional genetic algorithm, as shown in Fig. 6 The convergence curve of the traditional genetic algorithm is displayed in Fig. 7.

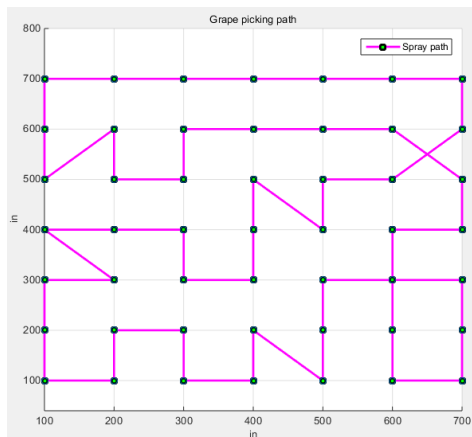


Fig. 6 - Path diagram of traditional genetic algorithm

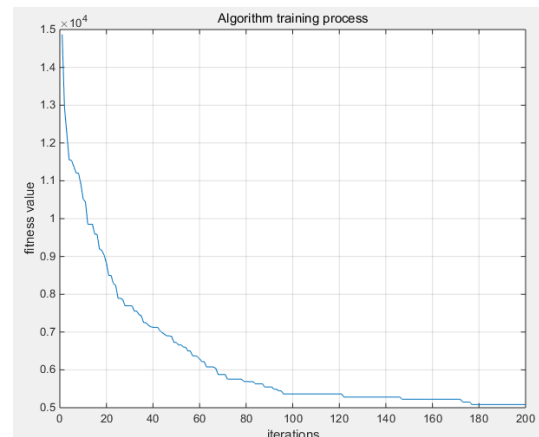


Fig. 7 - Convergence curve of traditional genetic algorithm

It could be observed that compared with the traditional genetic algorithm, the deep reinforcement learning algorithm was more exploratory and convergent, accompanied by the better value of the objective function.

Besides, the deep reinforcement learning algorithm performed better than the traditional genetic algorithm in the number of inflection points, convergence time and convergence algebra. In this study, an improved deep reinforcement learning algorithm was proposed to solve the traversal order of the grape picking robot in each picking area. First, a path quality evaluation function was established, the length of the coverage path was taken as an evaluation index to comprehensively score the coverage path planned in each round, and this score was used as the criterion for the subsequent reward assignment. Then, to enhance the global correlation of the model, the action value in each round was updated on the whole by setting an empirical repository, so as to accelerate the model learning efficiency in the initial stage. Finally, an empirical backtracking mechanism was established, and high-score paths were selected for empirical backtracking to enhance their positive guiding effect on the model. The model training results revealed that the deep reinforcement learning algorithm could complete convergence faster at the relatively optimal solution than the traditional genetic algorithm. Additionally, the navigation test results in the grape orchard manifested that the length of the coverage path obtained by the proposed method was reduced by 272.79in compared with the traditional genetic algorithm, with a reduction rate of 5.09%, and the total time consumption by navigation was 1549.24 s, which was 83.15 s shorter than that consumed by the traditional algorithm. This indicates that the coverage path planning method raised in this study can effectively shorten the length of the grape picking robot's coverage length and improve the navigation efficiency of the grape picking robot.

CONCLUSIONS

Given the large number of picking tasks in orchards and the highly random fruit distribution, a set of virtual obstacle positions based on deep reinforcement learning were set for the sake of real-time efficient path planning. The results of the simulation experiment showed that the picking success rate reached above 95.5%. Besides, a reward function setting method was put forward, i.e., introducing the idea of target attraction and obstacle repulsion of the artificial potential field method, aiming to increase the success rate of obstacle avoidance during picking. Considering that the shortest path planning was affected by the range repulsion of the artificial potential field method, a directional penalty obstacle avoidance function and a robot collision analysis model were established, facilitating the robot to make correct decisions and prevent unnecessary penalties and improving the picking efficiency. To verify the effectiveness of the proposed method, the picking performance contrast experiments under different reward functions were designed. The results manifested that the length of the coverage length was 272.79in, which was 5.09% shorter than that obtained by the genetic algorithm, and the total time consumption by navigation was 1549.24 s, which was 83.15 s shorter than that obtained by the traditional algorithm. The model and method involved in this paper can quickly complete the path planning of grape picking tasks under various conditions, but there is still small probability of picking failure under harsh picking conditions, which has certain shortcomings. In the follow-up study, the picking situation under special conditions will be processed, and the path planning in the case of irregular shape obstacles will be discussed to further improve the robustness of the system.

REFERENCES

- [1] Ali, H., & De Silva, C.W. (2019). Path Planning for Agricultural Robots: Algorithms, Challenges, and Applications. *IEEE International Conference on Robotics and Automation (ICRA)*, pp. 1234-1241, Canada.
- [2] Bac, C.W., Hemming, J., & Van Henten, E.J. (2014). Stem localization of sweet-pepper plants using the support wire as a visual cue. *Computers and Electronics in Agriculture*, Vol. 105, pp. 111–120, United Kingdom.
- [3] Brogli, R., & Rucker, D. (2017). Robots in Agriculture: A Review of Current Applications and Future Opportunities. *Precision Agriculture*, Vol. 18, pp. 471-486, Netherlands.
- [4] Cao, X. M., Wu, B., & Chen, H., Chen, C.Y., Huang, X. (2023). Path planning for a six degree of freedom harvesting robot (六自由度采摘机器人路径规划). *China Science and Technology Information*, Vol.21, pp. 87-90, Beijing/China.
- [5] Chen, Y., & Zhang, J. (2021). Mechanical Design and Control of Robotic Systems for Agricultural Harvesting Tasks. *Frontiers in Robotics and AI*, Vol. 8, pp. 63, Switzerland.
- [6] Cong, C., Liang, Y. Q., & Liu, J. D., Chen, H.Y. (2024). Full Automatic Picking Robot for Soft Date Kiwifruit (软枣猕猴桃全自动采摘机器人设计). *Journal of Jiamusi University (Natural Science Edition)*, Vol. 41, pp. 106-109, Jiamusi/China.

- [7] Cui, R., Li, Y., & Yan, W. (2016). Mutual information-based multi-AUV path planning for scalar field sampling using multidimensional RRT. *IEEE Transactions on Systems, Man and Cybernetics: Systems*, Vol.46, pp. 993–1004, United States.
- [8] Devaurs, D., Siméon, T., & Cortés, J. (2016). Optimal Path Planning in Complex Cost Spaces with Sampling-Based Algorithms. *IEEE Transactions on Automation Science and Engineering*, Vol.13, pp. 415-424, United States.
- [9] Gupta, S., & Shankar, A. (2022). Artificial Intelligence for Harvesting Robots: A Comprehensive Review of AI-Based Approaches and Future Trends. *Artificial Intelligence in Agriculture*, Vol.5, pp. 88-105, Beijing/China.
- [10] Hernandez, J., & Calderon, R. (2018). Robotic Harvesting of Fruit Crops: A Review of the State of the Art and Future Directions. *Robotics*, Vol. 7, pp. 46, Switzerland.
- [11] Jiang, H., & Zhao, X. (2020). Robotic Harvesting Mechanisms: A Comprehensive Review of Designs, Control Strategies, and Applications. *Advanced Robotics*, Vol. 34, pp. 325-343, Japan.
- [12] Lehmann, A., & Fendt, J. (2020). Multi-Robot Systems in Precision Agriculture: Opportunities and Challenges for Automated Harvesting. *Journal of Field Robotics*, Vol.37, pp. 1169-1185, United States.
- [13] Li, B. H., Chen, B. D. (2022). An adaptive rapidly-exploring random tree. *IEEE/CAA Journal of Automatica Sinica*, Vol.9, pp. 283-294, Beijing/China.
- [14] Li, P., Lee, S. H., & Hsu, H. Y. (2011). Review on fruit harvesting method for potential use of automatic fruit harvesting systems. *Proceedings of the 2011 International Conference on Power Electronics and Engineering Application*, Vol. 12, pp. 351–366, Shanghai/China.
- [15] Liu, Z., & He, Z. (2022). Collaborative Harvesting Using Multiple Robots in Greenhouses: A Survey. *International Journal of Advanced Robotics Systems*, Vol. 19, pp. 102, Austria.
- [16] Luo, H., & Wei, G. (2015). System design and implementation of a novel robot for apple harvest. *INMATEH-Agricultural Engineering*, Vol. 46, pp. 85-94, Romania.
- [17] Luo, L., Tang, Y., Zou, X., Ye, M., Feng, W., & Li, G. (2016). Vision-based extraction of spatial information in grape clusters for harvesting robots. *Biosystems Engineering*, Vol. 151, pp. 90–104, United Kingdom.
- [18] Ma, X.J., Shi, X.Y., & Xiao, W.X., Ren, M.T., Bao, M.L. (2024). Multi-objective continuous picking path planning for citrus based on TSP__RRT algorithm (基于 TSP__RRT 算法的柑橘多目标连续采摘路径规划). *Acta Agriculturae Universitatis Jiangxiensis*, Vol. 46, pp. 490-501, Nanchang/China.
- [19] Mohanan, M. G. & Salgoankar, A. (2018). A survey of robotic motion planning in dynamic environments. *Robotics and Autonomous Systems*, Vol. 100, pp. 171-185, Netherlands.
- [20] Nguyen, T., & Liu, W. (2020). Trajectory Planning for Autonomous Agricultural Robots in Dynamic Environments. *Journal of Field Robotics*, Vol.37, pp. 955-973, United States.
- [21] Nof, S. Y., & Sgobbi, F. (2022). Challenges in Robotic Harvesting of Soft Fruits: A Survey on Perception, Control, and Automation. *Robotics and Autonomous Systems*, Vol. 134, pp. 103617, Netherlands.
- [22] San Juan, V., Santos, M., & Andújar J. M. (2018). Intelligent UAV Map Generation and Discrete Path Planning for Search and Rescue Operations. *Complexity*, Vol.17, pp. 6879419, United States.
- [23] Sun, Y. X., Zhang, C. R., Sun, P. C. (2020). Safe and smooth motion planning for mecanum-wheeled robot using improved RRT and cubic spline. *Arabian Journal for Science and Engineering*, Vol.45, pp. 3075-3090, Saudi Arabia.
- [24] Wang, J., & Zhang, Y. (2021). Deep Learning for Agricultural Robotics: Applications in Harvesting, Monitoring, and Control. *Computers and Electronics in Agriculture*, Vol.183, pp.105964, United Kingdom.
- [25] Wei, W., Ouyang, D. T., Lu, S., & Feng Y.X. (2011). Multiobjective path planning under dynamic uncertain environment. *Jisuanji Xuebao/Chinese Journal of Computers*, Vol. 34, pp. 836–845, Beijing/China.
- [26] Xie, L., & Liu, H. (2019). A Review of Vision-Based Approaches for Fruit Detection and Localization in Robotic Harvesting. *Computers and Electronics in Agriculture*, Vol.158, pp. 49-61, United Kingdom.
- [27] Xu, N., & Zhou, W.M. Research on Global Coverage Path Planning of Picking Robot Based on Adaptive Ant Colony Algorithm (采摘机器人全局覆盖路径规划研究——基于自适应蚁群算法). *Journal of Agricultural Mechanization Research*, Vol. 45, pp. 213-216, Haerbin/China.
- [28] Zhang P., Song J., Gong S., & Muham, P.D. (2014). A kinematic analysis and simulation based on ADAMS for eggplant picking robot. *INMATEH-Agricultural Engineering*, Vol. 43, pp. 51-60, Romania.

- [29] Zhao, J.Z., Wang, H.C., & Yu, Y.H., Li, J.P. (2023). Design of Safety Protection for Deep Reinforcement Learning Picking Robot(深度强化学习采摘机器人安全防护设计). *Computer Simulation*, Vol. 40, pp. 448-453, Beijing/China.
- [30] Zhou, J., & Yu, C. (2023). Future Directions in Agricultural Robotics: Emerging Technologies for Smart Harvesting. *Journal of Field Robotics*, Vol.40, pp. 501-520, United States.

RESEARCH ON THE INFLUENCE OF THE MAIN VIBRATION-GENERATING COMPONENTS IN GRAIN HARVESTERS ON THE OPERATOR'S COMFORT

CERCETĂRI PRIVIND INFLUENȚA PRINCIPALELOR COMPONENTE GENERATOARE DE VIBRAȚII DIN CADRUL COMBINELOR DE RECOLTAT CEREALE ASUPRA CONFORTULUI CONDUCĂTORULUI

Eugen MARIN¹⁾, Petru CÂRDEI¹⁾, Valentin VLĂDUȚ¹⁾, Sorin-Ștefan BIRIȘ²⁾, Nicoleta UNGUREANU²⁾, Sorin Tiberiu BUNGESCU³⁾, Iulian VOICEA¹⁾, Dan CUJBESCU¹⁾, Iuliana GĂGEANU¹⁾, Lorena-Diana POPA⁴⁾, Simona ISTICIOAIA⁴⁾, Gheorghe MATEI⁵⁾, Sorin BORUZ⁵⁾, Gabriel TELIBAN⁶⁾, Cristian RADU⁵⁾, Onder KABAS⁷⁾, Ioan CABA¹⁾, Joński MACIEJ⁷⁾

¹⁾INMA Bucharest / Romania; ²⁾University POLITEHNICA Bucharest/ Romania; ³⁾USV "King Mihai I" Timișoara / Romania; ⁴⁾ARDS Secuieni / Romania; ⁵⁾University of Craiova / Romania; ⁶⁾University of Life Sciences Iași / Romania; ⁷⁾Akdeniz University / Turkey;

⁷⁾Warsaw University of Life Sciences / Poland

E-mail: petru_cardei@yahoo.com, valentin_vladut@yahoo.com, okabas@akdeniz.edu.tr; cabaioan@yahoo.com

DOI: <https://doi.org/10.35633/inmateh-74-71>

Keywords: harvesters, "vibration effects", driver, comparison, human body

ABSTRACT

The research aims to estimate the influence of the main vibration sources in grain harvesters on the combine operator. The study also has a comparative aspect, including two harvesters, a conventional one (C 110H) and one with an axial flow (CASE IH). The main sources of vibration considered were the thresher, chassis, and header for both types of harvesters, with the addition of the shaker as a source for the conventional harvester. The receiver is considered to be the operator's seat. The emission spectra of each source are recorded according to ISO 2631-1:2001 and ISO 2631-5:2018, as well as the spectrum received at the operator's seat. To estimate the influence of vibration sources on the operator's seat, interspectral correlations and influence coefficients were studied. The conclusions are useful for ranking the intensity of vibration sources affecting the operator's comfort and for comparing the comfort level between two grain harvesters with different operational technologies. What the paper introduces as new in the field of estimating the exposure time limit to harvester vibrations is the calculation algorithm for the exposure time limit and vibration intensity estimators.

REZUMAT

Cercetările vizează estimarea influenței principalelor surse de vibrații ale combinelor de recoltat cereale asupra conducătorului combinei. Studiul are și un caracter comparativ, incluzând două combine, una clasică (C 110H) și una cu flux axial (CASE IH). Ca surse principale de vibrații s-au considerat batoza, șasiul și hederul, la ambele tipuri de combine, în plus, la cea clasică fiind considerată ca sursă și scuturătorul, receptorul fiind considerat scaunul conducătorului. Spectrele de emisie ale fiecărei surse sunt înregistrate conform ISO 2631-1:2001 și ISO 2631-5:2018, ca și spectrul recepționat la scaunul conducătorului. Pentru estimarea influenței surselor de vibrație la scaunul conducătorului s-au studiat corelațiile interspectrale și coeficienții de influență. Concluziile sunt utile pentru ierarhizarea intensității surselor de vibrație asupra confortului conducătorului și pentru compararea confortului conducătorului pe două combine de recoltat cereale cu tehnologii diferite de funcționare. Ceea ce introduce nou lucrarea, în domeniul estimării timpului limită de expunere la vibrațiile combinelor este algoritmul de calcul al timpului de expunere limită și estimatorii intensității vibrației.

INTRODUCTION

The issue of estimating the effects of vibrations, waves, and shocks on humans, and generally on all living beings and the environment, benefits from a vast and long-standing literature (Zander, 1972).

The problem of estimating the effects of vibrations has theoretical solutions (Chen et al., 2020; Xinjie et al., 2002; Godzhaev et al., 2020; Pang et al., 2019), but the most reliable ones remain experimental or theoretical-empirical solutions (Vlăduț et al., 2006; Vlăduț et al., 2013; Almosawi et al., 2016; Pang et al., 2019; Zare et al., 2019; Feijoo et al., 2020; Yanchun et al., 2017; Xu et al., 2019; Jiangtao Jet al., 2020), or mixed approaches (Sirotin et al., 2019; Tang et al., 2018; Li et al., 2021). Many studies have focused on the vibrations of a single component of grain harvesters (Yanchun et al., 2017; Zare et al., 2019; Xinjie et al., 2002). Comprehensive studies and research have addressed the harvester operator's seat as a subject (Xu et al., 2019; Jahanbakhshi et al., 2020).

Theoretical-empirical models for harvesters have been developed for practical purposes, succeeding in improving their operational quality (Zhang and Peng, 2018). The works (Chuan-Udom S., 2010;2019; Pang et al., 2019) are dedicated to the redesign of cutting blades in grain harvesters to reduce vibrations and material losses. The vibrations of a bearing in the straw chopper of a harvester form the subject of an article that seeks to increase its reliability (Jotautiene et al., 2019). Other authors have developed modern systems for measuring the vibrations of grain harvesting combines (Yilmaz and Gokduman, 2020).

Regarding the estimation of the exposure time limit to vibrations from grain harvesters for their operators, this field is also present in the literature (Almosaw et al., 2016).

Vibration measurements have been conducted on most types of combine harvesters, some of the most well-known being Laverda L 6261, New Holland TX 66, New Holland TC 56, Topliner 4075, Bizon Record Z 058, Sema 140 M, C 110H, CASE IH (Vlăduț et al., 2006). Tsujimura et al., (2015), conducted research on a wide range of farm equipment used in rice cultivation, including harvesters.

The issue of human body exposure to vibrations is studied in well-known laboratories, resulting in interesting reports and studies for practical applications as well as for establishing equivalencies between various evaluation systems (Silsoe Research Institute, 2005; Guidance on Regulations, 2005; HaSPA, 2012; ISO 5008, 2002; ISO 2631-1, 1997; ISO 2631-5, 2018). An alternative to calculating the exposure time limit to vibrations as done by Vlăduț et al., (2006), Biriş et al., (2022), is the calculation of the effect of exposure to vibrations, as described, for example, in (<https://www.safeworkaustralia.gov.au>). Their equivalence or conversion remains to be established.

To increase the functional performance of agricultural machines, the producers of agricultural machines find solutions to limit the exposure of agricultural operators to vibrations (Vlăduț et al., 2013; Sorică et al., 2017; Zhiming et al., 2021; Junming et al., 2021). Also, they are looking for solutions to improve the comfort of the tractor operator, such as: cab suspension systems, front suspensions, or active seats (Cârdei et al., 2023; Vlăduț et al., 2014).

Our contributions to analysing the effects of vibrations on the driver and the quality of the combined work are focused in four directions. The first direction of the study was the development of a method for estimating the intensity of the effect of each vibration source on the combine on the driver's seat (implicitly the driver). In this sense, linear multivariate statistical analysis was used. The linear regression coefficients were assimilated with the influence coefficients.

A second contribution was formulating a mathematical model for the diagram of the limit times of exposure to vibrations of the human body. This model was used to estimate the limit working times of drivers, objectively, facilitated by the mathematical formulation (the mathematical model). A third contribution consisted of using an older measure of the effect of vibrations, namely the vibration intensity. This measure was also used to estimate the effect of vibrations on the driver. The last contribution is the comparison of the performances of the two combines analysed, which highlighted the superiority of the CASE IH combine, of more recent construction and with technological solutions that eliminate important sources of vibrations.

MATERIALS AND METHODS

- *Research material*

The research material consists of the spectra recorded in both stationary and working modes for the C110H and CASE IH harvesters.



Fig.1 - C 110H harvester, perspective view

To measure the vibrations produced by a machine or agricultural equipment on the operator, the vibrations transmitted to the operator's seat are determined.

The vibrations transmitted to the operator's seat represent the vibrations produced by the harvester's thresher, header, and shakers, transmitted through the chassis to the cabin, and from its platform to the seat.

This was achieved using Bruel & Kjaer accelerometers, Analog Devices amplifiers, a DAP 2400 data acquisition system, and a Laptop, which measured longitudinal, transverse, and vertical accelerations for two operating conditions where significant vibrations occur: stationary and during operation (wheat harvesting), using a medium-capacity harvester with a tangential threshing system – the C 110H (Figure 1).

The transducers (accelerometers) were mounted on flat surfaces, as level as possible, and as close as possible to the working part whose vibrations were to be measured. These accelerometers were not mounted directly on the working parts since most of the harvester's vibration-producing components are in motion: the shakers, cleaning system, threshing drum (rotor), etc., except for the header, where the moving working parts are incorporated into it.

As can be observed, both in the case of measuring the vibrations produced by the shakers (Figure 2), transmitted to the harvester, and those produced by the other working parts of the machine, mainly transmitted to the operator's seat, as well as those produced by the threshing drum (Figure 3), the attempt was made to mount the accelerometers measuring the accelerations in all three directions as close as possible to the source of the vibrations, in such a way that other conditions were also respected: the surface on which they were mounted had to be smooth and not inclined.



Fig. 2 - Accelerometers mounted near the shaker drive shaft



Fig. 3 - Accelerometers mounted near the threshing drum rotor drive wheel

When measuring the vibrations on the harvester's chassis (Figure 4) and its header (Figure 5), the accelerometers were mounted on the rigid chassis frame, which was considered to absorb most of the vibrations transmitted from the other working parts of the harvester, or directly on the side surface of the header, where there were no issues with flat surfaces, etc.



Fig. 4 - Accelerometers mounted on the harvester chassis

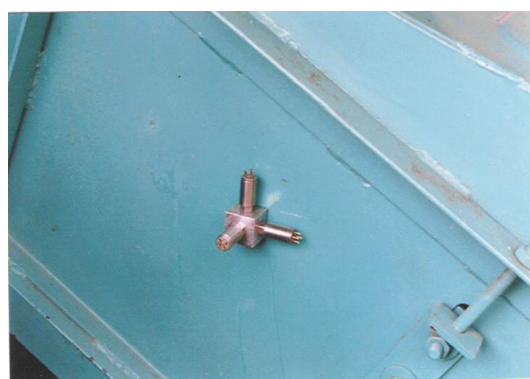


Fig. 5 - Accelerometers mounted on the harvester header

The main purpose of the measurements was to determine to what extent the vibrations produced by the main components of the harvester affected the health of the operator. For this, the vibrations transmitted to the harvester seat (Figure 6) were measured for both the C 110H and CASE-IH harvesters.



Fig. 6 - Accelerometers mounted on the harvester seat

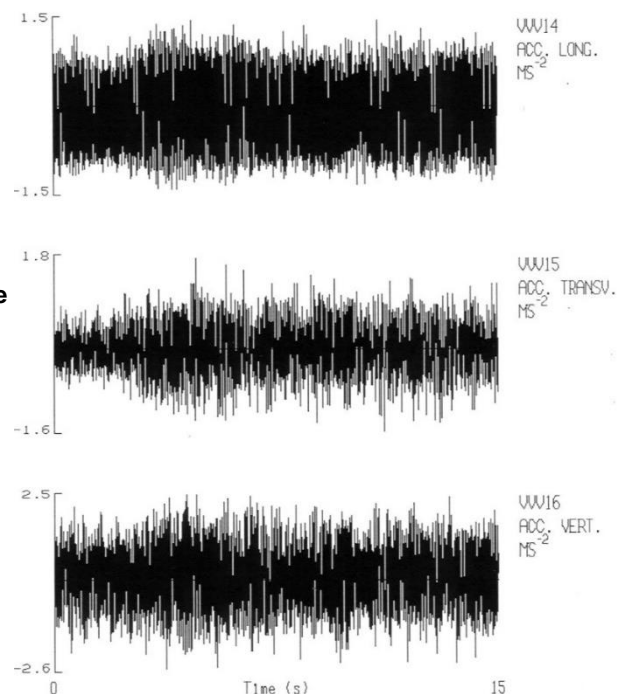


Fig. 7 - CASE-IH harvester, perspective view

The measurements were conducted in parallel for the two types of harvesters: tangential flow and axial flow, to highlight if one type of system and the harvester construction derived from its use produce fewer vibrations than the other type.

The vibrations were measured in three directions: x, y, and z, recording longitudinal, transverse, and vertical accelerations corresponding to the three directions simultaneously (Figure 8).

Fig. 8 - Measuring vibrations in the three directions: x, y, and z



After collecting the data, the processing began, resulting in nomograms that include: the variation of accelerations in the three directions depending on the measurement time (the entire signal), and to visualize the signal shape more clearly, a portion of the signal was taken where the following were determined: maximum value, minimum value, and the average values (Figure 8). The final step of this processing was the visualization of the accelerations on a diagram (third-octave analysis) depending on the frequency band.

For the C 110H harvester, the spectral data included in the study are presented graphically in Figures 9-13.

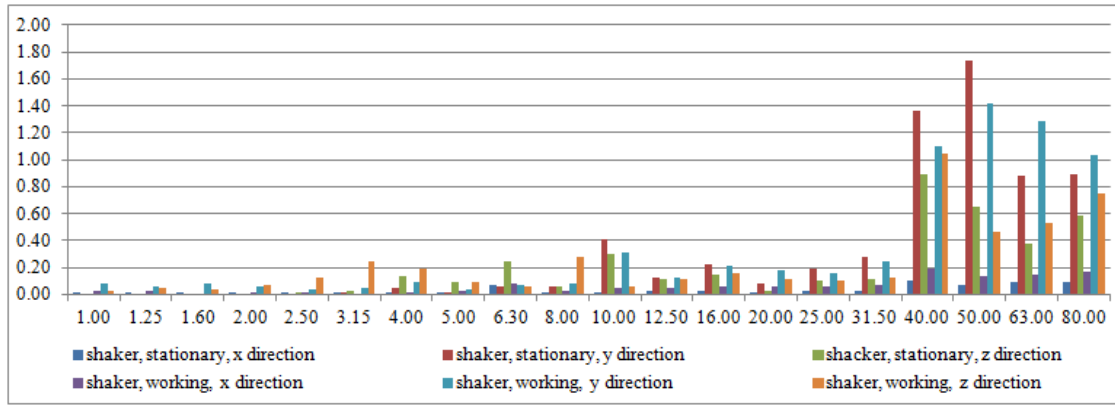


Fig. 9 - Typical spectrum generated by the shaker of the C 110H harvester
(horizontal axis: frequency in Hz; vertical axis: RMS acceleration, m/s²)

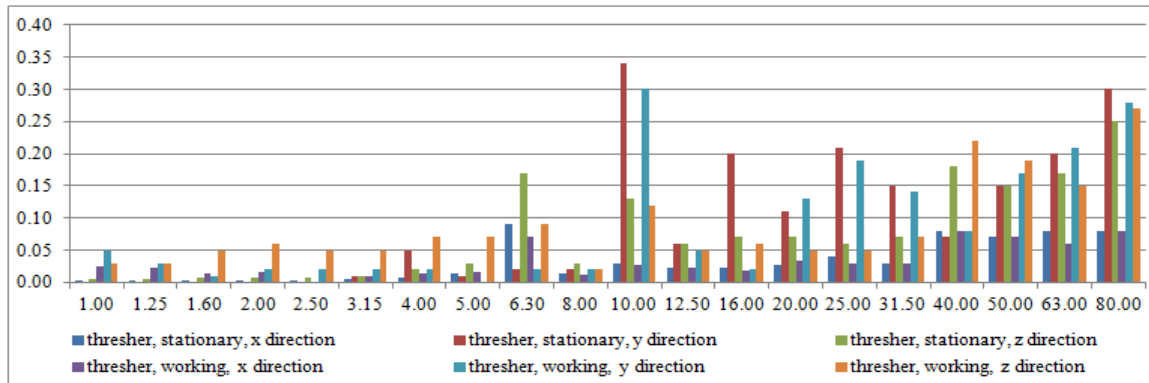


Fig. 10 - Typical spectrum generated by the thresher of the C 110H harvester
(horizontal axis: frequency in Hz; vertical axis: RMS acceleration, m/s²)

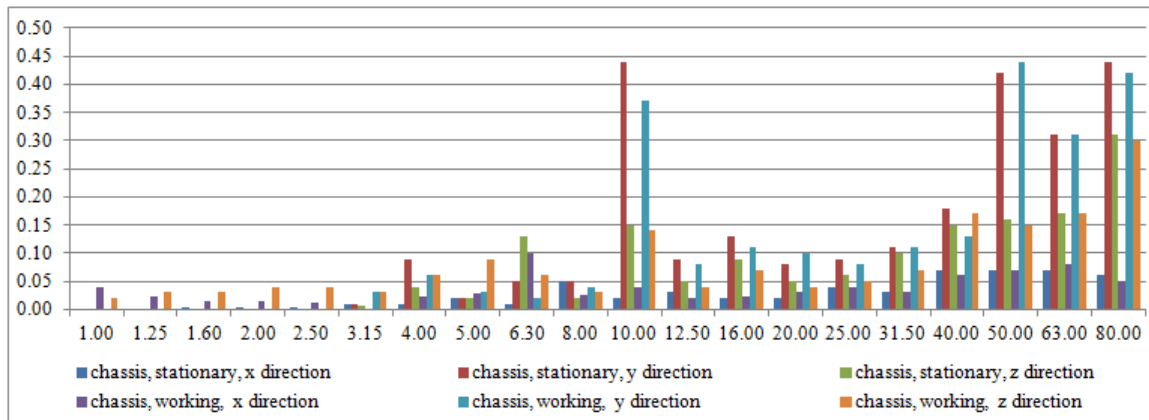


Fig. 11 - Typical spectrum generated by the chassis of the C 110H harvester
(horizontal axis: frequency in Hz; vertical axis: RMS acceleration, m/s²)

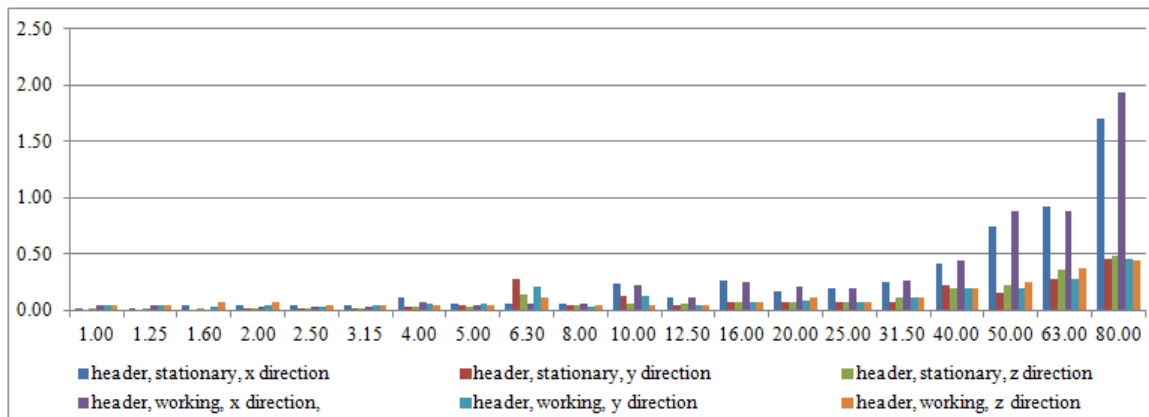


Fig. 12 - Typical spectrum generated by the header of the C 110H harvester
(horizontal axis: frequency in Hz; vertical axis: RMS acceleration, m/s²)

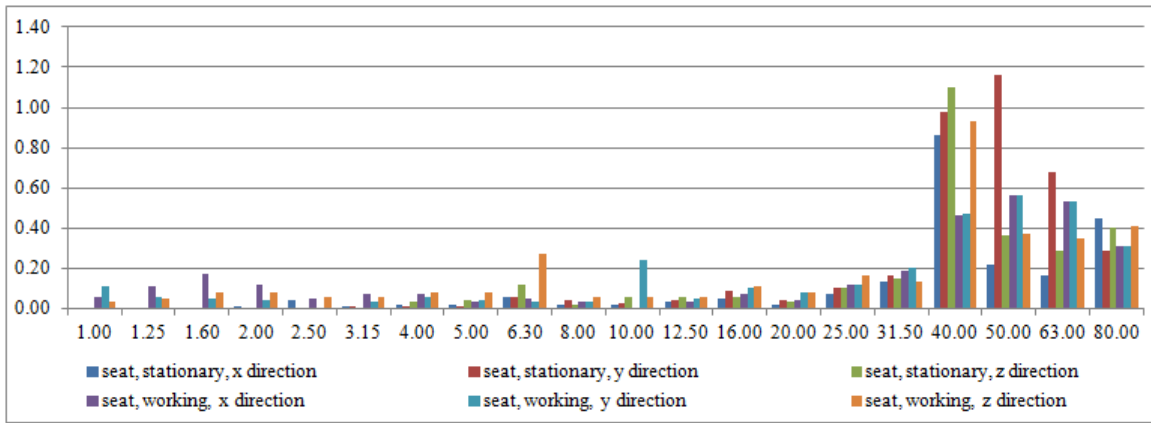


Fig. 13 - Typical spectrum received at the operator's seat of the C 110 H harvester
(horizontal axis: frequency in Hz; vertical axis: RMS acceleration, m/s²)

For the CASE IH harvester, the spectra of the main sources and the receiver are shown in Figures 14-17.

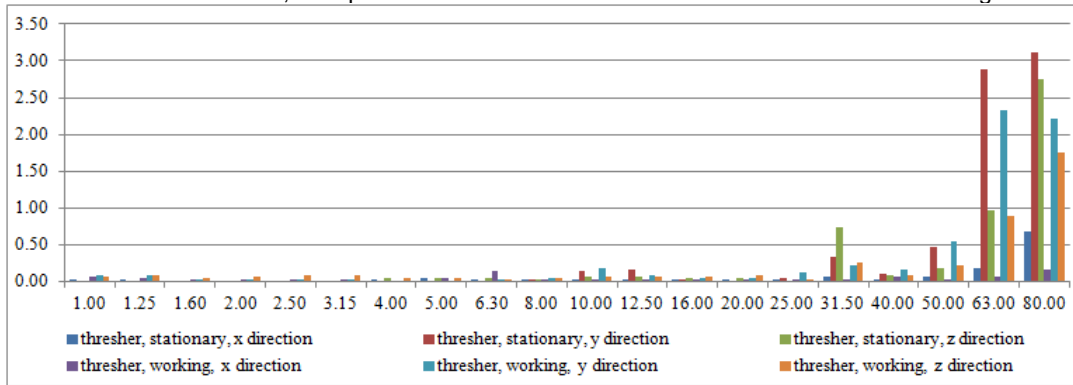


Fig. 14 - Typical spectrum generated by the thresher of the CASE IH harvester
(horizontal axis: frequency in Hz; vertical axis: RMS acceleration, m/s²)

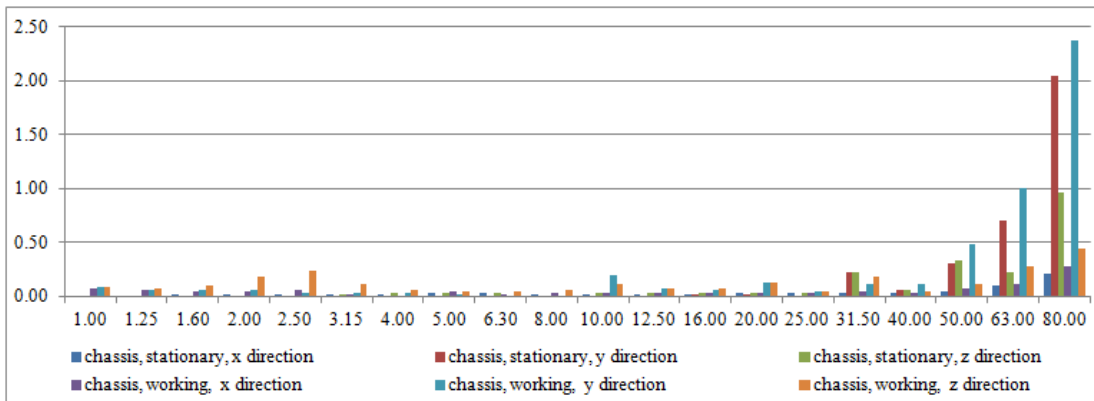


Fig. 15 - Typical spectrum generated by the chassis of the CASE IH harvester
(horizontal axis: frequency in Hz; vertical axis: RMS acceleration, m/s²)

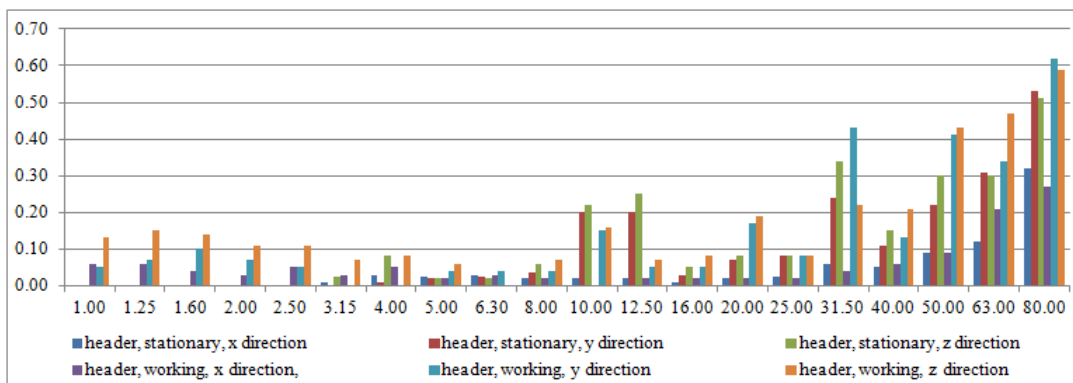


Fig. 16 - Typical spectrum generated by the header of the CASE IH harvester
(horizontal axis: frequency in Hz; vertical axis: RMS acceleration, m/s²)

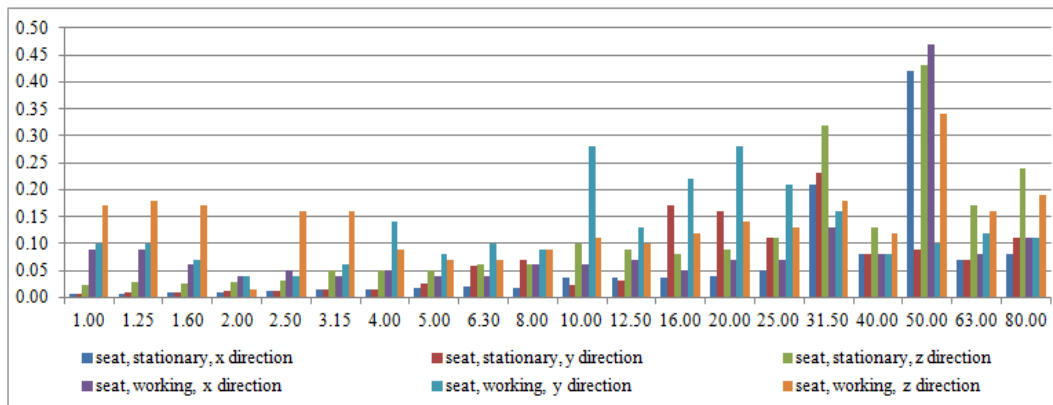


Fig. 17 - Typical spectrum received at the operator's seat of the CASE IH harvester (horizontal axis: frequency in Hz; vertical axis: RMS acceleration, m/s²)

• Data processing method

The three main objectives of the research are related to the influence of the main vibration sources on the harvester operator: *interspectral correlations*, *influence coefficients*, and *the operator's exposure time limit to vibrations*. Additionally, a *coherence degree* between the generating spectra and the receiver is defined, somewhat similar to the correlation between the same spectra. Along with these estimators of the effects of harvester vibrations on the operator, other factors include *vibration intensity*, *perception degree*, and *perception coefficient*, defined similarly to those in *Buzdugan et al., (1982)*.

RESULTS

• Interspectral correlations

One method to study the influence of a vibration source on a receiver is to calculate the correlation between the source spectrum and the receiver spectrum. When there are multiple sources, even if the absolute value of the correlation between the spectrum of one source and that of the receiver does not provide very interesting information, comparing the correlations for multiple sources allows for the ranking of the influence of the considered sources on the receiver.

Table 1

Correlations between the vibration spectra from the operator's seats and the generating sources in the harvesters

Operator's seat	Acceleration	Working mode	C 110H harvester				CASE IH harvester		
			<i>shaker</i>	<i>thresher</i>	<i>chassis</i>	<i>header</i>	<i>thresher</i>	<i>chassis</i>	<i>header</i>
			<i>ax</i> [m/s ²]	stationary	0.778	0.661	0.69	0.56	0.151
	in operation	0.799	0.728	0.54	0.657	0.012	0.189	0.238	
<i>ay</i> [m/s ²]	stationary	0.963	0.281	0.606	0.517	0.194	0.253	0.403	
	in operation	0.969	0.643	0.804	0.676	-0.028	-0.022	0.11	
<i>az</i> [m/s ²]	stationary	0.912	0.685	0.604	0.583	0.476	0.637	0.794	
	in operation	0.907	0.809	0.668	0.629	0.287	0.284	0.615	
Resultant	stationary	0.953	0.504	0.615	0.598	0.357	0.422	0.649	
	in operation	0.93	0.635	0.636	0.592	0.343	0.345	0.697	

• Coherence degree

Similar information regarding the influence of vibration sources on seat vibrations can be obtained using a measure similar to the coherence degree (*Shin and Hammond, 2008*), defined for the power spectra of the sources and the receiver, but applied to the spectra in the database presented in Figures 1-9. The coherence degree values between the spectra of the harvester operators' seats (receivers) and the source spectra are given in Table 2.

Table 2

Coherence degree of the vibration spectra from the operators' seats and the generating sources in the harvesters

Operator's seat	Acceleration	Working mode	C 110H harvester				CASE IH harvester		
			<i>shaker</i>	<i>thresher</i>	<i>chassis</i>	<i>header</i>	<i>thresher</i>	<i>chassis</i>	<i>header</i>
			<i>ax</i> [m/s ²]	stationary	0.681	0.558	0.577	0.456	0.104

	a_y [m/s ²]	in operation	0.803	0.743	0.621	0.597	0.253	0.333	0.344
		stationary	0.942	0.258	0.515	0.434	0.159	0.171	0.436
		in operation	0.955	0.655	0.786	0.694	0.131	0.131	0.381
	a_z [m/s ²]	stationary	0.86	0.59	0.518	0.496	0.335	0.504	0.789
		in operation	0.896	0.789	0.677	0.637	0.27	0.623	0.729
	Resultant	stationary	0.93	0.45	0.542	0.515	0.263	0.302	0.647
in operation		0.884	0.545	0.56	0.509	0.227	0.278	0.656	

• **Influence coefficients**

Regarding the influence of vibration generators in harvesters on the receiver (operator's seat), the study follows a unique approach that does not adopt the calculation of statistical influence, as the vibrations in our research are not entirely random. Instead, they include the fundamental components of systematic vibrations generated by the harvester's subassemblies during operation or with its components working in stationary mode. For this reason, in an initial attempt to estimate the major specific contributions of the main vibration-generating subassemblies of the harvester, the relationship between the operator's seat vibration spectrum and the spectra of the vibration generators (thresher, chassis, and header for both harvesters, and the shaker for the C110H harvester) is estimated using the least squares method.

If the vibration spectra measured on the five components of the C110H harvester and the four components of the CASE IH harvester are denoted by $S_s, S_{sc}, S_b, S_{sa}, S_h$:

$$\{S_{s_i}, S_{sc_i}, S_{b_i}, S_{sa_i}, S_{h_i}\}_{i=1, \dots, 81} \tag{1}$$

then the linear regressions have the following formulas:

$$SsI_i = 1.047Ssc_i + 0.51Sb_i - 0.389Ssa_i - 0.369Sh_i, i = 1 \dots n \tag{2}$$

for the C110H harvester in operation, respectively:

$$SsI_i = -0.265Sb_i + 0.401Ssa_i + 0.755Sh_i, i = 1 \dots n \tag{3}$$

for the CASE IH harvester in operation, with n being the number of frequencies contained in the experimental data. The maximum error per element, reported to the average value and the number of frequencies in the typical recorded spectrum (Figures 9-17) is:

$$e_i = \frac{100|Ss_i - SsI_i|}{Ss \cdot N} \tag{4}$$

where e_i is the error for each sample, and the maximum average error is:

$$\varepsilon = \max_{i=1 \dots N} e_i \tag{5}$$

Although they are not specifically designed for the approximate calculation of the spectrum at the operator's seat, for relations (2) and (3), the error values obtained according to formula (5) are specified: 2.988% for the C110H harvester, and 5.007% for the CASE IH harvester. To further highlight the contributions of the harvester's vibration generators, *contribution ratios* are constructed as follows:

$$rsc_i = \frac{1.047Ssc_i}{SsI_i}, rb_i = \frac{0.51Sb_i}{SsI_i}, rsa_i = \frac{-0.389Ssa_i}{SsI_i}, rh_i = \frac{-0.369Sh_i}{SsI_i}, i = 1, \dots, n, \tag{6}$$

for the C110H harvester, respectively:

$$rb_i = \frac{-0.265Sb_i}{SsI_i}, rsa_i = \frac{0.401Ssa_i}{SsI_i}, rh_i = \frac{0.755Sh_i}{SsI_i}, i = 1, \dots, n \tag{7}$$

In formulas (6) and (7), SsI represents the interpolated spectrum corresponding to the operator's seat, obtained using formula (2) for the C110H harvester and formula (3) for the CASE IH harvester. It is noted that the ratios defined in (6) and (7) are precisely the terms of the regressions (2) and (3) relative to the operator's seat spectrum, in the interpolated version.

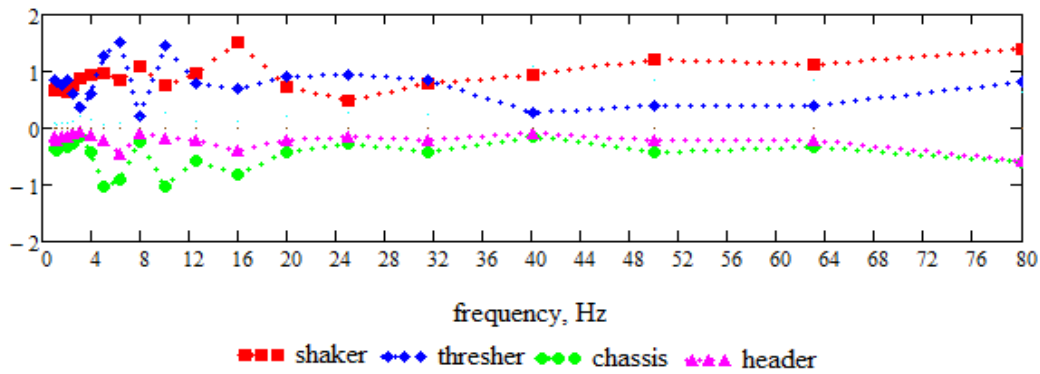


Fig. 18 - Variation of contribution ratios to the operator's seat spectrum for the C110H harvester

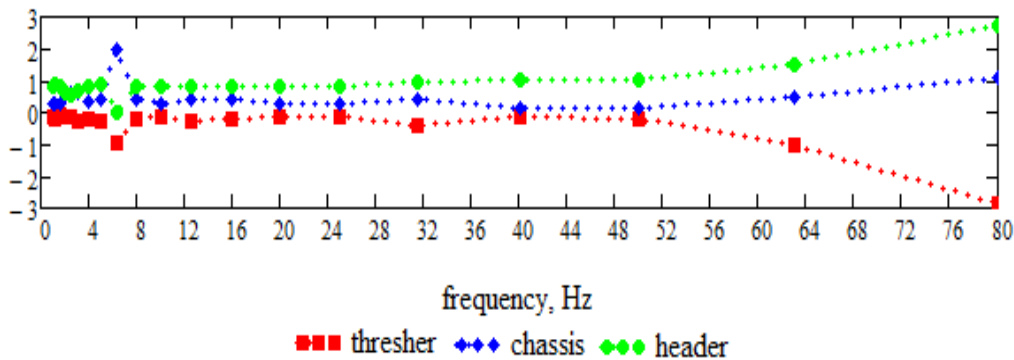


Fig. 19 - Variation of contribution ratios to the operator's seat spectrum for the CASE IH harvester

• **Exposure time limit to harvester vibrations for the operator**

To estimate the operator's work time limit on the harvester, the diagram method was used, which provides the maximum allowable limits for vibration exposure on the vertical axis. This diagram, of experimental origin, is taken from *Brüel & Kjaer, 1984*, but is not used in its graphic form; instead, a family of curves representing the time exposure boundaries was interpolated. The family of curves depends on the time parameter T and has the formula:

$$a(v, T) = \begin{cases} a_s(T), v \leq 4 \\ a_c(T), 4 < v < 8 \\ a_d(T), v \geq 8 \end{cases} \quad (8)$$

where:

$$\begin{aligned} \alpha(T) &= -1.796 \exp(-1.487T^{0.288}), \beta(T) = 0.636 \exp(-1.444T^{0.288}), \\ a_c(T) &= 5.312 \exp(-1.505T^{0.282}), a_s(T) = a_c(T) + (v - 4)tg(\alpha(T)), \\ a_d(T) &= a_c(T) + (v - 8)tg(\beta(T)) \end{aligned} \quad (9)$$

The graphic representation of nine curves from the family of curves (8)-(9) is shown in Fig.12. Similarly, the family of curves for the horizontal vibration exposure time limit diagram is derived. Some of the curves from this family are presented in Fig.13. Using the equation for the family of curves (8), the exposure time limit for the operator in different operating conditions was determined. Similarly, using the equations of the family of plane curves from the horizontal vibration exposure time limit diagram, the respective times for the C110H and CASE IH harvesters were obtained, in both operating modes considered (stationary and in operation). The horizontal acceleration (in the xOy plane) is the resultant plane acceleration:

$$a_o = \sqrt{a_x^2 + a_y^2} \quad (10)$$

where a_x is the acceleration in the direction of the harvester's forward movement, and a_y is the lateral acceleration. Clearly, a_z is the vertical acceleration. The values for the exposure time limit to the vibration regime for each of the two harvesters, as well as the critical acceleration and corresponding frequency, are given in Table 3 for each of the two operating modes considered (stationary and in operation).

The calculation of the exposure time limit to the vibration regime, in each case, is done by solving, approximately graphically, the equation:

$$a(v, t) = a_{cc} \tag{11}$$

for each harvester, each operating mode, with a_{cc} being the horizontal or vertical acceleration provided by the data spectra recorded during the experiments.

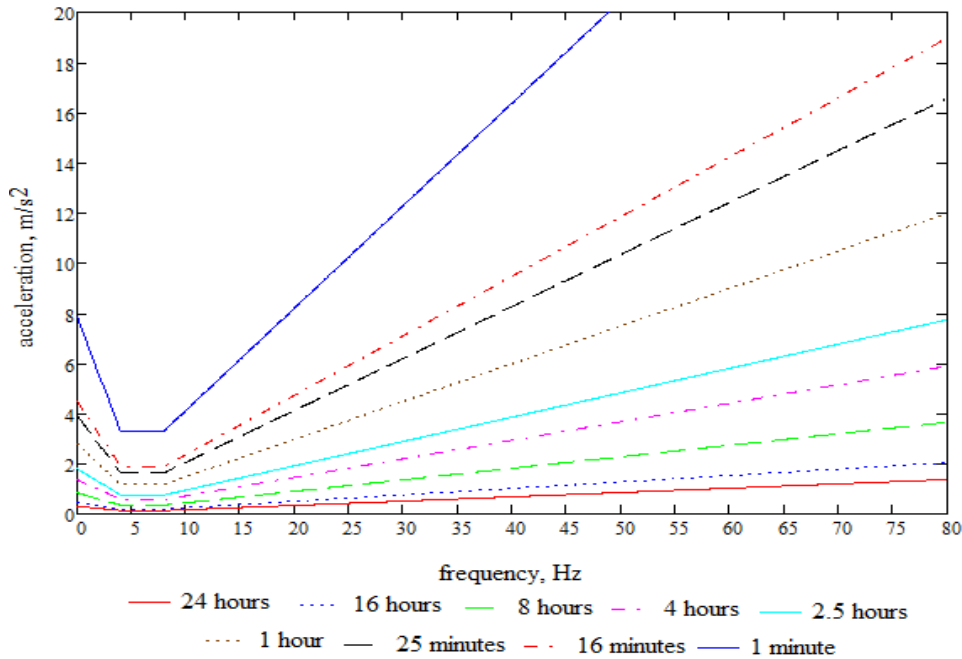


Fig. 20 - Diagram of exposure time limits to vibrations for the human body, in the vertical direction

Table 3

• Exposure time limits to vibration regimes for the harvester operator

Harvester	Working mode	Maximum tolerance time for the driver (hours)	Critical frequency (Hz)	Acceleration at critical frequency (m/s ²)
C110H, vertical acceleration	stationary	14.5	40.00	1.1000
	in operation	11.0	6.30	0.2700
CASE IH, vertical acceleration	stationary	35.0	10.00	0.1000
	in operation	23.0	3.15	0.1771
C110H, horizontal acceleration	stationary	60.0	2.50	0.0398
	in operation	12.0	1.60	0.1772
CASE IH, horizontal acceleration	stationary	104.0	2.00	0.0144
	in operation	16.5	1.25	0.1370

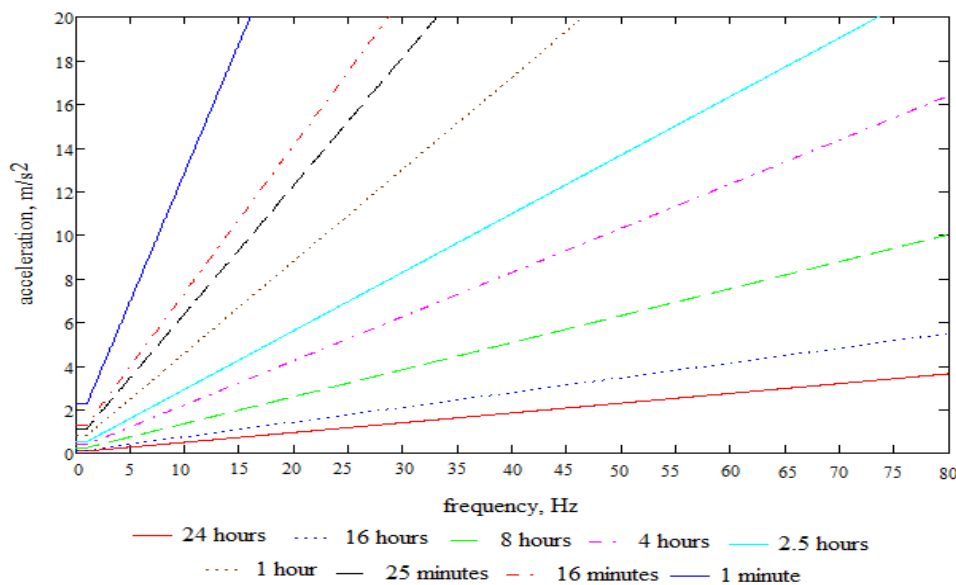


Fig. 21 - Diagram of exposure time limits to vibrations for the human body, in the horizontal direction

• **Vibration intensity**

In the paper (Buzdugan et al., 1982), several measures of vibration intensity are provided. Vlăduț et al., (2006), show that to characterize a vibration, kinematic quantities - displacement, velocity, acceleration - as well as temporal quantities - frequency, period, or pulse, are usually used. It is indicated that if the motion is harmonic, knowing one of the amplitudes (displacement, velocity, or acceleration) and the frequency is sufficient to characterize the vibration. However, harmonic motion is generally rare in engineering and nature. For this reason, a series of quantities have been proposed to characterize vibrations, which can be interpreted as criteria for assessing their effects. Among these estimators, the most well-known are: vibration intensity (in cm²/s³), vibration intensity in “vibrar”, perception degree, and perception coefficient.

Since the available data in our case consists of acceleration amplitude and frequency, it is initially chosen, from (Harris and Crede, 1976), the estimator called vibration intensity, according to (Zeller, 1933):

$$Z = \frac{a_0^2}{f} \tag{12}$$

for the case where vibration intensity is measured in cm²/s³.

To express it in “vibrar”, vibration intensity is calculated using the formula:

$$S = 10 \lg \left(\frac{Z}{Z_s} \right) \tag{13}$$

If Z_s=0.1 cm²/s³ is considered, then:

$$S = 10 \lg(10Z) \tag{14}$$

The perception degree is defined by the formula:

$$P = 10 \lg \left(\frac{Z}{Z_1} \right) \tag{15}$$

and taking Z₁=0.5 cm²/s³, it is obtained:

$$P = 10 \lg(2Z) \tag{16}$$

which is measured in “Pal Units” (Zeller, 1933).

The perception coefficient is also defined in Buzdugan et al., (1982); among the formulas suggested by the authors, due to the structure of our data, it is used:

$$K = a_{ef} \frac{\alpha}{\sqrt{1 + \left(\frac{f}{f_0}\right)^2}} \tag{17}$$

where α_{ef} is the effective acceleration in m/s², f is the vibration frequency, in Hz, f₀=10 Hz, α=18.0 m²/s.

The estimated values of vibration intensity at the operator's seat for the C110H and CASE IH harvesters in operating mode are provided in Table 4.

Table 4

Estimated values of vibration intensity at the operator's seat for C 110H and CASE IH harvesters

Harvester type	Working mode	Vibration intensity (according to Zeller), Z [cm ² /s ³]	Vibration intensity S [vibrar]	Perception degree, P	Perception coefficient, K
C110H	stationary	4.265	16.299	49.309	5.265
	in operation	12.884	21.101	54.111	3.516
CASE IH	stationary	2.3	13.617	46.628	1.232
	in operation	17	22.304	53.315	2.273

The calculation of the perception coefficient has been simplified by considering, for each frequency, an effective acceleration value of 0.707 from the value given in the source spectra, since an exact calculation is not possible without time recordings available.

Discussions

In *Buzdugan et al., (1982)*, it is stated that the effects of mechanical vibrations are not only measured by the deformations and unit stresses of elastic materials. Vibrations are transmitted to people, buildings, machines, and installations, producing effects ranging from unpleasant to dangerous and destructive. Generally, taking into account a series of measurable parameters that characterize vibrations, their effects on people, buildings, and machines are assessed based on the results of long-accumulated experience.

In *Brüel & Kjaer, (1984)*, it is asserted that the human body is both physically and biologically a "system" of an extremely complex nature. When viewed as a mechanical system, it contains a number of linear as well as nonlinear "elements," and the mechanical properties vary significantly from person to person.

An elementary mathematical model, linear elastic of the human body, largely appears in the literature dedicated to the effects of vibrations and shocks on humans (*Brüel & Kjaer, 1984; Harris and Crede, 1969*).

The values of the **interspectral correlations** (Table 1) show that the vibrations of the operator's seat in the C110H harvester are primarily influenced by the shaker, then by the chassis and the thresher, and, to a lesser extent, by the header. The analysis of the acceleration components shows that the lateral and vertical components at the operator's seat are most intensely correlated with the vibrations of the shaker. This statement refers to variation and not necessarily to intensity. After the shaker, the vibrations of the thresher are most intensely correlated with the vertical vibrations of the operator's seat. The CASE IH harvester is much "quieter." This harvester has an axial flow and does not have a shaker. As a result, considering the results in Table 1, it follows that the most influential components, especially in operation, for the CASE IH harvester are the header and the chassis, with the influence of the thresher being lower. This reduction in influence at the operator's seat may also be due to better vibration isolation of the cabin and seat in the CASE IH harvester compared to the C110H harvester.

Regarding the **coherence degree**, it is sufficient to specify that between Table 1 and Table 2, the correlation value is 0.921, which means that the assessments made from the perspective of this estimator are similar to the assessments provided by the correlation.

The **influence coefficients** also show that, in operation mode for the C 110H harvester, the shaker and the thresher have the strongest influences on the vibrations of the operator's seat - relation (2), while for the CASE IH harvester, the sources with the greatest influence on the vibrations of the operator are the header and the chassis - relation (3). The clearer influence of the sources from the perspective of the influence coefficients is made through the construction of the ratios defined in relations (6) and (7), whose variation along the experimental frequency spectrum is graphically presented in Figs. 10 and 11. With the help of these graphs, the frequencies at which a particular component of the harvester dominates the signal transferred to the operator's seat can be identified. It is worth noting that in the C 110H harvester, the chassis and header vibrate during operation, thus reducing the vibration transmitted to the seat (see also the negative coefficients in relation (2)), which is done by the thresher in the CASE IH harvester.

The study on the influence of the vibrating components of the C110H harvester on the driver's seat shows that:

1) 7 influence links are detected by the multiple regression method, both during stationary operation and while in working mode.

2) Among these seven links in each operating mode, for stationary operation, 4 influences are felt at the seat along the Ox axis, 2 along the Oy axis, and 1 along the Oz axis. During working operation, 2 influences are felt at the seat along the Ox axis, 3 along the Oy axis, and 2 along the Oz axis.

3) During stationary operation, the header does not introduce significant influences at the driver's seat. However, in working mode, the header has a significant influence on the seat.

4) During stationary operation, the most intense influences (the highest coefficients of the multi-linear regression components) on the driver's seat come from the chassis, while in working mode, the influences come from the chassis on the Ox and Oz axes and from the thresher on the Oy axis.

5) The frequency spectra of the harvester's vibrating components interact with the chassis, and the chassis interacts with the driver's seat. These interactions depend on where the components are mounted on the chassis, as well as on the mounting characteristics (detachable or fixed, with additional damping or isolation, and whether or not there is clearance).

6) In stationary operation, the major influences on the driver's seat come from the chassis (the components with the highest coefficients in the structural regression equations (1)-(6)).

7) In working mode, the major influences on the driver's seat still come from the chassis along the Ox and Oz axes, while along the Oy axis, the strongest influence comes from the thresher, as indicated by the structural equations (7)-(9).

The exposure time limit to vibrations for the operator in working mode is calculated using the methodology utilized in *Viăduț et al., 2006*. Contrary to this methodology and in general to the literature, the diagrams experimentally deduced from *Brüel & Kjaer, (1984)*, were used, in an interpolated form described in relations (8)-(11). The calculation of exposure time is done separately for horizontal and vertical vibrations. The lowest values for exposure time are obtained for the C 110H harvester: 11 hours for vertical vibrations and 12 hours for horizontal vibrations, both during operation (Table 3). For the two scenarios for the CASE IH harvester, the values obtained are 23 and 16.5 hours. These values are reassuring for normal working conditions, as a normal work schedule does not exceed 10 hours a day.

The **vibration intensity** estimators also provide a measure that characterizes vibrations at the source (in this case, the operator's seat). In general, with the exception of the vibration intensity measured in [vibrar] the values in Table 4 indicate that the C 110H harvester is more demanding on the operator than the CASE IH harvester, or that the CASE IH harvester is more comfortable than the C110H one. According to the results in Table 4 and the indications from *Buzdugan et al., (1982)*, regarding the levels of vibration perception, the C110H harvester presents vibrations that are *strongly* and *very strongly perceptible*, while the CASE IH harvester is at the level of *well-perceptible*.

Similar issues to those addressed by the authors of this paper have been highlighted and solutions were found and applications provided in *Almosawi et al., (2016)*, which considers not only the working mode (harvesting) but also the parking, transport, and movement between plots modes. Each of these modes involves different operating conditions for the harvester components and the external environment (rolling surface, resistance of the harvested material, etc.). The authors of *Almosawi et al., (2016)*, find that the maximum influence on the intensity of the harvester's vibrations comes from the header, which in this paper was found in the CASE IH harvester but not in the C110H. They found maximum acceleration values of 1.97 m/s², while in our study, the maximum values were below 2 m/s², with very few exceptions (under 1% of values). In extremely uncomfortable operating conditions, maximum acceleration values of 2.65 m/s² were found. The research was conducted on a CLAAS Dominator harvester.

In *Viăduț et al., (2006)*, accelerations were measured in three directions for different harvesters, in stationary, transport, and operation modes. For the C140 (M SEMA 140M) harvester, the maximum recorded acceleration value was in transport mode, at 1.11 m/s². For the New Holland TC 56, the maximum acceleration value is found to be 0.43 m/s² in stationary mode, in the longitudinal direction. In *Viăduț et al., 2006*, it was also found for the Deutz-Fahr TopLiner 4075 a maximum acceleration value of 0.75 m/s² but situated in a dangerous frequency zone for the human body (fortunately only during transport in the longitudinal direction). According to the same research, the Laverda L 6261 harvester had acceleration peaks of over 1.2 m/s², in frequency zones that limit the duration of exposure to vibrations, in stationary mode. Peaks of 0.5 - 1.0 m/s² also appear in the records given in *Viăduț et al., (2006)*, for the New Holland TX 66, also in dangerous frequency ranges. Thus, the data obtained led for the SEMA 140M harvester to a limitation of 16 working hours for the safety of the operator's health, for the New Holland TC 56, a limitation of 20 working hours, for the Laverda L 6261, 18 hours, and only 6 hours for the New Holland TX 66. In *Tsujimura et al., 2015*, maximum accelerations with values between 0.65 and 1.71 m/s² for a wide range of agricultural machines used in rice cultivation, including combine harvesters, were found. For calculating the exposure limit to vibrations, the authors of *Tsujimura et al., (2015)*, used the ELV algorithm, defined in (<https://www.castlegroup.co.uk/guidance/vibration-exposure-limits/>), according to (<https://www.hse.gov.uk/vibration/hav/regulations.htm>) and (<https://www.legislation.gov.uk/uksi/2005/1093/contents/made>).

CONCLUSIONS

The conducted research shows that both harvesters provide a maximum exposure time for the operator to vibrations that exceeds the maximum time of the usual work program in agriculture.

The CASE IH harvester ensures greater comfort for the operator compared to the C 110H harvester. This is due both to the fact that the CASE IH harvester does not contain one of the major vibrating components of the C 110H harvester (the shaker), and very likely to an additional and superior isolation of the operator's seat and cabin.

The estimators used in this work to assess the comfort quality of the harvester operator are all useful and, to a large extent, lead to the same conclusions.

It is important to note for future research that the acceleration spectrum corresponding to the engine needs to be measured, as it is an assembly or a vital component of the harvesters that certainly introduces vibrations into our study spectrum.

REFERENCES

- [1] Almosawi A.A., Alkhafaji A., Alqazzaz M. (2016), Vibration transmission by combine harvester to the driver at different operative conditions during paddy harvest, https://www.researchgate.net/publication/298559244_vibration_transmission_by_combine_harvester_to_the_driver_at_different_operative_conditions_during_paddy_harvest;
- [2] Biriş S.Şt., Constantin A.M., Anghelache D., Găgeanu I., Cujbescu D., Nenciu F., Voicea I., Matei Gh., Popa D., Duţu M.F., Ungureanu N., Zelazinski T., Perişoară L., Fodorean G. (2022). Considerations regarding the vibrations transmitted to the operator by an axial flow harvester combine. *INMATEH – Agricultural Engineering*, Vol.68(3), pp.747–756. DOI: <https://doi.org/10.35633/inmateh-68-74>.
- [3] Brüel & Kjaer (1984). *Mechanical Vibration and Shock Measurements*. K. Larsen & Søn. Denmark.
- [4] Buzdugan Gh., Fetcu L, Rades M. (1982), *Mechanical vibrations (Vibratii mecanice)*, Didactic and Pedagogical Publishing House, Bucharest, Romania.
- [5] Cârdei P., Constantin N., Muraru V., Persu C., Sfîru R., Vlăduţ N-V., Ungureanu N., Matache M., Muraru-Ionel C., Cristea O-D., Laza E-A. (2023). The random vibrations of the active body of the cultivators. *Agriculture*, 13(8), 1565. DOI: <https://doi.org/10.3390/agriculture13081565>.
- [6] Chen S., Zhou Y., Tang Z., Lu S. (2020), Modal vibration response of rice combine harvester frame under multi-source excitation, *Biosystems Engineering*, vol. 194, pp: 177:195;
- [7] Chuan-Udom S. (2010), Development of a Cutter Bar Driver for Reduction of Vibration for a Rice Combine Harvester, *KKU Res J*, 15(7), pp: 572-580;
- [8] Feijoo F., Gomez-Gil F.J., Gomez-Gil J. (2020), Application of Composite Spectrum in Agricultural Machines, *Sensors* 20(19), 5519; <https://doi.org/10.3390/s20195519>;
- [9] Godzhaev Z., Senkevich S., Kuzmin V., Ilchenko E., Chaplygin M., Alekseev I., Prilukov A. (2020), Simulation of the dynamic processes of a low-capacity combine harvester movement, *E3S Web Conferences*, 164, 06009;
- [10] Harris C.M., Crede C.E. (1976), *Shocks and vibrations. 2nd Edition*, McGraw and Hill Book Co. Publisher, 1218 pages;
- [11] HaSPA (Health and Safety Professionals Alliance), (2012). The Core Body of Knowledge for Generalist OHS Professionals. *Tullamarine, VIC*. Safety Institute of Australia;
- [12] ISO - International Organization for Standardization (2002), *ISO 5008. Agricultural wheeled tractors and field machinery-measurement of whole-body vibration of the operator*. Published (Ed.2, 2002), <https://www.iso.org/standard/1743.html>
- [13] ISO - International Organization for Standardization (1997). *ISO 2631-1. Mechanical vibration and shock. Evaluation of human exposure to whole-body vibration. Part 1: General requirements*. Published (Ed.2, 1997), <https://www.iso.org/standard/7612.html>
- [14] ISO - International Organization for Standardization (2018). *ISO 2631-5. Mechanical vibration and shock. Evaluation of human exposure to whole-body vibration. Part 5: Method for evaluation of vibration containing multiple shock*. Published (Ed.2, 2018) <https://www.iso.org/standard/50905.html>
- [15] Jahanbakhshi A., Ghamari B., Heidarbeigi K. (2020), Vibrations analysis of combine harvester seat in time and frequency domain, *Journal of Mechanical Engineering and Sciences* 14 (1), pp: 6251-6258, DOI:10.15282/jmes.14.1.2020.04.0489;
- [16] Jiangtao Ji, Jinpeng Hu, Shengsheng Wang, Ruihong Zhang, Jing Pang (2020). Vibration and impact detection of axial-flow threshing unit under dynamic threshing conditions. *INMATEH – Agricultural Engineering*. Vol.60(1), pp.183-192, Bucharest, Romania. DOI: <https://doi.org/10.35633/inmateh-60-21>;
- [17] Junming Hou, Weixue Hu, Wei Wang, Hongjie Zhu, Zhi Rende (2021). Fruit vibration harvesting technology and its damage. a review, *INMATEH – Agricultural Engineering*, 63 (1), pp. 155-168, Bucharest, Romania. DOI: <https://doi.org/10.35633/inmateh-63-16>;

- [18] Jotautiene E., Juostas A., Janulevicius A., Aboltins A. (2019), Evaluation of bearing reliability of combine harvester straw chopper, *Proceedings of International Conference "Engineering for Rural Development"*, Jelgava, pp: 625-629;
- [19] Li Y., Tang Z., Ren H., Zhou Y. (2021), Vibration Response of Combine Harvester Chassis Undergoing Multisource Excitation Force Distribution, *Mathematica Problems in Engineering*, <https://doi.org/10.1155/2021/8856094>;
- [20] Ministry of Labor and Social Solidarity (2002). *General labour protection rules (Norme generale de protecția muncii)*. TRIDONA Oltenița printing house, pp.180-181; 436-447;
- [21] Pang J., Li Y., Ji J., Xu L. (2019), Vibration excitation identification and control of the cutter of a combine harvester using triaxial accelerometers and partial coherence sorting, *Biosystems Engineering*, vol. 185, pp: 25-34, <https://doi.org/10.1016/j.biosystemseng.2019.02.013>;
- [22] Pang J., Li Y., Jin X., Xu L. (2019), Detection and Analysis of typical vibration load of grain harvester based on short-time Fourier method, *The International Journal of Electrical Engineering & Education* 60(1), pp: 37-39, <https://doi.org/10.1177/00207209231197934>;
- [23] Shin. K, Hammond. J. (2008). *Fundamentals of signal processing for sound and vibration engineers*. John Wiley & Sons Publishing;
- [24] Silsoe Research Institute and RMS Vibration Laboratory for the Health and Safety Executive (2005), *Whole-body vibration on agricultural vehicles of emission and estimated exposure levels*, Research Report 321, HSE BOOKS;
- [25] Sirotin P.V., Lebedinsky I.Yu., Sysoev M.I. (2019), Combine harvester-threshers operator workplace vibration load study and substantiation their secondary cushioning systems design principle, *AIP Conference Proceedings* 2188, 050030 (2019); <https://doi.org/10.1063/1.5138457>;
- [26] Sorică E., Vlăduț V., Cârdei P., Sorică C., Brăcăcescu C. (2017). Comparative analysis of the noise and vibration transmitted to the operator by a brush cutter. *Proceedings of the XIVth International Conference "Acoustics and Vibration of Mechanical Structures – AVMS-2017"*, 165–172, Timișoara, Romania. DOI: <https://doi.org/10.1007/978>.
- [27] Tang Z., Zhang H, Zhou Y. (2018), Unbalanced Vibration Identification of Tangential Threshing Cylinder Induced by Rice Threshing Process, *Shock and Vibration*, <https://doi.org/10.1155/2018/4708730>;
- [28] Tang Z., Zhang H., Zhou Y., Li Y. (2019), Effects of Stem Cutting in Rice Harvesting by Combine Harvester Front Header Vibration, *Advancing in Materials Science and Engineering*, Volume 2019, Article ID 6834269, 15 pages, <https://doi.org/10.1155/2019/6834269>;
- [29] Tsujimura H., Taoda K., Kitahara T. (2015), A field study of exposure the whole-body vibration due to agricultural machines in a full-time rice farmer over one year, *Journal of Occupational Health*, vol. 57(4), pp: 378-387;
- [30] Vlăduț V., Kiss I., Biris S., Bungescu S., Atanasov A. (2006), Research Regarding the influence of vibrations on the grain harvesters, *Annals of the Faculty of Engineering Hunedoara*, Tome IV, Fascicole 1, pp: 105-112;
- [31] Vlăduț V., Biriș S.Șt., Bungescu T., Herișanu N. (2013). Influence of vibrations on the operator in the grain harvesters. *Applied Mechanics and Materials*, Vol. 430, pp.290–296. DOI: <https://doi.org/10.4028/www.scientific.net/AMM.430.290>;
- [32] Vlăduț V., Pirnă I., Florea C., Popescu C., Brătucu Gh., Kabas O., Păunescu D. (2014). Influence of the vibration amplitude on the quality of shredded medicinal vegetal material subjected to sorting. *Proceedings of the 42nd International Symposium on Agricultural Engineering "Actual Tasks on Agricultural Engineering"*, pp. 273–282, Opatija, Croatia;
- [33] Xinjie N., Chengqian J., Peng L., Qinglun L., Yanpu C. (2002), Research on screening performance of double layer vibrating screen for soybean harvester based on discrete element method, *American Journal of Agricultural Research* 4 (68), pp: 1-17, <https://escipub.com/american-journal-of-agricultural-research/>;
- [34] Xu L., Chai X., Gao Z., Li Y., Wang Y. (2019), Experimental study on driver seat vibration characteristics of crawler-type combine harvester, *International Journal of Agriculture & Biology Engineering*, vol.12, pp: 90-97;
- [35] Yanchun Y., Zhenghe S., Yuefeng D., Xueyan Z., Enrong M, Fan L. (2017), Analysis of vibration characteristics and its major influenced factors of header for corn combine harvesting machine, *Transactions of the Chinese Society of Agricultural Engineering*, vol.33 (13), pp: 40-49;

- [36] Yilmaz D., Gokduman M.E. (2020), Development of a measurement system for noise and vibration of combine harvester, *International Journal of Agricultural and Biological Engineering*, vol.13 (6), pp: 104-108;
- [37] Zander J. (1972), *Ergonomics in machine design (a case -study of the self-propelled combine harvester)*, H. Veenman & Zonen N.V. Publishing – Wageningen;
- [38] Zare H.G., Maleki A., Rahaghi M.I., Lashgari M. (2019), Vibration modelling and structural modification of combine harvester thresher using operational modal analysis and finite element method, *Structural Monitoring and Maintenance*, vol. 6, pp: 33-46;
- [39] Zare H.G., Maleki A., Rahaghi M.I., Lashgari M. (2019), Vibration modeling the thresher unit of John Deere (955) combine harvester using operational modal analysis, *Journal of Agricultural Engineering* 42(1), pp: 109-125, <https://doi.org/10.22055/agen.2019.24782.1406>;
- [40] Zeller W. (1933). Proposal for a Measure of the strength of vibration, *Zeitschrift des Vereines Deutscher Ingenieure*, vol. 77, No.12, p.323.
- [41] Zhiming Shi, Tonghao Chen, Shoutai Li, Ling Yang, Mingjin Yang (2021). Impact of vibration on tillage performance of subsoilers using the discrete element method (DEM). *INMATEH – Agricultural Engineering* 64 (2), pp. 89-98, Bucharest, Romania. DOI: <https://doi.org/10.35633/inmateh-64-08>.
- [42] Zhang X., Peng K. (2018), Vibration control for crawler-type combine harvester, *Emirate Journal of Food and Agriculture* 30(10), pp: 873-882;
- [43] <https://www.castlegroup.co.uk/guidance/vibration-exposure-limits/>
- [44] <https://www.hse.gov.uk/vibration/hav/regulations.htm>
- [45] <https://www.legislation.gov.uk/uksi/2005/1093/contents/made>
- [46] ***(2005), Hand-arm vibration, The Control of Vibration at Work Regulation, *Guidance on Regulations, HSE*;
- [47] ***Guide to measuring and assessing workplace exposure to whole - body vibration, <https://www.safeworkaustralia.gov.au>.

RESEARCH ON DRIED DAYLILY GRADING BASED ON SSD DETAIL DETECTION WITH FEATURE FUSION

基于特征融合细节检测 SSD 的干制黄花菜分级研究

Xueli ZHANG^{1,2}, Haiyan SONG^{*1,2}, Decong ZHENG^{1,2}, Renjie CHANG^{1,2}, Chenfei LI^{1,2}, Yile SUN^{1,2}, Zonglin LIU^{1,2}

¹) College of Agricultural Engineering, Shanxi Agricultural University, Taigu 030801/ China;

²) Dryland Farm Machinery Key Technology and Equipment Key Laboratory of Shanxi Province, Taigu 030801/ China

Tel: +86 13994576078.; E-mail: yybbao@sxau.edu.cn

DOI: <https://doi.org/10.35633/inmateh-74-72>

Keywords: dried daylily, grading, SSD, ResNet50, feature fusion.

ABSTRACT

Daylily is widely used in medicine and diet therapy. In order to prolong the preservation period of daylily and make better use of its edible value, most of the daylily on the market are dried vegetables. Aiming at the problems of small size of dried daylily, similar color and texture between dried daylily, and difficulty in grading, this study proposes a method for grading dried daylily based on SSD. In the backbone feature extraction stage, the original backbone network VGG16 is replaced with the residual network model ResNet50 to realize the feature extraction of dried daylily. ResNet50 can deepen the network better and is more suitable for dried daylily feature extraction. Secondly, a feature fusion layer is added to improve the problem of insufficient utilization of shallow features in SSD network, which is more suitable for detail detection and improves the accuracy of dried daylily grading. Finally, the input image size is selected [512,512] to increase the image pixels, so that the network can capture more details of the dried daylily to improve the detection accuracy. The results show that the grading precision of the improved SSD algorithm is significantly improved compared with the traditional SSD, and the mean average precision is increased by 4.17%. At the same time, the same data set was used to test on the YOLOv5 model. Compared with YOLOv5s, YOLOv5s-CA and YOLOv5s-CBAM, the mean average precision was increased by 18.32%, 21.82% and 22.02% respectively, which further verified the precision and feasibility of the method and provided effective technical support for the grading of dried daylily.

摘要

黄花菜营养成分丰富，具有很高的食用和药用价值。鲜黄花菜因含有多种生物碱不宜多食，为了更好地利用其食用价值以及延长黄花菜的保存期，市面上的黄花菜大多是干菜。针对干制黄花菜体积小，黄花菜之间颜色和纹理相似，分级困难等问题，该研究提出了一种基于 SSD 的干制黄花菜等级分级的方法。该方法以 SSD 算法为基础，在主干特征提取阶段，将原主干网络 VGG16 替换为残差网络模型 ResNet50，实现对干制黄花菜的特征提取。ResNet50 可以更好地深化网络，更适用于干制黄花菜细节特征提取。其次，添加了特征融合层，改善了 SSD 网络中浅层特征利用不足的问题，更适合细节检测，提高了干制黄花菜分级的精度。最后，输入图像尺寸选取[512,512]，提高图像像素，使网络可以更好地捕捉干制黄花菜的细节信息，以提升检测精度。结果表明，改进后的 SSD 算法与传统 SSD 对比，分类精确度有明显的提升，平均精确度达到 97.52%，对比原 SSD 算法提高了 4.17%。同时，利用相同数据集在 YOLOv5 模型上进行试验，对比 YOLOv5s、YOLOv5s-CA、YOLOv5s-CBAM，平均精确度分别提升 18.32%、21.82%、22.02%，进一步验证了该方法的准确性和可行性，可以为干制黄花菜分级提供有效的技术支持。

INTRODUCTION

Daylily (*Hemerocallis citrina Baroni*) is an edible angiosperm of *Hemerocallis* in *Asphodelaceae*, which is a Chinese specialty. Daylily is rich in nutritional value, rich in protein, fat, sugar, etc. Daylily has high medicinal value. It has good functions of promoting diuresis and cooling blood, tranquilizing mind and improving acuity of vision, strengthening brain, anti-aging, and can significantly reduce serum cholesterol content. Because daylily contains a variety of alkaloids, which will cause diarrhea and other poisoning phenomena, its fresh flowers cannot be eaten too much. Therefore, it needs to be processed before eating. The main processing object of daylily is its flower bud; it is processed into dried vegetables by steaming (Xu, 2004), and then graded according to different quality, finally packaged for sale.

In recent years, the market demand for daylily has gradually increased. The grading of dried daylily has an important impact on the sales. Now, the sorting of dried daylily is still completely manual operation, as shown in Figure 1. The cost of the manual operation is high, the classification accuracy and the efficiency are low. Furthermore, the workers are in direct contact with daylily, which has certain food safety hazards. The grading problem restricts the development of daylily industry to a certain extent. With the expansion of the scale of the daylily industry, using automated grading equipment instead of manual labor to complete high-quality daylily external quality detection and grading will be of great significance for the realization of production automation and refinement in the daylily industry (Ma *et al.*, 2022), and also has a great impact on the price and sales of daylily.



Fig. 1 - Artificial classification workshop site of daylily

Image recognition based on machine learning is of great significance to the classification and identification of agricultural products. It has a wide range of applications in agriculture. There are many application objects in the field of agricultural product sorting, such as corn (Sun *et al.*, 2021), walnut (Zhang *et al.*, 2022), apple (Chen *et al.*, 2024) and so on. Because of the special shape and complex grading standards of daylily, the existing sorting machines on the market cannot be well applied. It is necessary to propose a proprietary sorting method for daylily.

Using deep learning to realize the classification and identification of agricultural products is an important direction of current research at home and abroad. Yin Chuan *et al.*, (2023), built a green tea quality detection algorithm based on YOLOv5s, and the mAP value reached 91.9%, which was 3.8% higher than the average accuracy of the basic YOLOv5s. Gui Zhiyong *et al.*, (2023), proposed a lightweight deep learning model for tea bud recognition based on YOLOv5. Compared with the original YOLOv5 model, the mAP value of the modified model increased by 9.66 %. Cao Shuo *et al.*, (2020), built an underwater live crab detection algorithm based on SSD, fused the feature pyramid with SSD to propose Faster MSSDLite, with an average accuracy of 99.01%. Sun Henan *et al.*, (2021), used SSD combined with MEAN module and Apple-Inception module to build a new apple leaf disease detection model, with an average accuracy of 83.12%.

Through the above literature research, it can be found that the mainstream deep learning model algorithm has high accuracy and has been applied in agriculture-related fields to a certain extent. However, there are still few studies on the classification of small agricultural products such as daylily. In this paper, aiming at the characteristics of dried daylily in the actual detection process, such as similar color texture and small size, a grade classification algorithm based on improved SSD is proposed. The algorithm replaces the VGG16 network in the traditional SSD with Resnet50, and adds a feature fusion layer to the network, which improves the accuracy of the algorithm. The commonly used input image size of SSD is increased from [300,300] to [512,512] to better detect small targets. The experimental results show that the proposed method can significantly improve the precision of dried daylily grading.

MATERIALS AND METHODS

Image data acquisition and preprocessing of dried daylily

Daylily of Yunzhou District, Datong City, Shanxi Province, China was selected as the detection target of this paper. According to the “National Standard of Daylily” and “Quality grading standard of dried daylily products in Datong”, through the comparison of color, shape and the degree of flowering crack at the top of daylily, daylily was divided into three grades: A-grade, B-grade and C-grade. The color of the A-grade daylily is uniform and shiny, it is golden or light yellow, the shape is symmetrical, and the head of the daylily does not bloom.

The B-grade daylily also has uniform color, golden or light yellow, the color may be slightly uneven but the shape is well, and the flowering degree of daylily's head is low. The C-grade daylily's color is uneven, the shape is irregular, and the head of daylily has a greater degree of flowering. Pictures of different grades of dried daylily are shown in Figure 2.

The images were captured in Agricultural Engineering College, Shanxi Agricultural University, using Hikvision CA060-10GC industrial camera. When collecting images, the background is single and the illumination is stable. A total of 860 images of daylily were collected. In order to avoid overfitting problems, the image data is enhanced by vertical flipping, 90° rotation, blurring processing and adding salt and pepper noise, so that the image data is increased by 8 times, that is, 6880 images. The target annotation tool Labellmg was used for data annotation, and the daylily image dataset was constructed. They were randomly divided into training set and test set according to the ratio of 8:1. The final quantity of daylily at all levels is shown in Table 1.

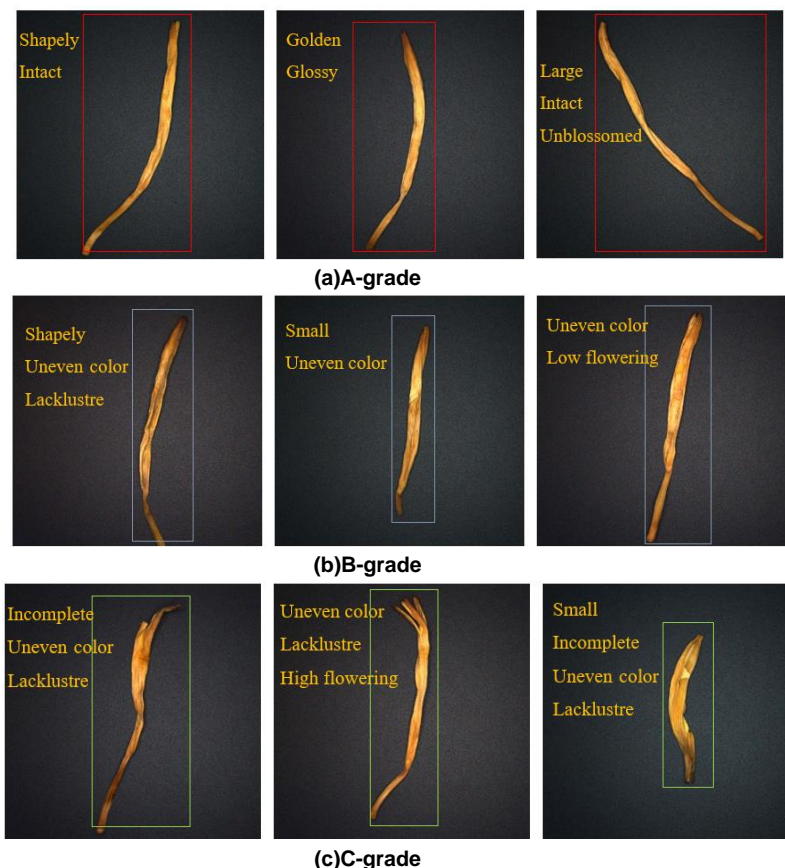


Fig. 2 - Examples of pictures of different grades of dried daylily

Table 1

The dried daylily dataset				
Dataset	Number	Number of each grade of Daylily		
		A-grade	B-grade	C-grade
Training set	6117	1565	2176	2376
Test set	763	195	272	296

SSD algorithm

Single Shot MultiBox Detector (SSD) algorithm is a fast and accurate target detection algorithm, which realizes the efficient detection of multi-scale targets by simultaneously detecting targets at different scales (Liu et al., 2016). The SSD algorithm mainly includes three parts: feature extraction network, prediction network and loss function. In the feature extraction network, the features of the image are extracted by convolution and pooling. In the prediction network, the location and category of the target are predicted by a multi-scale convolutional layer; in the loss function, the model parameters are optimized by calculating the loss function between the predicted results and the real labels.

The main design idea of SSD is multi-scale aspect ratio dense anchor point design and feature pyramid. The network structure of SSD is shown in Figure 3. SSD is based on a feedforward convolutional network, which generates a fixed-size bounding box set and the corresponding score of the target category in the box, and generates the final detection result according to the non-maximum suppression. SSD uses VGG16 as the base layer (Simonyan et al., 2014). The VGG16 network structure is shown in Figure 4. The Conv4_3 is selected as the first feature layer for target detection. In addition, SSD adds several additional feature layers for target detection. The FC7 (Fully Connected Layer7) in VGG16 is replaced by the convolutional layer Conv7, and several feature layers of Conv8, Conv9, Conv10, and Conv11 are added to perform target detection on multiple scales to improve detection accuracy. The idea of feature pyramid is realized. At the same time, SSD designs a large number of dense prior boxes to detect the entire image.

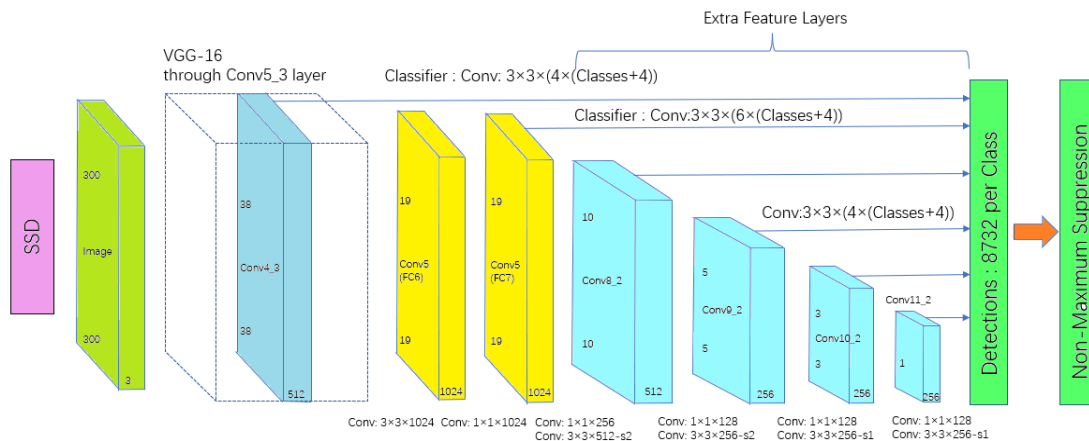


Fig. 3 - Network structure of SSD

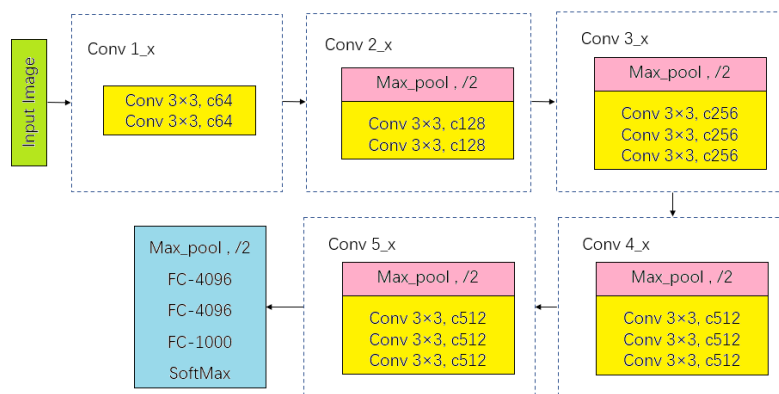


Fig. 4 - Network structure of VGG16

Improved SSD algorithm

In order to further improve the grading accuracy of dried daylily, the SSD algorithm was improved. The improved SSD network structure is shown in Figure 5. By replacing the original VGG16 with Resnet50 (He et al. 2016), the residual network can build a deeper network structure for detail detection, and improve the accuracy of daylily grading results. At the same time, the feature fusion layer is added. The small targets tend to rely more on shallow features. The feature fusion of SSD shallow information can enhance the characterization ability of features (Li et al., 2017), improve the model's understanding and expression ability of input data, and thus enhance the model's recognition ability of details (Tian et al., 2022). The image size is selected [512,512]. Improving the image pixels can provide more detailed information of daylily to the network (Tan et al., 2020), thereby improving the accuracy of grading. The network structure of the backbone network Resnet50 is shown in Figure 6. The improved SSD removes Conv5 and subsequent networks, and selects three feature maps generated by Conv2_3, Conv3_4, and Conv4_6 for feature fusion. Then the fusion results are sent to a series of additional feature layers to obtain multi-scale features, which are sent to the detector for detection. Finally, the prediction results are output by Non-Maximum Suppression.

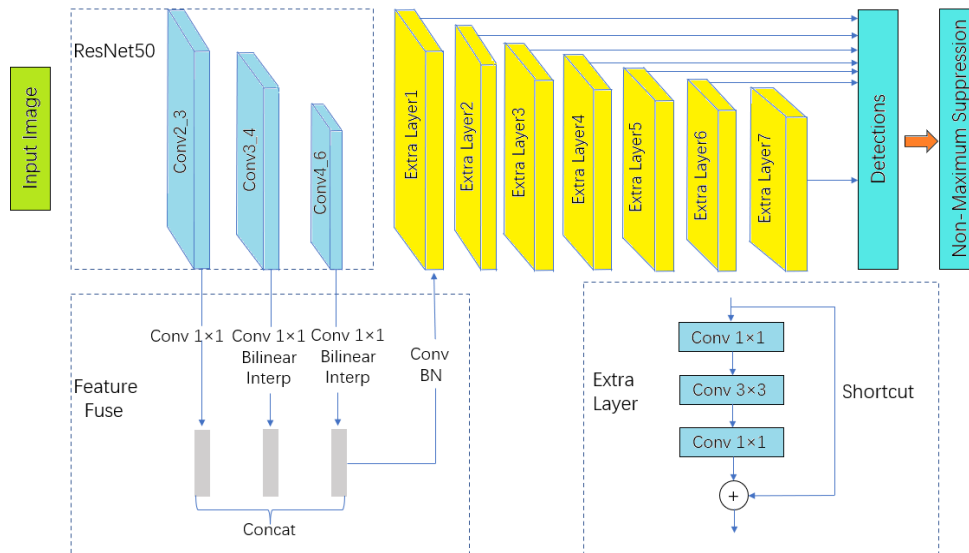


Fig. 5 - Network structure of the improved SSD

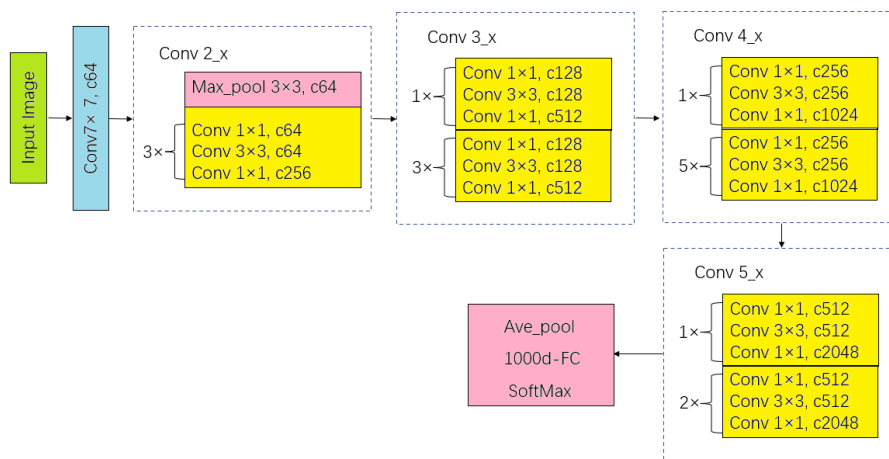


Fig. 6 - Network structure of ResNet50

Residual Network (ResNet) is one of the most commonly used convolutional neural network architectures. In deep learning training, with the deepening of the network, it is likely to appear the problem of gradient disappearance and gradient explosion. Using data initialization and normalization layer (BN) can solve the gradient problem, but the deepening of the network will also bring the problem of network degradation, that is, with the deepening of the network depth, the network performance will decrease instead. ResNet can be used to solve the degradation problem, and at the same time alleviate the problems of gradient disappearing and gradient explosion to a certain extent, and improve the performance of the network. Compared with the VGG network, Resnet can construct a deeper network structure. When the VGG network has a deeper network structure, the number of parameters is relatively large, which is prone to over-fitting. The number of Resnet parameters is relatively small, which reduces the risk of over-fitting. When training the deep network, Resnet is more stable, and the training and reasoning speed is relatively fast. The classical network structures of ResNet are: ResNet-18, ResNet-34, ResNet-50, ResNet-101, ResNet-152. In this paper, Resnet50 is selected as the backbone network.

Feature Fusion refers to the use of complementarity between features to fuse the advantages of features when features of different attributes are given, so as to improve the performance of the model. Although the SSD algorithm predicts features from different layers, SSD regards them as the same layer and predicts them directly, which cannot make full use of local detail features and global semantic features. Through feature fusion, shallow detail features and high-level semantic features can be combined to improve the prediction effect of the network. As shown in Figure 7 (a), SSD predicts directly on the feature of each layer, and there is no connection between each layer. After adding feature fusion, as shown in Figure 7 (b), the features of each layer are fused, and then the feature pyramid is generated from the fusion feature.

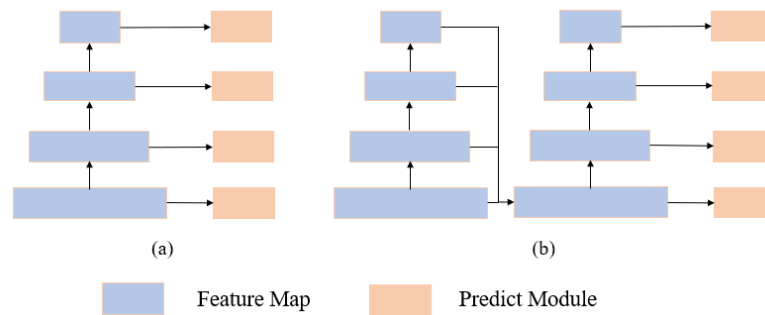


Fig. 7 - Feature information processing

RESULTS

In this paper, the Precision (P) and Mean Average Precision (mAP) are selected as the evaluation criteria of the algorithm. The Precision refers to the proportion of samples that are truly positive in all samples predicted by the classifier. The mAP provides a comprehensive measure to compare and evaluate the performance of different algorithms. The formulas are as follows.

$$P = \frac{TP}{TP+FP} \tag{1}$$

$$R = \frac{TP}{TP+FN} \tag{2}$$

$$AP = \int_0^1 P(R)dR \tag{3}$$

$$mAP = \frac{1}{K} \sum_{i=1}^K AP(i) \tag{4}$$

where:

P and R denote Precision and Recall. TP , FP and FN mean true positive, false positive and false negative, respectively. K is the number of detection classes.

The results of SSD

In this paper, the SSD algorithm and the improved SSD algorithm are used to classify the dried daylily. The experimental results are shown in Table 2. The results show that the improved SSD algorithm can effectively grade dried daylily. The mAP of the SSD512 reaches 97.52 %, which is 4.17 % higher than that of the traditional SSD algorithm. The examples of the grading results are shown in Figure 8.

Table 2

Experimental results of SSD and improved SSD

architecture	backbone	P (%)			mAP (%)	FPS
		AL	BL	CL		
SSD	VGG16	90.78	92.71	96.56	93.35	44
SSD300 r50	ResNet50	92.42	91.09	96.85	93.46	40
SSD512 r50	ResNet50	96.92	96.64	98.99	97.52	40



Fig. 8 - The examples of the grading results of SSD512

Comparison with YOLOv5 processing results

YOLOv5 is one of the YOLO (Redmon et al., 2016) series algorithms. It regards the target detection task as a regression problem, and directly predicts the bounding box and category probability through the convolutional neural network. YOLOv5 is mainly composed of four parts: Input, Backbone, Neck, and Head. The network structure of YOLOv5s is shown in Figure 9. In this paper, YOLOv5s algorithm is used for dried daylily grading.

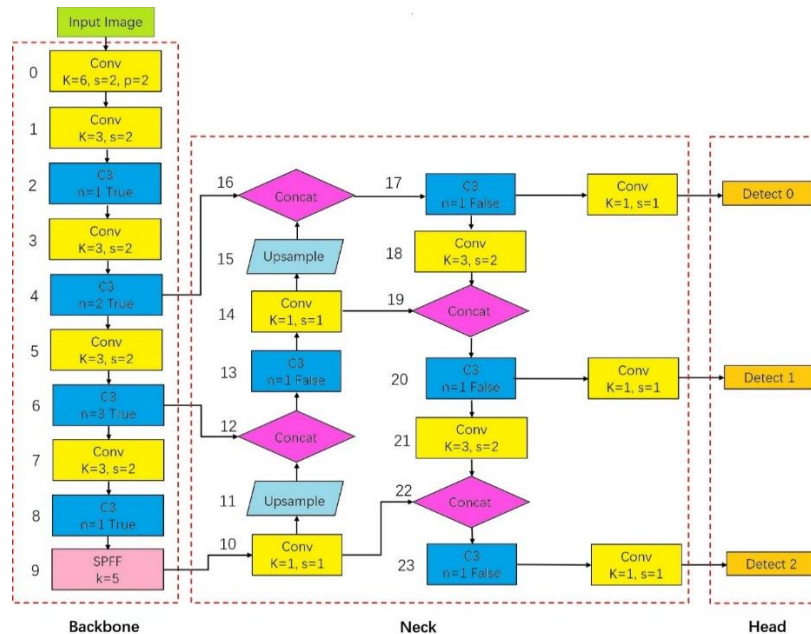


Fig. 9 - Network structure of YOLOv5s

In order to grade dried daylily better, the YOLOv5s network was improved by adding attention mechanism to the model (Wang et al., 2022). The attention mechanism is a computer science principle that imitates the human attention mechanism, which is mainly used to improve the performance of neural networks in processing sequence data (Xia et al., 2023). This paper selects two attention mechanisms: CBAM (Convolutional Block Attention Module) (Woo et al., 2018) and CA (Coordinate attention) (Hou et al., 2021). YOLOv5s-CA (Du et al., 2024) and YOLOv5s-CBAM (Dai et al., 2024) are used to process dried daylily data, respectively.

The processing results are shown in Table 3. The *P* value of each grade are not very high, and the *mAP* is lower than 80 %. Because the YOLO algorithm does not perform regional sampling directly, it extracts information through full-image detection. Therefore, YOLO has a good performance on global information, but a poor performance on small-scale information. The grading of dried daylily focuses on detailed information, so the precision of YOLOv5 is not high. After adding CBAM attention mechanism and CA attention mechanism to YOLOv5s, the two attention mechanisms have significantly improved the precision of A-grade, but the grading effect on B-grade is poor, resulting in a decrease in *mAP* value instead of an increase.

Table 3

Experimental results of YOLOv5s and improved YOLOv5s

architecture	P (%)			mAP (%)
	AL	BL	CL	
YOLOv5s	78.5	75.2	83.9	79.2
YOLOv5s-CA	80.4	63.5	83.9	75.9
YOLOv5s-CBAM	80.2	62.5	83.6	75.5

The comparison of the results of the SSD series algorithm and the YOLOv5 series algorithm is shown in Figure 10. For the problem of dried daylily grading, the classification effect of YOLOv5 algorithm is limited. The detail detection algorithm based on SSD proposed in this paper has obvious advantages in classification accuracy.

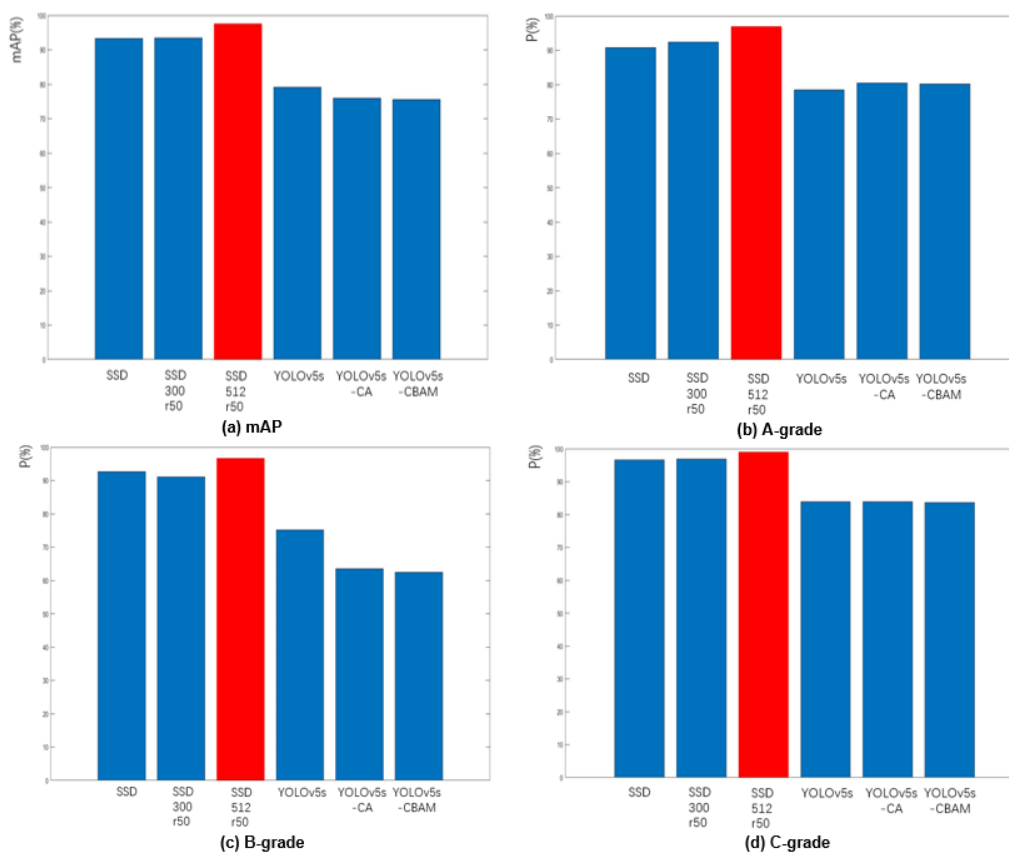


Fig. 10 - The comparison results of each algorithm

CONCLUSIONS

Daylily is small in size and similar in color and texture. The grading of dried daylily is extremely dependent on the ability to identify details. The manual sorting lacks specific quantitative criteria, the classification efficiency is low and the results are inaccurate. In terms of automatic grading, the requirement for the detail recognition ability of the algorithm is very high. The existing machine vision algorithm is mainly aimed at relatively large targets in the field of agricultural product recognition, and the ability of detail recognition is limited. This paper studies the grading algorithm of dried daylily based on deep learning, improves the detail recognition ability of the algorithm, establishes an efficient grading model, and realizes the automatic classification of daylily. The experimental results show that for dried daylily grading, the grading effect of YOLOv5 is relatively limited, while the SSD algorithm uses multi-scale feature extraction, that is, using multiple feature maps of different scales for target detection, which can effectively detect targets of various sizes, and the detection of small targets is more accurate. At the same time, SSD uses Default Boxes of different proportions and aspect ratios, which can better adapt to the target of various shapes. Therefore, this paper finally selects SSD algorithm as the grading algorithm of daylily. The improved SSD algorithm can effectively grade daylily with high precision. Compared with the original SSD algorithm, the precision is significantly improved, and the mAP is increased by 4.17%. At the same time, compared with YOLOv5s, YOLOv5s-CA and YOLOv5s-CBAM, the mAP increased by 18.32%, 21.82% and 22.02%, respectively. The improved SSD algorithm has good stability and reliability, and has a good application prospect, which can provide better technical support for the development of daylily industry.

ACKNOWLEDGEMENT

This work was supported in part by the Datong City and Shanxi Agricultural University Municipal Cooperative Scientific Research Project under Grant 2020HXDTHH05, in part by the Sub-Project of the National Key Research and Development Program of China under Grant 2021YFD1600301-4, and in part by the Earmarked Fund for Shanxi Modern Agro-Industry Technology Research System under Grant 2024CYJSTX08-18.

REFERENCES

- [1] Cao, S., Zhao, D., Liu, X. Y., & Sun, Y. P. (2020). Real-time robust detector for underwater live crabs based on deep learning. *Computers and Electronics in Agriculture*, Vol. 172: 105339.

- [2] Chen, Y. P., Niu, Y., Cheng, W. D., Zheng, L. N., & Sun, D. C. (2024). Apple detection method in the natural environment based on improved YOLOv5. *INMATEH - Agricultural Engineering*, 72(1), pp. 183-192. DOI: <https://doi.org/10.35633/inmateh-72-17>
- [3] Dai, J. X., Luo, Y. F., Shi, S. Y., Yang, D. T., & Zhao, Z. X. (2024). Design and experimental evaluation of an intelligent sugarcane stem node recognition system based on enhanced yolov5s. *Multimedia Systems*, 30(6), pp. 1-16.
- [4] Du, Y. H., Gao, A., Song, Y. P., Guo, J., Ma, W. & Ren, L. L. (2024). Young apple fruits detection method based on improved yolov5. *INMATEH - Agricultural Engineering*, 73(2), pp. 84-93. DOI: <https://doi.org/10.35633/inmateh-73-07>
- [5] Gui, Z. Y., Chen, J. N., Li, Y., Chen, Z. W., Wu, C. Y., & Dong, C. W. (2023). A lightweight tea bud detection model based on Yolov5. *Computers and Electronics in Agriculture*, Vol. 205: 107636.
- [6] He, K. M., Zhang, X. Y., Ren, S. Q., & Sun, J. (2016). Deep residual learning for image recognition. *Proceedings of the 2016 IEEE/CVF conference on Computer Vision and Pattern Recognition*. 770-778.
- [7] Hou, Q. B., Zhou, D. Q., & Feng, J. S. (2021). Coordinate attention for efficient mobile network design. *Proceedings of the 2021 IEEE/CVF conference on Computer Vision and Pattern Recognition*. pp.13713-13722.
- [8] Li, Z. X., & Zhou, F. Q. (2017). FSSD: feature fusion single shot multibox detector. *Computer Science. arXiv preprint arXiv: 1712.00960*.
- [9] Liu, W., Anguelov, D., Erhan, D., Szegedy, C., Reed, S., Fu, C. Y., & Berg, A.C. (2016). SSD: Single Shot MultiBox Detector. *Proceedings of the Computer Vision – ECCV 2016*. pp. 21-37.
- [10] Ma, C., & Chen, X. D. (2022). Dried daylily sorting method based on machine vision (基于机器视觉的黄花菜干菜分选方法研究). *Ningxia Journal of Agri. And Fores. Sci. &Tech*, 63(4), 61-65.
- [11] Redmon, J., Divvala, S., Girshick, R., & Farhadi, A. (2016). You Only Look Once: Unified, Real-Time Object Detection. *Proceedings of the 2016 IEEE conference on Computer Vision and Pattern Recognition*. pp.779-788.
- [12] Simonyan, K., & Zisserman, A. (2014). Very deep convolutional networks for large-scale image recognition. *Computer Science. arXiv preprint arXiv: 1409.1556*.
- [13] Sun, H., Qiao, J. B., Li, S., Li, M.Z., Song, D., & Qiao, L. (2021). Recognition of the maize canopy at the jointing stage based on deep learning(基于深度学习的玉米拔节期冠层识别). *Transactions of the Chinese Society of Agricultural Engineering (Trans. of the CSAE)*, 37(21), 53-61.
- [14] Sun, H. N., Xu, H. W., Liu, B., He, D. J., He, J. R., Zhang, H. X., & Geng, N. (2021). MEAN-SSD: A novel real-time detector for apple leaf diseases using improved light-weight convolutional neural networks. *Computers and Electronics in Agriculture*, Vol. 189: 106379.
- [15] Tan, L., & Gao, A. (2020). SSD object detection algorithm with feature enhancement of receptive field(感受野特征增强 SSD 目标检测算法). *Computer Systems & Applications*, 29(9), 149-155.
- [16] Tian, P. Y. (2022). FFSSD: feature fusion SSD algorithm with SE on traffic sign detection. *Procedia Computer Science*, Vol. 208, pp. 338-346.
- [17] Wang, Q. F., Cheng, M., Huang, S., Cai, Z. J., Zhang, J. L., & Yuan, H. B. (2022). A deep learning approach incorporating YOLO v5 and attention mechanisms for field real-time detection of the invasive weed *Solanum rostratum* Dunal seedlings. *Computers and Electronics in Agriculture*, Vol. 199: 107194.
- [18] Woo, S., Park, J., Lee, JY., & Kweon, I.S. (2018). CBAM: Convolutional Block Attention Module. *Proceedings of the Computer Vision – ECCV 2018*. pp. 3-19.
- [19] Xia, Y., Lei, X. H., Herbst, A., & Lyu, X. L. (2023). Research on pear inflorescence recognition based on fusion attention mechanism with YOLOv5. *INMATEH - Agricultural Engineering*, 69(1), pp.11-20. DOI: <https://doi.org/10.35633/inmateh-69-01>
- [20] Xu, X. D. (2004). Drying processing of daylily(黄花菜的干制加工). *Agricultural product processing*, 0(8), 31-31.
- [21] Yin, C., Su, Y. H., Pan, M., & Duan, J. S. (2023). Detection of the quality of famous green tea based on improved YOLOv5s(基于改进 YOLOv5s 的名优绿茶品质检测). *Transactions of the Chinese Society of Agricultural Engineering (Trans. of the CSAE)*, 39(8), 179-187.
- [22] Zhang, S. L., Zhang, L. P., Zheng, W. Q., Guo, Z., & Fu, Z. Q. (2022). Identification and localization of walnut varieties based on YOLOv5(基于 YOLOv5 的核桃品种识别与定位). *Journal of Chinese Agricultural Mechanization*, 43(7), 167-172.

PATH PLANNING RESEARCH ON GRAPE PICKING ROBOTIC ARM BASED ON IMPROVED RRT ALGORITHM

基于改进 RRT 算法的葡萄采摘机械臂路径规划研究

Yifan HU^{1,2)}, Jianjun QIN^{1,2*)}, Luyang WANG^{1,2*)}, Xifu CHEN^{1,2)}, Yue ZHAO^{1,2)}

¹⁾ Beijing University of Civil Engineering and Architecture, School of Mechanical-electronic and Vehicle Engineering, Beijing/China

²⁾ Beijing Engineering Research Center for Building Safety Monitoring, Beijing / China;

Tel: +86 18855174840; E-mail: qinjianjun@bucea.edu.cn

DOI: <https://doi.org/10.35633/inmateh-74-73>

Keywords: grape picking; improved RRT algorithm; robotic arm; path planning

ABSTRACT

The robot's operation in a grape orchard environment is often disrupted by obstacles such as vines and leaves, resulting in low fruit picking efficiency. To achieve stable obstacle avoidance, an improved RRT algorithm based on global adaptive step size and target-biased sampling was developed. First, the kinematic equations of the grape-picking robotic arm were established using the PoE method, and both forward and inverse kinematics calculations were performed to determine the robot's workspace. Then, to address the issues of lack of target orientation and other shortcomings in the traditional RRT algorithm when planning collision-free paths, dynamic updating and global adaptive step size strategies were proposed. Simulation experiments conducted using MATLAB software demonstrated that our improved RRT algorithm, compared to the RRT, RRT_informed, and RRT_star algorithms, offered advantages in terms of lower planning time, fewer sampling points, and shorter path lengths in both 2D and 3D map scenarios. Finally, grape-picking experiments were conducted in both a laboratory setting and a real orchard. The results demonstrated that the average path planning time using the proposed algorithm was shorter compared to baseline algorithms, effectively validating the efficiency and practicality of the algorithm.

摘要

机器人在葡萄果园环境中作业会受到藤枝叶等障碍物的干扰，导致果实采摘效率低。为实现稳定避障，研究出一种基于全局自适应步长与目标偏置采样的改进型 RRT 算法。首先，通过 PoE 法建立了葡萄采摘机械臂运动学方程，进行了正、逆运动学计算，并计算出了机械臂工作空间。然后，针对传统 RRT 算法在规划无碰撞路径时缺乏目标导向性等问题，提出了动态更新和全局自适应步长策略，应用 MATLAB 软件进行了仿真实验，验证了我们改进后的 RRT 算法相对于 RRT 算法、RRT_informed 算法和 RRT_star 算法在二维和三维地图场景中，具有规划耗时低、采样点个数少以及路径长度短的优点。最后，分别在实验室和真实果园进行了葡萄采摘试验，路径规划的平均时间相较于基线算法更短，有效验证了算法的高效性。

INTRODUCTION

Robotic technology has rapidly advanced, providing robotic arms with significant application prospects in agricultural harvesting (Zhang et al., 2022). For harvesting robotic arms, the performance of the path planning algorithm directly impacts the efficiency and accuracy of the harvesting process (Yang et al., 2023). In harvesting environments, immature fruits, vegetables, and grapevines are often randomly distributed around ripe fruits (Yu et al., 2022), increasing the difficulty of harvesting operations. Therefore, efficiently planning a high-quality obstacle-avoidance path for harvesting robotic arms is critical.

Among path planning algorithms for robotic arms, the Rapidly-exploring Random Tree (RRT) algorithm (LaValle S. et al., 1998) demonstrated superior exploration capabilities in high-dimensional spaces compared to algorithms such as A* (Hart P.E. et al., 1968), Ant Colony Optimization (Dorigo M. et al., 1996), and Artificial Potential Field (Khatib O. et al., 1986), including RRT-Connect (Kuffner J.J. et al., 2000), RRT* (Karaman S. et al., 2011), Informed RRT* (Gammell J.D. et al., 2014), and RRT*-Smart (Islam F. et al., 2012). These variants significantly enhanced search efficiency and path quality, driving continuous progress in the field of path planning. In the realm of RRT algorithm improvements, Gao et al. (2023), developed a path planning algorithm, BP-RRT*, based on backpropagation neural networks and an improved RRT* algorithm.

This algorithm introduced a distributed sampling method, transitioning from global search to local search in stages. A neural network model predicts the number of nodes required at each stage, improving the efficiency of path optimization. *Pohan et al., (2023)*, proposed a novel path re-planning method, RRT-ACS+RT, based on the Rapidly-exploring Random Tree Star (RRT-ACS) algorithm and Ant Colony System. This method incorporated a rule-template set based on the mobile robot in dynamic environmental scenarios during the path re-planning process. Through extensive experiments, the authors demonstrated that the proposed method outperforms other algorithms. *Shi et al., (2022)*, introduced a dual-arm robotic obstacle-avoidance path planning method, GA_RRT, based on target probability bias and cost functions. During random state generation, the algorithm calculated cost functions and selected the point with the lowest cost as a sub-node. For collision detection, the primary arm performed obstacle-avoidance path planning against static obstacles, while the secondary arm considered both static and dynamic obstacles, treating the primary arm as a dynamic reference point. *Mohammed et al. (2020)* proposed an improved RRT*N algorithm, which used a probabilistic distribution strategy to generate new nodes. Nodes closer to the target had a higher generation probability, forming a more focused tree structure along the robot-to-target connection. Simulations and experiments verified the effectiveness and robustness of the RRTN algorithm, demonstrating its potential in complex environments. *Cao et al. (2023)* proposed an enhanced RRT algorithm combining goal bias strategies and the Artificial Potential Field method, achieving significant improvements in iteration counts, planning speed, path length, and path smoothness. *Jia et al. (2023)* developed a collision-free bidirectional RRT algorithm (CGB-RRT) and a flexible obstacle-avoidance path planning strategy based on the RRT algorithm, successfully addressing obstacle-avoidance challenges in complex environments. *Alam et al. (2023)* proposed the FC-RRT* algorithm for energy-efficient motion planning in industrial robots, especially for pick-and-place tasks. The algorithm optimized motion trajectories by generating nodes along predefined directions and calculating energy consumption using a circular-point approach. By applying the work-energy principle to the rotational axes of a 6DOF industrial robot, energy consumption was reduced by 1.6% to 16.5% compared to kinematic solutions and the traditional RRT* algorithm. In addition, the intelligent fuzzy adaptive RRTN path planning method (FA-RRTN) was proposed by *Khattab et al. (2023)*, the waypoint simplification and smoothing RRT method (WSS-RRT) proposed by *Gültekin et al. (2023)*, and the algorithm combining the metaheuristic Salp Swarm Algorithm (SSA) with the RRT algorithm (IRRT-SSA) proposed by *Muhsen et al. (2024)* had all provided valuable insights for this paper.

When addressing complex obstacles, existing studies still face challenges in maintaining high harvesting efficiency. To further improve efficiency, an enhanced RRT algorithm for harvesting robotic arms was proposed. By introducing dynamic update strategies for the sampling area and a global adaptive step size strategy, the algorithm's performance was significantly improved. The effectiveness of the enhanced RRT algorithm was validated in both simulated orchard environments and real-world orchard experiments.

MATERIALS AND METHODS

Background

Standardized vineyards are primarily categorized into two types: trellis systems and pergola systems. As shown in Figure 1, trellis systems are typically constructed with one or two rows of vertical posts aligned along the grapevine rows. The distance between posts is generally 30–60 cm, with the trellis height ranging from 150 to 180 cm. The width between trellis rows usually measures 150–300 cm. The grape cluster picking points are typically located at a height of 80–150 cm from the ground. Currently, the grape-picking robot developed is designed for vineyards using trellis systems. In the future, an electric telescopic mechanism will be incorporated to meet the harvesting requirements of vineyards utilizing pergola systems.

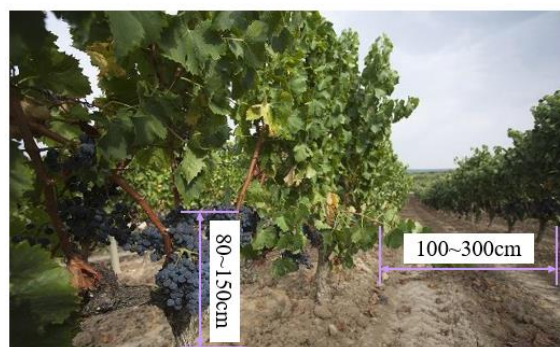


Fig. 1 - Standardized Vineyard - Trellis Structure

Forward kinematic analysis

To meet the requirements of grape harvesting, this study employed the Universal Robots UR3 robotic arm. The UR3 is a collaborative robotic arm with a payload capacity of 3 kg, a self-weight of 11 kg, a reach of 500 mm, and a repeatability of 0.1 mm. These performance parameters adequately satisfy the demands for flexibility and precision in grape harvesting.

For mathematical modeling of the UR3 robotic arm, the Product of Exponentials (PoE) method was adopted. Compared to the traditional Denavit-Hartenberg (DH) parameter method, the PoE method eliminated the need for complex coordinate frame establishment and instead focuses on the properties of each joint of the robotic arm. This made the modeling process more intuitive and concise, particularly well-suited for the multi-degree-of-freedom characteristics of the UR3 robotic arm.

To model using the PoE method, it was necessary to determine the end-effector pose in its initial configuration, the screw axes of all joints relative to the base frame (S1, ..., Sn), and the joint variables ($\theta_1, \dots, \theta_n$). Fig 2(a) illustrates the initial state of the robotic arm, from which the end-effector pose matrix E can be derived, as shown in Equation (1).

$$E = \begin{bmatrix} -1 & 0 & -1 & 0 \\ 0 & 0 & 0 & -192.8 \\ 0 & -1 & 0 & 691.95 \\ 0 & 0 & 0 & 1 \end{bmatrix} \tag{1}$$

The selection of the base coordinate system and end-effector coordinate system in Figure 2(a) follows the right-hand rule. Figure 2(b) illustrates the screw axes of each joint along with the points PPP on each axis, where the rotation direction of the screw axes is indicated by arrows. Since joints 1 to 6 are rotational joints, the coordinate values of any point on the joint axes are given in the base coordinate system. Typically, points with physical significance, such as the intersection of the joint and the link, are selected for this analysis.

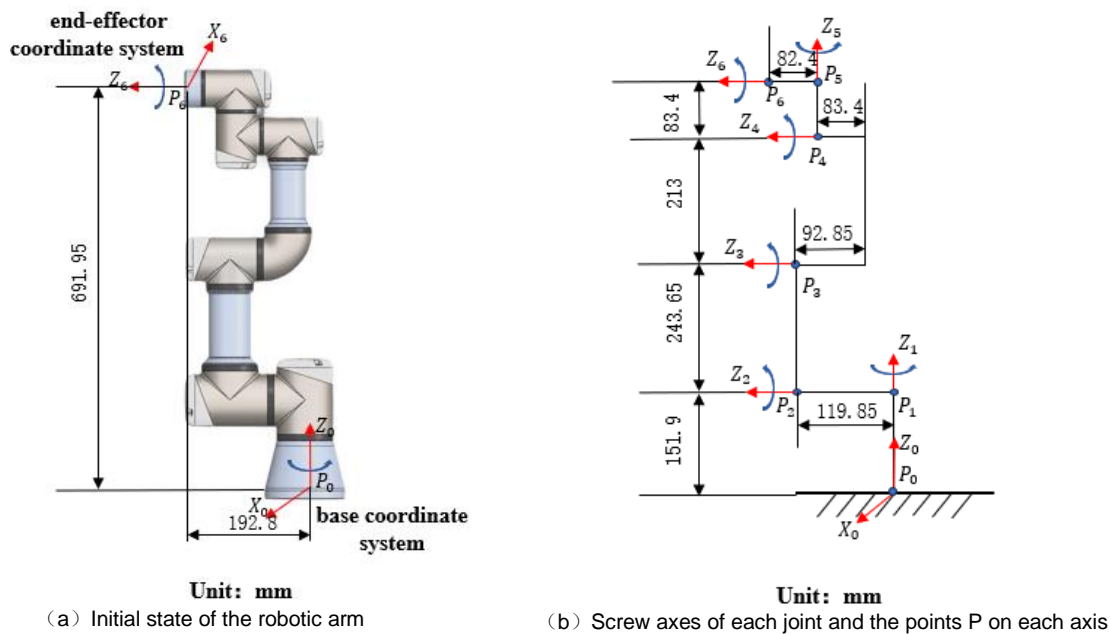


Fig. 2 - PoE modeling method

Table1

Parameter table of joints 1 to 6

n	w_n	P_n	v_n
1	(0, 0, 1)	(0, 0, 151.9)	(0, 0, 0)
2	(0, -1, 0)	(0, -119.85, 151.9)	(151.9, 0, 0)
3	(0, -1, 0)	(0, -119.85, 395.55)	(395.55, 0, 0)
4	(0, -1, 0)	(0, -110.4, 608.55)	(608.55, 0, 0)
5	(0, 0, 1)	(0, -110.4, 691.95)	(-110.4, 0, 0)
6	(0, -1, 0)	(0, -192.8, 691.95)	(691.95, 0, 0)

As shown in Table 1, the parameter table for the PoE method modeling is provided, $\omega_n \in \mathbb{R}^3$ and $v_n \in \mathbb{R}^3$ represents the angular velocity and linear velocity of joint n. \hat{s}_n denotes the unit vector along the positive direction of the joint axis, which represents the rotational axis of joint n relative to the base coordinate system. The velocity expression consists of two parts: the left part corresponds to the linear velocity caused by rotation, and the right part represents the linear velocity along the rotation axis. $[S_n]$ is the skew-symmetric matrix, calculated from S_n . As shown in Equation (2), $[S_n]$ is presented in Equation (3), and the homogeneous transformation matrix is given in Equation (4). Once T_6^0 is calculated, the forward kinematic analysis of the robotic arm is completed. The solution to the forward kinematics aids in the subsequent determination of the robotic arm's workspace.

$$S_n = \begin{bmatrix} w_n \\ v_n \end{bmatrix} = \begin{bmatrix} \hat{s}_n \\ -\hat{s}_n \times P_n \end{bmatrix} \tag{2}$$

$$[S_n] = \begin{bmatrix} [w_n] & v_n \\ 0 & 0 \end{bmatrix} \tag{3}$$

$$T_6^0 = e^{[S_1]\theta_1} \dots e^{[S_{n-1}]\theta_{n-1}} e^{[S_n]\theta_n} M \tag{4}$$

Inverse Kinematic Analysis

The inverse kinematics analysis of the robotic arm requires the known position and orientation of the robot's end-effector relative to the base coordinate system, in order to determine the six joint angles of the robotic arm. Assuming that the pose matrix of the robot's end-effector relative to the base coordinate system is given by Equation (5), the six joint angles of the robot can be derived from matrix calculations, as shown in Equation (6). The first three columns of the matrix in equation (5) represent the rotational relationship between the original coordinate system and the new coordinate system, while the last column of the first three rows indicates the translation of the origin of the new coordinate system relative to the original one. The final row ensures the matrix is in homogeneous form, enabling the unified representation of both rotation and translation transformations. There are a total of 8 solutions, with $\theta_1, \theta_2, \theta_4$ and θ_6 having unique solutions, and θ_3 and θ_5 each having two solutions. In Equation (6), s_i, c_i represents $\sin \theta_i, \cos \theta_i$, c_{ij}, s_{ij} represents $\cos(\theta_i + \theta_j), \sin(\theta_i + \theta_j)$, c_{ijk}, s_{ijk} represents $\cos(\theta_i + \theta_j + \theta_k), \sin(\theta_i + \theta_j + \theta_k)$, a_i denotes the link lengths, and d_i represents the link distances. The value of m,n,s,t is given in Equation (7). The aforementioned inverse kinematics calculations lay the foundation for the subsequent trajectory interpolation.

$$T_6^0 = \begin{bmatrix} n_x & o_x & a_x & p_x \\ n_y & o_y & a_y & p_y \\ n_z & o_z & a_z & p_z \\ 0 & 0 & 0 & 1 \end{bmatrix} \tag{5}$$

$$\left\{ \begin{array}{l} \theta_1 = A \tan 2(m, n) - \\ A \tan 2(-d_2 - d_4, \\ \pm \sqrt{m^2 + n^2 - (d_2 + d_4)^2}) \\ \theta_2 = A \tan 2(s_2, c_2) \\ \theta_3 = \pm \arccos\left(\frac{r_{14}^2 + r_{34}^2 - a_3^2 - a_2^2}{2a_2 a_3}\right) \\ \theta_4 = A \tan 2(s_{234}, c_{234}) - \theta_2 - \theta_3 \\ \theta_5 = \pm \arccos(s_1 a_x - c_1 a_y) \\ \theta_6 = A \tan 2(s, t) - A \tan 2(-s_5, 0) \end{array} \right. \tag{6}$$

$$\begin{cases} m = p_y - a_y d_6 \\ n = p_x - a_x d_6 \\ s = c_1 n_y - s_1 n_x \\ t = c_1 o_y - s_1 o_x \end{cases} \quad (7)$$

Design of the Robot Hardware

This study developed an experimental platform for the grape-picking robot. As shown in Figure 3, the 3D model of the main equipment primarily consists of a wheeled chassis and a robotic arm. The robotic arm is equipped with a self-designed end effector, two RealSense D435i depth cameras, and a 16-line LiDAR (model: Robosense RS-Helios-16P). The upper computer for the robotic arm is a laptop with 32GB of RAM and an RTX 3060 GPU, while the upper computer for the chassis is a Jetson Xavier NX with 64GB of memory.

For the task of grape picking, a specific end effector was designed. The end effector consists of an electric parallel two-finger gripper and electric scissors. The electric parallel two-finger gripper is the Z-EFG-20P model from HuiLing Technology, which offers an adjustable gripping force ranging from 30 N to 80 N. The electric scissors are self-designed, and their working principle involves a stepper motor driving a lead screw to control the opening and closing of the scissors. Additionally, a limit switch is used to fix the maximum and minimum opening angles of the scissors. The scissors blades extend 2 cm beyond the electric gripper, ensuring that grape clusters can be effectively cut. Both the electric gripper and electric scissors can be controlled via I/O, and after connecting them to the control cabinet of the UR3 robotic arm, the end tool can be controlled via the robotic arm teach pendant or the ROS2 in the upper-level computer. The 3D model of the end effector is shown in Figure 3. The distance from the TCP to the end of the flange is 176.2 mm. This distance, referred to as the TCP offset, is used when calculating the workspace of the robotic arm.

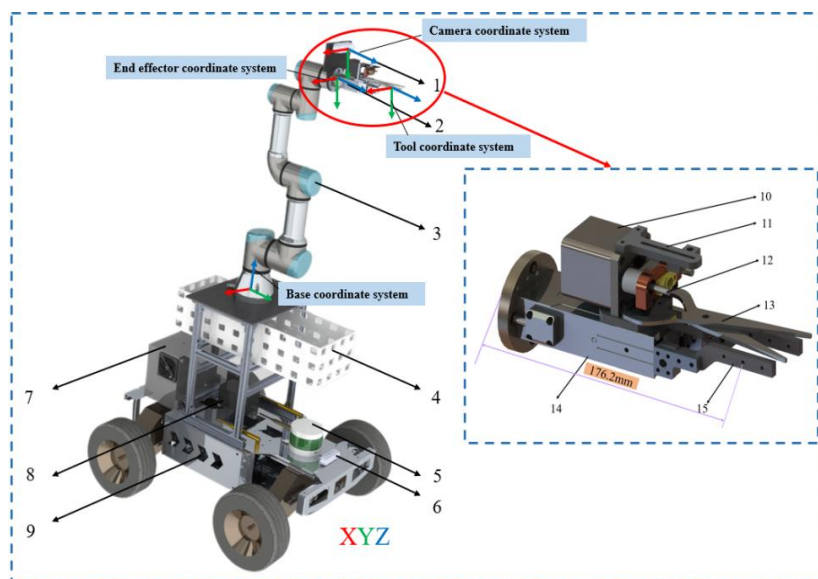


Fig. 3 - 3D Model of the Grape Picking Robot

1. RGB-D Camera; 2. End Effector; 3. UR3 Robotic Arm; 4. Storage Basket; 5. LiDAR; 6. RGB-D Camera;
7. Robotic Arm Control Cabinet; 8. Chassis Host Computer; 9. Chassis; 10. Stepper motor; 11. Limit switch;
12. Lead screw; 13. Picking scissors; 14. Electric parallel gripper; 15. Gripper extension section

Workspace analysis

The workspace refers to the set of all spatial points that the robot's end-effector can reach during the grape-picking process. Its shape and range are critical factors influencing the robot's operational performance. After completing the forward and inverse kinematics analysis of the robotic arm, the Monte Carlo method was employed in MATLAB to calculate the workspace of the UR3 robotic arm. The Monte Carlo method randomly generates multiple end-effector position coordinates using the forward kinematics equations (Equation 4), and then incorporates the TCP offset to obtain the workspace of the grape-picking robot (including the tool), as shown in Figure 4. The workspace of the UR3 robotic arm approximates an ellipsoid, with the range in the X and Y directions being approximately -600 mm to 600 mm, and the range in the Z direction being approximately -500 mm to 800 mm. When planning paths for grape-picking tasks using an improved RRT algorithm, the randomly sampled points should be confined within the workspace of the robotic arm.

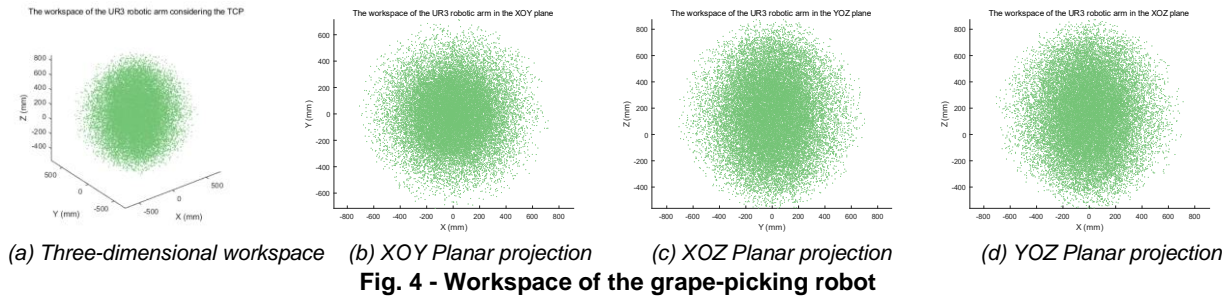


Fig. 4 - Workspace of the grape-picking robot

RRT algorithm improvement and simulation experiment

Improvement Strategies for RRT Algorithm

The RRT algorithm is a sampling-based path planning algorithm that uses the starting point as the root node, increases the number of nodes through random sampling and piling, and connects the nodes to generate a random tree. Nodes that do not satisfy the constraint requirements are discarded during the generation of subsequent nodes. When the random tree contains the goal point or enters the goal area, a route connecting the start point to the endpoint exists.

This paper proposes two improvement strategies for the traditional RRT algorithm: the sampling region dynamic update strategy and the global adaptive step size strategy, aimed at enhancing the algorithm's performance. First, the initial improvement strategy involved dynamically updating the sampling region. Traditional RRT algorithms often exhibited a lack of goal orientation when planning collision-free paths, sometimes growing in the reverse direction. This phenomenon primarily arose from random sampling in unsuitable regions, resulting in numerous ineffective branches. To address this shortcoming, a dynamic update mechanism for the sampling region was designed. The key to this strategy was to gradually reduce and optimize the sampling space as the random tree grows, particularly shifting focus to the region near the target point. This approach encouraged the random tree to grow toward the target point, defining positive growth as the expansion of random tree nodes toward the area between the current node and the target point. This helped continuously reduce the distance to the target point and ensured effective tree expansion. Conversely, if the growth was oriented toward the starting point, it is considered to have departed from the target point, thereby increasing the distance from it. This type of growth was defined as reverse growth and regarded it as a non-ideal form of expansion. Sampling only within the valid region may cause the algorithm to get stuck in a local optimum. Therefore, if the current node fails to expand after 30 iterations, it is considered invalid and removed from the random tree.

The second improvement strategy involved global adaptive step size adjustment. Traditional RRT algorithms typically utilize a predetermined fixed step size for tree expansion, failing to dynamically adjust this parameter based on the information gathered during the search process. This could result in improper selection of the step size, either too large or too small, adversely affecting the algorithm's convergence speed and the quality of the paths, particularly in narrow or obstacle-intensive regions, where exploration efficiency might be significantly diminished. The improved RRT algorithm considers the relationship between environmental complexity and obstacle characteristics by calculating factors such as the ratio of obstacle area to total area, the average distance between obstacles, and the reciprocal of the number of obstacles. In addition, different weighting coefficients were introduced to comprehensively determine the environmental complexity metric w_1 . This allowed the algorithm to self-calculate an adaptive initial step value to more effectively adapt to environmental changes.

$$step = step_{start} = \lfloor N_{size} * w_1 \rfloor \quad (8)$$

Then expand the new node q_{new} in steps, as shown in Equation (9):

$$q_{new} = step * \frac{|q_{nearest} - q_{rand}|}{\|q_{nearest} - q_{rand}\|} + q_{nearest} \quad (9)$$

In Equation (8) N_{size} was the map size, and $\lfloor N_{size} * w_1 \rfloor$ denotes $N_{size} * w_1$ rounded down to the calculation results, during the random expansion of the random tree, the strategy continuously acquired environmental information, and the improved RRT algorithm could adaptively adjust the step size in the region with more obstacles, as shown in Equation (10):

$$step = step * w_2 \quad (10)$$

In Equation (10), w_2 was the weight of step size reduction, and w_2 was selected according to the number of obstacles, in general, w_2 was taken as 0.7 for simple environment, and w_2 was taken as 0.3 for complex environment, and the initial step size would be restored after the extended tree covered the complex obstacle region, in summary the ability to realize the global adaptive step size strategy effectively increased the global search capability of the improved RRT algorithm. Below is the pseudocode for the improved RRT algorithm.

Algorithm:improved_rrt

Input: q_start , q_goal , M (map)
Output: Path from q_start to q_goal (if found)
 Initialize random tree with root q_start
 Set initial valid region near q_goal , invalid region elsewhere
while (random tree has not reached q_goal):
 Update Sampling Region
 if random tree grows towards q_goal :
 Shrink valid region toward target
 else if reverse growth:
 Expand valid region and remove invalid branches
 Sample q_rand within valid region
 Find nearest node $q_nearest$
 Calculate step size:
 if environment is complex:
 step = step * w_2
 else:
 step = step * w_1
 Steer towards q_rand :
 q_new = Steer($q_nearest$, q_rand , step)
 Check for collision:
 if ObstacleFree($q_nearest$, q_new):
 Add q_new to random tree
 if q_new is near q_goal , return path
if no path found after max iterations, return failure

Two-dimensional scene simulation

In this study, the traditional RRT algorithm, RRT_star algorithm, RRT_informed algorithm, and the improved RRT algorithm were used to plan paths on a two-dimensional map. Parameters such as the number of obstacles, the positions of obstacles, and the random seed were modified in MATLAB to test each algorithm 60 times, in order to validate the performance of the improved RRT algorithm for path planning in two-dimensional environments. The path-planning capabilities of the four algorithms were evaluated based on three indicators: planning time, number of sampling points, and path length. If an algorithm took less time, required fewer sampling points, and produced a shorter path, it was considered to have better path-planning performance. In the experiments, the two-dimensional map had dimensions of 450 cm by 450 cm, with the start point for path planning at (100 cm, 100 cm) and the endpoint at (300 cm, 300 cm). The fixed step size for the traditional RRT, RRT_informed, and RRT_star algorithms was set to 30 mm.

As shown in Figure 5, the hexagonal star shape represents the starting point of the path planning, and the pentagonal star shape represents the endpoint. The blue x symbols indicate randomly generated sample points, while the yellow circles and black rectangles represent obstacles. If a sample point is randomly generated inside an obstacle, it is not used during the path planning process. The black lines represent the connections between the sample points during the exploration of the random tree, the red line indicates the path before smoothing, and the blue line represents the path after smoothing.

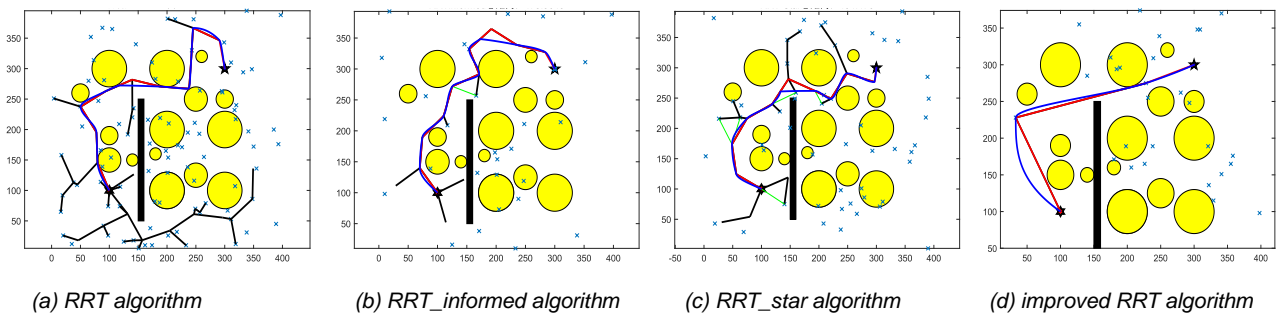


Fig. 5 - Comparison of four RRT algorithms in two-dimensional maps

Table 2

Comparison of indicators of four RRT algorithms for two-dimensional scenarios

Types of algorithms	Time consumption/s	Sampling points/each	Path length/cm
RRT	13.05	93	547.48
RRT_star	2.62	54	454.48
RRT_informed	2.93	45	475.96
Improved RRT	0.77	29	421.28

The results comparing the planning effects and indicators of the improved RRT algorithm presented in this paper with those of the other three RRT algorithms on two-dimensional maps were shown in Fig 5 and Table 2. Figure 5 shows that the traditional RRT algorithm generates numerous invalid nodes during path planning, resulting in directionless planned paths. The RRT_informed and RRT_star algorithms generate fewer nodes; however, the planned paths are more tortuous. Nevertheless, our proposed improved RRT algorithm not only significantly reduces the number of invalid sampling points but also efficiently plans smooth paths. Table 2 indicates that our improved RRT algorithm, compared to the traditional RRT algorithm, RRT_informed algorithm, and RRT_star algorithm, resulted in a 94.1%, 70.61%, and 73.72% decrease in planning elapsed time, a 68.82%, 46.3%, and 35.56% reduction in the number of sampling points, and a 23.78%, 7.31%, and 11.49% decrease in path length, respectively. In summary, compared to the other three RRT algorithms, the performance of our improved RRT algorithm has improved.

Three-dimensional scene simulation

The path planning in the three-dimensional scene of this study is similar to that in the two-dimensional scene. The length, width, and height of the three-dimensional map are 450 cm, with the starting point at (100 cm, 100 cm, 100 cm) and the endpoint at (300 cm, 300 cm, 300 cm). In the three-dimensional simulation scene, obstacles have been modified to colorful spheres and rectangular cuboids, while the other settings remain similar to those in the two-dimensional simulation scene. Similarly, several parameters were modified and the improved RRT algorithm was tested along with the three baseline algorithms in MATLAB, conducting 60 trials. The number of sampling points and the time recorded are the average values from the 60 trials, as shown in the Table 3.

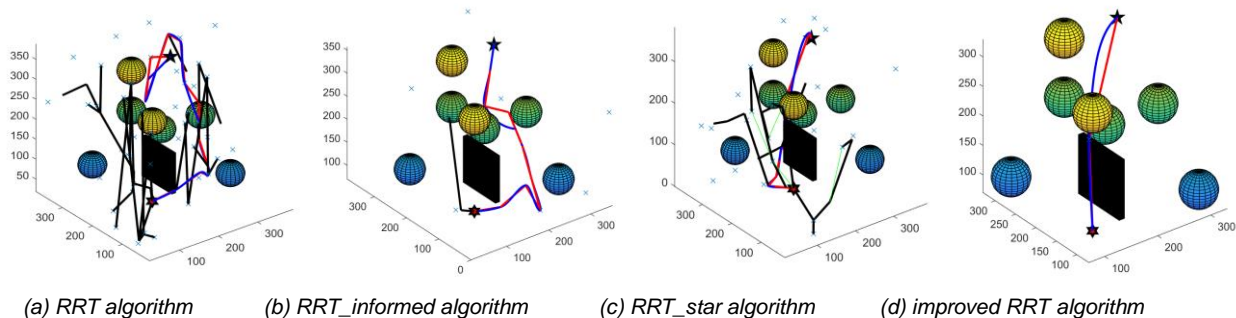


Fig. 6 - Comparison of four RRT algorithms in three-dimensional maps

Table 3

Comparison of indicators of four RRT algorithms for two-dimensional scenarios

Types of algorithms	Time consumption/s	Sampling points/each	Path length/cm
RRT	5.88	50	844.80
RRT_star	3.57	28	586.07
RRT_informed	0.74	12	555.36
Improved RRT	0.24	2	365.88

The results of the comparison of the planning effects and indicators between the improved RRT algorithm in this paper and the remaining three RRT algorithms on three-dimensional maps were shown in Figure 6 and in Table 3. Figure 6 and Table 3 indicate that the improved RRT algorithm presented in this paper, compared to the traditional RRT algorithm, RRT_informed algorithm, and RRT_star algorithm, results in a 95.92%, 93.28%, and 67.57% decrease in planning elapsed time, a 96%, 92.9%, and 83.33% reduction in the number of sampling points, and a 58.65%, 34.5%, and 34.12% decrease in path lengths, respectively. In summary, our improved RRT algorithm demonstrated strong planning capability on three-dimensional maps.

RESULTS

Planning system design

The simulation in MATLAB was conducted to validate the performance of the improved RRT algorithm. In real-world experiments, the MoveIt2 software in ROS2 and the OMPL library were primarily utilized to implement the RRT algorithm for planning and control. The real-world experiments were mainly divided into three parts: robotic arm path planning, target detection and localization, and the coordination between the chassis and the robotic arm. Figure 7(a) showed the hardware design and communication architecture of the grape-picking robot.

Path planning using the RRT and its variant algorithms involved five main processes: initializing the tree, random sampling, tree extension, path checking, and path optimization. In the real-world experiments, the host computer of the robot was connected to the UR3 robotic arm via an Ethernet cable, and the arm could be controlled using the MoveIt2 software. Various RRT algorithms were encapsulated in the OMPL library, which provided interfaces for path planning. The planned path required optimization, and MoveIt2 offered libraries to achieve trajectory smoothing and interpolation. Cubic spline interpolation was also used for trajectory optimization, and comparative results showed that it produced similarly smooth paths as those generated by the built-in MoveIt2 libraries. The 'ros2_control' framework had parsed planned trajectory into specific joint commands, which were then executed via hardware interfaces. Meanwhile, the execution status of the robotic arm was fed back to MoveIt2 through relevant ROS2 topics to enable real-time status monitoring and subsequent planning adjustments. Since multiple points were generated during trajectory interpolation, the inverse kinematics of the robotic arm was required to calculate the joint angles for these points (Equation (6)), allowing smooth movement along the generated trajectory. In most cases, path planning for the robotic arm was conducted in the joint space, but MoveIt2 also provides interfaces for planning based on the TCP (Tool Center Point) if required. The planning process was shown in Figure 7(b).

As shown in Fig 7(c), the target detection and localization process employed the YOLOv9 algorithm to identify grapes and their picking points. Once a picking point was detected by the RealSense D435i camera, the camera API was called to obtain the center position of the bounding box of the grape, along with its coordinates (x, y, z) in the camera coordinate system. Through hand-eye calibration and coordinate transformation of the robotic arm, the coordinates could be converted from the camera coordinate system to the end-effector coordinate system of the robotic arm. The transformed coordinates were then sent to MoveIt2 for path planning. The relevant coordinate systems of the robotic arm and the camera were shown in Figure 3.

The coordination between the chassis and the robot's host computer was achieved through a CAN bus. After the robotic arm completed the picking task for all recognizable grape clusters at the current location, the robot's host computer sent a signal to the chassis host computer to move the chassis forward by 15 cm. Once the chassis reached the new position, the robotic arm resumed the picking task, ensuring an efficient coordinated workflow, the process was detailed in Figure 7(b).

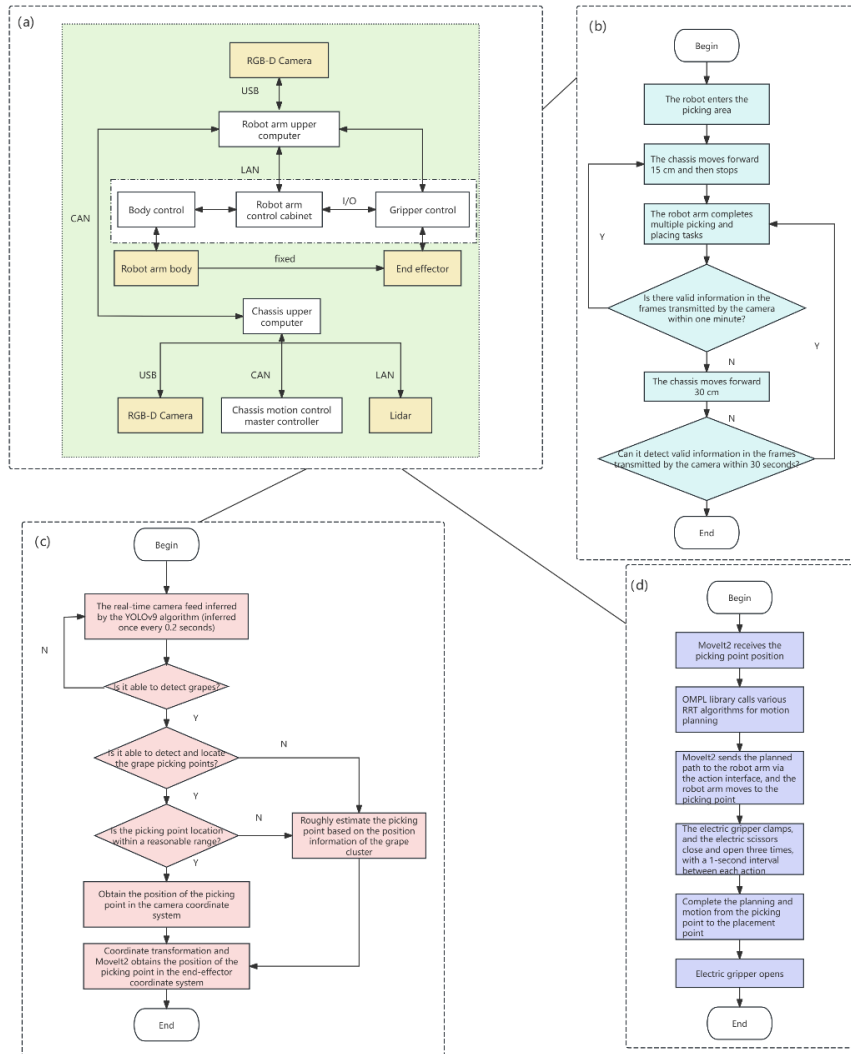


Fig. 7 - Hardware system of the grape picking robot and the process design of each module

(a) Picking Robot hardware design; (b) Chassis planning process;
 (c) Object detection and localization process; (d) Robotic arm planning and control process

Indoor experiment

The indoor picking experiment was conducted in a laboratory setting in September 2024, as shown in Figure 8. At the start of the experiment, 15 artificial grape bunches, each with an average weight of 200 g, were placed at varying heights on the vine. During the experiment, the RGB-D camera was first used to identify the grape bunches and locate the picking points. Then, the OMPL library in MoveIt2 invoked the specified algorithms for path planning. After planning, the robotic arm moved at a speed of 1 m/s to the vicinity of the nearest grape bunch for harvesting. Upon completion of the picking task, the upper computer planned a new path to place the grapes into the storage basket. As shown in Fig 8, the process of the picking experiment is illustrated. The three-fingered gripper used here was insufficient in gripping force, so in subsequent real-world experiments, it was replaced with a specialized gripper (Figure 3). For the indoor experiments, path planning was conducted within the joint space, and the use of the end-effector did not affect the validation of the planning algorithm.

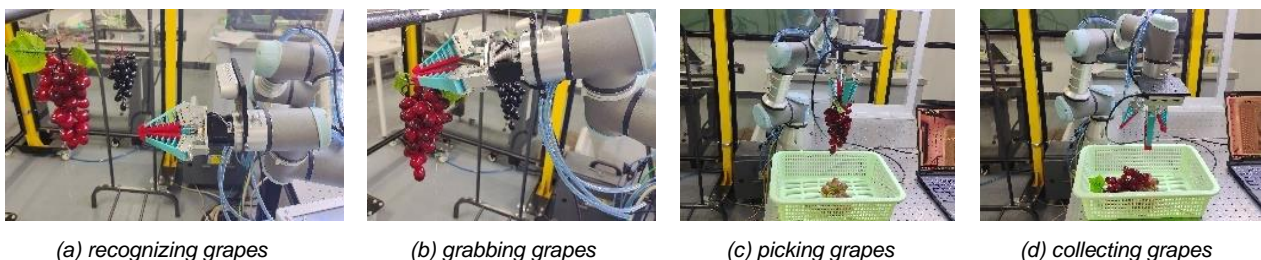


Fig. 8 - Picking process in the laboratory

The RRT algorithm, RRT_informed algorithm, RRT_star algorithm, and our improved algorithm were utilized for path planning. Each algorithm was tested 16 times, with 8 tests for picking and collecting a single grape bunch, and the remaining 8 for picking and collecting multiple bunches (averaging 4–5 bunches per experiment). The average time for each planning algorithm was recorded in every test. As shown in Table 4, our algorithm demonstrated improved planning efficiency compared to the other three baseline algorithms.

Table 4

Average Planning Time of Four Algorithms in Indoor Experiments

Type of Algorithms	Single-bunch grape picking experiment		Multi-bunch grape picking experiment
	Average Planning Time from Initial Position to Picking Point /s	Planning Time from Picking Point to Storage Basket /s	Total Average Planning Time for the Entire Process /s
RRT	0.42	0.58	5.44
RRT_informed	0.34	0.41	4.03
RRT_star	0.39	0.44	4.12
Ours	0.29	0.40	3.87

Outdoor experiment

In October 2024, a real-environment picking test was conducted at a grape picking garden in Fangshan District, Beijing, which covers an area of approximately 10 acres and uses a double-row trellis system, as shown in Fig 9. Four algorithms were used for the planning experiments, with each algorithm being tested 10 times for multi-bunch grape picking (averaging 6-7 bunches per test). The average planning time was calculated for each algorithm. As shown in Table 5, our improved algorithm still outperformed the other algorithms in terms of planning efficiency in the real-world scenario. However, due to the presence of obstacles in the real environment, the average path planning time for the robotic arm was longer compared to the indoor experiments.

Table 5

Average Planning Time of Four Algorithms in Outdoor Experiments

Types of Algorithm	Average Planning Time / s
RRT	8.53
RRT_informed	6.98
RRT_star	7.11
Ours	6.61



(a) recognizing grapes

(b) grabbing grapes

(c) picking grapes

(d) collecting grapes

Fig. 9 - Picking process in real orchard

CONCLUSIONS

(1) Compared to the traditional RRT algorithm, the improved RRT algorithm presented in this paper incorporates a dynamic sampling region update strategy and a global adaptive step size strategy. Simulation experiments conducted using MATLAB software demonstrated that the improved RRT algorithm required less planning time, utilized fewer sampling nodes, and generated shorter planning paths, thereby highlighting its superiority.

(2) Grape picking experiments were conducted in both laboratory and real orchard environments. In the laboratory setting, the average planning time for consecutive pickings was approximately 3.87 seconds, while in the real orchard, the planning time was 6.61 seconds. This increase in planning time in the real orchard environment is due to branches, leaves, and other obstacles that complicate the robotic arm's path planning. Overall, the path planning time using the improved RRT algorithm was shorter compared to the other three baseline algorithms.

ACKNOWLEDGEMENT

This paper was funded by the Special Funds Program for Basic Research Operating Expenses of Universities under Beijing Municipality (Grant No.X20060), Research Fund Project of Beijing Building Safety Monitoring Engineering Technology Research Center (Grant No.BJC2020K012) and Research on Intelligent Motion Control Design of Quadruped Robot (Grant No.PG2024139).

REFERENCES

- [1] Alam, M. M., Nishi, T., Liu, Z., et al. (2023). A Novel Sampling-Based Optimal Motion Planning Algorithm for Energy-Efficient Robotic Pick and Place. *Energies*, 16(19), 6910.
- [2] Cao, M., Zhou, X., & Ju, Y. (2023). Robot motion planning based on improved RRT algorithm and RBF neural network sliding. *IEEE Access*, 11, 121295-121305.
- [3] Dorigo, M. (1996). The Any System Optimization by a colony of cooperating agents. *IEEE Trans. System, Man & Cybernetics-Part B*, 26(1), 1-13.
- [4] Gammell, J. D., Srinivasa, S. S., & Barfoot, T. D. (2014). Informed RRT*: Optimal sampling-based path planning focused via direct sampling of an admissible ellipsoidal heuristic. *2014 IEEE/RSJ International Conference on Intelligent Robots and Systems*, 2997-3004.
- [5] Gao, Q., Yuan, Q., Sun, Y., & Xu, L. (2023). Path planning algorithm of robot arm based on improved RRT* and BP neural network algorithm. *Journal of King Saud University-Computer and Information Sciences*, 35(8), 101650.
- [6] Gültekin, Ayhan, Samet Diri, Yaşar Becerikli. (2023). Simplified and Smoothed Rapidly-Exploring Random Tree Algorithm for Robot Path Planning *Tehnički vjesnik*. 30.3 (2023): 891-898.
- [7] Hart, P. E., Nilsson, N. J., & Raphael, B. (1968). A formal basis for the heuristic determination of minimum cost paths. *IEEE Transactions on Systems Science and Cybernetics*, 4(2), 100-107.
- [8] Islam, F., Nasir, J., Malik, U., Ayaz, Y., Hasan, O. (2012). RRT*-smart: Rapid convergence implementation of RRT* towards optimal solution. *2012 IEEE International Conference on Mechatronics and Automation*, 1651-1656.
- [9] Karaman, S., & Frazzoli, E. (2011). Sampling-based algorithms for optimal motion planning. *The International Journal of Robotics Research*, 30(7), 846-894.
- [10] Khattab, O., Yasser, A., Jaradat, M., Romdhane, L. (2023). Intelligent Adaptive RRT* Path Planning Algorithm for Mobile Robots. *Advances in Science and Engineering Technology International Conferences (ASET)*. IEEE. DOI: 10.1109/ASET56582.2023.10180740
- [11] Khatib, O. (1986). Real-time obstacle avoidance for manipulators and mobile robots. *The International Journal of Robotics Research*, 5(1), 90-98.
- [12] Kuffner, J. J., & LaValle, S. M. (2000). RRT-connect: An efficient approach to single-query path planning. Proceedings 2000 ICRA. Millennium Conference. IEEE International Conference on Robotics and Automation. *Symposia Proceedings*, 2, 995-1001.
- [13] LaValle, S. (1998). Rapidly-exploring random trees: A new tool for path planning. Research Report 9811.
- [14] Mashayekhi, R., Idris, M.Y.I., Anisi, M.H., Ahmedy, I., Ihsan, A. (2020). Informed RRT*-connect: An asymptotically optimal single-query path planning method. *IEEE Access*, 8, 19842-19852.
- [15] Mohammed, H., Romdhane, L., & Jaradat, M. A. (2021). RRT* N: An efficient approach to path planning in 3D for Static and Dynamic Environments. *Advanced Robotics*, 35(3-4), 168-180.
- [16] Muhsen, Dena Kadhim, Firas Abdulrazzaq Raheem, and Ahmed T. Sadiq. (2024). Improved rapidly exploring random tree using salp swarm algorithm. *Journal of Intelligent Systems*. 33.1: 20230219.
- [17] Shi, W., Wang, K., Zhao, C., & Tian, M. (2022). Obstacle avoidance path planning for the dual-arm robot based on an improved RRT algorithm. *Applied Sciences*, 12(8), 4087.
- [18] Yu, F., Zhou, C., & Yang, X. (2022). Design and Testing of Tomato Picking Robot for Daylight Greenhouse (日光温室番茄采摘机器人设计与试验). *Transactions of the Chinese Society of Agricultural Machinery*, 53(1), 41-49.
- [19] Zhang, W., Zhang, B., & Gong, Y. (2022). Fruit and vegetable picking robotic arm research status and prospects (果蔬采摘机器人机械臂研究现状与展望). *Journal of Chinese Agricultural Mechanization*, 43(9), 232-237, 244.
- [20] Zhang, Y., Wen, Y., & Tu, H. (2023). A method for ship route planning fusing the ant colony algorithm and the A* search algorithm. *IEEE Access*, 11, 15109-15118.

DEEP LEARNING PREDICTIVE MODEL FOR SOIL TEXTURAL ASSESSMENT /

PAG TUKOY SA URI NG LUPA SA PAMAMAGITAN NG DEEP LEARNING MODEL

Karla Jane G. QUINOL¹⁾, Carolyn Grace G. SOMERA^{*2)}, Marvin M. CINENSE²⁾, Nemesio A. MACABALE Jr.³⁾

¹⁾Graduate Student, Department of Agricultural and Biosystems Engineering,
College of Engineering, Central Luzon State University, Philippines

²⁾Faculty, Department of Agricultural and Biosystems Engineering, College of Engineering,
Central Luzon State University, Philippines

³⁾Faculty, Department of Information and Technology, College of Engineering, Central Luzon State University, Philippines

E-mail: cqgsomera@clsu.edu.ph

Corresponding Author: Carolyn Grace G. Somera

DOI: <https://doi.org/10.35633/inmateh-74-74>

Keywords: *image processing, non-traditional methods, soil image classification, soil texture analysis*

ABSTRACT

The distribution of grain sizes in different soil samples is essential for agriculture and geotechnics, providing high-resolution soil maps crucial for land use planning. Traditional methods for soil texture analysis are reliable but often time-consuming and inconsistent. With that, this study aims to create an efficient predictive model for soil texture classification using deep learning techniques. A dataset of 4,556 images was extensively pre-processed and trained, with a model chosen for validation due to its low MSE value of 1.18. The model's performance, evaluated through Precision, Recall, and F1 Score, showed weighted averages of 88%, 78%, and 74%, respectively, and an overall accuracy of 94.56%. Validation using 456 images revealed high accuracy for Sandy and Clayey Soils but varying results for Loamy and Silty Soils. In Trial 1, the model achieved over 91% accuracy for all soil textures, with 100% accuracy for Sandy Soil. However, Trials 2 and 3 exhibited decreased accuracy for Loamy and Silty Soils, with the lowest accuracies at 61.40% and 65.78%, respectively. These results suggest that while the model is effective for certain soil textures, it requires further refinement and additional diverse training data to consistently match the reliability of traditional methods.

ABSTRAK

Ang pagtukoy sa uri ng lupa ay mahalaga sa larangan ng agrikultura at geotechnics. Ito ang nagbibigay ng maayos na mapa na siyang kritikal sa pagpapalano ng paggamit ng lupa. Ang mga tradisyunal na pamamaraan sa pagtukoy nito ay maaasahan, ngunit kadalasang matagal ang proseso at hindi pare-pareho. Dahil dito, ang pagsusuring ito ay naglalayong lumikha ng mabisang modelo para sa klasipikasyon ng uri ng lupa gamit ang makabagong teknolohiya na deep learning. Ang dataset na may 4,556 imahe ay sumailalim sa pag-proproseso, bago ginamit sa paghasa ng iba't ibang modelo, kung saan ang napili para sa balidasyon ay may mababang MSE value na 1.18. Ang bisa ng modelo na sinukat sa pamamagitan ng Precision, Recall, at F1 Score, ay nagpakita ng mga weighted average na 88%, 78%, at 74%, at may kabuuang accuracy naman na 94.56%. Sa balidasyon gamit ang 456 imahe, ipinakita ang mataas na accuracy para sa Sandy (Mabuhangin) at Clayey (Luwad) na lupa ngunit may iba't ibang resulta para sa Silty (Maalikabok) at Loamy (kumbinasyon ng tatlo) na lupa. Sa unang eksperimento, nakamit ng modelo ang 91% accuracy para sa lahat ng uri ng lupa, na may 100% accuracy para sa Sandy soil. Gayunpaman, ang ikalawa at ikatlong eksperimento ay nagpakita ng pagbaba ng accuracy para sa Loamy (61.40%) at Silty (65.78%) Soils. Ipinahihiwatig nito na habang ang modelo ay epektibo sa ilang uri ng lupa, kailangan pa itong mapabuti at dagdagan ng mas magkakaibang datos sa pag-hasa upang ganap na maitatag ang pagiging maaasahan nito.

INTRODUCTION

Soil texture is an important property influencing various physical, chemical, and biological characteristics of soils, which are crucial for agricultural productivity and geotechnical applications. It affects porosity, which determines properties such as water retention, drainage, nutrient availability, and erodibility, thus influencing soil fertility and agricultural productivity (Chakraborty and Mistri, 2015; Bhattacharyya et al., 2015). This puts us into the importance of understanding the distribution of soil particles categorized into fine earth (clay, silt, sand) and coarse fragments (gravels, stones) as it is essential in accurate land use planning and soil management.

Up until now, the most practiced method of determining soil texture analysis are the unconventional laboratory method which include sieving, hydrometer analysis, and oven drying. Although widely used, these processes present significant limitations because they are laborious, time-consuming, and prone to inconsistencies. As a result, the entire methods become less efficient in addressing the urgent need for precise soil analysis in light of global challenges like soil degradation and declining fertility (*Food and Agriculture Organization of the United Nations, 2020*).

The answer lies within the recent advancements in soil classification techniques which highlight the growing role of predictive and modelling approaches. Studies have demonstrated the value of statistical models, algorithms, and predictive frameworks, including deep learning and computer vision, in enhancing the accuracy and efficiency of soil texture analysis (*Barman, 2019; Han et al., 2016; Swetha et al., 2020*). These modern methods were proved to have great potential in overcoming the limitations of traditional techniques by enabling fast and consistent assessments of soil properties.

With that, this study aims to contribute to these advancements by developing a deep learning-based approach for soil texture analysis. The objective is to create a model, which could be incorporated into smartphone applications to deliver accurate and timely soil texture assessments. By addressing the inefficiencies of conventional methods, this research seeks to support farmers and land managers, particularly in regions with limited access to technical expertise and laboratory facilities, hence, promoting sustainable soil management and agricultural productivity.

MATERIALS AND METHODS

Sample Preparation

For the training and testing, a similar data set containing pre-determined soil samples from laboratory analysis were used. On the other hand, a different dataset for validation was collected in every town of Nueva Ecija province in Philippines during the year 2023. It underwent into oven-drying at 105°C (±5°C) for 24 hours, before subjected into sieving.

A total of 4,556 images were taken for training and testing via random sampling, equally distributed under different soil texture categories (Clayey, Silty, Sandy, and Loamy). Since a learning model can generally work with 100, 500, or even 10,000 images (*Barkved, 2022*), the study’s sample size was within the limit.

Ideally, a good accuracy in machine learning is anything greater than 70%; and, anything in 70-90% accuracy is not only ideal, but is also realistic (*Rosenbacher, 2022*). However, in soil related studies, the lowest accuracy obtained was 58% via Random Forest classifier (*Dornik et. al., 2018*), and several 100% accuracy in some researches (*Morais et. al., 2019, Han et. al., 2016*). Therefore, this study considered that any result as long as it is within the stated range of existing and published studies, would be considered acceptable and valid.

The soil samples were then taken using a smartphone with 108-megapixel resolution during daylight in a landscape camera-orientation and distance of 0.25 m vertically on top to capture the entire soil sample. A random splitting of data with ratio of 80:20 was used for training and testing. This is known as the rule of thumb in split training and testing of data in python – the language used in training the model.

Another randomly selected samples from dataset for validation (accounting to 10% of the total images used in training and testing) was used in order to avoid biasness that could happen in using similar set of data for validation (*Baheti, 2021*). There is no specific data split requirement in training, testing, and validation of soil classifications involved in machine learning. For example, *Anadan et. al. (2021)*, used different train-test-validate data split ratio on their two different studies (70-15-15 in 2021 using CNN and 60-20-20 in 2022 using hybrid CNN-LMO algorithm), while *Han et. al., (2016)*, used 10% of the total soil samples for their testing. With that, the researchers decided to follow the general rules governing data splitting of machine learning methods.

Table 1

Distribution of dataset for Training, Testing, and Validation

PRE-DETERMINED SOIL (4,556 SOIL SAMPLE IMAGES)		SOIL GATHERED IN NUEVA ECIJA, PHILIPPINES (NOT YET DETERMINED)
TRAINING (80%)	TESTING (20%)	VALIDATION (10% of training and testing)
3645	912	456

Training and Testing

The images were placed in separate folders for training and testing (training data, testing data) in order to have an organized segmentation of data used in designating labels for training and testing purposes. Each soil texture determined through laboratory analysis are also separated by folder. Studio Visual Code was the used IDE (Integrated Development Environment) for editing of codes as it supports and allows various usage of programming languages without the need to switch for editors. It served as the center and the most crucial element of establishing the predictive model for soil texture assessment.

The images underwent the process of Augmentation, Pre-processing with Hue, Saturation, and Value (HSV) extraction before subjecting to training.

To capture the hidden layers, Convolutional Neural Network was used. Structuring the CNN architecture of the study include Input Layer, Convolutional Layer, Pooling Layer, Flatten Layer, Fully Connected (Dense) Layers, and Output Layer. On the other hand, YOLO is employed for classes identification, brightness training, and for utilizing the Open Source Computer Vision Library (OpenCV).

Performance Evaluation and Data Analysis

In soil classification, the best matrix that showed the most favorable result was confusion matrix; this is both for binary and multiclass (*Srivastava et al., 2021*). This matrix is represented by rows and columns, wherein the actual labels are written in rows, and the predicted labels are in columns – a widely adopted convention in field of machine learning and statistics. True positive and true negative means correctly classified labels, while false positive and false negative represents the incorrectly classified labels.

In a confusion matrix, the performance metrics such as Precision, Recall, Accuracy, and F-measure were generated. Precision measured the fraction of the estimated soil patterns in a positive class that the model accurately identified as positive:

$$p = \frac{tp}{tp+fp} \quad (1)$$

where:

p denotes the precision, while tp implies the true positive, and fp represents the false positive.

Meanwhile, recall defines the ratio between positive soil patterns to the correctly classified soil patterns. It can be computed by the following formula:

$$r = \frac{tp}{tp+tn} \quad (2)$$

where:

r denoted recall, while tp and tn represents true positive and true negative, respectively.

Accuracy, on the other hand, is the ratio of right prediction made, over the number of examples evaluated:

$$acc = \frac{tp+tn}{tp+fp+tn+fn} \quad (3)$$

where:

acc represents the accuracy, while tp and tn defines the true positive and true negative, and fp and fn implies the false positive and false negative, respectively.

Finally, the f-measure represents the harmonic mean between the values of precision and recall. The best evaluation for these metrics should be one or closer to one.

$$fm = \frac{(2*p*r)}{p+r} \quad (4)$$

where:

f_m represents the f-measure, while p and r represent precision and recall.

During the training stage, the Mean Squared Error (MSE) can be determined which represents the difference between estimated solutions and the ones that are preferred. A low value of MSE is required to get better training results.

$$MSE = \frac{1}{n} \sum_{i=1}^n (P_i - A_i)^2 \tag{5}$$

where:

MSE means the mean squared error, while P_i is the predicted value, and A_i is the desired value.

Research Design and Statistical Analysis

In order to prove the consistency of the developed model when it comes to predicting soil textures, the study employed Analysis of Variance (ANOVA) under Complete Randomized Design (CRD) as treatment method to the gathered data. The process here is similar to the procedure of t-test. However, t-test can only determine differences between the means of two groups, while ANOVA can do with more groups (*Ardiansah et. al., 2021 & Zhang et. al., 2024*).

Therefore, this method is appropriate to identify the significant differences among three (3) validation sets for each independent metrics (accuracy, precision, recall, and F1 score). The conditions were set to reject the null hypothesis if p value result is less than 0.05. Since the researches wanted the readings across all validations to be consistent, the null hypothesis was set to: *there is no significant difference in the performance metrics observed across three validations*.

RESULTS

Training of Model

The training was commenced using 4,556 images which underwent into several trainings and re-trainings in order to optimize the result. The final training underwent 100 epochs with 179 steps per epochs and Batch size of 30.

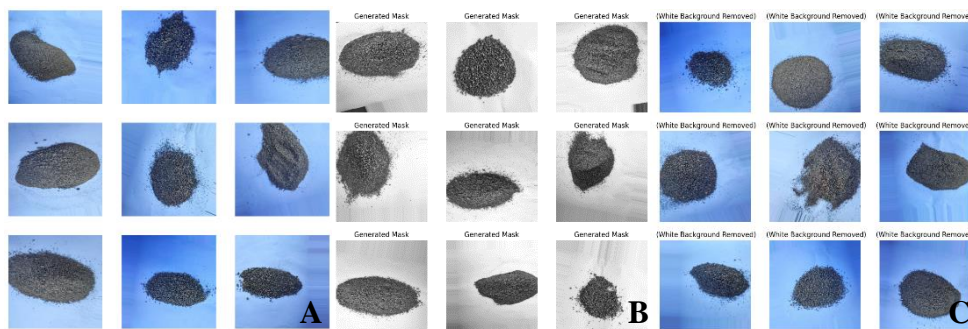


Fig. 1 – Pre-processed Images
A – Raw Image; B – Masked Image; C – Background Removed Image

The image samples underwent to pre-processing procedures and feature extractions (shown in Figure 1) which include masking, removing of image background, resizing of images into consistent resolutions in order to ensure uniformity of data; pixel normalization into 255 pixels; augmentation of data to increase the diversity of training data; cropping of images to focus on region of interest; color space conversion; and then noise reduction to clean and denoise the images before feeding the datasets to the model training.

Several models have been developed throughout the training as a result of utilizing different techniques to achieve the highest accuracy possible. In order to determine the predictive model to be chosen, the MSE of each model have been determined as shown in Figure 2.

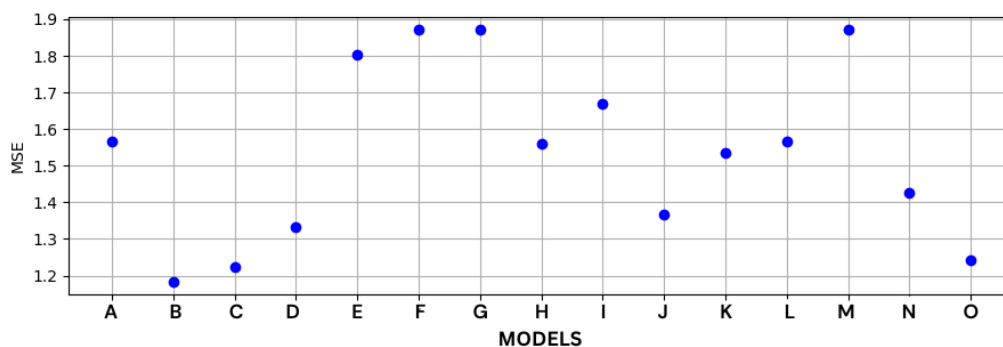


Fig. 2 – MSE of Different models developed throughout the course of training

Among the different training models, model B showed the lowest MSE value (1.18), hence it was considered to be the final model to be evaluated.

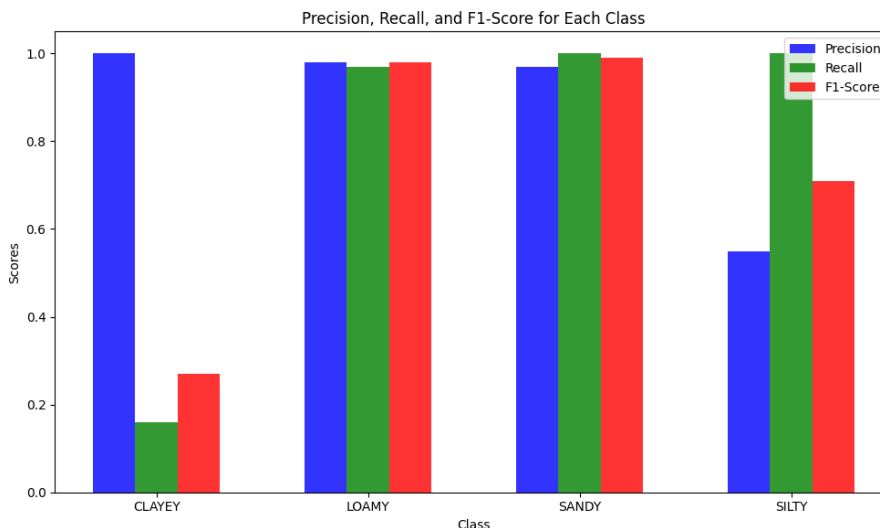


Fig. 3 – Precision, Recall, and F1 Score for each class of the best model

The different results of evaluation matrices for each class were shown in Figure 3. The weighted average of each evaluation matrices during the training of the model was 88% for Precision, 78% for recall, and 74% for the F-score. The overall accuracy of the training on the other hand, was 94.56%.

The interface of the developed predictive model (Figure 4) was run in an open-source app framework called *Streamlit*. It is a Python framework used in creating visualization for machine learning data. The interface was made user-friendly with written instructions on how to operate. User will upload an image through the ‘browse’ menu, and click ‘classify’ to obtain results (the predicted soil texture and some common suitable crop recommendations).

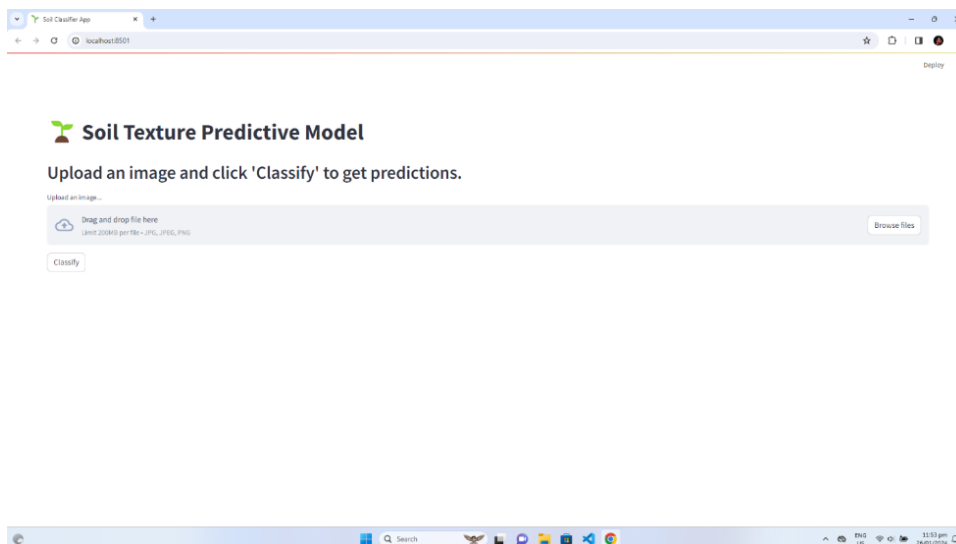


Fig. 4 – Interface of the predictive model in a local host

Actual Validation

For actual validation of data, three (3) validations were done in order to have a comparison of metrics gathered (accuracy, precision, recall, and F1 score). The validation images were 10% of the total number of images (Baheti, 2021).

Since a total of 4,556 images were used in training and testing, 456 images were used for validation (114 images for each soil texture categories). Shown in Table 2 is the summary of three validations made to determine if there are significant differences among the yielded results.

Table 2

	ACCURACY	PRECISION	RECALL	F1 SCORE
VALIDATION 1	0.96	0.96	0.96	0.96
VALIDATION 2	0.83	0.85	0.83	0.85
VALIDATION 3	0.79	0.78	0.79	0.79

The study considered four different levels (metrics) such as the Accuracy, F1 Score, Precision, and Recall. There are 12 observations in total, all of which were read and used in the analysis. Using Statistical Tool for Agricultural Research, the result of analysis was shown in Table 2.

Table 3

Source	Df	Sum of Squares	Mean Square	F value	Pr(>F)	CV (%)	Data Mean
Metrics	3	0.0001	0.0000	0.00	0.9996		
Error	8	0.0629	0.0079				
Total	11	0.0630				10.28	0.8625

The results of statistical analysis made revealed that there are no significant differences found among the metrics. This is because the p-value = 0.9996 is not less than 0.05, hence, the null hypothesis will not be rejected. It suggests that all metrics perform similarly with respect to the response variable. A coefficient of variance (CV) value of 10.28% or 0.1028 also suggested that the variation with respect to the mean is relatively low because a CV that is less than one is universally considered low variance. This means that the data points of performance metrics were relatively close to the mean value, hence, resulting in a smaller variation.

The data means (0.8625) for Accuracy, F1 Score, Precision, and Recall, which measures the central tendency, or the average value of overall data points, are very close, reinforcing the ANOVA result of no significant differences among the metrics. It shows that the data points exhibit relatively low variability around the mean value. As a result, there is a consistent level of performance across the different trials, with relatively minor fluctuations.

The analysis of the result reveals significant insight towards the performance of model in testing and actual validation of data. The testing was initiated with a dataset comprising of 4,556 images that underwent several iterations, trainings, and re-trainings to produce the best result. In order to determine which model has the best training result, the MSE should be low (*Srivasta et. al., 2021*) ranging from 1-10 for typical image processing that has pixel value range of 255. Since Model B has the lowest MSE value (1.18) as shown in Figure 2, it was the model chosen to be subjected into validation.

The performance of the final model was assessed using the standard evaluation metrics (*Srivasta et. al., 2021*): Precision, Recall, and F-score (Figure 3). The weighted averages for these metrics during training of the model were 88% for Precision, 78% for Recall, and 74% for F1 Score. These metrics, along with an overall accuracy of 94.56%, demonstrated the developed model's capability in correctly classifying the images. The accuracy of this model is inside the range of several studies related to soil image classification which utilized deep learning techniques.

Yu et. al., (2019), utilized 3D-CNN system that explored configurable liquid crystal filters (LCTF) which resulted in 99.59% accuracy. *Morais et. al. (2019)*, achieved an impressive 100% accuracy in classification and prediction using Digital Image Processing and MIA classifier. Other studies such as *Dornik et. al., (2018)*, and *Mengistu & Alemayehu, (2018)*, resulted in 58% and 89.7 accuracies respectively, which can be noted as much lower accuracies compared to the study.

For actual validation, 456 images (10% of the total dataset) were used, divided equally across the four soil texture categories (*Baheti, 2021*). Three validation runs were conducted to compare the performance metrics. The results showed varying degrees of accuracy, precision, recall, and F1 score across the validations (Table 2). Validation 1 exhibited the highest consistency with an accuracy, precision, recall, and F1 score of 0.96, while validations 2 and 3 showed lower but still acceptable performance levels.

To show how the developed model performed against the laboratory assessed samples, the number of predictions was listed in Table 4 below.

Table 4

Comparison of readings from Developed Predictive Model to the Laboratory Assessed samples

Laboratory Method Assessment Trial 1		Predictive Model Assessment Trial 1		
Texture	No. of Sample	Texture	No. of Predictions	Correct Predictions
Sandy Soil	114	Sandy Soil	114	100%
Silty Soil	114	Silty Soil	109	95.61%
		Clayey Soil	3	
		Loamy Soil	2	
Clayey Soil	114	Clayey Soil	104	91.23%
		Silty Soil	10	
Loamy Soil	114	Loamy Soil	111	97.37%
		Silty Soil	3	
Laboratory Method Assessment Trial 2		Predictive Model Assessment Trial 2		
Texture	No. of Sample	Texture	No. of Predictions	Accuracy
Sandy Soil	114	Sandy Soil	107	93.86%
		Loamy Soil	4	
		Silty Soil	3	
Silty Soil	114	Silty Soil	96	84.21%
		Loamy Soil	11	
		Sandy Soil	7	
Clayey Soil	114	Clayey Soil	100	87.72%
		Silty Soil	14	
Loamy Soil	114	Loamy Soil	76	67.67%
		Sandy Soil	5	
		Silty Soil	33	
Laboratory Method Assessment Trial 3		Predictive Model Assessment Trial 3		
Texture	No. of Sample	Texture	No. of Predictions	Accuracy
Sandy Soil	114	Sandy Soil	112	98.24%
		Loamy Soil	2	
Silty Soil	114	Silty Soil	70	61.40%
		Loamy Soil	30	
		Clayey Soil	9	
		Sandy Soil	5	
Clayey Soil	114	Clayey Soil	101	88.60%
		Silty Soil	13	
Loamy Soil	114	Loamy Soil	75	65.78%
		Silty Soil	33	
		Sandy Soil	6	

The model showed high accuracy for Sandy and Clayey Soils. On the other hand, Loamy and Silty soils have greater number of incorrect readings that varied across all soil textures. In Trial 1, the model achieved over 91% accuracy for all soil textures, with a perfect 100% accuracy for Sandy Soil. In Trial 2, accuracy declined for Loamy and Silty Soils, with Silty Soil reaching a low of 67.67%. Trial 3 showed further drops for Loamy and Silty Soils, with accuracies of 61.40% and 65.78%, respectively, while maintaining a high accuracy of 98.24% for Sandy Soil.

These findings indicate that while the developed model performs well in prediction of certain soil textures, it still needs refinement and additional data for diverse training in order to achieve a consistent and similar reliability reading of traditional methods.

CONCLUSIONS

The analysis of the model's performance reveals both strengths and areas for improvement for the study. Trained on a dataset of 4,556 images, the model was chosen for validation due to its lowest MSE value of 1.18. During training, the model achieved strong evaluation metrics, including 88% Precision, 78% Recall, 74% F1 Score, and an overall accuracy of 94.56%, which aligns with other deep learning studies in soil image

classification. However, the validation of 456 images in comparison to predetermined soil textures showed variable results, especially for Loamy and Silty Soils, with significant accuracy drops in Trials 2 and 3.

Despite that, the ANOVA analysis still indicated no significant differences among the evaluation metrics, and a coefficient of variation of 10.28% which suggested consistent performance overall. While the model demonstrated high accuracy for Sandy and Clayey Soils, its performance for Loamy and Silty Soils was inconsistent, indicating the need for further enhancement and more varied training data. In conclusion, the model showed strong potential for certain soil textures but still requires additional development to achieve consistent and reliable performance comparable to traditional laboratory methods.

ACKNOWLEDGEMENT

The authors would like to acknowledge the Department of Science and Technology – Science Education Institute (DOST-SEI) for funding this research through the Engineering Research and Development for Technology (ERDT) scholarship program.

REFERENCES

- [1] Anadan, K., Shankar, R., & Duraisamy, S. (2021). Convolutional Neural Network approach for the prediction of Soil texture properties. *Indian Journal of Science and Technology*, 14(3): 190-196. <https://doi.org/10.17485/IJST/v14i3.2047properties>
- [2] Anadan, K., Shankar, R., & Duraisamy, S. (2022). The Prediction of Soil Texture Properties Using Hybrid CNN-LMO Algorithm. *International Journal of Mechanical Engineering*, Vol. 7, No. 4: 1274-1281. ISSN: 0974-5823
- [3] Ardiansah, I & Bafdal, N., & Bono, A., Suryadi, E., & Husnuzhan, R. (2021). Impact of ventilations in electronic device shield on micro-climate data acquired in a tropical greenhouse. *INMATEH Agricultural Engineering*. Vol.63, pp.397-404. DOI: 10.35633/inmateh-63-40.
- [4] Baheti, P. (2021). *Train Test Validation Split: How To & Best Practices [2023]*. <https://www.v7labs.com/blog/train-validation-test-set#h1>
- [5] Barkved, K. (2022). *How To Know if Your Machine Learning Model Has Good Performance*. <https://www.obviously.ai/post/machine-learning-model-performance>
- [6] Barman, U. (2019). Prediction of Soil pH using Smartphone based Digital Image Processing and Prediction Algorithm. *Journal of mechanics of continua and mathematical sciences*, 14(2). <https://doi.org/10.26782/jmcms.2019.04.00019>
- [7] Bhattacharyya, R., Ghosh, B. N., Mishra, P. K., Mandal, B., Rao, C. S., Sarkar, D., Das, K., Anil, K. S., Lalitha, M., Hati, K. M., & Franzluebbers, A.J. (2015). Soil Degradation in India: Challenges and Potential Solutions. *Sustainability*, 7(4), 3528-3570. <https://doi.org/10.3390/su7043528>
- [8] Chakraborty, K., & Mistri, B. (2015). Importance of soil texture in sustenance of agriculture: a study in Burdwan-I CD Block, Burdwan, West Bengal. *Eastern Geographer*, 21(1), 475-482.
- [9] Dornik, A., Dragut, L., & Urdea, P. (2018). Classification of Soil Types Using Geographic Object-Based Image Analysis and Random Forests. *Pedosphere*, 28(6), 913–925. [https://doi.org/10.1016/S1002-0160\(17\)60377-1](https://doi.org/10.1016/S1002-0160(17)60377-1)
- [10] Food and Agriculture Organization of the United Nations. (2020). Soil testing methods manual. *Soil testing methods manual*. FAO. <https://doi.org/10.4060/ca2796en>
- [11] Han, P., Dong, D., Zhao, X., Jiao, L., & Lang, Y. (2016). A smartphone-based soil color sensor: For soil type classification. *Computers and Electronics in Agriculture*, 123, 232–241. <https://doi.org/10.1016/j.compag.2016.02.024>
- [12] Mengistu, A. D., & Alemayehu, D. M. (2018). Soil characterization and classification: A hybrid approach of computer vision and sensor network. *International Journal of Electrical and Computer Engineering*, 8(2), 989–995. <https://doi.org/10.11591/ijece.v8i2.pp989-995>
- [13] Morais, P. A. de O., Souza, D. M. de, Carvalho, M. T. de M., Madari, B. E., & de Oliveira, A. E. (2019). Predicting soil texture using image analysis. *Microchemical Journal*, 146, 455–463. <https://doi.org/10.1016/j.microc.2019.01.009>
- [14] Rosenbacher, J. (2022). *How many images do you need to train a model?* <https://blog.roboflow.com/images-train-model/>
- [15] Shukla, G., Garg, R. D., Srivastava, H. S., & Garg, P. K. (2018). An effective implementation and assessment of a random forest classifier as a soil spatial predictive model. *International Journal of Remote Sensing*, 39(8), 2637–2669. <https://doi.org/10.1080/01431161.2018.1430399>

- [16] Srivastava, P., Shukla, A., & Bansal, A. (2021). A comprehensive review on soil classification using deep learning and computer vision techniques. *Multimedia Tools and Applications*, 80(10), 14887–14914. <https://doi.org/10.1007/s11042-021-10544-5>
- [17] Srunitha, K., & Padmavathi, S. (2017). Performance of SVM classifier for image-based soil classification. *IEEE Xplore. International Conference on Signal Processing, Communication, Power and Embedded System, SCOPES 2016 - Proceedings*, 411–415.
- [18] Srunitha, K., & Sivasamy, P. (2016). Performance of SVM classifier for image-based soil classification. *IEEE Xplore. 2016 International Conference on Signal Processing, Communication, Power and Embedded System (SCOPES)*. 411–415. <https://doi.org/10.1109/SCOPES.2016.7955863>
- [19] Swetha, R.K., Bende, P., Singh, K., Gorthi, S., Biswas, A., Li, B., Weindorf, D.C., & Chakraborty, S. (2020). Predicting soil texture from smartphone-captured digital images and an application. *Geoderma*, 376. <https://doi.org/10.1016/j.geoderma.2020.114562>
- [20] Yu, Y., Xu, T., Shen, Z., Zhang, Y., & Wang, X. (2019). Compressive spectral imaging system for soil classification with three-dimensional convolutional neural network. *Optics Express*, 27(16), 23029. <https://doi.org/10.1364/oe.27.023029>
- [21] Zhang, J., Li, Z., Guo, G., Baikeli, Y., Wang, Y., Cai, J., & Wang, Z. (2024). Design and testing of a cotton stalk clamp-pulling test bench. *INMATEH Agricultural Engineering*. Vol.72, pp.699-709. DOI: 10.35633/inmateh-72-62.

STRUCTURAL DESIGN AND POWER SIMULATION OF TRACKED ELECTRIC TRACTOR BASED ON ECONOMY

基于经济性的履带式电动拖拉机结构设计与动力仿真

Qikang LI^{1,2}, Guodong NIU^{1,2*}, Yuanyi LIU^{1,2}, Xinyu SONG³

¹Shandong University of Technology, Collage of Agricultural Engineering and Food Science, Zibo, China

²Shandong University of Technology, Institute of Modern Agricultural Equipment, Zibo, China

³Shandong University of Science and Technology, Collage of Mechanical and Electronic Engineering, QingDao, China

Corresponding author: Guodong Niu

Tel: +86 13001512967; E-mail: niuguodong@163.com

DOI: <https://doi.org/10.35633/inmateh-74-75>

Keywords: Facility agriculture; Electric tractor; Finite element; Optimisation; Simulation

ABSTRACT

In view of the serious pollution of traditional fuel machinery in facility agriculture production, in order to facilitate the operation of tractors in greenhouses, in this study, a small tracked electric tractor suitable for facility agriculture was designed and analysed. In the early stage of design, the basic frame of pure electric tractor was established, the final chassis layout is determined through force analysis and layout setting; after the three-dimensional modeling of the tractor structure, the finite element analysis using the software Ansys verified that the stiffness and strength of the frame met the design requirements; the dual-motor drive structure was optimized. The maximum deformation of the track chassis frame was 0.685 mm, the maximum equivalent elastic strain of the track chassis frame was 0.0131 mm, and the maximum stress of the track chassis frame was 25.818 MPa, which was less than the yield stress of the selected material of the frame. ADVISOR was used to simulate the electric tractor during rotary ploughing and unladen transport operations. The simulation results showed that the dual-motor drive mode saved more than 20% of energy consumption compared with the single-motor mode and the transmission efficiency was improved by about 17%, which improved the operational efficiency of the tractor, and provided theoretical and data support for the subsequent prototype production.

摘要

针对设施农业生产中传统燃油机具污染较为严重的问题,为了便于在温室大棚内开展拖拉机作业活动,本研究设计并分析了一种适用于设施农业的小型履带式电动拖拉机。在设计前期,确立了纯电动拖拉机的基本框架,通过受力分析和布局设置,确定了最终底盘布局;在对拖拉机结构进行三维建模后,使用软件 Ansys 进行有限元分析验证了车架刚度与强度满足设计要求;其中履带底盘车架的最大变形为 0.685mm,履带底盘车架的等效弹性应变最大值为 0.0131mm,履带底盘车架的最大应力是 25.818MPa,小于车架选用材料的屈服应力。同时对双电机驱动结构进行优化,采用 ADVISOR 进行电动拖拉机在旋耕和空载运输作业时的模拟仿真,仿真结果表明,双电机驱动模式相比单电机模式能够节约能耗 20%以上,且传动效率提升了 17%左右,提高了拖拉机的作业效率,为后续样机试制提供了理论与数据支持。

INTRODUCTION

Facility greenhouse environment is relatively closed, crops on the environmental quality requirements are particularly high, in addition to the ground level, suitable moisture, good light conditions, as far as possible to reduce air pollution (Liu et al., 2022). For this reason, there is an urgent need for research on electric tractors with low energy consumption, low pollution, low noise, high efficiency and other advantages.

Crawler electric tractor has the following characteristics: low centre of gravity, higher coefficient of adhesion, better adhesion conditions under the same power, able to play a better traction performance with better trafficability (Matveev et al., 2013); differential steering mode more suitable for the structure of the dual-drive motor, with a smaller turning radius, able to operate in the narrow space of the facilities of agricultural operations; grounding ratio is low, able to reduce compaction of the soil structure, less likely to form a subsoil

Qikang Li, M.S. Stud. Eng.; Guodong Niu, Sen.Exp. M.S. Eng.; Yuanyi Liu, Prof. Ph.D. Eng.; Xinyu Song, Ph.D. Stud. Eng.

layer. Low ground specific pressure reduces compaction of the soil structure, making it less likely to form a plough subsoil when working in facility agriculture (Oelen et al., 1994).

Electric tractor refers to the tractor driven by electricity, including the energy system, drive system, the whole machine system, of which the energy system for electric tractor work to provide electric power, mainly composed of battery packs, can be used as auxiliary energy to improve the discharge performance through the range extender, fuel cell or supercapacitor, the direction of the electric power flow is controlled by the DC/AC converter. The drive system consists of drive motor, transmission system and travelling device, providing mechanical power for the whole machine to travel and traction. The complete machine system is an electric tractor whole that contains other parts such as the body and suspension device on the basis of the energy system and the drive system, and is used to realise the electric tractor driving, lifting agricultural implements as well as steering and braking according to the requirements (Song., 2023).

Drawing on the existing power transmission system structure of pure electric vehicles, the power transmission system of the whole machine in this paper is designed, and the preliminary design of the whole machine layout framework is shown in Fig. 1. Then, the electric drive system of the whole machine is designed, and the main components of the whole machine are identified.

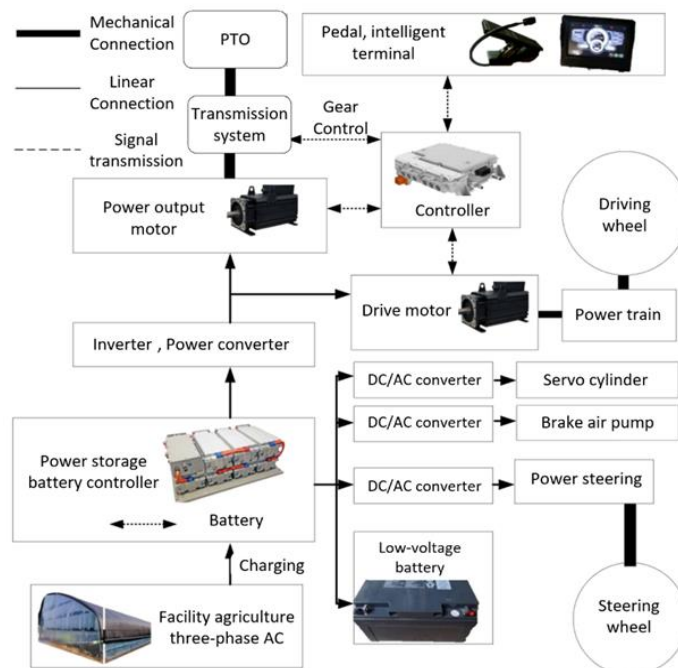


Fig. 1 - Basic frame of pure electric tractor

MATERIALS AND METHODS

Force Analysis

The force analysis of tracked electric tractor is shown in Fig. 2. The tractor is in contact with the ground through the track plate, the coefficient of friction is relatively high, the contact length is L_0 , the combined force of all the support reaction forces of the ground on the track plate is F_z , the distance between the centre of the combined force and the central axis of the drive wheel is x_y , the reaction forces in the vertical and horizontal directions when hanging and pulling the implement are F_y , F_D , the torque is M_z , and the point of force is at the centre of the track at the point O_I .

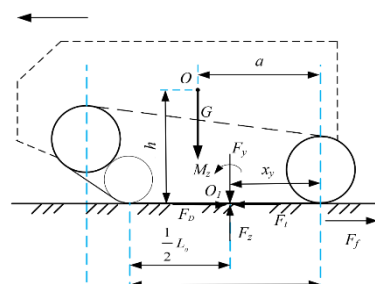


Fig. 2 - Force analysis of crawler electric tractor

The traction balance equation for a tracked motorised tractor in the horizontal direction is:

$$F_t = F_f + F_D \tag{1}$$

Balance of forces in the vertical direction equation:

$$F_z = G + F_y \tag{2}$$

The position of the centre of pressure can be obtained from the moment balance equation:

$$x_y = \frac{Ga + F_y(x_c + 0.5L_0) - M_z}{F_z} \tag{3}$$

When the centre of pressure of the track is located at the centre of the track, the soil will be subjected to the most uniform force, low compaction and small damage to the soil structure, so the centre of pressure should be located at the centre of the track as far as possible in the design of crawler type electric tractor (Song et al., 2023).

Facility agriculture-oriented electric tractor does not have a closed cab, a windshield, it has a simple shape and small windward surface, while being driven at a low speed, so the impact of air resistance on electric tractors is ignored. Based on the above analysis, the walking balance equation is established as follows:

$$F_t = F_f + F_i + F_j + F_D = mgf \cos \alpha_G + mg \sin \alpha_G + \delta m \frac{du}{dt} + F_D \tag{4}$$

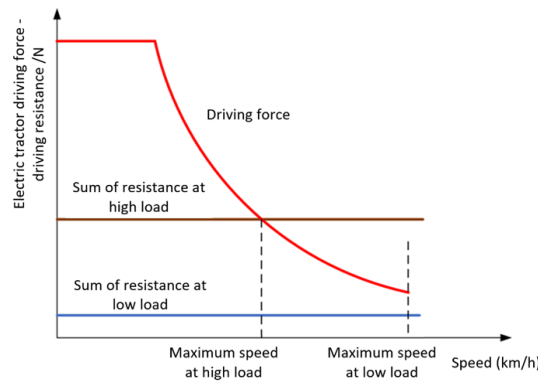


Fig. 3 - Driving force-resistance balance diagram

According to the above analysis to draw the driving force curve of the electric tractor shown in Figure 3, when the rolling resistance and traction force of the electric tractor is larger, the tractive force curve of the electric tractor and the intersection of the resistance curve corresponding to the speed of the electric tractor traction of the implement for the maximum speed, at this time (Song, 2023), the driving motor works in the constant power stage, the driving force is equal to the sum of the other resistances; when the tractor is unloaded or the ground conditions are better, the driving force is always greater than the sum of the resistance. The driving force of the tractor is always larger than the sum of resistances, at this time the maximum speed of the electric tractor is limited by the maximum speed of the drive motor, which can be obtained from:

$$u_{\max} = \frac{0.377rn_{\max}}{i} \tag{5}$$

In the facility agriculture field, the land is flat and the slope angle is small, so only the acceleration performance of agricultural electric tractor on flat ground is studied, which can be obtained according to the travelling balance equation of electric tractor operation:

$$a_j = \frac{F_t - F_D - F_f}{\delta m} \tag{6}$$

Structural Design

Through reasonable settings, the balanced distribution of traction force can be improved to overcome the problem of unbalanced force caused by the gravity balance of the rotary ploughing mechanism itself, and to avoid the situation of deviation and tilting of the travelling route in the course of the tractor, as shown in the structure of the electric crawler rotary ploughing machine in Fig. 4.

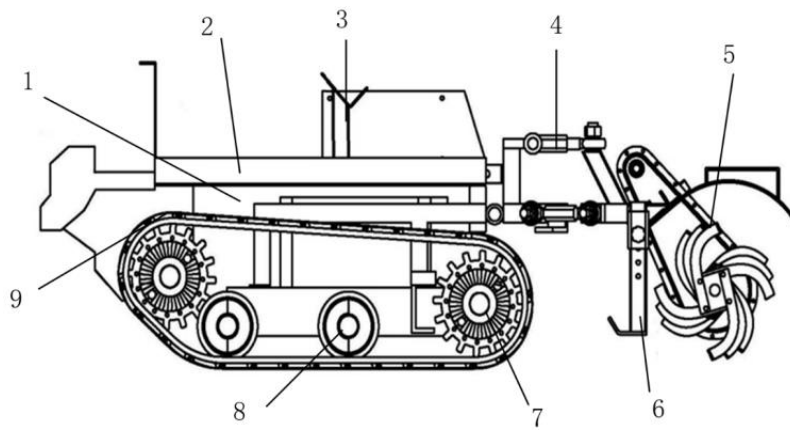


Fig. 4 - Crawler electric tractor structure diagram

- 1. Battery pack; 2. Rack; 3. Control system; 4. Suspension rack; 5. Rotary cultivator;
- 6. Support frame; 7. Drive wheel; 8. Support wheel; 9. Tracks

Frame Condition and Load Analysis

When the electric crawler tractor is working, the load situation of the frame is more complicated (Zhao *et al.*, 2022). This section focuses on analysing the changes of the frame architecture in the static state, and carrying out a static structural analysis of the force state of the frame when the crawler tractor is fully loaded. It is assumed that the electric crawler tractor carries out uniform linear motion on the ground with good road conditions (Gong *et al.*, 2021). At this time, the main sources of force on the frame are the gravity of each device and the frame, as well as the gravity of the mounted small rotary plough acting on the frame. The applied loads on the frame are shown in Table 1.

Table 1

Name	Specific loads for crawler tractors				
	Electromotor	Bodywork and transmission	Battery pack	Control system	Small rotary plough
Load size (kg)	100 kg*2	80 kg	45 kg	30 kg	120 kg

Considering the up and down bumps of the vehicle frame when driving a and operating on uneven road surface, the maximum dynamic load factor under full load bending condition should not be greater than 2.5. Since the electric tractor is mainly used in the gently sloping terrain of the facility agricultural plantation, in this paper, the dynamic load factor of the crawler chassis for driving and operating under bending condition is taken to be 2.

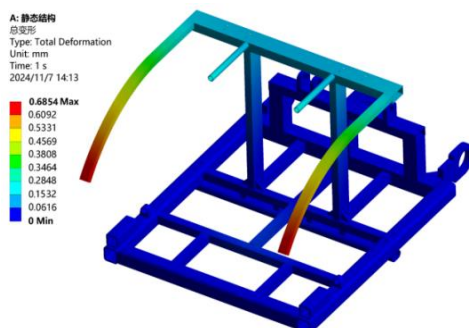


Fig. 5 - Total deformation

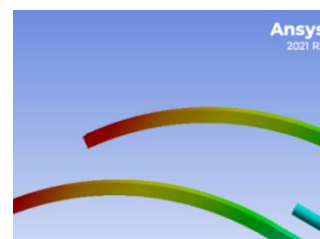


Fig. 6 - Maximum total deformation

As can be seen from Fig. 5 and Fig. 6, the maximum deformation of the tracked chassis frame is 0.685 mm, which is relatively small compared to the overall structure of the tracked chassis frame, so it can be assumed that the rigidity of the tracked chassis frame can satisfy the hydrostatic design requirements.

The maximum deformation occurs in the bumper at the upper end of the frame, because the engine is fixed to the two longitudinal beams at the front side, which is equivalent to the pressure exerted on a cantilever beam, and due to the deformation of the longitudinal beams at the front, the bumper is subjected to the tension force of the upper side wall, so it is reasonable that the maximum deformation occurs.

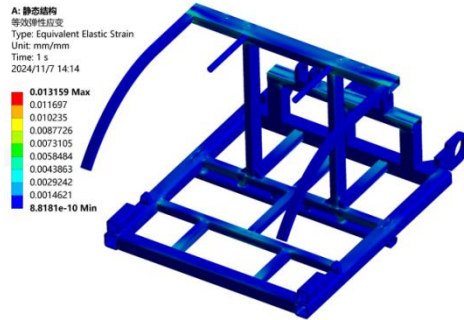


Fig. 7 - Equivalent elastic deformation

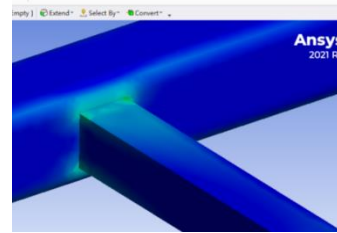


Fig. 8 - Maximum equivalent elastic deformation

Figure 7 and Figure 8 show that the maximum equivalent elastic strain of the tracked chassis frame is 0.0131 mm, which occurs below the connection between the front longitudinal beam and the front cross member, and is less than the maximum allowable deformation of the tracked chassis frame material. This indicates that the rigidity of the designed tracked chassis frame complies with the design conditions.

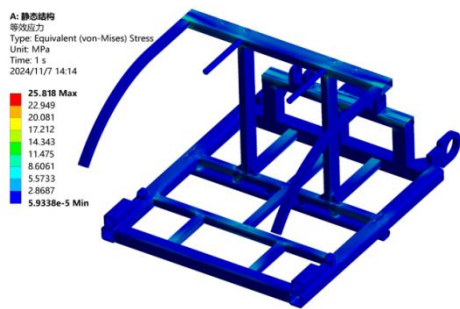


Fig. 9 - Equivalent stress

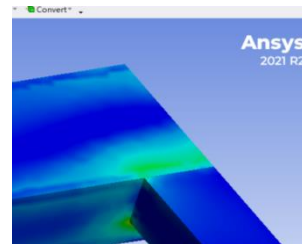


Fig. 10 - Maximum equivalent stress

According to Fig. 9 and Fig. 10, the maximum stress of the tracked chassis frame is 25.818 MPa, which is less than the yield stress of the materials selected for the frame, which indicates that the strength of the materials used for the tracked chassis frame is in accordance with the structural design requirements. The maximum stress occurs under the connection between the frame and the rear cross member, because the engine is mounted on the rear longitudinal beam, which is squeezed by the front longitudinal beam. In order to achieve the required stress reduction, it is possible to consider increasing the wall thickness in these areas or welding a rib plate. From the above analysis, the frame stiffness and strength of tracked electric tractor can meet the static design requirements under full load bending condition.

Whole Machine Power Simulation

Power Consumption and Power Utilisation of Crawler Tractors:

When calculating the rated traction, the tractor being in the ploughing and transport when the driving speed is slow, the tractor in the working state of the force analysis can be ignored when the air resistance, according to the horizontal direction of the force balance of the tension balance equation (Bing, 2021):

$$F_q = F_t + F_f \tag{7}$$

where: F_q - driving force, N; F_t - traction resistance, N; F_f - rolling resistance, N.

The traction resistance formula can be expressed as:

$$F_t = zb_1h_kk \tag{8}$$

where: z - number of ploughshares; k - soil specific resistance, N/cm²; h_k - depth of ploughing, cm; b_1 - width of individual ploughshares, cm.

As the tractor is mostly used for ploughing, its rated tractive effort is determined by the average tractive effort during ploughing. Since the tractor works in a complex environment and carries a wide range of ploughing implements, the resistance to work fluctuates accordingly, so it is necessary to retain a reserve of 10-20% of the traction capacity (Gao *et al.*, 2008). The rated traction force of an electric tractor can be expressed as follows:

$$F_{TN} = (1.1 \sim 1.2)F_T \quad (9)$$

Electric tractor in the work of the total energy consumed is equal to the energy output of the battery, so by the formula (7) on both sides multiplied by the tractor in the operation of the traveling speed, both the power arithmetic formula:

$$P = F_T \frac{V_j}{3.6} + F_f \frac{V_j}{3.6} w \quad (10)$$

where V_j - travelling speed during operation, km/h.

Determine the Chassis Layout

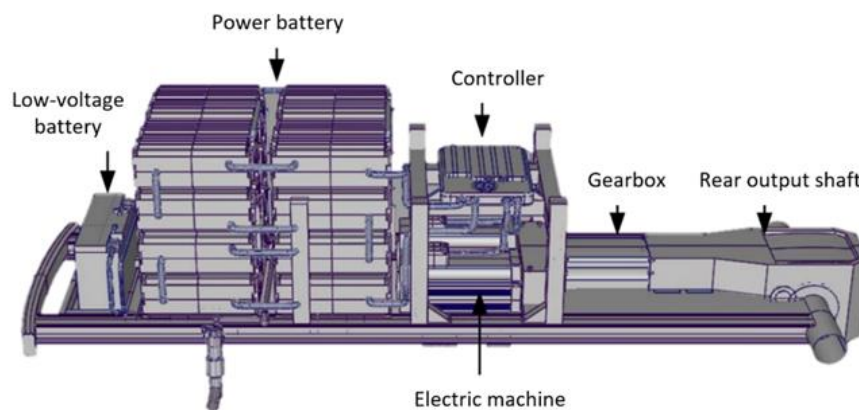


Fig. 11 - Chassis layout of the prototype

The electric tractor drive structure scheme designed in this paper is shown in Figure 11, two motors for steering drive at the same time, the two motors were installed to the left drive shaft and the right drive shaft, saving the space of the vehicle, the front drive motor is only responsible for the traction operation of the front wheels, the rear drive motor is responsible for the rear wheels of the traction operation and ploughing and other mechanical output. In this paper, the permanent magnet synchronous motor is chosen as the drive motor, with rated power of 5 KW and rated speed of 1500 min. The permanent magnet synchronous motor has the advantages of large starting torque, high efficiency, strong overload capacity, small volume, light weight, etc., and it can meet the requirements of the motor for the electric tractor in the special environment. The motor can meet the requirements of electric tractor in special environment.

Establish Simulation Test Conditions

ADVISOR was used to simulate the electric tractor during ploughing and transport operations, and the whole vehicle model, battery model, transmission controller model, and drive motor model were established. The whole vehicle model is based on the force analysis diagram under tractor traction operation. From the driving equilibrium equations, driving torque equilibrium equations and the load influence on the driving wheels, the whole vehicle simulation model is established in Simulink and then embedded into the ADVISOR simulation model. The battery model is composed of the battery charge equations and the loads on the drive wheels (Zhang *et al.*, 2017). The battery model is modelled in ADVISOR by the relationship between the state of charge (SOC) of the battery and the current, voltage and temperature, and the fuzzy inference algorithm is used to build the transmission simulation control model in Simulink and then embedded into ADVISOR. The drive motor model is built based on the relationship between the measured motor efficiency and the speed and torque. Due to the low travelling speed when the tractor is working, the air resistance is neglected in the model (Wang *et al.*, 2023).

The electric tractor can be roughly divided into two types of operation: unloaded transport and rotary ploughing, and this paper mainly establishes the simulation of these two working conditions, and the working conditions of transport operation are shown in Fig.12, with reference to the EUDC test conditions. The running time is 400 s in total, the running distance is 1.06 km, the maximal speed is 12.7 km/h, and the average speed is 9.42 km/h. Figure 12 shows the simulated working conditions of the rotary tillage operation of the electric tractor. Due to the complexity of the rotary tillage operation environment of the electric tractor, the traction force on the tractor will have a small range of changes, and the operating speed will remain unchanged while fluctuating up and down with the rated traction force as the benchmark to simulate the different conditions occurring in the operation of the tractor (Liu et al., 2023).

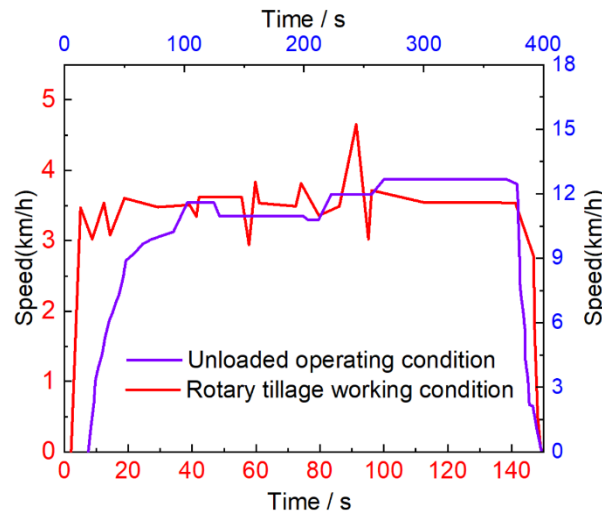


Fig. 12 - Unloaded operating condition and Rotary tillage working condition

RESULTS

Rotary Tillage Operations

The rotary ploughing conditions are determined by adjusting the controller to increase the resisting torque on the drive wheels so that the resisting torque is equal to the resisting torque of the tractor during ploughing, and by adjusting the accelerator pedal control to change the speed during operation, resulting in the drive wheel output torque, power consumption and transmission efficiency during ploughing. Figure 13 shows the output torque of the drive wheels, and the peaks appearing in the figure are the extra loads encountered by the tractor when ploughing. The two-motor drive uses a two-motor average torque distribution strategy to achieve the optimum drive effect.

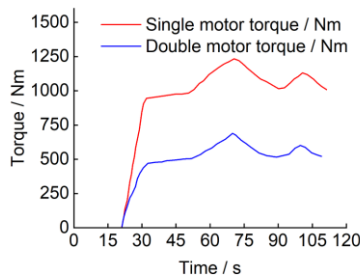


Fig.13 -Rotary tillage output torque

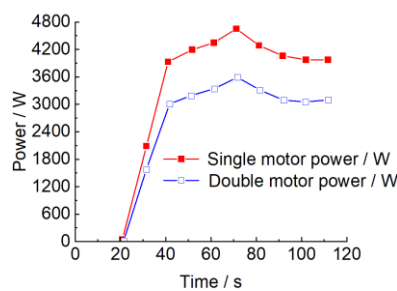


Fig. 14 - Output power

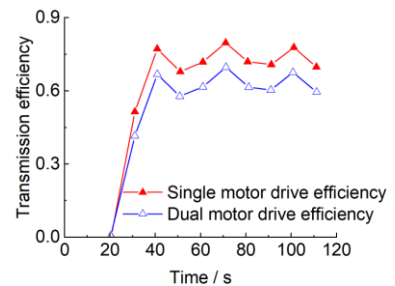


Fig. 15 - Transmission efficiency

Fig. 14 shows the power consumed by the two drive modes, the power consumed increases as the load increases, when the tractor and ploughs travel at a steady speed, the power consumed by the single motor drive mode is greater than that of the two-motor drive mode. The energy consumed by the tractor during operation is equal to the total energy output from the battery, and the power of the tractor is determined by multiplying the traction force by the travelling speed which gives the power consumed. From Fig.14, it can be seen that the average power consumed by the dual motors is 2876.95 W, and the average power in the single motor operation is 3725.3 W. Therefore, the dual motors save 22.7% of the energy consumption compared to the single motor operation.

Figure 15 shows the transmission efficiency of the two drive structures. Due to the two-motor drive structure designed in this paper, saving part of the transmission mechanism, reducing the energy loss caused by wear and tear of components, as can be seen from the transmission efficiency change curve in the figure, the transmission efficiency of the single-motor transport reaches an average of 0.61, the transmission efficiency of the double-motor operation averages 0.69. So, the transmission efficiency of the two-motor drive structure is 11.5% higher than that of the single-motor-driven structure.

Unloaded Operating Condition

The brake controller is adjusted so that the output torque at the drive wheels is equal to the load torque of 297 Nm for rated transport, yielding the power consumption, torque and transmission efficiency for normal driving (Chen et al., 2023).

As can be seen from Fig.16, when the tractor reaches the uniform speed driving state after acceleration, the vehicle output torque is relatively stable, with only minor fluctuations, and the dual-motor drive mode has a smaller torque than the single-motor drive mode.

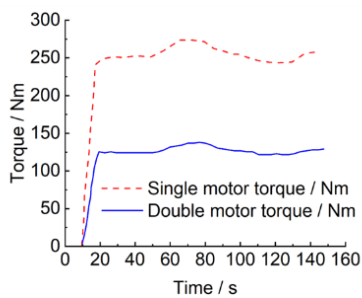


Fig. 16 - Unloaded motor torque

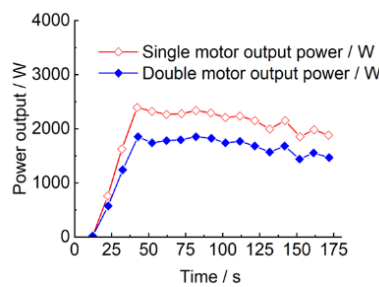


Fig. 17 - Output power

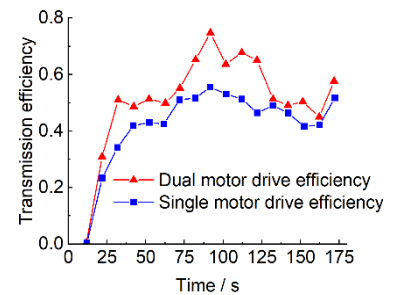


Fig. 18 - Transmission efficiency

From Fig.17, it can be seen that the power consumed by the tractor is relatively stable when driving at a constant speed, which is much smaller than that consumed during rotary ploughing operation, and the average power consumed during single-motor transport is 2012.3 W, while the average power consumed during dual-motor operation is 1609.2 W. The dual-motor drive mode saves 20.3% energy consumption compared with single-motor operation.

From the transmission efficiency shown in Fig. 18, it can be seen that the higher the tractor travelling speed, the greater the transmission efficiency, specific data are shown in the table2.

Table 2

Motor Efficiency Data				
Time/s	Dual motor	Average efficiency	Single motor	Average efficiency
11.75	0.01		0.00	
21.84	0.31		0.23	
32.20	0.51		0.34	
42.29	0.49		0.42	
52.13	0.51		0.43	
62.73	0.50		0.42	
72.10	0.55		0.51	
82.22	0.65		0.52	
91.82	0.75	0.52	0.55	0.43
101.71	0.64		0.53	
112.03	0.68		0.51	
121.87	0.65		0.46	
132.24	0.51		0.49	
141.84	0.49		0.46	
151.44	0.50		0.42	
162.05	0.45		0.42	
171.65	0.58		0.52	

Combining the graphs gives an average transmission efficiency of 0.43 for the single motor mode and 0.52 for the dual motor mode, with the dual electric drive mode having an average of 17% higher transmission efficiency than the single motor mode.

CONCLUSIONS

The power system of dual-motor electric tractor mainly includes the electric drive assembly with the drive motor as the core and the power output assembly with the power output. Compared with the single-motor centralised configuration, the rotational speed of the power output shaft is easier, and the application of the dual-motor also improves the tractor's dynamics, which is combined with the simulation analysis to determine the final chassis layout.

The crawler electric tractor was subjected to force analysis, layout setting, etc., and the frame structure was statically analysed by combining with Ansys software, and the stiffness and strength of the frame of the crawler electric tractor met the requirements of the static design under the working condition of full-load bending.

A simulation model of a small electric tractor for facility agriculture was constructed and the parameters of each component in the simulation model were set. The power consumed by the single-motor two-wheel drive mode is 1.29 times that of the two-motor drive mode in ploughing operation, and the power consumed by the single-motor drive is 1.25 times that of the two-motor drive mode in transport operation. The two-motor drive mode simplifies the transmission system, and the transmission efficiency is 52% in transport operation and 69% in ploughing operation, while the transmission efficiency of the single-motor drive mode is 43% in transport operation and 61% in ploughing operation. The simulation results verify the accuracy of the designed electric tractor parameter matching, and lay a foundation for the subsequent prototype trial production.

ACKNOWLEDGEMENT

The project supported by the Shandong Province agricultural machinery equipment research and development innovation plan project (No. 2018YF005).

REFERENCES

- [1] Bing K. (2021). Design and simulation of the overall scheme of small electric tractors for facility agriculture (面向设施农业的小型电动拖拉机整体方案设计及仿真模拟). *Shandong University of Technology*. <https://doi.org/10.27276/d.cnki.gsdgc.2021.000501>.
- [2] Cao Z. (2013). Future Orientation of Ecological Agriculture (生态农业未来的发展方向). *Chinese Journal of Eco-Agriculture*, 21(1), 29-38. <https://doi.org/10.3724/SP.J.1011.2013.00029>.
- [3] Chen Y. (2018). Study on Design and Drive Control Methods of Powertrain for Electric Tractor (拖拉机动力系统设计与驱动控制方法研究). PhD dissertation, *China Agricultural University*.
- [4] Chen A., Chen S., Shi A. (2021). Design of Torque Distribution Strategy for Dual-Motor Variable-Speed Drive Electric Tractor (双电机耦合驱动电动拖拉机转矩分配策略设计). *Journal of Agricultural Mechanization Research*, 43(11), 1-6. <https://doi.org/10.3969/j.issn.1003-188X.2021.11.002>.
- [5] Chen S., Hu M., Zhao J. (2023) Real-Time Torque Distribution Strategy for Dual-Motor Pure Electric Vehicle with Minimum System Loss (系统损耗最小的双电机纯电动汽车实时转矩分配策略). *Chinese Journal of Mechanical Engineering*, 1-13. <https://doi.org/10.3901/JME.2023.22.411>.
- [6] Dong X. (2019) Design of power dividing and converging device for dual-motor electric tractor based on virtual prototyping technology (基于虚拟样机技术的双电机电动拖拉机功率分汇流装置设计). *Henan University of Science and Technology*.
- [7] Gao H., Wang S., Zhu X., Zhao X. (2008) Test of driving force and transmission efficiency of electric tractor. *Transactions of the Chinese Society for Agricultural Machinery*, 39(10): 40-43.
- [8] Gong Jingfeng, Shan Dongsheng, Liu Hao, Li Xiuyuan. (2021). Design and Finite Element Analysis of Parametric Platform for Trapezoidal Frame of Truck (载货汽车梯形车架参数化平台设计及有限元分析). *Machinery Design and Manufacture*, Vol.16, Issue 7, pp. 6-9. <https://doi.org/10.3969/j.issn.1001-3997.2022.07.002>.
- [9] Huang Zhouwei. (2020) Strength Optimization Design of the Frame of a Three-wheeled Transport Vehicle in Greenhouse (某大棚三轮运输车车架强度优化设计). *Agricultural equipment and vehicle engineering*, Vol.59, Issue 6, pp. 63-68. <https://doi.org/10.3969/j.issn.1673-3142.2021.06.014>.

- [10] Liu M., Lei S., Zhao J., Meng Z., Zhao C., Xu L. (2022). Review of development process and research status of electric tractors (电动拖拉机发展历程与研究现状综述). *Transactions of the Chinese Society for Agricultural Machinery*, 53(S1): 348-364.
- [11] Liu Y. (2023). Design and Experimental Study of Dual Motor Drive System for Electric Tractor (拖拉机双电机驱动系统的设计及试验研究). *Journal of Agricultural Mechanization Research*, 45(11), 247-252. <https://doi.org/10.3969/j.issn.1003-188X.2023.11.041>.
- [12] Matveev A S, Hoy M, Katupitiya J. (2013) Nonlinear sliding mode control of an unmanned agricultural tractor in the presence of sliding and control saturation. *Robotics & Autonomous Systems*, 61(9): 973-987. <https://doi.org/10.1016/j.robot.2013.05.003>.
- [13] Michal M., Slawomir P. (2017) Comparison of computing efficiency of different hydraulic vehicle damper models. *Technical Transactions*, 10(8). <https://doi.org/10.4467/2353737xct.17.143.6894>.
- [14] Oelen W, Amerongen J V. (1994) Robust tracking control of two-degrees-of-freedom mobile robots. *Control Engineering Practice*, 2(2): 333-340. [https://doi.org/10.1016/0967-0661\(94\)90215-1](https://doi.org/10.1016/0967-0661(94)90215-1)
- [15] Rizzoni G., Guzzella L., Baumann B. (1999) Unified modeling of hybrid electric vehicle drivetrains. *IEEE/ASME transactions on mechatronics*, 4(3), 246-257. <https://doi.org/10.1109/3516.789683>.
- [16] Song X. (2023) Research on the structure layout and control strategy of electric tractor for protected agriculture (Research on the Structure Layout and Control Strategy of Electric Tractor for Protected Agriculture(面向设施农业的电动拖拉机结构布局及控制策略研究)). *Shandong University of Technology*. <https://doi.org/10.27276/d.cnki.gsdgc.2023.000684>.
- [17] Sun Y., Xu L., Jing B., Ding L., Xiao S. (2020) Development of a four-point adjustable lifting crawler chassis and experiments in a combine harvester. *Computers and Electronics in Agriculture*, 173(C). <https://doi.org/10.1016/j.compag.2020.105416>.
- [18] Wang Z., Xu S., Luo W. (2022) Research on Energy Management Strategy of Fuel Cell Vehicle Based on Dynamic Programming (基于动态规划的燃料电池车能量管理策略研究). *Acta Energiæ Solaris Sinica*, 52(09), 2077-2084. <https://doi.org/10.19912/j.0254-0096.tynxb.2022-0852>.
- [19] Wang Z., Zhou J., Rizzoni G. (2022) A review of architectures and control strategies of dual-motor coupling powertrain systems for battery electric vehicles. *Renewable and Sustainable Energy Reviews*, 62, 112455. <https://doi.org/10.1016/j.rser.2022.112455>.
- [20] Wang W., Shi J., Zhang Z., Lin C. (2018) Optimization of a dual-motor coupled powertrain energy management strategy for a battery electric bus. *Energy Procedia*, 145, 20-25.
- [21] Wang Z., Zhou J., Wang X. (2023) Research on Energy Management Model for Extended-range Electric Rotary-tilling Tractor (增程式电动拖拉机旋耕机组能量管理模型研究). *Transactions of the Chinese Society for Agricultural Machinery*, 54(4), 428-438. <https://doi.org/10.6041/j.issn.1000-1298.2023.04.045>.
- [22] Xiaofei Z. (2017). Design Theory and Performance Analysis of Electric Tractor Drive System. *International Journal of Engineering Research Technology (IJERT)*, pp. 235-238.
- [23] Xie B., Zhang C., Chen S., Wang Y., Lan Y. (2015). Transmission performance of two-wheel drive electric tractor. *Transactions of the Chinese Society for Agricultural Machinery*. 46(6), pp. 8-13. <https://doi.org/10.6041/j.issn.1000-1298.2015.06.002>.
- [24] Zhao D. (2022). Research and design of universal crawler based on HST in hilly areas (基于 HST 的山地丘陵履带式通用底盘研制). *Shandong University of Technology*.
- [25] Zhang Y., Lu M., Xie Q. (2017) Drive design of electric tractor based on economy (基于经济性的温室电动拖拉机驱动设计). *Xinjiang Agricultural Mechanization*. 37(05): 21-23. <https://doi.org/10.13620/j.cnki.issn1007-7782.2017.05.006>.

POTATO APPEARANCE DETECTION ALGORITHM BASED ON IMPROVED YOLOv8

/ 基于改进 YOLOV8 的马铃薯外观品相检测算法

Huan ZHANG¹⁾, Zhen LIU¹⁾, Ranbing YANG^{1,2)}, Zhiguo PAN^{*1)}, Zhaoming SU¹⁾, Xinlin LI¹⁾,
Zeyang LIU¹⁾, Chuanmiao SHI¹⁾, Shuai WANG¹⁾, Hongzhu WU³⁾

¹⁾ College of Electrical and Mechanical Engineering, Qingdao Agricultural University, Qingdao/ China

²⁾ College of Mechanical and Electrical Engineering, Hainan University, Haikou/ China

³⁾ Qingdao Hongzhu Agricultural Machinery Co., Ltd., Qingdao/ China

Tel: +8615318715305; E-mail: peter_panzg@163.com

Corresponding author: Zhiguo Pan

DOI: <https://doi.org/10.35633/inmateh-74-76>

Keywords: Classification of potato species, Automatic sorting, Target detection, YOLOv8, MobileNetV4

ABSTRACT

To meet the demands for rapid and accurate appearance inspection in potato sorting, this study proposes a potato appearance detection algorithm based on an improved version of YOLOv8. MobileNetV4 is employed to replace the YOLOv8 backbone network, and a triple attention mechanism is introduced to the neck network along with the Inner-CIoU loss function to accelerate convergence and enhance the accuracy of potato appearance detection. Experimental results demonstrate that the proposed YOLOv8 model achieves precision, recall, and mean average precision of 91.4%, 87.7%, and 93.7% respectively on the test set. Compared to YOLOv5s, YOLOv7tiny, and the original base network, it exhibits minimal memory usage while improving the mAP@0.5 by 1.1, 0.9, and 0.3 percentage points respectively, providing a reference for potato quality inspection.

摘要

为满足马铃薯分拣过程中对外观品相检测快速、准确的需求，本研究提出了一种基于改进 YOLOv8 的马铃薯外观品相检测算法。使用 MobileNetV4 替换 YOLOv8 主干网络，颈部网络引入三重注意力机制，Inner-CIoU 损失函数，加速收敛，提升马铃薯品相检测准确率。实验结果表明，提出的 YOLOv8 模型在测试集上的精确率、召回率和平均精度分别为 91.4%、87.7%、93.7%，相比较 YOLOv5s、YOLOv7tiny 和原基础网络，模型内存占用最少的同时的 mAP@0.5 分别提升了 1.1、0.9、0.3 个百分点，为马铃薯品质检测提供参考。

INTRODUCTION

Potatoes are the fourth largest staple crop in China. In 2023, the potato planting area in China was approximately 4,621 thousand hectares, with an annual production of fresh potatoes reaching 18.909 million tons. Due to the consumption habits of the Chinese population, fresh consumption accounts for more than 70% of the total potato consumption. Implementing scientific grading and classification strategies is crucial for the commercialization of fresh potatoes, meeting personalized needs, and enhancing economic value. Potato sprouting and surface damage are key factors affecting their market value and are important standards for determining potato grades. Therefore, timely and accurate detection of potato sprouting and surface damage is of significant importance in the grading, classification, and commercialization processes.

In most potato-producing regions of China, the sorting of fresh potatoes is primarily performed manually, resulting in high labor intensity and low efficiency. Therefore, the mechanization of rapid grading and sorting at production sites has become an inevitable trend. With the rapid advancement of computer technology, machine vision and deep learning have been widely applied in the agricultural sector. These methodologies are primarily founded on Convolutional Neural Networks (CNNs) and can be broadly categorized into two-stage detectors and one-stage detectors based on their processing workflows. They have significantly ameliorated the issues inherent in traditional object detection approaches.

In the realm of two-stage detection, the R-CNN series algorithms stand out as the most representative (Girshick R. et al., 2014; Ren S. et al., 2016; He K. et al., 2017). In the first stage, regions of interest (ROIs) are extracted from the input image, while in the second stage, each ROI undergoes object classification and bounding box regression. Arshaghi et al., (2023), proposed a deep learning model based on CNN for potato defect detection and classification.

Through large-scale image data training, it can accurately identify disease spots, cracks, insect eyes, etc. Data augmentation technology is introduced to improve the generalization ability of the model. Experiments show that the performance of the model is significantly better than the traditional method, and the recognition accuracy, speed and stability are excellent in complex environments.

Md et al. (2022) applied K-means segmentation technology combined with deep learning networks to predict and classify potato leaf diseases. The experimental results indicate that by utilizing the VGG16 model, the accuracy of their model reached 97%.

Geng et al., (2024) conducted research on an accurate and non-destructive detection method for potato sprouts that focuses on deformable attention. By embedding DAS (Deformable Attention Sampling), the approach enhances focus on relevant pixel image areas, thereby providing theoretical support for the non-destructive detection of sprouts in automated seed potato slicing.

Hatice et al., (2022) proposed a novel deep learning model called MDSCIRNet, which is based on the transformer architecture and deep separable convolutions for classifying potato leaf diseases. The experimental results show that this model improves the accuracy to 99.11% compared to the original model. *Zhao Yue et al.*, (2022), employed the Faster-RCNN model to identify potato leaf diseases, achieving early and accurate diagnosis, thereby enhancing diagnostic efficiency and ensuring the yield and quality of potatoes. Although the R-CNN series models boast high accuracy, their large size and slow detection speed render them unsuitable for real-time detection. In contrast, single-stage detection models, known for their rapid detection and strong scalability, are more suitable for practical applications. Among these, the YOLO series of models stands out as the most renowned and widely applied, with numerous researchers employing the YOLO series within the agricultural sector.

Zhang W. et al., (2022), utilized the YOLOv3-tiny network model to detect potato seed tuber eyes, achieving high precision in detection. On the NVIDIA Jetson Nano platform, the model achieves a real-time detection speed of 40 FPS, meeting the demands of embedded systems and providing technical support for subsequent automated segmentation detection.

Dai et al., (2022), introduced an optimized YOLO v5 model, named DA-ActNN-YOLOV5, aimed at researching potato diseases across multiple regions and periods. This model achieved a remarkable recognition accuracy of 99.81% for early and late blight on the test set, representing a significant improvement of 9.22% in average accuracy compared to the original model.

EIMasry et al., (2012), developed a fast and accurate system based on machine vision, which constructs an image database and extracts geometric features and Fourier shape parameters. The study identified roundness, range, and four Fourier descriptors as key classification features. Experiments demonstrated that the system achieved an average correct classification rate of 96.5% on the training set and 96.2% on the test set. Additionally, it achieved a 100% accuracy rate in classifying the size of potatoes, showcasing its significant potential in the automatic detection and sorting of deformed potatoes.

Yue et al., (2024), employed the YOLOv8n network for citrus detection, enhancing the feature extraction network to achieve a detection accuracy of 96.9%. These methods have garnered notable success in agricultural target detection, providing robust support for the realization of intelligent agricultural machinery.

The aforementioned scholars conducted a feasibility analysis of the application of object detection technology in the agricultural sector, highlighting certain challenges when identifying surface defects on potatoes. They noted that while object detection technology is effective, it is limited by the types and accuracy of defect identification. The subtle differences between various potato varieties make it difficult to extract more effective features, and the system's stability needs improvement. To address these issues, this paper proposes an improved model based on YOLOv8, named MTI-YOLOv8.

MATERIALS AND METHODS

Image acquisition system

To capture images of potato appearance features, an online detection device for potato appearance grading was designed, as shown in Figure 1. This device primarily comprised a potato conveying system and an image processing system. The potato conveying system consisted of a motor, roller conveyor belt, and belt conveyor. The image processing system included a depth camera, dedicated camera lighting, a Jetson TX2 board, data cables, power supply, and detection algorithms. The detection algorithm was deployed on the Jetson TX2 board, with images captured by the camera being transmitted to the TX2 board via data cables.



Fig.1 – Schematic diagram of the depth camera

Dataset producing

On the experimental platform at Qingdao Agricultural University in Shandong Province, a depth camera was used to collect image data of potatoes. The experiment selected the early-maturing and high-yielding Holland 15 potato variety from Heilongjiang, Inner Mongolia, and the Central Plains region as the test subjects. A total of 560 potato samples were randomly selected and placed in different environments for a period of time to observe potential surface damage. To obtain representative samples of surface damage, potatoes with varying degrees and areas of damage were sampled periodically. Given the significant impact of image quality on the model's detection performance, the collected images were screened to remove blurry ones, resulting in a selection of 2120 images that met the experimental standards. These images were saved in jpg format with a resolution of 2592×2048 pixels. For each potato, two clear and unblurred photos—one of the front and one of the back—were taken to ensure the completeness and accuracy of the data.

In the process of annotating surface damage on potatoes, any mislabeling of defects could have resulted in non-defective areas being incorrectly marked as defective. This could have led the model to learn inaccurate information, thereby reducing its recognition accuracy and affecting its performance in practical applications. In this study, when annotating potato images, sprouting or rotting potatoes were labeled as "rot," green discoloration on the surface was labeled as "green," surface cracks were marked as "break," and whole, undamaged potatoes were labeled as "intact" to differentiate between categories, as illustrated in Figure 2.



Fig. 2 – Potatoes with different degrees of sprouting and damage

a) Rot potato; b) Green potato; c) Break potato; d) Intact potato

Image preprocessing

Using the open-source software Labelimg, potato surface damage information was annotated, and the annotations were uniformly saved in the PASCAL VOC dataset standard format. To further enhance the model's generalization performance and robustness, as well as to reduce the risk of overfitting, data augmentation techniques were applied. These techniques included horizontal and vertical flipping, brightness enhancement and reduction, motion blur, and contrast enhancement, among others. After augmentation, a total of 4,071 sample images were obtained. These images were randomly divided into training, testing, and validation sets in a 7:2:1 ratio, respectively resulting in 2,849 images for the training set, 815 images for the testing set, and 407 images for the validation set. The training set was used to train the model, the validation set was employed to adjust the model's hyperparameters and conduct preliminary evaluations of the model's capabilities, and the testing set was utilized to assess the model's detection accuracy and evaluate its generalization ability.

THE IMPROVEMENT METHOD OF POTATO QUALITY DETECTION

My question is: When using the traditional YOLOv8 model for classifying potatoes, several challenges are encountered, such as the insignificant features affecting recognition accuracy, slow detection speed, poor system stability, and large weight file sizes impacting efficiency. To enhance detection performance and reduce computational costs, it is necessary to make deep optimizations and improvements across multiple areas. Firstly, to address the issue of excessive model computational load, the MobileNetV4 network structure is introduced to reduce the size of the weight files and improve the model's lightness. In addition to introducing the MobileNetV4 network structure, the integration of a Triplet Attention module is proposed to emphasize attention computation across dimensional interactions. This enhances feature representation and improves efficiency, aiding in the precise localization and identification of detection objects. Furthermore, by incorporating the Inner-CIoU loss function, classification information is embedded into the IoU (intersection over union) calculation to enhance the model's bounding box regression performance. These optimizations and improvements are based on a comprehensive analysis of current challenges, aiming to tackle each issue methodically, thereby bringing substantial improvements to the detection of potato appearance quality. The improved model is named the MTI-YOLOv8 network, with its model structure depicted in Figure 3.

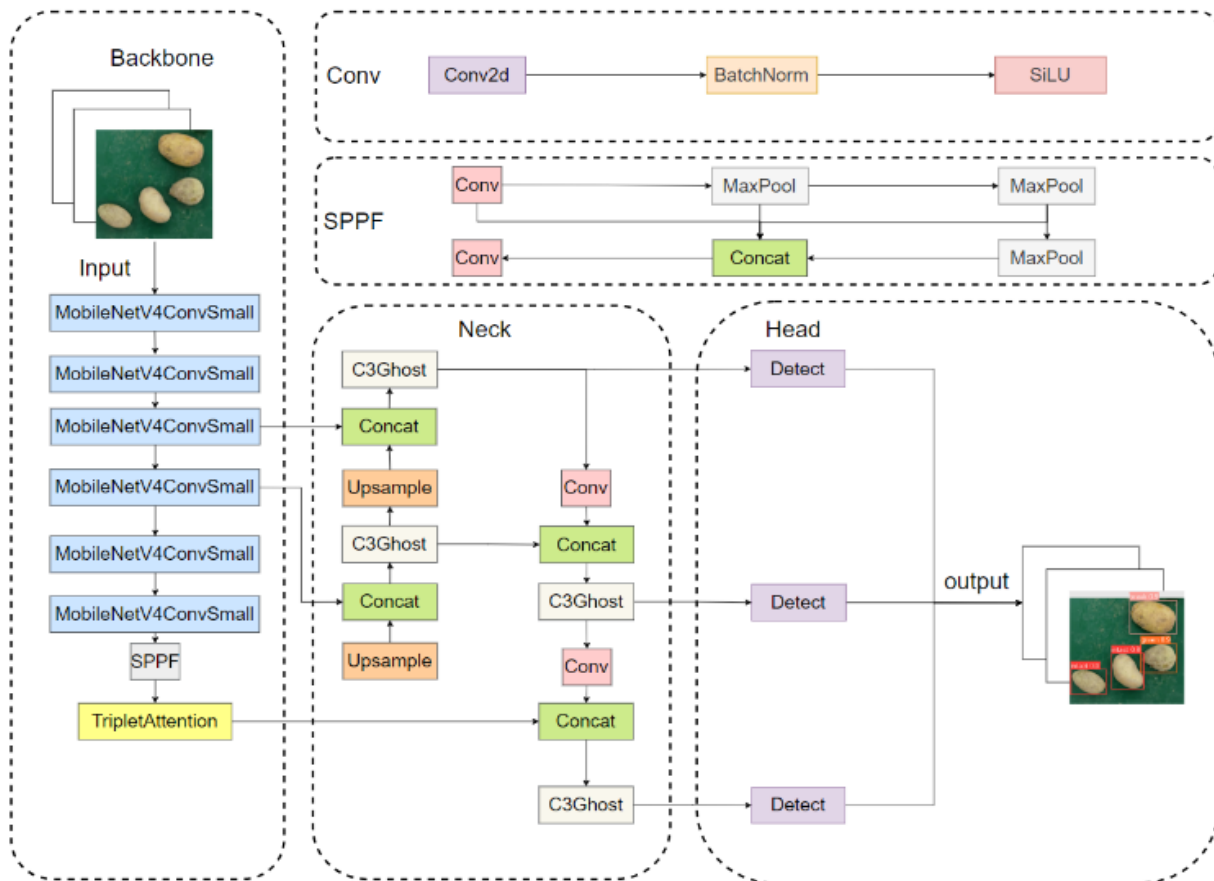


Fig. 3 – The structure of MTI-YOLOv8 model

MobileNetV4 backbone network

The original YOLOv8 model, while comprehensive in its capabilities, encounters challenges with a large number of parameters and accuracy that could be enhanced in the process of potato recognition. Experiments have revealed that the original YOLOv8 model exhibits high computational resource consumption and limited inference speed when handling complex and variable potato images. In response, an improvement strategy was implemented by replacing the backbone network of YOLOv8 with MobileNetV4, aiming to mitigate the issues of high model complexity and computational demand.

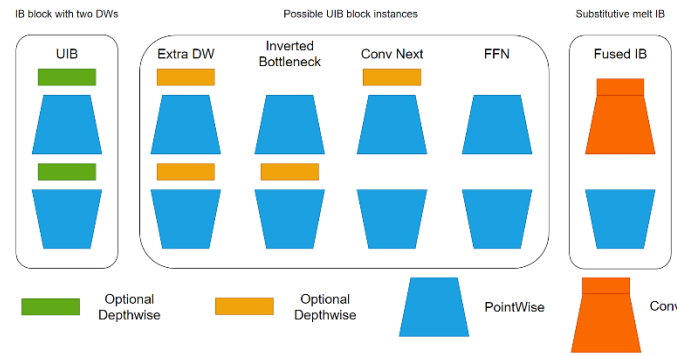


Fig. 4 – Universal Inverted Bottleneck (UIB) blocks

The improved model, by incorporating the MobileNetV4 backbone network, significantly reduces parameter count and computational load, enhancing inference speed and making it more amenable for deployment on edge computing and mobile devices. MobileNetV4 achieves lightweight performance while maintaining high efficiency through the innovative introduction of Universal Inverted Bottleneck (UIB) search blocks, Mobile MQA attention modules, and an optimized Neural Architecture Search (NAS) strategy. This enhances feature extraction capabilities and improves the accuracy and robustness of potato recognition. Additionally, the model demonstrates greater flexibility and reduced power consumption, eliminating the reliance on high-performance hardware and showcasing exceptional performance across diverse hardware platforms.

Triplet Attention module

In addressing the potato recognition task, the original YOLOv8 model, despite its comprehensive functionality, has shown significant shortcomings when faced with high environmental complexity, large weight files that impose storage burdens, and slow recognition speeds, as revealed by experiments. To mitigate these issues, this paper introduces the Triplet Attention mechanism as an improvement strategy.

In addressing the potato recognition task, the original YOLOv8 model, despite its comprehensive functionality, has shown significant shortcomings when faced with high environmental complexity, large weight files that impose storage burdens, and slow recognition speeds, as revealed by experiments. To mitigate these issues, this paper introduces the Triplet Attention mechanism as an improvement strategy. The Triplet Attention mechanism, with its unique tri-branch design, effectively captures cross-dimensional feature interactions between the spatial dimensions (H, W) and the channel dimension (C) of the input tensor. This endows the model with a more comprehensive image understanding capability, enabling it to precisely capture subtle and critical features in potato images. Compared to traditional attention mechanisms, Triplet Attention demonstrates significant advantages in computational efficiency by focusing on the interaction analysis among three elements rather than performing global computation on the entire input data. This greatly reduces the computational burden and time cost, making it especially suitable for the rapid processing of high-resolution potato images.

In complex scenarios where potatoes may exhibit different growth stages, morphological changes, and varying lighting conditions, the Triplet Attention mechanism enhances the model's ability to analyze cross-dimensional features. This significantly improves recognition accuracy and robustness, providing strong technical support for potato recognition tasks.

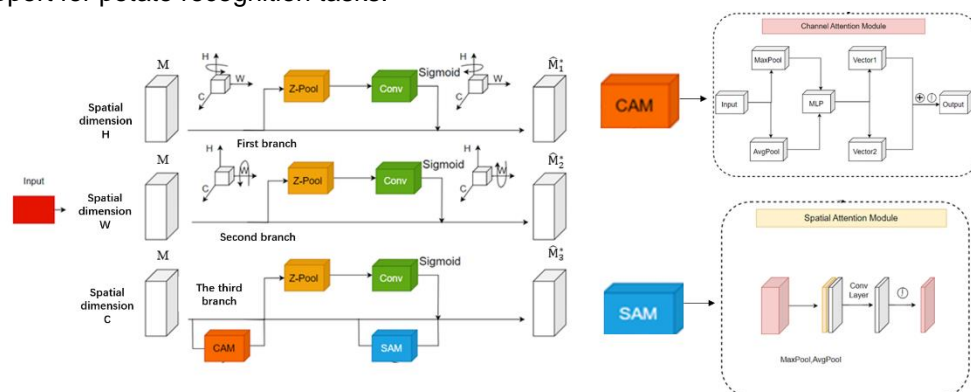


Fig. 5 – Triplet Attention structure

Triplet Attention consists of three parallel branches, and the input tensor $M \in \mathbf{R}^{C \times H \times W}$ is divided into three branches. In the first branch, the tensor M rotates 90° counterclockwise around the dimension H to obtain the rotation tensor \hat{M}_1 . After pooling, the tensor shape is $2 \times H \times C$, and then the convolution operation is performed. The attention weight is generated by the Sigmoid activation function. Finally, the rotation is 90° clockwise around the dimension H , and the output tensor \hat{M}_1^* is completed. The interaction between channel C and dimension H is completed. In the second branch, the tensor M rotates 90° counterclockwise around the dimension W , and the rotation tensor \hat{M}_2 is obtained.

After the pooling layer, convolution, and Sigmoid activation function, it rotates 90° clockwise around the dimension W , and the output tensor \hat{M}_2^* is completed. The channel C interacts with the dimension W . In the third branch, after the tensor M passes through the pooling layer, convolution, and Sigmoid activation function, the output tensor \hat{M}_3^* is obtained. Finally, the three tensors are averaged and aggregated to produce an output tensor y , as shown in equation (1).

$$y = \frac{1}{3} \left(\hat{M}_1 \sigma(\psi_1(\hat{M}_1^*)) + \hat{M}_2 \sigma(\psi_2(\hat{M}_2^*)) + M \sigma(\psi_3(\hat{M}_3^*)) \right) \quad (1)$$

In the formula: $\sigma(\cdot)$ is the Sigmoid activation function; $\psi_1(\cdot), \psi_2(\cdot), \psi_3(\cdot)$ are standard convolutions.

Inner-CIoU loss function

In analyzing the process and patterns of bounding box regression, the unique nature of the bounding box regression problem was observed. During the model training phase, using smaller auxiliary boxes to calculate loss can positively impact the regression of high IoU samples, while low IoU samples exhibit the opposite trend. This addresses the increased difficulty in potato recognition caused by occlusion of loss features due to complex environments during potato harvesting.

To enhance recognition accuracy and accelerate the speed of bounding box regression, the Inner-IoU Loss method is innovatively proposed. This method introduces a scale factor, ratio, to regulate the generation of auxiliary boxes of different sizes, which are then used for loss calculation. By integrating Inner-IoU Loss into existing IoU-based loss functions, faster and more accurate regression results can be achieved, as illustrated in Figure 6.

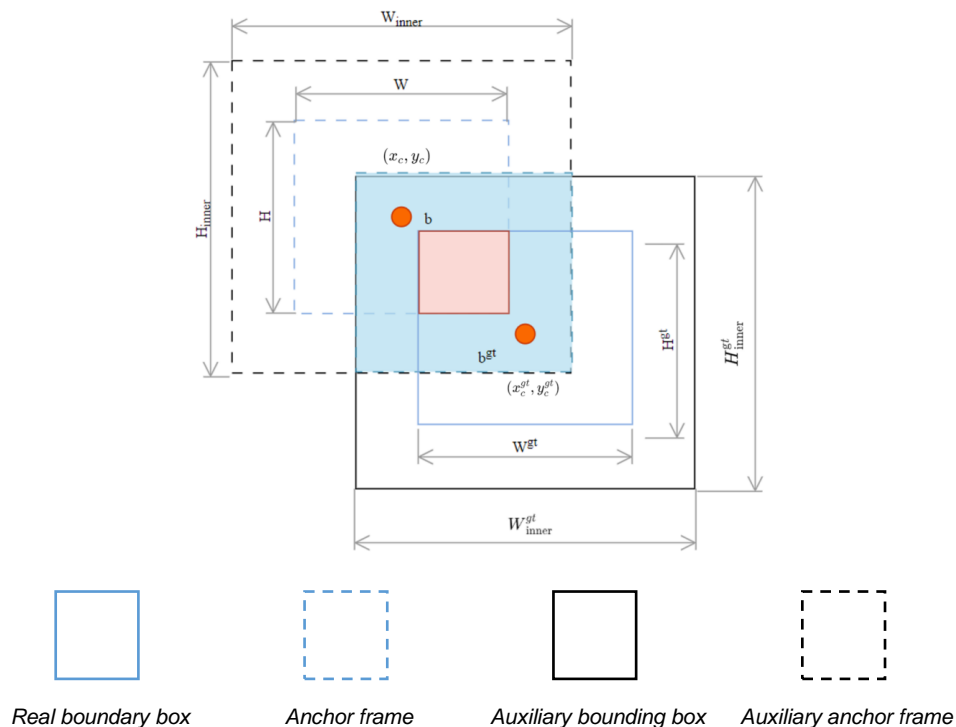


Fig. 6 – Inner-IoU loss function

Note : The real bounding box and the anchor box are represented by b^{gt} and b , respectively. The center point coordinates of the real bounding box is (x_c^{gt}, y_c^{gt}) , the center point coordinates of the anchor box is (x_c, y_c) , the width of the real bounding box is W^{gt} , the height of the real bounding box is H^{gt} , the width of the anchor box is W , the height of the anchor box is H , the width of the auxiliary bounding box is W_{inner}^{gt} , the height of the auxiliary bounding box is H_{inner}^{gt} , the width of the auxiliary anchor box is W_{inner} , and the height of the auxiliary anchor box is H_{inner} .

To enhance the generalization and convergence speed of the CloU loss function, Inner-IoU is introduced, utilizing auxiliary bounding boxes to calculate loss and thereby accelerating bounding box regression. Inner-IoU adjusts the auxiliary boxes through a scaling factor, allowing it to flexibly adapt to different datasets and detectors, and enhancing generalization capabilities in complex scenes.

RESULTS AND ANALYSIS

Test environment and parameter configuration

All experiments conducted in this study were trained on the same server, with the experimental platform operating on Windows 11. The CPU used was an Intel(R) Core(TM) i5-13500HX, supported by 16GB of memory. The graphics card was an NVIDIA GeForce RTX 4060 with 6GB of VRAM. The development language employed was Python 3.10, while the software environment comprised Pytorch 2.0.1, CUDA version 12.1, and CUDNN version 8.9. All other parameters adhered to the official default settings of YOLOv8.

Evaluating indicator

In order to comprehensively evaluate the detection performance of the proposed model, the following evaluation indicators were used: Precision, Recall, mAP @ 0.5, mAP @ 0.5 ~ 0.95, number of model parameters, and number of model floating-point calculations.

The calculation formula is as follows:

$$P = \frac{T_p}{T_p + F_p} \quad (2)$$

$$R = \frac{T_p}{T_p + F_n} \quad (3)$$

$$AP = \int_0^1 P(R) dR \quad (4)$$

$$mAP = \frac{\sum_{i=1}^N AP_i}{N} \quad (5)$$

In the formula, T_p represents the number of positive samples correctly predicted by the model; F_p represents the number of negative samples that are predicted to be positive by the model error. F_n represents the number of positive samples that are incorrectly predicted as negative by the model. AP_i denotes the AP value of category i ; n represents the number of data set categories.

Analysis of backbone network effectiveness

To evaluate the enhancement in performance of the MobileNetV4 backbone network within the MTI-YOLOv8 detection model, a comparative experiment was conducted. In this study, the conventional C3 and C2F detection backbones used in YOLO series models V5 and V8 were directly compared with the MTI-YOLOv8 model integrated with MobileNetV4 under identical testing conditions. The experimental data presented in Table 1 demonstrate that the MTI-YOLOv8 model, utilizing MobileNetV4 as its backbone network, exhibits significant advantages across several key performance metrics.

Specifically, the model achieved an accuracy of 91.4%, representing an improvement of 2.3% and 2.0% over the C3 and C2F detection backbones, respectively. In terms of recall, MobileNetV4 excelled with an impressive score of 87.7%, surpassing the C2F detection backbone by a notable 5.5%. Furthermore, regarding the mean Average Precision (mAP)—a critical metric for assessing overall detection accuracy—the MobileNetV4 model attained a score of 93.7%. This reflects a modest yet consistent increase compared to the 92.6% and 93.4% achieved by the C3 and C2F models, respectively.

In addition, regarding detection speed—an extremely important metric in practical applications—the model employing MobileNetV4 demonstrated faster processing speed, achieving 56 frames per second (FPS). This represents an increase of 6 FPS and 9 FPS compared to the C3 and C2F models, respectively, further validating its efficiency and superiority in the task of potato seedling detection. In summary, MobileNetV4 not only enhances detection accuracy and recall rate while maintaining a high mean average precision but also significantly accelerates detection speed, delivering a comprehensive performance improvement for the potato appearance detection model.

Table 1

Comparison test results of different detection backbones

backbone	P/%	R/%	mAP@0.5%	FPS
MobileNetV4	91.4	87.7	93.7	56
C3	89.1	92.6	92.6	50
C2F	89.4	82.2	93.4	47

Effectiveness analysis of attention mechanism

In our experiments on optimizing attention mechanisms for potato appearance detection tasks, it was observed that although CBAM, as an attention module integrating spatial and channel dimensions, has demonstrated excellent performance in other object detection studies, it did not significantly enhance accuracy in this study. Meanwhile, both the Global Attention Mechanism (GAM) and Dynamic Attention Transformer (DAT) contributed to considerable accuracy improvements; however, GAM resulted in increased model parameters and computational load, whereas DAT effectively alleviated these burdens. The EMA attention mechanism achieved a notable enhancement in detection accuracy, leveraging its ability to maintain the correlation between spatial and channel information and offering more stable feature representations. However, this improvement came with an approximate 9.09% increase in parameters and about a 20.5% rise in GFLOPs. In contrast, the Triplet Attention mechanism effectively enhanced feature representation by directly modeling inter-channel dependencies while maintaining lower model parameters and GFLOPs. This resulted in a 0.3% improvement in mAP@0.5, optimizing the model's detection accuracy. Therefore, for the task of potato appearance detection, the Triplet Attention mechanism demonstrates greater practicality and efficiency, making it a more suitable choice.

Table 2

Comparison of the results of different attention mechanisms

Attention Mechanism	mAP@0.5	mAP@0.5~0.95/%	Parameters /M	Floating Point Operation Quantity /G
—	93.4	73.1	3.01	8.1
Triplet Attention	93.7	72.8	2.61	7.0
CBAM	93.2	71.7	3.01	8.1
GAM Attention	93.3	71.7	4.62	9.4
EMA	94.2	73.3	12.10	28.6
DAT	93.3	71.4	2.46	6.8

Comparative test analysis of different algorithms

In order to verify the superiority of the research algorithm, the research algorithm MTI-YOLOv8 was compared with Faster R-CNN, Tood, YOLOv5s, YOLOv7-tiny, YOLOv8n, and another algorithm under the same conditions. The test results were shown in Table 3.

Table 3

Different model experiment results

Models	Recall/%	mAP@0.5	mAP@0.5~0.95/%	FLOPs/G	Parameters/MB	Model Size/MB
Faster R-CNN	65.1	71.5	38.4	137.20	41.36	315.46
Tood	67.1	87.8	54.7	126.96	32.03	244.13
YOLOv5s	88.8	92.6	70.9	15.8	7.02	14.5
YOLOv7-tiny	85.2	92.8	71.5	13.3	5.8	11.7
YOLOv8n	82.2	93.4	73.1	8.1	3.01	6.2
MTI-YOLOv8	87.7	93.7	72.8	7.0	2.61	5.54

Based on the experimental results presented in Table 3, it can be concluded that the two-stage object detection algorithm Faster R-CNN involves a relatively high number of floating-point operations and parameters, resulting in a larger model weight file. Therefore, it is considered that the two-stage object detection algorithm is not well-suited for the lightweight real-time detection requirements of this dataset.

YOLOv8 outperforms YOLOv7-tiny in terms of recall rate and mAP, while having fewer parameters and a smaller model size than other networks. The improved algorithm MTI-YOLOv8 enhances key metrics compared to the original YOLOv8n, with a 5.5% increase in recall rate and a 0.3% increase in average precision, while reducing the number of parameters and model size by 0.4 and 0.66, respectively. The experimental results clearly indicate that the MTI-YOLOv8 algorithm demonstrates excellent performance in potato object detection.



Fig. 7 – Comparison of model detection effects

Ablation test

In order to verify the effectiveness of each improved module of the algorithm in this study, the original model YOLOv8n was used as the baseline model, and the accuracy, recall rate, mAP @ 0.5, floating point operation amount and parameter number were used as evaluation indexes. The ablation test was carried out in different combinations of multiple improved modules, and the results were shown in table 4.

Table 4

Ablation experiment							
MobileNetV4	Triplet Attention	Inner-CIoU	P/%	R/%	mAP@0.5%	Parameters	FLOPs(G)
x	x	x	89.4	82.2	93.4	3264396	12.1
√	x	x	89.2	81.2	89.3	1740491	9.6
√	√	x	91.0	89.5	90.4	1632198	8.1
√	√	√	91.4	87.7	93.7	1632198	5.9

According to the analysis of the experimental results in Table 4, it can be seen that by improving the backbone network of the original YOLOv8n model using the MobileNetV4 model, the lightweight structure significantly reduces the number of floating-point operations and parameters of the model. However, this reduction comes at the cost of a decrease in detection accuracy, with mAP@0.5% dropping by 4.1%. The ablation experiments also show that on the basis of the improved backbone network model, adding the Triplet Attention mechanism significantly enhances recognition accuracy, while slightly reducing the model's parameters and floating-point operations. This indicates that the Triplet Attention mechanism performs better in balancing model performance and accuracy improvement. When the Inner-CIoU loss function is introduced, it aids in bounding box regression, improving the model's localization ability and accelerating model convergence, resulting in a 3.3% increase in mAP@0.5%.

In conclusion, compared to the original YOLOv8n baseline network model, the enhanced MTI-YOLOv8 model, while showing a modest improvement in mAP@0.5, achieved significant enhancements of 2 percentage points in precision and 6.5 percentage points in recall. Moreover, the model's floating-point operations and parameter counts were reduced by 1,632,198 and 6.2 GFLOPs, respectively, strongly demonstrating the effectiveness and efficiency of the improved algorithm proposed in this study.

CONCLUSIONS

This study developed a potato appearance detection model based on the improved YOLOv8n network. Detection results on the same dataset indicated that the enhanced model achieved an accuracy of 91.4%, a recall rate of 87.7%, and an average precision of 93.7% in potato detection, surpassing the original YOLOv8n network and other detection models. Field experiments conducted on a laboratory-constructed testing platform demonstrated that the improved YOLOv8n model can effectively detect potatoes in motion within a conveyor speed range of 3 to 5 m/min, providing a novel solution for rapid potato detection.

ACKNOWLEDGEMENT

The author has been supported by the “National Key R&D Program of China” (Project number: 2023YFD2000904), the “Industry Technology System of Modern Agriculture” (Project number: CARS-09-P32), and the “Qingdao Science and Technology Huimin Demonstration Project” (Project number: 23-2-8-xdny-2-nsh).

REFERENCES

- [1] Xia, Z., Pan, X., Song, S., Li, L. E., & Huang, G. (2022). Vision transformer with deformable attention. In *Proceedings of the IEEE/CVF conference on computer vision and pattern recognition*, 4794-4803.
- [2] Arshaghi, A., Ashourian, M., & Ghabeli, L. (2023). Potato diseases detection and classification using deep learning methods. *Multimedia Tools and Applications*, 82(4), 5725-5742.
- [3] Bochkovskiy, A., Wang, C. Y., & Liao, H. Y. M. (2020). Yolov4: Optimal speed and accuracy of object detection. *arxiv preprint arxiv:2004.10934*
- [4] Dai, G., Hu, L., & Fan, J. (2022). DA-ActNN-YOLOV5: Hybrid YOLO v5 Model with Data Augmentation and Activation of Compression Mechanism for Potato Disease Identification. *Computational Intelligence and Neuroscience*, 6114061.
- [5] ElMasry, G., Cubero, S., Moltó, E., & Blasco, J. (2012). In-line sorting of irregular potatoes by using automated computer-based machine vision system. *Journal of Food Engineering*, 112(1–2), 60-68. <https://doi.org/10.1016/j.jfoodeng.2012.03.027>
- [6] Geng B, Dai G, Zhang H, Qi S, Christine DEW. (2024). Accurate non-destructive testing method for potato sprouts focusing on deformable attention. *INMATEH - Agricultural Engineering: Vol.72*, pp. 402-413. DOI: 10.35633/inmateh-72-36.
- [7] Girshick, & Ross. (2015). [IEEE 2015 IEEE international conference on computer vision (ICCV) - Santiago, Chile (2015.12.7-2015.12.13)]. *IEEE international conference on computer vision (ICCV) - fast R-CNN*. 1440-1448.
- [8] Girshick, R., Donahue, J., Darrell, T., & Malik, J. (2014). Rich feature hierarchies for accurate object detection and semantic segmentation. In *Proceedings of the IEEE conference on computer vision and pattern recognition*. pp. 580-587.
- [9] He, K., Gkioxari, G., Dollár, P., & Girshick, R. (2017). Mask R-CNN. In *Proceedings of the IEEE international conference on computer vision*. 2961-2969.
- [10] Jocher, G., Stoken, A., Borovec, J., Changyu, L., Hogan, A., Diaconu, L., ... & Rai, P. (2020). YOLOv5: V3. 1-bug fixes and performance improvements. *Zenodo*. <https://zenodo.org/records/4154370>
- [11] Li, N., Wang, M., Yang, G., Li, B., Yuan, B., & Xu, S. (2024). DENS-YOLOv6: A small object detection model for garbage detection on water surface. *Multimedia Tools and Applications*, 83(18), 55751-55771.
- [12] Liu, Y., Shao, Z., & Hoffmann, N. (2021). Global attention mechanism: Retain information to enhance channel-spatial interactions. *arxiv preprint arxiv:2112.05561*.
- [13] Nishad, M. A. R., Mitu, M. A., & Jahan, N. (2022). Predicting and classifying potato leaf disease using k-means segmentation techniques and deep learning networks. *Procedia Computer Science*, 212, 220-229.

- [14] Ouyang, D., He, S., Zhang, G., Luo, M., Guo, H., Zhan, J., & Huang, Z. (2023). Efficient multi-scale attention module with cross-spatial learning. In *ICASSP 2023-2023 IEEE International Conference on Acoustics, Speech and Signal Processing (ICASSP)*. pp.1-5. IEEE.
- [15] Qin, D., Leichner, C., Delakis, M., Fornoni, M., Luo, S., Yang, F., & Howard, A. (2025). MobileNetV4: Universal Models for the Mobile Ecosystem. In *European Conference on Computer Vision*. pp. 78-96. Springer, Cham.
- [16] Redmon, J. (2016). You only look once: Unified, real-time object detection. In *Proceedings of the IEEE conference on computer vision and pattern recognition*.
- [17] Redmon, J. (2018). Yolov3: An incremental improvement. *arxiv preprint arxiv:1804.02767*.
- [18] Reis, H. C., & Turk, V. (2024). Potato leaf disease detection with a novel deep learning model based on depthwise separable convolution and transformer networks. *Engineering Applications of Artificial Intelligence*, 133, 108307.
- [19] Ren, S., He, K., Girshick, R., & Sun, J. (2016). Faster R-CNN: Towards real-time object detection with region proposal networks. *IEEE transactions on pattern analysis and machine intelligence*, 39(6), 1137-1149.
- [20] Wang, C.Y., Bochkovskiy, A., & Liao, H. Y. M. (2023). YOLOv7: Trainable bag-of-freebies sets new state-of-the-art for real-time object detectors. In *Proceedings of the IEEE/CVF conference on computer vision and pattern recognition*. 7464-7475.
- [21] Yue, K., Zhang, P., Wang, L., Guo, Z., & Zhang, J. (2024). Recognizing citrus in complex environment using improved YOLOv8n (基于改进 YOLOv8n 的复杂环境下柑橘识别). *Transactions of the Chinese Society of Agricultural Engineering*, 40(8), 152-158.
- [22] Zhang, W., Han Y., Huang, C., & Chen Z. (2022). Recognition method for seed potato buds based on improved YOLOv3-tiny. *INMATEH-Agricultural Engineering*, 67(2), pp.364-373
- [23] Zhao Yue, Zhao Hui, Jiang Yongcheng, Ren Dongyue, Li Yang, Wei Yong. (2022). Potato Leaf Disease Detection Method Based on Deep Learning(基于深度学习的马铃薯叶片病害检测方法). *Journal of Chinese Agricultural Mechanization*, (10), 183-189. doi:10.13733/j.jcam.issn.2095-5553.2022.10.026.

REAL-TIME MECHANICAL FLOWER THINNING EQUIPMENT, CONTROLLED BY ARTIFICIAL INTELLIGENCE

ECHIPAMENT PENTRU RARIREA MECANICĂ A FLORILOR ÎN TIMP REAL, CONTROLAT FOLOSIND INTELIGENȚA ARTIFICIALĂ

Mihai Gabriel MATACHE¹, Robert CRISTEA^{*1}, Ana ZAICA¹, Radu CIUPERCĂ¹, Adrian IOSIF², Gheorghe VOICU²

¹) INMA Bucharest/ Romania;

²) University "POLITEHNICA" Bucharest/ Romania;

Tel: +40 771 717 451; E-mail: robertcri@yahoo.com

DOI: <https://doi.org/10.35633/inmateh-74-77>

Keywords: YOLOv9, apple flowers counting, mechanical thinning, smart horticulture

ABSTRACT

In this paper, the designing and development of a novel mechanical flower thinning equipment, destined to increase the fruit production in orchards, is presented. The system integrates a ZED 3D camera with a dedicated controller for artificial intelligence running a custom trained YOLO9 algorithm, for real-time flower detection and counting. Based on the flower density data, the rotational speed of the thinning rotor is automatically adjusted to achieve the desired thinning ratio. Laboratory tests were conducted to evaluate the efficiency and adaptability of the YOLO9 algorithm to control the equipment in simulated flower density conditions. Results demonstrated potential improvements in thinning accuracy, contributing to optimized fruit development, and reduced manual labor. The proposed equipment offers an innovative approach to orchard management, ensuring sustainable practices by enhancing flower thinning precision while reducing labor costs.

REZUMAT

În această lucrare se prezintă proiectarea și dezvoltarea unui echipament inovator pentru rărirea mecanică a inflorescențelor, destinat creșterii producției de fructe în livezi. Sistemul integrează o cameră 3D ZED cu un controler dedicat procesării programelor de inteligență artificială, care rulează un algoritm antrenat special YOLO9 pentru detectarea și numărarea în timp real a florilor. Pe baza densității florilor, viteza de rotație a rotorului de rărire este reglată automat pentru a obține raportul dorit de rărire. Au fost realizate teste în laborator pentru a evalua eficiența și adaptabilitatea algoritmului YOLO9 de a controla echipamentul în condiții simulate de densitate florală. Rezultatele au demonstrat îmbunătățiri potențiale în ceea ce privește acuratețea răririi, contribuind la optimizarea creșterii fructelor și la reducerea lucrărilor manuale. Echipamentul propus oferă o abordare inovatoare pentru gestionarea livezilor, asigurând practici durabile prin creșterea preciziei răririi florilor și reducerea costurilor cu forța de muncă.

INTRODUCTION

In modern orchard management, mechanical thinning of flowers is essential to optimize fruit production ensuring balanced nutrient allocation and reducing competition among fruits (Smith et al., 2015). Thinning is essential for increasing fruit quality and yield, and several methods have been developed to address this need, including mechanical, manual, and chemical/hormone thinning techniques. Each approach presents distinct advantages and limitations, which are important to consider when selecting a thinning strategy for specific orchard conditions.

Manual thinning is a more traditional approach, often favored for its precision and flexibility. Workers can selectively remove flowers or fruitlets, ensuring that most promising fruits receive enough space and adequate nutrients. However, manual thinning is highly labor-intensive and subject to human error, resulting in inconsistencies and inefficiencies, particularly in large-scale operations (Hernandez et al., 2016). Furthermore, as labor shortages continue to affect agricultural industries globally, reliance on manual thinning becomes increasingly unsustainable (Gomez and Perry, 2019).

Chemical and hormone thinning, using substances like auxins and cytokinins, represents another popular technique for managing flower density. This approach is advantageous because it can be applied over large areas with relatively low labor requirements (Rodriguez et al., 2017).

However, its efficacy is highly dependent on environmental conditions such as temperature and humidity, which could lead to results that are not always as expected (Perez *et al.*, 2018). Besides, the overuse of chemical agents could have negative effects on tree health and on the environment (Huang and Lee, 2020), raising concerns about this method's long-term sustainability.

Mechanical thinning, including the method discussed in this paper, addresses many of the limitations of manual and chemical thinning. By using advanced technologies such as AI-based flower detection and real-time adjustments, mechanical thinning offers high precision and efficiency (Miller *et al.*, 2018). Unlike chemical methods, mechanical thinning does not depend on environmental conditions and avoids the potential ecological risks associated with chemical agents (Jensen and Roberts, 2021). Additionally, it significantly reduces the labor costs associated with manual thinning while providing more consistent results across large orchards (Zhang and Collins, 2019).

In summary, traditional manual thinning methods are labor-intensive and subject to inconsistencies, especially in large-scale orchard operations (Adam and Brown, 2008). Chemical thinning is less labor-intensive but could cause variable results and potential environmental harm. Mechanical thinning methods, particularly with AI enhancements, provide high efficiency and precision without the need for chemicals, making them promising solutions for modern orchard management. Studies have shown that effective thinning, including spatially managed approaches, can optimize crop load distribution, indicating potential benefits of precision strategies in orchard management (Manfrini *et al.*, 2009).

Over-thickened flower clusters can limit the quality and yield of fruits, because they compete for vital resources needed for growth. This fact has driven the demand for automated solutions, which are increasingly being adopted for precision agriculture (Lee *et al.*, 2021).

Latest advancements in automation, particularly the integration of artificial intelligence (AI) and machine learning algorithms, have revolutionized agricultural practices (Kramer *et al.*, 2000). Systems equipped with AI technologies offer real-time decision-making capabilities, enabling more precise interventions in vegetable crops, especially orchard management (Werner *et al.*, 2005; Matache *et al.*, 2022). Recent advancements also illustrate how non-destructive sensing technologies can further improve precision agriculture, integrating real-time data to optimize processes like thinning (Biegert and McCormick, 2024). Object detection algorithms such as YOLO (You Only Look Once) have been proven effective in real-time recognition tasks, including the detection and counting of flowers and fruits (Brown, 2010; Stern and Lars, 2009; Chen *et al.*, 2024). These algorithms, combined with advanced imaging systems like the ZED 3D camera, provide higher accuracy and adaptability in detecting flower clusters under varying conditions (Gonzalez and Turner, 2020).

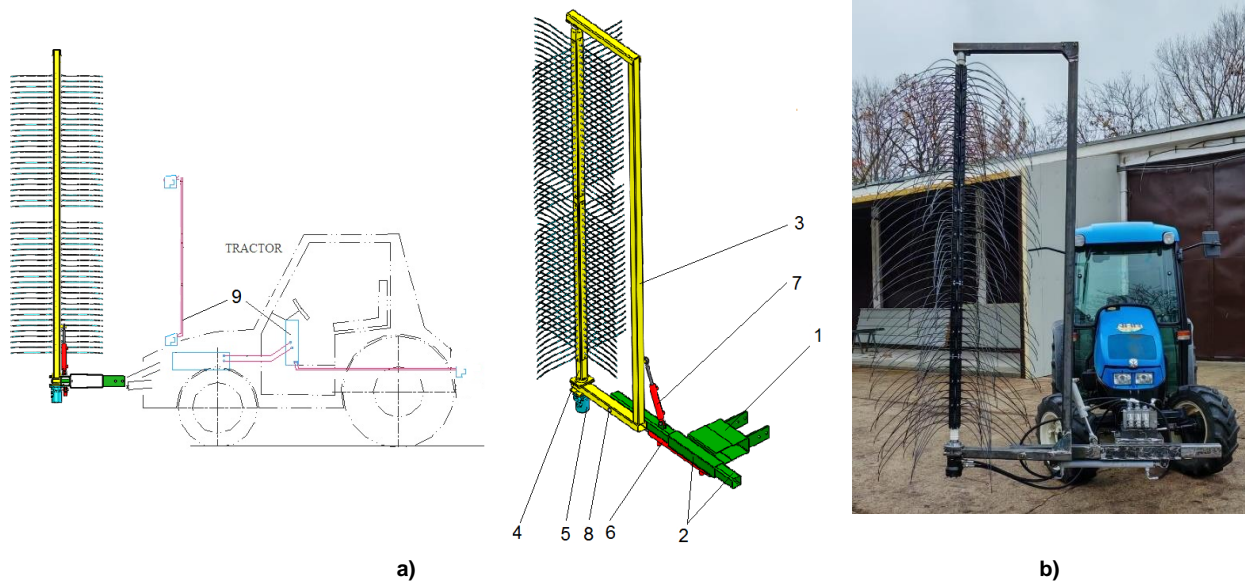
The development of AI-controlled mechanical thinning equipment offers several advantages, including increased operational efficiency, reduced labor costs, and enhanced precision in thinning flower clusters (Miller and Zhang, 2018). These systems ensure optimal thinning, promoting consistent fruit development and improved yields by automatically adjusting the rotational speed of the thinning rotor, based on real-time flower density detection (Lee *et al.*, 2021). Moreover, they contribute to the orchards sustainability, reducing the need for manual labor, which is increasingly scarce in agricultural sectors worldwide (Smith *et al.*, 2015).

This paper presents the design and development of an innovative mechanical flower thinning system that integrates a ZED 3D camera with a custom-trained YOLO9 AI algorithm on an open source dataset of apple flowers. The system was designed to detect and count flowers in real-time, adjusting its thinning action dynamically based on flower density. Laboratory tests were conducted to evaluate the system's accuracy and adaptability under controlled conditions. The results demonstrated potential improvements in thinning accuracy and operational efficiency, offering a promising solution for modern orchard management.

MATERIALS AND METHODS

Technical Equipment for Flower Thinning in Orchards, ERI-0, is designed for the thinning of flower clusters on fruit trees in orchards to optimize fruit development and production. The equipment can be used in orchard farms by commercial entities engaged in orchard maintenance, manufacturers of technical equipment for orchards, dealers, distributors, etc. The technical equipment for flower thinning, symbolized as ERI, performs the mechanical thinning of flower clusters on fruit trees, a necessary operation when the productivity of orchards is reduced because all nutrients are consumed for vegetative growth rather than fruiting. It also aims to reduce the costs of technological operations in plantations.

Figure 1 presents the compenence of the experimental model - technical equipment for flower thinning.



1. Welded support; 2. Guide assembly; 3. Rotor support; 4. Rotor shaft assembly; 5. Hydraulic motor; 6. Hydraulic cylinder, 500 mm stroke; 7. Hydraulic cylinder, 150 mm stroke; 8. Coupling bolt; Flower detection system – ZED 3D camera + controller

Fig. 1 - Technical Equipment for Flower Thinning in Orchards, ERI-0, in aggregate with the working tractor

a) Component elements; b) ERI-0 experimental model

The technical equipment for flower thinning in orchards, ERI, operates in combination with agricultural tractors with a power of approximately 45 HP. The equipment is mounted at the front of the tractor and is driven by its own hydraulic system, which is powered by the tractor's hydraulic outlets.

After coupling the ERI equipment to the tractor, it is transported to the work site. The equipment is raised to the maximum position using the tractor's hydraulic system, and adjustments are made to the rotor's inclination (position 4, fig. 1), the working distance of the rotor relative to the tree crown, and the penetration depth of the rotor equipped with wires. These adjustments are performed by operating the two hydraulic cylinders (positions 6 and 7, fig. 1) of the equipment.

Once these adjustments are made, the hydraulic motor that drives the rotor is connected to the tractor's hydraulic system, and the tractor transmission is initially set to a lower gear. The tractor-ERI unit is then set in motion, performing the flower thinning. Depending on the situation, the speed of movement and the position of the ERI equipment relative to the rows of trees can be adjusted.

The rotational speed of the thinning rotor is continuously and automatically adjusted, controlled by the flower detection system. This system is equipped with an intelligent video camera that records the density of the flower clusters, transmits the information to the analysis system, which then sends commands to the equipment's proportional distributor, thereby varying the rotor's speed. The rotor speed is programmed based on the flower density.

During one pass, the equipment thins half of the tree crown, with the other half being thinned on the return pass.

Main Technical Specifications of the Experimental Model:

- Purpose: for flower thinning
- Type of Equipment: mounted, three-point linkage
- Power Source / Required Power: minimum 45 HP wheel tractor
- Maximum Working Height, mm: 3000
- Height Adjustment, mm: hydraulic
- Oblique Rotor Inclination for Adjusting the Working Angle: approx. 18°
- Equipment Weight, kg: approx. 120
- Minimum Width, mm: approx. 2093
- Maximum Width, mm: approx. 2593

- Length, mm: approx. 875
- Height, mm: approx. 2220

The logical flow of the application for flower counting and controlling the thinning rotor speed follows a continuous cycle, starting from real-time image capture and ending with automatic adjustment of the rotor speed based on flower density.

The process begins with the ZED 3D camera, which captures images of the flowers in the orchard. ZED 3D camera provides enhanced depth perception, allowing for more accurate detection of flower clusters in complex environments like orchards. These raw images are then sent for pre-processing. In this stage, the application automatically adjusts the orientation of the images to ensure correct alignment, resizes the image to 640x640 pixels for compatibility with the YOLO9 model, and applies augmentations such as rotations and exposure adjustments. After the images have been pre-processed, they are sent to the YOLO9 model. The model analyzes the images to identify and count flower clusters. During this analysis, YOLO9 divides the image into grids and makes predictions for each section. If flower clusters are detected, the application proceeds to count them, comparing the identified visual characteristics with the reference patterns in the pre-trained model to ensure accuracy.

Based on the visual analysis results of YOLO model, the application adjusts the rotational speed of the thinning rotor in real-time. If the density of flowers is high, the rotor speed is increased to ensure effective thinning, while a lower density results in a slower rotor speed. This adaptive control mechanism allows the equipment to maintain optimal thinning, promoting balanced fruit development across the orchard.

The entire flow of the application operates in a continuous cycle, capturing images, pre-processing them, analyzing them to count flowers, and adjusting the rotor speed as needed. This ensures an efficient and automated system for managing flower thinning, reducing the need for manual intervention, and optimizing the overall process.

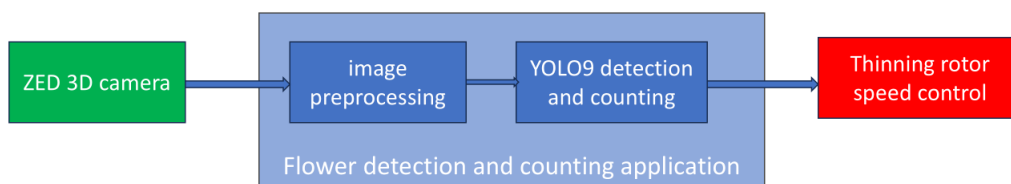


Fig. 2 – Flow diagram of the software application for the thinning equipment control

In order for the YOLO9 model to detect and count the flowers, it was trained using a dataset with pictures of apple flowers (Addineduws, 2024). Training the YOLO9 model involved optimizing the loss function to minimize errors in detecting and counting flower clusters. The model was trained using stochastic gradient descent (SGD) with an initial learning rate of 0.01, a momentum of 0.937, and a weight decay of 0.0005. The batch size was set to 16, and training was conducted for 300 epochs.

The performance of the YOLO9 model was evaluated using several metrics: **Precision (P)**, **Recall (R)**, **mean Average Precision (mAP)**, **inference time**, and **visual assessment**. These comprehensive evaluation metrics ensured a thorough assessment of the model’s performance in counting flowers, enabling reliable and effective control of the rotor speed based on real-time flower density. The calculation of these metrics considered the number of true positive samples (TP), false positive samples (FP), and the total number of samples (N). The **Average Precision (AP)** for each flower cluster category was derived using a specific formula, providing detailed insights into the model's accuracy across different categories.

For apple flowers on trellis systems, required density after thinning aims to balance the tree's capacity to support fruit growth while preventing overloading. Proper thinning typically retains about 5-10 cm of spacing between clusters, which effectively reduces the initial flower density by approximately 70-80%. This practice ensures that about 20-30% of the flowers are left, promoting optimal fruit quality and size (NIAB, 2024; Valent, 2024). This enhances light penetration and air circulation, leading to improved fruit quality.

Fruits spacing and load reduction also help to mitigate risks such as reduced flowering in the following seasons and potential damage to tree limbs (ISHS, 2024).

To correlate the YOLO9 output with the control thresholds for the thinning equipment, an adaptive mechanism was implemented to adjust the rotor's speed based on detected flower density. After analyzing the images captured by the ZED 3D camera, the YOLO9 model provided a real-time count of flower clusters, which was then used to determine the appropriate speed setting for the thinning rotor.

The system was designed around three predefined thresholds corresponding to 50%, 75%, and 100% of the nominal rotational speed, set at 400 rpm. These thresholds were directly linked to specific density ranges, which were set empirically for the purpose of laboratory tests of the equipment:

1. **Low Density:** When the YOLO9 model detected a low number of flower clusters (e.g., 0-10 per frame), the system activated the rotor at 50% speed, or 200 rpm. This ensured minimal thinning where fewer flowers were present.
2. **Medium Density:** For a moderate count (e.g., 11-20 clusters per frame), the rotor speed was adjusted to 75% (300 rpm), allowing more substantial thinning without full intensity.
3. **High Density:** If the model identified a high density of flowers (21 or more per frame), the equipment automatically operated at the maximum 400 rpm to ensure effective thinning across dense clusters.

This setup allowed for continuous real-time analysis in laboratory conditions, where the YOLO9 model was fed with test pictures to monitor the flower density as the equipment simulated the moving along the orchard rows. The control system dynamically adjusted the rotor speed based on the model's output, creating a simulated thinning process. This was done through a variable command signal for the hydraulic proportional valve which controlled the hydraulic motor.

The simulation tests were designed to evaluate how effectively the mechanical flower thinning equipment could adapt to different scenarios by using real-time data from the YOLO9 model. The laboratory tests aim was to see how well the system adjusted the rotor speed based on varying flower densities detected in the orchard.

Four distinct scenarios were set up to represent low, medium (usually met in orchards, 2 scenarios), and high flower densities, each testing the equipment's adaptive control mechanism.

- **Scenario 1: Low Density** In the first test, the YOLO9 model detected a low number of flower clusters, specifically 5 clusters, which was categorized as a low-density situation. Based on this input, the control system set the rotor speed to 200 rpm, or 50% of the nominal speed of 400 rpm. This ensured minimal thinning, which was appropriate for areas where fewer flowers were present, preventing over-thinning.
- **Scenario 2: Medium Density** The second scenario simulated a moderate density, with the YOLO9 model identifying 15 flower clusters per frame. This was classified as medium density, prompting the system to adjust the rotor to 300 rpm, or 75% of the nominal speed.
- **Scenario 3: High Density** In the third test, a high-density scenario was simulated. The YOLO9 model detected 25 flower clusters, indicating a dense area that required more intensive thinning. The control system responded by setting the rotor to its maximum speed of 400 rpm, ensuring thorough thinning across the dense clusters.
- **Scenario 4: Medium Density Revisited** The final scenario revisited a medium-density situation, where the YOLO9 output showed 18 clusters. As with the earlier medium-density test, the system adjusted the rotor speed to 300 rpm, providing a consistent thinning performance.

To simulate the presence of flowers on branches, artificial markers representing flower clusters were placed in the lab setup, for the 4 scenarios. These included, bright pink and white colored stickers mimicking the size and positioning of real flower clusters. The YOLO9 model detected these markers, and the equipment responded as if they were actual flowers. After the thinning operation, the remaining markers were counted to verify the thinning efficiency.

The laboratory tests involved capturing "before" and "after" images during the simulation. By comparing the number of markers detected by YOLO9 before the equipment was activated and after the thinning process, the percentage of simulated flower clusters removed was calculated. Efficiency was assessed using a simple formula:

$$TE (\%) = \frac{NBT - NAT}{NBT} \quad (1)$$

where:

TE – thinning efficiency, *NBT*- number of detected clusters before thinning,
NAT – number of detected clusters after thinning.

Through this laboratory-based approach, the effectiveness of the thinning equipment was tested even in the absence of flowering trees. This method provided a comprehensive evaluation of the system’s performance, ensuring it was ready for real-world deployment during the flowering season.

RESULTS

The YOLOv9c model was trained on a laptop ASUS ROG Strix SCAR 18, G834JY-N6046X, 18-inch, QHD+ 16:10 (2560 x 1600, WQXGA), 13th Gen Intel® Core™ i9-13980HX Processor 2.2 GHz (36M Cache, up to 5.6 GHz, 24 cores: 8 P-cores and 16 E-cores), with NVIDIA® GeForce RTX™ 4090 graphic card and DDR5 64GB RAM, on UBUNTU 22.04.4 LTS operating system. The software environment comprised PyTorch 2.0.0, Cuda 11.8, Cudnn 8.6.0, and Python 3.8.

In figure 1, the confusion matrix created after model training is presented.

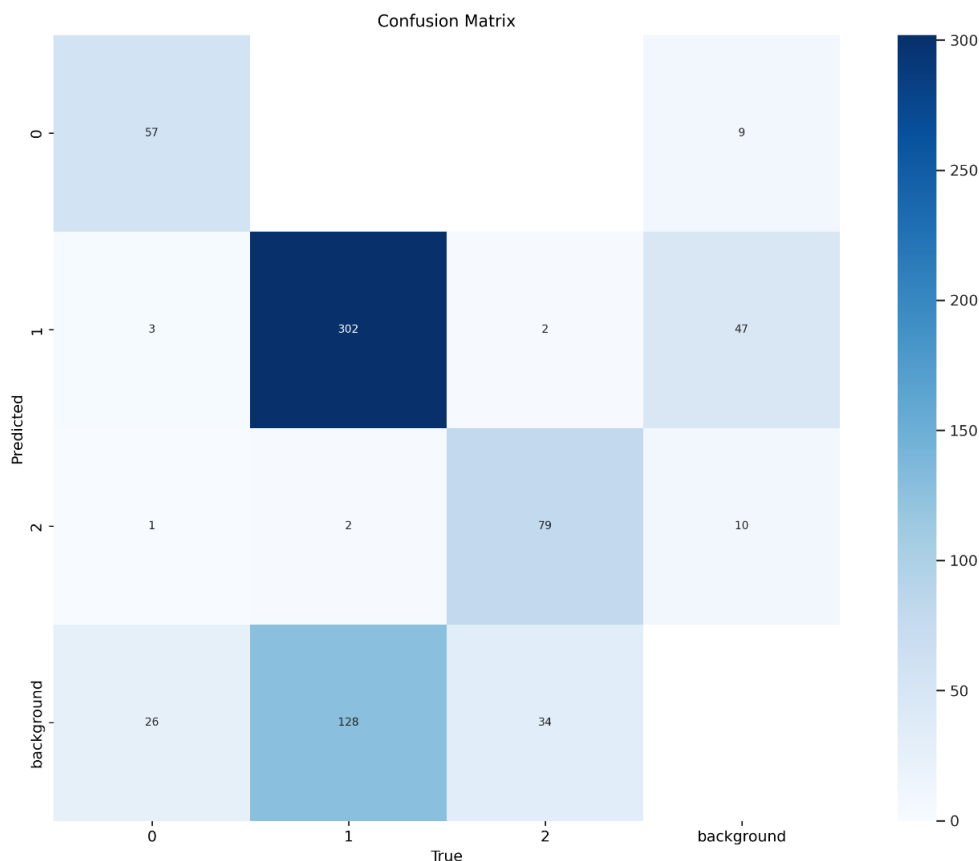


Fig. 3 – Confusion matrix after YOLO9c training

The confusion matrix offered valuable information about the performance of the model across different flower-related classes. The dataset included three main classes: bud (Class 0), flower (Class 1), and middle (Class 2), along with a category for background elements. For the **Class 0 – Buds**, the model showed a reasonable ability to identify buds, correctly classifying 57 instances. However, there were some misclassifications, with 9 buds incorrectly labeled as background. This suggests that while the model was able to recognize the features of buds effectively, there was still some confusion, likely due to overlapping characteristics or background elements that closely resembled buds. Flowers, classified as Class 1, were the most accurately detected, with 302 instances correctly identified. This high true positive rate indicates that the model learned to distinguish flowers effectively. However, there were still a few misclassifications: 3 were mistaken for buds (Class 0), 2 for the middle section (Class 2), and 47 were classified as background. The relatively high number of misclassifications as background suggests that, in certain situations, the model might have struggled to differentiate flowers from non-floral elements, possibly due to environmental noise or the complexity of the scene. The middle sections of the flower, or Class 2, were recognized with moderate success, with 79 instances correctly classified. There were minor misclassifications: 1 instance was mistaken for a bud, 2 for flowers, and 10 were labeled as background.

These errors indicate that the model could be facing challenges in distinguishing the middle parts, which might require more training data or clearer feature separation from other classes. The background category experienced significant misclassifications. Although 34 instances were correctly recognized as background, there were considerable errors where background elements were incorrectly labeled: 26 as buds, 128 as flowers, and 34 as the middle section. The high misclassification rate, particularly with flowers, suggests that the model may over-detect objects, interpreting random patterns or elements in the background as flowers. This could point to a need for further training to improve background discrimination or to refine the dataset with more diverse background examples. In table 1 are presented the metrics obtained after model training.

Table 1

Metrics obtained for the trained model	
Metrics	YOLOv9c
Precision – P (%)	0.8306
Recall – R (%)	0.6861
F1-score (%)	
mAP50 (%)	0.7803
mAP50-95 (%)	0.4861
Inference time	1.1ms preprocess, 64.5ms inference, 0.8 ms postprocess per image at shape (1, 3, 512, 640)

The performance metrics obtained from the YOLOv9c demonstrate strong precision and solid average precision, but they also highlight areas for potential improvement.

Precision was high at 83.06%, indicating that the model accurately identified buds, flowers, and middle sections without many false positives. This level of precision is important for ensuring that the thinning equipment responds correctly to actual flower clusters, avoiding unnecessary adjustments based on incorrect detections. However, the **recall rate**, at 68.61%, was a little bit lower, meaning that the model missed some instances that should have been detected. Improving recall would help ensure that no significant clusters are overlooked during the thinning process. The model's performance was also reflected in the **mean Average Precision (mAP50)** score of 78.03%, which describe its reliability in detecting and localizing flower components across different conditions. A score above 75% indicates that the model has learned to generalize well, effectively recognizing objects even in complex scenarios. However, the **mAP50-95 score**, which was 48.61%, was low. This metric considers a wider range of intersection over union (IoU) thresholds, highlighting that the model's localization accuracy could still be improved. Still, for our equipment which has a more general approach on the all vertical side of the tree, this metric value is acceptable. In terms of **inference time**, the model demonstrated impressive efficiency, with 1.1 ms for preprocessing, 64.5 ms for inference, and 0.8 ms for post-processing per image. These quick processing times indicate that the system can operate in near real-time, which is essential for the adaptive control of the thinning equipment. This speed allows the equipment to respond dynamically to changes in flower density, ensuring smooth and consistent thinning.

In figure 4 are presented the results obtained by YOLOv9c model after it was fed the test images with various instances of apple flowers. The results displayed in the image represented the outcomes of the YOLO model after training, showing how effectively the model was able to detect and classify different components of apple flowers. The bounding boxes in the images indicated where the model detected instances of each class, providing a visual representation of its performance. YOLO model demonstrated a strong capability to identify and differentiate between buds, flowers, and middle sections. In many cases, the bounding boxes accurately and tightly surrounded the relevant objects, highlighting that the model had learned to localize these features effectively. For example, the buds (Class 0) were consistently detected in images showing early-stage flowers, and full blooms were correctly identified as flowers (Class 1). This indicated that the model could reliably classify each class across different scenarios. The detection was observed to be consistent across multiple environmental conditions, including different lighting scenarios and varied backgrounds, proving that the training process, which included data augmentation, helped the model generalize well. Even in more complex scenes, where flower clusters were dense, the model was able to identify multiple instances of flowers, showing it could handle scenarios with close-packed objects. Despite the overall strong performance, there were some instances where the model misclassified objects or incorrectly labeled them. For example, in certain images, buds might have been mistakenly classified as middle sections, or the bounding boxes overlapped significantly, suggesting the model sometimes struggled to distinguish overlapping features. These issues pointed to areas where further fine-tuning could improve accuracy, especially in distinguishing subtle differences between classes.



Fig. 4 – Identification results after YOLO9c training

To evaluate the performance and adaptive capabilities of the mechanical flower thinning equipment, a series of simulation tests were conducted under controlled laboratory conditions. Given the absence of flowering trees during the testing period, the system was tested using bright pink and white colored stickers mimicking the size and positioning of real flower clusters. In table 2 are presented the results observed during these tests, highlighting the equipment's ability to adapt to different levels of flower density.

Table 2

Simulation tests for the system functioning

Test Scenario	Detected Flower Clusters (YOLO9 output)	Density Classification	Rotor Speed Setting (rpm)	Thinning Efficiency (%)	Comments
Scenario 1	5	Low density	200	30	Minimal thinning, suitable for low-density sections.
Scenario 2	15	Medium density	300	60	Moderate thinning, appropriate for medium-density areas.
Scenario 3	25	High density	400	90	Maximal thinning, effective in dense flower clusters.
Scenario 4	18	Medium density	300	65	Consistent thinning achieved for medium-density patches.

The simulation tests demonstrated that the adaptive control system of the thinning equipment could effectively adjust rotor speeds based on real-time flower density data from the YOLO9 model. The system responded appropriately across different scenarios, from low to high-density areas, ensuring that the thinning process was efficient and precise. By fine-tuning the rotor speed to match the detected flower density, the equipment was able to optimize thinning, promoting uniform fruit development and reducing the need for manual intervention.

CONCLUSIONS

The development and testing of the mechanical flower thinning equipment demonstrated the potential of using artificial intelligence to enhance precision and efficiency in orchard management. The integration of a ZED 3D camera and the YOLO9 model enabled real-time detection and counting of flower clusters, providing accurate data to control the thinning process in an adaptive manner. Laboratory simulations showed that the system effectively adjusted rotor speeds based on detected flower densities, ensuring consistent thinning across various scenarios.

The results indicated that the adaptive control mechanism could reliably manage low, medium, and high-density flower clusters by setting appropriate rotor speeds, from minimal thinning at 200 rpm to maximum thinning at 400 rpm. This feature is mandatory for maintaining optimal flower spacing, promoting uniform fruit development, and reducing the need for manual intervention. Furthermore, the YOLO9 model achieved a high degree of accuracy in identifying and classifying apple flower components across various conditions. While the model performed well, some misclassifications, especially concerning background elements, suggested that further refinements could enhance performance. Expanding the dataset to include more diverse environmental conditions and refining the model's ability to differentiate overlapping features would likely reduce errors and improve reliability.

This study has shown that AI-enhanced mechanical thinning equipment can be a promising solution for modern orchard management, offering a balance of precision, adaptability, and efficiency. Future developments should focus on real-world field testing during the flowering season to validate laboratory results, and fine-tuning the system to address any challenges that arise under natural conditions. This approach will help ensure that the technology is ready for practical deployment, enabling sustainable and cost-effective orchard practices.

ACKNOWLEDGEMENT

This work was supported by a project of the Ministry of Research, Innovation and Digitization, through Program NUCLEU - Project: PN 23 04 01 05 - Innovative technology for the maintenance of fruit plantations, contract no. 9N/ 01.01.2023.

REFERENCES

- [1] Adam J., Brown P. (2008). Advances in Orchard Management Technologies. *Journal of Agricultural Innovation*. vol. 5, no. 2, ISSN 1234-5678, pp. 112-120.
- [2] Addineduws. (2024). Apple Flower 7 237 Dataset. Open Source Dataset, Roboflow Universe, *Roboflow*, Available at: https://universe.roboflow.com/addineduws/apple_flower_7_237.
- [3] Biegert K., McCormick R.J. (2024). Non-destructive sensors and modelling to detect apple fruit and tree properties, *Acta Horticulturae*, International Society for Horticultural Science. DOI: 10.17660/ActaHortic.2024.1395.12.
- [4] Brown P. (2010). Real-Time Detection in Agricultural Systems. *Transactions of the Agricultural Engineering Society*. vol. 9, no. 1, ISSN 9876-5432, pp. 55-63.
- [5] Chen Y., Niu Y., Cheng W., Zheng L., Sun D. (2024). Apple detection method in the natural environment based on improved YOLOv5. *INMATEH Agricultural Engineering*, vol. 72, no.1, pp. 183-192.
- [6] Gomez J., Perry M. (2019). Labor Challenges in Fruit Production: A Global Perspective. *Journal of Agribusiness Management*. vol. 17, no. 3, ISSN 1234-5678, pp. 220-230.
- [7] Gonzalez J., Turner K. (2020). Machine Vision for Precision Agriculture: A Comprehensive Review. *Journal of Automation in Agriculture*. vol. 18, no. 3, ISSN 6543-8765, pp. 45-60.
- [8] Hernandez P., Foster L., Kim S. (2016). Manual Thinning Practices in Modern Orchards, *Agricultural Labor Studies*, vol. 12, no. 1, ISSN 9876-5432, pp. 100-110.

- [9] Huang Z., Lee A. (2020). Environmental Impact of Chemical Thinning Agents in Fruit Orchards, *Journal of Agricultural Sustainability*, vol. 15, no. 4, ISSN 6543-8765, pp. 300-315.
- [10] ISHS (2024). Influence of Tree-Adapted Flower Thinning on Apple Yield and Fruit Quality, *International Society for Horticultural Science*, Available at: <https://www.ishs.org>
- [11] Jensen A., Roberts M. (2021). Advances in Mechanical Thinning Technologies for Fruit Orchards, *International Journal of Agricultural Robotics*, vol. 9, no. 2, ISSN 8765-4321, pp. 145-160.
- [12] Kramer H., Werner L., Smith R. (2000). Mechanized Flower Thinning: A Review of Methods, *Journal of Orchard Systems*, vol. 11, no. 4, ISSN 8765-4321, pp. 178-186.
- [13] Lee J., Chang R., Li S., (2021), Advances in Autonomous Systems for Orchard Management, *Journal of Agricultural Robotics*, vol. 14, no. 2, ISSN 3456-7890, pp. 25-40.
- [14] Manfrini L., Taylor J.A., Grappadelli L.C., (2009), Spatial analysis of the effect of fruit thinning on apple crop load, *European Journal of Horticultural Science*, 74(2), pp. 54-60.
- [15] Matache M., Marin F., Gurau C., Gurau G., Marin M., Gageanu I., Ionescu A., (2022), Neural network testing for spot-application of phytosanitary substances in vegetable crops using a self-propelled electrical sprayer, *INMATEH Agricultural Engineering*, vol. 68, no.3, pp. 471-480.
- [16] Miller D., Zhang X., (2018), AI-Powered Orchard Management Systems: Precision and Efficiency, *Proceedings of the International Conference on Agricultural Engineering*, vol. 12, ISSN 1234-5678, pp. 105-115.
- [17] Miller P., Zhang X., (2018), Automated Systems for Orchard Management: A Comprehensive Review, *Agricultural Systems Journal*, vol. 13, no. 1, ISSN 5432-2109, pp. 55-70.
- [18] NIAB, (2024), *Apple Best Practice Guide*, NIAB Publications, Available at: <https://applegrowing.niab.com>
- [19] Perez J., Rodriguez L., Alvarez F., (2018), The Role of Environmental Factors in the Success of Chemical Thinning Applications, *Agricultural Science Review*, vol. 22, no. 2, ISSN 7654-3210, pp. 140-150.
- [20] Rodriguez L., Perez J., Alvarez F., (2017), Chemical Thinning in Apple Orchards: A Review, *Journal of Horticultural Science*, vol. 21, no. 3, ISSN 9876-4321, pp. 210-220.
- [21] Smith P., Zhao Y., Han Q., (2015), Orchard Mechanization and the Future of Fruit Production, *Agricultural Systems Review*, vol. 22, no. 1, ISSN 8765-3210, pp. 34-48.
- [22] Stern A., Lars B., (2009), Automation in Fruit Production: A New Frontier, *Proceedings of the International Symposium on Agricultural Robotics*, vol. 7, ISSN 8765-3210, pp. 90-100.
- [23] Valent, (2024), Apple Thinning is Science and Art: How to Create a Plan, *Valent Grower Insights*, Available at: <https://www.valent.com>
- [24] Zhang H., Collins P., (2019), AI-Enhanced Mechanical Thinning Systems: A Field Study, *Journal of Smart Agriculture*, vol. 16, no. 4, ISSN 6543-1234, pp. 115-125.
- [25] Werner L., Stern A., Kramer H., (2005), Precision Thinning Using Machine Vision and AI, *Journal of Automated Agricultural Systems*, vol. 8, no. 3, ISSN 6543-2109, pp. 200-210.

DEVELOPMENT OF FOGPONICS CULTIVATION SYSTEM FOR MICROGREENS WITH INTERNET OF THINGS MONITORING SYSTEM AND MACHINE LEARNING AUTOMATION

/

PAGLINANG NG SISTEMA NG FOGPONICS PARA SA PAGTATANIM NG MGA MICROGREENS NA MAY SISTEMA NG PAGSUBAYBAY SA PAMAMAGITAN NG INTERNET OF THINGS AT AWTONASYON NG MACHINE LEARNING

Jamal Omar S. SARANGANI¹⁾, Carolyn Grace G. SOMERA-ALMEROL^{*2)}, Marvin M. CINENSE²⁾,
Khavée Augustus W. BOTANGEN³⁾

¹⁾ Department of Agricultural and Biosystems Engineering, College of Engineering,
Central Luzon State University, Science City of Muñoz, Nueva Ecija, Philippines

²⁾ Faculty of Department of Agricultural and Biosystems Engineering, College of Engineering,
Central Luzon State University, Science City of Muñoz, Nueva Ecija, Philippines

³⁾ Faculty of Department of Information Technology, College of Engineering,
Central Luzon State University, Science City of Muñoz, Nueva Ecija, Philippines

Corresponding Author: Carolyn Grace G. Somera-Almerol; E-mail: cggsomera@clsu.edu.ph

DOI: <https://doi.org/10.35633/inmateh-74-78>

Keywords: Fogponics, Microgreens, Machine Learning, Internet of Things

ABSTRACT

New technologies are emerging every day to improve the productivity of food production to meet rising demands. Microgreens have gained popularity nowadays and are known for being nutritious and easy to cultivate. Fogponics is one of the emerging technologies that atomizes the nutrient solutions into fine mist, improving the oxygenation and reduces water usage that lacks from traditional farming methods. The study developed an automated fogponics system for microgreens production using machine learning automation and internet of things monitoring systems. The model's evaluation output proves that the system is reliable and capable of predicting an appropriate direction given the datasets acquired from temperature and humidity while the plants are thriving over time. The system has successfully reduced the temperature fluctuation ranging from 26°-33°C to 27°-30°C and stabilized humidity levels from 75-100% to 90-96%. As a result, the performance of the model effectively yielded the microgreens to flourish in its environmental parameters by incorporating machine learning automation and IoT-based monitoring systems. This study strengthened the importance of contributing a promising alternative for sustainable microgreens production. This prototype represents its significant advancement in agricultural strategies for indoor microgreens cultivation, offering a potential alternative for efficient and scalable production.

ABSTRAK

Araw-araw may mga makabagong pamamaraan sa pagtatanim ang umuusbong upang mapabuti ang produksyon ng pagkain para matugunan ang tumataas na pangangailangan nito. Ang microgreens ay nagiging popular ngayon dahil sa taglay na sustansya at madaling paraan ng pagtatanim. Ang fogponics ay isa sa mga umuusbong na teknolohiya na mekanismong pagkontrol para sa awtomasyon ng nutrient solution sa pamamagitan ng usok, ito ay nakakatulong upang mapabuti sa oxygenation at mababang pagkonsumo ng tubig na kulangan sa mga tradisyunal na pamamaraan ng pagsasaka. Ang layunin ng pananaliksik na ito ay bumuo ng automated fogponics system para sa produksyon ng microgreens, gamit ang machine learning automation at internet of things monitoring systems. Ang resulta sa pagsusuri ng modelo ay napatunayan na ang sistema ay may kakayahan upang malaman ang angkop na direksyon batay sa mga datos na nakalap mula sa temperatura at halumigmig habang ang mga halaman ay simisibol. Ang sistema ay matagumpay na napanatili ang pagbabagu-bago ng temperatura mula 26°C-33°C naging 27°C-30°C at napanatili ang antas ng halumigmig mula 75%-100% naging 90%-96%. Bilang resulta, ang prototype ay epektibong nakapag-ani ng microgreens na yumabong sa pamamagitan ng pagsasama ng machine learning automation at IoT-based monitoring systems. Ang prototype na ito ay kumakatawan sa makabuluhang pag-aambag sa pag-unlad ng mga estratehiya sa agrikultura para sa indoor microgreens cultivation, may potensyal bilang alternatibong pamamaraan para sa mahusay at pangmalakihang produksyon.

INTRODUCTION

In 2017, the Food and Agriculture Organization (FAO) projected that the global population could reach 10 billion by 2050, representing a 34% increase from where it is now. Consequently, global food production must increase by 70% by 2050 to meet this demand. While population growth undeniably contributes to the rising demand for food, its impact is further intensified by shifts in consumption patterns. This connection between emerging food demands highlights the necessity for innovative approaches to agricultural production, particularly in addressing both the quantity and quality of the food supply. To address this growing need for more and better food, it is crucial to intensify and industrialize agricultural practices while also maximizing the efficiency of water and other resources.

Microgreens are gaining popularity nowadays due to their nutraceutical potential, ease of cultivation, year-round availability, and culinary versatility (Jambor *et al.*, 2022). These young plants provide higher nutraceutical benefits than their mature counterparts due to their delicate texture, distinctive tastes, and excellent quantity of different nutrients (Xiao *et al.*, 2012). Microgreens are cultivated and harvested before their true leaves emerge; they are usually harvested when they reach the height of 1 – 3 inches or between 5 – 21 days after germination. It should not be confused with sprouts and baby greens. Unlike sprouts, which are grown without light and harvested earlier, or baby greens, which are harvested between 20 – 40 days, microgreens offer unique advantages (Partap *et al.*, 2023).

Various cultivation systems and growing media have been studied for microgreens farming, including soil and soilless cultivation systems and alternative growing medium (Eswaranpillai *et al.*, 2023; Gunjal *et al.*, 2024). Understanding of the most commonly used cultivation system for microgreen farming is gained from the work of Paglialunga *et al.* (2023), who shed light on the significance of soil-less or hydroponics cultivation system. Although the hydroponics cultivation system has advantages in growing microgreens, it also has drawbacks such as mold and yeast development due to overexposure of seeds to the nutrient solution and inadequate air circulation (Li *et al.*, 2021; Ocho Bernal *et al.*, 2023). These issues can be mitigated by using an aeroponics cultivation system, which enhances oxygenation and water efficiency by spraying nutrient solutions directly onto the seeds or roots. It expedites the delivery of nutrients up to 135% for emitting droplets compared to the latter (Eka Putri *et al.*, 2023).

On the other hand, a gentler nutrient delivery mechanism is imperative to cultivate microgreens to yield its optimal growth. The ultrasonic aeroponics or simply fogponics cultivation system manages these matters by atomizing the nutrient solution into a fine fog. It rests on the notion that the maximum particle capacity for a plant's nutrient absorption is between 1 – 25 micrometers in size (Gandham *et al.*, 2022) whereas, this process fosters improved growth of the plants as it robust absorption of nutrients through its roots (Gao *et al.*, 2016; Lakhier *et al.*, 2018). Thereby, fogponics cultivation system was found to significantly minimizes consumption of water up to 50% (Al-Kodmany, 2018).

In spite of the existing advantages, various factors can affect the ability of the plant to thrive through its process (Abbasi *et al.*, 2024). This method also poses challenges for the need to maintain adequate nutrient absorption and manage root zone temperature as well. Thus, appropriate management of nutrient solution and parameters such as light intensity, temperature, and humidity is essential for a successful cultivation especially when conducting the fogponics cultivation system (Lakhier *et al.*, 2018).

Managing laborious tasks in agriculture is evident in the possibilities for enhancement made by integrating emerging technologies like machine learning-based automation and IoT monitoring systems. Furthermore, to yield the ideal growth of the plant, algorithms of machine learning optimize actuator settings. The work of Ardiansah *et al.* (2023) provides valuable insights into IoT monitoring systems, in which it facilitates real-time monitoring by overseeing its sensors, environmental conditions, and transmitting the data straight to the cloud. It also enables users to access the recorded readings of sensors through the application or the internet (Ardiansah *et al.*, 2022). In the study of Sarmphim *et al.* (2022), the researchers use Blynk application as an IoT for accessing sensor data and as an automation. Blynk application is an IoT platform that is user-friendly that can be access via smartphones.

This study aims to develop a prototype fogponics system design to establish productive indoor cultivation of microgreens by leveraging machine learning automation to optimize environmental conditions and resource usage, and IoT monitoring system to provide real-time data. Given the expressed significance to address the challenges encountered in traditional farming such as resource inefficiency and limited scalability, it is pertinent to explore such factors to contribute to a more sustainable and productive agricultural practices.

MATERIALS AND METHODS

In the development of automated fogponics system for microgreens, the researchers split the methodology into data gathering phase and training and validation phase. Data gathering phase is where the system is built and the data is collected for the training of the machine learning model. On the other hand, the training and validation phase is where the model is trained and subsequently the fogponics system is tested to assess the model's effectiveness.

Main setup

The automated fogponics system for microgreens consists of two containers namely nutrient tank and the growing box, along with a mainframe, LED lights, a power supply, and a control system (see Fig. 1). The nutrient tank, constructed from a plastic container, includes an ultrasonic fogger, blower fan, and water level sensor. It creates and transfers the atomized nutrient solution to the growing box. The growing box contains a seedling tray for holding seeds and the nutrient solution. The mainframe is built from PVC pipes and fittings. It supports the LED light, control system, and power supply. Meanwhile, the control system features a microcontroller that operates actuators and gathers sensor data, while the microprocessor interprets this data to predict actuator combinations; the Blynk application enables real-time monitoring, data logging, and machine learning model development.

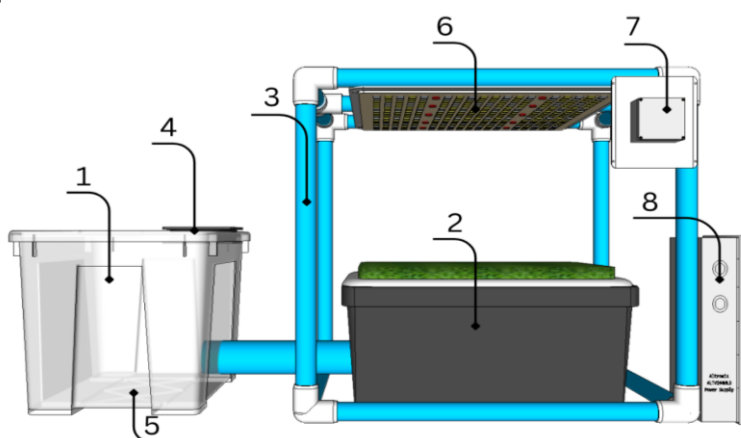


Fig. 1 - Fogponics system setup

1 - nutrient tank, 2 - seedling box, 3 - main frame, 4 - fan, 5 - ultrasonic fogger, 6 - LED light, 7 - control system, 8 - power supply

Circuit Diagram

Fig. 2 provides the comprehensive control and power circuit diagram of the study powered by ESP32 microcontroller. The ESP32 receives the data from the water level sensor, light sensor, and temperature and humidity sensor. The microcontroller ensures the interaction between various sensors and actuators. It uses a relay module to control the fogger and blower and uses PWM for adjusting the brightness of LED light. The buck converter provides needed voltages for the control system.

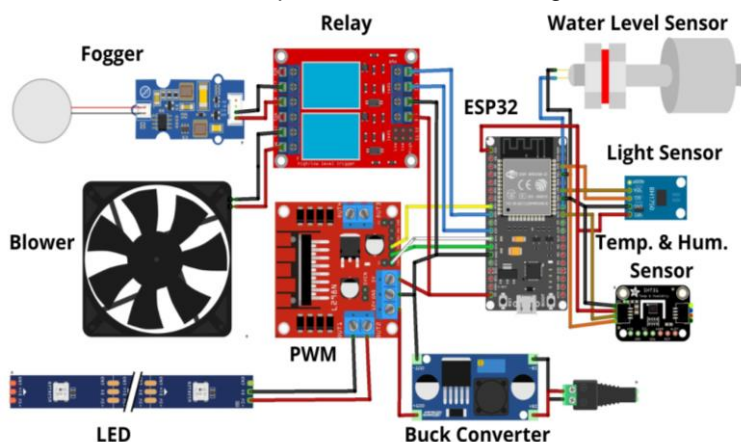


Fig. 2 - Control and power circuit diagram

Control System Diagram

In Fig.3A, the control system acquires data from actuators and sensors while the fogponics system operates, turning actuators on and off based on a researcher-set frequency.

A microcontroller, interfaced with various sensors and actuators, manipulates environmental conditions effectively. The Blynk application offers a user interface for monitoring, controlling the system, visualizing data, and logging data for machine learning model training.

Meanwhile, Fig.3B illustrates system automation, integrating both the microprocessor and microcontroller. The microcontroller, connected to sensors like temperature, humidity, light, and water level, gathers real-time data, relayed to the microprocessor for processing and decision-making. The microcontroller also controls actuators such as the blower, ultrasonic fogger, and LED lights. Additionally, the Blynk application provides a user interface for data visualization and manual system control.

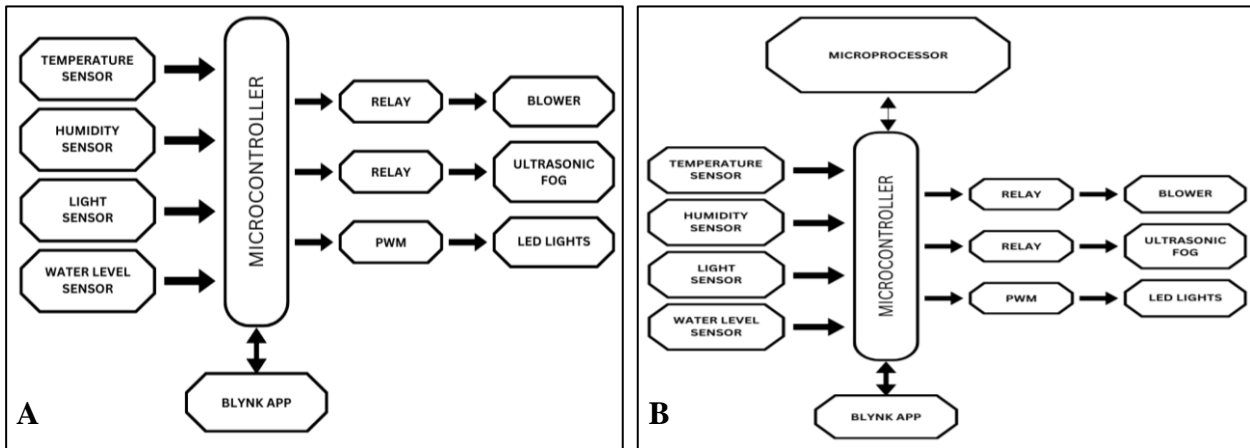


Fig. 3 - Control system diagram

System Flow Diagram

The Fig. 4A illustrates the phase 1 system flow diagram, starting with system initialization. The system includes the Blynk application which allows manual control of actuators, real-time data visualization, data logging, and simple automation. The microcontroller manages the actuator control and sensor data.

On the other hand, Fig. 4B depicts the phase 2 system flow diagram for automated fogponics systems, integrating both automated and manual controls. This phase is divided into microprocessor, microcontroller, and Blynk application subsystems. The process begins with component initialization. The microprocessor requests data from Blynk, processes it, and predicts necessary actions for the system. These actions are then communicated to the microcontroller, which controls the actuators and sensor reading. The application provides manual override capabilities, data visualization, and logging for real-time monitoring of system performance and environmental conditions.

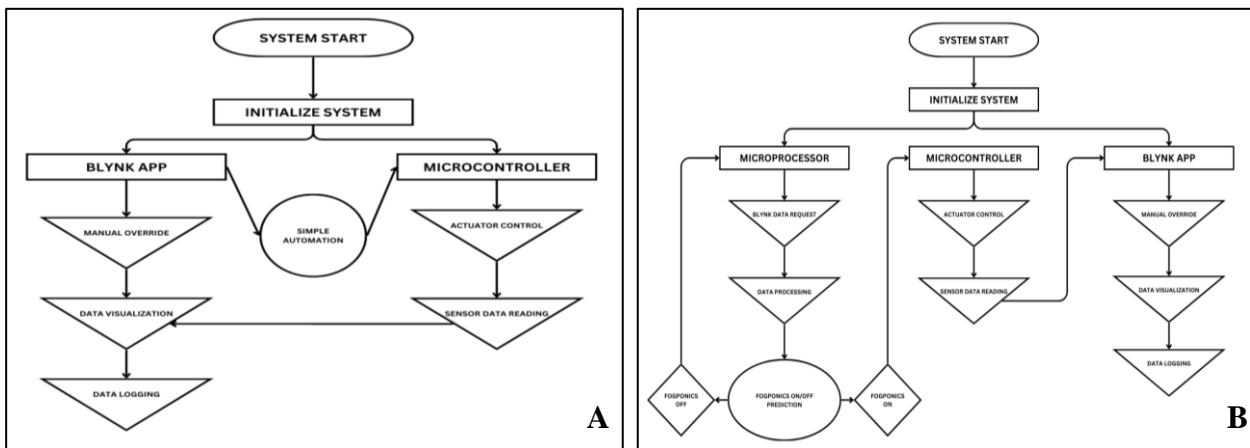


Fig. 4 - System flow diagram

Machine Learning Model

After gathering data in phase 1, it undergoes cleaning and processing using Python. K-means clustering algorithm is used to categorize environmental data and set controls for the fogponics system. Normalization is performed by subtracting the mean and dividing by the standard deviation of each feature, ensuring equal feature contribution to the clustering process. The model is then fitted with the normalized data, assigning each data point to one of two clusters: 1 for system "ON" or 0 for system "OFF." The processed data is saved to a CSV file for training the automation model.

The next step is the model training, where the random forest regression is used as a machine learning algorithm. During the training phase, it generates many decision trees. In order to measure a random subset of characteristics in each partition, a random subset of the data set is used to construct each tree. The combination of multiple decision trees makes it a stable and accurate prediction model.

Model Validation

The validation of accuracy and performance of the model is requisite to ensure the effectiveness of the model in predicting the values derived from the datasets. Thus, different methods are used to validate the model. Whereas, the data is split into 80% training data and 20% test data of the whole datasets. The training data is used to train the model while the test data is used to validate the model. The accuracy of the model is validated using metrics such as Precision, Recall, and F1-Score. On the other hand, the reliability of the model is validated using Root Mean Squared Error (RMSE) and R-squared (R^2).

Root Mean Squared Error (RMSE)

Prediction error metrics like Root Mean Squared Error (RSME), is the square root of MSE. It gives an approximation of the average variations between the predicted and actual results in the dataset.

$$RSME = \sqrt{\frac{1}{n} \sum_{i=1}^n (y_i - \hat{y}_i)^2} \quad (1)$$

where:

n denotes number of observation, y_i represents the actual value of i^{th} observation, and \hat{y}_i implies the predicted value of the i^{th} observation.

R-squared (R^2)

R-squared (R^2) measures how well the model explains how much variation of a dependent variable is explained by an independent variable in a regression model. Values closer to 1 means better model fit.

$$R^2 = 1 - \frac{RSS}{TSS} \quad (2)$$

where:

$R^2 = \text{coefficient of determination}$ denotes the coefficient of determination, RSS represent the sum of squares of residuals, and TSS stands for total sum of squares.

Precision

Accuracy metrics like Precision evaluate the accuracy of the ratio of true positive predictions to the total of predicted positives.

$$\text{Precision} = \frac{\text{True Positives}}{\text{True Positives} + \text{False Positives}} \quad (3)$$

Recall

Recall is measuring the model's ability to recognize the positive instances. It is solved as the ratio of true positive predictions to the total actual positives.

$$\text{Recall} = \frac{\text{True Positives}}{\text{True Positives} + \text{False Negatives}} \quad (4)$$

F1 Score

F1-Score on the other hand, is the harmonic mean of precision and recall. It is solved using this formula.

$$F1 \text{ Score} = 2 \times \frac{\text{Precision} \times \text{Recall}}{\text{Precision} + \text{Recall}} \quad (5)$$

RESULTS

Data Distribution

The Fig. 5A illustrates the data distribution of the state of temperature and humidity data during the data gathering phase of the study. Most of the temperature data clusters toward the middle range, with most values being around 28°C. The normal distribution of the temperature data is beneficial in training the machine learning model, this data helps the algorithm to process and learn the data efficiently. The baseline for predicting the average temperature conditions is due to the concentration of temperature at 28°C. While the humidity data is showing a heavily skewed distribution towards higher values. The data of humidity depicts values ranging from 75 to 100%, with 100% being the most frequent. This skewed distribution can influence the prediction accuracy of the model in humidity.

Consequently, Fig. 5B presents the distribution of temperature and humidity data when the machine learning model was applied to the system. The temperature histogram displays a more uniform distribution, with values ranging from 26.5°C to 30°C and a recurring value of 27.5°C. The temperature data reveals a steadier distribution, having a periodic value of 27.5°C. It shows the notable disparity in temperature compared to the initial data. Meanwhile, the humidity histogram shows a broader range from 84% to 98%, with the most frequent value around 94%. The humidity graph has shown a significant change in the distribution of data. The humidity data is showing a much stable distribution, with values ranging from 84% to 98%.

The shown data indicates the effectiveness of implementation of machine learning models in the system. In addition, the system has successfully reduced the frequency of extreme values of environmental factors, effectively regulated the environmental conditions within the favorable range that contributes to plant growth.

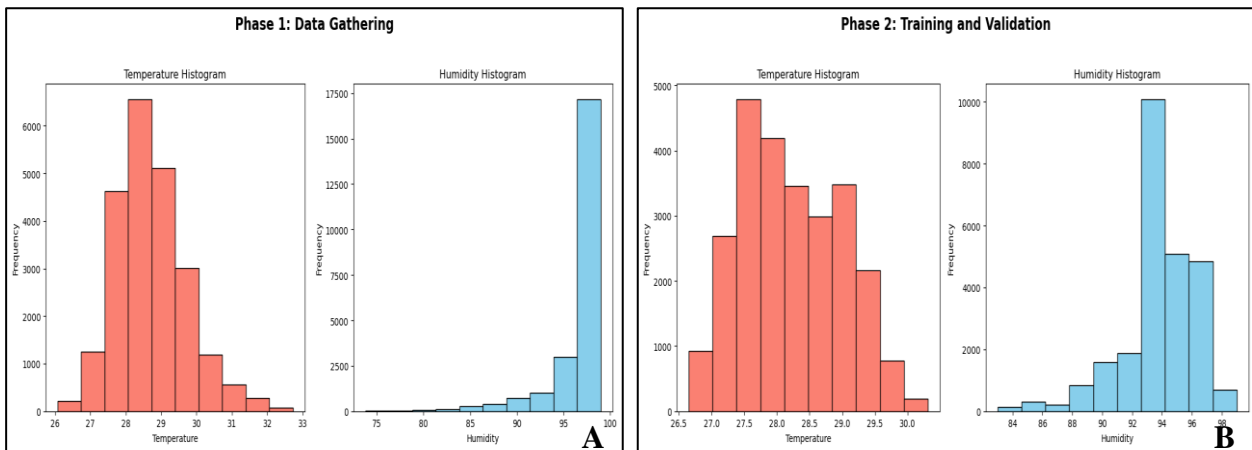


Fig. 5 - Temperature and Humidity histogram

Data Over Time

The graph depicted in Fig. 6 shows the data log from the Blynk application before implementing the machine learning model. The first graph illustrates the temperature variations over time, showing fluctuations of highs and lows. The temperature values are ranging from 26°C to 33°C in general. Thus, there is a notable rise in temperature as time progresses, suggesting a warming trend over the observed period.

On the other hand, the second graph illustrates the humidity levels over time. In the first part, the humidity stays close to 100% but it suddenly drops around 75%. After this, it demonstrates a more variability in values that range around 75% to 100%.

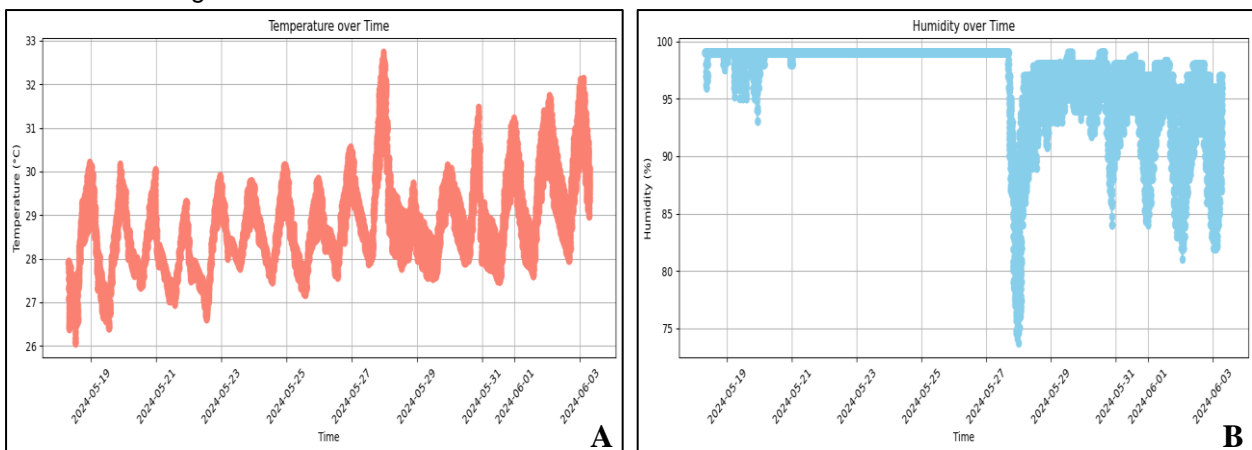


Fig. 6 - Phase 1: Temperature and Humidity over time data

The graph illustrated in Fig. 7 shows the data log of using machine learning in the fogponics system. The temperature graph shows that the fluctuation of temperature is between 27°C to 30°C. The graph also suggests that temperature peaks consistently around midday, while declining during the night. There is also a slight downward shift of temperature at the end of the period. Alternatively, the graph of humidity over time period remains relatively in the range of 90% to 96%, with a slight variation in the early part of the graph ranging from 84% to 98%.

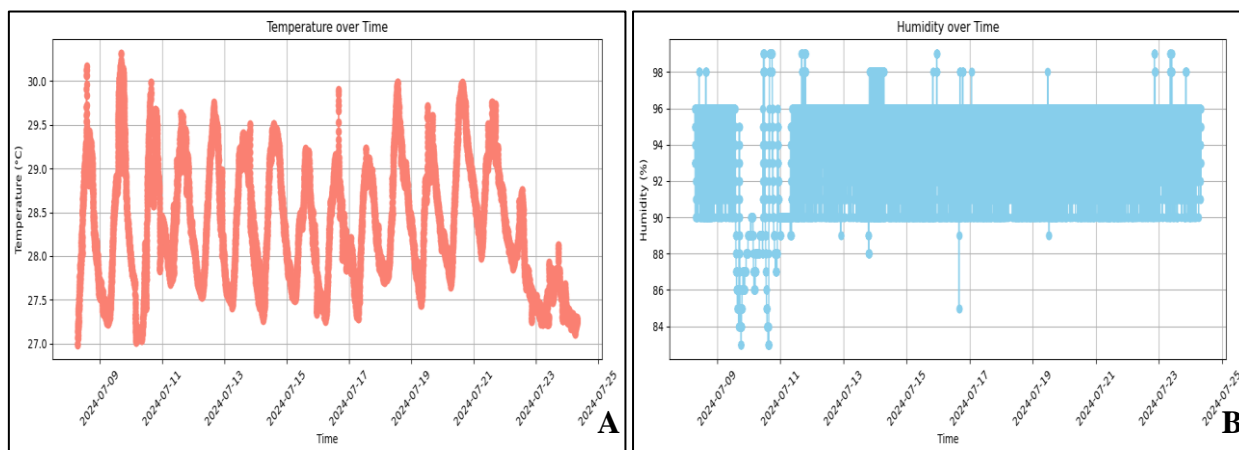


Fig. 7 - Phase 2: Temperature and Humidity over time data

The performance of the fogponics system with machine learning automation is assessed by comparing the temperature and humidity before and during the implementation of the machine learning model. The temperature fluctuation has decreased from 26°C to 33°C. The temperature is more consistent and exhibits a more stable pattern.

Meanwhile, this indicates the model’s effectiveness in regulating the environmental conditions. This wider range, seen in first phase, suggests that the machine learning model is actively controlling the humidity levels more dynamically, making sure they stay within a range that is favorable for plant growth. The humidity had a significant change in fluctuation from values that range around 75%-100% respectively 90%-96%. Whereas, the humidity level is more consistent and less erratic. Plants need at least 90% relative humidity for it to be enough, but root zone temperature will be increased as atomization time increases which will result in abnormal plant growth. Thus, the improvement suggests that the implementation of the machine learning model was effective in upholding a more regulated and balanced environment.

Machine Learning Model Evaluation

Table 1

Result of machine learning model evaluation

Root Mean Squared Error	R-squared (R2)	Precision	Recall	F1 Score
0.0362	0.9884	0.9917	0.9983	0.9950

The table presents the performance evaluation of the random forest regression algorithms which is implemented in the study for automating the fogponics system. Through the combination of multiple decision trees, it establishes the model’s precise prediction. Thus, the metrics above provides an overview of the machine learning model performance.

For the first metric of machine learning model evaluation, which is Root Mean Squared Error (RMSE) that calculates the average deviation of predicted values from the actual values. An RMSE of 0.0362 suggests that, on average, the prediction of the model has a deviation of 0.0362. This implies the model’s capability to predict environmental parameters such as humidity and temperature with high accuracy. Following this is the R-squared (R2) where its value indicates how much variation of dependent variables is explained by an independent variable in the machine learning model. An 0.9884 R-squared value means 98.84% of the variance in the outcome can be explained by the model. It measures the model’s ratio of true positive predictions out of all positive predictions. An 0.9917 precision indicates that 99.17% of the positive predictions of the model were correct. The other metric is Recall. It assesses how the model can correctly identify the true positive from all the actual positive data. A recall of 0.9983 implies that 99.83% of all actual positives are correctly identified. The final metric of machine learning model evaluation is the F1 Score, which indicates the balance ratio of precision and recall. An F1 score of 0.9950 means that the model’s overall performance is exceptionally good.

As has been demonstrated, the analysis of the result of machine learning model evaluation reveals that the model is highly effective in predicting the appropriate action of the fogponics system based on the temperature and humidity data. The high value of precision (0.9917), recall (0.9983), and F1 score (0.9950) reflects its reliability in making correct predictions. It further confirms by having low RMSE (0.0362) and high R-Squared value (0.9884) the significant predictive accuracy of the model.

Microgreen Growth Stage

The pictures shown in Fig. 8 illustrate the growth progression of microgreens before implementing the machine learning model. The growth of microgreen is somewhat uneven and less robust. The lack of uniform growth and the sparse density of the microgreens suggest that the environmental conditions are not optimal.



Fig. 8 - Phase 1: Gathering of training data

The pictures shown in Fig. 9 illustrate the growth of microgreens under the implementation of machine learning automation of the fogponics system. The microgreens are more uniform and appear healthier. This indicates that the environmental factors needed by the microgreens are met. The machine learning model is effective in producing microgreens in this kind of setup.



Fig. 9 - Phase 2: Machine Learning Implementation

Before and during the implementation of the machine learning model, it is shown that the microgreens have grown after 15 days of cultivation. In Fig. 8, although the microgreens have developed further, the growth is somewhat uneven. The uneven growth of plants may be due to the overwatering of the system. In contrast, in Fig. 9, the microgreens appear more uniform, denser and healthier. It indicates that the system has effectively cultivated microgreens indoors and significantly improved the control of the environmental parameters by incorporating machine learning automation and IoT-based monitoring systems.

Despite the fact that the machine learning model used in automating the fogponics system in this study is effective, further studies should be implemented to improve and assess the system's effectiveness. It is recommended to utilize image recognition to greatly enhance the capability of the system to recognize patterns and automate the system. In addition, implementing the system to a larger scale and different microgreens will evaluate the extent of the automated fogponics system.

CONCLUSIONS

The automated fogponics system for cultivating microgreens was developed to introduce potential alternatives for sustainable agricultural production. The use of the internet of things through Blynk application as a monitoring system has provided the ease of visualizing the different environmental parameters, and made the systems parts such as sensors and actuators interconnected. Whereas, the automation model of the system is trained using the random forest regression algorithm which maintains the parameters needed by microgreens to thrive. Based on the result of this study, using machine learning and internet of things in fogponics systems for microgreens production have been proven to be effective. The purpose of this study to develop an automated fogponics system for microgreens using machine learning automation and internet of things monitoring system has been accomplished. This study will introduce the potential alternative method of producing microgreens.

ACKNOWLEDGEMENT

The authors would like to express their gratitude to the Central Luzon State University - Engineering Research and Development for Technology (CLSU-ERDT) and the Department of Science and Technology – Science Education Institute (DOST-SEI) for providing financial support for the completion of this study.

REFERENCES

- [1] Abbasi, F., Khandan-Mirkohi, A., Ahmad, A. H., Kafi, M., & Shokrpour, M. (2024). Optimization of Aeroponic and Ultrasonic Soilless Culture Systems in Terms of Timing and Growth Characteristics of Liliium OT Hybrid. *International Journal of Horticultural Science and Technology*, 11(2), 269–284. <https://doi.org/10.22059/IJHST.2023.361423.658>
- [2] Al-Kodmany, K. (2018). The Vertical Farm: A Review of Developments and Implications for the Vertical City. *Buildings* 2018, 8(2), 24. <https://doi.org/10.3390/BUILDINGS8020024>
- [3] Ardiansah, I., Bafdal, N., Bono, A., Suryadi, E., & Nurhasanah, S. (2022). An Overview of IoT Based Intelligent Irrigation Systems For Greenhouse: Recent Trends And Challenges. *Journal of Applied Engineering Science*, 20(3), 657–672. <https://doi.org/10.5937/JAES0-35224>
- [4] Ardiansah, I., Calibra, R. G., Bafdal, N., Bono, A., Suryadi, E., & Nurhasanah, S. (2023). An IoT-Enabled Design for Real-Time Water Quality Monitoring and Control of Greenhouse Irrigation Systems. *INMATEH - Agricultural Engineering*, 68(3), 417–426. <https://doi.org/10.35633/INMATEH-69-39>
- [5] Eka Putri, R., Fauzia, W. A., & Cherie, D. (2023). Monitoring and Control System Development on IoT-Based Aeroponic Growth of Pakcoy (*Brassica rapa* L.). *Jurnal Keteknik Pertanian*, 11(2), 222–239. <https://doi.org/10.19028/JTEP.011.2.222-239>
- [6] Eswaranpillai, U., Murugesan, P., & Karuppiyah, P. (2023). Assess the impact of cultivation substrates for growing sprouts and microgreens of selected four legumes and two grains and evaluation of its nutritional properties. *Plant Science Today*, 10(2), 160–169. <https://doi.org/10.14719/PST.2058>
- [7] FAO. (2017). *The future of food and agriculture and challenges*. Food and Agriculture Organization of the United Nations. <https://openknowledge.fao.org/server/api/core/bitstreams/2e90c833-8e84-46f2-a675-ea2d7afa4e24/content>
- [8] Gandham, V. V. S. K., Manohar, B. S. P. S., & Dhal, P. K. (2022). Esperanza-Expectation Leads to Inventions in Space. *International Journal of Recent Advances in Multidisciplinary Topics*, 3(3), 120–126. <https://journals.ijramt.com/index.php/ijramt/article/view/1883>
- [9] Gao, J., Zhang, J., & Lu, D. (2016). Design and Atomization Experiments of an Ultrasonic Atomizer with a Levitation Mechanism. *Applied Engineering in Agriculture*, 32(4), 353–360. <https://doi.org/10.13031/AEA.32.11029>
- [10] Gunjal, M., Singh, J., Kaur, J., Kaur, S., Nanda, V., Mehta, C. M., Bhadariya, V., & Rasane, P. (2024). Comparative analysis of morphological, nutritional, and bioactive properties of selected microgreens in alternative growing medium. *South African Journal of Botany*, 165, 188–201. <https://doi.org/10.1016/J.SAJB.2023.12.038>
- [11] Jambor, T., Knizatova, N., Valkova, V., Tirpak, F., Greifova, H., Kovacik, A., & Lukac, N. (2022). Microgreens as a functional component of the human diet: A review. *Journal of Microbiology, Biotechnology and Food Sciences*, 12(1), <https://doi.org/10.55251/JMBFS.5870>

- [12] Lakhiar, I. A., Gao, J., Syed, T. N., Chandio, F. A., & Buttar, N. A. (2018). Modern plant cultivation technologies in agriculture under controlled environment: a review on aeroponics. *Journal of Plant Interactions*, 13(1), 338–352. <https://doi.org/10.1080/17429145.2018.1472308>
- [13] Li, T., Lalk, G. T., & Bi, G. (2021). Fertilization and Pre-Sowing Seed Soaking Affect Yield and Mineral Nutrients of Ten Microgreen Species. *Horticulturae*, 7(2), 14. <https://doi.org/10.3390/HORTICULTURAE7020014>
- [14] Ocho Bernal, T. G., Lyttle, N., & Jung, Y. (2023). Microbiological quality of microgreen seeds purchased from online vendors and evaluating seed decontamination techniques available online. *Frontiers in Sustainable Food Systems*, 7, <https://doi.org/10.3389/fsufs.2023.1264472>
- [15] Paglialunga, G., El Nakhel, C., Proietti, S., Moscatello, S., Battistelli, A., Formisano, L., Ciriello, M., Del Bianco, M., De Pascale, S., & Roupael, Y. (2023). Substrate and fertigation management modulate microgreens production, quality and resource efficiency. *Frontiers in Sustainable Food Systems*, 7, <https://doi.org/10.3389/FSUFS.2023.1222914>
- [16] Partap, M., Sharma, D., HN, D., Thakur, M., Verma, V., Ujala, & Bhargava, B. (2023). Microgreen: A tiny plant with superfood potential. *Journal of Functional Foods*, 107, <https://doi.org/10.1016/J.JFF.2023.105697>
- [17] Sarmphim, P., Sutthiphon, N., Jaroensong, P., Sirisathitkul, C., & Sirisathitkul, Y. (2022). IoT Based soil moisture management using capacitive sensor and user-friendly smartphone application. *INMATEH - Agricultural Engineering*, 66(1), 159–166. <https://doi.org/10.35633/INMATEH-66-16>
- [18] Xiao, Z., Lester, G. E., Luo, Y., & Wang, Q. (2012). Assessment of vitamin and carotenoid concentrations of emerging food products: Edible microgreens. *Journal of Agricultural and Food Chemistry*, 60(31), 7644–7651. <https://doi.org/10.1021/jf300459b>

OPTIMISATION AND TESTING OF STRUCTURAL PARAMETERS OF INTERNAL TANGENT CIRCLE EXTERNAL GROOVED WHEEL FERTILISER DISCHARGER

内切圆外槽轮式排肥器结构参数优化与试验

Shubin YAN¹⁾, Wendong ZHONG¹⁾, Guifang WU^{*1)}, Xiangping BAI²⁾, Jianing DI¹⁾, Xiangpeng ZHAO¹⁾

¹⁾Inner Mongolia Agricultural University, College of Mechanical and Electrical Engineering, Hohhot/China;

²⁾Inner Mangolia Autonomous Region Agricultural and Pastoral Technology Extension Center, Hohhot/ China

Tel: 13274851436; E-mail: 13274851436@163.com; wgfsara@126.com

DOI: <https://doi.org/10.35633/inmateh-74-79>

Keywords: Granular Fertilizer Discharger, Discrete Element Model, Optimization, Field Oriented Control Algorithm

ABSTRACT

Aiming at the problem of traditional external grooved wheel type fertilizer discharger, which discharges fertilizer unevenly, an internal tangent circle external grooved wheel type granular fertilizer discharger is designed. Firstly, the 19-19-19 NPK compound fertilizer produced by Stanley Company in China is selected, and the pulsatility of the straight groove wheel, external tangent circle groove wheel, and internal tangent circle groove wheel is compared and analyzed using the Hertz-Mindlin (no-slip) model in the EDM2020 simulation, then the structural parameters are optimized for the better type of groove wheel. Finally, the Field Oriented Control (FOC) algorithm is used to control the brushless motor to further optimize the coefficient of uniform volatility. The four factors and three levels response surface simulation test was conducted with the groove tooth inclination angle, number of grooves, diameter of the inner tangent circle and angular velocity of groove wheel as test factors. Simulation results showed that when the groove tooth inclination angle was 38.341° , the number of grooves was 9.999, the diameter of the inner tangent circle was 13.154 mm, and the angular velocity of groove wheel was 5.998 rad/s, the coefficient of uniformity of fluctuation of the discharged fertilizer was 4.11%. Based on practical considerations, the groove tooth inclination angle was set to 38° , the number of grooves to 10, the diameter of the inner tangent circle to 13 mm, and the groove wheel angular velocity to 6 rad/s for a bench validation test. The bench test results showed that the optimized internal tangent circle groove wheel fertilizer applicator achieved a uniform fluctuation coefficient of 6.32%, while incorporating FOC algorithm motor control further reduced the coefficient to 4.62%, meeting the design requirements for the fertilizer applicator.

摘要

针对传统外槽轮式排肥器排肥不均匀的问题,设计了一种内切圆外槽轮式颗粒肥料排肥器。首先,选用中国史丹利公司的复合肥(19-19-19),通过EDM2020仿真采用了Hertz-Mindlin(无滑移)模型对比分析直槽轮、外切圆槽轮和内切圆槽轮的脉动性,然后针对较优型槽轮进行结构参数优化设计,最后利用FOC算法控制无刷电机进一步优化排肥均匀波动性系数。以槽轮槽齿倾角、槽轮槽数、内切圆直径和槽轮角速度为试验因素,进行四因素三水平响应面仿真试验。仿真试验结果表明:当内切圆槽轮槽齿倾角为 38.341° 、槽轮数目为9.999、内切圆直径为13.154mm、槽轮角速度为5.998rad/s时,排肥均匀波动性系数较优值为4.11%。根据实际情况取倾角为 38° 、槽轮槽数为10、内切圆直径为13mm、槽轮角速度为6rad/s进行台架验证试验。台架验证试验结果表明:优化后的内切圆槽轮排肥器,排肥均匀波动性系数为6.32%,而增加FOC算法电机控制后的排肥均匀波动性系数为4.62%,符合排肥器设计要求。

INTRODUCTION

Precision agriculture technology is an agricultural production method based on information technology, which carries out real-time monitoring and data collection of the farmland environment through the use of modern sensors, communication networks, computers and other technological means, and applies these data to agricultural production decisions.

Shubin Yan, master degree; Wendong Zhong, Ph.D.; Guifang Wu, Prof. Ph.D.;*Corresponding authors: wgfsara@126.com; Shubin Yan and Wendong Zhong contributed to the work equally and should be regarded as co-first authors;

Precision agriculture technology can help farmers realize refined management, improve production efficiency and quality, and reduce resource waste and environmental pollution. Fertilizer application is an important part in the application process of precision agriculture technology (Liao et al., 2023). Precision fertilization not only reduces the use of chemical fertilizers and lowers production costs, but also avoids land pollution and ecological damage caused by over-fertilization. Therefore, how to realize precision fertilization has become an important direction of precision agriculture technology research.

At present, fertilizer dischargers are mainly classified into external chute wheel type, spiral type, disc type and collector-excluder type and so on. Among them, the external grooved wheel type fertilizer discharger is simple in structure, with simple and precise displacement adjustment, which is widely used in China's fertilizer application machinery. In order to improve the accuracy of the fertilizer discharger displacement, many scholars have explored the two aspects of structure and control, respectively. In terms of structure, Wang Yubing has designed the opposed double-spiral external grooved wheel fertilizer discharger for the problem of pulsation of traditional external grooved wheel fertilizer discharger (Wang et al., 2022). Wang Jinfeng used the discrete element method to qualitatively and quantitatively study the influence of the grooved wheel structural parameters on the fertilizer transport process (Wang et al., 2023). Wen Fujun proposed a spiral grooved wheel fertilizer application device (Wen et al., 2024). In fertilizer application control, Zhou Liming designed an online monitoring system for fertilizer application flow based on the principle of capacitive detection (Zhou et al., 2022). Dong Guoqiang achieved precise control of fertilizer discharge by gradually extruding the fertilizer using a variable diameter and variable pitch structure (Dun et al., 2023). Mondal proposed a novel sensorless field-oriented control (FOC) method for sensorless motor control (Mondal et al., 2024).

In summary, improvement of the groove wheel structure and addition of a fertilizer application control system can effectively improve the pulsation of the external groove wheel fertilizer discharger, thus improving the accuracy and continuity of the discharger. Therefore, this paper designs a new type of trough wheel and builds a FOC control system for it.

MATERIAL AND METHODS

External Grooved Wheel Fertilizer Discharger

The external grooved wheel type fertilizer discharger is a kind of agricultural machinery (as shown in Fig.1), which is used for spreading fertilizers evenly into the soil. The main structure of the outer grooved wheel type fertilizer discharger includes: fertilizer box, fertilizer discharging insert plate, arc base, grooved wheel.

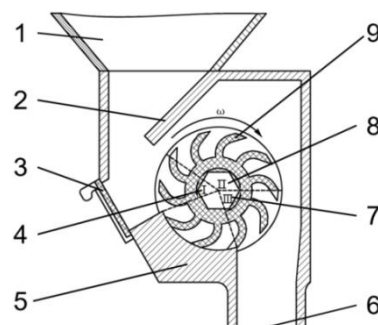


Fig. 1 - External Grooved Wheel Fertilizer Discharger

1. Fertilizer box; 2. Deflector plate; 3. Fertilizer unloading insert; 4. Fertilizer filling area; 5. Arc base; 6. Fertilizer discharge opening; 7. Fertilizer feeding area; 8. Fertilizer carrying area; 9. Trough wheel

The fertilizer discharger operates with side filling, directing granular fertilizer from the fertilizer box along the guide plate into the shell, where it enters the grooves of the groove wheel within the filling area. In the process of rotating the groove wheel, it passes through the fertilizer carrying area and fertilizer feeding area, and forcibly drives the granular fertilizer in the groove to be discharged from the fertilizer discharging port. Compared with the traditional groove wheel, this design can not only increase the range of particles into the groove, but also avoid the fertilizer sliding down automatically by gravity (Zhang et al., 2015).

Trough Wheel Designs

Trough wheels are the key component in an external trough wheel fertilizer discharger, and their primary function is to deliver fertilizer uniformly to the soil through rotation. The design of the chute wheel ensures uniform fertilizer delivery, and many external chute wheel fertilizer dischargers allow for adjustments in rotational speed and replacement of the chute wheel to accommodate different fertilizer types and application needs.

Among the factors of groove wheel structure that affect the operating effect of the groove wheel fertilizer discharger, the number of grooves, the effective working length, the radius of the groove wheel, and the cross-sectional shape of the individual grooves are the main factors (Zhu *et al.*, 2018). The appropriate cross-section shape and volume of the grooves can improve the filling effect of granular fertilizer, and when the filling rate of the grooves is maximized, the displacement per minute of the groove wheel no longer increases with the increase of rotational speed (Wang *et al.*, 2018). In order to be able to improve the pulsation of the fertilizer discharger without changing the structure of the discharger housing and the effective length of the grooved wheel, and to make the discharging of fertilizer more uniform, this paper optimizes the design of the grooved wheel in terms of the shape of the groove tooth cross-section and the number of grooves, and designs the following different kinds of grooved wheels, which are shown in Fig. 2 as a comparison with the straight groove wheel. The length of the grooved wheel is 60 mm, the diameter of the outer circle Φ is 65 mm, and the diameter of the inner circle D is 35mm. d_1 is the diameter of the external tangent circle groove wheel (the outer tangent circle is tangent to the outer circle Φ); d_2 is the diameter of the inner tangent circle (the inner tangent circle is tangent to the inner circle D); and the groove tooth inclination angle θ is the angle between the grooved tooth and the diameter of the inner tangent circle (the said diameter is parallel to the tangent line between the inner tangent circle and the inner circle).

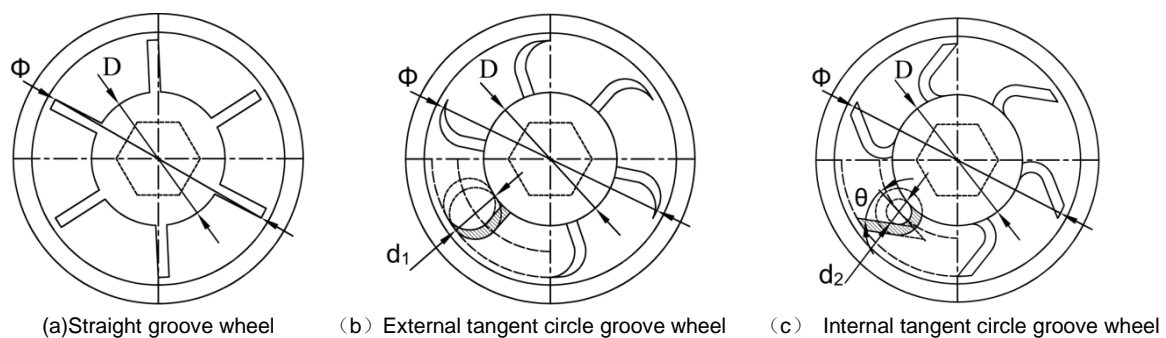


Fig. 2 - Different types of groove wheels

Discrete element simulation

Determination of simulation parameters and modelling

Pellet plant setup

In this experimental study, the 19-19-19 NPK compound fertilizer produced by Stanley Fertilizer Jilin Co., Ltd (measured average diameter of 100 grains 1.64 mm, standard deviation 0.18 mm, density 1.86 g·cm⁻³) was selected as the test fertilizer, the particle modelling used pure spherical and non-agglomerated particles, and the material of fertilizer discharger was PLA plastic, and through the review of the relevant literature (Li *et al.*, 2023), the relevant parameters of simulation model were set as shown in Table 1.

Table 1

Global Variable Parameter Setting		
Item	Property	Value
Fertilizer particles	Poisson ratio	0.25
	shear modulus/Pa	1.00×10 ⁷
	densities/(kg·m ⁻³)	1 861
Groove wheel, Shell	Poisson ratio	0.394
	shear modulus/Pa	3.18×10 ⁸
	densities/(kg·m ⁻³)	1 240
Pellet-Pellet	coefficient of restitution	0.11
	coefficient of static friction	0.30
	coefficient of rolling friction	0.10
Pellet-wheel, Shell	coefficient of restitution	0.41
	coefficient of static friction	0.32
	coefficient of rolling friction	0.18

Simulation analysis of pulsation of fertilizer discharger

Using SolidWorks 2022 to model the single screw fertilizer discharger and simplify the unnecessary structure, the model in SolidWorks 2022 is converted into STL file and imported into EDEM2020 software, and the model is built by filling in the parameters according to Table 1. A total of 50,000 fertilizer particles were generated in the fertilizer box, simulating a particle factory. All particles were released once the fertilizer applicator began to rotate. The relationships between the fertilizer particles and the fertilizer discharger casing, as well as between the fertilizer particles themselves were modeled using Hertz-Mindlin (no-slip) model, and the Auto Grid Resizing option in EDEM software was selected.

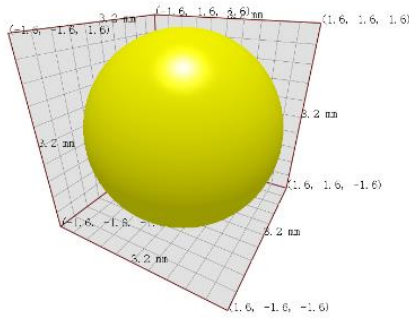


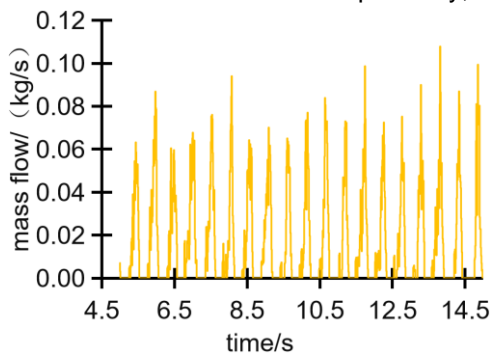
Fig. 3 - Fertilizer granules



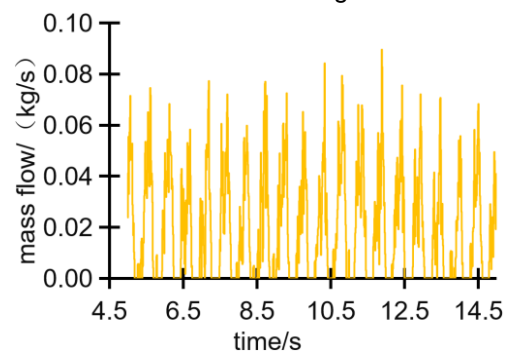
Fig. 4 - Fertilizer discharge pulsatility simulation

Pulsatility analysis

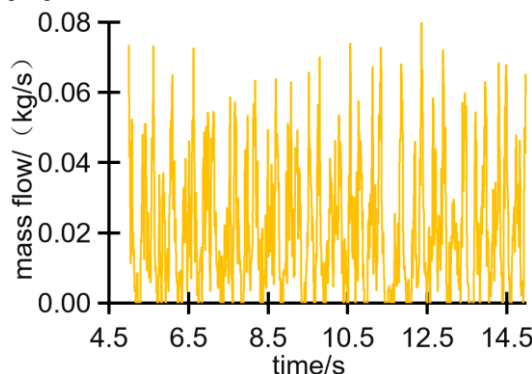
In order to better observe the pulsation phenomenon of various grooved wheels when discharging fertilizers, three types of grooved wheels were set up for the simulation test: straight groove wheel, external tangent circle groove wheel and internal tangent circle groove wheel. The number of grooves was set to 6, and the angular velocity of groove wheel was set to 3.14 rad/s. In order to obtain a complete and accurate instantaneous discharge of the particle flow, a cylindrical virtual discharge sensor grid was set at the bottom of the grooved wheel at a position of 3 mm vertically downward, which was used for the detection of the instantaneous discharge of the particles. Fertilizer discharge pulsatility simulation is shown in Fig. 4, the cylindrical grid has a radius of 50 mm (detection range of 100 mm, larger than the fertilizer discharge port), a height of 30 mm, and a detection time interval of 0.01 s. The fertilizer discharger using three types of grooved wheels was simulated for 15 s respectively, and 4.5-14.5 s of them were taken to obtain Fig. 5.



(a) Mass flow rate of straight groove wheel



(b) Mass flow rate of external tangent circle groove wheel



(c) Mass flow of internal tangent circle groove wheel

Fig. 5 - Pulsation of different grooved wheels

This pulsation phenomenon is described in terms of the amplitude and time interval of the pulsation. The amplitude of the pulsation is the difference between the maximum value and the minimum value of the instantaneous displacement, the larger the amplitude of the pulsation, the more uneven the displacement. The time interval refers to the time difference between the maximum value and the minimum value of the instantaneous displacement of two adjacent times, the larger the time interval, the more obvious the pulsation, the more likely to cause the leakage of the application (Song *et al.*, 2021). From Fig. 5, it can be concluded that the internal tangent circle groove wheel discharging fertilizer pulsation amplitude is smaller, and the pulse time interval is smaller, so the internal tangent circle groove wheel discharging fertilizer is more uniform and has better fertilizer discharging effect in the case of a certain angular velocity of groove wheel and the number of grooves.

Response surface simulation test

Single factor test

Fertilizer discharger with different parameters of the grooved wheel was modeled, and the model was converted into STL file and imported into EDEM, and the parameters were set according to Table 1, and the particle factory was established in the fertilizer box, and a total of 50,000 fertilizer particles were generated, and the fertilizer discharger started to rotate after the generation of all the fertilizer particles. The angular velocity of groove wheel was set to 3.14 rad/s. The relationships between the fertilizer particles and the fertilizer discharger casing, as well as between the fertilizer particles themselves were modeled using Hertz-Mindlin (no-slip) model, and the Auto Grid Resizing option in EDEM software was selected. The grid method was used to count the data on the uniform volatility of fertilizer discharge (Sugirbay *et al.*, 2020), and the coefficient of uniform volatility was used as the evaluation index (the smaller the coefficient of uniform volatility represents the more uniform fertilizer discharge). A mass sensor was set on the conveyor belt and divided into 30 portions, each portion with a length of 350 mm and a width of 20 mm. the conveyor belt was moved at a speed of 0.2 m/s (this speed is only for the study of fertilizer dischargers) (Dun *et al.*, 2024), and the data were recorded at intervals of 0.01 s. The EDEM simulation model of the external grooved wheeled fertilizer discharger is shown in Fig. 6.

The coefficient of uniform volatility σ_u is as follows:

$$m_a = \frac{\sum_{i=1}^{30} m_i}{n} \quad (i = 1, 2, \dots, 30) \quad (1)$$

$$\sigma_u = \sqrt{\frac{\sum_{i=1}^{30} (m_i - m_a)^2}{m_a^2 (n-1)}} \times 100\% \quad (i = 1, 2, \dots, 30) \quad (2)$$

In the formula (1)~(2): m_i is the mass of fertilizer particles in the i -th grid, (g); n is the number of evenly divided grid cells in the monitoring area, $n=10$; m_a is the average mass of fertilizer particles in the grid cells, (g); σ_u is the coefficient of uniformity of volatility of fertilizer discharges, (%).

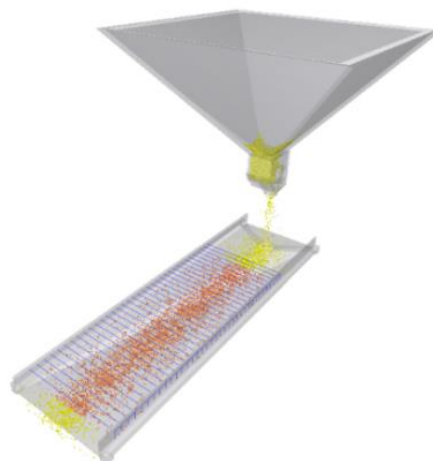


Fig. 6 – Single factor test process

In order to study the influence of each parameter of the trough wheel on the coefficient of uniform volatility, the degree of influence of the four factors affecting the coefficient of uniform volatility was taken and analyzed according to the actual use. The results are shown in Fig. 7.

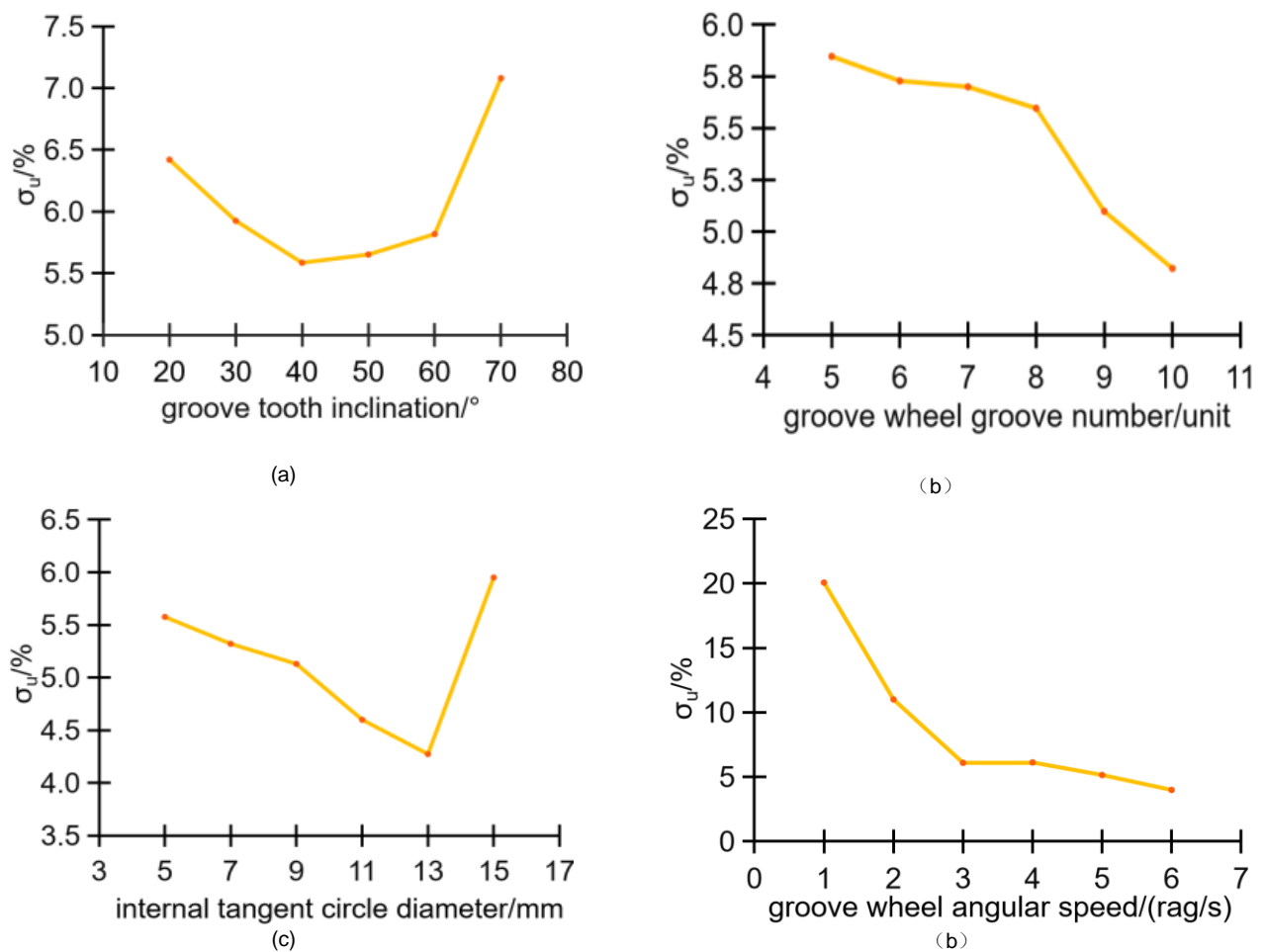


Fig. 7 – Results of Single factor test

It can be seen from Fig. 7(a) that with the increase of the inclination angle of the groove teeth, the uniform volatility coefficient of fertilizer discharge decreases and then increases; in Fig.7(b) it can be seen that with the increase of the number of grooves, the uniform volatility coefficient of fertilizer discharge decreases; Fig.7(c) shows that with the increase of the diameter of the inner tangent circle, the uniform volatility coefficient of fertilizer discharge decreases and then increases; Fig.7(d) shows that with the increase of the angular velocity of groove wheel, the uniform volatility coefficient of fertilizer discharge decreases.

Multifactor test

According to the preliminary pre-test and one-factor finding, the groove tooth inclination angle A , the number of grooves B , the diameter of the inner tangent circle C and the angular velocity of groove wheel D are the key factors affecting the coefficient of uniformity and volatility of the fertilizer discharger. In order to find the best working parameters of the fertilizer discharger, the four factors and three levels experimental design was used, and the factors and levels are shown in Table 2, and the experimental scheme and experimental results are shown in Table 3.

Table 2

Test factors and coding considerations				
Encodings	A / °	B / unit	C / mm	D / (rad/s)
-1	30	5	11	1
0	40	7	13	3.5
1	50	9	15	6

Table 3

Test Scheme and Results					
Experiment Serial number	Experimental factors				
	A	B	C	D	σ_u
1	30	10	13	5	5.52678
2	40	8	15	5	5.53912
3	40	9	13	5	4.73283
4	40	9	11	6	5.08475
5	40	10	13	4	5.25807
6	50	8	13	5	6.59669
7	40	9	11	4	6.33458
8	40	9	13	5	4.89352
9	40	10	13	6	4.11044
10	50	9	11	5	7.0583
11	40	8	13	6	5.3971
12	40	9	13	5	4.98372
13	40	8	13	4	5.28156
14	30	9	13	4	6.60464
15	50	9	13	4	5.90993
16	30	8	13	5	4.97249
17	30	9	13	6	5.31614
18	40	9	15	6	4.50924
19	50	9	15	5	5.81091
20	30	9	11	5	5.76912
21	40	10	11	5	5.10965
22	40	9	15	4	5.96199
23	40	8	11	5	6.27953
24	50	9	13	6	6.83487
25	40	10	15	5	5.22641
26	30	9	15	5	5.33301
27	50	10	13	5	4.90294

The results of the test were analyzed by quadratic regression ANOVA and the results are shown in Table 4. According to the significance test, the F-value of the model was 5.98, $P < 0.01$, indicating that the quadratic regression model was highly significant. The coefficient of determination of the model, $R^2 = 0.8746$, proved that the model was well fitted. The significance of each factor was analyzed and the quadratic polynomial regression equation for the coefficient of uniform volatility was obtained as:

$$\begin{aligned}
 \sigma_u = & 4.87 + 0.2993 \times A - 0.3077 \times B - 0.2714 \times C - 0.3415 \times D \\
 & - 0.562 \times AB - 0.2028 \times AC + 0.55334 \times AD - 0.2143 \times BC \\
 & - 0.3158 \times BD - 0.057 \times CD + 0.7808 \times A^2 - 0.0236B^2 \\
 & + 0.4534 \times C^2 + 0.2767 \times D^2
 \end{aligned}
 \tag{3}$$

Table 4 shows that the influence of each factor is $D > B > A > C$. It is shown that there is an interaction between the groove tooth inclination angle and the number of grooves, the groove tooth inclination angle and angular velocity of groove wheel.

Table 4

Analysis of variance of the coefficient of uniform volatility						
Source	Sum of Squares	df	Mean Square	F-value	p-value	
Model	12.08	14	0.8629	5.98	0.0018**	
A	1.07	1	1.07	7.45	0.0183*	
B	1.29	1	1.29	8.93	0.0113*	
C	0.8831	1	0.8831	6.12	0.0293*	
D	1.4	1	1.4	9.7	0.0089**	
AB	1.26	1	1.26	8.76	0.0119*	
AC	0.1645	1	0.1645	1.14	0.3066	
AD	1.22	1	1.22	8.49	0.013*	
BC	0.1837	1	0.1837	1.27	0.2813	
BD	0.3989	1	0.3989	2.76	0.1223	
CD	0.0103	1	0.0103	0.0713	0.7939	
A²	3.25	1	3.25	22.53	0.0005**	
B²	0.003	1	0.003	0.0206	0.8883	
C²	1.1	1	1.1	7.6	0.0174*	
D²	0.4084	1	0.4084	2.83	0.1183	
Residual	1.73	12	0.1443			
Lack of Fit	1.7	10	0.1699	10.52	0.0899	
Pure Error	0.0323	2	0.0162			
Cor Total	13.81	26				

Note: * denotes significant difference, ** denotes significant difference.

Analysis of the effect of interaction factors on the coefficient of uniform fluctuation of the fertilizer discharge

Interaction of groove tooth inclination angle and the number of grooves

Fig.8(a) shows the response surface diagram of the interaction between the inclination angle of the groove teeth and the number of grooves when the angular velocity of the groove wheel is 4 rad/s and the diameter of the inner tangent circle is 13 mm. When the groove tooth inclination angle is 30~40°, with the increase of the number of grooves, the coefficient of uniform volatility shows an increasing trend; when the groove tooth inclination angle is 40~50°, with the increase of the number of grooves, the coefficient of uniform volatility shows a decreasing trend. The reason is: when the groove tooth inclination angle is 30~40°, the bigger the number of grooves, the smaller the opening of the grooves, the more difficult to fill the fertilizer, the coefficient of uniform volatility shows an increasing trend. When the groove tooth inclination angle is 40~50°, the size of the groove opening meets the condition of filling fertilizer, so the coefficient of uniformity and volatility of fertilizer discharge shows a decreasing trend. Therefore, when the groove tooth inclination angle is 35~40° and the number of grooves is 9~10, the coefficient of uniform volatility is smaller.

Interaction of groove tooth inclination angle and angular velocity of groove wheel

Fig.8(b) shows the response surface of the interaction between the groove tooth inclination angle and angular velocity of groove wheel. When the number of grooves is 9 and the diameter of the inner tangent circle is 13 mm. When the groove tooth inclination angle is 30 ~ 40°, the angular velocity of groove wheel increases, the uniform volatility coefficient of fertilizer discharge presents a decreasing trend; when the groove tooth inclination angle is 40 ~ 50°, the angular velocity of groove wheel increases, the uniform volatility coefficient of fertilizer discharge presents an increasing trend.

The reason is as follows: fewer grooves lead to a shorter fertilizer filling time. Groove tooth inclination angle is 30 ~ 40°, the tangential force acting on the fertilizer is greater, which helps with fertilizer filling, so filling the fertilizer will not be affected by the filling time, showing a decreasing trend. Groove tooth inclination angle of 40 ~ 50°, the fertilizer tangential force is small, leading to insufficient filling. In this case, the filling process is more sensitive to time, showing an increasing trend. Therefore, the coefficient of uniform volatility is smaller when the groove tooth inclination angle is 35~40° and the angular velocity of groove wheel is 5 rad/s ~ 6 rad/s.

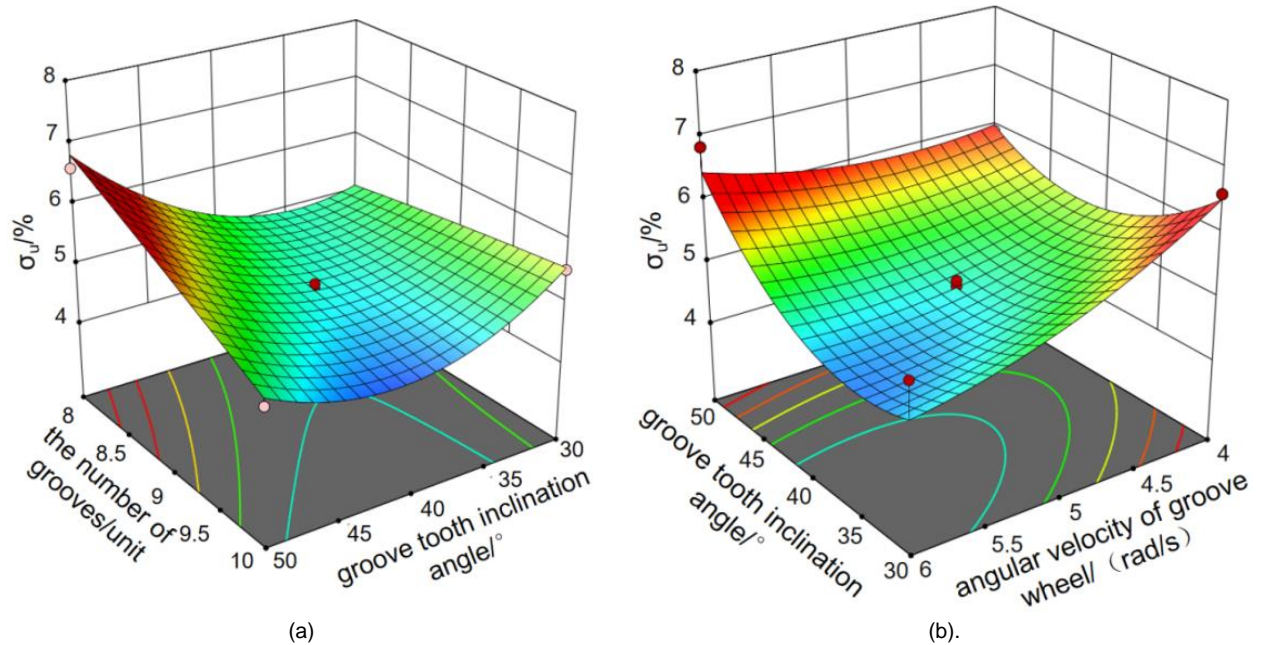


Fig. 8 – Effect of interaction factors on the coefficient of uniform fluctuation of fertilizer discharge

Optimization of grooved wheel parameters

In order to ensure that the external grooved wheel type fertilizer discharger has a good performance of fertilizer discharge, the coefficient of uniform volatility is taken as an evaluation index, to optimize the structural parameters of the external grooved wheel. The objective function and constraints are:

$$\begin{cases} \min \sigma_u \\ \text{s.t.} \begin{cases} A \in [-1,1] \\ B \in [-1,1] \\ C \in [-1,1] \\ D \in [-1,1] \end{cases} \end{cases} \quad (4)$$

Optimization-Numerical module in Design-Expert 13 software was used to solve the optimization problem, and the results showed that the coefficient of uniformity of fertilizer discharge fluctuation was better when the groove tooth inclination angle was 38.341°, the number of grooves was 9.999, the diameter of the inner tangent circle was 13.154 mm, and the angular velocity of groove wheel was 5.998 rad/s. The coefficient of uniform volatility was better by 4.11%.

FOC algorithm

Brushless electric motor

The internal components of a brushless DC motor are the rotor and stator. The rotor, which can be considered as a permanent magnet (Fig.9), is located in the center of the motor and has magnets attached. The coil winding fixed at the inner edge of the motor serves as the stator. A three-phase, three-winding, two-pole internal rotor motor is modeled. When the direction of the current passed through the three-phase winding of the stator changes, the direction of the magnetic field generated by the stator also changes, and the rotor rotates under the influence of the magnetic force.

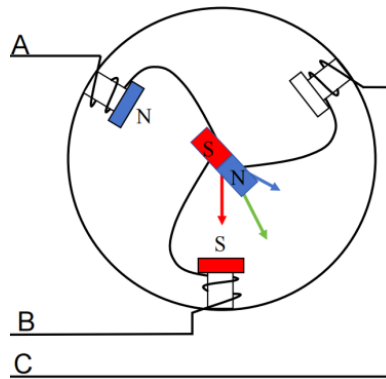


Fig. 9 – Brushless motor schematic

FOC Principle

The FOC (Field-Oriented Control) algorithm is an efficient motor control strategy, the core of which is to decompose the current of the motor into two components related to the orientation of the magnetic field, so as to realize the independent control of the motor speed and torque. The whole operation process of the FOC algorithm is a continuous feedback and adjustment process (Figure 10). It can adapt to load changes and changes in motor parameters to maintain efficient and stable operation of the motor.

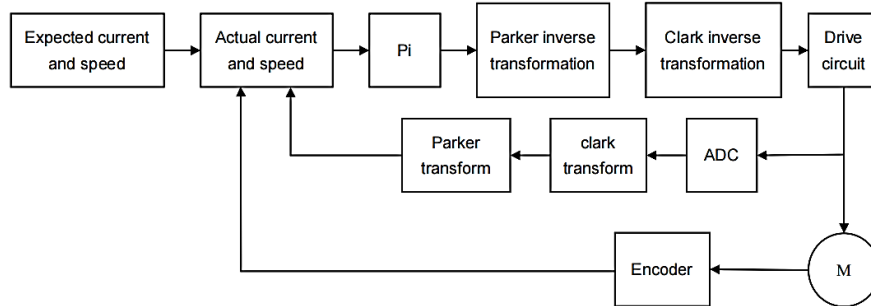


Fig. 10 – FOC Algorithm Schematic

FOC Realization

The AC power supply is converted from 220V AC to 24V DC by the power adapter to supply power to the FOC driver board, which has a built-in voltage regulator circuit to supply power to the ESP32 microcontroller and the encoder respectively, and the ESP32 microcontroller receives the real-time motor position data and the motor current data (of which the position data is provided by the encoder and the current data is provided by the FOC driver board). All the data are calculated by the ESP32 microcontroller and then PWM signals are sent to the FOC driver board, which outputs high-power PWM current to drive the motor according to the PWM signals. The specific electrical connection is shown in Figure 11.

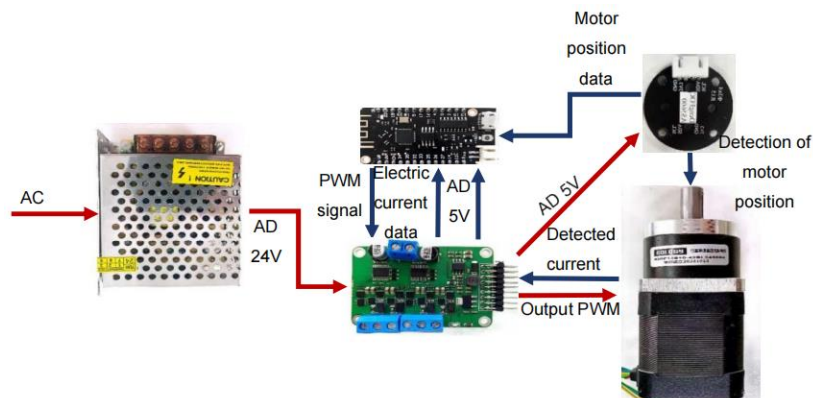


Fig. 11 – Electrical connection

This design takes Arduino SimpleFOCLibrary to implement the FOC algorithm. The FOC driver board increases the current when the brushless motor is subjected to resistance, and its current versus speed relationship when the brushless motor receives a load is shown in Figure 12 below.

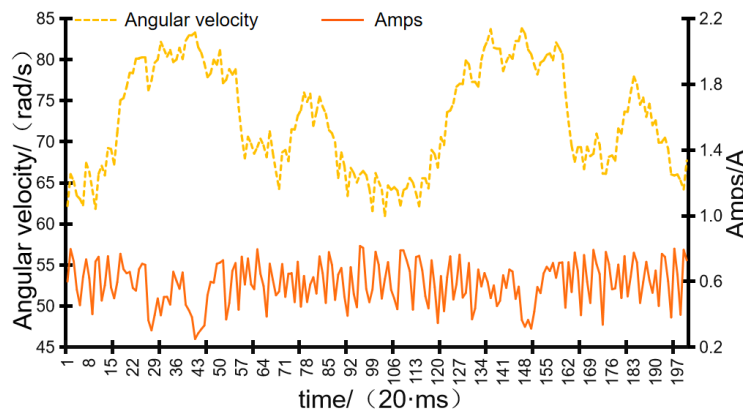


Fig. 12 – Current vs. speed under load

RESULTS

Bench Test

Based on the above parameter optimization results, for better machining and better control of rotational speed, the following parameters are taken: groove tooth inclination angle of 38°, number of grooved wheels of 10, diameter of the inner tangent circle of 13 mm, angular velocity of groove wheel of 6 rad/s. The grooved wheel parts and other related parts of the fertilizer discharger are processed by a 3D printer with the optimum parameter combination, and the conveyor belt is processed by using an aluminum profile. The bench-scale validation test of the external grooved wheel fertilizer discharger under the optimal combination of mechanism parameters was carried out indoors using conventional PWM motor control, as shown in Fig. 13.

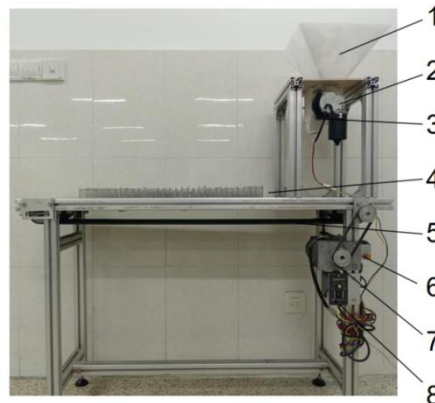


Fig. 13 - Bench Test

- 1 Fertilizer box 2 Discharger 3 Discharger motor 4 Fertilizer collection box 5 Conveyor belt
- 6 Fertilizer Discharger Motor Speed Controller 7 Belt Motor 8 Belt Speed Controller

The speed of the angular velocity of groove wheel was set to 6 rad/s and the speed of the conveyor belt was set to 0.2 m/s. When the fertilizer was discharged, the fertilizer collection box was put into the conveyor belt from the right side of the conveyor belt; and when it reached the left side of the conveyor belt, the fertilizer collection box was taken out. Repeat the process 5 times and calculate the coefficient of uniform volatility. Verify that the coefficient of uniform volatility is 6.32%, replace the motor and control system of the fertilizer discharger with the electronic control system shown in Fig. 11, and carry out this experiment for 5 more times. The coefficient of uniform volatility obtained from the validation test was 4.62%. The test results are more consistent with the prediction model within the error range, as shown in Table 5.

Table 5

Bench test results						
	1	2	3	4	5	average value
PWM motor control	8	4.4	7.2	6.3	5.7	6.32
FOC algorithm	4.8	4.7	4.2	4.9	4.5	4.62

CONCLUSIONS

In this study, the internal tangent circle groove wheel granular fertilizer discharger is designed for the problem of uneven fertilizer discharge of the traditional outer grooved wheel type fertilizer discharger. The pulsatility of straight groove wheel, external tangent circle groove wheel and internal tangent circle groove wheel is analyzed using the Hertz-Mindlin (no-slip) model in the EDM2020 simulation. The structural parameters are optimized for the best type of grooved wheel. Finally, the FOC algorithm is used to control the brushless motor to further optimize the coefficient of uniform volatility. The following conclusions are drawn from the simulation and experimental studies:

(1) The discrete element simulation platform of the working process of the external grooved wheel fertilizer discharger was constructed by EDEM2020 software, and the pulsation of the external tangent circle groove wheel, internal tangent circle groove wheel and straight grooved wheel was compared. The simulation test shows that the internal tangent circle groove wheel discharges fertilizer more evenly.

(2) The four factors and three levels response surface simulation test was carried out using the groove tooth inclination angle, the number of groove wheels, the diameter of the inner tangent circle and the angular velocity of groove wheel as test factors. The simulation results show that when the groove tooth inclination angle is 38.341° , the number of grooves is 9.999, the diameter of the inner tangent circle is 13.154 mm, and the angular velocity of groove wheel is 5.998 rad/s, the improved value of the coefficient of uniform volatility is 4.11%.

(3) According to the optimal combination of structural parameters, the groove tooth inclination angle is 38° , the number of grooves is 10, the diameter of the inner tangent circle is 13 mm, and the angular velocity of groove wheel is 6 rad/s. The bench test and the whole machine test are carried out. The bench test and the whole machine test were carried out. The bench test showed that: the coefficient of uniform volatility by the traditional PWM motor was 6.32%; the coefficient of uniform volatility by the FOC motor was 4.62%.

The results of the discrete element method (DEM) simulation provide a theoretical basis for the design of the motor control strategy, enabling uniformity control of fertilizer discharge in practical applications.

ACKNOWLEDGEMENTS

This study was supported by the National Natural Science Foundation of China (32060414), Inner Mongolia Natural Science Foundation (2022MS05049), Inner Mongolia Autonomous Region 's first-class discipline research special project (YLXKZX-NND-046) and Ordos City Key R & D Program (YF20240031).

REFERENCES

- [1] Chen, K. K., Yuan, Y. W., Zhao, B., Zhou, L. M., Niu, K., Dong, X., Jin, X., & Zheng, Y. J. (2022). Design of dynamic compensation system for corn seeding position based on fuzzy PID control and analysis of bench test. *INMATEH-Agricultural Engineering*, 67(2), 394-405. <https://doi.org/10.35633/inmateh-67-40>
- [2] Dun, G. Q., Wu, X. P., Ji, X. X., & Wei, Y. H. (2023). Design and experiment of an electric control spiral-pushing feed mechanism for field fertilizer applicator. *Applied Sciences*, 13(23), 12628. <https://doi.org/10.3390/app132312628>
- [3] Dun, G., Li, X., Ji, X., Sheng, Q., & Ji, W. (2024). Optimization and experiment of co-rotating and double-spiral fertilizer feeder (同向双螺旋排肥器优化设计与试验). *Journal of Huazhong Agricultural University*, 05, 278-287. <https://doi.org/10.13300/j.cnki.hnlkxb.2024.05.031>
- [4] Li Xin, Jiang Xinbo, Ji Xinxin, Dun Guoqiang, Zhao Yu, & Du Jiaying. (2023). Optimization design and experiment of spiral double-wheel fertilizer applicator based on genetic algorithm (基于遗传算法的螺旋双轮排肥器优化设计与试验). *Journal of Henan Agricultural University*, 06, 1026-1034. <https://doi.org/10.16445/j.cnki.1000-2340.20230619.001>
- [5] Liao, Z. Q., Dai, Y. L., Wang, H., Ketterings, Q. M., Lu, J. S., Zhang, F. C., & Fan, J. L. (2023). A double-layer model for improving the estimation of wheat canopy nitrogen content from unmanned aerial vehicle multispectral imagery. *Journal of Integrative Agriculture*, 22(7), 2248-2270. <https://doi.org/10.1016/j.jia.2023.02.022>
- [6] Mondal, S., Roy, P., Banerjee, A., & Mondal, U. (2024). A CKF-based sensor-less FOC integrated with gh-SVPWM for PMSM drives. *Electrical Engineering*, 106(3), 3461-3473. <https://doi.org/10.1007/s00202-023-02169-8>
- [7] Shi, Y. Z., Yu, J. J., Liu, M. H., Zhang, G. L., Lu, F. X., Qin, Z. X., Fang, P., & Chen, X.F. (2022) Design and experiment of cam-linkage self-cleaning fertilizer apparatus. *INMATEH-Agricultural Engineering*,

- 68(3), 424-434. <https://doi.org/10.35633/inmateh-68-42>
- [8] Song Cancan, Zhou Zhiyan, Wang Gguobin, Wang Xunwei, & Zang Ying. (2021). Optimization of Structural Parameters for the Slot Wheel of a Fertilization Drone Slot-Wheel Type Applicator (优化施肥无人机槽轮式排肥器槽轮结构参数优选). *Transactions of the Chinese Society of Agricultural Engineering*, 22, 1-10. <https://doi.org/10.11975/j.issn.1002-6819.2021.22.001>
- [9] Su, N., Xu, T. S., Song, L. T., Wang, R. J. & Wang, Y. Y., (2015). Variable rate fertilization system with adjustable active feed-roll length. *International Journal of Agricultural & Biological Engineering*, 8(4), 19-26. <https://doi.org/10.3965/j.ijabe.20150804.1644>
- [10] Sugirbay, A. M., Zhao, J. J., Nukeshev, S. O., & Chen, J.J. (2020). Determination of pin-roller parameters and evaluation of the uniformity of granular fertilizer application metering devices in precision farming. *Computers and Electronics in Agriculture*, 179, 105835. <https://doi.org/10.1016/j.compag.2020.105835>
- [11] Wang Zaiman, Huang Yichun, Wang Baolong, Zhang Minghua, Ma Yuexin, Ke Xinrong, & Luo Xiwen. (2018). Design and experiment of rice precision metering device with sowing amount stepless adjusting (播量无级调节水稻精量排种装置设计与试验). *Transactions of the Chinese Society of Agricultural Engineering (Transactions of the CSAE)*, 34(11), 9-16. <https://doi.org/10.11975/j.issn.1002-6819.2018.11.002>
- [12] Wang, B. W., Che, G., Wan, L., Zhao, N. C., & Guan, Z. N. (2023). Design and experiment of impeller type variable fertilizer discharger device based on EDEM simulation. *INMATEH-Agricultural Engineering*, 71(3), 734-744. <https://doi.org/10.35633/inmateh-71-64>
- [13] Wang, J. F., Fu, Z. D., Jiang, R., Song, Y. L., Yang, D. Z., & Wang, Z. T. (2023). Influences of grooved wheel structural parameters on fertilizer discharge performance: Optimization by simulation and experiment. *Powder Technology*, 418, 118309. <https://doi.org/10.1016/j.powtec.2023.118309>
- [14] Wang, Y. B., Liang, F., Xu, F., Deng, W. H., & Yu, Y. Z. (2022). Discrete element simulation and experiment of opposed double helix outer sheave fertilizer discharger. *INMATEH-Agricultural Engineering*, 68(3), 617-628. <https://doi.org/10.35633/inmateh-68-61>
- [15] Wen, F. J., Wang, H. H., Zhou, L., & Zhu, Q. C. (2024). Optimal design and experimental research on the spiral groove wheel fertilizer apparatus. *Scientific Reports*, 14(1), 510. <https://doi.org/10.1038/s41598-024-51236-y>
- [16] Xu, B., Cui, Q. L., & Zheng, D. C. (2023). Improvement design and simulation analysis on centrifugal disc organic fertilizer spreader. *INMATEH-Agricultural Engineering*, 70(2), 328-336. <https://doi.org/10.35633/inmateh-70-32>
- [17] Yang Zhou, Zhu Qingchuang, Sun Jianfeng, Chen ZhaoChun, & Zhang zhuowei. (2018). Study on the performance of fluted roller fertilizer distributor based on EDEM and 3D printing (基于 EDEM 和 3D 打印成型的外槽轮排肥器排肥性能研究). *Journal of Agricultural Mechanization Research*, 40(5): 175-180. <https://doi.org/10.3969/j.issn.1003-188X.2018.05.032>
- [18] Zhang Minghua, Wang Zaiman, Luo Xiwen, Jiang Enchen, Dai Yizheng, Xing He, & Wang Baolong. (2018). Effect of double seed-filling chamber structure of combined type-hole metering device on filling properties (组合型孔排种器双充种室结构对充种性能的影响). *Transactions of the Chinese Society of Agricultural Engineering (Transactions of the CSAE)*, 34(12), 8-15. <https://doi.org/10.11975/j.issn.1002-6819.2018.12.002>
- [19] Zhou, L. M., Niu, K., Chen, K. K., Yuan, Y. W., Xue, B., & Wang, L. L. (2022). Design and test of real-time monitoring system for non-contact fertilization flow. *INMATEH-Agricultural Engineering*, 66(1), 351-360. <https://doi.org/10.35633/inmateh-66-35>
- [20] Zhu Qingzhen, Wu Guangwei, Chen Liping, Zhao Chunjiang, & Meng Zhijun. (2018). Influences of structure parameters of straight flute wheel on fertilizing performance of fertilizer apparatus (槽轮结构参数对直槽轮式排肥器排肥性能的影响). *Transactions of the Chinese Society of Agricultural Engineering (Transactions of the CSAE)*, 34(18), 12-20. <https://doi.org/10.11975/j.issn.1002-6819.2018.18.002>

DESIGN AND EXPERIMENT OF THE RECIPROCATING ADJUSTABLE STRIKING-VIBRATING COMBINED DEVICE for ROOT-SOIL SEPARATION of *GENTIANA*

往复调节式龙胆根土分离敲-振组合装置设计与试验

Hongguang CUI ¹⁾, Guangshuo CHEN ¹⁾, Zhanqiu XIE ¹⁾, Wenzhong HUANG ²⁾, Weiming BIAN ²⁾,
Liyan WU ¹⁾, Cuihong LIU ^{1*)}

¹⁾ Shenyang Agricultural University, College of Engineering, Shenyang / China;

²⁾ Fushun Agricultural and Rural Development Service Center, Fushun / China

Tel: +8615942060166; E-mail: cuihongliu77@syau.edu.cn

DOI: <https://doi.org/10.35633/inmateh-74-80>

Keywords: Agricultural Machinery; Gentian; Root-Soil Separation; Crank Slider Mechanism; Reciprocating Adjustable mechanism; Striking-Vibrating Combination

ABSTRACT

In order to solve the problem of low efficiency and potential damage in the separation of *Gentiana* roots from soil, a reciprocating adjustable striking-vibration combined device was designed, along with its performance testing. The ranges of working parameters for the vibration mechanism, striking mechanism, and adjustable reciprocating mechanism were determined through dynamic analysis of the mechanisms and materials. The effects of vibration frequency (X_1), crank speed (X_2), and screw feed speed (X_3) on the threshing efficiency (Y_1) and damage percentage (Y_2) were studied using a ternary quadratic regression orthogonal combination experimental method, combined with response surface analysis to explore the interaction effects of these factors on the indicators. A regression model was established through variance analysis. The significant factors affecting Y_1 were X_2 , X_3 , and X_1 in that order, while the significant factors affecting Y_2 were X_1 , X_3 , and X_2 . In the interaction of factors, X_1X_2 significantly affected both Y_1 and Y_2 ; X_1X_3 had extremely significant impact on both Y_1 and Y_2 ; and X_2X_3 had extremely significant impact on Y_1 . The optimal working parameters for the root-soil separation device of *Gentiana* were determined to be vibration frequency of 6 Hz, crank speed of 204 r/min, and screw feed speed of 15 mm/s. With this combination of parameters, experimental tests yielded a threshing efficiency of 90.8% and a damage percentage of 5.9%. The relative errors compared with the theoretical optimization results were less than 5%. This study meets requirements for the root-soil separation of *Gentiana*.

摘要

为解决龙胆脱土效率低、易损伤的问题，设计了一种往复调节式敲-振组合的龙胆根土分离装置，并对其进行了设计和性能试验。对敲击机构进行动力学分析，对龙胆根土复合体在振动筛上的受力进行分析，确定振动机构、敲击机构及调节式往复运动机构的工作参数范围。采用三元二次回归正交组合试验方法，以振动装置振动频率、敲击装置曲柄转速、调节式往复运动装置丝杠进给速度为试验因素，以脱净率、损伤率为试验指标，实施试验并对其结果进行分析，建立影响因素与评价指标回归模型。结果表明：龙胆根土分离装置最优工作参数为振动频率 6 Hz、曲柄转速 204 r/min、丝杠进给速度 15 mm/s，在此参数组合下进行试验台试验，得到龙胆根系脱净率为 90.8%，损伤率为 5.9%，与理论优化结果相对误差均小于 5%。能够满足龙胆根土分离田间作业要求。

INTRODUCTION

Gentiana (*Gentiana scabra* Bunge.) is a typical Chinese medicinal material, belonging to the Gentianaceae family of perennial herbs, and its rhizome is used medicinally for its effects in purging excessive fire from the liver and gallbladder (Gao et al., 2020). As an herbaceous root-type medicinal material, it is planted with a small spacing between plants, leading to a tangle of root systems from multiple plants in the later stages of growth. Compared to single-stemmed medicinal materials, the harvesting of *Gentiana* is challenging in terms of soil removal. During the harvesting process, it is difficult to achieve complete root-soil separation with field excavation and harvesting machinery, resulting in a large number of *Gentiana* root-soil complexes. Root-soil separation is an important post-harvest production step. Currently, farmers employ a significant labor force for manual separation of *Gentiana* roots and soil, which is labor-intensive, has low work efficiency, and is costly. Researching the mechanical separation of root-soil complexes for root-type medicinal materials, to achieve a higher root-soil threshing efficiency and lower root damage percentage during harvesting, is of great significance for the grading of medicinal materials, increasing the economic income of farmers, reducing the time for washing and drying medicinal materials, and minimizing the loss of effective components.

Overseas research on rhizome-type medicinal material harvesting and separation devices is relatively scarce, while numerous scholars in China have conducted relevant research on rhizome-type harvesting and separation devices and achieved certain results. For instance, *Liu Zhixin et al. (2024)* addressing the issues of separation damage in potato harvesters, designed a three-stage potato soil low-loss separation device, which was optimized through EDEM simulation to reduce the rate of damaged potatoes. *Yang Ranbing et al. (2024)* designed a low-damage fresh-eating sweet potato combine harvester based on a two-segment potato-soil separation device, which reduced the skin-breaking rate and impurity rate of sweet potato. *Liu Yafeng et al. (2024)* realized the harvesting and root-soil separation of rakkyo through roller differential crushing and brush-type conveying separation, which improved the root-soil separation rate and reduced the damage percentage. *Yan Shuai et al. (2023)* designed a drum-type experimental platform for separation of *Codonopsis pilosula* roots and soil, and through kinematic analysis, simulation analysis, and experimental platform testing, they optimized the design parameters of the root-soil separation device, achieving efficient damage reduction. *Tao Guixiang et al. (2022)* addressing the issues of low root-soil separation rate and high rhizome damage rate in the harvesting of *Isatis indigotica*, designed a combined oscillating type *Isatis indigotica* root-soil separation device, and through parameter optimization, enhanced the ability to crush and screen soil. *Chen Xueshen et al. (2015)* designed a two-roller root soil separation device for the root soil removal of Chinese medicinal material *Polygonum cuspidatum*. The team of *Zhang Zhaoguo* at Kunming University of Science and Technology has researched the *Panax notoginseng* harvesting and separation device, conducting an analysis of the working mechanism and parameter optimization of the *Panax notoginseng* harvester's conveying and separating device. They have used a secondary vibrating screen, a finger-like rubber lifting rod structure, and a two-stage lifting transmission method for the separation and cleaning of *Panax notoginseng* roots and soil (*Wang et al., 2023; Cui et al., 2018, Xue, 2022*).

Currently, traditional Chinese medicinal material harvesters have the advantages of high work efficiency and low energy consumption. However, due to the diversity of Chinese medicinal products, they are not suitable for the separation and harvesting of the root-soil complex of *Gentiana* (RSCG), which have dense and intertwined root systems and soil. In this paper, a root-soil separation device targeting RSCG is developed, which combines striking and vibration separation methods and is equipped with an adjustable reciprocating mechanism. This allows the striking mechanism to descend with the height reduction of the root-soil complex, thereby improving work efficiency and soil threshing efficiency, reducing root damage percentage, and enhancing the quality of operation. Through dynamic analysis, key components are designed and parameters are selected. Orthogonal tests are conducted on the prototype's threshing efficiency and damage percentage to seek optimal working parameter combinations, aiming to provide technical references for the mechanized root-soil separation of *Gentiana*.

MATERIALS AND METHODS

Mechanism design and working principle

The root-soil separation device of *Gentian* is primarily composed of three parts: the striking mechanism, the vibrating mechanism, and the adjustable reciprocating mechanism. The striking mechanism and the vibrating mechanism are driven by crank-slider mechanisms, while the adjustable reciprocating mechanism is driven by a ball screw. The structural diagram is illustrated in Figure 1.

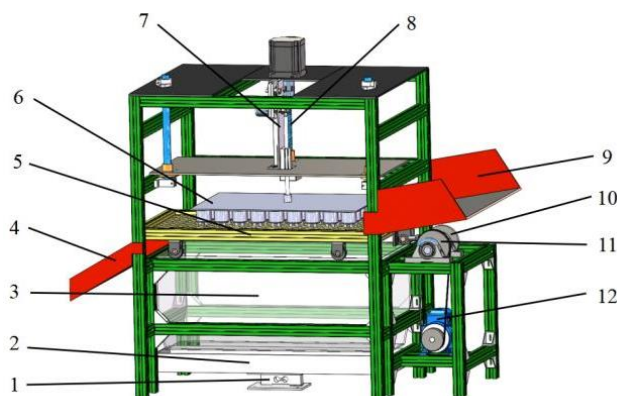


Fig. 1 - Structure diagram of root-soil separation device of Gentian

1-Weighing sensor; 2- Soil weighing tray; 3- Soil retaining box; 4- Discharge outlet; 5- Vibrating screens; Striking plate; 7- Striking mechanism; 8- Adjustable reciprocating mechanism; 9- Feed Inlet 10- Eccentric Wheel; 11- Belt Pulley; 12- Electric Motor

Working principle

The incompletely separated RSCG scattered in the field after the field harvester's operation are placed on the vibrating screen of the root-soil separation device of *Gentian* through the feed inlet. The striking mechanism drives the striking plate to hit RSCG, while the adjustable reciprocating mechanism moves downward at a preset speed, achieving dynamic adjustment of the distance between the striking plate and RSCG as their height decreases. Under the reciprocating vibration of the vibrating mechanism, the crushed soil falls through the mesh holes of the vibrating screen into the soil weighing tray, while the gentian roots, being larger than the diameter of the mesh holes, remain on the surface of the vibrating screen. Driven by the friction force of the vibrating screen, the *Gentian* roots move towards the discharge outlet, thereby achieving the separation of *Gentian* roots and soil. With the reciprocating motion of the striking mechanism, a large quantity of *Gentian* can be processed, enhancing work efficiency and saving labor, while achieving better processing results for RSCG.

Design of Striking Mechanism

Due to its ability to achieve reciprocating striking motion, simple structure, easy processing, and good adjustability of follower motion laws, the crank-slider mechanism is selected as the driving mechanism for the striking mechanism. The schematic diagram of the mechanism is shown in Figure 2, where AB represents the crank, BC represents the connecting rod, and the rectangle represents the striking plate C . During operation, the crank-slider mechanism ABC reciprocates under the rotation of the crank, causing the striking plate C to reciprocate and tap RSCG on the vibrating screen, thereby separating the *Gentian* roots from the soil aggregates. The structure and operating parameters of the crank-slider mechanism directly affect the striking effect, which is analyzed specifically in this paper.

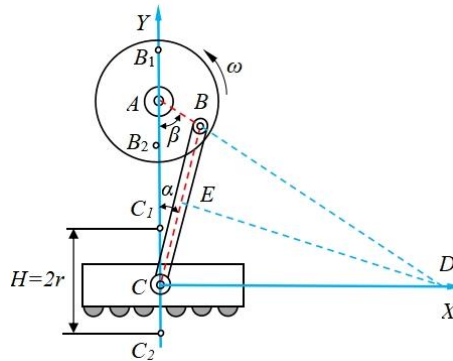


Fig. 2 - Schematic diagram of Crank slider mechanism

A rectangular coordinate system is established with the origin at point A , which is the rotary center of the crank in Figure 2, and with the frame AC collinear with the Y -axis. The angles α and β represent the angles between BC and the Y -axis, and AB and the Y -axis, respectively (Feng et al., 2023; Luo et al., 2018, Tang et al., 2020). Point E is the midpoint of the connecting rod BC , while Point D is the instantaneous center of velocity for the connecting rod BC . Therefore, the trajectory coordinates of the points C is $y_C = y_B - l_{BC} \cos \alpha$.

Due to the limitations of the frame's spatial structure and the installation position of the striking mechanism, the initial length range of the crank is determined to be $40 \text{ mm} \leq l_{AB} \leq 50 \text{ mm}$, and the connecting rod length l_{BC} is 85 mm. Establish the velocity equation of the striking mechanism's motion. Given the displacement equation of the striking mechanism, the first derivative of displacement with respect to time is velocity. By taking the first derivative of the displacement equation, the velocity of point C can be obtained.

$$Y'_C = l_{AB} \cdot l_{BC} (\beta' \sin \beta \cos \alpha + \alpha' \sin \alpha \cos \beta) \quad (1)$$

Establish the acceleration equation for the striking mechanism's motion. According to the first derivative of displacement with respect to time being velocity, and the second derivative being acceleration. Solve the second derivative of equation (1) to obtain the acceleration at point C .

$$Y''_C = l_{AB} \cdot l_{BC} [(\alpha'^2 + \beta'^2) \cos \alpha \cos \beta - 2\alpha'\beta' \sin \alpha \sin \beta] \quad (2)$$

From the acceleration formula (2), it can be seen that the acceleration of the striking mechanism is related to the rotational speed of crank and the lengths of l_{AB} and l_{BC} (Zou, 2023; Lu, 2022).

The angular velocity of the crank AB is ω_A , the angular velocity of the connecting rod BC is ω_C , and the angular velocity of the instantaneous center of velocity D is ω_D . According to the kinematic principles of plane motion of a rigid body, it can be derived:

$$v_B = l_{AB} \omega_A \tag{3}$$

$$\omega_D = \frac{v_B}{l_{BD}} = \frac{l_{AB} \cdot \omega_A}{l_{BD}} \tag{4}$$

$$v_C = l_{CD} \omega_D = \frac{l_{CD} \cdot l_{AB} \cdot \omega_A}{l_{BD}} \tag{5}$$

Let the moment of inertia of *AB* about point *A* be J_1 , and the moment of inertia of *BC* about its centroid *E* be J_2 . The moment of inertia of *BC* about its instantaneous center of velocity *D* is J_C , according to the kinetic energy theorem, the total kinetic energy of this system of particles is:

$$T = T_{AB} + T_{BC} + T_C \tag{6}$$

where: $T_{AB} = \frac{1}{2} J_1 \omega_A^2$, $T_{BC} = \frac{1}{2} m_{BC} v_E^2 + \frac{1}{2} J_C \omega_E^2$, $T_C = \frac{1}{2} m_C v_C^2$, substituting T_{AB} , T_{BC} and T_C into equation (6) yields

$$T = \frac{1}{2} J_1 \omega_A^2 + \frac{1}{2} m_{BC} v_E^2 + \frac{1}{2} J_C \omega_E^2 + \frac{1}{2} m_C v_C^2 \tag{7}$$

where: $v_E = \omega_D \cdot l_{DE}$, $\omega_E = \frac{2v_E}{l_{BC}}$, $J_1 = \frac{1}{3} m_{AB} l_{AB}^2$, $J_C = \frac{1}{12} m_{BC} l_{BC}^2$.

The soil crushing by striking is an instantaneous collision process, and the collision process always satisfies the law of conservation of energy, neglecting the work done by the impact force generated during the collision process in the direction of deformation of RSCG and the energy consumed by the frictional force of the mechanism (Qian, 2015; Zhao et al., 2013). Based on the previous impact test of RSCG, the striking energy is determined to be 1.4 J. According to the kinetic energy theorem for the system of particles, the formula is obtained:

$$\Delta E_k = C \tag{8}$$

$$\Delta E_k = T_{AB} + T_{BC} + T_C \tag{9}$$

When the angle β is 45° , the range of the crank length is $40 \text{ mm} \leq l_{AB} \leq 50 \text{ mm}$, and the length of the connecting rod is 85 mm. The masses of the crank, connecting rod, and striking plate are measured to be 0.01 kg, 0.06 kg, and 3 kg, respectively. Substituting these values, the range of the crankshaft speed is calculated to be $168 \text{ r/min} \leq n \leq 240 \text{ r/min}$.

Design of Vibrating Mechanism

The vibration mechanism is shown in Figure 3. Under the drive of the motor, the crank disc performs uniform circular motion, which leads the connecting rod to move periodically. Through the action of the connecting rod on the vibration screen, the screen surface is driven to move periodically. This causes RSCG to move back and forth in front of the screen, with the forward movement distance being greater than the backward movement distance. This ensures that RSCG moves from the material feed inlet to the material discharge outlet (Li et al., 2024), thereby achieving the planar reciprocating vibration of the vibration screen. The struck root-soil complex of *Gentian* is affected by the vibration frequency of the vibration mechanism during the movement of the sieve mesh. If the vibration frequency is too low, RSCG cannot generate relative motion with the sieve mesh. The soil that is struck and falls cannot spread out on the sieve surface, preventing the separation of the *Gentiana* root system from the soil. If the vibration frequency is too high, RSCG moves too quickly on the sieve mesh, leading to RSCG being carried away without sufficient screening. Both excessively low or high vibration frequencies can result in poor screening effects. Therefore, designing reasonable parameters for the vibration mechanism is crucial for improving the soil removal effect.

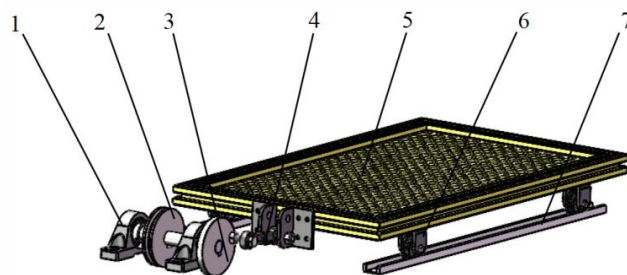


Fig. 3 - Structure diagram of Vibrating mechanism

- 1- Bearing housing; 2- Pulleys; 3- Crank disc; 4- Connecting rod;
- 5- Sieve body; 6- Sieve wheel; 7- Track

Motion Analysis of RSCG

The main form of motion for RSCG on the screen surface is the reciprocating motion of the composite along the screen surface. The reciprocating motion of RSCG along the screen surface is related to the frictional forces between the composite and the screen surface, as well as the composite and the striking plate. In order to continuously direct RSCG towards the discharge outlet, the force propelling the composite towards the discharge outlet along the screen surface must be greater than the force pushing it towards the feed inlet. To improve the screening efficiency, it is necessary to increase the distance RSCG travels on the screen surface. Therefore, the composite must be able to move along the screen surface towards the feed inlet. The force analysis of RSCG's motion on the screen surface is shown in Figure 4 (Cui *et al.*, 2021).

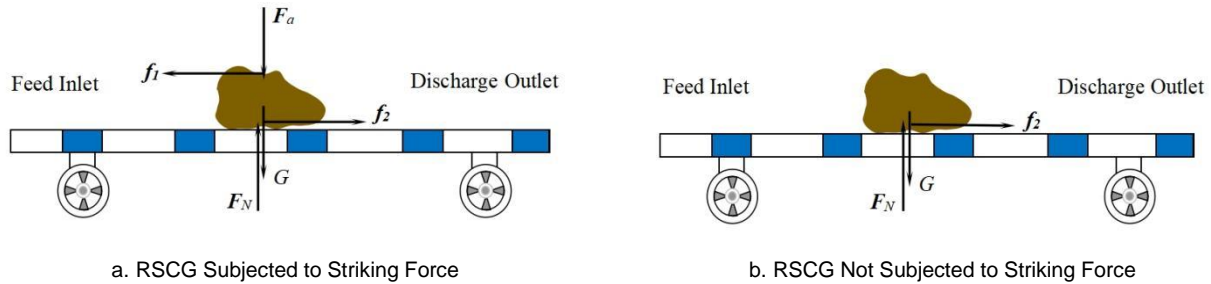


Fig. 4 - Force analysis diagrams of RSCG along the screen

Note: F_N represents the supporting force of the screen surface on the material, N ; F_a represents the striking force of the striking plate on the material, N ; f_1 represents the frictional force of the striking plate on the material, N ; f_2 represents the frictional force of the screen surface on the material, N ; G represents the material gravity, N .

The motion of RSCG includes movement from the feed inlet to the discharge outlet of the vibrating screen, as well as root-soil separation (Wei *et al.*, 2019, Wei *et al.*, 2023, Lv *et al.*, 2022, Wei *et al.*, 2018). When the vibrating screen is not subjected to vibration, the shape of its screen surface can be approximated to a straight line (Quan *et al.*, 2013). RSCG is considered as a rigid body. If air resistance is neglected, the force analysis is shown in Figure 4. When RSCG is subjected to a striking force, f_2 is the resistance for the composite to move towards the feed inlet. The dynamic equation in this state is:

$$f_1 - f_2 = ma_{x1} \quad (10)$$

$$f_1 = \mu_1 F_a \quad (11)$$

$$f_2 = \mu_2 F_N \quad (12)$$

$$F_N = F_a + G \quad (13)$$

$$f_2 = ma_0 = mA\omega^2 \cos(\omega t) \quad (14)$$

where: m is the mass of RSCG, kg; g is the acceleration due to gravity, taken as 9.8 m/s²; μ_1 is the coefficient of friction between the striking plate and RSCG; μ_2 is the coefficient of friction between the screen surface and RSCG; a_{x1} is the tangential acceleration of RSCG when subjected to the striking force, m/s².

Substitute equations (11) and (14) into equation (10) and then rearrange to obtain.

$$\mu_1 F_a - mA\omega^2 \cos(\omega t) = ma_{x1} \quad (15)$$

Similarly, when RSCG is not subjected to a striking force, f_2 is the driving force for the composite to move towards the discharge opening. The dynamic equation in this state is:

$$f_2 = ma_{x2} \quad (16)$$

$$f_2 = ma_0 = mA\omega^2 \cos(\omega t) \quad (17)$$

$$f_2 = \mu_2 F_N \quad (18)$$

$$F_N = G \quad (19)$$

Collation available:

$$mA\omega^2 \cos(\omega t) = ma_{x2} \quad (20)$$

where: a_{x2} represents the tangential acceleration of RSCG when it is not subjected to a striking force, m/s².

Analysis indicates that the reciprocating motion of RSCG along the screen surface is related to the screen vibration amplitude A , the rotational angular velocity of the crank disc ω , the mass of RSCG m , and the frictional force experienced by RSCG a . The back-and-forth motion of RSCG on the vibrating screen can extend the travel distance of the composite on the screen surface, which is beneficial for root-soil separation. When RSCG is subjected to a striking force, it moves along the screen surface towards the feed inlet; reducing the screen vibration amplitude A and increasing the rotational angular velocity of the crank disc ω are beneficial for the movement of RSCG towards the feed inlet. Similarly, when RSCG is not subjected to a striking force, it moves along the screen surface towards the discharge outlet; increasing the screen vibration amplitude A and decreasing the rotational angular velocity of the crank disc ω are beneficial for the movement of RSCG towards the discharge outlet. Preliminary tests have determined that when the vibration frequency of the vibrating screen is within the range of 4 Hz to 8 Hz, the *Gentiana* root system after soil removal can move along the screen surface towards the discharge outlet.

Adjustable reciprocating mechanism

The adjustable reciprocating mechanism is composed of a ball screw pair, with the purpose of adjusting the distance between the striking plate and RSCG. As RSCG is reduced in size by the striking plate, if the striking plate always remains stationary, it would result in the striking plate being unable to strike RSCG. The role of the ball screw is to dynamically adjust the distance between the striking plate and RSCG. The adjustable reciprocating mechanism is shown in Figure 5.

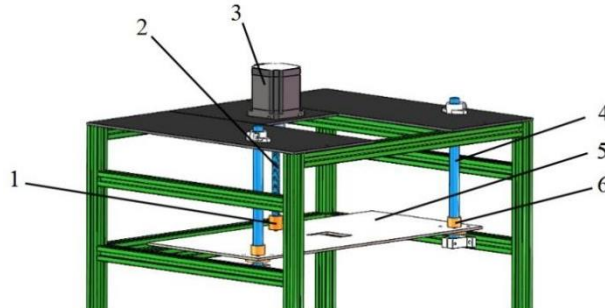


Fig. 5 - Structure diagram of Adjustable reciprocating mechanism

1. Optic axis; 2- Stepping motor; 3- Ball screw; 4- Nut; 5- Carrier platforms; 6- Ball round flange linear bearings

By calculation, the range of the crankshaft speed is determined to be 168 r/min $\leq n \leq$ 240 r/min. Taking the midpoint of the crankshaft speed, $n=204$ r/min, it is found that the time required for the striking mechanism to strike once is 0.3 seconds. Through preliminary impact tests, the average range of height difference Δh is determined to be 3.07 mm to 6.03 mm. Calculations are performed using equation (21), the range of the descending speed for the adjustable reciprocating mechanism is determined to be 10~20 mm/s.

$$v = \frac{\Delta h}{t} \quad (21)$$

where: v is the descending speed of the lead screw, mm/s; Δh is the average height difference of RSCG, mm; t is the time for the striking mechanism to strike once, s.

Experiment design

Experiment condition and equipment

The experimental site is the laboratory of the College of Engineering at Shenyang Agricultural University. The experimental materials are sourced from the *Gentiana* planting base in Qingyuan Manchu Autonomous County, Fushun City. To adapt to the root-soil separation device and operational requirements, the stems and leaves of the *Gentiana* are removed before the experiment, and the root blocks are divided into appropriately sized root-soil complex. The experimental method refers to GB/T5667-2008 "Agricultural Machinery Production Test Methods." The test indicators are the threshing efficiency and damage percentage of the *Gentiana* root system. Natural air drying is utilized to maintain the moisture content of the *Gentiana* root-soil composite between 10% and 15%.

Main experimental equipment and instruments: root-soil separation device of Gentian test bench, one laptop computer, a laser tachometer (range 1–9999 r/min, accuracy $\pm 0.02\%$), a weighing sensor (range 50 kg, accuracy 0.02 kg), a multifunctional electronic stopwatch, and a steel tape measure (range 3 m, accuracy 1 mm), as shown in Figure 6.



Fig. 6 - Test bench for root-soil separation of *Gentiana*

- 1- High-speed camera; 2- Real-time weight detection system for detached soil;
- 2- Striking mechanism; 4- Vibrating mechanism; 5- Adjustable reciprocating mechanism

Experiment factors and indexes

Based on the results of single-factor experiments and the design of mechanisms, it has been determined that the vibration frequency (X_1), crank speed (X_2), and screw feed speed (X_3) are the three most significant factors affecting the performance of the root-soil separation device of *Gentiana*, and the range of levels for the test factors has been established. According to the Box-Behnken three-factor three-level experimental design in Design-Expert 12.0 software, the work performance of the root-soil separation device of *Gentiana* was studied, with the root threshing efficiency and damage percentage as the response values. The levels of the test factors are shown in Table 1. The main indicators for evaluating the efficiency of the root-soil separation of *Gentiana* are the threshing efficiency and damage percentage of the *Gentiana* root system, and the calculation formulas for the evaluation indicators are shown in equations (22) and (23).

$$Y_1 = \frac{m_0 - m_1}{m_0 - m_2} \times 100\% \tag{22}$$

$$Y_2 = \frac{m_3}{m_2} \times 100\% \tag{23}$$

where: Y_1 is the threshing efficiency of *Gentiana* roots, %; Y_2 is the damage percentage of *Gentiana* root system, %; m_0 is the total mass of RSCG before the test, kg; m_1 is the total mass of RSCG after the test, kg; m_2 is the total mass of the net root system without residual soil, kg; m_3 is the mass of damaged *Gentiana* roots after root-soil separation, kg.

Table 1

Factors and levels of combination experiment

Levels	Factors		
	Vibration frequency	Crank speed	Screw feed speed
	[Hz]	[r·min ⁻¹]	[mm·s ⁻¹]
	X_1	X_2	X_3
-1	4	168	10
0	6	204	15
1	8	240	20

RESULTS

The orthogonal test plan includes 17 test points, among which there are 12 analysis factors and 5 zero-point estimation errors. The test design scheme and test results are shown in Table 2. Based on the experimental data in Table 2, the Design-Expert 12.0 software is used to perform a multivariate regression fitting analysis on the experimental data, establishing a second-order polynomial regression model for the test indicators of *Gentiana* root threshing efficiency Y_1 and damage rate Y_2 against the three test factors of vibration frequency X_1 , crank speed X_2 , and screw feed speed X_3 .

Table 2

Experimental plan and results

No.	Vibration frequency [Hz]	Crank speed [r·min ⁻¹]	Screw feed speed [mm·s ⁻¹]	Y_1 [%]	Y_2 [%]
1	-1	1	0	91.7	6.1

No.	Vibration frequency [Hz]	Crank speed [r·min ⁻¹]	Screw feed speed [mm·s ⁻¹]	Y ₁ [%]	Y ₂ [%]
2	0	0	0	94.9	3.7
3	0	0	0	94.7	3.5
4	-1	0	-1	91.6	5.6
5	1	0	1	91.6	5.4
6	1	-1	0	92.8	4.5
7	1	0	-1	92.9	3.9
8	0	0	0	94.3	3.4
9	-1	0	1	94.4	5.2
10	-1	-1	0	93.9	4.8
11	0	-1	1	94.1	5.3
12	1	1	0	92.2	4.6
13	0	1	1	91.7	5.7
14	0	0	0	94.4	3.3
15	0	-1	-1	92.1	4.6
16	0	0	0	94.8	3.6
17	0	1	-1	92.2	4.6

Experiment results variance analysis

According to the analysis of variance results in Table 3, it can be seen that the model P for the threshing efficiency (Y_1) and damage percentage (Y_2) are both significantly less than 0.01, and the P for the lack of fit are both significantly greater than 0.05. The model determination coefficients R^2 are 0.9847 for the threshing efficiency and 0.9764 for the damage percentage. In summary, it can be concluded that the regression model is significant and has a good fit, making the model reliable.

Table 3

Data significance experiment and analysis of variance

Source of variation	The threshing efficiency Y_1					The damage percentage Y_2				
	SS	DF	MS	F value	P value	SS	DF	MS	F value	P value
Model	25.77	9	2.86	50.04	<0.0001**	12.33	9	1.37	32.24	<0.0001**
X_1	0.5512	1	0.5512	9.63	0.0172*	1.36	1	1.36	32.03	0.0008**
X_2	3.25	1	3.25	56.83	<0.0001**	0.4050	1	0.4050	9.53	0.0176*
X_3	1.13	1	1.13	19.66	<0.0030**	1.05	1	1.05	24.74	0.0016***
X_1X_2	0.6400	1	0.6400	11.19	0.0123*	0.3600	1	0.3600	8.47	0.0226*
X_1X_3	4.20	1	4.20	73.45	<0.0001**	0.9025	1	0.9025	21.24	0.0025*
X_2X_3	1.56	1	1.56	27.31	<0.0012**	0.0400	1	0.0400	0.9412	0.3643
X_1^2	3.68	1	3.68	64.34	<0.0001**	2.29	1	2.29	53.89	0.0002**
X_2^3	4.51	1	4.51	78.83	<0.0001**	2.45	1	2.45	57.60	0.0001**
X_3^2	4.73	1	4.73	82.69	<0.0001**	2.61	1	2.61	61.44	0.0001**
Residual	0.4005	7	0.0572			0.2975	7	0.0425		
Lack of Fit	0.1325	3	0.0442	0.6592	0.6187	0.1975	3	0.0658	2.63	0.1864
Pure error	0.2680	4	0.0670			0.1000	4	0.0250		
Total sum	26.17	16				12.63	16			

On the basis that the model is significant without loss of fitting, the non-significant terms in the model are eliminated, and the regression equation is obtained, as shown in equations (24) and (25).

$$Y_1 = 94.62 - 0.263X_1 - 0.638X_2 + 0.375X_3 + 0.4X_1X_2 - 1.03X_1X_3 - 0.625X_2X_3 - 0.935X_1^2 - 1.04X_2^2 - 1.06X_3^2 \quad (24)$$

$$Y_2 = 3.50 - 0.413X_1 + 0.225X_2 + 0.363X_3 - 0.3X_1X_2 + 0.475X_1X_3 + 0.1X_2X_3 + 0.738X_1^2 + 0.763X_2^2 + 0.788X_3^2 \quad (25)$$

Analysis of influencing factors

The response surface plots were obtained using Design-Expert 12.0 software as shown in Figure 7, which further investigate the impact patterns of the test factors (vibration frequency, crank speed, and screw feed rate) and their interactions on the test indicators (threshing efficiency Y_1 and damage percentage Y_2).

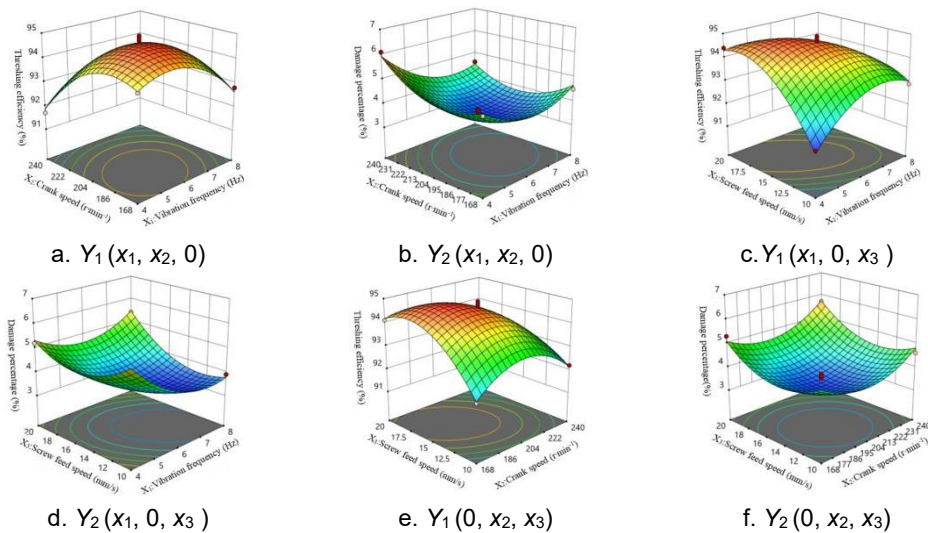


Fig. 7 - Response surface analysis of the factors' interaction effect on the index

Figures 7a and 7b are the response surface plots showing the interactive effects of vibration frequency (X_1) and crank speed (X_2) on the threshing efficiency (Y_1) and damage percentage (Y_2). The interaction is significant. When the vibration frequency ranges from 4 to 8 Hz and the crank speed ranges from 168 to 240 r/min, the threshing efficiency is relatively optimal and the damage percentage is relatively low. When the screw feed speed (X_3) is at the central level ($X_3 = 15$ mm/s), at a given vibration frequency, the threshing efficiency first increases and then decreases with the increase of the crank speed, showing a significant change; the damage percentage first decreases and then increases with the increase of the crank speed, showing a significant change; when the crank speed is constant, the threshing efficiency first increases and then decreases with the increase of the vibration frequency, and the change amplitude is higher than the influence of the crank speed change. The damage percentage first decreases and then increases with the increase of the vibration frequency, and the change amplitude is lower than the influence of the crank speed change.

Figures 7c and 7d are the response surface plots showing the interactive effects of vibration frequency (X_1) and screw feed speed (X_3) on the threshing efficiency (Y_1) and damage percentage (Y_2). The interaction is significant. When the screw feed speed ranges from 10 to 20 mm/s and the vibration frequency ranges from 4 to 8 Hz, the threshing efficiency is relatively optimal and the damage percentage is relatively low. When the crank speed (X_2) is at the central level ($X_2 = 204$ r/min), at a given screw feed speed, the threshing efficiency first increases and then decreases with the increase of the vibration frequency, showing a significant change; the damage percentage first decreases and then increases with the increase of the vibration frequency, showing a significant change; when the vibration frequency is constant, the threshing efficiency first increases and then decreases with the increase of the screw feed speed, and the change amplitude is significantly higher than the influence of the vibration frequency change; the damage percentage first decreases and then increases with the increase of the screw feed speed, and the change amplitude is significantly lower than the influence of the vibration frequency change.

Figures 7e and 7f are the response surface plots showing the interactive effects of crank speed (X_2) and screw feed speed (X_3) on the threshing efficiency (Y_1). The interaction is significant. When the screw feed speed ranges from 10 to 20 mm/s and the crank speed ranges from 168 to 240 r/min, the threshing efficiency is relatively optimal and the damage percentage is relatively low. When the vibration frequency (X_1) is at the central level ($X_1 = 6$ Hz), at a given screw feed speed, the threshing efficiency first increases and then decreases with the increase of the crank speed, showing a significant change; the damage percentage first decreases and then increases with the increase of the crank speed, showing a significant change; when the crank speed is constant, the threshing efficiency first increases and then decreases with the increase of the screw feed speed, and the change amplitude is significantly higher than the influence of the crank speed change; the damage percentage first decreases and then increases with the increase of the lead screw feed speed, and the amplitude change is slightly higher than the influence of the crank speed change.

Parameter optimization and verification test

Utilizing Design-Expert 12.0 software to conduct target optimization for the parameter combination of the root-soil separation of Gentian, based on the working conditions of the root-soil separation device

of Gentian and the variance analysis results of the root threshing efficiency and damage percentage, the parameter optimization constraints are determined as.

$$\begin{cases} \max Y_1(X_1, X_2, X_3) \\ \min Y_2(X_1, X_2, X_3) \\ \text{s.t.} \begin{cases} 4 \leq X_1 \leq 8 \\ 168 \leq X_2 \leq 240 \\ 10 \leq X_3 \leq 20 \end{cases} \end{cases} \quad (26)$$

After analysis with Design-Expert 12.0 software, the optimal working parameter combination obtained is a vibration frequency of 6 Hz, a crank speed of 204 r/min, and a lead screw feed speed of 15 mm/s. At this point, the predicted threshing efficiency is 94.9%, and the damage percentage is 3.5%.

The verification experiment was conducted in the laboratory of the College of Engineering at Shenyang Agricultural University. The working parameters of the root-soil separation test bench of Gentian were set to a vibration frequency of 6 Hz, a crank speed of 204 r/min, and a lead screw feed speed of 15 mm/s. The experiment was carried out a total of 8 times, and the results were averaged.

The average threshing efficiency of the *Gentiana* root system was 90.8%, and the average damage percentage was 5.9%. Compared with the simulation test, the relative errors were 4.1% and 2.4%, respectively. The root-soil separation effect was good. The threshing efficiency in the test bench experiment was slightly lower, but the result difference was within a reasonable range, indicating that the regression model has good reliability.

CONCLUSIONS

1) This paper addresses the existing problem of difficulty in separating *Gentiana* roots from soil, and designs a root-soil separation device of *Gentian*, which mainly includes a striking mechanism, a vibration mechanism, and an adjustable reciprocating mechanism. The crank-slider mechanism is used to drive the striking and vibration mechanisms, and the ball screw mechanism is used to drive the adjustable reciprocating mechanism to complete the root-soil separation operation.

2) Kinematic analysis of the striking mechanism is conducted to obtain a crank speed range of 168 r/min $\leq n \leq$ 240 r/min. The forces acting on RSCG on the vibrating screen are analyzed to determine the vibration frequency range of the vibrating screen to be 4 Hz~8 Hz. Based on the early impact tests, the average height difference of RSCG was determined. Taking the midpoint of the crank speed, the operating speed range of the adjustable reciprocating mechanism was set to 10~20 mm/s.

3) The Box-Behnken response surface optimization test method is used to analyze the effects of vibration frequency, crank speed, and screw feed speed on the threshing efficiency and damage percentage, to establish a regression model, and to analyze their interactions. Finally, a multi-objective optimization design of the regression model for the test indicators is carried out, and the optimal working parameters combination is determined to be: vibration frequency 6 Hz, crank speed 204 r/min, screw feed speed 15 mm/s. Verification tests are conducted with these parameters, and the *Gentiana* root system threshing efficiency is found to be 90.8%, and the damage percentage is 5.9%. The relative errors compared to the theoretical optimization results are both less than 5%, indicating that the parameter optimization regression model is reliable.

ACKNOWLEDGEMENT

This research was mainly supported by the support of the Basic Scientific Research Program of the Education Department of Liaoning Province (LJKMZ20220998). National Natural Science Foundation of China (52275264). The authors thank relevant scholars for their assistance in the literature.

REFERENCES

- [1] Chen Xueshen, Ma Xu, Chen Guorui, Qi Long, Wu Tao, Zeng Lingchao. (2015), Research on soil-rhizome separating device of deep-rhizome Chinese herbal medicines (深根茎类中药材根土分离装置的研究), *Mechanical Design*, vol.32, no.7, pp.65-70.
- [2] Cui Zhenmeng, Zhang Zhaoguo, Wang Fa'an, Cheng Yiqi, Yang Haihui, Yang Yating, Gao Qingsheng. (2018), Kinematic analysis and optimization design of vibration-type device for panax notoginseng root-

- soil separation (振动式三七根土分离装置的运动学分析及优化设计), *Journal of Northwest Agriculture and Forestry University (Natural Science Edition)*, vol.46, no.11, pp.146-154.
- [3] Cui Zhichao, Guan Chunsong, Xu Tao, Fu Jingjing, Chen Yongsheng, Gao Qingsheng. (2021). Design and experiment of transplanting machine for cabbage substrate block seedlings, *INMATEH-Agricultural Engineering*, vol.64, no.2, pp.375-384.
- [4] Gao Song, Sun Wensong, Wen Jian, Li Xiaoli, Yang Zhengshu, Li Ling. (2020), Diversity of Rhizosphere Bacterial and Function Predicted Analysis in *Gentiana scabra* Replanting Soil (连作龙胆草根际土壤细菌多样性及功能预测分析), *Journal of Shenyang Agricultural University*, vol.52, no.1, pp.102-108.
- [5] Feng Xin, Wang Lijun, Yu Kunmeng, Gao Yunpeng, Bi Shengying, Wang Bo. (2023), Design and Experiment of Mechanism of Wave Screen for Maize Grain Cleaning (玉米籽粒清选波浪筛机构设计与试验), *Transactions of the Chinese Society for Agricultural Machinery*, vol.54, no.4, pp.142-154.
- [6] Li Dongjie, Hou Jialin, Wang Dongwei, Chang Zengcun. (2024). Design and testing of peanut sieving prototype machine, *INMATEH-Agricultural Engineering*, vol.73, no.2, pp.760-770.
- [7] Liu Yafeng, Fang Zhichao, Xia Haifeng, Qu Yongbo, Wu Mingliang. (2024), Design and Experiment of a Opposite Roller Extrusion Type Allium Chinese Harvester (对辊拨刷式蒜头收获机设计与试验), *Journal of Agricultural Science and Technology*, vol.26, no.6, pp.72-81.
- [8] Liu Zhixin, Shang Shuqi, Ma Shikuan, Hou Yaxiu, Dong Tongtong, He Xiaoning. (2024). Optimisation by coupled RECURDYN-EDEM simulation: Optimisation tests of a three-stage low-loss separation device for potato soil, *INMATEH-Agricultural Engineering*, vol.72, no.1, pp.138-147.
- [9] Lu Dequan, Liu Qingliang, Mao Hongwei. (2022), The Design and Simulation Analysis of Impact Sampler for Deep Sea Mineral Deposit (深海矿床冲击式破碎器的结构设计及仿真分析), *Journal of Ocean Technology*, vol.41, no.1, pp.84-91.
- [10] Luo Wei, Wang Jikui, Niu Hailong, Luo XinYu, Burlen-Halebek, Duan Wenxian, Li Yang. (2018), Design and Test on Debris Clean-up Device of Clamping Finger-chain Type Device for Recycling Agricultural Plastic Film (夹指链式残膜回收机清杂装置的设计与试验), *Journal of Agricultural Mechanization Research*, vol.40, no.2, pp.75-79.
- [11] Lv Jinqing, Yang Xiaohan, Lv Yining, Li Zihui, Li Jicheng, Du Changlin (2022) Analysis and Experiment of Potato Damage in Process of Lifting and Separating Potato Excavator (马铃薯挖掘机升运分离过程块茎损伤机理分析与试验), *Transactions of the Chinese Society for Agricultural Machinery*, vol.51, no.1, pp.103-113.
- [12] Qian Zhenjie; Zhang Dingguo. (2015), Frictional impact dynamics of flexible manipulator arms (含摩擦碰撞柔性机械臂动力学研究), *Journal of Vibration Engineering*, vol.28, no.6, pp.879-886.
- [13] Quan Longzhe, Zhang Dan, Zeng Baigong, Tong Jin, Chen Donghui. (2013), Modeling and optimizing dither mechanism for conveying corn stubble (玉米根茬抖动升运机构的建模与优化) *Transactions of the Chinese Society of Agricultural Engineering*, vol.29, no.3, pp.23-29.
- [14] Tao Guixiang, Zhang Ziheng, Yi Shujuan, Xia Chunlong, Ma Yongcai. (2022), Design and Test of Combined Swing Radix isatidi Root-soil Separation Device (板蓝根收获机组合筛面摆动式根土分离装置设计与试验), *Transactions of the Chinese Society for Agricultural Machinery*, vol.53, no.4, pp.109-119.
- [15] Tang Yongfei, Zhao Yongman, Wang Jikui, Wang Zheng. (2020), Design and experiment of film removing device for clamping finger-chain type residual film collector (夹指链式残膜回收机脱膜装置设计与试验), *Transactions of the Chinese Society of Agricultural Engineering*, vol.36, no.13, pp.11-19.
- [16] Wang Faan, Wen Bo, Xie Xiaohong, Xie Kaiting, Guo Siwei, Zhang Zhaoguo. (2023), Operation Mechanism Analysis and Parameter Optimization of Conveying and Separating Device of *Panax notoginseng* Harvester (三七收获机输送分离装置作业机理分析与参数优化), *Journal of Agricultural Machinery*, vol.54, no.S1, pp.201-211+259.
- [17] Wei Zhongcai, Li Hongwen, Sun Chuanzhu, Li Xueqiang, Liu Wenzheng, Su Guoliang, Wang Faming. (2018), Improvement of potato harvester with two segment of vibration and wave separation (振动与波浪二级分离马铃薯收获机改进), *Transactions of the Chinese Society of Agricultural Engineering*, vol.34, no.12, pp.42-52.
- [18] Wei Zhongcai, Li Hongwen, Su Guoliang, Sun Chuanzhu, Liu Wenzheng, Li Xueqiang. (2019), Development of potato harvester with buffer type potato-impurity separation sieve (缓冲筛式薯杂分离马铃薯收获机研制), *Transactions of the Chinese Society of Agricultural Engineering*, vol.35, no.8, pp.1-11.
- [19] Wei Zhongcai, Wang Xinghuan, Li Xueqiang, Wang Faming, Li Zhihe, Jin Chengqian. (2023) Design and Experiment of Crawler Self-propelled Sorting Type Potato Harvester (履带自走式分拣型马铃薯收获机设计

- 与试验), *Transactions of the Chinese Society for Agricultural Machinery*, vol.54, no.2, pp.95-106.
- [20] Xue Haotian. (2022), The Whole Machine Design and Simulation Test of Key Components of Panax notoginseng Combined Harvester (三七联合收获机整机设计及关键部件的仿真试验), *Kunming University of Science and Technology*.
- [21] Yang Ranbing, Wu Minsheng, Xu Peng, Pan Yongfei, Lv Danyang, Zha Xiantao. (2024). Design and experiment of sweet potato combine harvester based on two-segment potato soil separation device, *INMATEH-Agricultural Engineering*, vol.74, no.3, pp.509-525.
- [22] Yan Shuai, Cui Qingliang, Zhang Yanqing, Li Guang, Zhao Zhihong, An Nan. (2023), Design and testing of a drum-type root-soil separator for Codonopsis pilosula harvesting (党参收获滚筒式根土分离试验台的设计与试验), *Journal of Gansu Agricultural University*, vol.58, no.2, pp.226-234.
- [23] Zhao Zhan, Li Yaoming, Chen Yi, Liang Zhenwei, Liu Lixia. (2013), Impact Mechanical Characteristics Analysis of Rice Grain (水稻籽粒碰撞力学特性研究), *Transactions of the Chinese Society for Agricultural Machinery*, vol.44, no.6, pp.88-92.
- [24] Zou Yagang (2023) Mechanism Analysis and Parameter Optimization of Tea Shaking Screen Machine (茶叶抖筛机的机理分析与参数优化), *Anhui Agricultural University*.

DESIGN AND TESTING OF SEEDING QUALITY MONITORING SYSTEM FOR COTTON HILL-DROP PLANTER

棉花精量穴播器播种质量检测系统设计与试验

Liming ZHOU^{1,2}, Yuxi JI^{1,2}, Shenghe BAI^{1,2}, Gaoyong XING^{1,2}, Liang WEI^{1,2}, Yanwei YUAN^{1,2}, Bo ZHAO^{1,2}, Kang NIU^{1,2}, Yangchun LIU^{1,2}

¹) Chinese Academy of Agricultural Mechanization Sciences Group Co., Ltd, State Key Laboratory of Agricultural Equipment Technology, Beijing 100083, China;

²) China Agricultural University, Beijing 100083, China.

Tel: +86-18600073162; E-mail: lyc327@163.com

DOI: <https://doi.org/10.35633/inmateh-74-81>

Keywords: Cotton, Monitoring system, Precision hill-drop planter, Seeding quality

ABSTRACT

To address the limitations of seeding quality monitoring methods under the seeding operation mode of cotton hill-drop planter without grain, this paper designed a seeding quality monitoring system that can eschew the traditional reliance on seed conductor. The system realizes real-time monitoring based on the differences in the cotton seeds' absorption of light of different wavelengths, and achieves accurate evaluation of seeding quality by obtaining the seeding quality parameters with multiple types of sensors. Bench tests showed the lowest accuracy of seeding rate monitoring was 97% and the highest accuracy of missed seeding monitoring was 95% while the field tests showed that the highest drop in the accuracy of seeding rate monitoring was 2.03 percentage, but the lowest accuracy of missed seeding monitoring is still above 91%. The system does not require the transformation of the equipment carrier, but has a high degree of equipment adaptability, which can meet the requirements on monitoring of cotton seeding. The monitoring method is effective and feasible, with high accuracy and stability.

摘要

针对棉花精量穴播器无导种管播种作业模式下的播种质量检测方式的局限性, 本文摒弃依赖导种管的监测方式, 提出播种质量监测系统。该系统基于棉种对不同波长光吸收特性的差异性实现实时监测, 并采用多种形式传感器获取播种质量计算参数, 完成播种质量精准评估。台架试验表明, 播量检测准确率最低为 97%, 漏播量检测准确率达 95%; 田间试验表明, 播量检测准确率最高下降幅度为 2.03 个百分点, 漏播判定准确率最低仍维持在 91% 以上水平。系统无需对机具载体进行改造, 具有高度机具普适性, 并满足棉花播种状态监测要求, 监测手段有效可行, 准确率和稳定性较高。

INTRODUCTION

Cotton is the main cash crop in China, which is widely used in the production of cotton textiles, being an important strategic material that bears on the national economy and people's livelihood. With agricultural modernization, cotton planting in Xinjiang has been refined according to local conditions, where the mulch-covered precision hill-drop seeding effectively improves the seeding quality and efficiency and reduces the cost (Shen *et al.*, 2022). In order to realize the refined management of seeding, a seeding quality monitoring system has been developed to assist the monitoring of the planter's seed discharge and the early warning of failures. The problems such as missed seeding, repeated seeding and blockage can be timely identified and solved in a targeted manner, which is important to speeding up accurate and efficient mechanization and integrated development in cotton production (Majcher *et al.*, 2023; Liao *et al.*, 2017).

In precision seeding, the research and development of special high-precision sensors and intelligent measurement and control terminals for agriculture are of great significance to promoting rapid development of smart agriculture and improving the precision of seeding device (Wen *et al.*, 2022). Online accurate seeding monitoring methods can be divided into photoelectric detection (He *et al.*, 2021), piezoelectric detection (Zhao *et al.*, 2020), capacitance detection (Zhang *et al.*, 2022; Xu *et al.*, 2022), machine vision detection (Dong *et al.*, 2023), etc. according to the different detection principles of sensors.

Among them, machine vision detection is accurate, but is mostly used in laboratory evaluation other than fields with complex operating environments. Piezoelectric detection and capacitive detection have high requirements for device stability, and are weak in detecting subtle changes of seeds, which makes them not suitable for detection of small-particle seeds (Mapoka *et al.*, 2019). Photoelectric detection is widely used in the monitoring of seeding due to its high accuracy and good stability, and has broad application prospects.

Scholars have conducted considerable research on the seeding monitoring system, and achieved real-time monitoring by installing photoelectric sensors at seed conductor to capture the seed discharge signals. The SeedStar TM series precision agriculture operating system by U.S. John Deere is mature in the development of seeding monitoring products. Its user-friendly interface visually displays the information of seeding monitoring and operatable parameters, which guides farmers' seeding operation by providing detailed seeding decision based on the status of field plots.

Besharatia (2019) developed an infrared sensing system composed of infrared light-emitting diodes and photodiodes based on the physical characteristics of different types of seeds (chickpeas, wheat, alfalfa), but failed to achieve high monitoring accuracy on small-particle seeds due to diameter limitations of optical components. Previous studies (Ding *et al.*, 2020; Ding *et al.*, 2021; Wang *et al.*, 2023) demonstrated real-time monitoring of small-particle seed flow and the perception of high-throughput seed flow signals could be achieved by enhancing the resolution of the detection sensitive system with piezoelectric thin films and thin-surface laser-silicon photocell modules. Regarding the monitoring of double overlapping seeds, Xie *et al.* (2021) proposed the use of a laser sensor as the signal capture source, and used a triode to improve the drive force and anti-interference ability.

Yin (2018) proposed adoption of a distributed information structure to reduce the average response time of the system. In summary, there is rapid progress of current research on the monitoring system of small-particle seeds, but it is difficult to realize the commercialization of the seeding monitoring system or fully cover all types of seeders on the market. Especially, there is weak research on the monitoring of seeding by mechanical planter without a seeding conductor. Therefore, it is urgent to address the problems with real-time monitoring in single operation without a seed conductor.

The primary objective of this study was to develop a real-time seeding quality monitoring system for mechanical precision hill-drop planter by leveraging the light absorption characteristics of cotton seeds, thus eliminating the traditional reliance on seed conductor. A secondary objective was to enable the visualization and remote access of monitoring information on both vehicle terminal and cloud storage platform. Tests will be conducted to demonstrate that the monitoring accuracy meets the criteria for cotton seeding state monitoring. Ultimately, this research will contribute to addressing the challenges of seeding monitoring in planters without seed tubes and enhance the precision and efficiency of seeding operations.

MATERIALS AND METHODS

Overall system design

As the hill-drop planter is dragged by an auxiliary tractor at a working speed, some duckbill devices dig holes in the ground, while the seed tray inside the planter rotates and capture cotton seeds from the pile below. Due to gravity, the cotton seeds fall out of the pits and further slide out of the duckbills along the spacer sleeve before finally dropping into the hills. The system consists of four parts, namely, seeding rate monitoring module, basic parameter monitoring module, vehicle terminal (including touch screen, data acquisition module and STM32 master control unit), cloud storage platform, as shown in figure 1.

The seeding rate monitoring module is the core of the monitoring system to realize the monitoring of the seeding status of the hill-drop planter; on the basis of the machine's operating parameters collected by the basic parameter monitoring module, the information of the seeding quality and the planter positioning in the field is obtained. The display control terminal system is composed of the STM32 master control unit and its peripheral circuitry, and can achieve the visualization of seeding quality, BDS message analysis, integration, packaging and remote transmission of the information of seeding quality and positioning, users can access the operation information of the planter through the agricultural machinery operation platform.

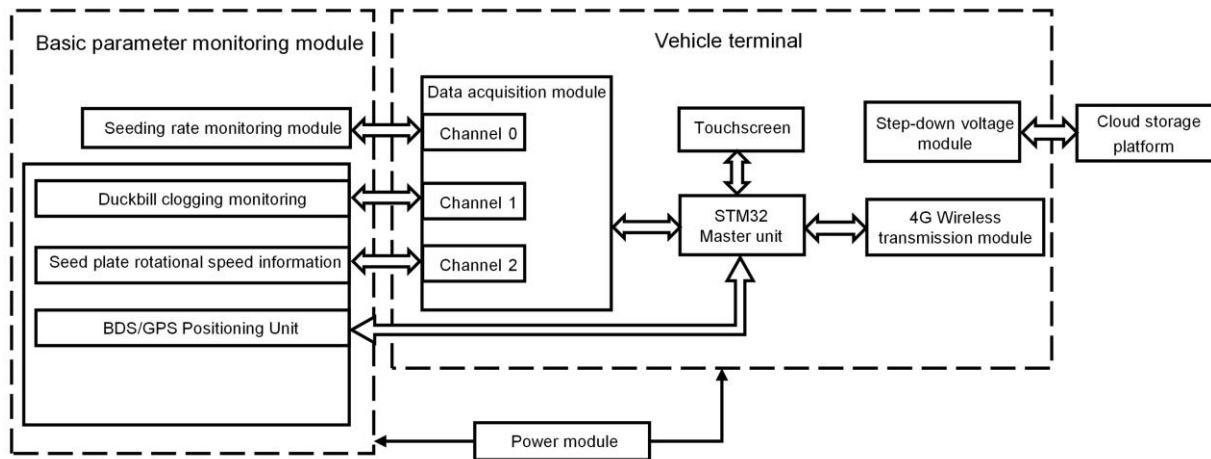


Fig. 1 - Monitoring system structure diagram

System hardware design

● **Hill-Drop seeding rate monitoring module design**

The hill-drop seeding rate monitoring module is composed of a color marker sensor and its peripheral circuitry, which operates based on the principle that different colored objects have varying reflectance to light (Lu et al., 2021). Three primary color light-emitting diodes are selected to provide the light source. The color marker sensor is of a Y-shaped optical fiber probe structure to adapt to the small space, transmits the light of specific color, and identifies the color according to the difference in the absorption of light of different wavelengths by the surface of the detection area (Petzi et al., 2023). The sensor’s receiving element is embedded with a filter to suppress interference of ambient light, and effectively receives diffuse reflected light signals from the detection area; the sensor’s color recognition system filters and amplifies the signal after photoelectric conversion, and the A/D converter converts the analog signal into a digital signal and outputs the RGB value for comparison with the standard color to identify cotton seeds. The structure of the color mark sensor is shown in figure 2.

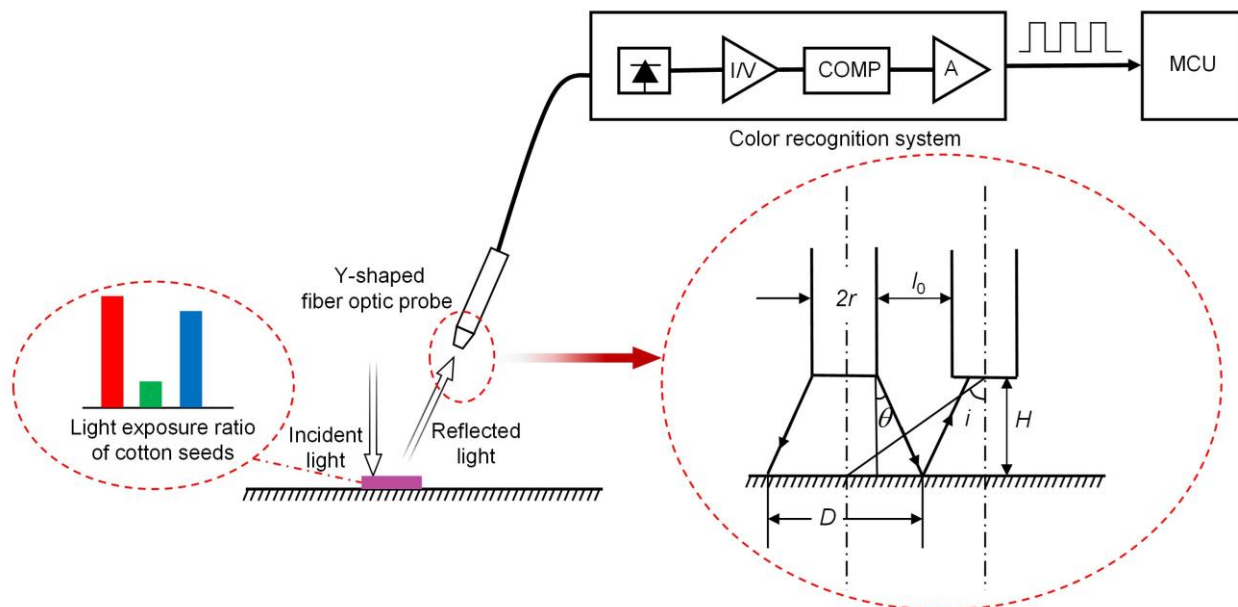


Fig. 2 - Structural composition of color sensor system

The distance of the sensor (optical fiber probe) from the pit in the detection area is the same as the working distance of the optical fiber probe of the color marker sensor. The operating area of the hill-drop planter’s seed tray is a closed dark space, and lit only by the light-emitting diode, where the interference of ambient light on the spectral response of the sensor and the reflection characteristics of the object surface can be ignored.

The seed tray is made of reinforced nylon, and can be simplified to a Lambertian scatterer, that is, the incident energy is evenly reflected in all directions and the surface radiation intensity satisfies Lamber's cosine law (Vazquez et al., 2020; Oguntosin et al., 2019).

The detection height of the Y-shaped optical fiber probe is H , and a three-color light source lights the reflective surface of the detection area. When the diffuse reflectance of the surface of the detection area is ρ , there is:

$$B = \rho E_0 \tag{1}$$

where B is the surface brightness of the detection area; E_0 is the illuminance of the light source.

The diameter of optical fiber core of Y-shaped optical fiber probe is $2r$, the aperture angle is θ_r , and the distance between the two sets of optical fibers in the probe is l_0 . The reflected luminous flux F in the detection area received by the color marker sensor in any reflection direction i is obtained:

$$B = \frac{\rho E_0 \cos^2 i}{\pi H^2} \tag{2}$$

To ensure that the information of diffuse reflection of the detection surface obtained by the color mark sensor is not distorted, the installation height H of the color sensor from the detection center should satisfy $H \gg (l_0 + 2r)$. At this time, i tends to 0, and there is:

$$F = \frac{\rho E_0}{\pi H^2} \tag{3}$$

When the reflectance ρ is fixed, the luminous flux F received by the sensor's light probe is related to the installation height H , where $F \propto H^2$. In practical applications, the luminous flux reflected to the sensor should be increased as much as possible. For curved detection areas, the installation height should be adjusted within the working range of the sensor to avoid blocking and shading, and the operating of the seed tray should not be affected, as shown in figure 3, where R_m is the radius of the outer ring of the seed tray; r_m is the distance from the concave point of the pit of the seed tray to the center of the seed tray; θ_m is the angle of the tangent line at the intersection of the concave extension cord and the outer ring.

The installation height of the sensor is determined: $H = \min \{ (R_m - r_m) \sin^{-1} \theta_m, H_0 \}$ ($H_0=50\text{mm}$). This is to obtain the maximum luminous flux to achieve the best detection effect. By reference to the design data of the hill-drop planter (Zhang et al., 2021; Jiang et al., 2021), the values of $R_m=110$ mm, $r_m=67.5$ mm, and $\theta_m = 30^\circ$ were substituted into the formula, and $H=21.25$ mm.

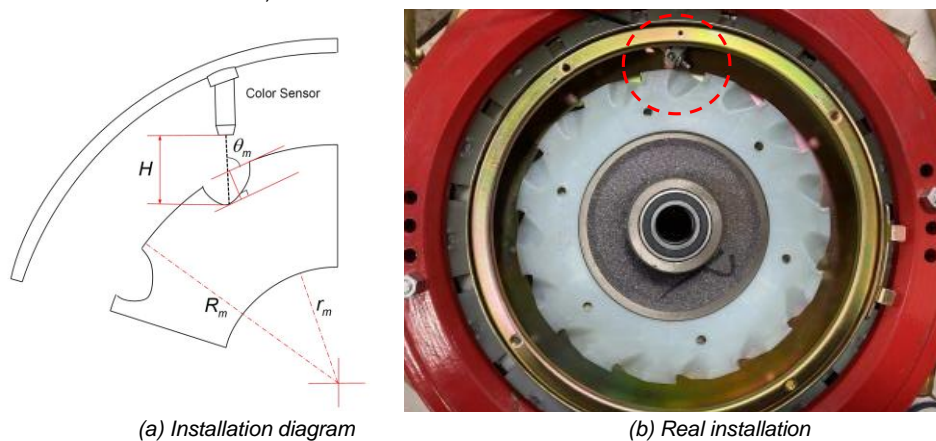


Fig. 3 - Installation of the color sensor

$$H \geq R_m - r_m \sin^{-1} \theta_m \tag{4}$$

The photoelectric conversion element of the color marker sensor are TCS34725 series whose peripheral circuit is as shown in figure 4.

The color marker sensor communicates with the STM32 master control unit through a 7-bit I²C bus, where the communication clock is 100 kbit/s. A read command is issued to the internal RGBC channel data register (0x14~0x1B) to access and obtain RGB values.

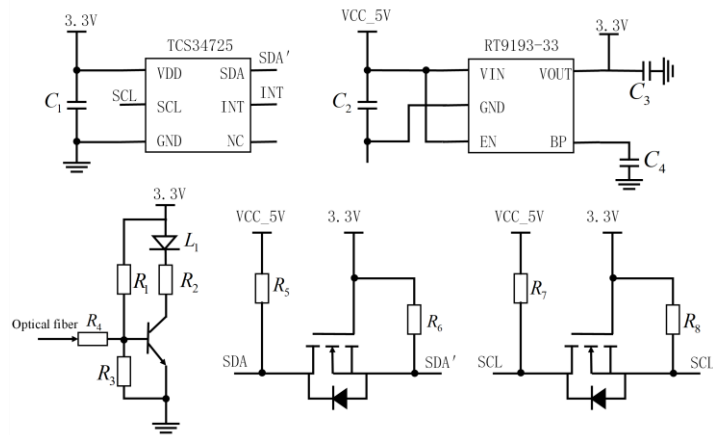


Fig. 4 - Peripheral circuitry of the color sensor

The sensor sequentially gates the filters to obtain the frequency pulse signals of the three primary colors R, G, and B, calculate their light intensity ratio and compare it with the RGB range interval of cotton seeds. If the detected values fall within the reference range, the sensor micro-processing unit directly outputs the TTL high level through the GPIO. The RGB component range (dimensionless) of fuchsia-coated cotton seeds was determined to be 120~200, 30~100 and 120~200 by the comparison with standard colorimetric cards, and the light receiving ratio was close to 4:1:4.

● **Basic parameter monitoring module**

The basic parameters include the duckbill clogging state, the speed of seed discharge tray (that is, the forward speed of the machine), other parameters for calculation of seeding quality, and the field positioning information of the planter. The infrared diffuse reflection photoelectric sensor transmits and receives continuous infrared light, and uses the intensity of the reflected light to perceive the opening and closing of the duckbill, thereby identifying the blockage. The speed measuring encoder captures the speed information of the seed discharge plate. Inside the encoder, there is usually a grating code plate engraved with an equidistant opaque grating, and the light-emitting diode illuminates the moving grating code plate to produce Moir stripes, where two columns of speed information fed back by pulse are generated alternately. BDS/GPS positioning unit receives and solves the field positioning of the planter through the antenna.

(1) Infrared diffuse reflection photoelectric

Through the infrared diffuse reflection photoelectric sensor M18 series (NPN-NC detection distance is 30-300 mm), the infrared signals are transmitted to the surface of the duckbill, and received and compared with the light intensity threshold, whereby whether there are seeds in the channel interfering the closing of the duckbill can be judged from the sensed opening and closing state. As shown in figure 5, when the duckbill is set to open, the detection distance d reaches the threshold distance d_{TH} . At this time, the reflected light intensity I_{TH} is the light intensity threshold, and an infrared signal is triggered. After judgment based on the gate logic circuit, high voltage is output. After being stabilized by the voltage regulator T_1 , a 5V pulse is detected at U_1 . At the same time, the diode D_1 is turned on and the clogging alarm light is on, if there is no seed in the channel and the early warning trigger condition is not reached, the output at U_1 is 0V.

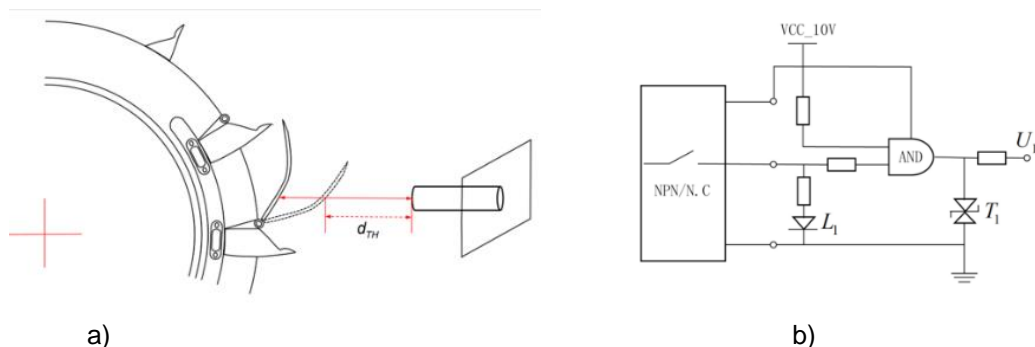


Fig. 5 - Blockage detection monitoring module

(a) Blockage state monitoring model (b) Blockage sensor circuit

(2) Incremental rotary encoder

The speed parameters of the seed discharge plate of the hill-drop planter are collected through the incremental rotary encoder E6B2-CWZ6C type (hereinafter referred to as the encoder). The encoder is fixed to the edge of the moving disc through a spring bracket. The silicone wheel on the encoder is directly in contact with the moving disc of the hill-drop planter, without slide between the surfaces. The moving disc drives the rotation of silicone wheel and further causes the rotation of encoder shaft, whereby the A and B sets of periodic pulse sequences with a phase difference of 90° are output. The data acquisition module captures the output pulse of encoder at a sampling rate of 20 kHz, and uploads it to the display control terminal through RS485 two-wire communication for discrimination of seeding status.

The counter counts the number on the rising and falling edges, which improves the resolution by 4 times. Since the encoder is installed by the side of the moving disc, the formula for calculating the speed of the hill-drop planter is obtained:

$$V_n = \frac{v_n r_n}{R_y} = \frac{T_n r_n}{4T_y R_y} \times 60 \tag{5}$$

where:

v_n is the encoder speed, r/min; T_n is the number of output pulses of the encoder; T_y is the number of pulses generated by the encoder in a complete rotation; r_n is the radius of the encoder’s synchronous wheel; R_y is the radius of the moving disc of the hill-drop planter.

(3) Vehicle terminal

The on-board terminal is mainly composed of FZ4050 series data acquisition module, STM32 master control unit, 4G wireless transmission module and Guangzhou Dachai serial port touch screen, and can achieve data processing and cloud storage of the information of the planter’s seeding quality and positioning information, and realizes the visualization of monitoring information and touch screen human-computer interaction. The system is powered by an external 12V power supply, and the step-down chip TPS5430DDAR provides a 3.3V/5V regulated power supply for each sensor and the master control unit chip.

The master-slave communication between data acquisition module and the STM32 master control unit are based on the RS485 Modbus protocol (RTU transmission mode) (Yan et al., 2023). The data acquisition module plays the role of a slave station in the communication with the STM32 master control unit. The Modbus protocol specifies that the slave station provides services in the form of a function code based on the request/response communication mode, and its message frame structure is shown in table 1. "0000~0002" was assigned as the input address range of CH0~CH2 channel in the Modbus register. The device address of the FZ4050 data acquisition module as a slave was 0x01. During transmission, it responded to the request of the STM32 master control unit through the 03 function code and read the channel data.

Table 1

Modbus RTU message structure

Address code	Function code	Data zone	Checksum
8-bit	8-bit	Nx8-bit	16-bit

System software design

The on-board terminal software is designed to realize the monitoring and management of the seeding, which covers system hardware driver, terminal human-computer interaction design, acquisition and process of seeding quality and positioning information, and database cloud management, etc. The software process is shown in figure 6. After the system is turned on, the hardware peripherals are initialized. The working status of sensor is checked circularly; the GPIO general input and output are defined, and the cloud platform connection is initialized. Cloud_Int () is called to establish a cloud platform connection, and the IP address (j.caams.org.cn) and port information (9926) are passed. The TCP/IP protocol stack is initialized. The cloud platform automatically assigns dynamic ports to the display control terminal according to the current equipment scheduling. Then, C/C++ is used to write a data transmission and reception script, and an AT command is sent to configure the 4G wireless transmission module for entry into the working mode. The information of seeding quality and the planter positioning is fused and written remotely to the cloud platform.

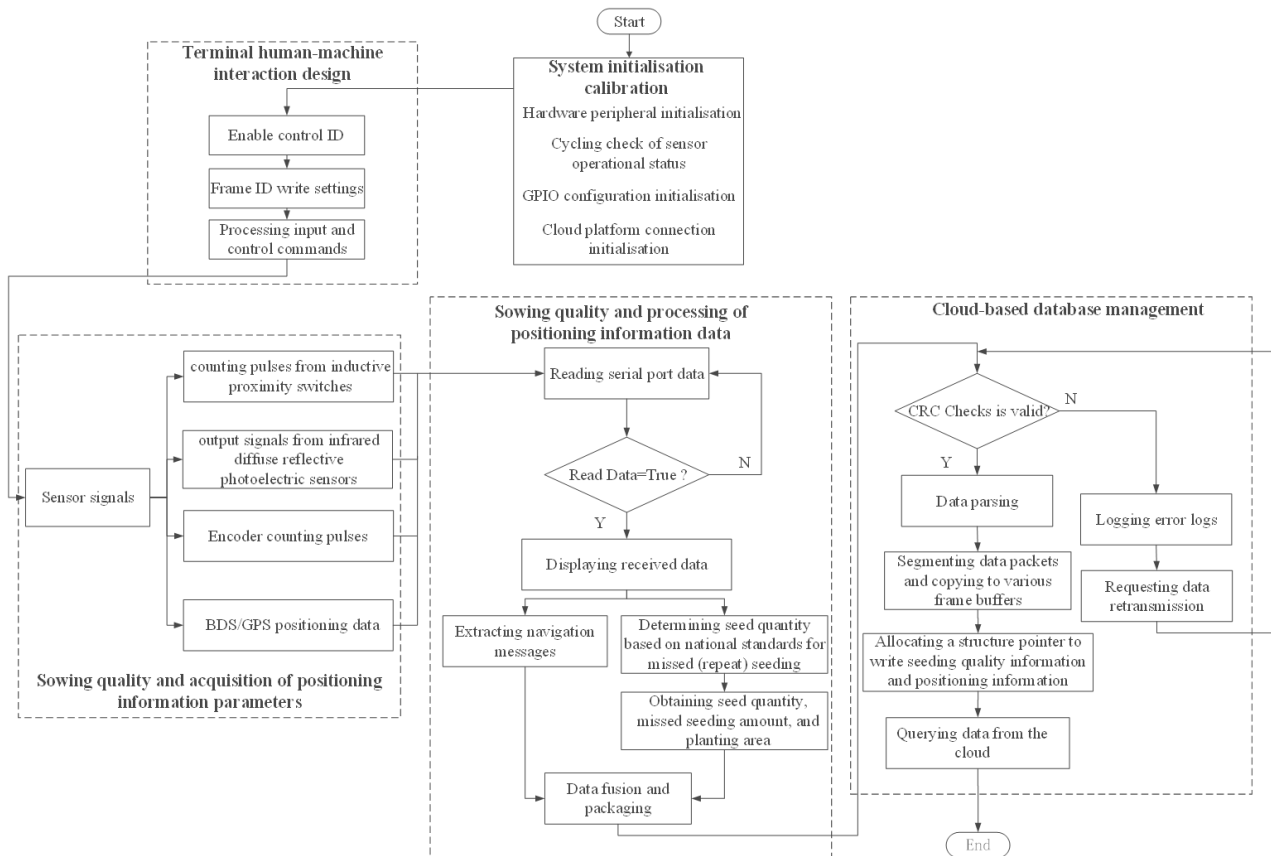


Fig. 6 - System software design process

● Acquisition of seeding quality information

The timer TIM2 is configured to external counting mode, and a double-edge trigger mode is adopted to monitor 6 channels of signal quality information. The system clock source is specified as the PLL output, with a clock frequency of 168 MHz. The AHB bus clock divider is set to 1, the PCLK1 divider to 4, and the PCLK2 divider to 2. The seeding quality discrimination result is written to the touch screen in real time.

After the forward speed v_1 of the machine is obtained, the actual seeding distance S_d of the two adjacent seeds is calculated:

$$S_d = \frac{v_1 \Delta t_1}{1000} \tag{6}$$

The seeding area A_I is calculated:

$$A_I = P_0 S_0 L_0 \tag{7}$$

where:

P_0 is the theoretical seeding rate; L_0 is the working width of the planter. By reference to GB/T 6973-2005 Single Grain (Precision) Planter Test Method, theoretical seeding distance S_0 is taken, and the actual seeding distance is S_d .

The judgment criteria is:

$$\begin{cases} 0.5S_0 < S_d \leq 1.5S_0 \text{ (Normal)} \\ S_d \leq 0.5S_0 \text{ (Repeated seeding)} \\ S_d > 1.5S_0 \text{ (Missed seeding)} \end{cases}$$

The touch screen human-computer interaction interface visualizes the operation results, as shown in figure 7.

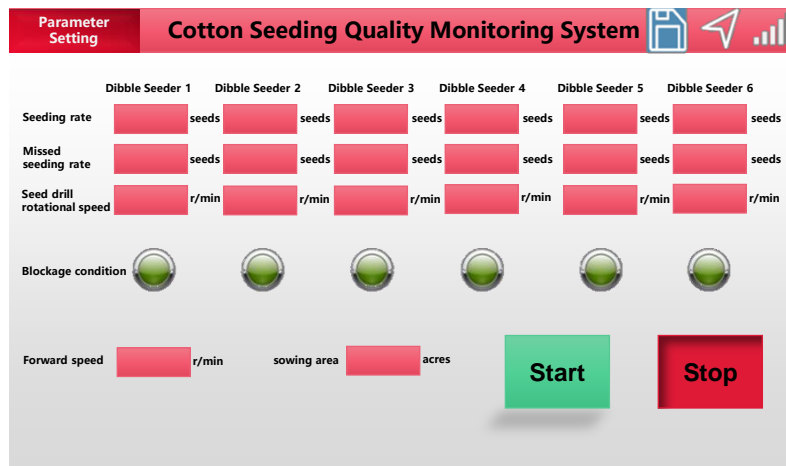


Fig. 7 - Cotton seeding quality monitoring software

● Acquisition and remote transmission of positioning

The serial port UART3 interruptedly collects the planter’s field positioning information on the GNSS positioning module. The data format of the planter’s positioning information is NMEA-0183. On the basis of 4G wireless transmission module, the serial port UART2 is defined to send the integrated data packets to the remote server regularly. The database schema design is shown in Table 2.

Table 2

Database schema design		
Field name	Data type	Field definition
AllotPort	Int	Terminal identifier
ltime	Verchar	Timestamp
Latitude	Double	Seeder latitude information
Longitude	Double	Seeder longitude information
Seeded_area	Double	Sowing area
Seeded_P1	Int	Sowing rate of the first row
Seeded_Q1	Int	Missed sowing rate for the first row
Seeded_P6	Int	Sowing rate for the sixth row
Seeded_Q6	Int	Missed sowing rate for the sixth row

RESULTS AND ANALYSIS

Bench tests

Xinluzao No. 78 cotton seeds (with a mass of 84.40 g per thousand grains and a moisture content of 4.45%, approximate ellipsoidal shape with a major axis of 1.2 cm and a minor axis of 0.5 cm) were used in the test. A test bench was built to simulate the forward movement of field machines, so as to test the system’s monitoring performance. The equipment includes a test bench for double-chamber cotton hill-drop planter with turntable vertical disc, a stepper motor controller, and a cotton seeding quality monitoring system.

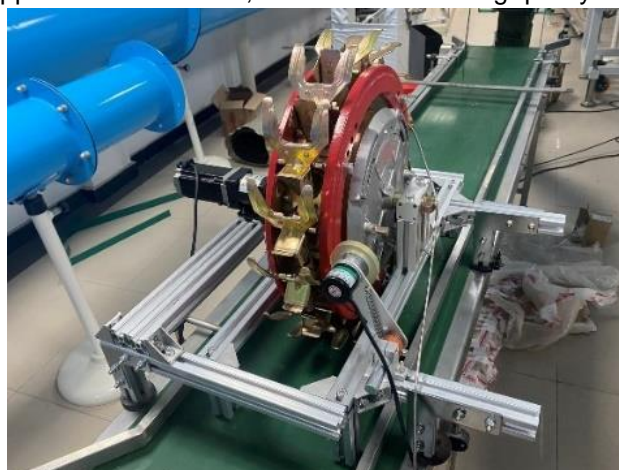


Fig. 8 - The seeding monitoring system test bench

By reference to NY/T 987-2006 Operation Quality of Film-laying Hill-drop Planter, the hill-drop planter is set to operating at 20, 25 and 30 r/min within the normal seed discharge interval in 6 repeated tests. The manual counts of the seeds were the real value, and the measured value was displayed on the industrial computer interface. The computer system determined the accuracy and measurement error.

(1) Test of the accuracy of seeding rate monitoring

In the test of the accuracy of seeding rate monitoring, the monitoring system started counting after the device was in stable operation for 10 minutes. The seed tray of the hill-drop planter has 15 pits, and the seeding rate was counted for every 20 laps of rotation.

After the monitoring is completed, cotton seeds in the bag are counted as the actual seeding rate, thereby the accuracy of the system’s seeding rate monitoring is calculated:

$$\eta_1 = \left(1 - \frac{|P_0 - P_1|}{P_0} \right) \times 100\% \tag{8}$$

where η_1 is the accuracy of seeding rate monitoring; P_0 is the theoretical (actual) seeding rate; P_1 is the system’s monitored seeding rate. The monitoring results of the system at different speeds were obtained, as shown in Table 3.

Table 3

Seed driller seeding rate monitoring results at different speeds

Rotation speed (r·min ⁻¹)	No.	Actual seeding rate	Monitored seeding rate	Monitoring accuracy of seeding rate (%)	Mean (%)	Standard Deviation (10 ⁻³)
20	1	302	298	98.67	99.33	4.724
	2	304	303	99.67		
	3	298	295	98.99		
	4	296	296	100		
	5	299	297	99.33		
	6	306	304	99.35		
25	1	300	302	97.39	98.08	4.750
	2	302	295	97.68		
	3	307	302	98.37		
	4	305	299	98.03		
	5	300	296	98.67		
	6	297	303	98.32		
30	1	296	291	98.31	97.79	5.123
	2	295	300	98.33		
	3	309	317	97.41		
	4	300	306	98.00		
	5	306	297	97.05		
	6	294	287	97.67		

With the increase of the rotation speed, both accuracy and precision of seeding monitoring decreased slightly. The reason is that the higher speed will cause some smaller cotton seeds fail to completely enter the pit, as a result of which they are not detected by the sensor. The overall accuracy of seeding rate monitoring maintained at over 97%, and the standard deviation of the monitoring results at different speeds was low, which indicates that the system’s seeding rate monitoring accuracy is high.

(2) Test of accuracy of missed seeding rate monitoring

In order to further evaluate the seeding quality and evaluate the stability and reliability of the system’s detection of missed seeding, the monitoring accuracy of missed seeding rate is subject to quantitative analysis according to formula (8). At each operating speed, the cotton seeds on the seed tray were reduced manually to increase missed seeding rate. Then, actual missed seeding on the planting bed was manually counted, and compared to the monitored value of the system to determine the error range. The monitoring results of missed seeding rate at different speeds are shown in Table 4.

Table 4

Missed seeding monitoring results of seed driller at different speeds

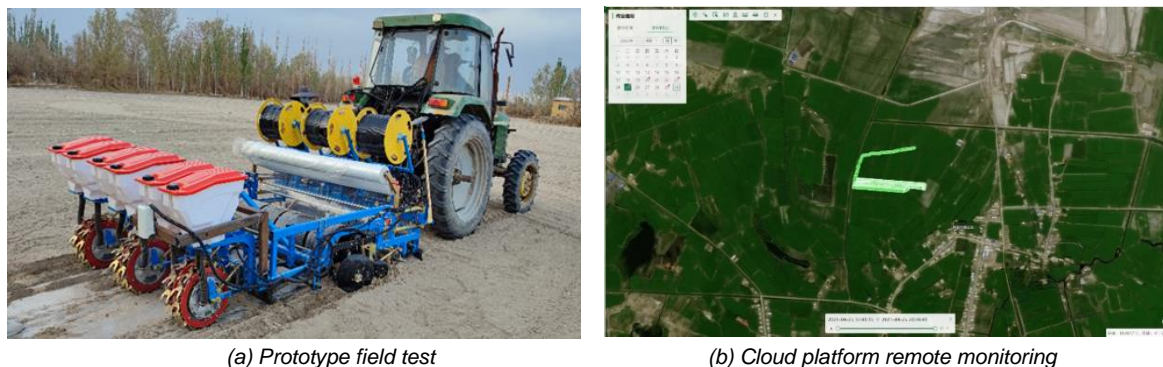
Rotation speed (r·min ⁻¹)	No.	Actual missed seeding rate	Monitored missed seeding rate	Monitoring accuracy of missed seeding rate (%)	Mean (%)	Standard deviation (10 ⁻³)
20	1	303	295	97.36	97.55	2.912
	2	292	285	97.60		
	3	307	300	97.72		
	4	295	302	97.84		
	5	297	306	97.06		
	6	302	309	97.73		
25	1	305	295	96.72	96.76	3.869
	2	303	294	97.03		
	3	299	310	96.45		
	4	301	291	96.68		
	5	297	308	96.30		
	6	303	295	97.36		
30	1	315	302	95.87	95.82	2.915
	2	299	287	95.99		
	3	293	306	95.75		
	4	303	315	96.19		
	5	299	285	95.32		
	6	308	295	95.78		

With the increase of the rotation speed, the accuracy of monitoring of missed seeding rate exhibited a slight downward trend. The comparison found that the accuracy of missed seeding rate monitoring was slightly lower than that of seeding rate monitoring, but it was still above 95%. The reason is that the higher speed of the seed discharge plate caused multiple collisions between the seed flow and the seed tray, which caused a small amount of broken seeds (shell of cotton seeds) that led to misdetection by the sensor. The manual operation to increase the missed seeding rate inevitably interfered with the seeding process of the hill-drop planter and affected the original trajectory of the seed flow. However, judging from the standard deviation of the monitoring results, the system's monitoring accuracy of the missed seeding rate still maintained at a high level, that is, the monitoring results are reliable.

Field tests

The test plot was 100 m long and 20 m wide, with soil suitable for cotton planting. The tested equipment was cotton precision planter (one membrane and 6 rows) pulled by John Deere 804 tractor. The seeding quality monitoring system was installed on the planter to obtain the seeding parameters in real time. By reference to the national machinery industry standard JB/T 7732-2006 Membrane Planter and the national agricultural industry standard NY/T 987-2006 Membrane Planter Operation Quality, the system was powered on before the start of the test, and the data was cleared after the system was initialized and calibrated. Finally, the machine was started for the tests.

During the test, the basic speed of John Deere 804 tractor was fast first gear speed (about 2 km/h, and the diameter of the hill-drop planter was 420 mm). By adjusting the throttle to control the speed, the speed of the seed discharge plate was set to 20, 30, and 40 r/min, respectively, the tractor moved 100 m (15 hills per lap, 75.8 laps, 1137 hills per ridge). The cotton seeds in soil were counted manually and seeding rate was monitored, thereby calculating the monitoring accuracy of the seeding rate; 100 hills were selected randomly on each ridge as the observation points (600 observation points in total at each rotation speed), and the current missed seeding monitoring result of the system was recorded for comparison, thereby finally counting the times of correct judgment at each rotation speed and calculating the accuracy of the system's judgment. At the same time, the location of the planter in the field, the operation area of the agricultural machinery, the operation path, and seeding status etc. were fed back to the agricultural machinery operation cloud platform, which provides users with remote monitoring channels, as shown in figure 9.



(a) Prototype field test

(b) Cloud platform remote monitoring

Fig. 9 - Field Seeding Monitoring Test Site

The monitoring results of each ridge at different speeds are shown in table 5.

Table 5

Field Monitoring Results of the System

Rotation speed (r-min-1)	No.	Actual seeding rate	Monitored seeding rate	Monitoring accuracy of seeding rate (%)	Mean (%)	Standard deviation (10-3)	Judgment accuracy of missed seeding (%)
20	1	1137	1105	97.19	97.48	5.419	95.00
	2	1130	1160	97.35			
	3	1137	1155	98.42			
	4	1139	1103	96.84			
	5	1140	1170	97.37			
	6	1145	1171	97.73			
25	1	1138	1077	94.64	95.33	5.569	91.67
	2	1130	1087	96.19			
	3	1137	1193	95.07			
	4	1142	1173	95.53			
	5	1133	1083	95.59			
	6	1143	1085	94.93			
30	1	1134	1201	94.09	93.79	6.814	91.67
	2	1145	1072	93.62			
	3	1131	1068	94.43			
	4	1137	1199	94.55			
	5	1130	1208	93.10			
	6	1132	1052	92.93			

The field test results showed that the accuracy of seeding rate monitoring at different speed is reduced to different extent compared to the bench test results. At low speed (20 r/min), the monitoring results were almost consistent, with a decrease of 0.07 percentage; at high speed (30 r/min), the accuracy decreased more significantly by 2.03 percentage points, and the data variability (standard deviation) also increased. This is because the increase in the amplitude of machine jittering in the field tests and the inconstant moving speed of the machine caused the reduced sensor monitoring accuracy. Nonetheless, the accuracy of seeding rate monitoring in the field tests was still slightly above 93%, and the judgment accuracy of missed seeding at high operating speed also be maintained above 91%, which indicates that the monitoring system exhibits satisfactory accuracy, reliability and performance in the fields.

CONCLUSIONS

In this paper, a seeding monitoring system suitable for mechanical precision cotton hill-drop planter was designed, and a test bench for double-chamber cotton hill-drop planter with turntable vertical disc was established for the performance test regarding the system’s accuracy in monitoring the seeding rate and missed seeding rate. Meanwhile, the reliability and stability of the system’s monitoring performance is further verified through field tests.

(1) This paper proposed the establishment of a seeding rate monitoring module with color marker sensor as the core, thereby realizing the identification and counting of cotton seeds based on the differences in their absorption of light of different wavelength. Accounting the counting test, the counting accuracy could reach 95%. Compared with the traditional laser beam detection method, the one-sided installation layout is more suitable for the small and compact space inside the hill-drop planter and requires no adjustment to the mechanical structure, which achieves satisfactory adaptability.

(2) The BDS/GPS positioning module was used to collect the field positioning information of planter; a rotary encoder was adopted to monitor the speed of seed discharge plate; an infrared diffuse reflection photoelectric sensor was provided to identify the clogging of the equipment; and a peripheral unit monitoring module was established to obtain their operation parameters in real time for seeding status discrimination. The judgment accuracy of missed seeding at high speed was above 91%. The information can be uploaded remotely to the terminal through the 4G wireless communication module, which provides the information traceability support to refined management of seeding operations.

(3) The reliability and accuracy of the monitoring system were verified through bench tests and field tests, separately. In the bench tests, the system's lowest seeding rate monitoring accuracy was 97%, and the missed seeding rate monitoring accuracy rate was 95%; in the field tests, seeding rate monitoring accuracy was above 93%, and the judgment accuracy of missed seeding was above 91%. In general, at different operating speed, the accuracy of field monitoring was reduced to different extent compared to the indoor tests: the accuracy of seeding rate monitoring at high speed (30 r/min) in field was reduced by 2.03 percentage compared to the bench test results, and that at the low speed (20 r/min) was reduced by 0.07 percentage without significant difference. The system exhibits satisfactory and stable monitoring performance.

ACKNOWLEDGEMENT

This work was supported by the National Key Research and Development Program (Project No. 2022YFD2002400) and Key scientific and technological projects in key areas of Corps (Project No. 2023AB014).

REFERENCES

- [1] Besharati, B., Navid, H., Karimi, H., Behfar, H., & Eskandari, I. (2019). Development of an infrared seed-sensing system to estimate flow rates based on physical properties of seeds. *Computers and Electronics in Agriculture*, 162, 874–881. <https://doi.org/10.1016/j.compag.2019.05.041>
- [2] Ding, Y., Chen, L., Wang, D., Liu, X., Xu, C., Wang, K., & Ding, Y. (2021). Design and test of monitoring system for rapeseed sowing quality (油菜播种质量监测系统设计与试验). *Transactions of the Chinese Society of Agricultural Engineering (Transactions of the CSAE)*, 42 (06), 43-51.
- [3] Ding, Y., Wang, K., Du, C., Liu, X., Chen, L., Liu, W., & Ding, Y. (2020). Design and experiment of high-flux small-size seed flow detection device (高通量小粒径种子流检测装置设计与试验). *Transactions of the Chinese Society of Agricultural Engineering (Transactions of the CSAE)*, 36 (13), 20-28.
- [4] Dong, W. (2023). *Research on machine vision hybrid rice intelligent constant seeding device based on embedded system (基于嵌入式系统的机器视觉杂交稻智能恒量播种装置研究)*. [Doctoral dissertation, Huanan Agricultural University].
- [5] He, Z., Liu, Q., & He, Z. (2021). Principles and applications of optical fiber distributed acoustic sensors. *Laser and Optoelectronics Progress (光纤分布式声波传感器原理与应用)*, 58(13), 11-25.
- [6] Hu, F., Liu, Y., Chen, C., Yin, W., Li, Y., Pu, H., & Hu, F. (2019). Design of vegetable precise seedling monitoring system based on LabVIEW (基于 LabVIEW 的蔬菜精密播种监测系统设计与试验). *Transducer and Microsystem Technologies*, 38(10), 114-117.
- [7] Jiang, M., Liu, C., Du, X., Dai, L., Huang, R., Yuan, B., & Liu, C. (2021). Development of seeding rate detection system for precision and small amount sowing of wheat (小麦精少量播种播量检测系统研制). *Transactions of the Chinese Society of Agricultural Engineering (Transactions of the CSAE)*, 37(05), 50-58.
- [8] Liao, Q., Lei, X., Liao, Y., Ding, Y., Zhang, Q., Wang L., & Liao, Q. (2017). Research progress of precision seeding for rapeseed (油菜精量播种技术研究进展). *Journal of Agricultural Mechanization Research*, 48(09), 1-16.

- [9] Lu, Q., Zhang, Y., Huo, X., Tang, Z., & Lu, Q. (2022). Design of automatic verification system for diaphragm gas meter based on color code sensor (基于色标传感器的膜式燃气表自动检定系统设计). *Instruments and Automation Equipment*, 38(10), 68-76.
- [10] Majcher, J., Kafarski, M., Szyplowska, A., Wilczek, A., Lewandowski, A., Skierucha, W., & Staszek, K. (2023). Prototype of a sensor for measuring moisture of a single rapeseed (*Brassica napus* L.) using microwave reflectometry. *Measurement*, 214, 112787. <https://doi.org/10.1016/j.measurement.2023.112787>
- [11] Mapoka, K., Birrell, S., & Tekeste, M. (2019). A comprehensive survey of nondestructive sensing technologies for the detection of corn seeds in a closed trench and measuring planting depth to augment the conventional method. *Computers and Electronics in Agriculture*, 158, 249–257. <https://doi.org/10.1016/j.compag.2019.02.010>
- [12] National Agricultural Machinery Standardization Technical Committee. (2005). GB/T6973-2005 *Testing methods of single seed drills (precision drills)*. China Agriculture Press.
- [13] National Agricultural Machinery Standardization Technical Committee. (2006). NY/T 987-2006 *Operating quality grain film-covering hill-drop drill*. China Agriculture Press.
- [14] Oguntosin, V., & Akindede, A. (2019). Design of a joint angle measurement system for the rotary joint of a robotic arm using an Incremental Rotary Encoder. *Journal of Physics. Conference Series*, 1299(1), 012108. <https://doi.org/10.1088/1742-6596/1299/1/012108>
- [15] Petzi, M., Liemert, A., Ott, F., Reitzle, D. (2023). Radiance and fluence in a scattering disc under Lambertian illumination. *Journal of Quantitative Spectroscopy & Radiative Transfer/Journal of Quantitative Spectroscopy & Radiative Transfer*, 310, 108728. <https://doi.org/10.1016/j.jqsrt.2023.108728>
- [16] Vazquez-Gutierrez, Y., O'Sullivan, D. L. (2020). Small-Signal modeling of the incremental optical encoder for motor control. *IEEE Transactions on Industrial Electronics*, 67(5), 3452–3461. <https://doi.org/10.1109/tie.2019.2916307>
- [17] Shen, L. (2022). Present situation and application of cotton precision sowing technology (棉花精量播种技术现状及应用). *Agricultural Technology and Equipment*, 388(04), 84-86.
- [18] Tu, Y., Tu, B., Zhu, H., Li, S., & Zhu, H. (2023). Error analysis of intelligent verification system of pointer pressure gauge and measurement accuracy evaluation method (指针压力表智能检定系统误差分析及检测精度评价方法). *Industrial Instrumentation and Automation*, (04), 98-102.
- [19] Wang, D. (2023). *Design and experiment of remote monitoring system for unmanned seeding operation of rapeseed direct seeding unit (油菜直播机组无人播种作业远程监测系统设计与试验)*. [Master's dissertation, Huazhong Agricultural University].
- [20] Wen, B., Song, P., Li, J., Huang, Y., Cen, H. (2022). Design and test of seeding monitoring and compensating system for belt-spoon type potato seed metering device (带勺式马铃薯排种器漏播检测与补种系统设计与试验). *Journal of Agricultural Mechanization Research*, 53(02), 36-46.
- [21] Xie, C., Yang, L., Zhang, D., Cui, T., Zhang, K. (2021). Seeding parameter monitoring method based on laser sensors (基于激光传感器的播种参数监测方法). *Transactions of the Chinese Society of Agricultural Engineering (Transactions of the CSAE)*, 37(03), 140-146.
- [22] Xie, C., Zhang, D., Yang, L., Cui, T., He, X. (2021). Precision seeding parameter monitoring system based on laser sensor and wireless serial port communication. *Computers and Electronics in Agriculture*, 190, 106429. <https://doi.org/10.1016/j.compag.2021.106429>
- [23] Xu, L., Hu, B., Luo, X., Ren, L., Guo, M., Mao, Z., Cai, Y., Wang, J. (2022). Development of a seeding state monitoring system using interdigital capacitor for cotton seeds (叉指电容式棉花穴播取种状态监测系统研制). *Transactions of the Chinese Society of Agricultural Engineering*, 38(23): 50-60.
- [24] Yan, P. (2023). *Eight-channel high-precision data synchronization acquisition module design (八通道高精度数据同步采集模块设计)*. [Master's dissertation, University of Electronic Science and Technology of China].
- [25] Yin, Y., Chen, L., Meng, Z., Li, B., Luo, C., Fu, W., . . . Qin, W. (2018). Design and evaluation of a maize monitoring system for precision planting. *International Journal of Agricultural and Biological Engineering*, 11(4), 166–170. <https://doi.org/10.25165/ij.ijabe.20181104.3517>

- [26] Yue, M., Cheng, W., Huang, J., Long, L., Hao, Y., & Yue, M. (2014). Development of intelligent detection system for operation distance of photoelectric proximity switch (光电式接近开关动作距离智能检测系统的研制). *Modern Manufacturing Engineering*, 29(09), 122-125.
- [27] Zhang, X., Chen, Y., Shi, Z., Jin, W., Zhang, H., Fu, H., Wang, D., & Zhang, X. (2021). Design and experiment of double-storage turntable cotton vertical disc hole seeding and metering device (双仓转盘式棉花竖直圆盘穴播排种器设计与试验). *Transactions of the Chinese Society of Agricultural Engineering (Transactions of the CSAE)*, 37(19), 27-36.
- [28] Zhang, X., Zhang, H., Shi, Z., Jin, W., Chen, Y., Yu, Y., & Shi, Z. (2022). Design and experiments of seed pickup status monitoring system for cotton precision dibblers (棉花精量穴播器取种状态监测系统设计与试验). *Transactions of the Chinese Society of Agricultural Engineering*, 38(05), 9-19.
- [29] Zhao, B., Fan, X., Zhou, L., Li, Y., Che, Y., Niu, K., & Zhou, L. (2020). Design and test of piezoelectric flow sensor for pneumatic seeder (气流输送播种机压电式流量传感器设计与试验). *Journal of Agricultural Mechanization Research*, 51(08), 55-61.

STRUCTURAL PARAMETERS OPTIMIZATION AND EXPERIMENT OF TRENCHING BLADES VIA DEM

基于 DEM 的开沟刀结构参数优化与试验

Haochao TAN, Congcong SHEN, Zhaoyang GUO, Deyu LI, Shuai MA, Liming XU¹

College of Engineering, China Agricultural University, Beijing 100083/China

Corresponding author: Liming XU

Tel: +86 010-62737291; E-mail: xulimingcoe@cau.edu.cn

DOI: <https://doi.org/10.35633/inmateh-74-82>

Keywords: trenching blades; structural parameter optimization; DEM; experimentation

ABSTRACT

This study developed a chain counter-rotating trenching and backfilling device to reduce high tillage resistance in orchard operations. A 3D mathematical model of the trenching blade was created using Cartesian coordinate transformation. Taking curvature (β), curve angle (α), bend radius (R), and cone residual angle (θ) as experimental factors, and soil cutting resistance as the evaluation index. The optimized parameters were $\beta=95^\circ$, $\alpha=10^\circ$, $R=24$ mm, $\theta=39^\circ$. Bench tests were performed with the optimal parameters, and the results showed that the optimized ditching blade reduced the resistance by 18.7% compared to the ordinary trenching blades. Field test results showed a 9.64% reduction in furrowing torque.

摘要

针对果园开沟过程中耕作阻力大的问题, 本文提出了一种链条反向旋转开沟回填装置。通过笛卡尔坐标系变换, 建立开沟刀的三维数学描述模型。以曲率(β), 曲线角度(α), 弯折半径(R)和锥余角(θ)为试验因素, 以切土阻力为评价指标进行试验, 优化后的参数为 $\beta=95^\circ$, $\alpha=10^\circ$, $R=24$ mm, $\theta=39^\circ$ 。以最优参数进行台架和田间试验, 台架试验表明, 相对于普通开沟刀, 优化后的开沟刀阻力减少了 18.7%, 田间试验表明, 相对于普通开沟刀, 装配有 BS 刀的开沟扭矩降低了 9.64%。

INTRODUCTION

Tillage has been a long-standing practice in agricultural production (Sadek *et al.*, 2021), and the continuous improvement of tillage techniques has been a key focus in the agricultural industry (Green *et al.*, 2023). The use of agricultural machinery in the tillage process has significantly enhanced operational efficiency, reduced manual labor, lowered costs, and improved the overall quality of agricultural production (Li *et al.*, 2023; Wang, Zhou *et al.*, 2024). Trenching and fertilization are an important part of crop growth. For deep-rooted crops such as grapes, the trench depth is generally deeper, often requiring 60 cm. Disc-type trenching equipment struggles to achieve such depths, making chain-type trenching devices a good choice for agricultural deep trenching.

The trenching blade is a key operating component in chain-type trenching devices, and studying the interaction between the tool and the soil is crucial for optimizing and improving its performance. Reasonably designed parameters can significantly enhance operation efficiency, reduce operational resistance, minimize trenching torque, and promote sustainable agricultural development (Liu, *et al.*, 2023; Wang, Zhang *et al.*, 2024; Wei *et al.*, 2024). Reducing the tillage resistance agricultural components has always been the goal pursued by agricultural experts. Hu Zhiyong *et al.*, (2017), conducted a structural statics, dynamic modal, and harmonic response analysis of a variant form of trenching blades using finite element analysis. The results showed that the trenching blades would not experience body forging and distortion during operation. Wang Xu, *et al.*, (2023), analyzed the force exerted on trenching blades during trenching, straw burial, and soil backfilling processes using a chain trenching device but did not optimize the structure parameters of the trenching blades. Kim *et al.*, (2019), applied a chain trenching device underwater and employed genetic algorithms for multi-objective optimization of the trenching machine, aiming to minimize power and weight during operation. Sitorus *et al.*, (2016), developed a kinematic and dynamic analysis model and designed a chain trenching machine for underwater applications.

¹ Haochao Tan, Ph.D.; Congcong Shen, Ph.D.; Zhaoyang Guo, Ph.D.; Deyu Li, Ms.; Shuai Ma, Associate professor Ph.D.; Liming Xu, Professor, Ph.D.

They analyzed the effects of cutting tools, material conditions, working parameters, and structural parameters on forces, torques, weight, and power components. *Azimi-Nejadian et al., (2022)*, used the DEM to study the influence of plow design parameters, plow depth, and operating speed on the burial depth of weed seeds. *Zhang et al., (2022)*, used the DEM to establish an interaction model between soil and rotary tiller roller, analyzed the dynamic process of soil cutting by the rotary tiller blade, and obtained the changes in soil deformation area, cutting energy, cutting resistance, and soil particle movement. *Ma et al., (2024)*, designed a double-disk trencher, utilized a 3D scanner to scan the trenching blade, established a 3D model of the trenching blade, and analyzed stress and strain conditions. The results showed that the maximum stress was 55.48 MPa, and the average deformation was 0.38 mm, meeting the usage requirements of the trenching blade. *Song et al., (2022)*, established a furrow opener model using 3D software. Through simulation experiments, they compared and analyzed the soil disturbance behavior of the furrow opener under different positions, speeds, and working depths. The results showed that the relative errors of the cross-sectional area for the front and rear furrow openers were 0.25% and 5.2%, respectively. The simulation results accurately reflected the soil disturbance during the furrowing process. *Zeng et al., (2024)*, have designed a standard ditching blade with a self-excited vibration device. A simulation model of soil and the ditching blade was established and experiments were conducted. The results show that compared to common ditching device, the self-excited vibration device reduces resistance by 12.3%. *Song et al., (2024)*, designed a trenching blade that combines cutting and throwing actions. Through simulations, the main factors affecting trenching performance were identified, the trenching blade was fabricated, and the tests were conducted. The results show that the trenching power consumption is 0.668 kW, and the soil fragmentation rate is 92.4%, meeting the quality requirements for trenching.

The aforementioned scholars have investigated the relationships between different soil-engaging components and the soil, reducing overall furrowing resistance, which holds significant research importance. However, there is still a lack of precise in-depth analysis concerning the trenching blades used in chain-type trenching devices, necessitating an analysis and optimization of the structural characteristics of the trenching blades. In response to the above issue, this study aims to establish a mathematical description model of the trenching blades, systematically design and optimize the structural parameters of the trenching blades, and manufacture new trenching blades (hereinafter referred to as BS blades) based on the optimal parameters. Subsequently, the practical effects of BS blades in reducing soil cutting resistance and torque will be verified through field trials, providing theoretical and technical support for achieving efficient and energy-saving furrowing operations.

MATERIAL AND METHODS

Structure and working principle

This article proposes a novel chain reverse rotation trenching device to meet the requirements of trenching, fertilizing, and backfilling. The overall structure is shown in Fig.1a. It mainly consists of a frame, ground wheel, hydraulic cylinder, and trenching blade (Material is 65Mn). The trenching depth is adjustable by extending the hydraulic cylinder, and the trenching blade is fixed in reverse with the blade edge facing downward, to achieve downward cutting of the soil. During this process, the trenching blade is an important component in the operation.

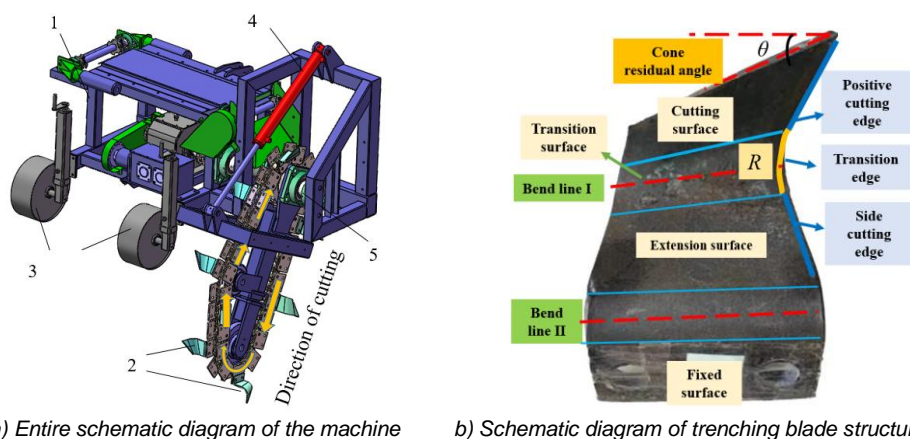


Fig. 1- Trenching machine structure

1-Frame; 2-Trenching blade; 3- Ground wheel; 4-Hydraulic cylinder; 5-Drive shaft

Fig.1b is a structural diagram of the ditching blade, which includes the cutting surface, transition surface, extension surface, fixation surface, side cutting edge, transition edge, and positive cutting edge. Among them, the positive cutting edge directly participates in cutting the soil, while the side cutting edge has almost no cutting effect. The transition edge is in an arc shape, realizing the transition from the positive cutting edge to the side cutting edge. The cutting surface, where the positive cutting edge is positioned, serves as the primary cutting role. The cone residual angle (θ) is an important parameter affecting the size of the cutting area. The transition surface is a curved surface, achieving the transition from the cutting surface to the extension surface. It participates in a small part of the cutting. The size of bend radius(R) affects the area of the cutting surface and the transition surface. The extension surface does not participate in cutting and its main function is to extend the cutting surface outward to achieve different trench widths. Based on the length of the extension surface, the ditching blades can be classified into models of 12, 15, 20, 25, and 30 cm. Different models of ditching blades only differ in the length of the extension surface; the cutting surface parts are exactly the same.

Analysis of trenching blades structure parameters

To facilitate the analysis of the formation process of the trenching blade, a right-handed coordinate system $X'''Y'''Z'''$ was established (Fig.2a), the X''' -axis coincides with the bending line l and points towards the positive cutting edge. The Y''' -axis coincides with the cutting surface and is perpendicular to the direction of bending line l . The Z''' -axis is perpendicular to the cutting surface and points towards the fixation surface. In this coordinate system, rotate it β degrees in the negative direction of the X''' axis to obtain the coordinate system $X''Y''Z''$, indicated by a single dashed line. Then, rotate it α degrees in the negative direction of the Z'' axis to obtain the coordinate system $X'Y'Z'$, indicated by a double dashed line. At this point, the unfolding diagram of the trenching blade is obtained (Fig. 2b).

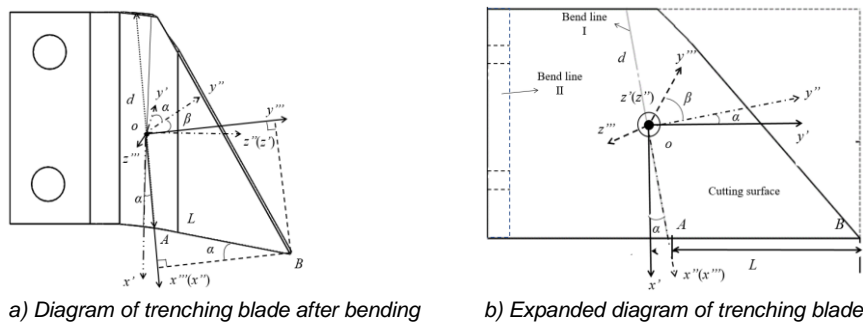


Fig. 2- Bending diagram of trenching blades

Note: A and B represent the two endpoints of the cutting edge; d represents the length of bend line l , mm; L represents the distance between A and B points, mm; α represents the inclination angle of bend line l , ($^\circ$); β represents the bending angle of the cutting surface, ($^\circ$).

In the $X'''Y'''Z'''$ coordinate system, the position of the positive cutting edge can be described by its two endpoints, A and B . We can solve for the coordinates of the two endpoints A and B using Equation(1):

$$A = \begin{pmatrix} \frac{d}{2} \\ 0 \\ 0 \end{pmatrix} \quad B = \begin{pmatrix} \frac{d}{2} + L \sin \alpha \\ L \cos \alpha \\ 0 \end{pmatrix} \tag{1}$$

The equation for the relationship between the coordinates of points A and B in the $X'Y'Z'$ coordinate system, as shown in Equation (2), can be derived.

$$C = \text{Rot}(Z'', \alpha) \text{Rot}(X''', \beta) i \tag{2}$$

where i is the coordinate value to be converted, and C is the converted coordinate value, specifically expanded as (3):

$$\begin{pmatrix} x' \\ y' \\ z' \end{pmatrix} = \begin{pmatrix} \cos \alpha & -\sin \alpha & 0 \\ \sin \alpha & \cos \alpha & 0 \\ 0 & 0 & 1 \end{pmatrix} \begin{pmatrix} 1 & 0 & 0 \\ 0 & \cos \beta & -\sin \beta \\ 0 & \sin \beta & \cos \beta \end{pmatrix} \begin{pmatrix} x''' \\ y''' \\ z''' \end{pmatrix} \tag{3}$$

where x', y', z' and x''', y''', z''' are the coordinates of points A and B in the coordinate systems $X'Y'Z'$ and $X'''Y'''Z'''$ respectively.

Solving equations 1 and 3, the coordinates of points A and B on positive cutting edges are obtained, respectively:

$$A = \begin{pmatrix} \frac{d}{2} \cos \alpha \\ \frac{d}{2} \sin \alpha \\ 0 \end{pmatrix} \quad B = \begin{pmatrix} \cos \alpha (\frac{d}{2} + L \sin \alpha) - L \cos^2 \alpha \sin \alpha \\ \sin \alpha (\frac{d}{2} + L \sin \alpha) + L \cos^3 \alpha \\ L \cos \alpha \sin \alpha \end{pmatrix} \quad (4)$$

The position of the positive cutting edge varies, leading to different angles of entry into the soil and consequently different cutting resistances. From equation (4), it can be observed that the factors affecting the variation in the position of the positive cutting edge primarily include the bending line angle α , the curvature β , the length of the positive cutting edge L , and the length of the bending line d . The length of the positive cutting edge is typically around 45 mm, so L can be considered as a constant. According to the Chinese national standard GB/T1243-2006, a 32A chain with a pitch of 50.8 mm is used for chain trenching devices. The parameter d is related to pitch, so the focus can be on the influence of α . Based on the analysis in the two sections above, the factors influencing the trenching blade cutting process include α , β , R , and θ .

Experimental design

By optimizing these parameters, the efficiency and functionality of the trenching blades can be improved. Central Composite Design (CCD) experiments were conducted with α values of 5°, 10°, 15°, 20°, and 25°, β values of 75°, 94°, 112°, 131°, and 150°, R values of 10, 15, 20, 25, and 30, θ values of 0°, 10°, 20°, 30°, and 40° to optimize the parameters of the trenching blade structure. A total of 30 experiments were conducted, including 24 experiments with different combinations of structural parameters and 6 repeated experiments. The cutting resistance (F_1) of the trenching blade fully entering the soil was chosen as the test index. Based on the structural parameters, SolidWorks (2016) was utilized to generate three-dimensional models for 24 distinctively shaped trenching blades intended for the experiment (Fig. 3a exhibits only 12 of them) and preserved them in .step format. Afterward, they were imported into the discrete element simulation software, employing the parameters outlined in Table 2 for the discrete element simulation. Given the reduced space necessary for single-blade soil cutting tests, the trench box dimensions in EDEM were configured to 2000 mm x 400 mm x 600 mm (Fig.3b). To expedite the computation process, the simulation duration was set to 0.5 seconds with a time step of 0.01 seconds.

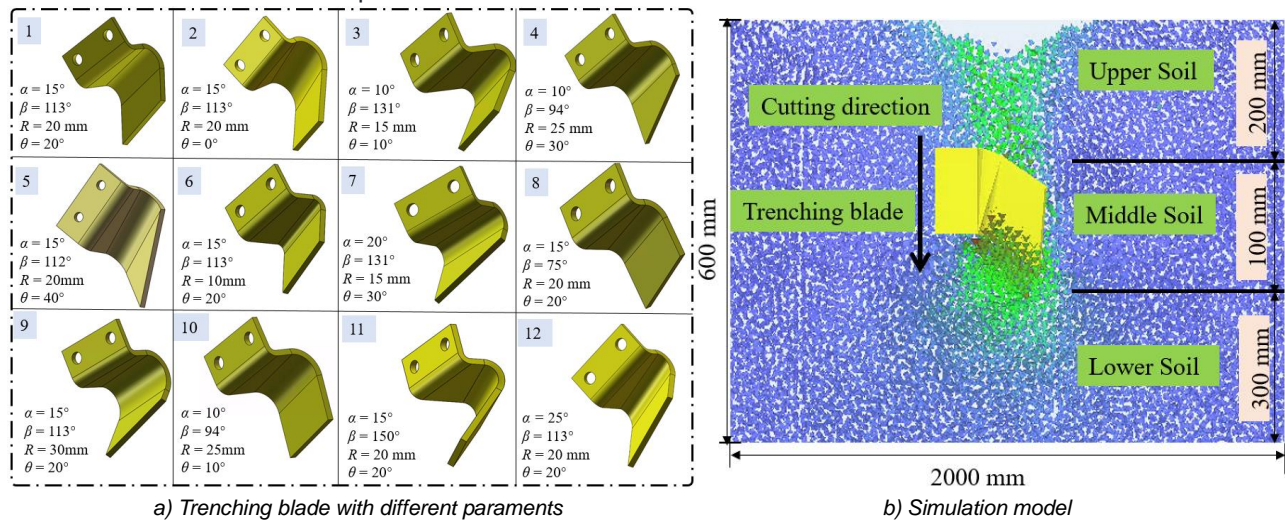


Fig. 3 - The models of the trenching blades with different structural parameters

Table 1

The experimental factors and level designs for the Central Composite Design

No.	Actual factor level				Coded factor level				Test indicators
	Curvature $\beta / ^\circ$	Bending line angle $\alpha / ^\circ$	Bend radius R / mm	Cone residual angle $\theta / ^\circ$	Curvature $\beta / ^\circ$	Bending line angle $\alpha / ^\circ$	Bend radius R / mm	Cone residual angle $\theta / ^\circ$	Cutting resistance F_1 / N
0	1	2	3	4	5	6	7	8	9
1	131.25	10	15	30	1	-1	-1	1	648.58
2	131.25	20	25	10	1	1	1	-1	1038.48
3	131.25	20	15	30	1	1	-1	1	739.59
4	75	15	20	20	-2	0	0	0	588.46
5	150	15	20	20	2	0	0	0	799.9

0	1	2	3	4	5	6	7	8	9
6	131.25	10	25	30	1	-1	1	1	690.02
7	112.5	15	30	20	0	0	2	0	881.06
8	93.75	10	25	10	-1	-1	1	-1	688.05
9	93.75	10	15	10	-1	-1	-1	-1	599.48
10	112.5	5	20	20	0	-2	0	0	546.6
11	112.5	15	20	40	0	0	0	2	600.82
12	131.25	20	25	30	1	1	1	1	878.17
13	112.5	15	10	20	0	0	-2	0	664.47
14	112.5	25	20	20	0	2	0	0	1011.97
15	93.75	20	15	30	-1	1	-1	1	666.01
16	93.75	10	25	30	-1	-1	1	1	477.76
17	93.75	20	25	30	-1	1	1	1	783.87
18	131.25	10	15	10	1	-1	-1	-1	689.38
19	131.25	10	25	10	1	-1	1	-1	809.58
20	93.75	20	25	10	-1	1	1	-1	931.76
21	93.75	20	15	10	-1	1	-1	-1	848.69
22	112.5	15	20	0	0	0	0	-2	890.63
23	131.25	20	15	10	1	1	-1	-1	795.3
24	93.75	10	15	30	-1	-1	-1	1	619.99
25	112.5	15	20	20	0	0	0	0	754.56

Table 2

Parameters of discrete element simulation for soil

Type	Static friction coefficient	Rolling friction coefficient	Restitution coefficient	Adhesive energy density / (J m ⁻³)
Upper soil	0.6	0.07	0.47	2694
Middle soil	0.5	0.17	0.52	4266
Lower soil	0.5	0.21	0.62	4432
65Mn- Upper soil	0.72	0.33	0.44	-
65Mn- Middle soil	0.8	0.16	0.54	-
65Mn- Lower soil	0.7	0.32	0.51	-

Validation test

The experiment consists of two parts: the first part involves using a universal testing machine to measure the cutting resistance of the trenching blade. The purpose is to compare the cutting resistance of BS blade with that of a conventional one (hereinafter referred to as CS blade). The second part involves the mean trenching torque. During field operations, the trenching process is the result of the combined action of multiple trenching blades. All trenching blades are driven by a drive shaft, so measuring the torque of the drive shaft can effectively reflect the resistance during the entire trenching process.

The cutting resistance measurement scene is shown in Fig.4, mainly including a computer, universal testing machine, trenching blade, soil box, pressure head, resistance sensor (Range:0~30 kN, accuracy 1%), etc. Before the experiment, the soil moisture content was adjusted to 13.6%, and the compaction level was adjusted to 450 kPa (consistent with field conditions). The soil was filled into the soil box and compacted, excess soil was scraped off with a shovel. The universal testing machine was set to move at a speed of 250 mm/min. The trenching blade cut through the soil under the forced action of the pressure head (Fig.4b). The resistance sensor transmitted the measured cutting resistance to the computer in real time until the entire trenching blade was pressed into the soil, ending the test process. Then, it was adjusted to its original state, and CS blade was tested in the same manner.

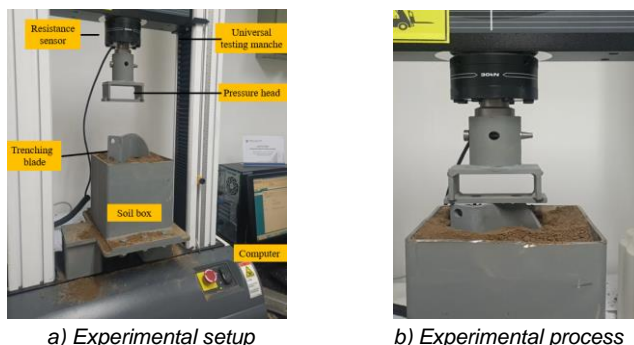


Fig. 4 - Single trenching blade test

To validate the optimization results, it is necessary to conduct on-site experiments to measure the mean trenching torque of the entire trenching system. The experiments are conducted at Yifeng Machinery Co., Ltd. in Gaomi City, Shandong Province. The soil at the experimental site is the same as that of the vineyard soil. Before the experiment, soil density was measured using the ring knife method, which was approximately 1500 kg/m³. The soil moisture content was determined to be around 13.6% using a moisture meter (TDR150, American Spectrometer, accuracy 3%, resolution 0.1%). The soil compaction measured using the Soil Compaction Meter (SC900, American Spectrometer, maximum depth 45 cm) is between 400-500 kPa. To accurately obtain the torque, a torque sensor (HCNJ-101 type, Beijing Haibohua, range 0~800 Nm, accuracy 0.5%) was used as the information perception component (Fig. 5a). The tractor provides power for the trenching device, and under the drive of the trenching shaft, the torque sensor rotates synchronously, and the output electrical signal is converted into a voltage value through the F/V conversion module. The data acquisition card displays the voltage signal on the computer with a sampling frequency of 20 Hz. The specific torque value was then determined using a linear mapping relationship (Fig.5b).

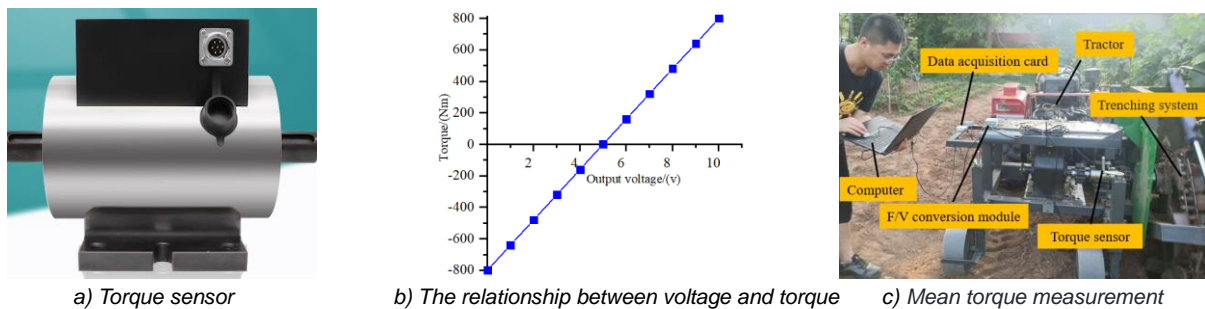


Fig. 5 - Field test

During the experiment, the CS blades were first tested, followed by testing the BS blades on the same land while maintaining the same operating parameters (Fig. 5c). Data analysis was performed during the stable working stage in the middle. The experiment was conducted three times, and the average value was selected as the final value.

RESULTS

Optimization and simulation analysis were conducted on the structural parameters of the trenching blades in order to obtain the variance analysis results for cutting resistance, as shown in Table 3. Based on the variance results, regression fitting was performed on the response variables, leading to the regression equations shown in Eq. (5).

Table 3

Analysis of variance for maximum cutting force					
Dependent variable	Source of variance	Sum of square	Degree of freedom	F value	P value
F ₁	β	47915.73	1	41.72	<0.0001**
	α	242800	1	211.39	<0.0001**
	R	54898.32	1	47.80	<0.0001**
	θ	93793.76	1	81.67	<0.0001**
	$\beta\alpha$	2679.87	1	2.33	0.1450
	βR	11031.83	1	9.61	0.0065**
	$\beta\theta$	899.55	1	0.78	0.3885
	αR	12696.22	1	11.06	0.0040**
	$\alpha\theta$	1858.69	1	1.62	0.2204
	R θ	7892.99	1	6.87	0.0179**
	β^2	9504.22	1	8.28	0.0105**
	R ²	53.15	1	0.046	0.8322

Note: ** represents factor with a highly significant influence on the index (P < 0.05)

$$F_1 = 768.83 + 44.68\beta + 100.57\alpha + 47.83R - 62.51\theta - 12.94\beta\alpha + 26.26\beta R + 7.5\beta\theta + 28.17\alpha R - 10.78\alpha\theta - 22.21R\theta - 18.43\beta^2 - 6.24R^2 \tag{5}$$

From the variance analysis results in the table, it can be noted that the factors α , β , R , and θ all have a significant impact on the maximum cutting force (F_1). Additionally, the interactions between the radius (R) and bending line angle (α), the radius R and the cone residual angle (θ), as well as the radius (R) and curvature (β), have a significant influence on F_1 .

Single Factor Analysis

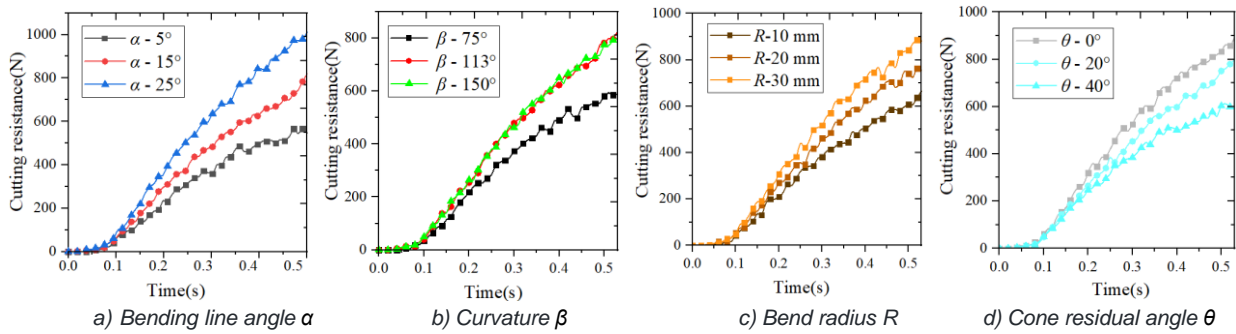


Fig. 6 - Single factor analysis

Keep three factors at middle levels, and the remaining factors at low, medium, and high levels respectively. Analyze the influence of each structural parameter on the cutting resistance. As illustrated in Fig. 6(a)–(c), during the initial 0.07 seconds, the trenching blade did not penetrate the soil, resulting in zero cutting resistance. From 0.07 to 0.55 seconds, the cutting resistance gradually increased and reached its maximum at the final moment. As demonstrated in Fig(a)–(c), the bending line angle α and radius R showed a positive correlation with cutting resistance; with the increase in α and R , the cutting resistance on the trenching blade increased, peaking when α was 25° and R was 30 mm. Analysis from Fig(b) indicated that the cutting resistance was minimum at 588 N when angle β was 75° . Although the resistance increased for β at 113° and 150° , the relationship weakened, indicating that the resistance did not increase linearly with β . Conversely, the cone residual angle θ had a negative correlation with cutting resistance; when θ was at its maximum, the cutting resistance was at its minimum. This is because θ directly determines the size of the cutting surface; a larger θ results in a smaller cutting surface, reducing the interaction area with the soil and thus decreasing the force, which aligns with the results of the mechanical analysis.

Interaction Analysis

The significant interaction terms are analyzed. From fig. 7(a)–(c), it can be noticed that regardless of the levels of β , α , and θ , F_1 gradually increases with an increase in R . When β and α are at a higher level, the increase in F_1 is much greater compared to when they are at a lower level (Fig.7(a) and (b)). Conversely, when θ is at a higher level, the increase in F_1 is lower compared to when it is at a lower level. Similarly, regardless of the radius level, the changes in F_1 are positively correlated with α and β and negatively correlated with θ , consistent with the findings of the single-factor analysis of F_1 . Additionally, it was found that reducing α is easier in lowering F_1 compared to reducing β or increasing θ . Hence, to achieve a lower F_1 , it is preferable to choose smaller values of α and β and a larger value of θ .

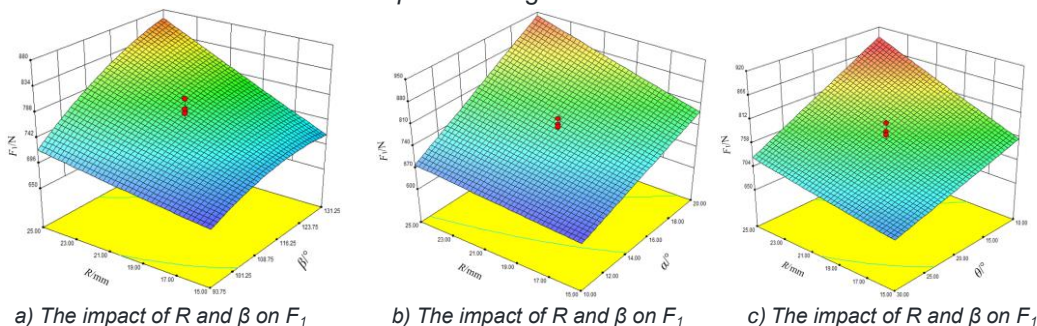


Fig. 7 - Response surfaces of F_1

Parameter Optimization and Experimental Verification

Considering the interaction among different factors and in order to obtain the optimal combination of trenching blade structural parameters, the minimization of cutting resistance was adopted as the optimization criterion to determine the parameter values of each factor. The calculation objective is as shown in formula (6).

$$\begin{cases} \min F_1 \\ 93.75^\circ \leq \beta \leq 131.75^\circ \\ 10^\circ \leq \alpha \leq 20^\circ \\ 15 \leq R \leq 25 \\ 0^\circ \leq \theta \leq 40^\circ \end{cases} \quad (6)$$

Through numerical optimization, the optimized values for the curvature (β), bending line angle (α), radius (R), and cone residual angle (θ) that minimize F_1 are found to be 95° , 10° , 24 mm, and 39° respectively. According to the solution parameters, the trenching blade is processed (BS blades), as shown in Fig. 8 in comparison with CS blades.

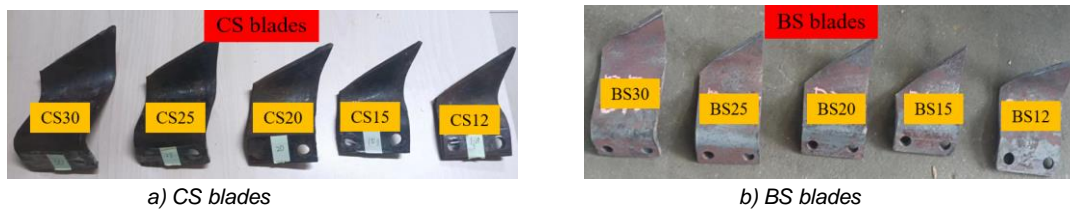


Fig. 8 - Comparison between the CS and BS blades

The only difference between different models of trenching blades was the length of the extending surface, while the cutting surface was the same. The optimized parameters mentioned above belonged to the optimization of the cutting surface. Therefore, according to the method shown in Fig. 4, it was only necessary to select the same model of BS and CS trenching blades (model 25) for the physical experiment. The test results were shown in Fig. 9, which illustrates the forces acting on the trenching blades over time. From the graph, it can be seen that as time increased, the force on the trenching blades also gradually increased, and the force curves of the two types changed in a similar manner. The force change was relatively slow in the 5-12 second stage, and it sharply increased in the 12-20 second stage. The force curve of the BS blade was lower than that of the CS blade, indicating that the trenching blades processed according to the optimized parameters could reduce the cutting resistance. The force on the BS blade peaked at 532.19 N, compared to 654.3 N for the CS blade, a reduction of 18.7%. This reduction indicates that the optimized trenching blade exhibits superior operational characteristics.

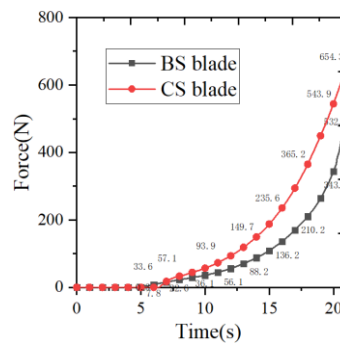


Fig. 9 - Results of soil cutting test

Field experiment

In LabVIEW (2018) software, a program was created and written through the graphical programming environment for cyclic acquisition of torque sensor signals. The CS and BS trenching blades were subsequently fixed to the chain trenching device using bolts, and field tests were conducted, with the test scene shown in Fig.10. The tractor output shaft speed is 540 r/min. For the convenience of data processing and analysis, the torque data from the middle 60 seconds was selected as a reference, dividing this 60-second period into six stages, each lasting 10 seconds. The average torque value for each stage was calculated within that stage, and the average values from these six stages were aggregated to serve as the final measurement result, as shown in Table 4.



Fig. 10 --Field experiment

According to Table 4, the average torque when using the CS trenching blade was 461.01 Nm, and when using the BS trenching blade, it was 416.66 Nm. Compared to CS blade, the mean torque was reduced by 9.62%. This indicates that the optimized trenching blade can significantly reduce the resistance of the entire trenching system and achieve excellent operational performance.

Table 4

Type	Time/s						Mean torque/Nm
	0-10	10-20	20-30	30-40	40-50	50-60	
CS blades	470.60	471.14	445.02	448.98	491.43	441.14	461.01
BS blades	395.85	419.06	374.99	87.77	461.94	461.89	416.66

CONCLUSIONS

To address the issue of high tillage resistance during deep ditching, our study proposed a chain type reverse-rotary trenching device, and reached the following conclusions:

(1) A three-dimensional mathematical model for the trenching blade was established by transforming into the Cartesian coordinate system. Analyzing the structure of the trenching blade, the structural parameters affecting the efficiency of the trenching operation were identified as curvature, bending line inclination, bend radius, and cone residual angle.

(2) A simulation experiment was conducted with curvature, bending line inclination, bend radius, and cone residual angle as experimental factors, and soil cutting resistance as the index. Through single-factor and interaction analysis, the influence patterns of each factor on soil cutting resistance were determined. Employing a multi-objective optimization algorithm, the optimal parameter combination for the trenching blade was obtained as: $\beta=95^\circ$, $\alpha=10^\circ$, $R=24\text{ mm}$, $\theta=39^\circ$.

(3) According to the optimal parameters, the trenching blades were processed and tested for validation. Measurements from a universal testing machine showed that the BS blades experienced less resistance than the CS blades, with a reduction of 18.7%. Field trenching test data indicated that the mean torque of the trenching device equipped with BS blades was 416.66 Nm, while that with CS blades was 461.01 Nm, which shows a decrease of 9.62%. This demonstrates that the trenching blades optimized through experimental testing can effectively reduce operational resistance and exhibit good operational performance.

ACKNOWLEDGEMENTS

This study was supported by Key Research and Development Program of Shandong Province (Science and Technology Innovation Boosting Action Plan for Rural Revitalization, Project Name: Research and Development of Intelligent Equipment for Grapes; Project Number: 2022TZXD001102-2), and China Agriculture Research System of MOF and MARA (CARS-29).

REFERENCES

[1] Azimi-Nejadian, H., Karparvarfard, S. H., & Naderi-Boldaji, M. (2022). Weed seed burial as affected by mouldboard design parameters, ploughing depth and speed: DEM simulations and experimental validation. *Biosystems Engineering*, vol. 216, pp.79-92, Iran.

[2] Green, L., Webb, E., Johnson, E., Wynn, S., & Bogen, C. (2023). Cost-effective approach to explore key impacts on the environment from agricultural tools to inform sustainability improvements: inversion tillage as a case study. *Environmental Sciences Europe*, vol.35, pp.79-94, Germany.

[3] Hu, Z.Y., Guo, Y.K., & Ming, Y. (2017). Finite element analysis of a chain-type orchard fertilizer

- trenching machine's trenching blade (一种链式果园施肥开沟机开沟刀的有限元分析). *Jiangsu Agricultural Sciences*, vol. 45, pp. 231-237, Jiangsu/China.
- [4] Kim, J., Kwon, O.S., Hai, N.L.D., & Ko, J.H. (2019). Study on the Design of an Underwater Chain Trencher via a Genetic Algorithm. *Journal of Marine Science and Engineering*, vol. 7, pp. 429, Korea.
- [5] Li, J., Li, H., Chen, Y., Lin, P., Zhang, Q., Cheng, Y., Yang, Z., & Huang, G. (2023). Research on Ditching Mechanism of Self-Excited Vibration Ditching Machine. *Agronomy*, vol. 13, pp. 905, Guangdong / China.
- [6] Liu, G., Yao, J., Chen, Z., Han, X., & Zou, M. (2023). Mesoscopic analysis of drag reduction performance of bionic furrow opener based on the discrete element method. *Plos One*, vol.18, pp. e293750, Jilin/China.
- [7] Ma, T., Qi, B., Sun, X., Liu, Y., Ren, Y., Sun, J., Zhang, B., & Wu, Q. (2024). Design and experiment of self-propelled multifunctional trenching and fertilizing machine. *INMATEH Agricultural Engineering*. vol.74, pp.449-459, Bucharest / Romania.
- [8] Sadek, M. A., Chen, Y., & Zeng, Z. (2021). Draft force prediction for a high-speed disc implement using discrete element modelling. *Biosystems Engineering*, vol. 202, pp. 133-141, Canada.
- [9] Sitorus, P.E., Ko, J.H., & Kwon, O.S. (2016). Parameter study of chain trenching machines of Underwater Construction Robots via analytical model. In MTS/IEEE OCEANS 2016 Monterey, pp.1-6, Korea.
- [10] Song, C., Zhang, X., Li, H., Lv, Y., Li, Y., Wang, X., Wei, Z., & Cheng, X. (2022). Effect of tine furrow opener on soil movement laws using the discrete element method and soil bin study. *INMATEH - Agricultural Engineering*, vol.68, pp.350-366, Bucharest / Romania.
- [11] Song, Y., Xu, J., Xing, J., Wang, X., Hu, C., Wang, L., & Li, W. (2024). Research and Experiment on the Ditching Performance of a Ditching and Film-Covering Machine in the Yellow Sand Cultivation Mode of Solar Greenhouses. *Agronomy*, vol.14, pp.1704-1731, Xinjiang/China.
- [12] Wang, J., Xu, Y., Wang, C., Xiang, Y., & Tang, H. (2023). Design and simulation of a trenching device for rice straw burial and trenching based on MBD-DEM. *Computers and Electronics in Agriculture*, vol.207, pp.107722, Harbin/China.
- [13] Wang, L., Zhou, B., Wan, C., & Zhou, L. (2024). Structural parameter optimization of a furrow opener based on EDEM software. *International Journal of Agricultural and Biological Engineering*, vol.17, pp.115-120, Xinjiang/China.
- [14] Wang, X., Zhang, S., Du, R., Zhou, H., & Ji, J. (2024). Recent Advances in Biomimetic Methods for Tillage Resistance Reduction in Agricultural Soil-Engaging Tools. *Agronomy*, vol. 14, pp. 2163, Henan/ China.
- [15] Wei, L., Huang, W., Liu, J., Li, M., Zheng, Z., Wang, S., Du, D., & Zhang, Y. (2024). DEM simulation of subsoiling in tropical sugarcane fields: Effects of opposing subsoiler design and model parameters. *Smart Agricultural Technology*, vol.9, pp.100593, Guangdong/China.
- [16] Zeng, Y., Li, J., Li, H., Zhang, Q., Li, C., Li, Z., Jiang, R., Mai, C., Ma, Z., & He, H. (2024). Research on the ditching resistance reduction of self-excited vibrations ditching device based on MBD-DEM coupling simulation. *Frontiers in Plant Science*, vol.15, Guangdong/China.
- [17] Zhang, X., Zhang, L., Hu, X., Wang, H., Shi, X., & Ma, X. (2022). Simulation of Soil Cutting and Power Consumption Optimization of a Typical Rotary Tillage Soil Blade. *Applied Sciences*, vol.12, pp.8177, Xinjiang/China.

OPTIMIZING TRENCHING DEVICE OPERATIONAL PARAMETERS VIA MBD-DEM COUPLING FOR ENERGY SAVINGS

基于 MBD-DEM 耦合法优化开沟装备作业参数以减少能源消耗

Haochao TAN, Congcong SHEN, Junlong MA, Chunlin WU, Liming XU, Shuai MA¹

College of Engineering, China Agricultural University, Beijing 100083 / China

Tel: +86- 17710628251; E-mail: mashuaicoe@cau.edu.cn

Corresponding author: Shuai MA

DOI: <https://doi.org/10.35633/inmateh-74-83>

Keywords: trenching device; operational parameter; MBD-DEM; energy saving

ABSTRACT

This study addresses the challenges of high resistance, energy consumption, and complex operations in deep trenching in orchards by proposing a reverse trenching and backfilling scheme. A reverse-rotating chain trencher was designed for integrated trenching and backfilling. Through mechanical analysis and MBD-DEM coupled simulation, operating parameters affecting the process were identified. A three-factor, three-level test with forward speed (v), rotation speed (n), and working angle (γ) determined the optimal parameters as $v=0.29$ km/h, $n=393$ r/min, $\gamma=15^\circ$. Field tests yielded specific energy consumption of 0.328 kWh m^{-3} and mean torque of 416.66 Nm, with simulation errors of 2.18% and 4.03% , respectively.

摘要

本研究针对果园深开沟作业中存在的阻力大、能耗高及作业复杂等问题，提出了反向开沟与回填作业方式，设计了反向旋转链式开沟回填一体机。通过力学分析与 MBD-DEM 联合仿真，明确了影响该作业方式运行的主要参数。通过三因素三水平正交试验确定了前进速度 (v)、刀轴转速 (n) 和工作角度 (γ) 的最佳参数组合为 $v=0.29$ km/h、 $n=393$ r/min、 $\gamma=15^\circ$ 。田间试验得到的比能耗为 0.328 kW·h m^{-3} ，平均扭矩为 416.66 Nm，仿真误差分别为 2.18% 和 4.03% 。

INTRODUCTION

Trenching and fertilizing are critical aspects of orchard management, particularly for deep trenching operations, which aid in promoting root growth, enhancing water retention capabilities, and improving nutrient distribution efficiency. Currently, the commonly used disc trenching machines primarily focus on a trenching depth of approximately 45 cm, but this depth often comes with high energy consumption issues. Therefore, reducing the resistance and energy consumption during the trenching process has become a key focus for agricultural experts (Chen et al., 2024; Liu et al., 2022; Yang et al., 2023). Liu et al., (2024), analyzed the power consumption of the counter-rotating trenching machine's cutter roll, explored the power consumption and resistance of the cutter roll under different soil particle diameters, and provided reference for the cutter roll-soil coarse-grained model. Zeng et al., (2024), addressed the issue of high-power consumption in blade trenching by designing a layered cutting and throwing trenching blade set. They optimized the working parameters of the trenching blade and conducted field tests, showing that the specific energy consumption of the optimized blade set was reduced by 8.31% . Liu et al., (2023), designed a counter-rotating twin-shaft spiral trenching machine. They analyzed the effects of different working parameters on the trenching performance and power consumption of the cutting knife. After optimizing the operating parameters of the trenching machine, they conducted field tests with the optimal parameters, obtaining a trenching qualification rate of 91.4% and an average soil crushing rate of 72% . Wang et al., (2024), studied the effects of forward speed, blade trenching angle, and width on trenching resistance based on the discrete element method, optimized the optimal parameters, and found that the minimum trenching resistance was 58.54 N under the optimized parameters, with an error of less than 10% between simulation and experimental values.

¹ Haochao Tan, Ph.D.; Congcong Shen, Ph.D.; Junlong Ma, Ph.D.; Chunlin Wu, Ms.; Liming Xu, professor, Ph.D.; Shuai Ma, associate professor Ph.D.

Although the aforementioned scholars have optimized the parameters of trenching machines through a combination of numerical simulation and field tests, reducing operational energy consumption, the depth of these trenching machines is generally shallow and unable to meet the 60 cm trenching depth required for deep-rooted crops like grapes.

While chain trenching machines can achieve trenching up to 100 cm, they have high resistance and energy consumption and are relatively complex to operate. Therefore, to address these issues, this paper proposes a chain counter-rotating trenching solution that simultaneously accomplishes trenching and backfilling. The feasibility of this solution has been demonstrated through MBD-DEM coupled simulation, and on this basis, operational parameters of the trenching machine have been optimized to reduce working energy consumption, with the optimization results validated through field tests.

MATERIAL AND RESEARCH METHODS

Structure and working principle

Traditional chain trenchers (hereinafter referred to as traditional trenchers) rotate in a forward direction, piling soil in front of the implement and forcing the accumulated soil to the sides through a spiral soil-separating wheel (Fig.1a). Subsequent backfilling is required to return the soil to the trench, making the process cumbersome. To achieve simultaneous trenching and backfilling, this paper proposes a reverse-rotating chain trencher (hereinafter referred to as reverse trencher) (Fig.1b). This device attempts to throw soil back into the trench by reversing the rotation of the trenching chain, thereby achieving the simultaneous process of trenching and backfilling. The device does not leave deep trenches on the ground surface after completing its operation. The specific backfilling effect of this innovative idea still requires subsequent simulation verification to confirm its feasibility.

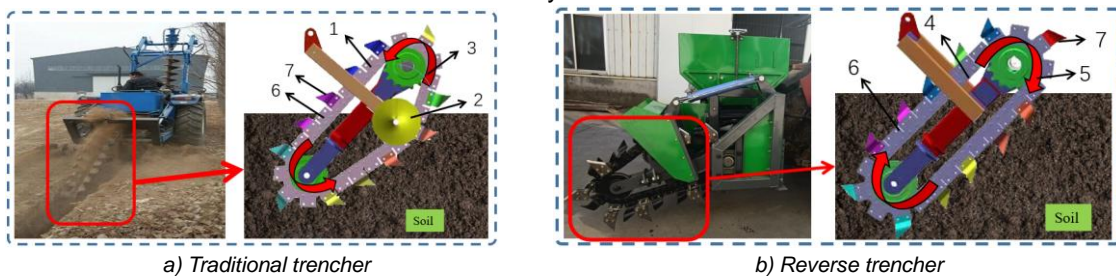


Fig. 1 - Trencher comparison

1- Traditional chain trencher; 2- Spiral soil separator wheel; 3- Forward rotation; 4- Reverse trencher; 5- Reverse rotation; 6- Trenching chain; 7- Trenching blade

Force analysis during the soil cutting process

To reduce the energy consumption of the reverse trencher, it is necessary to determine the operational parameters affecting soil cutting through mechanical analysis of the operation process. The main stages of reverse trench operation include: cutting stage (oc), convert stage (cd), soil lifting stage (da), and idling stage (ao) (Fig.2). The main force-bearing stages are the cutting stage and the soil lifting stage, so analysis of these two stages is required.

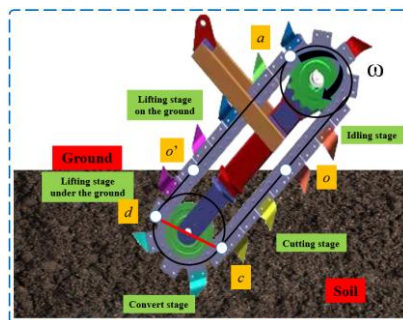


Fig. 2- Schematic diagram of the operating stage of the reverse trencher

Mechanical analysis of the cutting stage

According to Fig. 2, during the cutting stage, the trenching blade operates at a certain angle with the ground. Therefore, the force analysis will be based on the normal working state. The force analysis is shown in Fig. 3. On the cutting surface, the Y-axis is parallel to the positive cutting edge of the trenching blade, the Z-axis is perpendicular to the positive cutting edge and points upward, and the X-axis is perpendicular to cutting surface.

Thus, a coordinate system XYZ is established, wherein the advantage of this coordinate system is that most of the forces lie on the coordinate axes. Taking the forward direction as Y'-axis, the direction perpendicular to the ground and upward as Z'-axis, and the direction perpendicular to the forward direction as the X'-axis, a coordinate system X'Y'Z' is established. The purpose of this coordinate system is to ensure that the gravity of the soil block is parallel to the Z'-axis, facilitating subsequent decomposition.

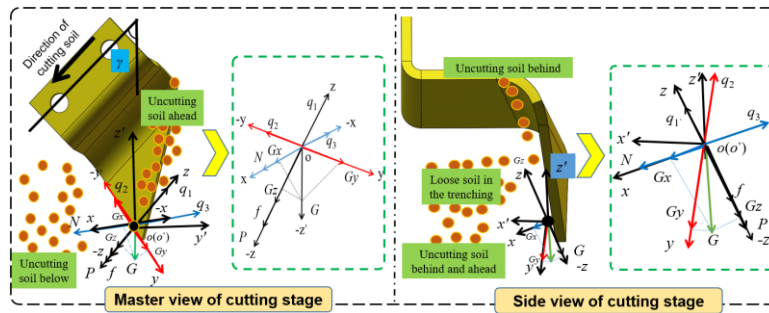


Fig. 3- Mechanical analysis of the soil cutting stage

In the diagram, $-x$, $-y$, $-z$, and $-z'$ represent the negative directions of the x , y , z , and $-z'$ axes, respectively, while o and o' represent the origins of the coordinate systems xyz and $x'y'z'$, respectively. With this understanding, the force equation for the cutting stage is established as follows:

$$\begin{cases} \sum F_x = G_x + N - q_3 \\ \sum F_y = G_y - q_2 \\ \sum F_z = q_1 - G_z - f - P \end{cases} \quad (1)$$

where: N represents the support force of the trenching blade on the soil, P represents the cutting force of the blade on the soil, q_1 represents the resistance of the uncut soil below, q_2 represents the resistance of the uncut soil in front, q_3 represents the resistance exerted by the loose soil inside the furrow, f represents the frictional force of the soil on the blade during motion, F_x , F_y and F_z represent the total forces experienced along the x , y and z axes respectively, G_x , G_y and G_z represent the components of force G along the x , y and z axes. These components are related to the structure parameters of the trenching blade, specifically the bending line inclination angle and the curvature, as shown in equation (2) and (3):

$$\begin{cases} G_x = G(\sin \beta \sin \gamma - \sin \alpha \cos \beta \cos \gamma) \\ G_y = -G[\sin \gamma(\cos^2 \alpha \sin \beta + \sin^2 \alpha \cos \beta) + \sin \alpha \sin \beta \cos \gamma] \\ G_z = -G[\cos \alpha \cos \gamma - \sin \gamma \sin \alpha \cos \beta(\cos \alpha \sin \beta + \sin \alpha)] \end{cases} \quad (2)$$

$$f = \mu N = \mu N_L [dL \cos \alpha + d^2 L^2 (1 - \tan \theta)] \quad (3)$$

where, G represents the soil weight of the soil being cut, μ represents the friction coefficient, θ represents the cone residual angle, which affects the size of the cutting surface of the trenching blade. N_L represents the support force on the unit cutting surface area. α and β denote the bending line angle and curvature of the trenching blade (Tan et al., 2024), while γ represents the working angle of the reverse trencher.

From (1)~(3), it can be seen that the main factors affecting soil cutting resistance are the gravity (G) of the soil block, the cone residual angle (θ), curvature (β), and bending line angle (α). Among them, the gravity (G) is related to the forward speed (v) and rotational speed (n). The faster the forward speed, the greater the length of the soil block in the Y'-direction per unit time. Similarly, the faster the chain rotation speed, the greater the length of the soil block in the Z'-direction per unit time, resulting in a greater gravity of the soil block. Therefore, the gravity can be determined by the forward speed (v) and rotational speed (n).

Mechanical analysis of the soil lifting stage

In Fig. 4, $-x'$ and $-y'$ represent the negative directions of the x' and y' axes, respectively. In this stage, including the above-ground soil lifting and the underground soil lifting, the focus will be on analyzing the complex force distribution in the underground soil lifting section. Some of the soil will move along with the movement of the trenching blades. The force analysis is shown in Fig. 4, and the force equations are as follows:

$$\begin{cases} \sum F_x = -q_{x'y'} \cos \theta_5 + N_{x'y'} \cos \theta_4 - f_{x'y'} \cos \theta_6 \\ \sum F_y = -q_{z'y'} \cos \theta_1 + N_{z'y'} \cos \theta_2 + f_{z'y'} \cos \theta_3 \\ \sum F_z = -G - q_{z'y'} \sin \theta_1 + N_{z'y'} \sin \theta_2 + f_{z'y'} \sin \theta_3 \end{cases} \quad (4)$$

where, $q_{x'y'}$, $f_{x'y'}$, and $N_{x'y'}$ represent the projections of q_2 , f , and N on the $X'O'Y'$ plane. $q_{z'y'}$, $f_{z'y'}$, and $N_{z'y'}$ represent the projections of q_2 , f , and N on the $Z'O'Y'$ plane. θ_1 to θ_6 represent the angles between the projection forces and the coordinate axes. The presence of $N_{z'y'} \sin \theta_2$ and $f_{z'y'} \sin \theta_3$ forces allows the soil to lift off the ground and move upward. The presence of $N_{z'y'} \cos \theta_2$ and $f_{z'y'} \cos \theta_3$ forces causes the lifted soil to move along the direction of the trencher operation. Therefore, in the $Y'O'Z'$ plane, the motion of the soil is a combined motion in the forward direction and vertically upward, and the trajectory of the motion approximates that of the trenching blades. At this stage, the values of θ_1 to θ_6 are determined by the working state of the blades, and they remain constant as long as the working state remains unchanged. The working state of the blades is determined by three factors: α , β , and γ , so the influencing factors of this stage can still be considered to be determined by α , β , and γ .

Based on our analysis, key trenching parameters were identified as α , β , γ , R , θ , n , and v . In previous work, the structural parameters α , β , R , and θ were optimized, enhancing blade performance. Now, the aim is to optimize the operational parameters γ , n , and v to reduce energy consumption and find the optimal combination.

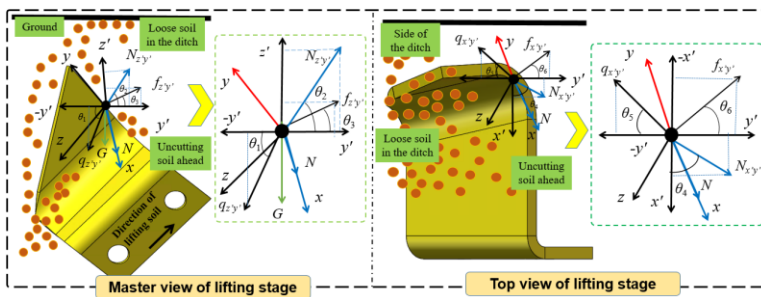


Fig. 4 - Mechanical analysis of the soil lifting stage

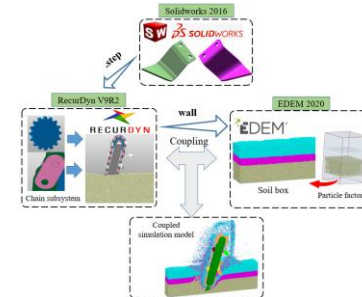


Fig. 5 - Schematic diagram of simulation model building

The establishment of a simulation model

In this study, the bidirectional MBD-DEM coupling method is employed to optimize the operating parameters. The soil is considered as discrete element particles (Kešner et al., 2021; Tamás & Bernon, 2021; Wang et al., 2020), and the size of soil particles is simplified, setting the diameter of soil particles to 5 mm (Wang et al., 2023). A Hysteretic Spring model and Linear Cohesion model were used as the contact models between particles (Ma et al., 2021). A soil-box model was built with dimensions of 4000 mm in length, 600 mm in width, and 650 mm in height. First, the forward and reverse rotation of the trencher chain in RecurDyn are set. This is to analyze the feasibility of real-time soil backfilling by the reverse trencher. The simulation runs for 7 seconds, saving data every 0.2 seconds. Based on the feasibility, the operating parameters are optimized to reduce the reverse trencher energy consumption. In this study, 3D models of the trenching blade were designed using SolidWorks and were saved in "Step" format. These models were then imported into the RecurDyn interface. The "chain" command in RecurDyn software was utilized to establish a chain drive system. Based on the operational requirements, rotational and translational joints and driving speeds were set for the chain, and the dynamic system was exported to EDEM software in ".wall" format. The complete simulation model and process are shown in Fig. 5, the discrete element parameters were determined as shown in Table 1 (Tan et al., 2024).

Table 1

Parameters of discrete element simulation				
Type	Static friction coefficient	Rolling friction coefficient	Restitution coefficient	Adhesive energy density / (J m ⁻³)
Upper soil	0.6	0.07	0.47	2694
Middle soil	0.5	0.17	0.52	4266
Lower soil	0.5	0.21	0.62	4432
65Mn- Upper soil	0.72	0.33	0.44	-
65Mn- Middle soil	0.8	0.16	0.54	-
65Mn- Lower soil	0.7	0.32	0.51	-

Experimental design

A simulation test with three factors (operating speed $v=0.2, 0.4, \text{ and } 0.6$ km/h, rotational speeds $n=200, 300, \text{ and } 400$ r/min, and working angles $\gamma=15^\circ, 25^\circ, \text{ and } 35^\circ$) and three levels was conducted, using the mean driving torque (T) of the reverse trencher and the specific energy consumption (Q) as evaluation indicators. 17 simulation experiments (Box-Behnken Design) were designed, including 5 repeats, with factors and results shown in Table 2. Among them, the calculation formula for specific energy consumption is shown as Eq.5.

$$Q = \frac{Tn}{9550 v k s} \quad (5)$$

where, Q represents specific energy consumption (kWh m^{-3}); T represents mean torque (Nm); n represents rotational speed (r min^{-1}); v represents forward speed (m/h); P represents the driving power (kW); k represents the trench width (mm); s represents the trench depth (mm).

Table 2

The experimental factors and level designs								
No.	Actual factor level			Coded factor level			Results	
	Forward speed v (km h^{-1})	Rotational speed n (r min^{-1})	Working angle γ ($^\circ$)	Forward speed v (km h^{-1})	Rotational speed n (r min^{-1})	Working angle γ ($^\circ$)	Mean torque T (Nm)	Specific energy consumption Q (kWh m^{-3})
1	0.2	200	25	-1	-1	0	1006	0.585
2	0.6	400	25	1	1	0	433.95	0.168
3	0.4	400	15	0	1	-1	334.17	0.194
4	0.4	400	35	0	1	1	428.2	0.249
5	0.6	300	35	1	0	1	433.37	0.126
6	0.2	300	35	-1	0	1	381.68	0.333
7	0.4	200	15	0	-1	-1	887.72	0.258
8	0.6	200	25	1	-1	0	992.56	0.192
9	0.4	200	35	0	-1	1	730.84	0.212
10	0.6	300	15	1	0	-1	690.39	0.201
11	0.2	300	15	-1	0	-1	631.57	0.551
12	0.2	400	25	-1	1	0	390.68	0.455
13	0.4	300	25	0	0	0	557	0.218

RESULTS

Reverse trencher feasibility analysis

To verify the feasibility of the proposed reverse trencher, simulations for both forward and reverse rotations were conducted. Based on the simulation model built in Fig. 5, the sprockets were set to rotate forward and backward at a speed of 250 r/min, with a forward speed of 1 km/h. To observe the movement of soil particles under these two motion modes, a region with dimensions of 300 mm in length, width, and height was selected at the midpoint of the simulation time, as shown in Fig. 6. Analysis was conducted for the time period from 3.8 to 4.6 s, as during this time interval, the trenching device passes through this area precisely.

According to Fig. 6, soil particles near the trenching blade have higher movement speeds, while those further away have lower speeds, indicating that the trenching blade is the main cause of soil movement. From Fig. 6(a), it can be seen that in the forward rotation mode, soil particles move upward and forward along with the trenching blade. At 4.4 seconds, some soil particles continue moving with the trenching blade, while others accumulate forward due to the obstruction of the shell; at 4.6 seconds, a small amount of soil entering the shell moves to the rear of the trenching device and backfills into the trench, while most soil particles continue to accumulate forward, as shown in Fig. 6(c). Continuous soil accumulation obstructs the forward movement of the trenching device, increasing the trenching resistance. Therefore, this traditional forward rotation trenching device usually needs to be equipped with a spiral conveyor structure to continuously transport accumulated soil to the sides of the trench, clearing the soil ahead. From Fig. 6(b), it can be seen that soil particles in the designated area move downward and backward with the trenching blade, and at 4.6 seconds, almost all soil is thrown to the rear, as shown in Fig. 6(d). In the reverse trenching mode, soil ahead of the trenching device is not accumulated but directly thrown backward. Although some soil may enter behind the shell under the action of the trenching blade, it eventually backfills into the trench due to collision with the shell, resulting in almost no change in soil height inside the trench.

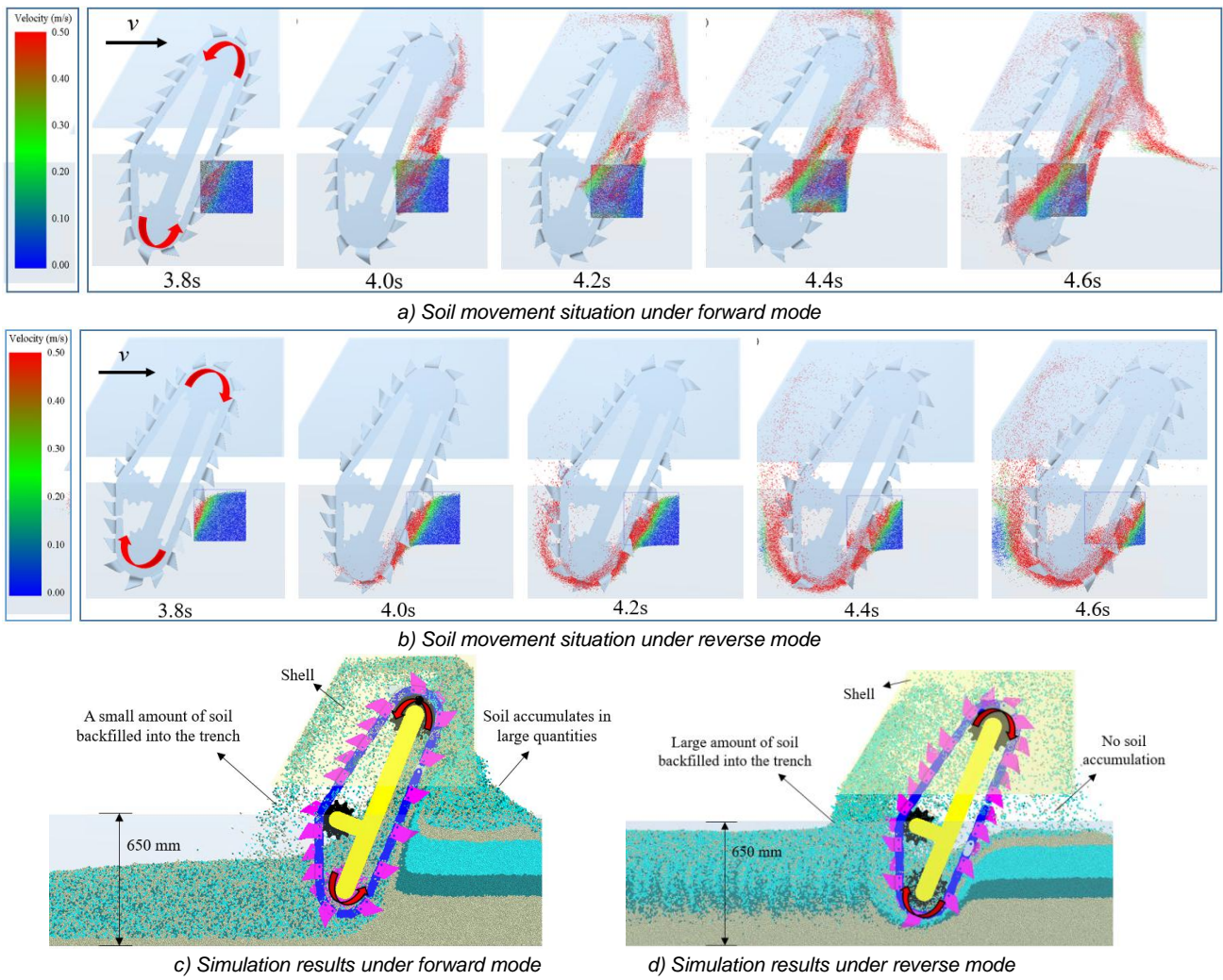


Fig. 6 - Soil movement trajectory

Particle Motion Velocity Analysis

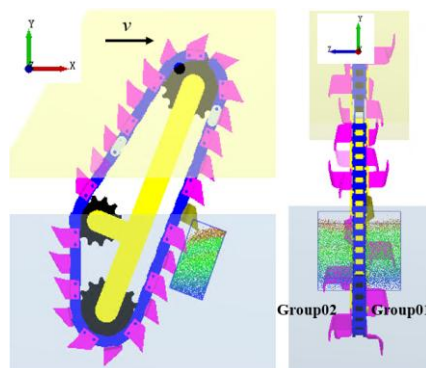


Fig. 7 - Schematic diagram of the selected area

In order to further illustrate the feasibility of verifying the reversed trenching, two Groups with length, width, and height of 150, 300, and 150 mm were set up, respectively. The Groups are parallel to the chain in the XOY plane, and are located on the left and right side of the trench in the ZOY plane, respectively. They are named as Group01 and Group02, respectively, as shown in Fig. 7, which are used to react to the movement pattern of soil particles on both sides.

The time period during which the trenching blades exactly pass through this position is from 3.8 to 4.4 seconds. The average motion speeds of particles in the XYZ directions for two groups (Group01 and Group02) within this time period are shown in Fig. 8. From Fig. 8(a) ~ (c), it can be seen that within Group01, the magnitudes of speeds in the XYZ axes under both forward and reverse rotation modes are basically the same, but the directions are completely opposite.

In the forward rotation mode, the speeds in the XY axes are positive, indicating that the soil particles have a tendency to move forward and upward. In the reverse rotation mode, the speeds are negative, indicating that the soil moves downward and backward, which is consistent with the motion trajectory described in Fig. 6. In the forward rotation, negative Z-axis speed indicates soil particles spread outward from the ditch, throwing some soil to the left. In reverse rotation, positive Z-axis speed signifies soil particles converge inward into the ditch, transporting soil into it. Since Group01 and Group02 are located in symmetric positions, the trend of soil particle speed changes in Group02 is generally consistent with that in Group01 (Fig. 8(d) and (f)), but the magnitudes are slightly different. The difference is that along the Z-axis, in forward rotation, the speed is positive, indicating a tendency for soil particles to be thrown to the other side of the ditch, while in reverse rotation, the speed is negative, indicating a tendency for soil particles to converge inward towards the ditch under the influence of the trenching blade.

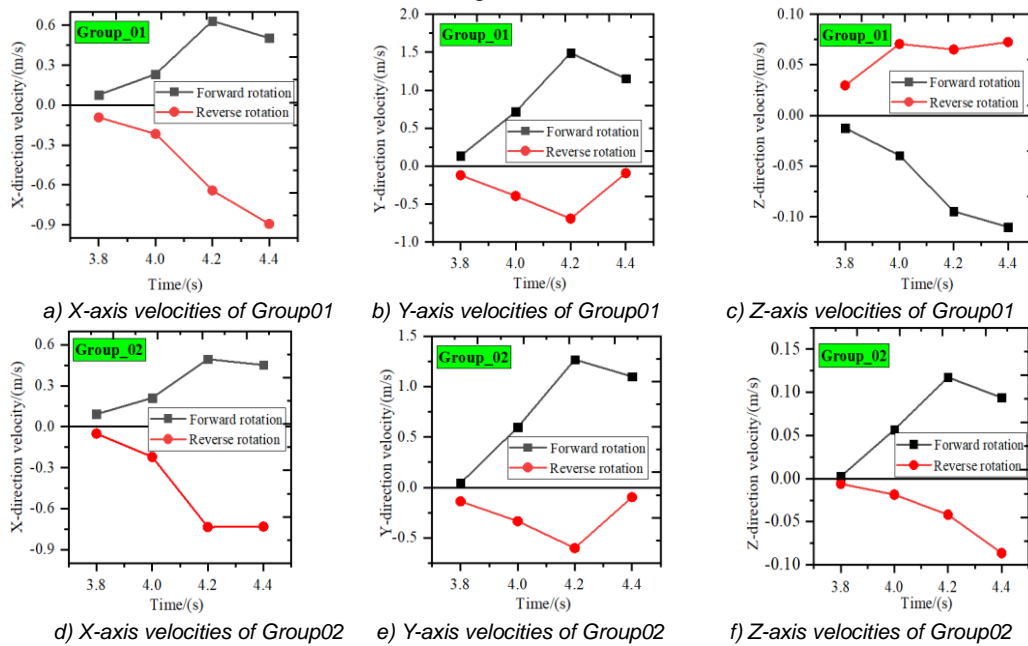


Fig. 8 - Velocity analysis of soil particles

Based on the analysis of soil particle motion speeds described above, the distribution of soil particles along the Z-axis at 4.4 seconds is observed (Fig. 9). From the figure, the position distribution of soil particles can be visually observed. In the same coordinate system, during forward rotation, the particle positions in the two groups are opposite: Group01 is mainly negative, and Group02 is mainly positive, indicating soil spreading outward. During reverse rotation, soil particles in both groups converge towards the center, facilitating easier backfilling of soil into the furrow. Based on the above analysis, this study proposes for the first time that the reverse trencher can meet the soil backfilling requirements. The reverse rotation mode is feasible, and subsequent field trials will be conducted using this new operational method.

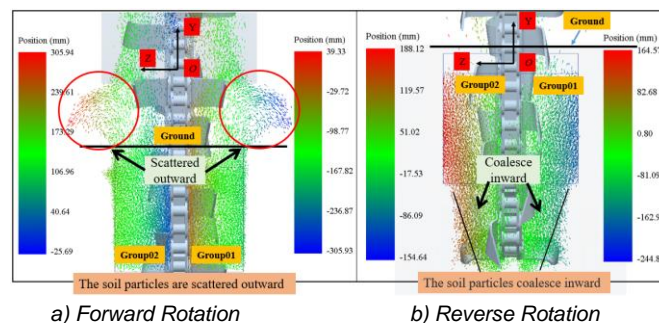


Fig. 9 - Distribution angle of Soil Particles along the Z-axis

Analysis of significance

Based on the results in Table 2, an analysis of variance (ANOVA) was conducted on the experimental factors, with the results shown in Table 3. Among the single factors, forward speed has a significant impact on energy consumption, and rotation speed has a significant impact on the mean torque.

Among the interaction terms, the interaction between rotation speed and working angle significantly impacts energy consumption, and the interaction between forward speed and working angle significantly impacts the mean torque. The impact of other factors is not significant. The regression equations for the response values can be expressed as Equation (6) and (7):

$$Q = 0.26 - 0.15v - 0.023n + 0.00267\gamma + 0.027vn + 0.036v\gamma + 0.025n\gamma + 0.087v^2 - 0.035\gamma^2 - 0.075v^2\gamma \quad (6)$$

$$T = 600.59 + 17.54v - 253.77n - 15.71\gamma + 14.18vn + 62.73n\gamma + 90.46n^2 - 81.08\gamma^2 - 111.02v^2\gamma \quad (7)$$

Table 3

The ANOVA of specific energy consumption and mean torque					
Dependent variable	Source of variance	Sum of square	Degree of freedom	F value	P value
Q	v	0.19	1	207.46	< 0.0001**
	n	4.147e-3	1	4.50	0.0715
	γ	2.056e-5	1	0.022	0.8854
	vn	2.836e-3	1	3.08	0.1227
	nγ	5.133e-3	1	5.57	0.050
	n ²	2.517e-3	1	2.73	0.1423
	γ ²	0.032	1	34.57	0.0006**
	v ² γ	5.093e-3	1	5.53	0.0510
T	v	2461.91	1	0.95	0.3589
	n	515200	1	198.28	< 0.0001**
	γ	987.53	1	0.38	0.5547
	vn	804.01	1	0.31	0.5932
	vγ	15738.96	1	6.06	0.0392**
	v ²	34552.7	1	13.30	0.0065**
	γ ²	27758.19	1	10.68	0.0114**
	v ² γ	24648.66	1	9.49	0.0151**

Interaction analysis

In order to further analyze the effects of various factors on torque and specific energy consumption, an interaction analysis was conducted. One factor is fixed at a 0 level and the effects of remaining two factors on Q and T is observed. From Fig. 10(a), it is evident that as rotational speed (n) and forward speed (v) increase, Q gradually decreases. When n is fixed at a certain level, Q increases rapidly with a decrease in v, showing a steep slope in response surface along the v direction. When v is fixed at a certain level, Q decreases with an increase in n, and when v is at a lower level, the increase in n has a minimal effect on Q. This indicates that the interaction between n and v has a non-significant impact on Q. The same trend can be observed from Fig. 10(b), where Q decreases with an increase in v and working angle (γ), but the magnitude of change is small, suggesting a weak interaction effect between the two factors.

From Fig. 10(c), it can be seen that T increases with an increase in v and a decrease in n. Regardless of the level at which n is fixed, T remains relatively stable with changes in v. Similarly, regardless of the level at which v is fixed, T remains stable with changes in n. This indicates that the interaction between n and v does not significantly affect T. This is consistent with the results reflected in Table 3. Conversely, from Fig. 10(d), when n is at a lower level, T decreases with an increase in γ. However, when n is at a higher level, T increases with an increase in γ. This suggests that the presence of n changes the impact of γ on T, indicating a significant interaction effect between n and γ. Therefore, to reduce T, consider a higher value of n and a smaller value of γ.

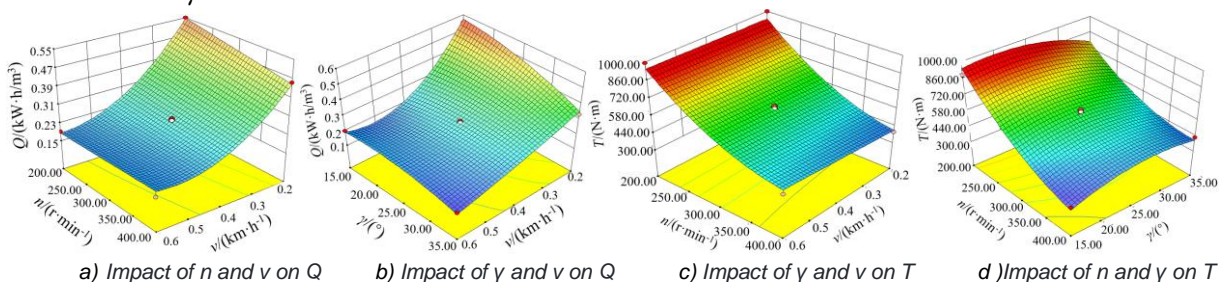


Fig. 10 - Response surfaces of T and Q under different v, n, and γ

Operation parameter optimization analysis

In the optimization process of reverse trencher operational parameters, a multi-objective optimization method was used to obtain the best parameter combination. The optimization equation can be expressed as follows:

$$\begin{cases} \min Q \\ \min T \\ 0.2 \leq v \leq 0.6 \\ 200 \leq n \leq 400 \\ 15^\circ \leq \gamma \leq 35^\circ \end{cases} \quad (8)$$

By solving the equation, the optimal speed $v = 0.29 \text{ km}\cdot\text{h}^{-1}$, rotational speed $n = 394 \text{ r}\cdot\text{min}^{-1}$, and angle $\gamma = 15^\circ$ were found that minimize torque and specific energy consumption, achieving the best system performance. Subsequently, a coupled simulation test using the MBD-DEM method was performed with these optimal parameters. Under the optimal parameters, the mean torque and specific energy consumption were found to be 434.15 Nm and $0.321 \text{ kW}\cdot\text{h m}^{-3}$, respectively.

Field validation test

Field tests were conducted in the vineyard of Shandong Gaomi Yifeng Machinery Co., Ltd. to validate the optimized operating parameters of the reverse trencher. During the tests, a torque sensor was used to connect the output shaft of the gearbox (with a reduction ratio of 1:4) to the trenching drive shaft, powered by the 12V battery of the tractor. The tractor's forward speed was adjusted to 0.29 km/h, and the working angle of the ditching machine was set to 15° by adjusting the hydraulic cylinder. The tractor's output shaft speed was 550 rpm (after the gearbox reduction, the speed was approximately 393 rpm). A data acquisition card was used to collect the voltage signals from the torque sensor at a sampling frequency of 20 Hz, converting these signals into torque values displayed on a computer. The operating scenario and results are shown in Fig.11.

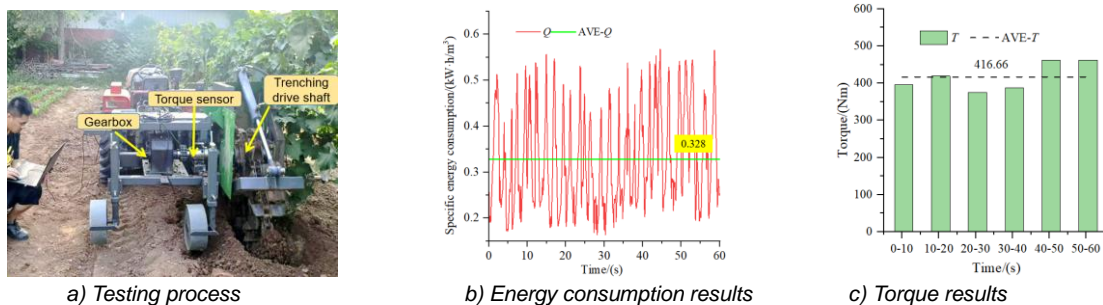


Fig. 11 - Field trial validation

The results of the field test show that under the optimized operating parameters, the energy consumption (Q) of the reverse trencher is $0.328 \text{ kW}\cdot\text{h m}^{-3}$, with an error of 2.18% from the simulation results, and the mean torque is 416.66 Nm, with an error of 4.03% from the simulation results, which indicates that the operating parameters of the reverse trencher optimized on the basis of the test are accurate and reliable.

CONCLUSIONS

1. A reverse-rotating chain trencher was proposed, and a force analysis was conducted during the soil cutting and lifting stages of the device. The key operating parameters affecting trenching were identified as forward speed v , rotational speed n , and working angle γ . An MBD-DEM coupled simulation model of the trencher was established and simulated. Comparative analysis was performed on the characteristics of traditional trencher and the reverse trencher in terms of soil particle motion trajectories, velocities, and positions, demonstrating the feasibility of the reverse-rotating furrowing and backfilling scheme proposed in this study. A comparative analysis was conducted on the characteristics of traditional trenchers and reverse trenchers in terms of soil particle motion trajectories, velocities, and positions. The study demonstrated the feasibility of the reverse trencher scheme proposed.

2. The operating parameters of the reverse trencher was analyzed and optimized using the response surface method. Significant factors affecting mean torque and specific energy consumption were identified. Based on minimizing specific energy consumption and mean torque, multi-objective parameter optimization was conducted, determining the optimal operating parameter combination for the reverse trencher as follows: $v = 0.29 \text{ km h}^{-1}$, $n = 394 \text{ r min}^{-1}$, $\gamma = 15^\circ$. Simulating with these optimal parameters yielded a specific energy consumption of $0.321 \text{ kW}\cdot\text{h m}^{-3}$ and an average torque of 434.15 Nm under the optimal operating conditions.

3. To verify the accuracy of the simulation results, field tests were conducted with the optimal parameters. The field tests measured specific energy consumption and mean torque as $0.328 \text{ kW}\cdot\text{h m}^{-3}$ and 416.66 Nm , respectively, with errors of 2.18% and 4.03% compared to the simulation results. These relatively small errors validate the accuracy of the optimization results.

ACKNOWLEDGEMENT

This study was supported by the National Natural Science Foundation of China (32301710) and China Agriculture Research System of MOF and MARA (CARS-29).

REFERENCES

- [1] Chen, W., Ren, J., Huang, W., Chen, L., Weng, W., Chen, C., Zheng S., (2024). Design and Parameter Optimization of a Dual-Disc Trenching Device for Ecological Tea Plantations. *Agriculture*, vol.14, pp.704, Fujian/China.
- [2] Kešner, A., Chotěborský, R., Linda, M., Hromasová, M., Katinas, E., & Sutanto, H., (2021). Stress distribution on a soil tillage machine frame segment with a chisel shank simulated using discrete element and finite element methods and validate by experiment. *Biosystems Engineering*, vol.209, pp.125-138, Suchdol/Czech Republic.
- [3] Liu, D., Gong, Y., Zhang, X., Yu, Q., Zhang, X., Chen, X., Wang Y., (2022). EDEM Simulation Study on the Performance of a Mechanized Ditching Device for Codonopsis Planting. *Agriculture*, vol.12, pp.1238, Xinjing/China.
- [4] Liu, J., Jiang, P., Chen, J., Zhang, X., Xu, M., Huang, D., Shi Y., (2023). Optimal Design of and Experiment on a Dual-Spiral Ditcher for Orchards. *Agriculture*, vol.13, pp.1628, Hunan/China.
- [5] Liu M., Xie F., Liu D., & Wang X., (2024). Analysis and Experiment on Power Consumption of Counter-rotating Ditcher Knife Roller Based on Particle Scaling Effect (基于颗粒放尺效应的逆旋开沟机刀辊功耗分析与试验). *Transactions of the Chinese Society of Agricultural Engineering*, vol.40, pp.83-92, Hunan/China.
- [6] Ma, S., Niu, C., Yan, C., Tan, H., & Xu, L., (2021). Discrete element method optimisation of a scraper to remove soil from ridges formed to cold-proof grapevines. *Biosystems Engineering*, vol.210, pp.156-170, Beijing/China.
- [7] Tamás, K., & Bernon, L., (2021). Role of particle shape and plant roots in the discrete element model of soil–sweep interaction. *Biosystems Engineering*, vol.211, pp.77-96, Hungary.
- [8] Tan H., Ma S., Shen C., Ma J., Zhou H., Xu L., (2024). Development and Experiment of Organic Fertilizer Chain Reversing Ditching and Fertilizing Machine for Vineyard (葡萄园有机肥链式反转开沟施肥机研制与试验). *Transactions of the Chinese Society of Agricultural Engineering*, vol.40, pp.12-23, Beijing/China.
- [9] Wang, J., Xu, Y., Wang, C., Xiang, Y., & Tang, H., (2023). Design and simulation of a trenching device for rice straw burial and trenching based on MBD-DEM. *Computers and Electronics in Agriculture*, vol.207, pp.107722, Harbin/China.
- [10] Wang, L., Zhou, B., Wan, C., & Zhou, L., (2024). Structural parameter optimization of a furrow opener based on EDEM software. *International Journal of Agricultural and Biological Engineering*, vol.17, pp.115-120, Xinjiang/China.
- [11] Wang, Y., Li, N., Ma, Y., Tong, J., Pflering, W., & Sun, J., (2020). Field experiments evaluating a biomimetic shark-inspired (BioS) subsoiler for tillage resistance reduction. *Soil and Tillage Research*, vol.196, pp.104432, Jilin/China.
- [12] Yang, Y., Hu, Z., Gu, F., & Ding, Q., (2023). Simulation and Experimental Study of the Tillage Mechanism for the Optimal Design of Wheat Rotary Strip–Tiller Blades. *Agriculture*, vol.13, pp.632, Beijing/China.
- [13] Zeng Y., Jiang X., Wu M., Zhao Z., Tang L., & Li P., (2024). Development of layered cutting and throwing ditching cutter group based on DEM-MBD for *Camellia oleifera* forest (基于DEM-MBD的油茶林分层切抛式开沟刀组研制). *Transactions of the Chinese Society of Agricultural Engineering*, vol.40, pp.30-42, Hunan/China.

MECHANIZATION OF GRASSLAND FARMING BY TECHNOLOGICAL VARIANTS WITH MINIMAL INPUTS. A REVIEW

MECANIZAREA LUCRĂRILOR AGRICOLE PE PAJIȘTI PRIN VARIANTE TEHNOLOGICE CU INPUTURI MINIME. REVIEW

Vasile MOCANU¹⁾, Tudor Adrian ENE¹⁾, Eugen MARIN²⁾, Neluș-Evelin GHEORGHÎĂ³⁾

¹⁾ Research-Development Institute for Grasslands, 500128 Brasov / Romania;

²⁾ The National Institute of Research – Development for Machines and Installations Designed for Agriculture and Food Industry – INMA Bucharest / Romania

³⁾ University Polytechnic of Bucharest, Department of Biotechnical Systems, Faculty of Biotechnical Systems Engineering, 006042 Bucharest / Romania;

Correspondence: Tel: +40728941786; E-mail: vasmocanu@yahoo.com

Tel: +40735713143; E-mail: tudorene@yahoo.com

DOI: <https://doi.org/10.35633/inmateh-74-84>

Keywords: grasslands management; minimal inputs; sustainability; productivity; fertilizing

ABSTRACT

Grassland farming plays a vital role in sustainable agricultural systems, providing forage resources for livestock production and contributing to environmental conservation. However, the labor-intensive nature of grassland management requires significant challenges for farmers. The adoption of appropriate mechanization technologies can improve efficiency, reduce labor requirements, and enhance overall productivity. This paper investigates the mechanization of grassland farming through technological variants with minimal inputs. The incorporation of sensor technologies and data analytics facilitates real-time monitoring of grass growth, enabling farmers to make decisions regarding grazing rotations and forage quality. Additionally, the utilization of smart sensors for soil moisture and nutrient content allows for targeted application of inputs, reducing waste and optimizing resource utilization. Overall, this article highlights the potential of mechanization and technological variants with minimal inputs to make efficient the grassland farming, improving productivity, sustainability and the livelihoods of farmers.

ABSTRACT

Gospodărirea pajiștilor joacă un rol vital în sistemele agricole durabile, oferind resurse furajere pentru animale și contribuind la conservarea mediului. Cu toate acestea, natura intensivă a forței de muncă pentru gestionarea pășunilor ridică provocări semnificative pentru fermieri. Adoptarea tehnologiilor adecvate de mecanizare poate îmbunătăți eficiența, poate reduce cerințele de muncă și poate crește productivitatea generală. Această lucrare analizează și promovează mecanizarea lucrărilor agricole pe pajiști prin variante tehnologice cu inputuri minime. Utilizarea tehnologiilor cu senzori și a analizei datelor facilitează monitorizarea în timp real a creșterii ierbii, permițând fermierilor să ia decizii cu privire la rotația pășunatului și la calitatea furajelor. În plus, utilizarea senzorilor inteligenți pentru umiditatea și conținutul de nutrienți ai solului permite aplicarea corectă a intrărilor, reducerea risipei și optimizarea utilizării resurselor. În general, acest articol evidențiază potențialul mecanizării și al variantelor tehnologice cu inputuri minime pentru eficientizarea valorificării pajiștilor, îmbunătățind productivitatea, durabilitatea acestora și mijloacele de trai ale fermierilor.

INTRODUCTION

According to FAO statistics, pastures—including open grasslands, herbaceous shrubs, and savannas—cover approximately 40 % of the Earth's land surface (O'Mara, 2012; Wilsey, 2018). Of this, 31.2 % are in America, 30.9% in Asia, 15.8% in Africa, 13.5% in Europe, and 8.6% in Oceania (FAOSTAT, 2024). Grasslands are among Earth's most valuable ecosystem complexes due to their vital ecological and socio-economic roles (Hobohm et al., 2021). They support biodiversity, provide habitats for countless species, and act as key regulators of the carbon and water cycles. In particular, permanent pastures serve as essential reservoirs of biodiversity and ecological stability, making them indispensable for nature conservation (Dengler et al., 2014; Frenzel et al., 2024; Feurdean et al., 2018).

Despite their importance, grasslands have significantly declined since the mid-20th century. This decline is largely driven by the intensification of extreme climatic events, such as prolonged droughts, heavy rainfall, and heatwaves, all of which have become more frequent due to global climate change (*Easterling et al., 2000; Pepin et al., 2022; Zhang et al., 2024*).

These adverse conditions have not only led to the degradation of permanent grasslands but have also critically impacted soil properties, including organic matter content, nutrient balance, and microbial activity. These factors are essential for maintaining grassland productivity and resilience (*Xinxia, 2024; Lu, 2024*).

Managing grasslands effectively presents a significant challenge for farmers. Balancing productivity with environmental sustainability requires adopting efficient strategies that optimize resource use and preserve ecosystem health (*Wróbel et al., 2023; Zhang et al., 2021; Wang et al., 2021*). Such approaches are crucial for ensuring consistent livestock productivity and improving forage quality, which is vital for meeting the nutritional needs of animals (*Chand et al., 2022*). At the same time, these practices must address environmental concerns, such as reducing greenhouse gas emissions linked to grazing and livestock activities (*Wan et al., 2024*) and preventing soil degradation through erosion, compaction, and nutrient depletion (*Bogunovic et al., 2022*). Technological advancements in monitoring and grazing systems provide promising solutions to these challenges, offering farmers tools to manage grasslands more effectively (*Liu & Shao, 2024*).

Beyond addressing immediate agricultural concerns, grassland management plays a broader role in tackling global socio-ecological issues. Proper management not only ensures the sustainability of rural livelihoods but also helps conserve areas unsuitable for conventional agriculture, thereby maintaining ecological balance (*Li et al., 2022; Dong et al., 2012*). Grasslands also provide valuable forage resources to support livestock production and enhance land use efficiency, which maximizes the productivity of available resources (*Anca, 2012; Buzhdygan et al., 2020*). By implementing effective strategies, farmers can contribute to preserving these critical ecosystems and preventing their overexploitation (*Peters et al., 2001*).

Innovative technologies, particularly sensor systems and data analysis, are transforming grassland management. Although adopting these tools can be challenging for farmers, they offer significant benefits when implemented successfully (*Polichshuk et al., 2023; Bikker et al., 2014; Creighton et al., 2011*). For instance, the development and performance of small power electric tractors, as demonstrated by *Matache et al. (2020)*, highlight the potential of renewable energy-powered machinery to achieve efficient and environmentally friendly outcomes. These tractors not only reduce emissions but also provide cost-effective alternatives for operations like ploughing, aligning with sustainability goals. Similarly, advanced sensors enhance grazing quality by improving soil and vegetation monitoring, which positively impacts livestock foraging behavior (*Amorim et al., 2020; Kennedy et al., 2007*). Furthermore, smart sensors designed to monitor soil moisture and nutrients enable precise input applications, reduce waste, and improve crop yields through informed decision-making (*Krueger et al., 2021; Cao, 2024; Tadesse et al., 2021*).

Conservation-focused technologies have also proven effective in improving grasslands. These approaches significantly boost biomass production and species richness, enhancing ecosystem stability and resilience (*Hakimovich and Alishovich, 2023; Li et al., 2022; Hautier et al., 2014; Isbell et al., 2015; Wagg et al., 2017; Wang et al., 2019*). Importantly, such advancements preserve soil properties, ensuring long-term productivity and sustainability (*Maron et al., 2011*). These methods not only support environmental goals but also enhance the livelihoods of farmers by improving economic returns and ecological outcomes (*Xiong et al., 2023; Dong et al., 2023*).

Despite the availability of advanced technologies, many grassland management practices still rely on universal agricultural machinery designed for crops like cereals or industrial plants (*Huang and Fu, 2024; Collins et al., 2017*). While these tools have their benefits, they are often not tailored to the specific needs of grasslands, limiting their effectiveness. Developing specialized equipment for grassland restoration could significantly enhance the efficiency of such efforts (*Lyons et al., 2023; Tindale et al., 2024; Xie et al., 2023*).

Traditional methods for maintaining degraded grasslands have several shortcomings, including negative impacts on soil health such as erosion, nutrient imbalances, and biodiversity loss (*Mocanu et al., 2021; Baritz et al., 2018*). Inappropriate technologies can exacerbate these issues, leading to inefficiencies like increased fuel consumption and reduced soil carbon sequestration, both of which contribute to environmental degradation (*Song et al., 2023; Gorris et al., 2024; Ibrahim et al., 2010*). Recent studies, such as those examining the random vibrations of active cultivator components, underscore the importance of understanding mechanical dynamics to improve agricultural machinery performance and reliability. Such insights can guide the development of more efficient tools that better align with sustainable agricultural practices (*Cardei et al., 2023*). Addressing these challenges requires a shift toward sustainable, targeted interventions.

Grassland degradation is a global concern with widespread consequences. Tackling this issue and restoring these vital ecosystems is a priority for protecting biodiversity and ensuring the well-being of dependent communities (Marușca *et al.*, 2020; Oprea and Marușca, 2023).

Strategies like overseeding and complete restoration using perennial grass and legume seeds have shown great potential in transforming low-yield grasslands into productive and resilient landscapes (Marușca, T., 2022; Marin *et al.*, 2023).

The application of organic fertilizers, facilitated by specialized machinery, is another important component of grassland restoration. This approach improves soil fertility and supports sustainable vegetation growth, effectively combating degradation (Ștefan *et al.*, 2021; Ștefan *et al.*, 2019). Recent advancements in grassland technologies, developed through scientific research, offer practical solutions for improving the productivity and sustainability of these ecosystems while minimizing environmental impact.

Within this paper are presented new technologies for the maintenance and improvement of grasslands, which include efficient mechanization solutions with a reduced ecological impact, developed with minimal inputs and promoting a minimal soil processing system.

A. GRASSLANDS MANAGEMENT EQUIPMENT

1. Fertilizing equipment EF 2.5 type

The EF 2.5 fertilizing equipment (Figure 1), is used for the administration of solid mineral fertilizers simultaneously with the execution of other compatible operation for grassland farming.

1.1. Description

The EF 2.5 fertilizing equipment consists of the following main parts: assembled frame (pos.1, Fig.1); fertilizer boxes with metering devices and agitator drive shaft (pos. 2, Fig. 1); the mechanism of movement transmission to the fertilizer metering devices and agitator drive shaft of the equipment (pos.3 and 4, Fig.1) (Mocanu and Hermenean, 2008).

1.2. Operation mode

When advancing the aggregate composed of the fertilizing equipment (mounted on the frontal three-point hitch of tractor), the pivoting drive wheel (pos. 3, Fig. 1), which runs on the ground, being kept in contact with the ground by an adjustable spring), transmits the rotational movement through two chain transmissions and a cardan shaft to the Northon type gearbox (pos. 4, Fig. 1).

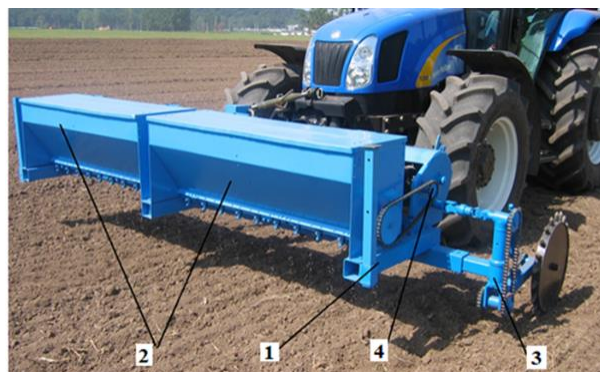


Fig. 1 - Fertilizing equipment EF 2.5 type
(Mocanu and Hermenean, 2008).

From the output of the gearbox, the movement is transmitted through a chain transmission to the agitator shaft of the fertilizer box (pos. 2, Fig. 1) whence, through a gear-driven transmission, the movement is transmitted to the axis of metering device that spread out the fertilizer directly on the ground. The Northon type gearbox allows adjusting the desired rate of fertilizer.

The pivoting drive wheel is a patented original construction that allows the movement to be transmitted even when the aggregate moves in a curve, for a left or right turning angle (inclination) of maximum 35 °, a value that exceeds the turning angle of the tractor steering wheels. The drive through this pivoting wheel has the great advantage that it gives the possibility to use the equipment even when moving the aggregate in a curve, a situation frequently encountered in the maintenance operations of grasslands by cleaning of weeds and worthless vegetation, in the preparation of the germinal bed, in reseeding degraded grasslands etc.

2. Fertilizing equipment EF 3.75 type; Sowing equipment ESR 3.75 type

The EF 3.75 fertilizing equipment (Fig. 2) is used for the administration of solid mineral fertilizers simultaneously with the execution of other compatible maintenance and improvement grassland farming operations (Mocanu and Hermenean, 2008). The ESR 3.75 seeding equipment is the same as the EF 3.75, except that the fertilizer metering device is replaced with seed metering device for grassland plant seeds.

2.1. Description

The EF 3.75 fertilizer equipment is a modular agricultural equipment (with three modules) that can be used as a separate equipment carried on rear three-point hitch of tractor or mounted on the equipment for grassland levelling, thus forming a complex aggregate for cleaning and fertilizing the grasslands (Fig. 3). The ESR 3.75 seeding equipment is intended for the administration of forage plant seeds of grasslands (oversowing) simultaneously with the execution of cleaning operation of mole hills, animal dung, leveling the nano relief and grass sward aeration with the help of the equipment for grassland levelling (grassland planer, Fig. 3). The norm of forage plant seeds distributed can be varied from 6 to 300 kg/ha.

The EF 3.75 fertilizing equipment consists of the following main parts: assembled frame (pos.1, Fig. 2); fertilizer boxes (pos.2, Fig. 2); the movement transmission mechanism to metering devices and agitator drive shaft (pos. 3 and 4, Fig. 2).

2.2. Operation mode

When advancing the aggregate composed of the equipment (mounted on the rear three-point hitch of tractor), the pivoting drive wheel (pos. 3, Fig. 2), which runs on the ground (being kept in contact with the ground by an adjustable spring), transmits the rotational movement through one chain transmissions, two equal bevel gear transmissions and a coupling nut to the Norton type gearbox and further to the agitators and metering drive shaft of the devices for dosing the fertilizers (EF 3.75) or grass seeds (ESR 3.75).



Fig. 2 - Fertilizing equipment EF 3.75 type; Sowing equipment ESR 3.75 type (Mocanu and Hermenean, 2008).

The pivoting drive wheel is another original construction, also patented, that allows the movement to be transmitted even when the aggregate moves in a curve, for a left or right turning angle (inclination) of maximum 35° , a value that exceeds the turning angle of the tractor steering wheels.

Usually, this equipment is mounted on the grassland planer (Fig. 3), thus forming agricultural aggregates that perform several grassland farming operations in a single pass.



Fig. 3 - Grassland planer in aggregate with fertilizing equipment EF 3.75 type or sowing equipment ESR 3.75 type (Mocanu and Hermenean, 2008).

Fertilizers or grass seed are distributed on the surface of the land, before the action of the active tools of the grassland planer start working. The action of the planer active tools produces the mixing (incorporation) of fertilizers (grass seeds) with soil, thus creating optimal conditions for plant growing.

3. Equipment for grassland levelling (grassland planer)

Grassland planer is intended for breaking up and spreading on the ground the mole hill, hummocks, droppings, micro uneven grounds and aerating the grassy carpet of grasslands (Mocanu and Hermenean, 2008).

3.1. Description

The grassland planer (Fig. 4), is an equipment carried on the three-point hitch of drive tractors. It consists of the following main parts: the frame with the coupling triangle on the tractor (pos. 1, Fig. 4); 3 work devices (pos. 2, Fig. 4).

Each working section is equipped with two rows of vertical chisel-type knives (pos. 3, Fig. 4, b) and two rows of inclined horizontal blades (pos. 4, Fig. 4, b). The vertical chisel knives are adjustable for vertical position and can be inclined to the direction of advance. The two rows of inclined horizontal blades are mounted behind the chisel knives, in two different planes and with opposite inclinations.



Fig. 4 - Grassland lever (Mocanu et al., 2022).
a) aggregate view; b) detailed view of the work section

3.2. Operation mode

When advancing the aggregate, the chisel-type vertical knives perform the fragmentation of the hummocks, nano relief and droppings in the vertical-longitudinal plane, and the inclined horizontal blades perform the horizontal cutting and uniform spreading of the resulting fragments on the ground.

4. The harrow with rigid tines GCF 4.0 type

The harrow with rigid tines (Fig. 5) is used for aerating the grasslands after winter period, as well as for cleaning/spreading manure after the end of each grazing cycle (Mocanu et al., 2022).



Fig. 5 - Harrow with rigid tines (Mocanu et al., 2022)

4.1. Description

The machine is an agricultural machine of the type carried on the rear three-point hitch mechanism of drive tractors. This complete harrow consists of tines grouped together in a frame and 4 of these frames grouped together.

The main component parts of the harrow with fixed tines are: assembled frame (pos. 1, Fig. 5); 4 individual harrows with a working width of 1 m (pos. 2, Fig. 5) linked to the frame with support chains (pos. 3, Fig. 5).

To reduce the gauge width during transport, the machine is equipped with a mechanism (pos. 4, Fig. 5) for lifting and descending the side harrows for transport and operation position respectively.

4.2. Operation mode

When advancing the aggregate, the rigid tines of harrows performs a superficial tillage, allowing aeration of the grassy carpet and spreading of animal dung and mole hills after each grazing cycle. It is generally a simple operation, but with a great effect for grassy plant growing.

5. Planer-grader equipment, RGP-2,0 type

Planer-grader equipment, RGP-2,0 type, is intended for the cleaning of annual and multi-annual hummocks, of animal dung and the micro-leveling of the land of degraded permanent pastures (Mocanu et al., 2022).

5.1. Description

The machine is a semi-carried agricultural machine during transport and respectively trailed during the operation.

The main components of the levelling-grader equipment, RGP-2,0 type (Fig. 6), are: assembly frame (1), left levelling blades (2), right levelling blade (3), posterior levelling blade (4), front disc battery (5), left side disc battery (6), right side disc battery (7) the mechanism of lifting-descending for posterior leveling blade (8), hydraulic (9).

5.2. Operation mode

During operation, the aggregate formed by the tractor and the planer-grader equipment for grassland, the battery with frontal discs fragment in vertical-longitudinal plane the annual, multiannual earth hummocks, mole-hills and the animal manure.

Alternative left and right movement of the fragmented material, thanks to leveling blades, and under the action of the lateral disc batteries, intensifies the process of cutting it, being evenly distributed on the surface of the ground by the rear leveling blade.

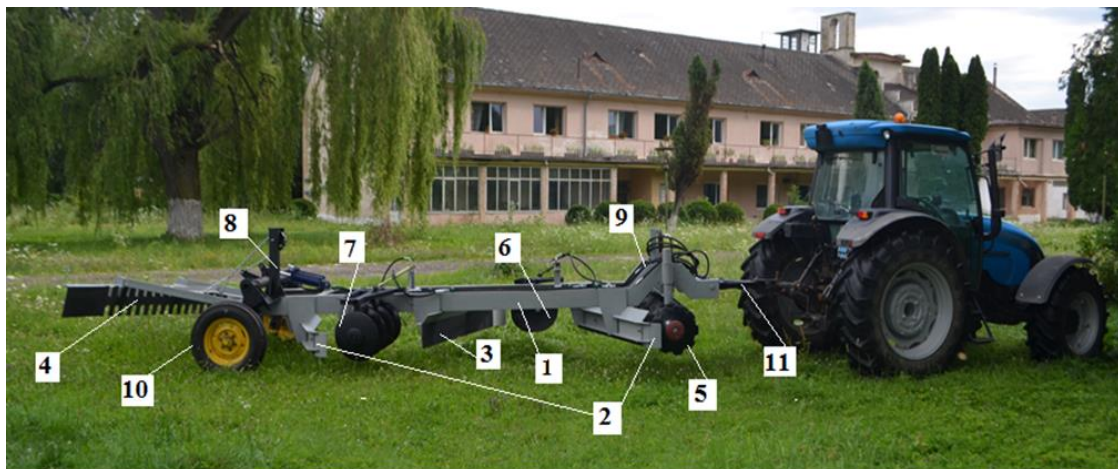


Fig. 6 - Side view of the aggregate tractor and planer-grader equipment RGP-2.0 type (Mocanu et al., 2022)

6. Rotary toppers for cleaning the grasslands

They are intended for cutting, chopping and spreading on the ground the hillocks, mole hills and worthless vegetation from pastures or green areas in parks and recreational or sports grounds or on the side of roads. The MCP-2 and MCP 2.5 type rotary cleaning machines are representative (Fig. 7) (Ștefănescu et al., 1982; Pop et al., 1994).

2.6.1. Description

The MCP-2 and MCP 2.5 grassland rotary cleaning equipment (Fig. 7) are machines carried on the three-point hitch mechanisms of drive tractors, have the active working tools of the vertical rotor type with articulated knives and are operated from the power take-off of tractors.

The main component parts of the rotary toppers MCP 2.0 and MCP 2.5 are: machine casing (pos. 1, Fig. 7), with the coupling frame to the tractor, with the grill with fingers and the support devices; the rotor with the active working tools (pos. 2, Fig. 7); support and adjustment wheels (pos. 3, Fig. 7); movement transmission system (pos. 4, Fig. 7).

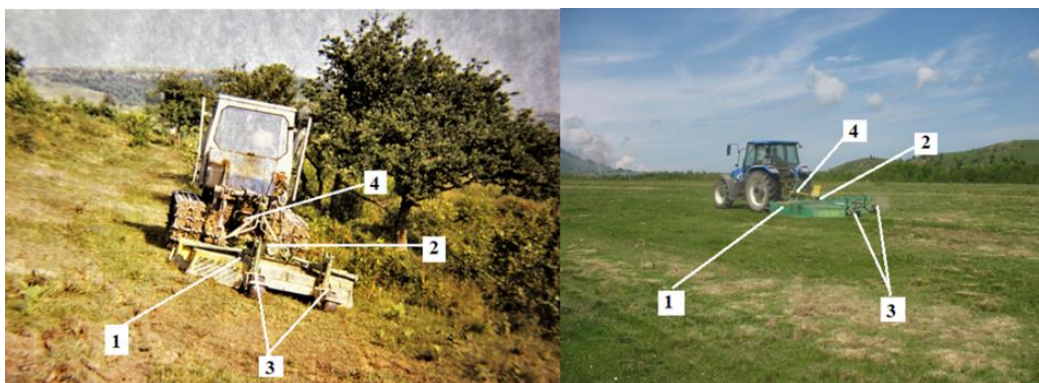


Fig. 7 - Rotary toppers for cleaning the grasslands (Pop et al., 1994)

a) MCP 2.0 type; b) MCP 2.5 type

6.2. Operation mode

When the aggregate is moving forward, the knives on the rotating rotor cut and shred the hummocks and worthless vegetation. The "Z"-shaped knives cut hillocks and worthless vegetation, and the "J"-shaped ones shred them and spread the fragments on the ground (Hermenean and Mocanu, 1986). The finger grate allows the passage and spreading on the ground only of the fragments that have the appropriate shredding sizes (less than 10 cm), the larger ones being further chopped until the passing size is obtained, which facilitates obtaining the desired degree of shredding.

7. Direct drilling seeder MSPD 2.5 type

Direct drilling seeder MSPD 2.5 type (Fig. 8) is intended for oversowing of degraded grasslands by opening furrows, metering, distributing and introducing the grassy seeds in the opened furrows and settling the sown row (Hermenean et al., 2003; Hermenean and Mocanu, 2002).

7.1. Description

The machine is rear mounted on the drive tractor. The main component parts of the direct drilling seeder MSPD 2,5 type are: assembled frame (pos. 1, Fig. 8); equipment for opening the seed slots (pos. 3, 4, 5, Fig. 8); sowing equipment (pos. 2, Fig. 8); movement transmission mechanism to the sowing equipment (pos. 6, Fig. 8); press wheels for settling the sown slots (pos. 7, Fig. 8) (Hermenean et al., 2003; Hermenean and Mocanu, 2002).

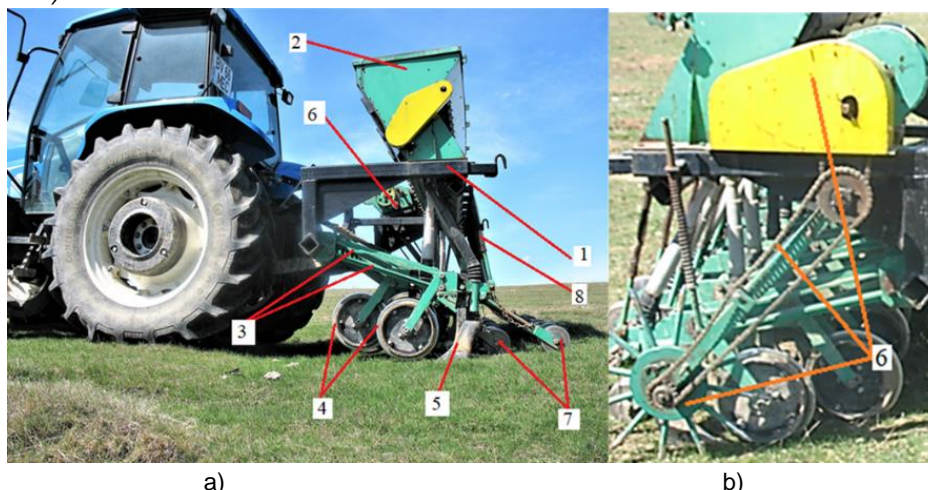


Fig. 8 - Side view of direct drilling seeder MSPD2.5 type

(Hermenean et al., 2003; Hermenean and Mocanu, 2002)

a) -left side; b) right side

7.2. Operation mode

When the tractor-oversowing machine aggregate is working, the rimmed discs of the furrow opening sections (pos. 4, Fig. 8) fractionate the old sward in a vertical-longitudinal plane, and the coulters (pos.5, Fig. 8) open the slot and insert, at the desired depth, the seed of the grassland fodder plants distributed by the sowing equipment of the machine. The press wheels achieve intimate contact between the seed and the soil, on each seeded row. The mounting on the frame of the slot opening sections by parallelogram drag arms (pos.3, Fig. 7) allows, on the one hand, to maintain the constant angle of attack of the coulters during work, and

on the other hand to copy the unevenness of the land within the limits of ± 10 cm. The loading springs (pos. 8, Fig. 7) achieves the force necessary to maintain the pressure and penetration on/into the soil of the rimmed disc wheels and the coulters. The rim on the disc wheels allows a constant sowing depth of the seeds during work time (Hermenean et al., 2006; Hermenean et al., 2006).

8. Combined grassland rotary tiller-drill machine MCT 2.5 M type

The MCT 2.5 combined machine is intended for the destruction of the old vegetal carpet and preparing seedbed, simultaneously with the sowing of grassland fodder plants.

By improving some of the components, the new modernized machine MCT 2.5 M type allows the removal of all the deficiencies reported in the old variant machine. Thus, a higher quality of the work can be obtained, the number of passes required for a good seedbed preparation is reduced etc. (Hermenean et al., 1994).

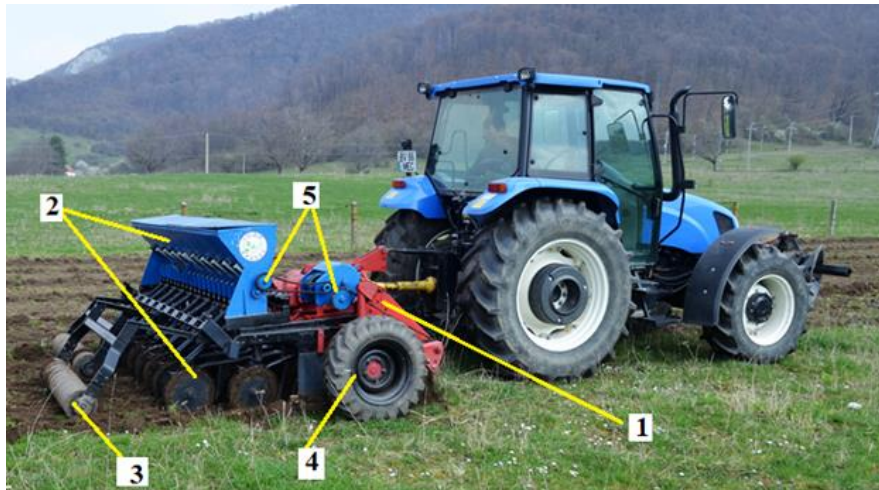


Fig. 9 - Combined grassland rotary tiller-drill machine MCT 2.5 M type (Hermenean et al., 1994)

8.1. Description

The machine is rear mounted on the drive tractor and operated from the power take-off of tractors. The improved combined machine MCT 2.5 M type (Fig. 9), consists of the following main parts: equipment for destroying the old sward and preparing the seedbed, rotary milling type (pos.1, Fig. 9); sowing equipment (pos. 2, Fig. 9); 2 light rollers for pressing the soil after sowing (pos. 3, Fig. 9); running wheels (pos. 4, Fig. 9); mechanism for transmission of movement to the sowing equipment (pos. 5, Fig. 9).

8.2. Operation mode

During work, the rotary milling equipment, which is driven by the independent power take-off of 1000 rpm. of the tractor, destroys the old vegetal carpet and prepares the seedbed. The sowing equipment, which is driven from the right wheel of the machine, distributes the adjusted seed rate and introduces it into the soil with the help of the double disc coulters. The use of double disc coulters eliminates the deficiency of the old coulters, namely that of clogging caused by large fragments of soil and no shredded sward. The light rollers mounted on the back of the sowing equipment allow rolling after sowing, thus creating optimal conditions for seed germination. The use of two articulated rollers allows better copying of the ground on the working width.

B. GRASSLANDS MANAGEMENT TECHNOLOGIES

1. The purpose of new technologies

The purpose of the new technologies for the mechanization of grassland maintenance and improvement operations consists in: creating favorable conditions for developing the valuable fodder plants; increasing the fodder quantity and quality; limiting or removing the phenomenon of degradation of the vegetal carpet; reducing and stopping the phenomenon of erosion on grasslands located on sloping land; conservation and restoration of grassland biodiversity; making available favorable conditions for the mechanization of grassland farming and in particular those for harvesting fodder; reducing the physical effort and labor required for the maintenance and improvement of degraded pastures; reducing the degree of the environment pollution (soil, air, water) as a result of reducing the specific fuel consumption and the passes number of the aggregates; increasing economic efficiency by reducing the cost per improved surface unit; promoting an ecological agriculture and improving the eco-landscape beauty by reducing the phenomenon of erosion and re-introducing the degraded surfaces into an agro-pastoral circuit (Hermenean and Mocanu, 2009; Mocanu and Hermenean, 2013).

2. Technologies for maintenance of grasslands

The maintenance of grasslands consists of: cleaning the hillocks and worthless vegetation, fertilizing during the years of exploitation, cleaning the plant residues after each grazing cycle.

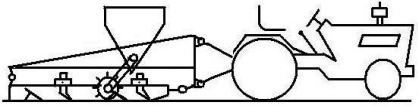
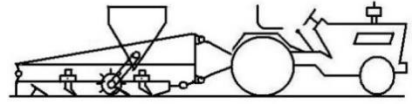
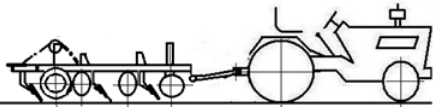
Depending on the degree of cover with anthill, mole hills, hummocks, grassy and non-valuable woody vegetation and their sizes, the following situations are found in practice:

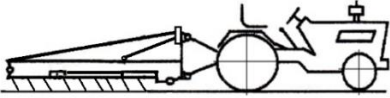
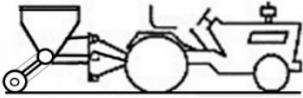
- a- grassland is invaded by hillocks and animal droppings after each grazing cycle;
- b- grassland is invaded by large hillocks and with a high cover degree per hectare;
- c- grassland is invaded by weeds and worthless vegetation with a diameter that does not exceed 4 cm;
- d- grassland area includes the plant residues after the end of a grazing cycle.

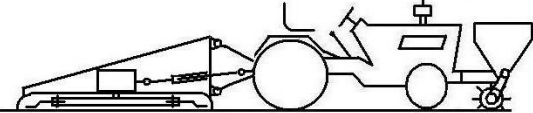
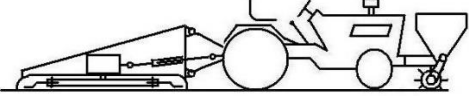
The new maintenance technologies, shown schematically in table 1, use combined aggregates that perform two or three operations in a single pass, namely: cleaning of mole hill, hillocks and chemical fertilization; cleaning of worthless vegetation, of hillocks and chemical fertilization; cleaning of the plant residues after grazing and phased chemical fertilization.

Table 1

New technological variants for maintenance of grasslands (Mocanu and Hermenean, 2013)

a. Grassland is invaded by hillocks and animal droppings after each grazing cycle			
Operations and recommended aggregates	Working capacity [ha/daily operating time]	Necessary labor force [man hour/ha]	Fuel consumption [l/ha]
Cleaning of mole hill, anthill, animal droppings, grass sward aeration and chemical fertilization  Wheel tractor of 48-60 kW (65-80 HP) + Grassland lever + Equipment for fertilizing EF 3.75 type	8.0	 1.00	4.6
b. Grassland is invaded by large hillocks and with a high cover degree per hectare			
Variant b1			
Cleaning of mole hill, anthill, animal droppings, grass sward aeration and chemical fertilization  Wheel tractor of 48-60 kW (65-80 HP) + Grassland lever + Equipment for fertilizing EF 3.75 type - two perpendicular passes with the administration of chemical fertilizers on the second pass	4.5	 1.78	8.8
Variant b2			
Cleaning of mole hills, large hillocks, animal droppings  Wheel tractor of 48-60 kW (65-80 HP) + Planer-grader equipment. RGP-2.0 type	5.6-8.2	 1.02-1.42	12.5-16.5
Chemical fertilization of grassland  Wheel tractor of 25-33 kW (35-45 HP) + Equipment for fertilizing EF 3.75 type	12.0-14.5	 0.55-0.66	3.5-4.5
Total variant b2	x	1.57-2.08	16.0-21.0

Variant b3			
Cleaning of mole hill, anthill, animal droppings, grass sward aeration  Wheel tractor of 25-33 kW (35-45 HP) + Harrow with rigid tines GCF 4.0 type	11.2-18.0	 0.44-0.72	3.8-6.1
Chemical fertilization of grassland  Wheel tractor of 25-33 kW (35-45 HP) + Equipment for fertilizing EF 3.75 type	12.0-14.5	 0.55-0.66	3.5-4.5
Total variant b3	x	0.99-1.38	7.3-10.6

c. Grassland is invaded by weeds and worthless vegetation with a diameter that does not exceed 4 cm;			
Cleaning of worthless vegetation, hillocks and fertilizing with chemical fertilizers  Wheel tractor of 60 -74 kW(80-100CP) + Rotary toppers for cleaning the grasslands MCP 2.5 type+ Equipment for fertilizing EF 2.5 type	3.8-4.5	 1.78-2.10	15.0-21.0
d. Grassland area includes the plant residues after the end of a grazing cycle			
Cleaning of refused plants after grazing and periodic chemical fertilization  Wheel tractor of 60 -74 kW(80-100CP) + Rotary toppers for cleaning the grasslands MCP 2.5 type+ Equipment for fertilizing EF 2.5 type	7	 1.14	8.50

3. Technologies for improving the degraded grasslands by oversowing method

Oversowing improvement technologies are part of the category of technologies for improving degraded pastures by surface operations focused on creating better seed growing conditions for valuable grassland plants, without destroying the existing vegetal sward. They are simple, easy to apply and in most cases, less expensive (Mocanu et al., 2021; Dragos et al., 2023; Mitev, 2023).

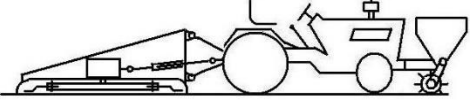
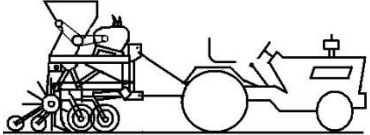
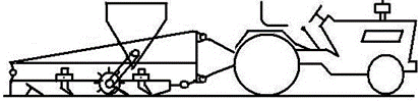
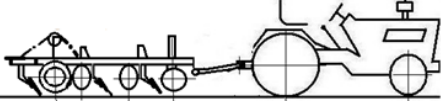
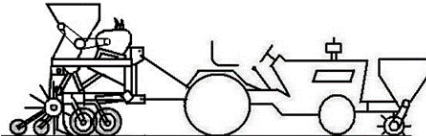
Oversowing operation consists of introducing the seeds of valuable perennial grasses and/or legumes into the old vegetal carpet by partial processing of sward (Cujbescu et al., 2021; Ene et al., 2023).

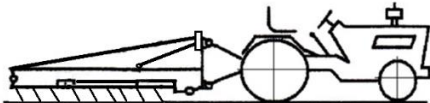
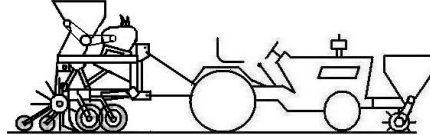
In general, in order to meet the agro-technical requirements, this is done with special overseeding machines (Hermenean and Mocanu, 2009; Ene et al., 2023). The grasslands indicated for overseeding are those surfaces characterized by: a low level of vegetation cover; inappropriate floristic composition (weedy); reduced edaphic volume; peaty or heavy soils on which processing by ploughing is difficult (Ungureanu et al., 2019) lands exposed to erosion and landslides; land without vegetation after: worthless woody vegetation control; destruction of hillocks; removing stones; levelling operation; paddocking surfaces; the surfaces on which, for the protection of the environment, total soil processing works are not indicated (by ploughing, deep milling etc.) (Vlăduț et al., 2023).

Table 2 shows the options for mechanizing the operation within the new technology for oversowing the degraded grasslands.

Table 2

**New technological variants for improving degraded grasslands
by oversowing method (Mocanu and Hermenean, 2013)**

Operations and recommended aggregates	Working capacity [ha/daily operating time]	Necessary labor force [man hour/ha]	Fuel consumption [l/ha]
Variant 1. Grassland is invaded by hillocks and worthless vegetation with a diameter that does not exceed 4 cm			
Controlling the competition of the old sward by cleaning of worthless vegetation, hillocks, micro unevenness, droppings and chemical fertilization (phosphorus and potassium)  Wheel tractor of 60 -74 kW(80-100CP) + Rotary tillers for cleaning the grasslands MCP 2.5 type+ Equipment for fertilizing EF 2.5 type	3.8-4.5	 1.78-2.10	15.0-21.0
Actual overseeding  Wheel tractor of 60 -74 kW(80-100CP) + Direct drilling seeder MSPD 2.5 type	8-10.5	 0.76-1.00	7.5-8.5
Total Variant 1	x	2.54-3.10	22.5-29.5
Variant 2. Grassland is invaded by mole hill, anthill, animal droppings			
Cleaning of mole hill, anthill, animal droppings, grass sward aeration and oversowing operation  Wheel tractor of 48-60 kW (65-80 HP) + Grassland lever+ Equipment for seeding ESR 3.75 type - two perpendicular passes with the administration of seed mixture on the first pass	4.5	 1.78	8.8
Variant 3. Grassland is invaded by mole hills, large hillocks, animal droppings			
Cleaning of mole hills, large hillocks, animal droppings  Wheel tractor of 48-60 kW (65-80 HP) + Planer-grader equipment, RGP-2.0 type	5.6-8.2	 1.02-1.42	12.5-16.5
Actual oversowing and chemical fertilization (phosphorus and potassium)  Wheel tractor of 60 -74 kW(80-100CP) + Direct drilling seeder MSPD 2.5 type + Equipment for fertilizing EF 2.5 type	7.0-9.0	 0.88-1.14	8.5-9.5
Total Variant 3	x	1.90-2.56	21.0-26.0

Variant 4. Grassland is invaded by mole hill, anthill, animal droppings			
Cleaning of mole hill, anthill, animal droppings, grass sward aeration  Wheel tractor of 25-33 kW (35-45 HP) + Harrow with rigid tines GCF 4.0 type	11.2-18.0	 0.44-0.72	3.8-6.1
Actual oversowing and chemical fertilization (phosphorus and potassium)  Wheel tractor of 60 -74 kW(80-100CP) + Direct drilling seeder MSPD 2.5 type + Equipment for fertilizing EF 2.5 type	8-10.5	 0.76-1.00	7.5-8.5
Total Variant 4	x	1.2-1.72	11.3-14.6
Variant 5. Degraded grasslands with thin fertile soil layer and thin sward			
Decreasing competition from old sward, the seedbed preparing by a low disturbance of soil, oversowing, rolling after sowing and fertilization with chemical fertilizers  Wheel tractor of 60 -74 kW(80-100CP) + Combined grassland rotary tiller-drill machine MCT 2.5 M type + Equipment for fertilizing EF 2.5 type	3.2-3.6	 2.22-2.50	25-30

These agricultural aggregates, depending on the needs, execute through a single pass, either the cleaning operations of hillocks and worthless vegetation along with chemical fertilization, or the cleaning of plant residues resulted after grazing simultaneously with periodical chemical fertilization.

CONCLUSIONS

New technologies or technological sequences for the mechanization of the maintenance and improvement of degraded grasslands, presented in this paper, are based on the composition of complex aggregates, using machines and equipment specific to the mechanization of grassland farming.

Compared to the classic technology, the new technology of mechanization of grassland improvement works by oversowing method use complex aggregates that perform two operations in a single pass, which allows reducing the number of passes of the aggregates. Thus, at the same time with execution of cleaning the hummocks, the old vegetation and to reduce the competition of the old sward before the actual oversowing, the fertilization with chemical fertilizers is also performed.

Compared to classic technologies, the new technologies and technological solutions for mechanization of the maintenance works and those for the improvement of degraded grasslands require lower fuel and work force consumptions with a lower number of passes of the aggregates.

Thus, fuel consumption is reduced by:

- 3.0-3.5 l/ha for grassland maintenance operations;
- 10.7 l/ha for improvement operation by oversowing the degraded grasslands;

By using the new technologies labor consumption is reduced with:

- 0.49 -1.176 man hours/ha for grassland maintenance operation;
- 2.316 man hours/ha for the improvement operations by oversowing;

When using the new technological variants, the number of passes of the aggregates for carrying out the operations under study is reduced as follows:

- for grassland maintenance operation from 2 passes to one pass;
- for the improvement operations by oversowing method from 4 passes to 2 passes;

By reducing fuel consumption and the number of passes, the new technologies and the technological sequences for mechanization of grassland farming have a reduced ecological impact, environmental pollution (air, water, soil) is lower, and the cost is reduced proportionally, the inputs being reduced.

ACKNOWLEDGEMENT

The results presented in this article were obtained with the support of MADR through the "Sectoral Plan - ADER 2026", financing contract no. 15.3.2 / 17.07.2023, ADER project 15.3.2. *Research on the development and promotion of mechanization technologies for the reconstruction, maintenance of permanent meadows, environmental protection and biodiversity maintenance using new specific equipment*, managed by the Research-Development Institute for Grasslands Brasov - Mechanization Laboratory.

REFERENCES

- [1] Amorim H.C., Ashworth A.J., Moore Jr P.A., Wienhold B.J., Savin M.C., Owens P.R., Jagadamma S., Carvalho T.S. and Xu S., (2020), Soil quality indices following long-term conservation pasture management practices. *Agriculture, Ecosystems & Environment*, 301, pp. 107060;
- [2] Anca B., (2012), The low-input concept in grasslands, *Romanian Journal of Grasslands and Forage Crops*, 5, pp. 7;
- [3] Baritz R., Wiese L., Verbeke I. and Vargas R., (2018), Voluntary guidelines for sustainable soil management: global action for healthy soils, *International yearbook of soil law and policy 2017*, pp.17-36;
- [4] Bikker J.P., Van Laar H., Rump P., Doorenbos J., Van Meurs K., Griffioen G.M. and Dijkstra J., (2014), Evaluation of an ear-attached movement sensor to record cow feeding behavior and activity. *Journal of dairy science*, 97(5), pp. 2974-2979;
- [5] Bogunovic I., Kljak K., Dugan I., Grbeša D., Telak L.J., Duvnjak M., Kusic I., Kapović Solomun M. and Pereira P., (2022), Grassland management impact on soil degradation and herbage nutritional value in a temperate humid environment. *Agriculture*, 12 (7), pp. 921;
- [6] Buzhdygan O.Y., Meyer S.T., Weisser W.W., Eisenhauer N., Ebeling A., Borrett S.R., Buchmann N., Cortois R., De Deyn G.B., de Kroon H. and Gleixner G., (2020), Biodiversity increases multitrophic energy use efficiency, flow and storage in grasslands. *Nature Ecology & Evolution*, 4 (3), pp. 393-405;
- [7] Cao M., (2024), *Soil matters: evaluating soil water dynamics and soil greenhouse gas emissions under climate-smart agriculture* (Doctoral dissertation, University of British Columbia);
- [8] Cardei P., Constantin N., Muraru V., Persu C., Sfiru R., Vladut N.V., Ungureanu N., Matache M., Muraru-Ionel C., Cristea O.D., Laza E.D., (2023), The Random Vibrations of the Active Body of the Cultivators. *Agriculture*, 13 (1565), DOI: [10.3390/agriculture13081565](https://doi.org/10.3390/agriculture13081565);
- [9] Chand S., Indu Singhal R.K. and Govindasamy P., (2022), Agronomical and breeding approaches to improve the nutritional status of forage crops for better livestock productivity, *Grass and Forage Science*, 77 (1), pp.11-32;
- [10] Creighton P., Kennedy E., Shaloo L., Boland T.M. and O'Donovan M., (2011), A survey analysis of grassland dairy farming in Ireland, investigating grassland management, technology adoption and sward renewal, *Grass and Forage Science*, 66 (2), pp. 251-264;
- [11] Collins M., Moore K.J., Nelson C.J. and Barnes R.F., (2017), Preservation of forage as hay and silage. *Forages*, 1, pp. 321;
- [12] Cujbescu D., Biriş S.Şt., Voicu Gh., Matache M., Paraschiv G., Vlăduţ V., Ungureanu, N., Bularda, M., (2020), Determination of sowing precision in simulated laboratory conditions, *INMATEH – Agricultural Engineering*, vol. 61, no. 2, Edited by: INMA Bucharest/Romania, pp. 209–216., DOI: <https://doi.org/10.35633/inmateh-61-23>;
- [13] Cujbescu D., Găgeanu I., Persu C., Matache M., Vlăduţ V., Voicea I., Paraschiv G., Biriş S.Şt., Ungureanu N.; Voicu G.; Ipate G., (2021), Simulation of sowing precision in laboratory conditions. *Applied Sciences - Basel*, vol. 11, Edited by: INMA Bucharest/Romania, art. ID 6264., <https://doi.org/10.3390/app11146264>;

- [14] Dragoş M.M.M., Andreoiu A.C., Mocanu V., Ene T.A., Zevedei P., Comşia C., Porr C., (2023), The influence of some type of mixtures, available for different uses, on forage quality in Brasov County, *Journal of Mountain Agriculture on the Balkans*, 26 (6), Edited by: RIMSA Troyan/Bulgaria, pp. 140-159, ISSN 1311-0489 (Print), ISSN 2367-8364 (Online);
- [15] Dengler J., Janišová M., Török P. and Wellstein C., (2014), Biodiversity of Palaearctic grasslands: a synthesis. *Agriculture, Ecosystems & Environment*, 182, pp. 1-14;
- [16] Dong S., Zhang Y., Shen H., Li S. and Xu Y., (2023), Grassland Social-Ecological Systems. In *Grasslands on the Third Pole of the World: Structure, Function, Process, and Resilience of Social-Ecological Systems*, Cham: Springer International Publishing, pp. 231-268;
- [17] Dong S., Lassoie J.P., Wen L., Zhu L., Li X., Li J. and Li Y., (2012), Degradation of rangeland ecosystems in the developing world: tragedy of breaking coupled human-natural systems. *International Journal of Sustainable Society*, 4 (4), pp. 357-371;
- [18] Easterling D.R., Meehl G.A., Parmesan C., Changnon S.A., Karl T.R. and Mearns L.O., (2000), Climate extremes: observations, modeling, and impacts, *Science*, 289 (5487), pp. 2068-2074;
- [19] Ene T.A., Mocanu V., Andreoiu A.C., Dragoş M.M.M., Blaj V.A., (2023), Technological solutions for improving the grasslands in the mountain zone, *Journal of Mountain Agriculture on the Balkans*, 26 (6), Edited by: RIMSA Troyan/Bulgaria, pp. 98-115, ISSN 1311-0489 (Print), ISSN 2367-8364 (Online);
- [20] Ene T.A., Mocanu V., Ionescu A., (2023), Sowing machine for experimental plots, MSCE 9 type, *Proceedings of International Symposium ISB-INMA TEH 2023*, Edited by: INMA Bucharest/Romania, ISSN 2537-3773 (Print), ISSN 2537-3773 (Online), pp. 124-129;
- [21] Feurdean A., Ruprecht E., Molnár Z., Hutchinson S.M. and Hickler T., (2018), Biodiversity-rich European grasslands: Ancient, forgotten ecosystems. *Biological Conservation*, 228, pp. 224-232;
- [22] Frenzel T., Wörsdörfer A., Khedhiri S., Di Giulio M., Leus F., Lipperts M.J., Martin D. and Fischer K., (2021), Grassland fallows as key for successful insect conservation, *Insect Conservation and Diversity*, 14 (6), pp. 837-850;
- [23] Gorris P., Bodin Ö., Giralt D., Hass A.L., Reitalu T., Cabodevilla X., Hannappel I., Helm A., Prangel E. and Westphal C., (2024), Socio-ecological perspective on European semi-natural grassland conservation and restoration: key challenges and future pathways, *Available at SSRN 4909041*;
- [24] Hakimovich H.H. and Alishovich K.B., (2023), Development of high-performance nature conservation: effective mechanized technology and pre-planting regional seeder parameters for the restoration and improvement of degraded desert pastures. *Spectrum Journal of Innovation, Reforms and Development*, 17, pp. 47-57;
- [25] Hautier Y., Seabloom E.W., Borer E.T., Adler P.B., Harpole W.S., Hillebrand H., Lind E.M., MacDougall, A.S., Stevens C.J., Bakker J.D. and Buckley Y.M., (2014), Eutrophication weakens stabilizing effects of diversity in natural grasslands. *Nature*, 508 (7497), pp.521-525;
- [26] Hermenean I., Mocanu V., (2009), New technological links for low-input mechanization of grassland farming (Noi verigi tehnologice de mecanizare cu inputuri reduse a lucrarilor de intretinere a pajistilor), *Farm Journal (Revista Ferma)*, no. 3-4, Agris Publishing House, Bucharest/Romania, ISSN 1011-7296, pp. 6-10;
- [27] Hermenean I., Mocanu V., Constantin N., Cojocar I., (2006), Mechanized overseeding of degraded grasslands (Supraînsămânţarea mecanizată a pajiştilor degradate), *"Cereals and Industrial Plants" Journal (Revista "Cereale și Plante Tehnice")*, nr. 3, AGRIS Publishing House, Bucharest/Romania, ISSN 1220-1197, pp. 15-18;
- [28] Hermenean I., Mocanu V., Maruşca T., (2006), The improvement of the degraded grasslands with the new machine for oversowing MSPD 2,5, *21st General Meeting of the European Grassland Federation "Sustainable Grassland Productivity"*, Badajoz/Spain, ISBN 84-689-6711-4, pp. 793-795;
- [29] Hermenean I., Mocanu V., Popescu S., (2003), Realization and testing a new machine for grassland oversowing, *Proceedings of International Congress on Information Technology in Agriculture, Food and Environment*, Ege University Press, Izmir/Turkey, pp. 670-673;
- [30] Hermenean I., Mocanu V., (2002), Mechanization technologies for over-sowing degraded lawns (Tehnologii de mecanizare pentru supraînsămânţarea pajiştilor degradate), *Agricultural Mechanization Journal (Revista Mecanizarea Agriculturii)*, Nr. 5, AGRIS Publishing House, Bucharest/Romania, ISSN 1011-7296, pp. 26-32;
- [31] Hermenean I., Mocanu V., Manailescu P., Tintea N., Alexandru M., (1994), Comparative trials with different technological variants of mechanization for reseeding and overseeding grasslands (Încercări

- comparative cu diferite variante tehnologice de mecanizare a lucrărilor de reînsămânțare și supraînsămânțare a pajiștilor), *Scientific papers of ICPCP Brasov (Lucrări științifice ICPCP Brașov)*, Brasov/Romania, vol. XVI, pp. 271-286;
- [32] Hermenean I., Mocanu V., (1986), Research on the mechanization of grasslands clearing of hummocks and worthless vegetation (Cercetări privind mecanizarea lucrărilor de curățire a pajiștilor de mușuroaie și vegetație nevalorosă), *Newletter of ASAS (Buletin informativ al ASAS)*, Nr. 17, Agricultural Technical Distribution Editorial (Redacția de Propagandă Tehnică Agricolă), Bucharest/Romania, pp. 183-202;
- [33] Hobohm C., Janišová M. and Vahle H.C., (2021), Development and future of grassland ecosystems: do we need a paradigm shift?, *Perspectives for Biodiversity and Ecosystems*, pp. 329-359;
- [34] Ibrahim M., Guerra L., Casasola F., Neely C., Abberton M., Conant R. and Batello C., (2010), Grassland carbon sequestration: management, policy and economics. In *FAO. Proceedings of the Workshop on the role of grassland carbon sequestration in the mitigation of climate change. Integrated Crop Management*, Vol. 11;
- [35] Isbell F., Craven D., Connolly J., Loreau M., Schmid B., Beierkuhnlein C., Bezemer T.M., Bonin C., Bruelheide H., De Luca E. and Ebeling A., (2015), Biodiversity increases the resistance of ecosystem productivity to climate extremes. *Nature*, 526 (7574), pp. 574-577;
- [36] Kennedy E., O'Donovan M., Murphy J.P., Delaby L. and O'Mara F.P., (2007), Effect of spring grazing date and stocking rate on sward characteristics and dairy cow production during midlactation, *Journal of Dairy Science*, 90 (4), pp. 2035-2046;
- [37] Krueger E.S., Ochsner T.E., Levi M.R., Basara J.B., Snitker G.J. and Wyatt B.M., (2021), Grassland productivity estimates informed by soil moisture measurements: Statistical and mechanistic approaches, *Agronomy Journal*, 113 (4), pp. 3498-3517;
- [38] Li T., Cui L., Lv W., Song X., Cui X. and Tang L., (2022), Exploring the frontiers of sustainable livelihoods research within grassland ecosystem: A scientometric analysis, *Heliyon* (10);
- [39] Liu K. and Shao X., (2024), Grassland Ecological Management and Utilization for Sustainability, *Agronomy*, 14 (1), p. 149;
- [40] Li Y., Wang J., Shen C., Wang J., Singh B.K. and Ge Y., (2022), Plant diversity improves resistance of plant biomass and soil microbial communities to drought, *Journal of Ecology*, 110 (7), pp. 1656-1672;
- [41] Lu X., (2024), Degraded grassland vegetation and soil characteristics: Challenges, opportunities, and sustainable development, *Advances in Resources Research*, 4 (2), pp. 205-220;
- [42] Lyons K.G., Török P., Hermann J.M., Kiehl K., Kirmer A., Kollmann J., Overbeck G.E., Tischew S., Allen E.B., Bakker J.D. and Brigham C., (2023), Challenges and opportunities for grassland restoration: A global perspective of best practices in the era of climate change, *Global Ecology and Conservation*, 46, pp.e02612;
- [43] Manea D., Voicu G., Farcaș N., Paraschiv G. and Marin E., (2017), Ecological Technology with Low Inputs for Regenerate the Degraded Grasslands, *Romanian Biotechnological Letters*, 22 (1), pp. 12274;
- [44] Manea D., Gheorghe V., Paraschiv G. and Marin E., (2016), November. Performances evaluation of direct seeder for grasslands. In *proceedings of the international scientific conference*, No. 15, Latvia University of Agriculture.
- [45] Manea D., Voicu G., Paraschiv G. and Marin E., (2015), Experimental comparative study between two types of mechanism used in grassland drills transmission, *INMATEH-Agricultural Engineering*, 47 (3), pp. 5-12;
- [46] Marin E., Manea D., Gheorghe G.V., Mateescu M., Bălțatu C., Cismaru E.M. and Dumitru D.N., (2023), Research on trends in the construction of technical grass sowing equipment., *Proceedings of ISB-INMATEH' 2023, International Symposium on Agricultural and Mechanical Engineering*, Bucharest, Romania, 5-6 October 2023, pp. 342-345;
- [47] Maron J.L., Marler M., Klironomos J.N. and Cleveland C.C., (2011), Soil fungal pathogens and the relationship between plant diversity and productivity, *Ecology letters*, 14 (1), pp. 36-41;
- [48] Marușca T., (2022), Long-term effect of technological improvement factors of subalpine grasslands of *nardus stricta* from the Carpatians mountains, *Romanian Journal of Grasslands and Forage Crops*, 26, pp. 15-25;
- [49] Marușca T., Ionescu I., Taulescu E., Simion I. and Malinas A., (2020), Contributions to the evaluation of the productivity of permanent grassland from North Oltenia. *Romanian Journal of Grassland and Forage Crops*, 21, pp. 49-59;

- [50] Matache M. G., Cristea M., Găgeanu I., Zapciu A., Tudor E., Carpus E., Popa L. D., (2020), Small power electric tractor performance during ploughing works, *INMATEH Agricultural Engineering*, vol. 60, no. 1, pp. 123–129, <https://doi.org/10.35633/inmateh-60-14>;
- [51] Mitev D., (2023), On the Behavior of Certain Artificial Grasslands on the Slopes of the Central Balkan Mountain in Bulgaria, *Global Journal of Science Frontier Research: D, Agriculture and Veterinary*, Volume 23, Issue 5, Version 1.0, Global Journal Publisher, ISSN: 2249-4626 (Online);
- [52] Mocanu V., Ene T.A., Hermenean I., (2022), Achievements regarding the mechanization of Grassland Farming (Realizări privind mecanizarea lucrărilor agricole pe pajiști), *ACTA AGRICOLA ROMANICA, ASAS Bucharest, Field Plant Culture Series*, Tome 4, Year 4, No. 4, ISSN 2784-0948, pp. 61-85;
- [53] Mocanu V., Dragomir N., Blaj V.A., Ene T.A., Tod Monica Alexandrina, Mocanu Victoria, (2021), *Romania's Grasslands – Resources, Improvement and Utilization Strategies (Pajiștile României - Resurse, Strategii de îmbunătățire și valorificare)*, Brașov/Romania, Transylvania University Publishing House, ISBN 978-606-19-1414-2;
- [54] Mocanu V., Ene T.A. and Blaj V.A., (2021), Technological Solutions and Specific Equipment for Improving the Degraded Grasslands by Total Reseeding. *Technology in Agriculture*, pp.167-186, DOI: 10.5772/intechopen.99403;
- [55] Mocanu V., Hermenean I., (2013), Grassland Mechanization – Technologies, machines and equipment (*Mecanizarea lucrărilor agricole pe pajiști - Tehnologii, mașini și echipamente*), Brașov/Romania, Transylvania University Publishing House, ISBN 978-606-19-0237-8;
- [56] Mocanu V., Hermenean I., Marusca T., (2008), Ecological and economical technology for mechanization of grassland improvement works, *Proceeding of the 22nd General Meeting of the European Grassland Federation "Biodiversity and Animal Feed – Future Challenges for Grassland Production"*, Uppsala/Sweden, ISBN 978-91-85911-47-9, pp. 144-146;
- [57] Mocanu V., Hermenean I., (2008), Technologies for Mechanization with Low Input System of Maintenance and Improvement Grassland Works (Tehnologii pentru mecanizarea cu inputuri minime a lucrarilor de intretinere si imbunatatire a pajistilor), Transilvania University Publishing House, Brașov/Romania, ISBN 978-973-598-348-2;
- [58] O'Mara F.P., (2012), The role of grasslands in food security and climate change. *Annals of botany*, 110 (6), pp.1263-1270;
- [59] Oprea A. and Marusca T., (2023), *Contribution to the assessment of mountain grasslands productivity from Râmnicu Sărat River Basin*. SSRN.
- [60] Pepin N.C., Arnone E., Gobiet A., Haslinger K., Kotlarski S., Notarnicola C., Palazzi E., Seibert P., Serafin S., Schöner W. and Terzago S., (2022), Climate changes and their elevational patterns in the mountains of the world, *Reviews of Geophysics*, 60 (1), pp.e2020RG000730;
- [61] Peters M., Horne P., Schmidt A., Holmann F., Kerridge P.C., Tarawali S.A.O, Schultze-Kraft R., Lascano C.E., Argel P., Stür W. and Fujisaka S., (2001), The role of forages in reducing poverty and degradation of natural resources in tropical production systems;
- [62] Polichshuk Y., Derepaskin A., Binyukov Y., Laptev N. and Komarov A., (2023), Improvement of the technological scheme of the implement for strip overseeding of grass seeds and selection of a combined tillage tool for leveling the soil in the strip and seeding. *Bulgarian Journal of Agricultural Science*, 29 (1).
- [63] Pop M., Hermenean I., Mocanu V., (1994), The improvement of degraded grasslands invaded by vegetable hills in the Juniperus mountainous zones, *Proceeding of the International Scientific Conference, Agricol Science University, Bucharest/Romania*, pp. 167-171;
- [64] Shaloo L., O'Donovan M., Leso L., Werner J., Ruelle E., Geoghegan A., Delaby L. and O'leary N., (2018), Grass-based dairy systems, data and precision technologies, *Animal*, 12 (s2), pp. 262-271;
- [65] Song Z., Hautier Y. and Wang C., (2023), Grassland stability decreases with increasing number of global change factors: A meta-analysis. *Science of the Total Environment*, 898, pp.165651;
- [66] Stefan V., Sfiru R. and Popa L., (2019), Experimental results on the solid organic fertilizer machine MG 5, In *E3S Web of Conferences*, EDP Sciences, Vol. 112, pp. 03007;
- [67] Stefan V., Zaica A. and Losif A., (2021), Research on the uniformity degree of solid organic fertilizers distribution, *INMATEH Agriculture Engineering*, 65, pp. 495–504;
- [68] Ștefănescu Șt., Neçulescu V., Hermenean I., (1982), Research regarding the development of new machines for grassland cleaning (Cercetări privind realizarea de noi mașini pentru curățirea pajiștilor), *Scientific papers of ICPCP Brasov (Lucrări științifice ale ICPCP Brașov)*, vol. VIII, pp. 245-258;

- [69] Tadesse M., Simane B., Abera W., Tamene L., Ambaw G., Recha J.W., Mekonnen K., Demeke G., Nigussie A. and Solomon D., (2021), The effect of climate-smart agriculture on soil fertility, crop yield, and soil carbon in southern Ethiopia. *Sustainability*, 13 (8), p. 4515.
- [70] Tindale S., Cao Y., Jin S., Green O., Burd M., Vicario-Modrono V., Alonso N., Clingo S., Gallardo-Cobos R., Sanchez-Zamora P. and Hunter E., (2024), Tipping points and farmer decision-making in European permanent grassland (PG) agricultural systems, *Journal of Rural Studies*, 110, p.103364;
- [71] Ungureanu N., Vlăduț V., Cujbescu D., (2019), Soil compaction under the wheel of a sprayer, 8th International Conference on Thermal Equipment, *Renewable Energy and Rural Development, Web-of-Conferences*, vol. 112, art. ID, 03027, <https://doi.org/10.1051/e3sconf/201911203027>;
- [72] Vlăduț N.V., Ungureanu N., Biriș S.Șt., Voicea I., Nenciu F., Găgeanu I., Cujbescu D., Popa L.D., Boruz S., Matei Gh., Ekielski A., Teliban G.C., (2023), Research on the identification of some optimal threshing and separation regimes in the axial flow apparatus. *Agriculture*, vol. 13, no. 4, art. ID 838. *Special Issue "Beyond Agriculture 4.0: Design and Development of Modern Agricultural Machines and Production Systems"*, <https://doi.org/10.3390/agriculture13040838>;
- [73] Wagg C., O'Brien M.J., Vogel A., Scherer-Lorenzen M., Eisenhauer N., Schmid B. and Weigelt A., (2017), Plant diversity maintains long-term ecosystem productivity under frequent drought by increasing short-term variation. *Ecology*, 98 (11), pp. 2952-2961;
- [74] Wang Y., Cadotte M.W., Chen Y., Fraser L.H., Zhang Y., Huang F., Luo S., Shi N. and Loreau M., (2019), Global evidence of positive biodiversity effects on spatial ecosystem stability in natural grasslands, *Nature communications*, 10 (1), p. 3207;
- [75] Wan L., Liu G. and Su X., (2024), Different grazing management strategies change greenhouse gas emissions and global warming potential in global grasslands, *Geography and Sustainability*;
- [76] Wang J., Li Y., Bork E.W., Richter G.M., Chen C., Shah S.H.H. and Mezbahuddin S., (2021), Effects of grazing management on spatio-temporal heterogeneity of soil carbon and greenhouse gas emissions of grasslands and rangelands: Monitoring, assessment and scaling-up, *Journal of cleaner production*, 288, pp.125737;
- [77] Wilsey B., (2018), *The biology of grasslands*, Oxford University Press;
- [78] Wróbel B., Zielewicz W. and Staniak M., (2023), Challenges of pasture feeding systems—opportunities and constraints, *Agriculture*, 13 (5), pp. 974;
- [79] Xie B., Jin Y., Faheem M., Gao W., Liu J., Jiang H., Cai L. and Li Y., (2023), Research progress of autonomous navigation technology for multi-agricultural scenes, *Computers and Electronics in Agriculture*, 211, pp. 107963;
- [80] Xinxia L., (2024), Degraded grassland vegetation and soil characteristics: Challenges, opportunities, and sustainable development, *Advances in Resources Research*, 4 (2), pp. 205-220;
- [81] Xiong D., Chen F., Lv K., Tan X. and Huang Y., (2023), The performance and temporal dynamics of vegetation concretes comprising three herbaceous species in soil stabilization and slope protection, *Ecological Engineering*, 188, pp. 106873;
- [82] Huang X. and Hou F., (2024), Principle, technique and application of grassland improvement. *Journal of Environmental Management*, 369, pp.122264;
- [83] Zhang Y., Lu Y., Sun G., Li L., Zhang Z. and Zhou X., (2024), Dynamic Changes in Vegetation Ecological Quality in the Tarim Basin and Its Response to Extreme Climate during 2000 – 2022. *Forests*, 15 (3), pp. 505;
- [84] Zhang R., Wang J. and Niu S., (2021), Toward a sustainable grazing management based on biodiversity and ecosystem multifunctionality in drylands, *Current Opinion in Environmental Sustainability*, 48, pp. 36-43;
- [85] Data on Land Cover (Grassland), FAOSTAT, (2024), Available online: <https://www.fao.org/faostat/en/#data/LC> (accessed on 02 Dec. 2024).

RESEARCH ON THE VISCO-ELASTIC BEHAVIOUR OF SOME VARIETIES OF CHEESE WITH MOLD, RIPENED UNDER SPECIFIC CONDITIONS

CERCETĂRI PRIVIND COMPORTAREA VÂSCOELASTICĂ A UNOR SORTIMENTE DE BRÂNZĂ CU MUCEGAI, MATURATE ÎN CONDIȚII SPECIFICE

Grațiela-Florinela PANĂ, Paula TUDOR, George IPATE, Mihaela BEGEA,
Elena-Mădălina ȘTEFAN, Gheorghe VOICU*)

National University of Science and Technology POLITEHNICA Bucharest, Romania

Tel: 004-0724-715585; E-mail: ghvoicu_2005@yahoo.com

DOI: <https://doi.org/10.35633/inmateh-74-85>

Keywords: ripened cheese, cheese with mold, creep test, pressing cylinder, linear distribution

ABSTRACT

Mold-ripened cheeses exhibit complex mechanical behavior, influenced by factors such as degree of ripening, water content, fat content, and type of mold (white or blue). This study explored the viscoelastic behavior of four types of mold-ripened cheeses to highlight their physicochemical properties, taking into consideration that the viscoelasticity influences their texture, stability and behavior during storage and processing. Analyzing the local pressures applied to the cheese samples, for a contact surface with the cheese samples of approximately 51.5 mm², the pressure levels vary between 40 kPa (for Roquefort cheese) and 50 kPa (for Dorblu cheese); the pressure for the other two types of cheese falls within this range. The data obtained from this study confirmed that penetration resistance and yield stress values provide valuable information in cheese production, in particular for the texture and firmness of cheeses at various stages of the manufacturing process.

REZUMAT

Brânzeturile maturate cu mucegai prezintă un comportament mecanic complex, influențat de factori precum gradul de maturare, conținutul de apă, conținutul de grăsime și tipul de mucegai (alb sau albastru). Această lucrare a avut scopul de a studia comportamentul vâscoelastic a patru tipuri de brânzeturi maturate cu mucegai, pentru a le evidenția proprietățile fizico-chimice, ținând cont de faptul că vâscoelasticitatea influențează textura, stabilitatea și comportamentul acestora în timpul depozitării și prelucrării. În urma analizei presiunilor locale aplicate pentru brânzeturile analizate, la o suprafața de contact cu mostrele de brânză de circa 51,5 mm², presiunea a înregistrat valori între 40 kPa pentru brânza Roquefort și 50 kPa pentru brânza Dorblu. Datele obținute din acest studiu au confirmat că rezistența la penetrare și tensiunea de biocurgere oferă informații valoroase în producția de brânzeturi, în diferite etape ale procesului de fabricație.

INTRODUCTION

Brie, Camembert, Roquefort and Dorblu are all well-known cheeses, but they differ significantly in their ingredients, manufacturing process, texture, taste and origin.

*Brie cheese originates from Île-de-France region of France and is made from cow's milk (usually pasteurized, but it can also be unpasteurized). It has a soft, creamy texture with an edible white mold rind (*Penicillium candidum*) and is typically aged for 4 to 6 weeks. The flavor is smooth, delicate, slightly buttery, with hints of nuts and fruit. It is placed in a large round shape, with a diameter of 23-36 cm and a thickness of 2.5-3 cm.*

*Camembert cheese originates from France, specifically from the Normandy region, and is made from cow's milk (usually unpasteurized for traditional Camembert). It also has a soft, creamy texture with an edible white mold crust (*Penicillium candidum*) and a maturation period of about 3 to 5 weeks. The taste is intense, fruity, slightly salty, with flavors of mushrooms and cream (Linton, 2008).*

*Roquefort cheese also originates from France, specifically from Roquefort-sur-Soulzon region, and is made from sheep's milk (Lacune sheep milk). It has a semi-hard, crumbly texture, with blue mold veins (*Penicillium roqueforti*) and an intense, spicy, salty taste with flavors of nuts and mushrooms. The maturation period is longer, usually between 3 and 6 months. It is shaped in a cylindrical form, with a diameter of about 19-20 cm a thickness of 8-10 cm.*

Dorblu cheese originates from Germany and is made from cow's milk (pasteurized) with a semihard, creamy texture, blue mold veins (*Penicillium roqueforti*), and a salty, slightly spicy taste with flavors of cream and mushrooms, typically shaped in round molds. The maturation period is usually between 2 and 3 months.

At a storage temperature of 4-10°C, the storage time (about 77 days) has a significant impact on the rheological behavior of blue mold cheeses, which does not occur at different storage temperatures. The compression force with large deformation and the viscoelastic moduli show values that decrease with storage time, while the nonlinear viscoelastic behavior increases. Results obtained by the authors of the study (Joyner, 2017) indicated that the microstructure of the samples weakened and was easily deformed as storage time increased. Thus, blue cheese can be stored at 4-10°C without significant changes in its composition or mechanical behavior.

The amount of mold in blue cheese has a significant influence on the quality of the cheese. The quantity and distribution of mold inside the cheese influence its appearance, color, structure, taste, and smell, and are evaluated by experts with appropriate sensory knowledge and skills. The authors of the studies (Brosnan and Sun, 2004; Caccamo et al., 2004; Jelinski et al., 2007; Kulmyrzaev et al., 2008; Ganchovska et al, 2019; Ganchovska et al, 2021) propose a computerized method for evaluating the appearance (color and structure).

It has also been found that the physical parameters of blue mold cheeses (such as Valdeon) are affected by the maturation time. Cheese aged for 120 days shows higher values of the elasticity moduli G' , G'' , and G^* , and a more elastic disposition, but also lower values of fracturability and chewiness (Diezhandino et al., 2016).

The storage modulus (G') and loss modulus (G'') of cheeses show increasing values from the surface towards the interior, while strain and $\tan \delta$ decreased, as reported in the study (Karoui et al, 2003).

For uniaxial creep behavior in cheddar cheeses with different fat contents, tests were conducted at 1, 3, 6, and 12 weeks of age, at a temperature of 40°C and a stress of 1119.5 Pa. The creep data were modelled using a six-element Kelvin model, and the instantaneous slope of the creep curve was defined as the viscoelasticity index. The results from the study show that the estimated viscoelasticity index could be used to predict cheese melting (Kuo et al, 2000).

Studying the rheological behavior of cheeses provides information related to texture and structure that can be useful for a better understanding of the complex aging behavior of cheese. Different authors show that fat content, testing temperature, and aging time have a significant impact on the viscoelastic parameters of cheeses, critical stress and strain, complex modulus G^* , and breaking stress, and they present positive correlations with phase angle and breaking strain (Bagher et al., 2020).

In the uniaxial compression process of rectangular pieces of processed cheese with cream, the applied force was measured using the Hounsfield H1KS equipment. The Maxwell model for creep/constant stress experiments shows that stress increases linearly with time, and experimental force-displacement curves were plotted for the slow strain-stress test. The Maxwell viscoelastic model was validated by comparing numerical results with experimental data (Ipate G., et al., 2019).

Experiments on stress relaxation, after a 10% compression on an Instron-type equipment, performed on Cheddar cheeses with four different fat contents, two different moisture contents, and four storage durations, showed that Peleg's empirical models better describe the stress relaxation behavior of processed cheese (at over 50°C), and eight-element Maxwell models better describe the cheese behavior than three- or six-element Maxwell models. The stress relaxation experiments showed viscoelastic differences in cheeses due to reduced fat content, increased moisture, and melting temperature or cheese aging (Venugopal V., Muthukumarappan K., 2001).

Physico-mechanical analyses for mold cheese involve evaluating the physical and mechanical properties that can affect the quality, texture, consistency, and behavior of the cheese both during the manufacturing process and throughout storage and consumption.

These analyses may include compression tests to determine texture, where the cheese's resistance to compression is measured, which is an important indicator of cheese firmness, as well as penetration tests to evaluate how easily an object can penetrate the cheese, providing data on its softness or hardness (Calzad et al., 2014).

Cheese elasticity is the property that indicates the cheese's ability to return to its original shape after being subjected to deformation. Elasticity tests are important to evaluate how the cheese behaves during handling and slicing (Garcia C.A. et al., 2018; Vandenberghe E. et al., 2013; Hassan L.K. et al., 2020). Cheese cohesion refers to the cheese's ability to remain compact without crumbling, which is essential to ensure that the cheese does not break apart when cut or chewed. Additionally, adhesion refers to how well the cheese sticks to different surfaces. This can influence how the cheese behaves when used in various culinary

preparations. Furthermore, the analysis of water content and humidity is important because these factors influence the cheese's texture, as well as its ability to spread or melt.

This study characterizes four types of mold cheeses, matured at temperatures and periods corresponding to the technological process recommendations for each type, after compression tests with a cylinder of 8.1 mm in diameter, at constant speeds, determining the variation of force-deformation parameters. The results presented in this paper, as well as the results of other researchers' studies in the field, can provide valuable information to specialists in the production and research of these cheeses.

MATERIALS AND METHODS

A fundamental understanding of the behavior of food products under mechanical stresses is essential for determining the energy requirements for various processing operations, as well as for designing machines, equipment, and facilities that process these products (Ionescu, M. et al., 2016).

For four types of mold-ripened cheese (Brie, Dorblu, Camembert, and Roquefort) purchased from commercial networks, viscoelastic behavior tests were conducted using the Hounsfield/Tinius Olsen H1-KS mechanical testing apparatus, equipped with a 1000 N load cell and an 8.1 mm diameter pressing cylinder.

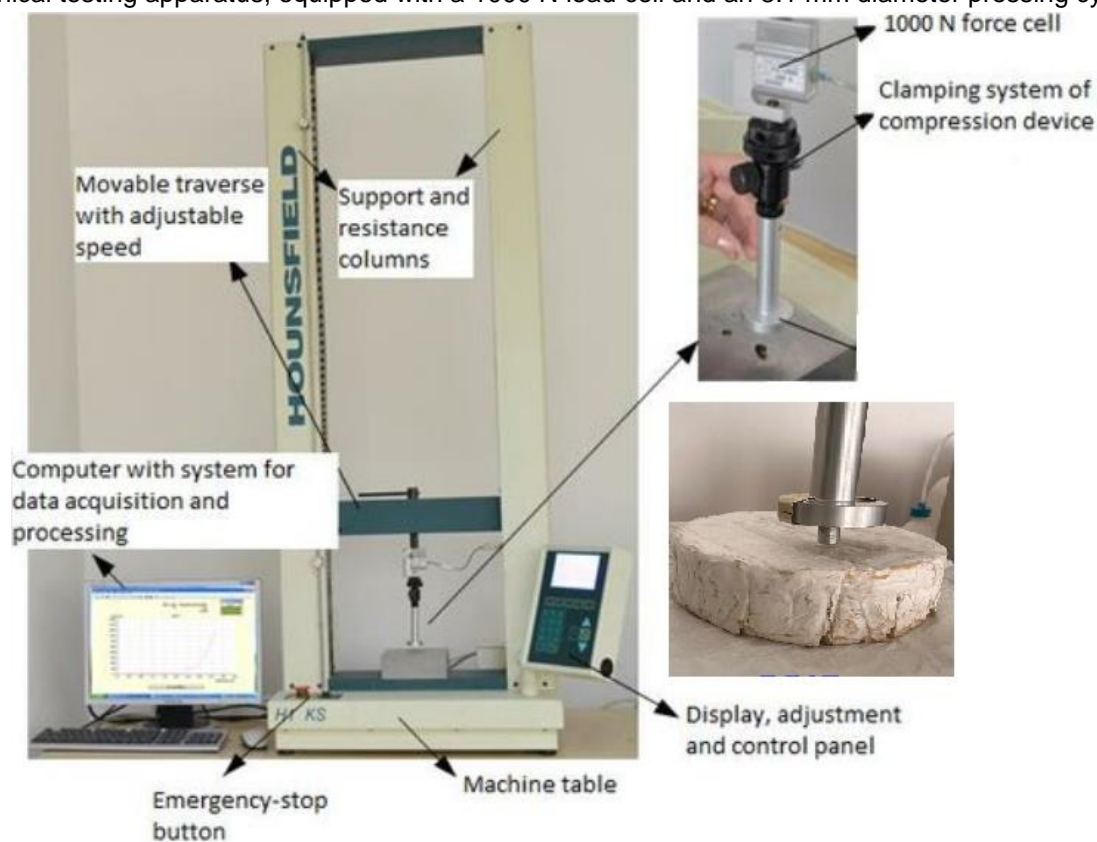


Fig. 1 - Hounsfield / Tinius Olsen model H1 KS device for mechanical tests

The main components of the equipment are: support columns; a fixed flat plate for supporting the sample; a pressing head with a movable flat plate parallel to the base plate; a display, adjustment, and control panel; a load cell; and a data acquisition system (computer) with QMAT software (Fig. 1).

In the case of the used apparatus, the resistant force exerted by the tested material sample is measured by a load cell, which can be easily and quickly changed through a special mechanism depending on the material being tested. For measuring displacement, the apparatus has a precision of ± 0.001 mm, and the movement speed can range from 0.001 mm/min to 1000 mm/min.

In the QMAT program, the parameters used in the experiments were set. First, the pressing head speed was set to 100 mm/min, the loading range was set to 25 N, the extension range was set to 5 mm, the hold load target was set to 2.5 N, and the hold load time was set to 180 s.

After acquisition, the samples of cheese were stored in the refrigerator at an average temperature of 8°C. The determination was performed at ambient temperature (by the end of the measurements, the temperature did not exceed 19.7 °C). Each type of cheese requires specific preservation treatment and optimal conditions to ensure quality and safety during storage (Najera A.I. et al., 2021).

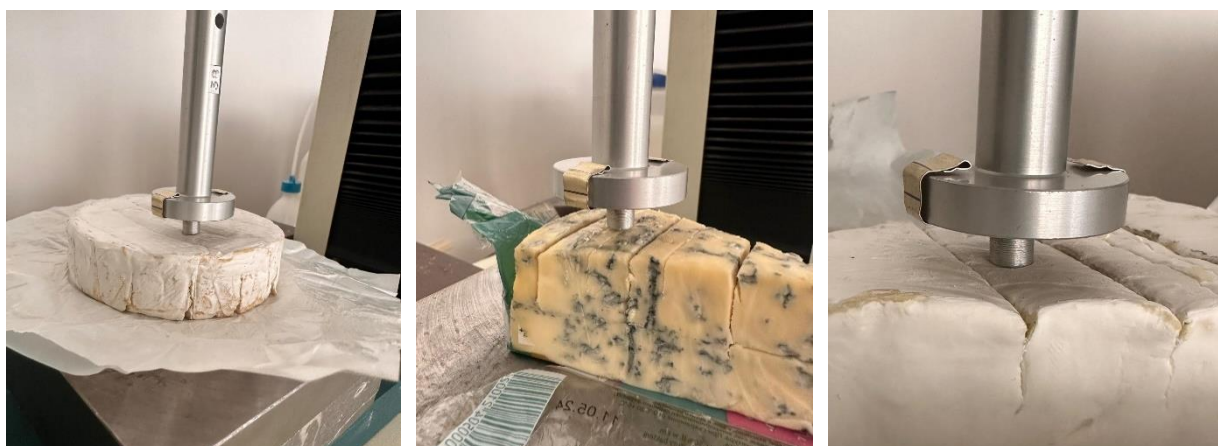


Fig. 2 – Aspects of the tests conducted on mold-ripened cheeses

Additional details about the analyzed cheeses can also be mentioned, for which prior tests were conducted in the faculty's laboratories (Table 1).

Table 1

Physical characteristics of the analyzed cheese samples

Cheese type	Camembert	Brie	Dorblu	Roquefort
Maturation period (days)	30	30	60	75
Mass of analyzed samples (g)	249	200	100	100
Height of samples (mm)	40	50	60	60
Width (mm) (at which the cuts were made)	100	75	55	80
	110	60	35	60
	90	50	20	50
Nutritional value (kcal)	216	334	413	346
pH	6.7	7.5	6.2	6.0
Fat (g/100g)	13.5	17	29	29.8
Total proteins (g/100g)	23.5	20	19	21.1
Dry matter (%)	45.5	45	48	48
Salt (g/100g)	1.5	1.3	1.7	3.5

After setting up the equipment as mentioned, the cylinder was positioned and adjusted in the apparatus to make contact with the sample to be analyzed, and it was ensured that the force and extension/displacement were set to 0. Then, the 'START' button was pressed to begin the analysis.

For the set movement speed and small displacements of the pressing head (at intervals of 0.01 mm), the apparatus recorded the resistant force. For Brie and Dorblu cheeses, the final displacement was on the order of 2-3 mm, for Camembert cheese on the order of 5-6 mm, and for Roquefort cheese, the test continued as far as the apparatus allowed, up to displacements on the order of 10 mm, as presented in Table 2.

The regression line of the displacement of the testing head correlated with the resistant force has the form:

$$F = a \cdot d + b \text{ (N)} \quad (1)$$

where:

F is the resistant force at a displacement d (mm) of the testing cylinder, in N; a – is the slope of the regression line, which gives the angles relative to the two axes; b – is the intercept on the origin of the considered line.

This phenomenon occurs mainly in the first part of the experiment because as the testing cylinder penetrates deeper into the sample, the shape of the force-displacement curve changes.

Regarding the influence of pressure on cheeses, it is particularly important to conduct tests on the behavior of cheeses under various pressure categories, as in the tests performed and presented in this paper.

RESULTS

The mechanical or rheological tests performed on cheeses can be used as study tools to characterize cheese functionality, and the results of these analyses can guide necessary adjustments in the manufacturing process to achieve a consistent and high-quality product.

The evaluation of the force required to cut the cheese is an indicator of its texture. Softer cheeses require less cutting force, while harder ones require more force (*Skordaris G. et al., 2022; Goh S.M. et al., 2005*). Moreover, the texture density of the cheese can provide information about its composition, including the ratio of solids to liquids, and the tensile strength test measures resistance to forces that tend to tear the cheese, which is relevant for cheeses that need to maintain structural integrity in various applications. All these tests are part of the rheological profile analysis of cheeses and provide information about viscoelasticity and beyond.

Each type of cheese requires specific preservation treatments and application conditions to ensure the quality and safety of the cheese during storage. High hydrostatic pressure processing (HHP) is an advanced non-thermal technology used for food processing, including cheeses. During the treatment, the product is subjected to high pressure (400–600 MPa - on an industrial scale) for 10–20 minutes at a temperature below 45°C, and the applied pressure is transmitted instantly throughout the food, regardless of its size, shape, and composition (*Nájera A.I. et al., 2021; Koutsoumanis K., et al., 2022*). However, the literature confirms that the timing of the high-pressure (HP) treatment (400-600 MPa, 7 min) is also important because it can lead to significant changes or not in microbiology, proteolysis, instrumental texture, and sensory parameters (*Delgado F.J. et al., 2012*). Thus, the timing of the treatment can result in changes in the appearance, smell, and texture, as well as the aroma and elasticity of the cheese.

The experimental test results show displacements on the order of 0.01 mm, for which the resistant forces were recorded in N. Based on these values, the force-deformation curves were plotted. The paper selects and presents the most significant values of these curves, highlighting changes in their trajectory (shape).

From the analysis of the data in Table 2, it can be observed that for the same values of displacement of the pressing cylinder, the resistant force differs among the four types of cheese (at least for the tested samples). For displacements of about 1.5 mm and approximately 3.2 mm, the resistant force for Dorblu and Brie cheeses is relatively similar, around 2.5 N. For Camembert cheese, this force value is only reached at a displacement of approximately 5 mm, while for Roquefort cheese, this value is not achieved even at a displacement of nearly 10 mm (referring here to the average values from the three measurements performed).

Table 2

The values of the characteristic points of the average curves for the tests on the cheeses

Roquefort		Brie		Camembert		Dorblu	
Extension, mm	Force, N						
0	0	0.07	0.015	0	0.030	0.01	0.030
0.40	0.133	0.5	0.077	0.22	0.110	0.40	0.763
0.50	0.227	0.75	0.280	0.45	0.257	0.50	0.840
1.00	0.673	1.00	0.532	0.67	0.373	0.75	1.313
1.50	1.053	1.50	1.085	0.90	0.497	1.00	1.757
2.00	1.267	2.00	1.622	1.12	0.603	1.25	2.257
2.50	1.367	2.28	1.733	1.35	0.687	1.49	2.545
3.00	1.447	2.50	1.963	1.57	0.790		
3.50	1.533	2.74	2.105	1.80	0.880		
4.00	1.600	3.00	2.390	2.02	0.967		
4.50	1.643	3.19	2.500	2.25	1.057		
5.00	1.663			2.47	1.183		
5.50	1.69			2.70	1.300		
6.00	1.700			2.92	1.393		
6.50	1.723			3.15	1.500		
7.00	1.733			3.37	1.590		
7.50	1.747			3.60	1.703		
8.00	1.767			3.82	1.847		
8.50	1.750			4.05	1.947		
9.00	1.823			4.20	2.053		

Roquefort		Brie		Camembert		Dorblu	
Extension, mm	Force, N						
9.50	1.987			4.27	2.187		
9.71	2.067			4.33	2.267		
9.92	2.115			4.50	2.360		
				4.72	2.390		
				4.95	2.460		
				5.03	2.430		

This phenomenon aligns with information from the literature, which states that cheeses with white mold (such as Brie or Camembert) are generally softer than blue mold cheeses (such as Roquefort, Gorgonzola, or Stilton). Brie and Camembert have a creamy, soft texture, almost like butter, and are covered with a fine white mold crust. In contrast, blue mold cheeses, while they can also be creamy, are usually firmer and sometimes even crumbly. Dorblu cheese has a creamy but firm texture; it is not as soft as Brie or Camembert but also not as crumbly as some of the more mature blue mold cheeses.

Based on the measured values in the laboratory and summarized in Table 2, the graphs presented in Figures 3 and 4 were plotted.

From the analysis of the graphs in Figure 3, it is observed that for small displacements of the sample cylinder, the variation in resistant force as a function of the sample head displacement is relatively linear. This phenomenon was observed both for each of the three (or four) tests conducted and for their average.

The analysis of the graphs reveals that, for Brie cheese, the inclination of the regression line relative to the horizontal axis ranges between 44-47°, with a regression coefficient R^2 of over 0.994.

For Camembert cheese, the deformation is slightly higher for the same values of resistant force compared to the previous case, and the angle of the regression line relative to the deformation axis ranges from 25-27°, with a regression coefficient $R^2 > 0.992$. In the case of Dorblu cheese, the regression lines for the three measurements show angles relative to the displacement axis between 58-63°, with a regression coefficient $R^2 > 0.987$. However, for the average values of the three measurements, the regression line shows an angle of 26.2°, with a correlation coefficient $R^2 = 0.994$, which is as expected given the previously stated values.

All this occurs, however, for the considered units of measurement, namely mm for displacements and N for resistant forces, at small displacements of the test head, as mentioned earlier.

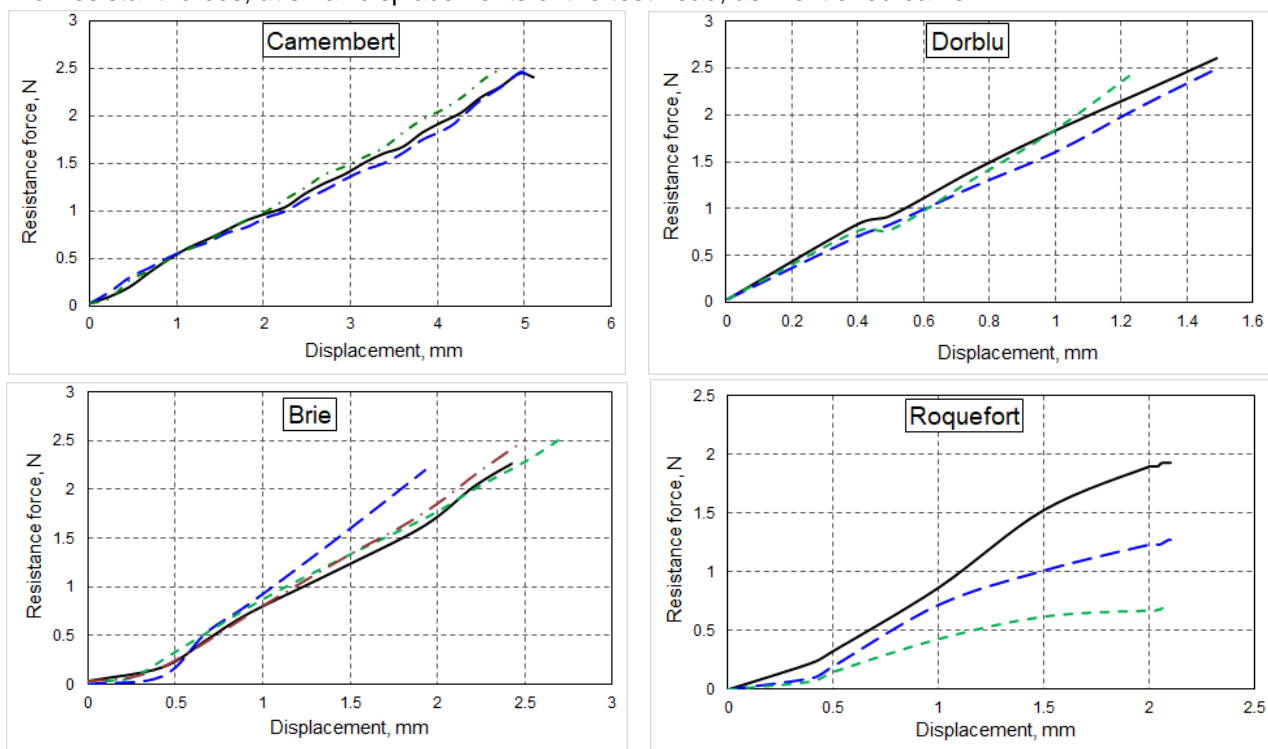


Fig. 3 – Resistive force correspondence – displacement for small displacement values, for the analyzed cheeses

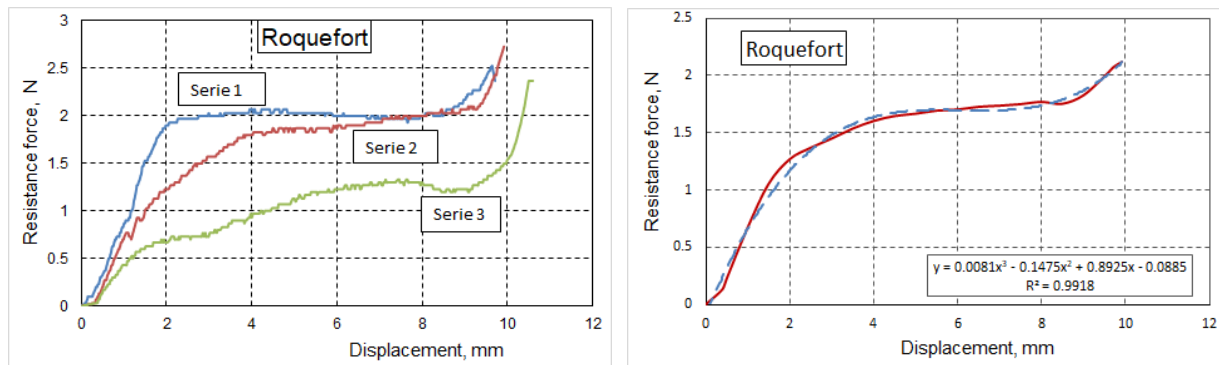


Fig. 4 – The final shape of the force-deformation (creep) curves for Roquefort mold cheese

For Dorblu cheese, the regression line equation for the average values of the three measurements has a correlation coefficient $R^2=0.997$, with a slope of 1.7254 and an intercept of 0.0278.

For Roquefort cheese, the situation is slightly more complex. A linear variation between displacement and the resistant force during pressing can only be observed at very small displacements of the test head. The angles in this part of the curves are less than 45° , specifically ranging between $19-44.5^\circ$, with a correlation coefficient $R^2>0.970$. This result reflects the texture of the cheese, which varies at different points on the samples.

However, in this type of cheese, the shape of the force-deformation curves is more sophisticated, initially presenting a relatively linear increase up to displacements of about 2-3 mm, followed by a relatively constant variation, with a pronounced increase in force in the final part of the curves, for small displacement variations.

Cheeses with mold have varied textures, and their reaction to a simple finger press can provide clues about the type and degree of ripeness of the cheese. When pressed, Brie or Camembert cheeses are quite soft and yield easily under pressure, but depending on the degree of ripeness, the center can be either firm or very creamy, almost liquid. The white mold crust may be slightly firmer, but it also yields under pressure, revealing the creaminess beneath.

In blue mold cheeses (Dorblu, Gorgonzola, Roquefort), the texture is firmer than in white mold cheeses, but they still yield easily under pressure, especially the creamier ones. However, more matured cheeses can be crumblier and denser. Generally, softer mold cheeses will yield easily under pressure, while more mature and dense ones will offer more resistance.

Mold cheeses react differently to various levels of pressure, depending on the type and degree of ripeness. Thus, the degree of ripeness plays an essential role in the cheese's reaction to pressure. Fresh cheeses are more elastic and yield more easily, while matured ones become denser and crumblier. The moisture content of the cheese also influences its reaction to pressure; moister cheeses (such as the less matured ones) will deform more easily and flow more quickly under pressure.

Under high pressure, Brie and Camembert cheeses will flatten significantly, and the creamy layer inside will flow freely, compromising the structure. In contrast, mature blue mold cheeses present resistance and will crumble or crack, with the texture becoming crumbly.

Analyzing the local pressures applied to the cheese samples, the contact surface with the cheese samples is approximately 51.5 mm^2 , and the pressure levels range between 40 kPa (for Roquefort cheese) and 50 kPa (for Dorblu cheese). The pressure for the other two types of cheese falls within this range.

The pressure-deformation curves for mold cheeses reflect how these cheeses react to the application of pressure. Depending on the type of cheese and its degree of ripeness, the curves can vary considerably in terms of shape as well as values, as previously observed.

In white mold cheeses (Brie, Camembert), the curve initially has a steep slope (large deformation for small pressure), reflecting the fact that the cheese is very soft and yields easily. As the pressure increases, the curve flattens, the initial deformation becoming proportional to the applied pressure, with reduced elasticity. When the cheese reaches a critical point, the deformation increases rapidly as the structure gives way.

In blue mold cheeses (such as Dorblu), the curve is less steep than in soft cheeses (as seen in fig. 3), indicating greater resistance to pressure. However, there is still a zone where the cheese will begin to yield more quickly to increasing pressure, with the deformation also increasing.

If the regression curve of the average force-deformation values for Roquefort blue mold cheese is analyzed (fig. 4, right), it can be observed that the shape of the curve can be approximated by a third-degree equation. However, it is difficult to determine which parameters each coefficient of the mathematical expression depends on (structure, texture, moisture, ripening period, temperature, etc.).

As general observations, it can be said that softer cheeses have steeper pressure-deformation curves at the beginning, indicating easy deformation under small pressures, while in matured and denser cheeses, a more extensive elastic zone is found with more controlled deformation up to a critical point, after which a sudden failure occurs (as observed in fig. 4).

CONCLUSIONS

It can be stated that the physical-mechanical tests and analyses applied to cheeses, especially those with mold, are crucial for assessing their functionality and determining whether the technological process has been adequate.

The physical-mechanical characteristics of moldy cheeses depend not only on the manufacturing process but also on the conditions of maturation and subsequent storage.

When testing the rheological characteristics of these cheeses, especially through flow tests, the force-deformation curves show variations depending on the type of cheese and the maturation period. It should be noted, however, that the initial part of the curves is relatively linear, with a more or less steep slope that varies depending on the specific type of cheese.

The results obtained confirm that white mold cheeses (Camembert and Brie) are generally softer than blue mold cheeses (Roquefort and Dorblu). In the cutting tests, it was observed that soft cheeses with a higher water content and a lower degree of ripening, such as Camembert and Brie, exhibit increased elasticity and progressive deformation.

The flow tests can be used to adjust maturation parameters such as temperature, humidity, and duration to achieve the desired characteristics of the cheese. Flow tests are essential in the cheese industry for understanding and controlling the physical properties of the final product, thus contributing to maintaining its quality and uniformity.

ACKNOWLEDGEMENT

The tests and analyzes presented in this paper are part of the set of physico-chemical, mechanical and rheological tests carried out during the doctoral internship, and I hereby thank all those who supported me in their realization and in the elaboration of the thesis.

REFERENCES

- [1] Bagher Seighalani, F.Z., Joyner, H.S., Ross, C.F. (2020). Relationships among rheological, sensory, and wear behaviors of cheeses, *Journal of Texture Studies*, 51(1), <https://doi.org/10.1111/jtxs.12547>;
- [2] Brosnan, T., Sun, D-W. (2004). Improving quality inspection of food products by computer vision - A review. *Journal of food engineering*, 61, pp. 3-16
- [3] Caccamo M., Melilli C., Barbano M. D., Portelli G., Marino G., Licitra G. (2004). Measurement of gas holes and mechanical openness in cheese by image analysis. *Journal of Dairy Science*, 87, pp. 739-748;
- [4] Calzad, J., Del Olmo, A., Picón, A., Gaya, P., Núñez, (2014). M. Effect of high-pressure-processing on the microbiology, proteolysis, texture and flavour of Brie cheese during ripening and refrigerated storage, *Int. Dairy Journal*, 37:64–73, doi: 10.1016/j.idairyj.2014.03.002.
- [5] Delgado, F.J., Crespo J.G., Cava, R., and Ramírez, R. (2012). Changes in microbiology, proteolysis, texture and sensory characteristics of raw goat milk cheeses treated by high-pressure at different stages of maturation, *LWT - Food Science and Technology*, vol. 48, Iss.2, pp. 268-275, doi: 10.1016/j.lwt.2012.03.025
- [6] Diezhandino, I., Fernández, D., Sacristán, N., Combarros-Fuertes, P., Prieto, B., Fresno J.M. (2016). Rheological, textural, colour and sensory characteristics of a Spanish blue cheese (Valdeón cheese), *LWT*, 65(5):1118-1125, <https://doi.org/10.1016/j.lwt.2015.10.003>;
- [7] Gančovska V., Danev, A., Bosakova-Ardenska, A., Panayotov, P., (2019). Blue cheese cut surface evaluation by images analysis: Application of image processing for analysis the mold distribution on cut surface of blue cheese, *CompSysTech '19: Proceedings of the 20th International Conference on Computer Systems and Technologies*, pp.169 – 174, <https://doi.org/10.1145/3345252.3345280>;

- [8] Ganchovska, V., Danev, A., Bosakova-Ardenska, A., Panayotov, P. Kostadinova-Georgieva, L. Boyanova, P. (2021). Application of thresholding algorithms in blue cheese cut surface evaluation, *Journal of Hygienic Engineering and Design*, 33: 22-27;
- [9] Garcia, C.A., Bermúdez, A.A., Arrazola, G. (2018). Mechanical and Viscoelastic Properties of Mozzarella Cheese, *Advance Journal of Food Science and Technology*, 15(SPL):113-116, doi: 10.19026/ajfst.14.5881
- [10] Goh, S.M., Charalambides, M.N., Williams, J.G. (2005). On the mechanics of wire cutting of cheese, *Engineering Fracture Mechanics*, 72(6):931-946, doi: 10.1016/j.engfracmech.2004.07.015
- [11] Hassan, L.K., Saady, S., Saadon F.A. (2020). Utilizing of the guar gum for improving the physiochemical, rheological and sensory properties of low-energy Mozzarella cheese, *Annals of Tropical Medicine and Public Health*, 23(16), doi: 10.36295/ASRO.2020.231622.
- [12] Ionescu, M., Voicu, G., Biris, S.-S. Stefan E.M, Ungureanu, N., Dinca, M. (2016). Determination of some mechanical properties for oilseeds using uniaxial compression tests, *INMATEH – Agricultural Engineering*, 49(2): 71-76.
- [13] Ipate, G., Biris, S.S., Voicu, G., Vladut, V., Zabava, B., Udriou, N.A. and Pihurov M. (2019). Numerical simulation and experimental evaluation of the rheological behaviour of cheese, *Conference: Research people and actual tasks on multidisciplinary sciences*, Lozenec, Bulgaria, 5 p.
- [14] Jelinski, T., Jin Du, C., Sun, D-W., Fornal, J. (2007). Inspection of the distribution and amount of ingredients in pasteur-ized cheese by computer vision. *Journal of food engineering*, 83, pp. 3-9;
- [15] Joyner, H.S., Francis, D., Luzzi, B., Johnson J.R. (2017). The effect of storage temperature on blue cheese mechanical properties *Journal of Texture Studies*. 49(8), <https://doi.org/10.1111/jtxs.12301>;
- [16] Karoui, R. Dufour, É. (2003). Dynamic testing rheology and fluorescence spectroscopy investigations of surface to centre difference in ripened soft cheeses, *International Dairy Journal*, 13(12):973-985, [https://doi.org/10.1016/S0958-6946\(03\)00121-3](https://doi.org/10.1016/S0958-6946(03)00121-3);
- [17] Koutsoumanis, K., Alvarez-Ordóñez, A., Bolton, D., et al., (2022). The efficacy and safety of high-pressure processing of food, *EFSA J*. 20(3): e07128, doi: 10.2903/j.efsa.2022.7128.
- [18] Kulmyrzaev, A., Bertrand, D., Dufour, É. (2008). Characterization of different blue cheeses using a custom-design multispectral imager. *Dairy Science Technology*, *EDP sciences/Springer*, 88, (4-5), pp.537-548
- [19] Kuo, M.I., Wang Y.C., Gunasekaran S. (2000). A viscoelasticity index for cheese meltability evaluation, *Journal of Dairy Science*, 83(3):412-7, [https://doi.org/10.3168/jds.S0022-0302\(00\)74897-1](https://doi.org/10.3168/jds.S0022-0302(00)74897-1);
- [20] Linton, M., Mackle, A.B., Upadhyay, V.K., Kelly, A.L., Patterson, M.F. (2008). The fate of *Listeria monocytogenes* during the manufacture of Camembert-type cheese: A Comparison between raw milk and milk treated with high hydrostatic pressure, *Innov. Food Sci. Emerg. Technol.*, 9:423–428. doi: 10.1016/j.ifset.2008.01.001.
- [21] Najera, A.I., Nieto, S., Barron, L.J.R., Albisu, M.A. (2021). Review of the preservation of hard and semi-hard cheeses: quality and safety, *Int. J. Environ. Res. Public Health*, 18(18): 9789, <https://doi.org/10.3390/ijerph18189789>
- [22] Skordaris, G., Vogiatzis, K., Kakalis, L., Mirisidis I., Paralidou, V., Paralidou, S. (2022). Increasing the life span of tools applied in cheese cutting machines via appropriate micro-blasting, *Coatings*, 12(9):1343, doi: 10.3390/coatings12091343
- [23] Vandenberghe, E., Choucharina, S., Luca, S., Ketelaere, B., Baerdemaeker, J., Claes, J.E. (2013). Spatio-temporal changes of physicochemical parameters during cheese ripening, *Inside Food Symposium*, Leuven, Belgium, 6 pag.
- [24] Venugopal, V., Muthukumarappan, K. (2001). Stress relaxation characteristics of Cheddar cheese, *International Journal of Food Properties*, 4(3):469-484, DOI:10.1081/JFP-100108649.

TRENDS IN THE DEVELOPMENT OF CONSERVATION / ECOLOGICAL AGRICULTURE IN THE CONTEXT OF CURRENT CLIMATE CHANGE – A REVIEW

TENDINȚE ÎN DEZVOLTAREA AGRICULTURII CONSERVATIVE / ECOLOGICE ÎN CONTEXTUL SCHIMBĂRILOR CLIMATICE ACTUALE - O SINTEZĂ

Nicolae-Valentin VLĂDUȚ¹⁾, Atanas ATANASOV^{*2)}, Nicoleta UNGUREANU^{*3)}, Larisa-Victoria IVAȘCU⁴⁾, Lucian-Ionel CIOCA^{5,6)}, Lorena-Diana POPA⁷⁾, Gheorghe MATEI⁸⁾, Sorin BORUZ⁸⁾, Valerian CEREMPEI⁹⁾, Victor ȚÎȚEI¹⁰⁾, Florin NENCIU¹⁾, Oana-Elena MILEA¹⁾, Ștefan DUMITRU¹⁾, Ioan CABA^{*1)}

¹⁾ INMA Bucharest / Romania; ²⁾ University of Ruse / Bulgaria; ³⁾ National University of Science and Technology Politehnica Bucharest / Romania; ⁴⁾ P.U. Timișoara / Romania; ⁵⁾ Lucian Blaga University of Sibiu / Romania; ⁶⁾ Academy of Romanian Scientists / Romania;

⁷⁾ ARDS Secuieni / Romania; ⁸⁾ University of Craiova / Romania; ⁹⁾ State Agrarian University of Moldova / Moldova;

¹⁰⁾ Alexandru Ciubotaru National Botanical Garden (Institute) of Moldova State University, Chișinău / Moldova

*E-mail corresponding author: aatanasov@ru.acad.ru; nicoletaung@yahoo.com; inmatm_caba@yahoo.com

DOI: <https://doi.org/10.35633/inmateh-74-86>

Keywords: *climate change, agroecology, sustainable farming, regenerative agriculture, carbon sequestration, teledetection*

ABSTRACT

In the context of severe climate change over the past 20 years, which has led to reduced rainfall and reduced crop yields, identifying solutions to meet these challenges has become a priority for agricultural researchers. Thus, conservation and ecological, organic farming practices have emerged, which can mitigate and even improve crop productivity, even in these harsh conditions for agriculture. This paper is a synthesis of 433 papers published worldwide (Europe, North America, South America, Africa, Asia and Australia) and analyzes how conservation and organic farming practices have influenced the increase in soil quality and health through: no-tillage, covering land with agricultural residues, crop rotation etc.

REZUMAT

În condițiile schimbărilor climatice accentuate din ultimii 20 ani, care au condus la reducerea precipitațiilor și scăderea randamentului culturilor, identificarea unor soluții care să răspundă acestor provocări a devenit o prioritate pentru cercetătorii din domeniul agricol. Astfel, au apărut practicile agriculturii conservative și ecologice, organice, care pot atenua și chiar îmbunătăți productivitatea culturilor, chiar în aceste condiții vitrege pentru agricultură. Această lucrare reprezintă o sinteză a 433 lucrări publicate în întreaga lume (Europa, America de Nord, America de Sud, Africa, Asia și Australia) și analizează modul în care practicile agriculturii conservative și ecologice au influențat creșterea calității și sănătății solului prin: lucrări no-tillage, acoperirea terenurilor cu reziduuri din agricultură, rotația culturilor etc.

INTRODUCTION

Agriculture plays a crucial role in sustaining life on Earth, being the foundation of global food security and local economies. By providing the resources needed for human and animal nutrition, agriculture supports not only daily life but also economic development, accounting for a significant share of the GDP of many countries, especially in rural regions. In addition, the agricultural sector supports social cohesion and the sustainable development of communities, being of vital importance for our collective future.

On the other hand, agriculture has a direct impact on the environment, being responsible for the use of natural resources such as water, soil and energy. In addition, agriculture contributes significantly to global greenhouse gas emissions (GES), not only through methane and nitrous oxide, but also through land use and emissions from industry and transport.

Estimates of agriculture's contribution to global emissions may vary depending on the methodologies used and data sources. According to data provided by the United States Environmental Protection Agency (EPA), the "Agriculture, Forestry, and Other Land Use" sector was responsible for approximately 22% of global GES in 2019, from agricultural activities, such as crop cultivation and animal husbandry, as well as from deforestation and other land use changes (US EPA, 2019). According to the Sixth Assessment Report of the Intergovernmental Panel on Climate Change, in 2022, agriculture was responsible for 10.8% of GES in the European Union (IPCC, 2023).

The Intergovernmental Panel on Climate Change has highlighted the importance of farmers implementing climate change mitigation measures to help reduce GES (Van Wyngaarden et al., 2024).

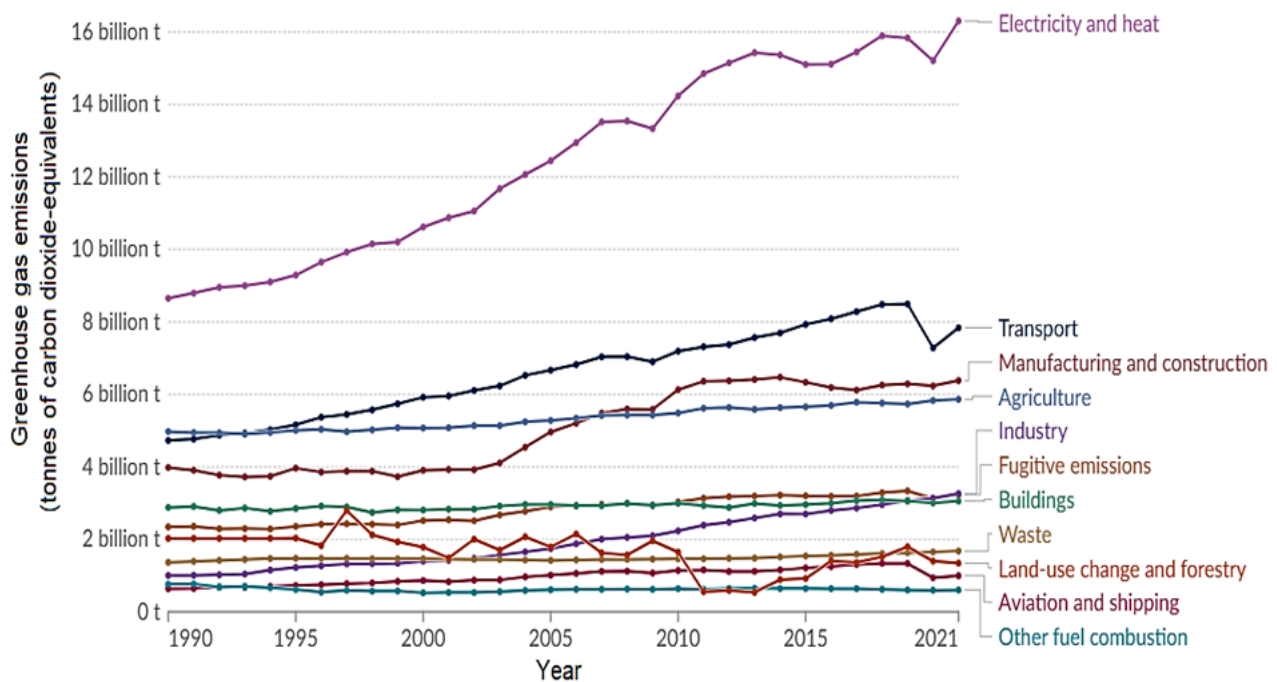


Fig. 1 – Greenhouse gas emissions by sector, worldwide (*Our World in Data, 2024a*)

✓ The impact of climate change on water availability and quality

Agriculture is the largest consumer of water globally. The irrigation sector is responsible for more than 70% of global water withdrawals from surface and groundwater sources (*Ungureanu et al., 2020b*), but this percentage can vary by region and season. Irrigation plays a critical role in increasing crop yields, particularly in arid and semi-arid regions of Asia, but also in developed countries (*Serra et al., 2023*). Traditional pollutants that could exceed irrigation water quality criteria include particulate matter, certain toxic metals (such as Cd, Cu, and Zn), synthetic organic chemicals (such as agrochemicals and polycyclic aromatic hydrocarbons), and waterborne pathogens (*Deng et al., 2021*).

Drought is one of the most severe types of natural disasters and one of the most significant consequences of climate change on ecosystems and human populations (*Zeng et al., 2022*). In recent years, concerns about the risks of hydrological drought and the reliability of irrigation water supplies have increased, especially in regions with Mediterranean climates (*Gómez-Limón et al., 2023*). Annual global economic losses caused by drought are estimated at over \$6 trillion, which represents about one-third of the total impact of natural disasters.

In many regions of the world, including the southern hemisphere, climate change is causing changes in precipitation, leading to a decrease in the total amount of water available and a change in the timing of its occurrence (*Norwood, 1994; Nielsen et al., 2005; Torres et al., 2019*). Global warming is also affecting Arctic regions through accelerated melting of glaciers and sea ice, which contributes to global sea level rise. These changes have major implications for local ecosystems and can influence global ocean and atmospheric circulations (*Yamanouchi et al., 2019*). In mountain regions, cryosphere water resources, originating from melting glaciers and snow, are threatened, which represent an important source of freshwater for downstream regions, especially in arid and semi-arid areas. This water contributes to maintaining river flows during dry periods, thus supporting agriculture, drinking water supply and hydropower production. Rapid glacier retreat, attributed to human-induced climate change, is a global phenomenon observed, and projections indicate a significant loss of glacial mass by the end of the 21st century, affecting mountain regions such as Central Europe, the Caucasus, Mountain Asia and the Southern Andes (*Jones et al., 2019*).

Climate change may also threaten the viability of fisheries, with significant changes in ocean conditions predicted, including increases in sea surface temperatures, water acidification, changes in ocean currents, weather patterns and ecosystems (*Fatima et al., 2023*). Microplastic pollution poses a significant threat to aquatic and terrestrial ecosystems, affecting the health of organisms and the entire food chain. Even if microplastics are effectively removed in sewage treatment plants, most of them end up in the generated sludge, which is then used as fertilizer on agricultural land, leading to soil contamination (*Lofty et al., 2022*).

Research suggests that in areas where lupins are grown there is an increased risk of contamination of drainage water and soil with indole and quinolizidine alkaloids, chemical compounds produced by this plant (Hama *et al.*, 2023).

✓ Degradation of agricultural land

Physical processes of soil degradation include deterioration of soil structure, crusting, compaction, erosion and desertification. Chemical processes include leaching, acidification, salinization and pollution. Biological processes of soil degradation include carbon reduction and decline in soil biodiversity.

Ongoing land degradation directly affects approximately 25% of the Earth's surface. Recent research suggests that approximately 2 billion hectares of land are severely degraded (some of them irreversibly), leading to serious damage to local ecologies and contributing significantly to climate change in recent years. Globally, at least one in three people is affected by land degradation in one way or another, and approximately 75 billion tons of soil material are lost each year as a result of this degradation. The European Commission's Soil and Food Mission Committee recently launched the report "Caring for Soil is Caring for Life", which highlighted that 60–70% of soils in the European Union are currently in an unhealthy state (Ungureanu *et al.*, 2024).

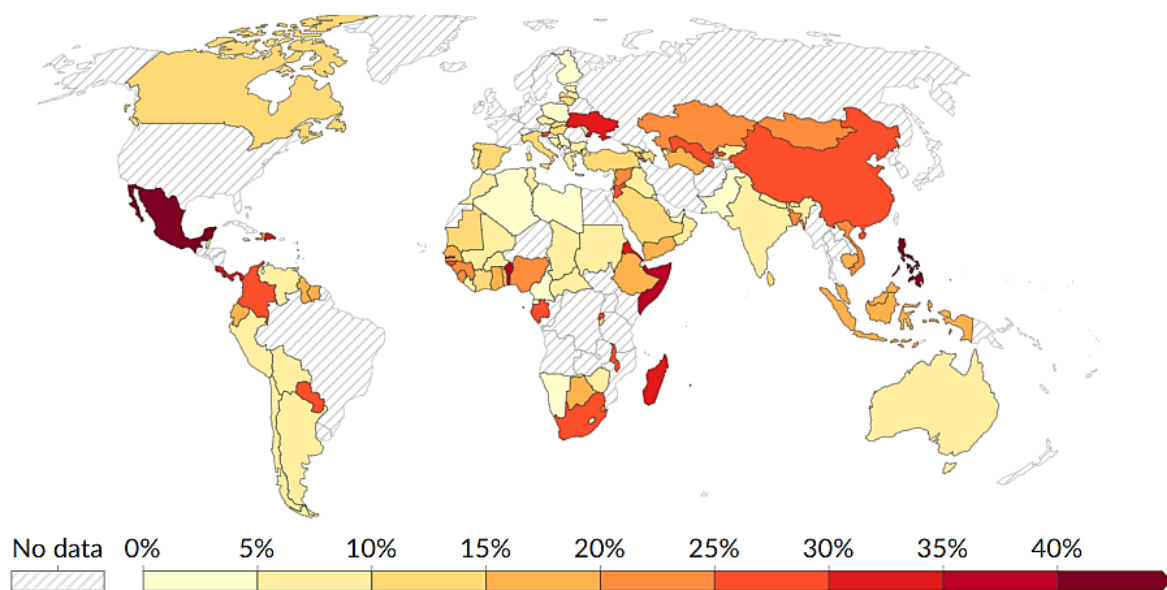


Fig. 2 – Proportion of land that is degraded over total land area (%), worldwide (Our World in Data, 2024b)

Drought can affect the structural stability of the soil, destroying macroaggregates and reducing the protection of organic matter. This effect is evident in Mediterranean grasslands, especially in winter, when agricultural activities are stopped, and the soil is exposed to extreme dryness. The decomposition of aggregates allows microorganisms to access organic carbon, a process that increases CO₂ emissions and leads to the loss of organic matter, affecting the carbon cycle and reducing the soil's capacity to sequester carbon (Quintana *et al.*, 2023).

Erosion of fertile soil has a negative impact on land productivity and the environment, affecting soil structure and vegetation, through the loss of essential nutrients, such as carbon, nitrogen and phosphorus. Soil erosion also influences the global carbon cycle and can cause climate change (Feeney *et al.*, 2022).

Grasslands cover approximately 40% of the Earth's land surface and 70% of agricultural land, playing an important role in storing soil organic carbon. Intensive grazing practices, which lead to overexploitation of vegetation and soil compaction, can prevent carbon sequestration and increase emissions of the greenhouse gases methane and nitrous oxide. In addition, high grazing intensity can reduce plant productivity, favoring fewer valuable species and affecting soil fauna (Abdalla *et al.*, 2018). For example, intensively managed grasslands in the Netherlands are affected by high nitrogen emissions from intensive agriculture, which harms biodiversity and water quality. This has led to a "nitrogen crisis", which requires a political response in the context of farmer protests. Changing agricultural practices to restore biodiversity is complex, involving economic and governmental factors. In this sense, a better understanding of farmers' behavior could improve the efficiency of agri-environmental governance (Westerink *et al.*, 2024).

✓ **Pollution with chemical fertilizers and chemical phytosanitary products**

The intensive use of chemical fertilizers in agriculture has become a widespread practice, with the aim of increasing crop productivity. However, the environmental side effects are significant and complex. In the soil, excessive accumulation of nitrogen and phosphorus from fertilizers can lead to nutritional imbalances, acidification and structural degradation. These factors affect the soil's ability to support microbial life essential for natural fertility. Over time, soils become less productive and more vulnerable to erosion.

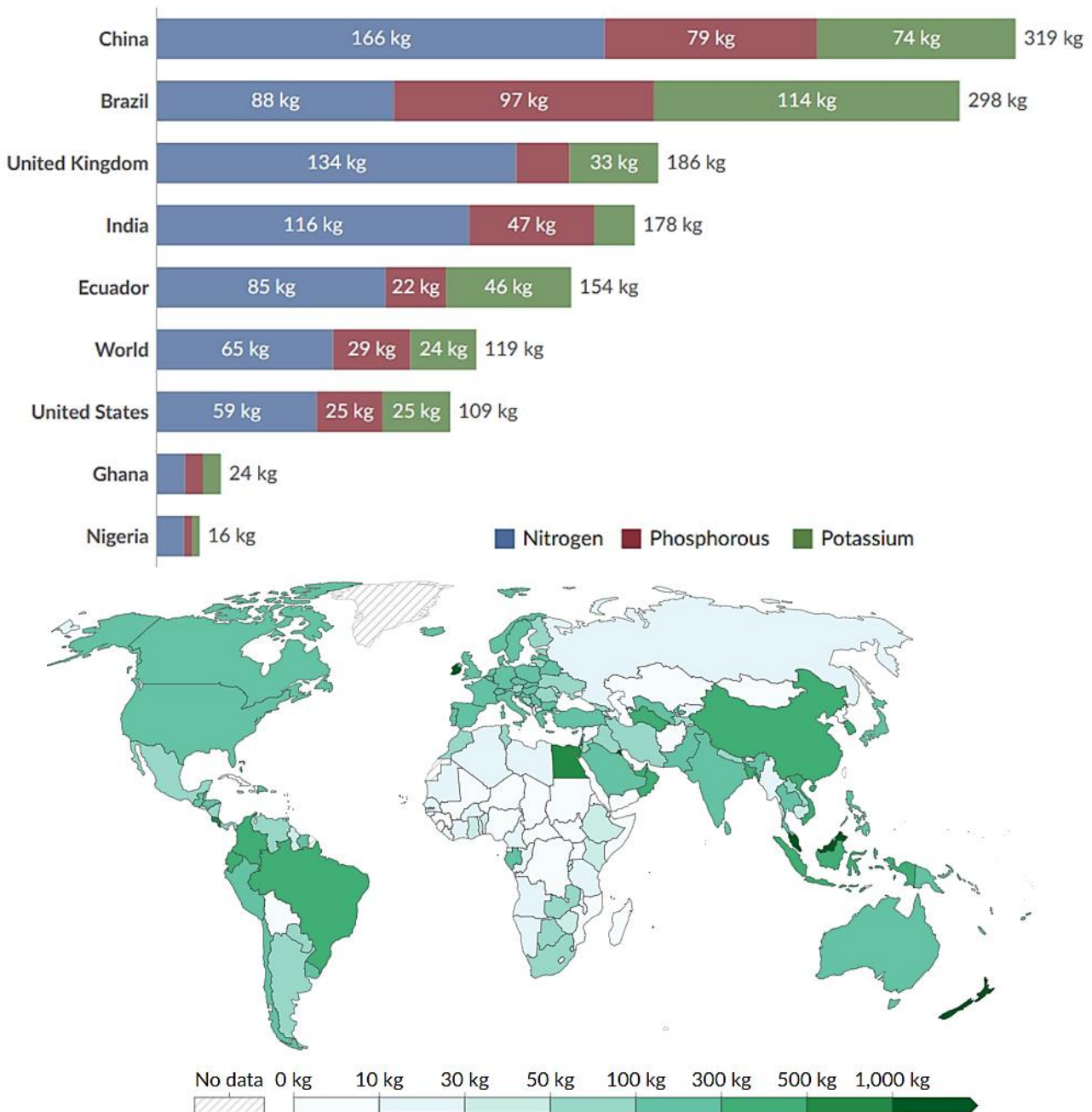


Fig. 3 – Fertilizers use per hectare of arable land in 2022, worldwide (Our World in Data, 2024c)
 (Fertilizer products cover nitrogenous, potash, and phosphate fertilizers, including ground rock phosphate. Animal and plant manures are not included. Application rates are measured in kilograms per hectare)

In addition to the impact on the soil, agricultural activities influence the quality of surface water and groundwater through sources of NO₃ pollution originating from synthetic NH₄⁺ fertilizers together with organic nitrogen in the soil (Li et al., 2022). NO₃ contamination can lead to risks of acidification and eutrophication, with negative impacts on the aquatic environment and toxic effects on animals, and in humans it can cause conditions such as methemoglobinemia and cancer (Kruisdijk, 2022).

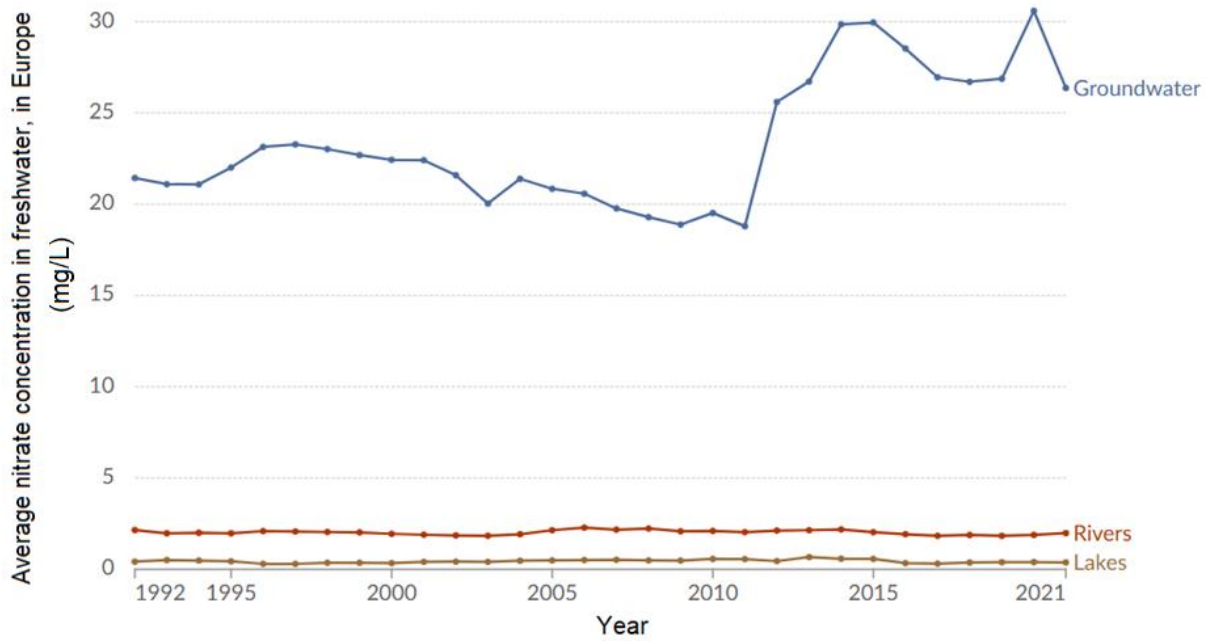


Fig. 4 – Average nitrate concentration in European freshwaters (*Our World in Data, 2024c*)

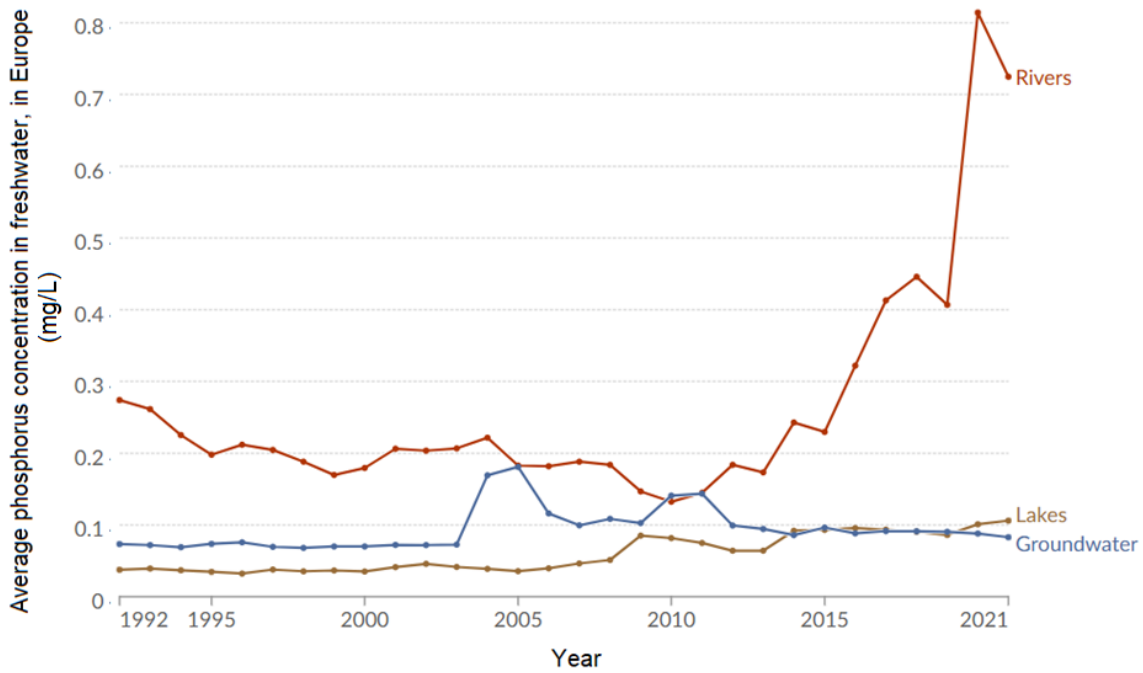


Fig. 5 – Average phosphorus concentration in European freshwaters (*Our World in Data, 2024c*)

In the air, the use of nitrogen-based fertilizers contributes to greenhouse gas emissions, such as nitrous oxide, which is about 300 times more potent than carbon dioxide. These emissions amplify climate change, and volatile particles also affect air quality, with a direct impact on human health. Chemical fertilizers reduce the diversity of wild plants and affect the natural habitat of pollinating insects. These changes disrupt food chains and the balance of ecosystems, reducing their ability to self-regulate

An extensive analysis of the impact of fertilizers on the environment, crops and human health was recently presented by *Ungureanu et al. (2024)*, concluding that a more sustainable approach, such as the use of biofertilizers and organic farming practices, could help reduce these harmful effects and protect the environment for future generations.

Herbicides, pesticides and fungicides are essential in protecting crops from pests and diseases, contributing significantly to increasing agricultural production and ensuring food security. These chemicals help to quickly and effectively control problems that can affect crops, thereby increasing yields and reducing losses. However, the long-term use of these products can have negative effects on the environment and human health, such as soil and water contamination, the development of pest resistance and the reduction of biodiversity.

Therefore, it is crucial to implement sustainable management strategies and use these substances responsibly to minimize their negative impacts.

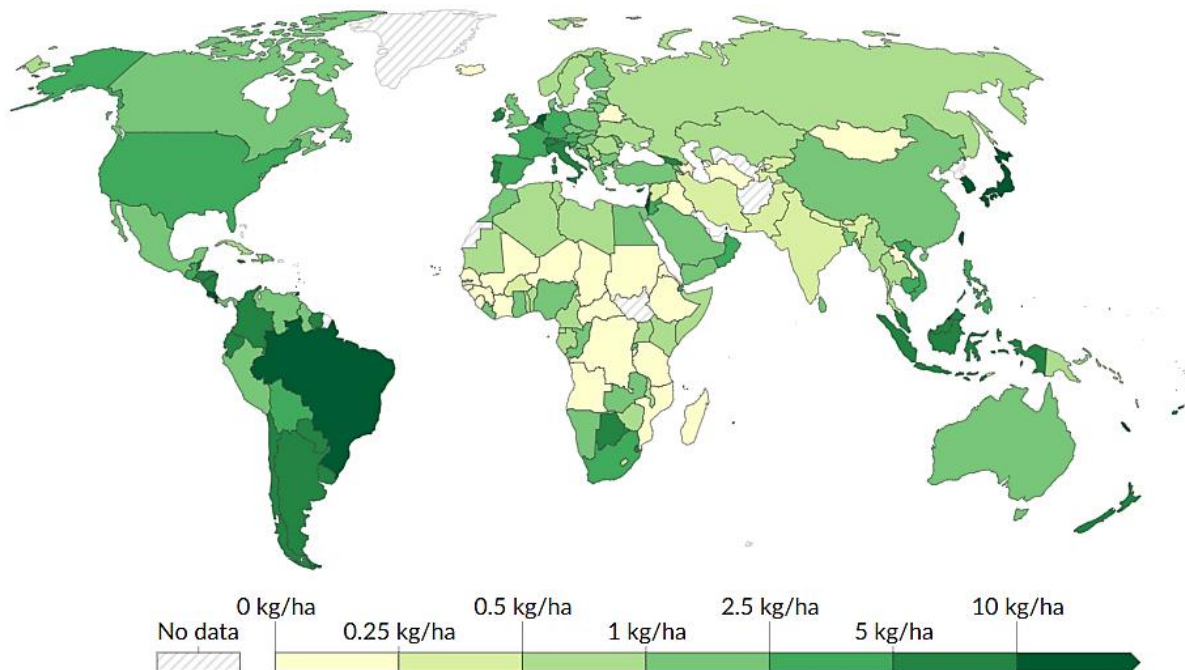


Fig. 6 – Pesticides use per hectare of cropland arable land in 2021, worldwide (Our World in Data, 2024d)

A major problem for farmers in any crop production system is weeds, which ultimately lead to reduced productivity and profitability. After the 1950s, most weed management strategies in developed countries were based on chemical (classical) weed control because it is the simplest and most effective method. Herbicides have been, along with mechanization and plant breeding, one of the cornerstones of modern high-yield agriculture (Liebman *et al.*, 2003). However, over time, weed resistance to herbicide chemicals has increased significantly, leading to an increase in the number of treatments and, implicitly, to excessive dependence on them. On the other hand, major problems have begun to arise on soil quality and health as a result of the excessive use of these substances over a long period of time (decades), which also affects human health (Sharma *et al.*, 2021).

Some studies have revealed that chemical compounds used to prevent crop diseases, such as fungicides, can negatively influence the health of bees by contaminating pollen and nectar, their essential food resources, causing physiological and behavioral problems. The degree of exposure varies depending on the species and biological characteristics of the bees (Zioga *et al.*, 2023).

The application of insecticides such as chlorpyrifos and carbaryl near homes can contribute to their presence in dust, with higher concentrations at distances of 2-4 km, and other chemicals such as cyfluthrin and phosmet have been detected more frequently in dust inside homes located up to 4 km from agricultural areas (Madrigal *et al.*, 2023). In addition, herbicide residues (such as triasulfuron, chloresulfuron, clopyralid and pyroxasulfone) significantly reduce nodulation and nitrogen fixation, affecting root and stem growth. Even at very low concentrations, triasulfuron can have negative effects on several legume crops (Yates *et al.*, 2024).

In view of the above, but also in the global context marked by climate change, pollution, rapid population growth, technological innovations and societal transformations, the adaptation of agriculture in the coming decades to new challenges and the implementation of innovative technologies are crucial for maintaining a balance between human needs and environmental protection (Soane *et al.*, 2012; Debonne *et al.*, 2022). The doubling of global food demand by 2050 brings huge challenges for the sustainability of food production, but especially of terrestrial and aquatic ecosystems and the services they provide to society (Tilman *et al.*, 2002).

For these reasons, farmers are looking for new, more efficient and productive methods, practicing intensive agriculture to meet the growing demand for products, which may lead to irreversible changes on the Earth's surface in the coming decades. To combat climate change and ensure environmental protection while improving crop yields, food security and human health, incentives and policies must be sought that ensure the sustainability of agriculture and ecosystem services (Palm *et al.*, 2014; Gonzalez-Sanchez *et al.*, 2016).

Given these pressing environmental challenges, it becomes increasingly clear that conventional agricultural practices must evolve toward more sustainable alternatives. In this context, conservation and ecological agriculture emerge as viable solutions, offering methods that not only mitigate the negative impact of farming but also promote long-term soil health, biodiversity, and climate resilience. The following sections explore the principles, benefits, and challenges of these approaches, highlighting their potential to transform modern agriculture.

CONSERVATION AGRICULTURE

Conservation agriculture began as a response to the Dust Bowl crisis of the 1930s and 1940s in the United States, which was marked by extensive soil erosion and agricultural destruction throughout the American Great Plains. This led to a paradigm shift toward farming methods that put an emphasis on soil health, reduce soil disturbance, and improve long-term ecological resilience (*Román-Vázquez et al., 2025*).

In the last 20–30 years, climate change has been increasingly acute, and its effects on agriculture have had a significant impact from year to year, especially due to prolonged droughts, culminating in disastrous effects in recent years, which led to the partial or almost total collapse of agricultural production (*Popescu et al., 2022*). Conservation agriculture has gained momentum especially in the last 20 years, with the area cultivated in the conservation system increasing from year to year, largely due to the decrease in annual rainfall (*Kassam et al., 2009*), and there is also a fundamental change in the thinking of the production system.

Conservation agriculture is a way to increase the competitiveness of an agricultural farm by reducing production costs, while adapting the work carried out to climate change, sustainable soil and water management (*Stagnari et al., 2009; Verhulst et al., 2010*).

Conservation agriculture is a more sustainable and environmentally friendly management system for growing various crops (*Hobbs et al., 2007; Thomas et al., 1990*). Through conservation agriculture, "sustainable agricultural systems" are used, which, when implemented, lead (over time) to the restoration of soil fertility (*Aguilera et al., 2021*). By permanently covering the soil surface with a layer of plants and practicing a rotation with a wide diversity of the basic crops grown, one can contribute to the conservation of soil and natural resources in a few years (*Gabriel et al., 2013*).

One of the measures with a long-term effect in mitigating climate change may be the application of conservation agriculture in areas strongly affected by successive droughts (and not only), because this type of agriculture has numerous advantages, including:

- it increases soil permeability for water and improves overall soil drainage;
- it reduces soil erosion; plant residues remaining on the soil surface contribute to moisture conservation, the growth of soil fauna and flora and improved productivity (*Fageria et al., 2005*);
- soil structure is restored, and surface and deep compaction are reduced (*Vlăduț et al., 2017; Ungureanu et al., 2017*);
- it increases the organic matter content of the soil, and in the long term, increases fertility (*Robert and Chan, 1990; Popescu et al., 2022*);
- the quality of groundwater and surface water is maintained (*Cârdei et al., 2021*);
- air quality is maintained by reducing fossil fuel emissions (diesel) used for classic energy-intensive works and by reducing carbon released into the atmosphere (being fixed by increasing organic matter in the soil);
- soil work time is reduced by 2-4 times;
- fuel consumption per unit area is reduced by 30–50%;
- the need for agricultural machinery per unit area is reduced (*Ungureanu et al., 2016*).

Given that agriculture will need to produce a greater quantity of food in the coming years, sustainably, using less agricultural land, by making natural resources more efficient, with low environmental impact, to meet the ever-increasing demands of the ever-growing population, the promotion and adoption of management systems of conservation agriculture can help achieve this objective (*Braim et al., 1992*). However, financial institutions are often reluctant to promote agricultural projects that use this conservation system (*Dauphin, 2003*). The promotion of conservation agriculture focuses on the development of alternative crops, crop rotation and residue management (*Paulitz et al., 2010*). Conservation agriculture plays an important role in sustainable agriculture, aiming to achieve minimal soil disturbance (no-till), to achieve continuous soil coverage (with mulch) combined with crop rotation, so as to function as a more sustainable cultivation system for the future.

Climatic conditions, the date of crop establishment, plant density per hectare and agronomic management practices affect the yields obtained, research carried out on different tillage techniques using conservation soil cultivation methods has highlighted that the yield varies depending on the type of plant cultivated before the crop to be established in a conservation system (*Di Ciocco et al., 2008*) and in addition, when residues from previous crops are used as mulch, higher yields are obtained (*Nematzadeh et al., 2022*), these can influence both the fungal communities in conventionally cultivated soils and those in the no-tillage system (*Beare et al., 1993*), including carbon sequestration (*Duiker and Lal, 2002; Franzluebbers, 2010; Gonzalez-Sanchez et al., 2012*). At the same time, the implementation of integrated and sustainable livestock systems is a priority, considering the adaptation of agricultural practices to climate change. Particular attention is recently paid to the potential of dry biomass crops in areas where there is demand for the biofuel industry, thus contributing to an economic and ecological balance.

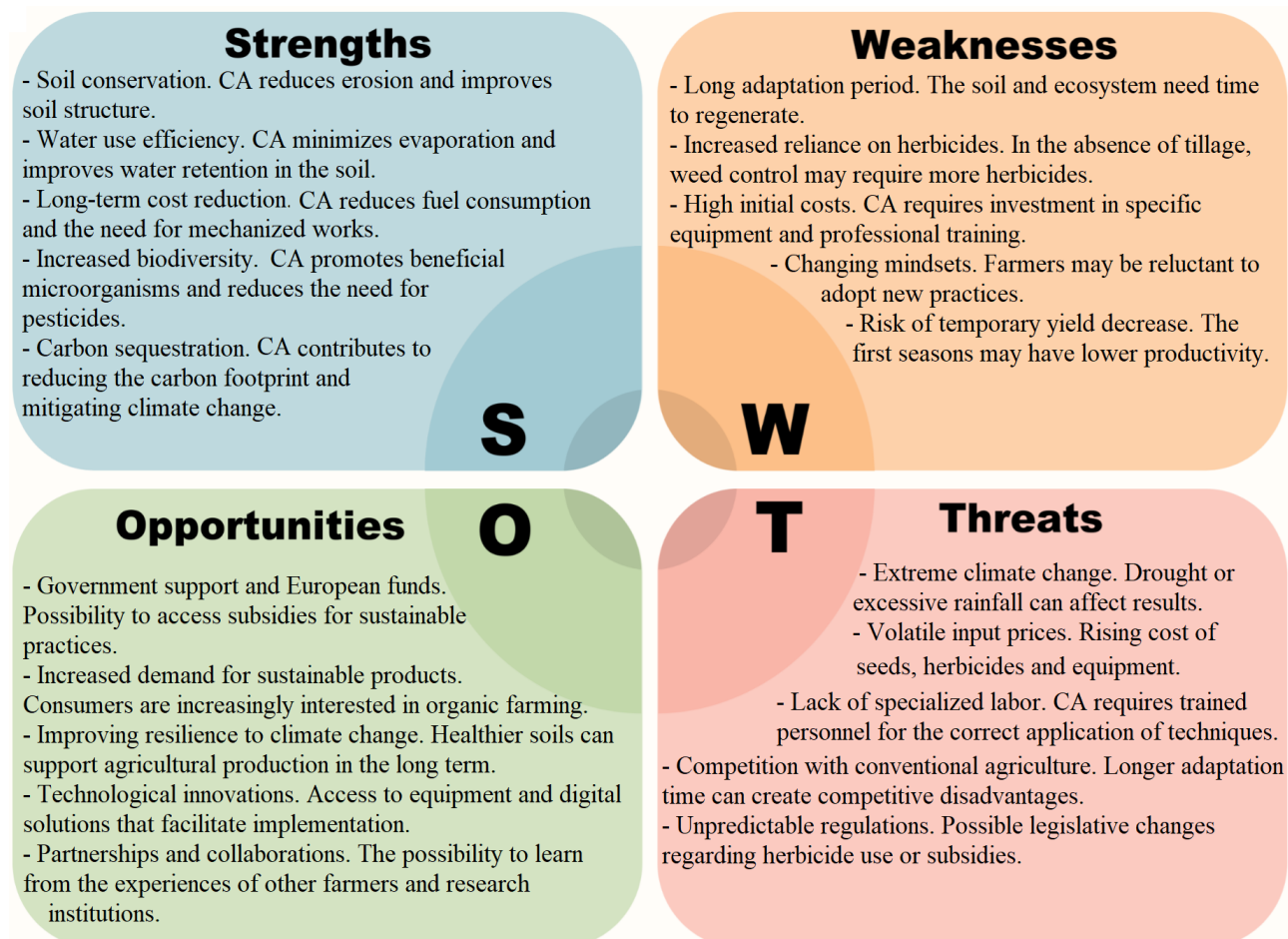


Fig. 7 – SWOT analysis of implementing conservation agriculture

PRINCIPLES OF CONSERVATION AGRICULTURE

Conservation agriculture is based on a series of practices designed to protect and improve soil health while reducing negative environmental impacts. This approach aims to maintain natural fertility, increase crop resilience to climate change, and optimize the resources used in agricultural production. By applying specific principles, conservation agriculture contributes to a more sustainable and efficient agriculture in the long term. There are three core principles in conservation agriculture (*Ruiz-Espinosa et al., 2024*): conservation tillage by minimum soil disturbance (soil disturbed area < 15 cm wide or 24% of the cropping area); permanent soil organic cover (>30% soil cover with cover crops, crop residues or mulch); crop diversification (includes a lot of break crops or non-cereal crops, particularly legumes).

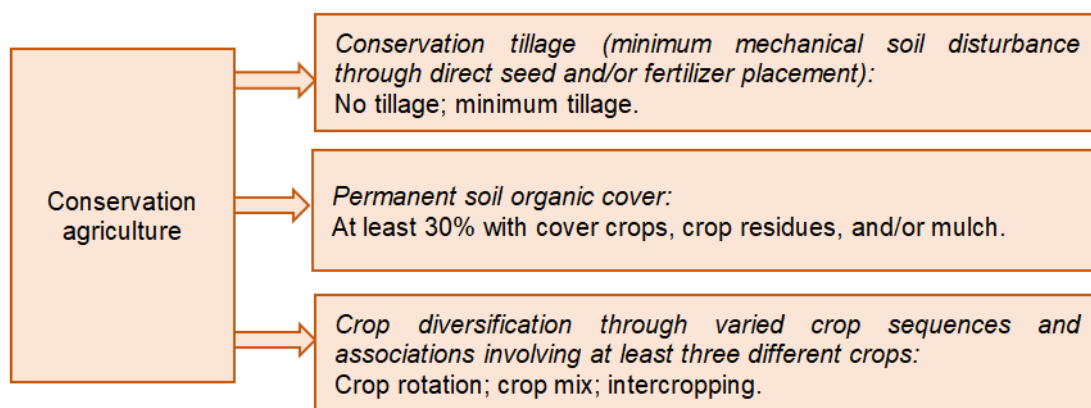


Fig. 8 – Three core principles of conservation agriculture

The following are the main principles underlying conservation agriculture.

✓ **Storage of organic carbon in the soil**

Given the continuous population growth and the events caused by climate change in recent years, more and more studies are focusing on increasing the capacity of agriculture to store (sequester) organic carbon in the soil, carbon having a major impact on the physical and chemical properties of the soil, respectively its yield (Page et al., 2020).

Carbon storage in agricultural soil is essential for climate change mitigation, contributing to reducing the concentration of carbon dioxide in the atmosphere. At the same time, it improves soil fertility, water retention capacity and the resilience of agricultural ecosystems, supporting long-term sustainable production.

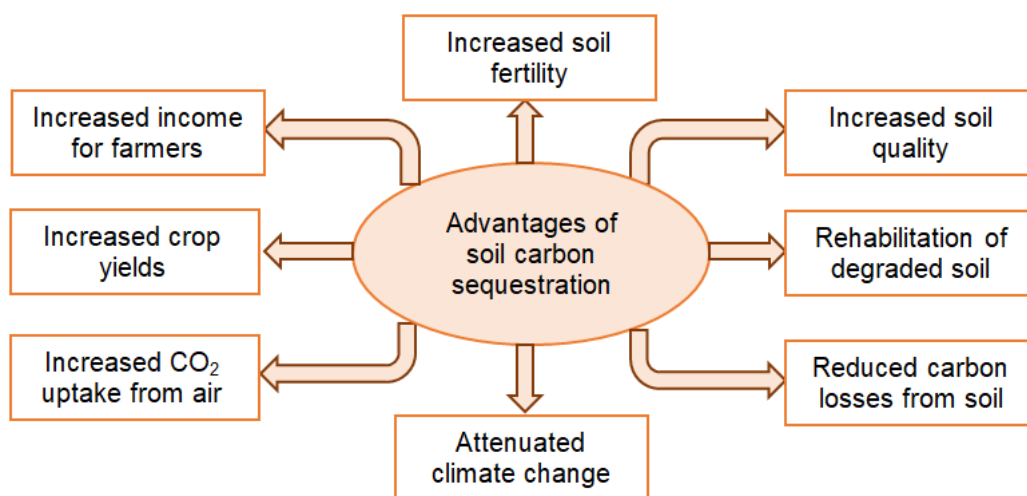


Fig. 9 – The advantages of carbon sequestration practices

Since Mediterranean lands are seasonally dry agroecosystems with low soil organic carbon content and high risk of land degradation and desertification, urgent measures are required to manage soil carbon, thus mitigating climate change and adapting Mediterranean cropping systems to practices that support these measures (Steinbach and Alvarez, 2006; Aguilera et al., 2013; Garcia-Palacios et al., 2019), of which conservation tillage practices (no-tillage and minimum till) did not have high effects on degradation but carbon sequestration was good and on the other hand the use of practices that combine the use of organic amendments with cover crops or conservation tillage had very good performances in carbon fixation (Luo et al., 2010).

A solution for storing soil organic carbon using nitrogen fertilizers and conservation tillage was studied by Alvarez (2006), field trials conducted worldwide (137 locations and 161 sites) tracking the impact of management practices on carbon sequestration. The model used considered the following independent variables: cumulative nitrogen fertilizer rate; rainfall, temperature, soil texture and crop intensity index and found that carbon sequestration increased as more nitrogen was applied to the system and as rainfall or crop intensity increased, and in areas with higher average temperatures and fine-textured soils, carbon

sequestration decreased. Carbon sequestration when conservation tillage practices were applied was independent of climate, soil texture or crop rotation (Angers *et al.*, 1995; Bayer *et al.*, 2006b).

Agricultural management also impacts soil organic carbon storage, and in wet and dry climates of temperate and tropical regions (USA), estimates of its impact have been obtained through a centralized carbon approach that tracks the impact of long-term cultivation, the removal of a portion of land from crop production, modification of tillage management, and soil carbon input through modification of harvesting practices (Ogle *et al.*, 2004; Tarkalson *et al.*, 2006).

The impact of tillage practices on organic carbon and nitrogen sequestration was studied on cold and wet soils in eastern Canada (Angers *et al.*, 1997) and the results highlighted the fact that the storage capacity of soil organic matter depends on (Bayer *et al.*, 2006a): soil type, climate and agricultural management practices (Teliban *et al.*, 2022), while also determining the effects of different tillage systems on the storage of organic C and N, on different soils, for corn and cereal crops. It was thus found that under the conditions of the studied area, crop production and agricultural waste residues were not affected by tillage, with reduced tillage systems not having a significant impact on the storage of soil organic matter in the first years of the study.

✓ **Conserving water in the soil**

Soil water conservation is a key principle of conservation agriculture, with a direct impact on the efficiency of natural resource use and the long-term sustainability of agricultural systems. Through practices such as reduced tillage and maintaining a layer of crop residues, conservation agriculture helps improve soil structure, preventing excessive evaporation and facilitating water retention in the soil. These measures not only reduce the need for supplemental irrigation, but also help protect the soil from erosion, thus ensuring more efficient and sustainable management of water resources in agriculture.

Understanding the role of soil management practices in increasing water use efficiency has been studied very often in recent years, as there is a high concern about the availability of water resources in irrigated agriculture and beyond (Ungureanu *et al.*, 2020b), and there is increased interest in understanding how to improve water use efficiency, namely how agricultural systems can be modified to be more efficient (Hatfield *et al.*, 2001). Thus, soil management practices can influence evapotranspiration by modifying the energy and water available in the soil profile or the exchange rate between the soil and the atmosphere.

In humid and semi-arid temperate regions, there has been a need to conserve soil moisture and reduce soil erosion through conservation tillage practices that are mainly based on covering the soil surface with residues (Carter, 1994; Montgomery, 2007; Verhulst *et al.*, 2011), respectively evaluating the potential for managing soil aggregation for storing and sequestering organic matter (Angers and Carter, 1995; Du *et al.*, 2017). The most important advantages of conservation tillage practices in humid climates are their continuity of living soil cover (especially during non-crop periods), the use of mulches, the incorporation of residues, and the speed and efficiency of crop establishment. In addition to their ability to conserve soil, conservation practices in humid regions must also consider the sustainability of the agricultural system in terms of energy conservation and nutrient management.

✓ **Crop rotation**

Although crop rotation has been used since ancient times, in the 1950–1960's it was found that chemical fertilizers and pesticides could largely replace this crop rotation without major yield losses, but later, based on more in-depth studies, it was found that crop rotation still has its role, because in the long term it increases yield and profit and allows for sustained production (Bullock, 1992; Karlen *et al.*, 1994; Waldhoff *et al.*, 2017; Chamberlain *et al.*, 2020).

Crop rotation is an essential practice in conservation and organic agriculture, helping to improve soil health, reduce erosion and limit the proliferation of weeds and pests. Diversified crop rotation helps maintain soil fertility and optimize nutrient cycles, thus reducing dependence on chemical inputs and promoting long-term sustainability.

The impact of tillage combined with crop rotation on soil carbon dynamics and storage has been a longstanding research focus for agricultural specialists (Huggins *et al.*, 2007), as soil organic carbon levels are closely linked to both cropping systems and the intensity of soil disturbance. Reduced tillage and diversified crop rotations have been shown to enhance carbon sequestration by minimizing organic matter decomposition and promoting microbial activity. Understanding these interactions is essential for developing sustainable agricultural practices that improve soil health and mitigate climate change.

✓ Use of cover crops and crop residue management

The use of cover crops has grown rapidly in the last 20 years, and is closely linked to climate change (Kaye *et al.*, 2017), as they have the potential to reduce erosion, fix atmospheric nitrogen, reduce nitrogen runoff and improve soil health. Soil health measures, such as increasing soil cover, reducing tillage and soil conservation practices (especially no-till or strip-till) (van Bruggen *et al.*, 2006), used in combination with soil conservation practices (crop rotations for soil conservation and cover crops), can lead to a number of benefits such as: increased agricultural productivity, increased drought resistance and a better environmental impact (Panigrahy and Sharma, 1997; Moraru *et al.*, 2013; Claassen *et al.*, 2018).

Using field-level data, new tillage practices could be adopted without disturbing the soil, partially or completely eliminating tillage operations. This allowed an assessment of tillage intensity (STIR, for mulching) as well as adoption rates for practices that affect soil cover – including cover crops, soil conservation crop rotations, double cropping, fencing and residue harvesting, or grazing (Sun *et al.*, 2019).

Crop residues have several important functions in conservation agriculture, the most important of which are: preserving soil moisture, restoring soil organic carbon and preventing erosion, and the degree of residue coverage on the soil surface highlights the result of the intensity of soil work and crop management practices (Hively *et al.*, 2018). Management of crop residues is an integral part of many soil conservation systems and at the same time, one of the solutions for reducing soil erosion and increasing the percentage of organic carbon in the soil. Through appropriate management of crop residues, positive effects on agricultural production can be achieved, since they (mulch, etc.) have positive effects on plant growth, weed reduction, soil conservation and the environment (Mesgaran *et al.*, 2017). Maintaining straw on the soil is a widespread solution because it is an environmentally friendly practice for managing carbon sequestration in agricultural ecosystems (Liu *et al.*, 2014), with straw return being an effective way to increase soil organic carbon accumulation, soil quality and crop yield (Radford and Thornton, 2011).

Although methods have been sought and various methodologies have been developed to allow a rapid, accurate and inexpensive assessment of the degree of soil cover with plant residues, this has not yet been fully achieved. Due to the fact that classical methods for quantifying crop residue cover are only partially adequate for characterizing the spatial variability of residue cover in fields and over large areas, Daughtry *et al.* (2005) evaluated several spectral indices for measuring crop residue cover using remote sensing (hyperspectral ground and aerial data), aiming to classify the intensity of soil work in agricultural lands based on crop residue cover. Authors Uri (2001) and Daughtry and Hunt (2008) conducted research to determine the effects of water content on remote estimates of crop residue cover, proposing a method to mitigate the effects of water content on remote estimates of crop residue cover, using advanced multispectral or hyperspectral imaging systems.

Satellite imagery is increasingly being used to estimate crop residue coverage using Landsat residue indices. A new normalized difference residue index (NDRI) was evaluated using multiple image data from 2005–2006 on soils in the state of Iowa (USA), which were processed using an automated method for field boundary delineation (Gelder *et al.*, 2009). Another method for modeling and mapping crop residue was based on the use of Landsat, ALI, Hyperion (Galloza *et al.*, 2013).

Gao *et al.* (2020) developed a novel Within-Season Termination (WIST) algorithm to map cover crop termination dates using imagery from the Vegetation and Environment Monitoring New Micro-Satellite (VEN μ S). Another method for mapping crop residue and tillage intensity is the use of shortwave infrared residue indices using the WorldView-3 satellite, which is a space-based platform for collecting narrowband SWIR reflectance images capable of measuring the absorption characteristics of cellulose and lignin. Images acquired with the WorldView-3 satellite allow for SWIR reflectance measurements that demonstrate the utility of clearly mapping crop residue cover after harvest (Hively *et al.*, 2018).

The use of cover crops and living mulches is one of the basic works in conservation agriculture, as they can bring many benefits, which is why there is an increased interest in annual winter cover crops (e.g. winter rye and fescue), for soil cover and soil erosion control (Hartwig and Ammon, 2017), because the integration of these cover crops in a relay cropping / over-seeding / inter-seeding / double cropping system can provide and conserve nitrogen (Zhou *et al.*, 2018) for subsequent cereal crops, respectively reduce soil erosion, weed pressure and increase the organic matter content in the soil (Hartwig and Hoffman, 1975), knowing that no-tillage cultivation practices can result in better soil aggregation (higher levels of organic matter), compared to conventional practices (Beare *et al.*, 1994).

Fescue has an increased availability of nitrogen for subsequent crops and increases soil organic matter, improving soil structure and water infiltration capacity, reducing surface runoff (*Tisdall and Oades, 1982*), while lowering soil surface temperature and water evaporation, improving weed control and increasing soil productivity (*Frye et al., 1988*). Research on the use of living perennial mulches, such as crownvetch (*Hartwig, 1983*) but also birdsfoot trefoil, flatpea and white clover (*Ammon et al., 1995*) has highlighted the advantages of using ground covers that eliminate the need for annual reseeding.

Legume cover crops are suitable as precursors for crops that consume a large amount of nitrogen – maize because they have the potential to fix nitrogen. Even if the crop is established after these cover crops, this excess nitrogen is not lost and is preserved for the following year's crop that can use it (*Hooda et al. 1998*) and the long-term influence of soil conservation on the chemical properties of the surface horizon and the yield of legume crops in a Vertisol in southern Spain was studied by *Bravo et al. (2007)* and *Nyagumbo et al. (2017)*.

✓ No-till agriculture

No-till, or no-tillage agriculture, or farming without soil processing, is a key practice in conservation agriculture, which involves direct seeding crops without turning the soil over through plowing. This method helps reduce soil erosion, increase water retention capacity, and maintain microbial biodiversity. By reducing energy inputs and soil disturbance, no-till farming promotes long-term soil sustainability and health.

Over time, numerous studies have been conducted on the implications of no-tillage soil management on carbon sequestration, soil fertility and crop yields, but a synthesis on the impact of no-tillage systems on soil physical properties, based on a comprehensive analysis of published studies worldwide, is not yet available. The analysis of changes in soil physical properties after the adoption of no-tillage technology is important for managing soils, agricultural production and environmental quality; by comparing soil physical property data between no-tillage, minimum tillage and conventional systems, the factors influencing the effects of the soil tillage system were tracked and research needs were highlighted (*Blanco-Canqui and Ruis, 2018*). It was thus found that no-tillage management generally improves soil physical properties and the benefits for improving soil properties increase over time and accompanying practices (e.g. cover crops) can enhance no-tillage performance and in general, the single tillage of the soil in a no-tillage system does not negatively affect soil properties.

No-tillage systems represent a solution to restore the structure and health of agricultural soils, by identifying how chemical gradients and topsoil acidification can determine how the chemical properties of a clay soil can be affected by the no-tillage system (*Limousin et al., 2007*). It was found that yields were not negatively affected by the no-tillage system in the long term and the organic carbon content increased, therefore this system can be an economic choice for wheat and corn crops in temperate environmental conditions.

In order to determine the efficiency of soil nitrogen use in the long-term use of no-tillage systems, soil nitrogen changes and its use efficiency were studied in an experimental plot over a period of over 40 years (1968–2013), using completely randomized tillage practices (conventional mechanical tillage and no-till), crop residue management (burned residues and retained residue), and nitrogen fertilization (0, 30 and 90 kg N/ha) on a Vertisol (Ustic Pellusert) (*Dalal, et al., 2011*).

The fact that farmers have started to leave more crop residues on the soil surface helps to reduce soil erosion, conserve energy, retain soil moisture and increase crop yields, but on the other hand, many plant pathogens in the soil survive in these residues, so diseases are more problematic under reduced tillage conditions (*Bockus and Shroyer, 1998*). Thus, reduced tillage can favor pathogens by: protecting the pathogen refuge in the residue from microbial degradation (*Angers et al., 1993*), lowering soil temperature, increasing soil moisture and leaving the soil undisturbed. However, it is recommended that crop rotation be coupled with reduced tillage, through this practice controlling many diseases, and also allowing as much of the crop residues as possible to be retained on the soil surface.

Conservation tillage technologies can be an effective tool to increase the yield of certain agricultural crops, under conditions of stress caused by prolonged drought. Thus, studies have been conducted on the effect of applying tillage strategies on soybean production (*Hosseini et al., 2016; Huang et al., 2021*).

Tillage is also important for a good understanding of field conditions in terms of drainage and soil pathogens and determining the need for tillage in cropping systems (*Rajana et al., 2022*). It has been shown that even by improving plant genetics, there are practically no consistent changes in the response to tillage compared to no-tillage systems (*Arora et al., 2011*). Currently, technologies exist that allow planting and weed control without tillage practices, and selective fungicidal seed treatment can further increase the profitability of

no-tillage systems (*Wu and Babcock, 1998; Liebhard et al., 2022*), but there are also certain constraints in adopting these systems in developing countries (*Lal, 2007*).

To investigate the long-term (20-year) effects of no-tillage on soil properties and productivity in maize compared to conventional tillage, *Ismail et al. (1994)* studied how the lack of soil disturbance in no-tillage systems changes some of the most important basic soil properties. The comparative analysis showed that soil organic carbon was restored to the soil level after a decline of almost 20%, whereas grain yields, which had declined with organic carbon, did not recover.

In comparative studies on conventional tillage for 13 years versus no-tillage, the impact of crop residue retention versus burning, as well as nitrogen fertilizer application (23-69 kg N/ha/year) versus no-tillage, on organic carbon content, total nitrogen, mineralizable nitrogen, pH, electrical conductivity, and other chemical properties in a fine-textured Vertisol was analyzed. It was found that tillage and residue management significantly influence soil organic matter, microbial activity, and water relations, even in a fine-textured Vertisol (*Dalal, 1989; Dou et al., 2008; Mangalassery et al., 2015; Mbuthia et al., 2015*).

In conservation agriculture, sowing is done with minimal or no tillage. In study a by *Baker et al. (2007)*, the authors made an analysis of no-tillage technologies, emphasizing no-tillage seed drilling, but also address the issue of soil carbon and how its fixation/sequestration interacts with soil tillage and no-tillage, how traffic control on agricultural lands can help no-tillage, the role of band fertilization on no-tillage, but also the economics of no-tillage, forage cropping by no-tillage and a method for risk assessment of different levels of machine sophistication (*Triplett and Dick, 2008*).

Although it is recognized that conservation agriculture has beneficial effects on soil health in the medium and long term, the combined effects of no-tillage practices and residue management on soil properties remain a subject of research.

MECHANIZATION OF SOIL WORKS IN CONSERVATION AGRICULTURE

An essential component of agricultural development is mechanization, which plays a primary role in responding to the needs of farmers. Due to the fact that a large part of agricultural land is subject to erosion, salinization, etc., increasing yield per hectare is crucial for increasing agricultural productivity (*Emadodin et al., 2012*).

Carter (1991) conducted research to evaluate shallow tillage of spring cereal crops over a 4-year period in the Canadian province of Prince Edward Island on a fine sandy loam soil (orthic podzol), which is not very suitable for direct seeding. Tillage was performed with a furrow plough and shallower tillage with a disc harrow (to a depth of 10 cm) followed by direct seeding. Compared to conventional ploughing (furrow ploughing), shallow tillage reduced machinery and energy costs by 25-48% for seeding, with the advantage of increasing the potential area that can be prepared for seeding in the short early spring period, eliminating some of the constraints associated with direct establishment and providing an alternative to conventional ploughing.

Soil tillage equipment has a high influence on soil compaction (*Ungureanu et al., 2015*), sowing precision (*Cujbescu et al., 2021*) and therefore the technologies developed within conservation agriculture must respond and solve these challenges through specific characteristics and design (*Croitoru et al., 2015; Croitoru et al., 2016*), reduce resistance to advancement (*Duiker and Beegle, 2006; Vlăduțoiu et al., 2016; Vlăduțoiu et al., 2023*) using active vibrating parts (*Cârdei et al., 2023a*) and in conjunction with the introduction of new plant varieties that are more drought-resistant and have high productivity (*Matei et al., 2020*), which also have an impact on ecosystem conservation (*Nenciu and Vlăduț, 2021b*), from whose residues other products with high added value can be obtained (*Nenciu et al., 2021a*).

The use of deep soil loosening equipment (*Matache et al., 2015; Croitoru et al., 2017*) can partially solve the problem of deep decompaction, so that water can also reach the lower layers of the soil. At the same time, the use of soil cover residues (including algae), resulting from the production of the main products (e.g. biogas, bioethanol), can be a solution for maintaining water in the soil and increasing soil fertility over time (*Rhoton, 2000; Ungureanu et al., 2020a*).

In many cases, the use of plant residues in conservation agriculture represents a challenge for farmers because the so-called clogging with crop residues occurs, which leads to low soil cultivation due to the stalk residues used as mulch (*Li et al., 2022*); thus, it was necessary to design a combined towed machine for subsoiling and land preparation by crushing the stalk residues, simultaneously incorporating them into the soil, using grooved coulters and a crushing roller, a solution for soil cultivation in a conservation system.

Another solution for conservation soil cultivation in hilly and mountainous areas in China consisted in the development of a mini-tiller that performs soil cutting with rotary blades (*Xiao et al., 2024*), based on the

analysis and simulation of soil cutting optimization with such equipment, using the ANSYS/LS-DYNA program. Solutions were sought to reduce the cutting resistance and energy consumption of the rotary blade of the mini-tiller, the cutting process of the rotary blade being analyzed through numerical simulation, taking into account parameters such as: tangential bending radius, bending angle and thickness of the rotary blade edge, in order to optimize it.

The development of a precision, strip-type, no-till soybean planting equipment that performs seed metering for the Huang-Huai-Hai region of China was analyzed by *Ma et al. (2024)*, who performed parameter optimization through simulation and functionality was verified through bench testing.

In general, large agricultural equipment manufacturers have developed solutions and equipment for soil cultivation in a conservation system, but less often such equipment for medium and small farms. Especially in small farms in hilly and mountainous areas, the implementation of conservation practices is lower due to the lack of specific equipment for the application of such practices. In this regard, *Li et al. (2023)* developed and tested a furrow opening device for a two-row seeder, analyzing the general structure and operating principle while optimizing the soil structural parameters

For sowing small vegetables in greenhouses, a single disc multi-row seeder was developed in which the airway disc structure was redesigned so that the negative pressure air chamber was divided into three separate air chambers. This solved the problem of the high pressure requirements of the traditional single air chamber seed metering device, adapting the solution with several smaller separate chambers for low-power machines (*Zhang et al., 2023*).

For no-till seeders, a problem is the adhesion of wet and sticky soil to the working parts entering the soil, the soil sticking practically blocking these parts and affecting the quality of sowing (*Fu et al., 2023*). Research aimed to improve the anti-adhesion properties of the seeding monomer, so that it can also work in wet soils, using the "Theory of Inventive Problem Solving", based on the systemic-functional analysis of the seeding depth limitation device and the analysis of the force of the measuring wheel during operation, a new type of depth measuring wheel with a large hole was designed.

Cârdei et al. (2023b) analyzed the intensity of traction forces in the supports of the working parts of a cultivator taking into account the fact that the distribution of traction resistance forces on the working parts of a complex cultivator is unpredictable, using the validation of the random nature of the force loading the active parts to indicate the mathematical model to be followed for the research of the soil cultivation system.

Conservation agriculture aims, among other things, to reduce soil compaction, which is the result of successive passes with the tractor - agricultural machine aggregate during agricultural work, harvesting etc., especially since in recent decades equipment has been developed that works on increasingly larger and therefore much heavier surfaces.

Cujbescu et al. (2019) investigated the influence of specific compaction factors: tire pressure, wheel load and contact pressure on the tire-soil contact area, as well as obtaining 2D and 3D maps of the pressure distribution in the contact patch of a Romanian agricultural tractor - U445, at five tire pressures: 100, 150, 200, 250 kPa. The study was later extended to other types of agricultural machinery.

Bularda et al. (2020) carried out an in-depth analysis of the effects of the conservation mechanized work system, minimum-till (heavy and scarified disc) and no-till (direct sowing), compared to the conventional system (plowing), highlighting their influences on the soil and plants, ways to reduce technological costs, improve soil quality indices by accumulating organic matter and increasing the supply of humus, the need to reduce mechanical equipment traffic and the possibilities of reducing fuel consumption, improving the conditions for retaining water reserves in the soil, reducing working times and the need for labor.

REMOTE SENSING IN MODERN AGRICULTURE: TECHNOLOGY FOR SUSTAINABILITY

Quantifying crop residue coverage, identifying tillage intensity, and assessing the effectiveness of conservation management practices are essential aspects of modern agriculture. Traditional methods for assessing these parameters are often costly, time-consuming, and require skilled labor.

Studies and research on the impact of conservation agriculture on reducing environmental degradation through sustainable management of agricultural lands show that since the 1990s, agricultural research has focused on remote sensing technologies, but less on the use of conservation management practices (*Roper and Gupta, 1995; Ge et al., 2011; Sonmez and Slater, 2016; Ahmed et al., 2024*).

Remote sensing is a technology that involves the collection and analysis of data about the Earth's surface without direct contact, using sensors mounted on satellites, aircraft, or drones, to monitor and assess various environmental characteristics.

The use of remote sensing and advanced visual technologies in agriculture allows for rapid and accurate monitoring of crops and soil conditions (Zheng *et al.*, 2014). The data obtained, including information on soil carbon, water retention capacity and evapotranspiration, are essential for optimizing the use of resources such as water, fertilizers and pesticides. These modern methods support the early detection of plant stress and diseases, contributing to increasing the productivity and sustainability of agricultural systems.

Satellite remote sensing has been found to be very useful for spatially interpolating and estimating cover crop biomass and nitrogen uptake in a small watershed (Xu *et al.*, 2018). Authors Beeson *et al.* (2016) monitored and evaluated crop residue coverage and tillage intensity in a watershed in central Iowa (USA) for three years (2009-2011), using multispectral satellite imagery. The determination of crop residues using remote sensing was studied by Beeson *et al.* (2020), who used Landsat Thematic Mapper Series platforms to track global temporal and spatial coverage starting in the mid-1980s, for 10 years, in the states of South Dakota, North Dakota and Minnesota, using the Normalized Difference Tillage Index (NDTI) and then validating the results against field-level survey data (Zheng *et al.*, 2013).

In a study by Gowda *et al.* (2008), a set of linear logistic models based on Landsat Thematic Mapper (TM) were presented, which had been previously used for mapping tillage practices and verified with an independent dataset (South *et al.*, 2004). Another approach for mapping conservation tillage practices was through the use of artificial neural networks (Sudheer *et al.*, 2010).

Conservation agriculture is closely related to precision agriculture because the use of field data such as: vegetation index (VI), normalized difference vegetation index (NDVI), green normalized difference vegetation index (GNDVI) and soil adjusted vegetation index (SAVI), to examine the vegetation vigor for each crop, helps farmers make quick and efficient decisions, which are vital for obtaining high yields for each crop. To determine these indices, Candiago *et al.* (2015) used an unmanned aerial vehicle - hexacopter (UAV) on which a Tetracam camera was mounted that allowed obtaining multispectral data, after processing obtaining triband orthoimages of the scanned areas, subsequently extracting the previously mentioned indices.

The influence of soil properties on soil tillage, and on soil quality parameters in a tallgrass prairie area, was addressed in studies by Van Deventer *et al.* (1997) and by Brye and Pirani (2005), the authors analyzing the physical, chemical and biological properties of the soil at depths of up to 10 cm, in the Grand Prairie region of east-central Arkansas, on six native pastures, these being then compared with the data obtained in the adjacent cultivated agricultural lands (11 combinations of land use from prairie-agriculture). Thus, it was found that the soil organic matter and total N and C concentrations were much lower, and the soil pH, electrical conductivity and extractable soil (K, P, Fe, Mg and Ca) were higher in the cultivated agricultural lands than in the native prairie lands, but the mechanization of intensive agriculture and its associated practices negatively affected the quality of the native soil in this region.

Chen and Wang (2010) used satellite sensing to observe land cover changes in a mountainous area of China near the Three Gorges Dam (TGA) over a 10-year period (1987-2006), developing a specific procedure that uses a decision rule-based classification method and post-classification change detection techniques, combining spectral and spatial knowledge in multi-temporal image classification. The responses of soil chemical and microbial indicators to conservation tillage were also monitored compared to conventional tillage in the North China Plain, with the results showing that after a 6-year period, conservation tillage improved soil quality (by improving its chemical and microbial properties), as well as the geometric mean of the tested enzymes, microbial biomass C, microbial biomass N and β -glucosidase (Qin *et al.* 2010).

In the case of winter cover crops also, one of the monitoring methods is satellite remote sensing to approximate the efficiency of nutrient uptake from them (Hively *et al.*, 2009), and to estimate the effect of these cover crops on nitrogen fixation in the soil, using in addition cost recording data and Soil and Water Assessment Tool modeling (Hively *et al.*, 2020) or by using Landsat and SPOT satellite images in conjunction with USDA cropland data (Hively *et al.*, 2015), so that the extent and quantity of winter green vegetation can be assessed on agricultural fields in four counties in Pennsylvania / USA, over a 4-year period (2010-2013). Analysis of winter satellite imagery revealed significant increases in vegetative ground cover over the study period, indicating that farmers have increasingly adopted practices such as cover crops that promote winter vegetation.

Remote sensing is a valuable tool for assessing and mapping the level of soil cover with post-harvest agricultural residues and cover crops, including during non-growing periods, based on multitemporal satellite imagery and spectral detuning techniques (Laamrani *et al.*, 2020; Prabhakara *et al.*, 2015). Given that understanding spatial variability in the adoption of cover crop practices, and their impact on soil, water and soil nutrients, is an important step in determining and prioritizing areas within a watershed to effectively utilize this

practice, and that data are often lacking, the development of a method for assessing cover crops, using remote sensing based on spatial assessment models, was studied by *Kc et al. (2021)*, who used images collected by Landsat 5, 7 and 8 satellites, during the period 2008-2019 in the Google Earth Engine platform.

By monitoring tillage practices, soil quality and production trends can be tracked, respectively their impact on environmental quality, but this depends largely on the existence of accurate maps of agricultural residues, one solution being the mapping of soil cultivation technologies using spatial information techniques. In this regard, in a study by *Paul Obade and Gaya (2020)* an empirical model for mapping surface agricultural residue cover was created by integrating line-transect % residue cover field measurements with information obtained from soil spectroradiometers and Advanced Wide-Field Sensor satellite images, the map being then validated using the fractional component of non-photosynthetic vegetation extracted through spectral mixture analysis.

ADOPTION OF CONSERVATION AGRICULTURE AT THE GLOBAL LEVEL: PROGRESS AND CHALLENGES

Although soil health practices such as cover crops, crop rotation, and conservation tillage certainly provide economic and ecological benefits on farms where they are implemented and indirectly on the environment, the implementation of these practices is still not widespread enough, and researchers are analyzing what may be the causes that lead to this situation (*Carlisle, 2016*).

From the analysis of recommendations for increasing the adoption of soil health practices, it was found that a complementary approach that combines education, policy, research, equipment adaptation measures, and efforts to address the farm and food system context may be the key to wider adoption of these practices among farmers. Soil conservation practices play an important role in restoring soil quality (organic carbon, microorganisms, etc.) but there is still reluctance among farmers regarding how these practices will influence production. The results of a study by *Anderson et al. (2020)* highlighted that both no-tillage and cover crops can help reduce production risk for farmers, while reducing soil and nutrient losses.

However, applying the principles of conservation agriculture does not automatically lead to better results in every situation, because under certain conditions (e.g. cold, wet environments, poorly drained soils) or if the practices have not been well adapted to the specific conditions of the area, the conservation management system may not be successful. Farmers need to have access to tools and resources that allow them to identify those principles of conservation agriculture that are appropriate for their situation and to well-established, locally adapted systems to successfully overcome the agronomic, social and economic challenges that may arise at a given time.

At European Union level, sustainable land management practices, which balance competitive agricultural production and environmental protection, have been supported in recent years through policies and subsidies, but the adoption of these practices that regulate biogeochemical cycles requires further studies, especially due to the effects of local pedo-climatic variability. A research study by *Camarotto et al. (2018)* aimed to analyze the influence of conservation agriculture and practices using cover crops to regulate water, carbon and nitrogen cycles in the Venetian lowland.

In Turkey, in the last two decades, agricultural land degradation due to intensive farming has increased greatly and therefore it has become necessary to apply conservation practices that protect both land and production, by establishing urgent measures and a national strategy to promote conservation agriculture throughout the country (*Altikat et al., 2018*), while also pursuing the various economic aspects of the conservation agriculture system (no tillage - direct seeding) that may influence farmers' decisions (*Kan et al., 2018*).

In Serbia, government authorities have also begun to align with European Union policies on stimulating and promoting the adoption of conservation soil cultivation practices, because although these practices (no-tillage, minimum tillage) have been available for many years, their adoption in Europe has not had the desired expansion (*Harper et al., 2018*), so the promotion of new technologies and the dissemination of agricultural innovations has required a commitment and close collaboration between all the factors involved: government, farmers, agricultural enterprises, advisory services and research.

Quantification of soil water storage and crop yield using different tillage systems was analyzed in dry semi-arid Mediterranean conditions in Spain during 1987–1992 (*Lampurlanés et al., 2016*). Their study highlighted that in semi-arid pluvial conditions, soil water storage increases with the use of conservation systems, being amplified with the degree of aridity of the site.

Studies on tillage systems in Mediterranean crops (Greece, Italy, Spain and Morocco) and soil organic carbon sequestration were carried out in 15 locations, aiming to identify biophysical and agronomic variables

associated with the rate of carbon sequestration and it was found that tillage, crop rotation and fertilization were the most important factors affecting the sequestration rate (*Francaviglia et al., 2017*).

A comparative multidimensional evaluation study of conservation agricultural systems, carried out for an area in southern Italy, highlighted the fact that conservation agriculture can be a viable alternative to conventional systems, and in the Mediterranean area it has the advantage of good yields even in dry years (conservation practices preserve water in the soil for crops). In addition, European public authorities (including policymakers) need to recognize the positive benefits of conservation agriculture and support them as ecosystem services within good agri-environmental practices and current CAP subsidies (*Vastola et al., 2017*).

In the USA, the adoption of conservation agriculture practices began about 40 years ago (*Nowak, 1987*), with research highlighting the fact that the variables positively associated with the adoption of these practices by farmers were those related to: financial non-involvement, attitude towards the environment, previous adoption of other conservation practices, etc. (*Prokopy et al., 2019*). Of course, the adoption of cover crops (*Arbuckle and Roesch-McNally, 2015*), the use of conservation practices (*Barbercheck et al., 2014*), best management practices (*Baumgart-Getz et al., 2012*) and the adoption of no-plow tillage (*Belknap and Saupe, 1988*), supported by voluntary agricultural policies to protect water quality (*Bosch et al., 1995*) although supported by the government, has always encountered resistance from farmers to the adoption of best management practices in certain regions (*Burnett, 2014*), because the transition to sustainability implies a change in thinking about changing food systems (*Hinrichs, 2014*), the modern world with current agri-food systems not always supporting sustainability (*Buttel, 2006; Gillespie et al., 2007*).

The continued decline in soil productivity in certain areas of the USA has been one of the main factors influencing the adoption of soil health practices by farmers (*Knowler and Bradshaw, 2007; Kara et al., 2008; McCann et al., 2015; Carlisle, 2016; Liu et al., 2018*), along with the adoption of agricultural production practices in pilot farms (lessons learned), supported by the Department of Agriculture (*Caswell et al., 2001; Singh et al., 2018*) or through incentive payments to encourage farmers to adopt water quality protection practices (*Cooper and Keim, 1996*). As a result, the conservation behavior of farmers following participation in these voluntary incentive programs has changed (*Kraft et al., 1996; Napier et al., 2000; Lichtenberg, 2004; Fishbein and Ajzen, 2010; Mase et al., 2016; Stallman and James, 2017; Dayer et al., 2018*), and a modeling of multiple adoption decisions within a common framework has been achieved (*Dorfman, 1996*), inevitably emerging new trends regarding the attitude towards the environment (*Dunlap et al., 2000; Gifford and Sussman, 2012*), including that of cattle breeders (*Kim et al., 2005; Lambert et al., 2014; Medwid, 2016*), and the perception regarding the use of cover crops among farmers has also changed (*Gottlieb et al., 2015; Dun et al., 2016*).

The USA is currently one of the largest and most powerful countries with a highly developed agriculture. In order to have a sustainable agriculture, a balance must be achieved between productivity, profitability and environmental health. *Davis et al. (2012)* have shown that by increasing the diversity of cropping systems, a balance can be achieved between these three important indices, taking into account that in the USA the vast majority of crop production systems are characterized by low species diversity and management, the large-scale use of fossil energy and chemicals having a major negative impact on the environment. Starting from the hypothesis that the diversification of crop systems can promote ecosystem services, as they can supplement and subsequently replace external synthetic inputs used to increase crop productivity, a field study was conducted during 2003–2011 (in the state of Iowa, USA), including three contrasting systems, where the length of the crop sequence and inputs varied and in the end it was found that grain yields, the mass of harvested products and implicitly the profit in diversified systems were similar or higher than those in the conventional system, even though chemical inputs were reduced, even weeds being effectively eliminated in all systems, but the toxicity of water in the soil on the lands where diversified systems were used was lower than in the conventional system by two orders of magnitude. Basically, the study highlighted the fact that more diversified cropping systems, although using reduced amounts of synthetic agrochemical inputs, can become powerful tools that allow regulating, rather than boosting, the performance of agroecosystems, while outperforming less diverse systems.

Given that the USA is one of the largest and most powerful countries with a highly developed agriculture, in recent years it has become a priority to identify and quantify the adoption of conservation practices on agricultural lands, by precisely monitoring soil health trends at the regional and national levels, in efforts to mitigate climate change (*Hagen et al., 2020*). In this regard, a mapping of conservation management practices for corn crops was carried out, using an operational soil cultivation information system (OpTIS) and a denitrification-decomposition model (DNDC). The USA has vast agricultural lands, characterized by large

monocultures where intensive agriculture is practiced, supported by chemical fertilizers and pesticides, so as to maintain high productivity (Schipanski *et al.*, 2016), but over time, with all the inputs, productivity has decreased and farmers have adopted a regenerative model of agricultural production that promotes soil health and biodiversity, while producing nutrient-rich but profitable agricultural products (LaCanne and Lungren, 2018).

No-tillage agriculture is promoted as one of the management practices that maintains the amount of and water, respectively the increase of organic carbon in the soil, compared to conventional tillage practices. Considering that the Great Plains region of the USA is an area with low rainfall, the crop that is best suited is wheat but even in these conditions satisfactory yields cannot be obtained without irrigation, so the adoption of no-tillage cultivation practices has become a necessity because it has led to more efficient storage and use of precipitation and implicitly to improvements in soil properties and increased productivity, in conjunction with a more diverse crop rotation (Hansen *et al.*, 2012).

For carbon sequestration in the soil, no-tillage agriculture represents a solution. Christopher *et al.* (2009) conducted a study on the effects of no-tillage on carbon sequestration in the Midwestern United States, and the results highlighted that most information on carbon sequestration in no-tillage systems was based on measurements in the surface layer of the soil (<30 cm) and the level of carbon sequestration at greater depths (up to 60 cm) is unknown. An analysis of the soil profile distribution of carbon and associated properties in no-till along a precipitation gradient in the semi-arid Central Great Plains of the USA and Canada was conducted in many studies (Tessier *et al.*, 1990; Puget and Lal, 2005; Blanco-Canqui *et al.*, 2011). Soil carbon storage and soil structural properties (aggregate stability and soil strength at 1 m depth) were evaluated in three long-term experiments (over 20 years) using no-tillage and conventional systems. It was found that no-tillage does not increase soil organic carbon stock, but increases wet aggregate stability and reduces aggregate tensile strength at the soil surface, and the impact of no-till management on soil carbon storage varies depending on soil structural properties, precipitation, equipment used, and cropping system (Olson, 2013).

In general, dryland crops do not produce large amounts of residues, and in this case the effects of no-tillage technology on infiltration, runoff and water conservation on land are generally small. In order to have the most accurate results, these effects were compared over a period of 12 years with those resulting from stubble mulch tillage in the state of Texas, USA (Jones *et al.*, 1994), with terminal infiltration rates being similar for both tillage systems. Despite the higher surface runoff from the no-tillage system compared to the conventional one, soil management in the no-tillage system led to improved water conservation due to reduced evaporation.

Given that the central US has some of the most productive agricultural land in the world and relatively large areas, and the stored carbon and greenhouse gas emissions due to agriculture represent a significant percentage of the entire country (Johnson *et al.*, 2005), the assessment of the greenhouse gas contribution and mitigation potential of agriculture in this region was studied, by converting agricultural land to grass, increasing the percentage of soil organic carbon sequestration. The assessment of the potential for reducing greenhouse gases: carbon dioxide (CO₂), nitrous oxide (N₂O) and methane (CH₄) through the application of sustainable management practices in eastern Canada and the northeastern US was studied by Gregorich *et al.* (2005), who synthesized the most recent information on the contribution of agricultural soils to atmospheric levels of these gases.

Most of Australia is affected by drought and cultivated agricultural areas are highly subject to erosion, and Australian farmers were among the first to implement conservation agriculture practices and even came up with innovations to increase yields with these systems (Belloti and Rochecouste, 2014). The first experiments by farmers with conservation agriculture began as early as the 1960s and have continued to the present day, when about 80-90% of Australia's winter crops are grown using conservation agriculture principles. This is also due to continuous investments in agricultural research and development, but especially to the innovation of farmers who adopted conservation agriculture (through waste management practices) because it satisfied their needs, maintaining productivity and profitability, having a positive impact on the chemical and microbiological properties of the soil (Pankhurst *et al.*, 2002; Thomas *et al.*, 2007) and sustainably increasing production with better environmental outcomes (O'Leary and Connor, 1997).

In Australia, no-tillage has been widely used in regions suitable for cereal cultivation over several decades (Llewellyn *et al.*, 2012), this paper analyzing the factors favoring the adoption of no-tillage systems, demand-driven innovation by farmers and agricultural researchers, which led to the development of high-performance agronomic technologies (herbicide and crop disease resistance, extension processes and economic influences); the impact of conservation tillage on soil quality and health (Pankhurst *et al.*, 1995),

including soil-borne crop diseases (*Rahman et al., 2007*), in semi-arid cereal cropping systems was also studied (*Page et al., 2013*). At the same time, changes in soil water storage in the no-tillage system and the maintenance of agricultural waste on a Vertisol were monitored, respectively their impact on productivity and profitability, over a period of 50 years (*Page et al., 2019*).

Analysis of differences in soil organic carbon levels following different tillage and stubble management practices in a continuous cropping system on a red soil in the New South Wales (Wagga Wagga) region, Australia, was studied in a wheat/lupine rotation experiment over a 10-year period (*Chan et al., 1992*). During this period, stubble burning and tillage had the same impact on reducing the total amount of organic carbon in the upper soil (0-2 m horizon), with no significant differences between conventional (3-crop) and reduced-tillage (1-crop) systems (*Loch et al., 1984*).

Although conservation farming practices are largely implemented by farmers in northeastern Australia, they often resort to an occasional tillage operation - strategic tillage - to combat the constraints of no-tillage systems (*Dang et al., 2015; Dang et al., 2018*), suggesting that there must be a tillage strategy in conservation farming systems. In order to validate this strategy, 14 experiments were established over a 4-year period (2012-2015), in farms that had implemented no-tillage systems for several years, so that there would be unity in: quantifying the associated risks and benefits on crop productivity, soil health and the environment, respectively exploring the key factors that must be taken into account to implement this strategy in a no-tillage system, the results highlighting the fact that the introduction of the strategy reduced weeds and improved crop productivity and profitability in the first year after soil cultivation, with no impact in the following 4 years, this strategy being viable for managing the constraints of no-tillage systems, with reduced short-term costs for the soil and the environment and some benefits (short-term farm productivity and profitability and reduced dependence on herbicides).

Farmers in developed countries in North and South America and Australia have implemented conservation agriculture on a large scale, achieving high profitability through a combination of increased agronomic productivity and reduced input costs (*Thomas et al., 1995*). Building on these results, smallholder farmers in sub-Saharan Africa and South Asia have also adopted conservation agriculture practices for a wide range of crops and farming systems, even though there are major differences between the biophysical and socio-economic environments in these regions (*Brouder and Gomez-Macpherson, 2014; Pannell et al., 2014; Pheap et al., 2019*). Based on the data evaluated from the reviewed studies, a minimum set of generic, relatively inexpensive and easy-to-implement data was proposed, which would allow quantifying and explaining crop and crop system performance.

In Portugal, the main constraints of agricultural production in the Mediterranean region were analyzed and the importance of conservation agriculture to mitigate them, having an even more important role, taking into account long-term studies carried out with these practices, studies that highlighted an increase in soil organic matter, improved aggregate stability and continuity of biological porosity along the soil profile (*Carvalho and Lourenço, 2014*). It was found that changes in soil properties help overcome edaphic and climatic constraints in Mediterranean conditions, improve saturated hydraulic conductivity which allows for better drainage during wet winters and better soil traversability, and highlight the fact that conservation agriculture can be economically and environmentally advantageous, contributing to the sustainability of rainfed agriculture.

In Brazil, conservation agricultural practices based on no-tillage systems were introduced over 35 years ago, initially in the southern state of Paraná, as a means of reducing erosion, and subsequently, research was conducted to study crop residue management and its effects on soil fertility, phosphorus management as a means of controlling soil acidity, and establishing how manure can be applied in a more localized manner (*Bernoux et al., 2006*). The spread of conservation agriculture in Brazil has involved major expansion works, with the area worked in no-tillage systems increasing, especially in the center and north of the country, occupying over 20 million hectares, covering a diversity of environmental conditions, cropping systems and management practices that track the interactions of conservation systems on soil organic carbon and soil fertility (*Sa et al., 2009*).

The soil conservation movement in Brazil has been the main driver for the continuous identification of new agricultural systems that are more sustainable than existing ones, especially in tropical and subtropical areas, and the development and adoption of Zero Tillage Conservation Agriculture has been key to the success of this movement, generating numerous agricultural, environmental and societal benefits (*Freitas and Landers, 2014*). This led to a major transformation of agriculture in Brazil through the development and adoption of conservation no-till agriculture, which now accounts for over 50% of the total cultivated area. This was due to the work and innovation of all those involved: farmers, agronomists, researchers, consultants, etc., as farmers

realized that erosion control required continuous soil cover, protecting it from torrential storms common to these regions. *Zero Tillage Conservation Agriculture* has stopped land and soil structure degradation by eliminating conventional tillage, thus improving its physical and chemical characteristics, this being achieved by promoting cover crops and permanent soil coverage with crop residues (*Raphael et al., 2016*), crop rotations and complementary technologies, appropriate for soil management.

By increasing soil carbon supply and stabilizing it, soils can become reservoirs of atmospheric CO₂-C, thus helping to mitigate global warming, in which case the combined role of no-tillage systems in storing and stabilizing soil carbon is essential (*Conceição et al., 2013*). A study conducted by *Veloso et al. (2018)* aimed to evaluate the sequestration and stabilization of carbon in a subtropical Acrisol from the Eldorado do Sul region, Brazil, which was conventionally worked for 18 years and subsequently with the no-tillage system, with two cropping systems: black oats (*Avena strigosa* Schreb) - winter cover crop and corn (*Zea mays* L.) - summer cereal crop, respectively black oats + vetch (*Vicia villosa* Roth) - winter cover crops and summer corn interspersed with cowpea (*Vigna unguiculata* (L.) Walp) - cover crop. Their results demonstrated that the no-tillage system is recommended for sustainable soil management and to increase soil carbon accumulation, the potential of cropping systems based on legume cover crops being used concurrently.

In tropical and subtropical mountainous areas there are many problems related to the sustainability of agriculture due to erosion and reduction of soil fertility, a long-term solution to these problems being the tillage in a conservation system, residue management and crop rotation (*Govaerts et al., 2007; Steward et al., 2018*). Both environmental conditions and microflora played an important role in the biology and expression of soil pathogens in the subtropical semi-arid and pluvial mountainous areas of central Mexico, along with the positive effects of no-tillage, crop rotation, and crop residue retention compared to conventional agricultural practices (*Govaerts et al., 2008*).

The implementation of conservation agricultural practices in the mountainous areas of central Mexico, especially through the use of crop residues, has been stimulated by the authorities through social and income crop compensations (*Beuchelt et al., 2015*). Due to the fact that a large part of farmers have low incomes, they use crop residues not only for soil cover but also as fodder or as an additional source of income, which largely explains the low adoption of conservation agriculture in some regions due to crop residue management in mixed crop-animal systems.

Climate change affects the livelihoods of people dependent on agriculture, causing migration, political instability and economic losses (*Linke et al., 2021*). In areas such as South Africa and Kenya, the tendency of residents is to use traditional knowledge to predict the weather, determine wind speed and preserve seeds, having a significant impact in reducing climate change affecting agricultural activities (*Apraku et al., 2021*). The need to identify appropriate weather conditions that directly influence soil cultivation processes led to the development of an automated climate prediction system for smart agriculture that uses a hybrid Deep Belief Network based on the Pelican Optimization algorithm, which has a maximum accuracy of 95.03% (*Punitha and Geetha, 2023*).

Although conservation agriculture has been heavily promoted in Africa as an alternative to the need for high food production based on more sustainable agricultural practices, its success in adopting it on farms is still limited, even though investments in research and development have been made over the last three decades (*Corbeels et al., 2014*). Smallholder farmers in Africa have not widely adopted conservation agriculture (*Brown et al., 2017; Thierfelder et al., 2018*), the main factor in the negative assessment of these conservation agriculture practices being the feasibility of implementation, primarily due to the fact that the resources required for their implementation (financial, physical, human and informational) are limited by community and institutional constraints and cannot be overcome by interventions aimed at addressing household resources.

To understand the impact and adoption of conservation agriculture in Africa, a multi-scale analysis must be carried out that takes into account the results obtained in previous and ongoing experiences, in a set of case studies, so that ultimately the reasons for the limited adoption of conservation agriculture practices on this continent can be better understood. Potential causes include: the lack of immediate income growth for farms that apply conservation practices, with small farmers often having short-term time horizons because future benefits do not adequately exceed their immediate needs, and conservation agriculture does not bring immediate benefits; in mixed livestock systems, crop residues are often used as animal feed and can no longer be used for soil cover; lack of good markets for purchasing inputs and selling products.

A large part of African countries are affected by drought (*Tekle, 2016*) and therefore the adoption of conservation tillage technologies may represent a solution (*Mrabet et al., 2012; Abdulai, 2016*). Some research

has sought to highlight the impact of conservation technologies on the well-being of farmers in Zambia and southern Africa, tracking the main factors that can determine the improvement of the situation of these farmers (Rusinamhodzi *et al.*, 2011; Sithole and Magwaza, 2019). Thus, an endogenous switching regression model was used to estimate the impact of technology on outcomes (agricultural production, transfer accounting ratio, poverty gap, poverty severity, etc.) and in addition farmers were educated, taught to access social networks, how to access credit, benefited from extension services and equipment to see how soil quality is positively influenced by the adoption of conservation technologies.

Also, in Malawi, on-farm evaluations were carried out on the yield and economic benefits of short-term legume intercropping systems in conservation agriculture (Ngwira *et al.*, 2012; TerAvest *et al.*, 2019). In other countries in southern Africa, such as Malawi and Zimbabwe, farmers began to adopt soil and water conservation measures starting in the 1990s, and then promoted them on a large scale (Andersson and D'Souza, 2014), but they did not expand as desired, with the use of these practices still being quite limited.

Given that much of Ethiopia is mountainous, extremely high volumes of runoff occur on cultivated land when it rains, and in this case the research aimed to see the medium-term effects (2005–2010) of applying cropping systems based on conservation agriculture on sustainable soil, water and crop productivity management in the highlands (Araya *et al.*, 2012). No-tillage systems, crop rotation and post-harvest residues in combination with conventional systems were tested in Ethiopia, for several types of crops and in the end it was found that runoff was reduced simultaneously with an increase in crop yield (higher in recent years).

In recent years, conservation agriculture has also been promoted in subhumid and semi-arid areas of Zimbabwe, from the point of view of increasing water use efficiency for crops and stabilizing yields (Baudon *et al.*, 2012; Nyamangara *et al.*, 2014), over three consecutive seasons, tracking the comparative short-term performance of conservation agriculture and current agricultural practices on small farms, in addition to biophysical measurements, farmers' perceptions of the technology were also assessed. Given that most soils in the study area fall into the dry and highly compacted category, farmers perceived conventional tillage as necessary in drier years (to maximize water infiltration) and conservation tillage systems as more beneficial in wetter years, which is incorrect because by applying conservation practices, crust formation and soil compaction can be avoided. This can be achieved through better crop management (adequate fertilization, timely planting, crop protection) in combination with intercropping.

A global perspective on the application of conservation agriculture in smallholder farming in southern Africa and Southeast Asia was presented by Ares *et al.*, (2015), who examined the potential benefits as well as the biophysical and socio-economic constraints that the expansion of conservation agriculture could bring to farmers in these areas. Although conservation agriculture systems around the world share many common principles, there are important differences depending on geographical location, climatic conditions, soil, and type of farming systems, crop-animal interactions, and farmers' access to resources, highlighting the effects of such differential conditions on the development of conservation systems.

Recent research in sub-Saharan Africa and South Asia, in dryland areas with smallholder farms, has sought to highlight the limits of productivity and the potential of conservation agriculture principles in these areas (Vanlauwe *et al.*, 2014; Pittelkow *et al.*, 2015; Pittelkow *et al.*, 2020; Rosenstock *et al.*, 2024). This is due to the fact that the population in these areas has grown rapidly in the last 20 years, but the conditions are not exactly conducive to developed agriculture, making these principles all the more suitable, with reduced external input and minimal impact on the environment, in variable and extreme climatic conditions (Tifton *et al.*, 2012). Conservation agriculture in these areas aims not to reduce production, but under certain conditions, this no-tillage system can produce equivalent or higher yields than conventional agriculture because when the no-tillage system is applied combined with the other two principles of conservation agriculture: maintaining agricultural residues and crop rotation, its negative impact is minimized and at the same time increases the productivity of rainfed crops in dry climate areas, which leads us to the idea that this can be an important future strategy for adapting agriculture to climate change in countries located in dry areas (Seufert *et al.*, 2012).

In Central Asia, the use of cover crops as a conservation agriculture practice for climate change mitigation and adaptation has gained momentum over the last 50 years, with concerns for increasing sustainability and efficient use of land and resources over a longer period of time (Kienzler *et al.*, 2012), however, given the diversity of institutional, socio-economic and agro-ecological contexts, a geographically differentiated approach to the dissemination of conservation agriculture practices must be taken, also considering a change in research paradigms (more participatory approaches with farmers). In Nepal, the introduction of sustainable crop establishment practices has increased profitability and yields in rice and wheat crops (Devkota *et al.*, 2019).

To understand the long-term impact of conservation tillage on soil structure and productivity, the effects of no-tillage practices and residue mulching compared to conventional tillage were analyzed over a 15-year period in northern China (*Li et al., 2007*), finding that crop yield and water use efficiency tended to be higher when using the no-tillage system combined with agricultural waste mulching compared to the conventional tillage system, especially during periods of low rainfall, highlighting that the modification of soil structure provided a better environment for crop development. Thus, the data obtained over this 15-year period highlight the fact that no-tillage is a more sustainable agricultural system, which over time can improve soil structure and increase crop yield, with positive environmental impacts in dryland agricultural areas. Also, maintaining residues on the soil and minimally cultivating it improves the physical soil environment in cultivated lands (*Li et al., 2019*), tracking the effects of soil conservation practices on soil physical properties, including soil bulk density, aggregate size and stability, hydraulic properties, and soil pH.

One way to conserve soil water is to till the soil as little as possible (in a single pass, if possible), without turning the furrow. To this end, researchers in Indonesia have developed a soil tillage and seedbed preparation equipment for small farms in mountainous areas (*Mustaqimah et al., 2021*), so that farmers can benefit from a mechanized solution that retains water in the soil.

The assessment of the problems and prospects of adopting conservation agriculture in Bangladesh (Jamalpur and Bogra districts) was studied by *Dhar et al. (2018)*, the research being conducted on a group of 120 farmers (20 from the focus group and 100 from the control group), surveyed to collect the necessary data and information and a combination of descriptive statistics and mathematical techniques was used for data analysis. The farmers in the target group followed the basic principles of conservation agriculture, and the farmers in the control group continued conventional crop cultivation practices, it was found that the focused farmers were more profitable compared to the farmers in the control group in terms of wheat and bean production.

In India, considerable efforts have been made in the last 30 years to develop and promote agricultural technologies based on conservation tillage systems and although significant progress has been made, there are still many constraints affecting the adoption of conservation agriculture, even though in principle it involves minimal soil disturbance, permanent coverage of the soil with crop residues or cover crops, and crop rotations to achieve higher productivity (*Bhan and Behera, 2014*). It was found that there are more benefits than trade-offs for adopting conservation technologies, offering opportunities to reduce production costs, save water and nutrients, increase yields, increase crop diversification, improve resource efficiency and benefit the environment. Obviously, there are also constraints to promoting conservation technologies, especially due to the lack of adequate equipment (seeders) for small and medium-sized farmers (*Pradhan et al., 2018*). In the semi-arid regions of India, the effects of conservation agriculture on soil properties and crop productivity were studied simultaneously with the maintenance of residues on the soil, under different heating systems, and it was observed that the average moisture content improved, the degree of compaction was reduced, and the organic carbon content in the soil increased (*Somasundaram et al., 2019*).

Given that intensive tillage combined with crop residue burning in the rice-wheat system is widely used in northwestern India, representing a serious problem that causes soil degradation and environmental pollution, losing large amounts of organic carbon, the no-tillage system has been recommended on a large scale as an alternative to improve soil carbon sequestration, biological properties and crop productivity (*Vandenbygaart et al., 2003; Jat et al., 2019*). It has been found that adopting climate-smart agricultural practices involving no-tillage, crop establishment, residue management and crop diversification in the rice-wheat system can significantly improve the productivity of the systems by increasing the percentage of soil organic carbon and soil health (*Jat et al., 2014*).

In Azerbaijan and Iran, the effects of tillage systems on productivity (dryland winter wheat–chickpea rotation) were also studied, as data on the success of intensive cropping systems in relation to conservation tillage management were insufficient (*Hemmat and Eskandari, 2004*), and tests were carried out to determine the effect of five tillage systems on crop yield in a winter wheat–chickpea rotation, over a 3-year period on a loamy-clayey soil.

From the analysis of these studies, it can be concluded that the adoption of conservation agricultural practices is influenced by a combination of environmental, economic, social, and institutional factors. Soil characteristics, climate variability, and water availability play a crucial role in determining the feasibility and effectiveness of these practices in different regions. Economic considerations, such as initial investment costs, long-term financial benefits, and access to subsidies or financial incentives, significantly impact farmers' willingness to transition.

Social and cultural factors, including traditional farming practices, peer influence, and knowledge transfer through extension services, also shape adoption rates. Additionally, institutional support, including government policies, availability of technical assistance, and access to appropriate machinery, can either facilitate or hinder implementation. Understanding these key factors is essential for designing targeted interventions that promote the widespread adoption of conservation agriculture.

ECOLOGICAL AGRICULTURE

Ecological agriculture is a sustainable production system aimed at maintaining and improving the health of soils, ecosystems and human communities. This model of agriculture is based on the use of ecological processes, biodiversity and natural cycles adapted to local specificities, instead of resorting to inputs with potential negative impacts. By integrating tradition, innovation and scientific knowledge, ecological agriculture aims to protect the environment, promote social equity and ensure a higher quality of life for all stakeholders.

Ecological or organic agriculture contributes to increasing the resilience of agroecosystems to climate change by creating sustainable agricultural systems that protect the soil and adapt to temperature fluctuations and drought. It also promotes ecological conservation and restoration practices, being a less expensive method compared to conventional agriculture (Gamage et al., 2023).

According to the most recent data, globally, at least 4.5 million farmers manage more than 96 million hectares of agricultural land (mainly due to growth in Australia) in 188 countries that practice organic agriculture (Trávníček et al., 2024).

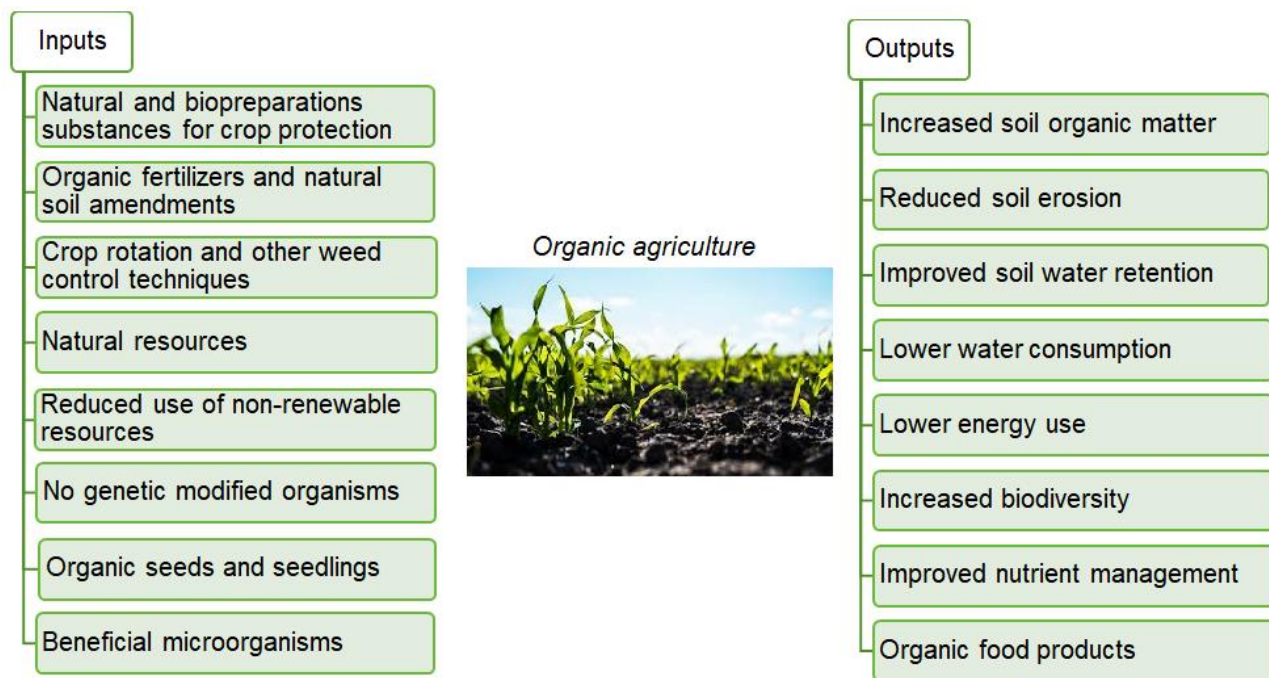


Fig. 10 – Inputs and outputs of organic agriculture

Although it promotes biodiversity and is generally more sustainable, organic farming has a significantly lower temporal stability of yield (-15%) per production unit compared to conventional farming (Knapp and van der Heijden, 2018).

In addition, ecological farming faces significant challenges, including limited access to resources, technical knowledge and markets for organic products. It is essential that government policies support the transition to more sustainable agricultural practices through financial incentives, education and research (FAO, 2018; Ding, 2018).

Diversifying cropping systems in conservation and organic agriculture is essential for improving biodiversity, preventing soil erosion and managing nutrients efficiently. It also contributes to the stability of agricultural ecosystems, reducing risks associated with pests and diseases, while supporting natural resource conservation practices.

An essential aspect of sustainable agriculture in dryland farming systems is the integration of well-nodulated legumes, which can provide nitrogen through a symbiotic process with root nodule bacteria (*Lupwayi et al., 2001*). Incorporating legumes into crop rotations helps reduce agricultural risks, lowering nitrogen fertilizer costs and allowing for better management of herbicides, pests and diseases (*Yates et al., 2024*).

Agroecology is one of the most used terms lately when farmers want to obtain organic production using ecological systems, being a system of practices that allow food production in a sustainable way without the use of agrochemicals. So ecological / organic farming also translates into a more ecologically sustainable and socially equitable agriculture.

Agroecology can also be defined as the application of ecological concepts and principles to the design and management of sustainable agroecosystems, with conversion to sustainable agriculture involving three levels of investigation: improving the efficiency of conventional agricultural inputs and practices in ways that reduce their quantities and the environmental impact of their use; replacing conventional inputs and practices with alternatives that meet broader environmental standards, i.e. the agroecosystem is redesigned to operate on a new set of ecological processes (*Gliessman, 2004*). Agroecology can be considered as the solution to the many challenges of the agricultural and food system, and can become a model for transforming agriculture towards more sustainable and resilient agri-food systems, with an important role played by new and emerging technologies related to digitalization and reproduction (*Ewert et al., 2023*).

Organic and regenerative agriculture is gaining ground in response to the negative environmental impacts of commercial agriculture, focusing on sustainable practices that improve biodiversity, water efficiency, and climate resilience. Global organic agriculture has grown significantly and its market has reached high values, with the US having the largest market share (*Boris and Lal, 2015; Mpanga et al., 2021*).

The Water-Energy-Food Framework (WEF) is a system developed to guide cross-sectoral policymaking, maximizing synergies and minimizing conflicts between water, energy and food systems (*Almulla et al. 2021*). In recent decades, European cities have even begun to reintegrate urban farms and gardens into their plans, promoting policies that support urban agriculture to meet the demands for local food, biodiversity and sustainable development (*Fox-Kämper et al., 2023*).

Adoption of sustainable agricultural practices depends on factors such as household wealth, age of household head, education and size (*Okello et al., 2021*). Studies suggest that authorities and agricultural development agencies should focus on increasing household assets and promoting training programs to support the adoption of these new practices (*Oyetunde-Usman et al., 2021*). Because the adoption of agri-environmental management mechanisms is somewhat of a voluntary process, it presents implementation difficulties for individual producers (*Van Wyngaarden et al., 2024*).

Ecological farming has gained considerable attention in recent decades, especially in the context of global climate change. It not only promotes sustainable practices, but also contributes to the reduction of greenhouse gas emissions (*Smith et al., 2014; Sun et al., 2020; Alhassan et al., 2021*). Studies show that organic farming can significantly reduce the carbon footprint of the agricultural sector (*Garnett et al., 2015*).

Another essential aspect of organic farming is crop diversification, which helps increase the resilience of agricultural systems to climate change (*Altieri and Nicholls, 2017*). By using crop rotation and perennials, farmers can improve soil health and reduce erosion, critical issues in the context of extreme weather events (*Kremen and Miles, 2012*). Ecological farming also promotes the use of renewable resources and water management techniques, which is crucial in the face of increasingly frequent droughts (*Lal, 2015*). Agroecological practices, such as agroforestry, contribute to carbon sequestration and improve biodiversity (*Milder et al., 2016*). Another important benefit of ecological / organic farming is its ability to support local communities and promote food security. By reducing dependence on chemical inputs and promoting local products, organic farming can contribute to circular economies and sustainable development (*Gliessman, 2015*).

A study by *Seitz et al. (2019)* evaluated the effect of different agricultural practices on soil erosion, comparing ecological farming, conventional farming, and no-tillage farming. The results indicated that ecological farming reduces sediment delivery by 30% compared to conventional farming, and the use of reduced tillage in ecological farming decreases sediment loss by 61% compared to intensive tillage.

According to *FAO (2018)*, organic agriculture plays a vital role in adapting to and mitigating the effects of climate change. By promoting sustainable practices, it not only helps protect the environment, but also contributes to the well-being of rural communities and global food security. It is essential that agricultural policies integrate the principles of organic agriculture to respond to the challenges posed by climate change and ensure a sustainable future for future generations.

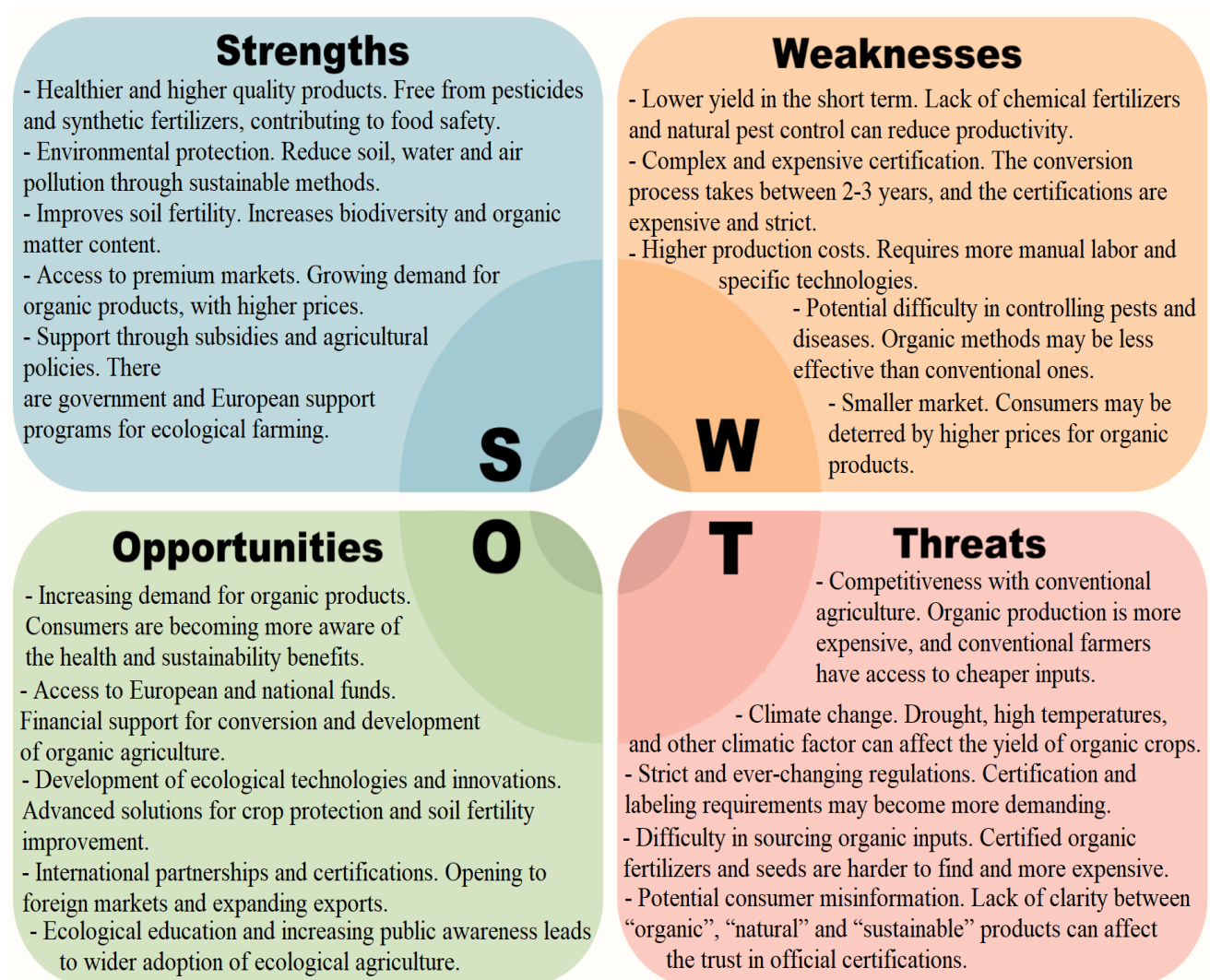


Fig. 11 – SWOT analysis of implementing ecological agriculture

ECOLOGICAL SOLUTIONS FOR SOIL FERTILIZATION AND CROP PROTECTION

Biofertilizers used in organic farming have numerous benefits (they eliminate chemical fertilizers) but also limitations (they do not have the same effect on weeds and pests as chemicals) (*Ritika and Utpal, 2014*), so that always, a correct analysis must be made regarding the final impact on agricultural production, regardless of how much is used (*Carvajal-Muñoz and Carmona-Garcia, 2012; Nabti et al., 2016*).

Biofertilizers can also be obtained from the algae used in the treatment of dairy wastewater and pig manure (*Mulbury et al., 2008*). To increase soil fertility using organic fertilizers, soil health boosters (Kaur, 2020) based on micro and macro algae (*Chapman, 2013; Silva and Bahcevandzjev, 2019; Chittora et al., 2020; Ammar et al., 2022*) can be used, proposing an effective approach, replacing inorganic and organic fertilizers that have a polluting impact on the soil (*Gonçalves, 2021*). The use of microalgae has also been extended to the cultivation of tomatoes in hydroponic cultures (*Zhang et al., 2017; Barone et al., 2019*) or in greenhouses (*Coppenes et al., 2016; Alobwede et al., 2019; Suleiman et al., 2020*) and not only that, they can have multiple applications as biofertilizers (*Chatterjee et al., 2017; Guo et al., 2020*) and even improve the productivity and salt stress tolerance of plants (*Hashem et al., 2019*), sandy and clay soil fertility (*Izzati et al., 2019*), they can have a biostimulatory role but also be a biofertilizer in vegetable crops (*Ronga et al., 2019*).

Another potential approach for sustainable crop production was studied by *Nosheen et al. (2021)*, who pursued the use of microbes as biofertilizers in agriculture, respectively for wastewater remediation using algae, simultaneously with the production of biofertilizers (*Zou et al., 2021*).

Ecological farming uses a variety of plant protection products approved by different countries, depending on local crops, pests and specific regulations. These products include biorational, inorganic, botanical, microbial, oil-based and soap-based pesticides, and some natural substances, such as nettle decoction, are

used for pest control. In addition, EU regulation 1107/2009 introduced the concept of "basic substances", which are not primarily intended for plant protection but can be legally used in organic farming, such as food products as vinegar or sunflower oil, with the exception of herbicides. (*El-Shafie, 2019*).

There is also a growing concern among agricultural scientists and the general public about the many problems associated with the use/reliance on herbicides, with direct threats to human health. Based on this concern, ecological management of agricultural weeds proposes alternative approaches, less dependent on herbicides and more on the understanding and manipulation of resources, allelopathy, disease, seed and seedling responses to soil cultivation and succession. Crop diversification can sustainably manage weeds in crop production systems, combined with the use of technological innovations that use non-chemical methods (*Teasdale, 1996*). As a result of crop diversification, weed density can be reduced by negatively impacting weed germination and subsequent growth. At the same time, diversified agricultural systems will be more resilient to climate change than monoculture systems and will provide better crop yields.

Combating trends in the use of synthetic fertilizers, pesticides and other plant protection substances is addressed within the framework of the European Union's Common Agricultural Policy, which aims for a 20% reduction in fertilizer use and a 50% reduction in pesticide use (*Slijper et al., 2023*).

WATER CONSERVATION THROUGH ECOLOGICAL AND SUSTAINABLE AGRICULTURAL PRACTICES

Water conservation is essential to protect water resources and ensure a sustainable future. Techniques such as efficient irrigation, mulching, crop rotation, and the use of cover crops reduce water loss and maintain soil moisture, preventing drought and land degradation. Ecological practices minimize water pollution from pesticides and chemical fertilizers, protecting aquatic ecosystems and drinking water quality. Adopting these methods not only supports agricultural production, but also the ecological balance, contributing to the resilience of communities in the face of climate change.

The creation and management of riparian buffer zones is considered an essential practice globally for improving the health of watercourses. In agricultural areas, they are often used as productive pastures, which can lead to increased levels of nutrients and sediment in the water, as well as reducing the capacity to sequester carbon and protect natural biodiversity (*Cambardella and Elliott, 1992*). An innovative approach to applying multisystem ecological and economic models, facilitating quantification at the property level, with reduced costs and greater speed, has been proposed by researchers *Malcher et al. (2023)*.

In the Northern Ireland region, short rotation coppice (SRC), grown as a riparian buffer in intensive agriculture, has been proposed as a solution to improve agricultural sustainability, contributing both to reducing greenhouse gas emissions and preventing water quality degradation, while the impact on food production remains minimal (*Livingstone et al., 2023*). In the coastal regions of the San Quintín Bay, salt marshes and seagrass have the ability to filter trace amounts of toxic elements from the environment. These plant ecosystems thus function as natural biofilters, protecting the environment from contaminants and helping to maintain the health of adjacent ecosystems (*Cuellar-Martinez et al., 2021*).

Retention lakes represent an innovative and sustainable solution for water management in agriculture, addressing the critical challenge of water availability during dry seasons (*Staccione et al., 2021*). These artificial or natural reservoirs are designed to capture and store excess water during periods of heavy rainfall, such as in the winter, and release it gradually for use in agricultural irrigation during droughts or dry seasons. This approach not only ensures a consistent water supply for crops but also helps mitigate the risks associated with water scarcity, which is becoming more frequent due to climate change. In addition to supporting irrigation, retention lakes play a crucial role in maintaining a minimum ecological flow in rivers, ensuring that aquatic ecosystems remain healthy even during periods of reduced rainfall. This is particularly important for preserving biodiversity and preventing the complete drying of riverbeds, which can have severe consequences for local wildlife and communities that depend on these water sources. Moreover, retention lakes can reduce the risk of flooding in agricultural areas by capturing excess runoff, protecting both crops and infrastructure. When integrated with other sustainable practices, such as efficient irrigation systems (e.g., drip irrigation) and crop rotation, retention lakes become a cornerstone of resilient water management strategies in agriculture. They not only improve water security but also contribute to the overall sustainability of farming systems, helping farmers adapt to the challenges posed by climate variability.

Micro-dams are used to reduce runoff, soil erosion and transport of crop protection products (CPPs) in agricultural fields. Research has shown that micro-dams can reduce runoff by an average of 62% (for corn and potatoes, the reduction was 62% and 81%, respectively), and soil erosion by an average of 73% (75% for corn and 89% for potatoes). PPP transport was also reduced by an average of 67%, with a significant reduction for

potatoes (91%). These results suggest that micro-dams can be integrated into environmental exposure assessments, by reducing the percentage of runoff, erosion and transport of CPPs or by decreasing the runoff curve number in numerical models (*Sittig and Sur, 2023*).

SOIL CONSERVATION THROUGH ECOLOGICAL AND SUSTAINABLE AGRICULTURAL PRACTICES

The European Commission, in the European Union Thematic Strategy for Soil, identified the following 7 soil functions that must be protected: biomass production, including in agriculture and forestry; storage, filtration and transformation of nutrients, substances and water; reservoir of biodiversity, such as habitats, species and genes; physical and cultural environment for people and human activities; source of raw materials; carbon sink; archive of geological and archaeological heritage.

Soil conservation and security gain global prominence as they are linked to crop production and global climate, soil contamination and human health, agriculture and ecosystem services, and the Millennium Sustainable Development Goals. Sustainable Development Indicator 15.3.1. assesses the degree of degradation by measuring soil carbon, land cover and productivity (*Thomas et al., 2023*).

Given that a large part of the population of developing and underdeveloped countries is dependent to a large extent on agriculture, animal husbandry and fishing, and modern and mechanized technologies are almost non-existent, their existence is directly linked to the quality of the land and its resources, and the role of sustainable management of agricultural land is of vital importance for the inhabitants of these states (*FAO, 2000; Alemu, 2016; Tey et al., 2017; Xiao et al., 2021*).

Ecological soil management is an alternative for healthy soils, based on the concept of “building soils as a solution for better crops” (*Magdof and Van Es, 2009*). Organic matter is the key to healthy soils and depending on the percentage of organic matter in the soil, we will benefit from a healthier soil. This is influenced by the physical properties of the soil, the degree of its degradation, but also by the cycles and flows of carbon and nutrients in the soil. Ecological soil management is influenced by factors such as: soil health, plant health and pests, and to obtain high-quality soils, organic matter management, diversification of crop systems, integration of crops and animals, use of composts, reduction of runoff and erosion, reduction of compaction, minimization of soil cultivation, water management: irrigation and drainage, and nutrient management must be taken into account.

Conservation tillage in ecological farming has several advantages, such as reducing soil erosion, improving macroporosity, carbon storage, increasing microbial activity, reducing nutrient runoff and fuel consumption, allowing for faster tillage. Disadvantages include increased pressure from perennial grasses, incompatibility with poorly drained or unstable soils, and limited crop options due to reduced nitrogen availability. The success of this method depends on the correct choice of crop rotation, management of weed and disease control, and adaptation to local soil and terrain conditions (*Peigné et al., 2007*).

Applying best management practices is a long-term conservation effort and can be achieved by adopting structural conservation practices to reduce soil erosion and surface water runoff (*Prokopy et al., 2008; Gedikoglu et al., 2011; Martins et al., 2021*). However, the geographical distribution of these practices is not very widespread, and for their digital mapping, timely and spatially explicit inventories of the areas to be mapped must be carried out. The development of such mapping is of real use for conservation programs, the geospatial inventory being easily accessible information for the evaluation of large-scale conservation practices on cultivated lands in a region / country.

Adopting regenerative agriculture practices on temperate arable lands can increase soil organic carbon concentrations without reducing yields, and can be considered a climate change mitigation strategy. Some studies in the UK show that the use of cover crops can increase stocks by an average of 10 t·ha⁻¹ within 30 years of adoption, sequestering approximately 6.5 megatons of carbon dioxide per year (Mt CO₂·y⁻¹) (*Powlson et al., 2016; Jordon et al., 2022*).

The application of biochar obtained by pyrolysis of corn straw instead of lime is a solution that has been shown to improve the physicochemical properties of the soil and its resistance to reacidification. The results showed that the application of biochar can significantly reduce soil acidity, from 8.2 ± 0.8 meq 100 g⁻¹ to 1.9 ± 0.3 meq 100 g⁻¹, considerably decreasing the bioavailability of nickel. (*Becerra-Agudelo et al., 2022*).

Within negative emission technologies, biochar obtained from forest residues represents a mature option for capturing and storing carbon in soils (*Ogle et al., 2019*). Studies show that biochar can generate negative CO₂ emissions, with additional benefits for agricultural yields and reduced air and marine pollution, but also some trade-offs regarding tropospheric ozone formation, land acidification and ecological toxicity. In

Norway, at the national level, biochar could offset between 13-40% of greenhouse gas emissions from the agricultural sector (*Tisserant et al., 2022*).

The aim of a research study by *Devine et al. (2022)* was to develop a guide for estimating the “time to trafficability” of soil (the period during which the soil is suitable for agricultural work and traffic), using data from soil surveys and hydroclimatological models. The study showed that fine and loamy soils have a longer time to trafficability in the cold months, and seasonal effects were more pronounced in loamy soils. The models developed allow mapping of typical time to trafficability and can help in decision-making regarding the management of aquifer recharge and soil compaction risks.

Cruz-Ramírez et al. (2012) studied the role of conservation agriculture in reducing soil erosion in olive groves and soil protection with cover crops between rows. Given the high erosion of olive soils in Spain and especially in the Andalusian area, the authorities have taken subsidy measures and developed regulations to stimulate the establishment of cover crops between rows in olive groves, using a method based on multi-objective neural networks to classify olive trees, bare soil and different cover crops, respectively, using remote sensing data recorded in spring and summer.

THE IMPACT OF CONSERVATION AND ECOLOGICAL AGRICULTURE ON BIODIVERSITY

Although biodiversity is a key factor for sustainable agriculture, measures to protect it are rarely put into practice by farmers, the main causes being different perceptions between scientists and farmers regarding the importance and implementation of these measures (*Maas et al., 2021*).

A key aspect of ecological / organic farming is its beneficial impact on biodiversity. Organic practices, such as crop rotation, the use of perennials, and the avoidance of chemical pesticides, play a crucial role in creating and maintaining a diverse habitat for numerous plant and animal species (*Kremen and Miles, 2012*). This biological diversity contributes not only to the health and resilience of ecosystems, but also to the improvement of ecosystem services, such as natural pest control and soil fertility, and to a stable food supply.

Organic farms have between 46-72% more semi-natural habitats, 30% more species, and 50% more individuals than non-organic farms, depending on altitude (*Pfiffner and Balmer, 2011*).

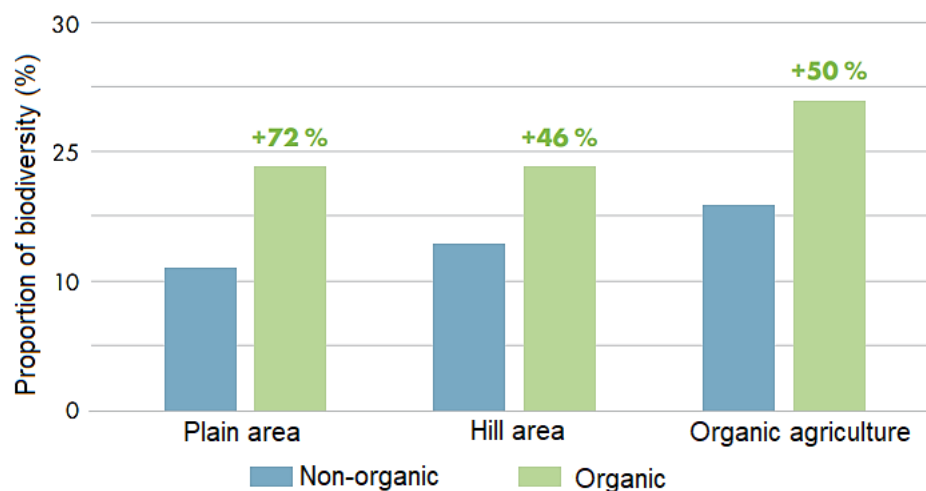


Fig. 12 – Proportion of biodiversity by altitude, in non-organic vs. organic farms (*Pfiffner and Balmer, 2011*)

A notable example is the support provided by biological diversity to the pollination process, an indispensable element for global food production. Increased biodiversity ensures the presence of a diverse range of pollinators, such as bees, butterflies and other beneficial insects, which, in turn, directly influence the quality and quantity of agricultural crops (*Potts et al., 2016*). In addition, organic systems reduce the risk of ecological imbalances caused by the intensive use of chemicals, thus protecting vulnerable species and contributing to the long-term regeneration of agricultural ecosystems.

Understanding how soil biology can influence soil health, soil properties and biological processes contributes to the sustainability of agriculture and ecosystem services. Through appropriate soil management (no-tillage) it is possible to influence (increase) microbial biomass and modify community profiles in soil aggregates (*Helgason et al., 2010*), this aggregation being important for soil functioning, as it provides physical protection of organic matter and microbial inhabitants and tillage disturbs aggregates, increases soil erosion (wind and water) and exposes previously protected organic matter to decomposition and loss.

Lehman et al. (2015) have analyzed how soil biology can be manipulated to increase nutrient availability for high-yield, high-quality crops, protect crops from pests, pathogens, weeds, and manage other factors that can limit production, the provision of ecosystem services, and stress resistance. Such an understanding and improvement of soil biological health may be the solution to reversing soil degradation (*Lal, 1994; Eswaran et al., 2001*).

The effects of tillage practices on the populations, functions and interactions of soil organisms depend on tillage systems that can affect the physical and chemical soil environment in which soil organisms live, directly affecting them (*Kladivko, 2001*). These practices alter soil water content, temperature, aeration and the degree of mixing of crop residues in the soil matrix (*Rochette, 2008*), affecting soil organisms, and understanding the impact of management on the complex interactions of all organisms at the soil level is a challenge for soil ecology research. Through the implemented practices, conservation agriculture can contribute to improving the ecology of aquatic ecosystems and increasing biodiversity (*Voicea et al., 2024*). It is true that soil conservation agricultural practices have been promoted and used mainly to improve soil health and mitigate soil loss, but an additional benefit of these practices has been to reduce the negative impact of agricultural runoff on aquatic ecosystems (*Lizotte et al., 2021*).

Analyzing ecological responses to conservation agriculture practices, it emerged that in about 40% of the studies there was a positive response to these practices – increased biodiversity (*Zedler, 2003; Moore and Palmer, 2005; Cullum et al., 2006; Moore et al., 2007a; Moore et al., 2007b; Schäfer et al., 2007; Smith et al., 2007a; Smith et al., 2007b; Maret et al., 2008; Smiley et al., 2008; Ellison et al., 2009; Knight et al., 2010; Lizotte et al., 2010a; Lizotte et al., 2010b; James et al., 2011; Christensen et al., 2012; McKinney, 2012; Sarkar et al., 2012; Seger et al., 2012; Knight et al., 2013; Withers et al., 2014; Smiley and Rumora, 2015; Ullah et al., 2015; Bullerjahn et al., 2016; Gbaguidi et al., 2016; Hall et al., 2017; Hunt et al., 2017; Kovalenko et al., 2019; Larned and Schallenberg, 2019; Moran et al., 2019; Goeller et al., 2020; Smith et al., 2020; Sander, 2021; and in almost 41% of the studies it had no visible ecological impact (*Boesch et al., 2001; Zablotowicz et al., 2001; Knight and Welch, 2002; Paerl et al., 2003; Knight and Welch, 2004; Carey et al., 2005; Carey et al., 2007; Moore et al., 2007c; Knight et al., 2008; Stephens et al., 2008; Utley et al., 2008; Todd et al., 2009; Smiley and Gillespie, 2010; Todd et al., 2010; Zablotowicz et al., 2010; Brooks et al., 2011; Smiley et al., 2011; Lizotte et al., 2012a; Lizotte et al., 2012b; Lizotte et al., 2012c; Lizotte et al., 2012d; Smiley et al., 2012; Knight and Cullum, 2014; Knight et al., 2015; Pearce and Yates, 2015; Porter et al., 2015; Whittaker et al., 2015; Wronski et al., 2015; Holmes et al., 2016; Álvarez et al., 2017; Wainger et al., 2017; Tsaboula et al., 2019; Lüring and Mucci, 2020) and in two out of two studies the influences were negative (*Chapman et al., 2008; Sarkar et al., 2020*).**

In almost all developed countries (USA, European Union, Japan, Canada, etc.) there are agricultural agencies that support farmers with programs to implement a variety of practices for agricultural conservation and in recent years their actions have also been directed to counteract the loss of habitat, biodiversity and ecosystem services, correlated with increased eutrophication and harmful algal blooms that are directly influenced by global population growth and climate change.

Therefore, conservation and ecological / organic agriculture not only supports sustainable food production, but also actively contributes to protecting biodiversity and maintaining the health of ecosystems, offering a viable solution to the challenges generated by climate change and the loss of natural habitats. However, it should be noted that activities aimed at expanding conservation agriculture and implementing these types of agriculture, although contributing considerably to solving ecological problems and preserving soil fertility, are also linked to the creation of favorable conditions for the development of harmful organisms.

THE IMPACT OF CONSERVATION AND ECOLOGICAL AGRICULTURE ON FOOD SECURITY AND LOCAL ECONOMIES

Conservation and ecological agriculture is increasingly recognized as a cornerstone of sustainable development, particularly in the face of climate change and economic instability. By prioritizing soil health, water conservation, and biodiversity, this model ensures that farming systems remain productive and adaptable over time. Practices such as crop rotation, cover cropping, and reduced tillage not only improve soil fertility but also enhance the capacity of the land to withstand extreme weather events like droughts or floods. For vulnerable communities, where access to resources is limited, ecological agriculture offers a cost-effective alternative to conventional methods reliant on expensive synthetic inputs. Farmers can cultivate healthy and diverse crops (*Gliesman, 2015*) using locally available organic fertilizers, pest management techniques, and traditional knowledge, reducing dependency on external inputs and market fluctuations.

A significant benefit of ecological / organic farming is its positive impact on local economies. By promoting local products and reducing dependence on external inputs, organic farmers contribute to circular economies and sustainable development. This not only supports the local economy, but also reduces the carbon footprint associated with transporting food. For example, recent studies highlight that organic farming can generate higher incomes for small farmers, due to the increased demand for organic products and the premium prices they attract (FAO, 2020). At the same time, by stimulating local markets and short supply chains, organic farming reduces the vulnerability of rural communities to global food price fluctuations (IPES-Food, 2021).

Thus, conservation and ecological farming represents not only a solution for sustainable food production, but also an opportunity to strengthen local economies, reduce inequalities and protect natural resources for future generations. Through its integrated approach, this agricultural model can respond to both economic and environmental challenges.

CONCLUSIONS

Conservation and organic agriculture plays a fundamental role in shaping the future of sustainable agriculture, having a significant impact on soil health, agricultural productivity and ecosystems.

By implementing practices such as crop rotation, the use of cover crops, and reduced tillage, these methods contribute to the conservation of natural resources while promoting biodiversity, reducing greenhouse gas emissions, and combating climate change. At the same time, organic agriculture supports food security and local economic development by reducing dependence on chemical inputs and stimulating circular economies. However, the success of these practices depends on close collaboration between farmers, researchers, authorities and civil society. Only through a collective effort to integrate these methods into a sustainable and accessible framework will the people be able to ensure a healthier, more equitable and more resilient agricultural future for future generations.

However, for effective large-scale implementation, further research is needed to address the technical, economic and social challenges associated with these systems. A key area of research is the optimization of crop rotations and permanent soil cover for different climatic conditions and soil types. Future studies should assess how specific combinations of cover crops and nitrogen-fixing plants influence soil fertility and agricultural productivity in the long term. Further investigation is also needed into the mechanisms by which conservation and organic agriculture can contribute to increased soil carbon sequestration. Research should determine the long-term impact of these practices on greenhouse gas emission reduction and climate change adaptation.

ACKNOWLEDGEMENT

This paper was financed by the European Union-NextGenerationEU, through the National Recovery and Resilience Plan of the Republic of Bulgaria, project № BG-RRP-2.013-0001-C01 and by the Ministry of Agriculture and Rural Development through the project ADER 25.1.2 - Innovative technology for minimum agricultural land processing adapted to current climate changes, contr. 25.1.2 / 14.07.2023.

REFERENCES

- [1] Abdalla, M., Hastings, A., Chadwick, D.R., Jones, D.L., Evans, C.D., Jones, M.B., Smith, P.E.T.E. (2018). Critical review of the impacts of grazing intensity on soil organic carbon storage and other soil quality indicators in extensively managed grasslands. *Agriculture, Ecosystems & Environment*, 253, 62–81. DOI: <https://doi.org/10.1016/j.agee.2017.10.023>.
- [2] Abdulai, A.N. (2016). Impact of conservation agriculture technology on household welfare in Zambia. *Agricultural Economics*, 47(6), 99, 729–741. DOI: 10.1111/agec.12269.
- [3] Aguilera, E., Lassaletta, L., Gattinger, A., Gimeno, B.S. (2013). Managing soil carbon for climate change mitigation and adaptation in Mediterranean cropping systems: a meta-analysis. *Agriculture, Ecosystems & Environment*, 168, 25–36. DOI: 10.1016/j.agee.2013.02.003.
- [4] Aguilera, E., Reyes-Palomo, C., Díaz-Gaona, C., Sanz-Cobena, A., Smith, P., García-Laureano, R., Rodríguez-Estévez, V. (2021). Greenhouse gas emissions from Mediterranean agriculture: Evidence of unbalanced research efforts and knowledge gaps. *Global Environmental Change*, 69, 102319. DOI: <https://doi.org/10.1016/j.gloenvcha.2021.102319>.
- [5] Ahmed, Z., Shew, A., Nalley, L., Popp, M., Green, V.S., Brye, K. (2024). An examination of thematic research, development, and trends in remote sensing applied to conservation agriculture. *International Soil and Water Conservation Research*, 12, 77–95. DOI: <https://doi.org/10.1016/j.iswcr.2023.04.00>.

- [6] Alemu, M.M (2016). Sustainable land management. *Journal of Environmental Protection*, 7(4). DOI: 10.4236/jep.2016.74045.
- [7] Alhassan, A.M., Yang, C., Ma, W., Li, G. (2021). Influence of conservation tillage on Greenhouse gas fluxes and crop productivity in spring-wheat agroecosystems on the Loess Plateau of China. *PeerJ*, 12(9), e11064. DOI: 10.7717/peerj.11064. PMID: 33954028.
- [8] Almulla, Y., Ramirez, C., Joyce, B., Huber-Lee, A., Fuso-Nerini, F. (2022). From participatory process to robust decision-making: an agriculture-water-energy nexus analysis for the Souss-Massa basin in Morocco. *Energy for Sustainable Development*, 70, 314–338. <https://doi.org/10.1016/j.esd.2022.08.009>.
- [9] Alobwede, E., Leake, J.R., Pandhal, J. (2019). Circular economy fertilization: Testing micro and macro algal species as soil improvers and nutrient sources for crop production in greenhouse and field conditions. *Geoderma*, 334, 113–123. DOI: <https://doi.org/10.1016/J.GEODERMA.2018.07.049>.
- [10] Altieri, M.A., Nicholls, C.I. (2017). Agroecology and the design of climate change resilient farming systems. *Agronomy for Sustainable Development*, 37(1), 1-15.
- [11] Altikat, S., Kuş, E., Küçükerdem, H.K., Gülbe, A. (2018). The importance of the conservation agriculture for Turkey. *Journal of the Institute of Science and Technology*, 8(2), 73-80.
- [12] Alvarez, R. (2005). A review of nitrogen fertilizer and conservation tillage effects on soil organic carbon storage. *Soil Use and Management*, 21(1), 38–52. DOI: 10.1079/SUM2005291.
- [13] Álvarez, X., Valero, E., Santos, R.M.B., Varandas, S.G.P., Sanches Fernandes, L.F., Pacheco, F.A.L. (2017). Anthropogenic nutrients and eutrophication in multiple land use watersheds: best management practices and policies for the protection of water resources. *Land Use Policy*, 69, 1-11. DOI: <https://doi.org/10.1016/j.landusepol.2017.08.028>.
- [14] Ammara, E.E., Aioub, A.A.A., Elesawy, A.E., Karkour, A.M., Mouhamed, M.S., Amer, A.A., El-Shershaby, N.A. (2022). Algae as bio-fertilizers: between current situation and future prospective. *Saudi Journal of Biological Sciences*, 29, 3083–3096. DOI: <https://doi.org/10.1016/j.sjbs.2022.03.020>.
- [15] Ammon, H.U., Garibay, S., Bohren, C. (1995). The use of dead or living mulch in maize and its suppression with herbicides. *Proceedings of the 9th European Weed Research Society Symposium*, Budapest, Hungary, 527-534.
- [16] Andersson, J.A., D'Souza, S. (2014). From adoption claims to understanding farmers and contexts: a literature review of Conservation Agriculture (CA) adoption among smallholder farmers in southern Africa. *Agriculture, Ecosystems & Environment*, 187, 116–132. DOI: 10.1016/j.agee.2013.08.008
- [17] Anderson, A. E., Hammac, W.A., Stott, D.E., Tyner, W.E. (2020). An analysis of yield variation under soil conservation practices. *Journal of Soil and Water Conservation*, 75(1), 103–111. DOI: 10.2489/jswc.75.1.103.
- [18] Angers, D.A., N'dayegamiye, A., Côté, D. (1993). Tillage-induced differences in organic matter of particle size fractions and microbial biomass. *Soil Science Society America Journal*, 57(2). DOI: 10.2136/sssaj1993.03615995005700020035x.
- [19] Angers, D.A., Carter, M.R (1995). Aggregation and organic matter storage in cool, humid agricultural soils. *Structure and Organic Matter Storage in Agricultural Soils*, 1st Edition, 19 p. DOI: 10.1201/9781003075561-9.
- [20] Angers, D.A., Carter, M.R., Gregorich, E.G., Bolinder, M.A., Donald, R.G., Voroney, R.P., Drury, C.F., Liang, B.C., Simard, R.R., Beyaerf, R.P. (1995). Agriculture management effects on carbon sequestration in eastern Canada, NATO ASI Series, 33. https://link.springer.com/chapter/10.1007/978-3-642-79943-3_17.
- [21] Angers, D.A., Bolinder, M.A., Carter, M.R., Gregorich, E.G., Drury, C.F., Liang, B.C., Voroney, R.P., Simard, R.R., Donald, R.G., Beyaert, R.P., Martel, J. (1997). Impact of tillage practices on organic carbon and nitrogen storage in cool, humid soils of eastern Canada. *Soil and Tillage Research*, 41(3–4), 191–201. DOI: 10.1016/S0167-1987(96)01100-2.
- [22] Apraku, A., Morton, J.F., Gyampoh, B.A. (2021). Climate change and small-scale agriculture in Africa: Does indigenous knowledge matter? *Insights from Kenya and South Africa*, *Scientific African*, 12, e00821. DOI: <https://doi.org/10.1016/j.sciaf.2021.e00821>.
- [23] Araya, T., Cornelis, W.M., Nyssen, J., Govaerts, B., Getnet, F., Bauer, H., Amare, K., Raes, D., Haile, M., Deckers, J. (2012). Medium-term effects of conservation agriculture based cropping systems for sustainable soil and water management and crop productivity in the Ethiopian highlands. *Field Crops Research*, 132, 53–62. DOI: 10.1016/j.fcr.2011.12.009.

- [24] Arora, V.K., Singh, C.B., Sidhu, A.S., Thind, S.S. (2011). Irrigation, tillage and mulching effects on soybean yield and water productivity in relation to soil texture. *Agricultural Water Management*, 98, 563–568. DOI: <https://doi.org/10.1016/j.agwat.2010.10.004>.
- [25] Arbuckle, J.G., Roesch-McNally, G. (2015). Cover crop adoption in Iowa: The role of perceived practice characteristics. *Journal of Soil and Water Conservation* 70(6), 418–429. DOI: 10.2489/jswc.70.6.418
- [26] Ares, A., Thierfelder, C., Reyes, M., Eash, N.S., Himmelstein, J. (2015). Global perspectives on conservation agriculture for small households. *Conservation Agriculture in Subsistence Farming: Case Studies from South Asia and Beyond*, 22–54. DOI: 10.1079/9781780644233.0022.
- [27] Baker, C.J., Saxton, K.E., Ritchie, W.R., Chamen, W.C.T., Reicosky, D.C., Ribeiro, F., Justice, S.E., Hobbs, P.R. (2007). No-tillage seeding in conservation agriculture. Second edition. Food and Agriculture Organization of the United Nations. <https://openknowledge.fao.org/server/api/core/bitstreams/5c811ec9-0b86-4eb3-b816-b88c099af857/content>.
- [28] Barone, V., Puglisi, I., Fragalà, F., Roberta Lo Piero, A., Giuffrida, F., Baglieri, A. (2019). Novel bioprocess for the cultivation of microalgae in hydroponic growing system of tomato plants. *Journal of Applied Phycology*, 31, 465-470. DOI: <https://doi.org/10.1007/s10811-018-1518-y>.
- [29] Baudron, F., Tiftonell, P., Corbeels, M., Letourmy, P., Giller, K. E. (2012). Comparative performance of conservation agriculture and current smallholder farming practices in semi-arid Zimbabwe. *Field Crops Research*, 132, 117–128. DOI: 10.1016/j.fcr.2011.09.008.
- [30] Baumgart-Getz, A., Prokopy, L.S., Floress, K. (2012). Why farmers adopt best management practice in the United States: A meta-analysis of the adoption literature. *Journal of Environmental Management*, 96(1), 17–25. DOI: 10.1016/j.jenvman.2011.10.006.
- [31] Bayer, C., Lovato, T., Dieckow, J., Zanatta, J.A., Mielniczuk, J. (2006a). A method for estimating coefficients of soil organic matter dynamics based on long-term experiments. *Soil and Tillage Research*, 91(1), 217-226. DOI: 10.1016/j.still.2005.12.006.
- [32] Bayer, C., Martin-Neto, L., Mielniczuk, J., Pavinato, A., and Dieckow, J. (2006b). Carbon sequestration in two Brazilian Cerrado soils under no-till. *Soil and Tillage Research*, 86(2), 237-245. DOI: 10.1016/j.still.2005.02.023.
- [33] Beare, M.H., Coleman, D.C., Pohlard, B. R., Wright, D.H. (1993). Residue placement and fungicide effects on fungal communities in conventional and no-tillage soils. *Soil Science Society of America Journal*, 57(2), 392-399. DOI: 10.2136/sssaj1993.03615995005700020018x.
- [34] Beare, M.H., Hendrix, P.F., Cabrera, M.L., Coleman, D.C. (1994). Aggregate-protected and unprotected organic matter pools in conventional - and no-tillage soils. *Soil Science Society of America Journal*, 58, 787-796.
- [35] Becerra-Agudelo, E., López, J.E., Betancur-García, H., Carbal-Guerra, J., Torres-Hernández, M., Saldarriaga, J.F. (2022). Assessment of the application of two amendments (lime and biochar) on the acidification and bioavailability of Ni in a Ni-contaminated agricultural soils of northern Colombia. *Heliyon*, 8(8). DOI: 10.1016/j.heliyon.2022.e10221.
- [36] Beeson, P.C., Daughtry, C.S.T., Hunt, E.R., Akhmedov, B., Sadeghi, A.M., Karlen, D.L., Tomer, M.D. (2016). Multispectral satellite mapping of crop residue cover and tillage intensity in Iowa. *Journal of Soil and Water Conservation*, 71, 385–395. DOI: <https://doi.org/10.2489/jswc.71.5.385>.
- [37] Beeson, P.C., Daughtry, C.S.T., Wallander, S.A. (2020). Estimates of conservation tillage practices using landsat archive. *Remote Sensing*, 12. <https://doi.org/10.3390/RS12162665>.
- [38] Belknap, J., Saupe, W.E. (1988). Farm family resources and the adoption of no-plow tillage in southwestern Wisconsin. *North Central Journal of Agricultural Economics*, 10(1), 13–23. DOI: <https://doi.org/10.2307/1349232>.
- [39] Bellotti, B., and Rochecouste, J.F. (2014). The development of conservation agriculture in Australia-Farmers as innovators. *International Soil and Water Conservation Research*, 2(1), 21–34. DOI: 10.1016/S2095-6339(15)30011-3.
- [40] Bernoux, M., Cerri, C.C., Cerri, C.E.P., Siqueira-Neto, M., Metay, A., Perrin, A.S., Scopel, E., Razafimbelo, T., Blavet, D., de Cassia Piccolo, M., Pavei, M., Milne, E. (2006). Cropping systems, carbon sequestration and erosion in Brazil, a review. *Agronomy for Sustainable Development*, 26(1), 1–8. DOI: 10.1051/agro:2005055.
- [41] Beuchelt, T.D., Villa, C.T.C., Gohring, L., Rodriguez, V.M.H., Hellin, J., Sonder, K., et al. (2015). Social and income trade-offs of conservation agriculture practices on crop residue use in Mexico's central highlands. *Agricultural Systems*, 134, 61–75. DOI: 10.1016/j.agsy.2014.09.003.

- [42] Bhan, S., Behera, U.K. (2014). Conservation agriculture in India – problems, prospects and policy issues. *International Soil and Water Conservation Research*, 2(4), 1–12. DOI: 10.1016/S2095-6339(15)30053-8.
- [43] Bockus, W.W., Shroyer, J.P. (1998). The impact of reduced tillage on soilborne plant pathogens. *Annual Review of Phytopathology*, 36, 485–500. DOI: 10.1146/annurev.phyto.36.1.485.
- [44] Boesch, D.F., Brinsfield, R.B., Magnien, R.F. (2001) Chesapeake Bay eutrophication: scientific understanding, ecosystem restoration, and challenges for agriculture. *Journal of Environmental Quality*, 30(2), 303–320. DOI: <https://doi.org/10.2134/jeq2001.302303x>.
- [45] Boris, B., Rattan Lal, R. (2015). Conservation Agriculture on Chernozems in the Republic of Moldova. *Soil Management of Smallholder Agriculture*, CRC Press, 203–221.
- [46] Bosch, D.J., Cook, Z.L., Fuglie, K.O. (1995). Voluntary versus mandatory agricultural policies to protect water quality: Adoption of nitrogen testing in Nebraska. *Review of Agricultural Economics*, 17(1), 13–24. DOI: <https://digitalcommons.unl.edu/usdaarsfacpub/1856>.
- [47] Braim, M.A., Chaney, K., Hodgson, D.R. (1992). Effects of simplified cultivation on the growth and yield of spring barley on a sandy loam soil. 2. Soil physical properties and root growth; root: shoot relationships, inflow rates of nitrogen; water use. *Soil and Tillage Research*, 22(1–2), 173–187. DOI: 10.1016/0167-1987(92)90030-F.
- [48] Bravo, C.A., Giraldez, J.V., Ordonez, R., Gonzalez, P., Torres, F.P. (2007). Long-term influence of conservation tillage on chemical properties of surface horizon and legume crops yield in a vertisol of southern Spain. *Soil Science*, 172(2), 141–148. DOI: 10.1097/ss.0b013e31802db198.
- [49] Brooks, R.P., Yetter, S.E., Carline, R.F., Shortle, J.S., Bishop, J.A., Ingram, H., Weller, D., Boomer, K., Stedman, R., Armstrong, A., Mielcarek, K., Constantz, G., Goslee, S.C., Vieith, T., Piechnik, D. (2011). Analysis of BMP Implementation Performance and Maintenance in Spring Creek, an Agriculturally Influenced Watershed in Pennsylvania; Riparia, Pennsylvania State University, *USDA Project Number: PENW-2006-03984*.
- [50] Brouder, S.M. și Gomez-Macpherson, H. (2014). The impact of conservation agriculture on smallholder agricultural yields: a scoping review of the evidence. *Agriculture, Ecosystems & Environment*, 187, 11–32. DOI: 10.1016/j.agee.2013.08.010.
- [51] Brown, B., Nuberg, I., and Llewellyn, R. (2017). Negative evaluation of conservation agriculture: perspectives from African smallholder farmers. *International Journal of Agricultural Sustainability*, 15(4), 467–481. DOI: 10.1080/14735903.2017.1336051.
- [52] Brye, K.R., Pirani, A.L. (2005). Native soil quality and the effects of tillage in the grand prairie region of eastern Arkansas. *The American Midland Naturalist*, 154, 1, 28–41. DOI: <https://www.jstor.org/stable/3566613>.
- [53] Bularda, M., Vișinescu, I., Ghiorghe, A., Vlăduț, V., Cujbescu, D. (2020). The effect of conservative agricultural works on soil and field plants and optimized mechanization technologies. *INMATEH - Agricultural Engineering*, 61(2), 35–42. DOI: <https://doi.org/10.35633/inmateh-61-35>.
- [54] Bullerjahn, G.S., McKay, R.M., Davis, T.W., Baker, D.B.; Boyer, G.L., D'Anglada, L.V., Doucette, G.J., Ho, J.C., Irwin, E.G., Kling, C.L., Kudela, R.M., Kurmayer, R., Michalak, A.M., D Ortiz, J., Otten, T.G., Paerl, H.V., Qin, B., Sohngen, B.L., Stumpf, R.P., Visser, P.M., Wilhelm, S.W. (2016). Global solutions to regional problems: collecting global expertise to address the problem of harmful cyanobacterial blooms. A Lake Erie case study. *Harmful Algae*, 54, 223–238. DOI: 10.1016/j.hal.2016.01.003.
- [55] Bullock, D.G. (1992). Crop rotation. *Critical Reviews in Plant Sciences*, 11(4), 309–326. DOI: <https://doi.org/10.1080/07352689209382349>.
- [56] Burnett, E.A. (2014). *The influence of farmer stress and hardiness on adoption of best management practices in the Maumee Watershed*. Master's thesis, 116 p., The Ohio State University, http://rave.ohiolink.edu/etdc/view?acc_num=osu1405694911.
- [57] Buttel, F.H. (2006). Sustaining the unsustainable: agro-food systems and environment in the modern world. *The Handbook of Rural Studies*, 213–229. London: SAGE Publications Ltd. DOI: 10.4135/9781848608016.n15.
- [58] Camarotto, C., Dal Ferro, N., Piccoli, I., Polese, R., Furlan, L., Chiarini, F., Morari, F. (2018). Conservation agriculture and cover crop practices to regulate water, carbon and nitrogen cycles in the low-lying Venetian plain. *Catena*, 167, 236–249. DOI: 10.1016/j.catena.2018.05.006.
- [59] Cambardella, J.C.A., Elliott, E.T. (1992). Particulate soil organic-matter changes across a grassland cultivation sequence. *Soil Science Society America Journal*, 56, 777–783. DOI: <https://doi.org/10.2136/sssaj1992.03615995005600030017x>.

- [60] Candiago, S., Remondino, F., De Giglio, M., Dubbini, M., Gattelli, M. (2015). Evaluating multispectral images and vegetation indices for precision farming applications from UAV images. *Remote Sensing*, 7(4), 4026–4047. DOI: <https://doi.org/10.3390/rs70404026>.
- [61] Carey, R., Vellidis, G., Lowrance, R., Pringle, C. (2005). Nutrient Enrichment and Stream Periphyton Growth in the Southern Coastal Plain of Georgia. *American Society of Agricultural and Biological Engineers (ASAE)*, Paper No. 052197, 1–13. DOI: 10.13031/2013.19021.
- [62] Carey, R., Vellidis, G., Lowrance, R., Pringle, C. (2007). Do nutrients limit algal periphyton in small blackwater coastal plain streams? *Journal of the American Water Resources Association*, 43(5), 1183–1193.
- [63] Carlisle, L. (2016). Factors influencing farmer adoption of soil health practices in the United States: a narrative review. *Agroecology and Sustainable Food Systems*, 40(6), 583–613. DOI: 10.1080/21683565.2016.1156596.
- [64] Carter, M.R. (1991). Evaluation of shallow tillage for spring cereals on a fine sandy loam. 1. Growth and yield components, N accumulation and tillage economics. *Soil and Tillage Research*, 21(1), 23–35. DOI: 10.1016/0167-1987(91)90003-G.
- [65] Carter, M.R. (1994). A review of conservation tillage strategies for humid temperate regions. *Soil and Tillage Research*, 31(4), 289–301. DOI: [https://doi.org/10.1016/0167-1987\(94\)90037-X](https://doi.org/10.1016/0167-1987(94)90037-X).
- [66] Carvajal-Muñoz, J.S., Carmona-Garcia, C.E. (2012). Benefits and limitations of biofertilization in agricultural practices. *Livestock Research for Rural Development*, 24, 1–8.
- [67] Carvalho, M., Lourenco, E. (2014). Conservation agriculture - a Portuguese case study. *Journal of Agronomy and Crop Science*, 200(5), 317–324. DOI: 10.1111/jac.12065.
- [68] Caswell, M., Fuglie, K.O., Ingram, C., Jans, S., Kascak, C. (2001). Adoption of Agricultural Production Practices: Lessons Learned from the US Department of Agriculture Area Studies Project. *Agricultural Economics Reports 33985*, Washington, USDA Economic Research Service.
- [69] Cârdei, P., Nenciu, F., Ungureanu, N., Pruteanu, A., Vlăduț, V., Cujbescu, D., Găgeanu, I., Cristea, O. (2021). Using statistical modeling for assessing lettuce crops contaminated with Zn, correlating plants growth characteristics with the soil contamination levels. *Applied Sciences – Basel*, 11(17), 8261. DOI: 10.3390/app11178261.
- [70] Cârdei, P., Constantin, N., Muraru, V., Persu, C., Sfiru, R., Vlăduț, N-V., Ungureanu, N., Matache, M., Muraru-Ionel, C., Cristea, O-D., Laza, E-A. (2023a). The random vibrations of the active body of the cultivators. *Agriculture*, 13(8), 1565. DOI: 10.3390/agriculture13081565.
- [71] Cârdei, P., Constantin, N., Muraru, V., Persu, C., Sfiru, R., Lateș, D. (2023b). Estimation of the random intensity of the soil tillage draft forces in the supports of the working bodies of a cultivator. *INMATEH - Agricultural Engineering*, 71(3), 58–65. DOI: <https://doi.org/10.35633/inmateh-71-58>.
- [72] Chapman, R.L. (2013). Algae: the world’s most important “plants” – an introduction. *Mitigation and Adaption Strategies for Global Change*, 18, 5–12. DOI: <https://doi.org/10.1007/s11027-010-9255-9>.
- [73] Chamberlain, L.A., Bolton, M.L., Cox, M.S., Suen, G., Conley, S.P., Ané, J.M. (2020). Crop rotation, but not cover crops, influenced soil bacterial community composition in a corn-soybean system in southern Wisconsin. *Applied Soil Ecology*, 154(7), 103603. DOI: 10.1016/j.apsoil.2020.103603.
- [74] Chan, K.Y., Roberts, W.P., Heenan, D.P. (1992). Organic carbon and associated properties of a red earth after 10 years rotation under different stubble and tillage practices. *Australian Journal of Soil Research*, 30(1), 71–83. DOI: 10.1071/SR9920071.
- [75] Chapman, L.J., Chapman, C.A., Kaufman, L., Witte, F., Balirwa, J. (2008). Biodiversity conservation in African inland waters: Lessons of the Lake Victoria region. *SIL Proceedings. Internationale Vereinigung für Theoretische und Angewandte Limnologie: Verhandlungen*, 30(1), 16–34. DOI: 10.1080/03680770.2008.11902077.
- [76] Chatterjee, A., Singh, S., Agrawal, C., Yadav, S., Rai, R., Rai, L.C. (2017). Role of Algae as a Biofertilizer (chapter 10). *Algal Green Chemistry. Recent Progress in Biotechnology*, 189–200. DOI: <https://doi.org/10.1016/B978-0-444-63784-0.00010-2>.
- [77] Chen, Z., Wang, J. (2010). Land use and land cover change detection using satellite remote sensing techniques in the mountainous Three Gorges Area, China. *International Journal of Remote Sensing*, 31(6), 1519–1542. DOI: <https://doi.org/10.1080/01431160903475381>.
- [78] Chittora, D., Meena, M., Barupal, T., Swapnil, P. (2020). Cyanobacteria as a source of biofertilizers for sustainable agriculture. *Biochemistry and Biophysics Reports*, 22. DOI: <https://doi.org/10.1016/J.BBREP.2020.100737>.

- [79] Christopher, S.F., Lal, R., Mishra, U. (2009). Regional study of no-till effects on carbon sequestration in the Midwestern United States. *Soil Science Society of America Journal*, 73(1), 207–216. DOI: 10.2136/sssaj2007.0336.
- [80] Christensen, V.G., Lee, K.E., McLees, J.M., Niemela, S.L. (2012). Relations between retired agricultural land, water quality, and aquatic community health, Minnesota River Basin. *Journal of Environmental Quality*, 41(5), 1459–1472. DOI: <https://doi.org/10.2134/jeq2011.0468>.
- [81] Claassen, R., Bowman, M., McFadden, J., Smith, D., Wallander, S. (2018). Tillage intensity and conservation cropping in the United States. *Economic Information Bulletin* no. 197, USDA - Economic Research Service. https://ers.usda.gov/sites/default/files/_laserfiche/publications/90201/EIB-197.pdf?v=48745
- [82] Conceição, P.C., Dieckow, J., Bayer, C. (2013). Combined role of no-tillage and cropping systems in soil carbon stocks and stabilization. *Soil and Tillage Research*, 129, 40–47. DOI: 10.1016/j.still.2013.01.006.
- [83] Cooper, J.C., Keim, R.W. (1996). Incentive payments to encourage farmer adoption of water quality protection practices. *American Journal of Agricultural Economics*, 78(1), 54–64. DOI: <http://hdl.handle.net/10.2307/1243778>.
- [84] Coppens, J., Grunert, O., Van Den Hende, S., Vanhoutte, I., Boon, N., Haesaert, G., De Gelder, L. (2016). The use of microalgae as a high-value organic slow-release fertilizer results in tomatoes with increased carotenoid and sugar levels. *Journal of Applied Phycology*, 28, 2367–2377. DOI: <https://doi.org/10.1007/S10811-015-0775-2>.
- [85] Corbeels, M., de Graaff, J., Ndah, T.H., Penot, E., Baudron, F., Naudin, K., Andrieu, N., Chirat, G., Schuler, J., Nyagumbo, I., Rusinamhodzi, L., Traore, K., Mzoba, H.D., Adolwa, I.S. (2014). Understanding the impact and adoption of conservation agriculture in Africa: a multi-scale analysis. *Agriculture, Ecosystems & Environment*, 187, 155–170. DOI: 10.1016/j.agee.2013.10.011.
- [86] Croitoru, Șt., Marin, E., Bădescu, M., Vlăduț, V., Ungureanu, N., Manea, D., Boruz, S., Matei, Gh. (2015). Agrotechnical and energetic characteristics of new designed subsoiler. *Proceedings of the 43rd International Symposium on Agricultural Engineering "Actual Tasks on Agricultural Engineering"*, 165–176, Opatija, Croatia.
- [87] Croitoru, Șt., Vlăduț, V., Marin, E., Matache, M., Dumitru, I. (2016). Determination of subsoiler's traction force influenced by different working depth and velocity. *15th International Scientific Conference "Engineering for Rural Development"*, 15, 817–825, Jelgava, Latvia.
- [88] Croitoru, Șt., Vlăduț, V., Voicea, I., Gheorghe, Gh., Marin, E., Vlăduțoiu, L., Moise, V., Boruz, S., Pruteanu, A., Andrei, S., Păunescu, D. (2017). Structural and kinematic analysis of the mechanism for arable deep soil loosening. *Proceedings of the 45th International Symposium on Agricultural Engineering "Actual Tasks on Agricultural Engineering"*, 207–216, Opatija, Croatia.
- [89] Cruz-Ramírez, M., Hervás-Martínez, C., Jurado-Exposito, M., Lopez-Granados, F. (2012). A multi-objective neural network based method for cover crop identification from remote sensed data. *Expert Systems with Applications*, 39(11), 10038–10048. DOI: <https://doi.org/10.1016/j.eswa.2012.02.046>.
- [90] Cujbescu, D., Ungureanu, N., Vlăduț, V., Persu, C., Oprescu, M.R., Gheorghiuță, N.E. (2019). Field testing of compaction characteristics for farm tractor Universal 445. *INMATEH - Agricultural Engineering* 59(3), 27–34. DOI: <https://doi.org/10.35633/inmateh-59-27>.
- [91] Cujbescu, D., Găgeanu, I., Persu, C., Matache, M., Vlăduț, V., Voicea, I., Paraschiv, G., Biriș, S.Șt., Ungureanu, N., Voicu, Gh., Ipate, G. (2021). Simulation of sowing precision in laboratory conditions. *Applied Sciences - Basel*, 11(14), 6264. DOI: 10.3390/app11146264.
- [92] Cullum, R.F., Knight, S.S., Cooper, C.M., Smith, S. (2006). Combined effects of best management practices on water quality in Oxbow lakes from agricultural watersheds. *Soil and Tillage Research*, 90(1-2), 212–221. DOI: <https://doi.org/10.1016/j.still.2005.09.004>.
- [93] Dalal, R.C. (1989). Long-term effects of no-tillage, crop residue, and nitrogen applications on properties of a vertisol. *Soil Science Society America Journal*, 53(5), 1511–1515. DOI: 10.2136/sssaj1989.03615995005300050035x.
- [94] Dalal, R.C., Wang, W., Allen, D.E., Reeves, S., Menzies, N.W. (2011). Soil nitrogen and nitrogen-use efficiency under long-term no-till practice. *Soil Science Society America Journal*, 75(6), 2251–2261. DOI: 10.2136/sssaj2010.0398.
- [95] Dang, Y.P., Balzer, A., Crawford, M., Rincon-Florez, V., Liu, H., Melland, A.R., Antille, D., Kodur, S., Bell, M.J., Whish, J.P.M., Lai, Y., Seymour, N., Carvalhais L.C., Schenk, P. (2018). Strategic tillage in conservation agricultural systems of north-eastern Australia: why, where, when and how? *Environment Science and Pollution Research*, 25, 1000–1015. DOI: 10.1007/s11356-017-8937-1.

- [96] Dang, Y.P., Seymour, N.P., Walker, S.R., Bell, M.J., Freebairn, D.M. (2015). Strategic tillage in no-till farming systems in Australia's northern grains-growing regions: I. Drivers and implementation. *Soil and Tillage Research*, 152, 104–114. DOI: 10.1016/j.still.2015.03.009.
- [97] Daughtry, C.S.T., Hunt, E.R., Doraiswamy, M.M. (2005). Remote sensing the spatial distribution of crop residues. *Agronomy Journal*, 97(3), 864–871. DOI: <https://doi.org/10.2134/agronj2003.0291>.
- [98] Daughtry, C.S.T., Hunt, E.R. (2008). Mitigating the effects of soil and residue water contents on remotely sensed estimates of crop residue cover. *Remote Sensing of Environment*, 112(4), 1647–1657. DOI: <https://doi.org/10.1016/j.rse.2007.08.006>.
- [99] Dauphin, F. (2003). Investing in conservation agriculture. *Conservative Agriculture*, 445–456. DOI: 10.1007/978-94-017-1143-2_54.
- [100] Davis, A.S., Hill, J.D., Chase, C.A., Johanns, A.M., Liebman, M. (2012). Increasing cropping system diversity balances productivity, profitability and environmental health. *PLOS One*, 7(10), e47149, 1–8. DOI: <https://doi.org/10.1371/journal.pone.0047149>.
- [101] Dawkins, M., Dolan, L., Fraser, D., Herrero, M., Hoffmann, I., Smith, P., Thornton, P. K., Toulmin, C., Vermeulen, S.J., Godfray, H.C.J. (2015). Sustainable intensification in agriculture: premises and policies. *Science*, 348(6230), 1–9.
- [102] Dayer, A.A., Lutter, S.H., Sesser, K.A., Hickey, C.M., Gardali, T. (2018). Private landowner conservation behavior following participation in voluntary incentive programs: recommendations to facilitate behavioral persistence. *Conservation Letters*, 11(2), 1–11. DOI: 10.1111/conl.12394.
- [103] Debonne, N., Bürgi, M., Diogo, V., Helfenstein, J., Herzog, F., Levers, C., Verburg, P. (2022). The geography of megatrends affecting European agriculture. *Global Environmental Change*, 75, 102551. DOI: <https://doi.org/10.1016/j.gloenvcha.2022.102551>.
- [104] Deng, Y. (2021). Pollution in rainwater harvesting: A challenge for sustainability and resilience of urban agriculture. *Journal of Hazardous Materials Letters*, 2, 100037. DOI: <https://doi.org/10.1016/j.hazl.2021.100037>.
- [105] Devine, S.M., Dahlke, H.E., O'Geen, A.T. (2022). Mapping time-to-trafficability for California agricultural soils after dormant season deep wetting. *Soil and Tillage Research*, 218, 105316. DOI: <https://doi.org/10.1016/j.still.2022.105316>.
- [106] Devkota, M., Devkota, K.P., Acharya, S., McDonald, A.J. (2019). Increasing profitability, yields and yield stability through sustainable crop establishment practices in the rice-wheat systems of Nepal. *Agricultural Systems*, 173, 414–423. DOI: 10.1016/j.agsy.2019.03.022.
- [107] Dhar, A.R., Islam, M.M., Jannat, A., Ahmed, J.U. (2018). Adoption prospects and implication problems of practicing conservation agriculture in Bangladesh: a socioeconomic diagnosis. *Soil and Tillage Research*, 176, 77–84. DOI: 10.1016/j.still.2017.11.003.
- [108] Di Ciocco, C., Coviella, C., Penón, E., Díaz-Zorita, M., López, S. (2008). Short communication. Biological fixation of nitrogen and N balance in soybean crops in the pampas region. *Spanish Journal of Agricultural Research* 6, 114–119. DOI: <https://doi.org/10.5424/sjar/2008061-5259>.
- [109] Ding, Y. (2018). The role of government policies in the adoption of conservation tillage in China: a theoretical model. *IOP Conference Series: Earth and Environmental Science*, 108(4), 1–8. DOI: 10.1088/1755-1315/108/4/042012.
- [110] Dorfman, J.H. (1996). Modeling multiple adoption decisions in a joint framework. *American Journal of Agricultural Economics*, 78(3), 547–557. DOI: <https://doi.org/10.2307/1243273>.
- [111] Dou, F., Wright, A.L., Hons, F.M. (2008). Sensitivity of labile soil organic carbon to tillage in wheat-based cropping systems. *Soil Science Society America Journal*, 72, 1445–1453. DOI: 10.2136/sssaj2007.0230.
- [112] Du, Z., Angers, D.A., Ren, T., Zhang, Q., Li, G. (2017). The effect of no-till on organic C storage in Chinese soils should not be overemphasized: a meta-analysis. *Agriculture, Ecosystems & Environment* 236, 1–11. DOI: 10.1016/j.agee.2016.11.007
- [113] Duiker, S.W., Lal, R. (2002). Mulch rate and tillage effects on carbon sequestration and CO₂ flux in an Alfisol in central Ohio (Chapter 5). *Agricultural Practices and Policies for Carbon Sequestration in Soil*, Lewis Publishers, Boca Raton, 53–61. DOI: 10.1201/9781420032291.pt2.
- [114] Duiker, S.W., Beegle, D.B. (2006). Soil fertility distributions in long-term no-till, chisel/disk and moldboard plow/disk systems. *Soil and Tillage Research*, 88, 30–41. DOI: 10.1016/j.still.2005.04.004
- [115] Dunlap, R.E., Van Liere, K.D., Mertig, A.G., Jones, R.E. (2000). New trends in measuring environmental attitudes: measuring endorsement of the new ecological paradigm: a revised NEP scale. *Journal of Social Issues*, 56(3), 425–442. DOI: <https://doi.org/10.1111/0022-4537.00176>.

- [116] Dunn, M., Ulrich-Schad, J.D., Prokopy, L.S., Myers, R.L., Watts, C.R., Scanlon, K. (2016). Perceptions and use of cover crops among early adopters: findings from a national survey. *Journal of Soil and Water Conservation*, 71(1), 29–40. DOI: 10.2489/jswc.71.1.29.
- [117] Ellison, C.A., Skinner, Q.D., Hicks, L.S. (2009). Assessment of best-management practice effects on rangeland stream water quality using multivariate statistical techniques. *Rangeland Ecology & Management*, 62(4), 371–386. DOI: 10.2111/08-026.1.
- [118] El-Shafie, H.A.F. (2019). Insect pest management in organic farming system. *Multifunctionality and Impacts of Organic and Conventional Agriculture*, 1–20. DOI: 10.5772/intechopen.84483.
- [119] Emadodin, I., Narita, D., Bork, H.R. (2012). Soil degradation and agricultural sustainability: an overview from Iran. *Environment, Development and Sustainability*, 14, 611–625. DOI: <https://doi.org/10.1007/s10668-012-9351-y>.
- [120] Eswaran, H., Lal, R., Reich, P.F. (2001). Land degradation: an overview. Responses to land degradation. *Proceedings of the 2nd International Conference on Land Degradation and Desertification*, Khon Kaen, Oxford Press, New Delhi.
- [121] Ewert, F., Baatz, R., Finger, R. (2023). Agroecology for a sustainable agriculture and food system: from local solutions to large-scale adoption. *Annual Review of Resource Economics*, 15, 351–381. DOI: <https://doi.org/10.1146/annurev-resource-102422-090105>.
- [122] Fageria, N.K., Baligar, V.C., Bailey, B.A. (2005). Role of cover crops in improving soil and row crop productivity. *Communications in Soil Science and Plant Analysis*, 36(19–20), 2733–2757. DOI: 10.1080/00103620500303939.
- [123] Food and Agriculture Organization of the United Nations - FAO. (2000). *Global Network on Integrated Soil*. Food and Agriculture Organization of the United Nations, Rome.
- [124] Food and Agriculture Organization of the United Nations - FAO. (2018). *The State of Food and Agriculture 2018*. Food and Agriculture Organization of the United Nations, Rome.
- [125] Food and Agriculture Organization of the United Nations - FAO. (2020). *The State of Food and Agriculture 2020: Overcoming Water Challenges in Agriculture*. Food and Agriculture Organization of the United Nations, Rome.
- [126] Fatima, N., Shuaib, S. E., Kong, J.D. (2023). Predicting adaptations of fish and fishing communities to rapid climate velocities in Canadian waters: a systematic review. *Environmental Advances*, 100452. DOI: <https://doi.org/10.1016/j.envadv.2023.100452>.
- [127] Feeney, C.J., Robinson, D.A., Thomas, A.R., Borrelli, P., Cooper, D.M., May, L. (2023). Agricultural practices drive elevated rates of topsoil decline across Kenya, but terracing and reduced tillage can reverse this. *Science of the Total Environment*, 870, 161925. DOI: <https://doi.org/10.1016/j.scitotenv.2023.161925>.
- [128] Fishbein, M., Ajzen, I. (2010). Predicting and changing behavior: the reasoned action approach. *Psychology Press*, Hove, UK, 538 p. DOI: <https://doi.org/10.4324/9780203838020>.
- [129] Fox-Kämper, R., Kirby, C.K., Specht, K., Cohen, N., Ilieva, R., Caputo, S., Béchet, B. (2023). The role of urban agriculture in food-energy-water nexus policies: insights from Europe and the US. *Landscape and Urban Planning*, 239, 104848. DOI: <https://doi.org/10.1016/j.landurbplan.2023.104848>.
- [130] Francaviglia, R., Di Bene, C., Farina, R., Salvati, L. (2017). Soil organic carbon sequestration and tillage systems in the Mediterranean Basin: a data mining approach. *Nutrient Cycling in Agroecosystems*, 107, 125–137. DOI: 10.1007/s10705-016-9820-z.
- [131] Franzluebbers, A.J. (2010). Achieving soil organic carbon sequestration with conservation agricultural systems in the Southeastern United States. *Soil Science Society America Journal*, 74, 347–357. DOI: 10.2136/sssaj2009.0079.
- [132] Frye, W.W., Blevins, B.L., Smith, M., Corak, S.J., Varco, J.J. (1988). Role of annual legume cover crops in efficient use of water and nitrogen, *Agricultural and Food Sciences. Environmental Science*, 129–153. ASA Special Publication No. 51. DOI: 10.2134/ASASPEC PUB51.C8.
- [133] de Freitas, P.L., Landers, J.N. (2014). The transformation of agriculture in Brazil through development and adoption of zero tillage conservation agriculture. *International Soil and Water Conservation Research*, 2(1), 35–46. DOI: 10.1016/S2095-6339(15)30012-5.
- [134] Fu, M., Li, R., Hao, Y., Meng, F., Zhou, J., Wang, C. (2023). Improved design and experiment of anti-clay adhesion for no tillage maize planter seeding monomer. *INMATEH - Agricultural Engineering*, 70(2), 33–40. DOI: <https://doi.org/10.35633/inmateh-70-33>.
- [135] Gabriel, J.L., Garrido, A., Quemada, M. (2013). Cover crops effect on farm benefits and nitrate leaching: Linking economic and environmental analysis. *Agricultural Systems*, 121, 23–32. DOI: 10.1016/j.agsy.2013.06.004.

- [136] Galloza, M.S., Crawford, M.M., Heathman, G.C. (2013). Crop residue modeling and mapping using landsat, ALI, Hyperion and airborne remote sensing data. *IEEE Journal of Selected Topics in Applied Earth Observations and Remote Sensing*, 6(2), 446–456. DOI: <https://doi.org/10.1109/JSTARS.2012.2222355>
- [137] Gamage, A., Gangahagedara, R., Gamage, J., Jayasinghe, N., Kodikara, N., Suraweera, P., Merah, O. (2023). Role of organic farming for achieving sustainability in agriculture. *Farming System*, 1(1), 100005. DOI: <https://doi.org/10.1016/j.farsys.2023.100005>.
- [138] Gao, F., Anderson, M.C., Hively, W.D. (2020). Detecting cover crop end-of-season using venms and sentinel-2 satellite imagery. *Remote Sensing*, 12, 1–22. DOI: <https://doi.org/10.3390/rs12213524>.
- [139] Garcia-Palacios, P., Alarcon, M.R., Tenorio, J.L., and Moreno, S.S. (2019). Ecological intensification of agriculture in drylands. *Journal of Arid Environment*, 167, 101–105. DOI: [10.1016/j.jaridenv.2019.04.014](https://doi.org/10.1016/j.jaridenv.2019.04.014).
- [140] Garnett, T., Appleby, M. C., Balmford, A., Bateman, I.J., Benton, T.G., Bloomer, P., Burlingame, B., Dawkins, M., Dolan, L., Fraser, D., Herrero, M., Hoffmann, I., Smith, P., Thornton, P.K., Toulmin, C., Vermeulen, S.J., Godfray, H.C.J. (2013). Agriculture. Sustainable intensification in agriculture: premises and policies. *Science*, 341(6141), 33–34. DOI: [10.1126/science.1234485](https://doi.org/10.1126/science.1234485).
- [141] Gbaguidi, H.M.A.G., Adite, A., Sossoukpe, E. (2016). Ecology and fish biodiversity of man-made lakes of Southern Benin (West Africa): implications for species conservation and fisheries management. *Journal of Environmental Protection*, 7(6), 874–894. DOI: [10.4236/jep.2016.76079](https://doi.org/10.4236/jep.2016.76079).
- [142] Ge, Y., Thomasson, J.A., Sui, R. (2011). Remote sensing of soil properties in precision agriculture: a review. *Frontiers of Earth Science*, 5(3), 229–238. DOI: <https://doi.org/10.1007/s11707-011-0175-0>.
- [143] Gedikoglu, H., McCann, L., Artz, G. (2011). Off-farm employment effects on adoption of nutrient management practices. *Agricultural and Resource Economics Review*, 40(2), 293–306. DOI: <https://doi.org/10.1017/S1068280500008078>.
- [144] Gelder, B.K., Kaleita, A.L., Cruse, R.M. (2009). Estimating mean field residue cover on midwestern soils using satellite imagery. *Agronomy Journal*, 101(3), 635–643. DOI: <https://doi.org/10.2134/agronj2007.0249>.
- [145] Gifford, R., Sussman, R. (2012). Environmental attitudes (Chapter 4). *The Oxford Handbook of Environmental and Conservation Psychology*, 65–80. DOI: <https://doi.org/10.1093/oxfordhb/9780199733026.013.0004>.
- [146] Gillespie, J., Kim, S., Paudel, H. (2007). Why don't producers adopt best management practices? An analysis of the beef cattle industry. *Agricultural Economics*, 36(1), 89–102. DOI: [10.1111/j.1574-0862.2007.00179.x](https://doi.org/10.1111/j.1574-0862.2007.00179.x).
- [147] Gliessman, S. R. (2015). Agroecology: the ecology of sustainable food systems. *CRC Press*.
- [148] Goeller, B.C., Febria, C.M., McKergow, L.A., Harding, J.S. (2020). Combining tools from edge-of-field to in-stream to attenuate reactive nitrogen along small agricultural waterways. *Water*, 12(2), 383. DOI: <https://doi.org/10.3390/w12020383>.
- [149] Gómez-Limón, J.A., Granado-Díaz, R. (2023). Assessing the demand for hydrological drought insurance in irrigated agriculture. *Agricultural Water Management*, 276, 108054. DOI: <https://doi.org/10.1016/j.agwat.2022.108054>.
- [150] Gonçalves, A.L. (2021). The use of microalgae and cyanobacteria in the improvement of agricultural practices: a review on their biofertilising, biostimulating and biopesticide roles. *Applied Sciences*, 11(2), 871. DOI: <https://doi.org/10.3390/APP11020871>.
- [151] Gonzalez-Sanchez, E.J., Kassam, A., Basch, G., Streit, B., Holgado-Cabrera, A., Trivino-Tarradas, P. (2016). Conservation agriculture and its contribution to the achievement of agri-environmental and economic challenges in Europe. *Aims Agriculture and Food*, 1(4), 387–408. DOI: [10.3934/agrfood.2016.4.387](https://doi.org/10.3934/agrfood.2016.4.387).
- [152] González-Sánchez, E.J., Ordóñez-Fernández, R., Carbonell-Bojollo, R., Veroz-González, O., Gil-Ribes, J.A. (2012). Meta-analysis on atmospheric carbon capture in Spain through the use of conservation agriculture. *Soil and Tillage Research*, 122, 52–60. DOI: [10.1016/j.still.2012.03.001](https://doi.org/10.1016/j.still.2012.03.001).
- [153] Gottlieb, P.D., Schilling, B.J., Sullivan, K., Esseks, J.D., Lynch, L., Duke, J.M. (2015). Are preserved farms actively engaged in agriculture and conservation? *Land Use Policy*, 45, 103–116. DOI: [10.1016/j.landusepol.2015.01.013](https://doi.org/10.1016/j.landusepol.2015.01.013).
- [154] Govaerts, B., Fuentes, M., Mezzalama, M., Nicol, J.M., Deckers, J., Etchevers, J.D., Figueroa-Sandoval B., Sayre K.D. (2007). Infiltration, soil moisture, root rot and nematode populations after 12 years of different tillage, residue and crop rotation managements. *Soil and Tillage Research*, 94(1), 209–219. DOI: [10.1016/j.still.2006.07.013](https://doi.org/10.1016/j.still.2006.07.013).

- [155] Govaerts, B., Mezzalama, M., Sayre, K.D., Crossa, J., Lichter, K., Troch, V., Vanherck, K., De Corte, P., Deckers, J. (2008). Long-term consequences of tillage, residue management, and crop rotation on selected soil micro-flora groups in the subtropical highlands. *Applied Soil Ecology*, 38(3), 197–210. DOI: 10.1016/j.apsoil.2007.10.009.
- [156] Gowda, P.H., Howell, T.A., Evett, S.R., Chavez, J.L., New, L. (2008). Remote sensing of contrasting tillage practices in the Texas Panhandle. *International Journal of Remote Sensing*, 29(12), 3477–3487. DOI: <https://doi.org/10.1080/01431160701581810>.
- [157] Gregorich, E.G., Rochette, P., Vanden Bygaart, A.J., Angers, D.A. (2005). Greenhouse gas contributions of agricultural soils and potential mitigation practices in Eastern Canada. *Soil and Tillage Research*, 83, 53–72. DOI: 10.1016/j.still.2005.02.009.
- [158] Guo, S., Wang, P., Wang, X., Zou, M., Liu, C., Hao, J. (2020). Microalgae as biofertilizer in modern agriculture. *Microalgae Biotechnology for Food, Health and High Value Products*, 397–411. DOI: https://doi.org/10.1007/978-981-15-0169-2_12.
- [159] Hagen, S.C., Delgado, G., Ingraham, P., Cooke, I., Emery, R., Fisk, J.P., Melendy, L., Olson, T., Patti, S., Rubin, N., Ziniti, B., Chen, H., Salas, W., Elias, P., Gustafson, D. (2020). Mapping conservation management practices and outcomes in the Corn Belt using the operational tillage information system (Optis) and the denitrification-decomposition (DNDC) model. *Land*, 9(11), 408, 1–23. DOI: <https://doi.org/10.3390/land9110408>.
- [160] Hall, K.R., Herbert, M.E., Sowa, S.P., Mysorekar, S., Woznicki, S.A., Nejadhashemi, P.A., Wang, L. (2017). Reducing current and future risks: using climate change scenarios to test an agricultural conservation framework. *Journal of Great Lakes Research*, 43(1), 59–68. DOI: 10.1016/j.jglr.2016.11.005.
- [161] Hama, J.R., Jorgensen, D.B.G., Diamantopoulos, E., Bucheli, T.D., Hansen, H.C.B., Strobel, B.W. (2022). Indole and quinolizidine alkaloids from blue lupin leach to agricultural drainage water. *Science of the Total Environment*, 834, 155283. DOI: <https://doi.org/10.1016/j.scitotenv.2022.155283>.
- [162] Hansen, N.C., Allen, B.L., Baumhardt, R.L., Lyon, D.J. (2012). Research achievements and adoption of no-till, dryland cropping in the semi-arid U.S. Great Plains. *Field Crops Research*, 132, 196–203. DOI: 10.1016/j.fcr.2012.02.021.
- [163] Harper, J.K., Roth, G.W., Garalejic, B., Skrbic, N. (2018). Programs to promote adoption of conservation tillage: a Serbian case study. *Land Use Policy*, 78, 295–302. DOI: 10.1016/j.landusepol.2018.06.028.
- [164] Hartwig, N.L., Hoffman, L.D. (1975). Suppression of perennial legume and grass cover crops for no-tillage corn. *Proceedings of the Northeastern Weed Science Society*, New York City, 82–88.
- [165] Hartwig, N.L. (1983). Crownvetch - a perennial legume “living mulch” for no-tillage crop production, *Proceedings of the Northeastern Weed Science Society* 37 (Suppl.), 28–38.
- [166] Hartwig, N.L., Ammon, H.U. (2017). Cover crops and living mulches. *Weed Science*, 50(6), 688–699. DOI: [https://doi.org/10.1614/0043-1745\(2002\)050\[0688:AIACCA\]2.0.CO](https://doi.org/10.1614/0043-1745(2002)050[0688:AIACCA]2.0.CO).
- [167] Hashem, H.A., Mansour, H.A., El-Khawass, S.A., Hassanein, R.A. (2019). The potentiality of marine macro-algae as bio-fertilizers to improve the productivity and salt stress tolerance of canola (*Brassica napus* L.) plants. *Agronomy*, 9(3), 146. DOI: <https://doi.org/10.3390/AGRONOMY9030146>.
- [168] Hatfield, J.L., Sauer, T.J., Prueger, J.H. (2001). Managing soils to achieve greater water use efficiency. *Agronomy Journal*, 93(2), 271–280. DOI: 10.2134/agronj2001.932271x.
- [169] Helgason, B.L., Walley, F.L., Germida, J.J. (2010). No-till soil management increases microbial biomass and alters community profiles in soil aggregates. *Applied Soil Ecology*, 46(3), 390–397. DOI: 10.1016/j.apsoil.2010.10.002.
- [170] Hemmat, A., Eskandari, I. (2004). Tillage system effects upon productivity of a dryland winter wheat–chickpea rotation in the northwest region of Iran. *Soil and Tillage Research*, 78, 69–81. DOI: 10.1016/j.still.2004.02.013
- [171] Hinrichs, C.C. (2014). Transitions to sustainability: a change in thinking about food systems change? *Agriculture and Human Values*, 31, 143–155. DOI 10.1007/s10460-014-9479-5.
- [172] Hively, W.D., Lamb, B.T., Daughtry, C.S.T., Shermeyer, J., McCarty, G.W., Quemada, M. (2018). Mapping crop residue and tillage intensity using WorldView-3 satellite shortwave infrared residue indices. *Remote Sensing*, 10(10), 1657. DOI: <https://doi.org/10.3390/rs10101657>.
- [173] Hively, W.D., Lang, M., McCarty, G.W., Keppler, J., Sadeghi, A., McConnell, L.L. (2009). Using satellite remote sensing to estimate winter cover crop nutrient uptake efficiency. *Journal of Soil and Water Conservation*, 64(5), 303–313. DOI: <https://doi.org/10.2489/jswc.64.5.303>.

- [174] Hively, W.D., Lee, S., Sadeghi, A.M., McCarty, G.W., Lamb, B.T., Soroka, A., Keppler, J., Yeo, I.Y., Moglen, G.E. (2020). Estimating the effect of winter cover crops on nitrogen leaching using cost-share enrollment data, satellite remote sensing, and Soil and Water Assessment Tool (SWAT) modeling. *Journal of Soil and Water Conservation*, 75(3), 362–375. DOI: <https://doi.org/10.2489/JSWC.75.3.362>.
- [175] Hively, W.D., Duiker, S., McCarty, G., Prabhakara, K. (2015). Remote sensing to monitor cover crop adoption in southeastern Pennsylvania. *Journal of Soil and Water Conservation*, 70(6), 340–352. DOI: <https://doi.org/10.2489/jswc.70.6.340>.
- [176] Hobbs, P.R., Sayre, K., Gupta, R. (2008). The role of conservation agriculture in sustainable agriculture. *Philosophical Transactions of the Royal Society B - Biological Sciences* 363, 543–555. DOI: <https://doi.org/10.1098/rstb.2007.2169>.
- [177] Holmes, R., Armanini, D.G., Yates, A.G. (2016). Effects of best management practice on ecological condition: does location matter? *Environmental Management*, 57(5), 1062–1076. DOI: 10.1007/s00267-016-0662-x.
- [178] Hooda, P.S., Moynagh, N., Svoboda, I.F., Anderson, H.A. (1998). A comparative study of nitrate leaching from intensively managed monoculture grass and grass-clover pastures. *The Journal of Agricultural Science*, 131(3), 267–275. DOI: <https://doi.org/10.1017/S0021859698005863>.
- [179] Hosseini, S.Z., Firouzi, S., Aminpanah, H., Sadeghnejhad, H.R. (2016). Effect of tillage system on yield and weed populations of soybean (*Glycin max* L.). *Anais da Academia Brasileira de Ciencinas*, 88, 377–384. DOI: <https://doi.org/10.1590/0001-3765201620140590>.
- [180] Huang, Y., Tao, B., Xiaochen, Z., Yang, Y., Liang, L., Wang, L., Jacinthe, P.A., Tian, H., Ren, W. (2021). Conservation tillage increases corn and soybean water productivity across the Ohio River Basin. *Agricultural Water Management*, 254, 106962. DOI: <https://doi.org/10.1016/j.agwat.2021.106962>.
- [181] Huggins, D.R., Allmaras, R.R., Clapp, C.E., Lamb, J.A., Randall G.W. (2007). Corn-soybean sequence and tillage effects on soil carbon dynamics and storage. *Soil Science Society of America Journal*, 71(1), 145–154. DOI: 10.2136/sssaj2005.0231
- [182] Hunt, L., Marrochi, N., Bonetto, C., Liess, M., Buss, D.F., Vieira da Silva, C., Chiu, M.C., Resh, V.H. (2017). Do riparian buffers protect stream invertebrate communities in South American Atlantic Forest agricultural areas? *Environmental Management*, 60(6), 1155–1170. DOI: 10.1007/s00267-017-0938-9.
- [183] Intergovernmental Panel on Climate Change – IPCC. (2023). *Climate Change 2023 Synthesis Report Summary for Policymakers*. https://www.ipcc.ch/report/ar6/syr/downloads/report/IPCC_AR6_SYR_SPM.pdf.
- [184] International Panel of Experts on Sustainable Food Systems - IPES-Food. (2021). *A long food movement: transforming food systems by 2045*. https://www.ipes-food.org/_img/upload/files/LongFoodMovementEN.pdf.
- [185] Ismail, I., Blevins, R. L., Frye, W.W. (1994). Long-term no-tillage effects on soil properties and continuous corn yields. *Soil Science Society of America Journal*, 58(1), 193–198. DOI: 10.2136/sssaj1994.03615995005800010028x.
- [186] Izzati, M., Haryanti, S., Setiari, N. (2019). The use of macroalga *Sargassum* sp. and *Gracilaria verrucosa* in improving sandy and clay soil fertility. *Journal of Physics. Conference Series*, 1217, 012179. DOI: <https://doi.org/10.1088/1742-6596/1217/1/012179>.
- [187] James, R.T., Havens, K.E., McOrmick, P., Jones, B., Ford, C. (2011). Water quality trends in shallow South Florida lakes and assessment of regional versus local forcing functions. *Critical Reviews In Environmental Science and Technology*, 41(S1), 576–607. DOI: 10.1080/10643389.2010.530581.
- [188] Jat, H.S., Datta, A., Choudhary, M., Sharma, P.C., Yadav, A.K., Choudhary, V., Gathala, M.K., Jat, M.L., McDonald, A. (2019). Climate smart agriculture practices improve soil organic carbon pools, biological properties and crop productivity in cereal-based systems of North-West India. *Catena*, 181, 104059. DOI: 10.1016/j.catena.2019.05.005.
- [189] Jat, R.K., Sapkota, T.B., Singh, R.G., Jat, M.L., Kumar, M., Gupta, R.K. (2014). Seven years of conservation agriculture in a rice–wheat rotation of Eastern Gangetic Plains of South Asia: yield trends and economic profitability. *Field Crops Research*, 164, 199–210. DOI: 10.1016/j.fcr.2014.04.015.
- [190] Johnson, J.M.F., Reicosky, D.C., Allmaras, R.R., Sauer, T.J., Venterea, R.T., Dell, C.J. (2005). Greenhouse gas contributions and mitigation potential of agriculture in the central USA. *Soil and Tillage Research*, 83(1), 73–94. DOI: 10.1016/j.still.2005.02.010.
- [191] Jones, O.R., Hauser, V.L., Popham, T.W. (1994). No-tillage effects on infiltration, runoff, and water conservation on dryland. *Transaction of ASAE*, 37(2), 473–479. DOI: 10.13031/2013.28099.
- [192] Jones, D.B., Harrison, S., Anderson, K., Whalley, W.B. (2019). Rock glaciers and mountain hydrology: a review. *Earth-Science Reviews*, 193, 66–90. DOI: <https://doi.org/10.1016/j.earscirev.2019.04.001>.

- [193] Jordon, M.W., Smith, P., Long, P.R., Bürkner, P.C., Petrokofsky, G., Willis, K.J. (2022). Can Regenerative Agriculture increase national soil carbon stocks? Simulated country-scale adoption of reduced tillage, cover cropping, and ley-arable integration using RothC. *Science of the Total Environment*, 825, 153955. DOI: <https://doi.org/10.1016/j.scitotenv.2022.153955>.
- [194] Kan, M., Partigoc, F., Gultekin, I., Arisoy, R.Z., Kaya, Y., Gultekin, S., Sahin, M., Aydogan, S., Ozdemir, F., Taner, A. (2018). Economical aspects of conservation agriculture (zero tillage – direct seeding) system in Turkey. *Fresenius Environmental Bulletin*, 27(5A), 3332–3341.
- [195] Karlen, D.L., Varvel, G.E., Bullock, D.G., Cruse, R.M. (1994) Crop rotations for the 21st century. *Advances in Agronomy*. 53(C), 1–45.
- [196] Kara, E., Ribaud, M., Johansson, R.C. (2008). On how environmental stringency influences adoption of best management practices in agriculture. *Journal of Environmental Management* 88(4), 1530–1537. DOI: 10.1016/j.jenvman.2007.07.029.
- [197] Kassam, A., Friedrich, T., Shaxson, F., Pretty, J. (2009). The spread of conservation agriculture: justification, sustainability and uptake. *International Journal of Agriculture Sustainability*, 7(4), 292–320. DOI: 10.3763/ijas.2009.0477.
- [198] Kaur, I. (2020) Seaweeds: soil health boosters for sustainable agriculture. *Soil Health*, 163–182. DOI: https://doi.org/10.1007/978-3-030-44364-1_10.
- [199] Kaye, J.P., Quemada, M. (2017). Using cover crops to mitigate and adapt to climate change. A review. *Agronomy for Sustainable Development*, 37(4), 1–17. DOI: 10.1007/s13593-016-0410-x.
- [200] Kc, K., Zhao, K., Romanko, M., Khanal, S. (2021). Assessment of the spatial and temporal patterns of cover crops using Remote Sensing. *Remote Sensing*, 13(14), 2689. DOI: <https://doi.org/10.3390/rs13142689>.
- [201] Kienzler, K.M., Lamers, J.P.A., McDonald, A., Mirzabaev, A., Ibragimov, N., Egamberdiev, O., Ruzibaev, E., Akramkhanov, A. (2012). Conservation agriculture in Central Asia - what do we know and where do we go from here? *Field Crops Research*, 132, 95–105. DOI: 10.1016/j.fcr.2011.12.008.
- [202] Kim, S., Gillespie, J.M., Paudel, K.P. (2005). The effect of socioeconomic factors on the adoption of best management practices in beef cattle production. *Journal of Soil and Water Conservation*, 60(3), 111–120.
- [203] Kladvik, E. J. (2001). Tillage systems and soil ecology. *Soil and Tillage Research*, 61(1–2), 61–76. DOI: 10.1016/S0167-1987(01)00179-9.
- [204] Knapp, S., van der Heijden, M.G. (2018). A global meta-analysis of yield stability in organic and conservation agriculture. *Nature Communications*, 9(1), 3632.
- [205] Knight, S.S., Welch, T.D. (2002). Ecological and water quality effects of the Mississippi Delta management systems evaluation area on Oxbow lakes. *Proceedings of the Mississippi Water Resources Conference*, 131–143, Raymond, MS, USA.
- [206] Knight, S.S., Welch, T.D. (2004). Evaluation of watershed management practices on Oxbow lake ecology and water quality. *Water Quality Assessments in the Mississippi Delta: Regional Solutions, National Scope*, Chapter 9, 119–132. DOI: 10.1021/bk-2004-0877.ch009.
- [207] Knight, S.S., Cullum, R.F., Cooper, C.M., Lizotte, R.E. (2008). Effects of suspended sediments on the chlorophyll-phosphorus relationship in Oxbow lakes. *International Journal of Ecology and Environmental Sciences*, 34(1), 1–6.
- [208] Knight, S.S., Lizotte, R.E., Smith, S., Bryant, C.T. (2010). Responses of *Hyalella azteca* to chronic exposure of Mississippi Delta sediments. *Journal of Environmental Science and Engineering*, 4(3), 1–12.
- [209] Knight, S.S., Locke, M.A., Smith, S. (2013). Effects of agricultural conservation practices on Oxbow lake watersheds in the Mississippi river alluvial plain. *Soil and Water Research*, 8(3), 113–123. DOI: 10.17221/45/2012-SWR.
- [210] Knight, S.S., Cullum, R.F. (2014). Effects of conservation practices on fisheries management. *Journal of Agriculture and Biodiversity Research*, 3(1), 1–8.
- [211] Knight, S., Cullum, R., Lizotte, R. (2015). The limnology of a Mississippi river alluvial plain Oxbow lake following the application of conservation practices. *Journal of Water Resource and Protection*, 7(9), 707–714. DOI: 10.4236/jwarp.2015.79058.
- [212] Knowler, D., Bradshaw, B. (2007). Farmers' adoption of conservation agriculture: a review and synthesis of recent research. *Food Policy*, 32(1), 25–48. DOI: 10.1016/j.foodpol.2006.01.003.
- [213] Kovalenko, K.E., Johnson, L.B., Brady, V.J., Ciborowski, J.J.H., Cooper, M.J., Gathman, J.P., Lamberti, G.A., Moerke, A.H., Ruetz, C.R., Uzarski, D.G. (2019). Hotspots and bright spots in functional and taxonomic fish diversity. *Freshwater Science*, 38(3), 480–490. DOI: <https://doi.org/10.1086/704713>.

- [214] Kraft, S.E., Lant, C., Gillman, K. (1996). WQIP: An assessment of its chances for acceptance by farmers. *Journal of Soil and Water Conservation*, 51(6), 494–498.
- [215] Kremen, C., Miles, A. (2012). Ecosystem services in biologically diversified versus conventional farming systems: benefits, externalities, and trade-offs. *Ecology Letters*, 15(12), 1505–1516.
- [216] Kruisdijk, E., Eisfeld, C., Stuyfzand, P.J., van Breukelen, B.M. (2022). Denitrification kinetics during aquifer storage and recovery of drainage water from agricultural land. *Science of the Total Environment*, 849, 157791. DOI: <https://doi.org/10.1016/j.scitotenv.2022.157791>.
- [217] Laamrani, A., Joosse, P., McNairn, H., Berg, A.A., Hagerman, J., Powell, K., Berry, M. (2020). Assessing soil cover levels during the non-growing season using multitemporal satellite imagery and spectral unmixing techniques. *Remote Sensing* 12(9), 1397. DOI: <https://doi.org/10.3390/RS12091397>.
- [218] LaCanne, C.E., Lundgren, J.G. (2018). Regenerative agriculture: merging farming and natural resource conservation profitably. *PeerJ* 6, e4428. DOI: 10.7717/peerj.4428.
- [219] Lal, R. (1994). Tillage effects on soil degradation, soil resilience, soil quality, and sustainability. *Soil and Tillage Research*, 27(1–4), 1–8. DOI: [https://doi.org/10.1016/0167-1987\(93\)90059-X](https://doi.org/10.1016/0167-1987(93)90059-X).
- [220] Lal, R. (2015). Sequestering carbon in soils of agro-ecosystems. *Food Policy*, 55, 1–10.
- [221] Lambert, D.M., Clark, C.D., Busko, N., Walker, F.R., Layton, A., Hawkins, S. (2014). A study of cattle producer preferences for best management practices in an east Tennessee watershed. *Journal of Soil and Water Conservation*, 69(1), 41–53. DOI: 10.2489/jswc.69.1.41
- [222] Lampurlanés, J., Plaza-Bonilla, D., Álvaro-Fuentes, J., Cantero-Martínez, C. (2016). Long-term analysis of soil water conservation and crop yield under different tillage systems in Mediterranean rainfed conditions. *Field Crops Research*, 189, 59–67. DOI: 10.1016/j.fcr.2016.02.010.
- [223] Larned, S.T., Schallenberg, M. (2019). Stressor-response relationships and the prospective management of aquatic ecosystems. *New Zealand Journal of Marine and Freshwater Research*, 53(12), 1–24. DOI: 10.1080/00288330.2018.1524388
- [224] Lehman, R.M., Cambardella, C.A., Stott, D.E., Acosta-Martinez, V., Manter, D.K., Buyer, J.S., Maul, J.E., Smith, J.L., Collins, H.P., Halvorson, J.J., Kremer, R.J., Lundgren, J.G., Ducey, T.F., Jin, V.L., Karlen, D.L. (2015). Understanding and enhancing soil biological health: the solution for reversing soil degradation. *Sustainability*, 7(1), 988–1027. DOI: <https://doi.org/10.3390/su7010988>.
- [225] Li, H., Gao, H., Wu, H., Li, W., Wang, X., He, J. (2007). Effects of 15 years of conservation tillage on soil structure and productivity of wheat cultivation in northern China. *Australian Journal of Soil Research* 45(5), 344–350. DOI: 10.1071/SR07003.
- [226] Li, J., Zhang, S., Zhang, P., Wang, W. (2022). Design and test of traction combined machine for subsoiling and land preparation, *INMATEH - Agricultural Engineering* 68(3), 283–294. DOI: <https://doi.org/10.35633/inmateh-68-28>.
- [227] Li, J., Zhu, D., Zhang, S., Yang, G., Zhao, Y., Zhou, C., Zou, S. (2022). Application of the hydrochemistry, stable isotopes and MixSIAR model to identify nitrate sources and transformations in surface water and groundwater of an intensive agricultural karst wetland in Guilin, China. *Ecotoxicology and Environmental Safety*, 231, 113205. DOI: <https://doi.org/10.1016/j.ecoenv.2022.113205>.
- [228] Li, Q., Feng, J., Ming, X. (2023). Design and experiment on the single-ditch and double-row opener for narrow row flat seeder. *INMATEH - Agricultural Engineering*, 70(2), 24–31. DOI: <https://doi.org/10.35633/inmateh-70-24>.
- [229] Li, Y., Li, Z., Cui, S., Jagadamma, S., Zhang, Q.P. (2019). Residue retention and minimum tillage improve physical environment of the soil in croplands: a global meta-analysis. *Soil and Tillage Research*, 194, 104292. DOI: 10.1016/j.still.2019.06.009.
- [230] Lichtenberg, E. (2004). Cost-responsiveness of conservation practice adoption: a revealed preference approach. *Journal of Agricultural and Resource Economics*, 29(3), 420–435. DOI: 10.22004/ag.econ.30920.
- [231] Liebman, M., Mohler, C.L., Staver, C.P. (2003). Ecological management of agricultural weeds. *Annals of Botany*, 91(4), 499–500. DOI: <https://doi.org/10.1093/aob/mcg042>.
- [232] Liebhard, G., Klik, A., Neugschwandtner, R.W., Nolz, R. (2022). Effects of tillage systems on soil water distribution, crop rates of soybean. *Agricultural Water Management*, 269, 107719. DOI: <https://doi.org/10.1016/j.agwat.2022.107719>.
- [233] Limousin, G., Tessier, D. (2007). Effects of no-tillage on chemical gradients and topsoil acidification. *Soil and Tillage Research*, 92(1–2), 167–174. DOI: 10.1016/j.still.2006.02.003.
- [234] Linke, A.M., Tollefsen, A.F. (2021). Environmental stress and agricultural landownership in Africa. *Global Environmental Change*, 67, 102237. DOI: <https://doi.org/10.1016/j.gloenvcha.2021.102237>.

- [235] Liu, C., Lu, M., Cui, J., Li, B., Fang, C. (2014). Effects of straw carbon input on carbon dynamics in agricultural soils: a meta-analysis. *Global Change Biology* 20(5), 1366–1381. DOI: 10.1111/gcb.12517.
- [236] Liu, T., Bruins, R., Heberling, R. (2018). Factors influencing farmers' adoption of best management practices: a review and synthesis. *Sustainability*, 10(2), 432. DOI: <https://doi.org/10.3390/su10020432>
- [237] Llewellyn, R.S., D'Emden, F.H., Kuehne, G. (2012). Extensive use of no-tillage in grain growing regions of Australia. *Field Crop Research*, 132, 204–212. DOI: 10.1016/j.fcr.2012.03.013.
- [238] Lizotte, R.E., Knight, S.S., Cooper, C.M. (2010a). Toxicity evaluation of a conservation effects assessment program watershed, Beasley Lake, in the Mississippi Delta, USA. *Bulletin of Environmental Contamination and Toxicology*, 84(4), 422–426. DOI 10.1007/s00128-010-9951-x.
- [239] Lizotte, R.E., Knight, S.S., Bryant, C.T. (2010b). Sediment quality assessment of Beasley Lake: bioaccumulation and effects of pesticides in *Hyalella Azteca*. *Chemistry and Ecology*, 26(6), 411–424. DOI: 10.1080/02757540.2010.522997.
- [240] Lizotte, R., Knight, S., Locke, M., Stienriede, W., Testa, S., Bryant, C. (2012a). Water quality monitoring of an agricultural watershed lake: the effectiveness of agricultural best management practices. *Design and Nature IV - WIT Transactions on Ecology and the Environment*, 160, 283–294. DOI: 10.2495/DN120251.
- [241] Lizotte, R.E., Shields, F.D., Testa, S. (2012b). Effects of a simulated agricultural runoff event on sediment toxicity in a managed backwater wetland. *Water, Air, and Soil Pollution*, 223(8), 5375–5389. DOI: 10.1007/s11270-012-1287-1.
- [242] Lizotte, R.E., Shields, F.D., Murdock, J.N., Knight, S.S. (2012c). Responses of *Hyalella azteca* and phytoplankton to a simulated agricultural runoff event in a managed backwater wetland. *Chemosphere* 87(7), 684–691. DOI: 10.1016/j.chemosphere.2011.12.058.
- [243] Lizotte, R.E., Knight, S.S., Locke, M.A., Steinriede, R.W. (2012d). Ten-year assessment of agricultural management and land-use practices on pesticide loads and risk to aquatic biota of an Oxbow lake in the Mississippi Delta, USA. *Agricultural Research Updates*, 2, 349–371.
- [244] Lizotte, R.E., Smiley, P.C., Gillespie, R.B., Knight, S.S. (2021). Agricultural conservation practices and aquatic ecological responses. *Water*, 13(12), 1687. DOI: <https://doi.org/10.3390/w13121687>.
- [245] Loch, R.J., and Coughlan, K.J. (1984). Effects of zero tillage and stubble retention on some properties of a cracking clay. *Australian Journal of Soil Research*, 22(1), 91–98. DOI: 10.1071/SR9840091.
- [246] Lofty, J., Muhawenimana, V., Wilson, C.A.M.E., Ouro, P. (2022). Microplastics removal from a primary settler tank in a wastewater treatment plant and estimations of contamination onto European agricultural land via sewage sludge recycling. *Environmental Pollution*, 304, 119198. DOI: <https://doi.org/10.1016/j.envpol.2022.119198>.
- [247] Luo, Z., Wang, E., Sun, O.J. (2010). Can no-tillage stimulate carbon sequestration in agricultural soils? A meta-analysis of paired experiments. *Agriculture, Ecosystems & Environment*, 139(1–2), 244–231. DOI: 10.1016/j.agee.2010.08.006
- [248] Lupwayi, N.Z., Arshad, M.A., Rice, W.A., Clayton, G.W. (2001). Bacterial diversity in water-stable aggregates of soils under conventional and zero tillage management. *Applied Soil Ecology*, 16(3), 251–261. DOI: 10.1016/S0929-1393(00)00123-2
- [249] Lüring, M., Mucci, M. (2020). Mitigating eutrophication nuisance: in-lake measures are becoming inevitable in eutrophic waters in the Netherlands. *Hydrobiologia*, 847, 4447–4467. DOI: <https://doi.org/10.1007/s10750-020-04297-9>.
- [250] Ma, C., Chen, W., Yang, S., Diao, P., Zhang, Y., Luo, Z., Wang, Z. (2024). Design and experiment of no-tillage precision planters with staggered seedling belts for soybean. *INMATEH - Agricultural Engineering*, 72(1), 193–202. DOI: <https://doi.org/10.35633/inmateh-72-18>.
- [251] Maas, B., Fabian, Y., Kross, S. M., Richter, A. (2021). Divergent farmer and scientist perceptions of agricultural biodiversity, ecosystem services and decision-making. *Biological Conservation*, 256, 109065. DOI: <https://doi.org/10.1016/j.biocon.2021.109065>.
- [252] Madrigal, J.M., Gunier, R.B., Jones, R.R., Flory, A., Metayer, C., Nuckols, J.R., Ward, M.H. (2023). Contributions of nearby agricultural insecticide applications to indoor residential exposures. *Environment International*, 171, 107657. DOI: <https://doi.org/10.1016/j.envint.2022.107657>.
- [253] Magdoff, F., van Es, H. (2009). Building soils for better crops: Ecological management for healthy soils. Fourth Edition. *Sustainable Agriculture Research & Education (SARE)*, Handbook Series Book 10, <https://s3.wp.wsu.edu/uploads/sites/2056/2023/05/Building-Soils-for-Better-Crops.pdf>.

- [254] Mangalassery, S., Mooney, S.J., Sparkes, D.L., Fraser, W.T., Sjögersten, S. (2015). Impacts of zero tillage on soil enzyme activities, microbial characteristics and organic matter functional chemistry in temperate soils. *European Journal of Soil Biology*, 68, 9–17. DOI: 10.1016/j.ejsobi.2015.03.001.
- [255] Maret, T.R., MacCoy, D.E., Carlisle, D.M. (2008). Long-term water quality and biological responses to multiple best management practices in Rock Creek, Idaho. *Journal of the American Water Resources Association*, 44(5), 1248–1269. DOI: <https://doi.org/10.1111/j.1752-1688.2008.00221.x>.
- [256] Martins, V.S., Kaleita, A.L., Gelder, B.K. (2021). Digital mapping of structural conservation practices in the Midwest U.S. croplands: Implementation and preliminary analysis. *Science of the Total Environment*, 772, 145191. DOI: <https://doi.org/10.1016/j.scitotenv.2021.145191>.
- [257] Mase, A.S., Gramig, B.M., Prokopy, L.S. (2017). Climate change beliefs, risk perceptions, and adaptation behavior among midwestern US crop farmers. *Climate Risk Management*, 15, 8–17. DOI: <https://doi.org/10.1016/j.crm.2016.11.004>.
- [258] Matache, M., Voicu, Gh., Cârdei, P., Vlăduț, V., Persu, C., Voicea, I. (2015). Accelerated test of MAS 65 deep soil loosening machine frame. *Proceedings of the 43rd International Symposium on Agricultural Engineering "Actual Tasks on Agricultural Engineering"*, 131–140, Opatija, Croatia.
- [259] Matei, Gh., Vlăduț, V., Dodocioiu, A.M., Toader, M. (2020). Study regarding the optimization of grain sorghum cultivation technology. *Scientific Papers-Series A-Agronomy*, 63(2), 152–145.
- [260] Mbuthia, L.W., Acosta-Martínez, V., DeBruyn, J., Schaeffer, S., Tyler, D., Odoi, E., et al. (2015). Long term tillage, cover crop, and fertilization effects on microbial community structure, activity: Implications for soil quality. *Soil Biology and Biochemistry*, 89, 24–34. DOI: 10.1016/j.soilbio.2015.06.016.
- [261] McCann, L., Gedikoglu, H., Broz, B., Lory, J., Massey, R. (2015). Effects of observability and complexity on farmers' adoption of environmental practices. *Journal of Environmental Planning and Management*, 58(8), 1346–1362. DOI: 10.1080/09640568.2014.924911.
- [262] McKinney, E.N. (2012). *Relative contribution of water quality and habitat to macroinvertebrate community composition in streams influenced by agricultural land use in the Cedar Creek Watershed, Indiana*. Master's Thesis, Purdue University Fort Wayne, U.S.A.
- [263] Medwid, L.J. (2016). *Incentives for best management practice adoption among beef cattle producers and effects on upland sediment loss: a case study in Southeastern Tennessee*. Master's thesis. University of Tennessee, Knoxville. http://trace.tennessee.edu/utk_gradthes/4057/.
- [264] Mesgaran, M.B., Madani, K., Hashemi, H., Azadi, P. (2017). Iran's land suitability for agriculture. *Scientific Reports*, 7, 1–12. DOI: <https://doi.org/10.1038/s41598-017-08066-y>.
- [265] Milder, J.C., et al. (2016). Agroecological practices for sustainable agriculture: a review of the evidence. *Agricultural Systems*, 149, 1–12.
- [266] Montgomery, D.R. (2007). Soil erosion and agricultural sustainability. *PNAS - Proceedings of the National Academy of Sciences of the United States of America*, 104(33), 13268–13272. DOI: 10.1073/pnas.0611508104.
- [267] Moore, A.A., Palmer, M.A. (2005). Invertebrate biodiversity in agricultural and urban headwater streams: implications for conservation and management. *Ecological Applications* 15(4), 1169–1177. DOI: <https://doi.org/10.1890/04-1484>.
- [268] Moore, M.T., Lizotte, R.E., Knight, S.S., Smith, S., Cooper, C.M. (2007a). Assessment of pesticide contamination in three Mississippi Delta Oxbow lakes using *Hyalella azteca*. *Chemosphere*, 67(11), 2184–2191. DOI: <https://doi.org/10.1016/j.chemosphere.2006.12.026>.
- [269] Moore, M.T., Lizotte, R.E., Smith, S. (2007b). Responses of *Hyalella azteca* to a pyrethroid mixture in a constructed wetland. *Bulletin of Environmental Contamination and Toxicology*, 78, 245–248. DOI: 10.1007/s00128-007-9135-5.
- [270] Moore, M.T., Lizotte, R.E., Smith, S. (2007c). Toxicity evaluation of diazinon contaminated leaf litter. *Bulletin of Environmental Contamination and Toxicology*, 78(2), 168–171. DOI: 10.1007/s00128-007-9032-y.
- [271] Moran, K., Anderson, B., Phillips, B., Luo, Y., Singhasemanon, N., Breuer, R., Tadesse, D. (2019). Water quality impairments due to aquatic life pesticide toxicity: prevention and mitigation in California, USA. *Environmental Toxicology Chemistry*, 39(5), 953–966. DOI: 10.1002/etc.4699.
- [272] Moraru, R.I., Babuț, G.B., Cioca, I.L. (2013). Study of methane flow in caved goafs adjacent to longwall faces in Valea Jiului coal basin. *Proceedings of the 13th Geoconference on Science and Technologies in Geology, Exploration and Mining - SGEM*, 1, 731–738, Albena, Bulgaria. DOI: 10.5593/SGEM2013/BA1.V1/S03.067.

- [273] Mpanga, I.K., Tronstad, R., Guo, J., LeBauer, D.S., Idowu, O.J. (2021). On-farm land management strategies and production challenges in United States organic agricultural systems. *Current Research in Environmental Sustainability*, 3, 100097. DOI: <https://doi.org/10.1016/j.crsust.2021.100097>.
- [274] Mrabet, R., Moussadek, R., Fadlaoui, A., van Ranst, E. (2012). Conservation agriculture in dry areas of Morocco. *Field Crops Research*, 132, 84–94. DOI: [10.1016/j.fcr.2011.11.017](https://doi.org/10.1016/j.fcr.2011.11.017).
- [275] Mulbry, W., Kondrad, S., Pizarro, C. (2008). Biofertilizers from algal treatment of dairy and swine manure effluents. *Journal of Vegetable Science*, 12(4), 107–115. DOI: http://dx.doi.org/10.1300/J484v12n04_08.
- [276] Mustaqimah, Ramayanty Bulan, S., Syafriandi, R., Imanda, R., Uzair, D., Sartika T.D., Sitorus, A. (2021). Development and testing of bed former implement powered by hand tractors. *INMATEH - Agricultural Engineering*, 65(3), 145–155. DOI: <https://doi.org/10.35633/inmateh-65-25>.
- [277] Nabti, E., Jha, B., Hartmann, A. (2016). Impact of seaweeds on agricultural crop production as biofertilizer. *International Journal of Environment Science and Technology*, 14, 1119–1134. DOI: <https://doi.org/10.1007/S13762-016-1202-1>.
- [278] Napier, T.L., Tucker, M., McCarter, S. (2000). Adoption of conservation production systems in three midwest watersheds. *Journal of Soil and Water Conservation*, 55(2), 123–134.
- [279] Nematzadeh, S., Mesri Gondoshmian, T., Besharati Moghadam, M.S., Azad, M. (2022). Optimization of mechanization of tillage and soybean cultivation operations using Taguchi approach. *Sustainable Agriculture Science Research*, 2, 50–60. DOI: <https://doi.org/10.30495/SARJ.2022.1959774.1072>.
- [280] Nenciu, F., Paraschiv, M., Kuncser, R., Stan, C., Cocârță, D., Vlăduț, V.N. (2021a). High-grade chemicals and biofuels produced from marginal lands using an integrated approach of alcoholic fermentation and pyrolysis of sweet sorghum biomass residues. *Sustainability*, 14(1), 402. DOI: <https://doi.org/10.3390/su14010402>.
- [281] Nenciu, F., Vlăduț, V. (2021b). Studies on the perspectives of replacing the classic energy plants with Jerusalem artichoke and Sweet Sorghum, analyzing the impact on the conservation of ecosystems. *International Conference on Sustainable Future and Environmental Science - IOP Conference Series-Earth and Environmental Science*, 635, 012002. DOI: [10.1088/1755-1315/635/1/012002](https://doi.org/10.1088/1755-1315/635/1/012002).
- [282] Ngwira, A.R., Aune, J.B., Mkwinda, S. (2012). On-farm evaluation of yield and economic benefit of short term maize legume intercropping systems under conservation agriculture in Malawi. *Field Crops Research*, 132, 149–157. DOI: [10.1016/j.fcr.2011.12.014](https://doi.org/10.1016/j.fcr.2011.12.014).
- [283] Nielsen, R.G.H., Unger, P.W., Millar, G. (2005). Efficient water use in dryland cropping systems in the Great Plains. *Agronomy Journal*, 97(2), 364–372. DOI: [10.2134/agronj2005.0364](https://doi.org/10.2134/agronj2005.0364).
- [284] Norwood, C. (1994). Profile water distribution and grain yield as affected by cropping system and tillage. *Agronomy Journal*, 86(3), 558–563. DOI: [10.2134/agronj1994.00021962008600030019x](https://doi.org/10.2134/agronj1994.00021962008600030019x).
- [285] Nosheen, S., Ajmal, I., Song, Y. (2021). Microbes as biofertilizers, a potential approach for sustainable crop production. *Sustainability*, 13(4), 1868. DOI: <https://doi.org/10.3390/SU13041868>.
- [286] Nowak, P.J. (1987). The adoption of agricultural conservation technologies: Economic and diffusion explanations. *Rural Sociology*, 52(2), 208–220. DOI: <http://hdl.handle.net/10919/68487>.
- [287] Nyagumbo, I., Mkuhlani, S., Pisa, C., Kamalongo, D., Dias, D., Mekuria, M. (2016). Maize yield effects of conservation agriculture based maize-legume cropping systems in contrasting agro-ecologies of Malawi and Mozambique. *Nutrient Cycling in Agroecosystems*, 105, 275–290. DOI: [10.1007/s10705-015-9733-2](https://doi.org/10.1007/s10705-015-9733-2).
- [288] Nyamangara, J., Marondedze, A., Masvaya, E.N., Mawodza, T., Nyawasha, R., Nyengerai, K., Tirivavi, R., Nyamugafata, P., Wutaet, M. (2014). Influence of basin-based conservation agriculture on selected soil quality parameters under smallholder farming in Zimbabwe. *Soil Use and Management*, 30(4), 550–559. DOI: [10.1111/sum.12149](https://doi.org/10.1111/sum.12149).
- [289] Ogle, S.M., Breidt, F.J., Paustian, K. (2005). Agricultural management impacts on soil organic carbon storage under moist and dry climatic conditions of temperate and tropical regions. *Biogeochemistry*, 72, 87–121. DOI: [10.1007/s10533-004-0360-2](https://doi.org/10.1007/s10533-004-0360-2).
- [290] Ogle, S., Alsaker, C., Baldock, J., Bernoux, M., Breidt, F., McConkey, B.G., Regina, K., Vazquez-Amabile, G.G. (2019). Climate and soil characteristics determine where no-till management can store carbon in soils and mitigate greenhouse gas emissions. *Scientific Reports*, 9, 11665. DOI: [10.1038/s41598-019-47861-7](https://doi.org/10.1038/s41598-019-47861-7).
- [291] Okello, D., Owuor, G., Larochelle, C., Gathungu, E., Mshenga, P. (2021). Determinants of utilization of agricultural technologies among smallholder dairy farmers in Kenya. *Journal of Agriculture and Food Research*, 6, 100213. DOI: <https://doi.org/10.1016/j.jafr.2021.100213>.

- [292] O'Leary, G.J., Connor, D.J. (1997). Stubble retention and tillage in a semi-arid environment: 1. Soil water accumulation during fallow. *Field Crops Research*, 52, 209–219. DOI: 10.1016/S0378-4290(97)00034-8.
- [293] Olson, K.R. (2013). Soil organic carbon sequestration, storage, retention and loss in U.S. croplands: Issues paper for protocol development. *Geoderma*, 195–196, 201–206. DOI: 10.1016/j.geoderma.2012.12.004.
- [294] Oyetunde-Usman, Z., Olagunju, K.O., Ogunpaimo, O.R. (2021). Determinants of adoption of multiple sustainable agricultural practices among smallholder farmers in Nigeria. *International Soil and Water Conservation Research*, 9(2), 241–248. DOI: <https://doi.org/10.1016/j.iswcr.2020.10.007>.
- [295] Paerl, H.W., Dyble, J., Moisaner, P.H., Noble, R.T., Piehler, M.F., Pinckney, J.L., Steppe, T.F., Twomey, L., Valdes, L.M. (2003). Microbial indicators of aquatic ecosystem change: current applications to eutrophication studies. *FEMS Microbiology Ecology*, 46(3), 233–246. DOI: 10.1016/S0168-6496(03)00200-9.
- [296] de Paul Obade, V., Gaya, C. (2020). Mapping tillage practices using spatial information techniques. *Environmental Management*, 66, 722–731. DOI: <https://doi.org/10.1007/s00267-020-01335-z>.
- [297] Page, K.L., Dang, Y., Dalal, R.C. (2013). Impacts of conservation tillage on soil quality, including soil-borne crop diseases, with a focus on semi-arid grain cropping systems. *Australasian Plant Pathology*, 42, 363–377. DOI: 10.1007/s13313-013-0198-y.
- [298] Page, K.L., Dang, Y.P., Dalal, R.C., Reeves, S., Thomas, G., Wang, W., Thompson, J.P. (2019). Changes in soil water storage with no-tillage and crop residue retention on a Vertisol: Impact on productivity and profitability over a 50 year period. *Soil and Tillage Research*, 194, 104319. DOI: 10.1016/j.still.2019.104319.
- [299] Page, K.L., Dang, Y.P., Dalal, R.C. (2020). The ability of conservation agriculture to conserve soil organic carbon and the subsequent impact on soil physical, chemical, and biological properties and yield. *Frontiers in Sustainable Food Systems*, 4. DOI: <https://doi.org/10.3389/fsufs.2020.00031>.
- [300] Palm, C., Blanco-Canqui, H., DeClerck, F., Gatere, L., Grace, P. (2014). Conservation agriculture and ecosystem services: an overview. *Agriculture, Ecosystems & Environment*, 187, 87–105. DOI: 10.1016/j.agee.2013.10.010.
- [301] Panigrahy, S., Sharma, S.A. (1997). Mapping of crop rotation using multirate Indian Remote Sensing Satellite digital data. *ISPRS Journal of Photogrammetry and Remote Sensing*, 52(2), 85–91. DOI: [https://doi.org/10.1016/S0924-2716\(97\)83003-1](https://doi.org/10.1016/S0924-2716(97)83003-1).
- [302] Pankhurst, C.E., Hawke, B.G., McDonald, H.J., Kirby, C.A., Buckerfield, J.C., Michelsen, P., et al. (1995). Evaluation of soil biological properties as potential bioindicators of soil health. *Australian Journal of Experimental Agriculture*, 35(7), 1015–1028. DOI: 10.1071/EA9951015.
- [303] Pankhurst, C.E., Kirby, J.M., Hawke, B.G., Harch, B.D. (2002). Impact of a change in tillage and crop residue management practice on soil chemical and microbiological properties in a cereal-producing red duplex soil in NSW, Australia. *Biology and Fertility of Soils*, 35, 189–196. DOI: 10.1007/s00374-002-0459-3.
- [304] Pannell, D.J., Llewellyn, R.S., Corbeels, M. (2014). The farm-level economics of conservation agriculture for resource-poor farmers. *Agriculture, Ecosystems & Environment*, 187, 52–64. DOI: 10.1016/j.agee.2013.10.014.
- [305] Paulitz, T.C., Schroeder, K.L., Schillinger, W.F. (2010). Soilborne pathogens of cereals in an irrigated cropping system: effects of tillage, residue management, and crop rotation. *Plant Diseases*, 94(1), 61–68. DOI: 10.1094/PDIS-94-1-0061.
- [306] Peigné, J., Ball, B.C., Roger-Estrade, J., David, C.J.S.U. (2007). Is conservation tillage suitable for organic farming? A review. *Soil Use and Management*, 23(2), 129–144.
- [307] Pittelkow, C.M., Liang, X., Linqvist, B.A., Van Groenigen, L.J., Lee, J., Lundy, M.E., Van Gestel, N., Six, J., Venterea, R.T., Van Kessel, C. (2015). Productivity limits and potentials of the principles of conservation agriculture. *Nature*, 517, 365–368. DOI: <https://doi.org/10.1038/nature13809>.
- [308] Pearce, N.J.T., Yates, A.G. (2015). Agricultural best management practice abundance and location does not influence stream ecosystem function or water quality in the summer season. *Water*, 7(12), 6861–6876. DOI: <https://doi.org/10.3390/w7126661>.
- [309] Pfiffner, L., Balmer, O. (2011). Organic agriculture and biodiversity. FiBL Research Institute of Organic Agriculture, Landbau.
- [310] Pheap, S., Lefevre, C., Thoumazeau, A., Leng, V., Boulakia, S., Koy, R., Hok, L., Lienhard, P., Brauman, A., Tivet, F. (2019). Multi-functional assessment of soil health under conservation agriculture in Cambodia. *Soil and Tillage Research*, 194, 104349. DOI: 10.1016/j.still.2019.104349.

- [311] Pittelkow, C.M., Liang, X., Linnquist, B.A., van Groenigen, K.J., Lee, J., Lundy, M.E., van Gestel, N., Six, J., Venterea, R.T., van Kessel, C. (2015). Productivity limits and potentials of the principles of conservation agriculture. *Nature*, 517, 365–368. DOI: 10.1038/nature13809.
- [312] Popescu, E., Nenciu, F., Vlăduț, V. (2022). A new strategic approach used for the regeneration of soil fertility, in order to improve the productivity in ecological systems. *Scientific Papers. Series E. Land Reclamation, Earth Observation & Surveying, Environmental Engineering*, XI, 277–284. DOI: <https://landreclamationjournal.usamv.ro/pdf/2022/Art33.pdf>.
- [313] Porter, P.A., Mitchell, R.B., Moore, K.J. (2015). Reducing hypoxia in the Gulf of Mexico: reimagining a more resilient agricultural landscape in the Mississippi river watershed. *Journal of Soil Water Conservation*, 70(3), 63A–68A. DOI: 10.2489/jswc.70.3.63A.
- [314] Powlson, D.S., Stirling, C.M., Thierfelder, C., White, R. P., Jat, M.L. (2016). Does conservation agriculture deliver climate change mitigation through soil carbon sequestration in tropical agro-ecosystems? *Agriculture, Ecosystems & Environment*, 220, 164–174. DOI: 10.1016/j.agee.2016.01.005.
- [315] Prabhakara, K., Dean Hively, W., McCarty, G.W. (2015). Evaluating the relationship between biomass, percent groundcover and remote sensing indices across six winter cover crop fields in Maryland, United States. *International Journal of Applied Earth Observation and Geoinformation*, 39, 88–102. DOI: <https://doi.org/10.1016/j.jag.2015.03.002>.
- [316] Pradhan, A., Chan, C., Roul, P.K., Halbrendt, J., Sipes, B. (2018). Potential of conservation agriculture (CA) for climate change adaptation and food security under rainfed uplands of India: a transdisciplinary approach. *Agricultural Systems*, 163, 27–35. DOI: 10.1016/j.agry.2017.01.002.
- [317] Prokopy, L.S., Floress, K., Klotthor-Weinkauff, D., Baumgart-Getz, A. (2008). Determinants of agricultural best management practice adoption: evidence from the literature. *Journal of Soil and Water Conservation*, 63(5), 300–311. DOI: 10.2489/jswc.63.5.300.
- [318] Prokopy, L.S., Floress, K., Arbuckle, J.G., Church, S.P., Eanes, F.R., Gao, Y., Gramig, B.M., Ranjan, P., Singh, A.S. (2019). Adoption of agricultural conservation practices in the United States: Evidence from 35 years of quantitative literature. *Journal of Soil and Water Conservation*, 74(5), 520–534. DOI: 10.2489/jswc.74.5.520.
- [319] Puget, P., Lal, R. (2005). Soil organic carbon and nitrogen in a Mollisol in central Ohio as affected by tillage and land use. *Soil and Tillage Research*, 80, 201–213. DOI: 10.1016/j.still.2004.03.018.
- [320] Punitha, A., Geetha, V. (2023). Automated climate prediction using pelican optimization based hybrid deep belief network for Smart Agriculture. *Measurement: Sensors*, 27, 100714. DOI: <https://doi.org/10.1016/j.measen.2023.100714>.
- [321] Qin, S.P., He, X. H., Hu, C.S., Zhang, Y.M., Dong, W.X. (2010). Responses of soil chemical and microbial indicators to conservational tillage versus traditional tillage in the North China Plain. *European Journal of Soil Biology*, 46(3–4), 243–247. DOI: 10.1016/j.ejsobi.2010.04.006.
- [322] Radford, B.J., Thornton, C.M. (2011). Effects of 27 years of reduced tillage practices on soil properties and crop performance in the semi-arid subtropics of Australia. *International Journal of Energy, Environment and Economics*, 19(6), 565–588.
- [323] Rahman, L., Chan, K.Y., and Heenan, D.P. (2007). Impact of tillage, stubble management and crop rotation on nematode populations in a long-term field experiment. *Soil and Tillage Research*, 95, 110–119. DOI: 10.1016/j.still.2006.11.008.
- [324] Rajanna, G.A., Dass, A., Suman, A., Babu, S., Venkatesh, P., Singh, V.K., Upadhyay, P.K., Sudhishri, S. (2022). Co-implementation of tillage, irrigation, and fertilizers in soybean: impact on crop productivity, soil moisture, and soil microbial dynamics. *Field Crops Research*, 288, 108672. DOI: <https://doi.org/10.1016/j.fcr.2022.108672>.
- [325] Raphael, J.P.A., Calonego, J.C., Milori, D.M.B.P., Rosolem, C.A. (2016). Soil organic matter in crop rotations under no-till. *Soil and Tillage Research*, 155, 45–53. DOI: 10.1016/j.still.2015.07.020.
- [326] Rhoton, F.E. (2000). Influence of time on soil response to no-till practices. *Soil Science Society of America Journal*, 64(2), 700–709. DOI: 10.2136/sssaj2000.642700x.
- [327] Ritika, B., Utpal, D. (2014). Biofertilizer, a way towards organic agriculture: a review. *Africal Journal of Microbiology Research*, 8(24), 2332–2343. DOI: <https://doi.org/10.5897/AJMR2013.6374>.
- [328] Roberts, W.P., Chan, K.Y. (1990). Tillage-induced increases in carbon dioxide loss from soil. *Soil and Tillage Research*, 17(1–2). DOI: [https://doi.org/10.1016/0167-1987\(90\)90012-3](https://doi.org/10.1016/0167-1987(90)90012-3).

- [329] Rochette, P. (2008). No-till only increases N₂O emissions in poorly-aerated soils. *Soil and Tillage Research*, 101(1–2), 97–100. DOI: 10.1016/j.still.2008.07.011.
- [330] Román-Vázquez, J., Carbonell-Bojollo, R.M., Veroz-González, Ó., Maraschi da Silva Piletti, L.M., Márquez-García, F., Cabeza-Ramírez, L.J., González-Sánchez, E.J. (2025). Global trends in conservation agriculture and climate change research: a bibliometric analysis. *Agronomy*, 15(1), 249. DOI: <https://doi.org/10.3390/agronomy15010249>.
- [331] Ronga, D., Biazzi, E., Parati, K., Carminati, D., Tava, A. (2019). Microalgal biostimulants and biofertilisers in crop productions. *Agronomy*, 9(4), 192. DOI: <https://doi.org/10.3390/agronomy9040192>.
- [332] Roper, M.M., Gupta, V.V.S.R. (1995). Management practices and soil biota. *Australian Journal of Soil Research*, 33(2), 321–339. DOI: 10.1071/SR9950321.
- [333] Rosenstock, T.S., Steward, P., Joshi, N., Lamanna, C., Namoi, N., Muller, L., Akinleye, A.O., Atieno, E., Bell, P., Champalle, C., English, W., Eyrich, A.S., Gitau, A., Kagwiria, D., Kamau, H., Madalinska, A., Manda, L., McFatrige, S., Mumo, E., Nduah, A., Ombewa, B., Poultouchidou, A., Rioux, J., Richards, M., Shuck, J., Ström, H., Tully, K. (2024). Effects of changing farming practices in African agriculture. *Scientific Data*, 11(1), 958. DOI: 10.1038/s41597-024-03805-z. PMID: 39227609.
- [334] Ruiz-Espinosa, L.I., Verhulst, N., van Ogtrop, F., Cross, R., Govaerts, B., van Rees, H., Trethowan, R. (2024). Quantifying the adoption of conservation agriculture: development and application of the Conservation Agriculture Appraisal Index. *Agricultural Systems*, 220, 104095. DOI: <https://doi.org/10.1016/j.agsy.2024.104095>.
- [335] Rusinamhodzi, L., Corbeels, M., van Wijk, M.T., Rufino, M.C., Nyamangara, J., Giller, K.E. (2011). A meta-analysis of long-term effects of conservation agriculture on maize grain yield under rain-fed conditions. *Agronomy for Sustainable Development*, 31, 657–673. DOI: 10.1007/s13593-011-0040-2.
- [336] Sa, J.C.D., Cerri, C.C., Lal, R., Dick, W.A., Piccolo, M.D., Feigl, B.E. (2009). Soil organic carbon and fertility interactions affected by a tillage chronosequence in a Brazilian Oxisol. *Soil and Tillage Research*, 104(1), 56–64. DOI: 10.1016/j.still.2008.11.007.
- [337] Sanders, K.E. (2012). *Relative importance of water quality and habitat to fish communities in streams influenced by agricultural land use in the Cedar Creek Watershed, Indiana*. Master's Thesis, Purdue University Fort Wayne, USA. DOI: <https://docs.lib.purdue.edu/dissertations/AAI1529918/>.
- [338] Sarkar, U.K., Pathak, A.K., Sinha, R.K., Sivakumar, K., Pandian, A.K., Pandey, A., Dubey, V.K., Lakra, W.S. (2012). Freshwater fish biodiversity in the River Ganga (India): Changing pattern, threats and conservation perspectives. *Reviews in Fish Biology and Fisheries*, 22(1), 251–272. DOI: 10.1007/s11160-011-9218-6.
- [339] Sarkar, U.K., Bakshi, S., Lianthuamluaia, L., Mishal, P., Das Ghosh, B., Saha, S., Karnatak, G. (2020). Understanding enviro-climatological impact on fish biodiversity of the tropical floodplain wetlands for their sustainable management. *Sustainable Water Resources Management*, 6(5), 96. DOI: 10.1007/s40899-020-00445-0.
- [340] Schäfer, R.B., Caquet, T., Siimes, K., Mueller, R., Lagadic, L., Liess, M. (2007). Effects of pesticides on community structure and ecosystem functions in agricultural streams of three biogeographical regions in Europe. *Science of the Total Environment*, 382(2–3), 272–285. DOI: 10.1016/j.scitotenv.2007.04.040.
- [341] Schipanski, M.E., MacDonald, G.K., Rosenzweig, S., Chappell, M.J., Bennett, E.M., Kerr, R.B., Blesh, J., Crews, T.E., Drinkwater, L.E., Lundgren, J.G., Schnarr, C. (2016). Realizing resilient food systems. *BioScience*, 66(7), 600–610. DOI: 10.1093/biosci/biw052.
- [342] Seger, K.R., Smiley, P.C., King, K.W. (2012). Influence of riparian habitat on aquatic macroinvertebrate community colonization within riparian zones of agricultural headwater streams. *Journal of Freshwater Ecology*, 27(3), 393–407. DOI: <https://doi.org/10.1080/02705060.2012.662470>.
- [343] Seitz, S., Goebes, P., Puerta, V.L., Pereira, E.I.P., Wittwer, R., Six, J., Scholten, T. (2019). Conservation tillage and organic farming reduce soil erosion. *Agronomy for Sustainable Development*, 39, 1–10.
- [344] Seufert, V., Ramankutty, N., Foley, J.A. (2012). Comparing the yields of organic and conventional agriculture. *Nature*, 10, 485(7397), 229–232. DOI: 10.1038/nature11069. PMID: 22535250.
- [345] Sharma, G., Shrestha, S., Kunwar, S., Tseng, T-M. (2021). Crop diversification for improved weed management: a review. *Agriculture*, 11(5), 461. DOI: <https://doi.org/10.3390/agriculture11050461>.
- [346] Silva, L.D., Bahcevandziev, K., Pereira, L. (2019). Production of bio-fertilizer from *Ascomyllum nodosum* and *Sargassum muticum* (Phaeophyceae). *Journal of Oceanology and Limnology*, 37, 918–927. DOI: <https://doi.org/10.1007/S00343-019-8109-X>.

- [347] Singh, A., MacGowan, B., O'Donnell, M., Overstreet, B., Ulrich-Schad, J., Dunn, M., Klotz, H., Prokopy, L. (2018). The influence of demonstration sites and field days on adoption of conservation practices. *Journal of Soil and Water Conservation*, 73(3), 276–283. DOI: 10.2489/jswc.73.3.276.
- [348] Sithole, N.J., Magwaza, L.S. (2019). Long-term changes of soil chemical characteristics and maize yield in no-till conservation agriculture in a semi-arid environment of South Africa. *Soil and Tillage Research*, 194, 104317. DOI: 10.1016/j.still.2019.104317.
- [349] Smiley, P.C., Gillespie, R.B., King, K.W., Huang, C. (2008). Contribution of habitat and water quality to the integrity of fish communities in agricultural drainage ditches. *Journal of Soil and Water Conservation*, 63(6), 218A–219A. DOI: 10.2489/jswc.63.6.218A.
- [350] Smiley, P.C., Gillespie, R.B. (2010). Influence of physical habitat and agricultural contaminants on fishes in agricultural drainage ditches. *Agricultural Drainage Ditches: Mitigation Wetlands of the 21st Century*, Kerula, India, Research Signpost, 37–73.
- [351] Smiley, P.C., King, K.W., Fausey, N.R. (2011). Influence of herbaceous riparian buffers on physical habitat, water chemistry, and stream communities within channelized agricultural headwater streams. *Ecological Engineering*, 37, 1314–1323. DOI: 10.1016/j.ecoleng.2011.03.020.
- [352] Smiley, P.C., King, K.W., Gillespie, R.B., Fausey, N.R. (2012). Influence of watershed scale atrazine reduction practices on pesticides and fishes within channelized agricultural headwater streams. *Journal of Sustainable Watershed Science & Management*, 1(2), 61–75. DOI: 10.5147/jswsm.2012.0068.
- [353] Smiley, P.C., Rumora, K.R. (2015). Planting grass filter strips: does it influence the structure and function of riparian habitats of agricultural headwater streams? *Riparian Ecology and Conservation*, 2(1), 58–71. DOI: <https://doi.org/10.1515/remc-2015-0002>.
- [354] Smith, S., Lizotte, R.E., Knight, S.S. (2007a). Pesticide body residues of *Hyalella azteca* exposed to Mississippi Delta sediments. *Bulletin of Environmental Contamination and Toxicology*, 78(1), 26–29. DOI: 10.1007/s00128-007-9020-2.
- [355] Smith, S., Lizotte, R.E., Moore, M.T. (2007b). Toxicity assessment of diazinon in a constructed wetland using *Hyalella Azteca*. *Bulletin of Environmental Contamination and Toxicology*, 79(1), 58–61. DOI: 10.1007/s00128-007-9215-6.
- [356] Smith, P., Clark, H., Dong, H., Elsiddig, E.A., Haberl, H., Harper, R., House, J., Jafari, M., Masera, O., Mbow, C., Ravindranath, N.H., Rice, C.W., Roble do Abad, C., Romanovskaya, A., Sperling, F., Tubiello, F. (2014). Agriculture, forestry and other land use (AFOLU) – chapter 11. *Climate Change 2014: Mitigation of Climate Change*. Cambridge University Press.
- [357] Smith, A., Tetzlaff, D., Gelbrecht, J., Kleine, L., Soulsby, C. (2020). Riparian wetland rehabilitation and beaver re-colonization impacts on hydrological processes and water quality in a lowland agricultural catchment. *Science of the Total Environment*, 699, 134302. DOI: 10.1016/j.scitotenv.2019.134302.
- [358] Soane, B.D., Ball, B.C., Arvidsson, J., Basch, G., Moreno, F., Roger-Estrade, J. (2012). No-till in northern, western and south-western Europe: a review of problems and opportunities for crop production and the environment. *Soil and Tillage Research*, 118, 66–87. DOI: 10.1016/j.still.2011.10.015.
- [359] Somasundaram, J., Salikram, M., Sinha, N.K., Mohanty, M., Chaudhary, R.S., Dalal, R.C., Mitra, N. G., Blaise, D., Coumar, M.V., Hati, K.M., Thakur, J.K., Neenu, S., Biswas, A.K., Patra, A.K., Chaudhari, S.K. (2019). Conservation agriculture effects on soil properties and crop productivity in a semiarid region of India. *Soil Research*, 57(2), 187–199. DOI: 10.1071/SR18145.
- [360] Sonmez, N.K., Slater, B. (2016). Measuring intensity of tillage and plant residue cover using remote sensing. *European Journal of Remote Sensing*, 49, 121–135. DOI: <https://doi.org/10.5721/EuJRS20164907>.
- [361] South, S., Qi, J., Lusch, D.P. (2004). Optimal classification methods for mapping agricultural tillage practices. *Remote Sensing of Environment*, 91, 90–97. DOI: <https://doi.org/10.1016/j.rse.2004.03.001>.
- [362] Stagnari, F., Ramazzotti, S., Pisante, M. (2009). Conservation agriculture: a different approach for crop production through sustainable soil and water management: a review. *Organic Farming, Pest Control and Remediation of Soil Pollutants. Sustainable Agriculture Reviews*, 1, 55–83. DOI: 10.1007/978-1-4020-9654-9_5.
- [363] Stallman, H.R., James, H.S. (2017). Farmers' willingness to cooperate in ecosystem service provision: Does trust matter? *Annals of Public and Cooperative Economics*, 88(1), 5–31.
- [364] Steinbach, H.S., and Alvarez, R. (2006). Changes in soil organic carbon contents and nitrous oxide emissions after introduction of No-Till in Pampean agroecosystems. *Journal of Environmental Quality*, 35(1), 3–13. DOI: 10.2134/jeq2005.0050.

- [365] Stephens, W.W.; Moore, M.T.; Farris, J.L.; Bouldin, J.L.; Cooper, C.M. (2008). Considerations for assessments of wadable drainage systems in the agriculturally dominated Deltas of Arkansas and Mississippi. *Archives of Environmental Contamination and Toxicology*, 55, 432–441. DOI: 10.1007/s00244-008-9136-3.
- [366] Steward, P.R., Dougill, A.J., Thierfelder, C., Pittelkow, C.M., Stringer, L.C., Kudzala, M., Shackelford, G.E. (2018). The adaptive capacity of maize-based conservation agriculture systems to climate stress in tropical and subtropical environments: a meta-regression of yields. *Agriculture, Ecosystems & Environment*, 251, 194–202. DOI: 10.1016/j.agee.2017.09.019.
- [367] Sudheer, K.P., Gowda, P., Chaubey, I., Howell, T. (2010). Artificial Neural Network approach for mapping contrasting tillage practices. *Remote Sensing*, 2, 579–590. DOI: <https://doi.org/10.3390/rs2020579>.
- [368] Suleiman, A.K.A., Lourenço, K.S., Clark, C., Luz, R.L., da Silva, G.H.R., Vet, L.E.M., Cantarella, H., Fernandes, T.V., Kuramae, E.E. (2020). From toilet to agriculture: fertilization with microalgal biomass from wastewater impacts the soil and rhizosphere active microbiomes, greenhouse gas emissions and plant growth. *Resources, Conservation and Recycling*, 161, 104924. DOI: <https://doi.org/10.1016/j.resconrec.2020.104924>.
- [369] Sun, L., Wang, R., Li, J., Wang, Q., Lyu, W., Wang, X., Ke Cheng, K., Mao, H., Zhang, X. (2019). Reasonable fertilization improves the conservation tillage benefit for soil water use and yield of rain-fed winter wheat: a case study from the loess plateau, China. *Field Crops Research*, 242, 107589. DOI: 10.1016/j.fcr.2019.107589.
- [370] Sun, W., Canadell, J.G., Yu, L., Yu, L., Zhang, W., Smith, P., Fischer, T., Huang, Y. (2020). Climate drives global soil carbon sequestration and crop yield changes under conservation agriculture. *Global Change Biology*, 26(6), 3325–3335. DOI: 10.1111/gcb.15001. PMID: 31953897.
- [371] Tarkalson, D.D., Hergert, G.W., Cassman, K.G. (2006). Long-term effects of tillage on soil chemical properties and grain yields of a dryland winter wheat-sorghum/corn-fallow rotation in the Great Plains. *Agronomy Journal*, 98(1), 26–33. DOI: 10.2134/agronj2004.0240.
- [372] Teasdale, J.R. (1996). Contribution of cover crops to weed management in sustainable agricultural systems. *Journal of Production Agriculture*, 9(4), 475–479. DOI: <https://doi.org/10.2134/jpa1996.0475>.
- [373] Tekle, A.T. (2016). Adaptation and constraints of conservation agriculture. *Journal of Biology, Agriculture and Healthcare*, 6(1), 1–14.
- [374] Teliban, G.C., Burducea, M., Mihalache, G., Zheljzkov, V.D., Dincheva, I., Badjakov, I., Bodale, I., Vlăduț, N.-V., Cojocaru, Al., Munteanu, N., Stan, T., Caruso, G., Stoleru, V. (2022). Morphological, physiological and quality performances of basil cultivars under farming management. *Agronomy*, 12(12), 3219. DOI: <https://doi.org/10.3390/agronomy12123219>.
- [375] TerAvest, D., Wandschneider, P.R., Thierfelder, C., Reganold, J.P. (2019). Diversifying conservation agriculture and conventional tillage cropping systems to improve the wellbeing of smallholder farmers in Malawi. *Agricultural Systems*, 171, 23–35. DOI: 10.1016/j.agry.2019.01.004.
- [376] Tessier, S., Peru, M., Dyck, F.B., Zentner, F.P., Campbell, C.A. (1990). Conservation tillage for spring wheat production in semi-arid Saskatchewan. *Soil and Tillage Research*. 18(1), 73–89. DOI: 10.1016/0167-1987(90)90094-T.
- [377] Tey, Y.S., Li, E., Bruwer, J., Abdullah, A.M., Brindal, M., Radam, A., Ismail, M.M., Darham, S. (2017). Factors influencing the adoption of sustainable agricultural practices in developing countries: a review. *Environmental Engineering & Management Journal (EEMJ)* 16(2), 337–349.
- [378] Thierfelder, C., Baudron, F., Setimela, P., Nyagumbo, I., Mupangwa, W., Mhlanga, B., Lee, N., Gérard, B. (2018). Complementary practices supporting conservation agriculture in southern Africa. A review. *Agronomy for Sustainable Development*, 38(16), 1–22. DOI: 10.1007/s13593-018-0492-8.
- [379] Thomas, J.K., Ladewig, H., McIntosh, W. (1990). The adoption of integrated pest management practices among Texas cotton growers. *Rural Sociology*, 55(3), 395–410. DOI: 10.1111/J.1549-0831.1990.TB00690.X.
- [380] Thomas, G.A., Gibson, G., Nielsen, R.G.H., Martin, W.D., Radford, B.J. (1995). Effects of tillage, stubble, gypsum, and nitrogen fertiliser on cereal cropping on a red-brown earth in south-west Queensland. *Australian Journal of Experimental Agriculture*, 35(7), 997–1008. DOI: 10.1071/EA9950997.
- [381] Thomas, G.A., Dalal, R.C., Standley, J. (2007). No-till effects on organic matter, pH, cation exchange capacity and nutrient distribution in a Luvisol in the semi-arid subtropics. *Soil and Tillage Research*, 94(2), 295–304. DOI: 10.1016/j.still.2006.08.005.
- [382] Tilman, D., Cassman, K.G., Matson, P.A., Naylor, R., Polasky, S. (2002). Agricultural sustainability and intensive production practices. *Nature*, 418, 671–677. DOI: 10.1038/nature01014.

- [383] Tisdall, J.M., Oades, J.M. (1982). Organic matter and water-stable aggregates in soils. *European Journal of Soil Science*, 33(2), 141–163. DOI: 10.1111/j.1365-2389.1982.tb01755.x.
- [384] Tiftonell, P., Scopel, E., Andrieu, N., Posthumus, H., Mapfumo, P., Corbeels, M., van Halsema, G.E., Lahmar, R., Lugandu, S., Rakotoarisoa, J., Mtambanengwe, F., Pound, B., Chikowo, R., Naudin, K., Triomphe, B., Mkomwa, S. (2012). Agroecology-based aggradation-conservation agriculture (ABACO): targeting innovations to combat soil degradation and food insecurity in semi-arid Africa. *Field Crops Research*, 132, 168–174. DOI: 10.1016/j.fcr.2011.12.011.
- [385] Trávníček, J., Schlatter, B. Willer, H., (2024). The World of Organic Agriculture 2024. FiBL & IFOAM - Organics International. Frick and Bonn.
- [386] Todd, M.J., Vellidis, G., Lowrance, R.R., Pringle, C.M. (2009). High sediment oxygen demand within an instream swamp in southern Georgia: Implications for low dissolved oxygen levels in coastal blackwater streams. *Journal of the American Water Resources Association*, 45(6), 1493–1507.
- [387] Todd, M.J., Lowrance, R.R., Goovaerts, P., Vellidis, G., Pringle, C.M. (2010). Geostatistical modeling of the spatial distribution of sediment oxygen demand within a Coastal Plain blackwater watershed. *Geoderma*, 159(1–2), 53–62. DOI: 10.1016/j.geoderma.2010.06.015.
- [388] Triplett, G.B., Dick, W.A. (2008). No-tillage crop production: a revolution in agriculture! *Agronomy Journal*, 100(S3), S153–S165. DOI: 10.2134/agronj2007.0005c.
- [389] Tsaboula, A., Menexes, G., Papadakis, E.-N., Vryzas, Z., Kotopoulou, A., Kintzikoglou, K., Papadopoulou-Mourkidou, E. (2019). Assessment and management of pesticide pollution at a river basin level part II: optimization of pesticide monitoring networks on surface aquatic ecosystems by data analysis methods. *Science of the Total Environment*, 653, 1612–1622. DOI: 10.1016/j.scitotenv.2018.10.270.
- [390] Ullah, S., Breitenbeck, G.A., Faulkner, S.P. (2005). Denitrification and N₂O emission from forested and cultivated alluvial clay soil. *Biogeochemistry*, 73(3), 499–513. DOI: <https://doi.org/10.1007/s10533-004-1565-0>.
- [391] Ungureanu, N., Croitoru, Șt., Biriș, S., Voicu, Gh., Vlăduț, V., Selvi, K.Ç., Boruz, S., Marin, E., Matache, M., Manea, D., Constantin, G., Ionescu, M. (2015). Agricultural soil compaction under the action of agricultural machinery. *Proceedings of the 43rd International Symposium on Agricultural Engineering "Actual Tasks on Agricultural Engineering"*, 31–42, Opatija, Croatia.
- [392] Ungureanu, N., Vlăduț, V., Voicu, Gh., Biriș, S.Șt., Ionescu, M., Dincă, M., Vlăduț, D.I., Matache, M. (2016). Influence of wheel load and tire inflation pressure on footprint area in static regime. *Proceedings of the 44th International Symposium on Agricultural Engineering "Actual Tasks on Agricultural Engineering"*, 99–110, Opatija, Croatia.
- [393] Ungureanu, N., Vlăduț, V., Biriș, S. (2017). FEM modelling of soil behaviour under compressive loads. *Materials Science and Engineering*, 163, 012001, 1–9. DOI: 10.1088/1757-899X/163/1/012001.
- [394] Ungureanu, N., Vlăduț V., Biriș, S.St. (2020a). Capitalization of wastewater-grown algae in bioethanol production. *19th International Scientific Conference Engineering for Rural Development*, 19, 1859–1864, Jelgava, Latvia. DOI: 10.22616/ERDev.2020.19.TF507.
- [395] Ungureanu, N., Vlăduț V., Voicu, Gh. (2020). Water scarcity and wastewater reuse in crop irrigation, *Sustainability*, 12, 9055. DOI: <https://doi.org/10.3390/su12219055>.
- [396] Ungureanu, N., Vlăduț, N.-V., Biriș, S.Șt., Gheorghită, N.E., Ionescu, M. (2024). The use of fertilizers in Romanian agriculture: the impact on the environment, crops and health, and possible solutions. *International Symposium ISB-INMA TEH International Symposium – Agricultural and Mechanical Engineering*, 428–445, 31.10–1.11.2024, Bucharest.
- [397] United States Environmental Protection Agency – US EPA. (2019). *Global Greenhouse Gas Overview*. <https://www.epa.gov/ghgemissions/global-greenhouse-gas-overview>.
- [398] Uri, N.D. (2001). The environmental implications of soil erosion in the United States. *Environmental Monitoring and Assessment*, 66, 293–312.
- [399] Utley, B.C., Vellidis, G., Lowrance, R., Smith, M.C. (2008). Factors affecting sediment oxygen demand dynamics in blackwater streams of Georgia's coastal plain. *Journal of the American Water Resources Association*, 44(3), 742–753. DOI: 10.1111/j.1752-1688.2008.00202.x.
- [400] Van Bruggen, A.H.C., Semenov, A.M., van Diepeningen, A.D., de Vos, O.J., Blok, W.J. (2006). Relation between soil health, wave-like fluctuations in microbial populations, and soil-borne plant disease management. *European Journal of Plant Pathology*, 115, 105–122. DOI: 10.1007/s10658-005-1250-8.

- [401] Vandenbygaart, A.J., Gregorich, E.G., Angers, D.A. (2003). Influence of agricultural management on soil organic carbon: a compendium and assessment of Canadian studies. *Canadian Journal of Soil Science*, 83, 363–380. DOI: 10.4141/S03-009.
- [402] Van Deventer, A.P., Ward, A.D., Gowda, P.H., Lyon, J.G. (1997). Using thematic mapper data to identify contrasting soil plains and tillage practices. *Photogrammetric Engineering & Remote Sensing*, 63(1), 87–93.
- [403] Vanlauwe, B., Wendt, J., Giller, K.E., Corbeels, M., Gerard, B., Nolte, C. (2014). A fourth principle is required to define conservation agriculture in sub-Saharan Africa: the appropriate use of fertilizer to enhance crop productivity. *Field Crops Research*, 155, 10–13. DOI: 10.1016/j.fcr.2013.10.002.
- [404] Vastola, A., Zdruli, P., D'Amico, M., Pappalardo, G., Viccaro, M., Di Napoli, F., Cozzi, M., Romano, S. (2017). A comparative multidimensional evaluation of conservation agriculture systems: a case study from a Mediterranean area of Southern Italy. *Land Use Policy*, 68, 326–333. DOI: 10.1016/j.landusepol.2017.07.034.
- [405] Veloso, M.G., Angers, D.A., Tiecher, T., Giacomini, S., Dieckow, J., Bayer, C. (2018). High carbon storage in a previously degraded subtropical soil under no-tillage with legume cover crops. *Agriculture, Ecosystems & Environment*, 268, 15–23. DOI: 10.1016/j.agee.2018.08.024.
- [406] Verhulst, N., Govaerts, B., Verachtert, E., Castellanos-Navarrete, A., Mezzalama, M., Wall, P.C., Chocobar, A., Deckers, J., Sayre, K.D. (2010). Conservation agriculture, improving soil quality for sustainable production systems. *Advances in Soil Science: Food Security and Soil Quality*, 137–208. DOI: 10.1201/EBK1439800577-7.
- [407] Verhulst, N., Nelissen, V., Jespers, N., Haven, H., Sayre, K. D., Raes, D., et al. (2011). Soil water content, maize yield and its stability as affected by tillage and crop residue management in rainfed semi-arid highlands. *Plant Soil*, 344, 73–85. DOI: 10.1007/s11104-011-0728-8.
- [408] Vlăduț, D.I., Vlăduț, V., Grigore, I., Biriș, S. (2017). Experimental research in qualitative indices of work for equipment for seedbed preparation in conservative system. *16th International Scientific Conference "Engineering for Rural Development"*, 1174–1179, Jelgava, Latvia.
- [409] Vlăduțoiu, L., Andrei, T., Marin, E., Vlăduț, V., Biriș, S.Șt., Matache, M., Fechete, L., Dumitru, I., Kiss, I. (2016). Determination of soil resistance related to wear of a chisel share. *Proceedings of the 44th International Symposium on Agricultural Engineering "Actual Tasks on Agricultural Engineering"*, 187–194, Opatija, Croatia.
- [410] Vlăduțoiu, L.C., Chișiu, G., Tudor, A., Vlăduț, N.-V., Fechete-Tutunaru, L., Marin, E., Grigore, I.-A. (2023). Tribological study of chisel knives of soil tillers. *Agriculture*, 13(6), 11235. DOI: 10.3390/agriculture13061235.
- [411] Voicea, I., Nenciu, F., Vlăduț, N.-V., Matache, M., Persu, C., Cujbescu, D. (2024). Exploring a self-sufficiency approach within a sustainable integrated pisciculture farming system. *Sustainability*, 16(18), 8055. DOI: 10.3390/su16188055.
- [412] Wainger, L., Loomis, J., Johnston, R., Hansen, L., Carlisle, D., Lawrence, D., Gollehon, N., Duriancik, L., Schwartz, G., Ribaud, M., Gala, C., (2017). Ecosystem service benefits generated by improved water quality from conservation practices. In Chapter: The Valuation of Ecosystem Services from Farms and Forests: Informing a Systematic Approach to Quantifying Benefits of Conservation Programs. *The Council on Food, Agricultural and Resource Economics (C-FARE) Report No. 0114-301; C-FARE: Washington, USA*, 2–57. DOI: 10.22004/ag.econ.260679.
- [413] Waldhoff, G., Lussem, U., Bareth, G. (2017). Multi-data approach for remote sensing-based regional crop rotation mapping: a case study for the RuR catchment, Germany. *International Journal of Applied Earth Observation and Geoinformation*, 61, 55–69. DOI: <https://doi.org/10.1016/j.jag.2017.04.009>.
- [414] Whittaker, G., Barnhart, B.L., Srinivasan, R., Arnold, J.G. (2015). Cost of areal reduction of gulf hypoxia through agricultural practice. *Science of the Total Environment*, 505, 149–153. DOI: <https://doi.org/10.1016/j.scitotenv.2014.09.101>.
- [415] Withers, P.J.A., Neal, C., Jarvie, H.P., Doody, D.G. (2014). Agriculture and eutrophication: Where do we go from here? *Sustainability*, 6(9), 5853–5875. <https://doi.org/10.3390/su6095853>.
- [416] Wronski, T., Dusabe, M.C., Apio, A., Hausdorf, B., Albrecht, C. (2015). Biological assessment of water quality and biodiversity in Rwandan rivers draining into Lake Kivu. *Aquatic Ecology*, 49, 309–320. DOI: 10.1007/s10452-015-9525-4.

- [417] Wu, J.J., Babcock, B.A. (1998). The choice of tillage, rotation, and soil testing practices: economic and environmental implications. *American Journal of Agricultural Economics*, 80(3), 494–511. DOI: <https://doi.org/10.2307/1244552>.
- [418] Xiao, L., Kuhn, N.J., Zhao, R., Cao, L. (2021). Net effects of conservation agriculture principles on sustainable land use: a synthesis. *Global Change Biology*, 27(24), 6321–6330. DOI: 10.1111/gcb.15906. PMID: 34583427.
- [419] Xiao, W., Niu, P., Wang, P., Xie, Y., Xia, F. (2024). Simulation analysis and optimization of soil cutting of rotary blade by ANSYS/LS-DYNA. *INMATEH - Agricultural Engineering*, 72(1), 22–32. DOI: <https://doi.org/10.35633/inmateh-72-02>.
- [420] Xu, M., Lacey, C.G., Armstrong, S.D. (2018). The feasibility of satellite remote sensing and spatial interpolation to estimate cover crop biomass and nitrogen uptake in a small watershed. *Journal of Soil and Water Conservation*, 73, 682–692. DOI: <https://doi.org/10.2489/jswc.73.6.682>.
- [421] Zablutowicz, R.M., Locke, M.A., Hoagland, R.E., Knight, S.S., Cash, B. (2001). Fluorescent *Pseudomonas* isolates from Mississippi Delta Oxbow lakes: in vitro herbicide biotransformations. *Environmental Toxicology*, 16(1), 9–19. DOI: 10.1002/1522-7278(2001)16:1.
- [422] Zablutowicz, R.M., Zimba, P.V., Locke, M.A., Knight, S.S., Lizotte, R.E., Gordon, R.E. (2010). Effects of land management practices on water quality in Mississippi Delta Oxbow lakes: Biochemical and microbiological aspects. *Agriculture, Ecosystems & Environment*, 139(1–2), 214–223. DOI: <https://doi.org/10.1016/j.agee.2010.08.005>.
- [423] Zedler, J.B. (2003). Wetlands at your service: reducing impacts of agriculture at the watershed scale. *Frontiers in Ecology and the Environment*, 1(2), 65–72. DOI: [https://doi.org/10.1890/1540-9295\(2003\)001\[0065:WAYSRI\]2.0.CO;2](https://doi.org/10.1890/1540-9295(2003)001[0065:WAYSRI]2.0.CO;2).
- [424] Zhang, J., Wang, X., Zhou, Q. (2017). Co-cultivation of *Chlorella* spp. and tomato in a hydroponic system. *Biomass Bioenergy*, 97, 132–138. DOI: <https://doi.org/10.1016/J.BIOMBIOE.2016.12.024>.
- [425] Zhang, Y., Yang, X., Li, X., Wang, Z., Zhou, H., Wang, J. (2023). Design and experiment of small vegetable seeder with single disc multi-row seeding and independent airway. *INMATEH - Agricultural Engineering*, 70(2), 3–10. DOI: <https://doi.org/10.35633/inmateh-70-03>.
- [426] Zheng, B., Campbell, J., Serbin, G., Daughtry, C. (2013). Multitemporal remote sensing of crop residue cover and tillage practices: A validation of the minNDTI strategy in the United States. *Journal of Soil and Water Conservation*, 68, 120–131. DOI: <https://doi.org/10.2489/jswc.68.2.120>.
- [427] Zheng, B., Campbell, J., Serbin, G., Galbraith, J. (2014). Remote sensing of crop residue and tillage practices: Present capabilities and future prospects. *Soil and Tillage Research*, 138, 26–34. DOI: <https://doi.org/10.1016/J.STILL.2013.12.009>.
- [428] Zhou, K., Cheng, T., Zhu, Y., Cao, W., Ustin, S., Zheng, H., Yao, X., Tian, Y. (2018). Assessing the impact of spatial resolution on the estimation of leaf nitrogen concentration over the full season of paddy rice using near-surface imaging spectroscopy data. *Frontiers of Plant Science*, 9, 964. DOI: <https://doi.org/10.3389/fpls.2018.00964>.
- [429] Zou, Y., Zeng, Q., Li, H., Kiu, H., Lu, Q. (2020). Emerging technologies of algae-based wastewater remediation for bio-fertilizer production: a promising pathway to sustainable agriculture. *Journal of Chemical Technology and Biotechnology*, 96, 551–563. DOI: <https://doi.org/10.1002/JCTB.6602>.
- [430] ***Our World in Data. (2024a). Greenhouse gas emissions by sector, World, <https://ourworldindata.org/is-organic-agriculture-better-for-the-environment>
- [431] ***Our World in Data. (2024b). Share of land that is degraded, <https://ourworldindata.org/grapher/share-degraded-land>.
- [432] ***Our World in Data. (2024c). Fertilizers, <https://ourworldindata.org/fertilizers>.
- [433] ***Our World in Data. (2024d). Pesticides, <https://ourworldindata.org/pesticides>.

RESEARCH AND OPTIMIZATION OF PARAMETERS CONCERNING THE INTERACTION MECHANISMS BETWEEN VERTICAL CUTTING BLADES AND STRAW IN CORN COMBINE HARVESTERS

玉米联合收获机纵置切刀-秸秆交互机理研究与参数优化

Zhu ZHAO^{1,2)}, Fengbo LIU¹⁾, Dongli SHUI¹⁾, Bintong ZHAO³⁾, Zhongnan WANG^{*1)}

¹⁾Liaoning Agricultural Technical College, Yingkou / China

²⁾ College of Agricultural and Animal Science, Tacheng Vocational and Technical College, Tacheng / China;

³⁾ College of Engineering, Shenyang Agricultural University, Shenyang / China;

Tel: +8604177020545; E-mail: zhaosynd@163.com

Corresponding author: Zhongnan Wang

DOI: <https://doi.org/10.35633/inmateh-74-87>

Keywords: Corn harvester, longitudinal straw shredding device, bionic cutting blades, cutting mechanism analysis, cutter-straw cutting simulation, finite element analysis

ABSTRACT

This study introduced a vertical straw shredding device that integrates both cutting and shredding functionalities, with the crucial components of the blade designed in a bionic serrated pattern. In order to explore the interaction mechanism between the vertical cutting blade and straw, a mechanical model of the cutting force has been developed. Based on the ANSYS-LYNA software, a cutting model for straw-bionic blades has been established. Regarding the test factors, i.e., the spindle speed, blade installation angle, forward velocity, and blade tilt angle, single-factor and orthogonal tests were also performed. Furthermore, the maximum equivalent stress experienced by straw was taken as the primary evaluation index. Accordingly, the results revealed the influencing parameters to be ordered as the blade installation angle > spindle speed > forward speed > blade tilt angle. The optimized parameters for the cutting blade were determined to be a spindle speed of 1400 r/min, an installation angle of 55°, a forward speed of 4.0 km/h, and a blade tilt angle of 0°. Similarly, the optimized parameters for the shredding blade were established as a spindle speed of 1400 r/min, an installation angle of 50°, a forward speed of 4.0 km/h, and a blade tilt angle of 0°.

摘要

本研究设计了一种集成切断和切碎功能于一体的纵向秸秆切碎装置，关键部件刀片设计为仿生刃形式。为探究纵置切刀-秸秆交互机理，建立纵置切刀切割力学模型。基于 ANSYS-LYNA 软件建立秸秆-仿生切刀切割模型，以刀轴转速、刀片安装角、前进速度和刀片倾斜角等试验因素，以切断刀和切碎刀切割秸秆过程秸秆所受最大等效应力为评价指标进行单因素和四因素四水平正交试验。试验结果表明刀轴转速、切刀安装角及行进速度对秸秆所受最大等效应力有显著影响，显著性顺序为切刀安装角>刀轴转速>行进速度>刀片倾斜角，切断刀在试验因素范围内的较优参数组合为刀轴转速 1400r/min、刀片安装角 55°、行进速度 4.0km/h 及刀片倾斜角 0°，切碎刀在切割试验因素范围内的较优参数组合为刀轴转速 1400r/min、刀片安装角 50°、行进速度 4.0km/h、及刀片倾斜角 0°。

INTRODUCTION

The straw shredding mechanism, which acts as an essential element within the combine harvester, significantly improves its operational capabilities (Liu et al., 2019). Generally, the design of straw shredding mechanisms is categorized as either vertical or horizontal (Zhang et al., 2021), employing a singular blade to process the entire straw. The straw cutting device faces issues such as poor cutting quality, high operational power consumption, and a tendency for the blades to wear out easily. The cutting of straw is closely related to the resource utilization of crop residues. Conducting research on the interaction process of cutting blades and straw is a significant aspect of the deep integration of agronomy and agricultural machinery, which has practical implications for agricultural production and ecological development (Wu et al., 2022; I. Aygun and E.Cakir, 2014).

¹ Zhao Zhu, Prof. Ph.D. Eng.; Liu Fengbo, Prof. Ph.D. Eng.; Shui Dongli, Lab.Techo. MA. Eng.; Zhao Bintong, MA. Stud. Eng.; Wang Zhongnan, Lab.Techo. MA. Eng.

The methodologies employed for straw cutting research are generally categorized into experimental and simulation approaches. Experimental investigations predominantly utilize mechanical testing apparatus (Ren et al., 2018), texture analysis devices (Huang et al., 2021), swing-cut testing platforms (Song et al., 2016), or the establishment of dedicated cutting test configurations and field trials to assess the influence of cutting parameters on various evaluation metrics. Standard evaluation metrics encompass cutting power consumption and cutting force. Simulation studies offer advantages such as low cost and high efficiency, serving as an effective complement to experimental research. Finite element software like ANSYS/LS-DYNA has been extensively applied in simulation studies of straw cutting (Gürkan Irsel, 2022). Wan et al. employed ANSYS/LS-DYNA to analyze the influence of device rotational speed, slope angle, and stem diameter on the maximum impact force and average power observed during the shredding process of mushroom grass (Wan et al., 2023). Xiao et al. performed computational simulations of the sugarcane cutting mechanism utilizing ANSYS/LS-DYNA software. Their findings revealed that with a cutter line speed of 38.8 m/s, a blade disk tilt angle of 11.66°, and a cutting edge angle of 25°, the minimum cutting power necessary was determined to be 0.80 kW (Xiao et al., 2022). Sun et al. utilized ANSYS/LS-DYNA software to simulate the branch cutting process, comparing the results with the cutting force curves obtained from bench tests, and concluded that the simulation results aligned well with those from the bench experiments (Sun et al., 2022). Zhang et al. employed ANSYS/LS-DYNA to investigate the rotary cutter's straw cutting process, identifying the parameters that minimize power consumption: a blade rotation speed of 1400 r/min, a cutting thickness of 7 mm, and a cutting edge angle of 20° (Zhang et al., 2016). Moreover, ABAQUS (Huang et al., 2021), the dynamic simulation software ADAMS, and discrete element method (DEM) technology (Li et al., 2016; Chen et al., 2024) have been utilized in various aspects of cutting performance research.

This study addresses the insufficient focus on the physical characteristics and cutting efficiency of straw shredding machinery, leading to issues like poor cutting quality, higher energy demands, and blade susceptibility. It proposes a design for a vertical straw shredding device equipped with biomimetic blades to enhance performance. It clarifies the cutting interaction dynamics between the vertical cutter and the straw, formulates a force model for the vertical cutter, and utilizes ANSYS-LYNA software to develop a biomimetic model of the cutter-straw interaction. The research performs simulation analyses of the cutting process involving the biomimetic cutter and straw, offering a theoretical basis for the design of straw shredding mechanisms in corn harvesting equipment.

MATERIALS AND METHODS

Structure and working mechanism

Considering the organizational structure and cutting characteristics of corn straw, a vertical straw shredding device has been engineered. This device is located below the ear-picking devices on the header, as depicted in Figure 1.

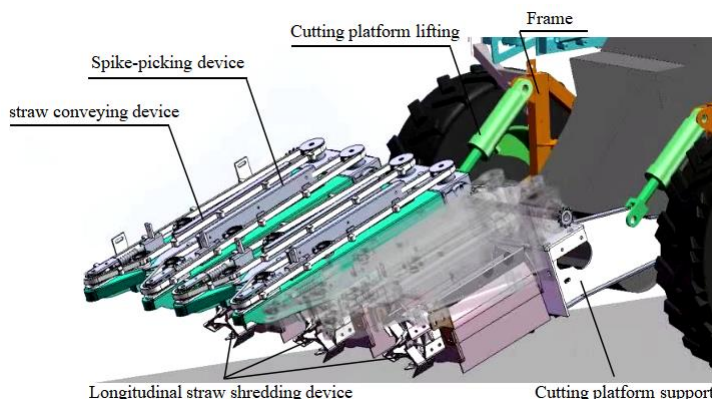


Fig. 1 - The installation diagram of longitudinal hob-type straw shredding device

The straw shredding device is composed of a cutting mechanism and a shredding mechanism. The cutting mechanism is made up of a cutting blade, a grass-cutting blade, and a cutting blade support. The shredding mechanism includes a shredding blade, shaft, and a shredding blade support, as illustrated in Figure 2. In the process of harvester operation, the blades of the cutting mechanism truncate the corn stalks at a reduced cutting height. As the harvester progresses, the stalks are directed into the shredding mechanism, where they are fragmented into smaller sections by the shredding blades.

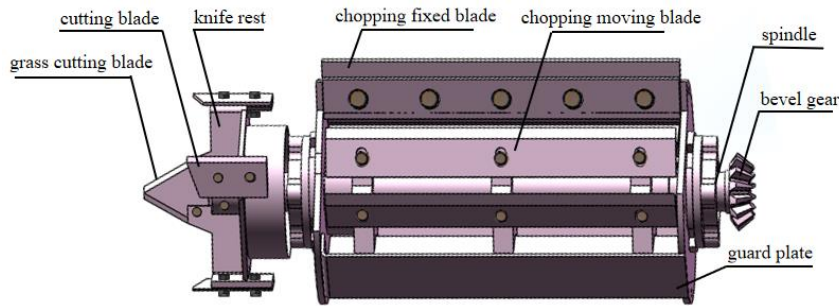


Fig. 2 - Structure diagram of straw shredding device

The cutting and shredding blades are engineered to emulate the mandibles of ants, featuring bionic serrations crafted into a suitable curvature that reflects the shape of the fourth tooth of an ant's jaw. The contour curve is expressed as a fifth-degree polynomial, and the configuration of the bionic blade is depicted in Figure 3, with specifications outlined in Table 1.

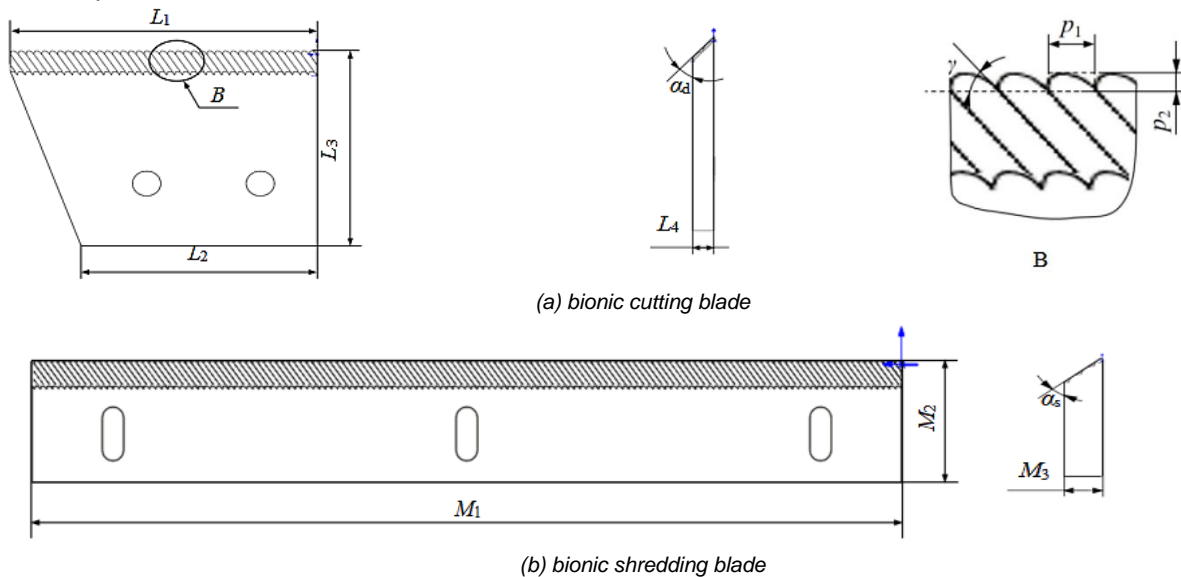


Fig. 3 - The structural of bionic blades

Note: p_1 represents the tooth spacing of the bionic blade, mm; p_2 indicates the tooth height of the bionic blade, mm; γ denotes the inclination angle of the tooth edge of the bionic blade, $^\circ$.

Table 1

The parameters of bionic cutting blade and shredding blade			
Project	Value	Project	Value
L_1 / mm	110	M_1 / mm	430
L_2 / mm	80	M_2 / mm	55
L_3 / mm	90	M_3 / mm	10
L_4 / mm	5	α_s / $^\circ$	38
α_d / $^\circ$	26	P_1 / mm	3
Material of cutting blade	T10	Material of shredding blade	65Mn

Construction of the cutting mechanics model for vertically cutting blades

The cutting process of the vertically cutting blade experiences complex forces. To facilitate the analysis of the forces acting on the blade, a uniformly distributed load applied across the blade's edge is assumed, focusing on the forces present during the extrusion stage and the initial cutting initiation. Establish a force diagram for the vertical cutting blade in a three-dimensional coordinate system, where the Oxy plane serves as the primary cutting surface, and the Oyz plane represents the secondary cutting surface, as depicted in Figure 4.

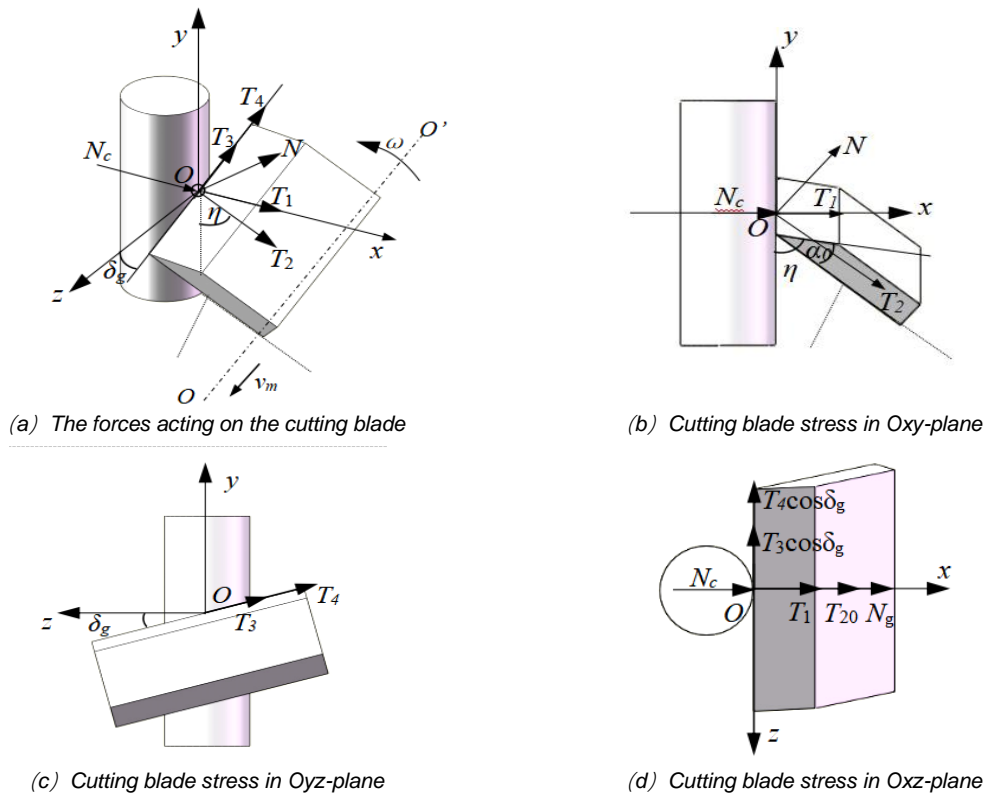


Fig. 4 -Force analysis diagram of longitudinal blade

Analysis of the compressive stress and construction of the mathematical model on the primary cutting plane

The compressive stress on the cutting blade at the primary cutting plane is illustrated in Figure 5.

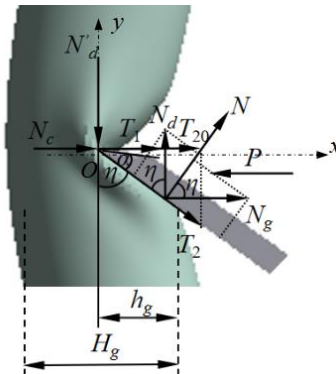


Fig. 5 -Force analysis of the main cutting surface of longitudinal blade

The reactive force N exerted on the cutting tool is:

$$N = N_g \cos \eta + N_d \sin \eta \tag{1}$$

where:

- N represents the pressure reaction force of the vertical cutting blade, (N);
- η denotes the blade installation angle, ($^\circ$);
- N_g stands for the horizontal reaction force N_d exerted on the vertical cutting blade, (N);
- N_d represents the vertical reaction force exerted on the vertical cutting blade, (N);

In the presence of the counteracting force N , the cutting tool produces a tangential frictional force T_2 .

$$T_2 = \mu_1 N = \mu_1 (N_g \cos \eta + N_d \sin \eta) \tag{2}$$

where:

- T_2 represents the tangential frictional force applied to the cutting blade, (N);
- μ_1 represents the horizontal friction coefficient between the blade and the straw.

Under the influence of the vertical reaction force N_d , the cutting blade's other cutting surface experiences a frictional force T_1 .

$$T_1 = \mu_1 N_d \tag{3}$$

The tangential friction component acting along the horizontal axis, denoted as T_{20} :

$$T_{20} = T_2 \sin \eta = \mu_1 (N_g \cos \eta + N_d \sin \eta) \sin \eta \tag{4}$$

It is clear that in the straw compression phase, the cutting blade is subjected to forces oriented horizontally along the x-axis. This encompasses the horizontal reaction force N_g induced by the compressed straw, the frictional force T_1 present on the blade's cutting surface, as well as the tangential friction force component T_{20} acting in the horizontal plane.

Analysis of the plastic deformation stress on the main cutting surface and the construction of a mathematical model

As the corn stalks experience plastic deformation, the cutting blade encounters a reaction force N_c :

$$N_c = \Delta_c L_c \sigma_c \tag{5}$$

where:

N_c denotes the reaction force of corn stalks on the cutting blade, (N);

Δ_c denotes the thickness of the cutting blade involved in the cutting process, (m);

L_c denotes the length of the cutting blade involved in the cutting process, (m);

σ_c denotes the critical yield strength of the corn straw, (N/m²).

To achieve the cutting of straw, the horizontal pressure P must meet the following conditions:

$$P \geq N_c + N_g + T_1 + T_{20} \tag{6}$$

By incorporating equations (3), (4), and (5) into equation (6), the minimum horizontal pressure, designated as P_{min} , is derived as follows:

$$P_{min} = \Delta_c L_c \sigma_c + N_g + \mu N_d + \mu (N_g \cos \eta + N_d \sin \eta) \sin \eta \tag{7}$$

Integrate the forces dN_g and dN_d acting on the thickness of the compressed straw layer unit, as illustrated in Figure 6.

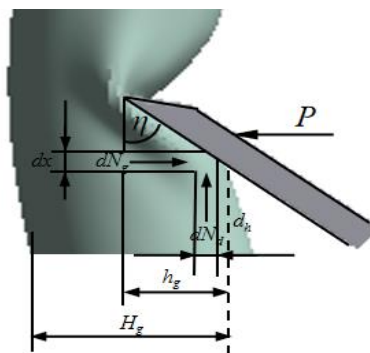


Fig. 6 - Integration force diagram of the main cutting surface

Assuming straw is regarded as an elastic material, according to Hooke's Law:

$$\varepsilon = \frac{\sigma}{E} = \frac{h_{gx}}{H_g} \tag{8}$$

where:

ε represents the relative deformation;

σ represents the normal stress experienced by the corn straw, (N/m²);

E represents the elastic modulus of the corn straw, (N/m²);

h_{gx} represents the depth of compression on the straw, (m);

H_g represents the total thickness of the straw cutting layer, (m).

In the lateral direction, the differential force dN_g exerted on the blade is:

$$dN_g = \sigma dx = E \varepsilon dx = E \varepsilon \tan \eta dh_x \tag{9}$$

Integrating both sides of the above equation yields:

$$N_g = \frac{E}{H_g} \tan \eta \int_0^{h_g} h_x dh_x = \frac{E}{2H_g} h_g^2 \tan \eta \tag{10}$$

The differential force acting on the cutter in the vertical direction:

$$dN_d = \varepsilon_1 E dh_x \tag{11}$$

where:

ε_1 represents the relative deformation of straw in the vertical direction. As is known from engineering mechanics:

$$\varepsilon_1 = \varepsilon \nu \tag{12}$$

Where:

ν represents the Poisson's ratio of corn stalks, (m).

Upon substituting equation (12) into equation (11) and performing integration on both sides of equation (11), the ensuing results are obtained.

$$N_d = \frac{\mu E}{H_g} \int_0^{h_g} h_x dh_x = \frac{E}{2H_g} h_g^2 \mu \tag{13}$$

Where:

E denotes the elastic modulus of corn stalks, (N);

H_g denotes the compression depth of the stalk before cutting, (m);

μ denotes the Poisson's ratio.

By integrating equations (5), (10), and (13) into equation (7), the pressure P is derived:

$$P = \Delta_c \sigma_c + \frac{E h_g^2}{2H_g} \left[\tan \eta + \mu \sin^2 \eta + \nu \mu (1 + \cos^2 \eta) \right] \tag{14}$$

Analysis of force on the side cutting surface and the construction of a mathematical model

The cutting blade undergoes forces on the Ozy plane, as illustrated in Figure 7, where the underside of the blade creates a frictional force denoted as T_3 .

$$T_3 = \mu_2 N = \mu_2 (N_g \cos \eta + N_d \sin \eta) \tag{15}$$

where: T_2 represents the tangential frictional force experienced by the blade, (N);

μ_2 represents the coefficient of longitudinal friction between the blade and the straw.

The blade produces a frictional force T_4 :

$$T_4 = \mu_2 N_d \tag{16}$$

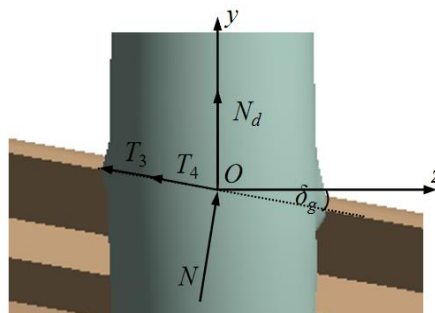


Fig. 7 - Force analysis of the secondary cutting surface of longitudinal blade

The component of friction acting in the direction of motion is:

$$T_0 = (T_3 + T_4) \cos \delta_g = \left[\mu_2 (N_g \cos \eta + N_d \sin \eta) + \mu_2 N_d \right] \cos \delta_g \tag{17}$$

It is clear that the forces exerted on the secondary cutting edge of the blade are influenced by the intrinsic material characteristics, the angles of cutting, and the blade's angle of inclination.

Establishment of the Cutter - Straw Cutting Model

To analyze the impact of experimental variables, including shaft rotation velocity, blade installation angle, travel speed, and blade inclination angle, on the peak equivalent stress encountered by corn straw during the cutting operation, dynamic cutting simulation tests were performed to identify the optimal operational parameters for the straw shredding devices.

A set of blades is selected for simulation cutting, removing the bolted attachment that links the cutter to the spindle and establishing a rigid connection between them. Disregarding the differences in the transverse geometry of corn stalks, assuming that maize stalks are represented as a dual-layer orthogonal isotropic cylindrical configuration featuring a uniform cross-sectional area, with a diameter specified at 27 mm. The internal fibers are considered to be uniformly and systematically arranged along the axial direction, resulting in a linear structure, with the straw length designated at 100 mm. The external layer and internal pith of the corn straw are intricately fused, with the thickness of the outer skin set at 1 mm.

Apply full constraints to both the base and top of the straw, with the cutting position set at a distance from the lower-middle section of the straw. A dual-layer representation of corn straw and a blade model were created utilizing SolidWorks software, subsequently saving it in .x_t format for incorporation into ANSYS LS-DYNA. Given LS-DYNA's proficiency in conducting numerical simulations of abrupt impact events, the duration for these simulations remains comparatively brief. In the context of the cutting model, it is optimal for the clearance between the blade and the corn straw to be precisely calibrated for contact. The material model selected for corn straw is categorized as a transversely isotropic elastic material, with the parameters of its material properties detailed in Table 2.

Table 2

Material parameter of corn stalk					
Part	Density/(kg·m ⁻³)	Elastic modulus/MPa	Poisson's Ratio	Shear modulus	Maximum equivalent failure stress
Straw husk	1120	3845.7	0.3	734	0.2
Straw pith	830	41.83	0.1	133	0.2

In the grid division process, the properties of the cutting tool and the corn straw material are defined, treating the cutter as a rigid body while designating the corn straw as a flexible entity. Frictional interactions occurring during the cutting action necessitate the assignment of a dynamic friction coefficient of 0.22 and a static friction coefficient of 0.45. The Body Sizing methodology is utilized for the model's grid division. To enhance the precision of the solution, additional control measures are applied to the grid elements of the corn straw, with the element size calibrated to 1.0 mm. The grid segmentation for the cutting simulation has been finalized, as depicted in Figure 8.

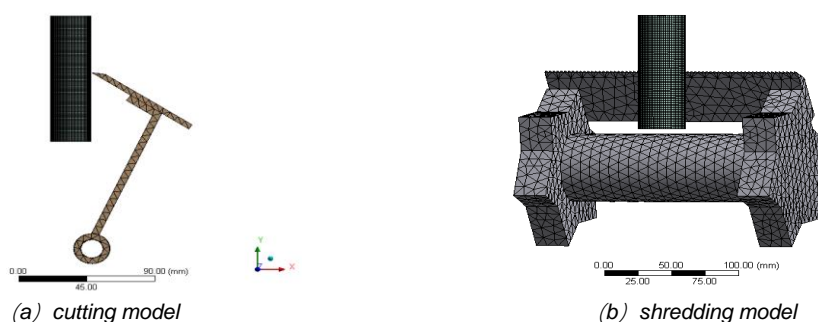


Fig. 8 - Model after meshing

The simulation duration is established at 0.005 seconds, with five CPUs designated and a memory allocation of 100 units. The output data is formatted as a series of equidistant points, each valued at 100, and the contact model selected is face-to-face erosion. Fixed constraints allowing full freedom of movement are imposed on both the top and bottom surfaces of the straw, effectively constraining any motion. Blade motion encompasses a combination of rotational movement around the blade's axis and longitudinal displacement. Specifically, the blade is programmed to translate along the Z-axis while simultaneously rotating about the Z-axis. The translation velocity is contingent upon the harvesting machine's operational speed and the stipulations of experimental design.

The rotational velocity of the blade shaft is modulated through variation in the blade's rotational angle, coupled with a distal displacement introduced at one end of the blade holder to restrict the plane of motion for the blade.

Experimental design

Single-factor experimental design

The blade installation angle is established at 50°, accompanied by a forward velocity of 3.0 km/h. The spindle rotation rates have been selected at 1000, 1200, 1400, 1600, 1800, and 2000 revolutions per minute to evaluate the resultant stress on corn stalks throughout the cutting operation. At a rotational speed of 1400 revolutions per minute and a feed rate of 3.0 kilometers per hour, various blade installation angles of 40°, 45°, 50°, 55°, 60°, 65°, and 70° are investigated to assess the peak equivalent stress experienced by corn stalks during the cutting process. When the blade installation angle is 55° and the spindle speed is 1400 r/min, the forward speeds are set at 1.5, 2.0, 2.5, 3.0, 3.5, 4.0, and 4.5 km/h to measure the equivalent stress of corn stalks during cutting. With a spindle speed of 1400 r/min, a forward speed of 3.0 km/h, and a blade installation angle of 55°, the blade inclination angles of 0°, 10°, 20°, and 30° are assessed to obtain the maximum equivalent stress of corn stalks during cutting.

Multi-factor orthogonal experimental design

To achieve the most effective combination of operational parameters for cutter performance during the cutting process, the experimental variables encompass spindle speed, feed rate, cutter mounting angle, and cutter tilt angle. The maximum equivalent stress experienced by corn stalks during the cutting operation serves as the assessment criterion for the orthogonal experiments conducted.

RESULTS AND ANALYSIS

Single-factor test

Effect of shaft rotational speed

Figure 9 delineates the maximum equivalent stress experienced by corn straw within the rotational speed range of 1000 to 2000 r/min. As the shaft speed increases, the maximum equivalent stress values fluctuate. At a rotational speed of 2000 r/min, the maximum equivalent stress experienced by the cutting blade and shredding blade on the straw peaks at values of 182.2 MPa and 186.5 MPa, respectively.

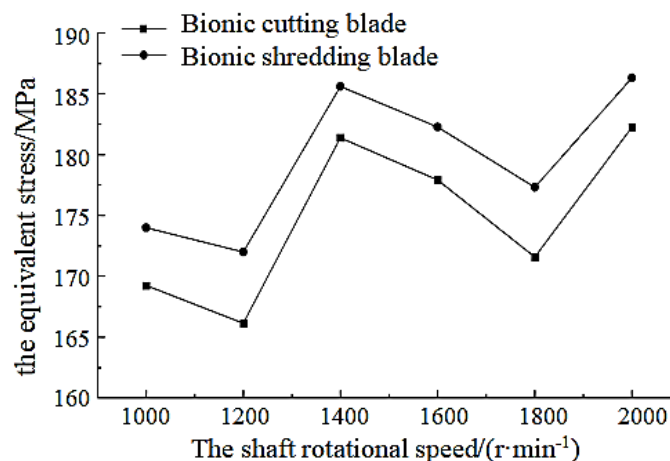


Fig. 9- The influence of spindle speed on test index

Effect of blade installation angle

As demonstrated in Figure 10, variations in the blade installation angle significantly impact the maximum equivalent stress during the straw cutting process. Initially, there is a gradual increase in this stress, followed by a subsequent decrease. The maximum equivalent stress rises from 167.23 MPa to 183.80 MPa, before diminishing to 175.05 MPa. The highest equivalent stress occurs at a blade installation angle of 55°. Additionally, when the angle of the biomimetic shredding knife is set to 50°, the equivalent stress on the corn stover peaks, reflecting a 9.17% increase compared to the maximum equivalent stress observed at a 70° angle.

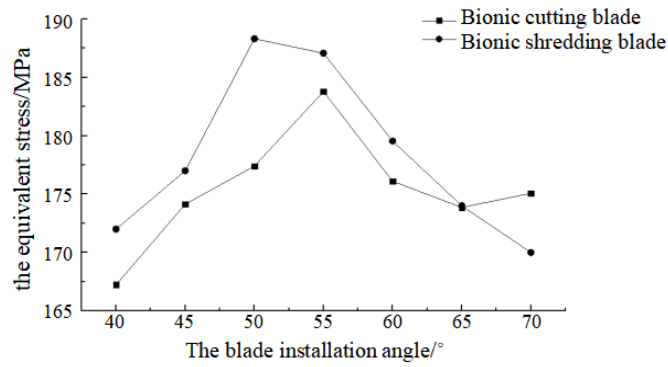


Fig. 10 -The influence of setting angle on test index

Effect of traveling speed

The effect of traveling speed on the maximum equivalent stress during the straw cutting process is shown in Figure 11. As the traveling speed increases, the maximum equivalent stress on the straw initially rises, then decreases, and subsequently shows an increasing trend again. When the cutting knife's travel speed is set at 2.5 km/h, the straw undergoes its peak equivalent stress, which is 4.50% greater than that at a speed of 1.5 km/h. Additionally, at a speed of 4.5 km/h, the bionic cutting knife subjects the straw to its highest equivalent stress. At a travel speed of 2.5 km/h, the stress is the second highest.

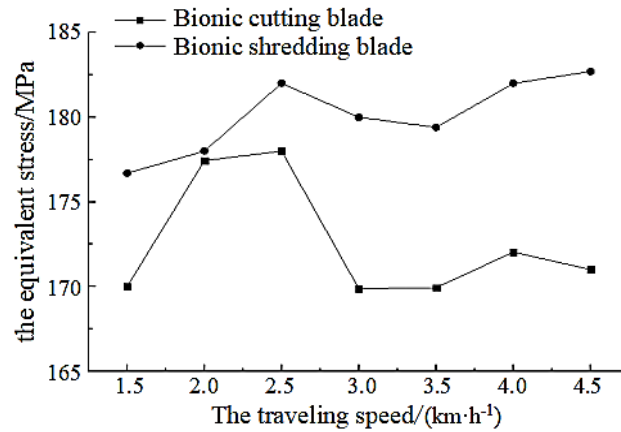


Fig. 11 - The influence of velocity on test index

Effect of blade tilt angle

Figure 12 presents the maximum equivalent stress endured by corn straw as the blade tilt angle changes from 0° to 30°. At a tilt angle of 0°, the maximum equivalent stress recorded for the cutting knife and shredding knife reaches its highest points, measuring 182.27 MPa and 188.78 MPa respectively. When comparing this to a tilt angle of 30°, the maximum equivalent stress values show an increase of 5.55% and 6.48%.

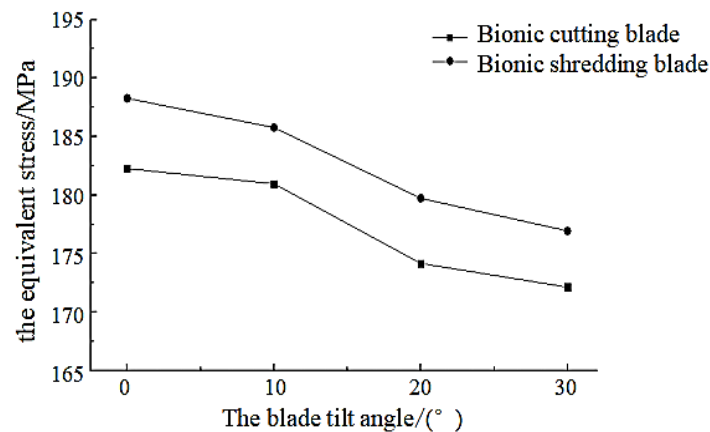


Fig. 12 - The influence of slant angle on test index

Multi-factor test

Based on the findings from the unifactorial experiment, the table coding the levels of factors has been generated and is displayed in Table 3. The protocols and findings are elaborated in Table 4.

Table 3

Levels	Shaft rotational speed A[r/min]	Blade installation angle B[°]	Traveling speed C [km/h]	Blade tilt angle D[°]
1	1600	60	4.0	15
2	1500	55	3.5	10
3	1400	50	3	5
4	1300	45	2.5	0

Table 4

Test No.	A	B	C	D	Vacant column	Equivalent stress of cutting straw/MPa	Equivalent stress of shredding straw/MPa
1	1	1	1	1	1	176.71	174.96
2	1	2	2	2	2	181.25	179.29
3	1	3	3	3	3	178.13	184.58
4	1	4	4	4	4	174.15	180.03
5	2	1	2	3	4	179.57	179.38
6	2	2	1	4	3	186.14	187.88
7	2	3	4	1	2	174.81	183.21
8	2	4	3	2	1	177.07	184.83
9	3	1	3	4	2	181.23	183.12
10	3	2	4	3	1	186.02	182.84
11	3	3	1	2	4	185.50	190.17
12	3	4	2	1	3	179.70	185.96
13	4	1	4	2	3	176.19	175.22
14	4	2	3	1	4	183.21	178.65
15	4	3	2	4	1	182.81	188.14
16	4	4	1	3	2	180.24	188.26

Note: A, B, C, and D represent the horizontal values of the tool spindle speed, blade installation angle, travel speed, and blade tilt angle, respectively.

Analysis of variance for experimental results

A variance analysis was conducted on the test results. As illustrated in Table 5, when the cutting blade processes straw, the hierarchy of the impact of the test variables on the maximum equivalent stress experienced by the straw is ranked as follows: blade installation angle > shaft rotation speed > traveling speed > blade inclination angle.

Table 5**Variance analysis table of maximum equivalent stress on stalk under cutting blade**

Sources	Squares	DF	MS	F value	P value	Significance
A	65.05	3	21.68	15.32	0.025	*
B	98.44	3	32.81	23.19	0.014	*
C	40.28	3	13.43	9.49	0.048	*
D	15.90	3	5.30	3.75	0.153	
Lake of Fit	4.245069	3	1.41502			

Note: *, significance level $0.01 < P < 0.05$; **, significance level $P < 0.01$.

The variance analysis presented in Table 6 regarding the maximum equivalent stress experienced by straw when cut by the shredding knife illustrates that the predominant factors affecting this stress, in order of significance, are: blade installation angle, knife shaft rotation speed, traveling speed, and blade inclination angle.

Table 6

Variance analysis table of maximum equivalent stress on stalk under shredding blade

Sources	Squares	DF	MS	F value	P value	Significance
A	71.95	3	23.98	13.46	0.030	*
B	158.20	3	52.73	29.57	0.010	*
C	50.29	3	16.76	9.40	0.049	*
D	37.86	3	12.62	7.08	0.071	
Lake of Fit	5.35	3	1.78			

Note: *, significance level 0.01 < P < 0.05; **, significance level P < 0.01.

Intuitive analysis for experimental results

The analytical outcomes pertaining to the maximum equivalent stress experienced by corn straw when affected by the cutting knife and the shredding knife are presented in Tables 7 and 8. When utilizing the cutting knife, the hierarchy of factors affecting the maximum equivalent stress on straw is $B>A>C>D$. Specifically, this pertains to the cutting knife installation angle, knife shaft rotational speed, travel speed, and blade inclination angle. The optimal configuration within the tested parameter range is $A_3B_2C_1D_1$, corresponding to a knife shaft rotational speed of 1400 r/min, a cutting knife installation angle of 55°, a travel speed of 4.0 km/h, and a blade inclination angle of 0°. When utilizing the shredding knife, the arrangement of factors affecting the maximum equivalent stress on straw is prioritized as $B>A>C>D$. The most effective parameter combination identified within the experimental factor limits is $A_3B_3C_1D_4$, which corresponds to a knife shaft rotational speed of 1400 r/min, a blade installation angle of 50°, a travel speed of 4.0 km/h, and a blade inclination angle of 0°.

Table 7

Maximum equivalent stress on stalk under cutting blade

Index	A	B	C	D
Mean value 1	177.56	178.43	182.15	178.61
Mean value 1	179.40	184.16	180.83	180.01
Mean value 1	183.11	180.31	179.91	180.99
Mean value 1	180.61	177.79	177.79	181.08
Range	5.55	6.37	4.36	2.48
Primary and secondary factors	$B>A>C>D$			
Optimal configuration	$A_3B_2C_3D_4$			

Table 8

Maximum equivalent stress on stalk under shredding blade

Index	A	B	C	D
Mean value 1	179.72	178.17	185.32	180.70
Mean value 1	183.83	182.17	183.19	182.38
Mean value 1	185.53	186.53	182.80	183.770
Mean value 1	182.57	184.77	180.33	184.79
Range	5.81	8.36	4.99	4.10
Primary and secondary factors	$B>A>C>D$			
Optimal configuration	$A_3B_3C_1D_4$			

Simulation of cutting corn straw with cutting blade and shredding blade

Figure 13 illustrates the procedure for severing straw utilizing the cutting blade.

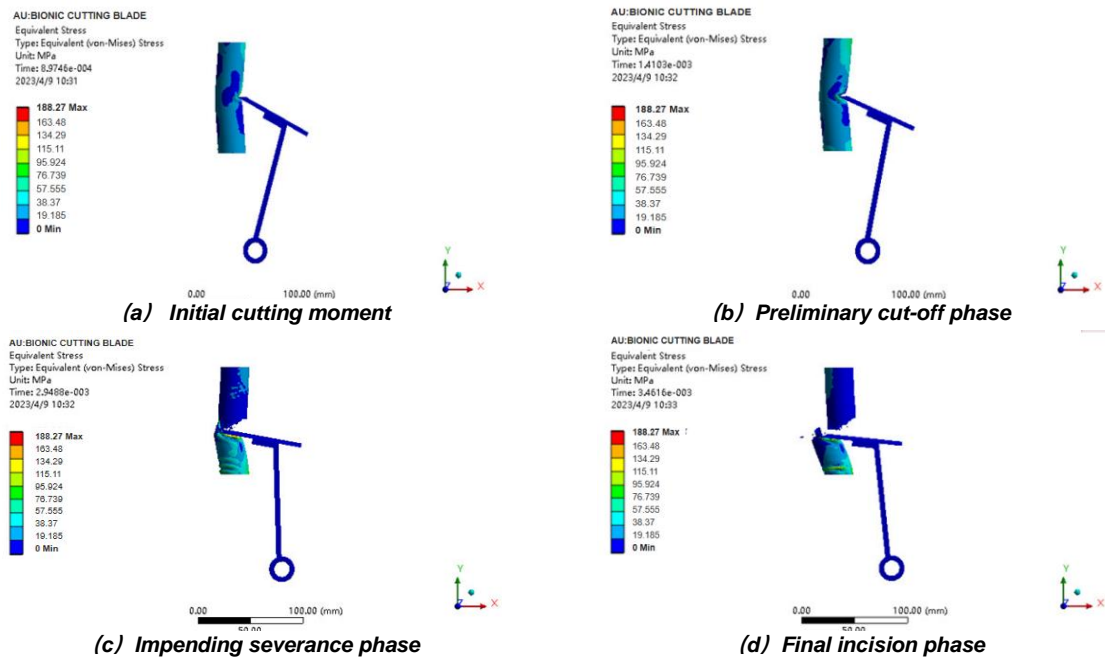


Fig. 13- Nephogram of equivalent stress of corn stalk during cutting process

Throughout the cutting procedure, the straw undergoes an initial compression, resulting in a progressive increase in the equivalent stress exerted on it. When this equivalent stress reaches a significant threshold, the cutting blade penetrates the straw, leading to substantial plastic deformation in the severed section. As the process advances, the equivalent stress on the straw decreases and fluctuates within a small range. Just before the straw is severed, the equivalent stress on the straw increases slightly. The maximum equivalent stress is localized at the severed section of the corn straw. Significant deformations are also observed in the upper and lower segments of the straw. During simulated cutting operations utilizing the bionic cutting knife, the peak equivalent stress recorded on the corn straw reaches 188.27 MPa.

Figure 14 illustrates the procedure for severing straw utilizing the shredding blade. The equivalent stress in corn straw is primarily localized at the point of incision. Additionally, the regions directly above and below the cut are subjected to variations in equivalent stress. During the corn straw cutting procedure, the straw is initially subjected to compression, resulting in a gradual increase in its equivalent stress. When this equivalent stress reaches its peak, the cutting blade penetrates the straw, leading to deformation in the section that has been severed. Following this, the equivalent stress begins to decrease and exhibits minor fluctuations until the conclusion of the cutting operation. The maximum recorded equivalent stress at the moment the cutting blade engages the corn straw is 193.25 MPa.

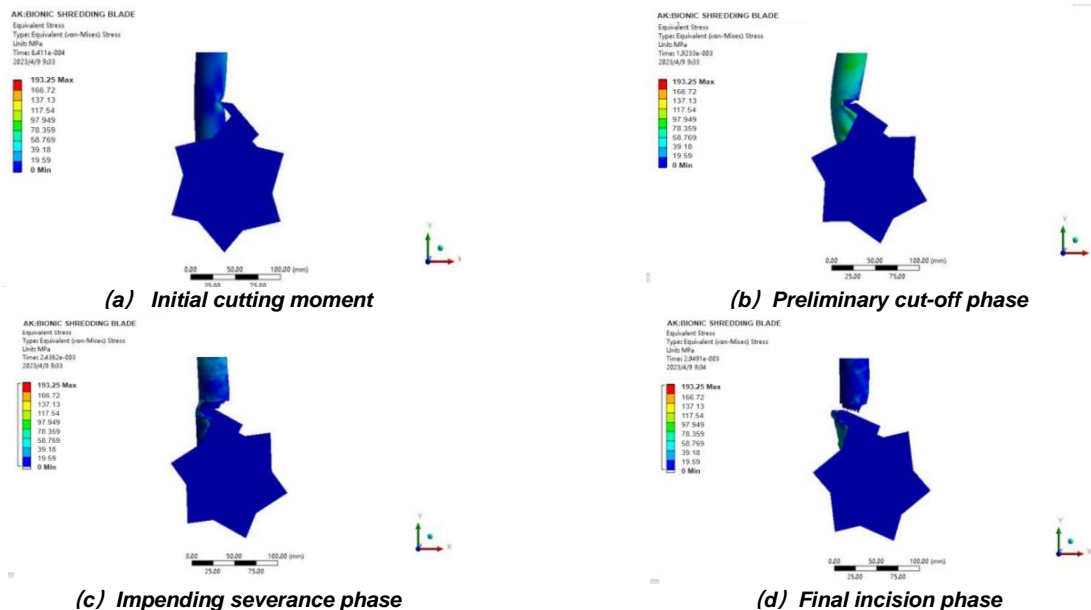


Fig. 14 - Nephogram of equivalent stress of corn stalk during cutting process

CONCLUSIONS

(1) This study presents the design of a longitudinal straw chopping apparatus for corn harvesters, alongside the development of a bionic blade for essential components. Furthermore, the force model in the horizontal direction during the extrusion phase of the primary cutting surface, as well as the force models relevant to both the primary and secondary cutting surfaces during the plastic deformation phase were established.

(2) A cutting model for a straw-bionic cutting knife has been developed using ANSYS-LYNA software. The model evaluates test factors including knife shaft rotational speed, blade installation angle, forward speed, and blade inclination angle through single-factor and four-factor, four-level orthogonal experiments. The primary evaluation metric is the maximum equivalent stress experienced by straw during the cutting operation of both bionic cutting and chopping knives. The findings indicate that the knife shaft rotational speed, cutting knife installation angle, and traveling speed exert significant influence on the maximum equivalent stress of straw, with the order of significance being blade installation angle > knife shaft rotational speed > traveling speed > blade inclination angle. The optimal parameters for the bionic cutting knife, within the tested factor range, are a knife shaft rotational speed of 1400 r/min, a blade installation angle of 55°, a traveling speed of 4.0 km/h, and a blade inclination angle of 0°. Conversely, the ideal parameter set for the bionic chopping knife is also a knife shaft rotational speed of 1400 r/min, a blade installation angle of 50°, a traveling speed of 4.0 km/h, and a blade inclination angle of 0°.

ACKNOWLEDGEMENT

This research was supported by the Natural Science Foundation of Liaoning Province (2024-BS-287), the "Enterprise Doctor Dual Innovation Plan" of Yingkou City (YKSCJH2023-015), and the scientific initiatives backed by Liaoning Agricultural Technical College (Lnz202216, Lnz202310).

REFERENCES

- [1] Aygun, I., Cakir. E., (2014). Development and determination of the field performance of stalk choppers equipped with different blade configurations. *Bulgarian Journal of Agricultural Science*, Vol. 20, pp.1268-1271, Izmir/ Turkey.
- [2] Chen B., Chu X., Huang B., Liu Y., Ge Y., (2024). Simulation and experiment of potato excavator. *INMATEH-Agricultural Engineering*, Vol. 74, pp. 526-534, Bucharest / Romania.
- [3] Gürkan Irsel., (2022). Strength-based design of a sunflower stalk cutter machine design using finite element analysis and experimental validation. *Proceedings of the Institution of Mechanical Engineers, Part C: Journal of Mechanical Engineering Science*, Vol.236, pp.1147-1168, Edirne/Turkey.
- [4] Huang W., Ren D.Z., Gong YJ., Bai XW., Shi H., Liu C.W., (2021). Coupling Separation Simulation Analysis and Test of Corn Stalk Rind-pith Based on Abaqus (基于 Abaqus 的耦合式玉米秸秆皮糠分离仿真与试验). *Transactions of the Chinese Society of Agricultural Machinery*, Vol.52, pp.124-133, Shenyang/China.
- [5] Huang WY., Qiu S., Ren D., Gong Y., Bai X., Wang W., (2021). Optimization of shearing parameters of corn stalks based on desirability function approach. *INMATEH-Agricultural Engineering*, Vol.64, pp.355-364, Bucharest / Romania.
- [6] Li B., Chen Y., Chen J., (2016). Modeling of soil-claw interaction using the discrete element method (DEM). *Soil and Tillage Research*, Vol.158, pp.177-185, Yangling/China.
- [7] Liu, P., Zhang Z., He J., Li H., Wang Q., Lu C., Lou S., Liu W., Cheng X. (2019). Kinematic analysis and experiment of corn straw spreading process. *INMATEH-Agricultural Engineering*, Vol. 58, pp. 83-92, Bucharest / Romania.
- [8] Ren Z., Bai X., Li J., Gong Y., Gao Y., (2018). Design and Test on Roller-teeth Husking Roller in Rind-pith Separation of Corn Stalks (玉米秸秆皮糠分离碾压揭皮辊设计与试验). *Transactions of the Chinese Society for Agricultural Machinery*, Vol.49, pp.93-99, Shenyang/China.
- [9] Song Z., Song H., Yan Y., Li Y., Gao T., Li F., (2016). Optimizing design on knife section of reciprocating cutter bars for harvesting cotton stalk(棉花秸秆往复切割器动刀片优化设计). *Transactions of the Chinese Society of Agricultural Engineering*, Vol.32, pp.42-49, Taian/China.

- [10] Sun, J., Xing, K., Yang, Z., Duan J., (2022). Simulation and experimental research on fruit branch pruning process based on ANSYS/LS-DYNA (基于 ANSYS/LS-DYNA 的果枝修剪过程仿真与试验研究). *Journal of South China Agricultural University*, Vol.43, pp.113-124, Guangdong/China.
- [11] Wan, J., Chen, W., Chen, C., Zheng, S., (2023). Analysis on power consumption model of hammer-JUNCAO mill system based on ANSYS Workbench/Ls-Dyna(基于 ANSYS Workbench/Ls-Dyna 的锤片 – 菌草粉碎系统的功耗模型分析). *Journal of Fujian Agriculture and Forestry University (Natural Science Edition)*, Vol. 52, pp.127-134, Fujian/China.
- [12] Wu, K., Song, Y., (2022). Research Progress Analysis of Crop Stalk Cutting Theory and Method(农作物茎秆切割理论与方法研究进展分析). *Transactions of the Chinese Society for Agricultural Machinery*, Vol.53, pp.1-20, Shandong/China.
- [13] Xiao, W., Lu, J., Deng, C., (2022). Research on power consumption model of sugarcane harvester cutting system based on ANSYS/Ls-Dyna(基于 ANSYS/Ls-Dyna 的甘蔗收获机切割系统功耗模型研究). *Journal of Chinese Agricultural Mechanization*, Vol.43, pp.116-121, Nanning/China.
- [14] Zhang, K., Zhang, W., Ma, J., Teng, S., (2021). Design and Experiment of Chopping Device for Corn Silage Test Bed (玉米青贮饲料试验台切碎装置设计与试验). *Forestry Machinery & Woodworking Equipment*, Vol.49, pp. 25-31, Gansu/China.
- [15] Zhang, Y., Diao, P., Du, R., Liu, L., Zhang, J., (2016). Design and Test of Stalk Chopping and Conveying Device for Corn Combine Reaping both Stalk and Spike (穗茎兼收型玉米收获机茎秆切碎与输送装置设计与试验). *Transactions of the Chinese Society for Agricultural Machinery*, Vol.47, pp. 208-214, Zibo/China.

RATIONALE OF THE OPTIMAL SHAPE AND PLACEMENT ANGLE VARIATION PATTERN OF THE TILLAGE ROTARY BLADE

Հողաստվածի Ֆրեզի Դաշնակի Օրիենտացիոն Զանգի և Տեղադրման Կոնցուրսի Փոփոխման Օրինակազմումից Հիմնարկում

Arshaluys TARVERDYAN¹⁾, Artur ALTUNYAN¹⁾, Albert GRIGORYAN¹⁾

¹⁾Scientific Research Institute for Agricultural Mechanization and Automation, Armenian National Agrarian University, Yerevan, Armenia

Tel: +37455327325; E-mail: arturaltunyan@gmail.com

Corresponding author: Artur Altunyan

DOI: <https://doi.org/10.35633/inmateh-74-88>

Keywords: tiller, streamlined blade, minimal resistance, installation angle, angle adjustment

ABSTRACT

The article addresses the issue of reducing the energy consumption and minimizing the ejection of loosened soil mass from the cultivated zone in gardening tillage rotary machines with a vertical rotation axis. Generally, rotary tilling machines with a horizontal rotation plane are characterized by high energy consumption. Additionally, during the rotary tilling process, there is an undesirable phenomenon of soil mass ejection caused by the blade, resulting in exposed areas and furrows in the already cultivated zone. This results in a disruption of the technological quality of soil cultivation. Considering that both the resistance moment of the rotor and the intensity of soil mass ejection are significantly influenced by several structural-technological and soil physico-mechanical factors, the comprehensive and simultaneous identification of these influences remains a relevant challenge. The solution to the problem is based on the theory of adjusting the angular positioning of rotary tiller blades and the results obtained. The theoretical solution to the issue of soil mass ejection from the cultivated area relies on the model of oblique impact between two bodies under viscous friction conditions. As a result, expressions were derived that allow determining an optimal angular positioning pattern for the tiller blades and an optimal shape of the blade body. These ensure that the technological process is carried out with minimal energy consumption and the least possible soil mass ejection.

ԱՍՓՈՓԱԳԻՐ

Հողվածում դիտարկվում է ուղղաձիգ պտտման առանցքով այգեգործական հողամշակ ֆրեզի էներգատարողության և մշակման գոտուց փխրեցված հողազանգվածի արտաշարտման նվազեցման հիմնախնդիրը: Ընդհանուր առմամբ հորիզոնական հարթության մեջ պտտվող հողամշակ ֆրեզ-մեքենաներին ներհատուկ է բարձր էներգատարողությունը, բացի այդ, հողի ռոտացիոն մշակման ընթացքում դիտվում է դանակի կողմից մշակված հողային զանգվածի շարտման անցանկալի երևույթ, որի պատճառով արդեն իսկ մշակված հողային գոտում ի հայտ են գալիս որոշ մերկացած տեղամասեր և ակոսներ, որոնց հետևանքով խաթարվում է հողի մշակման տեխնոլոգիական որակը: Հաշվի առնելով, որ ինչպես ռոտորի դիմադրության մոմենտը, այնպես էլ հողազանգվածի արտաշարտման ինտենսիվության վրա որոշիչ ազդեցություն են թողնում մեքենայի կառուցվածքա-տեխնոլոգիական և հողի ֆիզիկա-մեխանիկական հատկություններով պայմանավորված մի շարք գործոններ, որոնց ամբողջական ու միաժամանակյա ազդեցության բացահայտումը մնում է ակտուալ խնդիր: Խնդրի լուծման հիմքում դրված է հողամշակ ֆրեզի դանակների տեղակայման անկյան կարգավորման տեսությունը և ստացված արդյունքները: Մշակվող տարածքից հողազանգվածի արտաշարտման խնդրի տեսական լուծման հիմքում դրված է երկու մարմինների շեղ հարվածի մոդելը մածուցիկ շփման պայմաններում: Արդյունքում ստացվել են արտահայտություններ, որոնք հնարավորություն են տալիս սահմանել ֆրեզի դանակների տեղակայման անկյան կարգավորման այնպիսի օրինաչափություն և դանակի իրանի օպտիմալ ձև, որոնց դեպքում տեխնոլոգիական գործընթացն իրականացվում է նվազագույն էներգոծախսումներով և հողազանգվածի հնարավոր քիչ արտաշարտմամբ:

INTRODUCTION

Nowadays, the rotary tillers equipped with active operating parts have been widely used in the process of soil cultivation, in particular in the orchards and vineyards, to ensure the highest quality of the soil tillage

processes, weed control as well as to provide relevant agrotechnological requirements (Acharya et al. 2019; Manaenkov et al, 2017; Panov and Tokushev, 2005; Schjønning and Rasmussen, 2000).

The cutting angles of the blade in the separate locations of its movement trajectory significantly exceed the defined optimal cutting angles of the common operating parts of the rotary tiller with the vertical rotation axis (Sineokov and Panov; 1977; Koval, 2010; Kupryashkin and Gusev, 2020; Panov and Tokushev, 2005). The mentioned factor not only increases the energy consumption of the technological processes, but also negatively effects on the technological quality of the soil cultivation. The high energy consumption of the rotary tiller is connected also with the quite high cutting speeds of the soil's tillage process $(5,0 \pm 10,0) \frac{m}{s}$, in the course of it the technological characteristics of the interactions between the working part and cultivated soil changing significantly (Panov and Tokushev, 2005; Sineokov and Panov, 1977). This creates additional dynamic resistance, not only due to the soil cutting process but also due to the scattering of the cultivated soil mass. The aforementioned significant drawback is inherent in tillers with a vertical rotation axis (Kupryashkin and Gusev, 2020; Konstantinov, 2019).

Unlike the horizontal tillers, where the soil's cutting is a periodic process, in the case of the vertical tillers it is continuous and the knives are in the dense soil environment throughout the technological process.

In the case of the rigid fixation of the blade of the tiller with vertical rotation axis, the installation angles were selected by considering the fact that in the frontal area which is the most overloaded part of the knife's trajectory, the cutting angle was within the range of optimal values: $\beta = (20 - 30)^\circ$ (Akimov A.P. et al, 2013; Akimov A.P. et al, 2018; Grigoryan and Altunyan, 2021, Tarverdyan et al, 2022).

With this approach, the cutting angle almost doubles along the rest of the blade's movement trajectory, particularly in the tiller's rear area. As a result, highly undesirable processes such as scattering and scraping of the cultivated soil mass by the inner surface of the blade's handle are observed, negatively impacting technological quality. It is also important to note that changes in the cutting angle over such a wide range generate vibrations to the rotating parts, particularly the vibration of the tiller rotor, which is an undesirable phenomenon to ensure reliable machine operation.

The energy consumption of the technological process of the rotary tiller has been mainly defined by the geometric shape, location as well as the mutual positioning of the knives. This has been approved by many research studies and our own experiments (Panov, 2005; Koval, 2010; Konstantinov, 2019; Vorobyov and Marchenko, 1990; Chatkin, 2008; Mandal et al, 2013; Matin & Fielke, 2014; Raparelli et al, 2021; Grigoryan and Altunyan, 2021).

In addition, by considering the fact that the operational reliability of the existing machines is relatively low, especially in the types of terrain in the Republic of Armenia, which are characterized with the high content of stones and gravels, self-regulating blades for angular positioning were designed and developed, specifically for rotary tilling machines with a vertical rotation axis.

The patterns of variation in cutting angles and the conditions for maintaining them constant, in the case of a fixed positioning angle of the blade in a soil-cultivating rotary tiller with a vertical rotation axis, are detailed in the previous study (Tarverdyan A.P. et al, 2023).

In the study mentioned, an important conclusion was reached based on the review and analysis of scientific literature in the field. It highlights that the inherent shortcomings of soil-cultivating rotary tillers with a vertical rotation axis—namely, high energy consumption and the ejection of loosened soil from the cultivation zone—can be minimized. This can be achieved by optimizing the blade shape and adjusting the blade positioning angle throughout one rotation of the rotor.

The article aims to study the inherent drawbacks of rotary tillers with a vertical rotation axis, specifically high energy consumption and soil mass ejection from the cultivated zone, and to develop and justify an optimal blade body shape and a theoretical calculation for adjusting the angular positioning of the blades during one rotation of the rotor.

MATERIALS AND METHODS

As already mentioned, the high energy consumption and soil mass ejection of rotary tilling machines with a vertical rotation axis are primarily and mainly due to changes in the cutting angle of the blades during one rotation of the rotor, which, in turn, is related to the fixed angular position of the blades (Akimov A.P. et al, 2013, Damanauskas et al., 2019).

It is evident that a stable cutting angle during the operation of the tiller can only be ensured through the non-rigid fixation of the blades and the corresponding adjustment of their angular positioning.

The issue has been thoroughly discussed and resolved by us in (Tarverdyan A.P. et al, 2023), where analytical expressions were derived that substantiate the possibility of maintaining a constant cutting angle of the blades during one rotation of the rotor. Since this work also addresses the problem of blade angular positioning and, in particular, the optimal shape, it is necessary to present certain provisions and results from the mentioned work here.

During the operation of the rotary tiller when the rotor rotates at an angular speed ω ($\varphi = \omega t$) and makes a forward movement in the direction of the X axis at a speed of V_F (Fig. 1), an arbitrary point C of the rotary tiller draws an elongated cycloid (trochoid), the appearance of which is determined by the kinematic parameter of the rotary machine:

$$\lambda = \frac{V_C}{V_F} > 1, \quad (V_C = \omega R)$$

where V_F is the forward velocity of the machine [m/s] and V_C is the circumferential velocity of the blade [m/s], R - the rotation radius of the C point of blade, [m], ω - angular speed of the tiller blade, [min⁻¹].

In parametric form, the equation of C point motion in the XOY coordinate system is as follows in Eq. (1):

$$\left. \begin{aligned} x &= V_F t \pm R \sin \omega t, \\ y &= R \cos \omega t. \end{aligned} \right\} \quad (1)$$

where V_F is the velocity of forward movement of the aggregate [m/s], R - rotation radius of blade point (e.g. C point) [m], ω - angular speed of the tiller blade [min⁻¹]

The movement of the blade attached to the rotor during one full rotation is analyzed and it is assumed that the conventional starting point is the moment when the cutting edge of the blade crosses the y-axis (M point, Figure 1). The M point draws the MCANBF cycloid during one rotation, and since the blade is fixed to the rotary tiller disk at a constant angle γ with respect to the radius (OM), the cutting angles characterizing the technological process of soil cutting mass are constantly changing during the rotation.

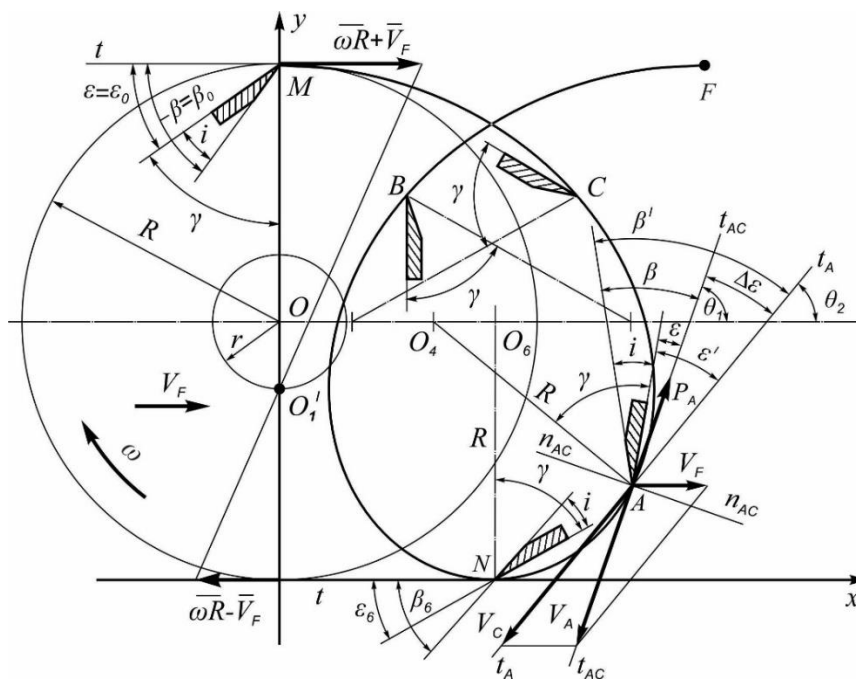


Fig. 1 - The changing scheme of the trajectory and cutting angles of the tiller's blade during one rotation of the rotor

The installation angle of the blade in an arbitrary position A of the trajectory - the angle γ - formed by the back plane of the knife arm and the radius $O_4A=R$ in that position is constant and unchanged, β'_4 is the front cutting angle; it is the angle formed by the tangent t_A of the front plane of the blade and the tangent at point A to the circle with radius $O_4A=R$, ϵ' is the angle formed by the back part of the blade and t_{AC} tangent, β_4 - real front cutting angle, it is the angle formed by the front plane of the blade and cycloidal tangent t_A across the A point, i - sharpening point of the blade.

The diagram (Figure 1) attests, that:

$$\beta' = \epsilon' + i; \quad \beta = \epsilon + i; \quad \beta = \beta' - \Delta\epsilon; \quad \epsilon = \epsilon' - \Delta\epsilon, \quad (2)$$

where $\Delta\varepsilon$ is the angle made by the cycloidal tangents (t_A and t_{AC}) to the circle at the given point (A).

Since the discussed objective seeks to provide the possible constant values of the blade's cutting angles during one rotation of the tiller, the only possible case is to reach the equilibrium of the changes of moment loads generated from the factors of the resistance forces applied on the rotor's shaft. It is obvious that in that case the blade installation angle γ has to be changed or adjusted.

As a result of the study of an arbitrary point trajectory on the tiller blade and the kinematic analysis of the drive mechanism, an analytical expression was derived for the precise determination of the change in the cutting angle of a rigidly fixed blade during one rotation of the rotor (Tarverdyan A.P. et al, 2023).

$$\Delta\varepsilon = \pm \arccos \frac{\lambda \pm \cos\varphi}{\sqrt{1 + \lambda^2 \pm 2\lambda\cos\varphi}} \quad (3)$$

Since, according to the condition of the discussed problem, the cutting angle of the blade must remain as constant as possible, the relationship between the blade's angular positioning γ and the change in the cutting angle $\Delta\varepsilon$ must be taken into account.

$$\gamma = \frac{\pi}{2} - \beta + i - \Delta\varepsilon, \quad (4)$$

The specified condition can only be met if the change in γ follows the same pattern.

The other essential aim of the discussed problem is to exclude or minimize the throwing process of the cultivated soil mass from the cultivated zones by the tiller's blade.

A straight flat blade of a rotary tiller with a vertical axis was chosen as the object of study.

When determining the angle of soil displacement and the relative and absolute velocities, it was assumed that the interaction between the blade and the soil is of impact nature under conditions of viscous friction.

The impact process between an individual soil particle and the vertical surface of the blade is considered. The blade has a cutting angle β , an inclination angle i , and an absolute velocity v_a (Fig. 2).

In the case of reversibility of the impact process, it can be assumed that the soil particle strikes the stationary blade with a velocity v_a at an angle of $90^\circ - (\beta - i)$ relative to the normal N of the blade vertical surface (Fig. 2a shows the pre-impact velocity v_a and the post-impact velocity u of the soil particle). After the impact, the velocity vector \bar{u} of the soil particle forms a reflection angle β' relative to the normal N .

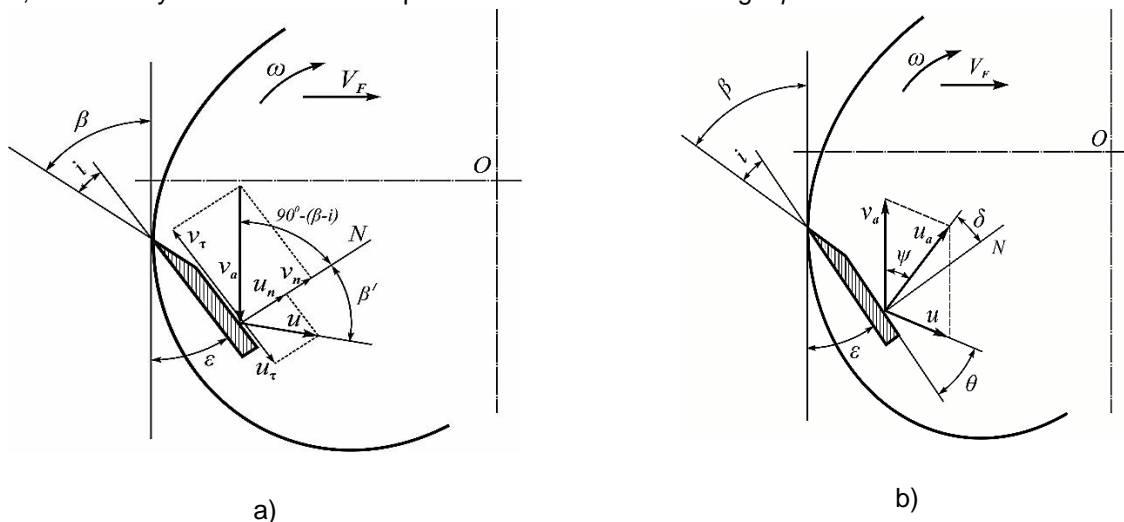


Fig. 2 - The case of a soil particle impact on the vertical flat surface of the blade:

- a) scheme for determining the relative velocity,
- b) scheme for determining the angle of the absolute velocity of particle displacement.

According to the classical theory of oblique impact for inelastic bodies, there is the following relationship between the normal components of the pre-impact and post-impact velocities of the particle (Ivanov A.P., 1992):

$$\mu = \frac{u_n}{v_n}, \quad (5)$$

where μ is the coefficient of restitution of the impacting body, $0 \leq \mu \leq 1$, v_n and u_n - the normal components of the pre-impact and post-impact velocities [m/s]. Moreover, the values $\mu = 0$ correspond to an absolutely inelastic impact, and $\mu = 1$ to an absolutely elastic impact.

Between the tangential components of the velocities, according to the hypothesis of viscous friction, the following relationship exists.

$$u_\tau = (1 - \varphi)v_\tau, \tag{6}$$

where v_τ and u_τ are the tangential components of the pre-impact and post-impact velocities [m/s], and φ - the instantaneous coefficient of friction during the impact.

After the impact, the relative velocity of the soil particle's motion, according to the scheme shown in Fig. 2a, will be:

$$u = \sqrt{u_\tau^2 + u_n^2}.$$

Considering that $u_\tau = v_a(1 - \varphi)\cos(\beta - i)$ and $u_n = v_a\mu \cdot \sin(\beta - i)$, after certain transformations it will be obtained:

$$u = v_a\sqrt{(1 - \varphi)^2\cos^2(\beta - i) + \mu^2\sin^2(\beta - i)}. \quad [\text{m/s}] \tag{7}$$

Regardless of which hypothesis is accepted for oblique impact - viscous or dry friction - the post-impact velocity of a material point after an oblique impact is determined as follows (Blekhman I.I., 1979):

$$u = v_a\mu \cdot \frac{\cos(\beta - i)}{\sin\beta'}. \tag{8}$$

According to the viscous friction hypothesis (Blekhman I.I., 1979), the angles of reflection β' and impact $[90 - (\beta - i)]$ are closely related by the following expression (Fig. 2a):

$$\text{tg}\beta' = \frac{1 - \varphi}{\mu} \text{tg}[90 - (\beta - i)]. \tag{9}$$

Since the blade is actually moving, and the soil particle is initially at rest before the impact, after the impact, the motion will also be transmitted to the soil particle in the direction of the impact. Therefore, the post-impact absolute velocity u_a of the soil particle will be determined as the vector sum of the translational velocity v_a and the relative velocity u (Fig. 2b).

$$u_a = \sqrt{u^2 + v_a^2 - 2uv_a\cos(90 + \beta - i - \beta')}. \tag{10}$$

The high values of the post-impact absolute velocity (u_a) of the soil particle are responsible for the ejection of the soil mass and also for the significant forces acting on the blade (Akimov A. P. et al, 2018). It should be noted that these factors are determined not only by the blade positioning angle but also by the geometric shape of the blade cross-section. Therefore, the blade positioning angle and the shape of its cross-sectional surface should be such that u_a is minimized.

RESULTS AND DISCUSSIONS

The process of the soil cutting, the cinematic and dynamic traits are characterized by the presented parameters in the arbitrary A point along with the trajectory (Fig.1 and 3).

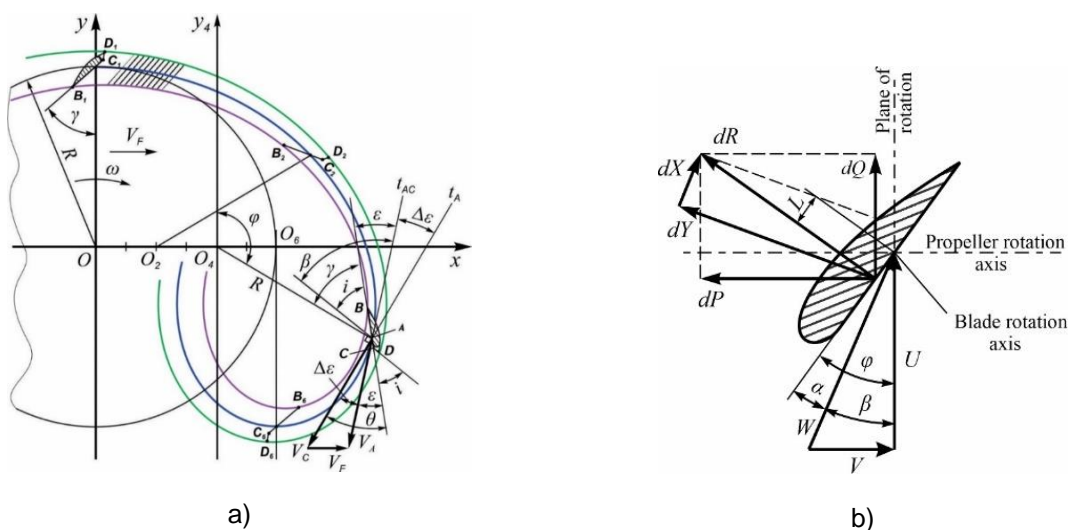


Fig. 3 - The scheme of the cutting angles changes of the tiller's blade with the streamlined form (a)
The scheme of the propeller location angles (according to Alexandrov V.L) (b)

During these investigations the goal is to elaborate certain scheme of the knife location to allow the cutting angles β and ε , by characterizing the main tillage procedure, to remain constant during one rotation and the location angle γ to be subjected with the designed adjusted changes, in respect with the Equation (11) (Tarverdyan A.P. et al, 2023)

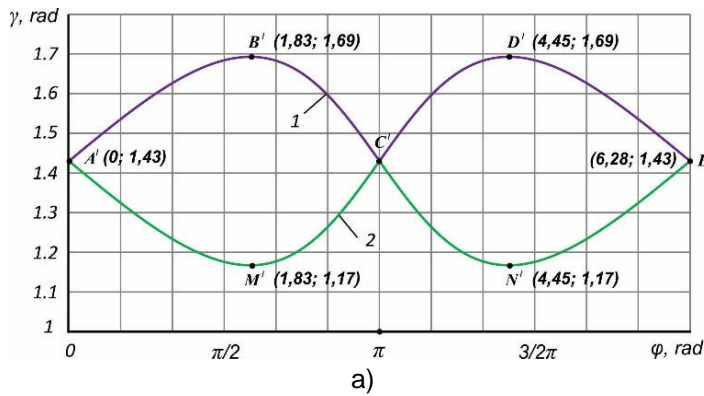
$$\gamma(\varphi) = \frac{\pi}{2} - \beta + i \mp \arccos\left(\frac{\lambda \pm \cos\varphi}{\sqrt{1 + \lambda^2 \pm 2\lambda\cos\varphi}}\right), \tag{11}$$

where i is the sharpening angle of the blade, it is constant in each specific problem; it is assumed that β is also constant as a precondition and hence assigning $K = \frac{\pi}{2} - \beta + i$ it can be written:

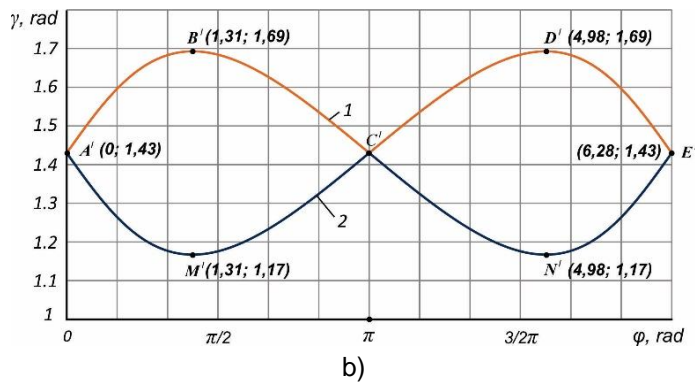
$$\gamma(\varphi) = K \mp \arccos\left(\frac{\lambda \pm \cos\varphi}{\sqrt{1 + \lambda^2 \pm 2\lambda\cos\varphi}}\right). \tag{12}$$

whereas $\mp \arccos\left(\frac{\lambda \pm \cos\varphi}{\sqrt{1 + \lambda^2 \pm 2\lambda\cos\varphi}}\right)$ member exhibits itself the changes of the cutting angles during one rotation period $\Delta\varepsilon$.

As it is known (Tarverdyan A.P. et al, 2023), the variation pattern of γ may depend on the rotor's rotation angle (φ) having the following form (Fig. 4):



1. $\gamma = 1,43 + \arccos\left(\frac{\lambda + \cos\varphi}{\sqrt{1 + \lambda^2 + 2\lambda\cos\varphi}}\right),$
2. $\gamma = 1,43 - \arccos\left(\frac{\lambda + \cos\varphi}{\sqrt{1 + \lambda^2 + 2\lambda\cos\varphi}}\right)$



1. $\gamma = 1,43 + \arccos\left(\frac{\lambda - \cos\varphi}{\sqrt{1 + \lambda^2 - 2\lambda\cos\varphi}}\right),$
2. $\gamma = 1,43 - \arccos\left(\frac{\lambda - \cos\varphi}{\sqrt{1 + \lambda^2 - 2\lambda\cos\varphi}}\right)$

Fig. 4 - The diagram of $\gamma = f(\varphi)$ function during one rotation of the rotor in case of constant cutting angles ($\lambda = 3,85$)

By following the presented pattern to ensure changes in the cutting angles, the tiller will operate stably and without vibrations. In this direction the research experiments continue to enhance the efficiency and productivity of the machine work.

However, it is essential to note, that the primary objective of the presented research is to solve the issue related to the soil throwing from the cultivated zone during the tillage. In fact, as it is mentioned, efforts were made to strengthen and ensure the streamlined shape of the blade.

Field experiments have revealed the fact that the high value of the absolute velocity (V_A) of the soil particle after hitting the surface of the knife determines the throwing of the soil mass as well as the high

resistance forces of the knife (Grigoryan and Altunyan, 2021; Akimov A.P., 2018; Tarverdyan A.P. et al, 2024; Konstantinov Yu.V., 2019; Raparelli T., 2021).

Considering equations 7 and 10, the post-impact absolute velocity of the soil particle is obtained:

$$u_a = v_a \sqrt{1 + m + 2\sqrt{m} \cdot \sin(\beta - \beta' - i)}, \quad [\text{m/s}] \quad (13)$$

where $m = (1 - \varphi)^2 \cdot \cos^2(\beta - i) + \mu^2 \cdot \sin^2(\beta - i)$:

Expression (13) implies that, in the case of a constant cutting angle, the absolute velocity of the post-impact soil particle remains approximately unchanged during one rotation of the rotor.

It must be considered that these factors have been related not only to the installed angles of the blade but also to the geometrical shape of its body plane. This indicates that its study and optimal configuration as well as the determination of its parameters becomes a vital issue.

It is important to define the exact knife shape (contours) for the required surface of the transverse incision of the blade to cause small resistance forces while moving in the soil and to have such a ratio of the tangential components and normal velocities of the different parts of the surface to result in a minimized throwing of the soil mass.

In the context of hydrodynamics and aerodynamics' similar problems, the movement of the bodies with streamlined abilities in the environment is considered (Landau and Lifshitz, 2001).

Research has defined that it is essential that the particles' detachment from the surface occur at the back edge of the body, where the "stormy" movements of the particles are minimal.

It is significant to mention that the field experiments and operation practices of the tiller have demonstrated that the amount of the soil thrown during its cultivation, is primarily connected with the physico-mechanical characteristics of the soil and its moisture content. In particular, the extent of throwing soil is minimal or completely absent in the wet and silty soil, whereas it is maximum in the dried soil that is characteristic for most orchards in Armenia.

Thus, the discussion refers to the example described above, and the behavior of dry, pulverized bulk soil mass can be assessed with the above mentioned analogy.

According to the prominent provisions of this analogy, it should be given such a form to the blade plane that the growing environmental resistance would occur slowly and smoothly along with its edge length.

The solution is to give elongated form to the plane of the blade so that that the streamlined surfaces gradually approach the cleaning direction by creating a sharp edge at the junction. In fact, the frontal part should have a rounded shape.

The mentioned conditions are totally provided by the prominent streamlined shape of plane (Figure 5).

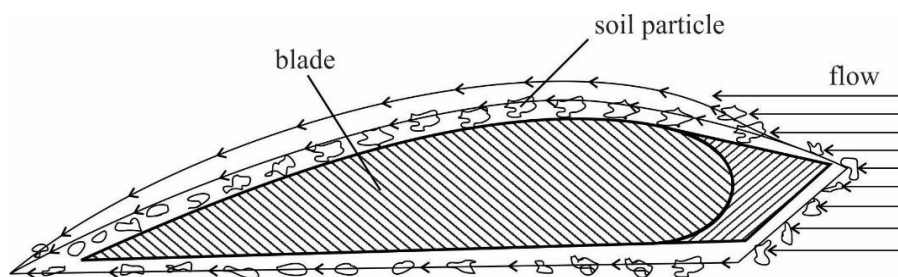


Fig. 5 - The scheme of the streamlined plane of the rotary tiller's blade

It is obvious, that the streamlined shape is related to the entire length of the blade body where the cutting edge should be fixed at the rounded part of the blade in the cutting zone of the soil layer.

Since the basis of the objective is to maintain the constant values of the cutting front and, consequently, the rear angles of the blade ($\beta = const$ or $\varepsilon = const$) during one rotation of the tiller rotor by regulating the angle of the knife location (γ), it is explicit from Equation (14) that:

$$\varepsilon = \frac{\pi}{2} - \gamma \pm \Delta\varepsilon = const. \quad (14)$$

In respect with the above mentioned analogy, it can be defined that during complex movement of the streamlined body in the resisting environment (e.g. air, water), the best streamlined ability of the body with the smooth movement of particles without removal from its surface, and their minimal "stormy" movement is ensured if the following conditions exist (Aleksandrov V.L., 1951):

$$\alpha = \varphi - \beta = \text{const} \quad (15)$$

The dimensions are demonstrated in the scheme given in Fig. 3b, where the location angles of the propeller and the forces exerted on it are represented.

By comparing the schemes depicted in fig. 3a and 3b it is clear, that in the mentioned case α is equivalent to ε , β is equivalent to $\pm\Delta\varepsilon$ and to φ , to θ or to the same like: $\frac{\pi}{2} - \gamma$.

In two different fields, the elaborated problems with nearly almost identical objectives and varying principles of solutions have shown substantial similarities. This allows assuming that in the discussed case, the obtained equilibriums and formulas can serve as the basis for the practical solutions of the mentioned objectives.

It is quite remarkable and interesting to mention that determining the optimal and favorable values of the location and cutting angles the tiller knife, in the perspective of the equality and minimum (Akimov A.P. et al, 2018; Ivanov A.P., 1992; Blekhman I.I., 1979) conditions of the resistance forces and on the basis of the streamlined ability and exclusion of throwing away the soil mass particles, leads to the same result for the stability of the cutting angles of the knife and with a very specific pattern of the changes for the location angle.

To verify and evaluate the results of the theoretical research, a laboratory soil-cultivating rotary tiller with a self-regulating blade positioning angle was designed and developed. The results and analyses of its testing will be presented in future studies.

CONCLUSIONS

1. The resistance moment or energy consumption of the rotor of a rotary tiller with a vertical rotation axis and the volumes of soil mass displacement from the cultivated area are interrelated and, under stabilized technological-kinematic parameters, are primarily determined by the angular positioning of the blades and the shape of their cross-sectional profile.

2. A significant reduction in the resistance moment of the rotary tiller and the velocity and volume of soil mass displacement is achieved during one rotation of the rotor by ensuring the stability of the cutting angle and using a streamlined cross-sectional shape of the blade body. The stability of the cutting angle is maintained through the adjustment of the angular positioning, according to the derived expression and established pattern. The streamlined cross-sectional shape of the blade body, in the case of complex motion, ensures the smooth movement of soil particles without detachment from the body surface until their separation at the sharp rear end. The pattern of the surface curve will be determined in future studies.

ACKNOWLEDGEMENTS

The work was supported by the Science Committee of MESCS RA, in the frames of the research project № 21APP-2D015.

REFERENCES

- [1] Acharya, B. S., Dodla, S., Gaston, L. A., Darapuneni, M., Wang, J. J., Sepat, S., et al. (2019). Winter Cover Crops Effect on Soil Moisture and Soybean Growth and Yield under Different Tillage Systems. *Soil and Tillage Research*, 104430. <https://doi.org/10.1016/j.still.2019.104430>.
- [2] Akimov A. P., Konstantinov Y.V., Turovskiy B.V. (2018). Mathematical Model of Interaction of Milling Knives with Soil (Математическая Модель Взаимодействия Фрезерного Ножа С Почвой). *Vestnik of Kazan State Agrarian University (Вестник Казанского ГАУ)*. (4), 67-71. https://doi.org/10.12737/article_5a5f06808b59a5.62332052
- [3] Akimov A.P., Konstantinov Yu.V., Feodorov D.I. (2013). Calculation method of resistance and moment of resistance to soil cutting (Методика расчета сопротивления и момента сопротивления резанию почвы) /Tractors and Agricultural Machines (Тракторы и сельхозмашины),-№3,-pp.32-35. <https://doi.org/10.17816/0321-4443-65880>
- [4] Aleksandrov V.L., (1951) *Air propellers (Воздушные винты)*, Moscow, Oborongiz (Обorongiz).-475 p.
- [5] Blekhman I.I. (1979). *Vibrations in Engineering: Handbook; Vol. 2. Oscillations of Nonlinear Mechanical Systems. (Вибрации в технике: Справочник. том. 2, Колебания нелинейных механических систем)*, Mechanical engineering (Машиностроение), Moscow. — 351 p.
- [6] Chatkin M.N., (2007) *Kinematics and dynamics of the working parts of the rotary tillers with screw elements (Кинематика и динамика ротационных почвообрабатывающих рабочих органов с*

- винтовыми элементами). Publishing house of Mordovia State University (Изд-во Мордовского ун-та), Saransk, 316 p.
- [7] Damanauskas, V., Velykis, A., and Satkus, A. (2019). Efficiency of Disc Harrow Adjustment for Stubble Tillage Quality and Fuel Consumption. *Soil & tillage Research*. 194, 104311, <https://doi.org/10.1016/j.still.2019.104311>
- [8] Grigoryan A.S., Altunyan A.V., (2021) The Effect of Some Factors on the Cutting Angle of the Vertical Blade during Rotary Soil Tillage (Влияние некоторых факторов на угол резания вертикального ножа при ротационной обработке почвы). *Agriscience and Technology (Агронаука и технология)*, №3/75, pp. 230-234, ANAU International Journal, <https://doi.org/10.52276/25792822-2021.3-230>
- [9] Ivanov A. P. (1992) Impact Energy with Friction. (Энергетика удара с трением), *Applied Mathematics and Mechanics (Прикладная математика и механика)* Volume 56, Issue 4, pp. 527-534
- [10] Konstantinov Yu. V., (2019) Calculation method of resistance and resistance moment to the soil cutting with a straight disk blade of the cutter (Методика расчета сопротивления и момента сопротивления резанию почвы прямым пластинчатым ножом фрезы). *Tractors and Agricultural Machinery (Тракторы и сельхозмашины)*, vol. 86 №5, p. 31-39. <https://doi.org/10.31992/0321-4443-2019-5-31-39>
- [11] Koval Zh.L., (2010) *Development of a rotary tiller with energy-saving cutting working parts (Разработка почвообрабатывающей машины с энергосберегающими фрезерными рабочими органами)*. Thesis for the Candidate of Mechanical Sciences, Moscow
- [12] Kupryashkin V.F., Gusev A.Yu., (2020) Justification of the parameters and operating modes of a self-propelled rotary tiller with combined rotation of active working parts (Обоснование параметров и режимов работы самоходной почвообрабатывающей фрезы с комбинированным вращением активных рабочих органов). *Scientific Review. International scientific and practical journal*. Saransk, - pp. 42-48. №2,
- [13] Landau L.D., Lifshitz E.M. (2001) *Theoretical Physics. Volume VI, Hydrodynamics (Теоретическая физика, Гидродинамика)*, Fizmatlit Publishing House (Физмат), Moscow .
- [14] Manaenkov K.A., Koldin M.S., Ankova Z.A., (2017), Improvement of tillage in row strips intensive gardens (Совершенствование обработки почвы в приствольных полосах интенсивных садов). *Technologies of food and processing industry. (Технологии пищевой и перерабатывающей промышленности)*, №3 (17) pp. 28-34
- [15] Mandal, S.K., Bhattacharyya, B., Mukherjee, S., & Chattopadhyay, P. (2013). Design & Development of Rotavator blade: Interrogation of CAD Method. *International Journal of Scientific Research in Knowledge, (IJSRK)*, 1(10), 439-447. <https://doi.org/10.12983/ijrk-2013-p439-447>
- [16] Matin M.A., Fielke J.M., Desbiolles Jacky M.A., (2014) Furrow parameters in rotary strip-tillage: Effect of blade geometry and rotary speed, *Biosystems Engineering*, Volume 118, Pages 7-15, ISSN 1537-5110, <https://doi.org/10.1016/j.biosystemseng.2013.10.015>
- [17] Panov I.M., Tokushev Zh.E., (2005) *Theory, design and calculation of rotary tilling machines (Теория, конструкция и расчет ротационных почвообрабатывающих машин)*. Publ. House of Kokshetau University, Kokshetau, 314 p.
- [18] Raparelli, T., Ivanov, A., Pepe, G. and Eula, G. (2021) "Analysis of the energy consumption of a rotary harrow", *Journal of Agricultural Engineering*, 52(2). <https://doi.org/10.4081/jae.2021.1132>
- [19] Schjønning, P., & Rasmussen, K. J. (2000). Soil Strength and Soil Pore Characteristics for Direct Drilled and Ploughed Soils. *Soil and Tillage Research*, 57, pp. 69-82. [https://doi.org/10.1016/S0167-1987\(00\)00149-5](https://doi.org/10.1016/S0167-1987(00)00149-5).
- [20] Sineokov G.N., Panov I.M., (1977) *Theory and calculation of tillage machines (Теория и расчет почвообрабатывающих машин)*, Mechanical engineering (Машиностроение), Moscow -322 p.
- [21] Tarverdyan, A.P., Altunyan, A.V., Grigoryan, A.S. (2023). Development and Justification of a Self-Regulating System for Adjusting the Angle of Rotary Tiller Blade with a Vertical Rotation Axis, "Agriscience and Technology", ANAU International Journal, №2/82, - pp. 117-123. <https://doi.org/10.52276/25792822-2023.2-117>
- [22] Tarverdyan, A.P., Altunyan, A.V., Grigoryan, A.S. (2024) Force analysis of a rotary tiller with a vertical rotation axis *INMATEH-Agricultural Engineering*, 71/2 <https://doi.org/10.35633/inmateh-72-40>

- [23] Tarverdyan, A.P., Grigoryan, A.S., Altunyan, A.V. (2022). Kinematic Study of Orchard Rotary Tiller with a Planetary Drive. *"Agriscience and Technology"*, ANAU International Scientific Journal, №3/79, -pp. 231-237. <https://doi:10.52276/25792822-2022.3-231>
- [24] Vorobyov, V.A. Marchenko, O.S., (1990). Rational Arrangement of Blades on the Tiller's Drum (Рациональная расстановка ножей на фрезерном барабане) *Machinery and Equipment for Rural Area (Техника в сельском хозяйстве)*. - №2, -pp. 19-25.

ADVANCING PRECISION AGRICULTURE WITH UAV'S: INNOVATIONS IN FERTILIZATION

PROGRESUL AGRICULTURII DE PRECIZIE CU UAV-URI: INOVAȚII ÎN FERTILIZARE

Gabriel-Valentin GHEORGHE, Dragoș-Nicolae DUMITRU, Radu CIUPERCĂ, Marinela MATEESCU, Stefano Andrea MANTOVANI, Elisabeta PRISACARIU, Alin HARABAGIU

INMA Bucharest/ Romania

E-mail: gabrielvalentinghe@yahoo.com

dumitrudragos.nicolae@gmail.com

DOI: <https://doi.org/10.35633/inmateh-74-89>

Keywords: drone, precision, agriculture, crop, plating, health, UAV

ABSTRACT

Unmanned Aerial Vehicles (UAVs) are revolutionizing precision agriculture, particularly in the domain of fertilization. Equipped with advanced sensors, mapping tools, and variable-rate application systems, drones enable farmers to precisely distribute fertilizers based on field variability. This targeted approach reduces waste, minimizes environmental impact, and optimizes crop yield. The integration of technologies such as multispectral imaging and AI-driven decision-making systems further enhances efficiency by allowing real-time assessment of soil and crop conditions. Despite their numerous advantages, challenges such as high costs, regulatory limitations, and technical scalability remain key barriers to widespread adoption. This article explores the innovations UAVs bring to precision fertilization, their benefits, and the obstacles hindering their broader application in agriculture.

REZUMAT

Vehiculele Aeriene Fără Pilot (UAV-uri) revoluționează agricultura de precizie, în special în domeniul fertilizării. Echipate cu senzori avansați, instrumente de cartografiere și sisteme de aplicare cu rată variabilă, dronele permit fermierilor să distribuie fertilizantii cu precizie, în funcție de variabilitatea terenului. Această abordare țintită reduce risipa, minimizează impactul asupra mediului și optimizează randamentul culturilor. Integrarea tehnologiilor precum imagistica multispectrală și sistemele de luare a deciziilor bazate pe inteligență artificială îmbunătățește eficiența prin evaluarea în timp real a condițiilor solului și ale culturilor. În ciuda numeroaselor avantaje, provocările precum costurile ridicate, limitările reglementărilor și scalabilitatea tehnică rămân bariere semnificative în calea adoptării pe scară largă. Acest articol explorează inovațiile aduse de UAV-uri în fertilizarea de precizie, beneficiile acestora și obstacolele care împiedică aplicarea lor extinsă în agricultură.

INTRODUCTION

The rapid growth of global agriculture demands innovative solutions to improve productivity, optimize resource usage and reduce environmental impacts. Traditional agricultural practices, especially in fertilization, often face challenges such as overuse of fertilizers, uneven application, labor shortages, and inefficiency in large-scale farming operations. To address these issues, smart agriculture, driven by advanced technologies, is emerging as a transformative approach to modern farming (Subeesh *et. al.*, 2021).

Drones, also known as Unmanned Aerial Vehicles (UAVs), have become a pivotal tool in smart agriculture due to their versatility, cost-effectiveness, and ability to perform precision-based tasks (Zhou *et. al.*, 2024). When integrated with technologies such as Global Positioning Systems (GPS), remote sensing, and artificial intelligence (AI), drones can revolutionize fertilization practices. They enable precise delivery of fertilizers, monitor crop health, and reduce waste, thereby enhancing yields and promoting sustainable farming (Zhou *et. al.*, 2023).

This review explores the role of drones in fertilization within smart agriculture systems. It discusses the technologies involved, benefits, challenges, and future trends. The integration of drone technology for fertilization not only ensures efficient use of agricultural inputs but also contributes to reducing environmental degradation and improving food security.

The global demand for food is steadily increasing due to population growth, which necessitates more efficient and sustainable agricultural practices (Gokool *et. al.*, 2024). Smart agriculture, driven by advancements in technology, aims to optimize farming processes (Van Klompenburg *et. al.*, 2020) by integrating tools such as sensors, data analytics, and unmanned aerial vehicles (UAVs), commonly known as

drones. Drones have emerged as a versatile solution for precision farming, offering applications in crop monitoring, irrigation management, and fertilization (Singh et al., 2024).

Smart agriculture, or precision agriculture, uses advanced technologies like sensors, GPS, drones, and AI to optimize farming practices. By collecting real-time data on factors such as soil moisture, crop health, and weather, farmers can make more informed decisions about irrigation, fertilization, pest control, and harvesting (Eckert et al., 2024).

This approach enhances farm efficiency, reduces waste, and minimizes environmental impact by applying resources like water and fertilizers precisely where needed. It also supports sustainability by lowering resource use while maintaining or increasing crop yields (Tanaka et al., 2024). Automation and robotics further improve productivity and reduce labor costs. Also, technologies like remote sensing, enhanced by cloud-based server-side processing of high-resolution satellite imagery, and Big Data analytics platforms such as Google Earth Engine (GEE), along with uncrewed aerial vehicles (UAVs), have significantly improved the ecological monitoring of natural habitats (Tripathi et al., 2024).

According to the International Society of Precision Agriculture (ISPA), precision agriculture is an approach to agricultural management that utilizes technology and agricultural data to enhance the quality, sustainability, and productivity of farming (Zualkernan et al., 2023).

Bhat et al., 2021, talks about achieving sustainable agricultural production, mentioning that the agriculture sector must adopt advanced technologies such as blockchain, IoT, and (Al Shadrin et al., 2019). With the progression of 6th generation (6G) communication (Sitharthan et al. 2023), new demands are emerging for integrated sensing and communication (ISAC) (Htun et al. 2024). Sensing improves communication accuracy by detecting nearby objects and delivering real-time feedback on relevant environmental information (Li et al., 2024).

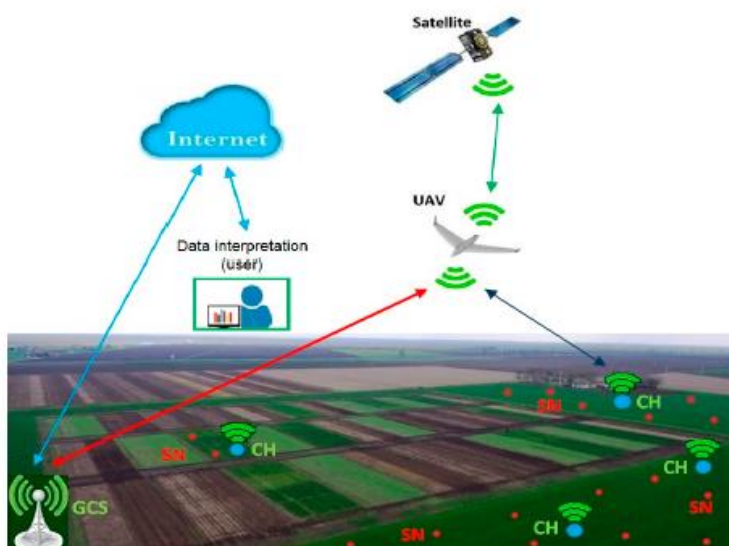


Fig. 1 - Concept of the integrated UAV

(Popescu et al., 2020)

As global food demand rises and resources like water and arable land become scarcer, there is an urgent need for efficient, sustainable agricultural practices (Sharma et al., 2020). Smart agriculture, or precision farming, uses technologies like sensors, GPS, drones, and AI to optimize crop management (Andreasen et al., 2022). This approach helps farmers use resources more efficiently, reduce waste, and minimize environmental impact (Yang et al., 2024). By providing real-time data on soil conditions and crop health, smart agriculture enables precise irrigation, fertilization, and pest control, improving yields and sustainability (Kumar et al. 2023). In the face of resource limitations and environmental challenges, smart agriculture is key to meeting food demand while protecting the planet (Chiu et al., 2024).

Ali et al., 2008, discusses the importance of water productivity, emphasizing its critical role in sustainable agricultural practices. By addressing factors such as soil quality, crop type, irrigation techniques, and climate conditions, the paper identifies opportunities to enhance water efficiency (Yang et al., 2020). The importance of improving water productivity lies in its potential to increase food production, conserve water resources, and ensure agricultural sustainability in the face of growing global water scarcity and demand (Chen et al., 2023).

To improve agricultural productivity and food management, there is an urgent need for precision agriculture monitoring on a larger scale (Murugan et al., 2017).

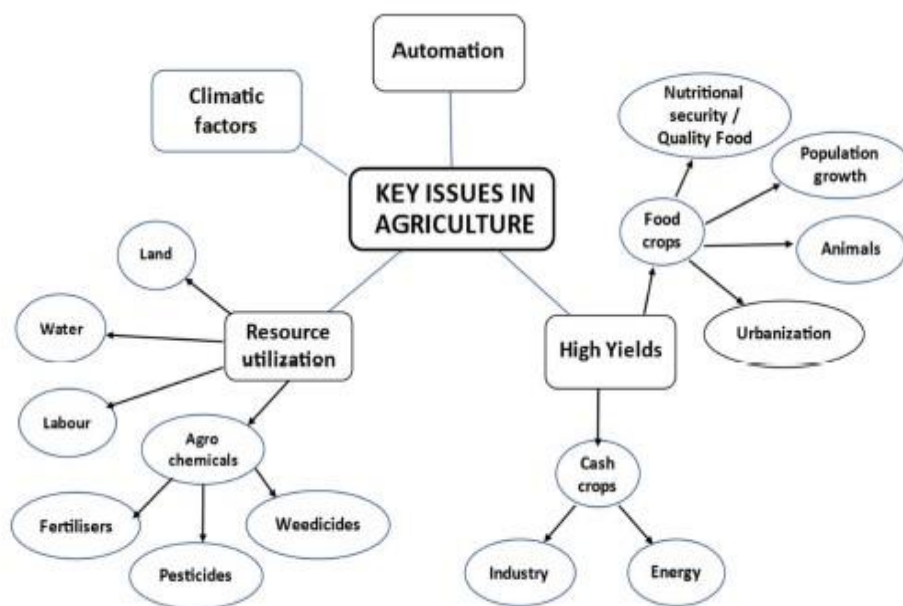


Fig. 2 - Key issues in Agriculture

(Dhanaraju et al., 2022)

In the agricultural context, Canicatti et al., 2024, says that vegetables play a vital role as protective foods, offering essential nutrients to the human diet. They are rich in vitamins, fibers, minerals, and nutraceuticals, contributing significantly to overall health and well-being.

Gokool et al., 2023, talks about precision agricultural practices supported by unmanned aerial vehicles. UAVs have gained significant traction in the agricultural sector and hold great potential for applications on smallholder farms (Albetis et al., 2019).

Drones, or Unmanned Aerial Vehicles (UAVs), are transforming precision agriculture by providing farmers with innovative tools for field management (Caballero et al., 2024). Equipped with advanced sensors and cameras, drones capture real-time aerial data, allowing farmers to monitor crop health, detect pests, and assess irrigation needs (Rejeb et al., 2022).

Drones also enable precise application of fertilizers, pesticides, and herbicides, reducing waste and environmental impact (Yacoob et al. 2024). By targeting specific areas (Dou et al., 2023), they help optimize resource use, improve yields, and lower costs. UAV systems represent, in most cases, the most efficient option to reach the inaccessible portions of the objects, providing a complete coverage of the infrastructure to be monitored (Massimo et al., 2024).

Dronova et al., 2021, talks about the fact that UAVs have become valuable tools in the global remote sensing community, functioning as small, flying robots capable of accessing hazardous or remote areas (Lee et al., 2024). They capture high-resolution imagery and support environmental monitoring and research (Couturier et al., 2021), spanning broad applications like agricultural management to specialized fields such as marine mammal behavioral ecology. UAVs are particularly advantageous for environmental monitoring (Shahi et al., 2022), (Shahi et al., 2023) as they overcome constraints in complex, dynamic, and limited-access environments that have traditionally been difficult to survey (Ming et al., 2024). Additionally, UAVs reduce the time and labor required for ground-based surveying and sampling, allowing for more focused managerial activities, such as restoration assessments, that might otherwise be neglected (Pereira et al., 2024).

UAVs provide high operational efficiency, excellent adaptability to various terrains, and safe applications (Nahiyoon et al., 2024).

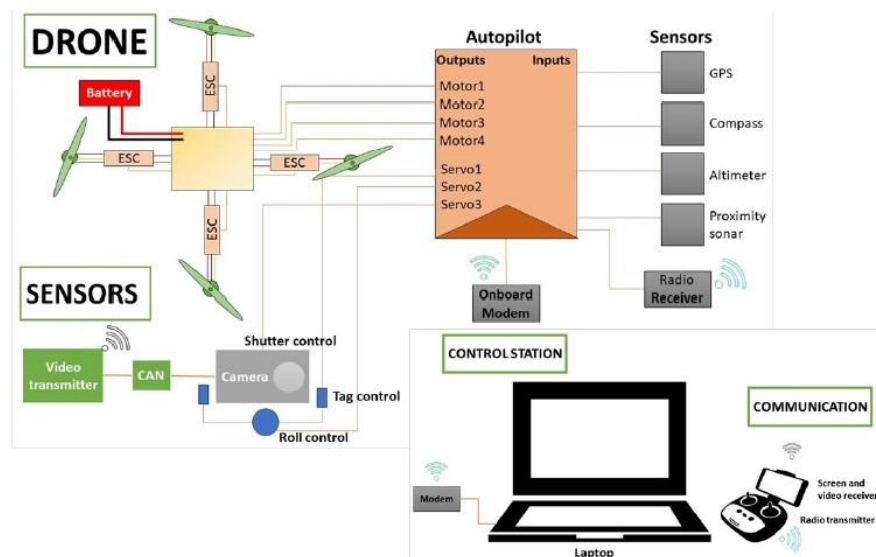


Fig. 3 - Block diagram of a drone system

(Guebsi et. al., 2024)

UAVs are already established across various fields (Khan et. al., 2021), and their market is projected to grow to \$200 billion in the coming years. Yamaha introduced its first UAV model, the Yamaha RMAX, designed for crop monitoring and pest control; however, production was discontinued in 2007 (Castro et. al., 2023). They developed a spray system integrated into a UAV platform, resulting in an autonomous spraying system used for pest management and vector control. Additionally, a Pulse Width Modulation (PWM) controller was implemented for UAV precision agriculture sprayers, enabling the UAV to be remotely controlled or operated autonomously through preprogrammed flight plans (Buters et. al., 2019).

Fertilization plays a fundamental role in enhancing crop productivity and maintaining soil fertility (Yuan et. al., 2024). However, traditional fertilization methods often lead to inefficiencies, including excessive fertilizer use, environmental pollution, and increased costs. Precision fertilization, enabled by drone technology, aims to address these issues by delivering the right amount of nutrients to crops in a targeted manner (Niu et. al., 2024).

Currently, there is excessive use of fertilizer and inadequate uniformity in the fertilizer distribution in corn fertilizer planters (Wang et. al., 2022).

Fertilization is essential for boosting crop yields by providing key nutrients like nitrogen, phosphorus, and potassium. These nutrients support plant growth, resulting in higher productivity and better-quality crops (Hasan et. al., 2020).

However, improper fertilization can harm soil health (Scherrer et. al., 2019). Overuse can lead to nutrient imbalances, soil degradation, and environmental issues like water pollution. Balanced and precise fertilization, based on soil testing, helps avoid these problems while maintaining soil fertility (Kannan et. al., 2024).

Chebrolu et. al., 2018, talks about the automated crop monitoring being a crucial component of precision farming, enabling farmers to make informed decisions about when, where, and how much fertilizer or pesticide to apply (Pu et. al., 2015). It also enhances yield estimation, contributing to improved efficiency and productivity in agricultural practices.

Esposito et. al., 2021, talks about precision agriculture utilizing technologies that integrate sensors, information systems, and data-driven management practices to enhance crop productivity while minimizing environmental impact. Nowadays, precision agriculture has diverse applications across various agricultural contexts, including pest control, fertilization, irrigation, sowing, and harvesting.

The knowledge of plant nutrient requirements and the use of inorganic fertilizer allow an increase in crop production (Farias et. al., 2020).

However, as drones began to be utilized in crop management (Valente et. al., 2013), challenges emerged regarding the standardization of operational parameters, such as height, speed, nozzle type, angle, flow rate, and spray width, as well as issues related to application drift and the type of agrochemicals used (Martínez-García et. al., 2023). To address these challenges, advanced precision technologies have been incorporated into drones for crop spraying, enhancing efficiency across multiple areas (García-Munguía et. al., 2024).

Drones equipped with advanced technologies, such as GPS, multispectral cameras, and variable-rate application systems, enable precision fertilization by delivering nutrients directly to targeted areas (Huang *et. al.*, 2024). This approach not only enhances fertilization accuracy but also reduces input costs and minimizes the environmental footprint, making it an attractive solution for modern agriculture (Carreño *et. al.*, 2024).



a)



b)

Fig. 4 - DJI Multispectral drones

(Panday *et. al.*, 2020)

(a) DJI P4 senseFly eBee SQ

(<https://www.dji.com/global/support/product/p4-multispectral>),

(b) fixed-wing drone

(<https://www.sensefly.com/solutions/drones/>)



a)



b)

Fig. 5 - DJI M600 Pro

(Panday *et. al.*, 2020)

Khanal *et. al.*, 2017, states that precision agriculture (PA) leverages advanced tools and technologies to detect variability in soil and crops within fields, aiming to enhance farming practices and optimize the use of agronomic inputs. Traditionally, optical remote sensing (RS), which uses visible light and infrared regions of the electromagnetic spectrum, has been a key component of PA for monitoring crops and soil conditions (Huang *et. al.* 2024). The use of agricultural drones not only helps reduce production costs but also boosts crop yields by minimizing losses during cultivation (Zhichkin *et. al.*, 2023).

This review aims to assess the application of drones in smart agriculture for fertilization, focusing on the technologies and methods utilized in drone-based fertilization, the efficiency and precision of these systems compared to traditional approaches, the environmental and economic benefits they offer, as well as the challenges and opportunities for future advancements.

MATERIALS AND METHODS

After full-text analysis, 80 studies were included in this review based on their relevance to drone-based fertilization in agriculture.

From the selected studies, data on drone type and sensor technologies, fertilization methods, operational efficiency, and case study results were extracted. Findings were organized into categories such as technological advancements, application accuracy, and environmental impacts. A qualitative synthesis of the findings was performed, focusing on recurring trends, technological improvements, and challenges in drone-based fertilization. Quantitative data, such as coverage efficiency and cost savings, were extracted for comparative analysis.

Data on drone types and sensor technologies

The DJI Phantom 4 Multispectral is a specialized drone designed for precision agriculture and environmental monitoring. It combines DJI's reliable drone technology with a multispectral imaging system to provide accurate data on crop health, soil condition, and vegetation analysis.



Fig. 6 - DJI Phantom 4 Multispectral
(Dong et. al., 2024)

DJI A3 System is a high-performance flight controller designed for professional drones, particularly in industrial applications, aerial photography, and custom drone builds. It provides advanced flight control, stability, and customization options for multirotor platforms



Fig. 7 - 6-rotor drone and spreading device controlled by DJI A3 system
(Han et. al., 2024)

The DJI Phantom 4 Pro is widely preferred in agriculture due to its compact design, affordability, and advanced features that make it ideal for various farming tasks.

Although the DJI Inspire 1 is less commonly used in routine agricultural operations compared to the Phantom 4 Pro, it remains valuable for specialized applications that require more advanced capabilities.



Fig. 8 - DJI Drones (Messina et. al., 2020)
(a) DJI Phantom 4 pro (b) DJI Inspire 1

Tabel 1

Features DJI Phantom 4 pro and DJI Inspire 1

Feature	DJI Phantom 4 Pro	DJI Inspire 1
Camera	20 MP, 1-inch sensor, 4K at 60 fps	4K camera with Zenmuse X3 or X5 gimbal (interchangeable lenses)
Flight Time	30 minutes	18-20 minutes
Speed	45 mph (72 km/h)	50 mph (80 km/h)
Flight Range	OcuSync (up to 4.3 miles or 7 km)	Lightbridge (up to 1.2 miles or 2 km)
Obstacle Avoidance	5 sensors (front, rear, downward)	Front and downward sensors only
Dual Control	No	Yes, dual operator control (pilot + camera operator)
Intelligent Flight Modes	ActiveTrack, TapFly, Return-to-Home	Follow Me, Waypoints, Point of Interest
Camera Control	Fixed camera	Interchangeable lenses with high control over the camera
Best For	General crop monitoring, field mapping, surveying, precision agriculture	Advanced inspections, professional-grade mapping, specialized tasks



Fig. 9 - Fixed-wing Drones
(Radoglou-Grammatikis et. al., 2020)

a) Fixed-wing UAVs

b) Rotary-wing UAVs

Tabel 2

Key differences between fixed-wing UAVs and rotary-wing UAVs

Aspect	Fixed-wing UAVs	Rotary-wing UAVs
Lift Mechanism	Lift generated by fixed wings during forward flight	Lift generated by rotating blades/rotors
Takeoff & Landing	Requires a runway or launch method (except VTOL models)	Vertical takeoff and landing (VTOL)
Flight Duration	Longer flight times due to higher efficiency	Shorter flight times due to energy-intensive hover
Speed	Faster, suitable for long-distance travel	Slower, more maneuverable
Maneuverability	Less maneuverable, limited to forward flight	Highly maneuverable, can hover and move in any direction
Applications	Long-range surveying, mapping, agriculture	Aerial photography, inspections, search and rescue

Sensor technologies

UAVs rely on advanced sensors to capture important data for various applications. Four key types of sensors used by UAVs include thermal, RGB, multispectral, and hyperspectral sensors.

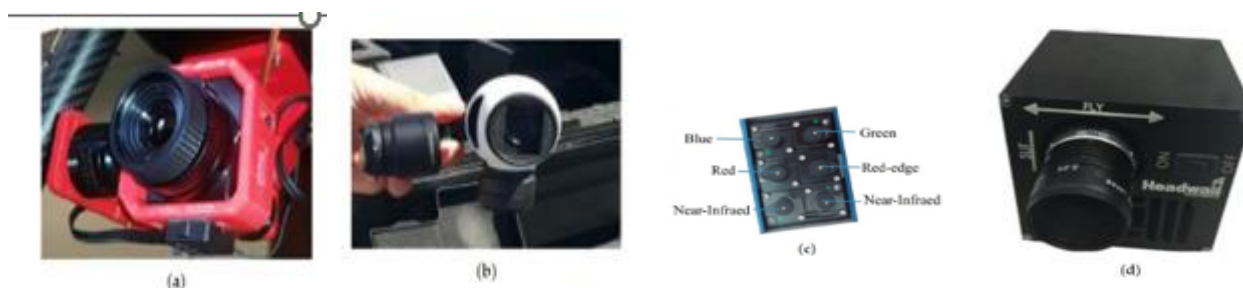


Fig. 10 - Examples of sensors used by UAVs

(Tsouros et al., 2019)

(a) thermal sensor, (b) RGB sensor, (c) multispectral sensors (d) hyperspectral sensor

Seeding methods



Fig. 11 - Seed metering device for aero sowing of forest pelleted seeds

(Lysych et al., 2021)

In this paper, *Lysych et al., 2021*, studied the design and simulation of a precision seed metering device tailored for aero sowing forest pelleted seeds. The system is developed to address the challenges of reforestation in difficult-to-access areas by leveraging drone technology. The seed metering device integrates advanced components, including a rotary seed metering mechanism, precise release systems, and simulation models to ensure uniform seed distribution. The design focuses on achieving optimal sowing accuracy, minimizing seed waste, and adapting to diverse terrain conditions. Results from simulations validate the system's efficiency, highlighting its potential for sustainable reforestation and ecological restoration efforts. This system uses balls with seed and fertilizer to help the seed develop.



Fig. 12 - Spraying system reservoir developed

(Barcelos et al., 2024)

Case Study Results

Han et al., 2024, studied the development of a rotor speed prediction model for multi-rotor unmanned aerial spraying systems (UASS) which enhances the efficiency and effectiveness of agricultural spraying. By predicting rotor speed based on real-time flight speed and payload, the system ensures stable flight and optimal spraying conditions. The study highlights the importance of matching rotor speed with the UASS load to optimize power consumption, performance, and reliability.

It also emphasizes the impact of rotor speed on the downwash field, which affects droplet deposition and spray effectiveness. Using a neural network for the prediction model demonstrates the potential of machine learning in precision agriculture, enabling real-time monitoring, adjustments, and improved operational efficiency, ultimately reducing waste and increasing crop yields.



Fig. 13 – Rotor speed prediction model for multi-rotor unmanned aerial spraying systems

(Han et. al., 2024)

a) TopXGun F16

b) UAV power system test platform

The rotor speed prediction model, developed using a neural network with real-time flight speed and payload as inputs, showed strong accuracy with correlation coefficients (R^2) of 0.728, 0.719, and 0.726 for training, validation, and test sets, respectively. A quadratic relationship between rotor speed and thrust was established, with a fitting parameter ($R^2 > 0.999$), indicating excellent alignment with test data. Under full-load conditions, the single-axis load capacity reached 50% of its maximum, increasing by over 75.83% compared to the no-load state, significantly affecting rotor speed and system performance. The model accurately predicted rotor speed, aligning well with theoretical calculations and test results. This study provides a reliable foundation for optimizing UASS performance and efficiency during continuous operation.

Jibon et. al., 2023, demonstrates that the use of an autonomous UAV greatly reduces the time and labor required for seed planting and fertilizer distribution. By operating without constant human intervention, the UAV ensures precise application, optimizing resource use and improving crop yields while minimizing waste. Equipped with ArUco markers and a computer vision-based control system, the UAV can navigate autonomously, enhancing its range and effectiveness. Automation of these processes reduces overall costs, making farming more economical, especially for small-scale farmers. Additionally, precise seed and fertilizer application reduces environmental impact, supporting sustainable farming practices. The UAV system is scalable and adaptable to different crops and field conditions, making it suitable for both small and large-scale agricultural operations.



Fig. 14 – System hardware architecture and autonomous flight plan

(Han et. al., 2023)

Liu et. al., 2021, study highlights the use of small fixed-wing and rotor-wing UAVs in precision agriculture, equipped with sensors to capture high-resolution images for monitoring crop health, detecting pests, and optimizing field practices. Deep learning (DL) techniques like CNNs and RNNs enable tasks such as crop classification, weed detection, and growth monitoring. The study emphasizes edge intelligence, combining AI with edge computing for real-time data processing on UAVs and IoT devices, reducing latency and bandwidth issues. Techniques like parameter pruning and quantization optimize DL models for resource-limited edge devices. It also

provides UAV-based remote sensing datasets for validating DL methods and suggests future research on advanced DL models, multi-source data integration, and improved edge intelligence to enhance precision agriculture scalability and performance.

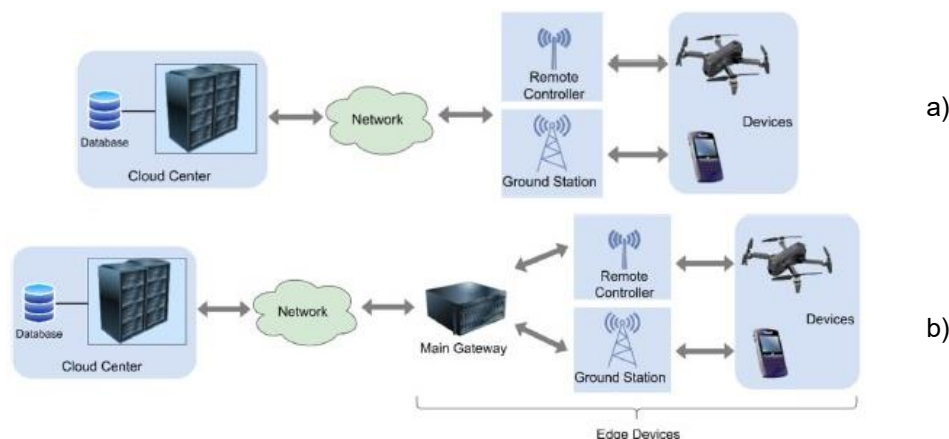


Fig. 15 - The use of small fixed-wing and rotor-wing UAVs in precision agriculture
(Liu et al., 2021)

a) Cloud computing paradigm

b) Edge computing paradigm for UAVs RS

Studies on precision agriculture highlight the benefits of integrating advanced technologies like GPS, remote sensing, and wireless sensors for real-time monitoring and data collection, enabling informed decisions on fertilization and irrigation (Lu et al., 2022). These technologies, along with variable rate technology (VRT), help optimize resource use, improve crop health, and reduce costs. Similarly, UAV-captured multispectral images can effectively estimate nitrogen concentration, uptake, and the nitrogen nutrition index (NNI) in grass seed crops, with NDRE and CIRE indices showing the best performance for predicting nitrogen status (Wang et al., 2019).

Research by Xu C. et al., 2017, found that increasing planting density boosted grain yield by 7% and improved nitrogen use efficiency by enhancing nitrogen remobilization, while reducing N₂O emissions and greenhouse gas intensity by 61.5% and 46.2%, respectively. Additionally, Xue X. et al., 2024, identified that sampling point height significantly affected droplet deposition rate, with UAV flight height and particle size having minimal impact. They used machine learning methods to predict droplet deposition and drift, with ELM showing the best prediction accuracy. The study also employed grid atomization technology to optimize droplet size, reducing drift and improving deposition for more effective spraying.



Fig. 16 - Spraying operations of the plant protection drone (Yu et al., 2023)

a) XAG V40; b) DJI T30 six-rotor electric; c) Knapsack Electric Sprayer

Yu et al., 2023, found that increasing spray volume from 60 L/ha to 120 L/ha significantly improved droplet density, coverage, and uniformity in the citrus canopy. The XAG V40 drone achieved 18.7–41.7 droplets/cm² with an 87.8% increase in coverage, while the DJI T30 reached 146.0–205.3 droplets/cm², with better penetration, particularly in the lower and middle canopy layers.

Droplet distribution uniformity improved, with the coefficient of variation decreasing by 22.0% for the XAG V40 and 26.8% for the DJI T30. In contrast, the knapsack electric sprayer (2400 L/ha) showed higher droplet density in the lower canopy but less uniform coverage (40.3%–42.4%).

RESULTS

A qualitative synthesis of the findings was performed, focusing on recurring trends, technological improvements, and challenges in drone-based. Quantitative data, such as coverage efficiency and cost savings, were extracted for comparative analysis.

This graph displays the qualitative analysis results for using drones in smart agriculture for fertilization. Each factor is rated on a scale from 1 to 5, with **efficiency, environmental impact, precision, and resource optimization** achieving the highest scores. Cost savings and scalability also show strong performance, highlighting the overall benefits of drones in precision fertilization.

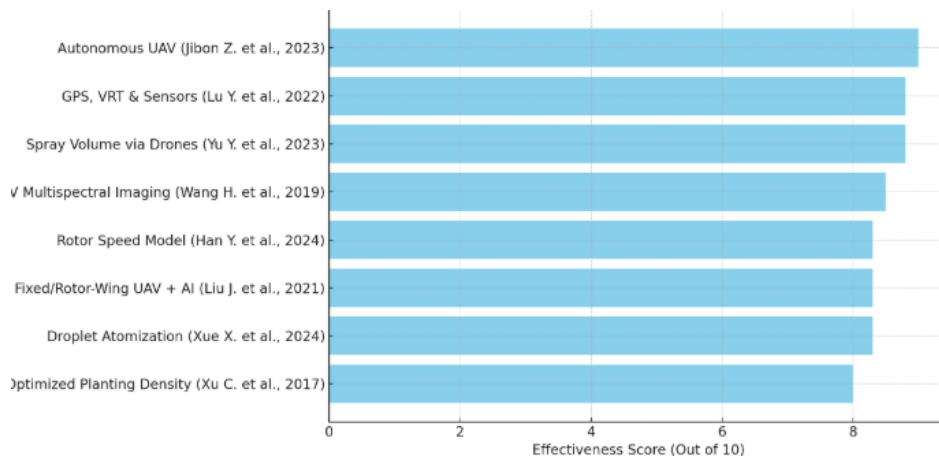


Fig. 17 - Comparative analysis for the case studies

The next table provides a comprehensive comparison of 8 UAVs used for liquid fertilizers application based on essential features such as payload capacity, spray efficiency, power source, battery life, spraying system, navigation, obstacle avoidance, durability, ease of use, and cost.

Tabel 3

Comprehensive comparison of 8 UAVs used for liquid fertilizers

Feature	DJI Agras T30	XAG P100 Pro	TTA M6E	Yamaha Fazer R	Hyllo AG-122	EAVision EAV-10	Walkera VITUS AG 18	Agribotix Hornet
Payload Capacity	30L	40L	16L	20L	20L	10L	18L	10L
Spray Efficiency	40 ha/day	16 acres/hour	Moderate	High	Moderate	Low	Low	Moderate
Power Source	Electric	Electric	Electric	Gas	Electric	Electric	Electric	Electric
Battery Life	~25 min	~20 min	~20 min	1-2 hours (gas tank)	~22 min	~25 min	~15-20 min	~25 min
Spraying System	High-precision, variable-rate spraying	Smart modular system	Smart flow control	Customizable nozzles	Autonomous sprayer	Target-specific sprayer	Targeted sprayer	Multi-purpose system
Navigation System	RTK GPS + AI mapping	RTK GPS + Wind Resistance	RTK GPS	Standard GPS	Fully autonomous GPS	Binocular vision + GPS	GPS	GPS
Obstacle Avoidance	Advanced (AI sensors)	Moderate	Basic	None	Moderate	Terrain sensing	Basic	Basic
Durability	Rugged and durable	Rugged and modular	Medium	High (gas-powered)	Medium	Designed for slopes	Compact	Medium
Ease of Use	User-friendly	Modular and flexible	Simple interface	More complex to operate	Very user-friendly	Plug-and-play design	Easy to operate	Easy to configure

Feature	DJI Agras T30	XAG P100 Pro	TTA M6E	Yamaha Fazer R	Hylío AG-122	EAVision EAV-10	Walkera VITUS AG 18	Agribotix Hornet
Cost approx.	High	High	Medium	High	Medium-high	Medium	Low	Medium

Observations:

Agricultural drones vary in payload, efficiency, durability, ease of use, specialization, and precision, catering to different farming needs. High-payload models like the XAG P100 Pro and DJI Agras T30 excel in large-scale operations, while specialized options such as the EAVision EAV-10 and Walkera VITUS AG 1 handle unique terrains, gas-powered drones like the Yamaha Fazer R ensure endurance, user-friendly models like Hylío AG-122 suit small farmers, GPS + RTK-equipped drones like Hylío AG-130 offer precision, and ground-based alternatives like the XAG R150 serve specific terrains, all optimizing fertilizer application, reducing waste, and enhancing efficiency.

Tabel 4

Versatility of drones in spreading solid fertilizers

Feature	DJI Agras T30	DJI Agras T40	XAG P100	XAG R150	Kisan Drone	Hylío AG-130	HSE Endurance	Yamaha RMAX	Krishna Drone	Drone AG Spreader
Payload Capacity (Kg)	30	40	60	60	10	25	20	28	15	10
Flight Time (Minutes)	20-25	25-30	30	Ground-based	15-20	25	30	90	15	20
Application Width (m)	7-9	10	10-12	Ground-based	5-8	8	7-8	6	5	6-8
Navigation System	GPS + RTK	GPS + RTK	GPS + RTK	GPS	GPS	GPS + RTK	GPS + RTK	GPS	GPS + Manual	GPS
Battery Type	Lithium-ion	Lithium-ion	Lithium-ion	Lithium-ion	Lithium-ion	Lithium-polymer	Lithium-ion	Combustion	Lithium-ion	Lithium-ion
Cost (USD)	~18,000	~20,000	~25,000	~30,000	~12,000	~18,000	~20,000	~80,000	~10,000	~15,000

CONCLUSIONS

The use of drones in smart agriculture for fertilization represents a significant advancement in agricultural technology, revolutionizing how farmers approach resource management. Drones equipped with advanced sensors and precision tools allow for the accurate application of fertilizers, ensuring that the right amount of nutrients is delivered to crops at the right time and place. This precision not only leads to higher crop yields but also helps reduce the overuse of fertilizers, minimizing environmental damage such as nutrient runoff and soil degradation.

This paper considers that the integration of drones in fertilization is a game-changer for modern agriculture, offering unparalleled precision and efficiency. The ability to monitor crop health and soil conditions in real time allows for targeted fertilizer application, reducing waste and maximizing productivity. From our perspective, this data-driven approach not only optimizes resource allocation but also improves farm profitability, making it a valuable tool for farmers of all scales.

Drones provide a **practical and scalable solution** for both small and large farming operations. Their autonomous capabilities **reduce labor costs and enhance efficiency**, while their adaptability to different crops and terrains makes them a versatile asset in agriculture. In our experience analyzing agricultural innovations, drones stand out as one of the most effective ways to **modernize and streamline fertilization practices**.

Furthermore, drone technology is seen as a **key contributor to sustainable agriculture**. By minimizing over-fertilization and reducing the environmental footprint of traditional methods, drones promote more **eco-friendly and responsible farming**. As technology continues to advance, drones will become even more essential in shaping the future of **efficient, sustainable, and environmentally conscious agriculture**.

ACKNOWLEDEMENT

This work was supported by a grant of the Romanian Ministry of Education and Research, through the project “Intelligent technology for high precision application of plant protection products, fertilizers and for seeding in hard-to-reach areas” – PN 23 04 01 01– Ctr. 9N/01.01.2023.

REFERENCES

- [1] Albetis, J., Jacquin, A., Goulard, M., Poilvé, H., Rousseau, J., Clenet, H., Dedieu, G., & Duthoit, S. (2019). On the Potentiality of UAV Multispectral Imagery to Detect Flavescence dorée and Grapevine Trunk Diseases. *Remote Sensing*, 11(1), 23. <https://doi.org/10.3390/rs11010023>
- [2] Ali M.H., Talukder M.S.U., (2008). Increasing water productivity in crop production—A synthesis. *Agricultural Water Management*, Volume 95, Issue 11, pp. 1201-1213, ISSN 0378-3774, <https://doi.org/10.1016/j.agwat.2008.06.008>
- [3] Andreasen C., Scholle K., Saberi M., (2022). Laser Weeding with Small Autonomous Vehicles: Friends or Foes. *Frontiers in Agronomy*, 4., DOI: 10.3389/fagro.2022.841086
- [4] Barcelos, C. O., Fagundes-Júnior, L. A., Mendes, A. L. C., Gandolfo, D. C., & Brandão, A. S. (2024). Integration of Payload Sensors to Enhance UAV-Based Spraying. *Drones*, 8(9), 490. <https://doi.org/10.3390/drones8090490>
- [5] Bhat S.A., Huang N., (2021) Big Data and AI Revolution in Precision Agriculture: Survey and Challenges. *IEEE Access*, vol. 9, pp. 110209-110222, 2021, doi: 10.1109/ACCESS.2021.3102227
- [6] Buters, T., Belton, D., & Cross, A., (2019). Seed and Seedling Detection Using Unmanned Aerial Vehicles and Automated Image Classification in the Monitoring of Ecological Recovery. *Drones*, 3(3), 53. <https://doi.org/10.3390/drones3030053>
- [7] Caballero-Martin, D., Lopez-Guede, J. M., Estevez, J., & Graña, M. (2024). Artificial intelligence applied to drone control: a state of the art. *Drones*, 8(7), 296. <https://doi.org/10.3390/drones8070296>
- [8] Canicatti M., Vallone M., (2024). Drones in vegetable crops: A systematic literature review. *Smart Agricultural Technology*, Volume 7, 100396, <https://doi.org/10.1016/j.atech.2024.100396>
- [9] Carreño Ruiz, M., Bloise, N., Guglieri, G., & D'Ambrosio, D. (2024). Toward Virtual Testing of Unmanned Aerial Spraying Systems Operating in Vineyards. *Drones*, 8(3), 98. <https://doi.org/10.3390/drones8030098>
- [10] Castro, G. G. R. d., Berger, G. S., Cantieri, A., Teixeira, M., Lima, J., Pereira, A. I., & Pinto, M. F. (2023). Adaptive Path Planning for Fusing Rapidly Exploring Random Trees and Deep Reinforcement Learning in an Agriculture Dynamic Environment UAVs., *Agriculture*, 13(2), 354. <https://doi.org/10.3390/agriculture13020354>
- [11] Chebrolu N., Läbe T., Stachniss C., (2018). Robust Long-Term Registration of UAV Images of Crop Fields for Precision Agriculture. *IEEE Robotics and Automation Letters*, pp. (99):1-1, DOI: 10.1109/LRA.2018.2849603
- [12] Chen B., Huang G., Lu X., Gu S., Wen W., Wang G., Chang W., Guo X., Zhao C., (2023) Prediction of vertical distribution of SPAD values within maize canopy based on unmanned aerial vehicles multispectral imagery. *Front Plant Sci.* 2023; 14:1253536. doi: 10.3389/fpls.2023.1253536. PMID: 38192698; PMCID: PMC10773710.
- [13] Chiu, M. S., & Wang, J. (2024). Evaluation of Machine Learning Regression Techniques for Estimating Winter Wheat Biomass Using Biophysical, Biochemical, and UAV Multispectral Data. *Drones*, 8(7), 287. <https://doi.org/10.3390/drones8070287>
- [14] Couturier A., Akhloufi M.A., (2021). A review on absolute visual localization for UAV. *Robotics and Autonomous Systems*. Vol.135, 103666, ISSN 0921-8890, <https://doi.org/10.1016/j.robot.2020.103666>.
- [15] Dhanaraju, M., Chenniappan, P., Ramalingam, K., Pazhanivelan, S., & Kaliaperumal, R. (2022). Smart Farming: Internet of Things (IoT)-Based Sustainable Agriculture. *Agriculture*, 12(10), 1745. <https://doi.org/10.3390/agriculture12101745>
- [16] Dong, P., Wang, M., Li, K., Qiao, H., Zhao, Y., Bacao, F., Shi, L., Guo, W., & Si, H. (2024). Research on the Identification of Wheat Fusarium Head Blight Based on Multispectral Remote Sensing from UAVs. *Drones*, 8(9), 445. <https://doi.org/10.3390/drones8090445>
- [17] Dou, W., Zhu, L., Wang, Y., & Wang, S. (2023). Research on Key Technology of Ship Re-Identification Based on the USV-UAV Collaboration. *Drones*, 7(9), 590. <https://doi.org/10.3390/drones7090590>
- [18] Dronova I., Chippie K., Zack D., Maggi K., (2021). A Review of Unoccupied Aerial Vehicle Use in Wetland Applications: Emerging Opportunities in Approach, Technology, and Data, *Drones*, 5, no.2: 45. <https://doi.org/10.3390/drones5020045>
- [19] Eckert, C., Hernandez-Jaramillo, D. C., Medcraft, C., Harrison, D. P., & Kelaher, B. P. (2024). Drone-Based Measurement of the Size Distribution and Concentration of Marine Aerosols above the Great Barrier Reef. *Drones*, 8(7), 292. <https://doi.org/10.3390/drones8070292>
- [20] Esposito M., Crimaldi M., Cirillo V., Sarghini F., Maggio A., (2021). Drone and sensor technology for sustainable weed management: a review. *Chem. Biol. Technol. Agric.* 8, 18, <https://doi.org/10.1186/s40538-021-00217-8>

- [21] Farias G.D., Dubeux Jr. J.C., Savian J.V., Duarte L.P., Martins A.P., Tiecher T., Alves L., Carvalho P.C., Bremm C., (2020). Integrated crop-livestock system with system fertilization approach improves food production and resource-use efficiency in agricultural lands. *Agronomy for Sustainable Development*, 40(39), DOI: 10.1007/s13593-020-00643-2
- [22] García-Munguía A., Guerra-Ávila P., Islas-Ojeda E., Flores-Sánchez J., Vázquez-Martínez O., García-Munguía A., García-Munguía O., (2024). A Review of Drone Technology and Operation Processes in Agricultural Crop Spray. *Drones*. 8. 674. DOI: 10.3390/drones8110674
- [23] Gokool, S., Mahomed, M., Clulow, A., Sibanda, M., Kunz, R., Naiken, V., & Mabhaudhi, T. (2024). Exploring the Potential of Remote Sensing to Facilitate Integrated Weed Management in Smallholder Farms: A Scoping Review. *Drones*, 8(3), 81. <https://doi.org/10.3390/drones8030081>
- [24] Gokool, S., Mahomed, M., Kunz, R., Clulow, A., Sibanda, M., Naiken, V., Chetty, K., & Mabhaudhi, T. (2023). Crop Monitoring in Smallholder Farms Using Unmanned Aerial Vehicles to Facilitate Precision Agriculture Practices: A Scoping Review and Bibliometric Analysis. *Sustainability*, 15(4), 3557. <https://doi.org/10.3390/su15043557>
- [25] Guebsi, R., Mami, S., & Chokmani, K. (2024). Drones in Precision Agriculture: A Comprehensive Review of Applications, Technologies, and Challenges. *Drones*, 8(11), 686. <https://doi.org/10.3390/drones8110686>
- [26] Han, J., Zhang, T., Liu, L., Wang, G., Song, C., & Lan, Y. (2024). Impact of Variable Device Structural Changes on Particle Deposition Distribution in Multi-Rotor UAV. *Drones*, 8(10), 583. <https://doi.org/10.3390/drones8100583>
- [27] Han, Y., Chen, P., Xie, X., Cui, Z., Wu, J., Lan, Y., & Zhan, Y. (2024). Rotor Speed Prediction Model of Multi-Rotor Unmanned Aerial Spraying System and Its Matching with the Overall Load. *Drones*, 8(6), 246. <https://doi.org/10.3390/drones8060246>
- [28] Hasan, R. I., Yusuf, S. M., & Alzubaidi, L. (2020). Review of the State of the Art of Deep Learning for Plant Diseases: A Broad Analysis and Discussion. *Plants*, 9(10), 1302. <https://doi.org/10.3390/plants9101302>
- [29] Htun, N. M., Owari, T., Tsuyuki, S., & Hiroshima, T. (2024). Detecting Canopy Gaps in Uneven-Aged Mixed Forests through the Combined Use of Unmanned Aerial Vehicle Imagery and Deep Learning. *Drones*, 8(9), 484. <https://doi.org/10.3390/drones8090484>
- [30] Huang, J., He, W., Yang, D., Lin, J., Ou, Y., Jiang, R., & Zhou, Z., (2024). Quantity Monitor Based on Differential Weighing Sensors for Storage Tank of Agricultural UAV. *Drones*, 8(3), 92. <https://doi.org/10.3390/drones8030092>
- [31] Huang X., Li Y., Ma H., Huang P., Zheng J., Song K., (2024) Fuel cells for multirotor unmanned aerial vehicles: A comparative study of energy storage and performance analysis, *Journal of Power Sources*, 613(6):234860, DOI: 10.1016/j.jpowsour.2024.234860
- [32] Jibon Z., Adnan M., Nora N., Akash M., Ahammed F., (2023) Development of an Autonomous UAV for Seed and Fertilizer Distribution in Precision Agriculture, *Conference: 2023 14th International Conference on Computing Communication and Networking Technologies (ICCCNT)*, DOI: 10.1109/ICCCNT56998.2023.10308182
- [33] Kannan, N., Martin, D., Srinivasan, R., & Zhang, W. (2024). Adjuvants for Drone-Based Aerial Chemical Applications to Mitigate Off-Target Drift. *Drones*, 8(11), 667. <https://doi.org/10.3390/drones8110667>
- [34] Khan S., Tufail M., Khan M.T., Khan Z.A., Iqbal J., Wasim A., (2021). Real-time recognition of spraying area for UAV sprayers using a deep learning approach. *PLoS One*. 2021;16(4):e0249436. doi: 10.1371/journal.pone.0249436. PMID: 33793634; PMCID: PMC8016340.
- [35] Khanal S., Fulton J., Shearer S., (2017). An overview of current and potential applications of thermal remote sensing in precision agriculture. *Computers and Electronics in Agriculture*, Vol.139, pp. 22-32, <https://doi.org/10.1016/j.compag.2017.05.001> .
- [36] Kumar, C., Mubvumba, P., Huang, Y., Dhillon, J., & Reddy, K. (2023). Multi-Stage Corn Yield Prediction Using High-Resolution UAV Multispectral Data and Machine Learning Models. *Agronomy*, 13(5), 1277. <https://doi.org/10.3390/agronomy13051277>
- [37] Lee, D-H., Seong, B-G., Baek, S-Y., Lee, C-G., Kang, Y-H., Han, X., & Yu, S-H. (2024). Coverage Estimation of Droplets Sprayed on Water-Sensitive Papers Based on Domain-Adaptive Segmentation. *Drones*, 8(11), 670. <https://doi.org/10.3390/drones8110670>
- [38] Li X., Liu Y., Zhang X., Huang J., Bian J., (2024). Characteristics Analysis and Modeling of Integrated Sensing and Communication Channel for Unmanned Aerial Vehicle Communications. *Drones*, 8(10):538 DOI: 10.3390/drones8100538
- [39] Liu, J., Xiang, J., Jin, Y., Liu, R., Yan, J., & Wang, L. (2021). Boost Precision Agriculture with Unmanned Aerial Vehicle Remote Sensing and Edge Intelligence: A Survey. *Remote Sensing*, 13(21), 4387. <https://doi.org/10.3390/rs13214387>
- [40] Lu, Y., Liu, M., Li, C., Liu, X., Cao, C., Li, X., & Kan, Z. (2022). Precision Fertilization and Irrigation: Progress and Applications. *AgriEngineering*, 4(3), 626-655. <https://doi.org/10.3390/agriengineering4030041>

- [41] Lysych, M., Bukhtoyarov, L., & Druchinin, D. (2021). Design and Research Sowing Devices for Aerial Sowing of Forest Seeds with UAVs. *Inventions*, 6(4), 83. <https://doi.org/10.3390/inventions6040083>
- [42] Martínez García, M., Ramos Cabral, S., Pérez Zúñiga, R., & Martínez Rodríguez, L.C.G. (2023). Automatic Equipment to Increase Sustainability in Agricultural Fertilization. *Agriculture*, 13(2), 490. <https://doi.org/10.3390/agriculture13020490>
- [43] Massimo F. and Monego M., (2024). A Drone-Based Structure from Motion Survey, Topographic Data, and Terrestrial Laser Scanning Acquisitions for the Floodgate Gaps Deformation Monitoring of the Modulo Sperimentale Elettromeccanico System (Venice, Italy)" *Drones* 8, no. 10: 598. <https://doi.org/10.3390/drones8100598>
- [44] Messina, G., & Modica, G. (2020). Applications of UAV Thermal Imagery in Precision Agriculture: State of the Art and Future Research Outlook. *Remote Sensing*, 12(9), 1491. <https://doi.org/10.3390/rs12091491>
- [45] Ming, R., Wu, T., Zhou, Z., Luo, H., & Hassan, S. G. (2024). Research and Design of an Active Light Source System for UAVs Based on Light Intensity Matching Model. *Drones*, 8(11), 683. <https://doi.org/10.3390/drones8110683>
- [46] Murugan D., Garg A., Singh D., (2017)., Development of an Adaptive Approach for Precision Agriculture Monitoring with Drone and Satellite Data, *IEEE Journal of Selected Topics in Applied Earth Observations and Remote Sensing*, pp. (99):1-7, DOI: 10.1109/JSTARS.2017.2746185
- [47] Nahiyoon, S. A., Ren, Z., Wei, P., Li, X., Li, X., Xu, J., Yan, X., & Yuan, H. (2024). Recent Development Trends in Plant Protection UAVs: A Journey from Conventional Practices to Cutting-Edge Technologies—A Comprehensive Review. *Drones*, 8(9), 457. <https://doi.org/10.3390/drones8090457>
- [48] Niu, Y., Xu, L., Zhang, Y., Xu, L., Zhu, Q., Wang, A., Huang, S., & Zhang, L. (2024). Enhancing the Performance of Unmanned Aerial Vehicle-Based Estimation of Rape Chlorophyll Content by Reducing the Impact of Crop Coverage. *Drones*, 8(10), 578. <https://doi.org/10.3390/drones8100578>
- [49] Panday, U. S., Pratihast, A. K., Aryal, J., & Kayastha, R. B., (2020). A Review on Drone-Based Data Solutions for Cereal Crops. *Drones*, 4(3), 41. <https://doi.org/10.3390/drones4030041>
- [50] Pereira, A., Warwick, S., Moutinho, A., & Suleman, A. (2024). Infrared and Visible Camera Integration for Detection and Tracking of Small UAVs: Systematic Evaluation. *Drones*, 8(11), 650. <https://doi.org/10.3390/drones8110650>
- [51] Popescu, D., Stoican, F., Stamatescu, G., Ichim, L., & Dragana, C. (2020). Advanced UAV–WSN System for Intelligent Monitoring in Precision Agriculture. *Sensors*, 20(3), 817. <https://doi.org/10.3390/s20030817>
- [52] Pu Q., Ananthanarayanan G., Bodik P., Kandula S., Akella A., Bahl P., Stoica I., (2015). Low Latency Geo-Distributed Data Analytics, ACM SIGCOMM Computer Communication Review, *Medium*, 45(5):421-434, DOI: 10.1145/2829988.2787505
- [53] Radoglou-Grammatikis P., Sarigiannidis P., Thomas Lagkas T., Moscholios I., (2020) A compilation of UAV applications for precision agriculture, *Computer Networks*, Vol. 172, 107148, ISSN 1389-1286 <https://doi.org/10.1016/j.comnet.2020.107148>.
- [54] Rejeb A., Abdollahi A., Rejeb K., Treiblmaier H., (2022). Drones in agriculture: A review and bibliometric analysis, *Computers and Electronics in Agriculture*, Volume 198,107017, ISSN 0168-1699, <https://doi.org/10.1016/j.compag.2022.107017>
- [55] Scherrer B., Sheppard J., Jha P., Shaw J., (2019). Hyperspectral imaging and neural networks to classify herbicide resistant weeds, *Journal of Applied Remote Sensing*, 13(04):1, DOI: 10.1117/1.JRS.13.044516
- [56] Shadrin D., Menshchikov A., Somov A., Bornemann G., Hauslage J., Fedorov M. (2019). Enabling Precision Agriculture Through Embedded Sensing With Artificial Intelligence, *IEEE Transactions on Instrumentation and Measurement*, pp(99):1-1, DOI: 10.1109/TIM.2019.2947125
- [57] Shahi, T. B., Dahal, S., Sitaula, C., Neupane, A., & Guo, W. (2023). Deep Learning-Based Weed Detection Using UAV Images: A Comparative Study. *Drones*, 7(10), 624. <https://doi.org/10.3390/drones7100624>
- [58] Shahi T.B., Xu C-Y., Neupane A., Guo W., (2022). Machine learning methods for precision agriculture with UAV imagery: a review, *Electronic Research Archive*, 30(12): 4277-4317, DOI: 10.3934/era.2022218
- [59] Sharma A. Jain A., Gupta P., (2020). Chowdary, Machine Learning Applications for Precision Agriculture: A Comprehensive Review, *IEEE Access*, pp. (99):1-1, DOI: 10.1109/ACCESS.2020.3048415
- [60] Singh N., Gupta D., Joshi M., Yadav K., Nayak S., Kumar M., Nayak S., Kumar M., Nayak K., Gulaiya S., Rajpoot A.S., (2024), Application of Drones Technology in Agriculture: A Modern Approach, *Journal of Scientific Research and Reports*, Volume 30, Issue 7, pp. 142-152, 2024; Article no.JSRR.118020ISSN: 2320-0227
- [61] Sitharthan R., Rajesh M., Vimal S., Saravana Kumar E., Yuvaraj S., Abhishek K., Jacob R. I., Vengatesan K., (2023). A novel autonomous irrigation system for smart agriculture using AI and 6G

- enabled IoT network, *Microprocessors and Microsystems*, Volume 101,104905, ISSN 0141-9331, <https://doi.org/10.1016/j.micpro.2023.104905>
- [62] Subeesh A., Mehta C.R., (2021) Automation and digitization of agriculture using artificial intelligence and internet of things, *Artificial Intelligence in Agriculture*, Volume 5, pp. 278-291, ISSN 2589-7217, <https://doi.org/10.1016/j.aiia.2021.11.004>.
- [63] Tanaka, T. S. T., Wang, S., Jørgensen, J. R., Gentili, M., Vidal, A. Z., Mortensen, A. K., Acharya, B. S., Beck, B. D., & Gislum, R. (2024). Review of Crop Phenotyping in Field Plot Experiments Using UAV-Mounted Sensors and Algorithms. *Drones*, 8(6), 212. <https://doi.org/10.3390/drones8060212>
- [64] Tripathi R.N., Ramachandran A., Tripathi V., Badola R., Hussain S.A., (2024). Optimizing Riparian Habitat Conservation: A Spatial Approach Using Aerial and Space Technologies, *IEEE Journal of Selected Topics in Applied Earth Observations and Remote Sensing*, pp. (99):1-20, DOI: 10.1109/JSTARS.2024.3454453
- [65] Tsouros, D. C., Bibi, S., & Sarigiannidis, P. G. (2019). A Review on UAV-Based Applications for Precision Agriculture. *Information*, 10(11), 349. <https://doi.org/10.3390/info10110349>
- [66] Valente J., Del Cerro J., Barrientos A., Sanz D., (2013). Aerial coverage optimization in precision agriculture management: A musical harmony inspired approach, *Computers and Electronics in Agriculture*, Volume 99, Pp. 153-159, ISSN 0168-1699, <https://doi.org/10.1016/j.compag.2013.09.008>.
- [67] Van Klompenburg T., Kassahun A., Catal C., (2020) Crop yield prediction using machine learning: A systematic literature review, *Computers and Electronics in Agriculture*, Volume 177, 105709, <https://doi.org/10.1016/j.compag.2020.105709>
- [68] Wang B., Wang Y., Wang H., Mao H., Zhou L., (2022). Research on accurate perception and control system of fertilization amount for corn fertilization planter, *Frontiers in Plant Science*, Vol. 13, DOI=10.3389/fpls.2022.1074945
- [69] Wang H., Mortensen A., Mao P., Boelt B., Gislum R., (2019) Estimating the nitrogen nutrition index in grass seed crops using a UAV-mounted multispectral camera, *International Journal of Remote Sensing*, 40:7, 2467-2482, DOI:10.1080/01431161.2019.1569783
- [70] Xu C., Huang S., Tian B., Ren J., Meng Q., Wang P., (2017). Manipulating Planting Density and Nitrogen Fertilizer Application to Improve Yield and Reduce Environmental Impact in Chinese Maize Production, *Front Plant Sci. 2017 Jul 12 8:1234*. doi: 10.3389/fpls.2017.01234. PMID: 28747925; PMCID: PMC5506086.
- [71] Xue X., Tian Y., Yang Z., Li Z., Lyu S., Song S., Sun D., (2024). Research on a UAV spray system combined with grid atomized droplets, *Frontiers in Plant Science*, vol. 14, DOI:10.3389/fpls.2023.1286332
- [72] Yacoob, A., Gokool, S., Clulow, A., Mahomed, M., & Mabhaudhi, T. (2024). Leveraging Unmanned Aerial Vehicle Technologies to Facilitate Precision Water Management in Smallholder Farms: A Scoping Review and Bibliometric Analysis. *Drones*, 8(9), 476. <https://doi.org/10.3390/drones8090476>
- [73] Yang M., Hassan M.A., Xu K., Zheng C., Rasheed A., Zhang Y., Jin X., Xia X., Xiao Y., He Z., (2020) Assessment of Water and Nitrogen Use Efficiencies Through UAV-Based Multispectral Phenotyping in Winter Wheat, *Frontiers in Plant and Science*, 11, DOI: 10.3389/fpls.2020.00927
- [74] Yang, S., Yuan, J., Chen, Z., Zhang, H., & Cui, X. (2024). Advances in Surveying Topographically Complex Ecosystems with UAVs: Manta Ray Foraging Algorithms. *Drones*, 8(11), 631. <https://doi.org/10.3390/drones8110631>
- [75] Yu Y., Yubin L., Guobin W., Mujahid H., Huizheng W., Xiaoqing Y., Changfeng S., Baoju W., Cancan S., (2023). Evaluation of the deposition and distribution of spray droplets in citrus orchards by plant protection drones, *Frontiers in Plant Science*, 14, DOI: 10.3389/fpls.2023.1303669
- [76] Yuan, J., Zhang, Y., Zheng, Z., Yao, W., Wang, W., & Guo, L. (2024). Grain Crop Yield Prediction Using Machine Learning Based on UAV Remote Sensing: A Systematic Literature Review. *Drones*, 8(10), 559. <https://doi.org/10.3390/drones8100559>
- [77] Zhichkin K., Nosov V., Zhichkina L., Anichkina O., Borodina I., Beketov A., (2023). Efficiency of using drones in agricultural production, *E3S Web of Conferences*, 381(2), DOI: 10.1051/e3sconf/202338101048
- [78] Zhou X., Minfeng X., Binbin H., Jinfei W., Yang S., Jiali S., Chunhua L., Min X., and Xiliang Ni., (2023). A Ground Point Fitting Method for Winter Wheat Height Estimation Using UAV-Based SfM Point Cloud Data. *Drones* 7, no. 7: 406. <https://doi.org/10.3390/drones7070406>
- [79] Zhou, X., Shi, G., & Zhang, J. (2024). Improved Grey Wolf Algorithm: A Method for UAV Path Planning. *Drones*, 8(11), 675. <https://doi.org/10.3390/drones8110675>
- [80] Zualkernan, I., Abuhani, D. A., Hussain, M. H., Khan, J., & ElMohandes, M. (2023). Machine Learning for Precision Agriculture Using Imagery from Unmanned Aerial Vehicles (UAVs): A Survey. *Drones*, 7(6), 382. <https://doi.org/10.3390/drones7060382>
- [81] <https://www.dji.com/global/support/product/p4-multispectral>
- [82] <https://www.sensefly.com/solutions/drones/>
- [83] <https://www.sensefly.com/solutions/drones/>
- [84] <https://www.dji.com/global/support/product/mavic-2>

INMATEH - Agricultural Engineering journal is indexed in the next international databases:
ELSEVIER /SciVerse SCOPUS, CLARIVATE - WEB of SCIENCE- Emerging Sources Citation Index (ESCI),
ULRICHS Web: Global Serials Directory, CABI, SCIPRO, Index COPERNICUS International, EBSCO Publishing,
Elektronische Zeitschriftenbibliothek

INMATEH - Agricultural Engineering

vol. 74, no.3 / 2024

e-ISSN: 2068 – 2239; p: ISSN: 2068 – 4215

<https://inmateh.eu/>

E-mail: inmatehjournal@gmail.com

Edited by: **INMA Bucharest**

Copyright: INMA Bucharest / Romania

National Institute for Research-Development of Machines and Installations
Designed for Agriculture and Food Industry - INMA Bucharest
6, Ion Ionescu de la Brad Blvd., sector 1, Bucharest, ROMANIA

WRITING INSTRUCTIONS

Article Types

Three types of manuscripts may be submitted:

1. **Regular articles:** These should describe new and carefully confirmed findings, and experimental procedures should be given in sufficient detail for others to verify the work. The length of a full paper should be the minimum required to describe and interpret the work clearly (max.10 pages, even number);
2. **Reviews:** Submissions of reviews and perspectives covering topics of current interest are welcome and encouraged (max.12 pages, even number).

Manuscripts should be written in English (American or British usage is accepted, but not a mixture of these) and submitted **electronically** at the following e-mail addresses: ***inmatehjournal@gmail.com***

Please be sure to include your full affiliation and e-mail address (see Sample manuscript)

The authors are responsible for the accuracy of the whole paper and references.

There are allowed 2 papers by each first author.

The text layout should be in single-column format. To avoid unnecessary errors it is strongly advised to use the "spell-check" and "grammar check" functions of your word processor.

Review Process

All manuscripts are reviewed by 2 members of the Scientifically Review Office. Decisions will be made as rapidly as possible and the journal strives to return reviewers' comments to authors in approx.3 weeks.

The editorial board will re-review manuscripts that are accepted pending revision.

NOTE:

Submission of a manuscript implies: that the work described has not been published before (excepting as an abstract or as part of a published lecture or thesis) that it is not under consideration for publication elsewhere.

1. REGULAR ARTICLES

- Manuscripts should be concise, in **1.15 line spacing**, and should have 2 cm all over margins. The font should be **Arial 10 pt.** Ensure that each new paragraph is clearly indicated, using **TAB at 1 cm.**
- Title will be **Arial 12 pt.** and explicit figures will be **Arial 9 pt.**
- Text will be written in English.
- Chapters' titles are written by **Arial 10 pt, Bold, Uppercase** (e.g. **INTRODUCTION, MATERIALS AND METHODS**), between chapters is left a space for 10 pt. At the beginning of each paragraph, TAB of 1 cm.
- The paper body will be written in **Arial 10 pt., Justify alignment.**

TITLE **Arial 12 pt., Uppercase, Bold, Center** (in English language) and **Bold Italic** (in native language).

Should be a brief phrase describing the contents of the paper. Avoid long titles; a running title of no more than 100 characters is encouraged (without spaces).

AUTHORS **ARIAL 9, Bold, Centre alignment**

Under the paper's title, after a space (enter) 9 pt., write **authors' names** and **affiliations (Arial 8 pt.-Regular)**

When the paper has more than one author, their name will be followed by a mark (Arabic numeral) as superscript if their affiliation is different. **Less than 6 authors.**

Corresponding author's name (next row), (**Arial 8 pt.**). Should be added also: phone, fax and e-mail information, for the paper corresponding author (**font: 8 pt., Italic**).

KEYWORDS (**In English**) about 4 to 7 words that will provide indexing references should be listed (**title: Arial 10pt, bold italic, text Arial 10 pt., italic**).

A list of non-standard **Abbreviations** should be added. In general, non-standard abbreviations should be used only when the full term is very long and used often. Each abbreviation should be spelled out and introduced in parentheses the first time it is used in the text. Standard abbreviations (such as ATP and DNA) need not to be defined.

ABSTRACT (**in English and Native language, Arial 10 pt.**), the title **bold**; the text of abstract: **italic**) should be informative and completely self-explanatory, briefly present the topic, state the scope of the experiments, indicate significant data, and point out major findings and conclusions. The Abstract should be max.250 words. Complete sentences, active verbs, and the third person should be used, and the abstract should be written in the past tense. Standard nomenclature should be used and abbreviations should be avoided. No literature should be cited.

INTRODUCTION (**Arial 10 pt.**) should provide a clear statement of the problem, the relevant literature on the subject, and the proposed approach or solution. It should be understandable to colleagues from a broad range of scientific subjects. We should refer to the current stage of researches performed in the field of the paper to be published, by quoting up-to-date specialty studies, preferably published after 2006, excepting certain referential specialty

books/studies, especially papers issued in magazines/journals/conferences/ISI quoted symposia or in other international data bases, which are well known and available.

MATERIALS AND METHODS (*Arial 10 pt.*) should be complete enough to allow experiments to be reproduced. However, only truly new procedures should be described in detail; previously published procedures should be cited, and important modifications of published procedures should be mentioned briefly. Methods in general use need not be described in detail.

RESULTS (*Arial 10 pt.*) should be clearly presented. The results should be written in the past tense when describing findings in the authors' experiments. Results should be explained, but largely, without referring to the literature. Discussion, speculation and detailed interpretation of data should not be included in the Results, but should be put into the Conclusions section.

CONCLUSIONS (*Arial 10 pt.*) The main conclusions drawn from results should be presented in a short Conclusions section. Do not include citations in this section.

Formulae, symbols and abbreviations: Formulae will be typeset in Italics (preferable with the Equation Editor of Microsoft Office 2003) and should be written or marked as such in the manuscript, unless they require a different styling. They should be referred to in the text as Equation (4) or e.g. (4). The formulae should be numbered on the right side, between brackets (*Arial 10 pt.*):

$$P = F \cdot v \quad (1)$$

Terms of the equation and the unit measure should be explained, e.g.

P is the power, [W];

F – force, [N];

v – speed, [m/s]

SI units must be used throughout.

Tables should be self-explanatory without reference to the text. The details of the methods used in the experiments should preferably be described in the legend instead of in the text. The same data should not be presented both in table and graph form or repeated in the text.

Table's title will be typed *Arial 9 pt, Bold, Centered*

In the table, each row will be written Arial 9 pt, single-spaced throughout, including headings and footnotes.

The table should be numbered on the right side, *Arial 10 pt.*

Figures (*Arial 9 pt., Bold, Center*) should be typed in numerical order (Arabic numerals). Graphics should be high resolution (e.g. JPEG). Figure number is followed by what represent the figure or graph e.g.:

Fig.1 – Test stand

Legend: *Arial 8 pt, Italic, Center, e.g.:*

1 - plansifter compartments; 2- break rolls; 3 – semolina machines; 4 – reduction rolls; 5 – flour

ACKNOWLEDGMENTS (*Arial 10 pt.*) of people, grants, funds etc should be brief (*if necessarily*).

REFERENCES (*Arial 10 pt.*)

(In alphabetical order, in English and in the original publication language).

Minimum 10 references, last 10 years, minimum 3 references from the last 2 years

It can be used “*References*” tool from the *Word Editor*. **APA Style (American Psychological Association)** <https://apastyle.apa.org/style-grammar-guidelines/references/examples>

All references must be provided in English

Authors are fully responsible for the accuracy of the references.

References should be **alphabetically**, with complete details, as follows:

Examples:

Books: <https://apastyle.apa.org/style-grammar-guidelines/references/examples/book-references>

Jackson, L. M. (2019). *The psychology of prejudice: From attitudes to social action* (2nd ed.). American Psychological Association. <https://doi.org/10.1037/0000168-000>

Kesharwani, P. (2020). *Nanotechnology based approaches for tuberculosis treatment*. Academic Press.

Sapolsky, R. M. (2017). *Behave: The biology of humans at our best and worst*. Penguin Books.

Torino, G. C., Rivera, D. P., Capodilupo, C. M., Nadal, K. L., & Sue, D. W. (2019). *Microaggression theory: Influence and implications*. John Wiley & Sons. <https://doi.org/10.1002/9781119466642>

In text:

- **Parenthetical citations:** (Jackson, 2019; Sapolsky, 2017)
- **Narrative citations:** Jackson (2019) and Sapolsky (2017)

Journal Article:

<https://apastyle.apa.org/style-grammar-guidelines/references/examples/journal-article-references>

Grady, J. S., Her, M., Moreno, G., Perez, C., & Yelinek, J. (2019). Emotions in storybooks: A comparison of storybooks that represent ethnic and racial groups in the United States. *Psychology of Popular Media Culture*, 8(3), 207–217. <https://doi.org/10.1037/ppm0000185>

In text:

- **Parenthetical citation:** (Grady et al., 2019)
- **Narrative citation:** Grady et al. (2019)

Conference or Symposium:

<https://apastyle.apa.org/style-grammar-guidelines/references/examples/conference-proceeding-references>

Duckworth, A. L., Quirk, A., Gallop, R., Hoyle, R. H., Kelly, D. R., & Matthews, M. D. (2019). Cognitive and noncognitive predictors of success. *Proceedings of the National Academy of Sciences, USA*, 116(47), 23499–23504. <https://doi.org/10.1073/pnas.1910510116>

In text:

- **Parenthetical citation:** (Duckworth et al., 2019)
- **Narrative citation:** Duckworth et al. (2019)

Dissertation / Thesis:

<https://apastyle.apa.org/style-grammar-guidelines/references/examples/published-dissertation-references>

Zambrano-Vazquez, L. (2016). *The interaction of state and trait worry on response monitoring in those with worry and obsessive-compulsive symptoms* [Doctoral dissertation, University of Arizona]. UA Campus Repository. <https://repository.arizona.edu/handle/10150/620615>

In text:

- **Parenthetical citations:** (Kabir, 2016; Miranda, 2019; Zambrano-Vazquez, 2016)
- **Narrative citations:** Kabir (2016), Miranda (2019), and Zambrano-Vazquez (2016)

<https://apastyle.apa.org/style-grammar-guidelines/references/examples/unpublished-dissertation-references>

Harris, L. (2014). *Instructional leadership perceptions and practices of elementary school leaders* [Unpublished doctoral dissertation]. University of Virginia.

In text:

- **Parenthetical citation:** (Harris, 2014)
- **Narrative citation:** Harris (2014)

Patents: Names and initials of authors, year (between brackets), patent title (Italic), patent number, country:

Grant, P. (1989). *Device for Elementary Analyses*. Patent. No.123456. USA.

Legal regulations and laws, organizations:

<https://apastyle.apa.org/style-grammar-guidelines/references/examples/iso-standard-references>

International Organization for Standardization. (2018). *Occupational health and safety management systems—Requirements with guidance for use* (ISO Standard No. 45001:2018). <https://www.iso.org/standard/63787.html>

Occupational Safety and Health Administration. (1970). *Occupational safety and health standards: Occupational health and environmental control: Occupational noise exposure* (OSHA Standard No. 1910.95). United States Department of Labor.

<https://www.osha.gov/laws-regs/regulations/standardnumber/1910/1910.95>

In text:

- **Parenthetical citations:** (International Organization for Standardization, 2018; Occupational Safety and Health Administration, 1970)
- **Narrative citations:** International Organization for Standardization (2018) and Occupational Safety and Health Administration (1970)

Web references: The full URL should be given in text as a citation, if no other data are known. If the authors, year, and title of the documents are known and the reference is taken from a website, the URL address has to be mentioned after these data.

Citation in text

Please ensure that every reference cited in the text is also present in the reference list (and vice versa).

Do not cite references in the Abstract and Conclusions !.

Unpublished results, personal communications as well as URL addresses are not recommended in the references list.

Making personal quotations (one, at most) should not be allowed, unless the paper proposed to be published is a sequel of the cited paper. Articles in preparation or articles submitted for publication, unpublished, personal communications etc. should not be included in the references list.

Citations style

Text: All citations in the text may be made directly (or parenthetically) as bellow.

- **single author:** the author's name (without initials, unless there is ambiguity) and the year of publication: "as previously demonstrated (*Brown, 2010*)".
- **two authors:** both authors' names and the year of publication: (*Adam and Brown, 2008; Smith and Hansel, 2006; Stern and Lars, 2009*)
- **three or more authors:** first author's name followed by "et al." and the year of publication: "As has recently been shown (*Werner et al., 2005; Kramer et al., 2000*) have recently shown"

Citations of groups of references should be listed first alphabetically, then chronologically.**Units, Abbreviations, Acronyms**

- Units should be metric, generally SI, and expressed in standard abbreviated form.
- Acronyms may be acceptable, but must be defined at first usage.

2. REVIEWS

Summaries, reviews and perspectives covering topics of current interest in the field, are encouraged and accepted for publication.

Reviews do not have the requirements for regular articles. However, should include: (*) an introductory chapter, (**) a careful and critical presentation of the relevant aspects of the topic approached and (***) emphasis of the aspects that aren't known and require further research to progress.

Reviews and perspectives covering topics of current interest in the field, are encouraged and accepted for publication. A review must have at least 80 references.

It might give a new interpretation of old material or combine new with old interpretations. Or it might trace the intellectual progression of the field, including major debates. And depending on the situation, the literature review may evaluate the sources and advise the reader on the most pertinent or relevant.

Literature reviews must contain at least three basic elements: an introduction or background information section; the body of the review containing the discussion of sources; and, finally, a conclusion and/or recommendations section to end the paper.

The following provides a brief description of the content of each: Introduction: Gives a quick idea of the topic of the literature review, such as the central theme or organizational pattern. Body: Contains your discussion of sources and is organized either chronologically, thematically, or methodologically. Conclusions/Recommendations: Discuss what you have drawn from reviewing literature so far.



Edited by: INMA Bucharest

6, Ion Ionescu de la Brad Blvd., sect. 1, Bucharest, ROMANIA

Tel: +4021.269.32.60; Fax: +4021.269.32.73

[https:// inmateh.eu](https://inmateh.eu)

e-mail: inmatehjournal@gmail.com